Ming Ronnier Luo

Editor

Encyclopedia of Color Science and Technology

Springer Reference

Handbook of Ultrasonics and Sonochemistry

Muthupandian Ashokkumar
Editor-in-Chief

Francesca Cavalieri • Farid Chemat
Kenji Okitsu • Anandan Sambandam
Kyuichi Yasui • Bogdan Zisu
Section Editors

Handbook of Ultrasonics and Sonochemistry

With 649 Figures and 99 Tables

Springer Reference

Editor-in-Chief
Muthupandian Ashokkumar
School of Chemistry
The University of Melbourne
Melbourne, VIC, Australia

Section Editors

Francesca Cavalieri
Department of Chemical Sciences and
Technologies
University of Rome "Tor Vergata"
Rome, Italy

Farid Chemat
Department of Chemistry
Universite d'Avignon et des Pays de
Vaucluse
Avignon cedex 1, France

Kenji Okitsu
Department of Materials Science
Osaka Prefecture University
Osaka, Japan

Anandan Sambandam
Department of Chemistry
National Institute of Technology
Tiruchirappalli
Tiruchirappalli, TN, India

Kyuichi Yasui
National Institute of Advanced Industrial
Science and Technology (AIST)
Nagoya, Japan

Bogdan Zisu
RMIT University
Melbourne, VIC, Australia

Printed on acid-free paper

Preface

Soundwaves, responsible for verbal communication between human beings and to some extent between living organisms, are capable of promoting chemical reactions and processing of materials. While many research articles, reviews, and books are available on selected aspects related to the topics covered in this Handbook, a single reference material that provides the current status of research areas ranging from fundamental aspects to various applications is missing in the literature. In order to overcome this shortfall, the *Handbook of Ultrasonics and Sonochemistry* (HBUS) has been developed with contributions from expertise in different areas of ultrasonics and sonochemistry.

HBUS consists of five sections: Fundamental Aspects, Nanomaterials, Environmental Remediation, Biomaterials, and Food Processing. Each section contains about ten chapters dealing with reviews of current literature and in some cases providing new results. While some chapters provide historical background of relevant topics, most focus on recent developments and current status of the research areas. The first section on fundamental aspects aims at providing the basics of acoustic cavitation. How ultrasound interacts with gas bubbles and grows them by rectified diffusion, theoretical aspects of cavitation, how the strong physical effects and chemical reactions are generated during cavitation, and what issues are still remaining unresolved are some topics covered in this section. In addition, acoustic cavitation in a microchannel, atomization, and a brief account of hydrodynamic cavitation are also included in this section. The section on nanomaterials deals with the synthesis of a variety of nanomaterials using the physical and chemical effects generated during acoustic cavitation and their applications. In addition to synthesizing materials, this chapter also deals with processing of materials such as micelles. There is a significant crossover between Sections II and III, which could be expected as materials are used in environmental remediation. In both sections, the advantages of using hybrid techniques are highlighted. A combination of ultrasound and electrochemistry or photocatalysis seems to offer synergistic effects under specific experimental conditions. Section III not only deals with processing of organic pollutants in aqueous environment, but also highlights the use of acoustic cavitation for the treatment of waste oils. In both sections, the use of hydrodynamic cavitation for synthesizing nanomaterials and environmental remediation is discussed. The physical and chemical events arising from acoustic cavitation have been extensively

used for synthesizing functional biomaterials, which is focused in Section IV. Ultrasonically synthesized core-shell materials are found to possess unique physical and functional properties as highlighted in this section. The last section of HBUS deals with one of the growing applications of ultrasound, food processing. In recent years, the physical forces generated during acoustic cavitation have been found useful for improving the functional properties of food and dairy systems. Food quality, functionality, nutritional properties, and storage stability are some processes that could be improved by sonication.

The high quality chapters in HBUS are contributed by leading researchers. The Editor-in-Chief and Section Editors sincerely acknowledge the authors for their time commitment and quality contributions. The Editor-in-Chief thanks the Section Editors for their involvement in HBUS project, who should take the full credit for organizing individual sections that include choosing leading researchers, sending invitations, organizing review processes, and completing the overall process on time. The Editor-in-Chief would also like to acknowledge Springer and its staff for their effort in making HBUS possible. In particular, Stephen Yeung, Tina Shelton, and Alexa Singh have been on our (Editor-in-Chief and Editors) toes to make sure we deliver what we promised, on time. And finally, it should be noted that HBUS is a great addition to academic literature and would help a wide range of communities including academic researchers, graduate students, and industries to understand and expand their knowledge in ultrasonics and sonochemistry from fundamentals to possible industrial applications.

<div align="right">
Muthupandian Ashokkumar
Editor-in-Chief
</div>

Contents

About the Editor-in-Chief

Muthupandian Ashokkumar is a Physical Chemist who specializes in Sonochemistry, teaches undergraduate and postgraduate chemistry subjects, and is a senior academic staff member of the School of Chemistry, University of Melbourne. He is the Associate Dean (Engagement and International) in the Faculty of Science. Ashok is a renowned sonochemist who has developed a number of novel techniques to characterize acoustic cavitation bubbles and has made major contributions of applied sonochemistry to the Food and Dairy industry. His research team has developed ultrasonic processing technology for improving the functional properties of dairy ingredients. Recent research also involves the ultrasonic synthesis of functional nano- and biomaterials including protein microspheres that can be used in diagnostic and therapeutic medicine.

Ashok is one of the Editors of *Ultrasonics Sonochemistry*, an international journal devoted to sonochemistry research. He has edited/coedited several books and special issues for journals, published ~310 refereed papers in high-impact international journals and books, and delivered over 150 invited/keynote/plenary lectures at international conferences and academic institutions. Ashok has successfully organized 10 national/international scientific conferences and workshops and managed a number of national and international competitive research grants. He has served on a number of University of Melbourne management committees and scientific advisory boards of external scientific organizations. Ashok is the recipient of several prizes, awards, and fellowships, including the Grimwade Prize in Industrial Chemistry. He is a Fellow of the RACI since 2007.

Ashok's research interests have been focused upon two key aspects: fundamental understanding of specific scientific problems and using the knowledge gained from fundamental projects to applied aspects that benefit the community. His research to date has been in multidisciplinary areas involving sonochemistry, sonoluminescence, materials chemistry, surface chemistry, radiation chemistry, photochemistry, and spectroscopy. His research focus has always been to address key issues in

energy, *environment*, and *health*. His research involved synthesis of advanced nanomaterials for solar energy conversion, fuel cell applications, and for environmental remediation. His recent work involves developing protein/polymer microspheres that have potential applications in targeted drug delivery. His work in the area of ultrasonic processing of dairy ingredients has received significant attention among dairy industries in Australia.

Section Editors

Francesca Cavalieri Department of Chemical Sciences and Technologies, University of Rome "Tor Vergata", Rome, Italy

Farid Chemat Department of Chemistry, Universite d'Avignon et des Pays de Vaucluse, Avignon cedex 1, France

Kenji Okitsu Department of Materials Science, Osaka Prefecture University, Osaka, Japan

Anandan Sambandam Department of Chemistry, National Institute of Technology Tiruchirappalli, Tiruchirappalli, TN, India

Kyuichi Yasui National Institute of Advanced Industrial Science and Technology (AIST), Nagoya, Japan

Bogdan Zisu RMIT University, Melbourne, VIC, Australia

Contributors

Ibrahim Alzorqi Manufacturing and Industrial Processes Research Division, Faculty of Engineering, University of Nottingham Malaysia campus, Semenyih, Selangor, Malaysia

Sambandam Anandan Nanomaterials and Solar Energy Conversion Lab, Department of Chemistry, National Institute of Technology, Tiruchirappalli, Tiruchirappalli, Tamilnadu, India

Daria V. Andreeva Physical Chemistry II, University of Bayreuth, Bayreuth, Germany

Muthupandian Ashokkumar School of Chemistry, The University of Melbourne, Melbourne, VIC, Australia

Sundaram Ganesh Babu SRM Research Institute, SRM University, Chennai, Tamilnadu, India

S. S. Barkade Department of Chemical Engineering, Sinhgad College of Engineering, Pune, India

Elisavet D. Bartzoka Department of Chemical Sciences and Technologies, University of Rome "Tor Vergata", Rome, Italy

Mehmet Başlar Faculty of Chemical and Metallurgical Engineering, Department of Food Engineering, Yıldız Technical University, Esenler, Istanbul, Turkey

Bhakar Bethi Department of Chemical Engineering, National Institute of Technology, Warangal, Telangana, India

Bhesh Bhandari School of Land and Food Sciences, The University of Queensland, Brisbane, Australia

Bharat Bhanvase Department of Chemical Engineering, Laxminarayan Institute of Technology, Rashtrasant Tukadoji Maharaj Nagpur University, Nagpur, Maharashtra, India

Hatice Biranger Yildirim Faculty of Chemical and Metallurgical Engineering, Department of Food Engineering, Yıldız Technical University, Esenler, Istanbul, Turkey

Daria C. Boffito Département de Génie Chimique, Polytechnique Montréal, Montréal, QC, Canada

Mark A. Borden Department of Mechanical Engineering, University of Colorado, Boulder, CO, USA

Patrick Braeutigam Center for Energy and Environmental Chemistry (CEEC), Institute of Technical and Environmental Chemistry, Friedrich-Schiller-Universität Jena, Jena, Germany

Carlos Cairós Drittes Physikalisches Institut, Georg August University Göttingen, Göttingen, Germany

Francesca Cavalieri Department of Chemical and Biomolecular Engineering, The University of Melbourne, Melbourne, VIC, Australia

Jayani Chandrapala Advanced Food Systems Unit, College of Health and Bio-medicine, Victoria University, Werribee, VIC, Australia

Farid Chemat Université d'Avignon et des Pays de Vaucluse, UMR 408, Equipe Green, Avignon, France

Pavel V. Cherepanov Physical Chemistry II, University of Bayreuth, Bayreuth, Germany

Pak-Kon Choi Department of Physics, Meiji University, Tama-ku, Kawasaki, Japan

Claudia Crestini Department of Chemical Sciences and Technologies, University of Rome "Tor Vergata", Rome, Italy

Zheng-Guo Cui Departments of Public Health, Graduate School of Medicine and Pharmaceutical Sciences, University of Toyama, Toyama, Japan

Diane Dalecki Department of Biomedical Engineering, University of Rochester, Rochester, NY, USA

Jackline Freitas Brilhante de São José Departamento de Educação Integrada em Saúde, Federal University of Espírito Santo, Vitória, Brazil

Tuna D. Dincer Food Science and Technology Program, School of Public Health, Faculty of health Sciences, Curtin University, Bentley, WA, Australia

G. Kumaravel Dinesh Department of Chemical Engineering, National Institute of Technology Tiruchirappalli, Tiruchirappalli, Tamilnadu, India

Salma A. Elgaili Department of Chemical Engineering, American University of Sharjah, Sharjah, UAE

Naoya Enomoto Department of Applied Chemistry, Faculty of Engineering, Kyushu University, Fukuoka, Japan

Mustafa Fatih Ertugay Department of Food Engineering, Erzincan University, Erzincan, Turkey

Frédéric Fine Terres Inovia, Pessac, France

Shengpu Gao China Animal Disease Control Center, Slaughter Technology Center of Ministry of Agriculture of China, Beijing, China

Aharon Gedanken Department of Chemistry and Kanbar Laboratory for Nanomaterials, Bar-Ilan University Center for Advanced Materials and Nanotechnology, Ramat-Gan, Israel

Department of Materials Science and Engineering, National Cheng Kung University, Tainan, Taiwan

Parag R. Gogate Chemical Engineering Department, Institute of Chemical Technology, Matunga, Mumbai, India

Veera G. Gude Department of Civil and Environmental Engineering, Mississippi State University, Mississippi State, MS, USA

Yacine Hemar School of Chemical Sciences, The University of Auckland, Auckland, New Zealand

The Riddet Institute, Plamerston North, New Zealand

Denise C. Hocking Department of Pharmacology and Physiology, University of Rochester, Rochester, NY, USA

Ghaleb A. Husseini Department of Chemical Engineering, American University of Sharjah, Sharjah, UAE

Salih Karasu Faculty of Chemical and Metallurgical Engineering, Department of Food Engineering, Yıldız Technical University, Esenler, Istanbul, Turkey

Sandra Kentish Department of Chemical and Biomolecular Engineering, The University of Melbourne, Melbourne, VIC, Australia

Li Ling Apple Koh Singapore University of Technology and Design, Singapore, Singapore

Takashi Kondo Departments of Radiological Sciences, Graduate School of Medicine and Pharmaceutical Sciences, University of Toyama, Toyama, Japan

Nobuki Kudo Graduate School of Information Science and Technology, Hokkaido University, Sapporo, Japan

Heiko Lange Department of Chemical Sciences and Technologies, University of Rome "Tor Vergata", Rome, Italy

Gang-Juan Lee Department of Environmental Engineering and Science, Feng Chia University, Taichung, Taiwan

Judy Lee Chemical and Process Engineering, University of Surrey, Guildford, Surrey, UK

Thomas Leong Faculty of Science, Engineering and Technology, Department of Mechanical and Product Design Engineering, Hawthorn, Swinburne University of Technology, Melbourne, Australia
School of Chemistry, The University of Melbourne, Melbourne, VIC, Australia
Department of Chemical and Biomolecular Engineering, The University of Melbourne, Melbourne, VIC, Australia

Gillian Lewis School of Biological Sciences, The University of Auckland, Auckland, New Zealand

J. Madhavan Department of Chemistry, Thiruvalluvar University, Vellore, Tamil Nadu, India

Richard Manasseh Swinburne University of Technology, Melbourne, VIC, Australia

R. V. Mangalaraja Faculty of Engineering, Advanced Ceramics and Nanotechnology Laboratory, Department of Materials Engineering, University of Concepcion, Concepcion, Chile

Sivakumar Manickam Manufacturing and Industrial Processes Research Division, Faculty of Engineering, University of Nottingham Malaysia campus, Semenyih, Selangor, Malaysia

Edith Martinez-Guerra Department of Civil and Environmental Engineering, Mississippi State University, Mississippi State, MS, USA

Ana M. Martins Department of Chemical Engineering, American University of Sharjah, Sharjah, UAE

Robert Mettin Drittes Physikalisches Institut, Georg August University Göttingen, Göttingen, Germany

Yoshiteru Mizukoshi Kansai Center for Industrial Materials Research, IMR, Tohoku University, Naka-ku, Sakai, Osaka, Japan

Nor Saadah Mohd Yusof Department of Chemistry, University of Malaya, Kuala Lumpur, Malaysia

Vijayanand S. Moholkar Department of Chemical Engineering and Center for Energy, Indian Institute of Technology Guwahati, Guwahati, Assam, India

Akihiro Morii Departments of Urology, Graduate School of Medicine and Pharmaceutical Sciences, University of Toyama, Toyama, Japan
Urology Department, Kurobe City Hospital, Kurobe, Japan

Ben Nanzai Faculty of Engineering, Kanagawa University, Kanagawa-ku, Yokohama, Japan

Bernaurdshaw Neppolian SRM Research Institute, SRM University, Chennai, Tamilnadu, India

Kim Truc Nguyen Division of Chemistry and Biological Chemistry, School of Physical and Mathematical Sciences, Nanyang Technological University, Singapore, Singapore

Susumu Nii Kagoshima University, Kagoshima, Japan

Ryohei Ogawa Departments of Radiological Sciences, Graduate School of Medicine and Pharmaceutical Sciences, University of Toyama, Toyama, Japan

Claus-Dieter Ohl School of Physical and Mathematical Sciences, Nanyang Technological University, Singapore, Singapore

Siew-Wan Ohl Institute of High Performance Computing, Singapore, Singapore

Kenji Okitsu Department of Materials Science, Graduate School of Engineering, Osaka Prefecture University, Sakai, Osaka, Japan

Gregory S. Patience Département de Génie Chimique, Polytechnique Montréal, Montréal, QC, Canada

Pankaj N. Patil Chemical Engineering Department, Gharda Institute of Technology, Ratnagiri, Maharashtra, India

Ilana Perelshtein Department of Chemistry and Kanbar Laboratory for Nanomaterials, Bar-Ilan University Center for Advanced Materials and Nanotechnology, Ramat-Gan, Israel

Nina Perkas Department of Chemistry and Kanbar Laboratory for Nanomaterials, Bar-Ilan University Center for Advanced Materials and Nanotechnology, Ramat-Gan, Israel

Nalenthiran Pugazhenthiran Nanomaterials and Solar Energy Conversion Lab, Department of Chemistry, National Institute of Technology, Tiruchirappalli, Tiruchirappalli, Tamilnadu, India

P. Sathishkumar Faculty of Chemical Sciences, Department of Organic Chemistry, University of Concepcion, Concepcion, Chile

R. A. Senthil Department of Chemistry, Thiruvalluvar University, Vellore, Tamil Nadu, India

S. Shaik Department of Chemical Engineering, National Institute of Technology, Warangal, Telangana, India

Anne-Gaëlle Sicaire Université d'Avignon et des Pays de Vaucluse, UMR 408, Equipe Green, Avignon, France

T. Sivasankar Sonochemical Intensification Laboratory, National Institute of Technology Tiruchirappalli, Tiruchirappalli, Tamilnadu, India

Younggyu Son Department of Environmental Engineering, Kumoh National Institute of Technology, Gyeongbuk, South Korea

Shirish Sonawane Department of Chemical Engineering, National Institute of Technology, Warangal, Telangana, India

Sivaramapanicker Sreejith Division of Chemistry and Biological Chemistry, School of Physical and Mathematical Sciences, Nanyang Technological University, Singapore, Singapore

Zeynep Hazal Tekin Faculty of Chemical and Metallurgical Engineering, Department of Food Engineering, Yıldız Technical University, Esenler, Istanbul, Turkey

Boon Mian Teo Interdisciplinary Nanoscience Center (iNANO), Aarhus University, Aarhus, Denmark

Institute of Biomedical Engineering (IBME), Oxford University, Oxford, UK

Kandasamy Thangavadivel Graduate School of Engineering, Osaka Prefecture University, Sakai, Osaka, Japan

J. Theerthagiri Department of Chemistry, Thiruvalluvar University, Vellore, Tamil Nadu, India

D. Thirumalai Department of Chemistry, Thiruvalluvar University, Vellore, Tamil Nadu, India

Ömer Said Toker Faculty of Chemical and Metallurgical Engineering, Department of Food Engineering, Yıldız Technical University, Esenler, Istanbul, Turkey

Maryline Vian Université d'Avignon et des Pays de Vaucluse, UMR 408, Equipe Green, Avignon, France

Rute F. Vitor Department of Chemical Engineering, American University of Sharjah, Sharjah, UAE

Hao Wang Laboratory for Biological Effects of Nanomaterials and Nanosafety, National Center for Nanoscience and Technology (NCNST), Beijing, China

Lei Wang Laboratory for Biological Effects of Nanomaterials and Nanosafety, National Center for Nanoscience and Technology (NCNST), Beijing, China

Akihiko Watanabe Departments of Urology, Graduate School of Medicine and Pharmaceutical Sciences, University of Toyama, Toyama, Japan

Jerry J. Wu Department of Environmental Engineering and Science, Feng Chia University, Taichung, Taiwan

Bin Xue Department of Chemistry, College of Food Science and Technology, Shanghai Ocean University, Shanghai, China

Guohai Yang State Key Laboratory of Analytical Chemistry for Life Science, School of Chemistry and Chemical Engineering, Nanjing University, Nanjing, People's Republic of China

Kyuichi Yasui National Institute of Advanced Industrial Science and Technology (AIST), Nagoya, Japan

Yanli Zhao Division of Chemistry and Biological Chemistry, School of Physical and Mathematical Sciences, Nanyang Technological University, Singapore, Singapore
School of Materials Science and Engineering, Nanyang Technological University, Singapore, Singapore

Meifang Zhou School of Chemistry, The University of Melbourne, Melbourne, VIC, Australia

Jun-Jie Zhu State Key Laboratory of Analytical Chemistry for Life Science, School of Chemistry and Chemical Engineering, Nanjing University, Nanjing, People's Republic of China

Bogdan Zisu School of Applied Sciences, College of Science, Engineering and Health, RMIT University, Melbourne, VIC, Australia

Part I

Fundamental Aspects

Bubble Dynamics and Observations

Robert Mettin and Carlos Cairós

Contents

Abstract

The dynamics of acoustic cavitation bubbles can be complicated due to their nonlinear nature. They comprise several aspects on different spatial and temporal scales: The interplay of bubble and sound field leads to volume oscillations and partly strong implosion of the gas phase, which induces further effects like chemical reactions and luminescence. Acoustic forces lead to bubble translation, interaction, and merging. Non-spherical shape modes can cause deformations and splitting, and the bubble collapse can take place with formation of a fast liquid jet in the case of rapid translation, adjacent bubbles, or solid objects. In multi-bubble systems, acoustic field geometries and bubble interactions lead to emergence of a variety of characteristic dynamical bubble structures. A brief review of these issues is given with an emphasis on observations in experiments.

R. Mettin (✉) • C. Cairós
Drittes Physikalisches Institut, Georg August University Göttingen, Göttingen, Germany
e-mail: robert.mettin@phys.uni-goettingen.de; carlos.cairos@phys.uni-goettingen.de

3

Introduction

A gaseous domain in liquid that is exposed to varying pressure can undergo complicated dynamics, including significant volume excursions, deformations, and interactions. A standard case where such conditions are met is in acoustic cavitation, i.e., the occurrence and dynamics of gas and vapor phase in sufficiently strong sound fields. Several review articles and monographs exist on acoustic cavitation, and many connected subjects are treated there in great detail [1–8]. In contrast, this chapter tries to sketch main aspects in brevity and with examples to provide the reader with a rapid overview, useful as a general background and for experiments involving cavitation. The main reference is to acoustic frequencies in the ultrasonic domain, although it should be noted that the phenomena discussed are not necessarily confined to this region. The presented features of bubble dynamics serve as well for an impression of the complexity involved. It is not sufficient to imagine "the" cavitation bubble as a standardized and unique entity in cavitating systems. Instead, a variety of bubble dynamics can occur at the same time in the same system, and furthermore a high sensitivity to external parameters may be found.

In the following, bubble dynamics is presented in a logical sequence from the generating sound field, nucleation, spherical bubble oscillation, and bubble collapse. Sections follow that report on acoustic (Bjerknes) forces, bubble translation and interaction, and non-spherical bubble dynamics. The dynamics of multi-bubble systems is briefly discussed, and finally some concluding remarks are given.

Bubble Dynamics

Sound Field

The generation of intense ultrasound in liquids is often done with one of two very common configurations: In an ultrasonic bath, several transducer elements are attached outside to the bottom and/or walls of a metal liquid container, typically of rectangular shape and with a free surface on top. The ultrasound develops roughly a plane standing wave pattern (although deviations and traveling wave parts can occur near the emitter). The second type of field is produced by an ultrasonic horn, i.e., an ultrasonically excited metal rod with shrinking diameter toward its end. The end tip oscillates with rather large displacements and is directly submerged into the liquid. This generates mainly a spatially decaying traveling wave field in front of the horn (reflections from container walls can also cause standing wave parts). Other geometries exist, like cylindrically or spherically focused (inner) fields or cylindrically decaying (outer) fields. Cavitation is generated in all cases, but details of the bubble

dynamics and bubble distributions can differ significantly. For example, the horn (also called sonotrode or disintegrator) is usually working only at lower ultrasonic frequencies ($\approx$20...50 kHz), while for higher frequencies (up to several MHz), bath-type reactors are common. Some previously reported influence of acoustic frequency on cavitation effects might actually be related to the different field geometries. Therefore, the sound field geometry should be included in any experimental report (in the same way as frequency and power settings), and the interpretation of frequency-related results should take place with sufficient care.

Nucleation

The strict notion of cavitation is an isothermal transition of the liquid-vapor phase boundary in a single component fluid due to a decrease of pressure [7, 9]. In other words, the cohesion between the fluid particles is overcome by an externally applied stress, which causes homogeneous nucleation of vapor. However, in most of the relevant cases, nucleation takes place in an inhomogeneous way, i.e., rupture of the liquid takes place at previously existing "weak points" that are generally called "nuclei." Potential nuclei are adhesive bonds to liquid or solid contaminants or to container walls. In aqueous systems, it is also common to find small pre-existing volumes of noncondensable gas. Such (sub-) microbubbles are apparently stabilized against surface tension-driven dissolution, and this might be achieved, e.g., by attachment to solids [10, 11] or by surface-active contaminants [12]. The presence of such gas nuclei is indicated by the possibility to suppress cavitation by degassing and by temporal application (and then release) of static overpressure [13]. True conditions for homogeneous nucleation might be encountered in the extreme case of sound-soft reflection of an acoustic shock wave: The inversion of the positive shock pressure leads to very large peak negative pressures. Figure 1a, b shows both types of nucleation in water initiated by a focused shock that is reflected at the free (water-air) surface. It should also be noted that ionizing radiation [2] or focused light [14] might as well cause weak spots in the liquid by local heating.

In continuously running ultrasonic setups, the origin of bubbles is typically heterogeneous and can be roughly classified into three phenomena: (i) spontaneous single-bubble creation at one of the described nucleus types; (ii) continuous bubble appearance from (often invisible) sources in the liquid or at walls, leading to formation of chains of translating bubbles (streamers); and (iii) splitting from existing bubbles, forming smaller fragments. Examples for these processes are illustrated by Fig. 1c–e. This classification does not have to be exclusive: A spontaneously nucleated single bubble can multiply itself into a bubble cluster, and a possible source of a continuously nucleated streamer can be another bubble attached to a crevice at a container wall, repetitively splitting off microbubbles [17, 18].

The sound intensity when the first cavitation occurs for increasing power is known as the cavitation inception threshold or simply cavitation threshold. It is influenced by the type and cleanliness of the liquid, its temperature, and content of
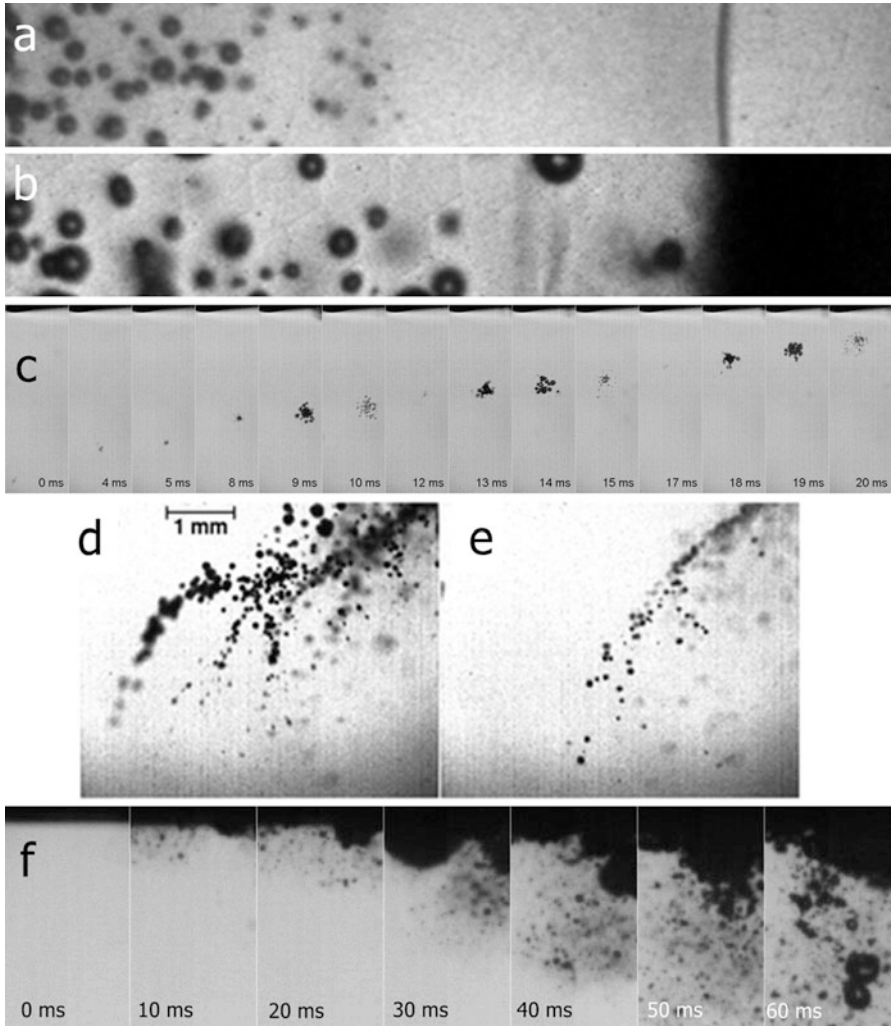
Fig. 1 (**a**) Nucleation in water caused by a focused acoustic shock wave (*dark line*), running from *left* to *right*. Individual bubbles occur in the trailing negative pressure edge wave (From [15]). (**b**) A similar shock wave after reflection at the water-air interface (to the *right*). Dark foamlike phase directly at the free surface appears. Images are rotated by 90°, exposure time 10 ns, and frame height 2 mm (From [15]). (**c**) Spontaneous nucleation of a bubble and subsequent bubble cluster formation in an ultrasonic field of 25 kHz. The visibility changes due to beat oscillation between bubbles and camera frame rate; frames without visible bubbles are left out. Exposure 1.5 μs and frame width 1.9 mm (After [16]). (**d**, **e**) Streamer formation due to localized repetitive nucleation; 25 kHz, scale indicated (From [16]). (**f**) Nucleation due to bubble splitting at a sonotrode just after switching on. First bubbles appear at the tip and fragment or shed smaller bubbles. The bubbly region drifts downward due to acoustic streaming (20.61 kHz, frame width 2.5 mm)

dissolved gas [6, 19]. Additional influence can be given by container walls or the sound field geometry. For higher acoustic frequencies, the threshold is generally higher, and it bears a hysteresis when the acoustic power is decreased. Furthermore, it is known that strong ultrasound in liquids will generate directional flows due to acoustic streaming [20, 21], and externally driven liquid flows might as well be present in a setup. Both will influence the distribution of nuclei in space and thus potentially as well the form of observed cavitation [22].

Spherical Bubble Oscillations

After its nucleation, the bubble is continuously exposed to the time varying local sound pressure. It responds with volume oscillations and potentially surface oscillations and translation in space. Neglecting the latter effects at first hand for a theoretical description, one can use the assumption of spherical bubble shape and stationary position in an infinite liquid at rest. Such an approximation is simplifying, but for many aspects sufficient. Then the excited bubble can be seen as a driven nonlinear oscillator with one degree of freedom, its momentary state being described by the radius $R(t)$ and the bubble wall velocity $dR/dt = U$ where d/dt denotes the derivative with respect to time t. From conservation of liquid mass and momentum and the boundary conditions at the bubble wall, a nonlinear ordinary differential equation of second order can be derived that describes the bubble wall motion under consideration of the liquid viscosity and surface tension: the Rayleigh-Plesset (RP) equation [7]. It has to be augmented by a model of the bubble interior where frequently a homogeneous ideal gas is employed. Several extensions of the RP equation exist, including for example compressibility of the liquid [23–25] or evaporation/condensation of liquid at the bubble wall [26, 27]. In any case, the response of the bubble for small driving can be linearized, yielding a harmonic oscillator with resonance frequency f_{res}. The linear resonance frequency depends reciprocally on the bubble size which is conveniently given by the rest radius (or equilibrium radius) R_0. Stated the other way around, for a fixed driving frequency f, one will find a linear resonant bubble size $R_{res} \sim 1/f$. The rest radius R_0 is the radius of the bubble in the absence of a sound field and represents a measure of the amount of noncondensable gas in the bubble. For small-amplitude volume oscillations, it corresponds to the time-averaged bubble radius, but for stronger oscillations, this average is shifted to larger values due to the nonlinear restoring forces of a bubble ("hardening spring" for compression and "softening spring" for expansion). In experimental imaging, the maximum radius during one bubble oscillation period, R_{max}, is usually the easiest to observe, while the minimum radius R_{min} frequently falls below space and/or time resolution of the imaging system. However, R_0 and R_{min} can sometimes be reconstructed from fitting recorded radius-time data to a spherical bubble model.

Due to the nonlinearity, periodically driven spherical bubbles can exhibit quite complicated dynamics when the exciting pressure is increased. The phenomena range from nonlinear resonances and hysteresis to period-doubling and deterministic
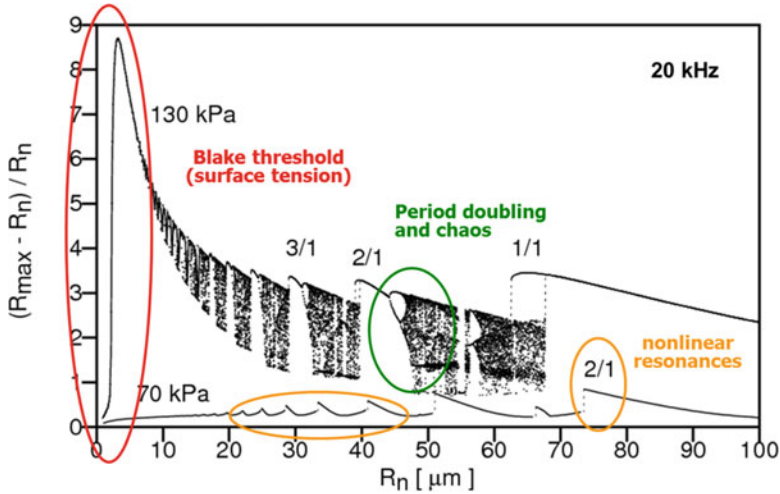
Fig. 2 Normalized response $(R_{max}-R_0)/R_0$ of a spherical bubble in water to a sinusoidal periodic driving pressure of 20 kHz (calculations based on the Gilmore model [23]). For each value of rest radius R_0, the maximum radius during one driving period is evaluated (after transients). If different maxima occur in sequential periods, the corresponding points are all included. Furthermore, hysteresis is found by scanning R_0 both up- and downward. The lower curve at 70 kPa driving pressure amplitude shows a chain of nonlinear resonances, each of which can be uniquely numbered [29, 30]. Further increase of driving amplitude to 130 kPa leads to stronger hysteresis, period-doubling sequences, and chaotic oscillations. Bubbles below the Blake threshold stay with small oscillations, while bubbles just beyond this surface tension threshold can show the largest relative expansions, causing an accordingly strong collapse (From [30], with kind permission from Springer Science + Business Media)

chaos [28]. Figure 2 exemplifies this in a bifurcation diagram where the bubble response is shown in dependence of the equilibrium radius. An important feature is the so-called (dynamical) Blake threshold, caused by surface tension: While the oscillation of very small bubbles is suppressed due to the high Laplace pressure, the bubble response grows enormously when the surface tension can just be overcome. The large expansion leads to an extreme collapse afterward with rapid high compression and heating of the bubble interior. The Blake threshold can be crossed by an increase of driving pressure, but as well by a growth of R_0, as shown in Fig. 2.

Spherical RP-like bubble models can describe experimental radius-time data with good quality as long as non-spherical shapes can be neglected and the details of collapse are not the prime interest. The typical nonlinear oscillation with large expansion and strong collapse of a bubble just beyond the Blake threshold is shown in Fig. 3a. The experimental data has been obtained from a single isolated bubble trapped in a standing wave field, and the Gilmore model can reproduce the radius-time history quite well. Further nonlinear phenomena like hysteresis, bifurcations, and chaotic oscillations are usually more difficult to observe directly in an undisturbed experiment with a single bubble, because the according system parameters are partly not accessible or the bubble becomes unstable. However, some data
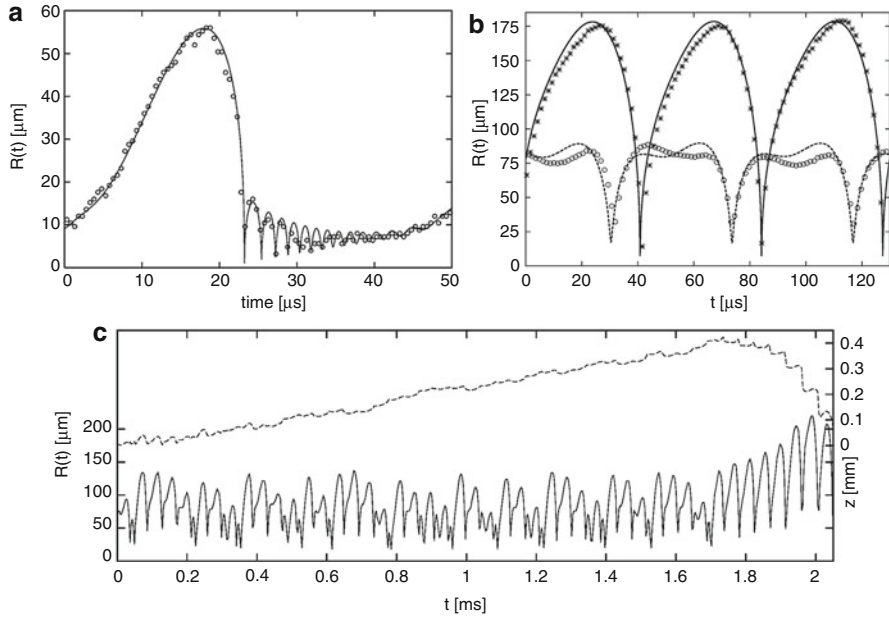
Fig. 3 (**a**) Radius-time observations (*circles*) of a bubble in water, trapped by an acoustic standing wave field at 21.4 kHz. The continuous line is a fit by the Gilmore model [23] from which a rest radius of $R_0 = 8.0$ μm and a driving pressure amplitude of 132 kPa can be inferred (From [8] with kind permission, copyright John Wiley & Sons, Inc. 1999). (**b**) Coexisting bubble dynamics (hysteresis) in sulfuric acid driven at 23 kHz: an oscillation with large bubble expansion can alternate with a pulsation of moderate amplitude and double maximum at otherwise unchanged conditions (*crosses* and *circles* represent experimental data, *continuous* and *broken lines* are coexisting attractors of a Keller-Miksis model [24, 32]). The smaller oscillation is shape unstable and shows surface modes, which leads to some variations of the measured bubble radius (*circles*) (Data courtesy of Andrea Thiemann [33]). (**c**) Chaotic volume oscillation and hysteresis of a bubble in phosphoric acid (near a sonotrode tip driven at 22 kHz [34]). The *solid line* is the measured bubble radius $R(t)$; the *dashed line* is the bubble position z. When the dynamics changes from chaotic to periodic ($t \approx 1.7$ ms), the direction of translation changes from *upward* to *downward*. After certain motion in negative z direction, the bubble dynamics switches to chaotic oscillation again, and it returns to the position shown in a periodic fashion (not shown)

from bubble traps are available [31], and relatively isolated bubbles in multi-bubble environments can be compared to model predictions for single bubbles as well. In such experiments it is found that the nonlinear features predicted by the models can indeed be observed, as is exemplified in Fig. 3b, c; see also section "Acoustic Forces and Translation."

Collapse Phenomena

The strong collapse is the most interesting but also challenging aspect of bubble dynamics with respect to the physical and chemical phenomena involved. It is the

key for many, if not all, applications of acoustic cavitation. When a spherical bubble is excited stronger and stronger, the bubble oscillation maximum is extended in time, while the minimum is shortened to an almost singular behavior. The accelerated inward wall motion is almost instantaneously reversed in the collapse peak to an expanding motion. This process can launch shock waves into the liquid and compress and heat the bubble interior to conditions where chemical reactions take place (sonochemistry [35]) and light emission may occur (sonoluminescence [36–38]). A direct experimental observation of the interior of the collapsing bubble is extremely difficult due to the small scales (below a μm) and the fast processes (below a ns). Therefore, indirect measures like shock waves in the liquid [39], chemical reactions [40], and the spectrum of emitted light [41] have been used to draw conclusions on the collapse conditions. Further insight comes from numerical simulations with advanced models that take into account a variety of chemical reactions in the gas and vapor phase or plasma physics; see, for instance, [42]. When the imploding bubble wall velocities reach very high values, the validity of RP-like models for the liquid side of the problem, as well as the usual assumptions on the gas, break actually down in the final moments of collapse. Then, partial differential equations should be employed for a full computational fluid dynamics approach, and the numerical effort grows significantly [43, 44]. An alternative of similar or even higher computational cost are molecular dynamics simulations [45]. However, RP-like models can at least provide an estimate of the collapse strength by the bubble compression rate $R_0/R_{\min}$ since the essential radius-time dynamics is reasonably captured. This is seen in the examples of the characteristic nonharmonic radius oscillations with periodically repeated collapse shown in Fig. 3. Note that the collapse peaks appear like singularities, but the curves run smoothly through the radial minimum, just on a very short time scale. Some experimental observations of collapse phenomena from isolated bubbles are presented in Fig. 4.

Acoustic Forces and Translation

The case of an isolated, strongly oscillating single bubble positioned stably in space, as in the illustrations of Fig. 4, is quite atypical in acoustic cavitation, and special setups have to be employed to realize it (so-called bubble traps). In most environments, the cavitation bubbles perform spatial translational motion and show interaction with adjacent bubbles. The reasons are "acoustic" forces caused by the volume oscillations of the bubbles in the sound field, the so-called Bjerknes forces [6, 48]. It turns out that bubble translation and interaction induced by Bjerknes forces are often dominant phenomena in multi-bubble systems. For example, acoustically driven bubble velocities usually supersede bulk flow velocities, and gas accumulation by bubble collision resulting from Bjerknes forces can be much faster than gas diffusion processes from the liquid into the bubble.

The basis of the Bjerknes forces is the same mechanism that leads to the rise of bubbles in a quiet liquid: A nonzero integral of the pressure forces over the bubble wall. By Gauss's theorem, this relates to the integral of the pressure gradient over the
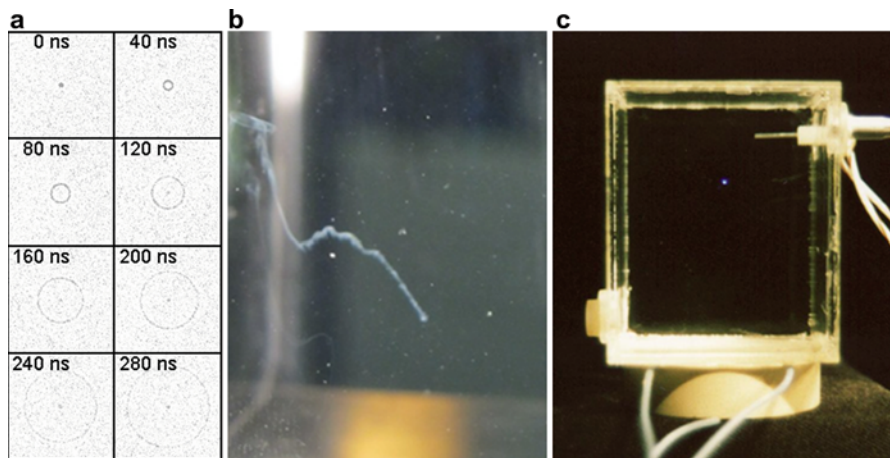
Fig. 4 Bubble collapse phenomena in experiments. (**a**) Spherical shock wave running outward from a fully collapsed bubble in water, captured in an acoustic bubble trap at 23 kHz (the bubble in the center is hardly visible; frame width 1.6 mm, timing indicated) (After [46], courtesy of R. Geisler). (**b**) Sonochemical reaction from a single bubble in a rectangular bubble trap (isomerization of maleic to fumaric acid, 18.5 kHz [47]). From the bubble, a *white* streak of insoluble product is emitted in *upper left* direction. (**c**) Sonoluminescence from a single bubble in a rectangular trap (water, 25 kHz; long-term exposure) (From [46], courtesy of R. Geisler)

bubble volume. In the case of spherical bubbles of small size compared to the spatial pressure variation, it is sufficient to consider the product of the bubble volume V and the pressure gradient at the center of the bubble (taken in the liquid for an absent bubble). In the case of a quiet water column, the hydrostatic pressure gradient results in the well-known buoyancy force $F_{\mathrm{buoy}} = V \rho g$ with the liquid density ρ and the gravitational acceleration g. If one assumes a periodic oscillation of both bubble volume and pressure gradient, the time-averaged force is of interest, which is called the primary Bjerknes force: $F_{B1} = <V(t) \, grad \, p(x,t) >_T$, where x is the position of the bubble center and $<.>_T$ denotes the time average over the period $T = 1/f$ of the oscillation with frequency f. Due to the correlation of the time variations of acoustic pressure, pressure gradient, and bubble volume, the primary Bjerknes force does typically not average out to zero. Indeed, it typically surpasses buoyancy by orders of magnitude. Still, its value and direction depend on the details of driving sound field and bubble response to the local pressure $p(x,t)$. If the limiting cases of plane traveling wave and plane standing wave are considered for small (linearized) bubble oscillations, one finds analytic expressions [5, 6] that describe the following behavior: Bubbles in a traveling wave are always pushed in the direction of the wave propagation, and the maximum forces occur for bubbles around the linear resonance size. In a standing wave field, a peculiar size sorting of bubbles takes place. Bubbles larger than linear resonance size are pushed to pressure amplitude minima (nodes), while the smaller ones are driven toward the pressure maxima (antinodes). At the nodes or antinodes, the pressure gradient and therefore also the primary Bjerknes

force vanish, and thus they form neutral positions. In the linearized theory, pressure nodes are stable for large bubbles ($R_0 > R_{res}$), while antinodes are stable for the smaller ones ($R_0 < R_{res}$).

The picture changes significantly if nonlinear bubble behavior is taken into account, which is important for stronger sound fields (compare Fig. 2). In comparison to the analytically given linear case, the large volume expansion and the shift of collapse phase relative to the driving pressure alter the time average with two important consequences: The absolute value of the force increases dramatically both in traveling and in standing waves (up to several orders of magnitude), and in standing waves the sign of the force can point away from pressure antinodes also for smaller bubbles [49, 50]. Then a stable positional equilibrium should exist between pressure nodes and antinodes: A location in the standing wave where the acoustic pressure is causing an oscillation form of the small bubbles is leading to zero primary Bjerknes force, and bubbles in the neighborhood of this position are pushed toward it. This is indeed the case if R_0 is sufficiently small. However, another generic feature occurs for the small bubbles of a size closer to the linear resonance size. The main resonance "bends over" to smaller equilibrium radii for higher driving pressure [51], and hysteresis of the radial oscillations sets in. This causes a bistability of the bubble dynamics, and a parameter range is formed where no positional equilibrium exists. Then the bubbles perform an oscillatory back-and-forth translation in space [52]. Further complications arise by the overlap of such hysteretic regions from adjacent nonlinear resonances and by emergence of chaotic bubble oscillations. This situation is illustrated by results from numerical calculations with a spherical single-bubble model in Figs. 5 and 6. Experimental evidence that reality is reasonably well captured is given by the examples of bistability, reciprocating translation, and chaotic volume oscillations in Fig. 3b, c.

When two or more oscillating bubbles come sufficiently close to each other, a mutual interaction takes place. Essentially, one bubble is reacting on the sound wave gradient emitted (i.e., scattered) by the other bubble, just in the way it behaves with respect to the incident (primary) sound field. This is why the generated force on the bubble is called secondary Bjerknes force. Apart from the scattered spherical (monopole) field, higher-order interaction terms come into play when one considers non-spherical bubble deformations or bubble translation, and potentially a mutual coupling of the adjacent bubbles by the emitted pressure becomes important [53–56]. In particular for close bubble encounters, the interaction can get involved then. Furthermore, the finite speed of sound might as well be considered, which leads to a time delay of the scattered waves [57, 58]. However, for two spherical bubbles "1" and "2" not too close nor too far apart, a reasonable approximation results in an expression of the secondary Bjerknes force as $F_{B2} = \rho / (4\pi\, d^2) < dV_1/dt\, dV_2/dt >_T$ where V_1 and V_2 denote the bubble volumes and d is the distance between the bubble centers [6, 59, 60]. From this notion, the case of linearized bubble oscillations in a fixed frequency acoustic field results in a mutual attraction of two bubbles if either both are smaller or larger than the linear resonance size R_{res}. For one bubble being smaller and the other larger than R_{res}, mutual repulsion occurs. For acoustically cavitating, i.e., strongly driven systems, important corrections
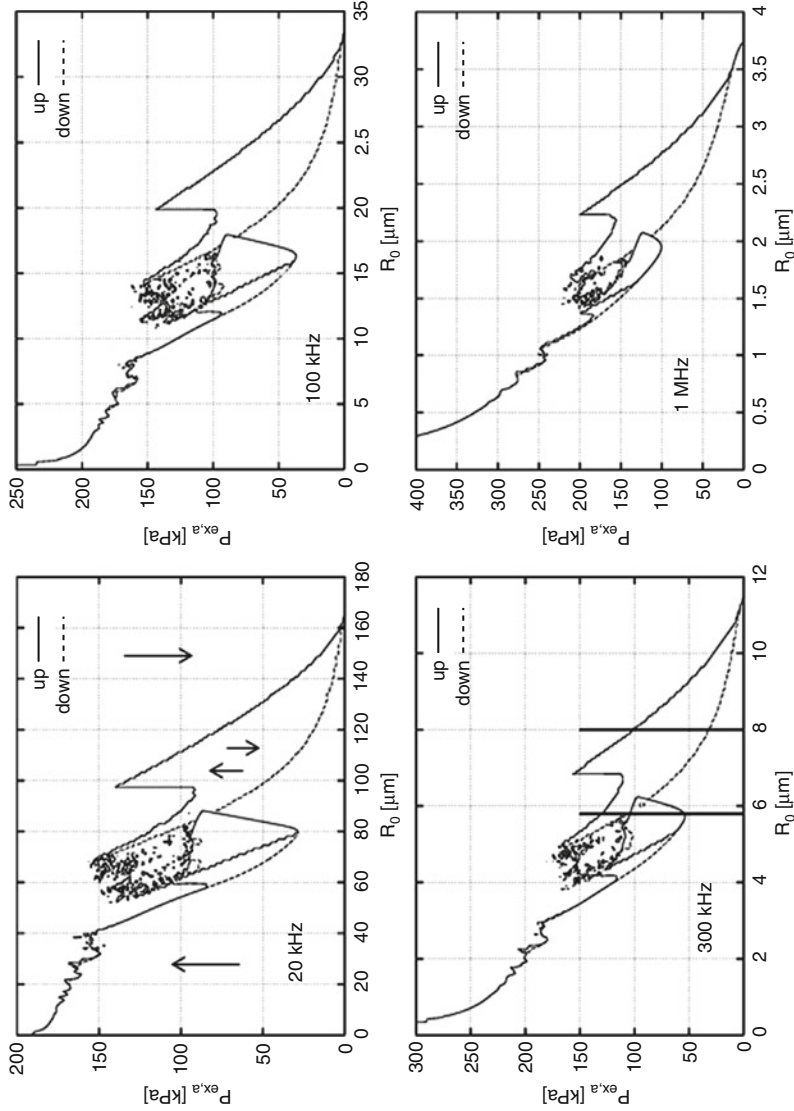
Fig. 5 Parameter planes of equilibrium bubble radius R_0 and acoustic pressure $P_{ex,a}$ in a standing wave, acoustic frequencies 20 kHz, 100 kHz, 300 kHz, and 1 MHz (water, normal conditions). *Lines* show the locations of zero primary Bjerknes force for increasing ("*up*," *solid*) and for decreasing ("*down*," *dashed*) driving pressure

of this picture result from the nonlinear bubble oscillations [60–62], similar as for the primary Bjerknes force. Again, the order of magnitude rises significantly, and the more complicated (non-sinusoidal) volume oscillations and nonlinear resonances lead to involved parameter patterns of attraction and repulsion. This is illustrated in Fig. 7.

Several experimental reports exist on quantitative measurements of the secondary Bjerknes forces and comparison with theory, see for instance [59, 63–66]. Like with tests of other features of bubble dynamics, it is notoriously difficult to prepare a controlled experimental system at desired parameters of bubble sizes, driving pressure and frequency. Furthermore, the forces are typically derived via measurement of translational bubble motion, and further model parameters are needed to correctly describe it (in particular drag force models, see, e.g., [7, 67]). Therefore the observational studies cover only a few selected parameter regions, but they give mostly a reasonable agreement with the theory [59, 63, 66]. Figure 8a, b shows data from an experiment with laser-seeded bubbles and their simulation with a spherical bubble model [64]. In this case, pressure amplitude and bubble sizes are in the range relevant for acoustic cavitation (i.e., strong collapse occurs), and a quite good reproduction of the observed bubble tracks is seen. This holds as well for the simulation of a multi-bubble streamer that has been stereoscopically recorded, see Fig. 8c [68]. At very close distances, however, also unexpected deviations have been reported [66]. Thus, experimental investigations and theoretical understanding of the interaction of driven bubbles remains a field of active research.

In any case, the dominant effect of the secondary Bjerknes force is the mutual attraction of neighboring bubbles of similar size, and this is the standard situation in acoustic cavitation. In spite of partly involved near-range interaction and notable exceptions, the close approach of bubbles then typically leads to coalescence. Bubble growth by collision is therefore an important factor for degassing of liquids by ultrasound [69], and the mechanism is controlled by the secondary Bjerknes force. Further observable effects of mutual bubble attraction occur in the formation of bubble clusters and structures of many bubbles, which is briefly discussed in section "Multi-bubble Systems."

Non-spherical Bubble Dynamics

Strongly oscillating spherical bubbles are an idealization. Even in an isolated and well-controlled situation like a bubble trap, a stronger collapse in gravity is expected to show deviations from a sphere due to a hydrostatic pressure gradient and minute

Fig. 5 (continued) scan. Parameter regions in the *lower left* part of the figures result in bubble motion toward higher driving pressure (toward the antinode), while parameters in the *upper right* region push to smaller amplitudes. In the *triangular* regions between *dashed* and *solid lines*, the direction of force depends on the initial conditions (bistability, force directions indicated by *vertical arrows* in the first plot). The *vertical lines* in the 300 kHz plot at 8 μm and 5.8 μm mark the parameter scans presented in Fig. 6 (From [52] with kind permission, copyright Elsevier 2009)
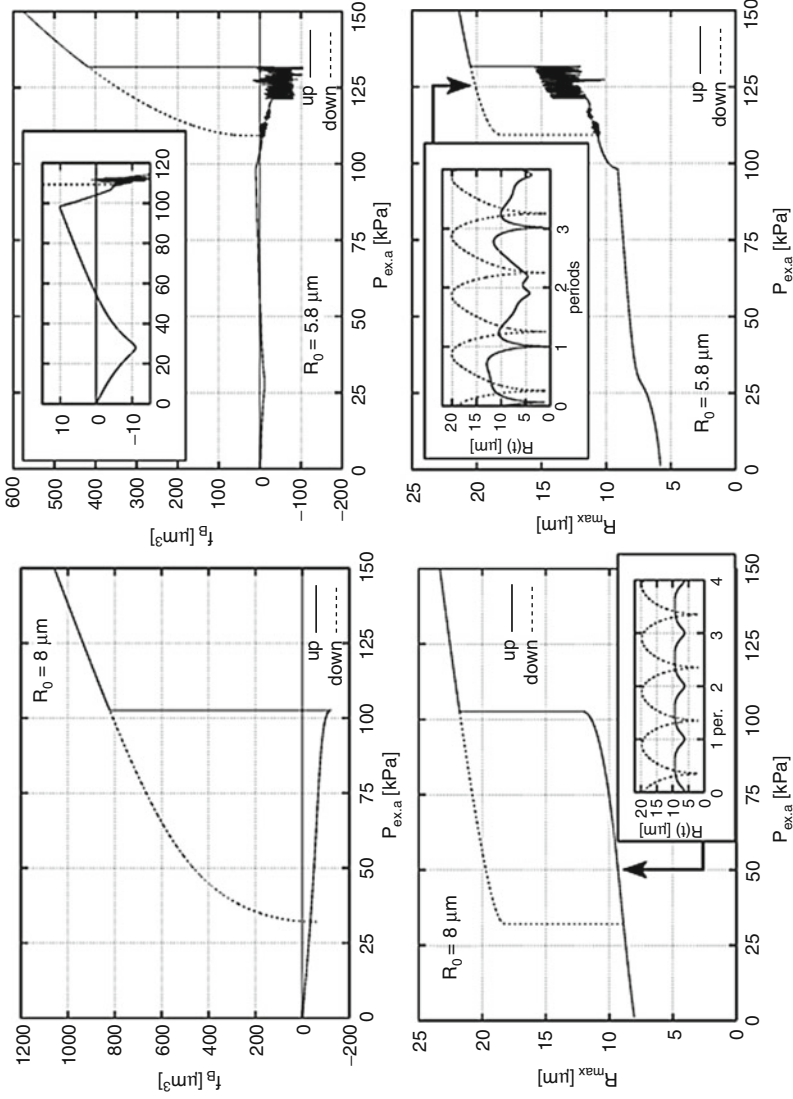
Fig. 6 *Left*: hysteresis in the Bjerknes force coefficient $f_B = < (4\pi/3)R^3(t)\cos(2\pi f\ t) >_T$ (*top*) and the maximum radius $R\max$ (*bottom*) for variable driving pressure amplitude $P_{ex,a}$ in a standing wave at $f = 300$ kHz, $R_0 = 8$ µm. Values resulting from upgoing (*downgoing*) pressure amplitude scan are given by *solid*
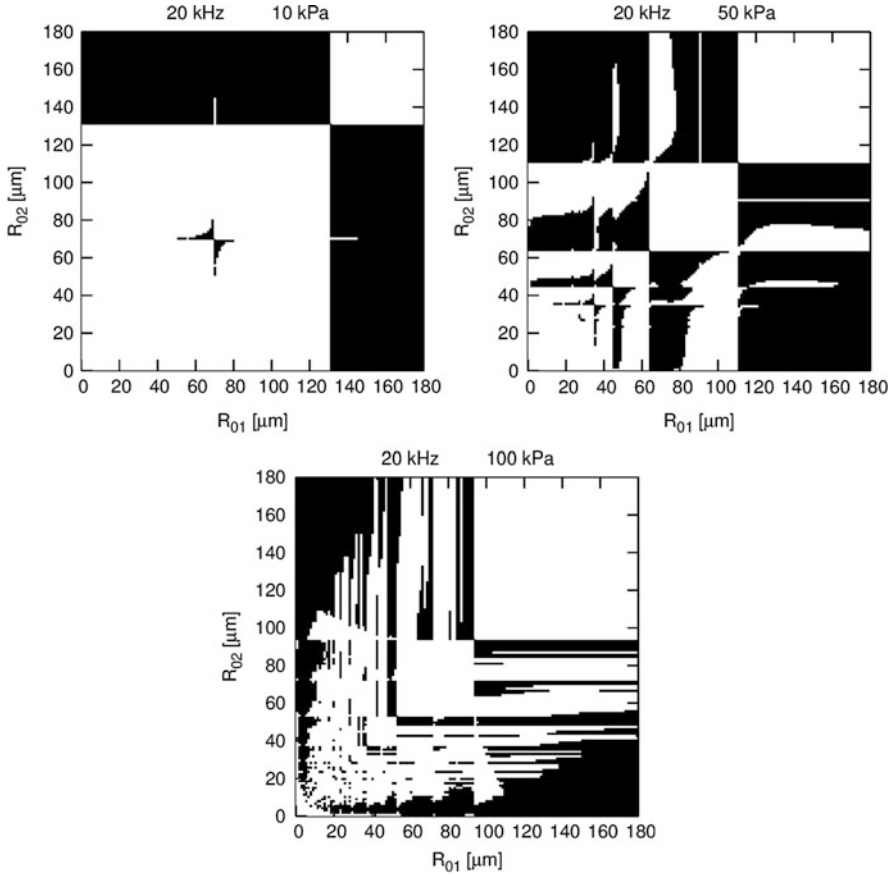
Fig. 7 Direction of secondary Bjerknes force between two spherical, nonmoving bubbles driven at 20 kHz (water, normal conditions). The *axes* indicate the equilibrium radii of the bubbles, R_{01} and R_{02}, and *white color* indicates their mutual attraction (*black color* mutual repulsion). For increasing driving pressure amplitude, the emergence of nonlinear resonances leads to a complicated alteration of attraction and repulsion. Effects from multi-stability are not included in the plots (From [16])

◀

Fig. 6 (continued) (*dashed*) lines. Positive (negative) f_B indicates a repulsive (attractive) pressure antinode, i.e., a primary Bjerknes force pushing the bubble to smaller (higher) driving pressures. The *inset* shows the bubble radius $R(t)$ vs. time in driving periods for the coexisting solutions at P_{ex}, $a = 50$ kPa. *Right*: hysteresis in f_B (*top*) and R_{max} (*bottom*) for variable $P_{ex,a}$ at $f = 300$ kHz, $R_0 = 5.8$ μm, notation as in *left* part of the figure. The *top inset* magnifies part of the graph, showing two finite pressure amplitudes with zero primary Bjerknes force. The *bottom inset* shows the bubble radius $R(t)$ vs. time in driving periods for the coexisting solutions at $P_{ex,a} = 125$ kPa, one oscillation being chaotic (From [52] with kind permission, copyright Elsevier 2009)
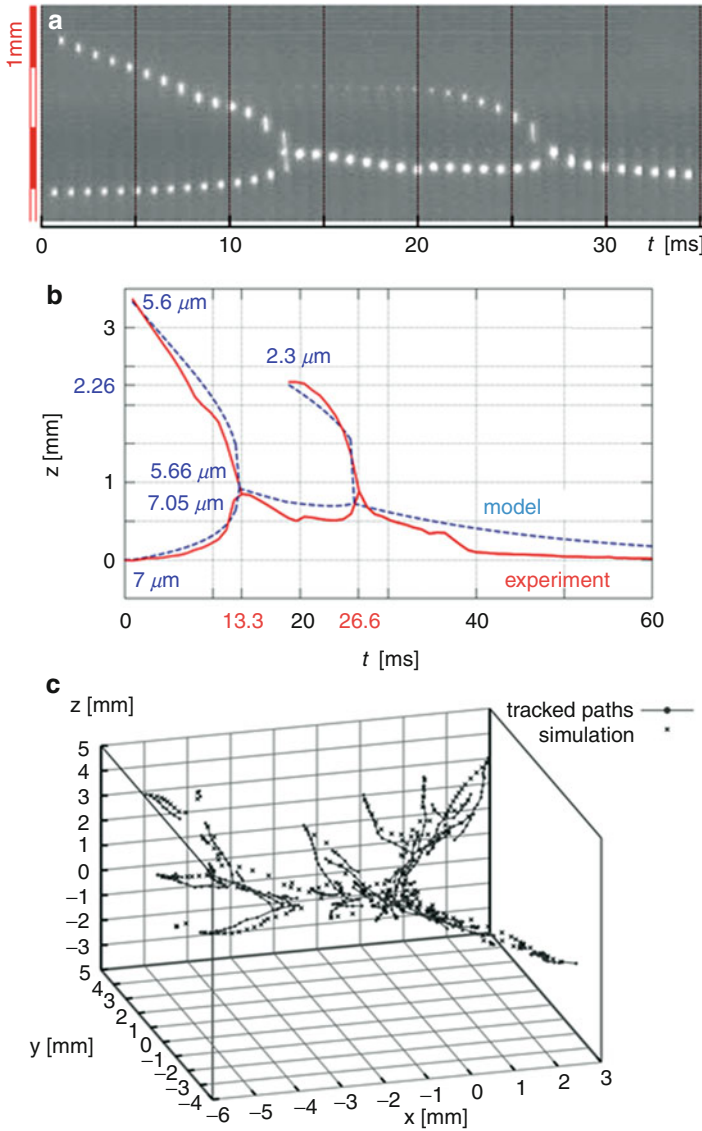
Fig. 8 Observation and modeling of mutual bubble attraction and collision caused by secondary Bjerknes forces. (**a**) Bubble positions (*bright spots*) versus time in a bubble trap experiment at 23 kHz acoustic driving, antinode pressure amplitude 120 kPa. One bubble is fixed at the pressure antinode (*bottom*), and a second bubble is seeded by a focused fs-laser pulse several mm apart. From this bubble, a fragment splits off around $t = 8$ ms. The larger bubbles merge at $t = 13.3$ ms, and the fragment joins at 26.6 ms (Courtesy of P. Koch, see also [64]). (**b**) Comparison of the experimental data (*continuous lines*) with a simulation (*dashed lines*) using spherical bubbles of the indicated rest radii (Courtesy of P. Koch, see also [64]). (**c**) Three-dimensionally tracked bubble motion (*lines* with points) near a pressure antinode (132 kPa, 22.8 kHz). All bubbles move toward the center, and some merge with neighbors. The tracks are simulated with spherical bubbles of $R_0 = 5$ µm (*crosses*) with reasonable agreement (From [68] with kind permission, copyright Elsevier 2004)

bubble motion [70, 71]. In fact, any relative motion of bubble and liquid during collapse will lead to a forward acceleration of the bubble. This happens since the relevant inertial component of the bubble momentum of translation is the added (or virtual) mass, connected with the liquid flow around the bubble [7]. When the bubble shrinks, so does the added mass, and the momentary conservation of momentum enforces the acceleration of the bubble. In the case of a strong collapse with nearly vanishing bubble volume (and massively shrinking added mass), the dramatic acceleration is not sustained, and a liquid jet develops that takes over the surplus momentum [72–74]. This jet shoots through the bubble in forward direction, pierces the opposite bubble wall, and can persist during the bubble re-expansion. Then the jet effect is visible as a characteristic sharp extrusion or "nose" of the bubble. Acoustic cavitation bubbles are frequently moving in space, driven by the Bjerknes forces, and the translation-induced forward jetting can partly be observed [75]. An example recorded in sulfuric acid is shown in Fig. 9a.

Other situations where the bubble develops a jet during collapse are neighboring bubbles [76–79], adjacent boundaries or objects [72, 80–82], or shock wave impact [83–85]. In all cases, the spherical symmetry of collapse is disturbed which provokes the jet flow. Examples for jetting collapses in experiments with laser-induced bubbles are given in Fig. 9b for adjacent bubbles and in Fig. 9c for a bubble next to a flat solid object. The peculiar aspherical collapse of bubbles at solid boundaries plays an important role in surface erosion [85, 86] and cleaning by cavitation [87–91].

The bubble deformation due to jetting has to be distinguished from non-spherical dynamics based upon instabilities of the spherical shape. The latter can occur without any perturbation of the symmetry (apart from microscopical disturbances). One type of spherical instability is based on unstable surface modes. The bubble shape can be decomposed into a series of modes, according to spherical harmonics functions [92]. Each mode is numbered with a natural number n with $n = 0$ being the radial mode. The mode $n = 1$ is the translation of the bubble's center of mass, $n = 2$ describes an oblate/prolate deformation, and so on (see, e.g., [6, 93]). For small bubble deformations, all higher modes are coupled only to the radial oscillation, and thus each mode is described by a separate driven harmonic oscillator. If the natural frequency of some mode is met by the radial oscillation frequency of the bubble, the mode can become unstable and grow, even from tiny starting values. The bubble shape then resembles the (oscillating) specific spherical harmonic function of n; see the second frame in Fig. 10a and frames 2 and 3 in Fig. 10b. Larger deformations can lead to splitting off of fragments, which happens almost symmetrically in the case shown in Fig. 10a. If the driving is stronger, several modes can be excited, and modes can couple with each other. The superposition of their oscillation causes irregularly appearing shapes with sharper peaks or cusps, and fragmentation happens more frequently, as illustrated by Fig. 10b. The fragments are typically bound to the core bubble by secondary Bjerknes forces ("satellite bubbles") and stay in the neighborhood. Very small ones dissolve, but larger satellites merge again with each other or with the central bubble after some time. If splitting occurs, the single-bubble system actually transforms into a multi-bubble system, and the notion of a "single bubble" becomes problematic. There are indications that the cavitation
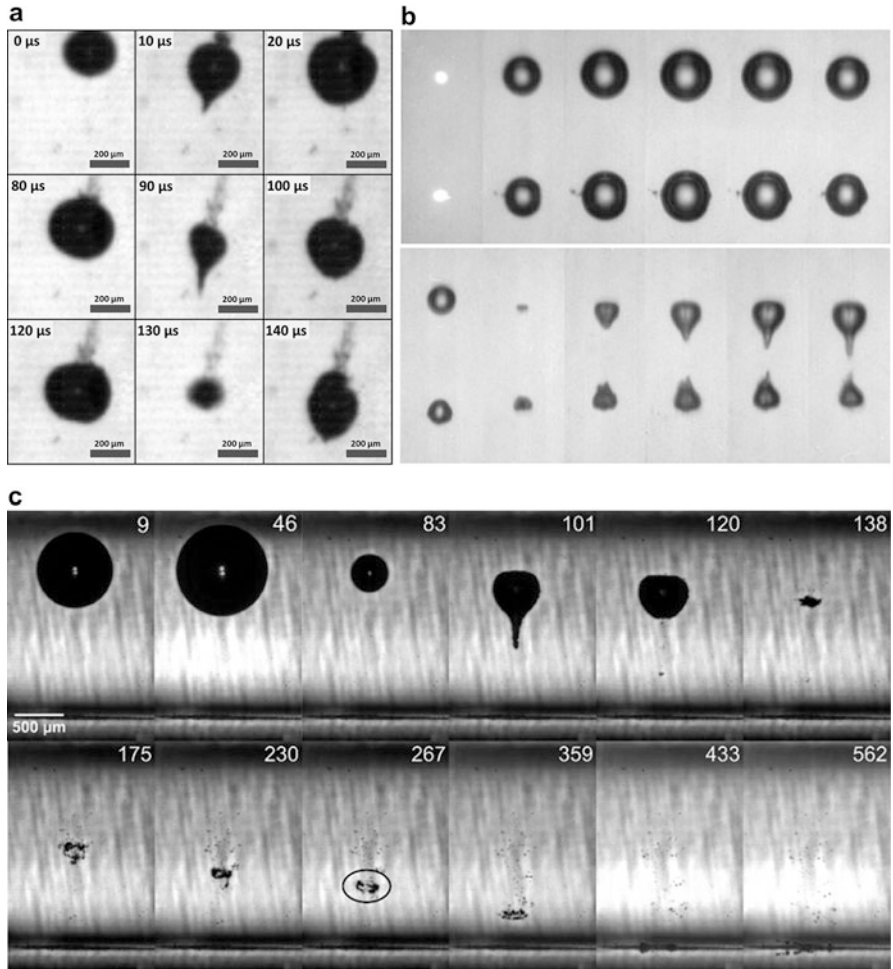
Fig. 9 Bubble collapse with a liquid jet flow through the bubble. (**a**) Fast translating bubble in sonicated sulfuric acid, subsequent collapses extracted from a high-speed recording. Acoustic frequency 23 kHz, frame width 650 μm, time indicated (Courtesy of A. Thiemann [33]) (**b**) Two laser-induced bubbles collapse next to each other, each with a jet toward the neighbor (interframe time 40 μs in the upper row and 20 μs later, initial bubble center distance 4.5 mm (After [79]). (**c**) Laser-induced bubble collapsing close to a solid boundary (at the *bottom*; time indicated in μs, scale given). The jet develops in the collapse (between 83 and 101 μs) toward the *solid*, and it persists during the rebound. The second collapse (≈138 μs) happens in a torus geometry (*ring bubble*) and leaves a downward traveling vortex flow that traps bubble remnants (encircled at 267 μs) (From [91] with kind permission, copyright Elsevier 2015)

effects can indeed change under this transition into a "small bubble cluster." See [47] for an example of the influence of bubble cluster dynamics on chemistry. If acoustic driving is increased even further, the mode of the unstable bubble with satellites can transform into a larger cluster of several similarly sized bubbles [95].
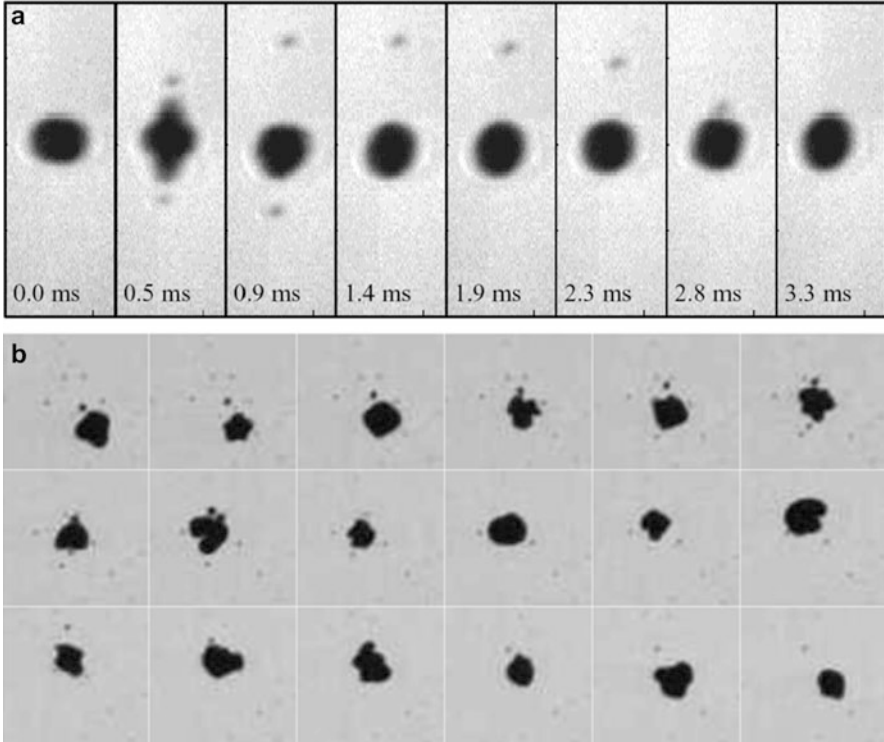
Fig. 10 High-speed recordings of trapped bubbles undergoing surface mode oscillations and splitting. (**a**) Alternating oblate/prolate shape ($n = 2$) and diametral ejection of two fragments in the second frame; later remerging of the fragments (each frame averaged over the exposure time of 444 μs, according to $\approx$11 driving periods at 25 kHz; frame width 1.2 mm) (From [94]). (**b**) Superposition of several modes leading to chaotic appearance of bubble shapes and to irregular splitting and merging of fragment bubbles (ca. 25 kHz, interframe time ca. 140 μs, exposure 1 μs, frame width ca. 2 mm). Frames 2 and 3 show modal shapes of $n = 5$ and $n = 4$ (Compare illustrations in [6])

The second type of spherical instability of the oscillating bubble is of Rayleigh-Taylor type. It is triggered by a sufficiently fast acceleration of the bubble wall in outward direction, i.e. acceleration of the lighter fluid (gas) into the heavier one (liquid). This instability therefore occurs during the bubble rebound and can destroy (fragment) the bubble. See [96–98] for a more detailed discussion.

Multi-bubble Systems

If few or many acoustically driven bubbles interact, the system dynamics can become considerably more complex than for a single bubble. This emerges not only because of the increase of degrees of freedom, but also due to the nonlinear

interaction laws and since bubble collisions and fragmentations are frequent processes. Bubble numbers are not conserved, and bubbles can form sources or sinks of other bubbles (compare Figs. 1, 8, 9, and 10). Even more, the bubble distribution can influence the acoustic wave propagation in the medium and thus cause a feedback reaction on itself [5]. For modeling purposes, approaches exist where the individual bubbles are captured (e.g., "particle models" [65, 68, 99–101]) and other methods where the bubble density and the gas void fraction are treated as time-dependent continuous fields in space [102–107]. Advanced modeling of acoustic cavitation is subject of active research, but it cannot be enlarged here; see the indicated references for further reading.

From the observational point of view, acoustic multi-bubble systems can form a variety of spatial patterns or structures that depend on the system parameters [95] and which partly still await a full explanation. In Fig. 11 two examples of structures in standing ultrasonic waves are given. Filamentary pictures as in (a) frequently arise if the bubbles are driven by primary Bjerknes forces toward a central region of higher acoustic pressure, e.g., an antinodal point or line (compare also Fig. 1d, e). The filaments are not static, but contain moving bubbles, which is why they are called "streamers." There exists also the term "acoustic Lichtenberg figures" (ALF) for the filamentary or "dendritical" structures due to their reminiscence of certain electrical discharge patterns [110, 111]. Numerical simulations can reproduce the shape of such filaments [65, 100, 101] and in special cases even the trajectories of the largest bubbles [68], compare Fig. 8c. Still, several aspects of the bubble dynamics in streamers remain to be clarified, see below. The other structure, shown in Fig. 11b, emerges in partly degassed liquid and consists of two bubbly layers that occur on opposite sides of pressure nodal regions. The layers have as well a filamentary structure when seen from the top [95]. Since the phase of the driving pressure jumps when the node of a standing wave is crossed, both bubble layers oscillate in antiphase. This can be seen on the inset of Fig. 11b. ALF filaments and double layers are common acoustic cavitation structures, but several other bubble distributions or arrangements can occur; see [95] for a (certainly incomplete) catalogue.

Cooperative bubble structures can be rich of complicated details that are revealed only at higher resolution of time and space. An example is the mentioned streamer, i.e., a line of bubbles traveling in one direction driven by primary Bjerknes forces. The streamer originates at some bubble source (e.g., nucleation point) and directs either toward a pressure antinode in a standing wave, as shown above, or in the direction of a propagating wave [112, 113]. The streamers can form junctions when they come close to each other, because the bubbles are mutually attracted by the secondary Bjerknes force. When the pressure antinode is a localized region in the liquid volume, streamers originating from distinct directions come automatically close to each other for geometrical reasons, and the ALFs occur as in Fig. 11a. Higher-resolution recordings show more details within a streamer. An example for a streamer junction (in aqueous sodium chloride solution with dissolved argon [113]) is shown in Fig. 12a. The acoustic field is a superposition of a standing and traveling wave at 90 kHz, and the streamers follow the direction of the traveling wave, which is downward in the image. Some individual bubbles that can be traced are marked by

Fig. 11 Bubble structures in standing acoustic waves in water. (**a**) Dendritic filament formed by bubbles that move from the outer regions toward the center of the cylindrical resonator cell (acoustic frequency 25 kHz). Such structures are also termed acoustic Lichtenberg figures (From [100], with kind permission from Springer Science + Business Media). (**b**) Double-layer structures in a 40 kHz ultrasonic bath. The layers arrange themselves in parallel to both sides of acoustic pressure nodal planes [108, 109]. The high-speed series in the inset highlights the composition out of many tiny bubbles and the antiphase oscillation of the layers (interframe time of 12.5 µs equals ¼ of the acoustic period, frame height 6.3 mm)
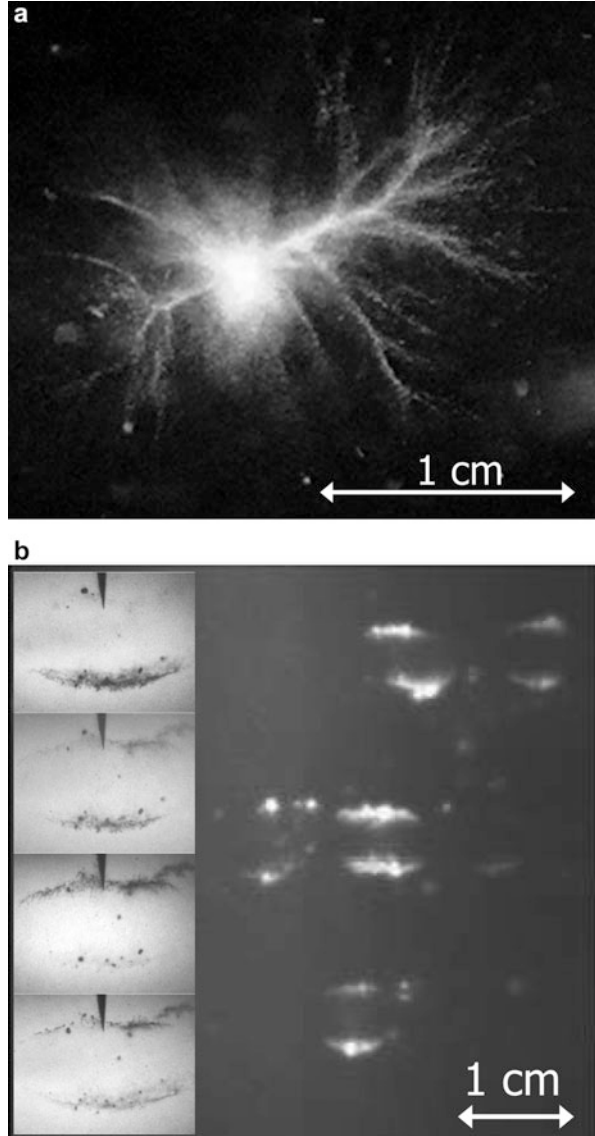
the arrows. The short exposure time leads to the correct impression of the momentary bubble size in each frame, making visible the composition of the bubble field and the strong volume oscillations. The largest maximum (expanded) bubble radii reach around 20 µm. Bubbles of different sizes follow each other on quite the same paths, but at potentially different speeds: The velocities cover a wide range from about 0.5 to 2.5 m/s. It turns out from observation at this scale that many coalescence events of bubbles take place, mostly at the junctions, but also within the streamer lines. As a
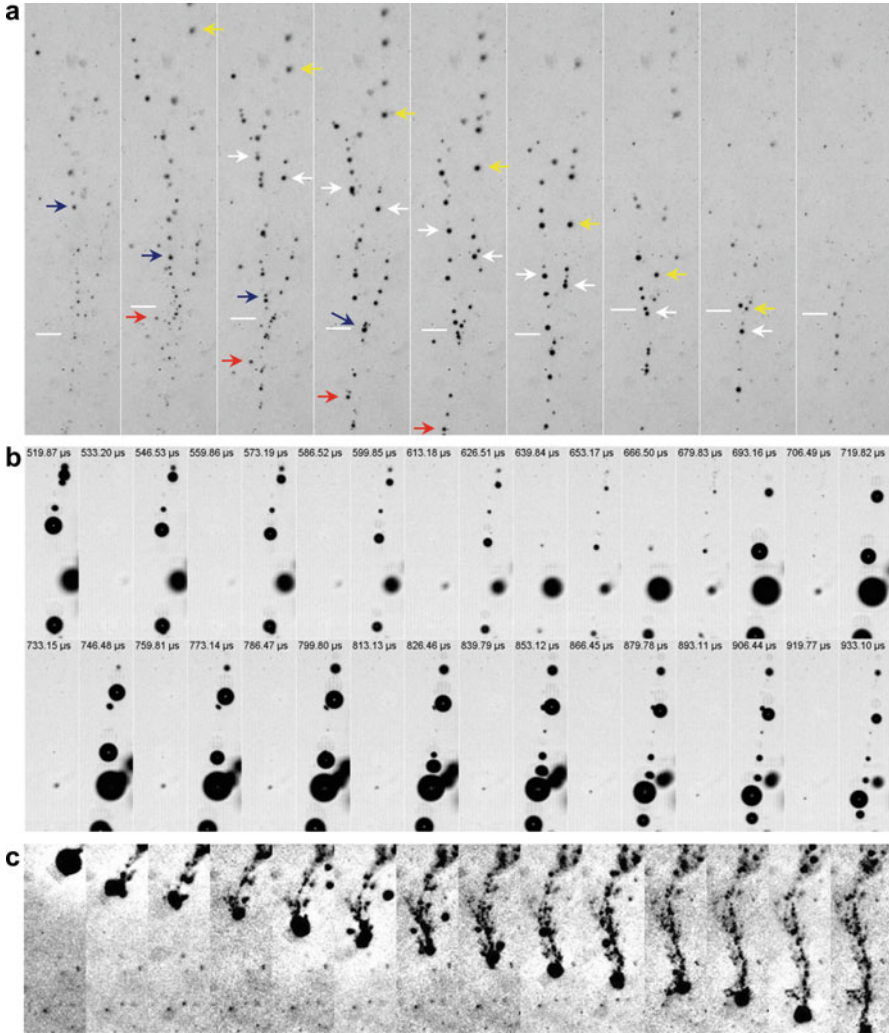
Fig. 12 Bubble motion in streamers, highly resolved in space and time. (**a**) Junction of two streamer arms, net flow of bubbles from *top* to *bottom* (aqueous 3 M NaCl solution with low continuous Ar flow, sonicated at 90.2 kHz, frame rate 7,000 fps, interframe time 142.8 μs, exposure 370 ns, frame width 650 μm, image turned 90°). Some bubbles are marked by *arrows* for identification which shows the dynamics of the structure. Bubble velocities range up to about 2.5 m/s. The point of confluence is indicated by a *horizontal line*. (**b**) Close-up of a *downward* directed streamer arm (phosphoric acid 85 %; low continuous air flow, 36.5 kHz; 75,000 fps; exposure 370 ns; frame width 170 μm; image turned 90°). Bubbles are nearly collapsed on every second frame and mostly fall below the optical resolution threshold then. The downward drift of the bubbles is temporarily stopped or inverted due to the mutual attraction that results in some coalescence events. Mean bubble velocities are in the region of 0.3 m/s. (**c**) Large bubble with surface instabilities and a trace of fragments (aqueous 3 M NaCl solution with high continuous Ar flow, other conditions like in (**a**); frame width 60 μm; image turned 45°). Large bubble velocity about 1.25 m/s. This kind of dynamics occurs for strong sparging of Ar in high dissolved salt concentration [113]

consequence the linear bubble number density (bubbles per streamer length) stays roughly the same in spite of the joined influx – bubble numbers are not conserved in this sense. A remarkable phenomenon is the longer-term positional stability of the confluence of the streamers, indicated by the horizontal lines. Its location fluctuates only on the scale of inter-bubble distances in the streamer arms. Possibly liquid flows induced by the fast bubble streams play a certain role here inasmuch as they might form longer living "channels," guiding the bubbles. The liquid flow would then be part of the observed bubble speed. Furthermore, the bubble velocities fluctuate due to mutual interactions, and even the momentary direction of bubble translation can change, although the primary Bjerknes force finally dictates an overall motion downward: When trailing neighbors approach, bubbles can temporarily stop or run backward, which evidences that the secondary Bjerknes force exceeds the primary one on the short inter-bubble distances. This is better illustrated in Fig. 12b where the relative bubble motion within another downward streamer (here in phosphoric acid driven at 36.5 kHz) is resolved: Some bubbles approach each other while others drift farther apart. The lowest bubble first moves down, but then changes direction and moves up to merge with several others (not shown).

The "fine structure" within streamers (and as well in other multi-bubble ensembles) shows that fluctuations of bubble number, size, and velocity always exist. Bubble populations in terms of, for instance, size or sonochemical activity distribution result from a dynamic process of mutual approach, coalescence, and potential splitting. Even if the finally observed bubble distribution appears (and possibly is) quasi-stationary, it becomes clear that it is based on a permanently fluctuating microstructure. This dynamic basis of bubble patterns bears part of the general sensitivity of acoustic cavitation to parameter changes. As an example, Fig. 12c demonstrates the susceptibility of the streamer structure to liquid and gas properties. The conditions are the same as in Fig. 12a, but the noble gas argon has been sparged at higher rate into the water/salt solution [113]. Now individual bubbles with a maximum radius around 20 μm occur that travel at medium speed and leave a plethora of smaller split-off fragment bubbles behind. The impression is reminiscent to the trace of fragments behind jetting bubbles in sulfuric acid (see Fig. 9a), but now the bubbles show rather non-spherical distortions originating from surface modes (stronger collapse and jetting might be involved, but is not resolved). The leftover fragments stay roughly in place, merge after a while, and form new larger bubbles that accelerate again. The overall picture of lines of traveling bubbles forming filaments has changed to a more hierarchical situation of "large" (faster moving) and "small" (nearly stagnant) bubbles, the smaller ones being seeded on the path of the larger ones. Apparently, the change of physicochemical liquid/gas parameters leads to significant changes of the microscopic single-bubble behavior (e.g., surface mode unstable dynamics) that in turn alters the bubble size distribution (e.g., many tiny fragments) and the emerging bubble structures (e.g., the streamer filaments of lined-up mainly spherical bubbles transform to individual non-spherical bubbles leaving a seeding trace). It is clear that global (averaged) measures of the system like bubble size distribution and spatial bubble densities are affected, and further consequences on sonoluminescence or sonochemical yields should be expected [47, 113].

Conclusions and Future Directions

This chapter has given a very brief overview of the dynamical aspects of acoustic cavitation bubbles. The focus has been set on qualitative descriptions and on observations to introduce the phenomena one has to expect and to illustrate how real cavitation bubbles may look like. Theoretical descriptions have been sketched, and it has been argued that Rayleigh-Plesset-like spherical bubble models are in some cases sufficient to capture essential features of the bubble dynamics: Oscillatory motions, including hysteretic and chaotic behavior, are well reproduced, and good estimates of Bjerknes forces can be obtained. Of course, more effort and extended models are necessary to obtain an adequate theoretical treatment of the exact conditions during strong bubble collapse, of bubble deformations due to surface modes and jetting, or for merging and splitting processes.

Although the dynamics of individual bubbles and the basics of their mutual interaction are therefore to a good part well known, the understanding, simulation, and prediction of the behavior of systems containing many acoustic cavitation bubbles are still a serious challenge. The following aspects contribute to this problem, all typical for "complex systems" [114, 115]:

Nonlinearity: Several nonlinear laws enter the description of cavitation, like the Rayleigh-Plesset equation or the distance dependence of the secondary Bjerknes force. Thus, already individual spherical bubble dynamics and few-bubble interaction are difficult to treat analytically, and complicated behavior can arise (e.g., in analogy to the famous gravitational three-body problem [116], since gravity follows the same distance law as the approximated secondary Bjerknes force). Furthermore, nucleation or activation of bubbles is a threshold process with respect to acoustic pressure, and bubble numbers change discontinuously.

Sensitivity: As a consequence of nonlinearity, bubble trajectories can show high sensitivity to slight changes of initial conditions. Sensitivity can also hold for the individual bubble oscillations (compare the hysteresis example above), although in important parameter regions, robust oscillation dynamics is seen where the bubbles mainly follow the external driving. Another relevant type of sensitivity of multi-bubble systems refers to liquid parameters. In particular, type and content of dissolved gas and solid contaminants play a role, since both potentially serve as nuclei and both are usually difficult to control in real-world systems.

Randomness: Some processes are so complicated or hardly controllable in their microscopic details that they appear as essentially random ingredients to acoustic cavitation. Examples are nucleation sites and nucleation frequencies, bubble fission fragment numbers and sizes, or acoustic wave field amplitudes in scattering environments (e.g., loaded cleaning bath). Ad hoc assumptions, observational data, or statistical methods are needed in such cases for a model.

Scales: Acoustic cavitation comprises phenomena on a huge variation of temporal and spatial scales. Time scales range from seconds (lifetime of collective bubble structures), milliseconds (bubble lifetime), and microseconds (acoustic period)

down to nano- and picoseconds (collapse phenomena). Spatial scales cover centimeter (liquid containers, acoustic wavelength, bubble structures), submillimeter (bubble sizes), and sub-micrometer ranges (collapsed bubble, bubble nuclei). All-comprising approaches are hardly possible, and typical modeling and simulation methods refer to only a certain part of this scale spectrum.

Emergence: Once many driven bubbles interact, collective phenomena can occur that are not existent or relevant in systems of individual or few bubbles. Among them are nonlinear sound wave propagation [104, 105], synchronization of bubble oscillations [117–119], and structure formation [95].

In conclusion, extended ("real") acoustic cavitation systems are complex which makes them difficult to analyze, to model, and to control. Considering a bottom-up approach, single bubbles serve as the fundamental building blocks that determine the global system properties by their dynamics and interaction. A good understanding of the individual bubble is necessary, but possibly not sufficient to reflect all collective effects. Mechanisms like nonlinearity and sensitivity have to be kept in mind if parameter dependences in acoustic cavitation are studied, and "dose laws" or expectations that "small input change causes small output effect" do not have to hold.

Future investigations will make use of the rapidly evolving experimental and numerical technologies. High-speed microscopic optical imaging is already developing toward a standard tool in experimental bubble dynamics. If the preparation techniques of suitable experimental cavitation setups develop as well, new and extended observations of, for instance, non-spherical bubble collapse and close bubble interactions are to be expected. Populations in multi-bubble systems will be evaluated highly resolved in time and space as a matter of routine. Special techniques like total internal reflection fluorescence microscopy [120] or X-ray imaging of liquid samples [121] can highlight bubble-surface interactions or microscopic cavitation processes, where so-called nanobubbles might play a role [122, 123]. Great progress will come from powerful computing where detailed simulations of bubble collapse and chemistry or of multi-bubble systems with individual bubble resolution are feasible; see [124] for an example from hydrodynamic cavitation. The same holds for advanced molecular dynamic methods that are able to explore nucleation [125, 126], collapse phenomena [45, 127], and further effects [128] on the nano- and potentially microscale. In conclusion, a better understanding of the complexity of acoustic cavitation, from a single bubble to large ensembles, will to a good part be based on the technological progress in imaging and computing, and in the perspective an adequate prediction of the cavitation phenomena in applications should be reached.

References

1. Flynn HG (1964) Physics of acoustic cavitation in liquids. In: Mason WP (ed) Physical acoustics, vol 1B. Academic, London, pp 57–172
2. Rozenberg LD (1971) High-intensity ultrasonic fields. Plenum Press, New York

3. Plesset MS, Prosperetti A (1977) Bubble dynamics and cavitation. Annu Rev Fluid Mech 9:145

4. Neppiras EA (1980) Acoustic cavitation. Phys Rep 61:159

5. Young FR (1989) Cavitation. McGraw-Hill, London

6. Leighton TG (1994) The acoustic bubble. Academic, London

7. Brennen CE (1995) Cavitation and bubble dynamics. Oxford University Press, New York

8. Lauterborn W et al (1999) Experimental and theoretical bubble dynamics. In: Prigogine I, Rice SA (eds) Advances in chemical physics, vol 110. Wiley, New York, pp 295–380

9. Trevena DH (1987) Cavitation and tension in liquids. Adam Hilger, Bristol

10. Crum L (1982) Acoustic cavitation. In: 1982 ultrasonics symposium. IEEE. pp 1–11

11. Mørch KA (2007) Reflections on cavitation nuclei in water. Phys Fluids 19:072104

12. Fox FE, Francis E, Herzfeld KF (1954) Gas bubbles with organic skin as cavitation nuclei. J Acoust Soc Am 26:984

13. Yount DE (1982) On the evolution, generation, and regeneration of gas cavitation nuclei. J Acoust Soc Am 71:1473

14. Lauterborn W, Vogel A (2013) Shock wave emission by laser generated bubbles, Chap. I.3. In: Delale CF (ed) Bubble dynamics & shock waves, vol 8, Shockwaves. Springer, Berlin, pp 67–103

15. Sankin G et al (2001) Early stage of bubble dynamics and luminescence in water in a converging shock reflected by a free surface. In: v. Estorff O (ed) Fortschritte der Akustik – DAGA 2001. DEGA, Oldenburg, pp 258–259

16. Mettin R (2007) From a single bubble to bubble structures in acoustic cavitation. In: Kurz T, Parlitz U, Kaatze U (eds) Oscillations, waves and interactions. Universitätsverlag Göttingen, Göttingen, pp 171–198

17. Krefting D (2003) Dissertation. Georg-August-University Göttingen

18. Fernandez Rivas D et al (2013) Ultrasound artificially nucleated bubbles and their sonochemical radical production. Ultrason Sonochem 20:510

19. Apfel RE (1970) The role of impurities in cavitation-threshold determination. J Acoust Soc Am 48:1179

20. Nyborg WL (1965) Acoustic streaming. In: Mason WP (ed) Physical acoustics, vol 2B. Academic, New York, pp 265–331

21. Zarembo LK (1971) Acoustic streaming. In: Rozenberg LD (ed) High-intensity ultrasonic fields part III. Plenum Press, New York, pp 137–199

22. Hatanaka S et al (2002) Influence of bubble clustering on multibubble sonoluminescence. Ultrasonics 40:655

23. Gilmore FR (1952) Collapse and growth of a spherical bubble in a viscous compressible liquid, Tech. Rep. No. 26-4, Office of Naval Research, Hydrodynamics Laboratory, California. Institute of Technology, Pasadena

24. Keller JB, Miksis M (1980) Bubble oscillations of large amplitude. J Acoust Soc Am 68:628

25. Prosperetti A, Lezzi A (1986) Bubble dynamics in a compressible liquid. Part 1. First-order theory. J Fluid Mech 168:457

26. Yasui K (1997) Alternative model of single-bubble sonoluminescence. Phys Rev E 56:6750

27. Storey BD, Szeri AJ (2000) Water vapour, sonoluminescence and sonochemistry. Proc Roy Soc Lond A 456:1685

28. Guckenheimer J, Holmes P (1982) Nonlinear oscillations, dynamical systems, and bifurcations of vector fields, vol 42, Applied mathematical sciences. Springer, New York

29. Lauterborn W (1976) Numerical investigation of nonlinear oscillations of gas bubbles in liquids. J Acoust Soc Am 59:283

30. Lauterborn W, Mettin R (1999) Nonlinear bubble dynamics: response curves and more. In: Crum LA et al (eds) Sonochemistry and sonoluminescence. Kluwer, Dordrecht, pp 63–72

31. Holt RG, Crum LA (1992) Acoustically forced oscillations of air bubbles in water: experimental results. J Acoust Soc Am 91:1924

32. Parlitz U et al (1990) Bifurcation structure of bubble oscillators. J Acoust Soc Am 88:1061

33. Thiemann A (2011) Dissertation. Georg-August-University Göttingen
34. Nowak T et al (2015) Acoustic streaming and bubble translation at a cavitating ultrasonic horn. In: Recent developments in nonlinear acoustics: 20th international symposium on nonlinear acoustics including the 2nd international sonic boom forum, AIP Conf. Proc. 1685, 020002-1-9 (2015); http://dx.doi.org/10.1063/1.4934382
35. Mason TJ, Lorimer JP (2002) Applied sonochemistry. Wiley-VCH, Weinheim
36. Gaitan DF et al (1992) Sonoluminescence and bubble dynamics for a single, stable, cavitation bubble. J Acoust Soc Am 91:3166
37. Putterman SJ, Weninger KR (2000) Sonoluminescence: how bubbles turn sound into light. Annu Rev Fluid Mech 32:445
38. Brenner MP, Hilgenfeldt S, Lohse D (2002) Single-bubble sonoluminescence. Rev Mod Phys 74:425
39. Holzfuss J, Rüggeberg M, Billo A (1998) Shock wave emissions of a sonoluminescing bubble. Phys Rev Lett 81:5434
40. McNamara WB, Didenko YT, Suslick KS (1999) Sonoluminescence temperatures during multi-bubble cavitation. Nature 401:772
41. Hiller R, Putterman S, Barber BP (1992) Spectrum of synchronous picosecond sonoluminescence. J Acoust Soc Am 92:2454
42. Yasui K et al (2008) The range of ambient radius for an active bubble in sonoluminescence and sonochemical reactions. J Chem Phys 128:184705
43. Wu CC, Roberts PH (1994) A model of sonoluminescence. Proc Roy Soc Lond A 445:323
44. Akhatov I et al (2001) Collapse and rebound of a laser-induced cavitation bubble. Phys Fluids 13:2805
45. Schanz D et al (2012) Molecular dynamics simulations of cavitation bubble collapse and sonoluminescence. New J Phys 14:113019
46. Geisler R (1998) Diploma thesis. Georg-August-University Göttingen
47. Mettin R, Cairós C, Troia A (2015) Sonochemistry and bubble dynamics. Ultrason Sonochem 25:24
48. Bjerknes VFK (1906) Fields of force. Columbia University Press, New York
49. Akhatov I et al (1997) Bjerknes force threshold for stable single bubble sonoluminescence. Phys Rev E 55:3747
50. Matula TJ et al (1997) Bjerknes force and bubble levitation under single-bubble sonoluminescence conditions. J Acoust Soc Am 102:1522
51. Thompson JMT, Stewart HB (1986) Nonlinear dynamics and chaos. Wiley, Chichester
52. Mettin R, Doinikov AA (2009) Translational instability of a spherical bubble in a standing ultrasound wave. Appl Acoust 70:1330
53. Zabolotskaya EA (1984) Interaction of gas bubbles in the field of a sonic wave. Akust Zh 30:618, transl. Sov. Phys. Acoust. 30, 365 (1984)
54. Luther S, Mettin R, Lauterborn W (2000) Modeling acoustic cavitation by a Lagrangian approach. In: Lauterborn W, Kurz T (eds) Nonlinear acoustics at the turn of the millennium. AIP conference proceedings, vol 524. AIP, Melville, pp 351–354
55. Harkin A, Kaper TJ, Nadim A (2001) Coupled pulsation and translation of two gas bubbles in a liquid. J Fluid Mech 445:377
56. Ilinskii YA, Hamilton MF, Zabolotskaya EA (2007) Bubble interaction dynamics in Lagrangian and Hamiltonian mechanics. J Acoust Soc Am 121:786
57. Mettin R et al (2000) Dynamics of delay-coupled spherical bubbles. In: Lauterborn W, Kurz T (eds) Nonlinear acoustics at the turn of the millennium, AIP conference proceedings, vol 524. AIP, Melville, pp 359–362
58. Doinikov AA, Manasseh R, Ooi A (2005) Time delays in coupled multibubble systems. J Acoust Soc Am 117:47
59. Crum LA (1975) Bjerknes forces on bubbles in a stationary sound field. J Acoust Soc Am 57:1363
60. Mettin R et al (1997) Bjerknes forces between small cavitation bubbles in a strong acoustic field. Phys Rev E 56:2924

61. Oguz HN, Prosperetti A (1990) A generalization of the impulse and virial theorems with an application to bubble oscillations. J Fluid Mech 218:143
62. Doinikov AA (1999) Effects of the second harmonic on the secondary Bjerknes force. Phys Rev E 59:3016
63. Barbat T, Ashgriz N, Liu C-S (1999) Dynamics of two interacting bubbles in an acoustic field. J Fluid Mech 389:137
64. Koch P et al (2003) Simulation of the translational motion of few cavitation bubbles in an ultrasonic field. In: Proceedings of IEEE international ultrasonics symposium, Honolulu, 5–8 Oct 2003, pp 1475–1478
65. Mettin R et al (2006) Modeling acoustic cavitation with bubble redistribution. In: 6th international symposium on cavitation – CAV2006, Wageningen, 11.15 Sept, paper no. 75
66. Yoshida K, Fujikawa T, Watanabe Y (2011) Experimental investigation on reversal of secondary Bjerknes force between two bubbles in ultrasonic standing wave. J Acoust Soc Am 130:135
67. Magnaudet J, Legendre D (1998) The viscous drag force on a spherical bubble with a time-dependent radius. Phys Fluids 10:550
68. Appel J et al (2004) Stereoscopic highs-peed recording of bubble filaments. Ultrason Sonochem 11:39
69. Kapustina OA (1973) Degassing of liquids. In: Rozenberg LD (ed) Physical principles of ultrasonic technology. Plenum Press, New York, Part IV
70. Longuet-Higgins M (1999) Particle drift near an oscillating cavity. In: Crum LA et al (eds) Sonochemistry and sonoluminescence. Kluwer, Dordrecht, pp 105–116
71. Obreschkow D et al (2011) Universal scaling law for jets of collapsing bubbles. Phys Rev Lett 107:204501
72. Benjamin TB, Ellis AT (1966) The collapse of cavitation bubbles and the pressures thereby produced against solid boundaries. Philos Trans R Soc Lond A260:221
73. Calvisi ML et al (2007) Shape stability and violent collapse of microbubbles in acoustic traveling waves. Phys Fluids 19:047101
74. Wang QX, Blake JR (2010) Non-spherical bubble dynamics in a compressible liquid. Part 1. Travelling acoustic wave. J Fluid Mech 659:191
75. Nowak T, Mettin R (2014) Unsteady translation and repetitive jetting of acoustic cavitation bubbles. Phys Rev E 90:033016
76. Tomita Y, Shima A, Sato K (1990) Dynamic behavior of two-laser-induced bubbles in water. Appl Phys Lett 57:234
77. Fong SW et al (2009) Interactions of multiple spark-generated bubbles with phase differences. Exp Fluids 46:705
78. Sankin GN, Yuan F, Zhong P (2010) Pulsating tandem microbubble for localized and directional single-cell membrane poration. Phys Rev Lett 105:078101
79. Han B et al (2015) Dynamics of laser-induced bubble pairs. J Fluid Mech 771:706
80. Plesset MS, Chapman RB (1971) Collapse of an initially spherical vapour cavity in the neighbourhood of a solid boundary. J Fluid Mech 47:283
81. Lauterborn W, Bolle H (1975) Experimental investigations of cavitation-bubble collapse in the neighbourhood of a solid boundary. J Fluid Mech 72:391
82. Blake JR, Gibson DC (1987) Cavitation bubbles near boundaries. Annu Rev Fluid Mech 19:99
83. Bourne NK, Field JE (1992) Shock-induced collapse of single cavities in liquids. J Fluid Mech 244:225
84. Ohl CD, Ikink R (2003) Shock-wave-induced jetting of micron-size bubbles. Phys Rev Lett 90:214502
85. Sankin GN et al (2005) Shock wave interaction with laser-generated single bubbles. Phys Rev Lett 95:034501. Tomita Y, Shima A (1986) Mechanisms of impulsive pressure generation and damage pit formation by bubble collapse. J Fluid Mech 169:535
86. Philipp A, Lauterborn W (1998) Cavitation erosion by single laser-produced bubbles. J Fluid Mech 361:75

87. Olaf J (1957) Oberflächenreinigung mit Ultraschall. Acustica 7:253
88. Agranat A, Bashkirov VI, Kitaigorodskii YI (1973) Ultrasonic cleaning. In: Rozenberg LD (ed) Physical principles of ultrasonic technology. Plenum Press, New York, Part III
89. Krefting D, Mettin R, Lauterborn W (2004) High-speed observation of acoustic cavitation erosion in multibubble systems. Ultrason Sonochem 11:119
90. Ohl C-D et al (2006) Surface cleaning from laser-induced cavitation bubbles. Appl Phys Lett 89:074102
91. Reuter F, Mettin R (2016) Mechanisms of single bubble cleaning. Ultrason Sonochem 29:550–562. doi:10.1016/j.ultsonch.2015.06.017
92. Prosperetti A (2011) Advanced mathematics for applications. Cambridge University Press, Cambridge
93. Kornfeld M, Suvorov L (1944) On the destructive action of cavitation. J Appl Phys 15:495
94. Krefting D, Mettin R, Lauterborn W (2001) Translationsdynamik levitierter Einzelblasen. In: v. Estorff O (ed) Fortschritte der Akustik – DAGA 2001. DEGA, Oldenburg, pp 252–253
95. Mettin R (2005) Bubble structures in acoustic cavitation. In: Doinikov AA (ed) Bubble and particle dynamics in acoustic fields: modern trends and applications. Research Signpost, Kerala, pp 1–36
96. Plesset MS (1954) On the stability of fluid flows with spherical symmetry. J Appl Phys 25:96
97. Sharp DH (1984) An overview of Rayleigh-Taylor instability. Phys D 12:3
98. Kull HJ (1991) Theory of the Rayleigh-Taylor instability. Phys Rep 206:197. Eller A, Flynn HG (1965) Rectified diffusion during nonlinear pulsations of cavitation bubbles. J Acoust Soc Am 37(3):493–503
99. Hinsch K (1975) The dynamics of bubble fields in acoustic cavitation. In: Akulichev VA et al (eds) Proceedings of 6th international symposium on nonlinear acoustics. Moscow University, pp 26–34
100. Mettin R, Ohl C-D, Lauterborn W (1999) Particle approach to structure formation in acoustic cavitation. In: Crum LA et al (eds) Sonochemistry and sonoluminescence. Kluwer, Dordrecht, pp 138–144
101. Mettin R et al (1999) Acoustic cavitation structures and simulations by a particle model. Ultrason Sonochem 6:25
102. Zabalotskaya EA (1973) Emission of harmonic and combination-frequency waves by air bubbles. Sov Phys Acoust 18:396
103. Commander KW, Prosperetti A (1988) Linear pressure waves in bubbly liquids: comparison between theory and experiments. J Acoust Soc Am 85:732
104. Caflisch RE et al (1985) Effective equations for wave propagation in bubbly liquids. J Fluid Mech 153:259
105. Kobelev YA, Ostrovsky LA (1989) Nonlinear acoustic phenomena due to bubble drift in a gas–liquid mixture. J Acoust Soc Am 85:621
106. Louisnard O (2012) A simple model of ultrasound propagation in a cavitating liquid. Part I: theory, nonlinear attenuation and traveling wave generation. Ultrason Sonochem 19:56
107. Jamshidi R, Brenner G (2013) Dissipation of ultrasonic wave propagation in bubbly liquids considering the effect of compressibility to the first order of acoustical Mach number. Ultrasonics 53:842
108. Mettin R et al (2002) Advanced observation and modeling of an acoustic cavitation structure. In: Rudenko OV, Sapozhnikov OA (eds) Nonlinear acoustics at the beginning of the 21st century, proceedings of 16th international symposium on nonlinear acoustics, vol 2. Moscow State University, Moscow, pp 1003–1006
109. Mettin R et al (2002) Bubble structures in acoustic cavitation: observation and modelling of a "jellyfish"-streamer. In: Forum acousticum Sevilla, Spain, 16–20 Sept 2002, Special Issue of the Revista de Acustica, Vol. XXXIII, 2002, ULT-02-004-IP
110. Lichtenberg GC (1777) Nova method natvram ac motvm fluidi electrici investigandi. Novi Commentarii Soc Regaiae 8:168–179

111. Merrill FH, Von Hippel A (1939) The atom physical interpretation of Lichtenberg figures and their application to the study of gas discharge phenomena. J Appl Phys 10:873
112. Thiemann A et al (2011) Characterization of an acoustic cavitation bubble structure at 230 kHz. Ultrason Sonochem 18:595
113. Cairós C et al (2014) Effects of argon sparging rate, ultrasonic power, and frequency on multibubble sonoluminescence spectra and bubble dynamics in NaCl aqueous solutions. Ultrason Sonochem 21:2044
114. Bar-Yam Y (1997) Dynamics of complex systems, vol 213. Addison-Wesley, Reading
115. Badii R, Politi A (1999) Complexity: hierarchical structures and scaling in physics. Cambridge University Press, Cambridge
116. Siegel CL, Moser J (1971) Lectures on celestial mechanics. Springer, New York
117. Ilinskii YA, Zabolotskaya EA (1992) Cooperative radiation and scattering of acoustic waves by gas bubbles in liquids. J Acoust Soc Am 92:2837
118. Parlitz U et al (1999) Spatio–temporal dynamics of acoustic cavitation bubble clouds. Philos Trans R Soc Lond A 357:313
119. Tervo JT, Mettin R, Lauterborn W (2006) Bubble cluster dynamics in acoustic cavitation. Acta Acustica United Acustica 92:178
120. Chan CU, Ohl C-D (2012) Total-internal-reflection-fluorescence microscopy for the study of nanobubble dynamics. Phys Rev Lett 109:174501
121. San Lee J, Weon BM, Je JH (2013) X-ray phase-contrast imaging of dynamics of complex fluids. J Phys D 46:494006
122. Tyrrell JW, Attard P (2001) Images of nanobubbles on hydrophobic surfaces and their interactions. Phys Rev Lett 87:176104
123. Chan CU et al (2015) Collapse of surface nanobubbles. Phys Rev Lett 114:114505
124. Rossinelli D et al (2013) 11 PFLOP/s simulations of cloud cavitation collapse. In: Conference for high-performance computing, networking, storage and analysis. IEEE, Denver, pp 1–13
125. Kinjo T, Matsumoto M (1998) Cavitation processes and negative pressure. Fluid Phase Equilib 144:343
126. Malyshev VL et al (2015) Study of the tensile strength of a liquid by molecular dynamics methods. High Temp 53:406
127. Shekhar A et al (2013) Nanobubble collapse on a silica surface in water: billion-atom reactive molecular dynamics simulations. Phys Rev Lett 111:184503
128. Fu H et al (2015) Sonoporation at small and large length scales: effect of cavitation bubble collapse on membranes. J Phys Chem Lett 6:413

Acoustic Bubbles, Acoustic Streaming, and Cavitation Microstreaming

Richard Manasseh

Contents

R. Manasseh (✉)
Swinburne University of Technology, Melbourne, VIC, Australia
e-mail: rmanasseh@swin.edu.au

Abstract

The phenomena of acoustic streaming and cavitation microstreaming can seem very complex, but underpinning them are fundamental concepts of fluid dynamics that are common to many similar systems. In this chapter, key aspects of fluid dynamics leading to bubble acoustics, acoustic streaming, and microstreaming are outlined. Basic concepts of sound are introduced, focusing on the special case of the sound waves produced by a bubble and how a bubble creates sound and responds to sound. The difference between linear and nonlinear theory for the time-dependent radius of an oscillating bubble is outlined. The concept of mean streaming is then introduced; this is when a purely oscillatory flow causes a net fluid motion. The origin of mean streaming is emphasized: the nonlinear term in Euler's momentum equation. It is explained that there are two classes of mean streaming: acoustic streaming, created when the ultrasonic power is high and has some gradient with distance, and microstreaming, created when the gradient is high on a small scale. Applications of acoustic streaming and microstreaming in biomedicine and engineering and the latest research are reviewed.

Fluid Dynamics

Introduction

Scientists and engineers who first encounter bubble physics are confronted by a bewildering variety of phenomena that can occur when a bubble's volume oscillates. In Fig. 1, a microstreaming flow can be seen around a bubble that is also undergoing oscillations in shape. The flow is three-dimensional and represents an interplay of forces controlled by three physical properties: compressibility, surface tension, and viscosity. Bubble oscillations account for observations as mundane as the splashing sound of running water and as exotic as the emission of light by a tiny bubble. Bubble oscillations – and the flows they drive – are used in technologies commonplace as the ultrasonic cleaning of jewelry and as specialized as the removal of gas from photographic coatings. Bubble acoustics has been applied to predict the severity of erupting volcanoes and the energy lost by breaking ocean waves. Bubble oscillations and microstreaming flows help to destroy kidney stones and tumors but also erode metal ship's propellers. Cavitation physics is used by shrimp to capture their prey. Bubble-acoustic microstreaming is thought to speed the dissolution of

Fig. 1 Acoustic microstreaming field created around a bubble of approximate radius 200 μm driven at 12.94 kHz (From Tho et al. [54]. Reprinted under a CSIRO Licence to Publish)
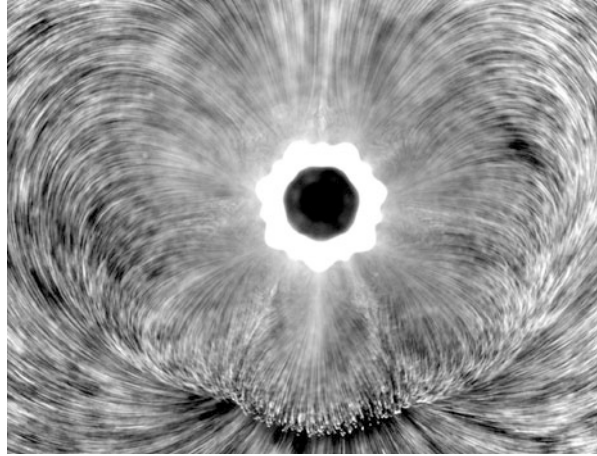
blood clots in the brain and to transport foreign genes into a cell for therapy. Some examples of this great variety of situations can be found in Manasseh and Ooi [32].

However, all these phenomena have a common explanation. Before delving into the specifics of bubble acoustics, cavitation, acoustic streaming, and microstreaming, it is important to understand that this "zoo" of diverse phenomena is really composed of members of the same family: the physics of fluids. Moreover, the origin of this behavior can be understood from just four fundamental equations, expressing the laws of conservation of mass, momentum, and energy and of the constitution of matter.

Basic Definitions

We first need to define a fluid. Colloquially, we could say "a fluid is a substance that can flow," but there is a more precise, scientific definition: a fluid is a substance that can deform indefinitely when a shear stress is applied. Both gases and liquids are fluids, and cavitation physics has been put to practical use in liquids as diverse as water, blood, mercury, molten lava, and the sap of trees. This attribute of indefinite deformation under shear stress is vital, because when we introduce the form of Newton's second law appropriate to a fluid, terms appear that are unique to fluids. These terms mean that fluids can not only transmit and respond to ultrasound, but also they can flow in response to ultrasound.

In contrast with fluids, when a shear stress is applied to a solid, it will deform to a certain extent that depends on its stiffness, then stop deforming. If the stress is increased sufficiently, the solid will fail – colloquially, we can say it has broken.

In the context of bubble acoustics and cavitation, there is a key difference between gases and liquids: gases are much more compressible than liquids.

This means that we will be able to capture the essential physics of bubble acoustics by initially assuming the gas in the bubble is compressible while the liquid surrounding it is incompressible – an important simplification.

The Constitutive Law Relating Pressure and Density

The extent to which *any* substance (a solid, liquid, or a gas) can be compressed is given by that substance's *bulk modulus*, K, where

$$K = \rho \frac{\partial p}{\partial \rho}, \tag{1}$$

where ρ is the density of the substance and p is the pressure applied to it. This is a fundamental relation between the density of a substance (for a given mass, a relation with the volume of a substance) and the pressure applied to it. This is an example of a *constitutive law of matter*. We will return to (1) when we consider sound propagation in liquids. However, for a gas, (1) can be simplified to the *ideal gas law*,

$$p_1 V_1^{\kappa} = p_0 V_0^{\kappa}, \tag{2}$$

where p is the pressure in the gas, V is the volume of the gas (the volume of the bubble), and κ is the *polytropic index*, which depends on the way with which the gas is compressed under the applied pressure. (If the pressure is less than ambient, the resulting negative compression is called *rarefaction*). The subscript 0 refers to the initial state of the gas, and the subscript 1 refers to the altered state of the gas after the compression; the subscript 0 often signifies the rest or equilibrium state when the bubble is not oscillating. In bubble acoustics, two extreme approximations for κ are sometimes used: either the compression is *adiabatic*, which means no heat is gained or lost by the gas in the bubble, or it is *isothermal*, which means the temperature of the gas in the bubble is a constant. In the adiabatic limit, $\kappa = \gamma \equiv Cp /Cv$, the ratio of specific heats of the gas, which is a fundamental property of the gas, depends only on the number of degrees of freedom of movement of the atoms that make up the gas molecule. For diatomic molecules like nitrogen and oxygen (which make up most of the atmospheric air), $7 = 7/5$. In the isothermal limit, $\kappa = 1$, and the ideal gas law is further simplified to Boyle's law,

$$p_1 V_1 = p_0 V_0, \tag{3}$$

first published by Robert Boyle in 1662. The adiabatic limit is often used for large bubbles undergoing small volumetric vibrations, while the isothermal limit is often used for small bubbles undergoing small volumetric vibrations. Cavitation bubbles may be small, but they often undergo large vibrations. Thus, a value of κ somewhere in between unity and 7 may need to be used.

Conservation of Mass

The law of conservation of mass for a continuum (a solid, liquid, or gas) is a mathematical statement of the fact that mass is neither created nor destroyed, under the assumptions of continuum mechanics. Only if we consider nuclear reactions, (or, at the very small scale, quantum effects), can mass be changed into energy (or appear and disappear). A fluid flow transports mass into and out of a volume. Because the fluid flow may be three-dimensional, the velocity is a vector, $\boldsymbol{u}$. By considering an infinitesimal element of fluid volume, it is easy to show that

$$\frac{\partial \rho}{\partial t} = -\boldsymbol{\nabla}.(\rho \boldsymbol{u}), \tag{4}$$

i.e., that the rate of change of density with time is equal to the divergence of the mass flux.

Conservation of Momentum

The law of conservation of momentum was first understood by Isaac Newton in 1687, who formulated it as *Newton's second law*,

$$\boldsymbol{F} = m\boldsymbol{a},$$

where $\boldsymbol{F}$ is the vector force applied to a mass m and $\boldsymbol{a}$ is the vector acceleration due to the application of the force. While Newton's second law applies to all matter, when written out for a fluid flow, the acceleration $\boldsymbol{a}$ in Newton's second law takes a more complex form that was derived by Leonhard Euler in 1757. The essential difference when a fluid accelerates, as opposed to a rigid solid, is that *fluid acceleration appears even if the velocity field does not change with time*, *when velocity changes with space*. This vital difference understood by Euler is what makes acoustic streaming and microstreaming possible. The conservation of momentum is expressed in *Euler's equation* as

$$\frac{\mathrm{D}(\rho \boldsymbol{u})}{\mathrm{D}t} = \nabla p + \rho \mathbf{g}, \tag{5}$$

where $\mathbf{g}$ is the acceleration due to gravity. By expanding the left-hand side of Euler's equation, (5), we can see how this unique property of a fluid is manifested,

$$\frac{\mathrm{D}(\rho \boldsymbol{u})}{\mathrm{D}t} = \frac{\partial(\rho \boldsymbol{u})}{\partial t} + \boldsymbol{u}\cdot\boldsymbol{\nabla}(\rho \boldsymbol{u}). \tag{6}$$

The term $\partial(\rho \boldsymbol{u})/\partial t$ is exactly the same for a fluid as for a solid. However, the term $\boldsymbol{u}\cdot\boldsymbol{\nabla}(\rho u)$ is the *nonlinear term* in Euler's equation that represents a fluid's ability to

change its velocity by changing its position in space. It is sometimes called the
advective term.

Finally, by the early nineteenth century, the work of Claude-Louis Navier and
George Gabriel Stokes leads to the inclusion of stresses due to viscosity, giving the
Navier-Stokes momentum equation

$$\frac{\mathrm{D}(\rho\boldsymbol{u})}{\mathrm{D}t} = \nabla \cdot \boldsymbol{\tau} + \rho\mathrm{g}, \tag{7}$$

where $\boldsymbol{\tau}$ is the *stress tensor*, a quantity that conveniently includes both the pressure
and the viscous shear stresses applied to the fluid.

Significance of the Nonlinearity in the Momentum Equation

Acoustic streaming and microstreaming phenomena are only possible because of the
nonlinear term in Euler's equation. In fact, as we will see in section "The Rectifica-
tion of Oscillation by the Nonlinear Term," acoustic streaming and microstreaming
phenomena are only some examples of very many other streaming phenomena that
can occur when waves are the primary flow. Let us see the significance of this
nonlinear term by looking at only the radial equation out of the three equations for
the three dimensions of the vector Euler's equation (5). For simplicity but not
necessity, assume the density is a constant and that forces due to gravity are in
balance, giving

$$\frac{\partial u}{\partial t} + u\frac{\partial u}{\partial r} = -\frac{1}{\rho}\frac{\partial p}{\partial r}, \tag{8}$$

where r is the radial direction in a spherical coordinate system (r, ϕ, θ). We need
only to examine the nonlinear term,

$$u\frac{\partial u}{\partial r},$$

in (8) to understand what is possible. The vital feature of this nonlinear term is that it
is a velocity multiplied by a velocity gradient. This means that for this term to exist,
there must be a gradient in the velocity. It is also quadratic in the velocity.

Jumping ahead of ourselves somewhat, let us imagine we have solved (4) and (7)
– or, at least, simplified versions of them – and have found a solution such that

$$u = U(r, \phi, \theta)\cos(\omega t). \tag{9}$$

In other words, a fluid flow that oscillates sinusoidally with time has radian fre-
quency ʊ and has any sort of field in space, $U(t, \phi, \theta)$. To arrive at such a solution,
we would probably have had to ignore the nonlinear term, by assuming it is
negligibly small (*linearize* the equation). Now, however, an interesting consequence

of the nonlinear term can be seen. Substituting (9) back into (8) and averaging over time, we can immediately see that the time average of the term $\partial u/\partial t$ is zero, because the average of a sine or a cosine is zero. However, the time average of the term $u\,\partial u/\partial r$ is not zero, because it varies with time as $\cos^2(\omega t)$, and average with time of a cosine squared is not zero.

Thus, any time we linearize the equations of fluid dynamics and arrive at a wave solution, the true nonlinear equations will generate a term that does not average to zero over time. Provided there is a gradient (i.e., $\partial u/\partial r$ is not zero), there will inevitably be a driver for net motion – a small but steady flow that continues over time, added to the much larger, primary oscillatory motion that cancels out over time. Small it may be, but it persists, and it is this persistence that has many interesting consequences to be outlined in sections "Acoustic Streaming" and "Acoustic Microstreaming."

The notion that there is a "second-order" nonlinear behavior superimposed on the "first-order" linear behavior proceeds directly from the mathematical approach of *perturbation theory*, in which the nonlinearity is assumed to be weak, so that it is only a modification to the primarily oscillatory linear behavior. Before mathematically deriving the first-order solutions such as (9), we should physically explain this nonlinear "rectification" of oscillatory motion.

The Rectification of Oscillation by the Nonlinear Term

As just noted, it is a fundamental feature of all fluid flows that admit waves that a primarily oscillatory motion can have a small net "drift" superimposed on it [47]. This holds true for waves in the ocean as well as for ultrasonic waves, and indeed for other classes of fluid wave motion, such as the large-scale waves in the atmosphere that affect our weather and climate. As a wave crest passes, it causes the fluid (and anything suspended in it) to move in one direction, and as a wave trough passes, the fluid is made to retrace its motion to its point of origin, as shown by the simple orbit on the left-hand side of Fig. 2. After the passage of each wave, there is no net displacement, at least according to the linear theory. This linear model of waves is, however, only exact if the amplitude of the waves is infinitesimally small.

In reality, the fluid does not return precisely to its starting point after the passage of each wave, as shown by the "incomplete" orbits on the right-hand side of Fig. 2. There is a rectification of the oscillatory motion due to the nonlinear term. Although the discrepancy in position of the fluid after each cycle is tiny compared with the motion it undergoes during each cycle, unlike the orbital motion, the discrepancy does not cancel out, and the discrepancies persist – and accumulate. Over many waves, the effect can be significant, and with ultrasonics, a million waves can pass in a second. The result is a net drift of the fluid – a streaming motion.

It is because of this fundamental physics that rip currents are created at ocean beaches, sand and flotsam are transported in the ocean, acoustic currents are created, and colloidal particles and biological cells are transported in ultrasonics.
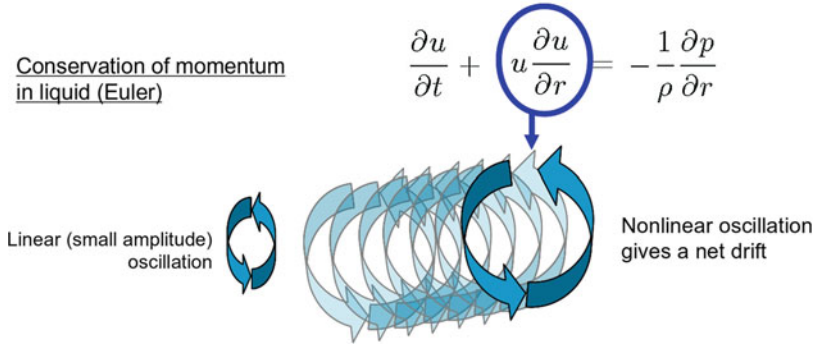
Fig. 2 Rectification of oscillatory motion by the nonlinear term in the fluid dynamics equation of motion, giving a net "drift" or "streaming" motion. The equation is (8), where, for simplicity, only one dimension of Euler's three-dimensional momentum (Eq. 5) is shown and the fluid is assumed to be of constant density and with gravitational forces in balance (Image by R. Manasseh)

As noted in section "Conservation of Momentum," the nonlinearity in the momentum equations of fluid dynamics creating this net motion is quadratic. This means that all streaming motions will be proportional to the wave amplitude squared and thus *proportional to the wave power*. Thus, the higher the power, the greater the net fluid motions, increasing in general linearly with power. The net motions are second-order effects. This means that although they vary with the square of the wave amplitude, their velocity is much weaker than the velocity with which the fluid oscillates as the waves pass.

Furthermore, the quadratic nonlinearity is actually a velocity multiplied by the gradient in velocity with distance. Thus, in order for the net motion to be possible, there should be a gradient in the wave velocity with distance. The larger the gradient, the larger is the local net motion.

The ocean rip current is induced by the dissipation as waves shoal onto a beach, leading to a gradient in the ocean wave power with distance. Analogously, acoustic streaming is induced by the dissipation due to viscous and scattering effects, leading to a gradient in the sound wave power with distance. Figure 3 shows a simple illustration of acoustic streaming over several tens of centimeters. Acoustic streaming will be further detailed in section "Large-Scale Acoustic Streaming."

Acoustics

Conservation of Mass and Momentum for the Sound Wave Case

Sound is a phenomenon in which a continuum (a solid, liquid, or a gas) is alternately compressed and expanded (or "rarefied") by waves propagating through it. Although the compressions and rarefactions are not obvious to the casual observer, scientists deduced that this was occurring by careful studies and experiments in the eighteenth
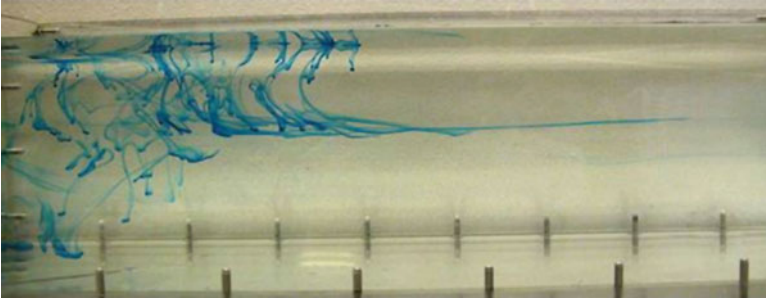
Fig. 3 Acoustic streaming in a water tank. Drops of dye released at the surface fall owing to their slightly greater density and are caught up in the acoustic streaming "jet" of speed roughly 0.02 m s^{-1} created by a 2.25 MHz transducer (at image *left*) driven by a continuous wave signal. Since the tank is of finite length, the flow created by the jet must recirculate, and evidence of the recirculation can be seen in the curvature of the dye lines above the jet. The bolts visible at the tank bottom are about 55 mm apart (Image courtesy of P. Lai; further details of this experiment are in Lai [21])

and early nineteenth centuries. The compressions and rarefactions are small, so that they would normally be neglected relative to other factors, such as advection and friction due to large flows or deformations. However, if the other factors are absent, only the compressions and rarefactions are left. Indeed, far away from active zones (such as near cavitating bubbles) where flows or deformations are large, sound is the only variation left, transmitting information about what happened in those zones throughout the continuum.

In both (4) and (7), the density is allowed to vary in space and time. This is necessary, since the propagation of sound inherently relies on the compressibility of a continuum. Compression (or "dilatation") changes the density of the continuum.

In general (4) and (7) are difficult to solve, particularly owing to the nonlinearity in (7). Fortunately, we know that for most sound waves the changes in density are small relative to the average density, $\rho 0$, and that the velocities are small. Hence, as anticipated in section "Significance of the Nonlinearity in the Momentum Equation," we can neglect terms in which small variables are multiplied together (linearize the equations). The mass conservation equation (4) becomes

$$\frac{\partial \rho}{dt} = -\rho_0 \nabla \cdot \boldsymbol{u}. \tag{10}$$

The momentum equation is likewise linearized, throwing away for the time being the interesting nonlinear term that we noted in section "Significance of the Nonlinearity in the Momentum Equation" which was the origin of acoustic streaming and microstreaming. Furthermore, assuming that friction is small eliminates the shear stresses from $\boldsymbol{\tau}$, leaving only the normal stress due to pressure, p; viscosity can be considered in a more detailed analysis. The gravity force can be neglected for now by assuming horizontal motion, but using a more detailed analysis, it is possible to show

that gravity is completely negligible no matter which way the sound propagates. Equation (7) then becomes

$$\rho_0 \frac{\partial \boldsymbol{u}}{\partial t} = -\boldsymbol{\nabla} p. \tag{11}$$

We have two vector equations involving three variables, ρ and p and the vector u. We can eliminate one of the variables by combining the mass and momentum conservation equations. Differentiating (10) with respect to time and taking the divergence of (11) gives

$$\frac{\partial^2 \rho}{\partial t^2} = -\rho_0 \boldsymbol{\nabla} \cdot \frac{\partial \boldsymbol{u}}{\partial t}, \tag{12}$$

$$\rho_0 \boldsymbol{\nabla} \cdot \frac{\partial \boldsymbol{u}}{\partial t} = -\boldsymbol{\nabla}^2 p, \tag{13}$$

and substituting (12) into (13) gives

$$\frac{\partial^2 \rho}{\partial t^2} - \boldsymbol{\nabla}^2 p = 0. \tag{14}$$

We now find the resulting momentum equation is *unclosed*: there is an additional variable, ρ. What is needed is the relation between normal stress (pressure) and volumetric strain (which is related to the density). We need a constitutive law relating stress and strain. This is the bulk modulus, K, that was given in (1). Integrating (1) with respect to ρ,

$$K \ln\rho = p + \text{const.}, \tag{15}$$

and using our initial condition that when $p = p_0$, $\rho = \rho_0$ gives the constant as $K \ln \rho_0 - p_0$. Inserting this constant and rearranging gives

$$K \ln \left(\frac{\rho}{\rho_0}\right) = p - p_0. \tag{16}$$

The natural log in (16) makes it a nonlinear relation. However, (14) was derived assuming the density only varies slightly from ρ_0, so it is consistent for us to make the same assumption regarding (16). Thus, we will apply the Taylor series expansion for the natural log function to (16). In this operation we will define the small variation in density as $\rho' = \rho - \rho_0$, so that

$$\ln \left(\frac{\rho}{\rho_0}\right) = \ln \left(1 + \frac{\rho'}{\rho_0}\right), \tag{17}$$

and remembering the Taylor series expansion for natural log for any small variation α about 1,

$$\ln(1+\alpha) = \ln(1) + \frac{1}{1+\alpha}\alpha - \frac{1}{(1+\alpha^2)}\alpha^2 + \dots,$$
$$\simeq 0 + \alpha - \alpha^2 + \dots,$$

where $\alpha = \rho'/\rho_0$, to first order (16) becomes

$$K\left(\frac{\rho - \rho_0}{\rho_0}\right) = p - p_0,$$
$$\Rightarrow \rho = \frac{\rho_0}{K}(p - p_0) + p_0. \tag{18}$$

Now that we have ρ as a function of p, we have our second equation. We need only to differentiate (18) twice with respect to time, and substituting into (14), we get

$$\frac{\partial^2 p}{\partial t^2} - c^2 \nabla^2 p = 0, \tag{19}$$

where $c = \sqrt{(K/\rho_0)}$.

Equation 19 is the linear one-dimensional *wave equation*. All small one-dimensional waves, whether they are electromagnetic waves, ripples on water, or sound waves as in our case, obey this equation. The constant c is the *speed of sound*. It is worth noting that the bulk modulus K can be related to the total pressure (including the atmospheric pressure) P_0 by $K = \gamma P_0$ where γ is the adiabatic index. Hence another expression for c is

$$c = \sqrt{(\gamma P_0/\rho_0)}. \tag{20}$$

Solution of the Wave Equation

To solve the wave equation, we can use one of two methods: the method of separation of variables or d'Alembert's method. Here, separation of variables will be used. This assumes that the pressure p can be split into two functions, one *only* of time and one *only* of space,

$$p = T(t)X(x). \tag{21}$$

For simplicity assume there is only one dimension in space, x. (The calculation below applies to three dimensions just as well.) Then, substituting into the one-dimensional version of (19) gives

$$\frac{\partial^2 T}{\partial t^2} X = c^2 T \frac{\partial^2 X}{\partial x^2}, \tag{22}$$

and dividing both sides by XT gives

$$\frac{1}{T}\frac{\partial^2 T}{\partial t^2} = c^2 \frac{1}{X}\frac{\partial^2 X}{\partial x^2}. \tag{23}$$

Now, the left-hand side of (23) is a function of t only, while the right-hand side is a function of x only. The only possibility is that both sides are equal to a constant, which we shall call $-\omega^2$, giving

$$\frac{\partial^2 T}{\partial t^2} = -\omega^2 T, \tag{24}$$

$$\Rightarrow T = A_1 \cos(\omega t) + A_2 \sin(\omega t). \tag{25}$$

Since both a sin and a cos are solutions of (24), we need to include both possibilities. (If we had assumed the constant was simply C say, a slightly longer but more general way to the answer is to say the solution is of the form $e^{\Omega t} \pm e^{-\Omega t}$ where $\Omega = \sqrt{C}$ is a complex number.) Likewise,

$$\frac{\partial^2 X}{\partial t^2} = -\frac{\omega^2}{c^2} X, \tag{26}$$

with solution

$$X = A_3 \cos(kx) + A_4 \sin(kx), \tag{27}$$

where $k = \omega/c$, giving the general solution

$$p = (A_1 \cos(\omega t) + A_2 \sin(\omega t))(A_3 \cos(kx) + A_4 \sin(kx)). \tag{28}$$

In general, we need to introduce boundary and initial conditions to get the four constants A_1, A_2, A_3, and A_4. Nonetheless, it is already clear that a solution to (19) consists of waves in both space and time. A further interesting property of the solution becomes apparent on applying some trigonometric identities (e.g., $\cos(\alpha + \beta) = \cos \alpha \cos \beta - \sin \alpha \sin \beta$ and so on) to (28). After some algebra we get

$$p = B_1 \cos(k(x - ct)) + B_2 \sin(k(x - ct)) \tag{29}$$

$$+ B_3 \cos(k(x + ct)) + B_4 \sin(k(x + ct)), \tag{30}$$

where B_1, B_2, B_3 and B_4 are constants made up of A_1, A_2, A_3 and A_4. The key property is that $x - ct$ and $x + ct$ are the arguments of the wave functions. This means that time

and space are interchangeable – we can always find a time t for a given point x where the waves look the same as at another point. And we can always find a point for a given time where the waves look the same at another time. All linear waves, be they electromagnetic waves, ocean waves, or sound waves, have this property.

The fact that we have both $x - ct$ and $x + ct$ means that a disturbance to the pressure field in a fluid propagates with the speed of sound both right and left from the source of the disturbance.

The frequency of the waves in radians per second is ω; the frequency in s^{-1} (Hertz) is given by $f = \omega/(2\pi)$, which is usually of more practical relevance since oscillations are usually measured in cycles per second. Similarly, the constant k in (30) is called the *wavenumber* and is related to the more physical *wavelength*, λ, by $\lambda = (2\pi)/k$; the wavelength is the distance in meters from one pressure maximum to the next. As for any waves, then, the speed of sound is related to the physical quantities of frequency and wavelength by

$$c = f\lambda. \tag{31}$$

Acoustic Impedance

Now that we have found the pressure in a sound wave, let us see what the velocity of the fluid u is. Remember, this is the velocity with which the fluid particles are set into motion by the passage of the wave. It is completely different to (and in the case of sound waves, much smaller than) the speed c with which the waves propagate. Let us go back to (11) and again assume one-dimensional motion for simplicity, so that (11) becomes

$$\rho_0 \frac{\partial u}{\partial t} = -\frac{\partial p}{\partial x}. \tag{32}$$

Now, substituting our solution in the general form of (30) into (32) and imagining the constants are chosen so that waves are propagating in one direction (say $+x$) gives

$$u = \frac{1}{\rho_0 c} p. \tag{33}$$

(Imagining the constants are chosen so the wave propagates with a negative speed, in the $-x$ direction, gives the same relation.) Note that the quantity $\rho_0 c$ called the *acoustic impedance* is a property of the fluid only. The relation (33), written as $p = \rho_0 c u$, makes it clear that we have an analogy with electromagnetic theory; with u the analog of electric current and p the analog of voltage, the acoustic impedance represents the resistance of the medium to the propagation of an alternating velocity field, just as electric impedance represents the resistance of a wire to the propagation of alternating current.

The Rayleigh-Plesset-Noltingk-Neppiras-Poritsky Equation

Rayleigh's Derivation of the Collapse of a Spherical Cavity

Rayleigh [45] considered the fluid dynamics of the collapse of a spherical cavity of liquid, motivated by problems of cavitation damage to ships' propellers. He considered the bubble to be at the center of a spherically symmetric coordinate system, which means that the only motions possible are radial. The conservation of mass (4) for a spherically symmetric system is given by

$$\frac{1}{r^2}\frac{\partial(r^2\rho u)}{\partial r} = -\frac{\partial\rho}{\partial t}, \tag{34}$$

where u is the outward velocity of the liquid induced by the pulsating bubble.

Now we will make a surprising assumption – that the liquid is incompressible. This is surprising because in section "Conservation of Mass and Momentum for the Sound Wave Case" we noted that sound waves certainly require compressibility to exist; we will later be using the frequency of the pulsating bubble for the frequency of the sound waves in the liquid. However, whether the liquid is compressible or incompressible has only a tiny influence on the pulsation of the bubble, which is dominated by the much greater compressibility of the gas. The right-hand side of (34) is thus zero. Integrating (34) with respect to r and noting that when r = $R(t)$, where $R(t)$ is the time-varying radius of the bubble, $u = \mathrm{d}R/\mathrm{d}t \equiv \dot{R}(t)$ gives

$$u = \frac{R(t)^2}{r^2}\dot{R}(t). \tag{35}$$

The equation of radial momentum balance is Euler's equation, (8), assuming incompressibility and spherical symmetry, and applied to the liquid only, and ignoring dissipation for simplicity. Substituting (35) into the derivatives in (8) gives

$$\frac{\partial u}{\partial t} = \frac{2R\dot{R}^2}{r^2} + \frac{R^2}{r^2}\ddot{R}, \text{ and } \frac{\partial u}{\partial r} = -2\frac{R^2}{r^3}\dot{R}, \tag{36}$$

and substituting these into (8) gives

$$\frac{2R}{r^2}\dot{R}^2 + \frac{R^2}{r^2}\ddot{R} - 2\frac{R^4}{r^5}\dot{R}^2 = -\frac{1}{\rho}\frac{\partial p}{\partial r}. \tag{37}$$

Now, we want to eliminate the spatial (r) dependence of (37), so integrate (37) from r = R to some arbitrary radius r = D giving

$$\left[-\frac{2R}{r}\dot{R}^2 - \frac{R^2}{r}\ddot{R} + \frac{1}{2}\frac{R^4}{r^4}\dot{R}^2\right]_R^D = -\frac{1}{\rho}(p(D) - p(R)). \tag{38}$$

Now send $D \to \infty$ and assume that at infinity $p = P_0$, giving

$$2\dot{R}^2 + R\ddot{R} - \frac{1}{2}\dot{R}^2 = -\frac{1}{\rho}(P_0 - p(R)). \tag{39}$$

Now $p(R)$ is the *absolute* pressure *in the liquid just outside the bubble*, and neglecting surface tension makes this the same as the pressure inside the bubble. Thus, using the ideal gas law (2),

$$p(R)V(R)^\kappa = P_0 V(R_0)^\kappa,$$

so that $p(R)$ is given by

$$p(R) = P_0(R_0/R)^{3\kappa},$$

and thus (39) becomes

$$R\ddot{R} + \frac{3}{2}\dot{R}^2 = -\frac{1}{\rho}\left(P_0 - P_0(R_0/R)^{3\kappa}\right). \tag{40}$$

Like the Euler momentum equation from which it was derived, (40) is a nonlinear equation: it has the quadratic nonlinearity due to fluid advection on its left-hand side, worsened by an additional nonlinearity that is due to the geometric spreading from a point source. Moreover, the bubble radius $R(t)$ appears on the denominator on the right-hand side, raised to a power that is, in general, a non-integer. If the bubble radius was to suddenly become small, very complex behavior would ensue, and indeed it does, as amply documented in the extensive literature on nonlinear microbubble dynamics (e.g., Lauterborn [24] and Leighton [25]). Rayleigh [45] stopped at the equivalent of (40), since he was concerned about the pressure created during the nonlinear collapse process rather than the natural frequency of the bubble.

Linearization Giving the Bubble Natural Frequency: The Minnaert Equation

To determine the natural frequency of the bubble, linearize (40) with the assumption $R(t) = R_0 + \delta(t)$ where $\delta \ll R_0$, and R_0 is the equilibrium radius of the bubble. Thus, δ is a perturbation in the bubble's radius that is *positive outward from the bubble*. The left-hand side of (40) becomes simply $R_0\ddot{\delta}$, while a Taylor series expansion gives

$$P_0(R_0/R)^{3\kappa} \simeq P_0(1 - (3\kappa/R_0)\delta), \tag{41}$$

and substituting this into (40) gives

$$R_0 \ddot{\delta} = -\frac{1}{\rho} P_0 (3\kappa/R_o)\delta, \tag{42}$$

giving the equation for simple harmonic motion

$$\ddot{\delta} = -\omega_0^2 \delta. \tag{43}$$

The radian frequency is now

$$\omega_0 = \sqrt{\frac{3\kappa P_0}{\rho}} \frac{1}{R_0}, \tag{44}$$

and the frequency in Hertz is

$$f_0 = \frac{1}{2\pi} \sqrt{\frac{3\kappa P_0}{\rho}} \frac{1}{R_0}. \tag{45}$$

It is worth noting that Minnaert (1933) derived (45) by heuristically assuming simple harmonic motion at the outset and balancing the kinetic and potential energies at each extreme of the motion. This obscures some of the assumptions, in particular the assumptions of an incompressible liquid, no dissipation of any kind, and small-amplitude behavior, giving linearity. Nonetheless, it was Minnaert who first quantified the relation between bubble size and its natural frequency, and hence (45) is called *Minnaert's equation*. The simple harmonic relation (43) expresses the essential physics of bubble acoustics: it can be thought of as a mass bouncing on a spring. The spring is a spherical spring consisting of the compressible gas, while the mass is the liquid surrounding the gas.

For bubbles of air (or nitrogen, oxygen, or indeed any diatomic gas) oscillating in water at approximately atmospheric pressure and room temperature, (45) can be approximated as

$$f_0 \simeq \frac{3.29}{R_0}, \tag{46}$$

so that, for example, the millimeter-sized bubbles one sees when pouring water into a glass naturally make sounds in the kilohertz range that we can hear: a 1 mm radius bubble makes a sound of about 3.3 kHz. This explains why humans can hear the sound of splashing and running water and of ocean waves breaking. Meanwhile, a 1 μm radius bubble, which is smaller than a blood cell, would have a natural frequency in the megahertz range, explaining why microbubbles are used as medical ultrasound contrast agents. (Bubbles this small have a frequency modified by other effects, as noted in section "Full Rayleigh-Plesset-Noltingk-Neppiras-Poritsky Equation.")

The linear approximation (41) shows that the *perturbation* in liquid pressure just outside a bubble, p', is given by

$$p' = -P_0(3\kappa/R_0)\delta. \tag{47}$$

This makes sense; if δ is positive, the bubble is expanded, so the liquid pressure is below P_0 and hence p' is negative. Equivalently, using (42) gives

$$p' = \rho R_0 \ddot{\delta}, \tag{48}$$

and the acceleration of the liquid, $a \equiv \ddot{\delta}$, is given by

$$a = \frac{1}{\rho R_0} p'. \tag{49}$$

Full Rayleigh-Plesset-Noltingk-Neppiras-Poritsky Equation

During the twentieth century, successive modifications and improvements were made to the derivation in section "Rayleigh's Derivation of the Collapse of a Spherical Cavity," and as a consequence the resulting equation is sometimes given all the names of the key workers contributing to its derivation, so that is it called the *Rayleigh-Plesset-Noltingk-Neppiras-Poritsky* (RPNNP) *equation*. An account of its derivation was given by Neppiras [36], and the background to each addition to Rayleigh's original work is covered by Leighton [25].

Surface tension and vapor pressure are included by modifications to the pressure term, giving

$$R\ddot{R} + \frac{3}{2}\dot{R}^2 = -\frac{1}{\rho}\left(\left(P_0 + \frac{2\sigma}{R} - p_v\right) - \left(P_0 + \frac{2\sigma}{R} - p_v\right)(R_0/R)^{3\kappa}\right), \tag{50}$$

where σ is the surface tension constant of the interface between the gas in the bubble and the surrounding liquid, and p_v is the vapor pressure due to those liquid molecules that have evaporated into the bubble. These are further constitutive properties of fluids, in addition to the constant κ from the ideal gas law, that are now considered. Including viscous damping means that the incompressible Navier-Stokes equation, (7), rather than Euler's equation, is now the form of the momentum equation being used. This gives

$$R\ddot{R} + \frac{3}{2}\dot{R}^2 = -\frac{1}{\rho}\left[\left(P_0 + \frac{2\sigma}{R} - p_v\right) - \left(P_0 + \frac{2\sigma}{R} - p_v\right)(R_0/R)^{3\kappa} + \frac{4\mu}{R}\dot{R}\right], \tag{51}$$

where μ is the dynamic viscosity of the liquid. Linearizing as in section "Linearization Giving the Bubble Natural Frequency: The Minnaert Equation," the natural frequency of the bubble including these effects [25] is now

$$f_0 = \frac{1}{2\pi} \sqrt{\frac{1}{\rho} \left[3\kappa \left(P_0 + \frac{2\sigma}{R} - p_v \right) - \left(\frac{2\sigma}{R} - p_v + \frac{4\mu^2}{\rho R_0^2} \right) \right] \frac{1}{R_0}}. \tag{52}$$

However, it is only for micron-sized bubbles that the frequency predicted by (52) differs notably from the Minnaert frequency (45). It is important to note that viscous dissipation is not the only source of energy loss from the bubble. Energy is also lost to sound radiation (here we finally acknowledge the compressibility of the liquid) and to heat loss; the latter may be accommodated by appropriately modifying κ [25].

During some cavitation conditions, the speed with which the bubble expands and contracts can be so large that it becomes a substantial fraction of the speed of sound. In this case, continuing to assume the liquid is incompressible is doubly inappropriate: not only does liquid compressibility radiate away energy, modifying the bubble's natural frequency, it alters the nonlinear terms in the momentum equation that can no longer be ignored. The only recourse to solution is then numerical. Researchers including Herring, Trilling, and Gilmore modified the RPNNP equation to include the effects of a finite speed of sound [36]. Presently, the equation most often used to represent all the effects noted above is the *Keller-Miksis equation*. The Keller-Miksis equation has been further modified to include the dynamics of a thin flexible shell encapsulating the bubble, modeling an ultrasound contrast agent, and to include the effects of multiple bubbles interacting [10]. Since the focus of this chapter is on acoustic streaming and microstreaming rather than the extremes of cavitation collapse, we will not further detail the fascinating but complex literature on highly nonlinear bubble oscillations. Acoustic streaming and microstreaming may be described as *weakly nonlinear* phenomena, which can be modeled by the perturbation theory concept described in general terms in section "Significance of the Nonlinearity in the Momentum Equation."

Bubble Trapped in a Narrow Tube

There have been several microfluidic applications in which an acoustically driven bubble trapped in a tube or microchannel has been proposed and tested as a flow actuator [6, 7, 56], and sonochemical reactions have been generated in such a system [52].

By following the same approach as in section "Rayleigh's Derivation of the Collapse of a Spherical Cavity," the linear natural frequency, ignoring surface tension and viscosity and assuming both the bubble and the liquid slug are long compared with the tube radius, is given by

$$f_0 = \left(\frac{1}{2\pi}\sqrt{\frac{\kappa P_0}{\rho}}\right)\frac{1}{\sqrt{L_0 S}}, \tag{53}$$

where L_0 is the equilibrium bubble length and S is the length of the liquid slug in the tube. In this simplistic example, the basic physics is even clearer than in the classical spherical bubble considered by Rayleigh and Minnaert: a mass of liquid contained in a tube is bouncing on the long "spring" formed by the bubble in the tube.

It is interesting to note that at a vastly greater scale than microfluidics, the same fundamental physics has been analyzed to predict the size of gas bubbles in Strombolian volcanoes, given measurements of the rumbling frequency. A bubble of gas is trapped in a tube, and above it is a mass of molten magma [58]. The size of the bubble may indicate the hazard presented by the impending eruption.

Two-Dimensional Planar Bubble

A two-dimensional or planar bubble could also occur in microfluidic contexts, for example, Liu et al. [30]. An equivalent would be a cylindrical bubble only capable of radial expansion and contraction. This system differs fundamentally from the three-dimensional bubble: the two-dimensional equivalent of the three-dimensional integration that leads from (38) to (39) is unbounded as $D \to \infty$, so that the domain size D is always a variable in the natural frequency. Thus, the two-dimensional bubble has a linear resonant frequency given by

$$f_0 = \left(\frac{1}{2\pi}\sqrt{\frac{2\kappa P_0}{\rho}}\right)\frac{1}{R_0\sqrt{\ln(D/R_0)}}, \tag{54}$$

whereas before R_0 is the equilibrium bubble radius and D is the radius of the liquid domain enclosing it.

Acoustic Streaming

Large-Scale Acoustic Streaming

Rayleigh [46] analyzed the acoustic streaming induced by sound waves propagating between parallel plates. This is usually called Rayleigh streaming. It was at this time that he applied the mathematical technique of perturbation theory to deal with the non-zero time-averaged flow created by the nonlinear term in Euler's equation, as described in section "Significance of the Nonlinearity in the Momentum Equation."
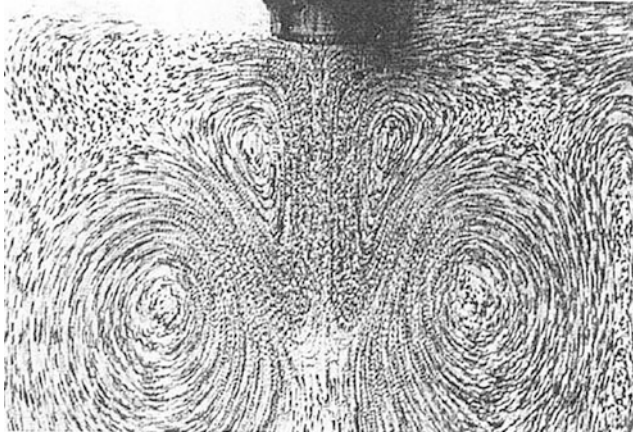
Fig. 4 Acoustic streaming field (Eckart streaming) created by a transducer 4 mm in diameter (seen at image *top center*) emitting 32 MHz pulses of 0.5 µs duration at 31 kHz pulse repetition rate into a $64 \times 64 \times 90$ mm *rectangular box*. Streaming speeds reach a maximum of about 15 mm s^{-1} (Reprinted from Nowicki et al. [39]. Copyright (1998), with permission from Elsevier)

Large-scale streaming due to ultrasound was originally called the "quartz wind" [11] owing to the quartz crystals used to produce ultrasound; it is also called Eckart streaming. Streak photographs of Eckart streaming extending a few centimeters from an ultrasonic transducer are shown in Fig. 4. Recall from section "The Rectification of Oscillation by the Nonlinear Term" that the only requirement for the nonlinear term to exist, and thus for streaming to occur, is that a gradient should exist in the first-order sound field. Any ultrasonic transducer will create a *near-field effect* (see, e.g., Kinsler and Frey [19]): owing to the finite size of the transducer, the field will change rapidly with distance away from it, gradually becoming more uniform at distances much greater than the transducer size. As distance from the transducer increases further, the field will eventually fall off simply, owing to geometric spreading. Thus one might expect some streaming even in the theoretical absence of dissipation.

Where the ultrasonic intensity is high enough to cause cavitation, as is usually the case when commercial sonotrodes or ultrasonic horns are used in chemical or biochemical preparations, acoustic streaming occurs together with cavitation. These systems can be extremely complex, with linear and nonlinear interactions between the cavitation bubbles and with the microstreaming associated with the microbubbles (see section "Basic Observations of Microstreaming") occurring at the small scale, as well as the large-scale streaming occurring. Significant power is lost from the sound waves in generating the cavitation bubbles, which locally absorb and scatter the sound waves. Thus, the effect of cavitation is to enhance the overall dissipation of energy from the sound waves, increasing the negative gradient in the acoustic field and reducing the distance from the source that the sound can penetrate. This may enhance the acoustic streaming closer to the source of the ultrasound, while limiting the extent to which the streaming penetrates.

Applications of Acoustic Streaming

It was suggested by Betheras [1] that the acoustic streaming created by a medical ultrasound scanner could be useful in medical diagnosis of cysts. A cyst is a lesion in the body that is often, though not always, filled with fluid. Ovarian cysts and related lesions in the body such as endometriomas could be benign or malignant, but the only true test is invasive biopsy or surgery [12]. If such cysts, which may be a few centimeters in size, contain fluid only, they are less likely to be malignant, but if they contain solid or more viscous matter, the risk of malignancy may be higher [12].

Medical scanners include a Doppler feature that permits them to measure the speed of blood flow. Normally, acoustic streaming caused by a medical ultrasound scanner is slower than blood flow, but in a cyst, there is no background flow at all, so the acoustic streaming can become visible. It is a complicated phenomenon because the scanner creates the streaming flow it is measuring. The velocity is a function of cyst size, location, shape, and the rheology of the fluid in the cyst. In addition to cysts of the female reproductive system, acoustic streaming has also been used in diagnoses of cysts in breast tissue [37].

Acoustic streaming flows in model cysts were studied by Zauhar et al. [62]. The velocity fields in an elastic spheroidal cavity were measured by Sznitman and Rösgen [51] using particle image velocimetry (PIV). A variety of acoustically transparent model cysts and rectilinear chambers were mounted at various locations in a much larger tank fitted with an ultrasonic transducer, and velocity fields were measured by PIV (Lai [21], as reported by Lai et al. [22]). It was found that the size and shape of the cavity in which the streaming occurred had a significant effect on the flow pattern. Furthermore, the streaming velocity profile depended on the location of the chamber relative to the transducer's focus point, as illustrated in Fig. 5.

High-power ultrasound has also been applied to molten metals, generating acoustic streaming (e.g., Kang et al. [17]) in an effort to improve the stirring and crystallization of the metal.

While acoustic streaming has these beneficial applications, when ultrasound is used to separate particles from liquid (see section "Motion of Particles Relative to Fluid" below), the acoustic streaming may disrupt the desired separation effect [27]. Hence, optimum power levels below which acoustic streaming is not detrimental need to be established.

Motion of Particles Relative to Fluid

The collection of fine rigid particles at the nodes of a standing wave sound field was clearly observed in the nineteenth century in the Kundt's tube, invented by Kundt in 1866. As just noted, Rayleigh [46] dealt with the nonlinearity in the governing equations using a perturbation approach. In Rayleigh's approach, the linear sound wave problem would be solved first, and the nonlinear streaming flow solved

Fig. 5 Effect of chamber location on profiles of acoustic streaming. Velocity component along the transducer axis is shown. The rectilinear chamber is 50 mm long and is immersed in a large tank driven by a 2.25 MHz transducer. *Lines* from top to bottom are, respectively, velocity along the central line of maximum cross-sectional velocity and averages over the central 12.5 %, 25 %, and 50 % of the chamber cross-section, with shading around the line indicating 95 % statistical confidence intervals. Note a different vertical scale on right-hand panel since velocities are lower farther from the transducer (From Lai [21]. Courtesy of P. Lai)

Cyst near face in <u>front</u> of transducer focus

Cyst far face <u>behind</u> transducer focus
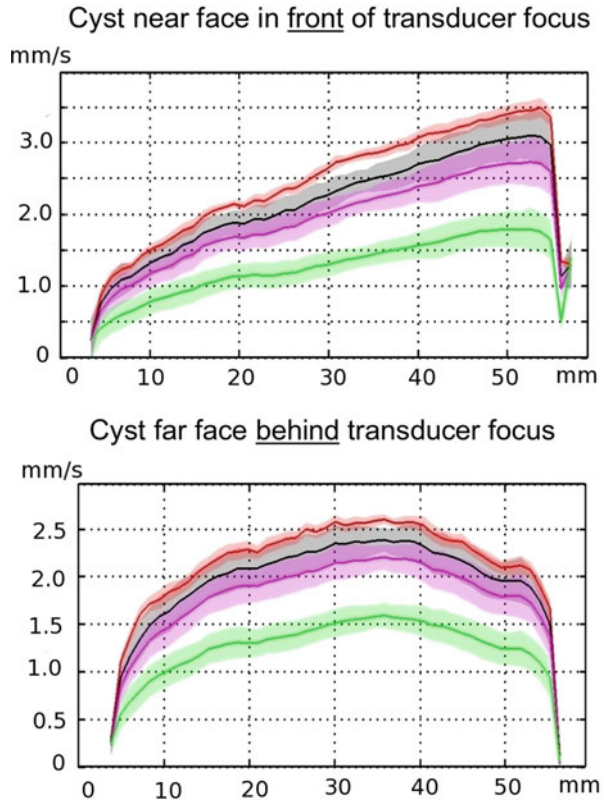
assuming that the linear solution, substituted into the nonlinear terms and time averaged, drove the streaming.

As will be outlined in section "Basic Observations of Microstreaming," it is the presence of a boundary layer and hence a non-zero gradient near the particle that makes a net motion possible. King [18] showed that particles could be made to drift in either traveling or standing waves. An appropriate second-order analysis leads to the derivation of an "acoustic radiation force" acting on particles with a different density or compressibility to their surrounds. King [18] calculated the radiation force on a rigid sphere much smaller than the sound wavelength. It was found that the radiation force would be an order of magnitude greater if the particle were in a standing wave field rather than a traveling wave field. If a standing wave field is created, particles will rapidly be attracted to the nodes or antinodes in the standing wave field depending on their density and compressibility relative to the carrier fluid. This phenomenon leads to the possibility of using ultrasound for separation.

Applications of ultrasonic separation to the food industry were outlined by Vilkhu et al. [59], and recent advances in ultrasonic separation were reviewed by Leong et al. [28].

Acoustic Microstreaming

Basic Observations of Microstreaming

Acoustic microstreaming is most usually called *cavitation microstreaming* in the literature. That is because it is most often created by a microbubble, and microbubbles are often created by cavitation. Acoustic microstreaming need not rely at all on the presence of microbubbles, but owing to the powerful effect microbubbles have on locally concentrating the sound field and thus creating large local gradients, acoustic microstreaming is most prominent when microbubbles are involved. Recall from section "Significance of the Nonlinearity in the Momentum Equation" that a gradient in the sound field is a prerequisite for any streaming.

While several types of acoustic streaming flow had been analyzed theoretically in the nineteenth and early twentieth centuries, the streaming flow around a sphere in a sound field – a typical particle in a Kundt's tube – was analyzed by Lane [23] using the approach of Rayleigh [46]. Significantly, Lane [23] recognized that there would be inner vortices (primary vortices) in the boundary layer (or *Stokes layer*) around a spherical particle in a sound field. These primary vortices would drive outer vortices (secondary vortices) over scales similar to several radii of the sphere (Fig. 6). Flow speeds in the primary vortices would be expected to be much higher than in the secondary vortices. Lane attempted an experiment with millimeter-sized spheres at audio frequencies, but had difficulty making observations and found the vortex size was overpredicted by theory.
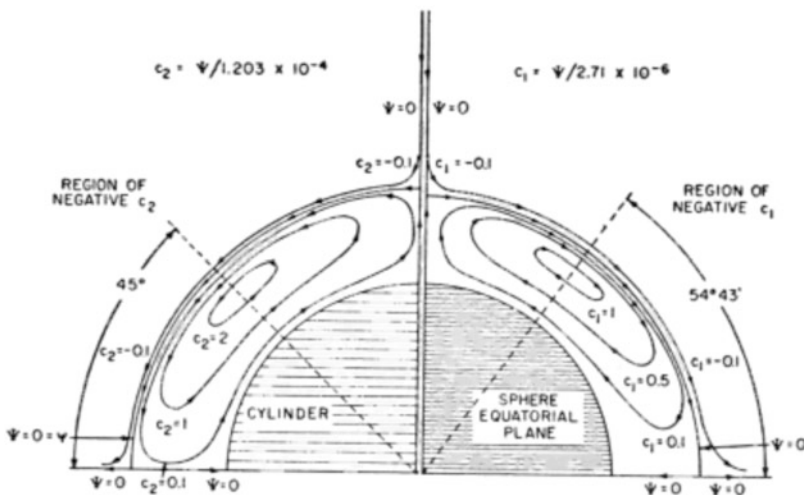
Fig. 6 Lane's original drawing of the primary microstreaming vortices around both a cylinder and a spherical particle. The innermost streamline of each secondary vortex is also shown, extending outwards at the top of the figure and at either side at the bottom. Note that the structure of the vortices is slightly different for the cylinder and the sphere (Reproduced with permission from Lane [23]. Copyright 1955, Acoustical Society of America)

Lane's identification of the primary and secondary vortices around a spherical particle was a first in acoustics, but is not unique in fluid dynamics. There are several other analogous flows at macroscopic scales, for example, when a circular cylinder is oscillated normal to its axis, primary vortices appear that are smaller than the cylinder, which in turn drive secondary vortices much larger than the cylinder (e.g., the experiment by Masakazu Tatsuno, published in van Dyke [57]). Engineers study such flows which might occur, for example, as ocean waves pass the leg of a platform in the sea. In a more recent example, centimeter-sized spheres were oscillated through amplitudes in the order of the sphere diameter and at frequencies in the order of a tenth of a cycle per second [42]. Both primary and secondary vortices were easily measured since the scales are in centimeters.

The Stokes layer thickness scales with $(2\ \mu/(\rho\omega))^{1/2}$, where ω is the applied frequency, and since for water $\mu/\rho \simeq 10^{-6}$, in the very low frequency experiment of Otto et al. [42], the Stokes layer thickness would be on the order of millimeters. However, an ultrasonic frequency, say 200 kHz, would result in a Stokes layer thickness around a micron – only a couple of wavelengths of light. Thus, since the boundary layer around ultrasonically driven microbubbles is so thin, it is only the secondary vortices that are usually observed in microstreaming around microbubbles – in cavitation microstreaming.

Cavitation microstreaming was first studied by Kolb and Nyborg [20], who allowed cavitation bubbles to form under the influence of various frequencies in the audible range, mostly 11.4 kHz and below. Kolb and Nyborg noted that streaming is most pronounced when the bubble is oscillating in its volumetric mode. This is consistent with the note above on the "concentrating" effect of bubbles: volumetric oscillations remove energy from the applied sound field, which at the scale of the bubble is in the form of plane waves, and reradiate sound as spherical waves that have a large local gradient. Kolb and Nyborg [20] also noted that microstreaming was pronounced when the bubble is on a solid boundary. The presence of a solid boundary can be modeled by a bubble interacting with its mirror image which is just touching it [32, 50], a situation that again would lead to a locally large gradient.

Research into cavitation microstreaming continued in the 1950s with the work of Elder [13], who used a precision hypodermic needle to inject bubbles of a controlled size of about 30 μm radius. The frequency was 10 kHz, and driving pressure amplitudes were varied in a range from about 0.2 to 0.9 kPa. Streaming velocities were visually estimated to be less than 0.0005 ms^{-1} – about half a millimeter per second. Elder [13] classified microstreaming into different regimes that were observed for different liquid viscosities and different sound amplitudes and frequencies. Although the boundary layers near the bubble surface were too thin to be observed, their importance was recognized by both Kolb and Nyborg [20] and Elder [13] by analogy with other acoustic streaming phenomena. Elder [13] also noted the earlier theory of Nyborg [40] that predicted the speed of the jet of liquid created between vortices.

Theoretical Analyses of Microstreaming

A key theoretical work was undertaken by Davidson and Riley [5]. They studied the streaming field around a drop or bubble that was oscillating in translation along an axis, but not oscillating volumetrically. An important feature of their analysis was that they considered only the second-order problem for the streaming, assuming the oscillatory motion due to the bubble and the incident sound field was prescribed. This approach follows logically from the mathematics of perturbation theory. Moreover, the streaming flow was assumed to be incompressible, which was consistent with the approach of Nyborg [40] and again dates back to Rayleigh [46].

The work of Davidson and Riley [5] was subsequently extended by Wu and Du [61] who made the same fundamental assumption as Davidson and Riley [5]: the streaming flow was incompressible and was driven by a prescribed bubble motion. Wu and Du [61] identified two modes of streaming. If the bubble is purely translating, the result is a microstreaming pattern of four vortices (a "quadrupole" pattern). However, if the bubble is undergoing volumetric pulsations, the result is a pattern of two vortices (a "dipole" pattern). They found that the streaming due to volumetric pulsation is stronger than that due to translation, which was consistent with the observation of Elder [13] that microstreaming was most pronounced near the bubble's resonance frequency. It is important to note that Wu and Du's calculations were *just outside* the Stokes layer and hence were calculations of the secondary vortices.

Longuet-Higgins [31] continued the approach of using perturbation theory with the same assumption of incompressible streaming driven by a prescribed velocity field. Although Longuet-Higgins did not explicitly say the calculations were outside the boundary layer, his boundary condition required the gradient of tangential velocity to become zero at the "bubble radius," effectively placing an artificial boundary at the streamline separating the primary and secondary vortices. Like Wu and Du [61], Longuet-Higgins found a quadrupole pattern when the bubble was translating and a dipole pattern when it was undergoing volumetric pulsations. He combined the two modes of oscillation; recalling that microstreaming results from nonlinear physics, this is not simply a matter of superposition. Indeed, Longuet-Higgins calculated that the microstreaming velocities are proportional to the product of the amplitudes of the two modes of oscillation and that the presence of volumetric pulsations enhanced the translation mode.

It is worth noting that, owing to the incompressibility assumption in all the works of Nyborg [40], Davidson and Riley [5], Wu and Du [61], and Longuet-Higgins [31], the streaming flow field was no different to what might be produced if, for example, a spherical toy balloon were pulsating in volume in a bathtub, in various combinations with and without to and from oscillations of the sphere, with no sound waves present. This assumption probably remains valid while the magnitude of the streaming velocity is small compared with the speed of sound.

The work of Wu and Du [61] was reevaluated by Doinikov and Bouakaz [8], who determined that Wu and Du's neglect of viscous effects outside the boundary layer caused a severe underestimation of the acoustic streaming velocity. Doinikov and Bouakaz [8] recalculated the radial and tangential components of the streaming velocity immediately outside the boundary layer for a case considered by Wu and Du [61]. Doinikov and Bouakaz [8] found that the true velocities were over an order of magnitude higher, reaching 0.03 ms^{-1} for a bubble of radius 33 μm driven at 100 kHz and about 55 kPa. This speed, at the boundary between the primary and secondary vortices, reached centimeters per second, contrasting with earlier predictions of fractions of a millimeter per second – and experimental measurements of secondary vortex speeds also in fractions of a millimeter per second.

It is important to recall that all these theories [5, 8, 31, 40, 61] were all predicated upon the perturbation method originally proposed by Rayleigh [46] for acoustic streaming: the linear first-order solution, once found (or simply prescribed), drives the second order where the streaming is manifested, and so on. This mathematical approach means that the analyses, while they have produced successful phenomenological comparisons with experiment, have an inherent disconnection between the acoustic behavior and the streaming behavior – a disconnect that is fundamentally due to the mathematical principle of perturbation theory. We might expect this approach to cause problems when the acoustic amplitude in the immediate vicinity of the microbubble is no longer predictable by linear theory; for example, when there is cavitation collapse or any other circumstance in which the amplitude with which the bubble radius is pulsating is large compared with its equilibrium radius. The assumption of incompressibility in the second-order streaming flows could also lose validity under the extremely nonlinear conditions commonly produced in sonochemical systems.

Even if the bubble dynamics is linear, the presence of many bubbles nearby could alter the local acoustic field owing to bubble-acoustic interactions (e.g., Nikolovska et al. [38]). The microstreaming field around a pair of microbubbles was calculated analytically by Wang and Chen [60], who found that radial streaming velocities were suppressed in favor of the tangential velocities.

Experimental Quantifications of Microstreaming

As noted earlier, the experiments of Kolb and Nyborg [20] and Elder [13] had already observed the secondary vortices around microbubbles, and Elder [13] had estimated streaming speeds. However they had not observed the primary vortices. Gormley and Wu [15] observed streaming around a 55 μm commercial contrast agent microbubble. The flow was revealed by fine particles forming streaks. Since the frequency was 160 kHz, the Stokes layer thickness and hence the primary vortices would have been too small to see, just as in the earlier studies. The work of Gormley and Wu [15] was significant in that the microstreaming flow was

photographed; the literature in the 1950s had presented sketches based on observations. Furthermore, Gormley and Wu's observations were around microbubbles that were not simple gas-in-liquid bubbles; they had a "shell" composed of a partially denatured protein, albumin.

Tho et al. [55] conducted micro-particle image velocimetry (micro-PIV) experiments on the microstreaming flows around microbubbles that were large enough, typically greater than 200 μm in radius, for detailed velocity fields to be quantified for the first time. The bubbles were sessile or pendant within a microchamber and thus had a contact circle with the chamber wall. The sound was applied by a piezoceramic disk that caused the chamber wall to flex. Applied frequencies were 2–13 kHz, and the pressure amplitudes were around 0.1–0.5 kPa.

Tho et al. [54] then studied cases where the bubble not only translated and pulsated but also underwent simultaneous translations around two orthogonal axes. Thus, the bubble center was made to trace out a circle, an ellipse or a line along a single axis, with or without volumetric pulsations, each selected by a particular frequency of insonation and bubble location in the microdevice. The path the bubble center traced out was also measured.

As theoretically predicted earlier [31, 61], translations along one axis corresponded to a quadrupole microstreaming pattern (Fig. 7), while volumetric pulsations corresponded to a dipole (Fig. 8). However, circular or elliptical paths created circular or elliptical vortices surrounding the bubble; as the minor axis of the bubble-translation-path ellipse tended to zero, the quadrupole pattern was recovered. As in previous studies, only the secondary vortices could be observed, with
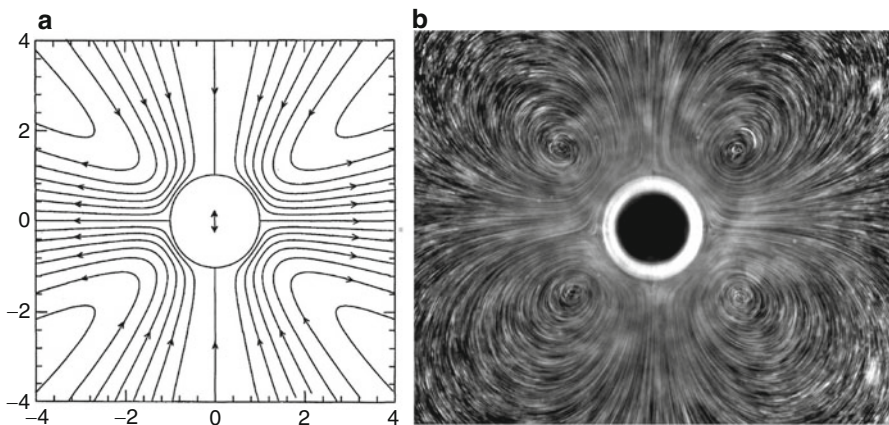
Fig. 7 Quadrupole microstreaming pattern for a bubble oscillating in translation only, showing the secondary vortex pattern. (**a**) Theoretical prediction for a bubble in an infinite domain (Reprinted from Longuet-Higgins [31] by courtesy of The Royal Society); (**b**) Experimental streak image around a bubble of radius 242 ± 10 μm attached to a microchamber wall and driven at 2.422 kHz, such that the bubble oscillated in translation only (From Tho et al. [54]. Reprinted under a CSIRO Licence to Publish)
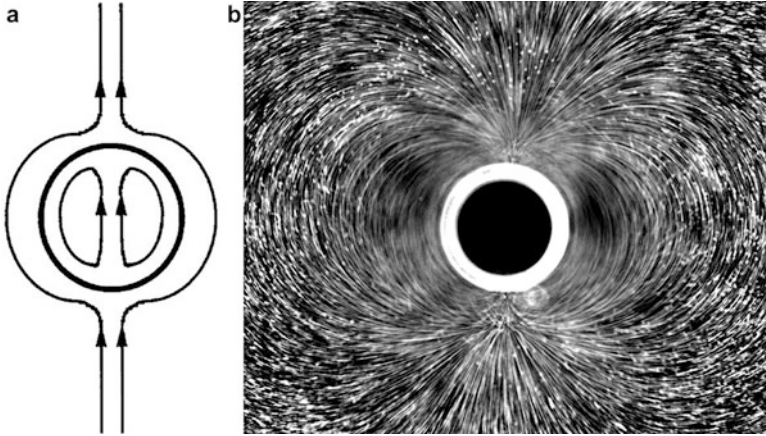
Fig. 8 Dipole microstreaming pattern for a bubble oscillating volumetrically only, showing the secondary vortex pattern. (**a**) Theoretical prediction for a bubble in an infinite domain (Reproduced with permission from Wu and Du [61]. Copyright 1997, Acoustical Society of America. Longuet-Higgins [31] only plotted results for volumetric plus translational oscillation); (**b**) Experimental streak image around a bubble of radius 271 ± 4 μm attached to a microchamber wall and driven at 8.658 kHz, such that the bubble oscillated volumetrically only (From Tho et al. [54]. Reprinted under a CSIRO Licence to Publish)

microstreaming speeds of up to 0.00045 ms^{-1} – less than half a millimeter per second. Although Tho et al.'s bubbles were about six times larger than those studied by Elder [13], frequencies and applied pressure amplitudes were similar, as were magnitudes of the measured velocities.

Microstreaming flows around multiple bubbles were also measured by Tho et al. [54], with up to four nearby bubbles studied. Flows around pairs of bubbles could be quadrupole (Fig. 9), dipole, or elliptical depending on the mode of oscillation, whereas Wang and Chen [60] later predicted predominantly tangential flows around a bubble pair.

In 2010, Collis et al. claimed to be the first to simultaneously observe and measure the primary vortices as well as the secondary vortices in an acoustically driven microbubble (Fig. 10). The primary vortex visualization was achieved by observing tracer particles adsorbed onto the bubble surface. For a 135 μm bubble driven at 28 kHz and 12 kPa (a pressure amplitude later calibrated by Leong et al. [26]), they estimated that the primary vortex speed 0.013 ± 0.002 ms^{-1} was two orders of magnitude higher than the secondary vortex speed. Although parameters were different from those studied at about the same time by Doinikov and Bouakaz [8], it is interesting that the primary vortex speed was also in the centimeters per second range predicted by Doinikov and Bouakaz [8].
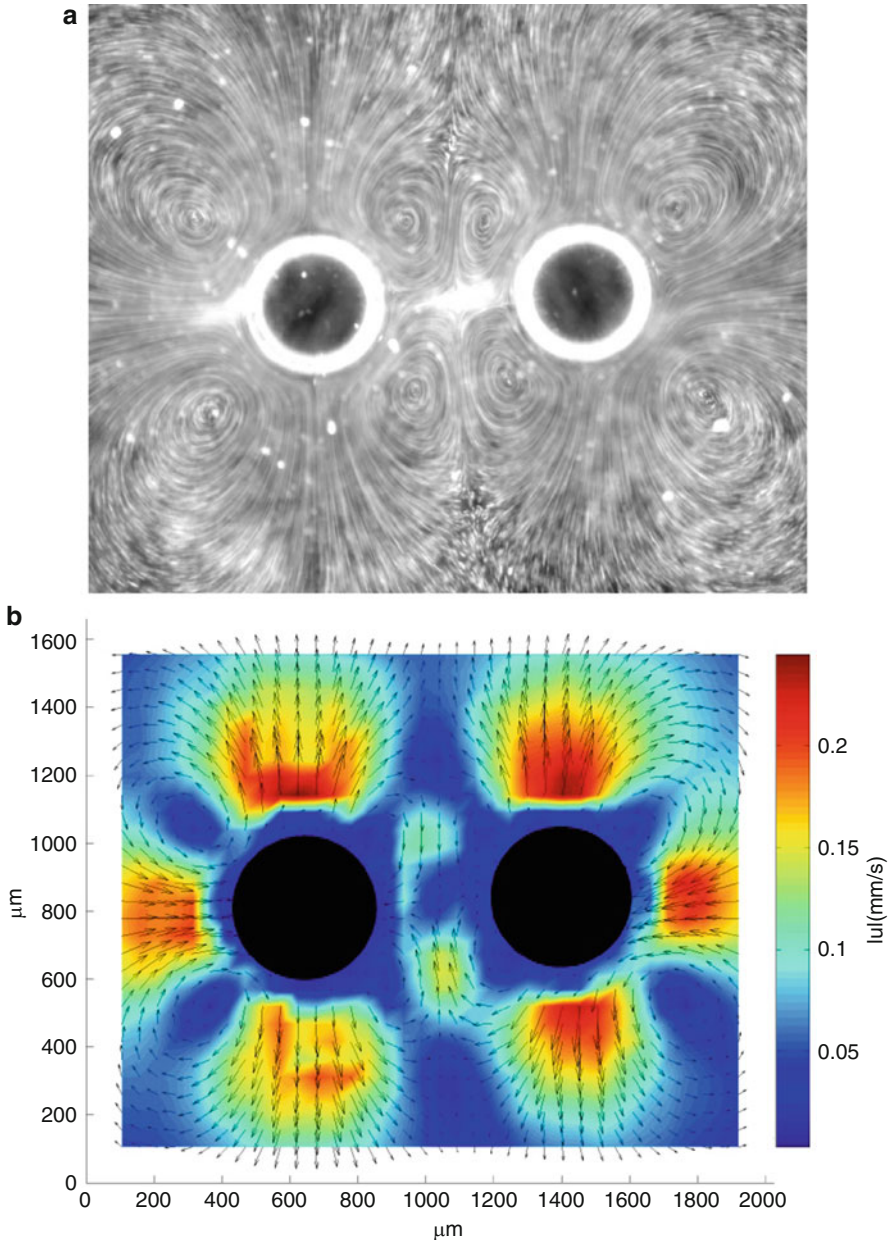
Fig. 9 Quadrupole microstreaming around a pair of bubbles. Left-hand bubble radius 212 μm, right-hand 208 μm, driven at 2.267 kHz. (**a**) Experimental streak image; (**b**) PIV data (From Tho [53], reprinted courtesy of P. Tho)
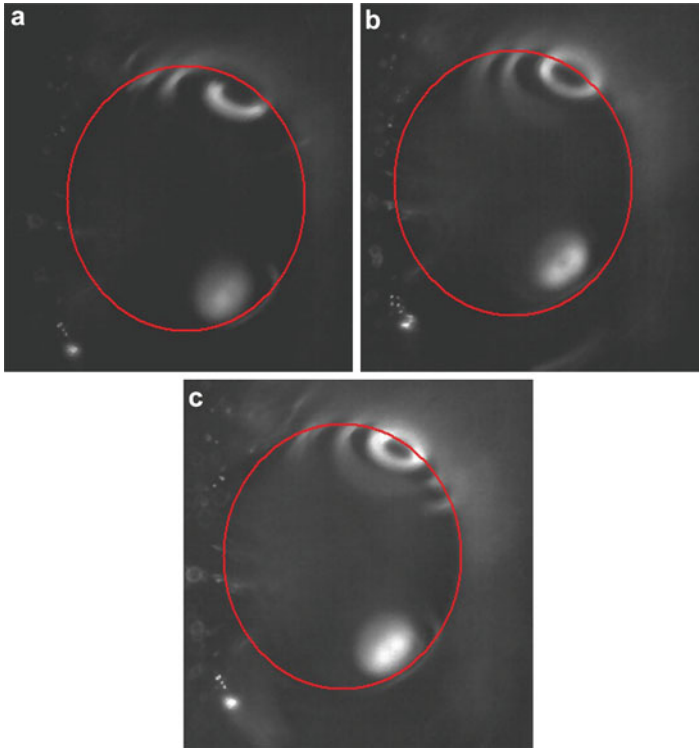
Fig. 10 Putative identification of the primary microstreaming vortices at a microbubble surface. A 135 μm radius bubble excited at 28 kHz was imaged with varying exposure times to estimate the velocity of primary vortices, giving 0.013 ± 0.002 ms^{-1}. Line approximately indicates the bubble surface. In the regime applied, vortices were irregular. Exposure times were (**a**) 5884 μs; (**b**) 8322 μs; (**c**) 11,767 μs (From Collis et al. [4]. Reprinted with the authors' permission)

Effects of Bubble Surface Properties on Microstreaming

As noted above, microstreaming is still observed when there is no gas-liquid interface of the bubble, rather a flexible "shell" material [15]. This can be expected, since all that is required for microstreaming is an acoustic boundary layer in which there is a large gradient in velocity. Thus, altering the properties of the surface might be expected to alter the velocity gradient in the boundary and thus the microstreaming. The effect of surfactants on microstreaming around a microbubble was studied by Leong et al. [26]. They carefully introduced different surfactant molecules such that the surface tension was maintained fixed while the molecular headgroup – the part of the molecule in the water – was altered in size. Microstreaming velocities were measured by micro-PIV. It was found that the surfactant molecule dodecyltrimethylammonium chloride (DTAC) caused significantly higher streaming velocities than other surfactants such as sodium dodecyl sulfate (SDS) or in plain water.

Bioeffects of Microstreaming

Cavitation microstreaming was noted to have a detrimental effect on cells in the 1950s, when "sonic destruction" of *Paramecium* cells was observed to be caused specifically by microstreaming flows [13]. This effect is distinct from the simple destruction of cells owing to the violence of cavitation collapse, which is utilized in commercial laboratory "cell disruptor" sonotrodes. Microstreaming from a microbubble was observed to disrupt an artificial vesicle – a model biological cell – by Marmottant and Hilgenfeldt [34].

Over the past decade, the relevance of microstreaming to beneficial ends has been proposed, particularly to the phenomena of sonoporation and sonothrombolysis (e.g., Manasseh et al. [33]).

It is important to understand the biological significance of the steady stresses due to microstreaming, compared to the transient stresses due to the first-order microbubble volumetric pulsation. The stresses due to the first-order linear or nonlinear bubble oscillation, which have been studied theoretically (e.g., Doinikov and Bouakaz [9]) in the sonoporation context, reverse every cycle. The primary oscillation cycles due to first-order ultrasound occur millions of times per second, whereas cell biological processes such as protein expression occur over timescales of minutes. Thus, the first-order ultrasound appears to be far too rapid to directly influence biological processes, unless, of course, the oscillatory stresses are high enough to cause permanent or semipermanent damage to the cell membrane. In contrast, the steady or quasi-steady stresses due to microstreaming are closer in timescale to the mechanical stresses known to influence cell processes [49].

The speed of flow in the primary vortices may have particular significance for the bioeffects of microstreaming. Collis et al. [3] proposed that the concept of surface divergence was relevant to sonoporation, sonothrombolysis, and kindred phenomena. The surface divergence metric, which can be extracted from micro-PIV measurements of microstreaming flows, could represent the extent to which a cell surface is being stretched or compressed by microstreaming flows. Such steady or at least quasi-steady stresses on cell membranes are known to cause, for example, stem cells to proliferate more rapidly and even differentiate into more specialized cell types [49].

Microstreaming in Micromixing and Microseparation

Mixing at microscale is a notorious problem. True mixing of two bodies of fluid containing different molecules is ultimately achieved by molecular diffusion. However, diffusion acts over short distances, thus taking a very long time in quiescent fluids to completely intermingle the two types of molecules. Fluid motion can stretch and fold the interface between the two fluids, thus allowing diffusion to do its work over a short distance. This stretching and folding is efficiently accomplished by turbulence, in which chaotic vortices at many scales create ever-longer boundaries between the two fluids and thus ever-shorter distances. Unfortunately, the absence of turbulence at microscale means that microscale stirring is necessary.

Microstreaming around a microbubble was demonstrated as a mechanism of micromixing in a microdevice by Liu et al. [30]. It was suggested by Manasseh et al. [33] that the micromixing due to microbubble-induced microstreaming could be responsible for the therapeutic benefits of ultrasound contrast agents, particularly in sonothrombolysis. Meanwhile, noting that what was needed for microstreaming was a large gradient in the sound field, which did not necessarily require a microbubble, Petkovic-Duran et al. [43] demonstrated effective micromixing within a drop with a small radius; by alternating "vortex" and "dipole" patterns of microstreaming, they also achieved a more efficient, "chaotic" micromixing. Subsequently, the micromixing due to drop-based microstreaming was able to improve the yield of RNA from a single cell by 100-fold [2]. The frequencies applied were so low, around 140–350 Hz, that they may have caused shape-mode resonances of the entire drop. However, similarly low frequencies were also shown to create microstreaming in a completely enclosed microchannel [41].

Microstreaming flows could also do the opposite of mixing; by creating a vortex, they can be used to trap particles [29, 44, 48].

Microstreamers in Cavitating Systems

It was noted by Blake in 1949 (as reported in Neppiras [36]) that cavitation microbubbles can form "streamers" in which the microbubbles appear to be mutually attracted into long, twisting ribbons or streams. Since microstreamers are composed of a large number of microbubbles, the scales of this motion are larger than the microstreaming around individual bubbles described in sections "Basic Observations of Microstreaming," "Theoretical Analyses of Microstreaming," "Experimental Quantifications of Microstreaming," "Effects of Bubble Surface Properties on Microstreaming," "Bioeffects of Microstreaming," and "Microstreaming in Micromixing and Microseparation." The streamer is thought to be formed by an attractive radiation force between bubbles, called the secondary Bjerknes force (e.g., Mettin et al. [16] and Jiao et al. [35]). However, we may speculate that microstreaming could contribute to maintaining the structure of the streamer. Highly ordered microstreamers can also be generated when microbubbles are created from ultrasonically excited pits [14].

Conclusions and Future Directions

The laws of fluid dynamics were introduced and applied to bubble acoustics, acoustic streaming, and cavitation microstreaming. The laws of conservation of mass and momentum and a constitutive law for the gas in the bubble, neglecting liquid compressibility, viscosity, surface tension, and vapor pressure, are sufficient to predict that a bubble will oscillate in volume with a natural frequency, called the Minnaert frequency. This natural frequency of bubble volumetric oscillation is inversely proportional to its size, and bubbles microns to tens of microns in size

oscillate at ultrasonic frequencies. The full form of the Rayleigh-Plesset-Noltingk-Neppiras-Poritsky equation for bubble acoustics also requires knowledge of the fluid constitutive properties of viscosity, surface tension, and vapor pressure, but these significantly alter the Minnaert frequency only for bubbles microns in size. For bubbles undergoing cavitation collapse, as well as for an accurate estimation of losses due to sound radiation, liquid compressibility must be considered, leading to the Keller-Miksis equation. The final modifications attempt to include the dynamics of a thin shell encapsulating the bubble, modeling medical ultrasound contrast agents.

The momentum equation for fluid dynamics in the absence of viscosity and liquid compressibility, Euler's equation, reveals the origin of acoustic streaming and microstreaming. These were shown to be due to the nonlinear term in Euler's equation. This nonlinearity represents the attribute that distinguishes a fluid from a solid: its ability to accelerate purely by moving into a region where the fluid velocity is different. The nonlinear term is the fluid velocity multiplied by the gradient with distance of the fluid velocity. If the fluid velocity is primarily oscillatory, which is the case with all fluid waves, including sound waves, the primary oscillation averages to zero. However, the nonlinear term does not average to zero over time. Thus there is a driver for a net streaming motion that, unlike the primary oscillation, does not average to zero.

Because the nonlinear term is a velocity multiplied by a velocity gradient, there are two ways in which the nonlinear term could be significant. The velocity could be high, in other words the ultrasonic power could be high, and this leads to acoustic streaming. However, even if the power is not particularly high, if the velocity gradient is high, as would occur in the immediate vicinity of an oscillating bubble, the nonlinear term could again be significant. This leads to cavitation microstreaming.

Future research should consider the effect of microstreaming on the relative motion of multiple bubbles or particles and the effects of interfacial chemistry on microstreaming. Furthermore, the ability of microstreaming to create stresses on biological surfaces needs further exploration.

References

1. Betheras FR (1990) Acoustic radiation force as a diagnostic modality. In: Proceedings of the 20th annual meeting of the Australian Society for Ultrasound in Medicine, p 69
2. Boon W, Petkovic-Duran K, White K, Tucker E, Albiston A, Manasseh R, Horne M, Aumann T (2011) Optical detection and quantification of micromixing of single-cell quantities of RNA. Biotechniques 50(2):116–119
3. Collis J, Manasseh R, Liovic P, Tho P, Ooi A, Petkovic-Duran K, Zhu Y (2010) Cavitation microstreaming and stress fields created by microbubbles. Ultrasonics 50(2):273–279
4. Collis J, Ooi A, Manasseh R (2010) Micro PIV analysis of secondary vortices with observations of primary vortices in single bubble cavitation microstreaming. In: 17th Australasian fluid mechanics conference, Auckland, 5–9 Dec
5. Davidson B, Riley N (1971) Cavitation microstreaming. J Sound Vib 15(2):217–233
6. Dijkink R, Ohl C-D (2008) Laser-induced cavitation based micropump. Lab Chip 8:1676–1681

7. Dijkink R, Van Der Dennen J, Ohl C, Prosperetti A (2006) The 'acoustic scallop': a bubble-powered actuator. J Micromech Microeng 16:1653–1659
8. Doinikov A, Bouakaz A (2010) Acoustic microstreaming around a gas bubble. J Acoust Soc Am 127(2):703–709
9. Doinikov A, Bouakaz A (2010) Theoretical investigation of shear stress generated by a contrast microbubble on the cell membrane as a mechanism for sonoporation. J Acoust Soc Am 128 (1):11–19
10. Dzaharudin F, Suslov S, Manasseh R, Ooi A (2013) Effects of coupling, bubble size and spatial arrangement on chaotic dynamics of microbubble cluster in ultrasonic fields. J Acoust Soc Am 134(5):3425–3434
11. Eckart C (1948) Vortices and streams caused by sound waves. Phys Rev 73(1):68–76
12. Edwards A, Clarke L, Piessens S, Graham E, Shekleton P (2003) Acoustic streaming: a new technique for assessing adnexal cysts. Ultrasound Obstet Gynecol 22:74–78
13. Elder S (1959) Cavitation microstreaming. J Acoust Soc Am 31:54–64
14. Fernandez Rivas D, Prosperetti A, Zijlstra AG, Lohse D, Garde-niers HJGE (2010) Efficient sonochemistry through microbubbles generated with micromachined surfaces. Angew Chem 49:9699–9701
15. Gormley G, Wu J (1998) Observation of acoustic streaming near Albunex (R) spheres. J Acoust Soc Am 104:3115–3118
16. Jiao J, He Y, Kentish SE, Ashokkumar M, Manasseh R, Lee J (2015) Experimental and theoretical analysis of secondary bjerknes forces between two bubbles in a standing wave. Ultrasonics 58:35–42
17. Kang J, Zhang X, Wang S, Ma J, Huang T (2015) The comparison of ultrasonic effects in different metal melts. Ultrasonics 57:11–17
18. King L (1934) On the acoustic radiation pressure on spheres. Proc R Soc Lond A Math Phys Sci 147(861):212–240
19. Kinsler LE, Frey AR (1962) Fundamentals of acoustics. Wiley, New York
20. Kolb J, Nyborg W (1956) Small-scale acoustic streaming in liquids. J Acoust Soc Am 28:1237
21. Lai P (2008) Acoustic streaming for medical diagnostics. Master's thesis, University of Melbourne, Department of Mechanical and Manufacturing Engineering
22. Lai P, Manasseh R, Ooi A (2009) Measurements of acoustic streaming velocity fields in model cystcavities. Ultrasound in Medicine and Biology. 35(8):S168
23. Lane C (1955) Acoustical streaming in the vicinity of a sphere. J Acoust Soc Am 27 (6):1082–1086
24. Lauterborn W (1976) Numerical investigation of nonlinear oscillations of gas bubbles in liquids. J Acoust Soc Am 59(2):283–293
25. Leighton TG (1994) The acoustic bubble. Academic, London
26. Leong T, Collis J, Manasseh R, Ooi A, Novell A, Bouakaz A, Ashokkumar M, Kentish S (2011) The role of surfactant head group, chain length and cavitation microstreaming on the growth of bubbles by rectified diffusion. J Phys Chem 115(49):24310–24316
27. Leong T, Johansson L, Juliano P, Mawson R, McArthur S, Manasseh R (2014) Design parameters for the separation of fat from natural whole milk in an ultrasonic litre-scale vessel. Ultrason Sonochem 21:1289–1298
28. Leong T, Johansson L, Juliano P, McArthur S, Manasseh R (2013) Ultrasonic separation of particulate fluids in small and large scale systems: a review. Ind Eng Chem Res 52 (47):16555–16576
29. Li H, Friend JR, Yeo LY (2007) Surface acoustic wave concentration of particle and bioparticle suspensions. Biomed Microdevices 9:647–656
30. Liu R, Yang J, Leningk R, Bonanno J, Grodzinski P (2004) Self-contained, fully integrated biochip for sample preparation, polymerase chain reaction amplification, and dna microarray detection. Anal Chem 76:1824–1831
31. Longuet-Higgins M (1998) Viscous streaming from an oscillating spherical bubble. Proc Roy Soc Lond A 454:725–742

32. Manasseh R, Ooi A (2009) Frequencies of acoustically interacting bubbles. Bubble Sci Eng Technol 1(1–2):58–74
33. Manasseh R, Tho P, Ooi A, Petkovic-Duran K, Zhu Y (2009) Cavitation microstreaming and material transport around microbubbles. Phys Procedia 3(1):427–432
34. Marmottant P, Hilgenfeldt S (2003) Controlled vesicle deformation and lysis by single oscillating bubbles. Nature 423:153–156
35. Mettin R, Akhatov I, Parlitz U, Ohl C, Lauterborn W (1997) Bjerknes forces between small cavitation bubbles in a strong acoustic field. Phys Rev E 56:2924–2931
36. Neppiras EA (1980) Acoustic cavitation. Phys Rep 61(3):159–251
37. Nightingale KR, Kornguth PJ, Trahey GE (1999) The use of acoustic streaming in breast lesion diagnosis: a clinical study. Ultrasound Med Biol 25(1):75–87
38. Nikolovska A, Manasseh R, Ooi A (2007) On the propagation of acoustic energy in the vicinity of a bubble chain. J Sound Vib 306:507–523
39. Nowicki A, Kowalewski T, Secomski W, Wojcik J (1998) Estimation of acoustical streaming: theoretical model, doppler measurements and optical visualisation. Eur J Ultrasound 7:73–81
40. Nyborg W (1958) Acoustic streaming near a boundary. J Acoust Soc Am 30(4):329–339
41. Oberti S, Neild A, Ng T (2009) Microfluidic mixing under low frequency vibration. Lab Chip 9:1435–1438
42. Otto F, Riegler EK, Voth GA (2008) Measurements of the steady streaming flow around oscillating spheres using 3d particle tracking velocimetry. Phys Fluids 20:093304
43. Petkovic-Duran K, Manasseh R, Zhu Y, Ooi A (2009) Chaotic micromixing in open wells using audio-frequency acoustic microstreaming. Bio Tech 47(4):827–834
44. Phan H, Sesan M, Alan T, Neild A (2014) Particle collection using vibrating bubbles. In: 19th Australasian fluid mechanics conference, RMIT University, Melbourne
45. Rayleigh (1917) On the pressure developed in a liquid during the collapse of a spherical cavity. Phil Mag 34:94–98
46. Rayleigh L (1884) On the circulation of air observed in Kundt's tubes, and on some allied acoustical problems. Philos Trans R Soc Lond 175:1–21
47. Riley N (2001) Steady streaming. Annu Rev Fluid Mech 33:43–65
48. Rogers P, Neild A (2011) Selective particle trapping using an oscillating microbubble. Lab Chip 11:3710–3715
49. Shah N, Morsi Y, Manasseh R (2014) Cell Biochem Funct 32(4):309–325
50. Strasberg M (1953) The pulsation frequency of nonspherical gas bubbles in liquid. J Acoust Soc Am 25(3):536–537
51. Sznitman J, Rosgen T (2008) Acoustic streaming flows in a cavity: an illustration of small-scale inviscid flow. Phys D: Nonlinear Phenom 237(14–17):2240–2246
52. Tandiono, Ohl S-W, Ow DSW, Klaseboer E, Wong VV, Dumke R, Ohl C-D (2011) Sonochemistry and sonoluminescence in microfluidics. Proc Natl Acad Sci U S A 108 (15):5996–5998
53. Tho P (2005) Cavitation microstreaming in single and two bubble systems. Master's thesis, University of Melbourne, Department of Mechanical and Manufacturing Engineering
54. Tho P, Manasseh R, Ooi A (2007) Cavitation microstreaming in single and multiple bubble systems. J Fluid Mech 576:191–233
55. Tho P, Zhu Y, Manasseh R, Ooi A (2004) Measurement of microbubble-induced acoustic microstreaming using micro particle image velocimetry. In: Biomedical applications of micro- and nanoengineering II, D. V. Nicolau (Ed), Proc. of SPIE international symposium on smart materials, nano-, and micro-smart systems, 12–15 Dec 2004. University of New South Wales Sydney, Australia, 5651:336–347
56. Torniainen ED, Govyadinov AN, Markel DP, Kornilovitch PE (2012) Bubble-driven inertial micropump. Phys Fluids 24, 122101(2012); http://dx.doi.org/10.1063/1.4769179
57. van Dyke M (1982) An album of fluid motion. Parabolic Press, Stanford
58. Vergniolle S, Ripepe M (2009) From Strombolian explosions to fire fountains at Etna Volcano (Italy): what do we learn from acoustic measurements? Geological Society Publishing, London

59. Vilkhu K, Manasseh R, Mawson R, Ashokkumar M (2010) Ultrasonic recovery and modification of food ingredients. Springer, New York, pp 345–368, chapter 13
60. Wang C, Chen J (2013) Cavitation microstreaming generated by a bubble pair in an ultrasound field. J Acoust Soc Am 134(2):1675–1682
61. Wu J, Du G (1997) Streaming generated by a bubble in an ultrasound field. J Acoust Soc Am 101(4):1899–1907
62. Zauhar G, Starritt HC, Duck FA (1998) Studies of acoustic streaming in biological fluids with an ultrasound doppler technique. Br J Radiol 71:297–302

The Growth of Bubbles in an Acoustic Field by Rectified Diffusion

Thomas Leong, Muthupandian Ashokkumar, and Sandra Kentish

Contents

T. Leong (✉)
Faculty of Science, Engineering and Technology, Department of Mechanical and Product Design Engineering, Hawthorn, Swinburne University of Technology, Melbourne, Australia

School of Chemistry, The University of Melbourne, Melbourne, VIC, Australia

Department of Chemical and Biomolecular Engineering, The University of Melbourne, Melbourne, VIC, Australia
e-mail: tshleong@unimelb.edu.au

M. Ashokkumar
School of Chemistry, The University of Melbourne, Melbourne, VIC, Australia

S. Kentish
Department of Chemical and Biomolecular Engineering, The University of Melbourne, Melbourne, VIC, Australia

Abstract

Rectified diffusion is a bubble growth phenomenon that occurs in acoustic fields. When subjected to a sound field (i.e., an oscillating pressure wave), a bubble of a suitable size range undergoes expansion and compression. During this bubble oscillation, the pressure within the bubble decreases as it expands and increases as it compresses. Consequently, gas and/or vapor diffuses in and out of the bubble due to the differences in pressure between the interior and exterior of the bubble. Several effects contribute to an unequal diffusion in and out of the bubble. The "area effect" refers to the influence of surface area on the mass diffusion. More gas tends to enter the bubble during bubble expansion when the surface area is larger, than out during bubble compression when surface area is smaller. The "shell effect" refers to the thickness of the liquid-air mass transfer boundary. During compression, this boundary layer increases in thickness, and vice versa during expansion. This difference in boundary layer thickness again tends to promote more gas to enter the bubble during expansion than out during compression. In simple air-water systems, these two effects are the primary contributors to rectified diffusion growth. In more complex fluid systems, the presence of surface-active molecules at the air-water interface can alter the surface tension, surface viscoelasticity, and resistance to mass transfer and increase fluid streaming effects around the oscillating bubble. All these effects can result in further enhancement to the accumulation of gas and hence faster bubble growth with time. This chapter provides an overview of the rectified diffusion process, detailing the basic physics of the event in both simple and complex fluid systems.

Introduction

Bubbles in an acoustic field can grow via two primary pathways: coalescence and/or rectified diffusion. Coalescence is the process by which two smaller bubbles combine to form a larger bubble. This is a phenomenon that also occurs in non-acoustic fields and has been studied in detail in this context [1, 2]. Studies by Lee [3] and Sunartio [4] have found that the effect of surface-active solutes on the coalescence behavior of bubbles in acoustic fields is similar to those reported in the absence of ultrasound. However, in an ultrasound field, coalescence can be complicated by competing forces. Two oscillating bubbles in the sound field can induce a force on one another known as the secondary Bjerknes force [5]. This net force can be attractive and bring the two bubbles together if the oscillations are in phase. If the oscillations are out of phase, then the net force is repulsive.

Rectified diffusion, on the other hand, is a bubble growth process that is unique to acoustic fields. This process is the growth of an individual bubble over time due to

uneven rates of mass transfer across the air/liquid interface during bubble expansion and compression as it is subject to an oscillating pressure field. This is a particularly interesting but challenging phenomenon to study and interpret, since most sonoprocessing systems contain many bubbles that will inevitably also result in coalescence. Multibubble sonoluminescence [6, 7] has been used to infer the growth of a large population of bubbles by rectified diffusion. This technique offers an indirect measurement, however, and careful interpretation must be considered to discern the influence of coalescence that will compete with rectified diffusion.

To study rectified diffusion most effectively requires the isolation of a single bubble in a sound field. In simple air-water systems, the process of rectified diffusion has been studied in great detail by using acoustic levitation techniques that enable the trapping of a single bubble within the center of an acoustic pressure antinode of a standing wave [8]. The bubble growth rates can be predicted by theoretical calculations with reasonable accuracy provided that the gas concentration, driving pressure, and acoustic frequency are known [9].

In sonoprocessing systems, fluids tend to be complex, i.e., they often contain surface-active solutes and/or other contaminants. These species can significantly influence the bubble growth behavior. Surface-active components, i.e., surfactants that self-assemble on the surface of the gas/liquid interface, will influence the mass transfer properties during bubble oscillation and modify the surface rheological properties such as surface elasticity and surface viscosity. Many investigations have studied the influence of surfactants to the rectified diffusion growth rate. Of interest is a significant increase in bubble growth rate in the presence of surfactants, when compared with a surfactant-free system. Furthermore, it has been shown that existing mathematical models [9–11] are insufficient to accurately account for the experimentally observed increase in growth rate. The reasons for this discrepancy have been alluded to by previous authors, with suggested reasons for the observed enhancement including a resistance to mass transfer provided by the surfactant layer at the interface [12], an enhancement of the acoustic microstreaming velocities of the fluid around the oscillating bubble [9, 13], and modification of the viscoelastic properties of the bubble surface [14].

This chapter provides an overview of the rectified diffusion process and some of the investigations that have been performed to understand its behavior in simple and complex fluid systems.

Theory and Background

It is prudent to establish the various processes of a bubble prior to, during, and after rectified diffusion growth to fully explain the process. In this section, the various mechanisms and aspects of bubble nucleation, bubble growth, and bubble collapse will be defined and explained. Some basic information pertaining to surfactants and their role in modifying rectified diffusion behavior will also be presented.

Bubble Formation in Acoustic Cavitation

In acoustic cavitation, sound waves impose a sinusoidal pressure upon existing cavities or bubbles in solution [15]. During the negative pressure cycle, the liquid is pulled apart at sites containing these gaseous impurities, which are known as "weak spots" in the fluid.

There are three known mechanisms for bubble formation [16]. One mechanism involves preexisting bubbles in the liquid which are stabilized against dissolution because the surface is coated with contaminants such as a skin of organic impurity. A second mechanism relies on the existence of solid particles (motes) in the liquid with gas trapped in these particles, where nucleation takes place. There can also be tiny crevices in the walls of the vessel or container where gas is trapped. The pressure inside a gas crevice is lower than the outside liquid pressure. Consequently, gas diffuses into the gas pocket, causing it to grow. A bubble is then created as the gas pocket departs from the crevice under the influence of acoustic radiation forces. The final mechanism is the generation of new bubbles by the fragmentation of a larger bubble.

The acoustic pressure at which nucleation occurs is often referred to as the Blake threshold, P_B, and is defined by Eq. 1 as [17]:

$$P_B = P_0 + \frac{8\sigma}{9} \left\{ \frac{3\sigma}{2[P_0 + (2\sigma/R_B)]R_B{}^3} \right\}^{1/2} \tag{1}$$

where P_0 is the ambient pressure, R_B is the Blake radius, and σ is the surface tension. Note that this expression does not involve the acoustic frequency and is simply an expression of the pressure required in excess of the ambient pressure to generate a bubble of a given size.

Cavitation Modes

Once nucleated, a bubble can exhibit different modes of behavior, dependent upon the oscillation frequency, the acoustic driving pressure, and the bubble radius.

For small bubbles at low driving pressures, the bubble undergoes low amplitude sinusoidal radial pulsations at the acoustic frequency [8, 18]. Under these conditions, rectified diffusion does not occur and the bubble simply dissolves away again over time (Fig. 1a). This is often referred to as a breathing mode.

As the acoustic pressure increases, a threshold is passed above which the bubble will undergo stable cavitation (Fig. 1b). In this mode, the bubble oscillates in a characteristic pattern which is far from sinusoidal, but is replicated identically for long periods of time. In this regime, rectified diffusion can occur, as can sonoluminescence (the generation of light from the bubble collapse). The transition from breathing mode to stable cavitation is referred to as the "lower stability threshold," or the rectified diffusion threshold. An equation developed by Safar [19] (Eq. 2)
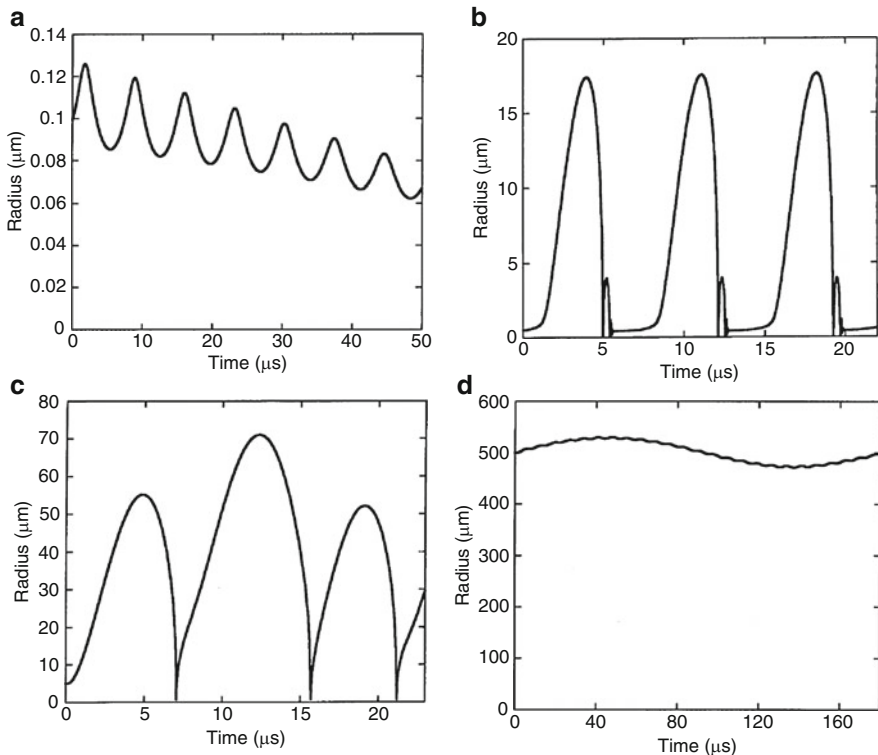
Fig. 1 Simulated radius-time curves at 140 kHz for (**a**) a dissolving bubble (initial radius 0.1 μm and acoustic pressure 500 kPa), (**b**) a bubble in stable cavitation (initial radius 0.5 μm and acoustic pressure 250 kPa), and (**c**) a bubble in transient cavitation (initial radius 5 μm and acoustic pressure 500 kPa). This bubble disintegrates into a mass of smaller bubbles just after the third collapse and (**d**) a "degas" bubble (initial radius of 500 μm and acoustic pressure of 500 kPa) (Reproduced with permission from Yasui (2002) [18]. Copyright 2002, Acoustic Society of America)

enables the prediction of this lower stability or rectified diffusion pressure threshold P_D for a bubble of radius R_D:

$$\frac{P_D}{P_0} = \frac{\left[3\eta\left(1 + \frac{2\sigma}{P_0 R_D}\right) - 2\sigma/P_0 R_D\right]\left[1 - \omega^2/\omega_r^2\right]\left[1 + \frac{2\sigma}{P_0 R_D} - C_i/C_0\right]^{1/2}}{[6(1 + 2\sigma/P_0 R_D)]^{1/2}} \quad (2)$$

Here, η is the solution viscosity, ω and ω_r the driving and resonance frequencies, respectively, and C_i and C_0 are the concentrations of dissolved gas in the liquid far from the bubble and at saturation, respectively.

At even higher acoustic pressures, the upper stability, or transient, cavitation threshold is passed and the bubble behavior becomes transient or unstable (Fig. 1c). Under these conditions, the bubble is no longer spherical and survives only a few cycles before disintegrating into a mass of smaller bubbles. Apfel develops an

expression that describes this inversely, as the threshold bubble radius, R_T, for a given acoustic pressure P_T/P_0 (Eq. 3):

$$R_T = \begin{cases} \dfrac{0.13}{\omega}\left(\dfrac{P_0}{\rho}\right)^{\frac{1}{2}}\left[\dfrac{P_T/P_0 - 1}{\sqrt{P_T/P_0}}\left[1 + \dfrac{2}{3}(P_T/P_0 - 1)^{\frac{1}{3}}\right]\right]; & \dfrac{P_T}{P_0} \leq 11 \\[4mm] \dfrac{0.13}{\omega}\left(\dfrac{P_0}{\rho}\right)^{\frac{1}{2}}\dfrac{2}{3}(P_T/P_0 - 1)^{\frac{1}{2}}; & \dfrac{P_T}{P_0} \geq 11 \end{cases}$$

(3)

Such transient cavitation collapse is a high energy event. Such events are often accompanied by local increases in temperature up to 10,000 K and pressure shockwave release of several hundred atmospheres. Under suitable conditions, the energy of the collapse can result in chemical reactions taking place including the formation of free radical species.

Yasui [18, 20] argues that the transitions to stable or transient cavitation are not directly related to the linear resonance radius, R_r, which is usually larger than that needed for stable cavitation to occur [21]. However, it is common practice to estimate the threshold for either stable or transient cavitation from this linear resonance radius, which itself is determined from Eq. 4:

$$R_r = \sqrt{\frac{3\gamma P_0}{\rho\omega^2}}$$

(4)

where γ is the specific heat ratio of the gas inside the bubble.

For the air-water system, Eq. 4 can be simply approximated by Eq. 5:

$$F \times R \approx 3$$

(5)

where F is the frequency in Hz and R is the bubble radius in m. Note that this equation gives only a very approximate estimation of the bubble sizes required for cavitation to occur and that there are many other factors at play [5, 22].

The fourth type of behavior is known as a "degas" bubble [18]. This occurs for larger bubbles, which are more affected by buoyancy forces and so rise rapidly to the surface. Such bubbles have too much inertia to undergo cavitation events at any acoustic pressure. These bubbles again exhibit a sinusoidal oscillation, but the main frequency of oscillation is the natural frequency of the bubble (Fig. 1d, where this oscillation period is 181 μs). There is also a smaller oscillation with ultrasonic frequency, which can be visualized in Fig. 1d as the oscillations of order 7 μs. These degas bubbles can grow through rectified diffusion, but do not sonoluminescence.

Both Apfel [23, 24] and Yasui [18] have used mathematical simulation to develop charts that predict the behavior of a bubble with a given radius at a defined acoustic pressure. Neppiras [25] developed similar predictions for the transient cavitation

thresholds based on Apfel's criterion for a bubble at the radius of the transient threshold and Blake's threshold pressure. This author used another expression from Safar [19] which included a multiplying factor that extended the formula so that it applied for bubbles through to resonance, not just $R_0 < R_r$.

Dynamics of a Single Bubble

Besant [27] first derived an equation for the motion of the bubble wall within an acoustic field in 1859 (Eq. 6):

$$\frac{P_L - P_0}{\rho} = R\ddot{R} + \frac{3}{2}\dot{R}^2 \tag{6}$$

where R is the radius of the bubble wall at any time, $\dot{R}$ is the wall velocity, P_0 is the pressure in the liquid at infinity, P_L is the pressure in the liquid at the bubble wall, and ρ is the liquid density.

Noltingk and Neppiras [28, 29] extended this fundamental equation to include the effects of surface tension due to the Laplace pressure of the bubble (Eq. 7). To take this into account, at $R = R_0$, the gas pressure in the bubble is $P_0 + 2\sigma/R_0$ where P_0 is the ambient pressure in the liquid and σ is the surface tension. Adiabatic heat transfer is assumed with γ being the ratio of specific heats of the gas.

$$R\ddot{R} + \frac{3}{2}\dot{R}^2 = \frac{1}{\rho}\left[\left(P_0 + \frac{2\sigma}{R_0}\right)\left(\frac{R_0}{R}\right)^{3\gamma} - \frac{2\sigma}{R} - P_\infty\right] \tag{7}$$

A viscosity term for the liquid was later added by Poritsky [30] and it was shown that this term arises only in the boundary conditions rather than through the Navier-Stokes equation. The equation then becomes:

$$R\ddot{R} + \frac{3}{2}\dot{R}^2 = \frac{1}{\rho}\left[\left(P_0 + \frac{2\sigma}{R}\right)\left(\frac{R_0}{R}\right)^{3\gamma} - \frac{2\sigma}{R} - \frac{4\eta\dot{R}}{R} + P_\infty\right] \tag{8}$$

where η is the viscosity of the liquid.

Equations 6, 7, and 8 are often referred to as the Rayleigh-Plesset equation and are commonly used as the basis from which the fundamental motion of a bubble in an acoustic field can be calculated. This model has been adapted into many different forms over the years, accounting for more varied effects such as heat transfer and bubble condensation/evaporation. A more in-depth derivation of the basic equations can be found in the book by Young [23].

If a bubble is subjected to a sound field such that the pressure P varies as:

$$P = P_0 - P_A \sin(\omega t) \tag{9}$$

where P_0 is the steady-state pressure (usually atmospheric pressure), ω is the angular frequency, and P_A is the amplitude of the driving pressure. The addition of this pressure term into Eq. 8 leads to:

$$R\ddot{R} + \frac{3}{2}\dot{R}^2 = \frac{1}{\rho}\left[\left(P_0 + \frac{2\sigma}{R_0}\right)\left(\frac{R_0}{R}\right)^{3\gamma} - \frac{2\sigma}{R} - (P_0 - P_A \sin(\omega t))\right] \qquad (10)$$

which is a useful fundamental equation that can be used to determine the radial dynamics of a gas bubble under the influence of an oscillating sound wave in simple air-water systems. Equation 10 and/or variations of it are often used as the starting point for numerical analysis of bubble dynamics in an acoustic field.

Rectified Diffusion Growth of a Single Bubble

The process of rectified diffusion is essentially a mass transfer phenomenon with a moving boundary layer. Growth occurs due to an unequal transfer of mass across the air/liquid interface during the rarefaction and compression phases of the sound wave cycle. Diffusion of gas occurs across the bubble interface such that more gas diffuses into the bubble during the expansion than out during the contraction [9]. The result is a net accumulation of gas within the bubble leading to growth over time.

During compression, the internal bubble pressure increases, causing gas to diffuse out of the bubble. In the expansion phase, the internal bubble pressure decreases and gas diffuses into the bubble (Fig. 2). Above the threshold pressure for rectified diffusion, bubbles grow until they are no longer shape stable at the driving pressure. Below this pressure, the bubble dissolves due to the Laplace pressure exerted on the bubble wall by surface tension. An elegant review of the history of the developments of the theory behind rectified diffusion is described in the work by Crum [9].

Eller and Flynn [10] accounted for this uneven mass transfer by describing two main effects, known as the "area" and "shell" effects. The "area" effect refers to the fact that diffusion of gas into the bubble occurs when the bubble is larger during the expansion phase, while diffusion out of a bubble occurs when the bubble is smaller during the compression phase. As the rate of diffusion across an interface is proportional to the surface area available for mass transfer, more gas diffuses into the bubble than out (Fig. 2).

The "shell" effect refers to the influence of the mass transfer boundary layer surrounding the bubble through which mass transfer occurs. As the bubble shrinks in the compression phase, this shell thickness increases. In contrast, as the bubble expands, the shell thins as depicted in Fig. 3. The concentration gradient of gas is lower when the bubble is in compression, but higher during expansion, thereby resulting in net accumulation of mass into the bubble.

The diffusion of gas in the liquid obeys Fick's law of mass transfer, but the solution to the rectified diffusion problem is complicated by the moving boundary layer as the bubble oscillates. This problem has been solved by various methods.

$$P_i = P_0 + 2\sigma/R \qquad\qquad P_i = P_0 + 2\sigma/R$$

$$P = P_0 - P_a \sin(\omega t) \qquad\qquad P = P_0 - P_a \sin(\omega t)$$

$$P_i < P_0 \qquad\qquad\qquad P_i > P_0$$

Gas diffuses into bubble   **Gas diffuses out of bubble**

P_0 P_i P_i P_0

P_a P_a

Rarefaction   **Compression**
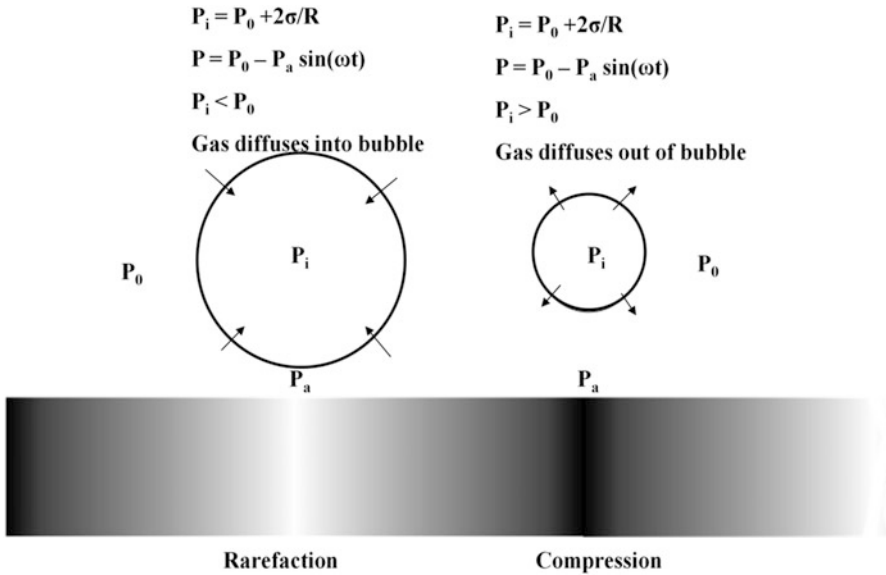
Fig. 2 During an acoustic cycle, gas diffuses into the bubble during the rarefaction (pressure minimum) and diffuses out of the bubble during the compression (pressure maximum). As the mass transfer is dependent on the surface area of the bubble, more gas diffuses in during bubble expansion than out during bubble compression. This will result in net growth of the bubble over time, provided that the acoustic driving pressure is above a threshold such that the accumulation of gas overcomes the depletion of gas from the bubble by Laplace pressure

Liquid shells

Gas

Bubble wall   **Bubble expanded, liquid shells compressed**   **Bubble compressed, liquid shells expanded**

Fig. 3 A depiction of the change in liquid shell thickness of a bubble during the expansion and compression cycles of an acoustic wave. The concentration gradient is enhanced during bubble expansion and reduced during bubble compression

Two different approaches have been described by both Eller and Flynn [10] and Hsieh and Plesset [31, 32]. Further details of their approaches can be obtained in their publications.

Eller and Flynn showed that the change in the number of moles n_g of a gas in a bubble is given by:

$$\frac{dn_g}{dt} = 4\pi DR_0 C_0 \left[\left\langle \frac{R}{R_0} \right\rangle + R_0 \left(\frac{\left\langle (R/R_0)^4 \right\rangle}{\pi D t} \right)^{1/2} \right] H \tag{11}$$

where H is defined by:

$$H = \frac{C_i}{C_0} - \left\langle \left(\frac{R}{R_0} \right)^4 \left(\frac{P_g}{P_0} \right) \right\rangle \bigg/ \left\langle \left(\frac{R}{R_0} \right)^4 \right\rangle \tag{12}$$

The pointed brackets in this case $\langle \rangle$ imply an average across the total growth time, t. C_i is the concentration of dissolved gas in the liquid far from the bubble, C_0 is the saturation concentration of gas in the liquid, and D is the diffusivity of the gas.

Crum [9] later used Eller's derivation and extended it to take into account the thermodynamics of the process. The end result for the change in bubble radius for a spherical bubble as a function of time t is:

$$\frac{dR_0}{dt} = \frac{Dd}{R_0} \left[\left\langle \frac{R}{R_0} \right\rangle \left(1 + \frac{4\sigma}{3P_0 R_0} \right)^{-1} \left(\frac{C_i}{C_0} - \left\langle (R/R_0)^4 (P_g/P_0) \right\rangle \bigg/ \left\langle (R/R_0)^4 \right\rangle \right) \right] \tag{13}$$

where $P_g = R_g T C_0 / P_0$. Here R_g is the universal gas constant and T is the temperature.

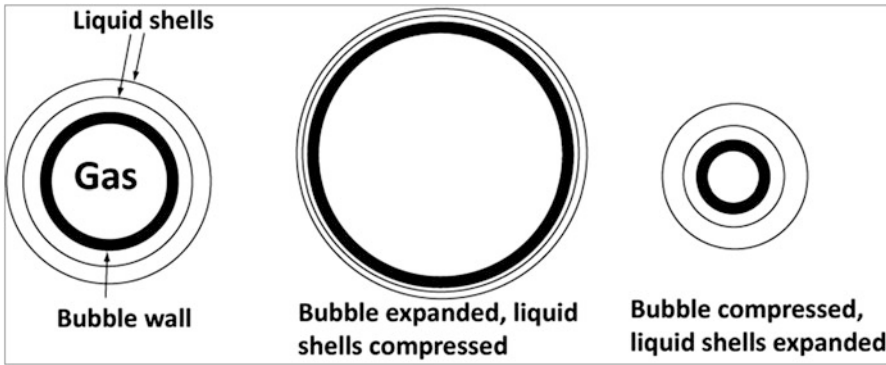An alternative mathematical analysis was presented by Fyrillas and Szeri [11, 12, 33] in a series of papers. Their derivation utilized Lagrangian rather than spherical coordinates in order to account for the moving boundary condition. The Henry's Law boundary condition describing the gas concentration at the surface of the bubble wall was also split into a smooth and oscillatory solution to the problem. They found that the oscillatory solution (i.e., accounting for individual bubble oscillations) contributed little relative to the overall mass transfer that occurs over the longer time frame.

To determine the rate of growth of a bubble by rectified diffusion directly, it is necessary to image and observe the growth of the bubble over time. Oscillations typically occur at ultrasonic frequencies, and the visualization of individual bubble oscillations would require high speed photography to capture effectively. This however is often not practical nor required, since the rectified diffusion process is often a slow effect that occurs over several minutes, i.e., many acoustic cycles.

A stroboscopic technique that delivers a simultaneous LED signal in synch to a particular point in the acoustic cycle of the bubble is one simple method that can be used to determine the growth rate of a bubble over time. In this technique, a consistent moment in the oscillation cycle can be used as the reference point over which the growth rate of the bubble can be determined.
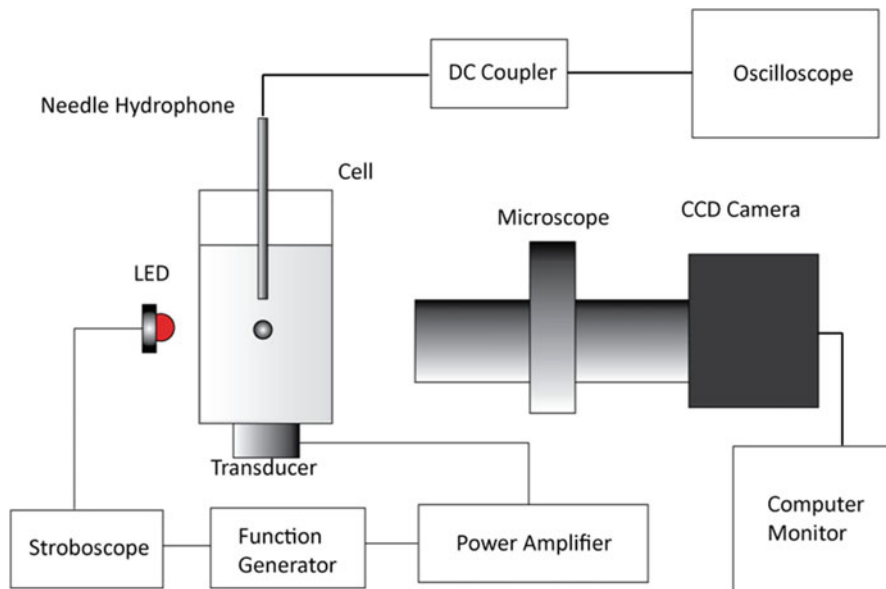
Fig. 4 Experimental setup for single-bubble rectified diffusion reprinted with permission from Leong et al. [35]. Copyright (2010) American Chemical Society

A typical setup that achieves this objective has been reported by Lee et al. [34]. A similar setup used by Leong et al. [35] is shown in Fig. 4.

A single-bubble imaging system typically consists of a visualization cell inside which an acoustic standing wave is established. A bubble injected or nucleated within the container will experience an acoustic radiation force that draws the bubble to the pressure antinode of the standing wave, provided that it is smaller than the resonance size. Visualization of the bubble over time can be recorded using appropriate microscopy and image-capturing equipment.

The rate at which a bubble grows is dependent on various parameters. These have been determined extensively by Crum [9] for simple air-water systems. In addition to the acoustic driving pressure as previously stated, the gas saturation and bubble radius are also important to the bubble growth. The degree of gas saturation is important as it defines the mass transfer concentration gradient around the bubble. A higher concentration of dissolved gas in the surrounding fluid of the bubble provides enhanced mass transfer and hence faster bubble growth. A degassed fluid may result in bubble dissolution when driven at equivalent pressure to a gas-saturated fluid.

Note that the parameters for growth are also dependent on the initial size of the bubble within the acoustic field, i.e., there exists a "threshold radius" for rectified diffusion growth (see Eq. 2). A smaller initial bubble size will have a higher threshold pressure requirement for rectified diffusion growth to occur. Bubbles driven at a pressure below the threshold requirement will dissolve into the bulk solution. At the threshold pressure, the bubble will neither grow nor shrink.

The experimental results reported by Crum achieved close agreement to the theory developed (Eq. 13) for simple air-water systems. However, this theory did not adequately predict the rectified diffusion growth rates when surface-active species such as long-chain surfactants and alcohols were present in the solution. When Crum performed single-bubble growth experiments in the presence of the commercial surfactant "Photoflo," the experimentally measured growth rates were significantly faster than the predicted growth rates. The surface tension term within Eq. 13 did not sufficiently account for the influence of the surface-active species. Lee et al. [34] showed similar increases in rectified diffusion growth rates when working with surfactants sodium dodecyl sulfate (SDS) and sodium dodecyl benzene sulfonate (SDBS). The reason for the enhancement in growth rate due to the presence of surfactant is not well understood but has been attributed to several possible causes. The following sections will detail some of the interesting effects resultant from solutions containing surfactants to bubble growth by rectified diffusion and elucidate some of the possible reasons for modifications to the observed rates of growth.

Rectified Diffusion Growth in Surfactant Solutions

This section details studies that have been made to understand the influence of surface-active solutes to the rectified diffusion growth in single-bubble and multibubble systems.

Surfactants

Surfactants are amphiphilic molecules which contain a hydrophilic head group, which can be charged (ionic) or polar (nonionic), and a hydrophobic tail consisting of a long hydrocarbon chain (see Fig. 5). Due to the difference in properties between these two portions of its structure, surfactants in aqueous solutions tend to aggregate by self-assembly as a monolayer at the air/liquid interface. The hydrophobic tail groups are arranged such that they point toward a gas interface and the hydrophilic head groups point toward the liquid interface, to minimize the free energy of the system [36].

This surfactant layer on the bubble surface results in a decrease of the interfacial tension (σ). The surface excess concentration (Γ_{surf}) for ionic surfactants in the absence of additional electrolytes (such as salt) can be calculated from this surface tension based on the Gibbs isotherm [36]:

$$\Gamma_{surf} = -\frac{1}{2R_G T}\left(\frac{\partial \sigma}{\partial \ln C_B}\right) \tag{14}$$

The expression differs by a factor of 2 for nonionic surfactants and ionic surfactants in the presence of added electrolyte:
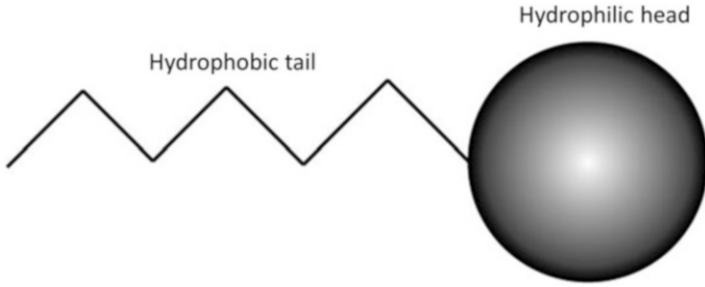
Fig. 5 Depiction of a surfactant molecule, which consists of a long-chain hydrocarbon tail that is hydrophobic and a polar or charged head group that is hydrophilic

$$\Gamma_{\text{surf}} = -\frac{1}{R_G T}\left(\frac{\partial\sigma}{\partial\ln C_B}\right) \tag{15}$$

Here R_G is the universal gas constant, T is the temperature, σ is the surface tension, and C_B is the bulk concentration of surfactant.

The surface excess concentration increases with increasing concentration of surfactant in the bulk, until the critical micelle concentration (CMC) of the surfactant is reached. After the CMC is exceeded, the surface excess remains essentially constant with further increase of the bulk concentration. This trend is reflected in the surface tension, which decreases until the CMC, and then also remains essentially constant. At the CMC, the surfactant molecules reach a saturation point on the surface of the interface and instead begin to form self-assembled structures called micelles in the bulk solution.

Effect of Soluble Surfactants on Rectified Diffusion

The rectified diffusion growth rates typical for water and for a 4.0 mM SDS measured by Leong et al. [35] using a stroboscopic technique are presented in Fig. 6a and b. The growth rate obtained here, for a bubble in water measured at a driving pressure of 0.27 ± 0.02 bar, is comparable to results obtained by Crum [9].

One experimental observation made by Crum [9] and others [35] is an increased ability for smaller bubbles to resist dissolution upon the addition of surfactant. That is, bubbles that dissolve in water will still grow in a surfactant solution, under the applied driving pressure. For pure water driven at 0.27 bar, the threshold radius for growth is approximately 30 ± 1 μm as predicted using Crum's model. However, as can be seen in Fig. 7, bubbles below 30 μm can grow via rectified diffusion in the presence of SDS in solution. This result was also observed by Suzuki et al. [37] in an investigation on the effect of SDS on the dancing behavior of bubbles. Suzuki et al. also found that bubbles in dilute SDS solutions were stabilized up to much higher driving pressures.
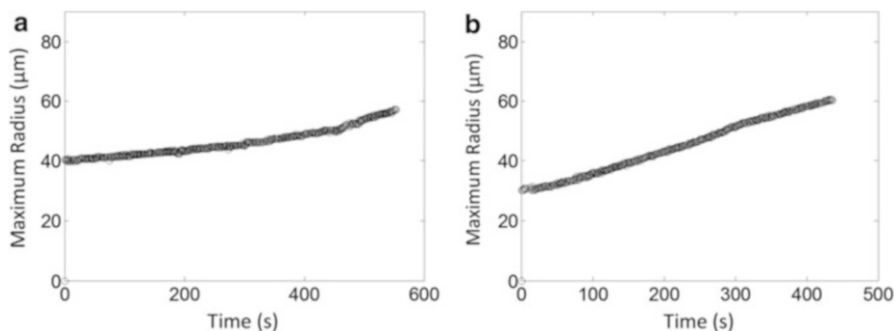
Fig. 6 Typical raw data curve determined for growth of a bubble over time for (**a**) pure water (**b**) 4.0 mM SDS bulk concentration solution. In both cases, bubbles are driven at an acoustic driving pressure of 0.27 bar. Each circular marker represents the radius size of the bubble strobed at the point of minimal pressure in the acoustic cycle (maximum radius) (Adapted with permission from Leong et al. [35]. Copyright (2010) American Chemical Society)

Fig. 7 Radius versus time growth curve for a bubble in 4.0 mM SDS surfactant solution. The growth of a bubble below the rectified diffusion threshold in water (30 μm) can be observed. (Adapted with permission from Leong et al. [35]. Copyright (2010) American Chemical Society)
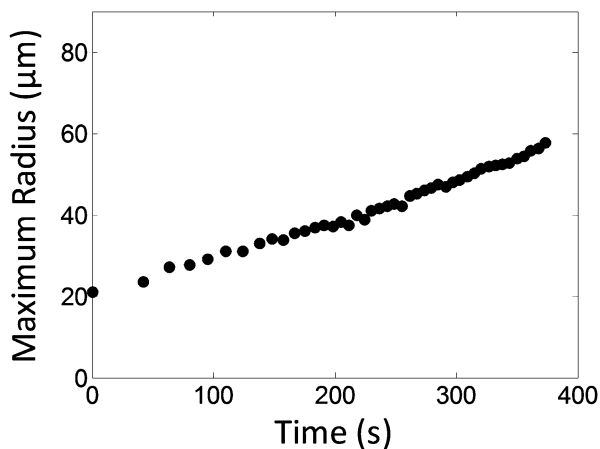
Influence of Electrostatic Interactions

The effect of adding 0.1 M NaCl salt electrolyte to the radius-time growth of bubbles is shown in Fig. 8a, b, and c. The addition of an electrolyte (salt) itself to pure water at concentrations up to 0.1 M has no ascertainable effect in influencing the growth rate by rectified diffusion, as can be seen in Fig. 8a. However, the addition of salt to solutions of SDS, an ionic surfactant, increases the growth rate when compared at the same bulk concentration. This enhancement effect is apparent in Fig. 8b and c.

The addition of electrolyte provides counterions which shield the negatively charged head groups present on SDS [3, 6, 38–40]. The dilution of this strong negative charge means that higher surface concentrations of surfactant can pack onto the interface, leading to a greater reduction in surface tension, an increase in surface viscoelasticity, and a lowering of the CMC. The net effect is an increase in the rate of rectified diffusion.
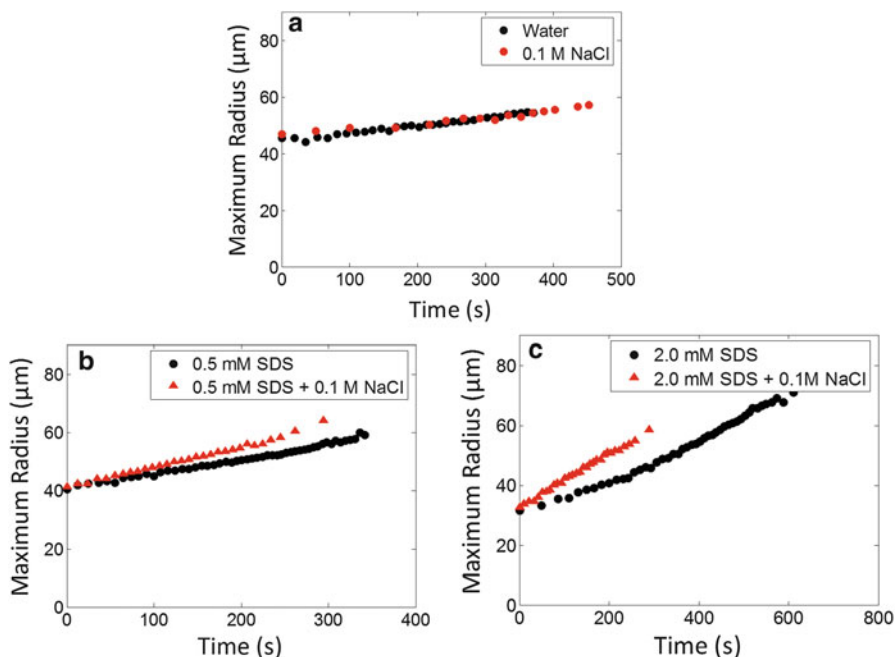
Fig. 8 (**a**) Plot of radius as a function of time for pure water and 0.1 M NaCl solution shows that there is no effect of salt in water. (**b**) For 0.5 mM bulk concentration of SDS, the addition of salt results in enhanced rectified diffusion growth. (**c**) At 2.0 mM SDS, the enhancement of growth with the addition of NaCl appears to be higher

The growth rate of a bubble within SDS solutions up to and beyond the CMC in the presence and absence of 0.1 M NaCl electrolyte are shown in Fig. 9. The growth rates of the bubbles presented here are for a 50 μm bubble strobed during the point of minimum pressure of the oscillation phase (i.e., maximum bubble expansion). It can be seen from these results that, beyond the CMC, there is minimal further enhancement of growth rate, as surfactant molecules have reached a saturation loading on the surface. In the same Figure, the enhancement in rectified diffusion growth is shown for SDS solutions with the addition of 0.1 M NaCl electrolyte. Similar to the case without electrolyte, the growth rates here also reach a plateau. However, the plateau occurs earlier here, reflecting the lower CMC due to the tighter packing of surfactant on the interface.

If the results for SDS with and without salt are compared as a function of the equilibrium surface tension (Fig. 10), a smaller difference between the two results can be observed. This confirms that rectified diffusion is strongly dependent on the surfactant loading on the bubble surface, which is directly related to the surface tension. However, while the rates are similar, in this case, the growth rate for SDS solutions with the addition of 0.1 M NaCl is actually lower than that of SDS solutions without the addition of the electrolyte. This suggests that there is a small contribution due to electrostatics from the SDS charge on the surface of the bubble,
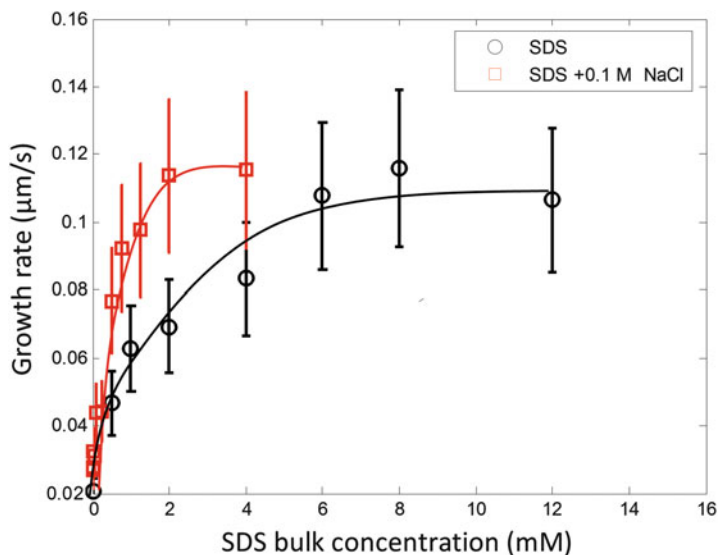
Fig. 9 Bubble growth rate as a function of SDS bulk concentration for a bubble at a maximum radius of 50 μm. The growth rate is determined by finding the instantaneous derivative of a bubble at this radius from the radius-time curves (Adapted with permission from Leong et al. [35]. Copyright (2010) American Chemical Society)
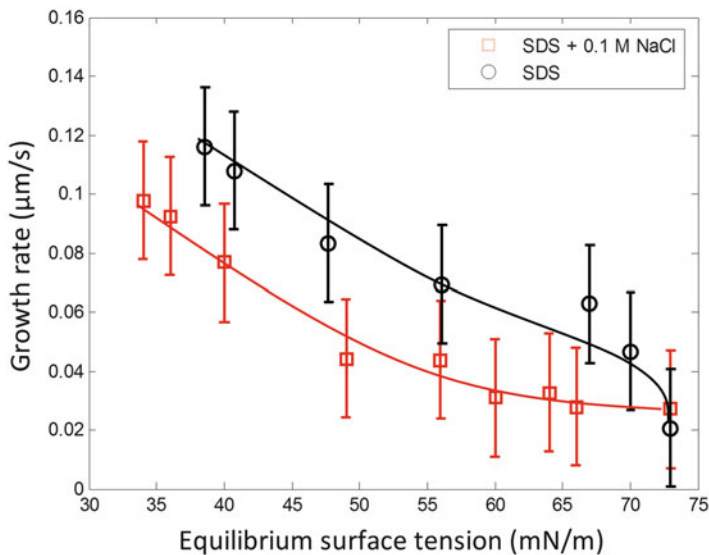
Fig. 10 Bubble growth rate as a function of equilibrium surface tension. There appears to be only a small difference between enhancement in growth rate for SDS with and without the addition of salt electrolyte when compared for similar surface loadings (Adapted with permission from Leong et al. [35])

Fig. 11 Comparison between growth rates for a 50 μm bubble in surfactant solutions of DTAC with and without the addition of 0.1 M NaCl electrolyte (Adapted with permission from Leong et al. [41]. Copyright (2011) American Chemical Society)
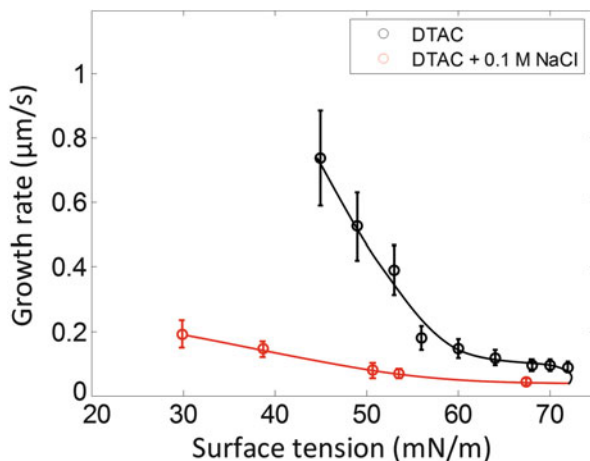
when comparing between two surfaces with approximately the same number of molecules. The system where charge is suppressed has a slightly smaller enhancement in growth rate. It is hypothesized that the charge on the surface of the bubble influences other phenomena such as the acoustic microstreaming and bubble stability.

To confirm the effect of electrostatics, the rectified diffusion growth rates of another charged surfactant, dodecyl trimethyl ammonium chloride (DTAC) with and without the addition of 0.1 M NaCl electrolyte, have been measured and are shown in Fig. 11.

Similar to the case of SDS, the addition of excess salt to the system in DTAC solution lowers the growth rate for the same equilibrium surface tension. In contrast to SDS though, the decrease in growth rate is much stronger with the suppression of the electrostatics. There is also a sudden increase in bubble growth rate for solutions below a surface tension of 55 mN/m, where DTAC without additional electrolyte resulted in the formation of strong surface oscillations. Such surface oscillations were not observed in the case where 0.1 M NaCl was added. Leong et al. [35] speculated that such a large difference exists in the case of DTAC due to the influence of the head group size or shape, which is discussed further below.

Role of Resistance to Mass Transfer

One of the effects alluded to by Crum [9] was that the presence of a surfactant layer at the bubble interface could provide a significant amount of resistance to mass transfer of gas such that it would enhance the rectification of gas during the bubble expansion and compression cycle. It has been reported by Mansfield [42] that during expansion of a surfactant film, more evaporation is attainable across the interface than when the monolayer is compressed. The density of surfactant packing becomes higher during bubble compression caused by a decrease in the surface area.
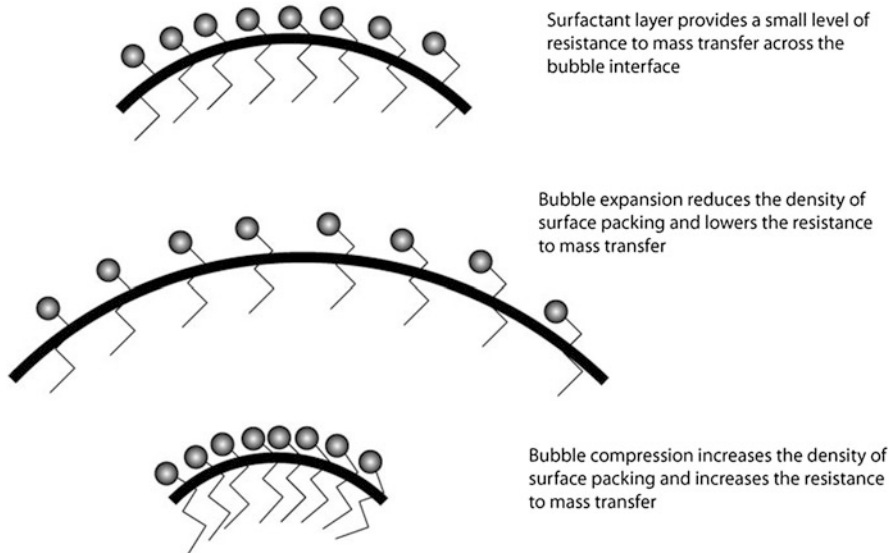
Fig. 12 Depiction of the change in surfactant packing density during bubble oscillation. During expansion, packing density decreases, lowering the resistance to mass transfer across the interface. During compression, packing density increases, increasing the resistance to mass transfer across the interface. As mass transfer into the bubble occurs during expansion, and mass transfer out of the bubble occurs during compression, a difference in mass flux is created that results in net accumulation of gas in the bubble

Similarly, during bubble expansion, the surface area of the bubble increases and the surface concentration decreases. This imbalance during expansion and compression enables rectification of gas to occur (Fig. 12).

Although the majority of literature suggests that high resistances to mass transfer exist only across condensed monolayers, Caskey and Barlage [43] have found that small but measurable resistances to mass transfer of carbon dioxide across a boundary layer could be determined for the surfactants SDS and DTAC. Even though the magnitude of the resistance determined for surfactants such as SDS and DTAC is small, for oscillations of the order > 20 kHz as experienced in an ultrasonic field, only small increases in the rectification is actually required each cycle for the growth rate to be significantly enhanced. Jayalakshmi [44] has suggested that, at these sufficiently high deformation rates, a monolayer of soluble surfactants can behave like an insoluble monolayer as the oscillations occur much faster than any observable relaxation at the surface by diffusion.

Fyrillas and Szeri [12] extended an analysis of the rectified diffusion process to include the effects of mass transfer resistance. In the case of SDS and DTAC, a significant increase in the rectified diffusion growth rates was calculated when mass transfer resistance was taken into account.

Leong et al. [41] compared the rectified diffusion growth rates across three surfactant solutions (SDS, DTAC, and DDAPS). Electrostatic effects for the ionic
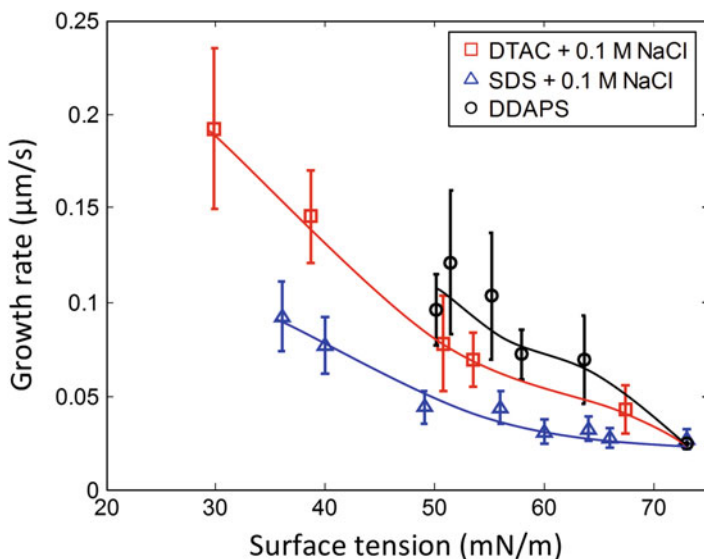
Fig. 13 A comparison between growth rates of surfactants. For DTAC and SDS, the head group charge is suppressed by the addition of 0.1 M NaCl, while DDAPS has a zwitterionic head group (no net charge). Without electrostatic charge, it appears that surfactants with "sterically bulkier" head groups provide greater enhancement in rectified diffusion growth, in the order SDS < DTAC < DDAPS (Adapted with permission from Leong et al. [41]. Copyright (2011) American Chemical Society)

surfactants (SDS and DTAC) were suppressed by the addition of 0.1 M NaCl. As shown in Fig. 13, even though these surfactants had identical chain length (C12), the growth rate varied, with SDS < DTAC < DDAPS.

As electrostatic effects are eliminated in all these cases, the trend in Fig. 13 must be explained by the head group size or "bulkiness," which would provide a resistance to mass transfer across the interface. DTAC is more bulky than SDS due to the presence of its trimethyl groups attached to a quaternary ammonium ion. Similarly, DDAPS is more bulky than DTAC due to the presence of a dimethyl group along with a propane sulfonate attached to its quaternary ammonium ion. Consistent with these results, Caskey and Barlage [43] also showed that DTAC provided a greater resistance to mass transfer compared to SDS.

In condensed monolayers, Healy and La Mer [45] have shown that the chain length of the surfactant also plays a dramatic role in influencing the ability of a surfactant monolayer to retard water evaporation. Caskey [46] has reported a trend of increasing chain length resulting in higher mass transfer resistance for soluble monolayers. Consistent with this trend, Leong et al. also show that a surfactant of long-chain length (SDS, C12) has a higher rectified diffusion growth rate than that of shorter chain surfactants with comparable head groups (pentane (C5) and octane (C8) sulfonate) (see Fig. 14).
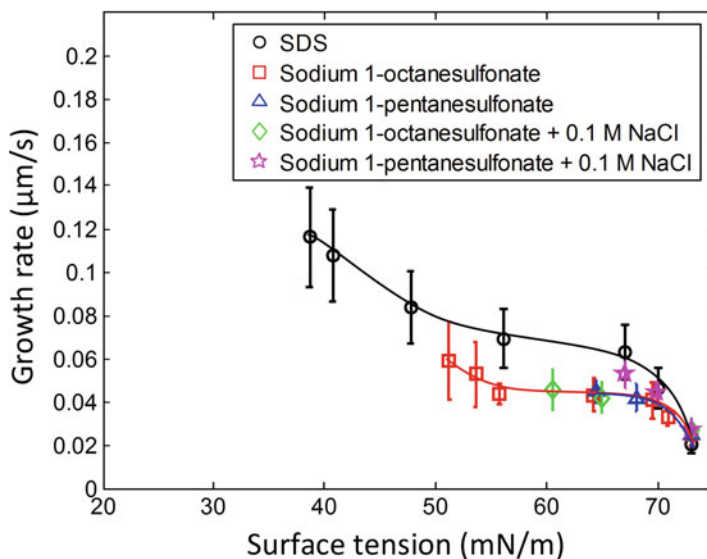
Fig. 14 Comparison between growth rate of SDS with shorter chain surfactants of sodium 1-octane sulfonate (C8) and sodium 1-pentane sulfonate (C5). Less enhancement in growth with the shorter chain surfactants is observed. The effect of the electrostatics appears to be negligible in the case of the C8 and C5 surfactant as the growth rate with the addition of NaCl appears to be unchanged (Adapted with permission from Leong et al. [41]. Copyright (2011) American Chemical Society)

Role of Viscoelasticity

Surface elasticity reflects the ability of a surface to restore the uniformity of the surface tension after a change [47]. During bubble expansion, this elasticity works to stabilize the bubble and thus slows the rate of the surface tension returning to a lower value. In contrast, the elasticity decreases the stability of the bubble during compression as it prevents the bubble from returning to a higher surface tension. The higher the surface elasticity, the more the surfactant layer behaves like an insoluble interface. Surface dilatational viscosity reflects the ability of surfactant molecules at the interface to "relax" from the interface during bubble oscillation. As such, this property is strongly dependent on the frequency at which the bubble oscillates.

Theoretical and experimental studies suggests that compression and expansion of a surface can result in either purely elastic or viscoelastic behavior when surfactants are present [48]. For example, Kloek [14] has shown that the presence of a surfactant monolayer significantly retards the rate at which small bubbles dissolve in solution. Kloek accounted for this by introducing a modified surface tension which depended on the viscous and elastic moduli of the surfactant. A similar retardation in dissolution is observed within the acoustic field, as shown in Fig. 7, where the threshold radius for bubble growth is significantly lowered in the presence of surfactant.

The mathematics of surface viscoelasticity and its impact upon bubble behavior is complex and will not be presented here. The reader is directed to the following references by Stride [49] and Church [50] for more discussion on this topic.

Role of Cavitation Microstreaming

Acoustic microstreaming, or cavitation microstreaming, refers to the small-scale streaming flow of fluid around an oscillating object such as a gas bubble. The fluid flow is generated from the vorticity caused by the oscillation of the boundary layer surrounding the bubble. This form of streaming should not be confused with "acoustic streaming," which is related to the attenuation of acoustic energy as a sound wave passes through the medium [51]. Microstreaming serves to enhance mixing effects around a bubble. In the context of rectified diffusion, microstreaming can significantly increase the rate of bubble growth since it drives fresh solution with higher gas concentration to the mass transfer boundary. Elder [52] observed that the addition of surfactants resulted in the formation of a thin film with a no-slip boundary condition. This boundary layer increased the amount of microstreaming around the bubble until it was broken by bubble pulsations. It has been shown by Gould [13] that enhanced microstreaming can lead to greater rectified diffusion growth rates. Gould however only saw dramatic increases in the rectified diffusion when surface mode oscillations were visible. Church [53] has shown numerically that taking microstreaming into account can dramatically increase the predicted rectified diffusion growth rate of a bubble.

Crum [9] suggested that the likely reason behind the enhanced rectified diffusion observed in surfactant solutions was due to surfactant-induced microstreaming. He speculated that microstreaming could be induced even without surface wave generation as seen by Gould. He suggested that the increased streaming due to the presence of surfactant at the air-water interface of the oscillating bubble would increase the growth rates at all acoustic amplitudes and bubble radii and would have no distinct inception threshold.

The determination of acoustic microstreaming patterns and velocities around the bubble can be achieved by the use of a technique called microparticle image velocimetry (micro-PIV) [41, 51, 54]. In this technique, fluorescent microspheres are moved by the acoustic streaming flows and tracked. A study performed by Leong et al. [41] using this technique related the flow velocities in various surfactant solutions to the rectified diffusion growth. The PIV images obtained for water and various concentrations of the surfactants SDS, DTAC, and DDAPS were analyzed to determine the mean and maximum streaming velocities in the flow field. A typical snapshot of a bubble along with its calculated vector field can be seen in Fig. 15.

Leong et al. [41] showed that the presence of surfactant in solution enhanced the microstreaming velocities around the bubble, even in the absence of noticeable bubble shape mode oscillations. The presence of DDAPS generated a faster streaming velocity than SDS when compared for a similar equilibrium surface tension (Fig. 16). The addition of sodium chloride electrolyte to SDS solution further
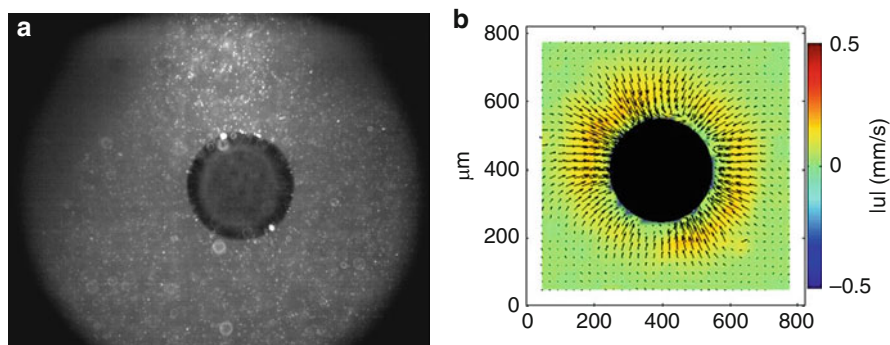
Fig. 15 Typical image snapshot of a bubble in the micro-PIV system (**a**) along with its calculated 2-dimensional vector field (**b**) (Taken with permission from Leong et al. [41] Copyright (2011) American Chemical Society)
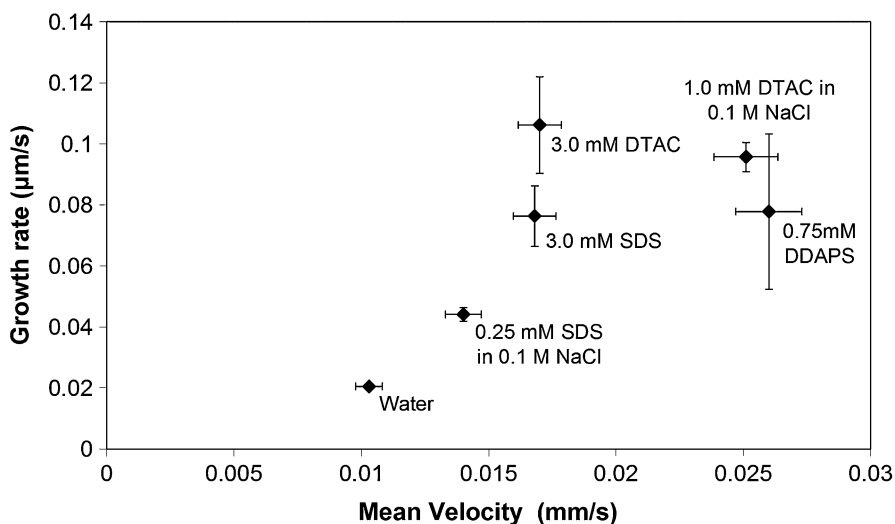
Fig. 16 Growth rate of a 50 μm bubble in various solutions as a function of the mean microstreaming velocity found using micro-PIV (Taken with permission from Leong et al. [41]. Copyright (2011) American Chemical Society)

reduced the mean streaming velocities, possibly because this reduced the repulsion between the head groups and hence created less disruption to the fluid flows. The velocities in the presence of 0.1 M NaCl correlated well with the bubble growth rates shown earlier in Fig. 13, as shown in Fig. 16.

There was a clear difference between microstreaming that occurred in the absence and presence of visible surface distortion. Tho et al. [51] showed previously using PIV that the streaming velocities achieved when surface distortion can be detected are two to three times higher than those of regular "breathing mode" volume
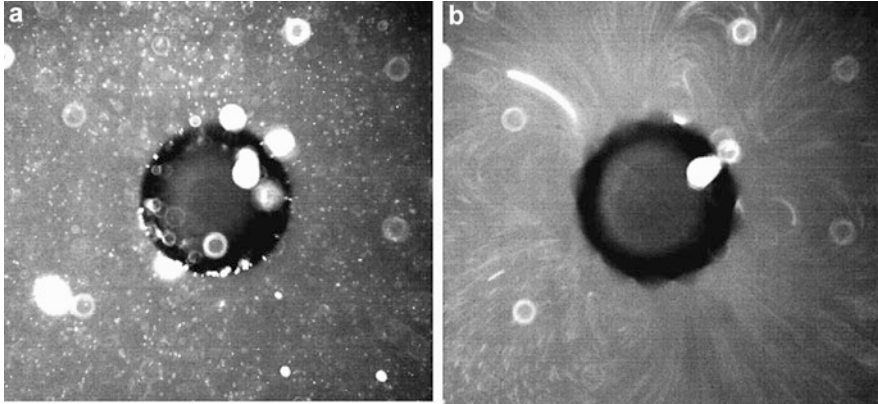
Fig. 17 (**a**) Streaming without surface oscillations; D = 225 μm, P = 5.2 kPa, Vmax = 0.24 ± 0.02 mm/s, Vmean = 0.047 ± 0.005 mm/s. (**b**) Streaming with surface oscillations; D = 225 μm, P = 7.6 kPa, Vmax = 11.1 ± 1 mm/s, Vmean = 5 ± 0.5 mm/s (Taken with permission from Leong et al. [41]. Copyright (2011) American Chemical Society)

oscillations. This is because the higher modes of oscillation lead to more random flow fields as can be seen in Fig. 17. Shape mode oscillations distort the bubble from appearing spherical in shape to those of various polygonal shapes [55]. The point at which these surface distortions begins to occur decreased in the presence of surfactant (Fig. 17), and once present, these surface distortions led to significantly enhanced growth rates.

Influence of Shape Mode Oscillations

Under the influence of a strong acoustic forces, bubbles commonly assume shapes that are distorted significantly from being spherical, due to an overshoot of the bubble wall resulting from inertia of the liquid [5, 56]. This departure from sphericity means that the radius of curvature is not the same at all points on the bubble wall. These changes in shapes can be described in terms of a perturbation of appropriately summed spherical harmonics which are superimposed on the spherical form. Oscillation continues to occur even when the bubble is distorted, tending to the spherical, as it seeks to minimize the energy of the system. A bubble experiencing such shape mode oscillations tends to become "unstable" in that it may experience dancing motion and/or pinch off daughter bubbles.

Shape mode oscillations have been studied theoretically. Rayleigh [57] first studied shape oscillations of small drops to predict the frequency of the shape oscillations and this work was later completed by Lamb [58]. More recently, theoretical derivations to describe shape mode instabilities have been developed by Plesset [59] and Hilgenfeldt [60]. The following equation taken from Plesset [59] gives the sum of the principle radii of curvature of a distorted bubble, R_1 and R_2:

$$\frac{1}{R_1} + \frac{1}{R_2} = \frac{2}{R} + \frac{(n-1)(n+2)}{R^2} a_n Y_n \qquad (16)$$

where n is the mode of the shape mode oscillation, a_n is the radial distortion amplitude, and Y_n is a zonal spherical harmonic. Plesset [59] and Hilgenfeldt [60] take the terms proportional to Y_n to give a second-order differential equation from which stability conditions may be deduced.

$$\ddot{a} + \left\{ \left[3\dot{R}/R \right] + \frac{2\nu}{R^2} \left[(n+2)(2n+1) - 2n(n+2)\frac{\delta}{R} \right] \right\} \dot{a} - Aa = 0 \qquad (17)$$

where A is:

$$A = \frac{[n(n-1)\rho_2 - (n+1)(n+2)\rho]R - n(n-1)(n+1)(n+2)\dfrac{\delta}{R^2}}{R[n\rho_2 + (n+1)\rho_1]}$$
$$+ 2n(n+2)(n-1)\frac{\delta}{R} \qquad (18)$$

Here, ρ_1 and ρ_2 are the gas and liquid densities, respectively, σ is the surface tension, ν is the kinematic viscosity of the liquid, and δ is the boundary layer thickness around the bubble approximated by:

$$\delta = \min \left(\sqrt{\frac{\nu}{\omega}}, \frac{R}{2n} \right) \qquad (19)$$

Based on similar equations, the stability threshold boundaries for shape mode oscillations were calculated by Hao and Prosperetti [61] for an air bubble in water driven at 20.6 kHz. Notably, they found that the oscillation stability threshold boundary displays complex features within the radius/pressure parameter space and arises due to the highly nonlinear behavior of the bubble wall motion predicted by the Rayleigh-Plesset equation used in the calculations.

It has been recently shown by Leong et al. [62] that the presence of surfactants can increase the viscoelastic effects and hence stabilize the bubbles, by both decreasing the oscillation amplitude and wall velocity of the bubble. The effect of this would be to shift the stability threshold upwards, such that the parameter space for a stable bubble is enlarged. This may explain why bubbles in SDS solution could grow by rectified diffusion even below the threshold radius for pure water (Fig. 7).

As a bubble grows by rectified diffusion, however, it will eventually enter the parameter space where the bubble becomes unstable and display surface oscillations. A surfactant-coated bubble may "shed" or release surfactant molecules rapidly from the surface when bubble shape mode oscillations occur. This shedding of surfactant may drive additional fluid flow in the vicinity of the bubble, stronger than in the absence of surfactant release. It may be a possible reason as to why stronger cavitation microstreaming flows have been observed around the bubble during

shape mode oscillations in the presence of surfactant, compared with cases in the absence of surfactants.

Multibubble Behavior in an Acoustic Field

In a multibubble system, the behavior of bubbles is more complex due to the multiple pathways in which a bubble can enter or leave the system and also different pathways in which it can grow or collapse. It is both difficult to predict theoretically and monitor experimentally the precise bubble behavior in such systems.

The main pathways for a bubble within a population under the influence of a sound field are depicted in Fig. 18. A bubble can meet another bubble in solution, combining via coalescence to form a larger bubble. In a gas-saturated solution such as water above the lower stability threshold (Eq. 2), individual bubbles can also grow with time over several acoustic cycles via rectified diffusion. If gas bubbles grow large enough, they can leave the system entirely due to buoyancy. This is termed degassing. Bubbles that reach the transient threshold may expand in an unstable fashion and collapse violently. This can sometimes be accompanied by fragmentation into smaller bubbles. Conversely, bubbles below the threshold pressure for rectified diffusion will dissolve into solution (Eq. 2).

Rectified Diffusion in Multibubble Systems

The imaging techniques employed to study rectified diffusion in single-bubble systems are difficult to apply to systems where multiple bubbles exist, due to competing processes such as bubble coalescence which will also influence the bubble growth rate. Instead, the sonoluminescence that is produced from cavitation within the acoustic field can be used to probe the growth of the overall bubble population in the system. In multibubble systems, the sonoluminescence (MBSL) is emitted from "clouds" of bubbles being driven at high amplitudes in gassed liquids. These clouds are not dispersed homogenously and instead form patterns due to interactions with the sound field and with other bubbles [63]. The most common pattern is the formation of filaments called streamers. In an acoustic standing wave, these streamers form a web-like pattern with a center located at the antinode.

Workers have shown using a pulsed ultrasound method [64] that the population of active bubbles takes time to grow to equilibrium, usually 20–50 pulses. Some typical initial growth behaviors of MBSL are shown in Fig. 19 [7]. The number of pulses, i. e., the buildup time required to reach a "steady-state" level (indicated by a horizontal line), can be used to judge the relative contributions due to coalescence and rectified diffusion [65]. Figure 19 further demonstrates that the addition of surface-active solutes, such as SDS, influences the initial sonoluminescence growth behavior. This is because the presence of solutes on the surface of the bubbles can modify the bubble-bubble interactions that occur within the acoustic field.
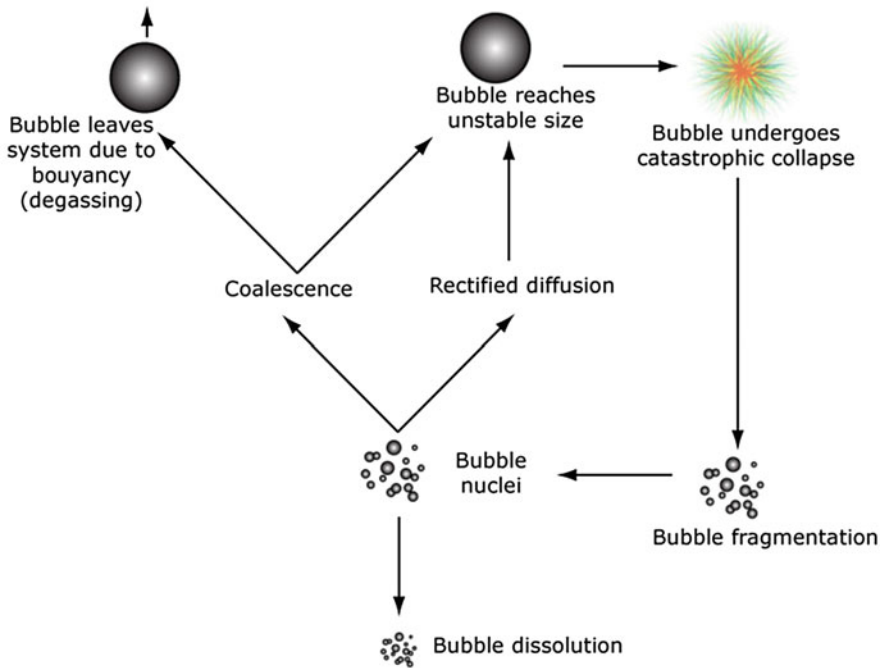
Fig. 18 Pathways for bubble nuclei under the influence of an acoustic sound field. Bubbles can grow via either coalescence or rectified diffusion, or dissolve into solution. Upon reaching an unstable size, a bubble will sometimes collapse, possibly fragmenting to form smaller bubbles. Bubbles that become larger may leave the system by buoyancy (Adapted with permission from Leong et al. [26])

In a multibubble field, there are two primary pathways by which bubbles can grow to reach a sustained population. In general, a coalescence pathway leads to an increase in the overall bubble population size range that is faster than rectified diffusion [6]. The presence of surface-active solutes such as SDS can inhibit the ability for bubbles to coalesce [4, 66]. For ionic surfactants, the inhibition can be explained by the electrostatic repulsion created by the charged head group located on the surface of the bubble. This means that, for the bubble population to reach a sufficient number of resonance-sized bubbles for sonoluminescence to occur, there requires a greater reliance from rectified diffusion. This is represented schematically in Fig. 20.

Since rectified diffusion is a slower process compared with coalescence, a larger number of ultrasound pulses are required for a steady-state population of resonance size-range bubbles to be achieved in solutions where coalescence is inhibited. Due to this behavior, the relative contributions of coalescence and rectified diffusion to the overall bubble growth in solutions containing different concentrations of surface-active solutes, such as ionic surfactants and some alcohols, can be inferred.
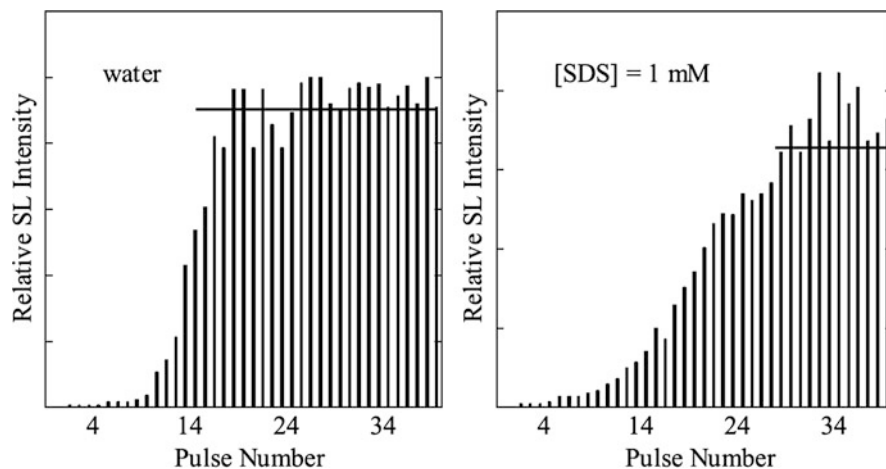
Fig. 19 The initial growth of MBSL as a function of number of acoustic pulses. Frequency = 515 kHz, duty cycle = 4 ms on, 12 ms off (Reprinted from Ashokkumar [7] with permission from Elsevier)
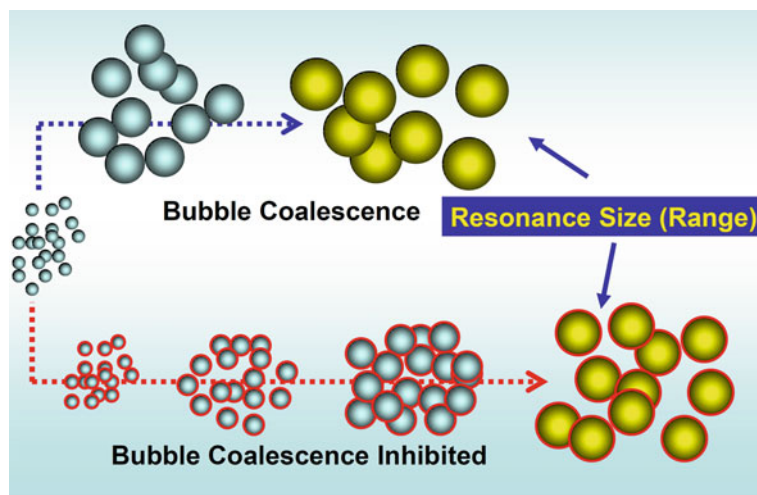
Fig. 20 Schematic representation of the inhibition of coalescence due to presence of surface-active solutes on the bubble surface (Adapted from Ashokkumar and Grieser [6] with permission of the PCCP Owner Societies)

Conclusions and Future Directions

Rectified diffusion is an interesting bubble growth phenomenon in acoustic fields. The results presented in this chapter explain some of the reasons as to why enhanced bubble growth is observed in the presence of surface-active materials. The results show the surface loading of the surfactant plays a key role on the enhancement of rectified diffusion growth. The electrostatic properties of charged surfactants also have an effect on the growth rate, with the likely reason being due to enhanced microstreaming in the presence of a charged surface. For surfactants with different chain lengths and head group size, longer chain lengths and larger head groups result in greater enhancer to the rectified diffusion growth rate. There however remains a need to further develop the theoretical predictions that take these effects into account. The behaviors described in this chapter hope to provide some improved insight to model the behavior of rectified diffusion in more complex fluids in future studies. Although the study of rectified diffusion in a single bubble is interesting, real-world applications of ultrasound processing involve multibubble fields where bubble-bubble interactions become important. Some information regarding bubble growth in these environments can be deduced from pulsed MBSL initial growth spectra; however, there still remains a missing link between the results obtained from bubble growth rates in a single-bubble system to those in industrial processes. The bridging of this missing link in future studies will be of high importance.

References

1. Liao Y, Lucas D (2010) A literature review on mechanisms and models for the coalescence process of fluid particles. Chem Eng Sci 65:2851–2864
2. Firouzi M, Howes T, Nguyen AV (2015) A quantitative review of the transition salt concentration for inhibiting bubble coalescence. Adv Col Int Sci 222:305–318
3. Lee J, Tuziuti T, Yasui K, Kentish S, Grieser F, Ashokkumar M, Iida Y (2007) Influence of surface-active solutes on the coalescence, clustering, and fragmentation of acoustic bubbles confined in a microspace. J Phys Chem C 111:19015–19023
4. Sunartio D, Ashokkumar M, Grieser F (2007) Study of the coalescence of acoustic bubbles as a function of frequency, power, and water-soluble additives. J Am Chem Soc 129:6031–6036
5. Leighton TG (1994) The acoustic bubble. Academic, San Diego
6. Ashokkumar M, Grieser F (2007) The effect of surface active solutes on bubbles in an acoustic field. Phys Chem Chem Phys 9:5631–5643
7. Ashokkumar M (2011) The characterization of acoustic cavitation bubbles–an overview. Ultrason Sonochem 18:864–872
8. Gaitan DF, Crum LA, Church CC, Roy RA (1992) Sonoluminescence and bubble dynamics for a single, stable, cavitation bubble. J Acoust Soc Am 91:3166–3183
9. Crum LA (1980) Measurements of the growth of air bubbles by rectified diffusion. J Acoust Soc Am 68:203–211
10. Eller A, Flynn HG (1965) Rectified diffusion during nonlinear pulsations of cavitation bubbles. J Acoust Soc Am 37:493–503
11. Fyrillas MM, Szeri AJ (1994) Dissolution or growth of soluble spherical oscilalting bubbles. J Fluid Mech 277:381–407
12. Fyrillas MM, Szeri AJ (1995) Dissolution or growth of soluble spherical oscillating bubbles – the effect of surfactants. J Fluid Mech 289:295–314

13. Gould RK (1974) Rectified diffusion in presence of, and absence of, acoustic streaming. J Acoust Soc Am 56:1740–1746
14. Kloek W, van Vliet T, Meinders M (2001) Effect of bulk and interfacial rheological properties on bubble dissolution. J Colloid Interface Sci 237:158–166
15. Goldberg BB, Liu J-B, Forsberg F (1994) Ultrasound contrast agents: a review. Ultrasound Med Biol 20:319–333
16. Ferrara K, Pollard R, Borden M (2007) Ultrasound microbubble contrast agents: fundamentals and application to gene and drug delivery. Ann Rev Biomed Eng 9:415–447
17. Blake FG (1949) Technical Memo. Harvard University
18. Yasui K (2002) Influence of ultrasonic frequency on multibubble sonoluminescence. J Acoust Soc Am 112:1405–1413
19. Safar MH (1968) Comment on papers concerning rectified diffusion of cavitation bubbles. J Acoust Soc Am 43:1188–1189
20. Leong TSH, Wooster TJ, Kentish SE, Ashokkumar M (2009) Minimising oil droplet size using ultrasonic emulsification. Ultrason Sonochem 16:721–727
21. Singla R, Ashokkumar M, Grieser F (2004) The mechanism of the sonochemical degradation of benzoic acid in aqueous solutions. Res Chem Intermed 30:723–733
22. Young FR (1989) Cavitation. McGraw-Hill, London
23. Apfel RE, Peter DE (1981) Methods in experimental physics. Academic, London, pp 355–411
24. Apfel RE (1981) Acoustic cavitation prediction. J Acoust Soc Am 69:1624–1633
25. Neppiras EA (1980) Acoustic cavitation thresholds and cyclic processes. Ultrasonics 18:201–209
26. Leong T, Ashokkumar M, Kentish S (2011) The fundamentals of power ultrasound–a review. Acoust Aust 39:54–63
27. Besant WH (1859) Hydrostatics and hydrodynamics. Deighton Bell, Cambridge
28. Noltingk BE, Neppiras EA (1950) Cavitation produced by ultrasonics. Proc Phys Soc B 63:674
29. Neppiras EA, Noltingk BE (1951) Cavitation produced by ultrasonics: theoretical conditions for the onset of cavitation. Proc Phys Soc B 64:1032
30. Poritsky P (1952) Proceedings of the 1st US National Congress in applied mechanics (ASME). The American Society of Mechanical Engineers, New York, p 813
31. Plesset MS, Hsieh DY (1961) Comments on the theory of rectified diffusion. J Acoust Soc Am 33:359–360
32. Hsieh DY, Plesset MS (1961) Theory of rectified diffusion of mass into gas bubbles. J Acoust Soc Am 33:206–215
33. Fyrillas MM, Szeri AJ (1996) Surfactant dynamics and rectified diffusion of microbubbles. J Fluid Mech 311:361–378
34. Lee J, Kentish S, Ashokkumar M (2005) Effect of surfactants on the rate of growth of an air bubble by rectified diffusion. J Phys Chem B 109:14595–14598
35. Leong T, Wu S, Kentish S, Ashokkumar M (2010) Growth of bubbles by rectified diffusion in aqueous surfactant solutions. J Phys Chem C 114:20141–20145
36. Rosen MJ (2004) Surfactants and interfacial phenomena. Wiley, New York
37. Suzuki H, Lee I-YS, Okuno Y (2010) Stability and dancing dynamics of acoustic single bubbles in aqueous surfactant solution. Int J Phys Sci 5:176–181
38. Lee J, Kentish S, Matula TJ, Ashokkumar M (2005) Effect of surfactants on inertial cavitation activity in a pulsed acoustic field. J Phys Chem B 109:16860–16865
39. Lee J, Yasui K, Tuziuti T, Kozuka T, Towata A, Iida Y (2008) Spatial distribution enhancement of sonoluminescence activity by altering sonication and solution conditions. J Phys Chem B 112:15333–15341
40. Lee JY (2005) The behaviour of ultrasound generated bubbles in the presence of surface active solutes. PhD thesis, The University of Melbourne
41. Leong T, Collis J, Manasseh R, Ooi A, Novell A, Bouakaz A, Ashokkumar M, Kentish S (2011) The role of surfactant headgroup, chain length, and cavitation microstreaming on the growth of bubbles by rectified diffusion. J Phys Chem C 115:24310–24316

42. Mansfield WW (1955) Influence of monolayers on the natural rate of evaporation of water. Nature 175:247–249
43. Caskey JA, Barlage WB (1972) Study of effects of soluble surfactants on gas absorption using liquid laminar jets. J Colloid Interface Sci 41:52–62
44. Jayalakshmi Y, Ozanne L, Langevin D (1995) Viscoelasticity of surfactant monolayers. J Colloid Interface Sci 170:358–366
45. La Mer VK, Healy TW, Aylmore LAG (1964) The transport of water through monolayers of long-chain n-paraffinic alcohols. J Colloid Sci 19:673–684
46. Caskey JA, Michelsen DL, To YP (1973) The effect of surfactant hydrophilic group on gas absorption rates. J Colloid Interface Sci 42:62–69
47. Lucassen J, Van Den Tempel M (1972) Dynamic measurements of dilational properties of a liquid interface. Chem Eng Sci 27:1283–1291
48. Lucassen-Reynders EH (1981) Anionic surfactants: physical chemistry of surfactant action. M. Dekker
49. Stride E (2008) The influence of surface adsorption on microbubble dynamics. Philos Trans R Soc Lond A Math Phys Eng Sci 366:2103–2115
50. Church CC (1995) The effects of an elastic solid surface layer on the radial pulsations of gas bubbles. J Acoust Soc Am 97:1510–1521
51. Tho P, Manasseh R, Ooi A (2007) Cavitation microstreaming patterns in single and multiple bubble systems. J Fluid Mech 576:191–233
52. Elder SA (1959) Cavitation microstreaming. J Acoust Soc Am 31:54–64
53. Church CC (1988) A method to account for acoustic microstreaming when predicting bubble growth rates produced by rectified diffusion. J Acoust Soc Am 84:1758–1764
54. Collis J, Manasseh R, Liovic P, Tho P, Ooi A, Petkovic-Duran K, Zhu Y (2010) Cavitation microstreaming and stress fields created by microbubbles. Ultrasonics 50:273–279
55. Kornfeld M, Suvorov L (1944) On the destructive action of cavitation. J Acoust Soc Am 15:495–506
56. Neppiras EA (1984) Acoustic cavitation series: part one: acoustic cavitation: an introduction. Ultra 22:25–28
57. Rayleigh L (1879) On the capillary phenomena of jets. Proc R Soc Lond 29:71–97
58. Lamb H (1924) Hydrodynamics. Cambridge University Press, London
59. Plesset MS (1954) On the stability of fluid flows with spherical symmetry. J Appl Phys 25:96–98
60. Hilgenfeldt S, Lohse D, Brenner MP (1996) Phase diagrams for sonoluminescing bubbles. PhFl 8:2808–2826
61. Hao Y, Prosperetti A (1999) The effect of viscosity on the spherical stability of oscillating gas bubbles. PhFl 11:1309–1317
62. Leong T, Yasui K, Kato K, Harvie D, Ashokkumar M, Kentish S (2014) Effect of surfactants on single bubble sonoluminescence behavior and bubble surface stability. Phys Rev E 89:043007
63. Lauterborn W, Kurz T, Geisler R, Schanz D, Lindau O (2007) Acoustic cavitation, bubble dynamics and sonoluminescence. Ultrason Sonochem 14:484–491
64. Lee J, Ashokkumar M, Kentish S, Grieser F (2005) Determination of the size distribution of sonoluminescence bubbles in a pulsed acoustic field. J Am Chem Soc 127:16810–16811
65. Leighton TG, Pickworth MJW, Walton AJ, Dendy PP (1989) The pulse enhancement of unstable cavitation by mechanisms of bubble migration. Proc Ins Acous 11:461–469
66. Lee J, Kentish SE, Ashokkumar M (2005) The effect of surface-active solutes on bubble coalescence in the presence of ultrasound. J Phys Chem B 109:5095–5099

Acoustic Cavitation in a Microchannel

Siew-Wan Ohl and Claus-Dieter Ohl

Contents

Abstract

Cavitation in confined geometries, such as microfluidic channels, allows an unprecedentedly detailed look on their dynamics with a much better control as compared to cavitation in the bulk. Another advantage is that only small amounts

S.-W. Ohl
Institute of High Performance Computing, Singapore, Singapore

C.-D. Ohl (✉)
School of Physical and Mathematical Sciences, Nanyang Technological University, Singapore, Singapore
e-mail: cdohl@ntu.edu.sg

of fluids are required. In these geometries, single or a few laser-generated bubbles are utilized for fundamental liquid processing such as mixing, sorting, and pumping. For acoustic cavitation, the bubbles need to be either injected a priori or generated through an entrainment process. Then cavitation can be utilized for emulsions, to lyse cells, to generate light (sonoluminescence), and to initiate chemical reactions. This review presents a summary of the effects of confinement on the bubble dynamics and how they can be utilized for research and applications.

Introduction

It is difficult to observe a completely spherical and symmetric cavitation bubble collapse. The cavitation bubble collapse is influenced by the hydrostatic pressure gradient, imperfection in the bubble generation process, and the wall of the liquid container; all of them induce some asymmetry. These factors cause instabilities to develop during the collapse phase. It is well known that when a bubble collapses near a rigid structure, a high-speed liquid jet directed toward the structure is generated. During its collapse phase, the initially spherical bubble moves toward the structure and becomes toroidal with a thin jet in the center which attends a high velocity up to about 100 m/s [1, 2]. In a confined geometry such as a microfluidic channel, influences from the walls are expectedly more pronounced.

Although single-bubble dynamics is well studied, in many practical applications, a large number of cavitation bubbles need to be generated and controlled. This can be achieved through the use of a strong acoustic field. In section "How to Generate Cavitation?," we will show the method to generate strongly oscillating bubbles in a microfluidic channel. Two technical "tricks" have been used to overcome the constraints, namely, the lack of gas nuclei in the small liquid volume and the issue of transport of acoustic energy into the channel.

In section "Effects of the Microchannel on the Bubble Dynamics," the effect of confinement is discussed. Previous theoretical and experimental works are reviewed. Then the interaction of the bubble with a nearby object (such as a bubble, a cell, or a droplet) is described. The section ends with detailed review of several fundamental controls of microfluidic flow. Various mechanics such as pumping, switching, and sorting in microfluidics are examined.

The last section is devoted to applications involving acoustic cavitation and microfluidics. These include physical applications such as emulsification and chemical processes such as sonoluminescence and sonochemistry. We will also present some biomedical-related use of acoustic cavitation on a chip.

How To Generate Cavitation?

Generation of Single Cavitation Bubbles in Microfluidics

Cavitation bubble dynamics in all aspects have been studied in great detail. They have been summarized in a number of textbooks and comprehensive review articles. For readers seeking an introduction, we recommend the review article by Lauterborn and Kurz [3]. In that article, most of the knowledge for bubble dynamics in large fluid volumes is covered. Our focus in this chapter is on the dynamics of bubbles confined by two and more walls.

Cavitation bubble may be generated from bubbles that are already in the liquid, from gas pockets that are entrained or added to the liquid, or by nucleation. There are several bubble nucleation techniques. These include deposition of energy, for example, through an intense laser beam, or by stretching the liquid, that is applying a negative pressure. A stable gas bubble can be converted into a cavitation bubble by expanding the bubble to about twice its original size [4]. This can be achieved by a short exposure of the bubble to a low-pressure field in which the bubble expands or by resonant excitation. Both methods of bubble nucleation work in confined geometries too. A venturi nozzle reduces the pressure of the liquid easily below the vapor pressure. Mishra and Peles [5] report on such kind of devices and their observation of the resulting cavitating flows. The pressure can also be reduced by evaporation of liquid with a pinned liquid meniscus. Evaporation causes the liquid droplet to pin to the solid surface by maintaining its surface area but reducing its contact angle. The liquid meniscus is therefore said to be pinned to the interface. Subsequently the droplet will shrink. Cavitation bubbles generated by pressure reduction from liquid droplet evaporation can be found in nanochannels [6], in synthetic trees [7], or in droplets trapped in drying hydrogels [8].

Resonant excitation of gas bubbles and their transformation can be achieved by irradiating the liquid in the microchannel with ultrasound. Many different approaches to achieve sufficient pressure inside the fluidic channel have been reported in literature. We are to highlight a few out of the long list. A straightforward approach is to use a sonicator and adapt it to a microfluidic channel [9]. A more integrated approach was developed by Tandiono et al. [10, 11] by attaching a piezoelectric transducer to the glass substrate that supports the microfluidic channels. In this design, the acoustic field serves two purposes; firstly, the sound field generates Faraday waves [12], which entrain bubbles into the liquid in the microfluidic channels. These bubbles then start to oscillate, resonantly, and create intense cavitation. Further discussion on acoustic bubbles is given in the following section.

Another method of generating cavitation bubbles in microfluidics is by energy deposition (Fig. 1). The laser source is a Nd:YAG laser and some part of the laser beam is utilized through an optical delay for illumination. Experimental results from single and multiple bubbles generated with a laser are presented in the next section.
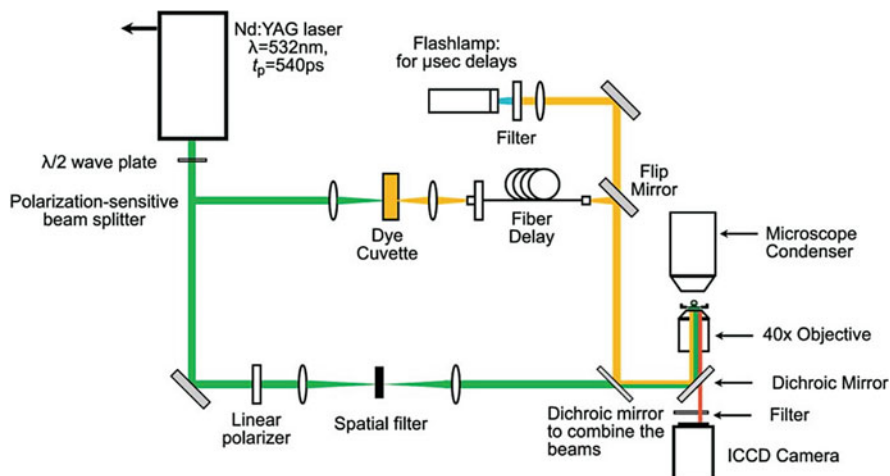
Fig. 1 Experiment setup for time-resolved fluorescence imaging

Before we come to the details, we want to highlight that several approaches have been utilized to create laser-induced bubbles in microfluidics: by linear absorption, by multiphoton absorption, and by plasmonic absorption. Linear absorption utilizes a liquid containing a dye with a high absorption coefficient at the laser wavelength [13]. This allows fine adjustment of the bubble size through the laser energy manipulation. The downside is that objects in the liquid may come into contact with the dye. This interaction is undesirable especially for biological cells. Nonlinear absorption [14] allows bubbles to be created in otherwise transparent liquids. However, the absorption process possesses a threshold, and therefore only relatively large bubbles can be generated. Plasmonic absorption can be achieved by deposition of a thin gold layer on the substrate. A green laser is then targeted to the gold layer for bubble nucleation. This approach is particularly attractive for studies with cells [15].

Acoustic Cavitation in Microfluidics

The bubbles used in microfluidics for mixing and pumping are often oscillating only gently. They are introduced either by direct injection [16] or trapped gas [17]. It is difficult to create cavitation bubbles in microfluidics by acoustics. Two main hurdles that have to be overcome are the lack of nucleation sites and the difficulty in transmitting high-pressure amplitude ultrasound into the microfluidic channels. The small volume of fluid in the microfluidic channels does not contain many pre-existing gas pockets or impurities which act as nucleation site of the cavitation bubbles. It is not practical to put an ultrasound transducer inside the microfluidic channels. Often the ultrasound is generated externally by transducers attached to the glass plate onto which the microfluidic channels are attached [10, 18]. The fragility

Fig. 2 The design and setup of the microfluidics device for the generation of intense cavitation. The transducer generating ultrasound is attached on the left side the microfluidic channel which is made of polydimethylsiloxane (PDMS) on a glass slide of 75×50 mm^2. The width of the T-junction is 50 μm and 100 μm for the gas and the main (water) channels, respectively. The main channel expands to 500 μm downstream. The height of the channel is 20 μm. The zoomed *inset* shows a typical configuration of the liquid–gas slugs in the channel (Reproduced with permission from Ref. [5], Fig. 1)
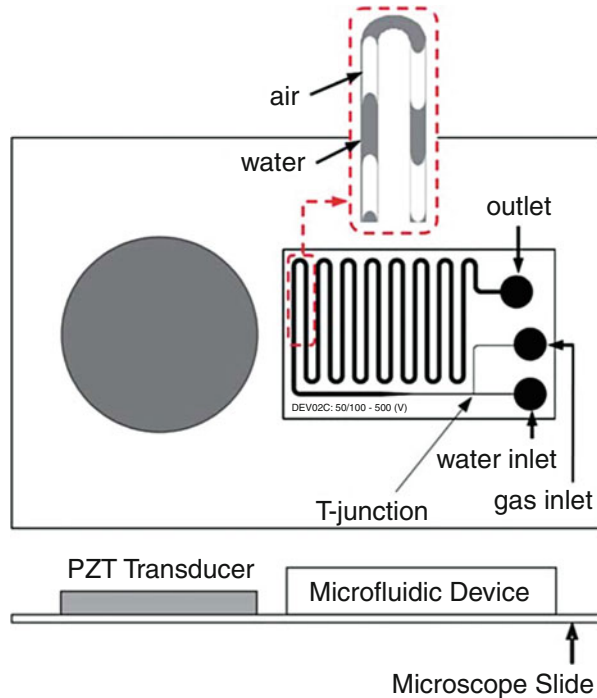
of the system (both the polydimethylsiloxane (PDMS) and the thin glass slide) prevents the use of high-intensity or large transducers.

Iida et al. [18] investigated the use of mild ultrasound (about 0.5 MPa) to generate cavitation bubble in a millimeter-sized channel or chamber. They used an external transducer which is attached to the bottom of their devices. They compare the results from these 1D channel and 2D chamber to that of a 3D (20 millimeter in height) glass tube. They measured the production of cavitation bubbles indirectly by monitoring the generation of fluorescent hydroxyterephthalate (HPTA) from the chemical reaction between terephthalate anion with OH radicals which are produced by ultrasonic cavitation. Higher ultrasonic power is needed to generate HPTA in the channel and chamber as compared to the tube.

Tandiono et al. [10] reported the first successful attempt to generate intense acoustic cavitation in a microfluidic channel. They overcome the problems mentioned by having a gas inlet (see Fig. 2). The gas pockets in the fluid form a large number of gas–liquid interfaces. The gas–liquid boundaries become the nucleation sites of the acoustic cavitation. On the same glass slide as the microfluidic channel, coin-shaped ultrasound transducers are attached. The ultrasound waves cause the gas–liquid interface to oscillate. At high-oscillation amplitude, these surface waves entrap gas pockets which expand and oscillate (see Fig. 3). The acoustic cavitation bubbles thus generated are used to create sonoluminescence and sonochemistry [11], cell disruptions or stretching [19, 20], and emulsification [21]. Details of these applications are given in the subsequent sections.
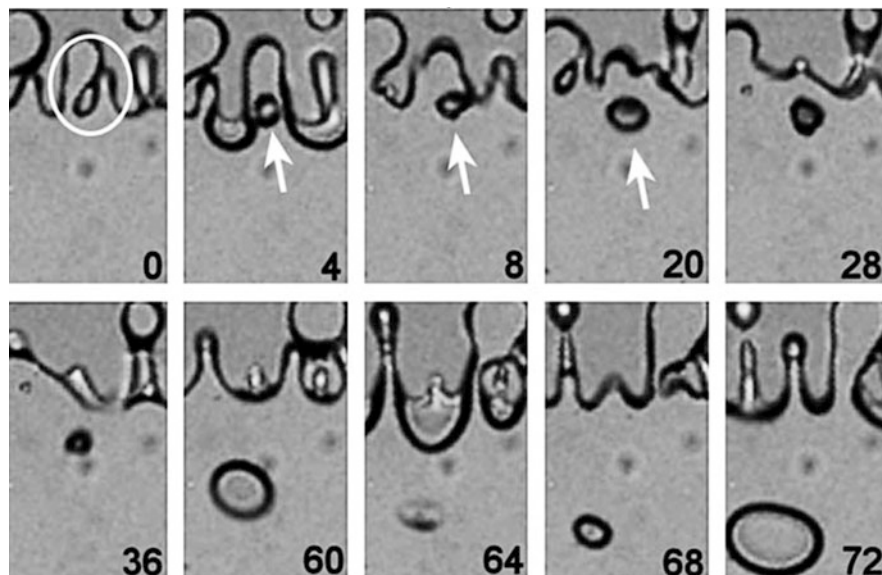
Fig. 3 The entrapment of gas pocket in a microfluidic channel. The air is on *top* and the water *below*. The number in each frame indicates the time in microsecond, and the frame width is 100 μm. The transducer is driven at 50 V, 100 kHz. In the first frame, the crest is *circled*. In the second, third, and fourth frames, the *arrows* point to the location where a gas nucleus is formed. The ultrasound causes this gas pocket to oscillate in the subsequent frames (Reproduced with permission from Ref. [5], Fig. 4)

Ultrasound Contrast Agents

Apart from cavitation bubbles, there is another type of bubble which is either generated in microfluidics or used in microfluidic research. It is known as the ultrasound contrast agent (UCA). These bubbles are typically in micron size (about 1–3 μm in radius). They are stable bubbles because of a lipid or polymer coating on the bubble surface. The bubble core is made of air or heavy gases such as perfluorocarbon.

The UCAs are used in ultrasound imaging for contrast enhancement [22]. They are injected intravenously into the blood circulation system. The bubbles oscillate and reflect the ultrasound. The echo generated allows the differentiation between the blood vessels and the surrounding tissues resulting in clear ultrasound images. Without the UCA bubbles, the echogenicity difference between the blood and its surrounding tissues is not strong.

Experiments with Ultrasound Contrast Agents (UCAs)

Experiments on UCA concentrate on the delivery of drug or gene into targeted tissue or cells. The loading of the drug or gene is performed in multiple ways. The drugs could be loaded on the surface of the microbubbles by ligands [23, 24]. The ligands

bind the drug molecules and the lipid layer on the bubble. Alternatively, the drug is dissolved in an oil layer within the microbubble [23]. In some cases, especially for gene transfection, the genetic material (e.g., plasmid DNA) is incorporated within the lipid layer [24].

After being injected into the bloodstream, the delivery of drug or gene is activated by ultrasound when the UCAs are detected by imaging to be near the targeted area (site of tumor, tissues to be transfected et cetera). The acoustic pressure waves cause the microbubbles to oscillate or collapse. The drug or gene is then dispensed from the bubbles to the surrounding tissues. Details of the mechanism of drug/gene delivery by UCA could be found in [24, 25].

These loaded UCAs have been studied to treat multiple illnesses and genetic disorders [23, 26, 27]. Since UCA has been developed initially for echocardiography, it is investigated for therapeutic treatment for the heart. Detail applications are presented and discussed in [23]. They include the use of UCA for sonothrombolysis and drug/gene delivery. Recent animal study from Wu et al. [28] suggests that the use of microbubbles (and ultrasound) and drug is a good treatment modality for heart attack (myocardial infarction). Datta et al. [26] present a systematic study of the use of ultrasound and microbubbles for the removal of blood clot. They find the ultrasonic bubbles enhance the removal of the blood clot and the delivery depth of the drug into the clot. While sonothrombolysis for heart and transcranial ultrasound surgery has been done for animal [28] and human trials [29], gene therapy is progressing at a slower pace. Successful tissue and animal trials have been reported [26, 30]. UCA gene delivery has the virtue of being nonviral and potentially noninvasive.

Effects of the Microchannel on the Bubble Dynamics

Single and Few Bubbles in Confined Environments

Cavitation bubbles in confined geometry have interesting properties to actuate and manipulate microfluidic fluid flow and the objects within the channels. These properties drive the research interest in this area. This chapter is organized by first introducing the simple models which describe the flow from single and multiple oscillating bubbles in a thin gap. We will then discuss the interaction of the bubbles with objects of interest before we address specific fluid flows created by single and few bubbles.

Modeling Approaches

We will first discuss a simplified approach to model bubbles by reducing the Navier–Stokes equation into an ordinary differential equation (ODE). Ignoring viscous and thermal effects, few-bubble systems can be described by a set of ODEs, including their transversal motion. However, particular qualities of the flow

Fig. 4 Side view of a bubble with lateral radius R being constrained by two horizontal plates separated by a distance h
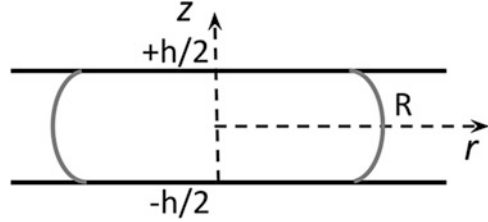
induced by the bubble cannot be described within above framework. Objects in the thin gap may undergo large shear. For this to occur, we need to account for the development of a nonuniform flow profile and, in particular, for the formation and separation of boundary layers. An example of the flow obtained from computational fluid mechanics is given resembling oscillatory flow in thin gaps.

Single-Bubble Ordinary Differential Equations

Next we derive a general ordinary differential equation describing the oscillation of a bubble in a thin gap with a planar flow following closely the derivation from Xiong et al. [31]. The radius of the cylinder is R and it is confined in a channel of height h. The geometry is sketched in Fig. 4.

We use an axisymmetric coordinate system (r, z, θ) and ignore translational motion of the bubble. Bubble motion will be discussed in section "Computational Fluid Dynamics (CFD) of Single Bubbles." The liquid is assumed incompressible; hence the fluid flow is given by the Navier–Stokes (NS) equation:

$$\frac{\partial u}{\partial t} + \left(\vec{u} \times \nabla \right) \vec{u} = -\frac{1}{\rho} \nabla p + \frac{\mu}{\rho} \nabla^2 \vec{u}, \tag{1}$$

where ρ is the density of the fluid, μ is the dynamic viscosity, $\vec{u}$ is the liquid velocity, and p is the pressure. As the problem is axisymmetric, i.e., $\partial/\partial\theta = 0$, planar flow depicts $u_z = 0$, and ignoring any swirl $u_\theta = 0$, we obtain the NS equation of the radial component:

$$\varrho \left(\frac{\partial u_r}{\partial t} + u_r \frac{\partial u_r}{\partial r} \right) = -\frac{\partial p}{\partial r} + \mu \left[\frac{1}{r} \frac{\partial}{\partial r} \left(r \frac{\partial u_r}{\partial r} \right) + \frac{\partial^2 u_r}{\partial z^2} - \frac{u_r}{r^2} \right] \tag{2}$$

As the continuity equation demands that $\nabla \cdot \vec{u} = 0$, one can show that the radial velocity component has the form $u_r = \frac{G(z,t)}{r}$, where G is an arbitrary function. Inserting this expression into Eq. 2, it simplifies into

$$\rho \left(\frac{\partial u_r}{\partial t} - \frac{u_r^2}{r} \right) = \frac{\partial p}{\partial r} + \mu \frac{\partial^2 u_r}{\partial z^2} \tag{3}$$

Equation 3 can be integrated once across the channel height to obtain

$$\rho\left(\frac{\partial \overline{u}_r}{\partial t} - \frac{\overline{u_r^2}}{r}\right) = -\frac{\partial p}{\partial r} + \frac{2\tau_w}{h}, \tag{4}$$

where $\tau_w = \mu \frac{\partial u_r}{\partial z}$ is the shear stress at $z = \pm h/2$, i.e., at the channel walls. Conservation of mass with the boundary condition at $u_z(r = R) = \frac{dR}{dt} = \dot{R}$ demands that the averaged velocity is $\overline{u}_r = R\dot{R}/r$. Inserting this expression into Eq. 4, we obtain an ordinary differential equation in R:

$$\frac{\rho}{r}\left(R\ddot{R} + \dot{R}^2\right) - \frac{\rho}{r^3}R^2\dot{R}^2 = \frac{\partial p}{\partial r} + \frac{2\tau_w}{h}. \tag{5}$$

We now integrate Eq. 5 from R_∞ to R in the radial direction resulting into

$$\left(R\ddot{R} + \dot{R}^2\right)\ln\frac{R}{R_\infty} + \frac{\dot{R}^2}{2}\left(1 - \frac{R^2}{R_\infty^2}\right) = \frac{p(R_\infty) - p(R)}{\varrho} + \frac{2}{h\varrho}\int_{R_\infty}^{R}\tau_w dr, \tag{6}$$

where $p(R)$ is the pressure in the liquid at the bubble surface. The logarithmic singularity in the first term of Eq. 6 prevents to set integrate to infinity but only to a finite size R_∞ which is typically the dimension of the microfluidic container.

The wall shear stress is not specified in Eq. 6 and depends on the velocity profile $u_r(z)$. Next we assume a Poiseuille-type flow, thus a quadratic flow velocity profile with no-slip at the channel walls τ_w and insert into Eq. 6, thus

$$u_r = \frac{f(r,t)}{2\mu}\left(z^2 - \frac{h^2}{4}\right). \tag{7}$$

Here the function $f(r, t)$ can be obtained from mass conservation. Therefore, Eq. 7 is integrated over the channel height and equated to the mass flux at the bubble wall:

$$2\pi Rh\dot{R} = 2\pi rh\overline{u}_r = 2\pi rh\left(-\frac{f(r,t)h^2}{12\mu}\right). \tag{8}$$

We can now solve Eq. 8 for the velocity $u_r(z)$, calculate the wall shear stress τ_w, and insert into Eq. 6:

$$\left(R\ddot{R} + \dot{R}^2 + \frac{12\mu}{h^2\varrho}R\dot{R}\right)\ln\frac{R}{R_\infty} + \frac{\dot{R}^2}{2}\left(1 - \frac{R^2}{R_\infty^2}\right) = \frac{p(R_\infty) - p(R)}{\varrho}. \tag{9}$$

Equation 9 is a Rayleigh–Plesset-type equation for a single bubble in a channel which accounts for viscous dissipation. We assume that the shape of the bubble does not change during the bubble oscillation; the bubble remains in a cylindrical shape with a constant contact angle Θ (liquid side). The pressure balance at the bubble wall

(ignoring normal viscous stresses) allows to relate the bubble pressure with the pressure in the liquid at the bubble wall:

$$p(R) = p_v + p_g - \Delta p = p_v + p_{g0}\left(\frac{R_0}{R}\right)^{3k} - \sigma\left(\frac{1}{R} + \frac{2\cos\Theta}{h}\right). \qquad (10)$$

Here, p_v is the vapor pressure, p_g is the gas pressure, and Δp is the jump due to surface tension. The gas pressure p_g is related to the gas pressure at equilibrium p_{g0} through the bubble radius R_0 at equilibrium and the polytropic exponent κ assuming an ideal gas law. The coefficient of surface tension is σ and the Laplace pressure has contributions from two radii of curvature.

Depending on the geometry, Eqs. 9 and 10 can be simplified, e.g., for sufficiently large channel gaps h; the contribution from viscosity in Eq. 9 and surface tension Eq. 10 may be ignored. A comparison of the bubble dynamics in a $h = 8$ μm and a $h = 700$ nm thick channel is presented in Fig. 5 as solid lines. The dashed lines show the dynamics in absence of the viscous contribution, while the symbols present experimental measurements.

During the initial expansion of the bubble from a size smaller than the gap height, the liquid flow will be a mixture of a 3D spherical and a 2D planar flow. To account for this, Leighton [32] provides corrections to the inertia term, i.e., LHS of Eq. 6.

Multiple Bubble Ordinary Differential Equations

If more than one bubble is present, interaction of the bubbles needs to be taken into account. The interaction between bubbles can be derived straightforwardly assuming potential flow of two or more cylindrical bubbles. A convenient approach to derive the equations of motion for the radial and the translational motion is the Lagrange formalism [33–35]. The geometry for two interacting bubbles is sketched in Fig. 6, together with the arbitrary origin O, and the variables used in the equations below. A full derivation is stated in Quinto-Su et al. [36]. The resulting equations of motions are

Fig. 5 (a) Comparing the radial dynamics of a bubble in the extended nanochannel with 8 μm (*hollow square*) with a viscid 2D model (*solid line*) and inviscid 2D model (*dashed line*). Left axis is for the bubble in extended nanochannel and the right one is for the bubble in a microchannel
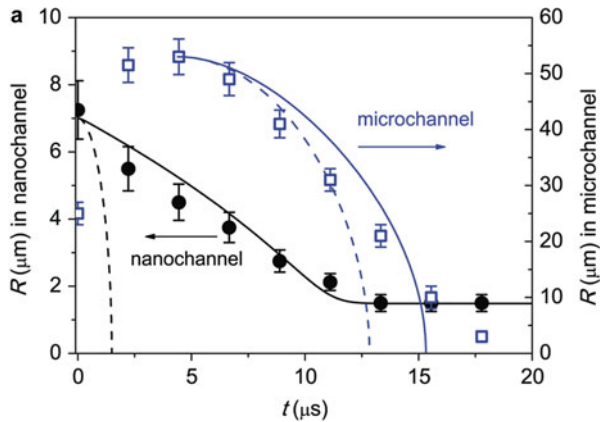
Fig. 6 Sketch of the bubble geometry and variables for bubble–bubble interaction. The positions of the bubbles 1 and 2 with radii R_1 and R_2 have their centers at r_{01} and r_{02} and translate with velocities U_1 and U_2 (Reproduced with permission from Ref. [36], Fig. 1)
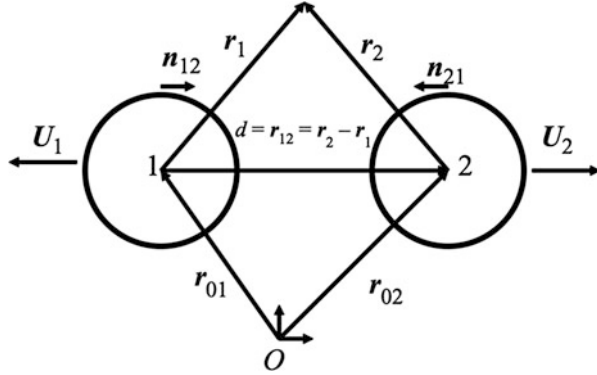
$$\left(\ddot{R}_i R_i + \dot{R}_i^2\right)\log\left(\frac{R_i}{R_\infty}\right) + \frac{\dot{R}^2}{2} = \frac{p}{\varrho} - \frac{\vec{U}_i^2}{2} - \sum_{k\neq i}\left(\ddot{R}_k R_k + \dot{R}_k^2\right)\log\left(\frac{r_{ik}}{R_\infty}\right), \quad (11a)$$

and

$$\ddot{\vec{r}}_{0i} = -\frac{2\dot{R}_i\,\vec{U}_i}{R_i} + \sum_{k\neq i}\frac{\vec{n}_{ki}\left(\ddot{R}_k R_k + \dot{R}_k^2\right)}{r_{ki}}. \quad (11b)$$

The pressure p in Eq. 11a is the pressure difference between the pressure at infinity and the pressure in the bubble. Equation 11a is a modified cylindrical Rayleigh equation for bubble i with two additional pressure terms on the RHS: the first is caused by the bubble translation and resembles a stagnation pressure and the second term is pressure induced by the neighboring bubble.

The sum in Eq. 11a includes all bubbles, except bubble i. A comparison of this model with two cavitation bubbles recorded with a high-speed camera at 500,000 frames is shown in Fig. 7. The bubbles are created with two laser foci at a distance of 70 μm with a smaller bubble on the left and a larger on the right, Fig. 7a. Both the radial and the translational models are well described using only the initial radial velocity of the bubbles as a fit parameter. For this example the pressure p in Eq. 11a was taken as the ambient pressure as laser-induced bubbles in water contains mostly condensable gas; surface tension and normal viscous stresses are not relevant. Yet, for more viscous liquid or gas bubble oscillations, a restoring gas pressure must be taken into account similar to Eq. 10.

Computational Fluid Dynamics (CFD) of Single Bubbles

Oscillating bubbles in a narrow gaps may not form a parabolic flow profile instantaneously as assumed in Eq. 7. The timescale to develop a flow field is given by the diffusion of vorticity which is of the order of $\Delta t = \rho l^2/\mu$, where l is a length scale, e.g., $h/2$, for the above $h = 8$ μm channel $\Delta t = 16$ μs which is of the order of the bubble oscillations.
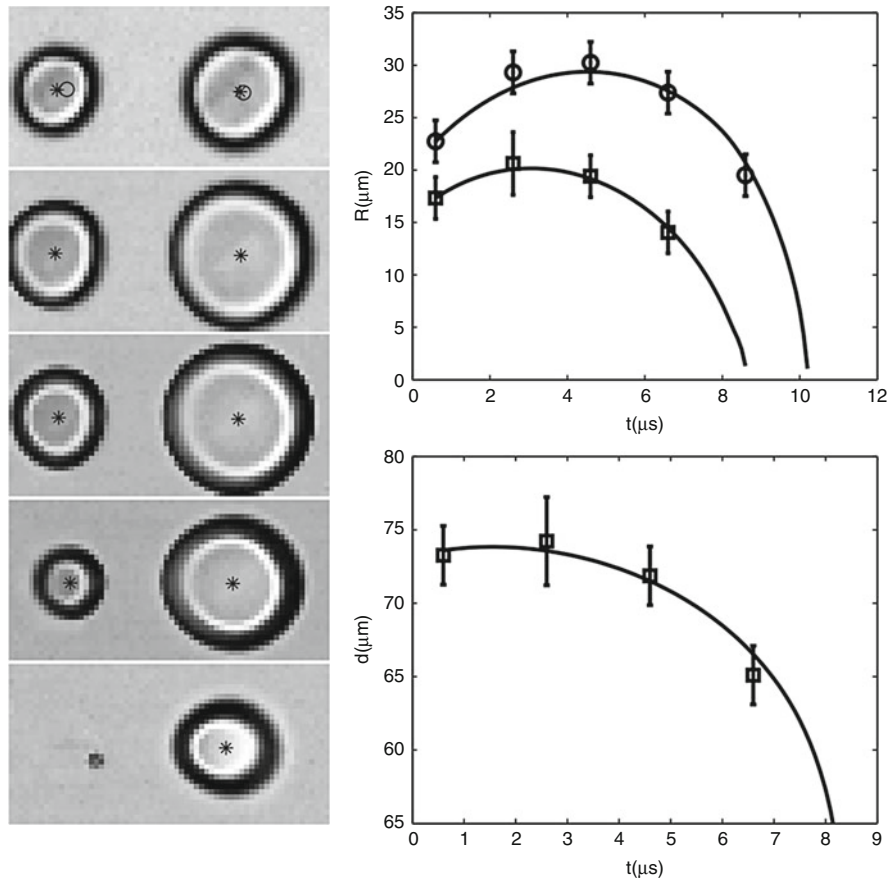
Fig. 7 Two unequal-sized bubbles created at a distance of 70 μm. The interval between two frames is 2 μs and the frame width is 128 μm. *Top right* figure denotes the radii in time for both bubbles. The *bottom right* figure shows the inter-bubble distance variation in time (Reproduced with permission from Ref. [36], Fig. 5)

We cannot therefore simply assume that the flow has developed. Additionally, during the initial expansion phase, the pressure inside the bubble might be higher than the surrounding fluid. During expansion, the pressure in the bubble drops, while the pressure far from the bubble might be higher, and an adverse pressure gradient builds up. The boundary layer may separate and give rise to a complex flow pattern with reverse flow, vorticity transport, and stagnation points inside the channel.

Axisymmetric radial flows of real fluids in narrow gaps have been studied experimentally and analytically in the past 50 years due to their relevance in industrial applications such as radial viscometers, radial diffusers, nonrotating air bearings, and disk-type heat exchangers, e.g., see Elkouh [37] and Von Kerczek [38] for analytical solutions to flows of a harmonically oscillating source at the center.

To demonstrate the importance of boundary layers, we present here a solution to the Navier–Stokes equation using the volume of fluid method with a level-set approach for the liquid–gas interface; for details see Li et al. [39]. The simulation starts with a pressurized spherical gas cavity in the center of a 20 μm high gap filled with a stagnant liquid (water).

Figure 8 depicts the temporal evolution of the bubble shape for 10 μs, thus an order of magnitude shorter than the vorticity diffusion time Δt. The spherical bubble quickly grows into a pancake shape, forming thin liquid films at the upper and lower solid walls. The maximum bubble radius is obtained after 4 μs. During bubble shrinkage, the convex interface flattens and only increases curvature after 8 μs, that is, when the internal pressure increases and dampens the collapse of the bubble. The bubble collapses to its minimum volume at t = 10 μs and rebounds afterward (not shown here). Right to the bubble profile in Fig. 8, the radial velocity profile at a distance of r = 50 μm from the bubble center is shown. Initially, the liquid is at rest and rapidly develops into a plug flow with strong wall shear stress. Gradually, a more parabolic profile develops. At the later expansion stage, the velocity near the walls is reduced and reversed in direction, while the liquid velocity in the center of the gap is still outward and positive. A more detailed study reveals that the adverse pressure gradient is responsible for the flow reversal.

Cavitation bubble dynamic modeling by solving the full Navier–Stokes equations in tubes has received more attention than in a planar gap. For example, Yuan and Prosperetti [40] and Ory et al. [41] have studied the pumping effect originating from vapor bubble expansion and collapse in tubes. Ye and Bull [42, 43] describe the therapeutical method of gas embolotherapy, where the expansion of liquid into a vapor shuts of nutrition supply to a malignant tumor. Their work [43] extends the

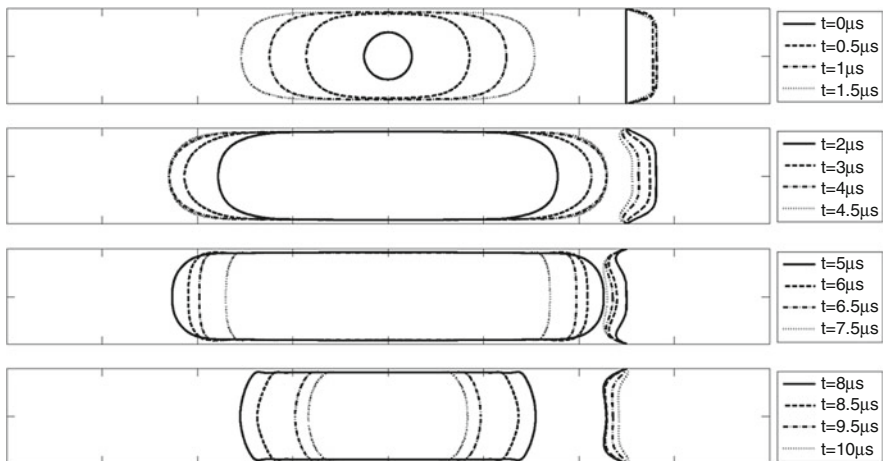**Fig. 8** Bubble shape evolution together with the radial liquid velocity profile at $r = 50$ μm from the center of the bubble. Please note the reversal of the flow direction near the boundaries occurring before the flow in the center of the gap

bubble oscillation into flexible tubes with the important finding that wall shear stress are greatly reduced once the constraining tube can elastically deform.

Effect of the Gap Height and Geometrical Shape on Bubble Dynamics

So far the bubble size considered is comparable and larger than the width of the gap, and the bubble center was located at the center of the gap. In many applications, bubbles are created close to one of the walls, e.g., on micro-heaters embedded in one of the plates. For narrow channels one can expect that the bubble fills quickly most of the gap. In contrast, if the gap is very large, the bubble is less affected and oscillates similarly to the situation where it is bounded by a single plate [44].

In a systematic study, Gonzales-Avila et al. [45] report about three scenarios and categorize them according to the nondimensional maximum bubble radius $\eta = h/R_x$, where h is the gap height and R_x the maximum bubble radius in the plate direction. Figure 9 depicts a collection showing that bubbles created in a very narrow gap expand and collapse by filling most of the channel, i.e., a disk-shaped bubble. For $0.4 < \eta < 1.0$, the bubble collapses onto the opposing side of the channel. The bubble migrates away from the plate it has been created. In the regime $1.0 < \eta < 1.4$, the bubble collapses mostly in the center of the channel, while for larger η-values, the collapse proceeds on the plate the bubble has been nucleated.

If the bubble is further constrained by lateral walls, complex jetting phenomena are observed. Zwaan et al. [46] showed that the bubbles can develop multiple jets. The number of jets corresponds to the number of nearby boundaries. Figure 10 depicts a bubble collapsing in a channel with two jets along the channel, three jets within an equilateral triangle, and four jets in a square chamber. The jets start from regions where there the largest volume of liquid is.

We have seen before that jets can be induced by a second nearby bubble which for a potential flow resembles a rigid boundary at half the distance between the bubbles. Another way to generate liquid jets is through an asymmetry of the bubble itself. This asymmetry can be conveniently generated with laser-induced bubbles, by either altering the shape of the focus or by creating multiple bubbles nearby which upon expansion coalesce and thereby form odd-shaped bubbles. An example for a toroidal bubble is shown in Fig. 11. There the laser focuses in on a circle resulting into to an annularly expanding bubble with a stagnation point in its center; see Lim et al. [47]. This specific laser focus was generated with a digital hologram and an objective lens acting as a Fourier lens.

Interaction of Single and Few Bubbles with Objects

Control over time and strength of the bubble dynamics enable the utilization of the bubble for manipulation of objects. In the paragraphs below, some of the work using cavitation bubble dynamics to study rheological properties of suspended objects are
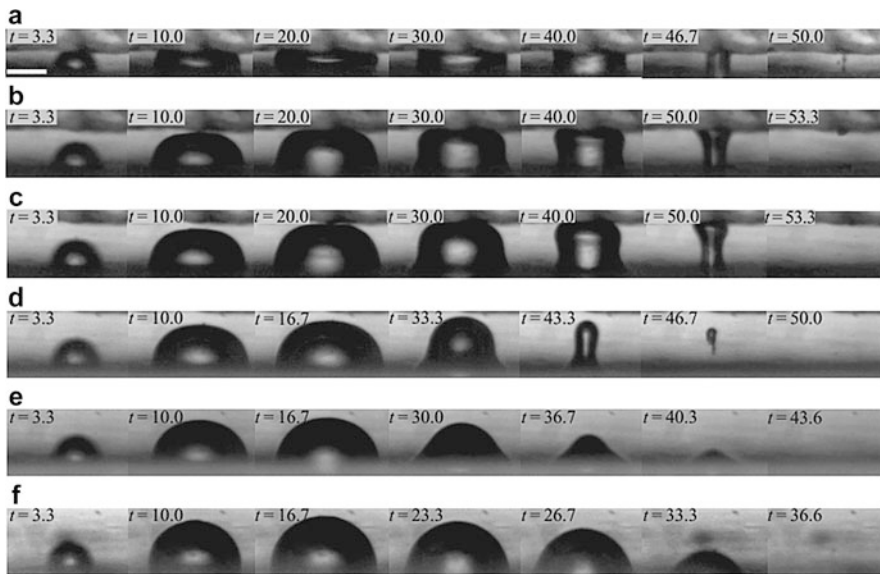
Fig. 9 Bubble dynamics as a function of channel height for bubbles with an approximate maximum horizontal bubble radius of $R_x = 140$ μm. The upper wall is visible in (**a**–**d**); the time in microseconds is shown on the *upper left* corner of each frame. (**a**) $\eta = h/R_x = 0.4$, bubble collapse between the two walls; (**b**) $\eta = 0.8$, bubble collapse onto the upper wall, at maximum expansion the bubble reaches the upper wall; (**c**) $\eta = 0.9$, bubble collapse onto the upper wall, the bubble does not reach the upper wall at maximum expansion; (**d**) $\eta = 1.2$, neutral collapse; (**e**) $\eta = 1.6$, non-spherical collapse onto the lower wall; and (**f**) $\eta = 7.3$, quasi-hemispherical collapse onto the lower wall. The scale bar indicates a length of 100 μm (Reproduced with permission from Ref. [45], Fig. 3)

discussed. First we will show the effect of the cavitation bubble dynamics on soft objects such as gas bubbles, biological cells, and droplets. Then an application will be presented to characterize the stiffness of some of the hardest fabricated material.

Interaction with Gas Bubbles

Gas bubble shock wave interaction is of major concern in medical applications such as shock wave lithotripsy [48–50], in cavitation damage research [44, 51], and in the study of explosives [52, 53]. In 2006, Chen et al. [13] devised a clever experiment where they generated first a gas bubble and then a cavitation bubble with a pulsed laser in a narrow gap filled with a light-absorbing liquid. The narrowness of the gap allowed a clear flow on the surface deformation, jetting, and breakup of the bubble resembling a cross-sectional cut; see Fig. 12. In a follow-up paper by Chen and Lin [54], they discussed the detailed fragmentation dynamics, yet more studies and comparison with analytical modeling of the fragmentation mechanics as well with numerical simulations may allow to make significant impact on our current understanding of shock wave–bubble interactions in liquids [55].
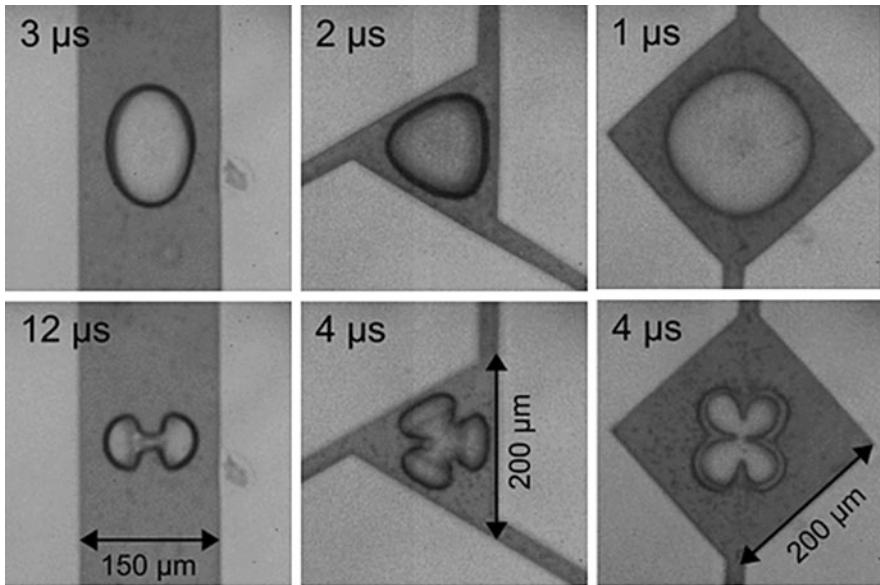
Fig. 10 Snapshots for three different geometries from *left* to *right*: single-bubble cavitation in a 150 μm wide and several millimeter long channel, in a 200 μm isosceles triangular structure with feeding channel attached to the corners and in a square chamber with 200 μm long sides (Reproduced with permission from Ref. [46], Fig. 5)
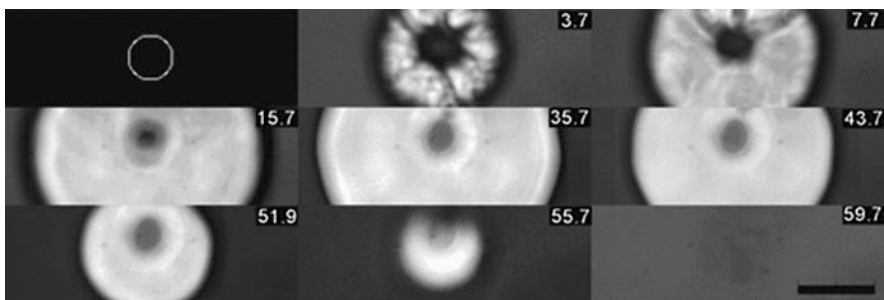
Fig. 11 Toroidal bubble created from a circular focus depicted in the first frame. The bubble expands initially with a rough surface likely due to separate bubbles which only coalesce in a later stage. Please note that the bubble retains its toroidal shape during the expansion and collapse cycle. The recording is taken at a frame rate of 250,000 fps. The black bar denotes a length of 100 μm and the time stamps in the *upper right* are given in microseconds (Reproduced with permission from Ref. [47], Fig. 8)

Interaction with Cells

The delivery of therapeutic agents into eucaryotic cells is hindered by the high selectivity of the cell membrane on foreign agents. In particular, uptake of large molecules such as DNA and RNA needs some active injection mechanics which
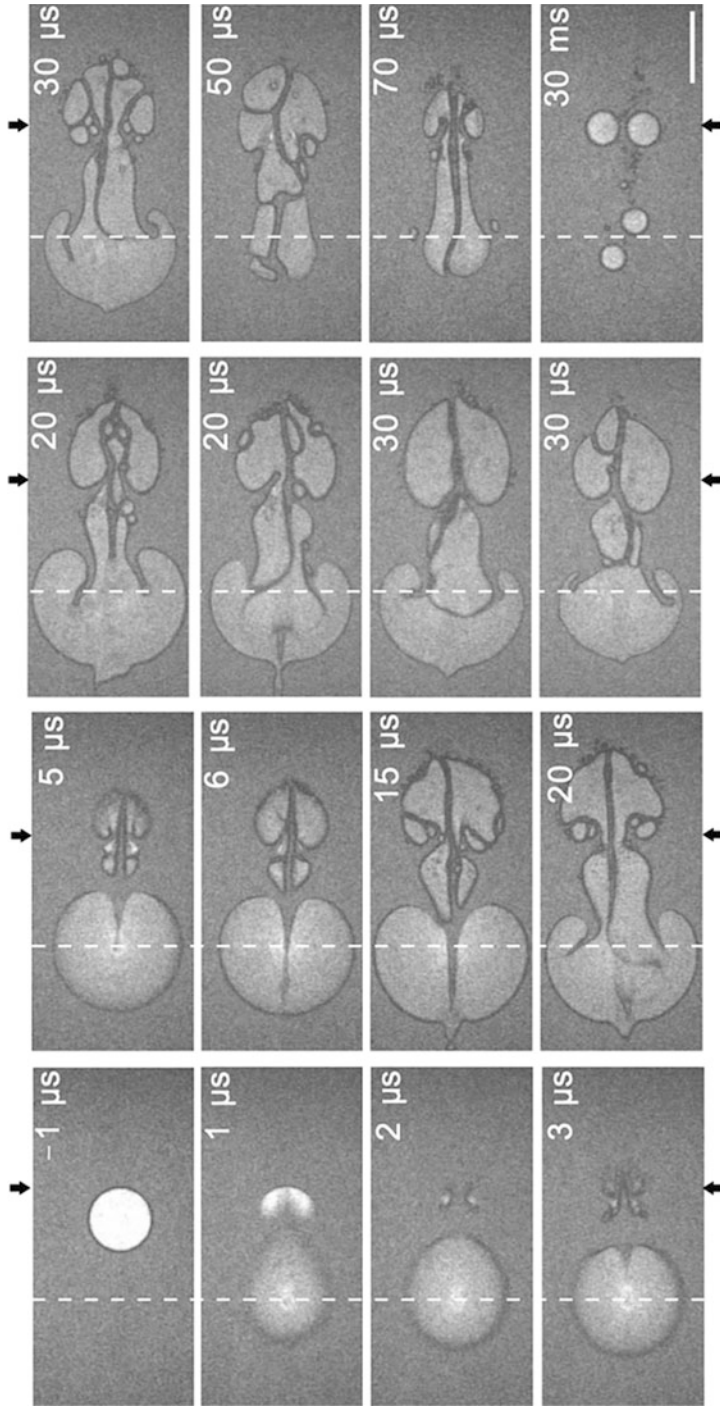
Fig. 12 Snapshots showing the bubble shape evolution for a gas bubble separated 0.225 mm from a cavitation bubble. The vertical dashed line and the arrows indicate the initial horizontal positions of the center of cavitation bubble and the right edge of the gas bubble, respectively. The length of the scale bar 0.2 mm (Reproduced with permission from Ref. [54], Fig. 12)

may be provided by viruses to deliver the molecular load through the plasma membrane. Transfecting single cells on demand would be a helpful tool in the development of novel medication and several approaches exist. Single-cell electroporation [56], optoporation [57], and sonoporation [58] have been developed. The latter two are based on focused laser light to directly form a tiny hole in the membrane and on creating/driving a bubble near to a cell to induce sufficient shear [58]. While in general the term sonoporation is used for driving a stable microbubble by ultrasound, they can also be generated with focused laser light in a microfluidic chip [59]. The technique has been considerably advanced using two laser pulses triggered at different times to create two bubbles with a high-speed jet [15, 60]. This tandem bubble technique has been carefully analyzed in the bulk liquid by Han et al. [61].

If the cavitation bubble is created within the cell, e.g., by focusing the laser pulse directly into the cell, cell lysis may be induced [62]. This technology may be suitable for collecting cellular content of single cells for µTAS systems. The strong shear flows (see section "Computational Fluid Dynamics (CFD) of Single Bubbles") created by an expanding cavitation can be utilized to test the rheological properties of cells. Quinto-Su et al. [63] demonstrated this in a study where original red blood cells were compared to cells that have been treated biochemically to soften and harden the plasma membrane. This nearly impulsive stretching of cells near to a cavitation bubble in a confined geometry can probe the cell's yield strength. Interestingly, maximum areal strain of a red blood cell is about an order of magnitude larger as compared to a quasi-static stretching [64, 65].

Generation and Coalescence Droplets

A pulsed laser-based droplet generator has been demonstrated by Park et al. [66]. The device consists of two parallel channels in which two immiscible fluids are flowing. They are connected by a nozzle and the laser is focused in one of the channels close to the nozzle. The expanding bubble accelerates some fluid into the second channel, thereby creating a droplet. The droplet size can be varied by changing the location of the laser focus and the laser energy allowing to produce highly repeatable droplets at rates of up to 10 kHz.

Having already a train of droplets and focusing a laser into that train, coalescence can be induced by the expanding bubble driving the interfaces into each other. Once the continuous phase separating the droplets ruptures coalescence is obtained. This technique has been demonstrated for on-demand droplet merging by Li et al. [67].

Interaction with Nano Objects

Two bubbles created simultaneously side by side in a microfluidic channel develop a liquid jet pointing toward each other, very similar to a single bubble created at half the distance to a rigid boundary. However, if one of the bubbles is considerably smaller, it will collapse and develop the jetting flow first. Once the second bubble collapses, it does not "see" the smaller collapsed bubble and shrinks more radially symmetric. The result is a directed flow from the smaller bubble to the larger bubble toward a stagnation point. A long object with dimensions oriented normal to the jet

flow direction will experience a largely nonuniform force which will bend the object. This allows to measure the elastic properties of suspended objects, such as multiwalled carbon nanotubes [68] and copper nanowires [69].

Generation of Fundamental Microfluidic Flows

A wide variety of flows can be generated by single and multiple bubbles. As described above, these flows can be used to separate cells, generate droplets, and deform thin objects. In microfluidic designs fundamental flows are combined to solve specific tasks. Here we'll provide a summary of fundamental flows cavitation bubbles can generate, i.e., mixing, pumping, switch, and cavitation induction. These flows may be combined, scaled, and optimized to solve a more complex microfluidic handling task.

Mixing

Mixing of miscible and low-viscosity fluids on large scale is a simple task; here the turbulent eddies support the entrainment the fluids such that molecular diffusion is occurring on a large interface. In microfluidics, surface forces keep flows even at rather high velocity laminar and therefore diffusion can only act on small interfacial areas. There are various ways to create these entraining eddies in microfluidics, one of them is to utilize the flow created by single cavitation bubbles. In the work of Hellman et al. [70], the horseradish peroxidase-catalyzed reaction is utilized to demonstrate rapid mixing after the collapse of a cavitation bubble. The bubble dynamics and liquid motion are shown in Fig. 13. Here two jets from along the channel direction meet and create a region of strong vorticity. This vortex region spreads and mixes both liquids over a timescale of milliseconds.

Pumping

When a cavitation bubble is expanding and collapsing in a channel, the location of expansion and collapse may differ if the bubble experiences different pressure boundary conditions during expansion (outflow of the tube into the reservoirs) and collapse (inflow). The reason is that for a finite Reynolds number, a jetting flow is generated during the bubble expansion, while during bubble collapse a sink flow is developed. Yuan et al. [40] model the flow for an arbitrary number of bubbles oscillating in the tube. They show that a single bubble being positioned not at the midpoint of the tube will create a net flow over one oscillation cycle, i.e., pump liquid to the side posing the lower resistance. The model has been refined by Ory et al. [41] considering the heat transfer and axisymmetric viscous flow.

A different pumping mechanism was used by Dijkink et al. [16]; they create a single bubble in chamber near to the exit channel. The channel width is considerably smaller than the chamber dimensions and the bubble at maximum expansion. Therefore the bubble dynamics is only little affected by the channel and shows a similar behavior as if it would collapse near a rigid boundary (see [71]): during bubble expansion it pushes some liquid into the channel; during early collapse,
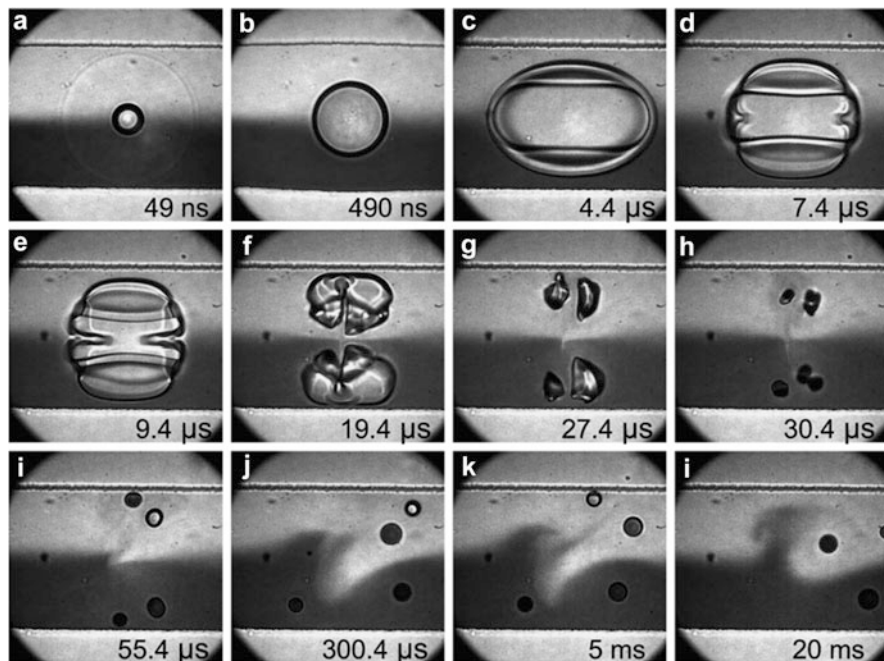
Fig. 13 Stroboscopic image series of a cavitation bubble expanding and collapsing and the subsequent mixing in a 200 μm wide microfluidic channel (Reproduced with permission from Ref. [70], Fig. 3)

liquid is sucked back into the chamber; and once the jet forms, liquid is pushed again into the chamber (Fig. 14). A net flux into the channel remains, resembling a positive displacement pump.

Switching and Sorting

Rapid switching of fluid flows allows the sorting of a stream of particles or droplets on demand. Wu et al. [72] demonstrated that a stream of particles can be deflected using the pressure generated from an expanding cavitation bubble. Their key idea is to separate the flow to be switched from a stagnant actuator chamber through an elastic membrane. Once a bubble is nucleated in the actuator chamber, it blocks the main flow which enters a y-region. At a suitable deflection strength, the particles or droplets can be switched between the two exit channels; see Fig. 15. This flow sorter was developed into a fluorescence cell sorter by Wu et al. [73].

Homogeneous Cavitation

During the early state of a violently expanding bubble, a shock wave is emitted which can be utilized for localized nucleation of secondary cavitation. An example of the shock wave emission is shown in frame (a) of Fig. 13. The initial pressure close to the bubble is of the order of gigapascals [74]. However it quickly drops to much lower pressures over time.
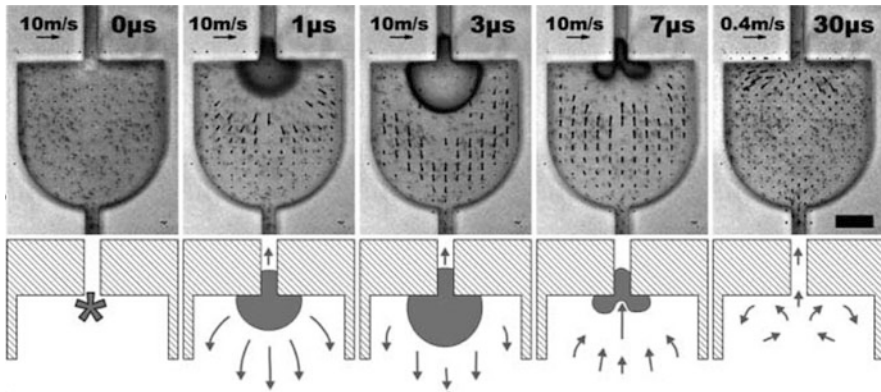
Fig. 14 Selected frames depicted the working principle a single bubble base pump displaying the microfluidic chamber (*below*), the bubble, and the channel (*on top*) into which the liquid is pumped. Overlayed are measured velocity vectors of the flow fields and a representation of the flow field is sketched below. The first image shows the chamber just before bubble initiation; 1 μs later the bubble is rapidly expanding, reaching its maximum size at 3 μs. Afterward the bubble starts to collapse creating a jet which is directed into the channel. In the last frame, the bubble has completely disappeared leaving some recirculating flow. The scale bar denotes 50 μm (Reproduced with permission from Ref. [71], Fig. 2)

Nucleation of secondary cavitation can be induced if the homogeneous cavitation threshold of the liquid is overcome. Although the precise value and the thermodynamic pathway for yield/rupture of water have not been settled [75], it is of the order of several hundreds of megapascals. The positive pressure pulse from the expanding bubble can be inverted by reflecting it at an acoustically soft boundary, e.g., a liquid–gas interface. The interface can be static as was shown in Ando et al. [74] or that of a neighboring expanding cavitation bubble as demonstrated by Quinto-Su and Ando [76]. In both cases the onset of homogeneous cavitation was found at -60 MPa and -20 MPa, respectively.

Applications Involving Bubbles in Confinement

In this section we present a brief discussion of a number of applications involving bubbles oscillating in a microfluidic environment. We focus on novel applications, such as using the ultrasonic bubbles to generate emulsions, and common biomedical applications involving cells.

Emulsification

When the cavitation bubbles in a microfluidic channel are excited strongly, they are capable of breaking up interfaces or fluid boundaries in a microfluidic channel or
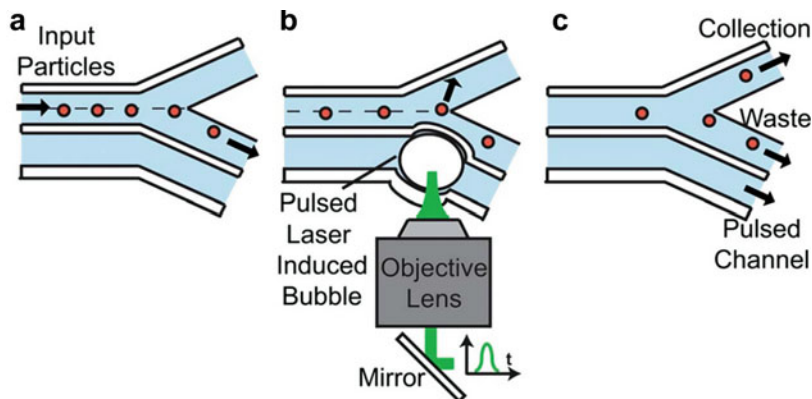
Fig. 15 Working principle of the cavitation bubble-based microfluidic switch. (**a**) Before switching, a train of particles/drops are transported into the waste channel. (**b**) A cavitation bubble is induced in the actuation chamber (pulsed channel) by a focused pulsed laser beam. The bubble expansion deforms the thin membrane and squeezes the fluid in the sample channel. (**c**) The selected particle is transported into the collection channel (Reproduced with permission from Ref. [72], Fig. 1)

chamber. Ohl et al. [21] report the use of the strongly oscillating bubbles to generate emulsions. Their setup is similar to that in Fig. 2 with the addition of a second liquid inlet. The two liquids are typically immiscible (e.g., oil and water) but not necessary so. The bubbles are generated as previously discussed (section "Ultrasound Contrast Agents"). However, in this case, there is an additional liquid–liquid interface.

Figure 16 shows the creation process of oil–water emulsion (viscosity ratio = 10:1). The liquid lining the microchannel is colored water, and a silicone oil is in the middle of the channel. The bubbles oscillate violently when the system is sonicated at its resonant frequency of about 100 kHz (driving voltage is about 200 V). They move along the channel rupturing the liquid–liquid interface, by creating high shear stress when oscillating and high-speed jets when collapsing. This process creates droplets in the channel. Further sonication causes the droplets to fragment into smaller droplets. It is found that the duration of ultrasound exposure is positively correlated to the uniformity of the emulsion and inversely correlated to the size of the droplets.

This system is highly efficient as submicron monodispersed emulsions as shown in Figs. 17 and 18 are created within milliseconds. Figure 17 shows a uniform emulsion of water in oil. Each of the droplet is about 1 μm in radius. A similar emulsion of oil in water is given in Fig. 18. In this case, the emulsion is slightly less uniform but longer sonication duration may increase the uniformity of the droplets formed. The system is highly versatile as emulsion of liquids with viscosity ratio up to 1000 has been produced.

Kentish et al. [77] use a sonic horn to generate nano-size droplets to form oil-in-water emulsions in a microfluidic chamber. Many other microfluidic emulsion generation systems make use of flow focusing instead on ultrasound and bubbles.
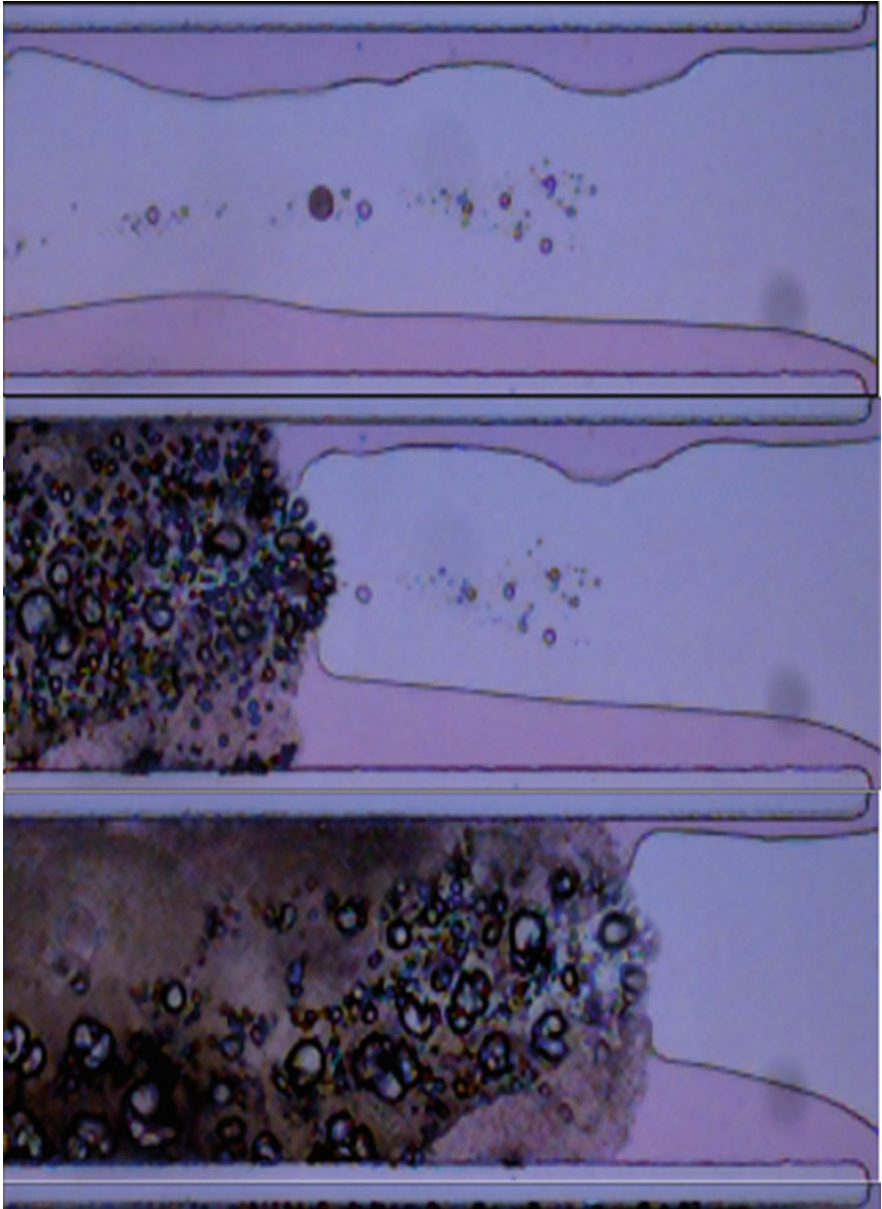
Fig. 16 The process of generating a water-in-oil emulsion. The bubbles are created as described in [10]. The flow in the channel induces the bubbles to move. They rupture the liquid–liquid interfaces, and droplets are formed
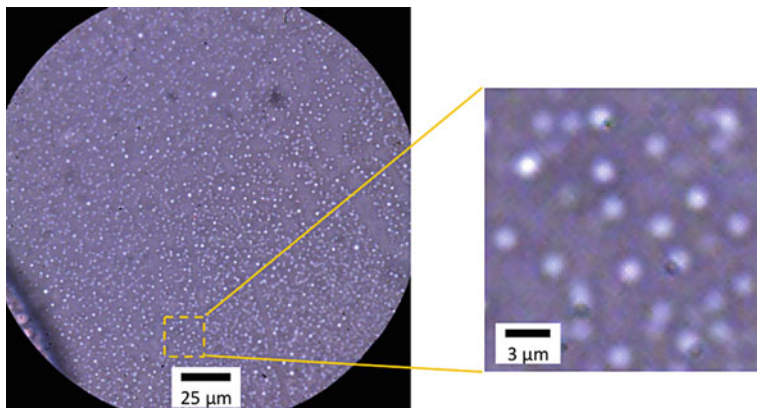
Fig. 17 Water-in-oil emulsion created in the microfluidic channel after sonification. The oil–water viscosity ratio is 100. The sub-figure on the *right* shows a magnified view of the area indicated
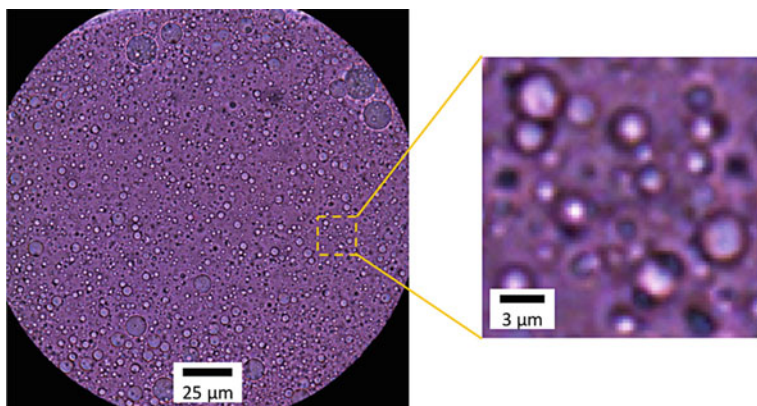
Fig. 18 Oil-in-water emulsion created in a microfluidic channel. The oil–water viscosity ratio is 100. The sub-figure on the *right* shows a magnified view of the region indicated

Some designs generate droplets through edifies or gaps in the microchannel, and others make use of mechanical parts such as a rotor to fragment the droplets. Recent reviews [78, 79] give good summaries of the current state of technology involved in the generation of emulsions in microfluidics.

Sonochemistry and Sonoluminescence

The strongly oscillating bubbles in a microfluidic channel generate transient regions of high temperature and pressure. Temperatures as high as 5000 °C and pressure as

high as 500 MPa have been measured [80]. The enormous energy concentrations in localized positions (where the bubbles collapse) enable chemicals to overcome reaction energy barrier. This branch of chemistry is known as sonochemistry. Sonochemistry is usually performed in bulk solution (within chemical flasks) using sonic horns. It is difficult to induce sonochemistry in microfluidics, due to the small volume of fluid and the problem of generating ultrasonic cavitation bubbles within the channels. Tandiono et al. [6] report the first success in generating chemiluminescence and sonoluminescence in microfluidics using a similar setup as described in Fig. 2.

The chemiluminescence described in [11] is the emission of light from the oxidation of luminol in a sodium carbonate base solution [81, 82]. The oxidation process is caused by the radicals H and OH which are produced by the ultrasonic bubbles from water (H_2O). The radicals subsequently trigger the formation of an unstable amino phthalate derivative with electrons in an excited state. As the chemical relaxes to lower-energy states, excess energy is emitted as a visible bluish light.

The image of the blue light emitted from chemiluminescence of luminol is captured by an intensified and cooled CCD camera (Fig. 19). The light is seen at the location where the cavitation bubbles are located (at the gas–liquid interfaces). The gray outline of the microfluidic channels which is taken with side illumination is superimposed to indicate the channel location. The green dash lines overlaid show the locations of the liquid slug.

Tandiono et al. [11] also show the evidence for sonoluminescence in their microfluidic system when it is strongly driven (driving voltage = 230 V). Sonoluminescence is the emission of light from the rapid heating of the bubble interior (during ultrasonic bubble collapse) without the use of chemicals. Figure 20 shows the light emission as detected by a photomultiplier. The microfluidic system is excited 100 times with 5000 cycles of ultrasound waves (on–off ratio is 0.01). It is noted that the amount of light detected in the sonoluminescence experiment is much lower than that from the chemiluminescence experiment. This is perhaps due to the fact that only a few of the bubble which collapses in the confined geometry of the microfluidic channels are sufficiently strong to induce sonoluminescence.

In a larger container, Rivas et al. [83] measure luminol chemiluminescence and sonoluminescence emission due to the oscillation and collapse of multiple bubbles generated from micromachined pits (15 μm in radius). Ultrasound is generated by a transducer placed at the bottom of a disk-shaped reactor and coupled to the glass bottom of the reactor. The plates containing the pits are arranged in several configurations and are submerged in the reactor and sonicated with different solutions. They report that the light emission is due to the transient cavitation nucleated by the microbubbles in the pits.

Tuziuti [84] investigate the effect of dissolved gas degree of saturation (DOS) on sonochemistry in a single microfluidic channel compared to a reactor which is millimeter in size. He measures the chemiluminescence intensity and finds that the sonochemical reaction in the microchannel needs lower power density for the same unit volume output. The 3D reactor requires higher power density and lower DOS to
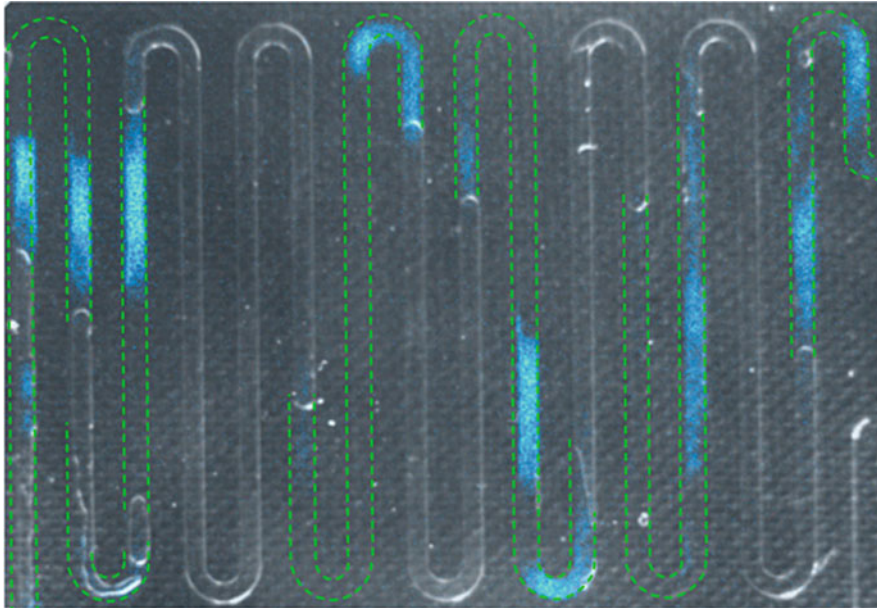
Fig. 19 Luminol chemiluminescence from cavitation bubble in microfluidic channels. The superimposed gray outline of the channel shows the distribution of the liquid and gas phases. The *green lines* indicate the locations of the liquid slugs. The bluish light from the oxidation of luminol is captured with an intensified and cooled CCD camera (Reproduced with permission from Ref. [11], Fig. 2a)

allow effective cavitation oscillations. He postulates that sonochemistry is more efficient and homogeneous in a microchannel.

Sonochemistry in microfluidics has the advantage of requiring only small amount of chemical fluids. The geometry allows direct observation of the relation between the ultrasonic bubbles, the sonochemistry, and the emission of light. The flexibility in microfluidic system design allows further optimization of these processes and customizations required for specific applications.

Biomedical Applications

Apart from chemistry-related applications, ultrasonic bubbles are utilized in various biomedical-related application of microfluidics. The small size of the channels is ideal for visualization of the manipulation of small objects such as cells and DNA. The controlled flow and ultrasound deployment allow for gentle handling of cells as well as applying localized shear stresses for cell lysis and fragmentation. In this section, several applications involving bacteria, yeast cell, red blood cells, and other biological tissues are discussed.
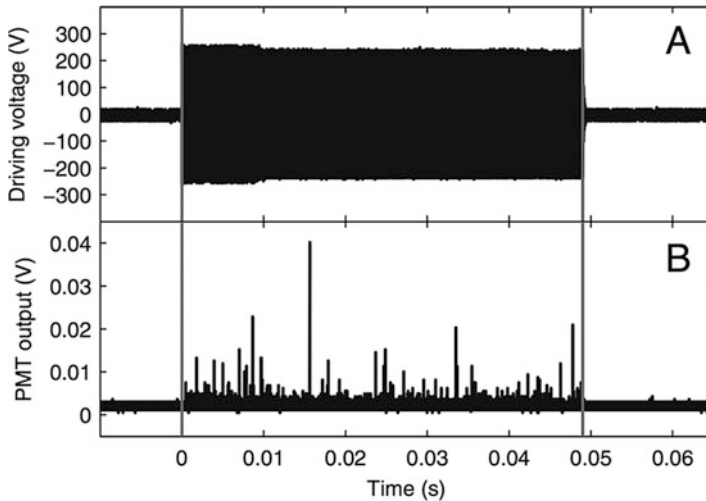
Fig. 20 Sonoluminescence signal from the microfluidic channels. (**a**) A driving voltage of 230 V is applied for 5000 cycles at the frequency of 103.6 kHz. (**b**) The light emission recorded by the photomultiplier from 100 repeated signals of (**a**). The light emission stops as soon as the ultrasound is turned off (Figure reproduced with permission from Ref. [6], Fig. 4)

Cell Stretching and Rupture

The harvesting of cellular content for analysis and profiling is an important process in biotechnology. Currently sonication is done in bulk medium using a vibrating probe which is inserted directly into the medium [85]. The ultrasound from the probe creates cavitation bubbles which oscillate and collapse. These bubbles generate mechanical shear stress on the cells and lyse them [86]. However this process is inefficient as some energy is lost as heat, and large amount of cells (medium in milliliter) is required.

Using microfluidics, however, the process is potentially more controlled. The cells could be lysed by different means in a microfluidic system: chemical [87], thermal [88], electrical [89], or mechanical [90]. Tandiono et al. [19] describe the use of a mechanical lysis of *Escherichia coli* bacterium and *Pichia pastoris* yeast cells using ultrasound in microfluidics. The gram-negative bacterium and the yeast cells are chosen because they are common microbial host cells that are used for screening of clones from genomic libraries and heterologous protein expression [91, 92]. Both cells allow the functional expression of multiple proteins in parallel in microplate assay. These proteins can be made amenable to microscale analysis.

The microfluidic system used in the experiment consists of a meandering channel, with two inputs (one for gas and one for liquid), and an outlet similar to the one in Fig. 2. The cells are mixed with the input liquid before the liquid comes into contact with the gas to form a slug after the T-junction. The main channel has a width of 500 μm and a depth of 20 μm. The ultrasound is generated by four transducers which are attached on the same glass slide as the PDMS (polydimethylsiloxane) slab

containing the microfluidic channels. Sonication is done in burst with 5-second intervals. The transducer is driven with 200 V at resonant frequency of the system (~130 kHz).

The effect of the sonication on the green fluorescent protein (GFP) expressing *E. coli* is shown in Fig. 21. Before the ultrasound is applied (Fig. 21a, left), the rod-shaped bacteria are seen to fluoresce in green. During sonication, the fluid movement and intense interaction between the bubbles and the cells are shown in the motion-blurred Fig. 21a (center). After the ultrasound is turned off, the flow in the channel stops. However it is clear that no intact bacteria remain (Fig. 21a, right). The supernatant appears greenish with the intracellular content from the lysed cells. Bright field microscopy (Fig. 21b) shows the microfluidic channel with the bacteria (left). After sonication, all of the bacteria are fragmented (right).

Tandiono et al. [19] also sonicate *Pichia pastoris* yeast cells using the same microfluidic system. The yeast cells harboring the pAcGFP1 (Clontech) and pGAP-EGFPd vectors are used. These cells have rigid extracellular cell wall which is made of a layered mesh of embedded glucans, chitin, and mannoproteins. The cell wall provides structural support that makes the yeast cell difficult to lyse.

Figure 22 shows the amount of DNA (deoxyribonucleic acid) released from the *P. pastoris* over time as quantified using qRT-PCR (real-time polymerase chain reaction) analysis. Both axes are logarithmically scaled. With longer sonication, the DNA concentration increases. It levels off after about 1 second. Further sonication leads to a decrease in DNA concentration measured. This may be an indication of DNA damage due to chemical exposure (such as the OH radicals) [11] or mechanical shear stress.

Marentis et al. [93] use a microfluidic ultrasound system, which they term microsonicator, to lyse mammalian cells (HL-60) and bacterial spores (*Bacillus subtilis*). The microfluidic channel used in [93] is 500 μm in width and 500 μm in height. It is sonicated from below by an attached transducer at 380 MHz. They report that 77.5 % of the HL-60 cells are lysed at a flow rate of 50 L/min. For the more difficult to lyse spores, at 5 L/min, 54 % of the *B. subtilis* spores are lysed. Many other microfluidic systems for cell lysis do not make use of ultrasound [94].

Another application of ultrasonic microfluidic system is for sorting and separation of cells or blood content [95–97]. In these systems standing waves are utilized. Augustsson et al. [95] use acoustophoresis to separate prostate cancer cells from white blood cells. Yang and Soh [96] develop an ultrasonic microfluidic system that sorts viable cells from a cell mixture containing both viable and nonviable cells. Ding et al. [97] use precisely controlled standing surface acoustic wave (SSAW) multichannel microfluidic system for cell sorting and processing. It is noted that these applications do not make use of ultrasonic bubbles.

When a laser-generated bubble is oscillating next to a red blood cell (RBC), it has been shown that the cell can be stretched [63] (also see Section "Interaction with Cells"). Tandiono et al. [20] extend the study by observing the interaction between one RBC and a single laser-generated cavitation bubble in a microfluidic chamber. The cell is placed in a microchamber which has a height of 20 μm. A pulsed laser is used to generate the cavitation bubble. Figure 23 shows the cell's response next to
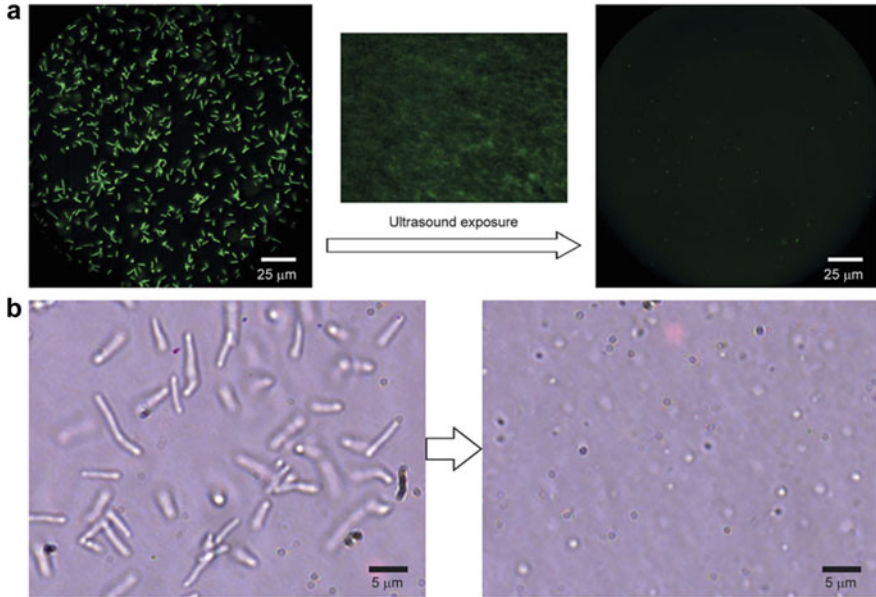
Fig. 21 Images of green fluorescent protein (GFP) *Escherichia coli* taken before and after sonication. (**a**) Fluorescence microscopy imaging of the bacteria before (*left*), during (*middle*), and after (*right*) ultrasound exposure. All bacteria are lysed with supernatant which appears greenish due to the intracellular content. (**b**) Bright field microscopy images of the bacteria before (*left*) and after (*right*) sonication. All bacteria are fragmented (Figure reproduced with permission from Ref. [19], Fig. 2)

the bubble. Initially (frame 1), the cell (4 μm in radius) is 84 μm away from the bubble center. As the bubble expands, the bottom of the cell is pushed away and the cell appears being "flattened" (frames 2–4). The bubble reaches its maximum size (100 μm in radius) at frame 4. After which, the bubble collapses. The flow generated by the rapid collapse of the bubble causes the RBC to stretch. Eventually it is seen to be elongated (frame 12).

Tandiono et al. [20] attempt to understand the stretching mechanism with numerical simulation. A boundary element method code is used to simulate the interaction of an elastic fluid vesicle and a vapor bubble. Details of the modeling methodology are reported in previous publications [98, 99]. The elasticity on the cell is described by an elasticity parameter, K, where $K = \frac{\sigma}{R_c p_\infty}$, σ is the surface tension, R_c is the cell radius, and p_∞ is the ambient pressure. Figure 24 shows the result of a cell with moderate elasticity ($K = 0.067$). The cell is flattened at the bottom and pushed up slightly as the bubble expands. When the bubble collapses, the cell bottom is initially stretched, and the whole cell is elongated at the end of the collapse.

For a rigid cell with $K = 1.33$, there is hardly any deformation on the cell throughout the bubble oscillation. As shown in Fig. 25, the rigid cell undergoes mild oscillation and returns to its original round shape after the bubble has collapsed. For a very "soft" cell with no surface tension ($K = 0$), it deforms as the bubble
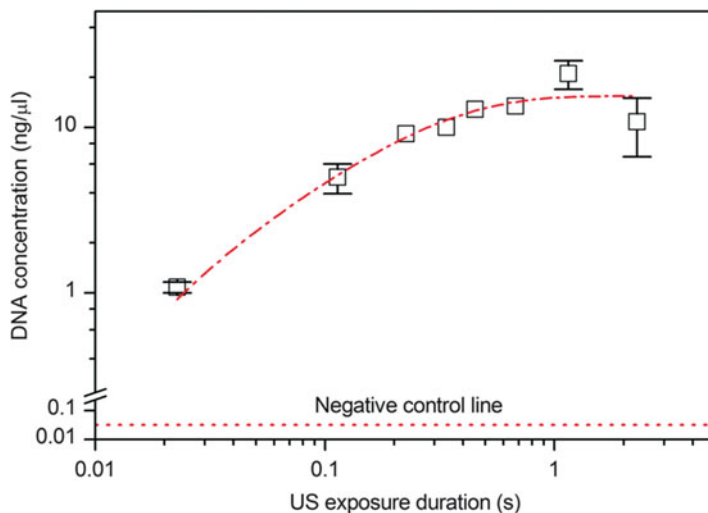
Fig. 22 DNA concentration of the treated *Pichia pastoris* yeast cell with increasing sonication. The error bars are obtained from multiple runs (2–4 runs). It is seen that DNA concentration increases with longer ultrasound exposure. After about 1 s, the amount of DNA levels is off. The negative control is obtained from untreated samples (Figure reproduced with permission from Ref. [19], (Fig. 6)

expands. But it regains its shape upon bubble collapse. From a parametric study, it is understood that only cells within certain elasticity range demonstrate the "stretching" phenomena. Also maximum elongation occurs when the oscillations of the bubble and cell are out of phase, that is, the bubble oscillates at half the oscillation time of the cell.

The ease of manipulating small entities, like cells, and the low volume of liquid needed (low-resource requirement) are important driving forces behind the use of microfluidics for biomedical technology. Diagnostic kits using microfluidics have been developed as a point-of-care device or as a substitute to the time-consuming laboratory testing [100–102] (note that no acoustic cavitation is used in these systems). For example, Chin et al. [100] use a microfluidic chip to perform ELISA-like assay for the detection of human immunodeficiency virus (HIV) in blood samples. The device requires only 20-minute processing time, needs small volume of blood (obtainable from a lancet puncture), and uses cheap photodetectors for rapid optical readout. Tests done using patient blood samples from a hospital in Rwanda show results that match the sensitivity and specificity of a rival laboratory-based ELISA test. Another clinical use of microfluidics is in the rapid purification and analysis of neutrophils. Warner et al. [101] design and utilize a microfluidic chip to isolate human blood polymorphonuclear cells (PMNs). These cells are then analyzed for gene expression using a commercial GeneChips. The results show unique genomic expression among patients with acute respiratory distress syndrome (as compared to healthy control subjects). Kotz et al. [102] make a microfluidic chip that is capable of isolating neutrophils from whole blood samples and "on-chip"
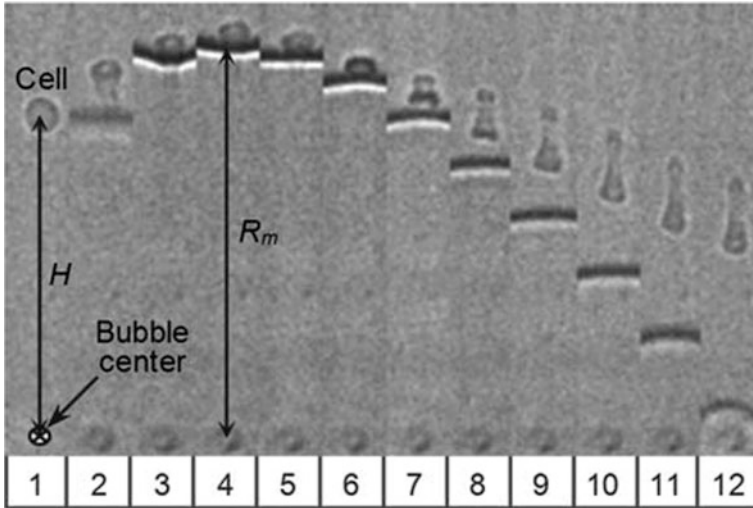
Fig. 23 A large cavitation bubble (partially seen) generated by a pulsed laser expands and collapses near a red blood cell. There are 12 frames shown taken at an interval of 2.78 ms (framing rate = 360,000 fps). The frame width is 16 μm. The cell is "flattened" during bubble expansion (frames 1–4) and then "stretched" during bubble collapse (Figure reproduced with permission from Ref. [20], Fig. 2)
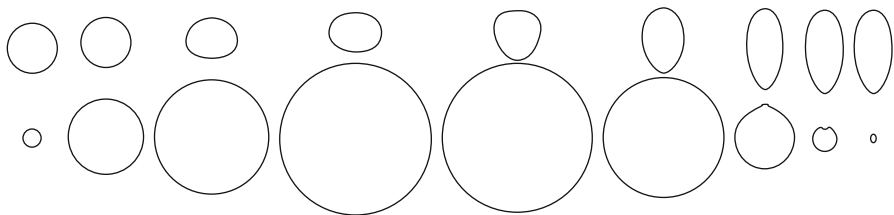
Fig. 24 Interaction of a "floppy" cell (*on top*) and a cavitation bubble (*below*). The cell has an elasticity parameter, $K = 0.067$. It is initially "flattened" when the bubble expands, and then it is "stretched" as the bubble collapses (Reproduced with permission from Ref. [20], Fig. 6)

processing for mRNA and protein isolation for genomics and proteomics. The device is tested on blood samples from trauma and burn patients with success. In conclusion, these microfluidic diagnostic techniques have the advantages of rapid processing, small sample volume requirement, and low-cost.

Conclusions

In general, the use of microfluidics as a research investigative tool has been expanded to practical and commercial products in recent years. It is used in fluid
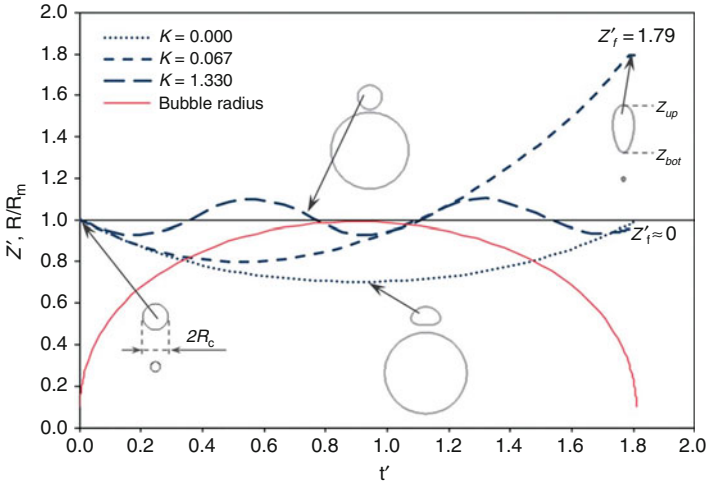
Fig. 25 The vertical deformation of the cell, Z', as a function of the dimensionless time, t': $Z' = \frac{z_{up} - z_{bottom}}{2R_c}$, where z_{up} is the top coordinate, and z_{bottom} is the lowest coordinate of the cell along the axis of symmetry, z. $t' = \frac{t}{R_m \sqrt{\rho_1/p_\infty}}$, where R_m is the maximum bubble radius, p_1 is the density of the fluid inside the cell, and p_∞ is the ambient pressure. The cell with no surface tension ($K = 0$) is flattened as the bubble expands but regains its shape upon bubble collapse. The rigid cell ($K = 1.33$) oscillates slightly as the bubble expands and collapses. Only the cell with moderate elasticity ($K = 0.067$) elongates after bubble collapses (Reproduced with permission from Ref. [21], Fig. 8)

dynamic studies for transport, sorting, mixing, emulsification, and the manufacturing of coated bubbles and droplets. It has also been used for chemical and biological analysis, clinical diagnostics, and treatment. In a 2006 *Nature* paper, Whiteside [103] has predicted that "(the) microfluidic technology will become a major theme in the analysis, and perhaps synthesis, of molecules." Indeed many microfluidic tools and systems have since been developed. However there are still limitations to be overcome, notably the lack of robustness and the difficulty in upscaling output volume. Most microfluidic devices that are made of PDMS (polydimethylsiloxane) are subjected to degradation after rapid use or thermal loading. The output volume of a microfluidic device is typically in the microliter, which is good for laboratory research or analysis but not practical for biotechnology processing and manufacturing. Nevertheless, it has remained an indispensable tool in scientific research. Its ability to facilitate visualization, its small input volume requirement, its potential for rapid processing and low-cost are advantages that will continue to fuel its development in the future.

A fruitful area for future study may be the simplification of current microfluidic designs which then would allow upscaling. Yet, to achieve this, electric engineers who are to integrate acoustic transducer, and fluid mechanics specialist and materials expert who are to design channels which can be mass produced, are needed. Then

instead of sonicating the bulk of a liquid with complex acoustics and bubble dynamics, simpler flows near to surfaces are obtained. We expect that breakthroughs in these geometries may be possible.

References

1. Blake JR, Taib BB, Doherty G (1986) Transient cavities near boundaries. Part 1. Rigid boundary. J Fluid Mech 170:479–497
2. Best JP, Kucera A (1992) A numerical investigation of non-spherical rebounding bubbles. J Fluid Mech 245:137–154
3. Lauterborn W, Kurz T (2010) Physics of bubble oscillations. Rep Prog Phys 73(10):106501
4. Flynn HG (1975) Cavitation dynamics: II. Free pulsations and models for cavitation bubbles. J Acoust Soc Am 58(6):1160–1170
5. Mishra C, Peles Y (2005) Cavitation in flow through a micro-orifice inside a silicon microchannel. Phys Fluids 17(1):013601
6. Duan C, Karnik R, Lu M-C, Majumdar A (2012) Evaporation-induced cavitation in nanofluidic channels. Proc Natl Acad Sci 109(10):3688–3693
7. Wheeler TD, Stroock AD (2008) The transpiration of water at negative pressures in a synthetic tree. Nature 455(7210):208–212
8. Vincent O, Marmottant P, Quinto-Su PA, Ohl C-D (2012) Birth and growth of cavitation bubbles within water under tension confined in a simple synthetic tree. Phys Rev Lett 108 (18):184502
9. Taylor MT, Belgrader P, Furman BJ, Pourahmadi F, Kovacs GTA, Northrup MA (2001) Lysing bacterial spores by sonication through a flexible interface in a microfluidic system. Anal Chem 73(3):492–496
10. Tandiono, Ohl S-W, Ow DS-W, Klaseboer E, Wong VVT, Camattari A, Ohl C-D (2010) Creation of cavitation activity in a microfluidic device through acoustically driven capillary waves. Lab Chip 10(14):1848–1855
11. Tandiono, Ohl S-W, Ow DSW, Klaseboer E, Wong VV, Dumke R, Ohl C-D (2011) Sonochemistry and sonoluminescence in microfluidics. Proc Natl Acad Sci 108 (15):5996–5998
12. Xu J, Attinger D (2007) Control and ultrasonic actuation of a gas–liquid interface in a microfluidic chip. J Micromech Microeng 17(3):609–616
13. Chen Y-H, Chu H-Y, Lin I (2006) Interaction and fragmentation of pulsed laser induced microbubbles in a narrow gap. Phys Rev Lett 96(3):034505
14. Vogel A, Venugopalan V (2003) Mechanisms of pulsed laser ablation of biological tissues. Chem Rev 103(2):577–644
15. Sankin GN, Yuan F, Zhong P (2010) Pulsating tandem microbubble for localized and directional single-cell membrane poration. Phys Rev Lett 105(7):078101
16. Dijkink R, Ohl C-D (2008) Laser-induced cavitation based micropump. Lab Chip 8 (10):1676–1681
17. Suh YK, Kang S (2010) A review on mixing in microfluidics. Micromachines 1(3):82–111
18. Iida Y, Yasui K, Tuziuti T, Sivakumar M, Endo Y (2004) Ultrasonic cavitation in microspace. Chem Commun 20:2280–2281
19. Tandiono T, Ow DS-W, Driessen L, Chin CS-H, Klaseboer E, Choo AB-H, Ohl S-W, Ohl C-D (2012) Sonolysis of *Escherichia coli* and *Pichia pastoris* in microfluidics. Lab Chip 12 (4):780–786

20. Tandiono T, Klaseboer E, Ohl S-W, Ow DS-W, Choo AB-H, Li F, Ohl C-D (2013) Resonant stretching of cells and other elastic objects from transient cavitation. Soft Matter 9 (36):8687–8696

21. Ohl S-W, Tandiono T, Klaseboer E, Ow D, Choo A, Li F, Ohl C-D (2014) Surfactant-free emulsification in microfluidics using strongly oscillating bubbles. J Acoust Soc Am 136 (4):2289–2289

22. Frinking PJA, Bouakaz A, Kirkhorn J, Ten Cate FJ, De Jong N (2000) Ultrasound contrast imaging: current and new potential methods. Ultrasound Med Biol 26(6):965–975

23. Unger E, Porter T, Lindner J, Grayburn P (2014) Cardiovascular drug delivery with ultrasound and microbubbles. Adv Drug Deliv Rev 72:110–126

24. Ferrara K, Pollard R, Borden M (2007) Ultrasound microbubble contrast agents: fundamentals and application to gene and drug delivery. Annu Rev Biomed Eng 9:415–447

25. Hernot S, Klibanov AL (2008) Microbubbles in ultrasound-triggered drug and gene delivery. Adv Drug Deliv Rev 60(10):1153–1166

26. Datta S, Coussios CC, Ammi AY, Mast TD, de Courten-Myers GM, Holland CK (2008) Ultrasound-enhanced thrombolysis using Definity® as a cavitation nucleation agent. Ultrasound Med Biol 34(9):1421–1433

27. Taniyama Y, Tachibana K, Hiraoka K, Aoki M, Yamamoto S, Matsumoto K, Nakamura T, Ogihara T, Kaneda Y, Morishita R (2002) Development of safe and efficient novel nonviral gene transfer using ultrasound: enhancement of transfection efficiency of naked plasmid DNA in skeletal muscle. Gene Ther 9(6):372–380

28. Wu J, Xie F, Lof J, Sayyed S, Porter TR (2015) Utilization of modified diagnostic ultrasound and microbubbles to reduce myocardial infarct size. Heart 101:1468–1474

29. O'Reilly MA, Hynynen K (2015) Emerging non-cancer applications of therapeutic ultrasound. Int J Hyperthermia 31(3):310–318

30. Guo H, Leung JCK, Chan LYY, Tsang AWL, Lam MF, Lan HY, Lai KN (2007) Ultrasound-contrast agent mediated naked gene delivery in the peritoneal cavity of adult rat. Gene Ther 14 (24):1712–1720

31. Xiong S, Chin LK, Ando K, Tandiono T, Liu AQ, Ohl CD (2015) Droplet generation via a single bubble transformation in a nanofluidic channel. Lab Chip 15(6):1451–1457

32. Leighton TG (2011) The inertial terms in equations of motion for bubbles in tubular vessels or between plates. J Acoust Soc Am 130(5):3333–3338, New York

33. Luther S, Mettin R, Lauterborn W (2000) Modeling acoustic cavitation by a Lagrangian approach. In: AIP conference proceedings, IOP Institute Of Physics Publishing Ltd, New York pp. 351–354

34. Harkin A, Kaper TJ, Nadim A (2001) Coupled pulsation and translation of two gas bubbles in a liquid. J Fluid Mech 445:377–411

35. Ilinskii YA, Hamilton MF, Zabolotskaya EA (2007) Bubble interaction dynamics in Lagrangian and Hamiltonian mechanics. J Acoust Soc Am 121(2):786–795

36. Quinto-Su PA, Ohl C-D (2009) Interaction between two laser-induced cavitation bubbles in a quasi-two-dimensional geometry. J Fluid Mech 633:425–435

37. Elkouh AF (1975) Oscillating radial flow between parallel plates. Appl Sci Res 30(6):401–417

38. Von Kerczek CH (1999) A note about the radial diffuser. Acta mech 135(3–4):229–233

39. Li F, Mohammadzadeh M, Ohl CD (2013) Shear stress induced stretching of red blood cells by oscillating bubbles within a narrow gap. Bull Am Phys Soc 58

40. Yuan H, Prosperetti A (1999) The pumping effect of growing and collapsing bubbles in a tube. J Micromech Microeng 9(4):402

41. Ory E, Yuan H, Prosperetti A, Popinet S, Zaleski S (2000) Growth and collapse of a vapor bubble in a narrow tube. Phys Fluids 12(6):1268–1277

42. Ye T, Bull JL (2004) Direct numerical simulations of micro-bubble expansion in gas embolotherapy. J Biomech Eng 126(6):745–759

43. Ye T, Bull JL (2006) Microbubble expansion in a flexible tube. J Biomech Eng 128 (4):554–563

44. Philipp A, Lauterborn W (1998) Cavitation erosion by single laser-produced bubbles. J Fluid Mech 361:75–116
45. Gonzalez-Avila SR, Klaseboer E, Khoo BC, Ohl C-D (2011) Cavitation bubble dynamics in a liquid gap of variable height. J Fluid Mech 682:241–260
46. Zwaan E, Le Gac S, Tsuji K, Ohl C-D (2007) Controlled cavitation in microfluidic systems. Phys Rev Lett 98(25):254501
47. Lim KY, Quinto-Su PA, Klaseboer E, Khoo BC, Venugopalan V, Ohl CD (2010) Nonspherical laser-induced cavitation bubbles. Phys Rev E 81(1):016308
48. Delius M (1994) Medical applications and bioeffects of extracorporeal shock waves. Shock waves 4(2):55–72
49. Sankin GN, Simmons WN, Zhu SL, Zhong P (2005) Shock wave interaction with laser-generated single bubbles. Phys Rev Lett 95(3):034501
50. Johnsen E, Colonius T (2008) Shock-induced collapse of a gas bubble in shockwave lithotripsy. J Acoust Soc Am 124(4):2011–2020
51. Dowson D, Taylor CM (1979) Cavitation in bearings. Annu Rev Fluid Mech 11(1):35–65
52. Field JE (1992) Hot spot ignition mechanisms for explosives. Acc Chem Res 25(11):489–496
53. Saurel R, Lemetayer O (2001) A multiphase model for compressible flows with interfaces, shocks, detonation waves and cavitation. J Fluid Mech 431:239–271
54. Chen Y-H, Lin I (2008) Dynamics of impacting a bubble by another pulsed-laser-induced bubble: jetting, fragmentation, and entanglement. Phys Rev E 77(2):026304
55. Delale CF (ed) (2012) Bubble dynamics and shock waves, vol 8. Springer, Berlin, Heidelberg
56. Khine M, Lau A, Ionescu-Zanetti C, Seo J, Lee LP (2005) A single cell electroporation chip. Lab Chip 5(1):38–43
57. Stevenson DJ, Gunn-Moore FJ, Campbell P, Dholakia K (2010) Single cell optical transfection. J R Soc Interface 7(47):863–871
58. Annemieke VW, Kooiman K, Harteveld M, Marcia E, Folkert J, Versluis M, De Jong N (2006) Vibrating microbubbles poking individual cells: drug transfer into cells via sonoporation. J Control Release 112(2):149–155
59. Gac SL, Zwaan E, van den Berg A, Ohl C-D (2007) Sonoporation of suspension cells with a single cavitation bubble in a microfluidic confinement. Lab Chip 7(12):1666–1672
60. Hsiao C-T, Choi J-K, Singh S, Chahine GL, Hay TA, Ilinskii YA, Zabolotskaya EA, Hamilton MF, Sankin G, Yuan F, Zhong P (2013) Modelling single-and tandem-bubble dynamics between two parallel plates for biomedical applications. J Fluid Mech 716:137–170
61. Han B, Köhler K, Jungnickel K, Mettin R, Lauterborn W, Vogel A (2015) Dynamics of laser-induced bubble pairs. J Fluid Mech 771:706–742
62. Quinto-Su PA, Lai H-H, Yoon HH, Sims CE, Allbritton NL, Venugopalan V (2008) Examination of laser microbeam cell lysis in a PDMS microfluidic channel using time-resolved imaging. Lab Chip 8(3):408–414
63. Quinto-Su PA, Kuss C, Preiser PR, Ohl C-D (2011) Red blood cell rheology using single controlled laser-induced cavitation bubbles. Lab Chip 11(4):672–678
64. Li F, Chan CU, Ohl CD (2013) Yield strength of human erythrocyte membranes to impulsive stretching. Biophys J 105(4):872–879
65. Li F, Chan CU, Ohl CD (2014) Rebuttal to a comment by Richard E. Waugh on our article "Yield Strength of Human Erythrocyte Membranes to Impulsive Stretching". Biophys J 106 (8):1832
66. Park S-Y, Wu T-H, Chen Y, Teitell MA, Chiou P-Y (2011) High-speed droplet generation on demand driven by pulse laser-induced cavitation. Lab Chip 11(6):1010–1012
67. Li ZG, Ando K, Yu JQ, Liu AQ, Zhang JB, Ohl CD (2011) Fast on-demand droplet fusion using transient cavitation bubbles. Lab Chip 11(11):1879–1885
68. Quinto-Su PA, Huang XH, Gonzalez-Avila SR, Wu T, Ohl CD (2010) Manipulation and microrheology of carbon nanotubes with laser-induced cavitation bubbles. Phys Rev Lett 104 (1):014501

69. Huang X, Quinto-Su PA, Gonzalez-Avila SR, Wu T, Ohl C-D (2010) Controlled manipulation and in situ mechanical measurement of single co nanowire with a laser-induced cavitation bubble. Nano Lett 10(10):3846–3851
70. Hellman AN, Rau KR, Yoon HH, Bae S, Palmer JF, Phillips KS, Allbritton NL, Venugopalan V (2007) Laser-induced mixing in microfluidic channels. Anal Chem 79(12):4484–4492
71. Lew KSF, Klaseboer E, Khoo BC (2007) A collapsing bubble-induced micropump: an experimental study. Sensors Actuators A Phys 133(1):161–172
72. Wu T-H, Gao L, Wei K, Chiou EPY (2008) Pulsed laser triggered high speed microfluidic switch. In: Optical MEMs and nanophotonics, 2008 IEEE/LEOS International conference on, IEEE, pp. 19–20
73. Wu T-H, Chen Y, Park S-Y, Hong J, Teslaa T, Zhong JF, Di Carlo D, Teitell MA, Chiou P-Y (2012) Pulsed laser triggered high speed microfluidic fluorescence activated cell sorter. Lab Chip 12(7):1378–1383
74. Ando K, Liu A-Q, Ohl C-D (2012) Homogeneous nucleation in water in microfluidic channels. Phys Rev Lett 109(4):044501
75. Azouzi MEM, Ramboz C, Lenain J-F, Caupin F (2013) A coherent picture of water at extreme negative pressure. Nat Phys 9(1):38–41
76. Quinto-Su PA, Ando K (2013) Nucleating bubble clouds with a pair of laser-induced shocks and bubbles. J Fluid Mech 733:R3 (12 pages)
77. Kentish S, Wooster TJ, Ashokkumar M, Balachandran S, Mawson R, Simons L (2008) The use of ultrasonics for nanoemulsion preparation. Innovative Food Sci Emerg Technol 9(2):170–175
78. Maan AA, Schroën K, Boom R (2011) Spontaneous droplet formation techniques for mono-disperse emulsions preparation–perspectives for food applications. J Food Eng 107(3):334–346
79. Zhao C-X (2013) Multiphase flow microfluidics for the production of single or multiple emulsions for drug delivery. Adv Drug Deliv Rev 65(11):1420–1446
80. Suslick KS (1990) Sonochemistry. Science 247(4949):1439–1445
81. Henglein A, Ulrich R, Lilie J (1989) Luminescence and chemical action by pulsed ultrasound. J Am Chem Soc 111(6):1974–1979
82. Hatanaka S-i, Mitome H, Yasui K, Hayashi S (2002) Single-bubble sonochemiluminescence in aqueous luminol solutions. J Am Chem Soc 124(35):10250–10251
83. Fernandez Rivas D, Ashokkumar M, Leong T, Yasui K, Tuziuti T, Kentish S, Lohse D, Gardeniers HJGE (2012) Sonoluminescence and sonochemiluminescence from a microreactor. Ultrason Sonochem 19(6):1252–1259
84. Tuziuti T (2013) Influence of degree of gas saturation on sonochemiluminescence intensity resulting from microfluidic reactions. J Phys Chem A 117(41):10598–10603
85. Smart EJ, Ying Y-S, Mineo C, Anderson RG (1995) A detergent-free method for purifying caveolae membrane from tissue culture cells. Proc Natl Acad Sci 92(22):10104–10108
86. Hughes DE, Nyborg WL (1962) Cell disruption by ultrasound. Streaming and other activity around sonically induced bubbles is a cause of damage to living cells. Science 138(3537):108–114
87. Schilling EA, Kamholz AE, Yager P (2002) Cell lysis and protein extraction in a microfluidic device with detection by a fluorogenic enzyme assay. Anal Chem 74(8):1798–1804
88. Waters LC, Jacobson SC, Kroutchinina N, Khandurina J, Foote RS, Ramsey JM (1998) Microchip device for cell lysis, multiplex PCR amplification, and electrophoretic sizing. Anal Chem 70(1):158–162
89. Wang H-Y, Bhunia AK, Chang L (2006) A microfluidic flow-through device for high throughput electrical lysis of bacterial cells based on continuous dc voltage. Biosens Bioelectron 22(5):582–588
90. Di Carlo D, Jeong K-H, Lee LP (2003) Reagentless mechanical cell lysis by nanoscale barbs in microchannels for sample preparation. Lab Chip 3(4):287–291

91. Boettner M, Prinz B, Holz C, Stahl U, Lang C (2002) High-throughput screening for expression of heterologous proteins in the yeast Pichia pastoris. J Biotechnol 99(1):51–62

92. Daly R, Hearn MTW (2005) Expression of heterologous proteins in Pichia pastoris: a useful experimental tool in protein engineering and production. J Mol Recognit 18(2):119–138

93. Marentis TC, Kusler B, Yaralioglu GG, Liu S, Hæggström EO, Khuri-Yakub BT (2005) Microfluidic sonicator for real-time disruption of eukaryotic cells and bacterial spores for DNA analysis. Ultrasound Med Biol 31(9):1265–1277

94. Nan L, Jiang Z, Wei X (2014) Emerging microfluidic devices for cell lysis: a review. Lab Chip 14(6):1060–1073

95. Augustsson P, Magnusson C, Nordin M, Lilja H, Laurell T (2012) Microfluidic, label-free enrichment of prostate cancer cells in blood based on acoustophoresis. Anal Chem 84 (18):7954–7962

96. Yang AHJ, Soh HT (2012) Acoustophoretic sorting of viable mammalian cells in a microfluidic device. Anal Chem 84(24):10756–10762

97. Ding X, Steven Lin S-C, Lapsley MI, Li S, Guo X, Chan CY, Chiang I-K, Wang L, McCoy JP, Huang TJ (2012) Standing surface acoustic wave (SSAW) based multichannel cell sorting. Lab Chip 12(21):4228–4231

98. Wang QX, Yeo KS, Khoo BC, Lam KY (1996) Strong interaction between a buoyancy bubble and a free surface. Theor Comput Fluid Dyn 8(1):73–88

99. Klaseboer E, Khoo BC (2004) An oscillating bubble near an elastic material. J Appl Phys 96 (10):5808–5818

100. Chin CD, Laksanasopin T, Cheung YK, Steinmiller D, Linder V, Parsa H, Wang J et al (2011) Microfluidics-based diagnostics of infectious diseases in the developing world. Nat Med 17 (8):1015–1019

101. Warner EA, Kotz KT, Ungaro RF, Abouhamze AS, Lopez MC, Cuenca AG, Kelly-Scumpia KM et al (2011) Microfluidics-based capture of human neutrophils for expression analysis in blood and bronchoalveolar lavage. Lab Invest 91(12):1787–1795

102. Kotz KT, Xiao W, Miller-Graziano C, Qian W-J, Russom A, Warner EA, Moldawer LL et al (2010) Clinical microfluidics for neutrophil genomics and proteomics. Nat Med 16 (9):1042–1047

103. Whitesides GM (2006) The origins and the future of microfluidics. Nature 442(7101):368–373

Importance of Sonication and Solution Conditions on the Acoustic Cavitation Activity

Judy Lee

Contents

Abstract

Acoustic cavitation is known to induce extreme physical and chemical effects, all of which derive from the creation and violent collapse of bubbles as the sound wave propagates through a liquid medium. In order to capitalize on the benefits of acoustic cavitation for specific physical and chemical process applications, it is important to understand how cavitation activity varies under different sonication

J. Lee (✉)
Chemical and Process Engineering, University of Surrey, Guildford, Surrey, UK
e-mail: j.y.lee@surrey.ac.uk

and solution conditions. This chapter will first provide an introduction on bubble growth by rectified diffusion and bubble coalescence, which leads to the evolution of sonoluminescence (SL) and sonochemiluminescence (SCL) activity, and how these can be quantified. This will then be followed by a comprehensive review on the current state of knowledge relating to the influence sonication and solution properties, such as power, frequency, pulsing, dissolved gases, and surface-active solutes, have on bubble growth, SL, and SCL. This chapter will demonstrate the sensitivity of cavitation activity to small changes in sonication and solution properties, and why an awareness into these effects is important for optimizing ultrasound applications.

Introduction

When ultrasonic waves pass through a liquid medium, it can induce the occurrence of a phenomenon known as acoustic cavitation. This term is used to describe the creation of cavities (bubbles) or the expansion of preexisting cavities induced by ultrasound [1], as well as other effects such as bubble growth by rectified diffusion and inertial collapse of bubbles. These collapsing bubbles are capable of generating extreme temperatures and pressures [2] which can lead to the emission of light known as sonoluminescence (SL) and generate OH radicals and H_2O_2 molecules [3] for sonochemiluminescence (SCL) from luminol and high energy chemistry. It is these physical and chemical effects that are responsible for the employment of ultrasound in numerous applications such as cleaning, emulsification, degradation of pollutants, and nanoparticle synthesis. Although applications of ultrasound in the industry appear promising, there is a need to better understand and control cavitation activity and improve the efficiency of these applications before it is economically viable.

Acoustic cavitation is both dynamic and complex system. Depicted in Fig. 1 is a simplified summary of the various processes that a bubble can undergo in an acoustic field. The pressure threshold for acoustic cavitation is well below the tensile strength of water; therefore, the general consensus to the cause of cavitation is from existing gas nuclei in the liquid [1, 4] such as small gas bubbles stabilized against dissolution by a skin of organic impurities [5], gases trapped in motes [6], or crevices in solid surfaces [7, 8]. Degassing and filtering have shown to increase the cavitation threshold [6], which provided evidence to support the theory for the preexisting gas nuclei in liquids as the inception of cavitation. In addition, shelled microbubbles can be added to act as bubble nuclei and have been observed to decrease cavitation threshold [9]. Once a certain threshold of acoustic pressure is applied, these existing bubbles grow, either via rectified diffusion or coalescence pathway, to reach the
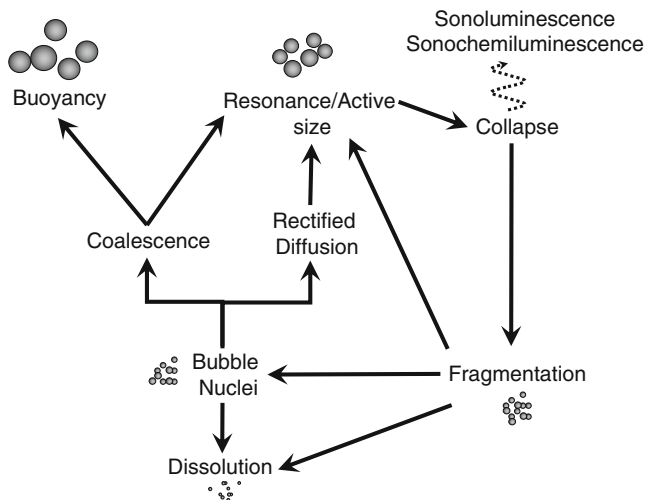
Fig. 1 Possible processes that a bubble in an acoustic field undergoes

resonance size for inertial collapse to take place, leading to the emission of light and sonochemical reactions. The collapse of the cavitation bubbles can fragment into smaller bubbles which can then act as bubble nuclei and undergo the cavitation cycle described in Fig. 1. Each of the pathways described in Fig. 1 is influenced by the solution conditions, such as dissolved gas concentration and presence of surface-active solutes, and sonication conditions such as frequency, power, and pulsing. These in turn can affect the population and spatial distribution of cavitation activity within the sonication reactor and hence the efficiency of the sonication system. The next few sections will provide an overview on the recent work and the current state of knowledge in this area.

Rectified Diffusion

When the acoustic pressure is above a certain threshold, a bubble will undergo a growth process known as rectified diffusion. This rectified diffusion process is used to describe the growth of bubbles by uneven mass transfer rate across the air-liquid interface [10]. This uneven growth was explained in terms of two effects [10], the "area" and the "shell" effect.

In the "area" effect, the rate of gas diffusion across the interface is proportional to the amount of surface area available for mass transfer. This surface area is greatest when the bubble is in the expanded state compared to when it is in the compressed state (Fig. 2). Hence, over a number of acoustic cycles, there is a net inflow of gas into the bubble resulting in a net growth. In the "shell" effect, consider a shell of liquid adjacent to the bubble wall (Fig. 2). As the bubble shrinks, the gas concentration near the bubble wall increases owing to Henry's law and the liquid shell
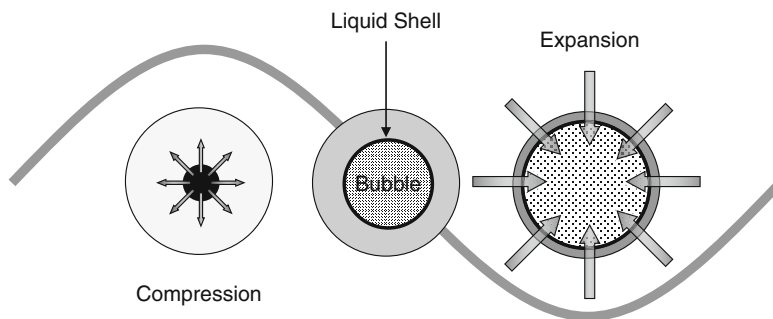
Fig. 2 The area and shell effects of rectified diffusion. The surface area available for mass transfer is larger during the expansion phase and smaller during the compression phase. The liquid shell is compressed during the expansion phase resulting in a higher gas concentration gradient (greater mass transfer driving force) as compared to the compression phase where the concentration gradient is small due to a larger liquid shell

becomes thicker. This increase in the shell thickness lowers the gas concentration gradient across the shell, which reduces the driving force for the mass transfer of the gas out of the bubble. Conversely, as the bubble expands, the concentration of gas near the bubble wall is reduced and the liquid shell is compressed. This thinning of the shell increases the gas concentration gradient across the shell, which results in a greater driving force for the mass transfer of the gas into the bubble. Both the "area" and "shell" effect contribute towards the net diffusion of gas into the bubble, or bubble growth, over time. The rate of growth by rectified diffusion has been studied experimentally by levitating a single gas bubble in a standing wave field to observe the change in the size of the bubble as a function of time, under various sonication conditions. Using this technique, Crum [10] experimentally measured the rectified diffusion growth and refined the existing theory on rectified diffusion to demonstrate a strong agreement between the theoretically predicted and experimentally measured values of pressure threshold and growth rate.

Total Bubble Volume and Bubble Coalescence

When water is sonicated, large visible bubbles are readily observed, mostly at the pressure nodes. Although bubbles do grow by rectified diffusion as described in the previous section, it is the coalescence of bubbles that is largely responsible for the large, visible bubbles or degassed bubbles. The coalescence of bubbles can have a significant influence on the population and size of cavitation bubbles [11–14]. For bubble coalescence to take place, bubbles need to first come into contact. Under an acoustic field, there are two acoustic forces that are responsible for driving bubbles towards each other, and these are the primary and secondary Bjerknes forces [15]. The primary Bjerknes force depends on the pressure gradient and the average

oscillation of a bubble within one cycle, and depending on the bubble size, it can force bubbles to move towards the pressure antinodes or pressure nodes [16]. The secondary Bjerknes force, which dominates at short ranges [17], can induce repulsion or attraction between two bubbles depending upon the average volume oscillation changes and the distance between them [16]. This secondary Bjerknes force could also be long range if there are many bubbles [18].

Theoretical studies have assumed if two bubbles are drawn together by Bjerknes forces, they will coalesce at encounter [19]. Crum [17] reported that coalescence of bubbles is normally observed under the influence of Bjerknes forces in a stationary wave field. However, Duineveld [20] demonstrated that this was not always the case and found when two equal size bubbles are driven near resonance, coalescence is inhibited. This was attributed to Bjerknes force-induced bubble oscillations causing the contacting surfaces to fluctuate too fast for coalescence to take place. A recent study [21] examined the coalescence time between two contacting bubbles driven at low frequencies and reported a much longer coalescence times for these bubbles compared to that calculated by the film drainage theory developed in the absence of ultrasound. These coalescence times were comparable with that predicted for rigid (surfactant coated) bubbles, even in the absence of surfactant. This suggests that the film drainage theory developed in the absence of ultrasound does not fully describe the coalescence process for two coalescing bubbles undergoing volume oscillations. The results are suggesting that the coalescence process could be statistical, with a distribution of film drainage times which is prolonged with increasing surface approach velocity and secondary Bjerknes force. Furthermore, bubbles oscillating in and out of phase to each other due to differences in the bubble sizes may influence film drainage time [21]. Although these experiments suggest that ultrasound hinders the coalescence process between two contacting bubbles, ultrasound does generate forces that are capable of driving bubbles into contact and increase the frequency of bubble coalescence. This explains the readily observed large degassed bubbles when water is sonicated.

In a multibubble field generated by ultrasound, bubble coalescence is much more complicated to experimentally evaluate. Labouret et al. [22, 23] demonstrated that hyperfrequency technique can be used to detect small voids induced by cavitation bubbles. By following the increase in the rate of void formation, information regarding bubble coalescence was obtained. Following this work, a capillary system was developed to detect similar bubble void rates [12] where the change in the total bubble volume (ΔV_T), formed after a volume of aqueous solution is sonicated, can be measured (Fig. 3). This volume change reflects the total volume of larger gas bubbles, generated mainly by the coalescence of cavitation bubbles during the sonication process.

Both the hyperfrequency and capillary system reported a linear rise in the void rate with time [24, 25]. This increase is related to the rise in the population of bubbles associated with sonication time which in turn leads to higher frequency of bubble coalescence and hence the increase in the volume of bubbles.

Fig. 3 A schematic diagram illustrating the capillary cell used to measure the change in liquid level (ΔV_T) that occurs during sonication
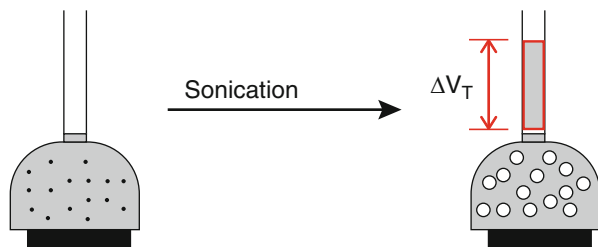
Sonoluminescence and Sonochemiluminescence

Single Bubble Systems

Much of our current fundamental understanding of SL only came about after the discovery of single bubble sonoluminescence (SBSL). The first report on SBSL was by Yoshioka and Omura [26] in 1962, but it was not until the report by Gaitan in 1990 [27] that led to an upsurge in experimental and theoretical research into this area. From these SBSL studies, it was shown that the light emitted is not continuous, but in fact flashes periodically during compression, just prior to the bubble collapsing to a minimum [28].

Ashokkumar and Grieser [29] demonstrated that the periodic flashes of SBSL can be used to photoexcite fluorescent solutes. By choosing different fluorescent solutes, the SBSL emission shifts to a particular wavelength depending on the type of fluorescent solute. Thus, it is possible to use SBSL to act as a pulsed picosecond light source and monitor the temporal emission profile of excited solutes.

There are various theories being proposed on SBSL. It was initially thought that SL emission was blackbody radiation from the heating of the internal bubble core up to temperatures of 10,000 k [30]. However, this theory required the dependence of the emission pulse width on wavelength which was shown not to be the case by Gompf et al. [31]. A much more convincing theory was provided by Suslick and coworkers where evidence was provided that the SL emission was from thermally excited chemical species, suggesting an optically opaque plasma core [32].

It is now accepted that the adiabatic collapse of the bubble allows the bubble core to heat up and initiate the hemolysis of water to produce H and OH radicals. This process is responsible for the much reported sonochemistry effects in the literature, one of which is SCL of luminol. Hatanaka et al. [33] have shown that the shape stable bubbles required for SBSL emission are in fact incapable of inducing chemical reactions for SCL of luminol. It was revealed that dancing bubbles, which does not emit SL, actually produces SCL of luminol. It is believed that the production of OH radicals may be enhanced by dancing single bubbles, and the generation of daughter bubbles allows OH radicals to be readily transported into the liquid.

Multibubble Systems

Evidence of possible light emission associated with cavitation activity was reported in the early 1930s when Marinesco and Trillat [34] discovered that photographic plates were darkened when immersed in liquid exposed to ultrasound. However, they

had concluded that chemical reactions, accelerated by the presence of ultrasound, may have caused the darkening effect. It was Frenzel and Schultes [35] who later attributed this darkening to the emission of light, later given the term sonoluminescence. SL intensity is usually captured using a light-sensitive photomultiplier tube (PMT) or photographically using a camera, with the images processed later to obtain a total integrated intensity. Often luminol is used to give off SCL as these intensities are much stronger compared to SL and can be captured with a normal commercial camera. For SL, a cooled CCD camera is required to capture the light emissions.

There are considerably more experimental studies on multibubble systems in the presence of ultrasound than in single bubble systems. This is presumably due to the simplicity in the setup required for multibubble systems and the greater range of practical applications for these systems. However, very little theoretical work has been done on multibubble systems due to the complexity of the system.

With the frequency in the kilohertz range, it is difficult to capture bubbles in a multibubble field without a high speed camera. Nevertheless, by measuring the intensity of the multibubble sonoluminescence (MBSL) or sonochemiluminescence (MBSCL) emitted, especially in pulse mode, one can gain an insight into the bubble dynamics. It has been shown that the initial MBSL or MBSCL intensity increases with time and reaches a steady state intensity (Fig. 4a). It is inferred that the time required to reach a stable level of MBSL [36] and MBSCL [37, 38] is related to the accumulation of active bubbles until a steady state population of active bubbles is reached. It was reported that the number of pulses required to reach this plateau (N_{crit}) increases with increasing presonication time and decreasing air concentration [38]. This was explained in terms of the removal of the stable nuclei by the presonication and deaeration process [38], which will contribute to an increase in the N_{crit} [37]. For fully degassed water, the solution becomes very difficult to cavitate (Fig. 4b) due to very few bubble nuclei in the system, and also bubble growth by rectified diffusion will be reduced. However, cavitation can be induced by the addition of shelled microbubbles, provided that the acoustic power is high enough to break the shell and release the gas (Fig. 4c, d) [9].

Crum et al. [39] showed using a 20 kHz horn that SL emissions were emitted from regions near the pressure antinodes in the standing wave field and from this concluded that the SL activity is from "stable" cavitation rather than "transient" cavitation. Generally, acoustic fields may be part standing wave and part traveling wave depending on the reflectivity of the interface as well as the attenuation effect of the medium [4]. Leighton et al. [40] demonstrated using an intensified CCD camera that a large amount of light was produced at the pressure antinodes when there is a high percentage of standing wave component in the acoustic field whereas in the case of a predominately traveling wave field, very little light was detected.

The spatial distribution of SL activity depends on the distribution of active bubbles in the vessel during sonication. This distribution of active bubbles primarily depends on the radiation forces, which can drive bubbles to a certain location depending on the size of the bubble and whether it is driven in a standing or a traveling wave field. For small radial amplitude oscillations, bubbles less than the
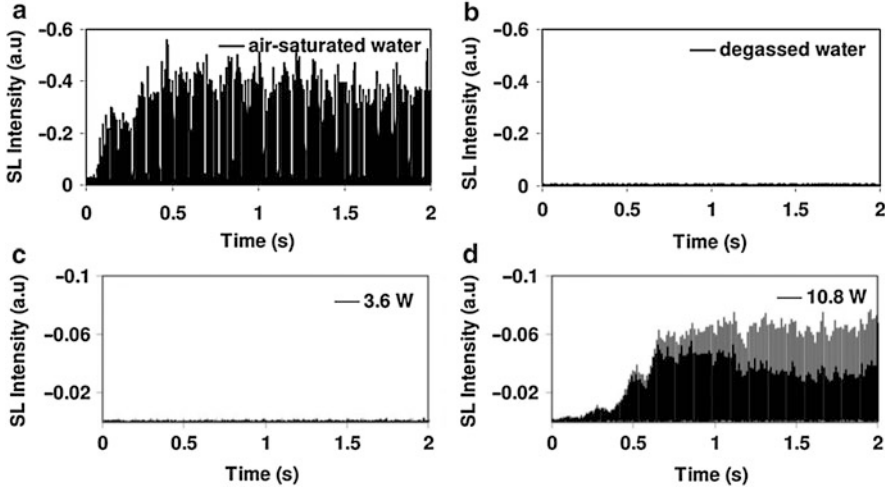
Fig. 4 Initial SL intensity observed as a function of time for (**a**) saturated water and (**b**) degassed water; (**c**) and (**d**) are degassed water with the addition of shelled microbubbles irradiated at acoustic powers of 3.6 W and 10.8 W, respectively (Reproduced from Ref. [9] with permission from the Royal Society of Chemistry)

resonance size are driven by the standing wave field to the pressure antinodes, whereas bubbles in the traveling wave field are transported in the direction of the propagating sound wave [4]. The force from the standing and traveling wave can be calculated using Eqs. 1 and 2 [4]:

$$\langle F_{TW} \rangle = \frac{3}{2} \frac{P_{TW}^2 V_o k}{R_0^2 \rho \omega_o^2} \frac{2 \frac{\beta_{tot}}{\omega}}{\left(\left\{ 1 - \left(\frac{\omega}{\omega_o} \right)^2 \right\}^2 + \left(2\beta_{tot} \frac{\omega}{\omega_o^2} \right)^2 \right)} \tag{1}$$

$$\langle F_{SW} \rangle = \frac{3 P_{SW} k R_{\varepsilon oa} V_o \sin(2ky)}{2R_o} \frac{(\omega_o^2 - \omega^2)}{\sqrt{(\omega_o^2 - \omega^2)^2 + (2\beta_{tot}\omega)^2}} \tag{2}$$

where F_{TW} and P_{TW} are the time-averaged force and acoustic pressure for the traveling wave, F_{SW} and P_{SW} are the time-averaged force and acoustic pressure for the standing wave, V_o is the equilibrium bubble volume, k is the wave number, β_{tot} is the dissipative constant, ω is the angular frequency, ω_o is the resonance angular frequency, R_o is the bubble radius, $R_{\varepsilon oa}$ is the radial amplitude of the bubble, y is the distance, and ρ is the density of the liquid. β_{tot} is evaluated using the approximation $\beta_{tot} = \omega_o/2Q$, where Q is the quality factor.

Acoustic waves are not always perfectly reflected, and with the presence of attenuation effects, the acoustic wave field is usually partially standing and partially
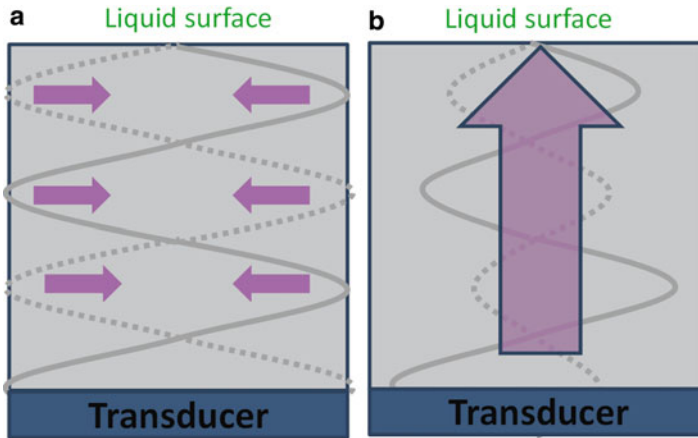
Fig. 5 A schematic illustrating the effect of (**a**) standing wave and (**b**) traveling wave field on the spatial distribution of cavitation bubbles

traveling wave [4]. Therefore, for simplicity, it is assumed that the sum of PTW and PSW is equal to the total acoustic pressure amplitude in the medium. At high percentage of standing wave, a bubble below the resonance size is strongly influenced by the force from the standing wave field. In this case, bubbles below the resonance size are more likely to be driven towards the pressure antinode (Fig. 5a). If the traveling wave component is dominant, active bubbles are more likely to be driven towards the liquid surface by the force from the traveling wave component (Fig. 5b). The percentages of the traveling and standing wave component can be determined experimentally using acoustic pressure distribution measurements and Eq. 3 [4]:

$$\% \, \text{Standing wave} = \frac{P_{antinode} - P_{node}}{P_{antinode} + P_{node}} \times 100 \tag{3}$$

where $P_{antinode}$ and P_{node} are the pressure maximum at the pressure antinode and the pressure minimum at the adjacent pressure node, respectively.

Cavitation Bubble Population and Size Distribution

The size and population of bubbles that is of interest are normally those that are capable of undergoing inertial collapse where the bubble expands significantly before collapsing violently leading to the emission of light or sonochemistry. The size in which inertial collapse occurs is often estimated by the Minnaert equation (4) for the linear resonance size [41]:

$$R_r = \sqrt{\frac{3\gamma P_\infty}{\rho \omega^2}} \tag{4}$$

Table 1 Bubble size ranges obtained from different techniques

Technique	Frequency (kHz)	Bubble size range (µm)
Hyperfrequency technique [23]	308	19–59
Sonoluminescence [13]	515	2.8–3.7
Sonoluminescence [45]	575	5.4–5.5
Sonochemiluminescence [45]	575	2.6–4.2
Sonochemiluminescence [45]	355	2.8–3.4
Laser light diffraction phase [49]	443	1–200
Laser light diffraction [46]	20 (horn)	1–20
Phase-Doppler techniques [46]	20 (horn)	2–40

where R_r is the linear resonance radius, γ is the specific heat ratio of the gas, and P_∞ is the ambient liquid pressure. These bubbles can be loosely described as "cavitation," "active," or "resonance" bubbles. However, it is shown by Yasui [42] using computer numerical simulations that there exists a range of bubble sizes, over an order of magnitude, for SL, and they do not coincide with the linear resonance radius predicted by Eq. 4. Yasui [42] also provided an acoustic pressure (P_a) and ambient bubble radius (R_o) map of various classifications of cavitation bubbles (dissolving, unstable SL, stable SL, unstable, and degassed bubbles).

In the absence of ultrasound, the size of bubbles is normally determined by photographic or acoustic methods [43]. However, acoustically generated cavitation bubble sizes are more difficult to measure due to the chaotic and fast oscillatory nature of acoustic cavitation. Various techniques, such as hyperfrequency [22], active cavitation detection [44], and pulsed ultrasound [13, 45], make use of the difference in dissolution rate between different size bubbles to predict the bubble size distribution and density. Another technique is the use of laser light diffraction phase-Doppler techniques [46–49] to examine the scattering from bubbles to estimate the size of cavitation bubbles. These techniques have shown that indeed there exists a range of bubble sizes for cavitation (Table 1) and support the findings reported by Yasui [42]. For the hyperfrequency and laser light diffraction and Doppler techniques, the bubble size range is larger than those obtained using pulsed ultrasound technique where SL and SCL intensity is measured as a function of pulse off time [13, 45]. This is because hyperfrequency and laser light diffraction and Doppler techniques measure both the active cavitation bubbles and the inactive, large degassed bubbles, whereas techniques using SL and SCL mainly capture bubbles that are capable of undergoing SL or SCL. In addition, care is needed when comparing size distribution obtained under different systems despite the same frequency and technique. Brotchie et al. [45] and Lee et al. [13] both used similar frequency but yielded different bubble size distributions. This was attributed to possibly differences in power, volume of solution, geometry, and transducer properties.

Table 1 also reveals differences between SL and SCL bubbles, where the latter had a size distribution that is smaller and broader [45]. It was concluded that there are
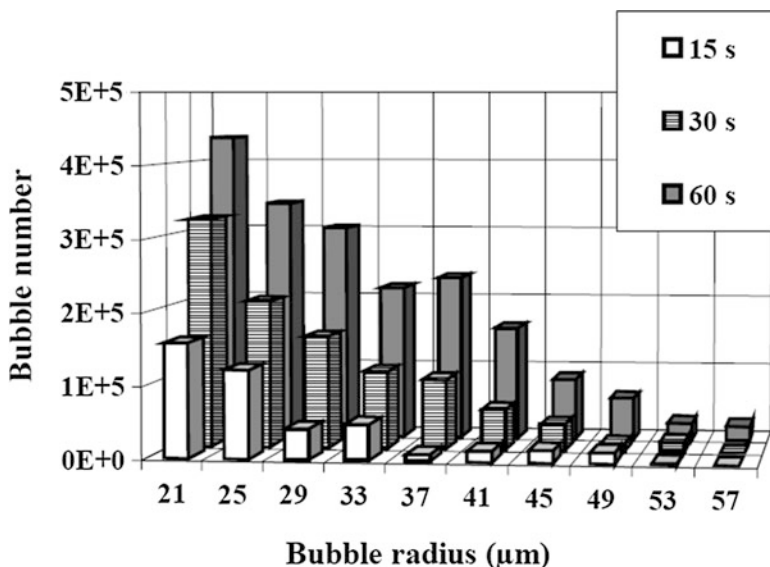
Fig. 6 Bubble number as a function of bubble radius under different sonication times. The solution was water, and the sonication frequency and power were 1 MHz and 0.21 Bars, respectively [23] (With kind permission of The European Physical Journal (EPJ))

two types of emissions, SL and SCL, each arising from different size bubble populations. This was attributed to different temperature required for SL and sonochemical reactions. For SL, temperature for ionization would be much higher compared to the sonochemical temperature needed for the dissociation of chemical bonds. It is thus inferred that larger cavitation bubbles would attain a greater temperature compared to smaller cavitation bubbles [45]. Differences in SL and SCL bubbles have been reported where it was found SCL of luminol was observed from dancing bubbles and not stable single bubbles [50], which is required for SL bubbles.

Labouret et al. [23] were able to use the total bubble volume and the dissipation rate of this volume to estimate the bubble number by assuming that the bubbles have reached their maximum size during their oscillations. For 1 MHz, they showed the increase in the bubble number as a function of time (Fig. 6).

Sonication Conditions

There are numerous reports in the literature on the effect of sonication conditions such as different frequency and power, on the cavitation efficiency. It has been shown that pulsing could also be an easy and effective method of optimizing the efficiency of ultrasound processes. This section will be devoted to work relating to different sonication conditions on the cavitation phenomena and characteristics

detailed in the Introduction on "Rectified Diffusion," "Total Bubble Volume and Bubble Coalescence," "Sonoluminescence and Sonochemiluminescence," and "Cavitation Bubble Population and Size Distribution."

Power

Rectified Diffusion

The effect of acoustic power on the threshold and growth rate of rectified diffusion is fairly well understood with strong agreement between experiment and theory. Experimental and theoretical calculations have both shown that with increasing acoustic pressure the bubble size threshold for rectified diffusion decreases [51, 52]. This is because as the acoustic pressure increases, the pulsation amplitude of the bubble becomes larger and allows a greater net rectified mass transfer per cycle. This thus allows smaller bubbles, which would have a stronger tendency to dissolve due to a higher Laplace pressure, to grow. Similarly, for a bubble above the threshold size but below the resonance size, increasing the acoustic pressure will effectively increase the rate of bubble growth by rectified diffusion [51, 52].

Total Bubble Volume and Bubble Coalescence

The total bubble volume has shown to increase with increasing acoustic power [53]; however, the degree of coalescence has been shown to be unaffected [53]. Although increasing acoustic power will increase the Bjerknes forces, the lack of influence on the degree of coalescence suggests that the increase in the total bubble volume with increasing acoustic power is attributed to the buildup in the population of cavitation bubbles. The pressure threshold for rectified diffusion increases with decreasing size of bubbles; therefore, a greater acoustic power would allow much smaller bubbles that would otherwise dissolve to cavitate and grow at a much higher growth rate, all of which can contribute to the increase in the total bubble volume.

Sonoluminescence and Sonochemiluminescence

For multibubble systems, unlike the single bubble systems where there exists a narrow range of acoustic power in which SL can occur, SL and SCL are readily observed provided a certain pressure threshold is exceeded [54]. It has been reported that the SL and SCL intensity both increases as a function of applied acoustic power [54]. The spatial distribution of such effect is illustrated in Fig. 7, which depicts a series of still photographs of SL and SCL under different input power [54]. The luminescence from the cavitation bubbles at the antinodes is clearly visible, and the increase in these luminescence bands with applied power is also evident.

It has been discussed in the previous sections that increasing power increases total bubble volume as well as the population of bubbles [23, 55]. This would effectively increase luminescence intensity as observed in the photographs. However, Hatanaka et al. [14] have shown that at excessive acoustic powers, quenching of the luminescence occurs. Still photographs comparing the cavitation bubbles and MBSL
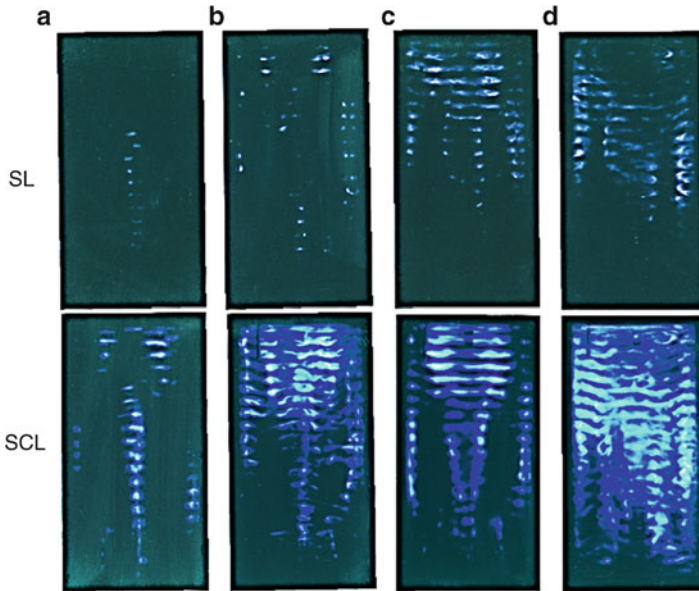
Fig. 7 Comparison of the spatial distribution of SL and SCL bubbles at 140 kHz for function generator power outputs of (**a**) 100 mV$_{pp}$, (**b**) 150 mV$_{pp}$, (**c**) 200 mV$_{pp}$, and (**d**) 300 mV$_{pp}$ (Reproduced from Ref. [54], Copyright © 2000 by The Japanese Journal of Applied Physics)

distribution under different pressures have attributed this decrease in the SCL at excessive powers to the expulsion of bubbles from the pressure antinode in the standing wave field (Fig. 8). It is believed that this repulsion is caused by the change in the primary Bjerknes force from attractive to repulsive as the pressure and the bubble size increase [14].

Cavitation Bubble Population and Size Distribution

Brotchie et al. [45], using the pulsed SL technique, observed an initial increase in the mean bubble size with increasing acoustic power. The bubble size then plateaus where further increase in power had negligible effect on the size. This invariant in the bubble size for a given acoustic power range is also reflected in the bubble size results obtained by Labouret et al. [23] using the void dissipation rate acquired via the hyperfrequency method. It is shown that increasing the power from 0.14 to 0.21 bars increased the bubble population from 75,000 to 240,000, especially for the smaller size bubbles (see Fig. 9), while the overall bubble size range remained the same. Yasui et al. [42, 56] have theoretically mapped out the region for different category of bubbles in the phase space of acoustic pressure versus equilibrium bubble radius and shown that in general increasing acoustic power widens the range of SL bubbles. This is attributed to the decrease in the Blake threshold radius, and Louisnard et al. [52] have theoretically shown that at high driving powers the rectified diffusion threshold radius merges with the Blake threshold radius. This
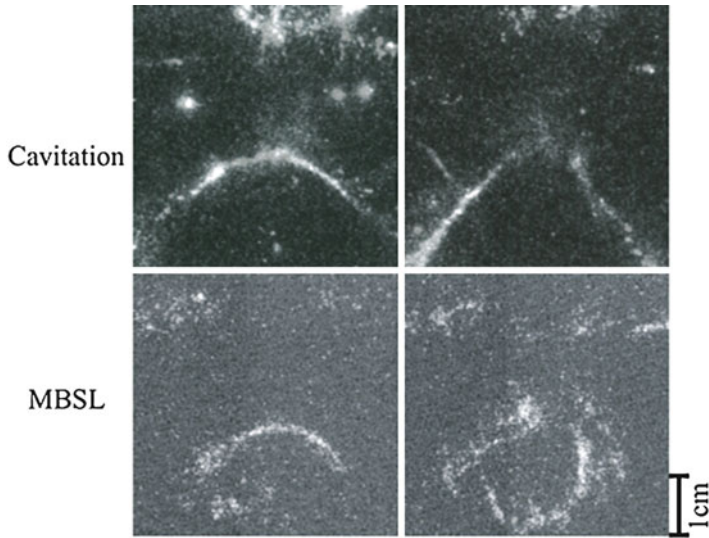
Fig. 8 Comparison between the spatial distribution of cavitation bubbles (*top*) and MBSL (*bottom*) under two function generator power outputs (**a**) 600 mV$_{pp}$ and (**b**) 900 mV$_{pp}$ (Reproduced from Ref. [14], Copyright (2001) by The Japanese Journal of Applied Physics)
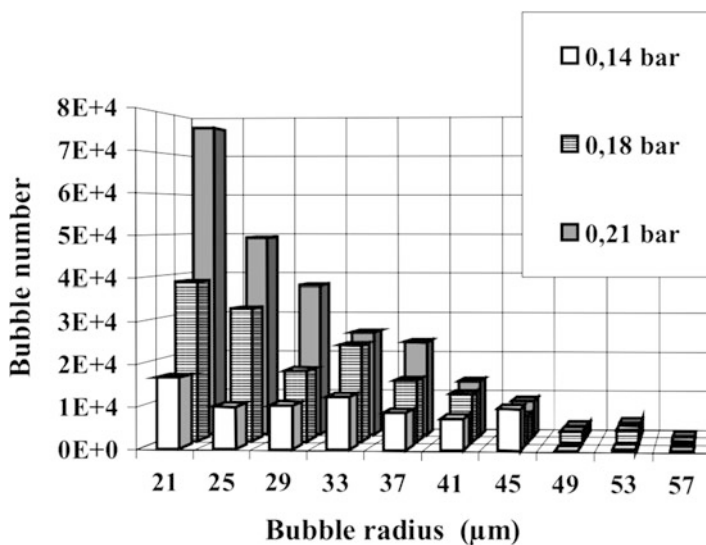
Fig. 9 The effect of the applied acoustic pressure on the bubble number and size distribution. The frequency and sonication time used were 308 kHz and 30 s [23] (With kind permission of The European Physical Journal (EPJ))

means much smaller bubbles will become active. Higher driving acoustic powers also induce stronger bubble collapse and increases the upper threshold bubble radius for SL. However, if the acoustic power is too great, stronger nonlinear pulsations at these powers can lead to bubble fragmentation and decrease the size of active bubbles. This may explain the lack of increase in the active bubble sizes at high acoustic powers.

Frequency

Rectified Diffusion

The effect of frequency on the threshold pressure for rectified diffusion is shown in Fig. 10 for two bubble sizes. It is evident from this graph that the threshold pressure decreases sharply as the frequency approaches the resonance frequency of the bubble. The exact form of the curve above and below resonance is unknown; hence the estimation is indicated by the dotted line. The trend appears to also suggest that the threshold pressure is generally greater for larger bubbles driven below its resonance frequency.

Theoretical studies by both Louisnard et al. [52] and Meidani et al. [58] have shown that the rectified diffusion growth rate is inversely proportional to the sonication frequency. This is owing to the decrease in the bubble expansion ratio with increasing frequency. This is illustrated in Fig. 11 where the average time variation of gas by rectified diffusion in a 70 μm radius bubble decreases with increasing frequency from 20 to 35 kHz (Fig. 11). Although 35 kHz is much closer to the resonance frequency of the bubble, the much higher average mass of gas observed for the lower frequency is attributed to the larger bubble pulsation amplitude by subharmonic resonance frequency.

There are very few experimental reports on the direct influence of frequency on rectified diffusion growth of a single bubble. However, initial SL pulse technique [59] revealed that in the presence of an ionic surfactant, sodium dodecyl sulfate (SDS), where coalescence is inhibited and growth is predominantly via rectified diffusion growth, a much longer initial growth in the active cavitation bubbles was observed at high frequencies. This indirectly implies that a much slower growth rate occurs at higher frequencies.

Total Bubble Volume and Bubble Coalescence

The total bubble volume or void measured can be attributed to mainly the coalescence of bubbles to form large degassed bubbles as the rate of growth by rectified diffusion pathway is slow in comparison to the coalescence process (Fig. 1). The effect of frequency on the rate of change in the total bubble volume (void rate) is shown in Fig. 12 where the void rate rises from approximately 3 to 8 μL/s when the frequency is increased from 168 to 726 kHz.

As discussed earlier, in order for coalescence to take place bubbles need to come into contact and the forces responsible are the Bjerknes forces. However, the magnitude of these forces diminishes with increasing frequency. In addition,

Fig. 10 Pressure thresholds
for rectified diffusion as a
function of frequency for a
100 % gas saturated solution
[57] (Copyright (1965)
Acoustical Society of
America)
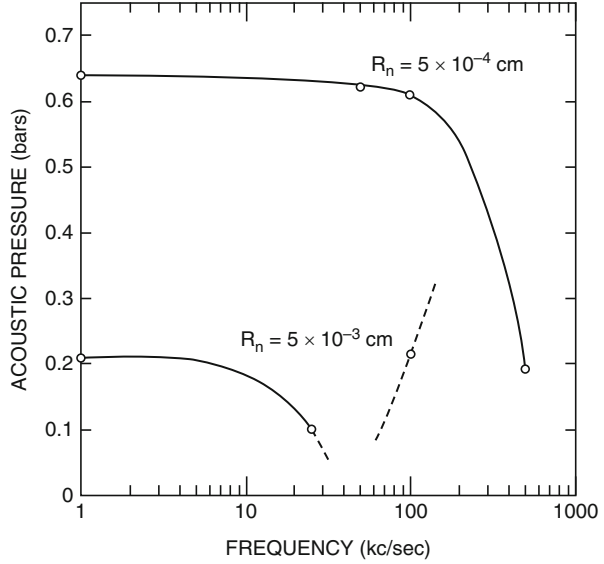
Fig. 11 Time variation of
average mass of gas contained
in the bubble with a radial size
of 70 μm for different acoustic
frequencies (Reprinted from
Ref. [58], Copyright (2004),
with permission from
Elsevier)
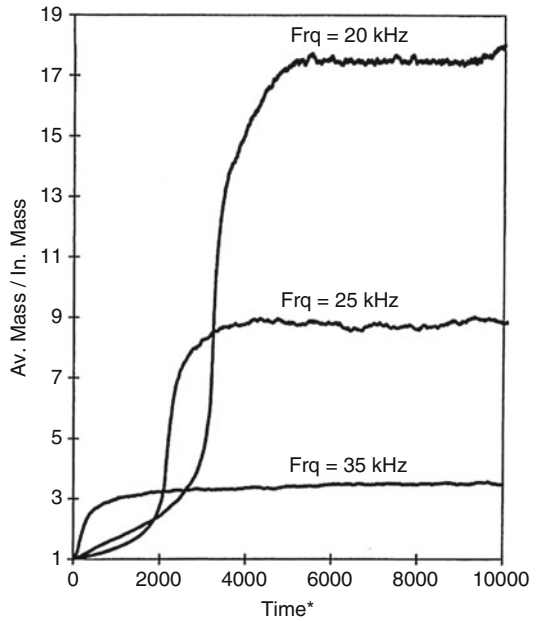
cavitation bubble size decreases with increasing frequency. Therefore, the rise in the
void rate observed is believed to be attributed to the higher number of anitnodes
associated with increasing frequency, which can result in a larger population of
cavitation bubbles and enhance the coalescence activity. Furthermore, higher

Fig. 12 Void generation rate at 168, 448, and 726 kHz for water. A driving power of 20 W was used for all systems (Data adapted from Ref. [60])
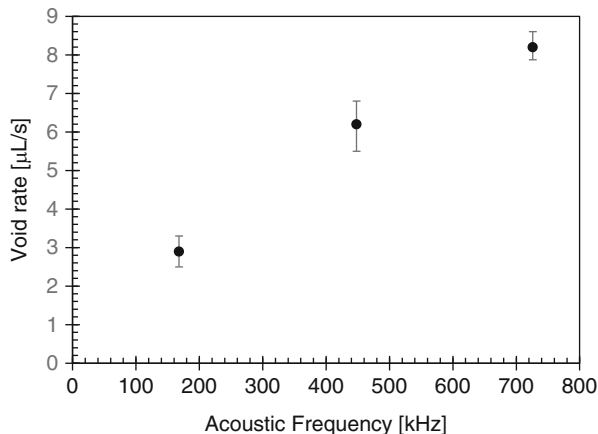
frequencies can lead to stronger attenuation of acoustic wave causing an increase in bulk acoustic streaming, which could further enhance the coalescence frequency.

Sonoluminescence and Sonochemiluminescence

As discussed in the Introduction on "Sonoluminescence and Sonochemilumi-nescence," MBSL and MBSCL initially increase in intensity as a function of sonication time before reaching a steady state intensity. It has been found that there exists an optimum frequency, between 200 and 300 kHz, at which the steady state intensity passes through a maximum [61]. As frequency increases, the wavelength of sound wave becomes shorter which can effectively increase the number of antinodes and hence larger population of SL and SCL bubbles [14]. On the other hand, at higher frequencies the shorter period causes the bubble to expand less (resulting in smaller ratio of R_{max}/R_o or R_o/R_{min}) and results in a weaker collapse intensity and lower SL and SCL [42] emission intensity. The range of bubble sizes capable of undergoing SL also becomes narrower with increasing frequencies as discussed earlier [42, 45]. It is this balance between the increase in the number of bubbles and the decrease in the range of bubble sizes capable of transient inertial collapse [42] that gives rise to the maximum SL intensity observed around 200–300 kHz.

The spatial distribution of SL bubbles as a function of frequency is presented in Fig. 13. Strong SL emission at the pressure antinodes is clearly demonstrated. The increase in the number of pressure antinodes is also evident at lower frequencies from 37 to 168 kHz, but less obvious at higher frequencies as the wavelength becomes too small to distinguish between the pressure antinode and nodes. With increasing frequency, the distribution of SL emission becomes localized towards the liquid surface.

The variations in the structure of the cavitation bubble distribution with increasing frequency are explained by the changes in the acoustic wave field from standing wave to traveling wave, brought about by the increase in the attenuation of the
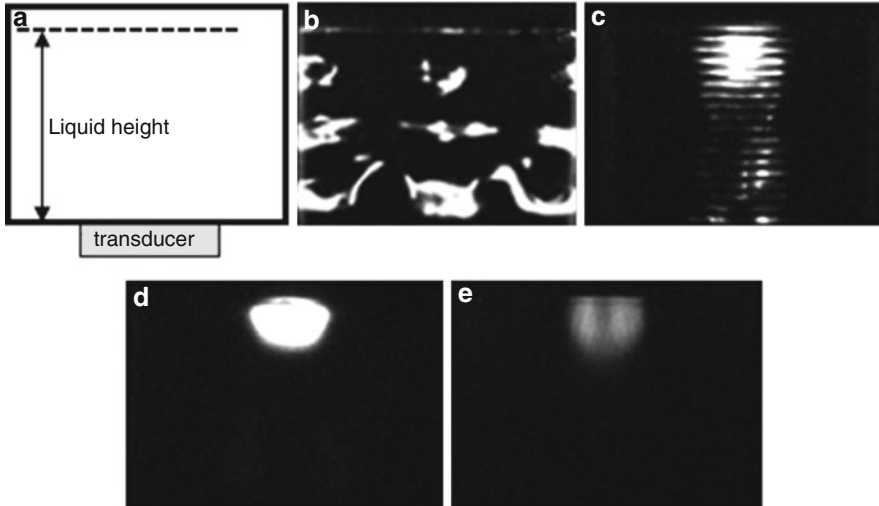
Fig. 13 Spatial distribution of SL intensity for different frequencies: (**a**) configuration of the sonication cell, (**b**) 37 kHz, (**c**) 168 kHz, (**d**) 448 kHz, and (**e**) 726 kHz [62, 63]. All images were taken with an exposure time of 30 s and power of 20 W, measured using a power meter (Reprinted in part from Ref. [62] with permission from the PCCP Owner Societies and from Ref. [63], Copyright (2010) (John Wiley and Sons))

acoustic wave. This attenuation is caused by the higher total bubble volume and dissipative constant (β_{tot}) as frequency increases. Also evident in Fig. 13 is the decrease in the SL intensity at higher frequencies.

Cavitation Bubble Population and Size Distribution

According to the Minnaert equation (4), the bubble's linear resonance size [41] reduces with increasing frequency. Yasui [42, 56] performed numerical simulations that took into account the conditions of multibubble sonoluminescence in water to obtain an acoustic pressure (P_a) and ambient bubble radius (R_o) map for different acoustic frequencies (Fig. 14). This P_a-R_o space maps out various classifications of cavitation bubbles (dissolving, unstable SL, stable SL, unstable, and degassed bubbles). It is evident from Fig. 14 that the bubble size range for stable and unstable SL decreases from 0.1–100 μm at 20 kHz to 0.1–3 μm at 1 MHz.

The calculations performed by Yasui [42, 56] were for SL bubbles. Experimental verification of this using the pulsed ultrasound technique was found to be difficult due to the sharp transition of SL intensity with increasing pulse separation at the different frequencies examined [64]. However, Brotchie et al. [45] were able to obtain experimental size distribution of SCL bubbles, which was much broader compared to SL bubbles, for a range of frequencies using the pulsed ultrasound technique [45]. As predicted by Yasui [42, 56], the cavitation bubbles were found to be much smaller compared to the linear resonance size calculated using Eq. 4. In
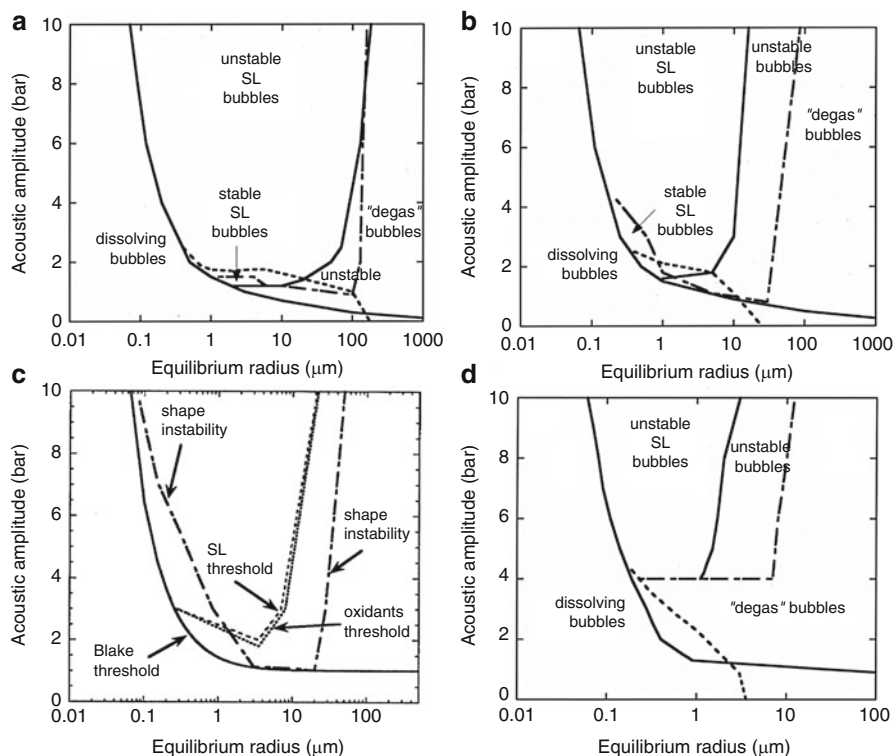
Fig. 14 The calculated thresholds for the different category of bubbles and shape instability in R_0-Pa plane for ultrasound frequency of (**a**) 20 kHz [42], (**b**) 140 kHz [42], (**c**) 300 kHz [56], and (**d**) 1 MHz [42]. Note the shorter range of the horizontal axis (R0) for (**c**) and (**d**) compared to that of (**a**) and (**b**) (Reprinted with permission from Refs. [42] and [56]. Copyright (2002), Acoustical Society of America, and Copyright (2008), American Institute of Physics)

addition, the experimental results show that the mean bubble size and size distribution become smaller and narrower with increasing frequency (Fig. 15), which is consistent with Yasui's numerical calculations [42, 56].

Pulsing

Sonoluminescence and Sonochemiluminescence

Systematic studies on the effect of pulsing were conducted by Henglein and coworkers [38], and it was reported that for a pulse of a given length, the SCL and sonochemical yield decreases with increasing pulse off time. This effect was explained in terms of a "cascade" effect where bubbles generated during the acoustic pulse on time survive through the shorter pulse intervals and thus act as further
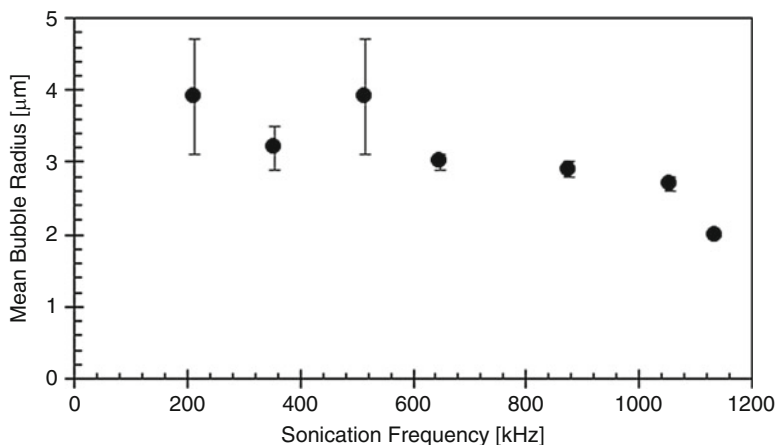
Fig. 15 Mean bubble radius as a function of sonication frequency. The error bars denote the width at half height of the normalized probability distribution curve. For all frequencies the acoustic power was fixed at 1.5 ± 0.4 W (Data extracted from Ref. [45])

cavitation nuclei for the subsequent pulse. This effect was captured using a high speed camera by Choi et al. [65]. As the pulse off time increases, bubbles can dissolve away before the subsequent pulse arrives and decrease the effective population of cavitation nuclei available to be grown to the active size during the pulse on time and effectively lower the overall cavitation activity.

It has been reported that there exists an appropriate pulse on and off ratio where a maximum SL [65, 66] and sonochemical reactions [67, 68] in terms of H_2O_2 production and enlarged SCL spatial distribution are observed. Figure 16 illustrates the enhancement in SL with increasing pulse off time. This broadening of the spatial distribution of cavitation activity has been attributed to the suppression in the generation of large coalesced bubbles, which would have otherwise attenuate the acoustic wave and allow a high amplitude of sound propagation and stronger standing wave field. If the pulse off time is too long, then the cavitation activity decreases due to the dissolution of cavitation bubble nuclei between the pulse on time as reported by Henglein et al. and coworkers [38].

The formation of the large degassed bubbles can be easily captured, and its structure has shown to reflect the spatial distribution of SL bubbles [60]. The effect of increasing pulse on or pulse off duration on the visible bubble structure is shown graphically in Fig. 17. It can be seen that as the pulse on duration increases for a given fixed pulse off time, the bubbles initially form a strong standing wave structure that extends from the transducer to the liquid surface and becomes disrupted by the onset of a force resulting in the standing wave structure to be limited to near the liquid surface. Similar development in the bubble structure is observed with increasing pulse off duration for a given fixed pulse on time. Figure 17 is categorized into three regions according to SL images reported in the literature [49, 66]. Region A is
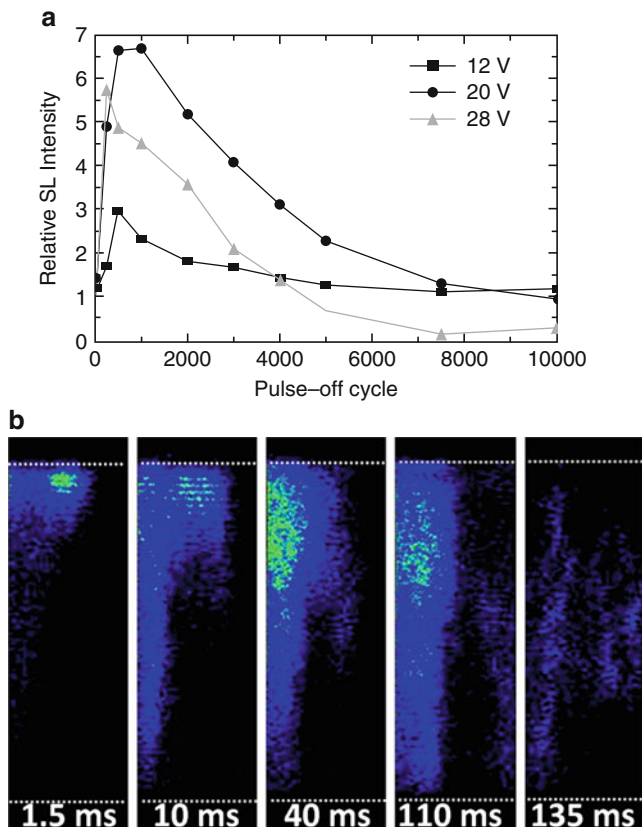
Fig. 16 (**a**) Relative SL intensity as a function of pulse off time for different acoustic powers, reproduced from Ref. [65] (Copyright © 2008 by The Japanese Journal of Applied Physics). (**b**) Images showing the effect of increasing pulse off time on the SL structure generated in saturated water at a frequency of 448 kHz and at a power of 1.1 W/cm². The pulse on time was fixed at 12 ms and exposure time was set to capture 100 pulses. The white dotted lines above and below the SL structure denote the liquid surface and the transducer position, respectively. The center of the vessel is located on the left side of the images (Reprinted with permission from Ref. [66]. Copyright (2008) American Chemical Society)

where SL is isolated to the liquid surface, region B is where the SL is homogeneously distributed in the vessel, and region C is where no SL activity is detected. Figure 17 demonstrates that there exits an optimum range of pulse on and off ratio for strong standing wave field and homogeneous distribution of active bubbles, which has been shown to translate to a higher sonochemical efficiency. If the pulse on and off ratio is in region A, the pulse on is sufficiently long or the pulse off is considerably short such that the system effectively behaves like a continuous system. If the pulse on and off ratio is in region C, the pulse on duration is inadequate for the generation of detectable bubbles. At the boundary between C and B where there is

Fig. 17 Visible bubble
structure for different pulse on
and off cycles captured in
saturated water at 448 kHz
and a driving power of 20 W.
Three regions have been
identified according to the SL
images reported in the
literature. *Region A* is where
SL is found isolated to the
liquid surface. *Region B* is
where SL is homogeneously
distributed. *Region C* is where
no SL activity was detected
(Reprinted from Ref. [60],
Copyright (2011), with
permission from Elsevier)
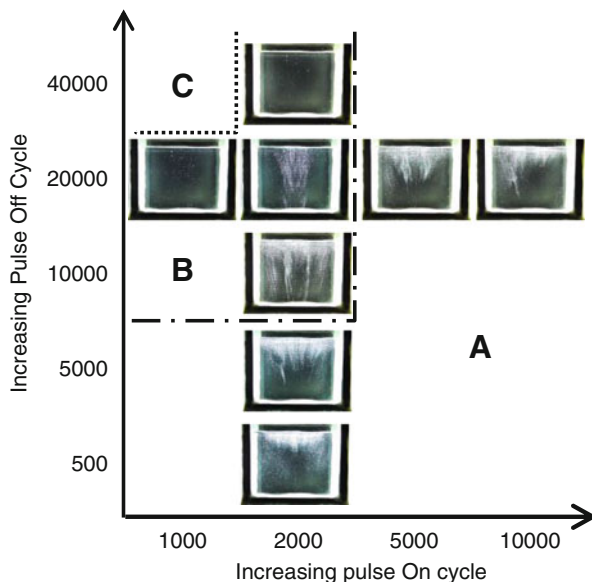
very few visible bubbles, it is not possible to determine if there is SL activity based
on optical photographs. At this region the SL structure will be that of a strong
standing wave pattern, but with increasing pulse off duration or decreasing pulse on
duration, SL diminishes. However, the boundary of A and B can be easily distin-
guished by optical photographs.

A different insight into pulse sonication induced enhancement was provided by
Choi et al. [65]. They reported that bubbles that survive during the pulse off time
were able to grow by the subsequent pulse to a size larger than that reached in
continuous mode. These larger bubbles are more susceptible to nonspherical col-
lapse and fragmentation into daughter bubbles. These daughter bubbles are much
smaller and collapse symmetrically which is thought to contribute to the enhance-
ment of the sonoluminescence. These were supported by the appearance of
subharmonics in pulsed sonication mode that were absent in continuous sonication
and a much higher broadband noise.

Solution Conditions

In many applications, the solution to be sonicated is not water, and depending on the
application, it may contain various solvents, dissolved gases, surface-active solutes,
and electrolytes. This section will discuss the importance of the solution conditions
such as concentration of the gases and solutes in the solution, and how these can
affect the process of rectified diffusion and degree of bubble coalescence, which in
turn influence the size distribution and population of cavitation bubbles as well as the
SL and SCL activities.

Dissolved Gases

Rectified Diffusion

It has been shown that the pressure threshold for rectified diffusion decreases with increasing dissolved gas concentration [51, 57]. This is due to the bubble's tendency to dissolve in under-saturated conditions, and this dissolution competes with the diffusion of gas by rectified diffusion. Therefore, to overcome the dissolution of the bubble as the concentration of dissolved gas decreases, a greater acoustic pressure is needed for rectified diffusion growth. Similarly, the rate of growth by rectified diffusion is also proportional to the concentration of dissolved gas. It has also been demonstrated that the type of dissolved gas also influences the rate of growth by rectified diffusion. Kang et al. [69] theoretically calculated the change in the bubble growth rate in various dissolved gases, namely, argon (Ar), hydrogen (H_2), and nitrogen (N_2), and found the growth rate to increase in the order of Ar, N_2, and H_2. This trend was attributed to diffusivity and thermal conductivity of the dissolved gases, with H_2 having the highest diffusivity and thermal conductivity, followed by N_2 having a higher thermal conductivity than Ar, but both N_2 and Ar have similar diffusivities. Currently there has not been any experimental verification on the effect of these gases on rectified diffusive growth. However, Kang et al. [69] found a strong correlation between the change in cavitation intensity and the bubble growth rate under these dissolved gases.

Total Bubble Volume and Bubble Coalescence

When the medium is totally degassed, insufficient number of bubble nuclei [38] coupled with high pressure threshold for rectified diffusion [10] results in very little SL activity. As the concentrations of dissolved air increase, the number of bubble nuclei available for cavitation activity increases [38], and SL and SCL activity is observed to reach a maximum, but further increase in the dissolved gas concentration towards saturation decreases the SL and SCL activity [66, 70].

As the air concentration increases, the number of bubble nuclei and frequency of bubble coalescence rises; this effect is observed in the increase in the total bubble volume as shown in Fig. 18. This coalescence of bubbles provides a faster pathway, compared to the rate of rectified diffusion, for small bubbles to reach the active size. As the air concentration approaches the saturation level, the number of bubbles increases dramatically, and excessive coalescence of bubbles can also lead to the loss of active bubbles as large degassed bubbles. The lower acoustic pressure at high air concentrations can also reduce the range of bubble sizes that can overcome the Blake threshold pressure [4], resulting in a lesser number of active bubbles.

Sonoluminescence and Sonochemiluminescence

The spatial distribution of SL bubbles formed under different dissolved oxygen concentration is displayed in Fig. 19 [66]. At very low dissolved oxygen concentration of 34 %, the SL activity is either nonexistent or too weak for the camera to detect. At 40 % saturation, the SL extends from the transducer to the liquid surface and intensifies until 50 % oxygen saturation where maximum total SL intensity
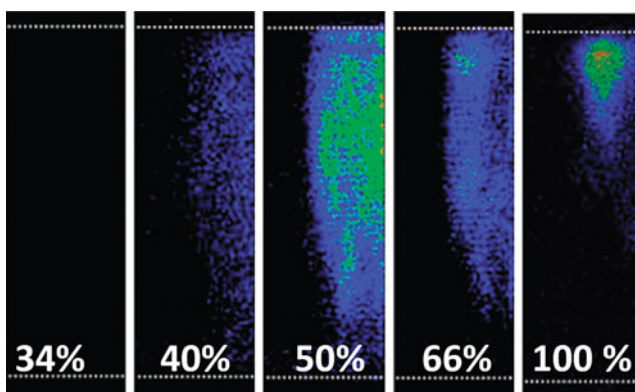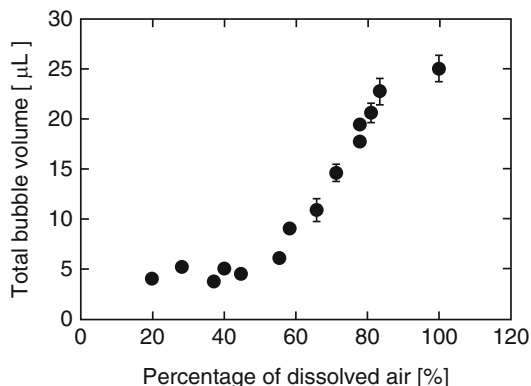
Fig. 19 The SL structure formed under different percentages of air-saturated water, sonicated in continuous mode at 448 kHz and at a power of 1.1 W/cm². An exposure time of 0.5 s was used for all images (Reprinted with permission from Ref. [66]. Copyright (2008) American Chemical Society)

occurs. This corresponds to the onset of total bubble volume shown in Fig. 18. As the level of dissolved oxygen increases to 100 %, the SL activity shifts towards the liquid surface. This change in the SL structure was explained by the variations in the percentage of standing and traveling wave established in the vessel. For saturated water, large coalesced bubbles decreased the average percentage of standing wave to below 30 %, and the dominant traveling wave component forced SL activity to be confined towards the surface of the liquid. For degassed systems where there are very few large coalesced bubbles present to attenuate the acoustic wave, a high percentage of standing wave averaging around 50 % is obtained.

   The type of dissolved gases also influences the intensity of SL as these dissolved gases will govern the gas content of cavitating bubbles. It has been shown that both the specific heat ratio (γ) and thermal conductivity of the gas content govern the bubble's core temperature and hence the intensity of SL. The effect of the specific

heat ratio on the temperature inside the bubbles can be seen in the following equation:

$$T_f = T_o \left(\frac{R_{max}}{R_{min}} \right)^{3(\gamma - 1)} \tag{5}$$

where T_f is the bubble's collapse temperature, T_o is the bubble's initial temperature, and R is the bubble radius. Gases with higher thermal conductivity allow higher loss of heat during the adiabatic collapse of the cavitation bubble, leading to a lower final bubble core temperature and hence a lower emission of light. Therefore, the SL intensity will increase with increasing specific heat ratio and decreasing thermal conductivity of the gas inside the collapsing bubble [71, 72].

Surface-Active Agents

Rectified Diffusion

The presence of surface-active solutes has been found to substantially enhance the rate of rectified diffusion [10, 73, 74] (Fig. 20), and this enhancement could not be accounted for by the surface tension term in the theory [10]. Several plausible causes for this anomaly have been given; the most probable cause being the surface-active solutes induces acoustic streaming at the bubble surface, even in the absence of surface oscillations. Recent work by Leong et al. [74, 75] explored the influence of surface-active solutes with different surface activity on the rectified diffusion growth rate and used particle-image velocimetry (PIV) to characterize the microstreaming around the bubble. They found a strong correlation between the growth rate of a bubble and microstreaming velocities (Fig. 20). In addition, at high surface excess concentrations, the bubble growth rates were significantly dependent on the type and charge of the surface-active solute's headgroup, with dodecyl trimethyl ammonium chloride (DTAC, cationic) giving the highest growth rate compared to sodium dodecyl sulfate (SDS, anionic) or dodecyl dimethyl ammonium propane sulfonate (DDAPS, zwitterionic). At low surface excess concentrations, no obvious differences were observed. It was concluded that DTAC had a bulkier headgroup, which leads to enhanced surface oscillations and microstreaming, and in addition surface-active solutes with a long chain length can enhance rectified diffusive growth by creating a greater mass transfer resistance which contributes to larger amount of rectification of gas into the bubble.

The increase in the rectified diffusion growth rate created by surface-active agents has been clearly demonstrated experimentally; however, the current theory still cannot account for the observed enhancements in the growth rate.

Total Bubble Volume and Bubble Coalescence

Total bubble volume method has been employed to examine the effect of various surface-active solutes on bubble coalescence in the presence of ultrasound [12]. The
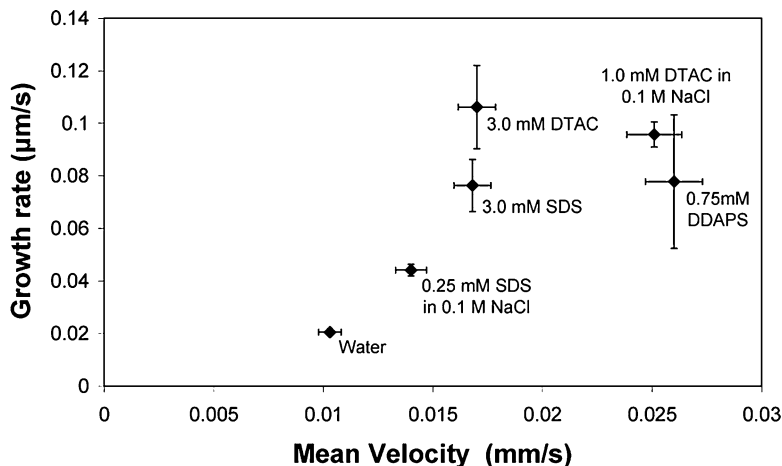
Fig. 20 Growth rate of a 50 μm bubble in various solutions as a function of the mean microstreaming velocity found using PIV (Reprinted with permission from Ref. [75]. Copyright (2011) American Chemical Society)

results show similarities with that obtained for bubble coalescence in the absence of ultrasound [76]. The sharp decline in total bubble volume observed as surface activity increases is indicative of coalescence inhibition by surface-active solutes. Shown in Fig. 21 is the bubble void rate under different frequency and SDS concentrations, and it demonstrates the decrease in the void rate when the coalescence is inhibited by SDS. However, at high SDS concentrations (10 mM), an increase in the void rate is recorded. The changes in the amount of large coalesced bubbles with the addition of different SDS concentration are illustrated by the still photographs shown in Fig. 21. The increase in total bubble volume at high concentrations of surface-active solute has also been recorded for alcohols [77]. This increase has been attributed to surfactant enhanced rectified growth as discussed in the previous section. For alcohols, its effect on the rectified diffusion has not been reported, but is speculated to have similar enhancement in the amount of gas being rectified.

Other surfactants have also been studied, and it was reported that for nonionic surface-active solutes, the coalescence inhibition is governed purely by the surface activity of the solutes and, more specifically for alcohols, by the length of the hydrocarbon chain. However, for charged surfactants, electrostatic effects also play a significant role in the extent of coalescence inhibition. For the four ionic surfactants studied, despite the dissimilarities in surface activity, all four exhibited the same magnitude of bubble coalescence inhibition. It was concluded that the cause of this behavior is the nonequilibrium adsorption of the surfactants at the bubble/liquid interface.

ΔV_T under different surface-active solute concentrations in the presence and absence of NaCl, as well as different frequencies and powers, were investigated
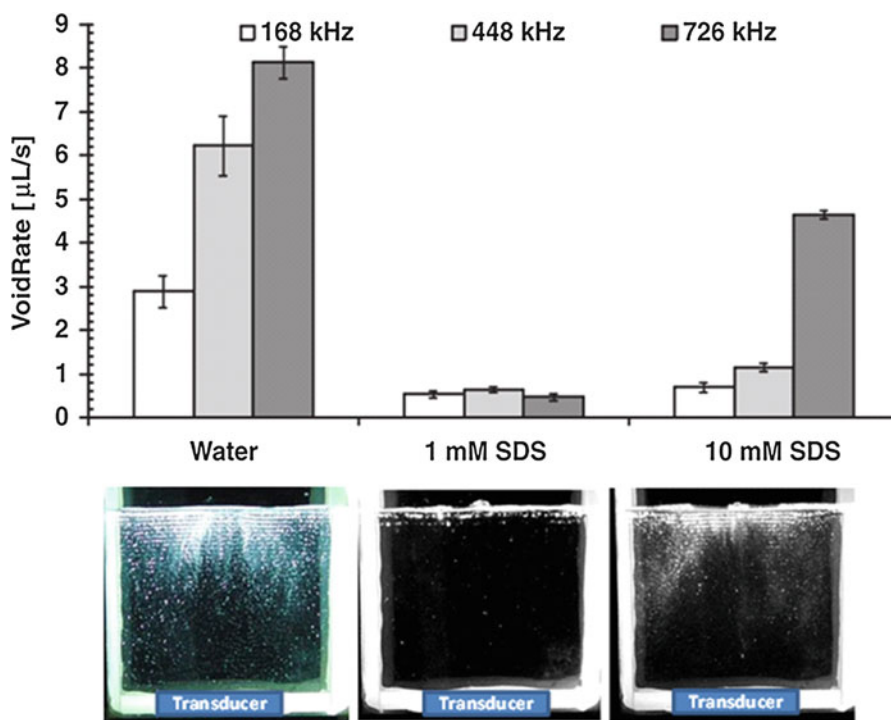
Fig. 21 Void generation rate at 168, 448, and 726 kHz for water, 1 mM SDS and 10 mM SDS. A driving power of 20 W was used for all systems. Below the graphs are the photographs of the reactor vessel showing the large degassed bubble structures for the different SDS concentrations (Reprinted from Ref. [60], Copyright (2011), with permission from Elsevier)

and reported by Sunartio et al. [53]. It was revealed that the relative change in the inhibition of bubble coalescence by increasing surface-active solute concentration was unaffected by power. However, it was reported that the coalescence was inhibited to a lesser extent at higher frequencies, and this was attributed to lower adsorption of SDS molecules onto the bubble/solution interface at higher frequencies. It was also estimated in this report that as the frequency increases from 213 to 1062 kHz, the maximum bubble lifetime and oscillation number varied from 0.35 to 0.1 ms and 70 to 110 oscillations, respectively.

Sonoluminescence and Sonochemiluminescence

Single Bubble Systems

Stottlemyer and Apfel [78] investigated the effect of two surfactants, a protein bovine serum albumin (BSA) and a nonionic surfactant Triton X-100. Two concentrations of BSA (50 % of critical micelle concentration (CMC) and at CMC) were investigated and found to allow the bubble to be driven at a higher acoustic pressure. This allowed the bubbles to reach a much larger maximum bubble size resulting in a

greater SL intensity compared to SBSL in water. This was attributed to BSA being able to dampen the interfacial motion and stabilize the bubble at higher driving pressures. However, for Triton X-100, which has been shown to lower the surface tension and allow free interfacial motion, at a concentration of 10 % CMC, a much smaller maximum bubble radius was reached, and the SL intensity measured was lower compared to the SL in water. Ashokkumar et al. [79, 80] extended the SBSL work to other surfactants such as an anionic surfactant SDS (0.38 % CMC), a cationic surfactant DTAC (0.15 % CMC), and a zwitterionic surfactant DAPS (0.75 % CMC). It was found that both the bubble dynamics and SL intensity were not affected by these surfactants; this was probably because the concentrations of the solutes were very low. Due to instabilities, higher concentrations of solutes were not possible.

The effect of alcohols on SBSL was also investigated [79, 81], and it was found that low concentrations of alcohols quench the SL emission. The alcohols do not alter the bubble dynamics significantly [79], and the quenching effect was observed both with increasing alcohol concentration and hydrocarbon chain length [79, 81]. This quenching is related to the equilibrium amount of solutes at the bubble surface (surface excess concentration) [79, 81].

Multibubble Systems

The initial growth in the cavitation activity can be affected by the presence of surface-active solutes. The initial time required to build up the MBSL intensity in water increases as a function of concentration of surface-active solutes such as alcohols and SDS but then decreases at high concentrations (Fig. 22). As discussed in the previous section, the addition of surface-active solutes can inhibit bubble coalescence. As a consequence of this, the population of bubbles is smaller in size, and the bubble growth is mainly via rectified diffusion. It is suggested that the decrease in the N_{crit} at higher surface-active solute concentrations [59, 77] may be caused by an increase in the bubble growth by rectified diffusion, since it is highly unlikely that at the higher concentrations of surface-active solutes there would be an increase in bubble-bubble coalescence. However, although there exists experimental evidence for the enhanced rectified diffusion growth by surfactants, there are no experimental reports on whether alcohols have the same effect. However, the ΔV_T data show that there is an increase in total bubble volume at higher concentrations of the alcohols [77] and SDS [53] to support the increase in the bubble size.

Also shown in Fig. 22b is the effect of frequency on the N_{crit}. For all frequencies, the increase in the N_{crit} with the addition of SDS is observed, and similarly, at high SDS concentrations, N_{crit} falls. However, the concentration at which N_{crit} starts to fall increases as the frequency shifts from 575 to 1136 kHz. This effect has been interpreted in terms of the changes to the oscillation time and lifetime of the bubbles [59]. As mentioned before, the decrease in the N_{crit} is related to the increase in bubble growth rate by rectified diffusion. It has been shown by Sunartio et al. [53] that an acoustic bubble in a multibubble field has a finite lifetime which decreases with increasing applied frequency. Thus as a result, the bubble growth by rectified growth will be slower for higher frequencies, giving rise to the shift in the maximum

Fig. 22 The effect of different surface-active solutes on the relative N_{crit} as a function of solute concentration: (**a**) different alcohols (Reprinted with permission from Ref. [77]. Copyright (2006) American Chemical Society) and (**b**) different concentrations of SDS for different sonication frequencies (Reprinted with permission from Ref. [59]. Copyright (2009) American Chemical Society)
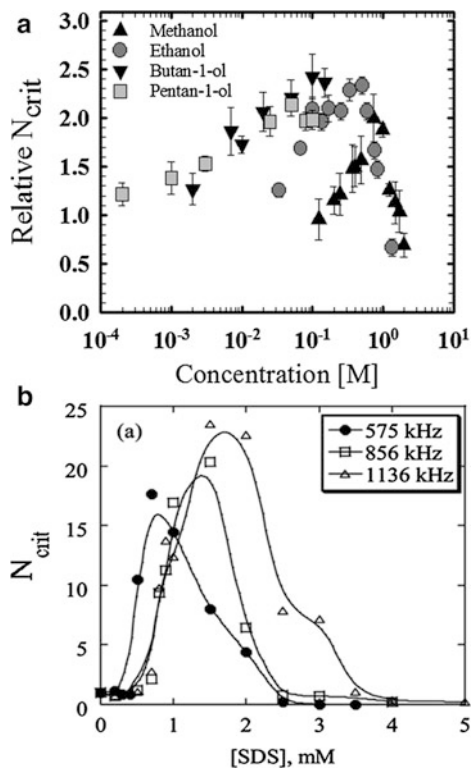
N_{crit} towards higher concentrations at higher frequencies. In addition, the maximum N_{crit} reached is also greater at higher frequencies.

What is not apparent in Fig. 22b is the rise and fall in the steady state MBSL intensity with increasing ionic surfactant concentration [82]. The SDS concentration at which the maximum MBSL is reached coincides with the concentration at which N_{crit} is a maximum. When 0.1 M of NaCl is added to SDS solutions, it is reported that no enhancement in the MBSL is observed [36, 82–84]. The physical explanation given is the acoustic impedance shielding effect (see Fig. 23). For a cluster of bubbles in water, the bubbles on the outside will impede the acoustic waves from reaching the inner bubbles. This hindrance will reduce the number of bubbles undergoing collapse and sonoluminescence. When charged surfactants are added, these surfactants will adsorb onto the bubble surface creating an electrostatic repulsion between the bubbles and lower the density of the bubble cloud, thus providing a more open cluster of bubbles that reduces the shielding effect. If NaCl is added or the concentration of ionic surfactant is high, the salt and excess surfactant will screen the electrostatic repulsion and bring the bubble cluster back to that in water. This electrostatic repulsion mechanism is supported by the lack of MBSL enhancement when a neutral, zwitterionic surfactant is used [82]. However, Segebarth et al. [84] showed that it is unlikely that less impedance shielding is the main cause of the

High impedance shielding   Low impedance shielding   High impedance shielding
Closed bubble cloud   Open bubble cloud   Closed bubble cloud

addition of small   addition of salt
concentrations of   Or
ionic surfactant   high concentrations of
                                  ionic surfactant
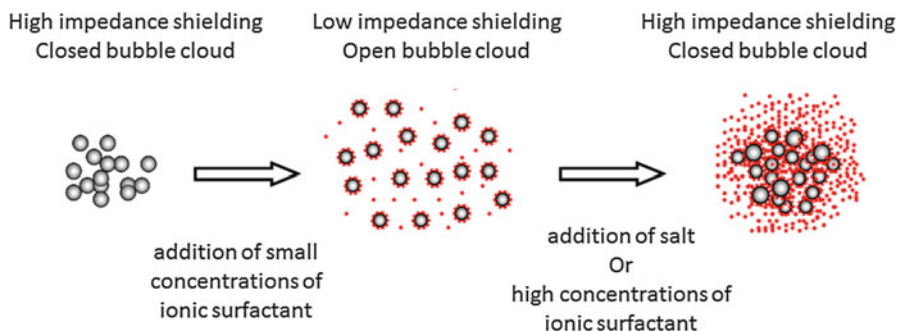
Fig. 23 An illustration of the influence of an ionic surfactant, with and without salt, on the impedance shielding effect of a bubble cluster

increase in the SL intensity. At 1 mM SDS, the Debye length is only 9.6 nm, and it was argued that for electrostatic repulsion to take effect, the local bubble density would need to be extremely high [84]. Nevertheless, Tronson et al. [36] argued that electrostatic effects within the streamers may lead to different spatial structures of the bubble cloud, i.e., a more "open" bubble cloud. Further experiments are required to fully understand the effect of surfactants and salt on bubble clusters.

The spatial distribution of SL activity upon the addition of SDS may provide another insight into the enhancement in the steady state MBSL. The effect of SDS on the spatial distribution of SL activity viewed from the side and from the top is shown in Fig. 24. The addition of 1 mM SDS broadened the SL activity from the liquid surface towards the transducer, expanding the regions of SL activity as seen with the effect of degassing and pulsing. This enlargement in the SL activity coincides with the increase in the integrated SL intensity reported in the literature for 1 mM SDS [82, 84]. Similar to the effect with degassing and pulsing, the enlargement in the SL activity is attributed to a lower attenuation of the acoustic wave brought about by the reduction in the formation of large coalesced bubbles that otherwise would attenuate the acoustic wave, resulting in the wave field being predominantly a standing wave field. Further increase in the SDS concentration to 10 mM SDS reverted the spatial distribution of SL bubbles to that of saturated water. This is in agreement with the reported integrated SL intensities which show high SDS concentrations resulted in the decrease in SL to an intensity comparable to water [82, 84]. The resemblance of the SL structure at 10 mM SDS to that obtained under saturated water is attributed to the increase in the population of large coalesced bubbles as supported by the increase in the ΔV_T at high SDS concentrations [53]. The attenuation of acoustic pressure by the increase in the bubble size at 10 mM SDS relative to 1 mM SDS thus lowers the percentage of standing wave field and causes the force from the traveling wave field to dominate.

The effect of alcohols, aliphatic esters, and ketones on the MBSL was reported by Price et al. [85] and Tronson et al. [36]. At 20 kHz, quenching was observed for the aliphatic esters and ketones, but not for the alcohols. It was speculated that alcohols have a stronger intermolecular interaction with water molecules, and therefore the
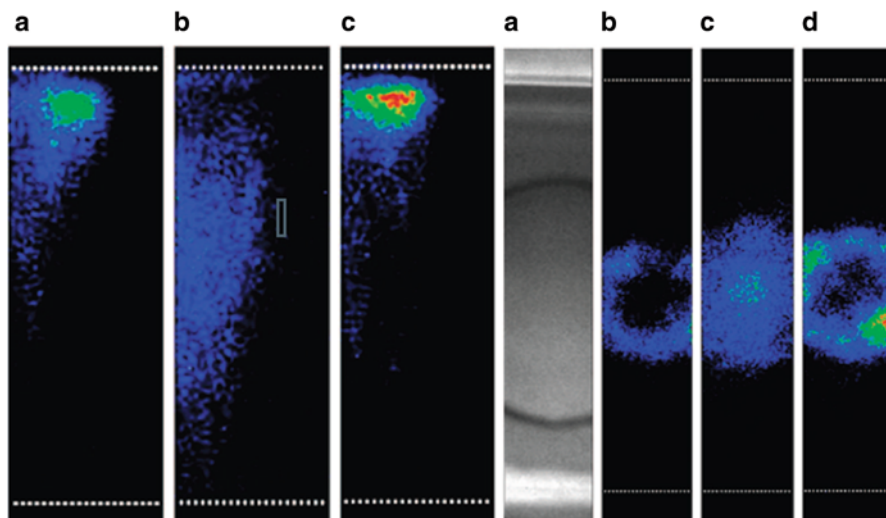
Fig. 24 Images showing the effect of SDS on the SL structure taken from the side and from the top of the vessel 448 kHz: (**a**) image of the vessel from the top, (**b**) water, (**c**) 1 mM SDS, and (**d**) 10 mM SDS. For both frequencies, continuous sonication at a power of 1.1 W/cm2 was used. Exposure time was set to collect 2×105 acoustic cycles. The white dotted lines denote the vessel wall (Reprinted with permission from Ref. [66]. Copyright (2008) American Chemical Society)

rate of evaporation of the alcohols into the bubble is retarded. In addition to this, at 20 kHz the cavitation is transient, meaning that the bubble only undergoes a few cycles before collapsing. This results in quenching being observed for aliphatic esters and ketones, which are more surface active and have a lower intermolecular interaction with water. However, prior to the quenching, a small enhancement in the SL was detected for aliphatic esters and ketones at 20 kHz [85]. It was concluded that there are two factors involved, SL quenching (a decrease in SL) and an increase in the population of active bubbles via coalescence inhibition (an increase in SL). At low solute concentrations, the latter is the dominating effect, and the former effect dominates at high solute concentrations. At 515 kHz, quenching was observed for all alcohols, aliphatic esters, and ketones. This is because at 515 kHz, the cavitation is stable, meaning that the bubble undergoes a number of cycles before collapsing. This allows time for the solutes to evaporate into the bubble and quench the SL.

Although it is commonly accepted that low frequencies generate transient cavitation and cavitation at high frequencies is predominate stable, a recent report by Ashokkumar et al. [62] provided evidence for a significant amount of stable cavitation at low frequencies (25 and 37 kHz) and existence of transient cavitation at high frequencies. In that study the proportion of standing and traveling wave distribution were altered by stabilizing the liquid surface to increase the strength of the standing wave field, and the MBSL and MBSCL intensity were measured to quantify the degree of quenching.

Cavitation Bubble Population and Size Distribution

The addition of a surface-active agent is known to inhibit the coalescence of bubbles. Figure 25 shows the decrease in the bubble size distribution induced by the addition of 1.5 mM of SDS, a surfactant concentration which corresponds to the minimum ΔV_T. Further increase in the SDS concentration to 4 mM resulted in an increase in the bubble size distribution, but the size still remains below that of water. This increase is consistent with the observed increase in the rectified diffusion and ΔV_T for high surfactant concentrations.

The bubble population for different SDS concentrations has been characterized by Iida et al. [49] using the Fraunhofer laser diffraction technique. The results from that study are shown in Table 2, which show a rise in the number of bubbles with increasing SDS concentrations. However, in that study, there is very little difference in the size of the bubbles for concentrations above 0.2 mM, and they are a lot larger compared to the sizes shown in Fig. 25. As mentioned in the Introduction on "Sonoluminescence and Sonochemiluminescence," laser diffraction technique will include both the degassed bubbles and cavitation bubbles; hence the size of the bubbles on average was larger than the cavitation bubbles measured using the sonoluminescence pulsing technique. Nevertheless, it provides an insight into the relative affects, which is the increase in the number of cavitation bubbles with the addition of surfactants.

Electrolytes

Total Bubble Volume and Bubble Coalescence

Bubble coalescence studies under an ultrasonic field using the total bubble volume measurements has shown that the transition electrolyte concentration, where 50 % of the bubble did not coalesce, is generally higher for acoustic bubbles compared to other non-acoustic systems [86]. Recent report by Browne et al. [86] used the total bubble volume measurements to evaluate the effect of different electrolytes and gas concentrations on the degree of bubble coalescence. A strong linear correlation was found between the total bubble volume change and the equilibrium gas solubility in different electrolytes and gases (Fig. 26). No obvious specific ion effects were observed, and it has been explained that the decrease in the total bubble volume change with decreasing gas content is related to the lower number of precursor gas nuclei that lead to stable final bubbles [86]. This effective increase in the inhibition of bubble coalescence by the addition of electrolyte is supported by the increase in the number of N_{crit} to reach equilibrium MBSL intensity [87] at high salt concentrations.

Sonoluminescence and Sonochemiluminescence

The effect of electrolytes in the study of acoustic cavitation has predominantly been at low concentrations of 0.1 M. This concentration has shown to have negligible effect on the SL activity [82]; however when added to charged surfactants such as
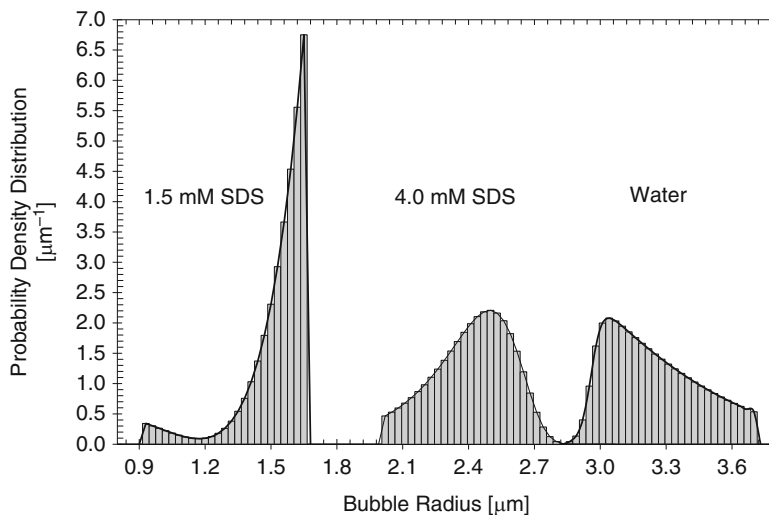
Fig. 25 The probability density distribution of the bubble size versus bubble radius for water, 1.5 mM and 4 mM SDS (Reprinted with permission from Ref. [24]. Copyright (2005) American Chemical Society)

Table 2 Estimated bubble number density using laser light scattering technique for different SDS concentrations, generated by 443 kHz and 20 W under pulsed conditions [49]

SDS concentration [mM]	D50 [µm]	Number of bubbles [cm^{-3}]
0.1	40	15
0.2	8	68
5	9	105
10	8	319

Fig. 26 Total bubble volume as a function of dissolved gas concentration under different concentrations of salts and gases. The circled data were obtained for pure water saturated with the different gases. The sonication conditions were 213 kHz, 19.5 W, and 10 s sonication time (Reprinted with permission from Ref. [86]. Copyright (2011) American Chemical Society)
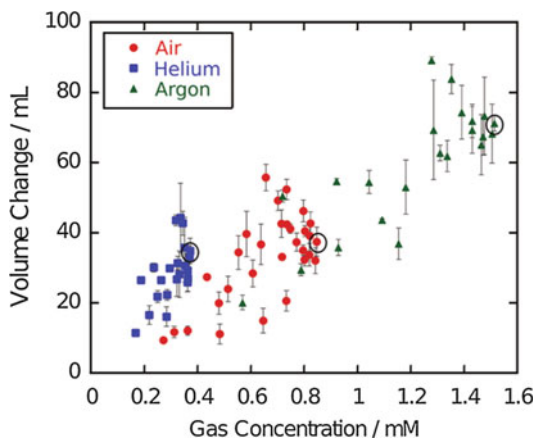
SDS, it can quench the SL enhancement as discussed in the Surface Active Agents section on "Sonoluminescence and Sonochemiluminescence" for "Multibubble Systems" and bring it to a level comparable to that of water. However, Wall et al. [87] have shown for various different electrolytes that increasing electrolyte concentration to the range between 1 and 3 M can enhance the SL intensity by 1.5–3 times that of water. Further increase in the electrolytes concentration past this maximum resulted in a sharp decrease in the SL intensity. Various physical characteristics such as solution viscosity, water vapor pressure, air-water interfacial tension, rate of bubble coalescence, and gas solubility were compared with the concentration when the maximum SL was recorded, and the only correlation was the extent of gas solubilization in the solution. However, Wall et al. [87] used the literature data for the rate of bubble coalescence that was obtained in the absence of ultrasound.

Scaling Up and Applications

For practical applications and scale-up of sonochemical reactors, effects such as type of transducers used, liquid height, and fluid flow are important. However, there are some contradicting reports on how these effects influence the cavitation activity. This is largely attributed to the complexities of overlapping affects these has on the proportion of standing and traveling wave in the wave field, degree of bubble coalescence, as well as the threshold for cavitation activity.

Type of Transducers

The spatial distribution of cavitation bubbles also varies depending on the type of ultrasound transmitters. Shown in Fig. 13 are from plate transducers, where the transducers are located at the bottom of the reactor vessel. Depicted in Fig. 27a is the spatial distribution of cavitation bubbles from a 20 kHz ultrasonic horn, where intense cavitation region is localized near the surface of the horn. Often this intense localization leads to surface erosion of the horn tip. Figure 27b shows the spatial distribution of cavitation bubbles generated by a high-intensity-focused-ultrasound (HIFU) transducer (Fig. 27b). It has been found that concentrated cavitation activity occurs just before and after the focal zone [88]. The lack of cavitation activity at the focus has been attributed to the shielding of the acoustic field by cavitation bubbles before the focus.

Liquid Height

The effect of liquid height was studied in both laboratory and large scale reactors [61, 89]. It was shown that as the liquid height increases, the sonochemical yield passes through a maximum, and for some frequencies there exists a second
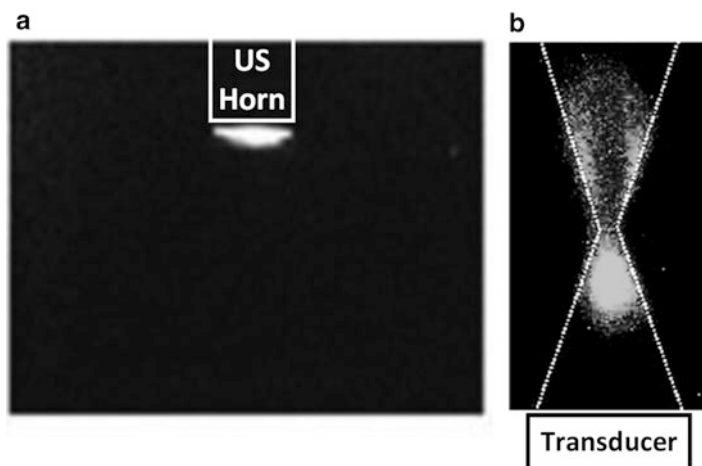
Fig. 27 Spatial distribution of SCL from luminol produced by (**a**) 20 kHz ultrasonic horn and (**b**) 750 kHz HIFU transducer (Reprinted from Ref. [88], Copyright (2010), with permission from Elsevier)
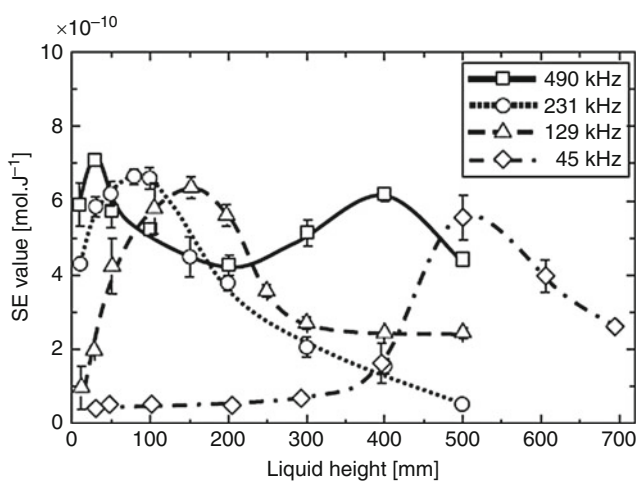
Fig. 28 Variation in the sonochemical yield as a function of liquid height for different ultrasonic frequencies (Reprinted from Ref. [61], Copyright (2008), with permission from Elsevier)

maximum (Fig. 28). A strong linear correlation between the liquid height corresponding to the first maximum in the sonochemical yield (h_{peak}) and the reciprocal of frequency was reported by Asakura et al. [61]. An empirical relation was fitted to yield the following relationship:

$$h_{peak} = 15.6\,\lambda - 22.9 \tag{6}$$

where λ is the wavelength of the acoustic wave. This expression, specific to the geometry and type of reactor used, suggests that the maximum sonochemical efficiency occurs at a liquid height that is approximately 15 times that of the wavelength.

Fluid Flow

Reports on the effect of fluid flow on sonochemical activity have been conflicting in that some reported an enhancement [90, 91] in the sonochemical activity by introducing flow whereas others have reported a decrease [92]. Bussemaker et al. [93, 94] have performed a systematic investigation for a range of frequency and power settings to elucidate the influence of fluid flow on sonochemical activities. It was found for 40 kHz, the sonochemical activity increased with increasing stirring speed [93]. This was attributed to the reduction in bubble coalescence which increases the population of cavitation bubbles. It was found that depending on the frequency and fluid flow rate, the flow of fluid had opposing effects [94]. In general for frequencies 376 and 995 kHz, the slower fluid flow does not interfere with the acoustic field and contributes towards increasing nonspherical bubble collapse, resulting in the observed enhancement in the sonochemical yield. However, with a faster fluid flow, the acoustic field was disrupted and attenuated; this subsequently reduced the sonochemical activity. At the higher frequency, negligible effect was observed with the different flow rates [94]. This was attributed to the active bubble size being much smaller and less prone to distortion or fragmentation, and therefore the cavitation system is less affected by the external flow.

Conclusions and Future Directions

In summary, acoustic cavitation is a complex and dynamic process where its spatial distribution and magnitude are very sensitive to the type of transducer used, frequency, power, mode of sonication, reactor geometry, volume of liquid, type and amount of dissolved gases, and the concentration and surface activity of the solutes in solution. There are other systems and conditions that were not covered in this review, such as dual frequency systems, chemical reactions, and solution temperature and viscosity, all of which will also be important for optimizing cavitation activity. Nevertheless, this chapter has provided an overview on the various methods for quantifying the cavitation activity and the influences different sonication and solution properties have on the cavitation activity that need to be considered for all applications of ultrasound. The reported effects are specific to the conditions used in those studies, and in order to optimize sonication processes for particular applications, it is important to conduct a systematic evaluation for that particular system. Much of the studies reported are laboratory and batch scale setups. In order for ultrasound applications to be fully integrated at larger industrial scales, more research into continuous and larger systems is required.

References

1. Young FR (1999) Cavitation. Imperial College Press, London
2. Ohl CD, Kurz T, Geisler R, Lindau O, Lauterborn W (1999) Philos Trans R Soc Lond A 357:269–294
3. Yasui K, Tuziuti T, Sivakumar M, Iida Y (2005) J Chem Phys 122:224706
4. Leighton TG (1994) The acoustic bubble. Academic, London
5. Fox FE, Herzfeld KF (1954) J Acoust Soc Am 26:984–989
6. Apfel RE (1970) J Acoust Soc Am 48:1179–1189
7. Winterton RHS (1977) J Phys D Appl Phys 10:2041–2056
8. Overton GDN, Trevena DH (1980) J Phys D Appl Phys 13:1309–1314
9. Zhou M, Cavalieri F, Ashokkumar M (2011) Soft Matter 7:623–630
10. Crum LA (1980) J Acoust Soc Am 68:203–211
11. Iida Y, Ashokkumar M, Tuziuti T, Kozuka T, Yasui K, Towata A, Lee J (2010) Ultrason Sonochem 17:480–486
12. Lee J, Kentish SE, Ashokkumar M (2005) J Phys Chem B 109:5095–5099
13. Lee J, Ashokkumar M, Kentish S, Grieser F (2005) J Am Chem Soc 127:16810–16811
14. Hatanaka S, Yasui K, Tuziuti T, Kozuka T, Mitome H (2001) Jpn J Appl Phys 40:3856–3860
15. Bjerknes V (1906) Fields of force. The Columbia University Press, New York
16. Mettin R, Akhatov I, Parlitz U, Ohl CD, Lauterborn W (1997) Phys Rev E 56:2924–2931
17. Crum LA (1975) J Acoust Soc Am 57:1363–1371
18. Yasui K, Iida Y, Tuziuti T, Kozuka T, Towata A (2008) Phys Rev E 77:016609
19. Pelekasis NA, Tsamopoulos JA (1993) J Fluid Mech 254:501–527
20. Duineveld PC (1996) J Acoust Soc Am 99:622–624
21. Jiao J, He Y, Yasui K, Kentish SE, Ashokkumar M, Manasseh R, Lee J (2015) Ultrason Sonochem 22:70–77
22. Labouret S, Frohly J (2000) Eur Phys J Appl Phys 10:231–237
23. Labouret S, Frohly J (2002) Eur Phys J Appl Phys 19:39–54
24. Lee J (2006) Bubble dynamics in the presence of ultrasound and surface active agents. PhD thesis, The University of Melbourne
25. Labouret S, Looten-Baquet I, Frohly J, Haine F (1998) Ultrasonics 36:603–606
26. Yosioka K, Omura A (1962) Proc Annu Meet Acoust Soc Jpn 125–126
27. Gaitan DF (1990) An experimental investigation of acoustic cavitation in gaseous liquids. PhD thesis, The University of Mississippi
28. Gaitan DF, Crum LA, Church CC, Roy RA (1992) J Acoust Soc Am 91:3166–3183
29. Ashokkumar M, Grieser F (2000) J Am Chem Soc 122:12001–12002
30. Noltingk BE, Neppiras EA (1950) Proc R Soc Lond Ser B 63:674–685
31. Gompf B, Günther R, Nick G, Pecha R, Eisenmenger W (1997) Phys Rev Lett 79:1405–1408
32. Flannigan DJ, Suslick KS (2005) Nature 434:52–55
33. Hatanaka S, Yasui K, Kozuka T, Tuziuti T, Mitome H (2002) Ultrsasonics 40:655–660
34. Marinesco N, Trillat JJ (1933) Proc R Acad Sci 196:858–860
35. Frenzel H, Schultes H (1934) Z Phys Chem 27b:421–424
36. Tronson R, Ashokkumar M, Grieser F (2002) J Phys Chem B 106:11064–11068
37. Henglein A, Ulrich R, Lilie J (1989) J Am Chem Soc 111:1974–1979
38. Henglein A, Herburger D, Gutierrez M (1992) J Phys Chem 96:1126–1130
39. Crum LA, Reynolds GT (1985) J Acoust Soc Am 78:137–139
40. Leighton TG, Pickworth MJW, Walton AJ, Dendy PP (1988) Phys Med Biol 33:1239–1248
41. Minnaert M (1933) Philos Mag 16:235–248
42. Yasui K (2002) J Acoust Soc Am 112:1405–1413
43. Pandit AB, Varley J, Thorpe RB, Davidson JF (1992) Chem Eng Sci 47:1079–1089
44. Chen WS, Matula TJ, Crum LA (2002) Ultrasound Med Biol 28:793–803
45. Brotchie A, Grieser F, Ashokkumar M (2009) Phys Rev Lett 102:084302

46. Burdin F, Tsochatzidis NA, Guiraud P, Wilhelm AM, Delmas H (1999) Ultrason Sonochem 6:43–51
47. Tsochatzidis NA, Guiraud P, Wilhelm AM, Delmas H (2001) Chem Eng Sci 56:1831–1840
48. Chapelon J, Newhouse V, Cathignol D, Shankar P (1988) Ultrasonics 26:148–154
49. Iida Y, Ashokkumar M, Tuziuti T, Kozuka T, Yasui K, Towata A, Lee J (2010) Ultrason Sonochem 17:473–479
50. Hatanaka S, Mitome H, Yasui K, Hayashi S (2002) J Am Chem Soc 124:10250–10251
51. Crum LA (1984) Ultrasonics 22:215–223
52. Louisnard O, Gomez F (2003) Phys Rev E 67:036610
53. Sunartio D, Ashokkumar M, Grieser F (2007) J Am Chem Soc 129:6031–6036
54. Hatanaka S, Yasui K, Tuziuti T, Mitome H (2000) Jpn J Appl Phys 39:2962–2966
55. Sunartio D, Yasui K, Tuziuti T, Kozuka T, Iida Y, Ashokkumar M, Grieser F (2007) Chem Phys Chem 8:2331–2335
56. Yasui K, Tuziuti T, Lee J, Kozuka T, Towata A, Iida Y (2008) J Chem Phys 128:184705
57. Eller AI, Flynn HG (1965) J Acoust Soc Am 37:493–503
58. Meidani AN, Hasan M (2004) Appl Math Model 28:333–351
59. Wu S, Leong T, Kentish S, Ashokkumar M (2009) J Phys Chem B 113:16568–16573
60. Lee J, Ashokkumar M, Yasui K, Tuziuti T, Kozuka T, Towata A, Iida Y (2011) Ultrason Sonochem 18:92–98
61. Asakura Y, Nishida T, Matsuoka T, Koda S (2008) Ultrason Sonochem 15:244–250
62. Ashokkumar M, Lee J, Iida Y, Yasui K, Kozuka T, Tuziuti T, Towata A (2009) Phys Chem Phys 11:10118–10121
63. Ashokkumar M, Lee J, Iida Y, Yasui K, Kozuka T, Tuziuti T, Towata A (2010) Chem Phys Chem 11:1680–1684
64. Brotchie AR (2010) Acoustic cavitation in dual frequency ultrasound fields. PhD thesis, The University of Melbourne
65. Choi P-K, Kaneko Y, Meguro T (2008) Jpn J Appl Phys 47:4111–4114
66. Lee J, Yasui K, Tuziuti T, Kozuka T, Towata A, Iida Y (2008) J Phys Chem B 112:15333–15341
67. Casadonte DJ Jr, Flores M, Petrier C (2005) Ultrason Sonochem 12:147–152
68. Tuziuti T, Yasui K, Lee J, Kozuka T, Towata A, Iida Y (2008) J Phys Chem A 112:4875–4878
69. Kang B-K, Kim M-S, Park J-G (2014) Ultrason Sonochem 21:1496–1503
70. Tuziuti T, Yasui K, Iida Y, Sivakumar M, Koda S (2004) J Phys Chem A 108:9011–9013
71. Young FR (1976) J Acoust Soc Am 60:100–104
72. McNamara WB, Didenko YT, Suslick KS (1999) Nature 401:772–775
73. Lee J, Kentish S, Ashokkumar M (2005) J Phys Chem B 109:14595–14598
74. Leong T, Wu S, Kentish S, Ashokkumar M (2010) J Phys Chem C 114:20141–20145
75. Leong T, Collis J, Manasseh R, Ooi A, Novell A, Bouakaz A, Ashokkumar M, Kentish S (2011) J Phys Chem C 115:24310–24316
76. Oolman TO, Blanch HW (1986) Chem Eng Commun 43:237–261
77. Lee J, Kentish S, Ashokkumar M, Grieser F (2006) J Phys Chem B 110:17282–17285
78. Stottlemyer TR, Apfel RE (1997) J Acoust Soc Am 102:1418–1423
79. Ashokkumar M, Crum LA, Frensley CA, Grieser F, Matula TJ, McNamara WB III, Suslick KS (2000) J Phys Chem A 104:8462–8465
80. Ashokkumar M, Guan J, Tronson R, Matula TJ, Nuske JW, Grieser F (2002) Phys Rev E 65:046310
81. Guan J, Matula TJ (2003) J Phys Chem B 107:8917–8921
82. Ashokkumar M, Hall R, Mulvaney P, Grieser F (1997) J Phys Chem B 101:10845–10850
83. Grieser F, Ashokkumar M (2001) Adv Colloid Interface Sci 89–90:423–428
84. Segebarth N, Eulaerts O, Reisse J, Crum LA, Matula TJ (2002) J Phys Chem B 106:9181–9190
85. Price GJ, Ashokkumar M, Grieser F (2004) J Am Chem Soc 126:2755–2762
86. Browne C, Tabor RF, Chan DYC, Dagastine RR, Ashokkumar M, Grieser F (2011) Langmuir 27:12025–12032
87. Wall M, Ashokkumar M, Tronson R, Grieser F (1999) Ultrason Sonochem 6:7–14

88. Hallez L, Touyeras F, Hihn J, Klima J, Guey J-L, Spajer M, Bailly Y (2010) Ultrasonics 50:310–317
89. Birkin PR, Leighton TG, Power JF, Simpson MD, Vincotte AML, Joseph PF (2003) J Phys Chem A 107:306–320
90. Hatanaka S, Mitome H, Yasui K, Hayashi S (2006) Ultrasonics 44:e435–e438
91. Matsuoka T, Asakura Y, Nishida T, Nii S, Koda S (2007) J Chem Eng Jpn 40:497–500
92. Gondrexon N, Renaudin V, Petrier C, Boldo P, Bernis A, Gonthier Y (1999) Ultrason Sonochem 5:125–131
93. Bussemaker MJ, Zhang D (2014) Ultrason Sonochem 21:436–445
94. Bussemaker MJ, Zhang D (2014) Ultrason Sonochem 21:485–492

Acoustic Bubbles and Sonoluminescence

Pak-Kon Choi

Contents

Abstract

In a multibubble field, the bubble dynamics is determined by acoustic field-bubble and bubble-bubble interactions. The latter plays an important role in a field of high acoustic pressure. The first part of this chapter discusses the high-speed observation of bubbles interacting with other bubbles. The theory of bubble-bubble interactions in an acoustic field is briefly described, and high-speed images representing bubble coalescence are presented. The bubble oscillation and bubble size are shown to be affected by surfactant molecules adsorbed at the bubble/liquid interface. The high-speed images indicate spherical bubble oscillation and a smaller size distribution upon adding sodium dodecyl sulfate. Further, the initial size distribution of sonoluminescence (SL)-emitting bubble is

P.-K. Choi (✉)
Department of Physics, Meiji University, Tama-ku, Kawasaki, Japan
e-mail: pkchoi@meiji.ac.jp

described on the basis of the experiment using a pulsed ultrasound. The second part deals with the dependence of bubble dynamics on the acoustic power in association with the variation of SL intensity. The method of acoustic power measurement is described. The intensity of SL (sonochemiluminescence, SCL) takes a maximum value at certain acoustic power at both 84 and 138 kHz. The high-speed shadowgraphy of bubbles revealed a transition from a bubble streamer to a cluster with increasing the power. The bubble cluster was found to be composed of a large nonspherical bubble and tiny bubbles that exhibit transient oscillation. The emergence of the bubble cluster is the main cause of the reduction in the SL (SCL) intensity.

Introduction

Let us consider the process from bubble generation to bubble cluster formation. A bubble nucleus adhering to dust particles in a liquid or to a container wall grows into a small bubble through the rectified diffusion of gas dissolved in the liquid under acoustic pressure. Some growing bubbles may dissolve in the liquid because of surface tension, and other bubbles may further grow into collapsing bubbles that oscillate violently. A collapsing bubble may cause nonspherical oscillation because of its strong nonlinearity, leading to fragmentation into small bubbles. Collapsing bubbles may cause each other to coalesce via the secondary Bjerknes force that acts between bubbles, and sometimes form a streamer. The conditions inside a collapsing bubble are a high temperature and a high pressure, which may result in light emission and hydroxyl (OH) radical production. OH radicals decomposed from water molecules transfer through the bubble/liquid interface and interact with foreign molecules surrounding the bubble. Further increase in acoustic pressure enhances the secondary Bjerknes force, resulting in the formation of bubble clusters.

The recent improvement of high-speed imaging techniques is helpful for understanding acoustic bubble oscillations and bubble-bubble interactions [1, 2]. The first part of this chapter gives a survey of bubble-bubble interactions followed by the experimental results of high-speed observation. We present high-speed images of bubble coalescence under the condition of an acoustic field, in which multibubble sonoluminescence (SL) can be observed. The effects of sodium dodecyl sulfate (SDS) surfactant on bubble oscillations and the distribution of the maximum bubble size are shown at a frequency of 82 kHz for various SDS concentrations.

Bubble-bubble interactions greatly change with the applied acoustic power. In the second part of this chapter, after introducing the fundamentals of acoustic power

measurements, we describe how SL and sonochemiluminescence (SCL) intensities depend on the acoustic power under various conditions of acoustic fields and how the bubble dynamics as collective motion depends on the acoustic power in association with the SL intensity.

Interactions of a Bubble with an Acoustic Field and Another Bubble

Primary and Secondary Bjerknes Forces

The fundamentals of cavitation bubble dynamics are described in books by Young [3], Leighton [4], and Brennen [5]. The physics of bubble oscillations and recent works on this topic have been thoroughly reviewed by Lauterborn and Kurz [6]. Bubbles generated in a strong acoustic field self-organize into structured ensembles in the form of filamentary patterns (sometimes called "streamers") [7–9] or clusters [10] consisting of many bubbles, depending on the acoustic power and frequency. These structures are formed by the attractive and repulsive forces generated by bubble-bubble interactions.

The interaction force of a bubble with an acoustic field is called the primary Bjerknes force. The time-averaged Bjerknes force on a spherically oscillating bubble under acoustic pressure $p(x, t)$ is given by

$$F_B = -\langle V(t)\nabla p(x,t)\rangle, \tag{1}$$

where $V(t) = (4\pi/3)R^3$ is the bubble volume and R is the bubble radius. The brackets $\langle \rangle$ indicate a time average over an acoustic cycle. We consider a bubble located at position x in a standing-wave pressure field of the form

$$p(x,t) = P_a \sin kx \cos \omega t, \tag{2}$$

where P_a is the pressure amplitude, k is the wavenumber, and ω is the angular frequency of the acoustic field. If the pressure amplitude is not very large, the bubble radius oscillates as

$$R(t) = R_0 - A \sin kx \cos (\omega t + \alpha), \tag{3}$$

where α is the phase difference between the pressure and bubble radius oscillation, which equals zero for bubbles smaller than the resonance radius or π for bubbles larger than the resonance radius. R_0 is the equilibrium radius in the case of no acoustic field, and A denotes the amplitude of radial oscillation. Then the Bjerknes force (Eq. 1) can be calculated as

$$F_B = \frac{3AP_a kV_0}{4R_0} \sin 2kx \cos \alpha, \tag{4}$$

where $V_0 = (4/3)\pi R_0^3$. Equation 4 shows that bubbles smaller than the resonant radius are subjected to a force directed toward a pressure antinode and that bubbles larger than the resonant radius are subjected to a force directed toward a pressure node. Figure 1 illustrates how small bubbles tend to shift toward a pressure antinode. If the pressure amplitude is sufficiently large for the bubbles to continue expanding during the compression phase of the acoustic cycle, the bubbles are repelled from the antinode. This repulsion occurs when the pressure amplitude is larger than 1.8 atm at 20 kHz [11].

If two bubbles exist in the vicinity of each other, the oscillation of a bubble with volume $V_1 = (4/3)\pi R_1^3$ produces pressure waves around the bubble that act as an additional force on the neighboring bubble. This is called the secondary Bjerknes force. Under a pressure gradient ∇p_1 caused by the first bubble, the second bubble of volume $V_2 = (4/3)\pi R_2^3$ is subjected to the force

$$F_{12} = -V_2 \nabla p_1 . \tag{5}$$

The time average of Eq. 5 gives the net force

$$\boldsymbol{F}_{B2} = -\frac{\rho}{4\pi d^2} \langle \dot{V}_1 \dot{V}_2 \rangle \mathbf{e}_r, \tag{6}$$

where ρ is the density of the liquid, d is the distance between the two bubbles, and $\mathbf{e}_r$ denotes the radial unit vector. For harmonic bubble oscillation, we obtain

Fig. 1 Bubbles smaller than the resonant size move toward a pressure antinode under the primary Bjerknes force F_B in a standing-wave field
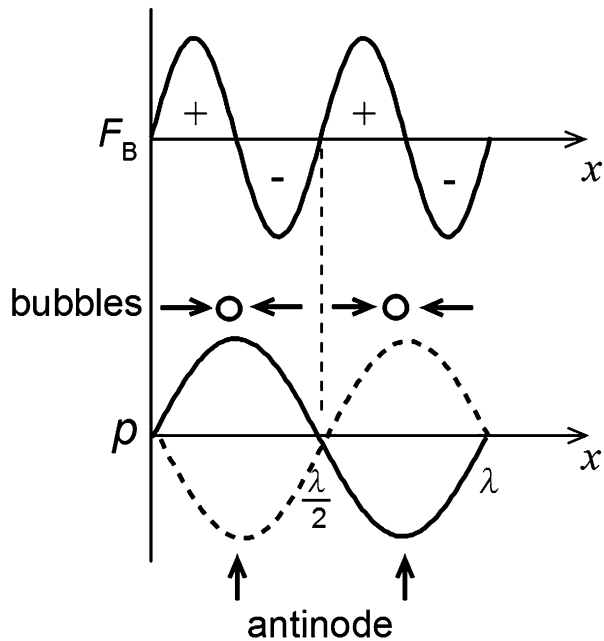
$$\boldsymbol{F}_{B2} = -\frac{\rho\omega^2}{8\pi d^2}V_{1A}V_{2A}\cos{(\varphi_1 - \varphi_2)}\mathbf{e}_r, \tag{7}$$

where V_{1A}, V_{2A}, and φ_1 and φ_2 are the magnitudes and phases of the volume oscillations, respectively. According to these equations, a bubble smaller than the resonance radius and a bubble larger than the resonance radius repel each other, while pairs of bubbles smaller or larger than the resonance radius attract each other. Mettin et al. [12] numerically investigated the secondary Bjerknes force in a strong acoustic field. They employed the model of Keller and Miksis [13] to calculate the oscillation of the second bubble using

$$\left(1 - \frac{\dot{R}_2}{c}\right)R_2\ddot{R}_2 + \left(\frac{3}{2} - \frac{\dot{R}_2}{2c}\right)\dot{R}_2^2 = \frac{1}{\rho}\left(1 + \frac{\dot{R}_2}{c}\right)(p_{2w} - p_0 - p_{sound})$$
$$+ \frac{R_2}{\rho c}\frac{d}{dt}(p_{2w} - p_{sound}) - \frac{1}{d}\left(2\dot{R}_1^2 R_1 + R_1^2\dot{R}_1\right), \tag{8}$$

where c is the sound velocity in the liquid, p_0 is the hydrostatic pressure, and p_{sound} is the external sound pressure. Here, p_{2w} is the pressure in the liquid at the bubble interface and is given by

$$p_{2w} = \left(p_0 + \frac{2\sigma}{R_{20}}\right)\left(\frac{R_{20}}{R_2}\right)^{3\gamma} - \frac{2\sigma}{R_2} - \frac{4\mu}{R_2}\dot{R}_2. \tag{9}$$

γ denotes the polytropic exponent, σ is the surface tension, μ is the viscosity of the liquid, and R_{10} and R_{20} are the equilibrium radii of the two bubbles. Figure 2 shows

Fig. 2 Secondary Bjerknes force coefficient plotted in the R_{10}-R_{20} plane for $d = 1$ mm and $P_a = 1.32$ atm. *White regions correspond to repulsion and the darker regions correspond to attraction between the two bubbles (Reprinted with permission from Ref. [12]. Copyright 1997, American Physical Society)
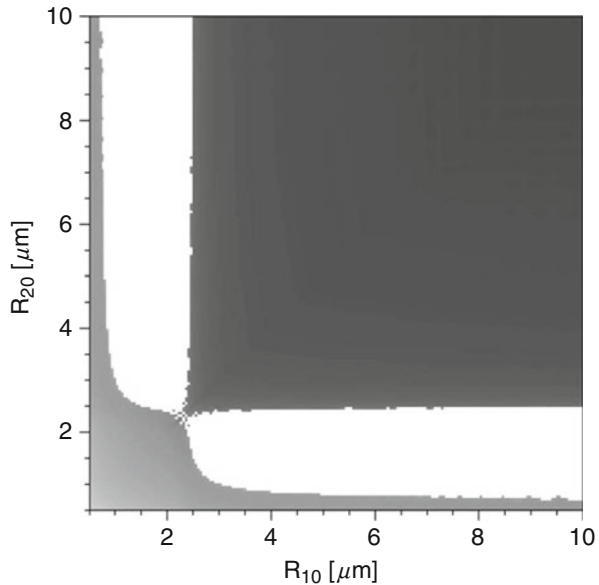
the secondary Bjerknes force coefficient $\frac{\rho}{4\pi}\langle \dot{V}_1 \dot{V}_2 \rangle$ represented in the R_{10}-R_{20} plane for a bubble distance of $d = 1$ mm and $P_a = 1.32$ atm. The white regions correspond to repulsion and the darker regions correspond to attraction between the two bubbles. The white regions become narrower when the two bubbles approach each other. The pairs of bubble radii corresponding to the white regions are smaller than the linear resonant radius, i.e., 0.15 mm at 20 kHz, which indicates an attractive force according to the linear theory expressed by Eq. 7. This apparent contradiction is explained by the fact that the nonlinear resonance radius decreases with increasing pressure amplitude.

High-Speed Observation of Two Interacting Bubbles

Jiao et al. [14] experimentally and theoretically studied the translational motion of two approaching bubbles. They used a cylindrical Pyrex resonator equipped with a 22.4 kHz transducer to trap two bubbles, which were injected near a pressure antinode. The movements of the bubbles were recorded using a high-speed camera at a frame rate of 2000 fps. Their relative velocity was measured at various distances between the bubbles. The experimental result is shown in Fig. 3 together with theoretical values calculated from the secondary Bjerknes force and drag force.
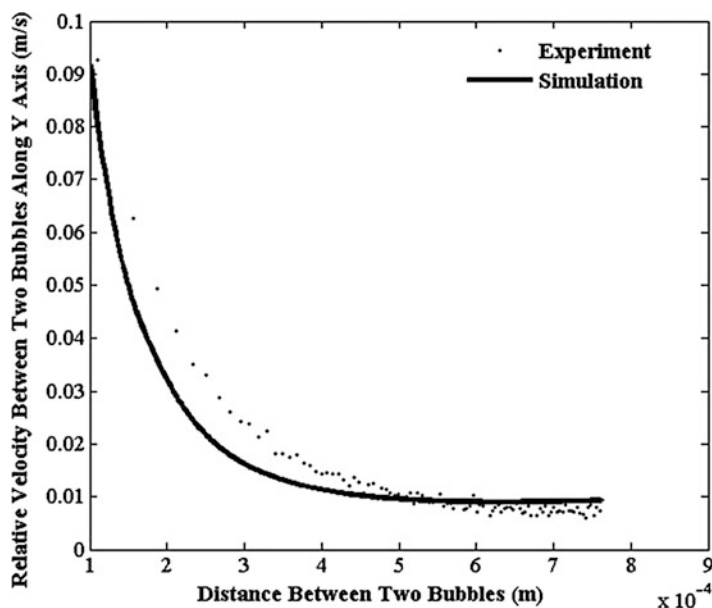
Fig. 3 Relative velocity of two bubbles as a function of the distance between them for a pressure amplitude of 40 kPa. The *solid line* denotes the values calculated from the secondary Bjerknes force (Reprinted with permission from Ref. [14]. Copyright 2013, American Chemical Society)
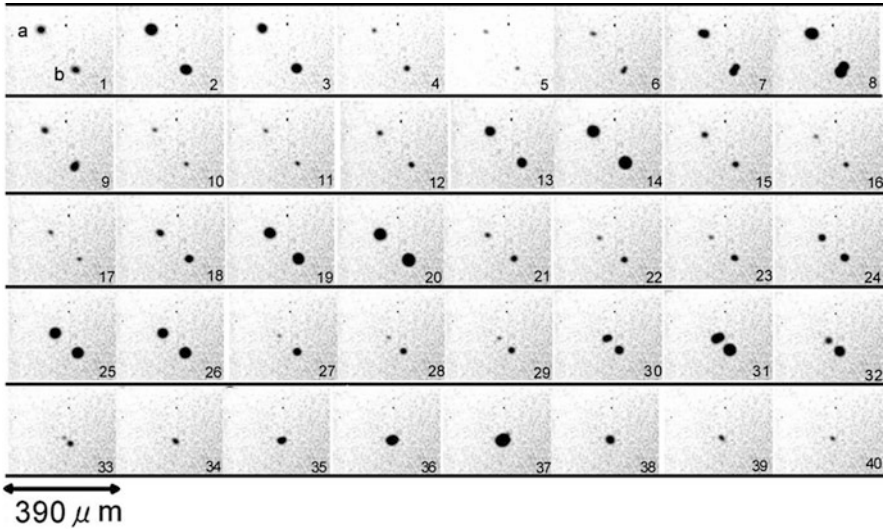
Fig. 4 Shadowgraphs of two bubbles exhibiting oscillations and coalescence in a 87 kHz standing-wave field in water. The acoustic power is about 5 W, and the time interval between images is 2 μs

The Keller-Miksis equation, Eq. 8, was used to calculate the radial oscillation of the bubbles. The experimental and simulation results have a reasonably strong correlation as shown in Fig. 3.

Choi and Deno [15] reported a high-speed movie of the coalescence of two bubbles interacting in a streamer in a standing-wave field of 87 kHz in water. Figure 4 shows selected images from the movie, which was taken at a frame rate of 1 M fps. Bubble a, which is located in the upper left of frame 1, approaches bubble b, which remains at almost the same position, while both bubbles repeatedly undergo expansion and contraction. The maximum sizes of the two bubbles are 50 μm, and the minimum sizes are approximately 9 μm. In frames 6–9, bubble b exhibits shape oscillation, although it exhibits spherical oscillation in the next acoustic cycle in frames 12–14. Bubble a also exhibits shape oscillation in frames 30–32. The two bubbles finally coalesce in frame 34. Figure 5 shows the time dependencies of the distance between the centers of the two bubbles and their relative velocity. Equation 6 predicts that the Bjerknes force between the bubbles is strong when the bubble volumes change rapidly. The velocity increases with decreasing the distance of the bubbles, corresponding to the rapid contraction of the two bubbles. The result is well explained by Eq. 6.

Several works on the oscillation of coated microbubbles, which are used in ultrasound contrast agents, have been reported. The nonspherical oscillation of a coated microbubble sonicated in the MHz range was observed by Versluis et al. [16], van der Meer et al. [17], and Dollet et al. [18]. Direct observations of the sonoporation of a viable cell membrane by cavitation bubbles [19] and coated microbubbles [20] were reported.
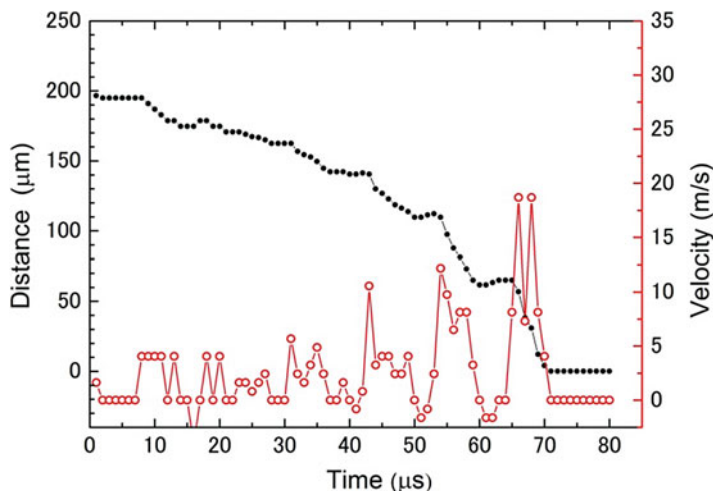
Fig. 5 Distance between the two bubbles (*closed circles*) and their relative velocity (*open circles*) as a function of time, which were obtained from the images in Fig. 4. The two bubbles coalesced at 70 μs

High-Speed Observation of Effects of Surfactant on Bubble Oscillations

The effects of surface-active solutes on cavitation bubbles have been extensively studied by Crum and others [21–23] and the group of Melbourne University [24, 25]. SL, sonochemistry, and acoustic emission have been used to monitor the effects of sodium dodecyl sulfate (SDS) molecules, adsorbed at a bubble/liquid interface. The effects are manifested in several ways. First, the bubble growth rate increases because of the resulting resistance to gas transfer across the interface, especially during the collapse phase of a bubble oscillation [26]. The inhibition of bubble coalescence also occurs due to the electrostatic effect caused by the adsorption of charged surfactant molecules at the bubble/liquid interface. This inhibition produces a sharp decrease in total bubble volume in a multibubble field [27]. The adsorption increases the number of active cavitation bubbles, which leads to the enhancement of multibubble SL, and also increases the symmetry of bubble oscillation, resulting in an increase in harmonic components in the acoustic emission spectrum [28].

A direct observation of the bubble oscillation in SDS solutions was reported by Deno and Choi [29]. Figure 6 shows the shadowgraph images of cavitating bubbles at their maximum sizes in water and 1 mM SDS solution captured with a high-speed camera (Shimadzu, HPV-2) at 1 M fps. The bubbles are streaming toward the lower right corner in a standing-wave field of 125 kHz. The bubbles in water (a) exhibit nonspherical oscillations, and those in SDS solution (b) exhibit spherical oscillations, confirming the speculation by Ashokkumar et al. [28], which was based on the acoustic emission spectrum.
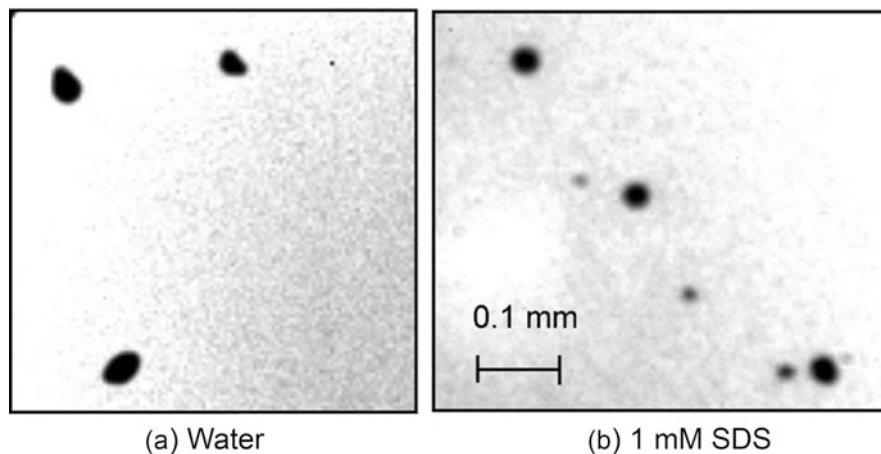
Fig. 6 High-speed images of cavitation bubbles in water (**a**) and 1 mM SDS solution (**b**) sonicated at 125 kHz and an acoustic power of 20 W. The bubbles are at their maximum sizes. The exposure time is 1 μs
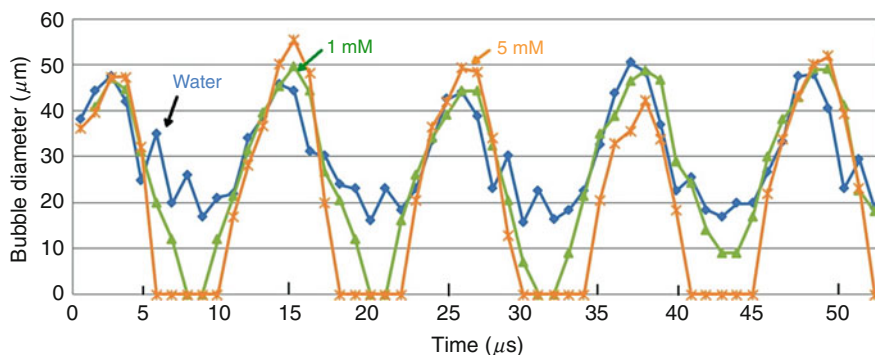
Fig. 7 Time sequences of bubble diameter obtained from high-speed movies captured at 1 M fps. The ultrasonic frequency is 87 kHz and the acoustic power is about 11 W. Diameters below 4.7 μm are plotted as zero

As shown in Fig. 7, the time sequences of bubble diameter were obtained from the high-speed images for water (blue) and 1 mM (green) and 5 mM (orange) SDS solutions at an ultrasonic frequency of 87 kHz. About 11 frames were captured in the period of ultrasound. Diameters below 4.7 μm are plotted as zero in these curves since the spatial resolution of the images was 4.7 μm. For water, oscillations with a shorter period appeared at compression phases. This was caused by the nonspherical oscillation of bubbles, which was observed very frequently in the high-speed movies. Conversely, for the 1 and 5 mM SDS solutions, the bubble oscillation curves in Fig. 7 resemble those obtained by the simulation of a single bubble.

This suggests that spherical oscillations preferentially occur in surfactant-adsorbed bubbles, in agreement with the high-speed images. The spherical oscillations can be explained by two factors [28]. First, the adsorption of the surfactant at the bubble/liquid interface dampens surface waves at the interface. Second, the electrostatic repulsion between bubbles leads to the "declustering" of the bubbles, which decreases the secondary Bjerknes force.

The distribution of the bubble size is also affected by a surface-active solute. The maximum diameters of cavitating bubbles can be estimated from high-speed images. Figure 8 shows a histogram of the maximum diameter under 87 kHz ultrasound with an acoustic power of about 11 W. In Fig. 8a, the maximum bubble diameter in water is distributed from 9 to 66 μm with an average of 31 μm, which is indicated by the arrow in the figure. Figure 8b–e show the histograms for SDS solutions with concentrations of 0.1, 1, 5, and 10 mM, respectively. The range of the maximum diameter decreases with increasing SDS concentration up to 5 mM then increases at 10 mM. The average maximum bubble diameter at 5 mM is 21 μm, which is the smallest value among the solutions investigated. At the concentration of 5 mM, the number of bubbles with diameters larger than 40 μm is significantly less than that in water. This is because bubble coalescence is inhibited when charged SDS molecules are adsorbed at the bubble/liquid interface. The direct observation of bubble oscillation demonstrated that the effects of SDS on bubble oscillation are most prominent at 5 mM, which is larger but in reasonable agreement with the value obtained by the observations of acoustic emission [28] and SL [30]. The effect of SDS adsorption may also depend on the acoustic frequency and power.

Size Distribution of Sonoluminescence Bubbles

Section "High-Speed Observation of Effects of Surfactant on Bubble Oscillations" describes the oscillations of bubbles regardless of the emission of SL. There is interest in the size of bubble that exhibits SL or SCL. Lee et al. [31] determined the size distribution of SL-emitting bubbles using a pulsed ultrasound at 515 kHz. They employed a 4 ms-duration (equivalent to 2060 cycles) ultrasound pulse so that a steady-state active bubble population is reached and a constant SL intensity is obtained. The active bubbles dissolve during a pulse off-time with a finite dissolution time depending on the initial bubble radius. If the successive ultrasonic pulses act upon the bubbles before the bubbles dissolve away, the bubbles can grow again to be in the active size range. The SL intensity at successive pulse on-time reflects the population of active bubbles. Thus, the decrease in the SL intensity during the pulse on-time as a function of pulse off-time gives a measure of the initial radius of active bubble. Lee et al. [31] obtained the experimental bubble radii of 2.8–3.7 μm for water and 0.9–1.7 μm for 1.5 mM SDS solution using the theory by Epstein and Plesset [32]. These values for water are smaller than the theoretical linear resonance size of 5.8 μm at 515 kHz. This is explained by the fact that nonlinear resonance size is smaller than the linear resonance size. Using a similar experimental technique, Brochie et al. [33] investigated the frequency and power dependencies of the size
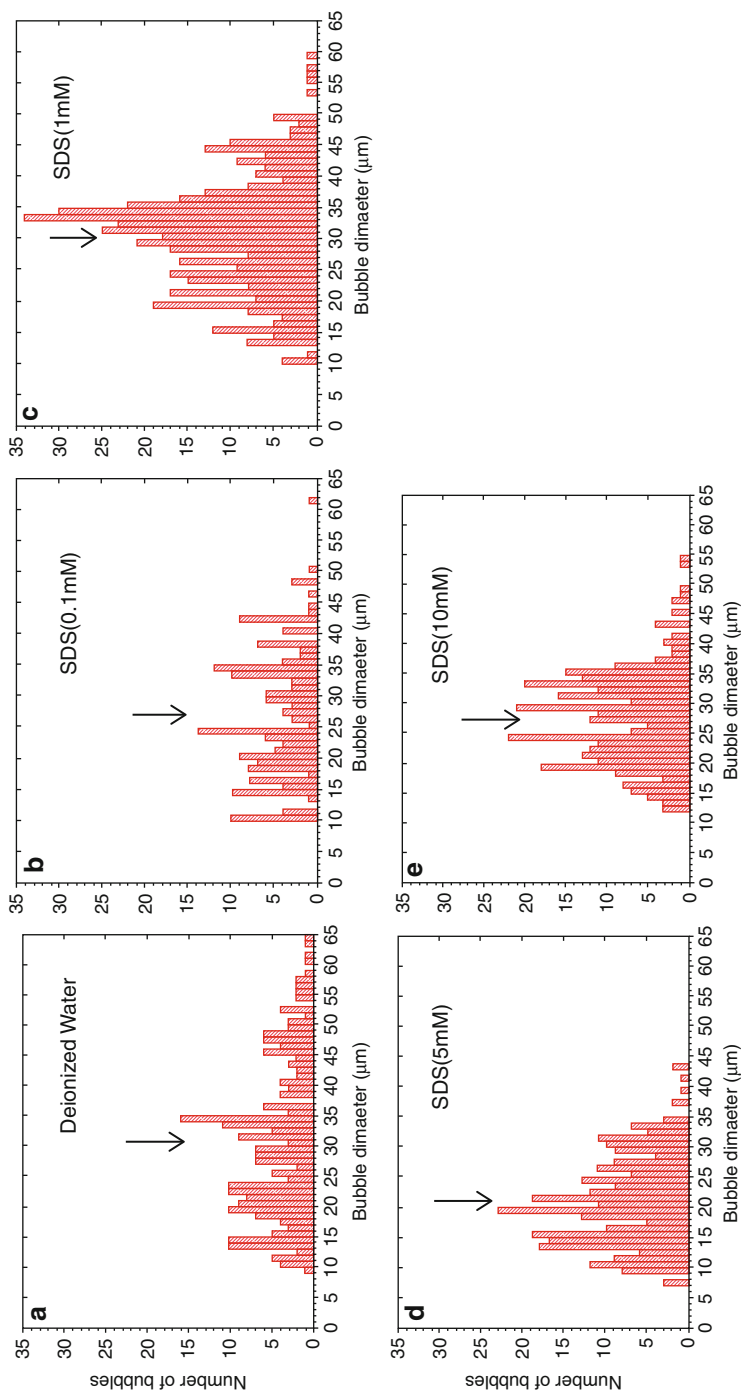
Fig. 8 Histogram of maximum diameter of cavitating bubbles under 87 kHz ultrasound with acoustic power of about 11 W. The diameters were obtained from high-speed images for water and SDS solutions with concentrations of 0.1, 1, 5, and 10 mM from (**a**) to (**e**), respectively. Each *arrow* indicates the average maximum diameter. The sample size is in the range of 178–463

distribution of SCL-emitting bubbles in a luminol solution. Figure 9 shows the results of the size distribution for several frequencies from 213 to 1136 kHz, indicating that the mean bubble size is smaller and the distribution becomes narrower with increasing frequency. It is noted that the bubble sizes in Fig. 9 are much smaller than those in Fig. 8 which shows the bubble sizes at their maxima. In Fig. 10, the active bubble size distributions are compared for SCL and SL at 575 kHz. The size is larger for SL bubbles than SCL bubbles. This indicates that there are two distinct classes of bubbles: larger bubbles which emit SL under a higher temperature condition at bubble collapse and smaller bubbles which produce OH radicals under a modest temperature condition at bubble collapse.

In a pulsed ultrasound experiment, the enhancement of SL intensity or OH radical production may occur by an appropriate choice of pulse on-time and pulse off-time. Choi et al. [34] reported the enhancement of SL intensity and acoustic emission spectra at 103 kHz. As shown in Fig. 11, they obtained the maximum amplification factor of 6.7 compared with continuous wave mode when the pulse on-cycle was 500 and pulse off-cycles were 500–10000. Lee et al. [35] and Tuziuti et al. [36] explained this enhancement by demonstrating the enlargement of SL and SCL spatial distributions with appropriate pulse-off times. The pulsed ultrasound may prevent the production of large degassing bubbles which absorb ultrasound energy, resulting in the increase in the active bubble population. Choi et al. [34] also reported the acoustic emission spectra, showing that subharmonic components and broadband
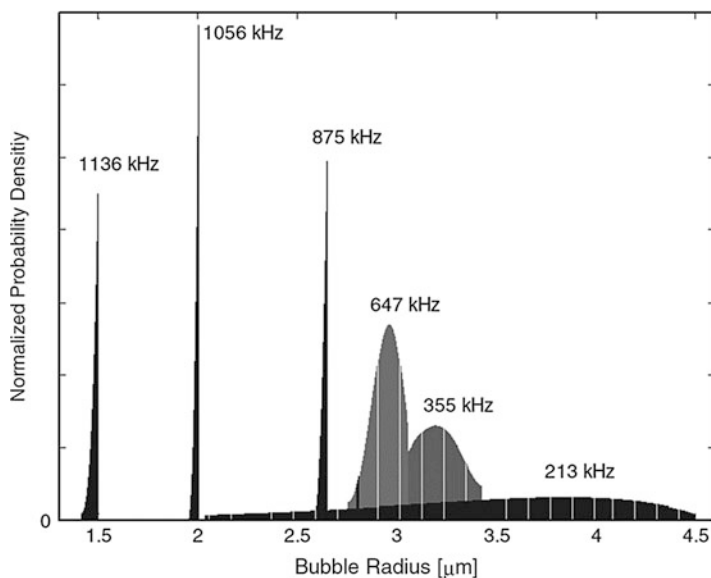
Fig. 9 The size distributions of SCL-emitting bubble at 213, 355, 647, 875, 1056, and 1136 kHz obtained using a pulsed ultrasound. The data for 875, 1056, and 1136 kHz have been scaled down by a factor of 4. The acoustic power of all frequencies is 1.5 W (Reprinted with permission from Ref. [33]. Copyright 2009, American Physical Society)
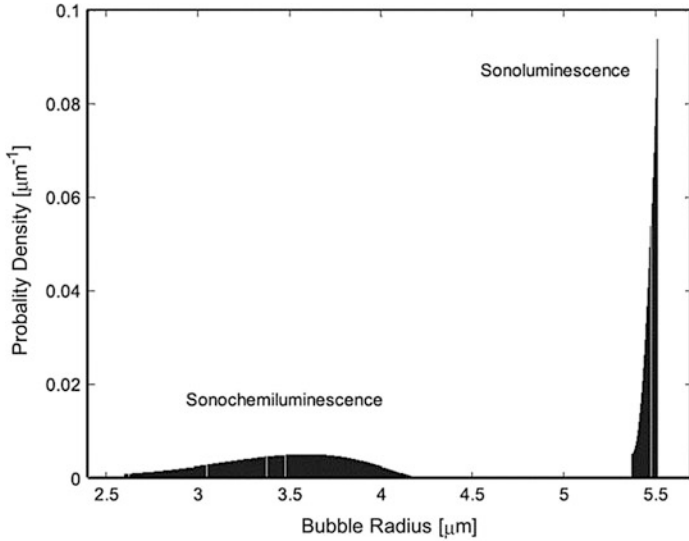
Fig. 10 The size distributions of SCL- and SL-emitting bubble at 575 kHz. The acoustic power was 2.8 W (Reprinted with permission from Ref. [33]. Copyright 2009, American Physical Society)
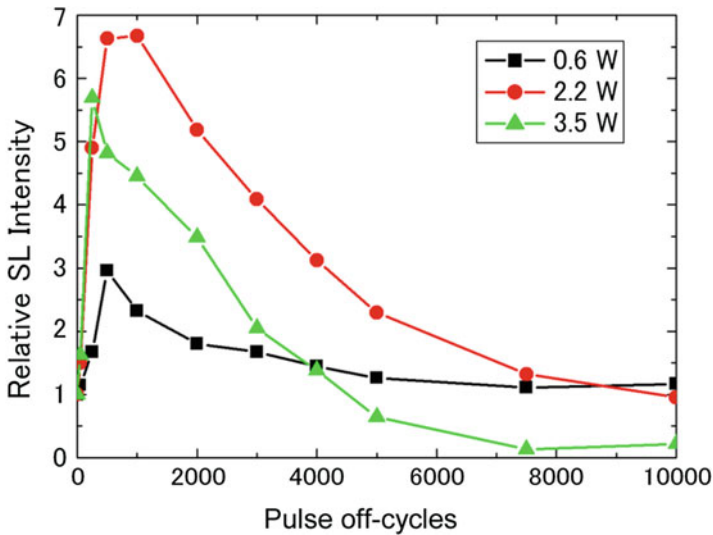
Fig. 11 The SL intensity in a pulsed wave mode normalized to that in a continuous wave mode as a function of pulse off-cycles. The ultrasound frequency is 103 kHz and the pulse on-cycles are 500 (Reprinted with permission from Ref. [34]. Copyright 2008, the Japan Society of Applied Physics)

noise increased for the pulsed mode compared with the continuous mode. The acoustic pressure in the pulsed mode may be larger than that in the continuous mode because of the lack of large degassing bubbles which absorb sound energy. This increases the subharmonic components and broadband noise [37]. Another possibility is that nonspherical bubble oscillations are favored in the pulsed mode. A complex bubble oscillation emitting many daughter bubbles was observed by using a high-speed camera. Further experiments are required to understand the mechanism which elucidates the SL enhancement in a pulsed ultrasound field. The observation of corresponding bubble dynamics will be helpful for that purpose.

Acoustic Power Dependencies of Bubble Dynamics in Relation to Sonoluminescence

Power Dependencies of Acoustic Cavitation

Acoustic cavitation produces extreme temperature and pressure conditions inside bubbles at collapse. These conditions induce SL and promote chemical reactions. Factors affecting acoustic cavitation include the acoustic frequency, applied acoustic power, dissolved gas, solution temperature, and environmental pressure. The use of optimal factors is especially important when developing large-scale reactors for sonochemical applications. The optimal frequency for SL and sonochemical activity has been explored [38]. Beckett and Hua [39] investigated the SL spectra from water and the chemical reactivity (1,4-dioxane decomposition and hydrogen peroxide formation) at frequencies of 205, 358, 618, and 1071 kHz. They concluded that 358 kHz was the optimal frequency for obtaining maximum SL intensity and chemical reaction rates. Koda et al. [40] reported that approximately 300 kHz was the most efficient frequency for the Fricke reaction and KI dosimetry on the basis of broadband measurements ranging from 19.5 to 1200 kHz. Kanthale et al. [41] showed that the SL intensity and hydrogen peroxide yield exhibited different frequency dependencies. This is because the SL intensity mainly depends on the maximum temperature within a bubble at collapse, whereas the hydrogen peroxide yield depends on the average temperature during bubble collapse as well as mass transfer effects. Yasui [42] numerically demonstrated that the mechanism of SL depends on the frequency. SL mainly originates from plasma emission at 1 MHz, whereas it originates from OH radical emission and plasma emission at 20 kHz.

A suitable acoustic power is also an important factor for efficient sonochemical reactions. The oxidation rate of iodide in aqueous KI solution has been shown to exhibit a nonlinear power dependence [43–46]. The oxidation of iodide has been used as a convenient method for evaluating the production of OH radicals. This method is called KI dosimetry. I^- ions are oxidized by OH radicals to give I_2. When excess I^- ions are present in the solution, I_2 reacts with the I^- ions to form I_3^- ions, which can be detected by their optical absorbance at 355 nm. Henglein and Gutierrez [45] demonstrated that the yield of iodine during KI oxidation showed a maximum
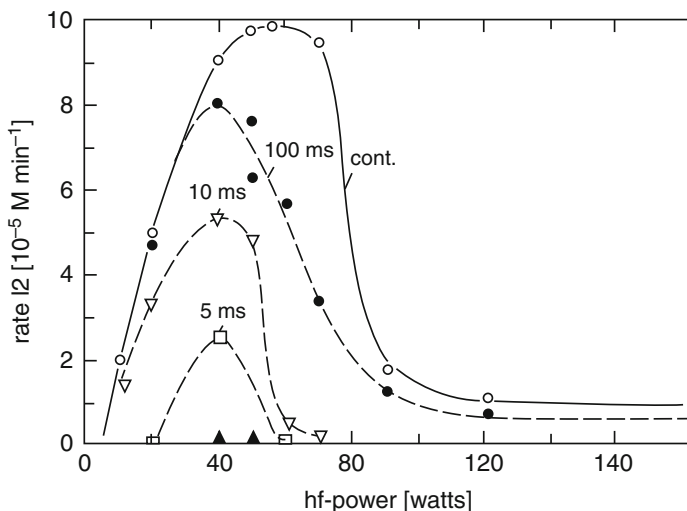
Fig. 12 Power dependence of the rate of iodine formation at 1 MHz. *Open circles* denote the yield of iodine in the continuous mode and other symbols denote the yield in the pulsed mode. The pulse duration times are indicated in the figure. The on/off ratio is 1:100 (Reprinted with permission from Ref. [45]. Copyright 1990, American Chemical Society)

when measured as a function of input power, as shown in Fig. 12. They used continuous- and pulsed-mode ultrasound at 1 MHz. The rate of iodine formation took a maximum at 60 W, which is equivalent to an acoustic power of 1.5 W/cm^2, in the continuous mode.

The dependence of the SL or SCL intensity on the acoustic power has only been investigated in a few intensive studies. Negishi [47] reported that the SCL intensity from a luminol solution suddenly decreased at an acoustic power of 2 W/cm^2 at 470 kHz. Recently, Hatanaka et al. [48] observed that the SL intensity at 132 kHz decreases at high powers, which they did not specify. Kanthale et al. [34] investigated the acoustic power and frequency dependencies of the SL intensity and hydrogen peroxide yield and showed that both quantities increase with the acoustic power up to 30 W. An increase in acoustic power increases the active bubble population and the maximum active bubble size, both of which enhance the sonochemical activity if the interaction among active bubbles is weak. If the acoustic power is sufficiently strong for bubble-bubble interactions to dominate, the dependence will show nonlinear behavior.

Measurement Method for Acoustic Power

When sound waves travel with velocity c through a liquid medium of density ρ, they transport the energy contained in them. This energy flow is characterized by the

sound intensity I. Suppose that the sound waves travel through an imaginary window of unit area perpendicular to the sound direction. The sound intensity is defined by the energy traveling through the window in a unit time and is sometimes called the "acoustic power." The sound energy density W is the energy per unit volume of the medium and is related to the sound intensity by

$$W = \frac{I}{c}. \tag{10}$$

The energy density W is composed of kinetic energy and potential energy. If both energies are taken per unit volume, the corresponding energy densities are

$$w_{\text{kin}} = \frac{1}{2}\rho u^2 \text{ and } w_{\text{pot}} = \frac{p^2}{2\rho c^2}, \tag{11}$$

where u is the particle velocity of the medium and p is the sound pressure. From the known specific acoustic impedance Z, which is defined for plane traveling waves as

$$Z = \frac{p}{u} = \rho c, \tag{12}$$

the total energy density is derived as

$$W = w_{\text{kin}} + w_{\text{pot}} = \frac{p^2}{\rho c^2} \left[\text{J/m}^3\right]. \tag{13}$$

Then, the sound intensity is obtained from Eqs. 10 and 13 as

$$I = \frac{p^2}{\rho c} \left[\text{W/m}^2\right]. \tag{14}$$

Note that the pressure is defined by the root-mean-square value in Eq. 14. If we use the pressure amplitude $\hat{p}$, Eq. 14 becomes

$$I = \frac{\hat{p}^2}{2\rho C} \left[\text{W/m}^2\right]. \tag{15}$$

The above equations hold for traveling sound waves. For standing sound waves, the energy density and sound intensity are respectively expressed by

$$W_{\text{stand}} = 2\frac{p^2}{\rho c^2}, I_{\text{stand}} = 2\frac{p^2}{\rho c}. \tag{16}$$

The acoustic power can be predicted from the measured sound pressure using Eq. 14 or 16. As an example, we consider plane sound waves with a pressure amplitude of 10^5 Pa ($=1$ atm) propagating in water. The corresponding acoustic power is

calculated from Eq. 14 to be 3.3×10^3 [W/m^2] or 0.33 [W/cm^2]. The unit of W/cm^2 is not based on the International System of Units but is customarily used.

In acoustic cavitation experiments, however, the accurate measurement of the acoustic pressure is practically difficult. Highly nonlinear phenomena such as cavitation cause the distortion of pressure waves, which results in the production of many harmonic and subharmonic components, complicating the pressure measurement. Instead, the calorimetric determination of the total sound energy delivered to the medium is frequently performed to estimate the acoustic power. When liquid with a mass of M kg is irradiated by ultrasound, the temperature in the liquid increases owing to the absorption of ultrasonic energy. The acoustic power I is obtained from the measured temperature rise ΔT during the irradiation time Δt using the known heat capacity C_p of the liquid at a constant pressure and is given by [49]

$$I = \left(\frac{\Delta T}{\Delta t}\right) M C_p. \tag{17}$$

The temperature is typically measured using a K type thermocouple. A resolution of 0.1 K is suitable for the measurement of acoustic powers of over 20 W. Alternatively, the electric power input to a transducer is sometimes used as a measure of the acoustic power dissipated in a liquid. The input electric power can be obtained from the measured applied voltage V and current A, and their phase difference θ as

$$I_e = VA\cos\theta. \tag{18}$$

An experimental system for calorimetric and electric power measurements is shown in Fig. 13a. Figure 13b shows an example of the temperature rise during ultrasound irradiation at 136 kHz in water with the mass $M = 0.326$ kg. The temperature rise from 1 min after the start of the system is switched on is nearly linear, giving an acoustic power of 30 W from Eq. 17. A comparison between the powers measured by calorimetric and electrical methods is shown in Fig. 14 for the cases of air-saturated water and degassed water samples.

In this experiment, a sandwich-type transducer with a fundamental frequency of 28 kHz was used; this transducer was attached to the stainless-steel sample container. The operation frequency was 116 kHz, which is one of the harmonics of the transducer. The electric powers, indicated by open symbols, are higher than the calorimetric acoustic powers, indicated by solid symbols, for both air-saturated and degassed water samples. Some of the electric power is consumed as the thermal loss within the transducer. The efficiency of electric to acoustic transduction is in the range of 50–90 %, which may depend on the input voltage and the method of transducer installation. The transduction efficiency decreases at higher applied voltages. The electric power is used for convenience to obtain an approximate value of the acoustic power, because the calorimetric measurement is more time consuming than the electric measurement. However, the existence of a difference between the calorimetric and electric powers should be kept in mind.
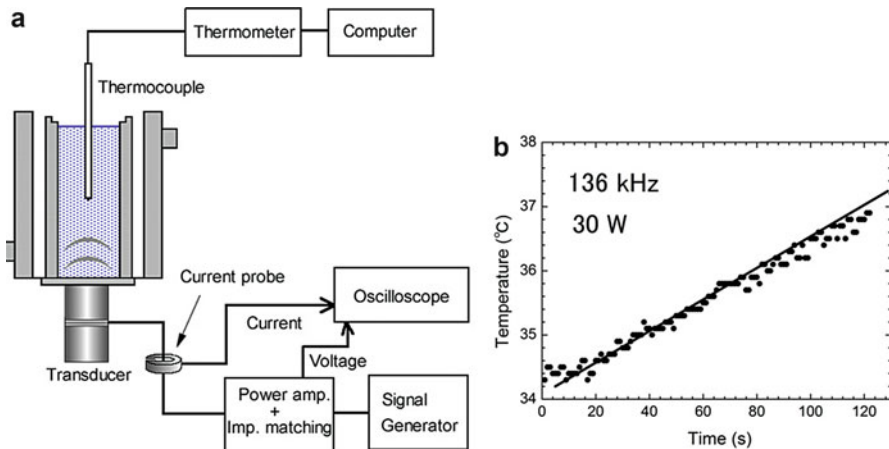
Fig. 13 (**a**) Apparatus for calorimetric and electric power measurements. (**b**) Temperature rise during ultrasound irradiation at 136 kHz. The gradient of the fitted line gives an acoustic power of 30 W
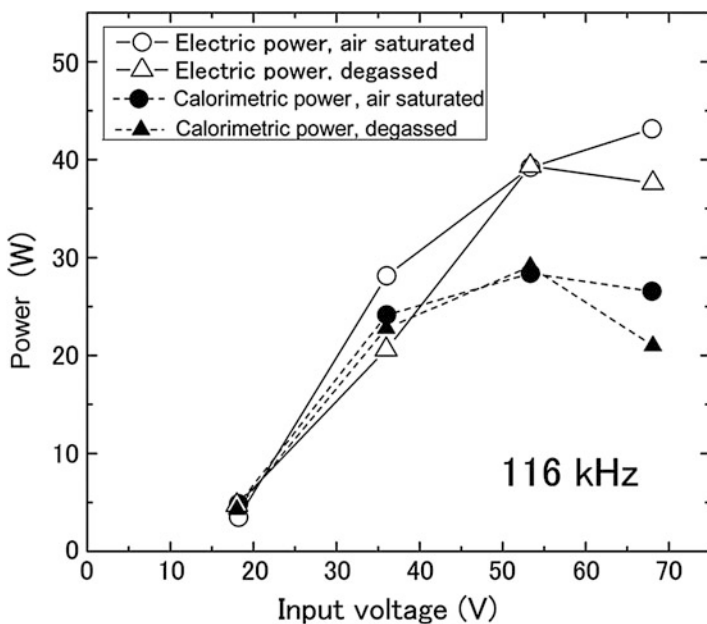
Fig. 14 Comparison of calorimetric power with electric input power for several input voltages. *Open* and *closed circles* represent the powers for air-saturated water, and open and closed triangles represent those for degassed water

Acoustic Power Dependencies of SL and SCL Intensities

The bubble dynamics in various acoustic fields should be clarified to determine the acoustic power dependencies of cavitation events. Negishi [47] carried out an extensive study on SL and SCL in various liquids. He observed a sudden decrease in SCL intensity in luminol solution at 470 kHz with increasing input voltage, as shown in Fig. 15. Similar decreases in SL intensity have been observed in all aqueous solutions of organic liquids and sodium salts investigated. Such a decrease in SL intensity was also observed by Hatanaka et al. [48], who attributed it to the formation of bubble clusters from their observation of bubble dynamics at 23 kHz using high-speed photography with a speed of 1000 fps. Ashokkumar et al. [50] compared the spatial distributions in SL and SCL images observed at frequencies of 170, 440, and 700 kHz and at various acoustic powers. They showed that the spatial distributions for SCL are much broader than those for SL at every power investigated. Sonochemically active bubbles were observed at relatively lower acoustic pressures than that required for SL bubbles to appear. The acoustic power required for the observation of the initial cavitation bubbles increased with an increase in the frequency. They observed a linear increase in SL intensity up to an electric power of 20 W at the three frequencies.

These studies on the power dependence of SL or SCL were performed under the boundary condition of a free liquid surface that is acoustically open ended. At high acoustic powers, the vibration or deformation of the liquid surface is frequently induced by the acoustic radiation force in the case of an open-type sample container in which acoustic waves are directed toward the liquid surface. The surface vibration or deformation may disturb the standing-wave field, causing a decrease in acoustic pressure. This hypothesis was tested by Lindström [44], who investigated the production of hydrogen peroxide under acoustic field conditions with free-surface and fixed-surface boundaries at 700 kHz. Hydrogen peroxide production saturated at high powers for the fixed-surface boundary and decreased at high powers for the

Fig. 15 Input voltage dependence of SCL intensity in a luminol solution for increasing and decreasing input voltage. The ultrasonic frequency is 470 kHz (Reprinted with permission from Ref. [47]. Copyright 1961, Physical Society of Japan)
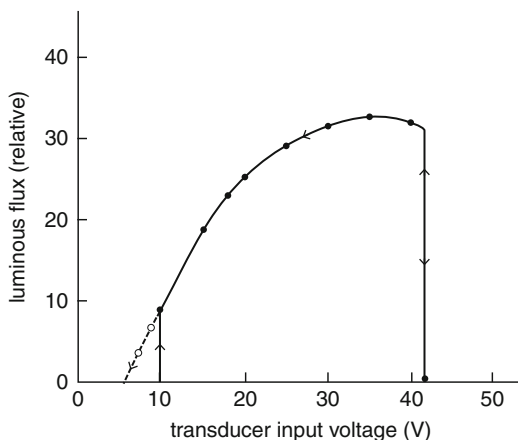
free-surface boundary. Tuziuti et al. [51] reported similar behavior for the SCL intensity. No decrease in SCL intensity was observed when the surface was covered with a thin layer of Teflon powder.

Lee and Choi [52] investigated the power dependencies of SL and SCL under three types of acoustic boundary condition at 83.8 and 138 kHz. The reactor used was a rectangular parallelepiped made of quartz glass (Fig. 16) with internal dimensions of 65 mm width, 65 mm depth, and 90 mm height. The sample volume was 320 mL. A sandwich-type Langevin transducer with a fundamental frequency of 28 kHz was cemented to the bottom of the reactor.

Figure 17 shows the spatial distributions of SL from argon-saturated water at 83.8 kHz. The images were captured using the reactor shown in Fig. 16 by a digital camera with an exposure time of 30 s and a sensitivity of ISO 16,000. The three types of liquid-surface boundary investigated were (a) a free-surface boundary, (b) a thin-film boundary, and (c) a stainless-steel (SUS 304) plate boundary. Boundaries (a) and (b) correspond to an acoustically free end, and boundary (c) corresponds to an acoustically fixed end. In the case of the free surface, the liquid surface vibrates at high powers owing to the acoustic radiation force. In the

Fig. 16 Rectangular parallelepiped reactor. A sandwich-type transducer is cemented to the bottom of the reactor. The amount of dissolved gas can be controlled by using an air-tight device
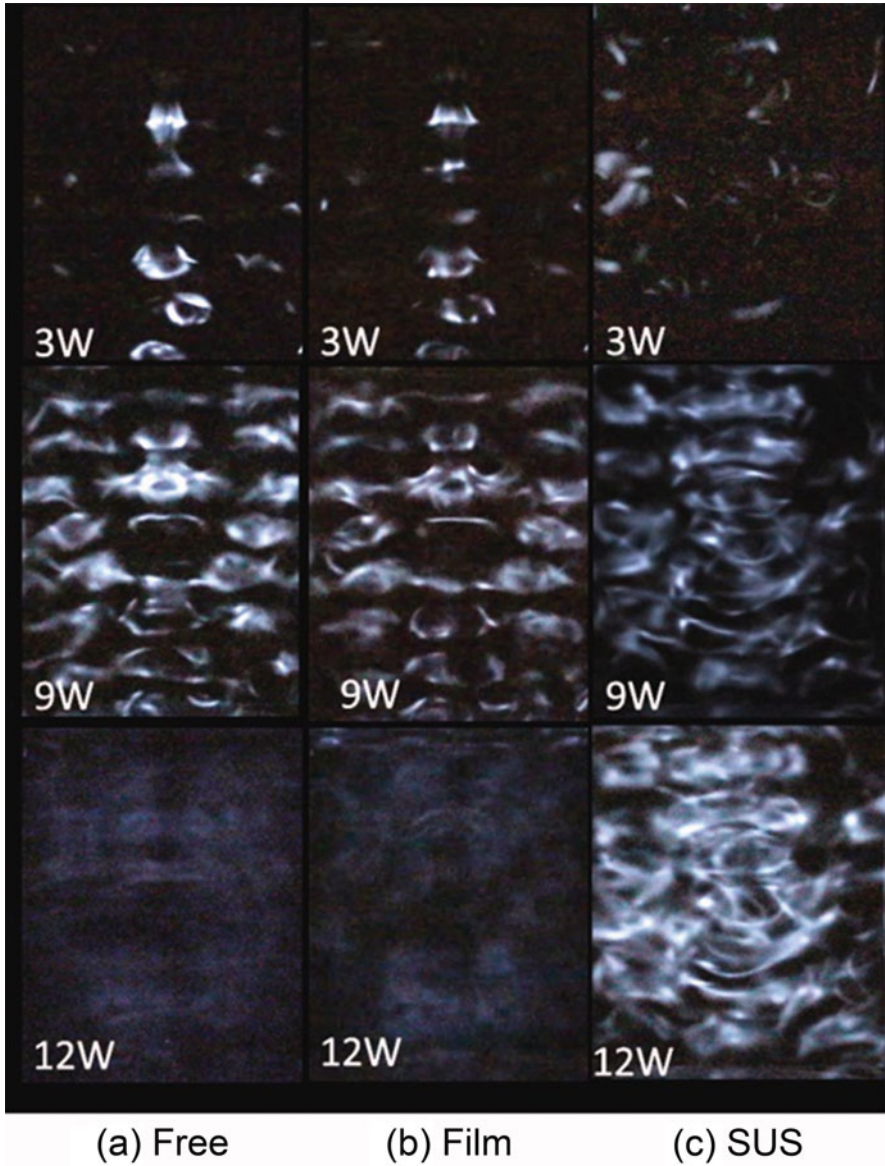
Fig. 17 Spatial distributions of SL from argon-saturated water at 83.8 kHz at electric powers of 3, 9, and 12 W, corresponding to acoustic powers of 1.8, 5.5, and 7.3 W, respectively. (**a**) Free-surface boundary, (**b**) thin-film boundary, and (**c**) stainless- steel boundary (Reprinted with permission from Ref. [52]. Copyright 2014, Elsevier Publishing)

case of the thin-film boundary, the liquid surface was covered with a polyethylene terephthalate (PET) film, suppressing the liquid-surface vibration. The film thickness was 0.1 mm, which was much smaller than the wavelength in PET, ensuring that the boundary was an acoustically free end. For the third type of boundary, the surface area was covered with an SUS plate of 17 mm thickness, equivalent to a quarter wavelength in the SUS plate at 83.8 kHz. This ensured that the boundary was perfectly rigid and was therefore an acoustically fixed end. For the free surface (Fig. 17a) and the film surface (Fig. 17b), the spatial distributions resemble each other because both cases correspond to the free boundary. The images suggest a decrease in SL at an electric power of 12 W in both cases. For the rigid boundary (Fig. 17c), the SL intensity did not decrease at 12 W but decreased at higher powers. The SL distributions are very complex, reflecting the antinode distribution of the three-dimensional standing waves in the reactor. The total SL intensity was obtained by integrating the brightness over each pixel of whole images using Image-J software. For a frequency of 138 kHz, the spatial distributions of SL and SCL were measured in the electric power range of 1–60 W using the reactor shown in Fig. 16. The selected images of SL and SCL for a free-surface boundary are shown in Figs. 18 and 19, respectively. The SL and SCL images were captured with different sensitivities, meaning that a direct comparison cannot be made between the SC and SCL intensities. Figure 20 shows the power dependencies of the integrated SL intensity at 83.8 kHz (a) and 138 kHz (b) for the three types of boundary. In Fig. 20a, the SL intensity increases up to 10–12 W and then decreases at higher powers. When the power increased to over 18 W, the SL intensity completely vanished. In Fig. 20b, the power dependencies of the integrated SL intensity at 138 kHz are similar to those at 83.8 kHz, and the power at which the SL intensity exhibits a maximum for a free liquid surface is 30 W, corresponding to an acoustic power of 0.77 W/cm^2. At 83.8 kHz, the acoustic power at the maximum SL intensity is 0.37 W/cm^2, which is smaller than that at 138 kHz. This result and those of previous studies at higher frequencies indicate that the acoustic power at which the SL intensity exhibits maximum increases with the frequency. The power dependencies of the integrated SCL intensity at 138 kHz are nearly the same as those of the integrated SL intensity at 138 kHz, suggesting that the power dependencies are independent on the bubble core temperature.

The increase in SL intensity with increasing power up to the SL maximum intensity can be explained as follows. An increase in power results in an increase in the number of active cavitation bubbles and also in the maximum size of individual bubbles. The increase in active bubble population can be clearly observed from the comparison of the SL images obtained at 3 and 9 W in Fig. 17. Kanthale et al. [41] examined the power dependencies of the SL intensity and H_2O_2 yield at four frequencies (213, 353, 647, and 1056 kHz). The maximum temperature at bubble collapse was estimated for each frequency on the basis of the single-bubble dynamics. In their study, the increase in SL intensity strongly correlated with the maximum temperature in their investigated power range of up to 30 W.

The deformation of a liquid surface by the acoustic radiation force disturbs the standing-wave field, which might cause a decrease in SL intensity. However, surface
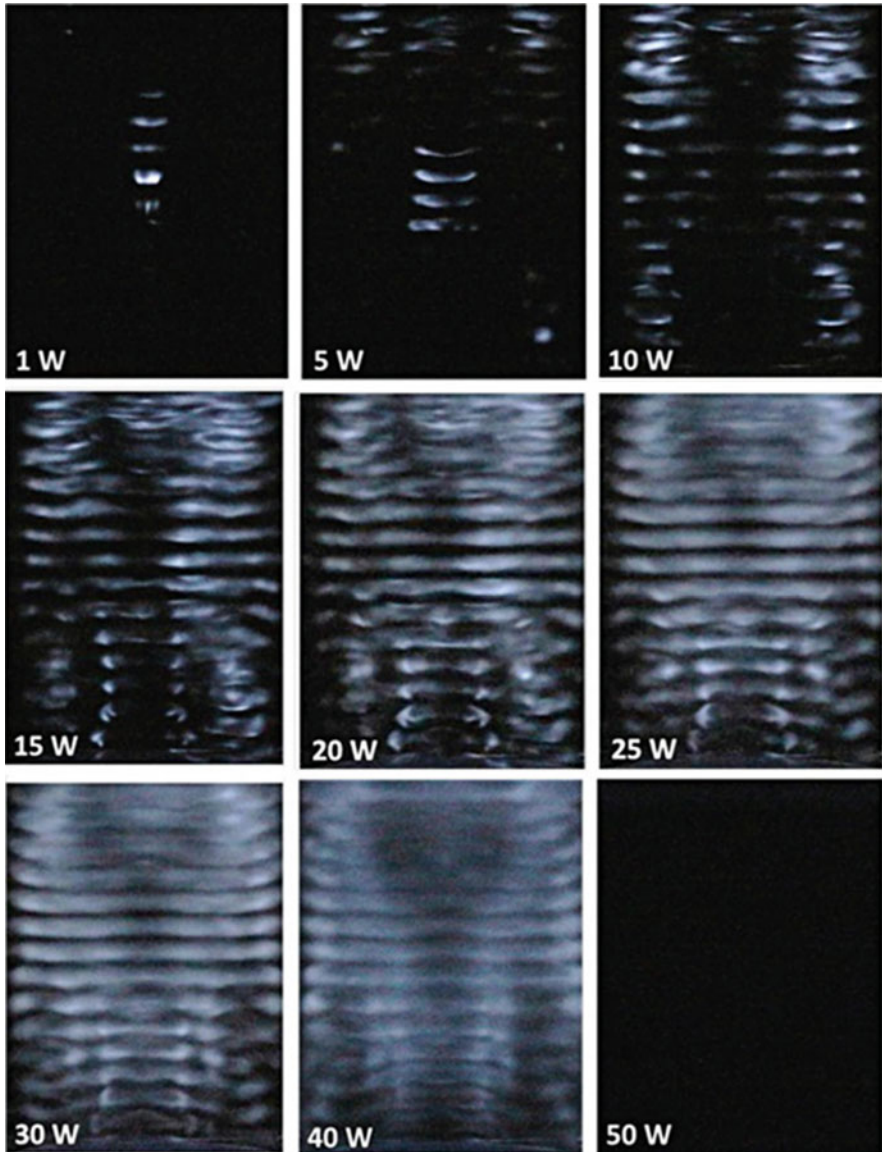
Fig. 18 Spatial distributions of SL from argon-saturated water at 138 kHz at electric powers of 1, 5, 10, 15, 20, 25, 30, 40, and 50 W. The images were captured using a Canon camera with ISO 16,000 and an exposure time of 30 s
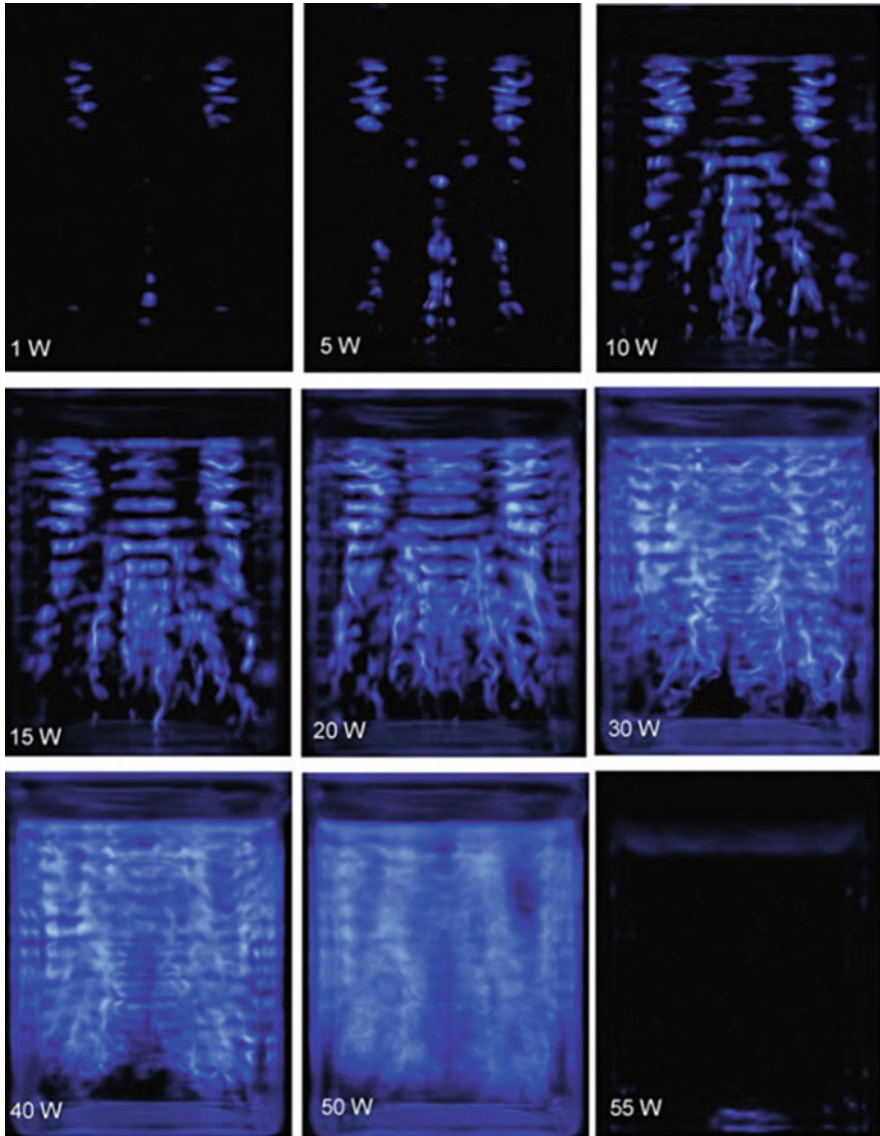
Fig. 19 Spatial distributions of SCL from argon-saturated luminol solution at 138 kHz at electric powers of 1, 5, 10, 15, 20, 30, 40, 50, and 55 W. The images were captured using a Canon camera with ISO 4,000 and an exposure time of 10 s

deformation is not the main reason why the SL intensity decreases at high powers, because such decrease was also observed under the rigid boundary condition, where no surface deformation occurs. Shortly after the decrease occurred, bubble clouds with a diameter larger than 1 mm appeared and the audible cavitation noise
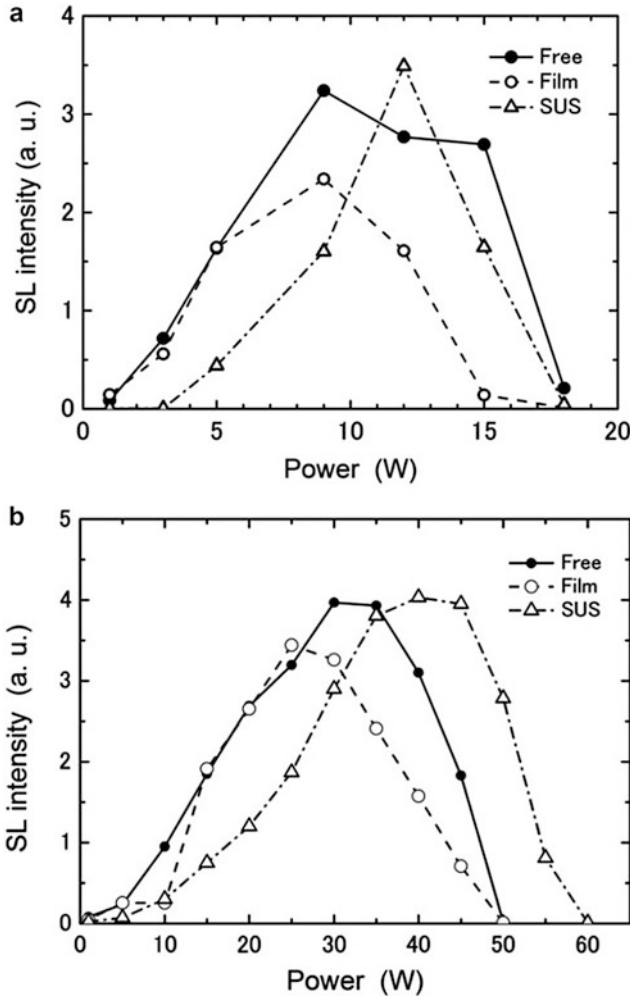
Fig. 20 Power dependence of integrated SL intensity at 83.8 kHz (**a**) and 138 kHz (**b**) for three types of acoustic boundary: a free liquid surface (*solid circles*), a liquid surface covered with a PET film (*open circles*), and a stainless-steel plate as a rigid boundary (*open triangles*) ((**a**): Reprinted with permission from Ref. [52]. Copyright 2014, Elsevier Publishing)

increased. Hanataka et al. [48] also suggested that the generation of bubble clusters is responsible for the decrease in SL intensity.

High-Speed Observation of Bubble Clusters

Lee and Choi [52] carried out high-speed observations of cavitation bubbles at 83.8 kHz and various powers, and investigated the transition of bubble dynamics.

Bubble shadowgraphs were captured by a high-speed video camera at a speed of 64,000 fps for the case of a free-surface boundary. Figure 21 shows the selected images of the bubble captured by high-speed shadowgraphy at powers of 3, 9, and 18 W. The videos are available in Ref. [52]. At a power of 3 W (Fig. 21a), only streaming bubbles with a low translation speed were observed. Four bubbles, indicated by the arrows in frame 1, finally coalesce into a single bubble, indicated by the arrow in frame 5. A larger bubble population at a power of 9 W than at 3 W and the frequent coalescences of streaming bubbles were observed. The expansion-to-contraction ratio for the streaming bubbles was sufficiently large for the bubbles to disappear during the contraction phases in the videos. The maximum size of the streaming bubbles was measured to be about 40 µm on average, and the minimum size during the contraction was less than the image resolution of 4.7 µm. With increasing power up to that giving the SL intensity maximum (9 W), the videos show that the active bubble population and bubble translational speed increase. The higher translation speed increases the rate of bubble coalescence. Thus, the increase in SL intensity up to the maximum at 9 W is due to the increase in the population of streaming bubbles oscillating with a large expansion-to-contraction ratio. In the intermediate power range of 9–18 W, where the SL intensity decreased, both bubble
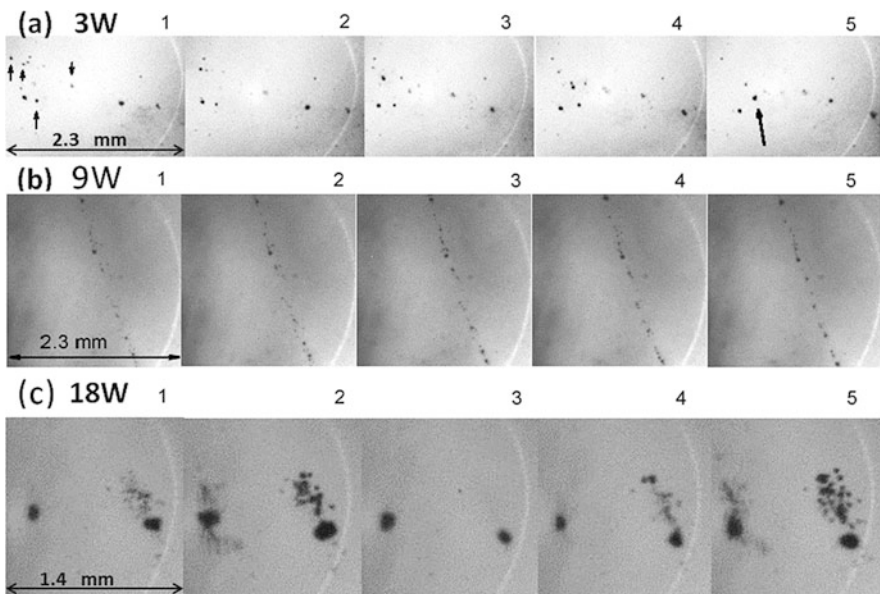
Fig. 21 Selected images obtained by high-speed shadowgraphy taken at a speed of 64,000 fps. (**a**) Streaming bubbles observed at a power of 3 W. Five frames with an interval of 190 µs were selected to illustrate bubble coalescence. The bubbles indicated by *arrows* in frame 1 coalesce into a single bubble in frame 5. (**b**) Streaming bubbles observed at a power of 9 W. The bubble population is greater than that in (**a**). The frame interval is 48 µs. (**c**) Two bubble clusters observed at a power of 18 W. The frame interval is 16 µs (Reprinted with permission from Ref. [52]. Copyright 2014, Elsevier Publishing)

streamers and a small number of bubble clusters were observed simultaneously. At a power of 18 W, no streaming bubbles and only bubble clusters were observed as shown in Fig. 21c. Since the frame interval is 16 μs and the acoustic period is 12 μs, the neighboring frames indicate bubble behavior having an acoustic phase difference of 480°. One large bubble, with a maximum size of about 200 μm, oscillates nonspherically. Tens of tiny bubbles followed the large bubble while undergoing expansion and contraction. The large bubble in the cluster does not contract violently, indicating that the temperature at bubble collapse is not high. Conversely, the tiny bubbles around the large bubble contract violently, disappear in a single cycle, and emerge at different positions in the next cycle, exhibiting "transient oscillations." This behavior differs from that for the streaming bubbles, which exhibit repeated expansion and contraction. While the sizes of the streaming bubbles and the tiny bubbles in the clusters are similar, the difference in the type of bubble oscillation may be responsible for the light extinction.

The mechanism involved in bubble cluster dynamics is very complex. Although there have been several numerical simulations on bubble cluster dynamics [53–56], a few experimental results [57, 58] have been reported. The synchronization of the periodicity and collapse phases of bubbles with different radii has been found. According to the cluster model assuming a monodisperse bubble radius, the interaction with neighboring bubbles dampens the oscillation of bubbles, which reduces the temperature at bubble collapse and also the production of OH radicals [59].

Conclusions and Future Directions

Fundamentals and some experimental results of bubble-bubble interactions have been presented. The size distribution of bubbles at their maximum radius revealed the decreasing effect in size upon adding surfactant molecules which adsorb bubble/liquid interface. The acoustic power dependencies on the SL and SCL intensity showed that not only bubble oscillation but also bubble-bubble interactions greatly affect the SL and SCL intensities on the basis of the direct observation of bubbles using a high-speed shadowgraphy. We have not yet enough knowledge to understand the whole diversity of bubble dynamics which depends on acoustic frequency and power. Especially, the elucidation of bubble cluster dynamics, which is crucial for high-power applications in sonochemistry, requires further studies involving theoretical and experimental works. A high-speed observation will be a key factor for that purpose.

References

1. Gelderblom EC, Vos HJ, Mastik F, Faez T, Luan Y, Kokhuis TJA, van der Steen AFW, Lohse D, de Jong N, Versluis M (2012) Rev Sci Instrum 83:103706
2. Versluis M (2013) Exp Fluids 54:1458
3. Young FR (1999) Cavitation. Imperial College Press, London
4. Leighton TG (1994) The acoustic bubble. Academic, San Diego/London
5. Brennen CE (1995) Cavitation and bubble dynamics. Oxford University Press, London

6. Lauterborn W, Kurz T (2010) Rep Prog Phys 73:106501
7. Doinikov AA (2001) Phys Rev E 64:026301
8. Appel J, Koch P, Mettin R, Krefting D, Lauterborn W (2004) Ultrason Sonochem 11:39
9. Zhang W, An Y (2013) Phys Rev E 87:053023
10. Krefting D, Mettin R, Lauterborn W (2004) Ultrason Sonochem 11:119
11. Yasui K (2015) In: Grieser F et al (eds) Sonochemistry and the acoustic bubble. Elsevier, Amsterdam, p 73
12. Mettin R, Akhatov I, Parlitz U, Ohl CD, Lauterborn W (1997) Phys Rev E 56:2924
13. Keller JB, Miksis M (1980) J Acoust Soc Am 68:628
14. Jiao J, He Y, Leong T, Kentish SE, Ashokkumar M, Manasseh R, Lee J (2013) J Phys Chem B 117:12549
15. Choi P-K, Deno S (2012) J Acoust Soc Am 131:3385
16. Versluis M, van der Meer SM, Lohse D, Palanchon P, Goertz DE, Chin CT, de Jong N (2004) Proc IEEE Ultrason Symp 207
17. van der Meer SM, Dollet B, Goertz DE, de Jong N, Versluis M, Lohse D (2006) Proc IEEE Ultrason Symp 112
18. Dollet B, van der Meer SM, Garbin V, de Jong N, Lohse D, Versluis M (2008) Ultrasound Med Biol 34:1465
19. Ohl C-D, Arora M, Ikink R, de Jong N, Versluis M, Delius M, Lohse D (2006) Biophys J 91:4285
20. Kudo N, Okada K, Yamamoto K (2009) Biophys J 96:4866
21. Crum LA (1980) J Acoust Soc Am 68:203
22. Asaki TJ, Thiessen DB, Marston PL (1995) Phys Rev Lett 75:2686
23. Stottlemyer TR, Apfel RE (1997) J Acoust Soc Am 102:1418
24. Ashokkumar M, Grieser F (2007) Phys Chem Chem Phys 9:5631
25. Ashokkumar M, Lee J, Kentish S, Grieser F (2007) Ultrason Sonochem 14:470
26. Lee J, Kentish S, Ashokkumar M (2005) J Phys Chem B 109:14595
27. Lee J, Kentish S, Ashokkumar M (2005) J Phys Chem B 109:5095
28. Ashokkumar M, Hodnett M, Zeqiri B, Grieser F, Price GP (2007) J Am Chem Soc 129:2250
29. Deno S, Choi P-K (2011) Proc 20th Annu Meet Jpn Soc Sonochem & Int Workshop Adv Sonochem: 92
30. Lee J, Vakarelski IU, Yasui K, Tuziuti T, Kozuka T, Towata A, Iida Y (2010) J Phys Chem B 114:2572
31. Lee J, Ashokkumar M, Kentish S, Grieser F (2005) J Am Chem Soc 127:16810
32. Epstein PS, Plesset MS (1950) J Chem Phys 18:1505
33. Brotchie A, Grieser F, Ashokkumar M (2009) Phys Rev Lett 102:084302
34. Choi P-K, Kaneko Y, Meguro T (2008) Jpn J Appl Phys 47:4111
35. Lee J, Yasui K, Tuziuti T, Kozuka T, Towata A, Iida Y (2008) J Phys Chem B 112:15333
36. Tuziuti T, Yasui K, Lee J, Kozuka T, Towata A, Iida Y (2008) J Phys Chem A 112:4875
37. Yasui K, Tuziuti T, Lee J, Kozuka T, Towata A, Iida Y (2010) Ultrason Sonochem 17:460
38. Portenlänger G, Heusinger H (1997) Ultrason Sonochem 4:127
39. Beckett MA, Hua I (2001) J Phys Chem A 105:3796
40. Koda S, Kimura T, Kondo T, Mitome H (2003) Ultrason Sonochem 10:149
41. Kanthale P, Ashokkumar M, Grieser F (2008) Ultrason Sonochem 15:143
42. Yasui K (2002) J Acoust Soc Am 112:1405
43. Weissler A, Cooper HW, Snyder S (1950) J Am Chem Soc 72:1769
44. Lindström O (1955) J Acoust Soc Am 27:654
45. Henglein A, Gutierrez M (1990) J Phys Chem 94:5169
46. Mark G, Tauber A, Laupert R, Schuchmann H-P, Schulz D, Mues A, von Sonntag C (1998) Ultrason Sonochem 5:41
47. Negishi K (1961) J Phys Soc Jpn 16:1450
48. Hatanaka S, Yasui K, Kozuka T, Tuziuti T, Mitome H (2002) Ultrasonics 40:655
49. Margulis MA, Margulis IM (2003) Ultrason Sonochem 10:343

50. Ashokkumar M, Lee J, Iida Y, Yasui K, Kozuka T, Tuziuti T, Towata A (2010) Chem Phys Chem 11:1680
51. Tuziuti T, Yasui K, Kozuka T, Towata A, Iida Y (2007) J Phys Chem A 111:12093
52. Lee H-B, Choi P-K (2014) Ultrason Sonochem 21:2037
53. Kanthale PM, Gogate PR, Pandit AB, Wilhelm AM (2003) Ultrason Sonochem 10:181
54. Doinikov AA (2004) J Acoust Soc Am 116:821
55. Nasibullaeva ES, Akhatov IS (2013) J Acoust Soc Am 133:3727
56. Yasui K, Iida Y, Tuziuti T, Kozuka T, Towata A (2008) Phys Rev E 77:016609
57. Tervo JT, Mettin R, Lauterborn W (2006) Acta Acust United Acust 92:178
58. Arora M, Ohl C-D, Lohse D (2007) J Acoust Soc Am 121:3432
59. Stricker L, Dollet B, Rivas DF, Lohse D (2013) J Acoust Soc Am 134:1854

Experimental Observation of an Acoustic Field

Nobuki Kudo

Contents

N. Kudo (✉)

Graduate School of Information Science and Technology, Hokkaido University, Sapporo, Japan
e-mail: kudo@bme.ist.hokudai.ac.jp

Abstract

In this section, optical techniques used for experimental observation of acoustic fields are reviewed. Acousto-optic interaction is discussed as a basic principle for visualizing inhomogeneity in refractive index fields. Light deflection and diffraction are also discussed as typical phenomena, especially in visualization of ultrasound fields. Three techniques, phase detection, Schlieren, and shadowgraph techniques, are mainly reviewed with discussion of the differences in the principles, optical systems, and acquired images. Background-oriented Schlieren technique, scanning laser Doppler vibrometry, and photoelastic techniques are also discussed as relatively new techniques for visualization of ultrasound fields. A technique that visualizes a distribution of temperature rise generated by ultrasound exposure is also introduced.

Introduction

The acousto-optic effect is used for visualization of ultrasound fields. Optical visualization of inhomogeneity in refractive index fields has a long history starting with the report by Hook about 350 years ago [1]. In contrast, application of optical techniques for visualization of ultrasound fields has a relatively short history of 85 years triggered by the invention of the Langevin transducer. Using high-intensity megahertz-range ultrasound fields generated by the transducer, Lucas and Biquard [2] and Debye and Sears [3] independently carried out experiments on light diffraction by a continuous ultrasound field in water. Theoretical studies on light diffraction in ultrasound fields were carried out by Raman and Nath [4–8].

Various types of optical methods have been developed and applied to a wide range of application fields [9–11]. Optical techniques specialized for visualization of ultrasound fields have also been developed and refined along with the development of ultrasound and optoelectronic technologies, which have made rapid progress in the past century. In the following section, interaction between light and ultrasound is discussed as the basics of optical visualization of acoustic fields. In sections "Phase Detection Techniques," "Schlieren Technique," and "Shadowgraphy," three specific techniques of ultrasound field visualization, phase detection, Schlieren, and shadowgraph techniques, are briefly reviewed with discussion of the differences in principles, optical systems, and acquired images. Other techniques are also discussed in section "Other Optical Techniques."

Acousto-optic Interactions

In this section, the basic principles of optical visualization of inhomogeneous refractive index distributions are briefly reviewed. Firstly, piezo-optic characteristics of water are discussed, and then Bragg and Raman–Nath diffractions of light by an acoustic field are discussed in the condition in which the field can be considered as a true phase grid that produces no brightness modulation just behind the grid. Deflection of light, which occurs in an acoustic field of a higher pressure range and causes brightness modulation, is also discussed.

Light Phase Modulation by a Phase Object

The most basic principle for optical visualization of ultrasound fields is detection of a change in the refracted index, i.e., change in light speed inside an object under sonication. The Lorentz–Lorenz equation theoretically describes the relation between the molar refractive index and density; however, the following empirical equation proposed by Eykman gives a better agreement with experimental data [12]:

$$C_{n_0} = \frac{\Delta n_{\mathrm{amp}}}{\Delta p_{\mathrm{amp}}} = \frac{(n_0 - 1)(n_0{}^2 + 1.4 n_0 + 0.4)}{(n_0{}^2 + 0.8 n_0 + 1)\rho c^2}, \tag{1}$$

where n_0 is the refractive index with no pressure perturbation and ρ and c are the density and sound speed of water, respectively. Δp_{amp} and Δn_{amp} are the applied pressure amplitude and amplitude of resulting change in the refractive index, respectively, and $C_{n_0} = \Delta n_{\mathrm{amp}}/\Delta p_{\mathrm{amp}}$ is the piezo-optic coefficient of water at n_0.

As shown in Fig. 1a, light ray incidents on a transparent object with a homogeneous refractive index propagate rectilinearly, and the wavefront of the incident light is maintained in the transmitted light. If the object has two locally different refractive indices as shown in Fig. 1b, the light that is transmitted through the portion with the lower refractive index n_1 is advanced in phase compared to that of the light transmitted through the other portion with the higher refractive index n_2. The wavefronts of light rays that are transmitted through the objects are parallel to those of the incident rays, indicating that the direction of the transmitted light rays is not changed in the condition of the refractive indices shown in Fig. 1b.

An important characteristic of ultrasound fields in their optical visualization is periodicity in pressure change. If a light source illuminates a sufficient number of ultrasound cycles in its beam, the ultrasound field works as a phase grating as shown in Fig. 1c. This grating induces two types of diffraction: Bragg diffraction and Raman–Nath diffraction.
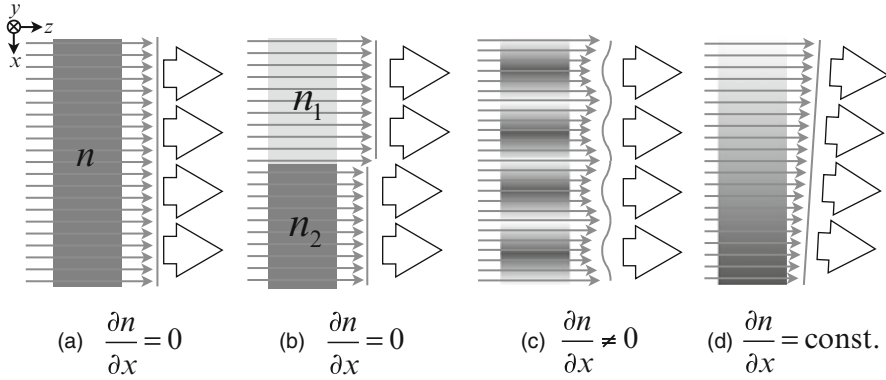
Fig. 1 Phase modulation of light transmitted through a phasic object. (**a**) $\partial n/\partial x = 0$. The wavefront of the incident wave is maintained. (**b**) Two objects with different refractive indices n_1 and n_2 but with $\partial n/\partial x = 0$. The wavefronts have a discontinuous phase change but the directions of propagation are the same. (**c**) $\partial n/\partial x \neq$ constant. The phase of the wavefront is modulated according to the change in the refraction index of the field, and the field with a periodic change works as a phase grid. (**d**) $\partial n/\partial x =$ constant ($\neq 0$). Linear increase in the refractive index causes a tilt in the direction of light propagation

Bragg Diffraction by an Acoustic Field

The phenomenon of an X-ray incident on a material with a thin multilayer structure making strong reflection at a specific angle is called Bragg diffraction (reflection). This phenomenon is also observed in the situation in which a light beam is incident on an ultrasound field. The Bragg diffraction becomes evident in the condition in which displacement of a light beam in the ultrasound field becomes sufficiently larger than an acoustic wavelength of the field. Bragg diffraction is typically observed at ultrasound frequencies above 100 MHz and is not observed at a light incident angle of $0°$.

Consider a condition in which a light beam of λ in light wavelength is incident on an ultrasound field of Λ in acoustic wavelength at an angle of θ_b (Fig. 2a). Different from a material that has a thin multilayer structure like a crystal, an ultrasound field has a gradual change in its refractive index and has no obvious interfaces that produce specular reflection. However, if we assume that ultrasound reflection occurs at wavefronts to produce maximum dp/dx, the rays reflected at the multiple wavefronts interfere with each other and produce strong peaks at the angle of θ_b defined by Eq. 2.

$$2\Lambda \sin \theta_b = m\lambda \; (m = 0, \; 1, \; 2, \; \cdots), \qquad (2)$$

where Λ and λ are wavelengths of acoustic and optical waves, respectively. A study that accounts for the continuity in the refractive index showed that the orders of reflected light are limited to 0th-order (transmitted) and 1st-order (reflected) light. Then, the relative intensities of the light are given by Eqs. 3 and 4:
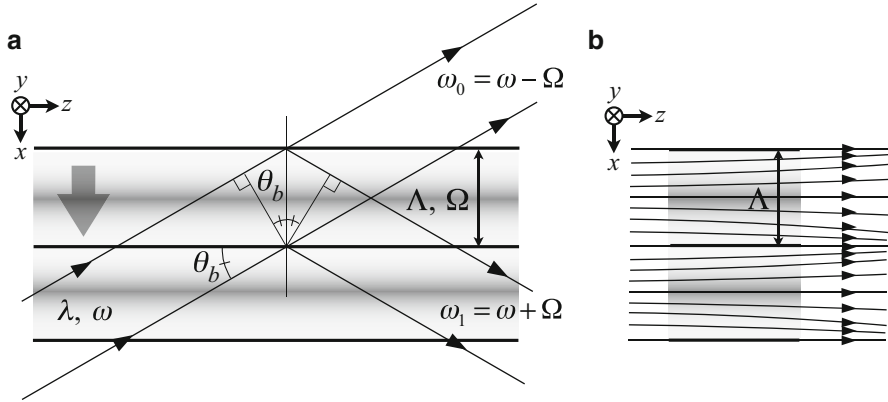
Fig. 2 Two types of diffraction of light in ultrasound field. (**a**) Bragg diffraction occurs under the condition in which the displacement of a deflecting light beam in an ultrasound field is sufficiently larger than the ultrasound wavelength. Typical ultrasound frequency is higher than 100 MHz. (**b**) Raman–Nath diffraction occurs under the condition in which the displacement of a deflecting light beam in an ultrasound field is sufficiently smaller than the ultrasound wavelength. Typical ultrasound frequency is lower than 10 MHz

$$i_0 = \cos^2\left(\pi w \Delta n_{\mathrm{amp}}/\lambda\right), \tag{3}$$

$$i_1 = \sin^2\left(\pi w \Delta n_{\mathrm{amp}}/\lambda\right), \tag{4}$$

where w is the width of the ultrasound beam. Equation 4 indicates that complete reflection occurs in the condition of $\pi w \Delta n/\lambda = \pi/2$.

Furthermore, propagation of wavefronts at sound velocity causes a Doppler shift in light frequency, and the angular frequency shifts ω_0 and ω_1 of the reflected and transmitted light, respectively, are given by Eqs. 5 and 6:

$$\omega_0 = \omega - \Omega, \tag{5}$$

$$\omega_1 = \omega + \Omega, \tag{6}$$

where ω and Ω are angular frequencies of the incident light and ultrasound, respectively.

Light Diffraction by an Acoustic Phase Grating

Another type of diffraction becomes evident in the condition in which displacement of a light beam in an acoustic field becomes sufficiently small compared to the wavelength of the acoustic field. Consider a situation in which a monochromatic plane wave light beam propagating in the z direction is incident to a continuous plane wave ultrasound field propagating in the x direction (Fig. 2b). Then, the ultrasound

field works as a phase grating, and the phase shift $\varphi(x,t)$ of the light beam that is transmitted through the field is given by Eq. 7:

$$\varphi(x,t) = w\,\Delta n_{\mathrm{amp}} \sin\left(\Omega t - \frac{2\pi}{\Lambda}x\right). \tag{7}$$

Using the phase shift $\varphi(x,t)$ and incident light $E_i(z,t)$ given by Eq. 8, the transmitted light $E_t(x,z,t)$ can be denoted as Eq. 9.

$$E_i(z,t) = E_0 e^{i\left(\omega t - \frac{2\pi}{\lambda}z\right)}, \tag{8}$$

$$\begin{aligned} E_t(x,\ z,t) &= E_i(z,t)e^{i\frac{2\pi}{\lambda}\varphi(x,t)} \\ &= E_0 e^{i\left(\omega t - \frac{2\pi}{\lambda}z\right)} e^{i\frac{2\pi w\Delta n_{\mathrm{amp}}}{\lambda}\sin\left(\Omega t - \frac{2\pi}{\Lambda}x\right)}, \end{aligned} \tag{9}$$

where E_0 is the amplitude of incident light. Then, using Jacobi–Anger expansion, the transmitted light can be rewritten as follows.

$$E_t(x,\ z,t) = E_0 \sum_{m=-\infty}^{\infty} J_m\left(\frac{2\pi w\Delta n_{\mathrm{amp}}}{\lambda}\right) e^{i(\omega+m\Omega)t} e^{-i2\pi\left(\frac{z}{\lambda}+\frac{x}{\Lambda}\right)}. \tag{10}$$

The equation indicates that the light transmitted through the grid is superposition of an infinite number of diffracted plane waves of m-th order ($-\infty < m < \infty$). The positive values of m represent the direction of ultrasound propagation. The m-th order wave is $\omega+m\Omega$ in angular frequency, $J_m^2(2\pi w\Delta n_{\mathrm{amp}}/\lambda)$ in intensity, and $\sin^{-1}(m\lambda/\Lambda)$ in propagation direction.

A standing wave field is generated in the situation in which forward and backward propagating waves are superimposed, and it therefore can be considered that the light transmitted through the standing field is diffracted by the two phase grids propagating in opposite directions. This means that diffraction patterns generated by propagating and standing waves are different.

As shown in Fig. 3, the ultrasound phase grating produces a Fresnel diffraction pattern on a screen placed at a near field and a Fraunhofer diffraction pattern on a screen placed at a far field. In the near field, the zeroth and a limited number of higher-order plane waves interfere mutually and generate a complex diffraction pattern. The pattern changes its shape and amplitude depending on the distance between the ultrasound field and the screen [13] because a number of higher-order diffraction waves that contribute to light interference depend on the distance. In the far field, all of the higher-order plane waves contribute to make separate peaks at the points at which the difference in light paths from two adjacent positions on the phase grid with the same phase becomes multiples of λ. This relation can be expressed using Eq. 11, indicating that a diffraction angle θ_d is determined using only λ and Λ.

$$\sin\theta_d = m\frac{\lambda}{\Lambda}. \tag{11}$$
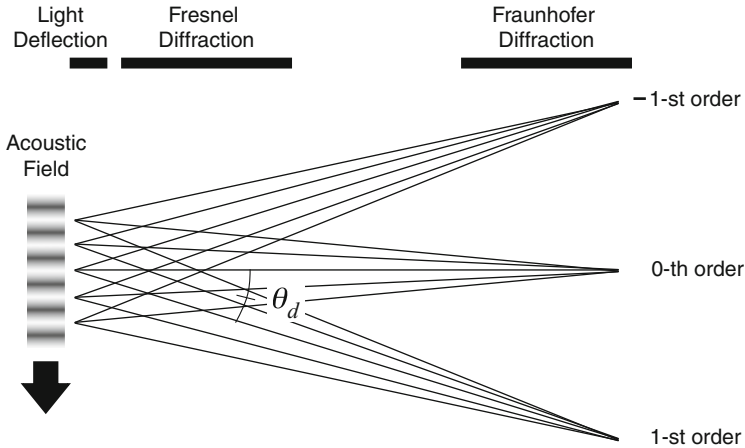
Fig. 3 Diffraction of light by an acoustic phase grating. Fresnel diffraction is observed at the near field, and Fraunhofer diffraction is observed at the far field. Effects of light deflection can be observed just behind the phase grating because the light intensity distribution generated by light deflection is not disturbed by light from adjacent cycles of the grating

In the condition of 1 MHz in frequency (ultrasound wavelength of 1.5 mm in water) and 500 nm in light wavelength, the diffraction angle θ_d becomes multiples of 3.3×10^{-4} rad.

Light Deflection by a Phase Object

If the transparent object has a refractive index field of a constant gradient, the phase of the transmitted light is linearly changed as shown in Fig. 1d, resulting in light deflection (or refraction). Consider a small region that has a refractive index of n at position x and a refracted index of $n+dn$ at position $x+dx$ as shown in Fig. 4. If light is incident on the field in the direction perpendicular to x, the light beams that are generated from point sources placed at different positions on the wavefront W_1 propagate at different speeds, and the wavefront W_2 will be tilted. Resulting light deflection is observed when a narrow light beam is made incident on an ultrasound field with a wavelength wider than the beam width. The angle of light deflection at a pressure gradient field of dp_{amp}/dx is given by Eq. 12 using the piezo-optic constant C_{n0} given by Eq. 1.

$$
\begin{aligned}
\tan \theta_r &= \frac{1}{n_0} \cdot \frac{dn_{\mathrm{amp}}}{dx} \cdot w \\
&= C_{n_0} \cdot \frac{1}{n_0} \cdot \frac{dp_{\mathrm{amp}}}{dx} \cdot w.
\end{aligned}
\tag{12}
$$

Fig. 4 Deflection of light at a pressure gradient field. The wavefront is tilted by spatial difference in the speed of light [11] (Copyright © 2015, The Japan Society of Applied Physics)
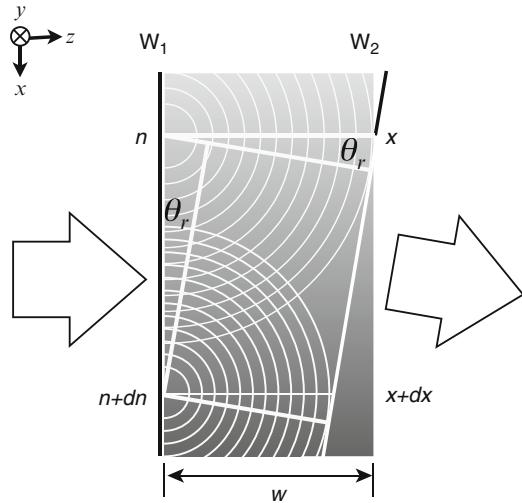
Then, the maximum angle of θ_r with exposure to a sinusoidal wave of 1 MPa in peak pressure and 1 MHz in frequency is calculated to be 2.4×10^{-3} rad by substituting $n_0 = 1.33$, $\rho = 1 \times 10^3$ kg/m^3, $c = 1,500$ m/s, and $w = 5$ mm. Further increase is expected if an ultrasound wave has high nonlinearity with a steep pressure increase at its wavefront.

Phase Detection Techniques

Basic Principle

A light ray that is transmitted through an inhomogeneous refractive index field will have a phase shift integrated over its propagation path. In the condition in which the light deflection can be neglected, the three-dimensional (3D) distribution of the refractive index can be determined by a computer tomography (CT) algorithm using profiles of phase shift taken from multiple directions. The technique visualizes an instantaneous ultrasound field by combining a stroboscopic technique that uses a short-pulsed illuminating light synchronized with ultrasound irradiation. Both continuous and pulsed ultrasound fields can be visualized because the technique does not utilize an ultrasound field as a phase grating.

Interferometry

A shift of light phase by an ultrasound field can be detected by an interferometer [14, 15]. Figure 5 shows a Michelson interferometer designed for visualization of ultrasound fields [14]. The phase shift integrated over a light path can be detected by
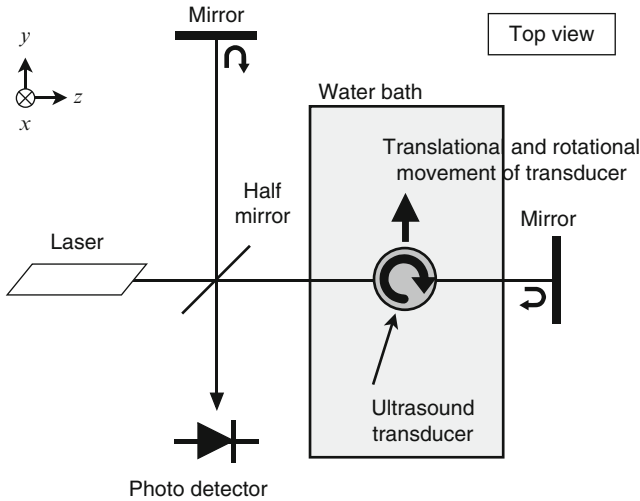
Fig. 5 Acquisition of phase shift profiles observed from multiple directions using a Michelson interferometer. Observation of the field from multiple positions is achieved by rotating the transducer

interference of the phase-modulated light with a reference light. A profile of the phase shift observed from one direction can be acquired by moving an ultrasound transducer in the translational direction, and profiles observed from multiple directions can be acquired by rotating the transducer at angles between 0 and 180°.

Fresnel Diffraction Technique

Light that is transmitted through a phase grating receives no amplitude modulation just behind the grating but receives phase modulation. However, projection of the phase-modulated image on a screen placed at the Fresnel region produces an intensity modulation image, i.e., Fresnel diffraction pattern. Results of several studies on the reconstruction of an ultrasound field from a Fresnel diffraction pattern have been reported [13, 16]. Patorski [16] evaluated a Fresnel diffraction pattern generated by a traveling plane wave of continuous ultrasound and showed that the depth of phase modulation can be determined by the amplitude of the fundamental frequency component of the Fresnel diffraction pattern.

Phase Contrast Technique

The phase contrast technique [17] is a method to convert a light phase modulation image into an amplitude modulation image. The technique is widely utilized in light microscopy for visualizing transparent biological cells but is also effective for
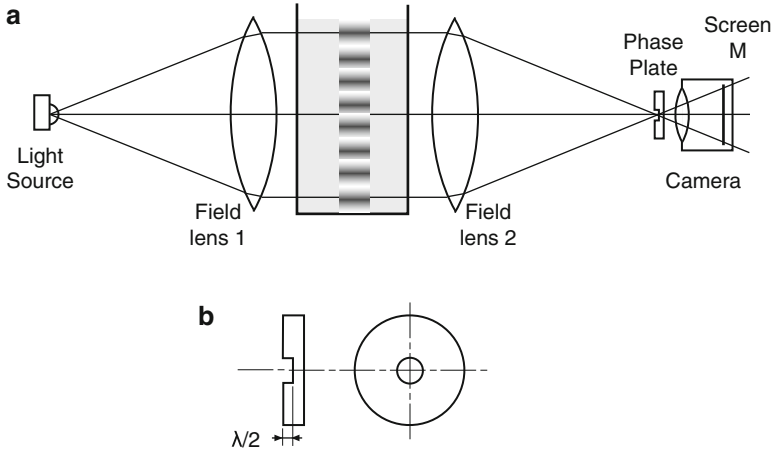
Fig. 6 Visualization of ultrasound fields using the phase contrast technique. (**a**) An optical system. An optical stop used in the Schlieren technique is replaced by a π/2 phase plate. (**b**) A schematic of the π/2 phase plate used to shift the phase of a zeroth-order diffraction light component

visualization of phase shift images generated by ultrasound fields [18, 19]. Figure 6a shows an optical system used for this purpose, in which the optical stop of the Schlieren optics was replaced by a phase plate. The phase plate is used to advance (or delay) the phase of zeroth-order diffraction light. Inclusion of zeroth-order light with a phase shift of π/2 at the focus position is for superimposing the reference light on a Schlieren image generated at the position of the camera screen. A region of light phase modulation in-phase with the reference light becomes a bright spot, and a region of antiphase becomes a dark spot. Figure 6b shows a schema of a phase plate. The diameter of the π/2 dip made at the center of the plate is determined to separate zeroth-order diffraction light and first-order diffraction light, and the depth is determined to the depth that produces a π/2 phase shift at the wavelength of light used for visualization.

Consider the situation in which an ultrasound field propagating in the x direction produces a phase shift of $\varphi(x,y,t)$ given by Eq. 13:

$$\varphi(x, y, t) = a(x, y) \sin\left(\Omega t - \frac{2\pi}{\Lambda}x\right), \tag{13}$$

where $a(x,y)$ represents spatial distribution of the pressure envelope function. Using $\varphi(x,y,t)$, the light $E_t(x,y,z,t)$ that is transmitted through the grid is denoted as follows:

$$
\begin{aligned}
E_t(x, \ y, z, t) &= E_i(z, t) e^{i\frac{2\pi}{\lambda}\varphi(x, y, t)} \\
&= E_0 e^{i\left(\omega t - \frac{2\pi}{\lambda}z\right)} e^{ia(x, y) \sin\left(\Omega t - \frac{2\pi}{\Lambda}x\right)}.
\end{aligned}
\tag{14}
$$

Under the condition of $\varphi(x, y, t) \ll 1$, Eq. 14 can be expanded using Taylor expansion, and omission of higher-order terms except for the 0th- and 1st-order terms gives Eq. 15.

$$E_t(x, \ y, z, t) \cong E_0 e^{i\left(\omega t - \frac{2\pi}{\lambda}z\right)}\left(1 + i\, a(x,y)\sin\left(\Omega t - \frac{2\pi}{\Lambda}x\right)\right). \qquad (15)$$

Since the phase plate gives the $\pi/2$ phase shift only to the 0th-order light, the light transmitted through the phase plate $E_t'(x, y, z, t)$ can be expressed using Eq. 16.

$$E_t'(x, \ y, z, t) \cong E_0 e^{i\left(\omega t - \frac{2\pi}{\lambda}z\right)}\left(e^{i\frac{\pi}{2}} + i\, a(x,y)\sin\left(\Omega t - \frac{2\pi}{\Lambda}x\right)\right). \qquad (16)$$

Finally, the phase shift distribution can be visualized as the intensity distribution $|E_t'(x, y, z, t)|^2$ as given by Eq. 17.

$$\left|E_t'(x, \ y, z, t)\right|^2 \cong E_0{}^2\left(1 - 2a(x,y)\sin\left(\Omega t - \frac{2\pi}{\Lambda}x\right)\right). \qquad (17)$$

Equation 17 indicates that the wavefront of the ultrasound field can be visualized using a stroboscopic technique; however, information on the ultrasound field is lost with temporally integrated observation. In the case of visualization of a standing wave field, intensity distribution $|E_t'(x, y, z, t)|^2$ is given by Eq. 18, and temporal integration also results in loss of information on the wavefronts.

$$\left|E_t'(x, \ y, z, t)\right|^2 \cong E_0{}^2\left(1 - 2a(x,y)\sin\Omega t \cos\frac{2\pi}{\Lambda}x\right). \qquad (18)$$

Figure 7 shows a non-axisymmetric therapeutic ultrasound field generated by a high-intensity focused ultrasound (HIFU) transducer of 75 mm in aperture and 1.07 MHz in center frequency [19]. The transducer consists of four piezo-electric elements electrically connected into two pairs, and the pairs are driven by signals with opposite phases. Phase contrast 2D images were acquired every 2° from 2 to 180°, and a 2D phase distribution image at the focus planes perpendicular to the transducer axis was reconstructed using a CT algorithm (Fig. 7a). A pressure amplitude distribution at the same plane was also visualized using a hydrophone-scanning technique (Fig. 7b), indicating good agreement in axis asymmetry. A quantitative comparison was carried out over axisymmetric trans-ducers, indicating that focal pressure values measured using the phase contrast image and the hydrophone show good agreement at the maximum pressure of 141 kPa [19].
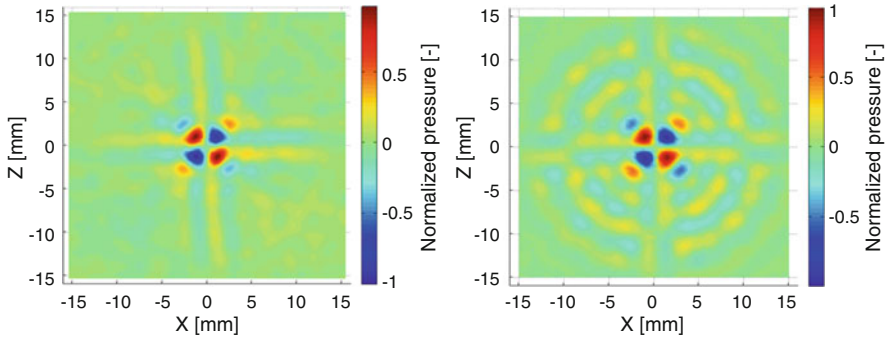
Fig. 7 Ultrasound pressure distributions generated by a non-axisymmetric-focused transducer. (**a**) Visualized using the phase contrast technique. (**b**) Measured using a hydrophone [19] (Copyright © 2013, The Japan Society of Applied Physics)

Schlieren Technique

Principle and Optical System

The Schlieren technique achieves sensitive visualization of an ultrasound field by utilizing Fraunhofer diffraction of light caused by an ultrasound field. Figure 8a shows a Schlieren optical system with two field lenses and an optical stop. Light emitted from a point light source is collimated by the first lens. A water bath is placed on a path of the collimated light, and a continuous or long-burst ultrasound field is irradiated from a transducer submerged in the bath. A camera takes an image of the acoustic phase grating.

Figure 8b schematically shows the principle. In the situation with no ultrasound pressure in the field, all of the light that is transmitted through the field converges on the focus of the second lens. Therefore, all of the light is projected on the screen M of the camera in the case without the optical stop, and no light is projected on the screen in the case with the optical stop. In the situation with ultrasound pressure in the field, the light is partially diffracted by the field, and the image of the grating is projected on the screen in the case without the optical stop. However, in the case with the optical stop, only the higher-order diffracted light comes to the screen, enabling sensitive detection of the ultrasound field.

Since the diffraction angle is 10^{-3} rad in its order, the Schlieren technique requires a high-quality optical system. A monochromatic light source with a high point light source property and the first lens with little aberration are important to illuminate the ultrasound field with a high-quality collimated beam. The second lens with little aberration is also important to make a clear diffraction pattern for the spatial filtering. High-quality thin lenses of more than one meter in focal length are typically used for this purpose. Parabolic mirrors, which are free from spherical and chromatic aberrations, are also frequently used for a Schlieren optical system. High-
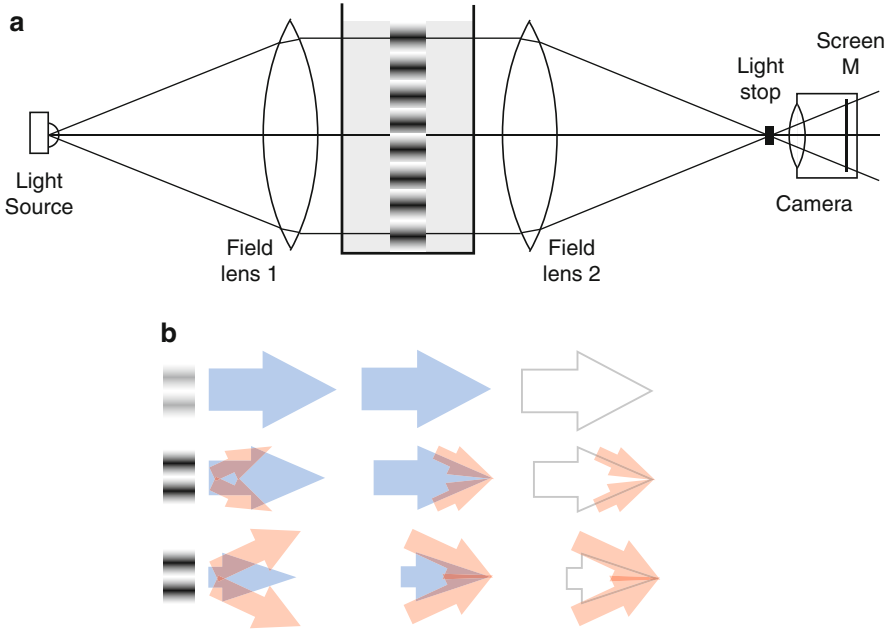
Fig. 8 Principle of the Schlieren technique. (**a**) A basic Schlieren optical system with two field lenses and an optical stop. (**b**) Sensitive detection of an ultrasound field image by elimination of non-deflected light using the optical stop [11] (Copyright © 2015, The Japan Society of Applied Physics)

quality optical windows also should be used for a water bath to maintain coherency of Schlieren optical systems.

A knife-edge is widely used for a spatial filter of a conventional Schlieren imaging system because generally there is no clear boundary between deflected light and non-deflected light in the diffraction pattern. Schlieren images show sensitive changes depending on the settings of the knife-edge. Again, consider a situation in which an ultrasound field propagating in the x direction produces a phase shift of $\varphi(x,t)$ given by Eq. 7. Then, the transmitted light $E_t(x,y,z,t)$ is given by Eq. 15 with the assumption of $\varphi \ll 1$, and the equation can be rewritten as shown in Eq. 19 [20].

$$E_t(x, \, y, z, t) \cong E_0 e^{i\left(\omega t - \frac{2\pi}{\lambda}z\right)} \left(1 + a(x,y)\frac{e^{i\left(\Omega t - \frac{2\pi}{\Lambda}x\right)} - e^{-i\left(\Omega t - \frac{2\pi}{\Lambda}x\right)}}{2}\right). \qquad (19)$$

On the right side of Eq. 19, the first term "1" in parentheses represents the 0th diffraction light spot and the other terms represent a pair of first-order diffraction light spots. Since a typical setting of the knife-edge is to place the edge at the center of the 0th-order light spot, half of the 0th-order light and one of the pair of the first-

order diffraction light spots are eliminated by the knife-edge. Therefore, the light transmitted through the spatial filter $E_t'(x, y, z, t)$ is given by Eq. 20,

$$E_t'(x, \ y, z, t) \cong E_0 e^{i\left(\omega t - \frac{2\pi}{\lambda}z\right)} \left(\frac{1}{2} + \frac{a(x,y)}{2} e^{i\left(\Omega t - \frac{2\pi}{\Lambda}x\right)} \right). \tag{20}$$

Then, the intensity distribution $|E_t'(x, y, z, t)|^2$ of the Schlieren image visualized in this condition is given by Eq. 21 because $a^2(x, y) \ll 1$.

$$\left| E_t'(x, \ y, z, t) \right|^2 \cong \left(\frac{E_0}{2} \right)^2 \left(1 + 2a(x,y) \cos \left(\Omega t - \frac{2\pi}{\Lambda}x \right) \right). \tag{21}$$

The equation indicates that stroboscopic observation can visualize wavefronts of a propagating ultrasound field, but time-averaging observation cannot do that.

A dot stop that only eliminates the 0th-order light is frequently used for visualization of ultrasound fields. In this case, the light transmitted through the spatial filter $E_t'(x, y, z, t)$ and intensity distribution of the Schlieren image $|E_t'(x, y, z, t)|^2$ are given by the following equations, respectively, because the first term "1" in the parentheses on the right side of Eq. 15 becomes zero.

$$E_t'(x, \ y, z, t) \cong i\, E_0\, a(x,y) \sin \left(\Omega t - \frac{2\pi}{\Lambda}x \right) e^{i\left(\omega t - \frac{2\pi}{\lambda}z\right)}, \tag{22}$$

$$\left| E_t'(x, \ y, z, t) \right|^2 \cong E_0^2 a^2(x,y) \sin^2 \left(\Omega t - \frac{2\pi}{\Lambda}x \right). \tag{23}$$

Equation 23 means that both stroboscopic and time-averaging observations can visualize the ultrasound field. Time-averaging observation visualizes the $a^2(x, y)$ component. Stroboscopic observation visualizes the $\sin^2(\Omega t - 2\pi x/\Lambda)$ component that can distinguish wavefronts of ultrasound, indicating that the ultrasound wavefronts visualized by stroboscopic observation have double frequency.

Figure 9 shows three Schlieren images of a focused ultrasound field visualized using different settings of the optical stop. A focused transducer of 1 MHz in resonant frequency was driven by 40-cycle burst pulses, and images of the focused field with ±0.3 MPa in peak pressures were acquired using zeroth-order light only (Fig. 9a), a half of zeroth-order light and 1st-order diffraction light (Fig. 9b), and 1st-order diffraction light only (Fig. 9c). The diffracted light eliminated from the image in Fig. 9a appeared in the image in Fig. 9c, and generation of a heated water flow adjacent to the transducer (white arrowheads) was visualized in the image shown in Fig. 9b. Figure 9b and c confirm that the Schlieren technique can visualize an envelope of the pressure field with no synchronization. Local contrast of the phase grating increases with increase in local ultrasound pressure, resulting in an increase in local brightness in the visualized Schlieren image.
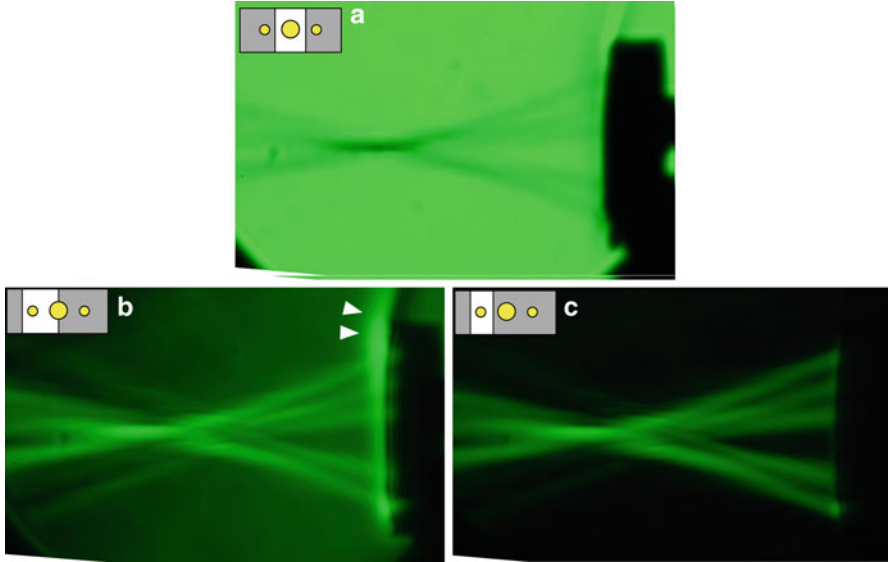
Fig. 9 Temporally averaged Schlieren images of a focused ultrasound field of 1 MHz in center frequency and 40 cycles in duration visualized using different settings of the optical stop. Images were acquired using (**a**) zeroth-order light only, (**b**) a half of zeroth-order light and first-order diffraction light, and (**c**) first-order diffraction light only (The images were taken by the courtesy of Prof. Shinichiro Umemura, Tohoku University, Japan)

Quantification

As discussed in the previous subsection, an intensity distribution of a time-averaged Schlieren image acquired using a dot stop is proportional to a square of a phase shift integrated over a light path. In the condition in which a pressure amplitude distribution P_{amp} has a 3D volumetric distribution, the intensity distribution of the Schlieren image is given by Eq. 24 [21, 22]:

$$I \propto \left(\int p_{amp} dz \right)^2, \tag{24}$$

where I is the light intensity and the integration term represents ultrasound pressure summarized over the light path interacting with the ultrasound field. In the condition in which light deflection is negligible, the 3D volumetric distribution of pressure can be calculated using a CT algorithm, which utilizes Schlieren images visualized from multiple directions.

Recent progress in electrooptic and optoelectronic devices such as laser diodes and CCD cameras has enabled high-quality quantitative image analysis. A compact and quantitative Schlieren system is commercially available (OptiSon®, Onda Corporation,

Fig. 10 Commercially available quantitative stroboscopic Schlieren system designed for visualization of both continuous and pulsed ultrasound fields (http://www.ondacorp.com/products.shtml, accessed Aug. 26, 2015)

Sunnyvale, CA, USA) [23, 24]. Figure 10 shows the system used for visualization of both continuous and pulsed ultrasound fields in the frequency range of 1–100 MHz at spatial and temporal resolutions of 50 µm and 150 ns, respectively. The primary importance of the equipment is instant visualization of the entire ultrasound field, but the secondary importance is supportive use for hydrophone measurements. Typically, focused ultrasound fields are characterized by parameters measured at the positions where they take spatial peaks. However, it is a time-consuming process to find the spatial peaks by 3D scanning of a hydrophone. Instant visualization of the field is therefore important to reduce the time-consuming process. The equipment also has a function to evaluate total output power using visualized field images. Measured values of the power have accuracy of ± 2 % in comparison with those measured using a radiation force balance in the range from 5 to 100 mW.

Stroboscopic Schlieren Technique

The stroboscopic Schlieren technique enables visualization of instantaneous ultrasound fields [21, 23–25]. Schlieren optics requires a coherent light source to produce a clear diffraction pattern by light interference. The stroboscopic Schlieren technique also requires the ability to produce light pulses that are sufficiently short compared to the period of ultrasound to be visualized. Laser diodes (LDs) are suitable for this
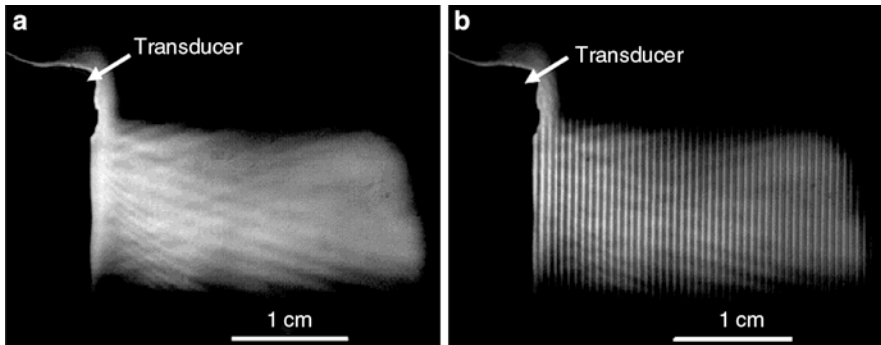
Fig. 11 Schlieren images of a continuous-wave ultrasound field generated by a disk transducer of 1.62 MHz in center frequency. (**a**) A time-averaged Schlieren image acquired using a continuous light source. (**b**) The same field visualized using short light pulses synchronized with the ultrasound phase [25] (Copyright © 2013, The Japan Society of Applied Physics)

application because they have a high point light source property with a large optical output and can generate narrow light pulses of several nanoseconds. Light-emitting diodes (LEDs) have increasing optical power; however, it is still difficult to utilize LEDs because they have low spatial coherency.

Figure 11 shows Schlieren images of a continuous-wave ultrasound field generated by a disk transducer of 1.62 MHz in center frequency [25]. The time-averaged Schlieren image shown in Fig. 11a was acquired using a continuous light source with no intensity modulation, and no wavefronts of propagating ultrasound are visualized. The Schlieren image shown in Fig. 11b is the same field but was taken using short light pulses synchronized with the ultrasound phase. The wavefronts are visualized as bright lines in the images. Since the images were taken using a ring knife-edge, their interval of the bright lines is $\Lambda/2$ as discussed on Eq. 23.

Shadowgraphy

Principle and Optical System

Shadowgraphy visualizes ultrasound fields by utilizing light deflection in an inhomogeneous refractive index field. A typical optical system for shadowgraphy shown in Fig. 12 has a point light source with a collimating lens and a screen on which the light transmitted through a phase object is projected.

The principle of shadowgraphy for visualizing an ultrasound field can be explained using Fig. 13. If the phase object has a constant refraction index ($\partial n/\partial x = 0$), light rays are straightly transmitted through the object and illuminate the screen with constant brightness as shown in Fig. 13a. If the phase object has a constant gradient of the refractive index ($\partial n/\partial x =$ const.), all of the light rays are deflected at the same angle and, again, the screen is illuminated by uniform brightness as shown
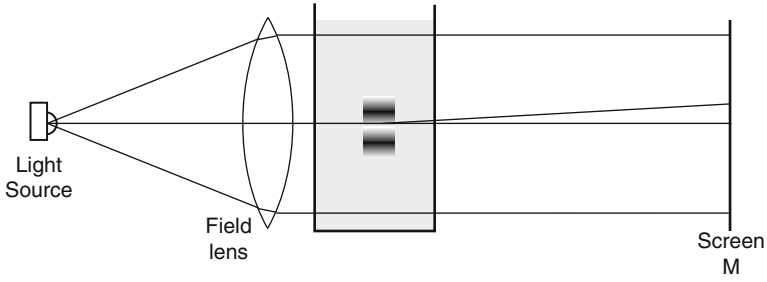
Fig. 12 An optical system for direct shadowgraphy with a collimated light source [11] (Copyright © 2015, The Japan Society of Applied Physics)
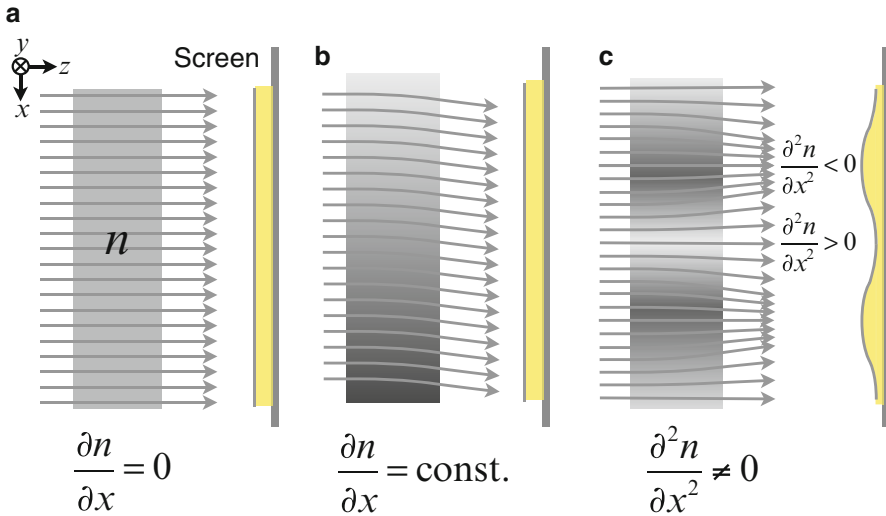
Fig. 13 Principle of the shadowgraph technique [11]. (**a**) In the condition of $\partial n/\partial x = 0$, no light deflection occurs, and a screen is uniformly illuminated. (**b**) In the condition of $\partial n/\partial x$ being constant, the incident light rays are deflected at the same angles. Also in this condition, the screen is uniformly illuminated. (**c**) In the condition of $\partial^2 n/\partial x^2 \neq 0$, convergence and divergence of the light rays produce an inhomogeneous light distribution on the screen (Copyright © 2015, The Japan Society of Applied Physics)

in Fig. 13b. Furthermore, under the condition of the phase object having a refractive index distribution of ($\partial^2 n/\partial x^2 \neq 0$) as shown in Fig. 13c, as it is for ultrasound fields, the transmitted light rays have a different deflection angle at each position, resulting in light ray convergence and divergence. In visualization of an ultrasound field, the brightness of the screen behind compressive pressure regions ($\partial^2 n/\partial x^2 < 0$) is increased and that behind rarefactional pressure regions ($\partial^2 n/\partial x^2 > 0$) is decreased.
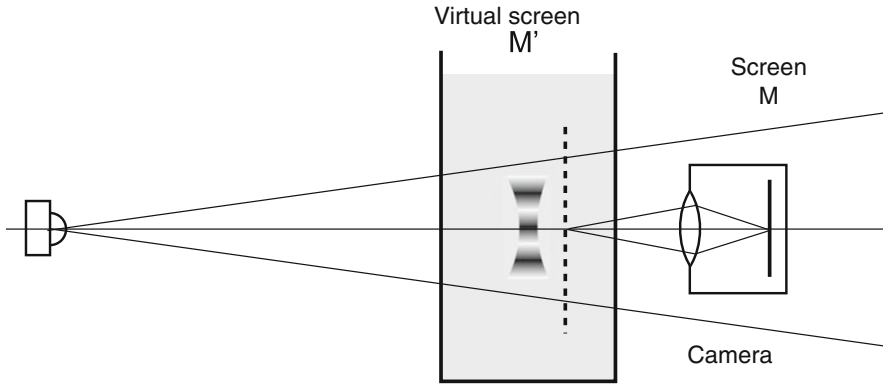
Fig. 14 A simple shadowgraphy optical system for ultrasound field visualization that uses only a point light source and camera [29] (Copyright © 2015, Elsevier)

Since shadowgraphy does not use light diffraction by an acoustic grating, optical coherency is not required for its optical systems.

As already mentioned, the Schlieren technique achieves sensitive detection of small changes in the refraction index field by eliminating non-diffracted light using optical spatial filtering. Shadowgraphy itself has no function of elimination but can have a similar effect by subtraction of images taken with and without ultrasound exposure because the subtraction image only contains deflected light.

Figure 14 shows a simple shadowgraphy system developed for ultrasound field visualization that only uses a point light source and a camera [26–29]. This is a variation of an optical system for direct shadowgraphy using a diverging light source [10] with the screen replaced by the camera. The camera works as a relay optics that transfers an image projected on a virtual screen to the image screen of the camera, enabling an independent setting of the virtual screen position and optical magnification of an image projected on the camera screen. In the proposed technique, the virtual screen is placed at a distance of several acoustic wavelengths behind the ultrasound field, minimizing image deformation caused by light deflection [29]. The camera with a short focus lens of small depth of field is placed near the ultrasound field to detect light with deflection angles larger by one order of magnitude than that of the diffraction angles.

Quantification

Sensitivity of visualization increases with increase in the distance between a pressure field and screen, but increase in the distance also increases image distortion. In the condition with a large distance between the ultrasound field and screen, deflected light affects the light distribution of the neighboring cycles of the grating, and the interference produces complex diffraction patterns. Under these conditions, it is basically difficult to perform quantitative estimation of ultrasound fields.
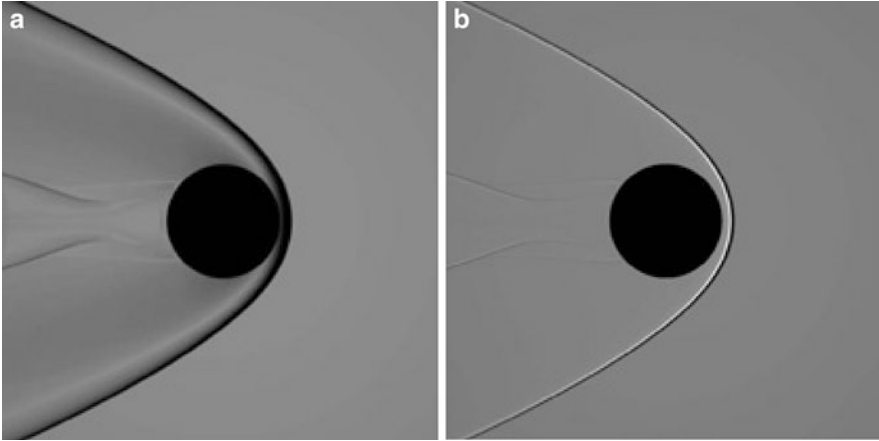
Fig. 15 Numerically calculated images of a pressure field generated around a flying sphere. (**a**) a Schlieren image and (**b**) a shadowgram [33] (Copyright © 2009, Springer)

In the condition in which light deflection is sufficiently small, change in local light intensity caused by a pressure amplitude distribution P_{amp} is expressed using the following equation [30–32]:

$$\frac{I_{on} - I_{off}}{I_{on}} \propto -l\frac{\partial n_{amp}}{\partial p_{amp}}\left(\frac{\partial^2}{\partial x^2} + \frac{\partial^2}{\partial y^2}\right)\int p_{amp}dz,\tag{25}$$

where I_{on} and I_{off} are the light intensities of shadowgrams taken in the conditions with and without ultrasound exposure, $\partial n_{amp}/\partial p_{amp}$ is the piezo-optic coefficient, and l is the distance between the ultrasound field to a shadow screen. The integration term shows integration of local pressure over a light propagation path. Therefore, the pressure integration term can be determined by second-order spatial integration of shadowgram light intensity.

Figure 15 shows numerically simulated Schlieren and shadowgraph images of a pressure field generated around a sphere flying at Mach 3.2 in air [33]. The pressure field was calculated by using a computational fluid dynamics program, and the images were calculated using a ray-tracing technique. The difference between the two techniques in their principles is clearly shown in the images: the Schlieren technique visualizes the first derivation of a refractive index field (Fig. 15a) and shadowgraphy visualizes the second derivation of a refractive index field (Fig. 15b).

Applications

The shadowgraph technique is often used for visualization of a shockwave or very high-pressure fields [34, 35]. Fields generated around high-speed flying objects, from a bullet to an aircraft, are visualized using shadowgraphy. The reason is
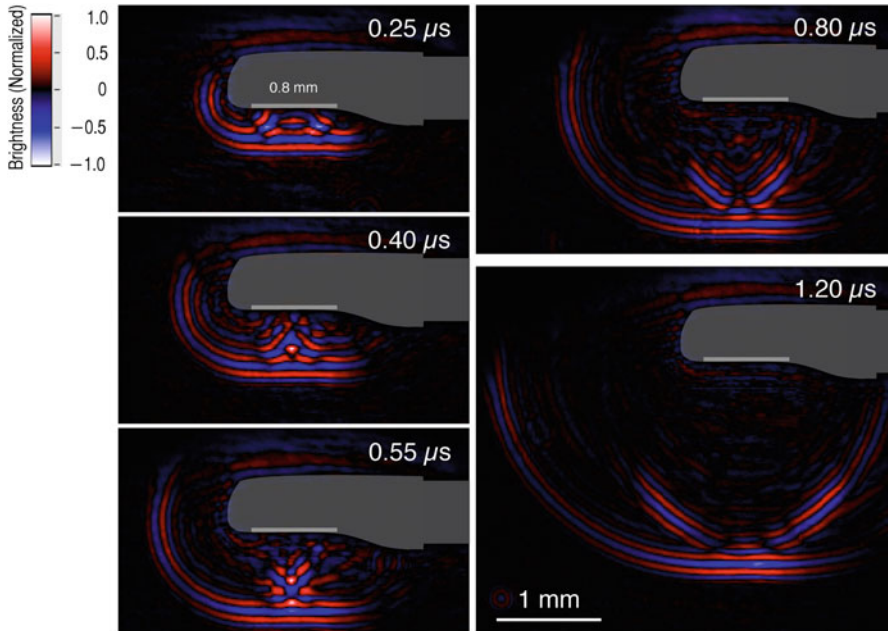
Fig. 16 High-frequency ultrasound fields irradiated from a flat-faced miniature transducer of 0.8 × 0.5 mm in size and 20 MHz in center frequency [29] (Copyright © 2015, Elsevier)

simplicity of the optics, which is important for visualization of a large object. The other reason is that sensitivity is not needed for shockwave visualization. Low sensitivity of shadowgraphy is caused by the fact that the technique itself has no function to eliminate non-deflected light.

Both continuous and pulsed ultrasound fields can be visualized using shadowgraphy, but the stroboscopic technique is essential. One of the important merits of optical visualization is the ability to visualize a high-frequency ultrasound field simply by increasing the optical magnification of the camera. Figure 16 shows high-frequency ultrasound fields irradiated from a flat-faced miniature transducer of 0.8 mm × 0.5 mm in size and 20 MHz in center frequency. These images were acquired using a simple shadowgraphy system with a macro lens [29]. Propagation of the field was visualized by taking a series of images at different time delays. Complex acoustic fields near the plane transducer, acoustic side lobes, and an edge wave that propagates in the horizontal direction can be visualized. The simple optics allows the use of optics of a microscope, enabling visualization of an ultrasound field up to 40 MHz [28].

Visualization of high-intensity ultrasound fields for therapeutic application is another important application of optical techniques that do not require placement of a physical device at the measuring position. Figure 17 shows continuous-wave therapeutic ultrasound fields generated by a focused transducer of 100 mm in
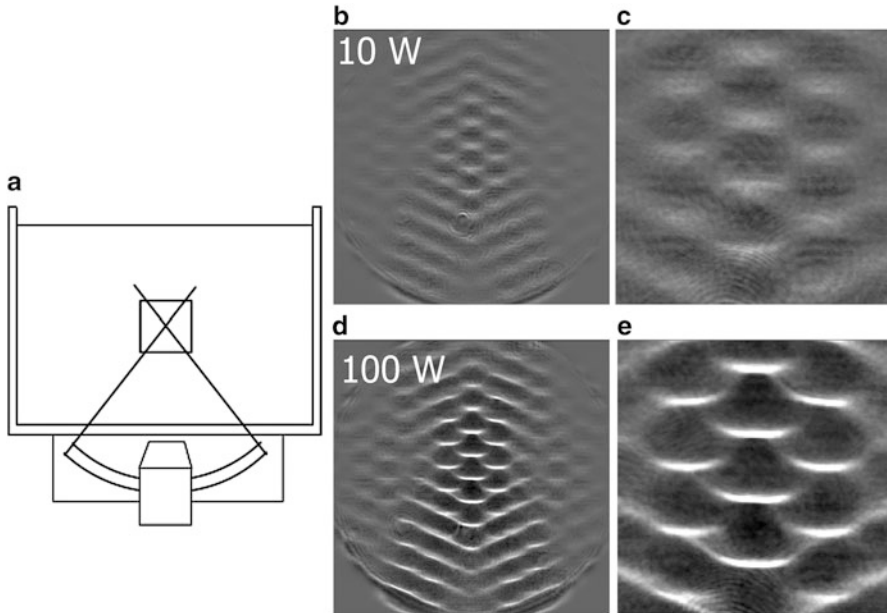
Fig. 17 Therapeutic ultrasound fields generated by a focused transducer of 100 mm in aperture and 110 mm in curvature with resonance frequency of 1.58 MHz. The acoustical intensity at the focus is 4,730 W/cm^2 at input power of 100 W [27]. (**a**) Experimental setting of an HIFU transducer and location of the observed regions. Schlieren images at input power of (**b**) 10 W and (**d**) 100 W. Expansion views in the focal region of (**c**) 10 W and (**e**) 100 W input power (Copyright © 2006, AIP Publishing)

aperture and 110 mm in curvature with a resonance frequency of 1.58 MHz [27]. The acoustical intensity estimated from electric input, transducer efficiency, and focus size is 4,730 W/cm^2 at the focus, indicating that such an intense field can be visualized using the simple technique.

Focused Shadowgraphy

Figure 18 shows a typical optical system called focused shadowgraphy [10], which is equivalent to the basic Schlieren optics without an optical stop. The technique is also used for ultrasound field visualization [31, 36–38]. The construction of typical optical systems for the phase contrast technique (Fig. 6), Schlieren technique (Fig. 8), and focused shadowgraph technique (Fig. 18) is the same except for the optical element placed at the focus of the second lens. A $\pi/2$ phase plate is used in the phase contrast technique, and light absorbers with luminous transmittances of 0 % and 100 % are used in the Schlieren and focused shadowgraph techniques, respectively.
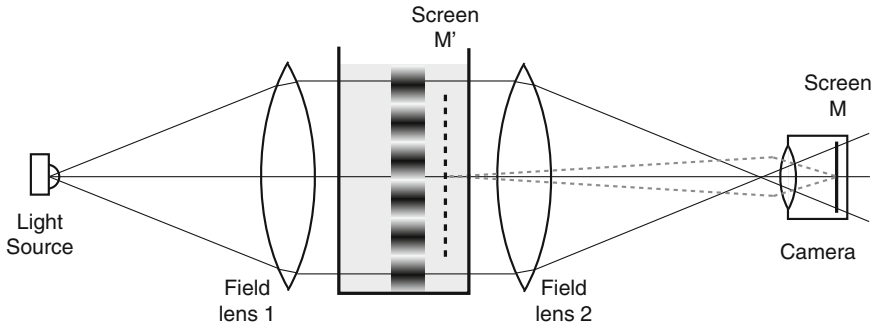
Fig. 18 An optical system for focused shadowgraphy. The system is equivalent to the system for the Schlieren technique except for the absence of a spatial filter at the focus of the second lens

Pitts et al. reported a technique to reconstruct an ultrasonically modulated phase image by a phase recovery technique that uses an iterating calculation algorithm [36]. Pulsed ultrasound fields of 2.5 MHz in center frequency were visualized in the pressure range of 6.59–111 kPa in peak pressure using Fresnel diffraction images acquired at a distance of 7.33 cm from the position just behind the field. Three-dimensional fields reconstructed using a CT algorithm showed good agreement with hydrophone measurements.

Other Optical Techniques

Background-Oriented Schlieren Technique

The background-oriented Schlieren (BOS) technique visualizes a refractive index distribution by detecting deformation of a background texture pattern caused by the inhomogeneous refractive index field that exists in the foreground [39]. The only optical requirement is to take a picture of a target field with a fine texture image in the background, and all other processes to estimate changes in the refractive index causing background pattern deformation are carried out by post-processing of an image.

Because of the small requirement for the optical system, the BOS technique is suitable for visualization of pressure disturbance in a large area. Visualization of a vortex field generated at the tip of a helicopter blade is one of the typical applications. Figure 19a, b show a background image taken immediately after departure of a helicopter and a foreground image taken during its hover flight. The background pattern was made by splashing droplets of white paint on a concrete ground, and the blade tip is shown in Fig. 19b, c shows a BOS image that visualizes the displacement vectors calculated using Fig. 19a, b. Figure 19d is an enlarged view of the image in Fig. 20c around the blade tip, and vectors shown in Fig. 19d indicate the direction and length of a displacement.
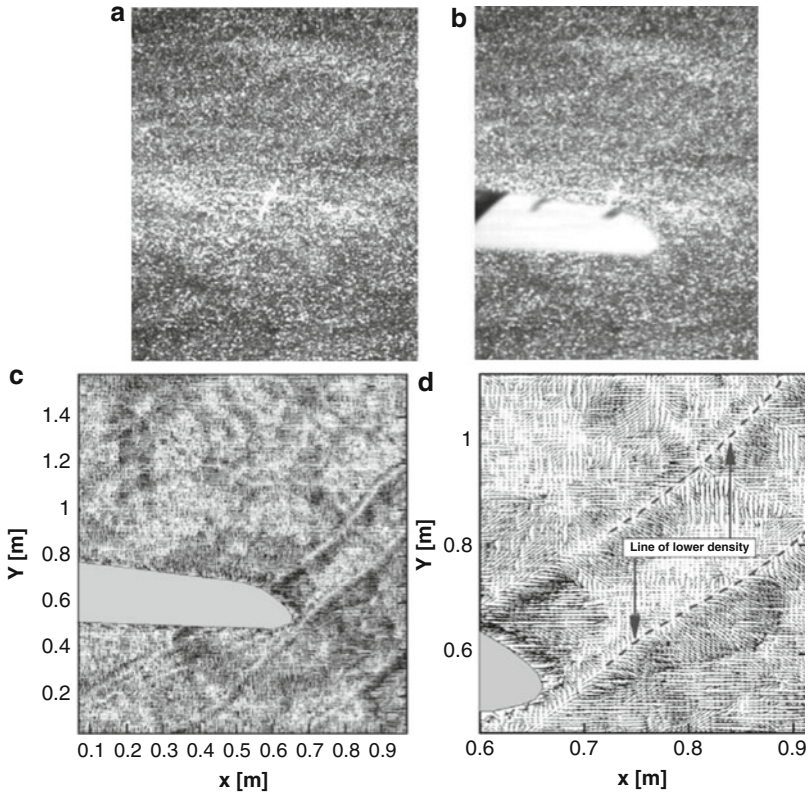
Fig. 19 Visualization of a vortex field generated by a helicopter blade using the background-oriented Schlieren (*BOS*) technique [39]. (**a**) A background image taken immediately after the departure of a helicopter, and (**b**) a foreground image taken during hovering before the departure. The blade tip is included in the image. (**c**) A BOS image calculated using the foreground and background images representing displacement of the background pattern. (**d**) An enlarged view around the blade tip shows vectors that show the direction and length of displacement (Copyright © 2001, Institute of Physics Publishing)

Another type of BOS technique, which does not use a random-dot pattern but uses a simple stripe pattern, is applied for visualization of a HIFU field [40]. The experimental system is simple as shown in Fig. 20: a transparent film with a black horizontal stripe pattern is placed in a water bath, and the pattern is illuminated by a backlight. The HIFU field generated in the water bath is then observed with the stripe pattern. Figure 21 shows the results of observation. The stripe pattern is distinguished in the condition without ultrasound exposure (Fig. 21a); however, the pattern behind the ultrasound focus is blurred with ultrasound exposure (Fig. 21b). The blurring is caused by light deflection in the ultrasound field, and the extent of the blurring reflects the magnitude of dp/dx.

Furthermore, subtraction of stripe images taken with and without ultrasound exposure gives the image shown in Fig. 22a. Light deflection caused by an

Fig. 20 An experimental
system that uses a stripe
pattern as a background
image. An image of the stripe
pattern behind an HIFU field
was taken with a focus on the
pattern
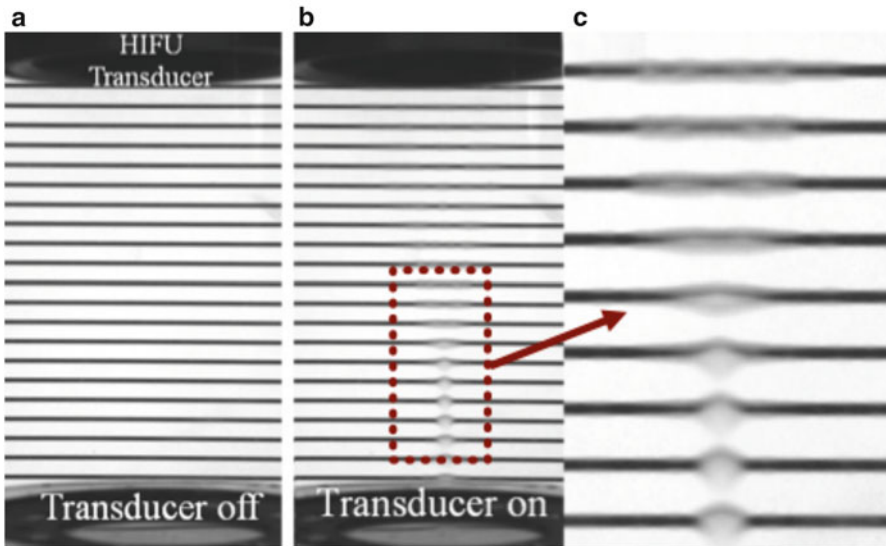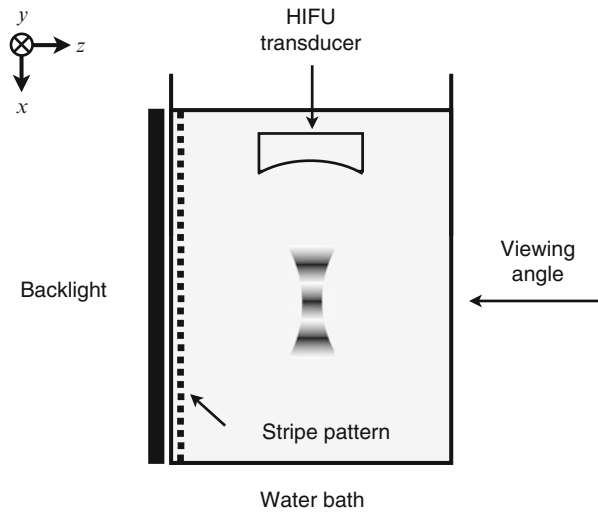
Fig. 21 Images taken using the experimental system that uses a stripe pattern for a background image. The transducer generates a focused ultrasound field of 1.07 MHz in center frequency; -3.8 and 15 MPa in peak negative and positive pressures, respectively; and 1,200 W/cm^2 in spatial peak intensity at the focus [40]. (**a**) An image taken without ultrasound exposure. (**b**) An image taken with ultrasound exposure. (**c**) An enlarged view around the focus, showing the stripes blurred by light deflection in the HIFU field (Copyright © 2010, IEEE)
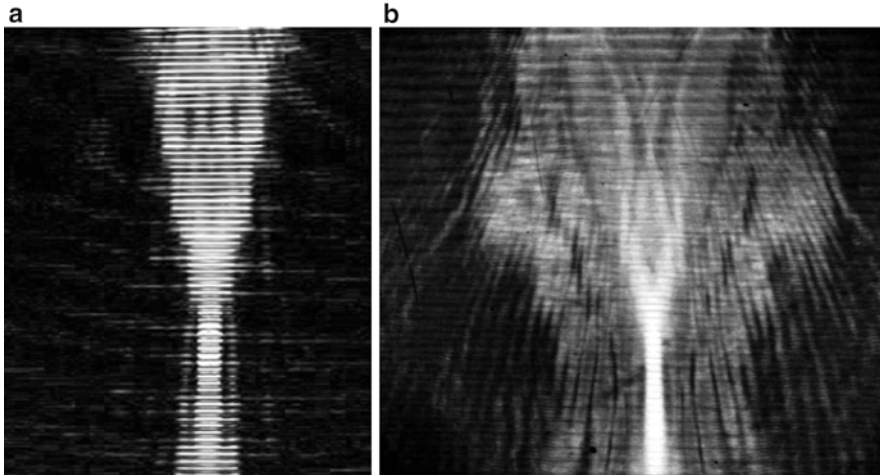
Fig. 22 A technique for sensitive visualization of the HIFU field [40]. (**a**) A single difference image is calculated by subtraction of the image taken without ultrasound exposure from the image taken with ultrasound exposure. (**b**) An image superimposing several difference images acquired using the same stripe pattern with a shifted phase. Effects of the stripe pattern disappear and details of the field appear (Copyright © 2010, IEEE)

ultrasound field can be visualized more clearly in the subtracted image. Although the image has discontinuity caused by the original stripe pattern, summation of images taken using the same stripe pattern with a shifted phase improves a field image as shown in Fig. 22b, indicating that the method has sufficiently high sensitivity to visualize details of complex HIFU fields. Hydrophone measurements are a gold standard for evaluation of an exact 3D ultrasound field; however, this technique cannot be used for 100 % inspection or for on-site daily inspection because hydrophone measurements require specialized equipment and take a long time. Therefore, optical visualization techniques are important especially for quality control purposes of ultrasound systems.

Scanning Laser Doppler Vibrometry

Laser Doppler vibrometry (LDV) is a technique for measuring vibration of a target spot illuminated by a laser beam. Velocity of the vibration is evaluated by detection of a frequency shift of the light reflected from the spot caused by the Doppler effect. A spatial distribution of the vibration can be visualized using LDV by mapping the laser spot at the surface of a target object. The Doppler shift can be detected by using a homodyne or heterodyne interferometer, which generally has a frequency bandwidth up to 10 MHz, and the technique can therefore be used for visualization of ultrasound fields within this frequency range.

Fig. 23 An experimental system for scanning laser Doppler vibrometry (*LDV*). The laser beam from the LDV head scans a retroreflective target. The light reflected from the non-vibrating target has a phase shift integrated over the light path interacting with the ultrasound field
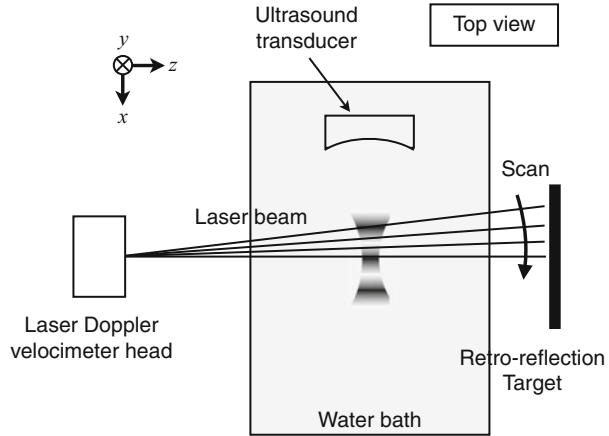
Figure 23 shows a schema of the experimental system used for visualization of an ultrasound field generated inside a water bath [41]. A laser head of a scanning LDV is placed in front of the water bath, and a retroreflective target is fixed at another side of the bath. The ultrasound irradiated from a transducer propagates in the horizontal direction. The LDV light beam is transmitted through the ultrasound field to illuminate the reflective target, and the reflected light is detected by the LDV head. Since the ultrasound pressure changes light speed in the water, light reflected from the non-vibrating reflector has a phase shift integrated over the light path interacting with the ultrasound field. Two orthogonal mirrors are used to scan the laser spot on the surface of the reflector in horizontal and vertical directions, and a 2D distribution of the light phase shift caused by the ultrasound field is measured. Figure 24 shows the results of visualization of the propagation of a burst pulse [41].

Photoelastic Technique

The property of a material having two different refractive indices depending on the polarized plane is called birefringence or double refraction, and a material that produces birefringence depending on the applied stress is called a photoelastic object. A technique that visualizes a stress distribution inside a transparent photoelastic object is called a photoelastic technique, and the technique is also utilized for visualization of an ultrasound field propagating inside a photoelastic object [42].

Figure 25 shows an optical system that utilizes a photoelastic technique for visualization of an ultrasound field propagating through a photoelastic object. The basic construction of the system is the same as that used for focused shadowgraphy; however, a polarizer and analyzer with $\lambda/4$ plates were inserted into the optical path preceding and succeeding to transmission of an ultrasound field. These polarizing plates are oriented in the orthogonal direction of polarization. The linear polarized
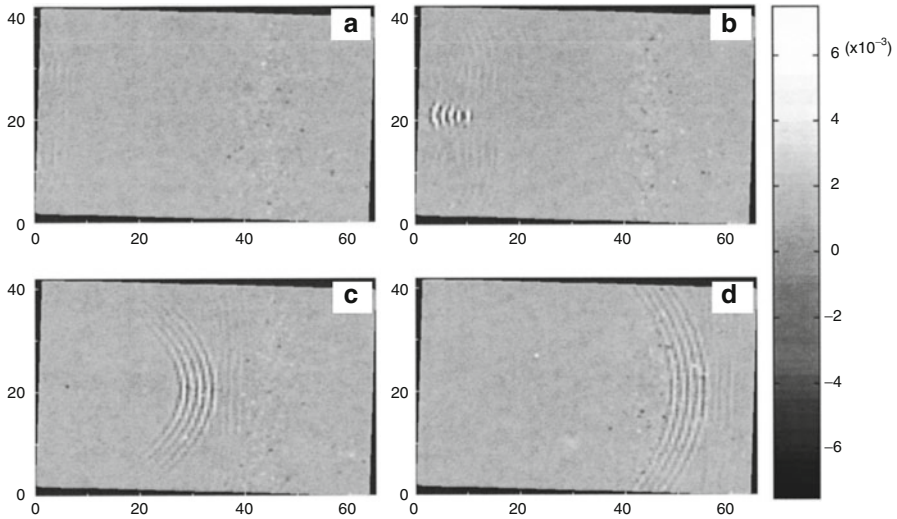
Fig. 24 Visualization of a tone-burst ultrasound pulse of 1 MHz in center frequency with five cycles generated by a focused transducer [41]. The images taken (**a**) 1.5 μs, (**b**) 50 μs, (**c**) 130 μs, and (**d**) 200 μs after insonation. The gray scale shows the rate of change in optical path length (m/s) (Copyright © 2004, Acoustical Society of America)
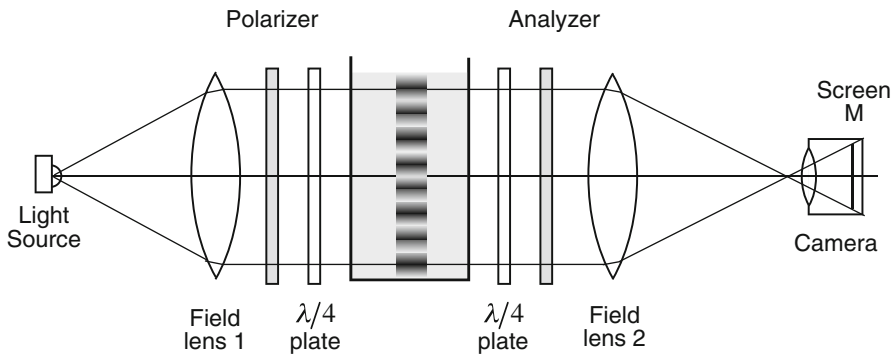
Fig. 25 An optical system for the photoelastic technique. A polarizer and analyzer with λ/4 plates were inserted into the optical path of the optical system for focused shadowgraphy

light that is transmitted through the polarizer is converted into circularly polarized light by the first λ/4 plate. In the condition in which no ultrasound pressure is applied to the photoelastic object, the second λ/4 plate converts the circularly polarized light into linear polarized light again, and the analyzer with the orthogonal polarizing plane does not transmit the light. In the case of ultrasound pressure being applied to the object, the linearly polarized light transmitted through the medium is converted into elliptic polarization, and the second λ/4 plate converts the elliptic polarized light
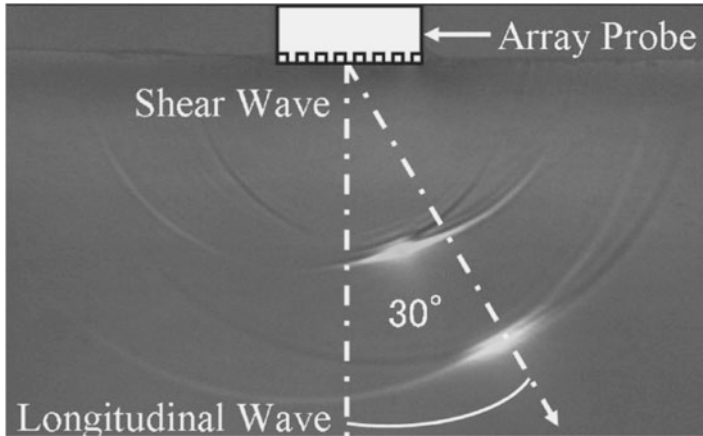
Fig. 26 Pressure distribution of a short ultrasound pulse generated by a 16-element-phased array transducer at a steering angle of 30° [43] (Copyright © 2012 The Japanese Society for Non-Destructive Inspection)

into linear polarized light with a different angle of polarization. The analyzer then transmits only a light component that has the same polarizing angle. The results show that the intensity of light that is transmitted through the photoelastic object increases with an increase in the phase difference between the two lights modulated anisotropically.

Figure 26 shows an ultrasound field generated by a phased array probe of 1 MHz in center frequency [43]. The transducer has 16 elements, which were driven to generate short-pulsed ultrasound at a beam-steering angle of 30°. Both longitudinal and shear waves are visualized in the image.

Techniques for Visualization of Temperature Elevation

Ultrasound irradiation causes temperature elevation in the propagating medium, which is determined by the ultrasound intensity multiplied by an absorption coefficient of the medium. Particularly in applications that utilize the temperature rise to promote chemical or therapeutic effects, direct visualization of the temperature rise distribution is more important than visualization of the pressure distribution.

A temperature elevation in biological tissue is one of the important issues in safety of diagnostic ultrasound and also in efficiency of ultrasound therapy. Typically, the temperature rise is estimated from an ultrasound intensity distribution measured in water; however, direct temperature measurement is also carried out using a tissue-mimicking phantom. A transparent phantom that becomes opaque when heated is used to visualize temperature rise caused by HIFU exposure. A polyacrylamide gel phantom supplemented with bovine serum albumin (BSA) has been developed for this purpose [44].
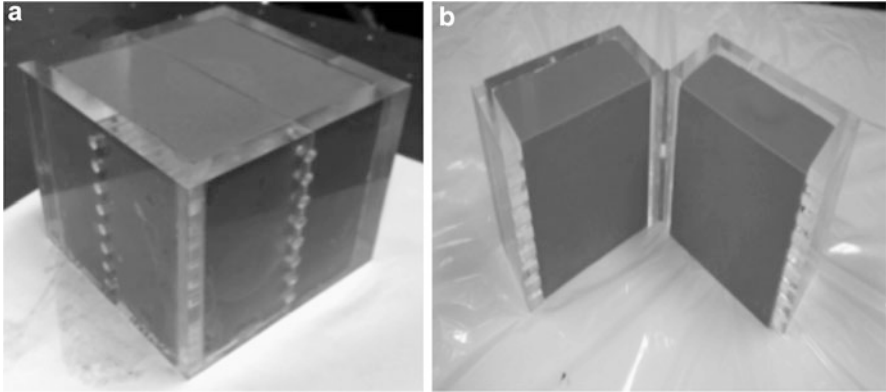
Fig. 27 A biological tissue-mimicking phantom designed for visualization of a temperature rise distribution [45]. (**a**) The phantom consists of two tissue-mimicking materials and is sonicated by an ultrasound transducer. (**b**) The phantom is split into two pieces, and an infrared camera takes a thermal image of the splitting interface (Copyright © 2015, The Japan Society of Ultrasound in Medicine)

An infrared camera and a specially designed phantom are also used for visualization of a temperature elevation caused by ultrasound exposure. The phantom consists of two tissue-mimicking materials (TMMs) with acoustic and thermal properties similar to those of a typical biological tissue. The two TMMs were sonicated with one united body as shown in Fig. 27a but were split into two TMMs after sonication as shown in Fig. 27b [45]. An image of temperature distribution that appeared at the splitting interface of the TMM is then taken by the camera. Figure 28 shows the temperature distributions generated by ultrasound exposure of 1-MHz in center frequency and 720 mW/cm^2 in spatially peak temporal-averaged intensity. Figure 28a, b show experimental results and simulation results calculated by a 3D finite difference time domain method [45]. The distributions are different in the near field because of the insufficient definition of the ultrasound source in the simulation, but they show good agreement in the far field, indicating the usefulness of the phantom for visualizing an arbitrary cross section of a 3D distribution of temperature rise.

Conclusions and Future Directions

Optical techniques have limitations in reconstruction of 3D ultrasound fields caused by light deflection and cannot replace conventional hydrophone measurements. However, an optical technique that can rapidly visualize ultrasound fields with no obstacle around the field is still attractive. Laser diodes and LEDs have made great progress recently, and the combination of a high-quality image sensor and digital image-processing techniques has totally changed the culture of photography. Optical
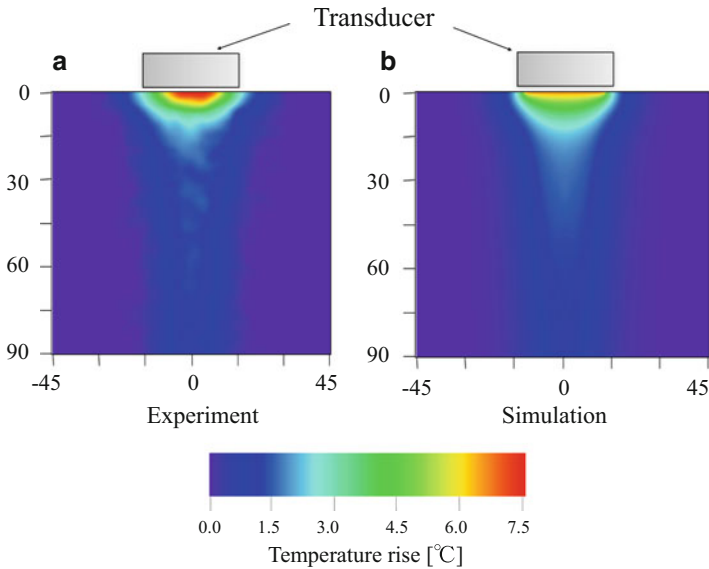
Fig. 28 Temperature rise distributions generated by non-focused ultrasound exposure of 1-MHz in center frequency and 720 mW/cm^2 in I_{SPTA} [45]. (**a**) Temperature distribution taken by the camera. (**b**) The distribution calculated by 3D simulation (Copyright © 2015, The Japan Society of Ultrasound in Medicine)

techniques have a long history for visualization of ultrasound fields; however, the techniques are now about to make a large step that utilizes these new technologies.

References

1. Rienitz J (1975) Nature 254:293
2. Lucas R, Biquard P (1932) J Phys Radium 3:464
3. Debye P, Sears F (1932) Proc Natl Acad Sci U S A 18:409
4. Raman CV, Nath NSN (1935) Proc Indian Acad Sci Sect A 2:406
5. Raman CV, Nath NSN (1936) Proc Indian Acad Sci Sect A 2:413
6. Raman CV, Nath NSN (1936) Proc Indian Acad Sci Sect A 3:75
7. Raman CV, Nath NSN (1936) Proc Indian Acad Sci Sect A 3:119
8. Raman CV, Nath NSN (1936) Proc Indian Acad Sci Sect A 3:459
9. Rienitz J (1997) Endeavour 21:77
10. Settles GS (2001) Schlieren and shadowgraph techniques: visualizing phenomena in transparent media. Springer, Berlin
11. Kudo N (2015) Jpn J Appl Phys 54:07HA01
12. Adler L, Hiedemann EA (1962) J Acoust Soc Am 34:410
13. Colbert HM, Zankel KL (1963) J Acoust Soc Am 35:359
14. Mizutani K, Ezure T, Nagai K, Yoshioka M (2001) Jpn J Appl Phys 40:3617
15. Obuchi T, Masuyama H, Mizutani K, Nakanishi S (2006) Jpn J Appl Phys 45:7152
16. Patorski K (1981) Ultrasonics 19:169
17. Zernike F (1942) Physica 9:686

18. Pitts TA, Sagers A, Greenleaf JF (2001) IEEE Trans Ultrason Ferroelectr Freq Control 48:1686
19. Harigane S, Miyasaka R, Yoshizawa S, Umemura SI (2013) Jpn J Appl Phys 52:07HF07
20. Núñez I, Ferrari JA (2007) Appl Opt 46:725
21. Hanafy A, Zanelli CI (1991) Proc IEEE Int Ultrason Symp 1223–1228
22. Pitts T, Greenleaf J, Lu J, Kinnick R (1994) Ultrason Symp 1665–1668
23. Schneider B, Shung K (1996) Ultrason Ferroelectr Freq Control IEEE Trans 43:1181
24. Charlebois T, Pelton R (1995) Med Electron 66–73
25. Azuma T, Tomozawa A, Umemura S (2002) Jpn J Appl Phys 41:3308
26. Kudo N, Ouchi H, Yamamoto K, Sekimizu H (2004) J Phys Conf Ser 1:146
27. Kudo N, Miyashita H, Yamamoto K (2006) AIP Conf Proc 829:614
28. Kudo N, Sanbonmatsu Y, Shimizu K (2010) Proc IEEE Int Ultrason Symp 829–832
29. Kudo N (2015) Ultrasound Med Biol 41:2071
30. Merzkirch W (1974) Flow visualization. Academic, London
31. Omura R, Shimazaki Y, Yoshizawa S, Umemura S (2011) Jpn J Appl Phys 50:07HC07
32. de Izarra G, de Izarra C (2012) Eur J Phys 33:1821
33. Kikuchi D, Sun M (2009) In: Choi H, Choi H, Yoo J (eds) Comput. Fluid Dyn. 2008 SE – 109. Springer, Berlin, pp 801–804
34. Boys CV (1893) Nature 47:440
35. Settles G, Grumstrup T (2005) Proc 5th Pacific Symp Flow Vis Image Process. 7 pages
36. Pitts TA, Greenleaf JF (2000) J Acoust Soc Am 108:2873
37. Neumann T, Ermert H (2006) Ultrasonics 44(Suppl 1):e1561
38. Shimazaki Y, Harigane S, Yoshizawa S, Umemura S (2012) Jpn J Appl Phys 51:07GF25
39. Richard H, Raffel M (2001) Meas Sci Technol 12:1576
40. Butterworth I, Shaw A (2010) Proc 39th Annu Symp Ultrason Ind Assoc UIA 2010
41. Harland AR, Petzing JN, Tyrer JR (2004) J Acoust Soc Am 115:187
42. Wyatt R (1972) Nondestruct Test 5:354
43. Washimori S, Mihara T, Tashiro H (2012) Mater Trans 53:631
44. Lafon C, Zderic V, Noble ML, Yuen JC, Kaczkowski PJ, Sapozhnikov OA, Chavrier F, Crum LA, Vaezy S (2005) Ultrasound Med Biol 31:1383
45. Tsuchiya T, Shimizu K, Endoh N Choonpa Igaku 10.3179/jjmu.JJMU.R.55, in print

Ultrasonic Atomization

Susumu Nii

Contents

Abstract

Ultrasound enhances dispersion of liquids into fine mist with a narrow size distribution. Such small liquid droplets and distributions are difficult to obtain with using conventional nozzles. Atomization occurs in the wide frequency range from 20 kHz to 10 MHz. Highlighted in this chapter is the phenomena occurring in MHz-range ultrasound because of the small mist size of submicrometer to several micrometers and enabling solute partitioning between mist and bulk liquid. The finding of surfactant enrichment in the mist brought a new aspect of separation in ultrasonic atomization. Targets of the separation range from ethanol, solid particles, and carbon nanotubes to rice wines. The chapter covers the basic mechanism of mist formation, solute-partitioning behavior, and recent topic of solid transfer into gas phase.

Keywords

Atomization, ultrasonic • Application, mist • Droplet formation • Droplet formation • Ethanol separation • Solute partitioning • Distillation, ultrasonically assisted • Droplet formation • Capillary wave hypotheses • Cavitation theory •

S. Nii (✉)
Kagoshima University, Kagoshima, Japan
e-mail: niisus@cen.kagoshima-u.ac.jp

Conjunction theory • Mist application • For preparing nanoparticles • For transferring solids to gas phase • Nanodroplets formation • Solute partitioning • Alcohol enrichment • Carrier gas • Droplet model • Enrichment ratio • Ethanol enrichment • Fuel atomization • Mass balance • Surfactant transport • Ultrasonic spray pyrolysis (USP)

Introduction

When liquid layer or dense liquid was subjected to a power ultrasound, fine mist would produce from liquid surface. The phenomenon is referred to as ultrasonic atomization or nebulization, which is firstly reported by Wood and Loomis [1] from liquids like benzene, water, and heavy transformer oil. The finding draws much attention from various fields which apply fine droplets or aerosols because of the characteristic of their diameter and the size distribution. Compared with conventional nozzles using a high shear to break up liquid, those droplets were ultrasonically produced, having smaller size and narrower size distribution [2–5]. The size is tunable by selecting ultrasonic frequency; many reports describe the range of several to several tens of micrometers under the irradiation of MHz frequency. The size range was difficult to obtain with pneumatic two-fluid nozzles.

From the aspect of fine droplet formation, ultrasonic atomization is characterized by the following points:

1. Very fine droplets whose size is from several to several tens of micrometer are obtained with narrower size distribution.
2. No need to pressurize fluid and the simplicity in equipment.
3. Easy to control the droplet density and transferring the droplets.

No. 1 is the greatest advantage in the use of droplets as a medium of mass-transfer or chemical reactions because of giving a large area per volume and the small path for diffusion of substances traveling between the surface and center of droplets. No. 2 and 3 will contribute for miniaturizing equipment and also saving the input energy for production. Ultrasonic atomization potentially improves the efficiency of an inhaler for drug delivery to the lung with very fine droplets whose diameter is in the 1–5 μm [6, 4, 7]. Therapeutic studies have carried out to deliver monoclonal antibodies or DNA-based vaccines [8]. Droplets have been utilized as precursor of inorganic and organic particles. Production of nanometer-sized particle requires much finer droplets and careful adjusting of droplet density. Thus, ultrasonic atomization becomes a key technique to obtain well-controlled solid particles [9–18].

Mechanism of Droplet Formation

Despite a substantial number of researches has been conducted, the mechanism of droplet formation under the irradiation of MHz range ultrasound is not fully understood. Two major theories and a conjunctive theory have been proposed. The first is

the capillary wave hypotheses delivered by Lang [12]. Droplets forms from crests of capillary waves on the liquid surface, into the gas phase. On the basis of Kelvin's equation [15], Rayleigh's instability [14] of liquid column or film, and stability limit wavelength, Lang had correlated his experimental data of the number-median diameter of droplets with the capillary wavelength. The average diameter was successfully predicted with the following equation:

$$d_{av} = a\lambda = a\left(\frac{8\pi\sigma}{\rho f}\right)^{1/3}$$

where d_{av} is average droplet diameter, a constant, σ interfacial tension, ρ liquid density, and f ultrasonic frequency. The equation indicates that the mean diameter is a constant fraction of the capillary wavelength. Lang determined the constant 0.34 for the number-averaged diameter of droplets produced with ultrasound of 10–800 kHz. For MHz-range ultrasound, the constant was modified to 0.96 by Yasuda et al. [15] for volume-averaged droplet diameter of aqueous alcohols solution, which was observed with laser diffraction method. When 1–2 MHz ultrasound was applied to atomization of aqueous solutions, the average droplet size predicted from Lang's equation would fall into several micrometers range. The calculated values accords fairly well with the observed values of laser diffraction method. It should be noted that lower detection limit of current laser diffraction method is approximately 0.1 μm. Since particles smaller than this size are unobservable, the "average diameter" depends on the observation method. Indeed, the presence of much finer droplets than the prediction of Lang's equation was reported by Yano et al. [16] with a small angle X-ray scattering. Also, Kobara et al. [17] applied a scanning mobility particle sizer, SMPS, to measure submicrometer-sized water droplets. From TiO_2 aqueous suspension, Sekiguchi et al. [18] separately observed submicrometer droplets with SMPS (Figs. 1, 2, and 3).

The second hypothesis is cavitation theory suggested by Sollner [19]. He conducted atomization of various liquids under degassed conditions and reduced or elevated temperature. The results indicated the close parallelism between emulsification and atomization, where cavitation provides destructive effects in dispersing liquids. Eknadiosyants [20] observed sonoluminescence from a liquid fountain during droplets emission and explained the occurrence of droplets as a result of frequent shockwaves from collapsing of cavities in the vicinity of liquid surface. This theory does not eliminate the possibility of capillary wave hypothesis. Indeed, Bograslavski and Eknadiosyants [21] proposed the conjunction theory, where the both mechanism are interrelated. They considered that breaking of crests of capillary waves is enhanced by periodical shockwaves near the liquid surface, which are produced by collapsing cavitational bubbles. In the earlier examination of atomization mechanism under the irradiation of MHz ultrasound, the theory has been sometimes rejected because of the high threshold power for cavitation in this frequency range.

Recent reports provide supporting evidence of occurring cavitation in MHz frequency. Frohly et al. [22] measured cavitation noise at a frequency of 1.6 MHz. During ultrasonic atomization of water by the irradiation of 2.4 MHz ultrasound,
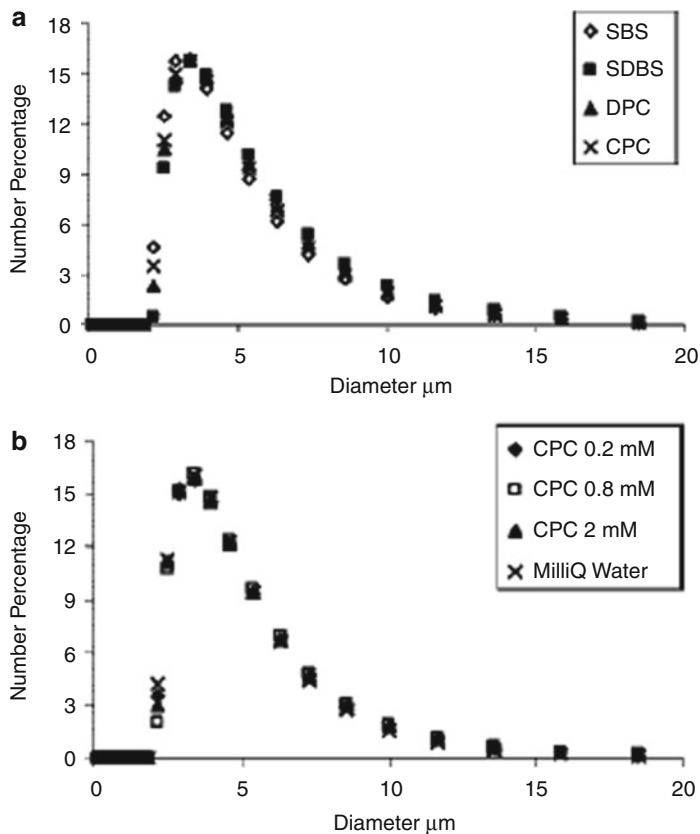
Fig. 1 Size distribution of aerosol droplets based on their percentage number, that was measured with a laser diffraction method: (**a**) Effect of surface activity of the surfactant, all solutions contained 0.2 mM surfactant. (**b**) Effect of solute concentration for cetylpyridinium chloride, CPC, surfactant. [29] Copyright (2008) ACS

Harada et al. [23] observed sonoluminescence and the spatial distribution of light. The brightest part was immediately below the bulk surface of the liquid. Since no light emission occurs without cavitation bubbles, their finding shows a clear evidence of occurring cavitation under the condition of atomization. Miller and Thomas [24] observed sonochemical oxidation of terephthalic acid under the irradiation of 1.6 MHz and the threshold power for the oxidation was 2 W/cm^2. Barreras et al. [25] showed pictures taken by a high-speed camera for atomizing from a mound of water by irradiating 1.6 MHz. The presence of dark spots near the water surface was reported and they suggested that the spots indicate the bubbles in water. Tsuchiya et al. [26] observed near the surface of liquid fountain from where liquid droplets form. The velocity of droplet ejection reached 5 m/s, which seems to be difficult to obtain from breaking up of capillary crests.
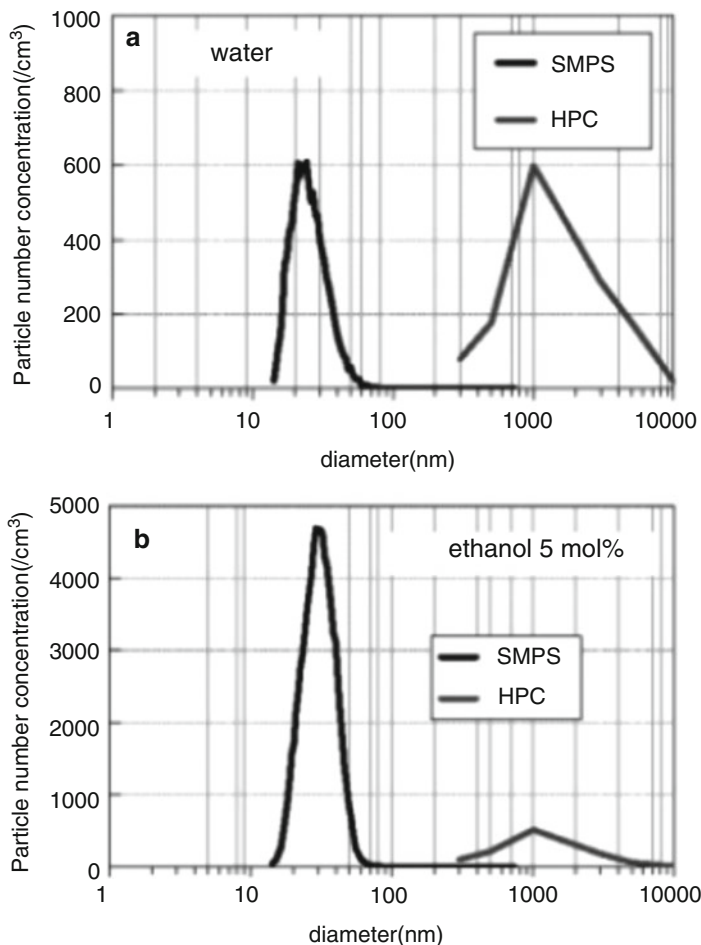
Fig. 2 Particle size distribution of mist generated by ultrasonic irradiation of (**a**) water, (**b**) ethanol 5 mol % at 20 °C and carrier-gas flow rate of 15 dm^3/min. HPC denotes handheld particle counter whose detection principle is laser diffraction. [17] Copyright (2010) AIChE

The above findings clearly show the existence of cavitation; however, it may not be the only mechanism of ultrasonic atomization. We carried out experiment to atomize degassed water at different levels of air contents and found no effect of degassing on the production rate of mist. The result suggests that the dominating effect might not be cavitation. There should be the influence of capillary wave. Therefore, at this moment we support the conjunction hypothesis for the mechanism of ultrasonic atomization (Figs. 4 and 5).

Because of the complexity lying in this phenomenon, determining the prevailing aspect depends too much on the condition. A more detailed observation is essential for elucidating the mechanism of ultrasonic atomization.

Fig. 3 Number concentration (N) as a function of particle diameter (D_p) measured with SMPS for ultrasonic mist containing particle, UMP, with or without heating by an electric furnace. [18] Copyright (2010) Elsevier
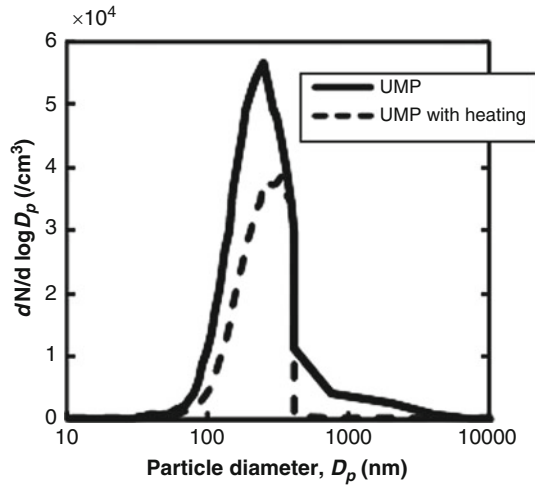
Fig. 4 High-speed image of perturbed water surface and ultrasonically atomized droplets under 1.65 MHz [25]. Copyright (2002) Springer
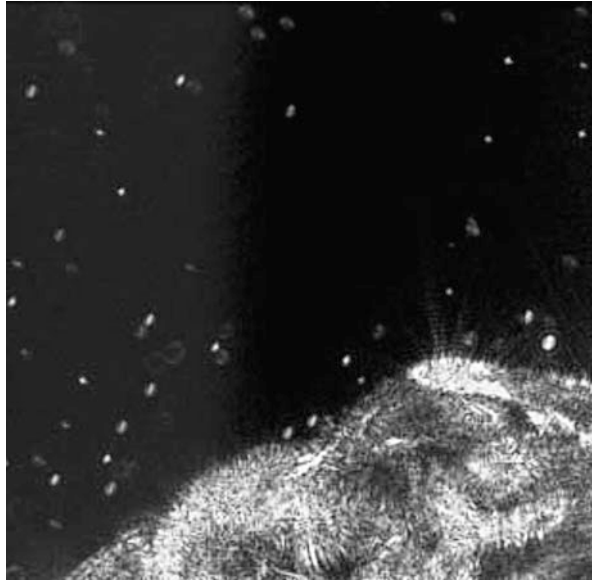
Solute Partitioning Between Mist and the Mother Solution

Unlike atomization of whole liquid from a thin layer on the surface of vibrating plates, the mist produced from thick liquid potentially contains matters at different composition from the mother liquid. When the liquid was a solution, partitioning of the solute could be found between the mist and the mother solution, which is a basic principle of separation. In this aspect, Rassokhin [27] firstly reported the selective
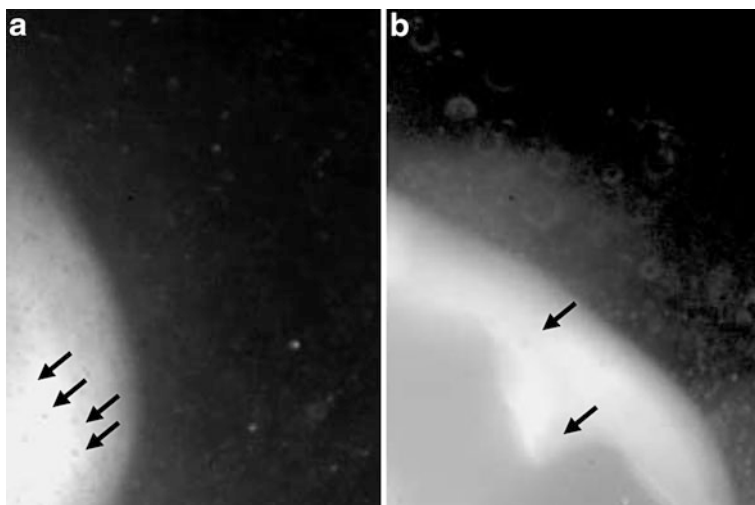
Fig. 5 Images where atomized droplets are visible together with bubbles, corresponding to dark spots (pointed by arrows), in the interior of the nonatomized water [25]. Copyright (2002) Springer

transport of a surfactant from the aqueous solution to mist produced by irradiating 724 kHz ultrasound. He successfully collected the mist and found that the surfactant concentration was as high as ten times of that for the mother solution. Takaya et al. [28] also reported the enrichment of surfactants in droplets ultrasonically atomized at 2.4 MHz which is higher than the above experiment. The enrichment ratio reached 5.2. Both ionic and nonionic surfactant showed a trend of increasing enrichment with decreasing surfactant concentration. In a system containing an anionic surfactant solution, salt addition changed dramatically the enrichment ratio from 1.6 to 4 due to the lowering of surface tension. The result indicates that the surface adsorption plays an essential role in the separation with ultrasonic atomization. To interpret this solute enrichment, Rassokhin [27] presented a droplet model, where the surfactant is adsorbed on the surface at its equilibrium condition, while the volume is occupied by the bulk solution. Jimmy et al. [29] carefully evaluated the model by predicting the enrichment with the observation of droplet diameter distribution. The calculated surfactant concentration was greater than the observed ones due to the partial achievement of adsorption equilibrium, surface excess. Comparison of diffusion time of the surfactant and the time for the wave propagation indicated that the surfactant enrichment is kinetically controlled [30].

Solutes of less surface activity than surfactants are also enriched in the mist produced by ultrasonic atomization. Suzuki et al. [31] reported that amino acids are concentrated in mist from aqueous solutions. Fuse et al. [32, 33] studied atomization of fuels for efficient combustion. When the fuels contained polar substances like ethanol or isopropanol, they found that enrichment of alcohols in the mist occurred from those tetradecane solutions. Surface excess of alcohols was assumed to be the reason for the enrichment. Yasuda et al. [15] conducted a

systematic study of alcohol enrichment from aqueous solutions. Methanol, ethanol, and 1-propanol were concentrated in the mist produced with irradiating 2.4 MHz. The alcohol content in the mist was in the order of 1-propanol > ethanol > methanol. It should be noted that the analysis of alcohol concentration was made with a mass balance.

Ethanol separation from the aqueous solution is a major subject of chemical engineering as well as solution chemistry because of the strong practical demand of its purification from azeotropic mixture with lower input energy. Sato et al. [34] presented a remarkable enrichment of ethanol in the mist produced with ultrasonic atomization from the aqueous solution. Under reduced temperature of 283 K, the mist contains almost pure ethanol from a feedstock whose ethanol concentration ranges from 7 % to 100 %. Significantly, the result indicates the possibility of breaking azeotrope with a simple technique. This finding triggered interests to elucidate separation mechanism and to develop practical applications. Due to the complexity in the phenomenon of atomization as well as the solution property of ethanol and water mixture, the separation mechanism is still under discussion. The practical application seems to be limited to high-value products because of the technical difficulty in the mist collection at production scale. Production of a premium grade Japanese rice wine from a feedstock of the normal grade has been carried out since 2003 [35]. The product is an ultrasonically atomized Japanese rice wine, which contains rich aroma and ethanol in comparison with the ones in ordinary grade. Since much less heat is applied than ordinary distillation, the flavors are retained in the atomized rice wine. There should be many opportunities to spark the idea for practical application of ultrasonic atomization (Figs. 6, 7, 8, and 9).

It has been pointed out that Sato's report is lacking of both direct analysis of ethanol concentration in the mist and experimental conditions such as operation time, solution volume, and the size of the container. Conditions that allow the remarkable enrichment have been carefully examined. They chose a high flow rate of air as a carrier gas, 25 L/min, temperature at 283 K, and the open system which makes the mist collection difficult. Interestingly, Matsuura [36], a coauthor of Sato's report [34], had reported only a slight enrichment of ethanol in the closed system shown below. It should be noted that collected mist was directly analyzed to determine ethanol concentrations.

In their experimental setup, the gas flows in the circulation mode to enhance the mist collection. No information of gas flow rate was given but it could not be as high as 25 L/min. The result showed a stark contrast of Sato's result. Even at 283 K, the enrichment is less remarkable. The atmosphere where atomization occurs may influence ethanol enrichment in the mist. When the mist was collected during the experiment, results similar to Matsuura's work have been published [37–40]. Particularly, Suzuki et al. [38–40] conducted experiment on the condition that mass balance was attained between atomized solution and the mist recovered. Under lower carrier gas flow rate, the degree of enrichment seems to be less remarkable than the Sato's report. Type of the carrier gas is also an important issue for

Fig. 6 Experimental setup of ultrasonic separation of ethanol from ethanol–water solution. Air flows one through the reservoir [34]. Copyright (2001) ACS publications

Oscillator

Air flow

Mist, vapor

Capillary waves

Ultrasonic vibrator (2.3 MHz)

Ethanol-water solution
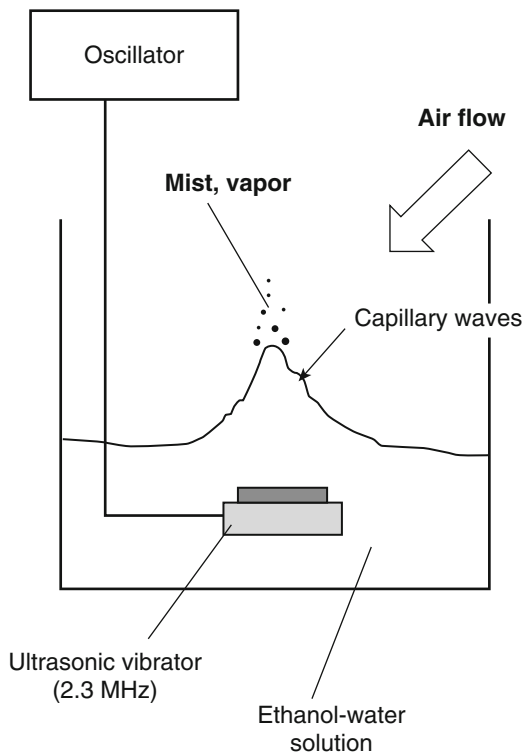
Fig. 7 Ethanol separation characteristics of ethanol–water solution. The horizontal axis is the concentration of ethanol in the aqueous solution and the vertical axis is the concentration in mist or vapor. The solid curve indicates the vapor–liquid equilibrium of ethanol–water solution under 101.3 kPa [34]. Copyright (2001) ACS publications

O 10°C ● 30°C □ 50°C

Ethanol mol concentration in mist (mol.%)

Ethanol mol concentration in solution (mol.%)
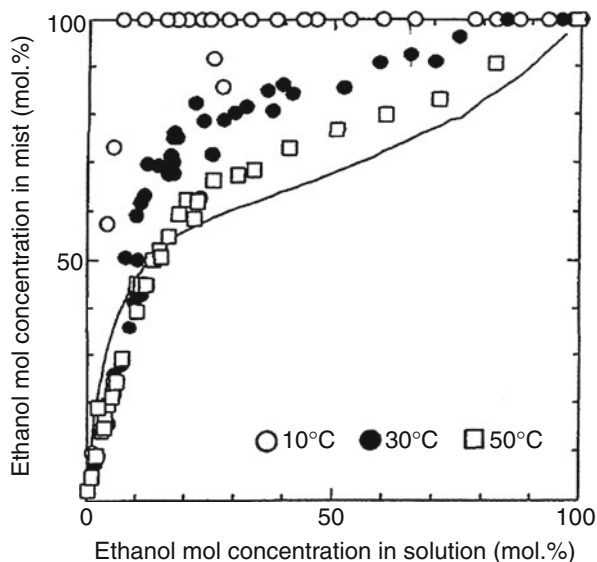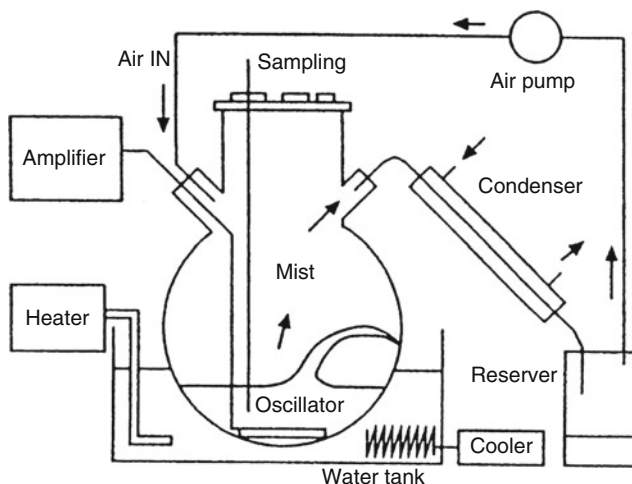
Fig. 8 Experimental setup of ultrasonic separation of ethanol from ethanol–water solution. Ultrasonic frequency is 1.6 or 2.3 MHz. Air is circulated in the system [36]. Copyright (1995) Society of Chemical Engineers Japan

Fig. 9 Ethanol separation characteristics of ethanol–water solution. Solid and dotted curve show the isobaric and the isothermal equilibrium curve, respectively. Closed circle: 283 K and 2.3 MHz, open circle: 303 K and 2. 3 MHz, closed triangle: 323 K and 2.3 MHz, and open triangle: 303 K and 1.6 MHz [36]. Copyright (1995) Society of Chemical Engineers Japan
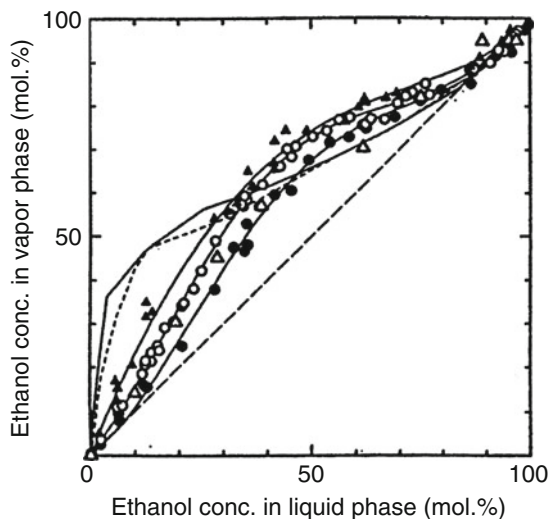
discussion. Spotar et al. [41] pointed out a possibility of condensing water vapor which was brought in the atomization column with supplying an air as a carrier gas. The accompanying of water lowers the concentration of ethanol in bulk solution as well as the selective transfer of ethanol from bulk solution to mist. Thus, the dilution effect results in overestimating the enrichment. They supplied dry nitrogen at

4–7.5 L/min to evaluate the performance of ethanol separation from water by using ultrasonic atomization and found that lower enrichment for hypothetical ethanol concentration in mist as well as for the mist recovered. Recently, Yasuda et al. [42] published a supporting data of remarkable enrichment of ethanol in droplets ultrasonically atomized by supplying dry nitrogen as a carrier gas at a high flow rate of 20 L/min. Despite the indirect analysis of the mist, their result showed that formation of droplet containing nearly 100 mol% ethanol from the feed aqueous solution of 60 mol%. A potential of enriching ethanol was ascertained even through rather short operation time of 5 min. As was pointed out by Spotar et al. [41], giving a carrier gas at such a high flow rate of 20 L/min makes difficult to recover product because of the high dilution and low cooling efficiency of gas. Thus, the product recovery is a major problem for the realization of the process. Nevertheless, further research should be conducted for elucidating the fundamental phenomena of ethanol separation.

Possible Mechanism for Ethanol Separation

Despite the fact that experimental observation shows a variation in the degree of ethanol enrichment, the separation mechanism is a center of interest of researchers. Complexity of the problem is due to the volatility of ethanol. Atomization of aqueous ethanol solution enhances the vaporization of ethanol because of the enlargement of surface area. When the vaporization occurs in a closed vessel and no foreign gas is in the vapor, ethanol concentration in the vapor reaches equilibrium at prevailing temperature and pressure. Thus, the benchmark of ethanol enrichment has been taken as vapor liquid equilibrium, VLE, for mixtures of ethanol and water. When the atomization increased ethanol concentration in the gas phase higher than the equilibrium concentration, there is a technical advantage in ultrasonic atomization than distillation. Therefore, possible routes for preferential transfer of ethanol than evaporation have been explored. Sato et al. [34] firstly supposed that droplets formation which are highly enriched with ethanol. Such droplets formed from the surface layer where ethanol is preferentially adsorbed. The point of discussion is the possibility of the presence of mist nearly pure ethanol.

It has been well known that the surface excess of ethanol occurs in ethanol and water mixture; however, the thickness of the layer is not as high as several molecules [43–45]. Yano et al. [16] have observed one nanometer-scale droplets from the mist of aqueous ethanol solution with a small angle X-ray diffraction method. The report shows one aspect of the mist. As discussed above, different observation method provides a different size of the mist. By using a laser diffraction technique, researchers also observed micrometer-scale droplets. Which distribution shows the actual property of the droplets is still a central problem in the discussion of separation mechanism. Yano et al. [16] speculated the fine nanometer-scale mist is enriched with ethanol. Wakisaka et al. [46] suggested that formation of clusters enriching with ethanol occurred in bulk solution, and on the basis of Yano's data, they assumed that the clusters were brought into the gas phase.

It is no doubt that atomization occurs at surface of liquids, bubble surface can also play a significant role in the enrichment. Researchers who support cavitation theory or conjunctive theory take this viewpoint. Kirpalani and Toll [37] proposed a hypothesis that ethanol selectively vaporizes inside bubbles through the bubble surface where ethanol is enriched during the traveling of microbubble clouds and the bubble collapse helps to form ethanol-rich mist. Suzuki et al. [47] attempted to evaluate their assumption quantitatively and developed a method to predict the ratio of liquid to vapor in the atomization product. They used salts as nonvolatile tracer to determine the amount of mist formation. Bubble and droplet model were proposed and bubbles of micrometer size can contribute ethanol enrichment. When surface excess layer in the bubbles were somehow brought into droplets, or there was ethanol evaporation from the layer, the ethanol enrichment could occur. Although we are still far from getting a clear picture of this enrichment, such a quantitative approach provided a step for the elucidation. Bubble surface might not be neat. It may be disturbed enough for giving very fine drops inside. Suslick's group [48, 49] proposed the formation of nanodroplets inside the bubbles. They have reported some supporting experimental results at ultrasonic frequencies lower than MHz region widely used for atomization. The finding may add a promising route to ethanol enrichment; however, the possibility should be carefully examined because of a large difference in conditions of timescale and size (Figs. 10, 11, and 12).

The idea of ultrasonically assisted distillation was further studied by Mahdi et al. [50] to intensify the separation of azeotropic mixture, which requires additional implements and operations for the distillation. They pointed out that micro-point vacuum condition is generated during bubbles formation and the change leads to alter the vapor composition inside bubbles. A mathematical model was developed and it was validated with comparing the prediction with experimental data for the
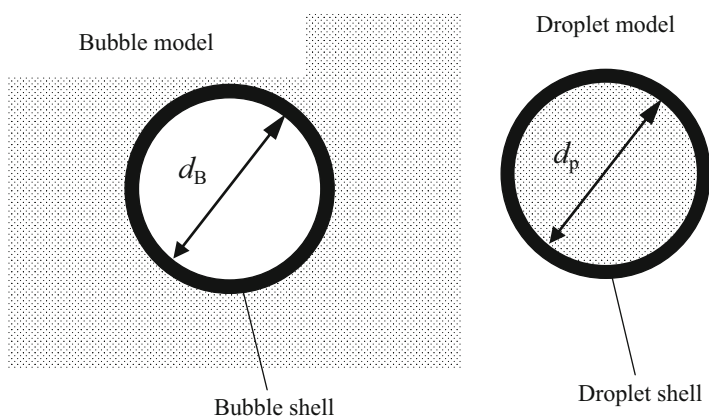
Fig. 10 Scheme of bubble and droplet model for ethanol separation from ethanol and water mixture [47]. Copyright (1995) Society of Chemical Engineers Japan
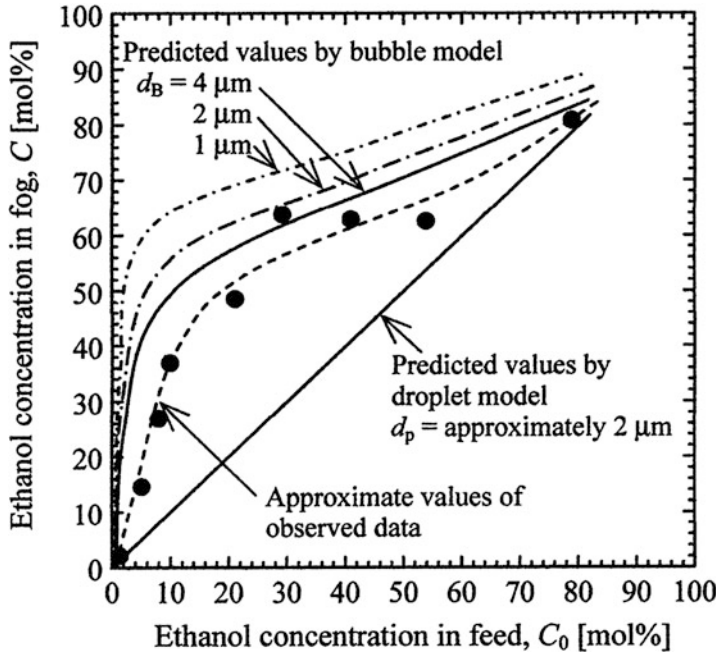
Fig. 11 Comparison of observed ethanol concentration in fog and predicted values by bubble or droplet model [47]. Copyright (1995) Society of Chemical Engineers Japan

Fig. 12 Scheme of injected droplet model in bubbles. Microdroplets of liquid are nebulized into the interior of bubbles by capillary waves on or microjets from bubble surface [48]. Copyright (2007) APS
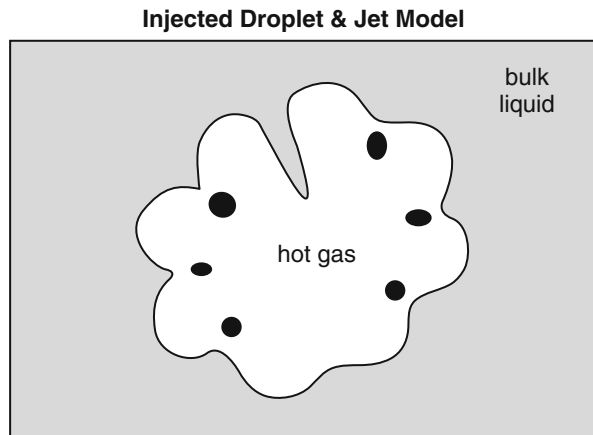
system of ethanol and ethyl acetate. The calculation indicated the elimination of azeotropic point. Though the benefit of reducing pressure to avoid azeotropic point is well known, this work presented the possibility of ultrasound in realizing the condition at ambient pressure.

Application of Mist for Transferring Solids to Gas Phase

With taking the advantage of well-controlled size and narrow size distribution of droplets, solid suspension was ultrasonically atomized to separate a specific particle or to provide a large surface area for VOC degradation. In this type of application, mist droplets work as a container to accommodate the target particle. Komatsu et al. [51, 52] found that ultrasonic atomization of a suspension of carbon nanotubes having different shapes of string, ring, and coil successfully enhanced the isolation of ring and coil carbon nanotubes. They were transferred into gas phase with the help of mist and carrier gas and then accumulated in the mist collection vessel. The size of those nanotubes was several hundred nanometers. It was speculated that droplets of a specific size accommodated those nanotubes. In this case, the mist recognizes the shape of solid.

Sekiguchi et al. [18, 53] reported that applying mist containing fine TiO_2 solid for enhancing photocatalytic decomposition of volatile organic compounds. When TiO_2 was brought into the mist, the working area for the photocatalyst was increased dramatically (Fig. 13).

In addition to the degradation of VOCs, complete capture of water-soluble intermediates was also achieved. This fact means that water also worked as a medium for reactions.

Nii et al. [54, 55] have shown that solid particles of a few hundred nanometers were separated from suspension with the help of ultrasonic atomization. Mixtures of
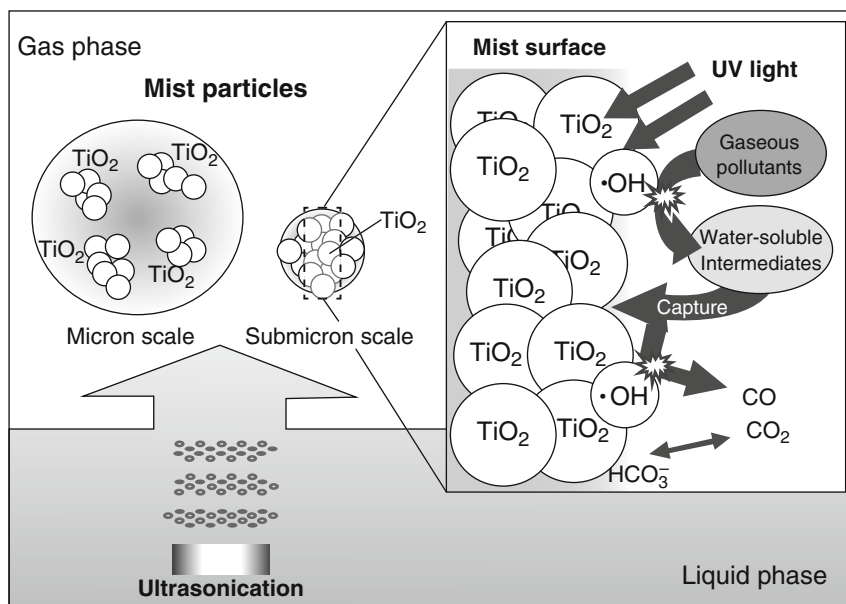
Fig. 13 Proposed mechanism for degradation of organic gases on ultrasonic mist containing TiO_2 particle, UMP surface [18]. Copyright (2010) Elsevier

different sizes SiO_2 or PS latex were suspended in water, and ultrasonically atomized mist was collected for analyzing the particle size. The size of collected particles fell in the limited range of diameter without depending on the type of solid. Interestingly, particles smaller than the range were not transferred into mist. Thus, mist recognizes size of particles of a few hundred nanometers. Moreover, the recognition ability of the mist diminished when the suspension was degassed. The fact demonstrates that cavitation plays a significant role in the size recognition of mist. It is a clue for solving such a complicated puzzle of the mechanism of particle size recognition of mist and even the atomization mechanism itself.

Application of Mist for Preparing Nanoparticles

Ultrasonic atomization has played a key role in fabrication of functional nanometer-sized particles. Ultrasonic spray pyrolysis, USP, is essential in the production of metal and metal oxides [10, 56–60] or carbon [61, 62], which are applied to electronic devices, electrodes for lithium and solar batteries, fuel cells, semiconductors, and capacitors. Better performance of these materials relies on particle properties, particle size, size distribution, and morphology. In USP processing, precursor solution is ultrasonically atomized to produce highly ordered droplets whose size and size distribution is tightly controlled. Ultrasonic frequency of 1.6, 1.7, and 2.4 MHz are generally used because of the high availability of the equipment, humidifier, or inhaler. The droplets are brought into tube furnace accompanied by the flow of carrier gas, where the droplets get pyrolysis. Since the process is operated continuously, controlling the mass and heat transfer is easier than the batch process. Because it is the solution process, there is a high flexibility in changing the composition of precursor and the residence time of droplets in the furnace. Furthermore, uniformity of the droplet diameter directly results in the homogeneous size and composition of the solid particle because of the uniformity of heat transfer. Advantages of UPS are enhancement in uniformity of the resulting particle size and size distribution and high flexibility in tuning the preparation condition. Drawbacks seem to be a limitation of viscosity of precursor solution to obtain a proper amount of mist and a difficulty in scaling up of the apparatus. To cope with the latter problem, one can take a numbering-up strategy. The number of publication on fabrication of nanoparticles is sharply increasing.

Early publication deals with producing metal oxides [56] from nitrate precursors due to the lower temperature for the decomposition. The trend developed from simple oxides to complex oxides with high crystallinity [57], which is utilized for electrode materials. In addition to producing solid particles, products were further processed to "ink" and used to coat substrate to prepare films such as flexible transistors and optoelectronic devices [59]. Recently, a dry processing was proposed [58] to coat the fiber surface with nanometer-sized MnO_2, where effluent from the tube furnace was directly sprayed on carbon fiber paper. SEM observation showed the fiber coated with MnO_2 fine particles.

Conclusions

This chapter illustrated some basic aspects of ultrasonic atomization as well as applications of separations for ethanol and solid particles, and even of reactions. Before the finding of surfactant or ethanol enrichment in the mist, the method has been only recognized as simply breaking up liquid into ordered size. It was an innovation to create a new value of ultrasonic atomization. As discussed above, there is still much room to explore in this phenomenon. Like most of the ultrasonic technique, scaling up to a practical stage requires big challenges to overcome problems in the low production amount per input power. However, turning our eyes to miniature-scale processing, atomization can enable spot transfer of target matters by taking advantage of simplicity in controlling the atomization amount, finely-tuned size of droplet, and matters selectively accommodated in the droplet. Researchers are welcomed to intensify knowledge for deeper understanding and various application of ultrasonic atomization.

References

1. Wood WR, Loomis AL (1927) The physical and biological effects of high-frequency sound-waves of great intensity. Philos Mag 7:417–436
2. Rajan R, Pandit AB (2001) Correlations to predict droplet size in ultrasonic atomization. Ultrasonics 39:235–255
3. Dobre M, Bolle L (2002) Practical design of ultrasonic spray devices; experimental testing of several atomizer geometries. Exp Therm Fluid Sci 26:205–211
4. Avvaru B, Patil MN, Gogate PR, Pandit AB (2006) Ultrasonic atomization: effect of liquid phase properties. Ultrasonics 44:146–158
5. Donnelly TD, Hogan J, Mugler A, Schommer N, Schnbmehl M, Bernoff AJ, Forrest B (2004) An experimental study of micron-scale droplet aerosols produced via ultrasonic atomization. Phys Fluids 16:2843–2851
6. Topp MN, Eisenklam P (1972) Industrial and medical uses of ultrasonic atomizers. Ultrasonics 10:127–133
7. Qi A, Friend J, Yeo L, Morton D, McIntosh M, Spiccia L (2009) Miniature inhalation therapy platform using surface acoustic wave microfluidic atomization. Lab Chip 9:2184–2193
8. Rajapaksa A, Ho J, Qi A, Bischof R, Nguyen TH, Tate M, Piedrafita D, McIntosh MP, Yeo L, Meeusen E, Coppel R, Friend JR (2014) Effective pulmonary delivery of an aerosolized plasmid DNA vaccine via surface acoustic wave nebulization. Respir Res 15:60
9. Ogihara T, Ookura T, Yanagawa T, Ogata N, Yoshida K (1991) Preparation of submicrometer spherical oxide powders and fibers by thermal spray decomposition using an ultrasonic mist atomizer. J Mater Chem 1:789–794
10. Suh WH, Suslick KS (2005) Magnetic and porous nanospheres from ultrasonic spray pyrolysis. J Am Chem Soc 127:12007–12010
11. Inukai A, Sakamoto N, Aono H, Sakurai O, Shinozaki K, Suzuki H, Wakiya N (2011) Synthesis and hyperthermia property of hydroxyapatite–ferrite hybrid particles by ultrasonic spray pyrolysis. J Magn Magn Mater 323:965–969
12. Lang RJ (1962) Ultrasonic atomization of liquids. J Acoust Soc Am 34:6–8
13. Lord Kelvin (Thomson W) (1871) On the equilibrium of vapor at a curved surface of liquid. Philos Mag 42:448–452

14. Rayleigh L (1892) On the instability of a cylinder of viscous liquid under capillary force. Philos Mag 34:145–154
15. Yasuda K, Bando Y, Yamaguchi S, Nakamura M, Oda A, Kawase Y (2005) Analysis of concentration characteristics in ultrasonic atomization by droplet diameter distribution. Ultrason Sonochem 12:37–41
16. Yano YF, Matsuura K, Fukazu T, Wakisaka A, Kobara H, Kaneko K, Kumagai A, Katsuya Y, Tanaka M (2007) Small-angle X-ray scattering measurement of a mist of ethanol nanodroplets: an approach to understanding ultrasonic separation of ethanol–water mixture. J Chem Phys 127:031101-1–031101-4
17. Kobara H, Tamiya M, Wakisaka A, Fukazu T, Matsuura K (2010) Relationship between the size of mist droplets and ethanol condensation efficiency at ultrasonic atomization on ethanol–water mixtures. AIChE J 56:810–814
18. Sekiguchi K, Noshiroya D, Handa M, Yamamoto K, Sakamoto K, Namiki N (2010) Degradation of organic gases using ultrasonic mist generated from TiO_2 suspension. Chemosphere 81:33–38
19. Sollner K (1936) The mechanism of the formation of fogs by ultrasonic waves. Trans Faraday Soc 32:1532–1536
20. Eknadiosyants OK (1968) Role of cavitation in the process of liquid atomization in an ultrasonic fountain. Sov Phys Acoust 14:107–111
21. Boguslavski YY, Eknadiosyants OK (1969) Physical mechanism of the acoustic atomization of a liquid. Sov Phys Acoust 15:14–21
22. Frohly J, Labouret S, Bruneel C, Looten-Baquet I, Torguet R (2000) Ultrasonic cavitation monitoring by acoustic noise power measurement. J Acoust Soc Am 108:2012–2020
23. Harada H, Iwata N, Shiratori K (2009) Observation of multibubble sonoluminescence from water saturated with various gases during ultrasonic atomization. Jpn J Appl Phys 48:07GH01-1–07GH01-4
24. Miller DL, Thomas RM (1993) Frequency dependence of cavitation activity in a rotation tube exposure system compared to the mechanical index. J Acoust Soc Am 93:3475–3480
25. Barreras F, Amaveda H, Lozano A (2002) Transient high frequency ultrasonic atomization. Exp Fluids 33:405–413
26. Tsuchiya K, Tanaka Y, Mori Y, Matsuura K (2009) Intensification of ultrasonic atomization process for ethanol separation and recovery. In: Proceedings of the 8th world congress of chemical engineering, Aug 23rd–27th 2009 Montreal, Paper no. 1795
27. Rassokhin DN (1998) Accumulation of surface-active solutes in the aerosol particles generated by ultrasound, J. Phys Chem B 102:4337–4341
28. Takaya H, Nii S, Kawaizumi F (2005) Enrichment of surfactant from its aqueous solution using ultrasonic atomization. Ultrason Sonochem 12:483–487
29. Jimmy B, Kentish S, Grieser F, Ashokkumar M (2008) Ultrasonic nebulization in aqueous solutions and the role of interfacial adsorption dynamics in surfactant enrichment. Langmuir 24:10133–10137
30. Jimmy B, Kentish S, Ashokkumar M (2011) Dynamics of counterion binding during acoustic nebulisation of surfactant solutions. Ultrason Sonochem 18:958–962
31. Suzuki A, Maruyama H, Seki H, Matsukawa Y, Inoue N (2006) Enrichment of amino acids by ultrasonic atomization. Ind Eng Chem Res 45:830–833
32. Fuse T, Kobayashi N, Hasatani M (2003) Performance of flammability and NO_x emission in premixed oil burner using ultrasonic atomization. J Chem Eng Jpn 36:852–859
33. Fuse T, Hirota Y, Kobayashi N, Hasatani M (2005) Characteristics of selective atomization of polar/nonpolar substances in an oleosus solvent with ultrasonic irradiation. J Chem Eng Jpn 38:67–73
34. Sato M, Matsuura K, Fujii T (2001) Ethanol separation from ethanol–water solution by ultrasonic atomization and its proposed mechanism based on parametric decay instability of capillary wave. J Chem Phys 114:2382–2386

35. Nii S, Matsuura K, Fukazu T, Toki M, Kawaizumi F (2006) A novel method to separate organic compounds through ultrasonic atomization. Chem Eng Res Des 84:412–415

36. Matsuura K, Kobayashi M, Hirotsune M, Sato M, Sasaki H, Shimizu K (1995) New separation technique under normal temperature and pressure using ultrasonic atomization. Jpn Soc Chem Eng Symp Series 46:44–49

37. Kirpalani DM, Toll F (2002) Revealing the physicochemical mechanism for ultrasonic separation of alcohol–water mixtures. J Chem Phys 117:3874–3877

38. Suzuki K, Kirpalani DM, Nii S (2011) Influence of cavitation on ethanol enrichment in an ultrasonic atomization system. J Chem Eng Jpn 44:616–622

39. Suzuki K, Kirpalani DM, McCracken TW (2006) Experimental investigation of ethanol enrichment behavior in batch and continuous feed ultrasonic atomization systems. Chem Eng Technol 29:44–49

40. Suzuki K, McCracken TW, Kirpalani DM (2008) Perspectives on intensification of ethanol-water separation process in a high frequency ultrasound system. J Chem Eng Jpn 41:855–861

41. Spotar S, Rahman A, Gee OC, Jun KK, Manickam S (2015) A revisit to the separation of a binary mixture of ethanol-water using ultrasonic distillation as a separation process. Chem Eng Process 87:45–50

42. Yasuda K, Mochida K, Asakura Y, Koda S (2014) Separation characteristics of alcohol from aqueous solution by ultrasonic atomization. Ultrason Sonochem 21:2026–2031

43. Li ZX, Lu JR, Styrkas DA, Thomas RK, Rennie AR, Penfold J (1993) The structure of the surface of ethanol-water mixtures. Mol Phys 80:925–939

44. Yano YF (2005) Correlation between surface and bulk structures alcohol-water mixtures. J Colloid Interface Sci 284:255–259

45. Bermudez-Salguero C, Gracia-Fadrique J (2015) Gibbs excess and the calculation of the absolute surface composition of liquid binary mixtures. J Phys Chem B 119:5598–5608

46. Wakisaka A, Matsuura K (2006) Microheterogeneity of ethanol–water binary mixtures observed at the cluster level. J Mol Liq 129:25–32

47. Suzuki K, Arashi K, Nii S (2012) Determination of droplet and vapor ratio of ultrasonically-atomized aqueous ethanol solution. J Chem Eng Jpn 45:337–342

48. Flannigan DJ, Suslick KS (2007) Emission from electronically excited metal atoms during single-bubble sonoluminescence. Phys Rev Lett 99:134301

49. Xu H, Eddingsaaas NC, Suslick KS (2009) Spatial separation of cavitating bubble populations: the nanodroplet injection model. J Am Chem Soc 131:6060–6061

50. Mahdi T, Ahmad A, Ripin A, Abdullah TAT, Nasef MM, Ali MW (2015) Mathematical modeling of a single stage ultrasonically assisted distillation process. Ultrason Sonochem 24:184–192

51. Komatsu N, Shimawaki T, Aonuma S, Kimura T (2006) Ultrasonic isolation of toroidal aggregates of single-walled carbon nano tubes. Carbon 44:2091–2093

52. Komatsu N (2009) Novel and practical separation processes for fullerenes, carbon nanotubes and nanodiamonds. J Jpn Pet Inst 52:73–80

53. Sekiguchi K, Yamamoto K, Sakamoto K (2008) Photocatalytic degradation of gaseous toluene in an ultrasonic mist containing TiO_2 particles. Cata Commun 9:281–285

54. Suzuki K, Hisaeda J, Nii S (2012) Application of ultrasonic atomization for fractionating particles in suspensions. J Chem Eng Japan 45:114–118

55. Nii S, Oka N (2014) Size-selective separation of submicron particles in suspensions with ultrasonic atomization. Ultrason Sonochem 21:2032–2036

56. Messing GL, Zhang S-C, Jayanthi GV (1993) Ceramic powder synthesis by spray pyrolysis. J Am Ceram Soc 76:2707–2726

57. Kinoshita T, Adachi M (2015) Submicron particle synthesis of $Gd_{0.1}Ce_{0.9}O_{1.95}$, NiO–$Gd_{0.1}Ce_{0.9}O_{1.95}$ and $La_{0.8}Sr_{0.2}CoO_3$ by ultrasonic spray pyrolysis. J Chem Eng Japan 48:238–244

58. Zhang Y, Huff LA, Gewirth AA, Suslick KS (2015) Synthesis of manganese oxide microspheres by ultrasonic spray pyrolysis and their application as supercapacitors. Part Part Syst Charact 32:899–906
59. Guo Y-X, Wu P, Cheng W-J (2015) Effect of boron doping on the optoelectronic properties of nanostructure SnO_2 thin film by ultrasonic spray pyrolysis on quartz substrate. J Mater Sci: Mater Electron 26:4922–4929
60. Das H, Sakamoto N, Aono H, Shinozaki K, Suzuki H, Wakiya N (2015) Investigations of superparamagnetism in magnesium ferrite nano-sphere synthesized by ultrasonic spray pyrolysis technique for hyperthermia application. J Magn Magn Mater 392:91–100
61. Skrabalak SE, Suslick KS (2006) Porous carbon powders prepared by ultrasonic spray pyrolysis. J Am Chem Soc 128:12642–12643
62. Arif AF, Balgis R, Ogi T, Mori T, Okuyama K (2015) Experimental and theoretical approach to evaluation of nanostructured carbon particles derived from phenolic resin via spray pyrolysis. Chem Eng J 271:79–86

Unsolved Problems in Acoustic Cavitation

Kyuichi Yasui

Contents

Abstract

It has long been believed that the main oxidant created inside a bubble at the bubble collapse in aqueous solutions under strong ultrasound is OH radical. However, numerical simulations of chemical reactions inside an air bubble in water indicate that the main oxidant is not always OH radical but sometimes H$_2$O$_2$ or O atom. The lifetime of O atom in the gas–liquid interface region is, however, unknown partly due to unknown temperature in the region. It has been experimentally reported that the upper levels of OH vibration are overpopulated inside a sonoluminescing bubble compared to the equilibrium Boltzmann distribution from the analysis of OH line spectra in SL. However, the reason is unknown although it could be due to the excitation through chemical reactions. The acoustic field inside a sonochemical reactor is also not fully understood because bubbles strongly attenuate ultrasound and radiate acoustic waves into the liquid. The spatial distribution of bubbles is strongly inhomogeneous. The number density of bubbles temporally changes due to fragmentation, coalescence, and dissolution. The liquid surface vibrates under ultrasound. The vibration of the container's wall also affects the acoustic field because acoustic waves are radiated

K. Yasui (✉)
National Institute of Advanced Industrial Science and Technology (AIST), Nagoya, Japan
e-mail: k.yasui@aist.go.jp

from the vibrating walls. The bubble–bubble interaction on pulsation of a bubble is also discussed.

Introduction

Ultrasonics are inaudible sound with its vibration frequency greater than 20 kHz (sometimes, the sound with its vibration frequency greater than 10 kHz is called ultrasonics for convenience). An acoustic wave (a sound wave) is a propagation of pressure oscillation in the medium with the velocity of sound (Fig. 1) [1]. The sound velocity in liquid water is about 1500 m/s, while that in air is about 340 m/s.

When a liquid is irradiated by a strong ultrasonic wave, the instantaneous local pressure becomes negative at the rarefaction phase of the ultrasonic wave. The negative pressure is a tension to expand the liquid element, which never occurs in gas phase. When negative pressure occurs in liquid adjacent to a solid surface (especially hydrophobic surface), gas bubbles are created at the solid surface (solid surface could be that of motes or dust particles in solution). Bubbles are more easily created at crevices of the solid, because inside a crevice the gas–liquid interface is concave with regard to the gas phase. Then the Laplace pressure caused by the
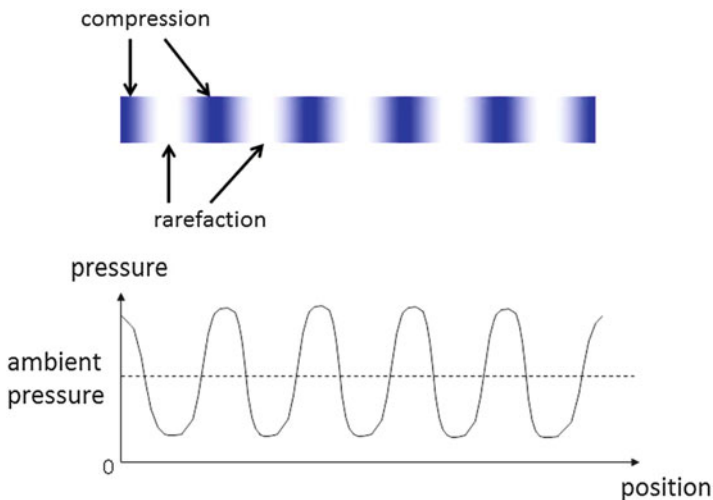
Fig. 1 An acoustic wave (Reprinted with permission from Yasui et al. [1]. Copyright (2004) by Taylor & Francis [http://www.informaworld.com])

surface tension *reduces* the internal gas pressure. Thus the dissolution of gas into the surrounding liquid is strongly retarded, and gas diffuses into the gas pocket in the crevice at the rarefaction phase of ultrasound due to the expansion of the gas pocket and decrease in the gas pressure [2].

Created bubbles repeat expansion and collapse according to the pressure oscillation of ultrasound. Sometimes the bubble collapse becomes very violent because of the spherically converging geometry and the inertia of the inwardly moving liquid [2]. The speed of such bubble collapse increases up to the sound velocity in the liquid near the bubble wall [3]. Such the bubble collapse is called the Rayleigh collapse. The creation and collapse of bubbles under ultrasound is called acoustic cavitation.

At the end of the Rayleigh collapse, the temperature and pressure inside a bubble dramatically increase up to a few thousand Kelvin and a few thousand atmospheric pressure or more, respectively. It is because the work done on a bubble by the surrounding liquid during the bubble collapse is mostly converted into the thermal energy inside a bubble as the bubble collapse is so fast that thermal conduction between the heated interior of the bubble and the surrounding liquid is not dominant. As a result, water vapor and oxygen gas (if present) are dissociated inside the heated interior of a bubble. Then, oxidants such as OH radicals, O atoms, H_2O_2, and O_3 are created inside a bubble. The oxidants diffuse out of the bubble into the surrounding liquid, and solutes such as pollutants are oxidized by them. Such chemistry is called sonochemistry. In addition, a faint light is emitted from a bubble as a pulse due to the high temperature, which is called sonoluminescence.

In the present chapter, mainly three topics are discussed focusing on unsolved problems in this field. One is the main oxidants created inside a bubble in water. Numerical simulations have indicated that not only OH radicals and H_2O_2 but also an appreciable amount of O atoms are created inside an air bubble. However, the lifetime of O atom in liquid water as well as its role in sonochemical reactions is unknown at present. Another is OH line emission in sonoluminescence. The topic is on the non-Boltzmann distribution of the vibrational population of OH radicals. Is it due to the nonequilibrium state of gas inside a bubble? Is it due to chemical excitation of vibrational states of OH radicals? (Is OH line emission originated in chemiluminescence?) The other is on an acoustic field. What is the influence of the attenuation of an acoustic wave due to bubbles on an acoustic field? How about the influence of acoustic radiation from vibrating walls of a container?

Main Oxidants (OH Radical, H_2O_2, and O Atom)

The main oxidant created inside a bubble in water under ultrasound has long been believed as OH radical [4]. Here we discuss that the main oxidant is not always OH radical but sometimes O atom and H_2O_2. In Figs. 2 and 3, the results of the numerical simulation of the pulsation of an isolated spherical air bubble in water irradiated with 300 kHz and 3-bar ultrasound are shown [5]. A bubble expands during the rarefaction phase of ultrasound and, violently, collapses during the initial compression
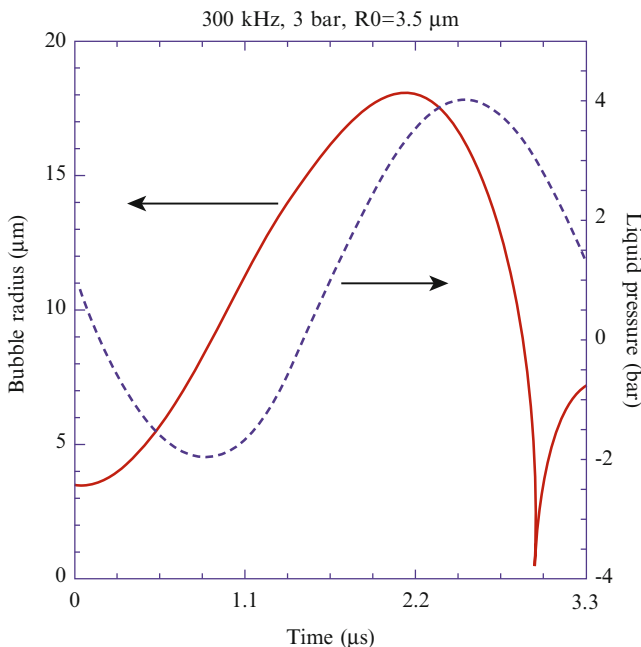
Fig. 2 The result of the numerical simulation on radius-time curve for one acoustic cycle (3.3 μs) when the frequency and pressure amplitude of an ultrasonic wave are 300 kHz and 3 bars, respectively. The ambient radius of an isolated spherical air bubble is 3.5 μm. The *dotted line* is the acoustic pressure (plus the ambient pressure) as a function of time (Reprinted with permission from Yasui et al. [5]. Copyright (2007), AIP Publishing LLC)

phase (Fig. 2). At the end of the bubble collapse (Rayleigh collapse), the temperature increases up to 5100 K (Fig. 3a). The density at the moment reaches 650 kg/m^3 which is in the same order of magnitude as that of the condensed phase (liquid density) (Fig. 3b). The pressure inside a bubble reaches 6×10^9 Pa (=6 GPa = 60,000 bar) at the moment. Most of water vapor and many of O_2 are dissociated inside the heated interior of a bubble, and many chemical products are created such as H_2O_2, HO_2, O, O_3, HNO_2, HNO_3, H_2, and OH radical (Fig. 3c). In this case, the main oxidant is H_2O_2 according to the numerical simulation. In the present numerical simulations, nonequilibrium effect of chemical reactions is taken into account. Rates of chemical reactions are calculated using the modified Arrhenius equations. Rates of backward reactions are also calculated. The chemical kinetic model used in the present simulations has been partially validated by hydrogen flame studies [6]. Furthermore, the present model of bubble dynamics including the chemical kinetic model has been validated by the study of single-bubble sonochemistry for which direct comparison between the numerical and experimental results is possible [7].

The results of many numerical simulations of chemical reactions inside an air bubble are summarized in Fig. 4 for various ultrasonic frequencies and pressure
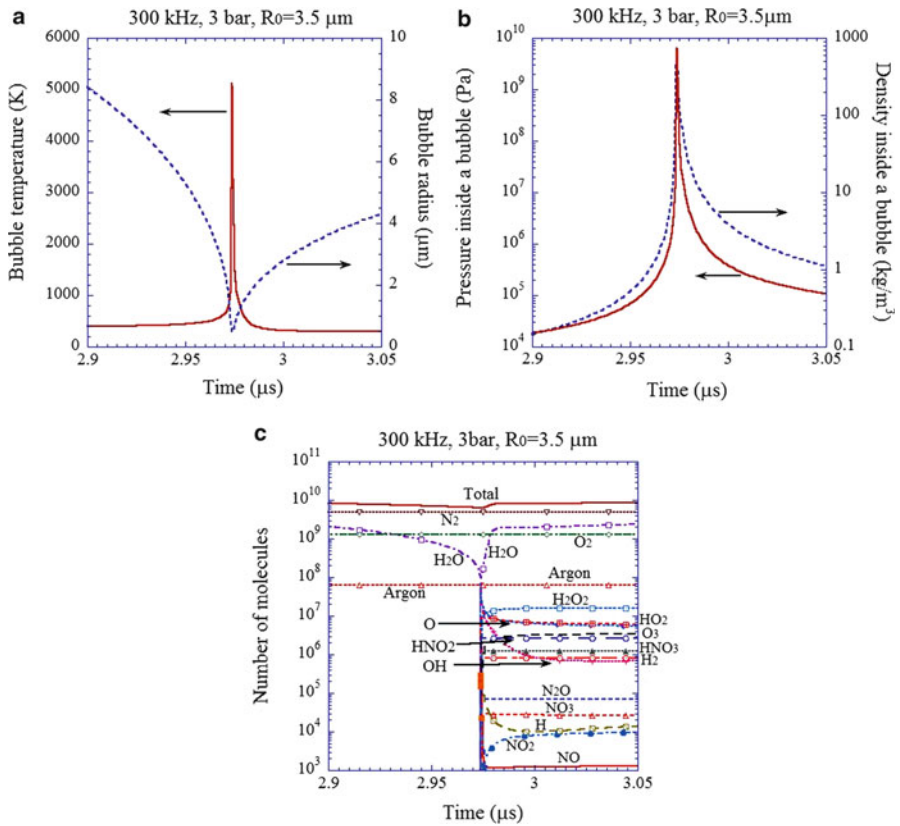
Fig. 3 The results of the numerical simulation under the condition of Fig. 2 at around the end of the bubble collapse. The horizontal time axis is only for 0.15 μs. (**a**) The bubble radius (*dotted line*) and the temperature inside a bubble (*solid line*). (**b**) The pressure (*solid line*) and the density (*dotted line*) inside a bubble with logarithmic vertical axes. (**c**) The number of molecules inside a bubble with logarithmic vertical axes. (Reprinted with permission from Yasui et al. [5]. Copyright (2007), AIP Publishing LLC)

amplitudes [5]. Rates of production of each oxidant as well as temperature inside an air bubble are shown as a function of acoustic amplitude. The ambient bubble radius, which is the bubble radius when ultrasound is absent, is assumed as 5 μm, 3.5 μm, 3.5 μm, and 1 μm for 20 kHz, 100 kHz, 300 kHz, and 1 MHz, respectively, as they are the typical values for each frequency.

For 20 kHz and 100 kHz, the bubble temperature takes a maximum value at relatively low acoustic amplitude and decreases as acoustic amplitude increases at relatively high acoustic amplitude. It is because the amount of water vapor inside a bubble increases due to larger expansion of a bubble [3]. Water vapor decreases the bubble temperature due to its endothermic dissociation as well as its larger molar heat than that of air. Thus we call a bubble filled mostly with water vapor a vaporous bubble, while a bubble with negligible amount of water vapor is called a gaseous
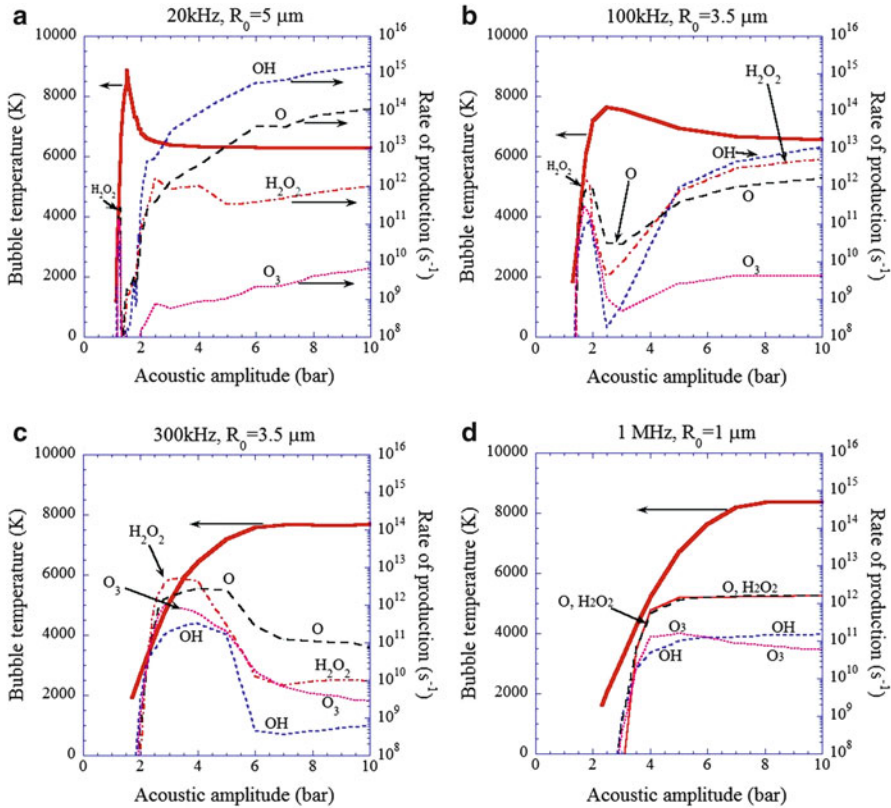
Fig. 4 The results of the numerical simulations on the rate of production of each oxidant inside an isolated air bubble per second estimated by the first bubble collapse as a function of acoustic amplitude with the temperature inside a bubble at the end of the bubble collapse (*the thick line*): (**a**) 20 kHz and $R_0 = 5$ μm. (**b**) 100 kHz and $R_0 = 3.5$ μm. (**c**) 300 kHz and $R_0 = 3.5$ μm. (**d**) 1 MHz and $R_0 = 1$ μm (Reprinted with permission from Yasui et al. [5]. Copyright (2007), AIP Publishing LLC)

bubble. Then the results in Fig. 4 are summarized as follows. For vaporous bubbles, the main oxidant is OH radical. For gaseous bubbles, on the other hand, the main oxidant is H_2O_2 when the bubble temperature at the collapse ranges from 4000 K to 6500 K. When the bubble temperature is higher than 6500 K in gaseous bubbles, the main oxidant is O atom. When the bubble temperature is higher than 7000 K, the oxidants are strongly consumed inside an air bubble by oxidizing nitrogen [8].

By the thermal dissociation of H_2O ($H_2O + M \rightarrow OH + H + M$, where M is the third molecule), the amount of H atoms is expected to be created by the same amount as that of OH radicals. However, the amount of OH radicals is much larger than that of H atoms (Fig. 3c). It is because the production of OH radicals is not only by the thermal dissociation of H_2O but also by the following reactions: $H_2O + O \rightarrow OH +$

Fig. 5 Experimental results
on the rate of production of
H_2O_2 in pure water and that of
I_2 in 1 M KI solution or 1 M
KI + 0.0005 M ammonium
molybdate solution under
various mixtures of argon and
oxygen dissolved in the
solution (Reprinted with
permission from Hart and
Henglein [9]. Copyright
(1985), American Chemical
Society)
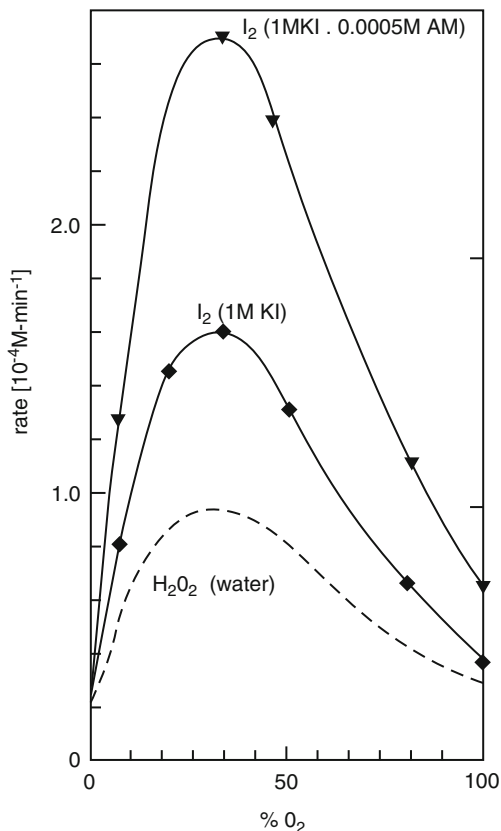
OH, $H_2O + H \rightarrow OH + H_2$ and $HO_2 + H \rightarrow OH + OH$ [7]. In addition, H atoms
are also consumed by the reaction $H + H \rightarrow H_2$.

In 1985, Hart and Henglein [9] suggested that the O atom created inside a bubble
may oxidize I^- ion in an aqueous KI solution in which the mixture of argon and O_2 is
dissolved. In their experimental results (Fig. 5), the amount of I_2 production in
aqueous KI solution ($2OH + 2I^- \rightarrow I_2 + 2OH^-$, and in the presence of ammonium
molybdate as catalyst $H_2O_2 + 2I^- \rightarrow I_2 + 2OH^-$), is considerably larger than that
of H_2O_2 in pure water ($2OH \rightarrow H_2O_2$). Thus they concluded that there should be
some oxidant other than OH radical and H_2O_2. They assumed that it is O atom
($O + 2I^- + 2H^+ \rightarrow I_2 + H_2O$). However, there has been no direct evidence on the
production of O atom in solution by cavitation bubbles.

Atomic oxygen (O atom) has eight electrons. Two of them are in the 1s orbitals.
Other two electrons are in the 2s orbitals. The rest of four electrons are in the 2p
orbitals when it is not highly excited (Fig. 6). The orbitals are characterized by the
quantum numbers n, l, m_l, and m_s, where n is the principal quantum number, l is the
orbital angular momentum, m_l is the magnetic quantum number, and m_s is the
secondary spin quantum number [10]. Orbitals are designated s, p, d, f, g
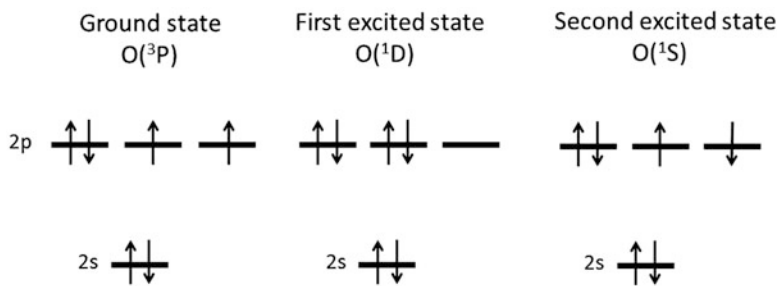
Fig. 6 Electronic configurations of ground state, first excited state, and second excited state of atomic oxygen. Two electrons in 1s state are omitted

corresponding to the orbital angular momentum $l = 0, 1, 2, 3, 4$, respectively. For an orbital with $n = 2$ and $l = 1$, it is called 2p orbital. For $n = 1$ and $l = 0$, it is 1s orbital. The number in front of the symbol for orbital angular momentum is the principal quantum number. The magnetic quantum number (m_l) can take the values of $-l$, $(-l + 1)$, ..., $(l-1)$, l. Thus for 2p orbital ($l = 1$), m_l can take the values of -1, 0, and 1. For each m_l state, two electrons can occupy (up-spin ($m_s = 1/2$) and down-spin ($m_s = -1/2$)).

When four electrons are in 2p orbitals, there are only three configurations as in Fig. 6 [11, 12]. According to Hund's first rule, the ground state is the configuration with the highest multiplicity. Only for the configuration at the left side in Fig. 6, the total spin angular momentum is nonzero ($S = \left| \sum m_s \right| = 1$). Thus, this corresponds to the ground state as the multiplicity is the highest as 3 (For the other two configurations, the multiplicity is 1). The total orbital angular momentum ($L = \sum l_i$ where the summation takes for all the electrons of O atom) can take the values of 0, 1, and 2 because the allowed values of the total angular momentum for the system of two angular momenta of j_1 and j_2 are $j = j_1 + j_2, j_1 + j_2-1, \ldots, |j_1-j_2|$ according to quantum mechanics [13]. It should be noted that the structure of two electrons in 2p orbitals is the same as that of four electrons in 2p orbitals because the structure of four electrons is equivalent to the closed-shell structure (six electrons in 2p orbitals as $L = S = 0$) minus the structure of two electrons in 2p orbitals [12]. The orbitals for $L = 0, 1, 2, 3, ..$ are referred to as S, P, D, F, .. [14]. When there are two parallel spin electrons as in the left side of Fig. 6, $L = 2$ is impossible due to Pauli's exclusion principle because the orbital angular momenta are also in parallel [15]. It is known that $L = 0$ is also impossible for this case due to Pauli's exclusion principle [12]. Thus, the ground state of O atom is for $L = 1$ and designated ^3P where the total spin angular momentum S is coded in the form of $2S + 1$ in the left superscript.

The first excited state of O atom is ^1D, because with the same multiplicity of 1 ($S = 0$) the configuration with the highest total orbital angular momentum (L) has the lowest energy (Fig. 6). For the first excited state, one of the 2p orbitals is empty. Thus, it is more easy to undergo bond-forming addition reactions than the ground
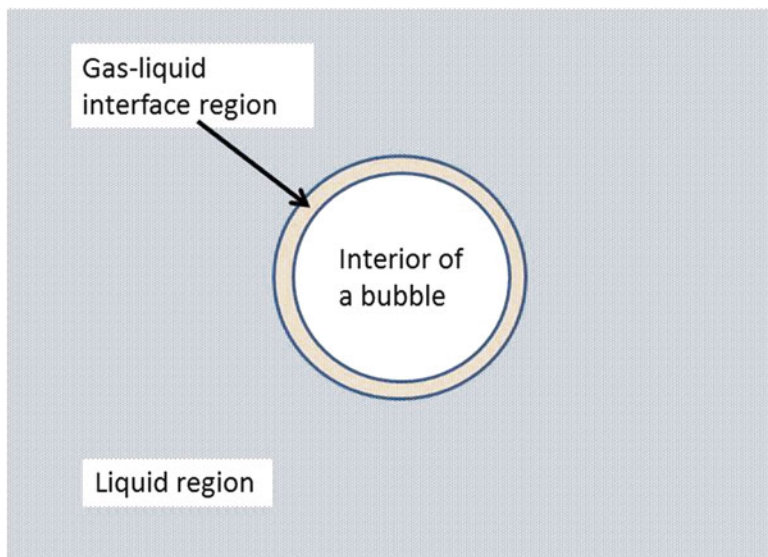
Fig. 7 Three regions for a cavitation bubble

state O atom. For example, the following reaction with water molecules is known to be very fast:

$$O(^1D) + H_2O \rightarrow H_2O_2. \tag{1}$$
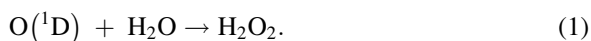
The rate constant for the reaction (1) with H_2O vapor is reported as $1.8 \pm 0.8 \times 10^{10}$ L/(mol s) [16]. If the rate constant is the same for the same reaction in liquid water, then the lifetime of $O(^1D)$ in liquid water is about 10^{-12} s $= 1$ ps. The diffusion length of O atom in this lifetime is only about 0.1 nm which is estimated by $2\sqrt{D\tau}$ where D is the diffusion coefficient of O atom in liquid water (10^9 m^2/s is assumed) and τ is the lifetime of O atom. Thus, $O(^1D)$ atom could be present only in the gas–liquid interface region of a bubble (Fig. 7).

On the other hand, the ground state $O(^3P)$ is a selective oxidant because it rather slowly reacts with molecules that have no unpaired electrons such as H_2O because such reactions violate the principle of spin conservation. With molecules that have unpaired electrons, $O(^3P)$ rapidly reacts. However, detailed reactivity and synthetic studies in solution are limited by lack of convenient and reliable methods for the generation and detection of $O(^3P)$ [17].

With regard to OH radical, the lifetime in solution is determined by the following reaction when the concentration of other solutes is not high:

$$OH + OH \rightarrow H_2O_2. \tag{2}$$

The rate constant is 5×10^9 L/(mol s). Thus the lifetime of OH radical in solution is determined by the concentration of OH radicals in this case. When [OH] is 5×10^{-3} mol/L [4], the lifetime of OH radical is 4×10^{-8}s $=$ 40 ns. When the concentration of other solutes is high, the lifetime of OH radical in solution is determined by the solute concentration. When it is 1 mol/L, the lifetime of OH radical in solution is 10^{-9}–10^{-8} s $=$ 1 ns – 10 ns because the rate constant is typically in the range of 10^8 to 10^9 L/(mol s). In the lifetime of 40 ns, the diffusion length of OH radical is about 10 nm. Thus OH radicals could be present only in the gas–liquid interface region (Fig. 7).

With regard to H_2O_2, the lifetime in solution strongly depends on the kind of solutes present. Without any solutes, H_2O_2 has a lifetime much longer than 30 min determined by the rate of the following reaction [18]:

$$H_2O_2 \rightarrow 1/2\ O_2 +\ H_2O. \tag{3}$$
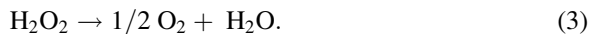
In the presence of OH radical, the following reaction takes place:

$$OH + H_2O_2 \rightarrow H_2O + O_2^- + H^+ \tag{4}$$
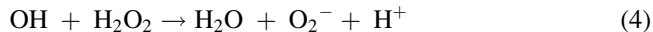
The rate constant of the reaction is $(2.7 \pm 0.3) \times 10^7$ L/(mol s) [19]. When the concentration of OH is 5×10^{-3} mol/L, then the lifetime of H_2O_2 is 7.4 μs. As the lifetime of OH is only 40 ns at this concentration, the time-averaged concentration of OH should be much lower. If it is 10^{-6} mol/L, then the lifetime of H_2O_2 is as long as about 40 ms. The diffusion length of H_2O_2 in this lifetime is about 10 μm. Thus H_2O_2 could be present not only in the gas–liquid interface region but also in the liquid region. If there are other kinds of radicals derived from solutes such as methanol by the reaction with OH radicals, however, the rate constant for the reaction of H_2O_2 is as high as 10^8–10^9 L/(mol s). Then the lifetime is as short as that of OH radical.

Physical and chemical properties of the gas–liquid interface region of a cavitation bubble are still under debate. Suslick et al. [20] suggested based on the experimental results of the vapor pressure dependence of sonochemical reaction rate at 20 kHz that the temperature of the gas–liquid interface region is as high as 1900 K. They also numerically calculated the temporal and spatial evolution of the liquid-zone temperature with a heat transport model. The model predicts a spatial and temporal average liquid-zone temperature of 2730 K. Furthermore, it predicts the width and the duration for the high temperature in the gas–liquid interface region as 200 nm and 2 μs, respectively. The author [21, 22] numerically calculated the temperature at the gas–liquid interface region based on a simple model. The model predicts the temperature at the gas–liquid interface increases up to the same order of magnitude with the maximum temperature inside a bubble (a few thousand Kelvin). The thickness and the duration for the high temperature region at the gas–liquid interface are estimated as only 4–10 nm and 2–6 ns, respectively. Further studies are required on this topic.

Not only experimentally but also numerically, chemical reactions of radicals in solution (liquid phase) have not yet been fully studied with regard to an acoustic cavitation bubble (sonochemistry). With regard to advanced oxidation processes such as O_3/H_2O_2, ultraviolet light/H_2O_2, and ultraviolet light/TiO_2, there are some numerical studies on the chemical reactions of OH radicals in solution [23]. Numerical simulations of chemical reactions in solution are required in sonochemistry.

OH Line Emission in Sonoluminescence

When H_2 gas reacts with O_2 gas in combustion, ultraviolet light is emitted by OH radicals. The wavelength of the light is about 310 nm, which is called OH line because the spectrum of the light is not continuum but a line (Fig. 8) [24]. The OH line emission in sonoluminescence could be observed through a quartz flask because the absorption of the light (310 nm) by a quartz flask is negligible (Fig. 9) [25].

There are two types in sonoluminescence [1, 26]. One is single-bubble sonoluminescence (SBSL) which is the light emission from a single stable bubble trapped near the pressure antinode of a standing ultrasonic wave in liquid by the acoustic radiation force called primary Bjerknes force. In SBSL, pulses of light are emitted periodically from a bubble with the period of ultrasound in a clocklike manner [27]. The other is multibubble sonoluminescence (MBSL) which is the light emission from a lot of bubbles in acoustic cavitation irrespective of standing or traveling ultrasonic waves. In MBSL, multiple pulses of light are periodically emitted with a half period of
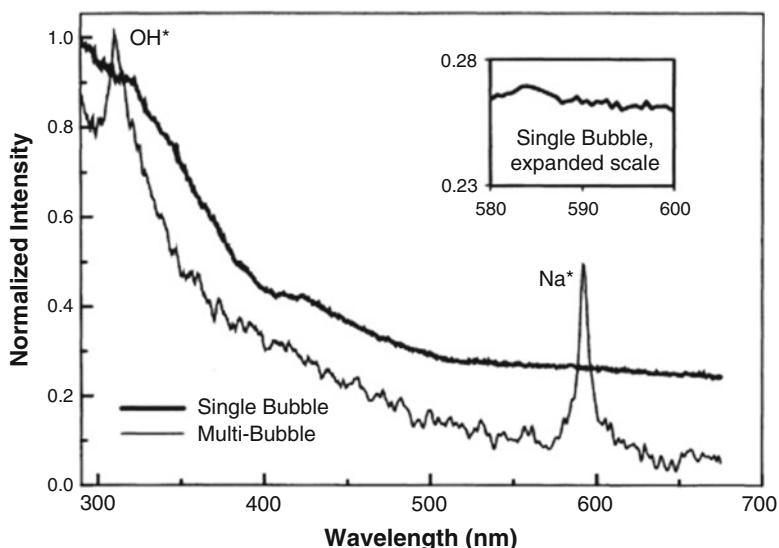
Fig. 8 Comparison of the background subtracted spectra of multibubble and single-bubble sonoluminescence in a 0.1 M sodium chloride solution (Reprinted figure with permission from Matula et al. [24]. Copyright (1995) by the American Physical Society)
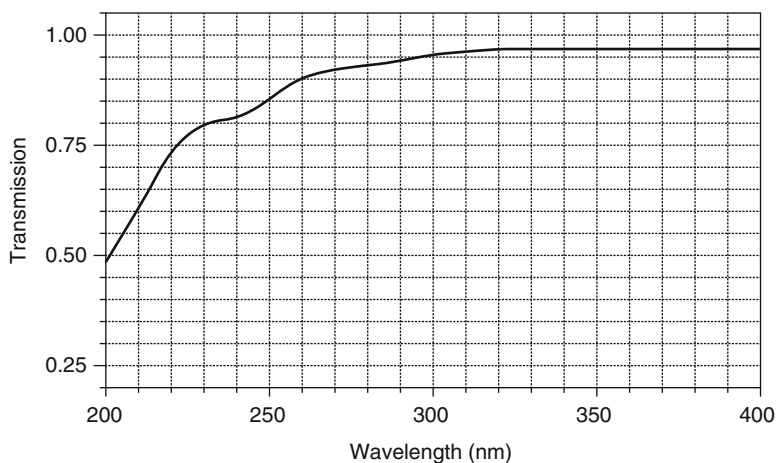
Fig. 9 Transmission of light through water and one wall of the quartz flask (Reprinted from Barber et al. [25], Copyright (1997), with permission from Elsevier)

Fig. 10 Average intensity dependence of argon single-bubble sonoluminescence spectral peaks (Reprinted figure with permission from Young et al. [28]. Copyright (2001) by the American Physical Society)
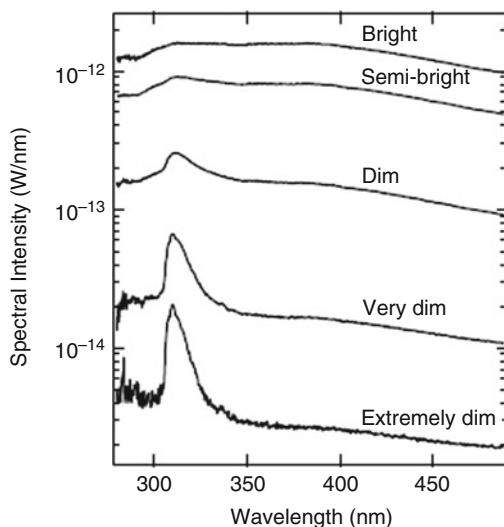
ultrasound because the light is emitted at around each pressure antinode for which pressure oscillation is in phase or in antiphase. It was reported that the OH line was not observed in SBSL but observed in MBSL in aqueous solutions (Fig. 8).

From very dark SBSL, however, the OH line was observed with an exposure of 5 days to a spectrometer, while spectra could be observed with an exposure of 100 min from bright SBSL (Fig. 10) [28]. In a dark room, bright SBSL could be seen with naked eyes like a star in a flask. Actually, the temperature inside a SBSL bubble increases to about 10,000 K at the end of the bubble collapse, which is similar to the

Fig. 11 The potentials for the A and X electronic states of OH (Reprinted with permission from Luque and Crosley [29]. Copyright 1998, AIP Publishing LLC)
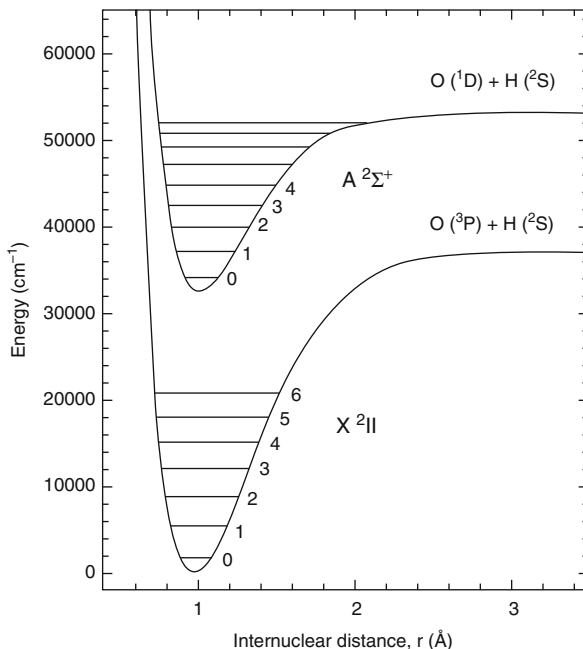
surface temperature of a star in the sky (the surface temperature of the sun is about 6000 K).

The OH line at about 310 nm in wavelength is emitted when electrons in the first excited state (A state) of OH radical are de-excited to the ground state (X state). It is called OH (A–X) band because both A and X states have various vibrational and rotational states of OH (Fig. 11) [29, 30]. The ground state of electrons in a molecule is usually labeled X, and the excited states are labeled A, B, C, . . .[13]. According to quantum mechanics, vibrational states of a molecule are quantized as 0,1,2,3,. . . (Fig. 11). The rotational states of a molecule are also quantized as J = 0,1,2,3,. . ., while they are not shown in Fig. 11 because the rotational energy levels $(10^{-4}$–10^{-2} eV) are much lower than that of the vibrational energy levels (0.1–1 eV) [14, 31]. The electronic energy levels are in several eV which correspond to the energy of visible to ultraviolet light. The vibrational energy corresponds to the energy of infrared light. The rotational energy corresponds to that of microwave. It should be noted that the energy of electromagnetic wave (light) is hc/λ, where h is the Planck constant $(6.6 \times 10^{-34}$ J s), c is the speed of light $(3.0 \times 10^{8}$ m/s), λ is the wavelength of light in meter, and 1 eV $= 1.6 \times 10^{-19}$ J.

In Fig. 11, the symbols Σ and Π show the total orbital angular momentum of electrons as L = 0 and 1, respectively. The total orbital angular momenta of 2, 3, .. are labeled Δ, Φ, .. as the Greek letters of Σ, Π, Δ, Φ, . . . correspond to S, P, D, F, .. The left superscript shows 2S + 1 where S is the total spin angular momentum as in the case of the atomic structure. The symbol "+" in the right superscript means that
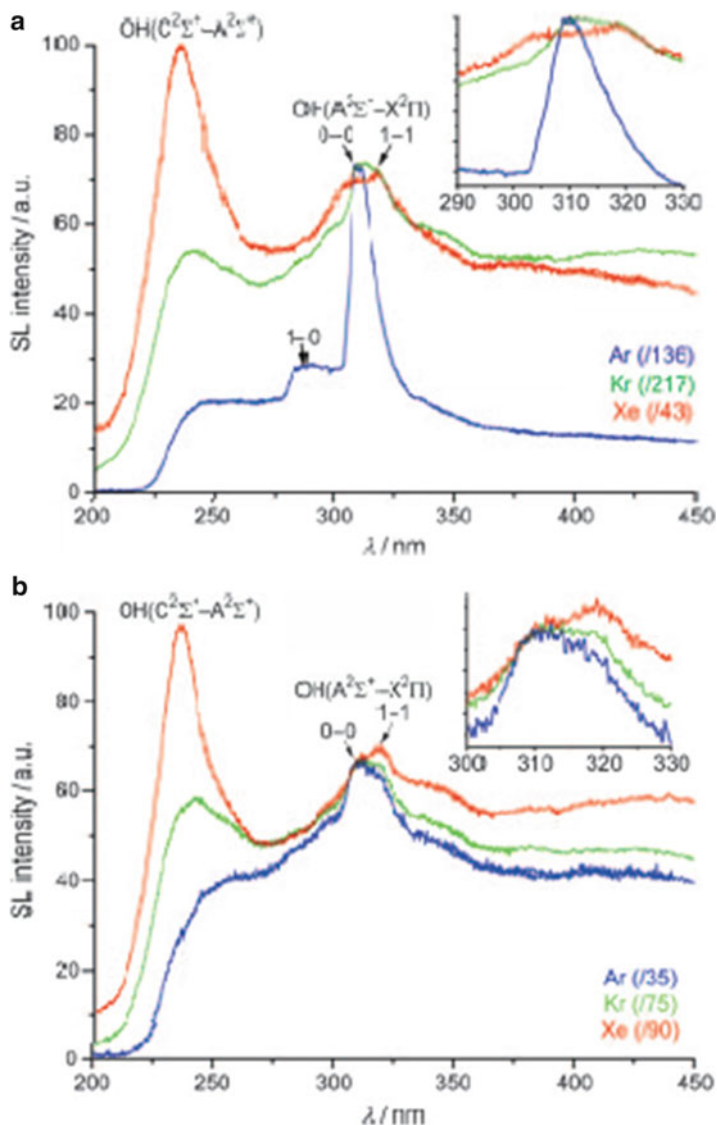
Fig. 12 Effect of the rare gas on the MBSL spectra from water at 20 kHz (**a**) and 607 kHz (**b**). (Reprinted from Pflieger et al. [32], Copyright (2010), with permission from Wiley-VCH)

the wave function of electrons does not change sign by reflection on the plane containing two nuclei of a molecule. ("-"means that the sign is changed.)

In 2010, Pflieger et al. [32] observed the emission from the third excited state (C state) of OH by the transition to the first excited state (A state), which is OH($C\ ^2\Sigma^+$ - A $^2\Sigma^+$) band in the range of wavelength of 225–255 nm (Fig. 12). The band has
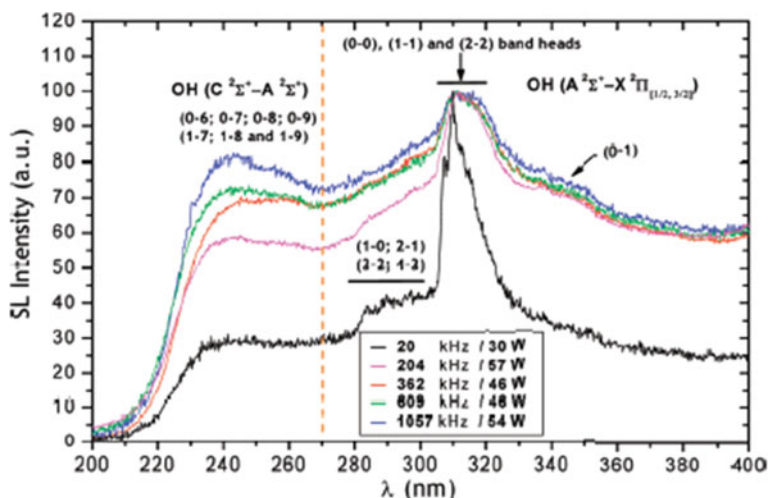
Fig. 13 Normalized MBSL spectra from water sparged with argon at 10–11 °C for different ultrasonic frequencies (Reprinted figure with permission from Ndiaye et al. [35], Copyright (2012) the American Chemical Society)

never been observed in normal combustion, while it has been observed in discharge in water vapor as well as γ-ray or electron irradiation of liquid water. Thus, Pflieger et al. [32] suggested that OH was excited to the third excited state by collisions with high-energy electrons created inside a bubble. It may be an evidence of the plasma formation inside a bubble under the condition of MBSL. The plasma formation inside a SBSL bubble in sulfuric acid has been experimentally confirmed by the observation of the emission lines of Ar^+ and O_2^+ [33, 34]. The difference and the similarity between SBSL and MBSL are still under debate and should be studied further in future.

Pflieger et al. [32] also found that OH emission depends on the noble gas species dissolved in water (Fig. 12). From Xe bubbles, the OH (C–A) band is stronger than OH (A–X) band. On the other hand, from Ar bubbles, the OH (A–X) band is stronger than OH (C–A) band. The reason may be the larger number of high-energy electrons inside a Xe bubble due to lower ionization potential and higher temperature compared to Ar caused by lower thermal conductivity of Xe resulting in a smaller amount of thermal conduction from the heated interior of a bubble to the surrounding liquid. Pflieger et al. [32] also found that OH line emission depends also on ultrasonic frequency (Fig. 12). The detailed mechanisms are, however, still under debate.

In 2012, Ndiaye et al. [35] in the same research group of Pflieger and Nikitenko derived the vibrational population distribution of OH (A $^2\Sigma^+$) from the analysis of the OH (A–X) band in MBSL spectra (Figs. 13 and 14). They also reported the dependence of the vibrational population distribution on ultrasonic frequency. They concluded that the vibrational population distribution deviated strongly from the
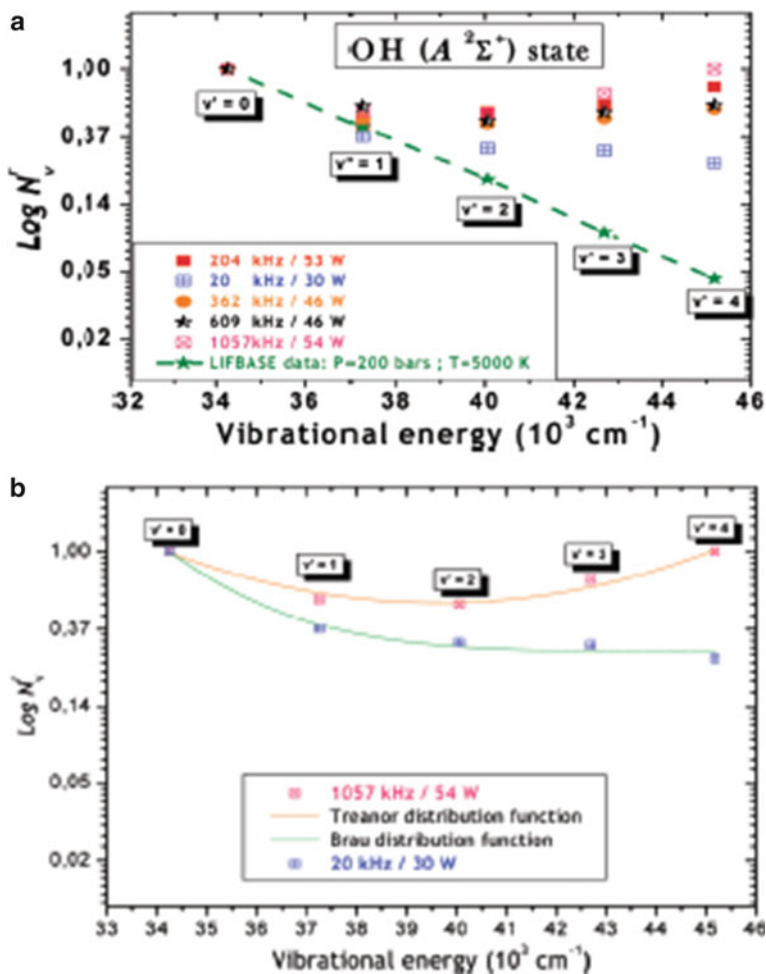
Fig. 14 Relative vibrational population distribution of the OH(A$^2\Sigma^+$) state as a function of vibrational energy for different ultrasonic frequencies. The dashed line in figure (a) shows the equilibrium Boltzmann distribution (Reprinted figure with permission from Ndiaye et al. [35], Copyright (2012) the American Chemical Society)

equilibrium Boltzmann distribution. It means that the vibrational population of OH (A $^2\Sigma^+$) is in nonequilibrium inside MBSL bubbles.

For equilibration, molecules and radicals need enough number of collisions among them. The number of collisions necessary to provide equilibrium distributions from strongly perturbed thermodynamic states of an assembly of particles is in the order of 10 for translational motion of particles [36]. It is in the order of 10^3 and 10^5 collisions for rotational and vibrational motion, respectively. For excitation and dissociation of molecules and radicals, it is in the order of 10^7. For ionization, it is in

the order of 10^9. Inside a sonoluminescing bubble, the concentration of molecules and radicals is in the same order of magnitude as that of the condensed phase (liquid state) and about 3×10^{28} m^{-3}. When the temperature inside a bubble is 10^4 K, the average velocity of each molecule is about 3×10^3 m/s. Then, the frequency of collision for each molecule or radical is about 5×10^{13} s^{-1} = $1.4 \times 0.4 \times 10^{-18}$ m^2 (cross section of a molecule or radical) $\times$ 3×10^3 m/s (mean velocity) $\times$ 3×10^{28} m^{-3} (number density). The time scale for the temperature change inside a sonoluminescing bubble is in the order of 0.1 ns $= 10^{-10}$ s. Thus, the number of collisions of a molecule or a radical is about 5×10^3 during the time. It is enough for equilibration of translational and rotational motion of molecules and radicals. However, it may be insufficient for the equilibration of vibrational population of molecules or radicals. Thus, it is possible that vibrational population distribution is in nonequilibrium inside a sonoluminescing bubble.

According to the experimentally derived distribution of vibrational population of OH (A $^2\Sigma^+$) inside sonoluminescing bubbles in Fig. 14, the population increases as the vibrational quantum number increases at relatively high quantum number. One of the examples of such distribution is the Treanor distribution (Fig. 15) [37]. The Treanor distribution is realized when the vibrational temperature is higher than the translational temperature of molecules for anharmonic oscillator (molecule) with decreasing energy interval between successive vibrational states for increasing quantum number for vibration. In this case, excitation and de-excitation of vibrational states of two colliding molecules are not in resonance when one of the molecules is in highly excited state of vibration and the other is in much lower energy state of vibration because the energy interval of successive states is quite different between them due to anharmonic nature of molecular vibration. For the excitation of the lower energy state of molecular vibration, not only the de-excitation of highly excited vibrational state but also the decrease of the energy of the translational motion is required. As a result, when the temperature of the translational motion is much lower than the temperature of the molecular vibration, the upper levels of vibration are overpopulated compared to a Boltzmann distribution. This is the Treanor distribution. There are some other similar distributions such as Brau and Bray distributions [38–40].

Inside a sonoluminescing bubble, the vibrational temperature may become higher than the translational temperature when a bubble re-expands after the violent collapse because the translational temperature may decrease faster. Then, could the Treanor distribution be realized during the re-expansion of a bubble after the violent collapse? According to the numerical simulations by An and Li [41], however, the OH emission is expected during the bubble collapse when the bubble internal temperature increases (Fig. 16). Thus further studies are required on whether the vibrational population distribution is really the Treanor one or not. If yes, why is the translational temperature lower than the vibrational temperature?

One possibility is the excitation of vibrational states of OH by chemical reactions. In this case, the electronic excitation of OH is also due to chemical reactions, and OH emission is chemiluminescence. It is widely known that molecular vibration is
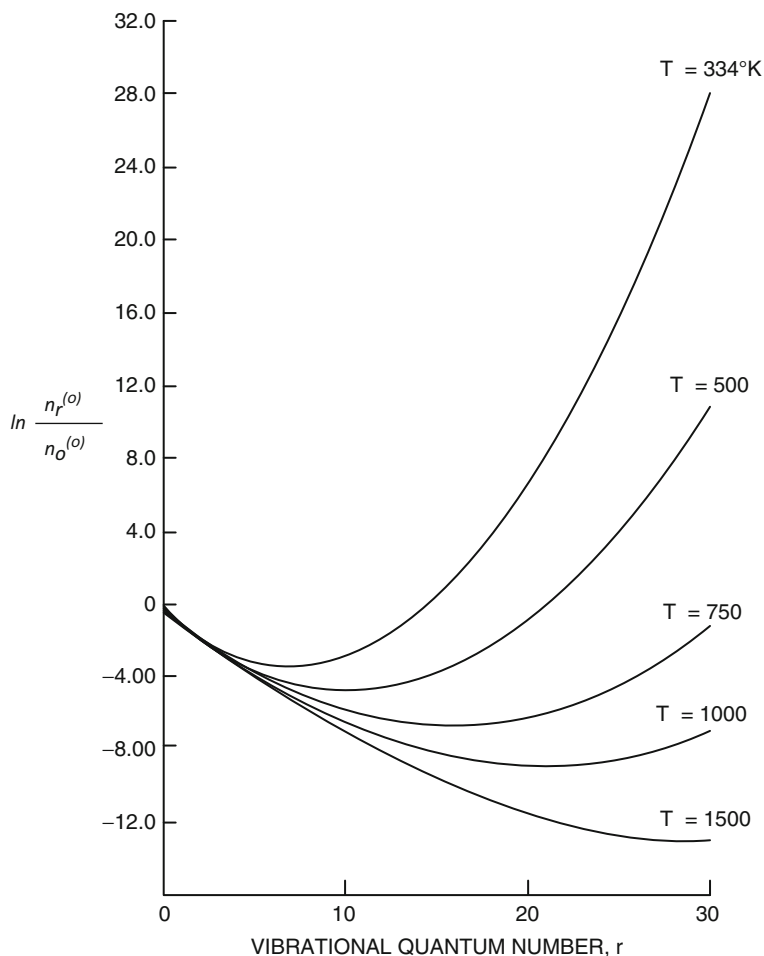
Fig. 15 Treanor distribution for various translational temperature for the vibrational temperature of 4000 K (Reprinted with permission from Treanor et al. [37]. Copyright 1968, AIP Publishing LLC)

preferentially excited through some kinds of chemical reactions [14]. According to the numerical simulations of bubble pulsation by the author [3], the density inside a sonoluminescing bubble is as high as that of the condensed phase (liquid phase). When the temperature inside such a bubble is as high as 10^4 K, molecules including electronically excited ones undergo many collisions. Then, non-radiative de-excitation, for which the energy is transferred to heat instead of light, takes place dominantly. It is called quenching. Thus, for strong radiative de-excitation, much more molecules should be electronically excited than the molecules undergoing non-radiative de-excitation (quenching). It may be only possible through chemical reactions. For OH, the following chemical reactions could produce
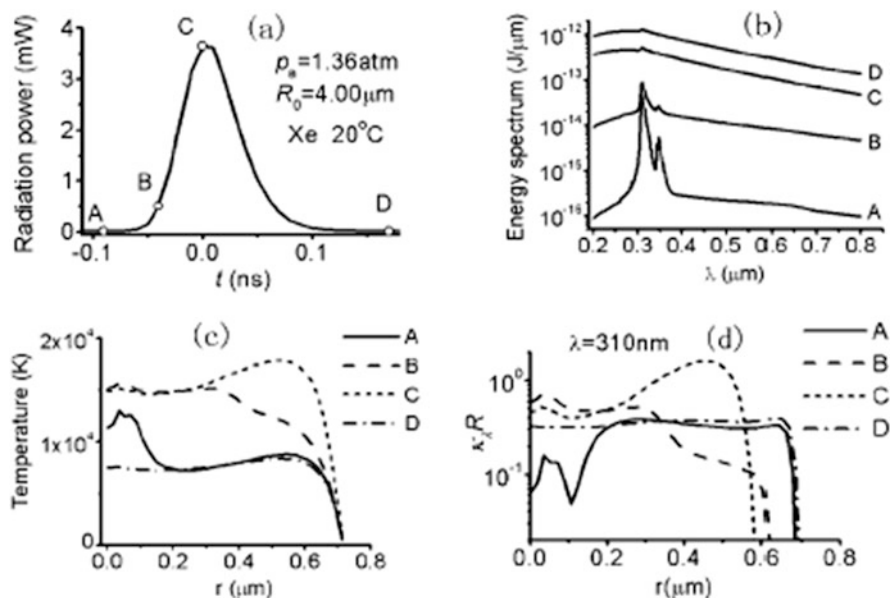
Fig. 16 The results of the numerical simulations for a Xe bubble in 20 °C water. (**a**) Optical radiation power of the bubble vs. time, (**b**) energy spectrum of sonoluminescence, (**c**) temperature vs. distance from the bubble center inside a bubble, and (**d**) absorption coefficient vs. distance from the bubble center inside a bubble (Reprinted figure with permission from An and Li [41], Copyright (2008) by the American Physical Society)

electronically excited OH (OH*): O + H + M → OH* + M and OH + H + OH → OH* + H_2O [3, 42].

Flannigan and Suslick [43] reported that the rotational temperature is much lower than the vibrational temperature of SO molecules which were determined from the SO emission spectra of SBSL in sulfuric acid (Fig. 17). Furthermore, Pflieger et al. [44] reported that the rotational temperature is significantly lower than the vibrational temperature for C_2 radicals which were determined from C_2 emission spectra of MBSL in aqueous t-BuOH solution (Fig. 18). The reason for the lower rotational temperature is, however, still under debate and should be studied in future.

In MBSL, there are a variety of bubbles which have different temperatures at the bubble collapse. Thus molecular emissions such as OH emissions could be from bubbles of different temperatures. In addition, even for a specified bubble, the temperature inside a bubble temporally changes dramatically (Fig. 3a). Thus the molecular emissions from bubbles are possibly at different temperatures. It may be one of the reasons for non-Boltzmann distribution for vibrational population of OH inside a SL bubble. However, the increase of population with the increase of the vibrational quantum number could not be explained by this effect. It suggests that vibrational population inside an SL bubble is actually in nonequilibrium.

Fig. 17 Experimental
spectrum of SO emission in
single-bubble
sonoluminescence from 80 wt
% H_2SO_4 as well as the
theoretical fits with the
rotational temperatures of
290 K and 2100 K (Reprinted
figure with permission from
Flannigan and Suslick [43],
Copyright (2012) the
American Chemical Society)
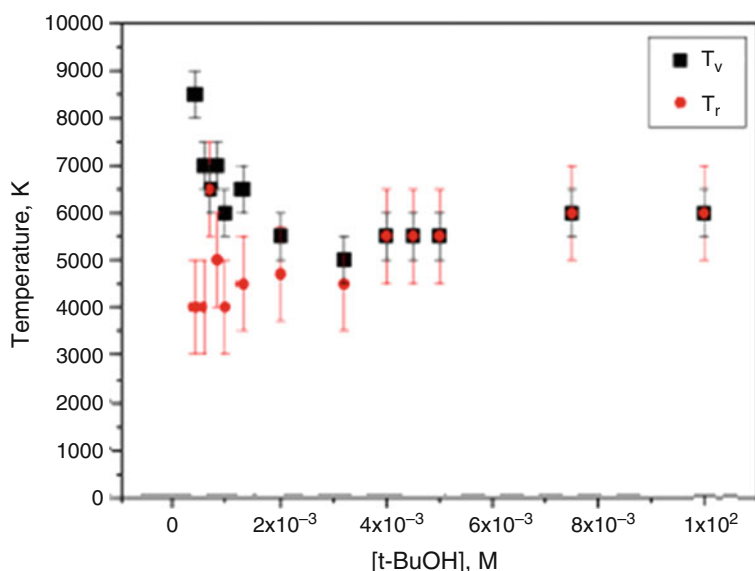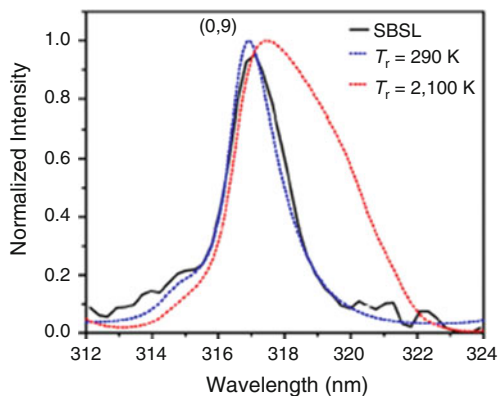
Fig. 18 Influence of t-BuOH concentration on C_2 vibrational and rotational temperatures in
multibubble sonoluminescence at 204 kHz, 32 W, and 6 °C (Reprinted figure with permission
from Pflieger et al. [44], Copyright (2015) the American Chemical Society)

Acoustic Field

The acoustic field in a sonochemical reactor is complex in general. The acoustic
cavitation bubbles strongly attenuate ultrasound and radiate acoustic waves into the
surrounding liquid by their pulsations. Furthermore, the bubbles move by acoustic
radiation forces. The speed of sound could be changed by the presence of bubbles. In
addition, the walls of the liquid container vibrate due to the pressure oscillation of

ultrasound. As a result, the walls radiate acoustic waves into the liquid. The liquid surface also vibrates under ultrasound. At the present stage, the whole system is not fully understood both theoretically and experimentally.

Here, we discuss the role of the vibration of the container's wall as well as the attenuation of ultrasound by bubbles by the FEM calculations of an acoustic field in a sonochemical reactor [45]. The basic equation is the wave equation (Eq. 5) with the boundary condition (Eq. 6):

$$\nabla^2 p - \frac{1}{c^2}\frac{\partial^2 p}{\partial t^2} = 0 \tag{5}$$

$$\frac{\partial p}{\partial n} = -\rho\frac{\partial^2 u_n}{\partial t^2} \tag{6}$$

where $\nabla^2 = \frac{\partial^2}{\partial x^2} + \frac{\partial^2}{\partial y^2} + \frac{\partial^2}{\partial z^2}$, p is the oscillatory component of the pressure, c is the velocity of sound, t is time, n is the length in the direction perpendicular to the boundary and is defined as positive in the direction into the liquid, ρ is the liquid density, and u_n is the displacement of the boundary (wall) in the direction perpendicular to the boundary. In the FEM calculations, the equations are expressed by an integral equation as follows:

$$\int_V W\left(\nabla^2 p - \frac{1}{c^2}\frac{\partial^2 p}{\partial t^2}\right)dV + \int_\Gamma W\left(\frac{\partial p}{\partial n} + \rho\frac{\partial^2 u_n}{\partial t^2}\right)d\Gamma = 0 \tag{7}$$

where V is the total volume of the liquid, W is an arbitrary weighting function, Γ is the boundary between the liquid and the solid (wall), and n is defined to be positive in the direction into the liquid. The solution of Eqs. 5 and 6 (p and u_n) automatically satisfies Eq. 7. It is an approximation that the solution of Eq. 7 (p and u_n) is regarded as that of Eqs. 5 and 6, which is called the method of weighted residuals. The method to solve Eq. 7 in the FEM calculations is described in Refs. [45, 46].

The calculations have been performed for a rectangular cell of 7 cm × 7 cm × 20 cm in internal dimensions filled with water at 20 °C [45]. The bottom of the cell is a vibrating plate which vibrates at frequency of 100 kHz, and the spatial distribution of its vibration amplitude has been assumed as a Gaussian distribution. At the center of the vibrating plate, the vibration amplitude has the maximum value of 0.1 μm. The liquid height is assumed as 13.9 cm unless stated, which is close to a resonance height of 13.875 cm. As the boundary condition, the applied pressure is assumed as zero (the free boundary condition) at the outer surface of the reactor's wall and the liquid surface. From the symmetry of the rectangular reactor, only 1/8 of the total volume has been considered in the calculation.

In Fig. 19, the calculated spatial distribution of the acoustic amplitude (the pressure amplitude) has been shown for the rigid wall and the glass wall (2 mm or 7 mm in thickness). The half width of the Gaussian distribution of the vibration amplitude has been assumed as 5 cm, while the side length of the vibrating plate is
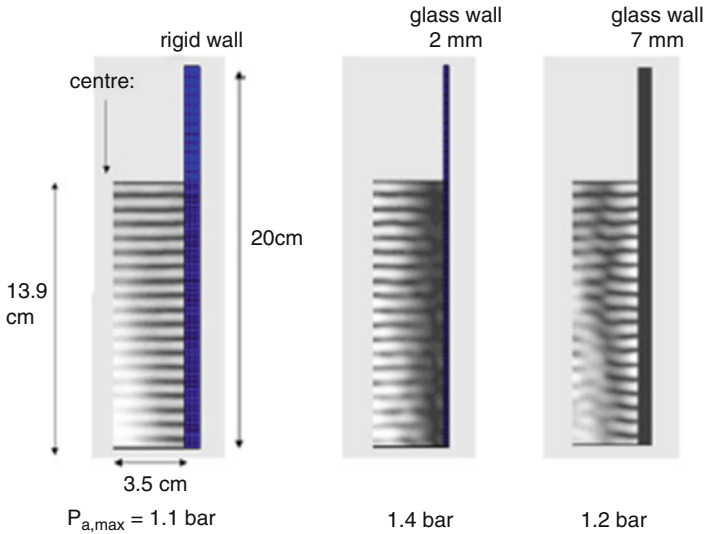
Fig. 19 The calculated spatial distribution of the acoustic amplitude for rigid wall and glass wall. The full width at half maximum for the Gaussian distribution of the vibration amplitude of the vibrating plate at the bottom is 5 cm. The attenuation coefficient is 5 cm^{-1}. The wall height is 20 cm, while the liquid height is 13.9 cm (Reprinted from Yasui et al. [45], Copyright (2007), with permission from Elsevier)

7 cm. The white and black regions show the region of the highest acoustic amplitude (pressure antinode) and that of zero (pressure node), respectively. At the liquid surface, the acoustic amplitude is always zero (pressure node) and shown with black line. At the vibrating plate at the bottom, it is a pressure antinode and shown with white because in this calculations the liquid height is nearly that of resonance. For the liquid container with thin glass walls (2 mm in thickness), the walls vibrate nearly freely. Thus, the pressure amplitude near the wall is nearly zero (pressure node) as seen in the middle of Fig. 19. For a thicker glass wall of 7 mm, on the other hand, the vibration of the wall is much less. As a result, the acoustic amplitude near the wall is not necessarily small although the vibration of the wall alters the acoustic field from the pure stripes seen in the case of the rigid wall.

The acoustic field also depends on the material of the wall. The glass wall vibrates more strongly than the stainless steel wall when the thickness of the wall is the same (Fig. 20). In other words, the glass wall is freer than the stainless steel wall. As a result, the acoustic amplitude near the glass wall is lower than that near the stainless steel wall.

The acoustic field strongly depends on the attenuation coefficient of ultrasound. At 100 kHz, the attenuation coefficient of ultrasound is only 2×10^{-4} m^{-1} without any bubbles in liquid water. However, with some amount of bubbles, the attenuation coefficient significantly becomes higher [47]. In Fig. 21, the calculated acoustic fields are shown for various attenuation coefficients of ultrasound. In the present calculations, the speed of sound in liquid water is assumed as constant, and its

Fig. 20 The calculated spatial distribution of the acoustic amplitude for stainless steel wall and glass wall. The full width at half maximum for the Gaussian distribution of the vibration amplitude of the vibrating plate is 16 cm. The attenuation coefficient is 5 m^{-1} (Reprinted from Yasui et al. [45], Copyright (2007), with permission from Elsevier)
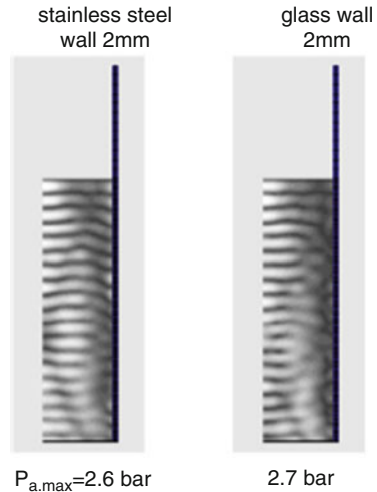
change due to the presence of bubbles is neglected because it is negligible at 100 kHz when the bubble volume fraction is less than about 0.01 [47]. Without any bubbles, the acoustic field is strongly perturbed by the vibration of the wall as seen in the right side of Fig. 21. The strongly vibrating wall radiates strong acoustic waves (ultrasound) into the liquid and strongly alters the acoustic field. As the attenuation coefficient increases, the effect of the vibration of the wall becomes smaller because the vibration amplitude of the wall decreases due to the decrease in acoustic amplitude. When the attenuation coefficient is larger than about 0.05 m^{-1}, the nearly stripe structure of the acoustic field is recovered. The photograph of sonochemiluminescence from an aqueous luminol solution shows the spatial distribution of OH radicals as well as H_2O_2 created by bubbles because the light emission is due to the chemical reaction of luminol with OH radical and H_2O_2 [48]. The spatial distribution of OH radicals reflects that of active bubbles. The spatial distribution of active bubbles reflects that of acoustic amplitude. Thus the photograph nearly shows the acoustic field. For the attenuation coefficient of 0.5–5 m^{-1}, the calculated acoustic field is similar to the spatial pattern of sonochemiluminescence because some horizontal stripes of pressure antinodes are disconnected. It suggests that under the experimental condition of sonochemiluminescence in Fig. 21, the attenuation coefficient in a bubbly liquid water is in the range of 0.5–5 m^{-1}. According to Dahnke and Keil [47], the attenuation coefficient of 0.5–5 m^{-1} at 100 kHz corresponds to the value for liquid water with the bubble volume fraction of 10^{-3}–10^{-2}.

In Fig. 22, the calculated results for the liquid height of resonance (13.875 cm) as well as that of antiresonance (14.25 cm) at 100 kHz are shown for rigid walls. For the both cases, the liquid surface corresponds to pressure node. For the case of resonance, the vibrating plate at the bottom corresponds to pressure antinode. On the other hand, for the case of antiresonance, it corresponds to the pressure node. Even for the case of antiresonance, a clear stripe pattern of an acoustic field is seen,

glass wall 7mm   glass wall 7mm   glass wall 7mm

Sonochemiluminescence from an aqueous luminol solution

$\alpha = 5$ (m^{-1})   0.5 (m^{-1}) 2×10^{-4} (m^{-1})

$P_{a.max} = 1.2$ bar   3.0 bar   6.5 bar
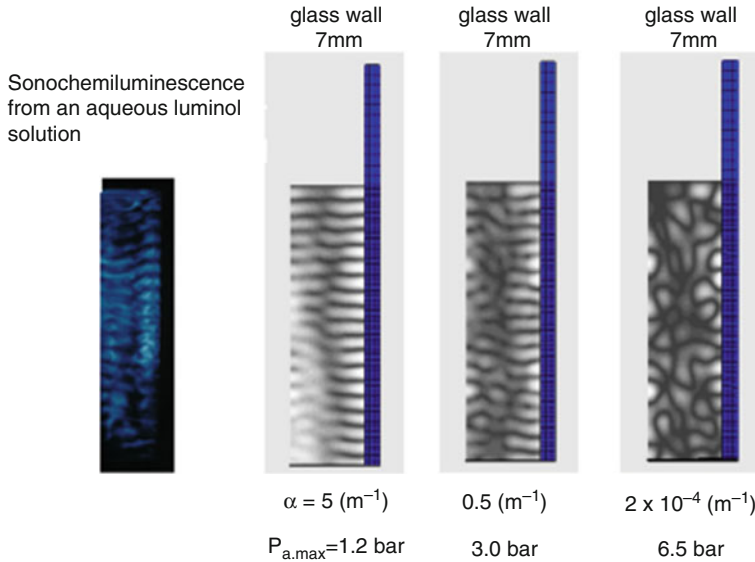
Fig. 21 The calculated spatial distribution of the acoustic amplitude for glass wall for various attenuation coefficients of ultrasound. The full width at half maximum for the Gaussian distribution of the vibration amplitude of the vibrating plate is 5 cm. The photograph of sonochemiluminescence from an aqueous luminol solution has been also shown for the corresponding half plane (Reprinted from Yasui et al. [45], Copyright (2007), with permission from Elsevier)

Fig. 22 The calculated spatial distribution of the acoustic amplitude for the resonance liquid height (13.875 cm) and the antiresonance one (14.25 cm) for the rigid wall. The bottom plate vibrates spatially uniformly. The attenuation coefficient is 5 m^{-1} (Reprinted from Yasui et al. [45], Copyright (2007), with permission from Elsevier)

rigid wall   rigid wall

13.875 cm   14.25 cm

$P_{a,max} = 1.7$ bar resonance   0.9 bar antiresonance
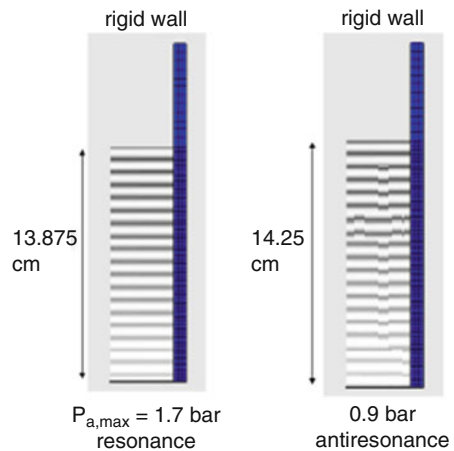
although the maximum acoustic amplitude of 0.9 bar is much lower than that of 1.7 bar for the case of resonance.

Without attenuation of ultrasound, an ideal standing wave is formed between the vibrating plate and the liquid surface. At the pressure nodes, the acoustic amplitude is exactly zero in an ideal standing wave. The distance between the successive nodes

Fig. 23 Spatial distribution of the pressure amplitude of a damped standing wave. The vibrating plate at the bottom of the liquid container is at the left side (x = 0). The liquid surface is at the right side where the pressure amplitude is zero (pressure node)
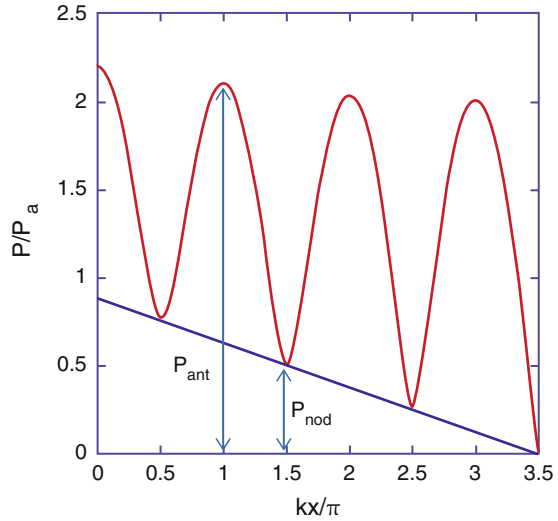
is a half wavelength of ultrasound. The distance between the successive node and antinode is a quarter wavelength. With attenuation of ultrasound, the acoustic amplitude at the nodes is nonzero except at the liquid surface. In Fig. 23, such an acoustic field is shown although the physical condition is different from those in Fig. 22. The solid line shows the pressure amplitude of ultrasound normalized with the amplitude of the reflected wave at the liquid surface at the right end of Fig. 23 as a function of the distance (x) from the vibrating plate in unit of kx/π where k is the wave number of ultrasound. Such an acoustic field is called a damped standing wave field [49]. A damped standing wave is composed of both traveling and standing waves. The straight line in Fig. 23 shows the traveling wave component. The percentage of the field which is the standing wave may be estimated by the following quantity [50]:

$$\frac{(P_{\mathrm{ant}} - P_{\mathrm{nod}})}{(P_{\mathrm{ant}} + P_{\mathrm{nod}})} \times 100 \ \% \tag{8}$$

where P_{ant} is the acoustic amplitude at the pressure antinode, and P_{nod} is that at the pressure node (Fig. 23). The value depends on the distance from the vibrating plate (or liquid surface) as seen in Fig. 23. The standing wave component is higher near the reflector such as the liquid surface at the right end of Fig. 23. The standing wave ratio (SWR) defined below may also be used to characterize the acoustic field [50]:

$$\mathrm{SWR} = \frac{P_{\mathrm{ant}}}{P_{\mathrm{nod}}} \tag{9}$$

The SWR varies between one for pure traveling wave and infinity for pure standing wave.

One of the problems in the present FEM calculations is the neglect of acoustic emissions from cavitation bubbles. In the presence of bubbles, the wave equation (Eq. 5) should be modified as follows [51, 52]:

$$\nabla^2 p - \frac{1}{c^2}\frac{\partial^2 p}{\partial t^2} = -\rho_l \sum_i N_i \frac{\partial^2 V_i}{\partial t^2} \tag{10}$$

where ρ_l is the liquid density, N_i is the number density of bubbles for a group i with the same bubble radius, and V_i is the volume of a bubble for a group i. In general, N_i and V_i are a function of the position ($\vec{r}$) and time (t). The volume of a bubble is related to the bubble radius (R_i) as $V_i = 4\pi R_i^3/3$. The bubble radius is calculated by the Rayleigh–Plesset equation (Eq. 11) or its modified version (Eq. 12) [2]:

$$R_i \ddot{R}_i + \frac{3\dot{R}_i^2}{2} = \frac{1}{\rho_l}\left(p_g - \frac{2\sigma}{R_i} - \frac{4\mu \dot{R}_i}{R_i} - p_0 - p\left(\vec{r},\, t\right)\right) \tag{11}$$

where the over-dot denotes the time derivative (d/dt), p_g is the pressure inside a bubble, σ is the surface tension, μ is viscosity, p_0 is the ambient static pressure, and $p\left(\vec{r}, t\right)$ is the acoustic pressure which is the solution of Eq. 10:

$$\left(1 - (\Lambda + 1)\frac{\dot{R}_i}{c}\right)R_i \ddot{R}_i + \frac{3\dot{R}_i^2}{2}\left(1 - \frac{1}{3}(3\Lambda + 1)\frac{\dot{R}_i}{c}\right)$$
$$= \frac{1}{\rho_l}\left(1 + (1 - \Lambda)\frac{\dot{R}_i}{c}\right)\left(p_B - p\left(\vec{r}, t\right) - p_0\right) + \frac{R_i}{c\rho_l}\frac{dp_B}{dt} \tag{12}$$

where Λ is an arbitrary constant which satisfies $|\Lambda| < c/|\dot{R}_i|$ ($\Lambda = 0$ for Keller equation, and $\Lambda = 1$ for Herring equation), and p_B is the liquid pressure at the bubble wall ($p_B = p_g - \frac{2\sigma}{R_i} - \frac{4\mu \dot{R}_i}{R_i}$).

Another problem is that in actual experiments, the liquid surface vibrates when the liquid is irradiated by ultrasound (Fig. 24). According to Tuziuti et al. [53], when the vibration amplitude of the liquid surface exceeds a quarter wavelength of ultrasound, the sonochemiluminescence (SCL) intensity strongly drops. The reason is probably the strong disturbance of a standing wave field by the liquid surface vibration. However, the influence of the liquid surface vibration on an acoustic field has not yet been fully studied as well as the physics of liquid surface vibration.

Another problem is the influence of pulsed ultrasound on an acoustic field. According to Tuziuti et al. [54], the spatial distribution of SCL intensity is strongly altered by using pulsed ultrasound (Fig. 25). With continuous ultrasound, the spatial distribution of SCL intensity is strongly inhomogeneous (Fig. 25d). On the other hand, with pulsed ultrasound (100 cycle On – 100 cycle OFF), the spatial distribution of SCL intensity is much more homogeneous (Fig. 25a). It is known that with pulsed ultrasound, the number of large degassing bubbles is much less than that with

a

b   —— 10 mm

c
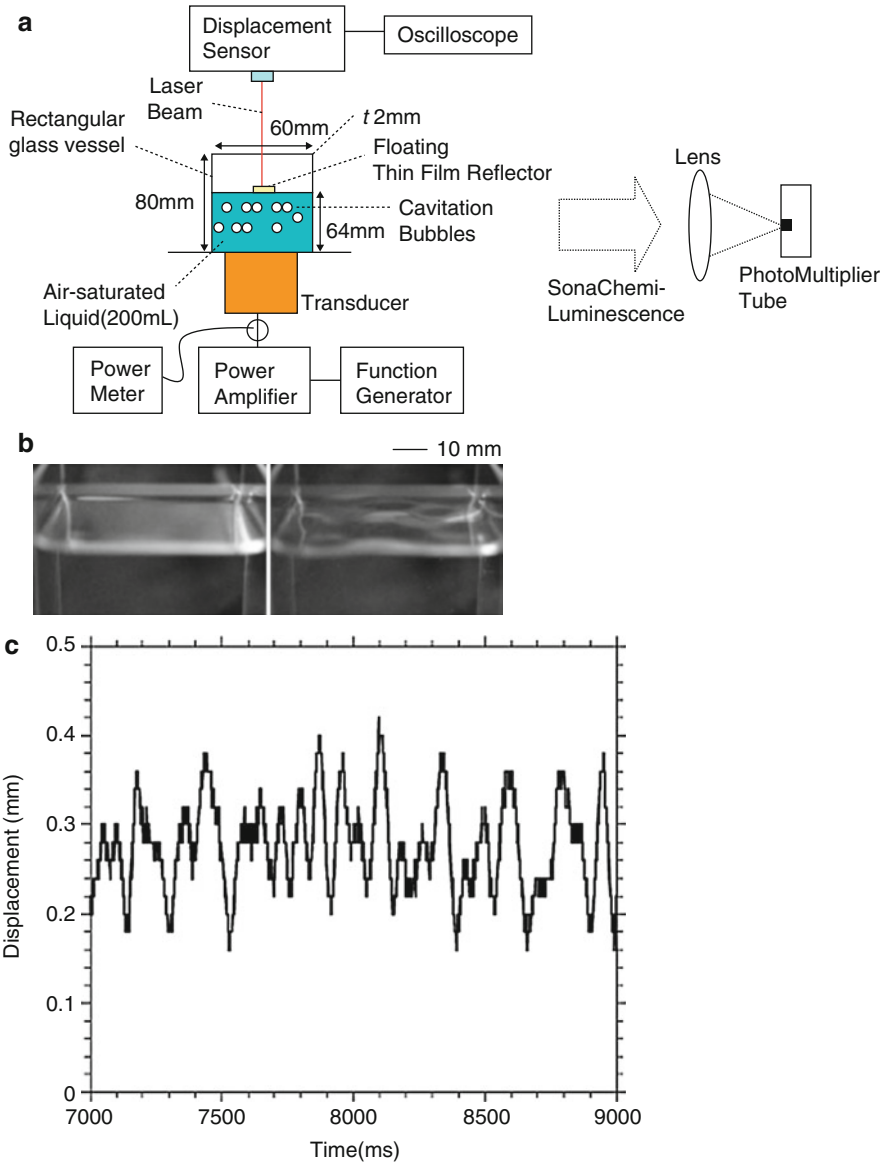
Fig. 24 The vibration of liquid surface by ultrasound irradiation. (**a**) Experimental apparatus. (**b**) The photograph of liquid surface without ultrasound (*left*) and with ultrasound (*right*). (**c**) Measured displacement of liquid surface as a function of time (Reprinted figures with permission from Tuziuti et al. [53], Copyright (2010) the American Chemical Society)

continuous ultrasound. The radii of degassing bubbles are larger than the resonance radius. Thus many of them are trapped at pressure nodes of a standing ultrasonic wave. It is expected that the degassing bubbles strongly alter the acoustic field which
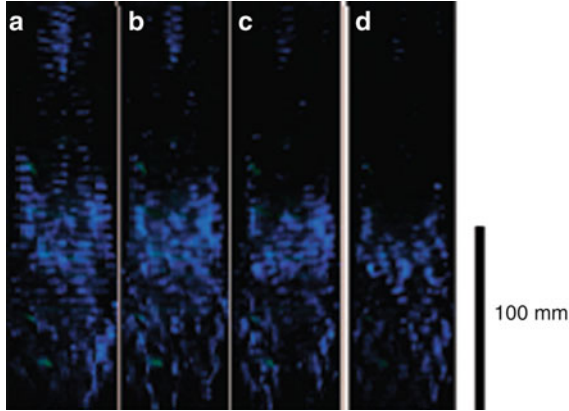
Fig. 25 The photographic images of luminol sonochemiluminescence (SCL) at 152 kHz with pulsed ultrasound repetition of (**a**) 100 cycle ON – 100 cycle OFF, (**b**) 1000 cycle ON – 1000 cycle OFF, (**c**) 10,000 cycle ON – 10,000 cycle OFF, and (**d**) continuous wave (CW) ultrasound. The exposure time for capturing the images was 3 min for (**a**), (**b**), and (**c**) and 1.5 min for (**d**) to equalize the net irradiation time between different conditions (Reprinted figure with permission from Tuziuti et al. [54], Copyright the American Chemical Society)

results in the inhomogeneous spatial distribution of the SCL intensity. However, detailed mechanism for the influence of degassing bubbles on the acoustic field has not yet been fully studied.

Finally, the bubble–bubble interaction is discussed (Fig. 26). Each pulsating bubble radiates acoustic waves into the surrounding liquid. It is like the sound radiation from a vibrating plate. The influence of acoustic waves which radiated from surrounding bubbles on the pulsation of a bubble is called the bubble–bubble interaction. The strength of the bubble–bubble interaction may be characterized by the following quantity named the coupling strength (S):

$$S = \sum_i \frac{1}{d_i} = \int_{l_{min}}^{l_{max}} \frac{4\pi r^2 n}{r} dr = 2\pi n \left(l_{max}^2 - l_{min}^2 \right) \approx 2\pi n l_{max}^2, \qquad (13)$$

where d_i is the distance between the bubble and another bubble numbered i, the summation is for all the surrounding bubbles, l_{min} is the distance between the bubble and the nearest bubble, l_{max} is the radius of the bubble cloud, n is the number density of bubbles, r is the distance from the bubble, and it is assumed that $l_{max} \gg l_{min}$ in the last equation. The coupling strength (S) can be experimentally estimated by measuring the number density of bubbles (n) and the radius of the bubble cloud (l_{max}).

The reason for the importance of this quantity is as follows. The pressure (p_i) of an acoustic wave which is radiated from a pulsating bubble is given by Eq. 14:
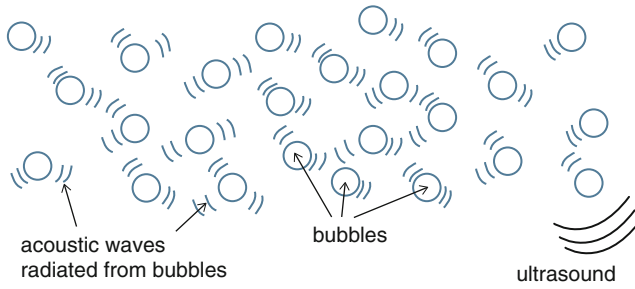
Fig. 26 The bubble–bubble interaction. Pulsation of a bubble is influenced by acoustic waves radiated by surrounding bubbles

$$p_i = \frac{\rho_l}{r_i}\left(R^2\ddot{R} + 2R\dot{R}^2\right) \tag{14}$$

where r_i is the distance from the bubble, and R is the instantaneous bubble radius. In Eq. 14, however, the time delay effect due to a finite speed of acoustic propagation is neglected. This approximation is valid only when the time delay (r/c) is much smaller than the acoustic period. The total pressure (P) of acoustic waves from all the surrounding bubbles is just the total sum of Eq. 14:

$$P = \sum_{i=1}^{N} p_i = \rho_l\left(R^2\ddot{R} + 2R\dot{R}^2\right)\left(\sum_{i=1}^{N}\frac{1}{r_i}\right) \tag{15}$$

where it is assumed that the bubble radius is the same for all the bubbles. This approximation as well as the approximation of the spatially homogenous distribution of bubbles used in Eq. 13 is called the homogenous bubble-cloud approximation. Under this approximation, Eq. 15 becomes Eq. 16 using Eq. 13:

$$P = \rho_l S\left(R^2\ddot{R} + 2R\dot{R}^2\right). \tag{16}$$

Thus, it is proportional to the coupling strength S. Under this approximation, $p\left(\vec{r},t\right)$ in Eq. 12 is expressed as Eq. 17:

$$p\left(\vec{r},t\right) = -p_a\sin\omega t + \rho_l S\left(R^2\ddot{R} + 2R\dot{R}^2\right) \tag{17}$$

where p_a is the pressure amplitude of ultrasound, ω is the angular frequency of ultrasound, and t is time. Thus, the factor S characterizes the strength of the bubble–bubble interaction and is called coupling strength of bubbles. In Fig. 27, the results of numerical simulations under the approximation of Eq. 15 are shown for the radius-time curves for various values of S. The bubble expansion is more strongly suppressed by the bubble–bubble interaction for a larger value of S.

Fig. 27 Results of numerical
simulations on the radius-time
curves for various coupling
strength (S) of bubbles. The
frequency and the pressure
amplitude of ultrasound are
20 kHz and 10 bar,
respectively. The ambient
pressure is 5 atm. The initial
bubble radius is 5 μm. The
liquid viscosity is 1 mPa s.
(Reprinted with permission
from Yasui et al. [56],
Copyright (2011), Acoustical
Society of America)
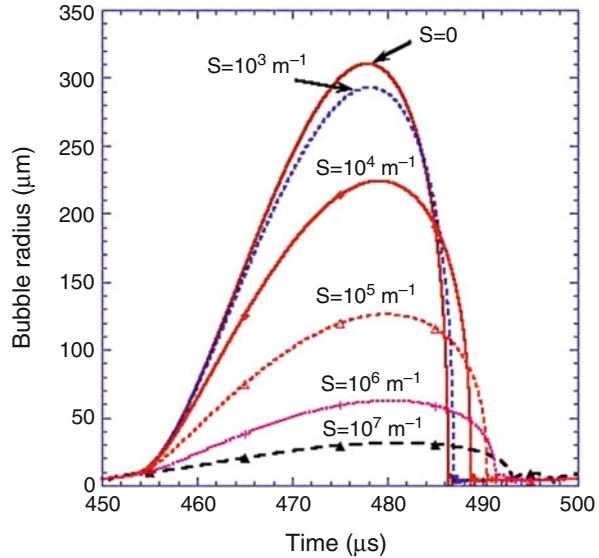
By linearizing Eq. 12 using the approximation of Eq. 17, the resonance frequency
of a bubble is derived as a function of S (Fig. 28). In Fig. 28, the resonance frequency
of an encapsulated microbubble used as a contrast agent in medical applications
(Albunex) is also shown. For both uncovered bubble (free bubble) and encapsulated
microbubble, the resonance frequency decreases as S increases above 10^5 m^{-1} due to
stronger bubble–bubble interaction.

Up to date, there has been no full numerical study of Eq. 10 taking into account
the nonuniform spatial distribution of bubbles; wide distribution of bubble size
(ambient bubble radii); movement of bubbles by radiation forces; temporal fluctu-
ation in the number density of bubbles by fragmentation, dissolution, and coales-
cence of bubbles [55]; vibration of the container's wall [45]; vibration of the liquid
surface [53]; presence of large degassing bubbles [54]; etc. Such studies are required
in future as well as experimental measurements of acoustic fields.

Conclusion and Future Directions

It has long been believed that the main oxidant created by acoustic cavitation
bubbles in aqueous solutions is OH radical. According to the numerical simulations
[5], however, the main oxidant is not always OH radical but sometimes H_2O_2 and O
atom. For vaporous bubbles for which the main bubble content at the bubble collapse
is water vapor, the main oxidant is OH radical according to the numerical simula-
tions. On the other hand, for gaseous bubbles for which the main bubble content at
the bubble collapse is permanent gas such as air, the main oxidant is H_2O_2 when the
bubble temperature at the collapse ranges from 4000 K to 6500 K. When the bubble
temperature is higher than 6500 K in gaseous bubbles, the main oxidant is O atom.

Fig. 28 The relationship between the coupling strength (S) of bubbles and the resonance frequency of a bubble (angular frequency ω_0). The result for encapsulated microbubble (Albunex) is also shown (Reprinted with permission from Yasui et al. [57], Copyright (2009), Acoustical Society of America)
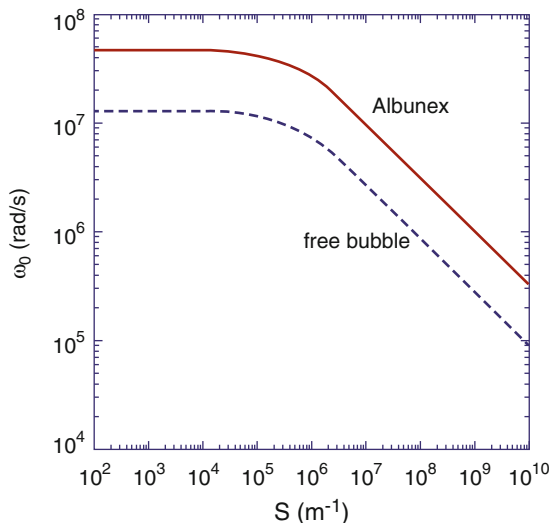
When the bubble temperature is higher than 7000 K in gaseous bubbles of air, the oxidants are strongly consumed inside a bubble by oxidizing nitrogen. Up to date, there has been no experimental confirmation on the presence of O atom in liquid water produced by bubbles. As the lifetime of O atom is expected to be very short, it may be only in the gas–liquid interface region of a bubble. In addition, the temperature as well as pressure of the gas–liquid interface region at the bubble collapse is still under debate. Numerical and experimental studies on the lifetime of O atom in the gas–liquid interface are required in future.

The experimental observation of OH line emission in multibubble sonoluminescence suggests that vibrational states of OH are in nonequilibrium inside a bubble at the collapse. The upper levels of OH vibration are overpopulated inside a bubble compared to the equilibrium Boltzmann distribution. Under some conditions, the population increases as the vibrational quantum number increases at relatively high quantum number. Such population could be realized when the translational temperature is much lower than the vibrational temperature known as Treanor distribution. Is the distribution of OH vibrational population inside an SL bubble really Treanor distribution? If yes, why is the translational temperature is much lower than the vibrational temperature? One possibility is that OH vibration is highly excited through chemical reactions inside a bubble. In this case, OH line emission could be due to chemiluminescence. Further studies are required on this topic.

The acoustic field inside a sonochemical reactor is not fully understood because bubbles strongly attenuate acoustic waves and radiate acoustic waves into the surrounding liquid. In addition, bubbles spatially move and the spatial distribution of bubbles is strongly inhomogeneous. The number of bubbles temporally changes by fragmentation, coalescence, and dissolution [55]. The vibration of the container's wall affects the acoustic field inside a sonochemical reactor because it radiates acoustic waves into the liquid [45]. The liquid surface also vibrates under ultrasound,

which influences the reflection of an ultrasonic wave at the liquid surface [53]. The experiments using pulsed ultrasound suggest that large degassing bubbles strongly alter an acoustic field [54]. Further studies are required on the acoustic field inside a sonochemical reactor both experimentally and numerically.

References

1. Yasui K, Tuziuti T, Sivakumar M, Iida Y (2004) Sonoluminescence. Appl Spectrosc Rev 39:399–436
2. Yasui K (2015) Dynamics of acoustic bubbles. In: Grieser F, Choi P, Enomoto N, Harada H, Okitsu K, Yasui K (eds) Sonochemistry and the acoustic bubble. Elsevier, Amsterdam, pp 41–83 (Chapter 3)
3. Yasui K (2001) Effect of liquid temperature on sonoluminescence. Phys Rev E 64:016310
4. Henglein A (1993) Contributions to various aspects of cavitation chemistry. In: Mason TJ (ed) Advances in sonochemsitry, vol 3. London, JAI Press, pp 17–83
5. Yasui K, Tuziuti T, Kozuka T, Towata A, Iida Y (2007) Relationship between the bubble temperature and main oxidant created inside an air bubble under ultrasound. J Chem Phys 127:154502
6. Kamath V, Prosperetti A, Egolfopoulos FN (1993) A theoretical study of sonoluminescence. J Acoust Soc Am 94:248–260
7. Yasui K, Tuziuti T, Sivakumar M, Iida Y (2005) Theoretical study of single-bubble sonochemsitry. J Chem Phys 122:224706
8. Yasui K, Tuziuti T, Iida Y (2004) Optimum bubble temperature for the sonochemical production of oxidants. Ultrasonics 42:579–584
9. Hart EJ, Henglein A (1985) Free radical and free atom reactions in the sonolysis of aqueous iodide and formate solutions. J Phys Chem 89:4342–4347
10. Richards WG, Scott PR (1976) Structure and spectra of atoms. Wiley, London
11. Ho RYN, Liebman JF, Valentine JS (1995) Overview of the energetics and reactivity of oxygen. In: Foote CS, Valentine JS, Greenberg A, Liebman JF (eds) Active oxygen in chemistry. Chapman & Hall, London, pp 1–23 (Chapter 1)
12. Slater JC (1960) Quantum theory of atomic structure, vol I. McGraw-Hill, New York
13. Atkins PW, Friedman RS (1997) Molecular quantum mechanics, 3rd edn. Oxford University Press, Oxford
14. McQuarrie DA, Simon JD (1997) Physical chemistry: a molecular approach. University Science, Sausalito
15. Herzberg G (1944) Atomic spectra and atomic structure, 2nd edn. Dover, New York
16. Biedenkapp D, Hartshorn LG, Bair EJ (1970) The O (^{1}D) + H_2O reaction. Chem Phys Lett 5:379–380
17. Carraher JM, Bakac A (2014) Generation of free oxygen atoms O(^{3}P) in solution by photolysis of 4-benzoylpyridine N-oxide. Phys Chem Chem Phys 16:19429–19436
18. Voitko K, Toth A, Demianenko E, Dobos G, Berke B, Bakalinska O, Grebenyuk A, Tombacz E, Kuts V, Tarasenko Y, Kartel M, Laszlo K (2015) Catalytic performance of carbon nanotubes in H_2O_2 decomposition: experimental and quantum chemical study. J Colloid Interf Sci 437:283–290
19. Christensen H, Sehested K, Corfltzen H (1982) Reactions of hydroxyl radicals with hydrogen peroxide at ambient and elevated temperature. J Phys Chem 86:1588–1590
20. Suslick KS, Hammerton DA, Cline RE Jr (1986) The sonochemical hot spot. J Am Chem Soc 108:5641–5642
21. Yasui K (1996) Variation of liquid temperature at bubble wall near the sonoluminescence threshold. J Phys Soc Jpn 65:2830–2840

22. Yasui K (1997) Alternative model of single-bubble sonoluminescence. Phys Rev E 56:6750–6760
23. Guo X, Minakata D, Niu J, Crittenden J (2014) Computer-based first-principles kinetic modeling of degradation pathways and byproduct fates in aqueous-phase advanced oxidation processes. Environ Sci Technol 48:5718–5725
24. Matula TJ, Roy RA, Mourad PD, McNamara WB III, Suslick KS (1995) Comparison of multibubble and single-bubble sonoluminescence spectra. Phys Rev Lett 75:2602–2605
25. Barber BP, Hiller RA, Lofstedt R, Putterman SJ, Weninger KR (1997) Defining the unknowns of sonoluminescence. Phys Rep 281:65–143
26. Young FR (2005) Sonoluminescence. CRC Press, Boca Raton
27. Brenner MP, Hilgenfeldt S, Lohse D (2002) Single-bubble sonoluminescence. Rev Mod Phys 74:425–484
28. Young JB, Nelson JA, Kang W (2001) Line emission in single-bubble sonoluminescence. Phys Rev Lett 86:2673–2676
29. Luque J, Crosley DR (1998) Transition probabilities in the A $^2\Sigma^+$ - X $^2\Pi_i$ electronic system of OH. J Chem Phys 109:439–448
30. Pearse RWB, Gaydon AG (1976) The identification of molecular spectra, 4th edn. Chapman and Hall, London, pp 264–265
31. Atkins P, Paula J (2014) Atkins' physical chemistry, 10th edn. Oxford University Press, Oxford
32. Pflieger R, Brau HP, Nikitenko SI (2010) Sonoluminescence from OH (C $^2\Sigma^+$) and OH (A $^2\Sigma^+$) radicals in water: evidence for plasma formation during multibubble cavitation. Chem Eur J 16:11801–11803
33. Flannigan DJ, Suslick KS (2005) Plasma formation and temperature measurement during single-bubble cavitation. Nature 434:52–55
34. Flannigan DJ, Suslick KS (2005) Plasma line emission during single-bubble cavitation. Phys Rev Lett 95:044301
35. Ndiaye AA, Pflieger R, Siboulet B, Molina J, Dufreche JF, Nikitenko SI (2012) Nonequilibrium vibrational excitation of OH radicals generated during multibubble cavitation in water. J Phys Chem A 116:4860–4867
36. Mavrodineanu R, Boiteux H (1965) Flame spectroscopy. Wiley, New York, pp 509–510
37. Treanor CE, Rich JW, Rehm RG (1968) Vibrational relaxation of anharmonic oscillators with exchange-dominated collisions. J Chem Phys 48:1798–1807
38. Brau CA (1972) Classical theory of vibrational relaxation of anharmonic oscillators. Physica 58:533–553
39. Bray KNC (1968) Vibrational relaxation of anharmonic oscillator molecules: relaxation under isothermal conditions. J Phys B 1:705–717 (Proc Phys Soc Ser. 2)
40. Fridman A (2008) Plasma chemistry. Cambridge University Press, Cambridge
41. An Y, Li C (2008) Spectral lines of OH radicals and Na atoms in sonoluminescence. Phys Rev E 78:046313
42. Yasui K (2001) Temperature in multibubble sonoluminescence. J Chem Phys 115:2893–2896
43. Flannigan DJ, Suslick KS (2012) Temperature nonequilibration during single-bubble sonoluminescence. J Phys Chem Lett 3:2401–2404
44. Pflieger R, Ndiaye AA, Chave T, Nikitenko SI (2015) Influence of ultrasonic frequency on swan band sonoluminescence and sonochemical activity in aqueous tert-butyl alcohol solutions. J Phys Chem B 119:284–290
45. Yasui K, Kozuka T, Tuziuti T, Towata A, Iida Y, King J, Macey P (2007) FEM calculation of an acoustic field in a sonochemical reactor. Ultrason Sonochem 14:605–614
46. Zienkiewicz OC (1977) The finite element method, 3rd edn. McGraw-Hill, London
47. Dahnke S, Keil F (1998) Modeling of sound fields in liquids with a nonhomogeneous distribution of cavitation bubbles as a basis for the design of sonochemical reactors. Chem Eng Technol 21:873–877
48. McMurray HN, Wilson BP (1999) Mechanistic and spatial study of ultrasonically induced luminol chemiluminescence. J Phys Chem 103:3955–3962

49. Kinsler LE, Frey AR, Coppens AB, Sanders JV (1982) Fundamentals of acoustics, 3rd edn. Wiley, New York
50. Leighton TG (1994) The acoustic bubble. Academic, London
51. Hamilton MF, Il'inskii YA, Zabolotskaya EA (1998) Dispersion. In: Hamilton MF, Blackstock DT (eds) Nonlinear acoustics. Academic, San Diego, pp 151–175, Chapter 5
52. An Y (2012) Nonlinear bubble dynamics of cavitation. Phys Rev E 85:016305
53. Tuziuti T, Yasui K, Kozuka T, Towata A (2010) Influence of liquid-surface vibration on sonochemiluminescence intensity. J Phys Chem A 114:7321–7325
54. Tuziuti T, Yasui K, Lee J, Kozuka T, Towata A, Iida Y (2008) Mechanism of enhancement of sonochemical-reaction efficiency by pulsed ultrasound. J Phys Chem A 112:4875–4878
55. Yasui K, Tuziuti T, Lee J, Kozuka T, Towata A, Iida Y (2010) Numerical simulations of acoustic cavitation noise with the temporal fluctuation in the number of bubbles. Ultrason Sonochem 17:460–472
56. Yasui K, Towata A, Tuziuti T, Kozuka T, Kato K (2011) Effect of static pressure on acoustic energy radiated by cavitation bubbles in viscous liquids under ultrasound. J Acoust Soc Am 130:3233–3242
57. Yasui K, Lee J, Tuziuti T, Towata A, Kozuka T, Iida Y (2009) Influence of the bubble-bubble interaction on destruction of encapsulated microbubbles under ultrasound. J Acoust Soc Am 126:973–982

Part II

Nanomaterials

Sonoelectrochemical Synthesis and Characterization of Nanomaterials

Guohai Yang and Jun-Jie Zhu

Contents

Abstract

Recent advances in nano-dimensional materials have been led by the development of new synthetic methods that provide control over size, morphology, and nanostructure. The sonoelectrochemical method, as a new environmentally friendly strategy, which combines sonochemistry and electrochemistry, has been proven to be a fast, simple, and effective route for shape-controlled synthesis of nanomaterials. During the acoustic cavitation process, high temperatures, pressures, and cooling rates can be achieved upon the collapse of the bubble, which permit access to a range of chemical reaction space normally not accessible, allowing for the synthesis of a wide variety of unusual nanostructured materials. It is commonly accomplished by applying an electric current pulse to nucleate and perform the electrodeposit, followed by a burst of ultrasonic wave to

G. Yang • J.-J. Zhu (✉)
State Key Laboratory of Analytical Chemistry for Life Science, School of Chemistry and Chemical Engineering, Nanjing University, Nanjing, People's Republic of China
e-mail: jjzhu@nju.edu.cn

295

remove the products from the sonic probe cathode. The shape and size of the nanomaterials can be adjusted by varying the operating parameters which include the ultrasonic power, current density, deposition potential, and ultrasonic versus electrochemical pulse times as well as the pH, temperature, and composition of the electrolyte in the sonoelectrochemical cell. Moreover, another setup that is the immersion of a conventional electrochemistry cell into a fixed position in the ultrasound bath is also introduced. Herein, we summarize the recent development of sonoelectrochemical synthesis and characterization of novel nanomaterials, including metals, semiconductors, polymers, and various nanocomposites. A brief look is also taken into the future enabling developments in this field.

Introduction

Nanomaterials have already revealed a great number of potential applications with possible uses in touch screens, capacitors, spintronic devices, fuel cells, batteries, sensors, transparent conductive films, high-frequency circuits, toxic material removal, and flexible electronics because of their unusual optical, magnetic, electronic, and chemical properties [1]. There are a range of methods of producing nanomaterials including radiation methods, thermal decomposition, vapor deposition, reduction in microemulsions, and hydrothermal methods [2]. Synthesizing various types of nanomaterials, including noble metals, metal oxides, multi-composition alloys and semiconductors, tuning over the crystalline structure of such materials, and accurately controlling the shape, size, and composition of composite materials have been developed. However, exploring new methods that involve mild conditions and convenient operations for the preparation of nanosized materials with desirable properties and controllable dimensions and morphologies is still a great challenge to both synthetic chemists and materials scientists. It is hoped that synthetic methods will not only expand the self-assembly of nanomaterials, particularly in the fast-developing field of building large-scale and long-range nanostructures from multicomponent and multidimensional nanomaterials, but also lead to the discovery of novel physical and chemical properties of the materials resulting from their geometrical characteristics.

Among a variety of approaches, the utilization of sonoelectrochemistry for nanomaterials synthesis has been extensively examined over many years and is now positioned as one of the most powerful tools in nanostructured materials synthesis [3]. It is a fast and simple synthetic strategy for the fabrication of nanomaterials and has received great success in the preparation of metals, alloys, semiconductors, and conductive polymers. Sonoelectrochemistry emerged as a new technique combing the sonochemistry and electrochemistry, becoming increasingly important in the last decade. The variety of induced effects on electrochemistry

processes by ultrasound waves can be attributed to the generation, growth, and collapse of microbubbles in the electrolyte. Ultrasound irradiation also offers a very attractive method for the shape-controlled preparation of various nanomaterials. In recent years, it has shown very rapid growth in its application to materials science due to its unique reaction effects. The advantages of this method include a rapid reaction rate, the controllable reaction conditions, and the ability to form nanoparticles with uniform shapes, narrow size distributions, and high purities. It has been extensively used to generate novel materials with unusual properties, because in many cases it causes the formation of particles with a much smaller size and higher surface area than those reported by other methods. During the reaction, high-temperature and high-pressure fields are produced at the centers of the bubbles. The implosive collapse of the bubbles generates a localized hotspot through adiabatic compression or shock wave formation within the gas phase of the collapsing bubbles. The conditions formed in these hotspots have been experimentally determined, with the transient temperature of ~5,000 K, pressure of >1,800 atm, and cooling rates in excess of 10^{10} K/s [4]. Meantime, ultrasound is not simply a source of activation; it also strongly influences the mass transport at the electrode–solution interface. Sonication of electrochemical cell results in a mass transfer enhancement and in activation of the surface of the working electrode. These effects can lead to an acceleration of electrochemical processes, an increase of electrolytic current, a change of the shape of voltammetric curves, and a change of the yield of electrolysis. Electrochemical processes, however, can also be used to synthesize and modify different components of these devices. Moreover, the activation (de-passivation) of the working electrode can enable to carry on preparative electrolysis even in the case, where, without sonication, the process would be hindered by adsorption of products on the electrode surface [5].

Mechanisms of Sonoelectrochemical Process

A number of different arrangements of the equipment have been used for the introduction of the ultrasound irradiation into the electrochemical systems. The two major sources of ultrasound utilized in electrochemistry are ultrasonic baths and ultrasonic immersion horn probes. The first setup is the immersion of a conventional electrochemistry cell into a fixed position in the ultrasound bath as shown in Fig. 1. An ultrasonic bath will be familiar in its capacity to clean electrode surfaces and assist dissolution. However, the power transmitted inside the electrochemistry cell is low, and the results depend strongly on its positioning because the distribution of the ultrasound field is not homogenous [6].

The most widely investigated setup is the introduction of an ultrasonic horn system (often referred to as a sonic probe) directly into an electrochemistry cell (Fig. 2). In these experiments, a titanium probe (usually at 20 kHz) acts both as a cathode and an ultrasound emitter. The electroactive part of the sonoelectrode is the planar circular surface at the bottom of the horn, and the immersed cylindrical part into the electrolyte is covered by an isolating plastic jacket. The ultrasound probe is

Fig. 1 The sonoelectrochemical deposition setup using a conventional electrochemistry cell under the ultrasonic bath
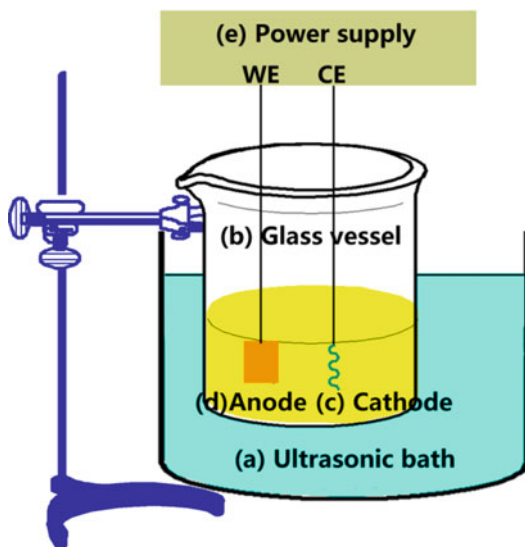
Fig. 2 Schematic of the pulsed sonoelectrochemical deposition setup
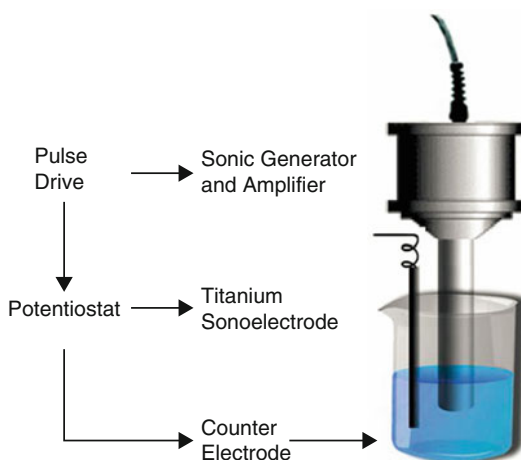
connected to a generator and a potentiostat using a pulse driver [7]. It is commonly accomplished by applying an electric current pulse to nucleate and perform the electrodeposition, followed by a burst of ultrasonic wave to remove the products from the sonic probe cathode. This method is also called the pulsed sonoelectro-chemical technique. The fundamental basis of the pulsed sonoelectrochemical technique for the production of nanomaterials is massive nucleation. At the cathode, a pulse of current (or potential) reduces a number of cations, depositing a high density of metal nuclei on the sonoelectrode surface, and the titanium horn works only as an

electrode during this time. This short electrochemical pulse is immediately followed by a short pulse of high-intensity ultrasound that removes the metal particles from the cathode surface and replenishes the double layer with metal cations by stirring the solution. Sometimes, an interval period without current or ultrasonic vibrations will be useful to restore the initial condition of the sonoelectrode surface. The ultrasonic irradiation differs in this sonoelectrochemical process from its traditional use as an energy source, because here it serves as a shaking element for the electrode. In other words, its mechanical power is used instead of the chemical energy that is used in sonochemistry to some extent. With the development of related techniques, sonoelectrochemistry system has been improved accordingly to overcome many limitations.

Sonoelectrochemistry allows the ultrasonic waves to be directed onto the electrode surface and provides much more efficient power control. There are also a number of environmental applications for sonoelectrochemistry, like the treatment of industrial waste waters, and the enhancement of electroanalytical techniques for the detection of pollutants and for process control, and improved metal recycling. However, the preparation of nanomaterials is the most important branch. Compared with the conventional methods, there are many advantages using the sonoelectrochemical method. Powder material can be obtained with the grain size in the nanometer scale while having a mass production; few restrictions are applied for the shape and size of anode nanomaterials; ultra-fine powder materials can be obtained in large quantities directly without subsequent complex process; the process is flexible and easy to control with reduced environmental pollution. Furthermore, this method can save energy and time and, thus, reduce the cost of final products [8–10]. The most significant effects produced by an ultrasonic field on an electrochemical system include the following: (a) A general improvement in hydrodynamics and the movement of species; (b) The alteration of concentration gradients at various points in the reaction profile and the consequent switching of kinetic regimes, with the resulting effect on mechanisms and reaction products; (c) A cleaning and abrading effect on the electrode surface, thus obviating fouling problems or altering the nature of any coatings that manage to form; (d) Sonochemically induced reactions of intermediate species that have been generated electrochemically; (e) The sonochemical formation of species that react electrochemically in conditions where the silent system is electro-inactive.

Up to now, plenty of nanomaterials have been prepared using the sonoelectrochemical method. The applications of sonoelectrochemistry to materials chemistry are diverse and rapidly increasing. The current review will focus on the preparation of nanomaterials using the sonoelectrochemical method, according to the related literature published to date. The criterion for the classification of nanomaterials is their chemical compositions. Thus, metals, semiconductors, polymers, nanocomposites, etc. will be introduced in this review. It is expected that it would provide a fundamental understanding of their basic principles and to demonstrate the powerful and unique aspects of sonoelectrochemistry in nanostructured materials synthesis.

Development in Sonoelectrochemical Synthesis and Characterization of Nanomaterials

The application of ultrasound in chemistry both for cleaning purposes and for acceleration of existing is well established, as well as for the introduction of new chemical reactions and processes. Nevertheless, in recent years the upsurges in the field of sonochemistry and exploring new fields of application have been observed. Hardcastle et al. [11] investigated the factors that dominated the presence and force of cavitation events at the interface of a macro-electrode, based on an electrochemical detection procedure using several models. It was found that a cavitation counting process based on the electrochemical detection of interfacial cavitation allowed a qualitative insight into the nature of interfacial and bulk cavitation processes. The most extreme and violent processes were clearly observed at a very close distance to the sound-emitting horn tip. They also compared the presence of interfacial cavitation at the electrode–solution interface with sonochemical processes, which occurred predominantly in the bulk solution phase. There was a correlation between the electrochemically detected cavitation violence and the sonochemical activity using a study of the sonochemical destruction of aqueous dilute cyanide solution (in 0.1 M NaOH). Factors that govern the violence of interfacial cavitation appear to be directly proportional to the factors that make cavitation in the bulk solution chemically efficient. Indeed, sonoelectrochemical processes under these extreme conditions may not only cause severe electrode surface erosion but also lead to the breakdown of conventional erosion process at the electrode–solution interface. The concept was applied to electrochemical reactions as well for the sonoelectrochemical production of nanomaterials.

Metals

Nanosized metals have attracted considerable interests in various fields of chemistry, because of their conspicuous physicochemical catalytic properties and their potential applications in microelectronic, optical, electronic, magnetic, and biological devices. The intrinsic properties of a metal nanostructure can be tuned by controlling its size, shape, and crystallinity [12]. Therefore, it should be critical to develop an effective preparation method of particles with well-controlled shapes and sizes. Sonoelectrochemical reduction of noble metal salts has many advantages over other traditional reduction methods (e.g., sodium borohydride, hydrogen, and alcohol): no chemical-reducing agent is needed, the reaction rates are reasonably fast. very small metal particles are produced, and various shapes of nanomaterials can be obtained as well.

Copper was one of the first metals to be synthesized using pulsed sonoelectrochemical methods. In 1994, Reisse et al. made the first sonoelectrochemical setup for the production of copper powders [13]. The sonoelectrochemical effects could be explained on the base of different physical mechanisms such as acoustic streaming, microstreaming and turbulence due to cavitation, and formation of microjets in the course of collapse of cavitation bubbles. Haas et al. [14] synthesized copper clusters

from an aqueous solution of $CuSO_4$ using poly(N-vinylpyrrolidone) (PVP) as a stabilizer. The as-prepared nanomaterials were systematically characterized. The PVP was found to greatly promote the formation rate of copper particles and to significantly reduce the copper deposition rate, thereby making monodispersed copper nanoparticles. The authors could control the particle size by adjusting various parameters such as current density, deposition, temperature, and sonic power and improve the homogeneity of the copper particles. The results also showed that the transfer rate of PVP-stabilized copper clusters from the cathodic vicinity to the bulk solution played an important role in the preparation of the monodispersed nanoparticles. It was proposed that the formation of the dendrites was accounted for the "drying-mediated self-assembly of nanoparticles" theory.

Zin et al. [15] reported the production of platinum nanoparticles from aqueous chloroplatinic solutions under galvanostatic conditions. The platinum nanoparticles produced were spherical with an average grain size ranging from 10 to 15 nm. These nanoparticles aggregated into secondary structures with a mean size ranging between 100 and 200 nm. It was observed that sonication enables the production of platinum nanoparticles with high purity, controlled structure, and homogenous nanometric crystalline size. The cathode efficiency for production of nanoparticles was also calculated. Three-dimensional dendritic Pt nanostructures (DPNs) which were built up by tens of primary nanoparticles with an average dimension of 3 nm were synthesized when PVP was used as stabilizer with a diameter of about 30 nm, which were produced with a current density of 10 mA cm^{-2}, ultrasound intensity of approximately 25 % of the rated power (about 20 W), and a reaction time of 1.5 h as shown in Fig. 3 [16]. The size and morphology of the final product could be controlled via simply adjusting the experiment parameters. The formation process of the DPNs was carefully studied and characterized by transmission electron microscopy (TEM), high-resolution transmission electron microscopy (HRTEM), scanning electron microscopy (SEM), energy-dispersive X-ray (EDX), and X-ray diffraction (XRD), and a spontaneous assembly mechanism was proposed based on the experimental results. The DPNs exhibited good activity for the electrooxidation of methanol and for the electrochemical detection of glucose, making them potentially useful in electrocatalytic applications such as in fuel cells or as biosensors. A major fact to emphasize is the easy and cheap scalable preparation of versatile nanomaterials with extraordinary properties.

Shaped silver nanoparticles with spheres, rods, and dendrites have also been prepared by a pulse sonoelectrochemical technique from an aqueous solution of $AgNO_3$ in the presence of nitrilotriacetate (NTA) [17]. The effects of electrosonic time on particle shape had been discussed. It was found that the concentration of $AgNO_3$ and NTA affected the shape of the Ag nanoparticles. There was no shaped Ag nanoparticles formed without NTA. Well-dispersed spherical Ag nanoparticles with a size of 20 nm, nanorod-structured Ag with a width of 10–20 nm in diameter, and highly ordered dendritic nanostructured Ag were observed at the different concentration of $AgNO_3$. Furthermore, Socol et al. used the same system ($AgNO_3$ + NTA) and proposed a model based on a suspensive electrode formation to explain the growth of dendritic structures [18]. It was the nanoparticles suspended in solution that obtain
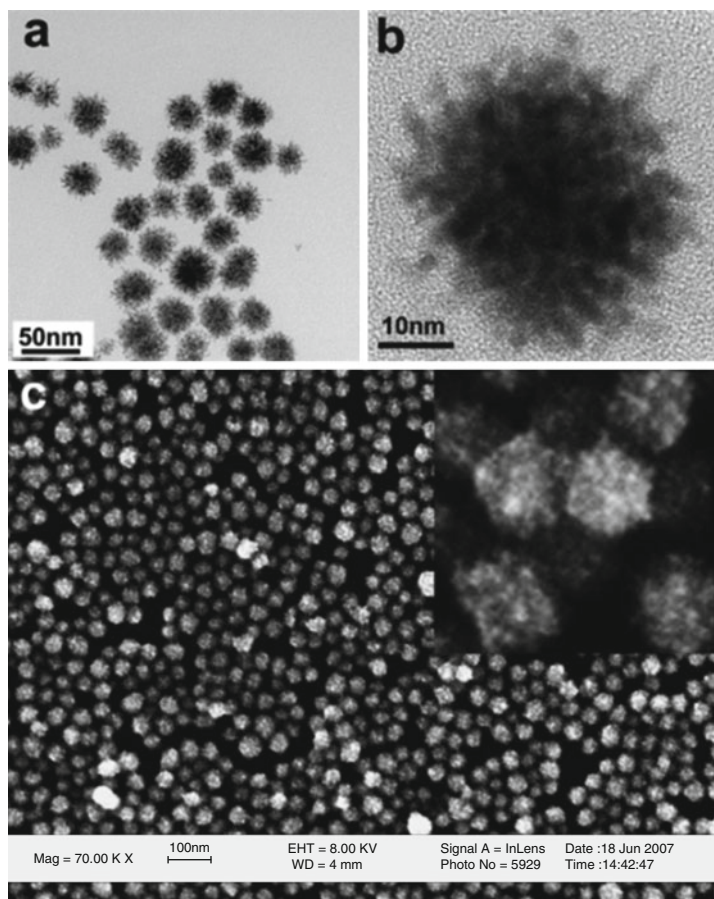
Fig. 3 TEM image in (**a**) low magnification, (**b**) high magnification, and (**c**) SEM image of DPNs; *inset* in (**c**) is the FESEM at high magnification (Reprinted with permission from Ref. [16]. Copyright (2008) American Chemical Society)

the electrode potential, thus act as part of the electrode. In details, particles expelled from the electrode surface as a result of the ultrasonic pulse into the solution where they can remain suspended, and then the suspended particles were moved in the solution by the sonic wave, hit the sonoelectrode, accept its potential, and travel back to the solution. These charged silver particles acting as part of the cathode could cause electrodeposition of silver ions and therefore grow. The major significance of this new insight was the opening up of new possibilities for sonoelectrochemical synthesis of the nanocomposite and core–shell materials.

Liu et al. have synthesized gold nanoparticles by a modified sonoelectrochemical method [19]. In their work, the bulk gold substrate was served as the sacrificial anode to obtain gold-containing complex solution. Then the bulk gold substrate was replaced by a Pt electrode, and a cathodic overpotential was applied under sonication
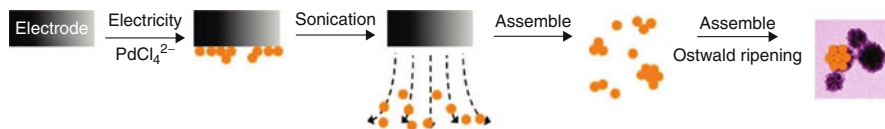
Fig. 4 Schematic illustration of the formation of palladium SSPs (Reprinted with permission from Ref. [21]. Copyright (2009) American Chemical Society)

to synthesize gold nanoparticles. The ultrasonic irradiation was performed by using an ultrasonic generator and was operated at 20 kHz with a barium titanate oscillator of 3.2 mm diameter to deliver a power of 100 W. Size-controlled gold nanoparticles, ranging from 2 to 15 nm in diameter, were prepared by authors. The particles size increased with the increase of the cathodic overpotential applied. However, there were some inconveniences in their reports. First, the gold precursor is the gold-containing complex which was obtained from the oxidation of the bulk gold substrate. Second, the working electrode must be replaced, which led to the relative complicated operation and the low production. Moreover, developing the sonoelectrochemical method to synthesize gold nanoparticles in the absence of stabilizers was still rarely concerned. Recently, Shen et al. reported a facile pulse sonoelectrochemical method to synthesize gold nanoparticles in the absence of any stabilizer [20]. The gold nanoparticles were produced with a current intensity of $16.3 \, \text{mA cm}^{-2}$, an ultrasound intensity of approximately 20 W, and a reaction time of 1.5 h. When the pH was 4, the uniform spherical gold nanoparticles with a diameter of about 20 nm were obtained. It was shown that the pH value of the precursor solution had a great effect not only on the size and shape of the Au nanoparticles but also on the dispersion of the gold nanoparticles. Finally, horseradish peroxidase was immobilized on the gold nanoparticles and fabricated a good biosensor response to H_2O_2.

Sonoelectrochemical method was used to realize the morphology-controlled synthesis of palladium nanostructures at room temperature [21]. The reaction conditions, such as the concentration, the molar ratio of reactants, and the pH value, were investigated, showing that sonoelectrochemistry could control the formation of the resultant samples. Palladium spherical nanoparticles, multi-twinned particles, and spherical spongelike particles (SSPs) were prepared using hexadecyltrimethyl ammonium bromide, PVP, and polydiallyldimethylammonium chloride as stabilizer, respectively. A spontaneous assembly mechanism was proposed for the formation of SSPs (Fig. 4). First, palladium ions were reduced by electricity to form palladium primary nanoparticles on the electrode. Then, the palladium primary nanoparticles were separated in the solution by ultrasonication. The primary nanoparticles could spontaneously assemble together and form small SSPs. With the increase of time and the continuous formation of primary nanoparticles, the small SSPs grew up and finally formed spherical SSPs. In addition, under the ultrasonic condition, the Ostwald ripening process was accelerated, which led to the small primary nanoparticles in favor of the crystallite reorganization. Electrochemical results demonstrated that the palladium SSPs nanostructures possessed excellent electrocatalytic properties and could be of great potential for direct alcohol oxidation

in alkaline media. The interconnected structure of palladium SSPs not only led to a high surface area but also provided enough absorption sites for involved molecules in a limited space.

Typically, zinc, nickel, and cobalt [9, 22] nanoparticles have also been successfully synthesized by pulsed sonoelectrochemical methods. Based on the tools and methods available now, it is expected that the application of ultrasound in areas as diverse as electroanalytical and synthetic electrochemistry will be beneficial, and new innovative approaches employing the various mechanical and chemical effects of ultrasound will result. With simple variations of reaction conditions and precursor compositions, a myriad of nanostructured materials with controlled morphologies, structures, and compositions could be successfully prepared by the application of sonoelectrochemistry. In another report, tungsten nanoparticles with high melting point have been synthesized by the sonoelectrochemical method [23]. A platinum slice was used as the anode and a titanium alloy horn as the cathode. An ultrasonic power density above the cavitation threshold of the electrolyte (about 500 kW m^2) was used. The ultrasound was pulsed with the duration ranging from 1 to 2 s. Due to the electrochemical reaction and the cavitation effect of the ultrasound, the iron–tungsten aggregates at the cathode were dispersed into the electrolyte, and iron atoms were dissolved in the acidic environment. In this way, body–center–cubic tungsten nanoparticles had been obtained by controlling the density of the electric current, the ultrasound pulse period, and the amplitude. The method of direct preparation by sonoelectrochemistry in a pressurized reactor can be utilized for efficient formation of metal structures to produce high-quality products in large quantities allowing further scaling and not requiring any aggressive chemicals. Therefore, it presents an environmentally benign method possibly attractive for industrial preparation.

Nanoparticles of very reactive metals with a high negative reduction potential, e. g., magnesium and aluminum, can also be synthesized using sonoelectrochemistry. No active reducing agents are known to reduce such active metals whose standard reduction potentials are negative. It is therefore clear that only electrolytic methods can lead to the reduction such as sonoelectrochemistry. Moreover, the present method is considered a promising technique for the fabrication of a large amount of nanometal particles. In 2008, 4 nm-sized and well-dispersed metallic magnesium particles were prepared by the sonoelectrochemical method, in which a plastic bag was used to avoid oxidation in the case of reactive metals [24]. In order to increase the ionic conductivity of the ether-based Grignard solutions, $AlCl_3$ was added to the solution in their contributions, in which the formed $MgCl^+$ in the reaction was an electrochemically active species. The Mg deposition was carried out using two different electrolyte solutions based on Grignard reagents (EtMgCl and BuMgCl) in ethers (tetrahydrofuran (THF) and dibutyl diglyme (DBDG)). The product efficiencies in THF and in DBDG were different at 41 % and 33 %, respectively, which might be ascribed to the difference in solution viscosity. Similarly, Mahendiran et al. also prepared aluminum nanoparticles with the similar experiment [25]. TEM analysis showed that the prepared aluminum nanoparticles ranged from 10 to 20 nm in size, and EDX results confirmed that the surface of the material was mainly

composed of aluminum. The selected area electron diffraction pattern showed the formation of ring patterns, which inferred the polycrystalline behavior of the materials and confirmed that the metal is Al. It should be noted that the current pulse used in the synthesis of aluminum and magnesium nanoparticles is much longer than those commonly used in the other nanometal synthesis (the duration of the current pulse was 600 s, and the off time of the current pulse was 60 s. The duration of the ultrasonic pulse was 240 ms. The ultrasound power intensity was 76 W). Maybe there is still space to improve in these studies.

Nanoalloys

The sonoelectrochemistry technique has been applied to the synthesis of binary and ternary alloyed nanopowders. Pure, binary and ternary alloyed iron, cobalt, and nickel nanopowders were obtained and characterized by Delplancke et al. [26] using a simple and inexpensive method. Binary and ternary alloys were deposited galvanostatically at 8,000 A m^{-2} and particles with a mean diameter of 100 nm were produced. Their composition and homogeneity were easily controlled by selecting the electrochemical and ultrasound parameters. It is worth noting that samples sonoelectrochemically prepared were different from that sonochemically prepared, which were studied by Mossbauer spectroscopy. Dabalá et al. presented a study on the synthesis of cobalt–iron alloy nanoparticles ($Co_{65}Fe_{35}$) using the sonoelectrochemical method to combine metallic electrodeposition with power ultrasound [27]. Temperature has an obvious influence on electrode kinetics, and the potential E is known to be temperature dependent. In these experiments, the temperature of the bulk solution was controlled and never rose above 298 $\pm$ 1 K during the sonoelectrochemical ran. The smallest particles had a mean dimension of about 5 nm, exhibited a bcc structure and strongly aggregated in three-dimensional clusters of about 300 nm. It was found that the faradaic yield was mainly affected by both the current density and the time management; the cathode efficiency was high and remained over 50 % or applied currents lower than −20 mA, but as the applied current increased by 50-fold, the cathode efficiency decreased tenfold.

Gold–silver alloy nanoparticles were also prepared by a novel sonoelectrochemical method from their bulk substrates without addition of any stabilizer due to their universe applications [28]. First, a silver substrate was roughened by a triangular wave oxidation–reduction cycle (ORC) in an aqueous solution containing HCl. Silver-containing complexes were found in the solution after the ORC treatment. Then a gold substrate was subsequently roughened by the similar ORC treatment in the same solution containing the silver complexes. After this procedure, Au- and Ag-containing complexes were left in the solution. Then the Au working electrode was immediately replaced by a Pt electrode, and gold–silver alloy nanoparticles, with the mean diameter of 5 nm and the content of Ag in the alloy nanoparticles being about 18 mol%, could be obtained at a cathodic overpotential of 0.6 V from the open circuit potential of ca. 0.75 V versus Ag/AgCl applied under sonification. The ultrasonic irradiation was performed by using an ultrasonic

generator and operated at 20 kHz with a barium titanate oscillator of 3.2 mm diameter to deliver a power of 100 W. The nature of the alloy was characterized by XPS. Variable contents of metal in alloy nanoparticles and size-controlled alloy nanoparticles could be easily synthesized by sonoelectrochemical reduction methods. The new sonoelectrochemical method has since been employed to produce numerous pure metals or alloy nanopowders with many advantages; however, to further improve the performance, how to synthesize higher-quality nanocrystals with morphology tunable is still a critical issue in this field.

Semiconductors

Semiconductor nanomaterials with superior characteristics of electronic, mechanical, optical, and transport nature are the foundations of modern electronics, finding applications in photochemistry, in dye-sensitized solar cells, in analog-integrated circuits, in the photocatalytic treatment of chemical waste, and so on [29]. One of the best bulk thermoelectric materials at room temperature are alloys of $A_2^V B_3^{VI}$ binary compounds such as Bi_2Te_3, Sb_2Te_3, Bi_2Se_3, which are doped with trace amount of other elements. This makes Bi_2Se_3 a good target material for developing heterojunction nanowires that have good potential to improve thermoelectric properties. Qiu et al. presented an alternative sonoelectrochemical route for the formation of striped Bi_2Se_3 nanowires [30]. The work was based on a previous setup using current densities in the range of 35.4–53.0 mA cm^{-2}. A nanowire junction with sharp interface could be clearly observed from the TEM image after a reaction of 15 min (Fig. 5a, b). It was confirmed that the heterogeneous nanowire was composed of two distinct phases of Bi_2Se_3. Moreover, a more exciting multijunction nanowire was found in the longer-sonicated samples, producing distinct phases within the nanowires. In this step, the solution was continuously sonicated for 1–3 h. The ultrasound pulse on/off ratio was 9:1 using a 0.6 cm diameter Ti horn at 20 kHz and 60 W cm^{-2}. The length of each phase is about 30 nm (Fig. 5c, d). The fabrication of one-dimensional superlattices in nanowires under ambient conditions was realized, and such nanowires were important to enhance the thermoelectric figure of merit.

Furthermore, highly uniform, single-crystalline, and pure PbTe nanorods with a diameter in the sub-10-nm regime were successfully prepared using NTA as stabilizer through a sonoelectrochemical method under ambient conditions (Fig. 6) [31]. The sonoelectrochemical method could achieve one-dimensional morphous control without any template, thereby practically overcoming the limitation of generating nanorods with diameters below 10 nm. Basically, the synthesis of PbTe nanorods consists of two steps: first, the electrodeposition of PbTe on the surface of the Ti sonication horn and, second, the dispersion of the PbTe nuclei into the solution by pulsed sonication. Pb^{2+}/NTA ratio played a key role in the synthesis of PbTe nanorods. Figure 6f showed that with very low concentrations of Pb^{2+} (2 mM), only spherical particles were observed and the increase in the concentration of Pb^{2+} ions caused the spheres to grow and rod-shaped morphologies to be formed. These very thin and cubic PbTe nanorods are promising building units for future thermoelectric devices.
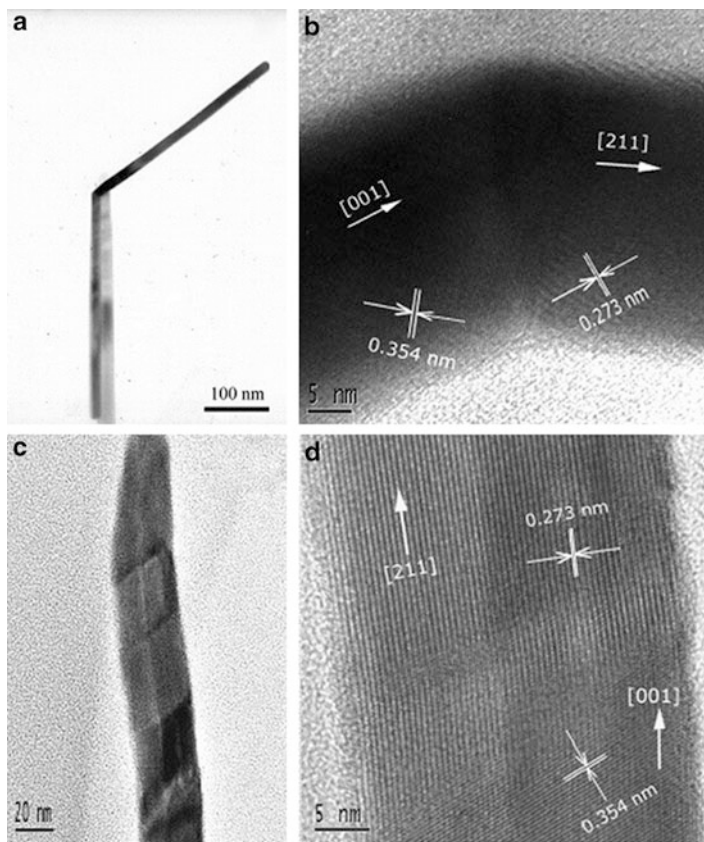
Fig. 5 (**a**) TEM image of a heterostructured Bi_2Se_3 nanowire. (**b**) HRTEM image of the heterojunction; the lattice spacing of phase 1 is 0.273 nm which corresponds to the [211] plane of the orthorhombic phase; the lattice spacing of phase 2 is 0.354 nm, which corresponds to the [001] plane of the hexagonal phase. (**c**) TEM of bismuth selenide multiple-heterojunction nanowire with periodic phase boundaries; the thickness of the nanowire is 29.2 nm, and the aspect ratio is 13.2. (**d**) HRTEM of the nanowire junction; lattice constant of phase 1 corresponds to orthorhombic Bi_2Se_3 along the [211] direction; the lattice constant of phase 2 corresponds to hexagonal Bi_2Se_3 along the [001] direction (Reprinted with permission from Ref. [30]. Copyright (2004) American Chemical Society)

Mancier et al. prepared Cu_2O nanopowders by ultrasound-assisted electrochemistry with a potentiostatic setup [32]. To produce nanopowders with control of the synthesis reaction, a classic three-electrode electrochemical setup with the sonotrode as the working electrode was employed. The reference electrode was a saturated mercury sulfate electrode (SSE). The work was based on a previous voltammetric study which showed that at an applied potential ranged between −0.65 and −1.0 V (vs. SSE). It was confirmed that only Cu_2O was formed, while there was neither metallic copper nor CuO formed at these potentials. Electron microscopy and centrifugation studies indicated that the powders consist of agglomerates of grains
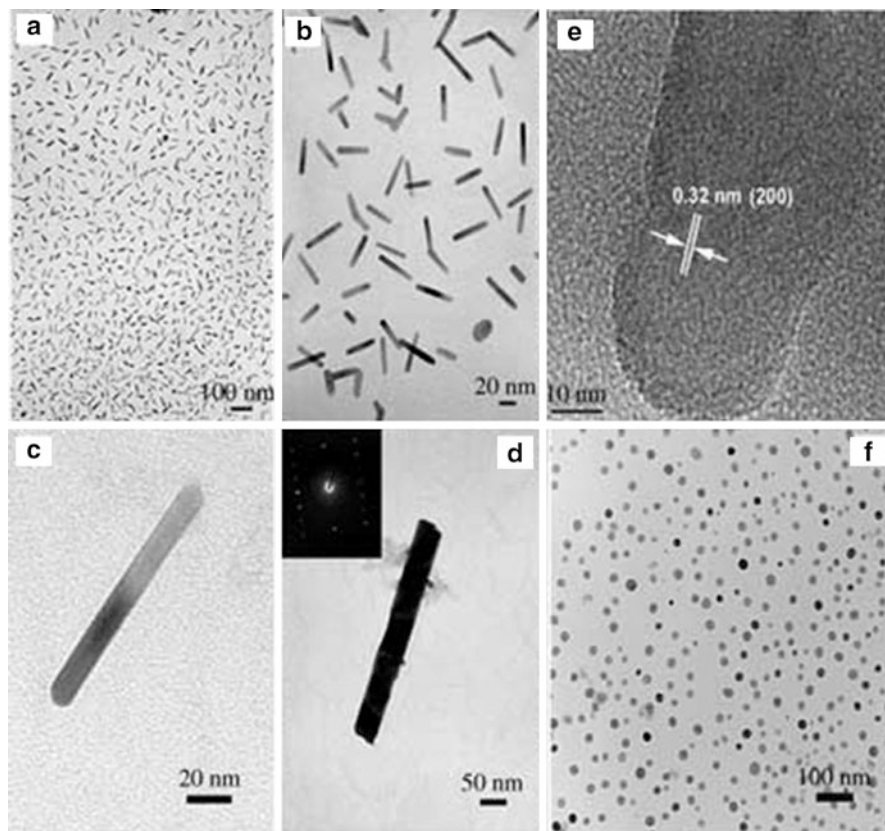
Fig. 6 (**a**) TEM image of PbTe nanorods prepared by sonoelectrochemistry at room temperature for 30 min. (**b**) Enlarged TEM image of PbTe nanorods prepared under identical conditions. (**c**) TEM image of a nanorod obtained after 45 min of reaction. **d** TEM image of a nanorod obtained after 1.5 h of reaction; the inserted selected area electron-diffraction pattern indicates the single-crystal nature of the shown nanorod. (**e**) HRTEM image of PbTe, a nanorod indicating the (200) lattice plane spacing. (**f**) Spherical PbTe nanoparticles synthesized under a low concentration of Pb^{2+} ions (2 mM) (Reprinted with permission from Ref. [31]. Copyright (2005) Wiley-VCH)

and isolated particles, which have a mean diameter of 8 nm. The specific surface areas determined by Brunauer–Emmet–Teller model are very high with a value close to 2,000 m^2 g^{-1}. The results showed that sonoelectrochemical methods have the potential to produce nanometer-scale semiconductive metal oxides.

Very recently, high-photoluminescent, water-soluble CdTe quantum dots were conveniently synthesized without precursor preparation and N_2 protection [33]. The mechanism of formation could be explained as follows: firstly, the Cd^{2+} and TeO_3^{2-} diffused toward the surface of the sonoelectrode; secondly, the TeO_3^{2-} ions were reduced to Te^{2-} by a controlled electric pulse; the Te^{2-} combined with Cd^{2+} to form CdTe nanoparticles immediately on the electrode surface; and then the CdTe nanoparticles were removed from the electrode surface by ultrasonic pulse.
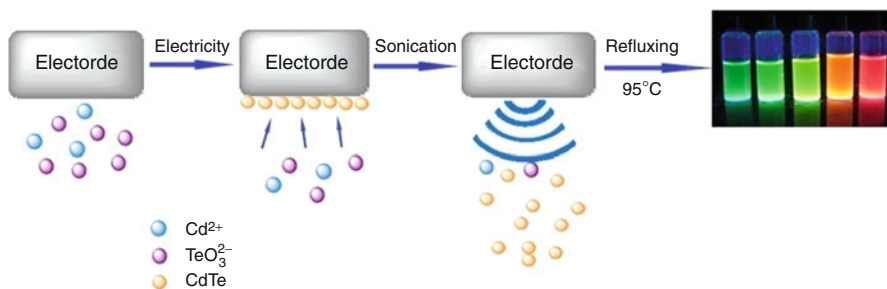
Fig. 7 The formation of CdTe quantum dots via sonoelectrochemistry (Reprinted with permission from Ref. [33]. Copyright (2014) Elsevier)

With the amount of primary CdTe nanoparticles increasing in the electrolyte, the Ostwald ripening exhibited as the dominant mechanism (Fig. 7). More importantly, because of the fast reduction for Te^{4+} to Te^{2-} occurred to supply the rapid nucleation of quantum dots on the sonoelectrode, no N_2 was used. The experimental results showed the photoluminescence emission wavelength and quantum yield of the water-soluble CdTe quantum dots could be effectively controlled by adjusting the synthetic parameters. In details, with the reaction time increasing, the photoluminescence peaks shifted to longer wavelengths; the photoluminescence quantum yield increased with the increase of reaction time due to the improvement of the crystallization and annealing effect of defects. However, further reaction resulted in a decrease in quantum yield due to broad distribution and relatively small surface/volume ratio of the obtained quantum dots. The red shift of the photoluminescence peak also occurred with the increase of current pulse width; when the current pulse width increased to 0.5 s, the highest photoluminescence quantum yield was obtained. However, as the current pulse width continued to increase, the CdTe nanoparticles formed on the sonoelectrode became larger but more surface defects occurred, resulting in lower photoluminescence quantum yield due to the production of the electronic traps. Such method can be expected to prepare more quantum dots as promising building blocks in solar cell, photocatalysis, sensors, and so on.

Self-ordered arrays of TiO_2 nanotubes of 30–100 nm in diameter and 300–1,000 nm in length could be rapidly synthesized under an applied potential of 5–20 V, with ultrasonic waves irradiated onto the solution to enhance the mobility of the ions inside the solution [34]. Briefly, nanotubular TiO_2 arrays were formed by anodization of the Ti foils in 300 mL of electrolytic solution using ultrasonic waves (100 W, 42 kHz). It was said that collapse of a cavitation bubble on or near to a solid surface generated a powerful liquid jet targeted at the surface during the reaction. This effect increased mass flow through the nanotubular surface and thus increased the rate of formation of the nanotubes. On the other hand, the formation of the nanotubes using conventional magnetic stirring was retarded by the formation of a double layer and diffusion-limited transport of the species. A better quality of nanotubes could be obtained through the sonoelectrochemical method, because the mass transfer throughout the process was uniform. The TiO_2 nanotubes synthesized

through the sonoelectrochemical route were then tested for photoelectrocatalytic generation of H_2 using water splitting and were found to have better activity than the nanomaterials prepared by the magnetic stirring technique due to the special structure.

MoS_2 has attracted a lot of attention for its promising semiconducting characteristics and potential applications in nanoelectronics and optoelectronics, as well as in energy storage and conversion. Mastai et al. exploited ultrasonic excitation, involving local bursts of very high temperature in and around collapsing bubbles (cavitation), to synthesize closed fullerene-like structures of MoS_2 by electrodeposition from thiomolybdate solutions onto an ultrasonic probe at room temperature [35]. The particles are typically several tens of nm in size, and most of the particles have sizes which are the same order of magnitude in all three dimensions according to the TEM results. Such closed structures usually require high temperatures for their formation to provide the high energy needed for their closure. While the combination of electrochemical and sonic processes facilitated the formation of fullerene-like structures. Either electrodeposition or ultrasonic irradiation alone results in X-ray amorphous Mo-S products, but the combination of both gives well-crystallized closed structures of MoS_2. It is promising to prepare atomically thick two-dimensional MoS_2 based on the above method which is a conceptually new class of nanomaterials. A series of semiconductors has been developed using sonoelectrochemistry, with the rapid heating and cooling of nebulized droplets that can easily create the rapid nucleation required. It is also desirable to develop more general synthetic routes to grow a broader range of semiconductor nanomaterials.

Conducting Polymers

Polymers, especially conducting polymers, exhibit not only electroconductivity but also unique optical and chemical properties [36]. The diversity of the properties exhibited by conducting polymers suggests that these materials can be used in numerous technological applications. Conducting polymer nanomaterials including polyacetylene, polypyrrole, polythiophene, polyaniline, and their derivatives can be synthesized through chemical or electrochemical routes. Chemical reactions usually produce powdery nanomaterials and can be easily scaled up; on the other hand, electropolymerization restricts the reactions on the surfaces of electrodes, and the nanostructures of conducting polymers are usually deposited on the electrode surface as films. Applications of ultrasound to materials chemistry have been further extended to polymers as well. The potential benefit of sonoelectrochemistry combining both sonochemistry and electrochemistry will facilitate the preparation of size- and shape-controlled conducting polymer.

Reyman et al. studied the effect of an ultrasonic field of 530 kHz frequency through a ceramic disk transducer mounted on a stainless steel plate on the electrodeposition of polythiophene in an acetonitrile solution using lithium perchlorate as background electrolyte [37]. Electrolysis was carried out at a constant temperature of 20 °C. As can be seen in Fig. 8, the surface obtained with ultrasound showed a more
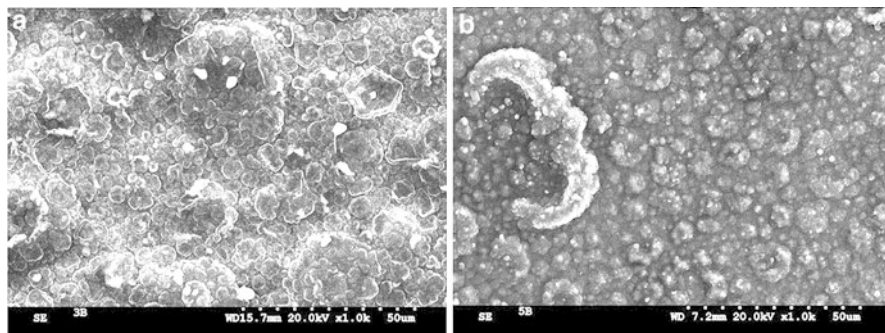
Fig. 8 SEM surface micrographs of polythiophene film obtained in 0.3 M thiophene and 0.03 M LiClO$_4$ in acetonitrile solution on tin oxide. (**a**) Without ultrasound, (**b**) with ultrasound (Reprinted with permission from Ref. [37]. Copyright (2007) Elsevier)

compact and homogenous morphology than that obtained without irradiation. This result could be explained by two parallel phenomena. The first was the diffusion of electroactive species to the electrode surface. In this case, the electropolymerization process was controlled by charge transfer and not by diffusion of the species from the bulk to the electrode–solution interface. The second phenomenon referred to other effects such as the formation of microflows close to a surface. The impact of microbubbles on the electrode surface caused the elimination of the points with the greatest energy, thus producing a certain cleaning of the surface, i.e., leveling all the surface and increasing its homogeneity. Moreover, they performed the sonoelectrodeposition of the polymer in the presence of the fluorophores Harmane (1-methyl-9H-pyrido[3,4-b]indole) or BCCM (9H-pyrido[3,4-b]indole-3-carboxylic acid methyl ester), while the films generated in the absence of ultrasound showed no fluorescence.

Ganesan et al. [38] reported the synthesis of polyaniline nanoparticles by oxidative polymerization using the sonoelectrode as anode without any costly dopants or surfactant. In the synthesis, a constant potential pulse of +1 V (vs. Ag/AgCl/3 M NaCl) was applied to a solution of 75 mL of 0.5 M aniline and 0.5 M HCl for 2 h. The duration of the potential pulse was 8,000 ms, and the off time of the potential pulse was 800 ms. The ultrasound power intensity was 76 W. Infrared and UV–vis spectra confirmed the formation of polyaniline nanostructures. Electron microscopy showed morphology of large particles with a diameter of 2–4 μm was made up of tiny polyaniline nanoparticles with an average size of 20–40 nm. The tiny polyaniline nanoparticles might be caused by the sonoelectro-pulse, which were nucleated and removed from the surface of the electrode. The resultant nanomaterial exhibited high capacitance, because the electrochemical utilization of the active nanomaterial on the electrode was responsible for a higher electrochemical activity, which benefited from the advantages of electrochemical technique.

Atobe et al. [39] reported the synthesis of nanosized poly(N-methylaniline) (PNMA) by the use of a pulsed sonoelectrochemical method (Fig. 9a). The platinum
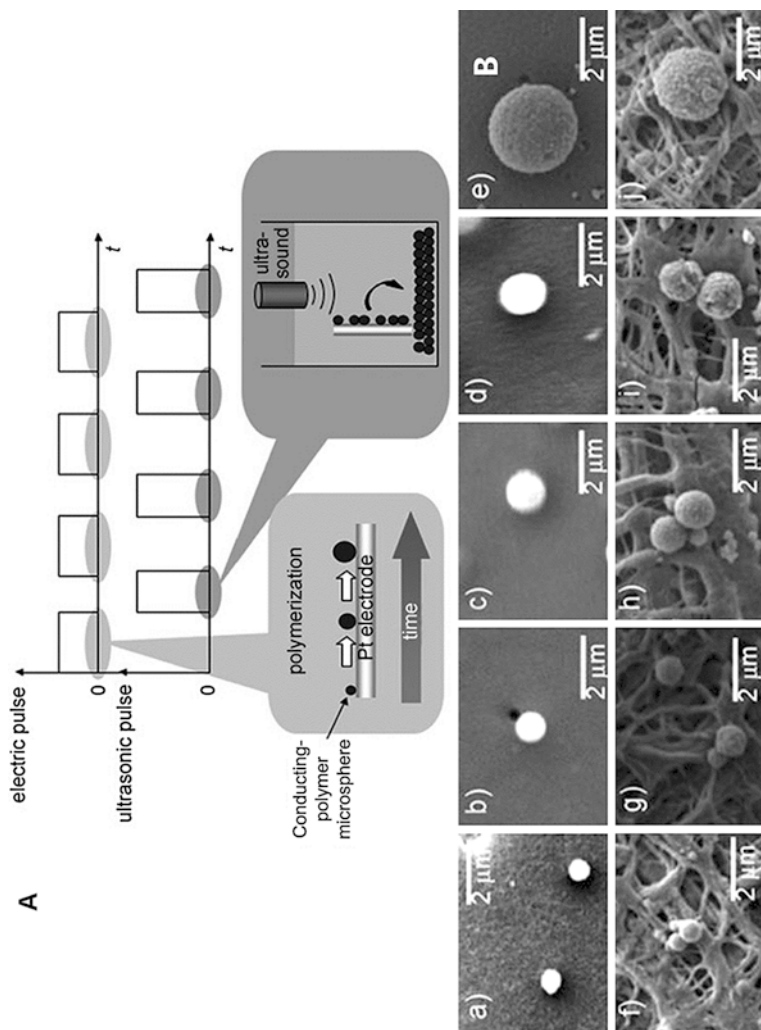
Fig. 9 (**a**) Pulsed sonoelectrochemical method for the production and recovery of conducting polymer microspheres; (**b**) SEM images of PNMA microspheres (**a**–**e**) as deposited on the anode surface by applying a potential pulse and (**f**–**j**) ablated from the anode surface by applying a subsequent sonic pulse. Experimental conditions: potential pulse, 0.75 V versus saturated calomel electrode; ultrasonic pulse density, 31 W cm^{-2}, duration of the ultrasonic pulse, 5 s; duration of the potential pulse, 10 (**a**, **f**), 20 (**b**, **g**), 30 (**c**, **h**), 40 (**d**, **i**), 90 s (**e**, **j**) (Reprinted with permission from 39. Copyright (2009) Wiley-VCH)

anode surface was positioned vertically to the propagating direction of ultrasonic waves. It was said that this arrangement overcame the drawback related to the use of an ultrasound horn in oxidation process. The experiment was carried out under a constant potential pulse of 0.75 V (vs. saturated calomel electrode) to the platinum electrode in an aqueous solution of methylaniline in HClO$_4$. The sonic pulse had a power of 31 W cm^{-2} with a duration of 5 s. PNMA microspheres were obtained, and the subsequent sonication had the sole role of ablating the microspheres from the anode surface and did not break them (Fig. 9b). When the electric pulse width was fixed during the sonoelectrochemical synthesis, the size of the spheres was well controlled and depended on the electric pulse width. This result suggested that the effective removal of the deposit from the anode by the sonic pulse occurred before the next electric pulse, thus preventing further growth of spheres. The redox properties of their solution-cast film on an indium tin oxide electrode were then investigated. The results revealed its high activities which might be ascribed to the effective charging and discharging of spheres. Thus it is expected that this new methodology will make a significant contribution not only to polymer chemistry but also to various device technologies.

Polypyrrole is one of the most studied conducting polymers due to its high electronic conductivity, good stability in air and aqueous media, and ease of preparation by either chemical or electrochemical polymerization. Dejeu et al. presented electrochemical synthesis of polypyrrole films under high-frequency sonication [40]. It was the first time to show that electrochemical polymerization of polypyrrole under high-frequency sonication (500 kHz) was possible on Si substrates, overcoming the problem to destroy the polymer film electrodeposited on substrate under 20 kHz sonication. The transmitted acoustic power was equal to 7.8 W. Systematical comparisons were made between the samples obtained with and without sonication. Important film parameters such as thickness, roughness, morphology, and adhesion were explored to observe the effects of sonication. SEM and mechanical probe profiling showed that sonication led to less rough and more homogenous surface structure. It was shown that the adhesion forces between sonicated polypyrrole films and Si substrates were very weak tested by atomic force microscopy, indicating that sonicated polypyrrole films were good candidates for applications in robotics since micromanipulation of robots needs the reduction and the minimization of adhesion forces between the micro-objects and the gripper.

In common, the wanted charge quantity under sonication is reached much faster than in silent conditions. The improvement of the mass transfer toward the electrode under sonication can be explained by the propagation of the ultrasound mechanical wave that creates a global convection within the liquid medium due to the energy losses. Therefore, it will increase mass transfer of the monomers in solution to the electrode. Moreover, an interface collapse of cavitation bubbles becomes asymmetric, and the formation of violent microjets directly toward the working surface enhances mass transfer to the electrode, allowing its activation by impingement. The monomers are thus brought to the electrode interface more efficiently, and electropolymerization is facilitated. Further work is needed in order for as-prepared polymers to become a successful class of multifunctional material.

Nanocomposites

In the last few decades, huge efforts have been made to synthesize versatile nanocomposite structures. In such systems, not only each component usually retains its original properties; new properties can also be attained by combining several materials. These nanomaterials prepared by various fabrication methods are widely employed in applications like biomedicine, electronics, optics, electrochemical energy conversion and storage, solar energy harvesting, and so on [41]. Nanocomposites, i.e., composite materials with one or more nanostructured components, containing hierarchically structured nanoparticles with single-particle precision may pave the path for next-generation nanodevices to meet the demands of future technologies. To obtain targeted functional nanocomposites, it is requisite not only to select the right nanoparticles as building blocks but also to develop approaches to assemble these artificial atoms over multiple length scale and, moreover, to be able to apply these approaches for nanoparticles with controlled shape, size, crystallinity, and functionality rather than the random mixtures. Therefore, this area of study within nanoscience still presents significant challenges for research before the goal of engineering nanomaterial properties is realized to its full potential. Sonoelectrochemistry provides the possibility for synthesizing related nanocomposites. For example, self-organized anodic TiO_2 nanotube arrays are functionalized with CdS nanoparticle-based perfusion and deposition through a single-step sonoelectrodeposition method [42]. A two-electrode system comprising a TiO_2 nanotube arrays working electrode (1×1 cm^2) and a Pt foil counter-electrode was employed. A mixed solution of 0.01 M $CdCl_2$ in dimethyl sulfoxide with saturated elemental sulfur is used as the electrolyte. First, the mixed solution was bubbled with flowing N_2 for 30 min in order to remove O_2 and any moisture within the solution. Second, the solution was persistently stirred for 2 h for an even mixing. Third, the mixed solution was irradiated using an ultrasonic with a frequency of 40 kHz and ultrasonic intensity of 2.4 kW m^{-2} for 2 h. The application of the sonoelectro-chemical technique led to better solar light harvest in the visible light region. Thus, the sonoelectrochemical method will provide a promising technique to fabricate excellent composite materials at lower temperature in organic solvent. Calcium phosphate was deposited sonoelectrochemically on carbon fabrics via superposition of the ultrasound on the electric field [43]. In this study, the addition of the ultrasonic wave generated more small crystals on the substrate surfaces compared to simple electrodeposition. In addition, the adhesive strength between the coating and carbon substrate was much higher than that obtained without sonication based on morphology and composition analysis. It was stated that the accelerated mass transfer and the degassing action on account of the ultrasound might provide a route for the generated hydrogen to escape from the electrodes. As a result, the internal stress could be released to a certain degree, causing the observed improvement of adhesion between the calcium phosphate coating and the carbon substrates. In vitro assessments showed the significant improvement in the cell attachment and proliferation was because of the phosphate deposits prepared by sonoeletrodepostion rather than the traditional silent one. Effects of different current densities and concentrations of electrolyte were also investigated. It was reported the morphology of the samples changed with the different experimental parameters.

Ashassi-Sorkhabi et al. synthesized sonoelectrochemically polypyrrole/multiwalled carbon nanotubes (MWCNTs)/chitosan nanocomposite with a standard three-electrode system for the first time [44]. Sonoelectro-polymerization of coatings on St-12 steel was carried out in an oxalic acid solution by a galvanostatic method. The aqueous electrolyte solution consists of oxalic acid (0.1 M), pyrrole monomer (0.1 M), dodecylbenzene sulfonic acid (100 mg L^{-1}), chitosan (0.02 g L^{-1}), and MWCNTs (0.05 g L^{-1}). It was prepared by dissolving appropriate volume of distilled pyrrole, dispersing MWCNTs, and dissolving chitosan in aqueous oxalic acid media under ultrasonic irradiation. SEM images indicated that the as-prepared nanocomposite looked condensed and homogenously covered the metal surface. It was considered the MWCNTs were the main component to build up the network of the polypyrrole/MWCNTs/chitosan nanocomposite. This study showed that the polypyrrole/MWCNTs/chitosan nanocomposite resulted in a good corrosion prevention, expanding the application field of the sonoelectrochemistry.

In another report, a simple, fast, reproducible and efficient one-step fabrication method was successfully developed to prepare gold nanoparticles/carbon nanosheet hybrids using sonoelectrochemistry [45]. The entire process was carried out in a homemade sonoelectrochemical device, which provided the high-intensity electric field and ultrasonic field. The electric and ultrasound fields played a crucial role in the production and dispersion of gold nanoparticles and the carbon nanosheet. The gold nanoparticles and carbon nanosheet formed must be rapidly transferred from the vicinity of the cathode and anode to the bulk solution to facilitate the self-assembly of gold nanoparticles on the surface of the carbon nanosheet. If the fabrication of gold nanoparticles/carbon nanosheet were carried out without an ultrasonic field, deposition of the gold nanoparticles and carbon nanosheet on the respective electrodes would occur (Fig. 10). The as-prepared gold nanoparticles/carbon nanosheet materials combined the unique properties of gold nanoparticles and carbon nanosheets and exhibited significant surface-enhanced Raman spectroscopy comparing to aromatic molecules. Considering the well-established sonoelectrochemical method in the preparation of nanomaterials, the present strategy might be applied in preparing other nanocarbon-based nanocomposites as well.

Graphene-based nanomaterials have generated enormous excitement in the areas of nanocomposites, specific optoelectronic, energy storage and conversion, as well as bioscience/biotechnologies, due to their extraordinary physicochemical and structural properties. Sonoelectrochemical technique was successfully applied to fabricate alloy–graphene nanocomposites [46]. It not only provided a simple way to synthesize alloy nanoparticles but also showed a general strategy for fabricating graphene-based nanostructures with anticipated properties. Pd was co-electrodeposited with Pt at different atomic ratios and then was anchored with reduced graphene oxide simultaneously in the presence of polydiallyldimethylammonium chloride acting as a stabilizer, disperser, and linker in the whole process. The morphologies and composition of the as-prepared nanocomposites were extensively investigated by TEM, SEM, XRD, and inductively coupled plasma–atomic emission spectroscopy. It was found that Pd_1Pt_3 alloy nanoparticles were uniformly dispersed on the reduced graphene oxide sheets with a mean particle size of 4.5 nm (Fig. 11). The electrochemical results
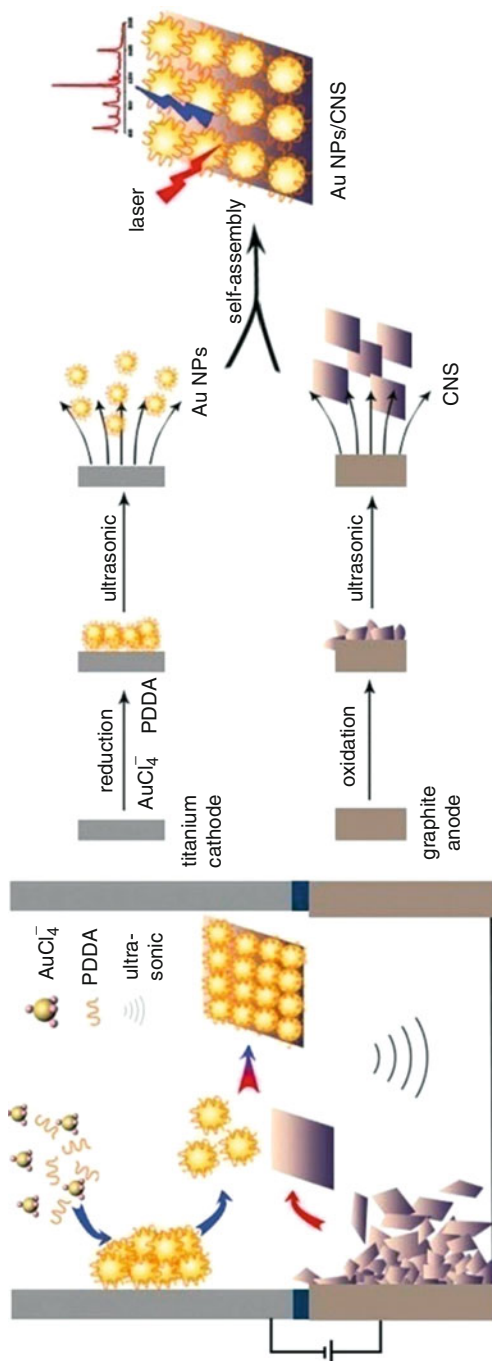
Fig. 10 Schematic illustration of the fabrication of the gold nanoparticles/carbon nanosheet hybrid by the one-step sonoelectrochemical method (Reprinted with permission from Ref. [45]. Copyright (2015) Royal Society of Chemistry)
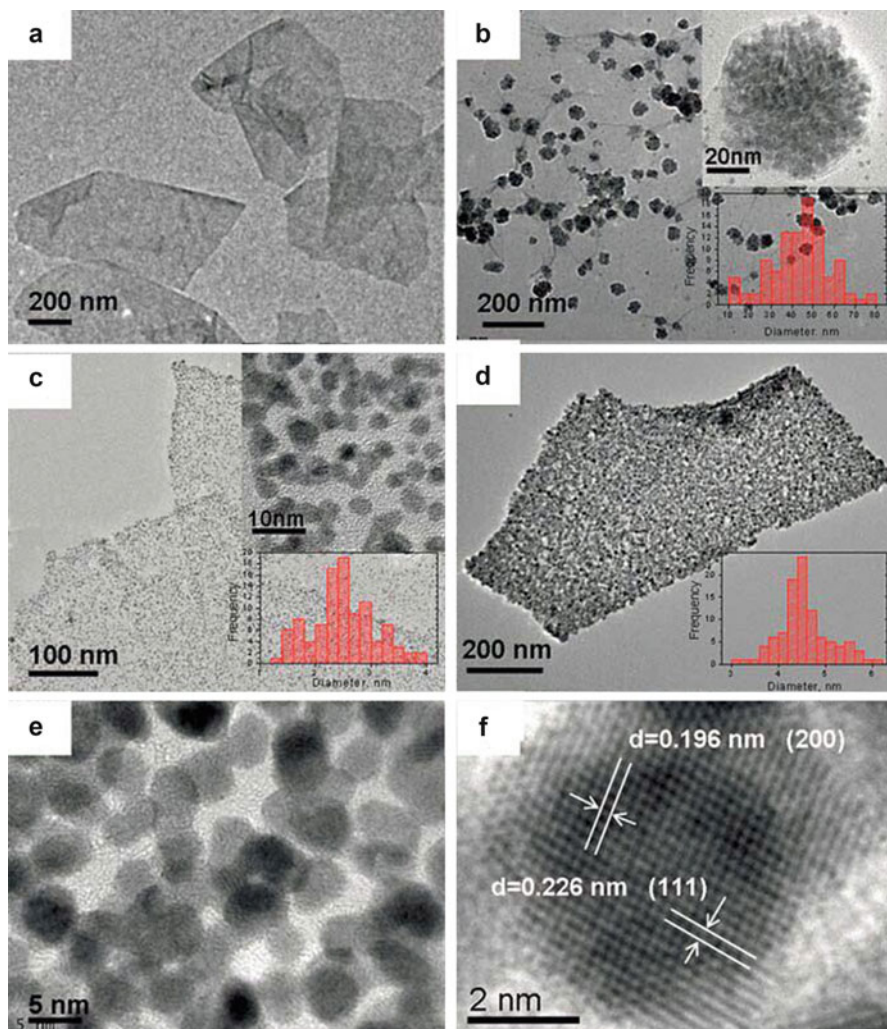
Fig. 11 TEM images of (**a**) the PDDA–RGO, (**b**) PDDA–RGO–Pd, (**c**) PDDA–RGO–Pt, and (**d**) PDDA–RGO–Pd$_1$Pt$_3$ and the HRTEM image of (**e, f**) the PDDA–RGO–Pd$_1$Pt$_3$. Image (**f**) shows the crystal structure of Pd$_1$Pt$_3$ in detail (Reprinted with permission from Ref. [46]. Copyright (2011) Royal Society of Chemistry)

showed that as-prepared nanocomposite had excellent electrocatalytic activities and stabilities for the electrooxidation of ethanol in alkaline media. It is anticipated to design graphene-based nanocomposites depending on the applications under similar conditions. Therefore, sonoelectrochemistry affords a technology which can be used to generate various nanostructured materials of significant commercial interest which encompass versatile properties.

Others

There are other nanomaterials prepared by sonoelectrochemistry not included above. As we know, mechanical effects induced by ultrasonication can be very helpful for the activation of electrochemical reactions. A new lead(II) complex [Pb(mq)$_2$] (mq = 2-methyl-8-hydroxyquinoline) in the presence of the 2-methyl-8-hydroxyquinoline ligand was prepared [47]. Studies based on HOMO and LUMO energy levels showed that a good level of luminescence would be sustained with this complex, indicating the complex could be used as a light emission layer in organic light-emitting diodes. The nanostructure was produced via sonoelectrochemical method, having rodlike morphology with diameters of about 60 nm and lengths of about 1–3 μm. The synthesis was conducted within a simple two-electrode-type electrochemical cell, using lead metal plate and a platinum wire as anode and cathode, respectively. While the single-crystal sample was also obtained under the electrochemical way in the absence of ultrasound for comparison. The electrochemical efficiency, defined as moles of metal dissolved per Faraday, in the sonoelectrochemical method was improved and was better than that of the conventional electrochemical method, because of the enhancement of the mass transfer at the electrode at constant current and time. The photoluminescence properties of the prepared compounds were investigated, and it was found the prepared compound as nanorods showed a blue shift in comparison to the single crystal one.

Fluorescent carbon-based nanomaterials have been widely investigated owing to their large surface area, good hydrophilicity, and low cytotoxicity. Some complex and expensive purification such as electrophoresis, ultrafilter, and dialysis has been used to remove salts after the oxidation in order to get pure fluorescent carbon nanoparticles (CNPs). Yao et al. prepared fluorescent CNPs in pure water by a novel electrolytic device [48]. It was peculiar with a very narrow gap of 2 mm between the anode and cathode. The electric field intensity offered was even higher than that in a normal capillary electrophoresis. Meanwhile, ultrasonic effect was also recommended into the electrolytic process (Fig. 12). Pure blue fluorescent CNPs were rapidly generated without any complex purification, benefiting from the combination of the high-intensity electric field and the ultrasonic field. Comparing to the normal electrolysis, the high-intensity electric field played a crucial role in improving the product purity. On the other hand, it was seen that the electrolytic efficiency was obviously enhanced, since the ultrasonic field could act synergistically with the high-intensity electric field. The scale of the CNPs was about 2–3 nm. The maximum fluorescence emission spectra of CNPs showed a maximum fluorescent intensity at 450 nm, while the maximum excitation wavelength was at 330 nm. The quantum yield was not very high (8.9 %); it would be interesting to explore the related properties if the reaction time be increased. Hence, the CNPs have the potential for application in bioimaging, immuno-labeling, and fluorescence detection. Such strategy can also be used to obtain other similar nanomaterials such as carbon dots or graphene quantum dots.

Electrochemical intercalation approaches for one-pot reactions are attractive for preparing reduced graphene nanosheets (RGN$_{SECM}$). It has been concluded that acoustic streaming in an ultrasonic field could promote the movement of the solution,

Fig. 12 Scheme of the sonoelectrolytic device (Reprinted with permission from Ref. [48]. Copyright (2014) Elsevier)
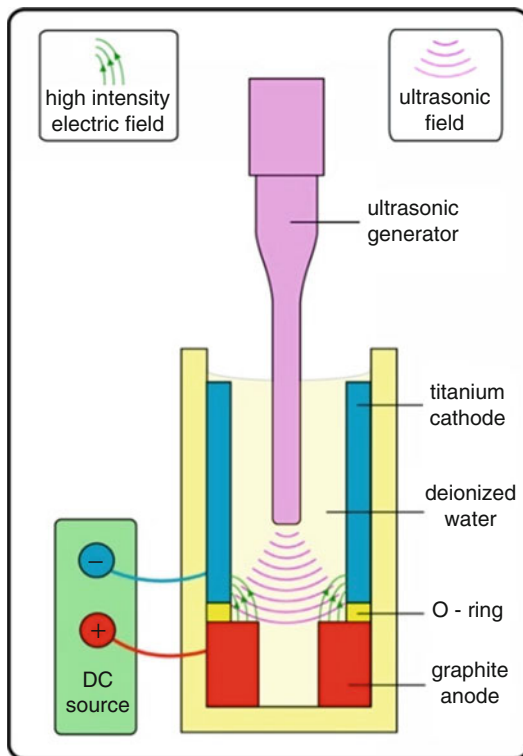
enhancing mass transfer of the electroactive compounds to the electrode surface and reducing the diffusion double layer. To increase the intercalation efficiency, sonoelectrochemical synthetic method is reported for rapidly preparing and dispersing RGN stabilized in an aqueous electrolyte, in which sodium *n*-dodecyl sulfate (SDS) was used in a one-pot reaction through fast intercalation of SDS into a graphite electrode in ultrasonicated aqueous electrolyte [49]. The X-ray photoelectron and Raman results demonstrated that the defects on RGN_{SECM} were predominantly physical and not similar to the chemical defects on reduced graphene nanosheets (RGN_{CM}) synthesized via chemical reduction of graphene oxide nanosheets based on the Hummer's method. It was shown that the in-plane crystallite size of RGN_{SECM} is 26.8 nm, larger than the 18.2 nm of RGN_{CM} (Fig. 13). What is more, the RGN_{SECM} with more physical defects-modified electrode showed better performance for H_2O_2 sensing and electroreduction reaction of oxygen, compared to that of the chemical defects-governed RGN_{CM}. The whole sonoelectrochemical process was long to some extent (8 h); however, such one-pot synthetic way could be extended to prepare graphene-based nanocomposites instead of other complicated and time-consuming procedures.

There are many experimental variables involved in the formation of nanoparticles via the sonoelectrochemical route in terms of particle size and process efficiency. Some of these including bath temperature, current density, the ultrasonic versus
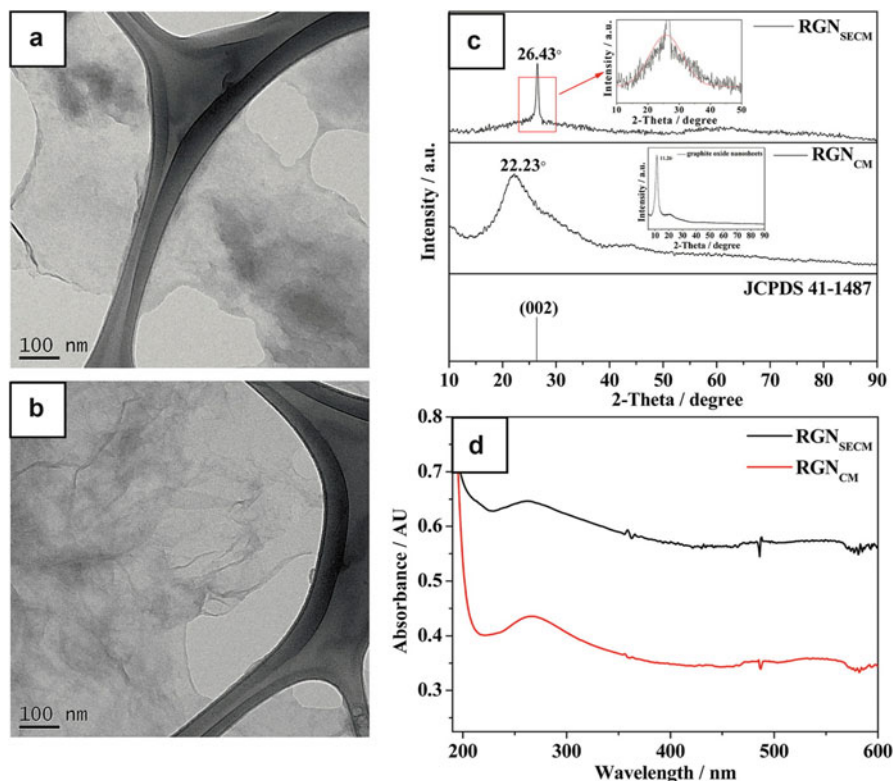
Fig. 13 Comparative TEM images, XRD patterns, and UV–vis spectra of RGNs synthesized using sonoelectrochemical and chemical method. (**a**) TEM image of RGN_{SECM}, (**b**) TEM image of RGN_{CM}, (**c**) XRD patterns (*inset* to the XRD ofGN_{CM}: XRD pattern of graphite oxide) and (**d**) UV–vis spectra (Reprinted with permission from Ref. [49]. Copyright (2015) Royal Society of Chemistry)

electrochemical pulse times, and ultrasound intensity and stabilizer have been discussed elsewhere [5]. Ultrasonic power, deposition potential, pH, and composition of the electrolyte in the sonoelectrochemical cell are also important as mentioned above. For example, the pH value was found to have an important effect on the size and dispersion of the obtained Au nanoparticles [20]. Figure 14 shows the TEM images of Au nanoparticles prepared in aqueous solution with different pH values. When the pH was 4, the agglomerated Au nanoparticles with a diameter in range of 20–100 nm were obtained (Fig. 14a). As the pH was increased to 7, the obtained Au nanoparticles were also aggregated (Fig. 14b), and the size was in the range of 10–50 nm. In solution of pH = 10, uniform Au nanoparticles with a diameter of 20 nm were produced (Fig. 14c). With the pH value was continuously increased to 12, the Au nanoparticles with a polyhedral shape were obtained (Fig. 14d). There are two reasons for this. First, there are more Cl^- anions which
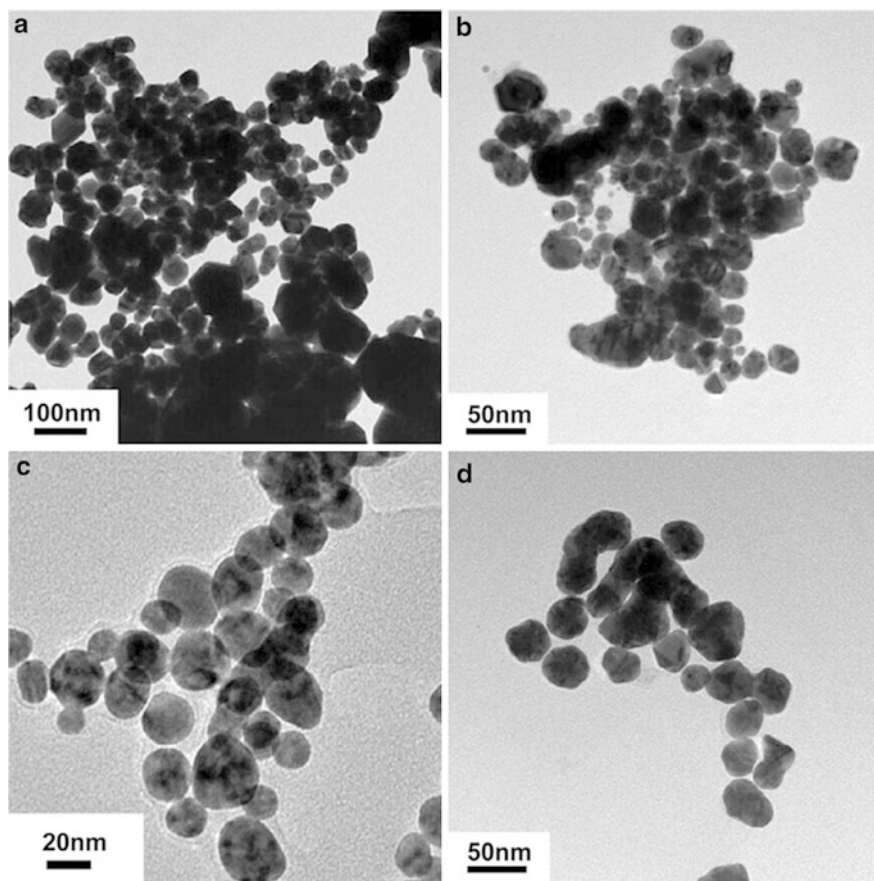
Fig. 14 TEM images of the Au NPs synthesized by sonoelectrochemical method at different pH values. (**a**) pH 4, (**b**) pH 7, (**c**) pH 10, (**d**) pH 12 (Reprinted with permission from Ref. [20]. Copyright (2011) Elsevier)

coordinate with Au^{3+} and thus inhibit the electroreduction of Au^{3+}. Second, the H^+ ions are more easily to be electrically reduced at a lower pH value, and the production of Au NPs is seriously inhibited. When the pH value of precursor solution is increased by adding NaOH, the Cl^- complex anion can be partially replaced by OH^-, facilitating the reduction of Au^{3+}. In general, parameters need to be optimized in order to get the best products with high yields.

Conclusions and Future Directions

Sonoelectrochemistry coupling of power ultrasound into an electrochemical experiment has been widely investigated. It provides not only an unusual sonochemical mechanism for generating high-energy chemistry (extremely high

local temperature and pressure, extraordinary heating and cooling rate) but also the merits of electrochemical methods. A considerable amount of literatures have demonstrated that sonoelectrochemistry is a powerful tool to synthesize functional nanomaterials during the past years. This chapter reviews the sonoelectrochemical synthesis and characterization of nanomaterials, including metals, semiconductors, polymers, nanocomposites, etc. The shape and size of the nanomaterials can be adjusted by varying the operating parameters which include ultrasonic power, current density, deposition potential, and the ultrasonic versus electrochemical time as well as the pH, temperature, and composition of the electrolyte in the sonoelectrochemical cell. Moreover, we try to examine the connection between the chemical and mechanical effects of sonoelectrochemical process and the dispersion, nucleation, and growth of nanomaterials in this chapter.

Great progress in this field has been achieved; however, there still remains much to explore in the sonoelectrochemical synthesis of nanostructured materials. We are only in the initial stages of these studies and there is a lot of potential waiting to be harnessed in the years to come [50]. While laboratory apparatus for sonoelectrochemical reactors is readily commercially available, large-scale equipment remains relatively uncommon. Although the production of ultrasound from electrical power can be extremely efficient, the coupling of ultrasound into electrochemical events remains a low-yield event. Changing the molecular arrangement and crystal structure for novel properties that are different from their bulk state is also a promising direction. In addition, the sonoelectrochemical synthesis of nanostructured materials is still limited to a few examples; hence, the development of new precursor materials and more systematical control over reaction parameters is highly desirable. Designing proper sonoelectrochemical equipment to take advantages of sonochemistry and electrochemistry should be beneficial with the development of the electrodeposition technology. More attentions should be paid to the mechanism and physics of sonoelectrochemistry, which may alleviate the current limitation. By monitoring the process and variation laws of the interactions between atoms or molecules during the reaction, the kinetics of real microscopic reactions can be revealed, which can be further applied for establishing a unified synthesis method for one or several types of materials. Last but not the least, developing new techniques to in situ study and characterizing the related change during the sonoelectrochemical reaction are of great significance, as these will allow us to investigate bond breaking and bond making and other processes as well as electron fluctuations during a sonoelectrochemical event.

In summary, ultrasonic irradiation produces a number of significant benefits to a wide range of electrochemical systems during the sonoelectrochemical process. Though this chapter cannot cover all the functional nanomaterials prepared by the sonoelectrochemical strategy ever reported in the literature, to some extent, it represents the latest progress in this field. In a word, compared with conventional methods, these novel sonoelectrochemical methods have a variety of advantages and will play an increasingly important role in materials science in the future.

References

1. Richards RM (2001) In: Klabunde KJ, Richards RM (eds) Nanoscale materials in chemistry, 2nd edn. Wiley-Interscience, New York, p 1
2. Buck MR, Schaak RE (2013) Angew Chem Int Ed 52:2
3. Mason TJ, Lorimer JP, Walton DJ (1990) Ultrasonics 28:333
4. Suslick KS, Price GJ (1999) Annu Rev Mater Sci 29:295
5. Sáez V, Mason TJ (2009) Molecules 14:4284
6. Brett C (2008) Sonoelectrochemistry. In: Arnau A (ed) Piezoelectric transducers and applications. Springer, Heidelberg, p 399
7. Compton RG, Eklund JC, Marken F (1997) Electroanalysis 9:509
8. Gedanken A (2004) Ultrason Sonochem 11:47
9. Reisse J, Caulier T, Deckerkheer C, Fabre O, Vandercammen J, Delplancke JL, Winand R (1996) Ultrason Sonochem 3:S147
10. Ashokkumar M, Lee J, Kentish S, Grieser F (2007) Ultrason Sonochem 14:470
11. Hardcastle JL, Ball JC, Hong Q, Marken F, Compton RG, Bull SD, Davies SG (2000) Ultrason Sonochem 7:7
12. Xia Y, Xiong Y, Lim B, Skrabalak SE (2009) Angew Chem Int Ed 48:60
13. Reisse J, Francois H, Vandercammen J, Fabre O, Kirsch-de Mesmaeker A, Maerschalk C, Delplancke JL (1994) Electrochim Acta 39:37
14. Haas I, Shanmugam S, Gedanken A (2008) Chem Eur J 14:4696
15. Zin V, Pollet BG, Dabalá M (2009) Electrochim Acta 54:7201
16. Shen Q, Jiang L, Zhang H, Min Q, Hou W, Zhu JJ (2008) J Phys Chem C 112:16385
17. Zhu JJ, Liu SW, Palchik O, Koltypin Y, Gedanken A (2000) Langmuir 16:6396
18. Socol Y, Abramson O, Gedanken A, Meshorer Y, Berenstein L, Zaban A (2002) Langmuir 18:4736
19. Liu YC, Lin LH, Chiu WH (2004) J Phys Chem B 108:19237
20. Shen Q, Min Q, Shi J, Jiang L, Hou W, Zhu J (2011) Ultrason Sonochem 18:231
21. Shen Q, Min Q, Shi J, Jiang L, Zhang J, Hou W, Zhu J (2009) J Phys Chem C 113:1267
22. Jia F, Hu Y, Tang Y, Zhang L (2007) Powder Technol 176:130
23. Lei H, Tang YJ, Wei JJ, Li J, Li XB, Shi HL (2007) Ultrason Sonochem 14:81
24. Haas I, Gedanken A (2008) Chem Commun 15:1795
25. Mahendiran C, Ganesan R, Gedanken A (2009) Eur J Inorg Chem 2009:2050
26. Delplancke J, Dille J, Reisse J, Long GJ, Mohan A, Grandjean F (2000) Chem Mater 12:946
27. Dabalá M, Pollet BG, Zin V, Campadello E, Mason TJ (2008) J Appl Electrochem 38:395
28. Liu Y, Lee H, Peng H (2004) Chem Phys Lett 400:436
29. Hoffmann MR, Martin S, Choi W, Bahnemann DW (1995) Chem Rev 95:69
30. Qiu X, Burda C, Fu R, Pu L, Chen H, Zhu J (2004) J Am Chem Soc 126:16276
31. Qiu X, Lou Y, Samia ACS, Devadoss A, Burgess JD, Dayal S, Burda C (2005) Angew Chem Int Ed 44:5855
32. Mancier V, Daltin AL, Leclercq D (2008) Ultrason Sonochem 15:157
33. Shi J, Wang S, He T, Abdel-Halim ES, Zhu J (2014) Ultrason Sonochem 21:493
34. Mohapatra SK, Misra M, Mahajan VK, Raja KS (2007) J Catal 246:362
35. Mastai Y, Homyonfer M, Gedanken A, Hodes G (1999) Adv Mater 11:101
36. Li C, Bai H, Shi G (2009) Chem Soc Rev 38:2397
37. Reyman D, Guereca E, Herrasti P (2007) Ultrason Sonochem 14:653
38. Ganesan R, Shanmugam S, Gedanken A (2008) Synth Met 158:848
39. Atobe M, Ishikawa K, Asami R, Fuchigami T (2009) Angew Chem Int Ed 48:6069
40. Dejeu J, Taouil AE, Rougeot P, Lakard S, Lallemand F, Lakard B (2010) Synth Met 160:2540
41. Kao J, Thorkelsson K, Bai P, Rancatore BJ, Xu T (2013) Chem Soc Rev 42:2654
42. Wang C, Sun L, Yun H, Li J, Lai Y, Lin C (2009) Nanotechnology 20:295601
43. Han H, Mikhalovsky SV, Phillips GJ, Lloyd AW (2007) N Carbon Mater 22:121

44. Ashassi-Sorkhabi H, Bagheri R, Rezaei-moghadam B (2015) J Mater Eng Perform 24:385
45. Zhang K, Yao S, Li G, Hu Y (2015) Nanoscale 7:2659
46. Shi J, Yang G, Zhu J (2011) J Mater Chem 21:7343
47. Shahrjerdi A, Davarani SSH, Amini MM, Najafi E, Janghouri M, Mohajerani E, Dehpour A (2014) J Mater Sci 49:441
48. Yao S, Hu Y, Li G (2014) Carbon 66:77
49. Chen C, Liu Z, Zhang Y, Ye J, Lee C (2015) RSC Adv 5:21988
50. Klima J (2011) Ultrasonics 51:202

Catalytic Applications of Noble Metal Nanoparticles Produced by Sonochemical Reduction of Noble Metal Ions

Kenji Okitsu and Yoshiteru Mizukoshi

Contents

Abstract

Noble metal nanoparticles have great potential for application as catalysts. Their catalytic properties depend sensitively on the size, structure, and shape of the metal nanoparticles and their combination with support materials. Sonochemistry is a possible approach for the efficient production of powerful noble metal nanoparticle-based catalysts. When an aqueous solution is irradiated by ultrasound, unique chemical effects (radical reactions and thermal reactions) and physical effects (shock waves and micro-jet flow) are simultaneously generated

K. Okitsu (✉)
Department of Materials Science, Graduate School of Engineering, Osaka Prefecture University, Sakai, Osaka, Japan
e-mail: okitsu@mtr.osakafu-u.ac.jp

Y. Mizukoshi
Kansai Center for Industrial Materials Research, IMR, Tohoku University, Sakai, Osaka, Japan

during acoustic cavitation. Inside the bubbles and the gas/liquid interfaces that occur during acoustic cavitation are specific reaction fields that can induce unique chemical reactions. In this chapter, the sonochemical reduction of noble metal ions, the synthesis of noble metal nanoparticles, and their immobilization on support materials are described. The applications of sonochemically prepared nanoparticles to catalytic hydrogenation reactions and photocatalytic reactions are also described. In addition, sonochemical synthesis and its application to noble metal–magnetic nanocomposites and to the catalytic growth behavior of sonochemically synthesized seed particles are introduced.

Keywords

Sonochemical reduction • Noble metal ions • Noble metal nanoparticles • Bimetal nanoparticles • Nanocomposite materials • Catalytic applications

Introduction

Noble metal nanoparticles are key materials in advanced nanotechnology because they can be useful in a wide variety of fields. For example, Pd nanoparticles can be used as catalysts for hydrogenation [1] and for alcohol oxidation in direct alcohol fuel cells [2]. The size and shape of metal nanoparticles control their catalytic properties by affecting the surface structure and electronic state. For example, the ratio of metal atoms on the facets, edges, and corners of nanoparticles are determined by the size and shape of the nanoparticles, resulting in different catalytic activities for structure-sensitive reactions.

A number of methods for synthesizing metal nanoparticles have been studied. Table 1 shows representative reductants and stabilizers or templates used in metal nanoparticle synthesis by the reduction of metal ions in solution. In most cases, selection of the stabilizer is the most important factor for controlling the size and shape of metal nanoparticles.

For example, Au nanoparticles can be synthesized by the reduction of Au(III) with $NaBH_4$ in an aqueous solution containing citrate [3]. The concentrations of Au (III), $NaBH_4$, and citrate and the reaction temperature affect the size of the Au nanoparticles formed. Recently, a microwave heating method was developed as an alternative to conventional heating during nanoparticle synthesis [4]. The result was homogeneous heating of the whole solution, which meant that the reduction of metal ions tended to proceed homogeneously. Consequently, microwave heating can more precisely control the size of metal nanoparticles than conventional heating methods can.

In addition to such heating methods, electrochemical [5, 6], photochemical [7, 8], plasma chemical [9, 10], radiation chemical [11, 12], and sonochemical methods have been studied for nanoparticle synthesis. The different experimental conditions that resulted could generate various types of reductants in situ. Sonochemical methods are unique because they can induce both thermal reactions and radical

Table 1 Representative reductants and stabilizers or templates for metal nanoparticle synthesis by the reduction of metal ions in solution

Using a reductant	$NaBH_4$, hydrazine, H_2, CO, aldehyde, citrate, ascorbic acid, alcohol under conventional, or microwave heating
Using an in-site generated reductant	Electrochemistry, photochemistry, plasma chemistry, radiation chemistry, sonochemistry
Using a stabilizer or template	Citrate, polyvinylpyrrolidone, sodium dodecyl sulfate, hexadecyl trimetylammonium bromide, hexadecyl trimethylammonium chloride, polyethylene(40)glycol monostearate, polyoxyethylene (20)sorbitan monolaurate, triphenylphosphine, disulfide, dendrimer, sodium polyacrylate, sodium 3-mercaptopropionate, dodecanethiol

reactions: thermal reactions are induced at extremely high temperatures during transient bubble collapse, and radical reactions are induced at room and/or relatively high temperatures. In addition, physical effects such as shock waves and micro-jet flow are also simultaneously generated during cavitation, thereby affecting both chemical reactions and the formation of metal nanoparticles.

This chapter introduces the synthesis of noble metal nanoparticles and their support materials via sonochemical reduction of metal ions. In addition, the catalytic activities of such nanoparticles with respect to the hydrogenation of olefins and the photocatalytic degradation of ethanol are described. Sonochemical synthesis and its application to noble metal–magnetic nanocomposites, and to the catalytic growth behavior of sonochemically synthesized seed particles, are also discussed.

Sonochemical Reduction of Metal Ions in Aqueous Solution and the Formation of Metal Nanoparticles

The reduction of metal ions or complexes in aqueous solution can be applied to the synthesis of the corresponding metal nanoparticles. In 1987, Gutierrez et al. [13] investigated the reduction of $AuCl_4^-$, Ag^+, and MnO_4^- in aqueous solution using 1-MHz ultrasound irradiation under a H_2–Ar mixed atmosphere in the absence of other additives. They found that the reduction proceeded most effectively under a 20 vol.% H_2 and 80 vol.% Ar mixed atmosphere, and the H radicals formed from sonolysis of water and H_2 were considered to be reductants.

In 1992, Nagata et al. [14] reported that the sonochemical reduction of Ag^+ proceeded in aqueous solution under Ar using a 200 kHz standing wave sonicator. By adding organic stabilizers such as surfactants [sodium dodecyl sulfate (SDS), polyethylene glycol (40) monostearate (PEG-MS), and polyoxyethylene (20) sorbitan monolaurate (Tween 20)], the preparation of Ag nanoparticles was achieved. In the presence of 2-propanol instead of surfactants, the rate of Ag^+ reduction was also enhanced in comparison with that in pure water, but the resulting particles tended to precipitate after several hours. In 1993, Yeung et al. [15] reported the sonochemical reduction of $AuCl_4^-$ in aqueous solution in the presence of

polyvinylpyrrolidone (PVP) and alcohols (methanol, 2-propanol, or pentanol). They used a 20 kHz horn sonicator, and the size of Au nanoparticles formed under Ar was affected by the type of alcohol used. The first research strategies reported by Gutierrez et al., Nagata et al., and Yeung et al. were based on gamma-ray irradiation chemistry, during which H and OH radicals were considered to be the key for the reduction of metal ions.

Following these pioneering studies, the sonochemical reduction of noble metal ions was further developed to produce metal nanoparticles with various sizes, structures, and shapes [14–22]. In 1996, Okitsu et al. [18] investigated the rate of sonochemical reduction of Pd(II) to Pd(0) in aqueous solutions in the absence and presence of PVP, SDS, PEG-MS, and Tween20 under Ar. In this report, the concentration of Pd(II) in the irradiated solutions was determined by an improved NaI colorimetric method. They reported that, with an initial Pd(II) concentration of 1 mM, the initial Pd(II) reduction rates were approximately 7 µM/min in the absence of additives, 87 µM/min with 1 g/L PVP, 130 µM/min with 8 mM SDS, 230 µM/min with 0.4 mM PEG-MS, and 400 µM/min with 5 g/L Tween20. The rates of Pd (II) reduction were, therefore, enhanced at least tenfold by the addition of organic stabilizers. In addition, the initial rates of Pd(II) reduction increased with increasing concentration of SDS: 30 µM/min with 0.1 mM SDS $<$ 100 µM/min with 1 mM SDS $<$ 130 µM/min with 8 mM SDS. The reduction rate was also enhanced by the addition of *tert*-butyl alcohol and *n*-pentanoic acid. Surfactants and various organic additives were thereby shown to act as precursors for the formation of reducing species.

Between 1996 and 2001, to determine the reduction mechanisms, the rates of radiolytic reduction of Pd(II), Au(III), Pt(II), and Pt(IV) under N_2O and the rates of the sonochemical reduction of these metal ions under Ar were investigated in the presence of organic compounds [16, 18–21]. Since pyrolysis radicals (methyl or alkyl radicals) were formed by the sonolysis of organic compounds in aqueous solutions [23], the following reactions were suggested to occur in aqueous sonication systems:

$$H_2O \rightarrow \ \cdot OH + \cdot H \tag{1}$$

$$RH + \ H_2O \ \rightarrow \text{pyrolysis radicals} \tag{2}$$

$$RH + \ \cdot OH \ (\cdot H) \rightarrow \text{reducing radicals} + \ H_2O \ (H_2) \tag{3}$$

$$M^{n+} + \text{reductants} \ \rightarrow M^0 \tag{4}$$

$$nM^0 \rightarrow \left(M^0\right)_n \tag{5}$$

$$M^0 + \ \left(M^0\right)_n \rightarrow \left(M^0\right)_{n+1} \tag{6}$$
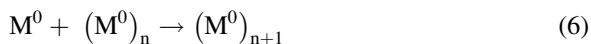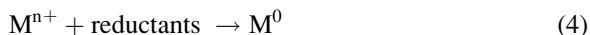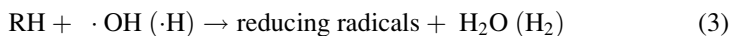
where RH is an organic additive such as a surfactant, water-soluble polymer, alcohol, or ketone and M^{n+} is a metal ion or complex. Equations 1 and 2, respectively, show the pyrolysis of water and an organic additive and the formation of primary radicals such as ·OH radicals, ·H radicals, and pyrolysis radicals. In this scheme, ·H radicals

and pyrolysis radicals can act as reductants for M^{n+}. In addition, reducing species and H_2 are secondarily formed from the abstraction reaction of RH with ·OH or ·H radicals, as shown in Eq. 3. Because ·OH radicals act as a strong oxidant, the presence of RH is important to convert OH radicals to reducing radicals, as shown in Eq. 3. It should be noted that the radicals formed in Eq. 2 are more/less reactive than those formed in Eq. 3. The reductants thus formed can reduce M^{n+}, as seen in Eq. 4. Consequently, the aggregation of M^0 atoms (nM^0) occurs to form $(M^0)_n$ (Eq. 5). When sonochemically formed M^0 is adsorbed on $(M^0)_n$, the formation of $(M^0)_{n+1}$ occurs (Eq. 6).

Effects of Various Parameters on the Rate of Sonochemical Reduction of Noble Metal Ions and on the Size of the Noble Metal Nanoparticles Formed

Table 2 shows the effects of general experimental parameters on the rate of sonochemical reduction of metal ions and on the size of the metal nanoparticles formed [14–22, 24–31]. The initial concentration of metal ions is a basic parameter. Just as with conventional synthetic methods, the use of lower concentrations of metal ions during sonochemical preparation tends to result in the formation of smaller metal nanoparticles within shorter reaction times. In addition, organic additives are effective in controlling the rate of reduction of metal ions and the sizes of the metal particles formed. When alcohols are used as additives, more

Table 2 Effects of general parameters on the rate of sonochemical reduction of metal ions and the formation of metal nanoparticles

Parameters	Types of starting metal ions or complexes	Effects on rate, size, or shape	Ref.
Initial concentration of metal ions or complexes or organic additives	Au(III), Pd(II)	Rate of reduction Size of particles	[14, 16, 24]
Types of alcohol (methanol, ethanol, propanol, ethylene glycol)	Au(III), Pd(II)	Rate of reduction Size of particles	[15, 16, 25]
Types of stabilizer (SDS, PVP, PEG-MS, Tween 20, CTAB, PMMA)	Ag (I), Au(III), Pd(II), Pt(II), Pt(IV)	Rate of reduction Size of particles	[16–22, 26]
Types of other organic additives (carbonic acids, ketones, sodium formate, hydrocarbon)	Au(III), Pd(II), Rh(III)	Rate of reduction	[16, 18, 19]
Types of metal oxides (alumina, silica, zeolite, titania, ferrite)	Au(III), Pd(II), Pt(II) Au(III)/Pd(II)	Rate of reduction Size of particles	[25, 27–31]
Types of inorganic salts and pH (NaCl, HCl, NaOH)	Au(III)	Size of particles Shape of particles	[24]

highly hydrophobic alcohols can enhance the rate of reduction of metal ions. The reason for this enhancement is that such alcohols can accumulate at the interface region of cavitation bubbles where high temperatures and local high concentrations of OH radicals exist, thereby facilitating the formation of reducing radicals. The addition of surfactants in the sonication system is also useful not only for the effective formation of reducing radicals but also for stabilization of the metal particles formed. For example, in the sonochemical reduction of Pt(II) ions, the average diameter of Pt nanoparticles synthesized in PEG-MS, SDS, and DBS is 1.0, 3.0, and 3.0 nm, respectively [21]. In the presence of polymethylacrylic acid, Ag nanoparticles smaller than 2 nm in diameter can be prepared by the sonochemical reduction of Ag(I) [26].

Table 3 shows the effects of experimental parameters peculiar to ultrasound on the rate of sonochemical reduction of metal ions and the formation of metal nanoparticles. The type of dissolved gas, the solution temperature, the ultrasound irradiation time, the ultrasound power, the ultrasound frequency, and the sonicator configuration are the primary parameters.

Cavitation bubbles originate from dissolved gas, the inherent characteristics of which affect the temperature of collapsing bubbles and their number. Important factors affecting the choice of gas are the ratio of the specific heats ($\gamma = C_p/C_v$), the thermal conductivity, and the solubility in water. Okitsu et al. reported that the sonochemical reduction rates of Au(III) under different gases were in the order $N_2 = He < Ne < Ar < Kr$ [32]: the higher the γ value and the lower the thermal conductivity of the gas, the higher the temperatures in collapsing bubbles. In addition, highly soluble gases increase the number of cavitation bubbles, resulting

Table 3 Effects of ultrasound parameters on the rate of sonochemical reduction of metal ions and the formation of metal nanoparticles

Parameters	Types of starting metal ions or complexes	Effects on rate, size, or shape	Ref.
Dissolved gas (He, Ne, Ar, Air, N_2)	Au(III)	Rate of reduction	[16, 32]
Solution temperature (2–40 °C)	Au(III)	Rate of reduction Size of particles	[32]
Irradiation time (0.5–120 min)	Au(III), Pd(II)	Size of particles Shape of particles	[16, 32, 33]
Ultrasound power (nominal power: 0–200 W)	Au(III)	Rate of reduction Size of particles	[32]
Ultrasound frequency (horn type 20 kHz, standing wave type 200 or 213–1062 kHz)	Au(III)	Rate of reduction Size of particles	[32, 34]
Configuration of sonicator (distance from oscillator, standing wave type and horn type)	Au(III)	Rate of reduction Size of particles	[32, 34]

in higher rates of sonochemical reactions. When sonication was performed under CO_2 and CH_4, the reduction of Au(III) did not occur because the temperature of the collapsing bubbles was not high enough to produce reducing radicals.

When the solution temperature was changed in the range 2–40 °C, the rate of Au (III) reduction increased with increasing temperature up to 20 °C, but it decreased at higher temperatures [32]. In the range 2–20 °C, the vapor pressure of water and alcohol molecules increasing with increasing temperature may result in the effective formation of reducing species for Au(III). When the temperature of the solution was increased from 20 to 40 °C, the temperature generated in collapsing bubbles likely failed to increase because of the cushion effect caused by the incorporation of excess water and alcohol molecules in the bubbles. Consequently, the concentrations of reducing species decreased in the higher temperature solutions.

Ultrasound irradiation time, ultrasound power, and ultrasound frequency are also important parameters affecting the sonochemical reactions. The effects of ultrasound power on the rates of Au(III) reduction were investigated under Ar at 20 °C in the presence of 20 mM 1-propanol. The rates increased with increasing power from 0.15 to 1.43 W cm^{-2}. For comparison, the rates of H_2O_2 formation in the sonolysis of water were investigated in the absence of Au(III) and 1-propanol. It was found that the number of cavitation bubbles and/or the temperature of collapsing bubbles, both of which affect reduction rates, increased with increasing ultrasound power.

The rate of Au(III) reduction under Ar decreases with increasing ultrasound frequency as follows: 213 > 358 > 647 > 1062 kHz [34]. The ultrasound frequency may affect the temperature and pressure of collapsing bubbles; the number, size, and lifetime of bubbles; the distribution of bubbles in a solution; and the dynamics and symmetry (shape) of bubble collapse. The above-mentioned effect on Au(III) reduction under Ar likely resulted from decreased numbers of active radicals forming in higher-frequency systems because there is not enough time for the accumulation of 1-propanol at the interface region or for the evaporation of water and 1-propanol to occur during the expansion cycle of bubbles [34]. However, the effects of ultrasound frequency are not clear at present, and further study is needed.

The configuration of the sonicator is another important factor because ultrasound attenuates when propagating in a medium. In addition, ultrasound reflection or overlapping can occur depending on the conditions. When indirectly irradiated ultrasound is applied, e.g., in a standing wave sonication system, the distance between the ultrasound oscillator and the reaction vessel affects the rate of sonochemical reactions. For example, the rate of Au(III) reduction under Ar in the presence of 20 mM 1-propanol at 20 °C was reported to be 75.8 μM/min with an oscillator–reaction vessel distance of 3.5 mm, 87.5 μM/min for 4.0 mm, and 49.2 μM/min for 4.5 mm [32]. Considering that 200 kHz ultrasound has a half-wavelength of 3.7 mm at 20 °C in water, the bottom of the reaction vessel should be 3.7 mm above the oscillator, because ultrasound can be effectively transmitted to the reaction vessel at half-wavelength distance. In addition, the characteristics of cavitation bubbles are different in low- and medium-/high-frequency sonication systems.

Table 4 The initial rate of Au(III) reduction, the average size of sonochemically formed Au nanoparticles, and the reduction ratio under various irradiation conditions (Reprinted with permission from [32]. Copyright 2002 The Chemical Society of Japan)

	Parameters			Initial rate of reduction / $\mu M\ min^{-1}$	Average size $\pm$ SD/nm	Reduction ratio[b]/%
Run	Intensity of ultrasound /Wcm^{-2}	Temperature of bulk solution/°C	Distance[a] /mm			
1	0.53	20	4.0	41.1	125.7 $\pm$ 52.7[c]	55
2	0.92	20	4.0	65.1	53.8 $\pm$ 16.6	78
3	1.20	20	4.0	71.3	50.8 $\pm$ 17.1	100
4	1.43	20	4.0	87.5	35.5 $\pm$ 8.0	100
5	1.43	20	3.5	75.8	33.3 $\pm$ 8.5	98
6	1.43	20	4.5	49.2	71.8 $\pm$ 16.4	84
7	1.43	40	4.0	37.0	71.5 $\pm$ 19.0	63
8	1.43	30	4.0	49.5	58.3 $\pm$ 16.1	74
9	1.43	2	4.0	50.2	40.3 $\pm$ 11.4	19
10	1.43	10	4.0	60.4	41.6 $\pm$ 10.1	100

[a]Distance between reaction vessel and oscillator
[b]Reduction ratio at 20 min irradiation
[c]The number of measurements are not enough

Tronson et al. reported that 20 kHz ultrasound generates predominantly transient cavitation, whereas 515 kHz ultrasound generates stable cavitation [35]. If the time for rectified diffusion into the bubbles with resonance size is short, the organic solute, i.e., the precursor of reducing radicals, cannot accumulate at the interface region, resulting in the formation of fewer reducing radicals.

Table 4 shows the average size of Au nanoparticles formed under different sonication conditions. The sonication time was fixed at 20 min and the concentration of 1-propanol was 20 mM. The variable parameters were ultrasound power, solution temperature, and distance between the bottom of the reaction vessel and the top of oscillator [32]. It was found that the size of the resulting Au nanoparticles was sensitively affected by the sonication conditions.

The average size of the Au nanoparticles in Table 4 can be plotted as a function of the rate of Au(III) reduction as shown in Fig. 1. The size of Au nanoparticles decreased with increasing rate of Au(III) reduction. A similar relationship was confirmed for the effects of ultrasound frequency, as shown in Fig. 2 [34]. The mechanical effects of ultrasound sonication, such as shock waves, may affect the resulting particle size. As ultrasound power increases and ultrasound frequency decreases, the strength of mechanical effects is suggested to become large. Because the fusion of metal nanoparticles was not observed in the above-described system [32, 34], the mechanical effects are likely insignificant when nanoparticles are exposed to relatively high-frequency ultrasound. In general, there is no direct
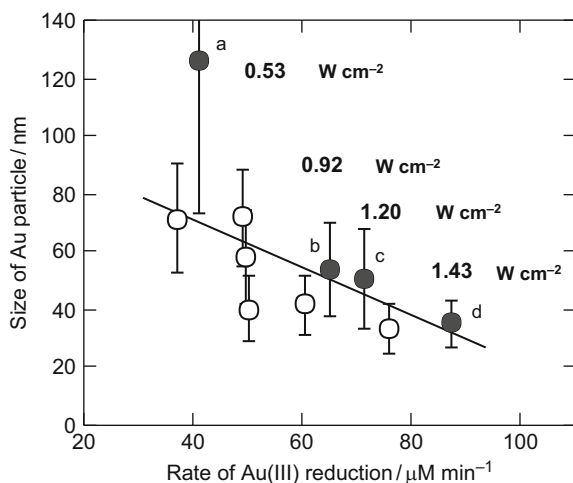
Fig. 1 Rate of Au(III) reduction and the average size of the gold particles formed. Error bars show the standard deviations of the gold particle sizes. This figure was prepared on the basis of the results in Table 4. Closed circles show that the rate of reduction increases with increasing ultrasound intensity: *a* 0.53 W cm^{-2}, *b* 0.92 W cm^{-2}, *c* 1.20 W cm^{-2}, *d* 1.43 W cm^{-2}. Initial concentration of Au(III): 1.0 mM (Reprinted with permission from Ref. [32]. Copyright 2002 The Chemical Society of Japan)

Fig. 2 Average size of Au nanoparticles as a function of the rate of Au(III) reduction. Error bars show the standard deviations of the gold particle sizes. Au(III), 0.2 mM; 1-propanol, 20 mM; atmosphere, Ar; ultrasonic power, 0.1 W mL^{-1}; irradiation time, 120 min. (Reprinted with permission from Ref. [34]. Copyright 2005 American Chemical Society)
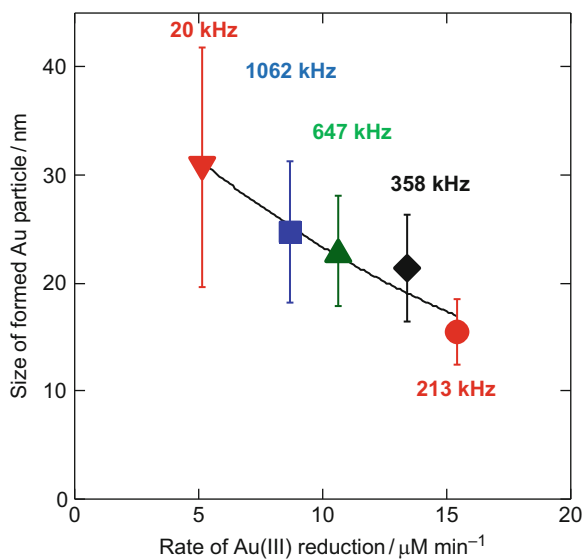
interaction between the sound field and any molecular species in solution. Similarly, in sonochemical processes, colloidal dispersions consisting of nanoparticles may be considered as a homogeneous system like any molecular species in solution.

Synthesis of Bimetal Nanoparticles and Nanocomposite Materials

When aqueous solutions containing Au(III) and Pd(II) in the presence of SDS are sonicated under Ar, Au core/Pd shell bimetallic nanoparticles can be synthesized. The reduction behavior of Au(III) and Pd(II) in such a system is shown in Fig. 3 [36]. A stepwise reduction of metal ions occurs: the reduction of Au(III) starts first, and then the reduction of Pd(II) starts after the reduction of Au(III) is complete. Based on the reduction mechanism described in section "Sonochemical Reduction of Metal Ions in Aqueous Solution and the Formation of Metal Nanoparticles," the sonochemical reduction of both Au(III) and Pd(II) should proceed simultaneously, but Fig. 3 shows that this is not the case. This behavior is caused by the different redox potentials of Au(III) and Pd(II): the following reaction would occur if Pd (0) were formed in the presence of Au(III):

$$3Pd(0) \ + \ 2Au(III) \rightarrow 3Pd(II) \ + \ 2Au(0)$$
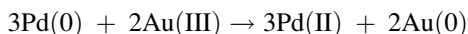
The formation of an Au core/Pd shell nanostructure was confirmed by analyzing the surface plasmon peaks and high-resolution transmission electron microscopy (HRTEM) images. The detailed formation mechanism and catalytic activities of Au/Pd nanoparticles are described in section "Application of Nanoparticles and Nanocomposites."

In general, catalytic activity decreases with reaction time. One reason for this phenomenon is the aggregation of metal nanoparticles. To avoid aggregation and

Fig. 3 Effects of the irradiation time on the concentrations of Au(III) and Pd(II) under an Ar atmosphere. Initial concentrations: 0.5 mM Au(III), 0.5 mM Pd(II), 8 mM SDS (Reprinted with permission from Ref. [36]. Copyright 1997 American Chemical Society)
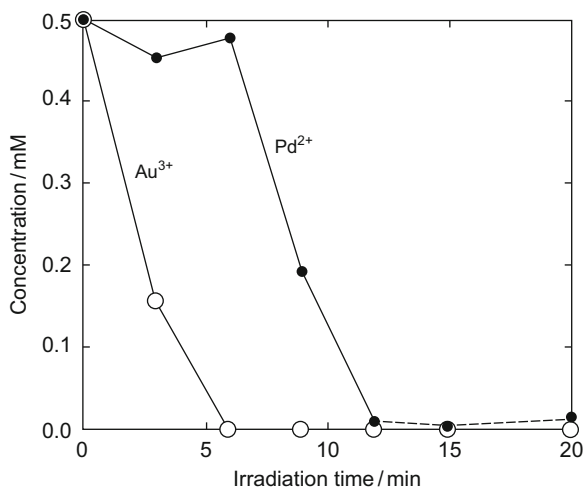
Fig. 4 Average size of Pd particles formed on Al_2O_3 surface and rate of sonochemical reduction of Pd (II). Conditions: 30 min irradiation time, 200 kHz ultrasound frequency, 1 mM Pd(II), 20 mM alcohol. Average rates for initial 5 min of irradiation were used (This figure was prepared on the basis of the results in Ref. [25]) (Reprinted with permission from Ref. [25]. Copyright 2000 American Chemical Society)
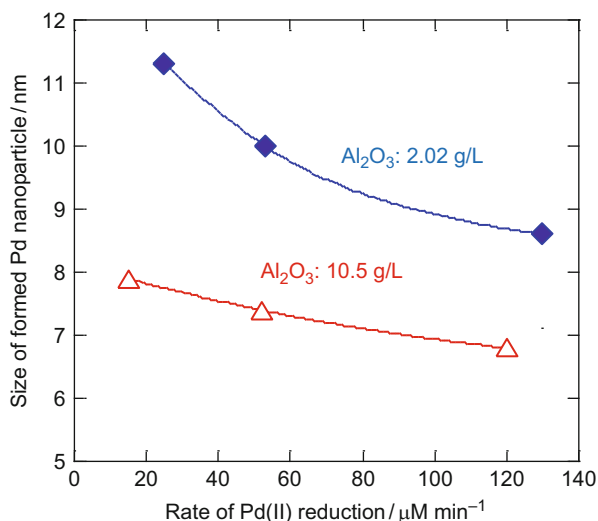
maintain good catalytic activity, metal nanoparticles are often immobilized on supports such as Al_2O_3, SiO_2, TiO_2, or zeolite. To synthesize such supported catalytic materials, the sonochemical reduction of metal ions has been investigated in the presence of various support materials. When such supports are added to an irradiated solution, the rate of reduction of metal ions may be affected. Therefore, it is important to consider the combination of different types of metal ions and supports. For example, when Al_2O_3 powder with low adsorption properties with respect to Pd(II) is used as a support, the rate of Pd(II) reduction and the size of the resulting Pd nanoparticles can be controlled. Figure 4 shows the relationship between the average size of Pd nanoparticles formed on Al_2O_3 and the rate of Pd (II) reduction. In this case, the Pd nanoparticles are immobilized on the surface of Al_2O_3 [25]. The rate of Pd(II) reduction changed by the types of alcohol added: the rate increased in the order of methanol < ethanol < 1-propanol. Although the rate of Pd(II) reduction did not change largely on the addition of Al_2O_3 powder, the size of the resulting Pd nanoparticles became smaller when the amount of Al_2O_3 was increased. In addition, the particle size decreased with increasing rate of Pd (II) reduction. These results indicate that the growth of Pd nuclei occurred in the bulk solution and then the growth and/or the agglomeration of Pd particles in the solution was suppressed by adsorption onto the Al_2O_3 surface. Consequently, the size of the resulting Pd particles decreased with increasing amounts of Al_2O_3. This mechanism was confirmed by analyzing transmission electron microscopy (TEM) images of samples taken during the synthesis of Pd/Al_2O_3 in the presence of methanol or 1-propanol (Fig. 5). Taking into account the formation mechanism, it should be noted that the Pd nanoparticles are immobilized only on the surface of Al_2O_3 powder. The catalytic activities of Pd/Al_2O_3 and other examples of supported catalysts are described in section "Application of Nanoparticles and Nanocomposites.".
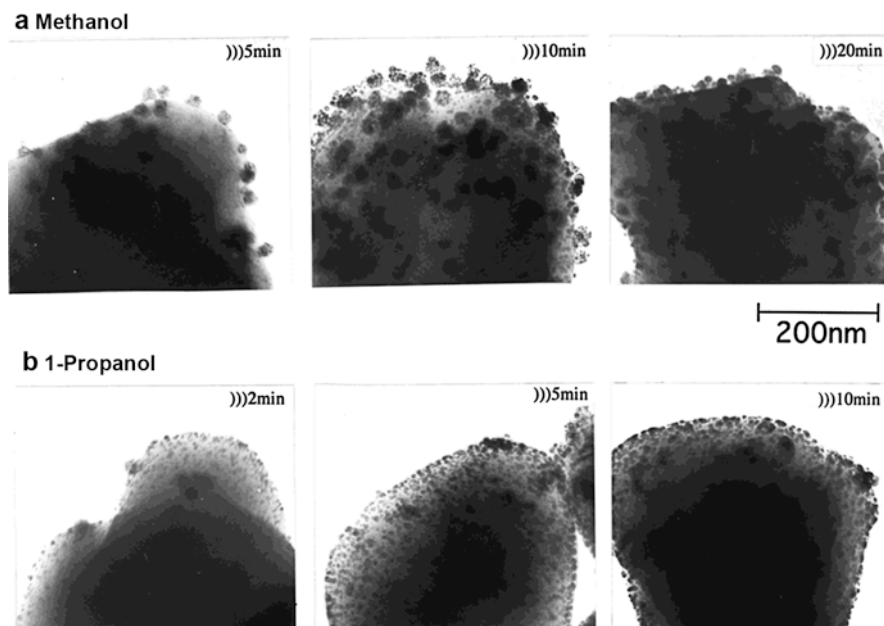
Fig. 5 TEM images of 5 wt% Pd/Al$_2$O$_3$ sonochemically formed in the presence of (**a**) methanol and (**b**) 1-propanol using different irradiation times. Conditions: 1 mM Pd(II), 20 mM alcohol, 2.02 g/L Al$_2$O$_3$, Ar atmosphere (Reprinted with permission from Ref. [25]. Copyright 2000 American Chemical Society)

Application of Nanoparticles and Nanocomposites

Catalytic Activity with Respect to Hydrogenation

The catalytic activities for hydrogenation of 4-pentenoic acid in water of unsupported sonochemically prepared Au/Pd core–shell nanoparticles with different Au/Pd ratios are shown in Fig. 6 [37]. Hydrogen uptake was monitored to determine the progress of hydrogenation. For comparison, the catalytic activities of sonochemically prepared Au and Pd monometallic nanoparticles and commercially available Pd black were also investigated: Au and Pd monometallic nanoparticles were mixed before hydrogenation experiments to yield the corresponding Au/Pd ratios. The rates of hydrogenation over Au/Pd core–shell nanoparticles were distinctly higher than those over the monometallic Pd nanoparticles. Au/Pd core–shell nanoparticles with a 1:4 Au/Pd ratio had the highest activities.

The catalytic activities were also investigated of Au core/Pd shell bimetallic nanoparticles immobilized on and inside SiO$_2$; the catalyst was synthesized by consecutive sonochemical and sol–gel processes [28]. Figure 7 shows the effect of Au/Pd composition on the rate of hydrogenation of cyclohexene in a 1-propanol
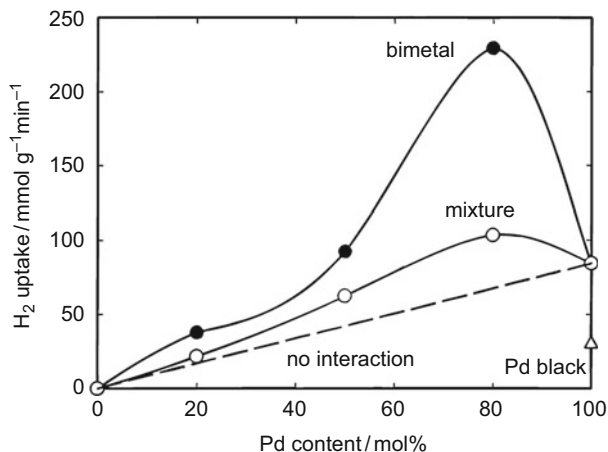
Fig. 6 Initial rates of catalytic hydrogenation of 4-pentenoic acid over bimetallic Au/Pd nanoparticles (●), Pd black stabilized by SDS (△), and mixtures of Au and Pd monometallic nanoparticles (○). The *dashed line* represents the rates estimated for mixtures of Au and Pd nanoparticles without mutual interaction (Reprinted with permission from Ref. [37]. Copyright 2000 American Chemical Society)
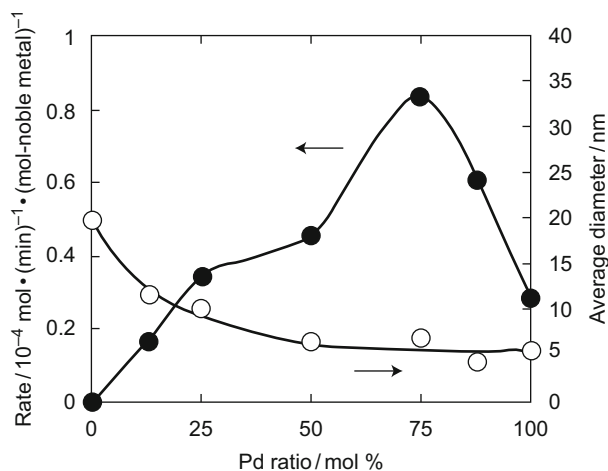
Fig. 7 Catalytic activities (●) for the hydrogenation of cyclohexene over catalysts with various Au/Pd compositions and average particle sizes (○). Reactions were carried out using a conventional closed system at $23 \pm 0.5\,°C$. Conditions: 1 atm initial H_2 pressure, 1.18 mmol cyclohexene, 30 mL 1-propanol solution (Reprinted with permission from Ref. [28]. Copyright 2000 The Chemical Society of Japan)

solution. For comparison, the average sizes of Au/Pd nanoparticles on and inside SiO_2 are also shown in Fig. 7. The catalytic activity was the highest at a composition of 75 mol% Pd and 25 mol% Au. This result is in good agreement with that of unsupported Au core/Pd shell bimetallic nanoparticles (Fig. 6). The catalytic activity

Fig. 8 H$_2$ consumption during 1-hexene hydrogenation over various Pd catalysts. Conditions: 1 atm H$_2$, 23 ± 0.5 °C. (×) Pd black, (△) conventional Pd/Al$_2$O$_3$, (□) Pd/Al$_2$O$_3$ sonochemically prepared in 20 mM methanol, (○) Pd/Al$_2$O$_3$ sonochemically prepared in 20 mM 1-propanol (Reprinted with permission from Ref. [25]. Copyright 2000 American Chemical Society)
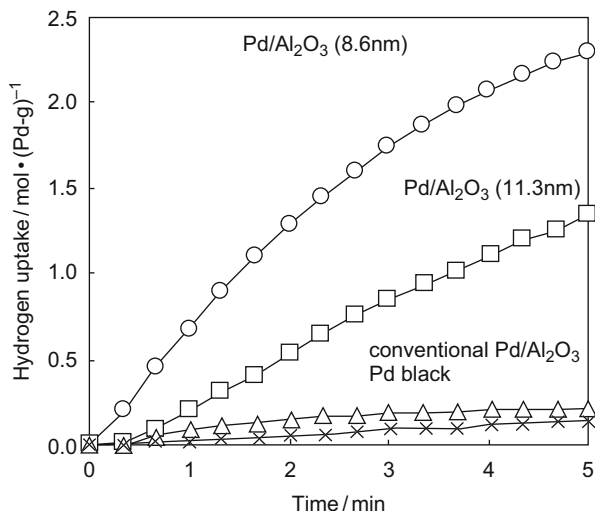
decreased significantly after heat treatment of catalyst samples at 400 °C. X-ray diffraction analysis showed that the core/shell structure changed to a random alloy structure at 400 °C. Therefore, it is clear that the core/shell structure is important to achieve high catalytic activity. The rate of hydrogenation is the highest at around 75–80 mol% of Pd in Figs. 6 and 7 because of the ligand effect: the electronegative double bond of the olefin is more easily adsorbed on the electropositive surface of the Pd shell on an Au core. Further mechanism details are described in section "Photocatalytic Activity."

Sonochemically formed Pd nanoparticles on Al$_2$O$_3$ have high catalytic activities for hydrogenation of olefins (1-hexene and 3-hexene) in a 1-propanol solution [25]. Figure 8 shows the hydrogen uptake during catalytic hydrogenation of 1-hexene. The catalytic activities of sonochemically prepared Pd/Al$_2$O$_3$ were 3–7 times higher than that of a conventional Pd/Al$_2$O$_3$ catalyst prepared by an impregnation method and 10–23 times higher than that of commercially available Pd black catalyst. The catalytic activity was higher for smaller Pd nanoparticles. Based on this result and the sonochemical formation mechanism described above, larger surface areas of Pd are important to achieve high catalytic activities. In addition, because the growth of Pd nanoparticles is suggested to occur in the bulk solution, sonochemically formed Pd nanoparticles are not exposed to high temperatures. Consequently, the surface structure of these Pd nanoparticles may have specific properties that are different from those of conventional Pd/Al$_2$O$_3$ catalysts prepared by an impregnation method. For example, Arai et al. reported that Pt/Al$_2$O$_3$ catalyst prepared using sodium tetrahydroborate as a reductant at ambient temperature had high activity and high selectively for the synthesis of cinnamyl alcohol in cinnamaldehyde hydrogenation [38]. They asserted that platinum sites for hydrogen adsorption/spillover may be different between catalysts prepared at ambient temperature and those prepared at high temperatures.

Photocatalytic Activity

Since Honda and Fujishima first reported the decomposition of water on the surface of a TiO_2 electrode in 1972 [39], considerable attention has been paid to photocatalysis. Photocatalysts have broad applications in fields as diverse as environmental protection and sanitary products. Photocatalysts are, in effect, transducers that transform illuminated light energy into chemically reactive species. For example, anatase titanium dioxide (TiO_2) can act as a photocatalyst when illuminated with UV light at wavelengths shorter than 387 nm. This wavelength corresponds to the bandgap, and illumination at wavelengths shorter than the bandgap results in the photogeneration of electrons and holes. If the electrons and holes migrate to the surface of the photocatalyst, they can reduce or oxidize chemical species, respectively, via the formation of hydroxyl radicals and superoxide anions. However, considerable numbers of electron–hole pairs recombine and are deactivated before migration to the surface of TiO_2 [40]. Some strategies have been proposed to minimize this undesirable recombination of the charge carriers. The enhancement of crystallinity is one approach, because defects in the photocatalyst structure act as recombination sites for electron–hole pairs [41]. Another strategy is the immobilization of noble metal nanoparticles, such as Pt, that have high work functions. When noble metals contact an n-type semiconductor such as TiO_2, the electrons photogenerated in TiO_2 move into the noble metal (the so-called Schottky model). In this model, nanoparticles are referred to as co-catalysts or promoters. Among the noble metals, Pt nanoparticles are effective because of their large work functions (Pt, 5.65 eV; Pd, 5.12 eV; Au, 5.10 eV) [42]. The proposed mechanism is that electrons move into Pt nanoparticles, but find it hard to return because of the high Schottky barrier [43].

In addition to the conventional effect of immobilized nanoparticles as electron acceptors, the plasmonic effects of nanoparticles immobilized on TiO_2 have recently attracted much attention. In this case, the direction of electrons is the opposite to that of conventional models: electrons in nanoparticles are excited by absorbing (visible) light, and the electrons move into the conduction band of TiO_2. The wavelengths of light that can be absorbed by the nanoparticles depend on the plasmon spectra of the immobilized nanoparticles [44].

In both the conventional and plasmonic models, immobilized nanoparticles are important for the enhancement of photocatalysis. Impregnation and photodeposition are the most common ways of immobilizing nanoparticles on the surfaces of TiO_2. Generally, the impregnation method involves several processes, i.e., the removal of solvents, drying, and the calcination and reduction of metal ions by hydrogen. High-temperature post-treatment induces sintering of the immobilized metal, meaning that it is not easy to disperse fine nanoparticles on the surface of TiO_2 using this method.

In contrast, sonochemical immobilization involves one-pot synthesis conducted by sonicating an aqueous solution containing noble metal ions, organic compounds (typically surfactants or alcohols), and appropriate supports such as TiO_2 powder. In this method, organic compounds are decomposed in or near the hot spots induced by ultrasound [16]. At the same time, noble metal ions coexisting in the sonicated
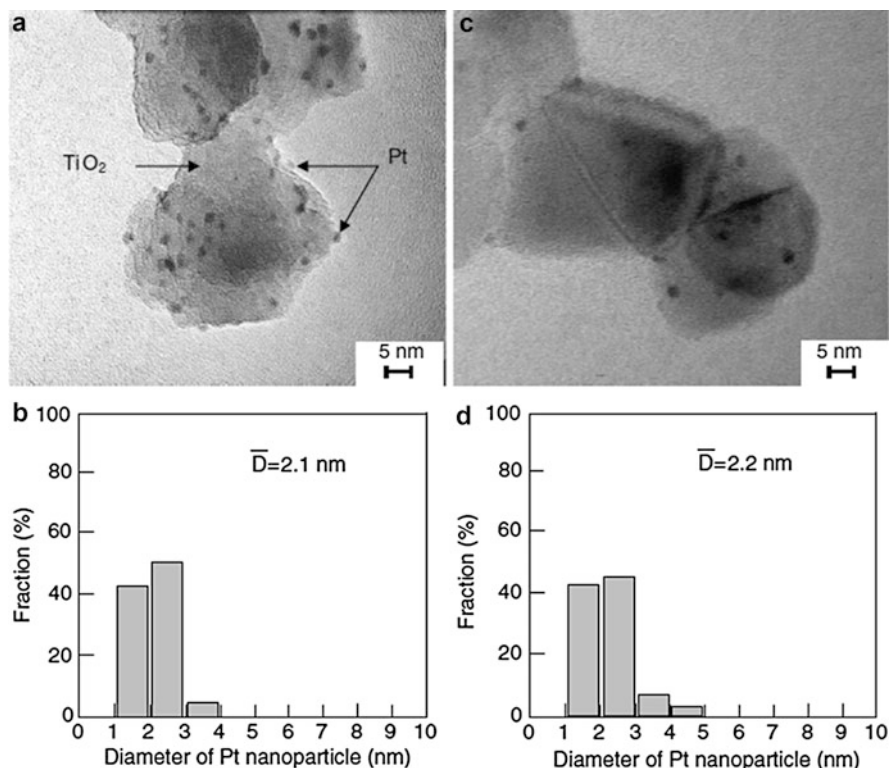
Fig. 9 TEM images of Pt/TiO$_2$ photocatalysts prepared using (**a**) sonochemistry and (**c**) impregnation. The size distributions of the respective supported Pt nanoparticles are shown in (**b**) and (**d**) (Reprinted with permission from Ref. [30]. Copyright 2007 Elsevier)

solution are reduced to form nanoparticles on the surface of the supports. Details of the sonochemical immobilization mechanism are described in sections "Synthesis of Bimetal Nanoparticles and Nanocomposite Materials," "Catalytic Activity with Respect to Hydrogenation," and "Preparation of Noble Metal–Magnetic Nanocomposites" [45].

Previously prepared nanoparticles can be immobilized on the surface of TiO$_2$ by mixing the nanoparticles with TiO$_2$ powders and employing prolonged sonication (a two-step method). When a dispersion of Pt nanoparticles prepared in the presence of PEG-MS was added to TiO$_2$ powders and underwent prolonged sonication, the white TiO$_2$ powder became a homogeneously grayish color because of Pt nanoparticles. The resulting gray powder was repeatedly washed with pure water, but the gray color did not fade. In addition, the filtrate was colorless and transparent, indicating that all Pt nanoparticles were successfully immobilized on the TiO$_2$.

Figure 9 shows TEM images of the product of the above-described two-step method and the conventional impregnation method and the corresponding size distributions of the immobilized Pt nanoparticles [30]. The average size and the
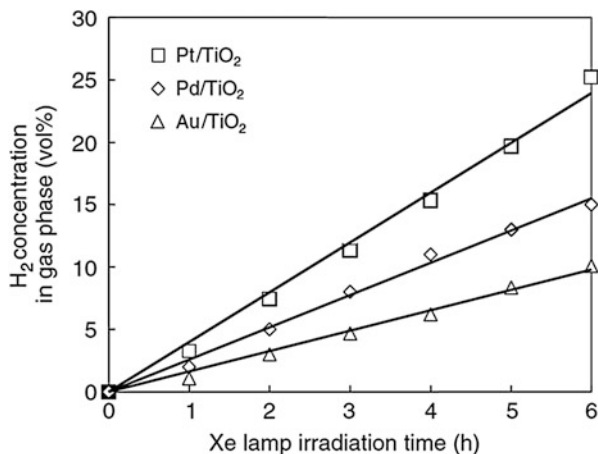
size distribution of the Pt nanoparticles were very similar to those of the nanoparticles before immobilization, meaning that Pt nanoparticles immobilized by sonication maintained their shape and size. The immobilization of previously prepared Pt nanoparticles is considered to result from shock waves generated during the collapse of cavitation bubbles [46]. The average size of the immobilized Pt nanoparticles was almost the same for both production methods, but the Pt size distribution of the conventionally produced catalyst was slightly broader. The number of Pt nanoparticles supported on TiO_2 by the conventional method is much lower than that by the sonochemical method. In addition, the surface of conventionally produced TiO_2 catalyst looks smoother than that of the sonochemically produced catalyst. The roughness of the sonicated surface probably results from the effect of ultrasound, which generates a clean surface.

The photocatalytic activities of sonochemically prepared Pt–TiO_2 were evaluated in the reforming of ethanol in aqueous solution. Typically, 15 mg of Pt–TiO_2 was dispersed in water using an ultrasound cleaning bath. An appropriate amount of ethanol was added and the reaction vessel was closed and purged with Ar to remove dissolved gases. The reaction mixture was stirred with a magnetic stirrer and illuminated with a Xe lamp (radiation intensity: 57 W/cm^2). H_2 was detected as a main product of the reforming. The evolution of H_2 proceeded linearly with the duration of UV illumination (Fig. 10). The results of Pd–TiO_2 and Au–TiO_2 catalysts prepared by sonochemical reduction are also given in Fig. 10. Pt–TiO_2 exhibited the highest activity, which can be explained by the high work function of Pt together with the smaller size of Pt nanoparticles.

The rates of H_2 production for sonochemically and conventionally synthesized Pt–TiO_2 are shown in Fig. 11. The horizontal axis denotes the Pt loading on TiO_2. During the impregnation or photodeposition processes, the sizes of immobilized Pt are changed by the reaction conditions, so that it is impossible to control the loading and the size of Pt simultaneously. In contrast, ultrasound can immobilize previously prepared Pt nanoparticles on TiO_2, and the size of nanoparticles remains virtually

Effect of Pt loading on H$_2$ formation rates. Axes: y-axis "H$_2$ production rate (mol/h·g·cat)", x-axis "Pt loading (wt%)". Legend: Pt/TiO$_2$(ultrasound), Pt/TiO$_2$(impregnation), TiO$_2$ only.
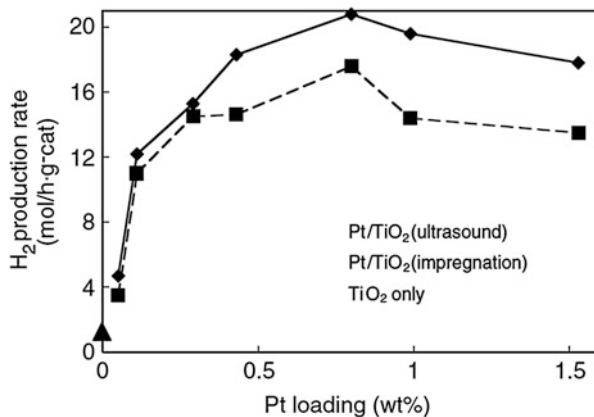
unchanged during the immobilization process. In other words, the size and the number of immobilized particles can be separately controlled, which is a major advantage of sonochemical preparation of noble metal nanoparticles immobilized TiO$_2$. As described later, bimetallic nanoparticles having a characteristic inner structure also can be immobilized using the sonochemical method. As shown in Fig. 11, the rate of H$_2$ evolution is significantly enhanced by the immobilization of Pt and depends on the Pt loading. This demonstrates that Pt nanoparticles are in direct contact with the TiO$_2$ photocatalyst, and photoexcited electrons can move between them. Photocatalysts prepared by the sonochemical method showed higher activities than those prepared by the impregnation method. This might result from the effects of sonication, which can clean the surface of TiO$_2$ and improve the dispersity of Pt–TiO$_2$.

Bimetallic nanoparticles have different properties depending not only on their composition, size, and shape but also on the distribution of each metal in the particles. Therefore, control of this distribution, i.e., control of the inner structure of the bimetallic nanoparticles, is considered to be a key technology for the development of efficient catalysts. Using sonochemical reduction, Au core/Pd shell bimetallic nanoparticles can easily be prepared [36]. The unique properties of bimetallic nanoparticles likely derive from their unusual electron distributions. In Au core/Pd shell particles, the electrons of the Pd shell are considered to be attracted to the Au core. This is reasonable from the viewpoint of the electron negativities. When measuring the absorption spectrum of Au/Pd bimetallic nanoparticles dispersed in water, a blue shift of the surface plasmon resonance absorption of Au was observed, indicating that the electron density of the Au core increased [47]. This phenomenon resulted in high catalytic activities for hydrogenation of olefins, as described in section "Catalytic Activity with Respect to Hydrogenation" [37].

TEM images of sonochemically prepared Au/Pd nanoparticles (25/75 mol ratio) immobilized on the surface of TiO$_2$ are shown in Fig. 12 [48]. The nanoparticles were prepared by the sonochemical reduction of an aqueous solution of Au(III)/Pd (II)/PEG-MS. After the reduction was complete, TiO$_2$ powder was added and
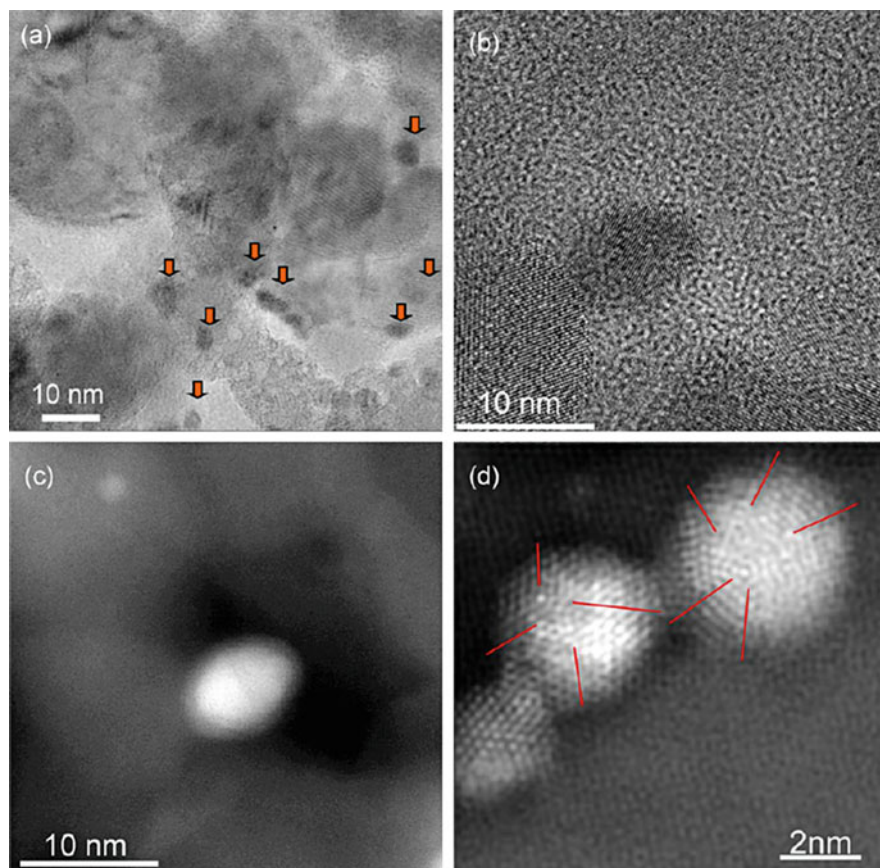
Fig. 12 TEM images of sonochemically prepared Au25/Pd75 (mol%) core–shell nanoparticles (*arrows*) immobilized on TiO$_2$: (**a**) TEM, (**b**) HRTEM, (**c**) HAADF-STEM (*red lines* indicate boundaries of the segments making up immobilized bimetallic nanoparticles), and high-resolution HAADF-STEM images (Reprinted with permission from Ref. [48]. Copyright 2010 Elsevier)

ultrasound irradiation was carried out. In Fig. 12a, the coarse particles shown in weak contrast are TiO$_2$, and the fine particles in strong contrast (as indicated by the arrows) are noble metals. Figure 12b and c is HRTEM and the corresponding high-angle annular dark field (HAADF)-STEM images, respectively, of the noble metal particles immobilized on TiO$_2$. In HAADF images, heavy atoms are brighter because the contrast of the observed object is proportional to the square of the atomic number. Therefore, it was concluded that the core of the immobilized particles is the heavier Au and the shell is Pd (the atomic numbers of Au, Pd, and Ti are 79, 46, and 22, respectively). According to the high-resolution HAADF-STEM image (Fig. 12d), immobilized bimetallic nanoparticles are composed of several segments forming icosahedrons, decahedrons, or truncated structures (multiple twin
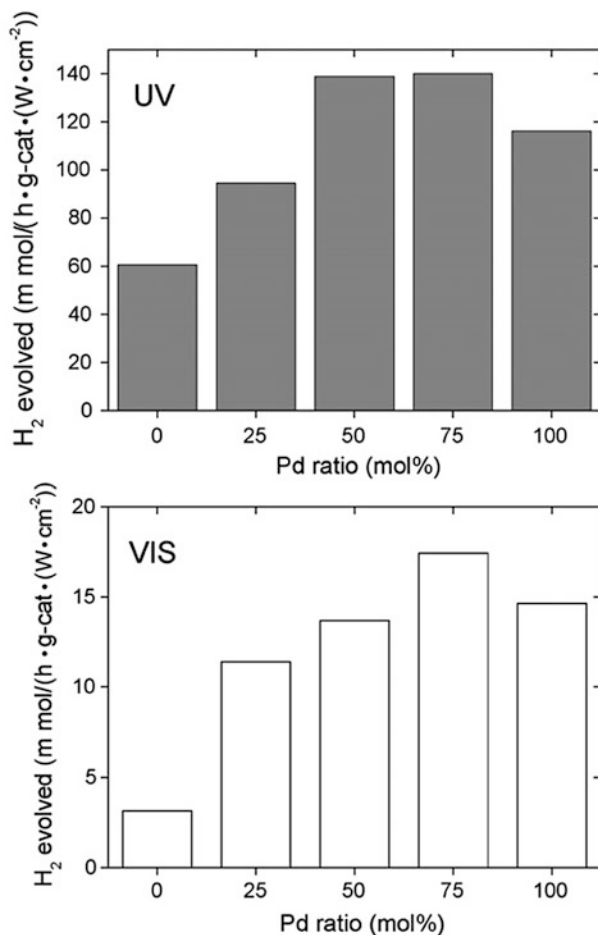
Fig. 13 Amounts of photocatalytically evolved H_2 from an aqueous ethanol solution under UV and visible (VIS) light illumination over Au/Pd bimetallic nanoparticles with different ratios of noble metals immobilized on TiO_2 (Reprinted with permission from Ref. [48]. Copyright 2010 Elsevier)

morphology). Red lines in the image denote the boundaries of segments. The average diameter of the immobilized bimetallic nanoparticles was 4.2 nm, based on the HAADF-STEM observations (Fig. 12).

The photocatalytic activities of the Au core/Pd shell bimetallic nanoparticles immobilized TiO_2 were evaluated using H_2 evolution from an aqueous ethanol solution. For Au/Pd ratios other than 25/75, HAADF-STEM imaging revealed that the immobilized particles also consisted of an Au core and a Pd shell. Figure 13 shows H_2 evolution with Au core/Pd shell bimetallic nanoparticles immobilized TiO_2 and also with monometallic Au (Pd ratio 0 %) and Pd (Pd ratio 100 %) nanoparticles. Interestingly, the photocatalytic activities depended on the Au/Pd ratio, and the sample containing 75 % Pd exhibited the highest activity under both

UV and visible light illumination. To investigate the origin of this high photocatalytic activity, it was prepared two other kinds of Au/Pd co-catalyst immobilized on TiO_2: (1) separately prepared Au and Pd monometallic nanoparticles and (2) bimetallic nanoparticles in which Au and Pd were homogeneously distributed. The ratio of Au/Pd was 25/75 in both samples. Sample (1) was prepared by sonochemical immobilization of a mixture of Au and Pd monometallic nanoparticles prepared by sonochemical reduction; this material cannot be synthesized by any other preparation method. Sample (2) was prepared by annealing Au core/Pd shell bimetallic nanoparticles immobilized on TiO_2 under H_2 gas flow (400 °C for 1 h). The result was the formation of random alloyed nanoparticles in which Au and Pd atoms were homogeneously distributed [29]. After annealing, the average diameter of the immobilized nanoparticles was 4.8 nm; significant increases in particles size as a result of sintering were not observed. The photocatalytic activities of these samples are displayed in Fig. 14.

Figure 14 clearly shows that the photocatalytic activities depend on the inner structures of the immobilized Au/Pd bimetallic nanoparticles even if the ratio of Au/Pd is the same. A mixture of monometallic Au and Pd nanoparticles immobilized on TiO_2 exhibited low photocatalytic activities under UV and visible light illumination. Core/shell bimetallic nanoparticles and random homogeneously distributed bimetallic nanoparticles immobilized on TiO_2 showed superior activity under visible light and UV, respectively. Recently, Su et al. reported simulation of the electron structures resulting from Au/Pd bimetallic nanoparticles on TiO_2 photocatalysts. They concluded that Au core/Pd shell nanoparticles are good co-catalysts because vacant d orbitals in Pd work as effective acceptors for photoexcited electrons generated by TiO_2 [49]. This interpretation based on the conventional role of nanoparticles on TiO_2 can explain photocatalytic activity under UV light. On the other hand, Shiraishi et al. reported that the low work function of the immobilized nanoparticles facilitates the plasmonic photocatalytic function [50]. The work function of an alloy is determined by the sum of the work functions of the metal components [51]. In addition, for nanoparticles, the work function depends on the particle size [52]. For smaller particles, the work function is larger. Because the work functions of Au and Pd are similar, i.e., 5.12 eV and 5.10 eV, respectively, the significant decrease of work function that facilitates the shift of photogenerated electrons from alloy nanoparticles to the conduction band of TiO_2 is not likely to occur.

Although the detailed mechanism of the enhanced photocatalytic activities induced by bimetallic nanoparticle co-catalysts remains unclear, the design of the inner structure of co-catalysts is an important factor in the development of new high-performance photocatalysts.

Preparation of Noble Metal–Magnetic Nanocomposites

The combination of multiple phases is one of the simplest approaches for fabricating novel functional materials. Among various functional materials, magnetic
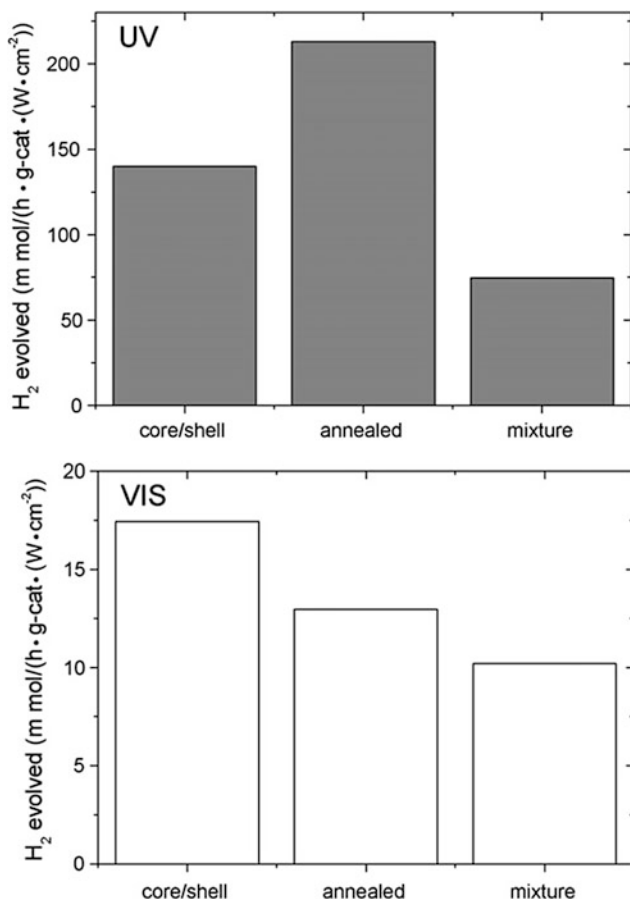
Fig. 14 Amounts of photocatalytically evolved H_2 from an aqueous ethanol solution under UV and visible (VIS) light illumination over Au/Pd nanoparticles [Au25/Pd75 (mol%)] immobilized on TiO_2. The catalysts were made using different methods, resulting in Au core/Pd shell bimetallic nanoparticles, bimetallic nanoparticles in which Au and Pd were homogeneously distributed, and a mixture of Au and Pd monometallic nanoparticles (Reprinted with permission from Ref. [48]. Copyright 2010 Elsevier)

substances are most familiar because they have been used as compasses, for example, since the Middle Ages. In contrast, the demand for noble metals, some of which are less well-known, has greatly increased because they are indispensable for IT industries and environmental remediation processes such as catalytic converters for automobiles. A general strategy to enhance catalytic activity is to fabricate nanosized noble metal particles, because specific catalytic reactions occur on the surfaces of noble metals, and small particles have high surface areas. However, it is difficult to retrieve small nanoparticles from reaction systems. If nanoparticles remain in the reaction system, they may contaminate the reaction products. From the viewpoint of

recycling noble metals, it is important to develop effective methodologies for retrieving noble metal as reusable catalysts.

To solve such problems, novel magnetically retrievable nanocatalysts consisting of a noble metal, such as Pd, and magnetic maghemite (gamma-Fe_2O_3) have been prepared by the sonochemical reduction method. The catalytic activities of these noble metal–magnetic nanocomposites can be evaluated by their effects on the reduction of nitrobenzene (NB). After their catalytic activities were evaluated, the catalysts were retrieved by a neodymium magnet, and activities on repeated use of the catalyst were evaluated to assess their durability.

Noble metal–magnetic nanocomposite catalysts can be prepared by one-pot sonochemical reduction. Briefly, an aqueous solution containing 0.5 mM Na_2PdCl_4, commercially available magnetic nanoparticles (gamma-Fe_2O_3), and PEG-MS was purged with Ar before sonication. Recently, some research projects focusing on magnetically retrievable heterogeneous catalysts have been reported [53–55]. Unlike conventional methods, such as impregnation, the sonochemical method can reduce noble metal ions and concurrently immobilize the resulting nanoparticles on the surface of supports without annealing. The avoidance of annealing reduces the possibility of increases in the size of the particles caused by unfavorable sintering [56]. In addition, good dispersity of the catalysts can be expected because of the physical effects of ultrasound.

When the sample solution was sonicated, the color of the solution changed from reddish brown, originating from pristine gamma-Fe_2O_3, to dark brown, indicating the formation of Pd nanoparticles [57] by the reduction of Pd ions. After 15 min of sonication, the sample solution was separated into magnetic and nonmagnetic fractions by a neodymium magnet.

The morphologies of the magnetic fraction were characterized by HAADF-STEM imaging. The image of the resulting Pd/gamma-Fe_2O_3 nanocomposite catalyst is shown in Fig. 15 [31]. Based on the atomic numbers of Pd (42) and Fe (26), the smaller particles with bright contrast are Pd nanoparticles, and the larger particles with dark contrasts are gamma-Fe_2O_3 particles. The distributions of Pd, Fe, and O analyzed using energy-dispersive X-ray spectroscopy are also shown in the figure. They reveal that the Pd nanoparticles are immobilized on the surface of gamma-Fe_2O_3 and that the average diameter of Pd nanoparticles is 3.8 nm.

To clarify where the seeds of Pd nanoparticles are generated and how they grow, HRTEM images of Pd/gamma-Fe_2O_3 and Au/gamma-Fe_2O_3 nanocomposites are displayed in Fig. 16, showing the interfaces between the noble metal particles and Fe_2O_3. The interfaces were found to be lines or planes, not points, suggesting that the growth of particles occurs on the gamma-Fe_2O_3 surface.

Figure 17 shows the progress of immobilization processes of Au nanoparticles on the surface of gamma-Fe_2O_3 with sonication time [45]. To obtain these data, the sonicated solution was periodically sampled and magnetically separated. The amount of Au (nanoparticles and ions) in the nonmagnetic fraction was determined by an improved colorimetric method [16]. The numbers of Au nanoparticles were calculated from the amount of Au in the magnetic fraction and the average diameter of nanoparticles measured from TEM images, assuming that the immobilized
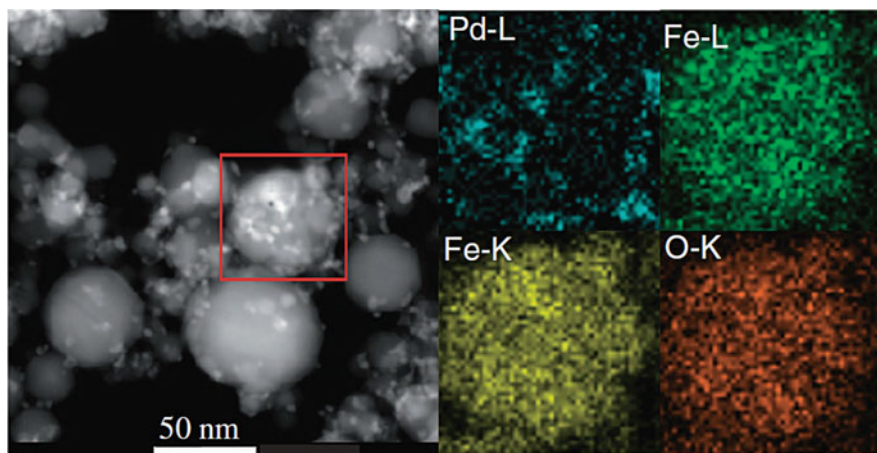
Fig. 15 HAADF-STEM image of fresh Pd/gamma-Fe$_2$O$_3$ nanocomposite catalyst and the corresponding energy-dispersive X-ray mappings (Reprinted with permission from Ref. [31]. Copyright 2008 The Chemical Society of Japan)
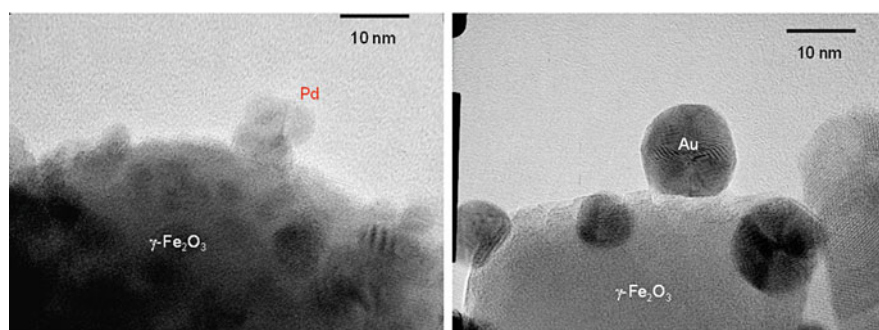
Fig. 16 TEM images of sonochemically prepared Pd/gamma-Fe$_2$O$_3$ (*left*) and Au/gamma-Fe$_2$O$_3$ (*right*) nanocomposites

nanoparticles are spherical and their density is the same as that of the bulk metal. The number of Au nanoparticles increased up to 3 min of sonication, and thereafter the number was almost constant. In contrast, the diameter of Au nanoparticles increased up to 9 min, suggesting that the nucleation of Au occurred in the early stage of sonication.

To elucidate the formation mechanism of such nanocomposites, the morphologies of Au/gamma-Fe$_2$O$_3$ prepared under various conditions were characterized. The results are summarized in Table 5 [45]. The numbers of immobilized Au nanoparticles listed in Table 5 were normalized using the number of Au nanoparticles (2.71×10^{14}) immobilized under standard reaction conditions (run 2). The values for Pt and Pd nanocomposites are also shown in the table.
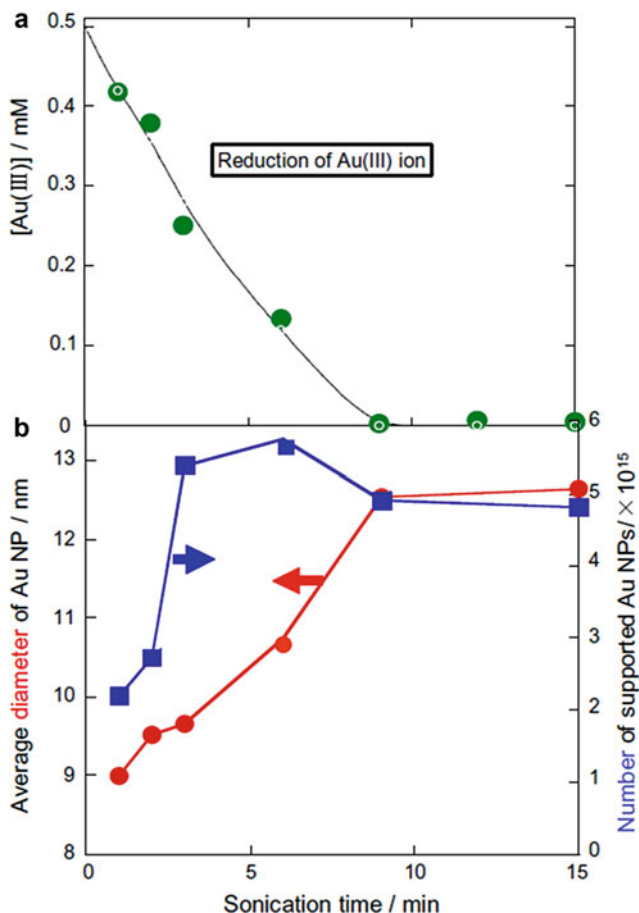
Fig. 17 Effects of the duration of sonication on the Au(III) ion concentration (**a**) and the average diameter and number of Au nanoparticles (NP) (**b**) immobilized on gamma-Fe_2O_3 (Reprinted with permission from Ref. [45]. Copyright 2008 Elsevier)

When the concentrations of $HAuCl_4$ (0.5 mM) and maghemite (gamma-Fe_2O_3) (0.1 g L^{-1}) were constant (runs 1–3), the normalized number of immobilized Au nanoparticles increased with increasing PEG-MS concentration. This is because PEG-MS is the precursor of the reductant in the sonochemical reduction. When the PEG-MS concentration was high, large numbers of reducing species were generated, and, as a result, the number of nuclei generated in the early stage of nanoparticle formation increased. Consequently, large numbers of small nanoparticles were produced.

In contrast, the effect of the amount of gamma-Fe_2O_3 on the number of immobilized Au nanoparticles was not significant (runs 2, 4, and 5). When the amount of gamma-Fe_2O_3 increased by a factor of 10, i.e., the surface area of gamma-Fe_2O_3 increased by a factor of 10, the number of immobilized Au

Table 5 Summary of the nanocomposite preparation conditions and the characteristics of the immobilized noble metal nanoparticles (Reprinted with permission from [45]. Copyright 2008 Elsevier)

Run no.	Starting materials						Immobilized noble metal	
	Noble metal (mM)		Maghemite (g L^{-1})	Ratio (w/w)	PEG-MS (mM)	Sonication time (min)	Diameter (nm)	Number (normalized)
1	HAuCl$_4$	0.5	0.1	1	0.04	15	13.3	0.62
2		0.5	0.1	1	0.4	15	12.5	1.00
3		0.5	0.1	1	4	15	9.6	2.03
4		0.5	0.5	0.2	0.4	15	12.1	1.01
5		0.5	1	0.1	0.4	15	10.4	1.61
6		0.1	0.1	0.2	0.4	9	6.7	1.21
7		0.2	0.1	0.4	0.4	15	8.5	1.17
8	Na$_2$PdCl$_4$	0.5	0.05	1	0.4	10	3.5	
9	(NH$_3$)$_4$Pd(NO$_3$)$_2$	0.5	0.05	1	0.4	10	3.8	
10	H$_2$PtCl$_6$	0.5	0.1	1	0.4	30	1.8	
11		0.5	0.1	1	0.1	60	2.3	

Fig. 18 Nitrobenzene consumption (*circles*) and aniline formation (*squares*) over Pt/gamma-Fe$_2$O$_3$ catalyst. *Triangles* indicate sum of nitrobenzene remained and aniline formed
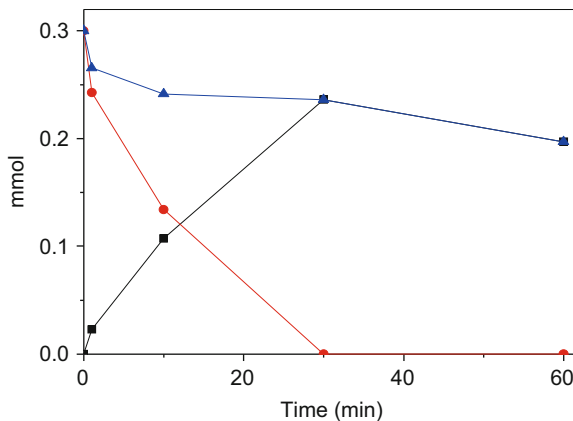
nanoparticles increased by only a factor of 1.6. This fact indicates that the nucleation of Au occurs in the bulk solution, not on the Fe$_2$O$_3$ surface.

The minor effect of the concentration of Au ions (runs 2, 6, and 7) was because the number of reducing species generated was much smaller than the number of Au ions. In fact, the generated amounts of CO and CH$_4$ were several micromoles per minute in the sonolysis of aqueous sodium dodecylbenzenesulfonate solution [21].

From the results in Table 5 and Fig. 17, the following sequence for the sonochemical immobilization of noble metal nanoparticles on the surface of gamma-Fe$_2$O$_3$ can be proposed: (1) small nuclei of noble metal nanoparticles are generated in the bulk solution (not on the surface of the Fe$_2$O$_3$) in the early stage of sonication, (2) the nuclei are immobilized on the surface of Fe$_2$O$_3$, and (3) the nuclei grow on the surface of Fe$_2$O$_3$.

The progress of the partial reduction of nitrobenzene (NB) over a Pd/Fe$_2$O$_3$ nanocomposite catalyst is shown in Fig. 18. The reduction of NB was conducted at 25 °C under 1 atm of H$_2$. The amounts of aniline (AN) formed and NB consumed were measured by high-performance liquid chromatography to monitor the progress of the reaction. NB was completely consumed after 30 min of the reaction and AN was formed. Blank tests indicated that AN was formed in the presence of H$_2$ and that some NB was adsorbed on the surface of the catalyst. This catalyst can be retrieved using an external magnetic field. The activities of the catalyst on repeated use and retrieval were assessed to investigate its reusability and durability. The results are given in Fig. 19 [31].

The changes in NB conversion [consumed NB(mol)/fed NB(mol)], AN selectivity [formed AN(mol)/consumed NB(mol)], and turnover frequency (TOF) of AN formation [formed AN(mol)/immobilized Pd(mol)/reaction time (h)] in four repeated uses of the same catalyst were evaluated. In the calculations of catalytic activities, the amount of NB adsorbed on the catalyst surface and reaction vessel (7 % of the fed amount), which was determined in a blank test in the absence of hydrogen, was subtracted from the consumption of nitrobenzene. NB conversion and AN selectivity averaged 100 and 87 %, respectively. The dispersion state of the
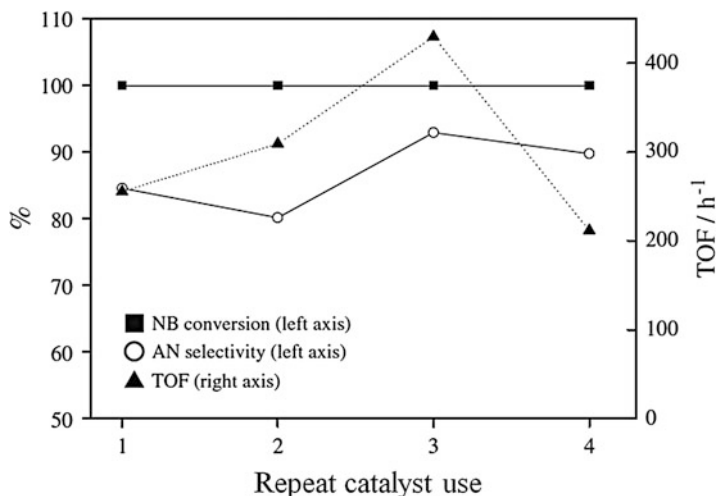
Fig. 19 Effect of repeated catalyst use on the catalytic activity of Pd/Fe$_2$O$_3$ nanocomposite particles during nitrobenzene reduction (Reprinted with permission from Ref. [31]. Copyright 2008 The Chemical Society of Japan)

catalyst might be the cause of the spread of TOF. The maximum TOF, 429.6 h^{-1}, and the average of the four repeated evaluations, 301.2 h^{-1}, are not inferior to the previous value for the activity of Pd/Ni catalysts reported by Nagaveni et al. [58]. Pd/gamma-Fe$_2$O$_3$ nanocomposite catalyst prepared by the sonochemical reduction method exhibited excellent catalytic activities for the reduction of NB and was high durable during repeated use/retrieval cycles.

In addition to their use as catalysts, noble metal nanocomposites can be utilized as magnetic nanocarriers. In the remainder of this section, Au/gamma-Fe$_2$O$_3$ nanocarriers will be introduced. Au nanoparticles have attracted much attention in the fields of nanobiotechnology in recent years because Au is generally harmless to the living body [59–61]. Moreover, biomolecules such as polypeptides and DNA can bond with Au via Au–S bonds without specific surface modification [62–64]. Magnetic beads are currently commercially available for the detection, separation, and manipulation of various biomolecules. However, to adsorb specific molecules on their surface, specific surface modifications of the beads with, for example, a polymer, are needed. In some cases, the use of such polymers might result in damage to biomolecules. If Au nanoparticles are coupled with magnetic particles, they can be utilized as versatile magnetic nanocarriers for biomolecules containing sulfur atoms, allowing such biomolecules to be selectively separated and manipulated by an external magnetic field.

Typical TEM images of sonochemically prepared Au/gamma-Fe$_2$O$_3$ nanocomposites are shown in Fig. 20 [65]. The Au/gamma-Fe$_2$O$_3$ nanocomposites were prepared from an aqueous solution containing HAuCl$_4$, PEG-MS, and gamma-Fe$_2$O$_3$ by a one-pot method. By using 2-propanol instead of PEG-MS, similar
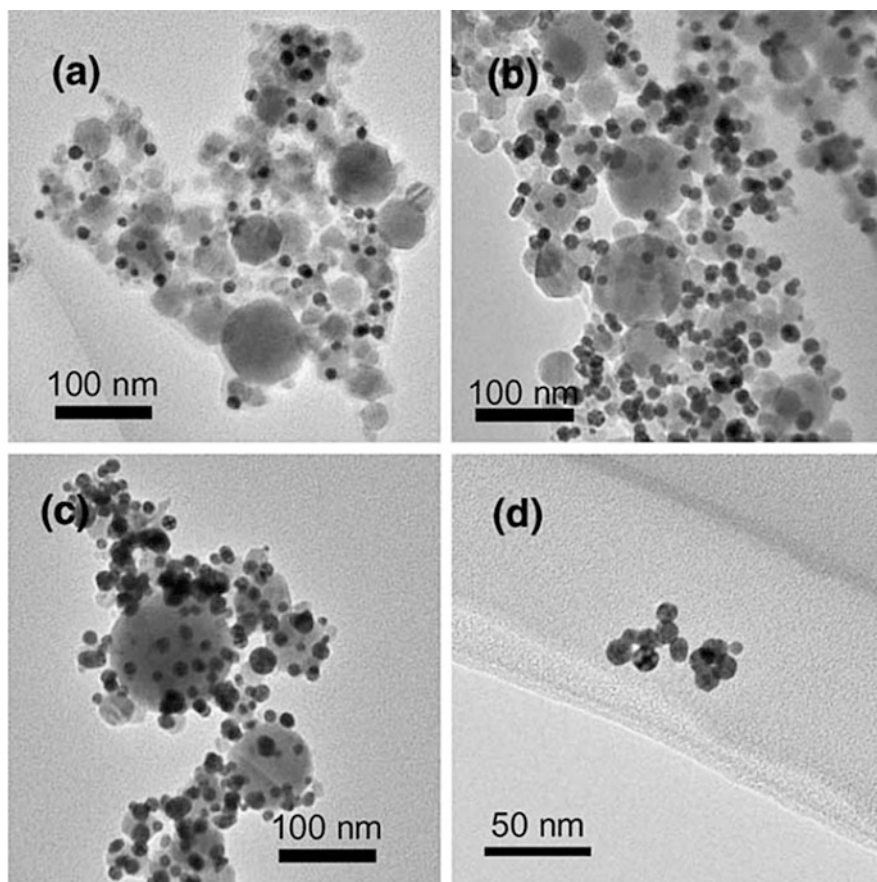
Fig. 20 TEM images of sonochemically prepared Au/gamma-Fe$_2$O$_3$ composite nanoparticles. Au/gamma-Fe$_2$O$_3$ ratios were (**a**) 1/10, (**b**) 1/5, and (**c**) 1/1. Au nanoparticles with no gamma-Fe$_2$O$_3$ are shown in (**d**) (Reprinted with permission from Ref. [65]. Copyright 2006 Elsevier)

nanocomposites can be obtained, but the immobilized Au nanoparticles are larger [66]. Using such Au/gamma-Fe$_2$O$_3$ nanocomposites, magnetic separation of gluta-thione [66], amino acids [65], and oligonucleotides [67] have been evaluated. Separability was tested as follows: known amounts of biomolecules were mixed with a dispersion of Au/gamma-Fe$_2$O$_3$. After mixing, the magnetic fraction was collected using an external magnetic field. Then, the amounts of biomolecules in the nonmagnetic fraction were determined. The difference between the initial amount of biomolecules and that remaining in the nonmagnetic fraction gave the amount magnetically separated.

Figure 21 shows the amounts of glutathione separated by a sonochemically prepared Au/gamma-Fe$_2$O$_3$ nanocarrier. By increasing the ratio of Au/gamma-Fe$_2$O$_3$, the amount of glutathione separated increased, indicating that the adsorption

Fig. 21 Effects of the Au/gamma-Fe$_2$O$_3$ ratio of the magnetic nanocarrier on the amounts of glutathione magnetically separated
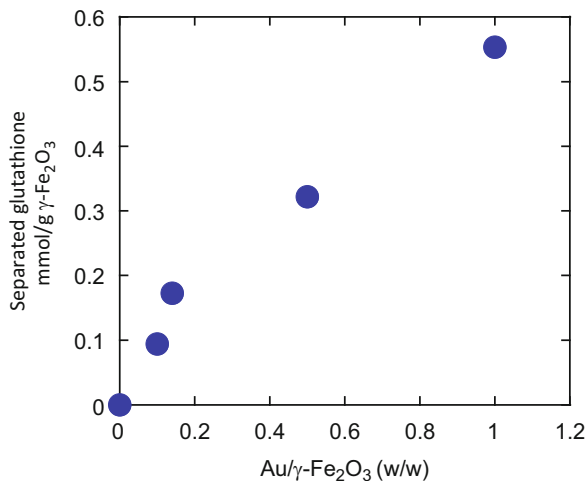
site of glutathione is Au, not gamma-Fe$_2$O$_3$. To assess amino acid separation, a standard amino acid solution was used that contained 17 alpha-amino acids: aspartic acid (Asp), threonine (Thr), serine (Ser), glutamic acid (Glu), glycine (Gly), alanine (Ala), valine (Val), cystine [(Cys)2], methionine (Met), isoleucine (Ile), leucine (Lue), tryptophan (Trp), phenylalanine (Phe), lysine (Lys), histidine (His), arginine (Arg), and proline (Pro). It should be noted that this standard solution contained the dimer of cysteine, cystine, rather than cysteine itself. The results for the separation of these amino acids are given in Fig. 22 [65]. Monolithic gamma-Fe$_2$O$_3$ nanoparticles were evaluated for comparison; they adsorbed almost all kinds of amino acids, but the amounts extracted were relatively small. However, relatively large amounts of aspartic acid and glutamic acid were separated by monolithic gamma-Fe$_2$O$_3$ nanoparticles, probably because of the carboxyl groups present in these amino acids [68]. Cystine and methionine contain sulfur, and remarkably high amounts of these two amino acids were separated by Au/gamma-Fe$_2$O$_3$. The separated amounts increased with increasing Au/gamma-Fe$_2$O$_3$ ratios. Au/gamma-Fe$_2$O$_3$ prepared in the presence of 2-propanol separated smaller amounts of amino acids and did not show selectivity for sulfur-containing amino acids, indicating that gamma-Fe$_2$O$_3$ covered with small Au nanoparticles is more effective for the selective adsorption of sulfur-containing compounds.

To assess oligonucleotide separation by Au/gamma-Fe$_2$O$_3$, thiol-modified oligonucleotides were incorporated as probes, which was substantially the same approach as that reported for monolithic Au nanoparticles by Mirkin et al. [69]. Thiol-modified 15-mer polythymine oligonucleotides were added to an Au/gamma-Fe$_2$O$_3$ aqueous dispersion to allow adsorption onto the gold nanoparticles via Au–S bonds. After removal of excess oligonucleotide, fluorescein isothiocyanate-labeled 15-mer polyadenine oligonucleotides, which were complementary to the probe, were added as the target. After stirring at 20 °C for 24 h, nonhybridized targets were removed by washing with phosphate-buffered saline solution. The target oligonucleotides were
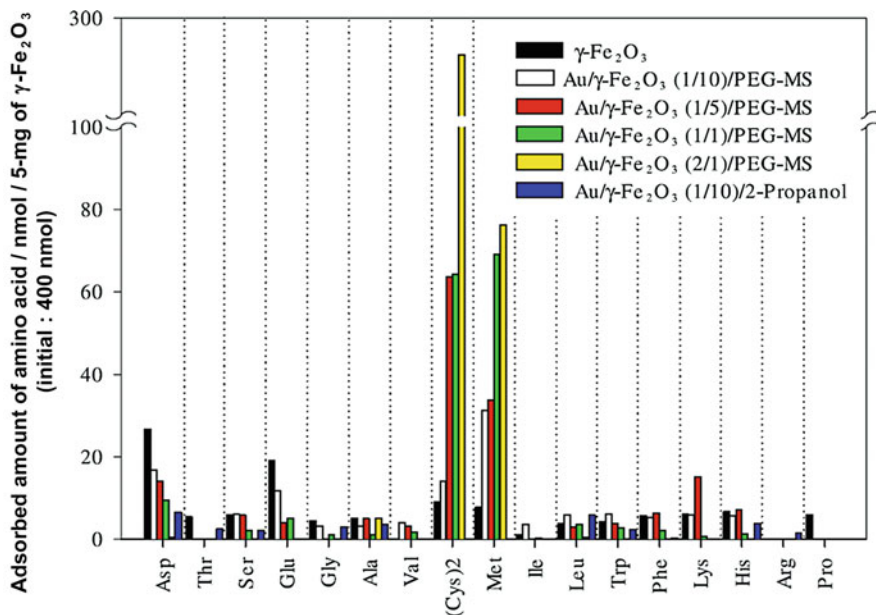
Fig. 22 Amounts of magnetically separated amino acids by Au/gamma-Fe$_2$O$_3$ composite nanoparticles with different Au/gamma-Fe$_2$O$_3$ ratios (Reprinted with permission from Ref. [65]. Copyright 2006 Elsevier)

eluted by heating at 60 °C for 10 min and were then magnetically separated from the Au/gamma-Fe$_2$O$_3$ by a magnetic separator. The amount of target oligonucleotides magnetically separated from Au/gamma-Fe$_2$O$_3$ was determined by a spectrofluorometer. Using this procedure, target oligonucleotide could be successfully collected. Analysis of the amounts of hybridized target oligonucleotides with respect to the total surface area of gold grains per milligram of Au/gamma-Fe$_2$O$_3$ showed that the hybridized amounts increased nearly linearly with the surface area of the gold grains [67].

Autocatalytic Growth of Au Seeds to Au Nanorods

Recently, a seed-mediated growth method for the synthesis of Au nanorods has been investigated. Au seeds act as a catalyst for the reduction of Au(I) with ascorbic acid, and thus Au seeds spontaneously grow to become Au nanorods [3, 70]. In this method, cetyltrimethylammonium bromide (CTAB) and AgNO$_3$ are added as effective capping agents for the growth of Au seeds to Au nanorods. Using a sonochemical reduction method, Au nanorods of different sizes and aspect ratios can be synthesized from identical starting materials [Au(I), CTAB, AgNO$_3$, and ascorbic acid] even for the same initial concentrations [33]. Here, the focus is on the

role of sonochemically formed Au seeds after short irradiation times and on the autocatalytic growth of these seeds to form nanorods.

When sample solutions containing Au(I), CTAB, $AgNO_3$, and ascorbic acid were irradiated under Ar, the extinction intensity of the sample solution increased with irradiation time and/or subsequent standing time, and finally two extinction peaks emerged at around 510–520 and 650–820 nm. These two peaks correspond to the surface plasmon resonances of Au nanorods, indicating that sonochemical reduction of Au(I) to Au(0) proceeded by reacting with reducing radicals formed via pyrolysis and/or radical reactions of CTAB, ascorbic acid, and water. As a result, Au seeds were formed, and then the formation of Au nanorods proceeded.

Figure 23a shows changes in the extinction peak intensity at the longitudinal plasmon resonance as a function of standing times after different ultrasound irradiation times (0.5, 1, 3, 10, and 15 min). Changes in the extinction intensity correspond to the formation of Au seeds and nanorods, meaning that a constant extinction intensity corresponds to completion of the formation of Au seeds and nanorods. For 15 min irradiation, the extinction intensity was almost constant at about 1.6 for standing times from 2 to 60 min, indicating that Au nanorods were formed within 15 min irradiation and 2 min standing time. For 0.5, 1.0, and 3.0 min irradiation, an induction period was observed before the extinction intensity started to increase, and the induction period became longer as the irradiation time became shorter. In addition, sigmoidal curves were observed. This means that autocatalytic growth of the sonochemically formed Au seeds took place, and the number and/or size of the Au seeds was affected by the irradiation time.

Figure 23b shows changes in the extinction peak wavelength of the longitudinal plasmon resonance as a function of standing time after different ultrasound irradiation times. This extinction peak wavelength is an index for the aspect ratio of the Au nanorods formed. At 1 and 3 min irradiation times, the peak wavelength first redshifted and then blueshifted with increasing standing times. Based on the literature [3, 70], this behavior can be explained by the aspect ratio of the Au nanorods first increasing and then decreasing during the standing time. In the conventional method, Au seeds 1–7 nm in diameter are used for nanorod synthesis [70–72]. Therefore, in the sonochemical reduction method, Au seeds with similar sizes are likely formed. In addition, as seen in Fig. 23, the optical properties (peak wavelength and peak extinction) of the resulting Au nanorods can be controlled by changing the irradiation time. Such optical properties could be applied in various fields of nanotechnology.

Figure 24a–e shows TEM images of Au nanorods grown from Au seeds formed with irradiation times of 0.5, 1, 3, 10, and 15 min, respectively. As the irradiation time decreased, the length and width of the resulting Au nanorods increased: the average length increased from 24 nm at 15 min to 53 nm at 0.5 min, and the average width increased from 7.9 nm at 15 min to 27 nm at 0.5 min. The reason that nanorods become larger for shorter irradiation times is that the number of sonochemically formed seeds becomes smaller, so that the remaining Au ions are distributed to a smaller number of seeds, resulting in the larger growth of each seed. In addition, the average aspect ratio decreased from 3.6 at 10 or 15 min to 2.0
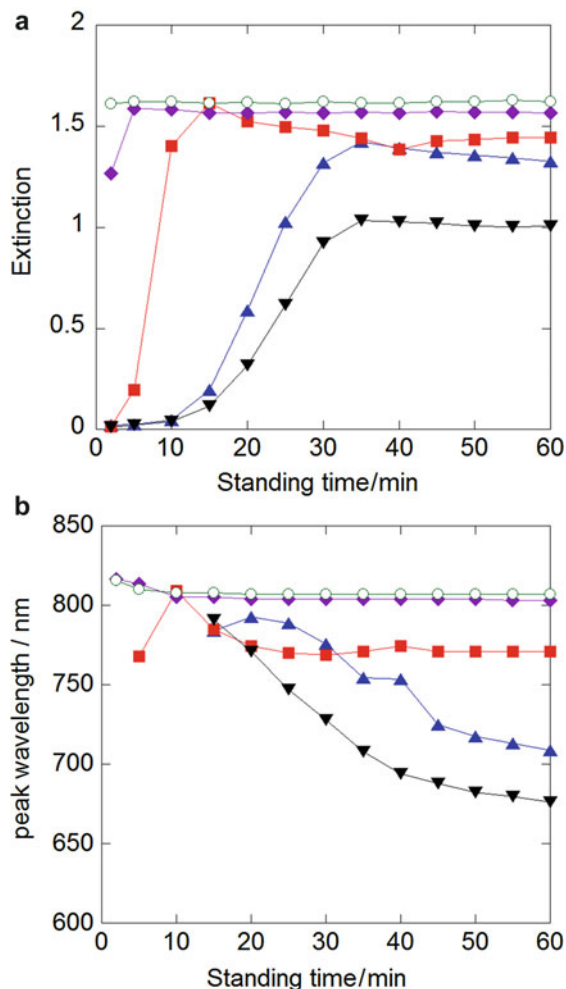
Fig. 23 Effects of irradiation time and subsequent standing time on (**a**) peak extinction and (**b**) peak wavelength of the longitudinal plasmon resonance of sample solution. Irradiation times: (▼) 0.5 min, (▲) 1 min, (■) 3 min, (◆) 10 min, (○) 15 min (Reprinted with permission from Ref. [33]. Copyright 2014 Elsevier)

for 0.5 min. The following formation mechanism of Au nanorods is proposed: relatively small Au seeds form at short irradiation times and rapidly grow to a critical size, and thus the size and aspect ratio of the resulting Au nanorods depend on the number of Au seeds attaining the critical size. This mechanism is supported by the following conjecture: the adsorption of CTAB on Au seeds that have just formed by the sonochemical method does not reach equilibrium, and thus the seeds rapidly grow to the critical size.
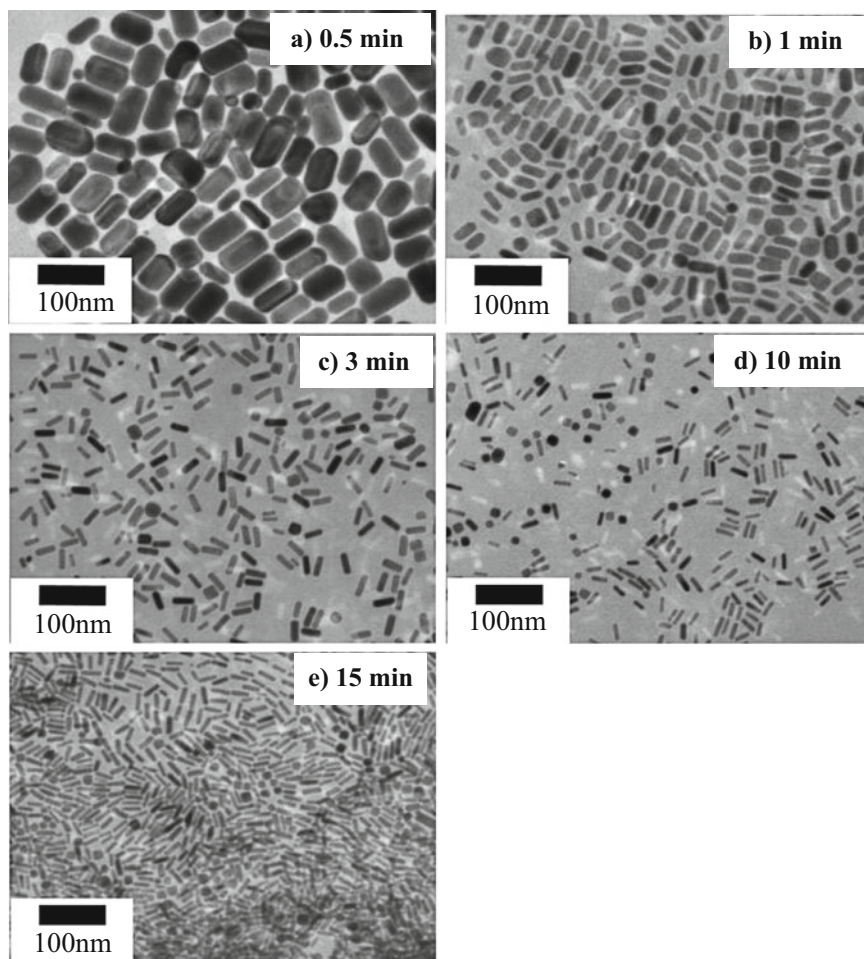
Fig. 24 TEM images of Au nanorods produced via Au seeds formed after (**a**) 0.5, (**b**) 1, (**c**) 3, (**d**) 10, or (**e**) 15 min of ultrasonic irradiation (Reprinted with permission from Ref. [33]. Copyright 2014 Elsevier)

Conclusions and Future Directions

The sonochemical reduction of noble metal ions or complexes proceeds effectively in the presence of an organic additive (RH), because reducing radicals such as H radicals and pyrolysis radicals are formed, and secondary radicals are formed from the abstraction reactions of RH with OH or H radicals. The rate of sonochemical reduction of metal ions can be controlled by changing the concentration of the organic additive. More highly hydrophobic organic additives tend to accumulate at the interface region of cavitation bubbles causing the reduction of metal ions to

proceed more rapidly. The rate of sonochemical reduction is dependent on the type of dissolved gas, the solution temperature, the ultrasound power and frequency, and the configuration of the sonicator. The sizes of metal nanoparticles tend to decrease with increasing rates of reduction of metal ions. In the presence of metal oxide powders, size-controlled monometallic or structure-controlled bimetallic nanoparticles formed by sonochemical reduction are immobilized on the metal oxide surface. The resulting supported catalysts can be applied to the catalytic hydrogenation of olefins and the photocatalytic degradation of alcohols to produce H_2 gas. Sonochemically prepared catalysts have higher catalytic activities than catalysts prepared by conventional impregnation methods. Catalysts consisting of immobilized noble metal nanoparticles can be prepared by ultrasound irradiation in a one-pot process, whereas the impregnation method for the synthesis of such catalysts needs several reaction vessels and several processes as well as heat treatments under H_2 gas. Taking into account these characteristics, the sonochemical method of catalyst preparation can be considered environment friendly. Noble metal–magnetic nanocomposites prepared by the sonochemical reduction method exhibited excellent catalytic activities for the reduction of nitrobenzene and high durability on repeated use/retrieval cycles. These nanocomposites also can be used for the separation of amino acids. In addition, by producing Au seeds with catalytic activity for the reduction of Au(I) with ascorbic acid, Au nanorods with specific lengths, widths, and aspect ratios can be prepared. Because short irradiation times are adequate for the synthesis of Au seeds, this is an energy-efficient method for the synthesis of metal nanoparticles. In the future, the development of simple one-pot sonochemical methods using short-duration ultrasound will be important for the synthesis of size-, shape-, and structure-controlled nanoparticles. When using the sonochemical method, the progress of chemical reactions can be easily controlled by switching the sonicator on and off. When the amounts and types of radicals formed can be more precisely controlled and the physical effects of cavitation bubbles are better under-stood, this method of nanoparticle synthesis will have great potential to advance a wide variety of industries through the application of nanotechnology.

References

1. Semagina N, Renken A, Laub D, Kiwi-Minsker L (2007) Synthesis of monodispersed palladium nanoparticles to study structure sensitivity of solvent-free selective hydro-genation of 2-methyl-3-butyn-2-ol. J Catal 246:308–314
2. Bianchini C, Shen K (2009) Palladium-based electrocatalysts for alcohol oxidation in half cells and in direct alcohol fuel cells. Chem Rev 109:4183–4206
3. Jana NR, Gearheart L, Murphy CJ (2001) Wet chemical synthesis of high aspect ratio cylindrical gold nanorods. J Phys Chem B 105:4065–4067
4. Baghbanzadeh M, Carbone L, Cozzoli PD, Kappe CO (2011) Microwave-assisted synthesis of colloidal inorganic nanocrystals. Angew Chem Int Ed 50:11312–11359
5. Yu YY, Chang SS, Lee CL, Wang CRC (1997) Gold nanorods: electrochemical synthesis and optical properties. J Phys Chem B 101:6661–6664
6. Mohamed MB, Ismail KZ, Link S, El-Sayed MA (1998) Thermal reshaping of gold nanorods in micelles. J Phys Chem B 102:9370–9374

7. Esumi K, Matsuhisa K, Torigoe K (1995) Preparation of rodlike gold particles by UV irradiation using cationic micelles as a template. Langmuir 11:3285–3287

8. Kim F, Song JH, Yang P (2002) Photochemical synthesis of gold nanorods. J Am Chem Soc 124:14316–14317

9. Saito N, Hieda J, Takai O (2009) Synthesis process of gold nanoparticles in solution plasma. Thin Solid Films 518:912–917

10. Mizukoshi Y, Masahashi N, Tanabe S (2014) Formation mechanism of noble metal nanoparticles in aqueous solution by solution plasma. Sci Adv Mater 6:1569–1572

11. Katsikas L, Gutiérrez M, Henglein A (1996) Bimetallic colloids: silver and mercury. J Phys Chem 100:11203–11206

12. Dey GR, El Omar AK, Jacob JA, Mostafavi M, Belloni J (2011) Mechanism of trivalent gold reduction and reactivity of transient divalent and monovalent gold ions studied by gamma and pulse radiolysis. J Phys Chem A 115:383–391

13. Gutierrez MS, Henglein A, Dohrmann JK (1987) H atom reactions in the sonolysis of aqueous solutions. J Phys Chem 91:6687–6690

14. Nagata Y, Watanabe Y, Fujita S, Dohmaru T, Taniguchi S (1992) Formation of colloidal silver in water by ultrasonic irradiation. J Chem Soc Chem Commun :1620–1622

15. Yeung SA, Hobson R, Biggs S, Grieser F (1993) Formation of gold sols using ultrasound. J Chem Soc Chem Commun :378–379

16. Nagata Y, Mizukoshi Y, Okitsu K, Maeda Y (1996) Sonochemical formation of gold particles in aqueous solution. Radiat Res 146:333–338

17. Grieser F, Hobson R, Sostaric J, Mulvaney P (1996) Sonochemical reduction processes in aqueous colloidal systems. Ultrasonics 34:547–550

18. Okitsu K, Bandow H, Maeda Y, Nagata Y (1996) Sonochemical preparation of ultrafine palladium particles. Chem Mater 8:315–317

19. Okitsu K, Mizukoshi Y, Bandow H, Maeda Y, Yamamoto T, Nagata Y (1996) Formation of noble metal particles by ultrasonic irradiation. Ultrason Sonochem 3:S249–S251

20. Mizukoshi Y, Oshima R, Maeda Y, Nagata Y (1999) Preparation of platinum nanoparticles by sonochemical reduction of the Pt(II) ion. Langmuir 15:2733–2737

21. Mizukoshi Y, Takagi E, Okuno H, Oshima R, Maeda Y, Nagata Y (2001) Preparation of platinum nanoparticles by sonochemical reduction of the Pt(IV) ions: role of surfactants. Ultrason Sonochem 8:1–6

22. Caruso RA, Ashokkumar M, Grieser F (2002) Sonochemical formation of gold sols. Langmuir 18:7831–7836

23. Alegria AE, Lion Y, Kondo T, Riesz P (1989) Sonolysis of aqueous surfactant solutions. Probing the interfacial region of cavitation bubbles by spin trapping. J Phys Chem 93:4908–4913

24. Sakai T, Enomoto H, Torigoe K, Sakai H, Abe M (2009) Surfactant- and reducer-free synthesis of gold nanoparticles in aqueous solutions. Colloids Surf A: Physicochem Eng Asp 347:18–26

25. Okitsu K, Yue A, Tanabe S, Matsumoto H (2000) Sonochemical preparation and catalytic behavior of highly dispersed palladium nanoparticles on alumina. Chem Mater 12:3006–3011

26. Xu H, Suslick KS (2010) Sonochemical synthesis of highly fluorescent Ag nanoclusters. ACS Nano 4:3209–3214

27. Okitsu K, Yue A, Tanabe S, Matsumoto H (2002) Formation of palladium nanoclusters on Y-zeolite via a sonochemical process and conventional methods. Bull Chem Soc Jpn 75:449–455

28. Okitsu K, Murakami M, Tanabe S, Matsumoto H (2000) Catalytic behavior of Au Core/Pd shell nanoparticles on silica prepared by sonochemical and Sol–gel processes. Chem Lett 29:1336–1337

29. Nakagawa T, Nitani H, Tanabe S, Okitsu K, Seino S, Mizukoshi Y, Yamamoto TA (2005) Structural analysis of sonochemically prepared Au/Pd nanoparticles dispersed in porous silica matrix. Ultrason Sonochem 12:249–254

30. Mizukoshi Y, Makise Y, Shuto T, Hu J, Tominaga A, Shironita S, Tanabe S (2007) Immobilization of noble metal nanoparticles on the surface of TiO_2 by sonochemical method: photocatalytic production of hydrogen from an aqueous solution of ethanol. Ultrason Sonochem 14:387–392

31. Mizukoshi Y, Sato K, Konno TJ, Masahashi N, Tanabe S (2008) Magnetically retrievable palladium/maghemite nanocomposite catalysts prepared by sonochemical reduction method. Chem Lett 37:922–923

32. Okitsu K, Yue A, Tanabe S, Matsumoto H, Yobiko Y, Yoo Y (2002) Sonolytic control of rate of gold(III) reduction and size of formed gold nanoparticles in an aqueous solution: relation between reduction rates and sizes of formed nanoparticles. Bull Chem Soc Jpn 75:2289–2296

33. Okitsu K, Nunota Y (2014) One-pot synthesis of gold nanorods via autocatalytic growth of sonochemically formed gold seeds: the effect of irradiation time on the formation of seeds and nanorods. Ultrason Sonochem 21:1928–1932

34. Okitsu K, Ashokkumar M, Grieser F (2005) Sonochemical synthesis of gold nanoparticles in water: effects of ultrasound frequency. J Phys Chem B 109:20673–20675

35. Tronson R, Ashokkumar M, Grieser F (2002) Comparison of the effects of water-soluble solutes on multibubble sonoluminescence generated in aqueous solutions by 20- and 515-kHz pulsed ultrasound. J Phys Chem B 106:11064–11068

36. Mizukoshi Y, Okitsu K, Maeda Y, Yamamoto TA, Oshima R, Nagata Y (1997) Sonochemical preparation of bimetallic nanoparticles of gold/palladium in aqueous solution. J Phys Chem B 101:7033–7037

37. Mizukoshi Y, Fujimoto T, Nagata Y, Oshima R, Maeda Y (2000) Characterization and catalytic activity of core-shell structured gold/palladium bimetallic nanoparticles synthesized by the sonochemical method. J Phys Chem B 104:6028–6032

38. Arai M, Usui K-I, Nishiyama Y (1993) Preparation of alumina-supported platinum catalyst at ambient temperature for selective synthesis of cinnamyl alcohol by liquid-phase cinnamaldehyde hydrogenation. J Chem Soc Chem Commun :1853–1854

39. Fujishima A, Honda K (1972) Electrochemical photolysis of water at a semiconductor electrode. Nature 238:37–38

40. Linsebigler AL, Lu G, Yates JT Jr (1995) Photocatalysis on TiO_n surfaces: principles, mechanisms, and selected results. Chem Rev 95:735–758

41. Agrios AG, Pichat P (2006) Recombination rate of photogenerated charges versus surface area: opposing effects of TiO_2 sintering temperature on photocatalytic removal of phenol, anisole, and pyridine in water. J Photochem Photobiol A 180:130–135

42. Michaelson HB (1977) The work function of the elements and its periodicity. J Appl Phys 48:4728–4733

43. Wang X, Yu JC, Yip H-Y, Wu L, Wong P-K, Lai S-Y (2005) A mesoporous $Pt/TiO2$ nanoarchitecture with catalytic and photocatalytic functions. Chem Eur J 11:2997–3004

44. Tian Y, Tatsuma T (2005) Mechanisms and applications of plasmon-induced charge separation at TiO_2 films loaded with gold nanoparticles. J Am Chem Soc 127:7632–7637

45. Mizukoshi Y, Tsuru Y, Tominaga A, Seino S, Masahashi N, Tanabe S, Yamamoto TA (2008) Sonochemical immobilization of noble metal nanoparticles on the surface of maghemite: mechanism and morphological control of the products. Ultrason Sonochem 15:875–880

46. Doktycz SJ, Suslick K (1990) Interparticle collisions driven by ultrasound. Science 247:1067–1069

47. Mulvaney P, Giersig M, Henglein A (1992) Surface chemistry of colloidal gold: deposition of lead and accompanying optical effects. J Phys Chem 96:10419–10424

48. Mizukoshi Y, Sato K, Konno TJ, Masahashi N (2010) Dependence of photocatalytic activities upon the structures of Au/Pd bimetallic nanoparticles immobilized on TiO_2 surface. Appl Catal Environ 94:248–253

49. Su R, Tiruvalam R, Logsdail AJ, He Q, Downing CA, Jensen MT, Dimitratos N, Kesavan L, Wells PP, Bechstein R, Jensen HH, Wendt S, Catlow CRA, Kiely CJ, Hutchings GJ, Besenbacher F (2014) Designer titania-supported Au–Pd nanoparticles for efficient photocatalytic hydrogen production. ACS Nano 8:3490–3497

50. Shiraishi Y, Sakamoto H, Sugano Y, Ichikawa S, Hirai T (2013) Pt–Cu bimetallic alloy nanoparticles supported on anatase TiO_2: highly active catalysts for aerobic oxidation driven by visible light. ACS Nano 7:9287–9297

51. Nakato Y, Ueda K, Yano H, Tsubomura H (1988) Effect of microscopic discontinuity of metal overlayers on the photovoltages in metal-coated semiconductor-liquid junction photoelectrochemical cells for efficient solar energy conversion. J Phys Chem 92:2316–2324

52. Wood DM (1981) Classical size dependence of the work function of small metallic spheres. Phys Rev Lett 46:749

53. Yi DK, Lee SS, Ying JY (2006) Synthesis and applications of magnetic nanocomposite catalysts. Chem Mater 18:2459–2461

54. Wang Z, Xiao P, Shen B, He N (2006) Synthesis of palladium-coated magnetic nanoparticle and its application in Heck reaction. Colloids Surf A 276:116–121

55. Guin D, Baruwati B, Manorama SV (2007) Pd on amine-terminated ferrite nanoparticles: a complete magnetically recoverable facile catalyst for hydrogenation reactions. Org Lett 9:1419–1421

56. Okitsu K, Nagaoka S, Tanabe S, Matsumoto H, Mizukoshi Y, Nagata Y (1999) Sonochemical preparation of size-controlled palladium nanoparticles on alumina surface. Chem Lett 28:271–272

57. Creighton JA, Eadon DG (1991) Ultraviolet–visible absorption spectra of the colloidal metallic elements. J Chem Soc Faraday Trans 87:3881–3891

58. Nagaveni K, Gayen A, Subbanna GN, Hegde MS (2002) Pd-coated Ni nanoparticles by the polyol method: an efficient hydrogenation catalyst. J Mater Chem 12:3147–3151

59. Mucic RC, Storhoff JJ, Mirkin CA, Letsinger RL (1998) DNA-directed synthesis of binary nanoparticle network materials. J Am Chem Soc 120:12674–12675

60. Storhoff JJ, Lazaorides AA, Mucic RC, Mirkin CA, Letsinger RL, Schatz GC (2000) What controls the optical properties of DNA-linked gold nanoparticle assemblies? J Am Chem Soc 122:4640–4650

61. Liu T, Tang J, Jiang L (2002) Sensitivity enhancement of DNA sensors by nanogold surface modification. Biochem Biophys Res Commun 295:14–16

62. Nuzzo RG, Allara DL (1983) Adsorption of bifunctional organic disulfides on gold surfaces. J Am Chem Soc 105:4481–4483

63. Mirkin CA, Letsinger RL, Mucic RC, Storhoff JJ (1996) A DNA-based method for rationally assembling nanoparticles into macroscopic materials. Nature 382:607–609

64. Kiang CH (2003) A DNA-based method for rationally assembling nanoparticles into macroscopic materials. Phys A 321:164–169

65. Mizukoshi Y, Seino S, Kinoshita T, Nakagawa T, Yamamoto TA, Tanabe S (2006) Selective magnetic separation of sulfur-containing amino acids by sonochemically prepared Au/gamma-Fe_2O_3 composite nanoparticles. Scr Mater 54:609–613

66. Mizukoshi Y, Seino S, Okitsu K, Kinoshita T, Otome Y, Nakagawa T, Yamamoto TA (2005) Sonochemical preparation of composite nanoparticles of Au/gamma-Fe_2O_3 and magnetic separation of glutathione. Ultrason Sonochem 12:191–195

67. Kinoshita T, Seino S, Mizukoshi Y, Nakagawa T, Yamamoto TA (2007) Functionalization of magnetic gold/iron-oxide composite nanoparticles with oligonucleotides and magnetic separation of specific target. J Magn Magn Mater 311:255–258

68. Sousa MH, Rubim JC, Sobrinho PG, Tourinho FA (2001) Biocompatible magnetic fluid precursors based on aspartic and glutamic acid modified maghemite nanostructures. J Magn Magn Mater 225:67–72

69. Demers LM, Mirkin CA, Mucic RC, Reynolds RA, Letsinger RL, Elghanian R, Viswanadham G (2000) A fluorescence-based method for determining the surface coverage and hybridization

efficiency of thiol-capped oligonucleotides bound to gold thin films and nanoparticles. Anal Chem 72:5535–5541

70. Park K, Drummy LF, Wadams RC, Koerner H, Nepal D, Fabris L, Vaia RA (2013) Growth mechanism of gold nanorods. Chem Mater 25:555–563

71. Jiang XC, Pileni MP (2007) Gold nanorods: influence of various parameters as seeds, solvent, surfactant on shape control. Colloids Surf A 295:228–232

72. Liu J, Duggan JN, Morgan J, Roberts CB (2012) Seed-mediated growth and manipulation of Au nanorods via size-controlled synthesis of Au seeds. J Nanoparticle Res 14:1289

Ultrasonic Synthesis of Polymer Nanoparticles

Boon Mian Teo

Contents

Abstract

Recent advances in nanomaterial synthesis have led to the search and development of new synthetic methods. The use of high-intensity ultrasound in chemistry offers a versatile and simple means of polymeric nanostructure synthesis. The chemical effects of ultrasound that are relevant to material synthesis arise from a phenomenon known as acoustic cavitation (the formation, growth, and violent collapse of bubbles under the influence of a sound field) which can create extreme conditions inside the collapsing bubbles, and this serves as the origin of sonochemistry. Herein, the fundamental concepts involving ultrasound, sonochemistry, and emulsion polymerization will be provided. In particular, special emphasis on sonochemical production of polymer nanocomposites and (bio)polymer microspheres and the biorelated applications of these microspheres will be given.

B.M. Teo (✉)
Interdisciplinary Nanoscience Center (iNANO), Aarhus University, Aarhus, Denmark

Institute of Biomedical Engineering (IBME), Oxford University, Oxford, UK
e-mail: bteo@inano.au.dk; boon.teo@eng.ox.ac.uk; boonmteo@gmail.com

Introduction

The application of high-intensity ultrasound in the field of chemistry has been shown to provide great promises in promoting a wide range of chemical processes such as the synthesis of polymer nanocomposites, the synthesis of proteinaceous or polymer-coated microspheres, metallic nanoparticle synthesis, and the degradation of a range of pollutants. The wide applications of ultrasound in chemical processes have attracted intense attention in various fields of chemistry, materials science, and chemical engineering. It exploits the effect of acoustic cavitation [1]; bubbles present in the solution grow and collapse when sound waves pass through a liquid. This results in the generation of radicals, excited-state species, enhancement of reaction rates, and excellent mixing of multiphase systems.

The aim of this book chapter is to introduce the reader to the key fundamental concepts involved in the field of ultrasound and sonochemistry. We aim to provide a detailed explanation on free radical polymerization and mechanism of emulsion polymerization and also review the recent progress and challenges in the use of high-intensity ultrasound on the synthesis of polymer particles and air- and oil-filled microspheres. In doing so, we hope to present the advancement and impact of the use of ultrasound in the field of fabricating polymeric colloidal systems over the past years. It does not provide an exhaustive literature review; rather, it provides an overview of some important research in this area.

Acoustic Cavitation and Sonochemistry

Ultrasound is a longitudinal wave that has wave frequency higher than human audible frequency range. Sound wave is classified according to the oscillating frequency, sound waves oscillating between 0.001 and 10 Hz are known as infra-sonic waves, and oscillating sound waves with frequencies higher than 16 kHz are known as ultrasound. Contrary to audible sound, ultrasound enacts several unique physical and chemical phenomena. The first report on the physical and biological effects of ultrasound was published in 1927 by Wood and Loomis [2], and the term sonochemistry was coined by Weissler in 1953 [3]. Both works are widely considered to give birth to the discipline of sonochemistry – a field in which chemistry and physics deal with the short-lived, localized high pressure and temperature produced through acoustic cavitation.

Acoustic cavitation (the formation, growth, and violent collapse of bubbles in a solution) is a process produced by irradiating a liquid with high-intensity ultrasound
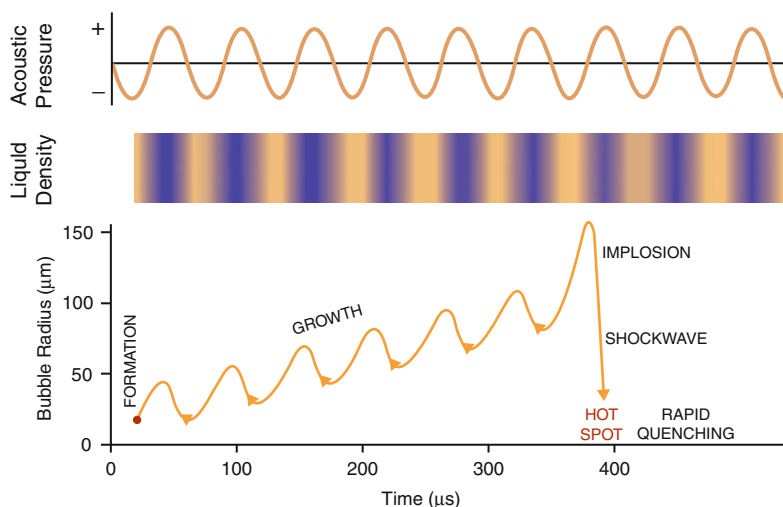
Fig. 1 Schematic representation of transient acoustic cavitation (Adapted from Adv. Mater., 2010, 22, 1039–1059 with permission. Copyright 2010, Materials Research Society)

with a frequency of 20 kHz to several MHz. Figure 1 shows the growth and violent collapse of microscopic bubbles in liquids under the influence of a sound field. During cavitation, the collapse of these bubbles is so intense to generate local heating, high pressures, and high-speed jets. Such intense and localized hot spots are responsible for many of the chemical reactions enacted by ultrasound irradiation. These bubbles grow from nuclei over several acoustic cycles through a process known as the rectified diffusion [4]. Rectified diffusion is explained by two contributing effects – area and shell effect. As the acoustic cycle alternates between the rarefaction and compression phases, gas is forced to diffuse in and out of the bubble. During the expansion cycle, the average surface area of the bubble is larger than that during the compression cycle. Due to that there is always a net flow of gas into the bubble over several cycles. The gas concentration gradient in the fluid shell around the bubble also contributes to this phenomenon. Since the diffusion rate of gases into bubbles is proportional to the concentration gradient of dissolved gas, the net inflow of gas will always be higher during the expansion stage of the bubble. Bubble growth is promoted by both the area and shell effects. When the bubbles reach a critical size range during the growth, they subsequently undergo a violent collapse.

Several theories have been postulated to explain the chemical effects of ultrasound: the hot spot theory [5] proposed by Noltingk and Neppiras and the electric discharge theory [6] by Margulis. The latter theory states that an electrical charge forms on the surface of the cavitation bubbles as it begins to break into tinier microbubbles, forming an electric field gradient across the bubbles. However, this theory has been discarded by several researchers [7]. The hot spot theory is to date the most accepted theory and that prior to the bubble collapse, bubble growth
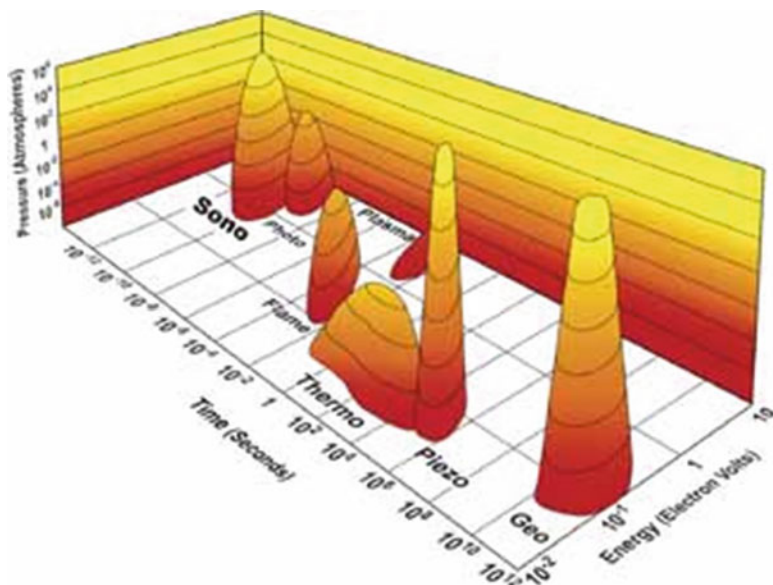
Fig. 2 Islands of chemistry as a function of time, pressure, and energy (Adapted from Adv. Mater., 2010, 22, 1039–1059 with permission. Copyright 2010, Materials Research Society)

proceeds under isothermal conditions, but the system becomes adiabatic upon bubble collapse, generating temperatures as high as a few thousands of degrees and pressures of over hundreds of atmospheres. Additionally, a secondary region of a thin layer of liquid surrounding the collapsed bubbles is also transiently heated. This region is approximately 200 nm thick and has been reported that it can get as hot as 2,000 K [8].

Ultrasound-induced cavitation in a liquid also gives rise to a number of physical effects, such as shock waves and microjets, and these phenomena can affect the efficiencies of chemical reactions. Shock waves created during a bubble collapse produce high mixing rates to the solution. In any heterogeneous system, the highly energetic collapse of bubbles will no longer be symmetrical as the solid surfaces prevent the homogenous flow of fluid, thus causing the collapse to often having a doughnut-like shape. This asymmetrical collapse results in jets of liquid directed at the solid surface at speeds of greater than 100 m s^{-1}. Shock waves and microjet agitation can create emulsions in systems that contain two immiscible liquids [9]. In comparison to other energy sources such as heat, and light, ultrasonic irradiation offers very unique reaction conditions (a short duration of extremely high temperatures and pressures in liquids) [10] (Fig. 2). The potential of this phenomenon will be discussed in the next sections.

Free Radical Polymerization

Among the many polymerization techniques, free radical polymerization is one of the most widely employed polymerization techniques and has been an important technological field for industrial production and applications. This technique is easy to perform and typically leads to high molecular weight polymers under relative mild reaction conditions. Many different free radical polymerization processes can be applied, such as bulk, solution, suspension or emulsion polymerizations. For a more detailed explanation on emulsion polymerization, the reader should refer to the work of Gilbert [11].

The mechanism governing a free radical polymerization process typically involves three steps: initiation, propagation, and termination [12]. As shown in Reaction 1 and Reaction 2, there are two steps involved in the initiation process: first, the dissociation of initiators to form free radicals and, second, the reaction of the free radical with a monomer molecule:

$$I \xrightarrow{k_d} 2R_i \qquad \text{(Reaction1)}$$

$$R_i + M \xrightarrow{k_i} M_i \qquad \text{(Reaction2)}$$

where R_i is the free radical formed, k_d is the rate constant for initiator decomposition, k_i is the rate constant for initiation process, M is the monomer, and M_i is the monomeric radical. The rate expression for initiation is given by Eq. 1:

$$\frac{d[R]}{dt} = R_i = 2fk_d[I] \qquad (1)$$

where R is the rate of initiation and f is the initiator efficiency.

The initiator efficiency is defined as the fraction of free radicals that can react with the monomer (Eq. 2). The value of f is usually less than 1 and typically falls in the range of 0.3–0.8. Once formed, free radicals can either recombine, terminate with another free radical, or initiate chain propagation. The initiation step plays a very important role in the overall rate of polymerization and also has an effect on the final molecular weight of the final polymer. The constant addition of monomer molecules to growing polymer radicals in the propagation stage takes place very rapidly (Reaction 3 and Reaction 4):

$$f = \frac{\text{rate of initiation of propagating chains}}{\text{rate of primary radical formation}} \qquad (2)$$

$$R + M \xrightarrow{k_p} M_i \qquad \text{(Reaction3)}$$

$$M_i + M \xrightarrow{k_p} M_{i+1} \qquad \text{(Reaction4)}$$

The propagation rate constant, k_p, usually falls in the range of 10^2–10^4 L mol^{-1} s^{-1} [12]. k_p is calculated using the experimental conversion and time data together with the initiator concentration measurements. The relationship is shown below (Eq. 3). The propagating polymer chains will stop growth and terminate after reaching a certain point. Termination of the radicals occurs by bimolecular reaction between two radicals (Reaction. 5) or, in another rare case, by disproportionation, whereby a hydrogen radical that is beta to one radical center is transferred to another radical center; this results in the formation of two polymer molecules (Reaction. 6):

$$\frac{dx}{dt} = k_p[R][I - x] \qquad (3)$$

where x is the mole fraction of the monomer.

$$M_i + M_j \xrightarrow{k_{tc}} P_{ij} \qquad \text{(Reaction5)}$$

$$M_i + M_j \xrightarrow{k_{td}} P_i + P_j \qquad \text{(Reaction6)}$$

where M_i and M_j are two different monomeric radicals and P_{ij}, P_i, and P_j are radicals.

The rate constant for termination depends on various parameters such as the overall composition and the chain length of the propagating species, and the value falls in the range of $10^6 - 10^8$ L mol^{-1} s^{-1}. The termination rate also decreases as the conversion to polymer increases. In some cases, chain propagation continues as the termination rate is decreased, and as a result, high molecular weight polymers are produced. This phenomenon is commonly referred to as the "gel effect" and is particularly evident in bulk polymerization reactions. In other cases, a polymer chain can also be prevented from growing by the removal of an atom from some substance present in the system to give a new radical, which may or may not start another new chain [13]. This process is known as chain transfer and can be represented by Reaction 7 and Reaction 8:

$$P_i + RX \rightarrow P_iR + X^{\cdot} \text{ Chain transfer reaction} \qquad \text{(Reaction7)}$$

$$X^{\cdot} + M \rightarrow P_i \text{ Generation of new kinetic chain} \qquad \text{(Reaction8)}$$
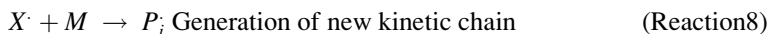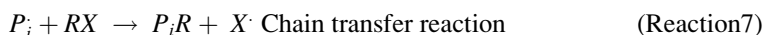
where RX represents solvent molecule and X• represents a univalent atom that was removed by the polymeric radical from the solvent molecule.

Free radical polymerizations can be classified as either homogeneous or heterogeneous reactions. In homogeneous polymerization, all components (the monomer, chemical initiator, and the polymer) are in the same phase throughout the reaction. In heterogeneous polymerization, at least one component is insoluble at some point during the reaction. For the purpose of this book chapter, heterogeneous polymerization will be the focus, and the reader is referred to this book of Odian on *Principles of Polymerization* [12] for homogeneous polymerization systems.

Heterogeneous Polymerization

While aqueous solution polymerizations are of considerable interest in the viewpoint of industrial applications, the number of water-soluble monomers available is limited. Heterogeneous polymerization processes are, in this case, more applicable to a wider range of monomers. Particularly, they offer more practical advantages over homogenous polymerization reactions. There are several different systems identified in heterogeneous polymerization process as outlined in Table 1. They differ for the initial state of polymerization mixture, the mechanism of particle formation, the size of the final polymer particles, and the polymerization kinetics. In the following section, a brief introduction to the three main important systems will be outlined, namely, suspension polymerization ("Suspension Polymerization" [14]), emulsion polymerization ("Emulsion Polymerization" [11, 14]), and miniemulsion polymerization ("Miniemulsion Polymerization").

Suspension Polymerization

In suspension polymerization, a water insoluble monomer is dispersed in the continuous aqueous phase as oil droplets by vigorous stirring while an oil soluble initiator is used to initiate the polymerization reaction inside the monomer droplets [14]. During the reaction, coalescence of the droplets and partially formed polymer particles are prevented by the presence of stabilizers. Stabilizers act to improve the dispersion by increasing the viscosity of the aqueous phase and preventing

Table 1 Different types of heterogeneous polymerization systems (Adapted from Ref. [14])

Type	Typical particle radius	Droplet size	Initiator	Continuous phase	Discrete phase (particles)
Emulsion	50–300 nm	≈1–10 μm	Water soluble	Water	Initially absent, monomer-swollen polymer particles form
Suspension	≥1 μm	≈1–10 μm	Oil soluble	Water	Monomer+formed polymer in pre-existing droplets
Dispersion	≥1 μm		Oil soluble	Organic	Initially, absent, monomer-swollen polymer particles form
Microemulsion	10–30 nm	≈10 nm	Water soluble	Water	Monomer, cosurfactant+formed polymer
Miniemulsion	30–100 nm	≈30 nm	Water soluble	Water	Monomer, cosurfactant+formed polymer

coalescence by steric effects. Each polymer particle behaves as an isolated reactor, and the kinetics is similar to that of a bulk polymerization. As a result, the droplet size and the amount of stabilizer do not affect the rate of reaction. The continuous aqueous phase acts to decrease the viscosity of the solution and to dissipate the heat generated during the reaction process. The size of the particles is usually in the range of 20–2,000 μm and is dependent on the stirring speed, volume ratio of monomer to water, amount of stabilizer involved, viscosity of both the aqueous and oil phases, and the design of the reactor.

Emulsion Polymerization

Emulsion polymerization finds application for the production of materials such as synthetic rubber, latex paints, adhesives, and coatings [11, 14]. It has been widely used due to its attractive advantages over bulk polymerization. For example, heat dissipation during the reaction can be easily controlled through heat transfer to the aqueous phase, and polymerization rate and conversation are usually higher. The resulting polymers usually have high molecular weights that can be easily controlled by the addition of chain transfer agents. In addition, the viscosity of the solution during emulsion polymerization is close to that of water since water is the continuous phase. Contrary to suspension polymerization, emulsion polymerization usually produces submicron-sized particles that can remain suspended in the aqueous medium, forming latex particles. In a typical emulsion polymerization, the mixture consists of water, hydrophobic monomers, surfactant, and a water-soluble initiator. In an emulsion polymerization, the stabilizer used to impart colloidal stability is surface active and composed of both hydrophobic and hydrophilic parts. The stabilizer adsorbs to the interface of the droplets and provides stabilization by electrostatic effect, steric effect, or both. When its concentration is above the critical micelle concentration (CMC), it forms micelles, which are normally swollen by the monomer. Secondly, the initiator in an emulsion polymerization is water soluble. Due to that the radicals are produced in the continuous aqueous phase in which the polymerization reaction is initiated. As a result of the solubility of the initiator, it affects the particle formation and the kinetics of polymerization. The monomer droplets act only as monomer reservoirs, and polymerization occurs through diffusion of the monomer molecules through the aqueous phase. Particle nucleation mechanism allows one to predict the final number of particles, N_p, to quantify the effect of various parameters such as the type and concentration of surfactant used, type and concentration of initiator, the nature of monomers, and reaction temperature. The compartmentalization of the propagation radicals within each separate particle complicates the polymerization kinetics. In an emulsion polymerization, the kinetics is not simply affected by the initiator, propagation, and termination as in a homogeneous radical polymerization. It is further complicated by the presence of two phases. The transfer of oligoradicals from the water phase into the particles, and vice versa, and the transfer of monomer have to be considered.

There are three stages to be considered in an emulsion polymerization reaction. Interval I is the particle formation stage, whereby there is an increase in the number of particles that remains constant during Interval II and III. Polymerization rate increases with time as the number of particle increases. Monomer molecules are constantly diffusing into the particles to replace the monomer molecules that have been polymerized. Interval I ends when the particle number stabilizes. This is a small fraction, typically about 0.1 % of the concentration of the micelles that are initially present in the system. As the polymer particles grow in size, they adsorb more surfactant to ensure the stability of particles in the solution. Surfactant concentration at this stage rapidly decreases below its CMC, and any micelles will become unstable and disappear due to dissolution of the micellar surfactant. By the end of Interval I and beginning of Interval II, almost all the surfactant molecules have been adsorbed on the polymer particles; any monomer droplets that remained in the system become unstable and coalesce if stirring ceases. Interval I is the shortest among the three intervals covering from 2 % to 15 % of the conversion. During Interval II the polymerization rate remains either constant or increases slightly with time. The latter behavior is due to the gel effect. Interval II ends when all the monomer droplets disappear, and the transition from Interval II to III occurs at lower conversions as the water solubility of the monomer increases and the extent of swelling of polymer particles increases. The particle number remains constant in Interval III, and polymerization continues at a decreasing rate as the monomer concentration in the polymer particles decreases. One hundred percent conversion of monomer to polymer can be usually achieved, and the final particles are typically in the size range of 50–300 nm.

The theory of emulsion polymerization relies on the following equation [12]:

$$R_p = k_p[M]_p N_p \tilde{n}/N_A \tag{4}$$

where R_p is the rate of polymerization, k_p is the propagation rate coefficient, $[M]_p$ is the concentration of monomer in a particle, ñ is the average number of radicals in a particle, N_p is the number concentration of particles, and N_A is Avogadro's constant.

The rate of polymerization, R_p, depends on the following parameters. The value of ñ is crucial in determining R_p. Through the mathematical analysis by Smith and Ewart, three scenarios can be considered in which the particle size and radical exit from the emulsion droplet rate may vary. The main differences between the three cases are (i) the occurrence of radical diffusion out of the particles, also known as desorption, (ii) the particle size, (iii) ways of termination, and (iv) rates of initiation and termination. The quantitative balance of these factors in this equation leads to the three scenarios.

In the first situation (Case 1), the polymer particles are small, the monomers are relatively soluble in water and desorption of radicals from the particles is likely to happen, ñ is very low, and polymerization is slow.

In the second situation (Case 2), radical exit is almost insignificant. When a radical enters a particle, polymerization occurs until the next radical comes along and both radicals instantaneously terminate (zero–one kinetics). Under such conditions, $\tilde{n} = 0.5$.

In the last situation (Case 3), the particles are larger than in the other two cases, such that more than two radicals can exist together in the particle without instantaneous termination. In this case, ñ may be greater than 1.

Compartmentalization

Compartmentalization in free radical emulsion polymerization is the term used to describe the situation whereby the radicals are kept in confinement within monomer droplets/latex particles [11]. In other words, the propagating radicals contained in a single polymer particle are physically separated from other radicals contained in another particle. As a result, bimolecular termination cannot occur between radicals in different particles.

Pseudo-bulk System

In this system, the number of radicals per particle is relatively high such that the emulsion polymerization resembles a bulk polymerization system [11]. The average number of radicals is always greater than 0.5. Compartmentalization does not affect the kinetics of polymerization in such a system, and termination is always diffusion controlled.

Zero–One System

The term zero–one typically describes the situation found in most emulsion polymerizations whereby all latex particles contain either zero or one active radical (i.e., two or more radicals cannot coexist in one particle) [11]. This is because the particles are very small and can result in instantaneous bimolecular termination. In other words, if an active radical enters a particle that already contains a radical, there will be an instantaneous termination of the two radicals. Therefore, the maximum value of the average number of radicals per latex particle, ñ, is 0.5. In such systems, compartmentalization becomes important in the kinetic events of emulsion polymerization.

Compartmentalized Pseudo-bulk System

This system, also known as the zero–one–two kinetics, is typical when termination is not instantaneous even when ñ is low [11]. Zero–one–two kinetics are favored by high propagation rate coefficients when radicals grow rapidly and bimolecular termination of radicals is no longer instantaneous. As the name implies, the latex particles may contain zero, one, or two radicals.

Miniemulsion Polymerization

There are two possible locations of particle formation in emulsion polymerization – within the micelles (micellar nucleation) and within the water phase (homogenous nucleation). Nucleation within the monomer droplets is not considered because of their large size and small droplet number, resulting in a very low probability to capture the water phase radicals. However if the droplets become sufficiently small,

they can compete for the radical entry and become the primary location of polymer particles formation. Such a system is known as the miniemulsion system. The miniemulsion polymerization is performed by vigorously stirring a mixture containing two immiscible liquids, one of which is an organic monomer and a hydrophobe and, the other, an aqueous surfactant solution. Monomer droplets of size ranging from 50 to 500 nm are usually obtained. The formation of miniemulsion droplets relies on the combination of the shear force treatment, the amount and type of surfactant, and the hydrophobe. The use of a hydrophobe or a cosurfactant is to enhance the stability of the small monomer droplets by limiting the coalescence by forming a barrier at the surface of the droplets by combination with surfactant and or preventing the diffusion of monomer from small to large particles by Ostwald ripening by building up an osmotic pressure within the droplets. The choice of a suitable hydrophobe is thus an important factor to consider for a successful miniemulsion polymerization. In an ideal scenario of a miniemulsion polymerization, the monomer droplet is the primary site of the polymerization reaction, and it is generally known as the 1:1 copy of the original monomer droplet to latex particle. Every monomer droplet acts as an independent nanoreactor, and polymerization inside the droplet occurs via a suspension polymerization-type reaction. Ugelstad et al. first introduced the concept of miniemulsion polymerization in 1973 when they successfully synthesized submicron-sized styrene particles using an emulsifier mixture of sodium dodecyl sulfate and cetyl alcohol [15]. The water-soluble initiator, potassium persulfate, was used as the chemical initiator for the polymerization reaction after the miniemulsion styrene droplets were formed. The sizes of the monomer droplets and the latex particles were observed to be similar, and it was proposed that nucleation occurred primarily inside the droplets.

An ideal miniemulsion polymerization, whereby each droplet is nucleated and transformed into a polymer particle, displays different kinetics from a classical emulsion polymerization process. A particle formation stage is observed which is followed by an increasing polymerization rate and increasing $\tilde{n} = 0.5$. During this stage, the polymerization follows a first-order kinetics with respect to monomer as in bulk, solution, or suspension polymerizations. Interval II in emulsion polymerization characterized by a constant polymerization rate does not occur in the ideal miniemulsion system as the transport of monomer is negligible. A last stage with increasing R_p and ñ is observed, which gives the typical gel effect (Fig. 3).

Ultrasonic Polymer Synthesis

Most synthetic polymers are prepared from monomers that contain a reactive double bond, which can undergo chain growth or addition reactions. The most common polymer synthesis method is via a free radical initiation process. It is known that ultrasound can be used as an initiating source for free radical polymerization reactions since, as already mentioned in section "Acoustic Cavitation and Sonochemistry," free radicals are produced during acoustic cavitation that involves the formation, growth, and collapse of bubbles. Due to that, the application of ultrasound to solutions containing vinyl monomers constitutes an alternative route to polymer synthesis.
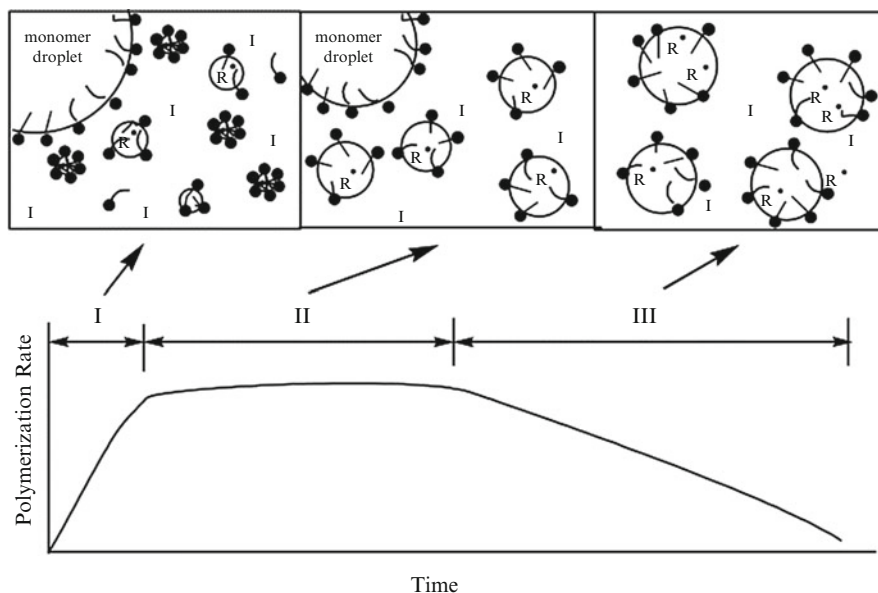
Fig. 3 The three intervals of an ab initio emulsion polymerization and their kinetics (Reprinted with permission from (Progress in Polymer Science, 2001, 26, 10, pp 2083–2134). Copyright (2001) Elsevier)

One of the earliest works on the chemical effects of ultrasound on macromolecules biopolymers, egg albumin, and plastein was reported by Florsdorf and Chambers in 1933 [16]. They found that the polymers in aqueous medium, when exposed to ultrasound, coagulated instantly at 30 °C and that the hydrolysis of sucrose was accelerated at temperatures as low as 5 °C comparable with the rate of the boiling point in the absence of polymerization. However, it was only in the early 1980s that extensive work on the effects of ultrasound on polymer systems was conducted. Ultrasound-initiated polymer synthesis can be divided into two categories: (i) homogenous systems commonly referred to as bulk polymerization with pure monomer and (ii) heterogeneous systems in which latex polymer particles formed are insoluble in the reaction medium. In this chapter, only polymerization in heterogeneous systems using ultrasound as an irradiation source will be discussed.

Sonochemical Polymerization in Heterogeneous Systems

As mentioned in section "Acoustic Cavitation and Sonochemistry," shock waves and microjet agitation from cavitating bubbles can generate emulsions in systems that contain two immiscible liquids. This constitutes an alternative method for sonochemical emulsion free radical polymerization. One of the major drawbacks in the classical emulsion polymerization is the use of chemical initiators and stabilizers that can alter the properties of the final product [17]. This can be prevented by using high-intensity ultrasound as a green method of polymerization as chemical initiators are not required in such systems. Due to the high localized

shear gradients generated through the cavitation bubbles, ultrasound allows very efficient stirring and dispersion of monomer droplets into the aqueous phase and thus prevents Ostwald ripening. It also helps to maintain a small and narrow distribution of monomer droplet sizes [17]. In addition, a unique feature of using ultrasound for polymerization reactions is that when the ultrasound is turned off, the polymerization reaction ceases. At fast polymerization rates with high monomer to polymer conversion at ambient temperature, polymers of high molecular weights can be produced, compared with conventional methods. The first report of applying ultrasound to this type of polymerization reaction dates back to the early 1950s. Ostroski and Stambaugh in 1950 reported that when a classical emulsion polymerization was conducted under sonication with frequencies of 15 and 500 kHz, better dispersion of styrene was obtained, which in turn dramatically enhanced the rate of polymerization [18]. They attributed the enhancement in the rate of styrene polymerization to a faster decomposition rate of the chemical initiator in the solution. As a result a stable emulsification is achieved by ultrasound in shorter times. Since then, the past decade has seen an extensive increase in the number of investigations undertaken to probe the mechanism of sonochemical emulsion polymerization reactions.

Biggs and Grieser conducted a mechanistic study on the synthesis of poly(styrene) latex particles by ultrasound irradiation at ambient temperature and drew the following observations: (i) the rate of polymerization reaction increased with increasing surfactant concentration, (ii) the average size of the latex particles was very small (approximately 50 nm), (iii) polymer molecular weights exceeded 10^6 g mol^{-1}, and (iv) there was a continuous formation of polymer particles [19]. They concluded that their sonochemical emulsion polymerization system bears similarities with the classical microemulsion polymerization system but with a much lower surfactant concentration. They extended their work to explore the effects of varying the acoustic intensity on the polymerization rate. An apparent increase in polymerization rate as a function of sonication time was observed as the intensity of ultrasound was increased. It was also reported that increasing the intensity did not affect the ensuing particle size range of the polymer particles, which was found to be in the range of 40–50 nm. They suggested that the narrow particle size range and high conversion rates obtained were due to a continuous nucleation of monomer droplets that then scavenged the sonochemically produced free radicals throughout the polymerization process. In another study, Cooper et al. found that by using a horn-type sonicator, it was possible to produce polymer latex particles with particle sizes smaller than those generated in the conventional process at low levels of or no surfactants. They observed a faster polymerization rate for butyl acrylate (BA) than vinyl acetate and ascribed it to the differences in the vapor pressures of the monomers [20]. Okudaira et al. reported a successful suspension polymerization using ultrasound with frequencies of 40 kHz and 200 kHz in the absence of surfactant and chemical initiator [21]. The styrene monomer was added dropwise into water and sonicated at 40 kHz to form monomer droplets dispersed in the aqueous phase. Polymerization of the monomer in the droplets was initiated by ultrasonic irradiation at 200 kHz. Both light-scattering data and TEM images indicated monodispersed polystyrene beads with an average diameter of 50 nm. They reported that no radical species were produced under
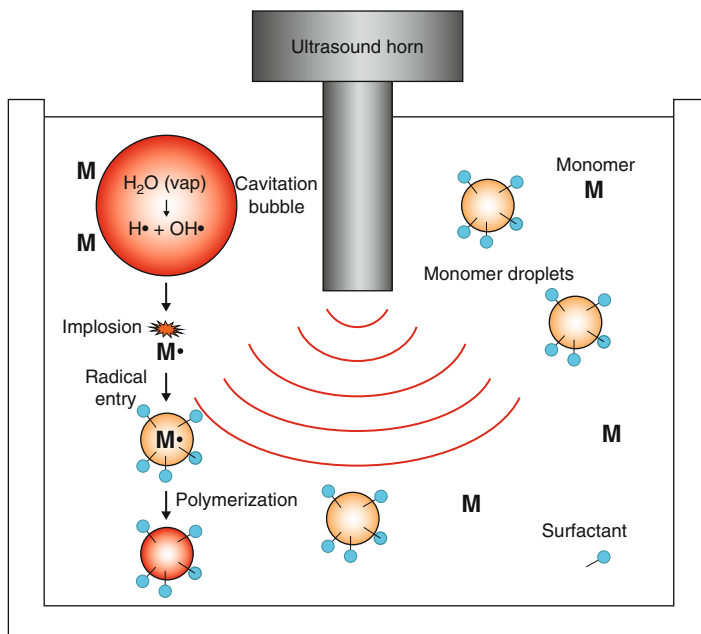
Fig. 4 Schematic diagram of proposed emulsion polymerization process induced by ultrasound. The scheme does not represent the true sizes of the system (horn, bubble, monomer, etc.) shown in the diagram (Reprinted with permission from (Ultrasonics Sonochemistry 2008, 15, 1, 89–94). Copyright (2008) Elsevier)

low-frequency irradiation at 20 kHz and it was exclusively used as a stirring technique to generate monomer droplets in aqueous phase while at 200 kHz, radicals were formed for the polymerization reaction.

Bradley and Grieser [17] conducted a mechanistic investigation of the sonochemical emulsion polymerization and gave a better insight to sonochemical polymerization in miniemulsion systems. They reported that the polymerization process is initiated by the reaction of the primary radicals with free monomer molecules, leading to the creation of monomeric radicals in the emulsion system (Fig. 4). The following reactions illustrate the initiation, propagation and termination processes of a sonochemical miniemulsion polymerization reaction. Upon collapse of the acoustic bubbles in an aqueous solution under the influence of a sound field, H• and •OH radicals are produced (Reaction 9). The monomer, methyl methacrylate (MMA), is volatile and can possibly evaporate into a cavitation bubble and be decomposed into hydrocarbon products. The H• and •OH radicals produced are captured by the solutes at the bubble–solution interface before they reach the aqueous phase. These solutes, present in the emulsion mixture, are mainly monomer and surfactant molecules. The primary radicals can react with the monomer adsorbed at the bubble–solution interface forming monomeric radicals in the bulk solution (Reaction 10). The monomeric radicals enter the monomer droplets and propagate

the polymerization process (Reaction 11). Reaction 12 and Reaction 13 represent a propagating radical undergoing polymerization. Termination of the polymerization reaction occurs when the growing radical reacts with another growing radical by disproportionation (Reaction 14).

Initiation:

$$H_2O \ )))) \ OH^{\bullet} \ + \ H^{\bullet} \qquad (Reaction\ 9)$$

$$OH^{\bullet} \ + \ M_s \rightarrow HOM_s^{\bullet} \equiv (M_s^{\bullet}) \qquad (Reaction\ 10)$$

$$H^{\bullet} \ + \ M_s \rightarrow HM_s^{\bullet} \equiv (M_s^{\bullet}) \qquad (Reaction\ 11)$$

Entry:

$$RM^{\bullet}(aq) \rightarrow RM^{\bullet}(d) \qquad (Reaction\ 12)$$

Propagation:

$$RM^{\bullet}(p) \ + \ M(p) \ \rightarrow P_2^{\bullet} \qquad (Reaction\ 13)$$

Termination:

$$P_i^{\bullet} \ + \ P_j^{\bullet} \rightarrow P_i + P_j \qquad (Reaction\ 14)$$
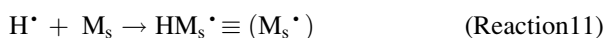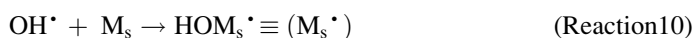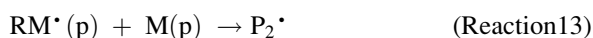
where M is the monomer; s is the surface of the cavitation bubbles; R represents the oligoradicals; d and p represent the monomer droplet and the polymer particle, respectively; P is the polymer chain; and i and j represent the length of different growing polymer chains.

Chou and Stoffer also performed a detailed investigation of ultrasound-initiated emulsion polymerization of MMA at ambient temperature using sodium dodecyl sulfate (SDS) as the surfactant [22]. They showed that the rate of polymerization and polymer yield were significantly improved under sonication compared to the classical emulsion polymerization methods at high temperature. The effects of several parameters such as acoustic intensity and surfactants on the ultrasound-initiated emulsion polymerization reaction were also investigated. Their conclusion was different from that of Bradley and Grieser [17] (surfactant molecules were degraded and acted as free radicals for the polymerization process). The rate of polymerization was found to be enhanced when the acoustic intensity, argon flow rate, and surfactant concentration were increased. The molecular weight of the polymer increased with an increase in the monomer concentration to a certain level and then became independent of the monomer concentration. From their experimental results, the molecular weight of the polymer decreased with an increase in the surfactant concentration, which was credited to an increase in the amount of radicals generated resulting from a higher number of surfactant molecules acting as initiators. However,

their assumption that the surfactant molecules serve as radicals for the polymerization reaction is unlikely because in the study conducted by Bradley and Grieser [17], they found that the surfactant molecules can be easily and successfully removed from the polymer samples simply by dialysis. This indicates that the surfactant does not play a major role in the initiation process for ultrasound-initiated emulsion polymerization.

Wang et al. [23] reported the sonochemical emulsion polymerization of MMA in an emulsion system with sodium dodecyl sulfate as the surfactant. They found that with higher surfactant concentration, the conversion of monomer to polymer increased significantly, but when no surfactant was added, no polymer was formed. From their experimental results, they suggested that the surfactant plays an important role in the initiation process. In addition, they observed an increase in monomer to polymer conversion when the reaction temperature was increased and that increasing the N_2 sparging rate increased the conversion percentage. They were able to obtain a monomer conversion of 67 % and polymer molecular weights of the order of several million daltons. They have also conducted an investigation of the ultrasonic emulsion polymerization of butyl acrylate (BA) to study the factors that affect the induction period and rates of polymerization and proposed a mechanism for sonochemical emulsion polymerization. They found that by increasing the N_2 sparging rate, temperature, surfactant concentration, and power intensity, and decreasing the monomer concentration, a decrease in the induction period and an increase in polymerization rate occurred. Under their experimental conditions, the conversion of BA to poly(butyl acrylate) (PBA) reached approximately 90 % within 10 min of sonication. They suggested that the mechanism of ultrasound-initiated emulsion polymerization was similar to a classical emulsion polymerization as a high surfactant concentration gives rise to a larger number of micelles, leading to more polymerization loci and increased the polymerization rates. Through analysis of the polymer product with nuclear magnetic resonance spectroscopy and Fourier transform infrared spectroscopy, their polymers were found to be slightly cross-linked and branched; hence, they concluded that the structure of the polymer particles obtained via sonochemistry was different from those obtained through the classical polymerization methods.

In a later study, Teo et al. reported the sonochemical polymerization of a family of methacrylate monomers. From their experimental results, they concluded that the physicochemical properties (e.g., vapor pressure and water solubility) of the monomers are crucial in determining the rates of polymerization in the sonochemical emulsion polymerization (Fig. 5) [15]. Their polymerization kinetic results also revealed a pseudo-first-order kinetics, supporting the use of a zero–one model for polymerization, in which the radical entering a particle already containing a growing oligoradical will lead to pseudo instantaneous termination. Particle size analysis showed that the sonochemical miniemulsion polymerization is consistent with a classical miniemulsion polymerization mechanism, such that there is a 1:1 copying of the monomer droplets into polymer particles.

Using the Keller–Miksis equation as a mathematical model for the radial motion of cavitation bubble, Moholkar and coworkers [24] concluded that several factors

Fig. 5 (a) Extent of monomer conversion; (b) pseudo-first-order kinetics data treatment (x as the fractional conversion of the monomer) as a function of sonication time for MMA, butyl methacrylate (*BMA*), and 2EHMA 2-ethylhexyl methacrylate at 25 mM SDS (Reprinted with permission from (Ultrasonics Sonochemistry 2008, 15, 1, 89–94). Copyright (2008) Elsevier)
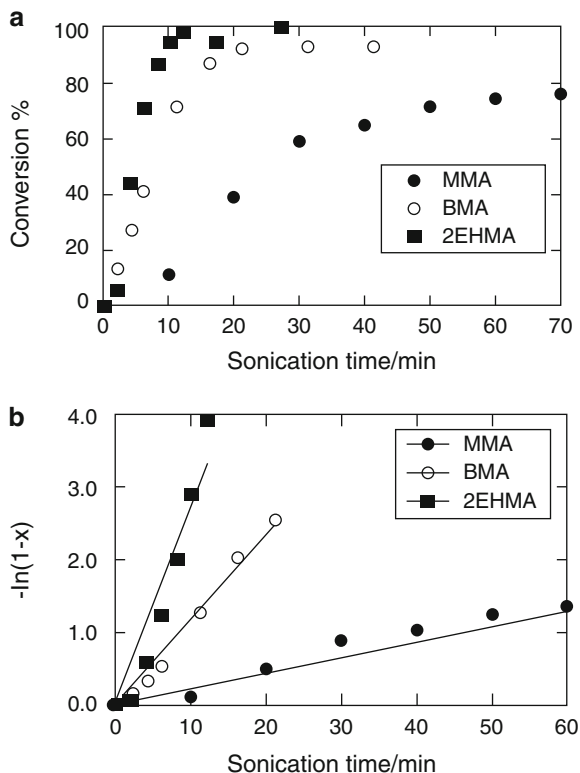
such as the extent of radical production from cavitation bubbles, magnitude of microturbulence and shock waves produced by the bubbles, glass transition temperature of the polymer, and the population density of the polymer particles all contributed to the final latex particle size and size distribution.

Bradley et al. [25] copolymerized MMA and BA using different MMA: BA ratios with ultrasound irradiation without chemical initiators. From the analysis of the polymers, they concluded that the microstructures of the copolymers were similar to those obtained in a classical copolymerization system. This indicated that ultrasound has no effect on the propagation step of the free radical polymerization.

Teo et al. reported the microemulsion polymerization of n-butyl methacrylate at a range of acoustic frequencies using ionic and nonionic surfactants [16, 17]. They reported that the properties of the polymer particles, such as the particle size and molecular weight, depended on the concentration and type of surfactants. The sonochemical microemulsion polymerization followed a continuous particle nucleation mechanism.

It has been shown by many authors [17, 19, 20, 26] that the molecular weights of the polymers prepared through sonochemical emulsion polymerization are generally higher than those prepared by conventional methods. Thus, it is important to be able to regulate the molecular weights of the polymers formed through the sonochemical

method. By using a range of organic solvents, Teo et al. were able to control the molecular weights of the polymers produced by ultrasound irradiation [26]. They showed that by changing the solvents used and its concentration, there is a pronounced decrease of the molecular weight of the polymer particles. This effect is due to a phenomenon known as the chain transfer reactions. Under specific experimental conditions, the chain transfer reaction may result in the production of a new radical, which may then continue the kinetic chain by reinitiation. While the molecular weight of the polymers was easily controlled by the addition of different organic solvents for a sonochemical emulsion polymerization method, the polydispersity index (PDI) remained high, and the limitation of this method is that the organic solvents used in this study were not considered "green."

Sonochemical Synthesis of Polymer Nanocomposites

The development of organic–inorganic nanocomposites, typically produced by grafting of synthetic polymers onto inorganic particles or simply by adding modified inorganic nanoparticles to polymer particles, finds applications in medicine and biotechnology to electronics and catalysis. The encapsulation of inorganic materials within a carrier polymer colloid is a significant innovation because polymer nanocomposite colloids have the potential to improve existing technologies. One main advantage of encapsulation is to protect and isolate the core from external harsh environments; an example is the encapsulation of probiotic bacteria from high-temperature food processing which protects enzymes from being denatured by solvents. Encapsulation is also used to deliver toxic materials such as pesticides and herbicides in agricultural and environmental applications. A second advantage of encapsulation is to allow the controlled release of incorporated loading in pharmaceutical and cosmetics applications. In the area of flavors, fragrance trapping systems, biocompatible microspheres can be used to entrap these molecules and allow for controlled time release.

Taking advantage of the miniemulsion polymerization process, polymeric nanocomposites containing inorganic nanoparticles can be incorporated within the core of the organic polymer shell. In order to successfully encapsulate hydrophobic materials within a latex particle, it is important to produce the appropriate latex particle size for encapsulation. In the first step, the core material must be hydrophobic to be dispersed in the organic monomer phase. Following this, emulsification of the organic phase is usually conducted by shearing the mixture with a homogenizer (or ultrasound), and subsequently, the monomer droplets containing the encapsulated materials are polymerized with free radical polymerization without changing their identity. The concept behind the miniemulsion process is that particle formation takes place via a droplet nucleation mechanism, whereby there is a 1:1 copy of the initial monomer droplets into the corresponding polymer particles. Thus, a miniemulsion droplet can be regarded as a nanoreactor, and the encapsulation of preformed polymer particles is effective.

Bradley et al. in 2003 described a one-pot sonochemical method to make fluorescent latex particles [24]. The monomer, methyl methacrylate, contained pyrene, 4-dicyanomethylene-2-methyl-6-(p-dimethylaminostyryl)-4H-pyran, or 1-bromo-

Fig. 6 (**a**) Pyrene (2×10^{-4} M) fluorescence decay in the monomer emulsion (10 wt. %): air ($\bigcirc$), oxygen ($\triangle$), and nitrogen ($\square$) atmospheres. The fluorescence decay in air is shown for the latex ($\cdot$) and is representative of the decay in all atmospheres. Excitation was at 337 nm, and fluorescence emission was monitored at 400 nm. (**b**) Constant first-order decay kinetics observed in latex particles exposed to the atmospheres listed in (**a**) (Reprinted with permission from (J. Am. Chem. Soc., 2003, 125 (2), pp 525–529). Copyright (2003) American Chemical Society)
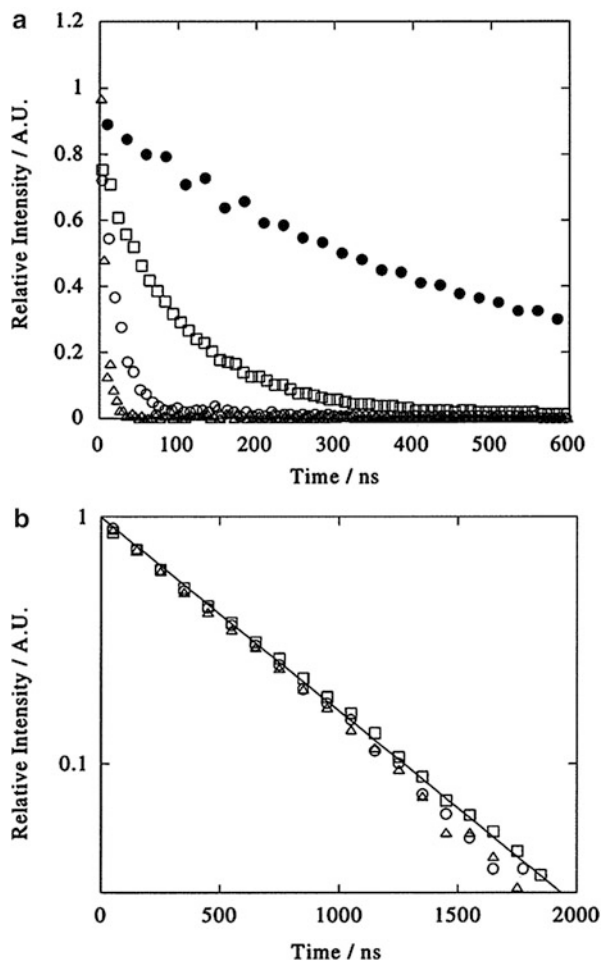
naphthalene, and subsequently exposed to ultrasound in an aqueous surfactant solution to produce 60 nm fluorescent latex particles. From fluorescence lifetime studies, they showed that the encapsulation of such fluorescent molecules into latex particles was effective and the polymer acts as a protecting layer for the fluorescent molecules from environmental influences such as dissolved gases (Fig. 6).

Qiu et al. prepared PS/Fe_3O_4 nanocomposites through sonochemical miniemulsion polymerization and reported that polymerization reaction rate increased with the number of Fe_3O_4 nanoparticles [27]. They attributed their finding to the increase in the number of radicals produced as a result of the presence of Fe_3O_4 nanoparticles. Their magnetic nanocomposites can be separated from the emulsion by an external magnetic field resulting in a milky white dispersion. However, the amount of Fe_3O_4 nanoparticles that were encapsulated into the polymer particles was very low. Teo et al. employed the sonochemical miniemulsion polymerization

technique to prepare magnetic polymer composite materials [28]. These magnetic nanocomposites are reported to exhibit excellent colloidal stability with strong magnetic properties. The sonochemical method of preparing magnetic polymer nanocomposites provides a simple one-pot fabrication process and does not require the addition of chemical initiators; this enables a clean and simple execution of the polymerization reaction. However, this method has its limitations: the distribution of magnetic nanoparticles between and within the polymer particles was inhomogeneous, and this could be due to the interactions between the magnetic nanoparticles and the destabilization of the monomer droplets.

Recently, Janus particles have attracted research interests for their unique properties such asymmetry and ability to impart different chemical and physical properties and directionality within a single particle. Owning to their unique structure, they have a potential in applications such as electronic displays, surfactants, and drug delivery. Most methods of preparation of such particles are template assisted or involve multiple steps in the procedure. Teo et al. reported on a sonochemical method of preparation of polymer/inorganic nanocomposite doublets composed of polystyrene/SiO_2 Janus particles [29]. The formation of these Janus particles was realized by the phase separation mechanism between the growing PS particles and tetraethoxysilane (TEOS). Figure 7 shows the TEM images of the sonochemically prepared Janus particles. Further optimization of their method allowed them to encapsulated 10 nm magnetic particles into one of the sides. As the result of the small dimensions of the miniemulsion droplets, small hybrid particles with size below 100 nm were synthesized. They have also demonstrated their application as Pickering emulsion stabilizers and their subsequent breaking via magnetic separation. For a more in-depth literature on Janus particles, the reader is referred to these review articles [30].

Sonochemical Preparation of Biopolymer-Based Microspheres

Another area of research based on the use of ultrasound in polymeric materials synthesis is the preparation of biopolymers, most notably, the synthesis of proteinaceous microspheres. Proteins are a class of nature-derived biopolymers that have several special functions and potential biorelated applications in nanomedicine. Nano- and microconstructs derived from proteins have several advantages such as biodegradability and nonantigenicity and can be easily surface modified and covalently conjugated to drugs and ligands. Several protein-based nano- and microconstructs have been fabricated and characterized for drug delivery, among them are albumin, silk fibroin, casein, lysozyme, and collagen.

Albumin is a globular protein and has been used as a versatile protein carrier for drug targeting and also for improving pharmacokinetic profile of bioactive compounds. It is the most abundant plasma protein ($35–50$ g L^{-1}) with a molecular weight of 66.5 kDa. Albumin is synthesized in the liver and is responsible for transport of fatty acids and other lipids that are insoluble in the circulating plasma. It is characterized by a low percentage of tryptophan, glycine, and methionine and a high percentage of cysteine (17 disulfide bonds and one sulfhydryl group) and charged amino acids, aspartic and glutamic acids, lysine, and arginine [31].
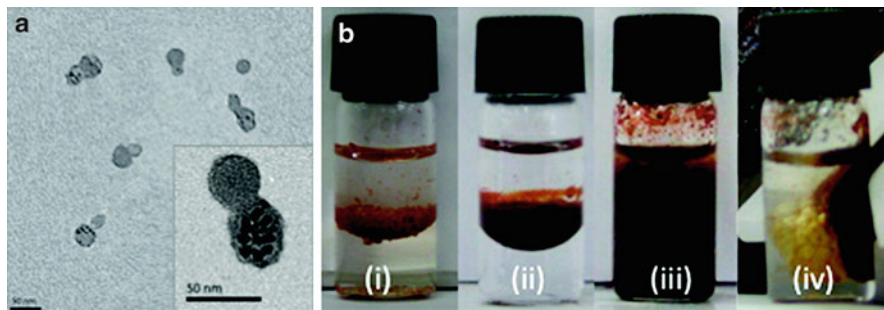
Fig. 7 (**a**) TEM images of the magnetite Janus particles. (**b**) Images of various forms of toluene−water−magnetic Janus particle systems: *i*) interfacial behavior at low loading with magnetic Janus particles; (*ii*) interfacial behavior at high loading with magnetite Janus particles in the water−toluene dual-phase system; (*iii*) an o/w emulsion from ii with asymmetric magnetite Janus particles, the emulsion was stable for at least 2 days; and (*iv*) manipulation of the magnetic Janus particle system in iii by an external magnetic field. The "magnetic" blob could be separated from the continuous phase by the external magnet, and the approximate amount of oil + water left in the vial was quantified with a syringe as 0.5 g. The separated oil can be seen between the dark meniscus and the beginning of the yellow emulsion phase (Reprinted with permission from (Langmuir, 2011, 27 (1), pp 30–33). Copyright (2011) American Chemical Society)

In the synthesis of oil-filled proteinaceous microspheres of bovine serum albumin (BSA), Suslick and Grinstaff showed that 3 min sonication of a biphasic system containing an aqueous solution of BSA and nonaqueous liquids was sufficient to form BSA protein microspheres including the organic liquids [32]. The proposed mechanism for the formation of these oil-filled microspheres is first due to emulsification by high-intensity ultrasound to disperse the nonaqueous phase into the aqueous protein solution. The authors ascertained that emulsification alone is not sufficient to form stable, long-lived microspheres and that a chemical process involving cross-linking of protein molecules through disulfide bond formation between cysteine residues was required. Based on chemical trapping experiments, superoxide (created during bubble collapse in the presence of oxygen) was identified as the cross-linking agent that renders the microspheres stable. The cross-linked shell of the microsphere was approximately ten protein molecules thick. In a later study by the same authors on sonochemical formation of air-filled microspheres, similar results were obtained [33].

Although many studies have concluded the importance of cysteine and the formation of S–S bonds in the creation of microspheres [32, 33], it has been shown by Avivi and Gedanken that proteins that do not contain a thiol group can also be used to make microspheres [34]. They applied this to the preparation of streptavidin microspheres and found that the microspheres were stable for many hours at room temperature and stable for at least a month at 4 °C. They found that no microspheres were formed when the pH was kept at 7; however, when the pH was lowered to 6.0, microspheres were formed. They hypothesized that hydrophobic or thermal denaturation of the protein after sonoemulsification assisted in the formation

of microspheres. By lowering the pH slightly, it neutralizes the basic COO- edges and creates a more favorable hydrophobic environment. To verify this hypothesis, poly(glutamic acid) protein was sonicated. This protein only carries carboxyl groups on the side chain. Microspheres of poly(glutamic acid) were formed only at a pH lower than 4.5, indicating that the hydrophobic interactions that become more dominant in an acidic medium are responsible for the production of microspheres. The microspheres formed without cysteine residues were stabilized by intermolecular interactions such as hydrogen bonding, van der Waals forces, and hydrophobic and electrostatic interactions. Their findings opened up a range of synthetic possibilities.

Since the first report of sonochemically synthesized proteinaceous microspheres, there has been a renewed interest in making such microspheres sonochemically. Gedanken and coworkers prepared magnetic proteinaceous microspheres that are useful for magnetic resonance imaging [35]. The microspheres composed of iron oxide-filled and iron oxide-coated BSA microspheres. In another work, they sonochemically synthesized DNA nanospheres of approximately 460 nm in size and successfully delivered genetic information that was encoded in the DNA nanospheres to competent cells and to human U2OS cancer cells and expressed in competent (*E. coli*) cells [36]. Han et al. [37] used the sonochemical method to make magnetic microspheres with chemically prepared magnetite embedded in polyelectrolyte multilayers, and these magnetized microspheres can be guided by an external magnetic field. They have also demonstrated the influence of a range of ultrasound parameters on the size and size distribution of the microspheres.

More recently in an elegant work conducted by Crestini and coworkers [38], they successfully fabricated lignin microcapsules with size range between 0.3 and 1.1 µm using ultrasound for potential in drug delivery. The mechanism responsible for the formation of lignin microcapsules is based on the synergistic effect of ultrasound-induced phenomena – emulsification and cross-linking. The first process arises from the collapse of cavitation bubbles generating high shear forces, and the latter is due to the cross-linking between lignin chains which was induced by the production of hydroxyl ($\cdot$OH) and superoxide ($HO_2^{-\cdot}$) radicals generated during the acoustic cavitation process (Fig. 8).

Cavalieri et al. successfully prepared stable lysozyme microbubbles using ultrasound-induced emulsification and cross-linking of chemically reduced lysozyme in aqueous solutions [39]. Their lysozyme-coated microbubbles were stable for several months and also retained the enzymatic activity of lysozyme. In a later work by the same authors, they successfully coated the lysozyme bubbles with gold nanoparticles and alkaline phosphatase for micro antimicrobial and biosensing devices [40]. Gold nanoparticle-coated lysozyme bubbles were able to significantly improve the antimicrobial efficiency of the bubbles against *M. lysodeikticus*, while the alkaline phosphatase-coated bubbles were used for detection of paraoxon in aqueous solutions as a novel sensing microdevice (Fig. 9). In another work, they reported a novel way to synthesize highly monodispersed nano- and micrometer-sized lysozyme bubbles for the application in diagnostics and gene therapy [41]. The method was based on a novel flow-through sonication technique whereby the active
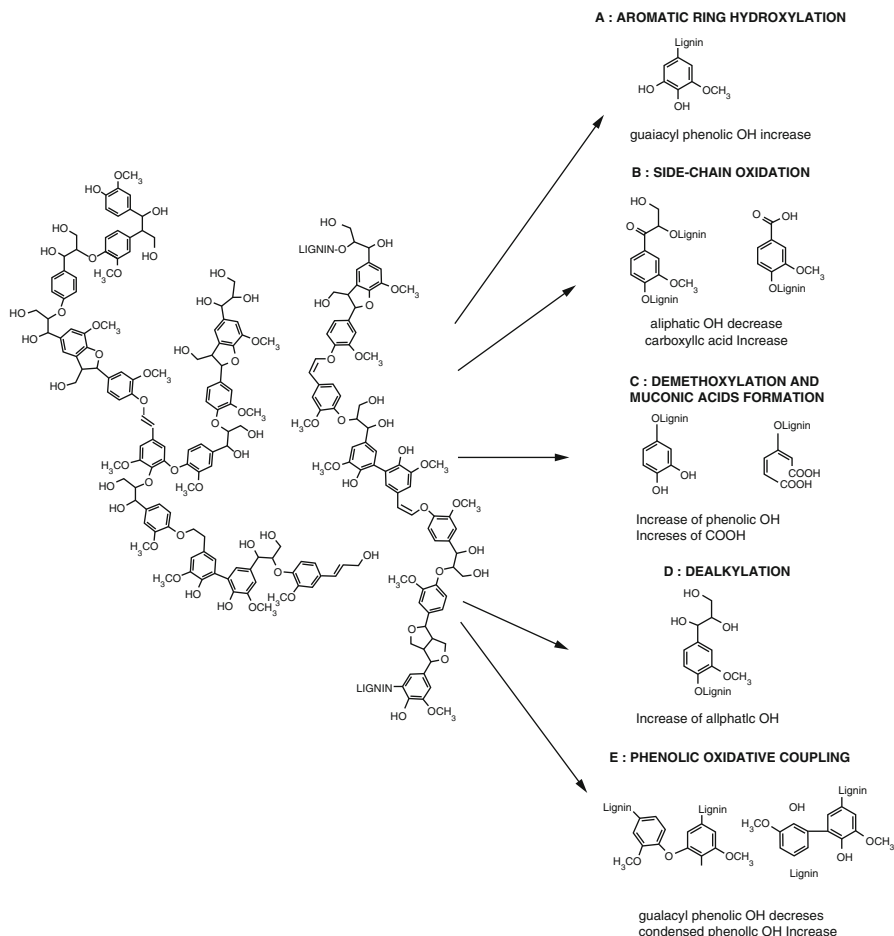
Fig. 8 Kraft lignin oxidation pathways in the presence of hydroxy and superoxy radical species at pH 8 (Reprinted with permission from (Biomacromolecules, 2014, 15 (5), pp 1634–1643). Copyright (2014) American Chemical Society)

cavitation zone is confined to the hole region and aqueous solution of lysozyme was flowed through the middle of the horn and continuous sprayed out highly stable cross-linked lysozyme bubbles between 400 and 700 nm (Figs. 10 and 11). Layer by layer (LbL) assembly of polyelectrolytes on these microbubbles to modify the surface properties of the microbubbles demonstrated the versatility of adsorbing potential drugs and/or biolabels for a range of therapeutic and diagnostic applications. In a later study, Zhou et al. demonstrated the ease of encapsulating a range of organic liquids into cross-linked lysozyme microspheres sonochemically [42]. From their results, they found that the size and the stability of their microspheres were dependent on the nature of the encapsulated organic liquids, demonstrating the potential usefulness of the sonochemical method in a range of medical and food industries.
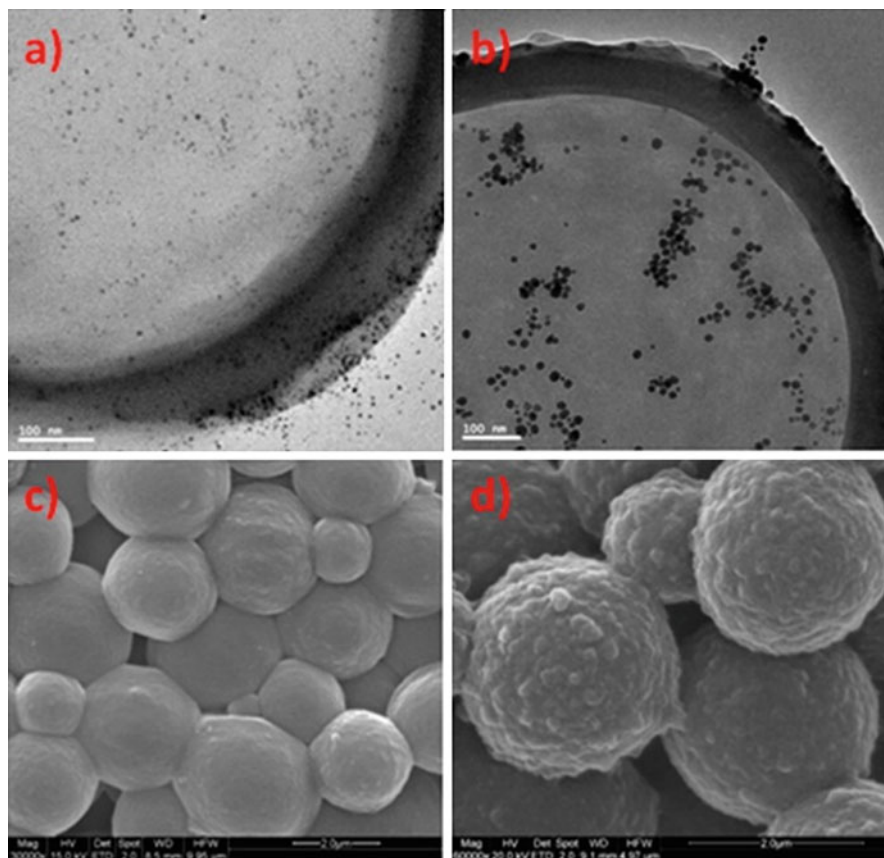
Fig. 9 (**a**) TEM image of LSMBs functionalized with BSA-AuNPs; (**b**) TEM image of LSMBs functionalized with PVP-AuNPs; (**c**) SEM image of LSMBs; (**d**) SEM image of LSMBs functionalized with BSA-AuNPs (Reprinted with permission from (ACS Appl. Mater. Interfaces, 2013, 5 (2), pp 464–471). Copyright (2013) American Chemical Society)

These air- and oil-filled microspheres have a range of biomedical applications such as the use in targeted drug delivery, as ultrasound contrast agents, as for magnetic resonance imaging, and as microencapsulation of pharmaceuticals and flavors. In the following section, the use of microspheres/microbubbles in biorelated applications will be outlined.

Drug Encapsulation Within Microspheres

There are several reports on the successful encapsulation of materials within sonochemically produced microspheres. Encapsulation of these molecules is typically conducted via a one-step process during the microsphere fabrication with the loading molecule either dissolved in the oil phase or the aqueous phase, resulting in either encapsulation within the oil core of the microspheres or the entrapment in the
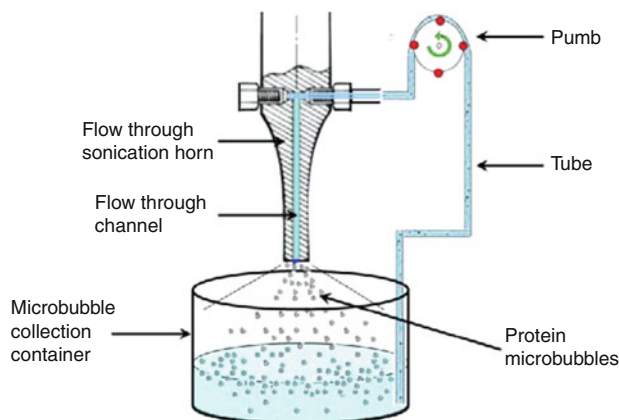
Fig. 10 Schematic representation of the formation of nano- and microbubbles using the flow-through sonication cell (Reprinted with permission from (ACS Macro Lett., 2012, *1* (7), pp 853–856). Copyright (2012) American Chemical Society)

protein shell. Gedanken and coworkers have encapsulated a mesitylene phase containing the drug, Taxol, within BSA spheres where a loading of over 90 % was achieved [43]. The taxol microspheres were tested for their anticancer activity against a mouse myeloma cell line, and it was found that when increasing the amount of drug loading, the death of cancer cells increased. Similar studies were carried out with gemcitabine, another anticancer drug, and tetracycline, an antibiotic, and in all these studies, the drug was loaded from the aqueous protein solution into microspheres containing an oil core [44, 45]. By sonication, the drug molecules partially solubilized in the oil core, and the loading was 30 % and 65 %, respectively. The gemcitabine microspheres were stable in a buffer solution at 37 °C, and the drug release over a period of 100 h was achieved by protease degradation of the protein shell. In another study, Silva et al. encapsulated a hydrophilic drug, piroxicam, within BSA or HSA microspheres using polyvinyl alcohol (PVA) as a stabilizer [45]. They reported that PVA acts to reduce the size of the microspheres due to steric stabilization during the fabrication of the microspheres and particularly the drug loading was enhanced in the presence of PVA. The PVA-BSA microspheres were stable over a period of several months, and the release of drug was performed during protease degradation. They reported that the release profile initially followed a burst release followed by a slower continuous release, thus suggesting that the release was first from the surface of the spheres followed by release from the inside of the protein sphere. Lentacker et al. fabricated perfluorocarbon gas-filled positively charged BSA microbubbles that were coated with a layer of poly(allylamine hydrochloride) (PAH) [46]. The surface functionalization of BSA bubbles with PAH renders the spheres with a positive charge, allowing the binding of DNA molecules. In another similar study carried out by Melino et al., the use of positively charged lysozyme to form microspheres allows DNA to bind to the surface of the spheres without the addition surface functionalization step [47].
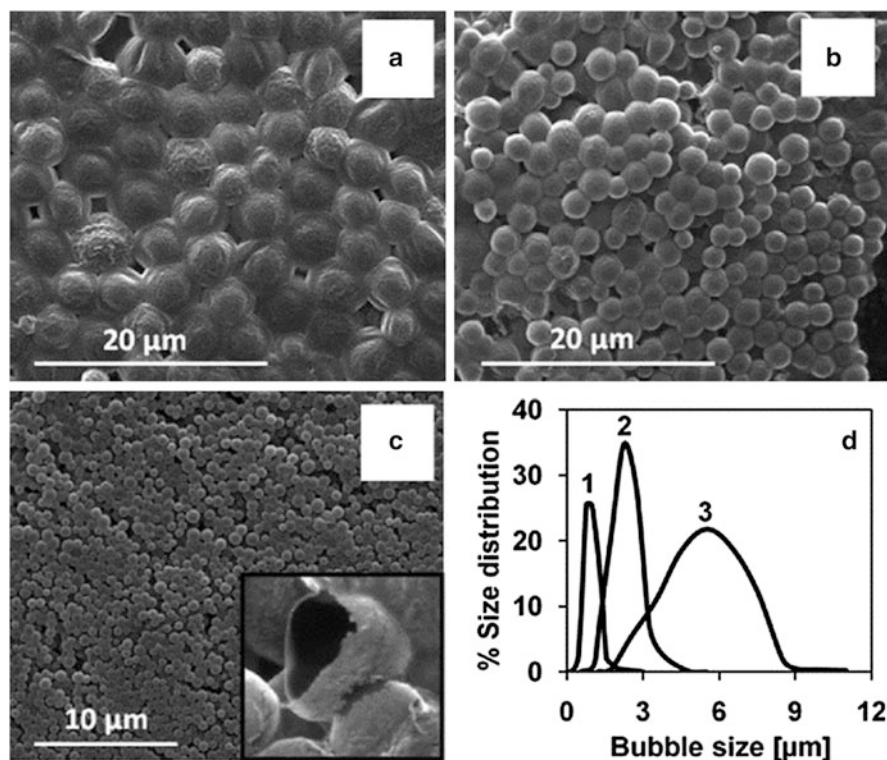
Fig. 11 SEM images of lysozyme microbubbles synthesized using (**a**) a 1 cm standard horn (160 W), (**b**) a 3 mm standard horn (120 W), and **c** a flow-through horn (240 W). Inset (**c**): Broken nanobubbles. Size distribution of lysozyme bubbles (**d**): (*1*) a flow-through horn, (*2*) a 3 mm diameter standard ultrasonic horn, and (*3*) a 1 cm standard horn (Reprinted with permission from (ACS Macro Lett., 2012, *1* (7), pp 853–856). Copyright (2012) American Chemical Society)

Bioactivity of Sonochemically Produced Microspheres

It is well known that irradiation of biopolymers (proteins) with high intensity can result in significant deactivation and aggregation of the proteins [48]. This inactivation of proteins under irradiation of ultrasound is caused by the denaturation of protein as a result of pyrolysis in the region of acoustic cavitation events such as the formation of free radicals. However, several researchers have shown that some enzymatic activity can still be retained in the microsphere after exposure to high-intensity ultrasound.

Gedanken and coworkers sonochemically fabricated decalin-filled α-amylase, α-chymotrypsin, and avidin microspheres, and they observed that while the enzymatic activity of the microspheres was reduced in all three cases, they were not totally destroyed [43, 44]. The secondary structure of the proteins is either left partially or wholly intact despite the large shear forces and the formation of intermolecular disulfide bonds. Similar results were also reported by Cavalieri

et al. [39, 40] The lysozyme microbubbles retained its enzymatic (antimicrobial) activity against *Micrococcus luteus*, and circular dichroism spectra of the native lysozyme protein and lysozyme microbubbles were similar, suggesting that either the protein had partially recovered its secondary structure or that the sonochemical synthesis method did not significantly alter the secondary structure of the protein [40].

The selective targeting of drug-loaded protein microspheres to tumors has been demonstrated by many researchers. Suslick and coworkers reported the modification of non-covalent, electrostatic LbL protein microspheres that can selectively target protein microspheres to the integrin receptors that are overexpressed in several tumors [45]. The protein microspheres are core–shell capsules consisting of a vegetable oil core and a BSA shell. Their research demonstrates the usefulness of these microspheres to targeted imaging and drug delivery systems.

Other Delivery Applications

Sonochemically produced microspheres have also been investigated as potential carriers of flavors and pesticides and fertilizers release. Gedanken and coworkers showed that fragrance molecules can be released over a period of 24 h when amyl acetate, a fragrant oil, was encapsulated with BSA microspheres [46]. This has potential in the development of next-generation fabric for slow release of fragrances built into fabrics.

Conclusions and Future Directions

This book chapter reviews the historical and current development and applications of polymer particles, (bio)polymer stabilized air- and oil-filled microspheres, as well as their preparation via the sonochemical approach. Recent reports in the literature on the application of ultrasound to polymer synthesis show that sonochemistry accelerates polymerization reactions and allows reactions to proceed at ambient temperatures without the need of additional chemical initiators. With these benefits, ultrasound stands out as an alternative technique for the synthesis of polymer nanoparticles and nanocomposites. The use of sonochemistry for the fabrication of proteinaceous microspheres has also seen remarkable development in the last decade. We anticipate that the sonochemical method together with recent advances in techniques for site-specific modification of proteins will expand exponentially. This will pave the way toward the continuous development of advanced multifunctional protein-based nano- and microspheres in a high-throughput manner. The myriad of benefits that ultrasound-initiated events offer as an alternative to existing polymerization processes demonstrates that it should become a technology of choice for new and improved polymerization processes. We hope that we have demonstrated in this chapter the importance and usefulness of ultrasound as an alternative and green method for the synthesis of a range of polymeric materials.

References

1. Leighton TG (1994) The acoustic bubble. Academic, London
2. Wood RW, Loomis AL (1927) Lond Edinb Dublin Philos Mag J Sci 4(22):417
3. Weissler A (1953) J Acoust Soc Am 25(4):651
4. Strasberg M (1961) J Acoust Soc Am 33(3):359. Din-Yu Hsieh, Milton S. Plesset (1961) J Acoust Soc Am 33(2):206
5. Noltingk BE, Neppiras EA (1950) Proc Phys Soc Sect B 63(9):674
6. Margulis MA (1995) Sonochemistry/cavitation. Taylor & Francis, London
7. Lepoint-Mullie F, De Pauw D, Lepoint T (1996) Ultrason Sonochem 3(1):73
8. Suslick KS, Hammerton DA, Cline RE (1986) J Am Chem Soc 108(18):5641
9. Lauterborn W, Vogel A (1984) Annu Rev Fluid Mech 16(1):223
10. Bang JH, Suslick KS (2010) Adv Mater 22(10):1039
11. Gilbert RG (1995) Emulsion polymerization: a mechanistic approach. Academic, London
12. Odian G (2004) Principles of polymerization. Wiley, Hoboken
13. Flory PJ (1937) J Am Chem Soc 59(2):241
14. Qiu J, Charleux B, Matyjaszewski K (2001) Prog Polym Sci 26(10):2083
15. Ugelstad J, El-Aasser MS, Vanderhoff JW (1973) J Polym Sci Polym Lett Ed 11(8):503
16. Flosdorf EW, Chambers LA (1933) J Am Chem Soc 55(7):3051
17. Bradley M, Grieser F (2002) J Colloid Interface Sci 251(1):78
18. Ostroski AS, Stambaugh RB (1950) J Appl Phys 21(6):478
19. Biggs S, Grieser F (1995) Macromolecules 28(14):4877
20. Cooper G, Grieser F, Biggs S (1996) J Colloid Interface Sci 184(1):52
21. Okudaira G, Kamogawa K, Sakai T, Sakai H, Abe M (2003) J Oleo Sci 52(3):167
22. Joe Chou HC, Stoffer JO (1999) J Appl Polym Sci 72(6):827
23. Wang Q, Xia H, Liao Y, Xu X, Baxter SM, Slone RV, Wu S, Swift G, Westmoreland DG (2001) Polym Int 50(11):1252
24. Morya NK, Iyer PK, Moholkar VS (2008) Polymer 49(7):1910
25. Bradley MA, Prescott SW, Schoonbrood HAS, Landfester K, Grieser F (2005) Macromolecules 38(15):6346
26. Teo BM, Ashokkumar M, Grieser F (2011) Phys Chem Chem Phys 13(9):4095
27. Guihua Qiu, Qi Wang, Chao Wang, Willie Lau, Yili Guo (2007) Ultrason Sonochem 14(1):55
28. Teo BM, Chen F, Hatton TA, Grieser F, Ashokkumar M (2009) Langmuir 25(5):2593
29. Teo BM, Suh SK, Alan Hatton T, Ashokkumar M, Grieser F (2011) Langmuir 27(1):30
30. Walther A, Müller AHE (2010) Chem Rev 113(7):5194. Shan Jiang, Qian Chen, Tripathy M, Luijten E, Schweizer KS, Granick S (2010) Adv Mater 22(10):1060
31. Paris G, Kraszewski S, Ramseyer C, Enescu M (2012) Biopolymers 97(11):889
32. Suslick KS, Grinstaff MW (1990) J Am Chem Soc 112(21):7807
33. Grinstaff MW, Suslick KS (1991) Proc Natl Acad Sci 88(17):7708
34. Avivi S, Gedanken A (2002) Biochem J 366:705
35. Avivi S, Felner I, Novik I, Gedanken A (2001) Biochim Biophys Acta Gen Subj 1527(3):123
36. Shimanovich U, Eliaz D, Aizer A, Vayman I, Michaeli S, Shav-Tal Y, Gedanken A (2011) Chem Biol Chem 12(11):1678
37. Han Y, Radziuk D, Shchukin D, Moehwald H (2008) J Mater Chem 18(42):5162
38. Tortora M, Cavalieri F, Mosesso P, Ciaffardini F, Melone F, Crestini C (2014) Biomacro-molecules 15(5):1634
39. Cavalieri F, Ashokkumar M, Grieser F, Caruso F (2008) Langmuir 24(18):10078
40. Cavalieri F, Micheli L, Kaliappan S, Teo BM, Zhou M, Palleschi G, Ashokkumar M (2013) ACS Appl Mater Interfaces 5(2):464
41. Zhou M, Cavalieri F, Caruso F, Ashokkumar M (2012) ACS Macro Lett 1(7):853
42. Zhou M, Leong TSH, Melino S, Cavalieri F, Kentish S, Ashokkumar M (2010) Ultrason Sonochem 17(2):333
43. Grinberg O, Hayun M, Sredni B, Gedanken A (2007) Ultrason Sonochem 14(5):661

44. Grinberg O, Gedanken A, Mukhopadhyay D, Patra CR (2013) Polym Adv Technol 24(3):294
45. Avivi, Nitzan Y, Dror R, Gedanken A (2003) J Am Chem Soc 125(51):15712
46. Lentacker I, De Geest BG, Vandenbroucke RE, Peeters L, Demeester J, De Smedt SC, Sanders NN (2006) Langmuir 22(17):7273
47. Melino S, Zhou M, Tortora M, Paci M, Cavalieri F, Ashokkumar M (2012) Amino Acids 43(2):885
48. Krishnamurthy R, Lumpkin JA, Sridhar R (2000) Int J Pharm 205(1–2)):23

Ultrasonic Synthesis of Ceramic Materials: Fundamental View

Naoya Enomoto

Contents

Abstract

This article is concerned with fundamental materials systems consisting of commonplace or ubiquitous elements (Si, O, Al, Fe, etc.), aiming at how to draw out the novel potentiality of sonochemistry to ceramic processing rather than to reach hurriedly to modern functional materials in popularity. Silica sphere synthesis is a main topic discussed in detail. Ultrasonication during the synthesis caused a curious agglomeration presumably due both to an ultrasonic-induced collision and to surface activity of silica spheres. Another type of sonication at very low intensity is newly proposed here to enhance the aging of starting solutions. This novel concept is based on a hypothesis that microscopic homogeneity is not guaranteed in a transparent solution. In the experimental facts, the

N. Enomoto (✉)
Department of Applied Chemistry, Faculty of Engineering, Kyushu University, Fukuoka, Japan
e-mail: enomoto@cstf.kyushu-u.ac.jp

395

aging of the starting solutions results in a delay of precipitation, narrowing of sphere size distribution, and increase of sphere size (i.e., decrease of nucleus number), which can be attributable to an increased microscopic homogeneity in the starting solutions. Other fundamental systems presented are crystallization from a supersaturated solution of alum (ammonium aluminum sulfate hydrate), solidification of molten inorganic salts (nitrate binary), and dissolution in and reprecipitation from a mother solution (ripening of aluminogels and oxidation of magnetic nanoparticles).

Introduction

One desirable goal for sonochemists concerned with materials science and materials engineering is possibly to discover a "superstar" material through sonoprocessing. "Superstar" in this case means to possess an excellent property for an outstanding performance, and hopefully it cannot be prepared by any routes other than the sonochemical route. It is true that an incredibly high temperature and pressure as well as an incredibly rapid mass flow are existing in the acoustic bubbles in a beaker at moderate condition, and also it seems that such an extreme condition is expected to attribute the "superstar" generation. However, it is not always easy to reach that goal.

Among so many reports and articles on sonoprocess of ceramic materials, an expression ". . . due to high temperature of 5,000 K during the bubble collapse, . . ." is quite often seen. However, direct connection between the experimental results and the extreme circumstance are not always supported by clear (or unclear) evidences. In this essay, I am talking to myself that an easy use of the expression, ". . . the 5,000 K bubbles enhance the materials process. . ." may hinder the essential development of sonochemistry. In order to know what really happens in sonoprocess, in my opinion, it is rather important to know what really happens in the absence of ultrasound in the materials system concerned. In this sense, I would like to start to review the most fundamental ceramic for the sonoprocess target. After reviewing the particular process of the sol-gel process of silica spheres a bit in detail, the other fundamental studies are introduced.

Ultrasonic Effects on Silica Sphere Synthesis from Alkoxide

Silicon dioxide (SiO_2) or silica is the most fundamental ceramic in that oxygen and silicon are the two top abundant elements around the earth's crust (two largest Clarke numbers). From a traditional study on clay and mineral to a modern research on

optical fibers, silica has been the key material for several applications. In this section, using ultrasonic irradiation in the synthesis of the silica sphere will be discussed. First, the definition of the sol-gel process will be given followed by a discussion of sol-gel process in the presence of ultrasound.

Why Silica Sphere?: Basis of the Sol-Gel Process of Silica

One of the most familiar items in a laboratory is a fused-silica cell for optical measurements. According to its name, it is in general prepared by melting pure silica above $\sim$1,700 °C to attain a homogeneous liquid structure that can preserved as a vitrified solid free from crystallization. In 1970s, there was an epoch in ceramic/ glass processing [1, 2]. It is named sol-gel process since then and has been inten- sively applied to various fields of ceramic materials production. In the sol-gel process of silica, a typical starting material is tetraethylorthosilicate (TEOS, Si $(OC_2H_5)_4$). TMOS ($Si(OCH_3)_4$) is also available, but one who uses this reagent must wear safety goggles in order to protect his/her eyes, because vaporization of TMOS is not negligible compared to TEOS. He/she should be surely cautioned if the following chemical reactions could proceed at around room temperature with mois- ture on his/her eyes:

$$\text{Hydrolysis} : Si(OR)_4 + 4H_2O \rightarrow Si(OH)_4 + 4ROH$$

$$\text{Polycondensation} : \quad \equiv Si - OH + HO - Si \equiv \rightarrow \equiv Si - O - Si \equiv + H_2O$$
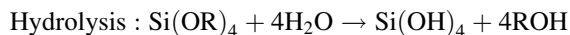
It should be noted that a three-dimensional network of silicon and oxygen (or, 3D connection of SiO4 tetrahedron) can be formed at near room temperature, of course in a solution in a beaker instead of the human eye surface. In the early stage of the network formation, the total solution should be called "sol" whereby very small particles are suspended in solvent. When the network is more formed, the total solution loses its fluidity; it is then called "gel." Thus the obtained gel looks bulky at a glance, but is not a bulk glass prepared above 1,700 °C, because it contains solvent, organic residue, and lots of pores. After heating the gel carefully, for instance, at about 800 °C, much lower than the melting temperature, we finally obtain a bulk silica glass. Here we need to realize that the "solvent" here is not water but alcohol; water is not a solvent but the reactant. Since alkoxide is fully hydrophobic, it cannot be miscible with water. In a usual sol-gel process, a cosolvent such as ethanol (preferably if the alkoxide is ethoxide) is employed to dissolve both alkoxide and water. At this point, ultrasound can have a definite role in this process to exclude the cosolvent by using its particular ability of emulsification. A gel prepared without cosolvent under ultrasonication is named "sonogel" [3, 4], which is also known to have less organic residue and higher density than the normally prepared "classical" gel. It can be a potential candidate for a superstar material if the exclusion of the cosolvent leads to an excellent performance in a certain material system.

Going back to the normal sol-gel process, imagine the following two species (a) and (b) are presented in the reacting solution in order to consider what is happening in it.

$$\text{(a)}\quad Si(OC_2H_5)_4 \quad \text{(b)}\quad Si(OC_2H_5)_3(OH)$$
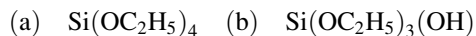
The former (a) is unreacted TEOS, and the latter (b) is a one-fourth hydrolyzed molecule. What will happen when the "next" water molecule attacks them?

In acidic or neutral conditions, as described in the previous paragraph, water attacks alkoxyl group (OC_2H_5 in this case), where the molecule (a) is a bit more likely to be attacked than the molecule (b) due to a larger number of non-attacked groups. Then, subsequent polycondensation gradually occurs among partially hydrolyzed molecules, loosely bonded, involving solvent molecules and unreacted groups inside the polymer. This is what we see as a sol-gel transition.

If the above reactions proceed under alkaline condition, the appearance is quite different from a slow gelling. In alkaline condition, OH^- attacks Si in a nucleophilic manner. Knowing that the "original" alkoxyl group is electron donating, while the "hydrolyzed" silanol group (OH bonded to Si) is electron attracting, (b) is much more likely to be attacked by OH^- due to the lower electron density of Si atom as well as less steric effect. Consequently, polycondensation in alkaline condition occurs among fully hydrolyzed molecules of,$Si(OH)_4$, thus the final product becomes dense. In a typical condition, the solution does not look like sol nor gel, but it looks like precipitation because rather dense silica particles are formed in the solution. However each particle can be regarded as a "gel" particle that loses fluidity inside itself. It should be emphasized that uniform silica spheres, as shown in Fig. 1, can be obtained if only the concentrations of reactants are right adjusted (denoted as the Støber process [5]). Such monodispersed spheres look so beautiful for ceramists
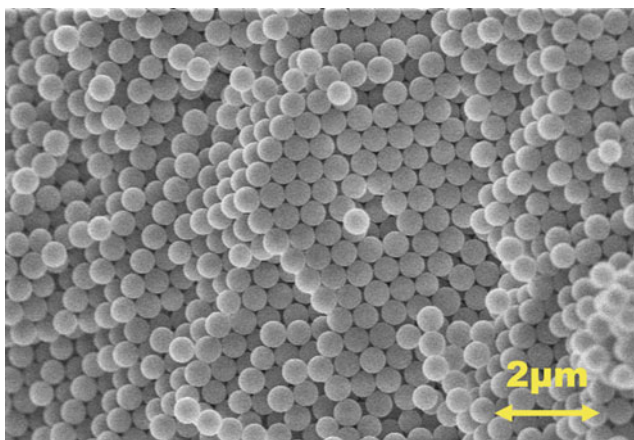
Fig. 1 Silica spheres synthesized normally (i.e., in the absence of ultrasound) from alkoxide

to realize an ideal closest packing in a green compact as well as for applied physicists to develop an optical modulation device [6–9]. Several successful results on the other types of spheres apart from silica spheres are reported so far [10–12]. However, other alkoxides are difficult to handle in general due to their high reactivity to moisture as well as high cost in a limited market. In our experience, it has not been easy to reproduce really monodispersed spheres other than silica. This simple process, where alkoxide and water (with catalyst) are separately dissolved in alcohol and then mixed, involves a fairly complicated issue, as will be discussed later in this section. In the next section, the synthesis of the silica sphere under alkaline conditions using ultrasound irradiation will be discussed.

Ultrasonication During the Synthesis of Silica Spheres

Agglomeration of Silica Spheres

In this section, the application of a 20 kHz horn-type ultrasound transducer for the synthesis of silica spheres will be discussed [13, 14]. Application of the horn-type ultrasound transducer during the synthesis of the silica sphere results in an interesting phenomenon. As shown in Figs. 2 and 3, the silica spheres were gradually agglomerated to form dense aggregates over time. In Fig. 3, the mechanical stirring (MS) in the absence of ultrasonic stimulation gave rise to spheres that grew monotonically, forming uniform spherical particles as shown in Fig. 1. The agglomeration behavior of the silica spheres in the presence of ultrasound can be observed in detail both with microscopic (TEM, transmission electron microscopy) and macroscopic (SALD, size analyzer by laser diffraction) techniques. It seems as follows: (I) in the beginning (0–10 min), no agglomeration occurred; (II) at the medium stage (10–30 min), rapid growth of aggregate occurred; and (III) in the final stage (30–90 min), the branched aggregates became gradually small as if they were sintered. In the SALD measurements, size distribution was also estimated by the ratio of D25/D75 (i.e., sharpness of the size distribution, or homogeneity of agglomeration size) as well as median diameter of D50. This result also supports that the deviation increased during the growth of the agglomerates (10–30 min) and decreased in the densification stage (30–90 min). Judging from the micrographs in Fig. 2, showing the spherical shape is preserved in the agglomerates, the particles were not dissolved/reprecipitated but collided to each other. Apparent densification and the size uniforming in the stage (III) may include breaking off of branched parts from the agglomerates and the pore elimination as if they are sintered. Considering the sizes of the cavitation bubbles and the agglomerates, it may be possible for the particles to enter the bubbles, although such phenomenon cannot ever be observed directly. The reason why the agglomeration did not occur in the beginning of the reaction could be due to the fact that the particles were too small to collide with sufficient energy. Doktycz and Suslick [15] reported that metallic particles (several μm in size) can be partially fused to agglomerate due to ultrasonic-driven collision. By changing the type of metals, it was found that, for instance, Ni (mp 1,453 °C) and
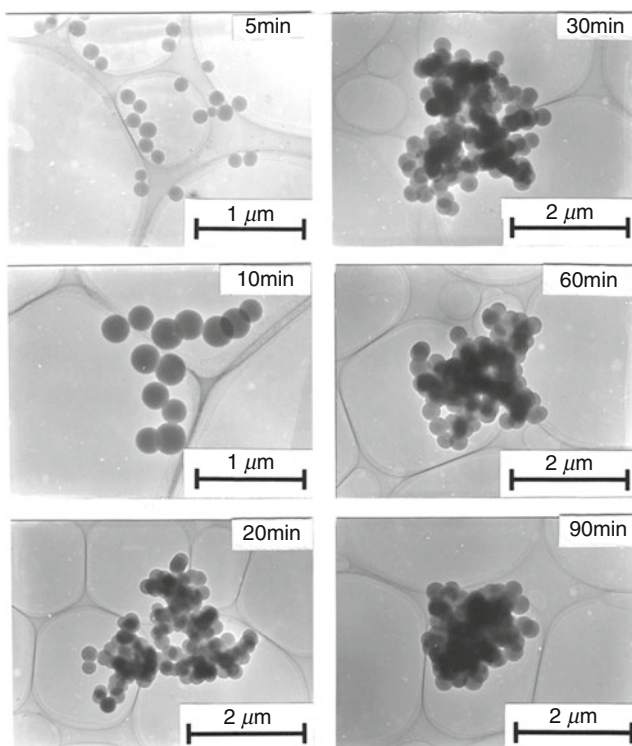
Fig. 2 Ultrasonic-induced agglomeration behavior of silica spheres. Small amount of the reacting solution was sampled at each reaction time into ethanol to quench the reaction and then sampled on TEM microgrid

Cr (mp 1,857 °C) showed a fair interparticle fusion while Mo (mp 2,617 °C) did not. From these results, they could estimate the temperature raise on the shock of collision. Compared to this interesting phenomenon concerning metals, the size of the silica spheres is much smaller and the density is much lower than the metallic particles. Another important feature of the silica sphere is the surface chemistry. The surface of the silica spheres is covered with silanol groups (Si-OH), and surface coverage is especially higher for smaller spheres. As a result, the interparticle connection among the silica spheres could be due to polymerization (or polycondensation) as described earlier in the section "Why Silica Sphere?: Basis of the Sol-Gel Process of Silica" in this chapter. It was also experimentally confirmed that further addition of TEOS can cause further agglomeration, suggesting that unreacted TEOS or some oligomers in the liquid phase can work as a glue to enhance the agglomeration [14]. These findings are summarized in Fig. 4.

Fig. 3 Ultrasonic-induced agglomeration behavior of silica spheres. Particle size distribution was measured by laser diffraction. D50 means the median diameter. D25 and D75 means the diameter at 25 % and 75 % at the accumulative curve of distribution. The ratio D25/75 represents the sharpness of the distribution (Reprinted with permission from [14]. Copyright 1997 Cambridge University Press)
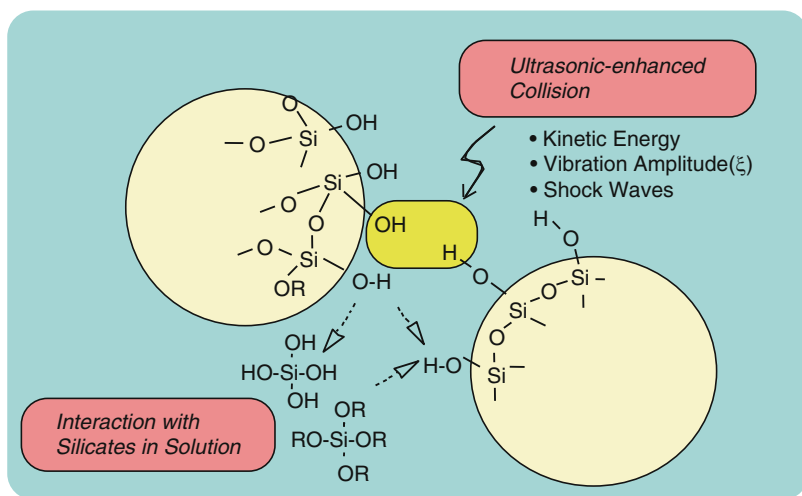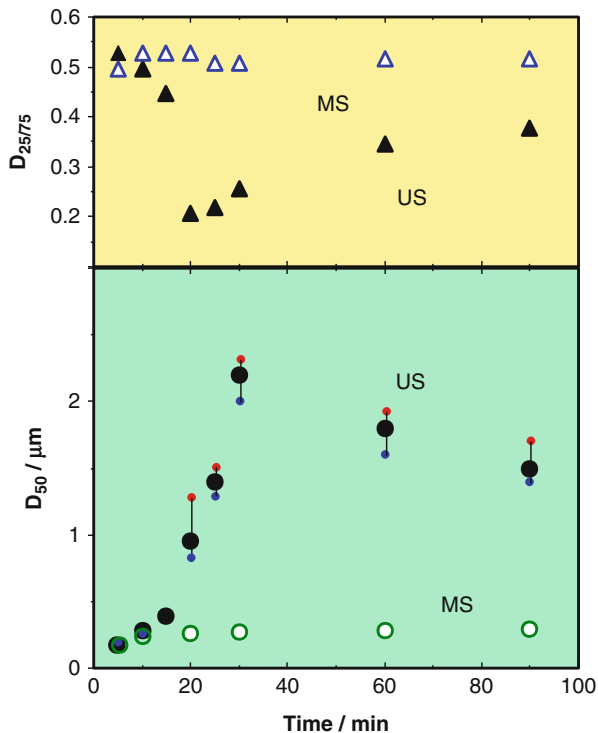
Fig. 4 Schematic of the ultrasonic-induced collision and the resultant agglomeration among silica spheres

Further Investigations on the Ultrasonic-Induced Agglomeration of Silica Spheres

If one would like to show the ultrasonic effect in a certain system, he/she must present a referential (or control) run in the absence of ultrasound where the other conditions fixed at the same. In this topic of the sphere agglomeration, the "MS" curves in Fig. 3 were presented without a detailed explanation because it could be impressively shown in Fig. 1 that this "particular" ultrasonic phenomenon in Fig. 2 is definite. The above information may be enough for description of the phenomenon only. However, one aim of this chapter is to survey a methodology of a sonoprocess study. When we compare the cases US and MS, ultrasound is usually irradiated throughout the reaction just as shown in Figs. 2 and 3. In such case as the behavior is not linear but changing, a "partial" sonication can offer new findings and deepen the sonoprocess.

To further examine the agglomeration behavior in this system, two series of experiments were run. They are named the US-MS test and the MS-US test.

In the US-MS test, the solutions were initially sonicated for t_{U-M} min, and then mechanically stirred afterward without a sonication. Such samples are denoted, for example if $t_{U-M} = 10$ min, as US10-MS. Figure 5 shows the agglomeration curves for various t_{U-M}. Note that the maximum value in the longitudinal axis of the graph is different from the previous ones. The curve US10-MS is similar to that of MS, from which it is reconfirmed that the sonication within the incubation period does not much influence the agglomeration. And then at $t_{U-M} = 15$–30 min, an abnormal agglomeration up to 8 µm was observed. It was confirmed that this agglomeration could not be broken by the SALD-attached sonicator (40 kHz, the power was not measured but would be much lower than the homogenizer used for the

Fig. 5 Changes of the particle size in the US-MS test; the samples were sonicated for initial 10 (■), 15 (△), 30 (+), and 90 min (●) and then subsequently mechanically stirred afterward (Reprinted with permission from [14]. Copyright 1997 Cambridge University Press)
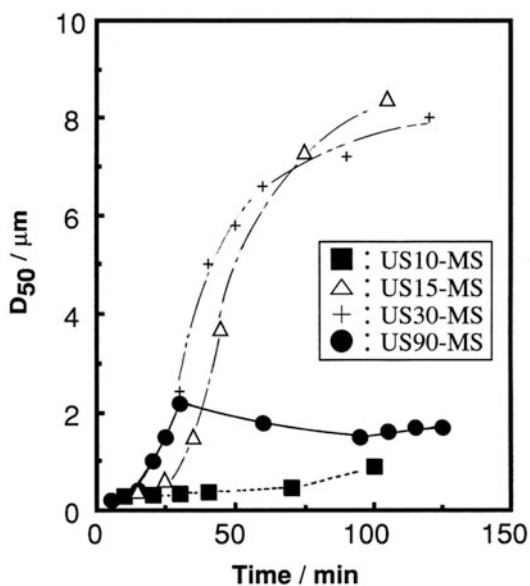
Fig. 6 Changes of the particle size in the MS-US test; the samples were mechanically stirred for initial 10 (▲), 15 (×), 30 (○), and 90 min (□) and then subsequently sonicated afterward (Reprinted with permission from [14]. Copyright 1997 Cambridge University Press)
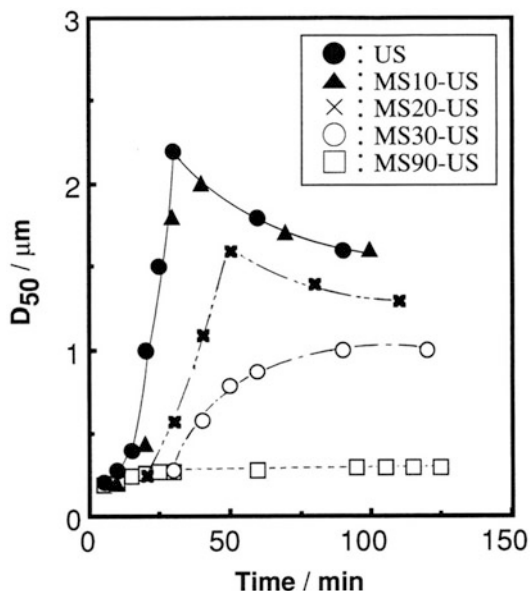
"agglomeration") but can be easily broken by the sonication using the homogenizer. Presumably, this agglomeration is caused by a tangling of the ramified particles. Finally at $t_{U-M} = 90$ min, the abnormal agglomeration could be scarcely observed because the agglomerates are no more ramified shaped at 90 min but rather round shaped as was shown in Fig. 2.

In this test, on the contrary to the US-MS test, the solutions were stirred only with a magnetic stirrer for the initial t_{M-U} min and then sonicated afterward. The samples in this series were named "MS10–US" or so. Figure 6 shows the agglomeration curves for various t_{M-U}. The curve at $t_{M-U} = 10$ min, which is within the incubation period, is almost similar to the basic US curve ($t_{M-U} = 0$ min). Thereafter, an increase of t_{M-U} caused a substantial lowering of the curve. Finally at $t_{M-U} = 90$ min, the agglomeration was rarely observed.

Another simple persistency is to change an ultrasonic intensity. Although it is easy to control the intensity of the horn-type sonication with an equipped knob, we need to spend some time to measure the actual output power by a global method, such as calorimetry [16], for a global comparison. Agglomeration curves at four different ultrasonic intensities, which were calorimetrically determined, are shown in Fig. 7. Only the weakest sonication (1.9 W/cm^2) resulted in a different behavior from the others. In the TEM observation of the samples sonicated at 1.9 W/cm^2, we saw non-agglomerated spheres as well as small agglomerates that are composed of a few spheres. It is inferred that the interparticle collisions were insufficient at this condition. Among the stronger sonications above 12.9 W/cm^2, similar behaviors of agglomeration were observed with similar agglomeration sizes at the maximum and at the equilibrium. It appears that, as the ultrasonic intensity increased, the
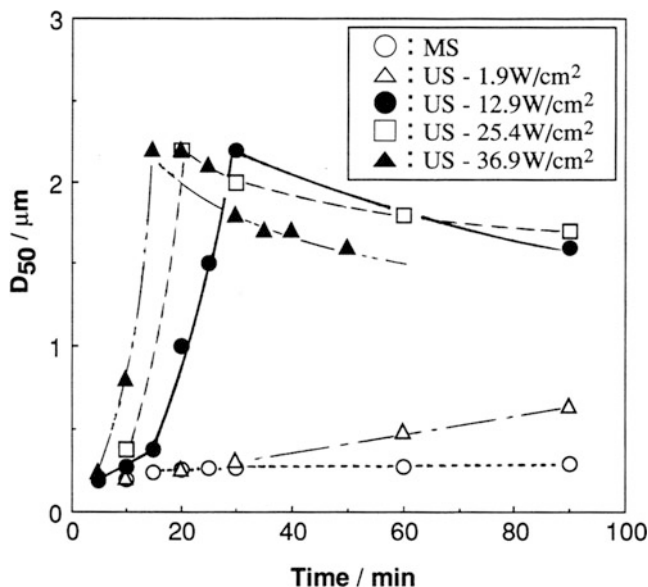
Fig. 7 Ultrasonic-induced agglomeration of silica spheres at various intensities. The intensity was measured by calorimetry (Reprinted with permission from [14]. Copyright 1997 Cambridge University Press)

incubation period (stage I) was reduced and the agglomeration size increased more rapidly at stage II.

Aging or Soft Sonication Prior to Synthesis of Silica Sphere [19, 20]

Ultrasound for chemistry is usually employed to generate cavitation at sufficient intensity of sound pressure. It is once stopped here in this section to think of cavitation. In this particular concept, weak ultrasound at very much lower than the cavitation threshold, which I denote as "soft sonication," will be presented. First section "Structure of a Water-Ethanol Mixture" below does not include ultrasound at all for the beginning to suggest the new concept. And most of the next section "Effect of Aging Starting Solution on Synthesis of Spherical Silica" is also free from ultrasound. In the final section "Soft Sonication to Starting Solutions for Spherical Silica Synthesis," a novel concept of soft sonication is shown.

Structure of a Water-Ethanol Mixture
In the beginning of this topic, I would like to propose a brand-new concept with a question, "*Are water and ethanol miscible with each other*?" Here we remind that both water and ethanol were used in the silica synthesis. Ethanol is a cosolvent and the water is a reactant. The synthesis process requires two starting solutions; one is ethanolic solution of TEOS, the other is ethanolic solution of water (with ammonia).

Fig. 8 Cold-spray ionication mass spectra (CSI-MS) of a water/ethanol mixture (W:E = 1:3 in volume) prepared on the measurement day (fresh) and previously (aged). Prior to measurement, whole sampling routes were renewed to avoid contamination. The spectrum was assigned as WmEn, where m and n are the number of water and ethanol molecules, assuming an ionized cluster of $H^+[H_2O]_m[C_2H_5OH]_n$, and $m/z = 18m + 46n + 1$
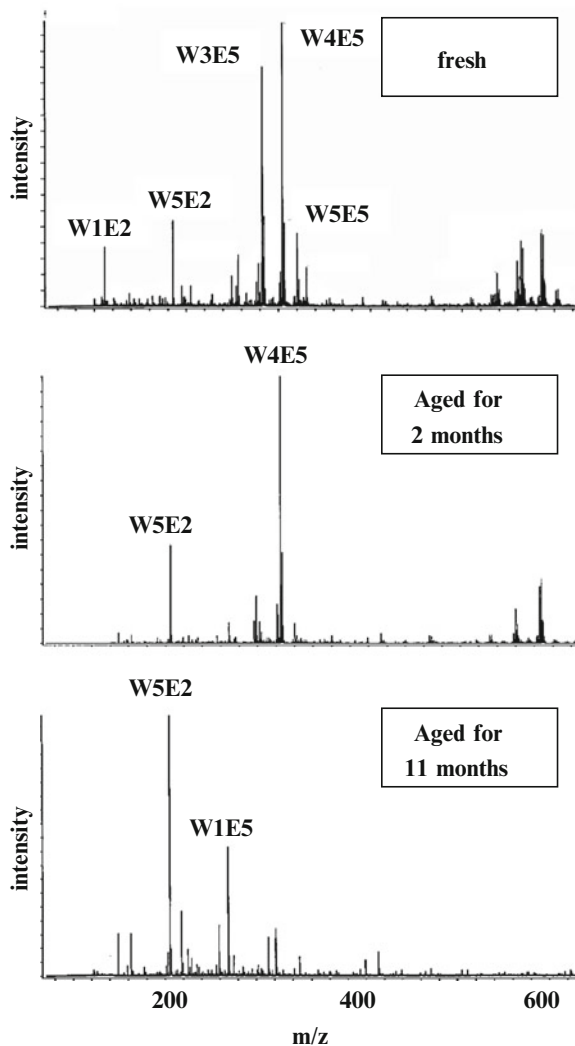
The answer to the above "*question*" is, of course, YES. However, if the number of carbon increases, say from ethanol to propanol, butanol, etc., the solubility of alcohol to water abruptly decreases. Then, ethanol is less miscible with water than methanol. One powerful and novel tool employed here is CSI mass spectroscopy (MS). CSI stands for cold-spray (or cryo-spray) ionization [17], which features a gentle ionization to preserve a weakly bonded structure like a hydrogen-bonded cluster among water and ethanol molecules. Assuming that such clusters are ionized as $H^+[H_2O]_m[C_2H_5OH]_n$, the mass spectrum can be assigned by the mass number $m/z = 18\ m + 46n + 1$. Figure 8 shows the CSI mass spectra of water/ethanol mixtures (W:E = 1:3 in weight) that were mixed on the measurement day (fresh) and

aged in a dark glass bottle for 2 and 11 months. In the upper "fresh" spectrum, large clusters at around $m/z = 600$ were clearly observed. On aging, this cluster decreased in the mixture aged for 2 months and disappeared in the mixture aged for 11 months. Looking at the lower $m/z = 200$–300, it was found that peaks in general shifted to lower mass number, in other words, smaller clusters. This tendency was reproducible when the other water/ethanol mixture at different composition was measured in the same manner.

Effect of Aging Starting Solution on Synthesis of Spherical Silica

Results depicted in Fig. 8 suggest that the solution structure may not be unchangeable on aging. This case is a most simplified one with water and ethanol only. If a solute were involved in the system, the interaction among solvent and solute molecules would be much more complicated and hardly investigated by CSI-MS due to a contamination problem.

A "stock" solution may be unconsciously used by those who study particle synthesis from a liquid phase. If we would like to run a series of the synthetic experiment, we prepare a suitably large amount of starting solution at a fixed concentration, and then a proper amount of the solution is taken out for each run. The stock solutions can be kept in a refrigerator, if necessary. It was our serendipity to find that the age of starting solutions has a drastic influence on precipitation behavior in a certain case [18]. On mixing of the starting solutions, precipitation occurred immediately if they are freshly prepared, while it was significantly delayed if they are aged in a stock solution container. Changing the container material did not influence it at all. The delay in the precipitation increased with an increasing aging time, but the resultant precipitates were basically the same. As our empirical knowledge, such a kind of aging effect is not observed in a fully aqueous system but more or less observed in a mixed solvent like water/ethanol. However, almost no attention is paid to the age of the stock solution as more attention is usually paid to the product than the process.

Now the story comes back to the silica sphere again. Figure 9 shows the experimental flow. This system includes both ethanol and water. Two starting solutions 1 and 2 were separately prepared. As either TEOS or (ammonia) water is quite soluble in ethanol, it is usual to start precipitation by mixing them soon after the preparation of the starting solutions.

What do you think will happen when we "wait" for a while even if the starting solutions are ready?

As indicated with the CSI-MS evidence, visible transparency does not guarantee the uniformity at a molecular level, which may be changed through aging (i.e., just to leave it after dissolving). What we expect here is that soft sonication at a very low intensity can enhance such an aging. If the ultrasound is strong enough to create cavitation, chemical actions such as sonolysis of water can occur, then the aging would be unfavorably complicated.

Figure 10 shows the effect of aging the starting solutions on the precipitation behavior, the monodispersity, and the final sphere size of silica particles. At first,
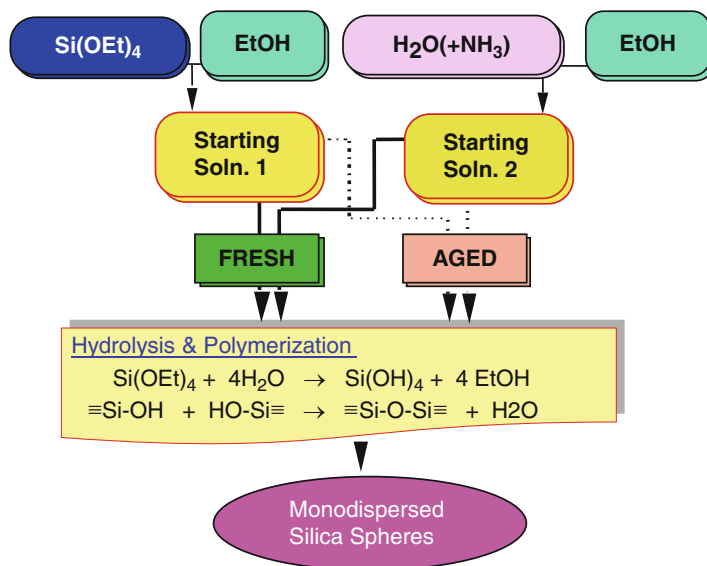
Fig. 9 Experimental flow of silica sphere synthesis. Usual process does not include aging since both solutes (TEOS and water) are quite soluble in the ethanol solvent

aging delays the occurrence of turbidity as previously mentioned [18]. Incubation time could be simply estimated by our naked eye. If only the solution is properly placed in front of a black wall, this rough estimation was found to be reproducible enough. Secondly, the size uniformity in monodispersed spheres was found to be intensified by the aging, when more than $\sim$300 spheres were measured on micrographs. It should be emphasized in this measurement that the uniform spherical shape of silica particles allows sufficiently reproducible results even if an SEM beginner operates to take the images with somewhat insufficient focusing and stigma adjustment. Thirdly, from the same data collected above, the median size of sphere was certainly increased by aging, too. Since the reaction time and the alkaline catalysis are sufficient, the whole TEOS initially added was fully precipitated to dense spheres by hydrolysis and polycondensation. Then, the obvious increment of the median sphere size means the decrease in the number of "nucleus" of silica spheres.

It is a bit difficult to specify what the sphere nucleus is. TEM image in Fig. 11 was taken by sampling the reacting solution at very early stage ($\sim$1 min), where nanoparticles less than 10 nm are observed to coagulate to form spheres (a few tens of nm in size). These spheres would be the "nuclei" of the final spheres. It should be compared with the 5-min image in Fig. 2, where no nanoparticles besides spheres were observed. Nanoparticles seen in Fig. 11 might be really existing at the early stage in the solution, or may be just precipitated after drying the solvent. Whichever the feature of these nanoparticles is, this coagulation would determine the number of spheres in the initial stage and then, without an extra nucleation, the

Fig. 10 Effect of aging the starting solutions for silica sphere synthesis. "Aged" means static aging, and "US" means soft sonication
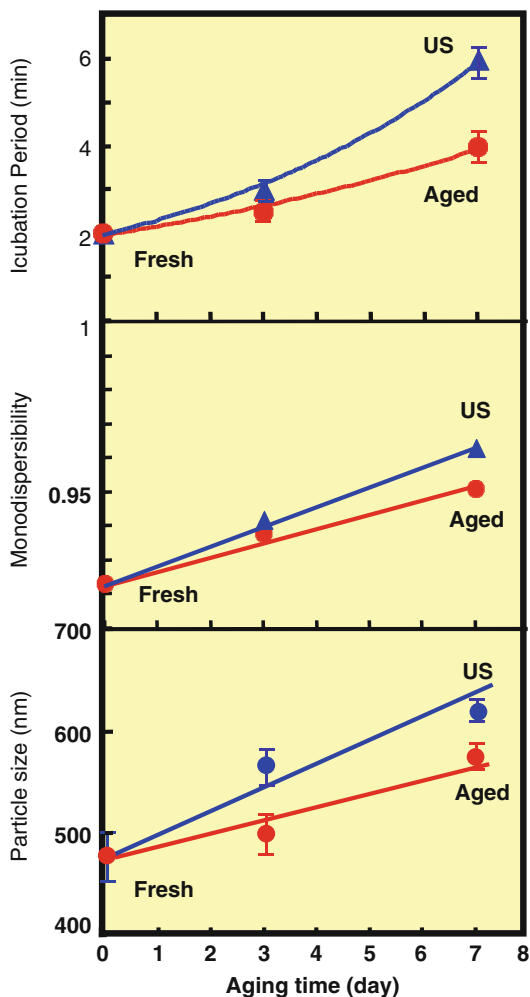
"monodispersed" spheres should only grow gradually through nourishing from liquid phase.

One may think that the size increment in the median size is not that much – only about 130 % at maximum for 7 days aging. However, it should be noticed that this is "one-dimensional" length. If we hit a calculator to convert length to volume, the value of $1/1.3^3 = 0.455...$ implies that the nucleation using the aged starting solutions became half as much as the fresh ones. I do emphasize that these results are quite reproducible, essential, and free from extra factors such as contamination from container or moisture in ethanol [18].

Figure 12 shows a rough illustration of the hypothesis to qualitatively explain the interesting results in Fig. 10. However a solute is soluble in (or miscible with) a solvent and however easy it is to obtain a transparent starting solution, it does not
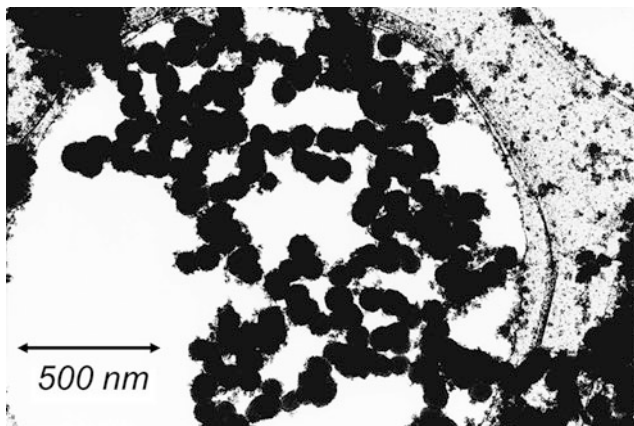
Fig. 11 Silica sphere synthesis at very early stage. Small particles less than 10 nm get together to form spheres. It should be noted such small particles were not observed in the 5-min sample in Fig. 2

guarantee the homogeneity at molecular level. If solute molecules are at first aggregated in the transparent solution, the aggregates may provide a heterogeneous nucleation, which is more likely to occur than homogeneous nucleation. Then, apparent precipitation would be enhanced to show earlier turbidity and more number of sphere nucleus. Monodispersity can be affected to lower side. On aging, such aggregates can be vanished, leading to longer incubation time, smaller number of nucleus (i.e., larger sphere size), and higher monodispersity.

One thing I left to mention in Fig. 10 is that "US" means soft sonication. That is, aging to decrease the sphere nucleus number and increase the sphere size does occur just by leaving it after preparation of the starting solution. And, soft sonication enhances the aging process or the modification of the solution structure. This will be discussed in the next section.

Soft Sonication to Starting Solutions for Spherical Silica Synthesis

Soft sonication was executed by using an aging plate (manufactured by Kyowa Interface Science Co., Ltd.), which is simply designed by gluing a piezoelectric vibrator (40 kHz) beneath a stainless plate, as shown in Fig. 13. Nominal ultrasonic power of this plate is less than mW, where ultrasonic cavitation can never happen. Glass containers of starting solution for silica sphere synthesis were placed on the plate with a small amount of glycerol to ensure a contact between the container bottom and the plate surface. In order to confirm the aging temperature, the whole plate was kept in an oven operating at 40 °C.

As mentioned in the section "Further Investigations on the Ultrasonic-Induced Agglomeration of Silica Spheres," it is absolutely important to compare MS and US in a fair manner. Previously in Fig. 10, quiet aging (i.e., without mechanical stirring) and soft sonication were compared. In order to connect the gap, a shaking incubator was employed for mechanical stirring of the same starting solution. It was confirmed
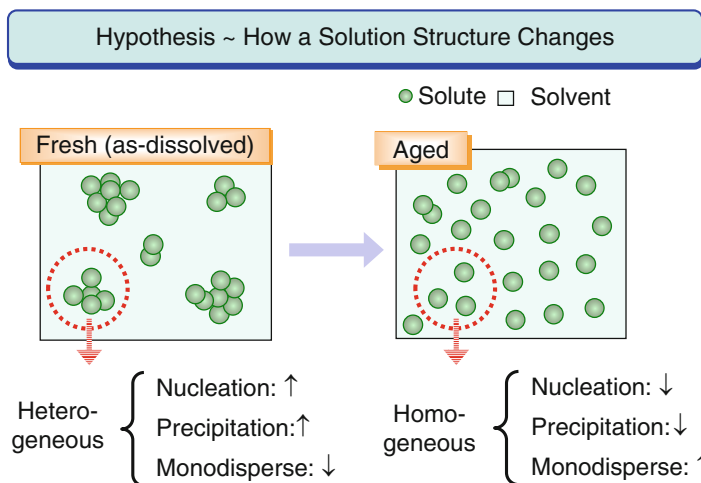
Fig. 12 Schematic illustration of a "transparent" starting solution for particles synthesis. Aging could possibly change the solution structure, thus the field of nucleation of particles
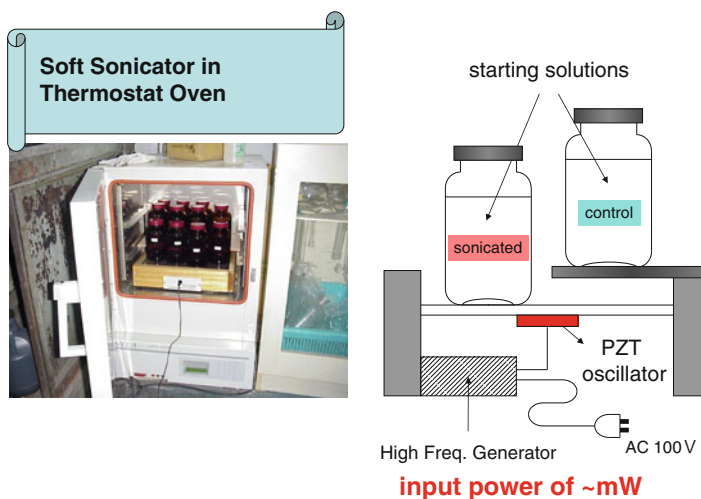
Fig. 13 A view and an illustration for soft sonication. Control and soft-sonicated solutions were treated exactly in the same manner besides the subtle vibration ($\sim$mW)

that mechanical shaking for a week had a similar effect as quiet aging at the same temperature, as shown in Fig. 14. Definite difference between soft sonication and mechanical shaking is the frequency. Compared to the mechanical shaking at $\sim$100 rpm ($=$ several cycle/s), the ultrasound (40,000 cycle/s) can provide very much more frequent "shaking" at very small vibration amplitude ($\sim$tens of nm) in the solution. The solution structure is a kind of black box for the synthesis of nanoparticles. When we prepare the starting solution for it, we scarcely think how
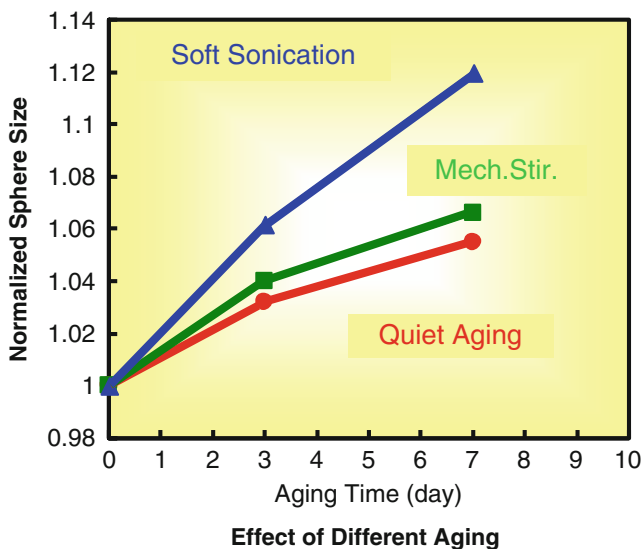
Fig. 14 Comparison with aging under mechanical stirring. Continuous mechanical stirring was conducted by using a labo shaker that was placed in the same oven as in Fig. 13

solvent molecules coordinate to solute molecules or ions, or how they are clustered. We are usually satisfied when the solvent dissolves the solute to a "transparent" level. Even if the solution looks transparent, repeatedly saying, it only means scattering-free from a visible light that has a wavelength of 400–700 nm. Size of a single water molecule is less than ~0.001 times smaller than the wavelength. Soft sonication can be a novel tool to enhance the micro-homogeneity in the solution as sketched in Fig. 12.

Additional Remarks: A Bird's-Eye View on the Time Scales

In this section "Ultrasonic Effects on Silica Sphere Synthesis from Alkoxide," various time scales had appeared. For example, the aging of 1 week equals to 7 days = 168 h = 1.01×10^4 min = 6.05×10^5 s, while the cycle of a 20 kHz ultrasound equals to 5.00×10^{-5} s and the proton exchange rate would be ~10^{-15} s. An idiom "*Not to see the forest for the trees*" is significantly instructive and comprehensive, for we often say to our students "When you take pictures with an electron microscope, take both at lower and higher magnifications," "See the forest as well as the trees, the leaves, the veins, the cells, and the molecules," and "Look at your work with a bird's-eye view." In a narrow sense, the idiom concerns with a length, having a dimension of meter (from km to nm). How about expanding the sense to time as shown in Fig. 15? Our dairy sense for usual experiments lies in the range from several minutes to several hours. We sometimes conduct a day~week experiment for aging, solid-state diffusion, or a fatigue test. With the aid of various

1 year = 32 Msec

| Very Long Process | 0   1 day   2 day .... week, month, year | Aging Degradation (Fatigue) |

| Long Process | 0   1 h   2 h   3h ....   24 | Growth Dissolution & Reprecipitation |

Experimentally Convenient

| Short Process | 0   1 min   2 min   3 min   ....   60 | Reaction Precipitation |

Elementary Processes

| Very Short Process | 0 10^{-15} 10^{-12} 10^{-9} 10^{-6} 10^{-3} 10^{0} sec |

visible light   ultrasound

atomic vibration   microwave   sound

Fig. 15 Time scale consideration for silica sphere synthesis

electromagnetic waves, on the other hand, we are able to measure various spectra and see what we cannot see with our naked eyes.

In the previous section, the aging of the starting solutions ($\sim$week$=10^{+6}$ s), ultrasonic vibration ($\sim 10^{-6}$ s/cycle), and clustering of water and ethanol molecules that is possibly related to protonic exchange rate ($\sim 10^{-15}$ s/cycle) were on the same table of the silica sphere synthesis, which were conveniently examined by the TEM sampling at the order of 10^{2}–10^{3} s. Compared to the ultrasonic vibration, a normal stirring has a frequency of 0.1–1 s/cycle. If those vibrations continue to 1 week, for example, the cycle number is 10^{12} for ultrasound and 10^{6} for mechanical stirring. The time scale in Fig. 15 may usually be considered separately except the lowest bar in logarithmic scale is quite often used to overview various electromagnetic waves. By adding the upper 3 bars, we could hopefully have another bird's-eye view on the sonochemical materials processing.

Sonochemical Effects on Nucleation and Growth

Nucleation from Solution

In this section, we focus on "phase change" without a change of chemical species. Most synthetic processes involve chemical changes that may look simple when described in a chemical equation, but are in fact fairly complicated. In the previous section on silica spheres synthesis, for example, the long explanation was, if described in chemical reactions, concerned with only two reactions (hydrolysis
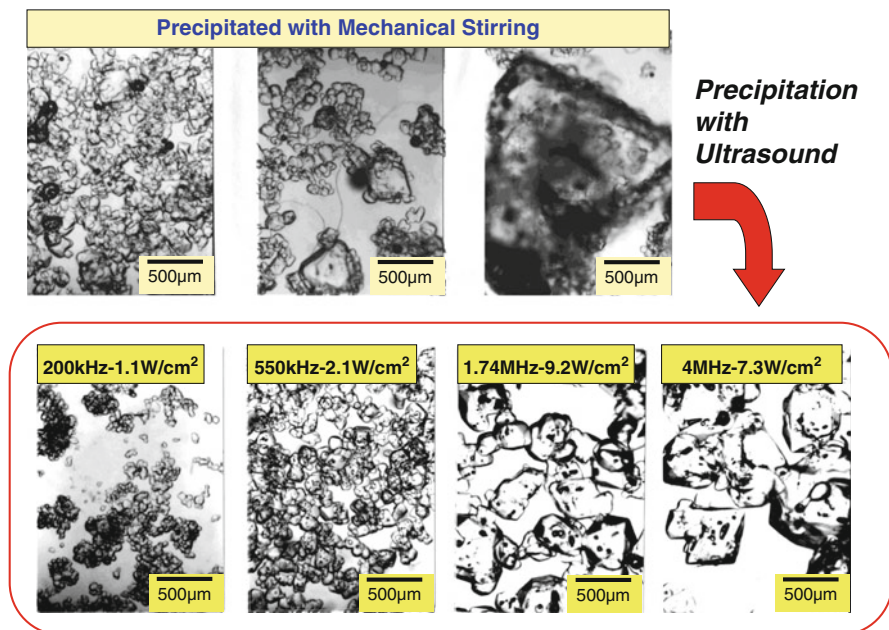
Fig. 16 Recrystallization of alum crystals from supersaturated solution in the absence and the presence of ultrasonic vibration

and polycondensation). As what we saw in Fig. 11, nanoparticles of an intermediate product, containing ∼1,000 SiO_4 tetrahedra, were accumulated to form spheres.

In order to look at the effect of ultrasound on nucleation and growth without chemical changes, we examined crystallization of alum (ammonium aluminum sulfate hydrate) from a supersaturated solution by cooling [21]. After going through a similar cooling history, the size of precipitated crystals was thoroughly influenced by agitation with or without ultrasound as shown in Fig. 16. Huge and large crystals were often observed with mechanical stirring, while the size distribution became quite uniform with ultrasonic agitation and median size could be controlled by the ultrasonic condition. The median size decreases with increasing intensity (Data not shown in Fig. 16). It is considered that a cavitation bubble can be a nucleation site and that the number of cavitation bubbles increases with increasing intensity of ultrasound. It is considered, moreover, that ultrasonic cavitation is likely to occur at lower frequency. The results shown in Fig. 16 suggest that not the nucleation but the growth was accelerated at higher frequency.

Solidification of Molten Salt

Bulk ceramic materials are produced by sintering a powder compact, while metallic materials are produced both by powder sintering (or powder metallurgy) and by

casting (solidification of molten metal). It is well known as *ultrasonic metallurgy* that microstructure of a casted metal ingot is drastically improved by an ultrasonic vibration during solidification. Since the dawn of ultrasonics to the present [22, 23], not a few papers are reported on the reduction of grain size, removal of dissolved gas in a melt, and the suppression of compositional segregation. As the properties of polycrystalline materials are absolutely dependent on their microstructure, it is widely recognized that ultrasonication fairly improves the properties of casted metals.

Why are ceramic materials NOT prepared through a melting and solidification process? Is that because ceramics have high melting temperature and high reactivity or corrosivity against the mold? Yes, it may be true in general, but it is not always true. The most essential reason I think is that ceramics are brittle and often thermally anisotropic. Sintering temperature of ceramics is in general known to be $\sim 0.8 \times$ [melting temperature in K]. If a ceramic melt are solidified, it must be exposed to the melting temperature itself. However the cooling rate is elaborated, grain growth in the bulk cannot help being significant. Then, essentially brittle ceramics are likely to be cracked due to thermal stress on cooling. If the technology of ultrasonic metallurgy is successfully applied to the development of "ceramic casting," there can be an innovation.

$NaNO_3$-$Ba(NO_3)_2$ binary system resembles to the Al-Si alloy system for a practical use. As a model inorganic, this nitrate binary system [24] was investigated with a horn-type sonicator equipped with furnaces as shown in Fig. 17. It is not
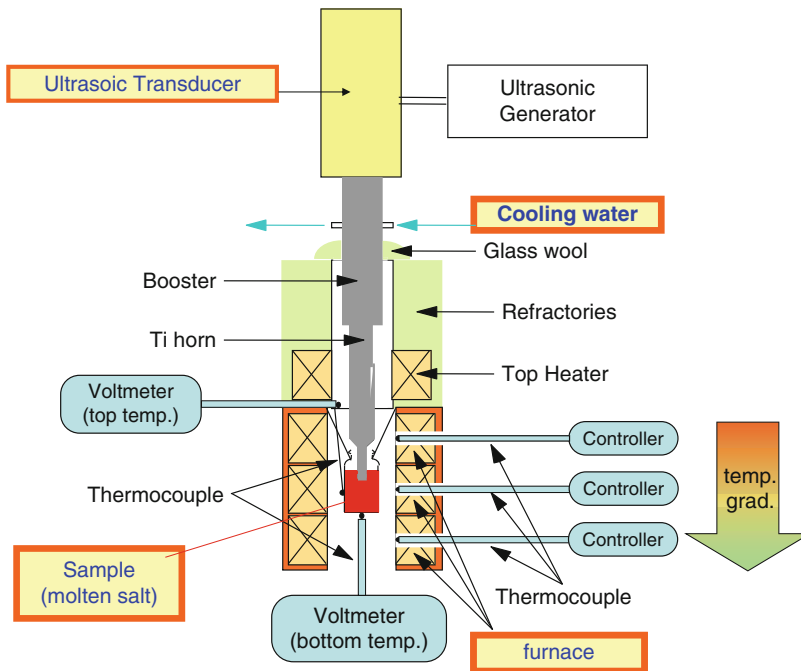
Fig. 17 Schematic of ultrasonic casting equipment

Fig. 18 Cast structure at 92% NaNO$_3$–8%Ba(NO$_3$)$_2$
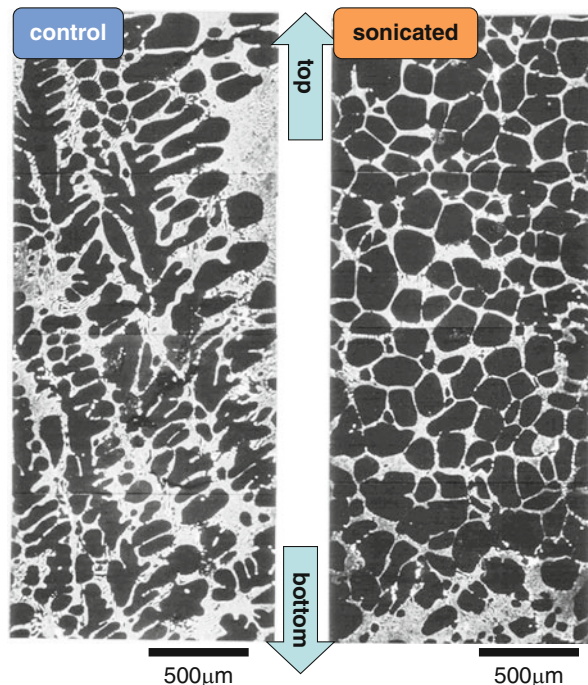
difficult to execute sonication at high temperature if only the horn is properly cooled, the horn tip and the vessel are durable enough, and suitable temperature gradient allows the solidification to occur at the bottom of the vessel. Prior to the binary, molten NaNO$_3$ alone was solidified for a preliminary test [24]. Although the result indicated the grain refinement like a metallurgy case and the alum case in the previous section, decomposition of NaNO$_3$ was accompanied to degrade the texture. It is necessary to find an available materials system. The binary system has a eutectic point at Ba(NO$_3$)$_2$ = 18 mass% and T = 290 °C. Figure 18 shows the casted structure at hypoeutectic at Ba(NO$_3$)$_2$ = 8 mass%. In this compositional image, black and white areas correspond to NaNO$_3$ and Ba(NO$_3$)$_2$, respectively. Obviously the large dendrite of NaNO$_3$ was successfully removed by the ultrasonic vibration.

Sonochemical Effects on Dissolution and Precipitation

One typical synthesis of ceramic particles is executed by mixing a cation-containing solution and a precipitating reagent such as ammonia, if the cation forms a hydroxide having a low solubility in the solvent. If the precipitation occurs immediately on mixing, the reaction appears to be very fast at a glance. In practice, however, it is not usual that a thermodynamically stable state can be achieved immediately at the first stage of the process and remained permanent. In most cases, the initial precipitates

would be dissolved in the mother solution and then reprecipitate to be in a more stable state. For example, Ostwald ripening occurs due to the difference in size and solubility. Ultrasonication is a powerful tool for enhancing dissolution without a single doubt, because effective dispersion of agglomerated substances absolutely increases the surface area as well as the mass transfer in solution is greatly accelerated by micro and straight flow. It is definite that a process involving a dissolution step can be significantly improved (or influenced) by ultrasound.

Ripening of Aluminogel

Alumina is the second abundant ceramic next to silica (Al: the third largest Clerk number) and is superior to silica as a high-temperature ceramic (m.p. of Al_2O_3 is more than 2,000 °C). In order to assure the performance of alumina at high temperature and for highly insulating application, high purity powder of alumina has been developed through a solution process. As solubility product of $Al(OH)_3$ is $K_{sp} = 5 \times 10^{-33}$, Al^{3+} ions in aqueous solution are promptly precipitated by adding ammonia water. If this is sampled soon after the precipitation, we do not see any crystalline phases in the precipitate of an amorphous aluminogel. However, if the precipitate is kept stirred (or ripened) in the mother solution for a long time, the gels can slowly dissolve into the mother solution and reprecipitate into crystalline phases depending on the ripening condition.

Figure 19 shows the effect of ultrasound on ripening detected as the formation of crystalline bayerite [25]. Compared to a control run (MS, standing for mechanical
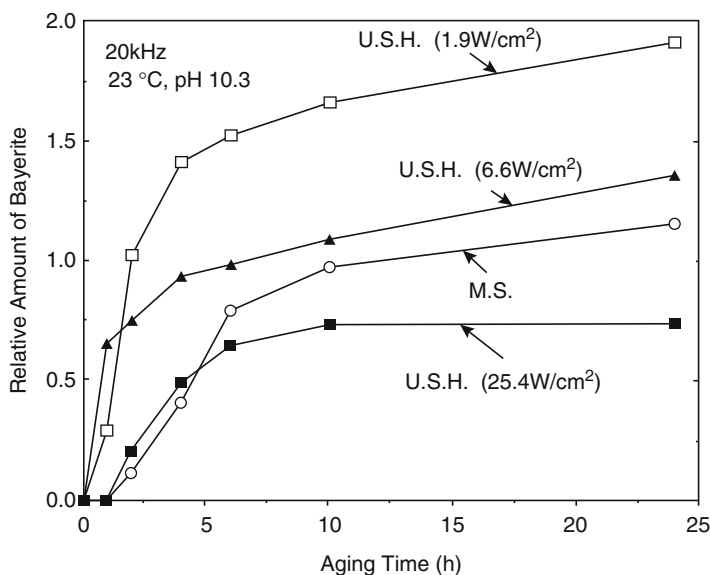
Fig. 19 Ripening of amorphous aluminogels under ultrasonic irradiation

stirring), it is obvious that the treatment with an ultrasonic homogenizer (denoted as USH) promoted the bayerite formation (appearance and final amount) at moderate intensity (1.9 W/cm^2), but suppressed it at higher intensity (25.4 W/cm^2). This ripening process occurs via the dissolution of aluminogel and subsequent precipitation of the crystalline phase. Even at the lower intensity, ultrasound was found to be effective in dissolving the gel. At higher intensity, however, it was found that a psuedoboehmite phase with lower crystallinity (i.e., poorly detected by X-ray diffractometry) was precipitated. This can be regarded as a *sonochemical switching* [26] from bayerite to psuedoboehmite according to ultrasonic intensity as a less-defined structure/phase is likely to form with a higher power sonication.

Magnetic Particle Processing Through Solution Oxidation

As a final topic, ultrasonic irradiation upon dissolution-reprecipitation process including an oxidation step, which was intensively studied for an industrial production of magnetic recording media [27–31]. In a typical process, an alkaline solution, such as NaOH aq. is added to a solution containing Fe^{2+}, and then a pale green precipitate of $Fe(OH)_2$ is immediately produced. By aging this suspension in the mother solution under constant stirring, the initial $Fe(OH)_2$ precipitate slowly dissolves to its ionic Fe^{2+} form again, which is then oxidized by dissolved oxygen to be precipitated as the oxidation product of magnetite (Fe_3O_4) or goethite (α-FeOOH). To start with Fe^{2+} is not roundabout but a sophisticated way to control the shape and the quality of product.

In order to consider the fundamental effect of ultrasound on oxidation, a $FeCl_2$ solution free from a NaOH precipitator was subjected to ultrasonication (20 kHz horn) in air or Ar (Fig. 20). The amount of Fe^{3+} was estimated by UV-vis spectrometry using a calibration curve with standard solutions containing a different amount of $FeCl_2$ and $FeCl_3$. In acidic conditions, air oxidation of Fe^{2+} without ultrasound ("MS" in the figure) is very slow (<2 % over 24 h). Despite the degassing (i.e., decreasing the amount of dissolved oxygen in solution) action of ultrasound, oxidation is promoted (>2 % over 4 h). Oxidation is further promoted by substituting air with Ar (>10 % over 4 h) because this gas increases the core temperature of cavitation bubbles and so enhances sonolysis processes for oxidative species like OH radical. This can cause another type of *sonochemical switching* [26] from a product with lower oxidation number (e.g., Fe_3O_4, magnetite) to that with higher oxidation number (e.g., α-FeOOH, goethite) provided the other conditions than sonication are all the same [27].

Figure 21 shows the effect of ultrasonic intensity (20 kHz, horn) on particle size of cubic magnetite. When MS (mechanical stirring) at zero intensity (i.e., no ultrasound) was used and compared to a moderate sonication at <10 W/cm^2, the particle size is increased due to the enhanced dissolution of the initial precipitate of $Fe(OH)_2$ and thus the supply of solute for reprecipitation. On increasing the ultrasonic intensity, the particle size decreased probably because the number of cavities to promote nucleation increased.

Fig. 20 Oxidation of (acidic) $FeCl_2$ aq. with or without ultrasound in air and Ar. (20 kHz, horn)
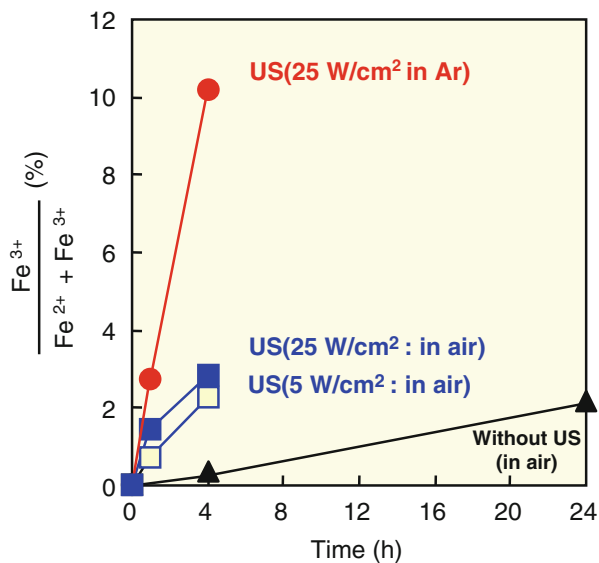
Fig. 21 Change in particle size of magnetite as a function of ultrasonic intensity (20 kHz horn). MS (intensity = 0) means the mechanical stirring without ultrasonics
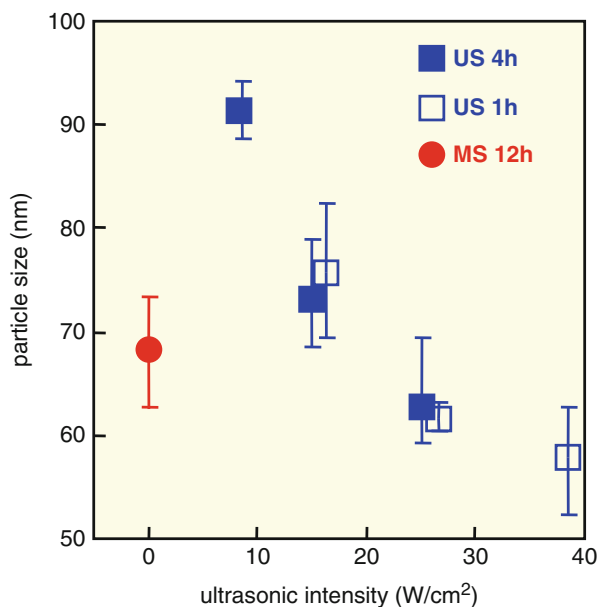
Dang et al. [27–30] successfully prepared monodispersed and stable magnetite nanoparticles by using a mixed solvent of water and ethanol with ultrasonic irradiation as shown in Fig. 22. Uniformly 30 nm-sized magnetite particles in the middle, which were prepared with ultrasound at ethanol/water = 2/8, showed high performance as a magnetic maker for a medical application. It should also be mentioned
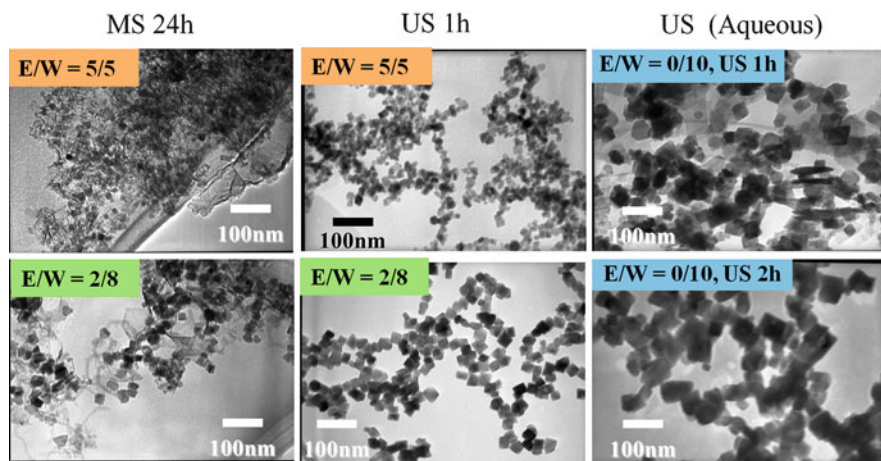
Fig. 22 Magnetite particles precipitated in various solvents (ethanol/water = 0/10, 2/8, 5/5) with or without ultrasound. 1 or 2 h were enough to complete the process in the presence of ultrasound. While in the absence of ultrasound, 24 h were barely required to finish the synthesis seemingly

Fig. 23 Magnetite nanoparticles (<10 nm) precipitated from a 0.001 M $FeCl_2$ and NaOH aq. under the standing-wave sonication at 200 kHz to 0.49 W. Products from the same solution under mechanical stirring and horn sonication were amorphous aggregates
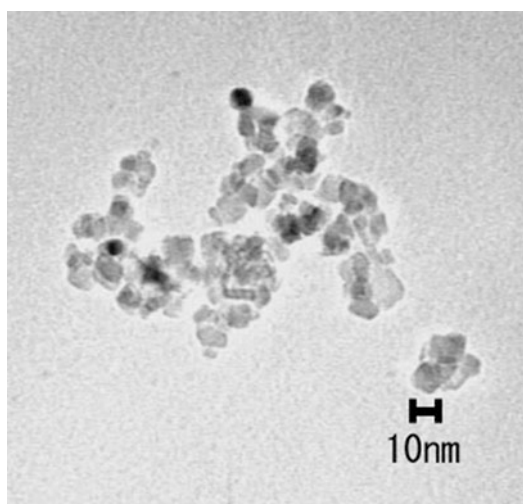
here that ultrasonication fairly reduce the time to complete the process. This is a great benefit for industrial related applications.

Here the topic of magnetite will be introduced. Particle size control is, of course, also available by changing the initial concentration of $[Fe^{2+}]$. The size decreases with the decreasing concentration in this case. At such lower concentration as $[Fe^{2+}] = 0.001$ M, the product was found to be amorphous gel instead of crystalline magnetite, in the absence and presence of ultrasound irradiation at 20 kHz. Crystalline magnetite of <10 nm, as shown in Fig. 23, was successfully obtained by using

standing-wave sonication at 200 kHz. It is inferred that the standing-wave can suppress an excessive macroscopic flow and localize the cavitation bubbles and thus the reaction site [30].

Conclusions and Future Directions

In this chapter, the author's intention was paid to deepen the fundamental aspect of the sonoprocess for ceramic materials. In spite of the incredibly high temperature and pressure as well as the incredibly rapid mass flow, ultrasonic cavitation is, at present, not a charm to facilitate every extreme reaction in every materials system.

In order to develop sonochemical technology for the "superstar materials" discovery in future, the following items are to be kept in mind:

1. To know what really happens in the absence of ultrasound. Chemical equations are just showing chemical names and the molar ratio.
2. To make a fair comparison with proper referential (control) runs.
3. Not only continuous irradiation but also partial one for appropriate stage.
4. Intensity effect can be either positive or negative.
5. Very low intensity may be workable in a case.

References

1. Dislich H (1971) New routes to multicomponent oxide glasses. Angew Chem Int Ed 10(6):363–434
2. Dislich H (1990) Sol-gel 1984–2004 (?). J Noncryst Solid 73:599–612
3. Rosa-Fox N, Esquivias L, Craievich AF, Zarzycki J (1990) Structural study of silica sonogels. J Noncryst Solid 121:211–215
4. Ramírez-Del-Solar M, Rosa-Fox N, Esquivias L, Zarzycki J (1990) Kinetic study of gelation of solventless alkoxide-water mixtures. J Noncryst Solid 121:40–44
5. Stöber W, Fink A, Bohn E (1968) Controlled growth of monodispersed silica spheres in micron size range. J Colloid Interface Sci 26:62–69
6. Míguez H, López C, Meseguer F, Blanco A, Vázquez L, Mayoral R, Ocaña M, Fornés V, Mifsud A (1997) Photonic crystal properties of packed submicrometric SiO_2 spheres. Appl Phys Lett 71:1148–1150
7. Wijnhoven JEGJ, Vos WL (1998) Preparation of photonic crystals made of air spheres in titania. Science 281(7):802–804
8. Arsenault AC, Míguez H, Kitaev V, Ozin GA, Manners I (2003) A polychromic, fast response metallopolymer gel photonic crystal with solvent and redox tunability: a step towards photonic ink (P-Ink). Adv Mater 15(6):503–507
9. Aguirre CI, Reguera E, Stein A (2010) Tunable colors in opals and inverse opal photonic crystals. Adv Funct Mater 20(16):2565–2578
10. Ogihara T, Nakajima H, Yanagawa T, Ogata N, Yoshida K, Matsushita N (1991) Preparation of monodisperse, spherical alumina powders from alkoxides. J Am Ceram Soc 74(9):2263–2269
11. Ikemoto T, Uematsu K, Mizutani N, Kato M (1985) Synthesis of monodispersed titania fine particles by hydrolysis of $Ti(OC_2H_5)_4$. J Ceram Soc Jpn 93(5):261–266
12. Ikemoto T, Mizutani N, Kato M, Mitarai Y (1985) Synthesis of monodispersed zirconia fine particles. J Ceram Soc Jpn 93(9):585–586

13. Enomoto N, Koyano T, Nakagawa Z (1996) Effect of ultrasound on synthesis of spherical silica. Ultrason Sonochem 3:S105–S109
14. Enomoto N, Maruyama S, Nakagawa Z (1997) Agglomeration of silica spheres under ultrasonication. J Mater Res 12(5):1410–1415
15. Doktycz SJ, Suslick KS (1990) Interparticle collisions driven by ultrasound. Science 247:1067–1069; Prozorov T, Prozorov R, Suslick KS (2004) High velocity interparticle collisions driven by ultrasound. J Am Chem Soc 126:13890–13891
16. Koda S, Kimura T, Kondo T, Mitome H (2003) A standard method to calibrate sonochemical efficiency of an individual reaction system. Ultrason Sonochem 10:149–156
17. Yamaguchi K (2003) Cold-spray ionization mass spectrometry: principle and applications. J Mass Spectrom 38:473–490
18. Enomoto N, Shiihara J, Hongo T, Nakagawa Z (1999) Effect of starting solutions on wet-chemical powder preparation using ethanolic solution of oxalic acid. J Ceram Soc Jpn 107(3):278–281
19. Enomoto N, Kumagai A, Hojo J (2005) Aging effect of starting solutions for spherical silica synthesis. J Ceram Soc Jpn 113(5):340–343
20. Enomoto N, Kumagai A, Hojo J (2005) Effect of soft sonication on starting solutions for spherical silica synthesis. J Ceram Process Res 6(4):286–289
21. Enomoto N, Sung TH, Nakagawa Z, Lee SC (1992) Effect of ultrasonic waves on crystallization from a supersaturated solution of alum. J Mater Sci 27:5239–5243
22. Hiedemann EA (1954) Metallurgical effects of ultrasonic waves. J Acoust Soc Am 26(5):831–842
23. Eskin GI, Eskin DG (2003) Production of natural and synthesized aluminum-based composite materials with the aid of ultrasonic (cavitation) treatment of the melt. Ultrason Sonochem 10(4–5):297–301
24. Enomoto N, Iimura Y, Nakagawa Z (1997) Microstructure of nitrate polycrystals solidified under ultrasonic vibration. J Mater Res 12(2):371–376
25. Enomoto N, Katsumoto M, Nakagawa Z (1994) Effect of ultrasound on the dissolution-precipitation process in the aluminum hydroxide- water system. J Ceram Soc Jpn 102(12):1105–1111
26. Ando T, Bauchat P, Foucaud A, Fujita M, Kimura T, Sohmiya H (1991) Sonochemical switching from ionic to radical pathways in the reactions of styrene and trans-b-methylstyrene with lead tetraacetate. Tetrahedron Lett 32(44):6379–6382
27. Enomoto N, Akagi J, Nakagawa Z (1996) Sonochemical powder processing of iron hydroxides. Ultrason Sonochem 3(2):97–103
28. Dang F, Kamada K, Enomoto N, Hojo J, Enpuku K (2007) Sonochemical synthesis of the magnetite nanoparticles in aqueous solution. J Ceram Soc Jpn 115:867–872
29. Dang F, Enomoto N, Hojo J, Enpuku K (2009) Sonochemical synthesis of monodispersed magnetite nanoparticles by using an ethanol-water mixed solvent. Ultrason Sonochem 16(5):649–654
30. Dang F, Enomoto N, Hojo J, Enpuku K (2010) Sonochemical coating of magnetite nanoparticles with silica. Ultrason Sonochem 17(1):193–199
31. Enomoto N, Yamada K, Dang F, Inada M, Hojo J (2009) Synthesis of magnetite nanoparticles understanding ultrasonication. J Jpn Soc Powder Powder Metall 56(4):194–198

Ultrasound-Assisted Synthesis of Nanoparticles for Energy and Environmental Applications

Sundaram Ganesh Babu, Bernaurdshaw Neppolian, and Muthupandian Ashokkumar

Contents

Abstract

Ultrasound causes high-energy chemistry that is accomplished through the process of acoustic cavitation. Ultrasound is used as an important source for the initiation or enhancement of catalytic reactions, in both homogeneous and heterogeneous systems. In this chapter, we focus on recent work on the ultrasound-assisted synthesis of metal nanoparticles for energy conversion applications and also for the environmental remediation.

Keywords

Sonochemistry • Dual frequency • Nanoparticles • Environmental remediation • Energy application

S.G. Babu • B. Neppolian (✉)
SRM Research Institute, SRM University, Chennai, Tamilnadu, India
e-mail: babuchemist007@gmail.com; neppolian.b@res.srmuniv.ac; b_neppolian@yahoo.com

M. Ashokkumar
School of Chemistry, The University of Melbourne, Melbourne, VIC, Australia
e-mail: masho@unimelb.edu.au

Introduction

Sonochemistry refers to ultrasound-assisted chemical reactions. The sonochemical effects in liquids are caused by the phenomenon of acoustic cavitation. The process of acoustic cavitation includes the growth of pre-existing bubbles and their collapse in a liquid. During the collapse of acoustic cavitation, intense heating of the bubbles occurs. These localized hot spots have temperatures of roughly 5,000 °C, pressures of about 2,000 atm, and lifetimes of a few microseconds [1]. Moreover, the shock waves from cavitation in liquid–solid slurries produce high-velocity interparticle collisions. The bubble growth due to the expansion–compression cycles is resulting in the formation of localized "hot spots" [2].

Loomis et al. firstly reported the details of chemical and biological effects of ultrasound [3, 4]. In the last few decades, ultrasound has emerged as a potential technology as it is widely used as an initiator of chemical reactions and physical transformations of materials. Ultrasound in the frequency range 20 kHz–1 MHz has been used in sonochemistry [5]. The physical and chemical effects of ultrasound have been effectively used in numerous applications such as cleaning, emulsification, polymerization, biomedicine, degassing, drilling, cutting, welding, flow measurements, imaging, automotive, food preservation, dairy industry, drug delivery, etc. [6, 7]. In addition, new opportunities have emerged for utilizing ultrasound for controlled synthesis of nanomaterials and porous materials and also for the degradation of organic pollutants, i.e., environmental remediation, namely, sonochemical oxidation of organic pollutants (wastewater treatment) [8–25].

In contrast to the traditional energy sources such as heat, light, and ionizing radiation, ultrasonic irradiation differs in the duration, pressure, and energy. Sonochemistry occupies a unique short-time, high-energy, and high-pressure space. Owing to the immense pressure and temperature, the extraordinary heating and cooling rates ($>10^9$ K/s) produced by the collapse of bubbles are high, and liquid jet streams generated travel at ~400 km/h [26].

This cavitation effect during sonolysis produces oxidative and reductive radicals that can initiate chemical reactions. The advantages of sonochemical reactions include higher reaction rates, higher reaction yields, efficient energy usage, switching of reaction pathways, performance improvement of phase-transfer catalysts, avoidance of phase-transfer catalysts, use of crude or technical grade reagents, activation of metals and solids, and increase in the reactivity of reagents or catalysts [27]. The major benefits of using ultrasound-assisted synthesis of materials with unusual properties include the preparation of samples with high purity, synthesis of materials with narrow particle size distribution, controllable reaction conditions, ability to form NPs with uniform shape, potentially low operating costs, and rapid reaction rate. Ultrasound is used widely in the following processes as given in Table 1 because of its superior effects compared to conventional techniques.

This chapter mainly focuses on ultrasound-assisted synthesis of NPs which are largely used for energy and environmental applications.

Table 1 Various applications of ultrasound

Different applications of ultrasound	Comments	Reference
Removal of organic contaminants from soil and water	Complete mineralization of organic contaminants in aqueous medium is achieved using ultrasound under diffused sunlight	[28]
Agglomeration of aerosols	Ultrasound is used for the sedimentation of superfine aerosol	[29]
Combined with bioremediation	Effect of low-frequency ultrasound in enzyme catalysis, biosensors, and biosludge processing	[30]
Isolation of potentially bioactive components from non-utilized by-product streams	Ultrasound can accelerate the internal diffusion, giving rise to an increased mass transfer, and allow a greater penetration of solvent into the sample matrix and thereby increase the extraction of bioactive compounds from plants and seeds	[31]
Preparation of activated metals by reduction of metal ions	Ultrasound is proven to be effective for the reduction of metal ions without any external reducing agents which is highly active in energy application	[32]
Impregnation of metals, metal oxides, or metal halides on supports	Ultrasound is effectively utilized for the impregnation of metal oxide nanocomposites on graphene oxide support	[32]
Reactions involving metals via in situ generated organoelement species	Ultrasound is used for the generation of organoelement species	[33]
Reactions involving nonmetallic solids	Use of high-power ultrasound in reactions involving nonmetallic solids is reviewed	[34]
Crystallization and precipitation of metals, alloys, zeolites, and other solids	Ultrasound is efficiently used to improve the metal sulfate precipitation from wastewater	[35]
Modification of surface morphology and particle size by high-velocity interparticle collisions	Flowerlike, rodlike morphologies can be achieved by simply altering the ultrasonication power and time without use of any external chemicals	[36]
Formation of amorphous nanostructured materials, including high surface area transition metals, alloys, carbides, oxides, and colloids		
Agglomeration of crystals		
Smoothing and removal of passivating oxide coating		
Micromanipulation (fractionation) of small particles		
Dispersion of solids	Ultrasound generates shear forces in the liquids, useful in the dispersion of solids	[33]

<div align="right">(continued)</div>

Table 1 (continued)

Different applications of ultrasound	Comments	Reference
Intercalation of guest molecules into host inorganic layered solids	A sonochemical approach is developed for the synthesis of $Fe_3O_4@SiO_2$ core–shell NPs with tunable properties	[37]
Sonochemistry of polymers	Sonochemical synthesis of nanosized metal–organic lead(II) polymer is reported which is used as a precursor for the preparation of nanostructured lead (II) iodide and lead(II) oxide	[38]
Degradation and modification of polymers		
Synthesis of polymers		
Sonolysis of organic pollutants in water	Sonolysis of water molecules generates highly reactive ·OH radicals that are efficiently used for the complete degradation of organic pollutants in aqueous medium	[39]

Sonochemical Synthesis of Nanoparticles and Their Applications

Nanoparticle Synthesis

Sonochemical Synthesis of rGO–Au Composite

High-frequency ultrasound at 211 kHz was found to be an effective tool for the synthesis of graphene-based nanoarchitectures. Vinodgopal et al. employed both simultaneous and sequential reduction steps to reduce the graphene oxide (GO) and a gold precursor, $HAuCl_4$, as shown in Fig. 1 [40]. Transmission electron microscopic results confirmed that the reduction process facilitated the formation of well-dispersed Au NPs on reduced GO (rGO) sheets. The rGO–Au composites exhibited a distinct surface enhancement of the graphene Raman bands by increasing the surface coverage of Au NPs.

Simultaneous and sequential reduction of GO and Au(III) were employed for the synthesis of rGO–Au nanocomposites. For simultaneous reduction process, $HAuCl_4$ was mixed with the GO suspension and sonicated for 5 h to make sure that both the GO and the Au salt were reduced. In the case of sequential reduction, the GO was reduced first (by sonicating for 3 h), and then $HAuCl_4$ solution was added to the rGO suspension and the sonication continued further for 2 h. In both cases, the reduction of the metal ions was rapid as evidenced by the appearance of the Au surface plasmon resonance band at 530 nm in the UV–vis spectrum. In the case of sequential reduction, complete reduction of the gold occurred within 1 h of addition of the Au (III) solution to the rGO suspension. Nevertheless, when the $HAuCl_4$ was sonicated simultaneously with the GO, reduction of the entire mixture was accomplished after 4 h. More importantly, the position of the Au plasmon absorption band was also unchanged in both reduction processes indicating that particle sizes were comparable without any aggregation effects.

The oxygen-rich functional groups on the GO surface served as a nucleation and binding center for the Au NPs. Homogeneous dispersion of Au NPs on the surface

Fig. 1 Sonochemical reduction of graphene oxide (*GO*) and gold precursor, HAuCl$_4$ (Reprinted with permission from Ref. [40]. Copyright 2010 American Chemical Society)
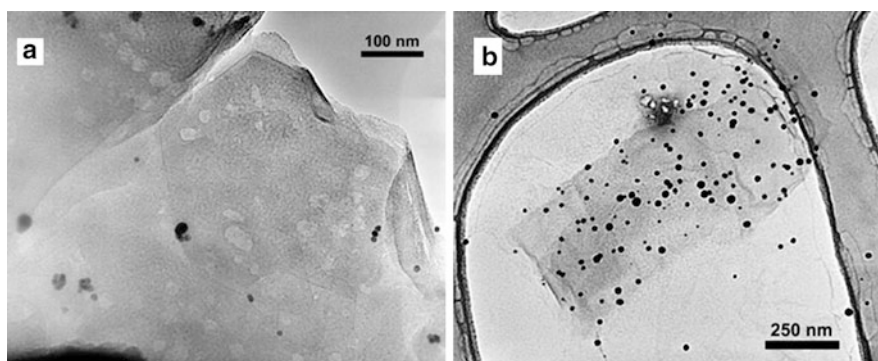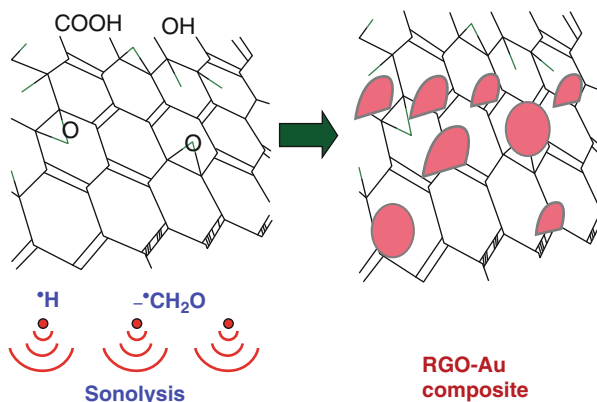
Fig. 2 TEM images of rGO–Au composite synthesized by (a) sequential and (b) simultaneous reduction methods (Reprinted with permission from Ref. [40]. Copyright 2010 American Chemical Society)

of the exfoliated graphene sheets was achieved by simple sonochemical reduction method which is a major advantage of ultrasound-assisted synthesis of nanostructured materials. The TEM images of Au–rGO composites (Fig. 2) showed the high dispersion of Au NPs on rGO surface. TEM images of both sequential and simultaneous reduction of rGO–Au composite showed different dispersities of Au NPs on rGO sheets. In the sequential reduction process, the particle size of Au NPs is smaller and existed as nanoclusters on graphene support. As the epoxide sites were firstly reduced, it prevented the strong binding of Au(III) ions to the graphene sheets. However, simultaneous reduction produced relatively well-dispersed Au NPs on the surface of rGO. Nonetheless, the particle size of Au NPs was found to be comparatively larger than the Au NPs obtained by sequential reduction process. Simultaneous reduction technique provided sufficient interaction between the Au(III) ions and GO due to the oxygen-rich functional groups in GO that served as a nucleation center for Au NPs. However, the slower reduction

rate in simultaneous reduction facilitated the growth of Au seeds which resulted in larger particle size. This difference in the particle size, dispersity, and density of the Au NPs on the rGO surface highlighted the merits of applying ultrasonication in two different manners.

Combined Effect of Ultrasound with Sol–Gel Technique

Ultrasound was effectively combined with sol–gel technique for the synthesis of 100 % rutile polymorph of nanostructured TiO_2 [41]. The effect of cavitation on the phase transformation, crystallite size, crystallinity, and morphological properties of the TiO_2 NPs was studied. Very interestingly, the yield of TiO_2 NPs was enhanced from 86 % to 95 % by the ultrasound-assisted synthesis. As expected, the complete phase transformation of the TiO_2 was observed with the use of ultrasound. The major advantage of this combined preparation technique is that the marked reduction in the required calcination temperature for obtaining 100 % phase transformation led to 70 % energy savings during calcination.

For Environmental Remediation

Ultrasound-Assisted Synthesis of Fe, Cr and Co, and Alloy NPs

Dissociation of metal–carbonyl bonds is one of the interesting strategies to produce individual elemental metal NPs. Ultrasonic irradiation of volatile compounds such as $Fe(CO)_5$ or $Cr(CO)_6$ in nonvolatile solvent results in dissociation of the metal–carbonyl bonds within the cavitation bubble core. Herein, the nonvolatile solvents played a vital role especially in absorbing the heat energy in the collapsing bubble. In a similar way, bimetallic alloy particles can also be prepared by simple sonochemical method. For instance, ultrasonication of $Fe(CO)_5$ and $Co(CO)_3NO$ led to the formation of Fe–Co alloy particles [42, 43]. Composition and metal ratio of the alloy was controlled by simply varying the ratio of the metal precursors. Typically, the alloy NPs exhibit higher catalytic performances toward the dehydrogenation of cyclohexane to benzene than that of the monometallic NPs. More importantly, ultrasound-assisted synthesis of alloy NPs shows high reactivity.

Sonochemically Synthesized MoS$_2$ Nanospheres

The major advantage of ultrasound-assisted NP synthesis is that it generates metal NPs with high surface area. Furthermore, hierarchically structured metal sulfide NPs can also be achieved by sonochemical synthesis. For example, MoS_2 nanostructured photocatalyst was prepared by sonication of $Mo(CO)_6$ with elemental sulfur in 1,2,3,5-tetramethylbenzene under Ar atmosphere [44]. The morphology of sonochemically synthesized MoS_2 is dramatically different from that prepared by a conventional wet chemical method. The conventional methodologies generate layered or platelike MoS_2, whereas the sonochemically synthesized MoS_2 NPs possessed spherical morphology with an average diameter of 15 nm. TEM analysis showed the presence of more defective sites and edges in the sonochemically prepared MoS_2. Importantly, the sonochemically prepared MoS_2 exhibited higher

catalytic activity toward the hydrodesulfurization of thiophene than the MoS_2 prepared by conventional wet chemical method. This increased catalytic hydrodesulfurization activity was mainly attributed to the higher surface area and more edges of the sonochemically prepared MoS_2.

Sonochemical Synthesis of Core–Shell Nanocomposites

Core–shell $TiO_2@C$ composite NPs were synthesized from a single precursor source, namely, titanium(IV) oxyacetylacetonate monohydrate by simple sonochemical method in a specially made Swagelok cell at various temperatures [45]. Different reaction time and temperature led to variation in carbon content in the catalyst samples. The prepared samples were characterized by XRD, diffuse reflectance UV–vis, Raman, TEM, HRTEM, and N_2 adsorption–desorption methods. It is evident from TEM analysis that the as-prepared samples had core–shell structure of TiO_2 anatase phase and C. The diameter of the prepared NPs was in the range of 15–35 nm. Few graphitic layers wrapped TiO_2 composite structure was evidenced by HRTEM analysis. These carbon layers were responsible for suppressing other phase formations of TiO_2 even at high temperature. The prepared samples were tested for their photochemical activities for 4-chlorophenol degradation. The sample prepared at 700 °C showed comparable activity for the degradation of 4-chlorophenol with that of Degussa P25. The photobleaching studies of methylene blue were also carried out under sunlight. It was found that the $TiO_2@C$ samples showed higher photocatalytic activity than Degussa P25.

Role of High-Intensity Ultrasound on the Synthesis of Mesoporous TiO_2 with a Bicrystalline Framework

Yu and his co-workers demonstrated the synthesis of mesoporous TiO_2 with a bicrystalline (anatase and brookite) framework directly under high-intensity ultrasound irradiation [46]. Titanium isopropoxide was used a starting material for the preparation of mesoporous TiO_2. Triblock copolymer ($EO_{20}PO_{70}EO_{20}$) was used to control the structure and morphologies of anatase and brookite TiO_2 catalyst. Effect of the addition of a triblock copolymer was studied. Very importantly, without thermal treatment, mesoporous TiO_2 was formed by the agglomeration of monodispersed TiO_2 sol particles. The resulting materials were characterized with different physiochemical techniques such as XRD, TEM, BET nitrogen adsorption–desorption studies, TGA/DTA, and FTIR. The brookite phase formation was achieved by this ultrasound irradiation-assisted synthesis method. The pore size and the crystalline sizes of anatase and brookite became larger, as the content of the brookite phase increased which was achieved by the use of different molar ratios of triblock copolymer. Both as-prepared samples exhibited better activities than the commercial photocatalyst Degussa P25 in the degradation of n-pentane in air atmosphere. The degradation rate using mesoporous TiO_2 synthesized by the ultrasound-assisted preparation procedure in the presence of triblock copolymer was about two times greater than that of commercial Degussa P25. The combined effect of three factors, namely, high brookite content, high surface area, and the existence of mesopores, is mainly responsible for the high activities of the mesoporous TiO_2 with a bicrystalline framework.

Ultrasound-Assisted Synthesis of Highly Visible Light-Induced Nanosized BiVO₄ Photocatalyst

Shang et al. reported an ultrasonic-assisted synthetic route for the preparation of nanosized $BiVO_4$ with high visible light-induced photocatalytic activity [47]. The overall synthesis was performed with $Bi(NO_3)_3 \cdot 5H_2O$ and NH_4VO_3 in 1:1 molar ratio as precursors in the presence of polyethylene glycol (PEG) under ultrasonic irradiation. The particle size of the as-synthesized $BiVO_4$ photocatalyst was ca. 60 nm as strongly supported by the TEM micrographs. The effects of ultrasonic irradiation and surfactant were investigated toward the degradation of organic dye under visible light illumination. The nanosized $BiVO_4$ exhibited excellent visible light-driven photocatalytic efficiency for degrading organic dye, which was increased to nearly 12 times than that of the products prepared by traditional solid-state reaction. In addition to the decoloring ability, the reduction of chemical oxygen demand (COD) concentration was also observed in the degradation of organic dye that further demonstrates the superior photocatalytic performance of $BiVO_4$ photocatalyst prepared by simple ultrasonication in the presence of PEG. The excellent stability of the prepared $BiVO_4$ photocatalyst was illustrated by recycling studies. The photocatalytic performance of the photocatalyst was remained the same after five recycles which confirming the photocatalyst was essentially stable. Close investigation revealed that the crystal size, BET surface area, and appropriate band gap of the as-prepared $BiVO_4$ are the responsible characteristic features that improve the photocatalytic activities.

Effective Doping of Metal NPs on TiO₂ by Simple Sonochemical Method

Synthesis of titanium dioxide NPs doped with Fe and Ce using sonochemical approach was developed, and its catalytic activity was compared with the conventional doping method [48]. Bare TiO_2 photocatalyst was prepared from titanium (IV) isopropoxide in propanol solution. For the doping of Fe and Ce onto TiO_2, ferric nitrate and cerium(III) nitrate were used as precursors, respectively. The effectiveness of the synthesized catalyst for the photocatalytic degradation of crystal violet dye was investigated by considering the crystal violet degradation as the model reaction. The metal NP-doped TiO_2 photocatalysts prepared by sonochemical method showed superior photocatalytic performance as compared to that of the photocatalysts that are prepared by the conventional wet chemical methods. In comparison with the photocatalytic performance of Ce-doped TiO_2 and Fe-doped TiO_2, Ce-doped TiO_2 exhibited maximum photocatalytic activity, and also the least activity was observed for bare TiO_2. The presence of Fe and Ce in the TiO_2 structure results in a significant absorption shift toward the visible region. Detailed investigations on the degradation indicated that an optimal dosage with 0.8 mol% doping of Ce and 1.2 mol% doping of Fe in TiO_2 results in higher extents of degradation. Kinetic studies also established that the photocatalytic degradation followed the pseudo first-order reaction kinetics. Overall, it was established that ultrasound-assisted synthesis of doped photocatalyst significantly enhances the photocatalytic activity.

Doping of Metal Oxide NPs on TiO_2 Nanotubes by Sonochemical Technique

Similarly, Fe-incorporated TiO_2 nanotube arrays (Fe–TiO_2 NTs) were prepared by an ultrasound-assisted impregnating-calcination method by Wu et al. [49]. Initially, vertically oriented TiO_2 nanotube (TiO_2 NTs) layers were prepared directly on Ti foils via electrochemical anodic oxidation in HF electrolyte with Pt foil as the counter electrode. Then, these as-prepared TiO_2 NT samples were immersed in aqueous solution of $Fe(NO_3)_3 \cdot 9H_2O$ and stimulated immediately by an ultrasonic generator to prepare Fe-doped TiO_2 NTs. The samples were subsequently annealed at different temperatures. SEM, TEM, XRD, XPS, and UV–vis DRS indicated that α-Fe_2O_3 nanoparticles were deposited into the TiO_2 nanotubes, and some Fe^{3+} ions were doped into TiO_2 lattice. The absorption of Fe–TiO_2 NTs in the visible light region increased with the increase of Fe content. The photocatalytic activity of Fe–TiO_2 NTs was evaluated by the degradation of methylene blue aqueous solution under visible light irradiation. The results demonstrated that the Fe–TiO_2 NTs exhibited significantly enhanced photocatalytic activity compared with pure TiO_2 NTs. Photoluminescence and electrochemical impedance spectroscopy analyses confirmed that the increased photocatalytic activity of the Fe–TiO_2 NTs was due to enhanced separation and transfer of photogenerated charge carriers.

Use of Ultrasound for the Preparation of Photocatalyst and Also for the Degradation Studies Under Diffused Sunlight

Ultrasound was used not only for the preparation of supported mixed metal oxide NPs but also for the effective degradation of dyes under diffused sunlight. In one of our recent works, low-frequency ultrasound was used for the preparation of reduced graphene oxide (rGO)-supported CuO–TiO_2 photocatalyst, and an ultrasonic bath was used for the complete mineralization of organic pollutant under diffused sunlight, as shown in Fig. 3 [28]. $Cu(NO_3)_2 \cdot 3H_2O$ and titanium tetraisopropoxide (TTIP) were used as precursors for the preparation of bare CuO–TiO_2 photocatalyst. A tenfold synergy is achieved for the first time by combining sonochemical and photocatalytic degradation under diffused sunlight. rGO loading augments the activity of bare CuO–TiO_2 more than twofold. The ability of rGO in storing, transferring, and shuttling electrons as well as the formation of a heterojunction between TiO_2 and CuO facilitated the separation of photogenerated electron–hole pairs as evidenced by the photoluminescence analysis. Total organic carbon analysis confirmed the complete mineralization of MO and the by-products within a short span of time. Reaction pathway was studied by LC-MS which inferred the hydroxyl radical-mediated degradation under diffused sunlight. Different organic pollutants, namely, methyl orange, methylene blue, and 4-chlorophenol, were degraded under diffused sunlight which indicated the versatility of the catalyst for the degradation of various pollutants. This novel investigation is likely to open new possibilities for the development of highly efficient diffused sunlight-driven TiO_2-based photocatalysts for the mineralization of organic contaminants.
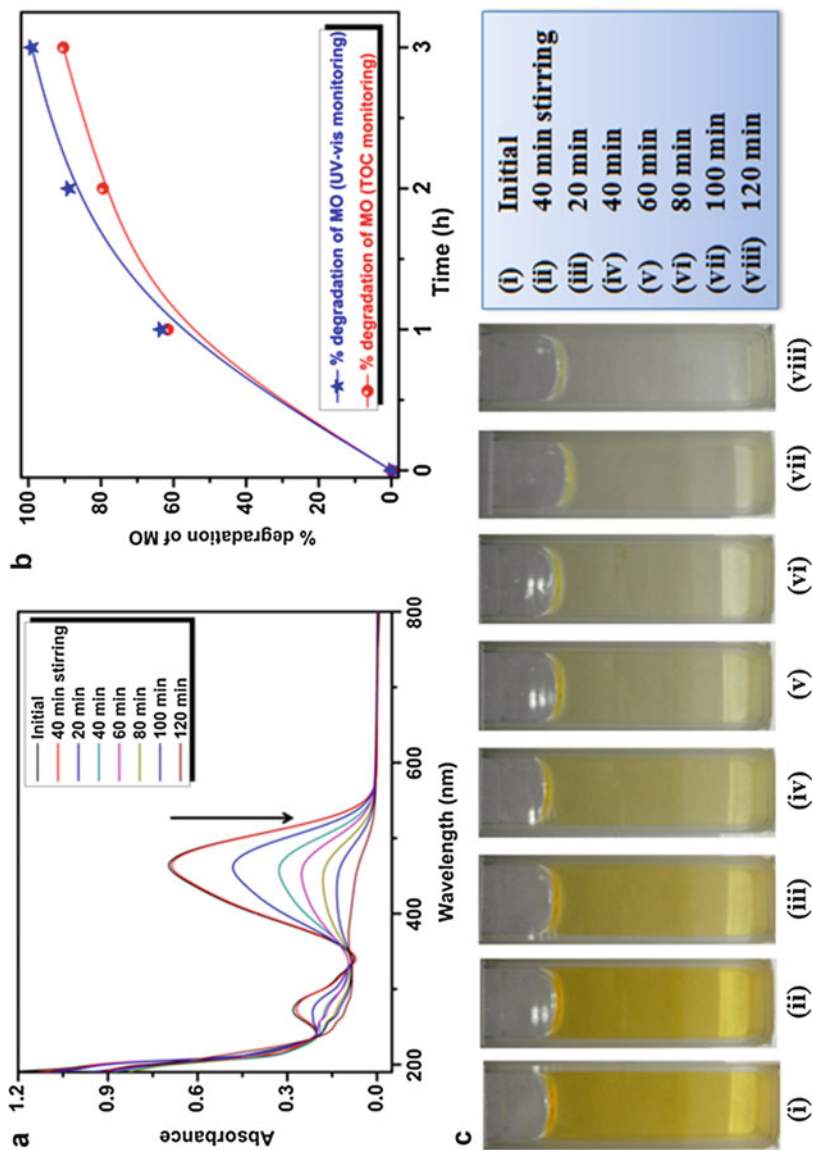
   The presence of mixed metal oxide nanoparticles on the surface of rGO was confirmed by TEM analysis as shown in Fig. 4. Furthermore, the complete utilization of metal oxide NPs on the rGO surface was also evidenced. The ultrasound assisted the complete distribution of the $CuO–TiO_2$ nanocomposites over rGO. More importantly, mesoporous TiO_2 was also prepared by sonochemical method which results in formation of TiO_2 with high surface area and crystallinity. It was further confirmed that $CuO–TiO_2$/rGO possesses distorted elliptical and spherical structures with narrow range of particle sizes. Crystal size distribution graph unveiled the particle size distribution of $CuO–TiO_2$/rGO ranging from 10 to 16 nm with an average of 13 nm.

   It is important to optimize the weight percentage loading of CuO and rGO in the photocatalyst. It was found that only 35 % degradation could be achieved by
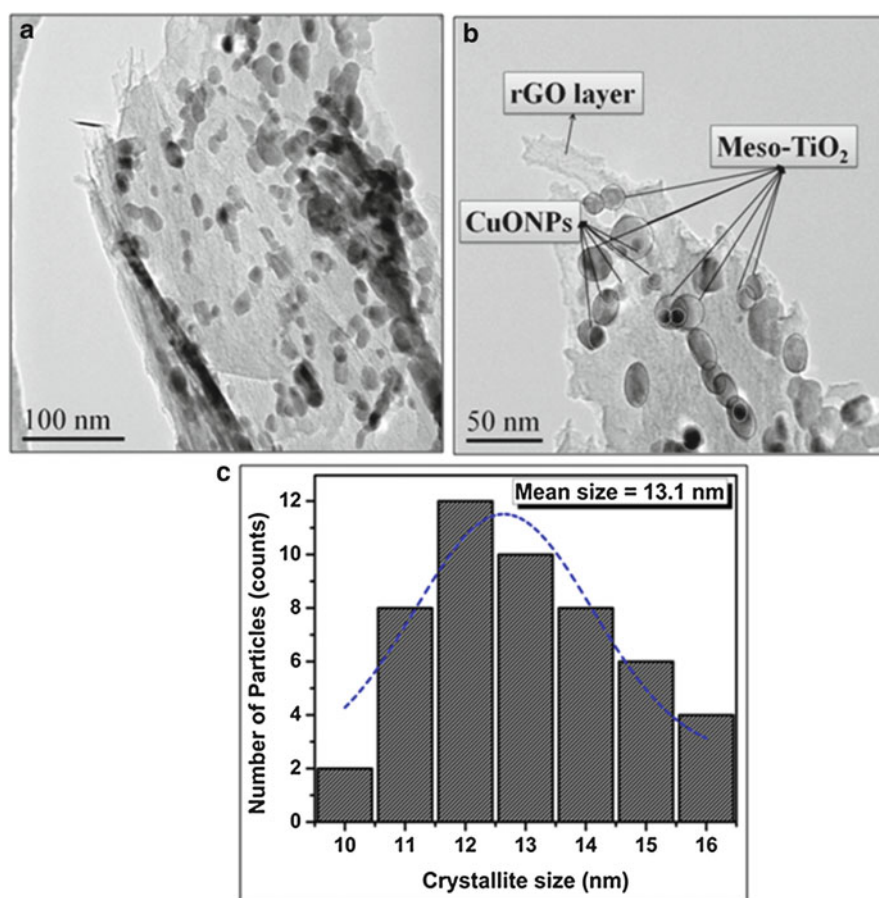
Fig. 4 TEM images of $CuO–TiO_2$/rGO nanocatalyst (**a**) 100 nm, (**b**) 50 nm, and the corresponding (**c**) crystallite size distribution graph (Reprinted with permission from Ref. [28]. Copyright 2015 Elsevier)

CuO–TiO$_2$ (without rGO), whereas rGO-loaded CuO–TiO$_2$ catalyst showed 89 % degradation highlighting the influence of rGO on the catalytic system. Photoluminescence studies and photocurrent results inferred that the increased photocatalytic performance of rGO-loaded photocatalyst was owing to the effective charge carrier separation in CuO–TiO$_2$/rGO photocatalyst. The optimum amount of rGO support was found out by performing different experiments with different amounts of rGO in fixed CuO–TiO$_2$ as shown in Fig. 5a. rGO loading was varied in the range 0, 1, 2, and 3 % with respect to CuO–TiO$_2$ content, and the corresponding MO degradation was found to be 35, 54, 89, and 41 %, respectively. The maximum catalytic activity was obtained with 2 wt.% GO loading. Higher loading of rGO decreased the efficiency of the catalyst which might be due to the mask or prevent the direct contact between the light and the surface of the catalyst. Hence, 2 wt.% of rGO was

Fig. 5 (**a**) rGO loading and (**b**) Cu loading effects on the ultrasound-assisted photocatalytic degradation of MO under diffused sunlight (Reprinted with permission from Ref. [28]. Copyright 2015 Elsevier)
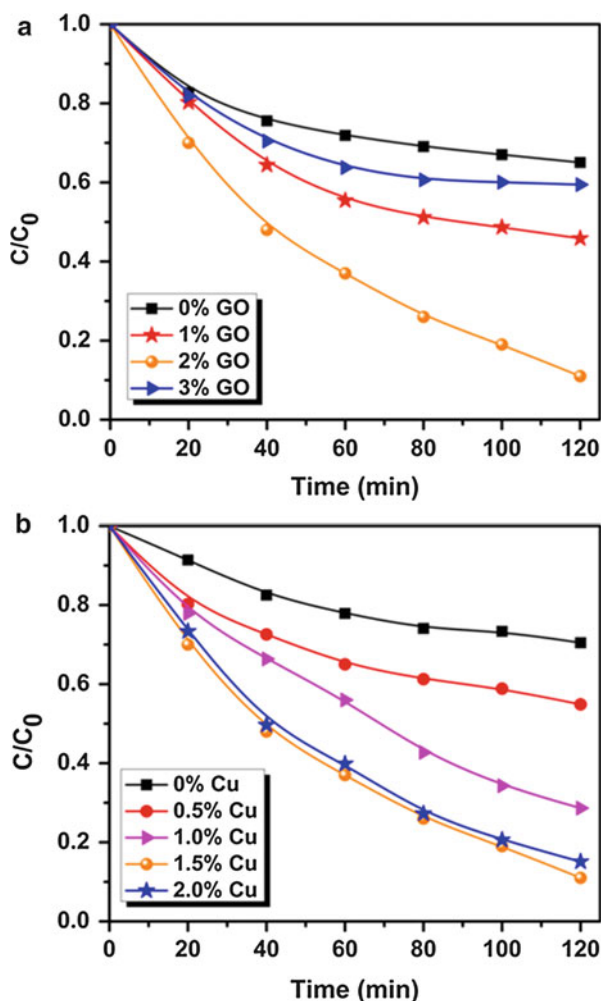
registered as the optimum loading. Similarly, the specific influence of CuO on the sonophotocatalytic degradation of MO under the diffused sunlight was studied with different CuO loading (0–2.0 wt.%) with TiO_2/rGO because the photogenerated electrons migrate from TiO_2 to CuO through rGO. Without CuO only a negligible sonophotocatalytic reaction was observed under the diffused light. Nevertheless, with the initial increase of Cu loading (0, 0.5, 1.0, and 1.5 wt.%), the MO degradation also increased gradually (35, 43, 80, and 89 %, respectively) and exhibited a maximum efficiency with 1.5 % Cu-loaded catalyst as given in Fig. 5b. This can be well explained by the fact that Cu loading (1.5 %) caused a shift in the effective band gap energy from 3.23 eV to 3.08 eV. However, further increase of Cu loading (2 % Cu) showed no much influence on the photocatalytic performance toward MO degradation. Hence, 1.5 % Cu-loaded photocatalyst [CuO–TiO_2/rGO (1.5 % Cu and 2 % rGO)] was used as an optimal amount for the photocatalytic degradation of MO in sonophotocatalytic degradation under diffused sunlight. Complete mineralization of methyl orange, methylene blue, and 4-chlorophenol was ascertained by the UV-vis spectrophotometer and TOC analysis.

Sonochemical Synthesis of Au–Ag/rGO Catalyst for 4-Nitrophenol Reduction

Neppolian and co-workers developed a simple and efficient sonochemical method for the synthesis of Ag and Au monometallic and Au–Ag bimetallic catalysts supported on rGO [50]. Low-frequency horn-type ultrasonicator was used for the loading of bimetallic catalysts containing different weight ratios of Au and Ag onto the surface of GO, whereas high-frequency ultrasonication was effectively utilized for the reduction of Ag(I) and Au(III) ions in the presence of PEG and 2-propanol. The rate of sonoreduction of both Au(III) and Ag(I) in the presence of GO was determined by UV–vis spectrophotometer. The absorption maxima of Ag and Au with GO were monitored around 320 nm and 520 nm, respectively. As the sonication time increased, the absorption intensity gradually increased and attained a maximum value that indicated the complete reduction of Au and Ag NPs. With further increase of sonication time, the absorption intensity value remarkably decreased which might be due to the aggregation of MNPs that led to settling of the particles as shown in Fig. 6.

It can be seen from the TEM images in Fig. 7 that the average particle size of Au NPs was about 50 nm, whereas the size of Ag particles was about 5 nm. Irrespective of the preparation protocol (either by simultaneous or sequential ultrasonication method), Au and Ag NPs were found separately in the form of islands of particles over rGO surface. Furthermore, the images revealed that there was neither a core–shell nor alloy material formed during the sonochemical method of preparation, whereas Anandan et al. reported that Ag–Au was formed as core–shell structure during sonochemical preparation method without rGO [51]. This preparation technique yielded a bimetallic nanocomposite with Ag particles surrounded by Au particles. TEM images clearly showed a higher amount of Au and Ag loading onto the surface of rGO support using dual-frequency ultrasonication. However,

Fig. 6 UV–vis absorption spectra of Au–rGO prepared by sonochemical method (Reprinted with permission from Ref. [50]. Copyright 2014 Elsevier)
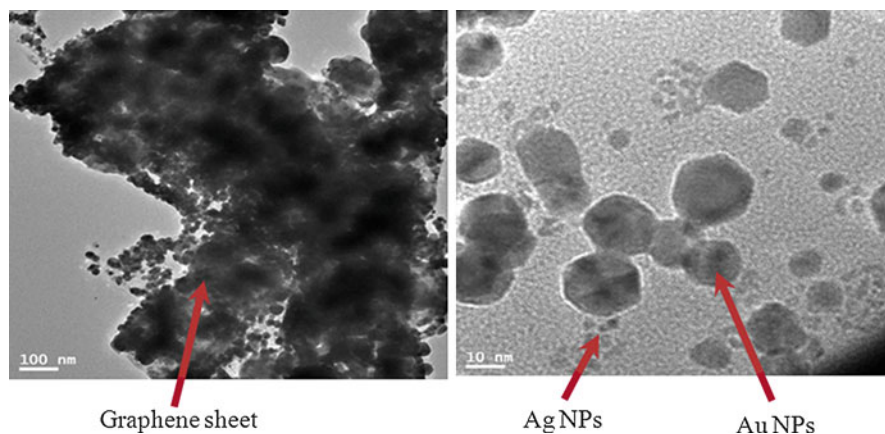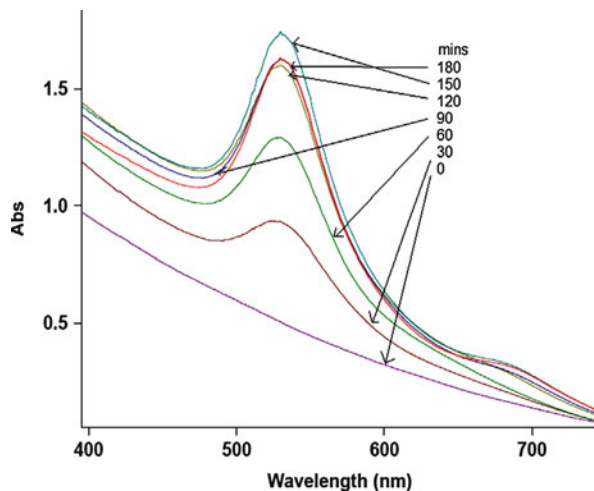
Fig. 7 TEM images of Ag–Au–rGO (2:1) bimetallic photocatalysts prepared by sonochemical method (Reprinted with permission from Ref. [50]. Copyright 2014 Elsevier)

the size, morphology, and shape of the particles are similar in both simultaneous and sequential sonochemical methods as evidenced by TEM analysis.

In order to compare the catalytic efficiency of the prepared catalysts, reduction of 4-nitrophenol (4-NP) and the subsequent formation of 4-aminophenol (4-AP) were carried out which was monitored by UV–vis spectrophotometry. The reduction of 4-NP to 4-AP is an industrially important organic reaction which converts the harmful 4-NP to pharmaceutically and chemically important 4-AP [52]. The results emphasized that the bimetallic catalysts (Au–Ag–rGO) showed higher activity for the reduction of 4-NP to 4-AP than the monometallic counterparts (Au–rGO and Ag–rGO). Similarly, different weight ratios of Au- and Ag (1:1, 1:2, and 2:1)-loaded

rGO catalysts were prepared and their reduction abilities were tested. Among the different weight ratios of Au- and Ag-loaded rGO catalyst, 1:2 (Au–Ag) catalyst exhibited maximum catalytic performance for the conversion of 4-NP to 4-AP. Complete reduction of 4-NP was achieved within short span of time using the catalyst prepared by Au–rGO that was reduced first followed by Ag reduction, whereas a lower reduction rate was observed with the catalyst in which Ag–rGO was reduced first and the results are given in Fig. 8. A similar result was observed for all ratios of bimetallic catalysts. Very importantly, applying dual-frequency ultrasonication was an effective way to prepare bimetallic catalysts that required comparatively low levels of added chemicals and producing bimetallic catalysts loaded on rGO surface with improved catalytic efficiency.

Ultrasound-Assisted Synthesis of Pt–TiO$_2$/rGO Photocatalyst

Ashokkumar and co-workers reported on ultrasound-assisted method for the synthesis of nanosized Pt–rGO–TiO$_2$ photocatalyst [53]. The pH swing method (multi-gelation method) was used to prepare TiO$_2$ nanosized particles along with surfactant under ultrasonic irradiation. Then, rGO–TiO$_2$ composite material was synthesized by an ultrasound-assisted hydrothermal method. Different weight percentage of Pt was doped into the rGO–TiO$_2$ photocatalysts by a photochemical reduction method. For this purpose, H$_2$PtCl$_6$ was dissolved in distilled water and mixed with rGO–TiO$_2$ photocatalyst and then irradiated with UV light for 2–3 h under the continuous stirring condition in an inert atmosphere. A schematic of Pt–rGO–TiO$_2$ photocatalyst is represented in Fig. 9.

The absorption edge of GO–TiO$_2$ was very slightly shifted to the near visible region of spectrum in comparison with bare TiO$_2$ as supported by the DRS studies. The topography and particle size distribution were analyzed by TEM and the results are shown in Fig. 10. The formation of a few layers of GO was confirmed by AFM
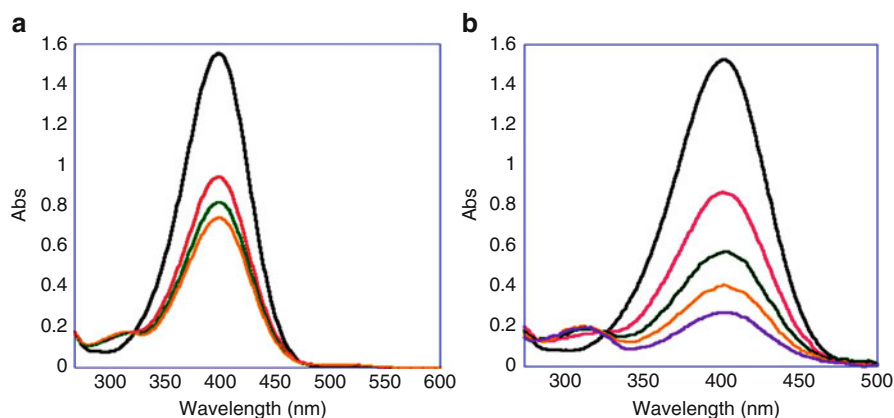
Fig. 8 UV–vis absorption spectra of 4-NP reduction with 1.0 mg of catalyst: (**a**) Au–Ag (1:1)–rGO (Ag reduced first with rGO); (**b**) Ag–Au (1:1)–rGO (Au reduced first with rGO) (Reprinted with permission from Ref. [50]. Copyright 2014 Elsevier)
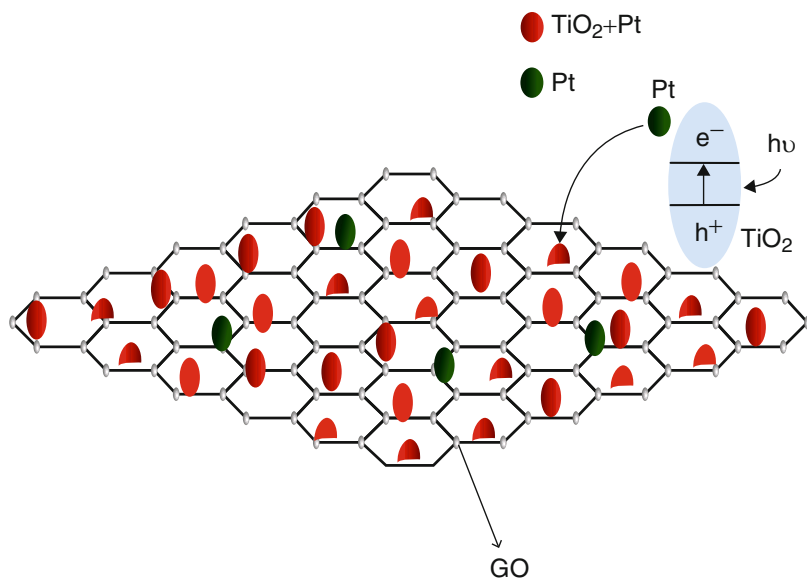
Fig. 9 A schematic representation of dispersion Pt and TiO$_2$ NPs on rGO sheets and the mechanism of photocatalysis (Reprinted with permission from Ref. [53]. Copyright 2012 Elsevier)

Fig. 10 TEM images of Pt–GO–TiO$_2$ (0.4 wt.% Pt) photocatalysts calcined at 650 °C (Reprinted with permission from Ref. [53]. Copyright 2012 Elsevier)
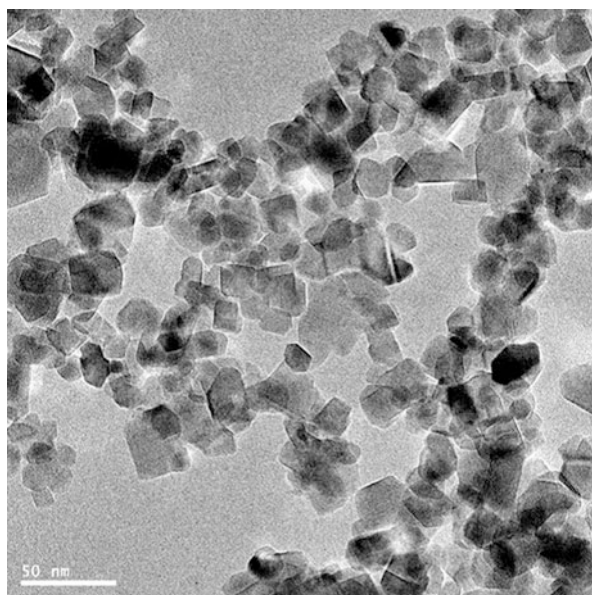
analysis which revealed that the thickness of the GO was around 4.1 nm that consisted of around two- to three-layer thickness of GO formed by this simple ultrasound-assisted synthesis. XRD analysis was performed to find out the crystalline nature of the photocatalysts which showed that Pt–rGO–TiO_2 consisted of 100 % anatase with a sharp peak for anatase at $2\theta = 25.5$. Similarly, the BET surface area analysis revealed that the surface area of TiO_2 was decreased slightly by the loading of GO and Pt which might be due to aggregation.

The photocatalytic and sonophotocatalytic degradation of a commonly used anionic surfactant, dodecylbenzenesulfonate (DBS), in aqueous solution was carried out using Pt–rGO–TiO_2 nanoparticles in order to evaluate the photocatalytic efficiency. DBS is a surfactant widely used in various applications as diverse as in the removal of contaminants from the surface of the human skin to the manufacture of textiles. They are also used in a range of industries including paper, polymer, and pharmaceutical and oil recovery [54]. Each year, large quantities of surfactants are produced worldwide for the above purposes to supply the required demand. For instance, the average annual production of detergent is ~8 million tons from the western world alone [55]. Hence, degradation of surfactant is an important process from an environmental point of view [56]. Photocatalytic degradation technique is one of the advanced oxidation processes for the mineralization of these types of environmental pollutions [57]. The Pt–rGO–TiO_2 photocatalyst showed higher degradation rate than P-25, TiO_2, and rGO–TiO_2 photocatalysts. Importantly, the mineralization of DBS was enhanced by threefold using Pt–rGO–TiO_2 photocatalyst in comparison to the degradation efficiency of P-25 (Fig. 11). GO loading augmented the degradation efficiency of TiO_2. The efficiency was further increased by the doping with Pt. The degradation of DBS was performed under visible light irradiation. Effect of initial pH was examined and it was found that it had a strong influence on photocatalytic oxidation of DBS, whereas no such effect was observed for sonochemical and sonophotocatalytic oxidation process in the presence of Pt–rGO–TiO_2. The mineralization route and intermediate products formed during the degradation of DBS were monitored using electrospray mass spectrometry. The authors concluded that the ability of rGO to serve as a solid support to anchor platinum particles on rGO–TiO_2 is useful in developing new photocatalysts.

Sonochemical Approach for the Synthesis of TiO_2/WO_3 Nanoparticle Photocatalyst

Anandan et al. synthesized TiO_2/WO_3 nanoparticle photocatalyst through an ultrasound-assisted method at room temperature [58]. The presence of monoclinic WO_3 and rutile TiO_2 nanoparticles was ascertained by the XRD analysis of the as-prepared TiO_2/WO_3 nanoparticles. Very interestingly, the sonochemically synthesized TiO_2/WO_3 nanoparticles consisted of mixed square and hexagonal shape particles about 8–12 nm in diameter which was clearly evidenced by TEM micrographs. Furthermore, the authors tested the photocatalytic activity of the prepared TiO_2/WO_3 nanoparticles for the degradation of a wastewater containing methylene blue under visible light irradiation. They concluded that the TiO_2-loaded WO_3 nanoparticle photocatalyst exhibited a higher degradation rate constant which is
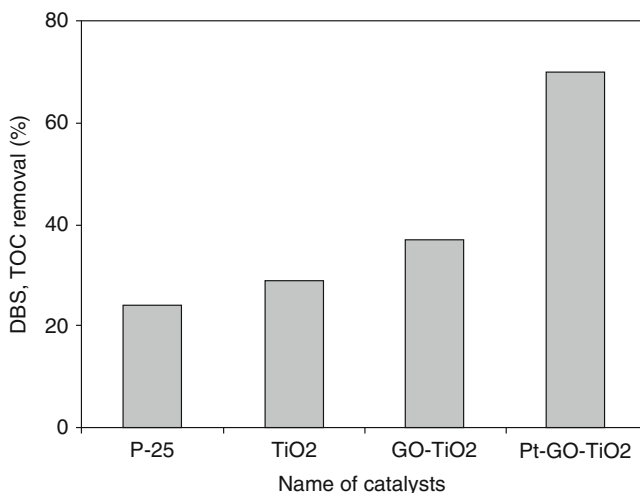
Fig. 11 TOC removal (%) of DBS by different TiO_2-based photocatalysts (Reprinted with permission from Ref. [53]. Copyright 2012 Elsevier)

about $6.72 \times 10^{-4} \, s^{-1}$ than the bare TiO_2 nanoparticles (ca. $1.72 \times 10^{-4} \, s^{-1}$) under identical experimental conditions.

By mixing titanium isopropoxide and sodium tungstate in acidic media, titanium isopropoxide was converted into titanium tetrahydroxide $[Ti(OH)_4]$, and in the same way, sodium tungstate was changed into tungstic acid (H_2WO_4). Then this mixture was subjected to ultrasonication. As a result of sonication, localized extreme conditions were generated at room temperature which led to the formation of coupled TiO_2/WO_3 nanoparticle photocatalyst. SEM and TEM analyses were executed to understand the morphology of the sonochemically synthesized TiO_2/WO_3 nanoparticle photocatalyst. The mixed square and hexagonal shape particles of size 8–12 nm in diameter were observed in SEM and TEM images (Fig. 12). The high resolution of the TEM images revealed that the particles are tightly attached together and making aggregates by sharing the corners or edges between them which probably due to the formation of Ti–O–W bonds [59–64]. The observed selected area electron diffraction (SAED) pattern is entirely different compared to pure monoclinic WO_3 and rutile TiO_2, indicating the formation of coupled TiO_2/WO_3 nanoparticles. From the EDX spectrum, no other impurity is identified which indicates that the formed TiO_2/WO_3 nanoparticles were 100 % pure.

After the complete characterization of the sonochemically synthesized TiO_2/WO_3 nanoparticles with XRD, SEM, SEM-EDX, TEM, and BET surface area and UV–vis diffuse reflectance spectroscopy (DRS), the photocatalytic activity of TiO_2/WO_3 nanoparticles was tested for the degradation of a wastewater pollutant. Photocatalytic degradation of organic pollutant is one of the best ways to mineralize hazardous organics from wastewater [65–70]. Concretely, the degradation of methylene blue under visible light illumination was monitored by recording the decrease
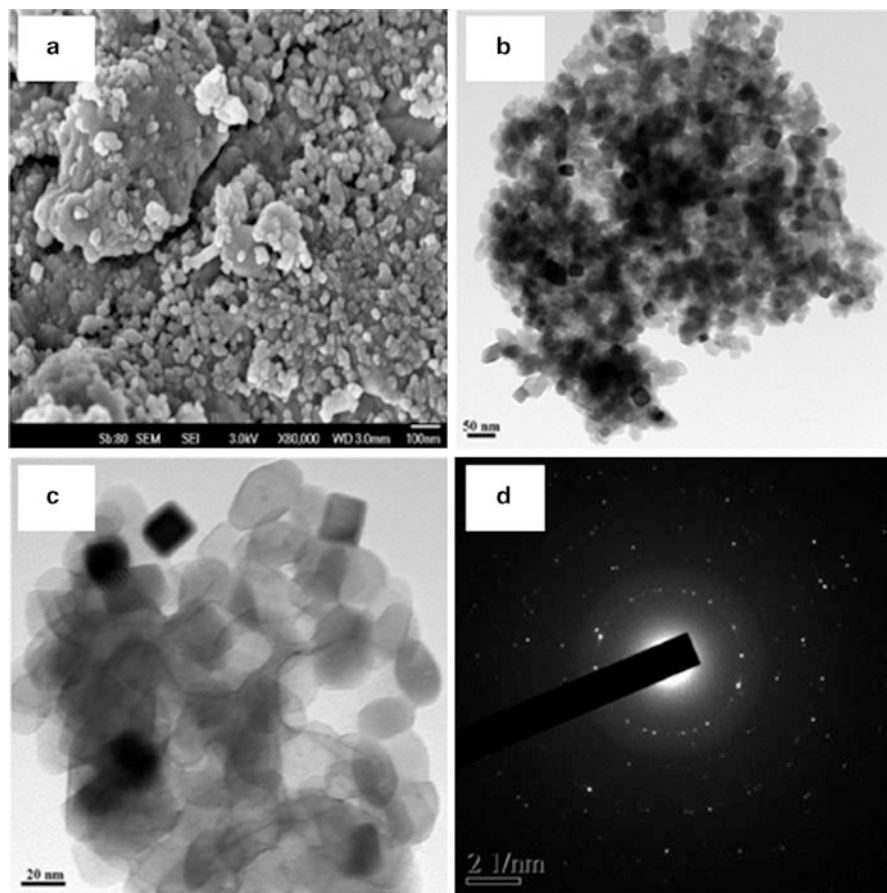
Fig. 12 (**a**) SEM, (**b, c**) HRTEM, and (**d**) SAED pattern of TiO_2/WO_3 nanoparticles (Reprinted with permission from Ref. [58]. Copyright 2014 Elsevier)

in the absorption of methylene blue ($\lambda_{max} = 664$ nm) (Fig. 13). As illustrated in the figure, the kinetics of the degradation of methylene blue with various amounts of TiO_2/WO_3 nanoparticle photocatalyst (0.25, 0.5, 0.75, and 1.0 g/L) was tested and found that pseudo-first-order kinetic was observed for the degradation of methylene blue with respect to the concentration of catalyst. The plot (C_0/C_t) vs. time gave the rate constants which were calculated for the different TiO_2/WO_3 concentrations and was being 5.22×10^{-4} s^{-1}, 6.18×10^{-4} s^{-1}, 6.72×10^{-4} s^{-1}, and 6.37×10^{-4} s^{-1} as the concentration increased from 0.25 to 1.0 g/L. Very importantly, the degradation rate was certainly higher for the reaction carried out with 0.75 g/L of the TiO_2/WO_3 nanoparticle photocatalyst which is very much higher than that measured for pristine TiO_2 nanoparticle photocatalyst (1.72×10^{-4} s^{-1}) under similar experimental conditions. The probable reason for the decreased activity of bare TiO_2
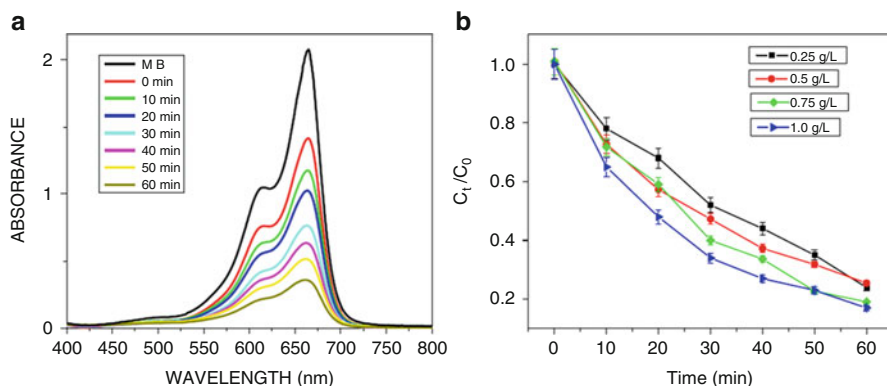
Fig. 13 (**a**) UV–vis absorption spectrum of methylene blue degradation over TiO_2/WO_3 nanoparticle photocatalyst under visible light irradiation and (**b**) kinetic plot [(C_t/C_0) vs. time] for various concentrations of TiO_2/WO_3 nanoparticle photocatalyst (0.25, 0.5, 0.75, and 1.0 g/L) (Reprinted with permission from Ref. [58]. Copyright 2014 Elsevier)

nanoparticle photocatalyst may be due to the recombination between the photogenerated charges and/or by the low adsorption of methylene blue on the surface, the reaction performed under visible light illumination, whereas the TiO_2 photocatalyst is active only in UV light and finally an impeded adsorption of reaction products or carbonaceous poisoning species. The advantage of TiO_2/WO_3 nanoparticle photocatalytic system was that it could adsorb higher amount of incident photons from the visible light. Besides, the recombination of electron–hole pair was significantly prevented in TiO_2/WO_3 nanoparticle photocatalytic system because the conduction band edge of WO_3 and TiO_2 photocatalysts was aligned in such a way that the photoexcited electrons migrated from TiO_2 to WO_3. The transferred electron to WO_3 was utilized for the reduction of W(VI) to W(V). In this way, the photogenerated electrons were trapped by WO_3 and limit the electron–hole pair recombination processes. Thereby, the freely available holes are actively involved in the degradation of methylene blue dye by generating hydroxyl radicals from the aqueous medium.

Ultrasound-Mediated Synthesis of Au–TiO₂ Nanoparticles for the Sonophotocatalytic Degradation

Ashokkumar et al. proved that ultrasound can be effectively used not only for the synthesis of nanoparticles but also can be used for the degradation of organic pollutants in the aqueous medium. In this context, they prepare Au–TiO₂ photocatalysts by simple sonochemical method and tested their sonophotocatalytic activity toward the degradation of organic pollutants in the wastewater [71]. The authors followed the sonochemical preparation in three different procedures for the preparation of same Au–TiO₂ photocatalysts however with different properties. Besides, they studied the effect of preparation procedure in terms of their photocatalytic and sonophotocatalytic efficiencies for the degradation of a

representative organic pollutant, nonylphenol ethoxylate (NPE) surfactant in aqueous solutions. As per the first procedure, the Au–TiO$_2$ photocatalysts were synthesized by doping sonochemically synthesized Au NPs on Degussa P25 Au–TiO$_2$ photocatalysts by stirring without an ultrasonic irradiation. Nonetheless, the Au NPs are sonochemically synthesized and simultaneously deposited on Degussa P25 Au–TiO$_2$ photocatalysts in the second procedure. However, in the third procedure, Au–TiO$_2$ photocatalysts were synthesized sonochemically by the simultaneous irradiation of an aqueous solution containing AuCl$_4$ and titanium tetraisopropoxide. The as-prepared NPs were characterized by UV–vis spectroscopy and TEM. The photocatalytic and sonophotocatalytic efficacy of these Au–TiO$_2$ photocatalysts which were prepared by three different procedures was compared for the degradation of a polydisperse nonylphenol ethoxylate, Teric GN9 under visible light/high-frequency ultrasound irradiation. However, the photocatalytic system failed to exhibit synergistic effect toward the sonophotocatalytic degradation of Teric GN9. This can be well explained by the fact that the interference of the degradation products is generated during the simultaneous irradiation by light and ultrasound which restrict the synergism.

Sonochemical irradiation of AuCl$_4$ aqueous solution led to the formation of Au NPs by the reduction process at room temperature. The formation of Au NPs by sonoreduction method for the reduction of AuCl$_4$ by the primary and secondary radicals generated during acoustic cavitation was well known and clearly explained in detail elsewhere [72]. As per the report, the hydrogen atoms and alcohol radicals reduced Au ions to produce Au NPs. The aqueous solution of Au NPs was of purple in color, and the UV–vis absorption spectrum of the sonochemically synthesized Au NPs exhibited a characteristic high intense surface plasmon absorption band at $\lambda_{max} = 530$ nm in the visible region, as shown in Fig. 14. Furthermore, Fig. 14 also showed the UV–vis spectra of Au–TiO$_2$ NPs. It can be well clear from the spectra that a redshift of 15–40 nm in the absorption maximum of Au plasmon absorption band was owing to the adsorption/deposition of Au NPs on Degussa P25 TiO$_2$ photocatalyst particles. Xu et al. also observed similar trend during the adsorption of Au NPs on (3-aminopropyl)trimethoxysilane [73].

TEM image of the sonochemically synthesized Au NPs is illustrated in Fig. 15. Very interestingly, the sonochemical synthesis resulted in the formation of Au NPs in spherical shape with particle size of 5 nm. More significantly, the sonochemically synthesized Au NPs exhibited fairly narrow particle size distribution. However, the transmission electron micrographs of the Au–TiO$_2$ NPs showed a variation in Au particle size which is in the range of 3–20 nm. Nevertheless, the TEM images of the conventional physical blending method of Au and TiO$_2$ NPs showed that the Au particle size has been slightly increased. This might be due to the agglomeration of Au NPs on TiO$_2$ surface during the drying/sintering process. But the simultaneous reduction/deposition of Au NPs on commercial Degussa P25 TiO$_2$ photocatalyst powder resulted in a slightly larger Au NPs on the surface of TiO$_2$ particles. The particle size of Au NPs in this particular case is estimated to be greater than 20 nm. An acceptable reason for the substantial increase in the Au particle size might be due to the coalescence of Au NPs on the surface of semiconductor particles. The Au–TiO$_2$ NPs
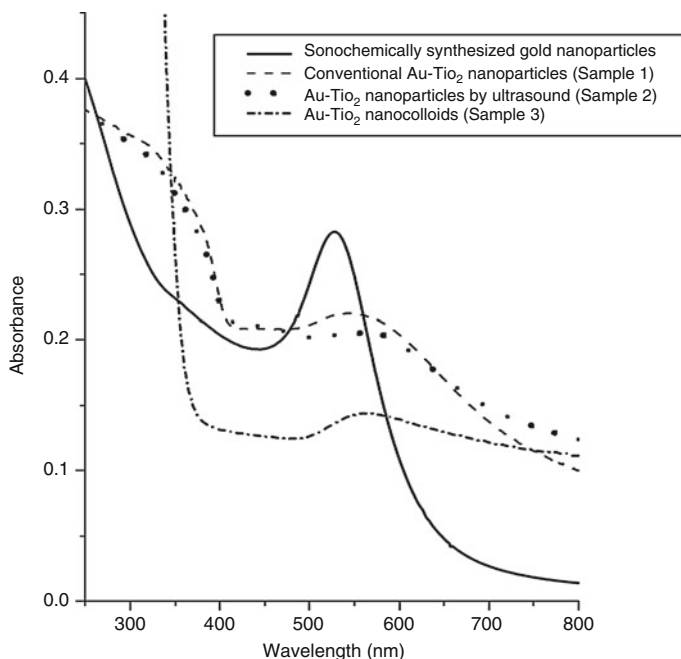
Fig. 14 Solid-state diffuse reflectance UV–vis spectra of (i) sonochemically synthesized Au NPs (—), (ii) conventional Au–TiO$_2$ NPs (-----), (iii) Au–TiO$_2$ NPs by ultrasound (.........), and (iv) Au–TiO$_2$ nanocolloids (-.-) (Reprinted with permission from Ref. [71]. Copyright 2009 Elsevier)

prepared by the simultaneous ultrasonication of titanium tetraisopropoxide and gold chloride ions clearly showed that 2–3 nm Au NPs were immobilized on the surface of TiO$_2$ particles without any aggregation. The formation/deposition of significantly smaller Au NPs could be attributed to the in situ reduction of AuCl$_4$ on the surface of TiO$_2$ particles during the sonication process.

The sonophotocatalytic degradation of Teric GN9 pollutant using the Au–TiO$_2$ NP photocatalyst prepared in the presence of ultrasonic irradiation was monitored through the HPLC analysis, and the respective three-dimensional plot of HPLC chromatograms is given in Fig. 16. The HPLC monitoring was not only restricted for this system alone but also performed for all the experiments. HPLC results implied that the degradation of Teric GN9 increased with increase in reaction time. Initially, the concentration of Teric GN9 was increased during the sonication time which might be due to the fact that desorption of Teric GN9 that adsorbed on the surface of the catalyst during the stirring of reaction medium in the dark to reach adsorption–desorption equilibrium. But High performance liquid chromatography (HPLC) results clearly suggested that the complete degradation was achieved by 3 h of sonophotocatalysis of Teric GN9 using Au–TiO$_2$ NP photocatalyst. With an increase in irradiation time, a substantial increase in hydrophilic products was
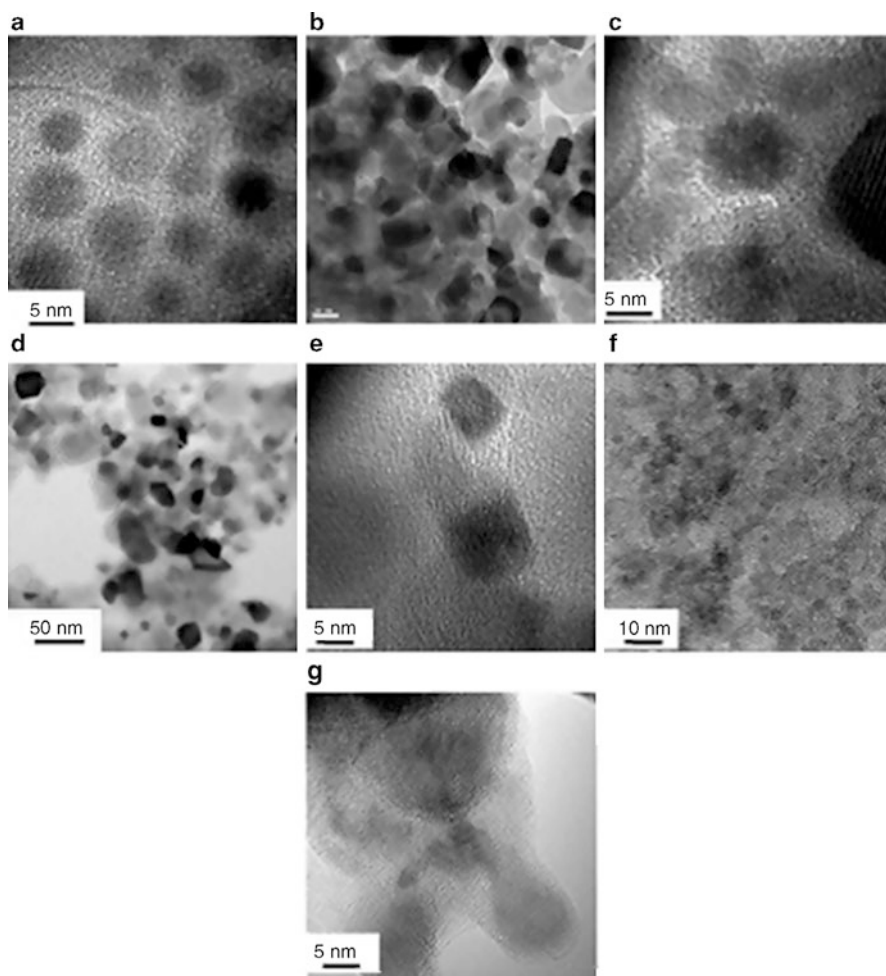
Fig. 15 TEM image of (**a**) sonochemically synthesized Au NPs, (**b**) conventional Au–TiO$_2$ NPs, (**c**) HRTEM image of conventional Au–TiO$_2$ NPs, (**d**) Au–TiO$_2$ NPs prepared in the presence of ultrasonic irradiation, (**e**) HRTEM image of Au–TiO$_2$ NPs prepared in the presence of ultrasonic irradiation, (**f**) Au–TiO$_2$ nanocolloids, and (**g**) HRTEM image of Au–TiO$_2$ nanocolloids (Reprinted with permission from Ref. [71]. Copyright 2009 Elsevier)

observed at short retention times [74]. In addition to this, a change in the shape of Teric GN9 band could be observed with increasing sonication time. The reason for this might be the polydispersity of Teric GN9 molecules with varying hydrophobicity. The molecules that are more hydrophobic (longer retention times) could be expected to degrade faster. This leads to the degradation of more hydrophobic Teric GN9 molecules that leads to a change in the HPLC band observed at a retention time of about 10 min.
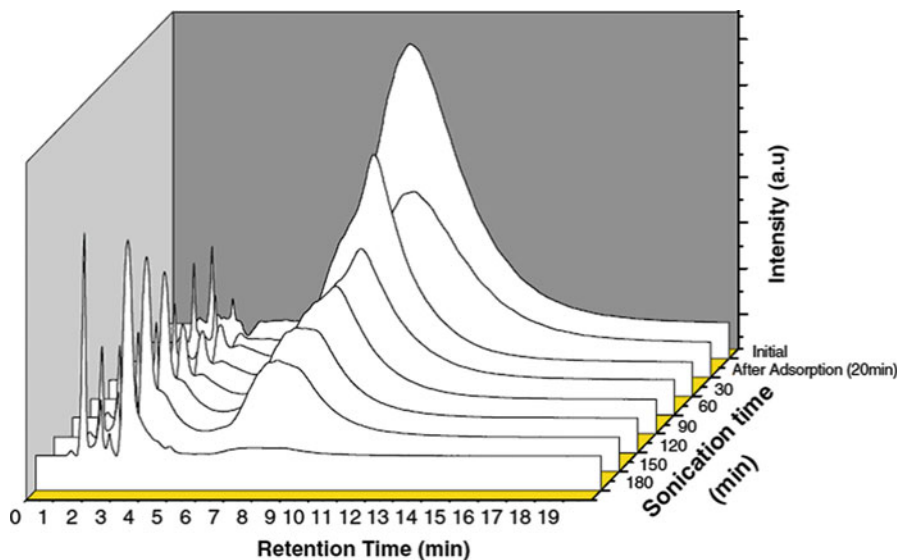
Fig. 16 Three-dimensional plot showing the evolution of the HPLC chromatogram as a function of irradiation and sonication time for sonophotocatalytic degradation of Teric GN9 surfactant $(1.5 \times 10^{-4}$ M) using Au–TiO$_2$ NPs prepared by the sonochemical deposition of Au NPs on Degussa P25 TiO$_2$ photocatalyst. Mobile phase: acetonitrile/water (60/40 v/v) and detection wavelength = 226 nm (Reprinted with permission from Ref. [71]. Copyright 2009 Elsevier)

The change in concentration of Teric GN9 as a function of irradiation time was calculated by integrating the area under the entire peaks in the HPLC spectrum. The data is plotted and is given in Fig. 17. Figure 17 shows the change in concentration as a function of reaction time for sonolytic, photocatalytic, and sonophotocatalytic degradation of Teric GN9 using the Au–TiO$_2$ photocatalyst prepared by conventional method. However, the similar experimental data were collected for the Au–TiO$_2$ photocatalysts prepared by the sonochemical deposition of Au NPs on Degussa P25 TiO2 photocatalyst surface and also for the Au–TiO$_2$ nanocolloidal photocatalyst. A decrease in the concentration of the Teric GN9 surfactant with respect to time during sonolysis, photocatalysis, and sonophotocatalysis is due to the oxidation of the surfactant molecules by ·OH radicals [75, 76]. A number of studies [75, 76] have shown the detailed mechanism of the degradation of organic compounds using sonolysis and photocatalysis. Based on these studies, it is proposed that the ·OH radicals attacked on the Teric GN9 surfactant are the initial reaction step during the degradation of the surfactants.

The plots of ln[Teric GN9] vs. time for sonolysis, photocatalysis, and sonophotocatalysis are shown for the degradation of Teric GN9 surfactant using Au–TiO$_2$ photocatalyst prepared by conventional method in Fig. 18. The linear relationship between ln(C/C$_0$) and irradiation time indicates that the degradation follows a first-order kinetics. Based on the slopes of ln(C/C$_0$) vs. reaction time, the first-order rate constants were also calculated degradation of Teric GN9 surfactant using Au–TiO$_2$ photocatalyst prepared by conventional method.
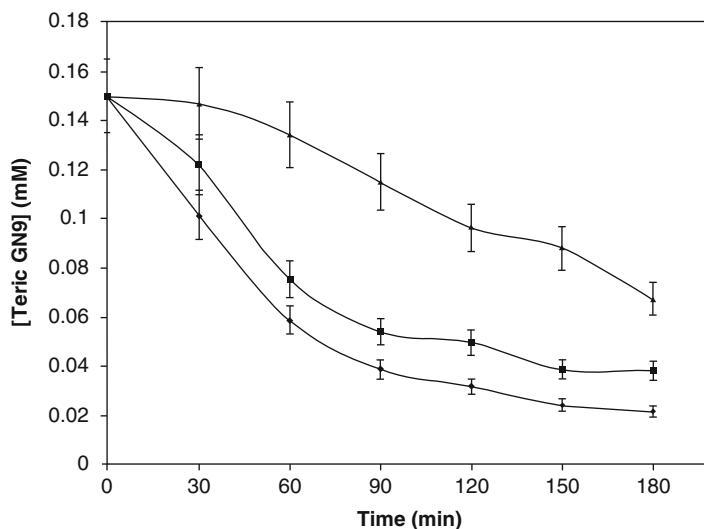
Fig. 17 The degradation plot for Teric GN9 surfactant $(1.5 \times 10^{-4}$ M) using conventional Au–TiO$_2$ NPs (prepared by conventional method) by photocatalysis (♦), sonophotocatalysis (■), and sonolysis (▲) methods. The degradation of Teric GN9 surfactant was monitored from the change in the peak area of the surfactant band in the HPLC chromatogram. The lines shown are just to guide the eyes to note the trend. These lines are not theoretical curves. The error bars shown are to indicate the deviation from an average value. Each data point is an average of two to four individual analytical data (Reprinted with permission from Ref. [71]. Copyright 2009 Elsevier)

For Energy Applications

Sonochemical Synthesis of rGO Supported Pt–Pd Alloy

Neppolian et al. recently reported the preparation of bimetallic NPs (Pt–Pd) supported on rGO by a simple sonochemical reduction method in the presence of polyethylene glycol as a stabilizing agent [77]. K$_2$PtCl$_4$ and Pd(OAc)$_2$ are used as the precursors for Pt and Pd, respectively. Fine tuning of particle composition without any significant changes in the particle size and degree of aggregation was achieved by this synthetic route. A novel dual-frequency technique was employed to achieve uniform deposition of Pt–Pd NPs with average diameter of 3 nm on rGO nanosheets as evidenced by the TEM image shown in Fig. 19.

Sonolysis of water molecules generates highly reactive H· and OH· radicals that are scavenged by the polyethylene glycol (PEG), leading to the generation of secondary reducing radicals. The secondary reducing radicals reduced the metal ions and GO simultaneously. PEG not only acted as a radical scavenger but also involved in stabilizing the metal NPs which were formed during the sonochemical reduction of metal precursors along with the reduction of GO nanosheets [39].

Pt–Pd/rGO composite prepared by the dual-frequency sonochemical method showed significant electrocatalytic activity for methanol oxidation, as shown in Fig. 20. Different Pt and Pd molar composition catalysts (1:1, 2:1, and 3:1) were
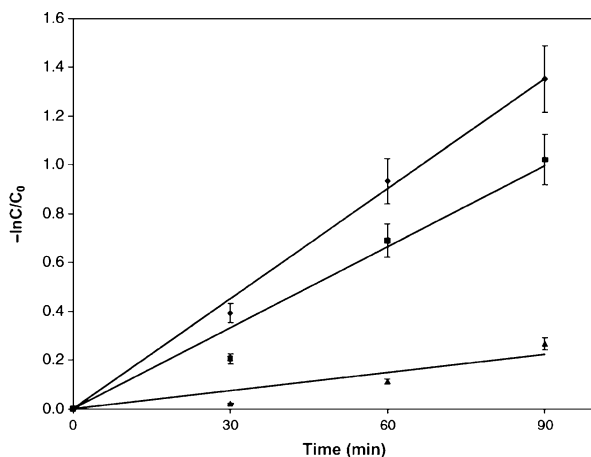
Fig. 18 The kinetics of Teric GN9 (1.5×10^{-4} M) degradation using conventional Au–TiO$_2$ NPs (prepared by conventional method) by photocatalysis (♦), sonophotocatalysis (■), and sonolysis (▲) methods. The degradation of Teric GN9 surfactant was monitored from the change in the area of the surfactant band in the HPLC chromatogram. The linear fits show that the reaction follows first-order kinetics. The error bars shown are to indicate the deviation from an average value. Each data point is an average of two to four individual analytical data [76] (Reprinted with permission from Ref. [71]. Copyright 2009 Elsevier)

Fig. 19 TEM image of Pt–Pd/rGO prepared by the simultaneous sonochemical method (Reprinted with permission from Ref. [77]. Copyright 2014 Springer)
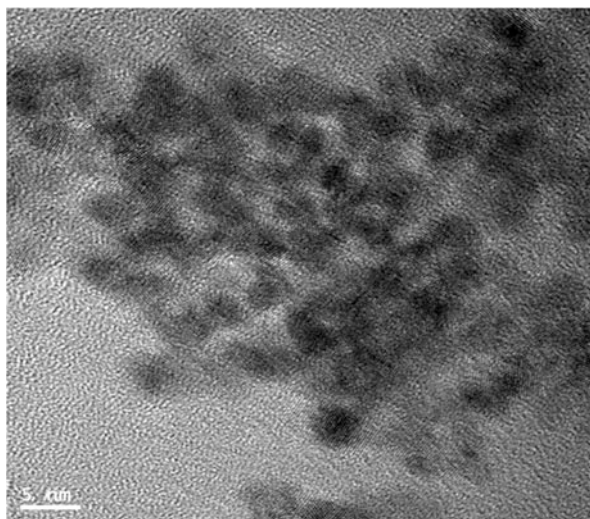
prepared, and their electrocatalytic activity toward methanol oxidation was tested, and the 1:1 ratio Pt–Pd catalyst showed the lowest onset potential which was about 0.25 V, whereas for the other two ratios (2:1 and 3:1), it is more positive than 0.3 V and generated a higher peak current density (36 mA). The peak current densities owing to methanol oxidation were found to be 36, 24, and 26 mA for 2.5, 3.3, and

Fig. 20 Cyclic voltammograms for Pt–Pd/rGO with three different catalyst loadings (low = 2.5 mg, medium = 3.3 mg, and high = 5.8 mg) on carbon Toray paper in 0.5 M H$_2$SO$_4$+250 mM methanol solutions; scan rate 10 mV/s (Reprinted with permission from Ref. [77]. Copyright 2014 Springer)
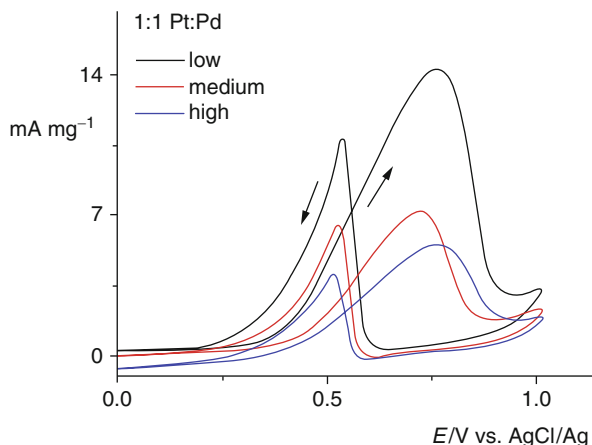
5.8 mg, respectively, of electrocatalyst (Pt–Pd=1:1) loadings on carbon Toray paper (used as a working electrode). Effect of catalyst dosage inferred that beyond a certain amount of catalyst loading, the catalytic activity was lowered which might be due to the aggregation of metal nanoparticles (MNPs) loaded on rGO nanosheets.

Sonochemical Synthesis of Ni-Doped ZSM

Vafaeian et al. developed a sonochemical method for the dry reforming of methane with an intension of reaching most efficient nanocatalyst. The as-synthesized nanocatalyst was tested for the carbon dioxide reforming of methane which is an important route for the synthesis of gas production over nanocatalyst [78]. The effect of Ni loading on Zeolite Socony Mobil-5 (ZSM-5) support was studied toward the carbon dioxide reforming of methane. Interestingly, the NiO XRD peak became sharper as the increase of Ni content over the support. The favorable influence of ultrasound-assisted procedure became more asserted for the preparation of nanocatalysts with lower metal content (3 % and 8 %). The observed reduction in particle size of Ni NPs and also the narrow particle size distribution of the Ni NPs over ZSM-5 support might be assigned to the use of ultrasound energy during the synthesis. For the preparation of Ni-doped ZSM-5 catalyst, the precursor solutions [Ni(NO$_3$)$_2$·6H$_2$O as Ni source and ZSM-5] were sonicated using low-frequency ultrasonicator under argon atmosphere. Nano-range particle size, narrow particle size distribution and high crystallinity of Ni NPs, and high surface area Ni-doped ZSM-5 catalyst were mainly owing to the use of ultrasonic irradiation for the synthesis. TEM analysis inferred the formation of nanocatalyst with the average metal particle size of about 43 nm. Moreover, nearly about 99 % of Ni metal particles size was less than 100 nm. This particular property is essential for the relative suppression of carbon formation on nanocatalysts. The effect of different feed ratios, gas hourly space velocities, and reaction temperatures was carried out for the reforming reactions to identify the influence of operational conditions. The nanocatalyst synthesized with 8 wt.% Ni under ultrasonication represents the

outstanding nanocatalyst among the other catalysts. The product yields remained at constant for the nanocatalyst prepared with 8 % Ni loading after 24 h of reaction time which implied the stability of the nanocatalyst prepared by sonochemical method under the given reaction condition.

Sonochemical Synthesis of rGO Supported Cu_2O–TiO_2 Photocatalyst for Increased H_2 Production

Recently, Babu et al. reported a simple, low-cost, and scalable preparation of reduced graphene oxide (rGO)-supported surfactant-free Cu_2O–TiO_2 nanocomposite photocatalysts by ultrasound-assisted wet impregnation method [32]. The combination of ultrasound-assisted synthetic route with wet impregnation technique possesses major advantages. For instance, unlike the conventional preparation techniques, simultaneous reduction of copper precursor and graphene oxide (GO) to rGO was achieved by ultrasonic method without addition of any external reducing agent which was ascertained by XRD and XPS analyses. The UV-vis DRS studies provided evidence that the loading of Cu_2O tailored the optical band gap of the photocatalyst from 3.21 eV to 2.87 eV. H_2 production via splitting of water was verified through the photoreactivity of the as-prepared Cu_2O–TiO_2/rGO photocatalyst in the presence of glycerol as a hole (h^+) scavenger under visible light irradiation, as shown in Fig. 21. The addition of rGO increased the carrier mobility at Cu_2O–TiO_2 p-n heterojunction which was evidenced from the lesser reduced luminescence intensity of Cu_2O–TiO_2/rGO photocatalyst. Hence, rGO astonishingly enhanced the photocatalytic activity as compared with pristine TiO_2 NPs and Cu_2O–TiO_2, by factors of ~14 and ~7, respectively. A maximum H_2 production rate of 110968 µmol h^{-1} g_{cat}^{-1} was obtained with a 1.0 % Cu and 3.0 % GO photocatalyst composition which is extremely superior than the previously reported graphene-based photocatalysts. More importantly, the present H_2 production rate is much higher than that of precious/noble metal (especially Pt)-assisted graphene-based photocatalysts.

Particle size and uniform distribution of Cu_2O–TiO_2 nanocomposites over rGO layer were investigated using TEM analysis, as shown in Fig. 22. As seen from the TEM images, very small and well-dispersed Cu_2O–TiO_2 were anchored tightly onto the surface of rGO layer. The particle size histogram of Cu_2O–TiO_2 demonstrated that the Cu_2O–TiO_2 nanocomposites have a fairly broad size distribution ranging from 13 to 21 nm with a peak centered at ca. 16.1 nm. Besides, the crystalline structure of Cu_2O–TiO_2 is noticed clearly from the TEM micrographs. It is interesting to see from the TEM images that no free Cu_2O–TiO_2 was found in the background, apart from the rGO layer, which confirmed the complete utilization of Cu_2O–TiO_2 nanocomposites.

To study the specific role of individual components such as TiO_2, Cu_2O, and rGO of the as-synthesized photocatalyst under ultrasonication, different photocatalysts were tested under identical condition toward the H_2 evolution, as depicted in Fig. 23. The relative order of photocatalytic activity for water splitting was Cu_2O/rGO (5060 µmol h^{-1} g_{cat}^{-1}) < TiO_2 NPs (7786 µmol h^{-1} g_{cat}^{-1}) < TiO_2/

Fig. 21 Cu_2O–TiO_2/rGO-catalyzed water splitting reaction (Reprinted with permission from Ref. [32]. Copyright 2015 Royal Society of Chemistry)
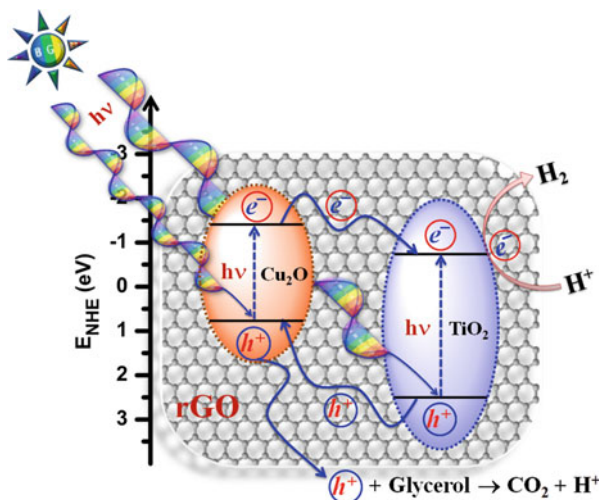
Fig. 22 TEM image of Cu_2O–TiO_2/rGO photocatalyst (Reprinted with permission from Ref. [32]. Copyright 2015 Royal Society of Chemistry)
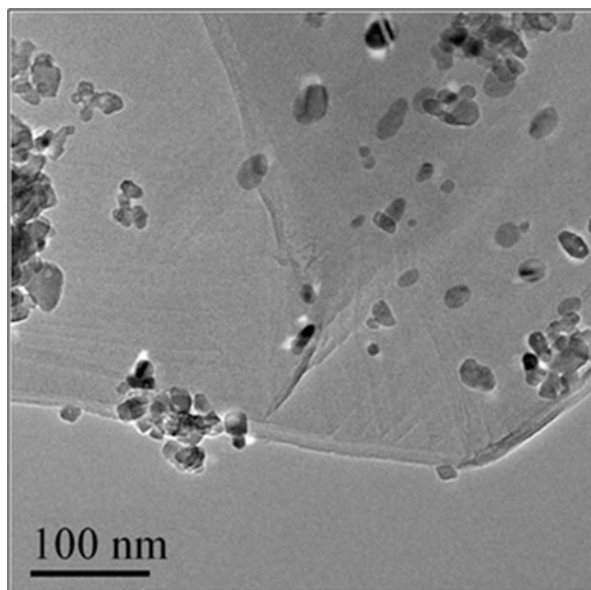
rGO (8226 µmol h^{-1} g_{cat}^{-1}) < Cu_2O–TiO_2 (16656 µmol h^{-1} g_{cat}^{-1}) < Cu_2O–TiO_2/rGO (110968 µmol h^{-1} g_{cat}^{-1}). The photocatalytic activity of the pristine TiO_2 NPs, rGO-loaded TiO_2, and rGO-loaded Cu_2O was insignificant as compared with the Cu_2O–TiO_2/rGO photocatalyst. However, the mixed metal oxide photocatalyst Cu_2O–TiO_2 showed comparable activity to some extent. But the final photocatalyst exhibited an enhanced photoactivity, in terms of highest H_2 production rate. Indeed, the effect of rGO on the photocatalyst activity was phenomenal which
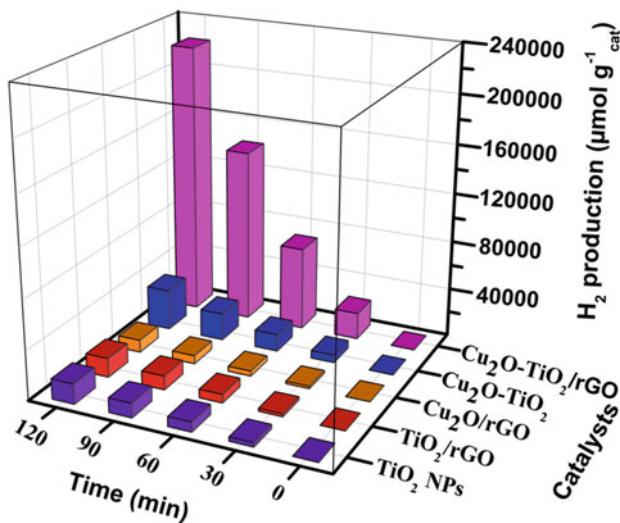
Fig. 23 Splitting of water using different photocatalysts (Reprinted with permission from Ref. [32]. Copyright 2015 Royal Society of Chemistry)

increased the H_2 evolution to approximately 94312 μmol h^{-1} g_{cat}^{-1}, i.e., from 16656 μmol h^{-1} g_{cat}^{-1} (for Cu_2O–TiO_2) to 110968 μmol h^{-1} g_{cat}^{-1} (for Cu_2O–TiO_2/rGO). In comparison with recently reported Cu_2O–TiO_2 photocatalyst which produced 18000 μmol h^{-1} g_{cat}^{-1} of H_2, the present photocatalytic system performed in the presence of Cu_2O–TiO_2/rGO photocatalyst exhibited more than sixfold enhancement.

Sonochemically Synthesized Pd–Cu/Al$_2$O$_3$ Nanocatalyst

The bimetallic Pd–Cu nanocatalysts with different Pd loadings and ultrasonic irradiation times were sonochemically synthesized by Estifaee and co-workers [79]. The authors investigated the catalytic activities of the as-synthesized Pd–Cu/ Al$_2$O$_3$ catalysts toward CO oxidation. The sonochemically synthesized catalysts were characterized with different spectroscopic, microscopic, and analytical characterization techniques such as XRD, FESEM, TEM, BET, FTIR, and TG-DTG. Very interestingly, formation of CuAl$_2$O$_4$ spinel with an average crystallite size of 4.9 nm was confirmed by XRD studies. Increase of ultrasonic irradiation time literally increased the uniform particle size and uniform pattern and also significantly reduced the agglomeration of particles which was strongly evidenced by FESEM images. TEM images also depicted the uniform distribution of active phases over alumina support as in good agreement with FESEM results. Very importantly, increasing Pd loadings do not significantly affect the surface area. However, the discrepancy in ultrasound irradiation time increases the BET surface area slightly as strongly supported by BET analysis. They studied the effect of different mole ratio of Pd and Cu over Al$_2$O$_3$ support for the CO oxidation. Among the catalysts prepared

with different weight percentage ratios of Pd and Cu, and different ultrasonication time, the catalyst Pd(1.5 %)–Cu(20 %)/Al_2O_3 with 95 min ultrasonic irradiation time showed excellent CO oxidation performance over the course of reaction. Authors strongly concluded that ultrasonic irradiation time played a vital role in CO conversion. They prepared different catalysts by varying the ultrasonication time, viz., 45 min, 70 min, and 95 min, and tested their catalytic CO conversion at 150 °C. Besides, increasing CO at feed composition revealed that among the sonochemically synthesized nanocatalysts with 0.5 %, 1 %, and 1.5 % of Pd, the catalyst synthesized with 1.5 % of Pd exhibited the best low-temperature activity.

Syngas Production Over Sonochemically Synthesized Ni/Al_2O_3–MgO Nanocatalyst

Haghighi et al. successfully synthesized Ni/Al_2O_3–MgO nanocatalyst by sonochemical method and used those catalysts for dry reforming of methane to produce syngas (nothing but H_2 and CO) [80]. The microscopic characterization especially the FESEM micrographs clearly revealed that particles of Ni/Al_2O_3–MgO nanocatalyst are in nanometer range and also confirmed the formation of nanocatalysts with uniform crystallite size. Furthermore, the TEM micrographs supported that the ultrasound-assisted preparation induced average Ni particle size of Ni/Al_2O_3–MgO catalyst as small as 21.4 nm with narrow particle size distribution. More significantly, the maximum CO_2 conversion was achieved using this nanocatalyst at higher temperatures ca. 750–800 °C and also proven that H_2/CO ratios were near thermodynamic equilibrium. The CO_2 conversion is 10 % higher than that of CH_4 in the reaction which is performed at the temperature range of 500–800 °C using the sonochemically synthesized Ni/Al_2O_3–MgO nanocatalyst. The CO_2 reforming of methane over Ni/Al_2O_3–MgO nanocatalyst can selectively produce the syngas with H_2/CO ratio of 1 that is near thermodynamic equilibrium which is a major merit of this CO_2 reforming system.

Sonochemically Prepared Supported Ru–Pt Catalyst for H_2 Production via Steam Reforming of Ethanol

Leong et al. reported a new synthetic route for the preparation of alumina (Al_2O_3)-supported ruthenium and ruthenium–platinum nanoparticles which was derived from sonochemical synthesis of organometallic cluster precursors [81]. They also found that the as-synthesized nanocatalyst exhibited highly efficiency for H_2 production via the steam reforming of ethanol. The nanocatalysts derived from organometallic cluster were more active and highly selective than the catalysts which are derived from other metal salts under similar reaction condition. Even the higher loading of metals with salt-derived catalysts is not comparable with the sonochemically synthesized organometallic cluster-derived catalysts. Among the different mole ratios of Ru- and Pt-loaded Al_2O_3 catalysts, the one which prepared with Ru(2.5):Pt(1) is a promising bimetallic cluster-derived catalyst. Very importantly, the present catalysts are highly active which exhibits the potential to outperform a commercial 5 wt.% Ru-loaded Al_2O_3 catalyst. The authors strongly believe that the excellent catalytic performances of these catalysts are owing to their

extremely small particle sizes of the cluster-derived nanoparticles. It was further supported by TEM analyses which evident the size of nanoparticles derived from organometallic nanoclusters that are nanometer size in range. Very importantly, the spent cluster-derived catalysts remained in the same particle size as revealed by the TEM studies. EDX analyses also strongly suggested that the presence of Pt might assist in suppressing coke formation over both cluster- and salt-derived catalysts. The authors also believe that the as-synthesized Ru–Pt bimetallic-loaded Al_2O_3 catalyst can be used in various applications, especially in H_2 production from proton exchange membrane fuel cells (PEMFCs).

Conclusions and Future Directions

A number of physical and chemical effects can be generated by sonochemical processes, which are favorable to the preparation or modification of NPs. The major advantage of sonochemical synthesis is that it required very few chemicals to carry out the process. The physical phenomenon responsible for the sonochemical process is acoustic cavitation. The MNPs prepared by sonochemical methods showed higher surface area and more active sites on the surface. Ultrasound-assisted synthetic route generated nanostructured materials with hierarchical structures, controlled morphologies, and desired composition by simple variations in reaction conditions and precursor compositions. In general sense, nanoparticles prepared by ultrasound-assisted method exhibit higher catalytic performance as compared with the nanoparticles prepared by traditional chemical synthesis. Ultrasound-mediated synthesis always possesses major advantages in preparing prominent catalyst materials. Some of the sonochemical synthetic routes for the synthesis of MNPs and their applications in energy and environmental remediation have been discussed in this chapter. In addition, the significance of simultaneous and sequential sonoreduction processes has been highlighted. In conclusion, sonochemical synthesis technique always played a crucial role in getting well-systematized high-performance materials.

References

1. Suslick KS (1990) Science 247:1439
2. Nieves-Soto M, Hernandez-Calderon OM, Guerrero-Fajardo CA, Sanchez-Castillo MA, Viveros-Garcia T, Contreras-Andrade I (2012) Biodiesel Curr Technol Ultrason Process Realistic Ind Appl. doi:10.5772/52384, InTech, ISBN: 978-953-51-0910-5
3. Richards WT, Loomis AL (1927) J Am Chem Soc 49:3086
4. Wood R, Loomis AL (1927) Phil Mag Ser 4:417
5. Ashokkumar M, Mason TJ (2007) Sonochemistry. Kirk-Othmer Encyclopedia of Chemical Technology. John Wiley & Sons, Inc
6. Ashokkumar M, Sunartio D, Kentish S, Mawson R, Simons L, Vilkhu K, Versteeg C (2008) Innov Food Sci Emerg Technol 9:155
7. Suslick KS (1988) Ultrasound: its chemical, physical and Biological effects, VCH Publishers, New York

8. Bang JH, Han K, Skrabalak SH, Kim H, Suslick KS (2007) J Phys Chem C 111:10959
9. Neppolian B, Celik E, Anpo M, Choi H (2008) Catal Lett 125:183
10. Neppolian B, Haeryong J, Choi H, Lee JH, Kang JW (2002) Water Res 36:4699
11. Neppolian B, Park JS, Choi H (2004) Ultrason Sonochem 11:273
12. Singla R, Grieser F, Ashokkumar M (2004) Res Chem Intermed 30:723
13. Singla R, Grieser F, Ashokkumar M (2009) J Phys Chem A113:2865
14. Vecitis CD, Wang Y, Cheng J, Park H, Mader B, Hoffmann MR (2010) Environ Sci Technol 44:432
15. Vinoth R, Babu SG, Bahnemann D, Neppolian B (2015) Sci Adv Mater 7:1443
16. Yang L, Sostaric JZ, Rathman JF, Weavers LK (2008) J Phys Chem B 112:852
17. Yang L, Rathman JF, Weavers LK (2005) J Phys Chem B 110:18385
18. Zhang GM, Zhang PY, Yang JM, Chen YM (2007) J Hazard Mater 145:515
19. Lim M, Son Y, Park B, Khim J (2010) Japan J Appl Phys 49:07HE06
20. Gultekin I, Tezcanli-Guyer G, Ince NH (2009) J Adv Oxid Technol 12:105
21. Hamdaoui O, Naffrechoux E (2008) Ultrson Sonochem 15:981
22. Guo ZB, Zheng Z, Zheng SR, Hu WY, Feng R (2005) Ultrason Sonochem 12:461
23. Little C, Hepher MJ, El-Sharif M (2002) Ultrasonics 40:667
24. Kim JK, Martinez F, Metcalfe IS (2007) Catal Today 124:224
25. Suh WH, Jang AR, Suh YH, Suslick KS (2006) Adv Mater 18:1832
26. Xu H, Zeiger BW, Suslick KS (2013) Chem Soc Rev 42:2555
27. Upadhyay K, Khandate G (2012) Univ J Environ Res Technol 2:458
28. Babu SG, Vinoth R, Neppolian B, Dionysiou DD, Ashokkumar M (2015) J Hazard Mater 291:83
29. Antonnikova A, Korovina N, Kudryashova O (2013) Open J Acoust 3:16
30. Rokhina EV, Lens P, Virkutyte J (2009) Trend Biotechnol 27:298
31. Baysal T, Demirdoven A (2012) Handbook on applications of ultrasound: sonochemistry for sustainability. CRC Press, Taylor & Francis Group, pp 163–182
32. Babu SG, Vinoth R, Kumar DP, Shankar MV, Chou HL, Vinodgopal K, Neppolian B (2015) Nanoscale 7:7849
33. Peters D (1996) J Mater Chem 6:1605
34. Mason TJ (1997) Chem Soc Rev 26:443
35. Davies LA, Dargue A, Dean JR, Deary ME (2015) Ultrason Sonochem 23:424
36. Xu L, Ding YS, Chen CH, Zhao L, Rimkus C, Joesten R, Suib SL (2008) Chem Mater 20:308
37. Morel AL, Nikitenko SI, Gionnet K, Wattiaux A, Him JLK, Labrugere C, Chevalier B, Deleris G, Petibois C, Brisson A, Simonoff M (2008) ACS Nano 2:847
38. Aslani A, Morsali A (2009) Inorg Chim Acta 362:5012
39. Adewuyi YG (2005) Environ Sci Technol 39:3409
40. Vinodgopal K, Neppolian B, Lightcap IV, Grieser F, Ashokkumar M, Kamat PV (2010) J Phys Chem Lett 1:1987
41. Prasad K, Pinjari DV, Pandit AB, Mhaske ST (2010) Ultrason Sonochem 17:409
42. Bellissent R, Galli G, Hyeon T, Magazu S, Majolino D, Migliardo P, Suslick KS (1995) Phys Scr T57:79
43. Suslick KS, Hyeon T, Fang M (1996) Chem Mater 8:2172
44. Mdleleni MM, Hyeon T, Suslick KS (1998) J Am Chem Soc 120:6189
45. Shanmugam S, Gabashvili A, Jacob DS, Yu JC, Gedanken A (2006) Chem Mater 18:2275
46. Yu JC, Zhang L, Yu J (2002) Chem Mater 14:4647
47. Shang M, Wang W, Zhou L, Sun S, Yin W (2009) J Hazard Mater 172:338
48. Shirsath SR, Pinjari DV, Gogate PR, Sonawane SH, Pandit AB (2013) Ultrason Sonochem 20:277
49. Wu Q, Ouyang J, Xie K, Sun L, Wang M, Lin C (2012) J Hazard Mater 199–200:410
50. Neppolian B, Wang C, Ashokkumar M (2014) Ultrason Sonochem 21:1948
51. Anandan S, Grieser F, Ashokkumar M (2008) J Phys Chem C 112:15102
52. Kuroda K, Ishida T, Haruta M (2009) J Mol Catal A Chem 298:7

53. Neppolian B, Bruno A, Bianchi CL, Ashokkumar M (2012) Ultrason Sonochem 19:9
54. Bandala ER, Pelaez MA, Salgado MJ, Torres L (2008) J Hazard Mater 151:578
55. Lea J, Adesina AA (1998) J Photochem Photobiol A Chem 118:111
56. Yang L, Rathman JF, Weavers LK (2006) J Phys Chem B 110:18385
57. Neppolian B, Choi HC, Sakthivel S, Arabindoo B, Murugesan V (2002) J Hazard Mater 89:303
58. Anandan S, Sivasankar T, Lana-Villarreal T (2014) Ultrason Sonochem 21:1964
59. Li Y, Chen L, Guo Y, Sun X, Wei Y (2012) Chem Eng 181–182:734
60. Shifu C, Lei C, Shen G, Gengyu C (2005) Powder Technol 160:198
61. Tada H, Kokrubu A, Iwasaki M, Ito S (2004) Langmuir 20:4665
62. Chai SY, Kim YJ, Lee WI (2006) J Electroceram 17:909
63. Yang XL, Dai WL, Guo C, Chen H, Cao Y, Li H, He H, Fan K (2005) J Catal 234:438
64. Kumar PS, Selvakumar M, Babu SG, Karuthapandian S, Chattopadhyay S (2015) Mater Lett 151:45
65. Gopiraman M, Babu SG, Khatri Z, Kim BS, Wei K, Karvembu R, Kim IS (2015) React Kinet Mech Catal 115:759
66. Karthik P, Vinoth R, Babu SG, Wen M, Kamegawa T, Yamashita H, Neppolian B (2015) RSC Adv 5:39752
67. Kumar PS, Selvakumar M, Babu SG, Jaganathan S, Karuthapandian S (2015) RSC Adv 5:57493
68. Babu SG, Athira SV, Neppolian B (2015) Mater Focus 4:272
69. Babu SG, Narayana PS, Bahnemann D, Neppolian B (2015) APL Mater 3:104415
70. Liu B, Wen L, Zhang H, Zhao X (2012) J Am Ceram Soc 95:3346
71. Anandan S, Ashokkumar M (2009) Ultrason Sonochem 16:316
72. Yeung SA, Hobson R, Biggs S, Grieser F (1993) J Chem Soc Chem Comm 378
73. Xu JZ, Zhao WB, Zhu JJ, Li GX, Chen HY (2005) J Colloid Interface Sci 290:450
74. Vinodgopal K, Ashokkumar M, Grieser F (2001) J Phys Chem B 105:3338
75. Pelizzetti E, Minero C, Maurino V, Sclafani A, Hidaka H, Sepone N (1989) Environ Sci Technol 23:1360
76. Brand N, Mailhot G, Bolte M (1998) Environ Sci Technol 32:2715
77. Neppolian B, Saez V, Gonzalez-Garcia J, Grieser F, Gomez R, Ashokkumar M (2014) J Solid State Electrochem 18:3163
78. Vafaeian Y, Haghighi M, Aghamohammadi S (2013) Energy Convers Manag 76:1093
79. Estifaee P, Haghighi M, Mohammadi N, Rahmani F (2014) Ultrason Sonochem 21:1155
80. Abdollahifar M, Haghighi M, Babaluo AA (2014) J Ind Eng Chem 20:1845
81. Koh ACW, Leong WK, Chen L, Ang TP, Lin J, Johnson BFG, Khimyak T (2008) Catal Commun 9:170

Synthesis of Inorganic, Polymer, and Hybrid Nanoparticles Using Ultrasound

S. Shaik, S. H. Sonawane, S. S. Barkade, and Bharat Bhanvase

Contents

S. Shaik • S.H. Sonawane (✉)
Department of Chemical Engineering, National Institute of Technology, Warangal, Telangana, India
e-mail: shabana89.chem@gmail.com; shirishsonawane@rediffmail.com;
shirishsonawane09@gmail.com; shirish@nitw.ac.in

S.S. Barkade
Department of Chemical Engineering, Sinhgad College of Engineering, Pune, India
e-mail: shrikantbarkade09@gmail.com

B. Bhanvase
Department of Chemical Engineering, Laxminarayan Institute of Technology, Rashtrasant Tukadoji
Maharaj Nagpur University, Nagpur, Maharashtra, India
e-mail: bharatbhanvase@gmail.com

Abstract

In this chapter, an attempt has been made to explain the role of ultrasonication in the synthesis of pure nanoparticles and nanoparticle-loaded polymers (i.e., hybrid). Ultrasound acts as an opportune method to synthesize metal, metal oxide nanoparticles, and hybrids with unique properties which are highly desirable for many applications. Extraordinary conditions such as temperature, pressure, heating, and cooling rates during the acoustic cavitation provide access to the range of chemical reaction conditions. These conditions generate the nanoparticles/hybrids with extremely large surface-to-volume ratio and specific surface area due to non-equilibrium conditions of cavitation interface. In this present chapter, new developments in ultrasound-assisted synthesis of inorganic nanomaterials and polymer-based hybrids had been discussed. In this chapter, the use of ultrasound atomization process for the production of the nanomaterials which are used in solar cells and electronics application was also discussed. The chapter also reports about the formation of the pigment dispersion which was an energy-intensive process when compared to planetary ball milling. Finally, the comparison of the acoustic cavitation and hydrodynamic cavitation was reported for nano-calcite production.

Keywords

Ultrasound • Nanoparticles • Ultrasound-assisted miniemulsion • Hybrid particles • Sonochemical processing • Nanostructures

Introduction

Sonochemistry is a branch of science that deals with the chemical and mechanical effects of ultrasound [1]. Ultrasound is an inaudible sound and its frequency of pressure oscillation is above 20 kHz [2]. The use of ultrasound in the form of irradiation had become increasingly popular during the last one-and-a-half decade for the synthesis of nanoparticles and hybrid materials. For the synthesis of nanoparticles and hybrid materials, the ultrasound irradiation appears to be more general than other activation techniques (e.g., microwaves, photochemistry, or high pressure) as the system requires essentially an ultrasound source and a liquid (either aqueous or organic). Ultrasound-assisted preparation methodology is the most

reliable and efficient preparative technique, primarily owing to its ability to concentrate the acoustic energy in a smaller volume [3]. The implosion of cavitation microbubbles results in the formation of millions of short-lived bubbles that had an extreme temperature and pressure conditions. Ultrasound helps in the formation of various morphologies of nanomaterials such as nanowires and nanospheres. A proper selection of ultrasonic irradiation parameters yields the satisfactory formation of nanomaterials [4].

Literature Review on Mechanism of Formation of Inorganic Nanoparticles and Hybrids Using Ultrasound

Firstly, Suslick and his coworkers successfully produced amorphous iron metal and colloidal iron nanoparticles within the size ranging from 10 to 20 nm by treating a nonaqueous solution of $Fe(CO)_5$ in the presence of ultrasound [5]. Cavitation effect induced by ultrasound waves imparts a distinctive molecular level interaction between energy and chemical species via the generation of millions of short-lived, localized bubbles which has corresponding temperatures in the region of 5000 K, pressures of about 1000 bar, and heating and cooling rates above 10^{10} K/s during the inertial bubble collapse phase. These intense conditions can result in very high-concentrated energy to accelerate and augment the chemical reactions that are usually not viable to be achieved by the traditional methods for the synthesis of wide range of unusual nanomaterials [6]. The violent and implosive collapse provides disruptive forces, liquid microjets, and shock waves outside the microbubbles, which considerably increase the mass transport. Further improved chemical reaction rates and decrease in the diffusion layer thickness are the additional benefits derived from the ultrasound. In addition, the generation of free radicals by the dissociation of water, penetration of solute, and reacting molecules reaches to active sites of catalyst surface due to microjets [7].

Ultrasound has been used for the generation of inorganic nanomaterials like silica and ceramic/oxide by sinking the micron-sized particles into nanosize. The use of ultrasound for the preparation of various nanostructured materials has become an important technique due to its advantages such as easy control of particle size at nanometer regime, monodisperse characteristics of particles, simple equipment and mild operating conditions, and ability to generate crystalline materials in many cases [8]. Pal et al. [9] reported the preparation of ZnO nanoparticles via an ultrasound-assisted method by using zinc (II) acetate dihydrate mixed in *N,N*- dimethylformamide and deionized water. The solution was sonicated at 150 and 300 W of dissipated power under Ar flow for 3 h; a white colloidal solution was obtained. This solution was carried out for centrifugation and washed with ethanol for several times. With the variation of ultrasound power, the average pore sizes of ZnO nanoparticles has been changed from 2.5 to 14.3 nm along with changes in the morphology [9].

In the current scenario, miniemulsion polymerization is a widely used method for the generation of smaller-size nanoparticles. Nanoparticles with higher surface area

were used for loading onto polymers as functional attachments [9]. Recently, ultrasound was used for miniemulsion polymerization [10]. For the formation of stable monomer droplets, ultrasound was one of most outstanding methods and it also avoids the aggregation and adhesion of polymer onto reactor wall during the suspension and emulsion polymerization process [11]. Physical effects and chemical effects are key parameters for the sonochemical reactions. In ultrasound-assisted emulsion process, very fine and stable uniform monomer droplets are normally formed at or near the interface of immiscible oil phase. These cavitation microjets assist in moving the radicals to the surface of micelle [12]. Several research groups have applied ultrasound technique for emulsion polymerization of various monomers such as styrene, aniline, methyl methacrylate, and butyl acrylate [13–16]. Ultrasound-assisted emulsion polymerization has several advantages over the conventional emulsion polymerization.

Ultrasound-Assisted Synthesis of Inorganic Nanomaterials

Ultrasound-Assisted Synthesis of TiO_2 Nanoparticles

The use of nanomaterials in this modern era has rapidly increased to fulfill the needs of the demands with special properties. The synthesis of nanomaterials had been started in the nineteenth century; Faraday synthesized gold nanoparticles in colloidal suspension in a fluid-like water [17]. Jing et al. [18] synthesized carbon-deposited TiO_2 nanoparticles by one pot hydrothermal method by using glucose and $TiCl_4$ solutions. The hydrolysis of $TiCl_4$ gives a high acidic condition for TiO_2 crystallite formation.

Sonawane et al. [19] synthesized TiO_2 using a sonochemical approach by using an ultrasound probe technique, taking titanium isopropoxide in 2-propanol as a main precursor and cerium nitrate as a reducing agent and sonicated by maintaining a constant temperature. Cerium nitrate solution and NaOH solution were added to the main precursor at equal interval of time. Thus, formed solution was kept undisturbed to settle the precipitate; later, the precipitate undergoes the following processes like centrifuge, filtration, drying, and calcinations at 450 °C temperature for about 3 h. Similar procedure was adopted for the synthesis of Fe-doped TiO_2, Ce-doped TiO_2 catalyst prepared by this process, exhibiting higher photocatalytic activity.

The X-ray diffraction (XRD) analysis (Fig. 1) was used to find out the presence of the compound and to know the phase structure of the compound. The XRD patterns of the TiO_2 show the main peak at 2Θ value of 25°, 38°, 47°, 55°, and 61° and hence conform that it was in crystalline form and it was of TiO_2. The XRD patterns of Fe-doped TiO_2 show its major peaks at 2Θ values of 25°, 36°, 48°, 54°, and 62°, representing anatase phase, which indicates that the doping of TiO_2 with metal ions does not affect the crystalline structure of the particle. Similarly, Ce-doped TiO_2 has its major peaks at 25°, 37°, 47°, 54°, and 62° of 2Θ values representing anatase phase and they are compared with JCPDS 21–1272 having crystalline plain values of (101), (004), (200), (211), and (204). The Fourier transform infrared spectroscopy
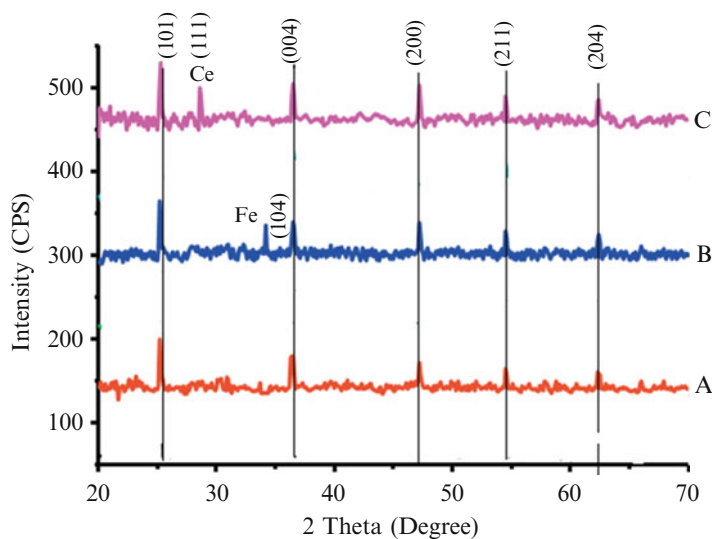
Fig. 1 XRD patterns of TiO_2 [A], Fe-doped TiO_2 [B] and Ce-doped TiO_2 [C] (Reprinted with permission from [20]. Copyright 2013 Elsevier)
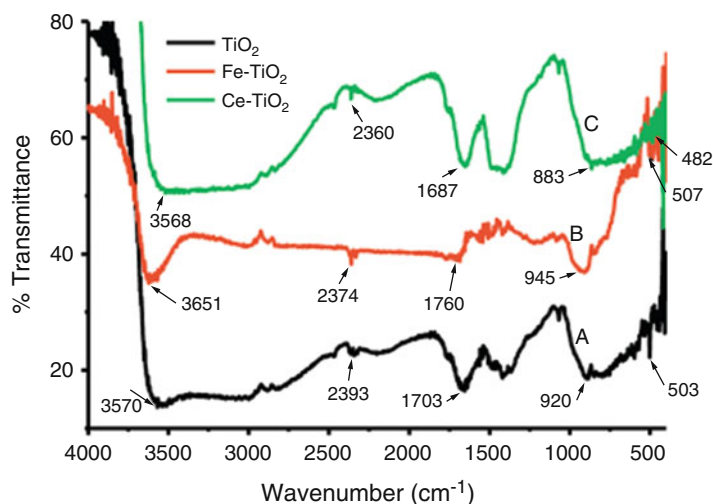
Fig. 2 FTIR spectras of TiO_2[A], Fe doped TiO_2 [B] and Ce doped TiO_2 [C] (Reprinted with permission from [20]. Copyright 2013 Elsevier)

(FTIR) spectra of TiO_2, Fe-doped TiO_2, and Ce-doped TiO_2 are shown in Fig. 2. The spectra in the range of 3420–3540 cm^{-1} show the stretching vibrations of amine bonds, whereas 1630–1640 cm^{-1} indicates the bending vibrations of hydroxyl group. The spectra in the range of 500–900 cm^{-1} indicate the presence of TiO_2.
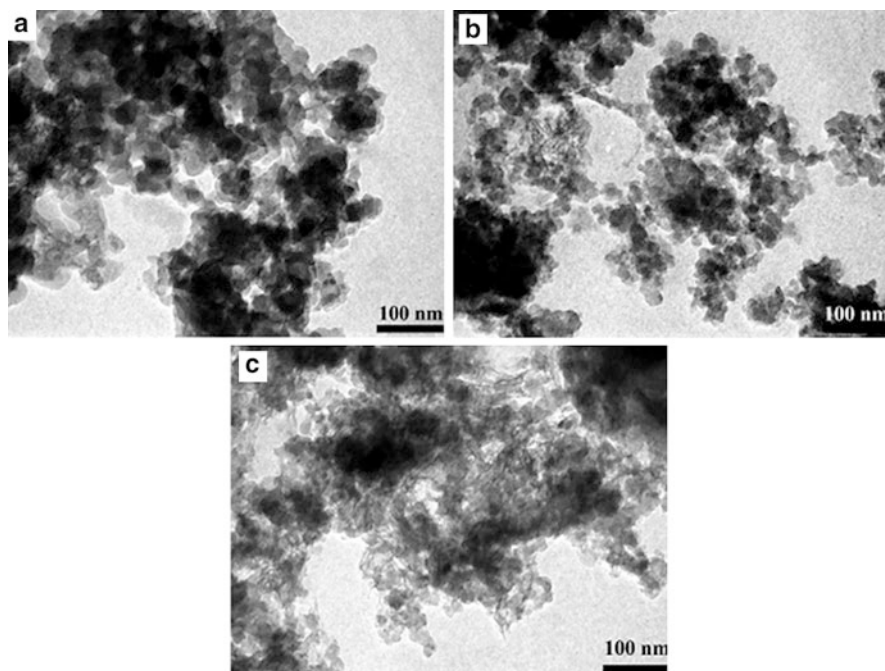
Fig. 3 TEM images of (**a**) pure TiO_2, (**b**) Fe-doped TiO_2, and (**c**) Ce-doped TiO_2 (Reprinted with permission from [20]. Copyright 2013 Elsevier)

Figure 3 illustrates the transmission electron microscopic (TEM) images of TiO_2[A], Fe-doped TiO_2[B], and Ce-doped TiO_2[C], and it shows the spherical nature of the nanoparticles. The average size of the particle was found to be in the range of 10–50 nm, and the individual particles agglomerated to form second larger particles. The particle sizes of the doped particles are a little larger than the undoped particles.

$CaCO_3$ Nanoparticles Synthesis by Ultrasonication

Calcium carbonate can be obtained in three forms: as calcite, aragonite, and vaterite, in which calcite was one of the prominent forms and can be used in pigments, fillers in plastics, rubber, paper, and paints. Calcite produced by the carbonation of calcium hydroxide finds application in lubricants, textiles, adhesives, waste water treatments, ink, ceramic materials, etc. It is also used as a building material and as a raw material in cement industries.

Romuald et al. [21] synthesized $CaCO_3$ nanoparticles by controlled precipitation method using Na_2CO_3 and $Ca(NO_3)_2$ solutions as precursors. The sodium carbonate was dissolved in sodium hydroxide and sodium nitrate solution. Later, the calcium nitrate solution was added to the above solution drop by drop with

continuous stirring at a constant speed for a set time by maintaining constant temperature. The solution was kept aside undisturbed to precipitate, and it was filtered and dried at room temperature. The effects of agitation rate, mixing time, and temperature were studied. Ghadami et al. [22] synthesized $CaCO_3$ nanoparticles by a reverse microemulsion technique with different surfactant at different concentrations. $CaCl_2$ and Na_2CO_3 were used in the synthesis of $CaCO_3$ nanoparticles. The precursor's solutions were prepared by mixing surfactant and toluene in reverse microemulsion method using stirring at room temperature. Microemulsion solutions were prepared by mixing two surfactants in a solvent by using any external force. Slowly, the prepared calcium chloride solution was added to the above mixture and continued with the stirring and processed for 12 h till emulsion was formed. A single phase calcite was formed and conformed from FTIR spectra shown at 712,881 cm^{-1}. Sargheini et al. [23] synthesized a simple one-step facile mechanochemical route for $CaCO_3$ synthesis using $CaCl_2$ and Na_2CO_3 as precursors without any subsequent heat treatment. The raw materials were finely grinded in planetary ball mill and attrition mill. The particles grow through nanosizes of particles 60–90 nm. Indeed, the surface area of the particles was 19 m^{2}g^{-1} analyzed from BET analysis. Shirsath et al. [24] prepared $CaCO_3$ by precipitation method by using continuous-stirred tank reactor along with sonication method. Sonawane et al. [24] prepared nano-calcite by using CO_2 gas as a carbonizing agent of $Ca(OH)_2$ under ultrasonication technique. The comparison between both the process with and without sonication was studied.

Calcium hydroxide and carbon dioxide are used as the precursors in the preparation of desired concentration of $Ca(OH)_2$, and it was well mixed under a magnetic stirrer at 500 rpm for 15 min. Then, the CO_2 gas was introduced through a sparger at the bottom of the tank. The inlet was fed continuously to the tank simultaneously; the outlet is withdrawn, and the pH and the conductivity of the reaction was measured [25, 26]. As the pH of the reaction mixture reaches seven, then the reaction is terminated. Different parameters like $Ca(OH)_2$ slurry concentration, flow rate on particle size, and morphology were studied at continuous mode (Fig. 4). The same concentrations of 1.96–5.66 wt% was carried out on both ultrasonication and conventional method by maintaining at the constant volumetric flow rate of 20 mL/min and gas flow rate of 45 L/h. The comparison morphology obtained from both processes was studied and shown in Fig. 5 and Table 1, and the XRD patterns have been shown in Fig. 6.

The SEM images of Fig. 5 were taken with different concentrations of $Ca(OH)_2$ slurry in both the methods with and without sonication. From the figure, it was observed that the shapes of the particles are rhombohedral in both cases. The particle size of calcite was decreased with an increase in concentration of calcium hydroxide in a sonication method. In conventional methods (stirring/without sonication), the particle size was decreased to an extent, and then there was an increase in size. When compared to sonicated and conventional methods, the particle size was less in the sonication method and it is clearly shown in Table 1. The X-ray patterns are shown in Fig. 6. These patterns are used to investigate the phase structures of the calcite nanoparticles. Both sonicated and conventional methods showed the major peak at
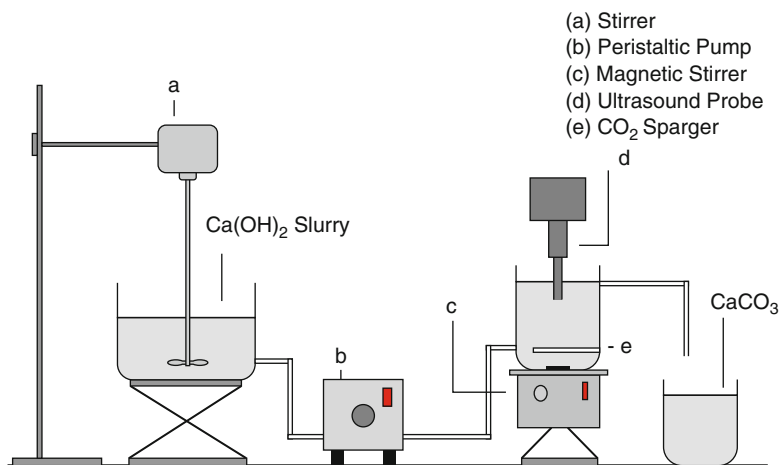
Fig. 4 Schematic diagram of continuous production of nano-calcite (Reprinted with permission from [24]. Copyright 2014 Elsevier)
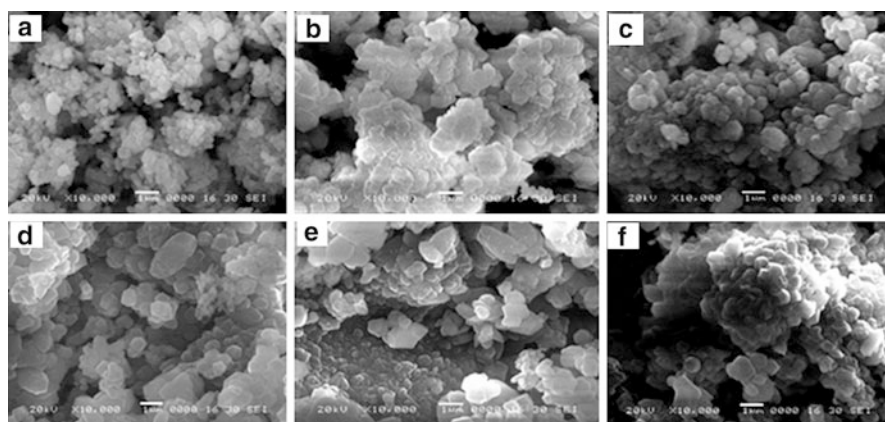
Fig. 5 SEM images of $CaCO_3$ particles with different $Ca(OH)_2$ slurry concentration with and without sonication. (**a**) 2.92 wt% (**b**) 3.85 wt% (**c**) 4.76 wt% with ultrasonication and (**d**) 2.92 wt% (**e**) 3.85 wt% (**f**) 4.76 wt% without sonication (Reprinted with permission from [24]. Copyright 2014 Elsevier)

$30°$ range of 2θ value. The other peaks at $23°$, $29°$, $43°$, $47°$, $48°$, $57°$, $60°$, and $64°$ and shows the calcite phase $CaCO_3$ formed during carbonization [27, 28].

Sonawane et al. also synthesized nano-calcite using sonochemical carbonization [29]. In this chapter, it is shown that the ultrasound creates a supersaturation of Ca^{2+} ions in the synthesis, leading to a rapid nucleation of $CaCO_3$ and improving the solute transfer rate. An innovative arrangement has been used for passing the gas through the ultrasound probe instead of the separate sparger tube which is described

Table 1 Tabulation of particle size with respect to change in different parameters (Reprinted with permission from [24]. Copyright 2014 Elsevier)

Parameter	Particle size (nm)	
	Stirring	Ultrasound
Slurry connection (wt %)		
1.96	1314	1018
2.92	1157	744
3.85	601	371
4.76	967	366
5.66	1151	858
CO₂ flow rate (L/h)		
35	575	132
45	601	371
55	521	373
Slurry flow rate (mL/min)		
12	971	685
16	691	423
20	601	371
24	577	244
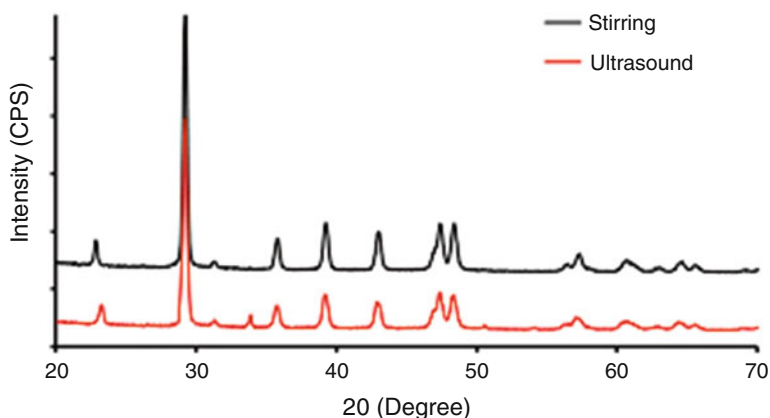
Fig. 6 XRD pattern of CaCO₃ particles with sonication and without sonication (stirring) (Reprinted with permission from [24]. Copyright 2014 Elsevier)

in the above paragraph. The XRD patterns of synthesized nano-calcite prepared by carbonization technique are shown in Fig. 7 for different processes with and without sonication. The major peaks were observed at 30°, 24°, 39°, 36°, 43°, 56°, and 58° having plane structure along (0 1 0) for all except 14 and 20 mm diameter probe with holes. The plane structure for both cases falls along (1 1 9).

From Fig. 8, it can be observed that the power change plays a vital role in the size of the particle via sonication technique. As the probe size increases, the power dissipation increases in liquids; therefore, the particle size is reduced. Due to its

Fig. 7 XRD patterns of nano-calcite crystals by carbonization method at different conditions. *A.* Without ultrasound *B* 10 mm probe without hole *C* 10 mm probe with hole *D* 14 mm probe without hole *E* 14 mm probe with hole *F* 20 mm probe without hole *G* 20 mm probe with hole (Reprinted with permission from [29]. Copyright 2008 Elsevier)
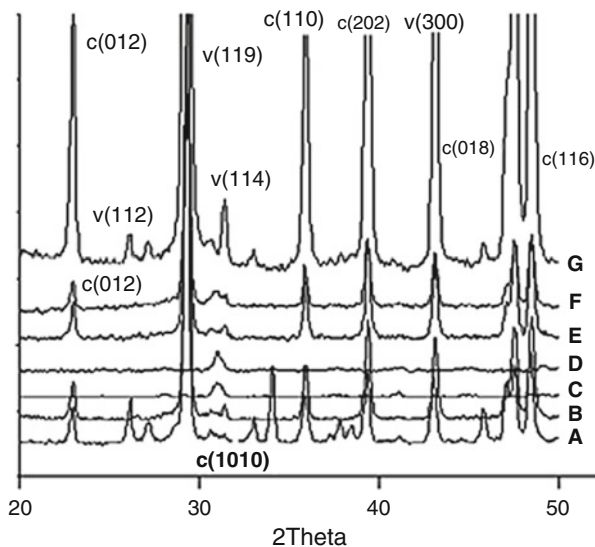
increased surface area, the probe with holes gives more power dissipation when compared to a normal flat probe. The effect of different parameters was tabulated in Table 2 for the reaction carried out on sonication with holes, without holes, and without sonication. When CO_2 gas was passed through the probe hole, the particle size has reduced gradually. The crystal size was also changed with the injection of CO_2 gas in the probe. The particle size and other parameters differ with sonication and without sonication.

Sonawane et al. [30] studied the effect of different surfactants such as polyacrylic acid, steric acid, sodium tripolyphosphate, and myristic acid on the synthesis of nano-$CaCO_3$. The use of ultrasound during synthesis of nanoparticles leads to an arrow distribution of particles. The minimum particle size was obtained for sodium tripolyphosphate as compared to other surfactants. The major peak was observed at 29° and it was the largest for the myristic acid because of its hydrophobic nature. The preferred orientation of nano-$CaCO_3$ was found at (1 0 1 0) plane for all the surfactants. The addition of sodium tripolyphosphate leads to increase in the rate of precipitation of calcite. The rate of the reaction is generally monitored with the use of pH and conductivity measurement. The rate of precipitation of carbonates using sodium tripolyphosphate, myristic acid, steric acid, and polyacrylic acid was 0.226, 0.222, 0.158, and 0.115, respectively. The pH effect with time was recorded for different surfactants, but at the initial stage, it was constant for all the surfactants, whereas it is independent of ion transfer rate. Surfactants reduce the agglomeration during nucleation process by reducing surface tension and nullifying the charges of the particles. Ultrasound and surfactants reduced the population of nuclei; hence, the reduction of particles took place. The ultrasound and the surfactants both act as active agents in reducing the particle size [31, 32].

Fig. 8 Particle size distribution of nano-calcite prepared by sonochemical carbonization technique (Reprinted with permission from [29]. Copyright 2008 Elsevier)
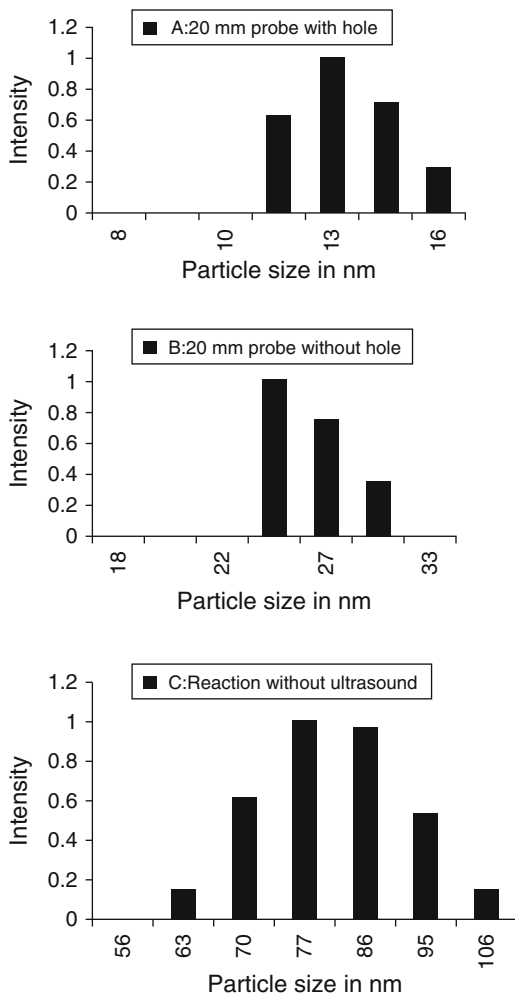
Ultrasound-Assisted Synthesis of Zinc Oxide Nanoparticles

Barkade et al. used ultrasound-assisted precipitation for the synthesis of ZnO nanoparticles [33]. The reaction between zinc sulfate heptahydrate and ammonia was carried out in the presence of an ultrasonic probe (750 W, 22 kHz, Sonics and Materials, USA) at 40 % amplitude. The total time for completion of the reaction was 28 min with the formation of milky precipitate. At the end, the solution had been centrifuged and then calcined at 400 °C in air to obtain the ZnO nanoparticles. Figure 9 showed the XRD pattern of the zinc oxide nanoparticles. The sharp nature of diffraction peak indicated the crystalline nature of ZnO nanoparticles. The ZnO nanoparticle's size calculated by using Scherrer's formula was found to be 90 nm. TEM image of ZnO indicated the average size of about 80–100 nm in Fig. 10.

Table 2 Effects of different parameters during synthesis of nano-calcite by carbonization method through sonication technique (Reprinted with permission from [29]. Copyright 2008 Elsevier)

Probe diameter	Description	Total power dissipated into the reactor (W/m^3)	Crystallite size in nm	Particle size distribution (nm)	Induction time (min)
20	With hole	18.5×10^3	35	11–16	20
20	Without hole	12.5×10^3	51	24–29	30
14	With hole	11.6×10^3	38	26–37	32
14	Without hole	8.9×10^3	53	50–77	35
10	With hole	9.3×10^3	48	41–70	40
10	Without hole	5.0×10^3	60	69–106	60
No probe used	Reaction without ultrasound	–	104	62–117	110
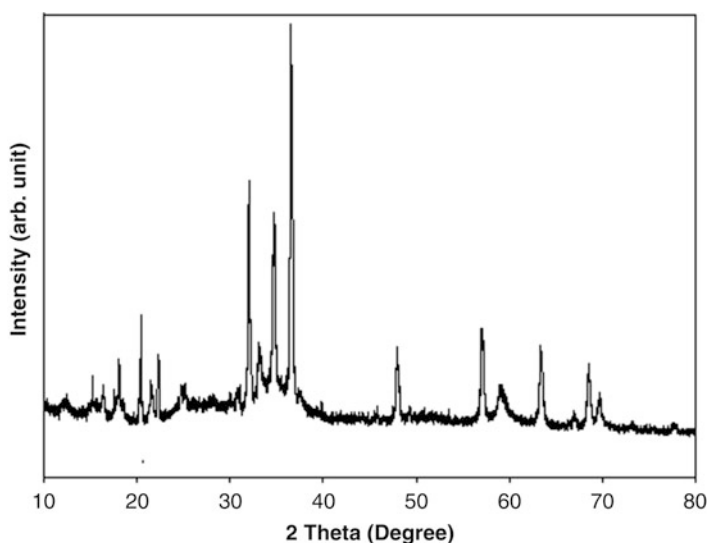
Fig. 9 X-ray of nanosized ZnO particles (Reprinted with permission from [33]. Copyright 2013American Chemical Society)

Ultrasound-Assisted Synthesis of SnO$_2$ Nanoparticles

Barkade et al. synthesized tin oxide nanoparticles by the combination of tin tetra-chloride and urea solutions (ratio 1:2) using an ultrasonic horn with an operating frequency of 22 kHz and rated output power of 750 W [34]. The system was operated with 50 % amplitude with energy dissipation rate as 375 W. The final white precipitate was separated by centrifugation, washed with distilled water for
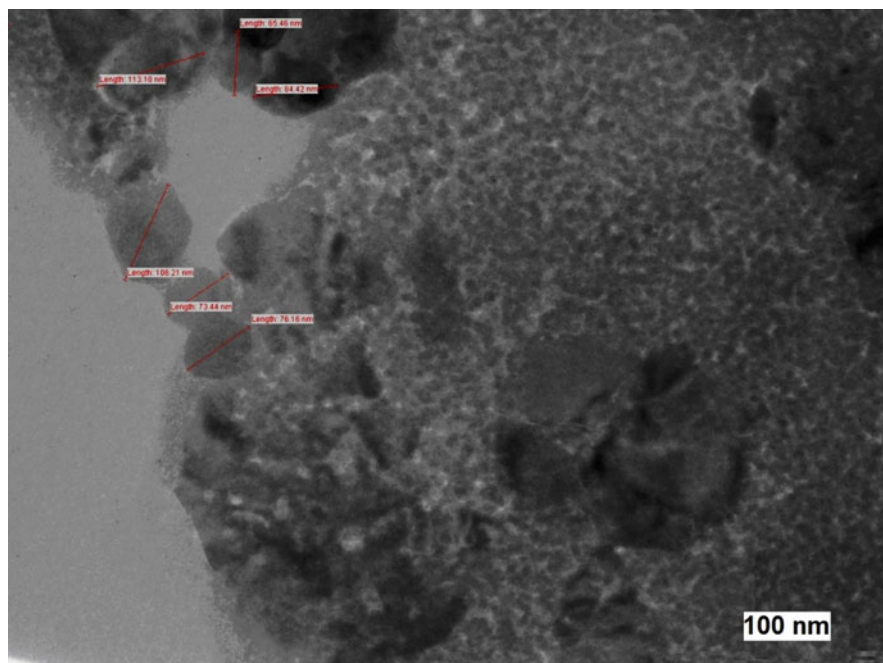
Fig. 10 TEM of ZnO prepared via ultrasound-assisted precipitation method (Reprinted with permission from [33]. Copyright 2013 American Chemical Society)

several times, and dried in an oven at 90 °C. Figure 11 shows the XRD pattern of the SnO_2 nanoparticles. XRD diffractogram match well with the standard SnO_2 tetragonal rutile structure (JCPDS:41–1445). The morphology of SnO_2 nanoparticles was shown in the TEM image (Fig. 12) with the diameter of 15–20 nm.

Sonochemical Preparation of Hybrid Nanomaterials

Hybrid nanomaterials are the composites consisting of two constituents at the nanolevel in which one compound may be organic and the other may be inorganic in nature. They can be classified based on the possible interactions connecting between the organic and inorganic materials. The term hybrid nanomaterials was used if the inorganic particles are formed in situ by molecular precursors. Composites that consist of inorganic hybrid nanomaterials in polymers are recently considered more due to the increase in its mechanical, thermal, biological, magnetic, optical, and optoelectronic properties [31]. In the following section, various hybrid nanocomposites are discussed. The metal oxide-incorporated poly (butylmethacrylate) latex can be used as a photoanode for the conversion of solar energy and polyaniline. $CaCO_3$ nanocomposite can be used for anticorrosion purposes for the mild substrate.
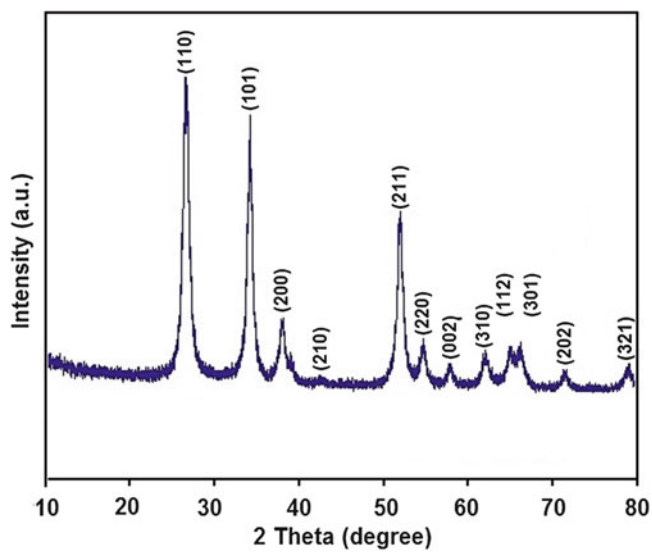
Fig. 11 X-ray diffraction of SnO_2 nanoparticles (Reprinted with permission from [34]. Copyright 2013 Elsevier)

Fig. 12 TEM image of SnO_2 nanoparticles (Reprinted with permission from [34]. Copyright 2013 Elsevier)
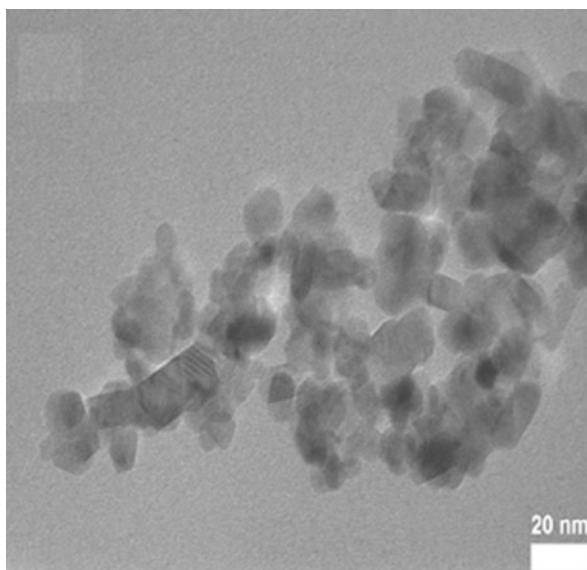
Preparation of Metal Oxide-Incorporated Poly(Butylmethacrylate) Latex by Miniemulsion Polymerization

Metal and metal oxide-loaded conducting polymers are used as photoanodes for the conversion of solar energy. There are two ways for the production of photoanode thin films. Metal oxides are deposited on a conducting glass at very high temperatures using chemical vapor deposition/electrochemical deposition method or semiconductor incorporating in conducting materials. The sonochemically synthesized semiconductor particle-loaded polymer matrix-produced photocurrent increases with an increase in loading percentage [35].

Sonawane et al. [35] used semiconductors in incorporating conducting polymers, such as polyaniline/polypyrrole/porphyrin, which were coated onto the nonconducting transparent matrix such as poly(methylmethacrylate) and polyethylene terephthalate. Different oxide semiconductors, such as TiO_2, ZnO, and Bi_2O_3/$ZrTiO_4$, were incorporated into poly(butylmethacrylate) latex particles via sonochemical polymerization method. Initially, butyl methacrylate and surface-modified oxide were mixed thoroughly and added into the ultrasonic reactor. The water-containing sodium dodecyl sulfate added to the reaction mixture and the entire solution was thoroughly deoxygenated by bubbling with argon for 45 min at room temperature. Inert argon gas was passed over the reaction mixture to avoid oxygen diffusion into the solution during the polymerization reaction. The liquid mixture was then subjected to sonication for carrying out the polymerization reaction. The reaction was said to be completed within less than 40 min. During the synthesis of latex, a small quantity of polyaniline was added for the transport of charge carriers.

TEM analysis revealed the particle sizes (Fig. 13a–c) of TiO_2, ZnO, and Bi_2O_3/$ZrTiO_4$ embedded into PBMA latex were found to be 21, 15, and 7 nm, respectively [35]. Fringes were also observed on the particles in the case of Bi_2O_3/$ZrTiO_4$ (Fig. 13d), which indicates that the semiconductor nanocomposite oxides synthesized using ultrasound-assisted methods are crystalline in nature. The reported cryo-TEM images in Fig. 14a and b showed that the nanosized TiO_2 and ZnO particles are incorporated into the polymer latex, respectively [35].

Synthesis of Polyaniline/CaCO₃ Nanocomposite via Semi-Batch Emulsion Polymerization Using Ultrasound Technique

Bhanvase and Sonawane [36] have carried out the synthesis of polyaniline/$CaCO_3$ nanocomposites by semi-batch in situ emulsion polymerization via indirect ultrasound technique (ultrasonication in bath). Distilled aniline acts as a monomer, ammonium persulfate as an initiator, and sodium lauryl sulfate as a surfactant. The course of reaction was in semi-batch mode (continuous addition of aniline during the course of reaction) for 90 min at 4 °C. Myristic acid-coated nano-$CaCO_3$ percentage was varied from 2 % to 8 % of monomer quantity.
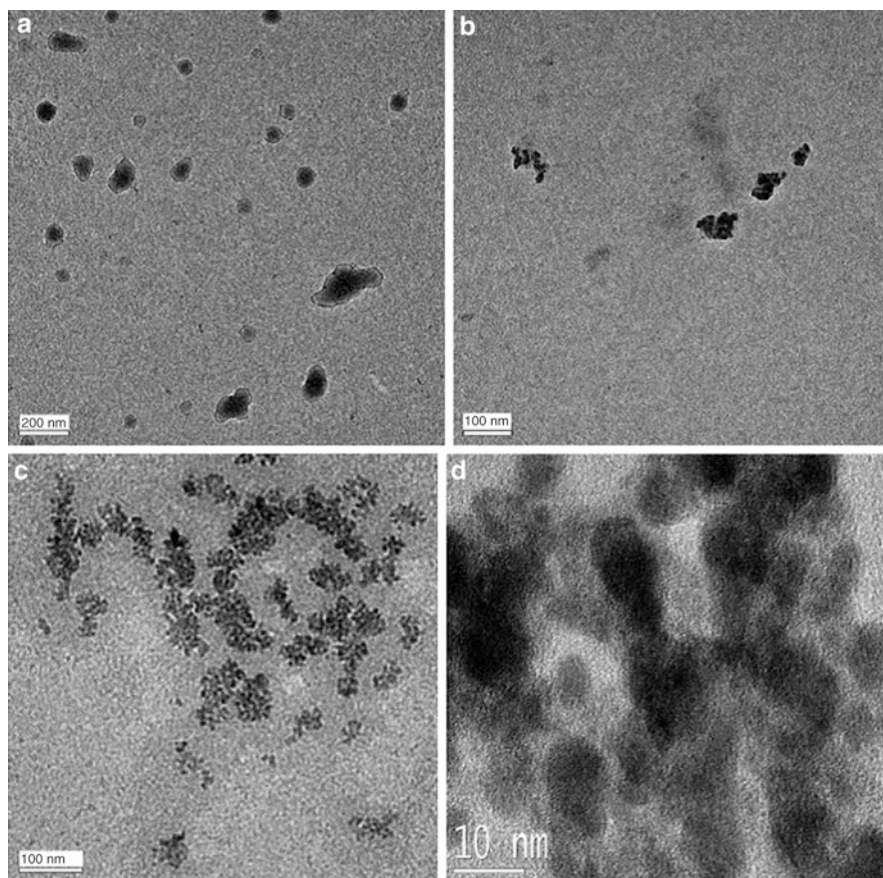
Fig. 13 (**a**) TEM image of TiO_2 nanoparticles embedded in the PBMA matrix. (**b**) TEM image of ZnO nanoparticles embedded in the PBMAmatrix. (**c**) TEM image of Bi_2O_3/ZrTiO4 nanoparticles in the PBMA matrix. (**d**) TEM image of Bi2O3/ZrTiO4 (Reprinted with permission from [35]. Copyright 2010 American Chemical Society)

Initially, functionalization of $CaCO_3$ was carried out by passing CO_2 gas through calcium hydroxide slurry, and myristic acid was introduced along with methanol (methanol:MA = 4:1wt basis) [30]. Then, the surfactant solution was prepared by adding sodium laurel sulfate in water, and further, nano-$CaCO_3$ (2–8 % of monomer) was added to the surfactant solution. The initiator was prepared by adding ammonium per sulfatein deionized water and then it was transferred to a semi-batch reactor. Initially, a small quantity of aniline was added to the reactor and then the remaining quantity was added in a dropwise manner. This addition process was completed within the time span of 70 min. The temperature of the reaction polymerization was maintained at 4 °C throughout the process. An ultrasonic bath sonicator (Sonics and Materials, 20 kHz, 600 W) was used to enhance their action rate and micro-mixing in the solution. As reaction progressed (after 20–30 min), the
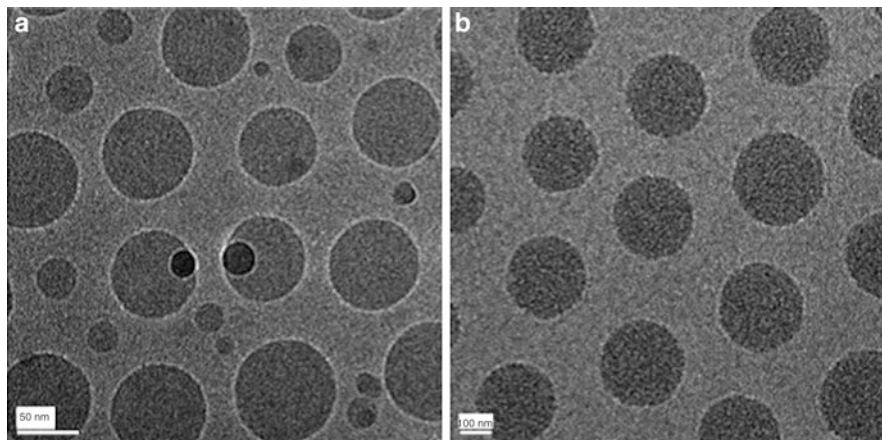
Fig. 14 Cryo-TEM image of (**a**) TiO2-PBMA latex particles and (**b**) ZnO-PBMA latex particles (Reprinted with permission from [35]. Copyright 2010 American Chemical Society)

formation of a thick orange solution was initially observed and later transformed into dark green suspension. Polyaniline was prepared by following the same process without the addition of nano-$CaCO_3$. Conversion of aniline monomer to polymer was measured gravimetrically and found to be more than 98 %.

In XRD analysis, the semi-crystalline nature of PANI/$CaCO_3$ nanocomposites was shown. It was reported that most of the $CaCO_3$ particles are finely dispersed in the PANI matrix. It may be due to the hydrophobic nature and micro-mixing created by ultrasound. Therefore, ultrasound produces fine $CaCO_3$-embedded emulsion droplets, which leads to the formation of finely dispersed PANI/$CaCO_3$ nanocomposites [37]. DSC reveals the interaction between $CaCO_3$ nanoparticle surface and polyaniline functionalities, resulting in the initiation of cross-linking reaction at lower temperature (Fig. 15). Reduction in ΔH (heat of reaction) indicates the decrease in exothermic polymer matrix due to the addition of $CaCO_3$ nanoparticles in PANI. The $CaCO_3$ particles are absorbing the heat of reaction in polymer; hence, the overall crystalline of nanocomposite increases. The heat of reaction for PANI is higher as compared to PANI/$CaCO_3$ nanocomposite. Fine dispersion of myristic acid-treated $CaCO_3$ in PANI/$CaCO_3$ nanocomposites had also been confirmed by TEM and EDAX analysis (Fig. 16).

Ultrasound-Assisted In Situ Emulsion Polymerization of Polyaniline-Encapsulated Nano $CaZn_2(PO_4)$ and Layer-by-Layer(LbL) Assembly of Nanocontainers

Nanocontainers were assembled using core and shell morphology by making the polyelectrolyte assembly, one of the important research areas for consistent and responsive release of the active agents. The active agents could be corrosion
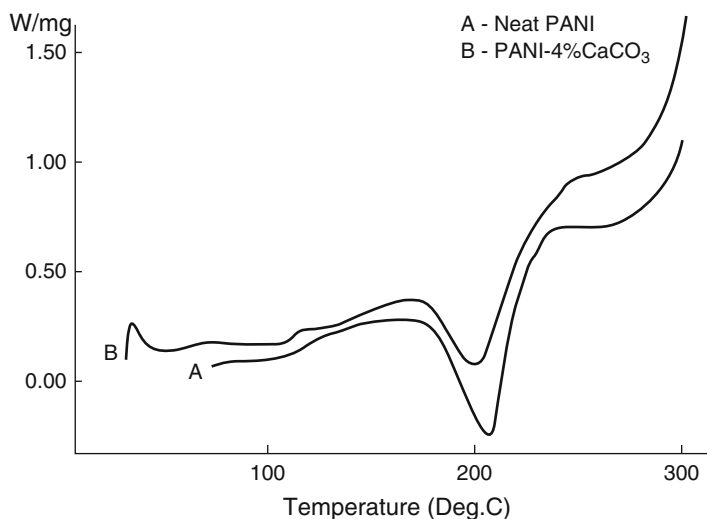
Fig. 15 DSC thermograms (**a**) Pure PANI, (**b**) PANI + 4 % CaCO$_3$ (Reprinted with permission from [36]. Copyright 2010 Elsevier)

inhibitors, drug molecules, oil, etc. The making of nanocontainer assembly was very important for the sustainable release of energy. In case of corrosion inhibitor release, the core itself can act as the inhibitor. The liquid inhibitors such as benzotriazole or other inhibitors can be added onto the assembly using polyelectrolyte solution. Using ultrasound cavitation, the inorganic pigment can be synthesized using precipitation technique. The polyelectrolyte assembly consists of water-soluble polymers; polyacrylic acid or polyvinyl acetate can be added over the core.

Bhanvase et al. encapsulated the polyaniline (PANI) on nano-CaZn$_2$(PO$_4$)$_2$, and layer-by-layer (LbL) assembly of nanocontainers has been achieved using ultrasonic irradiation. Also, calcium zinc phosphate nanoparticles were prepared via ultrasound-assisted coprecipitation technique. The complete encapsulation of polyelectrolyte on the nanopigment CaZn$_2$(PO$_4$)$_2$ was observed during preparation mainly due to the presence of ultrasonic irradiations [38].

Initially, CaZn$_2$(PO$_4$)$_2$ nanoparticles were functionalized using the myristic acid. Myristic acid functionalization generates negative charges on the surface of CaZn$_2$(PO$_4$)$_2$. The complete encapsulation of myristic acid on CaZn$_2$(PO$_4$)$_2$ (core) by positively charged PANI layer was accomplished in the presence of ultrasound [38]. Initially, surfactant solution was prepared by adding SDS, myristic acid, and modified CaZn$_2$(PO$_4$)$_2$ in water, which was subsequently transferred to an ultrasound reactor. Initiator solution was prepared separately by the adding of ammonium persulfate into deionized water, and then the solution was transferred to the reactor. Monomer aniline was added in a dropwise manner for 30 min, and the entire reaction mixture was sonicated in a reactor at 4 °C for 90 min. Finally, polyaniline-coated CaZn$_2$(PO$_4$)$_2$ nanocontainer particles were separated by centrifugation and washed with water. Then,
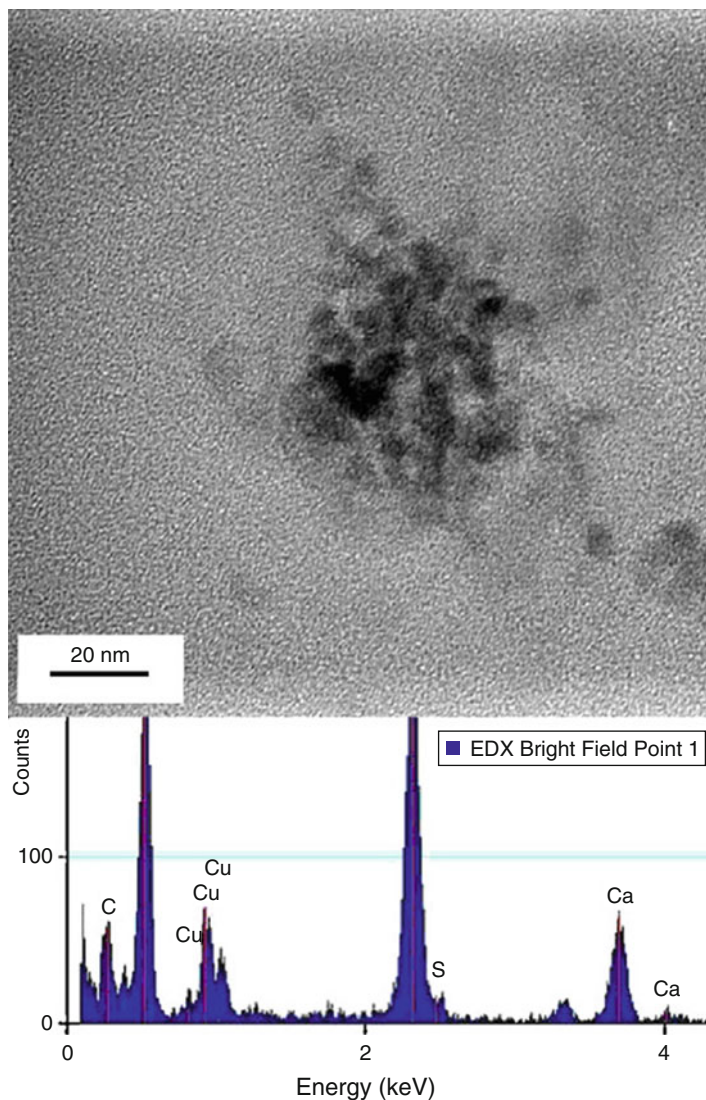
Fig. 16 EDAX analysis and transmission electron microscopic images of PANI/CaCO$_3$ nanocomposite (Reprinted with permission from [36]. Copyright 2010 Elsevier)

the drying was carried out at 60 °C in oven for 4 h. Further, the loading of positively charged benzotriazole layer on the surface of polyaniline-encapsulated CaZn$_2$(PO$_4$)$_2$ nanoparticles was done using benzotriazole in acidic media at pH 3 for 20 min using ultrasound-assisted method. At the end, polyacrylic acid polyelectrolyte layer was added on benzotriazole-loaded PANI-CaZn$_2$(PO$_4$)$_2$ nanoparticles using PAA solution in NaCl in the presence of ultrasound irradiation for 20 min.
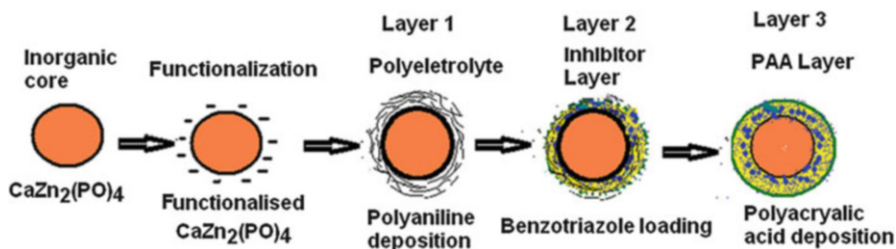
Fig. 17 Schematic illustration of the procedure for synthesis of $CaZn_2(PO_4)_2$ nanocontainer (Reprinted with permission from [38]. Copyright 2013 Elsevier)

Electrophoretic measurement indicates a drastic decrease in the surface charge of $CaZn_2(PO_4)_2$ nanoparticles after deposition of the polyaniline layer (from 32.8 to -61.9 mV) [38]. Zeta potential value was increased to -52.4 mV after deposition of positively charged benzotriazole layer on the surface of PANI-encapsulated $CaZn_2(PO_4)_2$. Therefore, it shows the adsorption of positively charged benzotriazole on the surface of polyaniline-encapsulated $CaZn_2(PO_4)_2$. Further increment in the zeta potential value to -38.3 mV is observed after the adsorption of positively charged polyacrylic acid (PAA) layer. Also, the coating of polyaniline layer on $CaZn_2(PO_4)_2$ nanoparticles showed the increment in the average particle size from 53.7 (core) to 134.5 nm. This clearly indicates the adsorption of polyaniline on the surface of $CaZn_2(PO_4)_2$ nanoparticles. The thickness of the coated PANI layer is estimated to be 40.4 nm. Finally, layer-by-layer assembly of nanocontainer was formed, and the average particle size of the hybrid was up to 493 nm (Fig. 17).

TEM analysis of $CaZn_2(PO_4)_2$ nanocontainers indicates (500 nm) the conformity of the size with the results obtained from particle size distribution analysis [38]. The dark-colored core $CaZn_2(PO_4)_2$ nanoparticles have been surrounded by the polyaniline, benzotriazole, and PAA layers in the formation of the nanocontainer process (Fig. 18).

Ultrasound-Assisted Preparation of Iron Oxide-Blended Sodium Zinc Molybdate Nanocontainer

Kapole et al. used a novel approach by combining two different cores in the formation of nanocontainer. In the presence of ultrasonic irradiations, the mixture of iron oxide and sodium zinc molybdate was prepared by adding iron oxide nanoparticle slurry in the aqueous mixture of sodium zinc molybdate [39]. Myristic acid was used for the functionalization of the iron oxide nanoparticles, and then it was blended with sodium zinc molybdate which represents the core of the nanocontainer. Ultrasound-assisted emulsion polymerization was used for the formation of polyaniline coating on the core. Then, the formation of the polyaniline-coated core of sodium zinc molybdate and iron oxide nanoparticles was done using imidazole in acidic media at pH 3. Then, the adsorption of negatively charged polyacrylic acid was carried out on imidazole-loaded polyaniline blend of sodium

Fig. 18 TEM Image of $CaZn_2(PO_4)_2$ nanocontainer (Reprinted with permission from [38]. Copyright 2013 Elsevier)
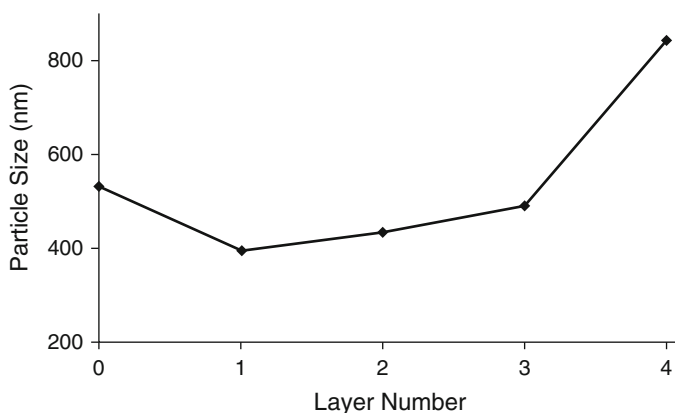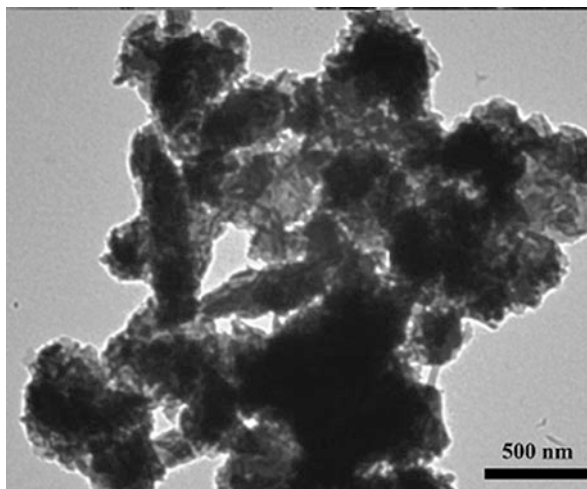
Fig. 19 Growth in particle size of nanocontainer during LbL assembly. Layer number 0: iron oxide-blended sodium zinc molybdate, *1* MA-treated iron oxide-blended sodium zinc molybdate, *2* iron oxide-blended sodium zinc molybdate/PANI, *3* iron oxide-blended sodium zinc molybdate/ PANI/imidazole, *4* iron oxide-blended sodium zinc molybdate/PANI/imidazole/PAA (Reprinted with permission from [39]. Copyright 2014, Taylor & Francis)

zinc molybdate and iron oxide nanoparticles. Particle size analysis data of the prepared nanocontainer shows the average particle size that gradually increases with an increase in the layer addition (Fig. 19).

XRD patterns of a core containing iron oxide-blended sodium zinc molybdate nanoparticles indicate the presence of sodium zinc molybdate and iron oxide in the region of 25–40 and 45–70 (2θ value). In XRD pattern of nanocontainer, the prominent peaks of the core are not observed which ultimately indicates the particles are completely covered with polymer (Fig. 20).
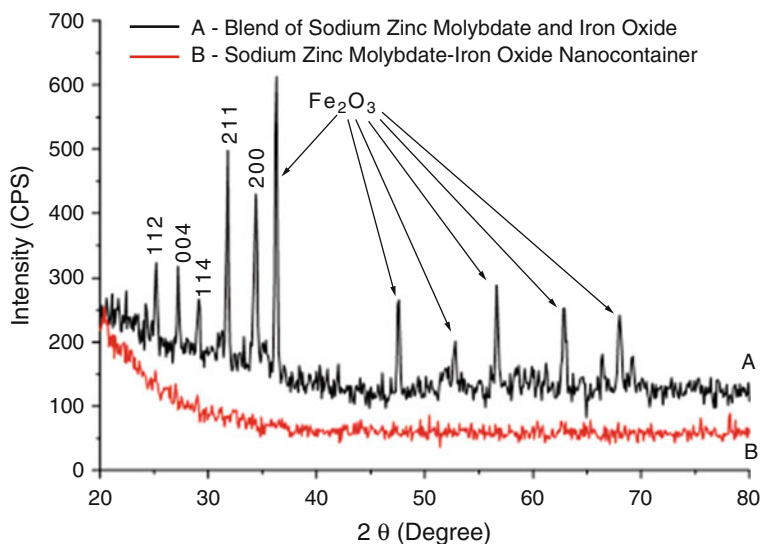
Fig. 20 XRD pattern of (**a**) iron oxide-blended sodium zinc molybdate nanoparticles and (**b**) iron oxide-blended sodium zinc molybdate nanocontainer (Reprinted with permission from [39]. Copyright 2014 Taylor & Francis)

Synthesis of Poly(Methylmethacrylate)/CaCO₃ Hybrid via Combination of the Conventional and Ultrasound-Assisted Polymerization

K. Prasad et al. prepared a polymethyl methacrylate (PMMA)/$CaCO_3$ hybrid using a combined method involving conventional and ultrasonic polymerization and also by individual techniques [40]. It has been observed that the excellent dispersion ability of ultrasound helped to obtain narrow size distribution and smaller average sizes in the PMMA/$CaCO_3$ systems. Initially, sodium dodecyl sulfate solution was taken in water and then methyl methacrylate (MMA) and KPS were added to the solution. Further, myristic acid-coated $CaCO_3$ was added to the solution of SDS in water and a uniform suspension of $CaCO_3$ was formed. Sonication equipment (Branson 450, 20 kHz) with a standard horn of 19 mm in diameter with a stainless steel tip was used. The ultrasound delivered at a pulsed input (0.7 s on, 0.3 s off) with 50 % amplitude with effective power delivery of 23 W. A combination of ultrasound and initiator potassium persulfate (KPS) was used to initiate polymerization. The polymerization mixture was sonicated for 20 s in continuous mode.

In combined polymerization, three types of radicals are generated, viz., the SO_4 radicals generated thermally, the H and OH radicals by the sonolysis of water, and the radicals created by the sonochemical degradation of the surfactant and monomer molecules [41, 42]. Therefore, theoretically, generation of more radicals had to give a high rate of conversion, but actually it was less due to interference of other
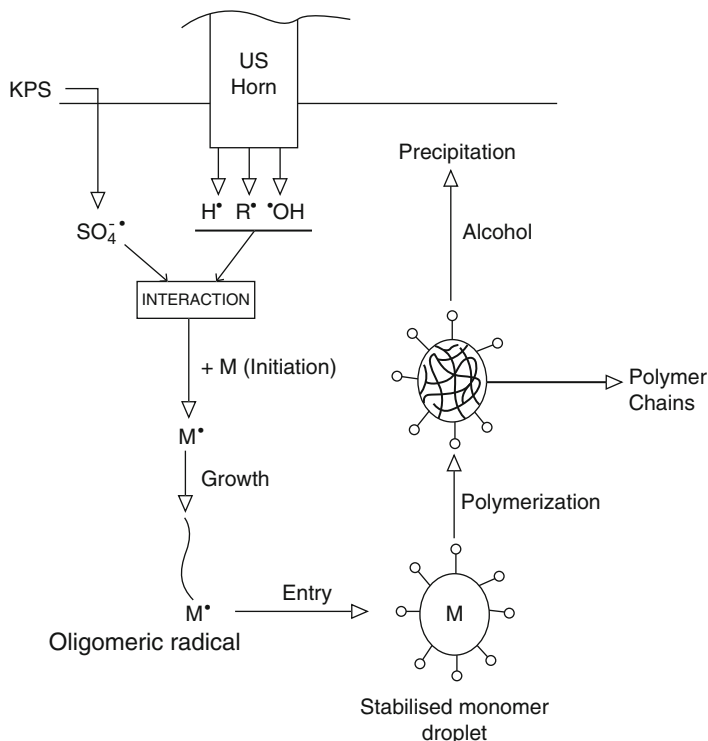
Fig. 21 Mechanism of USK (Ultrasound KPS - a Combination of ultrasound and KPS was used to initiate polymerization) polymerization and particle formation (Reprinted with permission from [40]. Copyright 2013 Elsevier)

reactions. Moderately higher rate of reaction with narrow particle size distribution and lower average particle size was obtained in the combination processes (Fig. 21).

TEM analysis of the hybrid clearly showed two distinct phases corresponding to the PMMA and the $CaCO_3$ (Fig. 22a). The spots on the image designate the formation of core–shell-like structures (magnified in Fig. 22b). Also, the darker $CaCO_3$ particles surrounded by the lighter PMMA particles indicated the core–shell morphology of the hybrid.

Ultrasound-Assisted Nanopigment Synthesis

Preparation of inorganic oxide nanopigments was a new area of research where many researchers paid attention due to their exceptional anticorrosive properties in the coating industry. The use of anticorrosive nanopigments instead of micron-sized pigments gives extreme change in the properties of the materials, which finds several applications in coating industries. Further, the change in the properties like particle surface area, size, shapes, and hydrophobicity makes these nanopigments more
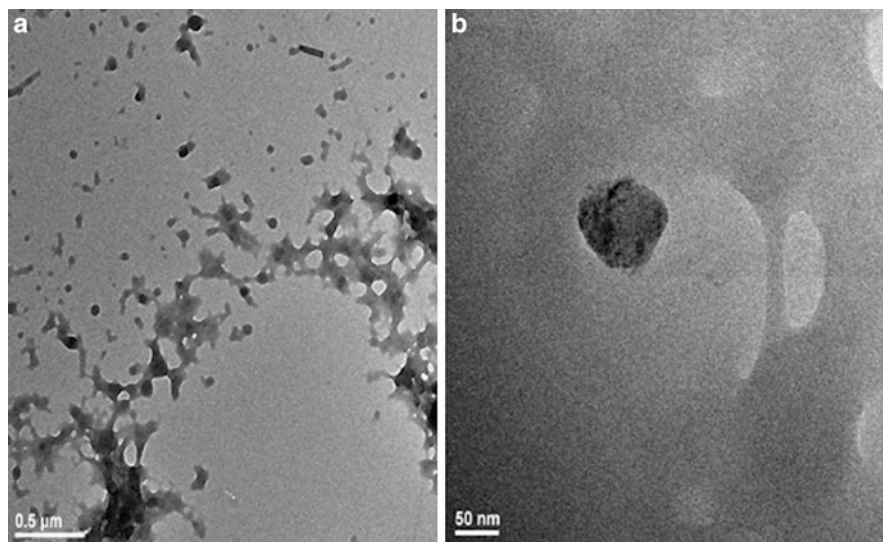
Fig. 22 TEM image of poly(methylmethacrylate)/CaCO$_3$ at (**a**) 500 nm (**b**) 50 nm (Reprinted with permission from [40]. Copyright 2013 Elsevier)

suitable for coating applications. Out of these inorganic nanopigments, many of them are prepared from toxic compounds such as cadmium, lead, chromium, or cobalt, which are harmful to living being. Therefore, it is required to search a substitute to these pigments with other environment-friendly or less toxic pigments. The sonochemical synthesis method for the preparation of nanopigments improves the product distribution and anticorrosion properties because of the smaller size, uniform, and fine dispersion of the nanopigments in the coatings with lesser dosage of nanopigments which would reduce the cost. Also, the shock waves produced due to ultrasonic irradiations prevents the agglomeration of the nanopigments and improves the dispersion ability in the coatings. The sonochemical precipitation method has been used as a useful method for the preparation of nanosized pigments. The extreme environments created due to cavity collapse, i.e., high temperature, pressure, and intense micromixing, lead to the formation of nanometer-sized particles with improved solute transfer and nucleation rate in aqueous suspension.

Karekar et al. [43] had studied the synthesis of zinc molybdate (ZM) and zinc phosphomolybdate (ZMP) nanoparticles using conventional and innovative sonochemical coprecipitation methods without any emulsifier. These new pigments are eco-friendly and they can be used as a substitute to lead, cadmium, and chromium pigment that contain carcinogenic species. In this, the preparation of ZMP was carried out using precursors such as sodium molybdate dihydrate, zinc sulfate heptahydrate, HNO$_3$ (oxidizing agent), and potassium dihydrogen phosphate in the presence of ultrasonic irradiation using an ultrasonic horn (Hielscher Ultrasonics GmbH, UP200S model, 24 kHz frequency, 200 W) at 50 % amplitude. Further, the preparation of ZM nanopigment was reported to be carried out using

sodium molybdate dihydrate and zinc chloride in the presence of ultrasonic irradiations.

Karekar et al. [43] reported that the growth of the primary particles was generally affected by the residence time of the particle in the reactor. As per this report, in the case of the conventional method of preparation of ZM and ZMP nanoparticles, the reported reaction time was 1.5 h, whereas the time for the preparation of these products using an ultrasound-assisted method was 1 h [43]. This reduction in the time might be due to the extreme pressure (>500 atm) and temperature ($>10,000$ K) with a cooling rate of $>10^{10}$ K/s conditions created by ultrasonic irradiation, which leads to extreme micromixing that enhances the solute transfer and nucleation rate in aqueous suspension and results in enhancement of the reaction rate.

The XRD patterns of the ZM shows that the ZM nanoparticles are crystalline in nature, and the observed phase of ZM nanoparticles are in scheelite phase. The intense and sharper diffraction peaks show a better crystalline nature of the formed products with smaller particle size. The reported crystallite size of ZM and ZMP nanoparticle is equal to 11.85 and 12.51 nm, respectively, which was calculated using Debye Scherrer's formula. Further, it has been reported that the XRD pattern of ZM and ZMP nanopigment prepared by ultrasound-assisted method shows less intensity peaks which was an indication of amorphous nature of the prepared product when compared to that of conventional method. The TEM analysis of zinc molybdate nanopigment confirms the rod-like structure in both cases of synthesis methods (sonochemically and conventionally). Further, the agglomeration was reported in the case of conventionally prepared ZM nanopigment which leads to the increase in particle size. Further, the considerable decrease in the particle size of sonochemically prepared ZM nanopigment without any agglomeration has been reported. The reason put forth was the use of ultrasonic irradiation. Further, the decrease in the particle size was due to lesser induction period, i.e., faster nucleation and improved control growth rate of the crystal due to the presence of ultrasonic irradiations in chemical precipitation method. Further, as per their report, the basically biphasic structure of sonochemically as well as conventionally prepared ZM nanoparticles has been reported. The rod-like structure was due to ZM phase inversion. The TEM image of conventionally synthesized ZMP nanoparticles shows agglomeration, and there was a significant reduction in the agglomeration as well as in the particle size of the sonochemically synthesized ZMP nanopigment. This happened due to the decrease in the agglomeration, efficient micro-mixing, and fast reaction kinetics created due to cavitational effects generated by ultrasonic irradiations. Further, the reported particle size of ZM and ZMP nanoparticles was higher in case of conventional method when compared to sonochemical method. This was again due to more induction period for the nucleation of these nanoparticles, which leads to uncontrolled growth in case of conventionally prepared ZM and ZMP nanoparticles. Further, agglomeration plays a key role in the increment of particle size of ZM and ZMP nanoparticles in the conventional as compared to ultrasound-assisted method. The reported range of the particle size of ZM nanopigment was 20–30 nm in case of sonochemical method of synthesis, whereas it was reported to be 75–120 nm in case of conventional method. Further, the particle size distribution reported is much broader for conventional

method due to drastic improvement in micro-mixing created by the physical effects of the ultrasonic irradiation which leads to faster reaction to form ZM nanopigment. The reported possible explanation for this was perhaps the fast kinetics of the ultrasound-assisted reaction, which does not give sufficient time for growth of particle and lead to the overall reduction in the particle size.

Ultrasound-Assisted Preparation of Nanofluid and Nanopigment Dispersion

Nanofluids have a number of applications in heat exchange fluid. Nanofluids are the fluids in which nanosize particles are dispersed into the base fluids such as water or ethylene glycol. The nanoparticles preferably loaded less than 10 % loading which gives the improvements in the thermal conductivity of base fluid. Copper, aluminum oxide, copper oxide, iron oxide, etc. and inorganic nanoparticles have been used in the base fluid. The preparation of the nanofluids is generally carried out by dispersing nanoparticles into base fluids; however, there was an issue of the dispersion instability or the particle settling which leads to decrease in the performance of the nanofluid. The instability was due to the presence of the surface charges on the nanoparticles. Therefore, the sonication and surfactants are used to break the agglomeration of the particles and bring the colloidal stability. Gurav et al. [44] reported the ultrasound-assisted synthesis of aniline miniemulsion polymerization using the ultrasound-assisted technique. The prepared polyaniline was used as the nanofluid. Polymerization was carried out in the sonochemical reactor, in which the cavitation enhances the polymerization. One of the important effects of cavitation was that the initial droplet size of emulsion was in nanometer range and hence the final polymer latex was also in the nanometer range. The polyaniline is a conducting polymer having enhanced thermal conductivity and can be used as nanofluid. They reported that the PANI nanofibers are in the range of 50–60 nm. The nanofibers are in the form of bundles. The structure of the nanofibers is impacting the thermal conductivity of nanofluids. They reported that the addition of 0.2 % of polyaniline into the base fluids shows the improvement in the heat transfer coefficient around 27 %, while 1.2 % addition of the PANI nanoparticles leads to improve the heat transfer coefficient around 64 %.

Nanopigment dispersion/pigment concentrates are important in the paints and coating industries for decorative, industrial paint application. The tinting strength is one of important criteria for the best pigment concentrate. It depends on the size of the pigment and the removal of agglomerates during the dispersion preparation process. Planetary ball milling was one of the preferred ways to prepare the organic dispersion. Pigment concentrates were prepared by adding the organic pigments into the solvents and then grinding using planetary milling process. Though industrially it was preferred to prepare the nanopigment dispersion using cavitation technique, ultrasound cavitation technique was one of the important techniques through which it is possible to prepare the pigment dispersion in nanosize without sacrifice of the energy. Smaller distribution of nanosize pigment shows better color strength and

stability of the polymer coatings. Badgujar et al. [45] had reported the pigment dispersion preparation using an ultrasound-assisted technique. They have taken phthalocyanine blue and phthalocyanine green organic pigment. They studied the nanopigment dispersion in aqueous as well as in organic solvents in the presence of the different surfactant such as Tween 80 and SDS, Oleic acid, etc. The ultrasound probe tip of 6, 10, and 20 mm diameter was used for the preparation of the tinter. In this chapter, it was reported that probe diameter of 10 and 20 mm showed better color strength. Finer dispersion was achieved using 20 mm probe tip diameter. 6 mm probe shows the particle size distribution in the range of 78–825 nm. Twenty millimeter probe shows narrow particle size distribution over the range 68–531 nm. The preparation of the fine concentrate of organic pigment in the presence of ultrasound probe was due to the physical effects of cavitation which involves the formation, growth, and implosive collapse of bubbles in the liquid medium resulting in the formation of fine dispersion of pigments.

Ultrasound-Assisted Atomization Process for Nanostructure Synthesis

Atomization is the process that breaks the liquids into fine droplet size. Atomization can be classified based on the energy used, for example, spinning disk atomization, nozzle atomization, and pressure atomization. The droplet formation and distribution of the droplets was important to the formation of the uniform film and the coatings on the surface of the substrate [46, 47]. Ultrasound atomization had large importance in the recent years due to formation of the narrow distribution of the droplets and formation of the uniform film thickness on the surface. Ultrasound atomization works on the principle of acoustic energy, converts the liquid films, and breaks into smaller droplets compared to other atomization process. There are two phenomena which are responsible for the droplet distribution: capillary hypothesis and cavitations hypothesis. In case of the solar panels, or electronics applications, the droplets discharged from the ultrasound atomizer convert into thin film when the surface temperature was above 150 °C. In ultrasound atomization process, viscosity of liquid, surface tension of the liquids, frequency of ultrasound and amplitude, and power of atomization are important parameters to atomize the liquids. Ramisetty et al. [48] reported the effect of different parameters of atomization and its effect on the droplet formation. They reported the new correlation for the formation of the droplet through ultrasound atomization process as follows:

$$d_P = 0.0154 \left(\frac{\pi\sigma}{\rho f^2}\right)^{0.33} \left[1 + \left(\frac{\pi\sigma}{\rho f^2}\right)^{-0.2} We^{0.154} Oh^{-0.111} I_N^{-0.033}\right] \quad (1)$$

d_p = Droplet diameter (m)
ρ = Density of the Liquid (Kg/m^3)
f = Ultrasonic Frequency (1/s)

σ = Surface Tension (N/m)

We = Modified Weber number = $(fQ\rho/\sigma)$

Oh = Modified Ohnesorge number = $(\mu/fA_m^2\rho)$

A_m = Tip Amplitude (m)

I_N = Intensity Number = $(f^2A_m^4/CQ)$

C = Velocity of Sound in Liquid medium (m/s)

Q = Volumetric Flow Rate (m^3/s)

Among the physical methods, spray pyrolysis is generally used for the synthesis of nanosized metal oxides, but spray pyrolysis approach requires high-pressure air to atomize precursor solution. In the ultrasound atomization process, the precursor solution is to be placed at a certain height so that the solution flows freely at any flow rates and therefore the overall operation can be energy efficient. Liu et al. [49] reported about the large production of the nanostructure materials using mist formation. They reported the production of ferric oxide as an example using ultrasound-assisted nebulization process. They had used the two different ultrasound atomization chambers for the precursor solution and the reaction was carried out in the form of mist, finally forming the nanoparticles of ferric oxide. Bang et al. [50] reported the formation of nanostructured oxide materials using the ultrasound-assisted spray pyrolysis process. This discussed about different ultrasound-assisted nebulization processes and effects onto the droplet distribution. They reported that ultrasound-assisted spray pyrolysis can be used for the formation of the metal oxides, semiconductor materials, inks, and nanostructure powder preparation.

Ultrasound-Assisted Preparation of Nanoclays and Nanocomposites

Natural clays such as bentonite clay and montmorillonite clay contain 1000 platelets, having the thickness of 1 nm size. If this is exfoliated or separated from each other, then it could be useful for the applications in barrier coatings and nanocomposite formation for structural applications. Bentonite is a natural clay and falls in the group of smectite clay. There are two forms of the nanoclay: (i) intercalated nanoclay and (ii) exfoliated nanoclay. In order to exfoliate the clay, it is necessary to apply the shear to clay tactoids. Hence, the ultrasound-assisted ion exchange technique was useful for the production of the exfoliated nanoclay. Sonawane et al. [51] reported about the formation of exfoliated nanoclay using natural bentonite as clay using an ultrasound-assisted technique. The cation exchange reaction using three different chemicals and intercalating agents such as tetrabutyl ammonium chloride, hexadecyltrimethyl ammonium chloride, and trimethyl ammonium bromide was carried out under an ultrasound-assisted cavitation technique. It was found that the nanoclay shows the platelets in the range of 30–50 nm. The presence of ultrasound waves and the intercalation of the long chain surfactant are facilitated, and exfoliation gives the nanoplatelet structure. It was observed that cetyltrimethylammonium bromide and cavitation technique gives better crystalline nanoplatelet structure. TBAC

shows the amorphous nanostructure from the XRD pictogram. FTIR reports the reaction of cation exchange occurred and the NH_2 and CH_2 groups are present on the clay platelets. It was found that due to sonication technique, the cation exchange capacity of the clay has also been drastically improved [51]. Sonawane et al. [52] reported the ultrasound-assisted synthesis of polyacrylic acid nanoclay nanocomposite synthesis. In this chapter, the synthesized nanoclay was exfoliated into the 40 % polyacrylic acid solution using the cavitation technique. Further, polymer chains are being intercalated into the gallery spacing, finally forming the uniform nanocomposite. Prepared nanocomposite was used for the adsorption of the dye solution.

Scale-Up Issues with Acoustic Cavitation: Case Study of Production Nanoparticles Using Hydrodynamic Cavitation

Cavitation comes in as an aid to solve the problem. The minute cavities are generated either by an acoustic medium such as ultrasound horn or by constriction of the flowing fluid by orifice. The cavitation can be classified into two major categories, hydrodynamic cavitations and acoustic cavitations. Since our process deals with the production of large-scale nanocalcium carbonate, this simple physical phenomenon was produced by creating a sudden pressure drop in the system by constricting the flow of the flowing fluid. This constriction was achieved by an orifice. Due to this sudden constriction, the pressure of the flowing fluid equals to its vapor pressure and cavities created. These cavities collapse and generate a tremendous pressure and temperature variation in the liquid and develop local hot spots which leads to the release of energy which can be further used for carrying various processes. With this basic idea in mind, the technique of hydrodynamic cavitation has been used for the multiphase reaction [26, 29, 30, 53, 54].

Inorganic nanoparticles such as calcium carbonate can be made possible to scale up in the large quantity using the hydrodynamic cavitation technique. There are a number of applications of calcium carbonate in many industries such as paper, paint, and coating industries. There is a requirement of large production of the calcite phase which have a number of applications. The reaction of calcite production is a three-phase reaction which involves the water (liquid) phase, calcium hydroxide as solid phase, CO_2 gas as gas phase. This is one of the important heterogeneous reactions. It is possible to produce the calcium carbonate nanoparticles using the cavitation technique. The dissolution of the CO_2 gas is one of the prime stages. The crystallization takes place during the reaction and forms the different phases such as calcite, vaterite, and aragonite due to the controlled dissolution of the CO_2 gas. The precipitation of $Ca(OH)_2$ slurry by bubbling of CO_2 is the most preferred method on large-scale production. The following is the reaction that takes place during the precipitation [26, 29, 30, 53, 54]:

$$Ca(OH)_2(s) \ + \ CO_2(aq) \ \rightarrow \ CaCO_3(s) \ + \ H_2O$$
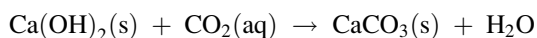
Table 3 Comparison of the hydrodynamic cavitation and acoustic cavitation for production of the calcium carbonate

	Acoustic cavitation	Hydrodynamic cavitation
Cavitation	Ultrasound (20–100 kHz)	Centrifugal pump Based on the cavitation number Cv defined less than 1
Device	Probe tip diameter 10–20 mm	Using Venturi or orifice
CO_2 insertion	Through probe	After the cavitation zone
Reaction Time	1 h	15 min
Batch size	500 mL	15 l
Phase	Calcite	Calcite
Particle size	45 nm	30 nm

The stable phase of calcite can be obtained in the hydrodynamic cavitation process if the reaction was carried out while considering the proper dilution of calcium hydroxide by adding CO_2 gas into it by inserting the CO_2 gas at the cavitation zone after the orifice or venture. The following are the limitations of acoustic cavitation for scale:

1. Power consumption per kg of the production of calcite is very high.
2. The effective utilization of CO_2 gas is the problem, most of CO_2 gas remains undissolved.
3. Compared to the conventional batch, reaction through time required in ultrasound cavitation technique is less; however, still time of reaction can be reduced using hydrodynamic cavitation technique.
4. Particle size distribution and optimization of the parameters is an issue in acoustic cavitation.

The above said disadvantages can be overcome by using hydrodynamic cavitations. The time required for the nucleation was quite small in hydrodynamic cavitations. While in acoustic cavitations, the time of nucleation was in minutes; hence, an acoustic cavitations-based carbonation process will produce large particle size due to Ostwald ripening process. As shown in Table 3, the acoustic cavitation requires more power while reaction time has large difference. The size of the batch process using hydrodynamic cavitations can go up to 500 l. Theproblem of conversion of single phase after the reaction along with the uniform particle size was handled by monitoring the process to the desired conditions in order to achieve a single certain phase, but this does not necessarily mean that the particle produced will be of larger surface area. Therefore, having a system which can give a single phase and a material with large surface area is the need of the day [29, 53, 54].

Iron Oxide Nanoparticles Using Hydrodynamic Cavitations

Iron(III) oxide is the inorganic pigment with the formula Fe_2O_3. It is one of the three main oxides of iron. There is large demand of the iron oxide pigment in paint, chemical, and coating industries. There are three different forms of iron oxide: yellow, red, and black. There is large demand for the yellow iron oxide pigment. The scale up of yellow iron oxide is also possible using the cavitation technique.

This is neutralization reaction, and iron precursor initially dissolved in the water later. It was neutralized using the NaOH solution. The solution of iron precursor is passed through the hydrodynamic cavitations, and NaOH addition was carried out in dropwise manner. The compressed air is also added after the cavitating zone. The existing commercial process requires time around 72 h. While using hydrodynamic cavitations, it is possible to produce the yellow iron oxide pigment within 4–5 h. The size of yellow iron oxide is in the range of 30–50 nm size. The shape of pigment is spherical in nature.

Conclusions and Future Directions

The use of ultrasound for the synthesis of nanomaterials rapidly increased due to special properties of nanoparticles obtained through sonochemical technique. With the example of the TiO_2 and doped TiO_2, it can be possible to conclude that sonication process can be used for sol-gel method. The structure of the TiO_2 particles and phases changes with the use of ultrasound. Doping is being affected by the ultrasound. The size of doped and undoped TiO_2 particles lies in the range of 10–40 nm. Sonochemical carbonation can be used for synthesis of specific shape (calcite) of calcium carbonate. Due to insertion, CO_2 gas through ultrasound probe leads to smaller bubble size and affects the final formation of the nano-calcite phase, which is one of the important conclusions for ultrasound-assisted precipitation reactions. It is also concluded that the formation of nano-calcite has an impact on the addition of the type and quantity of surfactant. Ultrasound has impact on the synthesis of inorganic oxide such as ZnO and SnO_2, specifically on the particle size distribution, shape, and structures. Using ultrasound-assisted miniemulsion polymerization, it is possible to make narrow distribution of the latex particle synthesis. The latex particle size has an impact on the surface tension of the monomer. The core-shell morphological hybrid materials was synthesized using ultrasound assisted miniemulsion polymerization.

The ultrasound-assisted technique has large opportunities in nanomaterial synthesis area. The structure and properties are impacting on the applications such as solar cells, gas sensors, electronics devices, etc. Ultrasound-assisted miniemulsion polymerization for hybrid nanoparticle area has ample opportunities to make hybrid nanoparticles, Janus nanoparticles which may be the future possible area in sonochemistry. Hydrodynamic cavitation can be used for the scale-up of the

nanoparticles, specifically for the precipitation and neutralization reactions. Hydro-dynamic cavitation and acoustic cavitation both will play important roles in the synthesis of the inorganic nanopigments such as $CaCO_3$, iron oxide, and making organic pigments into smaller size in the future.

References

1. Chen D, Sharma SK, Mudhoo A (2012) Handbook on applications of ultrasound: sonochemistry for sustainability. CRC Press, Boca Raton
2. Cheeke JDN (2002) Fundamentals and applications of ultrasonic waves. CRC Press, Boca Raton
3. Sanghi R, Singh V, Cann MC, Connelly ME (2000) Real-world cases in green chemistry. ACS, Washington, DC
4. Manickam S, Ashokkumar M (2014) Cavitation: a novel energy-efficient technique for the generation of nanomaterials. CRC Press, Boca Raton
5. Bang JH, Suslick KS (2010) Applications of ultrasound to the synthesis of nanostructured materials. Adv Mater 22:1039–1059
6. Suslick KS, Gawienowski JW, Suhubert PF, Wag HH (1983) Alkane sonochemistry. J Phys Chem 87:2299–2301
7. Suslick KS (2001) Sonoluminescence and sonochemistry. In: Meyers RA (ed) Encyclopedia of physical science and technology. Academic, San Diego
8. Mason TJ, Cordemans de Meulenaer E (1998) Synthetic organic sonochemistry. Plenum Press, New York
9. Pal U, Kim C, Jadhav N, Kang Y (2009) Ultrasound-assisted synthesis of mesoporous ZnO nanostructures of different porosities. J Phys Chem C 113:14676–14680
10. Forcada J, Ramos J (2010) Encapsulation of inorganic by miniemulsion ploymerization. In: Mittal V (ed) Miniemulsion polymerization technology. Wiley Scrivener, Salem
11. Teo BM, Prescott SW, Ashokkumar M, Grieser F (2008) Ultrasound initiated miniemulsion polymerization of methacrylate monomers. Ultrasound Sonochem 15:89–94
12. Kobayashi D, Matsumato H, Kuroda C (2008) Improvement of indirect ultrasonic irradiation method for intensification of emulsion polymerization process. Chem Eng J 135:43–48
13. Teo BM, Ashokkumar M, Grieser F (2011) Sonochemical polymerization of miniemulsions in organic liquids/water mixtures. Phys Chem Chem Phys 13:4095–4102
14. Xia H, Wang Q, Liao Y, Xu X, Baxter SM, Slone RV, Wu S, Swift G, Westmoreland DG (2002) Polymerization rate and mechanism of ultrasonically initiated emulsion polymerization of n-butyl acrylate. Ultrason Sonochem 9:151–158
15. Kojima Y, Koda S, Nomura H (2001) Effect of ultrasonic frequency on polymerization of styrene under sonication. Ultrason Sonochem 8:75–79
16. Wang R, Cheung HM (2005) Ultrasound assisted polymerization of MMA and styrene in near critical CO_2. J Supercrit Fluids 33:269–274
17. Chau HCJ, Stoffer JO (1999) Ultrasonically initiated free radical catalyzed emulsion polymerization of methyl methacrylate (I). J Appl Polym Sci 72:797–825
18. Grieser F, Ashokkumar M (2004) Sonochemical synthesis of inorganic and organic colloids. In: Caruso F (ed) Colloids and colloid assemblies. Wiley-VCH GmbH & CoKga A, Weinheim, pp 120–149
19. Jing J, Feng C, Jinlong Z (2010) Carbon-deposited TiO_2: synthesis, characterization, and visible photocatalytic performance. J Phys Chem C 114:933–939
20. Shirsath SR, Pinjari DV, Gogate PR, Sonawane SH, Pandit AB (2013) Ultrasound assisted synthesis of doped TiO_2 nanoparticles: characterization and comparison of effectiveness for photocatalytic oxidation of dyestuff effluent. Ultrason Sonochem 20:277–286

21. Romuald B, Hamoudi S, Larachi F, Belkacemi K (2012) Synthesis of $CaCO_3$ nanoparticles by controlled precipitation of saturated carbonate and calcium nitrate aqueous solutions. Can J Chem Eng 90:26–33
22. Aboutaleb GJG, Mohammad I (2013) Characterization of $CaCO_3$ nanoparticles synthesized by reverse microemulsion technique in different concentration of surfactants. Iran J Chem Eng 32:27–35
23. Sargheini J, Ataie A, Salili SM, Hoseinion AA (2012) One step facile synthesis of $CaCO_3$ nanoparticles via mechano-chemical route. Powder Technol 219:72–77
24. Shirsath SR, Sonawane SH, Saini DR, Pandit AB (2014) Continuous precipitation of calcium carbonate using sonochemical reactor. Ultrason Sonochem 24:132–139
25. Gomez-Diaz D, Navaza JM, Sanjurjo B (2006) Analysis of mass transfer in the precipitation process of calcium carbonate using a gas/liquid reaction. Chem Eng J 116:203–209
26. Wachi S, Jones AG (1991) Effect of gas–liquid mass transfer on crystal size distribution during the batch precipitation of calcium carbonate. Chem Eng Sci 46:3289–3293
27. Silva P, Bucea L, Moorehead DR, Sirivivatnanon V (2006) Carbonate binders reaction kinetics strength and microstructure. Cement Concr Compos 28:613–620
28. Sun Q, Deng Y (2004) Synthesis of micrometer to nanometer $CaCO_3$ particles via mass restriction method in an emulsion liquid membrane process. J Colloid Interface Sci 278:376–382
29. Sonawane SH, Shirsanth SR, Khanna PK, Pawar S, Mahajan CM, Paithankar V, Shinde V, Kapadnis CV (2008) An innovative method for effective micro-mixing of CO_2 gas during synthesis of nano-calcite crystal using sonochemical carbonization. Chem Eng J 143:308–313
30. Sonawane SH, Gumfekar SP, Meshram S, Deosarkar MP, Mahajan CM, Khanna P (2009) Combined effect of surfactant and ultrasound on nano calcium carbonate synthesized by crystallization process. Int J Chem React Eng 7:1–15
31. Li S, Toprak MS, Jo YS, Dobson J, Kim DK, Muhammed M (2007) Bulk synthesis of transparent and homogeneous polymeric hybrid materials with ZnO quantum dots and PMMA. Adv Mater 19:4347–4352
32. Askari S, Halladj R (2013) Effects of ultrasound-related variables on sonochemically synthesized SAPO-34 nanoparticles. J Solid State Chem 201:85–92
33. Barkade SS, Pinjari DV, Singh AK, Gogate PR, Naik JB, Sonawane SH, Pandit AB, Ashokkumar M (2013) Ultrasound assisted miniemulsion polymerization for preparation of polypyrrole zinc oxide (PPy/ZnO) functional latex for LPG sensing. Ind Eng Chem Res 52:7704–7712
34. Barkade SS, Pinjari DV, Nakate UT, Singh AK, Gogate PR, Naik JB, Sonawane SH, Pandit AB (2013) Ultrasound assisted synthesis of polythiophene/SnO_2 hybrid nanolatex particles for LPG sensing. Chem Eng Process 74:115–123
35. Sonawane SH, Neppolian B, Teo BM, Grieser F, Ashokkumar M (2010) Ultrasound-assisted preparation of semiconductor/polymer photoanodes and their photoelectrochemical properties. J Phys Chem C 114:5148–5153
36. Bhanvase BA, Sonawane SH (2010) New approach for simultaneous enhancement of anticorrosive and mechanical properties of coatings: application of water repellent nano $CaCO_3$–PANI emulsion nanocomposite in alkyd resin. Chem Eng J 156:177–183
37. Elik MC, Onal M (2007) Intercalated polyaniline/Na-montmorillonite nanocomposites via oxidative polymerization. J Polym Res 14:313–331
38. Bhanvase BA, Kutbuddin Y, Borse RN, Selokar NR, Pinjari DV, Gogate PR, Sonawane SH, Pandit AB (2013) Ultrasound assisted synthesis of calcium zinc phosphate pigment and its application in nanocontainer for active anticorrosion coatings. Chem Eng J 231:345–354
39. Kapole SA, Bhanvase BA, Pinjari DV, Kulkarni RD, Patil UD, Gogate PR, Sonawane SH, Pandit AB (2014) Intensification of corrosion resistance of 2 K epoxy coating by encapsulation of liquid inhibitor in nanocontainer core of sodium zinc molybdate and iron oxide. Compos Interfaces 21:469–486

40. Prasad K, Sonawane SH, Zhou M, Muthupandian A (2013) Ultrasound assisted synthesis and characterization of poly(methyl methacrylate)/CaCO$_3$ nanocomposites. Chem Eng J 219:254–261

41. Maruthamuthu P (1980) Absolute rate constants for the reactions of sulfate, phosphate and hydroxyl radicals with monomers. Macromol Chem Rapid Commun 1:23–25

42. Criquet J, Leitner NKV (2009) Degradation of acetic acid with sulfate radical generated by persulfate ions photolysis. Chemosphere 77:194–200

43. Karekar SE, Bhanvase BA, Sonawane SH, Deosarkar MP, Pinjari DV, Pandit AB (2015) Synthesis of zinc molybdate and zinc phosphomolybdate nanopigments by an ultrasound assisted route: advantage over conventional method. Chem Eng Process 87:51–59

44. Gurav P, Naik S, Bhanvase BA, Pinjari DV, Sonawane SH, Ashokkumar M (2015) Heat transfer intensification using polyaniline based nanofluids: preparation and application. Chem Eng Process 95:195–201

45. Badgujar NP, Bhoge YE, Deshpande TD, Bhanvase BA, Gogate PR, Sonawane SH, Kulkarni RD (2015) Ultrasound assisted organic pigment dispersion: advantages of ultrasound method over conventional method. Pigment Resin Technol 44:214–223

46. Yasuda K, Bando Y, Yamaguchi S, Nakamura M, Oda A, Kawase Y (2005) Analysis of concentration characteristics in ultrasonic atomization by droplet diameter distribution. Ultrason Sonochem 12:37–41

47. Wang WN, Purwanto A, Lenggoro IW, Okuyama K, Chang H, Jang HD (2008) Investigation on the correlations between droplet and particle size distribution in ultrasonic spray pyrolysis. Ind Eng Chem Res 47:1650–1659

48. Ramisetty KA, Pandit AB, Gogate PR (2012) Investigations into ultrasound induced atomization. Ultrason Sonochem 20:254–264

49. Liu R, Liu L, Liu J (2009) Massive production of nanoparticles via mist reaction. Physica E 41:1197–1200

50. Bang JH, Didenko YT, Helmich RJ, Suslick KS (2012) Nanostructured materials through ultrasonic spray pyrolysis. Mater Matters 7:15–18

51. Sonawane SH, Chaudhari PL, Ghodke SA, Parande MG, Bhandari VM, Mishra S, Kulkarni RD (2009) Ultrasound assisted synthesis of polyacrylic acid–nanoclay nanocomposite and its application in sonosorption studies of malachite green dye. Ultrason Sonochem 16:351–355

52. Sonawane SH, Chaudhari PL, Ghodke SA, Ambade SB, Gulig S, Mirikar A, Bane A (2008) Combined effect of ultrasound and nanoclay on adsorption of phenol. Ultrason Sonochem 15:1033–1037

53. Sonawane SH, Gumfekar SP, Kate SH, Meshram SP, Kunte KJ, Ramjee L, Mahajan CM, Parande MG, Ashokkumar M (2010) Hydrodynamic cavitation-assisted synthesis of nanocalcite, Int J Chem Eng 10:1–8

54. Sonawane SH, Kapadnis CV, Meshram S, Gumfekar SP, Khanna PK (2010) Sonochemical formation of CaCO$_3$ nanoparticles with controlled particle size distribution. Int J Green Nanotechnol PhysChem 2:69–79

Ultrasonic Modification of Micelle Nanostructures

Nor Saadah Mohd Yusof and Muthupandian Ashokkumar

Contents

Abstract

The tremendous attention given to micelles in recent technological advancements and industries is due to its amazingly stable and flexible physicochemical properties exhibited upon exposure to different stimuli. A concise review of micelle

N.S. Mohd Yusof (✉)
Department of Chemistry, University of Malaya, Kuala Lumpur, Malaysia
e-mail: adah@um.edu.my; adah.yusof@gmail.com

M. Ashokkumar
School of Chemistry, The University of Melbourne, Melbourne, VIC, Australia

structures and the effects of various stimuli on the structural properties of micelles with a particular focus on the effect of ultrasound are provided. While the use of conventional stimuli such as temperature, shear, etc., for controlling micelle structures is widely reported, the use of ultrasound as a stimulus has not been studied extensively. For this reason, a detailed discussion on the possibility of designing a variety of micelle nanostructures using ultrasound is provided. Using ultrasound as a stimulus is an advantage as it eliminates the need for adding external chemicals to the micellar system and the experimental parameters could be easily controlled. A case study of using cetyltrimethylammonium salicylate (CTASal) prepared from ion exchange process of equimolar mixture of cetyltrimethylammonium bromide (CTABr) and sodium salicylate (NaSal) is used in order to evaluate the efficiency of ultrasonics on controlling the micelles' aggregational structures. Further experiments and discussion imply that the transformation is mainly driven by the physical effect generated from sonication. Evidence from cryo-TEM indicates that the structural transformation took place according to the reptation and reaction Model proposed before.

Introduction

Surfactant with unique characteristics of amphiphilicity can self-assemble to form micelles. When a low concentration of micelle-forming surfactant is dissolved in a solvent, surfactant molecules exist as monomers. Once the concentration reaches its critical micelle concentration or cmc, monomers aggregate together forming a "micelle." Micelle has the unique ability to flexibly break and reform within a wide range of sizes, from nm to mm, as well as to different aggregational structures with pronounced properties. Hence, they are also termed based on their structures such as vesicle, liposome, gel, microemulsions, etc. The amphiphilic behavior and the flexible aggregational properties make them very useful in many areas. People are more familiar with their areas of application such as soap, detergent, wetting agent, bactericide, corrosion inhibitor, foaming agent, dispersant, emulsifier, antistatic agent, and many more.

Micelle is a remarkable system because of its ability to undergo self-aggregational transformation even with the slightest change, such as settling in a different environment (solvent), increasing/decreasing its monomer's concentration, or even by slightly changing the solution temperature. Their assembly and transformational processes are a net effect from the balance of their electrostatic, hydrophobic, van der Waals, and steric interactions.

Micelle Aggregation

One of the earliest evidence for micelle aggregation was reported in 1913 by McBain who observed abnormal viscosity in sodium palmitate solution [1]. Despite its significant viscosity, the system still exhibited normal electrical mobility, therefore initially termed as "colloidal ion" [1]. The aggregation relied solely on the amphiphilicity of molecules (monomers) in the solution. In aqueous solutions, the water loving identity is exposed, and the water hating identity is well hidden in the core, a region where it is believed to be completely free of water molecules. In nonpolar solvents such as oil, the aggregation is reversed, hence termed as a reverse micelle.

The concept behind the aggregation of micelles is simple. In any system, each molecule stably exists in its lowest potential energy required. Conflict arises when both parts – water loving and hating are exposed to the solvent, i.e., water molecules. Hence, this molecule has no option other than orienting its water hating part at the air-water interface with the tail projected away from the water. However, as a collective system, specifically above its critical micelle concentration (cmc) and Kraft temperature, they have a better option by aggregating together, known as the self-assembling process. Kraft temperature is the minimum temperature required for the surfactants to start aggregating to form micelle. At temperature below Kraft temperature, micelle will not form even at its high concentration. The hydrophilic heads form a shield to avoid any interaction or any close contact of their hydrophobic tails to water molecules, by an equilibrium process known as aggregation or micellization. This is shown by Eq. 1 where S represents the monomer and S_n represents the micelle. By forming micelle, they possess lower potential energy; therefore the aggregation is very stable.

$$nS \rightleftarrows S_n \tag{1}$$

Despite the use of the term "stable", it is important to understand that micellization itself is a dynamic process of formation and deformation of micelle-forming surfactant monomers, as illustrated in Fig. 1. This is described by the micelles' equilibrium (K_M) in Eq. 2 where k_f^M is the rate constant of micelle formation and k_d^M is the rate constant of micelle deformation.

$$K_M = k_f^M / k_d^M \tag{2}$$

A micelle can flexibly and reversibly grow to different structures in order to stay in its lowest energy state. For deeper understanding, two crucial governing factors are discussed below [2, 3]:

(i) Any course of increasing the tail-tail attraction will lower the cmc as well as promoting growth, vice versa.

Fig. 1 Micellization process
from monomers above cmc
and Kraft temperature
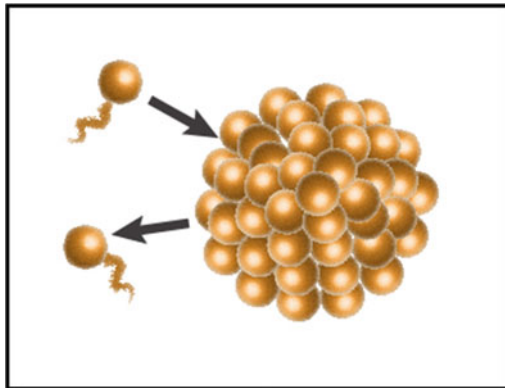
- Hydrophobic group – micelle-forming surfactant with a more hydrophobic nature will result in stronger attraction, therefore has a low cmc and promotes growth.
- The number of carbon atoms building a straight chain – more carbon atoms in a straight chain will increase the hydrophobicity of the molecule.
- Branched carbon chain – with the same number of carbon atoms, increasing branch(es) will increase the cmc. This is because the potential energy of branched micelle-forming surfactant aggregation is higher than the corresponding linear molecule.

(ii) Any course of decreasing the head-head repulsion will lower the cmc and promote growth, vice versa.

- Charge(s) of the head – increase in the head's charge(s) will result in a greater repulsion between them, resulting in a higher cmc.
- Number of hydrophilic group – increase in the hydrophilicity will also result in an increase in repulsion between the heads, resulting in a higher cmc.
- Electrolyte and nonelectrolyte additives – any additive that can reduce the head-head repulsion will reduce the cmc.

In concluding terms, micelles' structural aggregation relies heavily on hydrophobic attraction but limited by the repulsion between hydrophilic heads. The balance between these two results in a curvature growth in order to gain more space between the charged heads, hence the formation of spherical micelles above the cmc. Despite the repulsion of the heads, surfactant molecules are closely packed together to ensure that its hydrophobic core is free of water. Therefore, in examining such aggregation, the terms of "spontaneous curvature" or "critical packing" (CP) behaviors are usually used for discussion [4]. Optimum head group spacing and water-free hydrophobic core will promote growth and determine the flexible structure of micelle. The average length of micelle is also known as its contour length, denoted by $\bar{L}$.
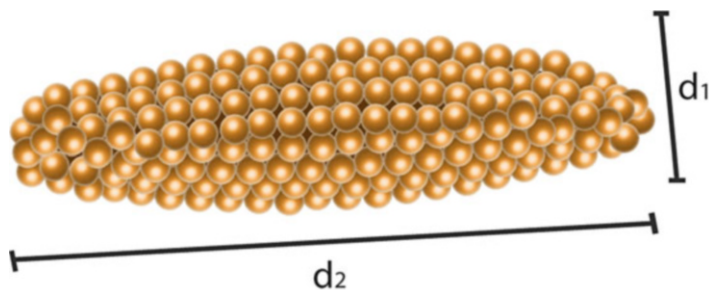
Fig. 2 The critical packing (CP) value is given by the ratio of the two diameters of the structure, d_1 and d_2
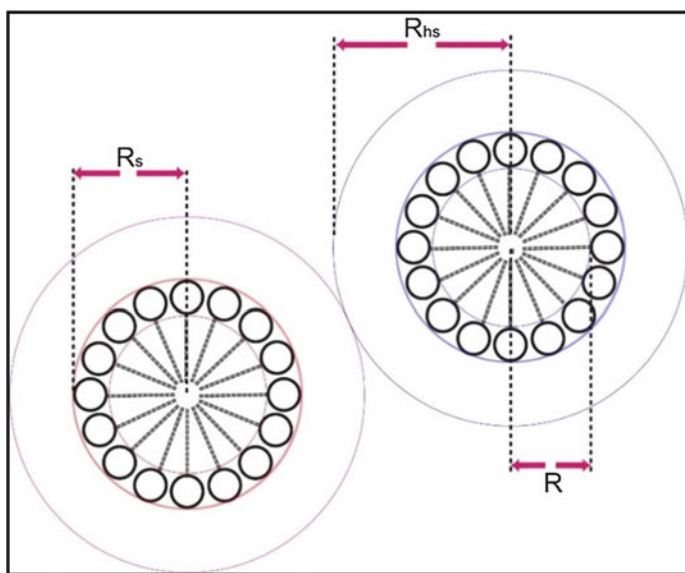
Fig. 3 The core radius (R), the shell radius (R_s), and the hard-sphere interaction radius (R_{hs}) of micellar aggregations in aqueous system

Micelle Aggregational Structures

Micelles can assemble by noncovalent interaction to different structures that are "energetically stable." The size of the aggregation can be described by their radii – the core radius (R), shell radius (R_S), and the hard-sphere interaction radius (R_{hs}) as shown in Fig. 3 [5]. However, when micelles grow (elongate), the critical packing (CP) process is usually described by the aspect ratio of the two diameters of the

Fig. 4 Illustration of
spherical micelles
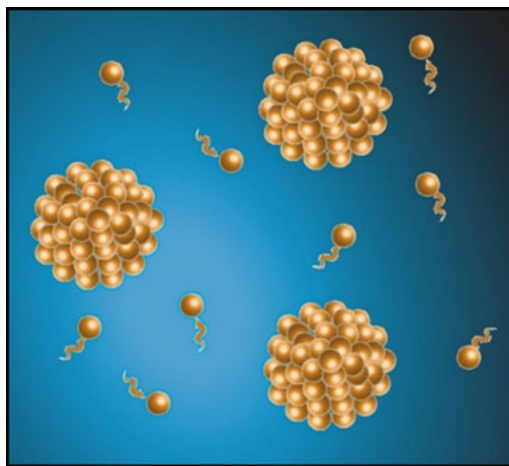
structure, d_1 and d_2 in Fig. 2 [6]. This highly relies upon the required energy to form the curvatures that determine the two diameters of a micelle aggregation, which is also known as the scission energy [7]. The two diameters are the horizontal and vertical diameters of a micelle structure.

In simple cases where there is no external disturbance on the system, the scission energy depends solely on the strength of surfactant-counterion interaction [7]. When there are more than one counterions present, the strength is also characterized by the ion exchange constant, K^X_Y (X and Y are the two competing counterions) value [8, 9]. This and the surfactant-counterion ratio have significant effect on the system's viscoelasticity [10]. The length of the micelle's structure is usually determined by direct visualization of cryo-TEM imaging [11], or determination by light and neutron scattering [12, 13]. As micelles can form many aggregational structures, some of the common ones are mentioned in this section.

Spherical Micelles

The most common structure of micelle aggregation usually formed right above its cmc and Kraft temperature is the spherical micelle. As its name infers, they form more or less a sphere structure as illustrated in Fig. 4.

Since they form immediately above their cmc, the size is remarkably homogenous throughout the system, with its radius being approximately equal to the hydrocarbon chain length of its monomer. The CP for this structure is $\leq 1/3$ [4]. The curvature growth of the micelle is due to its adaptation to two factors: providing more space for the strong repulsion effect between the charged heads and aiding the strong attraction between the hydrophobic chains of its core. Spherical micelle solution does not show any significant viscosity increase but usually exhibits shear-thinning rheological property.
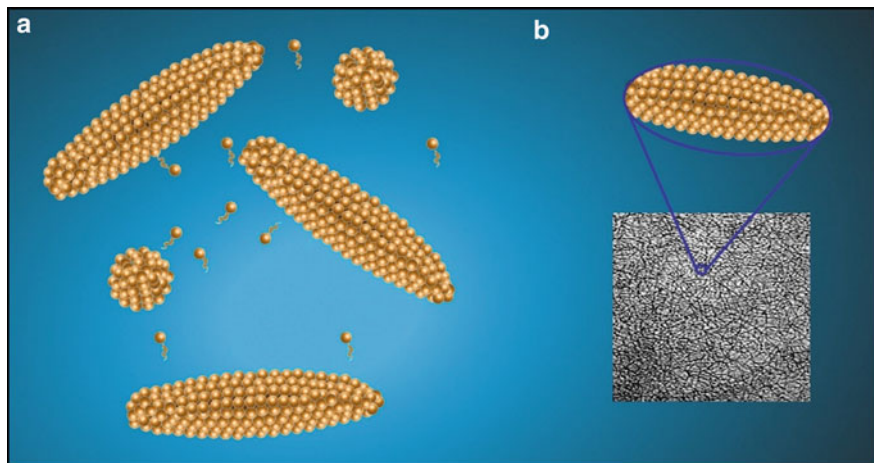
Fig. 5 Illustration of (**a**) rodlike and (**b**) wormlike micelles. Rodlike micelle is elongated micelle but does not entangle in a network. Wormlike micelle is much longer than rodlike micelle and entangled together

Rodlike and Wormlike Micelles

Within $1/3 \leq CP \leq 1/2$, a micelle can grow to rodlike or wormlike micelle as shown in Fig. 5 [4]. Such growth occurs by the natural act of the micelle aggregation process in order to reduce its total energetics by decreasing the proportion of its end caps over the linear portion [4]. This can only happen when energy for the spontaneous curvature of the end caps is higher than the energy of the curvature along its cylindrical structure. Compared to a spherical micelle, the core and shell radii of wormlike micelle is smaller [5]. The spherical micelle form rodlike micelle by its one-directional growth and continue to elongate depending on the condition [5].

The wormlike micelles tend to entangle together into a transient network. This entanglement results in its viscoelastic property [14]. Each of the wormlike micelle continues to break and reform either by itself or by interaction with its neighboring micelles within milliseconds timescale [15–17]. There have been many studies on such structures, due to their applications in many areas [17]. Researchers are mainly interested in the architecture of this structure because of its unique and beneficial reversible and flexible viscoelasticity.

Vesicles and Multilamellar

Lamellar structure is formed by fine alternating layers of different materials, or in the case of micelle aggregation are the alternating hydrophilic and hydrophobic layers as shown in Fig. 6b. When they form unilamellar structure with a hollow core, it is known as vesicle as in Fig. 6a. This kind of aggregation occurs when its $CP \geq 1/2$ [4].
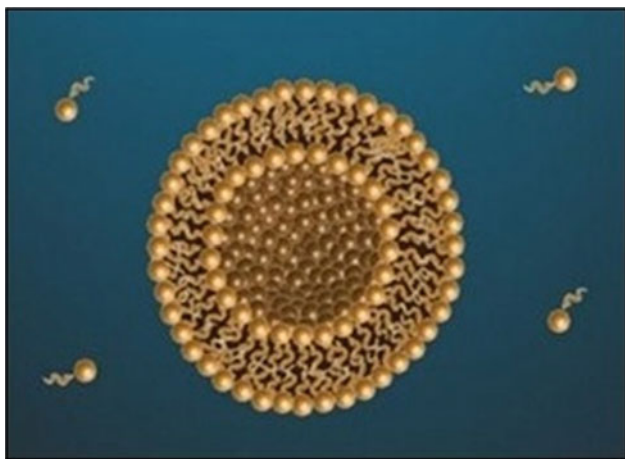
Fig. 6 Illustration of a vesicle
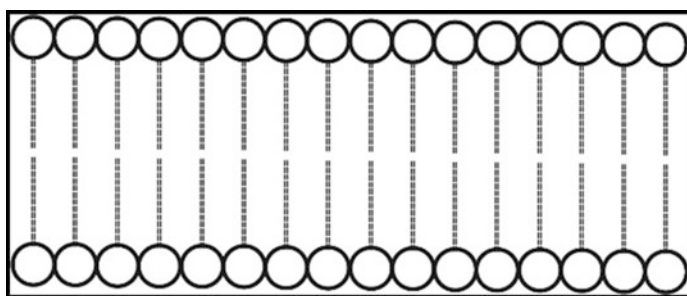
Fig. 7 A bilayer system formed by micelle forming surfactant

If the molecular assembly process is solely governed by the hydrophobic attraction, the monomers would prefer to aggregate to form a bilayer structure as shown in Fig. 7. However, due to the strength of hydrophilic repulsion of the hydrophilic head groups, the bilayer folds to form a vesicle with expected number of monomers to be less in the inner layer compared to the outer layer. This type of assembly can only form when the hydrophobic interaction is relatively much stronger than the head groups' repulsion. However, the inner heads are still assumed to be very closely packed. Transformation of micelle structure from wormlike micelle to vesicle can be easily detected by the significant and sudden viscosity reduction.

There has been many reports on micelle structural changes according to the order of the structures discussed above – monomer to spherical to rodlike/cylindrical to wormlike and to vesicle. In a simple system, e.g., the addition of strong binding counterions to a micelle solution can induce the aforementioned structural transformation. An example is the mixture of cetyltrimethylammonium bromide and
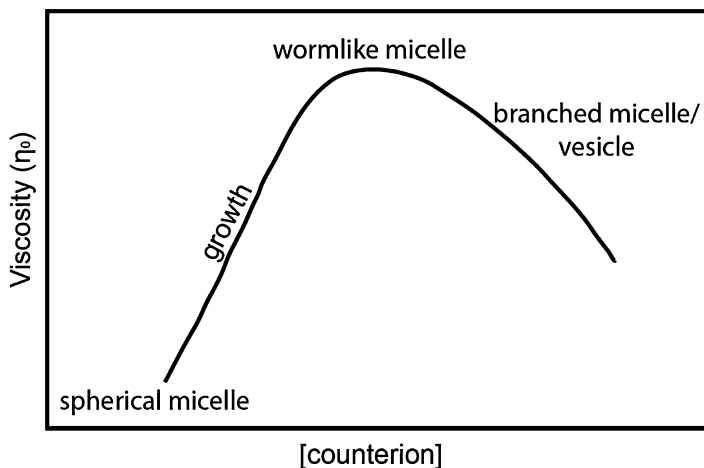
Fig. 8 The zero shear viscosity (η_0) of a micelle system upon increasing concentration of its counterion
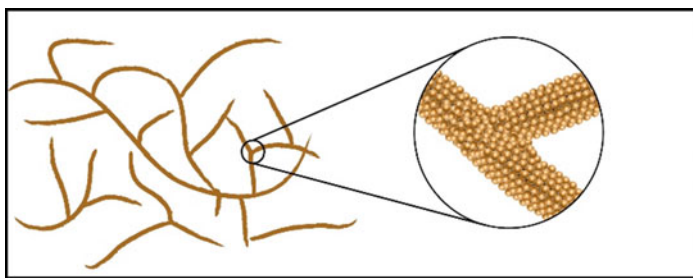
Fig. 9 Illustration of a branched micelle system

5-methylsalicylate [18]. Typically, this is detected by the viscosity measurement upon increasing counterion concentration as shown in Fig. 8.

There have been many studies that reported the formation of branched micelles (Fig. 9) instead of vesicles [2, 3, 19–25]. The branched micelle was found to exhibit a reduction in its viscosity value compared to the system of linear entangled wormlike micelle (Fig. 9).

The appearance of the branches in a micelle system is the way for a micelle to compensate the increase of its end cap energy, therefore having a mean curvature at the opposite direction of the original end caps [3, 5]. This is as a result of reptation reaction mechanism which will be explained in detail later. These intermicellar junctions have the ability to slide/diffuse effectively along the micelles' curvature length to release the stress also known as the relaxation process. This existence of this structure can only be confirmed by cryo-TEM imaging [2, 10].

Microstructural Transformation of Micelle

Micelle aggregational responses toward different stimuli have been studied extensively since the discovery of its viscoelasticity in the 1970s. The viscoelasticity of micelle system is a result from the aggregation forming wormlike micelles. Initially, such aggregational structure was formed at very high concentrations of surfactant. In 1976, it was first discovered that wormlike micelle structure can also be induced at surfactant's low concentration by adding certain additive such as salicylate and chlorobenzoates [26]. This discovery is not only beneficial due to the need of much lower concentration in achieving viscoelasticity, but it also contributes to unfolding the mystery of micelles' aggregational behavior. Eversince, the effect of other stimuli such as temperature, shear, UV-light, and solution pH were discovered to be able to induce micellar structural transformation. Since sonication will also result in the increase of temperature as well as generation of strong shear, these two stimuli will be briefly reviewed as below.

Temperature

In 1996, the ability of temperature change to induce micelle structural transition was first reported [27]. The system used was a mixture between CTAB and sodium hydroxynaphthalene carboxylate (SHNC) forming cetyltrimethylammonium hydroxynaphthalene carboxylate (CTAHNC). Upon temperature change from room temperature to 70 °C, vesicle (diameter = 1–10 μm [28]) to wormlike micelle transition was observed. This may be explained as below. At lower temperatures, the hydroxynaphthalene carboxylate (HNC^-) counter ion shows weak solubility in water. Therefore, it binds strongly to the CTA^+ (from CTAB) micelles' palisade layer resulting in the formation of vesicles. At higher temperatures, the solubility of the HNC^- increases, which then results in the two forms present: bound (HNC^-_{mic}) and unbound (HNC^-_{aq}). With less counterion binding in the micelle phase, the vesicles transform to wormlike micelle system. Similar observation was reported with the existence of salicylate ions [27]. Another example is the temperature effect on the cmc of a nonionic micelle system – the Tween surfactant series [29]. Its cmc was found to decrease with the increasing temperature up to 57 °C and slightly increase with further increase in temperature.

Shear

A year after the first discovery of the effects of temperature on micelle system, the effect of shear on the same micelle system was reported by Mendes et al. [30] Similar to the previous case, almost all of the vesicles transformed to wormlike micelle structure upon subjected to shear. This is usually evident by the increasing viscosity of the system. The appearance of shear induced structure (SIS) is also an indication of its response toward shear [7]. SIS can be clearly observed from shear thickening

rheological behavior in a flow curve plot. There are three stages involved in shear thickening of micelles: (i) induction; (ii) aggregation; and (iii) orientation [31]. However, such SIS phase is usually unstable and will relax to its original structure after a short period of time [32]. Unlike the system reported by Mendes et al., which was stable [30]. With shear applied, the micelle is stretched or extended. Therefore, the probability of their intermicellar interactions increases compared to its original state [33]. With sufficient shear, the scission energy can be overcome and the end caps will be broken, resulting in micelles with residual charges [7]. The micelles with residual charges then combine to form longer structure of micelle system [33].

Another example of vesicle to entangled wormlike micelle transition by the effect of shear was reported by Zheng et al. on cetyltrimethylammonium chloride (CTAC) and 3-methyl salicylate ion (CH_3Sal^-) [34]. The aim of the study was to imitate the blotting flow deformation process in the preparation cryo-TEM sample. Initially, the CH_3Sal^- counterions intercalated at the vesicle/water interface. As a strongly binding counterion, CH_3Sal^- is an effective species in reducing the electrostatic repulsion effect between the CTA^+ head groups and promotes the formation of vesicle. In flow field, the straining deformation of the experiment disrupted vesicle structure and altered the distribution of CH_3Sal^- counterions around the fragments of vesicles. This fragmentation is known as the vesicle division. The formation and dissociation in micelle equilibrium is now shifted, therefore altering the local preferred curvature of the aggregation. This initiates aggregational instability of the vesicles' fragments which then induces their reconstruction into the entangled wormlike micelle structure.

Ultrasonics and Micelles

The effect of ultrasound on micelle structure is an area that has not been investigated in detail. Though the propagation of ultrasound in a solution results in acoustic cavitation that generates extreme temperature and strong shear, the effect is more complex than simply applying heat and shear. Therefore, it is essential to study the effect of ultrasound on micelle system. One of the related publications reported in the literature is a study by Wang et al. [35] in 2009 on an amphiphilic diblock copolymer micelle system of poly(ethylene oxide)-*block*-poly(2-tetrahydropyranyl methacrylate) (PEO-*b*-PTHPMA). The ultrasound used in this study was a high-intensity focused ultrasound (HIFU) system operated at 1.1 kHz frequency and 200 W. The ultrasound system used was similar to the one used in therapeutic medicine. The choice of using PEO-*b*-PTHMA micelle is based on its sensitivity toward low pH condition and to thermal effect by hydrolysis process. The PEO-*b*-PTHPMA was found to undergo lysis and converted to poly(methacrylic acid) (PMAA) upon sonication due to the hydrolysis-induced cleavage of tetrahydropyran-2-ol [35]. This was initially detected by the pH reduction of the solution and confirmed by infrared analysis, dynamic light scattering, atomic force microscopy, and fluorescent measurements. The extent of micelle disruption was found to be governed on the power of sonication, solution volume and the size, as well as the location of the

targeted focal area on the system. Upon detailed study, they also reported that such observation did not take place in control experiments where no ultrasound was introduced, instead the solution was just heated at 90 °C, or just vigorously stirred for 4 hours. Therefore, they suggested that the phenomenon observed in their study was not purely the effect of heat generated, but also initiated by the mechanical effect of sonication. The effect of ultrasound in the study discussed above is mainly due to its ability in breaking the monomer forming the micelle system, instead of rearranging the monomers. This can be useful for designing drug delivery system [36, 37] given that none of sonicated product is dangerous to the human body.

This is followed by another publication on micelle structural change upon sonication on a catanionic (cationic/anionic) system of CTAB and 1-butyl-3-methylimidazolium octyl sulfate (Cmim) by Ghosh et al. [38] Pure Cmim in aqueous solution forms tiny micellar aggregation at around 3 nm in size [39]. However, once CTAB was introduced at different fraction, χ_{CTAB} ($\chi_{CTAB} = (V_{CTAB})/(V_{CTAB} + V_{Cmim})$), different types of micelle aggregational structures appeared, evident by the changes in the turbidity and appearance of the solutions. A similar observation has been reported before. A mixture of cationic and anionic micelle usually results in a neutral micelle assembly at equimolar mixing [40]. For mixtures other than their equal ratio, there will be excess charge that may spontaneously induce the formation of different sizes of vesicles [41, 42], independent of their formation path [43].

In this study, at χ_{CTAB} below 0.25, the solution was clear and possessed low viscosity, due to the existence of small micelles of pure Cmim and those mixed micelles formed by mixture with CTAB. However, at $\chi_{CTAB} = 0.25$–0.6, the system appeared to be bluish in color and showed turbidity behavior. This indicates the aggregation of vesicles in the system. At $\chi_{CTAB} = 0.6$, they reported the formation of large multilamellar vesicles with their size around 200–400 nm as evident by TEM images. The aggregation was described as an onion-like arrangement consisting of several concentric bilayers. From $\chi_{CTAB} = 0.7$–0.8, the system forms elongated micelle with viscoelastic property and above 0.8 they seemed to revert back to a clear micellar phase. Samples at $\chi_{CTAB} = 0.6$ was then further treated for spectroscopic study. The system was put under a few cycles of freezing and thawing and later sonicated using an ultrasonic probe for 20 min. The sonication was able to break the multilayer arrangement, resulting in the formation of a single layer vesicle in the size range of 90–125 nm [38].

Despite the interesting structural changes reported in this study, it only focuses on the ability of ultrasound to break micellar structure as reported by Wang et al. [35]. In addition, none of these publications discussed the mechanism of micelle structural changes (disruption) by ultrasound.

Ultrasound-Induced Structural Transformation of CTASal Micelle

The ability of ultrasound as a stimulus to induce micelles' microstructural transformation was recently investigated. In the study, the micelle system used was cetyltrimethylammonium salicylate (CTASal), prepared by an ion exchange process

Fig. 10 Cryo-TEM image of CTASal micelle structures before sonication (Reproduced from Ref. [44] with permission from the Royal Society of Chemistry)
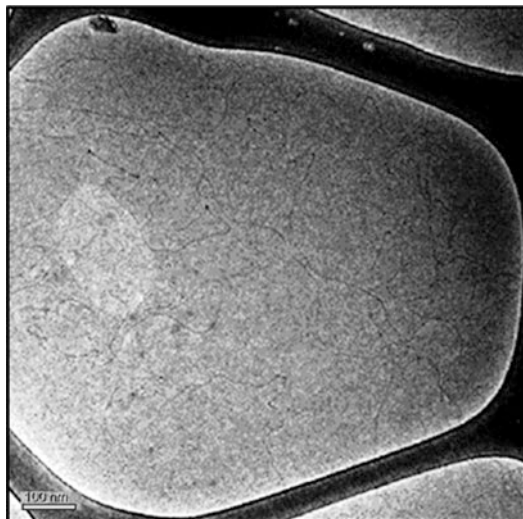
between cetyltrimethylammonium bromide (CTAB) and sodium salicylate (NaSal). A mixture of CTAB and NaSal was chosen over the commercially available CTASal due to the following reason. The existence of two counterions, i.e., bromide and salicylate ions would provide a better stability to the micelle system formed thereby inducing the formation of wormlike micelle even at lower concentrations. The effect of sonication on CTASal was investigated in the sonication frequency range of 20–1080 kHz and at applied power levels in the range of 10–70 W. Wormlike micelle structure was chosen by fixing the concentration ratio of 0.015 M CTAB and NaSal. The formation of wormlike micelle structure is evident from cryo-TEM imaging as shown in Fig. 10.

In addition, the effect of different sonication reactors on the CTASal micelle system has also been investigated. The reactors used were horn-, plate- and high-intensity focused ultrasound (HIFU)- type transducers. All three systems delivers different powers and from different directions. Horn and plate type transducers are standard commercially available units. However, the HIFU transducer used was custom built. The schematics of the three transducers are shown in Fig. 11.

The horn-type sonication reactor used was a Branson cell disruptor Model 450D. The frequency of this unit was 20 kHz with a maximum power output of 400 W. As shown in Fig. 11 (left), the ultrasound wave propagates through the medium from the horn transducer from the top direction. Since the depth of the transducer can be adjusted, the position was fixed throughout the experiment. The diameter of the horn used was 1 cm. The plate-type transducer used was an Allied Signal plate transducer combined with the ELAC RF generator. This is shown in Fig. 12. Four sets of transducers were used in order to vary the ultrasonic frequencies at 211, 355, 647, and 1080 kHz. The maximum applied power for this type of transducer was 100 W. For the purpose of comparing the frequencies, the applied power was fixed at
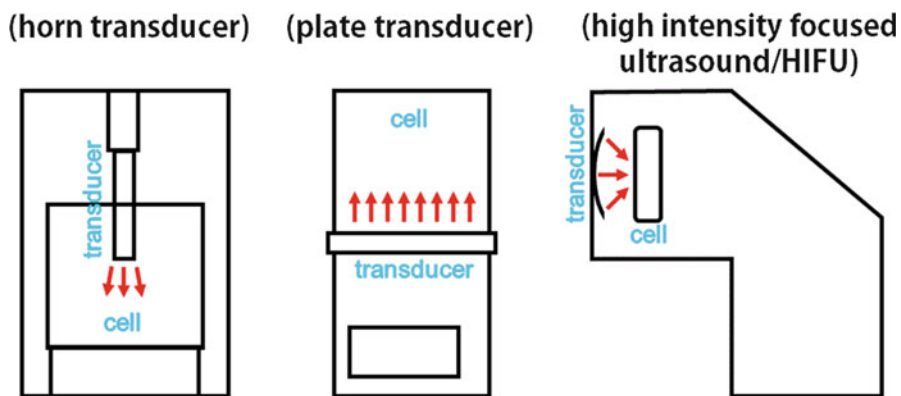
Fig. 11 The three ultrasonic reactors used in the study – horn-type transducer on the *left*, plate-type transducer in the *middle*, and high-intensity focused ultrasound (*HIFU*) on the *right*
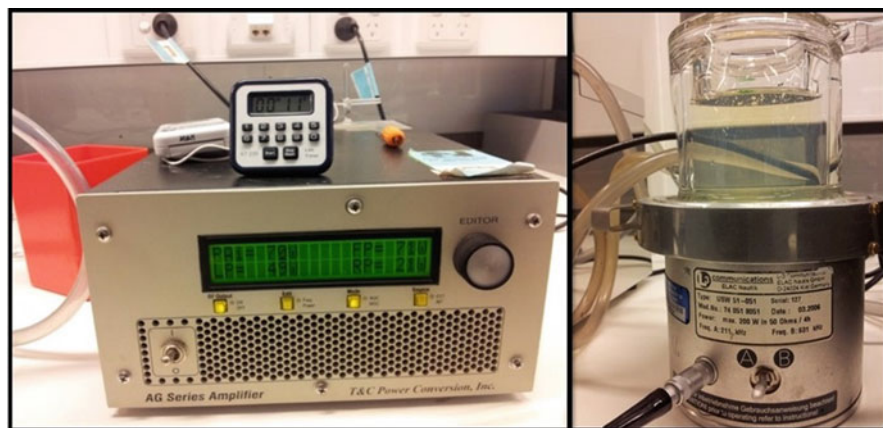
Fig. 12 The experimental setup of the sonication with the plate-type transducer. *Left*: function generator and amplifier; *Right*: transducer and glass cell

40 W. However, for the purpose of comparing the applied sonication power, few sets of experiments were carried out at 10, 40, and 70 W at 355 kHz.

For both transducers – the horn- and plate-type, 200 mL of micelle solution was used. The absorbed acoustic powers were measured by a calorimetric technique for all systems. The temperature of the experiments were maintained at 30 °C using a thermostated water jacket. Cryo-TEM images were taken for the sonicated micelle systems using a TF30 Transmission Electron Microscope from Tecnai, Heindoven, the Netherlands. The cryogenic treatment was essential due to the reversible nature of a micelle system. This will be discussed later. The rheological experiment was done using an AR-G2 Controlled Stress Rheometer from Anton Paar.
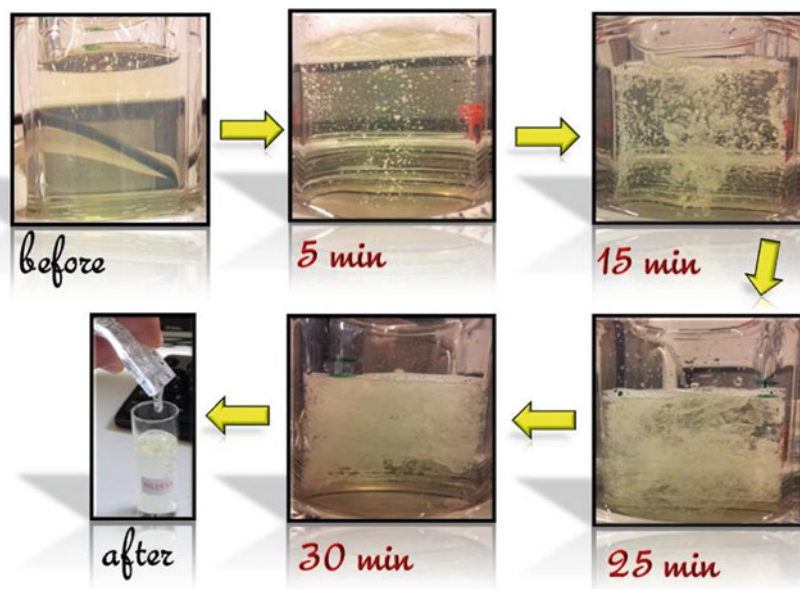
Fig. 13 The pictures of micelle solution over sonication time. The solution was homogenous before sonication started. When sonication started, small micelle agglomerates appeared and adhered together with increasing sonication time. This lead to the separated two layers of micelle system when sonication was stopped. The after image was taken during the transfer of the top layer from one cell to another (Reproduced from Ref. [44] with permission from the Royal Society of Chemistry)

Sonication at 211 kHz Frequency and 40 W Power

The first set of experiment was carried out using the plate-type transducer at 211 kHz frequency and 40 W of power. Upon sonication, the homogeneous micellar solution was transformed into two separated layers of micelle system with significant difference in their viscoelasticity. This is shown in the pictures taken at different sonication times in Fig. 13. The first image was taken for the micelle solution before sonication experiment. It was left overnight for equilibration. Within the first few minutes of sonication, the micelle agglomerates were visible and agglomeration increased with an increase in sonication time. These individual aggregates adhered together leading to phase separation. The two layers stayed separated when sonication was stopped. The aforementioned changes in were absent when blank experiments were carried out without ultrasonic irradiation, instead only with shear effect caused by stirring a magnetic stirrer. Therefore, it can be concluded that such changes were induced by sonication effect. By initial visual observation, the top layer of the sonicated micelle system was showing strong viscoelasticity. On the other hand, the bottom layer showed a water-like viscosity. The opaque top micelle
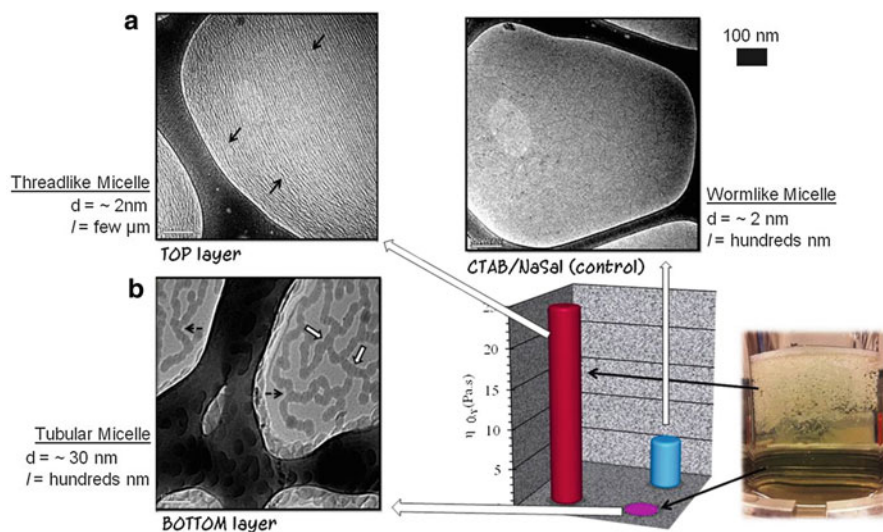
Fig. 14 The viscosity values and cryo-TEM images of CTASal micelle system before sonication and for the both top and bottom layers after sonication (Reproduced from Ref. [44] with permission from the Royal Society of Chemistry)

layer and the bottom, smaller aggregates in the aqueous micelle system were analyzed to determine their aggregational structure and viscoelasticity property.

The viscosity result and cryo-TEM images of the micelle system for both layers are presented in Fig. 14. The viscosity of the CTASal micelle system before sonication was measured to be around 6 Pa.s. However, after sonication, the top layer of the micelle system was found to exhibit viscosity value for almost four times greater (22.7 Pa.s) than that of before sonication and the bottom layer was found to exhibit more than 100 times less viscosity (0.04 Pa.s). The high viscosity shown for the top layer is due to the structural transformation of initial wormlike micelle to long and stable threadlike micelles. These micelles entangled together by the force of ultrasound from the plate transducer. On the other hand, the low viscosity observed of the sonicated bottom layer is due to the formation of vesicles and tubular micelles. The significant difference of viscoelasticity can be properly explained by looking at their cryo-TEM images.

Upon cryo-TEM imaging, it was found that the wormlike micelle initially formed by CTASal solution underwent significant transformation during sonication. The top layer of the sonicated micelle formed a very long threadlike micelle structure, thence exhibiting higher viscoelasticity. The structure has a diameter of ~2 nm and length of several μm. This was determined by examining the end caps of the micelles seen on the images. On the contrary, tubular micelles were observed at the bottom layer of the sonicated micelle system, thence the water-like viscosity shown. The diameter of the micelle is ~30 nm with a length of a few hundred nanometers.

With detailed inspection of the images, some important characteristics of micelle displayed can be detected. The long threadlike micelles formed in the top layer were

greatly aligned. The cause of this is sonication, rather than other factors during sample preparation. Despite being almost completely aligned, the occurrence of bond interchange between the individual micelles are obvious from the four-armed star junction points shown by the black arrows in Fig. 14. On the other hand, close examination of the tubular micelle in the bottom layer of sonicated micelle revealed that the tubular structure is due to the coalescence of vesicles in the system. At a given magnification, the coalesced vesicles building a tubular micelle can be clearly seen. The interaction results in the structure of tubular micelle with T-shape (white arrow) and Y-shape (dashed arrow) junctions. Some of the vesicles are still visible in the cryo-TEM images. Some examples are shown by the black circle in Fig. 14. This is due to the reversed process of tubular micelle formation caused by the effect of shear during the blotting process of the sample preparation. The process of vesicle coalescence takes a longer time than the relaxation of aligned micelles. This also indicates that the coalesced vesicles in this form are intermediates rather than stable structures. The detailed information revealed from cryo-TEM images will help in proposing the structural transformation of the micelle system to be discussed later.

Micellar Structural Transformation

The structural transformation of micelle as observed in the case study above may offer a great possibility in many technological advancement and improvements in industries. Despite the many discoveries of micelle structural responses toward different stimuli, the mechanism was never discussed in detail. In 1980s, early attempts to propose a theory for micelle transformation was done based on polymer system. However, due to significant difference of rigidity between polymer and micelle system, Cates came up with a refined theory in 1987 known as the Reptation Theory [45]. The model was refined by taking into account the continuous reptation and breakage of individual micelle [46]. The overview of micelle reptational and breakage processes are reviewed in this section.

Reptation Model

The resemblance of a system of elongated micelles, especially the entangled worm-like micelle to polymers has been proposed before, evidenced by the emerging publications on the analogy between these two [21]. Their appearance similarity emanate relaxation mechanism theory for micelle systems adapted from the well-known relaxation theory of polymers [45]. According to the original theory for a polymer in melt, the stress relaxation process of the polymer relies on the reptational diffusion of its long linear chains [45, 47]. This is a process when any given chain in a semidilute system gradually disentangles from its neighboring chains which creates a tube-like environment by diffusing along its own curvilinear silhouette [47]. The relaxation of the reptation process is given by Eq. 3. $\bar{L}$ is the fixed length of the particular polymer chain and D_0 is its mobility constant.

$$\tau_{rep} = \overline{L^3}/D_0 \tag{3}$$

According to the reptation theory for polymers, the self-diffusion coefficient has a direct influence to its aggregational property, according to Eq. 4 below. D_S is the self-diffusion coefficient, N is the number of monomers per chain, and c is the concentration of the monomer [46, 48].

$$D_S \propto N^{-2}c^{-1.75} \tag{4}$$

In such discussion, the polydisperse distribution focuses on its mean value, N_0, and is known to increase with the monomer's concentration according to the Eq. 5 [46].

$$N_0 \propto c^{0.5} \tag{5}$$

However, Eq. 5 is only true in an ideal case, when the interactions between the chains are completely ignored. Thus, the equation was later simplified as Eq. 6 [49].

$$N_0 \propto c \tag{6}$$

Therefore, from Eq. 6, the polydispersity distribution is represented in Eq. 7.

$$D_S \propto c^{-3.75} \tag{7}$$

However, in contrast to a polymer, micelle is a dynamic system with its ability to continuously break/dissociate and reform at equilibrium, K_M [45]. These processes are represented by Eq. 8. In this equation, k_f is the rate of micelle formation and k_d is the rate of micelle deformation.

$$K_M = k_f / k_d \tag{8}$$

The micelle formed undergo a reversible exchange of its monomers [50]. Due to this characteristic, such spontaneously formed system of elongated micelle has also been described as a type of "living polymer," examples include CTAB/KBr (cetyltrimethylammonium bromide/sodium bromide) and CTAC/NaSal (cetyltrimethylammonium chloride/sodium salicylate) [21, 51–53]. Micelle is also very different than a polymer in its number of monomers per aggregation or aggregational unit. Unlike a polymer, the length of a micelle chain will continuously change depending on many internal and external factors such as its concentration, additive(s) existence, and other stimuli. In realization to this, Cates proposed the modified relaxation theory of micelle in 1987 by taking into account its dynamic properties. Following the discussion, he has outlined a few kinetic assumptions of micelles' breaking and recombination processes as below [45]:

(i) A micelle chain can break with a fixed probability per unit time per unit length at any part in the chemical sequence.

(ii) Reversed reaction or recombination of two chains occur with a rate proportional to the concentration of the product of the two reacting subchains.

(iii) Rate constant involved is independent of the molecular weights of these two subchains.

(iv) There is no higher probability for a chain end to link up with the chain from which it was recently detached than with any other chain end in the vicinity.

With the aforementioned rules in mind, the stress relaxation model revolves around two important time scales which are the τ_{rep} and τ_{break}. This is the main difference of micelle system as compared to polymers. The τ_{rep} represents the survival time for the classical reptation process of a chain within the micelle's contour length to occur before it disappears due to recombination. On the other hand, the τ_{break} is the survival time of a chain within $\bar{L}$ before it breaks into two independent chains [45, 46]. These two are highly influential for the related discussion as their balance determines the micelle system's harmony [45].

In cases that the reptation time is less than its breaking ($\tau_{rep} < \tau_{break}$), the principal of stress relaxation process of a micelle system is merely by reptation process. When τ_{rep} is much less than τ_{break}, ($\tau_{rep} << \tau_{break}$), along with the continuous reptation, the chain is essentially unbreakable [50]. In this condition, any possible reaction can be considered as impossible. The particular chain will diffuse along its curvilinear distance and become completely free from its original tube [50]. However, in a steady state of a dynamic equilibrium of a micelle system, a chain can break in any interim along its length, as well as it can recombine with another chain in a short time interval. Cates has outlined the two principals in micelles' relaxation mechanism [45]:

(i) The chain can break within a certain length traveled.

(ii) The curvilinear diffusion may bring the new chain end past before it recombines.

In this discussion, the interaction between micelles is equally important and cannot be overlooked. In addition, neighboring chains are also expected to alter their arrangements under the same time scale. Elongated micelles in a semidilute system are usually entangled and continuously interacting with each other. In understanding this, two popular models are usually used for discussion purpose: (i) tube model and (ii) breathing modes model. According to the tube model, the neighbors of a particular chain in an entanglement provide a tube-like steric constraint that restricts the diffusive motion as the chain moves [46, 47, 49, 50, 54]. This has been briefly mentioned as part of the discussion before. This chain can break with roughly equal probability per unit time in any point along its length. The recombination point relies smoothly on the chain lengths that, by detailed balance, the lifetime of a broken end before recombination (τ_{rep}) is comparable to the lifetime of the original chain before breaking (τ_{break}) [45]. On the other hand, when there is a fluctuation in its tube length, the tube is said to be in a "breathing mode" where it

stretches in the Rouse-like motion that is shorter than the entanglement length. In this case, reptation to a specific tube segment is not required, instead the process is faster by the breathing fluctuation process [45]. Both models are considered possible under specific condition in the micelle system. However, in many cases, tube model is used to ease the discussion. But, in many cases, the neighboring chains are also expected to alter their arrangements under the same time scale [45].

In another case that the reptational time is greater than its breaking, $\tau_{rep} > \tau_{break}$, the chain will break at a point close enough to a given segment of tube for reptative relaxation to occur before the new chain end is lost by recombination. In other words, the chain breakage and reformation occur often before it has disengaged from its tube by ordinary reptation. In this case, the time scale for the stress relaxation mechanism, τ_R is given by Eq. 9 [45].

$$\tau_R = \left(\tau_{rep} \bullet \tau_{break}\right)^{0.5} \qquad (9)$$

When τ_{rep} is much greater than τ_{break}, $\tau_{rep} >> \tau_{break}$, the chain undergoes a number of breakages before it reptates out of its original tube [50]. This can be explained as below. As elucidated before, as the micelle is entangled in its semi dilute regime, each chain is constrained by a tube-like environment of its neighbors. With any small strain on the system, the particular micelle exists in nonequilibrium conformation or chaos and therefore induces the stress relaxation process. This takes place by the reptation diffusion process along its curvilinear length until the chain is out of its original tube, and enters a new tube, which at that point, is in equilibrium. At this point of the end of the chain, the particular micelle is said to be relaxed. From the discussion, even though the two time scales τ_{rep} and τ_{break} are important in understanding the stress relaxation mechanism of a micelle system; the stress relaxation time is simply represented by τ_{rep} [50]. The adsorbing ends of the chain segments make arbitrary jumps with appropriate transition probabilities or known as the recombination process.

Recombination of micelles can take place when two micelles come into contact with each other at some point with a sufficient energy available, such as the sudden change in the temperature or temperature jump in a system. There are three possible routes of recombination which are the reverse scission or end to end reaction, bond-interchange reaction, and the end-interchange reaction. Many factors were predicted to command any of the preferred routes between the three such as different chemical components, salinity, and temperature condition [50]. However, the discussion remains vague. The cases of all three possible recombination of micelles will be discussed separately in the section below. For the discussion, the breaking time of a micelle, τ_{break} is assumed to be independent of the concentration of surfactant and inversely vary with micellar length ($\tau_{break} \sim L^{-1}$) [45].
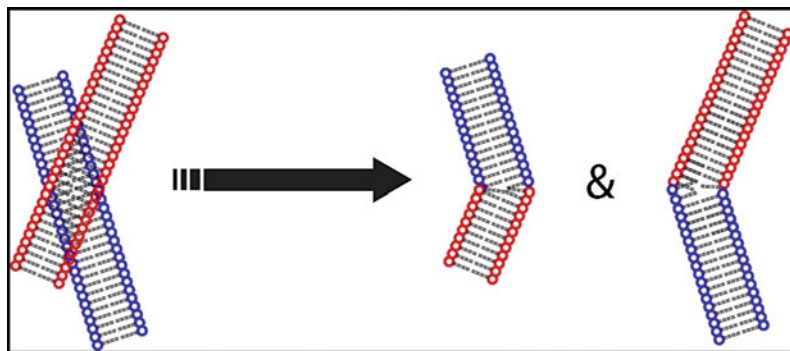
Fig. 15 Bond-interchange reaction between two elongated micelles

Reactions of Micelles

Bond-Interchange Reaction

Bond-interchange reaction is when two chains react and combine at some random point along their curvature length. This is evident by the appearance of a transient structure of a four-armed star junction, which can be detected by cryo-TEM imaging. This interaction results in the breaking of the structure to two new chains, with random exchange process of one part between the two of them. This is illustrated in Fig. 15. If this does not occur, both of them will break to form their original structures [50].

For bond-interchange reaction to occur, the timescale, τ_{break} is given by Eq. 10 where ϕ is the volume fraction of micelle and k_b is the rate constant [50].

$$\tau_{break} = \left(\phi \overline{L} kb\right)^{-1} \tag{10}$$

The τ_{break} is the supposedly needed time for one average chain to break. Considering the equilibrium of micelle aggregation as discussed before, τ_{break} is also comparable to the supposedly needed time for recombination reaction, τ_{rep}.

Even though the reaction is characterized by its rate constant, its overall rate is proportional to the square of its curvature length density. In this case, the lateral motion of the chains usually cannot be constrained by the entanglement of the system. Therefore, most of the time, through the bond-interchange reaction, micelle chain will pass through each other, or known as the "tube evaporation" process. In this unique process that cannot take place in polymer system, the entanglement of micelle is removed. Turner has summarized the relaxation time scale for different mechanisms of bond-interchange as Eq. 11 [50].

$$\tau \approx \begin{cases} \tau_{rep} & \text{for } \zeta \geq 1, \text{ "unbreakable" chains} \\ \zeta^{1/3}\tau_{rep} & \text{for } \alpha^{3/2} \leq \zeta \leq n1, \text{ reptative regime} \\ \alpha^{-2/5}\zeta^{3/5}\tau_{rep} & \text{for } \alpha^4 \leq \zeta \leq \alpha^{3/2}, \text{ breathing regime} \end{cases} \tag{11}$$

And by scaling, the relationship of τ with its micellar volume fraction, ϕ is given by Eq. 12 [50].

$$\tau \sim \begin{cases} \phi3.4 & \text{for } \zeta \geq 1, \text{ "unbreakable" chains} \\ \phi1.7 & \text{for } \alpha^{3/2} \leq \zeta \leq 1, \text{ reptative regime} \\ \phi1.2 & \text{for } \alpha^4 \leq \zeta \leq \alpha^{3/2}, \text{ breathing regime} \end{cases} \tag{12}$$

The attempt frequency is highest for the bond-interchange process compared to the other two which will be discussed below. But its activation energy is also found to be higher compared to others.

End-Interchange Reaction

End-interchange reaction is when the end of the first micelle chain "attack" and combine with the second chain at its random point along its curvilinear length. In this case, a transitory three-armed star junction forms and then break to two new chains. The first chain combines with a section from the second chain, and another section from the second chain breaks as a new independent chain. This is illustrated in Fig. 16.

The timescale for this particular reaction is given in Eq. 13 where C_e is the chain's density and k_e is the rate constant for the end-interchange reaction process.

$$\tau_{break} = \left(C_e \overline{L} k_e\right) - 1 = \left(\phi k_e\right)^{-1} \tag{13}$$

Even though the reaction is characterized by its rate constant, k_e, the overall rate is proportion to two parameters – the curvature length density and the density of end chains. The summary of the relaxation time scale for the different mechanisms of end-interchange reaction is shown in Eq. 14.

$$\tau \approx \begin{cases} \tau_{rep} & \text{for } \zeta \geq 1, \text{ "unbreakable" chains} \\ \zeta^{1/2}\tau_{rep} & \text{for } \alpha \leq \zeta \leq 1, \text{ reptative regime} \\ \alpha^{-1/4}\zeta^{3/4}\tau_{rep} & \text{for } \alpha^3 \leq \zeta \leq \alpha, \text{ breathing regime} \end{cases} \tag{14}$$

And the relationship of τ with its micellar volume fraction, ϕ is given by Eq. 15 below.

$$\tau \sim \begin{cases} \phi^{3.4} & \text{for } \zeta \geq 1, \text{ "unbreakable" chains} \\ \phi^{1.2} & \text{for } \alpha \leq \zeta \leq 1, \text{ reptative regime} \\ \phi^{0.58} & \text{for } \alpha^3 \leq \zeta \leq \alpha, \text{ breathing regime} \end{cases} \tag{15}$$

The attempt frequency of this mechanism is less than the frequency for bond-interchange mechanism, but more than the reverse scission which is explained below.
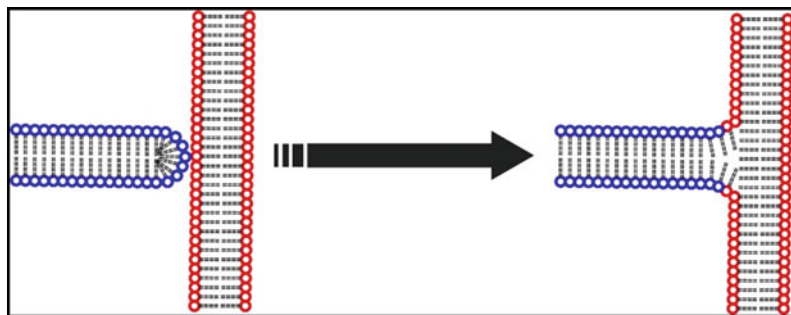
Fig. 16 End-interchange reaction

Fig. 17 Reversed scission or end to end reaction

Reverse Scission Reaction

Reverse scission reaction is when two micelles combine together at their ends thus sometimes termed as the end-to-end reaction. The bimolecular recombination reaction usually results in a longer linear unimolecular micellar chain. The reaction is illustrated in Fig. 17.

The timescale for this particular reaction is given in the Eq. 16 where k_s is its rate constant.

$$\tau_{break} = \left(\overline{L} k_s \right)^{-1} \tag{16}$$

For this reaction, k_s unit is per unit time per unit curvature length. However, it is speculated to be independent of its chain length.

The relationship of τ with its micellar volume fraction, ϕ is given by Eq. 17.

$$\tau \sim \begin{array}{ll} \phi^{3.4} & \text{for } \zeta \geq 1, \text{ ``unbreakable'' chain} \\ \phi^{1.4} & \text{for } \alpha \leq \zeta \leq 1, \text{ reptative regime} \\ \phi^{0.88} & \text{for } \alpha^3 \leq \zeta \leq \alpha, \text{ breathing regime.} \end{array} \tag{17}$$

The reverse scission reaction possess the lowest attempt frequency, but it also possesses much less activation energy as compared to bond-interchange and end-interchange reactions.

For all three cases, Turner has reported that the k_b, k_e, and k_s are independent on the chain length or concentration of micelle. Instead, they are highly dependent on the local motion of the chain's subsection [50]. It has also been reported that for the CTAB/KBr system, the temperature jump results only in reversible scission reaction.[50].

Mechanism

Based from the reptation and reaction model of micelle and the physical effects caused by sonication, the mechanism for ultrasound-induced structural transformation as observed in the case study of CTASal micelle is discussed in this section [44].

The propagation of ultrasound in liquid system causes a phenomenon known as the acoustic cavitation, which generates shear, heat, and reactive radicals upon bubble oscillation and implosion [55, 56]. In general, the physical forces generated during acoustic cavitation work according to the two categories – at "micro-" and "macro-" scales. The effect on the microscale is due to the cavitating and collapsing micron-sized bubbles at its antinodes. These processes generates strong shear due to the liquid system, known as the acoustic/cavitation microstreaming [55–57]. On the other hand, at the macroscale, the acoustic streaming pushes particles/materials in the system, causing separation of materials in accord to their sizes [58]. A number of theories have been proposed in describing the micellar structural transformation such as the reptation model of a polymeric micelle discussed in the section before [45, 59]. However, the explanations are considered as only speculations due to the missing experimental evidence at a molecular level. Therefore, the proposed mechanism for the case observed in this study in support of what was theoretically proposed earlier is crucial. Possible mechanisms of micelle structural changes are shown in Fig. 18.

The transitional processes are complementarily aided by the forces generated during sonication. IWM in Fig. 18 is the initial wormlike structure of CTASal that has been reported in earlier studies and shown in Fig. 10 of this book chapter [44]. LTM is the long threadlike micelle and TM is the tubular micelle structures observed for the top and bottom layers after sonication. The process of micellar aggregation to form long micelle structures is predicted to be similar to a polymerization process, but with the most important difference that the monomers continuously dissociate and reassociate forming a micelle structure [44, 45]. Due to this, unstable branching of micelles may form upon the changes in shear and temperature, and the micelles may revert back to the original IWM structure upon the removal of the stimuli. This is in contrast with the stable, aligned, very long threadlike micelles observed in the case study. In addition to the observation of these ultrasound-stimulated stable structures, the results also provide strong support to the reptation reaction model, which was initially proposed for polymer relaxation and extended by Cates [45] for wormlike micelles by considering the reversible breakdown and recombination of the structure [18, 60, 61]. Details of this model as according to the experimental evidence of the case studied are discussed below.

As shown in the mechanistic routes in Fig. 18, the nanostructural transition process starts with the entangled IWM prior to sonication at the center of the figure. As mentioned before, sonication results in the oscillation of microbubbles of different sizes from its minimum to maximum sizes, around less than 0.1–10 mm [62]. Some of these bubbles may be trapped in between the entangled IWM. The oscillation of these trapped microbubbles generates shear and acoustic microstreaming, which is favorable for the reptation process [45, 59]. According
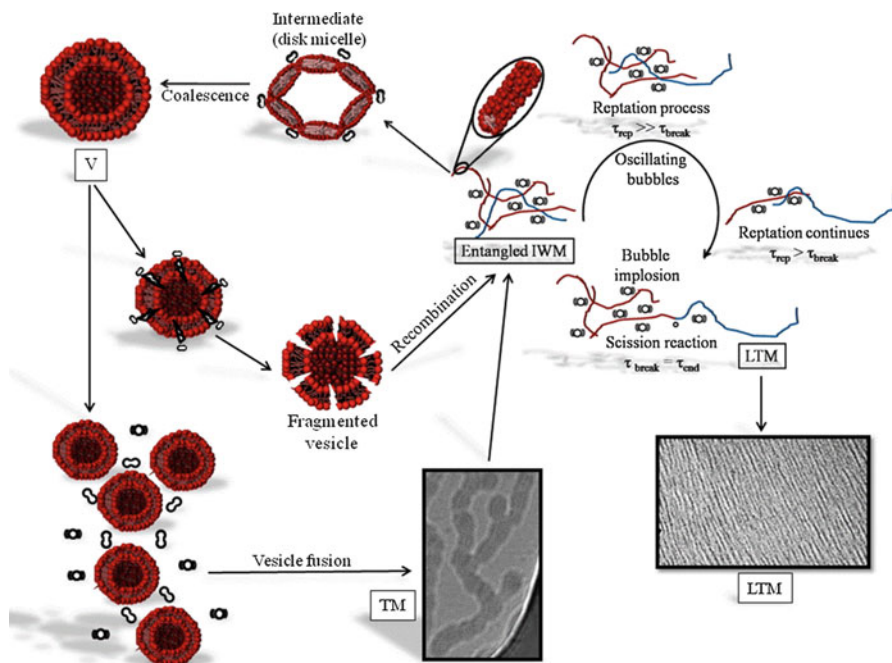
Fig. 18 The schematic illustration of the structural transitions of CTASal micelles from the initial wormlike structure to the long threadlike and tubular micelles (Reproduced from Ref. [44] with permission from the Royal Society of Chemistry)

to the reptation model of a micelle, the micelle forming surfactants may undergo reversible exchange reaction [59]. As reviewed earlier, the exchange reaction may take place by three means: (i) bond-interchange, (ii) end-interchange, and (iii) forward (scission) reactions. Bond interchange occurs when two wormlike micelles come into contact, break, and recombine as a four-armed star junction [50]. End-interchange reactions occur when the end of a wormlike micelle comes into contact with another wormlike micelle alongside, break and fuse to form a three-armed star junction [50]. This has not been observed in the case study. The forward reaction occurs when two wormlike micelles break at a random point along their length, reptate through and recombine at the end to end points of one another. Cates [45] has also mentioned that the highest probability of micelle interaction is the bond interchange reaction, however, the forward (scission) reaction possesses a much lower energy barrier compared to the other two reactions. The arguments put forward in this theory are fully supported by our experimental observations. The attempts for a bond interchange process are evident by the four-armed star junction. However, due to this structure being energetically unstable to recombine, the wormlike micelles continue to reptate through to be freed from the entanglement. This is majorly aided by the shear generated from microbubble oscillation. Mathematically, the process is due to the much larger relaxation time for the reptation process

compared to the relaxation process of the micelle breakage for recombination [50], thus reptation continues. In addition, the bubbles trapped in between the IWM achieve longer stability due to the IWM around them and continue to push the micelle free through reptation. As soon as the reptated micelle is released, the trapped bubbles are suddenly being freed from the entanglement and implode, inducing a temperature jump in the vicinity of the micelles, which causes the scission (end to end) reactions [26]. The breakage/recombination of micelles occur only when the reptation process finishes at the end of the micelles [50]. In other words, at the point when the ends of two micelles meet, breakage of the micelles occurs, which is followed by the recombination of the two of them. The whole process continues and results in the formation of LTM stabilized by the aligned patterned structure.

On the other hand, there is an equal probability of another case that the reptation process is agitated by a backward force from another oscillating bubble in the opposite direction, the micelles form a disk-like structure, which is known to be an intermediate to a vesicle [44]. The reorganization of disk micelles in a certain angle allows the bubbles to grow to their maximum size and collapse, resulting in a temperature jump in the vicinity of the micelles and recombination of the disk micelles forming vesicles (V). The vesicles then combine together forming tubular micelles™. The existence of TM agrees with the low viscosity but is higher than the viscosity of the vesicles, which is usually similar to water. TM is also known to be an intermediate in the structural transition process from vesicle to wormlike micelles as reported in the literature [35, 50]. From the above discussion, we may conclude that the processes shown at the right side of Fig. 18 build up the very viscoelastic top layer and the processes shown at the left side of Fig. 18 build up the less viscoelastic bottom layer as a function of sonication.

Sonication of CTASal Under Various Ultrasonic Conditions

A more comprehensive investigation on the effect of ultrasound frequency and power and the type of reactor on the structural changes was carried out [63]. Different structural responses were detected using rheological measurement and cryo-TEM images. These are shown in Table 1.

From Table 1, only sonication with plate-type transducers and at power more than 40 W resulted in the formation of two phases of micelle solutions with opposing degree of viscoelasticity. These two systems form separable layers and stay unmixed even after the sonication is stopped. The viscosity values and cryo-TEM images for these systems are shown in Figs. 19 and 20. For ease of discussion, Fig. 19 shows the experiments at different frequencies but at fixed power of 40 W, and Fig. 20 shows the experiments at different powers but at fixed frequency of 355 kHz.

Referring to the viscosity values in Fig. 20, it is clear that there is a decreasing viscosity trend with increasing frequency for the top layer system. On the contrary, an increasing viscosity was observed with increasing frequency for the bottom layer. To understand this, we need to examine the micelle structures formed in both layers,

Table 1 The effect of sonication parameters on the extent of micellar structural transformation

Transducer	Frequency	Power (W)	Phases(s)	η_0(Pa.s)	Micelles' structures
–	–	–	–	6.2	Wormlike micelle (control)
Horn (1 cm tip)	20	80	1	3.3	Rodlike micelle
Plate	211	40	2	24.7	Threadlike micelle
				0.1	Tubular micelle
	355	10	1	6.5	No change
		40	2	17.3	Threadlike micelle
				0.9	Tubular micelle
		70	2	21.0	Threadlike micelle
				1.0	Tubular micelle
	647	40	2	12.0	Threadlike micelle
				2.0	Tubular micelle
	1080	40	1	1.7	Vesicle
HIFU	643	10	1	4.9	Rodlike micelle
		40	1	4.3	Rodlike micelle
		70	1	4.3	Rodlike micelle

and understand the physical and chemical effects of sonication with increasing ultrasonic frequency along with the reference to the mechanism proposed.

Very long threadlike micelle structures were observed in the top layer for all three frequencies. They are ~2 nm in diameter and several μm in length. The cryo-TEM images for the threadlike micelles in all three systems seem to reveal some structural alignment. The threadlike micelle is the most aligned at 211 kHz and gets less coordinated with increasing frequency. The existence of tubular micelles can be seen from the cryo-TEM images of the bottom layers. The micelles are ~30–50 nm diameter and few hundred nm in length with the diameter increasing with the increasing frequency. At 211 kHz, despite the formation of the tubular micelle structure, the spherical shape of vesicle is still somehow visible, although not very clear. In other words, the micelle system forms a more stable tubular structure when sonicated at higher frequency. From sonication point of view, the wavelength is dependent on the ultrasonic frequency – longer at low frequency and shorter at high frequency. This results in the formation of larger microbubbles at low frequency when compared to those at higher frequencies. The oscillation of larger microbubbles results in the generation of relatively higher shear. As the frequency increases, microbubbles in the antinodes get smaller and generate relatively lower shear. Therefore, the shear decreases with increasing sonication frequency. According to the mechanism, the reptation of wormlike micelle is promoted by shear from the oscillating microbubbles. It seems logical that the threadlike micelle is the longest and most aligned at 211 kHz with highest viscoelasticity. To support the argument that the shear forces play a major role in causing changes to the structures and viscosity, let us look at the effect of sonication power. The shear is
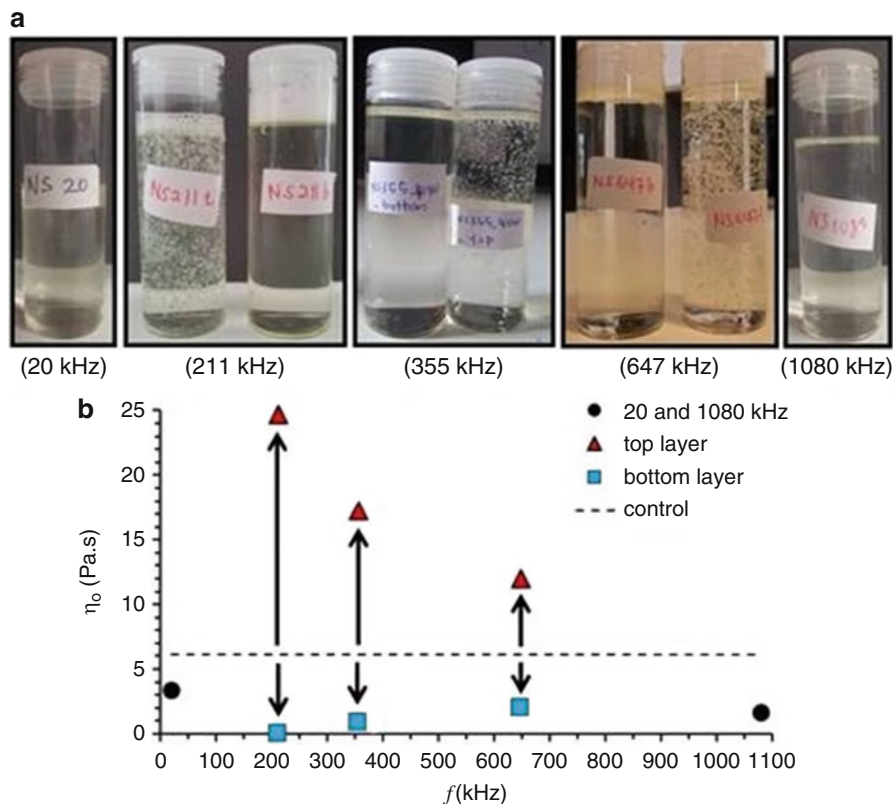
Fig. 19 (**a**) The top images are the sonicated CTASal micelle system at 20, 211, 355, 647, and 1080 kHz frequencies. 20 kHz uses horn-type transducer, and the rest are plate-type transducers. (**b**) At the bottom is the viscosity values of the systems (Reprinted from Ultrasonics Sonochemistry, 24, Nor Saadah Mohd Yusof, Muthupandian Ashokkumar, Ultrasonic transformation of micelle structures: Effect of frequency and power, 8–12 (2015), with permission from Elsevier)

known to increase with increasing power as the bubble size increases with an increase in power. Therefore, it can be expected that an increase in the micelle transformation from wormlike micelle to threadlike micelle occurs with increasing power, as shown in Fig. 20.

From Fig. 20, it can be seen that the shear forces generated at 10 W did not generate any structural changes in micelles. Sonication at 40 and 70 W results in the transformation of wormlike micelle and tubular micelle as observed before. The viscosity values increase with the increasing power. This supports the significant effect of shear in the formation of threadlike micelle from wormlike micelle upon sonication. The viscosity of the bottom layers did not show a significant change with increasing power from 40 to 70 W.

As also shown in the top left of Fig. 20, the sonication at 20 kHz of horn-type transducer results in only one phase of micelle, unlike the samples observed from
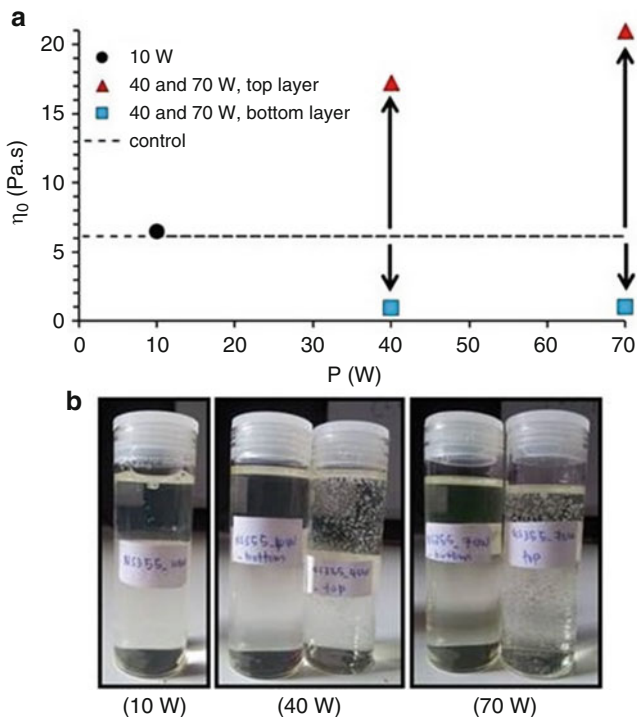
Fig. 20 The top is the viscosity values of CTASal micelle system at 355 kHz frequency and 10, 40, and 70 W of power. At the bottom are the images of the sonicated systems (Reprinted from Ultrasonics Sonochemistry, 24, Nor Saadah Mohd Yusof, Muthupandian Ashokkumar, Ultrasonic transformation of micelle structures: Effect of frequency and power, 8–12 (2015), with permission from Elsevier)

211 to 647 kHz. The viscosity was found to be at 3.3 Pa.s, about half of the original viscosity of CTASal before sonication. This is expected due to the very strong shear of such sonication system which may result in breaking of the micelles. The sonication using plate-type transducer at 1080 kHz also resulted in the formation of only one layer of micelle, with a much lower viscoelasticity observed. The viscosity value is just slightly above water (1.7 Pa.s) indicating the formation of vesicles and tubular micelles. As discussed earlier, the formation of long threadlike micelles take place through the reptation process of the wormlike micelles by the act of shear produced by the trapped oscillating microbubbles. On the other hand, when there are too many trapped microbubbles oscillating in opposite directions, the reptation process is disturbed, and micelle fragmentation occurs, resulting in the formation of disk-like micelles. They will then react together to form vesicles. A similar phenomenon is speculated at 1080 kHz. At this frequency, it is known that more microbubbles are formed by sonication, which may induce the formation of vesicles. This is supported by the viscosity value just above water shown.
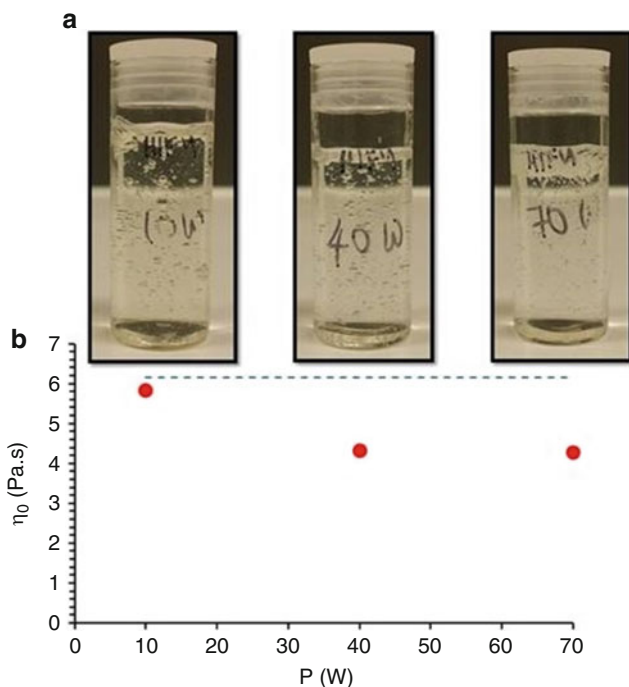
Fig. 21 (**a**) The images of sonicated CTASal micelle system using HIFU at 463 kHz frequency and applied power at 10, 40, and 70 W. (**b**) The viscosity values corresponding to (**a**)

Another type of sonicator used was the high-intensity focused ultrasound transducer, operated at 463 kHz frequency and at applied power of 10, 40, and 70 W. The pictures of the sonicated micelle system as well as their viscosity values are shown in Fig. 21.

As can be seen from Fig. 21, sonication of the micelle at all power levels results in only one phase of micelle. By visual observation, the viscoelasticity of these three systems cannot be distinguished. However, the viscosity values from rheological study showed a slight decrease in their viscosity in all three cases. We speculate that the breaking of CTASal micelles by HIFU took place, similar to the case proposed by Wang et al. [35] At 10 W, the viscosity was only slightly lower than the viscosity of CTASal before sonication. This is due to the weak shear forces generated below 25 W of power [64].

Conclusions and Future Directions

The basics of micelles and the effects of various stimuli on the structural and functional properties of micelles have been discussed in this chapter. The main focus of this chapter was to provide a comprehensive summary of the recently

completed study on the effect of ultrasound as a stimulus on the structural and functional properties of micelle systems. The data discussed in this chapter suggests that ultrasound can be used as an efficient stimulus in inducing micelle structural transformation in technological advancements. The following statements could be made from the data discussed in this chapter:

1. Ultrasonic irradiation of CTASal in the frequency range 211–647 kHz with power ranging from 10 to 70 W resulted in the transformation of wormlike micelle to long threadlike micelle and vesicle/tubular micelle, simultaneously.
2. According to the mechanism proposed, the direction of ultrasound-induced micellar changes and its extent of transformation are highly driven by the acoustic cavitation bubble oscillations.
3. The microbubble oscillation generates shear forces which drive the reptation process of the micelle. The temperature jump generated by microbubble implosion initiate recombination of micelles.
4. The transformation of CTASal micelle structure can be controlled by appropriate sonication experimental conditions as shown in Table 1. The structures are confirmed by the cryo-TEM images and rheological measurements.

The knowledge gained from this study can be applied in many technologies and applications. One of the examples is the Enhanced Oil Recovery (EOR) technology in oil drilling industry. In EOR technology, micelle with both behaviors of viscoelasticity and drag-reducing property are needed for different purposes. Therefore, both of the micelle characteristics are induced by different means of introducing different chemicals that does not only increase the cost of this industry, but could also be harmful to the environment. However, it is possible that by using ultrasound-induced micelle system, the required properties of micelle can be induced without the needs of introducing such harmful chemicals. If successful, this greener approach may eliminate the threats to the environment, as well as reduce the cost of EOR process.

References

1. Schryver SB et al (1913) Discussion. Trans Faraday Soc 9:93–107. doi:10.1039/TF9130900093
2. Croce V, Cosgrove T, Maitland G, Hughes T, Karlsson G (2003) Rheology, cryogenic transmission electron spectroscopy, and small-angle neutron scattering of highly viscoelastic wormlike micellar solutions. Langmuir 19:8536–8541. doi:10.1021/la0345800
3. Khatory A et al (1993) Entangled versus multiconnected network of wormlike micelles. Langmuir 9:933–939. doi:10.1021/la00028a010
4. Dreiss CA (2007) Wormlike micelles: where do we stand? Recent developments, linear rheology and scattering techniques. Soft Matter 3:956–970. doi:10.1039/B705775J
5. Guo L, Colby RH, Lin MY, Dado GP (2001) Micellar structure changes in aqueous mixtures of nonionic surfactants. J Rheol 45:1223–1243. doi:10.1122/1.1389315
6. Pérez-Juste J, Pastoriza-Santos I, Liz-Marzán LM, Mulvaney P (2005) Gold nanorods: synthesis, characterization and applications. Coord Chem Rev 249:1870–1901. doi:10.1016/j.ccr.2005.01.030

7. Vasudevan M, Shen A, Khomami B, Sureshkumar R (2008) Self-similar shear thickening behavior in CTAB/NaSal surfactant solutions. J Rheol 52:527–550. doi:10.1122/1.2833594

8. Yusof NSM, Khan MN (2010) Determination of an ion exchange constant by the use of a kinetic probe: a new semiempirical kinetic approach involving the effects of 3-F- and 4-F-substituted benzoates on the rate of piperidinolysis of anionic phenyl salicylate in aqueous cationic micelles. Langmuir 26:10627–10635. doi:10.1021/la100863q

9. Khan MN, Ismail E (2009) Kinetic evidence for the occurrence of independent ion-exchange processes in the cationic micellar-mediated reaction of piperidine with anionic phenyl salicylate. J Phys Chem A 113:6484–6488. doi:10.1021/jp902886z

10. Kim W-J, Yang S-M (2000) Effects of sodium salicylate on the microstructure of an aqueous micellar solution and its rheological responses. J Colloid Interface Sci 232:225–234. doi:10.1006/jcis.2000.7207

11. Magid LJ, Gee JC, Talmon Y (1990) A cryogenic transmission electron microscopy study of counterion effects on hexadecyltrimethylammonium dichlorobenzoate micelles. Langmuir 6:1609–1613. doi:10.1021/la00100a015

12. Arleth L, Bergström M, Pedersen JS (2002) Small-angle neutron scattering study of the growth behavior, flexibility, and intermicellar interactions of wormlike SDS micelles in NaBr aqueous solutions. Langmuir 18:5343–5353. doi:10.1021/la015693r

13. Magid LJ, Li Z, Butler PD (2000) Flexibility of elongated sodium dodecyl sulfate micelles in aqueous sodium chloride: a small-angle neutron scattering study. Langmuir 16:10028–10036. doi:10.1021/la0006216

14. Nakahara Y, Kida T, Nakatsuji Y, Akashi M (2005) New fluorescence method for the determination of the critical micelle concentration by photosensitive monoazacryptand derivatives. Langmuir 21:6688–6695. doi:10.1021/la050206j

15. Cates ME, Candau SJ (1990) Statics and dynamics of worm-like surfactant micelles. J Phys Condens Matter 2:6869

16. Cates ME (1990) Nonlinear viscoelasticity of wormlike micelles (and other reversibly breakable polymers). J Phys Chem 94:371–375. doi:10.1021/j100364a063

17. Magid LJ (1998) The surfactant−polyelectrolyte analogy. J Phys Chem B 102:4064–4074. doi:10.1021/jp9730961

18. Davies TS, Ketner AM, Raghavan SR (2006) Self-assembly of surfactant vesicles that transform into viscoelastic wormlike micelles upon heating. J Am Chem Soc 128:6669–6675. doi:10.1021/ja060021e

19. Koehler RD, Raghavan SR, Kaler EW (2000) Microstructure and dynamics of wormlike micellar solutions formed by mixing cationic and anionic surfactants. J Phys Chem B 104:11035–11044. doi:10.1021/jp0018899

20. Schubert BA, Kaler EW, Wagner NJ (2003) The microstructure and rheology of mixed cationic/anionic wormlike micelles. Langmuir 19:4079–4089. doi:10.1021/la020821c

21. Candau SJ, Hirsch E, Zana R (1985) Light scattering investigations of the behavior of semidilute aqueous micellar solutions of cetyltrimethylammonium bromide: analogy with semidilute polymer solutions. J Colloid Interface Sci 105:521–528. doi:10.1016/0021-9797(85)90327-3

22. Magid LJ, Han Z, Li Z, Butler PD (2000) Tuning microstructure of cationic micelles on multiple length scales: the role of electrostatics and specific ion binding. Langmuir 16:149–156. doi:10.1021/la990686c

23. Raghavan SR, Kaler EW (2000) Highly viscoelastic wormlike micellar solutions formed by cationic surfactants with long unsaturated tails. Langmuir 17:300–306. doi:10.1021/la0007933

24. Khatory A, Lequeux F, Kern F, Candau SJ (1993) Linear and nonlinear viscoelasticity of semidilute solutions of wormlike micelles at high salt content. Langmuir 9:1456–1464. doi:10.1021/la00030a005

25. Clausen TM et al (1992) Viscoelastic micellar solutions: microscopy and rheology. J Phys Chem 96:474–484. doi:10.1021/j100180a086

26. Gravsholt S (1976) Viscoelasticity in highly dilute aqueous solutions of pure cationic detergents. J Colloid Interface Sci 57:575–577. doi:10.1016/0021-9797(76)90236-8
27. Hassan PA et al (1996) Vesicle to micelle transition: rheological investigations. Langmuir 12:4350–4357
28. Mendes E et al (1997) Shear-induced vesicle to wormlike micelle transition. J Phys Chem B 101:2256–2258. doi:10.1021/jp962790y
29. Mahmood ME, Al-Koofee DAF (2013) Effect of temperature changes on critical micelle concentration for tween series surfactant. Glob J Sci Front Res Chem 13:1–7
30. Mendes E et al (1997) Shear-induced vesicle to wormlike micelle transition. J Phys Chem B 101:2256–2258
31. Prötzl B, Springer J (1997) Light scattering experiments on shear induced structures of micellar solutions. J Colloid Interface Sci 190:327–333. doi:10.1006/jcis.1997.4866
32. Chen S, Rothstein JP (2004) Flow of a wormlike micelle solution past a falling sphere. J Non-Newtonian Fluid Mech 116:205–234. doi:10.1016/j.jnnfm.2003.08.005
33. Cressely R, Hartmann V (1998) Rheological behaviour and shear thickening exhibited by aqueous CTAB micellar solutions. Eur Phys J B 6:57–62. doi:10.1007/s100510050526
34. Zheng Y et al (2000) Cryo-TEM imaging the flow-induced transition from vesicles to threadlike micelles. J Phys Chem B 104:5263–5271. doi:10.1021/jp0002998
35. Wang J, Pelletier M, Zhang H, Xia H, Zhao Y (2009) High-frequency ultrasound-responsive block copolymer micelle. Langmuir 25:13201–13205. doi:10.1021/la9018794
36. Pitt WG, Husseini GA, Staples BJ (2004) Ultrasonic drug delivery – a general review. Expert Opin Drug Deliv 1:37–56. doi:10.1517/17425247.1.1.37
37. Kost J, Leong K, Langer R (1989) Ultrasound-enhanced polymer degradation and release of incorporated substances. Proc Natl Acad Sci 86:7663–7666
38. Ghosh S et al (2013) Spontaneous transition of micelle–vesicle–micelle in a mixture of cationic surfactant and anionic surfactant-like ionic liquid: a pure nonlipid small unilamellar vesicular template used for solvent and rotational relaxation study. Langmuir 29:10066–10076. doi:10.1021/la402053a
39. Miskolczy Z, Sebők-Nagy K, Biczók L, Göktürk S (2004) Aggregation and micelle formation of ionic liquids in aqueous solution. Chem Phys Lett 400:296–300. doi:10.1016/j.cplett.2004.10.127
40. Silva BFB, Marques EF (2005) Thermotropic behavior of asymmetric chain length catanionic surfactants: the influence of the polar head group. J Colloid Interface Sci 290:267–274. doi:10.1016/j.jcis.2005.04.012
41. Kaler EW, Murthy AK, Rodriguez BE, Zasadzinski JA (1989) Spontaneous vesicle formation in aqueous mixtures of single-tailed surfactants. Science 245:1371–1374
42. Yatcilla MT et al (1996) Phase behavior of aqueous mixtures of cetyltrimethylammonium bromide (CTAB) and sodium octyl sulfate (SOS). J Phys Chem 100:5874–5879. doi:10.1021/jp952425r
43. Marques EF (2000) Size and stability of catanionic vesicles: effects of formation path, sonication, and aging. Langmuir 16:4798–4807. doi:10.1021/la9908135
44. Yusof NSM, Ashokkumar M (2013) Ultrasound-induced formation of high and low viscoelastic nanostructures of micelles. Soft Matter 9:1997–2002. doi:10.1039/C2SM27423J
45. Cates ME (1987) Reptation of living polymers: dynamics of entangled polymers in the presence of reversible chain-scission reactions. Macromolecules 20:2289–2296. doi:10.1021/ma00175a038
46. Messager R, Ott A, Chatenay D, Urbach W, Langevin D (1988) Are giant micelles living polymers? Phys Rev Lett 60:1410–1413
47. de Gennes PG (1971) Reptation of a polymer chain in the presence of fixed obstacles. J Chem Phys 55:572–579. doi:10.1063/1.1675789
48. Leger L, Hervet H, Rondelez F (1981) Reptation in entangled polymer solutions by forced Rayleigh light scattering. Macromolecules 14:1732–1738

49. Tanford C (1974) Theory of micelle formation in aqueous solutions. J Phys Chem 78:2469–2479. doi:10.1021/j100617a012
50. Turner MS, Marques C, Cates ME (1993) Dynamics of wormlike micelles: the "bond-interchange" reaction scheme. Langmuir 9:695–701. doi:10.1021/la00027a015
51. Candau SJ, Hirsch E, Zana R, Adam M (1988) Network properties of semidilute aqueous KBr solutions of cetyltrimethylammonium bromide. J Colloid Interface Sci 122:430–440. doi:10.1016/0021-9797(88)90377-3
52. Wunderlich I, Hoffmann H, Rehage H (1987) Flow birefringence and rheological measurements on shear induced micellar structures. Rheol Acta 26:532–542. doi:10.1007/BF01333737
53. Rehage H, Hoffmann H (1988) Rheological properties of viscoelastic surfactant systems. J Phys Chem 92:4712–4719. doi:10.1021/j100327a031
54. Leger L, Hervet H, Rondelez F (1981) Reptation in entangled polymer solutions by forced Rayleigh light scattering. Macromolecules 14:1732–1738. doi:10.1021/ma50007a023
55. Ashokkumar M, Mason TJ (2000) In: Kirk-Othmer encyclopedia of chemical technology. Wiley
56. Leighton T (1994) Academic Press, London
57. Tho P, Manasseh R, Ooi A (2007) Cavitation microstreaming patterns in single and multiple bubble systems. J Fluid Mech 576:191–233. doi:10.1017/S0022112006004393
58. Shoh A (1975) Industrial applications of ultrasound – a review I. High-power ultrasound. IEEE Trans Sonics Ultrason 22:60–70. doi:10.1109/T-SU.1975.30780
59. Patist A, Jha BK, Oh S g, Shah DO (1999) Importance of micellar relaxation time on detergent properties. J Surfactant Deterg 2:317–324. doi:10.1007/s11743-999-0083-6
60. Ziserman L, Abezgauz L, Ramon O, Raghavan SR, Danino D (2009) Origins of the viscosity peak in wormlike micellar solutions. 1. mixed catanionic surfactants. A cryo-transmission electron microscopy study. Langmuir 25:10483–10489. doi:10.1021/la901189k
61. Mohanty A, Patra T, Dey J (2007) Salt-induced vesicle to micelle transition in aqueous solution of sodium N-(4-n-octyloxybenzoyl)-l-valinate. J Phys Chem B 111:7155–7159. doi:10.1021/jp071312s
62. Brotchie A, Grieser F, Ashokkumar M (2009) Effect of power and frequency on bubble-size distributions in acoustic cavitation. Phys Rev Lett 102:084302
63. Ashokkumar M, Maspm TJ (2007) In: Kirk Othmer encyclopedia chemical tenchnology
64. Yusof NSM, Ashokkumar M (2015) Ultrasonic transformation of micelle structures: effect of frequency and power. Ultrason Sonochem. 24:8–12. doi:10.1016/j.ultsonch.2014.11.003

Ultrasound-Assisted Synthesis of Electrocatalysts for Hydrogen Production

Pavel V. Cherepanov and Daria V. Andreeva

Contents

Abstract

Hydrogen is a clean fuel that can be produced by means of hydrogen evolution reaction (HER) during water splitting process. HER requires the catalysts which could provide reversible binding of hydrogen that is energetically comparable with the process catalyzed by platinum (Pt). According to the most recent industrial reports, only 5 % of worldwide produced hydrogen is coming from electrolytic water splitting. One of the main obstacles is a very high onset overpotential which results in high energy consumption during hydrogen production process. Another problem is use of rather expensive precious metals and

P.V. Cherepanov • D.V. Andreeva (✉)
Physical Chemistry II, University of Bayreuth, Bayreuth, Germany
e-mail: daria.andreeva@uni-bayreuth.de

complicated multistep technological processes for synthesis of nanostructured materials. In this chapter, the main structural, compositional, and morphological aspects defining the efficiency of inorganic materials toward HER are summarized. Furthermore, materials containing earth-abundant transition and rare earth metals are highlighted as possible alternatives to Pt. It is demonstrated that alloys, nanoalloys, and near-surface alloys offer a number of potentially effective candidates toward HER. Use of high-intensity ultrasound for bottom-up synthesis of catalysts and especially for top-down structuring as well as activation of metal surfaces is discussed as a promising technological solution for the design of low-cost, robust, and efficient electrocatalysts.

Introduction

Hydrogen is an environmentally friendly energy carrier. Hydrogen evolution reaction (HER) is a process of hydrogen production from various sources including water. Technologically, production of molecular hydrogen via water splitting is a "green" process that does not produce harmful side products and uses renewable energy (grid, wind, solar, nuclear). Nowadays, one of the major needs for efficient electrolysis is the development of low-cost, active, and stable catalyst [1].

In the last few decades, there have been carried extensive studies on the subject of finding efficient, robust, and low-cost catalyst for electrocatalytic water splitting which could potentially replace widely used Pt electrocatalyst. Having found such catalyst would make overall process of highly pure hydrogen production by electrolysis preferable from the economical point of view in comparison to fossil fuel processing. Even though Pt is considered to be the most efficient material toward HER, it has two major disadvantages – low abundance in nature and high cost. Thus, the attention of scientists was drawn into investigation of potentially as efficient, less expensive, and significantly more abundant (Table 1) materials [2].

It was shown that nanoalloys consisting of transition metals potentially can have excellent catalytic properties for hydrogen production [3]. However, up to now, efficiency of electrocatalysts that were prepared using nanoalloys was found to be significantly lower as compared to Pt. Low efficiency of nanoalloys is probably related to low accessibility of active centers for hydrogen. Crystal structure and orientation of the potential electrocatalysts are discussed in section "Factors Defining the Efficiency of the Electrocatalytic Hydrogen Formation." Thus, it was proposed that nanostructures with particular orientation of the beneficial crystallographic planes that provides their maximum accessibility for hydrogen are desirable features of an efficient electrocatalyst. For example, exposure of the (100) edge planes of MoS_2 for hydrogen adsorption leads to a significant enhancement of its electrocatalytic properties [4].

Table 1 Abundance of selected transition metals in the Earth's crust

Element	Abundance in the Earth's crust (ppm)
Platinum	0.005
Molybdenum	1.2
Tungsten	1.25
Cobalt	25
Nickel	84

Recently, in order to enhance the efficiency of alloys for electrocatalysis, near-surface and surface alloys were proposed [5]. Near-surface alloys are characterized by different compositions of surface layer and support. Electrocatalytic properties of such alloys were demonstrated for a few systems that were prepared by deposition annealing procedure using transition metals and Pt (111) surface [6]. However, in many cases, near-surface alloys that are discussed in section "Potential Electrocatalytic Systems" require sophisticated and multistage preparation procedures. Furthermore, efficient structures are often sensitive to acidic or basic environment and change their surface composition upon hydrogen adsorption.

Nevertheless, recent achievements in structuring of inorganic materials demonstrated that alloys and especially near-surface alloys may become more attractive for industry if novel economically effective methods of manipulation of metal surface at atomic level can be proposed. In this chapter, the advantages of high-intensity ultrasound (HIUS) for the design of electrocatalysts are discussed in comparison to conventional methods of the formation of nanostructured materials.

HIUS is a unique technological approach for the synthesis of metallic nanomaterials and solid-state processing of metals [7–9]. HIUS provides extreme conditions for both bottom-up and top-down approaches to the design of nanomaterials.

Ultrasound-assisted bottom-up approach is based on decomposition of volatile precursors in the interior of a collapsing bubble. Collapsing cavitation bubbles creates μm-sized areas of high temperature and pressure. Suslick et al. [10] demonstrated that the mechanism of such synthesis has the following steps. First of all, organometallic compounds that are used as precursors for the synthesis of inorganic particles are decomposed inside a collapsing bubble. This process is followed by clustering of atomized metals and formation of nanostructures. A great success in sonochemical synthesis of catalytically active metal particles was an ultrasound-induced synthesis of amorphous Fe, Co, Ni particles; Fe–Co, Co–Ni, and Fe–Ni alloys [11]; as well as porous Mo_2C and W_2C [12]. However, amorphous phase is not suitable for electrocatalytic application. In order to transfer amorphous phase into crystalline one, the sonochemically formed metals were additionally heated.

Ultrasound-assisted top-down approach to solid-state structuring or restructuring of particles and surfaces at atomic scale is possible if HIUS is applied to heterogeneous systems [13]. In this case, ultrasonically induced shock waves stimulate intensive interparticle collisions [14]. Additionally, near liquid–solid interfaces, the cavity collapse is asymmetric and generates high-speed jets of liquid [15]. Impact of high-speed jets is pronounced if sonicated particles are larger than the size of cavitation bubbles (at 20 kHz, it is >100 μm) [10]. In this case, mechanical energy of ultrasound is directly transferred to surfaces through impact of high-speed jets.

Experiments of Suslick et al. on HIUS treatment suspensions of ~10 μm particles showed that cavitation creates large heating and local melting of metal surface of the collided particles [16]. The temperature reached at the point of impact during ultrasonically driven interparticle collisions was estimated at approx. 3000 °C. Andreeva et al. [17] showed that HIUS-induced local heating of metal surface of ~140 μm metal alloy particles can generate temperature gradient that enhances atomic diffusion in metals and grains' growth. In metallurgical industry, temperature-forced grain growth is leading to undesirable metal material softening [18]. In electrocatalysts, it is opposite; growth of crystallites is beneficial if it is accompanied by increasing of surface area and enhancing of accessibility of catalytically active sites [19].

Energy release/transfer from collapsing cavitation bubble depends on sonication medium [17]. It has been reported that temperature inside the cavitation bubble and its collapse intensity significantly depend on physical and chemical properties of sonication media. Sonication media with low vapor pressure and high viscosity result in an increased cavitation collapse intensity (ethylene glycol) [20]. A higher vapor pressure (water, ethanol) leads to higher vapor content inside the cavitation bubble and lower interior temperature of the collapsing bubble [21]. Therefore, by appropriate sonication medium choice during HIUS treatment, it might be possible to regulate the amount of cavitation energy that can be supplied to metal surface and achieve desirable microstructural and morphological properties of metals for electrocatalytic applications.

Additionally, HIUS treatment of sonication medium leads to its sonolysis – generation of free radicals [22]. In aqueous media, ultrasonically formed OH radicals can trigger surface redox reactions and thus be undesirable for electrocatalysis surface oxidation and passivation of electrode's surface. In contrast, HIUS treatment of metals in reductive media (ethanol, ethylene glycol) changes the crystal morphology of metals flowing up by reduction of metal oxide on the surface and, thus, increases accessibility of active centers and enhances electrocatalytic properties of material [23].

In this chapter, ultrasonically formed nanoalloys and near-surface alloys are highlighted as highly efficient alternatives to precious metal catalysts. Use of HIUS for the design of electrocatalysts is proposed as a promising technological solution for enhancement of catalytic efficiency and also for reduction of costs and negative environmental impact of energy production. Main aspects of ultrasound-assisted top-down and bottom-up approaches to synthesis and activation of potential electrocatalysts are compared to the other technologies. Additionally, the fundamental aspects of HER are presented, and factors defining the efficiency of the electrocatalytic hydrogen formation are summarized.

Overview of the Electrocatalytic Hydrogen Formation Mechanism

According to classical theory [24], overall HER on the metal electrocatalyst (M) surface in the acidic media may proceed via several elementary steps (Fig. 1). First, hydrogen-free surface of the electrocatalyst undergoes a primary discharge step defined as:

Fig. 1 Schematic presentation of elementary steps involved in electrocatalytic hydrogen formation process (Reprinted with permission from Ref. [19]. Copyright 2015 Royal Society of Chemistry)

$$H_3O^+ + e^- \rightarrow M\text{-}H_{ads} + H_2O \text{ (Volmer reaction)}$$
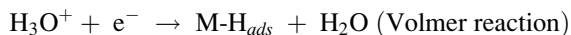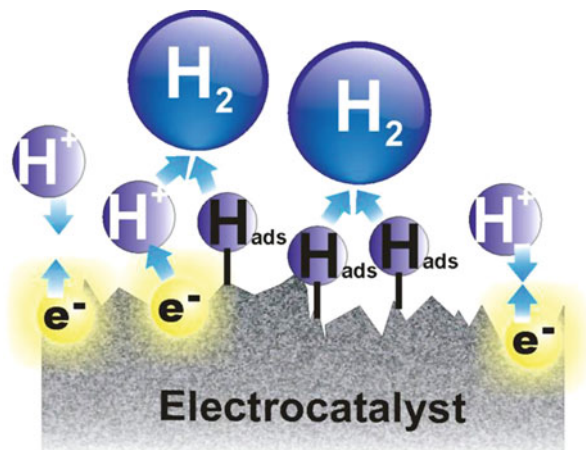
Generally, a primary discharge step leading to a formation of adsorbed hydrogen ($M\text{-}H_{ads}$) is believed to be fast and followed by either desorption step:

$$M\text{-}H_{ads} + H_3O^+ + e^- \rightarrow H_2 + M + H_2O \text{ (Heyrovsky reaction)}$$

or a recombination step:

$$M\text{-}H_{ads} + M\text{-}H_{ads} \rightarrow H_2 + M \text{ (Tafel reaction)}$$

Either reaction, Heyrovsky or Tafel, is considered to be a rate-limiting step. Thus, the HER mechanism may be represented as Volmer–Heyrovsky or Volmer–Tafel. Theoretically, inherent property of the electrocatalyst such as Tafel slope (b) which is arising Tafel equation:

$$\eta = b \log j + a,$$

where η is overpotential and j is current density, should be useful for revealing the actual rate-limiting step. Thus, evaluation of the linear part of the Tafel plot that fits to Tafel equation should make it possible to determine the overall HER mechanism.

Tafel slope (b) for primary discharge, desorption, and recombination steps are defined as the following:

$$b = \frac{2.3RT}{\alpha F} \approx 120 \text{ mV (Volmer)}$$

$$b = \frac{2.3RT}{(1+\alpha)F} \approx 40 \text{ mV (Heyrovsky)}$$

$$b = \frac{2.3RT}{2F} \approx 30 \text{ mV (Tafel)}$$

where R is the ideal gas constant, T is the absolute temperature, α is the symmetry coefficient, and F is the Faraday constant. In principle, if analysis of the linear part of Tafel plot results in the lower Tafel slope, this indicates that electrocatalyst requires a lower overpotential to generate reasonable current. Nevertheless, the Tafel plots should be interpreted cautiously, since the Tafel slope has a complex dependence on various parameters such as type of the catalyst, catalyst pre-activation, adsorption/desorption conditions to/from active sites, electrode modification, reaction pathway, etc. [25]. Another important parameter which can be estimated from the Tafel plot is the exchange current density (j_0) which is obtained from extrapolating linear part of the Tafel plot to zero overpotential. (j_0) is an extremely valuable parameter that represents the intrinsic rate of electron transfer between analyte and electrocatalyst [26].

Factors Defining the Efficiency of the Electrocatalytic Hydrogen Formation

Crystal Structure (Type and Orientation)

While developing the potential electrocatalytic system for water splitting, special attention should be given to its crystal structure and orientation on the surface (exposed edges). Based on the review of the existing electrocatalysts, majority of the most promising materials which could replace platinum utilize trigonal/hexagonal crystal structure. It is well known that in trigonal/hexagonal lattice system, there is one unique axis (called principal axis) which allows distinguishing between edge (parallel to the principal axis) and basal (perpendicular to the principal axis) planes. It is believed that electrochemical reactions preferentially occur on the edge planes [4, 27–30]. Based on the comprehensive review of Banks et al. [27], much of the electrocatalytic activity is attributed to surface edge plane sites.

Later, Yuan et al. demonstrated electrochemical behavior of the single-layer graphene-based electrodes depending on the type of the exposed plane. It was found experimentally that in contrast to graphene basal planes, edge planes exert significantly higher capacitance and faster rate of the electron transfer, resulting in at least two orders of magnitude higher current density values [28].

Another useful approach for identification of electrocatalytically active sites is density functional theory (DFT) calculations. Considering molybdenum (IV) sulfide MoS_2 nanoparticles as an analogue to hydrogen-producing enzyme, it was calculated that hydrogen is being adsorbed with a low barrier/low overpotential (~ 0.1 V.) to the edge planes, while basal planes of MoS_2 remain catalytically inactive [29]. These calculations support the experimental results for electrochemical hydrogen evolution on MoS_2 nanocatalyst, where the efficiency of HER activity directly correlates with the number of exposed edge sites [4]. Additionally, on the example of Mo–S catalyst,

it was shown that significant enhancement of HER activity is mainly attributed to thiomolybdate $[Mo_3S_{13}]^{2-}$ nanoclusters which expose a large number of electrocatalytically active edge sites [30].

Thus, it is highly recommended to consider the type of the catalyst crystal structure as well as surface orientation of the active sites for creating the electrocatalytically efficient material toward HER which could withstand the competition against platinum.

Keeping in mind that growth of crystals is a temperature-driven process, ultrasound can provide special conditions for manipulation of crystal morphology. Collapsing of cavitation bubbles near/on solid–liquid interfaces generates temperature gradients that propagate from metal surface into the metal interior and, therefore, stimulate atomic diffusion and crystal growth. The crystallite size analysis of catalytically active Al_3Ni_2 [19] phase using Scherrer abd Williamson–Hall methods reveals that the sonochemical impact of ultrasound on suspensions of metal particles is beneficial for HER activity increase.

Furthermore, it was shown that during HIUS treatment the average minimum temperature (the minimum temperature up to which a metal particle is heated during sonication) can be controlled by physical properties of the sonication medium such as vapor pressure and viscosity and is increasing in the row ethylene glycol < ethanol < water < decane [17]. Based on the obtained data, energy transfer from collapsing cavitation bubble to sonicated particle was estimated ~17 % more efficient in decane than in ethylene glycol. Additionally, it is demonstrated in Fig. 2 that for the suspensions with particle concentration <10 wt%, atomic diffusion and crystal growth were observed, while HIUS treatment of more concentrated suspensions (>10 wt%) led to melting processes and recrystallization indicating that average minimum temperature is exceeding the particle melting point.

Thus, HIUS can be used for the controllable manipulation of crystal morphology. Sonication medium, concentration of the used suspensions, and the initial size of particles affect the kinetics of crystal growth.

Surface Composition and Morphology

Undoubtedly, surface composition of the electrocatalyst plays a major role in defining its efficiency and potential use toward HER. Formation/presence of any compounds which could possibly passivate the water splitting process is highly undesirable. For instance, earth-abundant aluminum cannot be used for electrocatalysis simply due to the formation of protecting/passivating layer of aluminum oxide/hydroxide [23]. Another issue that can restrict electrocatalyst from its use for HER is the presence of amorphous phase on its surface. Amorphous phase as being irregular in structure inhibits the process of hydrogen formation significantly. Besides that, surface of the prospective catalyst should preferably consist of stable/chemically inert compounds which do not undergo oxidative dissolution or corrosion. As a result, some promising electrocatalysts in the first place do not last, and their efficiency drops drastically as in the case of WC or Mo_2C which is prone to oxidation [31] or Ni_2P which is subject to slow corrosion [32].
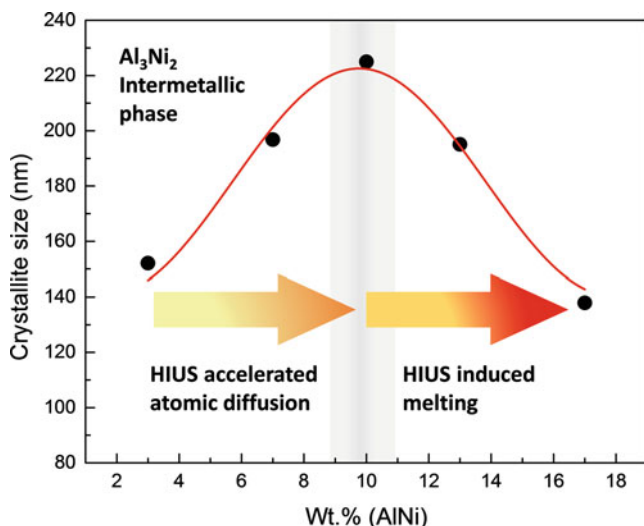
Fig. 2 Effect of HIUS on crystal size of metals. Plot of crystal size of the HIUS-treated Al_3Ni_2 intermetallic phase versus the concentration of AlNi particles in decane. Lower particle concentration (<10 wt%) leads to the process of atomic diffusion, while HIUS treatment of more concentrated suspensions (>10 wt%) results in remelting processes indicating that HIUS-generated average minimum temperature is exceeding the particle melting point (Reprinted with permission from Ref. [17]. Copyright 2015 Elsevier B.V.)

In addition to surface composition, morphology of electrocatalyst is also one of the parameters that define the efficiency of hydrogen evolution. To date, there have been made numerous attempts to achieve the enhancement of electrocatalytic water splitting process through the adjustment of catalyst's morphology. Thus, the potential catalysts were synthesized in the form of nanoparticles, nanowires, or as a porous-like structure simply to increase the surface area of the active phase.

Even though it is believed that high surface area should enhance the catalytic activity of the material, in the area of electrocatalysis, such assumption may not be accurate. For example, the effective current output of nickel nanowire-based HER catalyst is lower than that of planar nickel plate despite of its high surface area [33]. This can be explained in terms of limited HER active area. Clustered nickel nanowire structures only allow vertical bubble escape which interferes with electrolyte inflow to the bottom of the nanowires. Therefore, hindered electrolyte transport significantly reduces the efficiency of the prospective electrocatalyst.

Additionally, porous structures may also inhibit overall process of hydrogen production. In this case, newly formed hydrogen bubbles are trapped within the pores and considerably contributing in the electrolyte ohmic resistance, which results in noticeable catalytic HER activity loss [34]. With this in mind, it is important to consider full accessibility of the surface by electrolyte rather than high surface area when creating efficient electrocatalyst. This could be achieved,

for instance, by impregnation of a prospective catalyst in a well-spread support that would prevent electrolyte inflow interruption or hydrogen bubble trapping.

Regarding tuning of surface morphology and composition of catalysts, sonochemical approach is a versatile method of modification of metal surfaces. Use of different sonication media allows controlling of surface morphology and porosity of metal-based catalysts and, therefore, their electrochemical performance. In water, the interfacial redox reactions have a pronounced contribution to the particle modification process, and the formation of a rough metal oxide layer with high surface area (up to $125 \, m^2 g^{-1}$ for AlNi alloy particles) was observed [13]. Effect of reducing and oxidative media on the ultrasonically driven activation of the electrocatalyst's surface was investigated using AlNi in the presence of water, water–ethanol mixtures, and ethanol [23]. Surface analysis by X-ray photoelectron spectroscopy (XPS) revealed that the AlOx content decreased as the sonication medium was changed from pure water to pure ethanol. Additionally, XPS detected reduction of AlOx to Al, as well as reduction of NiOx to Ni upon sonication of AlNi alloy particles in ethanol.

The HER data (Fig. 3a) and the corresponding Tafel plots (Fig. 3b) showed that the use of oxidative aqueous media for the sonochemical preparation of electrocatalysts inhibited HER [23]. In contrast, electrochemical activity of AlNi particles was observed for the samples prepared in reductive medium of ethanol. For the HIUS treated in ethanol samples, noticeable current increase when the potential reached about -0.7 V with formation of the first hydrogen bubble at as low as -0.6 V was measured. Furthermore, HIUS treatment of AlNi alloy particles in ethanol resulted in nearly 146-fold increase in (i_0) and was 2.26 mA/cm^2. On the other hand, HIUS treatment in water decreased the (i_0) to almost half (0.0078 mA/cm^2).

Summarizing, HIUS affects both surface morphology and surface composition of metals. The choice of a suitable sonication medium for HIUS treatment of metals is crucial for their application in electrocatalytic water splitting. Use of oxidative sonication medium allows creating efficient hydrogenation catalyst with high surface area [13]. Reductive sonication medium provides important conditions for the formation of effective electrocatalysts with reduced oxide layer [23].

Electrocatalyst Pre-activation for Hydrogen Evolution

Often, as synthesized/fabricated catalytic materials do not perform well enough until they are properly activated, therefore, the process of activation is being an important step in catalyst preparation, significantly increasing its catalytic ability. Many of the electrocatalysts require activation for efficient hydrogen production.

According to hydrogen evolution mechanism, the first step in HER is an adsorption of hydrogen to the surface of the electrocatalyst (Volmer discharge step). It is known that first hydrogen bonds to the active site strongly and cannot be easily removed as required by HER mechanism. The phenomenon is taking
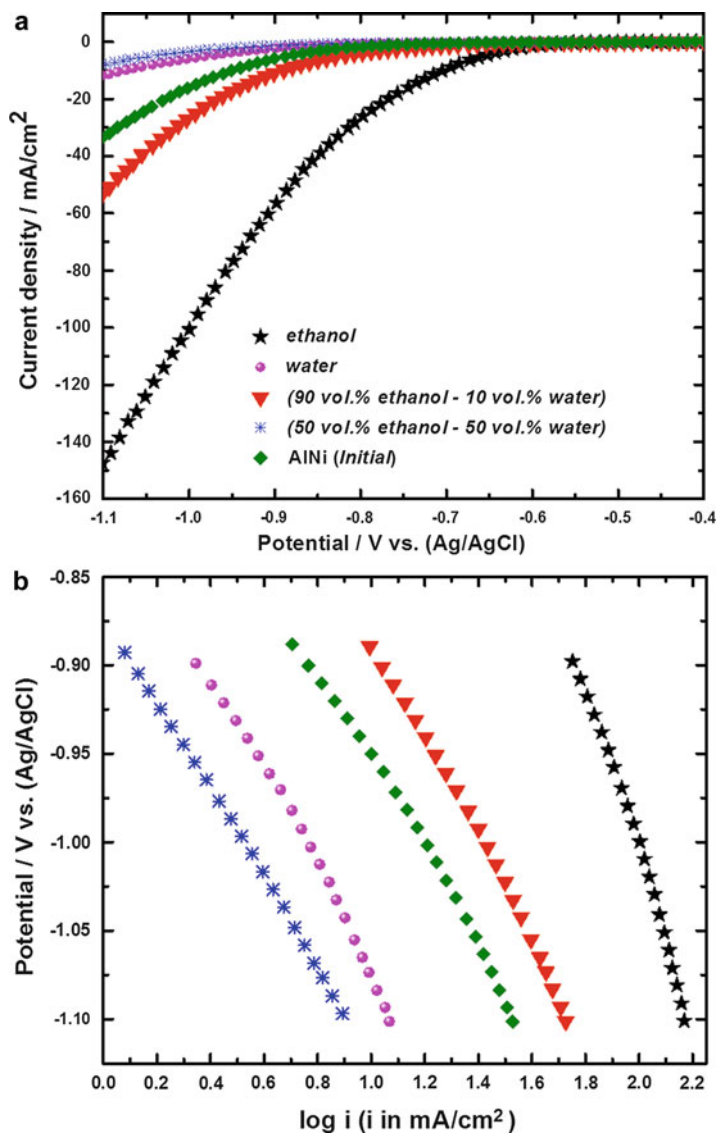
Fig. 3 HER current–potential profiles (**a**) and Tafel plots (**b**) for the initial and HIUS treated AlNi alloy particles (50 wt.% Ni) in different sonication media. Legend is valid for both (**a**) and (**b**) parts of the figure (Reprinted with permission from Ref. [23]. Copyright 2014 Elsevier B.V.)

place until specific for the particular catalyst hydrogen coverage is reached (normally 0.25) [4]. Upon reaching the necessary coverage value, the free energy of adsorption is lowering allowing the rest of the hydrogen atoms to be able to absorb with a significantly lower barrier or, with respect to HER, with a lower overpotential.

Thus, it would be desirable for catalyst to possess required hydrogen coverage before its use. This is normally achieved by purging hydrogen gas over the catalyst surface for an extended time of several hours or sometimes even days [35]. Once activated and all requirements are met (crystal structure, surface composition, and morphology), the prospective catalyst should ideally perform at the lower overpotential and initiate the considerable current.

HIUS-induced generation of free radicals followed by redox reaction on the metal surface significantly contributes to the process of catalyst pre-activation. It was demonstrated for the sonochemically activated AlNi hydrogenation catalyst [13]. The interfacial redox reactions on AlNi particles triggered by free radicals formed during water sonolysis led to metal surface oxidation and simultaneous generation of hydrogen. H_2 generated concomitantly with the catalyst production provides a self-activation of the catalyst.

Thus, application of sonochemical approach to the catalysts' formation can help to avoid additional activation step before use.

New Approach to Electrocatalyst Fabrication

At the present time, there are a variety of methods that are used for the creation of potentially efficient catalytic materials toward hydrogen evolution. Most of them employ wet chemistry approach, which can be quite sophisticated and lengthy. Among those are the catalysts which synthesize by means of carburization, solvothermal processing, microwave-assisted hydrothermal approach, ammonolysis, selenization, etc. Many of the synthesis pathways involve complex steps of nanoengineering to produce nanoparticles, nanosheets, or nanowires. Some also include the catalyst incorporation on various supports, such as impregnation into carbon nanotubes, mesoporous graphene foams, reduced graphene oxide sheets, etc. In addition to synthesis, majority of the catalysts must be activated prior their use, which overall extends the preparation time significantly and requires unnecessary power input. As a result, at the present time, it is unlikely to distinguish the simple method that could be used for creation of electrocatalyst as efficient as Pt from earth-abundant metals without utilizing rare elements or expensive precursors. Nevertheless, an unexpected solution of this issue may come from the area of acoustic chemistry.

Sonochemistry is the area that has been developing over the last few decades. Since 2014, its principals have been applied to materials' surface modification with respect to electrocatalytic water splitting [19, 23]. Sonochemistry is mainly associated with effect of cavitation, that is known to occur naturally and notorious for its destructive properties being a significant cause of wear in many engineering contexts. Surprisingly, artificially caused acoustic cavitation can serve as a simple and powerful tool for fabrication of HER active electrocatalyst.

Based on the recent achievements in the area of sonochemical processing of earth-abundant metal alloys (AlNi) for electrocatalytic applications [19, 23], ultrasound can be considered as an easy "one-pot" method of efficient electrocatalyst fabrication.
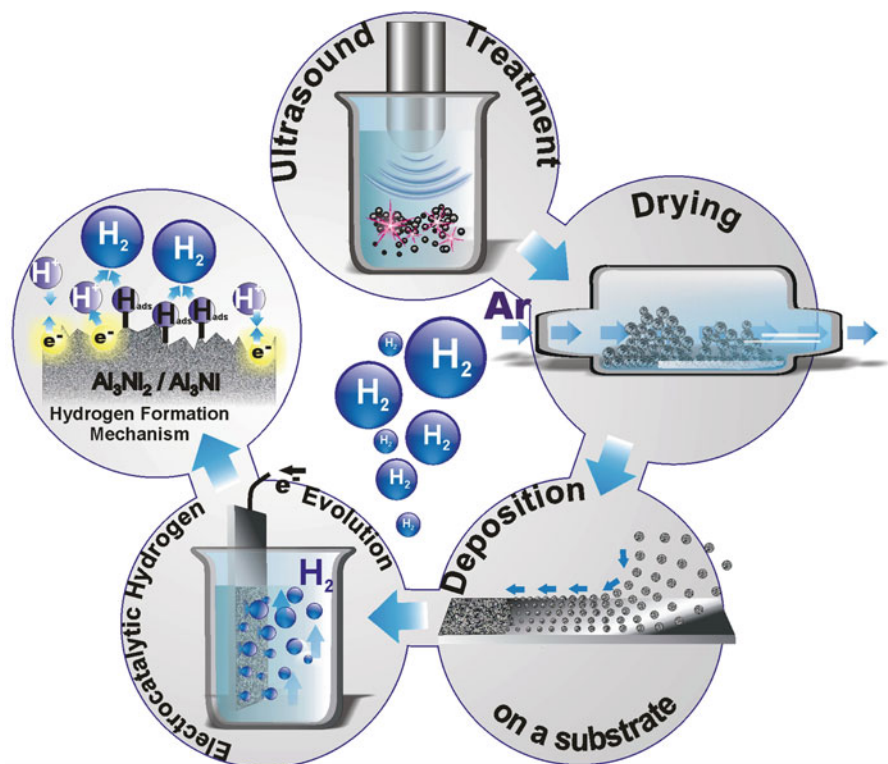
Fig. 4 Schematic illustration of the HIUS-assisted electrocatalyst preparation procedure (Reprinted with permission from Ref. [19]. Copyright 2015 Royal Society of Chemistry)

The recently developed by Andreeva et al. [19, 23] sonochemical approach to the electrocatalyst preparation is sketched in Fig. 4. First of all, 10 wt% suspensions of alloy particles (~140 μm) were sonicated in ethanol at a frequency of 20 kHz and intensity of 140 W/cm^2 for 1 h. This processing results in the activation of the catalyst surface (change in crystal structure, phase composition, and morphology). After that, the modified particles were centrifuged and dried in Ar atmosphere. The dried particles were deposited on a substrate and their electrocatalytic activity was evaluated.

Summarizing, single-step ultrasound modification of inexpensive earth-abundant AlNi alloy satisfies required catalytically active phase structuring (growth and exposure of HER active sites on the surface), controllably avoids creation of high surface area (prevention of hydrogen bubble trapping), as well as involves a very important step of catalyst activation by achieving the necessary hydrogen coverage that is incorporated to the surface of the catalyst from sonication media. Given these points, sonochemical processing may become a unique and elegant approach for fabrication of inexpensive, robust, and highly efficient electrocatalyst which could competitively replace platinum.

Potential Electrocatalytic Systems

Based on the results presented in the literature, the most promising electrocatalysts are those that contain one or more transition metals such as molybdenum, tungsten, cobalt, and nickel. Summary of the existing active catalysts (compounds/composites/hybrids) toward hydrogen evolution reaction is provided in the Table 2.

Molybdenum (Mo)-Based Electrocatalysts

The most common molybdenum-containing compounds for electrocatalytic water splitting are molybdenum sulfides, selenides, phosphides, as well as nitrides and carbides. Themselves, in the pure/bulk form, they do not possess outstanding electrocatalytic properties. Though being incorporated into various supports such as reduced graphene oxide (RGO) sheets and mesoporous graphene foams (MGF) or

Table 2 Most common transition metal-based catalysts for HER. The characteristics of Pt are given as a reference

Catalyst	Crystal structure/ coordination	Exchange current density (i_0) mA/cm^2	References
Pt	Cubic	2.2	[51]
MoS$_2$ nanoparticles on MGF	Hexagonal	3.01×10^{-3}	[26]
Mo$_2$C nanoparticles on CNT	Orthorhombic	0.014	[37]
MoP nanoparticles	Hexagonal	0.086	[38]
Cu$_2$MoS$_4$	Tetragonal	0.040	[39]
WC	Hexagonal	6.8×10^{-4}	[46]
WO$_3$ nanorods	Hexagonal	2.75×10^{-3}	[47]
WO$_3$ bulk	Hexagonal	8.57×10^{-4}	[47]
WO$_3$ nanowires	Hexagonal	6.61	[48]
WO$_3$ commercial	Hexagonal	0.265	[48]
W2MoC	Hexagonal	0.011	[31]
W4MoC	Hexagonal	0.029	[31]
CoSe$_2$ nanoparticles on carbon fiber paper	Cubic	4.9×10^{-3}	[51]
CoSe$_2$ film	Cubic	5.9×10^{-5}	[51]
Co$_{0.6}$Mo$_{1.4}$N$_2$	Trigonal/octahedral	0.23	[52]
Co$_{57}$Ni$_{43}$ alloy	–	0.048	[53]
Co$_{57.5}$Ni$_{36}$Y$_{6.5}$ alloy	–	0.067	[53]
Co$_{57}$Ni$_{35}$Ce$_8$ alloy	–	0.079	[53]
Ni nanowires	Cubic	–	[33]
Ni$_2$P nanoparticles	Hexagonal	0.49	[32]
NiS	Hexagonal	–	[54]
Ni$_3$S$_2$	Rhombohedral	–	[54]
Al$_3$Ni$_2$/Al$_3$Ni	Hexagonal/ orthorhombic	17	[19]

simply converted into nanoparticle/nanowire form, the resulting hybrid systems significantly improve HER performance.

For example, obtained by solvothermal method, molybdenum (IV) sulfide (MoS_2) nanoparticles from ammonium tetrathiomolybdate ((NH_4)$_2MoS_4$) exert enhanced HER properties (low overpotential, increased current output) when incorporated into MGF [25]. Such incorporation allows better accessibility of hydrogen to active edge sites [4, 27–30]. Besides the improved HER performance, the resulting catalyst is reasonably stable for at least 1000 voltammetric cycles.

Efficiency of molybdenum-based electrocatalyst can be increased by substituting sulfur with selenium. Thus, molybdenum (IV) selenide ($MoSe_2$) – the product of hydrothermal reaction between sodium molybdate (Na_2MoO_4) and hydrazine hydrate–Se – deposited on graphene reduced the overpotential of water splitting process by 20–30 mV [36] compared to MoS_2 on MGF.

Better electrocatalytic performance can be achieved when molybdenum (II) carbide (Mo_2C) nanoparticles are obtained by carburization of ammonium heptamolybdate tetrahydrate ((NH_4)$_6Mo_7O_{24}°4H_2O$) and impregnated into carbon nanotubes (CNT) [37]. Mo_2C nanoparticles on CNT demonstrate higher exchange current density as well as better stability – no activity loss after 3000 voltammetric cycles.

Another promising catalyst which could enhance water splitting reaction is molybdenum phosphide (MoP). It can be obtained through the formation of precursor from ammonium molybdate and ammonium hydrophosphate ((NH_4)$_2HPO_4$) and its following temperature-programmed reduction (TPR) under H_2/Ar atmosphere [38]. Resulted in such a way, closely incorporated network of MoP nanoparticles shows significantly improved stability (at least 24 h without change in HER activity) as well as increased value of exchange current density. Finally, molybdenum-based electrocatalyst with reasonable HER properties can also be obtained by simple precipitation of ammonium tetrathiomolybdate with Cu(I). Thus, precipitated copper (I) tetrathiomolybdate (Cu_2MoS_4) is among the promising alternatives to platinum catalyst [39].

Ultrasound was applied for both bottom-up and top-down preparation roots of Mo-based electrocatalysts. First of all, MoS_2 and Mo_2C were sonochemically synthesized by decomposition of metal carbonyl precursors. Suslick et al. prepared Mo_2S by ultrasonication (20 kHz) of suspensions of molybdenum hexacarbonyl and sulfur in 1,2,3,5-tetramethylbenzene (isodurene). The sonochemically prepared MoS_2 were porous agglomerates with an average diameter of 15 nm and average crystallite size of 1.6 nm after thermal treatment [40].

Furthermore, Suslick et al. proposed an ultrasound-assisted synthesis of Mo_2C. According to this synthesis, sonochemical decomposition of molybdenum hexacarbonyl in hexadecane leads to the formation of a black amorphous compound that became crystalline Mo_2C powder after heat treatment at 450 °C. The proposed mechanism of the formation of Mo_2C was based on the disproportionation of carbon monoxide on the active metal surface to form carbon and carbon dioxide [11]. The decomposition kinetics of $Mo(CO)_6$ induced by sonolysis in hexadecane solvent and the formation of Mo_2C was studied by Pandya et al. [41].

Top-down ultrasound-assisted approach to the formation of potentially active electrocatalysts is based on exfoliation/fragmentation of the layered structures of MoS_2. The process is similar to those for graphene and bulk graphite. The formation of nanosheets and nanoparticles of MoS_2 is desirable since it leads to different optical and electrical properties of nanostructures [42]. An ultrasound-assisted liquid exfoliation technique was proposed by Coleman et al. The technique was demonstrated for MoS_2, but the authors suggested that this approach can be applied for the exfoliation of other layered materials such as WS_2, $MoSe_2$, $MoTe_2$, $NiTe_2$, etc. [43]. Later on, this approach was optimized in order to avoid aggregation and restacking of exfoliated MoS_2. It was shown that surface energy, boiling point of solvent, as well as low solubility of the used compounds are the crucial parameters for the formation of well-dispersed Mo_2S particles with particular size. The MoS_2 nanosheets were fabricated by a simple ultrasound exfoliation method in dimethylformamide (22 h) [42], in N-methylpyrrolidone with posttreatment by chloroform [44], and in isopropyl alcohol [45].

The mechanism of exfoliation (see the schematic illustration in Fig. 5) has two main contributions: the separation of solids into single-layer or few-layer platelets and the fragmentation of the platelets due to breaking of the MoSMo bridges [45].

Gopalakrishnan et al. showed that exfoliated MoS_2 material loaded on gold electrode exhibited good electrocatalytic activity with a low onset potential of ~190 mV [44].

Tungsten (W)-Based Electrocatalysts

To date, there are varieties of tungsten containing electrocatalysts that exhibit decent efficiency toward hydrogen evolution reaction. Among those, the most studied are the electrocatalytic systems based on tungsten carbides, oxides, nitrides, as well as their combinations. Harnisch et al. synthesized tungsten carbide (WC) powder electrocatalyst [46] via carburization of tungsten (VI) oxide (WO_3) with improved efficiency for HER as compared to commercial WO_3. Moreover, they investigated 27 mixed catalysts containing different fractions of pure tungsten (W), tungsten (IV) oxide (WO_2), tungsten carbide (WC), and tungsten semicarbide (W_2C) and suggested that electrocatalytic performance of such systems to a high extent depends on the amount of WC, while presence of the other compounds play only a minor role.

It is important to note that they also reported on the stability of synthesized electrocatalyst, showing that WC undergoes slow oxidative dissolution in neutral media due to formation of soluble tungstate ion (WO_4^{2-}) and the process cannot be suppressed completely. Nevertheless, WO_3, used as a precursor for synthesis of WC, itself can serve as a potential electrocatalyst. Thus, Rajeswari et al. produced WO_3 nanorods [47] (130–480 nm in length and 18–56 nm in width) through thermal decomposition of tetrabutylammonium decatungstate $[((C_4H_9)_4N)_4W_{10}O_{22}]$.

Besides higher efficiency toward HER, WO_3 nanorods demonstrated reasonable stability in 1 M H_2SO_4. After performing 50 consecutive voltammetric cycles, the
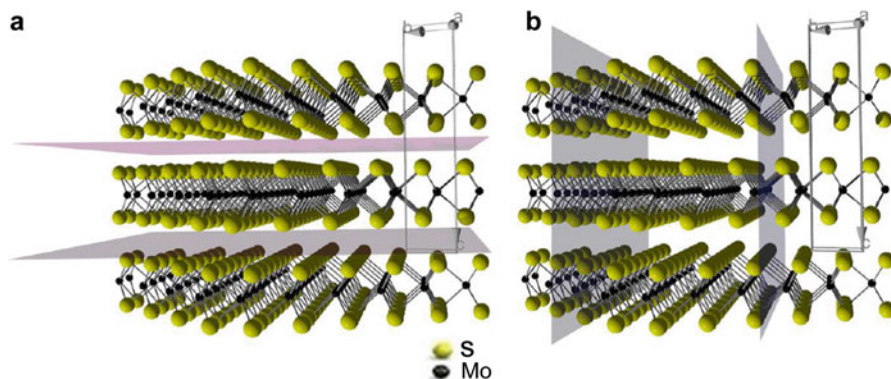
Fig. 5 Effects of HIUS on MoS$_2$ flakes dispersed in isopropyl alcohol: breaking between basal planes (**a**) and fragmentation of lamellae (**b**) (Reprinted with permission from Ref. [45]. Copyright 2015 American Chemical Society)

catalyst showed almost no change in activity. Additionally, WO$_3$ with enhanced electrocatalytic properties can be obtained by microwave-assisted hydrothermal processing of sodium tungstate dihydrate (Na$_2$WO$_3$°2H$_2$O) [48]. This method leads to the formation of hexagonal WO$_3$ nanowires with diameter of 5–10 nm which possess higher crystallinity and increased surface area. Such catalyst shows significantly improved HER efficiency in terms of exchange current density value compared to commercial WO$_3$ or even Pt.

Interestingly, combination of thermal processing and carburization can be used for creation of more sophisticated tungsten-based composite electrocatalyst. Xiao et al. showed formation of molybdenum tungsten complex oxide nanowires [31] through hydrothermal processing of ammonium heptamolybdate tetrahydrate ((NH$_4$)$_6$Mo$_7$O$_{24}$°4H$_2$O) with Na$_2$WO$_3$°2H$_2$O and their following carburization into molybdenum carbide–tungsten carbide composite nanowires (W2MoC, W4MoC). Both composites retain hexagonal crystal lattice of WC and Mo$_2$C and, after activation by cyclic voltammetry, demonstrated reasonable HER efficiency. In this particular case, electrochemical activation allows inducing hydrophilic carboxyl/epoxy interface to ensure improved electrocatalytic performance.

Sonochemical decomposition of tungsten hexacarbonyl in n-hexadecane leads to the formation of promising catalytic W$_2$C particles [12]. Comparing to conventional synthesis of carbides, the sonochemical approach is a simple and efficient procedure that allows significant reduction of reaction temperatures. The mechanism of sonochemical formation of tungsten carbide was proposed by Nikitenko et al. The authors studied the kinetics of W(CO)$_6$ sonolysis in diphenylmethane at 32 Wcm^{-2} intensity of ultrasonic treatment. The special role of solvent in the formation of carbide was highlighted. Kinetic study shows that sonolysis of W(CO)$_6$ leads to the formation of W nanoparticles and follows by their reaction with the products of sonochemical degradation of the used solvent [49].

The porous WO_3 nanoparticles were synthesized using a HIUS irradiation (100 W/cm^2 for 3 h at 5 °C) of WO_3 nanoparticles (80 nm) in ethanol. It is interesting that 2–5 nm uniform pores were formed in WO_3 nanoparticles without significantly changing the initial WO_3 nanoparticle sizes [50].

Cobalt (Co)-Based Electrocatalysts

Cobalt is not as commonly used for creation of electrocatalyst; nevertheless, there are systems where this non-noble transition metal enhances electrocatalytic process of water splitting. One of the examples is cobalt (IV) selenide ($CoSe_2$) nanoparticles [51] which are grown on carbon fiber paper. In the first place, pre-synthesized cobalt oxide nanoparticles are drop casted on carbon microfiber (pore size ~ 8 μm). After that, the system is selenized under Se atmosphere to produce highly stable electrocatalyst which shows no change in HER activity for at least 60 h. Important to note that use of carbon microfiber paper as a support allows for creation of a catalytic material with highly accessible pores for hydrogen adsorption.

Another example of using cobalt was shown in the work of Cao et al. where cobalt (II) molybdate ($CoMoO_4$) undergoes two-step ammonolysis: formation of intermediate Co_3Mo_3N and its following conversion into mixed close-packed cobalt molybdenum nitride ($Co_{0.6}Mo_{1.4}N_2$). As-prepared nanostructured catalyst shows improved HER activity that is comparable to one of platinum and reasonable stability – electrocatalytic activity is slightly decreasing over first 50 voltammetric cycles, while for the next 3000 cycles, it remains the same [52].

Additionally, cobalt-based electrocatalysts can be prepared using simple alloying method. Cobalt can form alloys with nickel and some rare earth metals such as yttrium, cerium, praseodymium, and erbium. It was found that the most promising toward HER are alloys of the following compositions: $Co_{57.5}Ni_{36}Y_{6.5}$ and $Co_{57}Ni_{35}Ce_8$ [53]. Thus, substituting a small amount of nickel with rare earth metals in parent $Co_{57}Ni_{43}$ alloy enhances electrocatalytic activity in the water splitting process.

Even though Co-based materials clearly show the potential to be used as a prospective electrocatalyst toward HER, there are almost no reports on using ultrasound processing as a method for fabrication/activation of such materials. Therefore, ultrasound treatment of Co-based materials might open the new prospective while searching for an inexpensive alternative to Pt.

Nickel (Ni)-Based Electrocatalysts

Nickel is among the most abundant transition elements in the Earth's crust. This makes its use for creation of electrocatalyst toward HER extremely attractive. Unfortunately, at the present time, nickel is not as studied as the other most common transition metals due to its low HER activity. Nevertheless, there have been several attempts to enhance electrocatalytic properties of this metal through the change of morphology or by synthesis of nickel sulfides and phosphides.

The change of morphology does not bring the desirable results. For example, nickel in the form of nanowires [33] still has a large overpotential value of ~1.2 V, which makes its use as an alternative to platinum economically unreasonable. Opposite situation is observed in the case of nickel phosphide (Ni_2P). Synthesized from nickel (II) acetylacetonate ($Ni(acac)_2$), Ni_2P nanoparticles exert significantly better electrocatalytic properties toward HER [32]. Specifically, the exchange current density value of Ni_2P is only one order of magnitude lower than the one of platinum. The only disadvantage of this catalyst is its stability – corrosion does take place during electrolysis which reduces overall HER activity.

Other examples of potential nickel-based candidates for HER are nickel sulfides. Prepared from $Ni(acac)_2$, NiS and Ni_3S_2 nanoparticles [54] also possess decent HER properties, although, as in the case of Ni_2P, nickel sulfide catalysts lack stability. As reported, hydrogen evolution activity was reduced after 3000 voltammetric cycles and continued reducing up to 5000 cycles. Even though the attempts of creating nickel-based electrocatalysts were not as successful, continued nanoengineering efforts and search of appropriate methods might evolve into creation of robust, efficient, and inexpensive electrocatalytic material for hydrogen evolution.

Ultrasound irradiation was applied in order to synthesize NiS nanoparticles. Spherical NiS nanoparticles with narrow size distribution and high purity were prepared by sonicating an aqueous solution containing metal acetates and thioacetamide in the presence of triethanolamine as a complexing agent. Use of ultrasound provides a fast and efficient once-step synthesis at mild condition [55].

The novel Ni-based electrode material consisting of NiS nanosheet array grown on the surface of nickel foam (named as NiS–NF) with excellent long-term electrochemical stability even under high current density was synthesized via immersion of $Ni(OH)_2$–NF into NaHS solution followed by treatment under ultrasonic conditions. The high stability of composite material was explained by the porous structure and strong contact force between nanosheets and the base that was probably achieved due to ultrasonic-assisted conditions. $Ni(OH)_2$–NF was converted to NiS–NF in the presence of ultrasound [56].

Metal Alloys and Nanoalloys

Metal alloys and nanoalloys including transition metals, non-transition metals, and rare earth metals are promising materials for electrocatalytic reactions compared to expensive platinum. Alloys are composite materials formed by a mixture of elements (metals and nonmetals) or intermetallic compounds. Alloying leads to the enhanced properties of materials including catalytic activity due to synergetic effects [57]. For example, in the case of Pt-containing alloys, the observed improved electrocatalytic performance is explained by geometric and electronic synergetic effects due to the lattice contraction and downshift of the d-band center of Pt in the bimetallic structures [58]. The term "nanoalloys" or "alloyed metal nanoparticles" describes metallic compositions with controllable properties and structures on the nanometer

scale. Similar to alloys, nanoalloys can be solid solutions that are formed by mixing of atoms and core–shell, multi-shell, or multilayered and Janus-like structures that consist of segregated metal atoms [59].

Metallic nanoalloys can be prepared by controllable clustering of metal atoms. Bottom-up approaches to formation of metallic nanoalloys include micelle synthesis [60]; block copolymer self-assembly [61], in the presence of surfactants including polymers and biopolymers [62]; and using inorganic templates, for example, porous carbons [63].

Controlled synthesis of catalytically active nanoalloys consisting of Pt, Pd, and Ni was preformed via convective heating by microwave [64–66], laser irradiation [67], and using sonochemical approach [68, 69].

Main advantage of use of microwave irradiation is rapid transfer of energy directly to the reactants with minimum temperature gradient effect. The interaction of the dipole moment of the molecules with the high-frequency electromagnetic radiation (2.45 GHz) leads to heating effect [65].

The mechanism of nanoalloy formation via laser irradiation is based on several aspects including (i) atomic transformations that are caused by localized heating of particles due to laser-induced resonant electron excitation [67, 70], (ii) reduction of metal ions by reducing agents in the close vicinity of the laser-heated nanoparticles, and (iii) melting of the reduced metal by heat transfer from the nanoparticles and therefore diffusion of the atoms and formation of alloy nanoparticles [64].

Pathways of chemical reactions in laser-treated solutions depend on pulse duration and solvent. Femtosecond laser irradiation of aqueous solutions leads to water decomposition and formation of solvated electrons and hydrogen and hydroxyl radicals along with reactive oxygen species (ROS) [70] that oxidize metals. If nanosecond laser is applied, shock waves trigger rapid dissociation of the peroxides and inhibit oxidation. In the presence of hexane, generation of reducing species – high energetic electrons – was observed [71].

A very interesting approach to the formation of metal nanocomposites is reaction-driven restructuring of nanoalloys. Tao et al. [72] revealed reversible changes of Rh–Pd nanoparticles in composition and chemical state in response to oxidizing or reducing conditions. Segregation of Rh and Pd atoms under oxidizing and reducing conditions was explained by the different surface energy of metals and different stability of metal oxides. The lower surface energy of Pd relative to Rh tends to drive Pd metal atoms to the surface. More stable Rh oxide provides preferential oxidation of Rh at the surface. This work illustrates the high sensitivity of the structure of bimetallic nanoparticle to external conditions.

Sonochemical approach was also used for the synthesis of bimetallic particles and nanoalloys. Ashokkumar et al. [68] and Griezer et al. [69] reported on the sonochemical synthesis of core–shell Pt–Ru nanoparticles by the sonochemical co-reduction of corresponding metal ions using 20 kHz ultrasound in aqueous solution of surfactants and polymers. Formation of core–shell morphology was explained by the different sonochemical reduction rates of metal ions. Polymeric radicals, produced by the reaction of ultrasonically generated primer radicals with a

polymer, reduce the metal ions to generate metal particles. Thus, application of ultrasound for the synthesis of nanoparticles allows using of mild reducing conditions.

Furthermore, use of ultrasound helps to simplify multistage fabrication procedures that are very common for the synthesis of composite materials. Simultaneous ultrasonically driven reduction of Pt and Sn salts and graphene oxide leads to the formation of electrocatalytically active Pt–Sn bimetallic particles deposited on reduced graphene oxide [68]. It was demonstrated that the one-step ultrasound-assisted synthesis of Pt–Sn/reduced graphene oxide composites led to the formation of the composites with well-distributed nanoparticles on graphene sheets.

Suslick et al. demonstrated in the early 1990s that high-intensity ultrasound can be used for the formation of alloys from metal carbonyls. Fe–Co nanostructured alloys were prepared from Fe–$(CO)_5$ and $Co(CO)_3(NO)$ precursors. The Fe–Co alloys had different compositions depending on the ratio of solution concentrations of the precursors. The as-prepared Fe–Co alloys were amorphous that is undesirable for electrocatalytic application. The crystalline form of the alloys was achieved by thermal posttreatment [11].

A number of nanoalloys were synthesized by Kwon et al. using ultrasonically optimized polyol method. More specifically, nanoalloys such as Pd–Co [73], Fe–Pt with different Pt shell thickness [74], Ni–Pt [75], and Pt–Pd [76] were synthesized using this approach. It was shown that polyol method of preparation of nanoalloys can be significantly improved by application of ultrasound. Among the possible reasons are the presence of reductive media (polyol) which under ultrasonic conditions promotes the reduction of metals from their corresponding salts and caused by acoustic cavitation temperature impact that is responsible for nanoalloy formation. Prepared under ultrasonic irradiation, core–shell structures were covered by Pt shell and, thus, demonstrate enhanced catalytic properties. In contrast, the conventional polyol method leads to the formation of particles with less active Co-, Fe-, Ni-, or Pd-enriched shell. Kwon et al. explained their results by different volatility of the used precursor compounds under ultrasonic irradiation. Additionally to the already listed advantages of the sonochemical approach, use of ultrasound allows high control over size and shape of nanoalloys, formation of particles with different thickness of Pt shell, as well as high content of non-noble component in an alloy.

Furthermore, acoustic cavitation was applied in order to enhance the process of electrodeposition of catalytic particles on electrodes. Enhanced mass transport in a cavitated liquid leads to a decrease in diffusion layer thickness and an increase in the rate of electrodeposition. Thus, better distribution of nanoparticles on an electrode's surface can be achieved [77].

Near-Surface and Surface Alloys

Near-surface alloys as one of the types of composite metallic gradient materials are very perspective catalysts and electrocatalysts [5]. It was predicted using density

functional theory that some near-surface alloys allow weak H binding and low H_2 dissociation barrier that is important for effective hydrogen production [78].

Formation of multicomponent gradient nanomaterials helps to achieve tuning of properties without changing particle size [79]. It was demonstrated that the Pt_3Ni (111) surface was even more active than the "gold standard" Pt/C catalysts for the polymer electrolyte membrane fuel cell [80]. The possible explanation for the enhanced catalytic activity of near-surface alloys besides the different electronic and geometric structure of metals in alloys comparing to pure metals was a number of surface effects. In such systems, formation of a rough catalyst surface with a larger number of active sites (increase of the active surface area) can be easily achieved [81]. However, up to now, such alloys were prepared by time- and energy-consuming deposition annealing procedure using transition metals and Pt(111) surface.

Recently, a novel ultrasound-assisted technological approach for near-surface structuring of AlNi alloys was proposed by Andreeva et al. [19, 23]. AlNi alloys are the mixture of various intermetallic phases which possess different and often opposite physical and chemical properties. For example, AlNi with 50 wt% of Ni contains Al, Al_3Ni, and Al_3Ni_2 phases. Using density functional theory, it was predicted that only Al_3Ni_2 phase has promise for HER characteristics [19]. However, the formation of the Al_3Ni_2 phase on the surface of AlNi alloys is kinetically restricted [82]. Therefore, surface of AlNi alloy is passivated by inactive Al_3Ni and Al phases.

Processing of AlNi surface by ultrasonically generated cavitation bubbles was found to be very effective for the activation of metal surface toward HER. HIUS triggers large local temperature gradients' propagation in the metal particles [19]. Such processing stimulates the desired phase transformations at the surface (see the sketches in Fig. 6) rather than in the particle interior according to the following reaction [82]:

$$\mathbf{Al_3Ni} \overset{1127\mathbf{K}}{\rightarrow} \mathbf{Al_3Ni_2} + \mathbf{L}_{15,\, 3 \text{ at. \% Ni}}$$
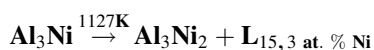
where $\mathbf{L}$ denotes the liquid of a corresponding composition upon equilibrium melting.

Thus, collapsing cavitation bubbles heat the surface above 1124 K and trigger the near-surface transformation of the catalytically inactive Al_3Ni phase into beneficial Al_3Ni_2. The surface of the catalyst before and after ultrasonic modification is shown in Fig. 6. Additional evidences of the microstructure refinement in the alloys after the ultrasonic treatment are provided by selected area electron diffractions (SAED) (see inserts in Fig. 6).

The ultrasonically generated high temperature in nm-thick surface layer of metal particles quenches extremely fast in the particles' interior. Analysis of the sizes of the crystallites of intermetallic phases using Scherrer and Williamson–Hall methods reveals that in the particle interior HIUS triggers crystal growth due to solid-state diffusion [83]. The estimated mean temperature in the particles' interior reaches
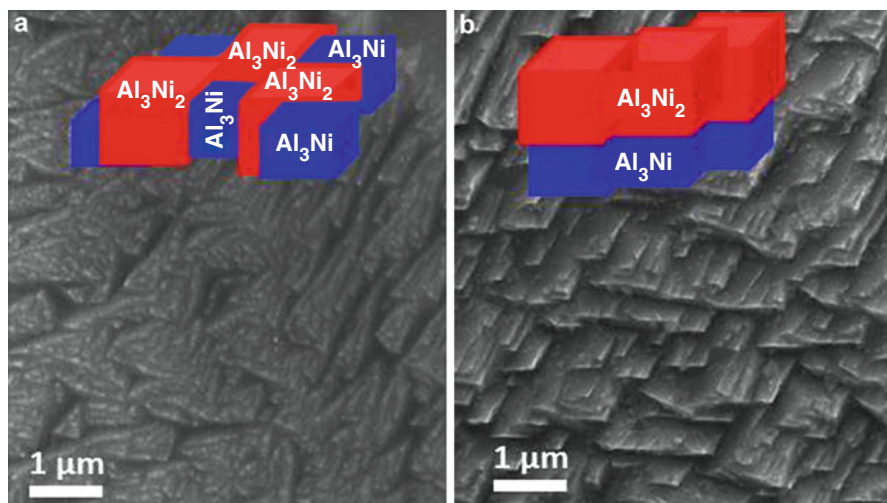
Fig. 6 Scanning electron microscopy images taken from the surface of AlNi (50 wt% Ni) before (**a**) and after (**b**) ultrasonication. The sketches illustrate the random phase distribution in the initial AlNi particles and the preferential clustering of the Al_3Ni_2 phase upon the HIUS treatment (Reprinted with permission from Ref. [19]. Copyright 2015 Royal Society of Chemistry)

824 K, which is well below the phase transformation temperature [83]. Thus, HIUS is a unique tool for the modification of metal surface at atomic level and the formation of materials with composition gradient.

Furthermore, the near-surface structured cheap and robust AlNi catalyst exhibited the onset overpotential of -0.25 V versus standard hydrogen electrode (SHE) (Fig. 7a) and exchange current density, $i_0 \approx 17$ mA/cm^2, that exceeds i_0 of catalysts prepared by using other approaches (see Table 2).

Summarizing, HIUS creates a special condition for near-surface structuring of metals and metal alloys and, thus, their activation for water splitting. The ultrasonically generated near-surface AlNi catalyst was found very robust and exhibited excellent stability in electrochemical use as it can be seen in Fig. 7b.

Conclusions and Future Directions

Sonochemical processing of metals/metal alloys is among the most promising methods for creation of active catalysts toward hydrogen evolution. Surprisingly, caused by acoustic wave cavitation phenomenon that is highly undesirable for industrial engineering, it has a great number of positive impacts in the area of catalytic material formation. In other words, method of ultrasound treatment is a perfect example of turning initially disadvantageous cavitation effects into highly beneficial ones.
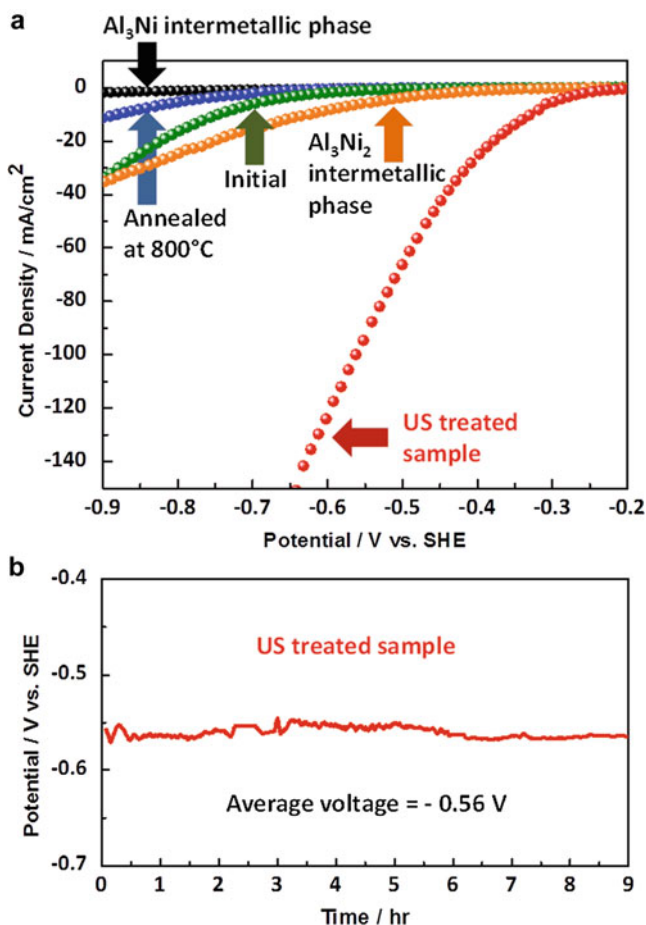
Fig. 7 HER current–potential profiles for the initial and ultrasonically modified AlNi (50 wt% Ni) alloys, bulk commercial Al_3Ni and Al_3Ni_2 phases, as well as AlNi alloy annealed at 800 °C (**a**). Galvanostatic HER profile for ultrasonically modified AlNi (50 wt% Ni) alloy (**b**) (Reprinted with permission from Ref. [19]. Copyright 2015 Royal Society of Chemistry)

Intensive studies on the subject of ultrasound processing of metal/metal alloy allowed revealing of numerous fundamental aspects such as temperature impact of cavitation bubble implosion, solid-state atomic diffusion, and morphological and compositional changes. The obtained fundamental knowledge was successfully implied for development of the material with significantly enhanced electrocatalytic properties. Thus, with respect to formation of electrocatalytically active interface, ultrasound treatment allows to satisfy several requirements that are important for the catalyst to be efficient.

First, HIUS treatment leads to overall structuring of HER active phases, namely, their growth and exposure on the catalyst surface due to accelerated solid-state

atomic diffusion caused by created temperature gradient. Second, through the appropriate choice of sonication medium, it is possible to controllably avoid the formation of porous surface for prevention of hydrogen bubble trapping and associated with it increased electrolyte ohmic resistance. Additionally, while sonicated, the catalyst surface is being activated which is required for the achievement of the necessary hydrogen coverage. This step may drastically reduce the applied overpotential of HER process. In summary, US treatment can be simply considered as a unique "one-pot" surface modification method which opens the new prospective for inexpensive earth-abundant metals such as aluminum and nickel to be used for fabrication of robust and highly efficient electrocatalyst alternative to platinum toward hydrogen evolution.

Nevertheless, despite the unraveled fundamental knowledge about cavitation and its impact on the formation of electrocatalytically active interface toward hydrogen evolution, there are several important points which should be addressed in the near future. The exact mechanism of hydrogen formation for a given ultrasonically modified system and its kinetic is still unclear and debatable, even though the elementary steps involved in the HER process are well known. Thus, the question about rate-limiting step still needs to be clarified.

In addition to that, more information should be revealed with respect to synergetic effects of HER non-active/active phases, especially in case of several possibilities for hydrogen adsorption, what phase adsorbs it first, and whether there is a migration from one phase to another during ultrasound treatment.

Besides that, other potential earth-abundant (tungsten, cobalt, molybdenum) metal systems should be investigated in terms of ultrasound-assisted enhancement of electrocatalytic properties. The knowledge that may come from these studies not only will help designate the promising HER active materials but, more importantly, will finally assist with the creation of "real" more efficient catalyst than platinum.

References

1. Hydrogen production. Overview of technology options. Report of Freedom Car Fuel Partnership (2009) https://www1.eere.energy.gov/hydrogenandfuelcells/pdfs/h2_tech_roadmap.pdf
2. It's elemental – the periodic table of elements. Jefferson Lab. (2007) http://education.jlab.org/itselemental
3. Skulason E, Tripkovic V, Björketun ME, Gudmundsdottir S, Karlberg G, Rossmeisl J, Bligaard T, Jonsson H, Norskov JK (2010) Modeling the electrochemical hydrogen oxidation and evolution reactions on the basis of density functional theory calculations. J Phys Chem C 114:18182–18197
4. Jaramillo TF, Jørgensen KP, Bonde J, Nielsen JH, Horch S, Chorkendorff I (2007) Identification of active edge sites for electrochemical H_2 evolution from MoS_2 nanocatalysts. Science 317:100–102
5. Greeley J, Mavrikakis M (2004) Alloy catalysts designed from first principals. Nat Mater 3:810–815
6. Knudsen J, Nilekar AU, Vang RT, Schnadt J, Kunkes EDL, Dumesic JA, Mavrikakis M, Nesenbacher F (2007) Cu/Pt near-surface alloy for water–gas shift catalysis. J Am Chem Soc 129:6485–6490

7. Skorb EV, Andreeva DV (2013) Bio-inspired ultrasound assisted construction of synthetic sponges. J Mater Chem A 1:7547–7557
8. Bang JH, Suslick KS (2010) Applications of ultrasound to the synthesis of nanostructured materials. Adv Mater 22:1039–1059
9. Skorb EV, Andreeva DV (2013) Surface nanoarchitecture for bio-applications: self-regulated intelligent interfaces. Adv Funct Mater 23:4483–4506
10. Suslick KS, Price GJ (1999) Application of ultrasound to materials chemistry. Annu Rev Mater Sci 29:295–326
11. Suslick KS, Hyeon T, Fang M (1996) Nanostructured materials generated by high-intensity ultrasound: sonochemical synthesis and catalytic studies. Chem Mater 8:2172–2179
12. Oxley JD, Mdleleni MM, Suslick KS (2004) Hydrodehalogenation with sonochemically prepared Mo_2C and W_2C. Catal Taday 88:139–151
13. Dulle J, Nemeth S, Skorb EV, Irrgang T, Senker J, Kempe R, Fery A, Andreeva DV (2012) Sonochemical activation of Al/Ni hydrogenation catalyst. Adv Funct Mater 22:3128–3135
14. Doktycz SJ, Suslick KS (1990) Interparticle collisions driven by ultrasound. Science 247:1067–1069
15. Lorimer JP, Mason TJ (1987) Sonochemistry part 1-the physical aspects. Chem Soc Rev 16:239–274
16. Prozorov T, Prozorov R, Suslick KS (2004) High velocity interparticle collisions driven by ultrasound. J Am Chem Soc 126:13890–13891
17. Cherepanov PV, Kollath A, Andreeva DV (2015) Up to which temperature ultrasound can heat the particle? Ultrason Sonochem 26:9–14
18. Conrad H, Narayan J (2000) On the grain size softening in nanocrystalline materials. Scr Mater 42:1025–1030
19. Cherepanov PV, Melnyk I, Skorb EV, Fratzl P, Zolotoyabko E, Dubrovinskaia N, Dubrovinsky L, Avadhut YS, Senker J, Leppert L, Kuemmel S, Andreeva DV (2015) The use of ultrasonic cavitation for near-surface structuring of robust and low-cost AlNi catalysts for hydrogen production. Green Chem. doi:10.1039/c5gc00047e
20. Rajan R, Pandit AB (2001) Correlations to predict droplet size in ultrasonic atomization. Ultrasonics 39:235–255
21. Ciawi E, Rae J, Ashokkumar M, Grieser F (2006) Determination of temperatures within acoustically generated bubbles in aqueous solutions at different ultrasound frequencies. J Phys Chem B 110:13656–13660
22. Anbar M, Pecht I (1964) On sonochemical formation of hydrogen peroxide in water. J Phys Chem 68:352–355
23. Cherepanov PV, Ashokkumar M, Andreeva DV (2015) Ultrasound assisted formation of Al-Ni electrocatalyst for hydrogen evolution. Ultrason Sonochem 23:142–147
24. Conway BE, Tilak BV (2002) Interfacial processes involving electrocatalytic evolution and oxidation of H_2, and the role of chemisorbed H. Electrochim Acta 47:3571–3594
25. Liao L, Zhu J, Bian X, Zhu L, Scanlon DS, Girault HH, Liu B (2013) MoS_2 formed on mesoporous graphene as a highly active catalyst for hydrogen evolution. Adv Funct Mater 23:5326–5333
26. Atkins P, Paula JD (2002) Atkins' physical chem, 7th edn. Oxford University Press, Oxford, New York
27. Banks CE, Davies JD, Wildgoose G, Compton RG (2005) Electrocatalysis at graphite and carbon nanotube modified electrodes: edge-plane sites and tube ends are the reactive sites. Chem Commun 7:829–841
28. Yuan W, Zhou Y, Li Y, Li C, Peng H, Zhang J, Liu Z, Dai L, Shi G (2013) The edge- and basal-plane-specific electrochemistry of a single-layer graphene sheet. Sci Rep 3:1–7
29. Hinnemann B, Moses PG, Bonde J, Jørgensen KP, Nielsen JH, Horch S, Chorkendorff I, Nørskov JK (2005) Biomimetic hydrogen evolution: MoS_2 nanoparticles as catalyst for hydrogen evolution. J Am Chem Soc 127:5308–5309

30. Kibsgaard J, Jaramillo TF, Basenbacher F (2014) Building an appropriate active-site motif into a hydrogen-evolution catalyst with thiomolybdate $[Mo_3S_{13}]^{2-}$ clusters. Nat Chem 6:248–253

31. Xiao P, Ge X, Wang H, Liu Z, Fisher A, Wang X (2015) Novel molybdenum carbide–tungsten carbide composite nanowires and their electrochemical activation for efficient and stable hydrogen evolution. Adv Funct Mater 25:1520–1526

32. Popczun EJ, McKone JR, Read CG, Biacchi AJ, Wiltrout AM, Lewis NS, Schaak RE (2013) Nanostructured nickel phosphide as an electrocatalyst for the hydrogen evolution reaction. J Am Chem Soc 135:9267–9270

33. Chen PC, Chang YM, Wu PW, Chiu YF (2009) Fabrication of Ni nanowires for hydrogen evolution reaction in a neutral electrolyte. Int J Hydrogen Energy 34:6596–6602

34. Kiuchi D, Matsushima H, Fukunaka Y, Kuribayashi K (2006) Ohmic resistance measurement of bubble froth layer in water electrolysis under microgravity. J Electrochem Soc 153:138–143

35. Chang Y-H, Lin C-T, Chen T-Y, Hsu C-L, Lee Y-H, Zhang W, Wei K-H, Li L-J (2013) Highly efficient electrocatalytic hydrogen production by MoS_x grown on graphene-protected 3D Ni foams. Adv Mater 25:756–760

36. Tang H, Dou K, Kaun CC, Kuang Q, Yang S (2014) $MoSe_2$ nanosheets and their graphene hybrids: synthesis, characterization and hydrogen evolution reaction studies. J Mater Chem A 2:360–364

37. Chen WF, Muckerman JT, Fujita E (2013) Recent developments in transition metal carbides and nitrides as hydrogen evolution electrocatalysts. Chem Commun 49:8896–8909

38. Xing Z, Liu Q, Asiri AM, Sun X (2014) Closely interconnected network of molybdenum phosphide nanoparticles: a highly efficient electrocatalyst for generating hydrogen from water. Adv Mater 26:5702–5707

39. Tran PD, Nguyen M, Pramana SS, Bhattacharjee A, Chiam SY, Fize J, Field MJ, Artero V, Wong LH, Loo J, Barber J (2012) Copper molybdenum sulfide: a new efficient electrocatalyst for hydrogen production from water. Energy Environ Sci 5:8912–8916

40. Mdleleni MM, Hyeon T, Suslick KS (1998) Sonochemical synthesis of nanostructured molybdenum sulfide. J Am Chem Soc 120:6189–6190

41. Mahajan S, Papish ET, Pandya K (2004) Sonolysis induced decomposition of metal carbonyls: kinetics and product characterization. Ultrason Sonochem 11:385–392

42. Wang X, Nan F, Zhao J, Yang T, Ge T, Jiao K (2015) A label-free ultrasensitive electrochemical DNA sensor based on thin-layer MoS_2 nanosheets with high electrochemical activity. Biosens Bioelectron 64:386–391

43. Coleman JN, Lotya M, O'Neill A, Bergin SD, King PJ, Khan U, Young K, Gaucher A, De S, Smith RJ, Shvetz IV, Arora SK, Stanton G, Kim H-Y, Lee K, Kim GT, Dueberg GS, Hallam T, Boland JJ, Wang JJ, Donegan JF, Grunlan JC, Moriarty G, Shmeliov A, Nocholls RJ, Perkins JM, Grieveson EM, Theuwissen K, McComb DW, Nellist PD, Nicolosi V (2011) Two-dimensional nanosheets produced by liquid exfoliation of layered materials. Science 331:568–571

44. Gopalakrishnan D, Damien D, Shaijumon MM (2014) MoS_2 quantum dot-interspersed exfoliated MoS_2 nanosheets. ACS Nano 8:5297–5303

45. Mascuso L, Cravanzola S, Cesano F, Scarano D, Zecchina A (2015) Optical, vibrational and structural properties of MoS_2 nanoparticles obtained by exfoliation and fragmentation via ultrasound cavitation in isopropyl alcohol. J Phys Chem C 119:3791–3801

46. Harnisch F, Sievers G, Schroeder U (2009) Tungsten carbide as electrocatalyst for the hydrogen evolution reaction in pH neutral electrolyte solutions. Appl Catal B 89:455–458

47. Rajeswari J, Kishore PS, Viswanathan B, Varadarajan TK (2007) Facile hydrogen evolution reaction on WO_3 nanorods. Nanoscale Res Lett 2:496–503

48. Phuruangrat A, Ham DJ, Hong SJ, Thongtem S, Lee JS (2010) Synthesis of hexagonal WO_3 nanowires by microwave-assisted hydrothermal method and their electrocatalytic activities for hydrogen evolution reaction. J Mater Chem 20:1683–1690

49. Gao C, Nikitenko SI (2012) Mechanism of $W(CO)_6$ sonolysis in diphenylmethane. Ultrason Sonochem 19:498–502

50. Rangari VR, Hassan TA, Mayo Q, Jeelani S (2008) Size reduction of WO_3 nanoparticles by ultrasound irradiation and its application in structural nanocomposites. Compos Sci Technol 69:2293–2300

51. Kong D, Wang H, Lu Z, Cui Y (2014) $CoSe_2$ nanoparticles grown on carbon fiber paper: an efficient and stable electrocatalyst for hydrogen evolution reaction. J Am Chem Soc 136:4897–4900

52. Cao B, Veith GM, Neuefeind JC, Adzic RR, Khalifah PG (2013) Mixed close-packed cobalt molybdenum nitrides as non-noble metal electrocatalysts for the hydrogen evolution reaction. J Am Chem Soc 135:19186–19192

53. Rosalbino F, Delsante S, Borzone G, Angelini E (2008) Electrocatalytic behaviour of Co–Ni–R (R = Rare earth metal) crystalline alloys as electrode materials for hydrogen evolution reaction in alkaline medium. Int J Hydrogen Energy 33:6696–6703

54. Chung DY, Han JW, Lim DH, Jo JH, Yoo SJ, Lee H, Sung YE (2015) Structure dependent active sites of NixSy as electrocatalysts for hydrogen evolution reaction. Nanoscale 7:5157–5163

55. Wang H, Zhang J-R, Zhao X-N, Xu S, Zhu J-J (2002) Preparation of copper monosulfide and nickel monosulfide nanoparticles by sonochemical method. Mater Lett 55:253–258

56. Yu L, Yang B, Liu Q, Liu J, Wang X, Song D, Wang J, Jing X (2015) Interconnected NiS nanosheets supported by nickel foam: soaking fabrication and supercapacitors application. J Electroanalyt Chem 739:156–163

57. Ferrado R, Jellinek J, Johnston RL (2008) Nanoalloys: from theory to applications of alloy clusters and nanoparticles. Chem Rev 108:845–910

58. Xia BY, Wu HB, Li N, Yan Y, Lou XW, Wang X (2015) One-pot synthesis of Pt–Co alloy nanowire assemblies with tunable composition and enhanced electrocatalytic properties. Angew Chem Int Ed 54:3797–3801

59. Wilcoxon J (2009) Absorption properties of dispersed gold and silver alloy nanoparticles. J Phys Chem B 113:2647–2656; Munoz-Florez BM, Kharisov BL, Jumenez-Perez VM, Martinez PE, Lopez ST (2011) Recent advances in the synthesis and main applications of metallic nanoalloys. Ind Eng Chem Res 50:7705–7721

60. Li ZY, Wilcoxon JP, Yin F, Chen Y, Palmer RE, Johnston RL (2007) Structures and optical properties of 4–5 nm bimetallic AgAu nanoparticles. Faraday Discuss 138:363–372

61. Mun JH, Chang YH, Shin DO, Yoon JM, Choi DS, Lee K-M, Kim JY, Cha SK, Lee JY, Jeong J-R, Kim Y-H, Kim SO (2013) Monodisperse pattern nanoalloying for synergistic intermetallic catalysis. Nano Lett 13:5720–5726

62. Brayner R, Vaulay MJ, Fievet F, Coradin T (2007) Alginate-mediated growth of Co, Ni, and CoNi nanoparticles: influence of the biopolymer structure. Chem Mater 19:1190–1198

63. Ghimbeo CM, Le Meins JM, Zlotea C, Vidal L, Schrodj G, Latroche M, Vix-Guteri C (2014) Controlled synthesis of NiCo nanoalloys embedded in ordered porous carbon by a novel soft-template strategy. Carbon 67:260–272

64. Abdelsazed V, Aljarash A, El-Shall MS, Al Othman ZA, Alghamdi AH (2009) Microwave synthesis of bimetallic nanoalloys and CO oxidation on ceria-supported nanoalloys. Chem Mater 21:2825–2834

65. Zhu J, Palchik O, Chen S, Gedanken A (2000) Microwave assisted preparation of CdSe, PbSe, and Cu_2-xSe nanoparticles. J Phys Chem B 104:7344–7347

66. Ma H, Wang H, Na C (2014) Microwave-assisted optimization of platinum-nickel nanoalloys for catalytic water treatment. Appl Cat B 163:198–204

67. Peng Z, Spiethoff B, Tesche B, Walther T, Kleinermanns K (2006) Laser-assisted synthesis of Au–Ag alloy nanoparticles in solution. J Phys Chem B 110:2549–2554

68. Anandan S, Manuvel A, Ashokkumar M (2012) One step sonochemical synthesis of reduced graphene oxide/Pt/Sn hybrid materials and their electrochemical properties. Fuel Cells 6:956–962

69. Winodgopal K, He Y, Ashokkumar M, Griezer F (2006) Sonochemically prepared platinum–ruthenium bimetallic nanoparticles. J Phys Chem B Lett 110:3849–3852

70. Besner S, Meunier M (2010) Femtosecond laser synthesis of AuAg nanoalloys: photoinduced oxidation and ions release. J Phys Chem C 114:10403–10409
71. Herbani Y, Nakamura T, Sato S (2011) Synthesis of near-monodispersed Au–Ag nanoalloys by high intensity laser irradiation of metal ions in hexane. J Phys Chem C 115:21592–21598
72. Tao F, Grass ME, Zhang Y, Butcher DR, Renzas JR, Liu Z, Chung JZ, Mun BS, Salmeron M, Somorjai GA (2008) Reaction-driven restructuring of Rh-Pd and Pt-Pd core-shell nanoparticles. Science 322:932–934
73. Jang J-H, Pak C, Kwon Y-U (2012) Ultrasound-assisted polyol synthesis and electrocatalytic characterization of Pd_xCo alloy and core-shell nanoparticles. J Power Sources 201:179–183
74. Jang J-H, Park J, Kim J, Hong S, Kwon Y-U (2013) Rational synthesis of core-shell $Fe_x@Pt$ nanoparticles for the study of electrocatalytic oxygen reduction reaction. Sci Rep 3:2872
75. Lee E, Jang J-H, Matin MA, Kwon Y-U (2014) One-step sonochemical syntheses of Ni@Pt core-shell nanoparticles with controlled shape and shell thickness for fuel cell electrocatalyst. Ultrason Sonochem 21:317–323
76. Matin MA, Jang J-H, Lee E, Kwon Y-U (2012) Sonochemical synthesis of Pt-doped Pd nanoparticles with enhanced electrocatalytic activity for formic acid oxidation reaction. J Appl Electrochem 42:827–832
77. Boopathi S, Kumar SS (2014) Impact of ultrasonic waves in direct electrodeposition of nanostructured AuPt alloys catalyst on carbon substrate: structural characterization and its superior electrocatalytic activity for methanol oxidation reaction. J Phys Chem C 118:29866–29873
78. Chen C, Kang Y, Huo Z, Zhu Z, Huang W, Xin HL, Snyder JD, Li D, Herron JA, Mavrikakis M, Che M, More KL, Li Y, Markovic NM, Somorjai GA, Yang P, Stamenkovic VR (2014) Highly crystalline multimetallic nanoframes with three-dimensional electrocatalytic surfaces. Science 343:1339–1343
79. Mizukoshi Y, Fujimoto T, Nagata Y, Oshima R, Maeda Y (2000) Characterization and catalytic activity of core–shell structured gold/palladium bimetallic nanoparticles synthesized by the sonochemical method. J Phys Chem B 104:6028–6032
80. Stamenkovic VR, Fowler B, Mun BS, Wang G, Ross PN, Lucas CA, Markovic NM (2007) Improved oxygen reduction activity on Pt3Ni(111) via increased surface site availability. Science 315:493–497
81. Stamenkovic VR, Mun BS, Mayrhofer JJ, Ross PN, Markovic NM (2006) Effect of surface composition on electronic structure, stability, and electrocatalytic properties of Pt-transition metal alloys: Pt-skin versus Pt-skeleton surfaces. J Am Chem Soc 128:8813–8819
82. Batalu D, Cosmeliata G, Aloman A (2006) Critical analysis of AlNi phase diagrams. Metalurgia Int 11:36–45
83. Cherepanov PV, Melnyk I, Andreeva DV (2014) Effect of high intensity ultrasound on Al_3Ni_2, Al_3Ni crystallite size in binary AlNi (50 wt% of Ni) alloy. Ultrason Sonochem 23:26–30

Sonophotocatalytic Degradation of Organic Pollutants Using Nanomaterials

J. Theerthagiri, R. A. Senthil, D. Thirumalai, and J. Madhavan

Contents

Abstract

The textile, cosmetic, and food industries use different organic compounds that are more toxic and non-biodegradable. These compounds are the most important source of water contamination, and hence the treatment of these wastewaters is important to protect the ecosystem. Sonophotocatalytic degradation is an effective method used for the removal of organic pollutant from wastewater. Sonophotocatalysis has received increased attention in advanced oxidation processes for the degradation of organic pollutants, which involves the combination of ultrasound waves and semiconductor photocatalyst to enhance the degradation rate. Different types of semiconductor photocatalysts are used in sonophotocatalysis; among these, the most widely used photocatalysts are TiO_2 and ZnO.

The degradation efficiency is low when sonolysis or photocatalysis is used alone. In order to increase the degradation efficiency, researchers focused on

J. Theerthagiri (✉) • R.A. Senthil • D. Thirumalai • J. Madhavan (✉)
Department of Chemistry, Thiruvalluvar University, Vellore, Tamil Nadu, India
e-mail: j.theerthagiri@gmail.com; senthil2551988@gmail.com; thirumalaid@gmail.com; jagan.madhavan@gmail.com

developing new materials by doping of metal ions or use of composite semiconductor materials. This chapter deals with a detailed analysis of research reports published so far on the nano-sized materials such as TiO_2, ZnO, metal sulfides, and composite materials used in sonophotocatalysis. The reaction mechanism of the sonophotocatalysis for the degradation of organic pollutants is also discussed in detail.

Introduction

Due to increasing revolution in science and technology, numerous groups of organic pollutants are discharged into the environment from various industrial processes posing a serious threat to the environment. Organic pollutants such as dyes, pesticides, chloro-organics, etc., released from textile, leather, cosmetic, food processing, pharmaceutical, woven pulp and paper, agricultural research, and electroplating industries are toxic in nature [1]. Their presence in the wastewater can change the oxygen levels drastically leading to severe problems in the ecosystem [2]. Hence, the remediation of organic pollutants in wastewater has received significant attention from the researchers. Though various physical and biological methods are successfully employed for the degradation and mineralizations of such organic pollutants, these methods have their own drawbacks. Most of the physical methods such as flocculation, reverse osmosis, and adsorption on activated charcoal are nondestructive, but can only transfer the organic pollutant into other secondary products which can lead to other serious environmental issues [3]. Biological aerobic treatment processes face major drawbacks such as (i) formation of large amounts of sludge and (ii) does not degrade the organic pollutant content to a satisfactory level [1]. Therefore, the researchers have proposed advanced oxidation processes (AOPs) to overcome the drawbacks of some conventional treatment methods. The most widely investigated AOPs for the degradation and mineralization of organics are semiconductor photocatalysis, Fenton and photo-Fenton oxidation, ozonation, UV/H_2O_2, sonolysis, etc., [4, 5]. AOPs work through the use of free radicals, particularly hydroxyl ($^{\bullet}OH$), and the superoxide ($^{\bullet}O_2$ or $^{\bullet}OOH$) radicals. These radicals are able to oxidize organic pollutants and form less or nontoxic products such as carbon dioxide (CO_2), water (H_2O), and inorganic mineral acids [6]. Among the AOPs, the semiconductor photocatalysis has received considerable attention in the area of environmental remediation due to its nontoxic nature, its ability to achieve complete mineralization, no waste disposal problem, low operational cost, and easy process conditions. Generally, photocatalysts are selected based on its stability, cost-effectiveness, and capability to harvest light in the visible region. Over the past few decades, various semiconductor materials such as metal oxides, metal sulfides, and

oxynitrides are employed for the degradation of organic pollutants [7–17]. The major reactions that occur in photocatalysis are shown below (Rxn. 1–5).

$$\text{Photocatalyst} \xrightarrow{h\nu} e^-_{CB} + h^+ \tag{1}$$

$$\text{Photocatalyst} \, (e^-_{CB}) + O_2 \rightarrow O_2^{\bullet-} \tag{2}$$

$$O_2^- + 2e^-_{CB} + 2H^+ \rightarrow {}^\bullet OH + OH^- \tag{3}$$

$$\text{Photocatalyst} \, (h^+) + H_2O \rightarrow H^+ + {}^\bullet OH \tag{4}$$

$$\text{Organic pollutant} + {}^\bullet OH + O_2^{\bullet-} \quad \rightarrow \quad \text{Degraded pollutant}$$
$$\downarrow$$
$$(CO_2 + H_2O + \text{Mineral acids}) \tag{5}$$
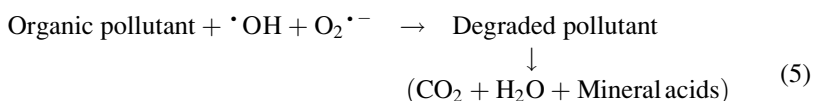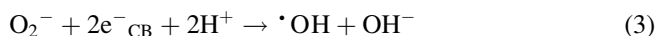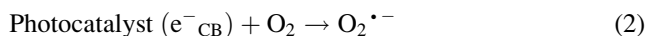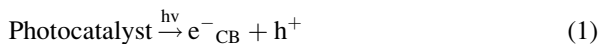
Over the last few years, sonolysis, a kind of chemical reaction taking place by the application of ultrasound (US) radiation (20 kHz–10 MHz), has also received much interest toward degradation of organic pollutants because of its advantages, viz., safety, cleanliness, and no requirement of additional chemicals [18, 19].

Ultrasound is an oscillating sound wave with a frequency greater than the upper limit of the human hearing range [20, 21]. Ultrasound is used in several fields such as the animal navigation and communication, detection of cracks, fetal scanning, and various other medical applications [22]. When the ultrasound wave is passed through an aqueous solution, the acoustic cavitation phenomena take place. The effects of cavitation induced by the ultrasound waves are shown in Fig. 1a.

The cavitation is responsible for many physical and chemical reactions such as the formation, growth, and subsequent collapse of micro-sized bubbles in a fraction of seconds, releasing large magnitudes of energy within the region of the micro-sized bubbles [24]. The micro-bubbles grow in successive cycles and reach to an unstable diameter that collapses violently, producing shock waves at around the temperature of 5000 °C and pressure of 2000 atm in few microseconds [22]. Figure 1b presents the development and collapse of the cavitation bubbles.

The high-energy chemical reaction of the sonochemical processes takes place in three different regions and is shown in Fig. 2 [25–27].

1. The region inside the cavity bubbles (gaseous region). Due to high temperature inside the bubble, volatile and hydrophobic molecules are degraded. (The cavitation bubble water molecules are pyrolyzed forming •OH and •H radicals in the gas phase. The substrate either reacts with the hydroxyl radical or undergoes pyrolysis.)
2. The region at the gas–liquid interface. Formation of hydroxyl radicals takes place in an aqueous phase. The primary radicals generated within the bubbles can react with solutes adsorbed at the bubble–solution interface, thereby initiating the degradation process.

3. The bulk liquid region. The free radicals migrate from the gas–liquid interface into the bulk liquid region to create secondary sonochemical reactions. (In bulk phase, the reactions are basically between the substrate and the •OH radical or H_2O_2.) The primary radicals can diffuse into the bulk solution and react with solutes. Thus, the sonochemical degradation pathway of a particular substrate will depend on its chemical nature, that is, its volatility, solubility, and surface activity.

The sonochemical process is one of the most efficient water treatment technologies for the degradation of organic pollutants. However, using sonolysis alone is limited in large-scale application due to its poor degradation rate which may be due to the high polarity of organic compounds. In order to improve the degradation, it is necessary to combine sonolysis with other AOP [4]. Among the various combined processes, the sonophotocatalysis (combination of sonolysis and photocatalysis) has gained significant attention in the last few years. Sonophotocatalysis is a process of combination of semiconductor photocatalyst which is active in UV or visible or UV-visible light. The sonophotocatalytic degradation of organic pollutants occurs mainly due to the synergistic effect of the sonolysis (US) and photocatalysis (UV).
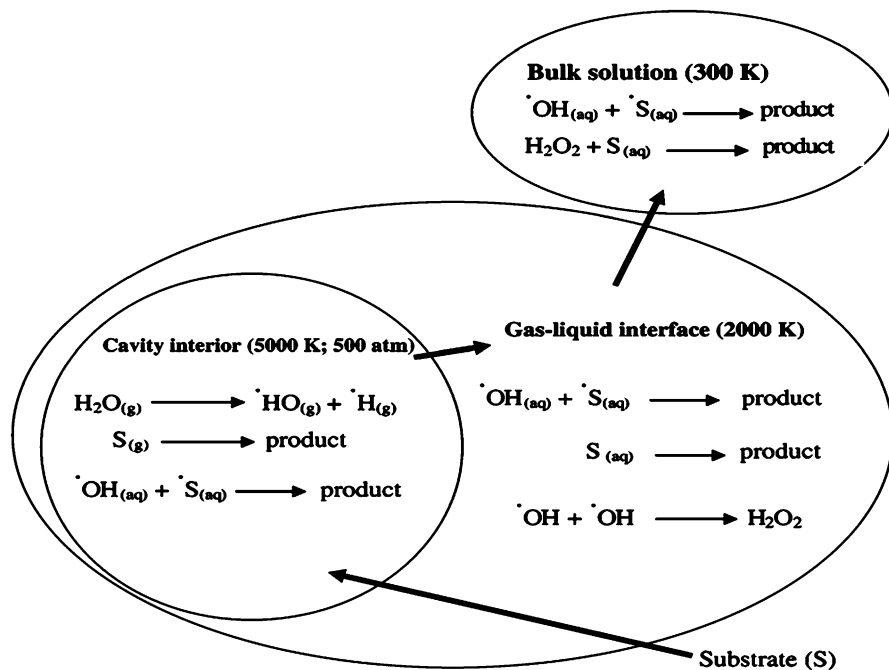
Fig. 2 The three different regions of sonochemical reactions [25] (Reprinted with permission from Ref. [25]. Copyright 2009, Elsevier)

The intermediates formed during ultrasound-assisted degradation are more stable than the parent compounds. As a result, the sonochemical degradation takes a long time for complete mineralization. If it combines with photocatalysis, the degradation of intermediates is very fast. The major advantages of combining these two processes are (i) additional generation of free radicals through both the band gap excitation of photocatalyst and sonolytic splitting of water molecules; (ii) application of ultrasound which continuously cleans the photocatalyst surface, so that the activity of the photocatalyst can be maintained over longer irradiation times; and (iii) its ability to achieve degradation of both hydrophilic and hydrophobic organic compounds. A quantitative way to evaluate the synergistic effect during multiple AOPs application is done by calculating the synergy index and can be calculated as follows [5].

$$\text{Synergy index} = \frac{R_{(\text{US}+\text{UV}+\text{TiO}_2)}}{R_{(\text{US}+\text{TiO}_2)} + R_{(\text{UV}+\text{TiO}_2)}} \qquad (6)$$

Synergy index values >1 indicate the combined process exceeds the sum of the separate processes. The synergy index was calculated from the degradation rates of sonocatalysis $R_{(\text{US}+\text{TiO2})}$, photocatalysis $R_{(\text{UV}+\text{TiO2})}$, and sonophotocatalysis $R_{(\text{US}+\text{UV}+\text{TiO2})}$. The combined process is shown to achieve greater degradation
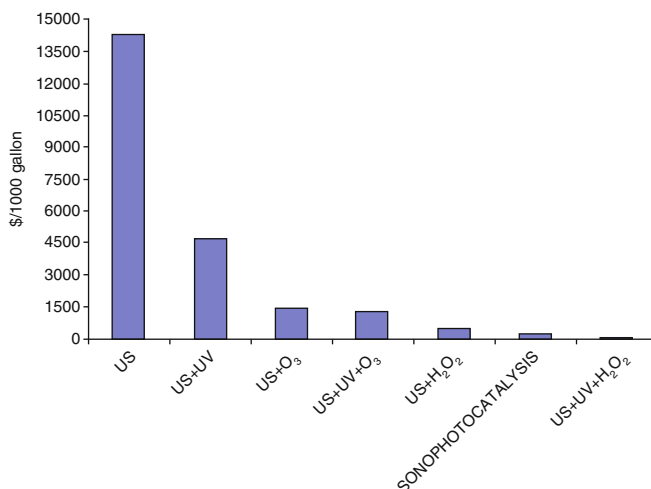
Fig. 3 The overall cost of degradation of organic pollutants using various processes [20] (Reprinted with permission from Ref. [20]. Copyright 2010, Elsevier)

efficiency, reduced cost of treatment, and application of scaling-up than the individual processes of sonolysis and photocatalysis. Mahamuni et al. investigated the technical and economical feasibility of ultrasound for the wastewater treatment on industrial scale [20]. They also reported that the cost of ultrasound for the degradation of organic pollutant was reduced when combined with photocatalysis (Fig. 3).

The following section of this chapter addresses the use of various nanomaterials such as metal oxides, metal sulfides, and composite photocatalysts in sonophotocatalytic degradation of organic pollutants in aqueous environment. The reaction mechanism of ultrasonic degradation of different organic pollutants in the presence of various photocatalysts is also discussed in detail.

Nanomaterials for Sonophotocatalysis

Out of the many photocatalysts, nano-sized TiO_2 and ZnO are widely used in sonophotocatalysis. Hence, the following section separately covers the applications of these materials in detail.

Nano-titanium Dioxide-Mediated Sonophotocatalysis

The titanium dioxide (TiO_2) has been widely studied for the degradation and mineralization of organic pollutants in aqueous media. TiO_2 has several advantages such as strong oxidizing ability, chemical stability, nontoxicity, and availability at low cost [28–39]. TiO_2 can be found in three crystal structures, such as anatase,
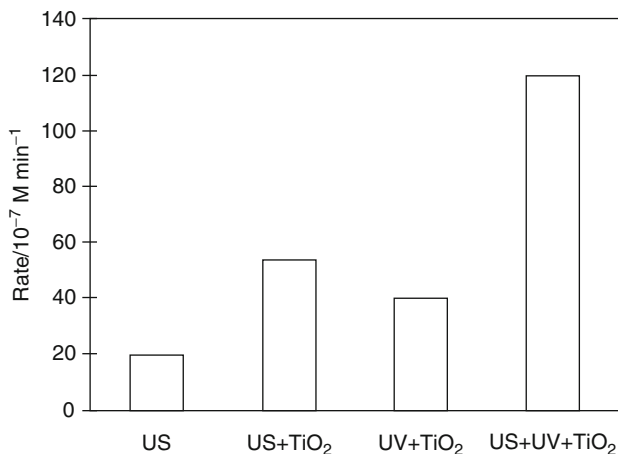
Fig. 4 Comparison of degradation rates of acid red 88 in the presence of TiO_2 (1 g L^{-1}) using different processes [40] (Reprinted with permission from Ref. [40]. Copyright 2010, Elsevier)

brookite, and rutile. Among these, the anatase form of TiO_2 has been mostly used in photocatalysis activity than the other two forms.

Madhavan et al. investigated the degradation of acid red 88 using sonolysis, photocatalysis, and sonophotocatalysis in the presence of TiO_2 (Degussa P25) [40]. The degradation of AR88 using US + TiO_2, UV + TiO_2, and US + UV + TiO_2 was performed with initial dye concentration of 0.09 mM and a fixed catalyst amount of 1 g/L. The obtained degradation rates of all the processes are shown in Fig. 4. The results showed the higher degradation rate observed for the sonophoto-catalysis. This may be due to the synergistic effect by the combination of ultrasonic irradiation, ultraviolet radiation, and a semiconductor photocatalyst.

Mishra et al. studied the sonophotocatalytic degradation of p-nitrophenol in the presence of TiO_2 as catalyst using low-frequency ultrasound waves (25 kHz) [41]. The effect of catalyst concentration on sonophotocatalytic degradation was investigated by varying the amount of TiO_2 from 0.5 to 4.0 g/L at pH 2.5 for p-nitrophenol (10 ppm) solution. A maximum of 76.4 % degradation was observed at TiO_2 concentration of 2.0 g/L. On further increase above 2.0 g/L of TiO_2, the degradation rate was decreased which may be attributed to the dominant screening effect of excess TiO_2 particles.

The pH of the solution is an important factor in determining the physical and chemical properties of a solution, which will affect the bubble dynamics. Hence, the process of sonophotocatalysis was investigated at different pH values of 2.5, 5.0, 7.0, 9.0, and 11.0. The maximum degradation of 76.4 % was obtained at a concentration of 10 ppm p-nitrophenol at pH 2.5, and the extent of degradation was decreased as the pH was increased. This may be attributed to the fact that under acidic conditions, both UV- and US-induced degradation favored to show enhanced degradation in the combined process. At lower pH values (higher acid concentration), there is

Fig. 5 First-order kinetic plots of AO8 degradation in the presence of TiO$_2$ nanoparticles using (**a**) sonolysis, (**b**) photocatalysis, and (**c**) sonophotocatalysis [42] (Reprinted with permission from Ref. [42]. Copyright 2002, Royal Society of Chemistry)
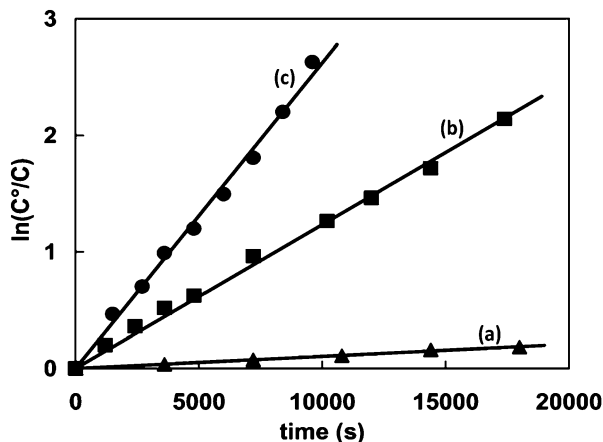
domination of the molecular form of p-nitrophenol. This molecular form of p-nitrophenol makes it possible to diffuse into the reactive zone (gas–liquid film region). Also, a small fraction of this molecular form may even evaporate into the cavity (gaseous) region from the gas–liquid interface. Thus, the overall decomposition of p-nitrophenol at low pH (higher acidic solution) took place in gaseous, interfacial film regions by pyrolysis and free radical attack. Therefore, the catalyst concentration and pH of the solution also affect the degradation rate of sonophotocatalysis.

Selli et al. studied the sonophotocatalytic degradation of acid orange 8 (AO8) using TiO$_2$ [42]. The first-order kinetic plots of AO8 degradation using sonolysis, photocatalysis, and sonophotocatalysis in presence of TiO$_2$ nanoparticles are shown in Fig. 5. It was observed that the degradation efficiency for the sonophotocatalysis was higher than the individual processes, and this may be due to the synergistic effect of sonolysis and photocatalysis.

Mishra et al. investigated the sonocatalytic and sonophotocatalytic degradation of rhodamine B (RhB) with different TiO$_2$ catalyst loadings ranging from 0.5 to 4.0 g/L [43]. The higher degradation was observed at a TiO$_2$ concentration of 3 g/L. Beyond which, the sonophotocatalytic degradation was lowered. Further, the degradation efficiency of sonocatalysis was found to be almost similar to that of sonophotocatalysis. The observed degradation efficiency for sonocatalysis was 92 %, while that for sonophotocatalysis was only 93 %. Berberidou et al. investigated the degradation of malachite green (MG) in aqueous solution using sonolytic, photocatalytic, and sonophotocatalytic process in the presence of TiO$_2$ [44]. The sonophotocatalysis was observed to be more efficient for the degradation of MG than compared to the individual processes due to the enhanced formation of reactive radicals as well as the possible ultrasound-induced increase of the available active surface area of the catalyst. Further, it was noted that the ecotoxicity of MG to marine bacteria was partially/fully eliminated depending on the conditions employed such as the concentration of the catalyst, pH, and power of the ultrasound. Kritikos

et al. carried out the sonophotocatalytic degradation of reactive black 5 (RB5) in the presence of TiO_2 nanoparticles [45] and achieved almost complete decolorization after 20 min of photocatalytic degradation under ultrasound irradiation (80 kHz, 135 W) at catalyst loading of 1.0 g/L. These results indicated that the coupling of photocatalysis with ultrasound irradiation significantly increased the degradation efficiency when compared to the individual processes operating at standard conditions.

Cheng et al. designed an ultrasound-intensified photocatalytic reactor and demonstrated the degradation of azo dye methyl orange (MO) using TiO_2 [46]. The obtained results showed higher efficiency for sonophotocatalysis due to the synergistic effect of sonolysis and photocatalysis. They also investigated the effect of operational parameters such as US power, TiO_2 dosage, and airflow rate on the degradation efficiency. The effect of US power on synergy was more significant which revealed the effects of physical and chemical parameters of US on photocatalysis. Selli et al. have evaluated the rate of 1,4-dichlorobenzene (1,4-DCB) degradation and mineralization in the aqueous phase under photocatalysis and sonophotocatalysis in the presence of Degussa P25 TiO_2 [47]. The higher degradation and mineralization rates were observed for the combined process of photocatalysis and sonolysis. The rate constant observed for the photocatalysis was $2.4 \pm 0.2 \times 10^{-4}$ s^{-1} and sonophotocatalysis was $3.8 \pm 0.2 \times 10^{-4}$ s^{-1}. Davydov et al. studied the effect of ultrasound on the photodegradation of salicylic acid with four different commercial TiO_2 powders such as Hombikat, Ishihara, Degussa, and Aldrich [48]. The smaller particle-sized Degussa P25 exhibited the higher activity for the sonophotocatalytic degradation of salicylic acid than other catalysts. The higher degradation rate was observed for the sonophotocatalysis, which may be due to the aggregate breakage of TiO_2 nanoparticles by the ultrasound. Ahmedchekkat et al. investigated the decolorization of RhB in aqueous solution using photocatalysis and sonophotocatalysis in the presence of Degussa TiO_2 [49]. About 98 % decolorization was obtained for sonophotocatalysis, whereas 90 % of degradation was observed in case of photocatalysis. A synergy index value of 1.4 was obtained from the degradation rates of sonolysis, photocatalysis, and sonophotocatalysis, which revealed the synergistic degradation of RhB. Madhavan et al. studied the degradation of paracetamol by the sonophotocatalysis in the presence of TiO_2 and reported on sonophotocatalysis that achieved the higher degradation efficiency than the individual processes [50]. The degradation rates obtained for the sonolysis, photocatalysis, and sonophotocatalysis were about 8.3, 30.2, and 40.2×10^{-7} M min^{-1}, respectively. The corresponding plot of degradation rates is shown in Fig. 6.

Yuan et al. synthesized TiO_2 nanotube array by anodic oxidation and investigated the degradation of methylene blue by sonophotocatalytic process [51]. It was observed that the ultrasound frequency had a significant effect on the synergy between sonolytic and photocatalytic degradation of MB. TiO_2 nanotube array catalyst showed a good recyclability and the synergy was as high as 22.1 % at 27 kHz irradiation. Saien et al. studied the degradation of styrene–acrylic acid copolymer (ASSC) in aqueous media using sono-assisted photocatalytic process
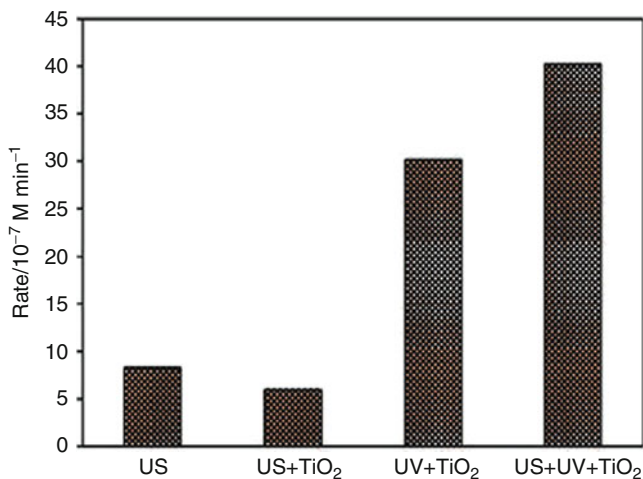
Fig. 6 The paracetamol degradation rates for different processes with and without ultrasound [50] (Reprinted with permission from Ref. [50]. Copyright 2013, Elsevier)

with Degussa P25 TiO_2 as a photocatalyst and evaluated the effect of TiO_2 dosage in the sonophotocatalytic degradation [52]. The results showed that the degradation efficiency increased with the increase in catalyst concentration from 0.01 to 0.07 g/L, and this may be due to more active species generated by absorbed fraction of the irradiated lights. The optimized catalyst amount of 0.03 g/L provided a distinct trend of variation of a nearly perfect degradation over a usual time of 60 min. Also, they reported the degradation and mineralization of 96 % and 91 %, respectively. Khokhawala et al. investigated the degradation of phenol using a sonophotocatalysis in the presence of TiO_2 [53]. The effect of concentration of TiO_2 on the degradation rate of phenol has been investigated over a concentration range of 0.5–2.5 g/L, and the obtained results are shown in Fig. 7. It showed that the extent of degradation of phenol increased almost linearly with an increase in the loading of the photocatalyst over the entire range of concentration. This was due to the fact that as the quantity of TiO_2 was increased, the number of active sites available for light-induced reaction also increased resulting in the enhanced reaction between the pollutant molecules and hydroxyl radicals. However, in sonophotocatalysis the maximum degradation was observed for 2.0 g/L of TiO_2. This investigation clearly showed that the amount of TiO_2 affects the degradation rate.

Jelic et al. studied the photocatalytic and sonophotocatalytic degradation of carbamazepine (CBZ) in the presence of TiO_2 nanoparticles [54]. The combined oxidation $UV/US/TiO_2$ resulted in a significant enhancement of CBZ degradation rate. Wu et al. investigated the decolorization of reactive red 2 (RR2) using sonocatalysis, photocatalysis, and sonophotocatalysis with TiO_2 nanoparticles [55] and observed the decolorization rates in the following order: $UV/US/TiO_2 > UV/TiO_2 > US/TiO_2$ at pH 7.0. This clearly showed that the $UV/US/TiO_2$ system effectively decolorized and mineralized RR2. They also investigated the effect of

Fig. 7 The photocatalytic and sonophotocatalytic degradation of phenol with different amounts of TiO_2 [53] (Reprinted with permission from Ref. [53]. Copyright 2010, Elsevier)
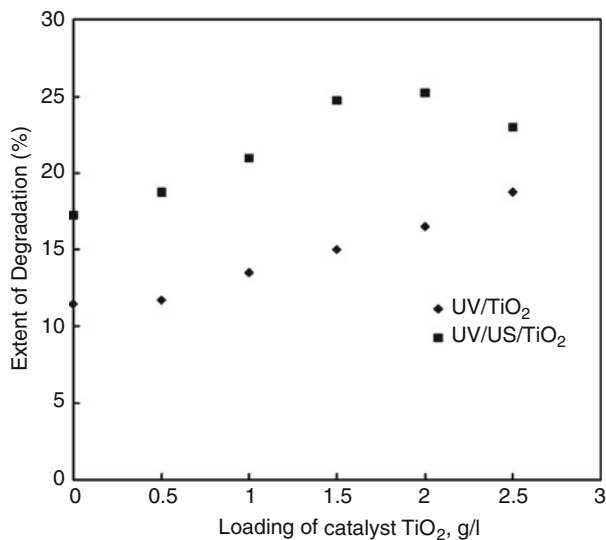
TiO_2 dosage, pH, and temperature on RR2 decolorization by the sonophotocatalysis, which supported the importance of combined treatment method for enhancing the degradation rate of organic pollutant in water. Taicheng An et al. investigated the sonophotocatalytic process for the decolorization of reactive brilliant orange K-R (RBOKR) and COD removal from the synthetic wastewater [56]. The results showed that the combination of sonolysis and photocatalysis could efficiently remove the color and reduce the COD from the synthetic dye-containing wastewater. Taghizadeh et al. studied the sonolytic, sonocatalytic, and sonophotocatalytic degradation of chitosan in the presence of TiO_2 nanoparticles using ultrasound irradiation (24 kHz), where an ultraviolet light source of 16 W was used for UV irradiation [57]. The observed results showed that the sonophotocatalytic degradation was faster than the individual processes due to the enhanced formation of reactive radicals as well as the possible ultrasound-induced increase of the active surface area of the photocatalyst. He et al. investigated the sonophotocatalytic degradation of p-chlorobenzoic acid (PCBA) in the presence of TiO_2 nanoparticles [58]. The degradation of 100 μM PCBA was carried out at two different solution pH values, viz., 2.0 and 10.0, for studying the effect of pH on the degradation rate. The rate constant and synergistic index of solution pH 2.0 was found to be higher when compared to pH 10.0. From the study, it was evident that the sonochemical degradation of PCBA was much in favor of acidic pH 2.0 than alkaline pH 10.0. Some studies on sonophotocatalytic degradation of organic pollutants using nano-sized TiO_2 are summarized in Table 1.

Though there are several reports on TiO_2 in sonophotocatalysis, the major disadvantages of TiO_2 that restrict its large-scale application are as follows: (i) it can only work in UV light irradiation with wavelength less than 380 nm (anatase form of TiO_2 owing its band gap 3.2 eV) and (ii) it has a faster rate of recombination

Table 1 Sonophotocatalytic degradation of pollutants using nano-sized TiO_2

S.No	Pollutant	Ultrasonic frequency	Ultrasonic power	Synergy index	Refs.
1	Acid red 88	213 kHz	55 mW mL^{-1}	1.3	[40]
2	Acid orange 8	20 kHz	20 W	0.49	[42]
3	2-Chlorophenol	20 kHz	20 W	0.07	[42]
4	Malachite green	80 kHz	150 W	0.14	[44]
5	Reactive black 5	80 kHz	135 W	Synergetic	[45]
6	Methyl orange	20 kHz	600 W	1.75	[46]
7	1,4-Dichlorobenzene	20 kHz	40 W	Synergetic	[47]
8	Rhodamine B	20 kHz	40 W	1.4	[49]
9	Paracetamol	213 kHz	13.8 W	1.0	[50]

of photogenerated electron–hole pairs. Therefore, numerous studies have been made to expand the visible light response of TiO_2 by doping of other metal or coupling with other semiconductor photocatalyst materials. The later part of this chapter deals about the composite materials for sonophotocatalytic applications.

Nano-Sized ZnO-Mediated Sonophotocatalysis

ZnO nanoparticles have attracted much attention as a potential catalyst in the field of environmental remediation because of its exceptional physical, chemical, and optical properties such as high UV absorption potential with wide band gap (3.37 eV), high bond energy (60 meV), and high thermal and mechanical stability [59–69].

Elena Selli investigated the synergistic effects on combination of ultrasound with ZnO photocatalysis [42]. The degradation of the azo dye acid orange 8 in aqueous solution was evaluated under sonolysis (US), photocatalysis (UV + ZnO), and sonophotocatalysis (US + UV + ZnO). The degradation rate of the azo dye was higher for the combined process when compared to the individual sonolysis and photocatalysis. The active surface area of ZnO was increased under ultrasonic irradiation which leads to an increase in the catalytic performance of ZnO. Which was more active than TiO_2 toward the degradation of azo dye due to the formation of active radicals and high synergistic effect? Ertugay et al. studied the sonocatalytic activity of nano-sized ZnO for the degradation of direct blue 71 [70]. The sonocatalytic activity of ultrasound/ZnO was higher than the sonolysis alone. Ultrasound played an important role in decomposing azo dye in the presence of ZnO. The degradation rate was also increased with amount of ZnO used. The degradation efficiency followed the order US/ZnO/H_2O_2 > US/H_2O_2 > US which corresponds to 98 %, 55 %, and 23 %, respectively. The higher degradation efficiency observed for US/ZnO/H_2O_2 was attributed to the promotion of ultrasound on ZnO-catalyzed decomposition of H_2O_2 to form active •OH radicals. When the production of •OH radicals increases, the degradation efficiency also increases. Anju et al. studied the
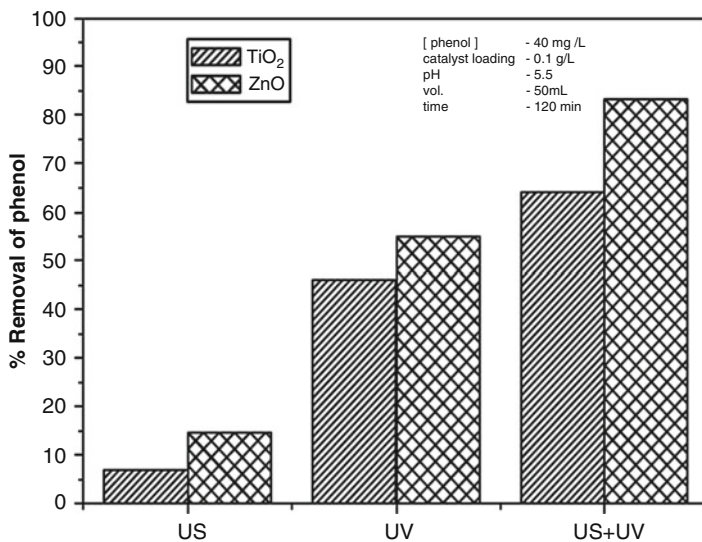
Fig. 8 Sonolysis, photocatalysis under UV light, and sonophotocatalysis process for the degradation of phenol in the presence of ZnO and TiO$_2$ nanomaterials [71] (Reprinted with permission from Ref. [71]. Copyright 2012, Elsevier)

ZnO-mediated sonophotocatalysis for the degradation of phenol in aqueous solution [71] and reported that the nano-sized ZnO was found to be more active than nano-sized TiO$_2$-mediated sonophotocatalysis than the individual processes. The comparative percentage of phenol degradation by various processes is shown in Fig. 8.

Talebian et al. synthesized ZnO nanoparticles by solvo-thermal method and investigated the morphology of ZnO with respect to the concentration of hydrazine hydrate [72]. SEM morphology (Fig. 9) showed granular, hexagonal granular, and rodlike nanoparticles for 5 wt%, 40 wt%, and 80 wt% of hydrazine hydrate. Depending on the shape and morphology, the degradation rate of chrome intra orange G was changed. The ZnO with nanorod structure materials showed the highest efficiency for the degradation of the azo dye. The ZnO-mediated sonophotocatalysis showed better performance than the ZnO photocatalysis, and this may be due to the presence of ultrasound, which promoted the deaggregation by increasing the active surface area of ZnO. From the study, it was evident that the shape, surface morphology, and size of the nanomaterials played an important role in influencing the efficiency of sonophotocatalysis for the degradation of organic pollutants.

Madhavan et al. investigated the degradation of diclofenac, a nonsteroidal anti-inflammatory drug in an aqueous environment using ZnO photocatalyst [73]. Total organic carbon (TOC) studies were compared for the degradation of diclofenac by sonolysis, ZnO photocatalysis, and sonophotocatalysis. 23 % of degradation of diclofenac was observed in sonolysis, 68 % of degradation was achieved using photocatalysis, whereas the sonophotocatalysis showed the highest degradation
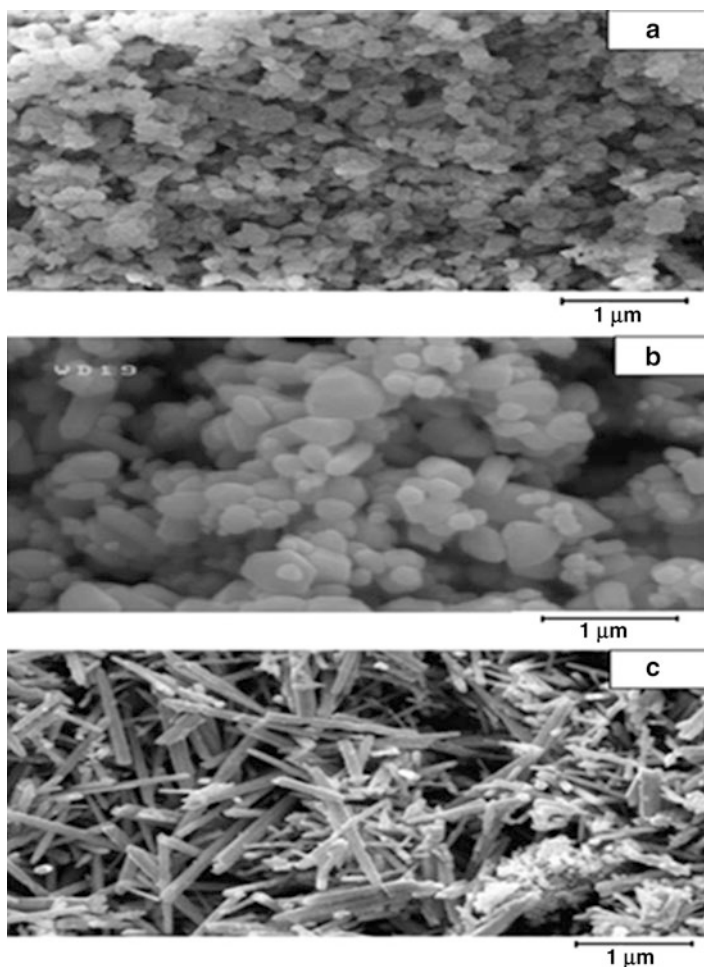
Fig. 9 A typical SEM images of ZnO nanoparticles obtained using the hydrazine hydrate aqueous solutions with different concentrations: (**a**) 5 wt%, (**b**) 40 wt%, and (**c**) 80 wt% [72] (Reprinted with permission from Ref. [72]. Copyright 2013, Elsevier)

efficiency of 73 % in 1 h. The corresponding normalized TOC vs. time plot for the degradation of diclofenac is shown in Fig. 10.

Wang et al. studied the sonocatalytic degradation of acid red B (ARB) in aqueous solution in the presence of nano-sized ZnO powder [74]. They also investigated the effect of degradation rate by the addition of other inorganic oxidants such as $KClO_4$, $KClO_3$, and $Ca(ClO)_2$. It was found that the inorganic oxidants can efficiently assist the sonophotocatalytic degradation of ARB in the presence of nano-sized ZnO powder. The order of degradation efficiency with oxidants was $KClO_4 >$ $KClO_3 >$ $Ca(ClO)_2$. The active site on the surface of ZnO nanoparticles can promote the decomposition of various oxidants under ultrasonic irradiation and generation of
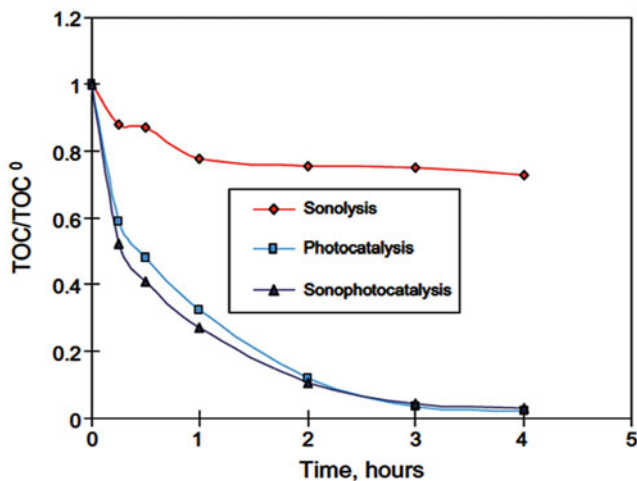
Fig. 10 Normalized TOC vs. time plot for the degradation of diclofenac with different techniques [73] (Reprinted with permission from Ref. [73]. Copyright 2010, Elsevier)

added •OH radicals. The reaction pathways to generate the •OH radicals by the inorganic oxidant-assisted ZnO sonocatalysis are as follows:

$$ClO_4^- + US/ZnO \rightarrow \ ^{\bullet}ClO_3 + \ ^{\bullet}O^- \tag{7}$$

$$^{\bullet}O^- + H^+ \rightarrow \ ^{\bullet}OH \tag{8}$$

$$ClO_3^- + US/ZnO \rightarrow \ ^{\bullet}ClO_2 + \ ^{\bullet}O^- \tag{9}$$

$$ClO^- + US/ZnO \rightarrow \ ^{\bullet}Cl + \ ^{\bullet}O^- \tag{10}$$

$$2 \ ^{\bullet}Cl \rightarrow Cl_2 \tag{11}$$

$$Cl_2 + H_2O \rightarrow ClO^- + Cl^- + 2H^+ \tag{12}$$
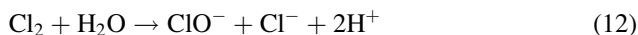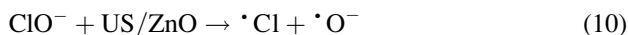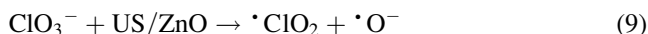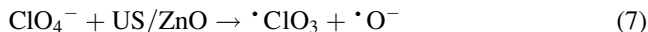
Chekma et al. synthesized ZnO- and Fe^{3+}-doped ZnO nanoparticles using ultrasound-assisted impregnation method [75]. The synthesized photocatalysts were subsequently employed for the sonophotocatalytic degradation of textile dyes such as ARB and MB. The results showed higher degradation activity for sonophotocatalysis than the individual processes. The doping of small amount of Fe^{3+} ions can function as a photogenerated hole trap, which inhibits the recombination of electron–hole pairs. The degradation of organic pollutant was increased when the Fe^{3+} ions reacted with oxygen and hydroxyl ions adsorbed on the catalyst surface to produce hydroxyl and superoxide radicals. In the presence of ultrasound, the sonochemically produced hydrogen peroxide might react with the Fe^{3+} thereby forming a Fenton reaction for the degradation of organic pollutant.
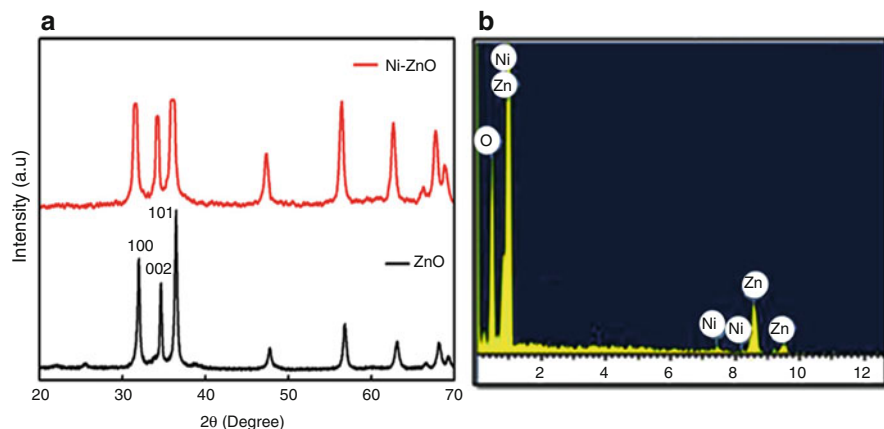
Fig. 11 (**a**) X-ray diffraction and (**b**) energy-dispersive X-ray spectrum of synthesized ZnO and Ni-doped ZnO nanoparticles [76] (Reprinted with permission from Ref. [76]. Copyright 2015, Elsevier)

Saharan et al. synthesized Ni-doped ZnO nanoparticles by simple coprecipitation method. They investigated the synergistic effect of Ni-doped ZnO particles and ultrasonication for the degradation of fast green (FG) and victoria blue (VB) dyes [76]. The synergistic effect of Ni–ZnO nanoparticles and ultrasound proved to be more effective in degrading the dyes than the pure ZnO photocatalysis and ultrasound alone. The substitutional doping of Ni in ZnO lattice had a positive influence on the electronic structure of ZnO which improved the sonocatalytic activity toward the degradation of organic pollutants. The X-ray diffraction and energy-dispersive X-ray spectrum of synthesized ZnO and Ni-doped ZnO nanoparticles are shown in Fig. 11. The phase formation and substitutional doping of Ni in ZnO were confirmed by these analyses.

Khataee et al. synthesized ZnO and Gd-doped ZnO nanoparticles using simple sonochemical method and demonstrated the degradation of AO7 in aqueous medium [77]. The application of pure ZnO sonocatalyst contains some drawbacks such as the fast recombination of the generated electron–hole pairs. In order to reduce the recombination and enhance the catalytic activity of ZnO nanoparticles, the Gd metal ions were incorporated into the ZnO structure. The 5 % Gd-doped ZnO nanoparticles with band gap of 2.8 eV exhibited the higher sonocatalytic activity with a degradation efficiency of 90 % at a reaction time of 90 min. The particle size distribution of Gd-doped ZnO nanostructure is shown in Fig. 12. It was seen that most of the nanoparticles ranged between 20 and 30 nm with frequency of 52.17 %. The frequency of the particle size range of <10, 10–20, and 30–40 nm is 2.17 %, 41.30 %, and 4.31 %, respectively. In another report by Khataee et al., ZnO and Pr-doped ZnO nanoparticles were synthesized using simple sonochemical process, and their sonophotocatalytic activity were investigated for the degradation of acid red 17 (AR17) under ultrasonic irradiation [78]. The degradation efficiency of sonocatalysis was found to be higher than the sonolysis alone.
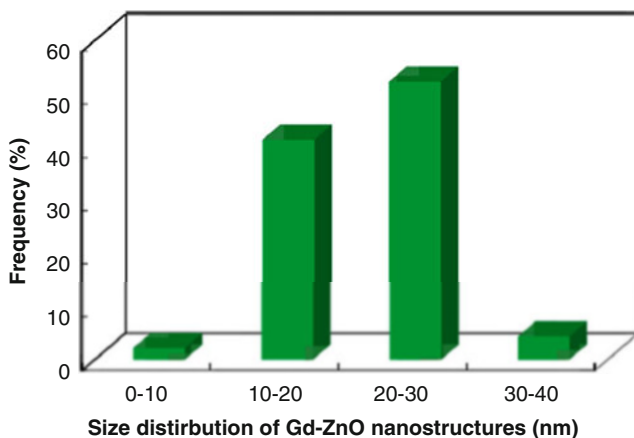
Fig. 12 The particle size distribution of Gd-doped ZnO nanostructure [77] (Reprinted with permission from Ref. [77]. Copyright 2015, Elsevier)

Metal Sulfide-Mediated Sonophotocatalysis

Very few reports are available in the literature, regarding metal sulfide-mediated sonocatalysis. Cadmium sulfide (CdS) nanoparticles, when combined with TiO_2 nanoparticles, can act as sonophotocatalyst. The CdS with ideal band gap energy (2.4 eV) is very unstable against photocorrosion in aqueous solution. Hence, it has been studied in combination with other materials such as TiO_2 or ZnO. CdS is widely considered as the most promising material for coupling with TiO_2 because of a slightly higher conduction band level compared to TiO_2. The coupling could prevent the recombination rate of electron–hole pairs and will improve the sonocatalytic activity.

Li et al. synthesized nano-sized CdS/TiO_2 with different morphologies and particle sizes by sonochemical method with different ultrasonic frequencies and investigated the sonophotocatalytic degradation of MO [79]. At lower frequencies, the CdS/TiO_2 was smaller, well crystallized, and even denser which corresponds to the lower sonophotocatalytic activity for the degradation of MO. However, at higher frequencies, the CdS/TiO_2 nanoparticles were larger, poorly crystallized, and looser which correspond to higher sonophotocatalytic activity for the degradation of MO. The TEM micrographs of sonochemically (35 kHz) synthesized CdS/TiO_2 nanocomposite and commercial TiO_2 are shown in Fig. 13. Compared to the commercial TiO_2, the nanocomposite formed has an average size of about 28.7 nm and the observable lattice fringes with spacing of about 0.31 and 0.35 nm, respectively, which correspond to the (101) plane of hexagonal CdS and anatase TiO_2, respectively.

Ghows et al. synthesized core–shell CdS/TiO_2 nanocrystal by the combination of ultrasound and microemulsion [80]. The synthesized CdS/TiO_2 core–shell was employed for the sonocatalytic degradation of reactive black 5 (RB5). In
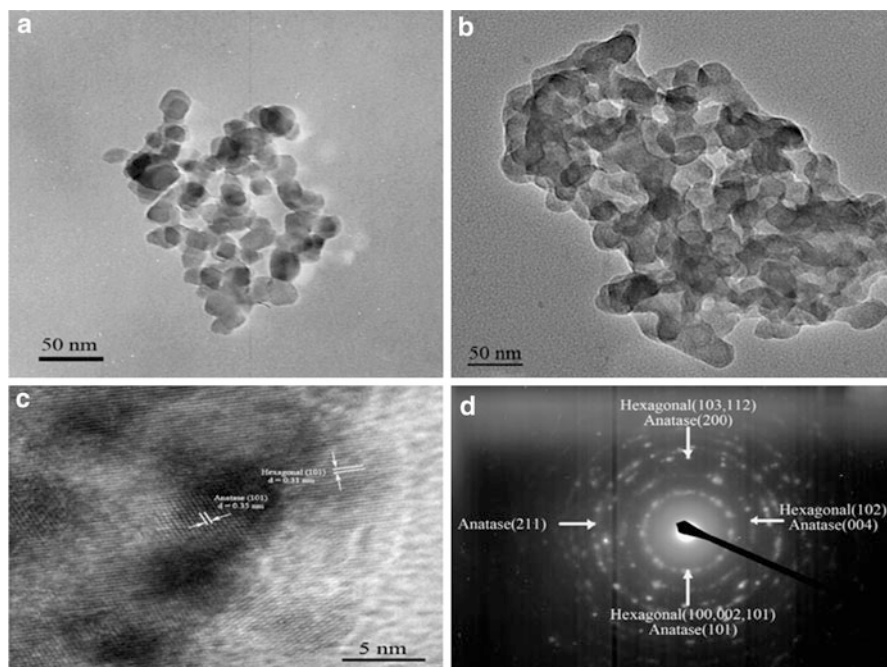
Fig. 13 TEM images of CdS/TiO2 nanoparticles, (**a**) commercial TiO2, (**b** and **c**) CdS/TiO2–35 kHz, and (**d**) SAED pattern of CdS/TiO2–35 kHz [79] (Reprinted with permission from Ref. [79]. Copyright 2012, Elsevier)

sonophotocatalytic degradation reaction, the first step is the conversion of the colored dye into an intermediate which is subsequently converted into colorless products. The core–shell CdS/TiO$_2$ particles showed a higher degradation efficiency than that obtained by sonolysis and photocatalysis. Zhu et al. investigated the MWCNT and CdS-modified TiO$_2$ for the degradation of RhB [81]. The catalyst was synthesized by the sol–gel method followed by solvo-thermal treatment at low temperature. The nano-sized CdS/CNT–TiO$_2$ photocatalyst showed an enhanced activity for the sonocatalytic degradation of RhB than the non-CdS-treated CNT–TiO$_2$. The sonocatalytic degradation mechanism of RhB over CdS/CNT–TiO$_2$ catalyst is shown in Fig. 14.

When CdS/TiO$_2$ was irradiated under ultrasonic radiation, the photogenerated electrons are excited from the valance band of CdS to the conduction band of TiO$_2$ through MWCNTs, simultaneously leaving the photogenerated holes in the valence band of CdS. The electrons react with O$_2$ to generate O$_2^{\bullet-}$, and the holes react with OH$^-$ or H$_2$O to generate •OH radicals.

$$CdS/TiO_2 + US \rightarrow CdS\,(h^+, e^-)/TiO_2 \qquad (13)$$
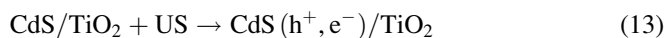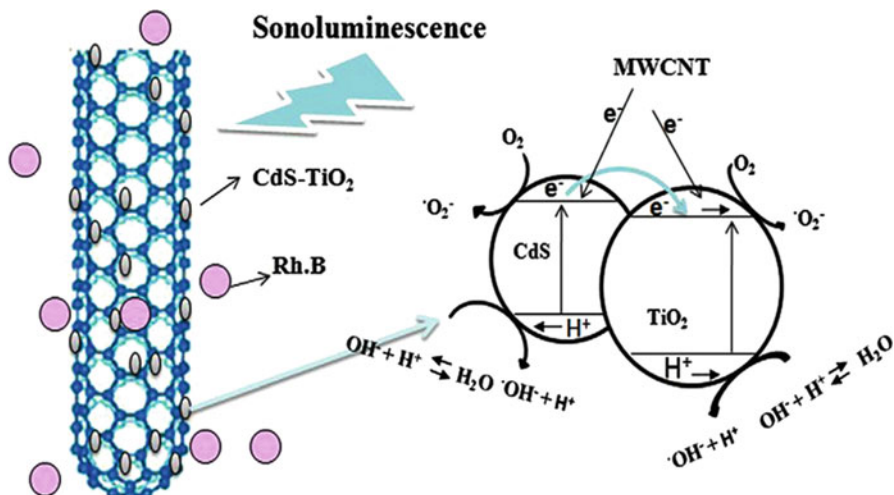
Fig. 14 Sonocatalytic degradation mechanism of RhB by CdS/CNT–TiO$_2$ composite [81] (Reprinted with permission from Ref. [81]. Copyright 2013, Elsevier)

$$CdS\,(h^+,\ e^-)/TiO_2 \rightarrow CdS\,(h^+)/TiO_2(e^-) \quad (14)$$

$$e^- + O_2 \rightarrow {}^{\bullet}O_2{}^- \quad (15)$$

$$h^+ + OH^- \rightarrow {}^{\bullet}OH \quad (16)$$

$$h^+ + H_2O \rightarrow {}^{\bullet}OH + h^+ \quad (17)$$
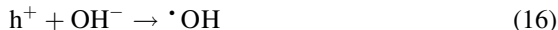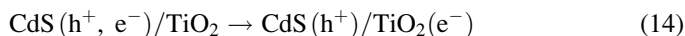
Based on available literature, the photocorrosion and instability nature of CdS in aqueous solution restricts its practical applications. Hence, coupling with other semiconductor materials such as TiO$_2$, ZnO, etc., is found to improve its stability as well as the degradation efficiency of organic pollutants. Some studies on sonophotocatalytic degradation of organic pollutants using ZnO and CdS nanomaterials are summarized in Table 2.

Other Catalytic Material-Mediated Sonophotocatalysis

Many potential sonophotocatalytic active semiconductor nanomaterials have been studied so far. In particular TiO$_2$ and ZnO are widely investigated materials for sonophotocatalysis as discussed above. Apart from these materials, there are many metal oxides and silver compounds which act as potential semiconductor catalysts in sonophotocatalysis.

The hydroxyl radicals are important in the catalytic degradation of organic pollutants. Wu et al. synthesized AgBr sonophotocatalyst by simple precipitation route, and it was investigated for the sonophotocatalytic degradation of organic

Table 2 Sonophotocatalytic degradation of pollutants using ZnO and CdS nanomaterials

S. No	Pollutant	Catalyst	Ultrasonic frequency	Ultrasonic power	Synergy index	Refs.
1	Acid orange 8	ZnO	20 kHz	20 W	0.59	[42]
2	2-Chlorophenol	ZnO	20 kHz	20 W	0.12	[42]
3	Phenol	ZnO	40 kHz	100 W	1.25	[71]
4	Acid red B, methylene blue	ZnO	40 kHz	200 W	Synergetic	[75]
5	Methyl orange	CdS/TiO$_2$	40 kHz	220 W	Synergetic	[79]
6	Reactive black	CdS/TiO$_2$	20 kHz,	41 W	Synergetic	[80]
7	Rhodamine B	CdS/ CNT–TiO$_2$	20 kHz	750 W	Synergetic	[81]

pollutants such as MB, RhB, and MO [82]. AgBr generates •OH radicals by the ultrasound in aqueous media, thus leading to the degradation of organic pollutants.

$$H_2O + US + AgBr \rightarrow {}^{\bullet}OH + {}^{\bullet}H \tag{18}$$

$$O_2(\text{bubbles}) + US + AgBr \rightarrow 2O^{\bullet} \rightarrow {}^{\bullet}O + H_2O + 2{}^{\bullet}OH \tag{19}$$

$$O_2(\text{bubbles}) + H^{\bullet} \rightarrow {}^{\bullet}O_2H \rightarrow H_2O_2 + O_2 \rightarrow H_2O_2 + US + AgBr + 2{}^{\bullet}OH \tag{20}$$

$${}^{\bullet}OH + \text{Organic pollutants} \rightarrow \text{Degradation products} \tag{21}$$
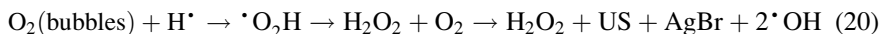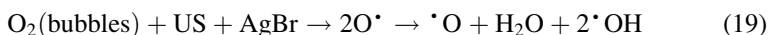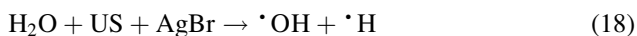
Song et al. synthesized silver tripolyphosphate (Ag$_5$P$_3$O$_{10}$) hydrothermally and used it as a sonophotocatalyst for the degradation of dyes such as RhB and MB [83]. The results showed that Ag$_5$P$_3$O$_{10}$ exhibited an excellent sonophotocatalytic activity due to the enhanced production of •OH radicals by combined UV and US radiations. A similar study on hydrothermally synthesized AgPO$_3$ microsphere for the degradation of RhB was reported by He et al. [84]. The microspheres of the AgPO$_3$ are shown in Fig. 15 (a–c and e–f), and the mean particle size distribution of AgPO$_3$ microsphere is shown in Fig. 15d. It was observed that the particle size of AgPO$_3$ was found in 3.67–4.93 μm and the mean particle size diameter was 4.23 μm.

Wang et al. synthesized magnetic Fe$_3$O$_4$ nanoparticles by simple coprecipitation method [85] and used it for the sonophotocatalytic degradation of RhB. The photocatalytic degradation efficiency of 95 % was achieved using Fe$_3$O$_4$-assisted sonophotocatalysis. The α-Fe$_2$O$_3$ is known to be a poor catalyst in usual photocatalytic reaction but it showed better performance when combined with sonolysis. According to Elshafei et al., 60 % sonocatalytic degradation of nitrobenzene was achieved using α-Fe$_2$O$_3$/CuO [86]. The collapse of micro-sized bubbles in cavitation produced more hydroxyl radicals.

Zhou et al. synthesized LuFeO$_3$ nanoparticles by a polyacrylamide gel route [87]. The phase formation, purity, and morphology of the LuFeO$_3$ nanomaterials are shown in Fig. 16. The XRD pattern showed that the LuFeO$_3$ formed in a orthorhombic perovskite structure, a sphere-like particle with an average size of
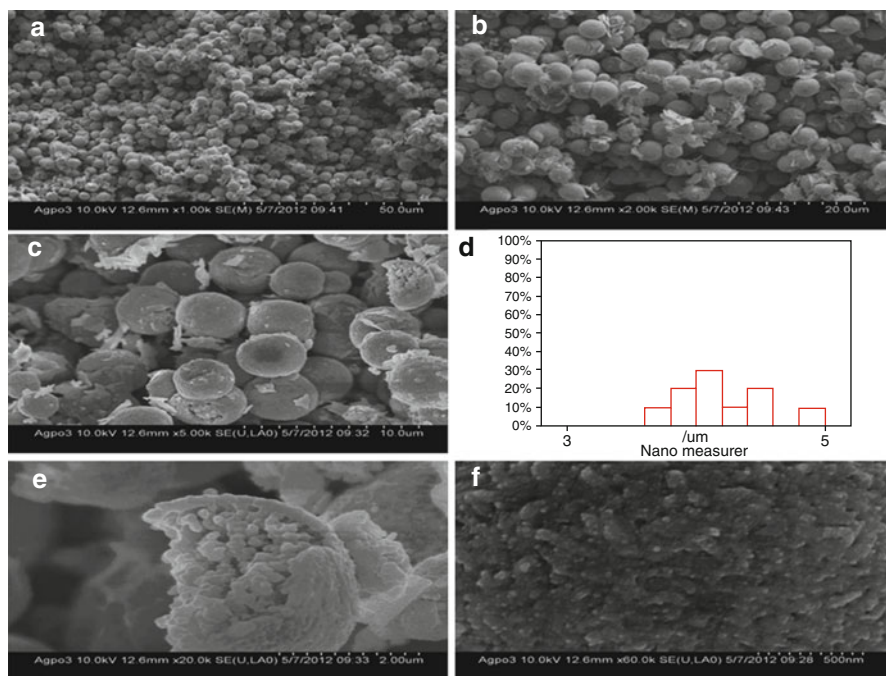
Fig. 15 (**a**–**b** and **e**–**f**) Typical SEM images of AgPO$_3$ (**d**) mean particle size distribution of AgPO$_3$ microspheres [84] (Reprinted with permission from Ref. [84]. Copyright 2014, Elsevier)

~200 nm. The sonocatalytic activity of LuFeO$_3$ nanoparticles showed better performance in degrading of RhB.

Nanocomposite Material-Mediated Sonophotocatalysis

The composites are the materials formed by coupling of two or more semiconductor photocatalysts. This is done to reduce the recombination rate of photogenerated electron–hole pairs and also to increase the visible light response of the catalytic materials. Thus, a higher photocatalytic activity is expected from these composite materials.

Ahmd et al. synthesized a series of ZnO nanoparticles decorated on multiwalled carbon nanotube (ZnO/MWCNT) composite by a facile sol method [88] to study the sonophotocatalytic degradation of RhB in the presence of ZnO and ZnO/MWCNT. They also compared the degradation by sonolysis and photocatalysis and observed that the sonophotocatalysis showed higher degradation efficiency than the individual processes. This may be due to the formation of higher •OH radicals and increased active surface area of ZnO/CNT composite. The reaction rate constant for the degradation of RhB over photocatalysis, sonolysis, and sonophotocatalysis method
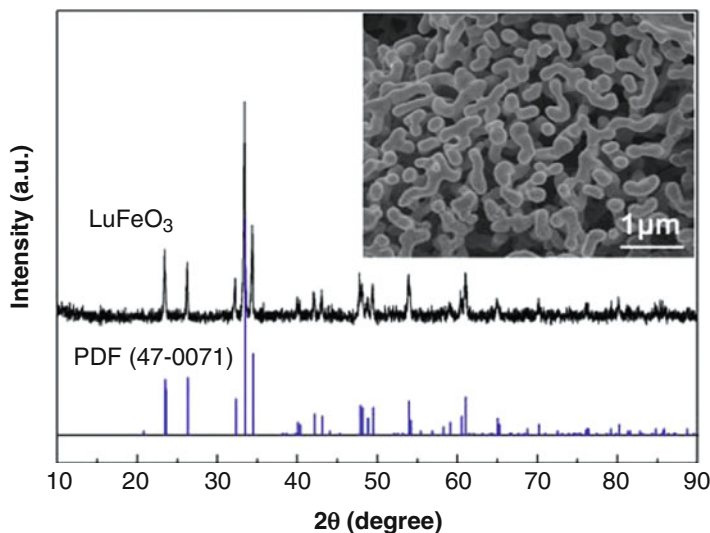
Fig. 16 XRD pattern of LuFeO₃ particles. *Inset* shows a SEM image of LuFeO₃ particles [88] (Reprinted with permission from Ref. [88]. Copyright 2015, Elsevier)

for the pure ZnO, MWCNTs, and different amounts of ZnO-loaded CNTs is shown in Fig. 17.

Zhang et al. prepared a high surface area of TiO_2–CNT composite catalyst by the deposition of TiO_2 particles on the surface of carbon nanotubes (CNTs) employing a modified sol–gel technique [89]. The as-prepared catalyst was used for the degradation of MB in aqueous solution using visible light and ultrasonic irradiation using a probe-type sonicator. The reaction for the formation of anatase TiO_2–CNT composite catalyst is shown in Fig. 18. The CNTs are functionalized with strong oxidizing group m-chloroperbenzoic acid. During the hydrothermal process, the carboxylic acid groups on CNT surface can react with alkoxide precursor of Ti under certain temperature to form the composite catalyst.

Wang et al. prepared various nano-sized metal oxide-dispersed TiO_2 (CeO_2/TiO_2, SnO_2/TiO_2, and ZrO_2/TiO_2) composite catalyst and compared the sonocatalytic activity toward the degradation of acid red B [90]. The order of the degradation activity was as follows: $CeO_2/TiO_2 > SnO_2/TiO_2 > TiO_2 > ZrO_2/TiO_2 > SnO_2 > CeO_2 > ZrO_2$. The highest degradation efficiency of 91.32 % was obtained for the CeO_2/TiO_2, which may be due to the reduction of recombination rate of electron–hole pairs in the composite catalysts. Neppolian et al. synthesized $Bi_2O_3/TiZrO_4$ nanoparticles by an ultrasonic-assisted hydrothermal method and investigated the oxidative degradation of 4-chlrophenol using sonolysis, photocatalysis, and sonophotocatalysis process [91]. It was found that the combined sonophotocatalytic degradation was simple to apply and proved as a potential process for the degradation of organic pollutants. Ghosh et al. synthesized CdSe–graphene composite by a simple hydrothermal method and studied the sonocatalytic degradation of
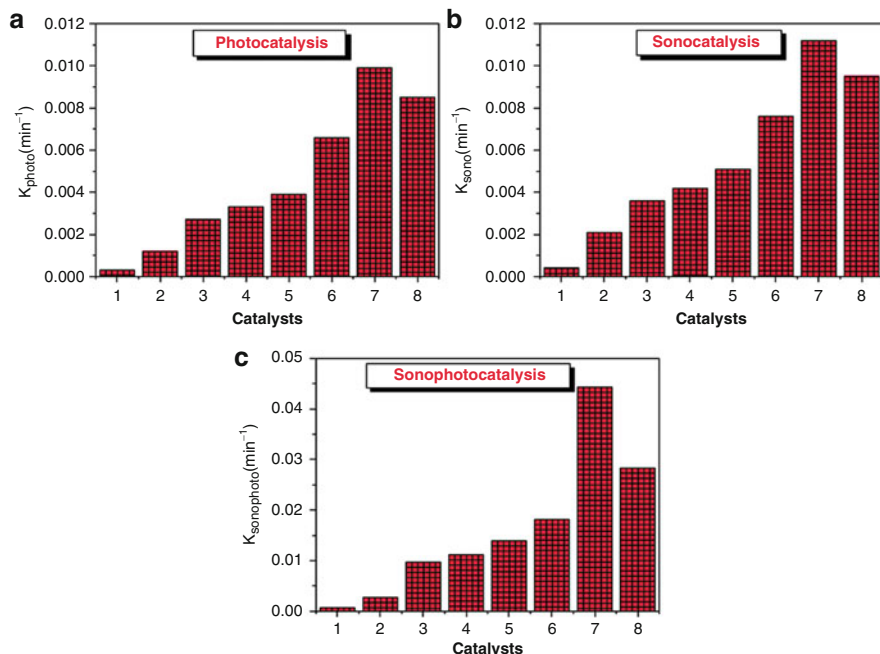
Fig. 17 Photocatalytic, sonocatalytic, and sonophotocatalytic rate constants in the presence of (*1*) no catalyst, (*2*) CNTs, (*3*) ZnO, (*4*) 1 wt% CNTs–ZnO, (*5*) 2 wt% CNTs–ZnO, (*6*) 5 wt% CNTs–ZnO, (*7*) 10 wt% CNTs–ZnO, and (*8*) 20 wt% CNTs–ZnO [89] (Reprinted with permission from Ref. [89]. Copyright 2014, Elsevier)
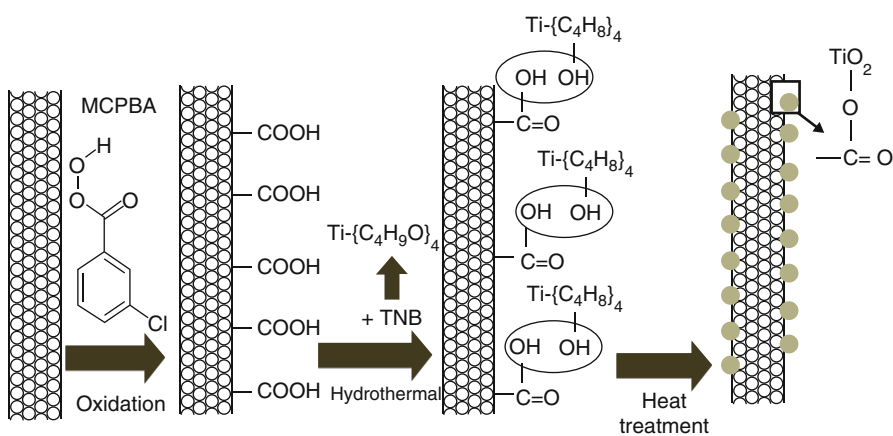
Fig. 18 Formation of anatase TiO_2–MWCNT catalyst [90] (Reprinted with permission from Ref. [90]. Copyright 2011, Elsevier)
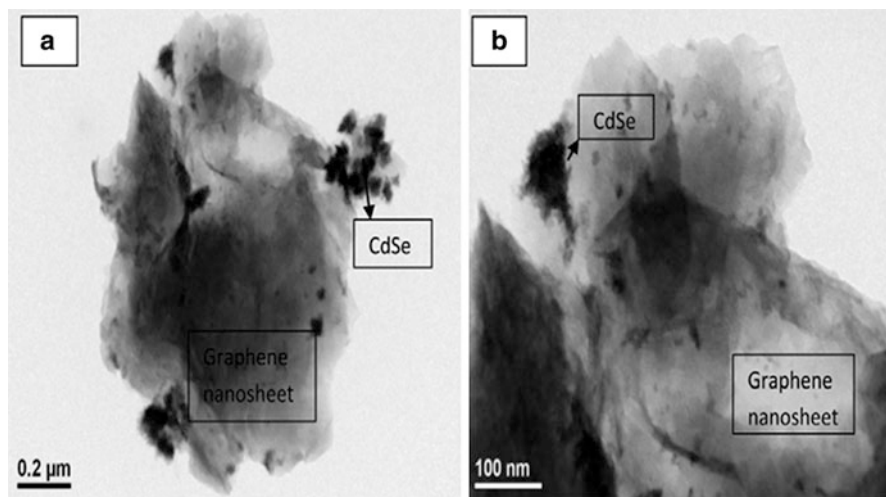
Fig. 19 TEM images of CdSe–graphene composite [93] (Reprinted with permission from Ref. [93]. Copyright 2013, Elsevier)

azo dyes, MO, and RhB [92]. The stability of the sonocatalyst was also investigated from the reusability tests. The TEM images of the CdSe–graphene composite are shown in Fig. 19.

Wang et al. investigated the silver-loaded TiO_2 nanoparticles for the sonophoto-catalytic degradation of MO [93]. The degradation of MO was enhanced in case of sonophotocatalysis, when compared to individual processes which may be due to the synergistic effect of sonolysis and photocatalysis. It was also observed that the degradation of MO increased with an increase in ultrasonic power. Zhang et al. prepared Fe/TiO_2–MWCNT by the deposition of MWCNTs with Fe and TiO_2 nanoparticles using modified sol–gel method [94]. The sonophotocatalytic degradation efficiency of TiO_2, Fe/TiO_2, and Fe/TiO_2–MWCNT catalysts were investigated for the degradation of MB. The enhanced formation of reactive radicals and ultrasound-induced active surface area increase of the catalyst was observed when Fe/TiO_2–MWCNT was used as a catalyst. Zhai et al. developed an Er^{3+}: $YAlO_3/TiO_2$–SnO_2, a novel sonocatalyst by the deposition of Er^{3+}:$YAlO_3$ on the surface of TiO_2–SnO_2 composite [95]. The obtained sonocatalyst was used for the degradation of acid red B. The heat-treatment temperature of the catalyst during the synthesis was observed as a main factor which influenced the sonocatalytic degra-dation activity. In another report by Gao et al., the Er^{3+}:$YAlO_3/TiO_2$–ZnO nanocomposite was used for the sonocatalytic degradation of acid red B [96]. The results showed that the temperature employed for the synthesis of composite catalyst played a significant role in the degradation of organic pollutants and also the Ti/Zn molar ratio that influenced the sonocatalytic activity of the catalyst. Zhao et al. synthesized CeO_2 and MnO_2 nanoparticles by simple precipitation method and prepared the MnO_2/CeO_2 nanocomposites by impregnation method [97], to

investigate the degradation of MO by sonocatalysis. The degradation efficiency of the composite catalyst was found to be enhanced due to the formation of excessive reactive radicals. The catalytic materials may act as a cavitation nucleus and enhance the ultrasonic cavitation effect. The resonance sizes of cavitation bubbles are compensable with the size of the catalyst.

Boutoumi et al. synthesized the titanium dioxide–montmorillonite/polythiophene–sodium dodecyl sulfate (TiO_2–Mt/PTP–SDS) nanocomposite via in situ intercalative oxidative polymerization of thiophene (TP) in TiO_2–Mt clay in the presence of anionic surfactant SDS [98]. The sonophotocatalytic degradation of Rh 6G was investigated using the TiO_2–Mt/PTP–SDS nanocomposite and found the sonophotocatalytic degradation was higher than the individual processes, which may be due to the synergistic effect between the sonolysis and photocatalysis. Sathishkumar et al. synthesized the rare earth nanocluster (Gd^{3+}, Nd^{3+}, and Y^{3+})-loaded TiO_2 and used for the sonophotocatalytic degradation of acid blue 113 under ultrasonic irradiation [99]. The higher degradation efficiency was observed for the Y^{3+}-loaded TiO_2 nanoparticles. Further, the degradation of acid blue 113 in the presence and absence of Y^{3+}-loaded TiO_2 ensured the following order: sonophotocatalysis > sonocatalysis > photocatalysis > sonolysis. The presence of ultrasound enhances the possibility of the effective interaction of AB113 with the electronic charges generated during the catalytic processes. Therefore, the maximum charge carrier initiation was achieved during the sonophotocatalytic degradation of AB113 in the presence Y^{3+}–TiO_2 nanophotocatalysts. Meng et al. prepared Fe-treated fullerene/TiO_2 nanocomposite by sol–gel method and investigated the catalytic activity by sonocatalytic degradation of MB [100]. The complete mineralization of MB was observed under ultrasonic irradiation in the presence of Fe-fullerene/TiO_2 nanocomposite, and the content of Fe also enhanced the degradation rate. For Fe–TiO_2 composites, the Fe particles lead to enhanced catalytic activity by trapping the e^- and h_{vb}^+ pairs. Iron doping increases the OH^- production by its capacity to act as h_{vb}^+ traps, which reduces the recombination; thus the chance for e^- and h_{vb}^+ to form oxidative radicals is improved. In sonolysis, the generated light or heat can be transferred to yield the e^- and h_{vb}^+ pairs on the surface of TiO_2, and some electrons are captured by Fe^{3+}, so the sonocatalytic of Fe–TiO_2 composite is obviously improved by doping Fe^{3+} ion. The TEM images of Fe-fullerene/TiO_2 nanocomposites are shown in Fig. 20.

Sathishkumar et al. synthesized nano-size gold-loaded visible light-driven TiO_2 (Au–TiO_2) sonophotocatalysis using bath-type sonicator (42 kHz) [101] for the sonophotocatalytic degradation of simazine. 1.65- and 1.38-fold enhancement in the mineralization was achieved for the sonophotocatalytic degradation of simazine when compared with the photocatalysis and sonolysis processes. Khataee et al. synthesized TiO_2/montmorillonite K10 (TiO_2/MMT) nanocomposite by hydrothermal method and employed toward sonocatalytic degradation of basic blue 3 (BB3) [102]. The obtained sonocatalytic activity of TiO_2/MMT nanocomposite was higher than that of pure TiO_2 and MMT nanoparticles. Ghodke et al. synthesized TiO_2/nanoclay nanocomposite by sonochemical method [103] and used it as a photocatalyst for the degradation of phenol under acoustic cavitation. The higher
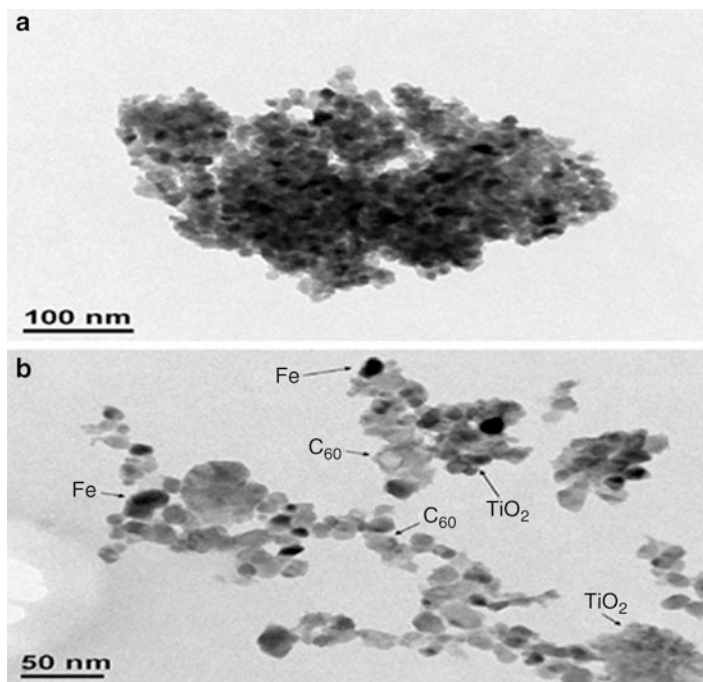
Fig. 20 A typical TEM images of Fe-fullerene/TiO$_2$ nanocomposites [101] (Reprinted with permission from Ref. [101]. Copyright 2011, Elsevier)

degradation efficiency (59 %) was obtained for the TiO$_2$/nanoclay nanocomposite, whereas the nanoclay alone achieved only 47 % degradation. Some studies on sonophotocatalytic degradation of organic pollutants using nanocomposite materials are summarized in Table 3.

Numerous efforts are needed for the development of new materials with high photocatalytic activity. Based on reports discussed so far, composite materials can be the promising materials to use in the sonophotocatalytic process for the degradation of organic pollutants present in the aqueous environment.

Reaction Mechanism of Sonophotocatalysis for the Degradation of Organic Pollutants

Photocatalytic degradation of organic compounds occurred through the OH• formed on the photocatalyst during the photochemical reactions. Thus, the combination of photocatalytic and ultrasonic irradiation (sonophotocatalysis) seems to enhance the degradation rate of the organic pollutants by the increased generation of OH•. The presence of a heterogeneous catalyst contributes to the increase in the rate of formation of cavitation bubbles by providing additional nuclei, which in turn

Table 3 Sonophotocatalytic degradation of organic pollutants using nanocomposite materials

S. No	Pollutant	Catalyst	Ultrasonic frequency	Ultrasonic power	Synergy index	Refs.
1	Rhodamine B	ZnO/CNTs	35 kHz	200 W	Synergetic	[88]
2	Methylene blue	TiO_2–CNT	28 kHz	50 W	Synergetic	[89]
3	4-Chlorophenol	$Bi_2O_3/TiZrO_4$	20 kHz	51 W	Synergetic	[91]
4	Rhodamine B	CdSe–graphene	20 kHz	750 W	Synergetic	[92]
5	Methylene blue	Fe/TiO_2–MWCNT	28 kHz	50 W	Synergetic	[94]
6	Acid red B	Er^{3+}:$YAlO_3$/TiO_2–SnO_2	40 kHz	50 W	Synergetic	[95]
7	Methyl orange	MnO_2/CeO_2	24 kHz	65 W	Synergetic	[97]
8	Acid blue 113	Y^{3+}, Gd^{3+}, Nd^{3+}–TiO_2	42 kHz	–	Synergetic	[99]
9	Methylene blue	Fe-fullerene/TiO_2	20 kHz	750 W	Synergetic	[100]
10	Simazine	Au–TiO_2	42 kHz	–	Synergetic	[101]
11	Basic blue 3	TiO_2/montmorillonite	40 kHz	–	Synergetic	[102]

increases the pyrolysis of H_2O molecules and OH• formation. These observations may propose the possibility of ultrasonic irradiation over the semiconductor catalyst that enhances the generation of OH•. Hence, this effect is found to be mediated by mechanisms similar to that of photocatalysis [88].

The reaction mechanism of sonophotocatalysis (UV + US) for the degradation of organic pollutants was mainly due to the synergistic effect between sonolysis (US) and photocatalysis (UV). The remarkable improvement in the degradation of organic pollutants by sonophotocatalysis may be due to the following reasons [73, 85].

1. The production of oxidizing species increases in the liquid phase due to the sonolytic cleavage of water.
2. Due to the shock wave propagation, the mass transport of the organic pollutant to the catalyst surface is increased.
3. The aggregation of catalyst particles in aqueous solution is prevented by the physical effects of acoustic cavitation which leads to an increase in the active surface area.
4. The surface of the catalyst is continuously cleaned by ultrasonic waves, which is used to maintain the catalytic performance of the photocatalyst.

The reaction mechanism of synergistic effect between the sonolysis and photocatalysis is shown in Fig. 21. The adsorbed dye molecule on the surface of photocatalyst reacts with the active radicals generated through photocatalysis. Subsequently desorption of dye molecules from the surface of the photocatalyst by the
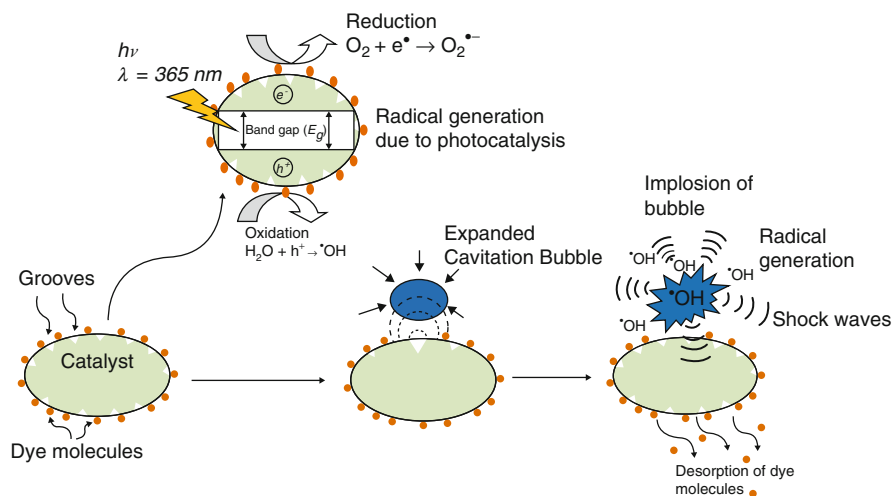
Fig. 21 The reaction mechanism of synergy between sonolysis, photocatalysis, and sonophoto-catalysis [75] (Reprinted with permission from Ref. [75]. Copyright 2015, Elsevier)

shock waves generated by the cavitation bubbles will take place, which reduces the interaction probability of dye molecule with the active radicals. On the other hand, the radicals generated by transient implosion of cavitation bubbles in the vicinity of the photocatalyst particles can cause degradation of the dye molecules. Generally, the smaller size and larger surface area of the nanoparticles increase the active sites, which are more advantageous for sonophotocatalysis.

Conclusions and Future Directions

Sonophotocatalytic degradation of organic pollutants is an emerging treatment process, which involves the combination of ultrasound with different semiconductor nanomaterials. The ultrasonic treatment for pollutant removal has become a popular technique due to its non-selective, not creating any secondary pollution, nontoxic, and irreversible degradation process. However, use of ultrasonic irradiation as individual process is limited for large-scale applications because of the inability to achieve high degradation efficiency to certain organic pollutants, particularly, hydrophilic compounds which are very hard to decompose by the cavitation phenomenon induced from the ultrasonic irradiation. In such cases, sonophotocatalytic processes are used to solve the problems related to the opacity and porosity of the catalyst support when compared to individual sonolysis and photocatalysis.

TiO_2 and ZnO are the most commonly used catalysts for sonophotocatalytic process because of its advantages, such as cost-effectiveness, nontoxic, thermal, and mechanical stability. The catalyst was activated by the ultrasonic irradiation, thus resulting in the generation of electron–hole pairs. It was found that the reduction

in the recombination rate can increase the degradation efficiency in sonophotocatalysis. Loading or doping of metal particles into conventional photocatalyst or their composites can reduce the recombination between electrons and holes produced during ultrasonic irradiation of catalyst to enhance the sonophotocatalytic degradation efficiency.

Most of the investigated photocatalysts are UV active. Intense investigations are required for efficient and large-scale applications of sonophotocatalysis. The replacement of UV light irradiation with visible light (sunlight) should be a global objective for efficient sonophotocatalysis. Hence, numerous catalysts should be investigated for the development of sonophotocatalysis under visible light irradiation. Apart from this, it is also necessary to optimize the influence of reaction parameters to obtain the maximum degradation efficiency and to reduce the overall cost of the sonophotocatalytic treatments. Thus sonophotocatalytic process can serve as a promising technique for the treatment of organic pollutants in degrading harmful pollutants into less or nontoxic products.

References

1. Lam SM, Sin JC, Abdullah AZ, Mohamed AR (2012) Degradation of wastewaters containing organic dyes photocatalysed by zinc oxide: a review. Desalin Water Treat 41:131–169
2. Bokhale NB, Bomble SD, Dalbhanjan RR, Mahale DD, Hinge SP, Banerjee BS, Mohod AV, Gogate PR (2014) Sonocatalytic and sonophotocatalytic degradation of rhodamine 6G containing wastewaters. Ultrason Sonochem 21:1797–1804
3. Ameta R, Benjamin S, Ameta A, Ameta SC (2013) Photocatalytic degradation of organic pollutants: a review. Mater Sci Forum 734:247–272
4. Balaji C, Moholkar VS, Pandit AB, Ashokkumar M (2011) Mechanistic investigations on sonophotocatalytic degradation of textile dyes with surface active solutes. Ind Eng Chem Res 50:11485–11494
5. Madhavan J, Grieser F, Ashokkumar M (2010) Degradation of formetanate hydrochloride by combined advanced oxidation processes. Sep Purif Technol 73:409–414
6. Pang YL, Abdullah AZ, Bhatia S (2011) Review on sonochemical methods in the presence of catalysts and chemical additives for treatment of organic pollutants in wastewater. Desalination 277:1–14
7. Theerthagiri J, Senthil RA, Priya A, Madhavan J, Michael RJV, Ashokkumar M (2014) Photocatalytic and photoelectrochemical studies of visible-light active α-Fe_2O_3–g-C_3N_4 nanocomposites. RSC Adv 4:38222–38229
8. Kohtani S, Kamoi Y, Yoshioka E, Miyabe H (2014) Kinetic study on photocatalytic hydrogenation of acetophenone derivatives on titanium dioxide. Catal Sci Technol 4:1084–1091
9. Zhu LP, Bing NC, Yang DD, Yang Y, Liao GH, Wang LJ (2011) Synthesis and photocatalytic properties of core–shell structured α-Fe_2O_3@SnO_2 shuttle-like nanocomposites. Cryst Eng Comm 13:4486–4490
10. Khedr MH, Halim KS, Soliman NK (2009) Synthesis and photocatalytic activity of nano-sized iron oxides. Mater Lett 63:598–601
11. Wang M, Xie F, Li W, Chena M, Zhao Y (2013) Preparation of various kinds of copper sulfides in a facile way and the enhanced catalytic activity by visible light. J Mater Chem A 1:8616–8621
12. Guan XH, Qu P, Guan X, Wang GS (2014) Hydrothermal synthesis of hierarchical CuS/ZnS nanocomposites and their photocatalytic and microwave absorption properties. RSC Adv 4:15579–15585

13. Zhang K, Guo L (2013) Metal sulphide semiconductors for photocatalytic hydrogen production. Catal Sci Technol 3:1672–1690
14. Du Y, Zhao L, Zhang Y (2014) Roles of TaON and Ta_3N_5 in the visible-Fenton-like degradation of atrazine. J Hazard Mater 267:55–61
15. Nakamura R, Tanaka T, Nakato Y (2005) Oxygen photoevolution on a tantalum oxynitride photocatalyst under visible-light irradiation: How does water photooxidation proceed on a metal-oxynitride surface. J Phys Chem B 109:8920–8927
16. Gaya UI, Abdullah AH (2008) Heterogeneous photocatalytic degradation of organic contaminants over titanium dioxide: a review of fundamentals, progress and problems. J Photochem Photobiol C 9:1–12
17. Theerthagiri J, Senthil RA, Priya A, Madhavan J, Ashokkumar M (2014) Synthesis of a visible-light active V_2O_5–g-C_3N_4 heterojunction as an efficient photocatalytic and photoelectrochemical material. New J Chem 39:1367–1374
18. Gedanken A (2004) Using sonochemistry for the fabrication of nanomaterials. Ultrason Sonochem 11:47–55
19. Madhavan J, Sathish Kumar P, Anandan S, Grieser F, Ashokkumar M (2010) Sonophotocatalytic degradation of monocrotophos using TiO_2 and Fe_3^+. J Hazard Mater 177:944–949
20. Mahamuni NN, Adewuyi YG (2010) Advanced oxidation processes (AOPs) involving ultrasound for waste water treatment: A review with emphasis on cost estimation. Ultrason Sonochem 17:990–1003
21. Liang J, Komarov S, Kasai NHE (2007) Recent trends in the decomposition of chlorinated aromatic hydrocarbons by ultrasound irradiation and Fenton's reagent. J Mater Cycles Waste Manag 9:47–55
22. Pilli S, Bhunia P, Yan S, LeBlanc RJ, Tyagi RD, Surampalli RY (2011) Ultrasonic pretreatment of sludge: a review. Ultrason Sonochem 18:1–18
23. Rivas DF, Cintas P, Gardeniers HJGE (2012) Merging microfluidics and sonochemistry: towards greener and more efficient micro-sono-reactors. Chem Commun 48:10935–10947
24. Joseph CG, Puma GL, Bono A, Krishnaiah D (2009) Sonophotocatalysis in advanced oxidation process: a short review. Ultrason Sonochem 16:583–589
25. Chowdhury P, Viraraghavan T (2009) Sonochemical degradation of chlorinated organic compounds, phenolic compounds and organic dyes-A review. Sci Total Environ 407:2474–2492
26. Ahmedchekkat F, Medjram MS, Chiha M, Al-bsoul AMA (2011) Sonophotocatalytic degradation of Rhodamine B using a novel reactor geometry: effect of operating conditions. Chem Eng J 178:244–251
27. Goel M, Hongqiang H, Mujumdar AS, Ray MB (2004) Sonochemical decomposition of volatile and non-volatile organic compounds-a comparative study. Water Res 38:4247–4261
28. Pandit AB, Gogate PR, Mujumdar S (2001) Ultrasonic degradation of 2:4:6 trichlorophenol in presence of TiO_2 catalyst. Ultrason Sonochem 8:227–231
29. Ismail AA, Bahnemann DW (2011) Mesoporous titania photocatalysts: preparation, characterization and reaction mechanisms. J Mater Chem 21:11686–11707
30. Lee SY, Park SJ (2013) TiO_2 photocatalyst for water treatment applications. J Ind Eng Chem 19:1761–1769
31. Park H, Park Y, Kim W, Choi W (2013) Surface modification of TiO_2 photocatalyst for environmental applications. J Photochem Photobiol C 15:1–20
32. Chong MN, Jin B, Chow CWK, Saint C (2010) Recent developments in photocatalytic water treatment technology: a review. Water Res 44:2997–3027
33. Ajmal A, Majeed I, Malik RN, Idriss H, Nadeem MA (2014) Principles and mechanisms of photocatalytic dye degradation on TiO_2 based photocatalysts: a comparative overview. RSC Adv 4:37003–37026
34. Kim J, Satoca DM, Choi W (2012) Simultaneous production of hydrogen with the degradation of organic pollutants using TiO_2 photocatalyst modified with dual surface components. Energy Environ Sci 5:7647–7656

35. Nakata K, Fujishima A (2012) TiO$_2$ photocatalysis: design and applications. J Photochem Photobiol C 13:169–189
36. Zhang L, Kanki T, Sano N, Toyoda A (2003) Development of TiO$_2$ photocatalyst reaction for water purification. Sep Purif Technol 31:105–110
37. Fujishima A, Rao TN, Tryk DA (2000) Titanium dioxide photocatalysis. J Photochem Photobiol C 1:1–21
38. Fujishima A, Zhang X, Tryk DA (2008) TiO$_2$ photocatalysis and related surface phenomena. Surf Sci Rep 63:515–582
39. Augugliaro V, Bellardita M, Loddo V, Palmisano G, Palmisano L, Yurdakal S (2012) Overview on oxidation mechanisms of organic compounds by TiO$_2$ in heterogeneous photocatalysis. J Photochem Photobiol C 13:224–245
40. Madhavan J, Sathish Kumar P, Anandan S, Ashokkumar M, Grieser F (2010) Degradation of acid red 88 by the combination of sonolysis and photocatalysis. Sep Purif Technol 74:336–341
41. Mishra KP, Gogate PR (2011) Intensification of sonophotocatalytic degradation of p-nitrophenol at pilot scale capacity. Ultrason Sonochem 18:739–744
42. Selli E (2002) Synergistic effects of sonolysis combined with photocatalysis in the degradation of an azo dye. Phys Chem Chem Phys 4:6123–6128
43. Mishra KP, Gogate PR (2011) Intensification of degradation of aqueous solutions of rhodamine B using sonochemical reactors at operating capacity of 7 L. J Environ Manage 92:1972–1977
44. Berberidou C, Poulios I, Xekoukoulotakis NP, Mantzavinos D (2007) Sonolytic, photocatalytic and sonophotocatalytic degradation of malachite green in aqueous solutions. Appl Catal B 74:63–72
45. Kritikos DE, Xekoukoulotakis NP, Psillakis E, Mantzavinos D (2007) Photocatalytic degradation of reactive black 5 in aqueous solutions: effect of operating conditions and coupling with ultrasound irradiation. Water Res 41:2236–2246
46. Cheng Z, Quan X, Xiong Y, Yang L, Huang Y (2012) Synergistic degradation of methyl orange in an ultrasound intensified photocatalytic reactor. Ultrason Sonochem 19:1027–1032
47. Selli E, Bianchi CL, Pirola C, Cappelletti G, Ragaini V (2008) Efficiency of 1,4-dichlorobenzene degradation in water under photolysis, photocatalysis on TiO$_2$ and sonolysis. J Hazard Mater 153:1136–1141
48. Davydov L, Reddy EP, France P, Smirniotis PG (2001) Sonophotocatalytic destruction of organic contaminants in aqueous systems on TiO$_2$ powders. Appl Catal B 32:95–105
49. Ahmedchekkat F, Medjram MS, Chiha M, AliAl-bsoul AM (2011) Sonophotocatalytic degradation of Rhodamine B using a novel reactor geometry: effect of operating conditions. Chem Eng J 178:244–251
50. Madhavan J, Grieser F, Ashokkumar M (2013) Sonophotocatalytic degradation of paracetamol using TiO$_2$ and Fe^{3+}. Sep Puri Technol 103:114–118
51. Yuan S, Yu L, Shi L, Wu J, Fang J, Zhao Y (2009) Highly ordered TiO$_2$ nanotube array as recyclable catalyst for the sonophotocatalytic degradation of methylene blue. Catal Commun 10:1188–1191
52. Saien J, Delavari H, Solymani AR (2010) Sono-assisted photocatalytic degradation of styrene-acrylic acid copolymer in aqueous media with nano titania particles and kinetic studies. J Hazard Mater 177:1031–1038
53. Khokhawala IM, Gogate PR (2010) Degradation of phenol using a combination of ultrasonic and UV irradiations at pilot scale operation. Ultrason Sonochem 17:833–838
54. Jelic A, Michael I, Achilleos A, Hapeshi E, Lambropoulou D, Petrovic M, Fatta-Kassinos D, Barcelo D, Perez S (2013) Transformation products and reaction pathways of carbamazepine during photocatalytic and sonophotocatalytic treatment. J Hazard Mater 263:177–186
55. Wu CH, Yu CH (2009) Effects of TiO$_2$ dosage, pH and temperature on decolorization of C.I. Reactive Red 2 in a UV/US/TiO$_2$ system. J Hazard Mater 169:1179–1183

56. An T, Fu J, Gu H, Xiong Y, Chen W, Zhu X, Sheng G (2003) Decolourization and COD removal from reactive dye-containing wastewater using sonophotocatalytic technology. J Chem Technol Biotechnol 78:1142–1148

57. Taghizadeh MT, Abdollahi R (2011) Sonolytic, sonocatalytic and sonophotocatalytic degradation of chitosan in the presence of TiO_2 nanoparticles. Ultrason Sonochem 18:149–157

58. He Y, Grieser F, Ashokkumar M (2011) Kinetics and mechanism for the sonophotocatalytic degradation of p-Chlorobenzoic Acid. J Phys Chem A 115:6582–6588

59. Zhou H, Zhang H, Wang Y, Miao Y, Gu L, Jiao Z (2015) Self-assembly and template-free synthesis of ZnO hierarchical nanostructures and their photocatalytic properties. J Colloid Interface Sci 448:367–373

60. Anbuvannan M, Ramesh M, Viruthagiri G, Shanmugam N, Kannadasan N (2015) Synthesis, characterization and photocatalytic activity of ZnO nanoparticles prepared by biological method. Spectrochim Acta Mol Biomol Spectrosc 143:304–308

61. Farbod M, Jafarpoor E (2014) Hydrothermal synthesis of different colors and morphologies of ZnO nanostructures and comparison of their photocatalytic properties. Ceram Int 40:6605–6610

62. Ramasamy P, Kim J (2013) Facile and fast synthesis of flower-like ZnO nanostructures. Mater Lett 93:52–55

63. Onwudiwe DC, Arfin T, Strydom CA (2015) Surfactant mediated synthesis of ZnO nanospheres at elevated temperature, and their dielectric properties. Superlattices Microstruct 81:215–225

64. Kim KJ, Kreider PB, Choi C, Chang CH, Ahn HG (2013) Visible-light-sensitive Na-doped p-type flower-like ZnO photocatalysts synthesized via a continuous flow microreactor. RSC Adv 3:12702–12710

65. Subash B, Krishnakumar B, Velmurugan R, Swaminathan M, Shanthi M (2012) Synthesis of Ce co-doped Ag–ZnO photocatalyst with excellent performance for NBB dye degradation under natural sunlight illumination. Catal Sci Technol 2:2319–2326

66. Kumar R, Anandan S, Hembram K, Rao TN (2014) Efficient ZnO-based visible-light-driven photocatalyst for antibacterial applications. ACS Appl Mater Interfaces 6:13138–13148

67. Kumar R, Kumar G, Umar A (2013) ZnO nano-mushrooms for photocatalytic degradation of methyl orange. Mater Lett 97:100–103

68. Saleh R, Djaja NF (2014) Transition-metal-doped ZnO nanoparticles: synthesis, characterization and photocatalytic activity under UV light. Spectrochim Acta Mol Biomol Spectrosc 130:581–590

69. Kaur J, Bansal S, Singhal S (2013) Photocatalytic degradation of methyl orange using ZnO nanopowders synthesized via thermal decomposition of oxalate precursor method. Physica B 416:33–38

70. Ertugay N, Acar FN (2014) The degradation of Direct Blue 71 by sono, photo and sonophotocatalytic oxidation in the presence of ZnO nanocatalyst. Appl Surf Sci 318:121–126

71. Anju SG, Yesodharan S, Yesodharan EP (2012) Zinc oxide mediated sonophotocatalytic degradation of phenol in water. Chem Eng J 189–190:84–93

72. Talebian N, Nilforoushan MR, Mogaddas FJ (2013) Comparative study on the sonophotocatalytic degradation of hazardous waste. Ceram Int 39:4913–4921

73. Madhavan J, Sathish Kumar P, Anandan S, Zhou M, Grieser F, Ashokkumar M (2010) Ultrasound assisted photocatalytic degradation of diclofenac in an aqueous environment. Chemosphere 80:747–752

74. Wang J, Jiang Z, Zhang Z, Xie Y, Lv Y, Li J, Deng Y, Zhang X (2009) Study on inorganic oxidants assisted sonocatalytic degradation of Acid Red B in presence of nano-sized ZnO powder. Sep Purif Technol 67:38–43

75. Chakma S, Moholkar VS (2015) Investigation in mechanistic issues of sonocatalysis and sonophotocatalysis using pure and doped photocatalysts. Ultrason Sonochem 22:287–299

76. Saharan P, Chaudhary GR, Lata S, Mehta SK, Mor S (2015) Ultra fast and effective treatment of dyes from water with the synergistic effect of Ni doped ZnO nanoparticles and ultrasonication. Ultrason Sonochem 22:317–325

77. Khataee A, Soltani RDC, Karimi A, Joo SW (2015) Sonocatalytic degradation of a textile dye over Gd-doped ZnO nanoparticles synthesized through sonochemical process. Ultrason Sonochem 23:219–230

78. Khataee A, Karimi A, Oskoui SA, Soltani RDC, Hanifehpour Y, Soltani B, Joo SW (2015) Sonochemical synthesis of Pr-doped ZnO nanoparticles for sonocatalytic degradation of Acid Red 17. Ultrason Sonochem 22:371–381

79. Li D, Wang J, Li X, Liu H (2012) Effect of ultrasonic frequency on the structure and sonophotocatalytic property of CdS/TiO_2 nanocomposite. Mater Sci Semicond Process 15:152–158

80. Ghows N, Entezari MH (2013) Kinetic investigation on sono-degradation of Reactive Black 5 with core–shell nanocrystal. Ultrason Sonochem 20:386–394

81. Zhu L, Meng ZD, Park CY, Ghosh T, Oh WC (2013) Characterization and relative sonocatalytic efficiencies of a new MWCNT and CdS modified TiO_2 catalysts and their application in the sonocatalytic degradation of rhodamine B. Ultrason Sonochem 20:478–484

82. Wu Y, Song L, Zhang S, Wu X, Zhang S, Tian H, Ye J (2013) Sonocatalytic performance of AgBr in the degradation of organic dyes in aqueous solution. Catal Commun 37:14–18

83. Song L, Zhang S, Wu X, Zhang S, Tian H, Ye J (2013) Preparation, characterization and sonodegradation properties of silver tyipolyphosphate catalyst. Catal Commun 30:27–31

84. He P, Song L, Wu X, Tian H, Wei Q, Ye J, Zhang L, Cui Y, Wang Y (2014) Fabrication and sonocatalytic property of $AgPO_3$ microsphere. Ultrason Sonochem 21:136–141

85. Wang N, Zhu L, Wang M, Wang D, Tang H (2010) Sono-enhanced degradation of dye pollutants with the use of H_2O_2 activated by Fe_3O_4 magnetic nanoparticles as peroxidase mimetic. Ultrason Sonochem 17:78–83

86. ElShafei GMS, Yehia FZ, Dimitry OIH, Badawi AM, Eshaq G (2014) Ultrasonic assisted-Fenton-like degradation of nitrobenzene at neutral pH using nanosized oxides of Fe and Cu. Ultrason Sonochem 21:1358–1365

87. Zhou M, Yang H, Xian T, Li RS, Zhang HM, Wang XX (2015) Sonocatalytic degradation of RhB over $LuFeO_3$ particles underultrasonic irradiation. J Hazard Mater 289:149–157

88. Ahmad M, Ahmed E, Hong ZL, Ahmed W, Elhissi A, Khalid NR (2014) Photocatalytic, sonocatalytic and sonophotocatalytic degradation of Rhodamine B using ZnO/CNTs composites photocatalysts. Ultrason Sonochem 21:761–773

89. Zhang K, Zhang FJ, Chen ML, Oh WC (2011) Comparison of catalytic activities for photocatalytic and sonocatalytic degradation of methylene blue in present of anatase TiO_2–CNT catalysts. Ultrason Sonochem 18:765–772

90. Wang J, Lv Y, Zhang L, Liu B, Jiang R, Han G, Xu R, Zhang X (2010) Sonocatalytic degradation of organic dyes and comparison of catalytic activities of CeO_2/TiO_2, SnO_2/TiO_2 and ZrO_2/TiO_2 composites under ultrasonic irradiation. Ultrason Sonochem 17:642–648

91. Neppolian B, Ciceri L, Bianchi CL, Grieser F, Ashokkumar M (2011) Sonophotocatalytic degradation of 4-chlorophenol using $Bi_2O_3/TiZrO_4$ as a visible light responsive photocatalyst. Ultrason Sonochem 18:135–139

92. Ghosh T, Ullah K, Nikam V, Park CY, Meng ZD, Oh WC (2013) The characteristic study and sonocatalytic performance of CdSe–graphene as catalyst in the degradation of azo dyes in aqueous solution under dark conditions. Ultrason Sonochem 20:768–776

93. Wang H, Niu J, Long X, He Y (2008) Sonophotocatalytic degradation of methyl orange by nano-sized Ag/TiO_2 particles in aqueous solutions. Ultrason Sonochem 15:386–392

94. Zhang K, Oh WC (2010) Kinetic study of the visible light-induced sonophotocatalytic degradation of MB solution in the presence of Fe/TiO_2-MWCNT catalyst. Bull Korean Chem Soc 31:1589–1595

95. Zhai Y, Li Y, Wang J, Wang J, Yin L, Kong Y, Han G, Fan P (2013) Effective sonocatalytic degradation of organic dyes by using $Er^{3+}:YAlO_3/TiO_2–SnO_2$ under ultrasonic irradiation. J Mol Catal A-Chem 366:282–287

96. Gao J, Jiang R, Wang J, Kang P, Wang B, Li Y, Li K, Zhang X (2011) The investigation of sonocatalytic activity of $Er^{3+}:YAlO_3/TiO_2$-ZnO composite in azo dyes degradation. Ultrason Sonochem 18:541–548

97. Zhao H, Zhang G, Zhang Q (2014) MnO_2/CeO_2 for catalytic ultrasonic degradation of methyl orange. Ultrason Sonochem 21:991–996

98. Boutoumi NK, Boutoumi H, Khalaf H, David B (2013) Synthesis and characterization of TiO_2–Montmorillonite/Polythiophene-SDS nanocomposites: application in the sonophoto-catalytic degradation of rhodamine 6G. Appl Clay Sci 80–81:56–62

99. Sathishkumar P, Mangalaraja RV, Rozas O, Mansilla HD, Pinilla MAG, Anandan S (2014) Low frequency ultrasound (42 kHz) assisted degradation of Acid Blue 113 in the presence of visible light driven rare earth nanoclusters loaded TiO_2 nanophotocatalysts. Ultrason Sonochem 21:1675–1681

100. Meng ZD, Oh WC (2011) Sonocatalytic degradation and catalytic activities for MB solution of Fe treated fullerene/TiO_2 composite with different ultrasonic intensity. Ultrason Sonochem 18:757–764

101. Sathishkumar P, Mangalaraja RV, Mansilla HD, Pinilla MAG, Anandan S (2014) Sonophoto-catalytic (42 kHz) degradation of Simazine in the presence of Au–TiO_2 nanocatalysts. Appl Catal B: Environ 60–161:692–700

102. Khataee A, Sheydaei M, Hassani A, Taseidifar M, Karaca S (2015) Sonocatalytic removal of an organic dye using TiO_2/Montmorillonite nanocomposite. Ultrason Sonochem 22:404–411

103. Ghodke S, Sonawane S, Gaikawad R, Mohite KC (2011) TiO_2/Nanoclay nanocomposite for phenol degradation in sonophotocatalytic reactor. Can J Chem Eng 9999:1–7

Ultrasonic Synthesis of Nanomaterials for Photocatalytic Removal of Pollutants from Wastewater

Bin Xue

Contents

Abstract

   Photocatalysis is an efficient and sustainable way to the removal of pollutants from wastewater. Ultrasound technology provides the opportunities for the quick and facile synthesis of photocatalytic nanomaterials. This paper is devoted to a comprehensive perspective of ultrasonic synthesis of nanomaterials for photocatalytic removal of pollutants from wastewater. Ultrasonic synthesis of the three categories of photocatalytic nanomaterials including semiconductors,

B. Xue (✉)
Department of Chemistry, College of Food Science and Technology, Shanghai Ocean University, Shanghai, China
e-mail: bxue@shou.edu.cn; binxue_chem@yahoo.com

doped semiconductors, and compound semiconductors is involved. Especially, the very recent developments in the ultrasonic synthesis of semiconductor materials such as heterostructures, hybrid semiconductors, noble metal-deposited semiconductors, sensitized semiconductors, and supported semiconductors are summarized. On this basis, the outlook on ultrasonic synthesis of photocatalytic nanomaterials is provided.

Introduction

Along with the rapid development of human society, environmental pollution is getting worse today than any other time. A large amount of wastewater worldwide is produced during industrial production and human life. Wastewater containing toxic pollutants such as dyes, pesticides, antibiotics, heavy metals, and so on seriously threatens human health and the environmental safety. The environmental remediation including the removal of wastewater has become very imperative. Biodegradation, chemical precipitation, adsorption, membrane filtration, ion exchange, flocculation, and electrodialysis are some conventional methods for the removal of wastewater. However, these methods have limitations with varying degrees in practical application owing to complex processes, expensive cost, high energy consumption, and low efficiency. In recent years, with the development of semiconductor nanomaterials, photocatalytic removal of wastewater has attracted wide attention [1]. In the process of photocatalysis, the semiconductor photocatalysts are excited by light to produce the separation of photogenerated electrons and holes. Then, various pollutants in wastewater are decomposed through the redox of highly active photogenerated electrons and holes. Namely, the semiconductor photocatalysts can efficiently realize the removal of wastewater using sunlight as a clean and sustainable energy. Therefore, semiconductor photocatalysis is a promising technology because of environmental friendliness and sustainable use of energy.

Size, morphology, and composition of the semiconductor nanomaterials strongly influence their photocatalytic properties. Currently, a lot of research work focused on the design and synthesis of semiconductor photocatalysts with highly photocatalytic activity. Among various synthesis approaches of nanomaterials, ultrasound-assisted synthesis is remarkable due to efficient, facile, and rapid characteristics [2]. The localized pressure (about 10^5 kPa), high temperature (about 10^4 K), and cooling rates (in excess of 10^9 K s^{-1}) generated from the collapse of cavitation bubbles under ultrasonic irradiation, which can promote the crystallization and reduce the particle size for nanomaterials. Not only that, more importantly, the semiconductor photocatalysts prepared by ultrasonic-assisted method tend to exhibit higher photocatalytic activity for the removal of wastewater. This will greatly facilitate the practical application of photocatalytic removal of wastewater.

In the paper, the recent situation of ultrasonic-assisted synthesis of nanomaterials for photocatalytic removal of wastewater was presented panoramically, mainly focusing on semiconductors, doped semiconductors, and compound semiconductors.

Ultrasonic Synthesis of Semiconductors

TiO$_2$

As an oxide of the abundant crustal elements, TiO$_2$ materials are widely used in photocatalytic removal of wastewater due to its high activity, inexpensive, stability, and environmental friendliness. So far, the research on TiO$_2$ is most thorough and comprehensive for photocatalytic removal of wastewater. Ultrasonic synthesis of TiO$_2$ photocatalysts is a popular object in early stages of photocatalysis research. As early as 2001, Yu et al. prepared TiO$_2$ nanoparticles with highly photocatalytic active under ultrasonic irradiation [3]. In the synthesis process, titanium tetraisopropoxide was added dropwise to pure water or EtOH-H$_2$O mixed solution and followed by ultrasonic irradiation in an ultrasonic bath. Finally, the TiO$_2$ nanoparticles consist of anatase and brookites were obtained after aging, drying, and calcination. Obviously, ultrasonic irradiation promoted the hydrolysis of titanium alkoxide, the nucleation of TiO$_2$, and the reduction of TiO$_2$ particle size. Moreover, photocatalytic activity of the TiO$_2$ nanoparticles can be enhanced because of better crystallinity, small particle size, and two-phase structure of the TiO$_2$ nanoparticles. However, unlike the above example, Colmenares et al. synthesized pure anatase TiO$_2$ nanoparticles by an ultrasound-assisted sol-gel method using titanium tetraisopropoxide as a Ti source and 2-propanol/water mixture as a solvent under alkaline (pH 9 with NH$_4$OH) conditions [4]. It can clearly be seen that crystallization of TiO$_2$ is closely related with the factors such as precursors, pH, and solvents under ultrasonic irradiation. Furthermore, ultrasonic sources and frequency have an important impact on particle size, pore structure, and photocatalytic activity of TiO$_2$ nanoparticles. Neppolian et al. prepared TiO$_2$ nanoparticles by an ultrasonic-assisted sol-gel method using bath- and tip-type ultrasonic sources, respectively [5]. The results indicated that TiO$_2$ nanoparticles prepared under tip-type ultrasonic condition possessed smaller particle size, higher specific surface area, and higher pore volume than the TiO$_2$ nanoparticles prepared under bath-type ultrasonic condition. However, the photocatalytic activity evaluation for degradation of 4-chlorophenol displayed that the photodegradation ability of TiO$_2$ nanoparticles prepared under bath-type ultrasonic condition was stronger than TiO$_2$ nanoparticles prepared under tip-type ultrasonic condition. This can be attributed to that TiO$_2$ nanoparticles prepared under bath-type ultrasonic condition have larger pore size. Unlike the case of bath-type ultrasonic condition, TiO$_2$ nanoparticles inside a reactor were directly subjected to the implosion of cavitation bubbles under tip-type ultrasonic condition. This difference in ultrasonic condition may cause different pore size of TiO$_2$ nanoparticles. Latt et al. prepared anatase TiO$_2$ nanoparticles via a sol-gel process under ultrasonic

Fig. 1 Schematic illustration of US-associated sol-gel TiO₂ process with reflection plate. *US* ultrasound, *RP* reflection plate Reprinted from [6], Copyright (2008), with permission from Elsevier
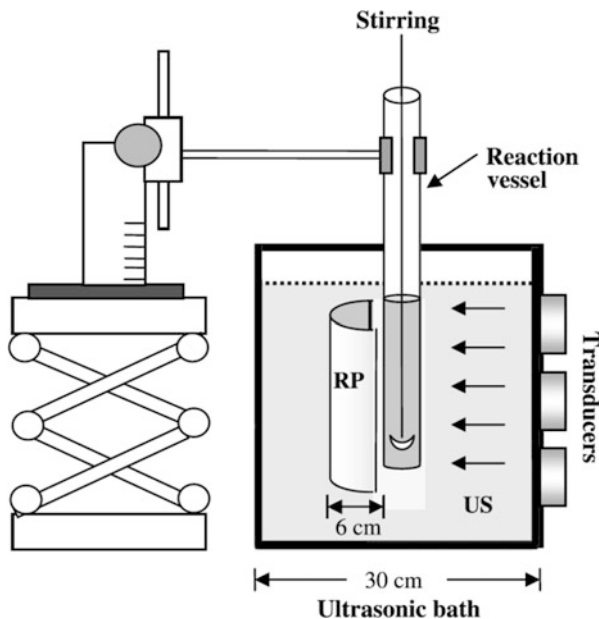
irradiation with different frequency [6]. They found that TiO_2 nanoparticles prepared under low ultrasonic frequency and low calcination temperature exhibited the higher photocatalytic activity for degradation of rhodamine 640 dye due to smaller particle size and larger specific surface area. In addition, the adoption of reflection plate behind the reaction vessel in ultrasonic bath could significantly affect size and textural properties of TiO_2 nanoparticles and improve the photocatalytic activity (Fig. 1).

As is well known, the presence of mesoporous structure of photocatalysts will significantly affect their photocatalytic activity. Sonication in the synthesis of TiO_2 helps to form mesoporous structure. Yu et al. prepared mesoporous TiO_2 nanocrystalline photocatalysts in pure water under irradiation with a high-intensity ultrasonic horn using tetrabutyl titanate as a precursor without any templates [7]. The ultrasound-prepared TiO_2 nanocrystalline photocatalysts possess a greater specific surface area, larger pore size, and smaller crystalline size than that of samples prepared by conventional hydrolysis. It is worth mentioning that TiO_2 gel has been transformed into nanocrystals under high-intensity ultrasound treatment before calcination. The phenomenon suggested that a great ultrasonic power has an important influence on the crystallization of TiO_2 in a sol-gel process.

The creation of oxygen vacancies on the surface of TiO_2 is one important way to induce its visible light-responsive photocatalytic activity. Usually, the synthesis of TiO_2 photocatalysts with oxygen vacancies requires expensive equipment, complicated procedures, and harsh conditions. However, the above synthesis can be easily achieved by ultrasound irradiation due to high-speed collisions between the precursors. Osorio-Vargas et al. reported the preparation of oxygen vacancies contained

TiO_2 nanoparticles with visible light absorption under low-frequency ultrasound irradiation using P25 TiO_2 nanoparticles as parent materials [8]. The facile route has promise for the large-scale preparation of visible light-responsive TiO_2 photocatalysts.

In summary, synthesis condition, crystallinity, size, textural properties, and photocatalytic activity of abovementioned TiO_2 photocatalytic materials are listed in Table 1.

Others

In recent years, other semiconductor materials with photocatalytic activity have been extensively studied. Similar to the case of TiO_2 photocatalysts, ultrasound treatment can effectively improve the crystallinity and control the morphology for the synthesis of other photocatalysts. Lai et al. reported the ultrasound-assisted hydrothermal synthesis of flowerlike ZnO nanostructures [9]. Sonication enhanced the dispersion of Zn^{2+} and the complexation between Zn^{2+} and citric acids (structure-directing agent) before hydrothermal reaction. The influence of ultrasound treatment on the morphology of flowerlike ZnO nanostructures is more obvious under conditions of low-dose citric acids. The flowerlike ZnO nanostructures exhibited good photocatalytic activity for rhodamine B (RhB) degradation under UV light irradiation. However, the photocatalytic activity of flowerlike ZnO nanostructures with ultrasonic assistance was less than that of counterpart without ultrasonic assistance due to the decrease of oxygen vacancy. Similar examples of ultrasound-assisted preparation also include the cases of $NaTaO_3$ and $AgMO_2$ (M = Fe, Ga). Perovskite-like $NaTaO_3$ can be synthesized under ultrasonic bath treatment and subsequent calcination [10]. Compared to $NaTaO_3$ prepared by conventional solid-state method, $NaTaO_3$ materials prepared via ultrasound-assisted route exhibited an unusual transient open circuit potential characteristic in neutral solution under UV light irradiation. The synthesis of $AgMO_2$ can be achieved by two different ultrasound-assisted routes [11]. Namely, α-$AgFeO_2$ was prepared by ultrasound-assisted coprecipitation in KOH solution using $AgNO_3$ and $Fe(NO_3)_3$ as precursors. Furthermore, β-$NaFeO_2$ and β-$NaGaO_2$ were translated into β-$AgFeO_2$ and α-$AgGaO_2$ via ultrasound-assisted ion exchange in $AgNO_3$ solution, respectively. These reactions occurred rapidly at room temperature owing to the employment of ultrasonic treatment.

Ultrasonic spray pyrolysis is also widely used in the preparation of non-TiO_2 photocatalytic materials. For example, Dunkle et al. prepared $BiVO_4$ photocatalysts with visible light-responsive photocatalytic by ultrasonic spray pyrolysis [12]. The $BiVO_4$ photocatalysts possess ball-in-ball or porous structures due to the evaporation of solvent and the decomposition of precursor during ultrasonic spray pyrolysis. These structural features are crucial for improving the photocatalytic activity of $BiVO_4$ photocatalysts. Mann et al. synthesized single-crystalline Bi_2WO_6 nanoplates through a solid-state metathesis reaction between colloidal BiOCl and Na_2WO_4 solution under ultrasonic spray pyrolysis [13]. The formation of single-

Table 1 Photocatalytic properties of TiO$_2$ photocatalytic materials synthesized via sonication for removal of pollutants from wastewater or air

Synthesis condition	Phase content/%	d^a/nm	S_{BET}^b/m^2 g^{-1}	d_p^c/nm	V_p^d/mL g^{-1}	Light source	Pollutant	Photocatalytic activity	Reference
Titanium tetraisopropoxide in water Ultrasonic bath, 47 kHz, 120 W, 1 h Calcination, 500 °C, 1 h	Anatase: 79.6 Brookite: 20.4	Anatase: 9.5 Brookite: 7.9	97.61	5.9	0.218	UV lamp, λ_{max} = 365 nm, 15 W	Acetone	Apparent rate constants 5.30 × 10^{-3} min^{-1}	[3]
Titanium tetraisopropoxide in 2-propanol/water Ultrasonic irradiation, 20 kHz, 300 W, 24 h Calcination, 500 °C, 6 h	Anatase	19	121	9.3	0.29	Medium pressure Hg lamp, λ_{max} = 365 nm, 125 W	3-Chloropyridine	Degradation of 65.9 % after 8 h	[4]
Titanium tetraisopropoxide in water Ultrasonic bath, 40 kHz, 157 W, 60 min Calcination, 500 °C, 3 h	Anatase: 90 Brookite: 10	11	Ca. 75	5.66	0.107	High pressure Hg lamp, λ_{max} = 254 nm, 4 W	4-Chlorophenol	Degradation of 83 %	[5]
Titanium tetraisopropoxide in water Tip-type ultrasonicator, 20 kHz, 30 W at 40 % amplitude, 90 min Calcination, 500 °C, 3 h	Anatase: 84 Rutile: 3.0 Brookite: 13	8.0	156	3.7	0.145	High pressure Hg lamp, λ_{max} = 254 nm, 4 W	4-Chlorophenol	Degradation of 80 %	[5]

Titanium tetraisopropoxide in ethanol-water Ultrasonic bath, 28 kHz, 175 W, 1 h Calcination, 300 °C, 1 h	Anatase:100	5	213	–	–	UV light beam, 1.5 mW	Rhodamine 640	Decomposition rate constants 0.077 min^{-1}	[6]
Tetrabutyl titanate in water High-intensity ultrasonic horn, 20 kHz, 1200 W/cm^2 at 50 % efficiency, 45 min (2 s on and 2 s off) Calcination, 500 °C, 2 h	Anatase: 63 Brookite: 37	10.9	97.3	9.1	0.222	UV lamp, λ_{max} = 365 nm, 15 W	Formaldehyde	Degradation of ca. 80 % after 50 min	[7]
							Acetone	Degradation of ca. 35 % after 50 min	

[a]Crystallite size
[b]BET specific surface area
[c]Pore size
[d]Pore volume

crystalline structure and platelike morphology of Bi_2WO_6 can be attributed to the synergistic effect between ultrasonic spray pyrolysis and solid-state metathesis reaction.

Ultrasonic Synthesis of Doped Semiconductors

Some pristine TiO_2, ZnO, SnO_2, WO_3, and ZnS materials have good UV light response; even so, they hardly exhibit photocatalytic activity under visible light irradiation owing to wide bandgap. The drawback seriously hinders practical applications of wide bandgap semiconductors in sunlight-driven photocatalytic process. Therefore, the design and synthesis of visible light-responsive photocatalysts have attracted keen research interest. In doping process, heteroatoms can be incorporated into the crystal lattice of wide bandgap semiconductors. This may cause the bandgap narrowing and the expansion of range of light response of wide bandgap semiconductors due to the shift in the valence and conduction band. Wherefore, metal or nonmetal heteroatom doping is an effective way to produce modified wide bandgap semiconductors with visible light-responsive photocatalytic activity.

In many cases, it is confirmed that sonication can contribute to the realization of doping. This could be attributed to that sonication affected crystallinity, morphology, size, and textural properties of photocatalysts as well as improved closely contact between precursors. For example, Fe-TiO_2 nanotube arrays with enhanced photocatalytic activity for the degradation of methylene blue (MB) under visible light irradiation were synthesized via an ultrasound-assisted impregnating-calcination route [14]. First, α-Fe_2O_3 nanoparticles were deposited into TiO_2 nanotubes under ultrasonic bath conditions. And Fe^{3+} ions were doped into TiO_2 lattice after calcination. Cr-doped TiO_2 supported on silica or zeolite photocatalysts were prepared by ultrasound-assisted impregnation method [15]. Ultrasonic bath promoted evaporation of the solvent in impregnation process. The Cr-doped TiO_2/silica (zeolite) photocatalysts exhibited good photocatalytic activities for the selective oxidation of glucose and total mineralization of phenol under visible light irradiation. The authors suggested that the ultrasound-assisted synthesis method plays a significant role on textural properties, morphologies, dispersion, and photocatalytic activities of photocatalysts. N-doped TiO_2 photocatalysts with good photodegradation activity for direct sky blue 5B under simulated sunlight irradiation were synthesized by a one-step sonochemical method [16]. In the preparation process of N-doped TiO_2 photocatalysts, the titanium horn of a sonicator directly immersed in the precursor solution. The nitrogen doping and crystallization of TiO_2 were completed after the ultrasound reaction up to 150 min. In addition, ultrasonic spray pyrolysis method can also be used for the preparation of doped photocatalysts. The ultrasonic spray pyrolysis preparation of ZnS:Ni^{2+} photocatalysts was reported by Bang et al. [17]. The results indicated the photocatalytic activity for H_2 production of ZnS:Ni^{2+} photocatalysts prepared by ultrasonic spray pyrolysis is distinctly higher and more stable than the counterpart prepared by traditional coprecipitation.

Apart from single doping, co-doped semiconductor photocatalysts can also be prepared by ultrasound-assisted method. Cheng et al. [18] and Khan et al. [19] reported ultrasound-assisted sol-gel synthesis of Mo, N-co-doped TiO_2 and Mo, and V-co-doped TiO_2 nanophotocatalysts, respectively. The aforementioned co-doped photocatalysts exhibited enhanced photocatalytic activities for decomposition of organic pollutants under visible light irradiation compared with single-doped or undoped photocatalysts.

At last, photocatalytic properties of abovementioned doped semiconductor photocatalytic materials for removal of pollutants from wastewater are summarized in Table 2.

Ultrasonic Synthesis of Compound Semiconductors

In order to obtain the new photocatalysts with visible light-induced photocatalytic activity for removal of wastewater, the fabrication of compound semiconductors is an effective approach. The compound semiconductor photocatalysts obtained through a series of modification strategies can significantly enhance the visible light-induced photocatalytic activity due to extension of the photoresponse range as well as reduction of the recombination of photogenerated electron-hole pairs in the interfaces between materials. These compound semiconductor photocatalysts with visible light-induced photocatalytic activity include several types of semiconductor heterostructures, hybrid semiconductors, noble metal-deposited semiconductors, and sensitized semiconductors. In addition, the construction of supported compound photocatalysts can improve photocatalytic activity, stability, and separability due to porous structure, mechanical strength, and magnetic properties of supports. Therefore, the development of compound semiconductor photocatalysts has brought new opportunities for photocatalytic removal of wastewater. Here, the applications of sonication in the synthesis of compound semiconductors were summarized.

TiO$_2$-Based Heterojunction

As a traditional photocatalytic material, TiO_2 is often chosen as the popular candidate material for the construction of composite photocatalyst systems with high photocatalytic activity. The synthesis of TiO_2 photocatalysts coupled with narrow bandgap semiconductor materials is a promising way to obtain composite photocatalysts with visible light-responsive photocatalytic activity. For example, Xue et al. prepared AgI/TiO_2 nanocomposite photocatalysts with high activity of photocatalytic degradation of methyl orange (MO) and killing of *E. coli* by an ultrasound-assisted precipitation process and subsequent low-temperature calcination [20]. Compared with counterparts prepared by conventional precipitation process, the AgI/TiO_2 nanocomposite photocatalysts possessed higher crystallinity, better dispersion, apparent blueshift phenomenon of the absorption band, and higher

Table 2 Photocatalytic properties of doped semiconductor photocatalytic materials synthesized via sonication for removal of pollutants from wastewater

Substrate materials	Doping elements	Synthesis condition	Textural properties	Optical properties	Light source	Pollutant	Photocatalytic activity	Reference
TiO$_2$ nanotube array	Fe	TiO$_2$ nanotube array in Fe(NO$_3$)$_3$•9H$_2$O solution Ultrasonic bath, 40 kHz, 2.4 kW m^{-2}, 5 min Calcination, 500 °C, 2 h	–	Broad band center at 540 nm	500 W tungsten-halogen lamp	MB	Decomposition rate constants 0.0043 min^{-1}	[14]
TiO$_2$ nanoparticles/ silica (zeolite)	Cr	Titanium (IV) isopropoxide in isopropanol, polyethylene glycol-400, silica or zeolite, C$_{15}$H$_{21}$CrO$_6$ in isopropanol Ultrasonic bath, 35 kHz, 560 W, 60 min Calcination, 500 °C, 4 h	TiO$_2$ nanoparticles/ silica: S_{BET} = 204 m^2 g^{-1}, d_p = 16 nm, V_p = 0.51 mL g^{-1} TiO$_2$ nanoparticles/ zeolite: S_{BET} = 672 m^2 g^{-1}, d_p = 0.7 nm, V_p = 0.44 mL g^{-1}	TiO$_2$ nanoparticles/ silica: absorption threshold at 577 nm TiO$_2$ nanoparticles/ zeolite: absorption threshold at 574 nm	Medium pressure Hg lamp, λ_{max} = 365 nm, 125 W	Phenol	Degradation of ca. 30 % after 240 min	[15]
TiO$_2$ nanoparticles	N	Urea in water + tetraisopropyl titanium in isopropyl alcohol Tip-type ultrasonicator, 150 min	–	Absorption band edge at ca. 460 nm	UV light: Hg lamp, 300 W Simulated sunlight: Xe lamp, 500 W	Direct sky blue 5B	UV light: color removal of 100 % after 50 min Simulated sunlight: color removal of 97 % after 60 min	[16]

TiO$_2$ nanoparticles	Mo, N	N doped TiO$_2$ in ammonium molybdate solution Sonication, 120 min Calcination, 500 °C, 4 h	–	Absorption band edge at ca. 520 nm	350 W arc xenon lamp with cutoff filter of 420 nm	Phenol	Degradation of 89.2 % after 2 h	[18]
TiO$_2$ nanoparticles	Mo, V	Titanium butoxide in ethyl alcohol + ammonium molybdate tetrahydrate and ammonium metavanadate in reverse osmosis water Ultrasonic bath, 40 kHz, 2 h Calcination, 550 °C, 1 h	$S_{BET} = 122.6 \text{ m}^2 \text{ g}^{-1}$, $d_p = 13.5$ nm, $V_p = 0.23$ mL g^{-1}	Absorption band edge at 489.4 nm	UV light: UVC lamp, $\lambda_{max} = 254$ nm Visible light: Hg medium pressure lamp, $\lambda_{range} = 410\text{–}660$ nm	MB	UV light: degradation of 98.5 % after 60 min Visible light: degradation of 95.2 % after 10 min	[19]
						Sulfamethoxazole	Visible light: degradation of 100 % after 10 min	
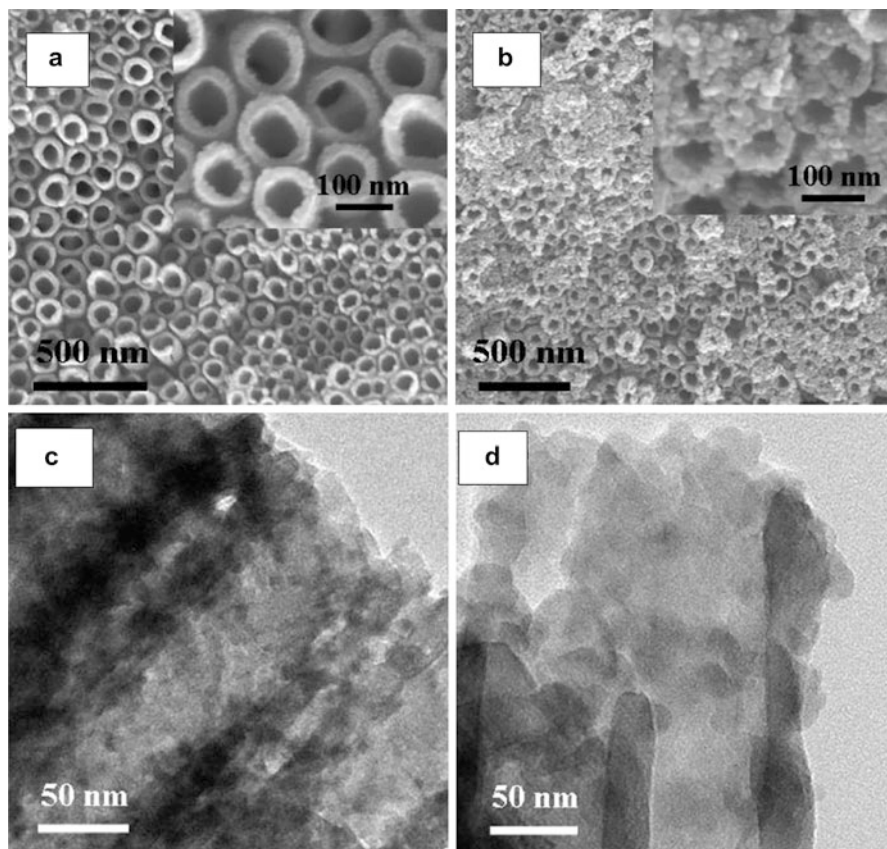
Fig. 2 FESEM and TEM images of (**a**, **c**) sonication-CdS/TNTAs and (**b**, **d**) CdS/ TNTAs Reprinted with permission from [22]. Copyright (2010) American Chemical Society

photocatalytic activity. Ghows et al. reported the synthesis of CdS/TiO$_2$ core-shell nanocrystals in microemulsion by means of ultrasonic irradiation and studied the effects of preparation method, sonication time, and sonication mode on the synthesis [21]. The results indicated that the use of titanium isopropoxide as a precursor led to form the core-shell structure. The increasing ultrasonic time helped to improve the degree of crystallinity of TiO$_2$. In addition, the CdS/TiO$_2$ core-shell nanocrystals formed under continuous sonication mode have larger specific surface area and smaller particle size in comparison with that formed under "on-off" sonication mode. Xie et al. synthesized the CdS quantum dot-sensitized TiO$_2$ nanotube arrays (TNTAs) by a sonication-assisted sequential chemical bath deposition approach [22]. The data clearly revealed that sonication can effectively promote the close deposition of CdS quantum dots on the TiO$_2$ nanotube walls and thereby avoid clogging the nanotube mouths (Fig. 2). The sonication-assisted prepared CdS/TNTAs exhibited higher photocurrent density and more negative photocurrent

onset than that of CdS/TNTAs prepared by conventional sequential chemical bath deposition approach under visible light irradiation. The results suggested that the dense distribution of CdS quantum dots on the sonication-CdS/TNTAs led to much enhancement in the photoelectrochemical and photocatalytic activity for the degradation of MO. Obviously, the common strategy of the above examples is that the heterogeneous component in situ was supported on a ready-prepared substrate materials. Unlike the above strategy, Li et al. one-step prepared TiO_2/In_2O_3 composite photocatalysts by an ultrasonic aerosol spray-assisted method using $TiCl_4$ together with $In(NO_3)_3$ as precursors [23]. The TiO_2/In_2O_3 composite photocatalysts showed excellent photocatalytic activity for degradation of MO under visible light irradiation. This work provides a facile and general route for the one-step synthesis of composite photocatalysts on a large scale.

In summary, synthesis condition, physicochemical properties, and photocatalytic activity of abovementioned TiO_2-based heterojunction photocatalytic materials are listed in Table 3.

g-C_3N_4-Based Heterostructures

Graphite-like carbon nitride (g-C_3N_4) is new metal-free polymer semiconductors and possesses a two-dimensional layered structure with weak interlayer van der Waals forces. Pure g-C_3N_4 is nontoxic, cheap, and stable and considered to be a kind of promising visible light-responsive photocatalysts for wastewater treatment due to suitable bandgap energy (~2.7 eV). However, pure g-C_3N_4 exhibits low photocatalytic activity under visible light irradiation due to high recombination rate of photogenerated electron-hole pairs. Therefore, it is necessary to construct semiconductor/g-C_3N_4 heterostructures in order to improve the potential application of g-C_3N_4.

Sonication plays an important role in the preparation of high activity g-C_3N_4-based heterostructure photocatalysts. On the one hand, sonication improves the dispersion of compositions in favor of close contact between g-C_3N_4 and other semiconductor materials. For example, Chen et al. dispersed mesoporous g-C_3N_4 (mpg-C_3N_4) into methanol by sonication, then added ZnO powder into the suspension of mpg-C_3N_4 under stirring, and finally prepared core-shell structure of ZnO@mpg-C_3N_4 [24]. The ZnO@mpg-C_3N_4 showed high photocatalytic activity for decomposition of MB under UV and visible light irradiation. The authors suggested that the hybridized effect between ZnO and mpg-C_3N_4 enhanced UV photocatalytic activity of ZnO@mpg-C_3N_4 photocatalysts. The enhancement of the visible light photocatalytic activity of ZnO@mpg-C_3N_4 photocatalysts could be attributed to the heterostructures induced by the match of lattice and energy level between g-C_3N_4 and ZnO.

On the other hand, the weak van der Waals interaction between layers of bulk g-C_3N_4 is destroyed to form a thin sheetlike nanostructures under sonication conditions. The thin sheetlike g-C_3N_4 nanostructures tend to show higher photocatalytic activity due to a large specific surface area and more exposed active sites. For

Table 3 Photocatalytic properties of TiO$_2$-based heterojunction photocatalytic materials synthesized via sonication for removal of pollutants from wastewater

Materials	Synthesis condition	Textural properties	Optical properties	Light source	Pollutant	Photocatalytic activity	Reference
AgI/TiO$_2$ nanocomposites	TiO$_2$ nanoparticles, AgNO$_3$, and KI in water Ultrasonic bath, 40 kHz, 300 W, 2 h Calcination, 350 °C, 2 h	–	Absorption band centered at 424 nm	250 W mercury blended lamp (4900 lm of photon flux) with filter (>420 nm)	MO	Degradation rate of 95.7 % after 2 h	[20]
CdS quantum dot-sensitized TiO$_2$ nanotube arrays	TiO$_2$ nanotube arrays, CdCl$_2$, and Na$_2$S in water Sonication-assisted sequential chemical bath deposition	–	Absorption edge of ~530 nm	Visible light	MO	Degradation rate of 61.4 % after 180 min	[22]
TiO$_2$/In$_2$O$_3$ composite	Pluronic P123, In (NO$_3$)$_3$, and TiCl$_4$ in ethanol Ultrasonic aerosol spray, 1.7 MHz, 30 W, 380 °C Calcination, 350 °C, 2 h	$S_{BET} = 131\ \mathrm{m^2\ g^{-1}}$, $d_p = 4.0$ nm, $V_p = 0.18\ \mathrm{mL\ g^{-1}}$	Extended absorption bands to approximately at 800 nm	300 W tungsten Halogen lamp with 400 nm cutoff filter	MO	Degradation rate of 93 % after 300 min	[23]
					RhB	Degradation rate of 95 % after 180 min	

example, Santosh Kumar et al. prepared N-doped ZnO/g-C_3N_4 hybrid core-shell nanoplates by an ultrasonic dispersion method [25]. At first, bulk g-C_3N_4 was exfoliated into pure g-C_3N_4 nanosheets via liquid-phase ultrasonic exfoliation. Next, previously prepared N-doped ZnO was added to the dispersion of pure g-C_3N_4 nanosheets. After stirring and evaporation, g-C_3N_4 nanosheets were wrapped on N-doped ZnO surface. The hybrid core-shell nanostructures exhibited enhanced visible light photocatalytic activity for the degradation of RhB and high photostability. The improved photocatalytic performance can be attributed to a large surface exposure area, energy band structure, and enhanced charge separation properties at the interface of N-doped ZnO and g-C_3N_4 nanosheets. Similarly, Zhang et al. achieved SnS_2 nanosheets coupled with g-C_3N_4 nanosheets through ultrasonic exfoliation of bulk g-C_3N_4 and subsequent deposition of previously prepared SnS_2 [26]. The two-dimensional heterojunction photocatalysts possessed high photocatalytic activity for RhB degradation. In addition, the thickness of g-C_3N_4 nanosheets can be effectively reduced by extending the ultrasonic time. Lu et al. prepared atomic layer g-C_3N_4 nanosheets through ultrasonication for 8 h [27]. Then, CdS nanoparticles in situ loaded on the atomic layer g-C_3N_4 nanosheets via solvothermal method. The atomic layer g-C_3N_4-CdS nanoheterojunctions showed significantly enhanced visible light-induced photocatalytic activity for MO degradation.

In summary, synthesis condition, physicochemical properties, and photocatalytic activity of abovementioned g-C_3N_4-based heterojunction photocatalytic materials are listed in Table 4.

Other Heterostructures

The ultrasonic synthesis of other semiconductor heterostructures also received widespread attention. Neppolian et al. reported the synthesis of visible light-responsive $ZrTiO_4/Bi_2O_3$ composite photocatalysts for 4-chlorophenol decomposition by an ultrasonic-assisted hydrothermal method [28]. First, the colloidal mixture solution formed using bismuth nitrate pentahydrate, titanium (IV) isopropoxide, and zirconium (IV) isopropoxide as precursors under ultrasonic condition. After hydrothermal reaction and succedent calcination, $ZrTiO_4/Bi_2O_3$ composite photocatalysts were obtained. However, the calcination is essential to improve the crystallinity of the product. Xu et al. fabricated crystalline CdS nanoparticles supported on the as-prepared ZnO hierarchical microspheres under high-intensity ultrasound irradiation [29]. The ZnO/CdS composite photocatalysts exhibited higher activity for photodegradation of RhB under nature sunlight. Li et al. prepared $Cu_2O/BiVO_4$ composite photocatalysts through the direct mixing of as-prepared Cu_2O and $BiVO_4$ under ultrasound irradiation [30]. The $Cu_2O/BiVO_4$ composite photocatalysts exhibited the photocatalytic activities for the decomposition of MB, MO, and phenol under visible light irradiation. Yu et al. achieved synthesis of $Co_3O_4/BiVO_4$ and $CuO/BiVO_4$ composite photocatalysts with high photocatalytic activity for the decomposition of acid orange II by an intense ultrasound irradiation approach [31]. The results proved that the metal salt precursors transformed completely into

Table 4 Photocatalytic properties of g-C$_3$N$_4$-based heterojunction photocatalytic materials synthesized via sonication for removal of pollutants from wastewater

Materials	Synthesis condition	Textural properties	Optical properties	Light source	Pollutant	Photocatalytic activity	Reference
ZnO@mpg-C$_3$N$_4$	mpg-C$_3$N$_4$ in methanol Ultrasonic bath, 30 min ZnO in mpg-C$_3$N$_4$ suspension Stirred, 24 h	—	Extended absorption bands to ca. 800 nm	UV light: 11 W UV light lamp, λ_{max} = 254 nm; Visible light: 500 W xenon lamp with 420 nm cutoff filter	MB	UV light: apparent rate constant of ZnO@mpg-C$_3$N$_4$-4 % is 0.135 min^{-1}; Visible light: apparent rate constant of ZnO@mpg-C$_3$N$_4$-20 % is 0.0205 min^{-1}	[24]
N-doped ZnO/g-C$_3$N$_4$ core-shell nanoplates	g-C$_3$N$_4$ in water Ultrasonic bath, 1 h N-doped ZnO in g-C$_3$N$_4$ suspension Stirred, 48 h	S_{BET} =45.17 m^2 g^{-1}	Absorption edge of ~410 nm	300 W Xe lamp with visible light region ranging from 400 nm to 700 nm and light intensity of 115 mW cm^{-2}	RhB	Apparent rate constant 0.0679 min^{-1}	[25]
SnS$_2$/g-C$_3$N$_4$ heterojunction nanosheets	g-C$_3$N$_4$ in methanol Ultrasonic bath, 30 min SnS$_2$ in g-C$_3$N$_4$ suspension Stirred, 36 h	S_{BET} =107.0 m^2 g^{-1}	Extended absorption bands to ca. 700 nm	300 W Xe lamp coupled with a cutoff filter (400 nm $< \lambda <$ 780 nm) (output density of ~ 300 mW/cm^2)	RhB / MO / 4-Nitrophenol	Degradation rate of 99.8 % after 20 min / Degradation rate of 95.0 % after 40 min / Degradation rate of 31.3 % after 120 min	[26]
g-C$_3$N$_4$-CdS nanoheterojunctions	g-C$_3$N$_4$ in ethanol Ultrasonic bath, 1 h Cd(CH$_3$COO)$_2$•2H$_2$O, thioacetamide in g-C$_3$N$_4$ suspension Hydrothermal reaction, 180 °C for 12 h	—	Absorption edge of ca. 440 nm	300 W Xe lamp with UV cutoff filter ($\lambda \geq$ 420 nm)	MO	Almost completely eliminate MO after 16 min irradiation	[27]

crystalline metal oxide by sonochemical hydrolysis and the crystallization process of $BiVO_4$ also occurred under intense ultrasonic irradiation. The crystallization behavior is closely related to high-intensity ultrasound conditions.

In summary, synthesis condition, physicochemical properties, and photocatalytic activity of abovementioned other heterostructure photocatalytic materials are listed in Table 5.

Semiconductor/Graphene (Derivatives)

Graphene is a two-dimensional material consisting of a single layer of sp^2-bonded carbon atoms arranged in a honeycomb structure. Graphene has received extensive attention because of the high electronic conductivity, large surface-to-volume atomic ratio, robust mechanical properties, and excellent chemical stability. Thus, graphene and its derivatives such as graphene oxide (GO) and reduced graphene oxide (RGO) are good platform for construction of hybrid semiconductor photocatalysts. Photogenerated electrons can be easily transferred to graphene in graphene-based composite photocatalysts; photogenerated electrons and holes are effectively separated, thereby improving photocatalytic activity.

Ultrasonic treatment is an efficient technology to improve dispersion of materials and close contact between graphene and semiconductors in mixture solution. For example, Thomas et al. reported a sonication and stirring method for decorating few-layer graphene with TiO_2 nanoparticles [32]. The few-layer graphene-TiO_2 composite photocatalysts showed higher degradation efficiency of RhB than bare TiO_2 nanoparticles under solar irradiation. The GO-P25 TiO_2 composite photocatalysts prepared by sonication exhibited an enhancement of mesoporosity and mesopore diameter owing to the formation of GO aggregates coated with P25 TiO_2 nanoparticles [33]. Compared to P25 TiO_2 nanoparticles, the first-order rate constant of MO photodegradation obviously increased for the GO-P25 TiO_2 composite photocatalysts under near-UV/Vis irradiation. Besides, Zhuo et al. reported the ultrasonic preparation of graphene quantum dots with upconverted emission [34]. The brief procedures are as follows: graphene was oxidized in concentrated H_2SO_4 and HNO_3, and then the mixed solution was treated ultrasonically for up to 12 h. Finally, graphene quantum dots were obtained after calcination. The corresponding rutile TiO_2/graphene quantum dots composite photocatalysts showed high photocatalytic rate for degradation of MB under visible light irradiation.

Furthermore, sonication also facilitates the conversion of precursor into nanocrystals, which deposits in situ on the surface of graphene. For example, Guo et al. reported the sonochemical synthesis of graphene-TiO_2 composite photocatalysts by means of the pyrolysis and condensation of $TiCl_4$ into TiO_2 nanoparticles [35]. Dong et al. achieved in situ ultrasonic-assisted growth of $ZnMoO_x$/RGO composite photocatalysts using $Zn(CH_3COO)_2$ as Zn sources and Na_2MoO_4 as Mo sources [36]. The $ZnMoO_x$/RGO composite photocatalysts exhibited a superior and recyclable natural-sunlight-driven photocatalytic activity for degradation of RhB and noticeable killing activity of *E. coli*.

Table 5 Photocatalytic properties of other heterostructure photocatalytic materials synthesized via sonication for removal of pollutants from wastewater

Materials	Synthesis condition	Textural properties	Optical properties	Light source	Pollutant	Photocatalytic activity	Reference
ZrTiO$_4$/Bi$_2$O$_3$ nanoparticles	Bismuth nitrate pentahydrate, titanium (IV) isopropoxide, and zirconium (IV) isopropoxide in isopropanol Ultrasonic bath (40 kHz), 1 h Hydrothermal reaction, 170 °C for 15 h Calcination, 450 °C	$S_{BET} = 48$ m^2 g^{-1}, $d_p = 17.0$ nm, $V_p = 0.200$ mL g^{-1}, $d = 7$ nm	Absorption region extended to ~560 nm	300 W Xe Arc lamp with UV cutoff filter ($\lambda \geq 410$ nm)	4-Chlorophenol	Degradation rate of 40 % after 1 h	[28]
ZnO/CdS hierarchical heterostructure	ZnO microspheres, cadmium chloride, and thiourea in water High-intensity ultrasound (100 W, 40 kHz), 2 h	–	Extended absorption bands to ~550 nm	Solar irradiation	RhB	Almost completely degradation after 200 min Apparent rate constant 0.0108 min^{-1}	[29]
Cu$_2$O/BiVO$_4$	Cu$_2$O in methanol Ultrasonic bath, 25 min BiVO$_4$ in Cu$_2$O suspension Stirred, 20 h	$S_{BET} = 4.35$ m^2 g^{-1}, $d_{BiVO_4} = 20.94$ nm, $d_{Cu_2O} = 32.53$ nm	Absorption region extended to ~540 nm	400 W metal-halide lamp ($\lambda_{max} = 588$ nm) with the combination of a cutoff filter ($\lambda > 400$ nm)	MB	Degradation rate of 89.1 % after 120 min, apparent rate constant 0.0182 min^{-1}	[30]
					MO	Degradation rate of 75.7 % after	

Material	Synthesis conditions	S_{BET}	Absorption	Lamp	Pollutant	Degradation	Ref.
Co$_3$O$_4$/BiVO$_4$	P123 nonionic surfactant, HNO$_3$, Bi(NO$_3$)$_3$ · 5H$_2$O, NH$_4$VO$_3$, copper acetate, or cobaltous acetate in water and alcohol	$S_{BET} = 8.03$ m^2 g^{-1}	Extended absorption bands to ~800 nm	300 W tungsten-halogen lamp with λ > 420 nm cutoff filter	Phenol	120 min, apparent rate constant 0.0118 min^{-1} Degradation rate of 56.5 % after 120 min, apparent rate constant 0.00693 min^{-1}	[31]
					Acid orange II	Degradation rate of 86 % after 5 h	
CuO/BiVO$_4$	Ultrasound irradiation with high-intensity ultrasonic probe (1.2 cm diameter, Ti horn, 20 kHz, 60 W/cm^2), 180 min	$S_{BET} = 8.78$ m^2 g^{-1}				Degradation rate of 78 % after 5 h	
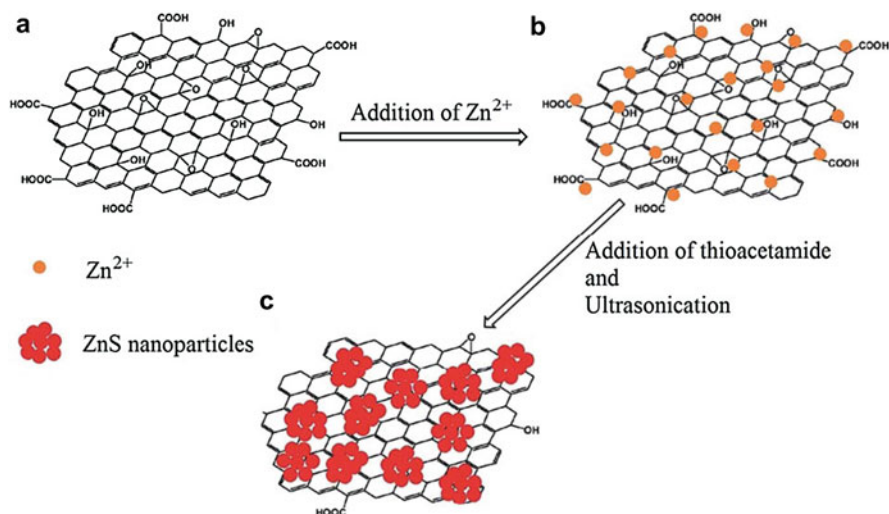
Fig. 3 Schematic illustration of formation mechanism for ZnSNPs-RGO composite via ultrasonic irradiation. Reproduced from [37] with permission from The Royal Society of Chemistry

In order to further suppress the recombination of photogenerated electron-hole pairs in GO-based composite photocatalysts, removal of the oxygen-containing groups from GO to obtain RGO has proved to be necessary. Ultrasonic treatment can effectively achieve reduction of GO. For example, as shown in Fig. 3, a mixture of zinc acetate dihydrate, thioacetamide, and GO was converted to ZnS nanosphere-RGO composite photocatalysts under ultrasonic irradiation [37]. Under ultrasonic conditions, highly reactive $H^\bullet$ and $^\bullet C(NH_2)CH_3$ radicals can be generated by the pyrolysis of water and thioacetamide molecules. While ZnS is anchoring in situ on the surface of GO, graphene oxide is reduced to RGO by reducing species such as $H^\bullet$ and $^\bullet C(NH_2)CH_3$ radicals (Eq. 1):

$$GO + \text{reducing species} (H^\bullet,\ ^\bullet C(NH_2)CH_3) \rightarrow RGO \tag{1}$$
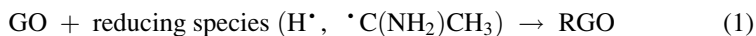
Obviously, ultrasonic treatment is a more safe and convenient way for the reduction of GO compared to hydrazine reduction and calcination.

In summary, synthesis condition, physicochemical properties, and photocatalytic activity of abovementioned graphene-based composite photocatalytic materials are listed in Table 6.

Semiconductor/Carbon Nanotubes

Carbon nanotubes (CNTs), a one-dimensional hollow carbon material, are considered as a perfect carrier for composite photocatalysts due to a large specific surface area and good electronic conductivity. The semiconductor/CNTs hybrid

Table 6 Photocatalytic properties of graphene-based composite photocatalytic materials synthesized via sonication for removal of pollutants from wastewater

Materials	Synthesis condition	Textural properties	Optical properties	Light source	Pollutant	Photocatalytic activity	Reference
TiO$_2$ nanoparticles/ few-layer graphene	TiO$_2$ and graphene in water Sonication, 30 min Stirred, 24 h	–	Absorption maximum shifted to 300 nm and the peak broadened	Two 15 W UVC tubes with main wave crest at 254 nm Sunlight (mainly in the summer at UV index >11) with measured light intensity between 77,000 and 85,000 luxes	RhB	UV light: degradation rate of 100 % after 20 min, apparent rate constant 0.226 min^{-1} Sunlight: degradation rate of 100 % after 8 min	[32]
GO-P25	GO and P25 TiO$_2$ in ethanol Ultrasonic bath, 1 h Calcination, 200 °C	S_{BET} = 55 ± 5 m^2 g^{-1}, d_p = 33.2 ± 0.5 nm, V_p (micro) = 0.02 ± 0.01 mL g^{-1}, V_p (meso) = 0.40 ± 0.02 mL g^{-1}	Extended absorption bands to ~600 nm	Medium pressure mercury vapor lamp (λ > 350 nm; 50 mW cm^{-2})	Diphenhydramine	Apparent rate constant 0.054 ± 0.003 min^{-1}	[33]
					MO	Apparent rate constant 0.207 ± 0.002 min^{-1}	
Rutile TiO$_2$/ graphene quantum dots nanocomposites	Graphene quantum dots: graphene in H$_2$SO$_4$ and HNO$_3$ Ultrasonic bath (300 W, 80 kHz), 12 h Calcination, 350 °C, 20 min Dialysis Rutile TiO$_2$/graphene quantum dots: rutile TiO$_2$ in graphene quantum dots solution Stirred, 30 min	–	–	350 W Xe lamp with 420 nm cutoff filter	MB	Degradation rate of 97 % after 60 min, apparent rate constant 0.0576 min^{-1}	[34]

(continued)

Table 6 (continued)

Materials	Synthesis condition	Textural properties	Optical properties	Light source	Pollutant	Photocatalytic activity	Reference
Graphene-TiO$_2$ composite	TiCl$_4$ and graphene oxide in ethanol and water. Sonication (high-intensity ultrasonic probe, Ti horn, 20 kHz, 100 W/cm^2), 3 h. Hydrazine reduction. Calcination, 450 °C, 3 h	S_{BET} = 49 m^2 g^{-1}	Extended absorption bands to ~800 nm	UV lamps (4 × 6 W)	MB	Apparent rate constant 0.0139 min^{-1}	[35]
ZnMoO$_x$/RGO composite	GO, Zn(CH$_3$COO)$_2$•2H$_2$O and Na$_2$MoO$_4$•2H$_2$O in water. Ultrasonic treatment, 150 min. Hydrazine reduction	S_{BET} = 2.5216 m^2 g^{-1}	Extended absorption bands to ~800 nm	Natural sunlight	RhB	Degradation rate of 99.8 % after 10 h	[36]
ZnS nanospheres-RGO composite	Zinc acetate dehydrate, GO, and thioacetamide in water. Sonication (ultrasonic horn, 20 kHz), 80 % amplitude, 15 min with 3 s pulse and 3 s relaxation cycle	S_{BET} = 66.81 m^2 g^{-1}, d_p = 2.3 nm, V_p = 0.2478 mL g^{-1}	–	UV lamps (5 × 8 W)	MB	Degradation rate of ~95 % after 180 min	[37]

photocatalysts can efficiently be prepared under ultrasonic condition. For example, Shi et al. fabricated a series of Ag/AgX-CNTs (X = Cl, Br, I) nanocomposite photocatalysts via an ultrasonic assistant deposition-precipitation route [38]. Compared to the pure AgX and CNTs, Ag/AgX-CNTs composite photocatalysts exhibited a remarkably enhanced visible light photocatalytic degradation efficiency of removal of 2,4,6-tribromophenol. The enhancement of photocatalytic activity is attributed to the effective transfer of photogenerated electron from AgX and Ag nanoparticles to CNTs. Zhai et al. prepared the Ag_3PO_4/CNT Pickering emulsions as a new kind of photocatalytic system [39]. In the preparation process, sonication employed for dispersing of the components and demulsifying. The Pickering emulsion-based composite photocatalysts showed a much higher efficiency for MB decomposition than traditional solution-dispersed photocatalysts under visible light irradiation.

In summary, synthesis condition, physicochemical properties, and photocatalytic activity of abovementioned CNTs-based composite photocatalytic materials are listed in Table 7.

Noble Metal/Semiconductor

Deposition with noble metal on semiconductors can improve photocatalytic activity under UV or visible light irradiation. However, the enhancement mechanisms of photocatalytic activity are different under different lighting conditions. Noble metals supported on semiconductors act as electron acceptors under UV light irradiation. The recombination of photogenerated electron-hole pairs is effectively suppressed due to the photogenerated electrons on semiconductors migrate to noble metal. Thus, the photocatalytic activity can be improved under UV light irradiation. Under visible light irradiation, noble metal nanoparticles supported on semiconductors can absorb resonant photons to enhance photocatalytic activity because of the localized surface plasmon resonance (LSPR).

Photochemical reduction is one of common methods for the preparation of noble metal nanoparticles. So, composite photocatalysts containing highly dispersed noble metal nanoparticles can conveniently be prepared by a combination method of ultrasound and photoreduction. For example, Sun et al. [40] and Gyawali et al. [41] synthesized Ag-TiO_2 nanotube array and Ag-$PbMoO_4$ composite photocatalysts under sonication and subsequent UV light irradiation, respectively. Sonication before photoreduction promotes uniform distribution of the precursors on the surface of supports and enhances interaction between noble metal ions and semiconductors. Thus, the size of noble metal nanoparticles on composite photocatalysts can be effectively reduced through ultrasound-assisted photoreduction routes. As shown in Fig. 4, the differences in particle size of samples made by different preparation routes unambiguously reveal the role of ultrasound in the above example of Ag-TiO_2 nanotube array [40].

Of course, one-step ultrasound-assisted synthesis of noble metal/semiconductor composite photocatalysts is more attractive due to facility and high efficiency. Zen

Table 7 Photocatalytic properties of CNTs-based composite photocatalytic materials synthesized via sonication for removal of pollutants from wastewater

Materials	Synthesis condition	Textural properties	Optical properties	Light source	Pollutant	Photocatalytic activity	Reference
Ag/AgCl-CNTs nanocomposite	KX (X = Cl, Br, I) and CNTs in water Ultrasonic bath (40 kHz), 20 min AgNO$_3$ and ammonia solution in above suspension Ultrasonic bath (40 kHz), 20 min Stirred, 24 h	S_{BET} = 50.3 m^2 g^{-1}, d_p = 16.8 nm, V_p = 0.289 mL g^{-1}	Extended absorption bands to ~800 nm	250 W metal-halide lamp with UV cutoff filter (λ < 400 nm), illumination intensity ~5 mW cm^{-2}	2,4,6-Tribromophenol	Degradation rate of 39 % after 130 min	[38]
Ag/AgBr-CNTs nanocomposite		S_{BET} = 20.8 m^2 g^{-1}, d_p = 26.0 nm, V_p = 0.142 mL g^{-1}				Degradation rate of 100 % after 50 min	
Ag/AgI-CNTs nanocomposite		S_{BET} = 18.4 m^2 g^{-1}, d_p = 35.9 nm, V_p = 0.159 mL g^{-1}				Degradation rate of 42 % after 180 min	
Ag$_3$PO$_4$/CNTs Pickering emulsions	MWNTs in isooctane + Ag$_3$PO$_4$ in water Sonication bath (100 W, 40 kHz), 20 min	–	–	500 W xenon arc lamp equipped with ultraviolet cutoff filter ($\lambda \geq$ 420 nm)	MB	Degradation rate of ~100 % after 10 min, apparent rate constant 0.48 min^{-1}	[39]
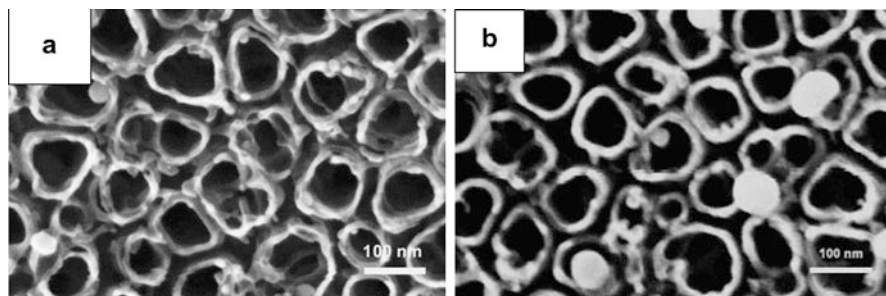
Fig. 4 SEM images of Ag-TiO$_2$ nanotube arrays made by (**a**) ultrasound-assisted photoreduction route and (**b**) photoreduction route Reprinted from [40], Copyright (2009), with permission from Elsevier
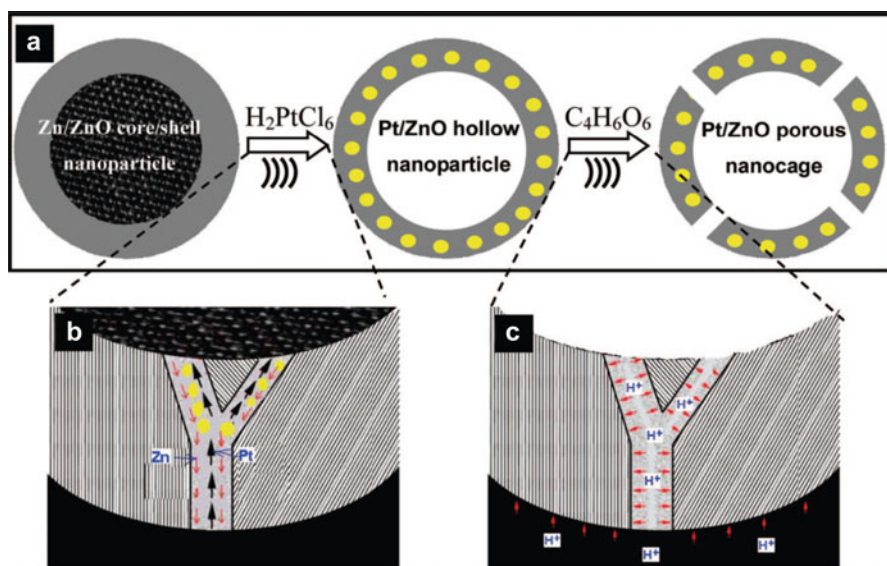
Fig. 5 Illustration of the formation mechanism of Pt/ZnO nanocages: (**a**) total process description, (**b**) H$_2$PtCl$_6$ etching-induced diffusion-redox-deposition process, and (**c**) tartaric acids (C$_4$H$_6$O$_6$) etching-induced nanoshell opening Reprinted with permission from [42]. Copyright (2008) American Chemical Society

et al. reported the fabrication of Pt/ZnO porous nanocages with good MO photodegradation activity by the two-step weak acid etching process under ultrasonic irradiation [42]. As shown in Fig. 5b, at first, Zn core of the Zn/ZnO core-shell nanoparticle colloids is oxidized by H$_2$PtCl$_6$ under sonication (Eq. 2). Simultaneously, the hollowing of Zn core and the in situ deposition of Pt nanoparticles occurred. Subsequently, as shown in Fig. 5c, ZnO shell is etching by H$^+$ from tartaric acid to form porous structures under sonication (Eq. 3). Finally, ultrafine Pt

nanoparticles were embedded on ultrathin porous ZnO shell layers to get the Pt/ZnO porous nanocages:

$$2Zn \; + \; Pt^{4+} \; = \; 2Zn^{2+} + \; Pt^0 \tag{2}$$

$$ZnO \; + \; 2H^+ \; = \; Zn^{2+} + \; H_2O \tag{3}$$
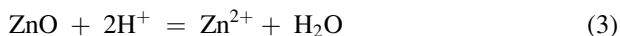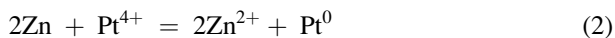
The ultrasonic irradiation provides the strong driving force and dispersing function for the redox reaction and etching. Also, the size of the Pt nanoparticles can be controlled by ultrasound power. Chen et al. synthesized Ag/AgCl nanocrystals by a one-step sonochemical approach using ethylene glycol (EG) as a solvent [43]. In the synthesis process, AgCl nanoparticles assembled into AgCl nanocubes and Ag^+ species in a surface of AgCl nanoparticles were reduced to Ag^0 by reducing radicals generated through sonolysis of EG under ultrasonic irradiation. Moreover, the Ag/AgCl nanocrystals exhibited excellent photocatalytic activities for degradation of MO, RhB, and MB under visible light irradiation. It is worth mentioning that the whole synthesis process of Ag/AgCl nanocrystals does not involve the external heat treatment nor additional reducing agents. Therefore, this sonochemical synthesis is convenient and efficient strategy. This work provides a general sonochemical method for the preparation of Ag-based composite photocatalysts using polyol process. Anandan et al. prepared Au-TiO$_2$ nanoparticles by three different sonochemical procedures [44]. In the first procedure, previously sonochemically prepared Au nanoparticles were deposited onto P25 TiO$_2$ nanoparticles under stirring. In the second procedure, Au nanoparticles in situ were deposited on P25 TiO$_2$ nanoparticles under sonication. In the third procedure, Au and TiO$_2$ nanoparticles were simultaneously synthesized by ultrasound irradiation using HAuCl$_4$ and titanium tetraisopropoxide as precursors. Between the above Au-TiO$_2$ nanoparticles, the particle size of Au nanoparticles in the sample prepared by the third method is the smallest and most uniform.

In summary, synthesis condition, optical properties, and photocatalytic activity of abovementioned noble metal/semiconductor composite photocatalytic materials are listed in Table 8.

Sensitized Semiconductors

Phthalocyanine dyes and π-conjugated organic molecules show strong absorption of visible light. The sensitization of phthalocyanine dyes and π-conjugated organic molecules on the surface of semiconductors can be to expand the visible light response range of semiconductors, thereby improving photocatalytic activity. Wang et al. in situ synthesized copper (II) phthalocyanine tetrasulfonate (CuPcTs)-sensitized TiO$_2$ photocatalysts by ultrasonic irradiation using TiCl$_4$ as Ti source [45]. The sonication not only promoted the crystallization of TiO$_2$ and completed the dispersion of CuPcTs on TiO$_2$ nanoparticles. The CuPcTs-sensitized TiO$_2$ photocatalysts possessed obvious visible light absorption. The measurement of

Table 8 Photocatalytic properties of noble metal/semiconductor composite photocatalytic materials synthesized via sonication for removal of pollutants from wastewater

Materials	Synthesis condition	Optical properties	Light source	Pollutant	Photocatalytic activity	Reference
Ag–TiO$_2$ nanotube array	TiO$_2$ nanotube arrays in AgNO$_3$ solution Ultrasonic bath (40 kHz, 0.96 kWm^{-2}), 30 min UV light reduction	LSPR peaks at around 400–650 nm	200 W high pressure mercury lamp ($\lambda_{max} = 365$ nm)	MB	Apparent rate constant ~0.025 min^{-1}	[40]
Ag–PbMoO$_4$ composite	Pb(NO$_3$)$_2$ and H$_2$MoO$_4$ in water Ultrasonic bath (20 kHz, 1000 W), 2 h AgNO$_3$ in above solution Ultrasonic bath UV light reduction	LSPR peaks at around 400–650 nm	Solar simulator	Indigo carmine	Apparent rate constant ~0.0263 min^{-1}, mineralization of 17.1 % after 120 min	[41]
Pt/ZnO porous nanocages	H$_2$PtCl$_6$ in Zn/ZnO colloid solution Ultrasonic irradiation, 30 min Tartaric acid in above solution. Ultrasonic irradiation, 30 min	–	125 W ultraviolet lamp, center wavelength of 365 nm	MO	Degradation rate of ~100 % after 90 min	[42]
Ag/AgCl nanocubes	AgNO$_3$ and PVP in EG Stirred, 45 min NaCl in above solution Sonication (Ti horn of 3.2 mm in diameter, 230 V/500 W, 20 kHz, 35–40 % amplitude, 5 min)	LSPR peaks at around 400–650 nm	visible light ($\lambda \geq 400$ nm)	MO	Apparent rate constant 0.21 min^{-1}	[43]
				RhB	Apparent rate constant 0.14 min^{-1}	
				MB	Apparent rate constant 0.03 min^{-1}	

Table 8 (continued)

Materials	Synthesis condition	Optical properties	Light source	Pollutant	Photocatalytic activity	Reference
Au-TiO$_2$ nanoparticles	HAuCl$_4$ •3H$_2$O and PVP in 1-propanol under nitrogen atmosphere Sonication (horn sonifier, 20 kHz, 80 W) P25 TiO$_2$ and the above solution containing Au nanoparticles Stirred, 66 h Calcination, 450 °C, 4 h	LSPR peaks at around 545–570 nm	150 W Xenon lamp, intensity of incident radiation 2.37 × 10^{-2} Einsteins m^{-1}	Polydisperse nonylphenol ethoxylate (Teric GN9) surfactant	Degradation rate constant 5.6 × 10^{-4} s^{-1}	[44]
	HAuCl4 •3H$_2$O, PVP and P25 TiO$_2$ in 1-propanol under nitrogen atmosphere Sonication (horn sonifier, 20 kHz, 120 W) Calcination, 450 °C, 4 h				Degradation rate constant 5.3 × 10^{-4} s^{-1}	
	HAuCl$_4$ •3H$_2$O, PVP, titanium tetraisopropoxide in isopropanol, and acidified water under nitrogen atmosphere Sonication (horn sonifier, 20 kHz, 160 W) Calcination, 450 °C, 4 h				Degradation rate constant 1.1 × 10^{-4} s^{-1}	

photodecomposition of MO indicated that photocatalytic activity of CuPcTs-TiO$_2$ is much more than that of CuPcTs or pure TiO$_2$ under visible light irradiation. Besides, sensitized semiconductor photocatalysts can be obtained easily by ultrasonic-assisted adsorption method of a mixed solution of semiconductor nanoparticles and sensitizers. Jiang et al. reported the synthesis of 7,7,8,8-tetracyanoquinodimethane (TCNQ)-sensitized TiO$_2$ photocatalysts with core-shell structure using the above strategy [46]. The TCNQ@TiO$_2$ photocatalysts exhibited visible light-induced photocatalytic activity of degradation of phenol.

In summary, synthesis condition, optical properties, and photocatalytic activity of abovementioned sensitized semiconductor photocatalytic materials are listed in Table 9.

Semiconductor/Support Materials

The support materials such as zeolites, clays, silica, alumina and activated carbon, etc. are also often used to build composite photocatalysts. The support materials do not exhibit photocatalytic activity; however, its presence can markedly enhance photocatalytic activity of composite photocatalysts due to the improvement of dispersion and stability for photoactive composition. For example, Liu et al. prepared SiO$_2$/TiO$_2$ composite photocatalysts using tetraethyl orthosilicate and tetrabutyl orthotitanate as precursors under ultrasonic treatment and subsequent calcination [47]. Embedding amorphous SiO$_2$ into TiO$_2$ matrix can suppress the increase of diameter of TiO$_2$ nanoparticles during calcination. The photocatalytic activity of the SiO$_2$/TiO$_2$ composite photocatalysts prepared with ultrasound obviously is higher than that of the counterparts prepared without ultrasound for the oxidation of formaldehyde in air under UV light irradiation (Fig. 6). The enhancement of the photocatalytic activity is attributed to improvement of ultrasonic irradiation for the hydrolysis of titanium and silicon alkoxide and the crystallization of the gel. Although the above example exhibited only high activity of SiO$_2$/TiO$_2$ composite photocatalysts prepared with ultrasound for photocatalytic decomposition of gas-phase pollutants, the results also suggested that sonication can play a positive role for preparation of other composite photocatalysts in photocatalytic removal of wastewater.

Hierarchical biological materials are ideal matrix supports for the fabrication of composite photocatalysts. The developed pore structure of hierarchical biological materials can provide a large number of accessible active sites for photocatalytic reactions. As a typical example, Mao et al. reported the preparation of mesoporous TiO$_2$/macroporous diatom frustule composite photocatalysts by sonochemical condensation of TiCl$_4$ and then calcination [48]. The TiO$_2$/diatom frustule composite photocatalysts showed high photocatalytic activity for degradation of MB under UV light irradiation due to hierarchical macro-/mesoporous structure. The unique pore structure facilitated efficiently the transports of MB molecules in the composite photocatalysts.

Table 9 Photocatalytic properties of sensitized semiconductors photocatalytic materials synthesized via sonication for removal of pollutants from wastewater

Materials	Synthesis condition	Optical properties	Light source	Pollutant	Photocatalytic activity	Reference
CuPcTs-sensitized TiO_2	$TiCl_4$, triethanolamine, and CuPcTs in ethanol and water Sonication (high-intensity ultrasonic probe, 1 cm diameter Ti horn, 20 kHz, 100 W/cm^2), 2 h	Absorption bands in the wavelengths of 600–700 nm	420 W halogen lamp with filter ($\lambda > 450$ nm)	MO	Degradation rate of ~80 % after 60 min	[45]
TCNQ@TiO_2	TCNQ and P25 TiO_2 in tetrahydrofuran and ethanol Ultrasonic bath, 1 h	Absorption edge at 455 nm, absorption peaks at 600 and 850 nm	500 W xenon lamp with 450 nm optical filters, average light intensity 23.6 mW/cm^2	Phenol	Apparent rate constant 0.2583 h^{-1}	[46]
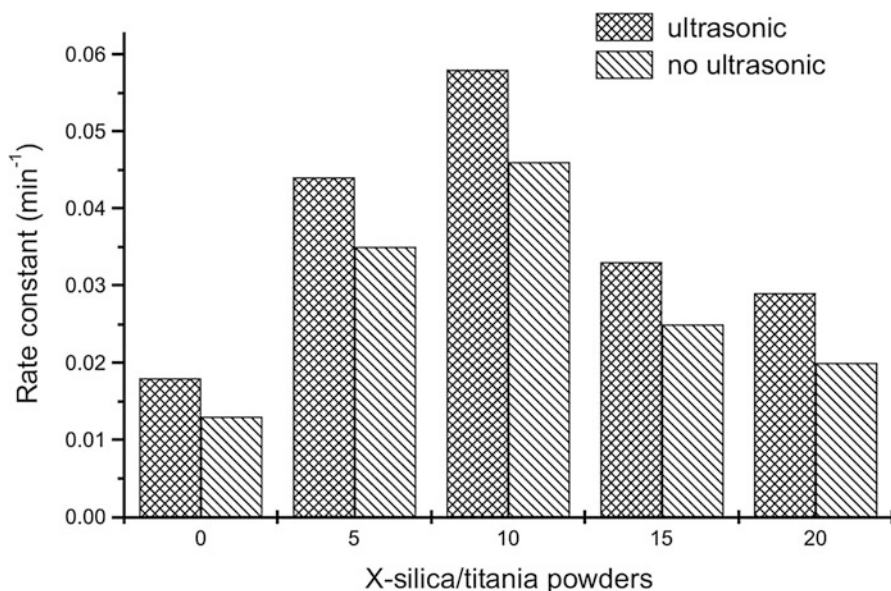
Fig. 6 The effect of ultrasonic irradiation on photocatalytic activity of the SiO_2/TiO_2 composite photocatalysts. Reprinted from [47], Copyright (2004), with permission from Elsevier

Magnetic Composite Photocatalysts

To overcome the difficulty in separating the powder photocatalysts from the aqueous solution, the fabrication of magnetically separating composite photocatalysts is an effective way in wastewater treatment. For example, Zhang et al. presented a method for preparing the MnO_2/Fe_3O_4 composite photocatalysts with a ferromagnetic nature by a mild ultrasonic means [49]. The composite photocatalysts composed of thin-layer MnO_2 nanosheets and Fe_3O_4 nanoparticles exhibited excellent photocatalytic activity and magnetically separating characteristic for the degradation of MB under UV-Vis light irradiation. More importantly, the MnO_2/Fe_3O_4 composite photocatalysts possessed a good acid resistance and stable recyclability during the photocatalytic process. Álvarez et al. prepared the $TiO_2/SiO_2/Fe_3O_4$ magnetically separated composite nanoparticles through an ultrasonic-assisted sol-gel route using commercial Fe_3O_4 nanoparticles as a support [50]. The results showed that the $TiO_2/SiO_2/Fe_3O_4$ composite photocatalysts have good photocatalytic activities for the degradation of acetaminophen (Ac) as well as the mixture of Ac, bisphenol A (BPA), metoprolol (Met), antipyrine (Ant), and caffeine (Caff) under UV irradiation. Moreover, the SiO_2 layers wrapped on Fe_3O_4 core improved the stability of the $TiO_2/SiO_2/Fe_3O_4$ composite photocatalysts owing to avoid photocorrosion of Fe_3O_4.

At last, synthesis condition, physicochemical properties, and photocatalytic properties of abovementioned semiconductor/support and magnetic composite photocatalytic materials are summarized in Table 10.

Table 10 Photocatalytic properties of semiconductor/support and magnetic composite photocatalytic materials synthesized via sonication for removal of pollutants from wastewater

Semiconductor	Support materials	Synthesis condition	Textural properties	Light source	Pollutant	Photocatalytic activity	Reference
TiO_2	SiO_2	Tetraethyl orthosilicate and tetrabutyl orthotitanate in water Ultrasonic cleaning bath (50 kHz, 80 W), 2 h Calcination, 500 °C, 1 h	$S_{BET} = 362 \ m^2 \ g^{-1}$, $d_p = 2.9$ nm, $V_p = 0.228 \ mL \ g^{-1}$	9 W 365 nm UV lamp	Formaldehyde	Rate constant 0.058 h^{-1}	[47]
TiO_2	Diatom	$TiCl_4$, Pluronic F127, CTAB, and diatom in water and ethanol Sonication (high-intensity ultrasonic probe, 20 kHz, 100 W/cm^2), 12 h Calcination, 550 °C, 5 h	$S_{BET} = 31.5 \ m^2 \ g^{-1}$	Four UV lamps (6 W each)	MB	Apparent rate constant 0.02415 min^{-1}	[48]
MnO_2	Fe_3O_4	Fe_3O_4 nanoparticles, 2-(N-morpholino) ethanesulfonic acid, and $KMnO_4$ in	–	250 W high pressure mercury lamp (wavelength range of 350–450 nm)	MB	Degradation rate of 98.2 % after 3 h	[49]

TiO$_2$	water Sonication, 40 min					
SiO$_2$/Fe$_3$O$_4$	Fe$_3$O$_4$ nanoparticle, NH$_4$OH, and ethanolic tetraethyl orthosilicate in isopropanol and water Ultrasonic bath, 3 h Titanium isopropoxide and above SiO$_2$/Fe$_3$O$_4$ in isopropanol and water Ultrasonic bath, 3 h Calcination, 400 °C, 1 h	$S_{BET} = 22$ m^2 g^{-1}	Low-pressure mercury lamp that emitted 254 nm radiation	Ac	Apparent rate constant $(9.79 \pm 0.21) \times 10^{-3}$ min^{-1}	[50]
				Mixture of Ac, BPA, Met, Ant, and Caff	Apparent rate constant Ac: $(7.44 \pm 0.20) \times 10^{-3}$ min^{-1} BPA: $(15.09 \pm 0.24) \times 10^{-3}$ min^{-1} Met: $(13.21 \pm 0.40) \times 10^{-3}$ min^{-1} Ant: $(9.97 \pm 0.16) \times 10^{-3}$ min^{-1} Caff: $(10.89 \pm 0.20) \times 10^{-3}$ min^{-1}	

Conclusions and Future Directions

In summary, ultrasound-assisted synthesis is a promising technology for the fabrication of nanomaterials. The local high temperature, pressure, and rapid cooling rates have contributed to the growth and assembly of nanomaterials under ultrasound conditions. Nanomaterials prepared by ultrasonication typically have excellent photocatalytic activity due to high crystallinity and dispersion. The rapid developments of ultrasonic synthesis have provided a good opportunity to design novel nanomaterials with high activity for photocatalytic removal of wastewater. In the paper, the recent research on ultrasonic synthesis of photocatalytic nanomaterials including single semiconductor, doped semiconductor, compound semiconductor (heterostructures and composites) roundly was summarized.

Although the evident progress has been achieved, ultrasound synthesis of photocatalytic nanomaterials still faces many challenges. Further work may be focused on the following points:

Firstly, the morphology, dimensions, and assembly of nanomaterials significantly affect their photocatalytic activity. Design and preparation of photocatalytic nanomaterials with a specific structure are a hot research area. However, the most reports of ultrasound synthesis of photocatalytic nanomaterials relate to the synthesis of nanoparticles and nanospheres; ultrasound synthesis of other nanostructures relatively is lacking. The researches on the synthesis of one-dimensional, two-dimensional, and high-energy crystal facets exposed photocatalytic nanomaterials are required under ultrasound conductions.

Secondly, current researches mostly focus on the effect of ultrasound on nucleation and growth of photocatalytic nanomaterials. In fact, the influence of ultrasound on structures and characteristics of photocatalytic nanomaterials is necessary to further exploration and improvement of photocatalytic activity for removal of wastewater. The roles of ultrasonic synthesis on the modulation of surface defects and interfacial properties of photocatalytic nanomaterials may be a notable research aspect.

Thirdly, as a promising new generation of photocatalysts, composite photocatalytic nanomaterials have been received extensive attention. However, compared with photocatalytic nanomaterials with single component, the understanding on the ultrasonic synthesis of composite photocatalytic nanomaterials is still preliminary. Thus, it is necessary to explore one-step synthesis, in situ load and multicomponent interaction of composite photocatalytic nanomaterials under ultrasound conditions.

In conclusion, ultrasonic technology brings new opportunities for the preparation of photocatalytic nanomaterials. Novel photocatalytic nanomaterials will play an important role in the field of energy and the environment. Meanwhile, the ultrasonic synthesis of photocatalytic nanomaterials is also full of challenges in practical application. Many interesting phenomena are waiting to be explored.

References

1. Han F, Kambala VSR, Srinivasan M, Rajarathnam D, Naidu R (2009) Appl Catal A 359:25
2. Colmenares JC (2014) ChemSusChem 7:1512
3. Yu JC, Yu JG, Ho WK, Zhang LZ (2001) Chem Commun 1942–1943
4. Colmenaresa JC, Aramendia MA, Marinas A, Marinas JM, Urbano FJ (2010) J Mol Catal A 331:58
5. Neppolian B, Wang Q, Jung H, Choi H (2008) Ultrason Sonochem 15:649
6. Latt KK, Kobayashi T (2008) Ultrason Sonochem 15:484
7. Yu JG, Zhou MH, Cheng B, Yu HG, Zhao XJ (2005) J Mol Catal A 227:75
8. Osorio-Vargas PA, Pulgarin C, Sienkiewicz A, Pizzio LR, Blanco MN, Torres-Palma RA, Pétrier C, Rengifo-Herrera JA (2012) Ultrason Sonochem 19:383
9. Lai YL, Meng M, Yu YF, Wang XT, Ding T (2011) Appl Catal B 105:335
10. Vázquez-Cuchillo O, Manzo-Robledo A, Zanella R, Elizondo-Villareal N, Cruz-López A (2013) Ultrason Sonochem 20:498
11. Nagarajan R, Tomar N (2009) J Solid State Chem 182:1283
12. Dunkle SS, Helmich RJ, Suslick KS (2009) J Phys Chem C 113:11980
13. Mann AKP, Skrabalak SE (2011) Chem Mater 23:1017
14. Wu Q, Ouyang JJ, Xie KP, Sun L, Wang MY, Lin CJ (2012) J Hazard Mater 199–200:410
15. Colmenares JC, Magdziarz A, Kurzydlowski K, Grzonka J, Chernyayeva O, Lisovytskiy D (2013) Appl Catal B 134–135:136
16. Wang XK, Wang C, Guo WL, Wang JG (2011) Mater Res Bull 46:2041
17. Bang JH, Helmich RJ, Suslick KS (2008) Adv Mater 20:2599
18. Cheng XW, Yu XJ, Xing ZP (2012) J Colloid Interface Sci 372:1
19. Khan H, Berk D (2014) J Photochem Photobiol A 294:96
20. Xue B, Sun T, Wu JK, Mao F, Yang W (2015) Ultrason Sonochem 22:1
21. Ghows N, Entezari MH (2011) Ultrason Sonochem 18:629
22. Xie Y, Ali G, Yoo SH, Cho SO (2010) ACS Appl Mater Interfaces 2:2910
23. Li CH, Ming T, Wang JX, Wang JF, Yu JC, Yu SH (2014) J Catal 310:84
24. Chen DM, Wang KW, Xiang DG, Zong RL, Yao WQ, Zhu YF (2014) Appl Catal B 147:554
25. Kumar S, Baruah A, Tonda S, Kumar B, Shanker V, Sreedhar B (2014) Nanoscale 6:4830
26. Zhang ZY, Huang JD, Zhang MY, Yuan Q, Dong B (2015) Appl Catal B 163:298
27. Lu ML, Pei ZX, Weng SX, Feng WH, Fang ZB, Zheng ZY, Huang ML, Liu P (2014) Phys Chem Chem Phys 16:21280
28. Neppolian B, Kim Y, Ashokkumar M, Yamashita H, Choi H (2010) J Hazard Mater 182:557
29. Xu F, Yuan YF, Han HJ, Wu DP, Gao ZY, Jiang K (2012) Cryst Eng Comm 14:3615
30. Li HQ, Hong WS, Cui YM, Hu XY, Fan SH, Zhu LJ (2014) Mater Sci Eng B 181:1
31. Yu CL, Yang K, Yu JC, Cao FF, Li X, Zhou XC (2011) J Alloys Compd 509:4547
32. Thomas RT, Rasheed PA, Sandhyarani N (2014) J Colloid Interface Sci 428:214
33. Morales-Torres S, Pastrana-Martínez LM, Figueiredo JL, Faria JL, Silva AMT (2013) Appl Surf Sci 275:361
34. Zhuo SJ, Shao MW, Lee ST (2012) ACS Nano 6:1059
35. Guo JJ, Zhu SM, Chen ZX, Li Y, Yu ZY, Liu QL, Li JB, Feng CL, Zhang D (2011) Ultrason Sonochem 18:1082
36. Dong SY, Hu LM, Feng JL, Pi YQ, Li QL, Li YK, Liu ML, Sun JY, Sun JH (2014) RSC Adv 4:64994
37. Golsheikh AM, Lim HN, Zakariad R, Huang NM (2015) RSC Adv 5:12726
38. Shi HX, Chen JY, Li GY, Nie X, Zhao HJ, Wong PK, An TC (2013) ACS Appl Mater Interfaces 5:6959
39. Zhai WY, Li GP, Yu P, Yang LF, Mao LQ (2013) J Phys Chem C 117:15183

40. Sun L, Li J, Wang CL, Li SF, Lai YK, Chen HB, Lin CJ (2009) J Hazard Mater 171:1045
41. Gyawali G, Adhikari R, Joshi B, Kim TH, Rodríguez-González V, Lee SW (2013) J Hazard Mater 263P:45
42. Zeng HB, Liu PS, Cai WP, Yang SK, Xu XX (2008) J Phys Chem C 112:19620
43. Chen DL, Yoo SH, Huang QS, Ali G, Cho SO (2012) Chem Eur J 18:5192
44. Anandan S, Ashokkumar M (2009) Ultrason Sonochem 16:316
45. Wang ZY, Mao WP, Chen HF, Zhang FA, Fan XP, Qian GD (2006) Catal Comm 7:518
46. Jiang WJ, Zhang M, Wang J, Liu YF, Zhu YF (2014) Appl Catal B 160–161:44
47. Liu ZY, Quan X, Fu HB, Li XY, Yang K (2004) Appl Catal B 52:33
48. Mao L, Liu J, Zhu SM, Zhang D, Chen ZX, Chen CX (2014) Ultrason Sonochem 21:527
49. Zhang LS, Lian JS, Wu LY, Duan ZR, Jiang J, Zhao LJ (2014) Langmuir 30:7006
50. Álvarez PM, Jaramillo J, López-Piñero F, Plucinski PK (2010) Appl Catal B 100:338

Part III

Environmental Remediation

Mathematical Models for Sonochemical Effects Induced by Hydrodynamic Cavitation

Vijayanand S. Moholkar

Contents

Abstract

Hydrodynamic cavitation has emerged as a potential alternative for acoustic cavitation. Extensive research in past two decades has demonstrated the efficacy of hydrodynamic cavitation for enhancement of numerous physical/chemical processes. Proper design and scale-up of the hydrodynamic cavitation reactors require deep mechanistic insight into the physics/chemistry of radial motion of cavitation bubble (or cavitation bubble dynamics) that leads to generation of the sonochemical effects. Development of mathematical models for bubble dynamics in hydrodynamic cavitation is therefore a crucially important component of efficient design of hydrodynamic cavitation reactors. In this chapter, a review

V.S. Moholkar (✉)
Department of Chemical Engineering and Center for Energy, Indian Institute of Technology Guwahati, Guwahati, Assam, India
e-mail: vmoholkar@iitg.ernet.in

of the developments of mathematical models for the hydrodynamic cavitation by our research group has been given. This chapter essentially presents a summary of five major studies published by our group, in which models for radial motion of cavitation bubbles in hydrodynamic cavitation were developed with successive incorporation of various physical aspects such as liquid compressibility, turbulent pressure fluctuations, bubble/bubble and bubble/flow interactions, and heat and mass transfer across bubble interface. Simulations of hydrodynamic cavitation carried out with these models have indicated relative influences of different design and process parameters on the radial motion of the bubbles. These models have helped in the identification of the conditions under which the radial motion in hydrodynamic cavitation resembles the one observed in acoustic cavitation. The major factor governing production of sonochemical effect by cavitation bubbles is pressure recovery profile, which in turn is influenced by three design and process parameters, viz., recovery (or discharge) pressure, permanent pressure head loss, and cavitation number. The simulations of hydrodynamic cavitation have also provided suitable guidelines for design, optimization, and scale-up of the hydrodynamic cavitation reactors for applications in different physical/chemical processes. This chapter is expected to be a useful source of collective information and critical analysis of the mathematical models for hydrodynamic cavitation to the research community in the field of hydrodynamic cavitation.

Keywords

Cavitation • Sonochemistry • Continuum mixture model • Turbulence modeling • Bubble Dynamics • Navier-Stokes equation • Rayleigh-Plesset equation

Introduction

To achieve physical or chemical change in a process essentially requires introduction of energy in the system. In addition to the quantity of the energy input to the system, the method of introduction of energy is also a critical factor that influences the overall efficiency of the process, i.e., extent of physical/chemical change achieved per unit energy input. The past two decades have witnessed development of several new technologies for safer, easier, and efficient means of energy introduction in the system. Cavitation technology is one such technology in which energy required for the physical/chemical transformation is introduced through cavitation phenomenon. The phenomenon of cavitation essentially refers to nucleation, growth, and implosive transient collapse of tiny gas–vapor bubble driven by variation in the bulk pressure in the medium. Variation of bulk pressure in the liquid medium required for occurrence of transient cavitation could be achieved by various means such as passage of an ultrasound wave in the form of compression/rarefaction cycles or change in the velocity of liquid due to change in the flow geometry. Cavitation generated by the acoustic or ultrasound wave is called acoustic cavitation, while

cavitation generated by changing flow geometry is called hydrodynamic cavitation. The most peculiar feature of cavitation technology that distinguishes it from other technologies is that transient collapse of cavitation bubbles creates intense energy concentration on an extremely small time and spatial scale, as explained in greater detail in subsequent section.

Occurrence of cavitation requires presence of nuclei in the medium. These nuclei could be small microbubbles already present in the medium or they could also be the gas pockets trapped in the crevices of the solid boundaries in the medium. These nuclei essentially grow into cavitation bubbles with fall of bulk pressure in the medium. Ultrasound passes through the medium in the form of compression/rarefaction cycles. The cavitation nuclei expand in the rarefaction half cycle and compress in the compression half cycle. If the pressure amplitude of the ultrasound wave is sufficiently high (typically greater than the static pressure in the medium), the expansion of the bubble in rarefaction half cycle is large – more than double of its initial size. In such situation, the bubble undergoes a transient collapse, which essentially is a fact and adiabatic compression to less than 1/10th of original size. During this adiabatic collapse, the temperature and pressure in the bubble reaches extreme, of the order of 5000 K and 500 bar, respectively. Ultrasound irradiation or sonication has been the conventional means of generating cavitation. Hydrodynamic cavitation is generated in flowing liquid due to variation in bulk pressure as a result of velocity variation in the flow induced by changing geometry of the conduit. For example, in the simplest case, hydrodynamic cavitation can be generated by throttling discharge of a pump through an orifice or venturi. As the pressure in the liquid flow falls downstream of the orifice plate or the throat of the venturi, the dissolved gas in the liquid gets released in the form of bubbles. If the fall of pressure in the downstream region of the conduit is sufficient, typically close to vapor pressure of the liquid at the bulk temperature, partial vaporization of liquid may also occur leading to formation of vapor bubbles. These gas or vapor bubbles subsequently oscillate and collapse with recovery of pressure in the liquid flow in the downstream region.

The nature of the radial motion of the cavitation bubble is influenced by the nature or profile of variation in bulk pressure. In acoustic cavitation, the variation in bulk pressure is of sinusoidal nature around the mean or ambient pressure. In hydrodynamic cavitation, the pressure variation is mostly of linear nature with fluctuations due to turbulence in the flow superimposed over the mean pressure. Since both types of cavitation have their origin in the characteristic radial motion of the bubble, theory of bubble dynamics can be applied for the analysis by proper choice of the mathematical term describing the time variation of bulk pressure in the liquid medium, which drives the radial bubble motion.

In last one decade, large amount of literature has been published on intensification of diverse physical and chemical processes with application of hydrodynamic cavitation. These processes include degradation of dyes [1–4], hydrolysis of oils [5–7], degradation of recalcitrant pollutants and wastewater treatment [8–14], enhancement of anaerobic digestion [15, 16], nanosynthesis [17–21], potable

water disinfection [22, 23], and microbial cell disruption [24–27]. State-of-the-art reviews by Gogate [28, 29] and Gogate and Pandit [30, 31] have given critical analysis of literature on hydrodynamic cavitation. Modeling of cavitation bubble dynamics in hydrodynamic cavitation has also been an active research area. These models form basis for optimization of the hydrodynamic cavitation process for large-scale applications. Several authors have also addressed issues of modeling and optimization of hydrodynamic cavitation [32–48].

The purpose of this chapter is to present a sequential and coherent depiction of various mathematical models of hydrodynamic cavitation developed by our group in past one decade along with the analysis. These models are essentially aimed at providing explanation to the "sonochemical and sonophysical effect" generated by hydrodynamic cavitation. The sonochemical effect is production of radical species through transient collapse of cavitation bubbles. These species are responsible for inducing chemical reactions in the medium such as degradation/oxidation of recalcitrant pollutants [49–56] or polymerization [57, 58] or synthesis of nanoparticles [59–62]. The sonophysical effect is generation of intense turbulence and shock waves due to transient motion of cavitation bubbles. This effect is manifested in terms of disruption of microbial cells, mass transfer enhancement or intense mixing, and generation of nanoemulsions [63–69]. We believe that this chapter will be a single and distinct source of information on the mathematical models of hydrodynamic cavitation.

Cavitation Bubble Dynamics and Pressure Recovery Profiles in Hydrodynamic Cavitation

Cavitation number: The phenomenon of hydrodynamic cavitation is characterized by a dimensionless parameter called *cavitation number*, which is defined as [70]:

$$C_i = \frac{P_2 - P_v}{\rho_L U_o^2 / 2} \tag{1}$$

Various notations are as follows: P_2 = recovery pressure (in the downstream region), P_v = vapor pressure of the liquid at temperature of operation, ρ_L = density of the liquid, and U_o = average velocity near the constriction in the downstream region (or the velocity at *vena contracta* in case of an orifice or the velocity at the throat of venturi or converging–diverging nozzle). It can be easily perceived from Eq. 1 that the pressure downstream of the orifice will fall at the vapor pressure of the liquid for $C_i = 1$. This will ensure generation of the vaporous cavitation bubbles in the liquid even if the liquid is devoid of any dissolved gas. This is cavitation inception number.

The characteristics of cavitation number are as follows [71]: (1) it is independent of the velocity in the pipe and shows dependence on the constriction sizes in the same pipe, (2) it increases linearly with the diameter ratio of orifice to pipe,

and (3) cavitation inception occurs at $C_i = 1$–2.5 depending on the size of the constriction and severity of the cavitation increases with a decrease in cavitation number.

Cavitation bubble dynamics: Cavitation essentially involves generation, oscillations, and transient collapse of small gas or vapor bubbles due to pressure variation or, in general, energy dissipation in the system. In the context of hydrodynamic cavitation, the pressure variation in the bulk flow is generated due to variation in the velocity of the flow induced due to changing flow geometry. In the simplest case, hydrodynamic cavitation can be generated by throttling the discharge of a pump through constriction such as venturi or orifice. As the bulk pressure in the flow falls in the downstream region of the constriction with concurrent rise in velocity, dissolved gas in the liquid can desorb, leading to formation of small bubbles. If the pressure in the flow falls to the vapor pressure of the liquid, as indicated by $C_i = 1$, vaporous cavitation occurs.

Radial motion of cavitation bubbles: The cavitation bubbles generated at vena contracta or throat of the venturi or converging–diverging nozzle flow along with the liquid in the downstream region and undergo oscillation as the bulk pressure recovers with reduction in velocity. The nature of the oscillations of the cavitation bubbles in hydrodynamic cavitation depends on the level of turbulence generated in the downstream region of the constriction through which the flow passes. The turbulence is generated due to the separation of the flow from the wall of the conduit, which results in pressure loss. The higher the pressure loss, the larger the magnitude of turbulence due to which the bulk pressure undergoes fluctuation. As explained in greater detail in the next sections, the pressure profile in hydrodynamic cavitation comprises of the mean pressure with turbulent pressure fluctuations superimposed over it. For flow geometries such as orifice plate, which involve large permanent loss in pressure head of the liquid, the level of turbulence is high. This makes the cavitation bubbles grow to large size (at least five to ten times original size) and the ensuing collapse is of transient nature, which generates high temperature and pressure peaks inside the bubble, $\sim$3,000 K and 100 bar, as in case of transient cavitation driven by ultrasound.

In case of flow geometries involving low pressure head loss, such as in venturi or converging–diverging nozzle, the level of turbulence is low. In this case, the bubble motion is essentially governed by the mean pressure in the flow, which undergoes a monotonous rise. Due to continuously increasing bulk pressure, the cavitation bubble does not undergo expansion. Instead, the bubble shows an oscillatory motion with sequence of several compressions and rebounces. The bubble motion is less energetic compared to that in orifice flow. However, the numerous oscillations of the bubbles give rise to pressure pulses of moderate magnitude (in the range of 2–20 bar), which are sufficient in accelerating reactions.

Before proceeding to discussion of different approaches to determine the pressure profile in hydrodynamic cavitation, we give below a brief discussion on various models of cavitation bubble dynamics. These models have been mostly developed for acoustic or hydrodynamic cavitation, but can well be applied for modeling of radial motion of cavitation bubbles in hydrodynamic cavitation.

The history of mathematical modeling of cavitation bubble dynamics dates back to 1917 when Lord Rayleigh [72] presented the first-ever analysis of an empty cavity collapsing under constant static pressure. This basic model was improved by several researchers in the later decades. Main developments in the model were incorporation of the physical properties of the liquid such as surface tension, vapor pressure, and viscosity of liquid. The effect of presence of non-condensable gas and solvent vapor inside the bubble was also accounted for. These developments resulted in a more rigorous model for cavitation bubble dynamics, which is named after its inventors as Rayleigh–Plesset–Noltingk–Neppiras–Poritsky (RPNNP) equation [73–75], written as follows:

$$R\frac{d^2R}{dt^2} + \frac{3}{2}\left(\frac{dR}{dt}\right)^2 = \frac{1}{\rho}\left[\left(P_o + \frac{2\sigma}{R_o} - P_v\right)\left(\frac{R_o}{R}\right)^{3\gamma} + P_v - \frac{2\sigma}{R} - \frac{4\mu}{R}\frac{dR}{dt} - (P_o + P(t))\right]$$

(2)

This model, however, did not account for the compressibility effect of liquid, which has major influence on radial motion of cavitation bubble during the final moments, when the bubble wall velocity reaches extreme and can even exceed the sonic velocity in the medium. The first model for cavitation bubble dynamics accounting for liquid compressibility effect (using Tait equation of state) was proposed by Gilmore [76], which was based on Kirkwood–Bethe hypothesis [77]. This hypothesis stated that for spherical waves with finite amplitude, the quantity $r\phi$ (r, radial coordinate; ϕ, velocity potential) propagates with a velocity equal to the sum of the velocity of the liquid and sonic velocity. Later years witnessed further developments in cavitation bubble dynamics, with most notable contributions from Keller and Kolodoner [78], Keller and Miksis [79], and Prosperetti and Lezzi [80]. Among several new equations for cavitation bubble dynamics, two primary equations, which have been extensively used in the literature of bubble dynamics and sonoluminescence, are:

1. Keller and Miksis equation [79, 81]:

$$\left(1 - \frac{\dot{R}}{c}\right)R\ddot{R} + \left(1 - \frac{3\dot{R}}{c}\right)\frac{3}{2}\dot{R}^2 = \frac{1}{\rho}\left(1 + \frac{\dot{R}}{c}\right)\left[p_g - P_o - P(t)\right] + \frac{\dot{R}}{\rho c}\frac{dp_g}{dt} - 4\nu\frac{\dot{R}}{R} - \frac{2\sigma}{\rho R}$$

(3)

2. Equation of Lofstedt et al. [82] and Barber et al. [83]:

$$R\ddot{R} + \frac{3}{2}\dot{R}^2 = \frac{1}{\rho}\left[p_g - P_o - P(t)\right] + \frac{\dot{R}}{\rho c}\frac{dp_g}{dt} - 4\nu\frac{\dot{R}}{R} - \frac{2\sigma}{\rho R}$$

(4)

Estimation of the sonochemical effect: The sonochemical effect essentially refers to induction/acceleration of a chemical reaction through energy concentration

created by transient cavitation. As noted earlier, the transient collapse of the cavitation bubble generates intense temperature and pressure peak in the bubble. At these conditions, the gas and vapor molecules present inside the bubble undergo thermal dissociation to produce numerous chemical species, some of which are radical species. These species can either diffuse out of the bubble or get released into the bulk liquid medium with collapse of the bubble and induce/accelerate chemical reactions. Transient radial motion of cavitation bubble also generates intense micro-convection in the medium, which are especially beneficial for the heterogeneous reaction systems (either liquid–liquid or liquid–solid). For the liquid–liquid systems, micro-convection leads to generation of fine emulsification in the reaction system, which enhances the interfacial area. For liquid–solid (or catalytic reaction systems), micro-convection can help desorption of the product species from catalyst surface (or cleaning of the catalyst surface), which helps in maintaining the activity of the catalyst during course of reaction. Micro-convection also causes dilution of the species that block the active catalyst sites and helps prevent catalyst poisoning.

Physical picture of sonochemical effect: The sonochemical effect or generation of radical species inside the bubble is mostly related to transport of solvent vapor across bubble interface during radial motion. Numerous authors have dealt with modeling of the vapor transport across bubble during radial motion with different approaches [84–93]. The general model for vapor transport and entrapment in the cavitation bubble, which relaxed all of the assumptions and limitations of the earlier models, was presented by Storey and Szeri [94]. Storey and Szeri [94] analysis revealed that water vapor transport in the bubble is a two-step process, i.e., diffusion to the bubble wall and condensation at the wall. During expansion of the bubble, evaporation of liquid occurs at the bubble interface, with diffusion of vapor molecules toward the core of the bubble. In the ensuing compression of the bubble, counter or reverse diffusion of the vapor molecules toward bubble interface occurs with condensation at the bubble wall. At the final moments of the bubble compression, the velocity of the bubble interface becomes extremely fast, and the vapor molecules present at or near the bubble core do not have sufficient time to diffuse toward bubble interface for condensation. Thus, in the final moments of bubble collapse, despite reduction in bubble volume, the composition of the bubble remains practically constant. Secondly, the "accommodation coefficient" (or the fraction of vapor molecules that stick to the bubble interface) at the bubble interface also becomes very low during final moment of bubble collapse. Hence, not all vapor molecules that have diffused toward the bubble interface stick to it for phase change (or condense). This gives rise to nonequilibrium phase change at the bubble interface, which also contributes toward "entrapment" of solvent vapor in the bubble.

The vapor transport across bubble interface is governed by the relative magnitudes of two time scales, viz., time scale of diffusion (t_{dif}) and time scale of condensation (t_{cond}) [95], with respect to the time scale of bubble dynamics, t_{osc}. In the initial phase of bubble collapse, the condition $t_{osc} \gg t_{diff}$, t_{cond} prevails, and the vapor molecules can diffuse toward the bubble interface to undergo equilibrium phase change at the bubble interface. At this stage, there is no concentration gradient of vapor inside the bubble, i.e., concentration of vapor molecules at the bubble

interface is essentially the same as that at bubble core. With acceleration of the bubble wall (or interface) during collapse, condition $t_{osc} \approx t_{dif}$ prevails and the rate of reduction of vapor molecules in the central region of the bubble is less than that at the bubble wall. In the final moments of bubble collapse, $t_{osc} \ll t_{diff}$ condition is reached, and the vapor molecules have insufficient time to diffuse to the bubble wall. This essentially results in fixed and uneven distribution of vapor molecules in the bubble. The vapor present inside the bubble at this stage gets essentially "trapped" in the bubble.

Storey and Szeri [94] have hypothesized that "trapping" vapor molecules inside the bubble is also contributed by the mechanism of nonequilibrium phase change at the bubble wall. In the final moments of bubble collapse, the bubble interface moves with very high velocity, and the condition $t_{osc} \ll t_{cond}$ (time scale of condensation) is reached. The condensation or phase change at the bubble wall becomes nonequilibrium in that not all vapor molecules that approach bubble wall undergo phase change (or condensation) and get trapped in the bubble. While determining the relative contribution of diffusion limitation or nonequilibrium phase change to the total vapor entrapment, Storey and Szeri [94] showed that during the radial bubble motion, condition $t_{osc} \ll t_{diff}$ is reached well before the condition of $t_{osc} \ll t_{cond}$. This essentially means that relative contribution to vapor entrapment from diffusion mechanism is more than the condensation mechanism, and vapor transport in the bubble is a diffusion-limited process. The temperature and pressure in the bubble reaches extreme at adiabatic collapse and the vapor and gas molecules present in the bubble undergo thermal dissociation generating several chemical species – some of which are radical species, which induce the sonochemical effect.

Formulation of diffusion-limited model: On the basis of principal outcome of Storey and Szeri's work [94, 96] that vapor transport and entrapment in the bubble was a diffusion-limited process, Toegel et al. [97] developed a new model for vapor transport comprising ordinary differential equations. This model, known as diffusion limited, uses boundary layer approximation and has been validated against the partial differential equation (PDE) model as well as reduced model of Storey and Szeri [94, 96]. The essential equations and thermodynamic data of the diffusion-limited ordinary differential equation (ODE) model are given in Table 1A, B [98]. The main components of this model are (1) Keller–Miksis equation for radical motion of cavitation bubbles, (2) equation for the diffusive flux of solvent vapor through the bubble wall, (3) equation for heat conduction across bubble wall, and (4) overall energy balance treating the cavitation bubble as an open system. The transport parameters for the heat and mass transfer are determined using Chapmen–Enskog theory with Lennard–Jones 12–6 potential at the bulk temperature of the liquid [99–101]. The thermal and diffusive penetration depths are estimated using dimensional analysis from the radial motion of cavitation bubbles assuming that the condensation of vapor molecules at bubble interface is fast enough to maintain equilibrium. A brief description of the dimensional analysis for estimation of the diffusive penetration depth is given below. Similar analysis also holds estimation of the thermal diffusion length.

Table 1 Diffusion Limited Bubble Dynamics Model

(A) Model equations

Variable	Equation	Initial value
1a. Radius of the bubble (R)	$$\left(1-\frac{dR/dt}{c}\right)R\frac{d^2R}{dt^2}+\frac{3}{2}\left(1-\frac{dR/dt}{3c}\right)\left(\frac{dR}{dt}\right)^2$$ $$=\frac{1}{\rho_L}\left(1+\frac{dR/dt}{c}\right)(P_i-P_t)+\frac{R}{\rho_L c}\frac{dP_i}{dt}-4\nu\frac{dR/dt}{R}-\frac{2\sigma}{\rho_L R}$$	$t=0$ $R=R_o$
1b. Bubble wall velocity (dR/dt)	Internal pressure in the bubble: $P_i = \frac{N_{\text{tot}}(t)kT}{\left[4\pi\left(R^3(t)-h^3\right)/3\right]}$	dR/dt $=0$
2. Number of solvent (water) molecules in the bubble (N_W)	$\frac{dN_W}{dt}=4\pi R^2 D_W\frac{\partial C_W}{\partial r}\big|_{r=R}\approx 4\pi R^2 D_W\left(\frac{C_{WR}-C_W}{l_{\text{diff}}}\right)$	$t=0$
	Instantaneous diffusive penetration depth: $l_{\text{diff}}=\min\left(\sqrt{RD_S/|dR/dt|},R/\pi\right)$	$N_W=0$
3. Heat transfer through bubble (Q)	$\frac{dQ}{dt}=4\pi R^2\lambda\frac{\partial T}{\partial r}\big|_{r=R}\approx 4\pi R^2\lambda\left(\frac{T_0-T}{l_{th}}\right)$	$t=0$
	Thermal diffusion length: $l_{th}=\min\left(\sqrt{R\kappa/|dR/dt|},R/\pi\right)$	$Q=0$
4. Temperature of the bubble (T)	$C_{V,\text{mix}}dT/dt=dQ/dt-P_i dV/dt+(h_W-U_W)dN_W/dt$	$t=0$
	Mixture heat capacity: $C_{V,\text{mix}}=\sum C_{V,i}N_i$	$T=T_o$
	Molecular properties of water:	
	Enthalpy: $h_W=(1+f_i/2)kT_o$	
	Internal energy: $U_W=N_W kT\left(3+\sum_{i=1}^{3}\frac{\theta_i/T}{\exp(\theta_i/T)-1}\right)$	
	Heat capacity of other species ($i=O_2/N_2/H_2O$): $C_{V,i}=N_i k\left(f_i/2+\sum\left((\theta_i/T)^2\exp(\theta_i/T)/(\exp(\theta_i/T)-1)^2\right)\right)$	

(B) Thermodynamic properties of gas and liquid species

Species	Degrees of freedom (translational + rotational) (f_i)	Lennard – Jones force constants		Characteristic vibrational temperatures θ (K)
		σ (10^{-10} m)	ε/k (K)	
N_2	5	3.68	92	3350
O_2	5	3.43	113	2273
H_2O	3	2.65	380	2295, 5255, 5400

Source: Refs. [99–101]

Notations: R radius of the bubble, dR/dt bubble wall velocity, c velocity of sound in bulk liquid medium, ρ_L density of the liquid, ν kinematic viscosity of liquid, σ surface tension of liquid, λ thermal conductivity of bubble contents, κ thermal diffusivity of bubble contents, θ characteristic vibrational temperature(s) of the species, N_W number of solvent molecules in the bubble, t time, D_W diffusion coefficient of solvent vapor, C_W concentration of solvent molecules in the bubble, C_{wR} concentration of solvent molecules at the bubble wall or gas–liquid interface, Q heat conducted across bubble wall, T temperature of the bubble contents, T_o ambient (or bulk liquid medium) temperature, k Boltzmann constant, N, number of molecules of any other species (oxygen/ nitrogen/ water) in the bubble, f_i translational and rotational degrees of freedom, $C_{V,i}$ heat capacity at constant volume, N_{tot} total number of molecules (gas + vapor) in the bubble, h van der Waal's hard core radius, P_o ambient (bulk) pressure in liquid

During radial motion, the surface temperature of the bubble exceeds bulk water temperature only for a period of $\sim$10 ns during final moments of collapse. With this observation, the total bubble volume can be divided into two parts: (i) a "cold" boundary layer in thermal equilibrium with liquid and (ii) a hot homogeneous core. An underlying assumption for this distinction is that equilibrium phase change at bubble interface (i.e., the condensation of water molecules at the bubble wall) is much faster than the time scale of bubble oscillations. The instantaneous diffusive penetration depth is given using dimensional analysis by $l_{\text{diff}} = \sqrt{D_{ij}t_{\text{osc}}}$, where D_{ij} is the binary diffusion coefficient and t_{osc} is the time scale of bubble oscillations given as $|dR/dt|/R$. The assumption of division of the bubble interior in two parts can be validated by analysis of the diffusive penetration depth during radial motion of the bubble. During growth phase and major part of compression, the $l_{\text{diff}} \geq R$ holds, which implies that the total bubble volume is in equilibrium with the liquid. During the final phase of compression, the bubble wall velocity becomes very high during which the condition $l_{\text{diff}} = 0.01\,R$ prevails. Thus, thickness of the boundary layer is negligible compared to the radius of the bubble, and hence the bubble can again be treated as a homogeneous core. Considering the major conclusion of Storey and Szeri [94, 96] that vapor transport in the bubble is always diffusion limited, and the other approximations stated above, the rate of change of water molecules in the bubble is given as:

$$\frac{dN_W}{dt} = 4\pi R^2 D_{ij} \frac{\partial C_W}{\partial r}\bigg|_{r=R} \approx 4\pi R^2 D_{ij} \left(\frac{C_{WR} - C_W}{l_{\text{diff}}} \right) \tag{5}$$

Notation: C_{WR} = equilibrium concentration of water molecules at the bubble wall, calculated using vapor pressure at the bulk temperature (T_o); C_W = actual concentration of water molecules in the bubble core.

Upper limit on diffusion length: The above analysis holds good for bubble in motion, where the bubble wall velocity, dR/dt, has a nonzero value. However, at the instances of maximum and minimum radius, the bubble wall velocity is zero, and we need an alternate expression for the diffusion length. For this purpose, we identify that for $dR/dt = 0$, the equation for vapor transport inside the bubble becomes a pure diffusion equation:

$$\frac{\partial C_W}{\partial t} = D_{ij} \left(\frac{\partial^2 C_W}{\partial r^2} + \frac{2}{r} \frac{\partial C_W}{\partial r} \right) \tag{6}$$

The boundary conditions for the above equation are (i) $r = 0$, $\partial C_W/\partial t = 0$ for $t \geq 0$; (ii) $r = R$, $C_W = C_{WR}$ for $t \geq 0$; and (iii) $C_W = C_{W0} = 0$ for $t = 0$ and $0 \leq r \leq R$. The analytical solution to the above problem is given by Crank [102]:

$$\frac{C_W - C_{W0}}{C_{WR} - C_{W0}} = 1 + \frac{2R}{\pi r} \sum_{n=1}^{\infty} \frac{(-1)^n}{n} \sin\left(\frac{nr}{R/\pi} \right) \exp\left(-\frac{n^2 D_{ij} t}{(R/\pi)^2} \right) \tag{7}$$

From the inspection of the above solution, the characteristic length for the diffusion is R/π, which is chosen as upper limit for diffusion length. Thus:

$$l_{\text{diff}} = \min\left(\sqrt{\frac{RD_{ij}}{|dR/dt|}}, \frac{R}{\pi}\right) \qquad (8)$$

For greater details on calculation of the diffusion coefficient and the effective thermal conductivity of the gas–vapor mixture inside the bubble, we refer the readers to our earlier papers [34, 35, 103]. Diffusion-limited model ignores the transport of non-condensable gas (or rectified diffusion) across the bubble during radial motion, as the time scale of gas diffusion is of order of milliseconds, while the time scale of bubble motion is of the order of microseconds. As a consequence of large difference in the two time scales, practically no diffusion of gas occurs across bubble interface during transient motion of cavitation bubbles [104].

For estimation of the sonochemical effect using diffusion-limited model of Toegel et al. [97], it is assumed that chemical equilibrium prevails in the cavitation bubble all throughout radial motion. This assumption is justified as follows: in transient motion, the collapse of the bubble occurs within few tens of nanoseconds ($\sim 10^{-8}$), as determined by Storey and Szeri [94, 96]. For a typical operational system in hydrodynamic cavitation (comprising argon bubbles and in water as the bulk liquid), as many as eight reactions are possible through thermal dissociation of water vapor entrapped in the bubble. The kinetic data (Arrhenius constants) for these reactions is given in Table 2A [105], while numerical values of specific rate constants calculated from Arrhenius equation at temperatures 1,000, 2,000, and 3,000 K (typical of those attained during the bubble collapse) are listed in Table 2B [105]. In addition, the concentrations of various species in the bubble at the moment of collapse are very high. An order of magnitude calculation done with representative numbers [$\sim 10^{10}$ molecules or 10^{-13} mol in a bubble with initial size 100 μm (or $\sim 10^{-4}$ m) compressed to 1/10th of its original size, i.e., $\sim 10^{-5}$ m] puts concentrations as ~ 100 mol/cm^3. As a conservative estimate, the time scale for the reaction (t_{react}) can be taken as ~ 1/specific reaction rate. Comparison of the time scale of bubble collapse (10^{-8} s) with the time scale of reactions listed in Table 2B reveals that the latter is at least two orders of magnitude smaller. Due to large difference in the time scales of the bubble motion and reaction kinetics, thermodynamic equilibrium should prevail till the point of minimum radius during collapse. The cavitation bubble attains extremely energetic and highly unstable state at the instance of maximum compression (or minimum radius) during radial motion and may undergo collapse. The word "*collapse*" essentially means fragmentation of the bubble [106, 107]. For all practical situations, fragmentation of cavitation bubble can occur at first compression during radial motion. The chemical composition of the cavitation bubble at collapse, i.e., equilibrium mole fractions of all species formed in the bubble through thermal dissociation of the gas and vapor molecules, can be determined using thermodynamic equilibrium approximation (Gibbs energy

Table 2 Rate constants for various radical reactions

(A) Parameters for Arrhenius equation for specific reaction rate

No.	Reaction	Forward reaction			Backward reaction		
		A	c	E_a/k	A	c	E_a/k
1.	$O + O + M \leftrightarrow O_2 + M$	1.2×10^{17}	-1	0	3.16×10^{19}	-1.3	59893
2.	$O + H + M \leftrightarrow OH + M$	5.0×10^{17}	-1	0	3.54×10^{17}	-0.9	51217
3.	$O + H_2 \leftrightarrow H + OH$	3.87×10^4	2.7	3150	1.79×10^4	2.7	2200
4.	$H + O_2 \leftrightarrow O + OH$	2.65×10^{16}	-0.7	8576	1.2×10^{17}	-0.3	-83
5.	$H + H + M \leftrightarrow H_2 + M$	1.0×10^{18}	-1	0	1.2×10^{17}	-0.8	52177
6.	$H + OH + M \leftrightarrow H_2O + M$	2.2×10^{22}	-2	0	1.2×10^{17}	-2	59980
7.	$OH + H_2 \leftrightarrow H + H_2O$	2.16×10^8	1.5	1726	1.2×10^{17}	1.3	9529
8.	$OH + OH \leftrightarrow O + H_2O$	3.57×10^4	2.4	1062	1.2×10^{17}	2.2	7693

(B) Numerical values of specific reaction rate at various temperatures

No.	Reaction	T = 1000 K		T = 2000 K		T = 3000 K	
		k_f	k_b	k_f	k_b	k_f	k_b
1.	$O + O + M \leftrightarrow O_2 + M$	1.2×10^{14}	3.88×10^{-11}	6.0×10^{13}	159.5	4.0×10^{13}	2.04×10^6
2.	$O + H + M \leftrightarrow OH + M$	5×10^{14}	4.03×10^{-8}	2.5×10^{14}	2.86×10^3	1.67×10^{14}	1.01×10^7
3.	$O + H_2 \leftrightarrow H + OH$	2.09×10^{11}	2.5×10^{11}	6.55×10^{12}	4.87×10^{12}	3.31×10^{13}	2.1×10^{13}
4.	$H + O_2 \leftrightarrow O + OH$	3.97×10^{10}	1.23×10^{13}	1.78×10^{12}	9.59×10^{12}	5.59×10^{12}	8.38×10^{12}
5.	$H + H + M \leftrightarrow H_2 + M$	1.0×10^{15}	6.5×10^{-8}	5.0×10^{14}	7.97×10^3	3.33×10^{14}	3.5×10^7
6.	$H + OH + M \leftrightarrow H_2O + M$	2.2×10^{16}	3.28×10^{-9}	5.5×10^{15}	8.67×10^3	2.44×10^{15}	8.46×10^7
7.	$OH + H_2 \leftrightarrow H + H_2O$	1.22×10^{12}	3.0×10^9	8.15×10^{12}	8.67×10^{11}	1.99×10^{13}	7.19×10^{12}
8.	$OH + OH \leftrightarrow O + H_2O$	1.64×10^{12}	1.52×10^{16}	5.08×10^{12}	1.49×10^{15}	1.13×10^{13}	1.01×10^{15}

Note: The above parameters correspond to the specific reaction rate constant equation $k_r = AT^c \exp(-E_a/kT)$. Units of A are either cm³ mol⁻¹ s⁻¹ (two species reaction) or cm⁶ mol⁻² s⁻¹ (three species reaction). E/k is the activation temperature in K. Data taken from Ref. [105]

minimization) at the peak temperature and pressure at collapse determined using diffusion-limited bubble dynamics model.

Modeling of the bulk pressure profile in hydrodynamic cavitation flow: As noted earlier, hydrodynamic cavitation can be generated by throttling of high pressure flow (e.g., discharge of a pump) through constrained geometries with varying flow areas such as venturi or orifice plate. The bulk pressure in the high Re number cavitating flow has two components: the mean flow velocity (U) and the turbulent fluctuating velocity ($\bar{u}'$). Thus, the instantaneous velocity in the flow downstream of the orifice is written as:

$$u = U + \bar{u}' \qquad (9)$$

The velocity of the mean flow at vena contracta (U_o) can be determined using the cavitation number defined earlier. After calculating U_o for an assumed value of C_i, the velocity in the pipe (u_p) is calculated from the orifice to pipe diameter ratio (β) as:

$$u_p = \beta^2 U_o \qquad (10)$$

The region of pressure recovery downstream of the orifice (L') extends to about eight to ten pipe diameters. Using the values of L', u_p, and U_o, the time of pressure recovery downstream of the orifice (t_{rec}) is calculated using Newton's equations.

Turbulence in the cavitating flow is essentially a manifestation of the energy dissipation in the flow (in the form of permanent pressure drop). Thus, the turbulent fluctuating velocity is of significance for flows with large pressure drop, such as the orifice flow. In case of venturi flows, the flow geometry shows gradual variation and the bulk flow separation does not occur – leading to relatively low pressure drop. On the other hand, the orifice flow involves sudden contraction and expansion – leading to separation of flow and large permanent pressure drop. In order to determine the second component of the instantaneous velocity, i.e., $\bar{u}'$, we use an algorithm based on the assumption that the rate at which large eddies supply energy to the smaller eddies is proportional to the reciprocal of the time scale of larger eddies [36, 108]. The amount of kinetic energy per unit mass is proportional to $\bar{u}'^2$ and the rate of energy transfer is assumed to be $\bar{u}'/l$, where l is the size of the largest eddies in the flow. The rate of energy supply is equal to the rate of energy dissipation and is given as $\approx \bar{u}'^2 \times \bar{u}'/l = \bar{u}'^3/l$. The main steps of the algorithm for determination of turbulent fluctuation velocity are:

1. The rate of turbulence energy dissipation per unit mass in the region of pressure recovery downstream of the orifice is estimated using the permanent pressure head loss in the flow and the volumetric flow rate. Moreover, we consider only axial velocity fluctuations in our calculations (neglecting radial and azimuthal fluctuations). This approximation is based on the measurements of the turbulent velocity field downstream an orifice by Morrison et al. [109], which shows that the axial variance (or mean square of axial velocity fluctuations) was much higher than the radial and azimuthal variance.

2. The length scale of the eddy is estimated using the Prandtl eddy model ($l = 0.08$ d_c), in which the conduit diameter d_c is taken as an average of orifice and pipe diameters.
3. The steady-state frequency of the turbulent fluctuating velocity, f_T, is obtained by multiplying the rate of energy transfer ($\bar{u}'/l$) by the time of pressure recovery, t_{rec}.

The exact calculation steps for mean turbulent fluctuating velocity $\overline{u'}$ in an orifice flow are as follows: The velocity of the mean flow at vena contracta (U_o) is determined from cavitation number. Liquid velocity in the pipe (u_p) is related to U_o by Eq. 10. The pressure in the flow downstream of the orifice recovers in a length of about eight to ten pipe diameters ($L' \approx 8d_p$). The rate of turbulence energy dissipation per unit mass in the region of pressure recovery downstream of the orifice is:

$$P_m = \frac{\left(P_{ups} - P_2\right)\left(\frac{\pi}{4}d_p^2 u_p\right)}{\left(\frac{\pi}{4}d_p^2 \cdot L' \cdot \rho_L\right)} \tag{11}$$

P_{ups} is the pressure of the flow upstream of the orifice (for negligible frictional pressure drop). d_p is the diameter of the pipe. P_{ups} can also be considered as the discharge pressure of the pump driving the liquid circulation. An approximate relation between recovered pressure P_2 and P_{ups} is given as [110] $P_{ups} = P_2/\beta^2$. $\left(P_{ups} - P_2\right)$ is the permanent pressure head loss in the flow and ($\pi d_p^2 u_p/4$) is the volumetric flow rate. The denominator, $\left(\pi d_p^2 \cdot L' \cdot \rho_L/4\right)$, is mass of the liquid in zone of pressure recovery. $\bar{u}'$ is then calculated as:

$$\overline{u'} = \left(P_m \times l\right)^{1/3} = \left(P_m \times 0.08\frac{d_o + d_p}{2}\right)^{1/3} \tag{12}$$

It could be perceived that the length scale of the eddy l is taken as 0.08 ($d_o + d_p$)/2, based on Prandtl eddy model, $l = 0.08\,d_c$. The diameter of the conduit, d_c, is taken as an average of orifice (d_o) and pipe diameters (d_p). The instantaneous frequency of the turbulent fluctuating velocity, f_T, is then obtained as:

$$f_T = \overline{u'}/l = \overline{u'}/\left(0.08 \cdot \left(d_o + d_p\right)/2\right) \tag{13}$$

Calculation of time profile of instantaneous bulk pressure (P_t): Using values of various quantities U_o, t_{rec}, $\bar{u}'$, and f_T, the instantaneous bulk pressure in the flow is calculated as follows:

1. In consideration of the experimental results of Yan et al. [71], the instantaneous mean bulk pressure P_t at any time t is first calculated assuming a linear pressure recovery between the pressure at vena contracta (P_{vc}) and an assumed recovery
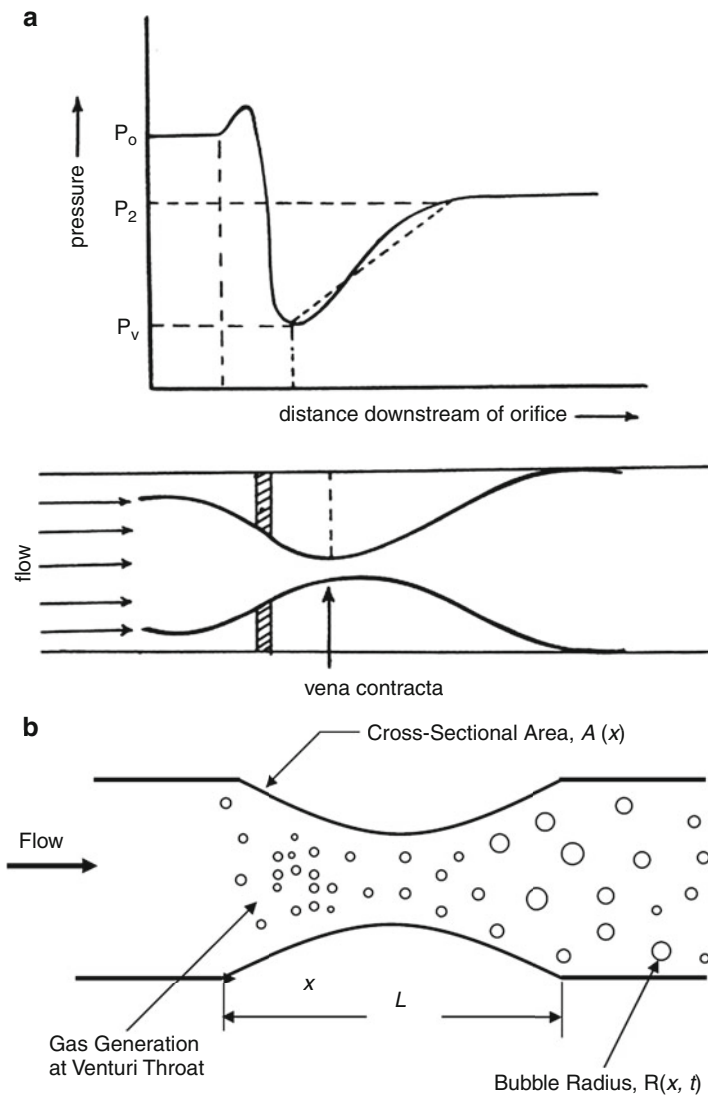
Fig. 1 (**a**) Schematic of pressure recovery profile in the downstream region of an orifice flow. (**b**) Schematic of the cavitating flow through a converging–diverging nozzle

pressure (P_2) downstream of the orifice (refer to Fig. 1a depicting the schematic of the pressure recovery profile):

$$P_t = P_{vc} + \frac{(P_2 - P_{vc})}{t_{rec}} t \tag{14}$$

2. The instantaneous mean velocity (U) corresponding to the above value of P_t is calculated using the Bernoulli equation between vena contracta and the point of full pressure recovery (eight pipe diameters downstream of the orifice):

$$U = \left(\frac{P_{ori} + \rho_L U_o^2/2 - P_t}{\rho_L/2}\right)^{1/2} \tag{15}$$

3. Variations in the turbulent fluctuation velocities are rather random. In the simplest case, we assume a sinusoidal variation for the turbulent velocity. The turbulent fluctuation velocity is essentially superimposed over mean velocity U to calculate the new value of the instantaneous velocity as:

$$u = U + \overline{u}' \sin\left(2\pi f_T t\right) \tag{16}$$

4. The bulk pressure in the flow is recalculated using Bernoulli equation:

$$P_t = \frac{1}{2}\rho_L U_o^2 + P_{vc} - \frac{1}{2}\rho_L u^2 \tag{17}$$

The above value of P_t is then substituted in the bubble dynamics equation (Eqs. 2, 3, or 4).

Early Models for Hydrodynamic Cavitation

Preliminary Model with Rayleigh–Plesset Model and Linear Pressure Recovery

In a preliminary study published by Moholkar et al. [111] in 1999, an attempt was made to study the radial motion of a cavitation bubble in hydrodynamic cavitation flow. This study was based on numerical solution of Rayleigh–Plesset equation to assess the radial motion of a bubble in hydrodynamic cavitation flow using a linear pressure recovery profile downstream of an orifice as given by Eq. 14. Simulations of cavitation bubble dynamics in hydrodynamic cavitation were compared against the simulations in acoustic cavitation. The effects of following parameters on radial motion of cavitation bubble in hydrodynamic cavitation flow were determined: (1) final recovery pressure downstream of the orifice, (2) time of pressure recovery, and (3) initial bubble radius. The cavitation number was assumed to be 1, at which both gaseous and vaporous cavitation occurs. A brief summary of the results of Moholkar et al. [111] is given below:

Final recovery pressure: The radial motion of cavitation bubble in hydrodynamic cavitation was found to be stable and oscillatory with small amplitude radial motion – against large amplitude transient motion seen in acoustic cavitation. The bubble undergoes several oscillations with reducing amplitude with recovery of pressure

downstream of the orifice. Such motion resulted in generation of large number of pressure pulses or peaks (of relatively smaller magnitude) inside the bubble. The amplitude of radial motion of the bubble and the magnitude of resultant pressure peaks or pulses were found to increase with recovery pressure.

Time of pressure recovery: With decreasing recovery times (i.e., faster pressure recoveries), the bubble life was found to increase, and also the magnitude of the pressure pulses obtained from the oscillations increased.

Initial bubble radius: Vaporization of liquid and desorption or liberation of dissolved gas in the liquid with fall of pressure in the downstream region gives rise to large number of bubbles of a wide size range. The typical range of the size of the bubbles could be 10–200 μm. The bubbles generated at *vena contracta* are in mechanical equilibrium with the surrounding, and hence, the pressure inside the bubble is $(P_v + 2\sigma/R_o)$. Simulations for bubbles of various sizes revealed that not all bubbles enjoy longevity in the flow with recovering pressure in the downstream region. The bubbles which are in mechanical equilibrium at the time of generation undergo oscillation till full pressure recovery, while nonequilibrium bubbles collapse prematurely.

In addition to the revealing interesting features of the radial motion of a cavitation bubble in hydrodynamic cavitation, the work of Moholkar et al. [111] also brought out interesting analogy between acoustic and hydrodynamic cavitation, as described below:

From simulation studies, an analogy between sonic and hydrodynamic cavitation can be developed. As depicted earlier, the sonic cavitation is a result of passage of ultrasound wave through the medium, while hydrodynamic cavitation is a result of the velocity variation in the flow due to changing geometry of the path of flow. Inspite of difference in the causes leading to generation acoustic and hydrodynamic cavitation, radial motion of the cavitation bubble showed similar trends with the variation of certain parameters in both types of cavitation. This similarity in radial motion formed the basis for analogy between acoustic and hydrodynamic cavitation. Two main features or aspects of radial motion in either acoustic or hydrodynamic cavitation are:

- The amplitude of oscillations of bubble radius, which has direct manifestation in the magnitude of the resultant pressure pulses.
- Duration for which the bubble undergoes oscillation before a transient collapse, which is manifested in terms of the distance traveled by the bubble before transient collapse. This feature essentially decides the size of the cavitationally active zone in which the physical/chemical effects of cavitation could be realized.

The parameters in acoustic cavitation and hydrodynamic cavitation that influence the above-mentioned features of radial motion of cavitation bubbles are:

Acoustic cavitation: Intensity of ultrasound and frequency of ultrasound
Hydrodynamic cavitation: Recovery pressure downstream of orifice and time of pressure recovery

The response shown by radial motion of cavitation bubble to variation in intensity of ultrasound in case of acoustic cavitation and the recovery pressure in case of hydrodynamic cavitation is essentially same. Increment in the amplitude of the radial motion of cavitation bubble is observed with increasing ultrasound intensities/recovery pressures. In a similar way, frequency of the ultrasound wave in acoustic cavitation and time of pressure recovery in hydrodynamic cavitation have analogous effects on radial motion of cavitation bubble. Increase in ultrasound frequency and reduction in time of pressure recovery results in an increment in duration for which the bubble undergoes oscillations before transient collapse. The preliminary analysis by Moholkar et al. [111] revealed that ultrasound intensity and recovery pressure and ultrasound frequency and time of pressure recovery are analogous parameters in acoustic and hydrodynamic cavitation.

Model Incorporating Turbulence Effect

In another contemporary paper, Moholkar and Pandit [108] assessed the influence of turbulent pressure fluctuations in the cavitating flow on the radial motion of the bubble. In this case, the Rayleigh–Plesset equation was solved using pressure profiles given by Eqs. 14 (linear pressure recovery) and 17 (pressure recovery with turbulent fluctuations). The comparison of the numerical solutions of Rayleigh–Plesset equation with the two pressure profiles provided an insight into the effect of turbulence on the transformation of the radial motion of the bubble. Influence of following design/process/physical parameters on the radial motion of the bubble in hydrodynamically cavitating flow has been evaluated: (1) recovery pressure downstream of the orifice (or discharge pressure of the pump), (2) effect of pipe size downstream of the orifice, (3) effect of orifice to pipe diameter ratio, and (4) effect of initial bubble radius. The major conclusion of this study was that turbulent pressure fluctuations cause drastic change in the nature of radial motion of the cavitation bubble in the flow downstream of the orifice. With turbulence, the oscillatory stable cavitation behavior transforms into a transient cavitation, similar to the acoustic cavitation. A brief description of the effect of each of the parameters listed above on radial motion of cavitation bubble is as follows:

1. It indicates that with an increase in the recovery pressure the maximum cavity size before collapse increases. The life of the bubble/cavity also increases.
2. With an increase in the pipe size, the maximum radius attained by the cavitation bubble before collapse increases, resulting in high pressure peak attained in the bubble. This result is attributed to increased scale of turbulence (which is a function of pipe and orifice diameters) which reduces the frequency of turbulence. Due to reduced frequency of turbulent pressure fluctuations, the cavitation bubbles grow to larger radius before the collapse.
3. With an increase in orifice to pipe diameter ratio, the life of the cavitation bubble (i.e., period for which it lasts before a transient collapse) increases. However, the

maximum radius attained by the cavitation bubble during radial motion does not alter significantly. This result can be explained as follows: orifice to pipe diameter governs the permanent pressure head loss in the cavitating flow, which is essentially manifested in generation of turbulence. For an orifice to pipe diameter ratio of 0.5, the permanent pressure head loss is 73 % of the orifice pressure differential. For an orifice to pipe diameter ratio of 0.75, the permanent pressure head loss is around 60 % of the orifice pressure differential. This essentially means that intensity of turbulence is inversely proportional to orifice to pipe diameter ratio. Therefore, increase in orifice to pipe diameter ratio decreases turbulent intensity, leading to increase in bubble life. However, the maximum bubble size attained before transient collapse does not show much alteration with orifice to pipe diameter ratio.

4. Simulations conducted using bubbles of two initial sizes, viz., 10 and 100 μm, revealed that expansion of the bubble over its initial radius (characterized by ratio R_{max}/R_o, where R_{max} = maximum size of the bubble attained during radial motion and R_o = initial size of the bubble) before collapse is higher for smaller bubbles. This implies that smaller bubbles make greater contribution to the cavitation intensity generated in the medium.

The study by Moholkar and Pandit [108] thus gave an important result that nature of radial motion of the cavitation bubble changes drastically under the turbulent flow conditions. Unlike the stable and oscillatory behavior under non-turbulent conditions, radial motion of the bubble in turbulent flow is of transient nature and resembles that under acoustic cavitation. This was an interesting result, which opened up new opportunities for design of hydrodynamic cavitation reactors for the so-called sonochemical effects. The simulations of Moholkar and Pandit [108] showed that intense energy concentration as achieved by transient motion of cavitation bubble in sonic reactors can be easily generated in a simple flow device like hydrodynamic cavitation reactor. Moreover, manipulation of the turbulence level in the flow offered a simple and effective method to control the intensity of transient collapse of the cavitation bubble.

The simulation studies of Moholkar and Pandit [108] also provided basic guidelines for effective control of the radial motion of cavitation bubble for generating maximum cavitation effect as follows: (1) increasing the discharge pressure, and hence, final recovery pressure would result in larger cavitationally active volume downstream of the orifice with higher cavitation intensity; (2) for a given discharge pressure, orifice to pipe diameter ratio provides another possible means of controlling cavitationally active volume without changing the cavitation intensity; and (3) in situ generated bubbles in the cavitating flow have a wide range of initial bubble size, which cannot be controlled. However, since small bubbles make greater contribution to the cavitation effect, such small bubble can be introduced externally in the flow through suitable gas distribution devices attached to the main geometry such as orifice or venturi.

Continuum Mixture Model Coupled with Rayleigh–Plesset Equation

The two models developed by Moholkar et al. [111] and Moholkar and Pandit [108] considered a single isolated bubble in cavitating flow. With this basic assumption, the earlier models could give a qualitative insight into the sonochemical effect induced by hydrodynamic cavitation. However, these models did not take into account the interactions between numerous bubbles that form simultaneously at *vena contracta*. The intermittent pressure waves emitted by oscillation/collapse of one bubble can affect dynamics of the other bubbles in its close vicinity. Secondly, the interactions between the flow and the bubble were also not considered. Under certain circumstances (explained in greater details subsequently), the bubble/flow interaction can lead to flashing of the flow. In order to account for these effects, Moholkar and Pandit [36, 112] proposed a new model based on coupling of continuum mixture model of van Wijngaarden [113, 114] and the Rayleigh–Plesset model used in our earlier papers. A summary of this study is given below – starting with description of the continuum mixture model:

In nonlinear continuum mixture model proposed by van Wijngaarden [113, 114], the Navier–Stokes equations for two-phase flow are coupled with Rayleigh–Plesset equation for cavitation bubble dynamics. This model is based on several assumptions as follows:

1. Incompressible liquid and no slip between the two phases.
2. No coalescence and further break up of bubbles in cavitating flow.
3. $\rho_L \gg \rho_G$, ρ_V. Hence, ρ_G and ρ_V are neglected.
4. Identical initial sizes (radii R_o) and spherical geometry of all bubbles.
5. No heat and mass transfer effects across the bubble (or bubble acts as closed system).
6. Uniform temperature and density in the bubble interior.
7. Bubbles in mechanical equilibrium with the surrounding after inception.

The mass density of gas–liquid flow, with gas bubbles of radii $= R(x,t)$, and bubble population per unit volume $= n$ is $\rho = \rho_L (1 - n V)$, where $V = 4/3\ \pi R^3(x,t)$ is the volume of a single bubble. The continuity and momentum equations of the two-phase flow are written as [115, 116]

$$\frac{\partial(\rho A)}{\partial t} + \frac{\partial(\rho u A)}{\partial x} = 0 \tag{18}$$

$$\frac{\partial u}{\partial t} + u\frac{\partial u}{\partial x} = -\frac{1}{\rho}\frac{\partial p}{\partial x} \tag{19}$$

The bubble void fraction in the flow defined as $\alpha(x,t) = \frac{4n\pi R^3(x,t)/3}{[1+4n\pi R^3(x,t)/3]}$. The initial bubble volume fraction is denoted by α_o. The bubble dynamics is modeled using

Rayleigh–Plesset equation with Lagrangian derivative $(D/Dt = \partial/\partial t + u\partial/\partial x)$, which also accounts for the bubble/flow interaction [117]:

$$\rho_L\left[R\frac{D^2R}{Dt^2} + \frac{3}{2}\left(\frac{DR}{Dt}\right)^2\right] = \left(P_o + \frac{2\sigma}{R_o} - P_v\right)\left(\frac{R_o}{R}\right)^{3k} - (P_o + P_t) - \frac{2\sigma}{R}$$
$$-\frac{4\mu}{R}\left(\frac{DR}{Dt}\right) + P_v \qquad (20)$$

The polytropic constant of the bubble contents, k, is assumed to be 1 on the basis of the analysis of Hilgenfeldt et al. [104]. The Navier–Stokes equations can be coupled to cavitation bubble dynamics by eliminating p in the momentum equation with P_t in cavitation bubble dynamics equation. A simple yet physically realistic method for solving the above system of equations is to assume steady-state cavitating flow for a constant mass flow rate [115].

Flow model for venturi or converging–diverging nozzle: A simple expression for the flow area in a converging–diverging nozzle of length L is [115]

$$A(x) = \left\{1 - \frac{1}{2}\delta\left[1 - \cos\left(\frac{2\pi x}{L}\right)\right]\right\}^{-1/2} \; for \; 0 < x < L \qquad (21)$$

Figure 1b shows the sketch of the converging–diverging nozzle with area given by above expression. The bubbles are generated at the throat of the nozzle with reduction in bulk pressure.

Flow model for orifice flow: As noted earlier, in case of high Reynolds number flow past an orifice plate, the velocity of the flow field has two components: the mean flow velocity and the turbulent fluctuating velocity superimposed over it. With calculation of mean turbulent fluctuation velocity, $\overline{u'}$, and its frequency, f_T, as per the algorithm described in section "Cavitation Bubble Dynamics and Pressure Recovery Profiles in Hydrodynamic Cavitation," the instantaneous fluid velocity u in Eqs. 18 and 19 is given by Eq. 16. With assumption of linear expansion of mean flow downstream of the orifice plate, the flow area $A(x)$ is written as:

$$A(x) = A_o + \left(A_p - A_o\right)x/L' \qquad (22)$$

Steady-state solutions: Under assumption of steady state, Eqs. 18, 19, and 20 are transformed as

$$\rho_L\left(1 - 4\pi nR^3/3\right)uA = \text{constant} \qquad (23)$$

$$u\frac{du}{dx} = -\frac{1}{\rho_L\left(1 - 4\pi nR^3/3\right)}\frac{dp}{dx} \qquad (24)$$

$$P_t = P_v - P_o + \left(P_o + \frac{2\sigma}{R_o} - P_v\right)\left(\frac{R_o}{R}\right)^{3k} - \frac{2\sigma}{R} - \frac{4u\mu}{R}\left(\frac{dR}{dx}\right)$$

$$- \rho_L\left[R\left(u^2\frac{d^2R}{dx^2} + u\frac{du}{dx}\frac{dR}{dx}\right) + \frac{3u^2}{2}\left(\frac{dR}{dx}\right)^2\right] \tag{25}$$

Replacing p in Eq. 24 by P_t in Eq. 25 gives a system of three simultaneous ODEs, which can be numerically solved as initial value problem. The simulations are terminated when Lagrangian bubble wall velocity ($u\ dR/dx$) becomes higher than velocity of sound in water (1500 m s^{-1}).

Pressure Gradients in Nozzle Flow and Orifice Flow: Comparative Evaluation

Nozzle flow: In a converging–diverging nozzle, the pressure in flow recovers from venturi throat at the expense of velocity of the flow. This change in velocity head of the flow takes place over the length of the nozzle (L). Velocity of the nozzle flow changes from U_o (at the throat) to u_p (in the pipe). For relatively low volume fraction of bubbles in the flow, $u_p \approx \eta^2 U_o$ where η is the ratio of diameters of nozzle throat and downstream pipe. Thus, approximate pressure gradient from throat of the nozzle to pipe, which drives the radial bubble motion, is $\rho_L(1 - \eta^2)^2 U_o^2/2L$. The bulk pressure in the nozzle flow increases monotonously, and hence, bubbles incepted at the throat never tend to grow as they move with the flow. However, a larger pressure gradient will cause higher compression of the bubble during radial motion resulting in larger peak pressure attained in the bubble.

Orifice flow: For relatively low bubble volume fraction in the flow, $u_p \approx U_o\beta^2$. However, the mean velocity is superimposed by the turbulent fluctuating velocity ($\overline{u'}$). The relative pressure magnitude and frequency of the turbulent fluctuations are denoted as I and f_T, respectively. Thus, the radial bubble motion in orifice flow is influenced by two pressure gradients: (1) the mean pressure gradient (similar to nozzle flow), $\frac{1}{2L}\rho_L(1 - \beta^2)^2 U_o^2$, and (2) the turbulent pressure fluctuation with peak amplitude, $I \approx \rho_L\overline{u'}^2/2$. As discussed in greater detail in section "Cavitation Bubble Dynamics and Pressure Recovery Profiles in Hydrodynamic Cavitation," the magnitude of the turbulent pressure gradient, which is oscillatory in nature, is a function of permanent pressure head loss in the flow. At sufficiently high pressure head loss, the magnitude of I is significant, due to which the mean pressure reduces during its negative oscillations of I. This results in growth of the bubble above its original size, as seen in the rarefaction half cycle of ultrasound in acoustic cavitation.

Simulations results and discussion: Simulations were carried out to assess effects of design parameters on radial bubble motion in the cavitating flow in converging–diverging nozzle and orifice plate. While choosing the simulation parameters listed in Table 3, the flow stability criterion given by Wang and Brennen [115] was checked a priori.

Table 3 Parameters for simulations of cavitation bubble dynamics using continuum mixture model

Figure number	Feature of cavitation bubble dynamics	Parameters for simulations
Fig. 2A	Nozzle flow: effect of recovery pressure	(A) $P_2 = 1$ bar; (B) $P_2 = 1.5$ bar; (C) $P_2 = 2$ bar
		Other parameters: $\eta = 0.84$, $\alpha_o = 2 \times 10^{-6}$, $C_i = 1$, $R_o = 100$ μm, $L = 0.1$ m.
Fig. 2B	Nozzle flow: effect of length of nozzle	(A) $L = 0.05$ m; (B) $L = 0.1$ m; (C) $L = 0.2$ m
		Other parameters: $\eta = 0.84$, $\alpha_o = 2.5 \times 10^{-6}$, $C_i = 1$, $R_o = 100$ μm, $P_2 = 1$ bar
Fig. 2C	Nozzle flow: effect of nozzle throat to pipe diameter ratio	(A) $\eta = 0.84$; (B) $\eta = 0.78$; (C) $\eta = 0.69$
		Other parameters: $P_2 = 1$ bar, $\alpha_o = 2 \times 10^{-6}$, $C_i = 0.9$, $R_o = 100$ μm, $L = 0.1$ m
Fig. 3A	Orifice flow: effect of recovery pressure	(A) $P_2 = 1$ bar ($I = 0.02$ bar); (B) $P_2 = 2$ bar ($I = 0.04$ bar); (C) $P_2 = 3$ bar ($I = 0.06$ bar)
		Other parameters: $f_T = 30.3$, $\beta = 0.5$, $\alpha_o = 2 \times 10^{-6}$, $C_i = 1$, $R_o = 100$ μm, $d_p = 0.05$ m
Fig. 3B	Orifice flow: Effect of orifice to pipe diameter ratio	(A) $\beta = 0.5$ ($I = 0.02$ bar, $f_T = 30.3$); (B) $\beta = 0.6$ ($I = 0.018$ bar, $f_T = 25.3$); (C) $\beta = 0.7$ ($I = 0.015$ bar, $f_T = 20.5$)
		Other parameters: $P_2 = 1$ bar, $\alpha_o = 2 \times 10^{-6}$, $C_i = 1$, $R_o = 100$ μm, $d_p = 0.05$ m
Fig. 3C	Orifice flow: effect of pipe size downstream of orifice	(A) $d_p = 0.05$ m ($I = 0.018$ bar, $f_T = 25.3$); (B) $d_p = 0.075$ m ($I = 0.018$ bar, $f_T = 25.3$); (C) $d_p = 0.1$ m ($I = 0.015$ bar, $f_T = 20.5$)
		Other parameters: $P_2 = 1$ bar, $\alpha_o = 2 \times 10^{-6}$, $C_i = 1$, $R_o = 100$ μm, $\beta = 0.6$

Results of Simulations of Nozzle Flow

Effect of recovery or upstream pressure: The results of simulations have been given in Fig. 2a with conditions for the simulations stated in the caption. Radial motion of the bubble in nozzle flow has oscillatory nature with dampening amplitude. The amplitude of bubble oscillations and hence the magnitude of the resultant pressure pulses increases with recovery pressure. This result is a consequence of higher pressure gradient in the nozzle with increasing recovery pressure.

Effect of length of nozzle: The results of simulations have been given in Fig. 2b with conditions for the simulations stated in the caption. Figure 2b depicts increase in the amplitude of bubble oscillations with reduction in length of the nozzle, with recovery pressure remaining the same. This effect is also a consequence of rise in the pressure gradient in nozzle with reduction in its length.

Effect of nozzle throat to pipe diameter ratio: The results of simulations have been given in Fig. 2c with conditions for the simulations stated in the caption. Reduction in nozzle throat to pipe diameter ratio results in rise in amplitude of bubble oscillations in the cavitating flow. The lesser the value of nozzle throat to pipe diameter ratio (for fixed recovery pressure and length of the nozzle), the larger is the pressure gradient across nozzle length. Therefore, the influence of nozzle throat to

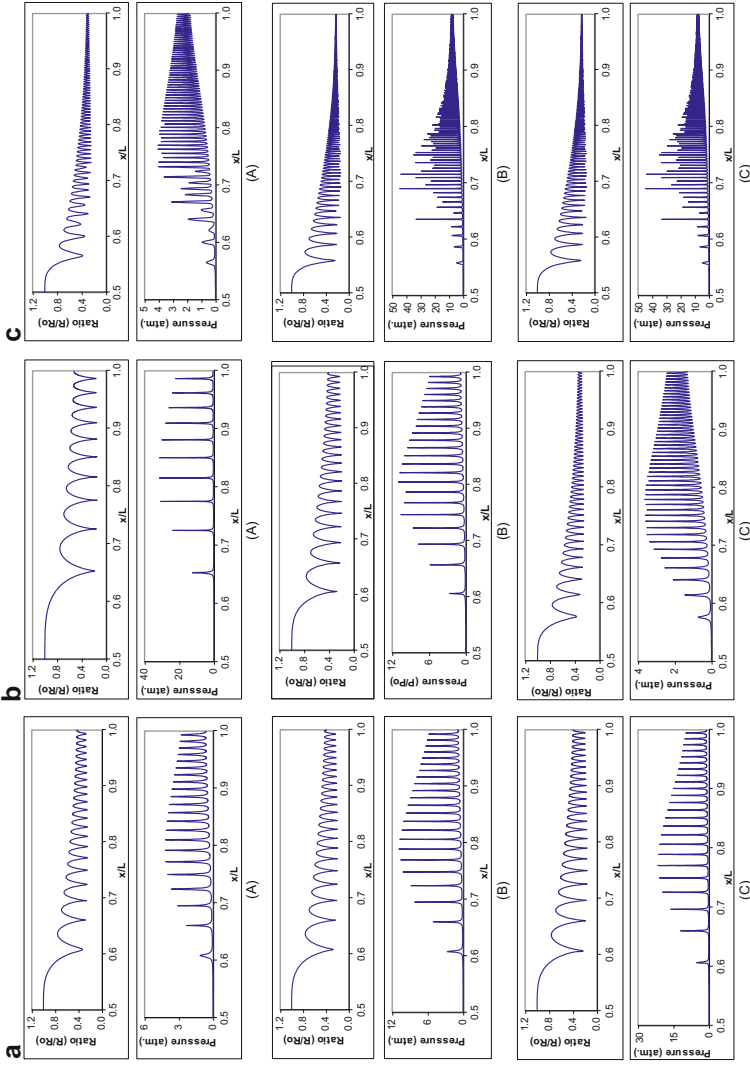**Fig. 2** (**a**) Simulations of cavitation bubble dynamics in nozzle flow with continuum mixture model: Effect of recovery pressure. (**b**) Simulations of cavitation bubble dynamics in nozzle flow with continuum mixture model: Effect of length of nozzle. (**c**) Simulations of cavitation bubble dynamics in nozzle flow with continuum mixture model: Effect of nozzle throat to pipe diameter ratio

pipe diameter ratio on radial motion of cavitation bubble is also attributed to rise in the pressure gradient.

Results of Simulations of Orifice Flow

Effect of the recovery pressure: The results of simulations have been given in Fig. 3a with conditions for the simulations stated in the caption. Figure 3a shows an interesting nature of the oscillations of cavitation bubble, which is a combination of oscillatory and transient type. The bubble undergoes small amplitude oscillatory motion initially, followed by large growth and an ultimate transient collapse. This motion is a manifestation of the two pressure gradients, viz., mean and turbulent, in the orifice flow, as mentioned earlier. During the initial stages of cavitating flow downstream of orifice, the mean pressure gradient dominates the bubble motion. The amplitude of the initial oscillatory motion of the bubble grows with rising recovery pressure. However, the explosive growth of the bubble thereafter remains essentially same, which is attributed to constant frequency of turbulent pressure fluctuations. Nonetheless, the intensity of the ultimate transient collapse of the bubble increases with rising recovery pressure, as indicated by the pressure pulse generated during collapse.

Effect of orifice to pipe diameter ratio: The results of simulations have been given in Fig. 3b with conditions for the simulations stated in the caption. As evident from Fig. 3b, the expansion of cavitation bubble during radial motion as well as the intensity of the subsequent collapse varies directly with the orifice to pipe diameter ratio. Increase in orifice to pipe diameter ratio causes reduction in both turbulent pressure gradient (due to lower $\overline{u'}$) and also frequency of the turbulent pressure fluctuations. However, the effect of latter parameter is higher in that the bubble grows to a larger size under influence of turbulent pressure fluctuations with reduced frequency. Larger expansion of the bubble during radial motion also results in collapse with higher intensity.

Effect of the pipe size downstream of orifice: The results of simulations have been given in Fig. 3c with conditions for the simulations stated in the caption. Increase in pipe size downstream of orifice has two principal effects on radial motion of the bubble: (1) number of small amplitude oscillations of the bubble and the resultant pressure pulses reduce, while the number of bubble oscillations before transient growth increase, and (2) the maximum size attained by the bubble during transient growth and hence the intensity of ensuing collapse increases. A plausible explanation for these trends can be given as follows: an increase in pipe diameter increases the length of pressure recovery zone downstream of orifice. This causes significant reduction in mean pressure gradient. The radial motion of cavitation bubble is essentially governed by turbulent pressure fluctuations. As a result, bubble grows to a larger size before more intense transient collapse.

Conclusions: Simulations of cavitating flow with continuum mixture model provided a deeper insight into the phenomenon of hydrodynamic cavitation revealing interesting features and trends of radial motion of the cavitation bubbles with design and process parameters. The radial motion of the bubble in the cavitating flow

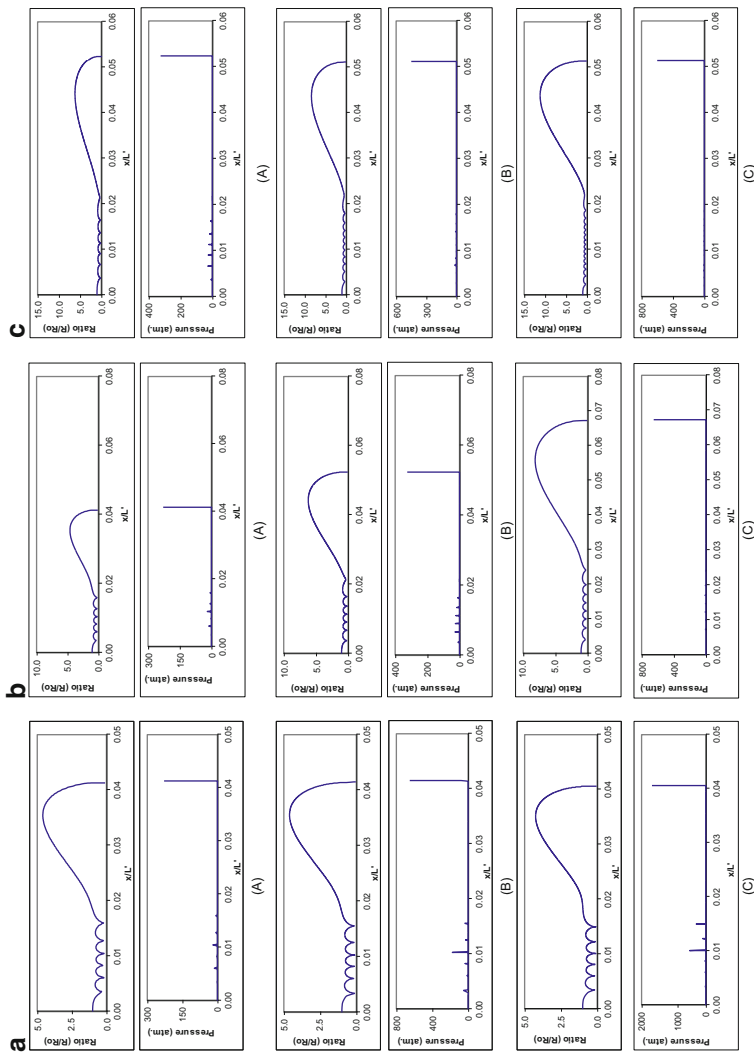**Fig. 3** (**a**) Simulations of cavitation bubble dynamics in orifice flow with continuum mixture model: Effect of recovery pressure. (**b**) Simulations of cavitation bubble dynamics in orifice flow with continuum mixture model: Effect of orifice to pipe diameter ratio. (**c**) Simulations of cavitation bubble dynamics in orifice flow with continuum mixture model: Effect of pipe size downstream of orifice

in venturi is of stable oscillatory type. The bubble motion in the orifice flow is found to be a combination of stable oscillatory motion and a transient motion (resembling the bubble motion in acoustic cavitation) as a result of two pressure gradients of different types, viz., the linear mean pressure gradient and the oscillatory turbulent pressure gradient. As such the cavitation intensity produced in an orifice flow is of much higher magnitude than that in a venturi flow. The results of these simulations also form guidelines for the optimization of hydrodynamic cavitation reactor for a given physical/chemical operation:

1. Hydrodynamic cavitation reactor with orifice flow configuration is suitable for only intense chemical reactions. For milder processes, requiring pressures in the range of 10–25 bar, nozzle flow configuration is sufficient.
2. For nozzle flow, the easiest technique for increasing cavitation intensity would be to reduce the length of the nozzle. It should be noted that this parameter could be limited by flow instability. Reduction in throat to pipe diameter is another option for increasing cavitation intensity.
3. For orifice flow configuration, the most convenient way of controlling the cavitation intensity will be to control the orifice to pipe diameter ratio (basically throttling the discharge of a pump through a valve).
4. Pipe diameter downstream of the orifice is another means for intensification of cavitation effects; however, the net throughput (or liquid volume handled per unit time) through the reactor also increases for operation at same cavitation number.

Recent Models for Hydrodynamic Cavitation

Diffusion-Limited Model Accounting for Heat and Mass (Vapor) Transfer

In a study published in 2006, Krishnan et al. [34] reported simulations of hydrodynamic cavitation reactors with orifice flow configuration using diffusion-limited model developed by Toegel et al. [97, 98]. Simulations of the radial dynamics of the bubble along with associated heat and mass transfer for various parameters sets, as given in Table 4A, were carried out. The pressure recovery profile downstream of the orifice was determined using the procedure outlined in earlier sections. The set of ordinary differential equations in the diffusion-limited model along with the thermodynamic data is given in Table 1A, B. The set of ordinary differential equations was solved using the initial conditions stated in Table 1A and the pressure profile given Eq. 17. The model system considered in these simulations was argon bubbles in the water flow. This study was distinct from earlier models because it directly provided a quantitative estimate of the sonochemical effect induced by hydrodynamic cavitation. The diffusion-limited model could provide the exact composition of the bubble contents (gas and vapor molecules) at transient collapse, along with the peak temperature and pressure reached in the bubble. Using this information, the

Table 4 Results of cavitation bubble dynamics simulations with diffusion-limited model

(A) Parameters for simulation

Set number	Parameters						
	P_2 (atm)	R_o (μm)	β	C_i	t_{rec} (s)	$\bar{u}'$ (m/s)	f_T (kHz)
Set 1	1	200	0.5	1	0.0462	1.316	0.432
Set 2	1.2	200	0.5	1	0.0421	1.398	0.459
Set 3	1	100	0.6	1	0.0425	1.129	0.347
Set 4	1	200	0.6	1	0.0425	1.129	0.347
Set 5	1	200	0.5	1.1	0.0485	1.316	0.432

(B) Equilibrium composition (mole fraction) of various species at pressure and temperature peak attained in the bubble at first compression

Species	Parameter set for simulation				
	Set 1	Set 2	Set 3	Set 4	Set 5
	Conditions at first compression of the bubble				
	$T_{max} =$ 2994 K	$T_{max} =$ 3103 K	$T_{max} =$ 2368 K	$T_{max} =$ 1527 K	$T_{max} =$ 1774 K
	$P_{max} =$ 603.8 atm	$P_{max} =$ 683.8 atm	$P_{max} =$ 70.7 atm	$P_{max} =$ 14.2 atm	$P_{max} =$ 26.8 atm
	$N_w = 6.8 \times 10^{14}$	$N_w = 3.9 \times 10^{14}$	$N_w = 9.8 \times 10^{12}$	$N_w = 9.6 \times 10^{13}$	$N_w = 1.2 \times 10^{14}$
H_2O	9.59×10^{-1}	9.49×10^{-1}	9.87×10^{-1}	9.99×10^{-1}	9.99×10^{-1}
H_2	1.98×10^{-2}	2.41×10^{-2}	6.87×10^{-3}	1.03×10^{-4}	5.30×10^{-4}
$OH^\bullet$	1.38×10^{-2}	1.75×10^{-2}	3.43×10^{-3}	2.01×10^{-5}	1.51×10^{-4}
O_2	6.42×10^{-3}	7.62×10^{-3}	2.58×10^{-3}	4.66×10^{-5}	2.27×10^{-4}
$H^\bullet$	8.76×10^{-4}	1.25×10^{-3}	1.34×10^{-4}	6.51×10^{-8}	1.27×10^{-6}
$O^\bullet$	3.57×10^{-4}	5.24×10^{-4}	4.38×10^{-5}	1.05×10^{-8}	2.75×10^{-7}
$HOO^\bullet$	7.55×10^{-5}	1.06×10^{-4}	5.81×10^{-6}	6.05×10^{-9}	8.99×10^{-8}
H_2O_2	3.20×10^{-5}	4.28×10^{-5}	2.21×10^{-6}	6.29×10^{-9}	6.34×10^{-8}
O_3	1.20×10^{-8}	2.03×10^{-8}	2.24×10^{-10}	4.14×10^{-15}	3.01×10^{-13}

Note: A pipe size of 2 in. is taken for all simulations. Liquid temperature is assumed to be 20 °C
Notation: T_{max} peak temperature attained in the bubble at transient collapse; P_{max} peak pressure attained in the bubble at transient collapse; N_w number of water vapor molecules entrapped in the bubble at transient collapse

equilibrium composition of various species generated from dissociation of gas and vapor molecules in the bubbles could be determined using Gibbs energy minimization technique. This study, therefore, provided a useful means of estimating number of radicals formed per cavitation bubble. The simulations of Krishnan et al. [34] also helped in understanding of the effect of the various operational parameters on the sonochemical effect, i.e., radical generation in the bubble.

The simulations results are presented in Fig. 4a–e and the summary of the simulation results is given in Table 4B that lists the collapse conditions (i.e., number of water molecules entrapped in the bubble and the peak temperature and pressure inside the bubble during first collapse) and the equilibrium composition of the various species at the conditions.

The time profiles of bubble radius and vapor molecules in the bubble depicted in Fig. 4a–e reveal that a large amount of water vapor enters the bubble during the expansion phase. Not all the water vapor that has entered the bubble during expansion can condense and escape the bubble during collapse. Significant amount of water molecules get entrapped in the bubble (as indicated by the number of water molecules in the bubble listed in Table 4B) and are subjected to extremes of temperatures and pressure at transient collapse. Equilibrium mole fraction of bubble contents calculated using Gibbs energy minimization technique (software FactSage, trial version) shows that $OH^{\bullet}$ is the dominant radical species of all species resulting from dissociation of water vapor. At the point of maximum compression (or minimum radius), the bubble, these radical species can diffuse out of the bubble. Alternatively, the bubble can undergo fragmentation at the point of maximum compression during radial motion, and the radical as well as other species get released in the bulk medium, where they induce/chemical reactions. Comparison of the simulations results in various parameter sets which give an insight into the effect of different design and process parameters on the extent of radical production and sonochemical effect induced by hydrodynamic cavitation.

Results of Simulations and Discussion

Effect of recovery pressure: Evaluation of results shown in Fig. 4a, b reveal that with rising recovery pressure, the maximum radius attained during the expansion phase remains unaltered. However, during the subsequent compression, more water vapor gets squeezed out of the bubble at higher recovery pressure, leading to rise in peak temperatures and pressures attained in the bubble. Due to higher temperature and pressure peak in the bubble, the equilibrium mole fraction of $OH^{\bullet}$ increases with recovery pressure and the net production of radicals reduces due to lesser entrapment of the water vapor at collapse.

Effect of orifice to pipe diameter ratio: Comparison of simulations depicted in Fig. 4a, d reveals the effect of the orifice to pipe diameter ratio on the bubble dynamics and associated sonochemical effect. Smaller orifice to pipe diameters favor sonochemical effect. Moreover, the extent of radical production is also very sensitive to this parameter. A relatively small rise in the orifice to pipe diameter ratio (from 0.5 to 0.6) results in significant quenching of the sonochemical effects. This result is attributed to the reduction in the magnitude turbulent pressure gradient, which is responsible for the growth of the bubble, as discussed in the previous section.

Effect of initial bubble radius: Simulations depicted in Fig. 4c, d reveal that smaller bubble (100 μm) undergoes more intense collapse, resulting in higher temperature and pressure peaks attained in the bubble. However, the amount of water vapor entrapped in the bubble is lesser. Nonetheless, lower water vapor entrapment in the bubble is compensated by larger equilibrium mole fraction of $OH^{\bullet}$ radicals due to higher temperature and pressure at collapse – which is approximately two orders of magnitude higher than the 200 μm bubble. The net radical

Fig. 4 (continued)

Fig. 4 (**a**) Simulations of cavitation bubble dynamics in orifice flow with diffusion-limited model: Results for parameter Set 1 (refer to Table 4A). (**b**) Simulations of cavitation bubble dynamics in orifice flow with diffusion-limited model: Results for parameter Set 2 (refer to Table 4A). (**c**) Simulations of cavitation bubble dynamics in orifice flow with diffusion-limited model: Results for parameter Set 3 (refer to Table 4A). (**d**) Simulations of cavitation bubble dynamics in orifice flow with diffusion-limited model: Results for parameter Set 4 (refer to Table 4A)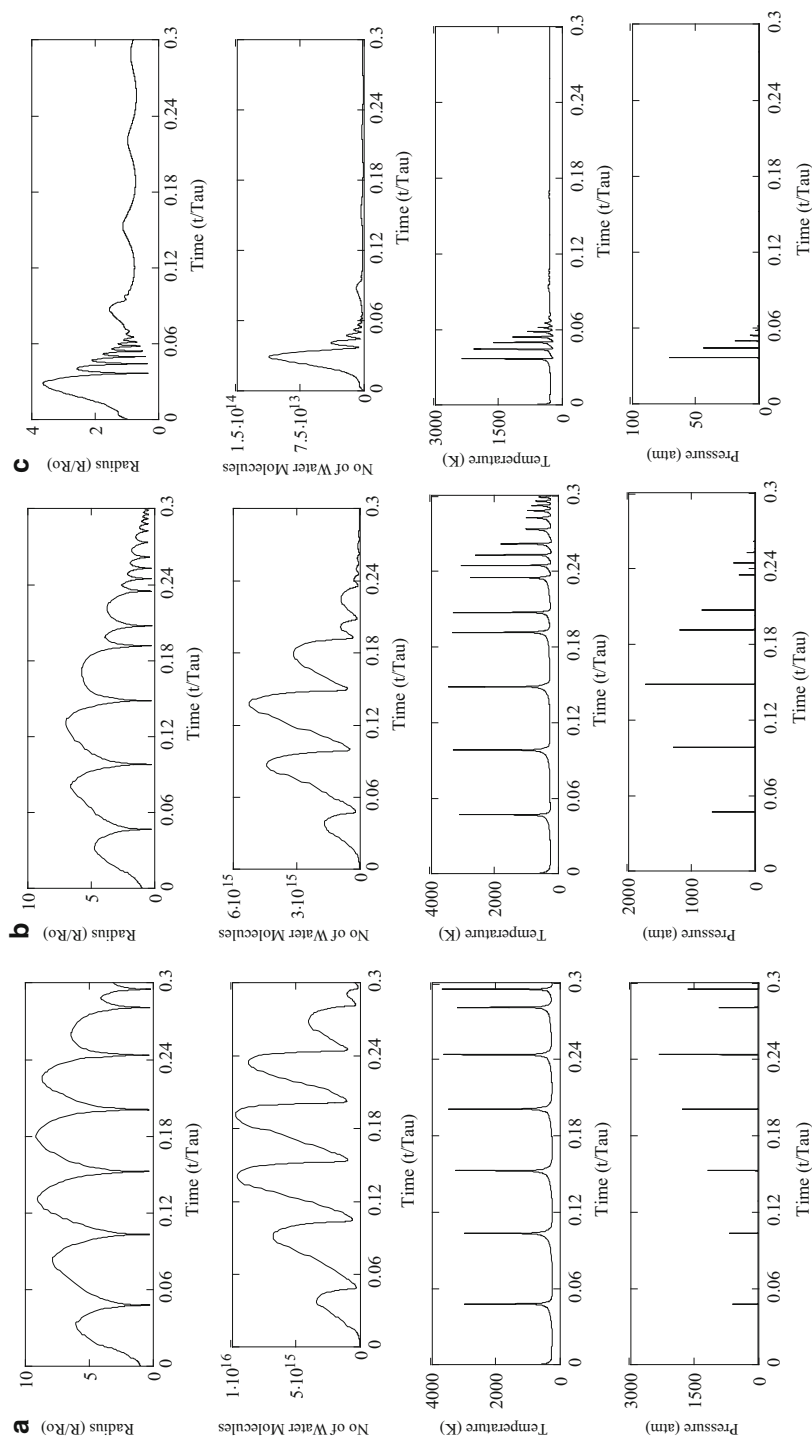. (**e**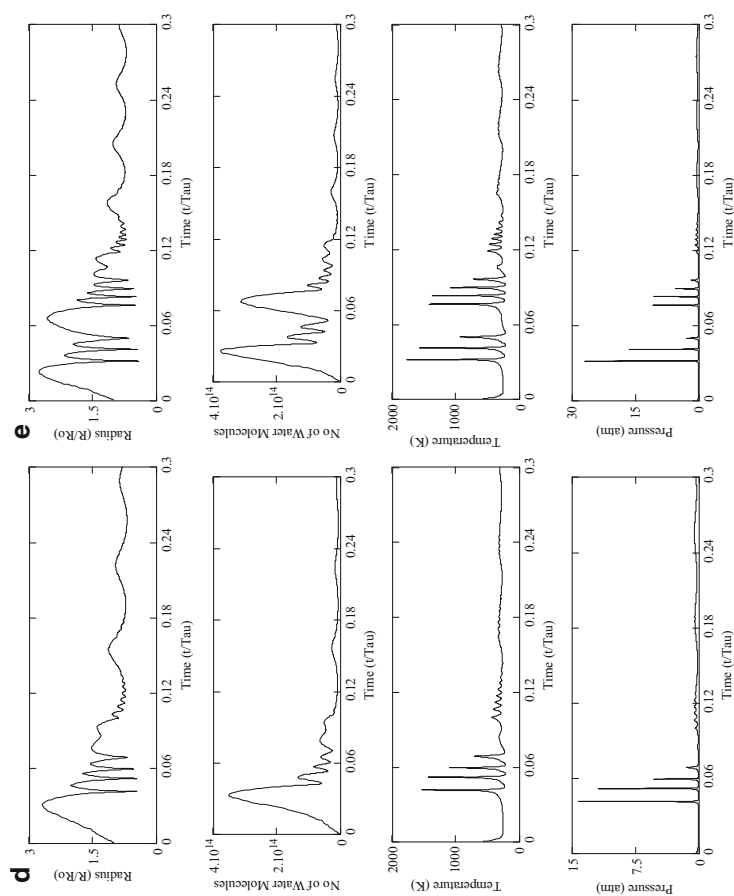) Simulations of cavitation bubble dynamics in orifice flow with diffusion-limited model: Results for parameter Set 5 (refer to Table 4A)

production per cavitation bubble is higher for smaller bubbles. Thus, smaller bubbles make greater contribution to the sonochemical effects.

Effect of cavitation number: Assessment of the simulation results depicted in Fig. 4a, e reveals effect of cavitation number on radial motion of the cavitation bubble and the sonochemical effect induced by it. Simulation results show that a small increment in the cavitation number 1.1 (Fig. 4e) from 1 (Fig. 4a) causes significant quenching of the sonochemical effect with $4\times$ reduction in water vapor entrapment and two orders of magnitude reduction in the equilibrium mole fraction of OH$^{\bullet}$ radicals. The main cause leading to these effects is the reduction in pressure gradient in the flow downstream of the orifice. Due to lesser pressure gradient, the expansion of the bubble and the ensuing collapse is less intense, resulting in reduced temperature and pressure peak attained in the bubble due to which the extent of radical production decreases.

Conclusions: The study of Krishnan et al. [34] gave a clear numerical evidence that, as in acoustic cavitation, the phenomena of water vapor entrapment and radical formation during bubble collapse also occurs in case of hydrodynamic cavitation. The entrapped water molecules are subjected to extreme temperature and pressure conditions attained in the bubble at transient collapse, resulting in thermal dissociation leading to radical production. OH$^{\bullet}$ radical is found to be the dominant radical species at conditions of bubble collapse. The peak temperatures reached in the bubble during transient collapse in all the five sets, however, are lesser than those reported for in case of acoustic cavitation ($\sim$5,000–7,000 K) [118].

These results could be a joint consequence of (1) higher entrapment of water vapor in the bubble due to which the net heat capacity of the bubble increases and (2) greater heat transfers from bubble to the surroundings during the bubble motion due to larger time scale of the radial bubble motion (of the order of millisecond against microseconds for acoustic cavitation). Changes in design and process parameters such as recovery pressure, orifice to pipe diameter ratio, and the cavitation number essentially influence the mean and turbulent pressure gradients in the cavitating flow, which is manifested in terms of the observed variations or differences in the characteristics of the radial motion of cavitation bubble and the associated effects. The findings of Krishnan et al. can be summarized as follows: (1) rise in the recovery pressure downstream of the orifice plate does not augment the sonochemical effect; (2) smaller bubbles make higher contribution to the sonochemical effect; and (3) sonochemical effect is critically sensitive to two parameters, viz., cavitation number and orifice to pipe diameter ratio. Small increment in these parameters causes significant quenching of the sonochemical effect.

Coupling Diffusion-Limited Model with Continuum Mixture Model

In a recent study, Kumar et al. [119] have coupled the continuum mixture model with diffusion-limited model. With this model, Kumar et al. [119] have developed the flow regime maps for hydrodynamic cavitation, which depict the prevalent mode of

operation of hydrodynamic cavitation reactor for different combinations of design and process parameters. Specific flow regimes have been identified depending on the energetics of the collapse of cavitation bubble as sonophysical, sonochemical, and stable oscillatory (no physical or chemical effect).

For development of the hybrid model combining diffusion-limited model and continuum mixture model, Kumar et al. [119] have simplified the basic equation for radial motion of cavitation bubble. The previous studies [36, 112] have indicated that during radial motion, the bubble wall velocity reaches or exceeds the sonic velocity for a very short duration ($\sim 10^{-6}$ s). Keller–Miksis equation in diffusion-limited model contains terms such as $(dR/dt)/c$ and $R(dP_i/dt)/\rho_L c$, which become significant only at the instance, where the bubble wall velocity is close to sonic velocity. Thus, the global dynamics of the bubble does not change if these terms are neglected. With this approximation, the simplified bubble dynamics equation becomes

$$\rho_L \left[R \frac{d^2R}{dt^2} + \frac{3}{2} \left(\frac{dR}{dt} \right)^2 \right] = P_i - P_t - \frac{2\sigma}{R} - \frac{4\mu}{R} \left(\frac{dR}{dt} \right) \tag{26}$$

Using Lagrangian derivative $D/Dt = \partial/\partial t + u\partial/\partial x$ in continuum mixture model, the equations of diffusion-limited model listed in Table 1A get transformed as

$$\rho_L \left[R \frac{D^2R}{Dt^2} + \frac{3}{2} \left(\frac{DR}{Dt} \right)^2 \right] = P_i - P_t - \frac{2\sigma}{R} - \frac{4\mu}{R} \left(\frac{DR}{Dt} \right) \tag{27}$$

$$\frac{DN_W}{Dt} = 4\pi R^2 D_W \frac{dC_W}{dr} \bigg|_{r=R} \approx 4\pi R^2 D_W \left(\frac{C_{WR} - C_W}{l_{\text{diff}}} \right) \tag{28}$$

$$\frac{DQ}{Dt} = 4\pi R^2 \lambda \left(\frac{T_o - T}{l_{th}} \right) \tag{29}$$

$$C_{v,\text{mix}} \frac{DT}{Dt} = \frac{DQ}{Dt} - P_i \frac{DV}{Dt} + (h_W - U_W) \frac{DN_W}{Dt} \tag{30}$$

The simulation parameters t_{rec}, $\overline{u'}$, and f_T for different combinations of design parameters P_2, C_i, and β were determined using the procedure described earlier. The mean liquid flow downstream of the orifice was assumed to expand linearly (as given by Eq. 22), and the instantaneous liquid velocity (u) was given by Eq. 16.

Steady-state solutions: While solving the model of one-dimensional two-phase flow with the nonlinear bubble dynamics, we make an assumption of steady-state cavitating flow with constant mass flow rate [115, 116]. With this assumption, the complete model for cavitating flow is described by following equations:

$$\rho_L \left(1 - 4\pi n R^3/3 \right) uA = \text{constant} \tag{31}$$

$$u\frac{du}{dx} = -\frac{1}{\rho_L\left(1 - 4\pi nR^3/3\right)}\frac{dp}{dx} \tag{32}$$

$$P_t = P_i - \frac{2\sigma}{R} - \frac{4\mu u}{R}\left(\frac{dR}{dx}\right) - \rho_L\left[R\left(u^2\frac{d^2R}{dx^2} + u\frac{du}{dx}\frac{dR}{dx}\right) + \frac{3u^2}{2}\left(\frac{dR}{dx}\right)^2\right] \tag{33}$$

$$u\frac{dN_W}{dx} = 4\pi R^2 D_{ij}\frac{\partial C_W}{\partial r}\bigg|_{r=R} \approx 4\pi R^2 D_{ij}\left(\frac{C_{WR} - C_W}{l_{\text{diff}}}\right) \tag{34}$$

$$u\frac{dQ}{dx} = 4\pi R^2\lambda\frac{\partial T}{\partial r}\bigg|_{r=R} \approx 4\pi R^2\lambda\left(\frac{T_o - T}{l_{\text{th}}}\right) \tag{35}$$

$$C_{v,\text{mix}}\frac{dT}{dx} = \frac{dQ}{dx} - P_i\frac{dV}{dx} + (h_W - U_W)\frac{dN_W}{dx} \tag{36}$$

The numerical values of the physical parameters in the model used during simulations were density (ρ_L) = 1,000 kg m^{-3}, surface tension (σ) = 0.072 N m^{-1}, and effective viscosity (μ) = 10^{-2} Pa–s. Damping of bubble oscillations during radial motion through various mechanisms were accounted for by larger value of the viscosity [115]. A representative initial bubble size of 100 μm was chosen for simulations. The mode of operation of hydrodynamic cavitation reactor, as represented by the radial motion, was scanned in extensive parameter space by choosing three typical values P_2, 4 values for β, three values of C_i, and four values of α_o, which are listed in Table 5A.

Criteria for mapping of flow regime and characterization of bubble motion: Flow regimes for cavitating flow were defined on the basis of characteristics of radial motion of the bubbles in the flow as follows: (1) stable oscillatory (OSC) regime inducing neither sonophysical nor sonochemical effect, (2) sonophysical (SP) regime, (3) sonophysical/ sonochemical (SPC) regime, and (4) Flash regime. In OSC regime, the expansion of the bubble during radial motion was less than 50 % of its original size $(\geq 1.5R_o)$ and the temperature in the bubble remained low (typically $\leq$ 400 K). For distinguishing between SP and SPC regimes, minimum temperature (in the pressure range between 500 kPa and 100 MPa) was determined at which the dissociation of water vapor will lead to formation of $^{\bullet}$OH radical, which is the predominant and most reactive radical species among all species formed after dissociation of water. Using Gibbs energy minimization technique (thermal equilibrium) [120, 121], the minimum temperature for formation of $^{\bullet}$OH radicals through dissociation of water molecules was determined as $\geq$900 K. Thus, SPC regime is characterized by transient bubble motion during which the peak temperature (T_{max}) attained inside the bubble is $\geq$900 K. The SP regime is characterized by moderately transient bubble motion for which 400 K $\leq T_{\text{max}} \leq$ 900 K. Characterization of the flashing regime is explained in the next section.

Flow stability (or flashing) criterion: Applying Bernoulli equation between vena contracta (point 0) and arbitrary location downstream of orifice (point x) gives for $C_i = 1$:

Table 5 Simulation parameters for continuum mixture model coupled with diffusion-limited model

(A) Range of simulation parameters	
Parameter	Representative values
1. Recovery pressure (P_2, kPa)	101.3 (1 atm), 202.6 (2 atm), 303.9 (3 atm)
2. Orifice to pipe diameter ratio (β)	0.3, 0.4, 0.5, 0.6
3. Cavitation number (C_i)	1.0, 1.1, 1.2
4. Initial bubble volume fraction (α_o)	1×10^{-8}, 2×10^{-8}, 1×10^{-7}, 2×10^{-8}

(B) Actual simulation parameters for different regimes[a]	Set of parameters			
Operating regime	P_2 (kPa)	C_i	β	α_o
1. Flashing regime	202.6	1	0.6	2×10^{-7}
2. Sonophysical regime (moderately transient behavior)	101.3	1	0.6	1×10^{-7}
3. Sonochemical regime (strongly transient behavior)	303.9	1	0.3	1×10^{-7}
4. Oscillatory behavior	101.3	1.1	0.6	2×10^{-8}

A pipe size of (0.0504 m or 2 in. ID) and an initial size of 100 μm have been considered for all simulations. Liquid temperature is assumed to be 293 K or 20 °C

[a]Graphical results of simulations are depicted in Fig. 5

$$P_x + \frac{1}{2}\rho u_x^2 = P_v + \frac{1}{2}\rho U_o^2 \tag{37}$$

Rearrangement gives the local cavitation number as: $C_x = (P_x - P_v)/(\rho U_o^2/2) = 1 - (u_x/U_o)^2$. Using continuity equation, the velocities can be related to bubble fractions (α) in the flow as: $U_o = \text{constant}/A_o(1 - \alpha_o)$ and $u_x = \text{constant}/A_x(1 - \alpha_x)$. With substitution of velocities in terms of bubble volume fraction, local cavitation number becomes: $C_x = 1 - [(1 - \alpha_o)A_o/(1 - \alpha_x)A_x]^2$. Moreover, defining area ratio as: $A_o/A_x = \beta_x^2$ gives: $C_x = 1 - [(1 - \alpha_o)\beta_x^2/(1 - \alpha_x)]^2$. It could be easily perceived that flashing of flow in the downstream region of orifice will occur if bulk pressure falls below vapor pressure leading to rapid expansion of the bubbles. Thus, the criterion for the flash regime is $C_x \leq 0$.

Results of Simulations and Formulation of Flow Regimes

Representative simulations of cavitation bubble dynamics for each of four categories, viz., OSC, SP, SPC, and Flash, are depicted in Fig. 5a–c. The parameters for simulations shown in Fig. 5a–c are listed in Table 5B. The complete flow regime maps for OSC, SP, and SPC regimes for the four values of α are shown in Figs. 6, 7, and 8, respectively. The flow regime maps are essentially contour plots of cavitation number (i.e., process parameter) against orifice to pipe diameter ratio and recovery pressure downstream of orifice (i.e., design parameters). Flow regime maps depict relative impact of recovery pressure (P_2), orifice to pipe diameter ratio (β), and
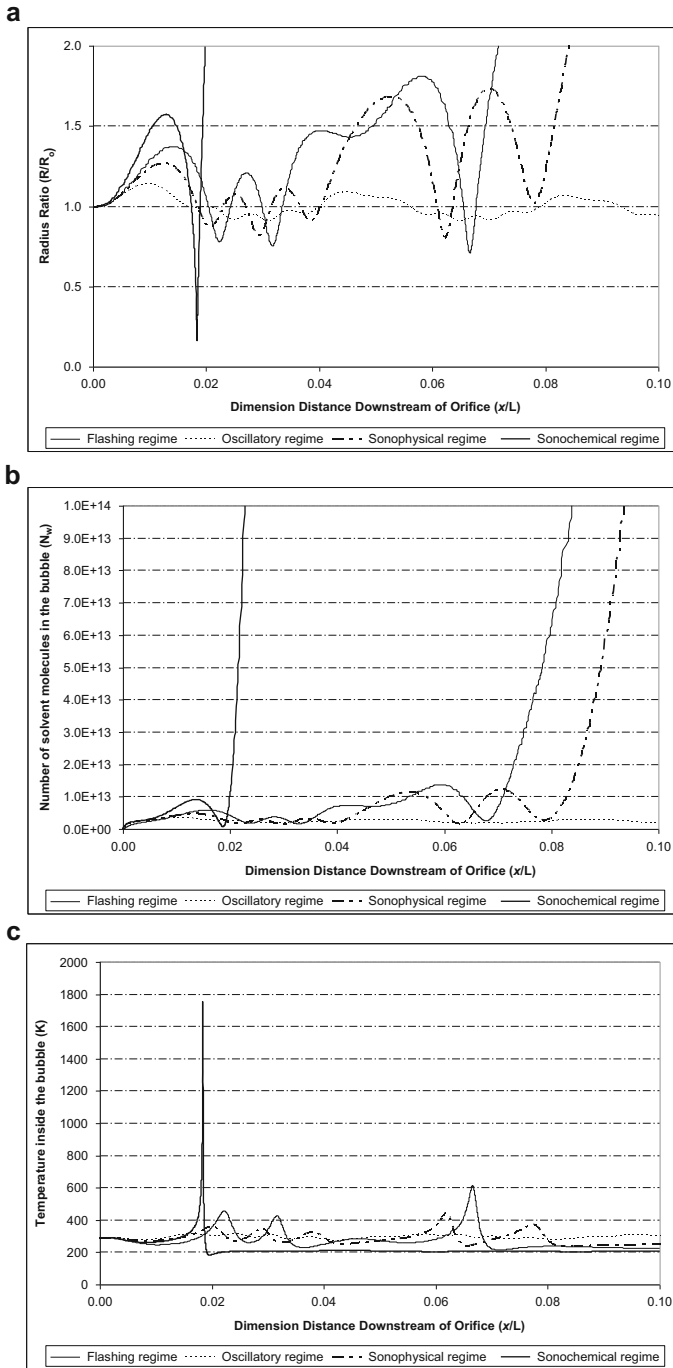
a

b
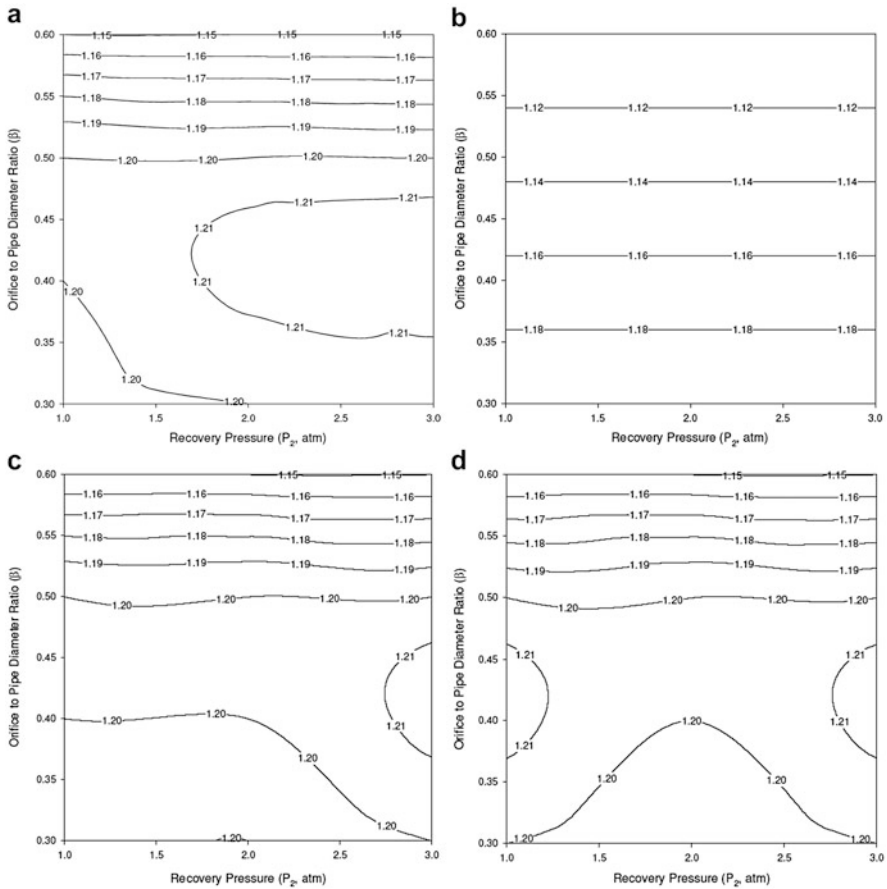

c

Fig. 5 (continued)

Fig. 6 Flow regime maps for OSC regime. The lines inside the figure indicate contours for cavitation number (C_i). (**a**) Map for $\alpha_o = 1 \times 10^{-8}$; (**b**) Map for $\alpha_o = 2 \times 10^{-8}$; (**c**) Map for $\alpha_o = 1 \times 10^{-7}$; (**d**) Map for $\alpha_o = 2 \times 10^{-7}$

cavitation number (C_i), on the nature of the cavitating flow. Some salient features of bubble behavior as evident from flow regime maps depicted in Figs. 6, 7 and 8 are:

1. The OSC regime extends for all values of α_o in the entire range of recovery pressure, orifice to pipe diameter ratios > 0.35, and cavitation number > 1.1.
2. The SP regime is seen for $C_i \approx 1$ for entire range of recovery pressures and orifice to pipe diameter range of 0.4–0.6. However, for same cavitation number, for

◀

Fig. 5 Results of simulations of cavitation bubble dynamics in different flow regimes using continuum mixture model coupled with diffusion-limited model. (**a**) Profile of (dimensionless) radius of cavitation bubbles; (**b**) profile of number of solvent (water) molecules in the cavitation bubble; (**c**) profile of temperature inside the cavitation bubble. Simulations parameters for different flow regimes are listed in Table 5B
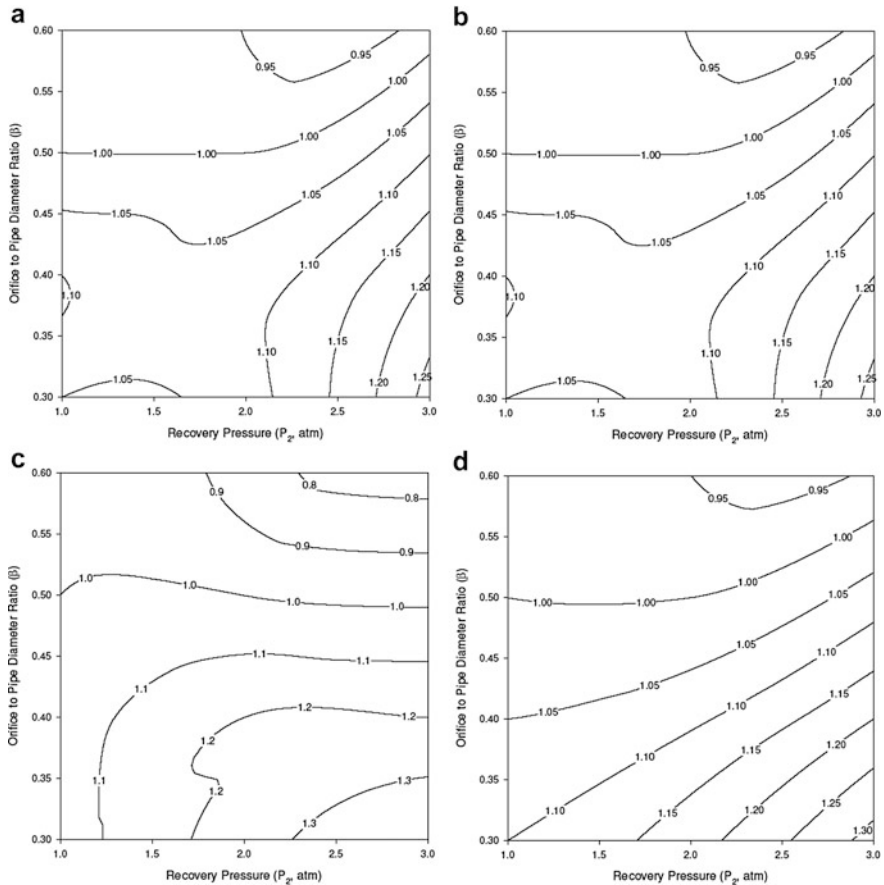
Fig. 7 Flow regime maps for SP regime (moderately transient bubble behavior giving sonophysical effects). The *lines* inside the figure indicate contours for cavitation number (C_i). (**a**) Map for $\alpha_o = 1 \times 10^{-8}$; (**b**) Map for $\alpha_o = 2 \times 10^{-8}$; (**c**) Map for $\alpha_o = 1 \times 10^{-7}$; (**d**) Map for $\alpha_o = 2 \times 10^{-7}$

higher values of recovery pressure (202.6 or 303.9 kPa), the space for SP regime is restricted for low values of orifice to pipe diameter ratio (<0.4).

3. The parameter space for SPC regime is more restricted, especially for higher initial bubble volume fractions of 1×10^{-7} and 2×10^{-7}. This regime is bounded by C_i range 1–1.1 and orifice to pipe diameter ratios of 0.4–0.6, for all recovery pressures considered in the simulations.

The influence of the design and process parameters on cavitation bubble behavior as seen from the simulation results is summarized below:

Influence of orifice to pipe diameter ratio (β): For all values of β used in simulations, moderately transient behavior of cavitation bubbles is seen for $C_i =$
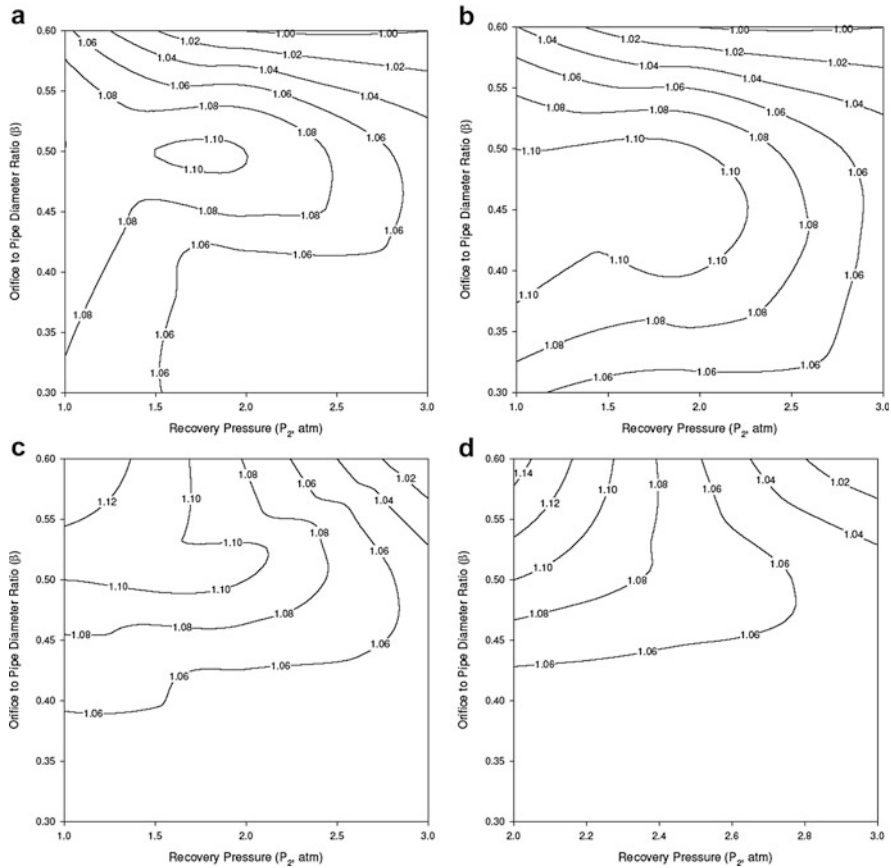
Fig. 8 Flow regime maps for the SPC regime (strongly transient bubble behavior giving sonochemical effects). The *lines* inside the figure indicate contours for cavitation number (C_i). (**a**) Map for $\alpha_o = 1 \times 10^{-8}$; (**b**) Map for $\alpha_o = 2 \times 10^{-8}$; (**c**) Map for $\alpha_o = 1 \times 10^{-7}$; (**d**) Map for $\alpha_o = 2 \times 10^{-7}$

1 and $P_2 = 101.3$ kPa. With increase in recovery pressure, cavitation number remaining the same, the intensity of cavitation bubble collapse increases. Flashing behavior of flow is seen at $P_2 = 202.6$ kPa and $\beta = 0.6$, for $\alpha_o = 1 \times 10^{-7}$ and 2×10^{-7}. For $\beta = 0.3, 0.4,$ and 0.5, the bubble undergoes a strong transient collapse giving sonochemical effect for all values of α_o. For recovery pressure of 303.9 kPa, the bubble motion becomes strongly transient for all values of α_o and β at $C_i = 1$.

Influence of cavitation number (C_i): For moderate recovery pressure of 101.3 kPa and $\beta = 0.3$, SP regime of cavitation bubble dynamics is seen for $C_i = 1$ and 1.1. With slight increase in cavitation number to 1.2, OSC regime is seen. This trend remains same for all values of α_o. At higher recovery pressures of 202.6 and 303.9 kPa, SPC regime is seen for $C_i = 1$ and 1.1, and SP/OSC regime is seen for $C_i = 1.2$. These trends essentially depict the sensitivity of the cavitation behavior

toward cavitation number at high recovery pressures. The highest sensitivity of the flow behavior toward C_i (for all α_o) is seen at high recovery pressures of 202.6 or 303.9 kPa and $\beta = 0.6$. A sharp transition in radial motion of bubble is seen with small change in C_i, e.g., from SPC regime at $C_i = 1$ to OSC regime at $C_i = 1.1$ or 1.2 or from Flash regime (at $\alpha_o = 1 \times 10^{-7}$ and 2×10^{-7}) for $C_i = 1$ to OSC regime at $C_i = 1.1$ or 1.2.

Influence of recovery pressure (P_2): Similar to the conclusions of earlier studies, the intensity of the transient collapse of cavitation bubble increases with P_2 at $C_i = 1$ for all values of α_o and β. However, some exceptions to this general trend are as follows: Flash regime is seen for $\alpha_o = 1 \times 10^{-7}$ and 2×10^{-7} for $P_2 = 202.6$ kPa and $\beta = 0.6$, while SPC regime is seen for $P_2 = 101.3$ and 303.9 kPa. For $C_i = 1.1$, the flow becomes stable (with no flashing) for all values of P_2 and β. At higher recovery pressures of 202.6 and 303.9 kPa, SPC regime is seen for $\beta = 0.3$, 0.4 and 0.5 at $C_i = 1.1$. However, for $\beta = 0.6$ at $C_i = 1.1$, and for all values of β at $C_i = 1.2$, OSC regime is seen. This indicates that flow regime becomes insensitive of recovery pressure for larger values of β and C_i.

Discussion: The ranges of parameter spaces in which certain flow regimes are observed can be justified on the basis of the dominant pressure gradient in cavitating flow. In an orifice flow, the mean pressure gradient at any location x can be determined as:

$$\frac{P_x - P_o}{x} \approx \frac{\rho U_o^2}{2x}\left(1 - \frac{u_x^2}{U_o^2}\right) = \frac{\rho U_o^2}{2x}\left[1 - \left(\frac{1 - \alpha_o}{1 - \alpha_x}\right)\beta_x^4\right]$$

$$\approx \frac{\rho U_o^2}{2x}\left[1 - \left(\frac{1 + 4n\pi R_x^3/3}{1 + 4n\pi R_o^3/3}\right)\beta_x^4\right] \tag{38}$$

The above expression indicates that larger expansion of the bubbles would tend to reduce the mean pressure gradient. As noted earlier, the mean pressure gradient is linearly increasing, and thus, it would not tend to grow a bubble above its original size at inception near vena contracta. The turbulent pressure gradient is of oscillatory nature. During the negative oscillations, it would tend to reduce the mean pressure gradient causing growth of the bubble. Growth of the bubbles in the flow would reduce the flow area for liquid causing rise in the velocity. This will further reduce the mean pressure gradient, which in turn would cause further growth of the bubble. In the limiting situation, the mean pressure in the flow could fall below the vapor pressure causing flashing of the flow.

The type of radial motion of cavitation bubble and the corresponding flow regime would depend on the relative magnitudes of the mean and turbulent pressure gradient. The magnitude of the mean pressure gradient depends on C_i, P_2, and α_o. For any combination of α_o and P_2, the largest mean pressure gradient occurs at $C_i = 1$. As C_i increases, the mean pressure gradient drops rapidly. The magnitude of turbulent pressure gradient depends on $\overline{u'}$, which varies inversely with β and C_i. Occurrence of SPC regime would require that bubble expands to at least twice of its original size followed by a rapid compression dominated by

inertial forces [84]. Such bubble motion is possible for moderate turbulent pressure gradient and high mean pressure gradient. If the turbulent pressure gradient is large and mean pressure gradient is moderate, the bubble collapse is only moderately transient as in SP regime due to excessively large expansion of the bubble, which is also accompanied by significant vaporization of solvent, which later on cushions the collapse and reduces the intensity of collapse. Examples of these flow regimes are as follows:

1. SPC regime at $C_i = 1$ for $P_2 = 101.3$ kPa and $C_i = 1$ or 1.1 at $P_2 = 202.6$ or 303.9 kPa
2. SP regime for $\beta = 0.3$, $C_i = 1$ and $P_2 = 101.3$ kPa, as the bubble collapse is only moderately transient, since the large turbulent pressure gradient causes large expansion of the bubble with significant evaporation of water in it. Strongly transient collapse of vapor filled gas bubble would require high mean pressure gradient, which is not available for $P_2 = 101.3$ kPa
3. OSC regime for $C_i = 1.2$. In this case, both mean as well as turbulent pressure gradients are small, due to which neither expansion nor compression of the bubble is appreciable, and the bubble essentially undergoes a small amplitude oscillatory motion in the flow
4. For higher P_2 of 303.9 kPa, and large orifice to pipe diameter ratios ($\beta = 0.5$ or 0.6), combination of large mean pressure gradient and small turbulent gradient gives SP regime of bubble dynamics

Conclusions: The flow regime maps proposed in the study of Kumar et al. [119] present a cogent and coherent picture of operation of hydrodynamic cavitation reactors. These maps essentially depict the trends in the intensity of transient collapse of the bubble with design/process parameters, which is responsible for inducing sonophysical or sonochemical effect. These design or process parameters essentially alter the intensities of the two pressure gradients, viz., mean and turbulent, in the orifice flow, which is reflected in the peak temperature and pressure reached inside the bubble at transient collapse. The flow regime maps reveal that intensity of transient bubble collapse is most sensitive to the cavitation number, among all process/design parameters. For $C_i \leq 1$, the radial motion of bubble is intense enough to induce sonochemical effect. For $C_i \geq 1$, the intensity of radial motion of bubble is rather low which is sufficient to induce physical effects which could be useful for operations such as extraction or emulsification.

Initial bubble volume fraction (α_o) in the flow is also a crucial parameter that influences the operation of the hydrodynamic cavitation reactors in different regimes. This parameter is difficult to measure or control. However, the new design of hydrodynamic cavitation reactor proposed by Kumar and Moholkar [35] introduces the concept of external introduction of gas bubbles in the flow – rather than in situ – generation, which is a random phenomenon. Introduction of external gas bubbles through suitable gas distribution devices (e.g., a glass frit) gives an efficient tool to control both quantity of gas volume fraction in the flow and also a control over the initial sizes of the bubbles.

Overall Conclusions

In this chapter, an attempt is made to give concise account of the developments in mathematical modeling of hydrodynamic cavitation to explain the sonochemical effects induced by it. The physical/chemical effects induced by cavitation are essentially manifestations of the radial motion of the cavitation bubble, which causes energy concentration. This radial motion is driven by the pressure variation profile in the system. The mathematical models for hydrodynamic cavitation have attempted to explore the factors that influence the pressure variation profile and hence the radial motion of cavitation bubbles. The models have also identified conditions under which bubble dynamics in hydrodynamic cavitation resembles that observed in acoustic cavitation. After the preliminary model for hydrodynamic cavitation proposed in 1999, the subsequent developments have been in terms incorporation of the turbulent pressure fluctuations and gradient, different flow geometries like orifice flow and converging–diverging nozzle, accounting for liquid compressibility, accounting for the bubble/bubble and bubble/flow interactions, incorporation of the heat and mass transfer effects and lastly the continuum mixture model coupled with diffusion-limited model that takes into account all factors. With higher level of rigor incorporated into successive models, the simulations of hydrodynamic cavitation have given deeper and more meaningful insight into the physics/chemistry of bubble dynamics phenomena and its influences in terms of intensification of the process. The principal design factors that govern the transient bubble dynamics in hydrodynamic cavitation that gives the sonochemical effect of generation of highly reactive radicals are recovery pressure, extent of permanent pressure head loss in the flow (which is manifested in terms of generation of turbulent pressure fluctuations in the flow), and cavitation number. The intensity of transient bubble motion increases with higher recovery pressure, smaller orifice to pipe diameter ration, and cavitation number <1. However, these factors are bound by the stability of the flow (avoiding flashing of the flow). The simulations of hydrodynamic cavitation have also outlined guidelines for optimization of these design parameters for maximizing the sonochemical effect. There are several avenues for furthering research on modeling of hydrodynamic cavitation. Some of these are as follows: (1) incorporation of the actual reaction kinetics in the bubble (relaxing the assumption of chemical equilibrium), (2) model for rectified diffusion of non-condensable dissolved gas in the liquid across the bubble, and (3) more rigorous modeling of the turbulent fluctuations in cavitating flows involving large pressure drops – as in orifice flow.

The models described in this chapter are very useful tool for design and optimization of the hydrodynamic cavitation reactors for physical and chemical processes. One major application of hydrodynamic cavitation reactors is in the area of wastewater treatments, where bio-recalcitrant pollutants are degraded effectively. This degradation occurs via production of the OH radicals which are strong oxidizing species with oxidation potential of 2.6 eV. The mathematical models for bubble dynamics described in this chapter can quantitatively predict the extent of formation of these radicals at different operating conditions and design parameters.

The simulations of hydrodynamic cavitation using these models could form useful guidelines for design and optimization of hydrodynamic cavitation reactors for effective degradation of larger variety of bio-recalcitrant pollutants.

References

1. Wang J, Wang X, Guo P, Yu J (2011) Degradation of reactive brilliant red K–2BP in aqueous solution using swirling jet–induced cavitation combined with H_2O_2. Ultrason Sonochem 18(2):494–500
2. Mishra KP, Gogate PR (2010) Intensification of degradation of rhodamine B using hydrodynamic cavitation in the presence of additives. Sep Purif Technol 75(3):385–391
3. Wang X, Wang J, Guo P, Guo W, Wang C (2009) Degradation of rhodamine B in aqueous solution by using swirling jet–induced cavitation combined with H_2O_2. J Hazard Mater 169(1–3):486–491
4. Sivakumar M, Pandit AB (2002) Wastewater treatment: a novel energy efficient hydrodynamic cavitational technique. Ultrason Sonochem 9(3):123–131
5. Pal A, Verma A, Kachhwaha SS, Maji S (2010) Biodiesel production through hydrodynamic cavitation and performance testing. Renew Energy 35(3):619–624
6. Sainte Beuve R, Morison KR (2010) Enzymatic hydrolysis of canola oil with hydrodynamic cavitation. Chem Eng Process 49(10):1101–1106
7. Kelkar MA, Gogate PR, Pandit AB (2008) Intensification of esterification of acids for synthesis of biodiesel using acoustic and hydrodynamic cavitation. Ultrason Sonochem 15(3):188–194
8. Schmid A (2010) MTBE degradation by hydrodynamic induced cavitation. Water Sci Technol 61(10):2591–2594
9. Pradhan AA, Gogate PR (2010) Removal of p–nitrophenol using hydrodynamic cavitation and Fenton chemistry at pilot scale operation. Chem Eng J 156(1):77–82
10. Chakinala AG, Gogate PR, Burgess AE, Bremner DH (2009) Industrial wastewater treatment using hydrodynamic cavitation and heterogeneous advanced Fenton processing. Chem Eng J 152(2–3):498–502
11. Braeutigam P, Wu Z–L, Stark A, Ondruschka B (2009) Degradation of BTEX in aqueous solution by hydrodynamic cavitation. Chem Eng Technol 32(5):745–753
12. Wang X, Zhang Y (2009) Degradation of Alachlor in aqueous solution by using hydrodynamic cavitation. J Hazard Mater 161(1):202–207
13. Benito Y, Arrojo S, Hauke G, Vidal P (2005) Hydrodynamic cavitation as a low–cost AOP for wastewater treatment: preliminary results and a new design approach. WIT Trans Ecol Environ 80:495
14. Kalumuck KM, Chahine GL (2000) The use of cavitating jets to oxidize organic compounds in water. J Fluids Eng 122(3):465–470
15. Biradar PM, Roy SB, D'Souza SF, Pandit AB (2010) Excess cell mass as an internal carbon source for biological denitrification. Bioresour Technol 101(6):1787–1791
16. Grubel K, Machnicka A (2009) Use of hydrodynamic disintegration to accelerate anaerobic digestion of surplus activated sludge. Water Environ Res 81(12):2420–2426
17. Sonawane SH, Gumfekar SP, Kate KH, Meshram SP, Kunte KJ, Ramjee L, Mahajan CM, Parande MG, Ashokkumar M (2010) Hydrodynamic cavitation–assisted synthesis of nanocalcite. Int J Chem Eng. doi:10.1155/2010/242963
18. Pinjari DV, Pandit AB (2010) Cavitation milling of natural cellulose to nanofibrils. Ultrason Sonochem 17(5):845–852
19. Patil MN, Pandit AB (2007) Cavitation – a novel technique for making stable nano–suspensions. Ultrason Sonochem 14(5):519–530

20. Find J, Emerson SC, Krausz IM, Moser WR (2001) Hydrodynamic cavitation as a tool to control macro–, micro–, and nano–properties of inorganic materials. J Mater Res 16(12):3503–3513

21. Moser WR, Sunstrom JE, IV, Marshik–Guerts B (1996) The synthesis of nanostructured pure–phase catalysts by hydrodynamic cavitation. In: Moser, WR (ed) Adv Catal Nanostruct Mater, Academic Press, San Diego, CA, USA, pp 285–306

22. Botha CJ, Buckley CA (1995) Disinfection of potable water: the role of hydrodynamic cavitation. Water Supply 13(2):219–229

23. Jyoti KK, Pandit AB (2003) Hybrid cavitation methods for water disinfection. Biochem Eng J 14(1):9

24. Save SS, Pandit AB, Joshi JB (1994) Microbial cell disruption: role of cavitation. Chem Eng J (Lausanne) 55:67B–72B

25. Balasundaram B, Harrison STL (2006) Disruption of Brewers' yeast by hydrodynamic cavitation: process variables and their influence on selective release. Biotechnol Bioeng 94(2):303–311

26. Balasundaram B, Harrison STL (2006) Study of physical and biological factors involved in the disruption of *E. coli* by hydrodynamic cavitation. Biotechnol Prog 22(3):907–913

27. Balasundaram B, Pandit AB (2001) Selective release of invertase by hydrodynamic cavitation. Biochem Eng J 8(3):251–256

28. Gogate PR (2002) Cavitation: an auxiliary technique in wastewater treatment schemes. Adv Environ Res 6(3):335–358

29. Gogate PR (2007) Application of cavitational reactors for water disinfection: current status and path forward. J Environ Manag 85(4):801–815

30. Gogate PR, Pandit AB (2001) Hydrodynamic cavitation reactors: a state of the art review. Rev Chem Eng 17(1):1–85

31. Gogate PR, Pandit AB (2005) A review and assessment of hydrodynamic cavitation as a technology for future. Ultrason Sonochem 12(1–2):21–27

32. Gogate PR, Pandit AB (2000) Engineering design methods for cavitation reactors ii: hydrodynamic cavitation. AIChE J 46(8):1641–1649

33. Kanthale PM, Gogate PR, Pandit AB, Wilhelm AM (2005) Dynamics of cavitational bubbles and design of a hydrodynamic cavitational reactor: cluster approach. Ultrason Sonochem 12(6):441–452

34. Krishnan JS, Dwivedi P, Moholkar VS (2006) Numerical investigation into the chemistry induced by hydrodynamic cavitation. Ind Eng Chem Res 45(4):1493–1504

35. Kumar KS, Moholkar VS (2007) Conceptual design of a novel hydrodynamic cavitation reactor. Chem Eng Sci 62(10):2698–2711

36. Moholkar VS, Pandit AB (2001) Modeling of hydrodynamic cavitation reactors: a unified approach. Chem Eng Sci 56(21–22):6295–6302

37. Vichare NP, Gogate PR, Pandit AB (2008) Optimization of hydrodynamic cavitation using a model reaction. Chem Eng Technol 23(8):683–690

38. Braeutigam P, Franke M, Wu Z–L, Ondruschka B (2010) Role of different parameters in the optimization of hydrodynamic cavitation. Chem Eng Technol 33(6):932–940

39. Morison KR, Hutchinson CA (2009) Limitations of the Weissler reaction as a model reaction for measuring the efficiency of hydrodynamic cavitation. Ultrason Sonochem 16(1):176–183

40. Mahulkar AV, Bapat PS, Pandit AB, Lewis FM (2008) Steam bubble cavitation. AIChE J 54(7):1711–1724

41. Amin LP, Gogate PR, Burgess AE, Bremner DH (2010) Optimization of a hydrodynamic cavitation reactor using salicylic acid dosimetry. Chem Eng J 156(1):165–169

42. Chatterjee D, Arakeri VH (1997) Towards the concept of hydrodynamic cavitation control. J Fluid Mech 332:377–394

43. Kumar PS, Pandit AB (1999) Modeling hydrodynamic cavitation. Chem Eng Technol 22:1017–1027

44. Gogate PR, Shirgaonkar IZ, Sivakumar M, Kumar PS, Vichare NP, Pandit AB (2001) Cavitation reactors: efficiency assessment using a model reaction. AIChE J 47:2526–2538
45. Chatterjee D (2003) Use of ultrasonics in shear layer cavitation control. Ultrasonics 41:465–475
46. Arrojo S, Benito Y (2008) A theoretical study of hydrodynamic cavitation. Ultrason Sonochem 15:203–211
47. Sharma A, Gogate PR, Mahulkar A, Pandit AB (2008) Modeling of hydrodynamic cavitation reactors based on orifice plates considering hydrodynamics and chemical reactions occurring in bubble. Chem Eng J 143:201–209
48. Kumar P, Moholkar VS (2011) Numerical assessment of hydrodynamic cavitation reactors using organic solvents. Ind Eng Chem Res 50(8):4769–4775
49. Sivasankar T, Moholkar VS (2009) Mechanistic approach to intensification of sonochemical degradation of phenol. Chem Eng J 149(1–3):57–69
50. Sivasankar T, Moholkar VS (2009) Physical insights into the sonochemical degradation of recalcitrant organic pollutants with cavitation bubble dynamics. Ultrason Sonochem 16(6):769–781
51. Sivasankar T, Moholkar VS (2008) Mechanistic features of the sonochemical degradation of organic pollutants. AIChE J 54(8):2206–2219
52. Sivasankar T, Moholkar VS (2010) Physical insight into the sonochemical degradation of 2,4–dichlorophenol. Environ Technol 31(14):1483–1494
53. Chakma S, Moholkar VS (2013) Physical mechanism of sono–fenton process. AIChE J 59(11):4303–4313
54. Chakma S, Moholkar VS (2014) Investigations in synergism of hybrid advanced oxidation processes with combinations of sonolysis + Fenton process + UV for degradation of Bisphenol–A. Ind Eng Chem Res 53(16):6855–6865
55. Chakma S, Moholkar VS (2015) Investigation in mechanistic issues of sonocatalysis and sonophotocatalysis using pure and doped photocatalysts. Ultrason Sonochem 22:287–299
56. Chakma S, Moholkar VS (2015) Sonochemical synthesis of mesoporous $ZrFe_2O_5$ and its application for degradation of recalcitrant pollutants. RSC Adv 5:53529–53542
57. Morya NK, Iyer PK, Moholkar VS (2008) A physical insight into sonochemical emulsion polymerization with cavitation bubble dynamics. Polymer 49(7):1910–1925
58. Kanmuri S, Moholkar VS (2010) Mechanistic aspects of sonochemical copolymerization of butyl acrylate and methyl methacrylate. Polymer 51(14):3249–3261
59. Reddy BR, Sivasankar T, Sivakumar M, Moholkar VS (2010) Physical facets of ultrasonic cavitational synthesis of zinc ferrite particles. Ultrason Sonochem 17(2):416–426
60. Choudhury HA, Choudhary A, Sivakumar M, Moholkar VS (2013) Mechanistic investigation of the sonochemical synthesis of zinc ferrite. Ultrason Sonochem 20(1):294–302
61. Goswami PP, Choudhury HA, Chakma S, Moholkar VS (2013) Sonochemical synthesis and characterization of manganese ferrite nanoparticles. Ind Eng Chem Res 52(50):17848–17855
62. Goswami PP, Choudhury HA, Chakma S, Moholkar VS (2013) Sonochemical synthesis of cobalt ferrite nanoparticles. Int J Chem Eng ID: 934234. (Online available at: http://www.hindawi.com/journals/ijce/aip/934234/)
63. Warmoeskerken MMCG, van der Vlist P, Moholkar VS, Nierstrasz VA (2002) Laundry process intensification by ultrasound. Colloids Surf A 210(2–3):277–285
64. Moholkar VS, Nierstrasz VA, Warmoeskerken MMCG (2003) Intensification of mass transfer in wet textile processes by power ultrasound. Autex Res J 3(3):129–138
65. Moholkar VS, Warmoeskerken MMCG, Ohl CD, Prosperetti A (2004) Mechanism of mass–transfer enhancement in textiles by ultrasound. AIChE J 50(1):58–64
66. Moholkar VS, Warmoeskerken MMCG (2004) Investigations in mass transfer enhancement in textiles with ultrasound. Chem Eng Sci 59(2):299–311
67. Midathana VR, Moholkar VS (2009) Mechanistic studies in ultrasound–assisted adsorption for removal of aromatic pollutants. Ind Eng Chem Res 48(15):7368–7377

68. Nalajala VS, Moholkar VS (2010) Investigations in the physical mechanism of sonocrystallization. Ultrason Sonochem 18(1):345–355

69. Chakma S, Moholkar VS (2011) Mechanistic features of ultrasonic desorption of aromatic pollutants. Chem Eng J 175:356–367

70. Shah YT, Pandit AB, Moholkar VS (1999) Cavitation reaction engineering, Plenum Chemical Engineering Series. Kluwer/Plenum Press, New York

71. Yan Y, Thorpe RB, Pandit AB (1988) Cavitation noise and its suppression by air in orifice flow. Proc Int Symp Flow Induced Vibration and Noise, ASME, Chicago

72. Rayleigh L (1917) On the pressure developed in a liquid during the collapse of spherical cavity. Philos Mag 34:94–98

73. Plesset MS (1949) Dynamics of cavitation bubbles. J Appl Mech (Trans ASME) 16:277–282

74. Poritsky H (1952) The collapse or growth of a spherical bubble or cavity in a viscous fluid. Proc 1st US National Congress Appl Mech (Ed. E. Sternberg) 813–821

75. Noltingk BE, Neppiras EA (1950) Cavitation produced by ultrasonics. Proc Phys Soc B 63:674–685

76. Gilmore FR (1954) Hydrodynamic laboratory report. California Institute of Technology, 26–4

77. Kirkwood JG, Bethe HA (1942) The pressure wave produced by an under water explosion. Off Sci Res Dev Rep. 558. Office of Scientific Research and Development [OSRD], Washington DC, USA

78. Keller JB, Kolodner II (1956) Damping of underwater explosion bubble oscillations. J Appl Phys 27:1152–1161

79. Keller JB, Miksis MJ (1980) Bubble oscillations of large amplitude. J Acoust Soc Am 68:628–633

80. Prosperetti A, Lezzi A (1986) Bubble dynamics in a compressible liquid. Part 1. First order theory. J Fluid Mech 168:457–477

81. Brennen CE (1995) Cavitation and bubble dynamics. Oxford University Press, Oxford

82. Lofstedt R, Weninger K, Puttermann SJ, Barber BP (1995) Sonoluminescing bubbles and mass diffusion. Phys Rev E 51:4400–4410

83. Barber BP, Hiller RA, Lofstedt R, Putterman SJ, Weninger KR (1997) Defining the unknowns of sonoluminescence. Phys Rep 281:65–143

84. Flynn HG (1964) Physics of acoustic cavitation in liquids. In: Mason WP (ed) Physical acoustics. Academic, New York, pp 57–172

85. Colussi AJ, Weavers LK, Hoffmann MR (1998) Chemical bubble dynamics and quantitative sonochemistry. J Phys Chem A 102(35):6927–6934

86. Colussi AJ, Hoffmann MR (1999) Vapor supersaturation in collapsing bubbles: relevance to mechanisms of sonochemistry and sonoluminescence. J Phys Chem A 103:11336–11339

87. Kamath V, Prosperetti A, Egolfopoulos FN (1993) A theoretical study of sonoluminescence. J Acoust Soc Am 94:248–260

88. Prasad Naidu DV, Rajan R, Kumar R, Gandhi KS, Arakeri VH, Chandrasekaran S (1994) Modeling of a batch sonochemical reactor. Chem Eng Sci 49(6):877–888

89. Gong C, Hart DP (1998) Ultrasound induced cavitation and sonochemical yields. J Acoust Soc Am 104:2675–2682

90. Sochard S, Wilhelm AM, Delmas H (1997) Modeling of free radicals production in a collapsing gas–vapor bubble. Ultrason Sonochem 4:77–84

91. Moss WC, Young DA, Harte JA, Levalin JL, Rozsnyai BF, Zimmerman GB, Zimmerman IH (1999) Computed optical emissions from sonoluminescing bubbles. Phys Rev E 59:2986–2992

92. Yasui K (1997) Alternative model for single–bubble sonoluminescence. Phys Rev E 56:6750–6760

93. Yasui K (1997) Chemical reactions in a sonoluminescing bubble. J Phys Soc Jpn 66:2911–2920

94. Storey BD, Szeri AJ (2000) Water vapor, sonoluminescence and sonochemistry. Proc R Soc London A 456:1685–1709

95. Eames IW, Marr NJ, Sabir H (1997) The evaporation coefficient of water: a review. Int J Heat Mass Transfer 40:2963–2973
96. Storey BD, Szeri AJ (2001) A reduced model of cavitation physics for use in sonochemistry. Proc R Soc London A 457:1685–1700
97. Toegel R, Gompf B, Pecha R, Lohse D (2000) Does water vapor prevent upscaling sonoluminescence? Phys Rev Lett 85:3165–3168
98. Toegel R (2002) Reaction diffusion kinetics of a single sonoluminescing bubble. PhD Dissertation, University of Twente
99. Hirschfelder JO, Curtiss CF, Bird RB (1954) Molecular theory of gases and liquids. Wiley, New York
100. Reid RC, Prausnitz JM, Poling BE (1987) Properties of gases and liquids. McGraw Hill, New York
101. Condon EU, Odishaw H (1958) Handbook of physics. McGraw Hill, New York
102. Crank J (1975) The mathematics of diffusion. Clarendon, Oxford
103. Sivasankar T, Paunikar AW, Moholkar VS (2007) Mechanistic approach to enhancement of the yield of a sonochemical reaction. AIChE J 53(5):1132–1143
104. Hilgenfeldt S, Lohse D, Brenner MP (1996) Phase diagrams for sonoluminescing bubbles. Phys Fluids 8(11):2808–2826
105. Lu X, Prosperetti A, Toegel R, Lohse D (2003) Harmonic enhancement of single bubble sonoluminescence. Phys Rev E 67:56310
106. Apfel RE (1981) In: Edmonds PD (ed) Methods in experimental physics, vol 19. Academic, New York, pp 355–413
107. Holland CK, Apfel RE (1989) An improved theory for prediction of microcavitation thresholds. IEEE Trans Ultrason Ferroelectr Freq Control 36:204–208
108. Moholkar VS, Pandit AB (1997) Bubble behavior in hydrodynamic cavitation: effect of turbulence. AIChE J 43:1641–1648
109. Morrison GL, DeOtte RE Jr, Nail GH, Panak DL (1993) Mean velocity and turbulence fields inside a $\beta = 0.5$ orifice flowmeter. AIChE J 39:745–756
110. Green DW, Perry RH (2008) Perry's chemical engineers' handbook. McGraw Hill, New York
111. Moholkar VS, Kumar PS, Pandit AB (1999) Hydrodynamic cavitation for sonochemical effects. Ultrason Sonochem 6(1–2):53–65
112. Moholkar VS, Pandit AB (2001) Numerical investigations in the behavior of one–dimensional bubbly flow in hydrodynamic cavitation. Chem Eng Sci 56(4):1411–1418
113. van Wijngaarden L (1968) On the equations of motion for mixtures of liquid and gas bubbles. J Fluid Mech 33:465–474
114. van Wijngaarden L (1972) One dimensional flow of liquids containing small gas bubbles. Annu Rev Fluid Mech 4:369–396
115. Wang Y–C, Brennen CE (1998) One dimensional bubbly cavitating flows through a converging–diverging nozzle. J Fluids Eng 120:166–170
116. Wang Y–C, Brennen CE (1999) Numerical computation of shock waves in a spherical bubble cloud of cavitation bubbles. J Fluids Eng 121:872–880
117. Plessset MS, Prosperetti A (1977) Bubble dynamics and cavitation. Annu Rev Fluid Mech 9:145–185
118. Brenner MP, Hilgenfeldt S, Lohse D (2002) Single bubble sonoluminescence. Rev Mod Phys 74:425–484
119. Kumar P, Khanna S, Moholkar VS (2012) Flow regime maps and optimization thereby of hydrodynamic cavitation reactors. AIChE J 58(12):3858–3866
120. Eriksson G (1975) Thermodynamic studies of high temperature equilibria – XII: SOLGAMIX, A computer program for calculation of equilibrium composition in multiphase systems. Chem Scr 8:100–103
121. FactWeb (Online Trial Version). Homepage: http://www.factsage.com (Accessed Nov 2009)

Sonophotocatalytic Mineralization of Environmental Contaminants Present in Aqueous Solutions

P. Sathishkumar, R. V. Mangalaraja, and Sambandam Anandan

Contents

Abstract

The wastewater released from the industrial sectors essentially needs the effective technology to avoid the hazardous effects associated with its discharge. The development of low cost and faster processing technology makes the mineralization of the environmental pollutants effective for the large-scale utilization. Various methodologies have been proposed and practiced for its commercialization; however, the generation of secondary pollutants was resulted. The

P. Sathishkumar
Faculty of Chemical Sciences, Department of Organic Chemistry, University of Concepcion, Concepcion, Chile
e-mail: sathishpanner2001@gmail.com

R.V. Mangalaraja (✉)
Faculty of Engineering, Advanced Ceramics and Nanotechnology Laboratory, Department of Materials Engineering, University of Concepcion, Concepcion, Chile
e-mail: mangal@udec.cl

S. Anandan
Nanomaterials and Solar Energy Conversion Lab, Department of Chemistry, National Institute of Technology, Tiruchirappalli, Tiruchirappalli, Tamilnadu, India
e-mail: sanand@nitt.edu

ultrasound-assisted mineralization of environmental contaminants gained the maximum interest from the public and research communities due to its enhanced efficiency of advanced oxidation processes (AOPs). The effective utilization of the ultrasound and its combination with the various AOPs achieved the maximum degradation for the wide spectrum of environmental pollutants and avoids the secondary pollutants generation. The current chapter summarizes the photocatalysis-, sonolysis-, sonocatalysis-, and sonophotocatalysis-assisted degradation of various environmental contaminants via single and coupled AOPs. The degradation of various colored and colorless environmental pollutants is discussed here. Among the AOPs reviewed herein, photocatalysis and sonophotocatalysis techniques were found to be very efficient for the degradation. The intermediates identified from the photocatalytic and sonophotocatalytic degradation of environmental contaminants are similar in most of the studies; however, a few of the intermediates were not observed in other AOP processes which indicates different pathway are followed during the degradation. The reasons for achieving synergy and detrimental effects from the coupled AOPs are analyzed. The development of visible light responsive nanocatalysts reduces the cost required for the commercialization of sonophotocatalysis. The cost estimation analysis was discussed here for the commercialization of the AOP techniques. In addition, recycling of the treated water reduces water consumption of various industries.

Keywords

Wastewater treatment • AOPs • Sonophotocatalysis • Synergy and cost estimation

Introduction

The indecent discharge of the industrial effluents and agrochemicals leads to increase the pollutant concentration in the environment. The presence of such high concentration of environmental contaminants tends to provoke the adverse effects on the ecosystem [1, 2]. The genetic damage, cancer, chromosomal abnormalities, birth defects, and few other health-related problems were identified due to the augmented concentration of environmental contaminants. The permissible quantity of the environmental contaminants is few parts per million, and in the case of colored organic contaminants very low level concentration can be visibly identified from its characteristic color [3, 4]. Hence, the mineralization of environmental contaminants was aimed by many research groups and started working towards the complete mineralization for the past five decades [5, 6]. The biological treatment, chemical precipitation and coagulation, thermal treatment/incineration, adsorption, ion exchange, sludge handling and disposal, and miscellaneous treatment processes are the techniques initially developed to remove the environmental contaminants; however, the unauthorized discharge of the materials utilized in the above-mentioned technologies causes the secondary pollution [7, 8]. To avoid the secondary pollutions and the perilous effects caused by the environmental contaminants, researchers discovered

the advanced oxidation processes (AOPs) or technologies (AOTs) for their removal from the environment.

Various kinds of AOPs are reported in the literature [9–12] for the degradation of environmental contaminants; however, the readily applicable techniques for the commercialization includes O_3/H_2O_2, Fe^{2+}/H_2O_2, UV/O_3, UV/H_2O_2, $UV/O_3/H_2O_2$, photocatalysis, catalytic ozonation, sonocatalysis, and sonophotocatalysis. The homogeneous catalysis of wastewater is not recommended since the concentration of metal ions on the aquatic environment tends to increase and fetch its adverse effects [13]. The semiconductor (TiO_2)-based photolysis technique for the water splitting in the presence of ultraviolet irradiation was first reported by Fujishima and Honda in 1972 [14]. The pioneering research work led to the origination of the semiconductor-based photocatalysis. The radical formation and the mechanistic investigation of the photocatalytic processes are well documented in the literature [15, 16]. As the time progresses, the research based on semiconductor photocatalysis has grown in various dimensions hence promising reports were achieved and further improved efficiencies were obtained in pilot plants. For example, Puma and Yue [17] reported the pilot scale photocatalysis slurry reactor for the mineralization of salicylic acid in which the mineralization of salicylic acid achieved 13-fold enhanced rate when compared to other techniques being practiced. The schematic representation of the reactor is shown in Fig. 1.

On the other hand, heterogeneous ozonation has emerged as the modern technology for the complete removal of organic pollutants. However, the drawbacks such as the loss of effective reaction sites, agglomeration of the nanosize semiconductor catalysts, and mass transfer rate of pollutants to the catalytic surface were need to be improved. Thus, in general, the advantages and disadvantages associated with the use of single-handed AOPs are presented in Table 1 [18]. The efficiency of single-handed AOPs needs to improve, further to minimize the operating cost as well as the processing time.

Sonolysis and Sonocatalysis

The schematic representation of sonolysis of water is presented in Fig. 2 [19], which describes the cavitation phenomenon followed by the formation of various free radicals. The extreme conditions produced during the sonolysis of water and the three reaction zones in the cavitation process were explained by Adewuyi [20]. The high temperature and pressure produced from the acoustic cavitation was proceeded by the water splitting reaction [21]. Among the various theories proposed to explain the phenomenon of acoustic cavitation [22–24], "hot spot theory" gave the satisfactory explanation. The presence of dissolved gas, nature of the substances, and other materials present near to the hotspot influence the generation of highly reactive radicals [25]. The radicals generated during the acoustic cavitation further initiates the production of secondary radicals and the degradation of contaminants present in its aquatic environment.
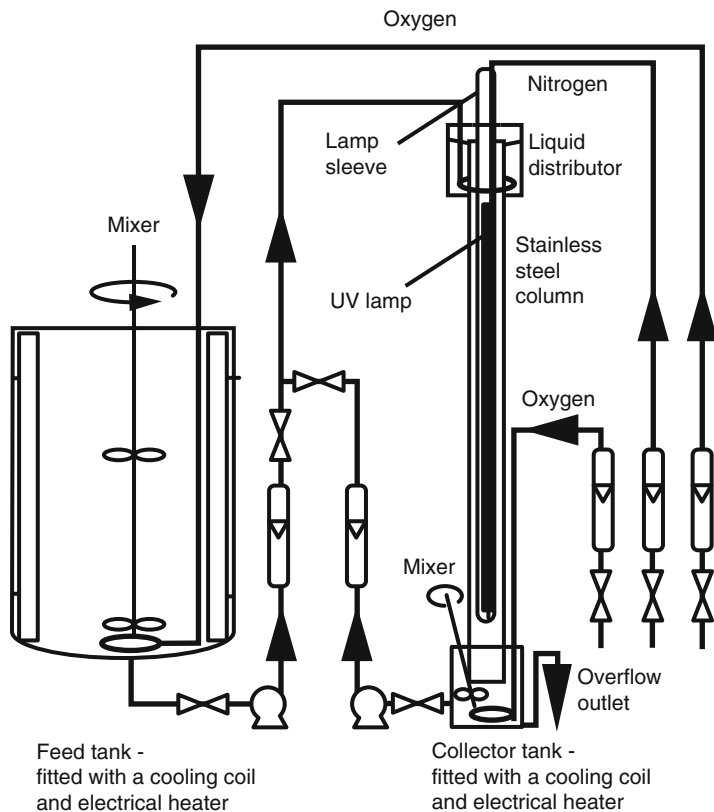
Fig. 1 Schematic representation of the pilot plant laminar falling film slurry photocatalytic reactor (Reprinted with permission from Ref. [17]. Copyrights (1999) American Chemical Society)

The complete removal of various environmental contaminants is not possible by the sonolysis alone since the sonolysis process suffers to oxidize the various environmental contaminants. The process needs a solid support for the effective interaction of the environmental pollutants with the various radicals produced during the sonolysis. In addition, the sonoluminescence produced from the sonolysis process can initiate the electronic charge creation from the semiconductor nanomaterials. Based on the cavitation phenomenon, the degradation of various contaminants was studied in order to prove that the ultrasound alone is more efficient for the degradation. Meng et al. [26] investigated the sonocatalytic degradation of Rhodamine-B in the presence of C_{60} coupled CdS-TiO_2 system. The pictorial representation for the mechanism of sonocatalytic degradation of Rhodamine-B was presented in Fig. 3. The direct band gap excitation of TiO_2 and CdS was accomplished during the ultrasound irradiation. However, in the absence of C_{60} the excited CdS injects the electrons into the conduction band of TiO_2 followed by the transfer of electrons to the dissolved oxygen to produce the superoxide radicals ($O_2^{\bullet-}$) in addition to the conduction band electrons produced from the TiO_2. The role

Table 1 Advantages and disadvantages of single-handed AOP systems adopted from Ref [18] and further references cited there in

S. No.	Process	Advantages	Disadvantages
A.	Biological	Cost-competitive option. Direct, disperse, and basic dyes have high level of adsorption on to activated sludge	Dyes are generally toxic and very resistant to biodegradation. Acid and reactive dyes are highly water soluble and have poor adsorption on to sludge
B.	Coagulation	Economically feasible; satisfactory removal of disperse, sulfur, and vat dyes	Removal is pH dependent; produces large quantity of sludge. May not remove highly soluble dyes; unsatisfactory result with azo, reactive, acid, and basic dyes
C.	Activated C adsorption	Good removal of wide variety of dyes, namely, azo, reactive, and acid dyes; especially suitable for basic dye	Removal is pH dependent; unsatisfactory result for disperse, sulfur, and vat dyes. Regeneration is expensive and involves adsorbent loss; necessitates costly disposal
D.	Ion exchange	Adsorbent can be regenerated without loss, dye recovery conceptually possible	Ion exchange resins are dye specific; regeneration is expensive; large-scale dye recovery cost prohibitive
E.	Chemical oxidation	Initiates and accelerates azo-bond cleavage	Thermodynamic and kinetic limitations along with secondary pollution are associated with different oxidants. Not applicable for disperse dyes. Negligible mineralization possible, release of aromatic amines, and additional contamination with chlorine (in case of $NaOCl$) is suspected
F.	Advanced oxidation processes, AOPs	Generate a large number of highly reactive free radicals and by far surpass the conventional oxidants in decolorization	AOPs in general may produce further undesirable toxic byproducts and complete mineralization may not be possible. Presence of radical scavengers reduces efficiency of the processes some of which are pH dependent. Cost prohibitive at their present stage of development
F-1.	UV/O_3	Applied in gaseous state, no alteration of volume. Good removal of almost all types of dyes; especially suitable for reactive dyes. Involves no sludge formation, necessitates short reaction times	Removal is pH dependent (neutral to slightly alkaline); poor removal of disperse dyes. Problematic handling, impose additional loading of water with ozone. Negligible or no COD removal. High cost of generation coupled with very short half-life and gas–liquid mass transfer limitation; suffer

(*continued*)

Table 1 (continued)

S. No.	Process	Advantages	Disadvantages
F-2.	UV/H_2O_2	Involves no sludge formation, necessitates short reaction times, and reduction of COD to some extent may be possible	Not applicable for all dye types, requires separation of suspended solid and suffers from UV light penetration limitation. Lower pH required to nullify effect of radical scavengers
F-3.	Fenton's reagent	Effective decolorization of both soluble and insoluble dyes; applicable even with high suspended solid concentration. Simple equipment and easy implementation. Reduction of COD (except with reactive dyes) possible	Effective within narrow pH range of <3.5; and involves sludge generation. Comparatively longer reaction time required
F-4.	Photocatalysis	No sludge production, considerable reduction of COD, potential of solar light utilization	Light penetration limitation, fouling of catalysts, and problem of fine catalyst separation from the treated liquid (slurry reactors)
F-5.	Electrochemical	Effective decolorization of soluble/insoluble dyes; reduction of COD possible. Not affected by presence of salt in wastewater	Sludge production and secondary pollution (from chlorinated organics, heavy metals) are associated with electrocoagulation and indirect oxidation, respectively. Direct anodic oxidation requires further development for industrial acceptance. High cost of electricity is an impediment. Efficiency depends on dye nature

of C_{60} in the CdS-TiO_2 system is to store the electronic charges as well to produce the enhanced surface area for the improved sonocatalytic degradation of Rhodamine-B. On the other hand, the holes produced from the direct band gap excitation of the semiconductor can quickly transfer to the bulk solution which can directly bleach the effluent, and it can split the water molecule to produce the hydroxyl radicals. In general, the enhanced population of hydroxyl radicals was observed from the sonocatalysis of C_{60} coupled CdS-TiO_2 system.

Moreover, Wang et al. [27] reported the sonocatalytic degradation of acid red B under different experimental conditions as shown in Fig. 4. The rutile TiO_2-assisted sonocatalytic degradation of acid red B gives the methoxy phenyl oxime and phthalic anhydride as the intermediates after sonication for 100 min; however, in the presence of anatase TiO_2 at the same experimental conditions even the so-called intermediates are degraded further to yield low molecular weight compound. From this, it is clear that the anatase and rutile phases of TiO_2 follow the different reaction mechanism during the sonocatalysis. Similarly, Khatae et al. [28, 29] utilized the
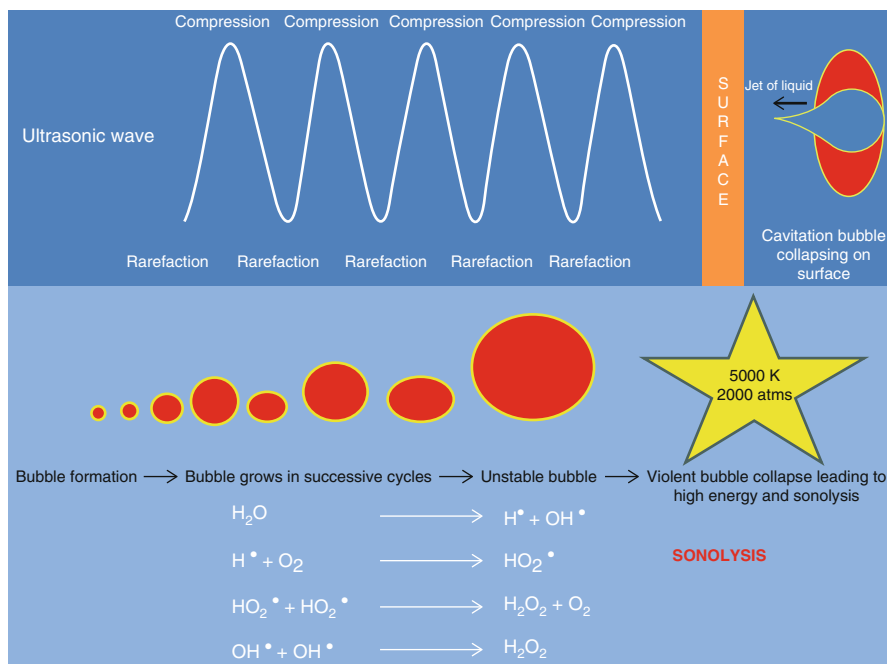
Fig. 2 Cavitation bubble formation at various stages and the production of various effective radicals during sonolysis of water (Reprinted with permission from Ref. [19]. Copyrights (2010) Elsevier Publications)

Gd and Pr doped ZnO for the sonocatalytic degradation of various textile dyes. In addition, Perozo-Rondon et al. [30] reported the ultrasound-assisted process is more efficient for the selective synthesis of chalcones.

Hybrid Advanced Oxidation Processes

The purpose of integrating or combing the two different advanced oxidation processes is to enhance the efficiency of the degradation as well as to reduce the operating cost and time required for the AOPs. The investigators coupled the AOPs in two different ways as (i) sequential or integrated and (ii) simultaneous or combined AOPs [31–33].

Sequential or Integrated AOPs

The sequential or integrated AOP means the treatment of the organic contaminants by an AOP is followed by another AOP process. The subsistence of the various advanced oxidation processes frequently extends the greater degradation rate, and
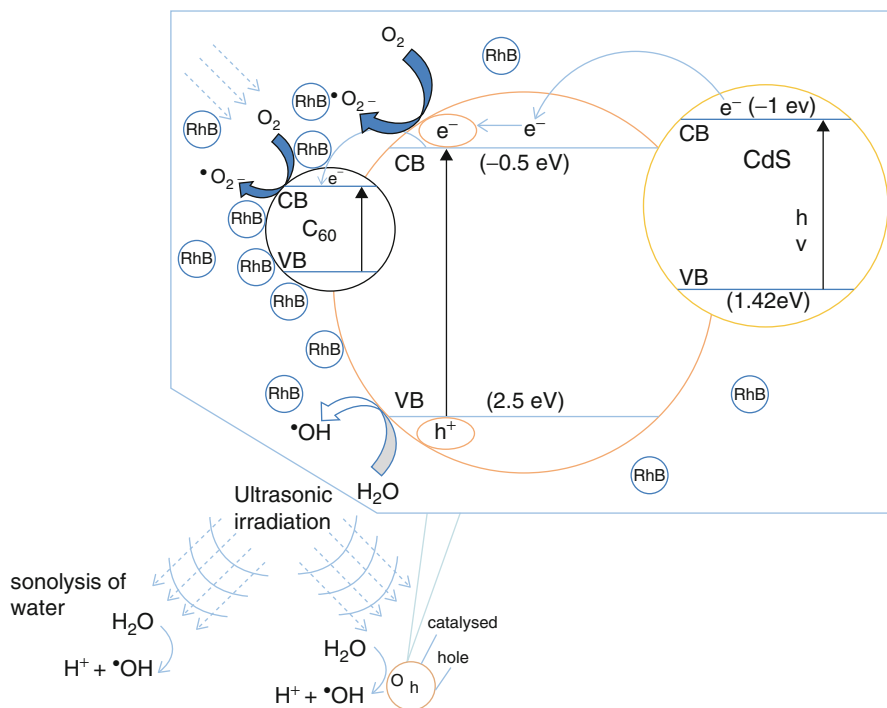
Fig. 3 Schematic representation of electronic charge separation at the interface of CdS-C_{60}/TiO$_2$ during ultrasound irradiation (Reprinted with permission from Ref. [26]. Copyrights (2012) Elsevier Publications)

the efficacy of the processes depends on the various factors. The wastewater treatment by the integrated AOPs was practiced at various scales and the results achieved during the processes are presented in Table 2 [34], which provides the detailed information about the various sequential processes studied in the literature. Moreover, a model schematic representation of the integrated sonophotolysis was given in Fig. 5 [35]; it describes the effluent treatment of photolysis followed by the sonolysis. However, the time span provided for the sequential treatment relaxes the electronic charges, radicals, as well as the mass transfer rate.

Simultaneous or Combined AOPs

In order to improve the efficacy further and to avoid the drawbacks associated with the utilization of single-handed and integrated AOPs, the combined AOP systems were developed. Ultrasound combined with photocatalyis, ozonation, Fenton, and electro-Fenton are the few combined advanced oxidation technologies developed for the degradation of environmental contaminants [36]. Stock et al. [31] and Neelavannan et al. [32, 33] attained the enhanced efficiency from the combined
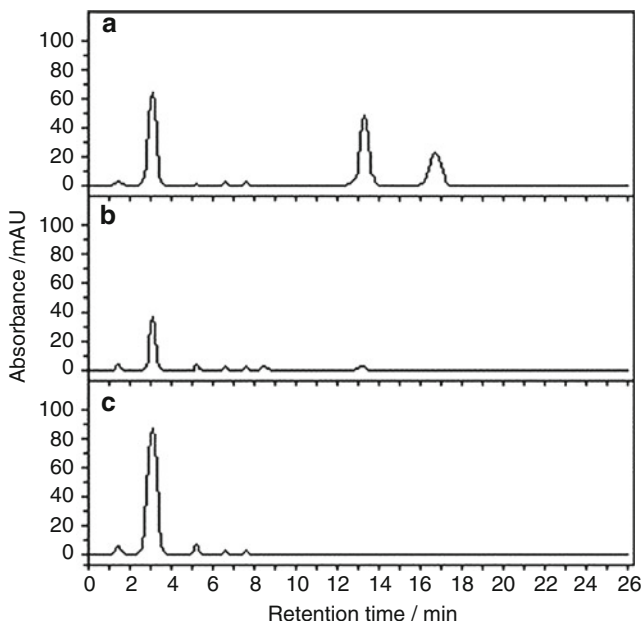
Fig. 4 HPLC chromatograms of acid red B solution under different conditions: (**a**) ultrasound (100 min) + rutile TiO$_2$; (**b**) ultrasound (100 min) + anatase TiO$_2$; and (**c**) original solution (Reprinted with permission from Ref. [27]. Copyrights (2007) Elsevier Publications)

processes when compared to the integrated processes. Among the various combined technologies, sonophotocatalysis received much consideration from various research communities due to its (i) enhanced efficiency for the mineralization of various environmental contaminants and (ii) the production of high temperature and pressure which resulted in the enhanced number of hydroxyl radicals for the degradation of environmental pollutants. Together, the application of ultrasound in the heterogeneous systems engenders the asymmetric cavitation. The asymmetric impulsive collapse of micro bubbles produced from the solvents leads to the microjet formation which reactivates the catalysts surface [37, 38].

The environmental contaminants are approximately classified into two categories based on the research articles published in the area of environmental purification. The colored pollutants' existence in very low concentration can be visibly identified from its characteristic color. Various analytical techniques are needed to prove the existence of the colorless pollutants in the aqueous environment. Therefore, we classified the degradation studies by the colored and colorless pollutants in the following section to easily understand the nature of the degradation pathway.

Perspective of Sonophtocatalytic Degradation of Colored Pollutants

The combined sonophotocatalysis provides a mean to develop the effective methodology for the degradation/mineralization of environmental contaminants. The effective reaction sites as well as the band gap excitation of the semiconductor

Table 2 Recent demonstrations of sequential treatment of real industrial effluents adopted from Ref. [34] and the references cited there in (Reprinted with permission from Ref. [34]. Copyrights (2014) Elsevier Publications)

Wastewater	Strength, kg COD m⁻³	Scale	Chemical treatment	Biological treatment	Main results
Pesticide-wash	0.5–1.4	Industrial	Solar photo-Fenton	IBR[a]	Best total DOC removal efficiency of 89 % (37.5 % after pretreatment). Pretreatment extended to achieve 40–50 % mineralization to deal with variability in real influent
Pesticide-wash	1.0–1.6	Pilot	Solar photo-Fenton	IBR[a]	Pretreatment increased BOD_5/COD from 0.3 to 0.6, total DOC removal efficiency of 82.5 % (50 % after pretreatment)
Filtered landfill leachate	3.0–4.0	Lab	Air stripping + Fenton	Sequential batch reactor	Air stripping removed 96 % ammonia and Fenton treatment removed 60 % COD. These pretreatments increased BOD_5/COD from 0.18 to 0.38
Vinasse	68.6	Lab	Ozonation	Anaerobic digestion	Pretreatment increased BOD_5/COD from 0.4 to 0.65; 15-min pretreatment also increased subsequent methane yield and production rate by 13 % and 41 %, respectively
Pyridine manufacturing	65	Lab	Fenton	*Putida* sp.[b]	Pretreatment increased BOD_5/COD from 0.037 to 0.79, total COD removal of 85 % (66 % after pretreatment)
3-Cyanopyridine manufacturing	25.6	Lab	Fenton	*Putida* sp.[b]	Pretreatment increased BOD_5/COD from 0.124 to 0.94, total COD removal of 94 % (84 % after pretreatment)
Pretreated landfill leachate	6.8–8.3	Pilot	Solar photo-Fenton	BOD_5, BOD_{28} and respirometry	Pretreatment increased the rate of oxygen uptake sevenfolds and increased BOD_5/COD from 0.16 to 0.37 and BOD_{28} (Zahn-Wellens) from 44–49 % to 89 % (330 mM H_2O_2)

Landfill leachate	1.2–1.8	Pilot and industrial	Fenton	BANF/BAF[c]	COD and TN removal >95%[e]. Fenton treatment contributed to more than 90 % of COD removal, but biological treatment was necessary to meet COD and N discharge limits
Refinery	1.2	Lab	Fenton	BOD_5	Pretreatment increased BOD_5/COD from 0.27 to 0.44
Winery	2.96 ± 0.07	Pilot	Solar photo-Fenton	IBR[a]	Pretreatment increased BOD_5/COD from 0.5 to 0.9 (80 mM H_2O_2) and BOD_{28} (Zahn-Wellen assay) from 78 % to 97 % (95 mM H_2O_2). Pretreatment also reduced the total treatment time necessary to meet discharge limits from 10 to 6 d
Pretreated landfill leachate	3.4–4.2	Pilot	Solar photo-Fenton	Activated sludge	Pretreatment increased BOD_{28} (Zahn-Wellen assay) from 4–20 to nearly 90 % depending on H_2O_2 dosage. Total DOC and dissolved nitrogen removal efficiencies of 90 % and 100%[e]
Pesticide manufacturing	28.1 ± 0.7	Lab	CWHPO[d]	Rotating biological contactor	Pretreatment increased BOD_5/COD from 0.07 to 0.13 and BOD_{17} (Zahn-Wellens assay) from 0 to 60 %. TOC removal of 78 % when the pretreated effluent was mixed with synthetic sewage (10 % vol.). Total nitrogen removal of 50 %

[a]IBR = aerobic immobilized biomass reactor
[b]*Putida* sp. = suspended *Putida pseudoalcaligenes*
[c]BANF/BAF = sequential biological anaerobic filter and biological aerated filter
[d]CWHPO = catalytic wet hydrogen peroxide oxidation
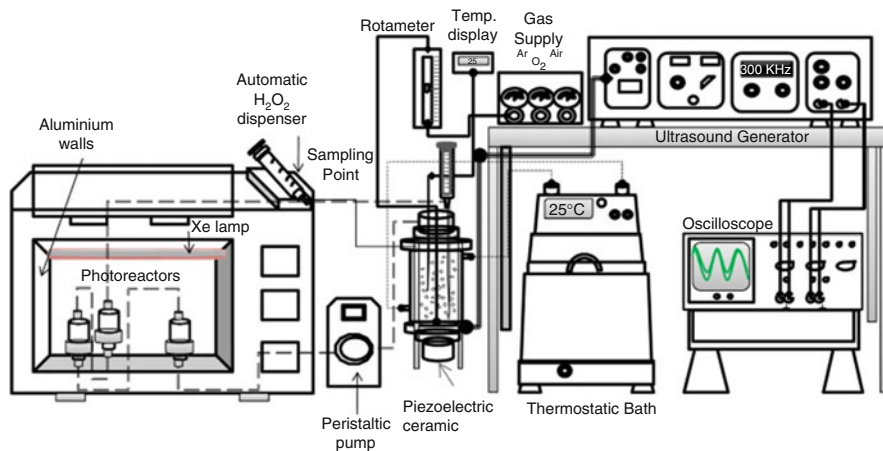[e]Methanol was added to support denitrification

Fig. 5 Experimental equipment and devices (Sun test for UV–vis irradiation, *left*, and sonolysis tank for ultrasound energy, *right*) (Reprinted with permission from Ref. [35]. Copyrights (2009) Elsevier Publications)

nanocatalysts enhance the efficiency of the processes. The semiconductor nanocatalyst undergoes the band gap excitation through the external light energy supplied (photocatalysis) or the light energy produced from the ultrasound (sonocatalysis). However, during the combined sonophotocatalysis the initiation of electronic charges via both the processes leads to enhance the overall efficiency of the microenvironment and avoids the disadvantages associated with the commercialization of single-handed as well as integrated AOPs. The band gap excitation of the semiconductor nanocatalysts using ultraviolet irradiation and the mechanism of sonolysis, sonocatalysis, and sonophotocatalysis for the degradation of acid red B and methylene blue were reported by Chakma and Moholkar [39]. The photocatalyst acts as the nucleation sites for the formation of microbubbles, and the band gap excitation leads to the initiation of various radicals as denoted in Fig. 6. The photocatalytic degradation of the adsorbed dye molecule was preceded along with the heterogeneous microjet formation results from the acoustic cavitation. Alternatively, the shock waves produced from the sonication decreases the number of dye molecules adsorbed on the catalysts surface thus enhances the mass transfer rate during the sonophotocatalysis. The authors used the following equation to calculate the synergetic effect produced from the combined sonophotocatalysis,

$$
\text{Synergy effect } (\%) = \frac{\left[\begin{array}{c}\text{Decolorization obtained} \\ \text{with hybrid AOP}\end{array}\right] - \left[\begin{array}{cc}\text{Decolorization with} & \text{Decolorization with} \\ \text{sonolysis} + & \text{photocatalysis}\end{array}\right]}{[\text{Decolorization with sonolysis } + \text{ Decolorization with photocatalysis}]} \times 100
$$

The sonophotocatalytic degradation of organic dyes was investigated in the presence of various ultrasound frequencies and power supplied during the processes
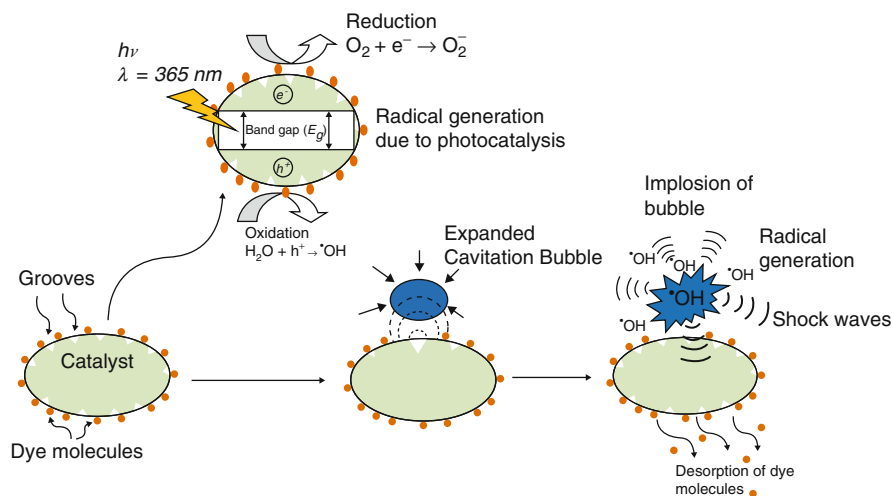
Fig. 6 Schematic depicting the synergy of physical mechanism between sonolysis, sonocatalysis, and sonophotocatalysis (Reprinted with permission from Ref. [39]. Copyrights (2015) Elsevier Publications)

Table 3 Effect of ultrasound power on the degradation of AR88 (0.09 mM) (Reprinted with permission from Ref. [40]. Copyrights (2010) Elsevier Publications)

S. No.	Power (mW mL^{-1})	Rate/10^{-7} M min^{-1}
1.	16	0.77
2.	35	19.5
3.	55	36.9
4.	64	47.7

or the effect of one parameter was investigated by keeping another constant. Madhavan et al. [40] reported the effect of power supplied during the sonophotocatalytic degradation of Acid Red 88 (AR88) by using the fixed ultrasound (213 kHz). The rate of AR88 degradation was found to increase when the power supplied for the degradation increases (Table 3). In order to achieve the optimum ultrasound required for the degradation of environmental contaminants, it can be investigated by keeping the power as constant since the optimized ultrasound frequency and power have a propensity to enhance the rate of degradation. The visible light-assisted sonophotolytic degradation of acid orange 7 was investigated by Ma et al. [41]. The synergetic effect was achieved for the sonophotolytic degradation of acid orange 7 when compared to the individual processes as presented in Fig. 7. The band gap energy of AO7 plays a vital role for achieving the synergetic enhancement since the band gap energy of the dye matches with energy of incident photons. Subsequently, the photo-induced reaction occurs which leads to achieve the synergetic enhancement. The band gap energy of the dyes which is not perfectly

Fig. 7 Temporal evolution of the removal percentage K under visible light irradiation (open *triangles*), ultrasound irradiation (open *circles*), and combination of visible light and ultrasound irradiations (closed *squares*) (Reprinted with permission from Ref. [41]. Copyrights (2006) Elsevier Publications)
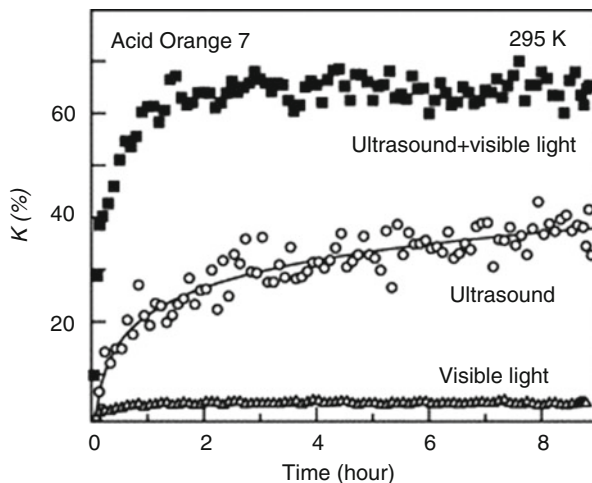
matched with the energy of incident photons cannot confer the synergetic effect during sonophotolytic degradation.

Mrowetz et al. [42] investigated the TiO$_2$-assisted sonophotocatalytic degradation of acid orange 8 (AO8), acid red 1 (AR1), and 2-chlorophenol (2-CP), and the pseudo–first-order rate constants observed for the degradation are presented in Table 4. The effect of initial concentration of substrate and photocatalyst was investigated in order to determine the origin of synergetic effect attained from the combination of two different AOPs. The synergy calculated (last entry in Table 4) from the degradation of the organic pollutants was mainly accounted from the scission of H$_2$O$_2$ produced from the photocatalysis and sonolysis. Thus increases the amount of effective radical produced during the degradation. The following equation is used to calculate the synergetic effect achieved during the degradation.

$$\text{Synergy} = \frac{(k_{US+UV+TiO_2}) - (k_{US+TiO_2} + k_{UV+TiO_2})}{(k_{US+UV+TiO_2})}$$

Sathishkumar et al. [43, 44] investigated the effect of rare earth dopants (RE^{3+}) on the sonocatalytic, photocatalytic, and sonophotocatalytic degradation of acid blue 113 (AB113). The influence of the rare earth dopants (Y^{3+}, Gd^{3+}, and Nd^{3+}) on the AB113 degradation was described in Table 5 [43]. Figure 8 demonstrates the enhanced rate achieved in the presence Er^{3+}, Sm^{3+}, and Pr^{3+} loaded TiO$_2$ upon compared to bare TiO$_2$ [44]. Among the doped nanocatalysts, Gd^{3+}-TiO$_2$ and Pr^{3+}-TiO$_2$ attained the maximum rate for the sonophotocatalytic degradation. The additive effect of the sonocatalytic and photocatalytic processes was observed for the sonophotocatalytic degradation. Nevertheless, the influence of 42 kHz ultrasound on the synthesis of rare earth doped TiO$_2$ and its catalytic performance was investigated. The surface modified RE^{3+}-TiO$_2$ nanocatalysts have demonstrated that the visible light is adequate to stimulate the visible light-assisted photocatalytic response. The

Table 4 Pseudo–first-order rate constants[a] of acid orange 8 (AO8), acid red 1 (AR1), and 2-chlorophenol (2-CLP) degradation under sonolysis in the presence of TiO_2 (US + TiO_2), photocatalysis (UV + TiO_2), and sonophotocatalysis (UV + US + TiO_2) (Reprinted with permission from Ref. [42]. Copyrights (2003) Elsevier Publications)

Substrate	C^{0b}/M	TiO_2 amount/g l^{-1}	$10^4 \times k_{US+TiO_2}$/s^{-1}	$10^4 \times k_{UV+TiO_2}$/s^{-1}	$10^4 \times k_{UV+US+TiO_2}$/s^{-1}	Synergy
AO8	2×10^{-5}	0.10	0.099 ± 0.005	3.93 ± 0.17	6.4 ± 0.2	0.37 ± 0.11
AO8	4×10^{-5}	0.10	0.105 ± 0.002	1.24 ± 0.02	2.61 ± 0.04	0.49 ± 0.04
AO8	6×10^{-5}	0.10	0.024 ± 0.017	0.44 ± 0.03	1.46 ± 0.09	0.68 ± 0.11
AO8	4×10^{-5}	0.20	0.089 ± 0.002	1.93 ± 0.09	3.57 ± 0.12	0.43 ± 0.10
AO8	4×10^{-5}	0.28	0.100 ± 0.001	1.81 ± 0.11	3.32 ± 0.09	0.42 ± 0.10
AR1	2.5×10^{-5}	0.10	0.038 ± 0.002	1.22 ± 0.03	2.89 ± 0.13	0.56 ± 0.09
2-CLP	4×10^{-4}	0.10	0.59 ± 0.02	0.88 ± 0.04	1.58 ± 0.06	<0.1

Irradiation intensity: 4.5×10^{-8} Einstein s^{-1} cm^{-2}

[a]Errors were estimated as standard errors of slope calculated from linear regression analysis

[b]C^0 = initial substrate concentration

Table 5 Degradation rate constant obtained for different processes using [nanocatalyst] = 1 g/L and [AB113] = 1×10^{-5} M (Reprinted with permission from Ref. [43]. Copyrights (2014) Elsevier Publications)

S. No	Process	Nanocatalyst	Rate, 10^{-4} s^{-1}
1	Photocatalysis	TiO_2	0.021
2	Sonocatalysis		0.532
3	Sonophotocatalysis		0.725
4	Photocatalysis	Y^{3+}-TiO_2	0.4
5	Sonocatalysis		0.88
6	Sonophotocatalysis		1.8
7	Sonophotocatalysis	Gd^{3+}-TiO_2	1.512
8	Sonophotocatalysis	Nd^{3+}-TiO_2	1.305

decolorization as well as mineralization of AB113 is significantly enhanced in combination with the ultrasound and the loaded RE^{3+} acts as the center for the recombination of electronic charges. The oxygen vacancies, oxidation state of oxides, and surface adsorbed hydroxyl ions predict the efficiency of RE^{3+}-TiO_2. The use of electron acceptors can further enhance the rate of mineralization.

Besides, the wide range of organic dye degradation/mineralization using various ultrasound combined processes is reported in the literature [45–48] using different experimental conditions. Among the various reports, few of them are presented in Table 6 adopted from Ref [4]. Table 6 provides an idea about the effect of various experimental parameters on the degradation of assorted dyes and the influence of ultrasound in the degradation processes. Table 6 shows the various advanced oxidation technologies investigated for the degradation of colored pollutants in addition to the sonophotocatalysis.

Perspective of Sonophtocatalytic Degradation of Colorless Pollutants

In continuation, the following equation can also be used to calculate the synergy for the combination of two advanced oxidation technologies, i.e., combined photocatalysis and sonophotocatalysis,

$$\text{Synergy} = \frac{k_{(\text{sonophotocatalysis})}}{k_{(\text{sonocatalysis})} + k_{(\text{photocatalysis})}}$$

Where, $k_{\text{sonophotocatalysis}}$, $k_{\text{photocatalysis}}$, and $k_{\text{sonocatalysis}}$ refer to the rate achieved during the sonophotocatalysis, photocatalysis, and sonocatalysis, respectively. The substitution of the appropriate rate value in the above equation will gives the synergy index obtained during the combined advanced oxidation processes. The synergy index reached more than one shows that the synergy is achieved during the combined processes, whereas the synergy index lower than one leads to the additive effect of the combined processes.

On the other hand, the accumulation of colorless environmental pollutants on the environment has dramatically increased due to its multiple usage such as pharmaceuticals, pesticides, etc., which seriously caused the adverse effects to the environment. Most of the colorless environmental contaminants are recalcitrant to natural biodegradation and phototransformation [49]. The continuous discharge and
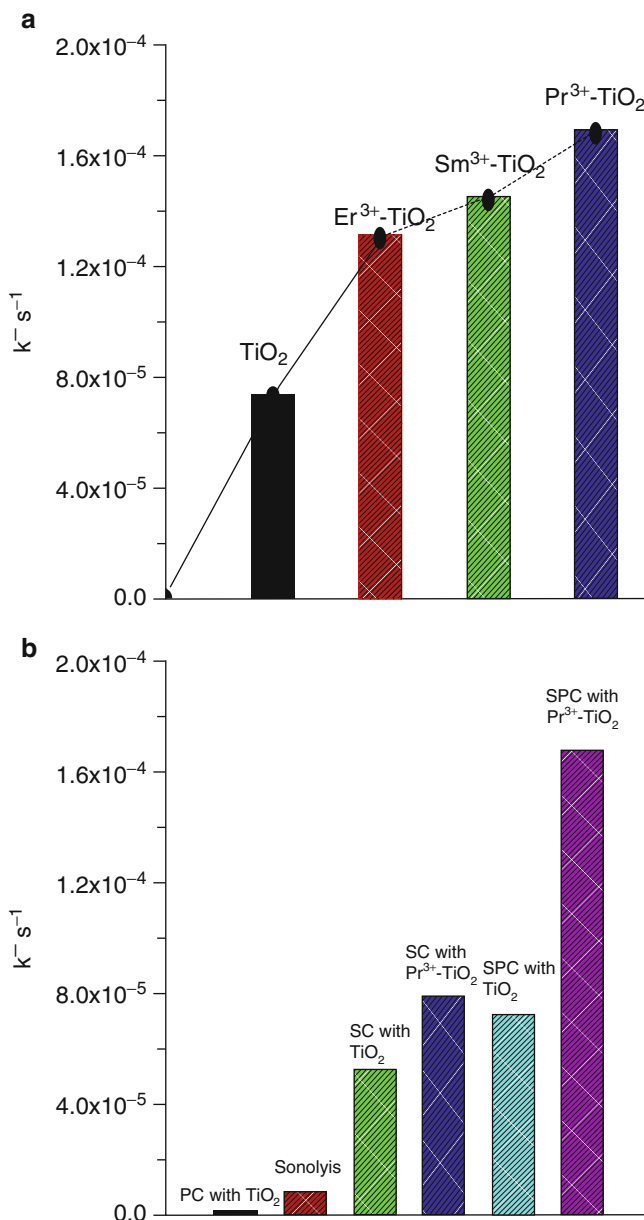
Fig. 8 (**a**) Comparison of apparent rate constants observed for the sonophotocatalytic decolorization of AB113 in the presence of various nanocatalysts and (**b**) Comparison of apparent rate constants observed for the various advanced oxidation processes. PC, SC, and SPC denote the photocatalytic, sonocatalytic, and sonophotocatalytic decolorization of AB113 (Reprinted with permission from Ref. [44]. Copyrights (2014) Elsevier Publications)

Table 6 Some recent studies which use ultrasound as a basic tool for dyestuff degradation in heterogeneous reactions (Adopted from Ref. [4] and the further references cited therein. Reprinted with permission from Ref. [4]. Copyrights (2004) Elsevier Publications)

Dye/initial concentration	Catalyst or adsorbent	Sonochemical conditions	Experimental conditions	Results
Acid red B (100 mg L^{-1})	1 g L^{-1} MnO$_2$, without pretreatment	50 kHz ultrasonic bath; Amplifier rating: 150 W; Reaction volume: 100 mL	Gas type: Argon–Oxygen; Temperature: 22 °C; Sonication time: 240 min; pH = 3	47.5 μm particle size before sonication; 3.2 μm particle size after sonication; 77.03 % and 90.88 % decolorization for MnO$_2$ and US/MnO$_2$; 11.89 % and 48.12 % TOC removal for MnO$_2$ and US/MnO$_2$
C.I. acid orange 7 (50 mg L^{-1})	1 g L^{-1} Fe^0 pretreatment with 1 M HCl;	20 kHz ultrasonic probe; Amplifier rating: 250 W.	Gas type: Nitrogen; Temperature: 20 °C; Sonication time: 30 min; pH = 5.	63 % and 91 % decolorization for Fe^0 and US/Fe^0;
Methyl orange (10 mg L^{-1})	500 mg L^{-1} anatase and rutile TiO$_2$ pretreatment with heating	40 kHz ultrasonic generator; Amplifier rating: 50 W; Reaction volume: 100 mL	Sonication time: 150 min; Temperature: 20 °C; pH = 3	41.36 % and 22.45 % decolorization for anatase TiO$_2$ with and without ultrasound
C.I. acid orange 7 (1000 mg L^{-1})	12 g Fe^0 and 2.3 g GAC (granular activated carbon) mixture	40 kHz ultrasonic bath; Amplifier rating: 100 W; Reaction volume: 100 mL	Preadsorption with GAC to prevent adsorption during sonication; Sonication time: 40 min; Temperature: 22 °C; pH = 4	80 % and 57 % color and TOC removal for US/Fe^0-GAC; 34 % and 28 % color and TOC removal for Fe^0-GAC
Rhodamine-B (5 mg L^{-1})	0.009 mol L^{-1} Fe$_2$O$_3$ core-shell nanowires	25 kHz ultrasonic bath; Amplifier rating: 100 W; Reaction volume: 50 mL	Gas type: Air; Sonication time: 60 min; pH = 2; For comparing Fe^{2+}, Fe^{3+}, Fe^0 addition	85 %, 76 %, 70 %, and 100 % color removal for Fe^{2+}, Fe^{3+}, Fe^0, and Fe@Fe$_2$O$_3$ with ultrasound; 24.1 %, 23.5 %, 19.1 %, and 60 % TOC removal for Fe^{2+}, Fe^{3+}, Fe^0, and Fe@Fe$_2$O$_3$ with ultrasound

Contaminant	Adsorbent/catalyst	Equipment	Conditions	Results
Methylene blue (50 mg L^{-1})	0.3 g/50 mL waste cellulosic materials without pretreatment	20 kHz ultrasonic equipment; Meas. exp. power[a]: 33 W cm^{-2}; Reaction volume: 50 mL	Temperature: 30 °C; Sonication time: 30 min	Equilibrium reaching 5 min and 30 min with and without ultrasound; Langmiur isotherm, sorption capacity (qm = 59 and 611 mg g^{-1} without and with ultrasound)
C.I. direct orange 39 (0.01 g L^{-1})	5 g L^{-1} geothite (α-FeOOH) washed before used	35 kHz ultrasonic equipment; Amplifier rating: 120 W; Reaction volume: 500 mL	Temperature: 25 °C (no cooling); Sonication time: 90 min; pH = 3; 5 g L^{-1} H_2O_2 addition	30 % adsorption and 47 % decolorization only goethite; 45 % adsorption and 83 % decolorization for goethite with US/H_2O_2. First-order rate constant: $k = 0.0189$ min^{-1} for goethite with US/H_2O_2
Direct scarlet 4BS (100 mg L^{-1})	0.6 g L^{-1} exfoliated graphite with pretreatment	28 kHz ultrasonic cleaner; Amplifier rating: 500 W; Reaction volume: 50 mL	Temperature: 50 °C; Sonication time: 90 min; pH = 2	28.9 % and 94.05 % decolorization for graphite and US/graphite
Methylene blue (0.3 mM)	2 g mL^{-1} TiO_2 and Al_2O_3 pellets without pretreatment	39 kHz ultrasonic generator; Amplifier rating: 200 W; Reaction volume: 5 mL	Sonication time: 60 min; Temperature: 20 ± 1 °C; pH = 7; 50 mM H_2O_2 addition	84.9 % and 22 % decolorization for TiO_2 and Al_2O_3 pellets presence of US/H_2O_2, while no degradation in US/H_2O_2 only
Malachite green (C.I. basic green 4) (10 mg L^{-1})	1 g/300 mL dead needles of Aleppo pine with pretreatment	40 kHz ultrasonic bath; Meas. exp. power[a]: 9 W; Reaction volume: 300 mL	Temperature: 30 °C; Sonication time: 9 h	Freundlich isotherm constants, $K_f = 1.96$ and 5.93 $mg^{1-1/n}$ $L^{1/n}$ g^{-1} for only adsorbent and US/adsorbent
C.I. reactive blue 19 (132–917 mg dm^{-3})	5 g dm^{-1} activated carbon (AC) without pretreatment	850 kHz ultrasonic transducer Meas. exp. power[a]: 190–760 W L^{-1}	Temperature: 20–47 °C; Sonication time: 15–18.34 min; pH = 4–12	36 %, 91 %, and 99.99 % decolorization for US, AC, and US/AC

Table 6 (continued)

Dye/initial concentration	Catalyst or adsorbent	Sonochemical conditions	Experimental conditions	Results
C.I. reactive black 5 (75 mg L^{-1})	0.2 g limestone without pretreatment	20 kHz ultrasonic equipment; Meas. exp. power[a]: 33 W cm^{-2}	Temperature: 40 °C; Sonication time: 10 min	Freundlich isotherm constants, $K_f = 28.2$ and 7.4 mg g^{-1} for only limestone and US/limestone for 20 kHz
Acid brown 348 (50 mg L^{-1})	2.0 g L^{-1} exfoliated graphite with pretreatment and activated carbon (AC)	25 kHz ultrasonic cleaner; Meas. exp. power[a]: 0.63 W; Reaction volume: 50 mL	Temperature: 40 ± 2 °C; Sonication time: 120 min; pH: 6; 4.08 g L^{-1} H$_2$O$_2$ addition.	74 % and 34 % decolorization for US/graphite and graphite; 21 % and 18 % decolorization for US/AC and AC; Langmuir and Freundlich isotherm applied.
Orange II (5 × 10^{-5} M)	100 g Au/TiO$_2$ with pretreatment;	40 kHz ultrasonic transducer; Meas. exp. power[a]: 0.045 W cm^{-2}, Reaction volume: 100 mL	Gas type: Argon; Sonication time: 30 min; Temperature: 22–28 °C; pH = 3.5	No degradation in the absence of catalyst; First-order rate constant $k = 0.0077 \pm 0.0008$ and 0.0178 ± 0.0014 min^{-1} for US/TiO$_2$ for US/TiO$_2$ and US/Au/TiO$_2$; 80 % TOC removal for US/Au/TiO$_2$ in 9 h
C.I. direct blue 168 (100 mg L^{-1})	2.0 g L^{-1} Fly ash, kaolinite, and diatomaceous earth	40 kHz ultrasonic bath; Amplifier rating: 250 W; Reaction volume: 50 mL	Temperature: 40 ± 2 °C; Sonication time: 90 min; pH = 3; 2.94 mM H$_2$O$_2$ addition	99 %, 92.2 %, and 88.3 % decolorization for fly ash, kaolinite, and diatomaceous earth with ultrasound

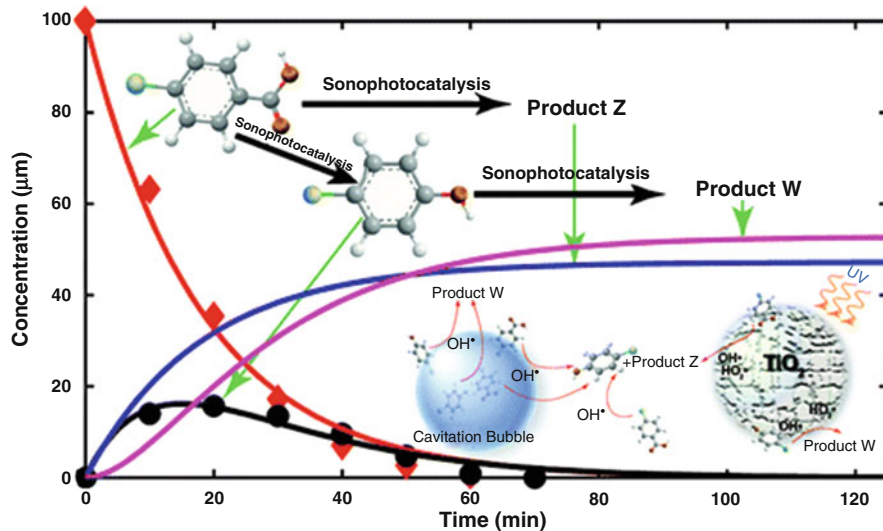[a]Meas. Exp. power: Measured experimental power

Fig. 9 Plot of sonophotocatalytic degradation of PCBA and the various intermediates produced from the degradation (Reprinted with permission from Ref. [51]. Copyrights (2011) American Chemical Society)

improper disposal of these environmental contaminants leads to increase its concentration [50]. Mineralization of these environmental contaminants was investigated using various AOPs; however, the complete mineralization using ultrasound-assisted treatment of the colorless environmental contaminants gained much interest from the environmental purification research groups. He et al. [51] investigated the kinetics and mechanism for the sonophotocatalytic degradation of p-chlorobenzoic acid (PCBA; Fig. 9). The sonolytic, photocatalytic, and sonophotocatalytic degradation of PCBA (X) produces the 4-choloro phenol (Y) as the derivative from the degradation (not shown in Fig. 9). The formation of product W (representative of all the products; stoichiometric molar ratio to Y is 1:1) and Z (represents all the products except Y formed during the degradation of X; stoichiometric molar ratio to X is 1:1) is explicated in Fig. 9. The red line shown in Fig. 9 indicates the progresses of the degradation. The hydroxylated products are the first intermediates produced from the degradation of X since the hydroxyl radicals are the major radicals produced from the sonolysis and photocatalysis; moreover, the hydroxyl radical undergoes the substitution of the aromatic ring. The HPLC analysis of He et al. [51] demonstrated the formation of hydroquinone, benzoquinone, and trihydroxybenzene as the major intermediates produced from the reaction between Y and hydroxyl radicals. The intensified supply of hydroxyl radicals during the sonophotocatalysis of X further converts the reactants into smaller products like CO_2, H_2O, and HCl.

Selli et al. [52] observed the efficiency of photolysis (UV), photocatalysis (UV + TiO_2), sonolysis (US), and sonophotocatalysis (US + UV + TiO_2) for the degradation of 1,4-dichlorobenzene (1,4-DCB). The energy consumption, percentage of

Table 7 Percentage of 1,4-DCB degradation attained after 6 h, time and energy required for attaining 60 % 1,4-DCB degradation under photolysis (UV), photocatalysis (UV + TiO$_2$), sonolysis (US), or sonolysis + photocatalysis (sonophotocatalysis, US + UV + TiO$_2$) (Reprinted with permission from Ref. [52]. Copyrights (2008) Elsevier Publications)

System	Light source	Photocatalyst	US power (W)	% Degradation[a]	Time[b] (min)	Energy[c] (kWh)
UV	I	–	–	25	>360	
UV	II	–	–	77	95	1.01
UV + TiO$_2$	I	P25	–	90	150	1.49
UV + TiO$_2$	I	TiO$_2$-300	–	72	263	2.61
UV + TiO$_2$	I	TiO$_2$-450	–	63	340	3.38
UV + TiO$_2$	I	TiO$_2$-600	–	58	>360	
UV + TiO$_2$	II	P25	–	100	64	0.73
US	–	–	20	72	206	0.66
US	–	–	40	79	142	0.49
US + UV + TiO$_2$	II	P25	40	100	41	0.58

Initial 1,4-DCB concentration: 2.7×10^{-4} M
[a]Percentage of 1,4-DCB degradation after 6 h
[b]Treatment time necessary to attain 60 % degradation
[c]Energy consumed to attain 60 % degradation, calculated on the basis of the effective power consumption of the light and/or ultrasound sources, and of the magnetic stirrer

degradation, and time required for attaining the 60 % degradation of 1,4-DCB are provided in Table 7. The authors employed two light sources (Jelosil, models HG 200, or HG 500) for the photocatalytic investigations, and 300, 450, and 600 given in the Table 7 indicates the calcination temperature of TiO$_2$ prepared by sol–gel synthesis starting from titanium isopropoxide. The UV-assisted TiO$_2$ photocatalysis achieved the maximum rate of 1,4-DCB degradation; however, the energy consumption during the process is relatively high when compared with the ultrasound. The authors reported the following order of energy consumption for the degradation of 1,4-DCB during various AOP treatments.

$$US(40 \text{ W}) < US + UV + TiO_2 < US(20 \text{ W}) < UV + TiO_2(\text{lamp II})$$
$$< UV(\text{lamp II}) < UV + TiO_2 \text{ (lamp I)}$$

Anandan and Ashokkumar investigated the visible light-assisted photocatalytic and sonophotocatalytic degradation of polydispersenonyl phenolethoxylate, Teric GN9 surfactant in the presence of Au-TiO$_2$ nanocatalysts [53]. The observed HPLC chromatogram after the irradiation and sonication time is shown in Fig. 10. The sonication tends to increase the mass transfer rate of Teric GN9 from the nanocatalyst surface to the bulk solution vice versa, and the complete degradation of Teric GN9 was achieved in about 3 h under sonophotocatalysis as evidenced from Fig. 10. The sonophotocatalytic degradation of Teric GN9 could not attain the synergetic enhancement due to the interference of the hydrophilic degradation products and polydisperse nature of Teric GN9. Therefore, it can be understood
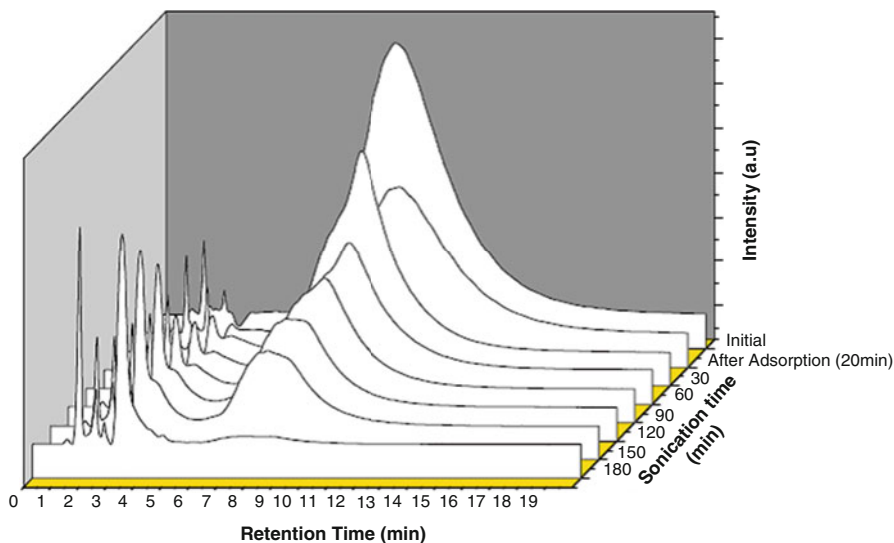
Fig. 10 3-D plot showing the evolution of the HPLC chromatogram as a function of irradiation and sonication time for sonophotocatalytic degradation of Teric GN9 surfactant (1.5×10^{-4} M) using Au-TiO$_2$ nanoparticles. Mobile phase: acetonitrile/water (60/40 v/v) and detection wavelength = 226 nm (Reprinted with permission from Ref. [53]. Copyrights (2009) Elsevier Publications)

that the nature of the substrate and nanocatalysts play a major role in accomplishing the synergetic effect.

Sathishkumar et al. [54] reported the sonocatalytic, photocatalytic, and sonophotocatalytic degradation of Simazine in the presence of Au-TiO$_2$ nanocatalysts. The HPLC chromatogram observed for the sonophotocatalytic degradation is presented in Fig. 11. From the HPLC chromatogram, formation of new products can be identified during the sonophotocatalytic degradation and the observed decrease indicates the degradation of Simazine. The order of degradation observed for the Simazine was sonophotocatalysis > sonocatalysis > photocatalysis. 1.65- and 1.38-fold enhanced mineralization was attained for the sonophotocatalytic degradation when compared with the individual AOPs. The proposed mechanism for the sonophotocatalytic degradation of Simazine in the presence of Au-TiO$_2$ nanocatalysts is shown in Fig. 12. Hydroxylated intermediates are the major products identified from the 2 h of the processed Simazine, further sonophotocatalytic treatment of Simazine leads to produce the intermediates III and IV as shown in Fig. 12. The 7 h sonophotocatalytic irradiation of Simazine tends to produce the intermediates VI and VII and identified that the mineralization of triazine-based skeleton is demanding more processing time.

Michael et al. [55] investigated the TiO$_2$-assisted photocatalysis under UV-A and simulated solar irradiation, and sonophotocatalysis of ibuprofen (IBP) and diclofenac (DCF). The Ultra-high performance liquid chromatography – Quadrupole-quadrupole time of flight – Mass Spectrum (UPLC-(−)
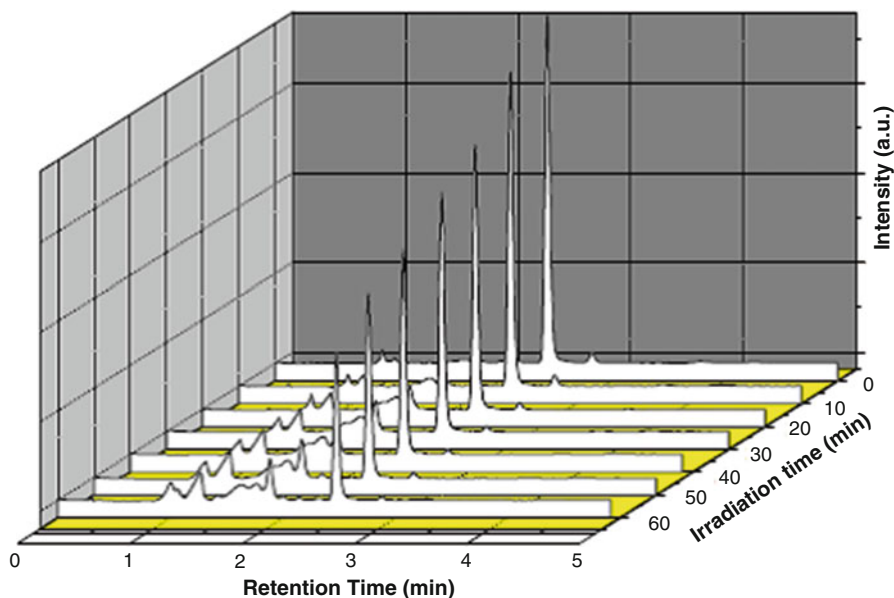
Fig. 11 3-D plot showing the evolution of the HPLC chromatogram for the sonophotocatalytic degradation of Simazine at its fixed initial concentration 5 mg/L and [Au–TiO₂] = 1.5 g/L (Reprinted with permission from Ref. [54]. Copyrights (2014) Elsevier Publications)

ESI–QqToF–MS) (Tables 8 and 9) analyses confirm the formation of seven transformation products (TP) from the degradation of IBP (TP1 to TP7) and DCF (TP*1 to TP*7). The tables provide the theoretical and experimental mass (m/z) values and retention time (t_R) for the transformation products. The analysis of the intermediates produced from the photocatalytic and sonophotocatalytic degradation of IBP and DCF shows that there is no difference in the nature of transformation products which indicates the involvement of similar reaction mechanisms.

Based on the experimental results, Michael et al. [55] proposed the tentative transformation pathway of IBP and DCF degradation by photocatalysis under UV-A and simulated solar irradiation, and sonophotocatalysis as shown in Figs. 13 and 14. The hydroxylation, demethylation, and decarboxylation are the major steps involved in the IBP degradation whereas the oxidation of DCF proceed by hydroxylation and oxidation between the chloroaniline and phenylacetic acid. Moreover, the cleavage of the aromatic rings leads to produce the transformation products with lower molecular mass.

Duran et al. [56] investigated the modeling and experimental investigation of sonophotocatalytic mineralization of carbamazepine. The degradation studies were carried using the $UV–H_2O_2$, $US–UV–H_2O_2$, and $US–UV–H_2O_2–Fe$ processes for the carbamazepine photo degradation process. The synergy index obtained between the UV-assisted degradation and sonolysis of carbamazepine was 27.7 %, which shows that the combined advanced oxidation processes can be effectively utilized for
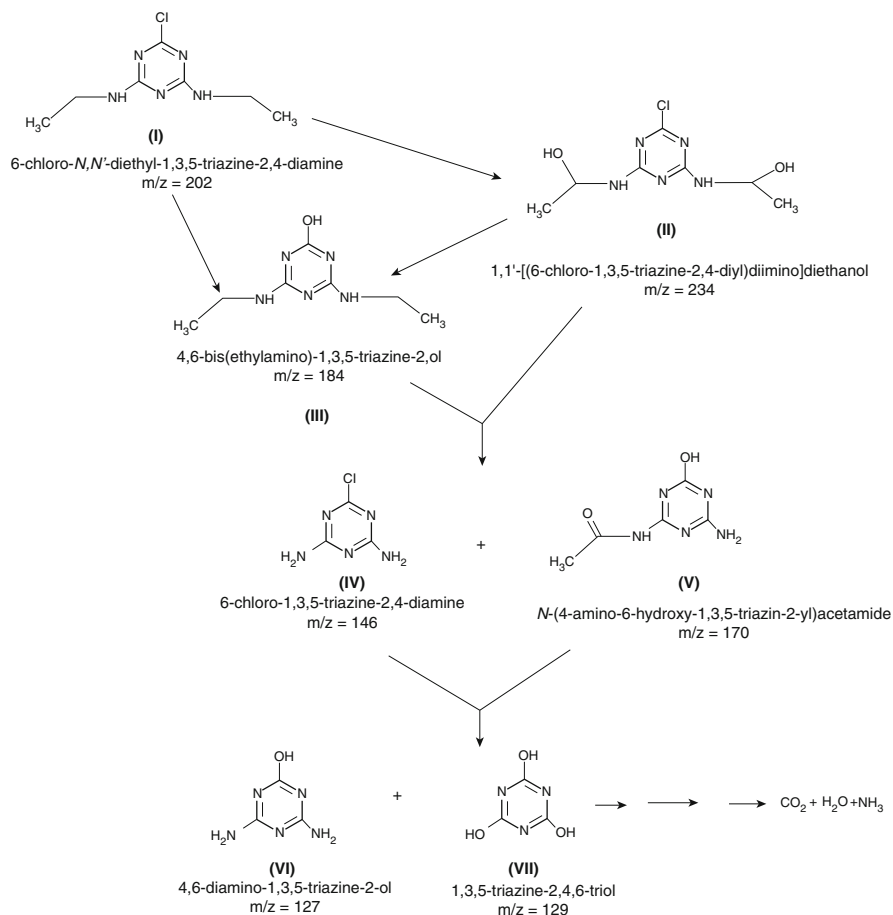
Fig. 12 Proposed pathway for the mineralization of Simazine during Au-TiO$_2$- assisted sonophotocatalysis (Reprinted with permission from Ref. [54]. Copyrights (2014) Elsevier Publications)

the carbamazepine degradation. In addition, the sonophotocatalytic experiments investigated in the presence of Fe leads to enhance the production of $^\bullet$OH radicals. The maximum total organic carbon removal attained in 35 min from the carbamazepine degradation in the presence of US–UV–H$_2$O$_2$–Fe system was 93 %. The enhanced degradation of carbamazepine shows that the developed system can be extended for the degradation of large quantity of the antiepileptic drug. The kinetic constants observed during the carbamazepine degradation were presented in Table 10.

In addition, Jelic et al. analyzed the various transformation products and reaction pathways of carbamazepine (CBZ) during sonolytic, photocatalytic [UV-A, solar irradiation (SSI)], and sonophotocatalytic degradation processes using (+)ESI-MS/

Table 8 Accurate mass measurements of the TPs of IBP as determined by UPLC-(−) ESI–QqToF–MS. Data for (pseudo)-molecular ions correspond to acquisitions in full-scan mode, those of fragment ions to product ion spectra of the protonated molecules (Reprinted with permission from Ref. [55]. Copyrights (2014) Elsevier Publications)

Compound	t_R (min)	Elemental formula	Mass (m/z)		Error		DBE[*]
			Theoretical	Experimental	mDa	ppm	
IBP	4.75	$C_{13}H_{17}O_2$	205.1229	205.1212	−1.7	−8.3	5.5
		$C_{12}H_{17}$	161.1332	161.1311	−1.9	−11.8	4.5
TP1	4.53	$C_{13}H_{17}O_3$	221.1178	221.1183	0.5	2.4	5.5
		$C_{12}H_{17}O$	177.1279	177.1274	−0.5	−3.1	4.5
		$C_{11}H_{14}O$	162.1045	162.1033	−1.2	−7.2	5
		$C_{10}H_{11}O$	147.081	147.0817	0.7	4.8	5.5
		$C_9H_{10}O$	134.0732	134.0719	−1.3	−9.4	5
		C_9H_8O	132.0575	132.0542	−3.3	−25.1	6
		$C_7H_6O_2$	122.0368	122.0358	−1	−8	5
		C_8H_7O	119.0497	119.0506	0.9	7.6	5.5
		C_6H_5O	93.034	93.034	0	−0.4	4.5
TP2	4.83	$C_{12}H_{15}O_2$	191.1061	191.1072	−1.1	−5.8	5.5
		$C_{12}H_{15}O$	175.1073	175.1123	−5.0	−28.5	5.5
		$C_9H_8O_2$	148.0513	148.0524	−1.1	−7.6	6
		C_7H_5O	105.0333	105.034	−0.7	−6.7	5.5
TP3	4.95	$C_{12}H_{15}O_3$	207.101	207.1021	−1.1	−5.4	5.5
		$C_{11}H_{11}O_3$	191.0697	191.0708	−1.1	−5.9	6.5
		$C_9H_8O_3$	164.0500	164.0473	2.7	16.2	6
		$C_8H_6O_3$	150.0306	150.0317	−1.1	−7.3	6
		$C_8H_7O_2$	135.0453	135.0446	0.7	5.1	5.5
		$C_7H_5O_2$	121.0293	121.029	0.3	2.9	5.5
		C_7H_6O	106.0453	106.0419	3.4	32.4	5
		C_6H_5O	93.0329	93.034	−1.1	−12.3	4.5
TP4	3.14	$C_{12}H_{17}O$	177.1284	177.1279	0.5	2.6	4.5
		$C_{11}H_{14}O$	162.1059	162.1045	1.4	8.9	5
		$C_9H_{10}O$	134.0726	134.0732	−0.6	−4.5	5
		C_9H_8O	132.0568	132.0575	−0.7	−5.4	6
		C_8H_7O	119.0492	119.0497	−0.5	−4.1	5.5
TP5	2.45	$C_{12}H_{15}O$	175.1108	175.1123	−1.5	−8.6	5.5
		$C_{12}H_{13}O$	173.095	173.0966	−1.6	−9.2	6.5
		$C_{12}H_{11}O$	171.0815	171.081	0.5	2.9	7.5
		$C_{11}H_8O$	156.0575	156.0575	0	0	8
		$C_{10}H_{11}O$	147.0814	147.081	0.4	2.8	5.5
		C_8H_7	103.0551	103.0548	0.3	3.2	5.5
TP6	3.03	C_9H_9O	133.0648	133.0653	−0.5	−3.8	5.5
		C_9H_7O	131.0489	131.0497	−0.8	−6.1	6.5
		C_7H_5O	105.0355	105.034	1.5	14.3	5.5
		C_8H_7	103.0549	103.0548	0.1	1	5.5
TP7	3.97	$C_9H_9O_2$	149.0605	149.0603	0.2	1.3	5.5
		$C_8H_6O_2$	134.0365	134.0368	−0.3	−2.1	6
		C_8H_7O	119.0487	119.0497	−1.0	−8.3	5.5

* DBE = Double bond equivalent.

Table 9 Accurate mass measurements of the TPs of DCF as determined by UPLC–(+)ESI–QqToF–MS. Data for (pseudo)-molecular ions correspond to acquisitions in full-scan mode, those of fragment ions to product ion spectra of the protonated molecules (Reprinted with permission from Ref. [55]. Copyrights (2014) Elsevier Publications)

| Compound | t_R (min) | Elemental formula | Error mass (m/z) | | Error | | DBE[a] |
			Theoretical	Experimental	mDa	ppm	
DCF	3.83	$C_{14}H_{12}Cl_2NO_2$	296.0245	296.0251	0.6	2.0	8.5
		$C_{14}H_{10}Cl_2NO$	278.0139	278.0134	0.5	2.5	8.5
		$C_{13}H_{10}Cl_2N$	250.0190	250.0185	1.2	−1.6	8.0
		$C_{13}H_{10}ClN$	215.0502	215.0496	0.8	−3.7	7.5
		$C_{13}H_{10}N$	180.0813	180.0808	1.0	1.0	7.5
TP*1 (A) and (B)	3.82	$C_{14}H_{11}Cl_2NO_3$	311.0116	312.0117	0.3	1.0	8.5
		$C_{14}H_{10}Cl_2NO_2$	294.0083	294.0089	0.5	2.1	8.0
		$C_{13}H_{10}Cl_2NO$	266.0134	266.0165	0.6	−0.5	8.5
		$C_{13}H_{10}ClNO$	231.0445	231.0478	1.5	−1.2	7.0
		$C_{13}H_{10}NO$	196.0757	196.0793	0.4	−2.4	6.0
TP*2 (A) and (B)	3.41	$C_{14}H_{12}Cl_2NO_4$	328.0138	328.0464	2.4	7.3	8.5
		$C_{14}H_{10}Cl_2NO_3$	310.0032	309.9882	−1.6	−4.9	8.5
		$C_{13}H_{10}Cl_2NO_2$	282.0083	282.0157	1.0	2.5	9.0
		$C_{13}H_{10}ClNO_2$	247.0395	247.0546	−2.3	−2.4	8.5
		$C_{13}H_{10}NO_2$	212.0706	212.0385	0.2	0.9	8.0
TP*3 (A) and (B)	3.86	$C_{13}H_{10}Cl_2NO$	266.0167	266.0139	2.8	10.5	8.5
		$C_{13}H_{10}ClNO$	231.0445	231.0451	−1.9	−8.2	9.0
TP*4	4.44	$C_{13}H_{10}NO_2Cl_2$	282.0062	282.0083	−2.7	−9.6	8.5
TP*5	4.49	$C_{13}H_8Cl_2NO_2$	280.0013	280.0052	−3.5	−0.5	8.5
		$C_{12}H_8Cl_2NO$	251.9977	252.0199	1.6	1.2	8.5
		$C_{12}H_8ClNO$	217.0289	217.0420	−2.1	−2.8	9.0
TP*6	4.49	$C_{14}H_{10}Cl_2NO_2$	293.7869	293.9630	1.3	2.6	8.0

(continued)

Table 9 (continued)

Compound	t_R (min)	Elemental formula	Error mass (m/z)		Error		DBE[a]
			Theoretical	Experimental	mDa	ppm	
		$C_{13}H_{10}Cl_2NO$	266.0134	265.9824	1.0	1.8	8.0
		$C_{13}H_{10}ClNO$	231.0445	231.0224	−1.2	0.8	7.0
		$C_{13}H_9NO$	195.0679	195.3815	0.5	1.7	7.0
TP*7	3.02	$C_6H_5Cl_2NO$	177.9825	177.9826	−0.1	−0.6	8.5
		C_6H_6ClNO	143.0132	143.0130	0.8	2.3	8.5

[a]DBE = Double bond equivalent
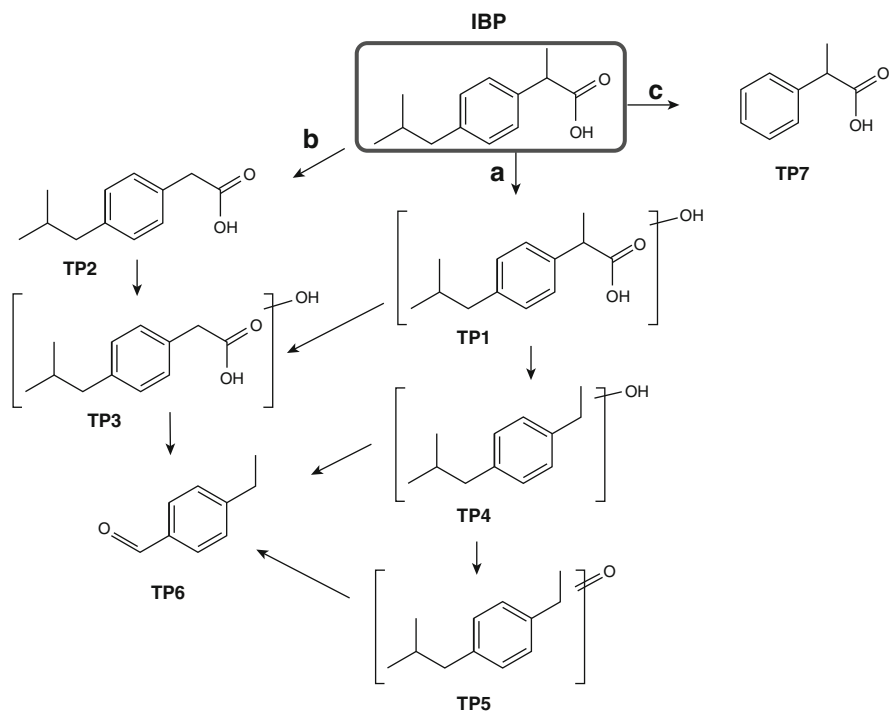
Fig. 13 Tentative transformation pathway of IBP degradation by photocatalysis under UV-A and simulated solar irradiation, and sonophotocatalysis. (Reprinted with permission from Ref. [55]. Copyrights (2014) Elsevier Publications)

MS analysis [57]. CBZ is an antiepileptic drug detected in surface, ground, and drinking water, which is potentially harmful to the aquatic organisms [58]. The solar driven TiO_2-photocatalysis, sonolysis, and sonocatalysis showed the lower rate of CBZ removal when compared to UV-A-assisted photocatalysis and sonophotocatalysis. Nine transformation products (TPs) are detected from the photocatalytic and sonophotocatalytic (UV-A) treatment processes, whereas eight transformation products are detected from the photocatalytic treatment under solar-simulated irradiation. Two isomeric forms of hydroxyacridine-9-carboxaldehyde(TP223) were detected during the photocatalytic and sonophotocatalytic treatment, which is not observed from the solar light irradiated photocatalysis due to the lower rate of CBZ degradation. The tentative pathway for the degradation of CBZ is shown in Fig. 15. The observed hydroxy and keto derivatives of CBZ during the analysis indicate the generation of large quantity of nonselective hydroxyl radicals. The identification of the same transformation products from the photocatalytic and sonophtocatalytic degradation of CBZ indicates that both the processes followed the similar reaction mechanisms.
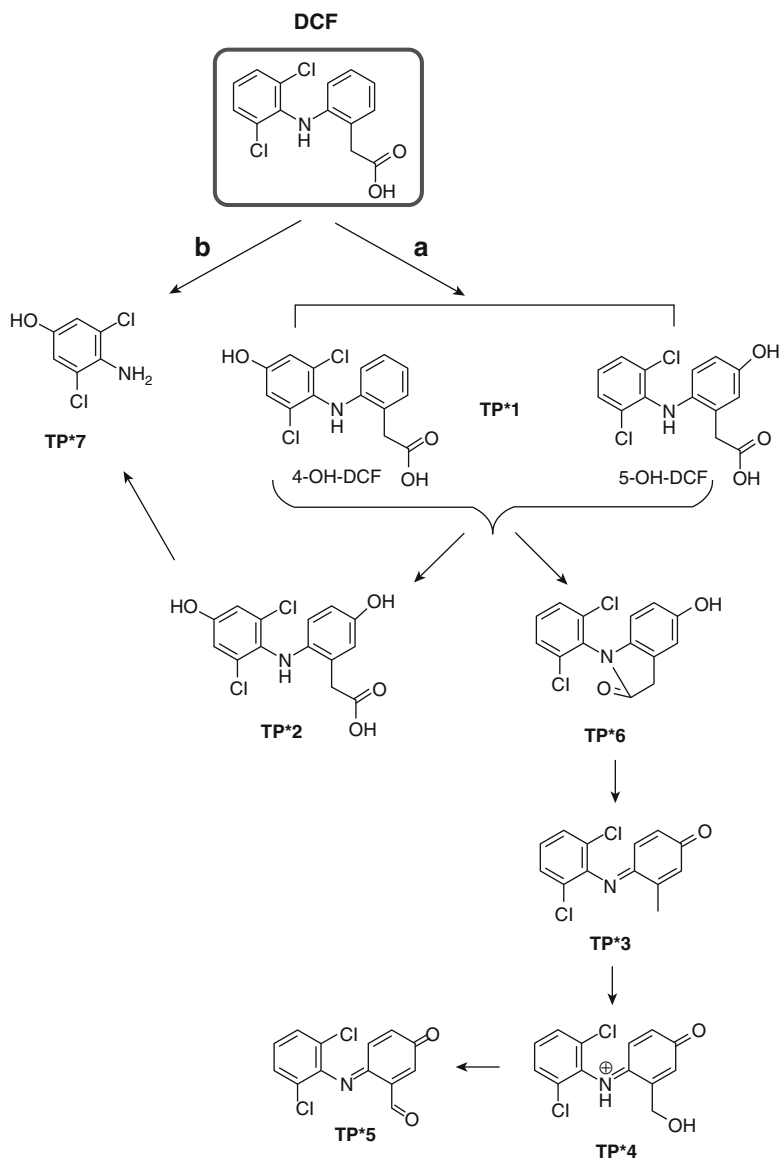
Fig. 14 Tentative transformation pathway of DCF degradation by photocatalysis under UV-A and simulated solar irradiation, and sonophotocatalysis. (Reprinted with permission from Ref. [55]. Copyrights (2014) Elsevier Publications)

Table 10 Calculation and values of constants in the model (Reprinted with permission from Ref. [56]. Copyrights (2016) Elsevier Publications)

Constant	Units	Information	Value for CBZ degradation	Value for TOC degradation
k_{UV}	min^{-1}	It is the direct photolysis rate constant ($[H_2O_2]_0 = 0$ mM)	0.028	0.0021
k_{US}	min^{-1}	It is the direct sonolysis rate constant ($[H_2O_2]_0 = 0$ mM	0.001	0.0034
k_1	min^{-1}	Represents the formation of H_2O_2 via US. It was found to be zero	~ 0	
k_2	min^{-1}	This pseudo–first-order rate constant was found to increase linearly with the initial concentration of H_2O_2	0.0848 (5 mM)	0.0022 (5 mM)
			0.1740 (7.5 mM)	0.0037 (7.5 mM)
			0.2089 (10 mM)	0.0158 (10 mM)
			0.4327 (15 mM)	0.0226 (15 mM)
k_3	min^{-1} mM^{-1}	Calculated [58]	0.0276	0.0013
k_4	min^{-1}	It is the overall constant for the UV/H_2O_2 process	Not needed to be calculated	
k_{scv}	min^{-1} mM^{-1}	Calculated in a self-developed spreadsheet minimizing the error between experimental data	0.0014 (0–15 min)	
			0.0012 (15–20 min)	
			0.00047 (20–25 min)	
			0.0004 (>25 min)	

Cost Estimation for Various AOPs

The cost estimation for the various AOPs is essential since the cost decides the feasibility of the commercialization of the processes. The effective commercialization technology needs low investment with the minimum processing time for the mineralization of the wide spectrum of environmental contaminants. However, the capital investment calculated for the degradation of a particular pollutant cannot be applicable for all the pollutants. Therefore, a separate analysis is needed to find out the cost required for the degradation of various pollutants present in the effluents released from industries. Patil and Gogate [59] investigated the cost required for the degradation of dichlorvos (2,2-dichlorovinyl dimethyl phosphate) which is a organophosphate, widely used as an insecticide to control household pests, by using various advanced oxidation processes (Table 11). The estimated cost required for the removal (83.12 %) of the contaminant was Rs. 0.70 per liter. The dichlorvos removal was reached 100 % at the cost of 0.73 (Rs/L); however, the proficiency of sonolysis suffers to oxidize the various intermediates produced during the
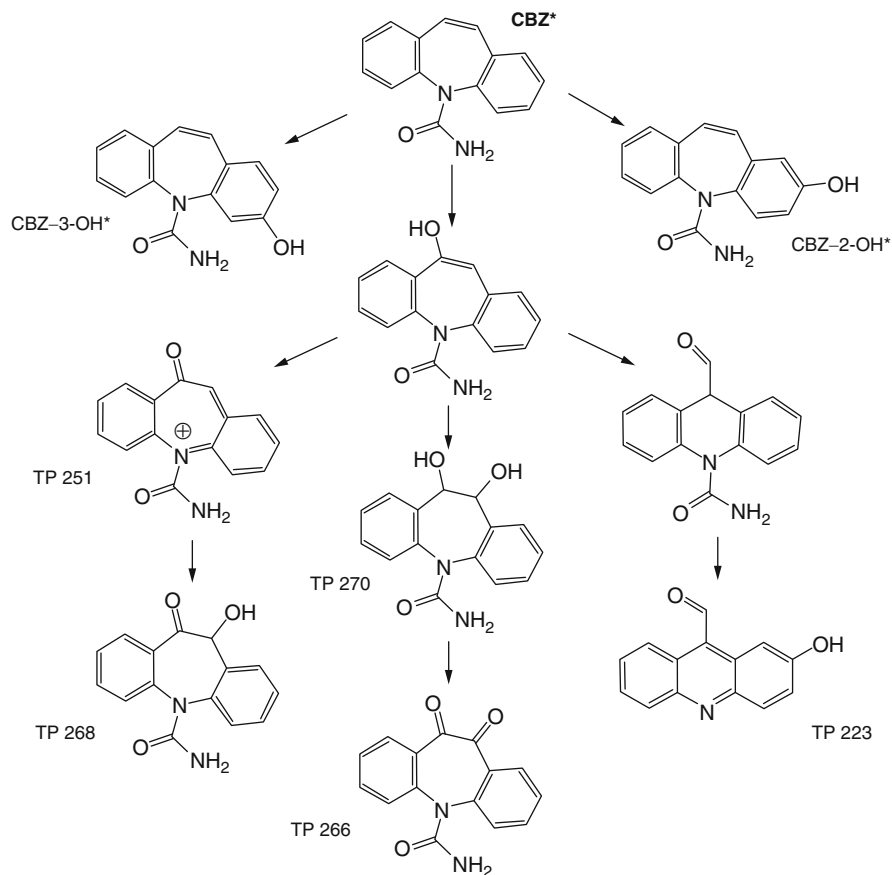
Fig. 15 Tentative transformation pathway of CBZ degradation by PC, SSI, and SPC (Reprinted with permission from Ref. [57]. Copyrights (2013) Elsevier Publications)

degradation [60]. Therefore, the sonophotocatalysis technique can be considered as the highly efficient technology for the complete removal of dichlorvos.

Mahamuni and Adewuyi [61] investigated the cost required for the commercialization of various environmental contaminants. The cost estimation analysis was reproduced in Table 12. The pollutants considered in this study were phenol, trichloroethylene (TCE), and azodyes. From the analysis, it can be understood that combined AOPs are economically attractive than the individual AOPs for the waste water treatment. However, the analysis provide further evidences that the higher cost may require for the commercialization of US + UV + O_3 process and US + UV technologies when compared to the existing technologies. Moreover, the sonophotocatalysis (US + UV + H_2O_2) technique requires less cost for its commercialization when compared to the other technologies for the azodye containing waste water.

Table 11 Comparison of energy efficiency and cost of treatment (Reprinted with permission from Ref. [59]. Copyrights (2014) Elsevier Publications)

Scheme	Degradation obtained (%)	Energy efficiency (mg/J)	Energy required per unit volume (J/L)	Energy required (kWh)	Total cost related to power (Rs/L)	Additive cost (Rs/L)	Total treatment cost (Rs/L)
Only US	6.4	8.30×10^{-6}	2.41×10^{6}	0.67	5.69		5.69
Only H_2O_2	2	7.78×10^{-6}	2.57×10^{6}	0.71	6.07	0.30	6.37
Only TiO_2	3	1.17×10^{-5}	1.71×10^{6}	0.48	4.05	0.11	4.16
Only Fenton	33.2	1.29×10^{-4}	1.54×10^{5}	0.04	0.37	0.11	0.47
US + H_2O_2	20	1.94×10^{-5}	103×10^{6}	0.29	2.43	0.30	2.73
US + TiO_2	7.45	7.24×10^{-6}	2.76×10^{6}	0.77	6.52	0.11	6.63
US + Fenton	81.19	7.89×10^{-5}	2.53×10^{5}	0.07	0.60	0.11	0.70
Solar + TiO_2	78.42	3.05×10^{-4}	6.55×10^{4}	0.02	0.15	0.11	0.27
US + solar + TiO_2	83.12	8.08×10^{-5}	2.47×10^{5}	0.07	0.58	0.11	0.70
Only ozone	100	6.48×10^{-5}	3.08×10^{5}	0.09	0.73		0.73
US + ozone	100	8.19×10^{-5}	2.44×10^{5}	0.07	0.58		

Table 12 Capital cost estimation ($) of various AOPs for degradation (Reprinted with permission from Ref. [61]. Copyrights (2010) Elsevier Publications)

Item	AOP reactor	Piping, valves, electrical (30 %)	Site work (10 %)	Subtotal	Contractor O&P (15 %)	Subtotal	Engineering (15 %)	Subtotal	Contingency (20 %)	Total capital	Amortized annual capital cost
For phenol											
UV	2.47E + 08	7.40E + 07	2.47E + 07	3.46E + 08	5.18E + 07	3.97E + 08	5.96E + 07	4.57E + 08	9.14E + 07	5.48E + 08	4.42E + 07
US	9.00E + 09	2.70E + 09	9.00E + 08	1.26E + 10	1.89E + 09	1.45E + 10	2.17E + 09	1.67E + 10	3.33E + 09	2.00E + 10	1.61E + 09
O$_3$	3.40E + 04	1.02E + 04	3.40E + 03	4.76E + 04	7.14E + 03	5.47E + 04	8.21E + 03	6.30E + 04	1.26E + 04	7.55E + 04	[a]7.55E + 04
US + UV	1.54E + 09	4.63E + 08	1.54E + 08	2.16E + 09	3.24E + 08	2.49E + 09	3.73E + 08	2.86E + 09	5.72E + 08	3.43E + 09	2.77E + 08
US + O$_3$	2.22E + 08	6.66E + 07	2.22E + 07	3.11E + 08	4.66E + 07	3.58E + 08	5.36E + 07	4.11E + 08	8.22E + 07	4.93E + 08	[b]3.98E + 07
UV + O$_3$	6.08E + 06	1.82E + 06	6.08E + 05	8.51E + 06	1.28E + 06	9.78E + 06	1.47E + 06	1.12E + 07	2.25E + 06	1.35E + 07	[b]1.12E + 06
US + UV + O$_3$	4.36E + 07	1.31E + 07	4.36E + 06	6.10E + 07	9.15E + 06	7.01E + 07	1.05E + 07	8.06E + 07	1.61E + 07	9.68E + 07	[b]7.83E + 06
US + H$_2$O$_2$ + CuO	2.35E + 08	7.05E + 07	2.35E + 07	3.29E + 08	4.94E + 07	3.78E + 08	5.68E + 07	4.35E + 08	8.71E + 07	5.22E + 08	4.21E + 07
Fenton	***	***	***	***	***	***	***	***	***	***	***
US + Fenton	7.14E + 07	2.14E + 07	7.14E + 06	1.00E + 08	1.50E + 07	1.15E + 08	1.72E + 07	1.32E + 08	2.64E + 07	1.59E + 08	1.28E + 07
UV + H$_2$O$_2$	1.32E + 07	3.96E + 06	1.32E + 06	1.85E + 07	2.77E + 06	2.13E + 07	3.19E + 06	2.44E + 07	4.89E + 06	2.93E + 07	2.36E + 06
Photocatalysis	1.40E + 09	4.21E + 08	1.40E + 08	1.97E + 09	2.95E + 08	2.26E + 09	3.39E + 08	2.60E + 09	5.20E + 08	3.12E + 09	2.51E + 08
US + photocatalysis	2.05E + 09	6.14E + 08	2.05E + 08	2.87E + 09	4.30E + 08	3.30E + 09	4.95E + 08	3.79E + 09	7.58E + 08	4.55E + 09	3.67E + 08
For reactive azo dye											
UV	–	–	–	–	–	–	–	–	–	–	–
US	8.23E + 09	2.47E + 09	8.23E + 08	1.15E + 10	1.73E + 09	1.32E + 10	1.99E + 09	1.52E + 10	3.05E + 09	1.83E + 10	1.47E + 09
O$_3$	2.04E + 05	6.12E + 04	2.04E + 04	2.86E + 05	4.28E + 04	3.28E + 05	4.93E + 04	3.78E + 05	7.55E + 04	4.53E + 05	[a]4.53E + 05

US + UV	2.64E + 09	7.91E + 08	2.64E + 08	3.69E + 09	5.54E + 08	4.25E + 09	6.37E + 08	4.88E + 09	9.77E + 08	5.86E + 09	4.72E + 08
US + O_3	8.63E + 08	2.59E + 08	8.63E + 07	1.21E + 09	1.81E + 08	1.39E + 09	2.08E + 08	1.60E + 09	3.19E + 08	1.92E + 09	[b]1.55E + 08
UV + O_3	5.04E + 06	1.51E + 06	5.04E + 05	7.06E + 06	1.06E + 06	8.11E + 06	1.22E + 06	9.33E + 06	1.87E + 06	1.12E + 07	[b]1.16E + 06
US + UV + O_3	6.74E + 08	2.02E + 08	6.74E + 07	9.43E + 08	1.41E + 08	1.08E + 09	1.63E + 08	1.25E + 09	2.49E + 08	1.50E + 09	[b]1.21E + 08
US + H_2O_2	2.40E + 08	7.20E + 07	2.40E + 07	3.36E + 08	5.04E + 07	3.86E + 08	5.80E + 07	4.44E + 08	8.89E + 07	5.33E + 08	4.30E + 07
UV + H_2O_2	4.09E + 07	1.23E + 07	4.09E + 06	5.73E + 07	8.59E + 06	6.59E + 07	9.88E + 06	7.58E + 07	1.52E + 07	9.09E + 07	7.33E + 06
US + UV + H_2O_2	3.60E + 07	1.08E + 07	3.60E + 06	5.04E + 07	7.55E + 06	5.79E + 07	8.69E + 06	6.66E + 07	1.33E + 07	7.99E + 07	6.44E + 06
Photocatalysis	1.20E + 08	3.60E + 07	1.20E + 07	1.68E + 08	2.52E + 07	1.93E + 08	2.90E + 07	2.22E + 08	4.44E + 07	2.67E + 08	2.15E + 07
US + photocatalysis	4.98E + 07	1.49E + 07	4.98E + 06	6.98E + 07	1.05E + 07	8.02E + 07	1.20E + 07	9.22E + 07	1.84E + 07	1.11E + 08	8.92E + 06
For TCE											
UV	2.35E + 06	7.04E + 05	2.35E + 05	3.28E + 06	4.93E + 05	3.78E + 06	5.67E + 05	4.34E + 06	8.69E + 05	5.21E + 06	4.20E + 05
US	5.24E + 07	1.57E + 07	5.24E + 06	7.34E + 07	1.10E + 07	8.44E++07	1.27E + 07	9.71E + 07	1.94E + 07	1.17E + 08	9.39E + 06
O_3	1.02E + 05	3.06E + 04	1.02E + 04	1.43E + 05	2.14E + 04	1.64E + 05	2.46E + 04	1.89E + 05	3.78E + 04	2.27E + 05	[a]226623.6
US + UV	1.34E + 07	4.03E + 06	1.34E + 06	1.88E + 07	2.82E + 06	2.16E + 07	3.25E + 06	2.49E + 07	4.98E + 06	2.99E + 07	2.41E + 06
UV + H_2O_2	3.13E + 05	9.40E + 04	3.13E + 04	4.38E + 05	6.58E + 04	5.04E + 05	7.56E + 04	5.80E + 05	1.16E + 05	6.96E + 05	5.61E + 04
Photocatalysis	2.34E + 06	7.03E + 05	2.34E + 05	3.28E + 06	4.92E + 05	3.77E + 06	5.66E + 05	4.34E + 06	8.68E + 05	5.21E + 06	4.20E + 05

[a]Since ozone generator is assumed to be replaced every year, amortized cost is taken as the same as that of the capital cost.
[b]Cost of ozone generator is added to the amortized cost of UV and US system amortized over 30 years at 7 % rate.

Conclusion

In summary, the industrial effluents discharged without proper treatment caused the environmental and health-related problems. The treatment of the recalcitrant pollutants by various techniques and the improvement needs for the enhanced efficiency of the processes are discussed here. The utilization of ultrasound as a tool for the degradation of various environmental contaminants increased the possibilities to degrade the contaminants into end products. The sonolytic, sonocatalytic, photocatalytic, and sonophotocatalytic degradation of various environmental contaminants using various experimental conditions are discussed herein. The combined ultrasound and photocatalysis technique provided an effective methodology for the mineralization; however, in the energy perspective, the utilization of ultraviolet irradiation increases the energy consumption of the sonophotocatalysis.

The visible light can be used as a source for the photocatalysis by making some modification in the photocatalysts during its synthesis which reduces the energy required for the sonophotocatalysis. Besides, the nanoparticles loaded to enhance the visible light response of the semiconductor nanocatalysts act as the center for the recombination of electronic charge carriers, a slight change in the do pant concentration significantly modify the efficiency of the nanocatalysts. On the other hand, the unselective nature of the radicals produced from the sonophotocatalytic microenvironment considerably increased the concurrent and unselective decomposition of various environmental pollutants. The identification of various intermediates during the sonophotocatalytic treatment increases the knowledge about the hazardous effects created by the intermediates, since in some cases, the derivative products are more toxic than the parent compounds.

Nevertheless, most of the sonophotocatalytic degradation of environmental pollutants documented are in the laboratory and pilot scales. The commercialization of sonophotocatalysis technique suffers from the cost of the ultrasonic equipments. The development of cost-effective ultrasonic transducers reduces the operating cost of the combined processes. The CO_2 and mineral acids present in the water are obtained as the final product after the sonophotocatalytic processes. The water can be recycled in the effluent industry to reduce the water consumption during the processes. However, the auxiliary chemicals present in the water needs to be removed for the effective recycling.

References

1. Auriol M, Filali-Meknassi Y, Tyagi RD, Adams CD, Surampalli RY (2006) Process Biochem 41:525
2. Belgiorno V, Rizzo L, Fatta D, Della Rocca C, Lofrano G, Nikolaou A, Naddeo V, Meric S (2007) Desalination 215:166
3. Kumar M, Puri A (2012) Indian J Occup Environ Med 16:40
4. Eren Z (2012) J Environ Manage 104:127
5. Devipriya S, Yesodharan S (2005) Sol Energy Mater Sol Cells 86:309

6. Burrows HD, Canle LM, Santaballa JA, Steenken S (2002) J Photochem Photobiol B: Biol 67:71
7. Wang C, Li J, Lv X, Zhang Y, Guo G (2014) Energy Environ Sci 7:2831
8. Hisaindee S, Meetani MA, Rauf MA (2013) Trends Anal Chem 49:31
9. Anandan S, Lee GJ, Chen PK, Fan C, Wu JJ (2010) Ind Eng Chem Res 49:9729
10. Surpateanu M, Zaharia C (2004) Cent Eur J Chem 2:573
11. Sathishkumar P, Pugazhenthiran N, Mangalaraja RV, Asiri AM, Anandan S (2013) J Hazard Mater 252–253:171
12. Madhavan J, Sathishkumar P, Anandan S, Zhou M, Grieser F, Ashokkumar M (2010) Chemosphere 80:747
13. Beltran FJ, Rivas FJ, Montero-de-Espinosa R (2003) Ind Eng Chem Res 42:3218
14. Fujishima A, Honda K (1972) Nature 238:37
15. Hoffmann MR, Martin ST, Choi W, Bahneman DW (1995) Chem Rev 95:69
16. Fox MA, Dulay MT (1993) Chem Rev 93:341
17. Puma GL, Yue PL (1999) Ind Eng Chem Res 38:3246
18. Shah M (2014) Int J Environ Bioremediat Biodegradation 2:231
19. Pollet BG (2010) Int J Hydrogen Energy 35:11986
20. Adewuyi YG (2001) Ind Eng Chem Res 40:4681
21. Harada H, Hosoki C, Kudo A (2001) J Photochem Photobiol A Chem 141:219
22. Suslick K (1990) Science 247:1439
23. Margulis MA (1992) Ultrasonics 30:152
24. Lepoint T, Mullie F (1994) Ultrason Sonochem 1:S13
25. Ashokkumar M, Lee J, Kentish S, Grieser F (2007) Ultrason Sonochem 14:470
26. Meng Z, Zhu L, Choi J, Park CY, Oh W (2012) Ultrason Sonochem 19:143
27. Wang J, Jiang Y, Zhang Z, Zhang X, Ma T, Zhang G, Zhao G, Zhang P, Li Y (2007) Ultrason Sonochem 14:545
28. Khataee A, Soltani RDC, Karimi A, Joo SW (2015) Ultrason Sonochem 23:219
29. Khataee A, Karimi A, Arefi-Oskoui S, Soltani RDC, Hanifehpour Y, Soltani B, Joo SW (2015) Ultrason Sonochem 22:371
30. Perozo-Rondon E, Martín-Aranda RM, Casal B, Duran-Valle CJ, Lau WN, Zhang XF, Yeung KL (2006) Catal Today 114:183
31. Stock NL, Peller J, Vinodgopal K, Kamat PV (2000) Environ Sci Technol 34:1747
32. Neelavannan MG, Revathi M, Ahmed Basha C (2007) J Hazard Mater 149:371
33. Neelavannan MG, Ahmed Basha C (2008) Sep Purif Technol 61:168
34. Guieysse B, Norvill ZN (2014) J Hazard Mater 267:142
35. Mendez-Arriaga F, Torres-Palma RA, Petrier C, Esplugas S, Gimenez J, Pulgarin C (2009) Water Res 43:3984
36. Augugliaro V, Litter M, Palmisano L, Soria J (2006) J Photochem Photobiol C Rev 7:127
37. Hamdaoui O, Chiha M, Naffrechoux E (2008) Ultrason Sonochem 15:799
38. Song YL, Li JT (2009) Ultrason Sonochem 16:440
39. Chakma S, Moholkar VS (2015) Ultrason Sonochem 22:287
40. Madhavan J, Sathishkumar P, Anandan S, Grieser F, Ashokkumar M (2010) Sep Purif Technol 74:336
41. Ma CY, Xu JY, Liu XJ (2006) Ultrasonics 44:e375
42. Mrowetz M, Pirola C, Selli E (2003) Ultrason Sonochem 10:247
43. Sathishkumar P, Mangalaraja RV, Rozas O, Mansilla HD, Gracia-Pinilla MA, Anandan S (2014) Ultrason Sonochem 21:1675
44. Sathishkumar P, Mangalaraja RV, Rozas O, Mansilla HD, Gracia-Pinilla MA, Meléndrez MF, Anandan S (2014) Sep Purif Technol 133:407
45. Xing TL, Chen GQ, Irl J, Chu KH (2009) Aatcc Rev 9:37–40
46. Chakinala AG, Gogate PR, Burgess AE, Bremner DH (2008) Ultrason Sonochem 15:49–54
47. Vinodgopal K, Peller J (2003) Res Chem Intermed 29:307e316
48. Minero C, Lucchiari M, Vione D, Maurino V (2005) Environ Sci Technol 39:8936–8942

49. Boreen AL, Arnold WA, McNeill K (2004) Environ Sci Technol 38:3933
50. Sorensen BH, Nielsen SN, Lanzky PF, Ingerslev F, Lutzhoft HCH, Jorgensen SE (1998) Chemosphere 36:357
51. He Y, Grieser F, Ashokkumar M (2011) J Phys Chem A 115:6582
52. Selli E, Bianchi CL, Pirola C, Cappelletti G, Ragaini V (2008) J Hazard Mater 153:1136
53. Anandan S, Ashokkumar M (2009) Ultrason Sonochem 16:316
54. Sathishkumar P, Mangalaraja RV, Mansilla HD, Gracia-Pinilla MA, Anandan S (2014) Appl Catal B Environ 160–161:692
55. Michael I, Achilleos A, Lambropoulou D, Torrens VO, Perez S, Petrovic M, Barcelo D, Fatta-Kassinos D (2014) Appl Catal B: Environ 147:1015
56. Duran A, Monteagudo JM, Exposito AJ, Monsalve V (2016) Chem Engg J 284:503
57. Jelic A, Michael I, Achilleos A, Hapeshi E, Lambropoulou D, Perez S, Petrovic M, Fatta-Kassinos D, Barcelo D (2013) J Hazard Mater 263P:177
58. Clara M, Strenn B, Gans O, Martinez E, Kreuzinger N, Kroiss H (2005) Water Res 39:4797
59. Patil PN, Gogate PR (2014) J Water Process Eng. doi:10.1016/j.jwpe.2014.10.012
60. Madhavan J, Sathishkumar P, Anandan S, Grieser F, Ashokkumar M (2010) J Hazard Mater 177:944
61. Mahamuni NN, Adewuyi YG (2010) Ultrason Sonochem 17:990

Advanced Oxidation Processes Using Ultrasound Technology for Water and Wastewater Treatment

Younggyu Son

Contents

Abstract

For decades, ultrasound technology using acoustic cavitation has been an issue and widely studied for many environmental/chemical engineering processes as one of emerging green technologies. Concentrated energy in tiny-scale cavitation bubbles releases when the bubbles collapse and various chemical and physical effects can be induced without the application of chemicals. In this chapter, previous researches regarding the optimization of sonochemical degradation/oxidation reactions for water and wastewater treatment processes are carefully reviewed. The basic principles of advanced oxidation processes and acoustic cavitation are introduced, and the effects of affecting factors on sonochemical oxidation/degradation reactions including input power, applied frequency,

Y. Son (✉)

Department of Environmental Engineering, Kumoh National Institute of Technology, Gyeongbuk, South Korea

e-mail: yson@kumoh.ac.kr

dissolved species, and target compounds' volatility are discussed in terms of engineering applications.

Advanced Oxidation Processes

Recently advanced oxidation processes (AOPs) have been widely investigated to develop effective treatment processes for the removal of emerging aqueous pollutants including natural organic matters (NOMs), disinfection by-products (DBPs), endocrine disrupting compounds (EDCs), pharmaceuticals and personal care products (PPCPs), and heavy metals [1–15]. Treatment guidelines for these compounds, detected at very low levels in natural ecosystem and water/wastewater treatment plants, have been issued to establish sustainable water supply systems and water reuse systems. AOPs can also effectively degrade other conventional recalcitrant pollutants such as phenols, dyes, and chlorinated compounds [16–29]. Highly reactive oxidizing species such as hydroxyl radical ($\cdot$OH), perhydroxyl radical ($\cdot$OOH), and hydrogen peroxide (H_2O_2) generated in AOPs are enable to effectively degrade and mineralize the above aqueous pollutants due to their high oxidation potentials as shown in Table 1 [30].

AOPs are divided into three categories. The first category is the chemical-based processes which include ozonolysis (O_3) and Fenton's oxidation (Fe^{2+} and H_2O_2). These chemical-based processes are considered as early-stage AOPs and involve the use of oxidizing chemicals and reactive radicals. The second category is the wave-energy-based processes, namely, photolysis (ultraviolet, UV), photocatalysis (UV/TiO_2), UV/H_2O_2 processes, sonolysis (ultrasound, US), and microwave (MW) processes. The third category is the combined processes of AOPs including sonophotolysis (UV/US), sonophotocatalysis (UV/US/TiO_2), UV/ozone processes, UV/Fenton processes, and US/Fenton processes. These combined AOPs can be synergistically effective in terms of reaction efficiency, input chemical consumption, energy consumption, and reaction time. Table 2 shows degradation/radical oxidation reaction mechanisms in various AOPs [2, 4, 16, 18, 28, 30–37].

For the last two decades, photocatalytic processes using TiO_2 have been designated as one of the most widely studied AOPs due to its high removal efficiencies for a wide range of aqueous pollutants, great potential to absorb solar energy, and for being stable/non-toxic/highly reactive [38]. The current research area of photocatalysis includes the optimization of processes, the modification of titanium-oxide photocatalysts for higher efficiency, the development of visible-light-sensitized photocatalysts, and the combination of other AOPs. However, it seems that the application of large-scale and continuous photocatalytic processes for water and wastewater treatment plants still needs further research due to two demanding issues: first is the separation and reuse of nano-size photocatalysts in aqueous phase.

Table 1 Oxidation potential of oxidizing species

Oxidizing species		Oxidation potential (V)
Fluorine	(F_2)	3.03
Hydroxyl radical	$(\cdot OH)$	2.80
Atomic oxygen	(O)	2.42
Ozone	(O_3)	2.07
Hydrogen peroxide	(H_2O_2)	1.78
Perhydroxyl radical	$(\cdot OOH)$	1.70
Permanganate	(MnO_4^-)	1.68
Hypobromous acid	$(HBrO)$	1.59
Chlorine dioxide	(ClO_2)	1.57
Hypochlorous acid	$(HClO)$	1.49
Chlorine	(Cl_2)	1.36

As shown in Fig. 1, the photocatalytically treated water on the right-hand side still looks much more contaminated than bisphenol-A (BPA) contaminated water on the left-hand side. It means that post treatment processes are always required to remove nanoscale particles from treated water when using photocatalytic processes. A variety of separation and reuse technologies of nano-size particles has been suggested. Nanoparticles with strong magnetic properties as shown in Fig. 2 were synthesized using diverse methods [6, 39, 40]. Yao et al. [6] used photocatalysis/microfiltration system for the removal of natural organic matter (NOM). Second is the application of extremely high dose of photocatalysts. It has been reported that the optimal dose of photocatalysts such as TiO_2 ranges from 240 to 1,000 mg/L [23, 25, 31, 36, 41–43]. As a result of this, the penetration distance of light (or effective distance from the light source such as a UV lamp) is very small due to large attenuation. Son et al. [37] reported that the half-light-intensity distance was only 0.5 cm for the TiO_2 concentration of 100 mg/L in a rectangular reactor (L, 600 × W, 110 × H, 250 mm^3) equipped with a commercial UV lamp module (254 nm, 6 W), while the half-intensity distance was 7.7 cm in the absence of TiO_2. On the other hand, no significant attenuation of ultrasound was observed for the TiO_2 concentration of 10, 50, and 100 mg/L in their study. In addition, the high dose of nano-size particles may cause adverse effects on ecosystems and human health. Samaee et al. [44] evaluated the toxicity of nano-size TiO_2 using zebrafish embryos for the TiO_2 concentration of 0, 1, 10, and 100 mg/L.

Recently, many environmental and chemical engineering researchers also have focused on ultrasound technology which is based on mechanical wave energy for drinking water treatments, municipal/industrial wastewater treatments, coagulation/flocculation, disinfection/sterilization, sludge dewatering/reduction, surface cleaning, contaminated soil washing, bioenergy production, and nanoscale material synthesis [7, 8, 45–62]. High-intensity ultrasound can induce various sonochemical and sonophysical effects without the use of chemicals. It is possible due to the acoustic cavitation phenomena, hence giving these microscale effects a potential to design varied novel and environmental friendly engineering processes. In Table 3,

Table 2 Degradation/radical oxidation reactions in AOPs

Treatment	Degradation/radical oxidation reactions	References
Ozonolysis	(i) Direct oxidation (ii) Radical oxidation from ozone decomposition $O_3 + OH^- \rightarrow O_2 \cdot^- + HO_2 \cdot$ $O_3 + HO_2 \cdot \rightarrow 2O_2 + \cdot OH$	Addamo et al. [31]
Fenton's oxidation	$Fe^{2+} + H_2O_2 \rightarrow Fe^{3+} + \cdot OH + OH^-$ $Fe^{3+} + H_2O_2 \rightarrow Fe^{2+} + \cdot OOH + H^+$	Esplugas et al. [32] and Parsons [30]
Photolysis	$P + h\nu \rightarrow P_{ox}$ ($h\nu$ is a unit light energy, photons) The reaction quantum yields of target compounds are considered	Chelme-Ayala et al. [33]
UV/H_2O_2 processes	$H_2O_2 + h\nu \rightarrow 2 \cdot OH$ UVC (254 nm) light is commonly used	Andreozzi et al. [34] and Pera-Titus et al. [4]
Photocatalysis	$TiO_2 + h\nu \rightarrow e^- + h^+$ (e^-, electron; h^+, hole) $\rightarrow \begin{array}{l} h^+ + P \rightarrow P_{ox} \\ e^+ + O_2 \rightarrow H_2O \end{array}$ Photocatalytic oxidation commonly occurs on the surface of photocatalysts	Parsons [30] and Agustina et al. [2]
Sonolysis	$H_2O + cavitation(US) \rightarrow \cdot H + \cdot OH$ Radicals are generated by pyrolysis and radical chain reactions induced by cavitation	Jiang et al. [18] and Lim et al. [19]
Microwave processes	Commonly used with oxidants such as H_2O_2 Enhance radical reactions by stimulating mechanisms such as rapid heating	Remya and Lin [35]
Combination processes	Optimal combination of wave energy technologies and chemical technologies Sonophotolysis (UV/US) Sonophotocatalysis (UV/US/TiO_2) Ozone/H_2O_2 UV/ozone UV/Fenton processes US/Fenton processes	Esplugas et al. [32], Pera-Titus et al. [4], Berberidou et al. [36], Bremner et al. [16], and Son et al. [37]

the applications of ultrasound technology in environmental and chemical engineering fields are summarized.

Acoustic Cavitation

When ultrasound at high enough intensity is irradiated in aqueous phase, a sound energy field is formed and the molecules in the sound field oscillate at their mean position. The sound pressure at each position changes sinusoidally, and this results in

Fig. 1 Bisphenol A contaminated water (1 mg/L) on the left-hand side and photocatalytically treated water (TiO$_2$ concentration: 500 mg/L) on the right-hand side
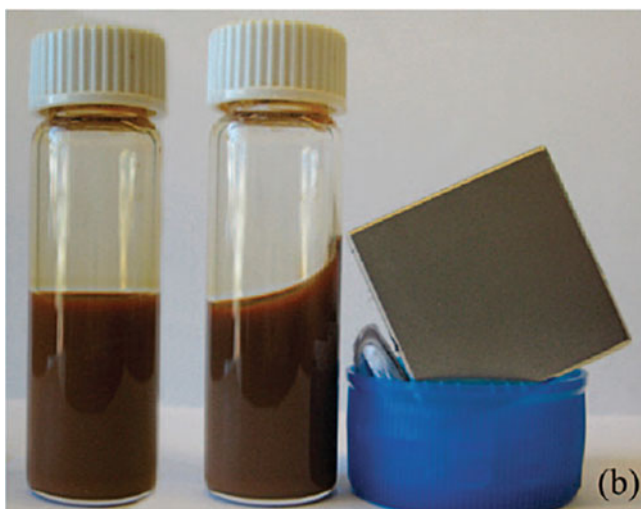

Fig. 2 Synthesized nanoparticles with strong magnetic properties [39]

the periodic repetition of the compression period (the sound pressure is positive) and the rarefaction period (the sound pressure is negative). The molecules are drawn apart in the rarefaction period and cavities are formed at high sound pressure which is enough to break the interaction of molecules. These cavities acting as bubbles, hence termed as cavitation bubbles, grow by diffusion and coalescence unless they are dissolved. At a maximum size, which is mainly determined by applied ultrasound frequency, the bubbles violently collapse. This microscale process is termed the acoustic cavitation (the formation, growth, and collapse of bubbles). A huge number

Table 3 The applications of ultrasound technology in environmental and chemical engineering fields

Fields	Ultrasonic processes
Drinking water	Micropollutants (NOMs, DBPs, EDCs, and PPCPs) removal
	Coagulation/flocculation
	Disinfection
Wastewater	Nonbiodegradable pollutants removal
	Heavy metals oxidation
Solid waste	Sludge dewatering/reduction
	Bioenergy (CH_4) production
	Spent nuclear fuel repressing
Contaminated soil	Soil washing/remediation
	Pollutants desorption/degradation
Lake/river	Water quality control
	Algae removal
Synthesis	Organic synthesis
	Nano-sized/nanostructured material synthesis
Mixing/mass transfer/separation	Violent mixing/agitation/homogenization
	Atomization
	Degassing
	Separation
Others	Surface cleaning
	Extraction

of cavitation events occur continuously and various chemical and physical cavitation effects can be observed in macroscale [37, 63–66].

It is generally known that the dissolved gas molecules such as dissolved oxygen molecules in water act as the nuclei for cavitation and the microscale particles act as the weak point for the breakage of the molecules interaction. Due to these impurities, the cavitation events occur under relatively low-pressure conditions (<20 atm), which can be induced by normal ultrasonic apparatus [63, 67]. (A negative pressure of approximately 1,500 atm is required to break the interaction of water molecules.) It was reported that much less cavitation occurred when ultrasound was irradiated in boiled distilled water including less dissolved gas molecules [13]. During bubble formation and growth, extreme conditions of very high temperatures ($\sim$ several thousand K) and pressures ($\sim$ several hundred atmospheres) develop inside cavitation bubble, and various radicals are generated by the pyrolysis of water molecules, dissolved gas molecules, and other volatile/hydrophobic molecules. They act as precursors for the generation of radical species and diffuse from the liquid into the bubble. At the last compression period, the bubble collapses, releasing highly concentrated energy and highly reactive radicals into the surroundings. During the cavitation events, both sonophysical effects including microjet, microstreaming, and shock wave and sonochemical effects including pyrolysis and radical reactions are
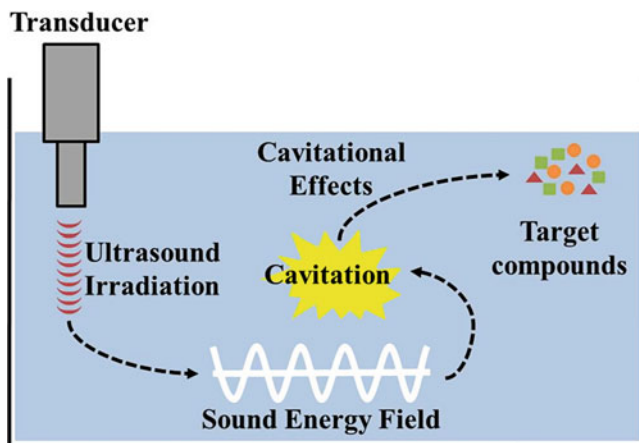
Fig. 3 A schematic of the cavitational reaction mechanisms of aqueous phase compounds by ultrasound irradiation
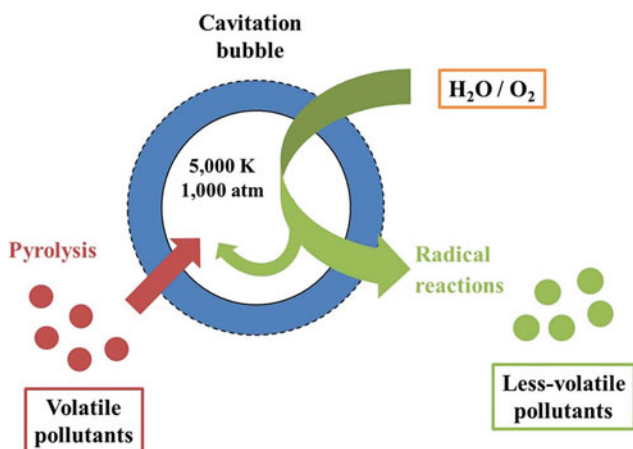

Fig. 4 Sonochemical effects including pyrolysis and radical reactions for the degradation of aqueous pollutants

simultaneously induced [49, 63, 68]. Figures 3 and 4 represent schematic diagrams of the cavitational reaction mechanisms and sonochemical effects for the degradation of aqueous pollutants, respectively. Light emission, called sonoluminescence, is also observed when the bubble collapses [65].

There are many different factors which affect the cavitation and the sonochemical degradation of pollutants, and they can be categorized into several groups as shown in Table 4 [63]. Ultrasonic factors in the first group determine the characteristics and the fate of cavitation bubbles, including applied frequency in single/multiple mode, input powers, and continuous/pulse irradiation mode. The factors in the second

Table 4 The different ultrasonic and environmental factors affecting the fate of cavitation bubbles and the sonochemical degradation

Groups	Affecting factors
Ultrasonic factors	Applied frequency
	Input power
	Single or multifrequency irradiation
	Continuous and pulse irradiation
Solution factors	Temperature, pressure, pH
	Dissolved gases and ions
	Particles and additives
Contaminant factors	Volatility/hydrophobicity
	Molecular structure/weight
	Initial concentration
	The presence of multiple contaminants
Geometric factors	Transducer type (horn type/plate type)
	Transducer location/array
	Irradiation distance (from sound source to reflecting boundary)
	Reactor shape/material
	Mixing/aeration/internal structures

group including temperature, pressure, pH, dissolved gases, dissolved ions, particles, and additives affect the degree of cavitation effects such as pyrolysis and radical reactions as well as the behavior of bubbles. These two groups above have been generally considered and widely investigated in sonochemistry. The factors in the third group representing the characteristics of contaminants are important to understand the degree of sonochemical degradation and the order of pollutants removal when multiple contaminants are present. The geometric factors of the last group have been recently focused due to the current demands for the scale up and industrial uses of ultrasound technology in environmental and chemical engineering fields. It was reported that the geometric factors could significantly change the formation of sound energy field and quite different cavitational effects were observed under the same ultrasonic conditions [13, 63, 69–73].

Quantification of Input Power

The input power of ultrasound is one of the most important affecting factors governing the acoustic cavitation. The quantification of ultrasonic power is required to quantitatively estimate and compare cavitational effects and resulting reactions. In sonochemistry many researchers have used the calorimetric method, known as calorimetry, to estimate the average ultrasonic power in the solution. The

calorimetric energy is quantified by measuring the temperature change of solution under ultrasound irradiation using the following equation [63, 69]:

$$P_{cal} = \frac{dT}{dt} C_P M \tag{1}$$

where P_{cal} is the calorimetric power, dT/dt is the rate of increase of the solution temperature, C_p is the specific heat capacity of the liquid (4.2 J/g·K for water), and M is the mass of the liquid. The temperature increase in the solution is mainly contributed by the attenuation/absorption of ultrasound in sonoreactors. It is theoretically known that the sound attenuation is a function of an irradiation distance, applied frequency, and solution characteristics as shown in following equations [13, 74]:

$$I = I_0 \times \exp(-2\alpha d) \tag{2}$$

$$\alpha = \frac{2\pi^2 f^2}{\rho c^3} \left\{ \frac{4}{3}\eta_s + \frac{(\gamma - 1)\kappa}{C_P} \right\} \tag{3}$$

where I is the sound intensity, I_0 is the initial sound intensity, α is the absorption/attenuation coefficient, d is the irradiation distance, f is the applied frequency, ρ is the density of the liquid, c is the sound speed in the liquid, η_s is the ordinary viscosity of the liquid, γ is the specific heat ratio, κ is the thermal conductivity, and C_p is the heat capacity at constant pressure. This equation only describes the sound energy loss due to frictional loss and thermal conduction in unconfined systems. On the other hand, the attenuation of ultrasound occurs mainly due to the boundaries including reactor walls, and the interface between air and liquid in relatively small-scale confined systems [13, 63, 67]. It is unclear whether the attenuation by boundaries can generate heat to noticeably increase the temperature of the liquid.

To quantify the ultrasonic energy using calorimetry, both the temperature increase in the transducer and the heat loss to the surroundings also should be carefully considered because of the following reasons: firstly, the ultrasound is irradiated by vibrating the transducer plate at a very fast period (20,000 times vibration for 20 kHz). As a result of this, the temperature of the transducer plate gradually increases and the heat dissipates into the solution. Secondly, the temperature change (ΔT) between the solution and the surroundings increases and the heat in the solution dissipates into the surroundings as the irradiation time elapses. Thus it is desirable to conduct calorimetry tests within a relatively short irradiation time to minimize the above two phenomena. Toma et al. [75] classified the total consumed energy into four categories including dissipated heat energy, atomization energy, heat energy stored at the transducer, and unquantified energy.

Koda et al. [76] tested calorimetry and three sonochemical oxidation methods including TPPS (5,10,15,20-Tetrakis (4-sulfotophenyl) porphyrin) dosimetry, KI (Potassium iodide) dosimetry, and Fricke dosimetry using several different sonoreactors under different frequency conditions and input power conditions.

They concluded that calorimetric power, a sort of wasted energy, did not appropriately represent the average ultrasonic powers and the degree of sonochemical reactions. It might be due to the different formation of sound energy field and the different behavior of sound attenuation in geometrically different sonoreactors. Asakura et al. [69] reported that measured calorimetric powers for four different frequency conditions significantly changed as the liquid height, the distance from the transducer to the water surface, increased in cylindrical sonoreactors equipped with the transducer at the bottom. On the other hand, Son et al. [63] reported that approximately constant calorimetric powers were measured for 36 and 108 kHz when the liquid height increased. Therefore, it seems that the relationship between calorimetric energy and average ultrasonic energy has not been proved.

It can be more appropriate to quantitatively compare the efficiencies of acoustic cavitation processes with those of other AOPs such as photocatalytic processes in terms of electrical energy consumption. Moreover the estimation of electrical energy consumption in sonochemical processes is required to design industrial-scale sonoreactors [3, 7, 77].

The input power in sonoreactors can be differently normalized depending on the ultrasonic apparatus types: the horn-type sonicator and the plate-type transducer module. For the horn-type ultrasound generator, ultrasound is intensively and concentrically irradiated from the small tip and the tip size can determine the behavior of ultrasound. Thus the input power can be normalized by the area of the tip and it is termed power intensity. The power intensity can be expressed as follows [67]:

$$\text{Power intensity} = \frac{P_E \ or \ P_{US}}{A_{Tip}} \tag{3}$$

where P_E is the electrical power, P_{US} is the ultrasonic power measured using calorimetry, and A_{Tip} is the area of the sonicator tip. On the other hand, it is not easy to estimate the irradiation area of the plate-type transducer module because the transducer is firmly attached to the metal plate with a larger surface area and the vibration of the plate induces relatively moderate ultrasound irradiation. In case of the plate-type transducer, the input power can be normalized using the total liquid volume as shown in the following equation, and it is termed power density [63, 72]:

$$\text{Power density} = \frac{P_E \ or \ P_{US}}{V_{liq}} \tag{4}$$

where V_{liq} is the liquid volume in the sonoreactor. Recently, the plate-type transducer modules are mostly used to induce sonochemical reactions because the cavitation-active zone induced by the horn-type sonicator is very small in spite of very high input energy consumption and only low-frequency (commercially 20–40 kHz range) ultrasound, which is suitable for sonophysical reactions, is generated by the horn-type sonicator [48, 78].

The Effects of Input Power on Sonochemical Reactions

As shown in Fig. 5, it is generally known that the efficiency of sonochemical reactions highly depends on the input power and the trends of sonochemical efficiency can be divided into several distinct phases including the lag phase, increase phase, stationary phase, and attenuation phase. At the lag phase, no significant sonochemical reactions are observed because the input power is less than a cavitation threshold power which is the minimum power to induce cavitation events. Then, the sonochemical efficiency increases with an increase in the input power at the increase phase and reaches the stationary phase with the observation of the maximal/optimal sonochemical efficiency. Finally, the sonochemical efficiency drastically decreases at the attenuation phase.

Jiang et al. [27] investigated the sonochemical degradation of volatile chlorinated aromatic compounds using a 500 kHz cylindrical sonoreactor (250 mL) and reported the linear relationships between the reaction rate constants and ultrasonic powers (5–50 W) measured by the calorimetry for 1,4-dichlorobenzene and 1-chloronaphthalene. Kirpalani and McQuinn [79] also reported that the concentration of iodine (I_2) increased as the power increased at 1.7 and 2.4 MHz using the KI dosimetry. The solution volume was 100 mL and the input power variations were 3–21 W and 8–18 W for 1.7 and 2.4 MHz, respectively. On the other hand, some researchers observed the drops of sonochemical efficiencies as shown in the attenuation phase above. Kang et al. [80] tested two frequencies of 205 and 358 kHz for the removal of MTBE (Methyl tert-butyl ether) using a cylindrical sonoreactor ($V = 500$ mL) and reported that both the pseudo first-order rate constants of 205 and 358 kHz increased as the power density increased up to 240 W/L. Over the power
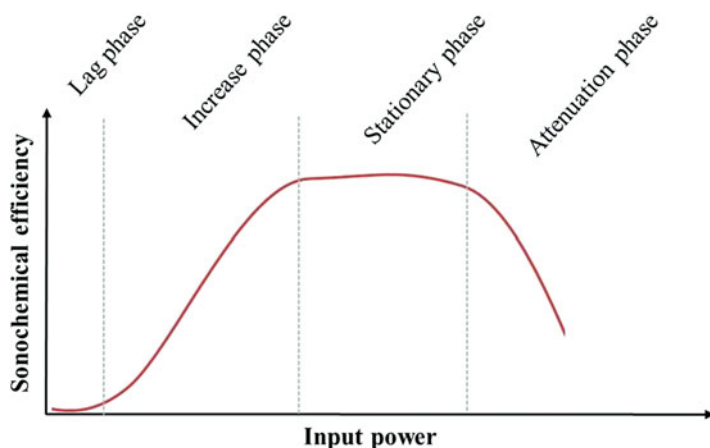
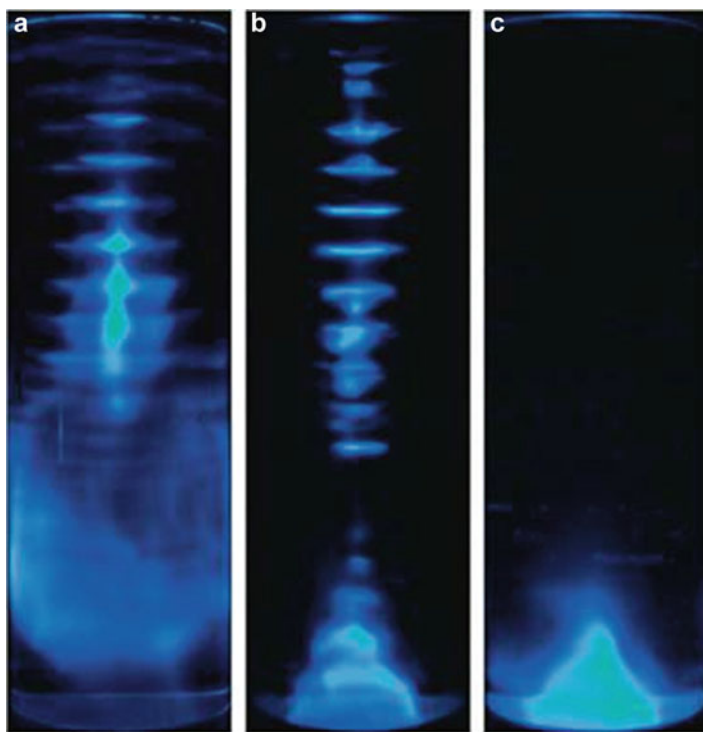**Fig. 5** Typical increase curve for the efficiency of sonochemical reactions

Fig. 6 The SCL images under (**a**) 30, (**b**) 60, and (**c**) 90 W in a cylindrical sonoreactor (frequency: 36 kHz, liquid height: 40 cm) [81]

density of 250 W/L, they found that the reaction constant of 358 kHz decreased, and they concluded that an optimum power density for the highest reactions rates could be determined from the bubble dynamics equations and their results. Sivakumar and Pandit [24] investigated the effect of power density on the sonochemical degradation of Rhodamine B using different ultrasonic apparatus including two horn-type sonicators (22.5 kHz) and a plate-type ultrasonic bath (22.5 kHz). They observed the decrease of sonochemical efficiencies for both the horn-type sonicator (over 15 W/cm^2) and the ultrasonic bath (over 0.063 W/mL).

Some researchers reported that the drop of sonochemical efficiencies in the attenuation phase might be due to the formation of cavitation bubble clouds, which are generated by the coalescence of cavitation bubbles, at relatively high-power conditions. The bubble clouds inhibit the ultrasound irradiation and the sonochemical reactions occur in a limited zone adjacent to the ultrasound source. Son et al. [81] visualized this inhibition in a 36 kHz cylindrical sonoreactors using luminol solution as shown in Fig. 6. The SCL (sonochemiluminescence) images were taken at different power conditions including 30, 60, and 90 W. It was found that the active zone shrunk to cone-shaped zone adjacent to the transducer and no standing wave field was observed at 90 W. Thus the attenuation of ultrasound by the

■ 23 W, ■ 40 W, ■ 82 W

Volume (L)	Intial concentration of KI (g/L)						
	0.05	0.1	0.5	1	2	5	10
0.05	460	460	460	460	460	460	460
0.1	400	400	400	400	400	400	400
0.2	200	200	410	410	410	410	200
0.3	133	273	273	273	273	273	273
0.5	80	164	164	164	164	164	164
1	82	82	82	82	82	82	82

Fig. 7 Determination of optimal input power condition for various initial concentration and volume conditions [72]. (The figure in each cell represents the power density of each condition)

formation of bubble clouds and the drops of the sonochemical efficiency seem to be related with the population of cavitation bubbles, and the control of the bubble population can be one of the key steps to optimize sonochemical processes. (The suggested sonochemical efficiency curve (Fig. 5) looks like the growth curve for a bacterial population.)

Lim et al. [72] investigated the geometric effect and the input power effect using the KI dosimetry at 291 kHz and found that the optimal power could be determined by considering both the input power and the solution volume as shown in Fig. 7. In their work the small input power of 23 W was the most effective for a small volume condition of 0.05 L, while higher input powers of 40 and 82 W were required to achieve the highest sonochemical efficiencies for larger volume conditions (0.1–1 L).

The Effects of Applied Frequency on Sonochemical Reactions

For the last two decades, many researchers have investigated the effect of frequency ranging from 20 kHz to 2.4 MHz on the various sonochemical reactions. As shown in Fig. 8, Beckett and Hua [82] suggested a scheme of the behavior of cavitation bubbles as a function of applied frequency in terms of the degree of bubble implosion (less symmetrical at low frequency), the degree of heat generated upon collapse (more intense at low frequency), the number of effective cavitation events per unit time (more at high frequency), the flux of gases and volatile species toward cavity (more rapid at high frequency), and the flux of active radical species outward (more rapid at high frequency). With these rules and their experimental results of 205, 358, 618, and 1,071 kHz, they determined the frequency of 358 kHz as the optimal frequency for both the degradation of 1,4-dioxane and the generation H_2O_2 due to the optimal combination of relatively less intensity of total energy inside the bubble and relatively more rapid mass transfer of dissolved gases/volatile species and active radical species. It is believed that this scheme explains the behavior of bubbles quite well and provides the intuitive mechanisms to analyze the sonochemical reactions from an overall viewpoint even though other affecting factors are not considered.
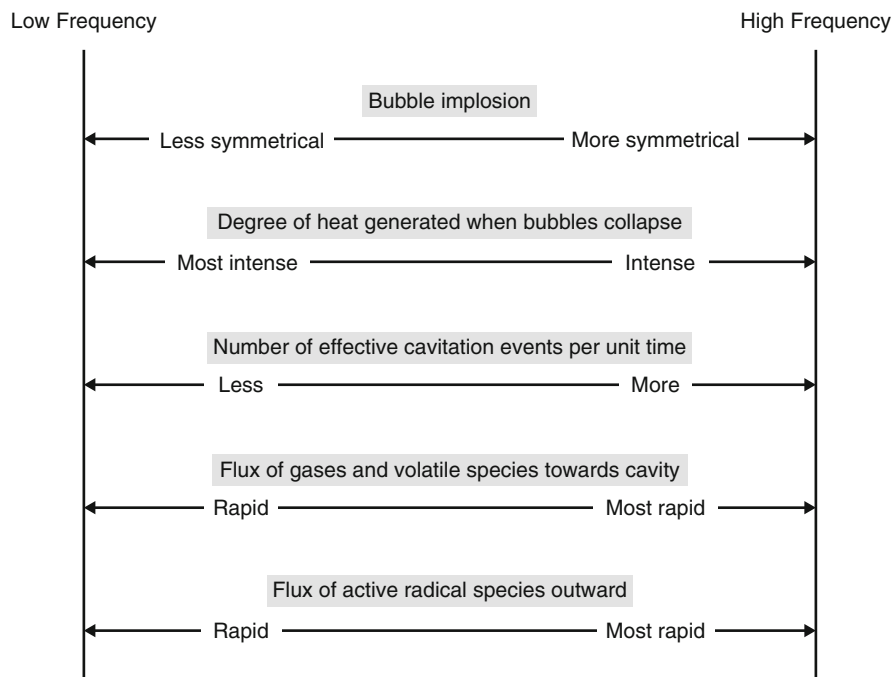
Fig. 8 Cavitation bubbles behavior as a function of applied frequency (Adapted from Beckett and Hua's work [82])

Hung and Hoffmann [83] tested six frequencies including 20, 205, 358, 500, 618, and 1,078 kHz for the sonochemical degradation of chlorinated hydrocarbons using three different sonoreactors and found that the highest degradation rate constant was obtained at 500 kHz. Entezari et al. [84] reported that for the sonochemical degradation of phenol, the initial rate constant of 500 kHz was 19 times and 4.4 times larger than that of 20 kHz and 35 kHz, respectively. Jiang et al. [18] reported that the order of initial degradation/generation rate of 4-chlorophenol and H_2O_2 was 200 kHz > 500 kHz > 800 kHz > 20 kHz. Koda et al. [76] tested three methods including the Fricke reaction, the KI dosimetry, and the TPPS dosimetry from 20 kHz to 1.2 MHz and revealed that the high values of the sonochemical efficiency (SE) were observed at the frequency conditions of 100–500 kHz. Among 35, 74, 170, 300, and 1,000 kHz frequencies, Lim et al. [85] found 300 kHz to be most effective for the sonochemical degradation of all three chlorinated compounds, namely, chlorobenzene, chloroform, and carbon tetrachloride. Therefore, from the literature reported, it would be reasonable to suggest that the optimal frequency ranges from 200 to 500 kHz for two kinds of sonochemical reactions including pyrolysis for volatile/hydrophobic compounds and radical reactions for less-volatile/hydrophilic compounds.

Recently, some researchers have focused on the use of higher frequencies (>500 kHz). Kirpalani and Mcquinn [79] tested the KI dosimetry at 1.7 and

2.4 MHz, and they found that cavitation yields at 1.7 MHz were significantly higher than those at 2.4 MHz with and without cooling. Leong et al. [86, 87] applied 600 kHz, 1 MHz, and 2 MHz frequency ultrasound to develop an ultrasonic fat separation process from natural whole milk in relatively large-scale sonoreactors. Yamamoto et al. [55] reported that high frequencies including 585, 864, and 1,146 kHz were more effective than 20 kHz ultrasound for the disruption of algal cells. Conventionally, the low-frequency ultrasound ranging from 20 to 40 kHz has known as the most effective frequency for sonophysical reactions such as surface cleaning, cell ruptures, and extraction.

Multifrequency systems can be considered to enhance the sonochemical efficiencies. It was reported that sonochemical efficiencies in multifrequency conditions were significantly higher than those in single-frequency conditions [71, 88–92]. However some previous researches revealed that multifrequency systems did not result in higher performances for all cases. Lee and Oh [71] observed the significant inhibition effect of sonochemical reactions in H_2O_2 generation while using a dual opposite irradiation system consisting of two 28 kHz transducers. Son et al. (201) [93] reported that the order of sonochemical efficiency normalized by each electrical input power followed the trend: 35 kHz > 35/500 kHz > 72 kHz > 1,000 kHz > 35/35 kHz > 35/1,000 kHz when KI dosimetry was tested in opposite irradiation systems. Gogate et al. [17] reported no significant synergistic effect for the sonochemical degradation of aqueous phenol in a triple irradiation system. The degradation efficiency for the triple (20/30/50 kHz) irradiation system was 21.4 % and each degradation efficiency for 20, 30, and 50 kHz was 11.7, 13.0, and 13.9 %, respectively. The reason for the low and ineffective sonochemical reaction efficiencies in multifrequency systems might be due to the lack of optimal design information on geometric effects, the arrays of transducers, and input power conditions [63, 71, 72].

Multifrequency ultrasound can be irradiated in a single-frequency irradiation mode. During the cavitation events, the cavitation bubble acts as secondary emitter and generates ultrasound of harmonics, subharmonics, and ultraharmonics of the fundamental driving frequency as shown in Fig. 9 [81, 94–97]. It is not clear whether harmonics and subharmonics can be involved in cavitation events and the resulting sonochemical reactions.

As discussed above, the high-frequency conditions ranging from 200 to 500 kHz seem to be optimal choices for sonochemical reactions. However the use of high-frequency ultrasound for large-scale sonoreactors still seems to require further investigation because the attenuation of high-frequency ultrasound is very severe, and it results in very small cavitation zone. Son et al. [74] measured the sound pressure of ultrasound for several frequency conditions including 35, 72, 110, and 170 kHz in a large-scale bath (L, 1.20 × W, 0.60 × H, 0.40 m^3) equipped with a transducer module on the side, and they found that the attenuation occurs much severe in higher frequency conditions as shown in Fig. 10. Asakura et al. [69] reported that high-frequency ultrasound conditions including 129, 231, and 490 kHz were not effective for higher liquid height conditions (larger volume conditions) under the similar calorimetric energy conditions. They also provided the SCL images showing sonochemical active zone in low- and high-frequency conditions.
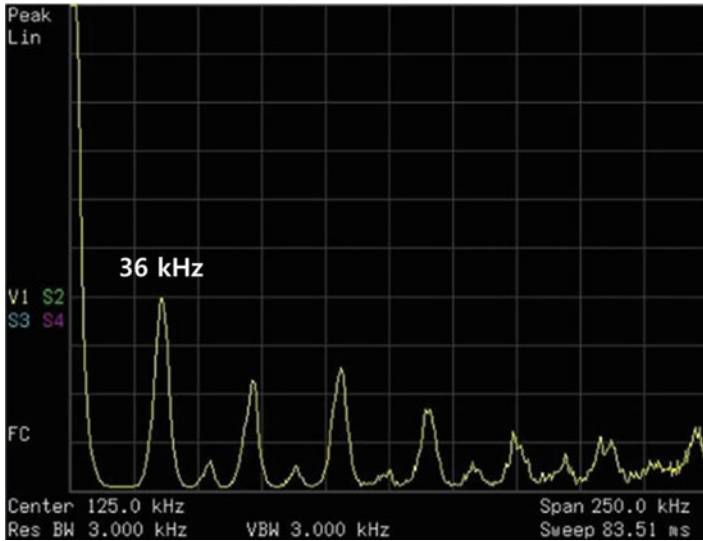
Fig. 9 Acoustic emission spectrum in a spectrum analyzer showing fundamental, harmonic, and subharmonic peaks when 35 kHz ultrasound is irradiated [81]
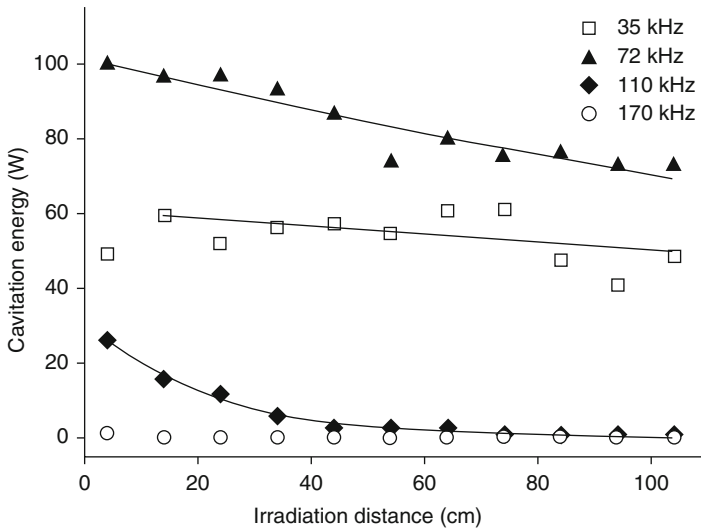

Fig. 10 Cavitation energy, equivalent to the sound pressure of ultrasound, distributions in a large-scale bath (250 L) for 35, 72, 110, and 170 kHz [74]

Other Factors Affecting Sonochemical Reactions

Dissolved Gases and Ions

In sonochemistry it is generally known that dissolved gases such as N_2, O_2, Ar, and air can noticeably affect sonochemical reactions due to the different maximum temperature and pressure inside the bubbles from the perspective of single bubble dynamics [28]. Recently, it was reported that the effectiveness of the dissolved gases for sonochemical reactions could be estimated depending on two cavitational degradation mechanisms: the gas with relatively high specific heat ratio such as Ar was more effective for direct pyrolysis, while O_2 and air resulted in higher reaction efficiencies for indirect radical reactions. Lim et al. [28] reported that Ar was the most effective for the sonochemical degradation of aqueous TCE (trichloroethylene) among air, N_2, and Ar. Pétrier et al. [68] reported that air and O_2 resulted in faster sonochemical degradation of 4-chlorophenol than Ar, while no significant difference was observed for the sonochemical degradation of chlorobenzene, which has higher Henry's law constant and is considered to be removed by direct pyrolysis. Rooze et al. [98] reviewed the effect of dissolved gas on ultrasonic cavitation. They compared the first-order degradation rate constants of various organic compounds using the results from previous researches for the saturating gas of Ar and air and found that Ar was mostly effective for chlorinated compounds, while air was more effective for chlorine-free compounds. They also considered two mechanisms, direct pyrolysis and indirect radical reactions, in terms of molecular bonds.

Some researchers investigated the effect of OH radical scavengers including alcohols, NOMs, and ion species to understand the inhibition and mechanisms of sonochemical reactions [15, 99–103]. Among various scavengers, naturally existing ion species such as NO_3^-, Cl^-, SO_4^{2-}, HCO_3^-, and Br^- are commonly detected in rivers, lakes, and water quality control systems including drinking water treatment facilities and municipal/industrial wastewater treatment plants. It was found that the sonochemical degradation of sulfamethazine was inhibited in the presence of NO_3^-, Cl^-, and SO_4^{2-} while the reactions efficiencies increased in the presence of HCO_3^- and Br^- [15]. The result that HCO_3^- ion inhibited sonochemical degradation was also reported. Gao et al. [104] observed that the sonochemical degradation of ametryn decreased in the order of $CO_3^{2-} > Cl^- > HCO_3^- > SO_4^{2-}$ in a UV/H_2O_2 process. The effects of these ion species on sonochemical reactions are required to do more investigation for environmental engineering applications because most previous researches regarding sonochemical degradation were conducted in deionized or distilled water systems.

Volatility/Hydrophobicity of Target Compounds

The effect of volatility of target compounds has been one of major topics in sonochemical degradation of aqueous pollutants, since it was revealed that a variety

of aqueous pollutants could be removed by acoustic cavitation. As Pétrier et al. [68] briefly summarized, it is believed that volatile compounds undergo direct pyrolysis inside the cavitation bubble, while less volatile compounds are degraded by highly reactive radical species such as OH radical on the bubble surface (Fig. 4). They reported interesting results showing the effect of volatility of target compounds on sonochemical degradation for three pollutant conditions of a volatile compound (chlorobenzene), a less volatile compound (4-chlorophenol), and a mixture of two compounds in a 300 kHz sonoreactor. They observed that the volatile compound-degraded faster than the less volatile compound when each compound existed alone. Moreover the less volatile compound rarely degraded until the volatile compound completely degraded in argon-saturated solution for the mixture of two compounds, while the sonochemical degradation of the less volatile compound was not retarded in the mixture condition when saturated with oxygen. As discussed in the section "Dissolved Gases and Ions," it seems the dissolved oxygen was the key component to significantly enhance the sonochemical degradation of less volatile compound in the mixture condition in their work. Nanzai et al. [105] compared sonochemical degradation of various aromatic compounds in a 200 kHz sonoreactor. They tried to establish a linear relationship between physical/chemical properties representing hydrophobicity including Henry's law constant, vapor pressure, and water solubility and sonochemical degradation rates and found the highest linearity in the relationship between log (vapor pressure) and the initial degradation rates. Previous researchers classified target compounds based mostly on Henry's law constant when they investigated the effect of volatility/hydrophobicity on sonochemical degradation [68, 85, 106, 107].

Geometric Effects on Sonochemical Reactions

Recently some researchers have focused on the optimization of geometric factors and the design of large-scale sonoreactors for industrial use. Koda's group tested several methods to quantify sonochemical reactions in various sonoreactors and investigated the effects of liquid heights and mechanical mixing on sonochemical oxidation using SCL images and KI dosimetry [69, 70, 76, 108]. Son's group observed the variation of sound energy field and corresponding sonochemical oxidation reactions depending on applied liquid heights under the same input power conditions as shown in Fig. 11. They also tried to determine optimal power density under various conditions including liquid heights/volumes, input powers, and initial reactant concentrations [13, 37, 63, 72, 74, 81]. Pandit and Gogate pointed out several limitations in recent sonochemistry research and suggested the strategies for the design and optimization of large-scale sonoreactors and hydrodynamic cavitation reactors in their review papers [88, 109–111].
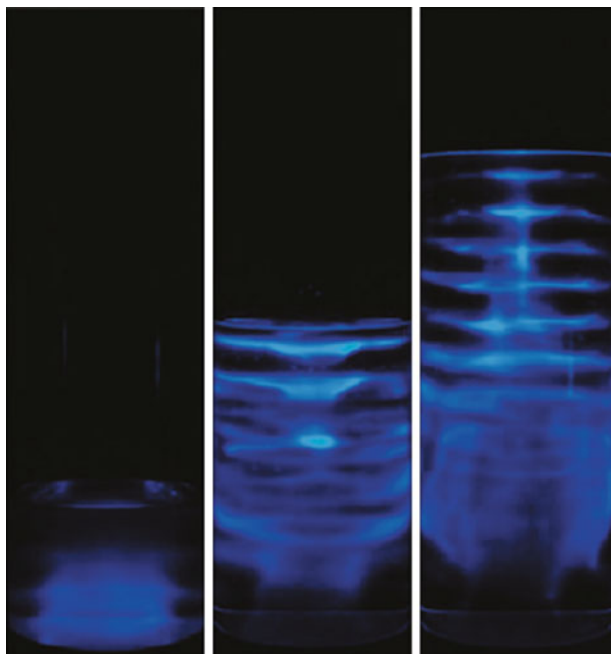
Fig. 11 Visualized ultrasound energy field using the SCL method for the different liquid heights of 10, 20, and 30 cm under the same input energy condition

Future Directions

Even though much data on acoustic cavitation and sonochemical reactions have accumulated for water and wastewater treatment applications, there are still some missing links between lab-scale sonochemical processes and industrial large-scale sonochemical processes. Following topics are required to be intensively investigated for industrial use:

1. Geometric effects including sonoreactor size/shape/material, transducer locations/array, reflector locations/material, and internal structures on sonochemical reactions
2. Determination of optimal effective range/volume for sonochemical reactions per unit transducer depending on applied frequency
3. Aqueous pollutants removal in terms of total organic carbon (TOC)
4. The optimization of sonochemical removal reactions for very low concentration range ($\sim \mu g/L$)
5. Sonochemical degradation/mineralization reactions in real surface water such as lake and river water and municipal/industrial wastewater
6. Development of continuous-flow sonochemical processes in large scale

References

1. Klavarioti M, Mantzavinos D, Kassinos D (2009) Environ Int 35:402
2. Agustina TE, Ang HM, Vareek VK (2005) J Photochem Photobiol C 6:264
3. Mahamuni NN, Adewuyi YG (2010) Ultrason Sonochem 17:990
4. Pera-Titus M, García-Molina V, Baños MA, Giménez J, Esplugas S (2004) Appl Catal B Environ 47:219
5. Chin A, Bérubé PR (2005) Water Res 39:2136
6. Yao P, Choo K-H, Kim M-H (2009) Water Res 43:4238
7. Park B, Cho E, Son Y, Khim J (2014) Ultrason Sonochem 21:1982
8. Kim I, Hong S, Hwang I, Kwon D, Kwon J, Huang CP (2007) Desalination 202:9
9. Esplugas S, Bila DM, Krause LGT, Dezotti M (2007) J Hazard Mater 149:631
10. Frontistis Z, Mantzavinos D (2012) Ultrason Sonochem 19:77
11. Liu Z-h, Kanjo Y, Mizutani S (2009) Sci Total Environ 407:731
12. Pétrier C, Torres-Palma R, Combet E, Sarantakos G, Baup S, Pulgarin C (2010) Ultrason Sonochem 17:111
13. Son Y, Lim M, Khim J, Kim L-H, Ashokkumar M (2012) Chem Eng J 183:39
14. Torres RA, Nieto JI, Combet E, Pétrier C, Pulgarin C (2008) Appl Catal B Environ 80:168
15. Gao Y, Gao N, Deng Y, Gu J, Gu Y, Zhang D (2013) Ultrason Sonochem 20:1401
16. Bremner DH, Molina R, Martínez F, Melero JA, Segura Y (2009) Appl Catal B Environ 90:380
17. Gogate PR, Mujumdar S, Thampi J, Wilhelm AM, Pandit AB (2004) Sep Purif Technol 34:25
18. Jiang Y, Petrier C, Waite TD (2006) Ultrason Sonochem 13:415
19. Lim M, Son Y, Cui M, Khim J (2009) Jpn J Appl Phys 48:07GH07
20. Pradhan AA, Gogate PR (2010) Chem Eng J 156:77
21. Maezawa A, Nakadoi H, Suzuki K, Furusawa T, Suzuki Y, Uchida S (2007) Ultrason Sonochem 14:615
22. Neppolian B, Choi HC, Sakthivel S, Arabindoo B, Murugesan V (2002) J Hazard Mater 89:303
23. Pekakis PA, Xekoukoulotakis NP, Mantzavinos D (2006) Water Res 40:1276
24. Sivakumar M, Pandit AB (2001) Ultrason Sonochem 8:233
25. Son Y, Cho E, Lim M, Khim J (2010) Jpn J Appl Phys 49:07HE05
26. Wawrzyniak B, Morawski AW (2006) Appl Catal B Environ 62:150
27. Jiang Y, Pétrier C, David Waite T (2002) Ultrason Sonochem 9:317
28. Lim M, Kim S, Kim Y, Khim J (2007) Ultrason Sonochem 14:93
29. Lim M, Son Y, Yang J, Khim J (2008) Jpn J Appl Phys 47:4123
30. Parsons S, Williams M (2004) In: Parsons S (ed) Introduction. IWA Publishing, London, p 1
31. Addamo M, Augugliaro V, García-López E, Loddo V, Marcì G, Palmisano L (2005) Catal Today 107:612
32. Esplugas S, Giménez J, Contreras S, Pascual E, Rodríguez M (2002) Water Res 36:1034
33. Chelme-Ayala P, El-Din MG, Smith DW (2010) Water Res 44:2221
34. Andreozzi R, Caprio V, Insola A, Marotta R (1999) Catal Today 53:51
35. Remya N, Lin J-G (2011) Chem Eng J 166:797
36. Berberidou C, Poulios I, Xekoukoulotakis NP, Mantzavinos D (2007) Appl Catal B Environ 74:63
37. Son Y, Lim M, Khim J, Ashokkumar M (2012) Ind Eng Chem Res 51:232
38. Schneider J, Matsuoka M, Takeuchi M, Zhang J, Horiuchi Y, Anpo M, Bahnemann DW (2014) Chem Rev 114:9919
39. Teo BM, Chen F, Hatton TA, Grieser F, Ashokkumar M (2009) Langmuir 25:2593
40. Zhang L, Wang W, Zhou L, Shang M, Sun S (2009) Appl Catal B Environ 90:458
41. Marugán J, Hufschmidt D, Sagawe G, Selzer V, Bahnemann D (2006) Water Res 40:833
42. Yang L, Yu LE, Ray MB (2008) Water Res 42:3480
43. Rincón AG, Pulgarin C (2003) Appl Catal B Environ 44:263

44. Samaee S-M, Rabbani S, Jovanović B, Mohajeri-Tehrani MR, Haghpanah V (2015) Ecotoxicol Environ Saf 116:121
45. Collings AF, Gwan PB, Sosa-Pintos AP (2010) Ultrason Sonochem 17:1049
46. Feng D, Aldrich C (2000) Adv Environ Res 4:103
47. Na S, Park Y, Hwang A, Ha J, Kim Y, Khim J (2007) Jpn J Appl Phys 46:4775
48. Son Y, Cha J, Lim M, Ashokkumar M, Khim J (2011) Ind Eng Chem Res 50:2400
49. Son Y, Nam S, Ashokkumar M, Khim J (2012) Ultrason Sonochem 19:395
50. Parag R G (2007) J Environ Manage 85:801
51. Na S, Kim Y-U, Khim J (2007) Ultrason Sonochem 14:281
52. Pérez-Elvira S, Fdz-Polanco M, Plaza FI, Garralón G, Fdz-Polanco F (2009) Water Sci Technol 60:1525
53. Cesaro A, Naddeo V, Amodio V, Belgiorno V (2012) Ultrason Sonochem 19:596
54. Blume T, Neis U (2004) Ultrason Sonochem 11:333
55. Yamamoto K, King PM, Wu X, Mason TJ, Joyce EM (2015) Ultrason Sonochem 24:165
56. Duckhouse H, Mason TJ, Phull SS, Lorimer JP (2004) Ultrason Sonochem 11:173
57. Zhang G, Zhang P, Fan M (2009) Ultrason Sonochem 16:334
58. Bang JH, Suslick KS (2010) Adv Mater 22:1039
59. Cavalieri F, Ashokkumar M, Grieser F, Caruso F (2008) Langmuir 24:10078
60. Neppolian B, Bruno A, Bianchi CL, Ashokkumar M (2012) Ultrason Sonochem 19:9
61. Vong F, Son Y, Bhuiyan S, Zhou M, Cavalieri F, Ashokkumar M (2014) Ultrason Sonochem 21:23
62. Zhou M, Cavalieri F, Ashokkumar M (2011) Soft Matter 7:623
63. Son Y, Lim M, Ashokkumar M, Khim J (2011) J Phys Chem C 115:4096
64. Ashokkumar M (2011) Ultrason Sonochem 18:864
65. Ashokkumar M, Grieser F (2004) ChemPhysChem 5:439
66. Ashokkumar M, Lee J, Kentish S, Grieser F (2007) Ultrason Sonochem 14:470
67. Mason TJ, Lorimer JP, Applied Sonochemistry-The Uses of Power Ultrasound in Chemistry and Processing, (Wiley-VCH Verlag GmbH, Weinheim, 2002), pp.25
68. Pétrier C, Combet E, Mason T (2007) Ultrason Sonochem 14:117
69. Asakura Y, Nishida T, Matsuoka T, Koda S (2008) Ultrason Sonochem 15:244
70. Khuyen Viet Bao T, Yoshiyuki A, Shinobu K (2013) Jpn J Appl Phys 52:07HE07
71. Lee M, Oh J (2011) Ultrason Sonochem 18:781
72. Lim M, Ashokkumar M, Son Y (2014) Ultrason Sonochem 21:1988
73. Little C, El-Sharif M, Hepher MJ (2007) Ultrason Sonochem 14:375
74. Son Y, Lim M, Khim J (2009) Ultrason Sonochem 16:552
75. Toma M, Fukutomi S, Asakura Y, Koda S (2011) Ultrason Sonochem 18:197
76. Koda S, Kimura T, Kondo T, Mitome H (2003) Ultrason Sonochem 10:149
77. Torres RA, Pétrier C, Combet E, Moulet F, Pulgarin C (2006) Environ Sci Technol 41:297
78. Dahlem O, Demaiffe V, Halloin V, Reisse J (1998) AIChE J 44:2724
79. Kirpalani DM, McQuinn KJ (2006) Ultrason Sonochem 13:1
80. Kang J-W, Hung H-M, Lin A, Hoffmann MR (1999) Environ Sci Technol 33:3199
81. Son Y, Lim M, Khim J, Ashokkumar M (2012) Ultrason Sonochem 19:16
82. Beckett MA, Hua I (2001) J Phys Chem A 105:3796
83. Hung H-M, Hoffmann MR (1999) J Phys Chem A 103:2734
84. Entezari MH, Pétrier C, Devidal P (2003) Ultrason Sonochem 10:103
85. Lim M, Son Y, Khim J (2011) Ultrason Sonochem 18:460
86. Leong T, Johansson L, Juliano P, Mawson R, McArthur S, Manasseh R (2014) Ultrason Sonochem 21:1289
87. Leong T, Juliano P, Johansson L, Mawson R, McArthur SL, Manasseh R (2014) Ultrason Sonochem 21:2092
88. Gogate PR, Mujumdar S, Pandit AB (2003) J Chem Technol Biotechnol 78:685
89. Liu H-L, Hsieh C-M (2009) Ultrason Sonochem 16:431
90. Zhao L, Ma J, Zhai X (2009) Environ Sci Technol 43:5094

 91. Hasanzadeh H, Mokhtari-Dizaji M, Zahra Bathaie S, Hassan ZM, Nilchiani V, Ultrason H (2011) Sonochemistry 18:394
 92. Lim M, Na S, Khim J, Son Y (2014) Jpn J Appl Phys 53:07KE02
 93. Son Y, Lim M, Cui M, Khim J (2010) Jpn J Appl Phys 49:07HE02
 94. Price GJ, Ashokkumar M, Hodnett M, Zequiri B, Grieser F (2005) J Phys Chem B 109:17799
 95. Matula TJ, Hallaj IM, Cleveland RO, Crum LA, Moss WC, Roy RA (1998) J Acoust Soc Am 103:1377
 96. Neppiras EA (1980) Acoustic cavitation. Phys Rep 61:159
 97. Yasui K, Tuziuti T, Lee J, Kozuka T, Towata A, Iida Y (2010) Ultrason Sonochem 17:460
 98. Rooze J, Rebrov EV, Schouten JC, Keurentjes JTF (2013) Ultrason Sonochem 20:1
 99. Taylor E Jr, Cook BB, Tarr MA (1999) Ultrason Sonochem 6:175
100. Laughrey Z, Bear E, Jones R, Tarr MA (2001) Ultrason Sonochem 8:353
101. Koda S, Taguchi K, Futamura K (2011) Ultrason Sonochem 18:276
102. Bokhale NB, Bomble SD, Dalbhanjan RR, Mahale DD, Hinge SP, Banerjee BS, Mohod AV, Gogate PR (2014) Ultrason Sonochem 21:1797
103. Sponza DT, Oztekin R (2014) Ultrason Sonochem 21:1244
104. Gao N-y, Deng Y, Zhao D (2009) J Hazard Mater 164:640
105. Nanzai B, Okitsu K, Takenaka N, Bandow H, Maeda Y (2008) Ultrason Sonochem 15:478
106. Colussi AJ, Hung H-M, Hoffmann MR (1999) J Phys Chem A 103:2696
107. Goel M, Hongqiang H, Mujumdar AS, Ray MB (2004) Water Res 38:4247
108. Kojima Y, Asakura Y, Sugiyama G, Koda S (2010) Ultrason Sonochem 17:978
109. Gogate PR, Sutkar VS, Pandit AB (2011) Chem Eng J 166:1066
110. Kumar A, Gogate PR, Pandit AB (2007) Ultrason Sonochem 14:538
111. Gole VL, Gogate PR (2012) Chem Eng Process 53:1

Metals Oxides and Doped Metal Oxides for Ultrasound and Ultrasound-Assisted Advanced Oxidation Processes for the Degradation of Textile Organic Pollutants

G. Kumaravel Dinesh, T. Sivasankar, and Sambandam Anandan

Contents

G.K. Dinesh (✉)
Department of Chemical Engineering, National Institute of Technology Tiruchirappalli, Tiruchirappalli, Tamilnadu, India

T. Sivasankar
Sonochemical Intensification Laboratory, National Institute of Technology Tiruchirappalli, Tiruchirappalli, Tamilnadu, India
e-mail: ssankar@nitt.edu

S. Anandan
Nanomaterials and Solar Energy Conversion Lab, Department of Chemistry, National Institute of Technology Tiruchirappalli, Tiruchirappalli, Tamilnadu, India
e-mail: sanand@nitt.edu

Abstract

This chapter deals with the different types of ultrasound-assisted advanced oxidation processes. The basic chemical principle involved in the production of OH radicals and its subsequent reaction with pollutants of the processes was discussed. The influence of ultrasound and their synergy toward other processes when coupled were highlighted to ensure complete and faster remediation of textile effluents. The ultrasound- and ultraviolet-mediated advanced oxidation processes have been classified based on the process conditions, especially the type of oxidant, Fenton's mechanism, catalyst usage, and so on, to implicate the method of sonolysis and photolysis, respectively, on the degradation of pollutants. The basic principle underlying every method of ultrasound-assisted advanced oxidation process along with the recent research findings were discussed in a holistic way to elucidate the degradation of organic pollutants. Different types of semiconductor metal oxides and doped metal oxides either metal- or nonmetal-doped catalysts were listed, and scope for ultrasonic degradation was presented. Emphasis has been given to the photocatalysts such as titanium dioxide (TiO_2), zinc oxide (ZnO), and bismuth oxide (Bi_2O_3) for their high-bandgap energy and photoactivity among others. Recent developments in various doping methods and their change in the nature of the catalyst in terms of size, shape, energy level, and degradation efficiency related to ultrasound process were focused. The significance of high-throughput-doped catalysts has been exemplified not only to explore novel and cheap catalysts but also to adopt facile doping methods in various processes pertaining to environmental remediation.

Introduction

The effluents having contaminants such as synthetic chemicals, dyes, organic matters, refractory organic waste, heavy metals, etc., are discharged to the nearest water bodies with or without any preliminary treatments. This causes serious damage to the dissolved oxygen level and ecological balance of the ecosystem of the nearby receiving water bodies. It is of utmost importance to dispose off these residues in a proper manner as well as to keep the concentration of chemicals in the effluent stream to a certain minimum level in order to comply with the environmental laws, which are becoming more stringent these days [1]. Thus, numerous studies are going on for finding a suitable technology to the wastewater treatment [2]. The conventional wastewater treatment has many limitations which favors for the new and advanced technologies for the treatment. High-density sludge was the final product of the conventional treatment such that the handling and disposal of this sludge were very difficult. The processes were too slow and a suitable environment has to be maintained in the process to take place. Merely this treatment process only transfers the pollutants from one phase to another leading to the dangerous secondary pollutant [3]. They are often too sensitive and produce unpredictable results for highly concentrated wastes hence ineffective in treating toxic effluents.

Research into new or more efficient wastewater treatment technologies so as to degrade the complex refractory molecules into simpler molecules is vital to combat the deteriorating water quality [4]. Hence, recent advanced research and treatment methodologies using single-chemical oxidants or the more effective destruction by the use of advanced oxidation processes (AOPs) have become popular and are most often studied [5, 6]. Also, in the last two decades, the emergence of AOPs have proved to be a promising solution due to their high potential for the ultimate destruction of many recalcitrant pollutants. These processes involve the formation of highly reactive free radical species, in particular hydroxyl radicals, far more powerful than the commonly used oxidants, like molecular oxygen and ozone [7]. The use of sequential or simultaneous AOPs called as hybrid configurations could reduce the final operation cost. Among the AOPs, those based on hydrogen peroxide, like Fenton, heterogeneous Fenton or catalytic wet peroxide oxidation (CWPO), photo-Fenton [2], TiO_2–H_2O_2–UV [8, 9], and solar-driven Fenton process [7, 10] that involve catalysis are receiving an increasing interest. Therefore, combinations of these processes can provide high efficiencies on a simple design basis since they operate under ambient or mild conditions. The efficacy of these processes involved in the generation of free radicals and further maximization of these radicals in the destruction of the pollutant molecules are the attractive advantages over conventional techniques.

The role of catalysts, especially photocatalyst, remains indispensable in case of AOPs as owing to its potential of enhancing the process of environmental degradation by means of its synergistic effect. The semiconductor photocatalyst such as titanium dioxide (TiO_2), zinc oxide (ZnO), and tungsten trioxide (WO_3) is presently employed often as photocatalyst. The method of mediating AOPs using solid

photocatalyst was referred to as heterogeneous photocatalysis. The catalysts require suitable light source for its excitation so as to initiate the photoreaction. The process involves breaking down of the pollutant molecule by simultaneous oxidation and reduction leaving no dye residues in the case of textile effluents, hence eliminating the problem of sludge disposal. The photocatalysts such as TiO_2, ZnO, Bi_2O_3, and so on, having wide bandgap energy, are commonly chosen for photoexcitation by visible, solar, or UV light spectrum. The selection of photocatalyst further depends on the catalyst properties, operation range, radiation source, targeted pollutants, and cost [11]. The mechanism of this photocatalysis effect can be well improved by assisting with ultrasonication. Thus, the sonophoto-catalysis offers the following required attributes such as (a) photocatalyst surface activation, (b) mass transport of organic compounds, and (c) aggregate breakage during degradation mechanism that will be dealt for highlighting the effect of ultrasound-assisted AOPs.

For applications pertaining to treatment of aqueous systems, photocatalyst necessitates the process of immobilization on the materials most commonly, transition metals. The direct usage of photocatalyst is usually prone to recombination of the electron/hole pairs during excitation. In order to ensure posttreatment recovery of the catalyst and to eliminate the shortcomings of the unmodified catalyst, chemical modification techniques generally known as "doping" could be used. The supported or doped photocatalyst tends to exhibit better photoactivity than unmodified catalysts, the reason of which is attributed to the higher surface area due to doping. The degradation of dye pollutants by means of doped photocatalyst has gained much potential for its high efficacy in degradation and mineralization of harmful organic dye pollutants. Another huge advantage of the doped photocatalyst is its tendency to improve the production of electron-rich species like $^{\bullet}OH$ radicals, which will subsequently help in oxidization of recalcitrant pollutants of textile effluent [12].

As the implication of nanotechnology is receiving much attention in a wide spectrum of applications, nanomaterial doping has been of much interest in present scenario. The nanomaterial or especially nanometal-doped catalyst ensures enhanced catalytic activity due to the enhanced surface to volume ratio and its structural ability compared to its pristine counterparts. The metal nanoparticles that have been doped on the photocatalysts involve storing of the excited electrons, thereby enabling efficient charge transfer when subjected to dye degradation in the presence of ultrasound irradiation. Moreover, the electron recombination time will be extended ensuring the higher catalytic efficiency [13]. The significance of doping has thus been elucidated in detail in this chapter based on the recent reports on catalyst modification especially using transition metals and nonmetals into the catalyst matrix. Developing novel photocatalysts from cheap sources of precursors, doping of prepared catalyst by facile and efficient methods, achieving desired process conditions by employing suitable oxidants, and combination and assistance of ultrasound have been discussed comprehensively based on the research findings.

Classification of Advanced Oxidation Processes

Advanced oxidation processes (AOPs) are one among the series of methods that generate highly oxidative $^\bullet$OH radicals to degrade persistent dye molecules. These include both non-photochemical and photochemical methods, both of which can be assisted by ultrasound for improved degradation mechanism. Some of these methods are explained below:

Non-photochemical Methods
1. Fenton's system (H_2O_2/Fe^{2+})
2. Ozonation at elevated pH (>8.5)
3. Ozone + hydrogen peroxide (O_3/H_2O_2)
4. Ozone + catalyst (O_3/CAT)
5. Electrochemical oxidation
6. Sonolysis
7. Radiolysis and treatment with electron beam

Photochemical Methods
1. O_3/UV
2. H_2O_2/UV
3. $O_3/H_2O_2/UV$
4. Photo-Fenton/Fenton-like systems
5. Photocatalytic oxidation (UV/CAT)
6. Sonophotolysis
7. Water photolysis in vacuum ultraviolet
8. Heterogeneous photocatalysis

Chemical Principle of AOPs

The treatment of effluents generated from various textile industries, dye industries, needs a clean and efficient technology for the possible discharge of zero toxic wastewater. The advanced oxidation processes can destroy these organic dye wastewater into less complex compounds such that their main approach was the complete removal of the pollutants from the wastewater without leaving secondary pollutants. The chemistry of AOPs could be essentially divided into three parts [14]:

1. Formation of $^\bullet$OH radicals
2. Initial attacks on target molecules by $^\bullet$OH radicals and their breakdown into fragments
3. Subsequent attacks by $^\bullet$OH radicals until ultimate mineralization

The main concept of the AOPs was the generation of the free radicals which are highly reactive species with the oxidation potential of 2.80 eV which can destroy

the complex waste contaminants into simpler and even very less toxic inorganic ions as the final product [15].

Non-photochemical Methods

Munter [13] classified non-photochemical methods as four well-known methods for generating hydroxyl radicals without using light energy. Two of the methods involve the reaction of ozone, while one uses Fe^{2+} ions as the catalyst. These methods are ozonation at elevated values of pH (>8.5), combining ozone with hydrogen peroxide, ozone + catalyst, and the Fenton system.

Ozonation at Alkaline pH

Oxidation of organic species occurs due to a combination of reactions with molecular ozone and reactions with $^{\bullet}OH$ radicals. When pH rises toward alkalinity, the decomposition rate of ozone in the water increases. The reaction between hydroxide ions and ozone leads to the formation of a superoxide anion radical (O_2^-) and hydroperoxyl radical ($HO_2^{\bullet}$). Due to the reaction between ozone and the superoxide anion radical, the ozonide anion radical O_3^- is formed, which decomposes immediately giving $^{\bullet}OH$ radical. Summarizing, three ozone molecules produce two $^{\bullet}OH$ radicals [8, 16–18]. At the alkaline pH along with ozone helped in complete degradation of the organic pollutants in wastewater treatment process.

$$3O_3 + OH^- + H^+ \rightarrow 2\,^{\bullet}OH + 4O_2 \tag{1}$$
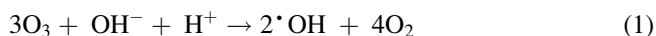
Ozone + Hydrogen Peroxide (O₃/H₂O₂) – (Peroxone)

The addition of hydrogen peroxide to ozone can initiate the decomposition cycle of ozone, resulting in the formation of $^{\bullet}OH$ radicals [17].

$$H_2O_2 \rightarrow HO_2^- + H^+ \tag{2}$$

$$HO_2^- + O_3 \rightarrow HO_2^{\bullet} + O_3^- \tag{3}$$
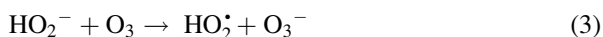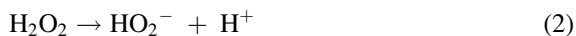
The reaction continues along the indirect pathway described above and $^{\bullet}OH$ radicals are produced. The combination of different reaction steps shows that two ozone molecules could produce two $^{\bullet}OH$ radicals,

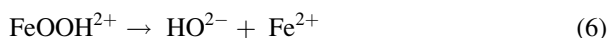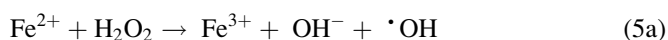$$2O_3 + H_2O_2 \rightarrow 2\,^{\bullet}OH + 3O_2 \tag{4}$$
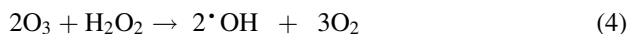
Several researchers [6, 19–21] have made different comparative studies in their experiments for the water purification and recovery methods by combining ozone and hydrogen peroxide.

Ozone + Catalyst (O_3/CAT)

Another opportunity to accelerate ozonation reactions is to use heterogeneous or homogeneous catalysts. Several metal oxides and metal ions (Fe_2O_3, Al_2O_3–Me, MnO_2, Ru/CeO_2, TiO_2–Me, Fe^{2+}, Fe^{3+}, Mn^{2+}, etc.) have been studied, and sometimes a significant acceleration in the decomposition of the target compound has been achieved [6, 22, 23]. Hoffman et al. [24] conducted ozonation reaction for the degradation of cyclohexane and indicated that the use of 2.5 mM ozone increases the degradation rate slightly faster.
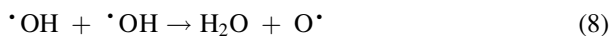
Fenton Process

The generation of $^{\bullet}OH$ radicals occurs when the iron salts are added with H_2O_2. The complete removal of the organic pollutants doesn't take place. The degradation follows an intermediate less reactive radical [4, 24–26], and these radicals slow down the degradation process.

$$Fe^{2+} + H_2O_2 \rightarrow Fe^{3+} + OH^- + {}^{\bullet}OH \tag{5a}$$

$$Fe^{3+} + H_2O_2 \rightarrow H^+ + FeOOH^{2+} \tag{5b}$$

$$FeOOH^{2+} \rightarrow HO^{2-} + Fe^{2+} \tag{6}$$

Sonolysis

Ultrasound is utilized to destroy the pollutants or used for the generation of free radical which further accelerates the degradation process. Recent studies proved that the sonolytic oxidation process [27] is more effective in wastewater treatment process when compared with other technologies. The use of ultrasound itself is a clean technology for treating wastewater. When ultrasound is used in combination with other technologies, it accelerates the degradation of the liquid phase contaminants. Further, ultrasound helps in complete degradation of the waste such that their toxicity can be reduced by breaking complex molecules into simple inorganic ions. The chemistry behind the sonolysis process is given as follows:

$$H_2O \xrightarrow{\text{)))}} {}^{\bullet}H + {}^{\bullet}OH \tag{7}$$

$${}^{\bullet}OH + {}^{\bullet}OH \rightarrow H_2O + O^{\bullet} \tag{8}$$

$${}^{\bullet}OH + H_2O \rightarrow H_2O_2 + H^{\bullet} \tag{9}$$
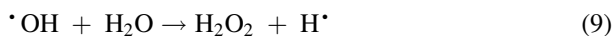
Researchers [4, 28–31] have done various studies in the field of sonochemistry involving cavitation process for the degradation of wastewater. Apart from the discussed non-photocatalytic processes, there are few other processes that were employed for wastewater treatment and were listed in Table 1 briefly.

Table 1 Non-photocatalytic process

Process	Reference	Highlights
Wet oxidation (WO), electrochemical oxidation (EO), and wet electrochemical oxidation (WEO)	[26]	WEO, the synergistic effects for both efficient removal of color and COD, were observed, possessing a high current efficiency higher than 100 %
Wet tube-type electrostatic precipitation	[27]	The decreasing trend of EDTA concentration with pH 3 and 5.5 was nearly the same up to 240 min of operation at 16.6 kV. The electrostatic precipitator works similarly an advanced oxidation reactor (equipped with ozone purging/UV radiation) which is capable of disintegrating EDTA
Advanced oxidation technology based on sulfate radicals	[11]	Co_3O_4 or GO alone exhibits little catalytic activity, their hybrid (Co_3O_4/GO) exhibits an unexpectedly high catalytic activity in the degradation of Orange II in water, and 100 % decomposition can be achieved in 6 min
Advanced oxidation process and biotreatment – Fenton's oxidation and coagulation with biochemical treatment (*T. ferrooxidans*)	[6]	The hybrid treatment system showed 97 % COD reduction and could be achieved within 2 days
Sonolysis	[31]	The presence of TiO_2 catalyst on the ultrasonic degradation of ofloxacin increases the efficiency of the degradation of ofloxacin
Sonocatalytic using Au/TiO_2	[32]	Sonocatalytic destruction of Orange II in aqueous solutions in the absence and presence of catalysts under Ar atmosphere. Almost no degradation was observed in the absence of catalyst. Au/TiO_2 can be used as an effective sonocatalyst. The mechanism involves both the enhanced oxidation and reduction by $^\bullet OH$ and $^\bullet H$ radicals

Photochemical Methods

Ultraviolet Irradiation

Photolytic degradation of wastewater is a simple process in which the compound present in the waste absorbs the radiations from the lamp such that the radiant energy on absorption make the molecule more active and the molecule's electrons move to the excited state to release free electrons. The free electrons excited from the compound undergo further breaking of molecular bond, and the chain reaction continues. These excited molecules undergo three different processes themselves in

breaking up of the molecules to the final degradation process. The processes are homolysis, heterolysis, and photoionization. Moreover, during the degradation process, some intermediate compounds form that do not absorb radiations, and hence, complete degradation is not achieved in photolysis itself [34]. Raj and Quen [17] used the low-pressure UV lamp for the degradation of tetrahydrofuran which is a nonbiodegradable compound.

$$Compound + h\nu \rightarrow intermediates \qquad (10)$$

$$intermediates + h\nu \rightarrow CO_2 + H_2O \qquad (11)$$
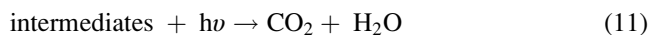
UV/H_2O_2

The efficiency of the photolysis process can be improved by the addition of oxidants. The photolysis helps in cleaving the O–O bond of hydrogen peroxide to generate $^{\bullet}$OH radicals. Chelme-Ayala et al. [34] studied the performance of UV/H_2O_2 for the dehydration of trifluralin. The combination of UV/H_2O_2 gave faster and higher degradation rate than the individual process. The results revealed that 97 % efficiency in 2 h than the individual process which took more than 4 h that to only 50 % efficiency based on the formation of $^{\bullet}$OH radicals by the photolysis of hydrogen peroxide and the subsequent propagation reactions. A relatively high dose of H_2O_2 and/or a much longer UV exposure time was required by individual processes [17, 19, 22]. With varying doses of H_2O_2 along with the combination of the UV light in the water purification system and found complete degradation of the organic pollutants in a very short period.

$$H_2O_2 \xrightarrow{h\nu} 2\ HO^{\cdot} \qquad (12)$$

Photocatalysis

In semiconductor photocatalysis, semiconductor material acts as a light-absorbing species. The electronic structure of most semiconductor materials comprises the valence band and the conduction band [20]. The valence band was the band occupied by electrons. Conduction band was the lowest band unoccupied by electrons. These two bands are separated by a region that was largely devoid of energy levels, and the difference between the two bands was called the bandgap energy. These bandgaps of semiconductor materials produce electron–hole pairs h^+ and e^- where they have the possibility of reacting with the surface of the absorbed species (Fig. 1).

Tong et al. [35] portrayed the various steps involved in the semiconductor photocatalysis. The major processes that occur when bandgap excitation occurs on a semiconductor photocatalyst in an aqueous solution containing dissolved oxygen and an oxidizable pollutant are:

1. Electron–hole recombination in a bulk
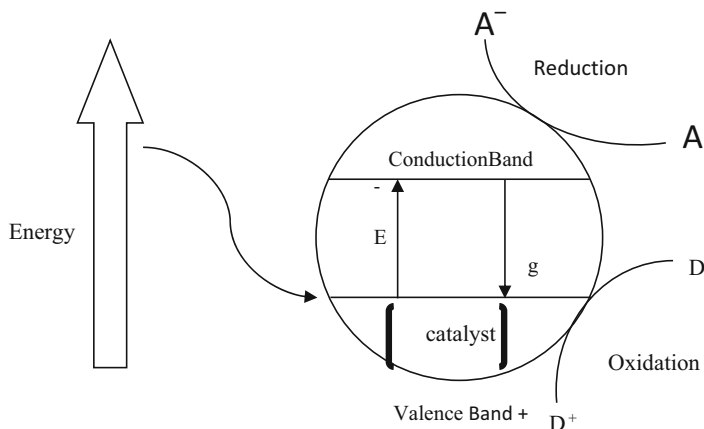2. Electron–hole recombination in the surface

Fig. 1 The schematic representation of the semiconductor photocatalysis process

3. Direct or indirect reduction of oxygen or oxidizing intermediates by the photogenerated electron at the surface of the semiconductor
4. Direct or indirect oxidation of the pollutant or an oxidized intermediate by the photogenerated hole on the surface of the semiconductor leading to the mineralization of the pollutant

Ideally, a semiconductor photocatalyst should be chemically and biologically inert, photocatalytically active, easy to produce and use [36], and activated by the UV/sunlight. It must be very essential to note that the process of electron transport is to be more effective. Their transport rate also depends upon the relative position of the conduction and valence bands and the redox potential of the adsorbed species.

The photoexcitation of semiconductor catalyst forms the basis for the photocatalysis process. The absorption of light by the semiconductor catalysts like ZnO, TiO_2, Bi_2O_3, WO_3, etc., involves the electrons in the valence band that move to the conduction band making an electron–hole pair in the valence band which readily induces the reduction or oxidation reaction in the aqueous solution [37]. Madani et al. [38] carried out various experiments for the study of degradation of diuron pesticide and found that the combined effect of UV and catalyst gave a higher removal rate in 30 min. This process is relatively slow compared to other AOPs and in some cases leads to incomplete mineralization of organics. Absorption of the radiation with the formation of electron–hole pairs initiates the reaction, and the reducing power of formed electrons allows metal reduction with the formation of the superoxide radical ion O^{2-}, whereas remaining holes are capable of oxidizing adsorbed H_2O or HO^- to reactive $HO^\bullet$ radicals. Many researchers [27, 39–41] used different combination of the AOPs for the degradation of complex dye removal from wastewater along with the photocatalytic process.

$$TiO_2 \rightarrow e^- + h^+ \tag{13}$$

$$TiO_2(h^+) + H_2O \rightarrow TiO_2(h^+) + HO^- + H^+ \tag{14}$$

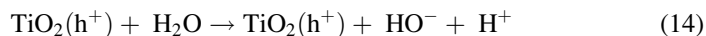$$TiO_2(h^+) + HO^- \rightarrow TiO_2 + HO^. \tag{15}$$

Photo-Fenton

Typical photo-Fenton process involves the irradiation of the Fenton system with UV light where the Fe(III) ion will be reduced to Fe(II) ion followed with the reaction of H_2O_2 to produce highly reactive hydroxyl radicals. Martin et al. [42] carried out photo-Fenton studies on the model mixture of four pesticides (laition, metasystox, sevnol and ultracid) and found that the complete degradation was attained by the combination of photo-Fenton reaction. The combined process removed the pesticides in wastewater by reducing the toxicity to 90 % and increased the biodegradability. The photolysis of Fe^{3+} complexes allows continuous Fe^{2+} regeneration.

$$Fe(OH)^{2+} \rightarrow Fe^{2+} + HO^{2-} \tag{16}$$
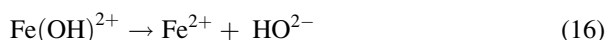
Sonophotolysis

The combination of both sonolysis and photolysis process helps in the faster scission of water molecules to form hydroxyl radicals, which are readily reactive species that help better in faster degradation when compared with the individual process [43]. The synergism of sonophotolysis was higher since the aggregation of compound and its further destruction by the formation of highly reactive intermediate species help much in the fragmentation of the complex compounds into various simple molecules at a very faster rate than other photochemical processes. Many researchers have contributed to the sonophotocatalytic degradation of the various dyes. Kaur and Singh [44] have reported that the synergism between sonolysis and photocatalysis in their study of the degradation of reactive red 198 gave synergistic index of 2.5 when compared with the individual process. Apart from the discussed photocatalytic processes, there are few other processes that were employed for wastewater treatment and were listed in Table 2 briefly.

Catalysts Used in AOP

The treatment of effluents needs better clean and efficient method. Though the AOPs were strong enough to break the recalcitrant pollutants, it is essential to remove these secondary pollutants before they reach the environment. The AOPs help in the degradation of the effluent but contain secondary pollutants, and they still in contact with the sludge and escape into the water bodies. They may require more time and not cost-effective in degrading process. They are limited by the slow rate potential or their tendency to form toxic secondary pollutants. The cost of application of the method increases if the reaction time increases. In certain compound like pesticides, quick degradation is required if the process takes some

Table 2 Photocatalytic process

Process	Reference	Highlights
Combination of catalytic wet peroxide oxidation and photocatalysis	[7]	The combination of catalytic wet peroxide oxidation and photocatalysis, with an iron-activated carbon-supported catalyst and titanium dioxide under light irradiation, allowed almost complete mineralization of phenol at medium-range concentration (200 mg L^{-1}) with the stoichiometric dose of H_2O_2 in ambient conditions
Sequential biological–advanced oxidation process using upflow anaerobic sludge blanket and UV/TiO$_2$/H$_2$O$_2$	[2]	UASB system was able to achieve 52.27 % substrate removal and 73.35 % COD removal at an hydraulic retention time of 6 h. In AOP posttreatment which was carried out for 1.5 h, the reaction preceded toward complete mineralization achieving 83.5 % substrate removal and 90 % COD removal
H_2O_2, H_2O_2/UV, UV, photocatalysis, ozonation, Fenton, and photo-Fenton	[8]	A high-dissolved organic carbon removal (94 %) was attained in the continuous operation of the combined processes (Fenton and photo-Fenton)
UV/H_2O_2 process for integration with biological waste treatment	[20]	Increase in pH favored total organic carbon reduction, which was sharply higher (31 %) at neutral pH when compared to that of the acidic range (18 % at pH 4). In the alkaline range, the increase in TOC reduction was marginal (35 % at pH 9 and 38 % at pH 11)
UV/TiO$_2$, UV/SnO$_2$, UV/TiO$_2$ + SnO$_2$, O$_3$, O$_3$ + MnO$_2$, UV/O$_3$ and UV/O$_3$ + TiO$_2$ + SnO$_2$	[18]	The reactive red 2 decolorization efficiency by UV/TiO$_2$ + SnO$_2$ was pH 7>pH 10>pH 4. Although SnO$_2$ displayed low activity because the UV light energy was insufficient to excite it in a single semiconductor system
Ferrioxalate–photo-Fenton [Fe(C$_2$O$_4$)$_3$/H$_2$O$_2$/UV-A; 300 nm >l>400 nm] and titanium dioxide-mediated heterogeneous photocatalytic (TiO$_2$/UV-A) treatment processes	[22]	Degradation of reactive red dye is faster using ferrioxalate–Fenton/UV-A oxidation, whereas the TiO$_2$/UV-A process is slightly better. The best TOC abatement occurs after a 1-hour treatment
Fe^{2+}/H$_2$O$_2$ molar ratio was selected as 1:5 (4 mM:20 mM) Fenton treatment at pH 3 along with UV	[9]	Results have demonstrated that during the Fenton treatment of the dye, decolorization was complete within minutes and accompanied with appreciable COD and DOC removals
Ozone/UV, ozone/H$_2$O$_2$, and ozone/UV/H$_2$O$_2$ on decolorization of acid red	[45]	In the advanced oxidation processes, ozone/UV/H$_2$O$_2$ treatment is more

(*continued*)

Table 2 (continued)

Process	Reference	Highlights
88, acid orange 7, acid orange 10, and acid red 73 dye effluents in the presence of sodium sulfate salt		efficient than other treatments in all the dye effluents except in acid red 88, where ozone/UV treatment gives a better result
UV, H_2O_2, UV/H_2O_2, Fenton, UV/Fenton and UV/TiO_2 varying pH, peroxide concentration, iron concentration, and TiO_2 loading	[5]	The degradation trends followed the order: UV/Fenton > UV/TiO_2> UV/H_2O_2> Fenton >H_2O_2>UV
UV/H_2O_2	[24]	UV radiation, in the absence of H_2O_2, led to barely 26 % degradation of the methyl orange dye in a period of 4 h. Similar conditions in the presence of H_2O_2, complete dye decomposition was achieved in a period of 3 min only

time to degrade the pollutant; the formation of stable secondary pollutant will affect the process nature, leading to the survival of the toxic intermediates. Though it was clear about the initial attack of reactive radicals on primary pollutants by AOPs, their further kinetics are unpredictable, and determination of optimal conditions is very uncertain. The application of catalyst results in the degradation of toxic compounds into CO_2 and water. When the catalysts are involved in the reaction mechanism, quick degradation by the generation of more hydroxyl radicals further results in faster degradation.

Advanced oxidation processes have been widely used in the presence of different catalysts and oxidants mainly for the enhanced generation of ${}^{\bullet}OH$ radicals such that ${}^{\bullet}OH$ radicals are extraordinary reactive species and attack the organic molecules at the rate of 10^6–10^9 $M^{-1}S^{-1}$ [23]. The fulfillment of several advanced oxidation processes depends on using significant catalyst for more generations of ${}^{\bullet}OH$ radicals which subsequently attack the organic compounds with faster degradation. The semiconductor photocatalysts have proven to be the most widely used processes in the degradation of various types of dyes due to its strong oxidizing power, nontoxicity, and long-term photostability.

Due to the largely insoluble nature of the catalysts during application, the area of semiconductor photocatalysis (SP) invariably constitutes a heterogeneous catalytic system that adheres to the five discrete processes associated with conventional heterogeneous catalysis:

1. Transfer of liquid or gaseous phase reactants to the catalytic surface
2. Adsorption of at least one reactant
3. Reaction in the adsorbed phase
4. Desorption of product(s)
5. Removal of products from the interface region

Various metal oxides (i.e., TiO_2, ZnO, Bi_2O_3, MoO_3, CeO_2, ZrO_2, WO_3, Fe_2O_3, and SnO_2) and metal chalcogenides (i.e., ZnS, CdS, CdSe, WS_2, and MoS_2) are used as catalysts in SP reactions. Many researchers have carried out their experiments by varying the parameters like catalyst loading, the pH, and dye concentration and succeeded in the degradation process [17, 30, 46, 47]. Chen and Huang [48] studied the various characteristics of TiO_2 along with different reactive, toxic, and nonbiodegradable dyes in the degradation process. Among the various catalysts reported, TiO_2, ZnO, and Bi_2O_3 have been considered as most promising and regularly studied catalysts for most advanced oxidation processes.

TiO_2 as Photocatalyst

The photocatalytic splitting of water on TiO_2 electrodes was discovered in 1972 by Fujishima and Honda [49]. This event ushered in a new era for heterogeneous photocatalysis with the utilization of TiO_2 as a semiconductor; however, it was not until the mid-1980s that research outputs started to flourish. Devilliers [70] conducted a detailed study on the photocatalytic activity of TiO_2. TiO_2 exhibits three distinct polymorphs (anatase, rutile, and brookite), of which only anatase is functional as a photocatalyst. Anatase is a typical n-type semiconductor and requires about 3.20 eV to be an electrical conductor. Photons with wavelengths shorter than 380 nm are sufficient in energy to excite electrons from the valence band to the conduction band of this material. Throughout the years, anatase has been the popular choice as semiconductor photocatalyst in research efforts, due to its nontoxicity, high photoactivity, mechanical stability, low cost, and favorable overlap with the ultraviolet portion of the solar spectrum, making it an attractive option for solar applications.

Ram et al. [28] and Tong et al. [35] devoted their experimental studies using TiO_2 as photocatalyst in degradation of procion yellow and methylene dye, respectively. The effect of process parameters, viz., pH [2–10], irradiation time, initial concentration of dye (50–200 ppm), UV intensity, and photocatalyst loading (0.62–1.5 g/L) on the degradation of dye has been assessed and found to be 30 %, while the sonophotocatalytic degradation of these dyes proved to be 90 % in the same conditions and with less irradiation time.

Chen and Huang [48] performed the sonophotocatalytic degradation studies of dinitrotoluenes (DNT) and trinitrotoluenes (TNT). Their experiments elucidated that the combined effect including sonication power, photo irradiation, and TiO_2 dosage helped in the complete mineralization of DNT and TNT wastewater in 8 h into carbon dioxide, nitrate ions, and water. They found that the sonophotocatalytic method with the combination of sonochemically synthesized TiO_2 for the degradation of TNT and DNT wastewater was a promising method.

ZnO as Catalyst

ZnO a semiconductor catalyst had found a profound application because of its wide bandgap which photolytically and sonochemically allows the formation of H_2O_2 which helps in the generation of $^{\bullet}OH$ radicals. Ultrasound-insisted synthesis of ZnO helps in the form of nanowires or nanorods with less bandgap. The surface of the catalyst will be readily available for the electron–hole pair formation in the degradation process.

Khataee and Zarei [50] and Muthirulan et al. [51] developed a simple model and low-cost ZnO as photocatalyst for degradation of diazo dye and alizarin cyanine green dye, respectively. They both have performed experiments using ZnO catalyst in combination with the activated carbon nanoparticles for better results under optimized condition like varying parameters such as pH, catalyst loading, and dye concentration. The dyes were quickly destroyed during the 90 min of ZnO process, yielding 92.7 % of decolorization efficiency, whereas at the same time UV/ZnO processes led to 69, 56, and 39 % decolorization efficiency, respectively. Chakrabarti et al. [52] and Akyol and Bayramoglu [53] investigated the photocatalytic degradation of model dyes in the presence of ZnO and UV light. Their results showed that decolorization and total organic carbon (TOC) removal are both affected in the same manner by the solution pH in the range $6-10$. They are inversely related to the dye concentration, an increase in power law with the light intensity. Decolorization is faster with 365 nm UV lamp. TOC removal is not affected by UV wavelength in the initial period up to 20 min, after which it progresses faster under 365 nm UV light radiation up to 90 % within a period of 20 min. These results indicate that the UV wavelength influences, especially the degradation rate of the intermediate products, generated during the initial period of the photocatalytic process. The dye-sensitized degradation is influenced by the amount of semiconductor, the intensity of UV radiation, and the amount of dye present. The potential of the use of a sensitizer together with the photocatalyst deserves more attention to enhance the feasibility of the technique.

Bi_2O_3 as Catalyst

Bi_2O_3 is an excellent semiconductor photocatalyst with the highest bandgap of 2.8 eV which is highly helpful in utilizing the visible light of 45 % of the solar radiations. The photocatalytic and sonolytic activity of the catalyst can be modified with the assistance of ultrasound during the synthesis process. Xie et al. [54] and Wu et al. [55] investigated the formation of Bi_2O_3 catalyst by precipitation method. Synthesized catalyst shows no changes in the structure and crystallinity even after doping with various ions. The optical absorption properties were also modified accordingly, resulting in the change of color from yellow

to pale orange because of its plate and polyhedral morphologies which proven to show higher photocatalytic activity than the needlelike crystals due to the better development of the active crystal faces with suppression of the preferred crystal growth habit.

Pugazhenthiran et al. [56] evaluated the degradation of acid orange under various influencing factors like ozonation, catalyst dosage, and the addition of oxidants. Sonochemically synthesized Bi_2O_3 catalyst showed a higher degradation rate when compared with other catalysts. A simple and inexpensive way of preparing nanocrystalline Bi_2O_3 was demonstrated which was in contrast to the widely reported fact that Bi_2O_3 mostly forms rod-shaped particles. A 3.5-fold enhancement in the rate of degradation of acid orange 10 upon addition of Bi_2O_3 during ozonation is attributed to the enhanced generation of active radicals at the Bi_2O_3 catalyst surface. Mineralization studies (TOC studies) revealed that Bi_2O_3 prepared by sonochemical method for the degradation of dyes such as acid orange 10 gave 40 % degradation within 30 min when compared with other catalyst.

Chemical Modification: Doping

Most of the nanomaterials find its applications because of its good optical properties. However, the highly efficient use of nanomaterials is sometimes prevented by its wide bandgap. The bandgap of these materials lies in the UV regime, which is only a small fraction of the sun's energy (<10 %). One of the goals for improvement of the performance of nanomaterials is to increase their optical activity by shifting the onset of the response from the UV to the visible region 426–428 nm. There are several ways to achieve this goal. Doping is nothing but the addition of some impurities to the nanomaterial such that the particle character changes its optical and electrical properties according to our need. The optical response of any material is largely determined by its underlying electronic structure. The chemical composition of nanophotocatalysts can be altered by doping [35].

The doping of nanomaterials influence the following changes:

 (i) Morphological, structural, optical, and electrical properties can be altered through doping of either anion or cation
(ii) Nanomaterials were doped so that they can realize their catalytic potential under solar irradiations

Addition of a very small amount of a foreign substance (impurity) to a very pure quantity allows the researchers to tailor its structural, morphological, optical, magnetic, and electrical properties.

Doping nanomaterials with other elements can narrow the electronic properties and, thus, alter the optical properties of nanomaterials. In addition, the modification of nanomaterial surface with other semiconductor can alter the charge transfer properties between the nanoparticle and the surrounding environment. Specifically,
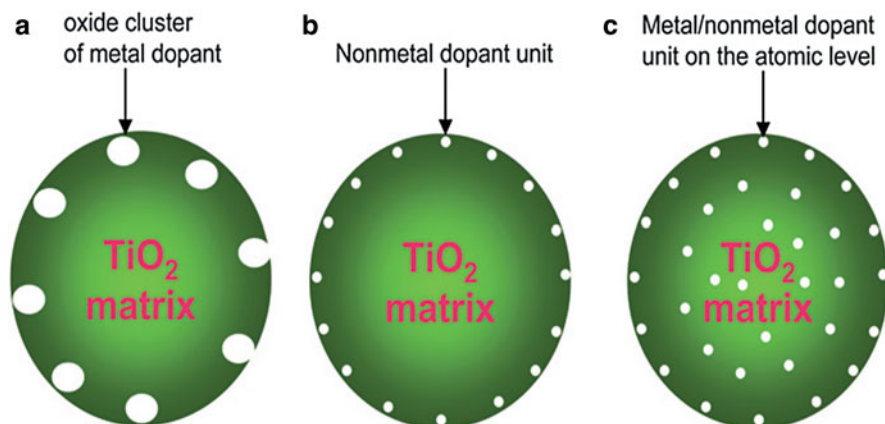
Fig. 2 Doping types on the TiO$_2$ catalyst [48]

the metal or the nonmetal component can be replaced in order to alter the material's optical properties [33]. It is desirable to maintain the integrity of the crystal structure of the photocatalytic host material and to produce favorable changes in electronic structure. It appears easier to substitute the cation with other transition metals, and it is more difficult to replace the anion with other anions due to differences in charge states and ionic radii. The small size of the nanoparticle is beneficial for the modification of the chemical composition due to a higher tolerance of the structural distortion than that of the bulk materials induced by the inherent lattice strain in nanomaterials.

Meng et al. [39] found that the photocatalysts in the presence of TiO$_2$ used in water splitting have some barriers. The mainly considered barriers for the photocatalysts are:

 (i) Rapid recombination of photogenerated electron–hole pairs
(ii) Backward reaction and poor activation of TiO$_2$ by visible light

Doping of the catalysts helps in overcoming these barriers by better photocatalytic activity due to better charge separation. Catalyst should have an open structure measuring big specific surface area leading to an increase in the degree of dispersion of active sites. TiO$_2$ acts as a stabilizer to stabilize the durability and active centers of the doped catalyst.

Types of Doping

The various types of doping in the catalyst structure can be illustrated through the following scheme (Fig. 2), and the comparison of types of doping was presented in Table 3.

Table 3 Comparison of types of doping

Surface doping	Homogeneous doping
1. Low visible light absorbance	1. High visible light absorbance
2. Wide-light absorption edge	2. Steep absorption edge
3. Low mobility of charge carriers	3. High mobility of charge carriers
4. Lower redox potentials of charge carriers with visible light than with UV	4. Same redox potentials of charge carriers with visible light as with UV
5. More flexible in modulating	5. Less flexible in modulating
6. Chemical states of surface dopants	6. Chemical states of bulk dopants
7. Easy to carry out	7. Hard to carry out

Various Doping Techniques

Nonmetal Doping

Most of the solar photons come under the visible region such that the ultraviolet is only 4–5 %, whereas 40 % of the photons are in the visible region. The large bandgap forms the pitfall of the nanomaterials. These nanomaterials will be activated upon the irradiation with photons in the UV regions which makes its usage practically impossible for the direct application of solar radiations. The nanoparticles can facilitate the visible light photon by changing its morphology with the help of doping. Nanocatalyst modified by nonmetal doping is gaining importance which helps in attaining the visible light absorption of a photocatalyst.

Nitrogen was proved to be a distinguished dopant. Xi et al. [57] found a novel single-step process of doping nitrogen with TiO_2 through sonochemical process. The catalyst was characterized by the XPS data, and the N-doped TiO_2 showed higher binding energy peak at 401.4 eV. The peak was assigned due to the presence of chemisorbed nitrogen incorporated in TiO_2. The photocatalytic activity of the obtained catalyst was investigated through the degradation of azo dye, direct sky blue 5B, where the degradation was 100 % in the presence of a doped catalyst within 50 min under UV light. The average size of the catalyst was found to be 10.8 nm, and the catalyst synthesized through sonication proved to an excellent catalyst for the degradation under the simulated sunlight.

Panda et al. [58] developed a multifunctional novel material of sulfur-doped ZnO through sonication process. The developed doped catalyst got an elongated grass (Fig. 3) like structure grown from a common center with a dimension of 150–250 nm width and 1.5–2 μm in length. The growth process and the clear structure were due to the sulfur incorporation on ZnO by the sonic energy. The photocatalytic activity of the catalyst was also increased that the absorption band shifted to 375 nm showing the blue shift helps in the visible region. Thus, it was revealed that the sonication involved doping of sulfur on ZnO helps in preparing a catalyst for solar-assisted photocatalytic reactions.
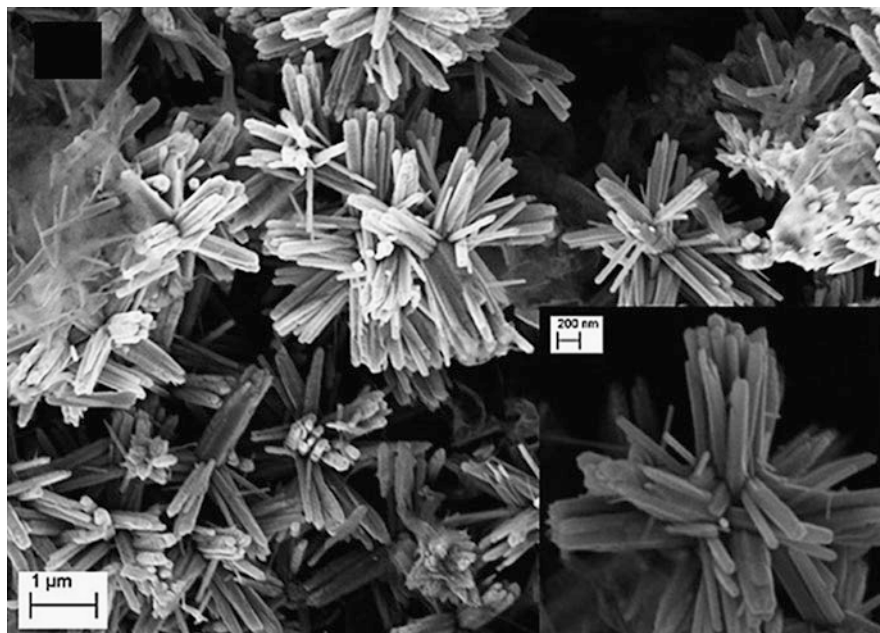
Fig. 3 Fe-SEM of sulfur-doped ZnO [58]

Nonmetal Co-doping

Nitrogen and fluorine (N–F)-co-doped TiO_2 has been explored in visible light photocatalysis due to similar structural preferences of the two dopants. In addition, the combined structure retains the advantages of N-doping in high visible light response and the F-doping significant role in charge separation. Furthermore, synergistic effects of the co-doping have been found. In fact, surface fluorination inhibits phase transformation from anatase to rutile and removal of N-dopants during annealing. In addition, it reduces the energy cost of doping and also the amount of oxygen defects in the lattice, as a consequence of the charge compensation between the nitrogen (p-dopant) and the fluorine (n-dopant) impurities. These effects stabilize the composite system and effectively reduce the concomitant electron–hole recombination that hampers the photocatalytic performance of singly doped N-TiO_2. The synergistic approach of the N–F doping has been further exploited employing a modified sol–gel technique based on a nitrogen precursor and a Zonyl FS-300 nonionic fluorosurfactant as both fluorine source and pore template material to tailor-design the structural properties of TiO_2. The obtained materials are active under visible light illumination and have been used for the photocatalytic degradation of a variety of pollutants in water. Very recently, these N–F-doped titania materials were successfully immobilized on glass substrates employing the dip-coating method with subsequent drying under infrared lamp, followed by calcination at 400 °C. The nanostructured titania-doped thin films preserve their

visible light-induced catalytic activity. Furthermore, comparative EPR measurements between the co-doped and reference samples identified distinct N spin species in N–F–TiO$_2$, with a high sensitivity to visible light irradiation. The abundance of these paramagnetic centers verifies the formation of localized intra-gap states in TiO$_2$ and implies synergistic effects between fluorine and nitrogen dopants.

The photocatalytic effect was increased by the combined doping effect of nitrogen- and fluorine-doped catalyst. This doping involves an opal reverse growth method using silica colloids for liquid phase deposition of N–F–TiO$_2$ where the catalyst grows in a hierarchical order in which macro-mesoporous structures were developed. These mixed multiple structures help in arriving stability and efficient photocatalysis through photon multiple scattering effect. Following another approach, recently the visible light active photocatalytic properties increased by the use of oxygen-rich catalyst through thermal decomposition of oxygen with the corresponding nanocatalyst wherein the catalyst has mixed proportions of catalyst with peroxo catalyst which has efficient visible light photocatalytic activity. It was found that the increased oxygen bond strength which gives way for upward shifting of the valence band (VB) helps to have improved photocatalytic shift for visible lights. Superconducting bandgap structures (~1.8 eV) control the activity and various other scattering effects.

Noble Metal and Transition Metal Deposition

The photocatalytic activity of TiO$_2$ can be improved by modifying it with transition metals such as Cr, Co, V, and Fe as these metals enable the spectral response of TiO$_2$ to be available better in the visible region. The transition metals may also cause a lowering of quantum efficiency of photocatalyst as it also acts as recombination sites for the photo-induced charge carriers. However, the reported research findings ensured that there has been an enhanced photocatalytic performance for Cr or V metal-deposited TiO$_2$ rather than bare TiO$_2$ during the nitrous oxide degradation under solar irradiation. There have been many literatures on modifying TiO$_2$ with a wide spectrum of transition metals, namely, Fe, Cu, Co, Ni, Cr, V, Mn, Mo, Nb, W, Ru, Pt, and Au (Fig. 4).

On account of incorporating such transition metals in the titania crystal lattice, new energy levels between the valence band and conductive band will be formed which further help in inducing light absorption to shift toward the visible light region. Based on the property and the amount of the doping agent, the photocatalytic activity differs. The main limitation inherent with transition metals is the effect of photocorrosion which further induces charge recombination at metal sites. In case of doping using noble metals like Ag, Au, Pt, and Pd, the photocatalytic efficiency of TiO$_2$ surface will be enhanced under visible light. This is attributed to the effect of doped TiO$_2$ that acts as an electron trap, thereby interfacial charge transfer gets promoted for delaying the recombination of electron–hole pair. The Pt doping on TiO$_2$ enabled trapping of photogenerated electrons for increasing the transfer rate of photo-induced electron at the interface.
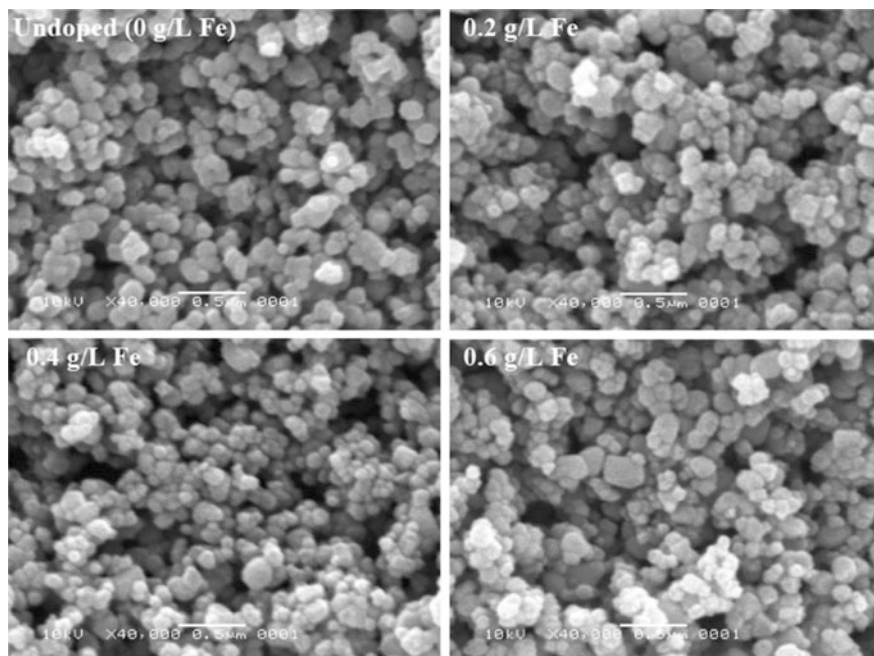
Fig. 4 SEM images of bare TiO_2 and varied concentration of Fe-doped TiO_2 [59]

The SEM results revealed that the morphology of the synthesized Bi_2O_3 and Fe-doped Bi_2O_3 was porous microspheres (Fig. 5). According to the results obtained using this synthesis method, the doped catalyst has strong visible light photoactivity in the range of 420–600 nm.

Sol–Gel Method

The sol–gel method of doping photocatalyst is one of the versatile, widely used methods by which the colloidal suspension called sol can be formed as a result of the hydrolysis and polymerization reactions of the precursors such as inorganic metal salts or metal organic compounds such as metal alkoxides. After complete polymerization, the depletion of solvent will enable the transition of liquid sol into a solid gel phase, which suggests the name of the method as "sol–gel." By optimizing the conditions of sol–gel formation, various nanomaterials can be synthesized and also can be doped with the transition metals.

Khataee et al. [61] and Wang et al. [62] prepared Pr-doped ZnO catalyst through sonochemical and sol–gel methods, respectively. The synthesis was the Pr-doped ZnO catalyst formed has different crystal size such that the minimum sizes of the formed crystal were 9.07 and 25.4 nm, respectively. In this, the sonochemically synthesized doped catalyst got very less crystal size of 9.07 nm due to the influence
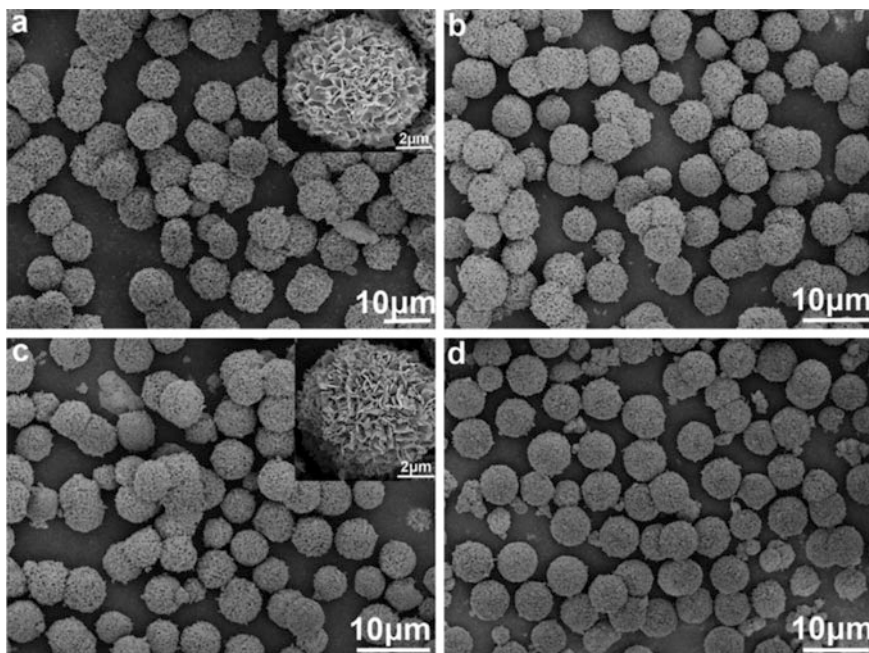
Fig. 5 SEM of bare Bi_2O_3 and Fe-doped Bi_2O_3 [60]

of the ultrasound during the synthesis process. The photocatalytic activity of the catalyst also varied due to the difference in the binding energies of the catalyst between the various synthesis routes. Different synthesis routes of catalyst when employed in the degradation of the model gave complete color removal when compared with the bare catalyst.

Hydrothermal Method

The method of hydrothermal synthesis is usually a reaction in aqueous solutions that takes place in autoclaves either coated or not coated with Teflon liners under controlled temperature and/or pressure. The temperature can be raised beyond the water boiling point, thus reaching up to the level of vapor saturation pressure. As the name suggests, this method depends mainly on the two factors such as the temperature and the amount of solution added to the autoclave for determining the production of internal pressure which eventually helps widely in the production of small particles in the ceramics industry. Chen et al. [63] synthesized Cu-doped ZnO through hydrothermal process, and their characterization results insisted the face selective crystal growth inhibition due to the intrinsic properties of Cu on incorporation on the ZnO surface. The catalyst formed a thin filmlike structure confirming the p-type Cu-doped ZnO fabricated rectifying diodes. The doping

also favored in the application of optoelectronic devices. The hydrothermal synthesis showed the crystal growth inhibition mechanism during the synthesis of Cu-doped ZnO. Khataee et al. [61] synthesized Eu-doped ZnO through sonochemical synthesis which exhibited hexagonal structure and slightly shifted toward the visible spectra showing the same characteristics of La-doped TiO_2, the particle size was found to be in the range of 20–30 nm much smaller than the undoped ZnO. The hexagonal structure of the Eu-doped ZnO was due to the successful incorporation of Eu^{3+} on the crystal lattice of ZnO through the assistance of ultrasound which enhanced the catalytic activity during the degradation of AR17 dye up to 90 %.

Solvothermal Method

The only difference between hydrothermal and solvothermal method is that in solvothermal method nonaqueous solvents are used. As any type of organic solvents even with higher boiling points can be employed in solvothermal method, this method has the advantage of elevating the temperature higher than that of hydrothermal method. The distribution of size and shape and also the crystallinity of the synthesized nanoparticles can also be controlled much better than that of hydrothermal method. With all these advantages, this method is chosen to be versatile for the synthesis of a wide range of nanoparticles of narrow size distribution. The solvothermal doping of metal nanoparticles is quite a challenging method as it consumes large time. Jovani et al. [64] synthesized a single-phase yellow ceramic pigment based on the Cr- and Sb-doped TiO_2 through microemulsion-mediated solvothermal method at temperature of 180 °C. The synthesized samples found to have good chemical and thermal stabilization. The spherical shape of the pigment was transited by the application of high temperature which helps in the change of the morphology of the rutile or anatase single phase of TiO_2.

Direct Oxidation Method

The doping of catalyst takes place through direct oxidation method at very high temperature. The samples prepared through this method are mostly used for fuel cell application. The electrode cells are synthesized through this doping technique such that the unstable nanomaterial can be stabilized by the insertion of the foreign ions or compounds into it. Synthesized gadolinia doped with Bi_2O_3 had promoted the catalytic activity in the methane oxidation. Bismuth oxide can be used extensively in industrial oxidation reactions; further they developed a novel ceramic system through this methane direct oxidation for the synthesis of anode materials which are highly responsible in the electricity generation without syngas production. The catalytic activity of the ceramic system increases over the pseudo-steady-state value, and this catalyst produces high CO_2 and H_2 at a lower temperature of 600 °C or lower.

Sonochemical Method

For the synthesis of a wide range of nanomaterials and also high-surface area transition metals, alloys, carbides, oxides, and colloids, ultrasound plays an important role. The chemical effects of ultrasound do not arise directly from an interaction with molecular species but arise from the acoustic cavitation constituting the formation, growth, and implosive collapse of bubbles in a liquid. During the incidence of cavitational collapse, higher temperature (5,000 K) as well as pressures (1,000 atm) and enormous heating and cooling rates ($>10^9$ K/s) occurs. Many researchers have reported that the synthesis of catalyst and doping of catalyst take place well in sonochemical method. Awati et al. [65] demonstrated the advantages of sonication versus the conventional method of preparing titania. They found that the more uniform distribution/dispersion of the nanoparticles, a marginally higher surface area, better thermal stability, and phase purity are some of the advantages of the preparation of nanocrystalline titania by the ultrasonication method.

Shirsath et al. [66] synthesized Fe- and Ce-doped TiO_2 through sonochemical approach and conventional doping method. The samples synthesized through sonochemical approach exhibited higher peaks in the XRD pattern than the conventional method revealing that the crystallinity of Fe-doped TiO_2 showed enhanced formation of crystalline particles. The photolytic property of the catalyst also shifts toward visible region which depends upon the method of preparation such that the absorption spectra shift in the visible range between 400 and 600 nm. The degradation studies of the Fe-doped TiO_2 show the effective degradation within 120 min under UV irradiation. Chakma and Moholkar [67] prepared Fe^{3+}-doped ZnO catalyst through ultrasound-assisted impregnation method. The sonochemical process helped in the formation of hexagonal wurtzite crystal structure in all Fe^{3+}-doped ZnO where the average particle size of the doped catalyst was found to be 56–60 nm. This smaller size and uniform distribution of the dopant on the catalyst was due to the contribution of sonication on the synthesis process. The BET surface area of the synthesized Fe^{3+} doped ZnO catalyst 4.34 m^2/g which is a reduced one due to the de-agglomeration caused by the sonication-assisted synthesis in the presence of surfactant. The degradation of acid red B dye with the doped catalyst gave higher decolorization of 80 %, which is twofolds higher than the individual process with the catalyst.

Eskandarloo et al. [68] studied through the ultrasound-assisted sol–gel synthesis of Co-doped TiO_2 that the sonication during sol–gel synthesis helped in morphology, size, and crystallinity of the particles and in-depth uniform distribution of dopant ions into the TiO_2 lattice. The TEM image of the doped catalyst confirms the mean particle size to be about 20 nm showing the role of ultrasound in the crystal growth and phase transformation of the catalyst during the synthesis. Further the spherical structure and slight agglomeration with uniform distribution of dopant ions on the surface of TiO_2 where ultrasound plays a key in the blue shift toward the visible region helping with higher photodegradation activity. The degradation of methyl orange showed maximum removal rate of 96.33 % achieved by the combination of ultrasound and successful synthesis method [69].

Conclusion and Future Directions

Advanced oxidation processes involving doped catalyst have gained more attention recently. The usage of doped catalyst in many applications for degradation studies and other catalytic studies has covered more areas in research. Many industries now look for the commercialization of these doped catalysts for various applications apart from wastewater treatment. The metal doping method has been used widely and being commercialized in the form of powders and colloidal solutions. The activity of the catalyst shifts from the UV region to the visible region. It has the ability to be used as antibacterial and self-cleaning applications with solar light. The major problem with doped catalyst is the loss of photocatalytic activity with repeated regeneration and recycling. The efficiency and storage properties depend upon the preparation method of the doped catalyst and the dopant used. The higher recombination rates of the metal ions sometimes lower the activity of the doped catalyst, thereby the activity of bare catalyst is even higher.

The difficulty faced by the nonmetal-doped catalyst is that the activity under visible light is much lower than the ultraviolet. The development of new optimized doped catalyst for more activities under visible light is more essential. The activity can be increased by changing the surface characteristics such that the chemical and physical stabilities are optimized to be better than the previous one. These materials together with the development of technically applicable self-aligning photocatalytic coating systems adaptable to the major substrates will represent a groundbreaking step change in this field particularly in the economic viability of a range of potential processes. Nonmetal doping seems to be more promising than metal-doped catalyst.

The cost analysis described about various advanced oxidation processes (AOPs) with respect to their operational costs. The studies reported that the overall cost constituting the capital, operating, and maintenance cost incurred for individual sonolysis seems to be economically unacceptable as only 34 % of electrical energy is being converted to cavitation energy during treatment of industrial effluents. However, sonolysis is considered superior among other AOPs in terms of efficiency and environmental safety in spite of its higher overall cost. Therefore, integration of other modes of energy like ultraviolet (UV) irradiation and combination of doped catalysts and chemical additives such as Fenton reagent, H_2O_2, or ozone along with sonolysis are found economical for efficient and economical wastewater treatment. Thus, the present research is throwing light on the investigation of possible combination and optimization of photocatalyst, UV, and other additives with sonolytic treatment.

To achieve higher treatment efficiency, the use of different catalysts and further exploration of novel catalysts are continuously being increased. Further, the use of sophisticated synthesized nanoassembled doped photocatalyst requires posttreatment recovery for possible commercialization of catalyst-assisted AOPs. To make recovery of the photocatalyst particles feasible after degradation of the aqueous effluent system, the method of forming nanostructures rather than nanoparticles for instance, TiO_2 nanotubes or nanowires will comply to the easier

recovery methods. The heterogeneous catalytic materials are presently gaining attention for their easy recovery, however, deterioration of their catalytic activity after prolonged usage. On employing catalyst during sonocatalytic degradation, ultrasonic irradiation creates an adsorption–desorption phenomenon with simultaneous cleaning of the catalyst surface. Hence, after completion of degradation, essential parameters of the catalysts like structural stability, reproducibility, and the extent of deactivation are needed to be analyzed. In case of adding chemical agents to conjugate with sonolysis, those that are capable of being hydrogen radical ($^{\bullet}$OH) scavenger such as H_2O_2, Fenton reagent at an optimum dosage is beneficial. Further, the optimization helps in such a way to not to produce secondary pollutants during effluent treatment. However, the optimum dosage generally depends on wastewater characteristics as the real-time effluent may typically contain various organic dyes and inorganic contaminants. On the other hand, it also depends on the ultrasonic operating conditions, namely, power density, operating frequency, and reactor configuration as these parameters will influence the effectiveness of free radical attack performed by the chemical agents.

References

 1. Zhao B, Lv M, Zhou L (2012) Environ Sci 24(4):774
 2. Dixit A, Tirpude AJ, Mungray AK (2011) Desalination 272:265
 3. Neppolian B, Kim Y, Ashokkumar M (2010) J Hazard Mater 182:557
 4. Gogate PR, Pandit AB (2004) Adv Environ Res 8:501
 5. Saritha P, Aparna C, Himabindu V, Anjaneyulu Y (2007) J Hazard Mater 149:609
 6. Mandal T, Maity S, Dasgupta D, Datta S (2010) Desalination 250:87
 7. Rey A, Carbajo J, Adana C, Faraldos M, Bahamonde A, Casas JA, Rodriguez JJ (2011) Chem Eng J 174:13
 8. Coelho A, Castro AV, Dezotti M, Sant Anna GL Jr (2006) J Hazard Mater 137:178
 9. Arslan Alaton I, Gursoy BH, Schmidt J (2008) Dyes Pigments 78:117
10. Pirkanniemi K, Sillanpaa M (2002) Chemosphere 48:1047
11. Shi P, Su R, Wan F, Zhu M, Li D (2012) Appl Catal B 123:265
12. Iyyapushpam S, Nishanthi ST, Pathinettam Padiyan D (2014) J Alloys Compd 601:85
13. Wang Y, He Y, Li T, Cai J, Luo M, Zhao L (2012) Chem Eng J 189:473
14. Mazille F, Schoettl T, Klamerth N, Malato S, Pulgarin C (2010) Water Res 44:3029
15. Jans U, Hoigné J (1998) Int Ozone Assoc 20:67
16. Munter R (2001) Proc Estonian Acad Sci Chem 50:59
17. Raj CBC, Quen HL (2005) Chem Eng Sci 60:5305
18. Wu C, Chang C (2006) J Hazard Mater B 128:265
19. Arslan I, Balciogilu IA, Bahnemann DW (2000) Dyes Pigments 47:207
20. Jamil TS, Ghaly MY, El-Seesy IE, Souaya ER, Nasr RA (2011) J Hazard Mater 185:353
21. Andreozzi R, Caprio V, Insola A, Marotta R (1999) Catal Today 53:51
22. Haji S, Benstaali B, Al-Bastaki N (2011) Chem Eng J 168:134
23. Kepa U, Stanczyk-Mazanek E, Stepniak L (2008) Desalination 223:187
24. Hoffman DJ, Oltmans SJ, Harris JM, Johnson BJ, Lathrop JA (1997) J Geophys Res 102:8931
25. Gupta AK, Pal A, Sahoo C (2006) Dyes Pigments 69:224
26. Zhou M, He J (2007) Electrochim Acta 53:1902
27. Tahir MS, Saleem M, Malik SR, Khan JR, Siebenhofer M (2012) Chem Eng Process 52:16
28. Ram C, Pareek R, Singh V (2012) Int Theor Appl Sci 4:82
29. Suslick KS, Choe SB, Cichowlas AA, Grinstaff MW (1991) Nature 353:414

30. Mahamuni NN, Adewuyi YG (2010) Ultrason Sonochem 17(6):990
31. Wang Y, Zhao D, Ma W, Chen C, Zhao J (2008) Environ Sci Technol 42:6173
32. Frontistis Z, Daskalakia VM, Hapeshi E (2012) J Photochem Photobiol A 240:33
33. Zhang Z, Yi JB, Ding J, Wong LM (2008) J Phys Chem C 112(26):9579
34. Chelme-Ayala P, Gamal El-Din M, Smith DW (2010) Chemosphere 78:557
35. Tong H, Ouyang S, Bi Y, Umezawa N, Oshikiri M, Ye J (2012) Adv Mater 24:229
36. Zhou H, Yi D, Yu Z, Xiao L, Li J (2007) Thin Solid Films 515:6909
37. Murugadoss G (2012) J Mater Sci Technol 28(7):587
38. Madani ME, Guillarda C, Perol N, Chovelon JM, El Azzouzi M, Zrineh A, Herrmann JM (2006) Appl Catal B 65:70
39. Meng Z, Juan Z (2008) Wastewater treatment by photocatalytic oxidation of nano-ZnO. Global Environmental Policy in Japan, No. 12, Internet Version, pp 1–9
40. Naveenraj M, Kumar S, Anandan S (2010) Adv Mater 1:51
41. Nenavathu BP, Krishna Rao AVR, Goyal A, Kapoor A, Dutta RK (2013) Appl Catal A 459:106
42. Martin MMB, Parez JAS, Lopez JLC, Oller I, Rodraguez SM (2009) Water Res 43:653
43. Li D, Wang J, Li X, Liu H (2012) Mater Sci Semicond Process 15:152
44. Kaur S, Singh V (2007) Ultrason Sonochem 14:531
45. Muthukumar M, Sargunamani D, Selvamani N (2005) Dyes Pigments 65:151
46. Akpan UG, Hameed BH (2012) Desalin Water Treat 43:84
47. Ali SAM, Abdullah AZ (2011) International conference on environment and industrial innovation, vol 12, IPCBEE. IACSIT Press, Singapore
48. Liu G, Wang L, Yang HG, Cheng HM, Lu QG (2010) J Mater Chem 20:831
49. Fujishima A, Honda K (1972) Nature 238:37–38
50. Khataee AR, Zarei M (2011) Desalination 278:117
51. Muthirulan P, Meenakshisundararam M, Kannan N (2013) J Adv Res 4(6):479
52. Chakrabarti S, Chaudhuri B, Bhattacharjee S, Das P, Dutta BK (2008) J Hazard Mater 154:230
53. Akyol A, Bayramoglu M (2005) J Hazard Mater 124:241
54. Xie J, Lu X, Chen M, Zhao G, Song Y, Lu S (2008) Dyes Pigments 77:43
55. Wu Y, Chaing Y, Huang C, Wang S, Yang H (2013) Dyes Pigments 98:25
56. Pugazhenthiran N, Sathishkumar P, Murugesan S, Anandan S (2011) Chem Eng J 168:1227
57. Xi Y, Megharaj M, Naidu R (2011) Appl Clay Sci 53:716
58. Panda NR, Acharya BS, Nayak P, Bag BP (2014) Ultrason Sonochem 21:582
59. Effendi M (2012) Int J Basic Appl Sci 12:107
60. Liang J, Zu G, Liu P, Luo X, Tan C, Jin L (2014) Superlattice Microst 72:272
61. Khataee A, Karimi A, Oskoui S, Darvishi R, Soltani C, Hanifehpour Y, Soltani B, Joo SW (2015) Ultrason Sonochem 22:371
62. Wang M, Zhao Z, Liu T (2015) J Alloys Compd 621:220
63. Chen C, Dai W, Lu Y, He H, Lu Q, Jin T (2015) Mater Res Bull 10:70
64. Jovaní M, Domingo M, Machado TR, Longo E, Beltran-Mir H, Cordoncillo E (2015) Dyes Pigments 116:106
65. Awati PS, Awate SV, Shah PP, Ramaswamy V (2003) Catal Commun 4:393
66. Shirsath SR, Pinjari DV, Gogate PR, Sonawane SH, Pandit AB (2013) Ultrason Sonochem 20:277
67. Chakma S, Moholkar VS (2015) Ultrason Sonochem 22:287
68. Eskandarloo H, Badiei A, Behnajady MA, Ziarani GM (2015) Ultrason Sonochem 26:281
69. Liu G, Wang L, Yang HG, Cheng HM, Lu GQ (2010) J Mater Chem 20:831
70. Devilliers (2006) Energia 17 1:6

Degradation of Organic Micropollutants by Hydrodynamic and/or Acoustic Cavitation

Patrick Braeutigam

Contents

Abstract

In recent years, micropollutants have become an emerging issue in natural water bodies, especially in industrialized countries. To treat those micropollutants, different advanced oxidation processes were developed and optimized. Some of the advanced oxidation processes need additional chemicals (catalysts, oxidation agents, pH control), which have to be separated, (re)

P. Braeutigam (✉)
Center for Energy and Environmental Chemistry (CEEC), Institute of Technical and Environmental Chemistry, Friedrich-Schiller-Universität Jena, Jena, Germany
e-mail: patrick.braeutigam@uni-jena.de

activated, or degraded after the treatment process often followed by a neutralization step accompanied with high salt loads. Cavitation processes belong to the group of advanced oxidation processes, due to the formation of highly reactive hydroxyl radicals by the homolytic cleavage of water molecules in the cavitation bubbles. Cavitation processes do not need any additional chemicals and do not rely on the salt content or turbidity. Moreover, the formation of hydroxyl radicals takes place in the whole volume of the treated water and is not restricted to a specific surface. However, the energy demand of cavitation processes is higher compared to other advanced oxidation processes. Therefore, new cavitation-based processes have to be developed to overcome the disadvantages. One possibility is the use of a combination of hydrodynamic and acoustic cavitation in one reactor, the so-called hydrodynamic-acoustic-cavitation. Within this, the effect of different parameters on the hydroxyl radical formation within a HAC setup is discussed and compared with literature data. Therefore, the oxidation of salicylic acid via hydroxyl radicals was used as model reaction (salicylic acid dosimetry). Moreover, a comparison concerning the synergy and the energy efficiency was done and research desiderata were derived.

Introduction

In recent years, micropollutants – for example, pharmaceuticals, endocrine disruptors, or industrial chemicals – in natural waters have become an emerging issue, especially in industrialized countries [1, 2]. Numerous investigations have been carried out on the occurrence, distribution, and fate of these substances [3, 4]. Micropollutants have been found in the aquatic environment around the world and were detected in surface water, groundwater, and even in drinking water [5, 6]. For example, up to now more than 130 pharmaceutical substances could be detected in the European aquatic environment [7]. The risk for living organisms is difficult to assess [2, 8], but the formation of resistances of microorganisms by antibiotics [9] or the feminization of fish populations by hormones [10] is discussed.

Therefore, as a preventive step, different techniques for the elimination of these substances were developed.

On the one hand, there exist methods which separate micropollutants from water without changing the chemical structure of the molecules, like adsorption or filtration processes [11, 12]. The main advantage of those techniques is that no (potentially toxic) transformation products are formed within the separation step, but disadvantages arise from additional purification steps of the concentrated pollutants or separation and/or reactivation of the adsorbents or filter materials.

On the other hand, there exists methods which degrade micropollutants in situ via different techniques, for example with biological, electrochemical, or photochemical processes [13–15]. Many of these methods can be summarized as advanced oxidation processes, where highly reactive hydroxyl radicals were formed [16]. Typical methods are photocatalysis [17], electrochemical oxidation with boron-doped diamond electrodes [15], Fenton reaction [18], UV/H_2O_2 [19], or cavitation [20], to name only a few. The advantage of those methods is that nearly all organic micropollutants were degraded in solution and in the best case no waste is produced (mineralization), but within the oxidative transformation processes in some cases toxic intermediates can be formed, which could lead to a secondary pollution. However, the toxic secondary pollution can be decreased based on degradation kinetics via retention time control.

Some of the advanced oxidation processes need additional chemicals (catalysts, oxidation agents, pH control), which have to be separated or degraded after the treatment process often followed by a neutralization step (accompanied with high salt loads). Only the electrochemical oxidation (with electrodes having a high O_2 overpotential), photooxidation via UV light, and cavitation processes work without additional chemicals. However, the success of electrochemical oxidation processes is connected with the available salt content (conductibility) and limited to electrode surface and mass transfer of the micropollutants to the electrode surface. Moreover, fouling processes at the electrode can decrease the effectiveness of the electrochemical oxidation with time [15]. UV oxidation is limited to the penetration depth of the UV light into the water (Lambert-Beer's law), which can be decreased with increasing turbidity [17].

Cavitation processes do not need any additional chemicals and do not rely on the salt content or turbidity [20]. Moreover, the formation of hydroxyl radicals takes place in the whole volume of the treated water. However, the energy demand of cavitation processes is higher compared to other advanced oxidation processes [21].

Cavitation is defined as the formation, growth, and subsequent collapse of gas- or vapor-filled bubbles in fluids [22]. In the collapse phase, high temperatures are generated in the bubbles (up to 5000 K) leading to homolytic cleavage of water molecules to form highly reactive hydroxyl or perhydroxyl radicals able to oxidize contaminants in aqueous systems [20, 23].

Cavitation can be initiated either by acoustic effects (ultrasound – AC) or through the utilization of hydrodynamic phenomena (HC) [24]. Both techniques have advantages and disadvantages, concerning scale-up, energy efficiency, collapse temperature, and bubble density [25, 26].

Cavitation is most commonly generated by ultrasonic transducers (acoustic cavitation), but problems concerning energy requirement and scale-up possibilities exist [27]. An alternative for generation of cavitation events is hydrodynamic cavitation, where bubbles are created due to a pressure drop caused by increasing fluid velocity (Bernoulli principle) and/or boundary layer separation [28, 29]. This technology offers a better scale-up possibility [30], a higher bubble density, and lower investment costs [31]. Investigations concerning the energy efficiency lead to different results with regard to the generation method (AC vs. HC) [25, 32, 33].
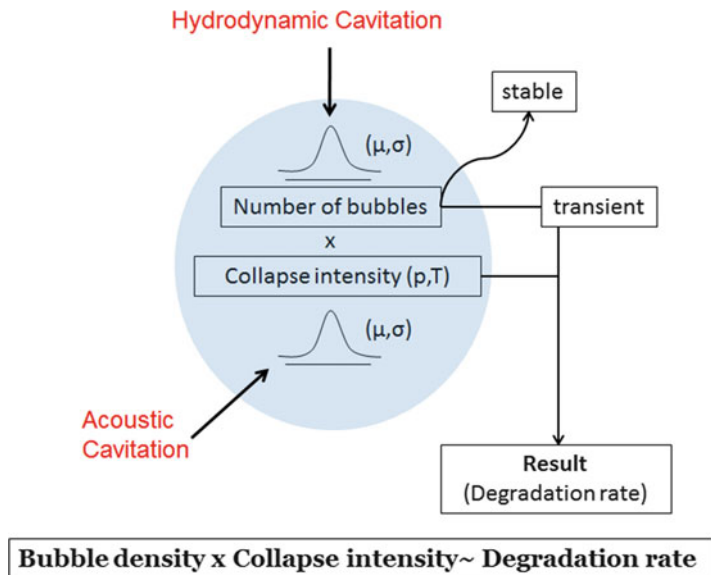
Fig. 1 Proposed mechanism of the hydrodynamic-acoustic-cavitation

However, the collapse intensity (temperature and pressure at the collapse) for hydrodynamic cavitation is lower in comparison to acoustic cavitation [34].

Therefore, a combination of both techniques in one reactor system (hydrodynamic-acoustic-cavitation – HAC) was introduced with the aim of using the advantages of each generation method (high bubble density and high collapse intensity) by avoiding the corresponding disadvantages. The proposed mechanism is related to the separation of bubble formation ans bubble collapse. Within hydrodynamic cavitation, which is the first step, a high bubble density is produced. At this step, a collapse of that bubbles is not intended due to the low collapse intensity at this stage. The bubbles will be transported to the acoustic field and collapse there under harsh conditions (Fig. 1). Moreover, bubble density as well as bubble size distribution can be varied within the transport due to different pressure-dependent effects like shrinking, growing, coalescence, or degassing.

Based on the proposed mechanism, hydrodynamic cavitation only generates a maximum value of bubbles (with the optimal critical size for acoustic cavitation), which are only collapsed within the acoustic field. With that approach, a high bubble density (reaction volume) could be connected with high collapse intensities (reaction conditions), leading to higher degradation rates and a more energy efficient process.

Up to now, only four publications exist, studying this combination, where always better results could be detected in the combined system for disinfection [35], the degradation of chloroform in water via a pyrolytic pathway [36], the oxidative degradation of the pharmaceutical carbamazepine in water [37], and the salicylic acid dosimetry [31]. However, the knowledge concerning this technology and the influencing parameters are limited and needs to be improved.

Within this study, the influence of different parameters, like reaction temperature, restriction specific parameters, the distance between the orifice and the sonotrode tip, amplitude, and pulsed ultrasound on the hydroxyl radical formation within a hydrodynamic-acoustic-cavitation setup will be discussed and compared with available literature data. A comparison of the HAC system with the individual methods regarding the OH-radical concentration as well as the cavitation-chemical efficiency will be shown, too.

Materials and Methods

This section contains the detailed description of the reagents used in this study (section "Chemicals"), the construction of the device used for the generation of HAC (section "HAC Reactor"), the orifices (section "Orifices") as well as the experimental procedures (section "Experimental Procedure"), and the analytical methods (section "Analytical Methods").

Chemicals

The chemicals used in this study are listed in Table 1 and were used as received. The water used for preparation of the stock solutions was purified by ion exchange resulting in a conductivity of 1.5 μS cm^{-1}.

HAC Reactor

The setup for creating HAC is shown in Fig. 2.

All parts of the setup, which were in contact with the solution, were constructed from stainless steel (SS 316). The loop setup consists of a reservoir (1) equipped with

Table 1 Overview of the chemicals used in this study

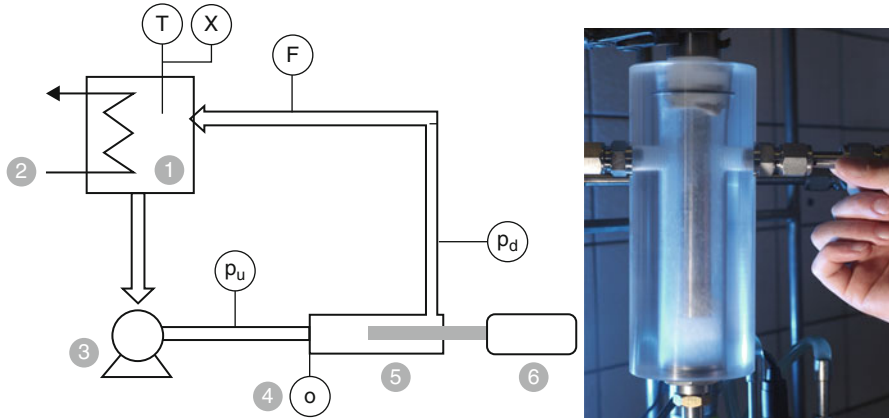| Compound	Formula	Structure	Purity	Supplier
Salicylic acid	$C_7H_6O_3$		>99 %	Sigma-Aldrich
2,3-Dihydroxybenzoic acid	$C_7H_6O_4$		>99 %	Sigma-Aldrich
2,5-Dihydroxybenzoic acid	$C_7H_6O_4$		>98 %	Sigma-Aldrich
Catechol	$C_6H_6O_2$		>99 %	Sigma-Aldrich
Phosphoric acid	H_3PO_4	–	>99.9 %	Sigma-Aldrich
Methanol	CH_3OH	–	>99.9 %	VWR

Fig. 2 Schematic overview of the HAC setup and a photo of the HAC reactor [37] ((*1*) reservoir, (*2*) cooling coil connected to a thermostat, (*3*) pump, (*4*) orifice, (*5*) HAC reactor, (*6*) ultrasound generator with sonotrode, (p_u) upstream pressure, (p_d) downstream pressure, (*F*) flow, (*T*) temperature, (χ) conductivity)

an inlet, sample port, and cooling coil connected to a thermostat ((2) – Proline RP 855, Lauda GmbH & Co. KG, Lauda-Königshofen, Germany, $-55 < T < 200\,°C$, accuracy: ± 0.2 K) to control the temperature of the solution. The reservoir was connected to the suction side of a pump ((3) – GY-028/II-LL-LA – centrifugal pump, 1.1 kW, 2800 min^{-1}, SPECK Pumps GmbH & Co KG, Roth, Germany). The pressure side of the pump was connected via pipes (inner diameter: 10 mm) to the HAC reactor (5) and a loop to the reservoir was installed. The up- (p_u) and downstream pressure (p_d, regarding HAC reactor) were measured with manometers (PGI series, Swagelok Germany, Markranstädt, Germany, accuracy: 0.5–2.5 %). The HAC reactor (self-made, cylindrical, ID 30 × 210 mm, stainless steel, 110 mL) consists of a replaceable orifice plate (4) at the entry of the reactor and a sonotrode connected to an ultrasound generator ((6) – UP200S, Hielscher Ultrasonics GmbH, Teltow, Germany, 24 kHz, 200 W, sonotrode: S14L2D, tip diameter: 14 mm, maximum amplitude: 125 μm). After the HAC reactor, the flow was measured (DRS-9250I4L4420, Kobold Messring GmbH, Hofheim, Germany, 0–40 L min^{-1}, accuracy: 1.5 %). Moreover, the electrical energy consumption was determined by an energy monitor (Voltcraft Energie Monitor 3000, Conrad Electronic SE, Hirschau, Germany, accuracy: ± 1 %) [37].

Orifices

In this study, different orifices (diameter: 12 mm, thickness: 2 mm, stainless steel (SS 316)) were used (Table 2).

The orifice-specific parameter β_0 describes the ratio of the cross-sectional area of the hole(s) to the cross-sectional area of the pipe and is given in percentage

Table 2 Overview of the orifices and specific parameters

Orifice number	Diameter of the hole (mm)	Area of the hole (mm^2)	β_0 (%)	δ (%)
1	2.3	4.15	5.29	0
2	2.5	4.91	6.25	0
3	2.9	6.60	8.41	0
4	3.0	7.07	9.00	0
5	3.2	8.04	10.24	0
6	3.5	9.61	12.25	0
7	3.7	10.75	13.69	0
8	4.0	12.56	16.00	0
9	4.5	15.90	20.25	0
10	5.0	19.63	25.00	0
11	10.0	78.54	100	0

(Formula 1) [38]. A β_0 of 30 % means that the orifice blocks 70 % of the cross-sectional area of the pipe and 30 % is available for the flow.

$$\beta_0 = \frac{A_h}{A_p} \cdot 100\% = \left(\frac{nr_h^2}{r_p^2}\right)_{circle} \cdot 100\% \tag{1}$$

Formula 1: Calculation of the orifice-specific parameter β_0.

   ((A_h) cross-sectional area of the hole, (A_p) cross-sectional area of the pipe, (n) number of holes on the orifice, (r_h) radius of the cross-sectional area of the hole(s) on the orifice, (r_p) radius of the cross-sectional area of the pipe).

   Another orifice-specific parameter called δ describes the radial displacement of the hole(s) on the orifice plate and is given in percentage, whereas a δ of 0 % means that the hole is in the center of the plate, and a δ of 100 % means that the hole is located next to the pipe wall [24].

Experimental Procedure

As a first step, an orifice was installed in the HAC reactor and the freshly prepared aqueous solution of salicylic acid (0.1 mM, 1 L) was filled into the reservoir. The temperature of the solution was adjusted to a desired value. The reservoir was closed and the pump as well as the ultrasound generator (for AC and HAC experiments) was switched on. For the experiments with acoustic cavitation as single method (AC) orifice plate number 11 was used, having the equal hole diameter as the pipe (10 mm). Samples were taken from the sample port before the reaction (0 min, initial concentration) and after 30 min reaction time. Each experiment was conducted at least two times and analyzed via HPLC-DAD (each at least as double determination).
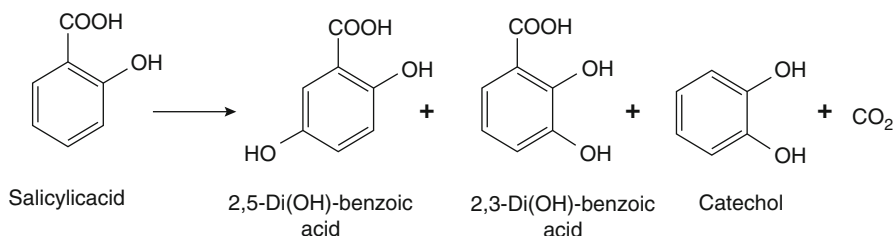
Fig. 3 Reaction schematic of salicylic acid dosimetry

Analytical Methods

This section describes the analytical methods for quantification of hydroxyl radicals in the HAC setup, starting with the description of the salicylic acid dosimetry as model reaction (section "Salicylic Acid Dosimetry") followed by the detection of the intermediates via HPLC-DAD measurements and calculation of the hydroxyl radical concentration (section "HPLC Measurements").

Salicylic Acid Dosimetry

For quantification of hydroxyl radical concentration, salicylic acid dosimetry was used in this study. Within that model reaction, salicylic acid is degraded through hydroxyl radical attack and formation of the hydroxylated intermediates 2,5-dihydroxybenzoic acid, 2,3-dihydroxybenzoic acid, and catechol (Fig. 3) [25].

The calculation of the reactive hydroxyl radical concentration can be done by the addition of the individual concentrations of the hydroxylated intermediates, which can be provided by HPLC-DAD measurements.

HPLC Measurements

HPLC measurements were carried out on a HPLC system (CD-2060 Plus column oven, PU-2080 Plus eluent pumps, AS 2055 Plus autosampler, JASCO Germany GmbH, Gross-Umstadt, Germany). The separation of salicylic acid and the corresponding hydroxylated intermediates (injection volume: 50 μL) was performed with a Kromasil C18 (250 mm $\times$ 4.6 mm $\times$ 5 μm) column, a flow rate of 1 ml min^{-1} (mobile phase (ultrapure water + phosphoric acid (pH 2)/methanol 40/60 (v/v)) and a column oven temperature of 35 °C. For the detection of the substances, a diode array detector (MD-2010 Plus multi-wavelength detector, JASCO Germany GmbH, Gross-Umstadt, Germany) was used working at 204 nm (salicylic acid (18.4 min), 2,3-dihydroxybenzoic acid (8.8 min), catechol (5.9 min) and 212 nm (2,5-dihydroxybenzoic acid (6.7 min)). The integrated peak areas correlate with the concentration of the corresponding substance. The quantitative analysis was done by external calibration with standards (see section "Chemicals"). Each analysis was repeated two times for quality control. A corresponding chromatogram is shown in Fig. 4.
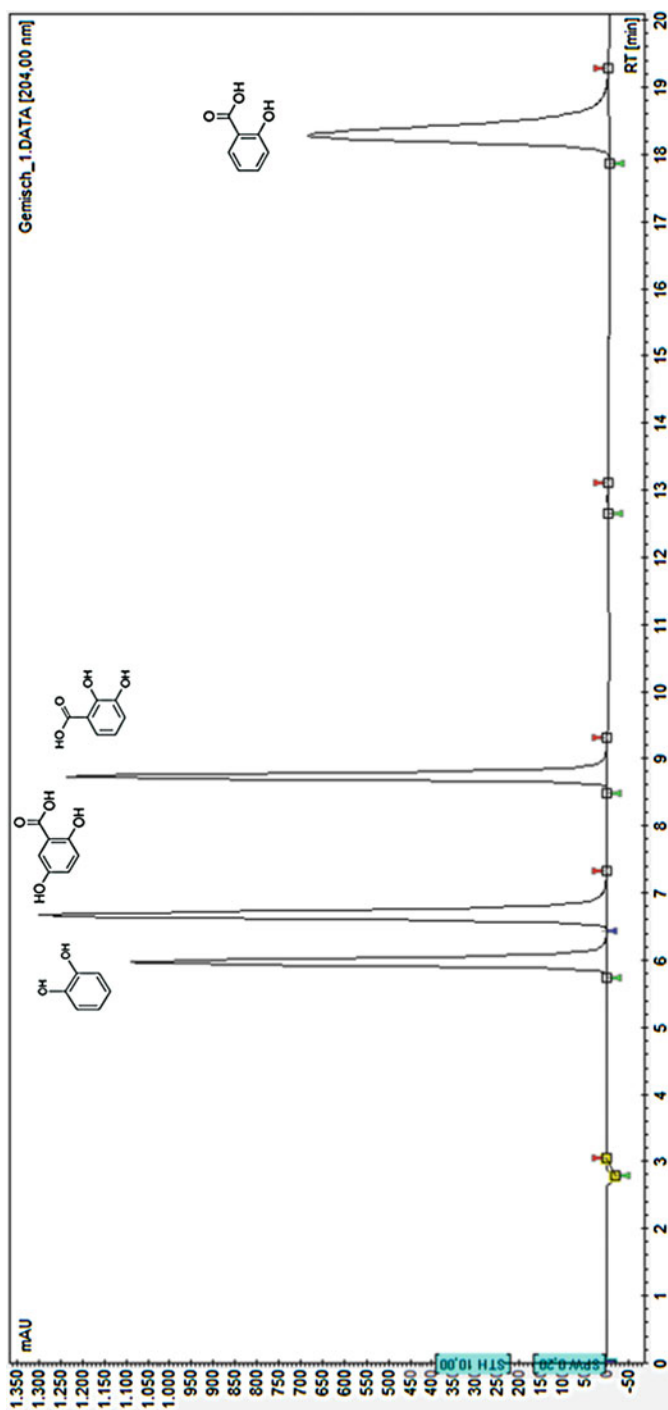
Fig. 4 Chromatogram of salicylic acid and the hydroxylated intermediates (Kromasil C18 (250 mm × 4.6 mm × 5 μm) column, water + orthophosphoric acid (pH 2)/methanol 40/60 (v/v), 1 mL min^{-1}, 35 °C, injection volume: 50 μL)

Results and Discussion

This section deals with the description of the effects of different parameters on hydroxyl radical formation in the hydrodynamic-acoustic cavitation setup. Therefore, the effects of the orifice-specific parameter β_0 (section "Effect of β_0 on the Hydroxyl Radical Formation") and the reaction temperature (section "Effect of Reaction Temperature on the Hydroxyl Radical Formation") are discussed. The effects of ultrasound specific parameters amplitude and pulse mode were described in the sections "Effect of Ultrasound Amplitude on the Hydroxyl Radical Formation" and "Effect of Pulsed Ultrasound on the Hydroxyl Radical Formation", respectively, followed by the effect of the distance between the orifice and the sonotrode tip (section "Effect of the Distance Between Orifice and Sonotrode Tip on the Hydroxyl Radical Formation"). At the end, a comparison of the combined method (HAC) with the individual methods (HC and AC) is done based on the hydroxyl radical concentration (section "Comparison of the Methods") and the energy efficiency (section "Energy Efficiency Assessment").

Effect of β_0 on the Hydroxyl Radical Formation

In this study, the effect of the orifice-specific parameter β_0 (see section "Orifices") was investigated in the range of 5.29–100 % with regard to the hydroxyl radical formation in the HAC setup (Fig. 5).

As can be seen in Fig. 5, a decrease in β_0 leads to a significant increase in the generated hydroxyl radicals. The single continuous ultrasound treatment ($\beta_0 = 100$ %) could produce a hydroxyl radical concentration of 0.34 μmol L^{-1}
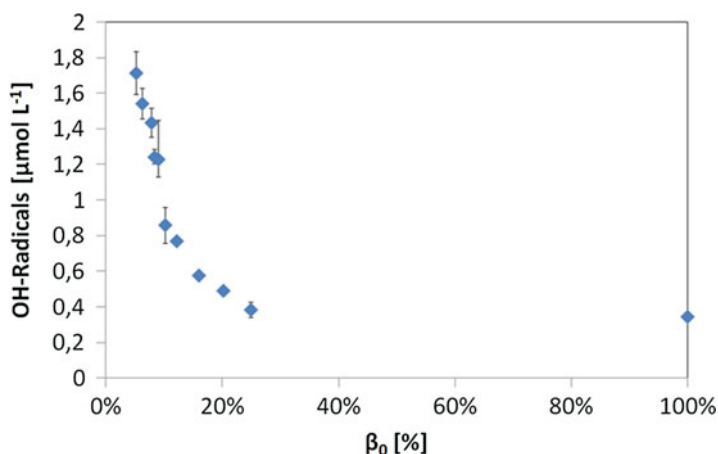

Fig. 5 Effect of β_0 on the hydroxyl radical formation in the hydrodynamic-acoustic-cavitation setup (1 L, 0.1 mM aqueous salicylic acid solution, orifice number 1–11, 24 kHz, 125 μm, distance HC-AC: 2.8 cm, 35 °C, 30 min)

within 30 min, whereas the HAC setup with a β_0 of 5.29 % (orifice number 1) could generate more than a fivefold amount (1.72 μmol L^{-1}) in the same time.

The effects of the orifice-specific parameter β_0 were mostly described in works concerning hydrodynamic cavitation as a single method. Here, β_0 is described as parameter, who affects the number of bubbles and collapse conditions. In many studies, it was found that an increase in β_0 leads to a decrease in fluid velocity accompanied with a decrease in the collapse conditions and number of bubbles generated, and therefore a decrease in β_0 was derived to reach higher degradation rates in advanced oxidation processes [32, 39].

Nevertheless, there exists other studies, where optimal values for β_0 were found [26, 36]. With a decrease in β_0, the pressure drop increases at constant flow rates, leading to a shift in the bubble size distribution to bigger bubble sizes, an increase in bubble density, and an increased possibility for degassing processes [40]. This could be a reason for optimal values of β_0, next to supercavitation phenomena, which become more probable with increasing pressure drops [30].

The effect of β_0 in the HAC system could be different compared to the effect of β_0 in the HC system. Within the HC system, the optimal operating point is based on the optimization of the number of bubbles as well as the collapse conditions, which are both influenced by the β_0 value. Within the HAC system, the generation of the bubbles and the collapse are separated in the best case. Therefore, β_0 has to be optimized with regard to the production of a high number of bubbles, having the critical radius when they reach the acoustic field for collapse. The effect of β_0 on the collapse (induced by HC) is not been focused on in the HAC approach.

Concerning the combined system of hydrodynamic and acoustic cavitation, only four publications exist [31, 35–37]. In two of them, the effect of β_0 was investigated. For the pyrolytic degradation of chloroform in water an optimal β_0 of 7.8 % was found [36], whereas in the oxidative degradation of the pharmaceutical carbamazepine optimal values for β_0 of around 6.3 % exist [37].

In this study, a decrease in β_0 leads to a continuous increase in hydroxyl radical formation. Based on the proposed mechanism for HAC, the HC unit is only responsible for the production of a high amount of bubbles. With decreasing β_0, the pressure drop increases continuously leading to continuously increased bubble density and bubble sizes. The bubble sizes, which are produced by acoustic cavitation, depend on the ultrasound frequency as well as on the acoustic power, where higher frequencies and higher power input lead to a narrow distribution with smaller bubbles, whereas lower frequencies and power inputs form broader distributions at higher bubble sizes [41]. Hence, the interaction of the acoustic field with the available bubbles (for example, produced by HC) is limited to those sizes.

With the HAC system (24 kHz, 200 W) used in this study, a wide range of comparable bigger bubbles could be used in the acoustic field. The bigger size of bubbles is correlated with a higher bubble density and therefore a higher reaction volume produced by the HC unit [40]. Based on the results, a higher density and bubble size after the orifice is preferable for hydroxyl radical production with low frequency ultrasound HAC systems. HAC systems using higher ultrasound
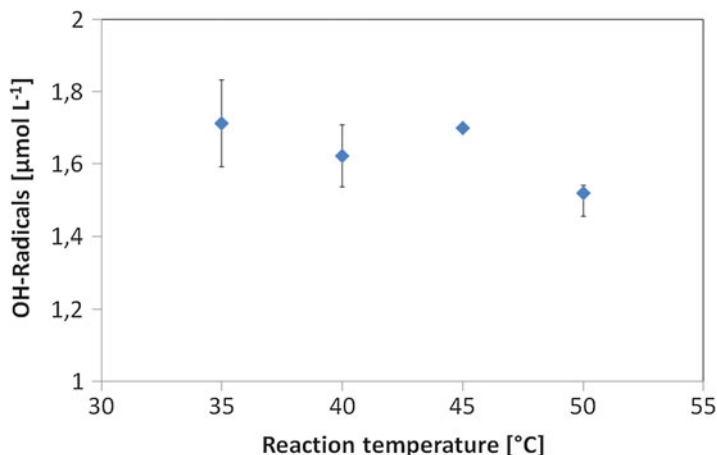
Fig. 6 Effect of the reaction temperature on the hydroxyl radical formation in the hydrodynamic-acoustic-cavitation setup (1 L, 0.1 mM aqueous salicylic acid solution, orifice number 1, 24 kHz, 125 μm, distance HC-AC: 2.8 cm, 35–50 °C, 30 min)

frequencies could show optimal results with orifices having different β_0 values, but this needs further experimental and theoretical confirmation.

Moreover, an optimum could be found with orifices having a $\beta_0 < 5$ % in this study, but this could not be investigated due to the temperature stability, which could not be guaranteed in this β_0 range. Another possible explanation for the different behavior in this study could be that the production of hydroxyl radicals needs harsher conditions than the oxidative or pyrolytic degradation of chloroform or carbamazepine in water and smaller β_0 values are preferable in this case. Based on the lack of experimental as well as theoretical studies, the effect of the parameter β_0 in the HAC system could not be elucidated in detail and needs further research activities.

For all further investigations, orifice number 1 having a β_0 of 5.29 % was used.

Effect of Reaction Temperature on the Hydroxyl Radical Formation

The effect of the reaction temperature in the range of 35–50 °C on the hydroxyl radical formation in the HAC setup is displayed in Fig. 6.

In Fig. 6, it could be seen that with increasing reaction temperature the hydroxyl radical formation decreases slightly from 1.72 μmol L^{-1} at 35 °C to 1.52 μmol L^{-1} at 50 °C.

Different physical-chemical parameters like vapor pressure, viscosity, surface tension, or gas solubility are temperature dependent and influence the cavitation process in terms of generation, growth, and collapse [42].

With increasing reaction temperature, the vapor pressure of water increases leading to an easier generation of cavitation bubbles accompanied with decreasing collapse conditions (Formula 2 and 3) [43], due to an increased vapor entrance into

the bubbles accompanied by decay of bubble collapse, resulting in decreased OH-radical concentration [44].

$$T_{\max} = T_f \left\{ \frac{P_m(K-1)}{P} \right\} \qquad (2)$$

Formula 2: Calculation of the maximum temperature at the bubble collapse [43].

(T_{max} – maximum gas temperature, T_f –fluid temperature, P_m – liquid pressure at transient collapse, K – ratio of specific heats for the gas, P – gas pressure in the bubble at its maximum size).

$$P_{\max} = P \left\{ \frac{P_m(K-1)}{P} \right\}^{K/K-1} \qquad (3)$$

Formula 3: Calculation of the maximum pressure at the bubble collapse [43].

(P_{max} – maximum gas pressure in the collapsing bubble, P – gas pressure in the bubble at its maximum size, P_m – liquid pressure at transient collapse, K – ratio of specific heats for the gas).

However, the rate constant depends on the reaction temperature, too. Thus, an increase in reaction temperature should lead to increased conversion, which means increased hydroxyl radical concentration. Therefore, optimal temperature ranges are expected for the formation of hydroxyl radicals within cavitation-based processes and could be shown, especially for high frequencies [44].

In the studies concerning HAC systems, only one paper deals with the effect of the reaction temperature on the degradation of carbamazepine, where an optimal temperature of 25 °C was found [37]. In this study, a slight decrease of hydroxyl radical formation was observed between 35 °C and 50 °C, which is consistent with the published results. Moreover, an optimum could be found at reaction temperatures <35 °C in this study, but this could not be investigated due to unfavorable heat transfer and temperature stability in this range.

Based on the available data, it is assumed that the effect of reaction temperature in HAC systems shows the same trends known from acoustic and hydrodynamic cavitation.

For all further investigations, a reaction temperature of 35 °C was used.

Effect of Ultrasound Amplitude on the Hydroxyl Radical Formation

In this study, the influence of ultrasound amplitude on the hydroxyl radical formation within a HAC setup was investigated in the range of 30–125 μm, which is the maximum for the applied ultrasound system (see section "HAC Reactor"). Moreover, experiments with the single HC method (amplitude = 0 μm) was done. The results are shown in Fig. 7.

In Fig. 7, it can be seen that with increasing ultrasound amplitude, the hydroxyl radical concentration increases nearly linear from 0.58 μmol L^{-1} at 30 μm to
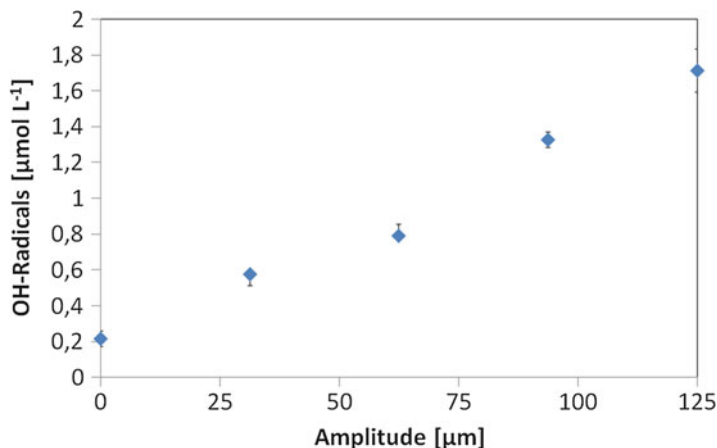
Fig. 7 Effect of the ultrasound amplitude on the hydroxyl radical formation in the hydrodynamic-acoustic-cavitation setup (1 L, 0.1 mM aqueous salicylic acid solution, orifice number 1, 24 kHz, 0–125 μm, distance HC-AC: 2.8 cm, 35 °C, 30 min)

1.72 μmol L^{-1} for 125 μm within 30 min. At a constant sonotrode area, the ultrasound amplitude is directly related to the power introduced into the liquid. An increase in the ultrasound amplitude leads to an increase of the total input power and to an expansion of the reactive volume and an increase in the generated bubble sizes [20, 41, 44]. Therefore, higher hydroxyl radical concentrations could be detected at higher ultrasound amplitudes. But, the hydroxyl radical concentration increases disproportionally lower with increasing amplitude, that means that with an amplitude of 60 μm a hydroxyl radical concentration of 0.79 μmol L^{-1} was reached, which is not the twofold of the hydroxyl radical concentration at an amplitude of 30 μm (0.58 μmol L^{-1}). This effect could be explained by the reactor geometry, since with higher amplitudes the interaction with the reactor wall (reflection, scattering) becomes more probable and therefore, a reduction of the effects could be observed. Other reasons could be an increasing probability for coalescence and degassing of bubbles with increasing amplitude, which leads to reduced reactive sides [41].

The single HC treatment leads to a hydroxyl radical concentration of 0.21 μmol L^{-1} and is lower than all HAC operating points. A comparison of the single AC treatment (see section "Effect of β_0 on the Hydroxyl Radical Formation", 0.34 μmol L^{-1} at 125 μm within 30 min ($\beta_0 = 100$ %)) with the HAC treatment at the same ultrasound amplitude of 125 μm (1.72 μmol L^{-1}) shows that the HAC system leads to a significant increase in hydroxyl radical formation. Moreover, all investigated HAC operating points (also with lower ultrasound amplitude and energy input) show a higher hydroxyl radical concentration than the single AC method at maximum amplitude.

The effect of the ultrasound amplitude in hydrodynamic-acoustic-cavitation systems was evaluated in only one more study, using the degradation of
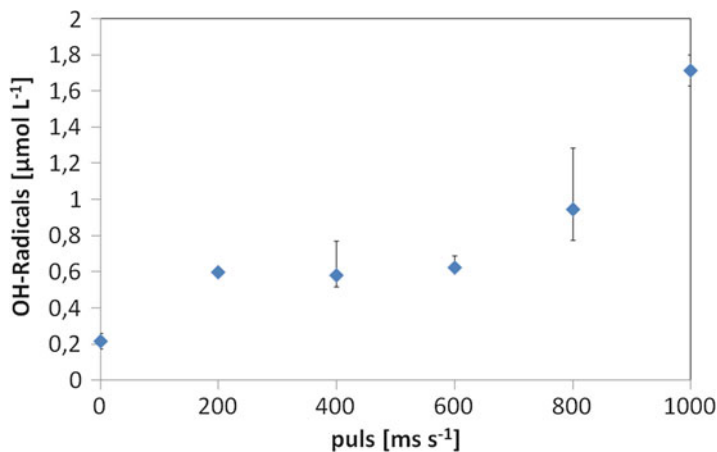
Fig. 8 Effect of pulsed ultrasound on the hydroxyl radical formation in the hydrodynamic-acoustic-cavitation setup (1 L, 0.1 mM aqueous salicylic acid solution, orifice number 1, 24 kHz, 125 μm, distance HC-AC: 2.8 cm, 35 °C, 30 min)

carbamazepine as model reaction [37]. Here, an increase in the amplitude leads to a nearly linear increase in degradation rate, too.

Based on the available data, the ultrasound amplitude plays an important role in HAC systems, whereas higher amplitudes lead to higher effects. Nevertheless, a lower amplitude is preferable in terms of stability (cavitation erosion) and energy consumption (disproportional lower OH-radical concentration with increasing amplitudes). Hence, more research is needed, for example, concerning the optimization of the ultrasound amplitude in connection with the reactor design.

The maximum available ultrasound amplitude of 125 μm was applied for all following experiments.

Effect of Pulsed Ultrasound on the Hydroxyl Radical Formation

In different studies, the effect of pulsed ultrasound was evaluated in various reactions for AC systems [45, 46]. The theoretical advantage of pulsed ultrasound is due to the use of active cavities in the breaks where no acoustic energy is introduced [20, 37]. Hence, the energy efficiency could be higher in comparison to continuous ultrasound.

In this study, the effect of pulsed ultrasound on the hydroxyl radical production was investigated in the range of 200–800 ms within 1 s. Moreover, experiments with the single HC method (puls = 0 ms s^{-1}) was done. The results are presented in Fig. 8.

With increasing pulse duration, the hydroxyl radical formation increases nearly continuously (with a slight deviation at 200 ms s^{-1}) from 0.6 μmol L^{-1} at 200 ms s^{-1} to 1.72 μmol L^{-1} for the continuous mode (1000 s ms^{-1}).

This enhancement seemed to be due to an increase in power, since the total input power increases linear with the pulse duration. Hence, no significant effect could be observed with pulsed ultrasound in the HAC setup.

The single HC treatment leads to a hydroxyl radical concentration of 0.21 μmol L^{-1} and is lower than all experimental data with pulsed ultrasound within the HAC setup. Also, the single AC treatment (see section "Effect of β_0 on the Hydroxyl Radical Formation", 0.34 μmol L^{-1} at 125 μm within 30 min ($\beta_0 = 100$ %)) shows significant lower values for hydroxyl radical formation than the HAC treatment at the same ultrasound amplitude of 125 μm (1.72 μmol L^{-1}). Moreover, all investigated HAC operating points (also with shorter pulse durations and therefore energy inputs) show a higher hydroxyl radical concentration than the single AC method at maximum amplitude.

Another study investigated the effect of pulsed ultrasound within a HAC setup, where same results could be observed for the oxidative degradation of carbamazepine in water [37].

Based on the few experimental data, the effect of pulsed ultrasound in hydrodynamic-acoustic-cavitation seems to be negligible for low frequency ultrasound. However, the effect should be proved in high frequency HAC systems due to possible energy savings.

For further experiments, the continuous ultrasound was used.

Effect of the Distance Between Orifice and Sonotrode Tip on the Hydroxyl Radical Formation

As described before, the proposed mechanism for hydrodynamic-acoustic-cavitation is based on the separation of bubble formation and bubble collapse. The orifice is used to produce a high bubble density. After that, the bubbles will be transported to the acoustic field and in the best case collapse there under harsh conditions (see Fig. 1). Starting with the creation of the bubbles by the pressure drop at the orifice, the bubbles will not only be transported but also changed in terms of bubble density as well as bubble size distribution due to different mainly pressure-dependent effects like shrinking, growing, coalescence, or degassing.

Since the bubble size distribution and bubble density distribution changes locally within transportation, the position of the sonotrode within the HAC setup should significantly influence the cavitation process.

Therefore, the distance between the orifice and the sonotrode tip was investigated in this study with regard to the hydroxyl radical formation within the HAC setup. The distance could be varied between 2.8 and 7.8 cm. Lower and higher distances could not be realized within the setup. The results are displayed in Fig. 9.

As could be seen in Fig. 9, the hydroxyl radical concentration slightly decreases by trend with increasing distance between orifice and sonotrode tip from 1.72 μmol L^{-1} at 2.8 cm to 0.97 μmol L^{-1} for 7.8 cm. This leads to the assumption that the bubble density is decreased with the distance due to degassing. Another assumption is that the bubble size distribution is shifted to higher or lower values,
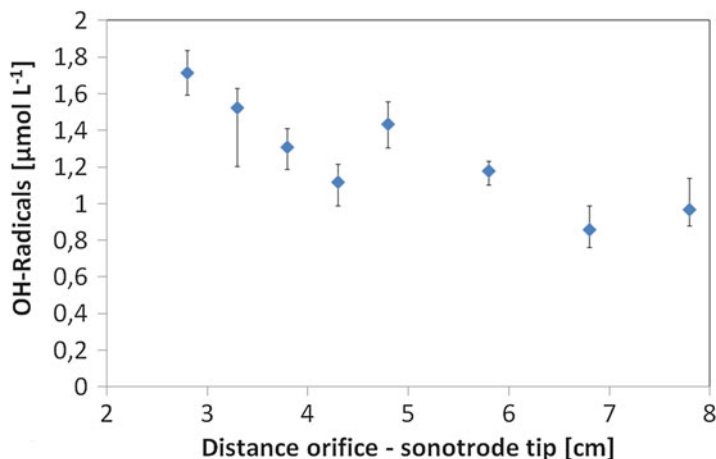
Fig. 9 Effect of the distance between orifice and sonotrode tip on the hydroxyl radical formation in the hydrodynamic-acoustic-cavitation setup (1 L, 0.1 mM aqueous salicylic acid solution, orifice number 1, 24 kHz, 125 μm, distance HC-AC: 2.8–7.8 cm, 35 °C, 30 min)

which are not useful for the applied ultrasound frequency of 24 kHz. This means also that the synergistic effect decreases with a successively increased local separation of HC and AC, where for higher distances a decoupling of both methods is expected, too. Therefore, lower distances are preferred for the hydroxyl radical formation within the HAC setup.

In another study, concerning on salicylic acid dosimetry at higher pressures (up to 4000 psi), an optimal distance of 1 cm was found and tracked back to the actual bubble radii at the entry in the acoustic field [31]. Best results were achieved if the bubbles were in the range of the critical radius. Thus, the next expression and compression phase of the ultrasound leads to the collapse. In any other case, the bubbles are smaller than the critical bubble radius and therefore the energy distributed by AC is used not only for the collapse but also for the growth of the bubbles (rectified diffusion). Thus, the hydroxyl radical concentration decreases since the number of collapses is lower. An optimal value for the distance in the range of 3–4 cm was also observed at the degradation of carbamazepine in a HAC setup and justified in the same way [37].

Based on the available data, it was found that the effect of the distance between orifice and the sonotrode tip has a significant influence in hydrodynamic-acoustic-cavitation. In general, smaller distances are found to be preferable, but also optimal values were obtained. At the moment, it is not clear why these differences exist. Due to the lack of experimental and theoretical studies, data concerning the bubble size distribution and bubble density distribution as a function of time and position are not available but needed for a more detailed insight in this technology. Moreover, the effect is mostly investigated for low frequency HAC setups. The coherences in high frequency HAC systems could be significantly different due to the smaller distribution of possible interacting bubble sizes.
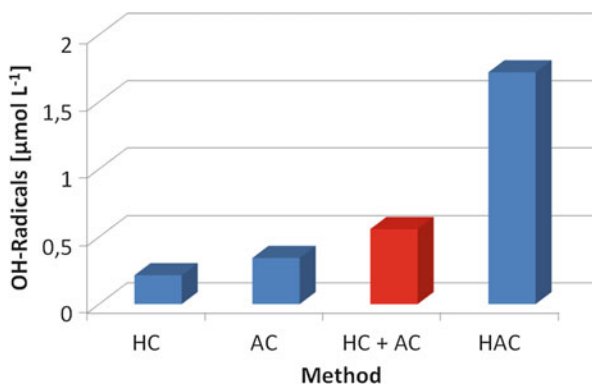
Fig. 10 Comparison of the single methods hydrodynamic cavitation and acoustic cavitation with the combined method of hydrodynamic-acoustic-cavitation in terms of the hydroxyl radical concentration (1 L, 0.1 mM aqueous salicylic acid solution, orifice number 1, 24 kHz, 125 μm, distance *HC-AC*: 2.8 cm, 35 °C, 30 min, *HC* hydrodynamic cavitation, *AC* acoustic cavitation, *HAC* hydrodynamic-acoustic-cavitation)

Based on the results, a distance of 2.8 cm was used in all subsequent experiments.

Comparison of the Methods

To elucidate synergistic effects of the optimized HAC setup ($\beta_0 = 5.29$ %, 35 °C, 125 μm ultrasound amplitude, continuous ultrasound, 2.8 cm distance between the orifice and the sonotrode tip), a comparison with the single methods (HC and AC) based on the hydroxyl radical concentration was done. The results are shown in Fig. 10.

As can be seen in Fig. 10, the single hydrodynamic cavitation (HC) leads to a hydroxyl radical concentration of only 0.21 μmol L^{-1}, whereas the acoustic cavitation (AC) leads to 0.34 μmol L^{-1} and the hydrodynamic-acoustic-cavitation (HAC) to 1.72 μmol L^{-1} within the same time.

The synergy for the combined HAC system could be calculated with regard to the sum of the single methods (HC + AC = 0.21 μmol L^{-1} + 0.34 μmol L^{-1} = 0.55 μmol L^{-1}) with Formula 4.

$$\text{Synergy} = \left(\frac{c_{OH}(HAC)}{c_{OH}(HC) + c_{OH}(AC)} - 1 \right) \cdot 100\% \qquad (4)$$

Formula 4: Calculation of the synergy of the hydrodynamic-acoustic-cavitation method.

(c_{OH} (HAC) – concentration of hydroxyl radicals generated by HAC method, c_{OH} (HC) – concentration of hydroxyl radicals generated by HC method, c_{OH} (AC) – concentration of hydroxyl radicals generated by AC method).

Based on the data, a high positive synergy of 212 % could be obtained within this HAC system. This means that by using hydrodynamic-acoustic-cavitation, the hydroxyl radical concentration could be increased more than threefold in the same reaction time compared to the hydroxyl radical concentration produced by both HC and AC.

In the four other HAC studies, a comparison with the single method was conducted, too. For the disinfection of microorganisms, the combined system was described to show a much higher disinfection compared to the individual techniques, but no concrete quantitative values are given [35]. In the study, which works with the high pressure HAC system and salicylic acid dosimetry, an increase in the extent of hydroxyl radical generation of 15 % for the combined system in comparison to the single HC system was observed [31]. In the study of Franke et al., the pyrolytic degradation of chloroform was investigated and a synergy was calculated on the basis of formula 4 to be 17 % [36]. Within the oxidative degradation of carbamazepine, a synergy of 63 % was calculated based on formula 4 [37]. Since the degradation process follows first order kinetics, the calculation of the synergy based on formula 4 is time dependent, and therefore a direct comparison of different devices or processes is not possible. A comparison based on the ratio of the rate constants [47] could be a solution and should be used on in further investigations.

Based on the available data, a positive effect could be detected by combining hydrodynamic and acoustic cavitation in one reactor for different chemical and biological processes. The hydrodynamic-acoustic-cavitation is believed to be a universal approach for intensification of cavitation processes. Based on the proposed mechanism (Fig. 1), the synergistic effect is connected with the matching of the individual advantages of the single methods. This means that the high bubble density, which could be produced by hydrodynamic cavitation, is combined with the high collapse intensity, which can be provided by acoustic cavitation. On the other hand, for example, effects of the (high) bubble density on the acoustic field distribution within the HAC reactor could also play a role in that complex method. Furthermore, there exist less experimental and theoretical studies which are needed to get a more precise insight in that interesting method.

Energy Efficiency Assessment

Next to the synergy of the HAC method, the energy efficiency is relevant not only for technical application. Therefore, the energy efficiency was assessed and compared in this study. The calculation for each method was done by using Formula 5.

$$EE = \frac{c_{OH}}{E/V} \tag{5}$$

Formula 5: Calculation of the energy efficiency for different methods.

(EE – energy efficiency, c_{OH} – concentration of hydroxyl radicals generated by the method, E – energy input of the method, V – reaction volume).
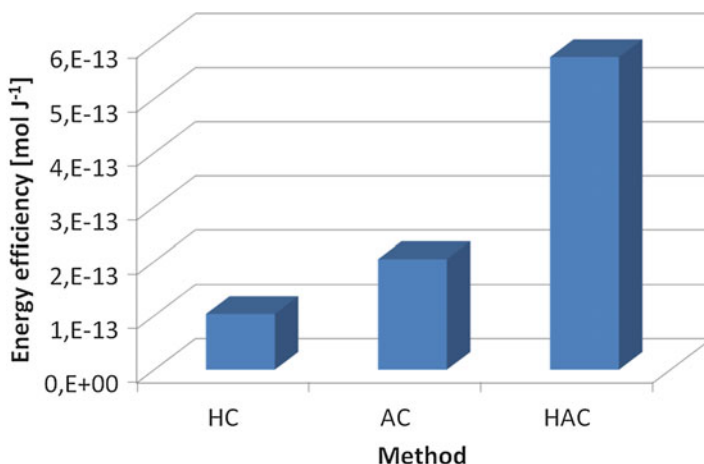
Fig. 11 Comparison of the single methods hydrodynamic cavitation and acoustic cavitation with the combined method of hydrodynamic-acoustic-cavitation in terms of the energy efficiency (1 L, 0.1 mM aqueous salicylic acid solution, orifice number 1, 24 kHz, 125 μm, distance HC-AC: 2.8 cm, 35 °C, 30 min, *HC* hydrodynamic cavitation, *AC* acoustic cavitation, *HAC* hydrodynamic-acoustic-cavitation)

Here, the generated hydroxyl radical concentration is related to the energy density and is given in mol J^{-1}. This is a useful term for the comparison of different scales of devices, too.

The results of the energy efficiency assessment are displayed in Fig. 11.

As can be seen in Fig. 11, the single HC method leads to an energy efficiency of only 1.03×10^{-13} mol J^{-1}, whereas the single AC methods show 2.04×10^{-13} mol J^{-1} and the HAC method 5.77×10^{-13} mol J^{-1}. The ratio of the energy efficiencies for HAC and AC is 2.83 (5.77/2.04 = 2.83). This means that within the HAC method, a 2.8-fold higher amount of hydroxyl radicals can be produced compared to the single AC method at an identical energy input. Based on these data, it can be seen that the HAC method is energetically preferred in comparison to the single methods.

Within the degradation of chloroform in water by HAC, the energy efficiency was calculated on the basis of the electrical energy input (energy efficiency I) and on the basis of the degree of efficiency (energy efficiency II). Concerning the energy efficiency I, the HAC shows a lower value compared to the single AC method, but in case of the energy efficiency II the HAC method is preferred in this study [36]. The study, which uses the degradation of carbamazepine in water, worked with the same energy efficiencies and found a ratio of the energy efficiency of the HAC to the AC method to be 2.43 (0.0017/0.0007 = 2.43) on the basis of energy efficiency I and 2.75 (0.011/0.004 = 2.75) on the basis of energy efficiency II. Here, the combined method shows significant higher values compared to the single methods for both energy efficiencies [37].

To sum up, the method of hydrodynamic-acoustic-cavitation is energetically preferred compared to the conventionally used single methods. The higher energy efficiency could be related to the proposed mechanism (Fig. 1), where more favorable reaction conditions for the acoustic cavitation are generated via hydrodynamic cavitation. As described before, the influence of the bubble density as well as the bubble size distribution on the acoustic field distribution and the cavitation field distribution within the HAC reactor could also be, next to others, an important factor for the HAC method. Moreover, from acoustic cavitation it is known that higher ultrasound frequencies are energetically favorable for hydroxyl radical production. Therefore, the introduction of higher frequencies to the HAC concept could be an interesting option. However, due to the lack of experimental and theoretical data, a deeper insight in the HAC method, the interaction between the single methods, or the distribution of the generated bubbles with regard to the position is not available at the moment and need further research activities.

Conclusions and Future Directions

It could be shown that technological as well as energetic advantages arise from hydrodynamic-acoustic-cavitation compared to the conventionally used single methods. The effect of different factors was studied with respect to the hydroxyl radical formation, compared with literature values and, if possible, general assertions were derived. Based on the proposed mechanism, it is assumed that the higher bubble density, produced via hydrodynamic cavitation by the orifice, is responsible for the synergistic effect. However, the main problem concerning the hydrodynamic-acoustic-cavitation is the lack of experimental as well as theoretical data, which is needed for a more detailed insight in this technology. Based on this study, four major research desiderata were derived.

1. Data concerning the bubble size distribution and bubble density distribution as a function of time and position after the orifice within the hydrodynamic cavitation unit are needed for the optimal adjustment of the single methods in the combined method.
2. Hydrodynamic-acoustic-cavitation is mostly investigated in low ultrasound frequency setups. The coherences in high frequency systems could be significantly different due to the smaller distribution of possible interacting bubble sizes, but experimental as well as theoretical studies are not available.
3. Hydrodynamic cavitation setups mainly use simple orifices for inducing the cavitation effect, where sheet cavitation could be observed. The pressure loss in those systems is very high and therefore the energy efficiency is comparably low. A change in the design of the orifice and of the pressures at the orifice could change the type of cavitation. By the use of an orifice without sharp edges and lower pressures behind the orifice, it is possible to produce cloud cavitation, accompanied with a continuous release of cavitation clusters. This cloud cavitation could lead to a higher energy efficiency (minimized pressure losses, higher cavitation effects) [48].

4. The interaction of the bubbles with the acoustic field in the HAC reactor is not fully understood. Through an optimized reactor design, improved cavitation conditions could arise. Therefore, more data concerning the fluid flow in conjunction with the acoustic field distribution as well as the cavitation field distribution is needed.

References

 1. Schwarzenbach RP, Escher BI et al (2006) The challenge of micropollutants in aquatic systems. Science 313:1072
 2. Kümmerer K (2008) Pharmaceuticals in the environment. Springer, Berlin
 3. Heberer T (2002) Occurrence, fate, and removal of pharmaceutical residues in the aquatic environment: a review of recent research data. Toxicol Lett 131:5
 4. Ternes TA (1998) Occurrence of drugs in German sewage treatment plants and rivers. Water Res 32:3245
 5. Stumpf M, Ternes TA et al (1999) Polar drug residues in sewage and natural waters in the state of Rio de Janeiro, Brazil. Sci Total Environ 225:135
 6. Vieno N, Sillanpää M (2014) Fate of diclofenac in municipal wastewater treatment plant – a review. Environ Int 69:28
 7. Bergmann A, Fohrmann R et al (2011) Zusammenstellung von Monitoringdaten zu Umweltkonzentrationen von Arzneimitteln. Umweltbundesamt, Dessau-Roßlau
 8. Galic N, Hommen U et al (2010) Potential application of population models in the European ecological risk assessment of chemicals II: review of models and their potential to address environmental protection aims. Integr Environ Assess Manag 6:338
 9. Baquero F, Martínez J-L et al (2008) Antibiotics and antibiotic resistance in water environments. Curr Opin Biotechnol 19:260
10. Kidd KA, Blanchfield PJ et al (2007) Collapse of a fish population after exposure to a synthetic estrogen. Proc Natl Acad Sci U S A 104:8897
11. Yüksel S, Kabay N et al (2013) Removal of bisphenol A (BPA) from water by various nanofiltration (NF) and reverse osmosis (RO) membranes. J Hazard Mater 263:307
12. Quinlivan PA, Li L et al (2005) Effects of activated carbon characteristics on the simultaneous adsorption of aqueous organic micropollutants and natural organic matter. Water Res 39:1663
13. Hata T, Shintate H et al (2010) Elimination of carbamazepine by repeated treatment with laccase in the presence of 1-hydroxybenzotriazole. J Hazard Mater 181:1175
14. Prieto-Rodriguez L, Miralles-Cuevas S et al (2012) Treatment of emerging contaminants in wastewater treatment plants (WWTP) effluents by solar photocatalysis using low TiO_2 concentrations. J Hazard Mater 131:211
15. Sirés I, Brillas E et al (2014) Electrochemical advanced oxidation processes: today and tomorrow. A review. Environ Sci Pollut Res 21:8336
16. Andreozzi R, Caprio V et al (1999) Advanced oxidation processes (AOP) for water purification and recovery. Catal Today 53:51
17. Chong MN, Jin B et al (2010) Recent developments in photocatalytic water treatment technology: a review. Water Res 44:1997
18. Neyens E, Baeyens J (2003) A review of classic Fenton's peroxidation as an advanced oxidation technique. J Hazard Mater 98:33
19. Cater SR, Stefan MI et al (2000) UV/H_2O_2 treatment of methyl *tert*-butyl ether in contaminated waters. Environ Sci Technol 34:659
20. Lifka J, Ondruschka B et al (2003) The use of ultrasound for the degradation of pollutants in water: aquasonolysis – a review. Eng Life Sci 3:253

21. Mahamuni NN, Adewuyi YG (2010) Advanced oxidation processes (AOPs) involving ultrasound for waste water treatment: a review with emphasis on cost estimation. Ultrason Sonochem 17:990
22. Suslick KS (1989) Sci Am 260:80
23. Didenko YT, McNamara WB III et al (1999) Hot spot conditions during cavitation in water. J Am Chem Soc 121:5817
24. Braeutigam P, Franke M et al (2010) Role of different parameters in the optimization of hydrodynamic cavitation. Chem Eng Technol 33:932
25. Arrojo S, Nerin C et al (2007) Application of salicylic acid dosimetry to evaluated hydrodynamic cavitation as an advanced oxidation process. Ultrason Sonochem 14:343
26. Braeutigam P, Wu Z-L et al (2009) Degradation of BTEX in aqueous solution by hydrodynamic cavitation. Chem Eng Technol 32:745
27. Gogate PR, Pandit AB (2004) Sonochemical reactors: scale up aspects. Ultrason Sonochem 11:105
28. Kumar PS, Pandit AB (1999) Modelling hydrodynamic cavitation. Chem Eng Technol 22:1017
29. Moholkar VS, Senthil Kumar P et al (1999) Hydrodynamic cavitation for sonochemical effects. Ultrason Sonochem 6:53
30. Gogate PR, Pandit AB (2005) A review and assessment of hydrodynamic cavitation as a technology for the future. Ultrason Sonochem 12:21
31. Amin LP, Gogate PR et al (2010) Optimization of a hydrodynamic cavitation reactor using salicylic acid dosimetry. Chem Eng J 156:165
32. Senthil Kumar P, Siva Kumar M et al (2000) Experimental quantification of chemical effects of hydrodynamic cavitation. Chem Eng Sci 55:1633
33. Suslick KS, Mdleleni MM et al (1997) Chemistry induced by hydrodynamic cavitation. J Am Chem Soc 119:9303
34. Gogate PR, Pandit AB (2004) A review of imperative technologies for wastewater treatment I: oxidation technologies at ambient conditions. Adv Environ Res 8:553
35. Jyoti KK, Pandit AB (2003) Hybrid cavitation methods for water disinfection. Biochem Eng J 14:9
36. Franke M, Braeutigam P et al (2011) Enhancement of chloroform degradation by the combination of hydrodynamic and acoustic cavitation. Ultrason Sonochem 18:888
37. Braeutigam P, Franke M et al (2012) Degradation of carbamazepin in environmentally relevant concentrations in water by Hydrodynamic-Acoustic-Cavitation (HAC). Water Res 46:2469
38. Vichare NP, Gogate PR et al (2000) Optimization of hydrodynamic cavitation using a model reaction. Chem Eng Technol 23:683
39. Gogate PR, Pandit AB (2000) Engineering design methods for cavitation reactors II: hydrodynamic cavitation. AIChE J 46:1641
40. Iben U, Wolf F et al (2015) Optical measurements of gas bubbles in oil behind a cavitating micro-orifice flow. Exp Fluids 56:114
41. Brotchie A, Grieser F et al (2009) Effect of power and frequency on bubble-size distributions in acoustic cavitation. Phys Rev Lett 102:084302
42. Mason TJ, Lorimer JP (2002) Applied sonochemistry: the uses of power ultrasound in chemistry and processing, vol 42. Wiley-VCH, Weinheim
43. Neppiras EA (1980) Acoustic cavitation. Phys Rep 61:159
44. Entezari MH, Kruus P (1996) Effect of frequency on sonochemical reactions II. Temperature and intensity effects. Ultrason Sonochem 3:19
45. Yang L, Rathman JF et al (2005) Degradation of alkylbenzene sulfonate surfactants by pulsed ultrasound. J Phys Chem B 109:16203
46. Henglein A (1995) Chemical effects of continuous and pulsed ultrasound in aqueous solutions. Ultrason Sonochem 2:115
47. Bagal MV, Gogate PR (2014) Degradation of diclofenac sodium using combined processes based on hydrodynamic cavitation and heterogeneous photocatalysis. Ultrason Sonochem 21:1035
48. Keil T, Buttenbender J et al (2012) On the transition from sheet to cloud cavitation. In: Proceedings of the 8th international symposium on cavitation (CAV2012), Singapore

Sonochemical Degradation of Aromatic Compounds, Surfactants, and Dyes in Aqueous Solutions

Kenji Okitsu, Ben Nanzai, and Kandasamy Thangavadivel

Contents

Abstract

Sonochemical degradation of hazardous organic compounds such as dyes, organic acids, aromatic compounds, and surfactants is summarized. The effects of dissolved gas, pH, and the initial concentration of organic compounds were evaluated in aqueous solutions mainly using a standing wave sonication system with 200-kHz ultrasound. The relationship between physicochemical properties of aromatic compounds and rates of degradation is discussed for a range of

K. Okitsu (✉)
Department of Materials Science, Graduate School of Engineering, Osaka Prefecture University, Sakai, Osaka, Japan
e-mail: okitsu@mtr.osakafu-u.ac.jp

B. Nanzai
Faculty of Engineering, Kanagawa University, Kanagawa-ku, Yokohama, Japan

K. Thangavadivel
Graduate School of Engineering, Osaka Prefecture University, Sakai, Osaka, Japan

aromatic compounds. The degradation mechanism and kinetics are described. The effects of various additives, such as inorganic ions, organic additives, inert solid particles, and reactive transition metal powders, and the effect of reaction vessel diameter on the rates of degradation are also addressed.

Keywords

Sonochemical degradation • Dye • Organic acid • Aromatic compound • Surfactant • Mechanism • Kinetics • Additive

Introduction

Advanced oxidation processes (AOPs), such as ozonation, the Fenton reaction, UV/photocatalysis, UV/H_2O_2, radiolysis, and sonolysis, among others, are being assessed as potential treatments of wastewater containing hazardous organic compounds. OH radicals formed in AOPs have high redox potential and high reactivity toward organic compounds. When aqueous solutions are irradiated by ultrasound, bubbles are formed. Quasi-adiabatic collapse produces extremely high temperatures and pressures within the bubbles. Sonochemical reactions induced by collapsing bubbles in water occur in three reaction zones:

(I) Inside the bubbles – temperatures of more than several thousands of degrees and pressures of more than hundreds of atmospheres exist. OH and H radicals are produced by the pyrolysis of water. Gases and volatile organic compounds are thermally degraded.

(II) Interface region of the bubble – relatively high temperatures exist that are intermediate between those inside the bubble and the bulk solution, and therefore thermal degradation of organic compounds takes place. Because the concentration of OH radicals is high, reactions with OH radicals also proceed.

(III) Bulk solution – ambient temperature and pressure exist, but unreacted radicals escaping from region (II) react with organic compounds.

Sonochemical degradation of organic pollutants in water proceeds not only via OH radical reactions but also via direct pyrolysis reactions in the hot spot of collapsing bubbles and at the interface region. In addition to chemical effects, physical effects of cavitation such as shock waves, micro-jets (about 100 m/s), acoustic streams, and intense micro- and macro-mixing are also generated in the solution.

Research is being conducted to assess the viability of sonochemical degradation as a wastewater treatment technology; it aims to (1) clarify the degradation mechanism by analyzing intermediate products (including safety assessment), (2) degrade persistent organic compounds that cannot be degraded by conventional technology (i.e., develop cutting-edge technology), (3) analyze degradation reaction kinetics, (4) produce large-scale processing plants, and (5) enhance the degradation rate (i.e., ensure high degradation efficiency).

In this chapter, sonochemical degradation of hazardous organic compounds such as dyes, organic acids, aromatic compounds, and surfactants is introduced. Degradation reactions are investigated in indirect sonication experiments in aqueous solutions mainly using a 200-kHz ultrasound system. The representative irradiation setup and the characteristics of the reaction vessel are shown in literature [1]. In this system, standing waves are formed by overlapping the irradiated ultrasound with the ultrasound that is formed by the reflection at the interface between the sample solution phase and the gas phase. The effects of dissolved gas, pH, and initial concentration of organic compounds are addressed. By investigating sonochemical degradation of various aromatic compounds, the relationship between the physicochemical properties of compounds and rates of degradation is discussed. The degradation mechanism and kinetics are also described. Because it is important to enhance the degradation rate, the effects of various additives, such as cations, anions, organic additives, inert solid particles, and reactive transition metal powders, and the effect of reaction vessel diameter on the rates of degradation are introduced.

Degradation of Dyes and Organic Acids

A range of dyes are used in the textile, paper and pulp, tannery, and Kraft bleaching industries [2]. Generally, it is reported that the acute toxicity of parent azo dyes is relatively low, but such dyes are cleaved by microorganisms under anaerobic conditions to form potentially carcinogenic aromatic amines [3]. The toxicity or endocrine-disrupting properties of azo dyes are under investigation [4]. To reduce dye pollution, it is important to develop effective treatment methods for wastewater containing such dyes. In this section, sonochemical degradation of azo dyes such as Reactive Red 22 (RR22) and methyl orange (MO) is introduced. Figure 1 shows the changes in RR22 concentration as a function of irradiation time using 200-kHz ultrasound under air or Ar at 20 °C [5]. The decrease of RR22 concentration with irradiation time indicates the progress of RR22 degradation. The degradation rate was faster under Ar than under air because the maximum temperature reached in the collapsing bubbles is higher under Ar. The maximum temperature in a collapsing bubble, T_{max}, can be theoretically determined as

$$T_{max} = \frac{T_0 P_{max}(\gamma - 1)}{P_0}$$

(1)

where T_0 is the temperature of the sample solution, P_{max} is the maximal pressure at the moment of transient collapse, γ is the ratio of the specific heats (C_p/C_v), and P_0 is the sum of the vapor pressures of the solvent and the atmospheric gas pressure [6]. Because γ for Ar (1.67) is higher than that for air (1.4), T_{max} in collapsing bubbles under Ar is higher than that under air. Figure 1 also shows the effect of initial RR22 concentration on the degradation rate (note that the concentration is plotted on a logarithmic scale). A linear relationship was observed for all plots in Fig. 1, suggesting that the degradation may follow pseudo-first-order kinetics. However, it

Fig. 1 Sonochemical decomposition of RR22 in aqueous solution. Ultrasonic irradiation was performed for initial concentrations of (○) 93.2 μM under air, (□) 19.0 μM under air, (△) 9.55 μM under air, (▽) 5.34 μM under air, (●) 93.0 μM under Ar, (■) 18.9 μM under Ar, (▲) 9.54 μM under Ar, and (▼) 5.13 μM under Ar (Reprinted with permission from Ref. [5]. Copyright 2005 Elsevier)
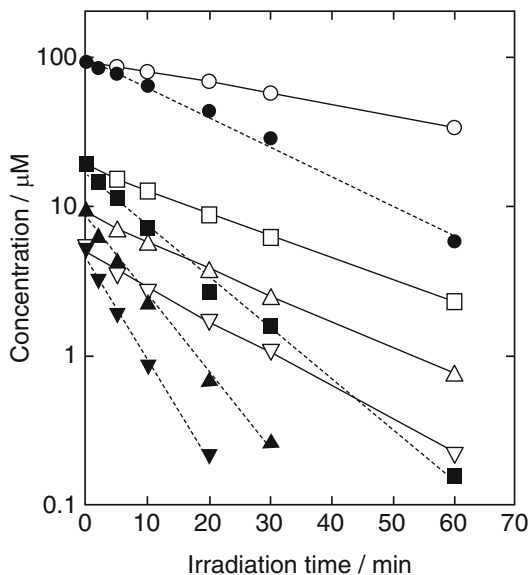
should be noted that the slopes of the plots became steeper as the initial concentration of azo dyes decreased. This means that the pseudo-first-order rate constants calculated from the slopes in Fig. 1 depend on the initial RR22 concentration, i.e., the kinetics observed in Fig. 1 deviate from first-order kinetics.

Sonochemical degradation of MO was also investigated; degradation rates for different initial MO concentrations were measured under Ar at pH 2.0 or 6.5 [5]. It was confirmed for all initial MO concentrations that the degradation rate of MO at pH 2.0 was faster than that at pH 6.5. The reason for this sensitivity to pH is that the chemical structure of MO changes: because the pKa value of MO at 25 °C is 3.44, its chemical structure is different at pH 6.5 and pH 2.0. When organic compounds undergo sonolysis in water, it is reported that hydrophobic compounds tend to accumulate in the interface region of cavitation bubbles [7–12]; consequently, such compounds are more readily pyrolyzed and/or degraded by OH radicals formed by water sonolysis. The octanol–water partition coefficient ($P = C_{octanol}/C_{water}$) indicates the hydrophobicity of a target organic compound, where $C_{octanol}$ and C_{water} are the concentrations of an organic compound in 1-octanol and water, respectively. From the distribution equilibrium of the binary system of 1-octanol and water, it was confirmed that MO at pH 2.0 had higher hydrophobicity than MO at pH 6.5. Therefore, the degradation of MO proceeded faster at pH 2.0 than at pH 6.5.

The behavior of MO degradation as a function of irradiation time at different pH levels was similar to that of RR22 (Fig. 1): the MO concentration decreased exponentially with irradiation time, suggesting that sonochemical degradation of MO obeys pseudo-first-order kinetics. However, the slopes of the lines became steeper as the initial MO concentration decreased, just as they did for RR22. Therefore, sonochemical degradation of MO, like that of RR22, deviated from real
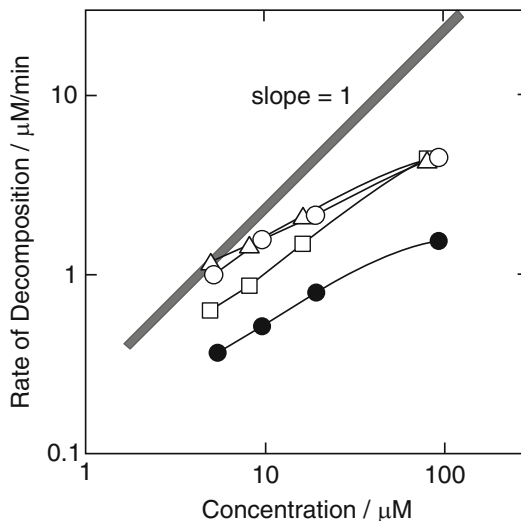
first-order kinetics. To determine the real reaction order, the initial degradation rates
of azo dyes are logarithmically plotted as a function of the initial dye concentration,
as shown in Fig. 2 [5]. The results indicated that the orders of the kinetics for both
RR22 and MO degradation are less than 1. If high initial concentrations of azo dyes
are used in sonochemical degradation experiments, it is possible that large amounts
of degradation intermediates or products will be formed. If this occurs, the kinetics
for degradation of the parent compounds will likely be affected by the intermediates
or products. To avoid such interference in the kinetics analysis, sonochemical
degradation experiments are performed with low initial concentrations of azo dyes
under the shortest possible irradiation times.

Okitsu et al. [5] reported that sonochemical degradation proceeds heteroge-
neously even in aqueous sonication systems with no solid particles present. The
following types of heterogeneity are involved: (1) gas/liquid heterogeneity caused
by cavitation bubbles formed in a liquid system, (2) concentration heterogeneity
caused by the local high concentration of OH radicals at the interface region of
cavitation bubbles [8, 12], (3) temperature heterogeneity caused by the formation of
high-temperature cavitation bubbles in a solution at ambient temperature, and
(4) concentration heterogeneity caused by the local high concentration of organic
solutes at the interface region of cavitation bubbles. The degree of accumulation
(or adsorption) of the organic solutes toward the interface region of the cavitation
bubbles is dependent on the hydrophobicity of the organic solutes [8].

These heterogeneities should affect the reaction kinetics of organic solute degra-
dation in water. A heterogeneous reaction model and the following assumptions
were taken into consideration [5]: (1) a local high concentration of OH radicals exists
at the interface region of collapsing bubbles [8, 12], and thus (2) oxidative degra-
dation of azo dyes quickly occurs in this region by reaction with OH radicals.
(A further experiment in which the effects of an OH radical scavenger were

Fig. 3 Sonolysis of RR22
and MO. Reciprocal plot of
decomposition rate versus
initial concentration. (●)
RR22 under air, (○) RR22
under Ar, (□) MO at pH 6.5,
and (△) MO at pH 2.0
(Reprinted with permission
from Ref. [5]. Copyright 2005
Elsevier)
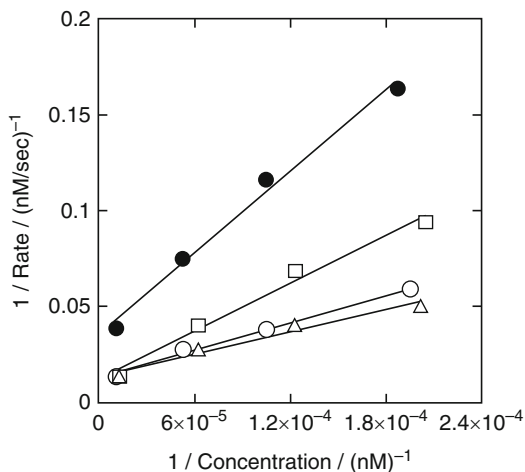
investigated to confirm that direct pyrolysis degradation of azo dyes is a minor
reaction and that degradation occurs mainly by reaction with OH radicals.) Because
the interface zone of cavitation bubbles has relatively high concentrations of OH
radicals and azo dyes, this zone can be considered as an effective reaction site for
sonochemical degradation. The equilibrium constant of azo dyes with respect to the
effective reaction site is defined as $K = k_1/k_{-1}$, where k_1 and k_{-1} correspond to
molecular adsorption (i.e., accumulation) at the site and molecular desorption from
the site before bubbles collapse. After bubbles have collapsed, it is considered that
azo molecules at the effective reaction site are degraded by OH radicals with pseudo-
rate constant k. Consequently, the degradation rate of azo dyes, r, can be determined
as [5]

$$r = \frac{kK[C]}{1 + K[C]} \tag{2}$$

where [C] corresponds to the initial concentration of azo dye. By inverting both sides
of Eq. 2, Eq. 3 can be obtained:

$$\frac{1}{r} = \frac{1}{kK} \frac{1}{[C]} + \frac{1}{k} \tag{3}$$

A plot of $1/r$ versus $1/[C]$ can be prepared as shown in Fig. 3 [5]. Straight line
relationships were observed, indicating that the degradation of azo dyes occurs at the
effective reaction site at the interface region of cavitation bubbles. Joseph
et al. investigated the sonochemical degradation of azobenzene, methyl orange, o-
methyl red, and p-methyl red at 500 kHz and 50 W under air, O_2, or Ar at 288 K;
degradation products and intermediates were identified by high-performance liquid
chromatography with a mass spectrometer through an electrospray interface [13].

Fig. 4 Sonochemical decomposition of butyric acid in aqueous solution of pH 2 under Ar atmosphere. Ultrasonic irradiation was performed for initial concentrations of (◇) 800 μM, (▽) 600 μM, (△) 400 μM, (□) 200 μM, and (○) 100 μM (Reprinted with permission from Ref. [14]. Copyright 2009 Elsevier)
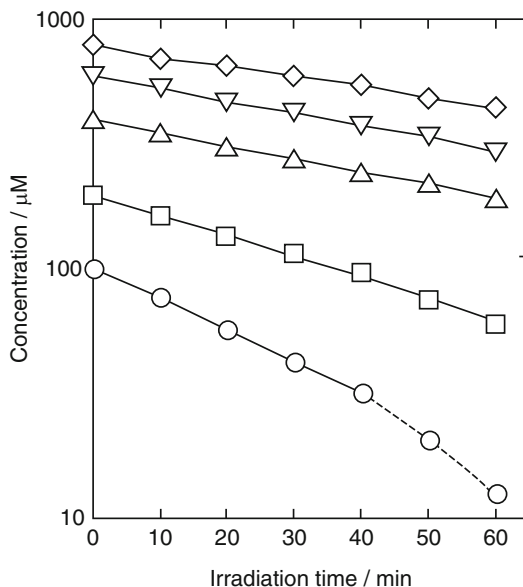
By analyzing the reaction products and intermediates, Joseph et al. proposed that degradation occurred mainly by reaction with OH radicals.

Next, sonochemical degradation of n-butyric acid was investigated using the same irradiation system with 200-kHz ultrasound. n-Butyric acid is an environmental pollutant with an offensive odor. Because n-butyric acid has a simple chemical structure with carboxyl and alkyl groups, it should serve as an effective probe to investigate more clearly the relationship between physicochemical properties and degradation rates of organic solutes.

Figure 4 shows changes in n-butyric acid concentration during sonication under Ar at pH 2. Different initial concentrations of n-butyric acid were used and the data were plotted semilogarithmically [14]. The degradation of n-butyric acid proceeded linearly (Fig. 4), but the slopes of the straight lines became steeper as the initial concentration of n-butyric acid decreased; the same result was found for RR22 and MO degradation described above.

Figure 5 shows the effects of pH on the amount of n-butyric acid degradation when 10-min sonication was performed under Ar at 20 °C [14]. The amount of degradation dramatically changed at around pH 4–5, and the amount of degradation was higher in acidic solutions below pH 4. The pKa value of n-butyric acid (C_3H_7COOH) is 4.63 at 25 °C [15]; as a result, the major chemical structure is C_3H_7COOH at pH less than 4 and $C_3H_7COO^-$ at pH greater than 5. Therefore, the more highly hydrophobic compound C_3H_7COOH was degraded faster than $C_3H_7COO^-$.

To determine the degree of direct pyrolysis of n-butyric acid in collapsing bubbles, the contribution of n-butyric acid vapor pressure must be considered. In solutions of pH greater than 5, $C_3H_7COO^-$ has no vapor pressure, and,

Fig. 5 Effect of pH on sonochemical decomposition of butyric acid under an Ar atmosphere. Irradiation time: 10 min (Reprinted with permission from Ref. [14]. Copyright 2009 Elsevier)
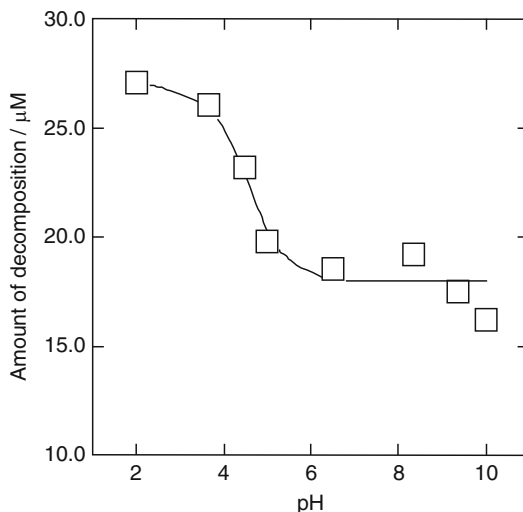

consequently, the pyrolytic degradation of $C_3H_7COO^-$ in collapsing bubbles would be negligible. On the other hand, the vapor pressure of C_3H_7COOH and water at 20 °C is 70.8 Pa and 2340 Pa [16], respectively. Although *n*-butyric acid is relatively volatile and possesses a strong odor, the net amount of *n*-butyric acid vapor is not so large compared to that of water vapor. Taking into account the low vapor pressure of C_3H_7COOH, it is suggested that the pyrolytic degradation of C_3H_7COOH in collapsing bubbles is also likely to be small. For comparison with *n*-butyric acid, sonochemical degradation of benzoic acid, an aromatic compound with a carboxyl group, was also investigated. With respect to the effects of pH and initial concentration of benzoic acid, similar results were obtained for *n*-butyric acid and benzoic acid degradation.

To establish the relative importance of reactions with OH radicals, the effect of OH radical scavenger *t*-butyl alcohol on the rate of *n*-butyric acid degradation was investigated. The sonochemical degradation of *n*-butyric acid (initial concentration: 100 μM) at pH 2 was suppressed by ca. 80 % in the presence of 3 mM *t*-butyl alcohol. This result suggests that *n*-butyric acid molecules are mainly degraded by reaction with OH radicals. Therefore, the degradation mechanism of *n*-butyric acid is considered to be similar to that of azo dyes. The degradation of *n*-butyric acid also followed Langmuir kinetics. An outline of the effective reaction zone for sonochemical degradation of *n*-butyric acid is shown in Fig. 6.

Degradation of Aromatic Compounds

Large amounts of aromatic compounds are used in industry and agriculture, e.g., phenols are used as raw materials for dyes, pharmaceuticals, agricultural chemicals, synthetic fibers, and synthetic resins, among others. However, most aromatic
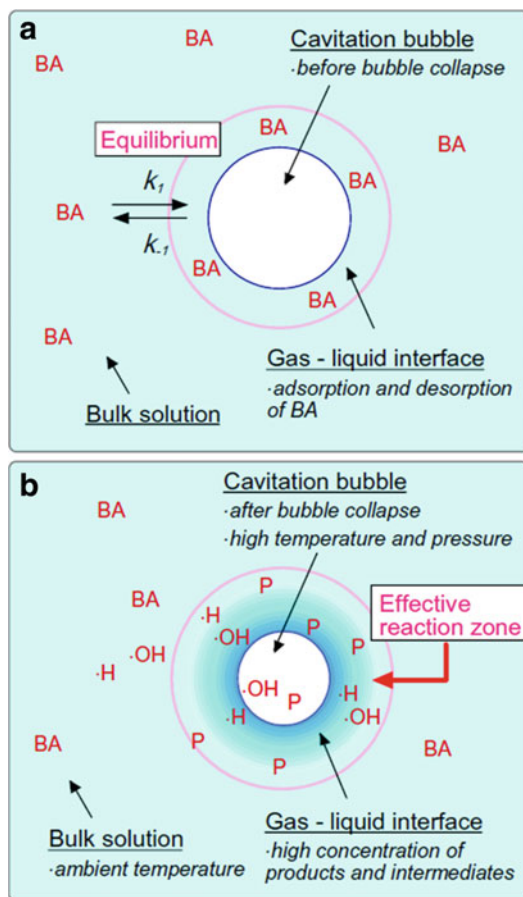
compounds are harmful [17, 18]; therefore, it is important to develop degradation techniques for such compounds. Nanzai et al. [19] reported the sonochemical degradation of 12 types of aromatic compounds (concentration: 100 μM) in water using a standing wave sonication system with 200-kHz ultrasound at 25 °C under Ar. It was confirmed that the initial degradation rate depended on the type of aromatic compound: the initial rate (in increasing order) was 2.2 μM min^{-1} for nitrobenzene, 2.7 μM min^{-1} for aniline, 4.1 μM min^{-1} for phenol, 4.3 μM min^{-1} for benzoic acid, 4.5 μM min^{-1} for salicylic acid, 6.5 μM min^{-1} for 2-chlorophenol, 7.0 μM min^{-1} for 4-chlorophenol, 8.8 μM min^{-1} for styrene, 8.9 μM min^{-1} for chlorobenzene, 9.3 μM min^{-1} for toluene, 11.2 μM min^{-1} for ethylbenzene, and 13.4 μM min^{-1} for *n*-propylbenzene.

To investigate the reasons for the above differences, the observed rates of sonochemical degradation for each aromatic compound were plotted as a function of various parameters. Figure 7 shows the relationship between the initial degradation rate of sonochemical degradation and the rate constants of reactions of aromatic

Fig. 7 Relationship between the rates of sonochemical decomposition of various aromatic compounds and rate constants of reaction of each organic compound with OH radicals (Reprinted with permission from Ref. [19]. Copyright 2008 Elsevier)
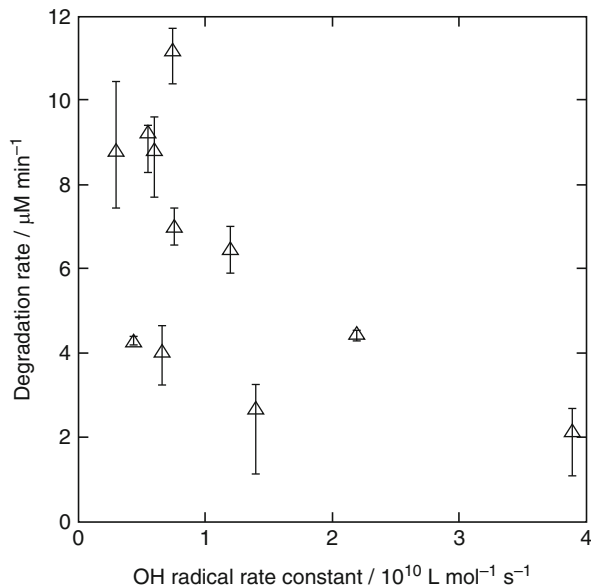
compounds with OH radicals; the rate constants were obtained from the literature [20] in which the rate constants were measured by methods other than sonochemical reactions. If aromatic compounds are mainly degraded by reactions with OH radicals, the rate of sonochemical degradation should increase with increasing OH radical rate constant. However, it is clear in Fig. 7 that the rates of degradation are not correlated with the rate constants.

Figure 8 shows the relationship between the initial rate of sonochemical degradation and vapor pressure of aromatic compounds. Figure 8 suggests that, for those with vapor pressures greater than 10^{-1} mmHg, aromatic compounds with higher volatility are more rapidly degraded. This is because highly volatile compounds can more readily vaporize into bubbles and undergo pyrolytic degradation on bubble collapse. The concentration of OH radicals inside the bubbles and in the interface region of bubbles is likely to be high, allowing degradation by OH radicals to proceed. When the relationship between the rate of sonochemical degradation and Henry's law constant of aromatic compounds was plotted instead of the vapor pressure, a similar pattern was observed [19]. Therefore, the vapor pressure and Henry's law constant of organic compounds are likely important parameters relating to the degradation rate.

Figure 9 shows the relationship between the initial degradation rate of sonochemical degradation of aromatic compounds and their log P values [19]. The log P values of the compounds are as follows: nitrobenzene (1.85), aniline (0.9), phenol (1.46), benzoic acid (1.87), salicylic acid (2.26), 2-chlorophenol (2.15), 4-chlorophenol (2.33), styrene (2.95), chlorobenzene (2.84), toluene (2.73), ethylbenzene (3.15), and n-propylbenzene (3.69). As described in section "Degradation of Dyes and Organic Acids," the hydrophobicity of an organic compound is important in determining the degree of degradation occurring in the effective reaction

Fig. 8 Relationship between the rates of sonochemical decomposition of various aromatic compounds and vapor pressure (Reprinted with permission from Ref. [19]. Copyright 2008 Elsevier)
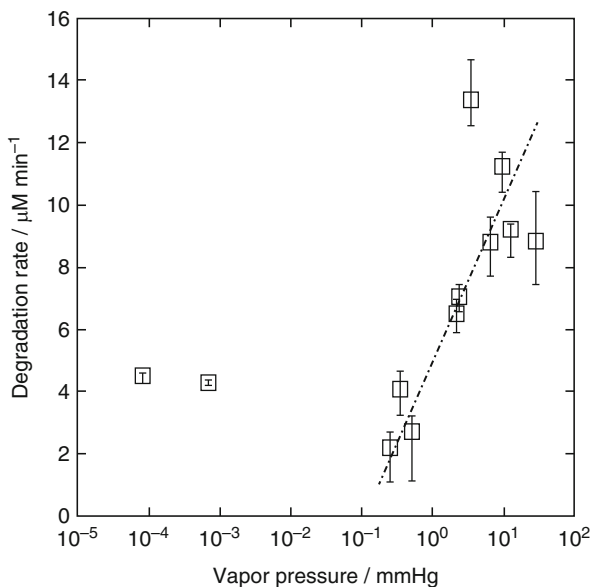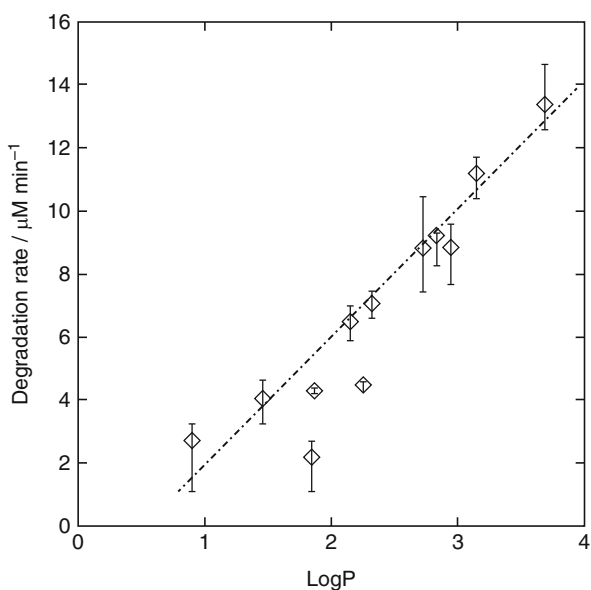

Fig. 9 Relationship between the rates of sonochemical decomposition of various aromatic compounds and log P (Reprinted with permission from Ref. [19]. Copyright 2008 Elsevier)

zone. Aromatic compounds with larger log P values correspond to compounds with higher hydrophobicity. From Fig. 9, it should be noted that a better correlation was observed between degradation rate and log P than between degradation rate and vapor pressure of aromatic compounds [19].

Several researchers have reported that log P is also a good indicator of degradation rate for substances other than these aromatic compounds, e.g., Kirschenbaum and Riesz [21] investigated sonochemical degradation of eight cyclic nitroxides, such as 2,2,6,6-tetramethylpiperidin-1-oxyl, in an Ar-saturated aqueous solution using a 354-kHz standing wave sonication system. They reported that the amount of degradation after 2 min of sonication was linearly correlated to the log P values of these cyclic nitroxides.

The surface excess may also be used as an indicator of the hydrophobicity of organic compounds [22–24]. An organic compound with high surface excess tends to exist at the gas–liquid interface with a high probability, and thus the surface excess may directly relate to the rate of sonochemical degradation when the degradation occurs at the gas–liquid interface of bubbles. In general, the surface excess is calculated (using the Gibbs–Duhem equation) from the change in surface tension of an aqueous sample solution of the target organic compound. If the solubility of a target compound is quite low, it is difficult to measure the change in surface tension. In such cases, log P would be appropriate to understand the hydrophobicity.

However, it should be noted that log P and surface excess are obtained only when the target organic compound is in equilibrium. In the sonochemical degradation, bubbles oscillate and finally collapse in an ultrasonic field in a short time. Such short time may not have time to reach the equilibrium of organic compounds to accumulate the interface region of cavitation bubbles. Further studies are needed to clarify the kinetics for the sonochemical degradation.

Degradation of Surfactants and Analysis of Interface of Cavitation Bubbles

As described above, during acoustic cavitation, the following two reaction sites are important for the effective degradation of organic compounds: (I) inside the bubbles and (II) the interface region of bubbles. Because the role and characteristics of the interface region of cavitation bubbles with respect to the sonochemical degradation of organic compounds are still unclear, the sonochemical degradation of linear alkylbenzene sulfonates (LASs, anionic surfactants) was investigated: the target compounds were p-octylbenzene sulfonate (LAS C_8), p-nonylbenzene sulfonate (LAS C_9), and p-dodecylbenzene sulfonate (LAS C_{12}) [25].

Figure 10 shows the rates of degradation of LAS as a function of LAS concentration in the range of 10–250 μM. The degradation rate in the low concentration range from 10 to 40 μM was in the following order: LAS C_8 > LAS C_9 > LAS C_{12}. This order was opposite to the order of the target compounds' hydrophobicities, which were deduced from the length of their alkyl chains as LAS C_8 < LAS C_9 < LAS C_{12}. Nanzai et al. [25] reported that the sonochemical degradation rates of LAS with shorter alkyl chains were higher because their diffusion rate is higher, meaning that they can more easily accumulate at the interface region of cavitation bubbles. These results are very similar to those of previous reports in which sonochemical

Fig. 10 Plot of initial LAS concentrations and degradation rates. Each value is the average of three to six sonication trials; error bars indicate the standard deviation (Reprinted with permission from Ref. [25]. Copyright 2009 American Chemical Society)
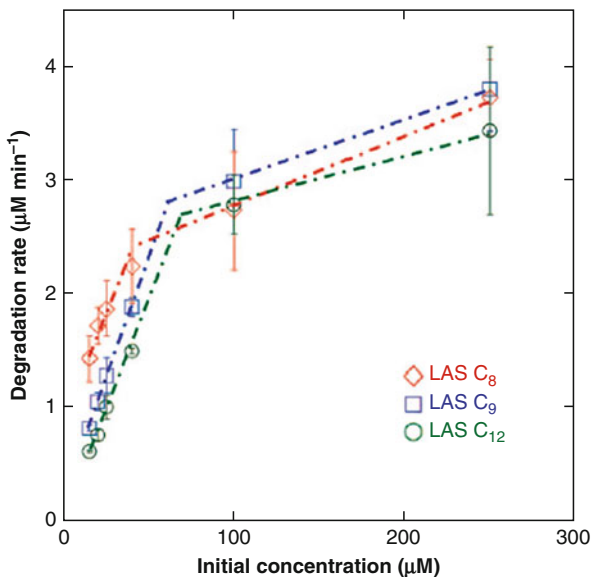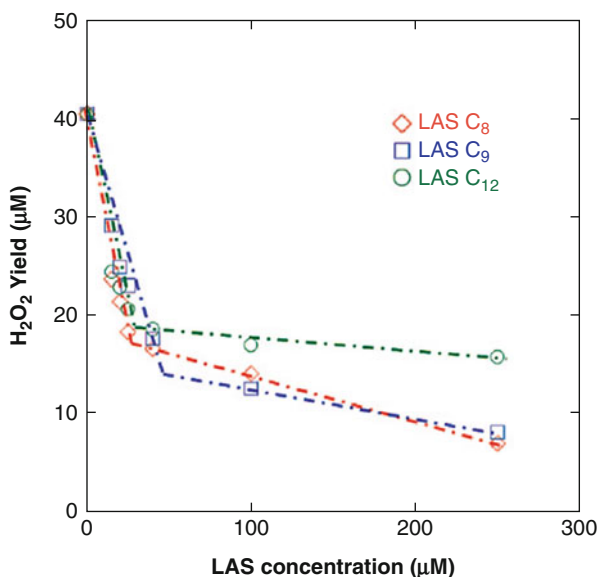

Fig. 11 Plot of LAS concentration and yield of H_2O_2 formed during sonochemical degradation of LAS (Reprinted with permission from Ref. [25]. Copyright 2009 American Chemical Society)

degradation of LAS C_8 and LAS C_{12} was investigated using continuous-wave ultrasound or pulsed ultrasound irradiation systems [26, 27].

To investigate quantitatively how the OH radicals are consumed by reactions with LAS, the yield of H_2O_2 was measured as a function of LAS concentration. Figure 11 indicates that the H_2O_2 yield decreases with increasing LAS concentration, and the H_2O_2 yield has an elbow point at 20–50 μM of LAS [25]. When the concentration of

LAS is lower than the elbow point, LAS reacts with OH radicals effectively. Because of their accumulation properties, direct thermal degradation of LAS should also occur. In the concentration range of 100–250 μM, the order of the degradation rates among LAS$_8$, LAS$_9$, and LAS$_{12}$ is unclear (Fig. 11). This may be a result of complex reactions, as described in the next paragraph.

LAS degradation rates reportedly obey Langmuir kinetics only at concentrations less than 40 μM; on the other hand, the rates do not obey Langmuir kinetics at concentrations higher than 40 μM [25]. This is because, for higher LAS concentrations, larger amounts of intermediates or products are formed, and these can affect reaction kinetics and cavitation dynamics. For example, when high LAS concentrations are used in sonochemical degradation experiments, the ratio of the rates of OH radical oxidation to pyrolysis reactions changes, and, consequently, the degradation mechanism changes. As a result, the types and amounts of intermediates or products also change, and this affects the characteristics of cavitation bubbles. In addition, when the amounts of intermediates or products increase, OH radical scavenging reactions occur by reactions with intermediates or products, thereby decreasing the LAS degradation rate. Furthermore, the temperature of collapsing bubbles is reduced by the production of gaseous intermediates or products, which generally have lower γ values than those of Ar or air.

The degradation rate at higher LAS concentrations was also investigated [28]. Figure 12 shows the relationship between the degradation rate and initial concentration of LAS. The degradation rate increased with increasing LAS concentration at lower concentrations, but the rate started to decrease at higher concentrations. The maximum rate was observed at 2.50 mM for LAS C$_8$, 1.25 mM for LAS C$_9$, and 0.25 mM for LAS C$_{12}$. The critical micelle concentration (CMC) of each LAS measured by an electrical conductivity method at 40 °C was 13.8 mM for LAS C$_8$, 7.1 mM for LAS C$_9$, and 1.0 mM for LAS C$_{12}$. The order of the degradation rate was the same as that of the CMC, but the concentration corresponding to the maximum rate was about four to six times lower than the CMC. Taking into account the accumulation properties of LAS, the concentration of LAS in the interface region of cavitation bubbles is likely higher than that of the bulk solution. If considerable amounts of LAS are concentrated in the cavitation bubble interface region, micelle formation may occur there even if the bulk concentration of LAS is less than the CMC.

Degradation of Perfluorooctane Sulfonates and Perfluorooctanoate

Perfluorooctane sulfonates (PFOS) have been commercially available in the form of PFOS salts and PFOS derivatives [29]. PFOS derivatives were mainly used to give grease, oil, and water resistance to materials such as textiles [29]. Perfluorooctanoate (PFOA) is similar to PFOS and had similar applications. Because of their extensive use in the past and their inertness in chemical and biological systems, PFOS and PFOA exist in the environment throughout the world [29–31]. The toxicity of PFOS and PFOA is under investigation [32, 33]. These compounds are generally difficult
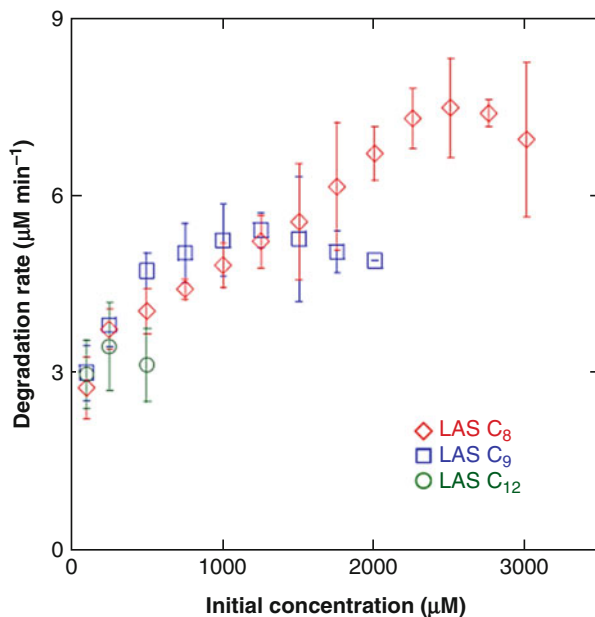
Fig. 12 Plot of initial LAS concentrations and degradation rates of LAS. Each value is the average of three to six sonication trials; error bar indicates the standard deviation (Reprinted with permission from Ref. [28]. Copyright 2009 Springer)

to degrade by conventional methods, and they therefore remain in the environment with very long half-lives. Consequently, PFOS and PFOA are categorized as persistent organic pollutants. Moriwaki et al. [34] reported the sonochemical degradation of PFOS and PFOA for the first time in 2005. They confirmed that the PFOS degradation rate followed pseudo-first-order kinetics and that PFOS degradation was faster under Ar than under air. Figure 13a, b show electrospray ionization mass spectrometry (ESI-MS) spectra of PFOS and PFOA solutions, respectively, after 60 min of sonication. Both figures show that the lengths of PFOS and PFOA alkyl chains become shorter as a result of ultrasonic irradiation [34]. Figure 14a, b show the concentrations of products and intermediates formed from the sonolysis of PFOS and PFOA, respectively. For PFOS, the amounts of PFOA, CF_3COO^-, and $C_2F_5COO^-$ increased with irradiation time. For PFOA, the amounts of CF_3COO^- and $C_2F_5COO^-$ increased with irradiation time. To clarify the degradation mechanism, the Fenton reaction (OH radical reaction induced by the reaction of Fe^{2+} with H_2O_2) was investigated. Because PFOS was not degraded by reaction with OH radicals generated by the Fenton reaction, it was confirmed that PFOS is thermally degraded at the interface region of cavitation bubbles [34]. Campbell et al. [35] and Cheng et al. [36] reported Langmuir kinetics for the sonochemical degradation of PFOS and PFOA. The effects of salts on the degradation of PFOA are discussed in the following section.
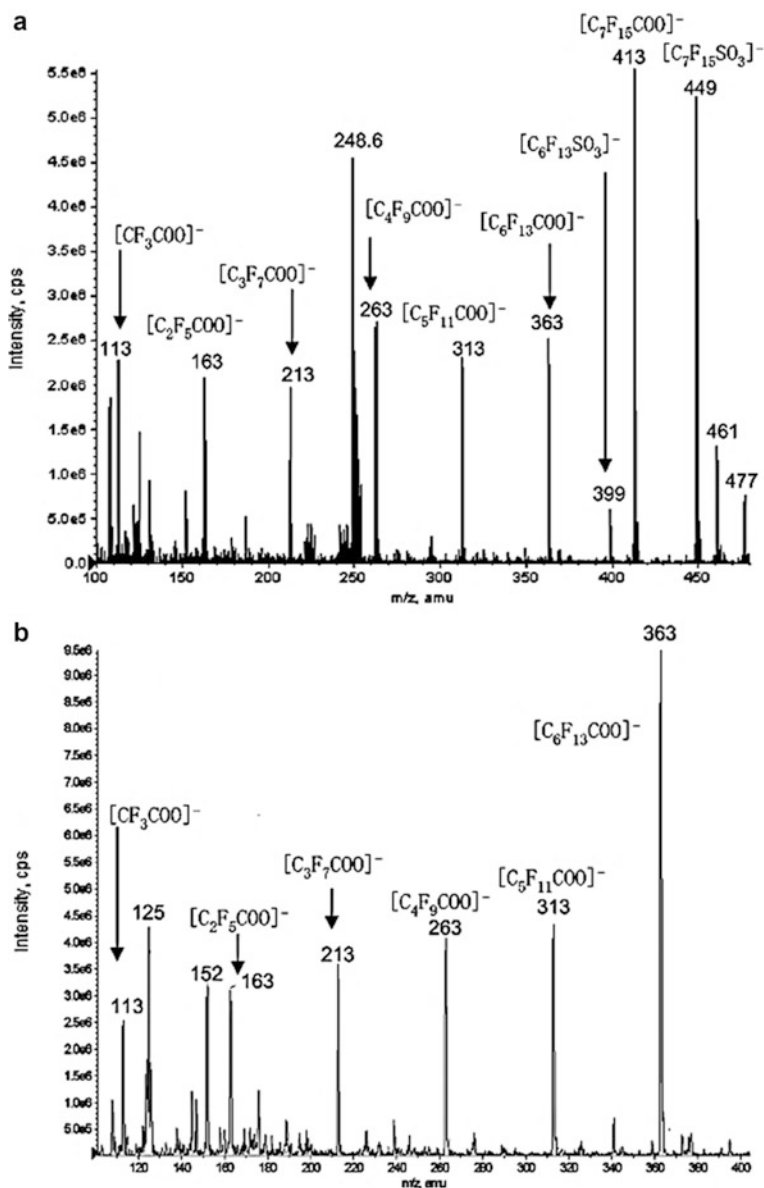
Fig. 13 (**a**) ESI-MS spectrum of PFOS solution after ultrasonic irradiation (60 min). A negative-ion mode was used. Scan range: 100–480. (**b**) ESI-MS spectrum of ion peaks assigned as products of PFOA degradation by ultrasonic irradiation (60 min). A negative-ion mode was used. Scan range: 100–410 (Reprinted with permission from Ref. [34]. Copyright 2005 American Chemical Society)

Fig. 14 Changes in
concentration of
$CF_3(CF_2)_nCOO^-$ (n = 0–5)
ions during sonication of
PFOS (a) and PFOA (b)
(Reprinted with permission
from Ref. [34]. Copyright
2005 American Chemical
Society)
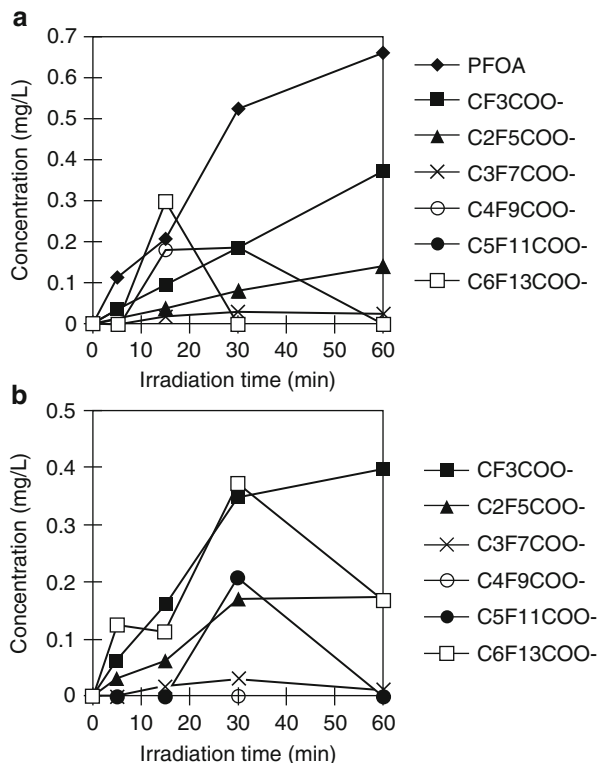
Effect of Inorganic Cations and Anions

As described above, a range of organic compounds can be degraded in water by ultrasonic irradiation via OH radical and/or pyrolysis reactions. However, at present, the rates of degradation are not high enough for practical application. Consequently, effort is being focused on accelerating the degradation rates. The effects of inorganic cations and anions are being actively investigated. For example, the addition of Fe^{2+} enhances the rate of sonochemical degradation of organic compounds [13, 37–39]. This is because the reaction of Fe^{2+} with sonochemically formed H_2O_2 occurs to form OH radicals as follows:

$$Fe^{2+} + H_2O_2 \rightarrow Fe^{3+} + \bullet OH + OH^- \tag{4}$$

Equation 4 is known as the Fenton reaction. Yim and Maeda reported the effect of added Fe^{2+} or Fe^{3+} on nonylphenol degradation under Ar and oxygen [39]. When the sonication of 30 μM nonylphenol was investigated as a function of Fe^{2+} concentration under Ar, the maximum degradation rate was observed in the range of 80–100 μM Fe^{2+}. For concentrations higher than 100 μM Fe^{2+}, the degradation rates became lower. This was likely because the reaction of OH radicals with Fe^{2+} occurred, decreasing the

amount of OH radicals available for nonylphenol degradation. In the presence of Fe^{3+} instead of Fe^{2+}, the maximum degradation rate was observed at around $50\,\mu M\ Fe^{3+}$. It is suggested that the following reactions occur:

$$Fe^{3+} + H_2O_2 \rightarrow Fe-OOH^{2+} + H^+ \tag{5}$$

$$Fe-OOH^{2+} \rightarrow Fe^{2+} + \bullet OOH \tag{6}$$
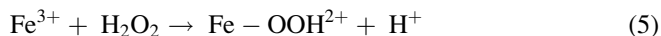
The resulting •OOH radicals react with nonylphenol. For Fe^{3+} concentrations higher than 50 μM, the reaction of •OOH radicals with Fe^{3+} takes place, thereby decreasing the amount of •OOH radicals available for nonylphenol degradation. In addition, the mineralization (conversion to inorganic compounds) ratio for nonylphenol sonolysis was larger under O_2 with Fe^{3+} than under Ar with Fe^{2+}.
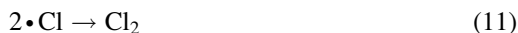
The addition of some anion types is also effective in enhancing degradation rates. Sonochemical degradation rates of Acid Blue 40 and methylene blue are reportedly enhanced by the addition of HCO_3^- or CO_3^{2-} [40]. This is because •OH radicals formed in the sonolysis of water react with HCO_3^- or CO_3^{2-} to produce CO_3^- radicals, which are then available for reactions. OH radicals and $•CO_3^-$ radicals have different reactivities and lifetimes; consequently, the effectiveness of these radicals for enhancing the degradation of organic compounds is different. For example, if organic compounds have some resistance against $•CO_3^-$ radicals, the degradation rate will become slower in the presence of CO_3^{2-}; conversely, the degradation rate of organic compounds that react with $•CO_3^-$ radicals will become faster in the presence of CO_3^{2-}. The sonochemical degradation rate of malachite green can be enhanced by the addition of Br^- [41]. The enhancement mechanism is similar to that for the addition of HCO_3^- or CO_3^{2-}: •OH radicals formed by water sonolysis react with Br^- to produce •Br radicals. Recently, it was reported that sonochemical degradation of PFOA was enhanced by the addition of carbonate ions [42] and sulfate ions [43]; the carbonate and sulfate radicals formed are suggested to act as effective reactants for PFOA.

The effects of NaCl or Na_2SO_4 on sonochemical degradation of organic compounds have also been investigated; however, the experimental results are sometimes contradictory. For example, Seymour and Gupta reported that sonochemical degradation rates of chlorobenzene, p-ethylphenol, and phenol were enhanced by the addition of NaCl under 20-kHz ultrasound irradiation [44]. In contrast, Chen and Smirniotis reported that the rates of sonochemical degradation of phenol decreased on the addition of NaCl or Na_2SO_4 under 20-kHz ultrasound irradiation [45]. Furthermore, the addition of NaCl or Na_2SO_4 slightly affected or did not enhance the rates of sonochemical degradation of Rhodamine B [46] and crystal violet [47]. Uddin and Okitsu recently investigated the effects of NaCl and Na_2SO_4 on the rates of sonochemical degradation of several phenolic compounds under Ar during 200-kHz ultrasound irradiation [48]. They suggested that two phenomena are induced by adding such salts in an aqueous solution. One phenomenon is that phenolic compounds tend to accumulate at the interface region of cavitation bubbles when such salts are added, resulting in the enhancement of the sonochemical degradation rate. The other phenomenon is that the solubility of Ar gas in aqueous

solutions decreases with increasing concentrations of such salts, resulting in a decreased sonochemical degradation rate. This is because of decreases in the number of cavitation bubbles and the rate of •OH radical formation.

Effect of Organic Additives

The addition of CCl_4 has been reported to enhance the degradation rates of organic compounds. Figure 15 shows the effect of CCl_4 concentration on MO degradation under Ar; the MO concentration sonicated in solution was determined spectrophotometrically. The MO degradation rate increased with increasing CCl_4 concentration [49]. The reason for this is that sonochemical degradation of CCl_4 produces active species as follows:

$$CCl_4 \rightarrow \bullet CCl_3 + \bullet Cl \tag{7}$$

$$\bullet CCl_3 \rightarrow : CCl_2 + \bullet Cl \tag{8}$$

$$2 \bullet CCl_3 \rightarrow C_2Cl_6 \tag{9}$$

$$2 : CCl_2 \rightarrow C_2Cl_4 \tag{10}$$

$$2 \bullet Cl \rightarrow Cl_2 \tag{11}$$

$$Cl_2 + H_2O \rightarrow HCl + HClO \tag{12}$$

Because CCl_4 is highly hydrophobic and volatile, it can be pyrolyzed inside collapsing cavitation bubbles and at their interface [50, 51]. Water pyrolysis also occurs

Fig. 15 Changes in MO concentration at pH 2 under ultrasonic irradiation in the absence and presence of CCl_4. (○) 0 ppm, (△) 50 ppm, (□) 100 ppm, and (●) 150 ppm (Reprinted with permission from Ref. [49]. Copyright 2008 Elsevier)
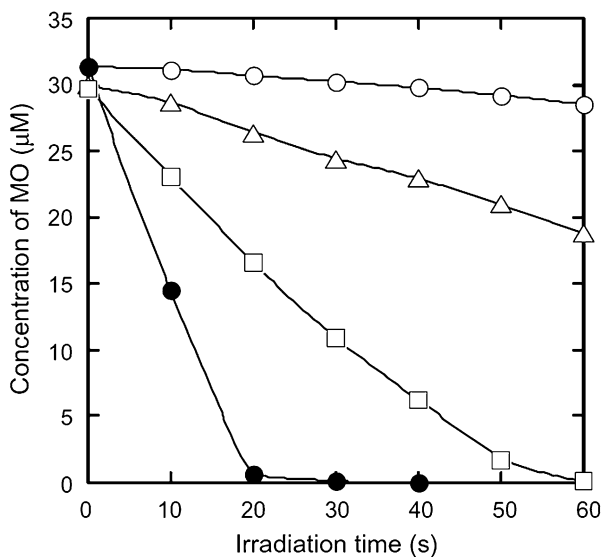
in the same regions, but the rate of the water pyrolysis is slow compared to that of CCl_4 pyrolysis because the bond energy of Cl–CCl_3 (288 kJ mol^{-1}) is much smaller than that of H–OH (497 kJ mol^{-1}) [52]. As a result, larger amounts of active species such as •Cl, Cl_2, and HClO are produced and effectively react with MO compared to the reaction with OH radicals. The addition of CCl_4 can reportedly enhance the degradation rate of Rhodamine B [45], C.I. Acid Orange 8 [53], methyl parathion (pesticide) [54], and dichlorvos (pesticide) [55]. However, because CCl_4 is highly toxic, more appropriate additives need to be explored.

A different analytical approach was developed to determine the concentration of CCl_4 spectrophotometrically by using the sonochemical decolorization of MO [56]: the concentration of CCl_4 in the range of 0.4–20 mg L^{-1} can be determined with a detection limit of 0.19 mg L^{-1}. The addition of CCl_4 is also useful to understand the chemical efficiency of hydrodynamic cavitation. Suslick et al. [57] reported that the chemical effects of hydrodynamic cavitation can be spectrophotometrically measured by analyzing the oxidation of I$^-$ in the presence of CCl_4. They found that the chemical effects of hydrodynamic cavitation are not high compared to those of acoustic cavitation [57].

There are many reports concerning the effects of t-BuOH on the sonochemical degradation rates of organic compounds. In general, t-BuOH acts as an OH radical scavenger; therefore the sonochemical degradation rate of a target organic compound decreases with increasing concentrations of t-BuOH. Recently, Ince et al. and Merouani et al. reported that the sonochemical degradation rate of nonylphenol [58] and Rhodamine B [46] was slightly enhanced by the addition of small amounts of t-BuOH. The reason for this enhancement is not clear at present. Further study is needed to clarify the mechanism of this phenomenon.

Effect of Unreactive Solid Particles

The effects of various types of particles on sonochemical reactions have been investigated with a view to enhancing the chemical effects of acoustic cavitation. Keck et al. [59] reported the effects of concentration and size of quartz particles on the sonolysis of terephthalic acid at ultrasound frequencies of 206, 353, 620, and 1028 kHz under Ar/O_2 (4:1). They found that quartz particles (concentration, 10 g/L; size, 3 μm) had a positive effect at 206 kHz, but had negative effects at 353, 620, and 1028 kHz. Keck et al. reported that the positive effect was likely caused by the formation of asymmetric bubbles with large surface areas. The increased surface area may enable more radicals to migrate from their formation site to the bulk solution and thereby react with more organic compounds in the bulk solution. Iida et al. reported that the sonochemical degradation rate of MO was enhanced by up to 50 % by the addition of appropriate α-alumina powder (average size: 56 μm) [60]. They also investigated the effects of activated alumina powders on the adsorption of MO and found that sonochemical degradation of MO simultaneously occurred in acidic solutions.

Nakui et al. [61] reported the effects of coal ash particles (size: 53–106 μm) on the rate of phenol degradation. The coal ash was mainly composed of SiO_2 62.0 wt%,

Fig. 16 Initial rate of sonochemical degradation of phenol as a function of amount of added coal ash. Initial concentration of phenol: 106 μmol/L (Reprinted with permission from Ref. [61]. Copyright 2007 Elsevier)
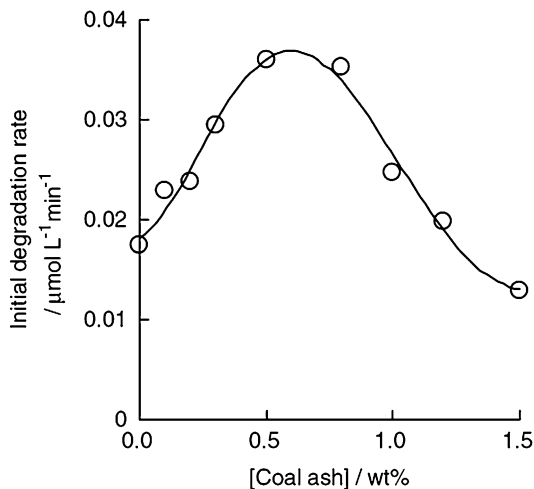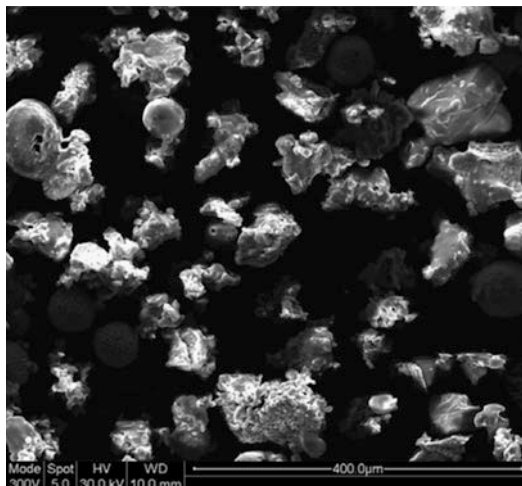

Fig. 17 Low-magnification scanning electron microscope image of coal ash (53–106 μm) (Reprinted with permission from Ref. [61]. Copyright 2007 Elsevier)

Al_2O_3 21.2 wt%, Fe_2O_3 3.9 wt%, and CaO 2.0 wt%. Figure 16 shows the effects of coal ash on the phenol degradation rate under air: the degradation rate doubled on the addition of 0.5 wt% of coal ash. Figure 17 shows a scanning electron microscope image of coal ash particles, indicating pores and uneven surfaces. Such pores and surface roughness act as nucleation sites for cavitation bubbles, resulting in the formation of larger numbers of bubbles than in the absence of coal ash particles. They also measured the effects of coal ash on the yield of H_2O_2 in the sonolysis of water in the absence of phenol. It was found that the yield of H_2O_2 was the highest at around 0.5 wt% of coal ash. This result was in good agreement with the results of phenol degradation in the presence of coal ash. The phenol degradation rate decreased with amounts of coal ash greater than 0.5 wt% (Fig. 16). This decrease

may result from ultrasound waves being scattered or absorbed by the coal ash, leading to the formation of weaker standing waves in the solution and thus lower numbers of cavitation bubbles.

The effects of TiO_2 particles on the degradation of organic pollutants have been investigated by several research groups. Shimizu et al. reported that the rate of sonochemical degradation of methylene blue was enhanced by the addition of TiO_2 particles when the experiments were performed in the dark [62]. In addition, because TiO_2 particles can act as a photocatalyst, the sonochemical degradation of organic pollutants in the presence of TiO_2 particles has also been investigated under UV light irradiation. This is called sonophotocatalysis. He et al. studied sonophotocatalytic degradation of methyl orange [63] and p-chlorobenzoic acid [64] in aqueous solutions, and the results were compared to those obtained from separate sonochemical and photocatalytic degradation. They reported that the intermediate products formed during sonophotocatalytic degradation were more effectively degraded to inorganic compounds compared to separate sonochemical or photocatalytic degradation. It has been suggested that sonochemical and photocatalytic degradation of organic pollutants occurs simultaneously in sonophotocatalytic degradation and that the physical effects of ultrasound are important in enhancing the mass transfer of the organic solutes and the surface cleaning of photocatalyst particles.

Effect of Reactive Transition Metal Powders

When aqueous solutions are irradiated by lower-frequency ultrasound, strong physical effects such as shock waves and micro-jets are formed. Such physical effects can be used to reduce the toxicity of hazardous chemicals [65–67]. Figure 18 shows the effects of Cu, Fe, and Zn powders on CCl_4 degradation under Ar using a 28-kHz ultrasound cleaning bath [67]. The result in the absence of metal powder is indicated as "none" in Fig. 18.

Fig. 18 Decomposition of CCl_4 by ultrasonic irradiation in the absence and presence of metal powders under Ar. Conditions: CCl_4, 1000 ppm; metal powder, 0.1 g; and 10-min irradiation by ultrasound cleaning bath at 28 kHz (Reprinted with permission from Ref. [67]. Copyright 2006 The Japan Society for Analytical Chemistry)
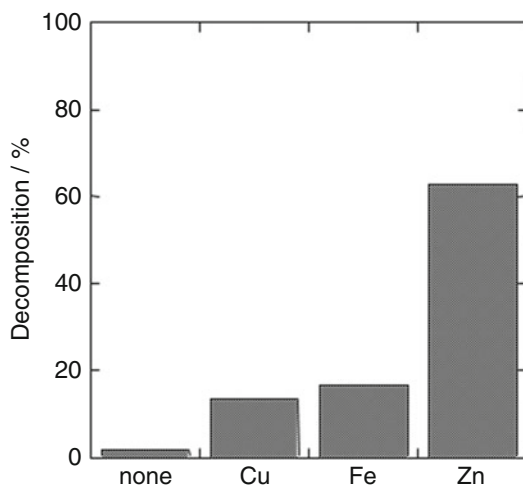
The degradation rates increased in the order none $<$ Cu $<$ Fe $<$ Zn, and the rate in the presence of Zn powder was about 33 times higher than that in the absence of metal powder. The effects of ultrasound frequency were also investigated: the results were that the degradation rate was in the order 100 kHz $<$ 45 kHz $<$ 28 kHz [67]. It could be considered that the stronger physical effects produced by the collapse of larger bubbles removed inactive oxide surfaces of metal powders or reduced the particle size, resulting in the enhancement of the reductive dechlorination reactions of CCl_4.

Effect of Reaction Vessel Diameter in an Indirect Sonication System

When ultrasound irradiation is performed indirectly, the reaction vessel is generally set above an ultrasound transducer to produce a standing wave in the irradiated solution. Although the transducer is of fixed size, the size and shape of the reaction vessel can be easily changed. Nanzai et al. reported the effects of reaction vessel diameter on the formation of H_2O_2 in the sonolysis of pure water and the formation of Cl^- in the sonolysis of 1,2,4-trichlorobenzene in aqueous solution under Ar. Figure 19 shows the sonication setup for a 200-kHz ultrasonic unit [68] and reaction vessels with diameters of 20, 50, 90, and 120 mm. For all experiments, the transducer diameter was 65 mm and the height of the solutions was kept at 36 mm. Figure 20 indicates the effects of the reaction vessel diameter on the yield of H_2O_2 and Cl^- during sonolysis of pure water and of 1,2,4-trichlorobenzene in aqueous solution, respectively. Both yields increased with increasing diameter up to 90 mm and then decreased for 120 mm. To address this phenomenon, the energy injected into the reaction vessel, the acoustic directionality coefficient as a function of ultrasound propagation angle, and the sonochemiluminescence emitted from luminol solutions were measured. When the 120-mm-diameter reaction vessel was used for sonication, the bubble nuclei likely escaped from the sonication zone to the outer nonsonication zone, and thus the number of active cavitation bubbles decreased [68]. Under indirect sonication, the ratio of the reaction vessel diameter to the transducer diameter may be the key to achieving optimum performance.

Conclusion and Future Directions

The sonochemical degradation rates of hazardous organic compounds are affected by the irradiation conditions. The type of dissolved gas is a major parameter because the gas is the origin of cavitation bubbles. Gases with high specific heat ratios (γ) and low thermal conductivities should be used to produce collapsing bubbles that attain high temperatures. The solubility of the gas also affects the number of cavitation bubbles. Therefore, these gas properties affect the sonochemical degradation rate of organic compounds. When considering the pH of the solution, the pKa value of the organic compound must be taken into account because the hydrophobicity of a compound affects its accumulation behavior at the interface of cavitation bubbles:
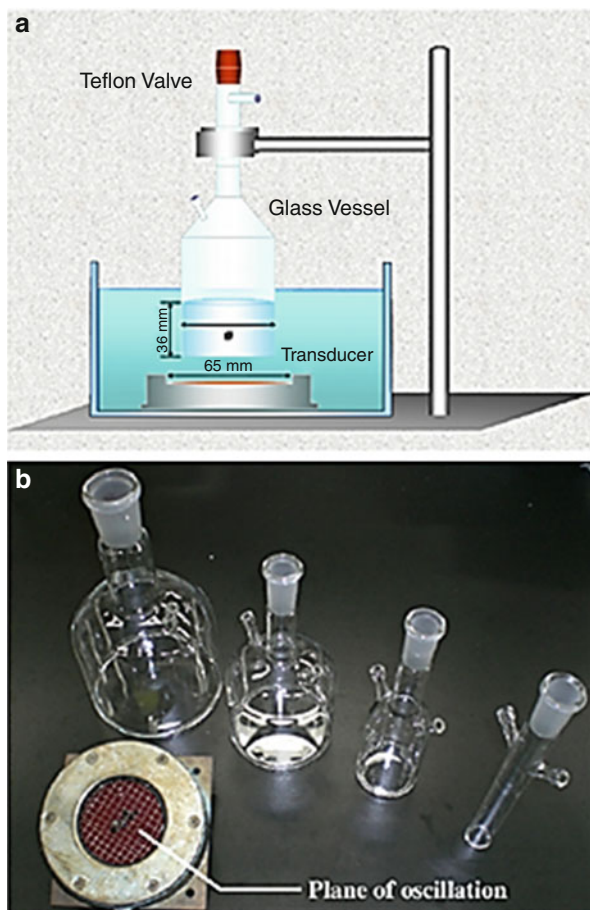
a compound with higher hydrophobicity tends to accumulate at the interface of cavitation bubbles and is quickly degraded. The sonochemical degradation rates of various aromatic compounds depended on their physicochemical properties. Highly volatile and hydrophobic compounds tend to be degraded at high rates. In particular, log P is a good index to indicate the degree of hydrophobicity of compounds. Analysis of the kinetics of sonochemical degradation of organic compounds should take into account several heterogeneities produced during the formation of cavitation bubbles. Langmuir kinetics can be applied to the sonochemical degradation of low concentrations of organic compounds. The addition of inorganic ions, organic additives, inert solid particles, and reactive transition metal powders is effective to control or enhance degradation rates. According to the literature, optimum amounts of appropriate additives enhance degradation rates, but degradation rates tend to decrease when large amount of additives are used. In addition, sonochemical degradation rates are sensitive to the diameter of the reaction vessel; consequently,
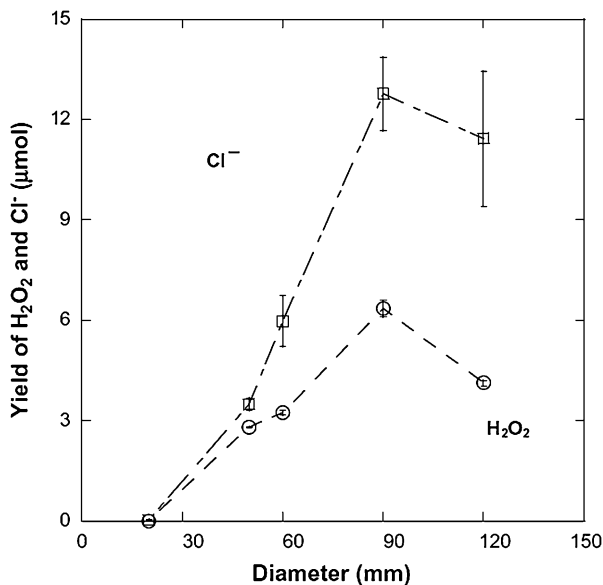
further parameters related to sonochemical reactor design should be investigated in the future.

The physicochemical properties of acoustic cavitation bubbles and the degradation rates of organic compounds should be analyzed more quantitatively in future research to better understand the physicochemical properties of acoustic cavitation bubbles and the behavior of organic solutes during sonication. In sonochemical degradation, the main reaction sites are the inside of cavitation bubbles and the surrounding interface region; therefore, it is important to develop techniques that make organic compounds accumulate effectively at these reaction sites. In addition, techniques to control the number of cavitation bubbles and their temperature are needed. The control of bubble temperature could be applied in the combined use of sonochemical degradation and catalyst technology to control the rate and selectivity of degradation reactions. If the combined use of sonochemical and catalyst technology is successful, valuable materials may be synthesized by the degradation of hazardous organic compounds.

References

1. Okitsu K, Yue A, Tanabe S, Matsumoto H, Yobiko Y, Yoo Y (2002) Sonolytic control of rate of gold(III) reduction and size of formed gold nanoparticles: relation between reduction rates and sizes of formed nanoparticles. Bull Chem Soc Jpn 75:2289–2296
2. Anjaneyulu Y, Chary NS, Raj DSS (2005) Decolourization of industrial effluents- available methods and emerging technologies- a review. Rev Environ Sci Biotechnol 4:245–273
3. Rehorek A, Tauber M, Gubitz G (2004) Application of power ultrasound for azo dye degradation. Ultrason Sonochem 11:177–182

4. Soriano JJ, Mathieu-Denoncourt J, Norman G, de Solla SR, VLanglois VS (2014) Toxicity of the azo dyes Acid Red 97 and Bismarck Brown Y to Western clawed frog (Silurana tropicalis). Environ Sci Pollut Res 21:3582–3591

5. Okitsu K, Iwasaki K, Yobiko Y, Bandow H, Nishimura R, Maeda Y (2005) Sonochemical degradation of azo dyes in aqueous solution: a new heterogeneous kinetics model taking into account the local concentration of OH radicals and azo dyes. Ultrason Sonochem 12:255–262

6. Neppiras EA (1980) Acoustic cavitation. Phys Rep 61:159–251

7. Gutierrez M, Henglein A, Ibanez F (1991) Radical scavenging in the sonolysis of aqueous solutions of I⁻, Br⁻, and N₃⁻. J Phys Chem 95:6044–6047

8. Henglein A, Kormann C (1985) Scavenging of OH radicals produced in the sonolysis of water. Int J Radiat Biol 48:251–258

9. Sostaric JZ, Riesz P (2002) Adsorption of surfactants at the gas/solution interface of cavitation bubbles: an ultrasound intensity-independent frequency effect in sonochemistry. J Phys Chem B 106:12537–12548

10. Nagata Y, Mizukoshi Y, Okitsu K, Maeda Y (1996) Sonochemical formation of gold particles in aqueous solution. Radiat Res 146:333–338

11. Sostaric JZ, Mulvaney P, Grieser F (1995) Sonochemical dissolution of MnO₂ colloids. J Chem Soc Faraday Trans 91:2843–2846

12. Yim B, Okuno H, Nagata Y, Nishimura R, Maeda Y (2002) Sonolysis of surfactants in aqueous solutions: an accumulation of solute in the interfacial region of the cavitation bubbles. Ultrason Sonochem 9:209–213

13. Joseph JM, Destaillats H, Hung H-M, Hoffmann MR (2000) The sonochemical degradation of azobenzene and related azo dyes: rate enhancements via Fenton's reactions. J Phys Chem A 104:301–307

14. Okitsu K, Nanzai B, Kawasaki K, Takenaka N, Bandow H (2009) Sonochemical decomposition of organic acids in aqueous solution: understanding of molecular behavior during cavitation by the analysis of a heterogeneous reaction kinetics model. Ultrason Sonochem 16:155–162

15. The Chemical Society of Japan (ed) (1993) Kagaku Binran Kisohen (Handbook of chemistry in Japanese), vol 2, 4th edn. Maruzen, Tokyo, p 321

16. The Chemical Society of Japan (ed) (1993) Kagaku Binran Kisohen (Handbook of chemistry in Japanese), vol 2, 4th edn. Maruzen, Tokyo, pp 123, 126, 135

17. Aruoja V, Sihtmäe M, Dubourguier H-C, Kahru A (2011) Toxicity of 58 substituted anilines and phenols to algae Pseudokirchneriella subcapitata and bacteria Vibrio fischeri: comparison with published data and QSARs. Chemosphere 84:1310–1320

18. Parka J-S, Brown MT, Han T (2012) Phenol toxicity to the aquatic macrophyte Lemna paucicostata. Aquat Toxicol 106–107:182–188

19. Nanzai B, Okitsu K, Takenaka N, Bandow H, Maeda Y (2008) Sonochemical degradation of various monocyclic aromatic compounds: relation between hydrophobicities of organic compounds and the decomposition rates. Ultrason Sonochem 15:478–483

20. Buxton GV, Greenstock CL, Helman WP, Ross AB (1988) Critical review of rate constants for reactions of hydrated electrons, hydrogen atoms and hydroxyl radicals (OH/O⁻) in aqueous solution. J Phys Chem Ref Data 17:513–886

21. Kirschenbaum LK, Riesz P (2012) Sonochemical degradation of cyclic nitroxides in aqueous solution. Ultrason Sonochem 19:1114–1119

22. Ashokkumar M, Hall R, Mulvaney P, Grieser F (1997) Sonoluminescence from aqueous alcohol and surfactant solutions. J Phys Chem B 101:10845–10850

23. Price GJ, Ashokkumar M, Grieser F (2004) Sonoluminescence quenching of organic compounds in aqueous solution: frequency effects and implications for sonochemistry. J Am Chem Soc 126:2755–2762

24. Caruso RA, Ashokkumar M, Grieser F (2002) Sonochemical formation of gold sols. Langmuir 18:7831–7836

25. Nanzai B, Okitsu K, Takenaka N, Bandow H (2009) Sonochemical degradation of alkylbenzene sulfonates and kinetics analysis with a Langmuir type mechanism. J Phys Chem C 113:3735–3739
26. Yang L, Rathman JF, Weavers LK (2005) Degradation of alkylbenzene sulfonate surfactants by pulsed ultrasound. J Phys Chem B 109:16203–16209
27. Yang L, Rathman JF, Weavers LK (2006) Sonochemical degradation of alkylbenzene sulfonate surfactants in aqueous mixtures. J Phys Chem B 110:18385–18391
28. Nanzai B, Okitsu K, Takenaka N, Bandow H (2009) Effects of initial concentration of LASs on the rates of sonochemical degradation and cavitation efficiency. Res Chem Intermed 35:841–849
29. Brooke D, Footitt A, Nwaogu TA (2004) Environmental risk evaluation report: perfluorooctanesulphonate (PFOS). Chemicals Assessment Section, Environment Agency, Wallingford
30. Zareitalabad P, Siemens J, Hamer M, Amelung W (2013) Perfluorooctanoic acid (PFOA) and perfluorooctanesulfonic acid (PFOS) in surface waters, sediments, soils and wastewater – a review on concentrations and distribution coefficients. Chemosphere 91:725–732
31. Hori H, Nagaoka Y, Yamamoto A, Sano T, Yamashita N, Taniyasu S, Kutsuna S (2006) Efficient decomposition of environmentally persistent perfluorooctanesulfonate and related fluorochemicals using zerovalent iron in subcritical water. Environ Sci Technol 40:1049–1054
32. Nakayama S, Harada K, Inoue K, Sasaki K, Seery B, Saito N, Koizumi A (2005) Distributions of perfluorooctanoic acid (PFOA) and perfluorooctane sulfonate (PFOS) in Japan and their toxicities. Environ Sci 12:293–313
33. Manzetti S, Van Der Spoel ER, Van Der Spoel D (2014) Chemical properties, environmental fate, and degradation of seven classes of pollutants. Chem Res Toxicol 27:713–737
34. Moriwaki H, Takagi Y, Tanaka M, Tsuruho K, Okitsu K, Maeda Y (2005) Sonochemical decomposition of perfluorooctane sulfonate and perfluorooctanoic acid. Environ Sci Technol 39:3388–3392
35. Campbell TY, Vecitis CD, Mader BT, Hoffmann MR (2009) Perfluorinated surfactant chain-length effects on sonochemical kinetics. J Phys Chem A 113:9834–9842
36. Cheng J, Vecitis CD, Park H, Mader BT, Hoffmann MR (2010) Sonochemical degradation of perfluorooctane sulfonate (PFOS) and perfluorooctanoate (PFOA) in groundwater: kinetic effects of matrix inorganics. Environ Sci Technol 44:445–450
37. Nagata Y, Hirai K, Bandow H, Maeda Y (1996) Decomposition of hydroxybenzoic and humic acids in water by ultrasonic irradiation. Environ Sci Technol 30:1133–1138
38. Nagata Y, Nakagawa M, Okuno H, Mizukoshi Y, Yim B, Maeda Y (2000) Sonochemical degradation of chlorophenols in water. Ultrason Sonochem 7:115–120
39. Yim B, Yoo Y, Maeda Y (2003) Sonolysis of alkylphenols in aqueous solution with Fe(II) and Fe(III). Chmosphere 50:1015–1023
40. Minero C, Pellizzari P, Maurino V, Pelizzetti E, Vione D (2008) Enhancement of dye sonochemical degradation by some inorganic anions present in natural waters. Appl Catal B Environ 77:308–316
41. Moumeni O, Hamdaoui O (2012) Intensification of sonochemical degradation of malachite green by bromide ions. Ultrason Sonochem 19:404–409
42. Thi L-AP, Do H-T, Lo S-L (2014) Enhancing decomposition rate of perfluorooctanoic acid by carbonate radical assisted sonochemical treatment. Ultrason Sonochem 21:1875–1880
43. Lin J-C, Lo S-L, Hu C-Y, Lee Y-C, Kuo J (2015) Enhanced sonochemical degradation of perfluorooctanoic acid by sulfate ions. Ultrason Sonochem 22:542–547
44. Seymour JD, Gupta RB (1997) Oxidation of aqueous pollutants using ultrasound: salt-induced enhancement. Ind Eng Chem Res 36:3453–3457
45. Chen Y-C, Smirniotis P (2002) Enhancement of photocatalytic degradation of phenol and chlorophenols by ultrasound. Ind Eng Chem Res 41:5958–5965
46. Merouani S, Hamdaoui O, Saoudi F, Chiha M (2010) Sonochemical degradation of Rhodamine B in aqueous phase: effects of additives. Chem Eng J 158:550–557

47. Duque FG, Petrier C, Pulgarin C, Penuela G, Torres-Palma RA (2011) Effects of sonochemical parameters and inorganic ions during the sonochemical degradation of crystal violet in water. Ultrason Sonochem 18:440–446

48. Uddin HM, Nanzai B, Okitsu K (2016) Effects of Na_2SO_4 or NaCl on sonochemical degradation of phenolic compounds in an aqueous solution under Ar: positive and negative effects induced by the presence of salts. Ultrason Sonochem 28:144–149

49. Okitsu K, Kawasaki K, Nanzai B, Takenaka N, Bandow H (2008) Effect of carbon tetrachloride on sonochemical decomposition of methyl orange in water. Chemosphere 71:36–42

50. Weissler A, Cooper HW, Snyder S (1950) Chemical effect of ultrasonic waves: oxidation of potassium iodide solution by carbon tetrachloride. J Am Chem Soc 72:1769–1775

51. Hua I, Hoffmann MR (1996) Kinetics and mechanism of the sonolytic degradation of CCl_4: intermediates and byproducts. Environ Sci Technol 30:864–871

52. Lide DR (ed) (2002) CRC handbook of chemistry and physics, 83rd edn. CRC Press, London, pp 9–75

53. Gültekin I, Tezcanli-Güyer G, Ince NH (2009) Sonochemical decay of C.I. Acid Orange 8: effects of CCl_4 and t-butyl alcohol. Ultrason Sonochem 16:577–581

54. Shriwas AK, Gogate PR (2011) Ultrasonic degradation of methyl parathion in aqueous solutions: intensification using additives and scale up aspects. Sep Purif Technol 79:1–7

55. Golash N, Gogate PR (2012) Degradation of dichlorvos containing wastewaters using sonochemical reactors. Ultrason Sonochem 19:1051–1060

56. Zhou R, Luo W, Zhu L, Chen F, Tang H (2007) Spectrophotometric determination of carbon tetrachloride via ultrasonic oxidation of iodide accelerated by dissolved carbon tetrachloride. Anal Chim Acta 597:295–299

57. Suslick KS, Mdleleni MM, Ries JT (1997) Chemistry induced by hydrodynamic cavitation. J Am Chem Soc 119:9303–9304

58. Ince NH, Gultekin I, Tezcanli-Guyer G (2009) Sonochemical destruction of nonylphenol: effects of pH and hydroxyl radical scavengers. J Hazard Mater 172:739–743

59. Keck A, Gilbert E, Koster R (2002) Influence of particles on sonochemical reactions in aqueous solutions. Ultrasonics 40:661–665

60. Iida Y, Kozuka T, Tuziuti T, Yasui K (2004) Sonochemically enhanced adsorption and degradation of methyl orange with activated aluminas. Ultrasonics 42:635–639

61. Nakui H, Okitsu K, Maeda Y, Nishimura R (2007) Effect of coal ash on sonochemical degradation of phenol in water. Ultrason Sonochem 14:191–196

62. Shimizu N, Ogino C, Dadjour MF, Murata T (2007) Sonocatalytic degradation of methylene blue with TiO_2 pellets in water. Ultrason Sonochem 14:184–190

63. He Y, Grieser F, Ashokkumar M (2011) The mechanism of sonophotocatalytic degradation of methyl orange and its products in aqueous solutions. Ultrason Sonochem 18:974–980

64. He Y, Grieser F, Ashokkumar M (2011) Kinetics and mechanism for the sonophotocatalytic degradation of p-chlorobenzoic acid. J Phys Chem A 115:6582–6588

65. Hung H-M, Hoffmann MR (1998) Kinetics and mechanism of the enhanced reductive degradation of CCl_4 by elemental iron in the presence of ultrasound. Environ Sci Technol 32:3011–3016

66. Hung H-M, Ling FH, Hoffmann MR (2000) Kinetics and mechanism of the enhanced reductive degradation of nitrobenzene by elemental iron in the presence of ultrasound. Environ Sci Technol 34:1758–1763

67. Okitsu K, Yoshioka Y, Tanabe S (2006) Effect of transition metal powder and low-energy ultrasound frequency on degradation rate of chlorinated hydrocarbons in water. Bunseki Kagaku 55:567–572

68. Nanzai B, Okitsu K, Takenaka N, Bandow H, Tajima N, Maeda Y (2009) Effect of reaction vessel diameter on sonochemical efficiency and cavitation dynamics. Ultrason Sonochem 16:163–168

Removal of Heavy Metal from Wastewater

Nalenthiran Pugazhenthiran, Sambandam Anandan,
and Muthupandian Ashokkumar

Contents

Abstract

The development of environmental remediation technologies targets to minimize the toxic effects of pollutants. Among developing remediation technologies, sonochemistry is an emerging technology for the removal of pollutants in aqueous environment. Primary reaction generated during acoustic cavitation is the homolytic cleavage of water molecules into atomic hydrogen (H) and hydroxyl (OH) radicals. Hydroxyl radicals unselectively oxidize target pollutant molecules. This chapter deals with technical feasibility of sonochemical process for the removal of heavy metal pollutants from aqueous environment. The removal of heavy metal pollutants using adsorption materials in the presence of ultrasonic

N. Pugazhenthiran • S. Anandan (✉)
Nanomaterials and Solar Energy Conversion Lab, Department of Chemistry, National Institute of Technology, Tiruchirappalli, Tiruchirappalli, Tamilnadu, India
e-mail: npugazhenthiran@gmail.com; sanand@nitt.edu

M. Ashokkumar
School of Chemistry, The University of Melbourne, Melbourne, VIC, Australia
e-mail: masho@unimelb.edu.au

irradiation shows better efficiency compared to reactions in the absence of ultrasonic irradiation. It is concluded that ultrasonic technology is a simple and possibly cost-effective alternative for the oxidation of heavy metals with and without assistance of external catalysts.

Introduction

The term "heavy metals" refers to any metallic element that has a relatively high density and is toxic or poisonous even at low concentrations. "Heavy metals" is a general collective term, which applies to a group of metals and metalloids with atomic density greater than 4 g cm^{-3} [1]. Although several adverse health effects of heavy metals have been known for a long time, exposure to heavy metals continues and is even increasing in some parts of the world. Heavy metals include lead (Pb), cadmium (Cd), zinc (Zn), mercury (Hg), arsenic (As), silver (Ag), chromium (Cr), copper (Cu), and iron (Fe) [2]. Emission of heavy metals to the environment occurs via a wide range of processes and pathways contaminating air (e.g., during combustion, extraction, and processing), water (via runoff and releases from storage and transport), and soil [2, 3]. Atmospheric contamination tends to be of greatest concern in terms of human health [3–5]. Lead emission is mainly related to road transport and thus most uniformly distributed throughout the atmosphere [2, 5]. Cadmium emission is primarily associated with nonferrous metallurgy and fuel combustion, whereas the spatial distribution of anthropogenic mercury emissions reflects the level of coal consumption in different regions [2, 5]. Moreover, discharge of heavy metal wastes into effluent over the past few decades has inevitably resulted in an increased flux of metallic substances into the global aquatic environment due to their acute toxicity, nonbiodegradability, and buildup in high concentrations [6]. Point and nonpoint source industrial runoffs from battery manufacturing, printing and pigments, tanneries, oil refining, mining smelting, electroplating, paintings, and most recently e-wastes have resulted in elevated levels and chronic toxicity of lead (Pb^{2+}), cadmium (Cd^{2+}), copper (Cu^{2+}), and iron (Fe^{2+}). Consequently, these heavy metals have been extensively studied and their effects on human health regularly reviewed by international bodies such as the WHO [2, 6]. The maximum permissible limit of these heavy metal ions (Pb^{2+}, Cd^{2+}, Cu^{2+}, and Fe^{2+}) in inland surface water and drinking water are 0.006, 0.01, 0.25, and 0.1 mg L^{-1}, respectively, according to the United State Environmental Protection Agency (USEPA) (Table 1) [7].

Table 1 United State Environmental Protection Agency (USEPA) maximum contamination levels for heavy metal concentration in air, soil, and water [7]

Heavy metal	Maximum concentration in air (mg m^{-3})	Maximum concentration in sludge (soil) (mg/Kg or ppm)	Maximum concentration in drinking water (mg L^{-1})	Maximum concentration in supporting aquatic life (mg L^{-1} or ppm)
Cd	0.1–0.2	85	0.005	0.008^c
Pb	…..	420	0.01^b (0.0)	0.0058^c
Zn^2	1, 5^a	7,500	5.00	0.0766^c
Hg	…..	<1	50	0.5
Ca	5	Tolerable	0.0	Tolerable >50
Ag	0.01	…..	0.01	0.1
As	…..	…..		…..

Value in bracket is the desirable limit
^{a}1 for chlorine fume, 5 for oxide fume; … no guideline available
^{b}WHO; EPA, July 1992
^{c}USEPA, 1987

Especially, wastes produced from the industrial activities not only bring about serious environmental effect but also threaten human health and ecosystem [5]. These heavy metals, for the convenience of analysis, reportedly fall into three families: toxic metals (Hg, Cr, Pb, Zn, Cu, Ni, Cd, As, Co, Sn, etc.), precious metals (Pd, Pt, Ag, Au, Ru, etc.), and radionuclides (U, Th, Ra, Am, etc.) [2, 3, 5, 8]. The methods for removing heavy metal ions from aqueous solution mainly consist of physical, chemical, and biological processes. Traditional physiochemical methods include chemical precipitation, oxidation or reduction, filtration, ion exchange, electrochemical treatment, reverse osmosis, membrane technology, and evaporation recovery [9–13]. Most of these are ineffective or excessively expensive when the metal concentrations are <100 mg L^{-1} [8, 14]. For example, usual physical pathways like ion exchange, activated carbon, and membrane adsorption belong to the latter costly group, especially when treating large amounts of wastewater [14]. In recent years, using ultrasonic technology to control and remove heavy metals has gained some attention [15–23]. Further, the combined effects of ultrasound with adsorbent materials show higher removal capacity. The adsorbent materials possess natural metal-sequestering features to decrease the concentration of heavy metal ions in solution from ppm to ppb level. It can effectively remove dissolved heavy metal ions and carry them out of dilute complex solutions with high efficiency; ultrasound features as an ideal candidate for treating high-volume and low-concentration complex wastewaters [24–31].

Compared with conventional treatment methods, sonochemical process has the following advantages [18–20, 22, 23]:

- High efficiency and selectivity for heavy metals in low concentrations
- Energy saving
- Broad operational range of pH and temperature

- Easy reclamation of heavy metal
- Easy recycling of catalysts

Heavy metal removal by sonochemical and ultrasound-assisted sorption processes has been investigated during the last several decades [15–17, 20–23, 26, 30, 31]. The capability of cavitation-generated radicals to oxidize metallic elements has first been observed from toxicological point of view [20, 23]. In addition, sorption materials such as activated carbon [25], bioinspired materials [24], etc., can passively bind metal ions via various physicochemical mechanisms. This discovery then led biosorption to an active research area for the removal of heavy metal. The ultrasound-assisted processes can be classified into the following categories: ultrasound only [15, 16, 18, 23], ultrasound coupled with sorption materials [24, 27, 31], and ultrasound with a combination of oxidizing agent [20, 21]. Researchers have focused on optimization, mechanism, and large-scale trails for the removal of heavy metals [25, 26].

The aim of this chapter is to present an overview of the current literature available in the area of ultrasound-assisted removal of heavy metals.

Conventional Technology for the Removal of Heavy Metal

Conventional physicochemical methods, such as activated carbon, precipitation, reverse osmosis, membrane separation, chemical oxidation, and ionic exchange, have been commonly used for the removal of heavy metals. However, most of those are less effective, excessively expensive, and eco-unfriendly when initial metal concentrations are in the range of 10–100 mg L^{-1}. For instance, chemical precipitation and electrochemical treatment are not very effective, especially when metal ion concentration in aqueous solution is among 1–100 mg L^{-1}, and also produce large quantity of sludge required to treat with still more great difficulty [32].

The advantages and limitations of these conventional methods are given below in detail:

Activated Carbon

It is a crude form of graphite with a random or amorphous structure, which is highly porous, exhibiting a broad range of pore sizes from visible cracks, crevices, and slits of molecular dimensions. With high specific surface area, microporous character, and chemical nature of the surface, activated carbon has been found to be a potential adsorbent for the removal of heavy metals from industrial wastewater [33–36]. In spite of its advantages, it also shows many shortcomings such as high cost to prepare, deactivation resulting in a loss of the carbon, performance type dependent of carbon, being nonselective, etc. Although modified/activated carbon can improve the selectivity, its preparation cost roars up subsequently [37]. Table 2 shows the effect of different metal concentrations (lead, cadmium, nickel, chromium, and zinc)

Table 2 The removal percentages of metals with different initial concentrations using activated carbon [38]

Element	Initial concentration (ppm)	Residual concentration (ppm)	Removal percentage (%)
Cd	30	4	86
	50	8	84
	100	30	70
	200	68	66
Pb	30	5	83
	50	13	74
	100	27	73
	200	61	70
Cr	30	15	51
	50	26	48
	100	70	30
	200	152	24
Ni	30	3	90
	50	6	88
	100	15	84
	200	32	84
Zn	30	5	84
	50	9	81
	100	24	77
	200	50	75

on the removal percentage of heavy metals. It can be seen that at low heavy metal concentration, the removal percentage is high and gradually decreases with an increase in heavy metal concentration. At 30 ppm of heavy metals, the removal percentages are 90 %, 86 %, 83.6 %, 83 %, and 51 % for Ni, Cd, Zn, Pb, and Cr, respectively. At 30 ppm, nickel shows the highest removal percentage at all concentrations, followed by cadmium, zinc, lead, and chromium. On the other hand, the highest heavy metal concentration (200 ppm) led to the lowest removal percentage of the heavy metals under consideration (66 %, 70 %, 24 %, 84 %, and 75 % for Cd, Pb, Cr, Ni, and Zn, respectively). Nickel shows the highest removal percentage at all concentrations, followed by other metals; however, the lowest removal percentage is the chromium at all concentrations [38].

Chemical Precipitation

This pathway is widely used for heavy metal removal from inorganic effluent. Typically, the metal precipitates from the solution in the form of hydroxide [39]. Since lime or calcium hydroxide is the most commonly employed precipitant

agent, this method gains availability at most corners of the world. Lime precipitation, another option, can be trusted to effectively treat inorganic effluent with a metal concentration of higher than 1,000 mg L^{-1} with a simple process. For instance, it helped to remove heavy metals such as Zn(II), Cd(II), and Mn(II) cations with initial metal concentrations of 450, 150, and 1,085 mg L^{-1}, respectively, in a batch continuous system [40]. In spite of its advantages, chemical precipitation requires a large amount of chemicals to reduce metals to an acceptable level for discharge. And generally it can hardly be used to handle low concentration of metal ion in wastewater, which is below 100 mg L^{-1}. Other drawbacks are its excessive sludge production that requires further treatment, the increasing cost of sludge disposal, slow metal precipitation, and the long-term environmental impacts of sludge disposal [41]. A variety of hydroxides have been used to precipitate metals from wastewater; based on the low cost and ease of handling, lime is the preferred choice of base used in hydroxide precipitation at industrial settings [42].

Chemical Oxidation and Reduction

Adding oxidizing or reducing agents makes toxic substances in wastewater being oxidized or reduced to nontoxic or low toxic substances. It has been reported that heavy metals such as Mn_2C, Cu_2C, Pb_2C, Cd_2C, Cr_3C, and Hg_2C could be effectively removed using potassium ferrate(VI) as oxidation and coprecipitation [43, 44]. However, currently chemical oxidation and reduction is generally used as a pretreatment for wastewater before the application of a powerful process.

Membrane Separation

Membrane separation methods like electrodialysis (ED), nano-filtration (NF), ultra-filtration (UF), and reverse osmosis (RO) [45] have received considerable attention for the treatment of inorganic effluent, since they are capable of removing not only suspended solid and organic compounds but also inorganic contaminants such as heavy metals [46]. Although it can be applied in occasions to low metal ion concentrations, for example, Tzanetakis et al. [47] illustrate the removal efficiencies of Co(II) and Ni(II) were 90 % and 69 %, at initial metal concentrations of 0.84 and 11.72 mg L^{-1}, respectively [47]. The main disadvantages of these processes are inadequate selectivity, high energy consumption, and immature technologies, which limit the popularization of this technology.

Ion Exchange

This is a method that uses an ion exchange resin or agent to exchange metal ions in dilute solutions to achieve the purpose of extraction or removal of certain metal ions. It is widely used for the recovery and removal of metals from process and waste

streams in chemical process industries [48]. In general, ion exchange is reportedly effective to treat inorganic effluent within a relatively wide range of metal ion concentrations from 10 to 100 mg L^{-1} [49, 50] or even up to higher than 100 mg L^{-1} [51]. Furthermore, unlike chemical precipitation, ion exchange does not present any sludge disposal problems [52]. Despite these advantages, it also has some limitations in treating wastewater laden with heavy metals ions. Suitable ion exchange resins are not available for all heavy metals ions, and the capital and operational cost is high [53].

Ultrasonic Removal of Heavy Metals

Application of ultrasound to chemical reactions and processes is termed as sonochemistry [54]. In recent years, sonochemical processes have received a lot of attention due to its special features. The mechanism causing sonochemical effects in liquids is the phenomenon of acoustic cavitation. The chemical effects of ultrasound are derived from acoustic cavitation, which is a nonlinear process that serves as a means of concentration of the diffuse energy of sound in liquids. This high-energy microenvironment is induced by the extreme conditions generated during acoustic cavitation leading to the generation of high-energy species (radicals) [17, 18, 20, 22–24, 31, 54, 55].

Cavitation is the formation, growth, and implosive collapse of bubbles in a liquid. Cavitation collapse produces intense local heating, high pressures, enormous heating and cooling rates, and liquid jet streams (~400 km h^{-1}) [54, 56]. These hot spots generated can reach temperatures above 5,000 K, pressures exceeding 1,000 atm, and heating and cooling rates in excess of 10^{10} K s^{-1}. These conditions are distinct from those generated by other conventional techniques such as photochemistry, wet chemistry, hydrothermal synthesis, or flame pyrolysis, making this technique unique for various applications. The effective lifetime of these localized hot spots may be only a few microseconds [54, 56–59].

In aqueous sonochemistry, chemical reactions occur at three regions (Figs. 1 and 2): (1) The cavitation bubble itself: Interior of collapsing bubbles where extreme conditions of temperature and pressure exist transiently, which induce chemical reactions yielding products that are typical of pyrolysis or combustion reactions in the gas phase. (2) Bubble/solution interface: Interfacial regions between the cavitation bubbles and bulk solution where a high temperature (lower than that in the bubble core). Nonvolatile solutes that accumulate in this region can undergo thermal decomposition and induce radical reactions. This interfacial reaction zone is estimated to be about 200 nm thick. (3) Bulk solution: Where the radicals, being produced in the interior of bubble and in the interfacial region, that survive migration from the interface can undergo reactions with solutes present in the bulk solution [54, 57–59].

Recently, Neppolian et al. [20, 23] reported on the effect of the sonochemical oxidation of As(III) to As(V) using a low-frequency horn-type ultrasonicator (frequency = 20 kHz; acoustic power range of 34–36 W; tip diameter = 19 mm).
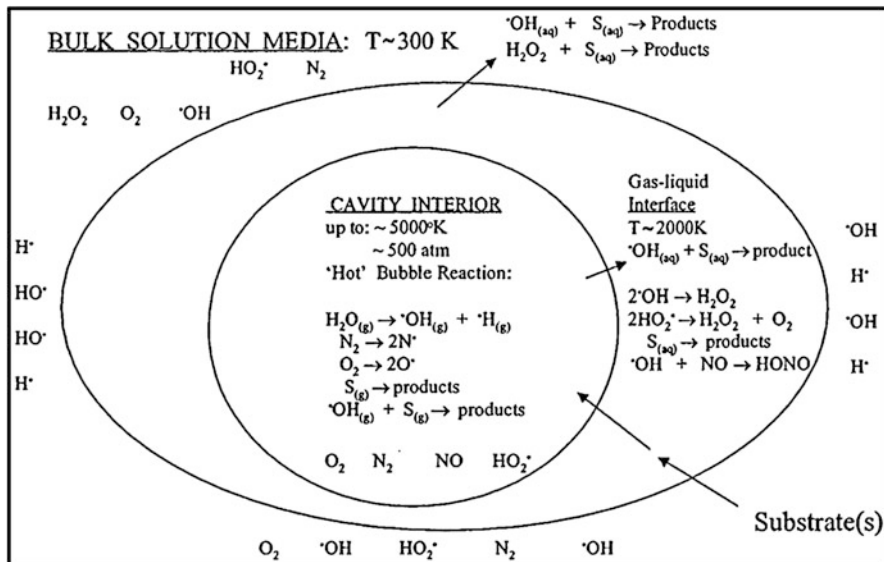
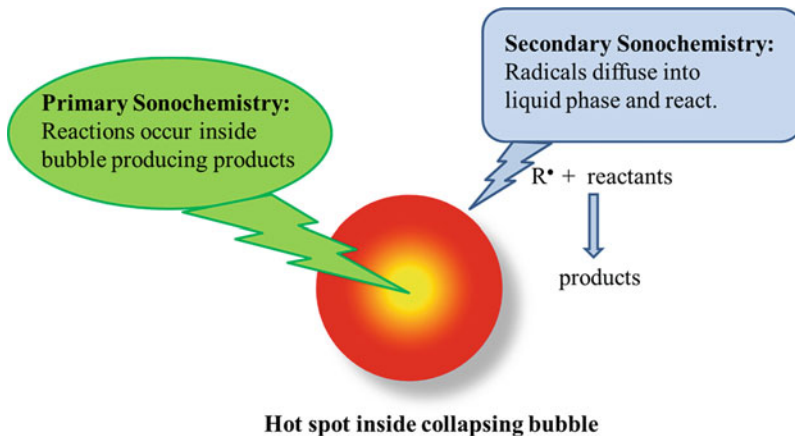**Fig. 1** Three reaction zones in the cavitation process [60]

Fig. 2 Primary sonochemistry and secondary sonochemistry for degradation of heavy metal ions [57]

The OH radicals effectively oxidize As(III) to As(V). They have investigated the effect of various experimental parameters on the sonochemical oxidation efficiency. With an increase in the initial concentration of As(III) (from 0.0013 to 0.0268 mM), the extent of oxidation of As(III) increases (Fig. 3). 325 ppb and 680 ppb of As(III)
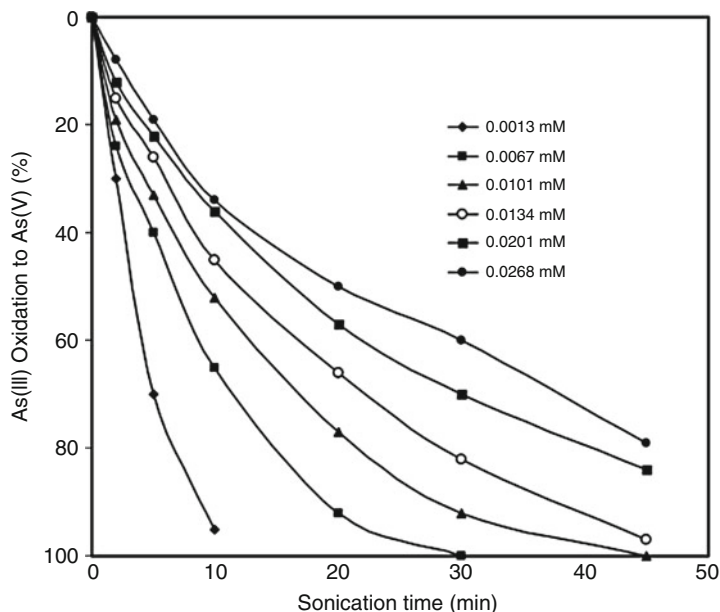
Fig. 3 Effect of the different initial concentrations of As(III) on the oxidation of As(III) to As(V). Experimental conditions: pH = 7, tip diameter = 19 mm, power = 36 W [23]

Table 3 Amount of As(III) oxidized into As(V) after sonication [23]

Initial [As] (ppb)	Amount oxidized in 10 min (ppb)	Amount oxidized in 30 min (ppb)
500	325	500
750	390	690
1,000	430	820
1,500	680	1,050
2,000	690	1,200

were oxidized into As(V) at 10 min sonication time when the initial concentration of As(III) was 500 ppb and 1,500 ppb, respectively. The same trend was observed for 30 min of sonication time (Table 3). The sonochemical oxidation of As(III) was carried out with different initial pHs of the reaction from 3 to 10.6. The rate of reaction was not altered when the initial pH of the medium was changed. The power density on the oxidation of As(III) was performed with different amplitudes from 15 % to 60 % (size of horn tip = 10 mm). Figure 4 shows that the % oxidation of As (III) gradually increases with increasing amplitude. The results were supported by an enhancement of the production of H_2O_2 with increasing amplitude from 15 % to 60 % is direct evidence for the formation of more OH radicals with increasing amplitude and yet another confirmation that OH radicals play an important role for the oxidation of As(III) to As(V) [23].
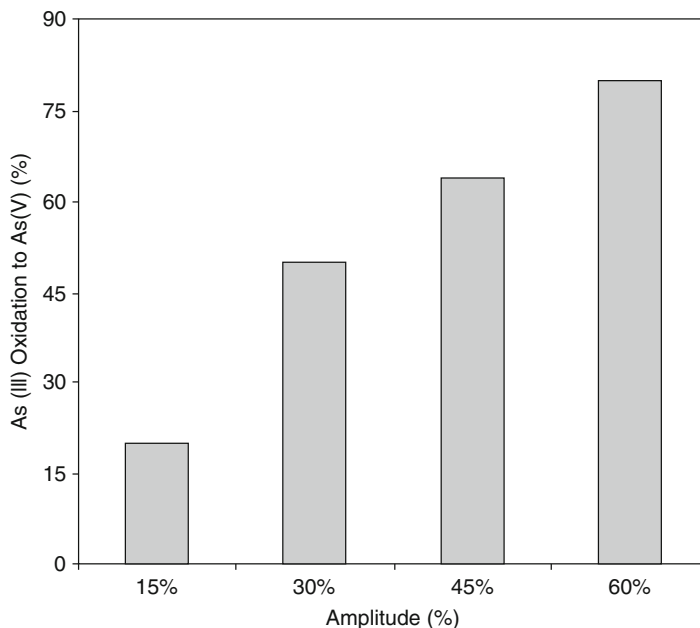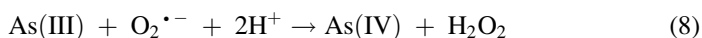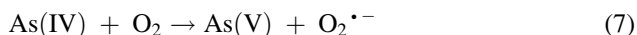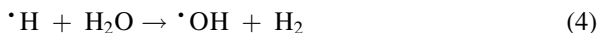
Fig. 4 Effect of acoustic power on the oxidation of As(III) to As(V). Experimental conditions: [As (III)] = 0.0101 mM; pH = 7; tip diameter = 10 mm; sonication time = 30 min [23]

In order to understand the effectiveness of pulsed mode on the oxidation of As (III) (0.5 s on and 0.5 s off), a remarkable increase in the rate of oxidation of As(III) was achieved using the pulse mode; ~85 % oxidation of As(III) was achieved within 20 min reaction time. This is almost two times higher compared to the rate of As(III) oxidation in continuous mode operation. The results suggest that "silent" oxidation reactions occur which are initiated by OH radicals. These occur effectively and separately and appear to be inhibited if the sonication is continuous. In addition to this, the number of active cavitation bubbles may also have increased in the pulsed sonication mode and as a result, an increase in the oxidation of As(III) [20, 23]. Further, the reaction rate was remarkably faster for the oxidation of As(III) to As(V) by ultrasound in combination with other oxidizing agents such as peroxodisulphate [20]. A detailed explanation is provided by considering the amount of OH radicals generated during sonication.

As mentioned earlier, highly reactive free radicals such as OH and H radicals are generated as shown in reactions 1–4 [20, 61]. H radical is largely converted to OH radical through reaction 4 [62, 63]. In the arsenic system, As(III) undergoes oxidation by donating an electron to the OH radical (reaction 5), as explained by Dutta et al. [64] and Xu et al. [65] The resulting As(IV) is highly unstable and readily undergoes further oxidation with either another OH radical or with dissolved oxygen forming the corresponding stable and less mobile As(V) ion (reactions 6 and 7) [66]. In addition to OH radicals, the superoxide radical anion, also an efficient

reactive radical, may also oxidize As(III) into As(IV) as shown in reaction 8. Thus, As(III) is rapidly oxidized to As(V) by reactions 1–8:

$$H_2O \xrightarrow{ultrasound} {}^{\bullet}OH + {}^{\bullet}H \tag{1}$$

$${}^{\bullet}OH + H \rightarrow H_2O \tag{2}$$

$${}^{\bullet}OH + {}^{\bullet}OH \rightarrow H_2O_2 \tag{3}$$

$${}^{\bullet}H + H_2O \rightarrow {}^{\bullet}OH + H_2 \tag{4}$$

$$As(III) + {}^{\bullet}OH \rightarrow As(IV) + OH^- \tag{5}$$

$$As(IV) + {}^{\bullet}OH \rightarrow As(V) + OH^- \tag{6}$$

$$As(IV) + O_2 \rightarrow As(V) + O_2{}^{\bullet-} \tag{7}$$

$$As(III) + O_2{}^{\bullet-} + 2H^+ \rightarrow As(IV) + H_2O_2 \tag{8}$$

In recent decades, ultrasound-assisted removal of heavy metal ions from contaminated soils and sediments through biosorbed materials have been reported [24, 27, 31]. In this context, ultrasound provides an alternative technology for the removal of heavy metals from heavy metal-contaminated environment. During the ultrasonic treatment of heavy metal-polluted sediment, Hg is released from the sediment into the aqueous phase. Once Hg is released by ultrasound, it could be recovered from aqueous solution by sorption techniques, such as activated carbon adsorption or biomass sorption [17, 24, 27, 31, 67–70]. Ziqi et al. [24] reported on the ultrasound-assisted removal of mercury in the presence biomass (transgenic C. reinhardtii). The observed results are shown in Fig. 5, ~18 % removal of Hg(II) was achieved within 15 min by ultrasonic irradiation in the presence of biomass. About 60 min time was taken for removal of ~14 % Hg(II) without ultrasound. This is attributed to ultrasonic effects on Hg(II) desorption and an increase in the mass transfer rate.

Mercury-contaminated marine sediment (NRC, Canada) used for field study and Hg removal by ultrasound with algal cells was conducted at pH 4.0 and 8.0. Figure 6 shows Hg desorption and removal by ultrasound with and without algal cells. Higher Hg removal was achieved with ultrasound in combination with algal cell and at pH 8.0. The efficiency was low at pH 4.0. In acidic conditions, a strong complexation between Hg and natural organic matter occurs lowering the efficiency. Gil et al. [67] reported on the removal of Hg(II) at trace level from water using an ultrasound-promoted reduction/volatilization process in the presence of formic acid. Formic acid played a major role for removal of Hg(II). Figure 7 shows that the Hg(II) removal increased on increasing formic acid concentration up to 0.9 mol L^{-1}.

The main reactions accounting for decomposition of formic acid such as thermal dehydration and decarboxylation occur as a result of the high temperatures existing in the adiabatic compression phase of cavitation bubbles. This temperature becomes lower with increasing formic acid content in the gas bubbles. Therefore, the Hg(II) removal decrease after a certain formic acid concentration [67].
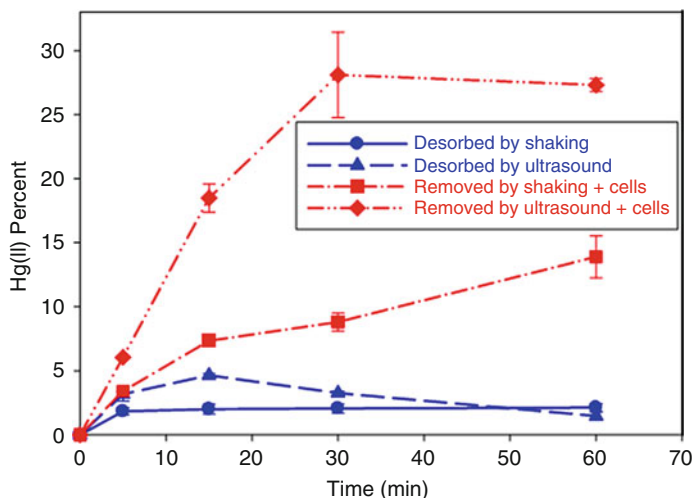
Fig. 5 Desorption and removal of Hg(II) from Al_2O_3 (pH = 5.0, $T = 20\,°C$, $I = 0.01$ M $NaNO_3$, [particle] = 16.7 g L^{-1}, [Hg(II)] initial on particle = 5.0 μmol g^{-1}, 4 mL transgenic cells, sonication intensity 20 W cm^{-2}) [24]
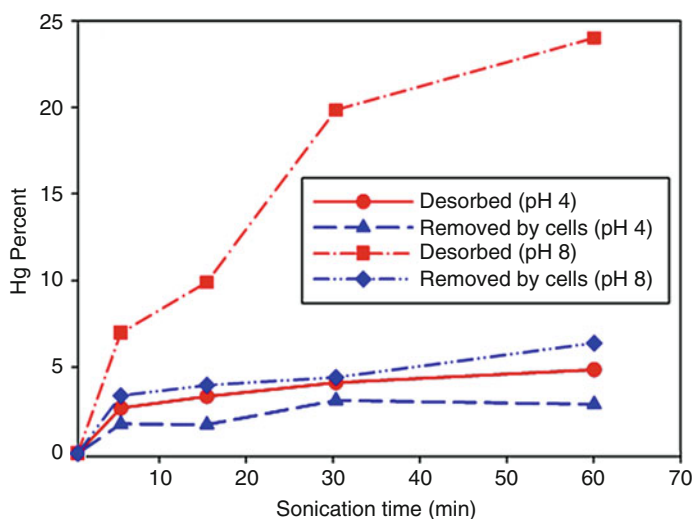

Fig. 6 Sonication of marine sediment for the removal of Hg [24]

Further, several anionic and cationic species present in water could influence the removal of heavy metal by using ultrasound treatments. The influence of foreign substance like alkaline, alkaline-earth salts, and transition metals for removal of mercury under ultrasound treatments has been reported recently [67]. The results are given in Table 4. Hg removal efficiency was decreased in the presence of NaCl, KCl,
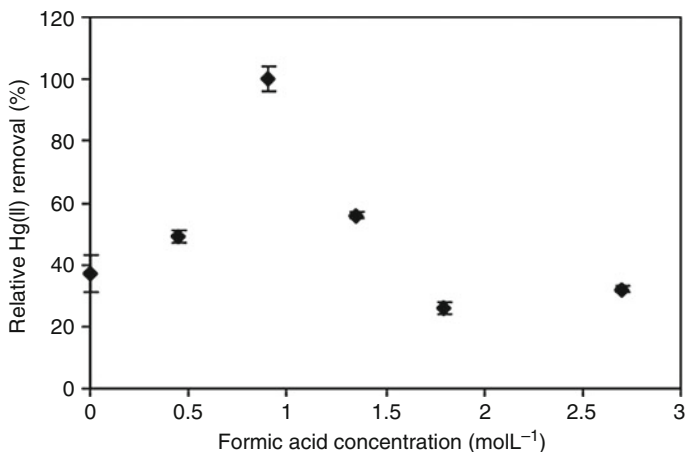
Fig. 7 Effect of formic acid concentration on Hg(II) removal $[Hg]^{2+} = 0.005$ mg L^{-1}; amplitude $=$ 50 %; sample volume $= 10$ mL; ultrasound irradiation time 10 min [67]

Table 4 Effect of foreign substances in water on the Hg(II) removal by ultrasound-promoted reduction [67]

Foreign substance	Concentration (mg L^{-1})	Effect on the Hg(II) removal (%)
NaCl	100	−34
Na$_2$CO$_3$	100	−50
KCl	100	−50
MgCl$_2$	100	−60
KNO$_3$	100	+1
MnCl$_2$	10	−37
Pd(NO$_3$)$_2$	10	−6
Ni(NO$_3$)$_2$	10	−9
(SO$_4$)$_2$Fe(NH$_4$)$_2$	10	−3
Cd(NO$_3$)$_2$	10	−3
CuCl$_2$	10	−50
Cr(NO$_3$)$_3$	10	−7

and MgCl$_2$ at 100 mg L^{-1} concentration, whereas no effect was observed for the 10 mg L^{-1} concentration of the abovementioned salts. On the contrary, KNO$_3$ did not cause any effect at 100 mg L^{-1} concentration. This is because chloride readily reacts with Hg(II) to form a stable compound, which in turn prevents the removal of Hg as Hg(0). Moreover, diminished Hg removal was also observed with Na$_2$CO$_3$.

Reducing radicals such as H radical formed during the sonolytic decomposition of water are responsible for the reduction reactions caused by ultrasonic irradiation. Addition of substances yielding additional reducing radicals can enhance reduction processes [17, 18, 20, 22–24, 31, 54, 55]. In this regard, Gil et al. have proposed a mechanism for removal of Hg with the help of formic acid in the liquid medium
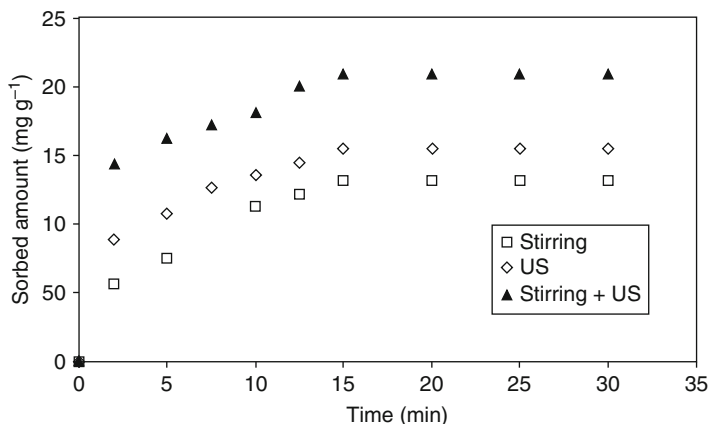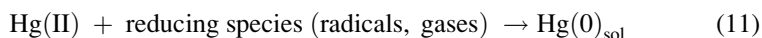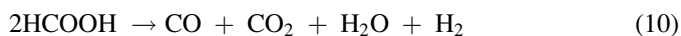
Fig. 8 Effect of the combination stirring and ultrasound on the sorption kinetics of cadmium by wheat bran ($C_0 = 100$ mg L^{-1}, sorbent dose $= 0.6$ g/300 mL, T $= 30$ °C) [70]

upon ultrasound irradiation [67]. The following mechanism is proposed for sonochemical reduction of Hg(II) to Hg(0):

Reactions 9–10 indicate the formation of reducing radicals and gases upon ultrasound irradiation. H radical and OH radical are produced as a result of the sonolysis of water (9), whereas COOH and H_2 are formed from the abstraction reaction of HCOOH with OH or H (reaction (10)). Formic acid can be degraded by pyrolysis occurring inside the cavitation bubbles to yield several gases and H_2O (reaction (10)). Finally, Hg(II) reduction (reaction (11)) proceeds by the reaction with several reducing species formed in earlier reactions:

$$HCOOH + {}^{\bullet}OH \, ({}^{\bullet}H) \rightarrow COOH^{\bullet} + H_2O \, (H_2) \tag{9}$$

$$2HCOOH \rightarrow CO + CO_2 + H_2O + H_2 \tag{10}$$

$$Hg(II) + reducing \; species \; (radicals, \, gases) \rightarrow Hg(0)_{sol} \tag{11}$$

Recently, many researchers [70] reported on the removal of cadmium through ultrasound-assisted sorption process using wheat bran [70], rubber powder [68], and olive leaf [71] as sorption material. A comparison of the removal efficiency in the presence and absence of ultrasound provided a clear evidence that ultrasonic irradiation changed the equilibrium leading to a higher removal of cadmium as shown in Figs. 8, 9, and 10. This observation was explained by the physical effects of cavitation process. The enhancement of sorption in the presence of ultrasound is due to enhanced mass transfer caused by turbulence, microstreaming, and other physical effects. In addition, micro-jetting may have caused additional adsorption sites on sorption materials leading to enhanced adsorption. Nouri et al. [70] and Hamdaoui [71] reported that the combination of ultrasound and mechanical stirring on the removal of cadmium ions in the presence of sorption materials enhances the

Fig. 9 Sorption isotherms of Cd(II) on the powder tire in the presence and absence of ultrasound (sorbent = 1 g; Cd(II) = 20.4 ppm): (•) stirring (30 °C), (■) stirring (40 °C), (▲) stirring (50 °C), (O) sonication (30 °C), (□) sonication (40 °C), and (Δ) sonication (50 °C) [68]

Fig. 10 Effect of sorbent dose on the sorption of cadmium by olive leaves (conditions: 300 mL of cadmium solution, initial concentration 100 mg L^{-1}, sorbent mass 0.2–1.0 g, acoustic power 10 W, stirring speed 400 rpm, pH 5.3, temperature 25 °C) [71]

Table 5 Comparison of sorption capacities of various sorbents for cadmium [71]

Sorbent	Q_m (mg g^{-1})
Olive leaves	
Conventional method	42.19
Sonication	55.87
Combined method	64.94
Wheat bran	
Conventional method	22.78
Sonication	35.09
Combined method	51.81

cadmium removal efficiency compared to conventional method as summarized in Table 5. This behavior could be explained by the strong convective currents occurring within the reactor. These effects associated with hydrodynamic effect of cavitation and mechanical stirring are responsible for the perfect mixing of the contents. A homogeneous mixing effect was thereby established under ultrasonic irradiation within the vessel. The thickness of the boundary layer between the fluid and solid decreases as the mass-transfer coefficient increases. Micro-jets and shockwaves produced by cavitation can disrupt the structure of the sorbent and lead to a higher sorption capacity. Additionally, extreme conditions produced by acoustic cavitation lead to high pressure and high temperature on the surface of the solid that can change the morphology of the surface and the biosorbent granulometry [17, 24, 27, 31, 67–71]. These phenomena might produce new sites for sorption that cause a higher removal of cadmium from aqueous solution.

Further, they have investigated the effect of temperature on the removal of cadmium in the presence and absence of ultrasound through sorption process. Entezari et al. [68] work indicates that the removal capacity of rubber in the presence of ultrasound was increased with an increase in temperature. The amount of cadmium removal capacity increased from 46 % to 66 % after 30 min ultrasound irradiation when the temperature was increased from 30 to 50 °C (Fig. 11). Loubna Nouri et al. [70] carried out experiments for removal of cadmium as a function of time at different temperatures (20, 30, and 50 °C) without and with the assistance of ultrasound. In both cases, the sorption capacity of wheat bran increased with increasing temperature (Fig. 12). Similar results were reported for the removal of cadmium by Hamdaoui (Fig. 13). This indicates that the sorption process is endothermic in nature. The rate of diffusion of the sorbate ions increased upon increasing the temperature, owing to a decrease in the viscosity of the solution. Such enhancement is due to the acceleration of the sorption process by the increased movement of metal ions from the bulk solution to the surface of the solid particles at higher temperatures. Additionally, in the presence of the ultrasonic irradiation, both the rate of sorption and the amount of cadmium sorbed are higher than those obtained in the conventional method for all the studied temperatures. Cavitation bubbles are more easily produced at high temperature because of a decrease of the liquid tensile stress and viscosity.
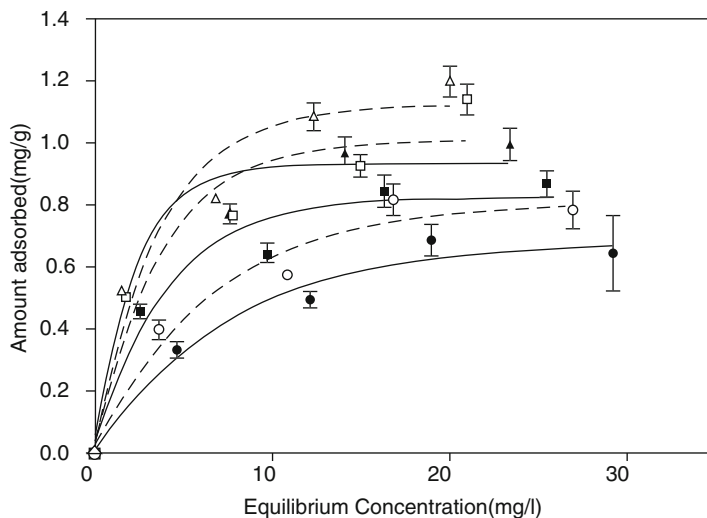
Fig. 11 Effect of temperature on the sorption of Cd(II) in the presence and absence of ultrasound (sorbent = 1 g; Cd(II) = 20.4 ppm): (•) stirring (30 °C), (■) stirring (40 °C), (▲) stirring (50 °C), (O) sonication (30 °C), (□) sonication (40 °C), and (Δ) sonication (50 °C) [68]
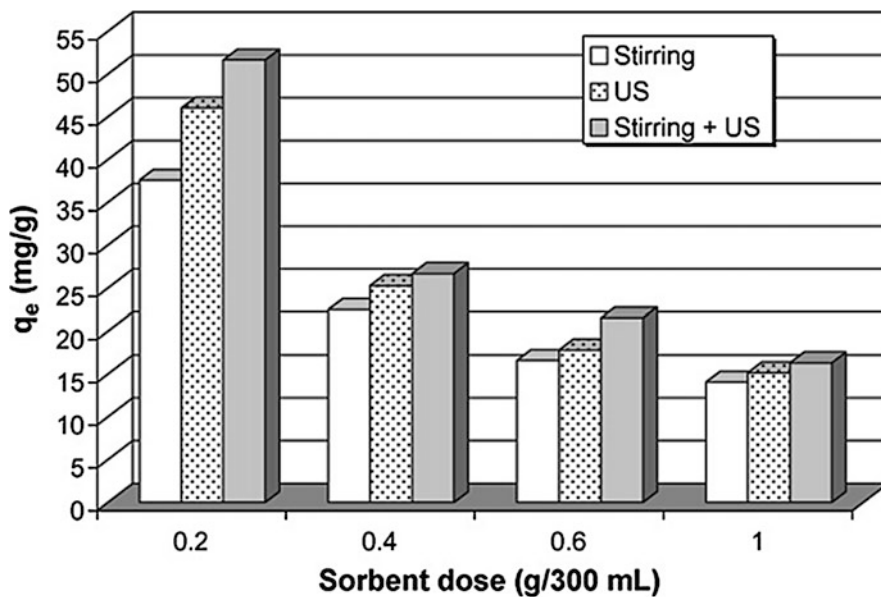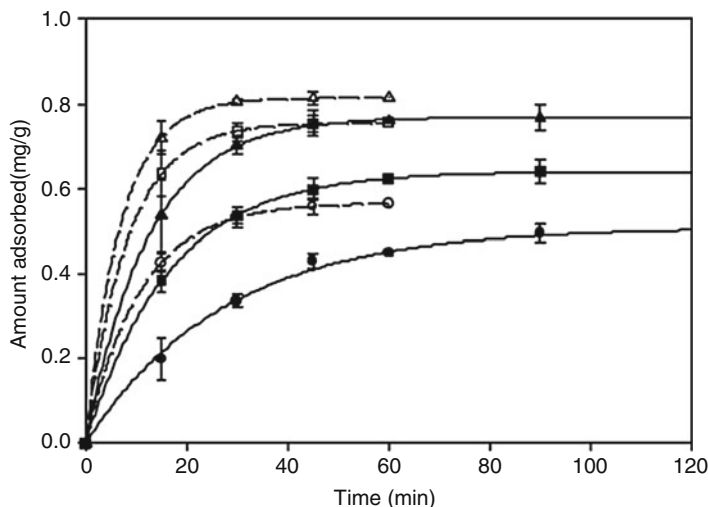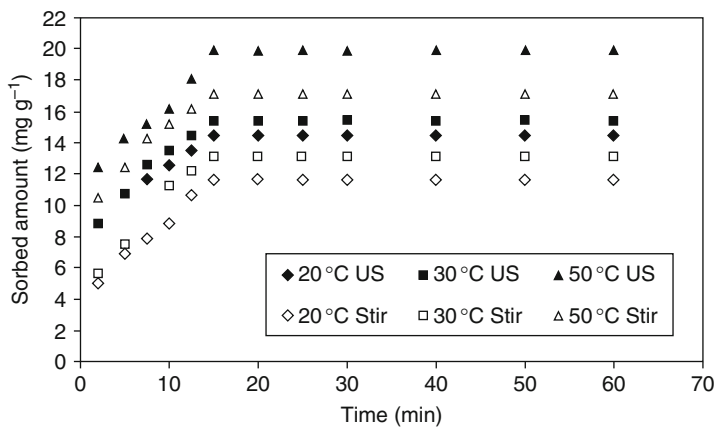

Fig. 12 Effect of temperature on the sorption kinetics with and without the assistance of ultrasound (C_0 = 100 mg L^{-1}, sorbent dose 0.6 g/300 mL, T 30 °C) [70]

Entezari et al. [72] investigated the influence of ultrasound for the removal of cadmium in two different ways: (a) constant sorbate concentration and variable amount of sorbent and (b) constant amount of sorbent and variable sorbate concentration in the presence and absence of ultrasound with the help of natural clay. As shown in Fig. 14, after 6 min, more than 95 % of the pollutant was removed in the presence of ultrasound. Figure 15 demonstrates that the slopes of the curves are
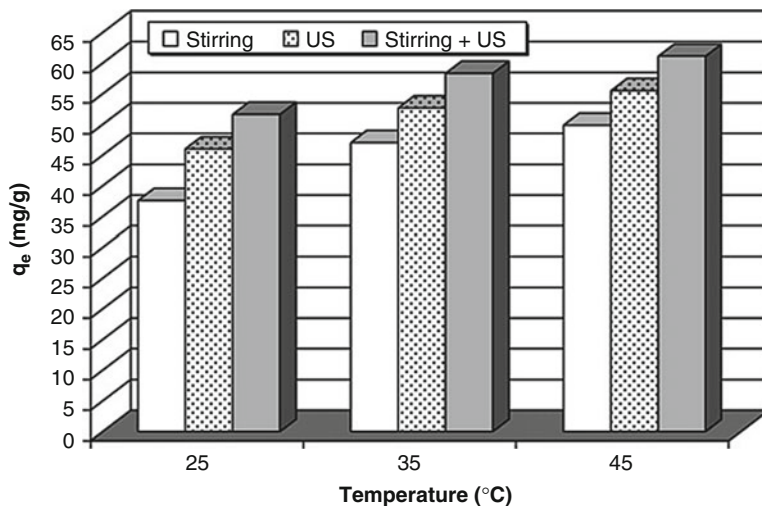
Fig. 13 Effect of temperature on the sorption of cadmium by olive leaves (conditions: 300 mL of cadmium solution, initial concentration 100 mg L^{-1}, sorbent mass 0.2 g, acoustic power 10 W, stirring speed 400 rpm, pH 5.3, temperature 25–45 °C) [71]
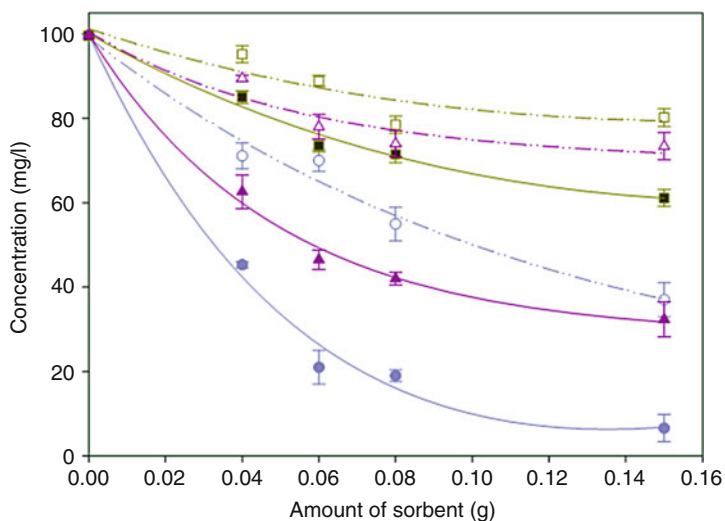
Fig. 14 Effect of amount of sorbent on the removal of cadmium ion (temp. = 27 °C, stirring speed = 300 rpm, C$_0$ = 99.6 mg L^{-1}, intensity = 25 %). (•) ultrasound (6 min), (o) classic (6 min), (▲) ultrasound (3 min), (Δ) classic (3 min), (■) ultrasound (1 min), and (□) classic (1 min) [72]

Fig. 15 Effect of amount of sorbent on the removal of cadmium ion ion (temp. = 27 °C, stirring speed = 300 rpm, C_0 = 93.25 mg L^{-1}, intensity = 25 %). (•) ultrasound (30 s), (o) classic (30 s), (▲) ultrasound (3 min), (Δ) classic (3 min), (■) ultrasound (6 min), (□) classic (6 min) [72]

higher in larger sorbate/sorbent ratio which is due to lower number of sites for sorption and higher concentration of sorbate. This condition can lead to a higher removal rate wh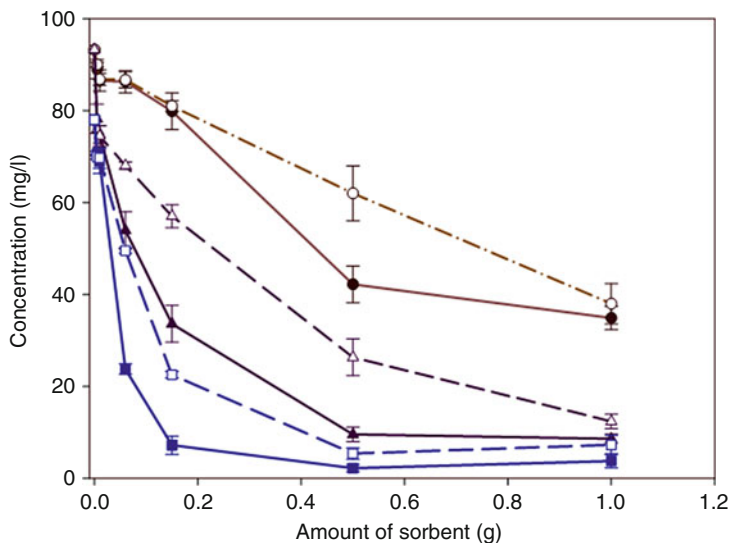ich could be related to a better contact between pollutant and sorbent sites. These slopes are also steeper in the presence of ultrasound which may be due to a better mass transfer in the presence of ultrasound. As a result, under appropriate experimental conditions, especially optimal intensity of ultrasound and sorbate/ sorbent concentration ratio, it is possible to remove cadmium ion from the solution quickly and efficiently. At higher intensity, a lower concentration ratio is more effective for longer times, but at lower intensity, a higher concentration ratio is more effective for shorter times.

Zhang et al. [73] reported on the effects of ultrasound on the adsorption capacity of Fe_3O_4 magnetic particle sorbent for a batch removal of chromate [Cr(VI)] from simulated wastewater. Comparison experiments were also performed in the presence and absence of ultrasound. The results shows that the Cr(VI) removal capacity of sorbent improved by a factor of about six times with ultrasonic irradiation (Fig. 16). Further, investigation such as the applied ultrasonic frequency and power in the context of Cr(VI) removal increased by about 230 % when the ultrasonic frequency was increased from 40 to 59 kHz and by 310 % when the ultrasonic power was increased from 40 to 200 W. This can be explained by the resonance size of the cavitation bubbles and the collapse times of the cavitation bubbles. It is well known that the ultrasonic frequency has a significant influence on cavitation [73].

The adsorption isotherm results were fitted with Freundlich and Langmuir isotherm models, which can be expressed as in Eqs. 13 and 14, respectively [73].
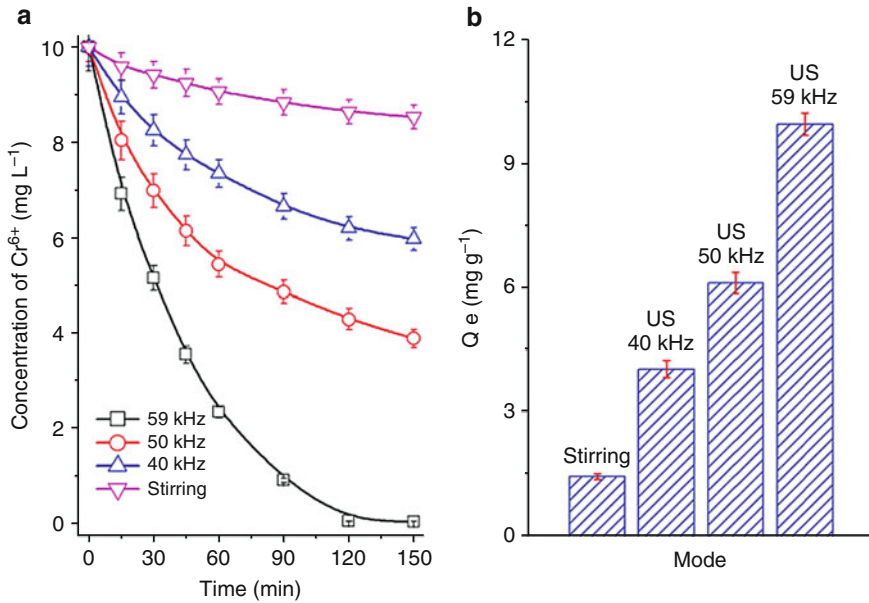
Fig. 16 Effect of ultrasonic frequency on the sorption of Cr(VI): (**a**) concentration of Cr(VI) in solution after adsorption versus time and (**b**) Qe versus ultrasonic frequency (sorbent, 0.05 g; pollutant, 10 mg L^{-1}; temperature, 318 ± 2 K; US, ultrasound; stirring rate, 600 rpm) [73]

Table 6 Adsorption isothermal constants calculated for the Langmuir and Freundlich models [73]

	Freundlich			Langmuir		
Mode	K_F	$1/n$	R^2	Q^0 (g mg^{-1})	K_L (L mg^{-1})	R^2
Ultrasound	16.14	0.40	0.90	12.04	19.70	0.99
Stirring	0.14	0.63	0.94	3.63	0.093	0.93

$$\frac{1}{Q_e} = \frac{1}{Q^0} + \frac{1}{K_L Q^0}\frac{1}{C_e} \tag{13}$$

$$\log Q_e = \log K_F + \frac{1}{n}\log C_e \tag{14}$$

The values of the correlation coefficients (R^2), K_L, K_F, and Q^0 calculated from the Langmuir model for Cr(VI) sorption on the Fe_2O_4 composite with ultrasonic assistance are listed in the Table 6. Comparison between the stirred and ultrasonic modes (Fig. 16) clearly shows that the application of ultrasound changes the equilibrium for each point to higher sorption. The values of Q^0 and K_L increased from 3.63 and 0.093 L mg^{-1} in stirring mode to 12.04 mg g^{-1} and 19.70 L mg^{-1}, respectively, in ultrasound mode due to the better sorbent distribution promoted by ultrasound. Entezari et al. [69] reported on the removal of chromium by ultrasound-assisted
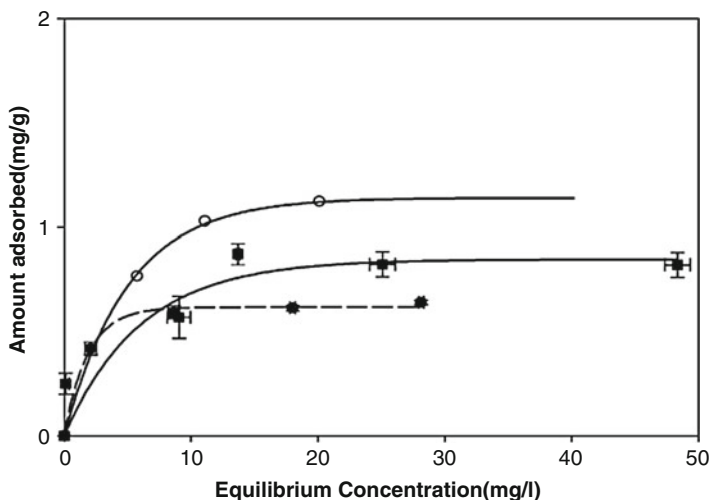
Fig. 17 Sorption isotherms of Cr(III) on tire powder in the presence of ultrasound, stirring, and a combination at 30 °C: (■) stirring, (•) sonication, (o) stirring + sonication [69]

sorption process. The removal of chromium through ultrasound-assisted sorption process by using rubber powder exhibited a Langmuir isotherm which clearly illustrates that ultrasonic irradiation changed the equilibrium leading to a higher removal of chromium compared to conventional treatment (Fig. 17). Further, Entezari et al. [69] have investigated the effect of temperature on the removal of chromium in the presence and absence of ultrasound through sorption process, and the results are shown in Fig. 18. The results indicate that the removal capacity of chromium in the presence of rubber and ultrasound was increased with an increase in temperature. The amount of chromium removal increased from 53 % to 100 % at 50 °C under 60 min sonication time.

It is known that energy is transferred upon cavitation bubbles growing and then collapsing during sonication. When a bubble collapses, strong localized physical forces are generated surrounding nearby solid particles of sorbent. These effects have a greater efficiency of interfacial mixing than conventional agitation, and therefore, ultrasound enhances the rate of sorption. In addition, the collapse of the bubble near the sorbent promotes dispersion of agglomerated magnetic particles, thereby increasing the surface area of the sorbent. The experimental data also reveal that the Langmuir isotherm fits the ultrasonic data more favorably than the data of stirring mode. Meanwhile, ultrasonic irradiation also produces more active sites for adsorption, which leads to a higher efficiency of chromium removal from aqueous solution and changes the equilibrium position [17, 18, 20, 22–24, 31, 54, 55, 69].

Milenkovic et al. [25] reported on the removal of Cu(II) ions from aqueous solution by ultrasound-assisted adsorption onto granular activated carbon obtained from hazelnut shells. The adsorption isotherms of Cu(II) ions on granular activated carbon from hazelnut shells at 25 °C in the absence of ultrasonic field as well as in
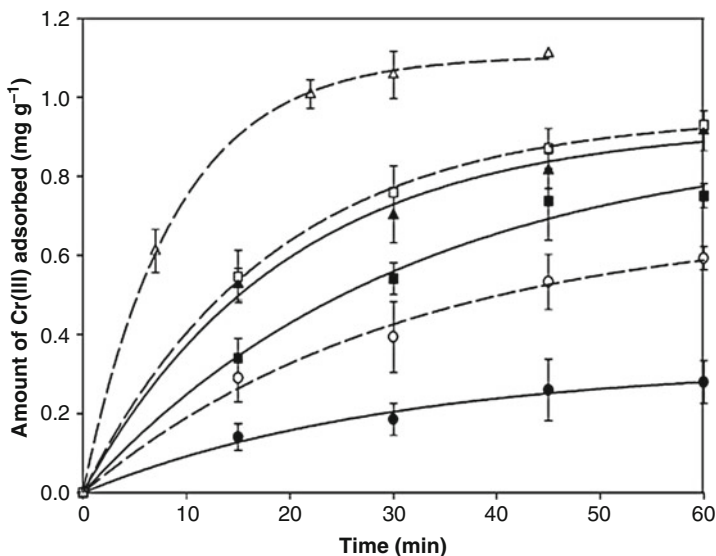
Fig. 18 Effect of temperature on the sorption of Cr(III) in the presence and absence of ultrasound (sorbent = 1 g, pollutant = 18.50 ppm): (•) stirring (30 °C), (■) stirring (40 °C), (▲) stirring (50 °C), (O) sonication (30 °C), (□) sonication (40 °C), (Δ) sonication (50 °C) [69]

the presence of ultrasonic field are shown in Fig. 19. As can be seen from Fig. 19, the amount of Cu(II) ions adsorbed on the granular activated carbon in the presence and absence of ultrasound is 3.77 mmol g^{-1} and 3.14 mmol g^{-1}, i.e., 20 % higher than that in the absence of ultrasound. The adsorption process in the absence and the presence of ultrasound obeyed pseudo second-order kinetics.

The major benefit of sonication is the increase in the adsorption capacity of the granular activated carbon due to the promotion of intraparticular diffusion. Further, investigation on the variations of initial concentration of Cu(II) ions a illustrates that ultrasound has significant influence on the kinetics of Cu(II) ions adsorption on granular activated carbon obtained from hazelnut shells. In the beginning of the adsorption process, Cu(II) ions were rapidly adsorbed, then the adsorption rate was slowed down, and finally an equilibrium was gradually reached. The highest rates of Cu(II) ion removal at the beginning are probably due to the larger surface area of hazelnut shells available for adsorption and probably the strong interaction between the Cu(II) ions and the surface of adsorbent. In the later periods, the surface adsorption sites become exhausted, and the removal rate is controlled by the rate of Cu(II) ions transportation from the exterior to the interior sites of the adsorbent particles. The cavitation process increased the diffusion process by the micro-jet and streaming produced in the collapse of the cavity. Ultrasound affected the distribution of the sites of energy (a homogeneous distribution) in addition to the effects of cavitation. Similar results are reported by Entezari et al. [74] on the effect of ultrasound on the sorption capacity of saffron corm for removal of Cu(II) ions.
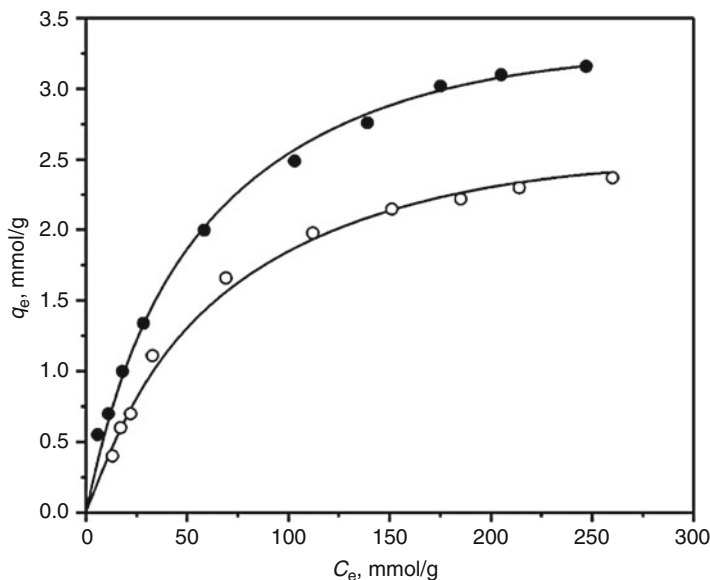
Fig. 19 Adsorption isotherms of Cu(II) ions on granular activated carbon from hazelnut shells in the absence (o) and in the presence of ultrasound (•) at 25 °C [25]

Langmuir isotherm model fits adequately the experimental data, and more than 60 % of copper ions was removed within 2 min from the solution in the presence of ultrasonic irradiation. Ultrasound-assisted recovery of copper from printed circuit board waste sludge has been reported by Xie et al. [28] They found that ultrasound-assisted separation efficiency of copper is higher than that of without assistance of ultrasound. The recovery efficiency of copper is ~98 % under optimized condition, such as pH 3.0, an ultrasonic generator power of 160 W, and time of 60 min. Further, the technique was successfully applied to industrial scaled applications in a heavy metal recovery plant in the city of Huizhou, China, for more than 2 years. Acoustic cavitation enhanced the dissolution of copper hydroxide into liquid phase.

Removal of Pb(II), a toxic heavy metal ion, onto styrene-divinylbenzene copolymer resin in the presence of ultrasound and classical method is reported by Entezari et al. [75] In the context of Pb (II) removal, batch experiments were conducted on the lead ion concentration versus contact time for a given concentration of sorbent (0.3 g) at different temperatures (Fig. 20). The initial concentration was 100 mg L^{-1} and the removal of lead ion was faster in the presence of ultrasound. As shown in Fig. 20, the amount of sorption of Pb(II) onto the resin increased rapidly at the beginning and then reached equilibrium. The sorption capacity of resin increased with increasing the temperature. This indicates that the sorption process is endothermic in nature and it is the reason for higher sorption at higher temperatures. In the presence of ultrasound, the lead is almost completely removed in 3 min at 50 °C which may be due to high interaction with resin especially in the presence of
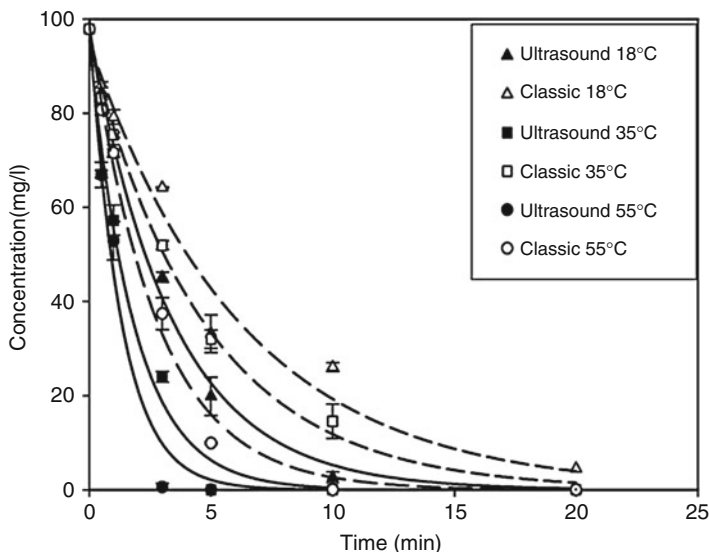
Fig. 20 Effect of contact time on the sorption of lead at different temperatures (stirring speed, 300 rpm; C_0, 100 mg L^{-1}; dose of sorbent, 0.3 g; acoustic power at position 25 %, 55.9 W) [75]

ultrasound. It is assumed that the shear forces generated in the medium due to the cavitation process may be the primary pathway for the morphology and the surface area changes of sorbent, which lead to higher removal rate. Langmuir model fitted better with the experimental data compared to Freundlich model. The kinetics of sorption was obeyed the pseudo first-order and first-order reversible models.

The simultaneous removal of copper and lead ions from a binary aqueous solution in the presence and absence of ultrasound has been reported recently [74]. The experiments under sonication were carried out using 20-kHz horn. Results indicated that the removal of copper and lead ions from a binary aqueous solution was greater in the presence of ultrasound, and the experimental data fitted very well with Langmuir model in the studied range of concentrations and temperatures. Second-order kinetic model could be used to describe the sorption process for both the ions. It was found that more than 90 % of lead and 60 % of copper ions were removed in <2 min time period. The affinity of lead ion was higher than copper ion with respect to the sorbent, and the ultrasound enhanced the removal of both ions from the binary solution. Further, the effect of ultrasound on the simultaneous removal of Cd^{2+} and Pb^{2+} ions from a binary aqueous solution in the presence of natural sorbent was studied by Entezari and Soltani [76]. It was found that the sorption efficiency of Cd^{2+} was decreased in the presence of Pb^{2+}. The observed differences in the removal of ions in binary solution can be due to solute–solute competition and solute–surface interactions. The results show that the functional groups on the surface of the sorbent had a relatively stronger affinity for Pb^{2+} than for Cd^{2+}. In the case of Pb^{2+}, the sorption is very fast and efficient which is due to the low activation energy. But this

Table 7 Optimal conditions analysis for heavy metal extraction by nitric acid assisted by ultrasound [15]

Heavy metal	Cu	Zn	Pb
Optimal duration of ultrasonication (min)	20	20	20
Optimal nitric acid concentration (mol L^{-1})	0.325	0.325	0.325
Extracted heavy metal content (mg kg^{-1})	27	1,033	656
Extraction efficiency (%)	9.5	82	87
Contribution proportion of ultrasonication (%)	22	19	18
Contribution proportion of nitric acid (%)	77	80	82

effect was important for the removal of Cd^{2+}. This ion was almost completely removed at 40 °C in the presence of ultrasound. Different multicomponent isotherm equations based on the Langmuir isotherm were used to predict the behavior multicomponent ion systems. In this study, the extended Langmuir model and the P-factor model were applied. Both models showed that the interaction and competition between the ions was negligible for the sorption of Pb^{2+}, but for Cd^{2+} the competition led to the decrease of removal of Cd^{2+} in the presence of Pb^{2+}.

Deng et al. [15] have investigated the removal of heavy metals such as copper, zinc, and lead from sewage sludge in the presence of nitric acid under the ultrasonic irradiation. The concentration of nitric acid was varied from 0 to 0.65 M under the ultrasonic irradiation. The results indicated that the removal efficiencies of Cu, Zn, and Pb increased with an increase in nitric acid concentration in the presence of ultrasonic irradiation. The optimal nitric acid concentration for heavy metal extraction was 0.325 M, while a 20 min sonication resulted in maximal heavy metal removal efficiency. The removal efficiencies of Cu, Zn, and Pb reached 9 %, 82 %, and 87 %, respectively, at the optimal concentration of nitric acid assisted by ultrasound for 20 min. Ultrasound alone was not effective enough to remove heavy metals from sludge, and the role played by nitric acid predominated over that of ultrasound. However, ultrasound was synergistic with nitric acid when these were used together to extract heavy metals from sludge. Optimal condition analysis for heavy metal extraction by nitric acid assisted by ultrasound is given in Table 7.

Conclusions

Nowadays, significant research has been focused on the search for alternative and innovative techniques for removal of heavy metals from aqueous environment. It has been shown that ultrasonic technology could be effective for the removal of heavy metals from aqueous solutions and sludges. In addition, a combination of ultrasound with adsorbent materials has exhibited excellent performance to remove heavy metals from the polluted environment, and this process is economic and eco-friendly. Acoustic cavitation-generated OH radicals play important role for removal of ions of heavy metals such as Arsenic. The physical effects of ultrasound and cavitation process also play a major role in ultrasound-assisted adsorption of

heavy metal contaminants. Increased mass transfer caused by the physical effects of cavitation is responsible for the observed enhancement in heavy metal removal. Despite lab-scale studies available in the literature, industrial scale processes have not been developed for heavy metal removal using ultrasound. Further optimization work and the development of custom-made ultrasonic equipment are necessary to move this technology to large-scale applications.

References

1. Tchounwou P, Yedjou C, Patlolla A, Sutton D, Luch A (ed) (2012) Heavy metal toxicity and the environment. Springer, Basel, p 133
2. Järup L (2003) Br Med Bull 68:167
3. Li Z, Ma Z, van der Kuijp TJ, Yuan Z, Huang L (2014) Sci Total Environ 468–469:843
4. Pacyna EG, Pacyna JM, Fudala J, Strzelecka-Jastrzab E, Hlawiczka S, Panasiuk D, Nitter S, Pregger T, Pfeiffer H, Friedrich R (2007) Atmos Environ 41:8557
5. Hu X-F, Jiang Y, Shu Y, Hu X, Liu L, Luo F (2014) J Geochem Explor 147(Part B):139
6. Hu Y, Liu X, Bai J, Shih K, Zeng E, Cheng H (2013) Environ Sci Pollut Res 20:6150
7. Duruibe JO, Ogwuegbu MOC, Egwurugwu JN (2007) Int J Phys Sci 5:112
8. Wang J, Chen C (2006) Biotechnol Adv 24:427
9. Nguyen TAH, Ngo HH, Guo WS, Zhang J, Liang S, Yue QY, Li Q, Nguyen TV (2013) Bioresour Technol 148:574
10. Chen M, Xu P, Zeng G, Yang C, Huang D, Zhang J (2015) Biotechnol Adv 33:745
11. Nancharaiah YV, Venkata Mohan S, Lens PNL (2015) Bioresour Technol 195:102
12. Tang W-W, Zeng G-M, Gong J-L, Liang J, Xu P, Zhang C, Huang B-B (2014) Sci Total Environ 468–469:1014
13. Hua M, Zhang S, Pan B, Zhang W, Lv L, Zhang Q (2012) J Hazard Mater 211–212:317
14. Ahluwalia SS, Goyal D (2007) Bioresour Technol 98:2243
15. Deng J, Feng X, Qiu X (2009) Chem Eng J 152:177
16. Hristozov D, Domini CE, Kmetov V, Stefanova V, Georgieva D, Canals A (2004) Anal Chim Acta 516:187
17. de La Rochebrochard S, Naffrechoux E, Drogui P, Mercier G, Blais J-F (2013) Ultrason Sonochem 20:109
18. Kazi TG, Jamali MK, Siddiqui A, Kazi GH, Arain MB, Afridi HI (2006) Chemosphere 63:411
19. Jonathan PM, Craig EB, Bruno GP (2014) Sonoelectrochemical synthesis of nanomaterials, cavitation: a novel energy efficient technique for the generation of nanomaterials. In Sivakumar M, Muthupandian A (eds), Pan Stanford Publishing, Singapore
20. Neppolian B, Doronila A, Ashokkumar M (2010) Water Res 44:3687
21. Wang X, Chen J, Yan X, Wang X, Zhang J, Huang J, Zhao J (2015) J Ind Eng Chem 27:368
22. Fontana A, Braekman-Danheux C, Jung CG (1996) Fuel Process Technol 48:107
23. Neppolian B, Doronila A, Grieser F, Ashokkumar M (2009) Environ Sci Technol 43:6793
24. He Z, Siripornadulsil S, Sayre RT, Traina SJ, Weavers LK (2011) Chemosphere 83:1249
25. Milenković DD, Dašić PV, Veljković VB (2009) Ultrason Sonochem 16:557
26. Lesa B, Aneggi E, Rossi G, Comuzzi C, Goi D (2009) J Hazard Mater 171:647
27. Şayan E (2006) Chem Eng J 115:213
28. Xie F, Li H, Ma Y, Li C, Cai T, Huang Z, Yuan G (2009) J Hazard Mater 170:430
29. Kalidhasan S, Santhana Krishna Kumar A, Vidya R, Rajesh N (2012) J Hazard Mater 213–214:249
30. Liu W, Zhang J, Cheng C, Tian G, Zhang C (2011) Chem Eng J 175:24
31. Zhang P, Ma Y, Xie F (2013) J Mater Cycles Waste Manag 15:530
32. Wang J, Chen C (2009) Biotechnol Adv 27:195
33. Bohli T, Ouederni A, Fiol N, Villaescusa I (2015) C R Chim 18:88

34. Luo X, Zhang Z, Zhou P, Liu Y, Ma G, Lei Z (2015) J Ind Eng Chem 27:164
35. Tao H-C, Zhang H-R, Li J-B, Ding W-Y (2015) Bioresour Technol 192:611
36. Dobrowolski R, Stefaniak E (2000) Adsorpt Sci Technol 18:97
37. Gomez-Serrano V, Macias-Garcia A, Espinosa-Mansilla A, Valenzuela-Calahorro C (1998) Water Res 32:1
38. Karnib M, Kabbani A, Holail H, Olama Z (2014) Energy Procedia 50:113
39. Tunay O (2003) Water Pollut Res 48:43
40. Charerntanyarak L (1999) Water Sci Technol 39:135
41. Jüttner K, Galla U, Schmieder H (2000) Electrochim Acta 45:2575
42. Wingenfelder U, Hansen C, Furrer G, Schulin R (2005) Environ Sci Technol 39:4606
43. Jain A, Sharma VK, Mbuya OS (2009) J Hazard Mater 169:339
44. Jiang JQ (2007) J Hazard Mater 146:617
45. Kurniawan TA, Chan GYS, Lo W-H, Babel S (2006) Chem Eng J 118:83
46. Ahn K-H, Song K-G, Cha H-Y, Yeom I-T (1999) Desalination 122:77
47. Tzanetakis N, Taama WM, Scott K, Jachuck RJJ, Slade RS, Varcoe J (2003) Sep Purif Technol 30:113
48. Fernández Y, Marañón E, Castrillón L, Vázquez I (2005) J Hazard Mater 126:169
49. Sapari N, Idris A, Hamid NHA (1996) Desalination 106:419
50. Álvarez-Ayuso E, García-Sánchez A, Querol X (2003) Water Res 37:4855
51. Lin SH, Kiang CD (2003) Chem Eng J 92:193
52. Dobrevsky I, Dimova-Todorova M, Panayotova T (1997) Desalination 108:277
53. Ahmed S, Chughtai S, Keane MA (1998) Sep Purif Technol 13:57
54. Suslick KS (1990) Science 247:1439
55. Kimura T, Sakamoto T, Leveque J-M, Sohmiya H, Fujita M, Ikeda S, Ando T (1996) Ultrason Sonochem 3:S157
56. Sehgal CM, Wang SY (1981) J Am Chem Soc 103:6606
57. Xu H, Zeiger BW, Suslick KS (2013) Chem Soc Rev 42:2555
58. Bang JH, Suslick KS (2010) Adv Mater 22:1039
59. Suslick KS, Price GJ (1999) Annu Rev Mater Sci 29:295
60. Adewuyi YG (2001) Industrial and engineering chemistry research 40:4681
61. Ashokkumar M, Grieser F (2004) ChemPhysChem 5:439
62. Anbar M, Pecht I (1964) J Phys Chem 68:1460
63. Mark G, Tauber A, Laupert R, Schuchmann H-P, Schulz D, Mues A, von Sonntag C (1998) Ultrason Sonochem 5:41
64. Dutta PK, Pehkonen SO, Sharma VK, Ray AK (2005) Environ Sci Technol 39:1827
65. O'Shea KE, Cardona C (1994) J Org Chem 59:5005
66. Lee H, Choi W (2002) Environ Sci Technol 36:3872
67. Gil S, Lavilla I, Bendicho C (2008) Ultrason Sonochem 15:212
68. Entezari MH, Ghows N, Chamsaz M (2006) J Hazard Mater 131:84
69. Entezari MH, Ghows N, Chamsaz M (2005) J Phys Chem A 109:4638
70. Nouri L, Hamdaoui O (2007) J Phys Chem A 111:8456–8463
71. Hamdaoui O (2009) Chem Eng Process Process Intensif 48:1157–1166
72. Entezari MH, Bastami TR (2008) Ultrason Sonochem 15:428–432
73. Zhang W-B, Deng M, Sun C-X, Wang S-B (2014) Ind Eng Chem Res 53:333–339
74. Entezari MH, Soltani T (2008) J Hazard Mater 160:88–93
75. Entezari MH, Bastami TR (2006) J Hazard Mater 137:959–964
76. Entezari MH, Soltani T (2009) Cadmium and lead ions can be removed simultaneously from a binary aqueous solution by the sono-sorption method. Ultrason Sonochem 16:495–501

Role of Process Intensification by Ultrasound

Bhakar Bethi, Shirish Sonawane, and Bharat Bhanvase

Contents

Abstract

Acoustic and hydrodynamic cavitations have proved a milestone as process intensification devices, especially in wastewater treatment processes. Generation of cavities and their subsequent collapse is a common principle of both types of

B. Bethi (✉) • S. Sonawane
Department of Chemical Engineering, National Institute of Technology, Warangal, Telangana, India
e-mail: shirishsonawane09@gmail.com

B. Bhanvase
Department of Chemical Engineering, Laxminarayan Institute of Technology, Rashtrasant Tukadoji Maharaj Nagpur University, Nagpur, Maharashtra, India
e-mail: bharatbhanvase@gmail.com

cavitations by which chemical and physical changes take place. There are a number of potential challenges which are not yet resolved in developing a water treatment technology using hydrodynamic and acoustic cavitation. When it is compared with the conventional water treatment technique, the cavitational approach shows significant difference in treatment time required and degradation efficiency of organic pollutants. In this book chapter, current trends of developments of hybrid wastewater treatment processes using ultrasound and hydrodynamic cavitation are discussed with examples: hybrid system development using hydrogel, ultrasound and hydrodynamic cavitation for degradation of dyes, and hybrid wastewater treatment system for adsorption of phenol using nanoclay and ultrasound. Water treatment using doped photocatalytic materials/hydrodynamic cavitation is discussed. The scale-up issues specifically for the development of wastewater treatment system using cavitation technique for mixed dyes are also reported.

Introduction

Day-to-day growth of urbanization, commercialization, and industrialization requires the need of fresh water. Release of wastewater from these sources consists of many harmful and toxic chemicals that adversely affect human and aquatic life. Treatment of wastewater from those polluting sources was concerned with the treatment of biodegradable organics and the degradation of pathogenic organisms via conventional methods (physical, chemical, and biological); however, these conventional treatment techniques failed to meet the demands of the newer environmental regulations. The water pollution from urbanization can be treated with the conventional treatment techniques, such as biological treatment techniques, which involve either aerobic or anaerobic biological treatment techniques. These biological treatment techniques are not suitable for treatment of textile wastewater as it contains complex organic chains and creates a toxic environment. Due to the presence of color in the form of organic components in the water, it is not suitable for any use. Even the presence of very less ppm of organic components in water shows toxicity to animals and plants. The most common dye used in dyeing industries contains 60–70 % of azo dyes [1]. However, studies on various azo dyes show that most azo dyes are carcinogenic, mutagenic, and toxic and resistant to biological and other conventional treatment techniques [2–5]. The conventional treatment technique includes physical, chemical, and biological treatment, such as adsorption [6–8], coagulation [9], and bio-sorption [10–12]. However, these treatment techniques usually involve high costs of treatment, longer treatment time, and lower percentage of removal/degradation, which limit the use of these techniques. This is applicable not only for dyes; some other wastewater sources also come under this category,

such as wastewater consisting of phenol, pesticides, etc. Hence, it is necessary to find an effective treatment technology that can degrade complex molecules or can break down into smaller molecules, which can be further degraded by conventional biological treatment techniques.

Researchers and technologists together had developed the efficient, economically feasible, time-saving process based on the oxidation technique called advanced oxidation process (AOP). Advanced oxidation process involves the generation of hydroxyl radicals which is the basis for the degradation of recalcitrant organic pollutants present in various industrial wastewaters. In the past, enormous research has been carried out on AOPs which includes photocatalysis, ozonation, UV/H_2O_2, etc. Acoustic and hydrodynamic cavitation has been considered as one of the advanced oxidation processes. It has been recognized as the most effective and energy-efficient treatment technique among other AOPs [4, 12]. Cavitation combined with other AOPs such as photocatalysis, H_2O_2, and ozonation has been proven to be an efficient treatment technique for complete mineralization of organic components [3].

Cavitation methods are mainly classified into four types based on the way of production of cavities.

(i) Acoustic cavitation

This is one type of cavitation technique; in this case, high-frequency ultrasound waves (usually 16 kHz–100 MHz) are the basis for the generation of cavities. The cyclic compression and expansion cycles create the cavities in the liquid medium. Generally, an ultrasonic probe or bath is used as a cavitating device for the production of cavities in the liquid. Subsequent growth and collapse of cavities generates the hydroxyl radicals [3].

(ii) Hydrodynamic cavitation

In this case, cavitation phenomena happen due to the pressure variations in flow line, which is obtained by changing the flow geometry in the pipeline flow. When a fluid flows through a narrow constriction which is provided in the line, the pressure at the narrow constriction falls below the vapor pressure of the liquid, and then cavities will form. The subsequent growth and collapse of cavities generates the hydroxyl radicals [13]. Usually an orifice and a venturi are used as cavitating devices to generate the cavities leading to hydroxyl radicals. Researchers also developed some new kinds of cavitating devices in the past decade such as the vortex diode, rotating disk, etc. [13].

(iii) Optic cavitation

This is one type of cavitation technique. It can be produced by passing photons of high-intensity light (laser) into the liquid continuum, where the photons rupture the liquid continuum and generate the small bubbles [14]. Application of the optic cavitation phenomena is not reported for the wastewater treatment due to less cavitation yield and high energy consumption.

(iv) Particle cavitation

In this case, cavities are produced by using a beam of elementary particles, e.g., a neutron beam rupturing a liquid, as in the case of a bubble chamber [14].

From these four types of cavitation, mainly acoustic and hydrodynamic cavitation generates the desired cavitational intensity that is suitable for chemical or physical processing.

Process Intensification

Process intensification can be defined as "any engineering development that leads to a substantially smaller in volume, cleaner, safer and more energy-efficient technology"[15]. It can be characterized by a huge reduction in plant volume by orders of magnitude. Stankiewicz and Moulijn [15] reported that as there is a growing worldwide competition in chemical production, it requires necessary changes in the ways of designing of plants and also suggests the important "key points" that would guide engineering developments in chemical industries. Key benefits from the process intensification involve reduction in capital investment, reduction in energy consumption, reduction in raw material cost, process safety, and better environmental performance [15].

Role of Ultrasound in Process Intensification

Ultrasound cavitation has two important effects in chemical transformations; in the case of water treatment, the generation of the radical is one important chemical effect, and higher shearing due to microjets introduces a drastic physical effect into the reactor. Due to these effects, a number of chemical reactions and processes can be intensified. In this book chapter, the role of cavitation as a process intensification device is discussed pertaining to wastewater treatment.

Recently ultrasonic irradiation is considered as an emerging advanced oxidation process since it generates the hydroxyl radicals as a result of ultrasonic vibrations [3]. The ultrasonic cavitation can be created by the transmission of ultrasonic waves in the range of 20–1000 kHz within the liquid [16]. The ultrasonic cavitation is defined as the formation, growth, and subsequent collapse of vapor- or gas-filled cavities which release enormous magnitudes of energy [13, 17]. During the cavity collapse process, the hydrophobic volatile nature of organic pollutants such as phenols or any other organic solvents in wastewater will undergo thermal pyrolysis in the gas phase inside the cavity, and the nonvolatile and hydrophilic organic polluted species can be degraded by $^\bullet$OH radical at the interface of the bubble surface in the bulk solution [3].

When ultrasonic waves are irradiated in a liquid medium, the molecules or particles swing at their mean positions. The molecules or particles come into contact with each other in the compression cycle and are drawn apart in the rarefaction cycle due to the variation of the acoustic pressure that involves a sinusoidal pattern [14]. If the applied acoustic pressure amplitudes are very large to break the molecular interaction, then cavities will form. This phenomenon is called as acoustic cavitation, due to the presence of the dissolved gas molecules and very fine suspended

particles acting as the extra nuclei for cavitation [14]. Under the extreme conditions, such as high temperatures of over several thousand Kelvin and high pressures of over several hundred atmospheres [14, 18–21], water molecules are thermally dissociated into hydrogen and hydroxyl radicals (H• and •OH) [18, 19]. With these intensifying techniques, researchers have recognized the cavitation as an emerging technology for wastewater treatment.

The combination of ultrasound irradiation with other AOPs such as photocatalytic oxidation [22], electrochemical [23], ozonation [24, 25], and particularly photo-Fenton and Fenton-like processes [26] has been reported to be a much more efficient and promising technique for the oxidative removal of recalcitrant organic pollutants compared to single AOPs.

The studies on various AOP's concluded that the single AOP's are inefficient,but the combination of below AOPs with the cavitation technique will work more efficiently:

- Ozone (O_3) [24]
- Hydrogen peroxide (H_2O_2) [27]
- Photo-Fenton system (Fe^{+3} + UV) [26]
- Photocatalysis (TiO2 + UV) [22]

Role of Hydrodynamic Cavitation in Water Treatment Processes

Reports on the applications of hydrodynamic cavitation are limited in the literature for the intensification of physical and chemical processes in various industries. But this technique has several advantages, which makes it a useful technique for industrial wastewater treatment application. Hydrodynamic cavitation can be easily scaled up to industrial application due to its capability of generating bulk hydroxyl radicals at ambient condition, and the fabrication cost makes this technique economically feasible to use in the industrial scale. In hydrodynamic cavitation, mainly cavities are formed due to the pressure variation in the flowing liquid in a pipe caused by a change in flow area by the incorporation of venturi and orifice plate in the liquid flow line [28]. According to the Bernoulli principle, when the liquid flows through the narrow constriction such as a venturi or an orifice, the kinetic head increases at the expense of the pressure head. If the throttling of the constriction is sufficient, the pressure which is present at the throat of the venturi equals or falls below the vapor pressure of that liquid, and then the vaporous cavities will form [13]. Further lowering the pressure, the cavities continue to grow and reach to its maximum size at minimum pressure, and whenever the liquid jet expands by reducing the flow velocity as a function of pipe length, the expanded pressure recovers at a particular point that results into the collapse of earlier formed cavities [28]. The microbubble/cavity collapse has the ability to generate localized "hot spots"; this phenomenon is known as the hot spot theory. These hot spots have a transient temperature of the order of 10,000 K and pressures of about 1000 atm over a microsecond interval [29]. Under this extreme conditions, water molecules dissociated into H• and •OH radicals. These •OH radicals are diffused into the bulk liquid medium where they

will react with organic pollutants [22]. The thermal decomposition of organic pollutants also occur in the hydrodynamic cavitation, the generated temperature and pressure through the cavity collapse are sufficient to break the bonds of organic molecules. Hence, the larger molecules can be broken down into smaller molecules [13]. The ability of developing cavitational condition by hydrodynamic cavitation is equivalent to that developed by acoustic cavitation, but the hydrodynamic cavitation technique is a capable and useful process-intensifying tool, which can be explored for the degradation of various organic pollutants at an industrial scale.

The hydrodynamic cavitation can scale up to the industrial scale for water treatment processes [6, 7]. The hydrodynamic cavitation can be described by using Bernoulli's theorem:

$$P_{static} + P_{Dynamic} = Constant\ = P_{static} + \frac{1}{2}\rho v^2$$

where P_{static} and $P_{dynamic}$ are static and dynamic pressures and ρ and v are the density and velocity of the liquid at the throat of the venturi or orifice. The sum of dynamic and static pressure is constant, and increase in dynamic pressure subsequently reduces the static pressure.

Ultrasound Cavitation-Based Hybrid Technique

Sono-sorption of Phenol Using Nanoclay

Case Study on Combined Effect of Ultrasound and Nanoclay on Adsorption of Phenol

Phenol is one of the most carcinogenic and nonbiodegradable common compounds found in many effluents of various industries especially from petrochemicals, pharmaceuticals, pesticides, paint, organic chemical manufacturing units, etc. A low ppm of phenol or the derivatives of phenol result in high levels of toxicity and also create foul odor to the water. It has been recognized as a major pollutant in the list of the EPA (USA). Many countries set the maximum allowable concentration of phenol or its derivates in the wastewater effluent streams which should be less than 1 ppm. Due to its nonbiodegradable and complex nature, phenol effluents are not suitable for the biological treatment. Various physicochemical treatment techniques such as electro-chemical degradation, chemical oxidation, membrane separation, and distillation are inefficient and involve high capital costs, high energy requirement, etc. Recently the cavitation technique either ultrasonic or hydrodynamic cavitation has been found as a process-intensifying device for the degradation of phenol or the derivatives of phenol in wastewater effluents [27].

Synthesis of Organically Modified Bentonite Nanoclay Under Sonication

Sonawane et al. [30] have studied the performance of organically modified bentonite nanoclay for the adsorption of phenol in the presence of an ultrasonic bath.

They have prepared different organically modified bentonite nanoclays from natural bentonite using TBAC, CTAB, and HDTMA surfactants for the adsorption studies of phenol on prepared nanoclays in the ultrasonic bath. Initially, TBAC-modified bentonite clay was prepared using 2.77 g of TBAC which was dissolved in 75 mL of distilled water containing a required quantity of hydrochloric acid. Instead of mechanical mixing, they used sonication for mixing at 80 °C for 30 min until a clear solution was obtained. In this way, they removed the ammonium salts which are present in the solution. Then, 3.25 g of bentonite was added to the above salt solution, and sonication was carried out for another 1.5 h. The precipitate which is formed after 1.5 h was carried out for filtration and again dispersed in hot water by mechanical stirring for 1 h. In the next stage chloride-free bentonite nanoclay has been obtained by the filtration. The final precipitate, they were thoroughly dried in an oven at 80 °C for 24 h to obtain the TBAC-modified bentonite nanoclay. The same procedure was used for the synthesis of CTAB- and HDTMA-modified bentonite nanoclays; they only changed the quantities of CTAB and HDTMA based on exchangeable ion content.

Adsorption of Phenol in Sonication Environment

Sonawane et al. [30] have carried out the sono-sorption of phenol in batch operation using an ultrasonic bath with the operating frequency of 22.5 kHz and a nominal power rate of 120 W (Ultrasonics Labline CL 500). The total acoustic power injected into the sample was calculated using the calorimetric method. The sono-sorption of phenol has been carried out for the stock solution of phenol containing 10 g/L. A 500 mL beaker containing 100 ml phenol solution was placed in the ultrasonic bath for the investigation of sono-sorption of phenol. Initial phenol concentration was considered in the range of 250–5000 mg/L. The mixture of phenol and nanoclay was irradiated for 10 min in the ultrasonic bath, and they observed that adsorption equilibrium has been reached in 1 h. Sono-sorption of phenol was carried out at room temperature in a batch mode using water circulation at the outer side of the bath.

It was reported that the method of synthesis also produces an effect on equilibrium adsorption. In the case of conventionally modified nanoclays, the sonosorption of phenol (2000 mg/L) was shown 37 % adsorption, whereas sonochemically synthesized clays show 50 % adsorption. They also reported that higher concentrations of phenol in liquid medium were irradiated under ultrasound for the three nanoclays showing that the equilibrium was achieved in a very short time (10 min). The concentration of phenol as a function of time in the hybrid technique (sonosorption) is shown in Fig. 1.

It was found that in the absence of ultrasonic irradiation, the equilibrium was achieved in 45 min, whereas for unmodified clay it has been found to be 40 min. The effect of different initial concentrations of phenol in sono-sorption, ranging from 250 to 5000 ppm, is shown in Fig. 2.

Irradiation of phenol in the presence of 0.5 g clay shown the better adsorption capacity. For all nanoclays, adsorption equilibrium time and adsorption time have been the same when 2000 ppm of phenol was used. 2000 ppm of phenol concentration was shown the equilibrium concentration. Therefor 2000 ppm concentration
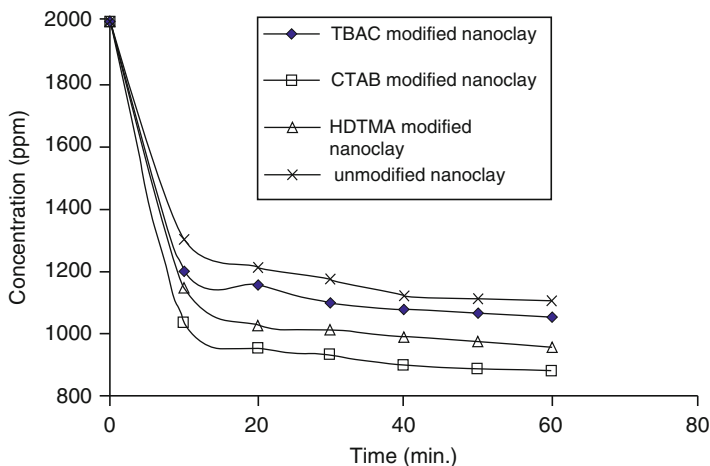
Fig. 1 Concentration of phenol as a function time in the hybrid technique (sono-sorption) [30]
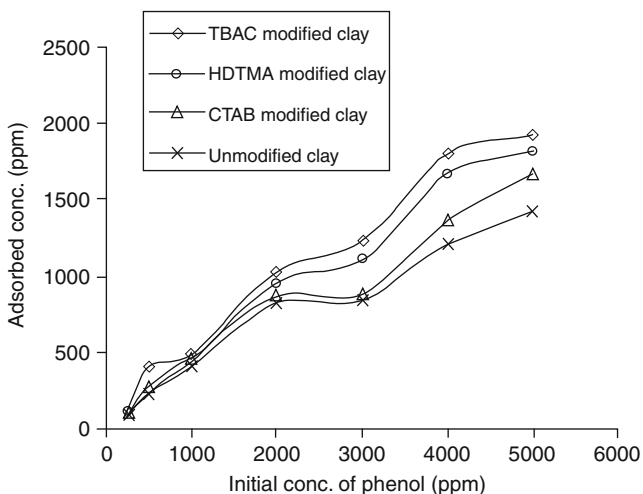
Fig. 2 Effect of different initial concentrations of phenol in sono-sorption, ranging from 250 to 5000 ppm [30]

were chosen as optimum concentration. It is found that the 2000 ppm concentration of phenol is sufficient to reach the equilibrium. This fact can be observed in Fig. 2. It will show over 5000 ppm of initial concentration of phenol; all the modified clays have shown the maximum adsorption of phenol below 2000 ppm on 0.5 g of each clay in 60 min of study. This point has been taken into consideration of 2000 ppm for the adsorption studies. With increase in phenol concentration, the adsorption rate in all three nanoclays increases. It was reported that ultrasonication is capable to alter the TBAC-modified clay which results into more exfoliation, hence the saturation of
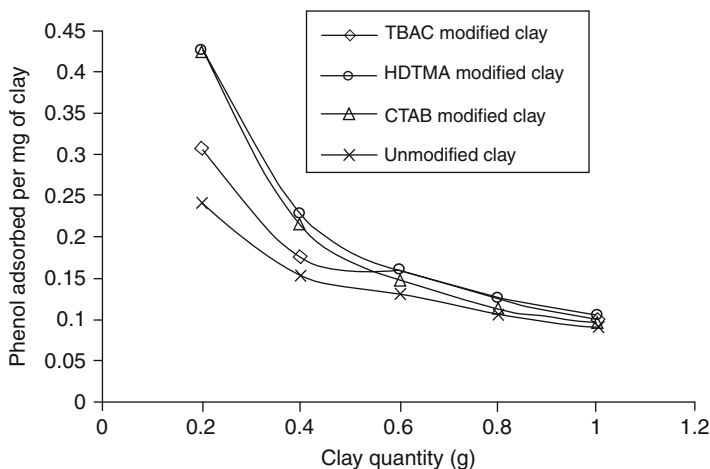
Fig. 3 Effect of nanoclay loading for the sono-sorption of phenol at 2000 ppm concentration [30]

adsorbent attained at early stage. The modified CTAB and HDTMA nanoclays take more time to get the phenol incorporated inside the clay platelets, hence there is more diffusion resistance to pass the phenol onto the nanoclay [31]. The effect of nanoclay loading for the sono-sorption of phenol at 2000 ppm concentration was shown in Fig. 3.

They also reported that, with the increase in clay loading into the ultrasonic bath, phenol adsorption has been decreased onto all three types of nanoclay. Two thousand ppm concentration of phenol has been considered as the optimum concentration for the sono-sorption using these three nanoclays. It was observed that TBAC-modified nanoclay is a suitable adsorbent for the adsorption of phenol, having the concentration of 2000 ppm in the phenolic water effluents.

Adsorption Isotherm Models
In order to understand the adsorption isotherm model for the three modified nanoclays, a Langmuir isotherm model linear plot of C_e/q_e versus C_e is shown in Fig. 4.

From the R^2 values, it was found that all three nanoclays do not favor the monolayer Langmuir adsorption isotherm. Linear plot of log q_e versus log C_e indicated that the sono-sorption follows the Freundlich isotherm model for all modified nanoclays. K and 1/n were calculated from the intercept and slope. If 1/n = 1, then the adsorption is linear, i.e., the adsorption sites are homogeneous in nature and there is no interaction between the adsorbed sites. If 1/n is less than 1, then the adsorption is favorable; it means that the adsorption capacity increases and a new adsorption site appears. For HDTMA-modified nanoclay, the value of 1/n was found to be 0.8544; it is less than 1, so it indicates favorable adsorption. A similar type of trend was also reported for the adsorption of phenol and dye onto bentonite clay [32, 33] and acid blue 193 dyes onto Na bentonite and HDTMA bentonite [34] and clay–wood sawdust mixture [35].
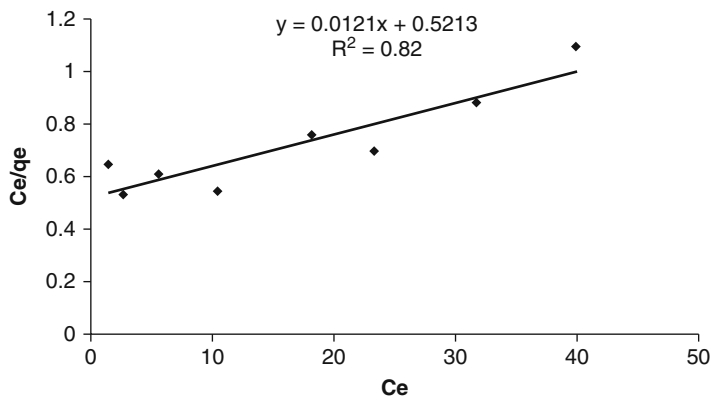
Fig. 4 Langmuir isotherm model linear plot of C_e/q_e versus C_e [30]

Case Study on Combined Effect of Ultrasound and Polymer Nanocomposite on Adsorption of Malachite Green Dye

Aqueous dye pollutants are released from various industries into the environment which causes serious problems on the ecosystem. The dyes which are used in dyeing industries are mainly azo dyes; these dyes are unable to degrade through biological treatment technique due to its biologically resistant nature. A number of techniques are available for the treatment of wastewater such as photocatalytic degradation, coagulation, electrocoagulation, and adsorption [36, 37]. Recently adsorption has been proven as a viable technique for the treatment of dye-contained wastewater. Recent studies have shown that apart from using single techniques, a combination of two or more techniques is more efficient for the treatment of wastewater [38, 39]. Adsorption is a more efficient and economically feasible technique for the removal of various contaminants by using various adsorbents such as activated carbons, activated alumina, palm ash, etc. [40, 41]. Researchers found many clay minerals (calcite, zeolite, bentonite, and kaolinite) and many composite materials for the adsorption of contaminants [42]. Li et al. [43] prepared the PAAm/laponite clay composite for the adsorption of cationic dyes from aqueous solution. Intercalation of iron oxide magnetic nanoparticles into polyacrylic acid has been attempted and investigated for the adsorption of methylene blue dye [44].

This case study deals with the sono-sorption of malachite green in the presence of polyacrylic acid as sonosorbent. Sonawane et al. [45] have synthesized the CTAB-modified bentonite nanoclay under ultrasound, and later they synthesized the PAA–nanoclay nanocomposite. The resultant nanocomposite was used for the removal of malachite green from the aqueous solution. In brief, batch sono-sorption experiments were carried out in the ultrasound reactor (frequency of 22.5 kHz and power of 120 W, Ultrasonics Labline CL 500) with inlet charge of 100 mL of dye solution along with 0.5 g of PAA–nanoclay nanocomposite. The effect of pH, initial MG dye concentration (250–1000 mg/L), and different quantities of PAA–nanoclay
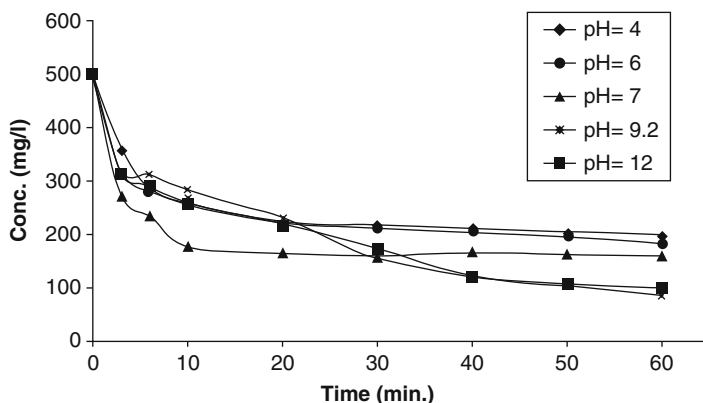
Fig. 5 The amount of the MG dye removed at different pH values [45]

nanocomposite (0.5–1.5 g) was studied for the adsorption performance of polyacrylic acid nanocomposite in the sonication environment. The effect of these parameters on the removal of MG dye will be discussed in detail after a few lines. The percentage dye removal and dye adsorbed per mg of adsorbent (q) were calculated using the following equations:

$$\text{Percentage removal} = \left[\frac{(C_o - C_e)}{C_o}\right] * 100 \tag{1}$$

$$q = \frac{[(C_o - C_e) * V]}{M} \tag{2}$$

where C_o and C_e are the initial and final concentrations of MG dye, V is the volume of dye solution, and M is the mass of PAA–nanoclay nanocomposite used for the dye removal.

Sonawane et al. [45] reported that with the increase of pH of the dye solution, the percentage removal of MG dye has been increased. The amount of the MG dye removed at different pH values is shown in Fig. 5.

The reason for obtaining such kind of profile is due to the competitive adsorption between H+ ions and MG dye molecules at the same adsorption site, and also the adsorption surface becomes less positive, so that the electrostatic attraction between MG molecules and nanocomposite surface increases [46].

Sonawane et al. [45] also studied the effect of PAA nanocomposite loading on sono-sorption of MG dye; the obtained results were shown in Fig. 6.

From those results, we can observe that the sono-sorption efficiency has increased with the increase in adsorbent loading. It was also reported that ultrasound in water also plays a key role in the degradation of MG dye by the generation of •OH and H• [47]. As per the mechanism of sono-sorption, both the radicals will help to improve the efficiency of the hybrid technique rather than use of single techniques such as sonolysis and adsorption. Among •OH and H•, the •OH radical will help in the
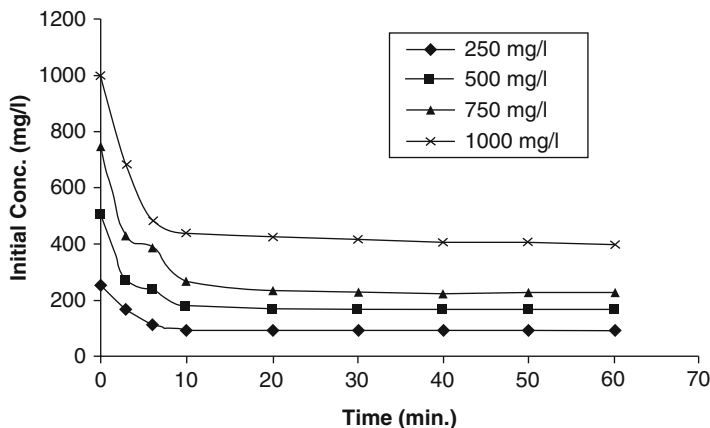
Fig. 6 Effect of PAA nanocomposite loading on sono-sorption of MG dye [45]

degradation of dye molecules, while H• will help to attach the dye molecule to form an intermediate complex that results into the adsorption of MG dye more efficiently.

Hydrodynamic Cavitation (HC)-Based Hybrid Techniques

Hydrodynamic Cavitation + H$_2$O$_2$

Case Study on Degradation of Imidacloprid Pesticide

Pesticides are mainly released into the environment by pesticide industrial effluent and agriculture runoff [48]. These pesticides are very toxic, hazardous, and carcinogenic and lead to adverse effects on the ecosystem. In this section, we will discuss about the degradation of imidacloprid, which belongs to a new class of insecticide called neonicotinoid, using hydrodynamic cavitation. Imidacloprid has high activity against sucking pests, including rice hoppers and white flies [49]. It has potential capability to create harmful effects on the aquatic environment [50, 51]. Water streams containing imidacloprid cause serious environmental problems due to its high solubility (0.58 g/L) and nonbiodegradable nature [52]. Biodegradation studies of imidacloprid have not shown satisfactory results in the past. Due to this reason, cavitation techniques have been considered as one of the most efficient degradation techniques in recent years because of its ability to degrade complex and nonbiodegradable organic pollutants into short-chain molecules.

Degradation of organic pollutants can be achieved in hydrodynamic cavitation through the free radical theory and thermal decomposition theory. Generation of hot spots in the hydrodynamic cavitation results from the cavity collapse and oxidation of organic molecules in the water due to the generation of reactive species like •OH and H•. It has been investigated that the degradation rate of organic pollutants is very

low when using cavitation alone than using additives such as H_2O_2 [53, 54], CCl_4 [55, 56], ozone [56–59], etc. Generally, combining cavitation with other additives has shown higher oxidation rates of target pollutants due to sufficient generation of the reactive species. Very few studies are reported on the degradation of imidacloprid in the past using various AOPs such as photo-Fenton [52, 60], photocatalytic [49, 60], photodegradation [61], and ozonation processes [62]. Hence, cavitation reactors or cavitation-based hybrid techniques have not yet been applied for the degradation of imidacloprid in the past. Raut-Jadhav et al. [63] have for the first time reported the cavitation-based degradation of imidacloprid. Their work mainly deals with the application of a hydrodynamic cavitation (HC)-based hybrid technique such as $HC + H_2O_2$ for the degradation of imidacloprid in the aqueous medium.

Raut-Jadhav et al. [63] studied the degradation of imidacloprid using a circular venturi as a cavitating device. They performed the experiments with 5 L of aqueous solution that contains imidacloprid having the concentration of 25 mg/L. The effect of inlet pressure on degradation of imidacloprid was studied by varying the inlet pressure from 5 to 20 bar (5, 10, 12.5, 15, 17.5, 20 bar) at a pH of 2.7. Degradation of imidacloprid solution was carried out at constant temperature throughout the process at 32 ± 4 °C by supplying water through the cooling jacket of the feed tank. They investigated that imidacloprid was degraded maximum at optimum inlet pressure of 15 bar. They also investigated the effect of pH on the degradation of imidacloprid by varying pH of feed solution as 2, 2.7, 3, 4, 6, and 7.5. It was reported that the imidacloprid was degraded maximum at a pH of 2.7. Higher degradation of imidacloprid is obtained due to the higher oxidation potential and lower rate of recombination of hydroxyl radicals under acidic conditions [64]. Hence, bulk quantities of hydroxyl radicals are readily available for the degradation. Under acidic conditions, the state of imidacloprid changes from molecular state to ionized state and thereby transferred itself from bulk to water–cavity interface, where the concentration of OH• radicals is high as compared to bulk liquid medium. Therefore, the degradation of imidacloprid is more in the acidic condition.

Degradation of Imidacloprid Using HC+ H_2O_2

Raut-Jadhav et al. [63] studied the combination of hydrodynamic cavitation and H_2O_2 on the degradation of imidacloprid at the initial concentration of 25 mg/L. Various molar ratios of imidacloprid–H_2O_2 were taken to observe the effect of H_2O_2 concentration on imidacloprid; the reported molar ratios of imidacloprid–H_2O_2 were like these: 1:1, 1:5, 1:10, 1:20, 1:30, 1:40, 1:50, and 1:60.

Effect of Cavitation Number

Raut-Jadhav et al. [63] investigated the effect of inlet pressure on cavitation and subsequent degradation of imidacloprid. For the calculation of cavitation number, inlet pressures were varied in the range of 5 to 20 bar and measuring the flow rate through the main line. Dimensionless cavitation number obtained can be used to characterize the flow conditions in the main line [65]. The cavitation number is defined as

$$C_v = \frac{\text{Pressure head}}{\text{Velocity head}}$$

$$C_v = \frac{P_2 - P_1}{\frac{1}{2}\rho v^2} \qquad (3)$$

where P_2 is the fully recovered downstream pressure after the circular venturi in kg/cm^2, P_1 is the vapor pressure of the liquid in kg/cm^2, ρ is the density of the dye solution in kg/m^3, and v is the velocity at the throat of the circular venturi in m/s. Velocity at the throat of the venturi can be calculated by knowing the flow rate in the main line and diameter of the throat. Flow characteristics of each inlet pressure through the cavitating device (circular venturi) are given in Table 1, which provides the information about the effect of inlet pressure on C_V.

Raut-Jadhav et al. [63] also studied the rate of mineralization achieved during the degradation of imidacloprid in various processes such as HC, H_2O_2, and HC + H_2O_2. The mineralization results obtained in various systems were shown in Fig. 7.

They carried out the mineralization study using HC alone and analysis has been carried out using TOC. From the results, they noticed that the mineralization rate achieved was very small in HC alone after 3 h of operation. It indicates that a very small amount of imidacloprid was degraded when using HC alone. They also observed the extent of mineralization to be 36.1 %, when using the hybrid technique of HC + H_2O_2. The reaction mechanism for the degradation of imidacloprid was also investigated by LC–MS analysis to identify the by-products formed from the degradation of imidacloprid when the combination of hydrodynamic cavitation and H_2O_2 process was used. Formation of by-products from the degradation of imidacloprid by LC–MS analysis is shown in Table 2.

Identification of by-products was also carried out in previous studies during photodegradation [61], photocatalytic degradation [49], and ozonation [62] of imidacloprid. Among the by-products identified in Raut-Jadhav et al.'s [63] work, 1-[(6-chloro-3-pyridinyl) methyl]-2-imidazolidinone [61] and 6-chloronicotinic aldehyde [62] have also been reported by other researchers.

Hydrodynamic Cavitation+Photocatalysis

Case Study on Decolorization of Malachite Green Dye

In this section, we are reporting the experimental work on decolorization of malachite green dye in the presence of the combination of hydrodynamic cavitation and photocatalysis. Initially graphene oxide (GO) was prepared from graphite powder by using modified Hummers' method [66] in the presence of ultrasonic irradiation using an ultrasonic horn (Dakshin ultrasonic probe sonicator, 22 kHz of frequency). The prepared GO and GO–ZnO nanophotocatalysts were characterized by XRD, FESEM, and TEM analysis. GO–ZnO nanophotocatalyst was used for the degradation of malachite green (MG) dye (500 mg/L) in aqueous solution using a hybrid

Table 1 Flow characteristics of each inlet pressure through the cavitating device (circular venturi) [63]

Inlet pressure (bar)	Vol. flow rate in LPH	Velocity (m/s)	Cavitation number (Cv)
3	340	30.063	0.215
5	410	36.252	0.148
7	470	41.557	0.112
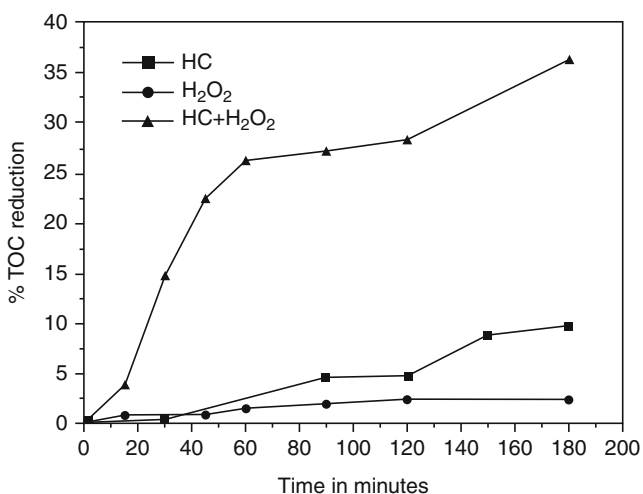
Fig. 7 Mineralization results obtained in various systems [63]

Table 2 Formation of by-products from degradation of imidacloprid by LC–MS analysis [63]

m/z by LC–MS	Degradation products	M_w
211	1-[(6-Chloro-3-pyridinyl) methyl]-2-imidazolidinone	211
185	6-Chloro-3-pyridylmethyl ethylenediamine	185
82	Imidazolone	82

advanced oxidation process which consists of hydrodynamic cavitation (HC) and GO–ZnO photocatalysis. A fixed volume of 5 L of solution containing 500 mg/L of MG dye was taken in the HC reactor. The temperature of the solution during experiments was kept constant in all cases at about 35 °C. Experiments were conducted at a constant inlet fluid pressure of 2 kg/cm^2. To observe the effect of solution pH on the degradation rate, experiments were performed at different pH values of 6, 8, 8.5 (natural pH), 9, and 10. As the pH increases from 6 to 10, the degradation time decreases. It can be seen that the degradation of MG is favored in basic media. From the results, it was observed that the percentage of the MG decolorization increased by increasing the pH of the dye solution. However, the optimum pH has been taken as 8.5, because beyond pH 9 malachite green had the pH transition stage.
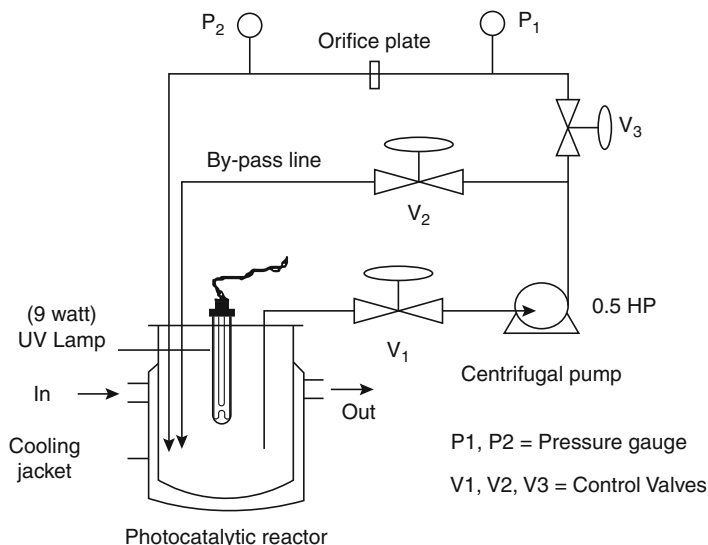
Fig. 8 Hydrodynamic cavitation setup with photocatalysis

Hydrodynamic cavitation setup consists of a centrifugal pump having the power rating of 0.5 HP, a 2 mm diameter orifice hole as a cavitation device, and a 9 W UV–visible light, and these were used in a typical hybrid advanced oxidation process. Typical experimental setup is shown in Fig. 8.

Two gram of GO–ZnO nanophotocatalyst were used for the degradation of MG. The degradation efficiency was 95 % when employing UV and hydrodynamic cavitations simultaneously. Decolorization of MG through hydrodynamic cavitation alone has been attained up to 93 %. It was observed that HC has shown more effect on decolorization of MG rather than the HC combined with photocatalysis. There are no reports in the literature on the effect of HC on the degradation of MG dye. Breakage of the chromophore group in the dye structure is the main thing for the decolorization of any dye. Due to the presence of a weaker chromophore group in MG dye structure, hence the dye has been decolorized more in HC than in HC plus photocatalysis.

Case Study on Decolorization of Crystal Violet Dye

To study the effect of ultrasonically prepared nanophotocatalysts on the decolorization of crystal violet (CV) dye, we used the sonochemical technique [67–69] to prepare the TiO_2, $Fe–TiO_2$, and $Ce–TiO_2$ nanophotocatalysts. The prepared nanophotocatalysts were characterized by XRD and TEM. The results obtained from XRD and TEM have shown the formation of uniform doping and small crystalline sizes of photocatalysts with the size of <100 nm. Initially decolorization of CV dye was studied using 50 mg/L of crystal violet (CV) dye from 5 L of crystal violet dye solution. Constant pressure (5 kg/cm^2 pump discharge pressure to the

cavitating device) and normal solution pH 6.5 were used for the study of CV decolorization. CV decolorization has been confirmed from the analysis of UV–Vis absorption spectrophotometer. It was observed that crystal violet dye was decolorized up to ~45 % when HC alone is used for 90 min. To investigate the decolorization rate in HC combined with photocatalysis, 0.6 g/L of 0.8 % Fe–TiO_2 and Ce–TiO_2 were used to study the decolorization rate of crystal violet dye at its solution pH of 6.5. Samples were taken, filtered, and tested using the UV spectrophotometer, after every 30 min of interval in the total decolorization time of 90 min. It was observed that 0.8 % Fe–TiO_2 showed the extent of decolorization to 98 %, whereas 1.6 % of Fe–TiO_2 showed the decolorization of 85 % in 90 min of treatment. Similarly 0.8 % Ce–TiO_2 showed the decolorization of ~84 %, whereas 1.6 % of Ce–TiO_2 showed the decolorization of ~82 %. It was observed that the Ce-doped TiO_2 did not show a significant effect on the degradation of crystal violet dye compared to the Fe-doped TiO_2. Higher catalytic activity has been reported for the Ce-doped TiO_2 materials for the photodegradation of dyes and other pollutants. Cerium oxides have attracted much attention due to the optical and catalytic properties associated with the redox pair of Ce^{3+}/Ce^{4+}. Cerium extends the photoresponse into the visible region; this can lead to an increase in the charge separation efficiency of surface electron–hole pairs. Earlier there are many reports of Fe doping on TiO_2 to improve its photocatalytic activity among a variety of transition metals, and also Fe on TiO_2 which acts as a Fenton reagent (Fe^{2+}) has shown better degradation performance of organic pollutants than other transition metals. So we have chosen these (Fe and Ce) better dopants among various transition metals for comparison.

HC Combined With Hydrogel Adsorption

The synthesis of hydrogel using cavitation technique was carried out as follows: Water (69 g) containing SDS (0.54 g) was added to the reaction mixture, and the entire solution was thoroughly deoxygenated by bubbling with argon for 45 min at room temperature. Initially 36 g of AA was added and the solution was irradiated for 10 min in the ultrasound reactor to form uniform monomer droplets. The temperature of the reaction mixture was maintained at 60 °C using a water bath. The liquid mixture was then subjected to sonication. 0.25 g of ammonium persulfate (APS) initiator in 5 mL of distilled water was added dropwise into the reaction mixture. The polymerization reaction was completed within 40 min. Within the initial 15 min of sonication, a viscous mass was formed, indicating the formation of pure polyacrylic acid hydrogel. The resulting polymerized hydrogel was then dried in an oven for 48 h at 85 °C. The photograph of polyacrylic acid hydrogel beads is shown in Fig. 9.

The reason for choosing the ultrasonic-assisted synthesis of polyacrylic acid hydrogel is that it takes less time for synthesis and has more dye adsorption capacities compared to the conventional synthesis of polymer hydrogels. Shirsath

Fig. 9 Polyacrylic acid hydrogel beads

et al. [70] have studied the dye adsorption capacities of both conventional and ultrasonic synthesis of polymer hydrogels.

Initially hydrodynamic cavitation-based degradation of malachite green was carried out using fixed solution volume of 5 L and for a constant circulation time of 90 min. The initial concentration of malachite green was 539 μM (500 ppm). The temperature of the solution during experiments was kept constant at 35 °C. The absorbance of malachite green was monitored using UV spectrophotometer (Shimadzu UV-1800), and then the concentration of dye was calculated by analyzing the absorbance of dye solution at the wavelength of 618 nm.

To know the effect on the degradation of MG using the combination (hybrid) of HC and hydrogel beads (such as polyacrylic acid hydrogel), the ultrasonically prepared polyacrylic acid hydrogel beads having the total weight of 25 g and 500 ppm of MG solution are used for carrying out the experiment. These beads are initially immersed in the hydrodynamic cavitation reactor for absorbing the MG dye present in the water. The fixed total time of 90 min has been kept for the degradation and adsorption of MG dye through HC and hydrogel, respectively. For every 15 min of time interval, samples are collected and analyzed for finding out the MG concentration present in the water. It has been observed that the degradation of MG is more in the combined HC and hydrogel than the single hydrodynamic cavitation technique. The degradation profile of MG in terms of concentration versus time for both single and hybrid process is shown in Fig. 10. The images of initial and final samples colors are shown in Fig. 11.

The swelling behavior of pure PAA hydrogels was studied. The weight of swollen pieces of hydrogels in the water was measured. The weight measurement of swollen hydrogels was carried out after the equilibrium was reached. The swelling ratio, S, was then calculated using the equation
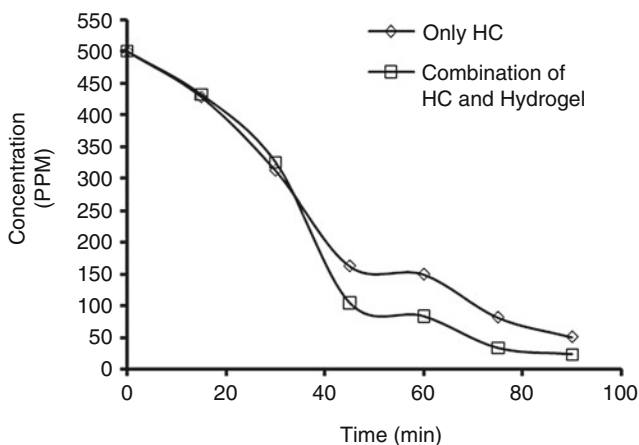
Fig. 10 MG degradation with respect to time
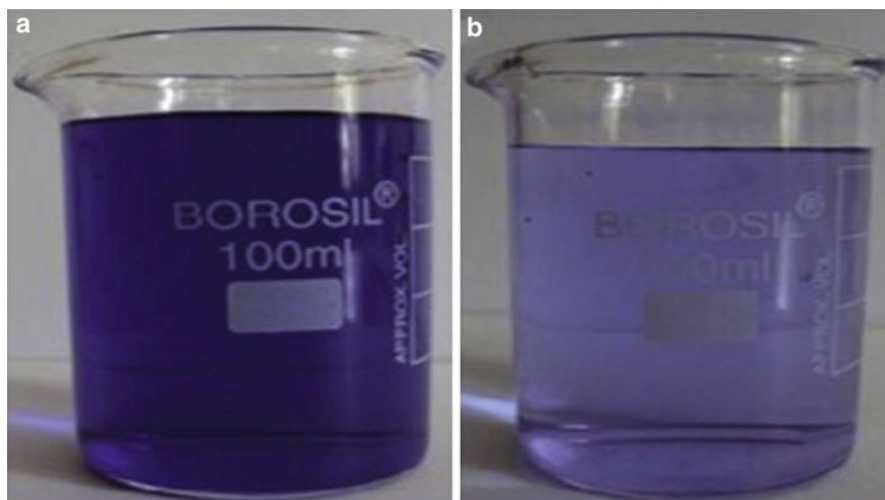
Fig. 11 (**a**) Initial MG color solution before degradation. (**b**) Final color after degradation

$$S = \frac{W_s - W_d}{W_d} \tag{4}$$

$$S = \frac{88.42 - 25}{25} = 2.53$$

where W_s and W_d were the swollen and dry weights of the hydrogel, respectively.

We also attempted the step for regenerating of polyacrylic acid hydrogel beads for reuse. The regeneration step has been carried in alkaline media (pH >14) for 24 h. Sample image of the regenerated PAA hydrogel bead is shown in Fig. 12.

Fig. 12 Regenerated PAA hydrogel bead

Mixture of Dye Degradation from Aqueous Solution Using Hydrodynamic Cavitation

As discussed in previous sections, ultrasonically induced cavitation has been successfully applied for the degradation of various pollutants on a laboratory scale of operation. However, the scale-up issue of ultrasonically induced cavitation is a problem due to its ineffective production of cavitation yield and distribution of the cavitational activity on a large scale of operation, and at a large scale of operation, transducers are ineffective and higher power dissipation/higher frequency is required. The scale-up of the degradation of organic pollutants through cavitation has been successfully applied on pilot scale recently using hydrodynamic cavitation. The application of hydrodynamic cavitation for the degradation of mixture of dyes is not investigated; hence, we have made the attempt. However, Chakinala et al. [26] for the first time reported the use of HC (liquid whistle reactor) in combination with the advanced Fenton process (AFP) for the treatment of real industrial wastewater.

In our studies, the experimental setup of hydrodynamic cavitation includes a 5 L holding tank; a centrifugal pump with a power rating of 3 HP was used for pumping the mixture of dye solution. The diameter of the main pipeline was 25 mm, and the orifice hole diameter was 6.25 mm; both were used for the degradation of tertiary dyes (methylene blue, brilliant green, crystal violet) with concentration of 200 mg/L of each dye. A total 5 L of dye stock solution were prepared and pumped through the orifice for 90 min. The temperature of the solution during experiments was kept constant in all cases at about 35 °C. Experiments were conducted at constant inlet fluid pressure of 2 kg/cm^2. Samples were withdrawn at a regular interval of 15 min,
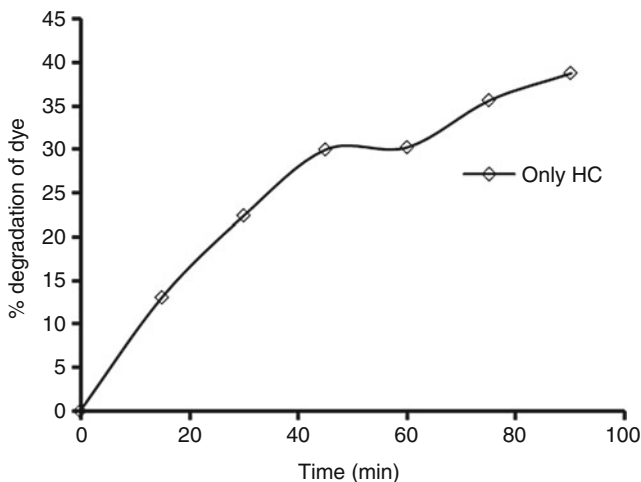
Fig. 13 Rate of decolorization of mixture of dyes as a function time in hydrodynamic cavitation

and the total time fixed for decolorization was 90 min. The decolorization and mineralization of dye mixture through hydrodynamic cavitation were analyzed using UV spectroscopy and TOC analysis. It was observed that decolorization of dyes in aqueous solution was obtained up to 38.79 %. The rate of decolorization of mixture of dyes as a function time in hydrodynamic cavitation is shown in Fig. 13.

The rate of mineralization was studied by carrying out total organic carbon (TOC) analysis (Shimadzu TOC-L). Combustion technique was used to identify the organic content in the liquid dye samples for every 15 min. It was observed that the percentage removal of TOC was obtained up to 54 % for HC alone. The effect of the addition of H_2O_2 on the rate of degradation of dyes in solution was also studied. Addition of 20, 40, 60, 80, and 100 mmol of H_2O_2 was carried out to know the degradation rate of dyes in aqueous solution. It was found that dyes were decolorized up to 65.35 %, and the removal of TOC was obtained up to 68.7 %. It was observed that the increase in addition of H_2O_2 concentration also increases the degradation of MG dye in hybrid technique. In this study, TOC removal is better than decolorization efficiency in the experiment, which is contradictory to the facts known. The reason why this type of contradiction is attained is mainly due to the use of tap water in carrying out the experiments. We analyzed the tap water for TOC content. The obtained results have shown that the TOC content of tap water is 79 ppm. The use of tap water for experiments has shown the effect on the final TOC removal results. If we deduct the tap water TOC value from the TOC results obtained in the experiments shown, the TOC removal percentages for HC and HC + H_2O_2 are 27.7 % and 51 %, respectively. The TOC removal rate obtained after deducting the values is shown to be lower than the decolorization rate. It almost justifies the facts known. Graphical representation of percentage removal of TOC is shown in Fig. 14.
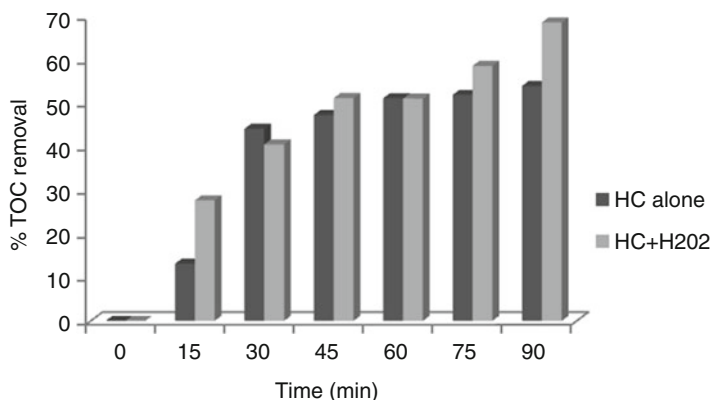
Fig. 14 Graphical representation of percentage removal of TOC in various systems

Scale-Up Issues for Wastewater Treatment Technique Using HC-Based Hybrid Processes

As we discussed in previous sections about the process intensification of wastewater treatment by cavitation techniques such as acoustic and hydrodynamic cavitation, from them one can observe that acoustic cavitations are unable to scale up to the industrial scale due to the production of less cavitational yield, difficult design, and material of construction; due to these drawbacks, no one has attempted to make a pilot-scale wastewater treatment using ultrasonic cavitation. Presently research is going in the way of making pilot-scale continuous wastewater treatment using ultrasonic cavitation; the imaginary design follows a plug flow reactor with the incorporation of ultrasound probe tips or transducers with the equal distances to cover the total length of the reactor. The distribution of probe tips or transducers in the plug flow reactor make the process continuous and treat the large volumes of wastewater by the uniform distribution of cavities throughout the length of the reactor. But this is not the possible way to treat the large volumes of wastewater due to high energy consumption and high capital investment. Hence, hydrodynamic cavitation can be used to treat the large volumes of wastewater. Hydrodynamic cavitation can be easy to scale up due to simplicity in design, less cost of material of construction, and higher cavitation yield which induce many researchers of this technique to scale up the process. It was also discussed in early stage that single treatment system is not as effective compared to the hybrid treatment system.

Cavitation and hydrogel technique discussed in section "HC Combined with Hydrogel Adsorption" has been used to treat 5 L of malachite green dye solution in the presence of hydrodynamic cavitation over the recirculation time of 90 min. It has been observed that color has been degraded up to 98 %. With this observation, we can scale up the treatment volume by changing the pump capacity and pipe size, orifice/venturi hole diameter, number of holes, and loading of hydrogel quantity.

Conclusion

It was concluded from the experimental studies on wastewater treatment sources such as phenol and dyes can be efficiently degraded with both the cavitation techniques (ultrasound and hydrodynamic cavitation). Apart from those cavitation techniques, hydrodynamic cavitation can be used to treat large volumes of wastewater compared to the ultrasonic cavitation technique. The operating parameters such as pH, inlet pressure, addition of H_2O_2, and type of photocatalysts dramatically change the rate of degradation of organic pollutants. Combining cavitation technique with other processes such as adsorption, photocatalysis, and H_2O_2 has shown the significant synergetic effects on the degradation of various organic pollutants in the aqueous solution.

References

1. Banat IM, Nigam P, Singh D, Marchant R (1996) Microbial decolorisation of textile dye containing effluents: a review. Bioresour Technol 58:217–227
2. Cho IH, Zoh KD (2007) Photocatalytic degradation of azo dye (Reactive Red 120) in TiO_2/UV system: optimization and modeling using a response surface methodology (RSM) based on the central composite design. Dyes Pigment 75:533–543
3. Song YL, Li JT, Chen H (2009) Degradation of C.I. Acid Red 88 aqueous solution by combination of Fenton's reagent and ultrasound irradiation. J Chem Technol Biotechnol 84:578–583
4. Kusic H, Koprivanac N, Srsan L (2006) Azo dye degradation using Fenton type processes assisted by UV irradiation: a kinetic study. J Photochem Photobiol A 181:195–202
5. Nilsson R, Nordlinder R, Wass U, Meding B, Belin L (1993) Asthma, rhinitis, and dermatitis in workers exposed to reactive dyes. Br J Ind Med 50:65–70
6. Gupta VK, Gupta B, Rastogi A, Agarwal S, Nayak A (2011) A comparative investigation on adsorption performances of mesoporous activated carbon prepared from waste rubber tire and activated carbon for a hazardous azo dye- Acid Blue. J Hazard Mater 186:891–901
7. Papic S, Koprivanac N, Loncaric Bozic A, Metes A (2004) Removal of some reactive dyes from synthetic wastewater by combined Al (III) coagulation/carbon adsorption process. Dyes Pigment 62:291–298
8. Yang CL, McGarrahan J (2005) Electrochemical coagulation for textile effluent decolorization. J Hazard Mater 127:40–47
9. Ellouze E, Ellouze D, Jrad A, Ben Amar R (2011) Treatment of synthetic textile wastewater by combined chemical coagulation/membrane processes. Desalination 33:118–124
10. Chen AH, Chen SM (2009) Biosorption of azo dyes from aqueous solution by glutaraldehyde-crosslinked chitosans. J Hazard Mater 172:1111–1121
11. Elisangela F, Andrea Z, Fabio DG, Cristiano RDM, Regina DL, Artur CP (2008) Biodegradation of textile azo dyes by a facultative Staphylococcus arlettae strain VN-11 using a sequential microaerophilic/aerobic process. Int Biodeter Biodegrad 63:280–288
12. Türgay O, Ersöz G, Atalay S, Forss J, Welander U (2011) The treatment of azo dyes found in textile industry wastewater by anaerobic biological method and chemical oxidation. Sep Purif Technol 79:26–33
13. Saharan VK, Pandit AB, Kumar PSS, Anandan S (2011) Hydrodynamic cavitation as an advanced oxidation technique for the degradation of Acid Red 88 dye. Ind Eng Chem Res 51:1981–1989
14. Young FR (1999) Cavitation. Imperial College Press, London

15. Stankiewicz AI, Moulijn JA (2000) Process intensification: transforming chemical engineering. Chem Eng Progr 96:22–34
16. Joseph CG, Puma GL, Bono A, Krishnaiah D (2009) Sonophotocatalysis in advanced oxidation process: a short review. Ultrason Sonochem 16:583–589
17. Cravotto G, Cintas P (2012) Harnessing mechano-chemical effects with ultrasound induced reactions. Chem Sci 3:295–307
18. Adewuyi YG (2001) Sonochemistry: environmental science and engineering applications. Ind Eng Chem Res 40:4681–4715
19. Thompson LH, Doraiswamy LK (1999) Sonochemistry: science and engineering. Ind Eng Chem Res 38:1215–1249
20. Mason TJ, Lorimer JP (2002) Applied sonochemistry – the uses of power ultrasound in chemistry and processing. Wiley, Weinheim
21. Suslick KS (1991) The temperature of cavitation. Science 253:1397–1399
22. Bagal MV, Gogate PR (2013) Degradation of 2,4-dinitrophenol using a combination of hydrodynamic cavitation, chemical and advanced oxidation processes. Ultrason Sonochem 20:1226–1235
23. Yang B, Zuo JN, Tang XH, Liu F, Yu X, Tang XY, Jiang H, Gan LL (2014) Effective ultrasound electrochemical degradation of methylene blue wastewater using a nanocoated electrode. Ultrason Sonochem 21:1310–1317
24. Zhao L, Ma J, Zhai XD (2010) Enhanced mechanism of catalytic ozonation by ultrasound with orthogonal dual frequencies for the degradation of nitrobenzene in aqueous solution. Ultrason Sonochem 17:84–91
25. Zhao L, Ma WC, Ma J, Yang JJ, Wen G, Sun ZZ (2014) Characteristic mechanism of ceramic honeycomb catalytic ozonation enhanced by ultrasound with triple frequencies for the degradation of nitrobenzene in aqueous solution. Ultrason Sonochem 21:104–112
26. Chakinala AG, Gogate PR, Burgess AE, Bremner DH (2009) Industrial wastewater treatment using hydrodynamic cavitation and heterogeneous advanced Fenton processing. Chem Eng J 152:498–502
27. Gogate PR (2008) Treatment of wastewater streams containing phenolic compounds using hybrid techniques based on cavitation: a review of the current status and the way forward. Ultrason Sonochem 15:1–15
28. Gogate PR, Pandit AB (2000) Engineering design methods for cavitation reactors II: hydrodynamic cavitation. AIChE J 46:1641–1649
29. Didenko YT, McNamara WB, Suclick KS (1999) Hot spot conditions during cavitation in water. J Am Chem Soc 121:5817–5818
30. Sonawane S, Chaudhari P, Ghodke S, Ambade S, Gulig S, Mirikar A, Bane A (2008) Combined effect of ultrasound and nanoclay on adsorption of phenol. Ultrason Sonochem 15:1033–1037
31. Mortland MM, Stephen SS, Boyd M (1986) Clay-organic complexes as adsorbents for phenol and chlorophenols. Clays Clay Miner 34:581–585
32. Banat F, Al-Asheh S, Al-Anbar S, Al-Refaie S (2007) Microwave- and acid-treated bentonite as adsorbents of methylene blue from a simulated dye wastewater. Bull Eng Geol Environ 66:53
33. Banat F, Al Bashir A, Al Aseh S, Hayajneh O (2000) Adsorption of phenol by bentonite. Environ Pollut 107:390
34. Ozcan AS, Erdem B, Ozacan A (2004) Adsorption of acid blue 193 from aqueous solutions onto Na–bentonite and DTMA–bentonite. J Colloid Interf Sci 280:44
35. Yeddou N, Bensmaili A (2005) Kinetic models for the sorption of dye from aqueous solution by clay-wood sawdust mixture. Desalination 185:499
36. Yapar S, Yilmaz M (2004) Removal of phenol by using montmorillonite, clinoptilolite, and hydrotalcite. Adsorption 10:287–298
37. Saquib M, Muneer M (2003) TiO_2-mediated photocatalytic degradation of a triphenylmethane dye (gentian violet), in aqueous suspensions. Dyes Pigment 56:37–49

38. Wang J, Hiang Y, Zhang Z, Zhao G, Zhan G, Ma T, Sun W (2007) Investigation on the sonocatalytic degradation of Congo red catalyzed by nanometer rutile TiO_2 powder and various influencing factors. Desalination 216:196–208
39. Kubo M, Matsuoka K, Takahashi A, Shibasaki-Kitakawa N, Yonemoto T (2005) Kinetics of ultrasonic degradation of phenol in the presence of TiO_2 particles. Ultrason Sonochem 12:263–269
40. Mane JD, Modi S, Nagwade S, Phadnis SP, Bhadari VM, Mane JD, Modi S, Nagwade S, Phadnis SP, Bhadari VM (2006) Treatment of spentwash using chemically modified bagasse and colour removal studies. Biores Technol 97:1752–1755
41. Atar N, Olgun A (2007) Removal of acid blue 062 in aqueous solution using calcinated colemanite ore waste. J Hazard Mater 146(1–2):171–179
42. Li M, Li JT, Sun HW (2008) Sonochemical decolorization of acid black 210 in the presence of exfoliated graphite. Ultrason Sonochem 15:37–42
43. Li P, Siddaramaiah NH, Kim S-B, Heo J-HL (2008) Compos Part B-Eng 39(5):756–763
44. Mak SY, Chen DH (2004) Fast adsorption of methylene blue on polyacrylic acid- bound iron oxide magnetic nanoparticles. Dyes Pigment 61:93–98
45. Sonawane SH, Chaudhari PL, Ghodke SA, Parande MG, Bhandari VM, Mishra S, Kulkarni RD (2009) Ultrasound assisted synthesis of polyacrylic acid–nanoclay nanocomposite and its application in sonosorption studies of malachite green dye. Ultrason Sonochem 16:351–355
46. Laizhou S, Jibin W, Qiuyan Z, Zunju Z (2008) Tsinghua Sci Technol 13(2):249–256
47. Ashokkumar M, Mason TJ (2007) Sonochemistry. In: Kirk-Othmer encyclopedia of chemical technology. Wiley VCH, NewYork
48. Daneshvar N, Aber S, Seyed Dorraji MS, Khataee AR, Rasoulifard MH (2007) Photocatalytic degradation of the insecticide diazinon in the presence of prepared nanocrystalline ZnO powders under irradiation of UV-C light. Sep Purif Technol 58:91–98
49. Mahmoodi NM, Arami M, Limaee NY, Gharanjig K (2007) Photocatalytic degradation of agricultural N-heterocyclic organic pollutants using immobilized nanoparticles of titania. J Hazard Mater 145:65–71
50. Malev O, Klobucar RS, Fabbretti E, Trebse P (2012) Comparative toxicity of imidacloprid and its transformation product 6-chloronicotinic acid to non-target aquatic organisms: microalgae desmodesmus subspicatus and amphipod. Pestic Biochem Phys 104:178–186
51. Tisler T, Jemec A, Mozetic B, Trebse P (2009) Hazard identification of imidacloprid to aquatic environment. Chemosphere 76:907–914
52. Segura C, Zaror C, Mansilla HD, Mondaca MA (2008) Imidacloprid oxidation by Photo-Fenton reaction. J Hazard Mater 150:679–686
53. Patil PN, Gogate PR (2012) Degradation of methyl parathion using hydrodynamic cavitation: effect of operating parameters and intensification using additives. Sep Purif Technol 95:172–179
54. Guo Z, Zheng Z, Zheng S, Hu W, Feng R (2005) Effect of various sono-oxidation parameters on the removal of aqueous 2,4-dinitrophenol. Ultrason Sonochem 12:461–465
55. Zheng W, Maurin M, Tarr MA (2005) Enhancement of sonochemical degradation of phenol using hydrogen atom scavengers. Ultrason Sonochem 12:313–317
56. Mahamuni NN, Pandit AB (2006) Effect of additives on ultrasonic degradation of phenol. Ultrason Sonochem 13:165–174
57. Wu Z, Franke M, Ondruschka B, Zhang Y, Ren Y, Braeutigam P, Wang W (2011) Enhanced effect of suction-cavitation on the ozonation of phenol. J Hazard Mater 190:375–380
58. Wu Z, Shen H, Ondruschka B, Zhang Y, Wang W, Bremner DH (2012) Removal of blue-green algae using the hybrid method of hydrodynamic cavitation and ozonation. J Hazard Mater 235–236:152–160
59. Jyoti KK, Pandit AB (2004) Ozone and cavitation for water disinfection. Biochem Eng J 18:9–19

60. Malato S, Blanco J, Caceres J, Fernandez-Alba AR, Aguera A, Rodriguez A (2002) Photocatalytic treatment of water-soluble pesticides by Photo-Fenton and TiO_2 using solar energy. Catal Today 76:209–220
61. Wamhoff H, Schneider V (1999) Photodegradation of imidacloprid. J Agric Food Chem 47:1730–1734
62. Bourgin M, Violleau F, Debrauwer L, Albet J (2011) Ozonation of imidacloprid in aqueous solutions: reaction monitoring and identification of degradation products. J Hazard Mater 190:60–68
63. Sunita R-J, Saharan VK, Pinjari DV, Sonawane S, Saini D, Pandit A (2013) Synergetic effect of combination of AOP's (hydrodynamic cavitation and H_2O_2) on the degradation of neonicotinoid class of insecticide. J Hazard Mater 261:139–147
64. Joshi RK, Gogate PR (2012) Degradation of dichlorvos using hydrodynamic cavitation based treatment strategies. Ultrason Sonochem 19:532–539
65. Kumar PS, Kumar MS, Pandit AB (2000) Experimental quantification of chemical effects of hydrodynamic cavitation. Chem Eng Sci 55:1633–1639
66. Hummers WS, Offeman RE (1958) Preparation of graphitic oxide. J Am Chem Soc 80:1339–1339
67. Shirsath SR, Pinjari DV, Gogate PR, Sonawane SH, Pandit AB (2013) Ultrasound assisted synthesis of doped TiO_2 nano-particles: characterization and comparison of effectiveness for photocatalytic oxidation of dyestuff effluent. Ultrason Sonochem 20:277–286
68. Perez IH, Maubert AM, Rendón L, Santiago P, Hernández HH, Díaz. Arceo L, Garibay Febles V, González EP, González-Reyes L (2012) Ultrasonic synthesis: structural, optical and electrical correlation of TiO_2 nanoparticles. Int J Electrochem Sci 7:8832–8847
69. Bethi B, Sonawane SH, Rohit GS, Holkar CR, Pinjari DV, Bhanvase BA, Pandit AB (2016) Investigation of TiO_2 photocatalyst performance for decolorization in the presence of hydro-dynamic cavitation as hybrid AOP. Ultrason Sonochem 28:150–160
70. Shirsath SR, Patil AP, Patil R, Naik JB, Gogate PR, Sonawane SH (2013) Removal of brilliant green from wastewater using conventional and ultrasonically prepared poly(acrylic acid) hydrogel loaded with kaolin clay: a comparative study. Ultrason Sonochem 20:914–923

Sonochemical Synthesis of Zinc Sulfide Photocatalysts and Their Environmental Applications

Jerry J. Wu and Gang-Juan Lee

Contents

Abstract

Different metal (Cu, Ag, Bi, Ga, In) ions doped into the lattice of ZnS spheres have been synthesized by sonochemical irradiation approach without using any template. The as-synthesized metal ion doped ZnS spheres were characterized by X-ray diffraction (XRD), field emission scanning electron microscopy (FE-SEM), high-resolution transmission electron microscopy (HRTEM), Fourier transform infrared spectra (FT-IR), and diffused reflectance spectroscopy (DRS). Among all, TEM images show that the prepared copper-doped ZnS crystallites have a hollow sphere-like self-assembled nanostructure. In FT-IR spectra, a noticed splitting of the ZnS peak at $1,110$ cm^{-1} into two peaks at $1,124$ and 998 cm^{-1} for copper-doped ZnS indicates that the copper atom can be partially

J.J. Wu (✉) • G.-J. Lee
Department of Environmental Engineering and Science, Feng Chia University, Taichung, Taiwan
e-mail: jjwu@mail.fcu.edu.tw; leeganjiuan@gmail.com

substituted in the zinc as $Cu - S - Zn$. Such a bonding interaction between copper and zinc ions toward sulfur was also confirmed from XRD and XPS analyses. Tuning of the band gap from 3.65 to 2.89 eV was successfully achieved upon doping copper ($0-5$ %) into ZnS. The band gaps of the ZnS doped with the different molar amounts of Ag, Bi, Ga, and In are all close to 3.54 eV, 3.58 eV, 3.66 eV, and 3.67 eV, respectively. The catalytic activity of hollow $Cu - ZnS$ nanostructures was tested by photosplitting of water containing Na_2S via visible-light irradiation. The hydrogen evolution rate of 4.0Cu/ZnS is 20.1 $\mu mol\ h^{-1}\ g^{-1}$. The doping sites could serve as the trapping pool for charge carriers, which is favorable for charge separation and photocatalytic activity enhancement. Therefore, the Cu doping into the lattice or interstitial of ZnS provides suitable heterogeneous energy levels to make it easier for the excited electrons from the valence band of ZnS to inject into the conduction band of ZnS, which results in easier water reduction to hydrogen. Furthermore, the degradation of the dye in an aqueous solution using 0.5 g/L ZnS photocatalyst at different desired doping metals of Cu, Ag, Bi, Ga, and In was significantly enhanced. Upon performing photocatalytic degradation of Orange II dye under UV light irradiation, the highest removal efficiency was obtained up to 95.9 % by 1.0Ga/ZnS photocatalyst.

Keywords

Introduction

Zinc sulfide (ZnS) is one of the most important II–VI wide band-gap semiconductor showing excellent physical properties, such as size-dependent electrical and optical properties, due to the quantum confinement [1]. In addition, ZnS has been intensively studied due to its rich morphologies at the nanoscale [1–3]. The morphology of ZnS at the nanoscale has been demonstrated to be one of the richest types among

all inorganic semiconductors [1]. ZnS has traditionally shown remarkable versatility and promise for novel fundamental properties and diverse applications, including light-emitting diodes (LEDs), electroluminescence, flat panel displays, infrared windows, sensors, lasers, and biodevices, etc. [1]. Atomic structure and chemical properties of ZnS are more comparable to widely known semiconductor, ZnO. However, certain properties pertaining to ZnS are unique, advantageous, and more suitable for visible blind ultraviolet light based devices (i.e., it can split hydrogen sulfide under ultraviolet irradiation only) [4]. Nevertheless, ZnS has some advantages, including excellent transport properties (reduction of the carriers scattering and recombination), an intrinsically n-type semiconductor, good thermal stability and high electronic mobility, nontoxicity, water insoluble, and comparatively inexpensive [5]. ZnS exists in two main crystalline forms. One is the cubic zinc blende (sphalerite) and the other is the hexagonal wurtzite [1]. In both crystalline forms, the coordination geometry at Zn and S are of tetrahedral crystal system, and their band gaps of 3.72 eV and 3.77 eV belong to cubic zinc blende and hexagonal wurtzite ZnS, respectively [1]. Hence, they are just only responsive to the UV light absorption (λ <340 nm). Furthermore, it undergoes photochemical decomposition into the components when irradiated in the absence of sacrificial electron donors [6]. Therefore, considerable attempts have been focused on developing visible-light-driven ZnS photocatalysts by using less energy but more abundant visible light (λ $\geq$420 nm) [7]. In order to harvest solar light efficiently, photocatalysts exhibiting an absorption band at longer wavelengths are highly desirable [8]. Many modifications have been performed in the development of visible-light-active photocatalysts that can efficiently utilize the maximum of solar light [9]. Thus, many researchers are interested in designing ZnS nanoparticles that could respond to visible-light irradiation. For that doping of foreign elements like Cu, Mn, Cd, etc., into UV-active nonoxide semiconductor could show necessary activity under visible-light irradiation [10–19]. Doping of Cu ions into zinc chalcogenides results wide range of tunable emission [10]. Further, doped Cu ion into ZnS could shift the absorption edge of ZnS into visible-light region [9]. A green luminescence peak was related with copper impurities, while two blue luminescence peaks can be attributed to native defects of ZnS. With increasing Cu^{2+} concentrations, the green emission peak is systematically shifted to longer wavelength [12]. Ag NPs have been known for their unique properties of high catalytic activity [20]. Bismuth doping in $NaTaO_3$ shows markedly enhanced photocatalytic hydrogen evolution under visible radiation [21]. The excellent performances of Bi–TiO_2 were attributed to their absorption ability in the visible-light region as well as effective charge carrier separation [22]. Doping of Ga into ZnO is expected to influence the separation rate of photoinduced charge carriers of ZnO due to the different structure of the electronic shell and size of Ga and Zn [23]. Doping of CdS with indium improves its visible-light absorption. Indium as the migration of photogenerated electrons from the former to the latter can occur in the composite system [24]. Furthermore, metal cations with the highest oxidative states in photocatalysts have d^{10} (Cu, Ag, Ga, In, and Bi) electronic configuration, while S shows its most negative states [6]. The bottom of the conduction band consists of the d and sp orbitals of the metal cations, while the

top of the valence band in metal sulfides is composed of S 2p orbitals, which are normally located at ca. +3 V (vs. NHE) or higher [6]. The solid solution of $Cd_{0.62}Zn_{0.16}S$ has the best activities of hydrogen production by water photocatalytic splitting under ultraviolet (16,320 µmol g^{-1} h^{-1}) and visible-light (2,007 µmol g^{-1} h^{-1}) irradiation due to preferential orientation of (1 0 1) plane, better crystallite size, and optimal band gap [25]. The photocatalytic H_2 evolution over the $Cd_{0.44}Zn_{0.56}S$ solid solutions under visible-light irradiation was investigated and the highest rate reached 2,640 µmol g^{-1} h^{-1} even without any cocatalysts [26]. Core/shell systems, such as CdSe/ZnS, ZnS/CdS, ZnSe/ZnS, and ZnS/ZnSe, could increase the stability of colloidal nanocrystals against chemical degradation. At the same time, the inverse structures with accounts of improved luminescence quantum yields, decreased fluorescence lifetimes, and benefits related to the tailoring of the relative band-gap positions between the two materials [27]. Moreover, the photocatalytic activity of semiconductor materials can be controlled by three key factors: (1) light absorption property, (2) rate of reduction and oxidation of reaction substrates by, respectively, electron and hole, and (3) rate of electron–hole recombination [28].

Transitional metal ions have been incorporated into ZnS nanostructure via thermal evaporation, sol–gel processing, coprecipitation, microemulsion, etc. Compared to the above conventional techniques, sonochemical method has emerged as a powerful tool for the fabrication of amorphous and crystalline nanosized materials [29]. When the compression of cavities occurs in irradiated liquids, the collapse is more rapid than thermal transport [30]. Ultrasound is a unique means of interacting energy and matter. The chemical effects of ultrasound do not come from a direct interaction with molecular species [30]. On the contrary, sonochemistry derives principally from acoustic cavitation. Acoustic cavitation can be considered to involve four stages: formation, growth, oscillation, and implosive collapse of gas bubbles in a liquid under proper conditions [29, 30]. Cavitation serves as a means of concentrating the diffuse energy of sound. Formation of cavities in liquids is a nucleated process. Nucleation of bubbles occurs at weak points in the liquid. With high-intensity ultrasound, a small cavity may grow rapidly through inertial effects. If its rate of expansion is sufficiently rapid, it will not have time to recompress during the positive-pressure half of the acoustic cycle. This process is called rectified diffusion and arises because the cavity's surface area is slightly greater during expansion than during compression; therefore, growth processes are slightly faster than shrinking processes. At some point, the cavity can reach a resonant size where it can efficiently absorb energy from the sound field. This size is determined by the frequency of the ultrasound. Such a cavity, if it is in phase with the sound field, can then grow rapidly in the course of a single expansion cycle. Once the cavity has overgrown, it can no longer efficiently absorb energy from the sound field and can no longer sustain itself. The surrounding liquid rushes in and the cavity implodes. Bubble collapse induced by cavitation produces intense local heating, high pressures, and very short lifetimes [29–33]. It is known that in liquids cavitation as a result of ultrasonic irradiation distorts the system integrity caused by the growth, the oscillation, and the collapse of gas bubbles. The collapse of cavitation bubbles generates localized hot spots with transient temperatures of above 10,000 K, pressure of about 1,000 atm or more, and heating

and cooling rates greater than 10^9 Ks^{-1}. Under such extreme conditions, it can obviously accelerate the hydrolysis or condensation reaction. In heterogeneous systems (liquid–solid), the high-speed shock waves and microjets may induce surface damage and promote the penetration of the particles into the matrix material [31–33]. The asymmetry of the environment near the interface induces a deformation of the cavity during its collapse. This deformation is self-reinforcing, and it sends a fast-moving stream of liquid through the cavity at the surface with velocities greater than 100 m/s. Such impingement of microjets and shock waves on the surface creates the localized erosion responsible for many of the sonochemical effects on heterogeneous reactions. The cavitational erosion of metals generates newly exposed, highly heated surfaces and ejects metal (in unknown form, perhaps as atoms or small clusters) from the surface. Microjet distortions of bubble collapse depend on a surface several times larger than the resonant bubble size. The turbulent flow and shock waves produced by intense ultrasound can drive metal particles together at sufficiently high speeds to induce effective melting at the point of collision. As a matter of fact, ultrasound can be used at room temperature and pressure to promote heterogeneous reactions, which normally occur only under extreme conditions of hundreds of atmospheres and hundreds of degrees. The high-velocity interparticle collisions produced in such slurries cause smoothing of individual particles and agglomeration of particles into extended aggregates. Then, various chemical reactions and physical changes occur and numerous nanostructured materials can be effectively synthesized with required particle size distribution. The ability of ultrasound to create highly reactive surfaces and thereby increase their catalytic activity has only just now been established. It is also likely that ultrasound can produce materials with unusual properties. The extraordinary temperatures and pressures reached during cavitational collapse, combined with the exceptionally high rates of cooling, may lead to the synthesis of novel solid phases difficult to prepare in other ways [29–33]. The physical and chemical effects generated by acoustic cavitation can be expected to significantly influence the properties of doped materials [32]. The effect of ultrasonic irradiation on the nanocomposite formation depends on the temperature, pressure, frequency and power of the sonoreactor, and the concentration of the components [31]. Sonochemistry may be able to initiate chemical reactions that are impossible to be done using conventional processing via selective heating of reactants. Then, various chemical reactions and physical changes occur and numerous nanostructured materials can be effectively synthesized with required particle size distribution [31–33]. Due to such principal reasons, sonochemical-assisted synthesis gives the advantages of room temperature, ambient pressure, and short reaction time to prepare metal-doped ZnS nanostructures.

Sonochemical Synthesis of Metal-Doped ZnS

Zinc acetate dihydrate and thioacetamide were used as the source of zinc and sulfur, respectively. Firstly, 0.5 M of $Zn(CH_3COO)_2 \cdot 2H_2O$ in 50 mL deionized water was prepared. Subsequently, 3.7568 g C_2H_5NS (0.5 M) was added into $Zn(CH_3COO)_2$
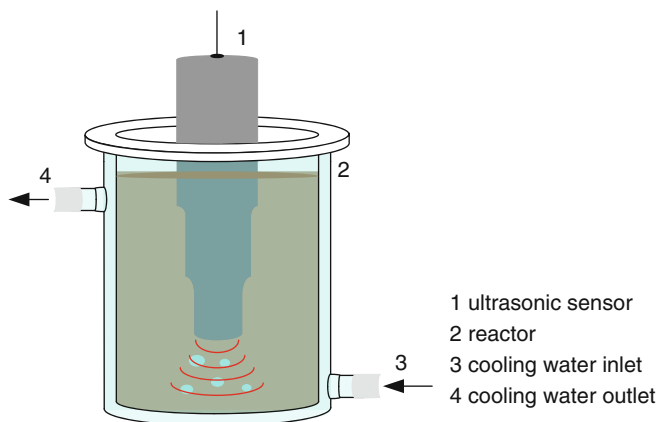
Fig. 1 Schematic diagram of sonochemical synthesis system
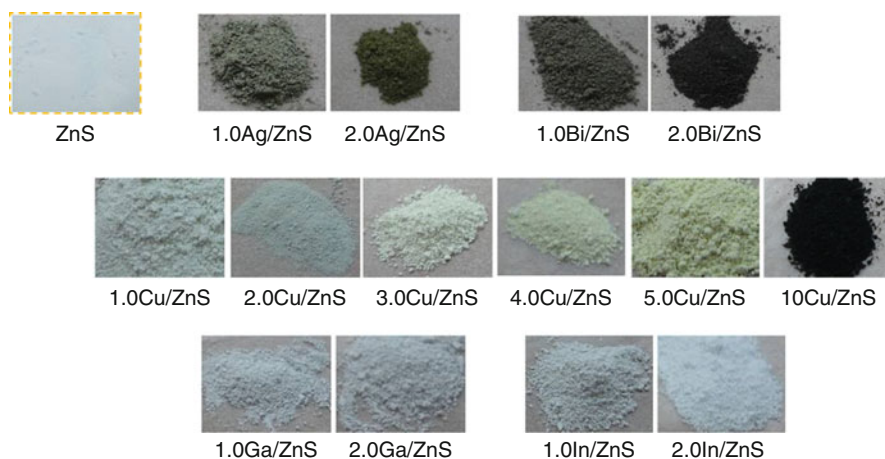
Fig. 2 Photos of the metal-doped ZnS powders by sonochemical method

solution by continuous stirring for 20 min (solution A). The different molar amounts of metallic solution in 50 mL deionized water (solution B) were also prepared. Under continuous stirring, solution B was added dropwise into solution A. The stirring was kept for 1 h to achieve complete reaction. Then, the mixture was irradiated with high-intensity ultrasound (600 W, 20 kHz) for 0.5 h as shown in Fig. 1. The temperature was maintained 15 °C by circulating cooling water. Finally, the metal-doped ZnS powders were centrifuged (10,000 rpm) and washed by ethanol and water for several times, and then dried at 60 °C in a vacuum oven overnight. The photos of metal-doped ZnS powders are presented in Fig. 2.
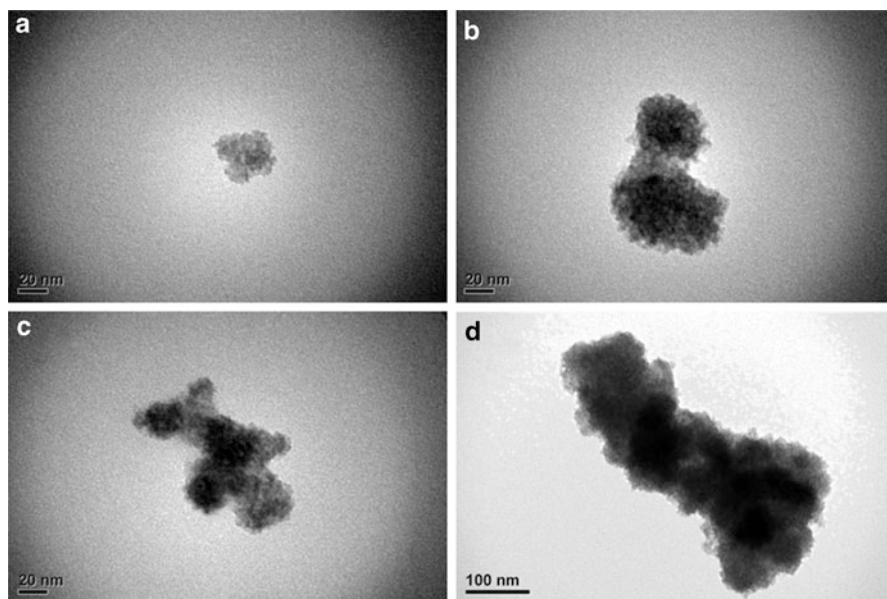
Fig. 3 Effect of irradiation time on ZnS at (**a**) 0.5 h, (**b**) 1.0 h, (**c**) 1.5 h, (**d**) 2.0 h

Effect of Irradiation Time on Synthesis of ZnS

The effect of ultrasonic irradiation time on the formation of as-synthesized ZnS nanostructure has been revealed in Fig. 3. It shows when ultrasonic time was prolonged, the amount of ZnS nanoparticles would gradually increase. When the ultrasonic time was applied for 0.5 h, the ZnS nanoparticles with size of 40 nm were formed. At the same time, from the XRD results as shown in Fig. 4, the major diffraction peaks at 28.91°, 48.00°, and 56.54° belonging to (111), (220), and (311) planes of ZnS nanostructures were observed and they match well with the cubic zinc blende phase structure (JCPDS card No. 05–0566, the cell parameters of a = 5.406 Å). The strong diffraction peaks indicate good crystallinity of the samples. No additional peaks in the XRD were observed, revealing the high purity of the prepared ZnS nanoparticles. Thus, it can be seen obviously that the as-synthesized ZnS nanoparticles have the same crystal structures.

XRD Analysis of Metal-Doped ZnS Nanostructures

The crystallinity and crystal phase of bare ZnS and metal-doped ZnS nanostructures were characterized by XRD as shown in Fig. 5. The major diffraction peaks of the ZnS clearly show the crystalline nature with assigned to the diffraction angles 28.91°, 48.00°, and 56.54° for (111), (220), and (311) planes, respectively. The
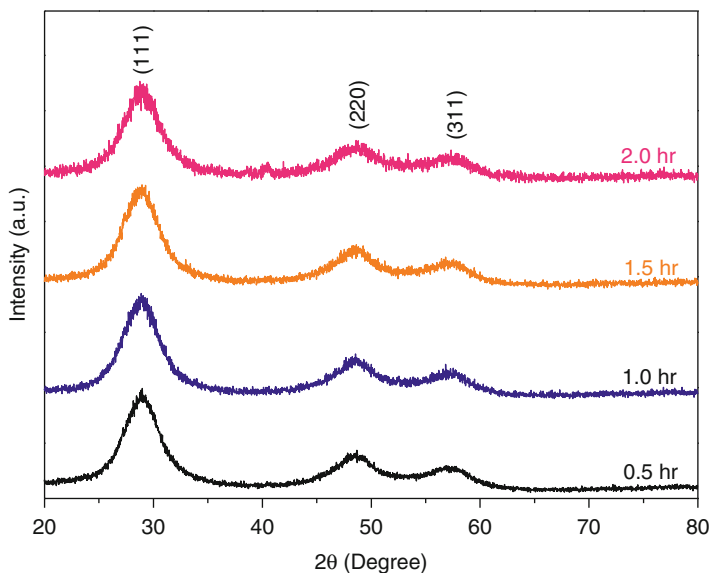
Fig. 4 XRD pattern of ZnS at different irradiation time

diffraction peaks indicate the cubic ZnS structure (JCPDS card No. 05–0566, the cell parameters of a = 5.406 Å) without any impurity and secondary phases. In addition, the significant broadening of the diffraction peaks is ascribed to the very small crystallite size [34]. The average crystallite size of the as-synthesized ZnS nanoparticles, D_{hkl}, can be calculated using the Debye Scherrer's equation, $D_{hkl} = k\lambda/(\beta_{hkl}\cos\theta_{hkl})$, where D_{hkl} is the particle size perpendicular to the normal line of (hkl) plane, k is a constant (0.9), λ is the wavelength of X-ray, β_{hkl} is the full width at half maximum of the (hkl) diffraction peak, and θ_{hkl} is the Bragg diffraction angle of (hkl) peak [19]. The microstrain (ε) can be calculated using the formula, $\varepsilon = (\beta_{hkl}\cos\theta_{hkl})/4$ [12]. The lattice constant a can be calculated using the formula, $d_{hkl} = a/[(h^2 + k^2 + l^2)^{1/2}]$, where d_{hkl} is d-spacings calculated from $\lambda = 2d_{hkl}\sin\theta_{hkl}$ formula [35]. The XRD pattern characteristics of the metal-doped ZnS nanoparticles were summarized in Table 1. The crystallite size of the metal-doped ZnS catalysts can be found to be less than 2 nm and confirmed the XRD results.

Furthermore, for Cu-doped ZnS nanostructures (molar ratio: 1.0–5.0), small shift was noticed in the peak positions towards the lower scattering angles, indicating an increase of lattice constant which can be attributed to the nonuniform substitution of copper ion into the zinc ion site as the radius of copper ion (0.057 nm) is smaller than that of the zinc ion (0.060 nm) [36]. Reduction of the lattice parameters in magnitude is called the lattice contraction that has important influences on physical and chemical properties of any material. In addition, the noticed broadening of diffraction peaks with the increase of copper concentrations may be due to the increase in microstrain. The lattice contraction occurs because of higher surface to volume ratio. This lattice contraction shows the existence of a surface stress. The surface atoms
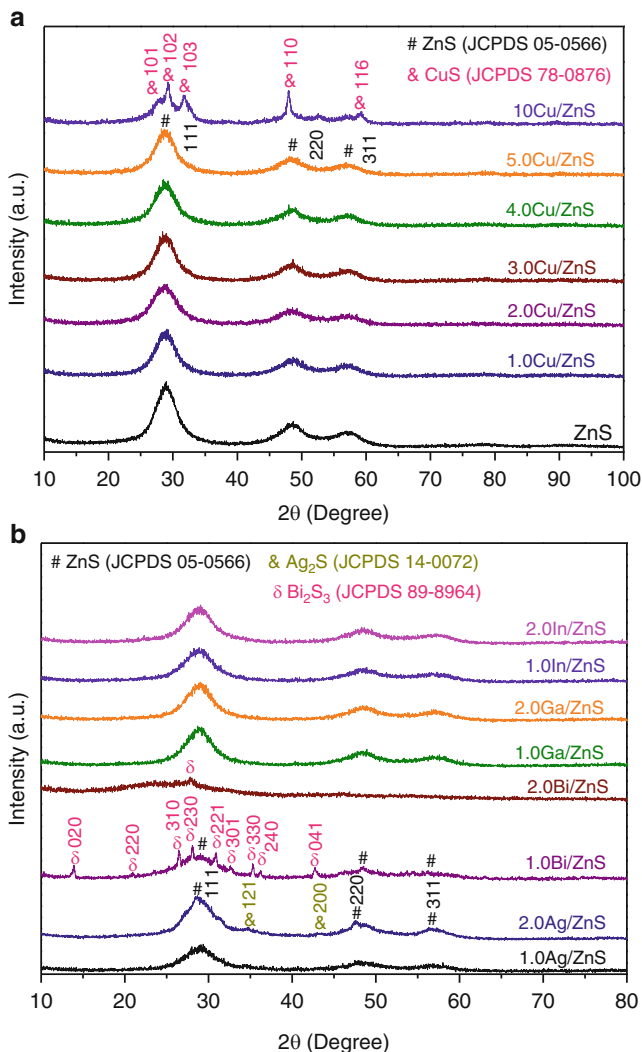
Fig. 5 X-ray diffraction patterns of the as-synthesized ZnS nanoparticles

form a large fraction of the material and hence the particles are in a strained condition due to the extra surface energy they possess. This may cause a contraction of the lattice without drastic change in the crystal structure [34]. At the same time, for the other metal-doped ZnS products, the peak positions also have the small shift towards the lower scattering angles (Ag, Bi, In-doped ZnS) or the higher scattering angles (Ga-doped ZnS) with the increase of metal concentrations (Ag, Bi, Ga, In) due to the increase of microstrain. In addition, the change in the lattice parameters could be understood by the substitution of metal ions [(Ag^+ = 0.100 nm, Bi^{3+} = 0.103 nm,

Table 1 Characteristics of the metal-doped ZnS nanoparticles from XRD patterns

Sample	2θ	d$_{111}$-spacing (Å)	Lattice parameter (*a*) (Å)	FWHM (β) (θ)	Crystal size (D$_{111}$) (nm)	Microstrain (ε) (10^{-3})
ZnS	28.92	3.087	5.347	4.279	1.919	18.076
1.0Cu/ZnS	28.85	3.095	5.361	4.007	2.049	16.929
2.0Cu/ZnS	28.82	3.098	5.365	4.066	2.020	17.178
3.0Cu/ZnS	28.82	3.099	5.367	4.231	1.941	17.877
4.0Cu/ZnS	28.79	3.101	5.371	4.284	1.917	18.101
5.0Cu/ZnS	28.77	3.104	5.376	4.748	1.729	20.062
10Cu/ZnS	29.47	3.031	5.250	5.749	1.430	24.255
1.0Ag/ZnS	28.87	3.093	5.357	4.576	1.795	19.334
2.0Ag/ZnS	28.87	3.093	5.357	4.651	1.766	19.650
1.0Bi/ZnS	28.65	3.116	5.397	6.339	1.295	26.796
2.0Bi/ZnS	23.80	3.739	6.475	22.117	0.367	94.412
1.0Ga/ZnS	28.84	3.096	5.362	4.099	2.003	17.318
2.0Ga/ZnS	28.87	3.093	5.357	4.135	1.986	17.469
1.0In/ZnS	28.83	3.097	5.364	4.345	1.890	18.358
2.0In/ZnS	28.83	3.098	5.365	4.388	1.871	18.542

In^{3+} = 0.062 nm) or (Ga^{3+} = 0.047 nm)] which are larger or smaller than that of Zn^{2+} ions (ionic radius = 0.060 nm) [36]. Detail results could be found in Table 1.

For Cu-doped ZnS, not only Cu^{2+} is crucial to the synthesis of hexagonal ZnS but also its concentration affects the crystal structure of ZnS. From Cu/ZnS hollow sphere nanostructures (molar ratio: 10 mol%) as shown in Fig. 5a, the observed major diffraction peaks close to 21.68°, 27.10°, 27.65°, 29.25°, 31.75°, 47.89°, 52.61°, and 59.24° belong to (004), (100), (101), (102), (103), (110), (108), and (116) planes of CuS, and they match well with the hexagonal CuS phase structure (JCPDS card No. 78–0876). According to the FE-SEM results as shown in Fig. 6, the copper-doped ZnS photocatalysts consist of irregular spheres and rectangular-shaped nanosheets with an average diameter of 40 nm and 60 nm, respectively, and seem to facilitate microsphere aggregation. The HRTEM results (Fig. 7) matched the XRD and SEM analyses. Based on the results above, the high doping amount of copper (10 mol%) could form two kinds of shapes, Cu/ZnS spheres and CuS nanosheet particles. For Ag-doped ZnS (2.0 mol%) as shown in Fig. 5b, the Ag$_2$S peaks present and match well with the acanthite Ag$_2$S structure (JCPDS card No. 14–0072). The major diffraction peaks close to 34.38° and 43.40° belong to (121) and (200) planes of Ag$_2$S. For Bi-doped ZnS nanostructures (2.0 mol%) as shown in Fig. 5b, the observed major diffraction peaks close to 14.15°, 20.91°, 26.54°, 28.15°, 31.04°, 32.49°, 35.23°, 36.19°, and 42.63° belong to (020), (220), (310), (230), (221), (301), (330), (240), and (041) planes of Bi$_2$S$_3$, and they match well with the orthorhombic structure of Bi$_2$S$_3$ particles (JCPDS card No. 89–8964). It also reveals that the higher doping amount of Bi (2 mol%) could not synthesize Bi/ZnS nanostructure and the phase of Bi$_2$S$_3$ would be present.

Fig. 6 FE-SEM image of the 10Cu/ZnS nanostructures. (*1*) *irregular spheres* of Cu/ZnS, and (*2*) *rectangular-shaped* nanosheets of CuS
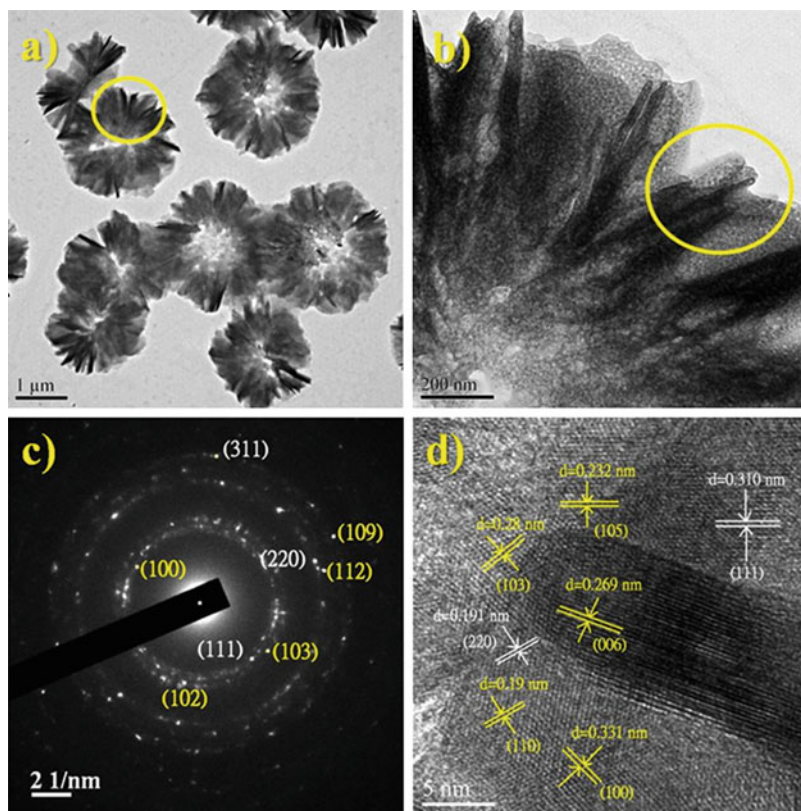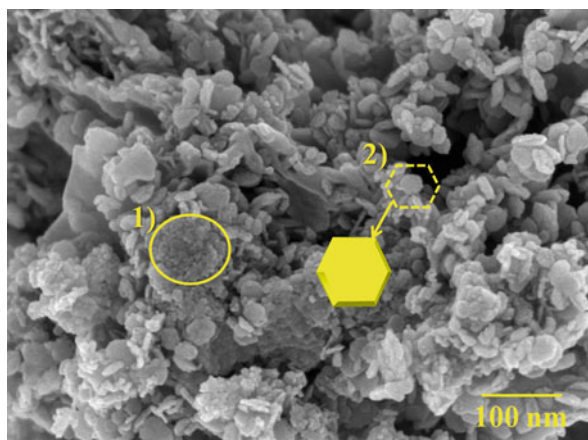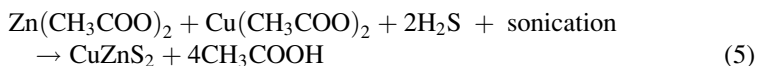

Fig. 7 (**a**) Typical HRTEM image, (**b**) magnified HRTEM image, (**c**) corresponding SAED pattern, and (**d**) lattice fringes of the 10Cu/ZnS nanostructures

Formation Mechanism

According to the references, sonochemistry has been proven to be an excellent approach in the preparation of amorphous and crystalline nanosized materials. The benefits of sonochemistry in creating nanostructural materials arise principally from acoustic cavitation, including the formation, growth, and implosive collapse of bubbles in a liquid. Bubble collapse stimulated by cavitation produces intense local heating and high pressures [37]. Therefore, based on the experimental results, the possible formation mechanism for the growth of the as-synthesized ZnS nanostructure could be explained by the self-assembled mechanism and a synergic effect of Ostwald ripening [38]. Initially, the amorphous fine particles were obtained as the precursor. The high-speed collision among precursors driven by high-intensity ultrasound irradiation produces the agglomerates and crystallization in the form of blende ZnS nanospheres. Since the equilibrium solute concentration at the surface of larger particles is lower than that of smaller ones and the resulting concentration gradients lead to solute ions flowing from small particles to larger ones, we obtained small nanocrystals of ~2 nm (compared with the 60 nm particles of bare ZnS) with self-supported ZnS nanospheres by carrying out ultrasounds irradiation of a homogeneous aqueous solution of zinc acetate and thioacetamide as the source of sulfide ions. The chemical process can be described by the following equation [39]:

$$Zn(CH_3COO)_2 + CH_3CSNH_2 + H_2O + sonication$$
$$\rightarrow ZnS + 2CH_3COOH + CH_3CONH_2 \tag{1}$$
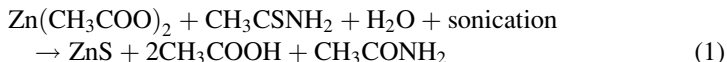
Furthermore, we also discussed the formation mechanism of the metal (Cu, Ag, Bi, Ga, and In)-doped ZnS nanostructures. According to the references, the effect of ultrasonic irradiation on the nanocomposite formation depends on the temperature, pressure, frequency and power of the sonoreactor, and the concentration of the components [29–33]. The remarkable effects of surface functionalization with various molecular weight ligands may bring different assembly behaviors [38]. It reveals that the metal-doped ZnS would result in the formation of different shapes. According to our experimental results, we attempted to describe and predict this behavior via atom-by-atom growth process. For Cu-doped ZnS nanostructures, at first from the EDX analysis as shown in Fig. 8 [40], it was observed that the Cu^{2+} ions have been successfully doped into the lattice of ZnS nanoparticles by sonochemical synthesis method. The chemical process can be described by the following equations [34]:

$$CH_3CSNH_2 + H_2O + sonication \rightarrow H_2S + CH_3(NH_2)C(OH) - SH \tag{2}$$

$$CH_3(NH_2)C(OH) - SH + H_2O + sonication \rightarrow CH_3(NH_2)C(OH)_2 + H_2S \tag{3}$$

$$CH_3(NH_2)C(OH)_2 + sonication \rightarrow CH_3(NH_2)C = O + H_2O \tag{4}$$

$$Zn(CH_3COO)_2 + Cu(CH_3COO)_2 + 2H_2S + sonication$$
$$\rightarrow CuZnS_2 + 4CH_3COOH \tag{5}$$
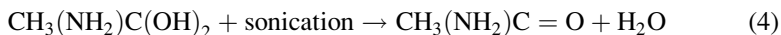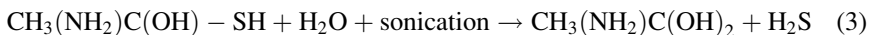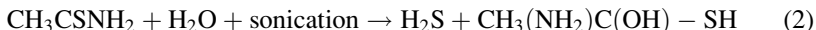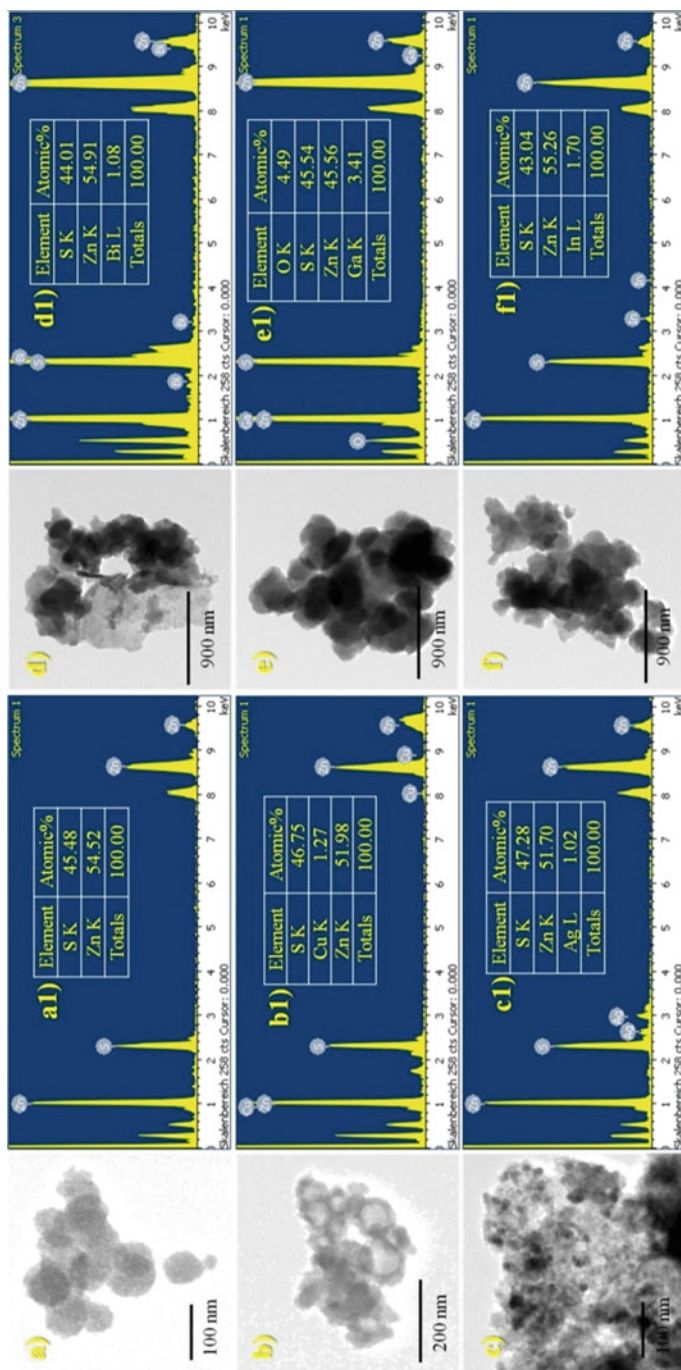
Fig. 8 TEM and EDX of the bare ZnS and metal-doped ZnS nanostructures [40] (**a**) ZnS, (**b**) 2.0Cu/ZnS, (**c**) 1.0Ag/ZnS, (**d**) 1.0Bi/ZnS, (**e**) 3.0Ga/ZnS, and (**f**) 1.5In/ZnS
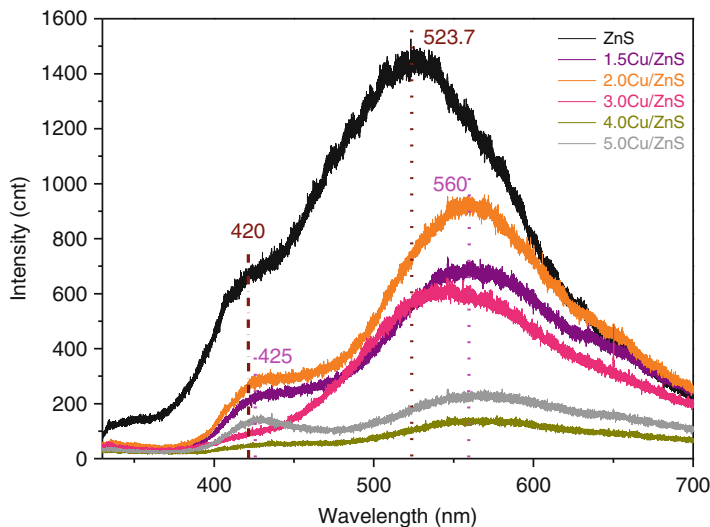
Fig. 9 Photoluminescence spectra of copper-doped ZnS and bare ZnS [40]

Thioacetamide is hydrolyzed and an intermediate and hydrogen sulfide is produced (reactions 2 and 3). The intermediate will lose water and produce acetamide ($CH_3(NH_2)CO$). Zinc acetate and copper acetate react with hydrogen sulfide and $CuZnS_2$ is produced. This indicates that the copper ions can be partially substituted between the zinc ions as Cu-S-Zn. There are some reasons that can be used to explain the binding of the modified ZnS with copper. First, the crystallite size decreased due to the doping copper as shown in Table 1, which implied that the crystal growth may be dominated by the oriented attachment mechanism, the direct self-organization of two particles into a single crystal by sharing a common crystallographic orientation [38]. Second, Cu^{2+} (0.057 nm) has nearly the same radius as Zn^{2+} (0.060 nm); therefore, the Cu^{2+} ions can readily substitute the Zn^{2+} ions in the host matrix, which makes the formation of $CuZnS_2$ hollow sphere nanostructures much easier in such extreme conditions by ultrasounds irradiation. Third, the photoluminescence spectra of the pristine ZnS and copper-doped ZnS (0–5.0 %) excited at 325 nm are shown in Fig. 9 [40]. Pristine ZnS shows a peak at 520 nm (green emission) and a shoulder at 420 nm (blue emission). However, for the copper-doped ZnS hollow nanostructures broad and red shifted peaks were noticed at 560 and 430 nm, which indicates indirectly the presence of more than one metal ions, probably (Cu-S-Zn). Moreover, the peak intensity at 420 nm is related with native defects (sulfur vacancy) [41]. When Cu^{2+} ions are doped into ZnS nanoparticles, more defect states will be introduced. Therefore, it is reasonable with some new peaks appeared in the longer wavelength side. The spectra show a broad emission spectrum around 400–600 nm. It is in agreement with earlier results in Cu/ZnS nanoparticles. With an increase of the Cu^{2+} concentration (from 0 % to 5.0 %), the green light position is systematically

shifted to longer wavelength. Furthermore, the intensity of the Cu/ZnS emission is decreased by higher concentration of the Cu^{2+}. When Cu^{2+} ions are incorporated successfully into ZnS host lattice, the luminescence centers of Cu^{2+} ions are formed [11, 12]. The decrease of luminescence intensity at the higher Cu^{2+} concentrations may be caused by the formation of CuS [10]. The evidence is that the nanocrystalline Cu/ZnS powder color was changed from almost light white to gray or light yellow when the doping concentration was increased from 1.0 % to 5.0 %. The CuS particles not only act as nonradiative recombination centers but also reduce the number of Cu^{2+} ions that are optically active luminescence centers in ZnS nanoparticles. Therefore, the emission intensity is considerably decreased with increasing Cu^{2+} concentration. Moreover, not only is Cu^{2+} crucial to the synthesis of Cu/ZnS but also its concentration effect on the hollow sphere nanostructures of ZnS. The Cu substitute Zn ions in ZnS crystals by introducing a trap energy level, where electron and hole can be trapped. An electron can undergo photoexcitation process in the host ZnS lattice of nanoparticles and consequently decay via a nonradiative transition from the sulfur vacancy level to the t_2 energy level of excited Cu^{2+} (d^9) [15].

It could be confirmed that the different morphology of Cu/ZnS from the TEM analysis as shown in Fig. 10 [40]. With increasing concentration of Cu^{2+} ions in the host, the hollow sphere structure gradually becomes flower-like structure until the concentration is 10 mol% (Fig. 10g2). Regarding copper-doped ZnS crystallites under TEM analysis, it looks like a hollow sphere-like nanostructure and flower-like structure with a diameter ranging from 50 to 100 nm and 2 μm, respectively.

The possible growth mechanism of Cu-doped ZnS nanostructures could be shown in Fig. 11. At first, the formation of these more complex spherical structures depends on an oscillative aggregation of nanocrystallites along the radial direction by ultrasounds irradiation. By a synergic effect of Ostwald ripening and the oriented attachment mechanism, the surface crystallites act as nucleation sites for the creation of the space between the core and shell. During the solid evacuation, crystallites immediately below the surface region are transported to these surface sites. Since the shells and cores have the same chemical constituents, the resultant structures are called "homogeneous core-shell" [42]. Then, the hollow nanospheres are formed through a solid evacuation and subsequent recrystallization process as shown in Fig. 11a.

Under such extreme conditions, the quicker release of the intermediate gas provides higher permeating pressure and faster permeating speed, which results in a broken shell of Cu/ZnS hollow spheres as shown in Fig. 11b. With increasing concentration of Cu^{2+} ions in the host, the hollow sphere structure gradually becomes flower-like structure until the concentration is 10 mol% as shown in Fig. 10g2. It can be seen that the sphere is constructed with cross nanoflakes as building blocks. The individual flower-like structure consists of aggregated nanoflakes. These nanoflakes, with a random array, are connected to each other to build a flower-like architecture [43]. The dark center of the flower indicates that the nanoflakes are accumulated tightly. Then, the components of primary crystallites in the cores are not exactly the same, ZnS and CuS hollowing of core can still take
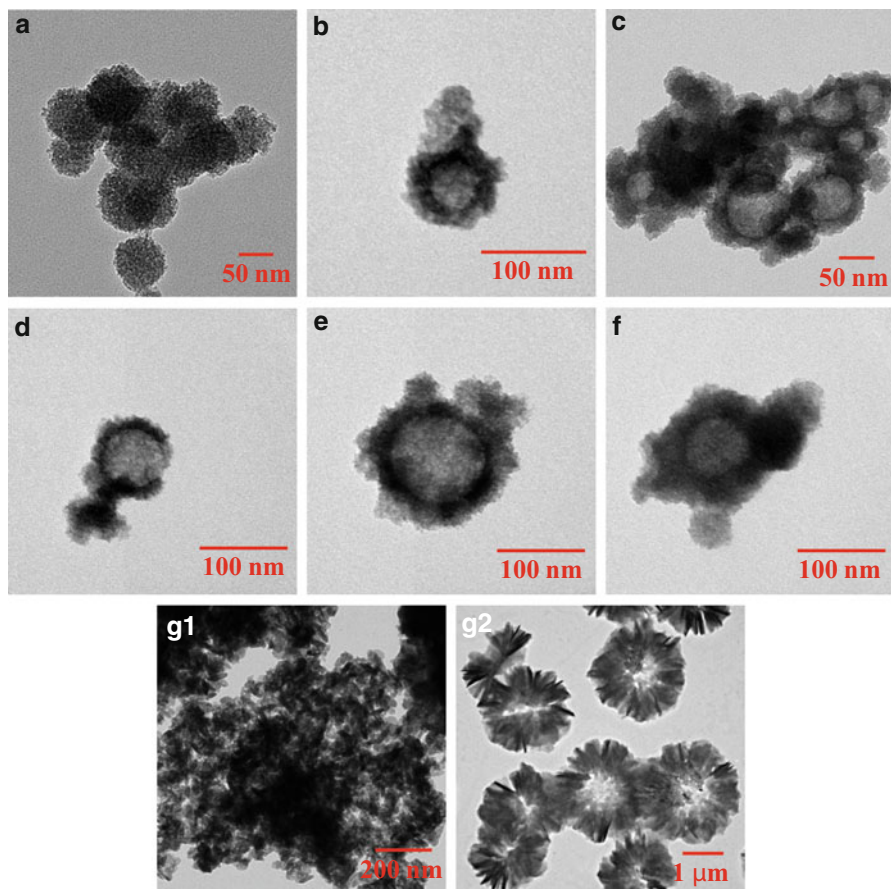
Fig. 10 TEM images of (**a**) ZnS, (**b**) 1.0Cu/ZnS, (**c**) 2.0Cu/ZnS, (**d**) 3.0Cu/ZnS, (**e**) 4.0Cu/ZnS, (**f**) 5.0Cu/ZnS, and (**g**) 10Cu/ZnS [40]

place, which will thus give even more complex space patterns as shown in Fig. 11c. Moreover, according to the Kirkendall effect, it is a consequence of the different diffusivities of Zn and Cu atoms in a diffusion couple causing a supersaturation of lattice vacancies. This supersaturation may lead to a condensation of extra vacancies in the form of so-called "Kirkendall voids" close to the interface [44]. But Kirkendall voids is a negative effect since the voids weaken the bonding strength and might cause failure of the electrical contact. Thus, flower-like structure will appear between the gaps during the growth. The element of Cu only existed in the cross nanoflakes, which results in a flower-like architecture. Based on the above results, we can synthesize the Cu/ZnS hollow sphere structure via facile one-pot and template-free hydrothermal routes by ultrasounds irradiation method.
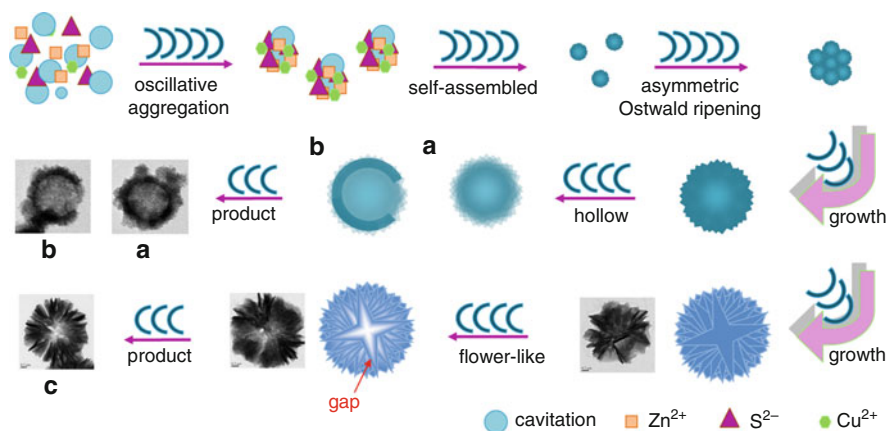
Fig. 11 Schematic illustration of possible growth mechanism of Cu/ZnS nanostructures. (**a**) and (**b**) the low doping amount (1.0–5.0 %), and (**c**) the high doping amount (10 %)

FT-IR Analysis of ZnS and Metal-Doped ZnS Nanostructures

FT-IR spectra of the synthesized ZnS were shown in Fig. 12. The broad band around 3,000–3,600 cm^{-1} is due to the OH stretching frequency (existence of water absorbed in the surface of nanocrystals). The peaks around 1,600–3,000 cm^{-1} is due to the microstructure formation of the samples [15, 45]. The bands at 1,420–1,565 cm^{-1} can be assigned to C $=$ O symmetric and asymmetric stretching modes arising from the absorption of atmospheric CO_2 on the surface of the nanocrystals [15, 46]. The characteristic ZnS vibration peaks can be noticed at 1,110 cm^{-1} and 672 cm^{-1} [15, 19]. However, the FT-IR spectrum of 2.0Cu/ZnS nanostructures shows similar peaks with respect to the bare ZnS nanoparticles, and in addition noticeable new peaks at 1,124 and 998 cm^{-1} may be due to arising resonance interaction among difference in vibrational modes of zinc and copper sulfide ions. This indicates that the copper ions can be partially substituted between the zinc ions as Cu-S-Zn, which may be responsible for splitting of original ZnS peak at 1,110 cm^{-1} into two new peaks, i.e., 1,124 and 998 cm^{-1}. Due to such competitive bonding interaction among copper and zinc ions towards sulfur, it causes initially formed agglomerated pristine ZnS spherical clusters into hollow sphere-like self-assembled nanostructure (Cu-ZnS) [15, 47]. In addition, the FT-IR spectrum of Ag-, Bi-, Ga-, and In-doped ZnS also show similar peaks as the spectrum of bare ZnS powder. The splitting of original ZnS peak at 1,110 cm^{-1} into two new peaks due to Ag-, Bi-, Ga-, and In-doped ZnS crystal. The peak at 860–998 cm^{-1} indicates the presence of resonance interaction between vibrational modes of sulfide ions in the crystal. It means that the doped Ag, Bi, Ga, and In would affect the structure of portion of the ZnS particles [15, 47].
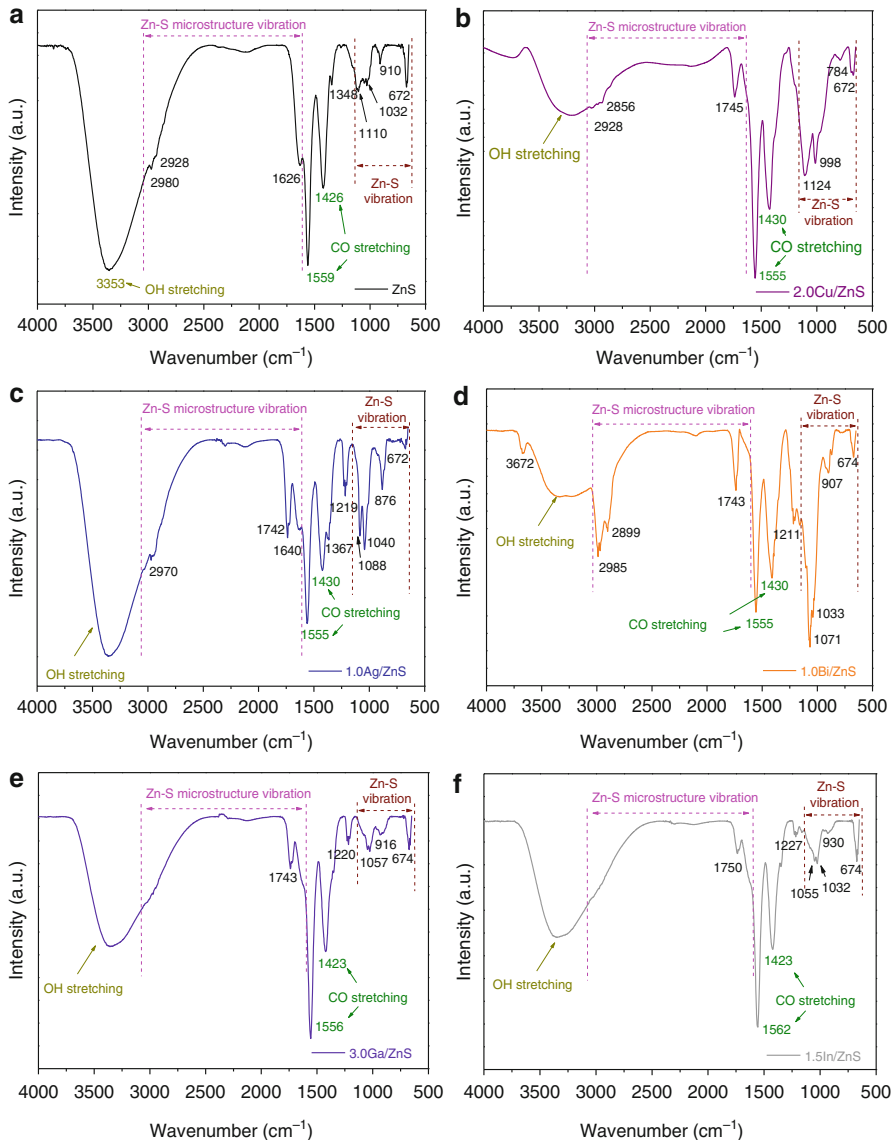
Fig. 12 FT-IR spectra of bare ZnS and metal-doped ZnS [40]

Optical Properties of ZnS and Metal-Doped ZnS Nanostructures

To better understand the chemical states of the elements, XPS analyses were performed and the typical XPS results are shown in Figs. 13 and 14. The XPS survey spectra of metal (Cu, Ag, Bi, Ga, In)-doped ZnS nanostructure show extra peaks for
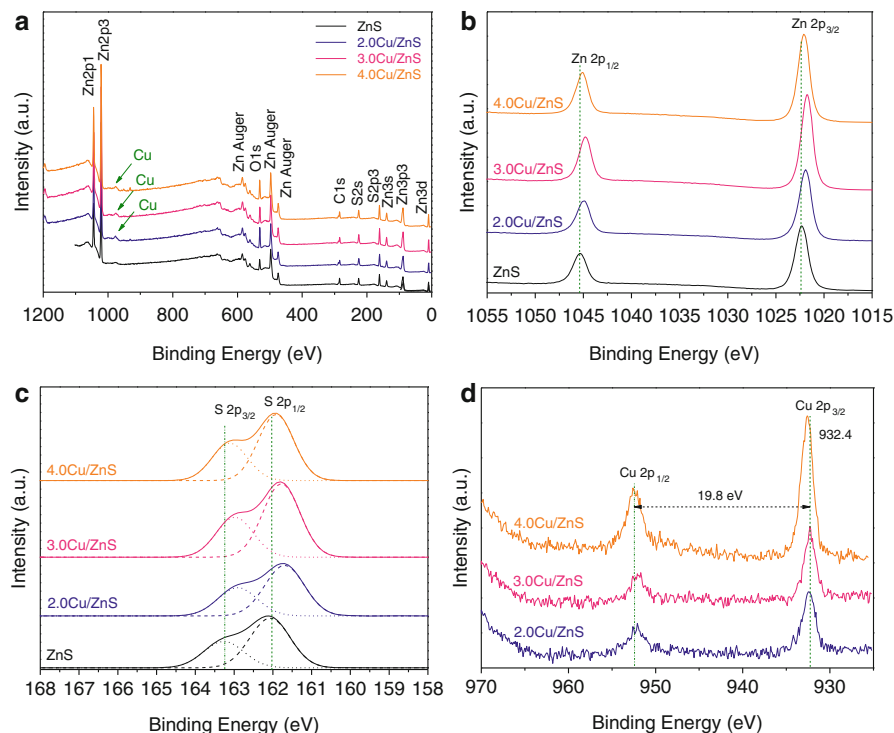
Fig. 13 (**a**) The survey spectra, and high-resolution XPS spectra of (**b**) Zn2p, (**c**) S2p, and (**d**) Cu2p of the synthesized composite photocatalysts

the element copper, silver, bismuth, gallium, and indium upon compared to pristine ZnS nanostructure. The peaks of Zn and S can also be noticed in both the survey spectra. The binding energy of Zn $2p_{3/2}$ and Zn $2p_{1/2}$ were found at 1,022.1 eV and 1,045.1 eV, belonging to the Zn^{+2} oxidation state in ZnS and in addition no noticeable shift after the metal doping as shown in Figs. 13b and 14b [48]. Moreover, the binding energy of S $2p_{3/2}$ and S $2p_{1/2}$ were clearly seen at 161.9 eV and 163.1 eV, which are consistent with the binding energy values as reported in the literature for sulfur as shown in Figs. 13c and 14c [48]. Meanwhile, for metal-doped ZnS nanostructures, whereas small shift was noticed in the peak positions of Zn and S towards the lower binding energy, indicating an increase of defects which can be attributed to the substitution of metal ion into the zinc ion site. Based on the above results, this observation is consistent with the doping-induced shift of the chemical potential. However, for the dopant copper, the binding energy of Cu $2p_{3/2}$ and Cu $2p_{1/2}$ are 932.4 eV and 952.2 eV, respectively, which can be assigned either to metallic or cationic Cu species based on available literature references as shown in Fig. 13d [48, 49]. However, Cu species detected in our hollow sphere-like self-assembled nanostructure may appear to be cationic (Cu-S-Zn) based on FT-IR studies stated in the above paragraph. The absence of satellite peaks (942 and 963 eV) indirectly indicates
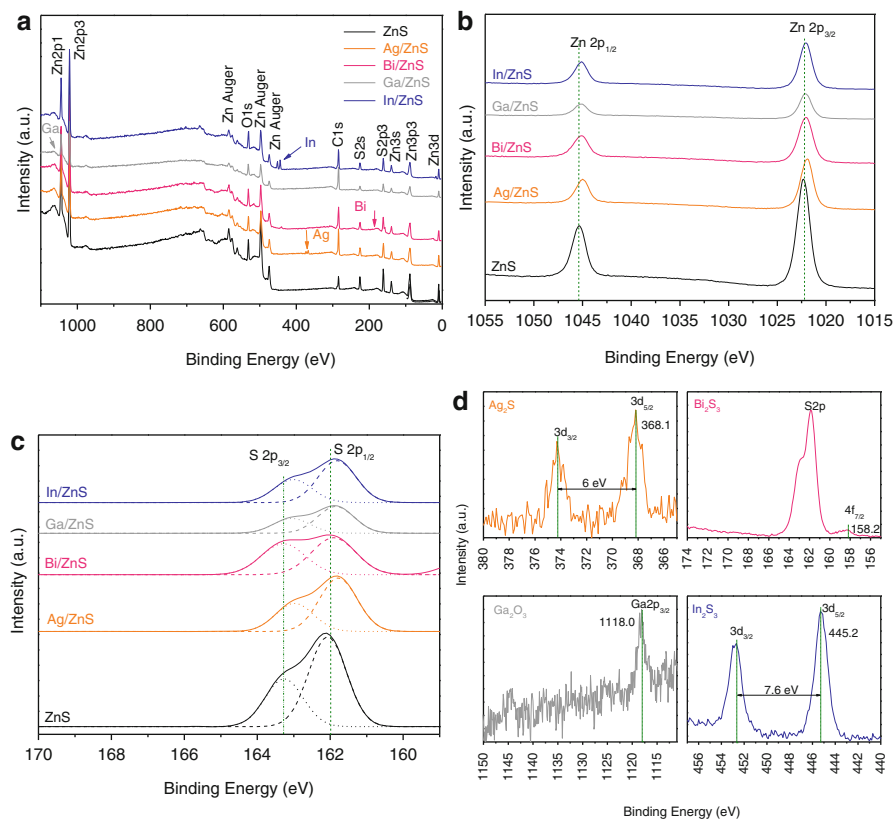
Fig. 14 (**a**) The survey spectra and high-resolution XPS spectra of (**b**) Zn 2p, (**c**) S 2p, and (**d**) metal of the synthesized composite photocatalysts

that the cationic species present in our system may be in +1 oxidation state (Cu^{+1}) although Cu^{2+} was used for the synthesis. Thus, all the characterization studies mentioned here clearly supports that there may be bonding interaction occurring between copper and zinc ions towards sulfur as Cu-S-Zn, which leads to hollow sphere-like self-assembled nanostructure. As for Ag, the binding energy of Ag $3d_{5/2}$ and Ag $3d_{3/2}$ are 368.0 eV and 374.1 eV, respectively. According to the XPS results in our analysis, the Ag species can be assigned to Ag^+ of Ag_2S [50]. As for Bi, the main Bi peaks (Bi $4f_{5/2}$, Bi $4f_{7/2}$) of the Bi_2S_3 exist at 163.0 eV and 158.0 eV, respectively. The Bi^{3+} peaks well agree with the reference [51]. The binding energy peak for Ga 3d is centered at 19.8 eV, which is attributable to the presence of gallium oxide [52]. As for In, the double spectral lines of In 3d located at 444.8 eV and 452.3 eV are ascribed to the binding energy of In $3d_{5/2}$ and In $3d_{3/2}$, respectively, which are coincided with indium oxide [53]. XPS measurement results demonstrate that Cu^{2+}, Ag^+, Bi^{3+}, Ga^{3+}, and In^{3+} have been successfully doped into the lattice of ZnS nanoparticles by sonochemical synthesis.
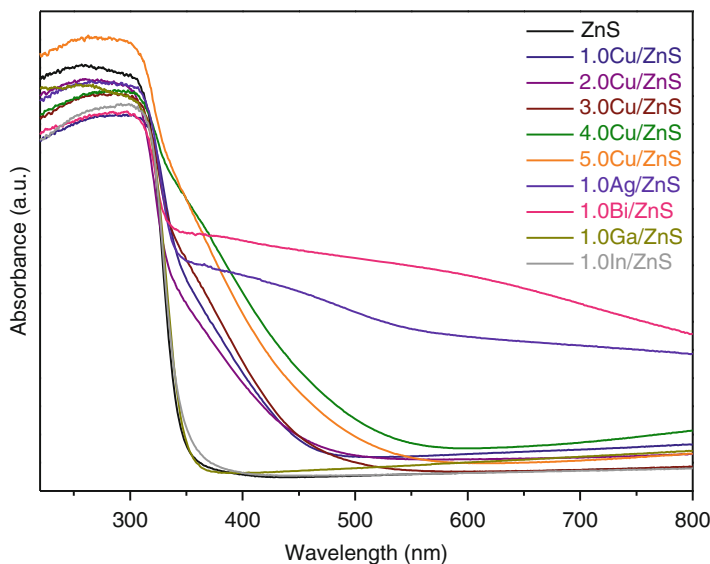
Fig. 15 UV–vis absorption spectra of metal-doped ZnS

UV–vis absorption of pristine ZnS and as-synthesized products are demonstrated in Fig. 15. The band gap energy was calculated using the Tauc's relation $[(\alpha h\upsilon)^{1/n} = A(h\upsilon - E_g)]$ [48]. The band gap of pristine ZnS is 3.69 eV. The observed red shift of the absorption edge for the hollow Cu-doped ZnS nanostructures compared to pristine ZnS revealed that copper doping can moderately benefit the optical property of bare ZnS which may be due to substitution of Cu ions on Zn lattice sites. The calculated band gap using the Tauc's relation starts decreasing from 3.69 to 2.89 eV upon increasing the concentration of copper dopant from 0 % to 5.0 % which indicates that Cu-doped ZnS may be used as a visible-light response catalyst for various applications, such as degradation of pollutants, photosplitting of water, etc. However, the band gaps of the ZnS doped with the different molar amounts of Ag, Bi, Ga, and In are all close to 3.54 eV, 3.58 eV, 3.66 eV, and 3.67 eV, respectively. It is apparent that the Ag and Bi can affect the absorbance property of the M/ZnS photocatalysts. Therefore, the red shift of the absorption edge of the M/ZnS photocatalysts is revealed and Ag and Bi doping can moderately benefit the optical property of bare ZnS.

EIS Analysis of ZnS and Metal-Doped ZnS Nanostructures

The as-synthesized ZnS products were subjected to electrochemical impedance spectroscopy (EIS) to determine the flat band potentials. The working electrode should exhibit favorable redox behavior within the analyte, reproducing electron transfer without electrode fouling. Meanwhile, the potential window over which the
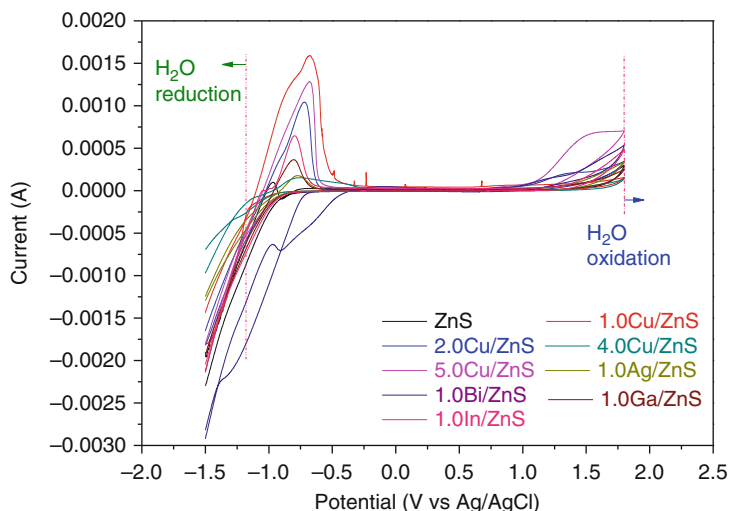
Fig. 16 Potential windows of the as-synthesized ZnS electrode

electrode performs in a given electrolyte solution should be as wide as possible to allow for the greatest degree of analyte characterization. In this section, experiments were carried out in 0.1 M Na_2SO_4 solution (pH = 7) within the potential region of -1.5 to 1.8 V versus Ag/AgCl of the working electrodes to select the great potential window for measurement. According to the CV curve results as shown in Fig. 16, with all of the experimental conditions remaining the same, sigmoidal shape was observed. This was the result of a steady-state condition between diffusion and electron transfer. Therefore, the next experiments were carried out in 0.1 M Na_2SO_4 solution at different frequencies (100, 200, 500, 1,000, 2,000, and 3,000 Hz) within the potential window of -1.2 to 1.8 V versus Ag/AgCl. The flat band potentials of the as-synthesized ZnS nanoparticles, E_{fb}, can be calculated using electrochemical impedance spectroscopy and the Mott $-$ Schottky equation, $C^{-2} = [2/(\varepsilon_s\varepsilon_0 eN_d)][E-E_{fb} - (k_BT/e)]$, where C is the interfacial capacitance, ε_s is the dielectric constant of the semiconductor, ε_0 is the permittivity of free space, e is the electronic charge, N_d is the donor density, E is the applied potential, E_{fb} is the flat band potential, k_B is the Boltzmann constant, and T is the absolute temperature [54]. Moreover, the flat band potential of the semiconductor and electrolyte interface can be obtained from the intercept on the potential axis, whereas the slope of the straight line is related to the carrier concentration. Based on the above experiments, the positive slope of the Mott–Schottky plots confirms the *n*-type semiconductor for our ZnS products in Fig. 17, and the flat band potential can be determined by extrapolating to C = 0. An average of the x-intercepts, at six different frequencies, produces flat band potentials for ZnS products with an estimated precision of ±0.1 V. As it is frequently the case, flat band potentials obtained from the Mott $-$ Schottky plots show a frequency dependency. At the same time, the nonconverging frequency dependency of the Mott–Schottky plot might originate from nonideality
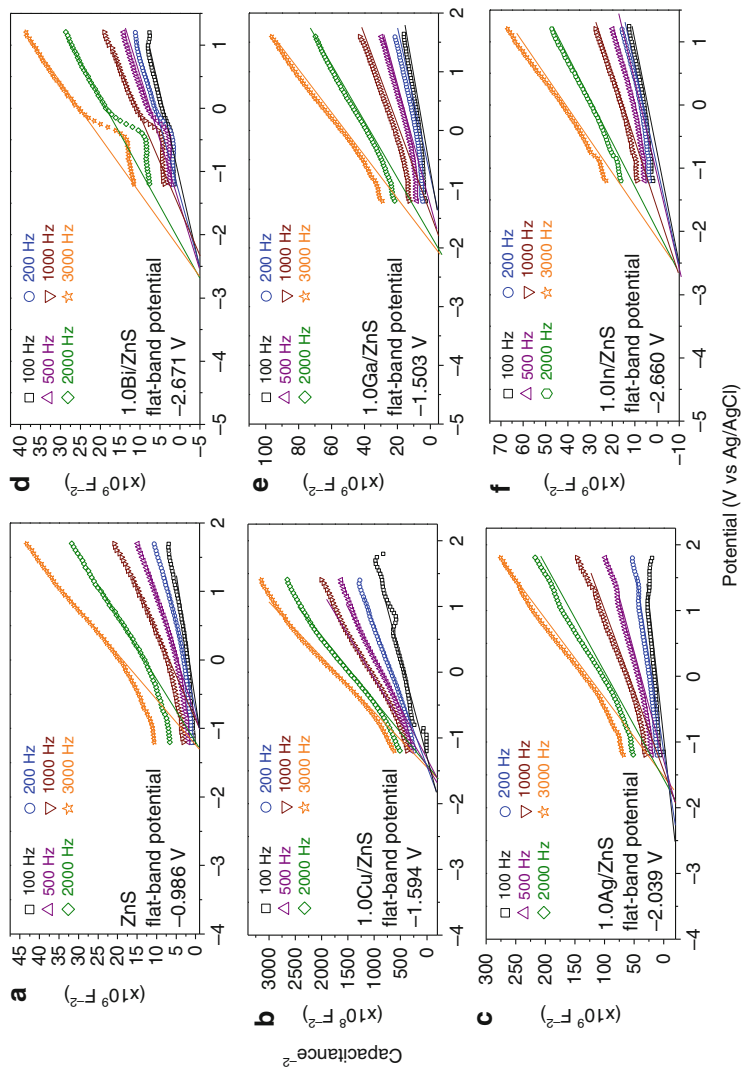
Fig. 17 Mott — Schottky plots for bare ZnS and metal-doped ZnS nanostructures
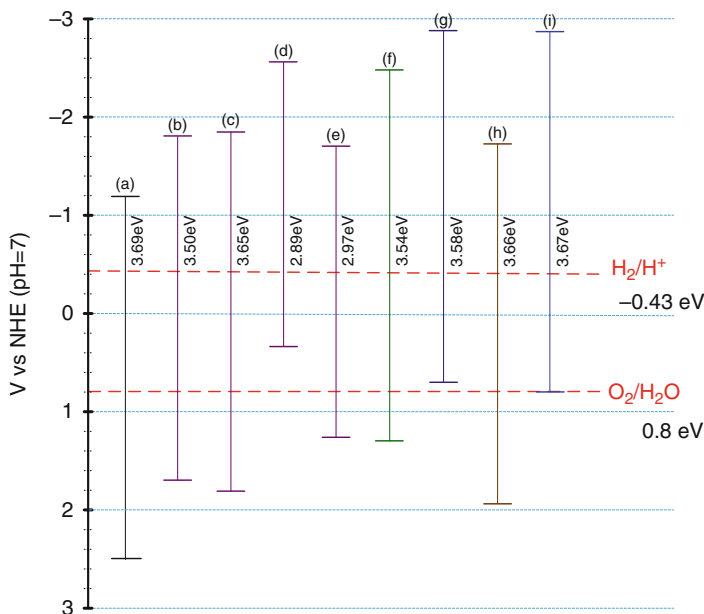
Fig. 18 Energy-level diagram showing the CB and VB edge positions of bare ZnS and metal-doped ZnS. (*a*) ZnS, (*b*) 1.0Cu/ZnS, (*c*) 2.0Cu/ZnS, (*d*) 4.0Cu/ZnS, (*e*) 5.0Cu/ZnS, (*f*) 1.0Ag/ZnS, (*g*) 1.0Bi/ZnS, (*h*) 1.0Ga/ZnS, i) 1.0In/ZnS

of the surface of a drop-cast semiconductor film on ITO for the capacitance measurement from the many grain boundaries of polycrystalline metal-doped ZnS and an inhomogeneous distribution of crystal sizes over the film surface [55].

The measured flat band potentials versus the Ag/AgCl in 3 M NaCl$_{(aq)}$ were converted to the reversible hydrogen electrode (RHE) scale via the Nernst equation, $V_{RHE} = V_{Ag/AgCl} + V^0_{Ag/AgCl \text{ vs NHE}} + 0.059 \times pH$, where V_{RHE} is the converted potential versus RHE, $V_{Ag/AgCl}$ is the experimental potential measured against Ag/AgCl reference electrode, and $V^0_{Ag/AgCl}$ versus NHE is 209 mV (3 M NaCl) at 25 °C [56]. Using the band gaps obtained from the action spectra and Tauc plots, along with the flat band potential and donor density obtained from the Mott − Schottky experiments, we were able to obtain a schematic of the band energies of ZnS composites as synthesized. Figure 18 shows the schematic of the conduction and valence band positions for ZnS composites structure. From the reference [57], we can understand that transition metal dopants influence wide band-gap semiconductor photocatalysts with at least two effects, including the change of the bulk electronic structure of the matrix semiconductor (changes in the position of the Fermi level, the formation of new energy levels by the interaction of the dopant with the matrix lattice, changes in the electron conductivity within the matrix semiconductor) and modification of the surface properties. Thus upon metal-ion doping, new energy states can be formed either within or beyond the band gap of

semiconductors. At first for copper-doped ZnS, as the impurity concentration (1.0–4.0 %) increases, the more negative reduction potential of the conduction band forms. When the Cu^{2+} cations are incorporated into the ZnS lattice by substituting Zn^{2+} cations, where the ionic radius of the Cu^{2+} is similar to that of Zn^{2+} and the electroneutrality as a whole requires the simultaneous formation of sulfur vacancies, the amount of which should be equal to half of the substitutional trivalent cation dopants incorporated at Zn^{2+} sites. The possible equation by the following equation holds [58]:

$$ZnS \rightarrow \left|Cu^{II}\right|_{Zn} + V_S^{\bullet\bullet} + S_S \tag{6}$$
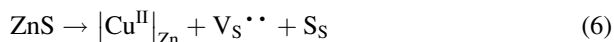
where $V_S^{\bullet\bullet}$ represents the sulfur vacancy, the energy level of which lies slightly below the CB edge; S_S denotes the sulfur atom at its normal lattice site. With increasing concentration of Cu^{2+} ions in the host, the potential of the conduction band becomes more positive until the concentration reaches 5.0 mol% as shown in Fig. 18e. The reason is that the Cu^{2+} will precipitate while the dopant Cu^{2+} exceeds in the matrix lattice and the decrease of lattice strain would result in the decrease of the vacancies. The data of PL can also further confirm the above results (Fig. 9). For Ag/ZnS, Bi/ZnS, Ga/ZnS, and In/ZnS catalysts, the reduction position of conduction band becomes more negative than that of bare ZnS. The band edge positions of the CB and VB are also responsible for the electronegativity of the dopants (electronegativity: Zn 1.65, Ag 1.93, Bi 2.02, Ga 1.81, and In 1.78) [59].

Photocatalytic Activity

The photocatalytic experiments of metal-doped ZnS catalysts were performed in two sections. One is for the photocatalytic hydrogen evolution of the visible-light-driven Cu/ZnS photocatalysts from an aqueous Na_2S solution under visible-light irradiation and the other is for the photocatalytic degradation of Orange II dye with metal (Cu, Ag, Bi, Ga, In)-doped ZnS catalysts under UV light irradiation.

Hydrogen Evolution

The photocatalytic activities of the prepared hollow copper-doped ZnS nanoparticles were evaluated for visible-light-driven hydrogen production by photosplitting of aqueous solution containing Na_2S as sacrificial agent as shown in Fig. 19. Obviously, copper-doped ZnS nanostructure (4.0Cu/ZnS) causes an improvement in the activity and liberates more amount of hydrogen (20.06 $\mu mol h^{-1} g^{-1}$), which may be due to the benefit in the optical property towards visible light while compared to pristine ZnS which absorbs only UV light (Fig. 15). The more negative reduction potential of the conduction band of 4.0Cu/ZnS leads to more efficient hydrogen generation than ZnS. Whereas the Cu doping into the lattice or interstitial of ZnS provides suitable impurity energy levels, which make it easier for the excited
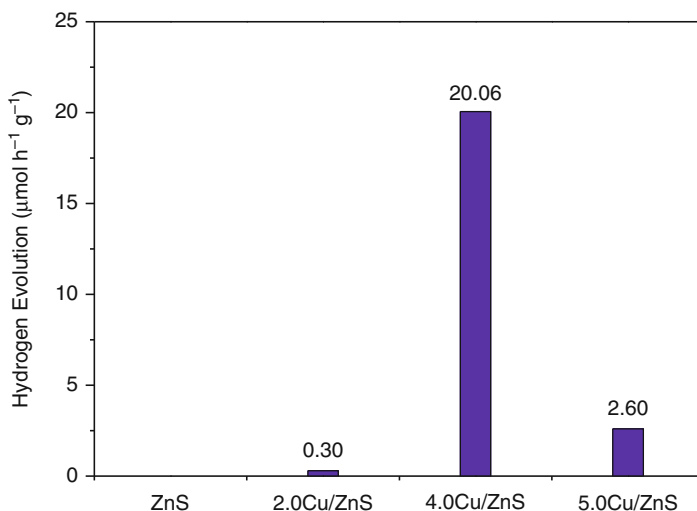
Fig. 19 Hydrogen evolution from an aqueous solution containing 0.1 M Na$_2$S catalyzed by Cu/ZnS and bare ZnS

electrons from the valence band of ZnS to inject into the conduction band of ZnS. The reason behind this is copper could form deep trap energy levels between valence band and conduction band of ZnS and by absorbing the external energy (visible light), electrons are excited from valence band (VB) to conduction band (CB) which then relaxed at shallow defect levels formed by impurity ions. The activated electrons will recombine with holes left in the CB or the holes transferred to copper trap energy levels by radiative transitions which give out photons [33, 43, 49, 60]. Thus the efficient interparticle charge transfer prevents the electron–hole recombination in copper-doped ZnS, resulting in superior photocatalytic activity towards photosplitting of S^{2-} ions. The existence of this charge gradient and uneven distribution of anionic S^{2-} ions may promote the charge separation of hole electron pairs and avoid their recombination in the bulk semiconductor, thus leading to significantly improved catalytic hydrogen production [61]. For 5.0 Cu/ZnS catalyst, the hydrogen production efficiency becomes poor (2.60 μmolh^{-1}g^{-1}), which may be attributed to the increase in number of impurity scattering centers, thus reducing mobility of the photogenerated charge carriers within the conduction and/or valence bands. The other reason is the potential of the conduction band becomes more positive. It is noted that electron transfer in 5.0 Cu/ZnS composite photocatalyst is less efficient, and the efficiency could not be further improved by doping high concentration of copper.

Photocatalytic Degradation of Dye

Photocatalytic degradation of Orange II dye under UV light irradiation was conducted to investigate the photocatalytic activities of the metal-doped ZnS
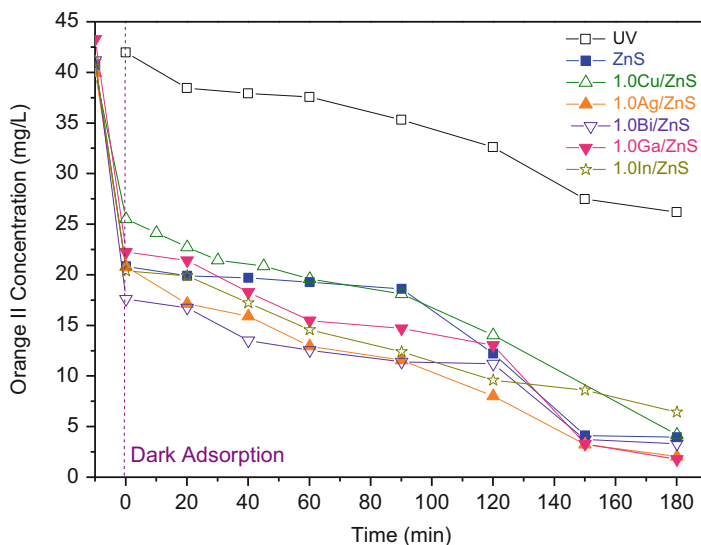
Fig. 20 Photocatalytic degradation of Orange II dye in the presence of bare and metal-doped ZnS photocatalysts

composite catalysts prepared at same dosages (1.0 mol%) of Cu/ZnS, Ag/ZnS, Bi/ZnS, Ga/ZnS, and In/ZnS. For comparison, the photocatalytic experiments under UV light were carried out and the efficient degradations of Orange II dye were presented in Fig. 20. The Orange II dye concentration was only decreased for 37.6 % after 180 min of irradiation in the absence of any photocatalyst. The removal percentages of the dye in an aqueous solution using 0.5 g/L ZnS photocatalyst at different desired doping metals of Cu, Ag, Bi, Ga, and In were significantly enhanced as shown in Fig. 20. Under similar experimental conditions, the removal efficiency of Orange II dye was obtained as 90.3 %, 89.5 %, 94.9 %, 91.9 %, 95.9 %, and 84.4 %, respectively, for ZnS, 1.0Cu/ZnS, 1.0Ag/ZnS, 1.0Bi/ZnS, 1.0Ga/ZnS, and 1.0In/ZnS. This reveals the optimal metal doping for efficient degradation of Orange II dye because doping the metals into the lattice of ZnS can separate photogenerated electrons and holes more effectively. Moreover, the TOC removal efficiency of Orange II dye was obtained as 60.4 %, 74.8 %, 50.0 %, 45.3 %, 53.3 %, and 53.9 %, respectively, for ZnS, 1.0Cu/ZnS, 1.0Ag/ZnS, 1.0Bi/ZnS, 1.0Ga/ZnS, and 1.0In/ZnS as shown in Fig. 21. The TOC concentration of Orange II dye was only reduced 12.6 % after 180 min of irradiation in the absence of any photocatalyst by UV light irradiation directly. According to the references, we could know that Cu, Ag, Bi, Ga, and In were considered to improve the photogenerated carrier separation efficiency, and Cu could play the role of a reduction site [41, 42, 47, 50, 62, 63]. Generally, the photogenerated electrons and holes transfer to the surface to react with the adsorbed reactants, and the migration direction of the photogenerated charge carriers greatly depends on the band edge position of semiconductors. Therefore, efficient interparticle charge transfer prevented electron–hole
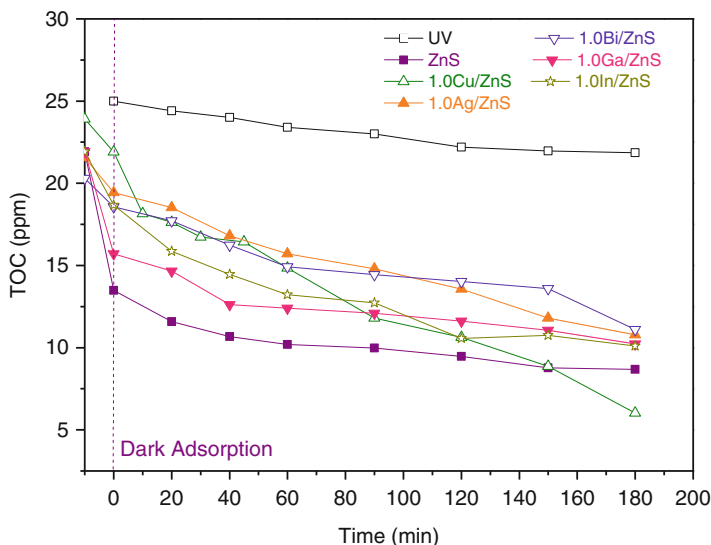
Fig. 21 TOC concentration of Orange II dye during photocatalytic reaction

recombination in ZnS, resulting in superior photocatalytic activities of metal (Cu, Ag, Bi, Ga, and In)-doped ZnS.

Based on the above results, the proposed mechanisms for Orange II dye (OII dye) degradation using the as-synthesis ZnS photocatalysts (M/ZnS denoted as Cu, Ag, Bi, Ga, and In-doped ZnS) are suggested as follows [41, 42, 47, 50, 62–66]:

$$M/ZnS + OII\ dye_{ads} + h\nu(UV-254\ nm)$$
$$\rightarrow M/ZnS(h^+_{vb}) + M/ZnS(e^-_{cb}) + OII\ dye_{ads}* \tag{7}$$

$$M/ZnS(h^+_{vb}) + M/ZnS(e^-_{cb}) \rightarrow M/ZnS + heat \tag{8}$$

$$OII\ dye_{ads}* + M/ZnS_{surf} \rightarrow OII\ dye_{ads}^+ + M/ZnS_{surf}(e^-) \tag{9}$$

$$M/ZnS_{surf} + M/ZnS(e^-_{cb}) \rightarrow M/ZnS_{surf}(e^-) \tag{10}$$

$$M/ZnS_{surf}(e^-) + O_{2ads} \rightarrow M/ZnS_{surf} + O_2^- \tag{11}$$

$$O_2^- + M/ZnS(e^-_{cb}) + 2H^+ \rightarrow H_2O_2 \tag{12}$$

$$H_2O_2 + M/ZnS(e^-_{cb}) \rightarrow OH + OH^- \tag{13}$$

$$M/ZnS(h^+_{vb}) + OH^-_{ads} \rightarrow OH \tag{14}$$

$$O_2^- + H_2O_2 + OH + OII\ dye_{ads}^+ \rightarrow degradation\ of\ OII\ dye \tag{15}$$
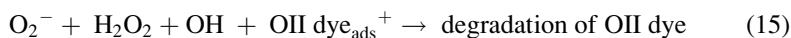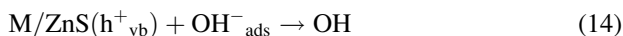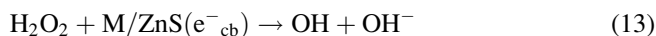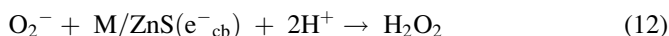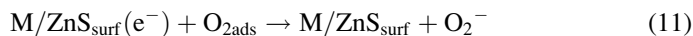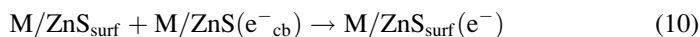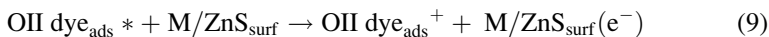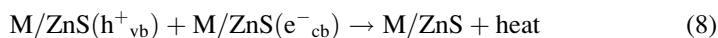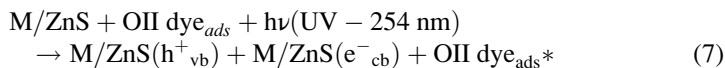
Since the M/ZnS catalyst is a strong adsorbent for Orange II dye in aqueous solution, a large amount of OII dye molecules are adsorbed on the surface of M/ZnS

catalysts due to the strong interactions between M/ZnS catalysts and OII dye. Under the UV-light irradiation, OII dye molecules can be activated to the excited state (OII dye*). Due to the strong electron affinity of M/ZnS catalysts, the electrons transfer from OII dye* to the M/ZnS catalysts. The metal (Cu, Ag, Bi, Ga, and In) doped into ZnS lattice as the modified photocatalysts makes the electrons move more freely without any scattering from atoms or defects. The moving electrons will be trapped when they encounter the metal (Cu, Ag, Bi, Ga, and In) islands. The electrons accumulated on the metal (Cu, Ag, Bi, Ga, and In) reduce the adsorbed oxygen species to superoxide anion radical (O_2^-) and the hole oxidize the adsorbed hydroxide ion into hydroxyl radical (OH•). The electrons accumulated on the conduction band reduce the superoxide anion radical and hydronium ion to dihydrogen dioxide (H_2O_2). Subsequently, OII dye is degraded by these active oxygen species. As a result, the metal (Cu, Ag, Bi, Ga, and In) can scavenge the injected electron and separate photogenerated electrons and holes more effectively, which are responsible for reduction of the photogenerated hole–electron recombination rate. Thus, the metal (Cu, Ag, Bi, Ga, and In) modified ZnS photocatalysts can improve the photocatalytic activity.

Conclusion and Future Directions

Hollow copper-doped ZnS self-assembled nanostructures were prepared by a facile sonochemical synthesis approach and provided suitable reasons for the observed morphology based on the characterization studies, i.e., the competitive bonding interaction between copper and zinc ions towards sulfur (Cu-S-Zn). The observed decrease in energy band gap shows that the copper-doped ZnS can better enhance the optical property of pristine ZnS by harvesting more visible light. The photosplitting of water in the presence of Na_2S indicates as prepared hollow Cu-ZnS self-assembled nanostructures may be an active visible response photocatalyst. Moreover, metal (Ag, Bi, Ga, and In) ions doped onto the lattice of ZnS spheres were synthesized by sonochemical irradiation approach without any template. Their UV light-assisted photocatalytic ability has been shown by the degradation of azo dye, Orange II. According to the experimental results, we inferred the possible structures of decomposed products and degradation pathway of Orange II dye. The active species (such as O_2^-, OH•, and H_2O_2) responsible for the degradation of Orange II dye were detected in the metal (Cu, Ag, Bi, Ga, and In)-doped ZnS photocatalytic system.

   Increasing specific surface area can provide more activity sites for better photocatalytic activities. For metal-doped ZnS catalyst, future research work will be expected to attempt by adding capping reagent, such as PVP, PEG, and CIT, in the synthetic solution to induce the formation of micelles that further become micro- or mesopores in the final catalyst product in sonochemical hydrothermal method. In this study, Ag, Bi, Ga, and In doped into the lattice of ZnS have provided a slight decrease in the ZnS band gap which is still larger than the emitting energy of visible light. To further improve photocatalytic activity within visible-light range, codoped

ZnS composite catalysts, such as ZnS/Ag:Ga, ZnS/Cu:In, or semiconductor materials of ternary chalcogenide compounds, such as $ZnGa_xS_y$ and $ZnIn_xS_y$, are strongly recommended to be synthesized in the future and to produce smaller band-gap semiconductor or electron–hole pairs separation.

References

1. Fang XS, Zhai T, Gautam UK, Li L, Wu L, Bando Y, Golberg D (2011) ZnS nanostructures: from synthesis to applications. Prog Mater Sci 56:175–287
2. Chen D, Huang F, Ren G, Li D, Zheng M, Wang Y, Lin Z (2010) ZnS nano-architectures: photocatalysis, deactivation and regeneration. Nanoscale 2:2062–2064
3. Ashkarran AA (2014) Absence of photocatalytic activity in the presence of the photoluminescence property of Mn–ZnS nanoparticles prepared by a facile wet chemical method at room temperature. Mat Sci Semicond Process 17:1–6
4. Maeda K, Domen K (2007) New non-oxide photocatalysts designed for overall water splitting under visible light. J Phys Chem C 111:7851–7861
5. Zhang H, Wei B, Zhu L, Yu J, Sun W, Xu L (2013) Cation exchange synthesis of ZnS–Ag_2S microspheric composites with enhanced photocatalytic activity. Appl Surf Sci 270:133–138
6. Zhu J, Zach M (2009) Nanostructured materials for photocatalytic hydrogen production. Curr Opin Colloid Interface Sci 14:260–269
7. Bao N, Shen L, Takata T, Domen K (2008) Self-templated synthesis of nanoporous CdS nanostructures for highly efficient photocatalytic hydrogen production under visible light. Chem Mater 20:110–117
8. Maeda K, Nishimura N, Domen K (2009) A precursor route to prepare tantalum (V) nitride nanoparticles with enhanced photocatalytic activity for hydrogen evolution under visible light. Appl Catal A-Gen 370:88–92
9. Karan NS, Sarma DD, Kadam RM, Pradhan N (2010) Doping transition metal (Mn or Cu) ions in semiconductor nanocrystals. J Phys Chem Lett 1:2863–2866
10. Murugadoss G (2012) Luminescence properties of Co-doped ZnS:Ni, Mn and ZnS:Cu, Cd nanoparticles. J Lumin 132:2043–2048
11. Peng WQ, Cong GW, Qu SC, Wang ZG (2006) Synthesis and photoluminescence of ZnS:Cu nanoparticles. Opt Mater 29:313–317
12. Muthukumaran S, Ashok kumar M (2013) Structural, FTIR and photoluminescence properties of ZnS:Cu thin films by chemical bath deposition method. Mater Lett 93:223–225
13. Begum R, Chattopadhyay A (2014) Redox-tuned three-color emission in double (Mn and Cu) doped zinc sulfide quantum dots. J Phys Chem Lett 5:126–130
14. Corrado C, Jiang Y, Oba F, Kozina M, Bridges F, Zhang JZ (2009) Synthesis, structural, and optical properties of stable ZnS:Cu, Cl nanocrystals. J Phys Chem A 113:3830–3839
15. Ummartyotin S, Bunnak N, Juntaro J, Sain M, Manuspiya H (2012) Synthesis and luminescence properties of ZnS and metal (Mn, Cu)-doped-ZnS ceramic powder. Solid State Sci 14:299–304
16. Hu L, Zhu L, He H, Guo Y, Pan G, Jiang J, Jin Y, Sun L, Ye Z (2013) Colloidal chemically fabricated ZnO:Cu based photodetector with extended UV-visible detection waveband. Nanoscale 5:9577–9581
17. Wang Y, Chen D, Wang Y, Huang F, Zhang J, Hu Q, Lin Z (2013) Tunable surface charge of ZnS:Cu nano-adsorbent induced the selective preconcentration of cationic dyes from wastewater. Nanoscale 4:3665–3668
18. Liu CC, Liu ZF, Li JW, Li YB, Han JH, Wang Y, Liu ZC, Ya J (2013) Cu-doping ZnO/ZnS nanorods serve as the photoanode to enhance photocurrent and conversion efficiency. Microelectron Eng 103:12–16

19. Goharshadi EK, Sajjadi SH, Mehrkhah R, Nancarrow P (2012) Sonochemical synthesis and measurement of optical properties of zinc sulfide quantum dots. Chem Eng J 209:113–117
20. Yan Y, Sun HP, Yao PP, Kang SZ, Mu J (2011) Effect of multi-walled carbon nanotubes loaded with Ag nanoparticles on the photocatalytic degradation of rhodamine B under visible light irradiation. Appl Surf Sci 257:3620–3626
21. Kanhere P, Tang Y, Zheng J, Chen Z (2013) Synthesis, photophysical properties, and photocatalytic applications of Bi doped $NaTaO_3$ and Bi doped $Na_2Ta_2O_6$ nanoparticles. J Phys Chem Solids 74:1708–1713
22. Bagwasi S, Tian B, Zhang J, Nasir M (2013) Synthesis, characterization and application of bismuth and boron Co-doped TiO_2: a visible light active photocatalyst. Chem Eng J 217:108–118
23. Zhong JB, Li JZ, Zeng J, He XY, Hu W, Shen YC (2012) Enhanced photocatalytic performance of Ga^{3+}-doped ZnO. Mater Res Bull 47:3893–3896
24. Sasikala R, Gaikwad AP, Sudarsan V, Gupta N, Bharadwaj SR (2013) Cubic phase indium doped cadmium sulfide dispersed on zinc oxide: enhanced photocatalytic activity for hydrogen generation from water. Appl Catal A-Gen 464–465:149–155
25. Xing C, Zhang Y, Yan W, Guo L (2006) Band structure-controlled solid solution of $Cd_{1-x}Zn_xS$ photocatalyst for hydrogen production by water splitting. Int J Hydrog Energy 31:2018–2024
26. Wang L, Wang WZ, Shang M, Yin WZ, Sun SM, Zhang L (2010) Enhanced photocatalytic hydrogen evolution under visible light over $Cd_{1-x}Zn_xS$ solid solution with cubic zinc blend phase. Int J Hydrog Energy 35:19–25
27. Goswami B, Pal S, Sarkar P (2008) A theoretical study on the electronic structure of ZnSe/ZnS and ZnS/ZnSe core/shell nanoparticles. J Phys Chem C 112:11630–11636
28. Soltani N, Saion E, Yunus WMM, Erfani M, Navasery M, Bahmanrokh G, Rezaee K (2014) Enhancement of visible light photocatalytic activity of ZnS and CdS nanoparticles based on organic and inorganic coating. Appl Surf Sci 290:440–447
29. Liu W, Gao L, Su G, Liu H, Wang X, Zhang L (2010) Ultrasound assisted synthesis of monoclinic structured spindle $BiVO_4$ particles with hollow structure and its photocatalytic property. Ultrason Sonochem 17:669–674
30. Suslick KS (1990) Sonochemistry. Science 247:1439–1445
31. Belova V, Borodina T, Möhwald H, Shchukin DG (2011) The effect of high intensity ultrasound on the loading of Au nanoparticles into titanium dioxide. Ultrason Sonochem 18:310–317
32. Shirsath SR, Pinjari DV, Gogate PR, Sonawane SH, Pandit AB (2013) Ultrasound assisted synthesis of doped TiO_2 nano-particles: characterization and comparison of effectiveness for photocatalytic oxidation of dyestuff effluent. Ultrason Sonochem 20:277–286
33. Kim TH, Rodríguez-González V, Gyawali G, Cho SH, Sekino T, Lee SW (2013) Synthesis of solar light responsive Fe, N co-doped TiO_2 photocatalyst by sonochemical method. Catal Today 212:75–80
34. Goharshadi EK, Mehrkhah R, Nancarrow P (2013) Synthesis, characterization, and measurement of structural, optical, and phtotoluminescent properties of zinc sulfide quantum dots. Mater Sci Semicond Process 16:356–362
35. Chen Z, Zhou S, Li Y, Li XX, Li Y, Sun W, Liu G, Chen N, Du G (2013) Strong blue luminescence of O^{2-}-doped ZnS nanoparticles synthesized by a low temperature solid state reaction method. Mater Sci Semicond Process 16:833–837
36. Shannon RD (1976) Revised effective ionic radii and systematic studies of interatomic distances in halides and chalcogenides. Acta Crystallogr A 32:751–767
37. Gedanken A (2004) Using sonochemistry for the fabrication of nanomaterials. Ultrason Sonochem 11:47–55
38. Zhang J, Huang F, Lin Z (2010) Progress of nanocrystalline growth kinetics based on oriented attachment. Nanoscale 2:18–34
39. Tomsa AR, Popovici EJ, Cadis AI, Stefan M, Barbu-Tudoran L, Astilean S (2008) Ultrasound-assisted synthesis of highly disperse zinc sulphide powders. J Optoelectron Adv Mater 10:2342–2345

40. Lee GJ, Anandan S, Masten SJ, Wu JJ (2014) Sonochemical synthesis of hollow copper doped zinc sulfide nanostructures: optical and catalytic properties for visible light assisted photosplitting of water. Ind Eng Chem Res 53:8766–8772

41. Kuppayee M, Vanathi Nachiyar GK, Ramasamy V (2011) Synthesis and characterization of Cu^{2+} doped ZnS nanoparticles using TOPO and SHMP as capping agents. Appl Surf Sci 257:6779–6786

42. Zeng HC (2007) Ostwald ripening: a synthetic approach for hollow nanomaterials. Curr Nanosci 3:177–181

43. Lei Y, Wang G, Song S, Fan W, Pang M, Tang J, Zhang H (2010) Room temperature, template-free synthesis of BiOI hierarchical structures: visible-light photocatalytic and electrochemical hydrogen storage properties. Dalton Trans 39:3273–3278

44. Fan HJ, Gosele U, Zacharias M (2007) Formation of nanotubes and hollow nanoparticles based on Kirkendall and diffusion processes: a review. Small 3:1660–1671

45. Ashwini K, Pandurangappa C, Nagabhushana BM (2012) Synthesis and optical properties of undoped and Eu-doped ZnS nanoparticles. Phys Scripta 85:065706–065710

46. Jindal Z, Verma NK (2008) Photoluminescent properties of ZnS:Mn nanoparticles with in-built surfactant. J Mater Sci 43:6539–6545

47. Rema Devi BS, Raveendran R, Vaidyan AV (2007) Synthesis and characterization of Mn^{2+}-doped ZnS nanoparticles. Prama-J Phys 68:679–687

48. Maji SK, Mukherjee N, Mondal A, Adhikary B, Karmakar B, Dutta S (2011) Synthesis and characterization of nanocrystalline zinc sulfide via zinc thiobenzoate-lutidine single-source precursor. Inorg Chim Acta 371:20–26

49. Chauhan R, Kumar A, Chaudhary RP (2014) Photocatalytic degradation of methylene blue with Cu doped ZnS nanoparticles. J Lumin 145:6–12

50. Hota G, Idage SB, Khilara KC (2007) Characterization of nano-sized CdS-Ag_2S core-shell nanoparticles using XPS technique. Colloid Surf A-Physicochem Eng Asp 29:5–12

51. Salavati-Niasari M, Ghanbari D, Davar F (2009) Synthesis of different morphologies of bismuth sulfide nanostructures via hydrothermal process in the presence of thioglycolic acid. J Alloy Compd 488:442–447

52. Cabello G, Lillo L, Caro C, Soto-Arriaza MA, Chornik B, Buono-Core GE (2013) Evaluation on the optical properties of Ga_2O_{3-x} thin films co-doped with Tb^{3+} and transitionmetals (Mn^{2+}, Cr^{3+}) prepared by a photochemical route. Ceram Int 39:2443–2450

53. Li Y, Duan G, Cai W (2007) Controllable superhydrophobic and lipophobic properties of ordered pore indium oxide array films. J Colloid Interf Sci 314:615–620

54. Bhattacharya C, Lee HC, Bard AJ (2013) Rapid screening by scanning electrochemical microscopy (SECM) of dopants for Bi_2WO_6 improved photocatalytic water oxidation with Zn doping. J Phys Chem C 117:9633–9640

55. Park HS, Kweon KE, Ye H, Paek E, Hwang GS, Bard AJ (2011) Factors in the metal doping of $BiVO_4$ for improved photoelectrocatalytic activity as studied by scanning electrochemical microscopy and first-principles density-functional calculation. J Phys Chem C 115:17870–17879

56. Tong L, Iwase A, Nattestad A, Bach U, Weidelener M, Götz G, Mishra A, Bäuerle P, Amal R, Wallace GG, Mozer AJ (2012) Sustained solar hydrogen generation using a dye-sensitised NiO photocathode/$BiVO_4$ tandem photo-electrochemical device. Energy Environ Sci 5:9472–9475

57. Zhang H, Chen G, Bahnemann DW (2009) Photoelectrocatalytic materials for environmental applications. J Mater Chem 19:5089–5121

58. Peng F, Cai LF, Yu H, Wang HJ, Yang J (2008) Synthesis and characterization of substitutional and interstitial nitrogen-doped titanium dioxides with visible light photocatalytic activity. J Solid State Chem 181:130–136

59. Zhang Z, Shao C, Li X, Sun Y, Zhang M, Mu J, Zhang P, Guo Z, Liu Y (2013) Hierarchical assembly of ultrathin hexagonal SnS_2 nanosheets onto electrospun TiO_2 nanofibers enhanced photocatalytic activity based on photoinduced interfacial charge transfer. Nanoscale 5:606–618

60. Anandan S, Madhavan J, Ashokkumar M (2010) The contribution of the nanotechnology to hydrogen. Nanotechnology for the energy challenge. Wiley-VCH Verlag GmbH & Co. KGaA, Wiley Online Library, DOI:10.1002/9783527629299. 5:111–136
61. Zhao L, Wang Y, Li X, Wang A, Song C, Hu Y (2013) Hydrogen production via decomposition of hydrogen sulfide by synergy of non-thermal plasma and semiconductor catalysis. Int J Hydrog Energy 38:14415–14423
62. Poormohammadi-Ahandani Z, Habibi-Yangjeh A, Pirhashemi M (2014) Ultrasonic-assisted method for preparation of Cu-doped ZnS nanoparticles in water as a highly efficient visible light photocatalyst. Phys Chem Res 2:76–89
63. Zhang W, Li D, Sun M, Shao Y, Chen Z, Xiao G, Fu X (2010) Microwave hydrothermal synthesis and photocatalytic activity of $AgIn_5S_8$ for the degradation of dye. J Solid State Chem 183:2466–2474
64. Rajabi HR, Khani O, Shamsipur M, Vatanpour V (2013) High-performance pure and Fe^{3+}-ion doped ZnS quantum dots as green nanophotocatalysts for the removal malachite green under UV-light irradiation. J Hazard Mater 370:250–251
65. Chen PK, Lee GJ, Anandana S, Wu JJ (2012) Synthesis of ZnO and Au tethered ZnO pyramid-like microflower for photocatalytic degradation of Orange II. Mater Sci Eng B 177:190–196
66. Liu Y, Chen X, Li J, Burda C (2005) Photocatalytic degradation of azo dyes by nitrogen-doped TiO_2 nanocatalysts. Chemosphere 61:11–18

Combined Treatment Processes Based on Ultrasound and Photocatalysis for Treatment of Pesticide Containing Wastewater

Pankaj N. Patil and Parag R. Gogate

Contents

Abstract

The research area of water purification/wastewater treatment has been extensively growing in the last few decades, especially as the water quality control and regulations against hazardous pollutants are becoming more stringent. Wastewater generated from the pesticide and chemical industries contains toxic and nonbiodegradable compounds, and it is imperative to develop efficient treatment approaches. A promising way to achieve/enhance the degradation of biologically

P.N. Patil
Chemical Engineering Department, Gharda Institute of Technology, Ratnagiri, Maharashtra, India
e-mail: pankaj.n.patil86@gmail.com

P.R. Gogate (✉)
Chemical Engineering Department, Institute of Chemical Technology, Matunga, Mumbai, India
e-mail: pr.gogate@ictmumbai.edu.in; paraggogate@yahoo.co.in

and chemically stable molecules like pesticides is by the application of advanced oxidation processes (AOPs). The chapter focuses on the application of sonochemical reactors and photocatalytic oxidation reactors, either operated individually or in combination, for the treatment of pesticide-containing wastewaters. Initially introduction to the sonochemical reactors has been presented along with the discussion about the benefits that can be obtained using different combinations of advanced oxidation processes based on the sonochemical reactors, Fenton's chemistry, ozonation, and use of hydrogen peroxide. Guidelines have been presented for the selection of optimum parameters for maximizing the process intensification benefits. Overview of earlier literature in the specific area of sonophotocatalytic oxidation has also been presented. In the last part of chapter, a case study related to the degradation of dichlorvos pesticide in aqueous solution using ultrasonic cavitation and photocatalytic oxidation has been discussed to highlight the methodology for optimization and the expected benefits that can be obtained using the combination approach. Overall it appears that using a combination of advanced oxidation processes under optimized conditions yields significant benefits as compared to the individual operations.

Introduction

Pesticide-Containing Wastewater

Groundwater contamination by pesticides is certainly a serious matter with reference to the Indian context considering that India is dominantly an agricultural country. A variety of pesticides are widely used in the fields for plant protection. The different categories of pesticides include herbicides, insecticides, fungicides, rodenticides, nematicides, and microbiocides. In general chemical processing industries are considered to generate wastewaters containing toxic and nonbiodegradable compounds, and the pesticide processing industries and sectors also contribute significantly to this environmental concern [1]. Industrial waste streams containing high concentrations of pesticides should ideally be treated at source. Contamination of soils and runoff water with the pesticides is also a very important problem worldwide and dominant for the agricultural countries as the pesticides/herbicides are widely used in the agricultural fields. During the application, the pesticides/herbicides are often not completely consumed meaning a significant quantum is likely to mix with the runoff waters from fields or slowly leach into ground. Different types of pesticides are used in agricultural fields for plant protection and among these, organo-chloro-phosphate compounds are the most widely used class of pesticides.

Pesticides are generally toxic and also sometimes carcinogenic leading to potential health hazards [2, 3]. Most of the active ingredients in the pesticides are resistant

to the simple chemical and/or biological degradation under typical operating conditions [4]. Due to the long-term stability of pesticides and the hazardous effects especially on human beings, it becomes imperative to develop effective treatment schemes for the removal of residual pesticides and avoid the problems of pesticide pollution in surface and groundwater that has been recognized for many years as an important issue in a number of countries.

Need of Efficient Treatment

The dreadful effects of pesticides on human and aquatic life impart the need of effectively treating the wastewater streams containing these toxic compounds. It is imperative to highlight the effects of pesticide so that the importance of the treatment can be established and some of the significant effects of pesticides are as follows:

- The long-term exposure to pesticides poses the risk of cancer. Associations have been found with leukemia, lymphoma, and other forms of cancer of brain, kidney, breast, prostate, pancreas, liver, lung, and skin. The risk is for both residential and occupational exposures, although it is dominant among farm workers who regularly apply these chemicals. Occupational exposure of mothers to pesticides during pregnancy can also lead to leukemia and brain cancer in the newborn.
- Pesticide exposure can also worsen the neurological system and result in a range of neurological health effects such as memory loss, loss of coordination, reduced speed of response to stimuli, reduced visual ability, altered or uncontrollable mood and general behavior, and reduced motor skills. The risk of developing Parkinson's disease is 70 % greater in those people exposed to even low levels of pesticides, insecticides, or herbicides.
- Pesticide exposure leads to birth defects, fetal death, and altered fetal growth. A number of pesticides have also been associated with impaired fertility in males.
- Other possible health effects include asthma, allergies, hypersensitivity, and hormone disruption.

Pesticides like methyl parathion, imidacloprid, triazophos, dichlorvos, and alachlor are highly toxic in nature and have an adverse effect on humans. As there is an extensive demand of these pesticides especially in the agriculturally dominated countries like India, the production of these pesticides is continuously increasing and so is the occurrence in the effluent streams from industries as well as in the runoff water streams from agricultural and domestic fields. Because of the potential hazards associated with these specific pesticides, control and remediation of pesticide-contaminated water is usually desired.

Methyl parathion ($C_8H_{10}NO_5PS$) is an organophosphorus pesticide that has been widely used as an agricultural insecticide in India and can result in significant water pollution due to its biorefractory nature and longer stability. Methyl parathion is used to control boll weevils and many biting insects found in the vicinity of agricultural

crops, primarily cotton. Methyl parathion, also known as the "cotton poison," is applied in the fields containing crops such as cotton, corn, apples, soybeans, rice, wheat, peaches, alfalfa, sunflower, and sweet corn [5]. Methyl parathion has only one structural isomer and its partition coefficient is 3 which suggest its high potential for bioaccumulation in the organisms. It readily degrades to methyl paraoxon in the human body which acts as acetyl cholinesterase inhibitor creating problems with nervous systems [6].

Imidacloprid ($C_9H_{10}ClN_5O_2$) is a systemic chloronicotinyl pesticide, generally used for the control of sucking insects and some of the chewing insects including termites, soil insects, and fleas on pets. It belongs to the class of neonicotinoid insecticides. Because of its high efficiency against many pests, its use is increasing worldwide. Due to its high toxicity, relatively high solubility (0.58 g/L), and stability in water, it has also created significant environmental concerns [7]. Acute toxicity of imidacloprid on the bee population (oral $LD_{50} = 0.0037$ μg/bee) and aquatic environment has been reported [8].

Triazophos is a common name for O,O-diethyl-O-1-phenyl-1H-1,2,4-triazol-3-yl phosphorothioate, which is generally used as an insecticide on various crops such as cotton and rice to control aphids, fruit borers, leafhoppers, and cutworms [9]. Triazophos is a moderately toxic and broad spectrum nonsystemic organophosphorus pesticide used in large quantities worldwide [10, 11]. Wastewater containing triazophos pesticide has typically significant toxic effects [12].

Dichlorvos (2,2-dichlorovinyl dimethyl phosphate), commonly known as Vapona, is a chlorinated volatile organophosphate compound with fumigant action and available as an oily colorless to amber-colored liquid, with an aromatic chemical odor. Dichlorvos is also commonly used to control insects in food storage areas, greenhouses, workplaces, and homes. It is widely used for crop protection mainly in greenhouses and for controlling parasites and insects in houses, aircraft, and outdoor areas [13]. Hydrolysis of dichlorvos is a slow phenomenon under natural conditions, which means that dichlorvos mixed with water will have a long shelf life and hence the residual concentrations will be significant resulting in severe water pollution. Dichlorvos is poisonous if inhaled, swallowed, or absorbed through the skin and eyes. Very large doses of dichlorvos may cause breathing problems, coma, and even death [14]. Chronic exposure from handling certain organochlorine and organophosphate pesticides including dichlorvos is linked with an increased risk of diabetes [15]. Dichlorvos has carcinogenic, neurotoxic, and genotoxic effects.

Alachlor (2-chloro-N-(2,6-diethylphenyl)-N-(methoxymethyl)acetamide) is a widely used herbicide from the chloroacetanilide family. The main applications of alachlor include control of annual grasses and broadleaf weeds in the fields used for the production of corn, soybeans, and peanuts. Alachlor has been classified as the carcinogen of B2 group by the EPA and has been known as a highly toxic endocrine-disrupting chemical. It is a persistent herbicide with a half-life in soil and in water of over 70 and 30 days, respectively. As alachlor is toxic to many organisms, conventional biological remediation processes are not suitable to remove the alachlor from contaminated water [16].

Existing Treatment Techniques

The technique of biodegradation, which is commonly used to counter the effects of water pollution, is not viable for majority of the biorefractory hazardous substances [17] including pesticides. Physical processes such as nanofiltration and reverse osmosis [18], activated carbon adsorption [19], as well as chemical oxidation processes based on the use of aqueous chlorine, ozone, hydrogen peroxide, and Fenton treatment [17, 20, 21] have been reported useful to a certain degree for the removal of pesticide residues. However, physical processes such as adsorption merely transfer pollutants from one phase to another phase creating problems of secondary pollution and chemical oxidation has a limitation in terms of the degree of destruction of pesticide and requirement of significant treatment times. Also, methods such as adsorption on activated carbon, extraction, and chemical oxidation suffer from disadvantages such as limited applicability and low efficiency [22, 23], thus imparting the need of research into alternative treatment techniques.

The research field of water purification/wastewater treatment has been extensively growing in the last few decades, as water quality control and regulations against hazardous pollutants are becoming more stringent. A promising way to achieve the degradation of biologically and chemically stable molecules is by application of advanced oxidation processes (AOPs) based on the "in situ" production of hydroxyl radicals under mild experimental conditions [24]. Among the AOPs, the commonly used techniques include the processes based on hydrogen peroxide (H_2O_2 + UV, Fenton, photo-Fenton, and Fenton-like processes), photocatalysis, processes based on ozone (O_3, O_3 + UV), and electrochemical processes [25]. Cavitation is another process being recently developed as an effective means of generating hydroxyl radicals through thermal hot spots and can be applied for wastewater treatment. A combination of treatment processes is also possible, which can achieve efficient removal of pesticides with near-complete mineralization. Detailed optimization studies are indeed required to minimize the treatment costs and achieve efficient mineralization.

The present work has focused on giving an overview on the application of cavitation-based approaches for wastewater treatment with a special emphasis on pesticides. Different guidelines for combination of treatment approaches (cavitation with different AOPs) have also been presented along with a detailed case study to highlight the optimization strategies required for obtaining an efficient treatment strategy.

Basic Aspects of Alternate Treatment Technologies

Advanced Oxidation Processes

The degradation of biologically and chemically stable molecules can be achieved more effectively by the application of processes based on the production of hydroxyl radicals under mild experimental conditions, which are also described as

AOPs [24, 26–28]. AOPs are in general based on the use of hydrogen peroxide, UV irradiations, Fenton's reagent, ozone, and ultrasound/cavitation.

AOPs Based on Hydrogen Peroxide

Hydrogen peroxide acts as a source of hydroxyl radicals which can intensify the degradation process as the oxidation potential of hydroxyl radicals is higher as compared to hydrogen peroxide. It is important to understand that the degree of intensification and requirement of hydrogen peroxide loading for optimum intensification is different for each pollutant under consideration and hence detailed laboratory-scale optimization studies for specific pollutants are important. Some of the processes based on the use of hydrogen peroxide are as follows [29]:

- Fenton's process (H_2O_2/Fe^{2+}): Fenton's reagent can be used to treat a variety of organic chemicals like phenols, formaldehyde, pesticides, wood preservatives, plastic additives, and rubber chemicals. The process may be applied to wastewaters and contaminated soils for a reduction in the toxicity to improve the biodegradability and for odor and color removal. The method involves the use of aqueous mixtures of ferrous iron salt (Fe^{2+}) and hydrogen peroxide (H_2O_2) under acidic conditions. The efficacy of using Fenton's reagent can be intensified based on the use of combined approaches employing irradiation which achieves an efficient conversion of Fe^{3+} to Fe^{2+}.
- Advanced Fenton process (H_2O_2/Fe solid): Similar to the Fenton process, advanced Fenton process can also be used with beneficial results for the degradation of pollutants, with possibly lower treatment costs due to the use of waste iron sheets or other forms such as slag. Fenton's reagent has a disadvantage in that the homogeneous catalyst, i.e., iron salt added into the solution, cannot be completely consumed in the degradation process and this results in the formation of a significant quantum of sludge. In recent years, homogeneous catalysts are being replaced by heterogeneous metal-supported catalysts giving advantages of easy separation and reduced sludge formation, and these processes are being described as the advanced Fenton processes.
- Photo-Fenton process ($H_2O_2/Fe^{2+}/UV$): Photo-Fenton is known to be able to improve the efficiency of dark Fenton or Fenton-like reagents by means of interaction of radiation (UV or Vis) with Fenton's reagent. This technique has been suggested to be feasible and promising to remove pollutants from natural and industrial waters and also increase the biodegradability of pollutant when used as a pretreatment to decrease the toxicity of water.
- H_2O_2/UV: Use of hydrogen peroxide alone for effluent treatment is not recommended due to the severe mass transfer limitations and limited oxidation capacity. The rate of formation of hydroxyl radicals is significantly enhanced when hydrogen peroxide is used in combination with UV and hence this combination can be more efficient as compared to only using hydrogen peroxide.
- Ultrasound/H_2O_2: Combination of hydrogen peroxide with ultrasound for possible intensification of water treatment process also works on similar principle as the UV/ H_2O_2 process. The enhanced formation of free radicals due to continuous

dissociation of hydrogen peroxide under the cavitating conditions coupled with intensified mass transfer due to the turbulence effects can result in the higher extent of removal of pollutants from the wastewater.

Combined Ozonation with Irradiations

Ozonation can also be an effective approach for the destruction of organics. Ozone with a standard reduction potential (E_0) of 2.07 V is capable of oxidizing organic and inorganic compounds [30]. Ozonation can also be combined with irradiation and this offers as a clean technology for removing different types of pollutants such as pesticides. The reaction of ozone with organic and inorganic pollutants follows two reaction mechanisms, viz., a direct reaction of molecular ozone and a radical type reaction involving $^\bullet$OH radicals induced by the decomposition of ozone in water under specific conditions (pH adjustment or combination with irradiation). The decomposition of ozone proceeds as chain reactions including initiation steps, propagation steps, and pollutant breakdown [31]. Combination of O_3 with other irradiation such as UV and ultrasound can be more effective as compared to only ozonation for the destruction of toxic and refractory organics present in water. The mass transfer limitations associated with only ozone can be eliminated based on the generation of turbulence when it is combined with ultrasound.

Electrochemical Treatment

In the electrochemical process [32], the pollutants are destroyed either by direct or indirect oxidation process. In direct anodic oxidation process, the pollutants are first adsorbed on the anode surface and subsequently destroyed by the anodic electron-transfer reaction. The efficacy of destruction strongly depends on the applied electric potential. In indirect oxidation process, stronger oxidants such as hypochlorite/chlorine, ozone, and hydrogen peroxide are electrochemically generated and the pollutants are then destroyed in the bulk solution by an oxidation reaction of the generated oxidant.

Cavitation

Cavitation is a phenomenon of generation, growth, and subsequent collapse of cavities in a liquid medium occurring in an extremely small interval of time (milliseconds) and releasing large magnitudes of energy locally with significantly higher energy densities [26]. The collapse of bubbles induces localized supercritical conditions such as high-pressure and high-temperature pulse ranging to about few thousands. The local effects of cavitation include generation of free radicals, hot spots, and intense turbulence coupled with liquid circulation currents. Cavitation can be generated by the passage of ultrasound in the liquid medium or by making use of the alternations in the velocity/pressure in the hydraulic systems. The intensity of cavitation and hence the net chemical effects are strongly dependent on the operating and design parameters such as reaction temperature, hydrostatic pressure, power dissipation, and equipment geometry. Cavitation can be combined with one or more

advanced oxidation techniques to give enhanced degradation of pollutants and possibly synergistic effects.

Types of Cavitation

Cavitation can be classified into four types based on the method of production of cavities, viz., acoustic, hydrodynamic, optic, and particle cavitation. Acoustic and hydrodynamic cavitation are due to the result of tensions prevailing in a liquid, while optic and particle cavitation are the consequence of the local deposition of a significant quantum of energy.

- *Acoustic cavitation*: In this case, cavitation is produced due to the pressure variation induced by the passage of sound waves usually over the frequency range of 16 kHz–2 MHz.
- *Hydrodynamic cavitation*: Cavitation is produced by pressure variation induced by changes in the geometry used for fluid flow.
- *Optic cavitation*: It is produced by photons of high intensity light (laser) rupturing the liquid continuum.
- *Particle cavitation*: It is produced by the beam of elementary particles, e.g., a neutron beam rupturing a liquid as in the case of a bubble chamber.

Out of these four techniques, acoustic and hydrodynamic cavitation are the most widely used approaches, as they are efficient in generating the required intensities for physical or chemical transformations. The overall cavitational effect depends on the intensity of turbulence and the number of cavities generated and these can be suitably optimized through the selection of operating and geometric parameters.

Acoustic Cavitation

Cavitation generated by use of ultrasound waves has been referred to as acoustic cavitation. The liquid molecules are stretched apart during the rarefaction phase of the ultrasound and pushed together during the compression phase. Cavities are formed in the liquid when the negative pressure created during the rarefaction phase exceed the tensile strength of the liquid and the molecules of the liquid are stretched beyond the critical molecular distance required to hold the liquid intact [33]. Subsequent compression and rarefaction cycles of the sound waves cause the bubble/cavity formed to expand, reach a maximum bubble size depending on the operating conditions, and then collapse releasing a large magnitude of energy creating conditions with very extreme temperatures and pressures (local hot spots) in the liquid. Environmental remediation by ultrasound involves pollutant destruction either directly via the thermal decomposition reactions or indirectly by the production of oxidative species such as hydroxyl radicals.

Hydrodynamic Cavitation

Hydrodynamic cavitation is based on the generation of cavitation using hydraulic means in a much more energy efficient manner. In this case, cavities are produced by

pressure variations, which can be obtained using changes in the geometry of the system. When the liquid passes through the constriction in a pipe, the kinetic energy of the liquid increases at the expense of local pressure and if the throttling is sufficient to cause the pressure around the point of vena contracta to fall below the threshold pressure for cavitation, cavities are generated. Subsequently, as the liquid jet expands, the pressure recovers and this drives the different stages of cavitation [34, 35].

Cavitation for Wastewater Treatment

The cavitational effects in terms of local hot spots and radical generation can be harnessed for degradation of complex chemicals present in the effluent. Cavitation has the potential to convert recalcitrant organic pollutants such as pesticides to biodegradable forms or even result in mineralization and hence cavitation has been applied for wastewater treatment. Various pollutants that have been degraded successfully using cavitational reactors include pesticides, dyes, phenols, cyanides, pharmaceuticals, etc. There have been some recent reports on the use of cavitation in combination with chemical disinfection techniques giving reduced treatment times and lower requirement of the chemical dosages [36, 37]. The combination approaches usually work in a synergistic manner if the controlling mechanisms are similar. The nature of pollutant and the physicochemical properties of solution greatly affect the efficiency of cavitational process and the controlling mechanism of oxidation. Intensification of the cavitational activity and hence the pollutant removal can be achieved based on the use of additives and optimization of operating parameters. The extent of intensification is dependent on the pollutant and hence the set of optimum operating parameters including the type of additives may or may not be applicable for other systems. Affinity of pollutant toward water plays a major role while discerning the mechanism of oxidation by cavitation. Hydrophobicity or hydrophilic nature decides the location of pollutant in the solution and hence the efficiency of cavitational degradation process. Also the physicochemical properties of the system decide the cavitational dynamics and hence the intensity. All these simultaneously acting mechanisms decide the final extent of degradation or mineralization.

The operating parameters like pH, temperature, and net power input can be optimized to enhance the extent of destruction. Also, some additives can be used to intensify the process of degradation based on the enhanced cavitational activity. Presence of additives in the system eases the process of cavity generation and hence can enhance the overall cavitational intensity. Different additives that can be used for intensification are H_2O_2, TiO_2, coal ash, activated carbon, supported TiO_2, salts (NaCl, Na_2SO_4), chloroalkanes, $CuSO_4$, $NiSO_4$, etc. The classification of different additives and their controlling mechanisms for the possible intensification are as follows:

- Salts: Due to high solubility in water, addition of salts like NaCl pushes the organic pollutant toward cavity giving an enhanced degradation.

- Gases: Gases like air, argon, and ozone provide additional nuclei and increase the overall cavitational activity as well as can provide additional radicals through reactions in the collapsing cavity which can enhance the degradation.
- Radical promoters: Use of additives as radical promoters help to increase the hydroxyl radicals or other oxidants in the system either by scavenging hydrogen radicals or by dissociation (for example hydrogen peroxide).
- Solid particles: Addition of solids provides additional nuclei for cavitation and also can generate additional hydroxyl radicals through the catalytic action (e.g., TiO_2).

Cavitational reactors offer significant promise for wastewater treatment, because of advantages like low processing time, high efficiency, etc., though the use of cavitation alone may not be enough for complete degradation of the complex chemicals like pesticides. Cavitation in combination with different AOPs could be quite effective and hence the following discussion is focused on the important aspects related to the combined processes.

Combination of Ultrasound and AOPs

Degradation of pesticides has been investigated using cavitational reactors either operated individually or in combination with additives and AOPs. A detailed discussion follows to understand the important design-related information and guidelines for the selection of optimum operating parameters.

Wang et al. [38] investigated the sonochemical degradation of methyl parathion using anatase titanium dioxide powder as a heterogeneous catalyst and the influence of parameters such as the type of TiO_2 and its loading, methyl parathion concentration, pH, ultrasonic intensity, ultrasonic frequency, and temperature on the extent of degradation have been investigated. Degradation of methyl parathion was shown to be strongly dependent on the loading of anatase TiO_2 catalyst, initial concentration of methyl parathion, operating pH, temperature, ultrasonic frequency, and intensity. It has been reported that the maximum extent of degradation of methyl parathion was more than 90 % within 50 min under optimum conditions. Shriwas and Gogate [6] also studied the ultrasonic degradation of methyl parathion in aqueous solutions and investigated the effect of the presence of different process-intensifying additives like TiO_2, CCl_4, H_2O_2 and Fenton's reagent on the extent of degradation. It was reported that the use of additives enhanced the degradation of methyl parathion significantly due to the generation of additional oxidizing species in the reactor. Fenton's reagent in combination with ultrasound was found to be the best treatment scheme. It has been reported that for large-scale operation of sonochemical reactors, it is better to use optimum levels of power dissipation. Also, use of larger transducer areas is recommended so as to get a uniform distribution of cavitational activity with minimal dead zones.

Fan et al. [39] investigated parathion degradation by Fenton process and analyzed the intermediate product formation. Comparison of the parathion degradation at

various Fenton dosages revealed that at initial Fe^{2+} concentrations of 0.5, 1.0, and 1.5 mM, the Fenton's reagent ratios ($[H_2O_2]/[Fe^{2+}]$) for optimum performance were established as 4, 3, and 2, respectively, and the corresponding removal efficiencies were 19 %, 48 %, and 36 % in the same order. Yao et al. [40] also studied the mechanism and kinetics of parathion degradation under ultrasonic irradiation and reported that the degradation rate of parathion decreased with an increase in the initial concentration and decrease in the power dissipation. Also the optimal frequency for parathion degradation was established as 600 kHz. It has also been reported that the gas/liquid interfacial regions are the real effective reaction sites for the sonochemical degradation of parathion. The main pathways for the parathion degradation by ultrasonic irradiation were also proposed by qualitative and quantitative analysis of organic and inorganic by-products.

Segura et al. [7] investigated the imidacloprid removal from wastewater using homogeneous photo-Fenton reactions based on the use of black light lamps and reported that imidacloprid degradation preceded via two distinctive kinetic regimes, an initial stage of rapid imidacloprid reduction, followed by a slower oxidation process finally resulting in a near-complete removal. Under optimal conditions, more than 50 % imidacloprid degradation was observed in about 1 min of treatment, and TOC and COD removals of 65 % and 80 %, respectively, were obtained. It was also reported that both acute toxicity and genotoxicity disappeared with considerable mineralization resulting in lower molecular weight by-products. Bourgin et al. [41] studied the degradation of imidacloprid by ozonation (ozone concentration in the inlet gas over a range of 25–100 g/m^3) and reported that imidacloprid degradation was a first-order reaction with respect to ozone. It has been reported that the kinetic rate constants approximately doubled following twofold increase in the concentration of ozone in the inlet gas.

Li et al. [12] studied the catalytic oxidation of triazophos using Fenton's reagent based on the use of simulated wastewater and also the actual industrial pesticide containing wastewater. The effect of reaction conditions including the dosages of $FeSO_4.7H_2O$, H_2O_2, pH and the stirring time on the COD removal have been investigated. For the actual industrial wastewater treatment, the COD removal efficiency of 85.4 % was obtained at the optimal conditions of pH as 4, loading of $FeSO_4 \cdot 7H_2O$ as 5.0 g/L, and loading of 30 % H_2O_2 solution as 75 mL/L. Lin and Yuan [42] studied the degradation kinetics and intermediate product formation and reported that the degradation of triazophos in unsterilized and sterilized sediments was 94.5 % and 20.5 %, respectively, during a treatment time of 6 days. The overall degradation was found to follow the first-order decay model. It was also observed that triazophos in sediment degraded faster under aerobic condition than under anaerobic one. Four major degradation products, namely, O,O-diethyl phosphorothioic acid, monoethyl-phosphorothioic acid, phosphorothioic acid, and 1-phenyl-3-hydroxy-1,2,4-triazole, have been identified in the work. Babu et al. [43] investigated the removal of pesticides (methyl parathion, atrazine, and triazophos) from wastewater using the electrochemical technique and reported that the reduction in the chemical oxygen demand (COD) was 76.2 % using electrooxidation, 88.4 % using electrocoagulation, and 81 % using electro-Fenton process. Final products

formed in all these three electrochemical techniques were of same in nature, although the intermediates varied indicating different routes of degradation. Overall electrocoagulation process showed excellent COD removal efficiency in terms of net COD reduction, energy consumption, and treatment cost and was recommended for the treatment of industrial effluents.

Schramm and Hua [44] studied the sonochemical degradation of dichlorvos in a batch reactor using 500 kHz ultrasound at input powers ranging from 86 to 161 W. It was reported that acoustic power and sparge gas are the two factors greatly affecting the sonochemical degradation efficiency. Increasing total acoustic power input from 86 to 161 W resulted in an increase in the rate constant from 0.018 ± 0.001 min^{-1} to 0.037 ± 0.002 min^{-1}. Total organic carbon and ion chromatographic analyses were employed in the work to determine and quantify the major degradation products, including dimethyl phosphate, formate, carbon dioxide, chloride, and phosphate.

Golash and Gogate [45] investigated the degradation of dichlorvos-containing wastewaters using sonochemical reactors and reported that low-frequency sonochemical reactors can also be effectively used for the treatment of pesticide wastewaters. Acidic conditions and optimum values of temperature and power dissipation have been reported to favor the degradation of dichlorvos. Complete removal of the pesticide has been reported using an optimized combination of ultrasound and Fenton's chemistry. Lu et al. [46] investigated the oxidation of dichlorvos using hydrogen peroxide in the presence of ferrous ion as catalyst. The study demonstrated that Fenton's reagent (Fe^{2+} and H_2O_2) induced the decomposition of dichlorvos via a two-stage process. The first stage was a Fe^{2+}/H_2O_2 reaction in which dichlorvos swiftly decomposed whereas in the second stage, dichlorvos decomposed somewhat less rapidly as the reaction involved the combination of Fe^{3+}/H_2O_2 as compared to the Fe^{2+}/H_2O_2 in the first stage. Oncescu et al. [47] investigated the photocatalytic degradation of dichlorvos in aqueous TiO_2 suspensions and reported that the calculated pseudo-first-order rate constants were dependent on the dissolved oxygen level at low O_2 flow rate, but somewhat independent of the initial pH. Decrease of pH during the irradiation was reported suggesting the formation of organic acids during the degradation. The presence of organic intermediates in the process was confirmed by TOC measurements. Shen et al. [48] studied ozonation induced degradation of dichlorvos and reported that more than 90 % of the dichlorvos was removed within the initial 5 min.

Bagal and Gogate [16] studied the sonochemical degradation of alachlor in the presence of process-intensifying additives such as hydrogen peroxide and carbon tetrachloride. It has been reported that acidic conditions favor degradation and also both the additives resulted into an enhanced extent of degradation. Torres et al. [49] studied the application of experimental design for optimizing the ultrasonic degradation of alachlor. The effect of power dissipation (20–80 W), pH (3–10), and substrate concentration (10–50 mg/L) was evaluated. Shiha et al. [50] studied the carbofuran degradation using ultrasound and Fenton processes. The effects of important operating parameters such as dosages of H_2O_2, Fe^{2+}, and initial carbofuran concentration have been established for different treatment schemes such as the ultrasound process, Fenton process, and a combined ultrasound/Fenton process.

Zapata et al. [51] used a mixture of five commercial pesticides commonly used in agriculture, viz., Vydate (10 % oxamyl), Metomur (20 % methomyl), Couraze (20 % imidacloprid), Ditimur-40 (40 % dimethoate), and Scala (40 % pyrimethanil), for understanding the degradation using the photo-Fenton process. The experiments were conducted in a solar pilot reactor attached with compound parabolic collectors. Irradiation time was kept as 50–100 min (normalized at 30 W/m^2 of light intensity) at 20 mg/L Fe^{2+} and it has been established that the treatment could completely eliminate the active ingredients. The parameters monitored for different approaches included time required for complete degradation of an active ingredient, time required for 75 % mineralization, and hydrogen peroxide consumed. Zero-order kinetics was found to fit well to the degradation data for each pesticide in the mixture treated by photo-Fenton. The results inferred that Ferrous ions were slightly more active than ferric which can be attributed to the Fe^{2+}/Fe^{3+} redox cycle inducing the formation of reactive radicals at a significant rate. Under identical conditions, photo-Fenton treatment was about 40 times faster as compared to the only Fenton-based treatment.

Combined Treatment Scheme of Ultrasound and Photocatalysis

The photocatalytic processes are of significant importance in the area of wastewater treatment, since these processes can result in complete mineralization with operation under mild conditions of temperature and pressure. The mechanistic details and overview of the applications of photocatalytic processes have been depicted in earlier reviews of Kamat [52] and Bhatkhande et al. [53]. Generally, two approaches being used for the oxidation are as follows:

- Photochemical oxidation: UV + Hydrogen peroxide
- Photocatalytic oxidation: Use of UV + solid photocatalyst such as TiO_2

Photocatalysis over TiO_2 or other semiconductor catalysts have been reported to be quite effective for wastewater treatment [53, 54]. Another advantage of photocatalytic oxidation-based processes lies in the possibility of using sunlight or near-UV light for irradiation, which can result in considerable economic savings especially for large-scale operations. Photocatalytic oxidation provides an interesting route for the destruction of toxic and hazardous pollutants like pesticides, and titanium dioxide (TiO_2) is the most widely accepted photocatalyst for such treatments [55, 56]. In the case of semiconductor catalyst like TiO_2, the highest occupied energy band (valence band) and lowest empty band (conduction band) are separated by a band gap. When the catalyst absorbs a photon of energy higher or equal to the band gap energy, an electron from the valence band is promoted to the conduction band with simultaneous generation of a hole in the valence band. The photogenerated holes have the ability to oxidize the organic molecule or they can react with OH^- or H_2O present in the effluent to form hydroxyl radicals. On the other hand, the photogenerated electrons can also react with oxygen to produce superoxide

radical anion $O2^{-\bullet}$ which can also lead to the formation of additional OH radicals [13]. By employing sunlight, the common drawback of the relatively high cost of UV lamps and operational electricity cost can be overcome.

The photocatalytic oxidation can also be combined with ultrasound for better removal of complex chemicals like pesticides. The combination results in the generation of sufficient quantity of hydroxyl radicals, which are able to completely oxidize the majority of complex compounds including the pesticides.

Overview of Literature in Recent Years

In this section, an overview on the reports of photocatalytic processes either operated alone or in combination with ultrasound for the treatment of pesticide-containing wastewaters is discussed.

Wang et al. [57] studied the sonocatalytic degradation of methyl parathion in the presence of micron-sized and nano-sized rutile titanium dioxide catalysts and observed that sonocatalytic performance of micron-sized TiO_2 powder was better than that of nano-sized rutile TiO_2 powder. Moctezuma et al. [58] investigated the photocatalytic degradation of methyl parathion and identified the reaction pathways and intermediate reaction products. It has been reported that the primary degradation product is methyl paraoxon, which eventually degraded to 4-nitrophenol. Under alkaline conditions, only 60 % of the TOC is converted to CO_2 after 6 h of reaction whereas at low pH, 90 % of TOC is converted to CO_2 in the same time. It has been also reported that the photocatalytic degradation of methyl parathion in deaerated water takes place at slower rates. Kitsiou et al. [59] studied the heterogeneous photocatalytic degradation of imidacloprid using artificial UV-A or visible range illumination. It has been reported that heterogeneous photocatalysis using TiO_2 under UV-A irradiation was a relatively slow process with measurable degradation of imidacloprid occurring in more than 240 min of reaction whereas the simultaneous use of TiO_2, Fe^{3+}, and H_2O_2 leads to significantly increased rates presumably due to the combined effects of homogeneous Fenton and heterogeneous photocatalytic reactions.

Malato et al. [17] studied the technical feasibility and performance of photocatalytic degradation of four water-soluble pesticides (diuron, imidacloprid, formetanate, and methomyl) at pilot-scale and reported that the degradation rate of organic pollutants was strongly accelerated by the combination of Fenton with UV–Vis light. The initial concentration levels investigated in the work were 50 mg/L for the case of imidacloprid, formetanate, and methomyl, whereas it was 30 mg/L for the diuron pesticide. The catalyst concentrations were 200 mg/L and 0.05 mM for the case of TiO_2 and iron, respectively. Total disappearance of the parent compounds and 90 % mineralization have been reported for all the pesticides studied in the work. Cernigoj et al. [24] investigated the effect of pH and ozone dosage on TiO_2 photocatalysis (combined process of $O_3/TiO_2/UV$). Aqueous solutions of neonicotinoid insecticides (thiacloprid and imidacloprid) were chosen as the model pollutants, since they exhibit a high threat for the aquatic systems. The combined photocatalytic ozonation ($O_3/TiO_2/UV$) was found to be the most efficient

process irrespective of the operating pH and also the degradation rate constants showed an increasing trend with an increase in the flow rates of ozone. Synergistic effect of ozone and TiO_2 photocatalysis was noticed at acidic and neutral pH, but the synergism was lost under basic conditions, probably due to the dominant self-decomposition of ozone under alkaline conditions. Under acidic conditions, the oxidation of chloride anions to chlorate (V) was also noticed in $O_3/TiO_2/UV$ and O_3/UV processes.

Aungpradit et al. [60] investigated the photocatalytic degradation of triazophos in aqueous titanium dioxide suspension and reported that the degradation of triazophos followed first-order kinetics with a half-life of 4.76 ± 0.42 h at a TiO_2 loading of 10 mg/L. Different degradation products were also identified based on the analysis using HPLC-UV, GC/MS/MS, HPLC/MS/MS, and IC. Two routes were proposed on the basis of observed transformation products, one based on the initial oxidative cleavage of $P = S$ bond to $P = O$ bond and the other on the basis of initial cleavage of the ester bonds. It has been reported that the photocatalytic degradation of triazophos showed great promise as a cost-effective treatment technology.

Evgenidou et al. [61] studied the removal of dichlorvos and dimethoate using a titanium dioxide-mediated photocatalytic process. The analysis of intermediates formed during the process led to the development of reaction mechanism. The results demonstrated that some of the formed transient intermediates (oxon derivatives, disulfide, chlorinated fragments), were more toxic as compared to the parent compounds though most of the other products were less toxic than the parent compounds. The increased toxicity of the dichlorvos-treated solution might be attributed to the presence of chlorinated photoproducts. The degradation of organic molecule followed Langmuir–Hinshelwood model. It was observed that the initial rate increases linearly with an increase in the amount of catalyst till an optimum loading beyond which no effect is seen. Above the optimum value, the suspended catalyst particles block the UV light passage and increase the extent of light scattering. Thus, any further increase in the amount of the catalyst has no positive effect on the photodegradation efficiency. At small concentrations, titanium dioxide appears to be more effective probably due to its larger surface area, but as the concentration increases, the light scattering, which is greater in the TiO_2 suspensions due to the smaller particle size, reduces the photocatalytic efficiency. It has also been established that temperature and pH also play a key role in deciding the rate of reaction. The addition of oxidants (H_2O_2 or $K_2S_2O_8$) to the TiO_2 suspension led to an increase in the extent of degradation. On the contrary, the addition of hydrogen peroxide in ZnO suspensions resulted in lower extents of degradation.

Photocatalyzed degradation of two selected pesticides, dichlorvos and phosphamidon, in aqueous suspensions of titanium dioxide was studied by Rahman and Muneer [62]. The degradation kinetics was investigated under different conditions of pH, catalyst concentration, substrate concentration, type of TiO_2, and addition of electron acceptor such as hydrogen peroxide (H_2O_2) besides molecular oxygen. It has been reported that the degradation rates were strongly influenced by all these parameters. The photocatalyst Degussa P25 was found to be most efficient as compared with other forms of TiO_2. Evgenidou et al. [63] also studied

semiconductor-sensitized photodegradation of dichlorvos in water using TiO_2 and ZnO as catalysts. Degradation of linuron by ultrasound combined with photo-Fenton treatment was studied by Katsumata and coworkers [64], and it was established that the degradation rate was strongly influenced by the initial concentration of Fe (II) and solution pH. The optimal Fe (II) concentration and pH were found to be 1.2×10^{-4} mol L^{-1} and 3.0, respectively [64]. Madhavan et al. [65] studied the application of different approaches based on ultrasound and ultraviolet irradiations for the degradation of monocrotophos in the presence of TiO_2 and Fe^{3+} and reported that the photocatalytic degradation rate using TiO_2 was lower than that of sonolysis alone due to the interference of phosphate ions formed as an intermediate product. On the other hand, a 15-fold enhancement in the degradation rate was found when photolysis was carried out in the presence of Fe^{3+} as compared to the rate observed with photolysis alone [65].

Sonophotocatalytic degradation of pesticides has not been studied by many authors, but some reports are available on the use of sonophotocatalysis for different organic compounds, which is discussed here to get an idea about the important design-related information. Bejarano-Perez and Suarez-Herrera [66] studied the sonochemical and sonophotocatalytic degradation of malachite green and compared the performance of different approaches such as sonolytic, photocatalytic, and sonophotocatalytic oxidation in the presence of carbon tetrachloride under a low-power ultrasonic field (<15 W) and using titanium dioxide as a photocatalyst. It has been reported that the simultaneous use of photocatalysis and sonolysis results in faster elimination of reaction intermediates. Oxidative degradation of dinitrotoluenes (DNTs) and 2, 4, 6-trinitrotoluene (TNT) in wastewater using ultrasonic irradiation combined with UV/TiO_2 was studied by Chen and Huang [67]. It was reported that the nitrotoluene contaminants could almost be completely eliminated by virtue of sonophotocatalysis, wherein TiO_2 serves both as photocatalyst and as nuclei for enhancing the quantum of cavitation bubbles. The mechanism of sonophotocatalytic degradation of methyl orange and its products in aqueous solutions has been studied by He et al. [68]. It was concluded that sonophotocatalysis is capable of yielding a more complete and faster mineralization of organic pollutants than the individual processes. Kaur and Singh [69] studied the visible light-induced sonophotocatalytic degradation of Reactive Red dye 198 using dye-sensitized TiO_2 and reported that a significant acceleration of the degradation of dye is achieved as activation of dye-sensitized TiO_2 under visible light has been achieved by ultrasonication.

Critical Analysis and Recommendations for Design Parameters

Based on the detailed review of the existing literature, following important recommendations can be drawn for the combined use of ultrasound and photocatalysis.

In the case of photocatalytic oxidation, the most common problem associated is the reduced efficiency of photocatalyst with continuous operation possibly due to the adsorption of contaminants at the surface and blocking of the UV-activated sites, which makes them unavailable for the degradation. Cavitational effects can induce

continuous cleaning of the catalyst surface during the operation and hence combination of these techniques can lead to higher extents of degradation. Also if the two modes of irradiation are operated in combination, more free radicals will be available for the degradation resulting into an increased rate. The different mechanisms for the expected synergism for the combination of these modes have been well explained by Gogate and Pandit [70] and summarized as below:

- Cavitational effects lead to the release of high energy (high temperature, high pressure, and intense turbulence) at the localized cavity implosion sites, which can enhance the rates of transport processes.
- Due to acoustic microstreaming, cleaning of the TiO_2 surface takes place, which gives more active catalyst sites.
- Surface area of catalyst is increased by fragmentation or pitting of the catalyst.
- Many radical intermediates are formed due to the high-temperature reactions under cavitating conditions, which participate in the destruction of organic compounds.
- The organic substrate reacts directly with the photogenerated surface holes and electrons under cavitating conditions.

Important factors that need to be considered while designing the reactors for sonophotocatalytic degradation and subsequent operation for better efficiency in terms of extent of degradation and energy requirement have been discussed in the following sections:

1. *Reactor design*
   The different reactor designs used so far for evaluating the synergism between ultrasound and UV irradiation have been mainly based on batch operations and at laboratory-scale operation. It has been established that the direct or indirect mode of UV radiation does not affect the expected synergism, which is an important point in the design particularly for having annular location of the UV tube. Design of continuous reactors rather than batch reactors or at least reactors operating in recirculating mode is preferred for the wastewater treatment application, as large quantities of effluents will have to be treated. In the case of design of photocatalytic part, usually immobilized or supported catalyst reactors are preferred but slurry reactors can also be used if better separation characteristics or lower loading of photocatalyst are achieved based on the use of ultrasound in synergy. The main point to be noted in the designing of photocatalytic reactor configuration is that uniform irradiation must be received by all the particles to get better results in terms of degradation efficiency. The sonochemical reactor configuration should be designed with power dissipation over a wider area, and hence ultrasonic bath-type reactors or parallel-plate reactors with multiple transducers are recommended.
2. *Ultrasonic power intensity*
   It is well known that the power intensity is an important operating variable in deciding the ultrasonic degradation of pollutants. The rate of degradation

generally increases with an increase in ultrasonic power intensity till an optimum level of power dissipation. An increase in the power intensity beyond the optimum results in a decrease in the rate of degradation. This may be attributed to the significant increase in the number of cavitation bubbles, close to the emitting surface of probe, due to a sharp increase in the power intensity. The considerable accumulation of bubbles around the emitting surface results in decoupling losses reducing the net cavitational intensity and hence lower extents of degradation are observed. Overall, it is recommended to optimize the ultrasound power for the specific geometry of the sonochemical reactor as well as the pollutant system under consideration.

3. *Sequential/simultaneous approach of irradiation*
   Combination of ultrasound and photocatalysis can be operated either in sequential or simultaneous approach. It is very important to operate simultaneously rather than having sequential irradiation of ultrasound followed by the photocatalytic oxidation, because the catalyst surface is kept clean continuously in the simultaneous operation due to the cleaning action of ultrasound in the operation. It results in maximum sites being available for the reaction and also the number of free radicals generated with simultaneous irradiation will be the maximum as compared to the sequential operation, thereby increasing the overall rates of degradation.

4. *Catalyst dosage*
   The generally used catalyst for the sonophotocatalytic degradation is TiO_2 though some studies have been reported with ZnO, CuO, and Al_2O_3. An increase in the dosage of catalyst till optimum loading results in an increase in the extent of degradation which may be attributed to the formation of more cavitating bubbles as the catalyst provides additional nuclei for the cavitation. Employing a significantly higher dosage of catalyst may result in the lower extents of degradation, as the higher concentration of catalyst powder may coagulate to form large particles, which may reduce the transfer of ultrasound energy leading to the reduction in the cavitational intensity. It is recommended to optimize the loading of catalyst based on the laboratory-scale studies as the optimum value will be dependent on the reactor configuration and the effluent composition.

5. *Stability of photocatalyst*
   Under ultrasonic irradiation, the crystal structure may be affected which may change the adsorption characteristics of pollutant molecules on the catalyst surface which in turn affects the rate of photocatalytic degradation. The stability of photocatalyst in terms of the size and shape and the structure are the important factors. The stability of catalyst support in case of supported photocatalyst is another critical factor affecting the extent of degradation. Accordingly, the aim should be at the development of proper supports for catalyst which are stable even in the presence of turbulence and acoustic streaming generated due to ultrasonic irradiation.

6. *Operating temperature*
   It is important to determine the suitable optimum temperature at which the maximum degradation efficiency of pollutants can be achieved. A careful

analysis of literature reveals that the degradation rate is higher at lower operating temperatures. This may be ascribed to cavitation intensity which reduces with an increase in the temperature possibly due to an increase in the solvent vapor pressure. Higher temperature also results in a decrease in the adsorption capacity of pollutants on the catalyst lowering the availability of the pollutants for the actual reaction in the adsorbed conditions.

7. *Operating pH*

   The operating pH is another crucial factor in deciding the rates of degradation and hence the overall efficacy of the treatment process. The effect of initial pH on the extent of degradation has been investigated in the past for an individual operation of ultrasonic irradiation as well as for photocatalytic oxidation. It has been observed that the extent of degradation is higher under acidic conditions as compared to that obtained under basic conditions for the sonochemically induced degradation [71]. The effect of pH on the rate of degradation is also dependent on the state of the pollutant molecule, i.e., whether the pollutant is present as ionic species or as a molecule. At a relatively lower pH, the pollutant is present in the molecular state and hence can easily enter the gas–water interfaces of bubbles and even vaporize into the cavitation bubbles, thereby enabling degradation by thermal cleavage along with free radical attack. Thus, the pollutant should be in the molecular state and the operating pH must be kept lower than the pKa value for the specific pollutant. Similar analysis is also valid for the photocatalytic oxidation and hence for the combined sonophotocatalytic degradation.

8. *Use of additives*

   Use of different additives either as inert solids or catalysts can result in an enhanced degradation. Different gases or solids have been used as additives with different degrees of intensification, and the following is the discussion about few of the important additives that are useful for the sonophotocatalytic oxidation.

   Addition of oxygen in the sonophotocatalytic process results in an enhanced degradation of components present in the wastewater because oxygen gas promotes the cavity formation by providing additional nuclei. The intensification may also be partially attributed to the enhanced generation of hydroxyl radicals through a series of reactions involving dissociation of molecular oxygen in the cavitation bubbles, formation of hydrogen peroxide at the gas/liquid interface of the bubbles, and subsequent dissociation into hydroxyl radicals.

   Introduction of air also results in higher extents of degradation in the case of the sonophotocatalytic oxidation. In addition to providing enhanced nuclei for the cavitation phenomena, one of the mechanisms explaining the observed enhancement is the possible formation of ozone as an additional oxidant based on the radical reactions driven by both ultrasound and UV irradiation. Aeration can also enhance the rates of ultrasonic degradation of organic pollutants possibly due to the availability of oxygen.

   The rate of sonophotocatalytic degradation can also be increased by the addition of H_2O_2, which can be attributed to the dissociation of hydrogen peroxide due to ultrasound and ultraviolet irradiation resulting in the generation

of enhanced quantum of free radicals. These radicals attack the pollutants and result in a higher degradation. Beyond a certain limit, an increase in the concentration of H_2O_2 does not result into an enhanced degradation as the undissociated excess H_2O_2 reacts with free radicals and reduces their usage for oxidation of the target pollutants. Besides, the free radicals if formed in excess undergo recombination thereby limiting the extent of available free radicals for the target oxidation. The optimum value of concentration of hydrogen peroxide will also depend on the initial concentration of pollutants and the type of pollutant.

Case Study: Combination of Ultrasound and Photocatalysis for the Degradation of Dichlorvos

A detailed case study based on our recent work on the application of the combined process of ultrasound and solar-based photocatalysis for degradation of dichlorvos [72] is presented for better understanding into different aspects of the optimization for the combined operation.

The sonochemical reactor equipped with a horizontal ultrasonic transducer (operating at a frequency of 36 kHz with the rated power output of 150 W) was procured from Roop Telsonic Ultrasonix Ltd., India. Schematic representation of the reactor is depicted in Fig. 1. The internal body of the reactor is made of stainless steel and dimensions of the reactor are 35 cm length, 12 cm width, and 20 cm height. A drainage valve is provided at the bottom of the reactor. For the photocatalytic and sonophotocatalytic approaches, solar irradiations have been used and the experiments were conducted between 11:00 AM to 2:00 PM when the solar intensity was the maximum and perpendicular to the surface.

The initial concentration of dichlorvos solution was kept constant, i.e., 20 mg/L in all the experiments. The reactor was filled with 7 L of dichlorvos solution in all the experimental runs. All the experiments were performed at pH 3 which was an optimized value as per the earlier laboratory-scale studies [45]. For obtaining uniform suspension of catalyst, a stirrer at an operating speed of 1300 rpm was used in all the experiments. The influence of addition of hydrogen peroxide as a process-intensifying additive on the degradation of dichlorvos in the presence of ultrasound was studied at different ratios of dichlorvos: H_2O_2 as 1:1 (20 mg/L H_2O_2), 1:10 (200 mg/L H_2O_2), 1:25 (500 mg/L H_2O_2), and 1:50 (1000 mg/L H_2O_2). In order to study the extent of intensification of degradation of dichlorvos using titanium dioxide, experiments were conducted using different amounts of TiO_2 as 0.01 g/L, 0.075 g/L, 0.1 g/L, and 0.2 g/L combined with sonication and also solar-based photocatalysis.

The concentration of dichlorvos was determined using nano-HPLC comprising of an autosampler, UV detector, and an HPLC column eclipse plus C18 having 2.1×50 mm cross section. Acetonitrile and deionized water (50:50) with a flow rate of 1 μL/min was used as the mobile phase for detection of dichlorvos. The wavelength used for UV detection was 210 nm and the retention time of dichlorvos in the analysis was around 2.35 min. The withdrawn samples were immediately
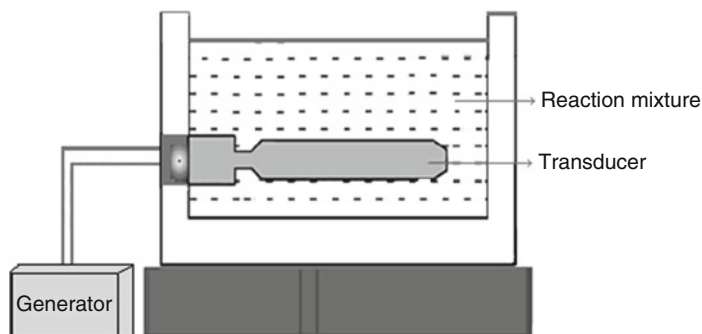
Fig. 1 Schematic representation of ultrasonic bath (Reprinted from Patil and Gogate [72] Copyright (2015), with permission from Elsevier)

analyzed using HPLC and the concentration was determined from the calibration chart obtained with known concentrations. All the experiments were repeated in duplicate and the experimental errors were within 2 % of the reported average value of the extent of degradation. Integral method of analysis was followed for fitting the kinetics of reaction. Extent of total organic carbon (TOC) removal was analyzed by using ANATOC II total organic carbon analyzer obtained from SGE International Pvt. Ltd., Australia.

The initial experiments were concentrated on analyzing the efficacy of individual treatment approaches. Degradation of 20 mg/L dichlorvos solution was studied using only sonication at an initial pH of 3. The variation in the extent of degradation with the treatment time has been depicted in Fig. 2. Only 6.4 % degradation of dichlorvos was achieved in 120 min with pseudo first-order rate constant of 0.54×10^{-3} min^{-1}. It is interesting to note that Golash and Gogate [45] reported a much higher extent of degradation using an ultrasonic horn at a laboratory scale with much higher values of power density (power dissipation per unit volume). In the present case, the power dissipation per unit volume is substantially lower as compared to ultrasonic horn and hence lower extents of degradation are expected as the cavitational effects are directly dependent on the power density. As the extent of degradation obtained by using only sonication was very low, combination of different AOPs has been attempted.

Combination of sonication and hydrogen peroxide was studied at different loadings of H_2O_2, i.e., 20, 100, 500, and 1000 mg/L using the ratios of dichlorvos, H_2O_2 as 1:1, 1:10, 1:25, and 1:50, and the obtained results are depicted in Fig. 2. It could be observed that the extent of degradation increased from 6.34 % (only sonication) to 20 % for the combination of sonication and hydrogen peroxide (1:25 ratio). As the loadings of hydrogen peroxide increased from a ratio of 1:1 to 1:25, extent of degradation also increased from 11.4 % to 20 % beyond which it decreased to 16.9 % for the ratio of 1:50. The maximum extent of degradation was observed at a loading of 1:25 and at this optimum loading, 12.5 % TOC removal was also observed from the TOC analysis studies. Thus, it has been established that there
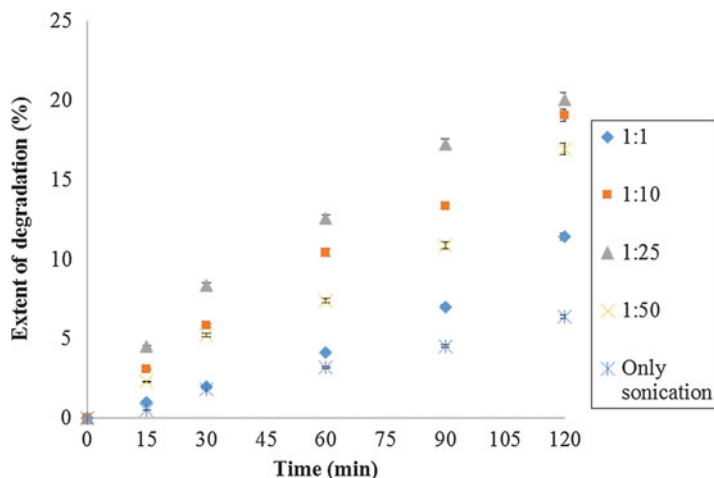
Fig. 2 Effect of loadings of H_2O_2 on extent of degradation of dichlorvos (Reprinted from Patil and Gogate [72] Copyright (2015), with permission from Elsevier)

exists an optimum concentration of hydrogen peroxide where the extent of decomposition of hydrogen peroxide into hydroxyl radicals is appreciable and scavenging action of residual hydrogen peroxide is not dominating. The optimum concentration of H_2O_2 also depends on the type of compound under study. Hydrogen peroxide is a strong oxidizing agent and has the capacity to oxidize the pollutants. Hence, experiments were conducted at the same optimized loading of H_2O_2 without cavitation to measure the effect of peroxide alone, but the total degradation obtained was only about 2 %. Thus, it can be concluded that ultrasonic irradiation results in a significant dissociation of hydrogen peroxide leading to the formation of hydroxyl radicals which have higher oxidizing action as compared to the individual oxidizing effect of hydrogen peroxide.

The kinetic studies (Table 1) for the combined approach of ultrasound and hydrogen peroxide showed that pseudo first-order rate constant increased from 0.9×10^{-3} min^{-1} to 2.03×10^{-3} min^{-1} with an increase in ratio of pollutant-to-hydrogen peroxide loading from 1:1 to 1:25 beyond which it decreased to 1.44×10^{-3} min^{-1} at a ratio of 1:50. Mishra and Gogate [73] investigated the ultrasonic degradation of Rhodamine B in the presence of different concentrations of hydrogen peroxide ranging from 200 to 800 mg/L and reported that the extent of degradation increased with an increase in the H_2O_2 concentration till an optimum loading of 500 mg/L. The results are also consistent with the results reported by Behnajady et al. [74] and Merouani et al. [75]. It is important to note here that the actual optimum value of hydrogen peroxide will be different depending on the pollutant and needs to be established using laboratory-scale studies. The results presented in the table 1 also confirm the enhanced degradation obtained based on latent remediation approach where the treated pollutant is kept for significantly longer durations for possible oxidation by the generated in situ oxidizing agents.

Table 1 Effect of loadings of hydrogen peroxide on kinetics of dichlorvos degradation (Reprinted from Patil and Gogate [72] Copyright (2015), with permission from Elsevier)

Experimental details: volume, 7 L; operation time, 120 min; temperature, $40 \pm 1\,°C$; initial concentration of dichlorvos, 20 mg/L; feed pH, 3 ± 0.5

Dichlorvos: H_2O_2	Extent of degradation (%)	Pseudo first-order rate constant $k \times 10^{-3}\ min^{-1}$	R^2
1:1	11.4	0.9	0.96
1:10	19.0	1.73	0.99
1:25	20.0	2.03	0.96
1:50	17.0	1.44	0.97
1:25 after 15 h	38.3	4.23	0.96
1:50 after 15 h	30.2	3.30	0.96

Experiments involving sonophotocatalytic degradation of dichlorvos using TiO_2 as the catalyst were conducted at different loadings of TiO_2 (0.01 g/L, 0.075 g/L, 0.1 g/L and 0.2 g/L). All the experiments were also conducted in the presence of only solar light. The obtained results with different loadings of TiO_2 are depicted in Fig. 3. It was observed that as the loading of TiO_2 increases from 0.01 to 0.1 g/L, the extent of degradation also increases from 34.7 % to 78.5 % beyond which the extent of degradation is nearly constant (77.5 % for 0.2 g/L). The maximum degradation in the presence of solar radiation is obtained at a TiO_2 concentration of 0.1 g/L (78.5 %) at 2 h of treatment time which then increased when the treatment time was increased to 3 h (total degradation was 91.3 %). It was also observed that the psuedo first-order rate constant increased with an increase in the loading of TiO_2 as shown in Table 2. Experiments were also performed using a combination of TiO_2 (0.1 g/L) and sonication, and it was observed that only 7.5 % degradation of dichlorvos was obtained. As shown in Table 2, highest degradation of 83.0 % was obtained by the combined operation involving sonication, solar light, and TiO_2 (0.1 g/L) in 120 min of reaction time with TOC removal of 71 %. Similar results have been reported by Taghizadeh and Abdollahi [76] for the degradation of chitosan using ultrasound/ultraviolet irradiation and its combination with heterogeneous catalyst (TiO_2). It has been reported that TiO_2-based sonophotocatalysis led to complete chitosan degradation in 60 min at an optimum catalyst loading.

In summary, the detailed study related to the degradation of dichlorvos using combined treatment processes based on ultrasonic cavitation at an operating capacity of 7 L revealed the following important findings:

- Addition of H_2O_2 for the treatment is not effective enough for degradation of dichlorvos since it gives only 20 % degradation at the optimum loading of hydrogen peroxide. The concept of latent remediation could be cost-effective using the sonication at industrial scales of operation.
- Use of the catalyst titanium dioxide results in an increased extent of removal only when combined with solar radiation. Treatment using titanium dioxide combined with sonication is not that effective as compared to the activation of titanium dioxide in the presence of solar radiation.
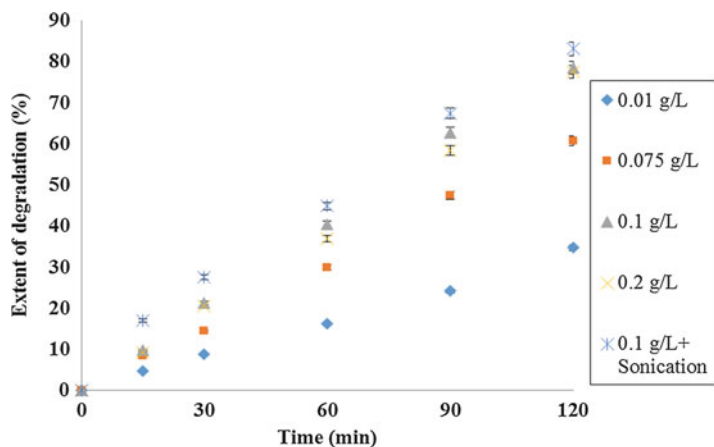
Fig. 3 Effect of TiO_2 loadings on degradation of dichlorvos in the presence of solar irradiation (Reprinted from Patil and Gogate [72] Copyright (2015), with permission from Elsevier)

Table 2 Effect of loadings of TiO_2 on the kinetic rate constant for degradation of dichlorvos (Reprinted from Patil and Gogate [72] Copyright (2015), with permission from Elsevier)

Experimental details: volume, 7 L; operation time, 120 min; temperature, uncontrolled; initial concentration of dichlorvos, 20 mg/L; feed pH, 3 ± 0.5			
Different approaches with varying loadings of TiO_2 (g/L)	Extent of degradation (%)	Pseudo first-order rate constant k $\times$ 10^{-3} min^{-1}	R^2
0.01 TiO_2+ solar	34.7	3.31	0.98
0.075 TiO_2+ solar	60.7	7.25	0.98
0.1 TiO_2+ solar	78.5	11.50	0.96
0.2 TiO_2+ solar	77.5	10.80	0.94
0.1 TiO_2+ sonication	7.5	0.59	0.97
0.1 TiO_2+ sonication + solar	83.0	13.33	0.96

- An optimized treatment scheme based on photocatalyst combined with ultrasonic irradiation in the presence of solar radiation can be used effectively for removal of dichlorvos at an operating capacity of 7 L.

Conclusions and Future Directions

A detailed analysis into different aspects of degradation of pesticides using ultrasonic cavitation in combination with photocatalysis has been performed. It was observed that cavitation in combination with different additives is more effective as compared to the individual process. The main principle of using these techniques in combination is to enhance the formation of free radicals in the water and also

eliminate the drawbacks associated with individual operations. Based on the analysis, the following important recommendations can be given for the use of cavitation in combination with photocatalysis.

- In the designing of the photocatalytic reactor, it is necessary that the uniform irradiation must be received by all the particles, whereas the sonochemical part should be designed with power dissipation over a wider area to get better results in terms of degradation efficiency.
- The effect of temperature on the extent of degradation in cavitation reactor is by way of two counteracting effects, viz., increased kinetic rates of reaction and reduced cavitational intensity due to higher volatility of the substances. Due to this dual effect, it is very important to optimize the operating temperature for specific compound under study.
- pH is the another important operating parameter that needs to be optimized as this has a major effect on degradation induced by cavitation as well as photocatalysis. Generally, under alkaline conditions, the extent of degradation is much lower than that observed under acidic conditions, though the exact recommended value will be dependent on the specific compound (pKa value) and also the natural pH of the solution.
- In the case of operation involving combination of cavitation and solar irradiation, enhanced extent of degradation is generally observed which can be attributed to the enhanced generation of hydroxyl radicals in combined cavitation /solar process as compared to cavitation and photocatalysis operated alone. Optimum loading of catalyst is required for synergistic results for the combination of cavitation with photocatalysis. The problem of catalyst fouling can also be avoided due to the turbulence generated under the cavitating conditions.

Overall, it can be said that the degree of intensification and requirement of oxidant loading is different for each compound and hence performing optimization studies for specific compound is very important for better reproducibility of treatment efficiency at commercial-scale operations. It can be said that combined processes based on cavitation offer significant promise for industrial wastewater treatment and can be a useful alternative to the conventional treatment approaches. The existence of synergism also points toward the important fact that the treatment costs at commercial scale of operation can be reduced by using the combined approaches.

References

1. Badawy MI, Ghaly MY, Gad-Allah TA (2006) Advanced oxidation processes for the removal of organophosphorus pesticides from wastewater. Desalination 194:166–175
2. Tamimi M, Qourzal S, Barka N, Assabbane A, Ait-Ichou Y (2008) Methomyl degradation in aqueous solutions by Fenton's reagent and the Photo-Fenton system. Sep Purif Technol 61:103–108

3. Mahmoodi NM, Arami M, Limaee NY, Gharanjig K, Nourmohammadian F (2007) Nanophoto-catalysis using immobilized titanium dioxide nanoparticles. Degradation and mineralization of water containing organic pollutant: case study of Butachlor. Mater Res Bull 42:797–806

4. Grover R, Cessna AJ (1991) Environmental chemistry of herbicides. CRC Press, Boca Raton

5. Edwards FL, Tchounwoul PB (2005) Environmental toxicology and health effects associated with methyl parathion exposure – a scientific review. Int J Environ Res Pub Health 2(3):430–441

6. Shriwas AK, Gogate PR (2011) Ultrasonic degradation of methyl Parathion in aqueous solutions: intensification using additives and scale up aspects. Sep Purif Technol 79:1–7

7. Segura C, Zaror C, Mansilla HD, Mondaca MA (2008) Imidacloprid oxidation by Photo-Fenton reaction. J Hazard Mater 150:679–686

8. Raut-Jadhav S, Saharan VK, Pinjari DV, Saini DR, Sonawane SH, Pandit AB (2013) Intensi-fication of degradation of imidacloprid in aqueous solutions by combination of hydrodynamic cavitation with various advanced oxidation processes (AOPs). J Envrion Chem Eng 1:850–857

9. Worthing CR, Hanrce RJ (1991) The pesticide manual: a world compendium, 9th edn. British Crop Protection Council, Farnham

10. Mingjing Q, Zhaojun H, Xinjun X, Lina Y (2003) Triazophos resistance mechanisms in the rice stem borer (Chilo suppressalis Walker). Pestic Biochem Physiol 77:99–105

11. Rani S, Madan VK, Kathpal TS (2001) Persistence and dissipation behavior of triazophos in canal water under Indian climatic conditions. Ecotoxicol Environ Saf 50:82–84

12. Li R, Yang C, Chen H, Zeng G, Yu G, Guo J (2009) Removal of triazophos pesticide from wastewater with Fenton reagent. J Hazard Mater 167:1028–1032

13. Sud D, Kaur P (2012) Heterogeneous photocatalytic degradation of selected organophosphate pesticides: a review. Crit Rev Env Sci Technol 42:2365–2407

14. Rangnarsdottir KV (2000) Environmental fate and toxicology of organophosphate pesticides. J Geol Soc 157:859–876

15. Montgomery MP, Kame F, Saldana TM, Alavanja MCR, Sandler DP (2008) Incident diabetes and pesticide exposure among licensed pesticide applicators: agricultural health study 1993–2003. Am J Epidemiol 167:1235–1246

16. Bagal MV, Gogate PR (2012) Sonochemical degradation of alachlor in the presence of process intensifying additives. Sep Purif Technol 90:92–100

17. Malato S, Blanco J, Caceres J, Fernandez-Alba AR, Aguera A, Rodriguez A (2002) Photocatalytic treatment of water soluble pesticides by photo-Fenton and TiO_2 using solar energy. Catal Today 76:209–220

18. Berg P, Hagmeyer G, Gimbel R (1997) Removal of pesticides and other micropollutants by nanofiltration. Desalination 113:205–208

19. Thacker NP, Vaidya MV, Sipani M, Kalra A (1997) A removal technology for pesticide contaminants in potable water. J Environ Sci Health B Pestic Food Contam Agric Wastes 4:483–496

20. Chiron S, Fernandez-Alba A, Rodriguez A, Garcia-Calvo E (2000) Pesticide chemical oxidation: state-of-the-art. Water Res 34(2):366–377

21. Zhang Y, Zhang W, Liao X, Zhang J, Hou Y, Xiao Z, Chen F, Hu X (2010) Degradation of diazinon in apple juice by ultrasonic treatment. Ultrason Sonochem 17:662–668

22. Martin MJ, Artola A, Balaguer MD, Rigola M (2003) Activated carbons developed from surplus sewage sludge for the removal of dyes from dilute aqueous solutions. Chem Eng J 94:231–239

23. Arslan I, Balcioglu IA, Bahnemann D (2000) W (2000) Advanced chemical oxidation of reactive dyes in simulated dyehouse by ferrioxalate-Fenton/UV-A and TiO_2/UV-A processes. Dyes Pigments 47:207–218

24. Cernigoj U, Stangar UL, Trebse P (2007) Degradation of neonicotinoid insecticides by different advanced oxidation processes and studying the effect of ozone on TiO_2 photocatalysis. Appl Catal B: Environ 75:229–238

25. Ayoub K, Van Hullebusch ED, Cassir M, Bermond A (2010) Application of AOPs for TNT removal: a review. J Hazard Mater 178:10–28
26. Gogate PR, Pandit AB (2004) Sonophotocatalytic reactors for wastewater treatment: a critical review. AIChE J 50(5):1051–1079
27. Gogate PR, Pandit AB (2004) A review of imperative technologies for wastewater treatment I: oxidation technologies at ambient conditions. Adv Environ Res 8:501–551
28. Song YL, Li JT, Chen H (2009) Degradation of C.I. Acid Red 88 aqueous solution by combination of Fenton's reagent and ultrasound irradiation. J Chem Technol Biotechnol 84:578–583
29. Marc PT, Verónica GM, Miguel AB, Jaime G, Santiago E (2004) Degradation of chlorophenols by means of advanced oxidation processes: a general review. Appl Catal B: Environ 47:219–256
30. Pillai KC, Kwon TO, Moon IS (2009) Degradation of wastewater from terephthalic acid manufacturing process by ozonation catalyzed with Fe^{2+}, H_2O_2 and UV light: direct versus indirect ozonation reactions. Appl Catal B: Environ 91:319–328
31. Legube B, Karpel Vel Leitner N (1999) Catalytic ozonation: a promising advanced oxidation technology for water treatment. Catal Today 53:61–72
32. Rajkumar D, Palanivelu K (2003) Electrochemical degradation of cresols for wastewater treatment. Ind Eng Chem Res 42:1833–1839
33. Moholkar VS, Shirgaonkar IZ, Pandit AB (1996) Cavitation and sonochemistry in the eyes of a chemical engineer. Ind Chem Eng B: Ind News 38(2B):81–93
34. Save SS, Pandit AB, Joshi JB (1997) Use of hydrodynamic cavitation for large scale microbial cell disruption. Food Bioprod Process 75:41–49
35. Gogate PR, Pandit AB (2001) Hydrodynamic cavitation reactors: a state of the art review. Rev Chem Eng 17(1):1–85
36. Duckhouse H, Mason TJ, Phull SS, Lorimer JP (2004) The effect of sonication on microbial disinfection using hypochlorite. Ultrason Sonochem 11:173
37. Blume T, Neis U (2005) Improving chlorine disinfection of wastewater by ultrasound application. Water Sci Technol 52:139
38. Wang J, Pan Z, Zhang Z, Zhang X, Wen F, Ma T, Jiang Y, Wang L, Xu L, Kang P (2006) Sonocatalytic degradation of methyl parathion in the presence of nanometer and ordinary anatase titanium dioxide catalysts and comparison of their sonocatalytic abilities. Ultrason Sonochem 13:493–500
39. Fan C, Tsui L, Liao M (2011) Parathion degradation and its intermediate formation by Fenton process in neutral environment. Chemosphere 82:229–236
40. Yao JJ, Gao NY, Li C, Li L, Xu B (2010) Mechanism and kinetics of parathion degradation under ultrasonic irradiation. J Hazard Mater 175:138–145
41. Bourgin M, Violleau F, Debrauwer L, Albet J (2011) Ozonation of imidacloprid in aqueous solutions: reaction monitoring and identification of degradation products. J Hazard Mater 190:1–9
42. Lin K-D, Yuan D-X (2005) Degradation kinetics and products of triazophos intertidal sediment. J Environ Sci 17(6):933–936
43. Babu BR, Meera KMS, Venkatesan P (2011) Removal of pesticides from wastewater by electrochemical methods: a comparative approach. Sustain Environ Res 21(6):401–406
44. Schramm JD, Hua I (2001) Ultrasonic irradiation of dichlorvos: decomposition mechanism. Water Res 35(3):665–674
45. Golash N, Gogate PR (2012) Degradation of dichlorvos containing wastewaters using sonochemical reactors. Ultrason Sonochem 19:1051–1060
46. Lu M-C, Chen J-N, Chang C-P (1999) Oxidation of dichlorvos with hydrogen peroxide using ferrous ion as catalyst. J Hazard Mater 65:277–288
47. Oncescu T, Stefan MI, Oancea P (2010) Photocatalytic degradation of dichlorvos in aqueous TiO_2 suspensions. Environ Sci Pollut Res Int 17:1158–1166

48. Shen J-M, Zhao Z-T, Chen Z-L, Liu Y, Ye M-M, Ren N-Q (2011) Efficiency and mechanism of dichlorvos removal by ozonation. J Harbin Inst Technol 43:19–23
49. Torres RA, Mosteo R, Petrier C, Pulgarin C (2009) Experimental design approach to the optimization of ultrasonic degradation of alachlor and enhancement of treated water biodegradability. Ultrason Sonochem 16:425–430
50. Ying-Shiha M, Chi-Fangaa S, Jih-Gawb LP (2010) Degradation of carbofuran in aqueous solution by ultrasound and Fenton processes: effect of system parameters and kinetic study. J Hazard Mater 178:320–325
51. Zapata A, Oller I, Bizani E, Perez J, Maldonado M, Malato S (2009) Evaluation of operational parameters involved in solar photo-Fenton degradation of a commercial pesticide mixture. Catal Today 144L:94–99
52. Kamat PV (1993) Photochemistry on non-reactive and reactive (semiconductor) surfaces. Chem Rev 93:267–300
53. Bhatkhande DS, Pangarkar VG, Beenackers AA (2002) Photocatalytic degradation for environmental applications: a review. J Chem Technol Biotechnol 77(1):102–116
54. Hoffmann MR, Martin ST, Choi W, Bahnemann DW (1995) Environmental applications of semiconductor photocatalysis. Chem Rev 95:69
55. Gaya UI, Abdullah AH (2008) Heterogeneous photocatalytic degradation of organic contaminants over titanium dioxide: a review of fundamentals, progress and problems. J Photochem Photobiol C: Photochem Rev 9:1–12
56. Maurino V, Minero C, Pelizzetti E, Vincenti M (1998) Photocatalytic transformation of sulfonylurea herbicides over irradiated titanium dioxide particles. Colloid Surf: A 151:329–338
57. Wang L, Zhu L, Luo W, Wu Y, Tang H (2007) Drastically enhanced ultrasonic decolorization of methyl orange by adding CCl_4. Ultrason Sonochem 14:253–258
58. Moctezuma E, Leyva E, Palestino G, de Lasa H (2007) Photocatalytic degradation of methyl parathion: reaction pathways and intermediate reaction products. J Photochem Photobiol A: Chem 186:71–84
59. Kitsiou V, Filippidis N, Mantzavinos D, Poulios I (2009) Heterogeneous and homogeneous photocatalytic degradation of the insecticide imidacloprid in aqueous solutions. Appl Catal B: Environ 86(1–2):27–35
60. Aungpradit T, Sutthivaiyakit P, Martens D, Sutthivaiyakit S, Kettrup AAF (2007) Photocatalytic degradation of triazophos in aqueous titanium dioxide suspension: Identification of intermediates and degradation pathways. J Hazard Mater 146:204–213
61. Evgenidou E, Konstantinou I, Fytianos K (2006) Study of the removal of dichlorvos and dimethoate in a titanium dioxide mediated photocatalytic process through the examination of intermediates and the reaction mechanism. J Hazard Mater 137:1056–1064
62. Rahman MA, Muneer M (2005) Photocatalysed degradation of two selected pesticide derivatives, dichlorvos and phosphamidon, in aqueous suspensions of titanium dioxide. Desalination 181:161–172
63. Evgenidou E, Fytianos K, Poulios I (2009) Semiconductor-sensitized photodegradation of dichlorvos in water using TiO_2 and ZnO as catalyst. Appl Catal B: Environ 59:81–89
64. Katsumata H, Kobayashia T, Kanecoa S, Suzuki T, Ohta K (2011) Degradation of linuron by ultrasound combined with photo-Fenton treatment. Chem Eng J 166:468–473
65. Madhavan J, Kumara PSS, Anandan S, Griesera F, Ashokkumar M (2010) Sonophotocatalytic degradation of monocrotophos using TiO_2 and Fe^{3+}. J Hazard Mater 177:944–949
66. Bejarano-Pérez NJ, Suárez-Herrera MF (2008) Sonochemical and sonophotocatalytic degradation of malachite green: the effect of carbon tetrachloride on reaction rates. Ultrason Sonochem 15:612–617
67. Chen W-S, Huang S-C (2011) Sonophotocatalytic degradation of dinitrotoluenes and trinitrotoluene in industrial wastewater. Chem Eng J 172:944–951
68. He Y, Grieser F, Ashokkumar M (2011) The mechanism of sonophotocatalytic degradation of methyl orange and its products in aqueous solutions. Ultrason Sonochem 18:974–980

69. Kaur S, Singh V (2007) Visible light induced sonophotocatalytic degradation of Reactive Red dye 198 using dye sensitized TiO_2. Ultrason Sonochem 14:531–537
70. Gogate PR, Pandit AB (2004) A review of imperative technologies for wastewater treatment II: hybrid methods. Adv Environ Res 8:553–597
71. Sivakumar M, Tatake PA, Pandit AB (2002) Kinetics of p-Nitrophenol degradation: effect of reaction conditions and cavitational parameters for a multiple frequency system. Chem Eng J 85:327–338
72. Patil PN, Gogate PR (2015) Degradation of dichlorvos using hybrid advanced oxidation processes based on ultrasound. J Water Proc Eng. 8:e58–e65
73. Mishra KP, Gogate PR (2011) Intensification of sonophotocatalytic degradation of p-nitrophenol at pilot scale capacity. Ultrason Sonochem 18:739–744
74. Behnajady MA, Modirshahla N, Tabrizi SB, Molanee S (2008) Ultrasonic degradation of rhodamine B in aqueous solution: influence of operational parameters. J Hazard Mater 152:381–386
75. Merouani S, Hamdaoui O, Saoudi F, Chiha M (2009) Sonochemical degradation of Rhodamine B in aqueous phase: effects of additives. Chem Eng J 158:550–557
76. Taghizadeh MT, Abdollahi R (2011) Sonolytic, sonocatalytic and sonophotocatalytic degradation of chitosan in the presence of TiO_2 nanoparticles. Ultrason Sonochem 18:149–157

Conversion of Refined and Waste Oils by Ultrasound-Assisted Heterogeneous Catalysis

Daria C. Boffito, Edith Martinez-Guerra, Veera G. Gude, and Gregory S. Patience

Contents

Abstract

Biodiesel synthesized with solid acid catalysts tolerates water and free fatty acids in the feedstock and can be easily separated versus alkaline homogeneous catalysts. Furthermore, corrosion rates are lower. Nevertheless, they are more than 4,000 times less efficient than basic catalysts. Ultrasound accelerates the conversion of oils to biodiesel in homogenous systems by a factor of 300 times (a few seconds of sonication) and reduces the time required by the acid-catalyzed heterogeneous reaction to less than 1 h. Cavitation bubbles form on solid

D.C. Boffito (✉) • G.S. Patience
Département de Génie Chimique, Polytechnique Montréal, Montréal, QC, Canada
e-mail: daria-camilla.boffito@gmail.com; daria-camilla.boffito@polymtl.ca; gregory-s.patience@polymtl.ca

E. Martinez-Guerra • V.G. Gude
Department of Civil and Environmental Engineering, Mississippi State University, Mississippi State, MS, USA
e-mail: em826@msstate.edu; gude@cee.msstate.edu; vgg25@msstate.edu

particles, but at the same time, the particles shield the ultrasonic waves so they do not penetrate as deeply into the liquid. Multiple transducers and designing the reactor can distribute the acoustic cavitation better. The literature focuses on classical sonochemical reactors for heterogeneous biodiesel production (baths and horns), whereas several optimized designs are available for homogeneous mixtures. We review the literature on heterogeneously catalyzed systems and include alternative reactor configurations for liquid mixtures that researchers have not yet adopted for solid catalyst systems. We report the effect of various alcohols and the combined action of ultrasound and microwaves to transesterify oil to biodiesel. Also, we discuss several catalyst/ultrasound systems that accelerate the reaction rates.

Introduction

Biodiesel has long been criticized as a renewable fuel because the feedstock, vegetable oil, competes with food and diverts arable land from edible crop cultivation. However, biodiesel commercial facilities are established worldwide with over 7,500 ML year^{-1} in the United States and about the same capacity in the European Community [1, 2]. Biodiesel is a biofuel with a low carbon footprint (closed CO_2 cycle), biodegradable. The emissions after combustion have 75–90 % less carcinogens compared with petrodiesel [3]. Transesterifying triglycerides is the only process at the commercial scale that converts nearly 100 % of the feedstock to liquid biofuels. Ethanol yields from biomass approach 50 % and yields from gasifying biomass followed by Fischer-Tropsch synthesis are even lower.

The drawbacks associated with biodiesel production on an industrial scale are well known and are mostly related to the limited miscibility of methanol and oil, which translates to low mass transfer rates. Homogeneous basic catalysts such as KOH, NaOH, and CH_3ONa are 4,000 times more efficient than acid catalysts; they require lower operating temperatures and are soluble in alcohol [4]. However, commercial processes to produce biodiesel still take up to 8 h per batch and suffer from drawbacks such as the need to dispose of the homogeneous catalyst after each batch operation, energy-intensive catalyst-product separation, and corrosion. Moreover, alkalis react with free fatty acids (FFA) to form soap. Both vegetable and waste oils contain FFA [5]. Refined vegetable oils can contribute up to 80 % of the overall biodiesel production cost [4]. Nonedible and waste oils are less expensive but require refining before the transesterification step. Therefore, alkali-catalyzed transesterification only accepts limited feedstocks, with low FFA and low moisture [2]. Acid catalysts, both homogeneous and heterogeneous, are FFA tolerant and active in the presence of water [6]. However, an acid catalyst would further slow down a reaction that is already both mass transfer limited (at the beginning) and then kinetically

controlled, as it approaches equilibrium [7]. A solid catalyst adds a phase which would reduce the mass transfer rate further.

Several process intensification techniques, among which the most common are cavitation (acoustic [8, 9], hydrodynamic [10]), microwaves [11]), and supercritical operation [12] increase the efficiency of both the traditional homogeneous alkali-catalyzed process [13–20] and the reactions promoted by acids and solid acid catalysts [6, 21–23].

The two main challenges of biodiesel production are:

- Increasing the mass transfer rate through process intensification
- Replacing homogeneous catalysts with heterogeneous catalysts

For the reasons highlighted above, these two objectives clash with respect to the additional phase that reduces global reaction rates.

Sonochemical techniques and ultrasound (US), in particular, increase the mass transfer rate, which addresses the major concern with heterogeneous catalysts.

Acoustic cavitation increases the transesterification by disrupting the boundary layer between the oil and the alcohol phases, which contains the catalyst. This creates an oil-alcohol emulsion that is finer than that generated by traditional mechanical stirring [8]. In the presence of an extended surface, such as a solid catalyst, acoustic cavitation bubbles form at the liquid-solid interface and collapse asymmetrically toward the solid surface. Therefore, in the case of a solid, there is a higher probability that the acoustic cavitation phenomenon is located in the vicinity of the reactive event, i.e., on the surface of the catalyst, than for a homogeneous catalyst. Moreover, solids act as cavitation bubble nuclei [24]. On the other hand, solids dissipate the power of the sound waves [25]. An optimized reactor design distributes the ultrasonic radiation minimizing the attenuation of the solid phase.

In this chapter, we review several reactor configurations to produce biodiesel from various feedstocks but emphasize solid-liquid systems. We examine both the FFA esterification and the triglyceride transesterification. Most of the data available in the literature on heterogeneous systems concern classic ultrasonic reactor configurations, such as ultrasonic baths (indirect sonication) and horns (direct sonication).

Ultrasonic Reactors for Biodiesel Production

Ultrasonic reactor's design criteria include:

- Type of sonication, (i) direct and (ii) indirect
- Batch, continuous, and semicontinuous operation type
- Reactor geometry
- Geometry of the transducers and their disposition
- Power
- Frequency

Fig. 1 Continuous ultrasonic reactor equipped with a Sonitube® device [27, 29]
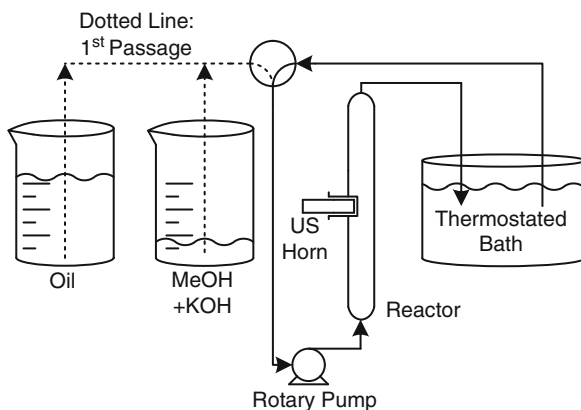
Ultrasonic horns or probes immersed in a solution generate the mechanical waves directly in the reaction medium, whereas ultrasonic baths have larger transducer areas that coincide with the bottom of the bath. The area where the cavitation is most efficient corresponds with the bottom of the bath and propagates toward the surface. Ultrasonic baths are indirect sonicators. The main challenge is to distribute the acoustic cavitation uniformly in the reactor whether or not it is with direct or indirect sonication.

An additional phase, such as a heterogeneous catalyst, adds more resistance to the mass transfer and attenuates the sounds waves, impeding their propagation [9].

Gole and Gogate [8] report that a direct sonicator penetrates into the liquid by 3–5 cm from the tip. Boffito et al. review many batch and continuous reactors for the production of methyl esters from vegetable oils [26]. They suggest that in the case of direct sonicators, loop technologies are the most promising to scale up. In loop technologies, high power fluxes are delivered to a small portion of the reactor, and the reagents are circulated frequently to this area (semicontinuous). Boffito et al. [27] report canola oil transesterification with selectivity to FAME (fatty acid methyl esters) over 90 % in 18 s of pulses (2 s on and 2 s off) with a Sonitube® loop-type reactor (Synetude, Chambery, France). Similarly, Somnuk reports FAME selectivity above 90 % in 18 s in a loop reactor from pre-esterified palm oil [28]. A typical loop reactor includes one or two feeding tanks for the oil and/or the alcohol (containing the catalyst), a pump, a tubular reactor hosting the direct sonicator (US horn), and a collecting tank (thermostated or not) that is larger than the reactor volume (Fig. 1).

Boffito et al. also report a new ultrasound semicontinuous loop-reactor design to treat vegetable and waste oils [29] (Fig. 2). The motor of the ball mill (A) rotates a mixing chamber, that is sonicated by a US horn. The rotation of basket creates turbulence in the mixing chamber. A rotative pump (2) feeds the reagents and the catalyst to the mixing chamber. The design ensures that oil and MeOH circulate in the vicinity of the US tip. US pulses (1 s on and 1 s off) convert more than 90 % of the oil to methyl esters in 1 min.

Fig. 2 Mini-fer (Netzsch) ball mill with an ultrasonic horn. (**a**) Ball mill (**b**) direct sonicator – ultrasonic horn (*1*) feed tank (*2*) feed pump (*3*) charging point (*4*) mixing chamber (*5*) discharging point (*6*) cooling water (*7*) micronizer motor (*8*) ultrasound control (Reprinted with permission from [29]. Copyright 2015 AIDIC)

Though loop technologies have proven to be efficient contactors for homogeneous systems, their efficacy for heterogeneous systems is undocumented. Gogate et al. [9] review sonochemical reactor designs and emphasize heterogeneous systems, including catalytic nanomaterials. They conclude that the presence of several phases in the system results in cavitational effects that are more pronounced with respect to systems with fewer phases, provided that the reactor configuration is optimized. Gole and Gogate also refer to the positive impact of impurities – solids act as cavitation nuclei [24]. On the other hand, the solid phase attenuates the kinetic energy of the mechanical waves [25]. Gogate et al. [9] also concluded that the tubular and hexagonal disposition of multiple transducers possibly operating at multi-frequencies is the best solution for large-scale operations. Calorimetry is an excellent tool to measure the extent of the dissipation [30] in both homogeneous and heterogeneous reactive systems. Gogate et al. [9] recommend intensities in the range 5–20 W/cm^2, depending on the reactor size and application.

At the lab scale, reactor designs that host heterogeneous systems are still limited to simple direct or indirect sonication devices, US horns, and baths, respectively (Table 1).

The literature on innovative ultrasonic reactor configurations for homogeneously catalyzed transesterification is abundant (Table 2). Besides the two configurations mentioned above [27, 29], (Figs. 1 and 2), several others are mentioned in the

Table 1 Direct and indirect sonication of heterogeneous transesterification

Ultrasonic variables	MeOH/oil mol ratio / Catalyst weight %	T, °C	S_{FAME}, %	Optimal condition time	Ref
20 kHz	*Jatropha c.* 5–28	Uncontrolled	7–94	MeOH 28	[6]
21–90 % of 400 W (n), direct	HPA/AC 2.5–4.5			3.5 cat	
				60 % Ampl.	
9″ on 3″ off				30 min	
20 kHz	*Jatropha c.* 20	Uncontrolled	71–87	20 % loading	[21]
75 % of 400 W (n), direct	15–25 % tungstophosphoric acid (TPA) supported on activated carbon (AC) 4 %			40 min	
10″ on 3″ off					
20 kHz	*Jatropha c.* 2–20 $H_3PW_{12}O_{40} \cdot nH_2O)/\gamma$-$Al_2O_3$ 3–4.5 %	Uncontrolled	34–84	25 % loading	[22]
45–90 % of 400 W (n), direct				MeOH 19	
				3.5 % cat	
9″ on 3″ off				60 % Ampl.	
				50 min	
30–90 % of 400 W (n), direct	*Jatropha c.* 5–20 $Cs_xH_{3-x}PW_{12}O_{40}$ ($x = 1$–3)	Uncontrolled	13–88	MeOH 25	[23]
				Cat $x = 1.5$, 3.5	
10″ on 3″ off	2.5, 3.5, 4.5			60 % Ampl.	
	Recycle			30 min	
22.5 kHz, 37 W (e) continuous	Alga *Scenedesmus* sp. 30–60	40–60	9–71	MeOH 60	[50]
	WO_3/ZrO_2 2–4			3 %	
				60 °C	
				20 min	
20 kHz, 500 W (n), direct continuous	*Nagchampa* 6–12	40–60	53–79	MeOH 10	[56]
	CaO 1–5			CaO 5 %	
				60 °C,	
				150 min	
20–25 kHz, 9–36 W (e), direct continuous	Soybean, *Jatropha c.* 5–9	50–65	51–95	MeOH 7	[57]
				5 %	
	$Na_2SiO_3@Fe_3O_4$ /C 1–9			55 °C	
				100 min	
20 kHz, 25–45 W (e) direct continuous	Soybean 9–18	30–50	70–95	MeOH 12	[58]
	9KF/γ-Al_2O_3 0.5–3			2 %	
				50 °C	
				40 min	

Table 1 (continued)

| Ultrasonic variables | MeOH/oil mol ratio | T, °C | S_{FAME}, % | Optimal condition time | Ref |
	Catalyst weight %				
22 kHz, 187.5 W (n) direct continuous	WCO 4–9	30–60	36–93	MeOH 6	[59]
	K_3PO_4, Na_3PO_4, Na_2HPO_4,			K_3PO_4 4 %	
	NaH_2PO_4, KH_2PO_4 1–4			60 °C	
				120 min	
22 kHz, 40 W (e), continuous	WCO	50–60	62–98	MeOH 9	[60]
	MeOH n.a.			Catalyst 3 %	
	Na^+/SiO_2 waste sponge 0, 1, 3, 6, 9			55 °C	
				30 min	
35 kHz, 35 W (e), continuous	*Jatropha c.* 6–18	45–75	22–93	MeOH 11	[61]
	CaO 3–7			5 %	
				64 °C	
				120 min	
35 kHz, 35 W (e), continuous	Soybean 6–18	40–60	1–85	MeOH 10	[62]
	CaO 1–7			CaO 6	
				60 °C	
				60 min	
35 kHz Power n.a., indirect continuous	Sunflower 6–20	75	39–56	MeOH 15	[63]
	Mesoporous tin-triflate based catalysts 1.5			SnTf-UVM-7[a]	
				120′	
35 kHz Power n.a., indirect continuous	Sunflower 4	72	8–51	20 % KF/Al_2O_3 activated at 450 °C	[64]
	10–30 % KF, LiF, CsF supported on MSU-Al_2O_3[b]				
	T activation = 350, 450 °C 1.2				
35 kHz Power n.a., indirect continuous	Sunflower, rapeseed 4	70	20–90	Sunflower MgO activated at 500 °C	[65]
	MgO nanosheets (111), MgO,				
	MgO aerogel 1.5				
	T activation = 310, 500 °C				

S_{FAME} selectivity to fatty acid methyl esters. The values of the power are meaningful if considered as power density (normalized by the volume), *n* nominal power, *e* effective (measured)
[a]SnTf-UVM-7 (Sn triftalate supported over bimodal mesoporous silica)
[b]MSU-Al_2O_3 mesoporous alumina

literature. Gole and Gogate [8] report 90 % conversion of *Nagchampa* oil in 40 min in a US bath with transducers in a triangular disposition. Boffito and coauthors achieved 95 % conversion of canola oil to FAME in 5 min with a Rosett cell reactor and US pulses [27]. In 5 min with a multi-frequency system with an ES300C SONOCHEMIST processor, 91 % of soybean oil reacts to biodiesel. The design of

Table 2 Direct and indirect sonication of homogeneous transesterification

Ultrasonic variables	MeOH/oil mol ratio / Catalyst weight %	T, °C	S_{FAME}, %	Optimal condition time	Ref
20 kHz, 150 W (n), pulse direct	WCO[a] 4.5–13.5	Uncontrolled	96–98	MeOH 9	[4]
	NaOH, 0.5–2			NaOH 1.25 %	
				100 % power	
				2 min	
20 kHz, 120 W (n)	WCO 4.5–13.5	Uncontrolled	88–90	MeOH 9	[13]
	NaOH 0.5–2			NaOH 0.5 %	
				100 % power	
				1.5 min	
20 kHz, 150 W (n), continuous direct	WCO 4.5–13.5	Uncontrolled	88–90	MeOH 9	[14]
	NaOH 0.5–2			NaOH 0.5 %	
				100 % power	
				1.5 min	
24 kHz, 400 W (n), direct continuous	Beef tallow 6	60	92	70 s	[15]
	KOH 0.5				
20 kHz, 150–250 W (n), indirect continuous	WCO 4–6	35–55	46–89.5	MeOH 6:1	[16]
	KOH 0.5–1.25			KOH 1 %	
				200 W 45 °C	
				40 min	
20 kHz, 2,200 W (n), continuous and pulsed	Soybean 5	40	87–96	Amplitude: 120 μm_{pp}, pulses 1.5 min	[17]
	NaOH 1				
20 kHz, 14.5 W (e), direct continuous	Soybean 3–9	25–60	82–92	MeOH 6	[18]
	KOH 1.5			40 °C	
				15 min	
Pulsed frequency, 0.4, – 200 W (n)	Soybean 3–16	25–45	69–100	MeOH 6	[19]
	NaOH, KOH na			1–100 W	
				45 °C	
				20 min	
28, 40 kHz, 60 % of 720 W (n), indirect continuous	Edible oil 6	36	75–98	NaOH, KOH 0.5 %	[20]
	NaOH, KOH 0.5–1.5			40 kHz	
				20 min	

S_{FAME} selectivity to fatty acid methyl esters. The values of the power are meaningful if considered as power density (normalized by the volume), n = nominal power, e effective (measured)
[a]Waste cooking oil

the ultrasonic reactor including a vessel with a parabolic bottom and a polyethylene acoustic membrane window concentrates US radiation in the reaction medium [31].

Push-pull sonicators have a design such that they vibrate longitudinally and produce an ultrasonic field that is more homogeneous compared to other types of applicators. Stavarache et al. report 95 % conversion of triglycerides to biodiesel in 10 min in 30 L to 75 L vessels [32].

Ultrasonic flow cells are flexible for both batch and continuous systems. In a batch flow cell, multiple transducers emit from several locations in the reactor to generate standing flow patterns [9]. In a continuous flow cell, the reagents circulate in and out of the reactor and the number and disposition of the transducers vary.

Manickam et al. adopted a flow cell with a hexagonal geometry and six transducers connected to each of the plates constituting the cell. The transducers on opposite walls had the same frequency, namely, 28, 40, and 70 kHz. The system operated at single, double, or triple frequency for a total of seven vibrating modes [33]. The authors report 93 % selectivity to biodiesel from palm oil in 15 min with a stoichiometric MeOH/oil ratio, and a mass fraction of catalyst of 1 %.

Another innovative design consists of a flow cell composed of a rectangular reaction chamber with three high-efficiency prestressed piezoelectric rings compressed between two ergal blocks as transducers, all operating at a maximum of 21.5 kHz. The authors report complete conversion of soybean oil to biodiesel in 1 h at a power density of 3 W/cm^2 [34].

Ultrasonic-Assisted Esterification and Transesterification

Ultrasound accelerates both homogeneous and heterogeneous reaction rates. In homogeneous solutions, the thermal effects of the acoustic cavitation produce radicals (reactive radicals such as H• and HO• from reactants or solvent molecules at the moment of bubble collapse) in most solvents that react or combine with other substrates or intermediates to generate products. In heterogeneous liquid-liquid systems (such as triglycerides and methanol), ultrasound forms fine emulsions that increase the available surface area between the two phases, thereby the reaction rate increases. In liquid-solid systems (such as heterogeneous catalysts for oil transesterification), the rapid and violent collapse of cavitational bubbles near the solid surface causes localized high temperatures and pressures that produce high-speed liquid jets near the solid surface and promote liquid-solid mass transfer [35]. More specifically, the chemical effects of ultrasound originate from the acoustic cavitation which is formation, growth, and implosive collapse of bubbles. In heterogeneous conditions, ultrasound reportedly increases reactivity up to 10^6 times [36]. For metal oxide catalysts such as barium oxide or strontium oxide in fine particulate form, the cavitational collapse produces shock waves that cause the particles to collide. For example, at 20 kHz, the diameter of the collapsing bubble is 150 μm, so microjets on particles smaller than this diameter will not form on the surface nor will the solids perturb the ultrasonic field [36], but will be influenced by the aforementioned phenomena.

Among the different types of catalysts to transesterify oils (alkali, acid, homogeneous, heterogeneous, and enzymatic), homogeneous ones (KOH, NaOH, CH₃ONa) are the least expensive. However, these catalysts are highly hydroscopic and absorb moisture from air during storage and transesterification. They also form water when mixed with an alcohol donor, which affects the biodiesel yields adversely. Heterogeneous catalysts, on the other hand, can be separated easily from the reaction mixture by settling or filtration. These catalysts are capable of simultaneously esterifying and transesterifying fats and oils and there is no need for pre-esterification. This renders these catalysts suitable for oils with high free fatty acids. The disadvantage is that the reaction rate is lower because it is limited by mass transfer between the liquid and solid phases, which can be overcome with ultrasound.

Other factors affecting the ultrasound-mediated reactions are ultrasound frequency, acoustic power, solvent, ultrasonic intensity, system vapor pressure, external temperature, and pressure. An increase in the frequency will decrease the cavitation effect mainly due to short rarefaction cycles which cannot produce large enough cavitation bubbles to collapse as well as creating a negative pressure. For this reason, the most commonly used frequencies vary between 20 and 50 kHz. Finally, different forms of energy can be generated through ultrasound application. When electrical energy passes through an ultrasonic probe, it is converted into heat and vibrational energy (i.e., mechanical energy). This vibrational energy is converted to cavitational energy in the reaction medium, and some of the vibrational energy is lost through sound reflection via harmonics and subharmonics [37]. The cavitational energy is further converted into chemical, physical, and biological energy depending on the application and reaction environment. In biodiesel processes, chemical and physical (thermal) effects have been noted by many researchers through a significant rise in the reaction temperature, reaction yields, and intense mixing in transesterification reactions using pure or used oil feedstock [11, 13, 38–41]. In some applications, destruction of cell membranes results in oil extraction such as in algae biodiesel production, which can be considered a biological effect [42–47].

Free Fatty Acid Esterification

Free fatty acids (FFA) react with KOH and NaOH to form soap [48, 49]. Which reduces the transesterification rate. FFA and methanol react over acid catalysts to fatty acid methyl esters (FAME): lowering the FFA concentration will increase the reaction rate and yield of biodiesel. Acid catalysts promote oil transesterification at temperatures beyond 120 °C [48]. However, transesterification at temperatures higher than 65 °C requires continuous addition of fresh MeOH [48] or pressures above atmospheric. Concurrent FFA esterification and triglyceride transesterification in one step with an acid heterogeneous catalyst are the main challenges of biodiesel production.
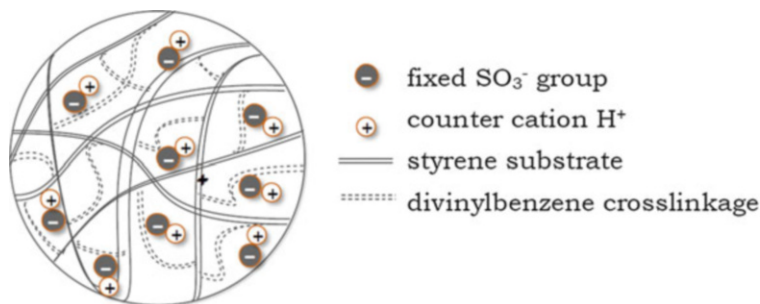
Fig. 3 Sulfonic ion-exchange resins of the Amberlyst®46 type as described in the reference [52] (Reprinted with permission from [52]. Copyright 2014 Elsevier)

Most articles concerning biodiesel production from raw or waste oils by ultrasonic transesterification report a FAME yield that includes FFA esterification and triglyceride transesterification [6, 21–23, 50]. However, none of these papers report the different extent of the two reactions as a contribution to the final biodiesel yield.

Tungstated zirconia transesterifies *Scenedesmus sp*. oil [50] with an acid value of 30 mg KOH/g, which suggests that the esterification occurred as well as transesterification. In fact, acid catalysts would activate the esterification rather than the transesterification at temperatures below 120 °C. Similarly, Badday et al. claim the transesterification of *Jatropha curcas* oil with a FFA weight concentration of 10.5 %. FFA esterification contributed without doubt to the overall oil conversion [6, 21–23].

As a conclusion, both homogeneous and heterogeneous acid catalysts tolerate the presence of FFA in the feedstock, and heterogeneous ones also the presence of moisture during the transesterification [6].

Few papers report the results exclusively related to FFA esterification in the presence of solid catalysts and ultrasound, in particular on immobilized lipase [51] and acid ion-exchange resins [52]. Jadhav and Gogate [51] report 97 % conversion of 100 % FFA of *Nagchampa* oil to FAME in 7 h at 30 °C in a batch reactor equipped with a US probe. The mechanical stirred process takes up to 8 h to achieve the same conversion above 60 °C [48]. Boffito et al. report [52] the conversion of FFA in tobacco and canola oil and a pure stream of oleic acid in 6 h in a batch reactor by direct sonication. Conversion was 70 %, 90 %, and 60 % at 63 °C, respectively. The catalyst was Amberlyst®46 (A46 – Dow Chemical). A46 is a copolymer of styrene cross-linked with divinylbenzene (DVB) functionalized with strong sulfonic acid groups, which are the active sites responsible for the esterification of the FFA. The A46 beads were 0.5–0.7 mm in diameter (Fig. 3).

A46 is sulfonated on the outer surface and not inside the pores [49]. This reduces the formation of subproducts, such as dialkyl ethers, from the auto-condensation of the molecules of the alcohol inside the pores [52]. Moreover, a high concentration of active sites located on the outer surface of the catalyst is beneficial for reactive systems that contain highly sterically hindered molecules, such as FFA [53].

For this system, Boffito et al. report that the Eley-Rideal kinetic model characterizes the experimental data ($R^2 > 0.97$ for canola and tobacco oils and > 0.99 for oleic acid). The expression of the concentration of the reacting species takes into account the mass transfer between the phases (Eq. 1):

$$r = \frac{k\left(C_{\text{FFA},s}C_{\text{MeOH},s} - \dfrac{C_{\text{H}_2\text{O},s}C_{\text{ME},s}}{K_{\text{eq}}}\right)}{1 + K_1 C_{\text{FFA},s} + K_3 C_{\text{H}_2\text{O},s}} \qquad (1)$$

where C_i and $C_{i,s}$ are the concentration of each of the four reacting species in the bulk and on the surface of the catalyst, k is esterification reaction constant, K_{eq} is the equilibrium constant between the esterification and hydrolysis reactions, and K_1 and K_3 are the equilibrium constants of the adsorption/desorption of the FFA and of the desorption/adsorption of H_2O on the catalyst (A46), respectively.

US increases the mass transfer rate by more than two times. They calculated the relative improvement, $k_{m,\text{US}}/k_m$, and the best fit parameters (Table 3). US increased the mass transfer coefficient in the raw tobacco oil 6.7 times and 4.1 times at 20 °C and 40 °C, respectively (Fig. 4).

Transesterification

Homogeneous Transesterification

Transesterification rates increase significantly with reaction temperature. However, ultrasound can transesterify oils at room temperature. In fact ultrasonic cavitation increases the medium temperature, thus an external heat source may be unnecessary. In conventional heating, the optimum temperature to transesterify oil is 65 °C, which is MeOH's boiling temperature. The temperature is higher for ethanol. During uncontrolled ultrasound transesterification, the bulk temperature of the emulsion does not necessarily represent the actual temperature since ultrasound produces localized high temperatures and pressures at a microscale and the heating and cooling cycles are so rapid that accurately measuring the surface temperatures is impossible. Table 2 compares studies using direct and indirect ultrasound under controlled and uncontrolled reaction temperature conditions. Higher reaction temperatures are unsuitable for ultrasound-mediated transesterification since the ultrasound energy drops increasing the solvent vapor pressure. At lower temperatures, ultrasound increases mass transfer rates both in liquid-liquid systems (homogeneous catalysis) and liquid-solid (homogeneous catalysis) systems. Therefore, solvents with a lower vapor pressure are better to transesterify oils and fats.

Heterogeneous Transesterification

Ultrasound-assisted heterogeneous transesterification is more efficient than mechanical stirring and requires a lower alcohol input [54]. The number of articles researchers are publishing increases year by year (Table 1). Most articles are about optimizing the reaction variables (alcohol/oil molar ratio, catalyst loading, and

Table 3 Best fit parameters estimates without US

Feedstock	ppm H_2O	T °C	k $L^2mol^{-1}min^{-1}$	K_{eq}	k_m L min^{-1}	$k_{m,US}$ L min^{-1}	$k_{m,US}/k_m$	k_{H2O} L min^{-1}	R^2	R^2_{US}
Oleic acid	0	63	0.0050	0.57	0.0034	0.0064	1.9	0.06	1.00	1.00
Canola	600	40	0.0009	0.073	0.0015	0.0040	2.6	0.05	0.98	0.97
Canola	600	63	0.0088	0.380	0.0017	0.0020	1.2	0.02	0.99	0.99
Tobacco	2,000	20	0.0005	0.007	0.0004	0.0024	6.7	0.02	0.99	0.97
Tobacco	2,000	40	0.0003	0.027	0.0019	0.0080	4.1	0.02	1.00	0.98
Tobacco	2,000	63	0.0027	0.050	0.0013	0.0026	2.0	0.01	0.99	0.98

k is the free fatty acid (*FFA*) esterification rate constant, K_{eq} is the equilibrium constant between the direct reaction (free fatty acids esterification) and the indirect reaction (hydrolysis), k_m is the mass transfer coefficient between the boundary layer around the catalyst and the bulk, k_{H2O} is the absorption coefficient of H_2O (Reprinted with permission from [52]. Copyright 2015 Elsevier)
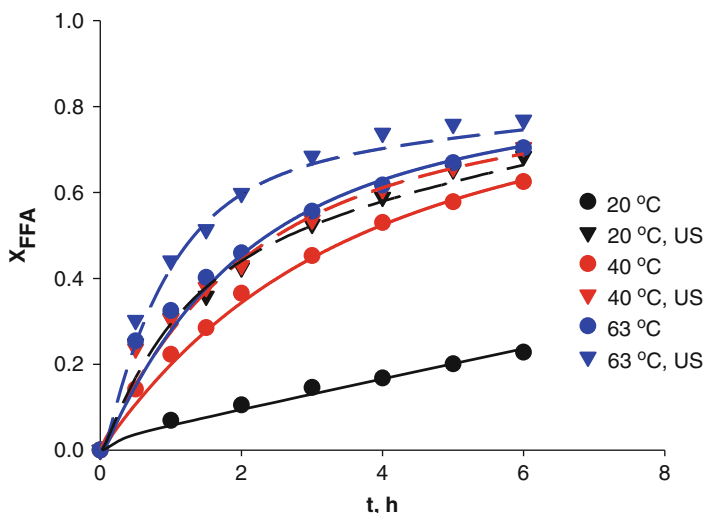
Fig. 4 Conversion with US and without US of tobacco seed oil. Catalyst: Amberlyst®46 [52]. The *lines* represent the model (Reprinted with permission from [52]. Copyright 2014 Elsevier)

temperature) rather than ultrasound variables (power, US pulses) and catalyst development.

Salamatinia et al. [55] report that the molecular composition of biodiesel obtained by US-assisted transesterification is the same as the one obtained by mechanical stirring. However, the former exhibits better clarity, less FFA, and less catalyst (traces).

The process with heterogeneous catalysts operates at 10–15 °C higher than the homogeneous processes (to achieve the same productivity) even in the presence of US. US does not compensate for the higher activation energy of heterogeneous versus homogeneous systems (compare Tables 1 and 2). Similarly, the required alcohol/oil molar ratios are higher for heterogeneous systems than homogeneous (>10 vs. <10). US finely emulsifies the methanol-aqueous phase – which contains the homogeneous catalyst – and the oil, whereas traditional mechanical stirring does not. As a consequence, US-assisted transesterification requires less alcohol to completely convert the oil in one step [27]. In heterogeneous systems, the catalyst is in a different phase than the MeOH-oil emulsion. Therefore, the reaction requires more alcohol to shift the equilibrium toward the products.

The power density (W/cm^3) to maximize triglyceride conversion is independent of the catalyst [6, 22, 23]. In most cases, it varies from 40 % to 70 % of the maximum power. The nominal power of commercial US is between 400 W and 1,500 W [26, 27]. The transesterification of triglycerides is slightly exothermic. Temperatures up to the boiling point of MeOH favor the kinetics and the solubility of MeOH in oil. Increasing the US power increases the temperature of the reaction medium and, as a consequence, the transesterification kinetics. US power increases the violence of the collapse of the cavitation bubbles, enhancing acoustic cavitation. However, there is

less dissolved gas to form cavitation bubbles and bubbles may exit the system before they cavitate [26, 27].

For homogeneously catalyzed systems, increasing the mass of catalyst (such as NaOH and KOH) dampens the conversion of triglycerides to biodiesel (Table 2) in both mechanically and ultrasonically stirred systems [29]. NaOH and KOH may saturate the oil-MeOH interface and hinder the contact between the reagents, in particular between the mono- or diglycerides and MeOH. In heterogeneously catalyzed systems (Table 1), the conversion of triglycerides to biodiesel reaches a maximum with respect to catalyst loading and remains constant thereafter rather than decreasing: heterogeneous catalysts do not interfere with the oil-MeOH interface.

Few papers report data on both basic [55–65] and acidic [6, 21–23, 50, 64, 65] heterogeneous catalysts. Verziu et al. [64] report that the activity of KF and CsF is higher compared to LiF supported on mesoporous bimodal alumina ($MSU-Al_2O_3$). $KF/MSU-Al_2O_3$ and $CsF/MSU-Al_2O_3$ are more basic than LiF. Increasing the loading of the active component on the support up to 20 % converts more triglycerides. Higher loadings decrease the conversion in the presence of US but not microwaves. The authors ascribed it to the leaching of the active components that is promoted by US but not MW and mechanical stirring.

Cesium-doped heteropoly acids ($Cs_xH_{3-x}PW_{12}O_{40}$, $x = 1–3$ %) convert 13–88 % of triglycerides to biodiesel in 30 min [6, 21, 23]. Replacing H with more Cs atoms in the heteropoly acid decreases the surface acidity and increases the specific surface area (SSA) [23]. As a general trend, the selectivity to biodiesel increases with the ratio surface acidity/SSA. High SSA does not increase the catalytic activity [53]. In fact, acidic or basic active sites should be located on the outer surface of the catalyst to be accessible for the triglycerides, which are sterically hindered.

Water leaches acid active groups from the support [48] making it less active, but also triglyceride hydrolysis may remove reagents from the transesterification reducing conversion.

Effect of Type of Alcohols

Methanol is more common as an alcohol donor [66] than ethanol, propanol, or butanol. The stoichiometric ratio of alcohol to oil is 3:1, but higher alcohol concentrations shift the equilibrium toward the products. Alcohol to oil ratios in the range of 4.5:1–15:1 are optimal for biodiesel yields with conventional heating. Lower molar ratios of 4.5: to 9:1 are optimal for ultrasound-mediated transesterification.

Reaction rates and yield are higher with methanol and ethanol compared to alcohols with a higher carbon number. Considering the long term, ethanol is a more environmentally friendly reactant for sustainable biodiesel production since it is derived from plants and crops [67, 68]. The extra carbon atom in the ethanol molecule slightly increases the heat content and the cetane number of ethyl esters compared to methyl esters. In addition, the ethyl esters generally have lower cloud and pour points than methyl esters [68]. Isopropyl esters lower the biodiesel pour

point and cloud point by about 10 °C and 20 °C, respectively, compared to methyl esters [69, 70].

Transesterification is limited by mass transfer at the beginning, and as the reaction proceeds, it is limited by reaction kinetics in the oil-methanol phase [71, 72]. Mass transfer between two organic phases (methanol and oil) plays a critical role during methanolysis and controls the reaction kinetics. Three kinetic regimes characterize the transesterification rate:

  (i) An initial mass transfer-controlled regime (slow)
 (ii) A chemically controlled regime (fast)
(iii) A final regime, close to equilibrium (slow) [7]

Therefore, the reaction consumes methanol inefficiently, due to the interfacial mass transfer resistance [73]. Efficient mixing, such as ultrasonic mixing, helps overcome the mass transfer limitations. Ultrasound increases the mass transfer rate between the two immiscible liquids [74]. Cavitation mainly affects the mass transfer rates and ensures a uniform distribution of the reactants. This enhances both the reaction rate and the equilibrium conversion, which is only observed after a few hours, when the biodiesel acts as a cosolvent (compatibilizer) [75].

Methanol is poorly miscible in oil, which limits mass transfer rates. However, methanol has a higher equilibrium conversion than any other alcohol, due to the higher reactive intermediate methyl group. On the other hand, ethanol has better solvent properties, besides the possibility to obtain it from renewable sources [76]. However, the emulsion of oil with ethanol makes the separation of ester difficult. The limitations with each of these alcohol donors can be overcome by combining the two alcohols to result in a beneficial effect. Methanol/ethanol mixtures in the transesterification reaction have both better solvent properties than methanol alone, and reaction kinetics are faster compared to ethanol itself. Moreover, esters of alcohols with a higher carbon number than MeOH have better lubricating properties. Finally, replacing methanol with ethanol will also make biodiesel production more sustainable by reducing the dependence on non-renewable methanol production [77].

Ultrasound provides superior mixing compared to conventional stirring in the transesterification reaction, promoting mass transfer between the oil and alcohols bigger than methanol.

A recent paper on the effect of pulsed sonication in the transesterification reaction of waste vegetable oil compares different alcohols [78]. The optimal conditions for ethanol or methanol or alcohol mixture (ethanol and methanol) were 9:1 alcohol to oil ratio, 1 % by weight of catalyst and nominal powers between 75 and 150 W. Methanol and ethanol transesterification gave similar selectivity to biodiesel (96 %) at an ultrasonic intensity of 10 W/cm^2, while ethanol-methanol (50–50 %) mixtures gave a higher biodiesel yield compared to ethanol or methanol, due to the combination of acoustic cavitation effect with the better solubility of ethanol at lower power density and US intensity.

Another recent paper by Boffito et al. reports canola oil conversion to methyl, ethyl, and propyl esters of 90 %, 65 %, and 40 %, respectively, within 1 min, at room

temperature, and with US pulses in the reactor described in the section "Ultrasonic Reactors for Biodiesel Production" [29]. Conversion in the presence of continuous US was 5–15 % lower. After 1 min with traditional mechanical stirring, no isopropyl esters were detected. Hanh et al. report a conversion less than 5 % in 25 min with i-propanol, at the same experimental conditions (1 % by weight of KOH as a catalyst, oil/iProH molar ratio = 1:6) [79, 80].

The benefits of ultrasonic irradiation, together with an optimized reactor design, increase process operational flexibility and productivity in larger-scale reactors. Since the biodiesel properties are reportedly better for the ethanol-methanol mixtures, additional research in this area would have a profound impact on current commercial processes. Finally, ethanol can be produced from renewable materials, which reduces the stress on existing methanol sources and associated gasoline price fluctuations, enhancing the sustainability of biodiesel production.

Ultrasound-Assisted Transesterification Kinetics

The scientific literature includes the kinetics of the transesterification reaction (also known as alcoholysis) with conventional methods for different feedstocks, including palm oil, rapeseed oil, soybean oil, vegetable oils, sunflower oil, *Jatropha curcas*, waste cooking oil, non-catalytic transesterification of soybean oils, oleic acid, *Pongamia* oil, and palm fatty acids [7, 81–94]. However, few studies report the kinetics of ultrasonic transesterification [18, 95]. Colucci et al. report a pseudo-second-order kinetic model for the hydrolysis of oils and reaction rate constants 3× to 5× higher than those of mechanical agitation [18]. Parker et al. compared the ultrasonic transesterification of soybean oil with conventional alkali-catalyzed reaction with mechanical stirring. They report the interrelation between mechanics of ultrasound/cavitation and the intrinsic behavior (represented by specific rate constant) of the transesterification reaction and propose a first-order kinetic model [95]. Mahamuni and Adewuyi [31] claim that the methanolysis of soybean oil to biodiesel in the presence of ultrasound at 35 °C is a second-order reaction (first order with respect to both oil and methanol). On the other hand, Georgogianni et al. [96] report the first- and second-order reaction rates with respect to TAG (triglycerides) for the base-catalyzed methanolysis of sunflower and cottonseed oils, at both low frequency ultrasonication and mechanical agitation, with the first-order reaction kinetics giving a better fit. Deshmane et al. [97] verified the agreement of experimental data with a first order followed by a second-order kinetic model with respect to fatty acids for the ultrasound-assisted acid-catalyzed esterification of palm fatty acid distillate. In another study, they also report a pseudo-first-order reaction kinetics for the transesterification of soybean oil over calcium methoxide [97]. Avramovic et al. report the results of the empirical modeling of ultrasound-assisted base-catalyzed sunflower oil methanolysis kinetics [98]. Vyas et al. measure the effects of molar ratio, alkali catalyst concentration, and temperature on the transesterification of *Jatropha* oil with methanol under ultrasonic irradiation by a first-order

kinetic model [99]. The transesterification of used soybean frying oil follows a first-order reaction kinetic [100].

Grant and Gude report the kinetics of waste cooking oil transesterification under ultrasound and with basic catalysts [101]. They estimate reaction rate constants and reaction orders with conversion versus reaction time data with the equations derived from the proposed model, considering eight different cases. In temperature-controlled reactions, the activation energy derives from reaction rate constants at different temperatures (45, 55, and 65 °C) for the base-catalyzed transesterification. The same study also proposed a mathematical model that could be applied to any biodiesel feedstock. The model reports the reaction rates with respect to individual reactants (oil and methanol), since they can assume different reaction orders in the transesterification.

Mathematical Analysis

Since the effect of ultrasound on the triglycerides and methanol (or other alcohol) can be different, reaction kinetic equations that include individual reaction rate orders with respect to the reactants in the reagents mixture (oil and methanol) must be considered [102]. The development of the reaction kinetic equations is as follows:

$$A + 3B \leftrightarrow P + R \tag{2}$$

Here, A refers to triglycerides; B, P, and R refer to methanol, biodiesel (fatty acid methyl esters), and glycerol, respectively.

The general rate equation for the transesterification reaction is:

$$-\frac{dC_A}{dt} = kC_A^{\alpha}C_B^{\beta} \tag{3}$$

where dC_A/dt is the consumption of reactant A per unit time, k is a rate constant, C_A is the concentration of A after time t, C_B is the concentration of B after time t, α is the order of reactant A, and β is the order of reactant B. In addition,

$$C_A = C_{A0}(1 - X) \tag{4}$$

$$C_B = C_{A0}(\theta_B - 3X) \tag{5}$$

$$\theta_B = \frac{C_{B0}}{C_{A0}} \tag{6}$$

where C_{A0} and C_{B0} are the initial concentrations of A and B, X is the conversion of triglycerides, and θ_B is the ratio of C_{B0} to C_{A0}. Equation 3 can be rewritten as:

$$\frac{dX}{dt} = kC_{A0}^{\alpha+\beta-1}(1 - X)^{\alpha}(\theta_B - 3X)^{\beta} \tag{7}$$

Eight different cases were considered to obtain the reaction order. These cases were ($\alpha = 0, \beta = 0$), ($\alpha = 1, \beta = 0$), ($\alpha = 0, \beta = 1$), ($\alpha = 1, \beta = 1$), ($\alpha = 2, \beta = 0$), ($\alpha = 0, \beta = 2$), ($\alpha = 2, \beta = 1$), and ($\alpha = 1, \beta = 2$). For each case, definite integrals of Eq. 6 were calculated from a conversion of $X = 0$ to a conversion of $X = X$ in the time span of $t = 0$ to $t = t$. The calculated equation for each case was then transferred into a linear equation passing through the origin ($y = mx$). The transferred equations for each of the case are as follows:

(a) Case 1: ($\alpha = 0, \beta = 0$)

$$C_{A0}X = kt \tag{8}$$

(b) Case 2: ($\alpha = 1, \beta = 0$)

$$\ln\left[\frac{1}{1-X}\right] = kt \tag{9}$$

(c) Case 3: ($\alpha = 0, \beta = 1$)

$$-\frac{1}{3}\left[\ln\frac{\theta_B - 3X}{\theta_B}\right] = kt \tag{10}$$

(d) Case 4: ($\alpha = 1, \beta = 1$)

$$\frac{1}{(\theta_B - 3)}\ln\left[\frac{(\theta_B - 3X)}{(1-X)\theta_B}\right] = kC_{A0}t \tag{11}$$

(e) Case 5: ($\alpha = 2, \beta = 0$)

$$\frac{X}{(1-X)} = kC_{A0}t \tag{12}$$

(f) Case 6: ($\alpha = 0, \beta = 2$)

$$\frac{X}{(\theta_B - 3X)\theta_B} = kC_{A0}t \tag{13}$$

(g) Case 7: ($\alpha = 2, \beta = 1$)

$$\frac{1}{(\theta_B - 3)}\left\{\frac{X}{(1-X)} - \frac{3}{(\theta_B - 3)}\ln\left[\frac{(\theta_B - 3X)}{(1-X)\theta_B}\right]\right\} = kC_{A0}^2 t \tag{14}$$

(h) Case 8: ($\alpha = 1, \beta = 2$)

$$\frac{1}{(3 - \theta_B)}\left\{\frac{3X}{(\theta_B - 3X)\theta_B} - \frac{1}{(3 - \theta_B)}\ln\left[\frac{(1-X)\theta_B}{(\theta_B - 3X)}\right]\right\} = kC_{A0}^2 t \tag{15}$$

Equations 10, 11, 12, 13, 14, and 15 are in the form $y = mx$, where t (for Eqs. 8, 9, and 10), $C_{A0}t$ (for Eqs. 11, 12, and 13), and $C_{A0}{}^2t$ (for Eqs. 14 and 15) are the abscissas. The y variable was plotted against the corresponding x variable and the coefficient of determination was estimated. In all cases for Eqs. 8, 9, 10, 11, 12, 13, 14, and 15, the slope is the reaction rate constant. The case that gave the highest correlation coefficient R^2 was used to determine the reaction order and reaction rate constants. Activation energy can be determined by using the Arrhenius equation which gives a relationship between the specific reaction rate constant (k), absolute temperature (T), and the energy of activation (E_a) as

$$k = A * \exp\left[-\frac{E_a}{RT}\right] \tag{16}$$

where A is the frequency factor and R is universal gas constant (J mol^{-1}K^{-1}). This equation can be rewritten as:

$$\ln(k) = -\frac{E_a}{RT} + \ln(A) \tag{17}$$

A number of experiments need to be conducted at different reaction temperatures to develop a plot of ln (k) versus $1/T$ (the Arrhenius plot) that gives a slope equal to ($-Ea/R$) from which activation energy can be determined.

Use of Model Equations

Grant and Gude [101] conducted several experiments to study the effect of reaction temperature on the conversion of waste cooking oil into biodiesel under ultrasonic irradiation. The reaction temperatures varied between 35 °C and 65 °C at 10° intervals. Figure 5 displays the biodiesel conversion as well as the glycerol, tri-, di-, and mono-glycerides concentrations for reaction times between 0 and 15 min. As reported in other papers [18, 81, 103], the transesterification reaction rate does not improve significantly after 10 min of reaction time, suggesting that shorter reaction times can be enough. Biodiesel conversion profiles and kinetics under ultrasonic mixing follow two regimes, the mass transfer-limited regime and the kinetics-controlled regime [97]. The profile (shape) corresponding to the two types of regime follows a sigmoidal curve during the products formation (i.e., FAME conversion). The data was divided into two sets to represent the two different regimes of the conversion profile (Fig. 5). The very fast triglyceride conversion in the first 2 min of reaction time followed by a slow conversion pattern between 2 and 15 min reaction time can be seen in (Fig. 5). In ultrasonic transesterification, higher temperatures do not reduce the time to reach the equilibrium, as other articles confirm [81, 97]. While the overall conversion of the transesterification did not change with temperature, the rate of the transesterification process increases with temperature. This means that the temperature improves the mass transfer thereby increasing the transesterification rate [104].

Fig. 5 *DMG* (di- and monoglycerides), *TAG* (triglycerides), FAME (fatty acid methyl esters), conversion profiles for waste cooking oil at different temperatures, catalyst: NaOH (Reprinted with permission from [101]. Copyright 2013 Elsevier)
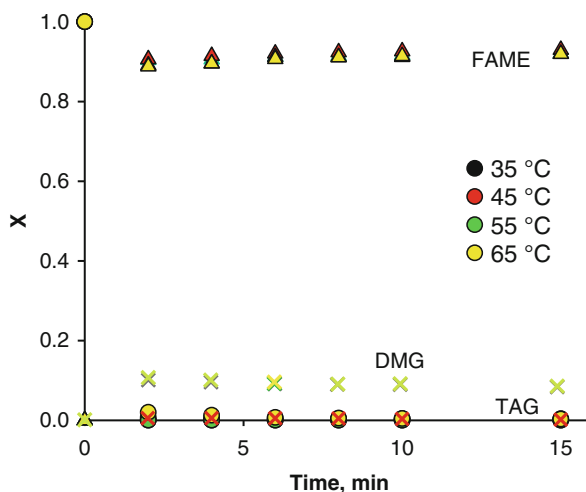

Table 4 The values of "R^2" for all eight cases of each data set in ultrasonic transesterification

Coefficient of correlation, R^2 for the eight cases for data set I				R^2 for the eight cases for data set II			
Temperature (°C)	35	45	55	65	35	45	55	65
Case 1	0.68	0.55	0.50	0.56	0.93	0.91	0.82	0.880
Case 2	0.93	0.70	0.61	0.78	0.93	0.92	0.84	0.883
Case 3	0.70	0.56	0.50	0.55	0.93	0.91	0.82	0.88
Case 4	0.85	0.64	0.56	0.70	0.93	0.91	0.84	0.88
Case 5	**0.99**	**0.88**	**0.77**	**0.97**	**0.93**	**0.92**	**0.85**	**0.88**
Case 6	0.34	0.39	0.41	0.39	0.93	0.91	0.82	0.88
Case 7	0.99	0.85	0.74	0.95	0.93	0.92	0.85	0.88
Case 8	0.71	0.55	0.51	0.60	0.93	0.92	0.84	0.88

Reaction Rates and Constants

Equations 8, 9, 10, 11, 12, 13, 14, and 15 can be used to determine the best fit of the reaction kinetics using eight different cases considering different reaction orders with respect to the individual reactants. These reaction orders represent different levels of activities of individual reactants (i.e., oil or methanol) under ultrasound irradiation. Table 4 reports the coefficients of correlation (R^2 values) for different cases at four reaction temperatures. The reaction order at each temperature was 2 with respect to oil at all the temperatures. It was 0 with respect to MeOH at all temperatures. The overall reaction order varied (Table 5). The reaction rate constants for both data sets at low reaction temperature (35 °C) were higher compared to the other temperatures. This is because the collapse of the cavitation bubbles is more powerful at low temperatures, although the viscosity is higher. At lower reaction temperatures, the physical effects of cavitation bubble dynamics (viz., micro-convection and shock

Table 5 Reaction order for each of the reactants, overall order, and rate constants. Rate constants I and II refer to data sets 1 and 2, respectively

Temperature (°C)	Overall order	Rate constant I	Rate constant II	Unit
35	2	10.5	1.00	$g \, mol^{-1} \, min^{-1}$
45	2	7.1	0.47	$g \, mol^{-1} \, min^{-1}$
55	2	8.0	0.72	$g \, mol^{-1} \, min^{-1}$
65	2	11.0	0.20	$g \, mol^{-1} \, min^{-1}$

waves) are more pronounced [95, 101]. The reaction at a temperature of 65 °C has about the same reaction rate constant, which can be attributed to the improved miscibility of heterogeneous mixture of oil and alcohol at higher temperature The reaction rate constants for different temperatures (35, 45, 55, and 65 °C) were 10.5 g^2 $mol^{-2} \, min^{-1}$ (reaction order 2 w.r.t. oil and 0 w.r.t. methanol), 7.1 (2, 0), 8.0 (2, 0), and 11.0 (2, 0) $g \, mol^{-1} \, min^{-1}$, respectively. The overall reaction order of the ultrasonic transesterification follows a second-order reaction kinetic, as the conventional transesterification process. Some papers report that a second-order or a pseudo-second-order mechanisms are more suitable for predicting FAME conversion at any reaction time [93]. The activation energy for the first data set was 19.6 $J \, mol^{-1} K^{-1}$, which was lower than the conventional heating method [18, 97, 100, 101]. In conclusion, the activation energy depends on the reaction mixture (quality of oil, alcohol catalyst) and the reaction conditions.

Synergistic Effects of Ultrasound and Microwaves

Microwaves, as well as ultrasound, increase the reaction rates in organic processes. The effect of microwaves in organic systems relates to both thermal and nonthermal effects. Microwaves enact phenomena such as dipolar momentum, ionic conduction, and dipolar polarization, which are a combination of both phenomena. Microwaves transfer energy into materials by dielectric heating (more specifically by dipolar polarization, ionic conduction, and interfacial polarization) and uniform and rapid heating of the reaction mixture [105, 106]. Methanol molecules have a dipole moment; therefore, when under microwave irradiation, the dipole tries to align with the applied electric field. Since the electric field is oscillating, the dipoles constantly try to realign to follow its movement. At 2.45 GHz, molecules have time to align with the electric field but not to exactly follow the oscillating field. This continual reorientation of the molecules results in frictions and consequently releases thermal energy. If a molecule is charged, then the electric field component of the microwave irradiation moves the ions back and forth through the sample while colliding at the same time. This movement, again, generates heat. In addition, since the energy continuously interacts with the molecules, they cannot reach a relaxation state, and the heat generated at a microscopic level by this phenomenon can be much greater than the overall recorded temperature of the bulk reaction mixture in the short time. In a word, there is instantaneous localized superheating.

Therefore, the bulk temperature is not an accurate measure of the temperature at which the actual reaction takes place. The interfacial polarization method can be considered as a combination of the conduction and dipolar polarization mechanism, which may also contribute to heat generation [107, 108].

Although microwaves accelerate thermal energy transfer, the inability to enhance mass transfer among the reactants is a limitation. Similarly, the inability to create high thermal energy to enhance process chemistry is a drawback of ultrasound. Simultaneous ultrasound and microwave irradiation can help overcoming the relative limitations. This combination of the two techniques provides the mechanical mixing required for mass transfer and high thermal energy at the same time. Both microwave and ultrasound irradiation can be controlled to deliver appropriate power effects to achieve desired reactions.

Abundant literature reveals that microwave and ultrasound have traditionally been adopted individually for various chemical applications. Although a few studies attempted to measure the effects of combining microwaves and ultrasound, detailed investigations are yet to be reported. Chemat et al. [109] first investigated the possibility of esterifying propanol in a microwave-ultrasound reactor followed by pyrolysis of urea. The combination of ultrasound and microwaves improved remarkably the products yield. Cravotto [110] later reported the combined effect of ultrasound and microwaves on the transesterification of vegetable oil and algal oil extraction. He reported that the two irradiation types, either alone or combined, give higher conversions and yields within short reaction times. Martinez-Guerra and Gude report in detail the effects of the combined technology in the biodiesel production process [14]. The beneficial effects are synergistic, meaning that the combined effect of both irradiations results in a greater effect than the sum of the individual irradiation effects (Fig. 6). Power density is defined as the ratio of the power supplied to the entire volume of the reaction (mL). In the work of Martinez-Guerra, the amount of sample included the methanol volume and the catalyst, besides the oil. Microwave and ultrasound irradiations had a total power output of 400 W (200 W for 2′ reaction time). The power densities were 3.8 W/mL, 5.1 W/mL, 7.7 W/mL, and 15.3 W/mL for volumes of 80, 60, 40, and 20 mL, respectively. Power density tests help optimize the approximate power output for a desired reaction. Higher power outputs do not necessarily result in higher reaction yields but rather in an increase of the energy cost and offset the net energy benefits, especially in biodiesel production [38, 111].

Energy Comparison and Design Considerations

Combining MW and US irradiation could significantly reduce the energy requirements for the transesterification compared to conventional heating and mixing such as water or oil baths or heating plates and mechanical mixers. The energy requirements depend on several factors such as the sample volume, nature of the medium (solvents), dissipation level of the microwave/ultrasound irradiation, and the depth of the reaction volume. Table 6 compares the energy requirements for different
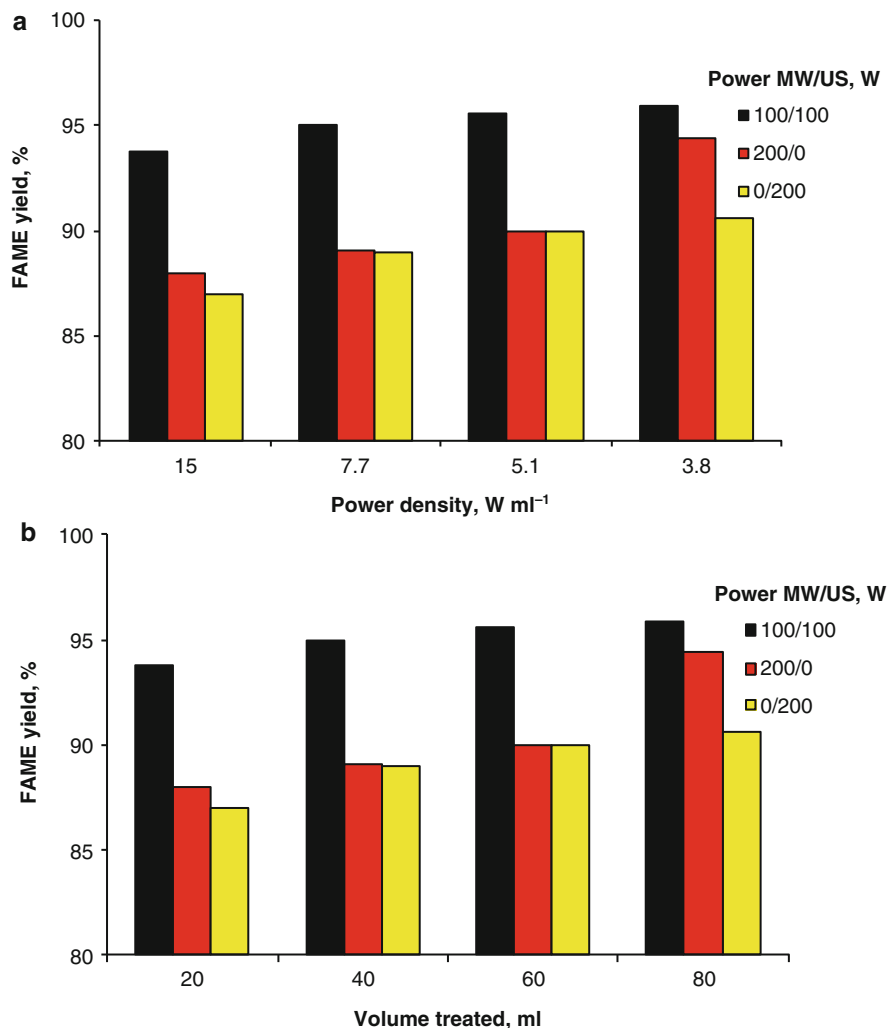
Fig. 6 Fatty acid methyl esters (*FAME*) yield as a function of power density and volume treated for combined MW/US and single MW and US processes, catalyst: NaOH (Reprinted with permission from [106]. Copyright 2014 Elsevier)

heating and mixing methods [13, 111–114]. Patil et al. [111] found that transesterification of the *Camelina sativa* oil was even successful at reduced microwave power levels using a domestic microwave unit. The efficient utilization of microwave power leads to process energy savings. The energy requirements for transesterification reaction are between 0.3 and 1.3 kJ/g for simultaneous MW-US irradiation, lower than other heating and mixing mechanism [114].

Simultaneous MW and US irradiations have a synergistic effect in small reactor systems, resulting in improved reaction rates and lower energy consumption. In large

Table 6 Comparison of energy requirements for transesterification reaction by different methods

Method	Experimental conditions	Energy consumption kJ/g	Ref
Conventional heating	*Camelina sativa* oil (500 W, 15′, 9 g of oil, KOH 1 % w/w)	50	[67]
Ultrasonic-assisted reactor	Vegetable oil (130 W, 30.7′, 52 g of oil, SrO 2.8 % w/w)	4.6	[70]
Direct sonication	Waste vegetable oil (300 W, 2′, 9 g of oil, NaOH 0.5 % w/w)	4	[16]
Microwave irradiation	Acidified waste cooking oil (360 W, 120′, 20 g oil, cation ion-exchange resin 3 g)	130	[69]
Microwave/ ultrasound	Waste vegetable oil (200 W (100 MW/100US), 2′, 18 g of oil, NaOH 0.75 % w/w)	1.3	[62]
Microwave/ ultrasound	Waste vegetable oil (200 W (100 MW/100US), 2′, 72 g of oil, NaOH 0.75 % w/w)	0.3	[62]
Pulse sonication	Waste vegetable oil (150 W, 1′n, 9 g of oil, NaOH 0.74 M)	1.0	[17]

batch reactors, ultrasound cannot always convey the desired chemical/physical effects to the entire reaction mixture, due to the difficulty in the scale up. The same applies to microwave irradiation [108]. The ability of microwaves to interact with different materials also limits its applications. Better process control logistics should be developed for microwave-ultrasonic reactors and process operations.

Ragaini et al. [115] report for instance a new type of US/MW reactor in which a coaxial dipole antenna delivers the MW, and a US horn delivers the sound waves. In the design by Pirola et al., both the US and MW emitters are at the same height from the bottom of reactor (5.5 cm) with a distance of 5 mm from each other. The axes of the emitters are nearly perpendicular. Ragaini et al. demonstrate that with the design proposed, the effects of US+MW are more than additive when US emits at 71 % of the nominal power (295 W). In this case the energy delivered to an organic system with low dipolar moment (cyclohexane) is more than 4 times and 3 times greater than US and MW alone (any MW power), respectively, at equal power consumption.

Ultrasonic-Assisted Synthesis of Catalysts for Oil Conversion

Few articles report the ultrasound-assisted synthesis of catalysts for oil conversion, either by transesterification or esterification, using ultrasound. The benefits of ultrasound in one or more steps of the manufacturing process of a nanomaterial and, in general, of a catalyst include:

- Increase of the rates of intercalation of a variety of species in a pre-existing structure.
- Increase of the nucleation rate, which is useful in the sol-gel syntheses.
- Increase of the specific surface area.

Table 7 Acid capacities, specific surface areas (SSA-BET) and porosity features (pore volume V_p and average diameter D_p), and elemental composition (EDX). Samples termed USZT refer to sulfated 80 %ZrO_2–20 %TiO_2 obtained with US. The name is followed by the US power, by the length of US pulses, and by the molar ratio of H_2O over precursors. For example, USZT_40_0.1_30 indicates a sample manufactured with US at 40 % of the maximum nominal power, with $0.1''$ on $0.9''$ off US pulses and H_2O/precursors molar ratio equal to 30 (Reprinted with permission from [53]. Copyright 2013 Elsevier)

Catalyst	meq H^+/g	SSA, m^2/g^{-1}	V_p, cm^3g^{-1}	Ave BJH D_p, nm	Zr:Ti weight ratio	S/(Zr+Ti) atomic ratio
SZ	0.30	107	0.20	6.0	100	0.090
SZT	0.79	152	0.19	5.0	79:21	0.085
SZT_773_6h	0.21	131	0.20	5.0	n.d.	n.d
USZT_20_1_30	0.92	41.7	0.12	12.5	80:20	0.095
USZT_40_0.1_30	1.03	47.9	0.11	9.5	81:19	0.067
USZT_40_0.3_30	1.99	232	0.27	4.5	81:19	0.11
USZT_40_0.5_7.5	1.70	210	0.20	5.0	78:22	0.086
USZT_40_0.5_15	2.02	220	0.20	5.0	80:20	0.13
USZT_40_0.5_30	2.17	153	0.20	5.0	78:22	0.12
USZT_40_0.5_60	0.36	28.1	0.10	10	79:21	0.092
USZT_40_0.7_30	1.86	151	0.16	5.0	78:22	0.11
USZT_40_1_15	3.06	211	0.09	7.0	80:20	0.15
USZT_40_1_30	1.56	44.1	0.09	7.0	80:20	0.17

- Improvement of the distribution of the active phase.
- Production of surface defects. The implosion of the cavitation bubbles on an extended surface or the impact with the mechanical waves or with other particles erodes the surface of the catalyst. This creates an uneven surface that is more likely to contain the active sites than a "smooth" surface. [49, 116].

Ultrasound is beneficial even when powered in a solution containing the finished catalyst [49], because it can still improve the dispersion of the active phase on the support.

Boffito et al. [53] report the increase of the specific surface area, porosity, and acidity for sulfated ZrO_2-TiO_2 systems and test them in the free fatty acid esterification. US pulses longer than $0.3''$ increases the acidity significantly along with the specific surface (Table 7). However the conversion of free fatty acids (FFA) was greater for the catalyst obtained with continuous US. In fact, for this catalyst the concentration of active sites normalized by specific surface area was the highest. Reactions as esterification and transesterification involving sterically hindered molecules such as triglycerides require catalysts that do not have a high surface area but that have a high concentration of active sites located on the external surface. Continuous ultrasound helps achieve these characteristics. However, ultrasonically assisted synthesis of catalysts for oil transformations still remains largely unexplored.

Pulsed US contributes to the increase of the surface area as well as to the increase of active sites on the surface (such as the sulfates in the work of Boffito et al., last column in Table 7). The outcome of this study is important to tune the properties of solid acid catalysts that activate many reactions such as isomerizations, alkylations, and esterifications.

Conclusion and Future Directions

Ultrasound increases the reaction rates of both free fatty acid esterification and triglyceride transesterification. Heterogeneous catalysts add an extra phase to a reactive system that is already limited by mass transfer. Nevertheless, the benefits of heterogeneous catalysts, in particular solid acids, are many: tolerance to free fatty acids (FFA) and moisture in the feedstock, eliminating a pre-esterification step, and no corrosion. Acid catalysts are 4,000 times less efficient than basic catalysts.

- Ultrasound helps overcome, at least in part, the drawbacks associated with heterogeneous acid catalysts. The presence of an additional phase is beneficial rather than negative in an ultrasound-fed system, because the solid surfaces act as active nuclei for the cavitation.
- Ultrasound and microwaves synergy increases the thermal energy delivered to the system with respect to either system alone. However, further efforts should be devoted to improving the design.
- Ultrasound to fabricate catalysts to treat oils could increase the dispersion of the active phase on the outer surface as well as increasing the concentration of the active sites on the outer surface. The active sites would be readily available to activate sterically hindered molecules like free fatty acids and triglycerides, neglecting the internal diffusion limitation phenomena. Further efforts should be devoted to use US to fabricate catalyst specifically designed to reduce mass transfer limitation, i.e., suitable to treat oils.

References

1. EIA Biodiesel producers and production capacity by state, http://www.eia.gov/biofuels/biodiesel/production/. Accessed on Jan 2015
2. Perego C, Ricci M (2012) Diesel fuel from biomass. Catal Sci Technol 2:1776–1786
3. Antolin G, Tinaut FV, Briceno Y (2002) Optimization of biodiesel production by sunflower oil transesterification. Bioresour Technol 83:111–114
4. Pirola C, Boffito DC, Carvoli G, Di Fronzo A, Ragaini V, Bianchi CL (2011) Soybean oil de-acidification as a first step towards biodiesel production. In: Krezhova D (ed) Biodiesel recent trends for enhancing the diversity and quality of soybean products. Intech, Rijeka, pp 321–345
5. Pirola C, Manenti F, Galli F, Bianchi CL, Boffito DC, Corbetta M (2014) Heterogeneously catalyzed free fatty acids esterification in (monophasic liquid)/solid packed bed reactors (PBR). Chem Eng Trans 37:553–558

6. Badday A, Abdullah A, Lee K (2013-1) Optimization of biodiesel production process from Jatropha oil using supported heteropolyacid catalyst and assisted by ultrasonic energy. Renew Energy 50:427–432
7. Stamenkovic OS, Todorović ZB, Lazić ML, Veljković VB, Skala DU (2008) Kinetics of sunflower oil methanolysis at low temperatures. Bioresour Technol 99(5):1131–1140
8. Gole VL, Gogate PR (2012) A review on intensification of synthesis of biodiesel from sustainable feedstock using sonochemical reactors. Chem Eng Proc 53:1–9
9. Gogate PR, Vinayak SS, Pandit AB (2011) Sonochemical reactors: important design and scale up considerations with a special emphasis on heterogeneous systems. Chem Eng J 166:1066–1082
10. Ghayal D, Pandit AB, Rathod VK (2013) Optimization of biodiesel production in a hydrodynamic cavitation reactor using used frying oil. Ultrason Sonochem 20:322–328
11. Martinez-Guerra E, Gude VG, Mondala A, Holmes W, Hernandez R (2014) Microwave and ultrasound enhanced extractive-transesterification of algal lipids. Appl Energy 129:354–363
12. Farobie O, Sasanami K, Matsumura Y (2015) A novel spiral reactor for biodiesel production in supercritical ethanol. Appl Eng 147:20–29
13. Gude VG, Grant GE (2013) Biodiesel from waste cooking oils via direct sonication. Appl Energy 109:135–144
14. Martinez-Guerra E, Gude VG (2015) Continuous and pulse sonication effects on transesterification of used vegetable oil. Energy Convers Manag 96:268–278
15. Teixeira LSG, Assis JCR, Mendonc DR, Santos ITV, Guimaraes PRB, Pontes LAM (2009) Comparison between conventional and ultrasonic preparation of beef tallow biodiesel. Fuel Process Technol 90:1164–1166
16. Hingu SM, Gogate PR, Rathod VK (2010) Synthesis of biodiesel from waste cooking oil using sonochemical reactors. Ultrason Sonochem 17:827–832
17. Chand P, Chintareddy VR, Verkade JG, Grewell D (2010) Enhancing biodiesel production from soybean oil using ultrasonics. Energy Fuel 24:2010–2015
18. Colucci JA, Borrero EE, Alape F (2005) Biodiesel from an alkaline transesterification reaction of soybean oil using ultrasonic mixing. J Am Oil Chem Soc 82:525–530
19. Ji J, Wang J, Li Y, Yu Y, Xu Z (2006) Preparation of biodiesel with the help of ultrasonic and hydrodynamic cavitation. Ultrasonics 44:411–414
20. Stavarache C, Vinatoru M, Nishimura R, Maeda Y (2005) Fatty acids methyl esters from vegetable oil by means of ultrasonic energy. Ultrason Sonochem 12:367–372
21. Badday AS, Abdullah AZ, Keat-Teong L (2014) Transesterification of crude Jatropha oil by activated carbon-supported heteropolyacid catalyst in an ultrasound-assisted reactor system. Renew Energy 62:10–17
22. Badday AS, Abdullah AZ, Keat-Teong L (2013-0) Ultrasound-assisted transesterification of crude Jatropha oil using alumina-supported heteropolyacid catalyst. Appl Energy 13:380–388
23. Badday A, Abdullah A, Lee K (2013) Ultrasound-assisted transesterification of crude Jatropha oil using cesium doped heteropolyacid catalyst: interactions between process variables. Energy 60:283–291
24. Mason TJ, Cordemans ED (1998) Practical considerations for process optimization. In: Luche JL (ed) Synthetic organic sonochemistry. Plenum, New York
25. Eckart C (1948) Vortices and streams caused by sound waves. Phys Rev 73:68–78
26. Boffito DC, Leveque JM, Pirola C, Bianchi CL, Vibert R, Perrier A, Patience GS (2014) Batch and continuous ultrasonic reactors for the production of methyl esters from vegetable oils. In: Fang Z, Smith RL, Qi X (eds) Production of biofuels and chemicals with ultrasound. Springer, Dordrecht
27. Boffito DC, Mansi S, Leveque JM, Pirola C, Bianchi CL, Patience GS (2013) Ultrafast biodiesel production using ultrasound in batch and continuous reactors. ACS Sustain Chem Eng 2013(1):1432–1439
28. Somnuk K, Smithmaitrie P, Prrateepchaikul G (2013) Two-stage continuous process of methyl ester from high free fatty acid mixed crude palm oil using static mixer coupled with high-intensity of ultrasound. Energy Convers Manag 75:3012–3310

29. Boffito DC, Galli F, Ruiz Martinez P, Pirola C, Bianchi CL, Patience G (2015) Transesterification of triglycerides in a new ultrasonic assisted mixing device. Chem Eng Trans 43:427–432

30. Mason TJ, Lorimer JP (1988) Theory, applications and uses of ultrasound in chemistry. Wiley, New York

31. Mahamuni NN, Adewuyi YG (2009) Optimization of the synthesis of biodiesel via ultrasound-enhanced base-catalyzed transesterification of soybean oil using a multifrequency ultrasonic reactor. Energy Fuels 23:2757–2766

32. Stavarache C, Vinatoru M, Maeda Y et al (2007) Ultrasonically driven continuous process for vegetable oil transesterification. Ultrason Sonochem 14:413–417

33. Manickam S, Arigela VND, Gogate PR (2014) Intensification of synthesis of biodiesel from palm oil using multiple frequency ultrasonic flow cell. Fuel Process Technol 128:288–293

34. Cintas P, Mantegna S, Calcio Gaudino E, Cravotto G (2010) A new pilot flow reactor for high-intensity ultrasound irradiation. Application to the synthesis of biodiesel. Ultrason Sonochem 17:985–989

35. Mikkola JP, Toukoniitty B, Toukonitty E, Aumo J, Salmi T (2005) Utilisation of on-line acoustic irradiation as a means to counter-effect catalyst deactivation in heterogeneous catalysis. Ultrason Sonochem 11:233–239

36. Doktycz SJ, Suslick KS (1990) Interparticle collisions driven by ultrasound. Science 247:1067–1069

37. Kasaai MR (2013) Input power-mechanism relationship for ultrasonic irradiation: food and polymer applications. Nat Sci 15:14–22

38. Martinez-Guerra E, Gude VG (2014) Transesterification of used vegetable oil catalyzed by barium oxide under simultaneous microwave and ultrasound irradiations. Energy Convers Manag 88:633–640

39. Somnuk K, Smithmaitrie P, Prateepchaikul G (2013) Optimization of continuous acid catalyzed esterification for free fatty acids reduction in mixed crude palm oil using static mixer coupled with high-intensity ultrasonic irradiation. Energy Convers Manag 68:193–199

40. Boey P-L, Ganesan S, Maniam GP, Ali DMH (2011) Ultrasound aided in situ transesterification of crude palm oil adsorbed on spent bleaching clay. Energy Convers Manag 52:2081–2084

41. Andrade-Tacca CA, Chang CC, Chen YH, Ji DR, Wang YY, Yen YQ et al (2014) Reduction of FFA in jatropha curcas oil via sequential direct-ultrasonic irradiation and dosage of methanol/sulfuric acid catalyst mixture on esterification process. Energy Convers Manag 88:1078–1085

42. Zheng H, Yin J, Gao Z, Huang H, Ji X, Dou C (2011) Disruption of chlorella vulgaris cells for the release of biodiesel-producing lipids: a comparison of grinding, ultrasonication, bead milling, enzymatic lysis, and microwaves. Appl Biochem Biotechnol 164:1215–1224

43. Araujo GS, Matos LJBL, Fernandes JO, Cartaxo SJM, Gonçalves LRB, Fernandes FAN et al (2013) Extraction of lipids from microalgae by ultrasound application: prospection of the optimal extraction method. Ultrason Sonochem 20:95–98

44. Neto AMP, Sotana de Souza RA, Leon-Nino AD, da Costa JDA, Tiburcio RS, Nunes TA et al (2013) Improvement in microalgae lipid extraction using a sonication-assisted method. Renew Energy 55:525–531

45. Adam F, Abert-Vian M, Peltier G, Chemat F (2012) "Solvent-free" ultrasound-assisted extraction of lipids from fresh microalgae cells: a green, clean and scalable process. Bioresour Technol 114:457–465

46. Wiyarno B, Yunus RM, Mel M (2010) Ultrasound extraction assisted (UEA) of oil from microalgae (Nannochloropsis sp.). Int J Eng Sci 1(3):65–71

47. Ma G, Hu W, Pei H, Jiang L, Song M, Mu R (2015) In situ heterogeneous transesterification of microalgae using combined ultrasound and microwave irradiation. Energy Convers Manag 90:41–46

48. Boffito DC, Pirola C, Bianchi CL (2012) Heterogeneous catalysis for free fatty acids esterification reaction as a first step towards biodiesel production. Chem Today 30:42–47

49. Pirola C, Bianchi CL, Boffito D, Carvoli G, Ragaini V (2010) Vegetable oil deacidification by Amberlyst: study of catalyst lifetime and a suitable reactor configuration. Ind Eng Chem Res 40:4601–4606

50. Guldhe A, Bhaskar S, Ismail R, Bux F (2014) Synthesis of biodiesel from *Scenedesmus* sp. by microwave and ultrasound assisted in situ transesterification using tungstated zirconia as a solid acid catalyst. Chem Eng Res Dis 92(8):1503–1511

51. Jadhav SH, Gogate PR (2014) Ultrasound assisted enzymatic conversion of non edible oil to methyl esters. Ultrason Sonochem 4:1374–1381

52. Boffito DC, Galli F, Pirola C, Bianchi CL, Patience GS (2014) Ultrasonic free fatty acids esterification in tobacco and canola oil. Ultrason Sonochem 21(6):1969–1975

53. Boffito DC, Crocellà V, Neppolian B, Cerrato G, Ashokkumar M, Bianchi C (2013) Ultrasonic enhancement of the acidity, surface area and free fatty acids esterification catalytic activity of sulphated ZrO2-TiO2 systems. J Catal 297:17–26

54. Ramachandran K, Suganya T, Nagendra Gandhi N et al (2013) Recent developments fo biodiesel production by ultrasonic assist transesterification using different heterogeneous catalyst: a review. Renew Sustainable Energy Rev 22:410–418

55. Salamatinia B, Abdullah AZ, Bhatia S (2012) Quality evaluation of biodiesel produced through ultrasound-assisted heterogeneous catalytic system. Fuel Proc Technol 97:1–8

56. Dubey SM, Gole VL, Gogate PR (2015) Cavitation assisted synthesis of fatty acid methyl esters from sustainable feedstock in presence of heterogeneous catalyst using two step process. Ultrason Sonochem 23:165–173

57. Zhang F, Fang Z, Wang YT (2015) Biodiesel production directly from oils with high acid value by magnetic $Na_2SiO_3@Fe_3O_4$/C catalyst and ultrasound. Fuel 150:370–377

58. Shahraki H, Entezari MH, Goharshadi EK (2015) Sono-synthesis of biodiesel from soybean oil by KF/gamma-Al_2O_3 as a nano-solid-base catalyst. Ultrason Sonochem 23:266–274

59. Pukale DD, Maddiheri GL, Gogate PR, Pandit AB, Pratap AP (2015) Ultrasound assisted transesterification of waste cooking oil using heterogeneous solid catalyst. Ultrason Sonochem 22:278–286

60. Hindryawati N, Maniam GP (2015) Novel utilization of waste marine sponge (Demospongiae) as a catalyst in ultrasound-assisted transesterification of waste cooking oil. Ultrason Sonochem 22:454–462

61. Choudhury H, Goswami P, Malani R, Moholkar V (2014) Ultrasonic biodiesel synthesis from crude Jatropha curcas oil with heterogeneous base catalyst: mechanistic insight and statistical optimization. Ultrason Sonochem 21(3):1050–1064

62. Choudhury H, Chakma S, Moholkar V (2014) Mechanistic insight into sonochemical biodiesel synthesis using heterogeneous base catalyst. Ultrason Sonochem 21(1):169–181

63. Verziu M, El Haskouri J, Beltran D, Amoros P, Macovei D, Gheorghe NG, Teodorescu CM, Coman SM, Parvulescu VI (2010) Mesoporous tin-triflate based catalysts for transesterification of sunflower oil. Top Catal 53(11-12):763–772

64. Verziu M, Florea M, Simon S, Simon V, Filip P, Parvulescu V, Hardacre C (2009) Transesterification of vegetable oils on basic large mesoporous alumina supported alkaline fluorides-Evidences of the nature of the active site and catalytic performances. J Catal 263(1):56–66

65. Verziu M, Cojocaru B, Hu J, Richards R, Ciuculescu C, Filip P, Parvulescu V (2008) Sunflower and rapeseed oil transesterification to biodiesel over different nanocrystalline MgO catalysts. Green Chem 10(4):373–381

66. Felizardo P, Neiva Correia MJ, Raposo I, Mendes JF, Berkemeier R, Moura Bordado J (2006) Production of biodiesel from waste frying oils. Waste Manag 26:487–494

67. Andrade Torres E, Cerqueira GS, Ferrer TM, Quintella CM, Raboni M, Torretta V, Urbini G (2013) Recovery of different waste vegetable oils for biodiesel production: a pilot experience in Bahia State, Brazil. Waste Manag 33:2670–2674

68. Encinar JM, Gonzalez JF, Rodrıguez JJ, Tejedor A (2002) Biodiesel fuels from vegetable oils: transesterification of Cynara cardunculus L. Oils with ethanol. Energy Fuels 16:443–450

69. Lee I, Johnson LA, Hammond EG (1995) Use of Branched-chain esters to reduce crystallization temperature of biodiesel. J Am Oil Chem Soc 75(10):1155–1160
70. Joshi RM, Pegg MJ (2007) Flow properties of biodiesel fuel blends at low temperatures. Fuel 86:143–151
71. Likozar B, Levec J (2014) Transesterification of canola, palm, peanut, soybean and sunflower oil with methanol, ethanol, isopropanol, butanol and tert-butanol to biodiesel: modelling of chemical equilibrium, reaction kinetics and mass transfer based on fatty acid composition. Appl Energy 123:108–120
72. Narvaez PC, Sanchez FJ, Godoy-Silva RD (2009) Continuous methanolysis of palm oil using a liquid-liquid film reactor. J Am Oil Chem Soc 86:343–352
73. Kai T, Mataki Y, Nakazato T, Takanashi H (2010) Optimization of reaction conditions of two-step batch operation for biodiesel fuel production using KOH catalyst. J Chem Eng Jpn 43(1):90–94
74. Leung DY, Wu X, Leung MKH (2010) A review on biodiesel production using catalyzed transesterification. Appl Energy 87(4):1083–1095
75. Likozar B, Levec J (2014) Effect of process conditions on equilibrium, reaction kinetics and mass transfer for triglyceride transesterification to biodiesel: experimental and modeling based on fatty acid composition. Fuel Process Technol 122:30–41
76. Issariyakul T, Kulkarni MG, Dalai AK, Bakhshi NN (2007) Production of biodiesel from waste fryer grease using mixed methanol/ethanol system. Fuel Process Technol 88:429–436
77. Kulkarni MG, Dalai AK, Bakhshi NN (2007) Transesterification of canola oil in mixed methanol/ethanol system and use of esters as lubricity additive. Bioresour Technol 98:2027–2033
78. Martinez-Guerra E, Gude VG (2014) Transesterification of waste vegetable oil under pulse sonication using ethanol, methanol and ethanol-methanol mixtures. Waste Manag 34:2611–2620
79. Hanh HD, Dong NT, Okitsu K, Nishimura R, Maeda Y (2009) Biodiesel production through transesterification of triolein with various alcohols in an ultrasonic field. Renew Energy 34(3):766–768
80. Hanh HD, Dong NT, Okitsu K, Nishimura R, Maeda Y (2009) Biodiesel production by esterification of oleic acid with short-chain alcohols under ultrasonic irradiation condition. Renew Energy 34(3):780–783
81. Darnoko D, Cheryan M (2000) Kinetics of palm oil transesterification in a batch reactor. JAOCS 77:1263–1267
82. Kusdiana D, Saka S (2001) Kinetics of transesterification in rapeseed oil to biodiesel fuel as treated in supercritical methanol. Fuel 80:693–698
83. Noureddini H, Zhu D (1997) Kinetics of transesterification of soybean oil. J Am Oil Chem Soc 74:1457–1463
84. Al-Zuhair S (2005) Production of biodiesel by lipase catalyzed transesterification of vegetable oils: a kinetics study. Biotechnol Prog 21:1442–1448
85. He H, Sun S, Wang T, Zhu S (2007) Transesterification kinetics of soybean oil for production of biodiesel in supercritical methanol. J Am Oil Chem Soc 84:399–404
86. Georgogianni KG, Kontominas MG, Pomonis PJ, Avlonitis D, Gergis V (2008) Conventional and in situ transesterification of sunflower seed oil for the production of biodiesel. Fuel Process Technol 89:503–509
87. Jain S, Sharma MP (2010) Kinetics of acid base catalyzed transesterification of Jatropha curcas oil. Bioresour Technol 101:7701–7706
88. Zheng S, Kates M, Dube MA, McLean DD (2006) Acid-catalyzed production of biodiesel from waste frying oil. Biomass Bioenergy 30:267–272
89. Dasari MA, Goff MJ, Suppes GJ (2003) Noncatalytic alcoholysis kinetics of soybean oil. JAOCS 80:189–192
90. Diasakou M, Louloudi A, Papayannakos N (1998) Kinetics of the non-catalytic transesterification of soybean oil. Fuel 77:1297–1302

91. Tesser R, Di Serio M, Guida M, Nastasi M, Santacesaria E (2005) Kinetics of oleic acid esterification with methanol in the presence of triglycerides. Ind Eng Chem Res 44:7978–7982

92. Karmee SK, Mahesh P, Ravi R, Chadha A (2004) Kinetic study of the base-catalyzed transesterification of monoglycerides from pongamia oil. JAOCS 81:425–430

93. Leevijit T, Wisutmethangoon W, Prateepchaikul G, Tongurai C, Allen M (2004) A second order kinetics of palm oil transesterification. The joint international conference on sustainable energy and environment (SEE), Hua Hin 3-025.

94. Aranda DAG, Santos RTP, Tapanes NCO, Ramos ALD, Antunes Octavio AC (2008) Acid-catalyzed homogeneous esterification reaction for biodiesel production from palm fatty acids. Catal Lett 122:20–25

95. Parkar PA, Choudhary HA, Moholkar VS (2012) Mechanistic and kinetic investigations in ultrasound assisted acid catalyzed biodiesel synthesis. Chem Eng J 187:248–260

96. Georgogianni KG, Kontominas MG, Alvonitis D, Gergis V (2006) Transesterification of sunflower seed oil for the production of biodiesel: effect of catalyst concentration and ultrasonication. WSEAS Trans Environ Dev 2(2):136–140

97. Deshmane VG, Gogate PR, Pandit AB (2009) Ultrasound assisted synthesis of isopropyl esters from palm fatty acid distillate. Ultrason Sonochem 16:345–350

98. Avramovic JM, Stamenkovic OS, Todorovic ZB, Lazic ML, Veljkovic VB (2012) Empirical modeling of ultrasound assisted base-catalyzed sunflower oil methanolysis kinetics. Chem Ind Chem Eng Q 18:2115–2127

99. Vyas AP, Verma JL, Subrahmanyam N (2011) Effects of molar ratio, alkali catalyst concentration and temperature on transesterification of jatropha oil with methanol under ultrasonic irradiation. Adv Chem Eng Sci 1:45–50

100. Lee K-W, Yu JX, Mei JH, Yan L, Kim Y-W, Chung K-W (2007) A kinetic study on the transesterification of glycerol monooleate and soybean used frying oil to biodiesel. J Ind Eng Chem 13:799–807

101. Grant GE, Gude VG (2013) Kinetics of ultrasonic transesterification of waste cooking oil. Environ Prog Sustain Energy 33:1051–1058

102. Singh AK, Fernand SD (2007) Reaction kinetics of soybean oil transesterification using heterogeneous metal oxide catalysts. Chem Eng Technol 30:1716–1720

103. Van Mang D, Chen YH, Chang CC, Chang MC, Chang CY (2011) Biodiesel production from Tung oil and blended oil via ultrasonic transesterification process. J Taiwan Inst Chem Eng 42:640–644

104. Helwani Z, Othman MR, Aziz N, Fernando WJN, Kim J (2009) Technologies for production of biodiesel focusing on green catalytic techniques: a review. Fuel Process Technol 90:1502–1514

105. Martinez-Guerra E, Gude VG, Mondala A, Holmes W, Hernandez R (2014) Extractive-transesterification of algal lipids under microwave irradiation with hexane as solvent. Bioresour Technol 156:240–247

106. Martinez-Guerra E, Gude VG (2014) Synergistic effect of simultaneous microwave and ultrasound irradiations on transesterification of waste vegetable oil. Fuel 137:100–108

107. Developments on microwave chemistry. (2005) Intellectual property report. Evaluserve analysis. http://www.rsc.org/images/evaluserve_tcm18-16758.pdf

108. Gude VG, Patil P, Martinez-Guerra E, Deng S, Nirmalakhandan N (2013) Microwave energy potential for biodiesel production. Sustain Chem Process 1(1):1–31

109. Chemat F, Poux M, Di Martino JL, Berlan J (2006) An original microwave-ultrasound combined reactor suitable for organic synthesis: application to pyrolysis and esterification. J Microw Power Electromagn Energy 31:19–22

110. Cravotto G, Boffa L, Mantegna S, Perego P, Avogadro M, Cintas P (2008) Improved extraction of vegetable oils under high-intensity ultrasound and/or microwaves. Ultrason Sonochem 15:898–902

111. Patil PD, Gude VG, Camacho LM, Deng S (2010) Microwave-assisted catalytic transesterification of Camelina sativa oil. Energy Fuels 24:1298–1304

112. Sáez-Bastante J, Pinzi S, Reyero I, Priego-Capote F, Luque de Castro MD, Dorado MP (2014) Biodiesel synthesis from saturated and unsaturated oils assisted by the combination of ultrasound, agitation and heating. Fuel 131:6–16
113. Zhang H, Ding J, Zhao D (2012) Microwave assisted esterification of acidified oil from waste cooking oil by CERP/PES catalytic membrane for biodiesel production. Bioresour Technol 123:72–77
114. Salamatinia B, Mootabadi H, Hashemizadeh I, Abdullah AZ (2013) Intensification of biodiesel production from vegetable oils using ultrasonic-assisted process: optimization and kinetic. Chem Eng Process 73:135–143
115. Ragaini V, Pirola C, Borrelli S, Ferrari C, Longo I (2012) Simultaneous ultrasound and microwave new reactor: detailed description and energetic considerations. Ultrason Sonochem 19(4):82–86
116. Suslick KS, Doktycz SJ (1990) The effects of ultrasound on solids. In: Mason TJ (ed) Advances in sonochemistry. JAI Press, New York

Part IV

Biomaterials

Ultrasonic Coating of Textiles by Antibacterial and Antibiofilm Nanoparticles

Ilana Perelshtein, Nina Perkas, and Aharon Gedanken

Contents

Abstract

In this chapter we review the antimicrobial functionalization of textile with nanoscale metal oxides. In view of the growing demands for the high-quality textile, much research has focused on the antimicrobial finishing of the fabrics

I. Perelshtein (✉) • N. Perkas
Department of Chemistry and Kanbar Laboratory for Nanomaterials, Bar-Ilan University Center for Advanced Materials and Nanotechnology, Ramat-Gan, Israel
e-mail: Ilana.Perelshtein@biu.ac.il; Nina.Perkas@biu.ac.il

A. Gedanken
Department of Chemistry and Kanbar Laboratory for Nanomaterials, Bar-Ilan University Center for Advanced Materials and Nanotechnology, Ramat-Gan, Israel

Department of Materials Science and Engineering, National Cheng Kung University, Tainan, Taiwan
e-mail: gedanken@mail.biu.ac.il; Aharon.Gedanken@biu.ac.il

967

protecting customers from pathogenic or odor-generating microorganisms. The metal nano-oxides have a large surface area and can be finely spread on the fabrics. This fact makes them a good alternative to the triclosan, quaternary ammonium salts, and other synthetic organic compounds that now dominate the antimicrobial market. The first section of the review scopes new publications on nano-oxides as antimicrobial agents in the textile finishing. The second section of the chapter explains the mechanism of the ultrasound-assisted deposition of nanoparticles on textile. The coating can be performed by an in situ process where the nanoparticles are formed and immediately thrown to the surface of the fabrics. This approach was used for ZnO, CuO, and Zn-CuO nanoparticles. In addition, the sonochemical process can be used as a "throwing stone" technique, namely, previously commercially synthesized nanoparticles will be placed in the sonication bath and sonicated in the presence of the fabric. The last achievements in the antimicrobial finishing of textile with metal nano-oxides by sonochemical method are provided in the third section. One of the proofs that the sonochemical method is one of the best coating methods is that the sonochemically coated fabrics were washed 65 cycles in hospital washing machines (75 or 92 °C) and have shown excellent antibacterial properties at the end of the process.

Introduction

With increasing population, the bacterial infection problems increased dramatically worldwide and affected the markets for the antimicrobial products [1]. Clothing and textile materials are good media for growth of microorganisms such as bacteria and fungi. Antimicrobial finishing of textiles protects users from pathogenic or odor-generating microorganisms, which can cause medical and hygienic problems, and protects textiles from undesirable aesthetic changes or damage caused by rotting, which can result in reduced functionality. As a consequence of their importance, the number of different antimicrobial agents suitable for textile application increased dramatically in the market [2].

The achievements in the field of antibacterial textiles in the previous decade were briefly described in a review of Gao and Cranston [3]. According to this data, metal and metal salts are one of the major classes of antibacterial and antifungal agents. Other organic compounds such as quaternary ammonium compounds, triclosan, chitosan, chlorine-containing N-halamine compounds, etc. are also widely used. The textile industry providing the antimicrobial finishing should consider not only the antimicrobial efficiencies of the agents that are important but the environmental, health, and safety aspects of their use [2]. Taking these worries into account, much research was focused on the synthesis of novel low toxic and effective antimicrobial agents.

In recent years, nanotechnology became one of the most important and exciting forefront fields in physics, chemistry, engineering, and biology. It showed great promise for providing in the near future many breakthroughs that will change the direction of technological advances in wide range of applications. One of the progressive applications of nanotechnology is the production of the antimicrobial textiles based on metals and metal oxides in their nanoscale [4–6].

The methods reported for stabilizing inorganic nanostructured materials on textile surfaces are based on multistep preparation processes that are time consuming for upscale consideration [4, 7–9]. Sometimes the binding molecules are toxic, for example, isocyanate groups, epoxides, acrylic acid esters, fluoropolymers, etc., and have to be applied to the textiles for the adherence of the nanoparticles [10–12]. Therefore, search for a new effective and environmentally friendly method for the antimicrobial finishing of the fabric is of high importance. This paper will scan the results in the field of antimicrobial functionalization of textile with nano-scale metal oxides for the last few years.

The current chapter is focused on the progress in the sonochemical coating of different kinds of textiles, such as cotton, wool, nylon, polyester, etc. with antimicrobial inorganic nano-oxides ZnO, CuO, and MgO and with a novel Zn-CuO. It is worth mentioning that ZnO, CuO, and MgO are recognized by the FDA as nontoxic for the human body.

In a previous review by our group, we described the development of the sonochemical technique for doping/deposition of nanoscale metal and metal oxides on ceramic and polymer substrates [13] and explained the unique properties that make ultrasound radiation an excellent technique for the adherence of nanoparticles to a large variety of substrates. Herein the advantages of sonochemistry as a one-step, environmentally friendly method for antimicrobial finishing of textile will be demonstrated.

Antimicrobial Functionalization of Textile with Nano-metaloxides

ZnO is one of the multifunctional inorganic nanoparticles exhibiting excellent electrical, optical, chemical, and antibacterial properties [14–17]. The advantage of using this inorganic oxide as an antimicrobial agent is that it is biocompatible and contains mineral elements essential to humans [18, 19]. Therefore, the application of ZnO nanoparticles to textile materials was the object of several studies aimed for producing antibacterial textiles.

Nanostructured inorganic oxides can be incorporated into textile by sol-gel technique, magnetron sputter coating, plasma sputtering, layer-by-layer coating, and other methods. One of the widely used techniques for coating textile substrates is the combination of the sol-gel synthetic procedure with the "pad-dry-cure" method. The synthesis process usually involves two main steps: synthesis of nanoparticles and their deposition on the fabric. For instance, for the incorporation of the ZnO nanorods on the cotton, the growing seeds were formed by coating ZnO nanosol using dip-coating, dip pad-curing, or spraying methods, and then the

hexagonally ordered ZnO nanorod arrays might be grown on fiber substrates [20]. In order to stabilize the precursor solution, triethylamine, with the same molar ratio as zinc acetate, was added to form a transparent homogeneous solution. The deposition of nano-ZnO onto cotton fabric was also performed by padding the textiles in the colloid formulation of the zinc oxide-soluble starch nanocomposite to impart the material with the antibacterial and UV-protection functions [21]. The conventional pad-dry-cure method was applied for grafting of reactive preformed polymers (PFP) along with ZnO nanoparticles to the cotton fabrics. PFP refers to monochlorotriazine β-cyclodextrin grafted with butyl acrylate [22].

A superhydrophobic ZnO nanorod array film on a cotton substrate was fabricated via a wet chemical route of subsequent modification with a layer of *n*-dodecyltriethoxysilane [23]. ZnO particles were prepared by the wet chemical method using zinc nitrate and sodium hydroxide as precursors and solubilized starch as a stabilizing agent. These NPs were impregnated onto cotton fabrics by the "pad-dry-cure" method using an acrylic binder.

Recently, some new publications reported on the modified wet chemical route antimicrobial functionalization of the textiles. The hydrolysis of zinc nitrate with ammonium chloride and urea at elevated temperature in presence of fabric was applied for finishing of cotton textile with ZnO nanostructures providing antimicrobial activity and ultraviolet (UV) protection [24]. To increase the stability of ZnO-coated textiles to the leaching, the polymer binding was applied. Thus, the bamboo pulp was impregnated with colloidal solution of ZnO nanoparticles with multi-amide polymer to provide the fabric with antibacterial and UV protective properties [25]. The effects of pretreatment with some polymeric binders to enhance chelation of nano-ZnO to viscose fabric for imparting antibacterial activity against *E. coli* and *Staphylococcus aureus* were reported in [26]. The authors claimed that the preliminary treatment of the textile or ZnO nanoparticles with polymer binders prolongs the superior reduction in the bacterial growth even after 20–40 washing cycle.

Copper is one of the relatively small numbers of metallic elements that is essential to human health. This element, along with amino and fatty acids and vitamins, is required for normal metabolic processes [27]. After the works of Gabbay et al. [28, 29], who prepared the cotton and polyester fibers with antifungal and antimicrobial properties by impregnation of CuO powder into polymer fibers during the masterbatch stage, some new publications appeared on the direct deposition of CuO nanoparticles on textile by wet chemical method.

Using copper sulfate and sodium hydroxide as precursors and soluble starch as stabilizing agent, the nano-copper oxide was microencapsulated by an ionic gelation and applied to plain weave cotton fabric by exhaustion as the first step and in the second step by the pad-dry-cure method [30]. High-purity and crystalline CuO nanoparticles were synthesized in situ by a direct precipitation method with particle size in the range 40–60 nm and were successfully applied onto cotton to obtain antimicrobial activity. The durability of the antimicrobial activity was increased up to 15 washings with the help of 1 % acrylic binder [31].

The antibacterial fixing of MgO nanoparticles is less studied compared to ZnO and CuO, because of high solubility of magnesium oxide in aqueous solution. Very

recently, the electrospinning method was applied for incorporation of MgO into Nylon 6, and the antibacterial activity of the obtained composite against *S. aureus* and *E. coli* was demonstrated [32]. The authors of [33] coated MgO nanoparticles on the cotton fabric using the silica nanosol as a binder. In other work, for the antibacterial and antifungal finishing of cellulose fabric with MgO nano-oxide, first the grafting of poly-N-vinyl-2-pyrrolidone polymer was cross-linked with cotton fabric using citric acid as cross-linker by pad-dry-cure method, and then MgO nanoparticles were deposited using starch as a stabilizing agent [34].

It can be resumed that most of the methods for finishing of textile with nano-oxide materials are based on a multistage procedure, including the preliminary synthesis of nanoparticles following the application of some templating agents for anchoring antibacterial nano-oxides to the substrates. This approach is rather complicated and can result in the release of some toxic compounds into the waste. The sonochemical method enables avoiding the use of the toxic binders and makes the coating procedure shorter, effective, and environmentally friendly.

Sonochemistry as a Perspective Method for Producing Antibacterial Fabrics

Sonochemistry is the scientific field that studies the chemical reactions that occur under ultrasound irradiation. In liquids, the sound waves generate bubbles that grow in size until they become unstable. Ultrasonic waves with the frequency range of 20 kHz to 1 MHz are responsible for the process of acoustic cavitation, i.e., the formation, growth, and explosive collapse of the bubbles. There are a number of theories that explain how 20 kHz ultrasonic radiation can break chemical bonds [35, 36]. One of the theories that explain why, upon the collapse of a bubble, chemical bonds are broken is the hot spot mechanism [37]. This theory claims that very high temperatures (5,000–25,000 K) are obtained upon the collapse of the bubble. Since this collapse occurs in less than a nanosecond, very high cooling rates in excess of 10^{11} K/s are obtained. These extreme conditions developed when the bubbles' collapse cause the chemical reactions to occur. The high cooling rate prevents the crystallization of the products. This is the reason why amorphous nanoparticles are formed when volatile precursors are used and the gas phase reaction is predominant.

However, from this explanation the reason for the formation of nanostructured material is not clear. Our explanation for the creation of nanoproducts is that the fast kinetics does not permit the growth of the nuclei, and in each collapsing bubble, a few nucleation centers are formed whose growth is limited by the explosive collapse. The dynamics of cavity growth and collapse during sonication is strictly dependent on the local environment. Cavity collapse in a homogeneous liquid is very different from cavitation near a liquid-solid interface. Suslick and Price [38] demonstrated that microjets and shock waves produced by acoustic cavitation are able to drive metal particles together at sufficiently high velocities to induce melting upon collision. This approach was developed further in our experiments on the deposition of NPs on different types of solid substrates [13]. Typically, the solid substrate was

introduced into the sonication cell containing the precursor solution, leading to the fabrication of nanoparticles under ultrasonic waves. The ultrasonic irradiation passes through the sonication slurry under an inert or oxidizing atmosphere for a specific period of time. This synthetic route is a single-step effective procedure. The microjets formed after the collapse of the bubble throw the just-formed NPs at the surface of the substrate at such a high speed that they strongly adhere to the surface, either via physical or chemical interactions, depending on the nature of the substrate, i.e., ceramic, polymer, or textile. The excellent adherence of the nanoparticles to the substrate is reflected, for example, in the lack of leaching of the nanoparticles from the substrate surfaces after many washing cycles. If, instead of forming the NPs sonochemically, we purchase them and use ultrasonic radiation just for "throwing stones" at a solid surface, a good adherence is still obtained, but the amount of the deposited material found on the surface is smaller by a factor of 3–4.

Our group developed ultrasound-assisted antimicrobial finishing of various kinds of textile with Ag nanoparticles [39], ZnO [40], CuO [41], and TiO$_2$ [42] nano-oxides by one-step "in situ" process and deposition of MgO nano-oxides by the "throwing stones" method [43]. The excellent antimicrobial properties of the coated fabrics as well as strong adherence of the nanoparticles to the textile substrates were demonstrated [44]. Recently, we developed a new method for formation and deposition of extremely effective antimicrobial Zn-CuO nanocomposite [45]. The following part of the current review will describe the details of the production of antibacterial textile by sonochemical method and our new achievements in this field.

It should be mentioned that the same sonochemical route was later used by other authors for antibacterial finishing of cotton with ZnO [46] and CuO nanoparticles [47].

Deposition of Metal Oxide Nanoparticles on Textiles by Ultrasound Irradiation

Synthesis and Deposition of ZnO

The antimicrobial activity of ZnO depends on the particle size: decreasing the particle size leads to an increase in the antimicrobial activity [48]. We have developed a simple new method for the preparation of cotton bandages with antimicrobial properties by immobilizing ZnO NPs on the fabric's surface via ultrasound irradiation [40]. The coating reaction was carried out with a high intensity ultrasonic horn (Ti horn, 20 kHz, 750 W at 70 % efficiency) under a flow of Ar. The sonication flask was placed in a cooling bath maintained at a constant temperature of 30 °C during the reaction. Our studies indicated that the yield of the product and the particle size are strongly dependent on the rate of particle collision and on the concentration of the reagents during sonochemical synthesis. Due to this, the experimental parameters such as time and concentration of the precursor were selected as important factors for the optimization of the sonochemical coating reaction. The aim of this work was to obtain a homogeneous coating of small ZnO NPs on the fabrics with a narrow size

distribution and to reach a minimal effective ZnO concentration that will still demonstrate antimicrobial activity. This process involves the in situ generation of ZnO under ultrasound irradiation and its deposition on fabrics in a one-step reaction. The sonication was performed in a water-ethanol solution in the presence of a cotton bandage. Zinc acetate was used as a precursor, and the pH was adjusted to 8–9 with the addition of $NH_3{\cdot}H_2O$.

Previous studies indicated that the product yield and particle size are strongly dependent on the rate of interparticle collision and on the concentration of the reagents during the sonochemical synthesis [49]. For this reason, experimental parameters such as time and concentration of the precursor were selected as important factors for the optimization of the sonochemical reaction. The XRD demonstrated that the ZnO NPs on the coated bandage are crystalline and the diffraction patterns matched the hexagonal phase of the wurtzite ZnO structure. No peak characteristics of any impurities were detected. The particle size estimated by the Debye-Scherrer equation is 30 nm. The morphology of the coated bandage before and after the deposition of ZnO NPs studied by HR-SEM is presented in Fig. 1. Figure 1a demonstrates the smooth texture of the pristine cotton bandage. After sonication, the bandage fibers were homogeneously coated with NPs (Fig. 1b). The inset image in Fig. 1b was taken at a higher magnification in order to obtain the particles' size distribution. The distribution of the particles is quite narrow, and primary particles are in a very low nanometric range (about 30 nm) that matches well with the XRD results. The selected-area HR-SEM image studied with the elemental dot-mapping technique is shown in Fig. 1c. The distribution of zinc and oxygen in the mapped area is presented in parts d and e of Fig. 1, respectively. These images verify a homogeneous coating of the fibers with ZnO NPs.

We considered the coating mechanism as follows: it involves the in situ generation of ZnO NPs and their subsequent deposition on fabrics in a one-step reaction via ultrasound irradiation. Zinc oxide is formed during the irradiation according to the following reactions:

$$Zn^{2+}{}_{[aq]} + 4NH_3{\cdot}H_2O_{[aq]} \rightarrow \left[Zn[NH_3]_4\right]^{2+}{}_{[aq]} + 4H_2O \qquad (1)$$

$$\left[Zn[NH_3]_4\right]^{2+}{}_{[aq]} + 2OH^-{}_{[aq]} + 3H_2O \rightarrow ZnO_{[s]} + 4NH_3{\cdot}H_2O_{[aq]} \qquad (2)$$
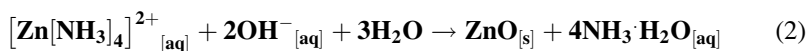
Ammonia works as the catalyst of the hydrolysis process, and the formation of zinc oxide takes place through the ammonium complex $[Zn[NH_3]_4]^{2+}$. The ZnO NPs produced by this reaction are thrown at the surface of the bandages by the sonochemical microjets resulting from the collapse of the sonochemical bubble.

As already mentioned above, the sonochemical irradiation of a liquid causes two primary effects, namely, cavitation (bubble formation, growth, and collapse) and heating. When the microscopic cavitation bubbles collapse near the surface of the solid substrate, they generate powerful shock waves and microjets that cause the effective stirring/mixing of the adjusted liquid layer. The after effects of the cavitation are several hundred times greater in heterogeneous systems than in
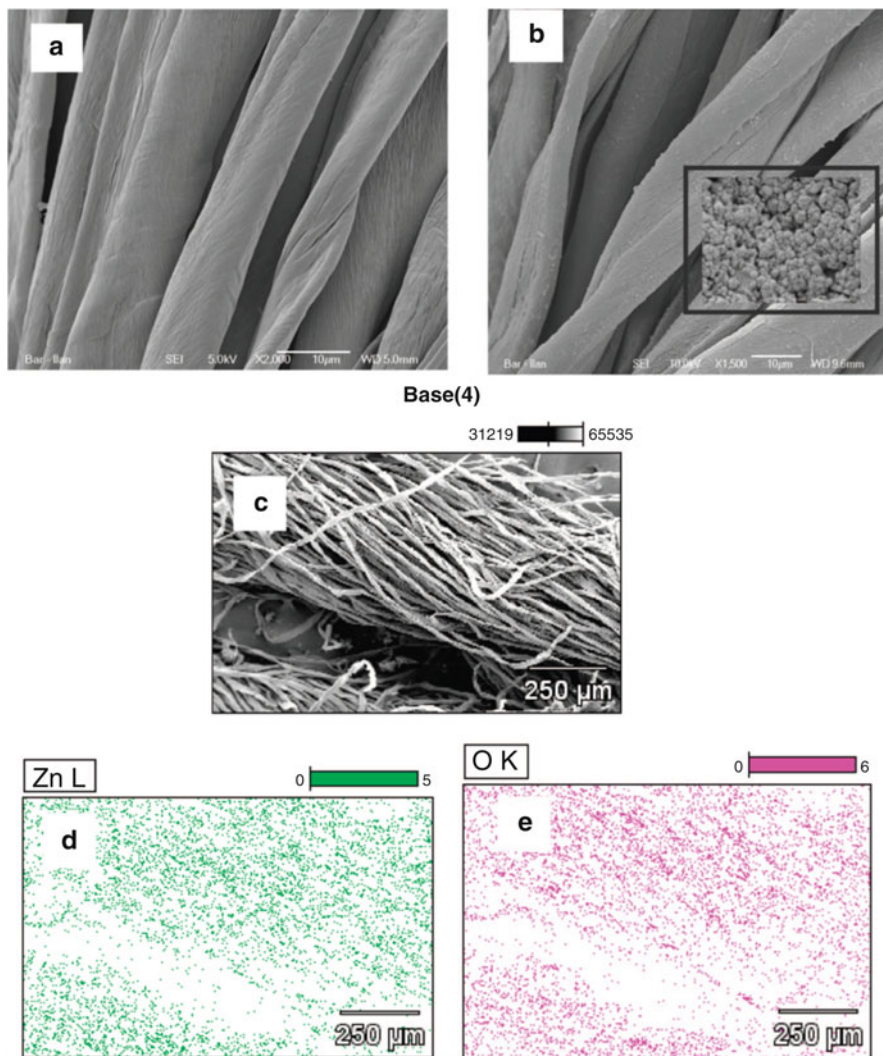
Fig. 1 HR-SEM images of (**a**) pristine bandages (magnification ×2K), (**b**) bandage coated with ZnO NPs (magnification ×1,500; the *inset* shows a magnified image (×50K) of the ZnO NPs on the fabric), (**c**) selected image for X-ray dot mapping, (**d**) X-ray dot mapping for zinc, (**e**) X-ray dot mapping for oxygen

homogeneous systems [35]. In our case, the ultrasonic waves promote the fast migration of the newly formed zinc oxide nanoparticles to the fabric's surface. This fact might cause a local melting of the fibers at the contact sites, which may be the reason why the particles strongly adhere to the fabric.

Here, the question rises as to whether sonication doesn't damage the fabric's substrate. Thus, the tensile mechanical properties of a cotton-impregnated fabric
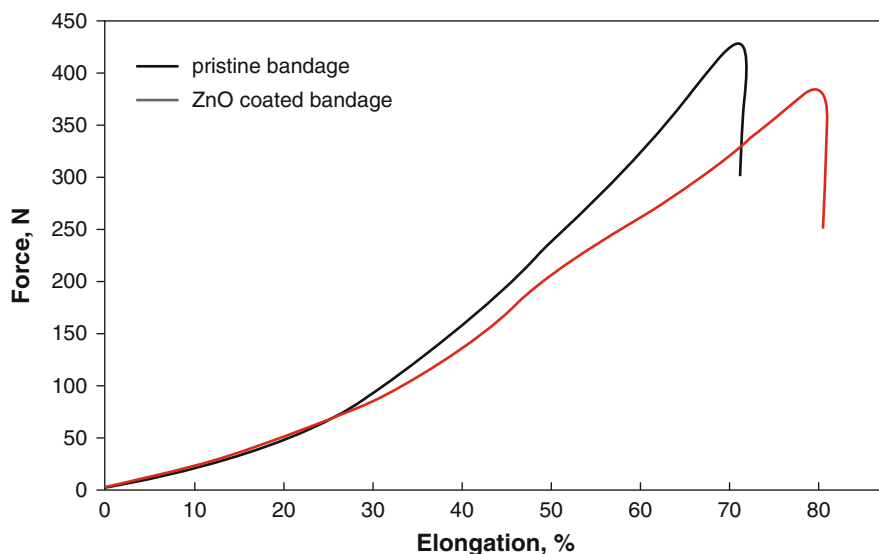
Fig. 2 Mechanical properties of the cotton bandage before and after the deposition

were studied on a universal testing machine, Zwick 1445. A fourfold fabric sample with a gauge length of 60 mm and a width of 40 mm was placed in special grips. The tensile force for the zinc oxide-coated sample was observed to be ~11 % less than that of the pristine bandage (Fig. 2). The observed changes in the mechanical behavior of the yarn are in a range that is acceptable for standard cotton fabrics. According to this result, we conclude that the sonochemical treatment of the bandage doesn't cause any significant change in the structure of the yarn.

One of the factors influencing the commercial exploitation of the antimicrobial bandages is the release of NPs into the surrounding environment. In light of a recent paper [50] where it has been found that silver NPs of 10–500 nm in diameter leach from sock fabric, we attempted to find the leached ZnO NPs in the washing solution. In the control experiments, we treated the coated bandages with an aqueous solution of 0.9 wt.% NaCl overnight at 37 °C. The leaching experiment indicated that only 16 % of the deposited zinc was removed under these conditions in an ionic form that is dictated by the low K_{sp} of zinc oxide in water. The dynamic light scattering (DLS) and TEM studies didn't reveal the presence of any nanoparticles in the washing solution. This indicates that the sonochemically deposited ZnO nanoparticles are strongly anchored to the textile substrate.

The excellent studies by Sawai and coworkers [51, 52] clearly showed that ROS concentrations increased with the ZnO content of slurries. Following the same paradigm, Applerot et al. [53] in an innovative study using electron spin resonance (ESR) coupled with the spin trapping probe technique monitored ROS, namely, hydroxyl radicals, and production in water suspensions of ZnO NPs. Their findings showed that hydroxyl radicals were present in water suspensions of ZnO and their amount was closely related to the size of the ZnO particles, with smaller sizes having
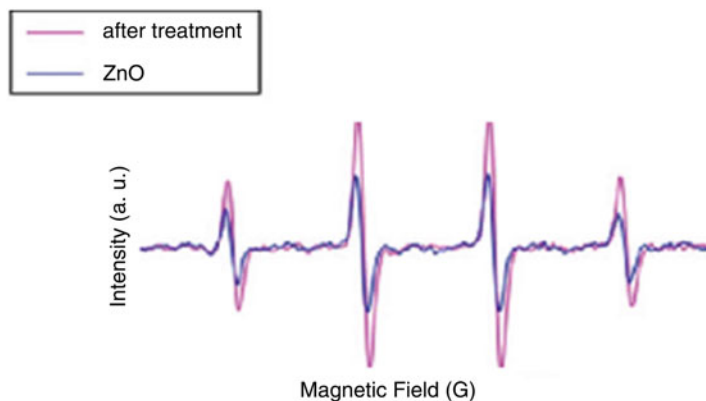
Fig. 3 ESR spectra demonstrating changes in hydroxyl radical concentrations upon antibacterial treatment of *E. coli* with a water suspension of ZnO

greater amounts of •OH on the basis of equivalent ZnO mass content. These results were correlated with the increase in the antibacterial effect of the small NPs. Thus, the small size and large specific surface area endow them with high chemical reactivity and intrinsic toxicity. Interestingly, combining Gram-negative bacterium *E. coli* and ZnO NP suspensions immediately enhanced the generation of •OH for up to an average of 142 % (Fig. 3). It appears that sublethal amounts of ROS may induce excessive intracellular oxidative stress, probably by disturbing the balance between oxidant and antioxidant processes.

We determined the antibacterial activity of the sonochemically coated cotton fabrics with 0.75 wt.% ZnO using the Gram-negative bacterium *E. coli* and the Gram-positive bacterium *S. aureus*. As shown in Table 1, treatment for 1 h with the coated cotton leads to the complete inhibition of *E. coli* growth. Regarding *S. aureus*, a 100 % reduction in viability was reached after 3 h, while after 1 h of treatment, a reduction of 60 % could be seen.

Zinc is an essential micronutrient for prokaryotic organisms. However, at super physiological levels, zinc inhibits the growth of many bacteria [54]. According to a leaching experiment with 0.9 wt.% NaCl, the concentration of Zn^{2+} in solution corresponds to 36.7 μM [40]. Compared to the minimum inhibitory concentration reported in the literature of 4–8 mM [55], the amount of zinc released from fabrics in our work is lower at least by a factor of 2. Therefore, we assume that the Zn ions have a minor influence on antibacterial activity. The major components responsible for the bactericidal effect are the ZnO nanoparticles. Although ZnO nanoparticles were not found in the solution, they can generate some species of oxyradicals [56]. In light of these results, the difference in the antibacterial action of ZnO-coated bandages on two strains of bacteria can be explained by the difference in their sensitivity toward oxyradicals. In this respect, it has been found recently that *S. aureus* contains a large amount of carotenoid pigment, which promotes a higher resistance to oxidative stress [57].

Table 1 Antibacterial activity test of ZnO-coated cotton[a]

Sample	Duration of treatment					
	1 h			2 h		
	CFU (ml^{-1})	N/N$_0$	Viability reduction (%)	CFU (ml^{-1})	N/N$_0$	Viability reduction (%)
E. coli						
Pristine fabric	$1.02 \cdot 10^{-7}$	0.98	0.98	$1.34 \cdot 10^{-7}$	1.28	−28.23
No fabric	$1.17 \cdot 10^{-7}$	1.14	−28.57	$1.23 \cdot 10^{-7}$	1.35	−35.16
0.75 wt.% ZnO on fabric	$1.71 \cdot 10^{-7}$	$1.58 \cdot 10^{-3}$	99.84	0	$0.9 \cdot 10^{-8}$	100
S. aureus	1 h			3 h		
Pristine fabric	$0.7 \cdot 10^{-7}$	0.71	20.46	$0.99 \cdot 10^{-7}$	1.125	−12.5
No fabric	$0.98 \cdot 10^{-7}$	1.10	−10.11	$0.67 \cdot 10^{-7}$	0.75	24.72
0.75 wt.% ZnO on fabric	$3.9 \cdot 10^{-6}$	0.34	66.4	$7.6 \cdot 10^{-3}$	$6.55 \cdot 10^{-4}$	99.93

[a]The viable bacteria were monitored by counting the number of colony-forming units [CFU]; N/N$_0$: survival fraction

Synthesis and Deposition of CuO

We extended the sonochemical approach for the deposition of CuO NPs on the textile fabrics, and, as in the case with ZnO NPs, the formation of copper oxide takes place through the ammonium complex. Copper ions react with a solution of ammonia to form a deep blue solution containing $[Cu[NH_3]_4]^{+2}$ complex ions [41]. This complex is hydrolyzed and crystalline CuO NPs are obtained. The CuO NPs produced by these reactions are thrown at the surface of the fabric by the above-described mechanism of the sonochemical microjets and are deposited on the surface of the substrate.

The morphology of the fiber surface before and after the deposition of copper oxide was studied by XRD and HR-SEM methods. The XRD revealed the monoclinic structure of CuO nanocrystals. The difference between pristine and coated cotton fabric is clearly demonstrated in Fig. 4. The inset image in Fig. 4b at higher magnification shows that the primary particles are in a very low nanometric range (~10–20 nm).

While Cu^{+2} is considered an environmentally safe ion, a much more important and serious issue is the leaching of CuO nanoparticles. DLS and TEM studies of the washing solution after treatment of the CuO-coated fabrics in 0.9 wt.% NaCl didn't reveal the presence of any nanoparticles. This means that the sonochemically deposited CuO nanoparticles are strongly anchored to the textile substrate, probably due to a local melting of the fibers at the contact sites. Similar results were obtained for the coating of various types of textiles, such as nylon, polyester, and composite types of textiles with ZnO and CuO NPs.

We tested the antimicrobial activity of the cotton bandages coated with CuO via ultrasonic irradiation against *E. coli* and *S. aureus*. Detailed investigations showed that after 1 h, the growth of both the strains was completely inhibited. One of the factors influencing the antibacterial activity of the developed coating is the release of the active phase into the surrounding medium, namely, copper ions and/or copper oxide nanoparticles. The examination of the leaching of the copper ions indicated that only a very low amount (~1.3 %) of the deposited copper was removed by washing with a 0.9 wt.% NaCl solution that corresponds to a concentration of Cu^{2+} 0.15 ppm. The slight solubility of copper oxide can be explained by the very low K_{sp} of CuO that dictates the very low concentration of Cu^{+2} in the solution. In order to examine the influence of copper ions on the antibacterial effect, a control antibacterial test was performed using a supernatant with the same concentration of Cu^{2+} instead of the coated cotton. After incubation for 24 h at 37 °C, no reduction in *E. coli* after 2 h was observed (Fig. 5).

This result indicates that the Cu^{2+} ions have no influence on the antibacterial activity. Thus, the antibacterial effect can be attributed to the copper oxide nanoparticles. It should be emphasized that no leaching of CuO nanoparticles to the environment was detected in these experiments. Although CuO nanoparticles were not found in the solution, they can generate some active species that are responsible for damaging the bacterial cells. These active species were detected in ESR studies conducted with and without the bacteria present in the ESR tube.
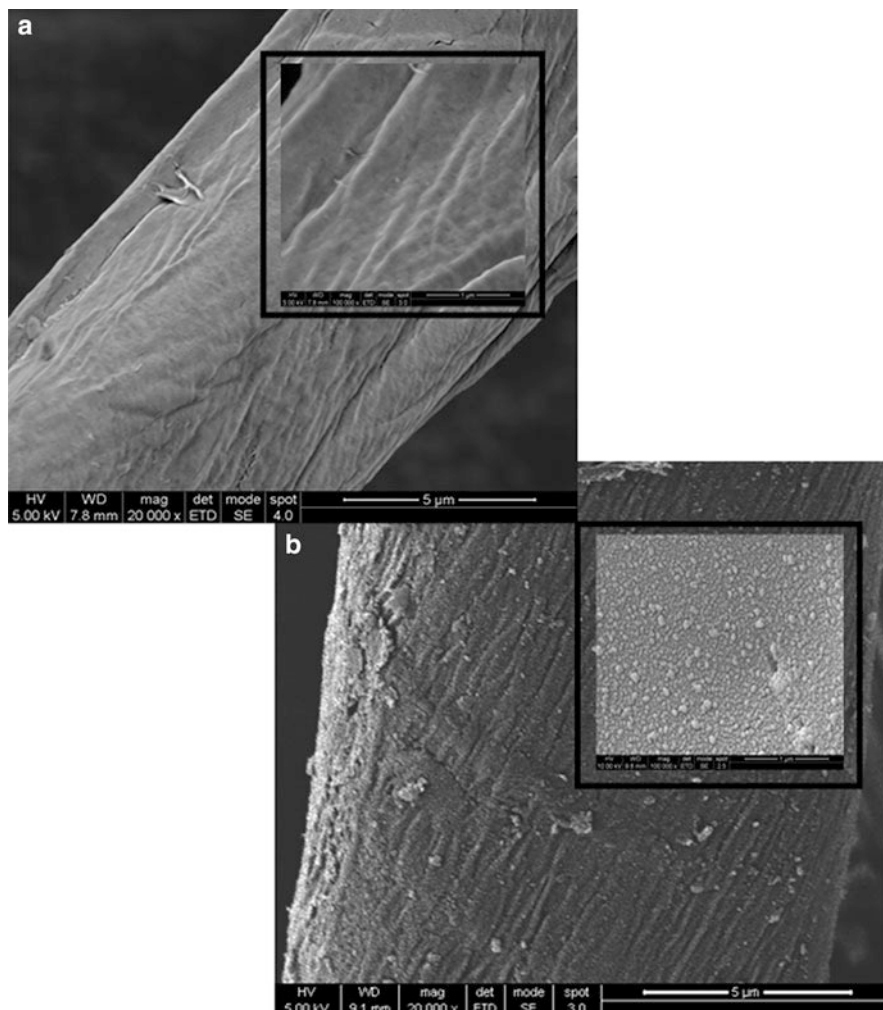
Fig. 4 HR-SEM images of cotton fibers: (**a**) pristine cotton; (**b**) cotton coated with CuO NPs (magnification ×20,000, *inset* images – magnification ×100,000)

Deposition of MgO

MgO is well known to have a strong antibacterial activity [58, 59]. Different methods have been reported on the synthesis of magnesium oxide NPs, such as the controlled speed of formation following the heating procedure [58], microwave-assisted synthesis [60], the formation of MgO from aqueous droplets in a flame spray pyrolysis reactor [61], sonochemically enhanced hydrolysis followed by supercritical drying [62], etc. However, there is no reported literature related to the deposition of magnesium oxide on textiles.
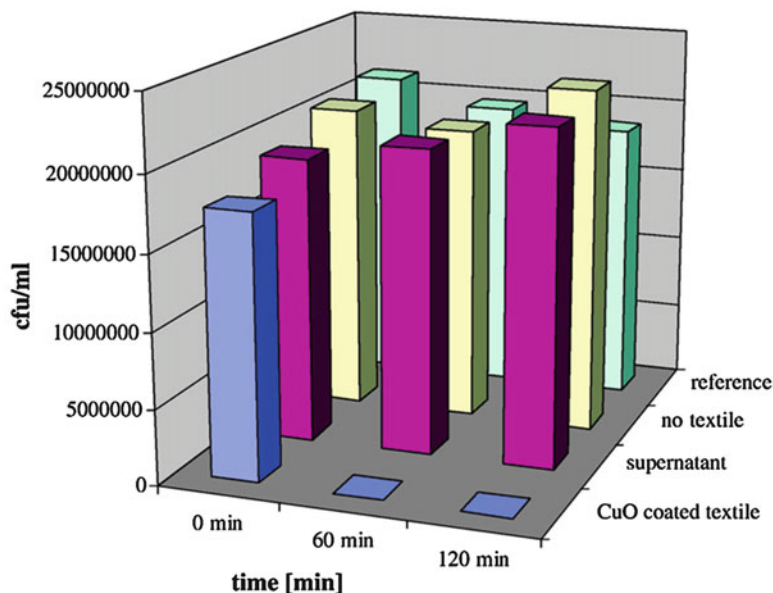
Fig. 5 Antibacterial test of CuO-coated cotton against *E. coli*

We have developed a method for depositing MgO nanoparticles on fabrics by ultrasound irradiation. In this case, ultrasound is used just for "throwing stones" at the fabric [43]. Namely, we took commercial MgO nanopowder (Aldrich, <25 nm) and sonicated it in the presence of a cotton fabric. The microjets formed after the collapse of the bubble throw the nanoparticles at high speed at the cotton yarn. This process is different from the deposition of ZnO and CuO where the nanoparticles were in situ generated and deposited on fabrics in a one-step reaction. The anchored amount for the commercial NPs was found to be smaller by a factor of 2–3 as compared to the one-stage deposition due to the fact that not all of particles are pushed by the microjets to the fabric surface. Nevertheless, using ultrasound as a "throwing stones" technique is an efficient process especially for nanoparticles that cannot be synthesized sonochemically.

The morphology of the fiber surface after the deposition of magnesium oxide nanoparticles studied by HR-SEM is presented in Fig. 6. Fibers after sonication are homogeneously coated with nanoparticles. The particle size was in the low nanometric range (~10–15 nm), and no aggregation was observed.

The antibacterial activity of cotton fabrics coated with 0.8 % of MgO was determined using the Gram-positive bacterium *Staphylococcus aureus* and the Gram-negative bacterium *Escherichia coli*. Treatment for 1 h with the MgO-coated cotton leads to a complete growth inhibition of *E. coli*. Regarding *S. aureus*, a 100 % reduction in viability was reached after 3 h, while after 1 h of treatment a reduction of 90 % could be seen.
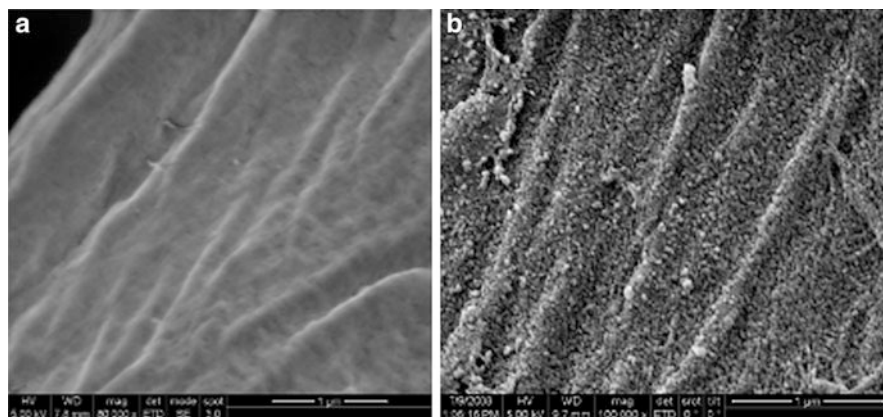
Fig. 6 SEM images of (**a**) pristine cotton bandage; (**b**) MgO-coated bandage

Sonochemical Synthesis of a Novel Zn-Doped CuO Nanocomposite: An Inhibitor of MDR Bacteria

Zinc oxide is known for its significant bacterial growth inhibition on a broad spectrum of bacteria, initiated by the formation of reactive oxygen species (ROS) produced in water [53, 63]. Very recently, it has been found that doping ZnO with Mg or Sb leads to a slight increase in the antibacterial activity of nanosized zinc oxide.

However, the effect of doping on the antibacterial activity of copper nano-oxide has not yet been reported. Prabhakaran et al. has reported on the synthesis of a Zn-doped CuO composite and characterized it only by chemo-physical properties such as its crystalline structure and magnetization as a function of temperature. During interaction with water, metal oxides produce reactive oxygen species (ROS) that are known to kill bacteria. The creation of ROS by metal oxides depends on the presence of defect sites in the structure of the metal oxide nanoparticles. The doped metal oxides are characterized by increased structural defects [64] that can make them rather effective antibacterial agents due to higher ROS production.

In the current part, the sonochemical synthesis and the antibacterial properties of zinc-doped copper oxide (Zn-CuO) were examined in powder or by deposition of the nanoparticles (NPs) on a cotton substrate [45]. This doped compound was also sonochemically deposited on teeth implant and had shown excellent antibiofilm properties against *Streptococcus mutans* bacteria [65].

In order to obtain the most active antimicrobial composite, various reaction conditions were tested. Mainly, the molar ratio between the reagents copper and zinc acetates was varied between 1:3, 1:2, 1:1, 2:1, and 3:1, respectively. Our results revealed that the highest antibacterial activity was obtained at a 3:1 M ratio (Cu:Zn), and this combination was further characterized.

The structure of the deposited material was studied by XRD, and the patterns are presented in Fig. 7. For comparison, the XRD patterns of sonochemically
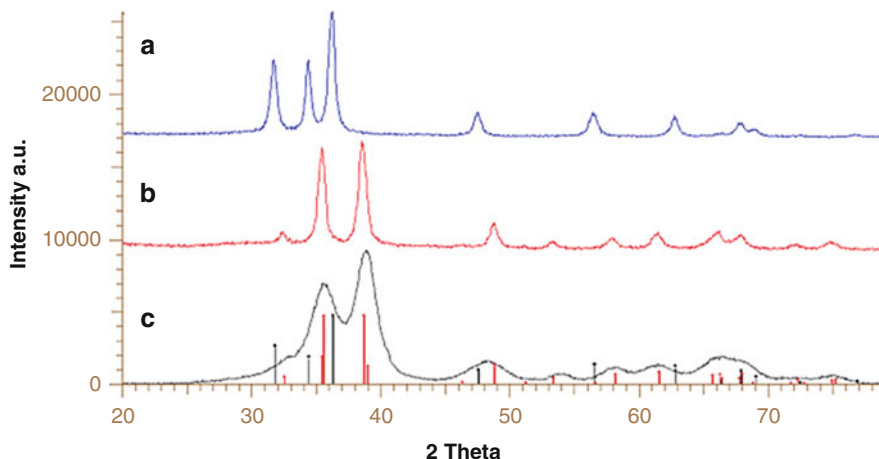
Fig. 7 XRD diffraction patterns of *a* ZnO, *b* CuO, and *c* Zn-CuO

synthesized ZnO and CuO are also presented (Fig. 7a, b). The peaks at 2θ angles = 32.8, 35.621, 38.851, 48.246, 58.077, 66.506, 67.850, 75.104 are assigned to the (111), (−111), (202), (204), (120), (313), (221), (315) reflection lines of the ZnO hexagonal wurtzite structure (PDF file 89-7102). The peaks at 2θ = 32.47, 35.49, 38.68, 48.65, 58.25, and 61.45 are assigned to the (110), (−111), (111), (−202), (202), and (−113) reflection lines of monoclinic CuO, respectively (PDF file 80-1916). Figure 7c presents the powder XRD of the material collected after the sonochemical reaction of a mixed solution of copper acetate and zinc acetate in a molar ratio of 3:1. All the peaks in the XRD spectra are assigned to monoclinic CuO. No peaks related to ZnO or any impurities were observed. It is apparent that the peaks of CuO were slightly shifted and broadened. The cell parameters of the CuO lattice were changed from $a = 4.6890$, $b = 3.4200$, and $c = 5.1300$ for CuO to $a = 4.6829$, $b = 3.4201$, and $c = 5.1429$ for the synthesized material. Calculations of the cell parameters were performed by the Rietveld method. The observed differences in the CuO lattice parameters can be explained as a result of the changes in the atomic composition of the lattice. One of the possible explanations for this phenomenon is that during the sonochemical reaction, the Zn^{+2} ions are doped in the unit cell of the monoclinic CuO lattice replacing the Cu^{+2} ions. This leads to formation of doped particles, marked as Zn-CuO. The doped structure is the preferred arrangement upon forming a mixture of separate phases of CuO and ZnO. The width of the diffraction patterns of Zn-CuO increased as compared to those of ZnO or CuO, indicating the formation of smaller particle grains, as well as due to defects and dislocations.

According to the XRD results, the crystalline phase of ZnO is not found in the product when a solution ratio of 3:1 between Cu and Zn was applied. Taking into account that the kinetics of $[Cu(NH_3)_4]^{2+}$ complex formation is faster as compared to the rate of formation of the $[Zn(NH_3)_4]^{2+}$ complex, we hypothesize that the CuO
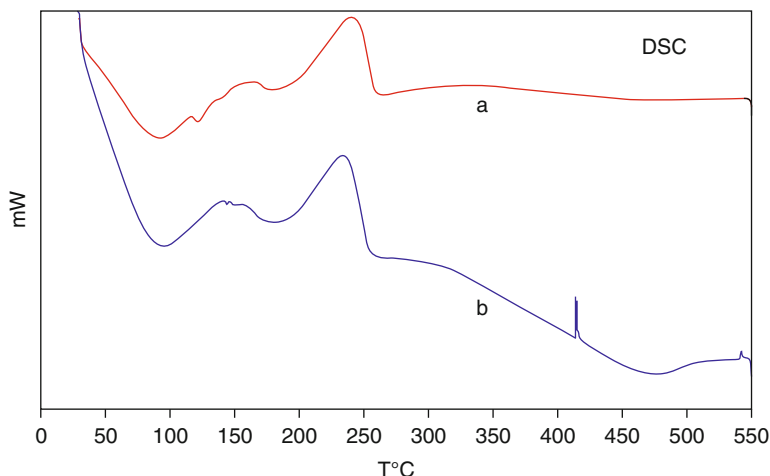
Fig. 8 DSC curves of the Zn-CuO composite: *a* under nitrogen; *b* under air

particles are formed initially and the zinc ions are later incorporated into the just-formed crystalline lattice of CuO. In support of this, we observed that when the ratio between Cu and Zn was varied as 1:1, 2:1, and 4:1, 2 separate phases of the CuO and the ZnO were revealed by XRD. Higher than 12 % Zn ions cannot be accommodated in the CuO unit cell. For lower concentrations of Zn^{+2}ions, similar XRD results are obtained, namely, ZnO diffraction peaks are not observed.

The Zn-doped CuO was characterized by the DSC method. DSC analysis, under both inert and oxidizing conditions, demonstrated one endothermic peak at 100 °C assigned to water evaporation and two exothermic peaks, a broad peak in the temperature range of 130–165 °C and a strong sharper exothermic peak at 240 °C (Fig. 8). The only difference between the two curves is the sharp exothermic peak appearing at 420 °C under air. The exothermic peaks at 130–165 °C and 240 °C are irreversible and don't appear in a second heating cycle. The two exothermic peaks can be attributed to the reordering of the crystals and the rearrangements of the vacancies formed due to the doping of Zn into the CuO crystal. Another possibility is that in addition to crystalline Zn-doped CuO, an amorphous product is also obtained. One of the DSC peaks most probably the 240 °C represents the crystallization of this product. Amorphicity by its nature means a less organized and more perturbed solid, adding to the formation of ROS. The appearance of the irreversible, very sharp peak at 420 °C under air can be explained by the filling of the defects in the crystal lattice by oxygen.

In order to emphasize that the defect sites in the nanoparticle crystal lattice are responsible for the formation of ROS, ESR measurements were performed on samples heated at various temperatures in air or nitrogen. It was revealed that after heating the NPs in air to 300 °C, no reduction in the ROS intensity was observed (Fig. 9b) within the experimental error (±10 %). However, increasing the temperature up to 550 °C under nitrogen led to a complete washout of the ESR spectrum
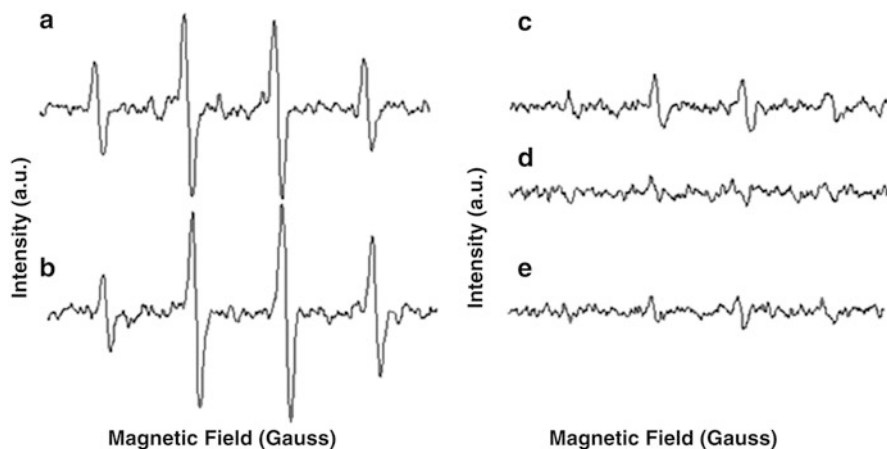
Fig. 9 ESR of (**a**) Zn-CuO (**b**) Zn-CuO after 300 °C under air (**c**) Zn-CuO after 550 °C under air (**d**) Zn-CuO after 550 °C under N2 (**e**) DMPO control

(compared to DMPO control – Fig. 9e) or the complete elimination of the ROS formation (Fig. 9d). Antimicrobial activity was not observed for the heated nanoparticles. The reason for this phenomenon can be attributed to the reorganization of the crystal lattice and the loss of the defects that are responsible for ROS formation. When the sample was heated to 550 °C under air, the subsequent reduction in the peak intensity was seen (Fig. 9c), unlike the heating under nitrogen, ROS still exist. It shows that the oxygen vacancies are only a minor factor in ROS formation, and the major factors are defects and dislocations in the crystal. From the results discussed above, it is clearly seen that the disappearance of the defects in the crystal by heating caused a reduction in ROS production, proving that the defects in the crystal are responsible for their formation. It is also clear that when compared to CuO, the crystal is more disturbed as a result of the presence of Zn. The importance of the unique activity of the $Cu_{0.88}Zn_{0.12}O$ is due to replacement of 12 % of the Cu atoms in the unit cell by Zn ions. The crystal cannot accommodate a higher number of zinc ions, which results in a lower number of ROS.

The antibacterial properties of the Zn-doped CuO were tested against *E. coli and S. aureus*. For both bacteria, after only 10 min of treatment with Zn-CuO, an inhibition of 6.1 and 5.37 orders of magnitude is observed for *S. aureus* and *E. coli*, respectively (Fig. 10). Pure CuO or ZnO nanoparticles induce much lower inhibition; one- and two-log reduction was observed on *S. aureus* for ZnO and CuO, respectively, and almost no effect was seen in *E. coli*. The viable bacteria were monitored by counting the number of colony-forming units (CFU). The results presented are an average of at least three independent experiments. As a control, an untreated (not coated) bandage was used.

These promising results led us to examine the antimicrobial activity of Zn-doped CuO nanoparticles against multidrug-resistant (MDR) bacteria. A methicillin-resistant *S. aureus* (MRSA) and a MDR *E. coli* were chosen for this characterization.
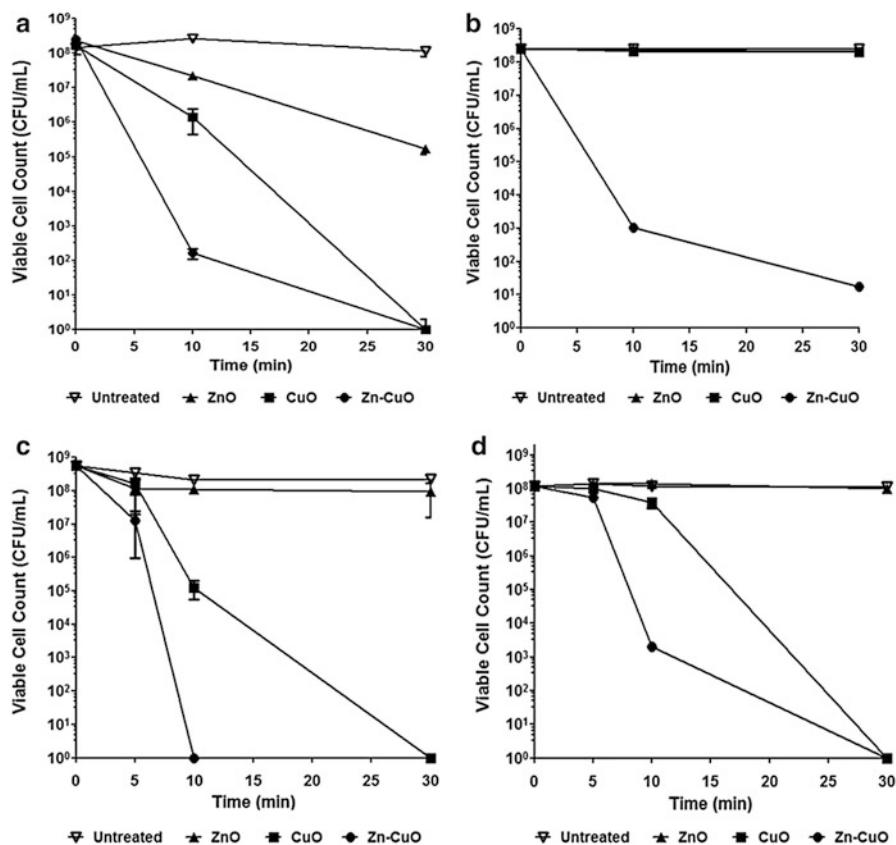
Fig. 10 Antimicrobial activity of Zn-CuO against bacteria. The antimicrobial activity of nanoparticle-coated fabrics was tested against sensitive (**a**) *S. aureus* and (**b**) *E. coli* and resistant (**c**) *MRSA* and (**d**) MDR *E. coli*

These bacteria are highly resistant to many of the commercially available antibiotics and thus are extremely hard to eradicate. The results presented in Fig. 10 clearly show that the Zn-doped CuO composite is more active than the CuO and ZnO treatments. For MRSA, complete killing was already evident in the Zn-doped CuO composites after ten minutes (the CuO only showed three-log killing, while the ZnO showed only one log reduction in bacteria CFUs during this time). For MDR *E. coli* complete killing was achieved after 30 min by both Zn-doped CuO and CuO; however, after 10 min the Zn-CuO already reduced the CFU by five logs, while CuO hardly affected cell viability. Taken together these results show superior activity for the Zn-doped CuO nanoparticles against multidrug-resistant bacteria.

To summarize, Zn-CuO NPs are capable of producing a larger amount of ROS as compared to the pure CuO or ZnO NPs. Using the DMSO scavenging, we suggest that OH radicals ($\geq$40 % of total ROS) are formed in Zn-CuO NPs. In pure CuO, the amount of OH• is lower than 15 %, while ZnO produces only OH radicals and no

superoxide anions. OH radicals, in addition to the singlet oxygen, may be formed through the interaction of Zn^{+2} and O^{-2} in the Zn-CuO unit cell. The results point out to the higher antimicrobial activity of the doped materials, as compared to ZnO and CuO nanoparticles. The higher activity is due to the higher total ROS production and subsequently higher OH radical, superoxide anions, and singlet oxygen formation by Zn-CuO NPs.

The Sonochemical Coating of Cotton Withstands 65 Washing Cycles at Hospital Washing Standards and Retains Its Antibacterial Properties: Upscaling of the Sonochemical Coating Process

Hospital-acquired nosocomial infections are a major health, and consequently financial issue, in the world healthcare system. The problem of bacterial infections in general, and in hospitals in particular, has led to extensive scientific and industrial efforts to fabricate antibacterial textiles. A sonochemical coating machine was developed and built and its ability to coat antibacterial nanoparticles (NPs) onto 40–50 m length of materials on a roll to roll basis at a speed of 22 cm/min [66]. Cotton coated sonochemically with copper oxide nanoparticles (CuO NPs) was found to maintain its antibacterial properties even after 65 cycles of washings [44] according to hospital protocols of hygienic washing (75 °C). This demonstrates the good quality and high stability of this sonochemically produced NP coating on textiles. Durable antibacterial textiles such as these may be suitable for widespread use in future hospital environments where hygiene control is of paramount importance.

Strips of cotton (10 m long and 10 cm wide) were coated with CuO NPs using a roll to roll feed with a machine that has been described elsewhere [66]. In Fig. 11, the photo image of the pilot installation during the coating of the cotton by CuO is presented. The front panel was open to show the change in the color of the fabric after coating with CuO nanoparticles. In the inset, one can observe that with the deposition of CuO nanoparticles, the color of the textiles was changed from white to brown. The configuration of the sonochemical coating machine allows coating of both sides of substrate.

The coated cotton fabric was sent to a commercial company which carried out the washings according to standard hospital practices at 75 °C using an ECOS detergent (Free & Clear Liquid Laundry Detergent/Earth Friendly Products, USA). For textile washing, the European standard EN ISO 6330 "Textiles – Domestic washing and drying procedure for textile testing" was applied.

The initial amount of CuO on fabrics was measured by ICP and was found to be ~0.7 % (wt%). In Fig. 12, the amount of CuO retained on the washed fabric as a function of the number of washing cycles as determined by ICP is presented. The error of the ICP method is around 8 %. A main decrease in the amount of coating occurs after 15 cycles of washing. Additional cycles don't affect significantly on the amount of the well-deposited coating. Although the amount of CuO after 65 cycles was reduced by half, we have already demonstrated in our previous study that this is
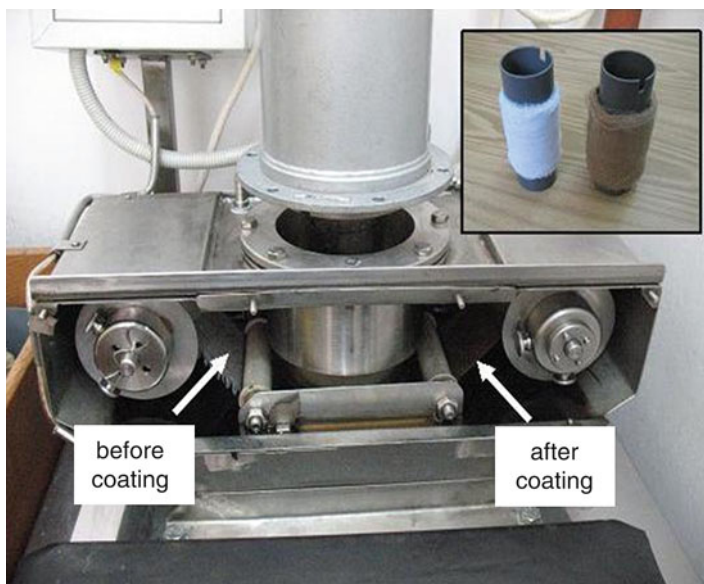
Fig. 11 Photo image of the pilot installation. In the *inset* of the figure, the CuO-coated and uncoated spools are shown
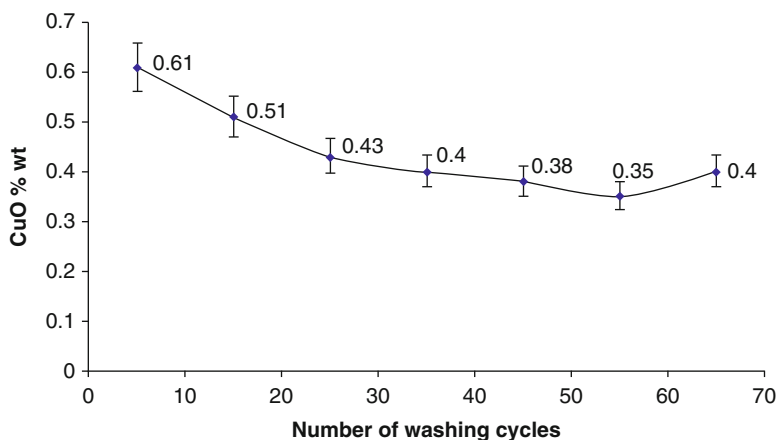

Fig. 12 Effect of number of washing cycles on the CuO content on the fabrics

not due to the leaching of nanoparticles. According to our explanation, the reduction in the amount of CuO on the fabric is due to the dissolution of Cu^{+2} ions in the washing solution. The slight solubility of CuO can be explained by the very low Ksp of CuO ($\sim 10^{-21}$ at room temperature) that dictates a very low concentration of Cu^{+2} in the solution. The washing in industrial washing machines is carried out at a high temperature (75 $°$C) that has led to an increase in the solubility of the copper.
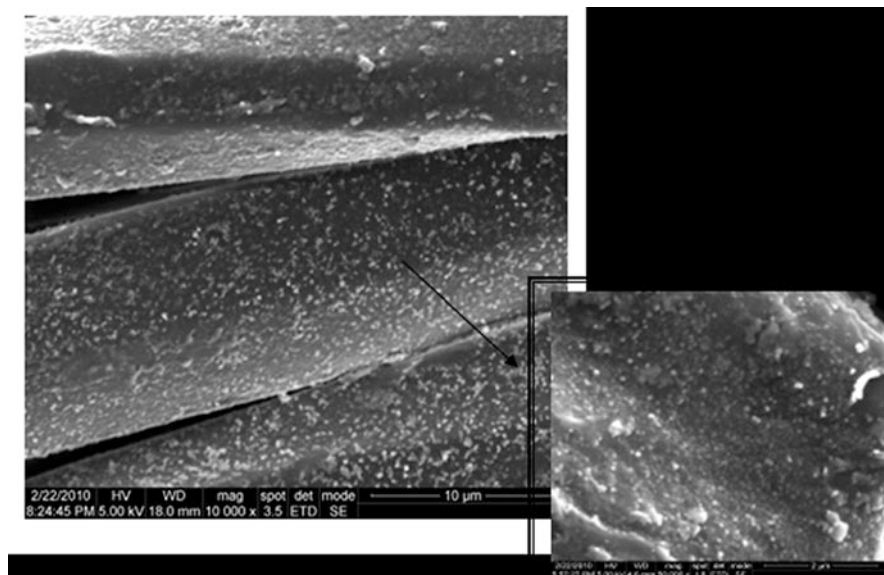
Fig. 13 SEM of CuO-coated cotton following 65 wash cycles. The *inset* image was taken in a higher magnification (MAGX50K)

To substantiate the ICP measurements and demonstrate that the CuO NPs are retained on the cotton fabric after washing, SEM measurements were carried out. The SEM images of cotton after 65 cycles illustrated in Fig. 13 indicate that the fibers are coated with NPs. The inset in Fig. 13 shows the coated fabric under higher magnification. A homogeneous monodispersed coating is observed with particles ranging in size from 20 to 50 nm. The particle size of the CuO NPs after the deposition was observed to be 60–80 nm; a few larger aggregates were also observed. It appears that the washing cycles and consequent dissolution of Cu have led to the reduction of the particle size and the elimination of aggregates. We have already shown that the particle size has a major effect on the antibacterial properties, and smaller NPs kill the bacteria more efficiently. It is therefore not surprising that the results obtained after washing were as good despite the loss of copper as measured by ICP.

One of the most efficient techniques available for the coating substrates in terms of stability is sonochemistry. This is due to the chemistry associated with acoustic cavitation collapse near to surfaces. This generates powerful shock waves and microjets that cause effective stirring and mixing of the liquid layer next to the surface. In our case, the ultrasonic waves promote the fast migration of the newly formed metal oxide nanoparticles to the fabric surface. The coating is not based on the creation of chemical bonds between the surface and the metal oxides but rather due to the physical impregnation of the NPs. This physical phenomenon is a result of the conditions developed by ultrasound irradiation.
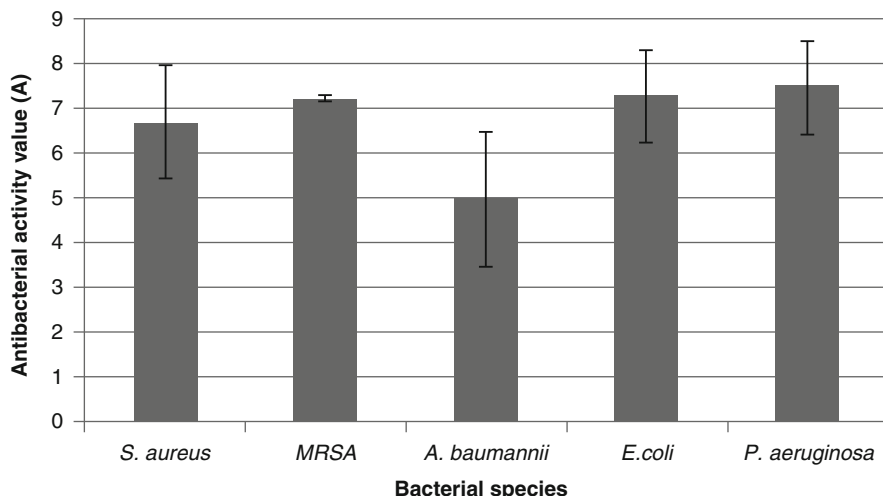
Fig. 14 Antibacterial activity values of CuO-coated fabrics against bacterial species commonly associated with hospital-acquired infections. The *error bars* show standard deviation, $n = 3$
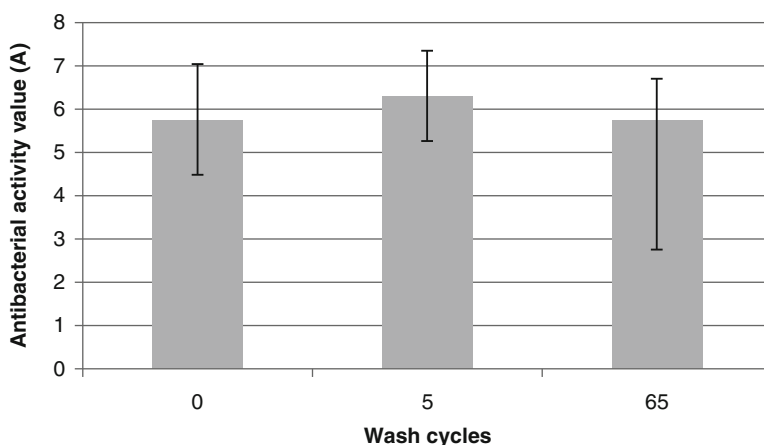
Fig. 15 Antibacterial activity values of washed CuO-coated fabrics against *Staphylococcus aureus* (ATCC 6538). Testing was carried out according to the absorption method from BS EN ISO 20743:2007. The *error bars* show standard deviation, $n = 3$

In Fig. 14, the antibacterial activity of the CuO-coated cotton against five different bacterial species is shown. An excellent level of antibacterial activity was observed against each of the test bacterial species. In each case, a greater than five-log reduction in bacterial numbers on CuO-coated cotton compared to plain cotton control samples was observed.
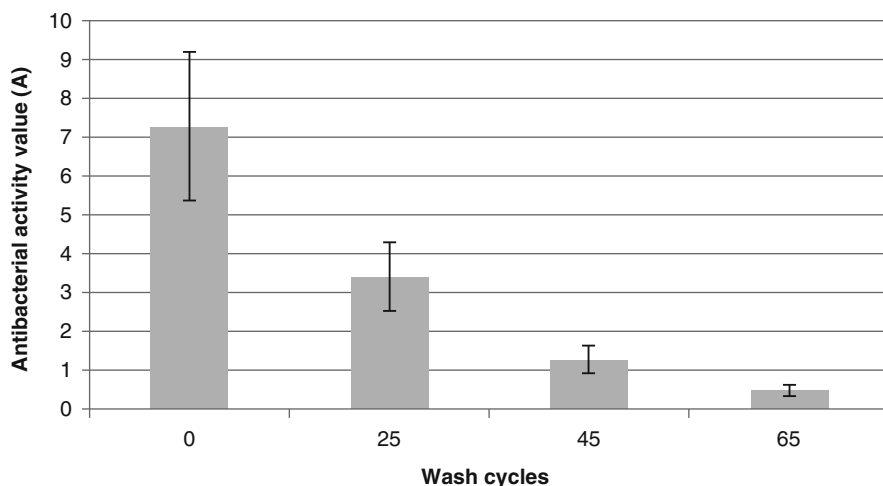
Fig. 16 Antibacterial activity values of washed CuO-coated fabrics against *Escherichia coli* (ATCC 8739). The *error bars* show percentage error, $n = 3$

The antibacterial efficacy levels of the CuO-coated cotton against *Staphylococcus aureus* following 0, 5, and 65 washing cycles are shown in Fig. 15. The levels of activity observed were very high in all cases with a greater than four-log reduction in bacterial numbers on CuO-coated cotton compared to uncoated plain cotton. Although there was some decrease in antibacterial activity after 65 wash cycles, the level was still well above the minimum acceptable antibacterial activity level of 2.

The antibacterial activity levels of the fabrics against the Gram-negative bacterium *Escherichia coli*, as indicated in Fig. 16, were not as good as against *Staphylococcus aureus* (which is a Gram-positive bacterium). The antibacterial activity decreased after each set of 20 wash cycles by nearly 60 %. After 25 washes, the fabrics had a good level of antibacterial activity, but this decreased to a poor value (0.5) after 65 wash cycles.

The two species of bacteria differ in that *E. coli* has a second outer lipid membrane. Once the antibacterial activity of the fabrics has been reduced by washing, this extra barrier layer may be enough to protect *E. coli* from the membrane damaging effects of the nanoparticles [28]. The amount of coating after 25 and 65 cycles is found to be almost the same and sufficient for the inhibition of *S. aureus* after 65 washing cycles, but not of *E. coli*. The explanation for the reduced killing of *E. coli*, despite the presence of the same amount of NPs on the fabric, might be because the production of ROS species after repeating washings is decreased and not enough ROS are formed for the inhibition of bacterium having two lipid membrane structure.

The results presented here show that by application of a sonochemical coating technology, it is possible to produce antibacterial fabrics that are durable enough to withstand 65 wash cycles under hospital washing conditions. The NPs are effectively embedded in the fabric and are resistant to removal by the washing cycles. The only loss appears to be due to the dissolution of Cu^{+2} ions which is very small even at 75 °C.

Conclusion

Nanoparticles with intrinsic antibacterial properties (ZnO, CuO Zn-CuO, and MgO) can be synthesized and uniformly deposited onto the surface of different kinds of textiles by the sonochemical method. The coating was performed by a simple, efficient, one-step procedure using environmentally friendly reagents. The physical and chemical analyses demonstrated that nanocrystals are finely dispersed onto the fabric surfaces without any significant damage of the structure of yarns. The mechanism of nanoparticle formation and adhesion to the textile was discussed. It is based on the local melting of the substrate due to the high speed at which the nanoparticles are thrown at the solid surface by sonochemical microjets causing local melting of the surface due to the high temperature. The performance of fabrics coated with low content of active nanomaterial (<1 wt.%) as an antibacterial agent was investigated, and their excellent bactericidal effect was demonstrated. The strong adhesion of metal nano-oxides to the substrate was demonstrated in terms of absence of leaching of the NP into the washing solution after 65 washing cycles. The washed coated textiles show high antibacterial activity.

References

1. (2012) The market for antimicrobial additives/biocides in plastics and textiles worldwide 2011–2025: development, strategies, markets, companies, trends, nanotechnology. http://www.hkc22.com/antimicrobials.html
2. Simoncic B, Tomsic T (2010) Text Res J 80:1721
3. Gao Y, Cranston R (2008) Text Res J 78:60
4. Moritz M, Geszke-Moritz M (2013) Chem Eng J 228:596
5. Hebeish A, Abdel-Mohdy FA, Fouda MMG, Elsaid Z, Essam, S, Tammam GH, Drees EA (2011) Carbohydr Polym 86 (4):1684
6. Zille A, Almeida L, Amorim T, Carneiro N, Esteves MF, Silva CJ, Souto AP (2014) Mater Res Express 1:032003
7. Wong YWH, Yuen CWM, Leung MYS, Ku SKA, Lam HLI (2006) AUTEX Res J 6:1
8. Dastjerdi R, Montazera M, Shahsavan S (2009) Colloids Surf A Physicochem Eng Asp 345:202
9. Rajendran R, Balakumar C, Ahammed HAM, Jayakumar S, Vaideki K, Rajesh EM (2010) Int J Eng Sci Technol 2:202
10. Kathirvelu S, D'Souza L, Dhurai B (2009) Mater Sci 15:75
11. Schäfer K (2009) Nanotechnology in textile finishing. www.exzellenz.nrw.de/highlights
12. Kim SS, Park JE, Lee J (2011) J Appl Polym Sci 119:2261
13. Gedanken A (2007) Ultrason Sonochem 14:418
14. Zhang Q, Dandeneau CS, Zhou X, Cao G (2009) Adv Mater 21:4087
15. Du X, Mei Z, Liu Z, Guo Y, Zhang T, Hou Y, Zhang Z, Xue Q, Kuznetsov AY (2009) Adv Mater 21:4625
16. Liu Y, He L, Mustapha A, Li H, Hu ZQ, Lin M (2009) J Appl Microbiol 107:1193
17. Jones N, Ray B, Ranjit KT, Manna AC (2008) FEMS Microbiol Lett 279:71
18. Li Z, Yang R, Yu M, Bai F, Li C, Wang ZL (2008) Phys Chem C 112:20114
19. Sousa CJA, Pereira MC, Almeida RJ, Loyol AM, Silva ACA, Dantas NO (2014) Int Endod J 47:416
20. Wang R, Xin JH, Tao XM, Daoud WA (2004) Chem Phys Lett 398:250

21. Vigneshwaran N, Kumar S, Kathe AA, Varadarajan PV, Prasad V (2006) Nanotechnology 17:5087
22. El Shafei A, Shaarawy S, Hebeish A (2010) Carbohydr Polym 79:852
23. Sivakumar PM, Balaji S, Prabhawathi V, Neelakandan R, Manoharan PT, Doble M (2010) Carbohydr Polym 79:717
24. Shateri-Khalilabad M, Yazdanshenas ME (2013) Text Res J 83:993
25. Zhang G, Liu Y, Morikawa H, Chen Y (2013) Cellulose 20:1877
26. Salama M, El-Sayed AA (2014) World App Sci J 32:392
27. Toxicological profile of copper (2004) U.S. Department of Health and Human Services, Public Health Service Agency for Toxic Substances and Disease Registry. Textiles 35:323–335
28. Borkow G, Gabbay J (2005) Curr Med Chem 12:2163
29. Gabbay J, Borkow G, Mishal J, Magen E, Zatcoff R, Shemer-Avni Y (2006) J Ind Text 35:323
30. Anita S, Ramachandran T, Rajendran R, Koushik CV, Mahalakshmi M (2011) Text Res J 81:1081
31. Gupta NK, Khurana NS, Adivarekar RV (2013) Int J Eng Res Technol 2:2278
32. Dhineshbabu NR, Karunakaran G, Suriyaprabha R, Manivasakan P, Rajendran V (2014) Nano-Micro Lett 6:46
33. Rajendran V, Dhineshbabu NR, Kanna RR, Kaler KVIS (2014) Ind Eng Chem Res 53:19512
34. Ramanujam K, Sundrarajan M (2004) World J Pharm Pharm Sci 3:1989
35. Suslick KS (1989) Sci Am 260:80
36. Mason TJ (1990) Sonochemistry. Royal Soc. Chem. Press, London
37. Suslick KS, Hammerton DA, Cline RE (1986) J Am Chem Soc 108:5641
38. Suslick KS, Price GJ (1999) J Annu Rev Mater 29:295
39. Perelshtein I, Applerot G, Perkas N, Guibert G, Mikhailov S, Gedanken A (2008) Nanotechnology. art. 19(24):245705
40. Perelshtein I, Applerot G, Perkas N, Wehrschetz-Sigl E, Hasmann A, Guebitz GM, Gedanken A (2009) ACS Appl Mater Interfaces 1:361
41. Perelshtein I, Applerot G, Perkas N, Wehrschuetz-Sigl E, Hasmann A, Guebitz G, Gedanken A (2009) Surf Coat Technol 204:54
42. Perelshtein I, Applerot G, Perkas N, Grinblat J, Gedanken A (2012) Chem Eur J 18:4575
43. Perelshtein I, Applerot G, Perkas N, Grinblat J, Hulla E, Wehrschuetz-Sigl E, Hasmann A, Guebitz G, Gedanken A (2010) ACS Appl Mater Interfaces 2:1999
44. Perelshtein I, Ruderman Y, Perkas N, Beddow J, Singh G, Vinatoru M, Joyce E, Mason TJ, Blanes M, Mollá K, Gedanken A (2013) Cellulose 20(3):1215
45. Malka E, Perelshtein I, Lipovsky A, Shalom Y, Naparstek L, Perkas N, Patick T, Lubart R, Nitzan Y, Banin E, Gedanken A (2013) Small 9:4069
46. Shahidi S, Zarei L, Elahi SM (2014) Fiber Polym 15:2472
47. El-Nahhal IM, Zourab SM, Kodeh FS, Semane M, Genois I, Babonneau F (2012) Nano Lett 2:14
48. Yamamoto O (2001) Int J Inorg Mater 3:643
49. Gedanken A (2004) Ultrason Sonochem 11:47
50. Benn T, Westernoff P (2008) Environ Sci Technol 42:4133
51. Sawai J, Kawada E, Kanou F, Igarashi H, Hashimoto A, Kokugan T, Shimizu M (1996) J Chem Eng Jpn 29:627
52. Sawai J, Shoji S, Igarashi H, Hashimoto A, Kokugan T, Shimizu M, Kojima H (1998) J Ferment Bioeng 86:521
53. Applerot G, Lipovsky A, Dror R, Perkas N, Nitzan Y, Lubart R, Gedanken A (2009) Adv Funct Mater 19:842
54. Soderberg T, Agren M, Tengrup I, Hallmans G, Banck G (1989) Infection 17:81
55. Lansdown ABG, Mirastschijski U, Stubbs N, Scanlon E, Agren MS (2007) Wound Repair Regen 15:2
56. Sengupta G, Ahluwalia HS, Banerjee S, Sen SP (1979) J Colloid Interface Sci 69:217
57. Liu GY, Essex A, Buchanan JT, Datta V, Hoffman HM, Bastian JF, Fierer J, Nizet V (2005) J Exp Med 202:209

58. Huang L, Li DQ, Lin YJ, Wei M, Evans DG, Duan X (2005) J Inorg Biochem 99:986
59. Ohira T, Kawamura M, Iida Y, Fukuda M, Yamamoto O (2008) J Ceram Soc Jpn 116:1234
60. Makhluf S, Dror R, Nitzan Y, Abramovich Y, Jelinek R, Gedanken A (2005) Adv Funct Mater 15:1708
61. Seo DJ, Park SB, Kang YC, Choy KL (2003) J Nanopart Res 5:199
62. Stengl V, Bakardjieva S, Marikova M, Bezdicka P, Subrt J (2003) Mater Lett 57:3998
63. Sawai E, Kawada F, Kanou H, Igarashi A, Hashimoto T, Kokugan MJ, Shimizu J (1996) Chem Eng Jpn 29:627
64. Smyth DM (2000) Solid State Ionics 5:129
65. Eshed M, Lellouche J, Gedanken A, Banin E (2014) Adv Funct Mater 24(10):1382
66. Abramov OV, Gedanken A, Koltypin Y, Perkas N, Perelshtein I, Joyce E, Mason TJ (2009) Surf Coat Technol 204:718

Ultrasound-Assisted Functionalization of Polyphenols

Elisavet D. Bartzoka, Heiko Lange, and Claudia Crestini

Contents

Abstract

Natural polyphenols are a class of compounds that are available in quantities from renewable resources. Natural polyphenols, among them especially lignins and tannins, thus represent important precursors for a variety of valorizations, ranging from the production of biofuel via the use as source for bulk aromatic chemicals to applications in material science areas. Ultrasonication has been used both for

E.D. Bartzoka • H. Lange • C. Crestini (✉)
Department of Chemical Sciences and Technologies, University of Rome "Tor Vergata", Rome, Italy
e-mail: crestini@stc.uniroma2.it

isolating and for subsequently valorizing natural polyphenols. This chapter introduces important structural characteristics of lignins and tannins in order to set the background for a series of applications of ultrasound in connection with polyphenols; these applications comprise isolation methods as well as valorization approaches.

Keywords

Lignins • Tannins • Ultrasonication • Isolation • Valorization

Introduction

The efficient use of biomass is essential for achieving the long-demanded sustainable way of life. Natural polyphenols, mainly present in nature in the form of lignins and tannins, are valuable renewable resources with a potential yet not fully exploited. Lignins and tannins offer a rather diverse selection of structural features besides their polyphenolic character. They thus represent emerging biomass-derived substrates for material science and chemistry. Both isolation and subsequent valorization can benefit from ultrasonication.

Hence this chapter will first briefly outline important characteristic features of the most important natural polyphenol "substrates," i.e., lignins and tannins, as well as important aspects of ultrasonication, before more specific examples are discussed in which ultrasonication was used either for isolating the polyphenols, or converting them in higher value substances and products.

Natural Polyphenols

The term "natural polyphenols" comprises a wide variety of polyphenolic compounds that are available from different types of biomass. In terms of abundances, lignins and tannins are the most important ones. Agricultural and forest biomasses contain large amounts of these substances, in monomeric, oligomeric, and polymeric forms, and utilization of these substances in the context of using renewable, hence sustainable resources is a long-standing issue. Natural complexity causing chemical peculiarities render the development of lignin and tannin-based applications a challenge.

Lignin

Payen scientifically described in 1838 a wood component that from our current perspective must have been a lignin-carbohydrate complex (LCC), connecting the term "lignin," which was introduced already before, closely to an isolable natural substance. In 1865 lignin was finally chemically defined by Schulze, who wrote about lignin as a polymer that was different from the cellulose components [1].

Lignin is the second most abundant component in forest biomass after cellulose. In contrast to cellulose, lignin is a comparably complex natural polymer, and this fact still hampers its exploitation. Old, "traditional" views on its structure and an admittedly tedious initial effort necessary to get an idea of the characteristics of a given lignin sample are significant facets of the problem. The isolation of lignin, its structural characterization, and its utilization have been subject to research activities around the globe for decades. Quite some of knowledge has been accumulated regarding lignin and its characteristics, and this knowledge is constantly refined with respect to technological advances in adjacent fields such as biorefinery, biotechnology, spectrometry, spectroscopy, etc., and the achievements are updated and regularly summarized in dedicated monographs and handbooks [1–3].

Lignin accounts for 15–35 % of the dry mass of wood, depending on the type of wood; it is thus the second most abundant natural polymer in forest biomass after cellulose in absolute numbers [4]. The rather hydrophobic polymer lignin is present in plant cell walls, where it interacts chemically and/or physically with cellulose and hemicellulose [5]: it is located in form of a mixture together with hemicellulose between the cellulose fibrils, putatively being fixed in lignin-carbohydrate complexes (LCCs) [6]. The tight interplay between these three major plant biopolymers results in an increased impermeability, mechanical strength, and rigidity of the plant cell walls, and thus serves to give stability to the plants; it also gives the cells a greater resistance to microbial attacks. Lignin content and lignin distribution vary in the plant between stem, branching points, branches, and leaves and between the different walls of the plant cells themselves [7]. The concentration of lignin in the middle lamella and the primary wall is higher than the concentration in the secondary wall. Nonetheless, the majority of the total amount of lignin present in the plant, 75–85 %, is located in the secondary wall, due to its considerably larger volume. The amount of lignin present in the plant varies from species to species, ranging from ca. 20 % in hardwoods, ca. 28 % in softwoods and herbaceous angiosperms, and ca. 15 % in monocots [5].

Accumulated current findings do at best contain hints of a sort of regulating system for lignin biosynthesis. Unlike cellulose, however, due to the absence of such a regulating system that would control the complex cascade of radical reactions underlying lignin formation, lignin does not display a regular repetition motif but a variety of different interunit bonding motifs, in which no preferred stereochemical pattern can be identified until now [8–11]. Moreover, structural variations are commonly found across plant types, plant parts, and even geographical origins of the same plant.

This natural variation is further fanned out by structural variations caused during the peculiarities of the various biorefinery processes yielding lignin streams. Often, the features inherent to the isolation process determine drastically the chemical and physical characteristics of lignins that are commercially available nowadays.

Current efforts utilize genetically modified model plants like *Arabidopsis thaliana* to improve understanding of the formation of lignin, its role in and for the plants, and its interaction with the other components in the cell walls [12–15]. The structure of lignins can, however, ultimately be described as a polymer

constructed of three monomers, called monolignols (Fig. 1a), namely, coumaryl alcohol (H-type lignin), coniferyl alcohol (G-type lignin), and sinapyl alcohol (S-type lignin), which are synthesized by the plants starting from L-tyrosine [8, 9, 16]. In vivo, these monolignols are enzymatically activated to undergo oxidative coupling reactions. Oxidative coupling of the monomers occurs preferentially at positions O-4, C-1, C-3, C-5, and C-β (IUPAC numbering), thus reflecting at least some selectivity of the activating enzymes involved in the lignin biosynthesis. The initial reaction is followed by downstream reactions that effectively yield the various interunit bonding motifs (Fig. 1b).

Depending on the natural source from which the lignin is isolated, the distribution of the different monomer types, as well as the nature and the distribution of the interunit bonding motifs, differ. Three different general types of lignin are distinguishable in spite of the natural differences: (i) softwood lignin, which is mainly comprised of G-type monomers and a small percentage of H-type monomers; (ii) hardwood lignin, which shows all three types of monomers in the typical ratio H/G/S = 1/1/3; and (iii) grass lignin, which contains all three monomer types with H-type monomers being the dominant one. It is currently still controversially discussed in the community which type of lignins are branched, and thus three-dimensional polymers, and which types rather consist of linear oligomeric chains (Fig. 2) [17, 18]. None of the isolated lignins available nowadays truly reflect the lignin oligomer/polymer as it is present in the living plant. Part of the research on lignin is thus directed to a better understanding of lignin formation in vivo and to structurally analyze lignin without eventually damaging and degrading isolation procedures in vivo.

Structurally understanding lignin is of obvious importance for rationalizing its physicochemical behavior; this is especially true for commercially available lignins such as kraft lignins, organosolv lignins, or steam explosion lignins, since a more rational understanding of the "structure-reactivity" relationships in lignin will foster meaningful valorizations, including ultrasonication-mediated approaches. Currently discussed and slightly outdated structures of some important commercially available lignins are given in Fig. 2.

Biological degradation of lignin can be effected by organisms outside the plant that host a special group of enzymes, which are called lignocellulolytic enzymes, namely, cellulases [19], hemicellulases [20], and ligninases [21–24]; the term ligninases thereby refers to enzymes that are selectively attacking lignin motifs and comprise laccase (phenol oxidases) and peroxidases (lignin peroxidase (LiP) and manganese peroxidase (MnP)) [25, 26]. Evolution of the enzymes and their parent organisms that serve to back-feed the different elements of woody biomass into the different element cycles of the planet started when the first vascular plants grew on dry landmass in the first half of the Paleozoic Era [26, 27]. The lignocellulolytic enzymes are commonly found in fungi, e.g., *Trichoderma reesei* (ascomycetes), *Phanerochaete chrysosporium* (white rot), and *Fomitopsis palustris* (brown rot) (both basidiomycetes phyla); in organisms specialized only on lignin degradation, e.g., *Ceriporiopsis subvermispora* [28], *Phlebia spp.* [29, 30], *Physisporinus rivulosus* [31], and *Dichomitus squalens* [30]; as well as in pathogenic species like
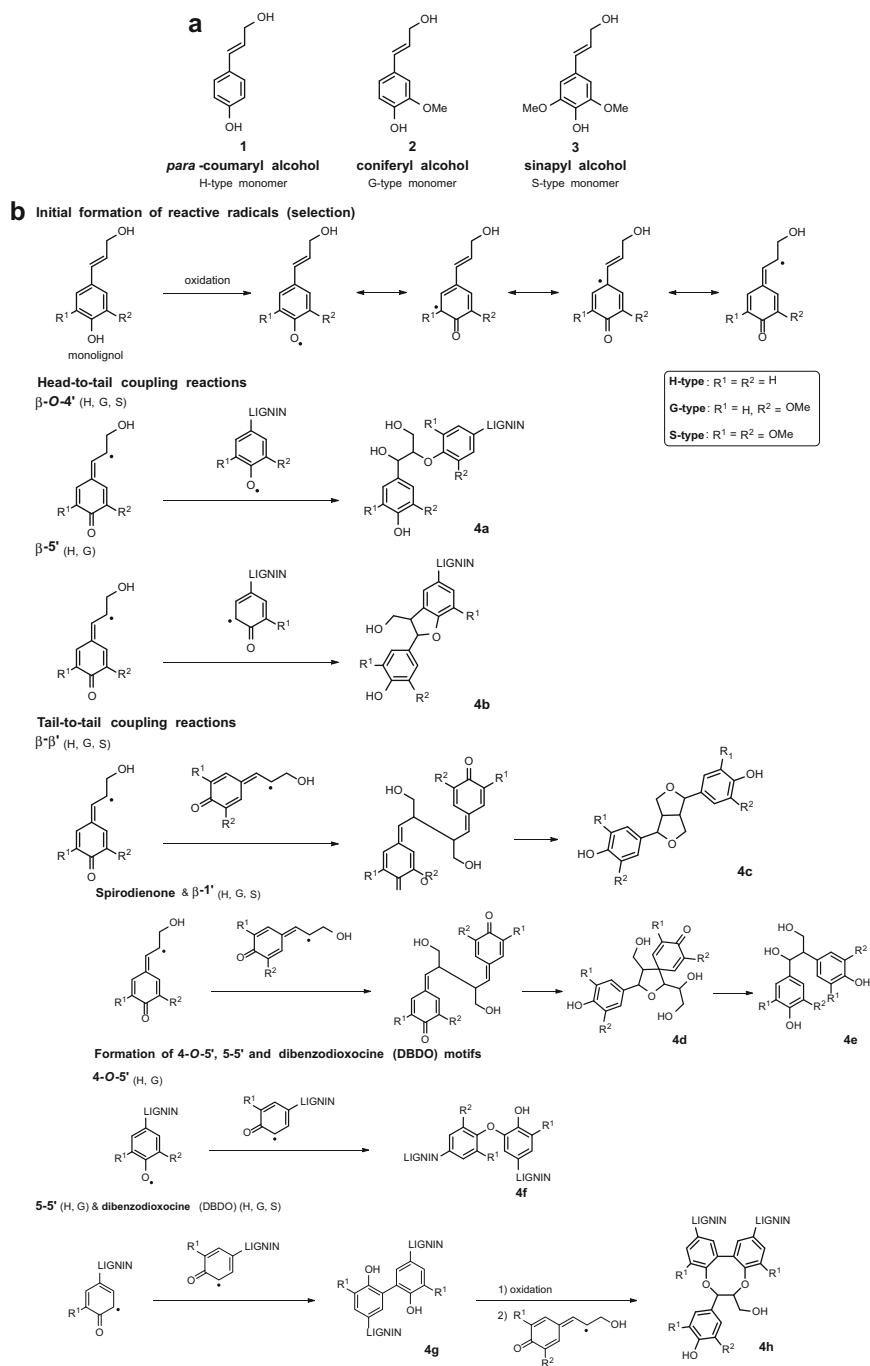
Fig. 1 (**a**) Monomeric building blocks of lignin. (**b**) Characteristic interunit bonding motifs and functional groups found in different lignins and their formation via radical intermediates
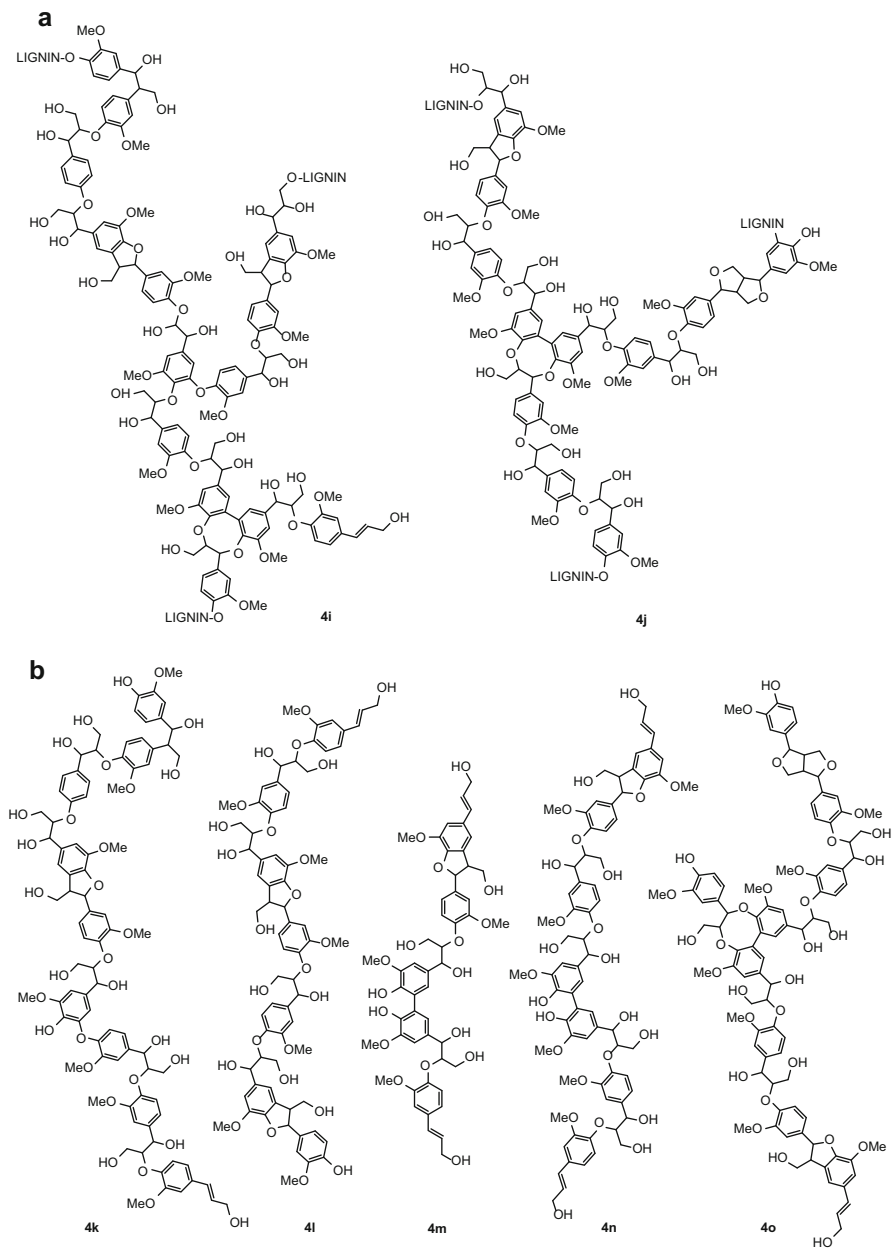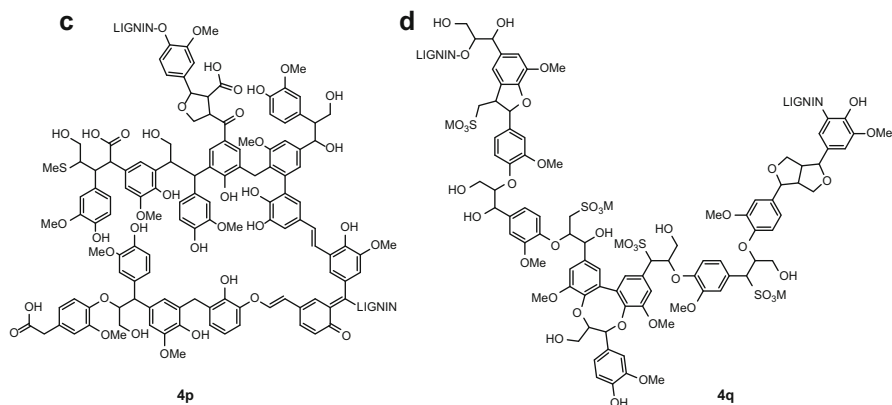
Fig. 2 (continued)

Fig. 2 Lignin structures showing characteristic interunit bonding motifs and functional groups for different types of lignin: (**a**) branched polymeric lignin (outdated view), (**b**) linear chains of oligomeric milled wood lignin (actual view), (**c**) kraft lignin (outdated view, revised structure to be published in due course), and (**d**) lignosulfonate

Fusarium solani f. sp. glycines [32]. The interested reader is encouraged to consult the recent literature on lignin degradation for further information on mechanistic details and adoption of underlying chemistries for the development of putative industrial processes for lignin valorization [33–36].

Tannins

A compound mixture exhibiting a bitter taste was reacted with iron solutions around the middle of the seventeenth century by the Italian chemist Giovannetti; these "astringents" were later shown to contain gallic acid, and further additional experiments finally led to the classification of these compounds that vary in the amount of gallic acid equivalents and its reactivity as tannins.

The name "tannins" thereby originated from the use of this class of compounds in the tanning process, based on their characteristic properties for the tanning. Tannins are usually brown, light yellow, or white amorphous powders or shiny, nearly colorless, loose masses, with a characteristic smell and astringent taste [1].

Tannins are natural polyphenols found in most of the higher plants around the globe, produced in almost all parts of the plant, such as seeds, roots, bark, wood, and leaves. Their fundamental role is to defend the plant against insects, infections, fungi, or bacteria, relying on a very characteristic feature of tannins: the capability to form non-reversible complexes with proteins [37, 38].

Traditionally, one distinguishes between tannins like gallotannins and ellagitannins on the one hand and "non-hydrolysable" or "condensed" tannins on

the other. While the first class of tannins is comprised of polyphenols that are soluble and cleavable into their components in hot water or in the presence of tannase, the second class comprises tannin species without carbohydrate moieties, i.e., proanthocyanidins, polyflavonoid tannins, catechol-type tannins, and pyrocatecholic-type tannins, which are stable under these conditions.

The most commonly used method to isolate tannins is their extraction using aqueous solutions of methanol, ethanol, ethyl acetate, or acetone [39–41], depending on the nature and the molecular weight of the target tannins. Commonly used extraction techniques comprise simple submersion of the tannin-containing material in a suitable solvent system under reflux conditions [42], maceration of the plant materials [41, 43], and classical Soxhlet extraction [44], with optional addition of inorganic salts to increase yields. For separating the tannins from other (poly) phenolic compounds present in the plants, i.e., lignans, lignols, and low molecular weight lignins, chromatography is most often used, employing as stationary phase C-18-type polymers and Sephadex LH-20, and as liquid phases ethanol followed by acetone/water.

Just as lignins, tannins are natural polyphenols that comprise a rather wide selection of particular structural motifs. Unlike the lignins, which are classified according to their origin and isolation methods, tannins are classified according to their reactivities into hydrolysable and non-hydrolysable species, as just discussed. These reactivities go hand in hand with structural features. Hydrolysable tannins are derivatives of gallic acid (3,4,5-trihydroxybenzoic acid), further subclassified according to the products of hydrolysis into gallotannins comprised of gallic acid and glucose and ellagitannins comprised of ellagic acid and glucose [45]. Most of the gallotannins isolated from plants contain a polyol residue derived from D-glucose [46]. Figure 3 gives an overview over the most important structural features of hydrolysable tannins.

Tannic acid [47] (**10**) is one of the most prominent representative of hydrolysable tannin(s). Tannic acid is nowadays understood to be a mixture of very similar substances, e.g., of penta-(digalloyl)-glucose and tetra-(digalloyl)-glucose or tri-(digalloyl)-di-(galloyl)-glucose [48]. Gallotannins are biologically synthesized in a cascade of five enzymatic reactions starting from the conversion of gallic acid to galloylglucose: enzyme studies by Hofmann and Gross have provided substantial evidence that 1-galloyl-β-D-glucose (β-glucogallin) serves as the general acyl donor in the entire biogenetic sequence from simple galloyl esters to complex gallotannins [49, 50].

The transition from "simple" galloylglucoses to complex gallotannins is marked by the addition of further galloyl residues to form first 1,2,3,4,6-pentagalloylglucose, that plays then a role as immediate precursor of more complex gallotannins [51], a process that can be formally seen as a continuation of the esterification reactions of the preceding steps [52]: formation of gallotannins, or depsidic metabolites, is essentially the galloylation of pentagalloylglucose to hexa-, hepta-, octa-, etc. galloylglucose derivatives by exploiting exclusively the phenolic hydroxyl groups [53].
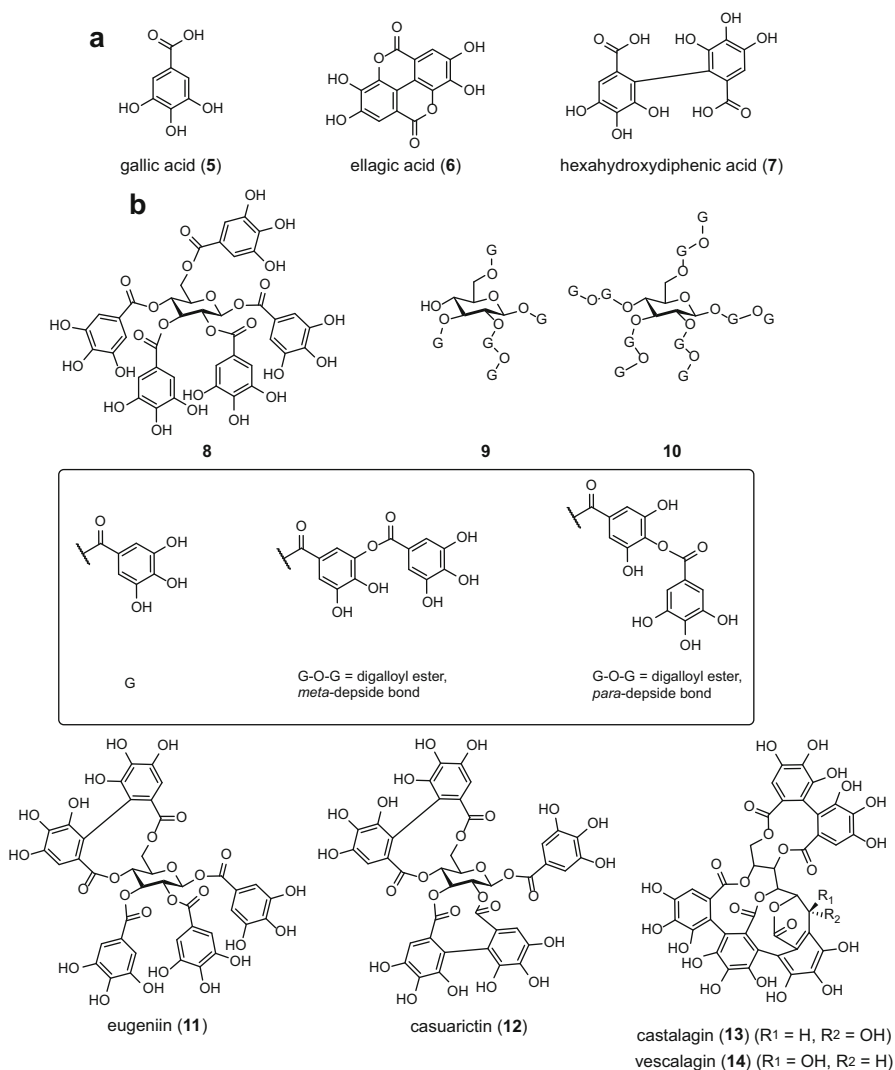
Fig. 3 Important structural aspects and representative examples for different hydrolysable tannins: (**a**) Name-giving structural elements in tannins: gallic acid (**5**), ellagic acid (**6**), hexahydroxy-diphenic acid (**7**); (**b**) Representative structures of hydrolysable tannins: pentagalloyl-*O*-*D*-glucopyranose (PGG) (**8**), PGG derivative (**9**), tannic acid (**10**), eugeniin, (**11**), casuarictin (**12**), and castalagin (R_1 = H, R_2 = OH) (**13**) and vescalagin (R_1 = OH, R_2 = H) (**14**)

With respect to gallotannins, ellagitannins contain additional bonding motifs that stem from additional oxidative coupling reactions between galloyl moieties (Fig. 3). Ellagitannin biosynthesis is thus an oxidative enzymatic progression of gallotannins comprising the formation of hexahydroxydiphenoyl (HHDP) units [54] and further

oxidation to form the dehydrohexahydroxydiphenoyl (DHHDP) motif. Moreover, subsequent oxidative transformations of the DHHDP motif yield several other subclasses of ellagitannins [55].

Condensed tannins are oligomeric and polymeric proanthocyanidins consisting of differently coupled flavan-3-ol (catechin) units (polymers with more than 50 units have been found), linked by carbon-carbon bonds not susceptible to hydrolytic cleavage. They are, however, decomposed to anthocyanidins through acid-catalyzed oxidation reactions upon heating in acidic alcohol solutions [56]. Condensed tannin rings are conventionally named as A, B, and C, and the most common interflavanol linkages are C-C bonds established between the C-4 of one flavanol unit ("extension" or "upper" unit) and the C-8 or C-6 of another unit ("lower" unit) (Fig. 4) [57].

Substitution may occur in either α- or β-position to C-4, depending on the stereochemistry of C-4. Linkage can also occur between C-4 of the upper unit and C-6 of the lower unit. In A-type proanthocyanidins, linkages occur between both C-2 and C-4 of the upper unit and the oxygen at C-7 and positions C-6 or C-8, respectively, of the lower unit [58], leading to differences in the reactivities based on differences in conformational flexibility [59, 60].

The substituents of the aromatic rings are either hydroxyl groups or hydrogen atoms; depending on the substitution pattern, different classes of flavanol polymers with differing responses to various assays (*vide infra*) can be distinguished. For example, procyanidins can be distinguished from prodelphinidins because prodelphinidins have a hydroxyl group at position 5 of the B-ring [61]. For example, an increase in the prodelphinidin/procyanidin ratio in a condensed tannin increases the ability of this tannin to complex with proteins [61]. The chemistry of the condensed tannin B-ring is closely related to that of the parent phenols like phenol, catechol, and pyrogallol [62, 63]. With respect to the use and the chemical modification of tannins, also the A-ring is important; also here, the hydroxyl groups play a crucial role. Biologically, production of condensed tannins follows the flavonoid pathway; in contrast to the hydrolysable tannins, they can occur as monomers or oligomers.

The first part of their biosynthesis coincides with the synthesis of anthocyanins: dihydroflavonol is first converted into leucoanthocyanidin by the dihydroflavonol reductase; then leucoanthocyanidin is reduced by the leucoanthocyanidin reductase to 2,3-*trans*-flavan-ol (catechin). Leucoanthocyanidin, however, is also the substrate for anthocyanidin synthase (ANS) that produces colored anthocyanidin, which is subsequently converted by anthocyanidin reductase (ANR) into the second precursor for condensed tannin, 2,3-*cis*-flavan-ol (epicatechin). Additionally, anthocyanidins can be glycosylated to form anthocyanins [38, 58]. The final steps in the biosynthesis of proanthocyanidins with various hydroxylation patterns, *ent*-isomers, and various coupling products are yet to be understood [64].

The second part of the biosynthesis of non-hydrolysable tannins is the polymerization of the precursors. It is, however, not clear whether this polymerization of the soluble precursors proceeds enzymatically, mediated by a phenol-oxidase like laccase, or nonenzymatically [65].
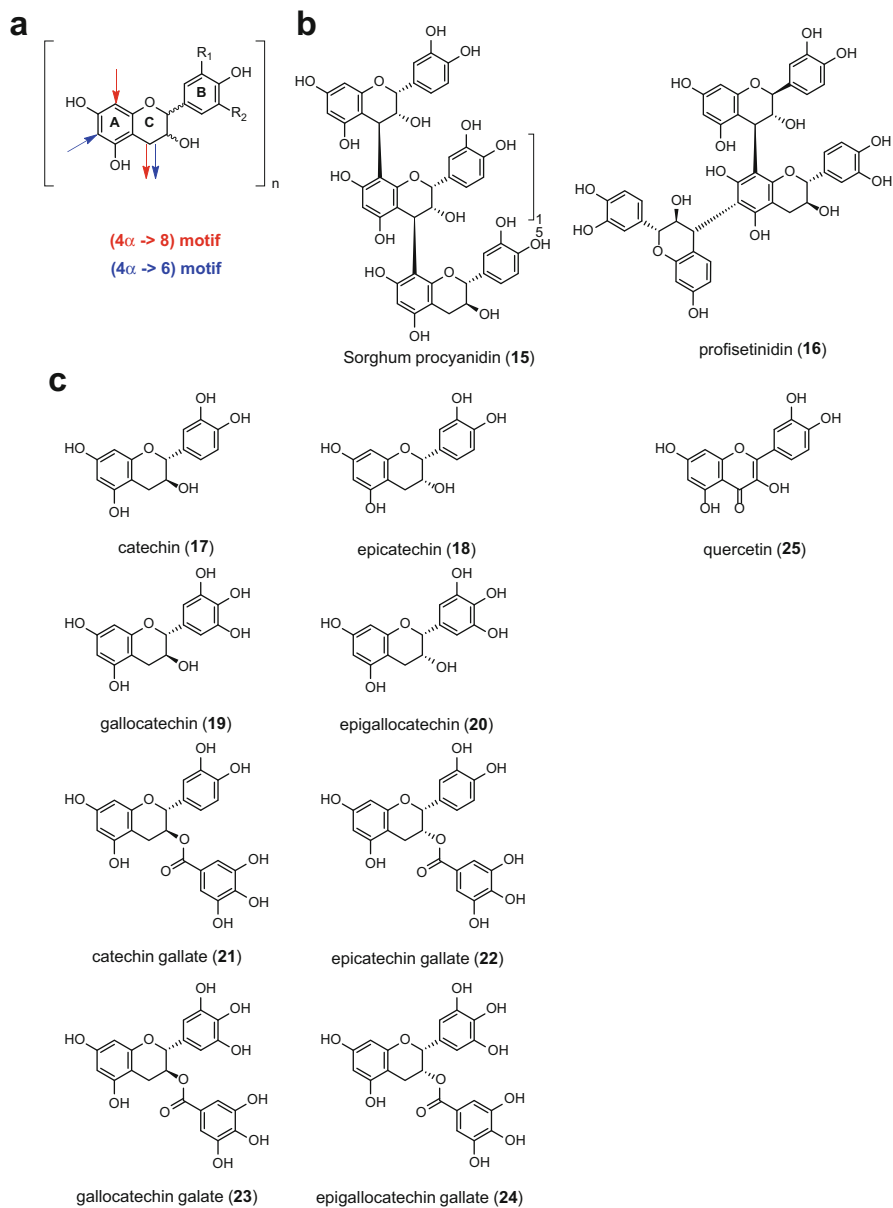
Fig. 4 Important structural aspects and representative examples for different condensed tannins: (**a**) "repetitive unit" of condensed tannins and bonding patterns found in oligomeric condensed tannins, (**b**) examples for condensed tannins such as sorghum procyanidin (epicatechin-[(4ß → 8)-epicatechin]₁₅-(4α → 8)-catechin) (**15**) and profisetinidin (*ent*-catechin-(4α → 8)-catechin-(6α → 4a)-fisetinidol) (**16**), and (**c**) historically important catechin tannin structures

The scaffold of the subclass of tannins called catechin tannins is very similar to that found in condensed tannins. Addition of a third phenolic group on the B-ring yields epigallocatechin and gallocatechin, while flavan-3-ols with a single phenolic group on the B-ring are less common [66–68]. Representative structures are given in Fig. 4c. Catechins are generally colorless, astringent, water-soluble compounds.

Gallocatechin (GC) **19** is a flaven-3-ol with gallate moiety in *trans*-configuration. The *cis*-configured isomer is called epigallocatechin (EGC) **20**; gallocatechin gallate (GCG) (**23**) and epigallocatechin gallate (EGCG) (**24**) are esters of gallic acid and GC and EGC, respectively.

The *cis*-configuration can be generally converted into its *trans*-configured epimer. This epimerization between such a pair of catechins is reversible [69]. It was found that this epimerization (as well as the degradation) of tea catechins follow first-order kinetics and that the rate constants of reaction kinetics for catechins followed the Arrhenius equation [70].

Elucidating Structural Features of Natural Polyphenols

As already emphasized before throughout the text, elucidation of structural features in lignins and tannins is essential for understanding physicochemical properties and thus for identifying promising valorization protocols by evaluating structural changes caused by various treatments. In case of lignins, structural elucidation is only possible by using a combination of different types of analysis techniques. Traditionally, systematic degradation and chemical modification using solvolytic methods such as acidolysis [71] and thioacidolysis [72] or oxidative methods like ozonolysis [73, 74] or the alkaline nitrobenzene oxidation [75] were used to determine structural features and composition of lignins in terms of the H/G/S ratios. Classic elemental analysis serves to determination the characteristic C9 formula of lignins.

Nondestructive methods such as ultraviolet (UV) and infrared (IR) spectroscopy, but especially nuclear magnetic resonance (NMR) spectroscopy are, however, the preferred analysis tools nowadays in order to gain structural insight.

Significant advances in the structural understanding of lignins and tannins were achieved by the use of advanced NMR spectroscopy on polyphenols, namely, in the form of quantitative ^{13}C NMR, quantitative ^{31}P NMR, and quantitative ^{1}H-^{13}C HSQC measurements [18, 76, 77].

Quantitative ^{31}P NMR spectroscopy basically substituted UV-based difference spectroscopy for the quantification of phenolic groups, ethylenic double bonds, non-condensed phenolic groups, and phenylcoumarans [78–80]: quantitative ^{31}P NMR on phosphitylated samples – 2-chloro-3,3,4,4-tetramethyl-1,3,2-dioxapho-spholane [81] is usually used as ^{31}P source – in the presence of an internal standard – e.g., cholesterol or *N*-hydroxy-5-norbornene-2,3-dicarboximide – is suitable to determine both the nature and the abundance of the various hydroxyl groups present in a natural polyphenols [76, 82]. Especially in the case of tannins, quantitative ^{31}P NMR on phosphitylated samples represented a huge step forward in delineating

structural features of pure tannins and compositions in case of mixed or polluted samples [83, 84]. Convenient monitoring of the various hydroxyl groups present in the natural polyphenols by means of quantitative ^{31}P NMR after phosphitylation is particularly interesting also with respect to valorizing these biomass components via ultrasonication methods, since the hydroxyl groups represent reactive centers.

Quantitative two-dimensional NMR spectroscopy is used nowadays for qualitatively and quantitatively determining interunit bonding types as well as H/G/S ratios in lignins. A quick-quantitative HSQC (QQ-HSQC) pulse sequence [85] or an approach consisting of a series of HSQC measurements with incremented repetition times and mathematical backward extrapolation, called $HSQC_0$ [86], can be adopted for the acquisition of lignin spectra [87]. While the results are comparable, the QQ-HSQC method has the drawback of being more difficult to be implemented, while the $HSQC_0$ method is significantly more time-consuming and bears an additional error source due to the necessary extrapolation. In any case, quantification is achieved based on the intrinsic standard represented by the distinct shifts of the aromatic hydrogen atoms in 2-position, which can be easily detected, summed up, and used as reference. Eventual solubility issues are conveniently evaded by working with acetylated samples [18, 87].

Quantitative ^{13}C NMR spectroscopy and in case of tannins also quantitative ^{13}C MAS NMR spectroscopy are used for validating results obtained by two-dimensional NMR studies and for determining structural features that are not, or simply not well visible in the aforementioned NMR techniques [76, 88, 89].

The determination of the molecular weight key figures for various polyphenols is nowadays achieved using size exclusion chromatography (SEC) in form of gel permeation chromatography (GPC) [90–93]. GPC is one of the major tools for following changes in the molecular weight key figures of natural polyphenols during a valorization protocol, despite some practical challenges: i) calibration of GPC setups with adequate standards reflecting the hydrodynamic volume properties of natural polyphenols; ii) setup depending solubility issues [94, 95]; and iii) despite a high sensitivity with respect to the choice of the detector system – commonly used UV-based detectors and refractive index detectors were shown to perform less well compared to molecular weight-sensitive detectors based on viscosimetry [96] or laser light scattering detectors [97–101]. More recently, MALDI-TOF mass analysis techniques were used for the determination of molar mass key data of lignins and tannins [102, 103]. At this point, the interested reader should once more refer to more dedicated literature for getting a complete overview regarding the analytical methods used for characterizing natural polyphenols.

Sonication

Sonochemistry is a term used to describe the use of sound energy to affect chemical processes. It is associated with sonication or ultrasonication, which is a technique based on the use of sound frequencies beyond the human hearing (16–18 kHz) to agitate particles in a liquid sample [104]. Ultrasound frequencies lie between 20 kHz

and many megahertz. Different frequency ranges have been applied in different fields ranging from 20 kHz to 1 MHz, to exploit both physical and chemical effect induced by sonication [105].

The main chemical and mechanical effects of ultrasonic energy arise from acoustic cavitation [106]. Acoustic cavitation is generated when moderate and high sound intensities are applied in a liquid as follows: as the ultrasound crosses the medium, dissolved gas in the liquid is forced to grow, forming bubbles. The bubbles then continue to expand by rectified diffusion [107] or coalescence pathways through a few acoustic cycles to reach resonance size, before collapsing violently on compression. The rapid collapse of the cavitation bubbles leads to the generation of localized "hot spots," in which high temperatures and pressures are created instantaneously, despite the normal conditions in the bulk solution [108]. Besides that, light is also emitted during the acoustic cavitation process, a phenomenon termed "sonoluminescence" [109].

High-power low-frequency waves favor the occurrence of physical and mechanical reactions that include microjets, shear forces, shock waves, and turbulence and enhance the movement of the reaction medium and the mass transport leading to higher reaction rates [110].

In low-power low-frequency waves, chemical reactions prevail. Highly reactive radical species are generated within the cavitation bubble in the liquid medium. In water, primary radicals such as OH· and H· are formed, whereas the presence of other volatile solutes, such as alcohols, induces the formation of various oxidative or reductive radicals that may initiate secondary chemical reactions [111].

More specifically, the ultrasound technique can be applied for the synthesis of new materials as eventual delivery nanosystems, since it reduces their size at the nanoscale, i.e., nanoemulsions or nanoparticles [112], and facilitates their loading with active agents. It is also used for degassing solutions, or in the extraction of valuable products, such as phytochemicals or microfossils [113] using appropriate solvents by concomitant mechanical agitation. Apart from the laboratory use, it is often utilized to assist industrial operations in pharmaceutical, cosmetic, water, food, fuel, wood product industries in order to maximize the efficacy of various chemical processes including emulsification, dispersion, grinding, milling, homogenization, and crystallization [114]. In biological applications, sonication can be used to disrupt biological materials [115] like membranes and urge the release of internal contents [116].

As a result, sonochemistry offers unique experimental conditions for a number of chemical and physical processes, as it offers simplified ways to achieve reactions that would otherwise require extreme reaction conditions as well as to avoid the use of toxic reagents or solvents. Controlling the parameters of the sonication treatment is, however, a rather challenging task as they are interdependent. Hence, a thorough understanding of the different cavitation processes is of paramount importance [117]. In higher frequencies (1–10 MHz) no chemical or physical reactions are noticed, rendering this range ideal for diagnostic purposes (diagnostic ultrasonics) in medicine [118].

Bond Cleavage Induced by Sonication/Isolation of Polyphenols

In addition to the generation of primary and secondary radicals that favor and accelerate chemical reactions and are mainly responsible for the synthesis of particles, cavitation also generates violent physical forces that include microjets, shear forces, shock waves, and turbulence that may cause disintegration and mass transfer of solid materials to a liquid system containing appropriate solvent or the disruption of cell walls due to bond cleavage that ease homolytic reactions and lead to better isolation of products. Ultrasound-induced cavitation bubbles present hydrophobic surfaces within the extraction liquid that increase the net hydrophobic nature of the extraction medium [119]. More in detail, shear forces induced by ultrasound waves support the diffusion solvents into the tissue, favoring the break of the cell and facilitating the mass transfer from the cell to the solvent. The abovementioned phenomenon is called "sponge effect" and is responsible for the liquid movement through the microchannels formed in the solid. Moreover, the particle size reduction that is induced by the cavitation increases the surface area in contact between the solid and the liquid phase and leads to increased extraction rates [120].

Food Processing

Ultrasound has proven to be a useful and effective tool in food processing, without affecting the food nature and quality. The food industry has shown great interest in developing novel emerging technologies such as sonication, as a result of the ever-increasing demands of the consumers for fresh food of high quality.

Ultrasound-Assisted Extraction (UAE)

Due to the abovementioned prevailing mechanism, ultrasound technology facilitates and renders more efficient the extraction of substances in food processing. Consequently it constitutes an appealing versatile technique that can be easily combined or adapted to other extracting approaches or even used as a pretreatment procedure. This type of food processing is called ultrasound-assisted extraction (UAE) and has been widely applied, due to the numerous advantages that it offers compared to conventional extraction methods. It is an effective way to increase extraction rates in shorter times that eventually result in worthwhile economic gains [121].

More specifically in the extraction of polyphenols, numerous applications in the food industry have been reported and involve the extraction of polyphenolic substances from fruits and juices. The key issues relating UAE have been identified and reviewed by Vilkhu et al. and refer to UAE mechanisms, application approaches, performance, process development, equipment, and design. Additionally, this review highlights the main concerns due to ultrasonic cavitation that propagate free radicals and can cause potential oxidative damage, as well as drawbacks on the potential scale up use of the UAE, as it is relatively easy to achieve on a lab scale whereas the industrial application still remains a challenging issue [122].

Various comparative studies have been carried out in order to achieve maximum amounts of phenolic extracts from pomegranate peel (*Punica granatum* L.) [123] or orange peel (*Citrus sinensis* L) [124] by sonication in the presence of appropriate food grade solvents. The latter study highlights optimized conditions for the method and demonstrates suitability for antioxidant-rich plant extraction.

Several other studies have focused on the optimisation of extraction conditions and the effect of different parameters on extraction kinetics and yield in order to achieve highest levels of polyphenols (from black chokeberry, *Aronia melanocarpa* berries) [125] and antioxidant activity that has been proved to be retained in elevated degrees through the ultrasound-assisted approach.

Furthermore, it has been underlined that UAE constitutes a nondestructive method regarding visual or chemical properties of the extracting material, as illustrated in the case of polyphenolic extraction from pomegranate juice [126]. Another study on the UAE has been realized in order to elucidate the differences in the sonication power and further assess the effects of direct and indirect sonication on the extracting material in comparison to more common thermal pretreatment methods. The conclusions of this work showed increased levels in the polyphenolic content extracted on olive paste upon ultrasound pretreatment [120].

Besides that, degradation pathway studies of polyphenolic compounds from various food origins demonstrated relatively low levels of degradation in the case of sonicated samples compared to conventional thermal processes that will eventually result in retention of nutritional quality [127]. Other advantages of the UAE process are mentioned in comparative studies of polyphenol extractions form grape seeds and include lower solvent consumption and decreased extraction times. In the case of wine processing, the extraction of aromatic and phenolic compounds from grape seeds is realized due to intense ultrasonic forces. All in all, UAE appears to be a rather rapid, repeatable, linear, and thus appealing process for the extraction of valuable polyphenols from grape seeds [128].

Extractions of tannins from *Caesalpinia coriaria* and *Anacardium occidentalis* has been studied using various methods including reflux extraction, microwave extraction, and sonication, and the results were confronted to those obtained by typical aqueous extraction methods. Similar results were obtained in the case of phytochemical extraction from the fruits of *Terminalia catappa* L [129] and extraction of tannins from *Rubus idaeus*, *Cydonia oblonga*, and *Rumex acetosa* [130].

To summarize, polyphenolic substances have been isolated via UAE processes from various plants, trees, and juices such as strawberries (*Fragaria x ananassa* Duch) [111], raspberry (*Rubus coreanus* Miq.) [131], star fruits [132], Chokanan mango (*Mangifera indica* L.) [133], and apple (*Malus x domestica*) [134], and their determination via UV showed elevated polyphenolic groups present, rendering this method ideal for this type of food processing.

Improvement of Food Quality

Sonication treatment has been reported to enhance the quality of the extracted compounds. Various studies on the potential application of ultrasound energy on food processing showed that a combination of blanching and sonication may in fact

be employed in the food industry to produce high-quality juices such as carrot juice with improved nutritional characteristics [135]. However, the sonochemical conditions shall be carefully controlled for the successful introduction of ultrasound technology in food processing, so as to avoid sonochemically induced hydroxylation of chemicals – this undesirable result can be eventually quenched by the addition of suitable radical chemicals [136]. Among various fruit juices, apple juice has been thoroughly investigated with respect to changes in its quality characteristics upon sonication treatment [137]. Another example is the use of ultrasonication as postharvesting treatment of grape fruits in order to obtain resveratrol-enriched grape juice [138]. Different studies suggest that sonication technique may be applied to improve phytonutrients content in fruit juices [134].

Lignocellulosic Conversion to Bioethanol

The pretreatment of lignin is an important initial phase in the biorefinery operation and the exploitation of lignocellulosic biomass. It separates the principal components of the biomass and degrades the extended polymer to smaller compounds. The structure of isolated lignin depends mainly on the nature of the pretreatment method. Success of biorefinery streams is highly dependent on the efficiency of biomass transformation. Hence, the isolation operations should ideally result in consistent types of lignin of high quality and purity that are representative of the native lignin.

Several methods have been developed to isolate lignins from biomass, such as acid or alkaline treatments, organosolv, pulping, pyrolytic, or steam explosion processes.

Ultrasound energy has been applied to increase lignin extraction yield and purity or to remove the major inorganic matter from the alkali lignin with no significant alteration in the characteristics of the isolated lignin samples, which is a promising result for the implementation of ultrasound treatment in biorefinery operations [139, 140]. Similar results were obtained by studies on organosolv lignin that also underline the potential use of ultrasound treatment as a pre-intensification step within the biorefinery process [141].

Seino et al. suggest that the majority of β-O-4 bonds are homolytically cleaved to some extent when ultrasonic irradiation of certain frequencies is applied [142].

More specifically, one type of application of ultrasound-assisted isolation of lignin within the biorefinery process that has been studied includes the conversion of lignocellulosic biomass into bioethanol by the exploitation of ultrasound energy for the homolysis of lignin-carbohydrate bonds [143]. This way, lignin and hemicellulose are released and cellulose is hydrolysed into sugars, hence improving the production of bioethanol based on lignocellulosic plant biomass [144].

Ultrasound technology can be used as a pretreatment step in the delignification process of lignocellulosic biomass. Alkaline pretreatments can be further enhanced by the application of ultrasound energy. This way, the process is optimized and higher yields of delignification and sugar reduction are achieved. Thus, sonication provides an environmentally friendly way for the isolation and exploitation of polyphenolic substances from the lignocellulosic biomass [145].

Bond Formation Induced by Sonication

Sonochemical formation of various types of nanostructures has been extensively studied in the last decades. The synthesis of nanomaterials is feasible mainly due to the unique reaction pathways and mechanisms induced by acoustic cavitation.

This versatile synthetic approach provides the possibility to obtain all types of nanomaterials by controlling various sonication factors, such as time, power, temperature, or consistence of bulk solution (i.e., mono- or biphasic system). These parameters are interdependent, rendering the control of the sonication synthetic method a rather challenging task [146]. However, this straightforward method offers numerous advantages such as shorter reaction times, no need for cross-linking agents or removal of non-biocompatible templates, as well as a narrower size distribution compared to other synthetic approaches [112].

Lignin

Lignin possesses an amphiphilic backbone due to the aliphatic and aromatic hydroxyl groups and the lipophilic aromatic rings that are abundant in its structure. Furthermore, lignin is known for its unique π-stacking and complexing properties [147, 148]. The supramolecular behavior and cross-linking characteristics of lignin, as well as the increased polydispersion index (PDI) in sonicated lignin samples [149], highlight the dynamic of the ultrasonic irradiation technique to functionalize such a natural polyphenol by the formation of nanostructured lignin-based materials.

Lignin Particles

Nanoparticles, micelles, and capsules possess great potential for the development of new materials. Wheat straw and sarkanda grass lignins were treated by sonication and the nanoparticles obtained had a significant reduction in diameter compared to untreated lignin samples [150]. This work presents a physical method to functionalize lignin by ultrasound energy in order to obtain particles in the range of 0.01–0.05 μm, along with a morphological and structural characterization due to sonication. The results imply that the modifications on lignin structures are due to the different nature and not due to the intensity applied. Additionally, a proposed mechanism for the possible degradation of lignin, consisting essentially in simultaneous oxidative processes that can alternatively produce side-chain cleavage with depolymerization or oxidative coupling with corresponding polymerization reactions.

Lignin is also reported to form supracolloidal particles from oil/water microemulsion precursors formed by sonication. More specifically, lignin particles in the size range of 1 μm were obtained as a result of emulsification induced by ultrasonic power followed by subsequent cross-linking of the lignin backbone achieved by the addition of cross-linking agents [151].

Another study on lignin functionalization via sonication focused on the synthesis of nanostructured lignin by ultrasound treatment that is afterwards embedded on

linen fabrics to be used as a UV-blocker, endowed with additional considerable properties such as antibacterial and antistatic [167].

Studies of Thomas et al. on the joint sonication of lignin-carbon nanotubes (CNT), as well as on the sonication of solely lignin solutions, demonstrate consequences for the morphology of lignins upon sonication treatment and provides a rather elucidating view on the lignin-CNT interactions [152].

Another work focused on the modification of the surface properties of wood fibers by free radicals generated by high-frequency ultrasound waves illustrates comparative experiments on the sonication of only hydrolytic lignin. The study summarizes changes in the surface properties of the sonicated samples and points up the effects of different operating parameters [153].

Lignin-Based Capsules

Recently lignin capsules were developed and investigated as promising carriers for hydrophobic active molecules, eventually applicable in the biomedical and cosmetic field (Fig. 5) [154]. Oil-filled microcapsules were efficiently obtained by sonicating a Kraft lignin emulsion containing a biocompatible oil, as a result of two ultrasound-induced phenomena: emulsification of the oil droplet in the aqueous solution which contained the polyphenolic matrix, followed by cross-linking of the lignin backbone at the oil/water interface.

The architecture of the capsules and the mechanism concerning the lignin orientation around the oily template, as well as the oxidative patterns that lignin
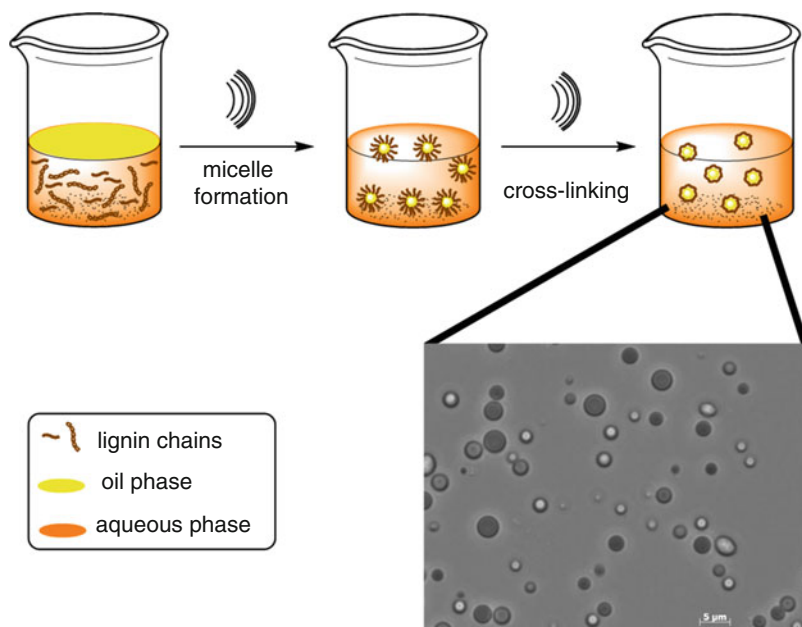
Fig. 5 Ultrasonication-based formation of lignin-based microcapsules (Adopted from Ref. [154])

undergoes during sonication, are asserted and presented in the published work by Tortora et al.^{31}P NMR analysis of phosphitylated lignin samples (*vide supra*) after sonication indicate that capsule formation is mainly attributed to lignin cross-linking along with polymerization and oxidative coupling reactions. The capsules could be filled with hydrophobic molecules which in turn could be released by the addition of surfactants. The development of such a system constitutes an encouraging discovery for the exploitation of natural polyphenols in general by the development of polyphenol-based capsules as delivery systems.

Tannins

Tannins are the second most abundant biopolymer in forest biomass after lignin. Up to date some studies on the sonicated assisted functionalization of tannins have been reported.

Tannic acid nanoparticles (NPs) have been obtained without stabilizers via a sonochemical route and have been subsequently deposited onto cotton substrates in a one-step process. The study describes the application of the sonication method for the formation of antimicrobial textiles coated with tannin nanoparticles that notably retained their initial functional features after the sonication treatment [155].

Another study demonstrates the functionalization of complex tannins with the polysaccharide hyaluronan (HA) via the combination of sonication and ultracentrifugation techniques to achieve the sedimentation of the tannin-HA complexed system and elucidates the interactions between the two substances by means of various analytical methods [156].

The compressive strength and impact resistance of tannin foams are reported to improve by the addition of small percentages of multiwalled carbon nanotubes after sonication treatment of a mixture of the components. This work focuses on the microscopical analysis of the functionalized system and assesses the distribution of nanotubes imbedded with respect to the different cell walls zones [157].

Ultrasonic Functionalization of Phenolic Compounds Mimicking Natural Polyphenols

A simple, versatile, one-pot sonochemical synthesis of polydopamine (PDA) nanocapsules from dopamine has been reported. Nanocapsules of 250 nm are obtained and their loading capacity of hydrophobic molecules has been evaluated [158].

A new approach for the preparation of drug nanocolloids based on the natural phenol curcumin that is individually isolated from plant extracts has been proposed via a sonication-assisted technique to initiate crystal nucleation in the presence of aqueous polycation. The nucleation is followed by polyelectrolyte layer-by-layer (LbL) technique to form the nanoshell. Higher intensities are proven to promote the drug particle growth in the initial steps [159].

The isoflavone genistein, which is commonly known as a phytoestrogen and chemoprotective agent, has been submitted under differential functionalization by an ultrasound treatment. The ultrasound-promoted functionalization of the phenolic groups in the genistein led to the synthesis of regioselective derivatives (esters and corresponding acids) and eliminated the need of phase-transfer catalysts or additional chemicals as protective groups. This study highlighted for the first time the potential use of this method in the selective structural modification of natural polyphenols in general, with subtle deviations that emerge from differences in acidity and spatial accessibility of phenolic hydroxyl groups [160].

Functionalization/Encapsulation Based on Polyphenols

Sonication of polyphenols may result in the encapsulation of these bioactive molecules either in mononuclear capsules or in a more aggregated system (particles). This modification may eventually improve some of their features, as the unpleasant taste can be easily masked before incorporating them to foods. The abundant work on encapsulation of polyphenols has been summarized and various features and morphologies of the system produced by the different encapsulation methodologies have been reviewed [161].

Liposomes obtained by combination of various methods with sonication were reported by various research groups and have efficiently encapsulated polyphenolic compounds, such as trans-resveratrol [162, 163].

Studies on the incorporation of catechins in phospholipids based on ultrasound-created microbubbles for ultrasound-triggered delivery exhibited satisfactory loading capacity and illustrated a promising method for the generation of potential ultrasound-promoted delivery systems [164].

Degradation

The two main ultrasound-induced phenomena that are responsible for the extraction processes are mass transfer intensification and increase in the fine grinding together with deagglomeration [165]. The positive effect of ultrasound technology is also reported in the sonochemical degradation of the monomeric phenolic compounds p-coumaric acid (CA) and p-hydroxybenzaldehyde (HBA). The degradation proceeds mainly due to the formation of hydroxyl radicals that lead to aromatic and ring cleavage reactions. As a result this method enhances the aerobic degradability of phenolic substances and eases the removal of p-CA and p-HBA, when used either as a standalone method or a pretreatment step to convert initially bioresistant compounds to more easily biodegradable ones. Furthermore, coupling of the ultrasound methodology with suitable catalyst or extra oxidant agents (such as H_2O_2 or Fe^{2+}/ Fenton-like processes), as well as the control of temperature and concentration of bulk solution, are supposed to improve the efficacy of this approach [165].

The sonodegradation and isolation of tannins have also been studied. Comparative results on the removal of total phenolics from grape-condensed tannins with and without sonication and in the presence and absence of oxidizing chemicals (e.g., hydrogen peroxide) introduced the most appropriate combination of conditions that would eventually provide maximum efficiency concerning destruction of polyphenols in general [166].

Conclusions and Future Directions

Natural polyphenols, especially lignins and tannins, are important compounds available in quantities from agricultural and forest biomass. Despite their complex structural features, it is possible to use ultrasonication for valorization purposes of these natural oligomeric and polymeric substances. Sonication allows the isolation or targeted removal of natural polyphenols from other biomass components in the processes of biorefinery and food processing. Sonication allows further the targeted functionalization of natural polyphenols, their conversion into fuels, as well as the exploitation of their unique structural features and related chemistries in more innovative fields of research like micro- and nanoparticle formation, encapsulation, and delivery vehicles. Encouraged by the promising results obtained by applying ultrasonication features for achieving the valorization of polyphenols, this emerging field is expected to see more seminal developments in the next years.

References

1. Sjöström E (1993) Wood chemistry: fundamentals and applications. 2nd edn, Academic Press, San Diego (CA)
2. Hu TQ (2002) Chemical modification, properties, and usage of lignin. Springer, New York
3. Heitner C, Dimmel D, Schmidt J (2010) Lignin and lignans: advances in chemistry, 1st edn. CRC Press, Boca Raton
4. Lewis NG, Yamamoto E (1990) Annu Rev Plant Physiol Plant Mol Biol 41:455
5. Lewis NG, Davin LB, Sarkanen S (1998) In: Lewis NG, Sarkanen S (eds) Lignin and lignan biosynthesis. American Chemical Society, Washington, DC, pp 1–27
6. Glasser WG, Sarkanen S (1989) Lignin: properties and materials. American Chemical Society, Washington, DC
7. ELC for C and Paper, The 8th international symposium on wood and pulping chemistry. 6–9 June 1995, Helsinki: Proceedings (Congrex, Blue & White Conferences, 1995)
8. Vanholme R, Demedts B, Morreel K, Ralph J, Boerjan W (2010) Plant Physiol 153:895
9. Boerjan W, Ralph J, Baucher M (2003) Annu Rev Plant Biol 54:519
10. Donaldson LA (2001) Phytochemistry 57:859
11. Akiyama T, Goto H, Nawawi DS, Syafii W, Matsumoto Y, Meshitsuka G (2005) Holzforschung 59:276
12. Romani A, Lattanzio V, Quideau S (2014) Recent advances in polyphenol research (vol. 4). Wiley, Chichester
13. Rogers LA, Campbell MM (2004) New Phytol 164:17
14. Anterola AM, Lewis NG (2002) Phytochemistry 61:221
15. Grima-Pettenati J, Goffner D (1999) Plant Sci 145:51

16. Whetten R, Sederoff R (1995) Plant Cell 7:1001
17. Holtman KM, Chang H-M, Jameel H, Kadla JF (2003) J Agric Food Chem 51:3535
18. Crestini C, Melone F, Sette M, Saladino R (2011) Biomacromolecules 12:3928
19. Bayer EA, Chanzy H, Lamed R, Shoham Y (1998) Curr Opin Struct Biol 8:548
20. Ljungdahl LG (2008) Ann N Y Acad Sci 1125:308
21. Weng J-K, Li X, Bonawitz ND, Chapple C (2008) Curr Opin Biotechnol 19:166
22. Kubicek CP (2012) Fungi and lignocellulosic biomass. Wiley-Blackwell, Oxford
23. Sánchez C (2009) Biotechnol Adv 27:185
24. Dashtban M, Schraft H, Qin W (2009) Int J Biol Sci 5:578
25. Ferm R, Kringstad KP, Cowling EB (1972) Sven Pap 75:859
26. Tien M, Kirk TK (1983) Science 221:661
27. Taylor TN, Osborn JM (1996) Rev Palaeobot Palynol 90:249
28. Guerra A, Mendonça R, Ferraz A, Lu F, Ralph J (2004) Appl Environ Microbiol 70:4073
29. Arora DS, Sharma RK (2009) BioResources 4:909
30. Fackler K, Gradinger C, Hinterstoisser B, Messner K, Schwanninger M (2006) Enzyme Microb Technol 39:1476
31. Hildén K, Hakala TK, Maijala P, Lundell TK, Hatakka A (2007) Appl Microbiol Biotechnol 77:301
32. Lozovaya VV, Lygin AV, Zernova OV, Ulanov AV, Li S, Hartman GL, Widholm JM (2007) Planta 225:665
33. Aresta M, Dibenedetto A, Dumeignil F (2012) Biorefinery: from biomass to chemicals and fuels. de Gruyter, Berlin
34. Sannigrahi P, Pu Y, Ragauskas A (2010) Curr Opin Environ Sustain 2:383
35. Argyropoulos DS (ed) (2007) Materials, chemicals and energy from forest biomass. ACS symposium series, no. 954. Oxford University Press, Oxford
36. Scultz TP (2000) Lignin: historical, biological, and materials perspectives. American Chemical Society, Washington, DC
37. Yoshida T, Ohbayashi H, Ishihara K, Ohwashi W, Haba K, Okano Y, Shingu T, Okuda T (1991) Chem Pharm Bull (Tokyo) 39:2233
38. Okuda T, Hatano T, Yazaki K (1983) Chem Pharm Bull (Tokyo) 31:333
39. Strumeyer DH, Malin MJ (1975) J Agric Food Chem 23:909
40. Arapitsas P, Menichetti S, Vincieri FF, Romani A (2007) J Agric Food Chem 55:48
41. Giner-Chavez BI, Van Soest PJ, Robertson JB, Lascano C, Reed JD, Pell AN (1997) J Sci Food Agric 74:359
42. Vieira MC, Lelis RCC, Da Silva BC, De Lima Oliveira G (2011) Floresta E Ambiente 18:1
43. Moreira J, Klein-Junior LC, Filho VC, Buzzi FC (2013) J Ethnopharmacol 146:318
44. Tian F, Li B, Ji B, Zhang G, Luo Y (2009) LWT -Food Sci Technol 42:1289
45. McLeod MN (1974) Nutr Abstr Rev 44:803
46. Khanbabaee K, van Ree T (2001) Nat Prod Rep 18:641
47. Fischer E (1919) Ber Dtsch Chem Ges B Ser 52:809
48. Arapitsas P (2012) Food Chem 135:1708
49. Mueller-Harvey I (2001) Anim Feed Sci Technol 91:3
50. Cammann J, Denzel K, Schilling G, Gross GG (1989) Arch Biochem Biophys 273:58
51. Feucht W, Nachit M (1977) Physiol Plant 40:230
52. Zhang LL, Lin YM (2008) Molecules 13:2986
53. Grundhöfer P, Niemetz R, Schilling G, Gross GG (2001) Phytochemistry 57:915
54. Tian L, Pang Y, Dixon RA (2008) Phytochem Rev 7:445
55. Hofmann AS, Gross GG (1990) Arch Biochem Biophys 283:530
56. Herderich MJ, Smith PA (2005) Aust J Grape Wine Res 11:205
57. Santos-Buelga C, Scalbert A (2000) J Sci Food Agric 80:1094
58. Xie D-Y, Dixon RA (2005) Phytochemistry 66:2127
59. Andersen OM, Markham KR (2005) Flavonoids: chemistry, biochemistry and applications. CRC Press, Taylor and Francis Group, Boca Raton (FL)

60. Rubanza CD, Shem MN, Ichinohe T, Fujihara T (2008) J Food Agric Environ 6:145
61. Schofield P, Mbugua DM, Pell AN (2001) Anim Feed Sci Technol 91:21
62. Laks PE (1989) In: Hemingway RW, Karchesy JJ, Branham SJ (eds) Chemistry and significance of condensed tannins. Springer, New York, pp 249–263
63. Laks PE (1989) In: Hemingway RW, Karchesy JJ, Branham SJ (eds) Chemistry and significance of condensed tannins. Springer, New York, pp 131–136
64. Gantulga D, Ahn YO, Zhou C, Battogtokh D, Bevan DR, Winkel BSJ, Esen A (2009) Phytochemistry 70:1999
65. Okuda T, Yoshida T, Hatano T, Ito H (2009) Chem Biol Ellagitannins 122:1
66. Mueller-Harvey I, Hartley RD, Reed JD (1987) J Sci Food Agric 39:1
67. Graham HN (1992) Prev Med 21:334
68. Francisco A (1995) Phytochem Anal 6:55
69. Wang R, Zhou W, Jiang X (2008) J Agric Food Chem 56:2694
70. Wang R, Zhou W, Wen RH (2006) J Agric Food Chem 54:5924
71. Pometto AL, Crawford DL (1985) Appl Environ Microbiol 49:879
72. Lapierre C, Monties B, Rolando C (2009) Holzforsch Int J Biol Chem Phys Technol Wood 40:47
73. Khudoshin AG, Mitrofanova AN, Lunin VV (2012) Russ J Phys Chem A 86:360
74. Sarkanen KV, Islam A, Anderson CD (1992) In: Lin DSY, Dence PEDCW (eds) Methods in lignin chemistry. Springer, Berlin/Heidelberg, pp 387–406
75. Chen C-L (1992) In: Lin DSY, Dence PEDCW (eds) Methods in lignin chemistry. Springer, Berlin/Heidelberg, pp 301–321
76. Heitner C, Dimmel D, Schmidt J (2011) Lignin and lignans: advances in chemistry. CRC Press, Taylor and Francis Group, Boca Raton (FL)
77. Guerra A, Filpponen I, Lucia LA, Argyropoulos DS (2006) J Agric Food Chem 54:9696
78. Aulin-Erdtman G (1954) Sven Pap 57:754
79. Aulin-Erdtman G, Hegbom L (1958) Sven Pap 61:187
80. El Mansouri N-E, Salvadó J (2007) Ind Crops Prod 26:116
81. Granata A, Argyropoulos DS (1995) J Agric Food Chem 43:1538
82. Saake B, Argyropoulos DS, Beinhoff O, Faix O (1996) Phytochemistry 43:499
83. Melone F, Saladino R, Lange H, Crestini C (2013) J Agric Food Chem 61:9307
84. Melone F, Saladino R, Lange H, Crestini C (2013) J Agric Food Chem 61:9316
85. Peterson DJ, Loening NM (2007) Magn Reson Chem 45:937
86. Hu K, Westler WM, Markley JL (2011) J Am Chem Soc 133:1662
87. Sette M, Lange H, Crestini C (2013) Comput Struct Biotechnol J 6
88. Landucci LL, Ralph SA, Hammel KE (2009) Holzforsch Int J Biol Chem Phys Technol Wood 52:160
89. Nimz HH, Robert D, Faix O, Nemr M (2009) Holzforsch Int J Biol Chem Phys Technol Wood 35:16
90. Obiaga TI, Wayman M (1974) J Appl Polym Sci 18:1943
91. Gellerstedt G (1992) In: Lin DSY, Dence PEDCW (eds) Methods in lignin chemistry. Springer, Berlin/Heidelberg, pp 487–497
92. Chen F, Li J (2000) J Wood Chem Technol 20:265
93. Salanti A, Zoia L, Tolppa E-L, Orlandi M (2012) Biomacromolecules 13:445
94. Lu F, Ralph J (1997) J Agric Food Chem 45:4655
95. Asikkala J, Tamminen T, Argyropoulos DS (2012) J Agric Food Chem 60:8968
96. Ringena O, Lebioda S, Lehnen R, Saake B (2006) J Chromatogr A 1102:154
97. Gidh AV, Decker SR, Vinzant TB, Himmel ME, Williford C (2006) J Chromatogr A 1114:102
98. Gidh AV, Decker SR, See CH, Himmel ME, Williford CW (2006) Anal Chim Acta 555:250
99. Fredheim GE, Braaten SM, Christensen BE (2002) J Chromatogr A 942:191
100. Braaten SM, Christensen BE, Fredheim GE (2003) J Wood Chem Technol 23:197
101. Cathala B, Saake B, Faix O, Monties B (2003) J Chromatogr A 1020:229
102. Bayerbach R, Nguyen VD, Schurr U, Meier D (2006) J Anal Appl Pyrolysis 77:95

103. Araújo P, Ferreira MS, de Oliveira DN, Pereira L, Sawaya ACHF, Catharino RR, Mazzafera P (2014) Anal Chem 86:3415
104. Mason TJ (1996) In: Siegel RJ (ed) Ultrasound angioplasty. Kluwel Academic Publishers, Norwell (MA), pp 25–54
105. Ashokkumar M, Mason TJ (2007) Sonochemistry. Kirk-Othmer Encyclopedia of Chemical Technology. Wiley VCH, New York
106. Leong T, Ashokkumar M, Kentish S (2011) Acoust Australia 39:54
107. Leong T, Collis J, Manasseh R, Ooi A, Novell A, Bouakaz A, Ashokkumar M, Kentish S (2011) J Phys Chem C 115:24310
108. Feng H, Barbosa-Canovas G, Weiss J (eds) (2011) Ultrasound technologies for food and bioprocessing. Springer, New York
109. Ashokkumar M, Crum LA, Frensley CA, Grieser F, Matula TJ, McNamara WB, Suslick KS (2000) J Phys Chem A 104:8462
110. Wu TY, Guo N, Teh CY, Hay JXW (2013) Advances in ultrasound technology for environmental remediation. Springer, The Netherlands, pp 5–12
111. Herrera MC, De Castro ML (2005) J Chromatogr A 1100:1
112. Manickam S, Ashokkumar M (2014) Cavitation: a novel energy-efficient technique for the generation of nanomaterials. CRC Press, Taylor and Francis Group, Boca Raton (FL)
113. Olivares M, Vallejo A, Irazola M, Murelaga X, Baceta JI, Tarriño A, Etxebarria N (2010) Talanta 83:605
114. Behrend O, Ax K, Schubert H (2000) Ultrason Sonochem 7:77
115. Guzmán HR, Nguyen DX, Khan S, Prausnitz MR (2001) J Acoust Soc Am 110:588
116. Muthukumaran S, Kentish SE, Stevens GW, Ashokkumar M (2011) Rev Chem Eng 22:155
117. Ashokkumar M, Grieser F (2011) Rev Chem Eng 15:41
118. Cavalieri F, Zhou M, Ashokkumar M (2010) Curr Top Med Chem 10:1198
119. Chandrapala J, Oliver CM, Kentish S, Ashokkumar M (2013) Food Rev Int 29:67
120. Jiménez A, Beltrán G, Uceda M (2007) Ultrason Sonochem 14:725
121. Ana Cristina Soria MV (2010) Trends Food Sci Amp Technol 323
122. Vilkhu K, Mawson R, Simons L, Bates D (2008) Innov Food Sci Emerg Technol 9:161
123. Yasoubi P, Barzegar M, Sahari MA, Azizi MH (2010) J Agric Sci Technol 9:35
124. Khan MK, Abert-Vian M, Fabiano-Tixier A-S, Dangles O, Chemat F (2010) Food Chem 119:851
125. D' Alessandro LG, Kriaa K, Nikov I, Dimitrov K (2012) Sep Purif Technol 93:42
126. Alighourchi HR, Barzegar M, Sahari MA, Abbasi S et al (2013) Int Food Res J 20:1703
127. Tiwari BK, O'Donnell CP, Patras A, Cullen PJ (2008) J Agric Food Chem 56:10071
128. Da Porto C, Porretto E, Decorti D (2013) Ultrason Sonochem 20:1076
129. Annegowda HV, Anwar LN, Mordi MN, Ramanathan S, Mansor SM (2010) Pharmacogn Res 2:368
130. Cobzac S, Moldovan M, Olah NK, Bobos L, Surducan E (2005) Ser F Chem 8:55
131. Teng H, Lee WY, Choi YH (2014) Food Anal Methods 7:1536
132. Annegowda HV, Bhat R, Min-Tze L, Karim AA, Mansor SM (2012) J Food Sci Technol 49:510
133. Santhirasegaram V, Razali Z, Somasundram C (2013) Ultrason Sonochem 20:1276
134. Abid M, Jabbar S, Wu T, Hashim MM, Hu B, Lei S, Zhang X, Zeng X (2013) Ultrason Sonochem 20:1182
135. Jabbar S, Abid M, Wu T, Muhammad Hashim M, Hu B, Lei S, Zhu X, Zeng X (2014) Int J Food Sci Nutr 65:28
136. Ashokkumar M, Sunartio D, Kentish S, Mawson R, Simons L, Vilkhu K, Versteeg CK (2008) Innov Food Sci Emerg Technol 9:155
137. Abid M, Jabbar S, Wu T, Hashim MM, Hu B, Lei S, Zeng X (2014) Ultrason Sonochem 21:93
138. Hasan MM, Yun H-K, Kwak E-J, Baek K-H (2014) Ultrason Sonochem 21:729
139. García A, Erdocia X, Alriols MG, Labidi J (2012) Chem Eng Process Process Intensif 62:150
140. Thomas R, Tripathi R, Kamat SD, Kamat DV (2012) Int J Pharm Sci Res 3:194

141. García A, Alriols MG, Labidi J (2012) Bioresour Technol 108:155
142. Seino T, Yoshioka A, Fujiwara M, Chen K-L, Erata T, Tabata M, Takai M (2001) Wood Sci Technol 35:97
143. Luo J, Fang Z, Smith RL Jr (2014) Prog Energy Combust Sci 41:56
144. Velmurugan R, Muthukumar K (2012) Bioresour Technol 112:293
145. Rehman MSU, Kim I, Chisti Y, Han J-I et al (2013) EEST Part Energ Sci Res 30:1391
146. Okitsu K, Ashokkumar M, Grieser F (2005) J Phys Chem B 109:20673
147. Contreras S, Gaspar AR, Guerra A, Lucia LA, Argyropoulos DS (2008) Biomacromolecules 9:3362
148. Guerra A, Gaspar AR, Contreras S, Lucia LA, Crestini C, Argyropoulos DS (2007) Phytochemistry 68:2570
149. Wells T, Kosa M, Ragauskas AJ (2013) Ultrason Sonochem 20:1463
150. Gilca IA, Popa VI, Crestini C (2015) Ultrason Sonochem 23:369
151. Nypelö TE, Carrillo CA, Rojas OJ (2015) Soft Matter 11:2046
152. Thomas D, Edwards J, Parker R, Ku CL, Bryan D, Liao YH, Liang R (2006) NSTI-Nanotech 1:290
153. Jayant RBG, Gadhe B (2006) Cellulose 13:9
154. Tortora M, Cavalieri F, Mosesso P, Ciaffardini F, Melone F, Crestini C (2014) Biomacromolecules 15:1634
155. Perelshtein I, Ruderman E, Francesko A, Fernandes MM, Tzanov T, Gedanken A (2014) Ultrason Sonochem 21:1916
156. Carn F, Guyot S, Baron A, Pérez J, Buhler E, Zanchi D (2012) Biomacromolecules 13:751
157. Srivastava VK, Li X (2013) Ind Crops Prod 43:636
158. Gil Yeroslavsky MR (2013) Chem Commun 49:5721
159. Zheng Z, Zhang X, Carbo D, Clark C, Nathan C-A, Lvov Y (2010) Langmuir 26:7679
160. Wang SF, Ye YH, Zhang Z, Tan RX (2006) Ultrason Sonochem 13:28
161. Fang Z, Bhandari B (2010) Trends Food Sci Technol 21:510
162. Isailović BD, Kostić IT, Zvonar A, Dordević VB, Gašperlin M, Nedović VA, Bugarski BM (2013) Innov Food Sci Emerg Technol 19:181
163. Bonechi C, Martini S, Ciani L, Lamponi S, Rebmann H, Rossi C, Ristori S (2012) PLoS One 7:e41438
164. Lu C-T, Zhao Y-Z (2008) J Drug Target 16:790
165. Vassilakis C, Pantidou A, Psillakis E, Kalogerakis N, Mantzavinos D (2004) Water Res 38:3110
166. Svitelska GV, Gallios GP, Zouboulis AI (2004) Chemosphere 56:981
167. Zimniewska M, Kozlowski R, Batog J (2008) Molec. Cryst Liquid Cryst 484:43

Ultrasonic Synthesis and Characterization of Polymer-Shelled Microspheres

Meifang Zhou, Francesca Cavalieri, and
Muthupandian Ashokkumar

Contents

Abstract

Ultrasound technique provides a simple, fast, versatile, and green pathway for synthesizing functionalized polymeric nanometer- and micrometer-sized core/shell structures. The core materials include gas, liquid, and solid materials. The microspheres' shell is composed of biopolymers such as proteins, polysaccharides, and biocompatible synthetic polymers. In this chapter, an overview of various reports available in the literature on ultrasonic synthesis and characterization of polymer-shelled microspheres is provided. Specific focus is given to how various experimental conditions could be used to fine-tune the physical and

M. Zhou (✉) • M. Ashokkumar
School of Chemistry, The University of Melbourne, Melbourne, VIC, Australia
e-mail: meifang.zhou@unimelb.edu.au

F. Cavalieri
Department of Chemical and Biomolecular Engineering, The University of Melbourne, Melbourne, VIC, Australia

functional properties of polymeric nano- and microspheres. It has been shown that their properties could be controlled by the power and frequency of ultrasound, the type of ultrasonic horn, and post-sonication technique. The importance of thiol functional groups for enhancing the stability of shell is also highlighted. The examples and discussion provided in this chapter indicate that ultrasound technology is versatile, simple, and efficient for synthesizing stable polymeric nano- and microspheres that have potential applications in biomedical and other areas.

Introduction

Polymer-based microspheres have been used for a wide range of applications including biomedical, food, and cosmetics. Polymer-shelled microspheres are suitable for encapsulation of contrast agents, drugs, dyes, flavors, and fragrances [1–4]. Different types of polymeric microspheres have been reported, including hollow polymer microbubbles [5–7] and core–shell polymer microspheres [8] as shown in Fig. 1.

Recently, ultrasonic technology has been applied for synthesizing biodegradable and biocompatible microspheres. Ultrasound synthesis offers a fast and facile pathway. In 1986, air-filled protein-shelled microbubbles were synthesized by Feinstein et al. [9–11] and used as contrast agents in echo sonography. Since then, intensive research has been conducted to develop a variety of biocompatible-shelled microspheres using proteins such as bovine serum albumin (BSA) and human serum albumin (HSA) [6, 7]. In 1990, liquid-filled microspheres were first made by Suslick and coworkers [12, 13] using BSA [12], HSA [6], and hemoglobin (Hb) [7] to encapsulate n-dodecane, n-hexane, and cyclohexane. These developments opened up a novel research pathway to explore new types of microspheres with a variety of functional shell and core materials. Recently, Cavalieri et al. reported on the synthesis of air-filled lysozyme [14] and thiolated poly(methyl methacrylate), PMA_{SH} [15] microbubbles. These systems can be used as contrast agents and drug and nutrient delivery systems due to their unique biodegradable and biocompatible properties. Zhou et al. [16] further investigated liquid-filled lysozyme and polymer-shelled microspheres. The core liquid materials included tetradecane, dodecane, sunflower oil, and perfluorohexane. Water-filled [17], oil-filled [16], solid-filled [18], and surface-functionalized [19] polymeric microspheres were developed using synthetic polymers for food and pharmaceutical applications.

The microspheres' shell material could also be post functionalized for imaging and drug delivery purposes. For example, air-filled lysozyme microbubbles were prepared for the immobilization of gold nanoparticles and an enzyme, alkaline
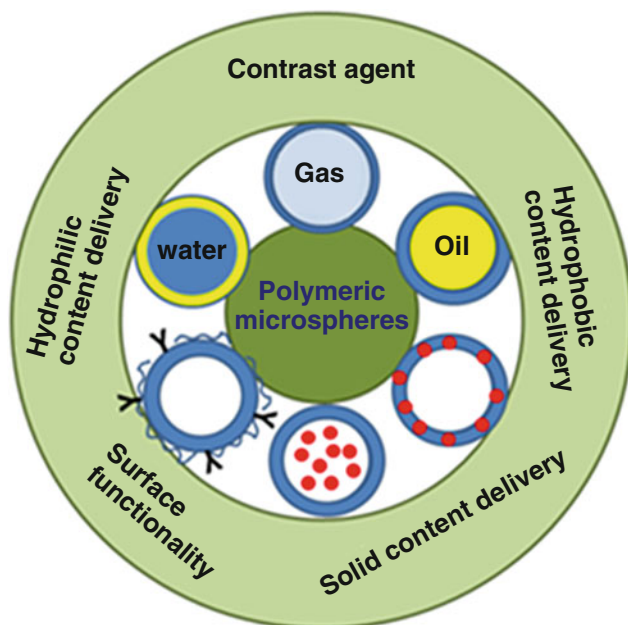
Fig. 1 Polymeric core/shell microspheres (gas-filled, oil-filled, water-filled, solid-filled, or surface functionalities) and their specific applications

phosphatase. These core–shell materials could be used as antimicrobial and biosensing devices [20]. A similar procedure was used for loading vitamin C for intravenously administrating high concentrations of vitamin C [21]. Overall, ultrasonic technique allows a one-step and efficient production of polymer-shelled microspheres to encapsulate a variety of compounds. The main focus of this chapter is to provide an overview of recent developments in ultrasonic/sonochemical synthesis of polymer-shelled nano- and microspheres and hybrid microspheres with particular attention to the mechanism, synthesis, and characterization. Although it is generally recognized that ultrasonic synthesis of colloidal systems generates particles with a wide size distribution, elegant and sophisticated ways to use ultrasonic equipment ranging from 20 kHz to 1 MHz to synthesize, modify, and characterize ultrasound-responsive micro-nanoparticles are discussed in this chapter.

Mechanism of Microsphere Formation

There are two key steps involved in the formation of air/oil-filled core–shell structures, which are ultrasound-induced emulsification and cavitation processes, as proposed by Suslick and coworkers [6, 13]. Ultrasonic emulsification creates micro-air bubbles or oil droplets dispersed in a protein solution to form protein
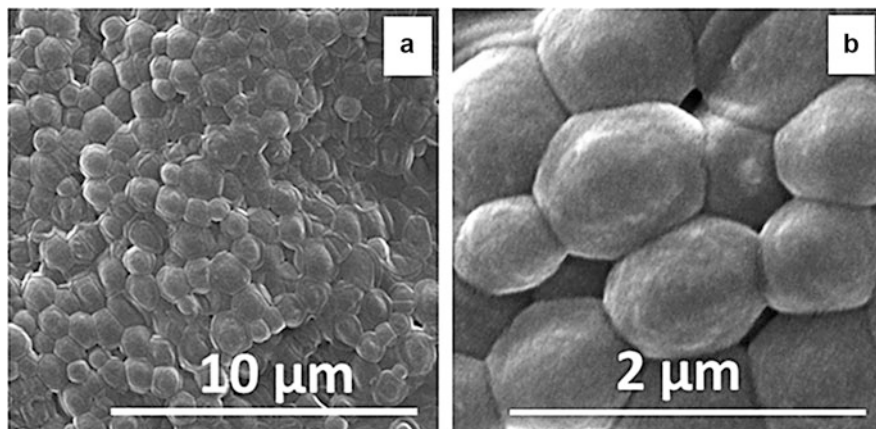
Fig. 2 SEM images of air-filled BSA microbubbles

microspheres. However, merely emulsification is not sufficient. Emulsions generated a same protein solution by vortexing failed to form stable polymeric microspheres. Suslick [6] found that protein microspheres are formed because of specific chemical reactions involving O_2 and other phenomena associated with the sonication treatment. Acoustic cavitation produced by ultrasonic irradiation in aqueous solution generates $H^{\bullet}$ and $OH^{\bullet}$, which can react further to produce H_2O_2 or HO_2 (in the presence of O_2) [22–24]. OH and HO_2 radicals are potential cross-linking agents. Through examination of the effects of various chemical traps [13], it was found that superoxide is responsible for microsphere formation. Superoxide is known to oxidize free cysteine [25]. The mechanism of the sonochemical formation of stable microspheres is due to the cross-linking of cysteine residues through disulphide bond formation.

Based on the mechanism discussed above, stable biopolymeric microspheres could be generated using those proteins bearing cysteine residues. For example, BSA, HSA, and Hb can form stable microspheres (Fig. 2) by ultrasound through chemical cross-linking of cysteine residues, whereas proteins, such as myoglobin, with no cysteine residues could not form the stable microspheres.

Cavalieri et al. [14] reported a new way to use a protein that does not have any free SH group to synthesize stable protein microspheres by ultrasound. Lysozyme, for example, has no free SH group in the molecular structure. Lysozyme is a globular protein containing 129 amino acids with four intramolecular disulfide bonds. When experiments were carried out with native lysozyme, stable microspheres could not be produced ultrasonically, possibly due to the absence of free thiol groups. It has been shown [26] that active thiol groups cannot be generated by thermal denaturation process. However, when a chemical reducing agent such as DL-Dithiothreitol (DTT) is used, partial denaturation of the protein could be achieved resulting in the formation of free thiol groups. Cavalieri et al. [14] used partial chemical denaturation by DTT to achieve stable microbubble formation. In addition to partial denaturation,
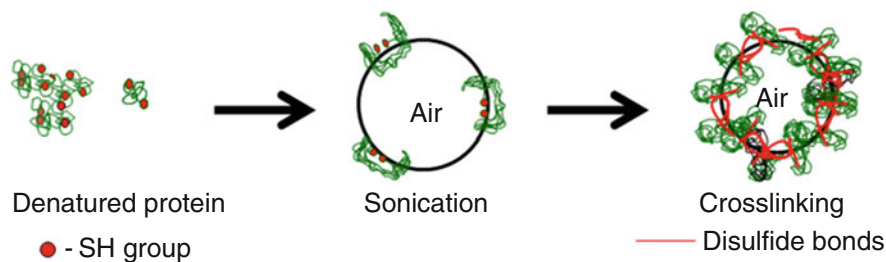
Fig. 3 Scheme of the formation of microspheres through cross-linking of disulfide bonds by ultrasound method

DTT treatment also increased the hydrophobicity of the protein, which is another important parameter for stable microbubble formation. The hydrophobic property would lead to the formation of surface active protein aggregates that migrate to air/liquid interface. Figure 3 shows a schematic representation of the events involved in the formation of protein-shelled microspheres. Another important finding in this study [14] was the establishment of a relationship between the extent of chemical reduction and the degree of cross-linking. DTT concentration and denaturation time significantly affected the stability, yield, and the size of microbubbles. The shorter chemical denaturation time resulted in the formation of larger size microbubbles. It is speculated that the degree of cross-linking is less under these experimental conditions.

In order to identify the importance of –SH functional groups for the formation of stable microspheres, Cavalieri et al. [15] used a synthetic polymer, poly(methacrylic acid) (PMA). In this study, PMA was thiolated to different extents. Stable microspheres could not be produced using pure PMA; however, using thiolated PMA stable microspheres could be ultrasonically produced (Fig. 4).

Using PMA and cystamine via carbodiimide coupling and subsequent reductions [27–30], PMA with 5–30 % -SH groups were produced. It was observed that non-thiolated PMA or PMA containing < 5 mol% thiol content did not produce stable microbubbles. It has been observed in this study that the amount of –SH substitution affected the size of the microspheres as well as the thickness of the polymer shell. Microbubbles made of PMA_{SH30} possessed a thicker shell compared to those prepared using PMA_{SH10}. In this study, Cavalieri et al. [15] have demonstrated for the first time that synthetic polymers containing sulfhydryl groups or disulfide bonds may be employed for the preparation of disulfide cross-linked shells. The sulfhydryl groups may preexist within the polymer structure or they may be introduced by a chemical reaction. However, a balance between the polymer hydrophobicity and the number of sulfhydryl moieties per chain was a crucial parameter for the successful synthesis of stable microbubbles. This is because sealing a gas phase into a microcavity by cross-linking a polymer at the air-water interface requires fine control over the chemical and physical properties of both the polymer and gas phase. Table 1 summarizes the possible mechanisms of the formation of stable polymeric microspheres in various studies.
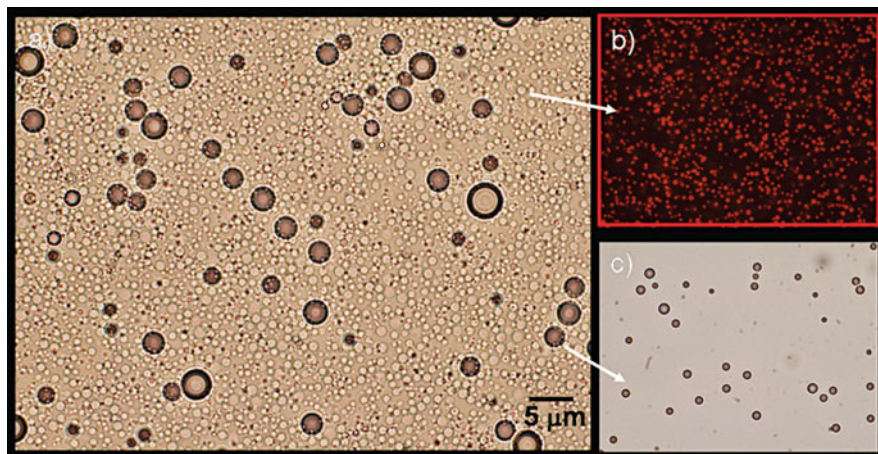
Fig. 4 (**a**) Optical microscopy image of PMA$_{SH}$ microbubbles and microcapsules synthesized by a one-pot ultrasonic synthesis. The smaller spheres (**b**) are microcapsules (labeled with fluorescent TRITC) and the larger spheres (**c**) are microbubbles (Reprinted with permission from Ref. [15])

Table 1 Summary of mechanism of formation of microspheres

Shell materials	Free SH group	S-S bond	Type of cross-linking	Core materials		Year/author/ref
				Gas	Liquid	
Bovine serum albumin (BSA), human serum albumin (HSA), and bovine hemoglobin (Hb)	Yes	Yes/no	Free SH groups	–	n-dodecane, n-decane, n-hexane, cyclohexane, toluene	1990/ Suslick/ [12, 13]
Lysozyme,	No	Yes	Breaking the S-S bond into two free SH groups	Air	–	2008/ Cavalieri/ [14]
Poly (methacrylic acid)	No	No	Chemically modified with free SH groups	Air	Perfluorohexane	2011/ Cavalieri/ [15]
Streptavidin Chitosan DNA	No	No	Hydrophobic interaction, hydrogen bond, intermolecular imine bond, van der Waals, electrostatic interactions	–	Decalin, soybean oil, dodecane	2002, 2010, 2011/ Gedanken / [31–33]

Apart from Suslick's disulphide cross-linking mechanism, Avivi and Gedanken [31] proposed other possible mechanisms of microspheres formation for those proteins that do not contain –SH groups. For example, it was found that hydrophobic interactions are responsible for the formation of poly(glutamic acid) and streptavidin microspheres in the absence of cysteine. In non-SH-containing polymers, such as chitosan, intermolecular imine cross-linking is found to be responsible for the generation of stable microspheres. Recently, Gedanken proposed [34] that the conversion of single-stranded DNA into microspheres is stabilized by electrostatic interactions while the conversion of long double-stranded DNA (ds-DNA) is prompted by a new covalent bond formation.

Gas- and Liquid-Filled Microspheres

Gas-filled microspheres (microbubbles) are used as contrast agents for ultrasound imaging [35–37]. Microbubbles with diameters between 1 and 5 μm have optimal acoustic responses in the MHz range. Microbubbles can change the acoustic impedance of the blood flow dramatically improving the echo contrast with the surrounding tissues [38, 39]. In addition, microbubbles made of biocompatible biopolymers could be used in drug and gene delivery applications [40]. In this respect, multifunctional and targeted microbubbles are uniquely suited as theranostic agents that allow molecular diagnosis, targeted drug delivery, and simultaneous monitoring and treatment of diseases. Nevertheless, when injected, micrometer-sized bubbles are constrained to the intravascular space because they are too large to exit the vasculature. Consequently microbubbles can access only targeted sites located either in the bloodstream or on the vascular endothelial surface. The development of nanobubbles for tumor imaging and therapy is therefore an attractive not yet pursued objective.

Liquid-filled microspheres are applied in biomedical fields and agriculture for the delivery of drugs, dyes, pesticides, and magnetic materials. The properties of microspheres generated could be controlled by selecting appropriate experimental conditions. The details of sonication conditions for preparing air-filled and liquid-filled microspheres with different shell materials are summarized in Tables 2 and 3. It could be seen in Table 2 that a slight variation in solution temperature could significantly affect the size of microsphere. In addition, acoustic power density, sonication time, and the size of horn were found to affect the size of polymeric microspheres.

Similar to air-filled microspheres, the size of oil-filled microspheres was also influenced by acoustic power, sonication time, and other experimental parameters as shown in Table 3. In most cases, a combination of protein denaturation, the extent of cross-linking, and the strength of shear forces were found to be responsible for the observed variations in size and size distribution of microspheres under the experimental conditions used in these studies.

Table 2 Summary of typical sonication conditions (20 kHz) for making air-filled microspheres

Shell materials	Sonication conditions					Comments on microspheres			Ref.
	Power	Time	Tip size	Temp. (initial)	pH	Size (μm)	Thickness (nm)		
Hb	Acoustic power: 150 W/cm^2	3 min	1.2 cm	23 °C	7.0	2.5	35		1994/Suslick [7]
BSA	Acoustic power: 200 W/cm^2	3 min	1.2 cm	50 °C	7.0	5	-		1991/Suslick [6]
HSA	Acoustic power: 200 W/cm^2	3 min	1.2 cm	50 °C	7.0	5	-		1991/Suslick [6]
BSA	Applied power: 180 W	30 s	3 mm	30 °C	8	2	-		2014/Vong [41]
Lysozyme	Applied power: 160 W	30 s	3 mm	25 °C	8	2.5	110		2011/Zhou [42]
PMASH	Applied power: 160 W	30 s	3 mm	25 °C	3	4.3 ~ 8	-		2011/Cavalieri [15]

Note: *Hb* bovine hemoglobin, *BSA* bovine serum albumin, *HSA* human serum albumin

Table 3 Summary of typical sonication conditions (20 kHz) for making liquid-filled microspheres

Shell materials	Type of liquid	Sonication conditions					Size of microspheres (μm)	Ref.
		Acoustic power	Time	Tip size	Temp. (initial)	pH		
BSA, HSA, Hb	Perfluorocarbon	150 W/cm²	3 min	1.2 cm	23 °C	7.0	–	1994/Suslick [7]
BSA	n-dodecane, n-decane, n-hexane, cyclohexane, toluene	200 W/cm²	3 min	1.2 cm	23 °C	7.0	2.5 ± 1	1990/Suslick [12]
Streptavidin	Decalin	150 W/cm²	3 min	1.2 cm	20 °C	6.0	5	2002/Gedanken [31]
BSA	Fragrant oil (amyl acetate)	150 W/cm²	3 min	1.2 cm	4 °C	–	1.3	2012/Gedanken [43]
Starch	Insulin + dodecane	150 W/cm²	3 min	1.2 cm	23 °C	–	0.6 ± 0.1	2010/Gedanken [44]
Avidin	Hexane	45 W/cm²	3 min	1.2 cm	25 °C	–	1.8, 3.4	2005/Gedanken [45]
α-amylase	Decalin	150 W/cm²	3 min	1.2 cm	20 °C	–	0.3, 2	2007/ Gedanken [46]
Lysozyme	Sunflower oil, tetradecane, dodecane perfluorohexane	300 W/cm²	30 sec	1.2 cm	25 °C	8	4–13, 3, 3–5.5, 2.5	2010/Zhou [16]
Lysozyme	NaCl water solution in tetradecane	14 W/cm²	30 s	1.2 cm	–	8	5	2012/Price [17]
RNA	Dodecane	26.7 W/cm²	3 min	1.2 cm	22 °C	7	0.05 to 0.60, 1 to 5	2011/Gedanken [47]
DNA	Dodecane, soybean oil	26.7 W/cm²	3 min	1.2 cm	22 °C	7	0.29–0.486	2011/Gedanken [33]

Note: *Hb* bovine hemoglobin, *BSA* bovine serum albumin, *HSA* human serum albumin

Solid-Filled Hybrid Microspheres

Solid-filled microspheres can be synthesized using a similar one-step ultrasonic procedure to encapsulate solid metals or metal oxides into polymer-shelled microspheres. For example, chitosan–TiO_2 hybrid microspheres [18] were generated by high-intensity ultrasound for antibacterial and photocatalytic applications. The experimental conditions were appropriately tuned to generate microspheres loaded with TiO_2 nanoparticles either in the shell or core. To encapsulate TiO_2 nanoparticles in the core, TiO_2 nanoparticles were first dispersed in an organic liquid (tetradecane). On the other hand, TiO_2 nanoparticles are dispersed in chitosan solution to entrap them in the shell as schematically shown in Fig. 5.

In this study, it has been shown that ultrasonic preparation technique is very simple and versatile. This procedure could be used to synthesize a variety of metal or metal oxide microspheres with hollow and porous structures for applications in paints and catalysis.
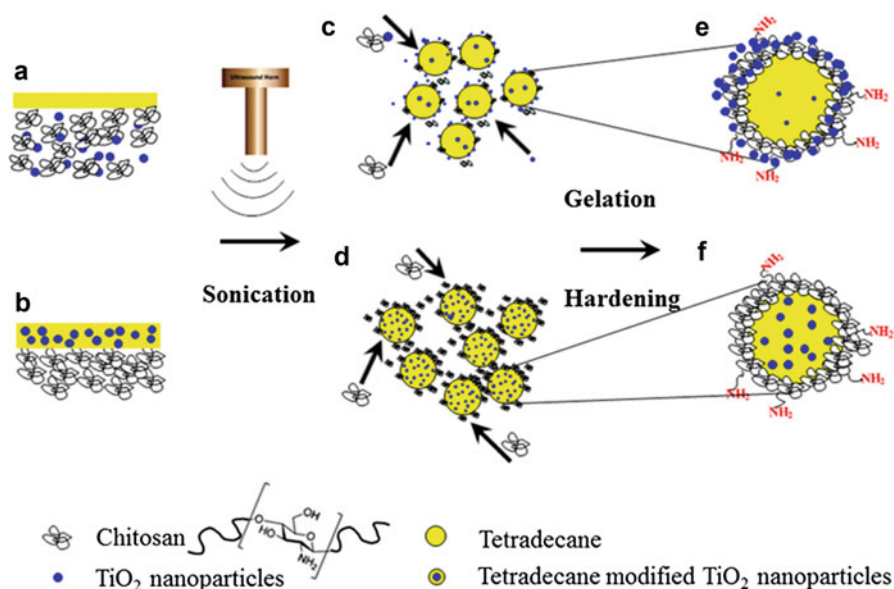
Fig. 5 Possible mechanism for the formation of TiO_2-loaded chitosan microspheres: (**a**) tetradecane layered on TiO_2 dispersed in aqueous chitosan solution, (**b**) TiO_2 dispersed in tetradecane layered on aqueous chitosan solution, (**c**) ultrasonically generated tetradecane droplets coated with TiO_2/chitosan, (**d**) ultrasonically generated TiO_2-loaded tetradecane droplets coated with chitosan, (**e**) TiO_2 loaded on chitosan shell of the microspheres, and (**f**) TiO_2 loaded in the core of chitosan microspheres (Reprinted with permission from Ref. [18])

Controlling the Properties of Polymeric Microspheres

The features of polymeric microspheres can be broken down into three categories: size, shell, and core materials. Each of these categories can be experimentally controlled and analyzed using different characterization techniques that are summarized in Fig. 6.

Size

The size and size distribution of polymeric microspheres can be controlled by sonication power, length of sonication time [42], different types and diameters of sonication horns [48], and post-sonication treatment [49]. Scanning electron microscopy (SEM) is used for the identification of the size changes in response to the sonication conditions.

Our recent investigation has shown that ultrasonic power and length of sonication could be used to control the size and size distributions of the microbubbles [42]. In Fig. 7, experimental data observed on the size and size distribution at various experimental conditions are shown. The corresponding SEM images are shown in Fig. 8. With an increase in ultrasonic power and length of sonication, it was observed that the size increases, the size distribution widens, and the size distribution changes

Fig. 6 Summary of characterization of polymeric microspheres
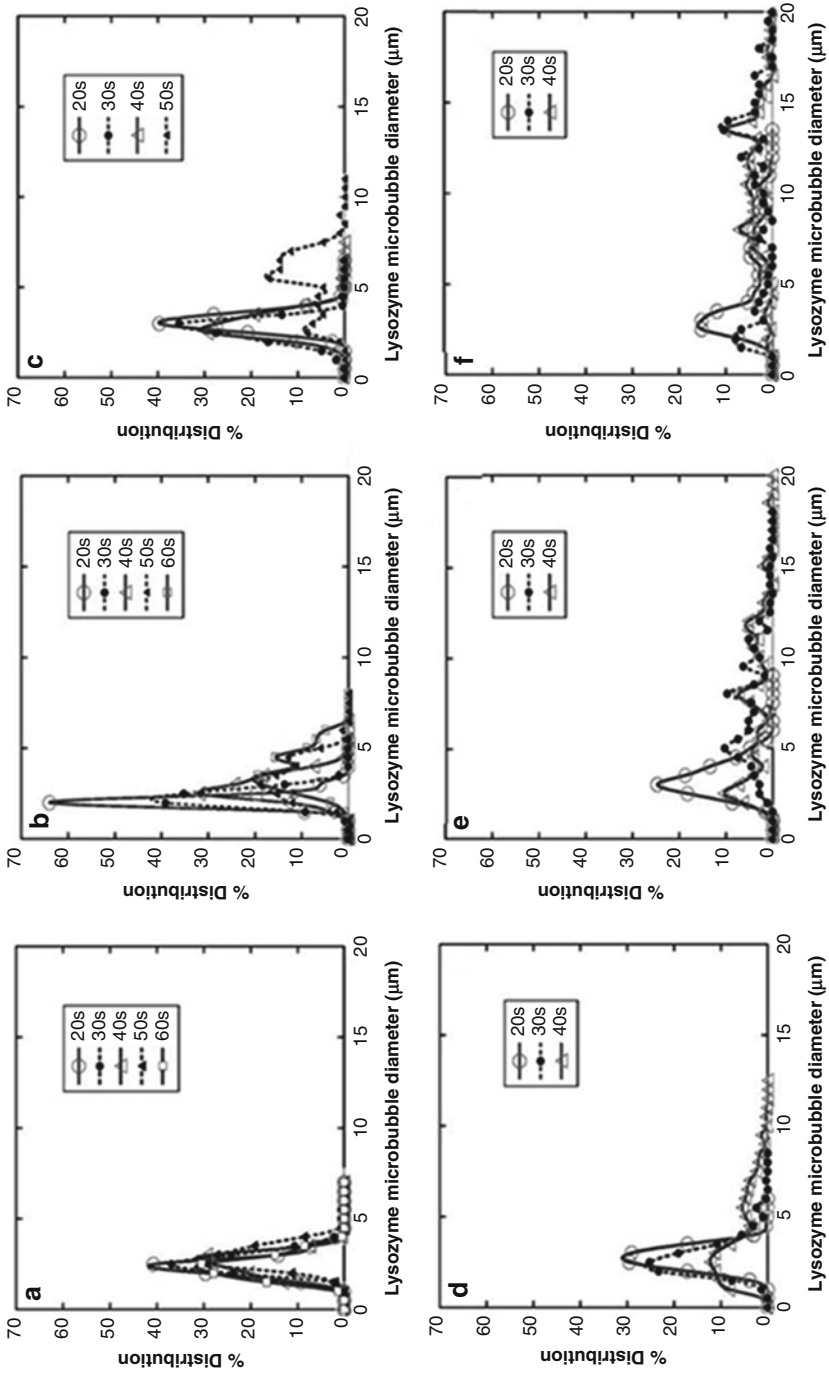
Fig. 7 The size distribution of lysozyme microbubbles sonicated at powers of 40 W (**a**), 80 W (**b**), 120 W (**c**), 160 W (**d**), 200 W (**e**), and 240 W (**f**) for different sonication times (Adapted from Ref. [42])
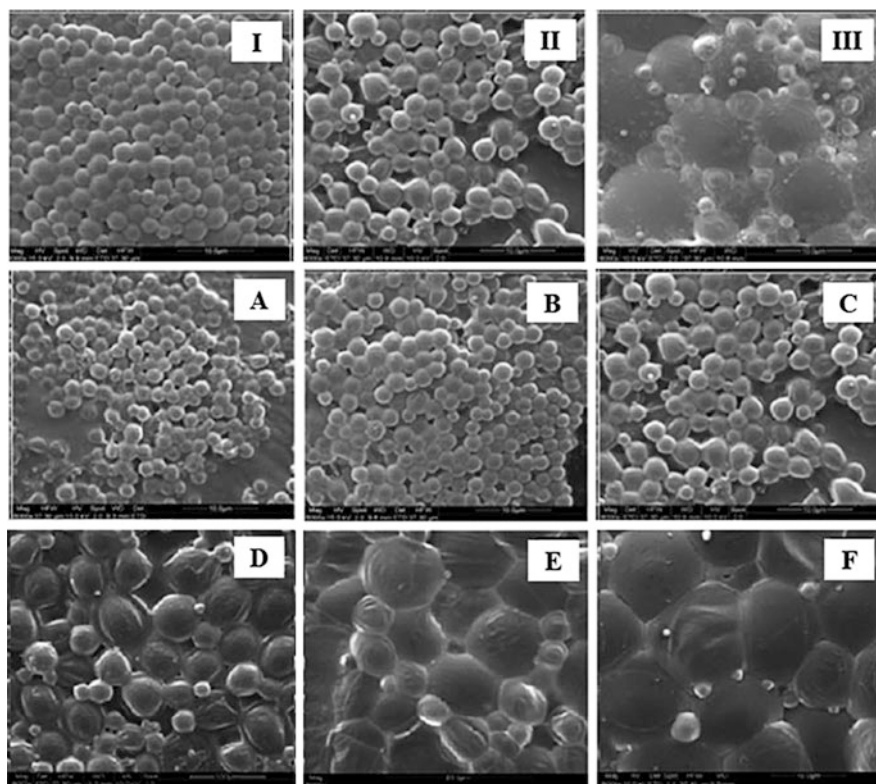
Fig. 8 SEM images of lysozyme microbubbles sonicated at 160 W for 20 s (I), 30 s (II), and 50 s (III) and powers of 80 W (**a**), 120 W (**b**), 160 W (**c**), 180 W (**d**), 200 W (**e**), and 240 W (**f**) for 30 s (Adapted from Ref. [42])

from monodispersion to a bi-/polymodal dispersion. The possible reasons have been discussed below.

As mentioned earlier, the sonochemical synthetic process for microbubbles involves two ultrasound-induced phenomena: emulsification and cavitation. It is expected that higher power generates stronger shear force creating small air bubble (droplet) emulsion in the sonication solution and also generates higher amount of HO_2 radicals to promote efficient cross-linking between the protein aggregates adsorbed at the interface of air and liquid solution, consequently, leading to the formation of small size of microbubbles.

However, in a real system, the influence of these two experimental parameters on the size and size distribution is more complex. As could be expected, efficient cross-linking between proteins would require a certain amount of oxidizing radicals that would lead to the formation of a stable shell. At very low power levels and short sonication times, there may not have been enough radicals generated due to acoustic cavitation. The results suggest that 10 s sonication time and 40 W acoustic power are

minimum requirements to produce stable microbubbles. Another aspect that is noticed in Fig. 7 is the narrow size distribution at 40 W independent of the length of sonication. It has been speculated that the physical forces generated are constant at a given power level independent of the length of sonication. At higher power levels, relatively monodisperse size distribution of microspheres is observed at short sonication times due to stronger shear forces. However, at long sonication times, bimodal distribution observed is linked to possible coalescence between bubbles [50–52] caused by strong shear forces and shockwaves generated during acoustic cavitation.

The synthesis of monodisperse stable nanobubbles is challenging task as the Laplace equation predicts that nanoscale bubbles have a very high inner gas pressure, and gas inside the nanobubble would rapidly dissolve in ambient liquid. A flow-through sonication technique was, for the first time, proposed by Zhou et al. for synthesizing stable nanometer-sized polymeric bubbles exploiting the confinement of acoustic cavitation processes.

Zhou et al. have shown that the size and size distribution of microspheres could be controlled by the type of ultrasonic horn used [48]. They [48] prepared lysozyme microspheres using 1 cm, 3 mm, and flow-through horns and discovered that the size and size distribution of microspheres were significantly affected by the type of horn used. As shown in Fig. 9, they found that 1 cm horn produced microspheres with a wide size distribution and relatively larger size range followed by 3 mm horn that produced smaller and narrow size distribution. Surprisingly, about 400 nm microspheres with a very narrow size distribution were produced when a flow-through horn was used. The observed results were discussed in terms of the active cavitation zones. They showed that the flow-through horn produced a two-dimensional cavitation zone leading to a relatively uniform physical force, which was responsible for the observed trend (Fig. 10).

A post-sonication method [49] was developed to control the size distribution of ultrasonically synthesized microbubbles. The size and shell properties of microbubbles are the most important factors for their acoustic response. The selective breakage of certain size microbubbles at selected ultrasound frequency has been used to modify the size distribution of microbubbles. The microbubbles with a certain size range might be broken under selected ultrasonic experimental conditions due to the acoustic force expanding the bubbles during the rarefaction cycles. The resonance size of the cavitation bubbles decreases with an increase in ultrasound frequency [53]. Polymer-shelled microbubbles may have a different resonance frequency compared to those of free cavitation bubbles [54]. However, the general size trend should be the same. Figure 11 shows that the size distribution of microbubbles can be selectively modified by post-sonication at various frequencies in the range 213–1056 kHz at 20 W for 20 s. For lysozyme microbubbles with an initial broad size range of 1.0 to 8.0 μm, most of large microbubbles were broken after sonication at all frequencies applied, and a relatively narrow size distribution of microbubbles was obtained. For instance, after post-sonication at 213 kHz, the average size of microbubbles was reduced to around 1.5 μm while for 647 and 1056 kHz to around 1.5–2.0 μm. Using post sonication technique, Smaller and
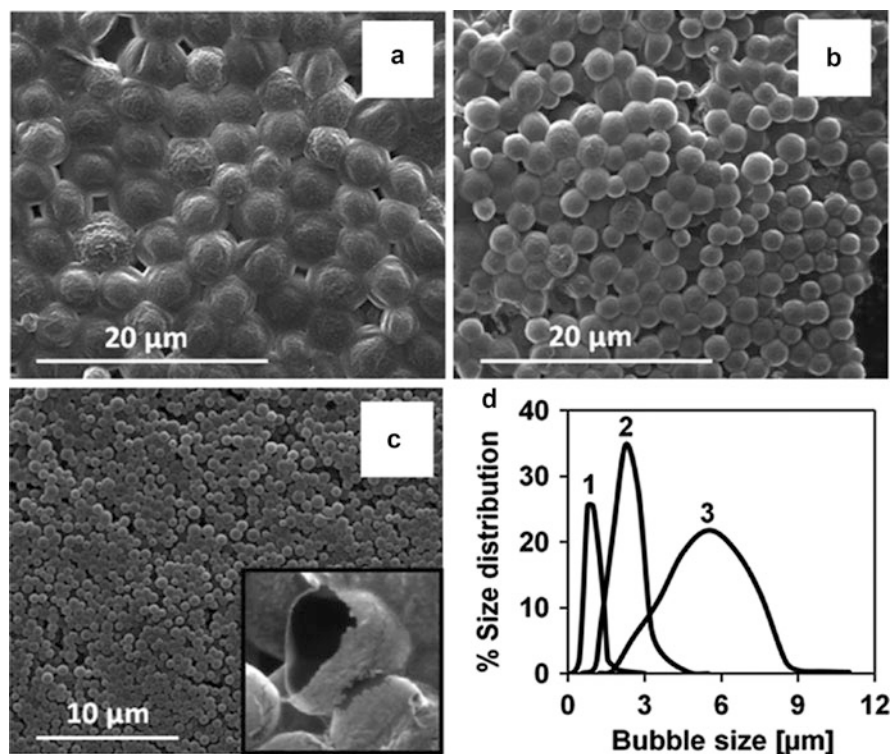
Fig. 9 SEM images of lysozyme microbubbles synthesized using (**a**) a 1 cm standard horn (160 W), (**b**) a 3 mm standard horn (120 W), and (**c**) a flow-through horn (240 W). Inset (**c**): Broken nanobubbles. Size distribution of lysozyme bubbles (**d**): (1) a flow-through horn, (2) a 3 mm standard horn, and (3) a 1 cm standard horn (Reprinted with permission from Ref. [48])

narrower size distribution of microbubbles can be obtained at low frequencies. The observed results were interpreted in terms of the physical forces generated by cavitation bubbles. It was speculated that the shear forces generated at lower frequencies are strong enough to break larger microbubbles. At very high frequencies, the shear forces are relatively weaker, and hence many larger bubbles survived the post-sonication process. The post-sonication not only changes the size distribution but also affects the population of microbubbles. The relative bubble population that survived after the post-sonication increases with an increase in the frequency (Fig. 11).

Shell

When controlling the properties of the shell of microspheres for a desired function, we must consider the following factors: stability, surface morphology, and thickness. Characteristics of microspheres are controlled by varying experimental conditions
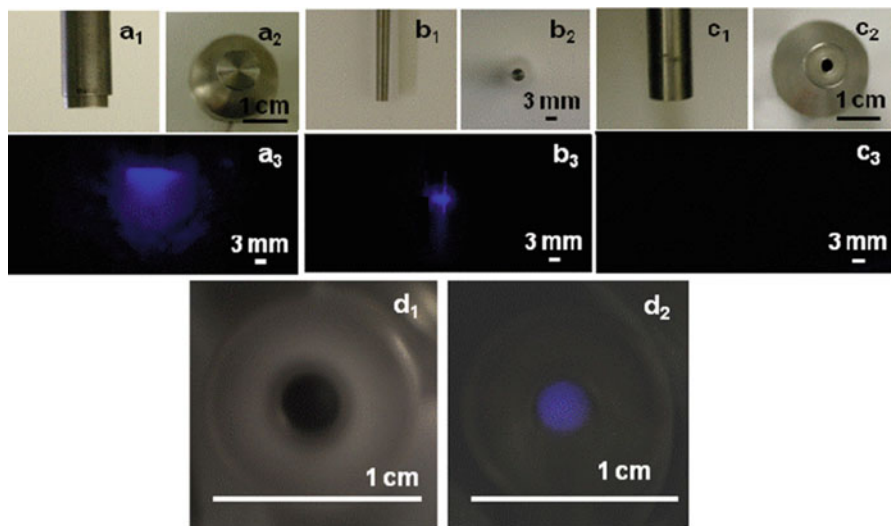
Fig. 10 Photographs of horns and SCL images: (**a**) a1 and a2 are side and head-on views, respectively, and a3 is a SCL image for a 1 cm horn; (**b**) b1 and b2 are side and head-on views, respectively, and b3 is a SCL image for a 3 mm horn; (**c**) c1 and c2 are side and head-on views, respectively, and c3 shows the (absence of) SCL image for a FT horn; (**d**) d1 is an enlarged bottom (head-on) view, and d2 is a SCL image (head-on) for a FT horn (Reprinted with permission from Ref. [48])
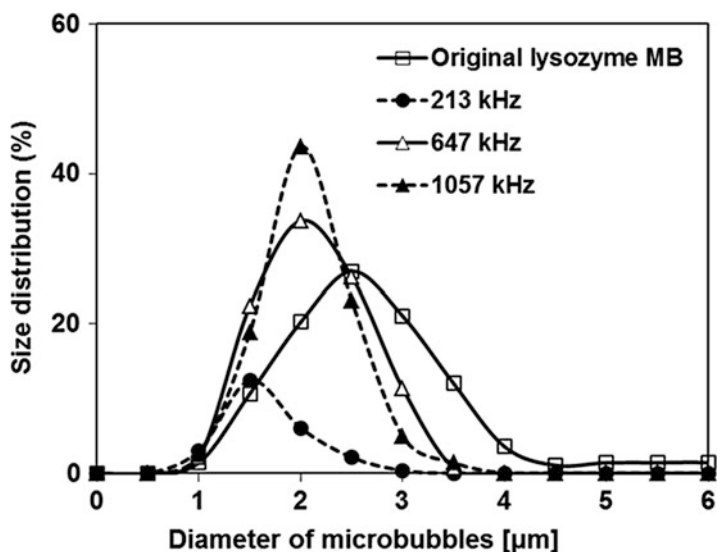
Fig. 11 Size distribution (%) of lysozyme microbubbles (*MB*) as a function of post-sonication ultrasound frequencies at 213, 647, and 1056 kHz (Adapted from Ref. [49])
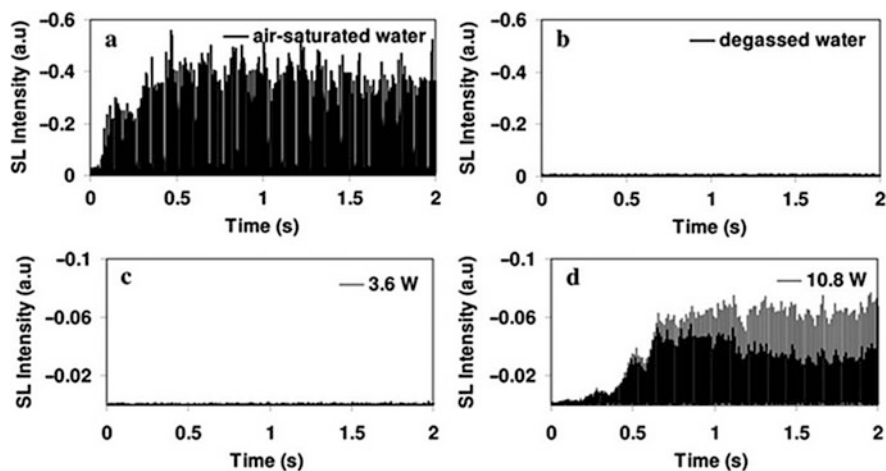
Fig. 12 Initial growth for lysozyme microbubbles at different acoustic power (Reprinted with permission from Ref. [42])

and assessed using techniques such as sonoluminescence (SL), SEM, and zeta potential measurements. A novel pulsed sonoluminescence technique [55] was developed to determine the strength of microbubble shell. It is known [56] that the initial growth of active cavitation bubbles takes a certain number of acoustic pulses. This is due to the fact that the gas bubbles present in a liquid are well below the resonance size and they grow by rectified diffusion over a number of acoustic cycles. As can be seen in Fig. 12, it takes about 20 acoustic pulsed for SL to reach a steady state in air-saturated water. When degassed water is used, no SL could be observed even after hundreds of acoustic cycles due to the absence of gas nuclei. The approach of the pulsed SL method is to use ultrasonically generated microbubbles as cavitation bubble source. If a protein-shelled microbubble is sonicated, gas trapped inside the microbubble could act as a source for cavitation bubbles provided the shell is broken and the gas is released. Obviously, a stronger shell would need higher acoustic pressure for breaking the shell and vice versa. Knowing the pressure required to break the shell, the relative strengths of shells of microbubbles generated under various experimental conditions could be determined using the pulsed SL technique. It is shown in Fig. 12 that microbubbles need higher acoustic pressures to break the shell. At 3.6 W, no SL could be observed whereas SL growth could be observed at 10.8 W.

Thus using pulsed SL technique, the relative strengths of ultrasonically generated microbubbles could be evaluated. In order to show that the bubbles are broken under high-frequency ultrasonication, SEM images were recorded. These images were also used to measure the shell thickness and surface morphology. Figure 13 shows SEM images of pre- and post-sonicated microbubbles.
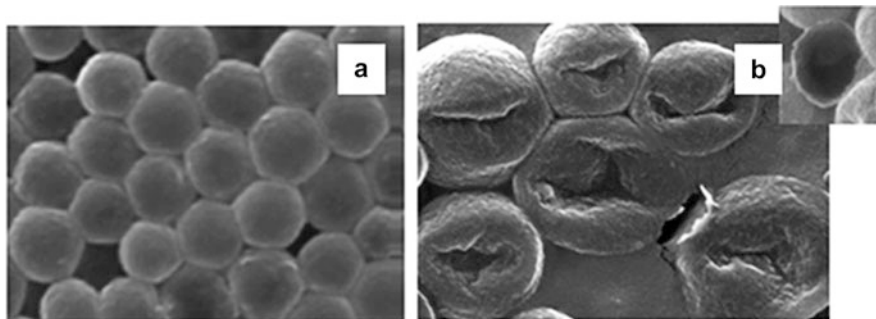
Fig. 13 SEM images of microbubbles before sonication (**a**) and post-sonication (**b**)

Morphology and Thickness of Microbubbles by Using SEM

The versatile applications of ultrasonically synthesized microspheres strongly depend upon their morphological characteristics, for example, drug-loading capacity, targeted delivery of the loaded drug, echogenic properties, etc.; microspheres could be significantly improved by controlling their morphological properties. Recent studies have shown that the morphology of polymeric microspheres could be controlled by varying the ultrasonic experimental conditions. Figure 14 shows that a rough surface morphology could be produced at low ultrasonic power and smooth-surfaced microspheres could be formed at higher power levels. It has been speculated that the strength of shear forces generated during acoustic cavitation plays a major role in controlling the surface morphology. A strong shear force at higher power levels leads to the generation of smoother surface and vice versa.

In addition to the acoustic power, the extent of cross-linking was also found to influence the morphology of the shell of polymeric microspheres [15]. It can be seen in Fig. 15 that the extent of thiolation in PMA and hence the extent of cross-linking affect the morphology. It was speculated that a higher –SH content in PMA lead to the formation of excess aggregation of polymeric nanoparticles on the surface leading to the formation of a rougher surface.

A similar observation was made in another study [42] where the ultrasonic power and length of sonication were found to influence the morphology of polymeric microspheres. With an increase in sonication power and time, the amount of oxidizing radicals increases. This would lead to an increase in the extent of cross-linking between protein nanoaggregates on the shell leading to a rougher surface. It can be seen in Fig. 16 that a rough surface morphology is obtained at higher power levels. It has also been observed in this study that the shell thickness decreased with an increase in the sonication power and sonication length. For instance, the thickness of microbubbles was approximately 110 nm for samples sonicated at 120 W for 20s, while samples sonicated at 240 W for 20 s–60 s resulted in microbubbles with 75 nm–20 nm thickness. These results indicate that higher power and longer sonication time led to a thinner shell. These results indicate that longer sonication time led to a thinner shell. The reason for this observation may be due to the coalescence within the sonication system and the
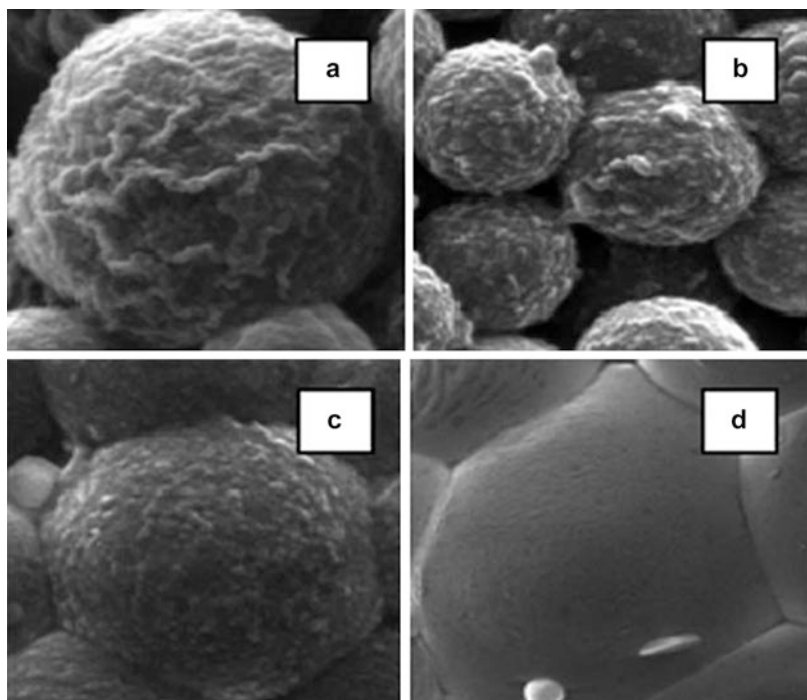
Fig. 14 Morphology of lysozyme microbubbles varied with sonication power and time (**a**) 40 W 50 s, (**b**) 80 W 20 s, (**c**) 120 W 30 s, and (**d**) 240 W 40 s (Reprinted with permission from Ref. [42])
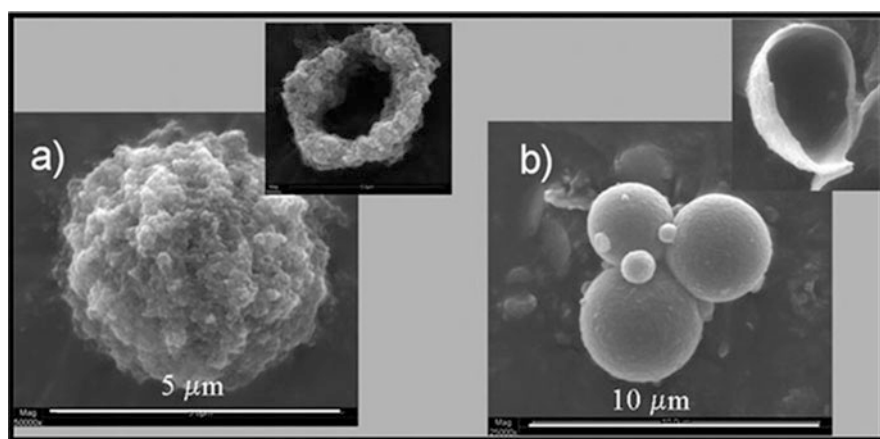
Fig. 15 SEM images of microbubbles composed of (**a**) PMA_{SH30} and (**b**) PMA_{SH10}, respectively (Reprinted with permission from Ref. [15])

Fig. 16 SEM image of
broken microbubbles
sonicated at 120 W for 30 s
(Reprinted with permission
from Ref. [42])
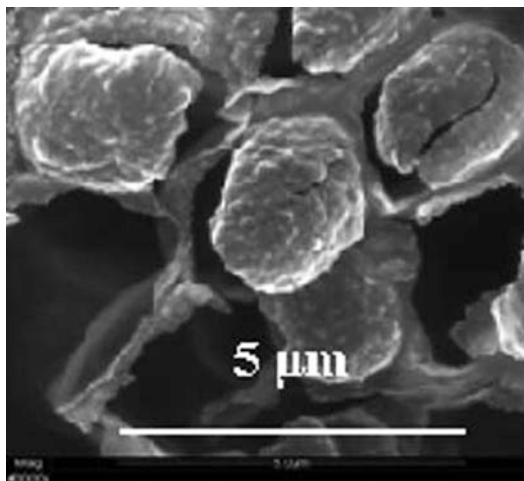
cavitation shear forces removing the protein aggregates from the surface of the
microbubbles prior to cross-linking.

Characterization of the Core Materials

The ability of microspheres to release the oil core can be studied using fluorescence
spectroscopy and microscopy. In order to probe the hydrophobic liquids encapsu-
lated inside the microspheres, organic dyes could be used. For example, Nile red was
used as a model fluorescence dye to characterize tetradecane core lysozyme-shelled
microspheres [16]. Fluorescence optical microscopy and the confocal laser scanning
microscopy (CLSM) were used to identify the dye-loaded tetradecane core. Fig-
ures 17 and 18 show that the fluorescence color is distributed homogeneously across
the cross-section of Nile red/tetradecane-filled lysozyme microspheres, indicating
that the microsphere is filled with tetradecane.

While the encapsulation of the core could be readily confirmed by microscopic
images, the release of the core into a medium when required needs a bit more careful
study. Steady-state fluorescence spectroscopy was used for this purpose [16].
Figure 19 shows the fluorescence spectrum of Nile red in tetradecane, which has
two main emission bands centered around 532 and 573 nm. The ratio between these
two bands seems to be influenced by the hydrophobic environment around Nile red.
Figure 19b shows that the ratio increases with an increase in the hydrophobicity of
the solvent environment.

The ratio observed for Nile red in encapsulated tetradecane core is similar to that
observed when Nile red is simply dissolved in tetradecane confirming that
tetradecane is protected by the protein shell when dispersed in water or
tetradecane/water mixture. However, when the shell is broken (by high intensity
ultrasound) and tetradecane is released, Nile red is exposed to the aqueous
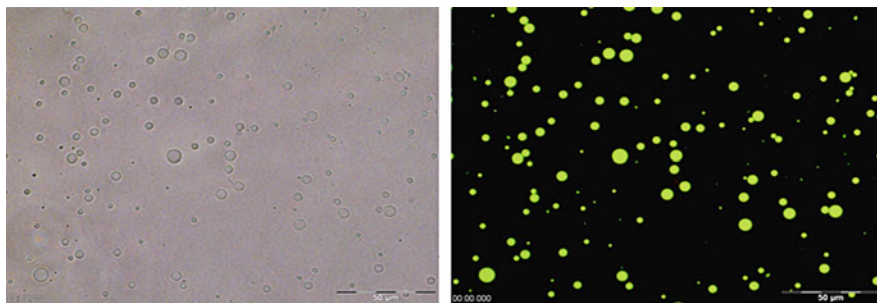
Fig. 17 Optical (*left*) and fluorescence (*right*) microscopy images of tetradecane-filled lysozyme microspheres

Fig. 18 Confocal laser scanning microscopic images of Nile red/tetradecane-filled lysozyme microspheres (Reprinted with permission from Ref. [16])
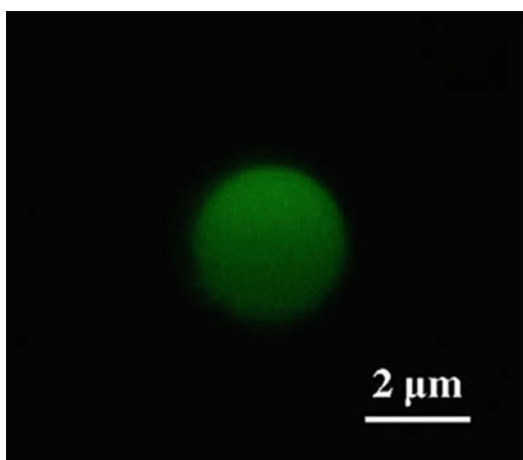
environment, and hence the ratio is increased as shown in Fig. 19b. These results prove that the encapsulated core materials could be released when needed.

Functional Properties of Polymer-Shelled Microspheres

Polymer-shelled microspheres offer a platform for further surface functionalization with biomolecules. The surface coating of positively or negatively charged microspheres is obtained using a deposition of proteins or polysaccharides, Alternatively, biomolecules can be coupled to the microspheres' surface exploiting chemical functionalities such as thiol, amine, or carboxyl groups. For instance, alkaline phosphatase was coupled to the surface of lysozyme microbubbles to obtain a floating biosensor for the detection of organophosphorus-based pesticides such as
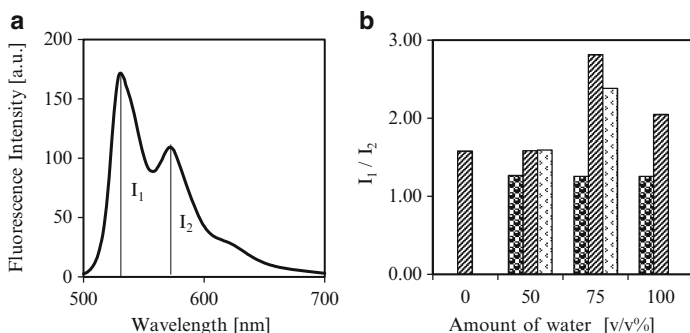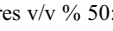
Fig. 19 (**a**) Fluorescence spectrum of nile red in tetradecane and (**b**) the intensity ratios of peak at 532 nm (I_1) and peak at 573 nm (I_2): ▨▨▨ – nile red in tetradecane mixed with 0, 50, 75, and 100 v/v% water. ▦▦▦ – unbroken nile red/tetradecane-filled lysozyme microspheres in tetradecane and water mixtures v/v % 50:50, 25:75 and 0:100. ▥▥▥ – broken nile red/tetradecane-filled lysozyme microspheres in tetradecane and water mixtures v/v% 50:50 and 25:75 (Reprinted with permission from Ref. [16])

paraoxon [20]. Gold nanoparticles were immobilized on microbubbles (Fig. 20) by exploiting the electrostatic interactions between serum albumin-stabilized gold nanoparticles and lysozyme microbubbles. In this work an ultrasound-responsive antimicrobial microdevice has been engineered for the first time by Cavalieri et al. [20]. Lysozyme microbubbles' antimicrobial activity is attributed to the strong interaction between microbubbles and bacteria. Microbubbles' surface hydrophobicity and cationic properties promote the interaction with the bacterial cell wall compromising its integrity and functions.

Gold nanoparticles immobilized on lysozyme microbubbles significantly improved the antimicrobial efficacy against *M. lysodeikticus*. Gold nanoparticles play a role in accelerating bacterial cell wall breakdown by acting as binding sites for bacteria and consequently increasing the interaction of *M. lysodeikticus* with the surface of microbubbles. The addition of gold nanoparticles and alkaline phosphatase did not compromise the echogenicity of lysozyme microbubbles.

Cavalieri et al. investigated the [57] association of lysozyme-shelled microbubbles (LSMB) and oil-filled lysozyme-shelled microcapsules (LSMC) with human breast adenocarcinoma cells (SKBR3). These studies showed that the positively charged LSMB and LSMC are not cytotoxic and can be readily internalized and degraded by the SKBR3 cells. The cellular internalization kinetics of LSMB and LSMC was evaluated using flow cytometry and confocal and scanning electron microscopic analyses (Fig. 21). Interestingly, LSMBs and LSMCs showed a different uptake kinetics and intracellular degradation pattern. Authors speculated that the assembly and deposition of the protein at the air–liquid or oil–liquid interfaces is different, resulting in a different biological behavior.
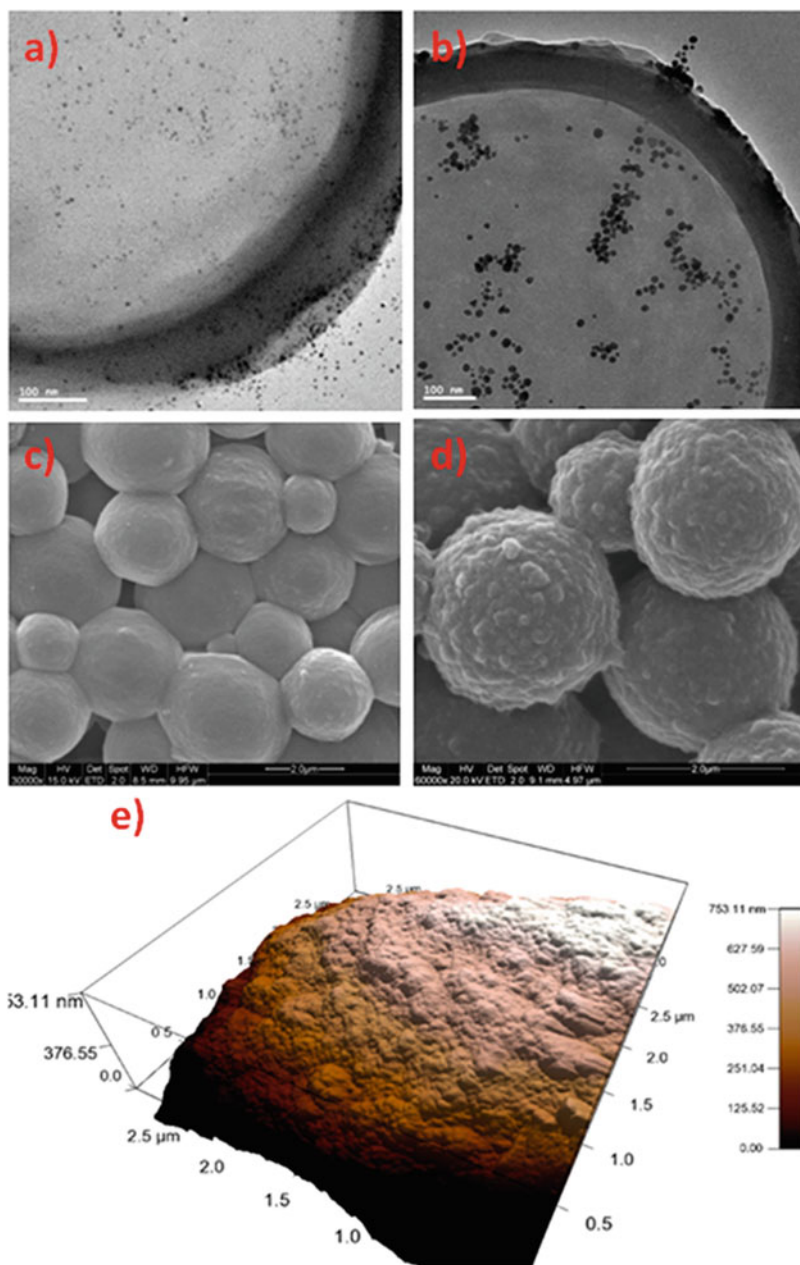
Fig. 20 (**a**, **b**) TEM image shows the presence of Au nanoparticles on lysozyme microbubbles surface; (**c**, **d**) SEM image confirms the presence of Au nanoparticles on the rough surface of microbubbles; (**e**) AFM image of lysozyme microbubbles decorated with Au nanoparticles (Reprinted with permission from Ref. [20])
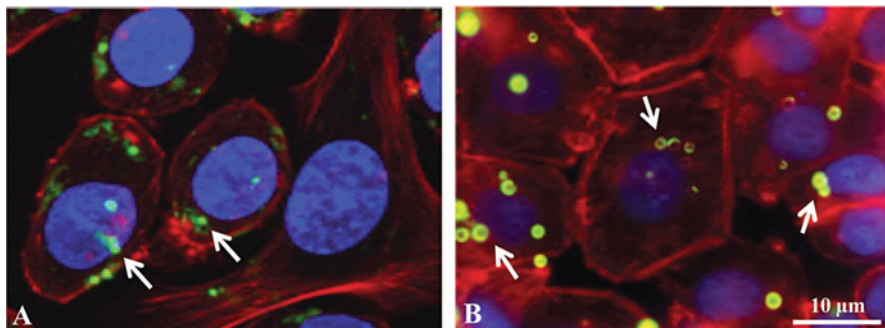
Fig. 21 CLSM image microparticles internalized into SKBR3 cells after incubation for 2 h with LSMB-FITC (**a**) and LSMC–FITC (**b**). *Green*, *red*, and *blue* indicate FITC-conjugated microparticles, actin filaments, and nuclei stained with Hoechst 33342, respectively (Reprinted with permission from Ref. [57])

Conclusions and Future Perspectives

A review of the work carried out by many researchers in the last decades to optimize the experimental parameters and fine tune the structural features of polymer-shelled microspheres and microcapsules is presented. A cross-linked polymer shell allows to control the mechanical properties of the microspheres and liquid-filled microcapsules providing a greatly increased stability and a higher loading capacity. The mechanisms involved in the formation of microbubbles and microcapsules highlighted the importance of the presence of thiol moieties on the polymer backbone for the ultrasonic synthesis of stable microspheres. Finally, innovative applications of polymer-shelled microspheres in different areas have been also highlighted. Although considerable advances have been made in the areas of synthesis and characterization of polymer-shelled microsphere, there are still significant issues that remain a challenge. For instance, in enhancing the versatility, the ultrasonic technique should be trialed using a variety of macromolecules with suitable amphiphilic properties and biocompatibility to generate multifunctional delivery vehicles.

References

1. Webb AG, Wong M, Kolbeck KJ, Magin RL, Wilmes LJ, Suslick KS (1996) Sonochemically produced fluorocarbon microspheres: a new class of magnetic resonance imaging agent. J Magn Reson Imag 6:675–683
2. Lee TM, Oldenburg AL, Sitafalwalla S, Marks DL, Luo W, Toublan FJ, Suslick KS, Boppart SA (2003) Engineered microsphere contrast agents for optical coherence tomography. Opt Lett 28:1546–1548
3. Langer R (1990) New methods of drug delivery. Science 249:1527–1533

4. Lee TK, Sokoloski TD, Royer GP (1981) Serum albumin beads: an injectable, biodegradable system for the sustained release of drugs. Science 213:233–235
5. Heidebach T, Forest P, Kulozik U (2009) Transglutaminase-induced caseinate gelation for the microencapsulation of probiotic cells. Int Dairy J 19:77–84
6. Grinstaff MW, Suslick KS (1991) Air-filled proteinaceous microbubbles: synthesis of an echo-contrast agent. Proc Natl Acad Sci U S A 88:7708–7710
7. Wong M, Suslick KS (1995) Sonochemically produced hemoglobin microbubbles. Mater Res Soc Symp Proc 372:89–94
8. Toublan FJ, Boppart S, Suslick KS (2006) Tumor targeting by surface-modified protein microspheres. J Am Chem Soc 128:3472–3473
9. Feinstein SB, Keller MW, Dick CD (1987) Successful transpulmonary contrast echocardiography in monkeys. J Am Coll Cardiol 9:111A
10. Keller MW, Feinstein SB, Briller RA, Powsner SM (1986) Automated production and analysis of echo contrast agents. J Ultrasound Med 5:493–498
11. Feinstein SB, Lang RM, Dick C, Neumann A, Al-Sadir J, Chua KG, Carroll J, Feldman T, Borow KM (1988) Contrast echocardiography during coronary arteriography in humans: perfusion and anatomic studies. J Am Coll Cardiol 11:59–65
12. Suslick KS, Grinstaff MW (1990) Protein microencapsulation of nonaqueous liquids. J Am Chem Soc 112:7807–7809
13. Suslick KS, Grinstaff MW, Kolbeck KJ, Wong M (1994) Characterization of sonochemically prepared proteinaceous microspheres. Ultrason Sonochem 1:S65–S68
14. Cavalieri F, Ashokkumar M, Grieser F, Caruso F (2008) Ultrasonic synthesis of stable, functional lysozyme microbubbles. Langmuir 24:10078–10083
15. Cavalieri F, Zhou M, Caruso F, Ashokkumar M (2011) One-pot ultrasonic synthesis of multifunctional microbubbles and microcapsules using synthetic thiolated macromolecules. Chem Commun 47:4096–4098
16. Zhou M, Leong TSH, Melino S, Cavalieri F, Kentish S, Ashokkumar M (2010) Sonochemical synthesis of liquid-encapsulated lysozyme microspheres. Ultrason Sonochem 17:333–337
17. Skinner EK, Price GJ (2012) Encapsulation and release of aqueous components from sonochemically produced protein microspheres. Chem Commun 48:9260–9262
18. Zhou M, Babgi B, Gupta S, Cavalieri F, Alghamdi Y, Aksu M, Ashokkumar M (2015) Ultrasonic fabrication of TiO_2/chitosan hybrid nanoporous microspheres with antimicrobial properties. RSC Adv 5:20265–20269
19. Cavalieri F, Zhou M, Tortora M, Ashokkumar M (2014) Ultrasound-assisted preparation of nanopolymeric and micropolymeric materials for the encapsulation of bioactive agents. In: Manickam S, Ashokkumar M (eds) Cavitation: a novel energy-efficient technique for the generation of nanomaterials. Pan Stanford Publishing Pte Ltd, Singapore, pp 227–261
20. Cavalieri F, Micheli L, Kaliappan S, Teo BM, Zhou M, Palleschi G, Ashokkumar M (2013) Antimicrobial and biosensing ultrasound-responsive lysozyme-shelled microbubbles. ACS Appl Mater Interfaces 5:464–471
21. Cavalieri F, Micheli L, Zhou M, Tortora M, Palleschi G, Ashokkumar M (2013) Electrochemical investigation of the interaction between lysozyme-shelled microbubbles and vitamin C. Anal Bioanal Chem 405:5531–5538
22. Weissler A (1959) Formation of hydrogen peroxide by ultrasonic waves: free radicals. J Am Chem Soc 81:1077–1081
23. Del Duca M, Jeager E, Davis MO, Hovarka F (1958) Isotopic technique in the study of the sonochemical formation of hydrogen peroxide. J Acoust Soc Am 30:301–307
24. Lippitt B, McCord JM, Fridovich I (1972) The sonochemical reduction of cytochrome c and its inhibition by superoxide dismutase. J Biol Chem 247:4688–4690
25. Asada K, Kanematsu S (1976) Reactivity of thiols with superoxide radicals. Agri Biol Chem 40:1891–1892

26. Touch V, Hayakawa S, Saitoh K (2004) Relationships between conformational changes and antimicrobial activity of lysozyme upon reduction of its disulfide bonds. Food Chem 84:421–428
27. Price AD, Zelikin AN, Wang Y, Caruso F (2009) Triggered enzymatic degradation of DNA within selectively permeable polymer capsule microreactors. Angew Chem Int Ed 48:329–332
28. De Rose R, Zelikin AN, Johnston APR, Sexton A, Chong S-F, Cortez C, Mulholland W, Caruso F, Kent SJ (2008) Binding, internalization, and antigen presentation of vaccine-loaded nanoengineered capsules in blood. Adv Mater 20:4698–4703
29. Sivakumar S, Bansal V, Cortez C, Chong S-F, Zelikin AN, Caruso F (2009) Degradable, surfactant-free, monodisperse polymer-encapsulated emulsions as anticancer drug carriers. Adv Mater 21:1820–1824
30. Zelikin AN, Li Q, Caruso F (2008) Disulfide-stabilized poly(methacrylic acid) capsules: formation, cross-linking, and degradation behavior. Chem Mater 20:2655–2661
31. Avivi S, Gedanken A (2002) S-S bonds are not required for the sonochemical formation of proteinaceous microspheres: the case of streptavidin. Biochem J 366:705–707
32. Skirtenko N, Tzanov T, Gedanken A, Rahimipour S (2010) One-step preparation of multifunctional chitosan microspheres by a simple sonochemical method. Chem Eur J 16:562–567
33. Shimanovich U, Eliaz D, Aizer A, Vayman I, Michaeli S, Shav-Tal Y, Gedanken A (2011) Sonochemical synthesis of DNA nanospheres. Chem Bio Chem 12:1678–1681
34. Silva R, Ferreira H, Azoia NG, Shimanovich U, Freddi G, Gedanken A, Cavaco-Paulo A (2012) Insights on the mechanism of formation of protein microspheres in a biphasic system. Mol Pharmaceutics 9:3079–3088
35. Dindyal S, Kyriakides C (2011) Ultrasound microbubble contrast and current clinical applications. Recent Pat Cardiovasc Drug Discov 6:27–41
36. Postema M, Helge Gilja O (2011) Contrast-enhanced and targeted ultrasound. World J Gastroenterol 17:28–41
37. Cavalieria F, Zhou M, Ashokkumar M (2010) The design of multifunctional microbubbles for ultrasound image-guided cancer therapy. Curr Top Med Chem 10:1198–1210
38. Gramiak R, Shah PM (1968) Echocardiography of the aortic root. Invest Radiol 3:356–366
39. Powsner SM, Keller MW, Sanfle J, Feinstein SB (1986) Quantitation of echo contrast effects. Am J Physiol Imag 1:124–128
40. Cavalieri F, Zhou M, Tortora M, Lucilla B, Ashokkumar M (2012) Methods of preparation of multifunctional microbubbles and their in vitro / in vivo assessment of stability, functional and structural properties. Curr Pharm Des 18:2135–2151
41. Vong F, Son Y, Bhuiyan S, Zhou M, Cavalieri F, Ashokkumar M (2014) A comparison of the physical properties of ultrasonically synthesized lysozyme- and BSA-shelled microbubbles. Ultrason Sonochem 21:23–28
42. Zhou M, Cavalieri F, Ashokkumar M (2011) Tailoring the properties of ultrasonically synthesised microbubbles. Soft Matter 7:623–630
43. Tzhayik O, Cavaco-Paulo A, Gedanken A (2012) Fragrance release profile from sonochemically prepared protein microsphere containers. Ultrason Sonochem 19:858–863
44. Grinberg O, Gedanken A (2010) The development and characterization of starch microspheres prepared by a sonochemical method for the potential drug delivery of insulin. Macromol Chem Phys 211:924–931
45. Avivi S, Gedanken A (2005) The preparation of avidin microspheres using the sonochemical method and the interaction of the microspheres with biotin. Ultrason Sonochem 12:405–409
46. Avivi S, Gedanken A (2007) Are sonochemically prepared a-amylase protein microspheres biologically active? Ultrason Sonochem 14:1–5
47. Shimanovich U, Volkov V, Eliaz D, Aizer A, Michaeli S, Gedanken A (2011) Stabilizing RNA by the sonochemical formation of RNA nanospheres. Small 7:1068–1074

48. Zhou M, Cavalieri F, Caruso F, Ashokkumar M (2012) Confinement of acoustic cavitation for the synthesis of protein-shelled nanobubbles for diagnostics and nucleic acid delivery. ACS Macro Lett 1:853–856
49. Zhou M, Cavalieri F, Ashokkumar M (2012) Modification of the size distribution of lysozyme microbubbles using a post sonication technique. Instrument Sci Technol 40:51–60
50. Lee J, Kentish SE, Ashokkumar M (2005) The effect of surface-active solutes on bubble coalescence in the presence of ultrasound. J Phys Chem B 109:5095–5099
51. Ashokkumar M, Lee J, Kentish SE, Grieser F (2007) Bubbles in an acoustic field: an overview. Ultrason Sonochem 14:470–475
52. Sunartio D, Ashokkumar M, Grieser F (2007) Study of the coalescence of acoustic bubbles as a function of frequency, power, and water-soluble additives. J Am Chem Soc 129:6031–6036
53. Brotchie A, Grieser F, Ashokkumar M (2009) The effect of power and frequency on acoustic cavitation bubble size distributions. Phys Rev Lett 102:084302-1-4
54. Khismatullin DB (2004) Resonance frequency of microbubbles: effect of viscosity. J Acoust Soc Am 116:1463–1473
55. Ashokkumar M, Hall R, Mulvaney P, Grieser F (1997) Sonoluminescence from aqueous alcohol and surfactant solutions. J Phys Chem B 101:10845–10850
56. Lee J, Ashokkumar M, Kentish SE, Grieser F (2005) Determination of the size distribution of sonoluminescence bubbles in a pulsed acoustic field. J Am Chem Soc 127:16810–16811
57. Cavalieri F, Colone M, Stringaro A, Tortora M, Calcabrini A, Zhou M, Ashokkumar M (2013) Influence of the morphology of lysozyme-shelled microparticles on the cellular association, uptake, and degradation in human breast adenocarcinoma cells. Part Part Syst Charact 30:695–705

Bioeffects of Ultrasound and Its Therapeutic Application

Ryohei Ogawa, Akihiro Morii, Akihiko Watanabe, Zheng-Guo Cui, and Takashi Kondo

Contents

Abstract

Ultrasound has been safely utilized in the medical field for a long time, and its application range is still growing widely nowadays.

Analyses of interactions between ultrasound and aqueous solution were studied for a long time. Free radical formation, an important chemical effect of ultrasound, which causes a major impact on bioeffects was discovered more than 30 years ago. However, the bioeffects caused by ultrasound cannot be

R. Ogawa (✉) • T. Kondo
Departments of Radiological Sciences, Graduate School of Medicine and Pharmaceutical Sciences, University of Toyama, Toyama, Japan
e-mail: ogawa@med.u-toyama.ac.jp

A. Morii
Departments of Urology, Graduate School of Medicine and Pharmaceutical Sciences, University of Toyama, Toyama, Japan

Urology Department, Kurobe City Hospital, Kurobe, Japan

A. Watanabe
Departments of Urology, Graduate School of Medicine and Pharmaceutical Sciences, University of Toyama, Toyama, Japan

Z.-G. Cui
Departments of Public Health, Graduate School of Medicine and Pharmaceutical Sciences, University of Toyama, Toyama, Japan

attributed only to free radical formation. They are interactions between the living body and a wide variety of very complex effects caused by ultrasound. Thus, one would have to say that mechanism underlying the ultrasound bioeffects is a long way from full clarification. However, analyzing how the living body could respond to ultrasound at a biomolecular level has become possible. Obtained results out of such analyses have advanced therapeutic ultrasound through its development, improvement, and assurance of safety. Thus, ultrasound in the medical field will be more and more dispensable from this time forward.

In this chapter, first we take a look at physical and chemical effects of ultrasound, which may provide some influence to the ultrasound bioeffects. Then, we move to ultrasound bioeffects and responses of cells and living tissues to ultrasound, particularly we review them at a biomolecular level. Later on, we discuss the therapeutic applications of ultrasound, including HIFU and LIPUS, which have already been applied clinically for cancer therapy and bone fracture healing, respectively. In addition to those, we also describe the latest research findings such as ultrasound-mediated gene therapy and drug delivery systems.

Introduction

The irradiation induced by ultrasound generates various effects. In particular, chemical effects may have strong bioeffects. The chemical effects of ultrasound using aqueous solutions are mainly caused by the impact of acoustic cavitation. Cavitation represents a complex phenomenon associated with the formation of small gas bubbles, which grow and eventually collapse in the medium. The very high temperature and pressure generated in connection with gas bubble collapse cause the pyrolysis of water molecules into hydroxyl (*OH) radicals and hydrogen (H) atoms. It should be stressed that investigations to understand the chemical effects of ultrasound in aqueous solutions are very important in terms of safety with respect to the use of ultrasound in addition to optimizing the therapeutic effects of ultrasound treatments. With knowledge of sonochemistry, the adverse events of ultrasound as a tool for diagnosis and therapy can be anticipated and minimized. In this chapter, we discuss the bioeffects of ultrasound associated with cell membrane and DNA damage in addition to gene expression profile changes and cell death resulting from chemical as well as other effects, including mechanical impacts.

Recently, analyses of the bioeffects of ultrasound at the molecular level have been widely conducted, and the obtained results have been used to advance clinical applications. Ultrasound has long been used as an imaging tool for diagnosis in medicine. Subsequently, taking advantage of the thermal and mechanical effects of ultrasound, high-intensity focused ultrasound (HIFU) cancer therapy and extracorporeal shock wave lithotripter therapy (ESWLT) were developed. These modalities
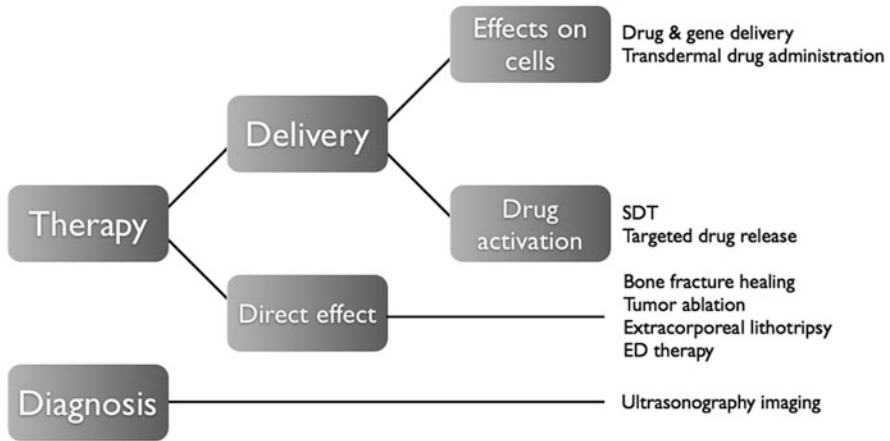
Fig. 1 Summary of medical applications of ultrasound

involve medical instruments that exert therapeutic effects by directly and violently acting on cells and/or tissues. The concept underlying the therapeutic use of ultrasound, in which energy is imparted to a target, has been advanced to the molecular level. For example, in terms of erectile dysfunction (ED), therapy with shock wave and bone fracture treatments with low-intensity pulsed ultrasound (LIPUS) provide feedback regarding the therapeutic effects and corresponding molecular mechanisms to advance the methodologies of these therapies. Meanwhile, other types of therapy applying ultrasound in which a bioactive substance is activated via sonication in a target area within a living body, including sonodynamic therapy and ultrasound-mediated gene therapy, facilitate drug activation and gene introduction (Fig. 1). Although many of these therapies remain under research, they are also being widely developed. Ultrasound is capable of noninvasively penetrating deep in the body and conferring energy to these locations. In addition, since ultrasound can be focused in small areas, it has the advantage of precisely providing the desired quantity of energy to small target areas within the body. Therefore, ultrasound is expected to be continuously and widely used in medicine.

In this chapter, the physical and chemical effects generated by ultrasound are reviewed, followed by the effects of ultrasound on cells and living tissues and finally recent advances in the therapeutic applications of ultrasound.

Bioeffects of Ultrasound

Bioeffects of Ultrasound

The biophysical modes of ultrasound can be divided into thermal- and nonthermal effects. Nonthermal effects are subsequently divided into cavitational and non-cavitational effects. All of these effects are dependent on the intensity of ultrasound. Cavitational effects are responsible for most of these consequences and

can be seen only above a certain intensity of ultrasound treatment. There is a threshold depending on the frequency, exposure time, medium composition, and so on. The intensity of ultrasound (I) is expressed by the following equation:

$$I = P^2/\rho c$$

where P is acoustic pressure (Pa), ρ is medium density (kg/m^3), c is the speed of sound (m/s), and ρc is the natural acoustic impedance (kg/m^2/s). The I in the SI unit is expressed in kg/m^2/s. The effects of ultrasound tend to be reflected at the interface; therefore, the equation reflects the intensity between two different tissues in the living body and provides a base for ultrasonography.

Ultrasound involves compression waves that, when traveling through biological tissues, shake and displace the molecules in the tissue. In addition, the adsorption of sound waves results in heat generation. The temperature rise per unit time is proportional to the ultrasound intensity times the adsorption coefficient. When applying focused ultrasound for diagnosis, heat is mainly generated at the focal point and subsequently diffuses due to the impact of thermal conduction and blood circulation.

The chemical effects of ultrasound in aqueous solutions are mostly attributed to the consequences of acoustic cavitation, which involves the formation, growth, and collapse of small gas bubbles. When such bubbles collapse, the generated high temperature and pressure result in the pyrolysis of water molecules, thus forming two free radical species of *OH radicals and H atoms. Sonochemical reactions progress at three different sites in cavitation bubbles. The first includes a reaction similar to that of combustive chemistry progressing at sites with high temperatures within collapsing gas bubbles. The second reaction is ongoing at the interface between the gaseous phase and aqueous phase. The third reaction progresses under usual temperatures in the aqueous solution around the gas bubble. In the last reaction, free radicals derived from inside the bubble react with solutes, including organic material in the aqueous solution, thereby producing substances such as those observed in aqueous radiation chemistry. It is reported that the physical impact of ultrasound resulting from the oscillation of cavitation bubbles is essential for the occurrence of the observed bioeffects. In addition, sonoporation occurring due to microjets generated when cavitation bubbles collapse is an important phenomenon for introducing macromolecules, including DNA, into cells.

The number of generated cavitation bubbles depends on the frequency and intensity of the applied ultrasound. The higher the ultrasound frequency, the smaller the size of formed cavitation bubbles. Ultrasound applied at higher frequencies is required for cavitation to occur. In cases treated with pulse ultrasound, the effects of rectified diffusion may make it difficult for cavitation bubbles to grow, as the duration is insufficient. Therefore, higher intensities are necessary for the generation of cavitation bubbles when using pulse ultrasound versus continuous ultrasound. Ultrasound with a frequency of 3–10 MHz is commonly used for the purpose of medical diagnosis at an intensity of 100 mW/cm^2. Under these conditions for ultrasound irradiation, cavitation bubbles should not form in vivo. Therefore, no ultrasound chemical effects are observed with diagnostic ultrasound irradiation.

In addition to the thermal and cavitation effects of ultrasound, there are the effects of radiation pressure, radiation force, radiation torque, and acoustic streaming. The contribution of these parameters to the biological effects of treatment depends on the experimental setup and usually requires special arrangements. Hence, there have been no previous studies explaining these effects comprehensively.

Free Radical Generation by Ultrasound

The very high temperature induced by cavitation bubble collapse facilitates the pyrolysis of water, resulting in the formation of $^*OH$ radicals and H atoms. This phenomenon can be confirmed according to the spin-trapping method with electron spin resonance (ESR). The ESR spin-trapping method using 5,5-dimethyl-1-pyrroline-N-oxide (DMPO) and alpha-4-pyridyl-1-oxide-N-tert-butylnitrone (POBN) as spin trap agents is a very strong tool for detecting free radicals [1]. For instance, by dissolving a rare gas with different thermal conductivity, it is possible to assess temperature-dependent processes in detail, such as the start of redox reactions attributable to $^*OH$ radicals and the generation of H atoms by ultrasound, in addition to pressure-dependent processes causing macromolecule dissociation or cell lysis.

The H atoms generated via ultrasound irradiation to aqueous solutions react immediately with oxygen molecules to form $^*H_2O$ radicals, even without the presence of oxygen molecules, thus producing superoxide ($^*O_2^-$). We previously showed that ultrasound irradiation applied to an ubiquinone solution saturated with Ar facilitated ubiquinol generation and that the reducing reaction was inhibited by an enzyme of superoxide dismutase [2]. It has also been reported that, under similar circumstances without oxygen molecules, the cytochrome C present in an Ar-saturated solution is reduced by $^*O_2^-$ following ultrasound irradiation. These results indicate that $^*O_2^-$ is formed after the application of ultrasound irradiation to solutions without oxygen molecules, as indicated in the following formula:

$$^*OH + \ ^*OH => O + H_2O, \ 2O => O_2$$
$$^*H + O_2 => \ ^*H_2O => \ ^*O_2^- + H^+$$
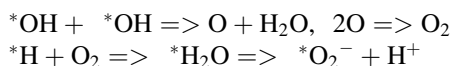
Artificial microbubbles of echo contrast agents used for ultrasonography enhancement significantly modify cavitational effects. Accordingly, the chemical effects of ultrasound are also modified. For instance, the echo contrast agents of Levovist (galactose crystal containing 0.1 % palmitic acid), PVC-AN (polyvinylidene chloride-acrylonitrile copolymer), and Albunex (albumin-coated small particles) at concentrations similar to those used to enhance ultrasonography decrease the threshold intensity required to generate hydrogen peroxide (H_2O_2) in air-saturated solutions. Meanwhile, it has been found that some contrast agents work as scavengers for $^*OH$ radicals and H atoms, suppressing the formation of H_2O_2 in an Ar-saturated solution following ultrasound treatment. Therefore, it should be taken into consideration that hazardous reaction products may be produced, even in the living body, when evaluating the effects of ultrasound as a modality applied in the clinical setting.

The sonolysis of sodium acetate, sodium propionate, amino acids, and sugars in Ar-saturated solutions has been investigated using the spin-trapping method over a

large range of concentrations. 3,5-dibromo-2,6-dideutero-4-nitrosobenzene sulfonate is used to detect potentially generated new radicals in the high-temperature zones surrounding the collapsing cavitation bubbles. At lower concentrations of these solutes, no evidence for specific new radicals has been found, and only radicals formed by *OH radical and H atom are detected. The radicals produced by UV photolysis in the presence of H_2O_2 are detected to identify the radicals present in Ar-saturated solutions by comparison. At higher concentrations of these solutes, new radicals, such as methyl radicals, are formed as a result of the high temperature generated by cavitation in some solutions. These findings indicate that the radicals generated by pyrolysis may be detected when nonvolatile solutes are present at high concentrations in the interfacial regions of cavitation bubbles.

The formation of pyrolysis radicals in sonicated Ar-saturated DNA solutions has also been examined. At lower nucleotide concentrations (0.05 mM or less), radicals detected with spin trapping are the products of reactions with H atoms and *OH radicals, mostly additional reactions to the 5,6 double bond of the base moiety. At a high concentration (1.0 mol dm^{-3}), pyrolysis radicals, mainly methyl radicals, for thymidine 5′-monophosphate, 2′-deoxy-uridine 5′-monophosphate, cytidine 5′-monophosphate, and uridine 5′-monophosphate are detected. These findings indicate that pyrolysis radicals can be formed due to high temperatures associated with cavitation when these nucleotides are present [3].

Ultrasound-Mediated Membrane Injury and Macromolecule Introduction into Living Cells

Ultrasound apparatuses with frequencies of 20–50 kHz have long been used for cell disruption in laboratories assessing cell biology and biochemistry. Therefore, ultrasound apparatuses are recognized by many researchers as tools for cell disruption.

Injury to the cell membrane is a frequent event, even under usual circumstances. The addition of mechanical stress to cells or living body tissues commonly results in membrane disruption, and the cells survive by repairing a certain level of such injury via various Ca^{2+}-dependent and Ca^{2+}-independent mechanisms [4]. Feccheimer and colleagues studied the effects of introducing macromolecules into cells, taking advantage of membrane damage repair mechanisms after sonication. They applied 20 kHz ultrasound irradiation to living amoebae of the cellular slime mold *Dictyostelium discoideum* at an intensity at which approximately 40 % of the cells survived and found that 10 % of the surviving cells were loaded with 40 kDa dextran labeled with fluorescent substances derived from the medium [5]. The authors successfully applied this technique for the transfection of mammalian cells, consequently sonicating adherent cells and floating cells in medium containing DNA [6]. Therefore, ultrasound can be used for transfection. Although the underlying mechanism has not been completely elucidated, gene transfer is considered to take place due to the mechanical effects generated when cavitation bubbles collapse as a result of ultrasound, presumably including microjets. Small pores may be formed on the cell membrane induced by microjets. If the pore is small enough, it is quickly repaired. At the time of pore formation and repair, macromolecules, including DNA, may be contained in the cell if such molecules exist in the vicinity. The streaming
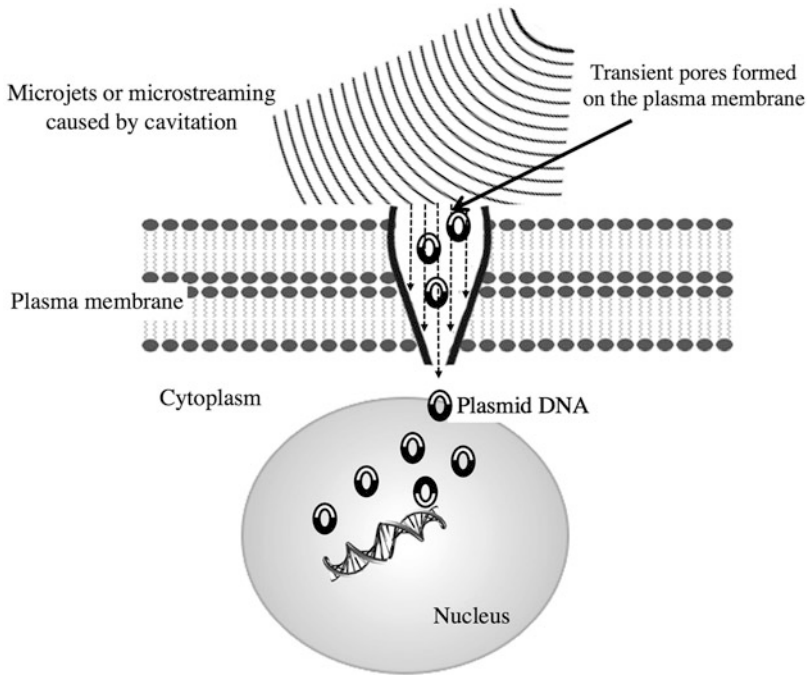
Fig. 2 A schematic illustration of a possible mechanism of ultrasound-mediated transfection. Microjet or microstreaming generated by cavitation may form transient pores on the plasma membrane through which plasmid DNA molecules put into cytoplasm or protruded into the nuclei of a cell. Completion of pore resealing after that results in transfection

force generated by the microjet might press the molecules into the cell through the pores (Fig. 2). This phenomenon is sometimes referred to as sonoporation, which may be analogous to electroporation. The macromolecule delivery facilitated by acoustic cavitation has become an active area of research as a non-viral gene transfer method aimed at gene therapy application. Further advancements in transfection efficiency achieved by increasing the dose of ultrasound irradiation exceeding a certain intensity may result in complete cell membrane disruption beyond restoration, leading to the disintegration of the cells. Therefore, the degree of cell viability should be taken into consideration when using this ultrasound-mediated transfection method.

Cell death induced by ultrasound is dependent upon the extent of injury and repair of the cell membrane. Figure 3 indicates the relationship among cell death, membrane damage, and membrane repair.

DNA Damage Caused by Ultrasound

For mammalian cells, just one double-strand break (DSB) of DNA may be lethal if not repaired. Therefore, DSB is one of the most severe forms of damage to life. It has long been known that ultrasound irradiation is capable of inducing DSBs if the
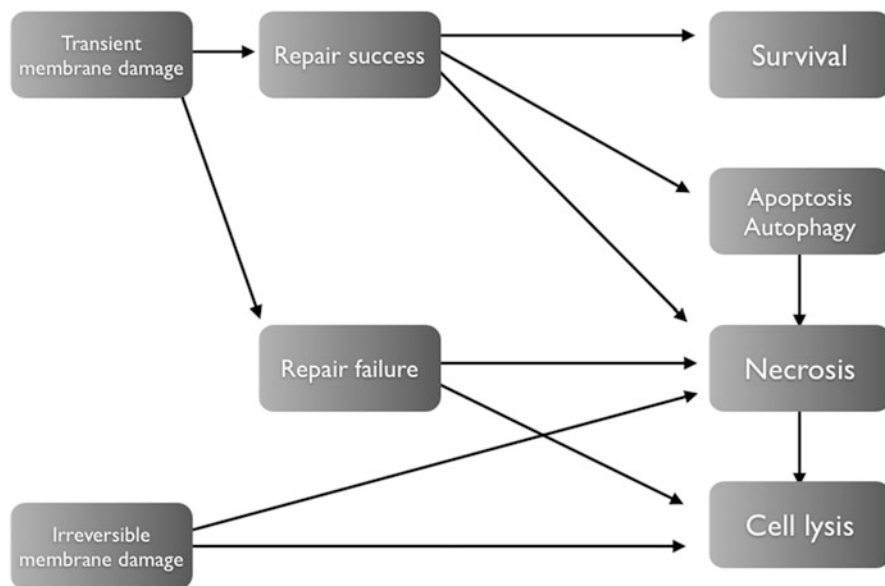
Fig. 3 Summary of membrane injury induced by ultrasound irradiation and their possible outcomes. This shows relations between membrane damages induced by ultrasound and mode of cell death subsequently caused. The membrane repair mechanism plays a critical role in a life-or-death decision

DNA is irradiated in solution, but not in the nuclei of a cell. This idea was established based on data obtained using a classical assay method called the neutral elution assay. However, this method is not completely reliable, as it can detect DSB only after cells are irradiated with approximately 100 Gy of ionizing radiation. We therefore applied a recently developed method to detect DSBs in cells induced by ultrasound. The aim of this method is to detect γH2AX foci with a corresponding antibody formed when DSBs occur. γH2AX foci are readily detected after sonication with 1 MHz ultrasound in cell lines derived from leukemia. This result was confirmed with a neutral comet assay that can detect DSBs when cells are irradiated with ionizing radiation at more than 2 Gy [7]. The DSBs induced by ionizing radiation are formed directly by the ionization of DNA with radiation or indirectly by the interaction of DNA with free radical species generated in the vicinity by radiation. The generation of DSBs in the cells induced by ultrasound irradiation is suggested to be involved in the process of cavitation, since they are not induced when N_2O, a triatomic gas, is saturated in the medium to suppress cavitation. Although the mechanical and chemical effects were found to be associated in this study, the addition of free radical scavengers, such as dimethyl sulfoxide (DMSO) or N-acetyl-L-cysteine (NAC), hardly affected the formation of γH2AX foci, indicating that ultrasound-induced DSB is not provoked by free radicals, unlike the effect that occurs with single-strand breaks [7]. Although the detailed mechanisms of DSB induction as a result of ultrasound have not been completely

elucidated, the mechanical effects caused by cavitation, including shear stress and high pressure, are expected to be involved.

Apoptosis Induced by Ultrasound

Apoptosis is a form of cell death controlled by genes. The process of cell death is regulated by programmed sequences of the gene expression, and fragments of the cells are finally phagocytosed by surrounding cells, thereby not releasing harmful substances into the environment. Apoptosis is a process of homeostasis, maintaining healthy individual cells and removing old, unnecessary, and damaged cells without changing the environment. Although it is widely known that stimulation, including ionizing that by radiation, chemicals, and hyperthermia, induces apoptosis, the induction of apoptosis by mechanical stimulation has scarcely been evaluated. Ultrasound-induced apoptosis was first reported by Ashushu and colleagues. They observed apoptosis in cells derived from leukemia exposed to focused 750 KHz frequency ultrasound at spatial-peak temporal-average intensities of 103.7 and 54.6 W/cm^2 [8]. Following this first observation, many reports on ultrasound-induced apoptosis assessed using different acoustic parameters have emerged. In one of these studies, for example, ultrasound was used at a frequency of 1.8 MHz and 0.22 W/cm^2 [9].

We performed analyses to identify the mechanisms underlying ultrasound-induced apoptosis using U937 cells, a cell line derived from human lymphoma. Using flow cytometry, apoptosis-related endpoints were examined 6 h after U937 cells were sonicated with 1 MHz ultrasound of continuous waves at an intensity of 4.9 W/cm^2. A fraction of cells with low mitochondrial membrane potential were observed after sonication. Additionally, significant $^*O_2^-$ and peroxide formation, increased caspase-3 activity, and DNA fragmentation were detected. Furthermore, as the incubation time increased, the rates of early apoptosis and secondary necrosis increased. In the results obtained 6 h after sonication, the ratio of early apoptosis reached the maximum when the cells were sonicated for 2 min and gradually decreased as the duration of sonication increased. On the other hand, secondary necrosis increased as the duration of sonication increased. When the effects of the dissolved gases Ar, N_2, O_2, air, N_2O, and CO_2 on free radical formation due to inertial cavitation were investigated with ESR spin trapping, H atoms and $^*OH$ radicals were detected in solutions saturated with Ar, N_2, O_2 and air, but not N_2O and CO_2. The apoptosis induced by ultrasound was found to be dependent on the dissolved gases in the approximate order of Ar = N_2 = O_2 = air $>> N_2O = CO_2$. These discoveries suggest that the ultrasound-mediated mitochondria-caspase pathway of apoptosis is involved in cavitation. However, the amount of generated free radicals was not affected by either early apoptosis or secondary necrosis. In addition, when ultrasound was irradiated to cells in the presence of Levovist, an echo contrast agent, at a dose of 20 mg/ml or more, the treatment synergistically enhanced secondary necrosis while being additive to early apoptosis. This result suggests that the agent worked to promote the formation of cavitation nuclei and enhance secondary necrosis due to the resulting increase in membrane damage.
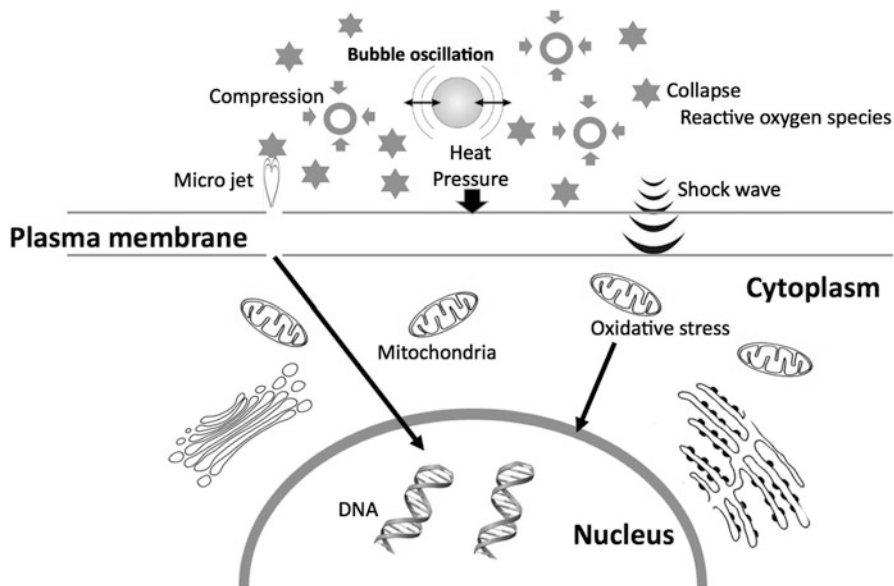
Fig. 4 Ultrasound bioeffects caused by a variety of microbubble actions and causing phenomena as results

The involvement of intracellular calcium ions ($[Ca^{2+}]_i$) in addition to reactive oxygen species (ROS), in the induction of apoptosis by ultrasound, has also been investigated. In one study, $[Ca^{2+}]_i$ was detected using digital imaging in addition to assessments of other apoptosis-related endpoints, including early apoptosis, secondary necrosis, loss of mitochondrial membrane potential, $^*O_2^-$ formation, caspase-3 activation, and DNA fragmentation. We also investigated the effects of BAPTA-AM (a $[Ca^{2+}]_i$ chelator), NAC (an antioxidant), verapamil (a calcium channel blocker), a buffer solution without $[Ca^{2+}]_i$, and Levovist. The results indicated (1) the mitochondria-caspase pathway and $[Ca^{2+}]_i$-dependent pathway may be involved, as BAPTA-AM treatment partially inhibited DNA fragmentation, mitochondria membrane potential loss, and caspase-3 activation; (2) ROS generated secondarily from mitochondria rather than directly via ultrasound irradiation are involved, as NAC treatment after sonication effectively suppressed apoptosis; (3) the increase in $[Ca^{2+}]_i$ may be derived from nonspecific influx, as the increase in $[Ca^{2+}]_i$ was not observed when a buffer solution without $[Ca^{2+}]_i$ was used [10] (Fig. 4).

Gene Expression Profile Changes Assessed Using Ultrasound

In 2004, the nucleotide sequence of human genomic DNA was read completely, which provided the basis of current bioinformatics, including DNA microarray analyses. DNA microarray is a very strong technique that can identify the gene expression profile of a whole genome. Moreover, microarray technologies coupled with bioinformatic tools have been used to obtain information regarding

genome-wide expression profiles, relevant biological functions, and gene networks according to gene expression data. We have continued analyses of the gene expression changes noted in cells in response to ultrasound stimulation.

The first trial to analyze gene expression changes in response to ultrasound stimulation was conducted among U937 cells of human lymphoma. The cells were sonicated with 1 MHz ultrasound in the presence of Ar or N_2O dissolved in medium, and gene expression changes were analyzed using a microarray.

Of the 9,182 genes whose probes were mounted on an array slide, only a decrease in the keratin gene expression was detected in the U937 cells sonicated in N_2O-containing medium without inertial cavitation. On the other hand, increases in five genes and decreases in two genes were detected in cells sonicated in Ar-containing medium with cavitation. Six of the seven genes were confirmed to be significantly increased using the RT-PCR method. The most upregulated gene was the heme oxygenase 1 (HO1) gene, showing a 6.6-fold expression and 4.0-fold expression after sonication using a microarray and RT-PCR, respectively. It is known that the HO1 gene expression is upregulated under oxidative stress conditions and demonstrates defensive functions in cells. These results indicate that inertial cavitation may affect the gene expression profile by modifying the expression of genes by changing their expressions in response to oxidative stress [11].

The gene expression profile changes in the Molt-4 cells of human leukemia were then investigated after nonthermal LIPUS treatment at a dose of 0.3 W/cm^2. The LIPUS treatment induced minimal cell lysis and approximately 24 % of apoptosis. In an analysis using a GeneChip type of microarray, genes encoding BCL2-associated athanogene 3, DnaJ homolog subfamily B member 1, heat shock 70 kDa protein 1B, and heat shock 70 kDa protein 6 showed increased expression levels, whereas those encoding isopentenyl-diphosphate delta isomerase and 3-hydroxy-3-methylglutaryl-coenzyme A synthase 1 showed decreased expression levels 3 h after LIPUS treatment. The expression levels of these six genes were further confirmed using a real-time PCR analysis. These two studies employing human leukemia cells are pioneering works on the application of microarray technologies to the field of medical ultrasound. Therefore, the changes in the gene expression profiles in response to LIPUS causing apoptosis were shown successfully. These findings provide the basis for achieving further clarification of the molecular mechanisms underlying the observed bioeffects of LIPUS [12].

In another study, Sonazoid was employed to determine how it modifies the bioeffects of ultrasound at concentrations similar to those used for clinical purposes. Sonazoid is a new echo contrast agent that is chemically stable and ultrasound resistant. The changes in the expression levels of genes responsive to ultrasound were evaluated by taking advantage of microarray technology and computational gene expression analysis tools. It was found that this combination enhanced cell killing, the mitochondrial pathway of apoptosis induction, and DNA damage. Furthermore, the addition of Sonazoid enhanced the expression of genes related to apoptosis and genes responsive to ultrasound. In the absence of ultrasound

treatment, Sonazoid alone had almost no effect on the cells or gene expression. Therefore, Sonazoid may be useful in the setting of cancer therapy when used in combination with ultrasound [13].

Application of Ultrasound for Therapy

Application of Ultrasound for Therapy

Ultrasound has long been used for application as a diagnostic modality in the clinical setting. Recently, it has been variously utilized as a therapeutic modality. For example, ultrasonic surgical devices and ultrasonic scalpels have been used in surgeries of digestive and cardiovascular organs, utilizing vibratory motion, a mechanical effect of ultrasound with a frequency of 20–40 kHz. Such devices are used for dissection and ablation and can be controlled with weak power in addition to stanching bleeding while being used for the purposes of dissecting and ablating. Therefore, this technique is very accurate and safe. In the field of ophthalmology, the crystal lens ultrasonic aspiration technique for treating cataracts has been widely used. This technique is performed with ultrasound of relatively low acoustic output. Ultrasound with a similar energy output has many clinical applications, such as tartar dental calculus scaling, liposuction, and thrombolysis. Moreover, low-intensity ultrasound is used in elastography for the purpose of diagnosis.

Ultrasound has also been employed as a heating device for treating hyperthermia, as applied for cancer therapy and physiotherapy. In addition, the application of intense focused ultrasound has been approved for extracorporeal lithotripsy and tissue ablation. Recently, LIPUS has been widely applied for bone fracture treatment in the field of orthopedics to accelerate bone regeneration and healing.

In the following sections, we discuss therapeutic modalities using ultrasound, both those routinely used in clinical practice, as mentioned above, and those still in the laboratory stage.

Focused Ultrasound Applications for Therapy

HIFU therapy is a type of thermal ablation therapy that removes diseased or damaged tissues scorched with heat of more than 90 °C generated by focusing the energy of high-intensity ultrasound. Although it requires very accurate control of ultrasound irradiation aided with a computer in addition to constant monitoring by a clinician, this method has little side effects on surrounding tissues, as the temperature drastically drops to approximately 50 °C in an area 5 mm apart from the focus. Moreover, it causes few complications and can be applied in a repetitive manner. This technique can be applied for therapy in elderly people and patients with recurrence after radiation therapy, as it carries only a small burden. The therapeutic HIFU system is usually composed of a probe involving a single- or multi-transducer system and a bag containing degassed water called a bolus in addition to a computer system that controls the ultrasound irradiation and focus localization. A magnetic resonance imaging (MRI) system installed in a parallel fashion to the HIFU system is commonly used for monitoring by the clinician. HIFU is a therapy utilizing the

thermal effects of ultrasound, the intensity of which surpasses the threshold required to generate cavitation. Cavitation reinforces target tissue breakdown but prevents sound wave transmission. Therefore, cavitation may be an obstacle to therapy and should thus be avoided. While HIFU was originally applied to treat benign diseases, such as uterine myoma and prostatic hyperplasia, the range of applications has widened to many kinds of malignant diseases, including prostate cancer, breast cancer, liver cancer, renal cancer, and pancreatic cancer.

Bone Fracture Therapy with LIPUS

Recently, LIPUS bone fracture therapy at a specific frequency, pulse width, pulse length, and intensity has been developed. It has been reported that this therapy facilitates a cure by significantly shortening the treatment duration up to 40 %. However, the target and sonication conditions must remain constant (in vitro or in vivo, methods of sonication, with or without standing wave, species of model animals, etc.). In addition, truly important factors mostly remain unknown. Therefore, making comparisons among experiments is difficult and standardization is an urgent necessity. Applying sonication for cells or animals with 1.5 MHz ultrasound at 30 mW/cm^2, 20 % duty factor (20 % pulse repetition frequency, thus 200 ms of pulse duration) for 20 m daily is a condition that may be appropriate from the aspect of the therapeutic effect and is frequently employed [14].

The biological phenomena mainly observed during ultrasound bone fracture therapy include cell proliferation and differentiation. However, small changes in the microenvironment of bone cells and tissues caused by the thermal and mechanical effects of ultrasound may also contribute to facilitating bone fracture healing [15]. Fracture healing involves a very complex process and involves four major events: (1) inflammation, (2) soft callus formation, (3) bone formation, and (4) bone remodeling [16]. LIPUS is considered to affect all of these phases to facilitate bone formation. Indeed, LIPUS has a positive effect to some extent in all phases. For instance, LIPUS mitigates the soft tissue phase in phases 1 and 2 and accelerates bone formation in phase 3. Moreover, it has been shown that LIPUS affects the biochemical properties of reformed bone tissues in phase 4. As mentioned above, it has been pointed out that, in the process of bone fracture healing, LIPUS affects the migration, proliferation, and differentiation of different types of cells, in addition to many other processes of bone reformation, including extracellular matrix generation and repair.

The use of in vitro cell culture systems remains of central importance for research at the cellular and molecular levels. In terms of bone fracture healing, many different effects of ultrasound may be involved. When sonicating cells with an ultrasound apparatus, the temperature of the interface between the transducer and cell culture dish may be raised to a few tenths of a degree to a few degrees. This temperature increase is sufficient to activate enzymes, including metalloproteinase, that could be involved in bone reformation [17]. The nonthermal effects of ultrasound may provide cells with strain and tense, in addition to the effects of liquid streaming arising from ultrasound irradiation. These effects are very important since their energy can be conveyed through a mechanosensing element into the cell, resulting in up- and downregulation of the gene expression. Once mechanical stimulation

generated by ultrasound irradiation is received by the mechanotransduction system of a cell, it is converted into chemical signals, thus activating the signal transduction pathway, which in turn induces gene expression profile changes in the cell. This causes phenotypic changes in the cell (or living body) for adaptation to the stimuli. Mechanoreceptors residing on the cell surface receive mechanical energy, which then activates molecules on the membrane and reorganizes the cytoskeleton network. These processes then increase $[Ca^{2+}]_i$ and activate a number of signal transduction pathways mediated via integrin-mediated focal adhesion with integrin molecules as the nucleus. It has been reported that LIPUS modifies the integrin activity [18] and contributes to the activation of molecules in the phosphatidylinositol 3-OH kinase/AKT pathway [19] downstream of integrin. Moreover, LIPUS facilitates the phosphorylation of ERK 1/2 of MAPK, which is further downstream. Activation of this pathway leads to the upregulation of genes, including MCP1, MIP1, and RANKL [18]. There are studies reporting that LIPUS has effects on healing bone fractures as mediated by the extracellular matrix.

In the inflammation phase, which begins immediately after bone fracture, LIPUS increases the proliferation of fibroblast cells [20] and facilitates the recruitment of osteoprogenitors and osteogenic precursor cells [21]. Moreover, LIPUS treatment induces osteoblastic cells of mouse or human origin to secrete IL-8 [20] and human osteoblastic cells and periphery monocytes to produce VEGF [20, 22], both of which are involved in angiogenesis. Likewise, LIPUS facilitates human osteoblastic cells to produce NO, probably due to iNOS activation [22].

In the relatively early period of bone fracture healing induced by LIPUS, the expression of IGF has been recognized in rat osteoblasts and a cell line derived from mouse bone marrow. Indeed, it has been reported that OSX, a gene downstream of IGF, which is involved in the differentiation of osteoblasts, is upregulated [23, 24]. Furthermore, it has been shown that c-Fos, c-Myc, and Egr-1 are involved in the proliferation and differentiation of osteoblasts and are upregulated in rat mesenchymal stem cells (MSCs) and osteoblasts after LIPUS treatment [25]. Osteogenic marker genes, including COL-1, OPN, BMB2, and ALP, have been found to be upregulated in osteoblastic cells within 24 h of LIPUS treatment [23].

The effects of LIPUS then advance to a stage in which the therapy facilitates osteoblast proliferation and differentiation. However, there are many contradictory reports regarding the proliferation of osteoblasts, in addition to effects on differentiation, and this finding is still controversial. Hence, the mechanism underlying the promotion of bone fracture healing induced by LIPUS in vivo is not clear as to whether the beneficial effects can be attributed to differentiation only or to a more complex activity associated with the proliferation of osteoblast cells.

It has been reported that a transcription factor called RUNX2, which plays an essential role in the process of ossification, is significantly increased a few days after LIPUS treatment applied to osteoblasts or MSCs [24]. It is known that RUNX2 regulates the differentiation of MSCs to the osteogenic lineage by directly controlling genes, including BSP, ALP, COL-1, MMP-13, OPN, and OC. Indeed, it has been observed that MC3T3-E1, a mouse osteoblast cell line, mouse MSCs, or other osteoblast-like cells upregulate the Alp, Opn, and Mmp-13 gene expression 10 days

after LIPUS treatment [26]. BMP-2, BMP-4, and BMP-7 are important proteins for bone fracture healing, as they regulate the differentiation of MSCs into the osteoblastic or chondroblastic lineage. BMP protein signals are transmitted through the SMAD transcription factor family, followed by MAPK members, such as p38 and ERK. It has been recorded that rat osteosarcoma cells upregulate the production of these proteins 5–7 days after treatment with LIPUS [24].

As the healing process reaches this stage, MSCs begin to differentiate into chondrocytic cells and ossification begins. One to a few weeks after LIPUS treatment, the production of COL-1, COL-2, COL-10, proteoglycan, and SOX-9, a transcription factor involved in cartilage differentiation, which are chondrogenic markers, is prominently increased [27]. Furthermore, both the differentiation and proliferation of rat, pig, and human chondrocytic cells are facilitated a few weeks after treatment [27]. Differentiated chondrocytic cells become hypertrophic and start to secrete ALP and initiate the mineralization process. Mineralized chondrocytic cells become scaffolds for osteoprogenitors to differentiate into bone tissue after forming bone-like tissue. Many studies evaluating bone fracture healing induced by LIPUS treatment have shown the expressions of OC and BS, mature osteoblast markers, and the deposition of calcium in the final process of ossification [28].

As described above, the effects of LIPUS are evident; however, the mechanisms by which LIPUS promotes bone fracture healing at the cellular and molecular levels have not been clearly clarified.

The gene expression changes that occur in response to LIPUS in MC3T3-E1 cells were recently analyzed using microarray technology. Although a single application of 20 min of LIPUS treatment with 1.5 MHz ultrasound at 30 mW/cm^2 was not shown to affect cell growth or the ALP activity, the mRNA expression levels of the Bglap gene in addition to those of 38 genes were upregulated, while those of 37 genes were downregulated more than 1.5-fold at 24 h after LIPUS treatment. A computational analysis performed with the Ingenuity Pathway Analysis tool showed that most of the upregulated genes belonged to a gene network of bone morphology in the category of the biological functions of skeletal and muscular system development. On the other hand, the downregulated genes were related to a gene network of the cell cycle as well as connective tissue development and functions [29].

Shock Wave for ED Therapy

The initial drug of choice for ED therapy is a phosphodiesterase type 5 inhibitor (PDE5i). This drug is a broadly prescribed medicine, with an improvement rate of approximately 70–80 % and showing high efficacy without pronounced side effects. However, in cases of organic ED associated with post-pelvic surgery and severe diabetes and/or cardiovascular disease, it is often difficult to obtain sufficient efficacy with PDE5i. In addition, this agent cannot be used with concomitantly administered oral medicines, such as nitrates. In such cases, although other remedies are available, their efficacy is usually not satisfactory for the patient. Moreover, all of these remedies, including PDE5i, are applied on demand and are often only effective for sexual intercourse just after application. These remedies are used for symptomatic treatment, not as a permanent cure to recover the penile function. Therefore,

currently available remedies for ED have not been developed as therapies designed to regain spontaneous penile erections. Although there are some studies reporting progressive improvements in the endothelial function with the daily oral administration of PDE5i, this treatment may have limitations.

Recently, LISWT has attracted attention as a new therapy for recovering the penile function or curing ED. The efficacy of LISWT to ED was first reported by Vardi et al. in a clinical study of 20 middle-aged vascular ED patients (average 56.1 years) whose international index of erectile function-erectile function (IIEF-EF) domain score was mild to moderate and who were identified to be responders to PDE5i [30]. Using a LISWT apparatus with shock wave irradiation at an intensity of 0.09 mJ/mm^2 and a repetition frequency of 120 waves/min, the treatments were performed following a protocol involving two 3-week applications consisting of two rounds of irradiation of 300 waves at five points (total 1,500 waves) in a region from the penis to the crus penis per week followed by a 3-week period of no treatment between the two treatment cycles. The average IIEF-EF domain score of the treated patients significantly increased, and the improved scores were maintained 6 months after treatment. In addition, improvements were observed on the nocturnal penile tumescence test (NPT) and in the flow-mediated dilatation (FMD) indicating the penile vascular endothelial function. Furthermore, 50 % of the patients regained their erectile ability without PDE5i. Subsequently, in an open-label single-arm prospective study including 29 ED patients (average 61.3 years) who were poor responders to PDE5i, the IIEF-EF domain scores, erection hardness scores, and penile vascular endothelial function all improved significantly, indicating the efficacy of LISWT in treating severe ED as well as mild ED [31]. There are two research groups reporting the results of prospective, randomized, double-blinded, placebo-controlled studies with treatment protocols identical to that mentioned above. Vardi et al. observed significant improvements in organic ED patients shown to be responders to PDE5i. Notably, the IIEF-EF domain scores in the treatment group versus the sham group were 6.7 ± 0.9 points versus 3.0 ± 1.4 points above the baseline, respectively, indicating a significant improvement in the treatment group [32]. Yee et al. also reported the results of their research in ED patients, including approximately 30 % severe ED cases based on a sexual health inventory for men score of $\leqq 7$ points, in which the IIEF-EF domain scores in the severe ED treatment group were most significantly improved versus that observed in the sham counterparts according to a subgroup analysis (7.1 points) [33].

Although the effects of LISWT in improving ED have not been completely elucidated, facilitation of the expressions and activities of factors related to angiogenesis, including VEGF, FLT-1, eNOS, and PCNA, may be involved [34]. Few studies have reported the findings of basic research on LISWT ED therapy. There are reports confirming these findings published after the clinical trials mentioned above. Qui and colleagues reported their results obtained with diabetic rats treated with streptozotocin. The authors used a LISWT apparatus with shock wave irradiation at an intensity of 0.1 mJ/mm^2 and repetition frequency of 120 waves/min applied to the rats in two sets of three 300 waves a week and subsequently evaluated the efficacy 2 weeks after the last treatment. The results confirmed a recovery of the

intracavernous pressure (ICP)/mean arterial pressure (MAP) index in addition to the proliferation of nNOS-positive cells, vascular endothelial cells, and smooth muscle cells detected using immunohistochemical staining. Furthermore, they confirmed an increase in the recruitment of MSCs, suggesting that the effects of LISWT treatment on ED may depend on a mechanism mediated via endogenous MSCs [35].

We previously found that ultrasound irradiation to vascular endothelial cells induces the HO1 gene expression. Approximately 33-fold upregulation of HO1 mRNA was observed when endothelial cells were exposed to 1 MHz ultrasound at 0.3 W/cm^2, DF 10 % for 20 s. The data obtained using a promoter and microarray analysis suggested that the NRF2/StRE signal pathway was involved in the observed upregulation. In addition, ultrasound stimulation to endothelial cells changed the gene expression profile, which modified the anti-inflammatory, antioxidant, and vasodilatory activities in addition to the pro-angiogenic and vascular reconstitution activities of endothelial cells [36]. As ultrasound irradiation upregulates the HO1 gene expression, we expect that this modality could be utilized for ED therapy via the induction of vasodilation as well as LISWT. As shown in Fig. 5, the CO produced by a hydrolysis reaction of heme stimulated by HO1 activates sGC, which in turn facilitates cGMP production, subsequently provoking vasodilation. Genes related to angiogenesis, including VDGF, are also downstream of HO1. Therefore, we consider that ultrasound might be useful for application to achieve a permanent cure in addition to symptomatic treatment.

LISWT treatment for ED is a promising technology, although it is still in its infancy, as only basic and clinical research has been started.

Application of Ultrasound for Gene Therapy

Gene transfer into mammalian cells via ultrasound was first reported by Fechheimer in 1987, as mentioned above, and 30 years has since passed [6]. This technique initially drew attention as a phenomenon and the mechanism gathered much interest, and continuous research has led to an increase in the efficiency and extension of applications, reaching one step short of practical realization.

It is expected that artificial microbubbles may facilitate transfection via low-intensity ultrasound, as it has been shown that these bubbles enhance the bioeffects of ultrasound. Hence, it is also expected that combining low-intensity ultrasound with such microbubbles will lead to site-specific gene transfer. In addition, we reported that the pretreatment of cells with local anesthesia or hyperthermia, which are known to be membrane fluidity facilitators, enhances the efficiency of ultrasound-mediated transfection in vitro and in vivo [37]. The enhancement of transfection efficiency requires cavitation (addition of Levovist) for both treatments. In addition, there are reports that both treatments promote the fluidity of the cell membrane. Therefore, the repair of pores formed on the cell membrane as a result of cavitation is presumed to be facilitated due to membrane fluidity, thereby repressing cell death via membrane disruption.

Although cavitation is essential for ultrasound-mediated transfection, it is difficult for this process to occur in a living body due to high viscosity. However, gene transfer into a living body is the first step forward for such therapy. Therefore,
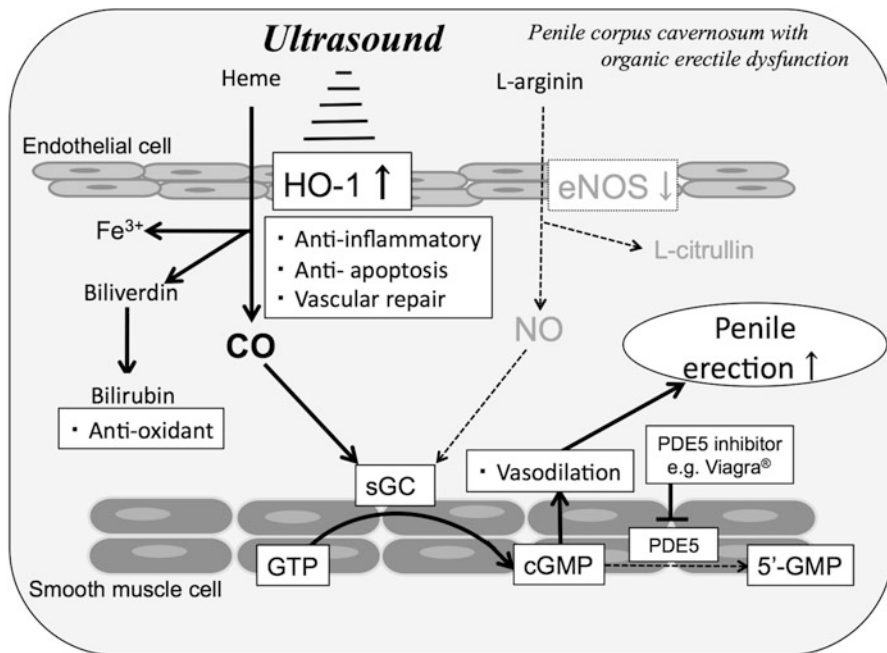
Fig. 5 A schematic illustration of a possible mechanism of vasodilation induced by HO1 upregulation by ultrasound. The hydrolysis reaction of heme by HO1 upregulated by ultrasound generates carbon monoxide (CO). It then stimulates soluble guanylyl cyclase (sGC) activity to facilitate cyclic guanosine monophosphate (cGMP) accumulation, inducing vasodilation

transfection has been applied with a high intensity of ultrasound and/or to tissues adjoining fluids, including the interior of the bladder and vascular endothelium as targets. Some authors have continued their research by conducting ex vivo transfection experiments targeting tissues or organs removed from animals. With respect to these problems, the potential of microbubbles has drawn the attention of researchers for ultrasound transfection, as they decrease the threshold for the onset of cavitation. Introducing and developing microbubbles has drastically improved the efficiency of transfection using ultrasound in a living body. A broad array of examinations for achieving higher transfection efficiency has since been applied, including the use of ultrasound irradiation with microbubbles, conditions varying the size and composition of microbubbles, targeting via the modification of surface molecules and combination therapy with other methods, and so on.

Initially, contrast agents for use in ultrasonography were mixed with genes and then applied for ultrasound-mediated transfection, successfully enhancing transfection efficiency. It is considered that these agents probably decreased the threshold intensity of ultrasound needed for cavitation. Furthermore, the transfection efficiency is further increased when negatively charged DNA molecules are attached to the surface of positively charged microbubbles. This may be because DNA is concentrated in the vicinity of pores formed on the cell membrane, as DNA

accumulates around cavitation bubbles as a result of the electrical force, even though the bubbles oscillate vigorously. Unglar and colleagues proposed the application of positively charged microbubbles to achieve tumor regression by introducing the IL-12 gene using a microbubble developed by this group [38]. Later, it was shown that a positively charged microbubble enhances the efficiency of ultrasound-mediated transfection 10- to 100-fold compared to that seen with an electrically neutral microbubble, although the degree of charge or other conditions may affect the findings [39]. The bubble liposome developed by Maruyama and colleagues is a microbubble formed with a water-soluble core that contains perfluoropropane droplets encapsulated with a positively charged lipid bilayer membrane [40]. The DNA to be delivered is electrostatically bound to the surface of the microbubble or encapsulated inside the microbubble. Specific targeting is also possible by adding ligand molecules to surface receptors or antigens [40]. Other microbubbles for transfection have also been developed, such as eLiposome, which is similar to the bubble liposome, although it contains perfluoropentane, and an echogenic liposome, which was originally designed as an echo contrast agent carrying a multi-membrane structure. It is also possible to mount the ligand molecules on the surface for targeting. Microbubbles consisting of lipid shell encapsulating gas are most frequently used for ultrasound-mediated transfection. The type of microbubbles can be prepared relatively easily. Therefore, improvements and modifications are also possible in the laboratory, and new microbubbles are expected to be developed continuously for different purposes.

Although almost all tissues and organs are targets for ultrasound-mediated transfection, the heart, muscle tissue, and vascular endothelium are targets that have been studied for a long period of time. Generally, it is difficult to introduce DNA into the blood vessel wall using a non-virus carrier as a result of prevention by the blood flow. However, ultrasound is effective for introducing DNA into the inner wall of the heart and inner wall of vascular vessels, since the process of formation and recovery of transient pores is rapid. It was succeeded that efficient gene introduction was achieved by providing ultrasound irradiation after administering a mixture of the stromal cell-derived factor-1 (SDF-1) gene with microbubbles into the blood vessels of ischemic muscle, effectively inducing capillary blood vessel formation. In another case, experimental therapy was conducted with ultrasound-mediated transfection for postischemic cardiac chamber dysfunction using mice as model animals. The researchers successfully introduced the tissue inhibitor of metalloproteinase-3 (Timp-3) gene, which appeases the symptoms of cardiac infarction in the myocardium, taking advantage of microbubbles mounted with anti-matrix metalloproteinase-2 antibodies on the surface targeting myocardium post-cardiac infarction. They consequently observed a significant increase in the volume of blood pumped out of the heart compared with that observed in mice treated identically except for microbubbles. In order to examine the ultrasound-mediated transfection of therapeutic genes into the heart or vascular endothelium, studies using small animals, such as mice and rats, as well as large animals, such as dogs and sheep, have been conducted applying the data for human use [41]. For instance, Yuan et al. introduced the hepatocyte growth factor (HGF) gene into the canine

myocardium using ultrasound and observed increases in capillary vessel density and blood flow, which successfully improved symptoms after cardiac infarction.

There are many published studies on the use of gene or drug delivery employing ultrasound and microbubbles designed for cancer therapy. Genes to be delivered include cytokine genes, such as the interferon-β gene, anti-angiogenesis peptide genes, so-called suicide genes, and others. Recently, there have been an increasing number of reports of the ultrasound-mediated delivery of siRNA or miRNA against genes promoting cancers, such as anti-apoptotic genes or oncogenes. In addition, there have also been many studies on cancer targeting microbubbles by mounting such bubbles on the surface with antibodies against cancer-specific antigens. Negishi and colleagues employed the AG73 peptide, which is composed of 12 amino acids derived from laminin α1 binding to syndecan 2, an antigen expressed on the endothelial surface of newly formed vessels, and placed the peptide on the surface of the bubble liposome. The application of this bubble liposome makes it possible to visualize tumors using diagnostic ultrasound, as they can bind to the endothelial cells of tumor vessels [42]. Furthermore, the authors reported successful gene introduction into primary endothelial cells via therapeutic ultrasound with bubble liposomes. It is expected that these bubble liposomes will serve as a new type of microbubble that may be used for diagnosis and therapy simultaneously [43].

One of the goals of gene therapy is to maximize the treatment efficacy and minimize hazardous side effects by expressing the required quantity of therapeutic genes in the tissue of greatest need when necessary. Therefore, a therapeutic system allowing for spatial control was recently developed by employing a tissue-specific and disease-specific promoter. Alternatively, using gene expression control with physical stimulation, it may be possible to develop a therapeutic system in which the gene expression is spatially and temporally controllable. Ultrasound energy can be precisely delivered to the deep portion of a living body without inducing prominent hazardous effects. Hence, using a promoter responsive to ultrasound, the expression of an introduced gene of interest may be spatially and temporally controlled.

Ultrasound energy can be easily converted to heat. Madio et al. took advantage of this phenomenon to control the gene expression using ultrasound [44]. They employed the promoter of the Hsp70B gene, whose degree of activation sensitively reflects the heat applied. As the rise in temperature determines the degree and duration of activation, the timing and quantity of transcription can be finely controlled with ultrasound irradiation. In addition, since the promoter has low tissue specificity, this gene regulation system has been successfully applied to treat different tissues, including the skin, muscle, prostate, and liver. MRI can be used to obtain reliable quantification of temperature changes in vivo using a relatively simple technique. Some of the latest HIFU systems are equipped with MRI to monitor its operation, and it has been reported that this technique can be applied to regulate the expression of genes of interest [45]. It has also been shown that the marker gene expression is steadily regulated by the promoter and that the therapeutic gene expression is controlled, showing curative effects in model animals [46]. Although there remain several problems left unresolved, including the thermotolerance of the

promoter and activation of the promoter by other forms of stimulation, it is a promising technology, as ultrasound irradiation into a living body has been conducted safely for a long period.

We developed an artificial promoter, other than the Hsp70B promoter, responsive to ultrasound. First, we focused our attention on intracellular oxidative stress caused by ultrasound and found that ultrasound stimulation activates an artificial promoter responsive to intracellular oxidative stress caused by ionizing radiation. We then constructed a promoter library by linking the TATA box to randomly combining binding sequences for NF-κB, AP-1, NF-Y, and CBF-A. Of 62 promoters in the library, we obtained two promoters responsive to ultrasound for which the expression of the luciferase gene linked downstream in HeLa cells of human cervical carcinoma was upregulated by more than tenfold after exposure to 1 MHz ultrasound at 0.5 W/cm^2, 10 % duty factor for 60 s [47]. Different types of cells respond differently to intracellular oxidative stress. Therefore, we chose OCT1, NF-κB, AP-1, p53, and NRF2 and successfully constructed a responsive promoter to ultrasound in LNCaP cells of human prostate cancer. The promoter similarly enhanced the expression of the luciferase gene linked to this promoter after sonication. A gene cassette composed of the promoter and the fcy::fur gene, a suicide gene, was successfully used for suicide gene therapy simulation in vitro, inducing a high cell death rate among cells transfected with the gene cassette after sonication in medium containing 5-FC, a prodrug processed by the product of the fcy:fur gene [48]. These newly developed promoters are still in the laboratory stage and may be improved or modified relatively easily, since they are artificially constructed promoters.

As microbubbles see further improvements by introducing a charge or mounting a ligand molecule on their surface, the realization of clinical application is approaching. However, there remain novel challenges, for instance, achieving fine control of sonication to deep targets in a living body, fusing ultrasound-mediated transfection in combination with other methods and/or preparing microbubbles made of novel materials. Further development is expected as researchers seek a safe and sophisticated method for gene therapy.

Application of Ultrasound for Drug Delivery Systems

The cellular membrane is the most important structure for interactions among ultrasound waves, drugs, and cells in the living body. Modes of interaction include (1) increased permeability, (2) transient pore formation (sonoporation), (3) drug release from carriers, and (4) drug activation. The effects of ultrasound on the lipid bilayer constitute potential benefits of therapeutic ultrasound. Ultrasound has been shown to disrupt packing of the bilayer, generating transient membrane pores. As discussed above, macromolecules, including DNA, are incorporated into cells, as mediated through (2) transient pore formation. We will now take a look at how these four modes are involved in drug delivery.

First, regarding (1) and (2), because the lipid bilayer is a highly effective barrier to the transport and exchange of substances between the cell interior and surrounding environment, the use of ultrasound to induce such deformations and/or pores would essentially enhance the uptake of molecules hardly trespassing the membrane owing

to size restrictions, such as that of DNA and RNA, solubility issues, such as that associated with hydrophilic drugs, and/or intended extrusion. The mechanism by which ultrasound affects membrane permeability can be attributed to the occurrence of inertial cavitation. Bubble oscillation and implosion result in microstreaming and the formation of high-speed microjets, respectively, which disrupt the cell membrane in the vicinity. These effects can irreversibly damage membranes and thus undermine the use of ultrasound as an adjuvant for drug delivery. Bubble oscillation alone may be adequate to temporarily perturb the membrane structure. Although the pressure gradient generated in the acoustic field has been suggested to be another mechanism for increasing membrane permeability, it may not have a significant contribution [49]. In addition, microstreaming and/or high-speed microjet formation may plunge molecules into the cell interior through sites of membrane perturbation or pores formed by cavitation. Such streaming forces may be very important on some occasions to internalize DNA or drugs since the cytosol is a colloidal solution and the diffusion of molecules occurs approximately fourfold slower than that seen in pure water. Therefore, it may be difficult to internalize DNA or drugs using only membrane deformation or pore formation.

As for (3), the use of ultrasound for delivery purposes in therapeutic applications enhances drug release from so-called ultrasound-responsive drug delivery systems. These systems include microbubbles, nanobubbles, liposomes, and micelles. The application of ultrasound with such systems enables the spatial and temporal control of drug release, which thus enhances bioavailability, decreases drug side effects, and, if combined with simultaneous membrane permeabilization, may boost therapeutic efficiency. Regarding (4), in addition to membrane modification, sonosensitizers are drugs activated by ultrasound irradiation and thereby manifest their effects on target cancer tissues in response to sonication, even in the living body. The combination treatment of ultrasound and a sonosensitizer is known as sonodynamic therapy (SDT). SDT has not been completed and is currently under development. If this technology is successfully completed, it would have advantages over currently available cancer therapies. Since this process is activated in response to ultrasound irradiation, the therapy can deliver its effects deep in the body, as long as ultrasound waves can reach these locations. The mechanisms required to activate the sensitizers remain to be elucidated, although some researchers have suggested the involvement of ROS. There is more than simply one universal mechanism explaining all actions of SDT, as different kinds of drugs have been suggested as possible sonosensitizers [50]. More investigations are needed to understand the mechanisms and complete this technology.

Conclusions and Future Directions

In this chapter, we reviewed the bioeffects and therapeutic applications of ultrasound, particularly for recent progresses. We took a look at many different very complex physical and chemical phenomena induced when ultrasound is irradiated

to aqueous solutions. We explored the detailed mechanisms underlying such phenomena, particularly related to clinical applications. In addition, we mentioned phenomena observed in cells or living tissues in the acoustic field of ultrasound and discussed possible interactions between ultrasound waves and cells or the living body. Ultrasound, of course, does not yield its effects individually on these tissues. In most cases, the various effects affect one another and induce complex interactions with the cells and living tissues. Moreover, ultrasound involves mechanical waves with a wide range of frequencies of more than 20 kHz and a combination of different conditions of intensity, duration, pulsation, and standing wave formation, giving rise to various effects. Therefore, the interactions between the effects of ultrasound on the organism are exceptionally complex. As a result, as ultrasound induces a broad array of bioeffects, we could not cover all of these topics, including immunomodulation, thrombolysis, blood-brain barrier opening, and wound healing. Although the biomolecular mechanisms of such bioeffects are progressing at a rapid rate, it is difficult to elucidate them completely due to their complexity. Indeed, some clinical applications are already available without knowing the underlying mechanisms, such as applications for bone fracture healing and ED therapy. As ultrasound is an easily accessible tool with low cost, research analyzing ultrasound bioeffects will continue. Novel ideas have shown that it is possible that ultrasound may activate the human brain or speed up the growth of fish. In particular, researchers have reported that the bioeffects of the latter issue may be obtained with whole-body ultrasound irradiation to the fish. It is of great interest to determine the effects when the whole human body is exposed to ultrasound, although this is a large challenge since its safety is not well established.

Ultrasound has a long history of use for diagnosis in the clinical setting and has obtained a reputation for safety at a diagnostic level. How safe is ultrasound with high intensity? HIFU is a therapy used to burn away the lesion. Therefore, its power is fierce at its focus. Irradiation to a normal tissue causes severe tissue damage. However, in a portion 5 mm apart from the center, the temperature difference is about 50 °C. Therefore, HIFU can be considered to be safe in terms of heat if the dose of irradiation is properly managed. Although there seems to be no hazardous effects of LIPUS used for bone fracture healing, this technique surely affects the gene expression profile. Hence, how safe is ultrasound for gene therapy and drug delivery, which require stronger intensity? Severe hazardous side effects have not been reported in the more than three decades that have passed since LISWT was introduced; however, it has been found that ultrasound irradiation induces DNA DSBs in cells. Does the same phenomenon occur in the living body? Answering these questions depends on the findings of future research.

Ultrasound is a modality that is superior in many ways to other modalities, and unknown bioeffects of ultrasound may be discovered in the near future. Taking advantage of these aspects of ultrasound techniques should lead to the development of unique and sophisticated therapies. Ultrasound will surely occupy a more important position in medicine in the future.

References

1. Makino M, Mossoba MM, Riesz P (1983) Chemical effects of ultrasound on aqueous solutions. Formation of hydroxyl radicals and hydrogen atoms. J Phys Chem 87:1369–1377
2. Kondo T, Riesz P (1996) Sonolysis of ubiquinone in aqueous solutions. An EPR spin-trapping study. Int J Radiat Biol 69:113–121
3. Riesz P, Kondo T (1992) Free radical formation induced by ultrasound and its biological implications. Free Radic Biol Med 13:247–270
4. Draeger A, Monastyrskaya K, Babiychuk EB (2011) Plasma membrane repair and cellular damage control: the annexin survival kit. Biochem Pharmacol 81:703–712
5. Fechheimer M, Denny C, Murphy RF, Taylor DL (1986) Measurement of cytoplasmic pH in Dictyostelium discoideum by using a new method for introducing macromolecules into living cells. Eur J Cell Biol 40:242–247
6. Fechheimer M, Boylan JF, Paker S, Sisken JE, Patel GL, Zimmer SG (1987) Transfection of mammalian cells with plasmid DNA by scrape loading and sonication loading. Proc Natl Acad Sci U S A 84:8463–8467
7. Furusawa Y, Fujiwara Y, Campbell P, Zhao QL, Ogawa R, Hassan MA, Tabuchi Y, Takasaki I, Takahashi A, Kondo T (2012) DNA double-strand breaks induced by cavitational mechanical effects of ultrasound in cancer cell lines. PLoS One 7:e29012
8. Ashush H, Rozenszajn LA, Blass M, Barda-Saad M, Azimov D, Radnay J, Zipori D, Rosenschein U (2000) Apoptosis induction of human myeloid leukemic cells by ultrasound exposure. Cancer Res 60:1014–1020
9. Lagneaux L, de Meulenaer EC, Delforge A, Dejeneffe M, Massy M, Moerman C, Hannecart B, Canivet Y, Lepeltier MF, Bron D (2002) Ultrasonic low-energy treatment: a novel approach to induce apoptosis in human leukemic cells. Exp Hematol 30:1293–1301
10. Honda H, Kondo T, Zhao QL, Feril LB Jr, Kitagawa H (2004) Role of intracellular calcium ions and reactive oxygen species in apoptosis induced by ultrasound. Ultrasound Med Biol 30:683–692
11. Tabuchi Y, Kondo T, Ogawa R, Mori H (2002) DNA microarray analyses of genes elicited by ultrasound in human U937 cells. Biochem Biophys Res Commun 290:498–503
12. Tabuchi Y, Ando H, Takasaki I, Feril LB Jr, Zhao QL, Ogawa R, Kudo N, Tachibana K, Kondo T (2007) Identification of genes responsive to low intensity pulsed ultrasound in a human leukemia cell line Molt- 4. Cancer Lett 246:149–156
13. Furusawa Y, Zhao QL, Hassan MA, Tabuchi Y, Takasaki I, Wada S, Kondo T (2010) Ultrasound-induced apoptosis in the presence of sonazoid and associated alterations in gene expression levels: a possible therapeutic application. Cancer Lett 288:107–115
14. Machado CB, de Albuquerque Pereira WC, Talmant M, Padilla F, Laugier P (2010) Computational evaluation of the compositional factors in fracture healing affecting ultrasound axial transmission measurements. Ultrasound Med Biol 36:1314–1326
15. Kruse DE, Mackanos MA, O'Connell-Rodwell CE, Contag CH, Ferrara KW (2008) Short-duration-focused ultrasound stimulation of Hsp70 expression in vivo. Phys Med Biol 53:3641–3660
16. Gerstenfeld LC, Cullinane DM, Barnes GL, Graves DT, Einhorn TA (2003) Fracture healing as a post-natal developmental process: molecular, spatial, and temporal aspects of its regulation. J Cell Biochem 88:873–884
17. Kusano K, Miyaura C, Inada M, Tamura T, Ito A, Nagase H, Kamoi K, Suda T (1998) Regulation of matrix metalloproteinases (MMP-2, -3, -9, and -13) by interleukin-1 and interleukin-6 in mouse calvaria: association of MMP induction with bone resorption. Endocrinology 139:1338–1345
18. Whitney NP, Lamb AC, Louw TM, Subramanian A (2012) Integrin-mediated mechanotransduction pathway of low-intensity continuous ultrasound in human chondrocytes. Ultrasound Med Biol 38:1734–1743

19. Takeuchi R, Ryo A, Komitsu N, Mikuni-Takagaki Y, Fukui A, Takagi Y, Shiraishi T, Morishita S, Yamazaki Y, Kumagai K, Aoki I, Saito T (2008) Low-intensity pulsed ultrasound activates the phosphatidylinositol 3 kinase/Akt pathway and stimulates the growth of chondrocytes in three-dimensional cultures: a basic science study. Arthritis Res Ther 10:R77

20. Doan N, Reher P, Meghji S, Harris M (1999) In vitro effects of therapeutic ultrasound on cell proliferation, protein synthesis, and cytokine production by human fibroblasts, osteoblasts, and monocytes. J Oral Maxillofac Surg 57:409–419

21. Kumagai K, Takeuchi R, Ishikawa H, Yamaguchi Y, Fujisawa T, Kuniya T, Takagawa S, Muschler GF, Saito T (2012) Low-intensity pulsed ultrasound accelerates fracture healing by stimulation of recruitment of both local and circulating osteogenic progenitors. J Orthop Res 30:1516–1521

22. Wang FS, Kuo YR, Wang CJ, Yang KD, Chang PR, Huang YT, Huang HC, Sun YC, Yang YJ, Chen YJ (2004) Nitric oxide mediates ultrasound-induced hypoxia-inducible factor-1alpha activation and vascular endothelial growth factor-A expression in human osteoblasts. Bone 35:114–123

23. Naruse K, Miyauchi A, Itoman M, Mikuni-Takagaki Y (2003) Distinct anabolic response of osteoblast to low-intensity pulsed ultrasound. J Bone Miner Res 18:360–369

24. Suzuki A, Takayama T, Suzuki N, Sato M, Fukuda T, Ito K (2009) Daily low- intensity pulsed ultrasound-mediated osteogenic differentiation in rat osteoblasts. Acta Biochim Biophys Sin (Shanghai) 41:108–115

25. Sena K, Leven RM, Mazhar K, Sumner DR, Virdi AS (2005) Early gene response to low-intensity pulsed ultrasound in rat osteoblastic cells. Ultrasound Med Biol 31:703–708

26. Unsworth J, Kaneez S, Harris S, Ridgway J, Fenwick S, Chenery D, Harrison A (2007) Pulsed low intensity ultrasound enhances mineralisation in preosteoblast cells. Ultrasound Med Biol 33:1468–1474

27. Lee HJ, Choi BH, Min BH, Son YS, Park SR (2006) Low-intensity ultrasound stimulation enhances chondrogenic differentiation in alginate culture of mesenchymal stem cells. Artif Organs 30:707–715

28. Ren I, Yang Z, Song J, Wang Z, Deng F, Li W (2013) Involvement of p38 MAPK pathway in low intensity pulsed ultrasound induced osteogenic differentiation of human periodontal ligament cells. Ultrasonics 53:686–690

29. Tabuchi Y, Sugahara Y, Ikegami M, Suzuki N, Kitamura K, Kondo T (2013) Genes responsive to low- intensity pulsed ultrasound in MC3T3-E1 preosteoblast cells. Int J Mol Sci 14:22721–22740

30. Vardi Y, Appel B, Jacob G, Massarwi O, Gruenwald I (2010) Can low-intensity extracorporeal shockwave therapy improve erectile function? A 6-month follow-up pilot study in patients with organic erectile dysfunction. Eur Urol 58:243–248

31. Gruenwald I, Appel B, Vardi Y (2012) Low-intensity extracorporeal shock wave therapy – a novel effective treatment for erectile dysfunction in severe ED patients who respond poorly to PDE5 inhibitor therapy. J Sex Med 9:259–264

32. Vardi Y, Appel B, Kilchevsky A, Gruenwald I (2012) Does low intensity extracorporeal shock wave therapy have a physiological effect on erectile function? Short-term results of a random- ized, double-blind, sham controlled study. J Urol 187:1769–1775

33. Yee CH, Chan ES, Hou SS, Ng CF (2014) Extracorporeal shockwave therapy in the treatment of erectile dysfunction: a prospective, randomized, double-blinded, placebo controlled study. Int J Urol 21:1041–1045

34. Nishida T, Shimokawa H, Oi K, Tatewaki H, Uwatoku T, Abe K, Matsumoto Y, Kajihara N, Eto M, Matsuda T, Yasui H, Takeshita A, Sunagawa K (2004) Extracorporeal cardiac shock wave therapy markedly ameliorates ischemia-induced myocardial dysfunction in pigs in vivo. Circulation 110:3055–3061

35. Qiu X, Lin G, Xin Z, Ferretti L, Zhang H, Lue TF, Lin CS (2013) Effects of low-energy shockwave therapy on the erectile function and tissue of a diabetic rat model. J Sex Med 10:738–746

36. Ogawa R, Watanabe A, Moriia A (2015) Ultrasound up-regulates expression of heme oxygenase-1 gene in endothelial cells. J Med Ultrason 42:467–475
37. Ogawa R, Kagiya G, Feril LB Jr, Nakaya N, Nozaki T, Fuse H, Kondo T (2004) Ultrasound mediated intravesical transfection enhanced by treatment with lidocaine or heat. J Urol 172:1469–1473
38. Anwer K, Kao G, Proctor B, Anscombe I, Florack V, Earls R, Wilson E, McCreery T, Unger E, Rolland A, Sullivan SM (2000) Ultrasound enhancement of cationic lipid-mediated gene transfer to primary tumors following systemic administration. Gene Ther 7:1833–1839
39. Wang DS, Panje C, Pysz MA, Paulmurugan R, Rosenberg J, Gambhir SS, Schneider M, Willmann JK (2012) Cationic versus neutral microbubbles for ultrasound-mediated gene delivery in cancer. Radiology 264:721–732
40. Suzuki R, Takizawa T, Negishi Y, Utoguchi N, Maruyama K (2008) Effective gene delivery with novel liposomal bubbles and ultrasonic destruction technology. Int J Pharm 354:49–55
41. Yuan QY, Huang J, Chu BC, Li XS, Si LY (2011) A visible, targeted high-efficiency gene delivery and transfection strategy. BMC Biotechnol 11:56
42. Negishi Y, Hamano N, Tsunoda Y, Oda Y, Choijamts B, Endo-Takahashi Y, Omata D, Suzuki R, Maruyama K, Nomizu M, Emoto M, Aramaki Y (2013) AG73-modified bubble liposomes for targeted ultrasound imaging of tumor neovasculature. Biomaterials 34:501–507
43. Negishi Y, Tsunoda Y, Hamano N, Omata D, Endo-Takahashi Y, Suzuki R, Maruyama K, Nomizu M, Aramaki Y (2013) Ultrasound-mediated gene delivery systems by AG73-modified bubble liposomes. Biopolymers 100:402–407
44. Madio DP, van Gelderen P, DesPres D, Olson AW, de Zwart JA, Fawcett TW, Holbrook NJ, Mandel M, Moonen CT (1998) On the feasibility of MRI-guided focused ultrasound for local induction of gene expression. J Magn Reson Imaging 8:101–104
45. Deckers R, Quesson B, Arsaut J, Eimer S, Couillaud F, Moonen CT (2009) Image-guided, noninvasive, spatiotemporal control of gene expression. Proc Natl Acad Sci U S A 106:1175–1180
46. Braiden V, Ohtsuru A, Kawashita Y, Miki F, Sawada T, Ito M, Cao Y, Kaneda Y, Koji T, Yamashita S (2000) Eradication of breast cancer xenografts by hyperthermic suicide gene therapy under the control of the heat shock protein promoter. Hum Gene Ther 11:2453–2463
47. Ogawa R, Lee SI, Izumi H, Kagiya G, Yohsida T, Watanabe A, Morii A, Kakutani S, Kondo T, Feril LB Jr, Ishimoto T (2009) Enhancement of artificial promoter activity by ultrasound-induced oxidative stress. Ultrason Sonochem 16:379–386
48. Watanabe A, Kakutani S, Ogawa R, Lee SI, Yoshida T, Morii A, Kagiya G, Feril LB Jr, Fuse H, Kondo T (2009) Construction of artificial promoters sensitively responsive to sonication. J Med Ultrason 36:9–17
49. Hassan MA, Campbell P, Kondo T (2010) The role of Ca^{2+} in ultrasound-elicited bioeffects: progress, perspectives and prospects. Drug Discov Today 15:892–906
50. Rosenthal I, Sostaric JZ, Riesz P (2004) Sonodynamic therapy- a review of the synergistic effects of drugs and ultrasound. Ultrason Sonochem 11:349–363

Lipid-Coated Nanodrops and Microbubbles

Mark A. Borden

Contents

Abstract

Lipid-coated microbubbles and nanodrops are used in many applications of biomedical ultrasound. They serve as ultrasound contrast agents, molecular imaging probes, targeted drug delivery vehicles, nucleic acid vectors, gas carriers, and enhancers of thermal ablation. Each application has a unique set of performance criteria – there is no "one size fits all" microbubble formulation. Rational design can be accomplished using the composition → processing → structure → property → performance paradigm first described by DH Kim for lipid-coated

M.A. Borden (✉)
Department of Mechanical Engineering, University of Colorado, Boulder, CO, USA
e-mail: mark.borden@colorado.edu

microbubbles over a decade ago. One notable example has been the synthesis of longer circulating microbubbles through centrifugal isolation of larger diameter microbubbles coated with long acyl chain phospholipids. The purpose of this chapter is to inform the reader of current knowledge of the effects of lipid composition and processing on microstructure, as well as the effects of microstructure on important physical properties, such as microbubble size and shell viscoelasticity. More research is necessary to further elucidate these interrelationships and to exploit them for innovative microbubble designs.

Introduction

The lipid monolayer is nature's solution to the problem of stabilizing a gas/water interface. The most prominent example is the lung: phospholipid is the main component of lung surfactant, which stabilizes the lung alveoli by reducing surface tension and providing mechanical rigidity [1]. Premature infants born without functional surfactant are unable to breathe properly and suffer from acute respiratory distress syndrome (ARDS). The treatment for neonatal ARDS is surfactant therapy, in which animal-derived and lipid-fortified surfactant is aspirated into the patient's lung. Another example is the eye: a lipid membrane coats and stabilizes the aqueous tear film against evaporation and rupture [2]. Dysfunction in the lipid layer of the eye can lead to ocular disease, such as dry eye. Lipids synthesized by specialized cells and excreted into the aqueous subphase spontaneously assemble into a monolayer at the air/water interface to provide these functions. It is therefore not surprising that scientists and engineers have utilized the lipid monolayer as an ideal self-assembling biomaterial to stabilize microbubbles and nanodrops used for applications in ultrasonics.

Lipid-coated microbubbles (1–10 μm) are used as echogenic contrast agents to illuminate the blood compartment on the ultrasound video screen [3–5]. Without microbubbles, the presence of blood is obscured by tissue scatter. When microbubbles are injected intravenously, the vascular structures and perfused tissue suddenly light up. The brightness on the video screen comes from the strong scattering amplitude of the microbubble. Microbubbles have a gas core that is highly compressible and pulsates with the passage of each mechanical acoustic wave. In fact, microbubbles resonate when driven at acoustic frequencies used by common diagnostic imaging scanners (1–10 MHz). Each microbubble is like a tiny bell, and modern ultrasound scanners employ specific pulse sequences to filter out the echo of each microbubble based on its peculiar tone. This has enabled enhanced ultrasound imaging of the blood pool in cardiology and radiology [6, 7], and more recently there has been a strong interest in ultrasound molecular imaging to assess the physiology of diseased vasculature [8]. Currently, a vast majority of the ultrasound contrast agents approved for clinical use are lipid-coated microbubbles.

Microbubbles are used also in ultrasound therapy. The response of a microbubble to ultrasound transitions from ringing (stable cavitation) to banging (inertial cavitation) as the acoustic intensity is increased. Inertial cavitation can be used to open up pores in the vasculature that allow drugs to move from the blood pool to the tissue compartment. Thus, the interaction of microbubbles with focused ultrasound allows one to manipulate the pharmacodynamics of a drug with excellent temporal and spatial control by virtue of when and where one points the acoustic focus. Additionally, the microbubble can be engineered to carry a drug payload that is simultaneously released with the opening of the vasculature [9]. Ultimately, the imaging and therapy functions of microbubbles can be combined for theranostic applications, such as image-guided cancer therapy.

The rich variety of ultrasonics applications that employ microbubbles calls for rational design, so that a specific microbubble formulation can be tailored to a particular use (Fig. 1). Dennis Heejong Kim, a student of David Needham at Duke University, first pioneered a set of design rules for lipid-coated microbubbles based on the general material science paradigm of composition → processing → structure → property → performance [10]. DH Kim first showed how lipid acyl chain length could be varied to control the surface shear properties of the monolayer film that coats each microbubble. He then went on to show that processing affects microstructure, which in turn controls the surface shear properties. Subsequent research has gone on to validate this approach by showing how other properties of the lipid shell, such as gas permeability and surface dilatational elasticity, as well as biomedical performance, depend on lipid composition and microstructure. The goal of this chapter is to provide the interested reader with an overview of this rational design paradigm for lipid-coated microbubbles and nanodrops.

Microbubble Composition

Uncoated Microbubbles Are Unstable

At the most basic level, a microbubble is simply a 1–10-μm-diameter gas sphere suspended in an aqueous medium. However, there is tension (σ) at the gas/water interface, and, owing to the spherical geometry, a pressure jump exists across the interface (Laplace pressure) [11]:

$$P_b - P_0 = \frac{2\sigma}{R} \tag{1}$$

where P_b is the pressure inside the bubble, P_0 is the hydrostatic pressure of the aqueous medium surrounding the bubble, and R is the bubble radius. For a 1.0-μm-diameter air bubble in water ($\sigma = 73\,\text{mN/m}$), the pressure inside the bubble is ~0.3 MPa greater than the surrounding medium. Thus, the gas molecules in the bubble have a much higher fugacity than those dissolved in the surrounding medium [12]. This sets up a chemical potential gradient that drives mass flux from the
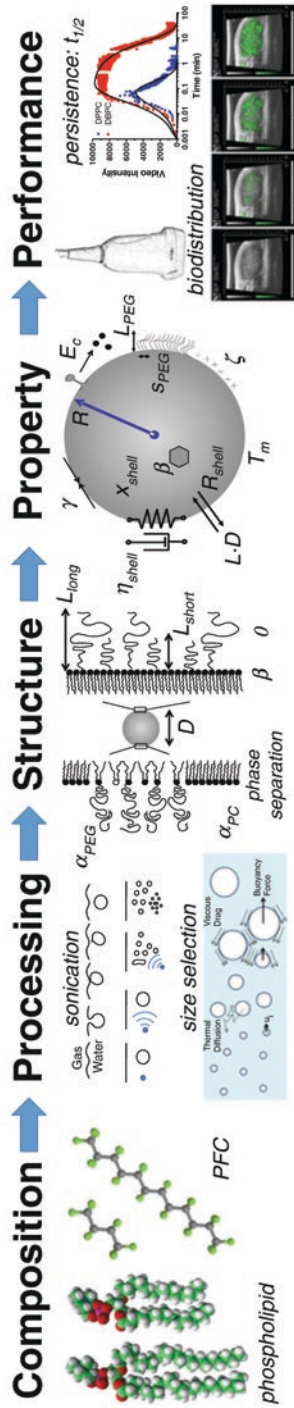
Fig. 1 Rational design of lipid-coated microbubbles. DH Kim first demonstrated the utility of employing the composition → processing → structure → property → performance paradigm to engineering lipid-coated microbubbles [10]. Research continues today to establish key structure–property–performance relationships for enhanced biomedical performance

microbubble – the microbubble is thermodynamically unstable. The rate of dissolution can be modeled by the Epstein–Plesset equation [13]:

$$-\frac{dR}{dt} = \frac{LD}{R}\left(\frac{1 + 2\sigma/P_0R - f}{1 + 4\sigma/3P_0R}\right) \tag{2}$$

where L is the Ostwald coefficient for the gas solubility, D is the gas diffusivity in water, and f is the solubility fraction of the gas in water. Equation 2 neglects the time to set up the concentration boundary layer, as this is very fast compared to the bubble wall velocity [14]. Epstein and Plesset's model predicts that, even when the aqueous solution is saturated with gas ($f = 1$) at hydrostatic pressure P_0, the Laplace pressure drives very rapid dissolution. Equation 2 predicts that a 1.0-µm-diameter air bubble in water dissolves within three milliseconds (Fig. 2). One may use less soluble gases to enhance stability. However, even perfluorobutane, which has a permeation coefficient (LD) ~300 times lower than that of air, cannot stabilize an uncoated microbubble for more than a minute [9]. Therefore, one may conclude that the uncoated microbubble is both thermodynamically and kinetically unstable.

The Lipid/PEG-Lipid Coating Provides Metastability

Needham et al. argued that a lipid monolayer coating between the gas and water phases effectively eliminates tension in the interface ($\sigma = 0$) in order to explain the "indefinite" persistence of lipid-coated air microbubbles in air-saturated aqueous media [14, 15]. Borden et al. initially disputed this claim, as the same lipid monolayers on the Langmuir trough were found to collapse at surface tensions well above zero [16]. However, it was later revealed by Witten et al. that the Wilhelmy plate method used with the Langmuir trough becomes inaccurate at very low surface tensions [17]; the method assumes the monolayer is a liquid with an isotropic stress distribution, but highly compressed lipid monolayers can act as solid elastic membranes with an anisotropic stress distribution, leading to artifacts in the measurement. The observation that most microbubbles are spherical under the microscope suggests that the lipid monolayer has some tension. One can estimate a lower limit for the surface tension by use of the Bond number (Bo), which is a ratio of the buoyant to surface tension forces:

$$Bo = \frac{\Delta\rho gR^2}{\sigma} \tag{3}$$

where $\Delta\rho$ is the density difference between the gas and aqueous phases and g is gravitational acceleration. The buoyancy force flattens the bubble out against the surface above, while the surface tension force contracts the bubble into a sphere. The fact that a resting lipid-coated microbubble is observed to be a sphere suggests that the Bond number is less than unity, and therefore the lower limit of the surface tension must be:

Fig. 2 Microbubble
dissolution curves in
air-saturated media. The
uncoated microbubble
dissolution curve (*red*)
was calculated using Eq. 2 with
$L = 0.02, D = 2 \times 10^{-5} \text{ cm}^2/\text{s}$,
$\sigma = 73$ mN/m, $P_0 = 10^5$ Pa,
and $f = 1$. The lipid-coated
microbubble dissolution curve
(*green*) was calculated using
Eq. 5, with $L = 0.02, D = 2$
$\times 10^{-5}$ cm^2/s, $\sigma = 3 \times 10^{-4}$
mN/m, $P_0 = 10^5$ Pa, $f = 1$,
and $R_{\text{shell}} = 10^3$ s/cm
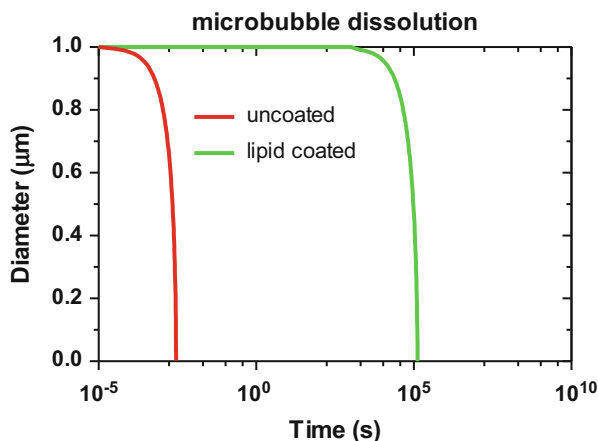
$$\sigma > \Delta\rho g R^2 \qquad (4)$$

For a 1.0-μm-diameter lipid-coated air bubble in water, this gives a lower limit of
$\sim 3 \times 10^{-6}$ mN/m. It is interesting to note that ~10-μm-diameter lipid-coated air
bubbles have been observed to flatten out during dissolution in unsaturated aqueous
media [18], indicating that the surface tension of the lipid monolayer coating may
become *less than* $\sim 3 \times 10^{-4}$ mN/m under compression. Both of these values are
extremely low and would hardly drive the microbubble to dissolve very fast. The
fugacity difference of the gas molecules in the bubble and medium at this low surface
tension would be only ~0.1 Pa. Thus, the gas core may be strictly thermodynami-
cally unstable, but the chemical potential gradient is very small.

The lipid monolayer also imposes an additional resistance to gas diffusion (R_{shell}
$\sim 10^3$ s/cm) [19], and this can be modeled by the following equation [18]:

$$-\frac{dR}{dt} = \frac{L}{R_{\text{shell}} + R/D}\left(\frac{1 + 2\sigma/P_0R - f}{1 + 4\sigma/3P_0R}\right) \qquad (5)$$

Using the values for σ and R_{shell} imparted by the lipid shell, Eq. 5 predicts that the
microbubble will last ~4000 years, an increase over the uncoated microbubble
lifetime by eight orders of magnitude! Thus, the lipid-coated microbubble is kinet-
ically trapped against dissolution, owing to the very slow diffusion. Since dissolu-
tion is a rate-limiting step in Ostwald ripening, this mechanism would likewise be
stalled by the lipid coating.

However, microbubble dissolution is driven not only by the chemical potential
gradient of the gas core but also that of the lipid molecules in the monolayer shell.
Lee et al. have measured the "equilibrium" surface tension of the lipid monolayer to
be ~25 mN/m for lipids above their main phase transition temperature (T_m) [20]. The
equilibrium surface tension increases as temperature decreases further and further

below T_m, ultimately approaching the value for a clean air/water interface ($\sigma = 73$ mN/m). This indicates that the lipid molecules are much more closely packed on the microbubble surface than they would be on a flat air/water interface, which reduces their translational entropy. The lipid molecules become packed this way on the microbubble surface during Laplace pressure-driven dissolution. The work used to condense the lipids is provided by the release in free energy as the gas molecules diffuse down their chemical potential gradient. Part of this free energy is stored in the compression state (reduced entropy) of the lipids. The system will tend to thermodynamic equilibrium as this free energy is released by lipids desorbing from the microbubble and reforming hydrated bilayers in the bulk aqueous phase. At present, we do not have a quantitative value of the energy barrier for this desorption process, but it must be rather high, as lipid-coated microbubbles have been observed to be stable over long timescales (at least 1 year in the author's laboratory).

Coalescence is another mechanism to release free energy stored in the microbubbles. Rapid coalescence would lead to thermodynamic equilibrium: complete phase separation of the gas and aqueous phases, where the lipids form bilayer structures within the aqueous phase. Coalescence is inhibited by a hydrated poly (ethylene glycol) (PEG) brush layer, extending away from the microbubble surface. Once the PEG brushes of two approaching microbubbles overlap, a strong steric/osmotic repulsion force arises that opposes the motion [21]. Thus, coalescence is prevented unless the inertia of the colliding bubbles is extremely high, or the approach is extremely slow (i.e., providing enough time to allow PEG-lipids to diffuse out of the contact zone [22]). The thickness of the PEG brush on the microbubble coating has been estimated from self-consistent field (SCF) theory to be ~10 nm [23]. Thus, the onset of this PEG brush-mediated repulsion is expected to occur with ~20 nm separation distance between the microbubble surfaces. It has been found that PEG-lipid is necessary as an "emulsifier" to generate microbubbles; lipid alone will not form a sufficient yield of microbubbles [24].

Lipid Composition and Molecular Structure

The discussion above concludes that two lipid components are necessary to form metastable microbubbles: (1) a main phospholipid species capable of achieving very low surface tension ($\sigma << 1$ mN/m) to inhibit dissolution and/or Ostwald ripening and (2) a PEG-lipid emulsifier capable of forming a hydrated brush of sufficient height and density to inhibit coalescence. Other emulsifiers may be substituted for PEG, but the fact remains that a long-range (tens of nm) repulsion force is necessary to inhibit coalescence over long and short timescales. PEG-lipid is the most common emulsifier used to synthesize microbubbles used in ultrasonics.

The main lipid species is often a saturated diacyl phosphatidylcholine (PC). This molecule has a cylindrical shape and self-assembles via hexagonal packing into planar monolayers and bilayers [11] (Fig. 3a). The cylindrical geometry is ensured by the roughly equivalent diameters of the acyl chains compared to the PC headgroup; the structure of a single acyl chain PC (lyso-lipid) is conical, which

induces curvature and disrupts the planar membrane geometry [25]. Additionally, the extra acyl chain doubles the hydrophobic cavity energy of the lipid molecule, thereby reducing its solubility (critical micelle concentration) by a factor of $e^2 = 7.4$, which helps pin the lipid to the gas/water interface. The fully hydrogenated chains can straighten out in the all-*trans* configuration during packing; a double bond would induce a kink that disrupts lipid packing. The acyl chain length can be manipulated to modulate molecular hydrophobicity and intermolecular van der Waals cohesion forces (Fig. 3a). In fact, PC acyl chain length is perhaps the most valuable molecular parameter for controlling the structure, properties, and performance of microbubbles in ultrasonics applications, as will be discussed throughout this chapter. The lower limit is C16; this is the shortest acyl chain that provides a lipid layer below T_m. PC lipids above T_m typically do not form stable microbubbles. On the other end of the spectrum is C24, which is the longest acyl chain PC lipid that is commercially available currently.

PC typically comprises 80–90 mol% of the lipid monolayer. The overall neutral charge of the PC headgroup limits lateral charge repulsion, allowing the molecules to pack tightly together. PC therefore acts as a monolayer matrix-forming lipid [10]. At the same time, the zwitterionic PC groups interact strongly with water, which is essential for reducing surface energy at the aqueous/lipid interface. The zwitterionic PC surface also is resistant to protein adsorption and opsonization [26], which ultimately helps biomedical performance.

Other lipid headgroups can be substituted for a fraction of PC, such as the negatively charged phosphatidic acid (PA) present in the commercially available ultrasound contrast agent Definity® (Lantheus Medical Imaging). The negative charge can mimic the double layer repulsion of the glycocalyx to minimize undesirable microbubble–cell interactions with red blood cells and endothelium. However, the negative charge can also promote opsonization [26]. On the other hand, positively charged lipid headgroups such as trimethylammonium-propane (TAP) can be used to adsorb negatively charged nucleic acids for gene delivery [27, 28]. These charged lipids rarely exceed 20 mol% of the total lipid owing to lateral charge repulsion that can destabilize the lipid shell, as well as the potential for increased opsonization [26].

The second critical component is the emulsifier, which is typically PEG-lipid (Fig. 3b). The PEG-lipid often comprises 10–20 mol% of the lipid coating. As mentioned above, the PEG-lipid is critical for forming a hydrated brush that inhibits microbubble coalescence. It appears that a PEG molecular weight of at least 2000 Da is necessary to stabilize the microbubbles [29]. At present, PEG molecular weights greater than 5000 Da have not been reported for lipid-coated microbubbles. Longer PEGs may lead to microbubble instability owing to the reduced overall hydrophobicity of the emulsifier molecule, allowing it to desorb more readily, as well as the possibility of a less dense PEG brush. It is also important to keep in mind that the PEG itself is polydisperse – there is a distribution of PEG chain lengths in most commercially available PEG-lipids, although this is rarely quantified with a polydispersity index.
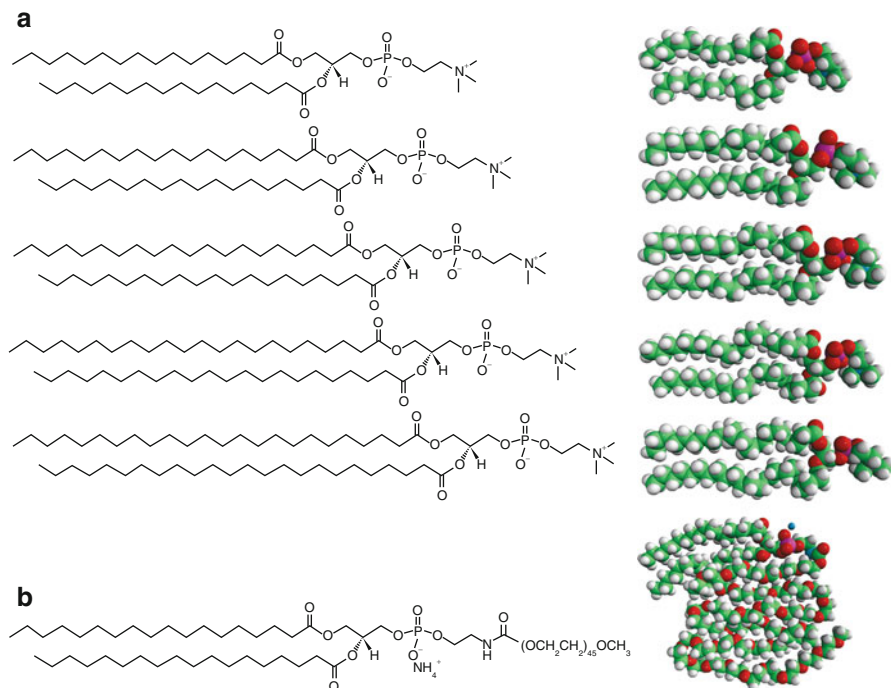
Fig. 3 Molecular structures of lipids commonly used to stabilize microbubbles and nanodrops. (**a**) Saturated diacyl phosphatidylcholine (*PC*) is the main lipid component and often comprises 80–90 mol% of the lipid shell. Shown is the homologous series from C16 to C24. (**b**) poly(ethylene glycol)-lipid serves as an emulsifying agent; shown here is C18 acyl chain length and 2000 Da PEG molecular weight (~45 ethylene oxide mers). These structures were taken from the Avanti Polar Lipids website (http://www.avantilipids.com/)

A secondary advantage of the PEG brush is that it may also inhibit opsonization and unwanted microbubble–cell interactions. On the other hand, the PEG serves as a tether for attaching targeting ligands [24] and nanoparticles [30–32]. Thus, the PEG emulsifier serves as an extremely useful component for more sophisticated microbubble designs.

Microbubble Fabrication

Now that the main lipid components have been identified and their use in microbubble stabilization has been justified, the next step in the rational design paradigm is to investigate processing techniques that lead to various microbubble structures. First, the main techniques to synthesize microbubbles are briefly reviewed. Then, a few postproduction processing steps are reviewed to fine tune and enhance the overall structure.

Microbubble Synthesis

As discussed above, the microbubble is a thermodynamically unfavorable structure. They do not self-assemble; equilibrium favors their disassembly into three separate phases of gas, aqueous medium, and hydrated bilayers. Rather, one must design a process that adds energy to synthesize them and then kinetically traps them in the most desirable state. Three of the more common microbubble fabrication methods are shown schematically in Fig. 4 and discussed in greater detail below.

Sonication

Sonication was the first method described to generate microbubbles for ultrasonics [33]. Sonication involves the high-frequency vibration (typically 20 kHz) of a horn tip at the gas/water interface. This vibration leads to entrainment and secondary breakup through cavitation in the bulk aqueous phase [34, 35]. Unfortunately, there is very little research into the details of bubble entrainment via sonication. It is generally known that low-power sonication with the tip submerged inside the aqueous medium leads to microbubble destruction (clarification) and breakup of the lipid structures from multi-lamellar vesicles (MLVs) into small unilamellar liposomes (SUVs). This is often a preparation step in generating microbubbles. Microbubbles are then generated by moving the probe tip to the gas/water interface and turning the system to full power. Sonication generates many microbubbles very rapidly: for example, 1 L volume of 10^{12}/L can be generated within 1 min. The stochastic processes of entrainment and breakup lead to a fairly polydisperse size distribution, which can be refined using centrifugation steps as outlined below [36]. Thus, sonication is a simple and economical method of generating microbubbles in high yield and admittedly is the preferred method used by the author's research group.

As mentioned above, low-solubility perfluorocarbon gases can be used to decelerate microbubble dissolution. This leads to higher microbubble yields, longer shelf-life, and longer in vivo circulation persistence (i.e., the so-called second-generation ultrasound contrast agents). In sonication, the gas is simply made to flow directly over the aqueous suspension.

A critical step in microbubble generation and stabilization is the adsorption of lipid onto the gas/water interface. This involves shuttling lipid from MLVs or SUVs through the aqueous phase to the newly formed microbubbles. One can model the adsorption process as a chemical reaction involving a particular collision frequency and activation energy. The collision frequency can be increased through increasing lipid concentration (e.g., more SUVs) and convection, which thins the concentration boundary layer. It has been found that 1 mg/mL lipid usually is sufficient to generate a microbubble suspension at 10^9/mL. Since the process necessarily exposes the hydrophobic acyl chains of the lipid molecules to water, there also is an activation energy barrier that limits the kinetics. Lipid adsorption to macroscopic interfaces under static conditions can take minutes or even days. However, as mentioned above, sonication can lead to lipid deposition rates of at least 10 m^2/min and possibly higher. Thus, sonication accelerates the reaction. Microstreaming and acoustic
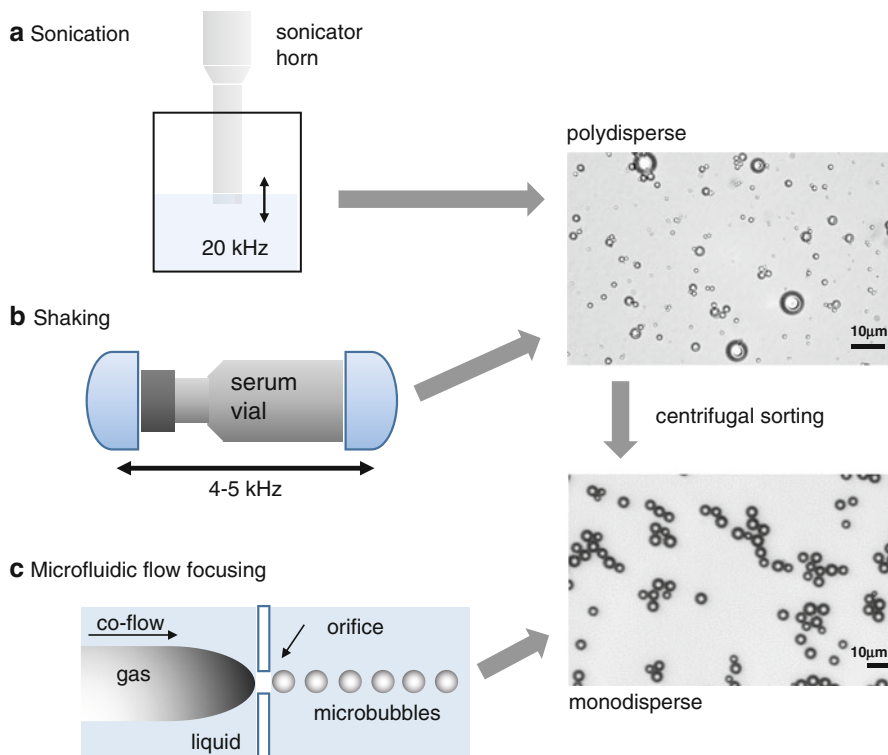
Fig. 4 Methods of microbubble synthesis and centrifugal sorting. Sonication (**a**) and shaking (**b**) produce polydisperse microbubbles very rapidly and economically, but they must be centrifugally sorted to a monodisperse size. Microfluidic methods (**c**) produce monodisperse microbubbles, but at relatively slow rates

radiation forces induce fluid flow that may increase the collision frequency between SUVs and the gas/water interface. Additionally, sonication may catalyze the reaction by highly localized (pico-liter volume) heating events at cavitation sites within the bulk phase. More research is necessary to better understand the bubble formation process during sonication, as well as how the sonication parameters affect microbubble size.

Shaking

Shaking is another process of mechanical agitation that is used to create microbubbles. Typically, a small volume ($\sim$1 mL) of lipid solution is sealed in a small vial with a gas headspace and placed in a dental amalgamator or similar mixing device. The device vibrates along the long axis of the vial at $\sim$4000 Hz. This method is used to generate Definity® microbubbles, for example. The benefit of the shaking method is that it can produce microbubbles rapidly ($\sim$10^9 in less than one minute) almost anywhere, on demand. The lipid suspension in the vial can be made at a

central facility, sterilized, and then shipped to the end user, who simply places the vial into the shaking device to generate the microbubbles. Thus, it is a very simple and economical method for multiple uses of small quantities of microbubbles. As with sonication, the bubble entrainment and breakup processes during shaking are poorly understood, but it is known that they lead to a polydisperse size distribution. Coincidentally, the size distribution of microbubbles formed by shaking tends to be remarkably similar to that of microbubbles formed by sonication, despite the very different geometry and characteristic frequency. More research is necessary to better understand the bubble formation process during shaking, as well as how the shaking parameters affect the microbubble size.

Microfluidics

More recently, researchers have begun investigating microfluidic techniques to generate microbubbles [37]. This follows advances in the design and fabrication of microfluidic devices, as well as empirical, theoretical, and computational work that has developed correlations to simplify the analysis of fluid mechanics in microfluidic flows. The main phenomenon exploited by microfluidic microbubble generation is flow focusing, in which a thread of gas sheathed by a liquid layer is forced to flow through a contraction and then expansion. The divergent flow leads to a capillary instability that breaks off microbubbles in a very regular pattern, leading to a monodisperse size distribution. The microbubble radius scales with flow rate in a planar flow-focusing device operating at high Reynolds number according to the following equation [38]:

$$\frac{R}{w} \propto \left(\frac{Q_{\text{gas}}}{Q_{\text{liquid}}}\right)^{2/5} \tag{6}$$

where w is the width of the nozzle and Q_{gas} and Q_{liquid} are the flow rates of the gas and liquid streams, respectively ($Q_{\text{liquid}} > Q_{\text{gas}}$). Thus, increasing the flow rate of the gas stream leads to a higher production rate, while increasing the relative flow rate of the liquid stream leads to smaller microbubbles.

The control over microbubble size and the possibility of directed assembly for more sophisticated structures are highly desirable aspects of microfluidic methods. Additionally, the devices are relatively easy to observe during operation with current high-speed imaging techniques, thus providing insight into the physics and engineering of the bubble formation. The main drawback is the relatively low yield (up to $\sim 10^6$/s). Additionally, microfluidic methods are relatively difficult and expensive to employ, as they require clean-room microfabrication facilities to build the device and some trial-and-error tuning and optimization of the relative gas and liquid flows to reproducibly generate the microbubbles. Typically, this is done with expensive microscopy and high-speed camera tools. More research is necessary to better understand the lipid coating process and how to engineer it for more efficient generation of stable microbubbles.

Postproduction Processing

Centrifugal Sorting

As shown below, size is a key structural feature of the microbubble that affects its acoustic properties and biomedical performance. Control of diameter is therefore essential to improving precision in ultrasonic applications employing microbubbles. As mentioned above, size can be controlled during microbubble synthesis with microfluidics by changing the gas and liquid flow rates and nozzle size [38]. However, microfluidics is not the only means of obtaining a monodisperse microbubble suspension. One can take the polydisperse suspensions obtained from sonication or shaking (or any other production method) and subject them to a series of centrifugation steps to isolate microbubbles of a select size [36]. The principle of operation is that microbubbles of different migration speeds under the centrifugal field fractionate into either a "cake" layer at the top or the aqueous subphase below. The migration rate of a microbubble is related to its size by the Stokes rise velocity (u) for low Reynolds number:

$$u = \frac{2\Delta\rho g R^2}{9\mu} \tag{7}$$

where μ is the viscosity of the aqueous phase. Note that the migration speed scales as R^2, which enhances the precision of this technique.

To isolate microbubbles above or below a certain size, one simply defines a cutoff radius and centrifugal strength (g) and then calculates the residence time (t) from the migration rate and height (h) of the centrifuge column (typically a stoppered syringe of 1–10 cm).

$$t = \frac{h}{u} \tag{8}$$

A centrifugal strength of 100–500 RCF (relative centrifugation to Earth's gravitational field) is sufficient to reduce the residence time to a few minutes without inducing an overly destructive hydrostatic pressure (P_0) on the microbubbles (see Eq. 5 above). Equation 7 is valid because viscous drag causes the microbubbles to accelerate and decelerate to the migration speed within a fraction of a second. One important consideration is that the microbubble suspension should be below 20 vol. % to avoid multi-bubble interactions that cause the migration rates to deviate from Eq. 7.

To sort microbubbles by this method, one simply performs multiple centrifugation steps, defining cutoff sizes above and below the desired radius. Microbubbles can be obtained from either the cake or the subphase; the PEG brush layer provides osmotic/steric stability against coalescence within the cake to preserve the size distribution. Once the desired size is isolated, the suspension can be refined by repeating centrifugations until the polydispersity index (the ratio of the volume-weighted mean radius to the number-weighted mean radius) drops to the desired

value. This is typically accomplished within an hour. With sufficient experience, very few microbubbles are lost during this procedure. Combined with sonication, this economical method provides a very high yield of low-polydispersity microbubbles of select size in a relatively short period of time.

Heat Treatment

As shown below, microstructure of the lipid coating can have a significant effect on the microbubble properties. Microstructure arises owing to crystallization of the lipids on the bubble surface to form domains (grains) surrounded by interdomain regions (boundaries) [10, 15]. The crystallization process follows classical nucleation–growth theory and terminates in a polycrystalline shell. Thus, one can use concepts from metallurgy to characterize and engineer the microbubble shell. Initially, crystallization occurs as the surface area is reduced (surface pressure increased) during Laplace pressure-driven dissolution of the newly formed microbubble, until it is stabilized by effectively zero surface tension. Since each microbubble has undergone its own peculiar formation and stabilization history, there may be a strong polydispersity in the microstructures. To improve uniformity and control microstructure, one can heat the microbubble suspension to a temperature above T_m of the main lipid species to melt the coating. One then cools the suspension at a certain rate, allowing the recrystallization. Slow cooling favors growth over nucleation, leading to a smaller number of large domains and therefore a low defect density. Rapid quenching favors nucleation over growth, leading to a larger number of small domains and therefore a high defect density. One can also anneal the polycrystalline shell (fuse the domains) by holding the microbubble suspension to a few degrees just below T_m [15].

Since the lipid coating is at least a binary mixture of phospholipid and emulsifier, there may be phase separation owing to the different nucleation and growth rates of the different species. This has been observed on lipid shells as domains of PC surrounded by interdomain regions of PEG-lipid [16, 29]. Fluorescent membrane dyes often partition with the PEG-lipid in the interdomain region, and the microbubbles appear like soccer balls under the microscope, with dark PC domains surrounded by bright PEG-lipid-enriched regions (Fig. 5).

Additionally, the selection of the PC lipid may influence the domain morphology and therefore defect density. For example, longer chain lipids may be kinetically trapped at high cooling rates as highly ramified dendritic (snowflake) domains, whereas shorter chains lipids may equilibrate to circular cloven domains when subjected to the same heat treatment [16]. More research is necessary to better understand and control the lipid crystallization process and the evolution of domain morphology over time.

Functionalization

Once microbubble size and microstructure of the lipid domains are set, one can further functionalize the microbubble by attaching molecules or nanoparticles to the surface. The simplest method is simple electrostatic adsorption, which can be used in layer-by-layer assembly to build polyelectrolyte multilayer shells [28]. Alternatively,
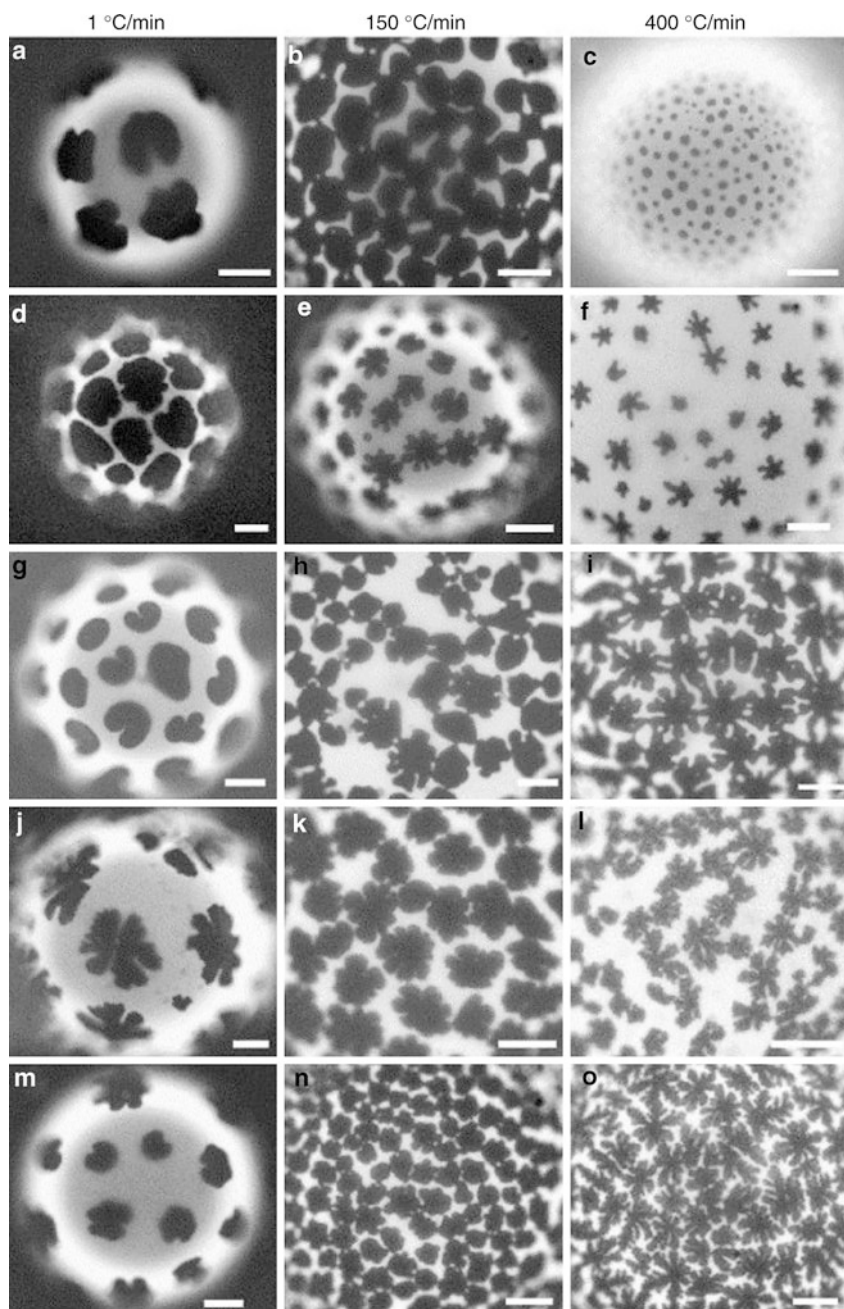
Fig. 5 Fluorescent micrographs of microbubbles heated to melt the lipid coating and then cooled at various rates. The lipid coating comprises a mixture of PEG40S:NBD-PC: (**a–c**) $diC_{16:0}PC$, (**d–f**) $diC_{18:0}PC$, (**g–i**) $diC_{20:0}PC$, (**j–l**) $diC_{22:0}PC$, (**m–o**) $diC_{24:0}PC$. Scale bars represent 20 μm (Taken from Borden et al. [16])

there are a variety of conjugation chemistries that have been described in the literature [24], including ligand–receptor avidin–biotin and covalent maleimide–thiol coupling. The advantage of these techniques is greater control over the loading density and configuration by virtue of the inherent specificity and stoichiometry of the chemical reactions. More sophisticated ligand expression can be achieved using tiered surface architectures to enhance exposure [39] or concealment [40] of the ligand. Additionally, there are many examples of nanoparticle loading onto microbubbles that have been reported in the literature [31, 41], including polymer, gold and iron oxide nanoparticles, quantum dots, liposomes, lipoplexes, and polyplexes.

Nanodrop Fabrication

Nanodrops are distinct from microbubbles in their size (submicron vs. micron) and the phase state of the interior fluorocarbon phase (liquid vs. gas). Otherwise, they are very similar in the sense that the lipid coating inhibits dissolution and coalescence to stabilize the aqueous emulsions. The nanodrop itself is not very echogenic or acoustically responsive owing to the relative small size and, more importantly, incompressibility of the liquid core. However, the nanodrop can be extremely ultrasound responsive if one can tune the composition and structure such that it vaporizes into a microbubble upon insonation (or some other stimulation). This is the so-called phase-change agent: a microbubble in a more compact form. Most fluorocarbons experience a fivefold change in radius upon vaporization. Thus, a 200-nm-diameter droplet can form a 1-µm-diameter microbubble. The smaller size of the droplets may provide new biomedical performance capabilities that were previously unavailable to microbubbles, such as longer circulation and accumulation in tumors owing to the enhanced permeability and retention effect. Additionally, the vaporization event itself is highly energetic and can be used to facilitate imaging, drug delivery, and ablation.

Two basic methods have been described to form phase-change nanodrops. The first method reported for longer chain fluorocarbons (perfluoropentane and above) was homogenization followed by extrusion [42]. All of the processing occurs with the fluorocarbon in the liquid phase. Unfortunately, however, the more cohesive fluorocarbons require relatively large acoustic energy (mechanical index) to induce a phase transition. More recently, a new method has been described to generate nanodrops of low-boiling fluorocarbons, such as F-propane and F-butane [42]. The method involves first generating a suspension of microbubbles and then cooling and pressurizing the suspension to induce a vapor-to-liquid phase transformation to form nanodrops [43]. The nanodrops are then brought back to standard pressure and temperature, where they remain remarkably metastable in the liquid form to phase change unless they are stimulated by a relatively small acoustic energy (Fig. 6). The superheated drops remain metastable owing to the need for homogenous nucleation and growth of a vapor embryo, making 90 % of the critical temperature the main trigger, rather than the boiling temperature [44]. Yet they can be vaporized acoustically at a clinically relevant mechanical index [45, 46]. One important advantage of

microbubbles
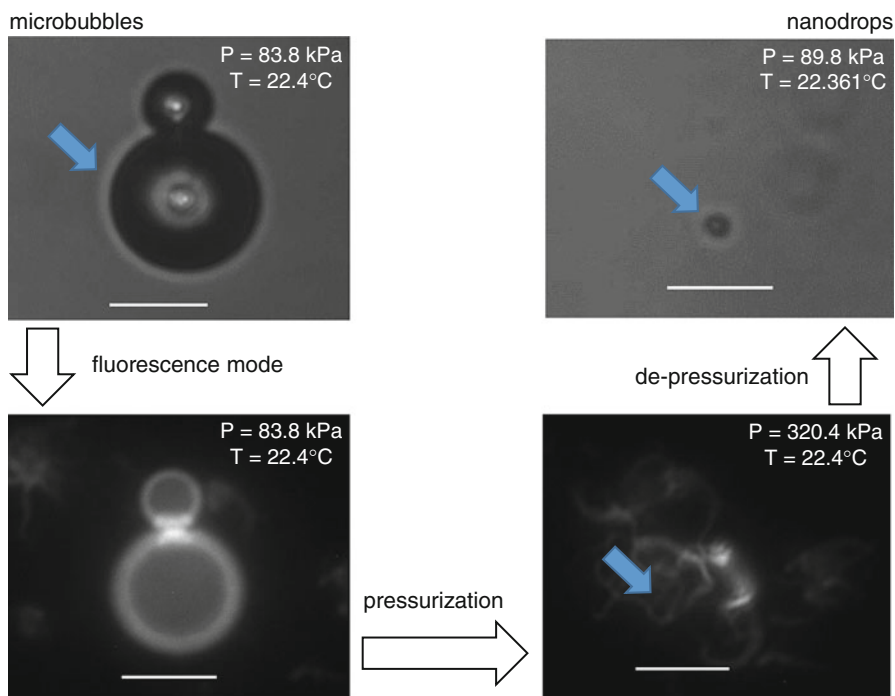
nanodrops

Fig. 6 Nanodrop synthesis by microbubble condensation. A relatively large microbubble (denoted by the *blue arrow*) shown in both bright-field and fluorescent microscopy modes (*left*) is pressurized to form a nanodrop (*bottom right*). Note the shedding of excess fluorescent lipid by this process. Upon depressurization back to standard conditions (*top right*), the nanodrop remains metastable in a superheated state (Images adapted from Mountford et al. [43])

the superheated droplets is the ability to engineer the formulation via control over microbubble composition and microstructure, as described throughout this chapter.

Structure–Property–Performance Relationships

Microbubble Size

Size is a key structural parameter of a microbubble that determines its acoustic properties and biomedical performance. For example, the acoustic response of a microbubble is most intense when driven at the resonance frequency [47]. The linearized eigenfrequency for small-amplitude oscillations of an uncoated microbubble (i.e., the Minnaert frequency) depends on the initial "resting" radius of the microbubble (R_0) according to the following equation [48]:

$$f_0 = \frac{1}{2\pi R_0}\left(\frac{3\gamma P_0}{\rho_0} + \frac{2(3\gamma - 1)\sigma}{\rho_0 R_0}\right)^{1/2} \tag{9}$$

where γ is the ratio of specific heats for the gas inside the bubble, P_0 is the hydrostatic pressure, and ρ_0 is the density of the surrounding aqueous phase. Equation 6 shows that, for an uncoated microbubble, the surface tension term (second term in the brackets) becomes significant as R_0 approaches one micrometer. Thus, the resonance frequency transitions from an R_0^{-1} dependence to an $R_0^{-3/2}$ dependence as the diameter decreases from 10 to 1 μm. Equation 9 predicts that the resonance frequency increases from 0.7 to 12 MHz as the microbubble diameter decreases from 10 to 1 μm. Thus, we expect that the echogenicity of a microbubble is highly dependent on its size. Indeed, it was found that 1–2-μm-diameter microbubbles provided a negative contrast (attenuation) when imaged in vivo at 40 MHz, while 6–8-μm-diameter microbubbles provided a positive contrast (scattering) under the same conditions [49]. This is partly owing to damping, discussed below. Polydispersity in the microbubble size distribution therefore presents an obstacle for quantitative imaging (e.g., molecular imaging), where it is desirable for the linearized video intensity to increase linearly with microbubble concentration. For contrast-enhanced ultrasound imaging, it is thus desirable to start with a microbubble suspension of uniform size matched to the resonance frequency of the ultrasound device.

The microbubble interaction volume scales as R_{max}^3, where R_{max} is the maximum radius experienced by the microbubble during an acoustically driven oscillation. Even when considering nonlinear bubble oscillations, R_{max} scales with R_0. According to the Marmottant model, for example, a 6-μm-diameter microbubble has an R_{max} value of 9.6 μm when driven at 1 MHz and 0.5 MPa peak negative pressure, whereas a 2-μm-diameter microbubble has an R_{max} value of 6.6 μm under the same conditions [50]. Thus, microbubble size is expected to significantly impact therapeutic efficiency. Indeed, larger microbubbles were observed to be more effective in vivo at blood–brain barrier (BBB) opening [51].

Microbubble size also affects microbubble stability and pharmacodynamics. As can be seen from Eq. 5, the dissolution rate increases with decreasing microbubble radius owing to the greater Laplace pressure, greater surface area-to-volume ratio, and a thinner concentration boundary layer; thus smaller microbubbles dissolve faster than larger ones. Indeed, smaller microbubbles were also observed to be more susceptible to destruction by fragmentation under acoustic stimulation [52]. Additionally, it has been found that larger microbubbles circulate in vivo much longer than smaller microbubbles [49].

Lipid Shell Elasticity

The elastic properties of the lipid coating can significantly affect the resonance frequency of the microbubble. The surface elasticity (χ) of a lipid monolayer is defined as [50]:

$$\chi = A \left(\frac{d\sigma}{dA} \right) \tag{10}$$

where A is the monolayer area and σ is the surface tension, as above. The linearized eigenfrequency of a lipid-coated microbubble with a shell elasticity undergoing small-amplitude oscillations (where $\sigma = 0$ at R_0, as shown above) is given by the following equation [53]:

$$f_0 = \frac{1}{2\pi R_0} \left(\frac{3\gamma P_0}{\rho_0} + \frac{4\chi}{\rho_0 R_0} \right)^{1/2} \tag{11}$$

Typical values of the lipid monolayer shell elasticity have been measured to be 0.5–1.0 N/m [53, 54]. Under these conditions, the shell term (second term in the brackets) dominates as R_0 approaches one micrometer, and the resonance frequency increases as $R_0^{-3/2}$. Experimental measurements have shown that the resonance frequency of a lipid-coated microbubble increases from 1 to 10 MHz as the diameter decreases from 10 to 1 μm [48]. It should be noted that microbubbles driven to large-amplitude oscillations deviate from Eq. 11 owing to shell rupture and buckling [50], which are not captured by the linearized model.

Elasticity of the lipid coating may affect not only the acoustic response but also the stability and pharmacodynamics of microbubbles. Sarkar et al. predicted that lipid shell elasticity may affect microbubble stability by resisting monolayer expansion and compression [55]. For example, elasticity of the lipid coating may explain the remarkable stability of small diameter (1–2 μm) microbubbles [56]. Experiments have confirmed that the lipid coating does have a significant effect on the growth and dissolution of a microbubble during gas exchange, and elasticity appears to be a function of both lipid composition and domain microstructure [57]. More research is necessary to better establish the effects of lipid composition and microstructure on shell elasticity and the exploitation of shell elasticity to achieve higher levels of performance in ultrasound applications.

Lipid Shell Viscosity

The surface viscosity of the lipid coating can affect the acoustic response and other properties of the microbubble. DH Kim et al. showed that lipid composition and microstructure have a profound effect on the surface shear yield and surface shear viscosity (η_s) of lipid-coated microbubbles [15]. The surface shear viscosity is expected to affect lipid buckling and folding during compression, thus altering stability. It was shown that increasing η_s (i.e., in-plane rigidity) by increasing phospholipid acyl chain length can cause a corresponding increase in microbubble stability against dissolution, acoustic destruction, and contrast agent half-life [58].

Additionally, the surface dilatational viscosity (κ_s) can affect microbubble expansion and is modeled to affect both expansion and contraction during oscillations under ultrasound stimulation. The linearized damping term for the microbubble shell is given by [53]:

$$\delta_{\text{shell}} = \frac{4\kappa_s}{2\pi f_0 \rho R_0^3} \qquad (12)$$

The shell damping term is a part of the overall damping coefficient:

$$\delta = \delta_{\text{shell}} + \delta_{\text{rad}} + \delta_{\text{visc}} \qquad (13)$$

where δ_{rad} and δ_{visc} are the damping coefficients corresponding to acoustic reradiation and viscous dissipation of the aqueous phase, respectively. These terms are given by [53]:

$$\delta_{\text{rad}} = \frac{2\pi f_0 R_0}{c} \qquad (14)$$

$$\delta_{\text{vis}} = \frac{2\mu}{\pi \rho f_0 R_0^2} \qquad (15)$$

where c is the speed of sound in aqueous media. Note that all of the damping terms depend on microbubble size, again pointing to the importance of monodispersity for more precise acoustics. The resonance frequency deviates from the eigenfrequency according to the following relationship [53]:

$$f_r = f_0 \sqrt{1 - \frac{\delta^2}{2}} \qquad (16)$$

The effect of lipid shell damping on the resonance frequency is rather small [53]; however, damping does effect the ratio of acoustic energy that is either scattered or attenuated (lost to heat dissipation). This explains the result mentioned above that smaller microbubbles can provide negative contrast, while larger microbubbles provide positive contrast for in vivo imaging at 40 MHz [49]. Damping also affects the lifetime of the signal (ring down) after the termination of the ultrasound pulse. Additionally, damping affects how much energy is converted from the acoustic wave to the local microenvironment by the microbubble, thus affecting therapeutic applications such as sonoporation and thermal ablation. Microbubble shell damping is an important property, but very little is known about the molecular mechanisms and microstructural effects of lipid monolayer rigidity and friction, particularly on microbubble shells. More research is needed to unravel these interrelationships and to put this knowledge to practice for advanced acoustic applications.

Viscoelastic Effects on Microbubble Stability

Sarkar et al. showed theoretically that viscoelasticity of the lipid monolayer shell can have a profound effect on microbubble stability [55]. Since changes in microbubble surface area are relatively slow for dissolution compared to ultrasonic oscillations, the

surface viscosity term often is assumed to have a negligible effect on microbubble stability. The surface elasticity, however, is expected to contribute significantly to microbubbles stability. In Sarkar's model, the elasticity resists both compression and expansion of the surface beyond the equilibrium state (equilibrium surface tension) of the phospholipid shell. Sarkar estimated, for example, an increase in the ratio of elasticity to the equilibrium surface tension (χ/σ_0) from 1.0 to 20 can increase the lifetime of a 2.5-μm-diameter air bubble from complete dissolution in ~20 s to almost no dissolution over 10^3 s [55]. Additionally, elasticity can explain the very long lifetimes observed for individual microbubbles. Sarkar estimated, for example, that an increase of χ/σ_0 from 1.0 to 1.05 was sufficient to explain the indefinite stability of submicron bubbles.

However, experimental data on microbubble growth and dissolution during gas exchange have indicated that the true situation for surface elasticity is much more complex than even the more advanced elasticity models employed by Sarkar [55, 59, 60]. In his doctoral dissertation experiment, JJ Kwan started with an SF_6 gas-filled microbubble suspended in an SF_6-saturated aqueous medium and then suddenly replaced the medium with air-saturated fluid. The microbubble was held in place with a hollow cellulose microfiber (dialysis tubing), which is highly permeable to dissolved gases, during the exchange of medium [61]. The medium exchange was ensured by using a low-volume, laminar-flow perfusion chamber. The microbubble was viewed under bright-field microscopy during the gas exchange process. Image analysis of the captured video frames was used to generate radius–time curves. Interestingly, the microbubble was found to initially grow owing to the influx of much faster diffusing and more soluble O_2 and N_2. Once the partial pressures equalized, the microbubble shank with the efflux of SF_6 (which was absent in the surrounding medium). The microbubble stopped shrinking near its initial radius. It then remained stable for some time before again dissolving to a smaller diameter (typically ~1–2 μm). These experimental radius–time curves were compared to predictions from a theoretical model that accounted for mass transport of each gas species to and from the microbubble. The model had been previously validated with Kwan's experimental setup by comparing growth and dissolution curves for the soluble surfactant sodium dodecyl sulfate (SDS) [61]. To fit the radius–time curves for lipid-coated microbubbles, the "apparent" surface tension was varied for each time step. The surface tension was then plotted as a function of microbubble surface area to determine the stress–strain relationships [57].

The resulting surface tension-area isotherms showed very complex elastic behavior. During the initial microbubble growth phase, the surface tension increased linearly with area, indicating a linear elastic regime. This linear behavior continued from essentially zero surface tension to a surface tension approaching ~72 mN/m, the surface tension of a clean air/water interface. Remarkably, the surface tension then started to decrease exponentially to 25 mN/m (curiously close to the equilibrium surface tension of a liquid expanded-phase phospholipid monolayer [20]), even as the microbubble continued to grow! Finally, during subsequent microbubble compression, the surface tension was found to decrease from 25 mN/m back to ~0 mN/m as the bubble approached its initial diameter. The decrease in surface tension appeared to be a linear function of area, but the slope (and therefore elasticity) was much lower than that found for the expansion phase. Thus, there is significant hysteresis between the expansion and compression curves.

The following sequence of microstructural events were used to explain this highly nonlinear elastic behavior: (1) the lipid monolayer expands elastically from the resting state to rupture; (2) the monolayer ruptures into domains (islands) of condensed lipids, which slowly dissolve to fill in the vacuum of free gas/water interface between the domains; (4) upon compression, the lipids repack into domains; and (5) the domains repack and halt dissolution at the initial, resting surface area. The latter step is a remarkable self-healing phenomenon. This explanation was supported by Langmuir trough data of phospholipid monolayers slowly compressed to the collapse plateau and then suddenly expanded. Taken together, these data show that the lipid shell elasticity depends highly on its particular microstructure, which in turn depends on the composition and processing history of the individual microbubble. Similar behavior is expected for lipid-coated, liquid-filled fluorocarbon nanodrops.

Lipid Shell Permeability

Microbubble stability is not solely governed by the lipid shell elasticity. Another property that affects the rate and extent of microbubble growth and dissolution is the monolayer permeability to gases. As mentioned above, prior experimental evidence showed that the lipid shell can impede oxygen transport [19]. This was shown using an ultra-microelectrode (UME) juxtaposed to a microbubble held by a micropipette. Voltage applied to the UME induced the reduction of dissolved oxygen in a diffusion-limited process, which induced oxygen release and transport from the nearby microbubble. The reaction rate could be monitored by following the current applied to the UME. A simple mass transport model was used to back out the permeability of the lipid monolayer shell from the steady-state current at each UME-microbubble separation distance. It was found that the lipid monolayer permeation resistance increased exponentially with increasing phospholipid acyl chain length, which confirmed prior work by VK La Mer and colleagues with fatty acids and alcohols on retardation of water evaporation [62]. La Mer favored an energy barrier model for monolayer permeation, in which it was predicted that increasing lipid hydrophobic chain length would lead to a greater activation energy owing to a deeper van der Waals intermolecular potential well. In other words, a smaller fraction of the gas molecules colliding with the monolayer had enough kinetic energy to punch through, according to the Boltzmann distribution, thus inhibiting gas transport. The effect of the lipid shell permeability on gas transport has also been modeled by Sarkar et al. [63, 64]. Again, similar effects are expected for lipid-coated, fluorocarbon liquid-filled nanodrops.

Conclusion and Future Directions

Over a decade ago, DH Kim first described the materials science paradigm of composition → processing → structure → property → performance for rational design of lipid-coated microbubbles. Since then, a significant body of work has

elucidated the effects of composition and processing on microbubble structure, as well as some structure–property–performance relationships. For example, only after centrifugal sorting to control size had been mastered was it possible to show that longer acyl chain lipids lead to better microbubble stability, acoustic longevity, and in vivo circulation persistence.

However, more research is necessary to fully unlock the mystery of how lipid composition and processing affect lipid domain microstructure. Moreover, it is important to further establish the interrelationships between lipid shell microstructure and key microbubble physical properties, such as the shell elasticity and viscosity. For example, the molecular mechanism for lipid shell friction must be elucidated, so that we can better avoid or exploit acoustic damping effects on microbubble performance in ultrasound imaging and therapy. Ultimately, greater flexibility and control over the lipid coating microstructure coupled with a better understanding of key microbubble structure–property relationships will enable true innovations in biomedical ultrasound.

References

1. Borden MA (2014) Microbubble dispersions of natural lung surfactant. Curr Opin Colloid Interface Sci 19(5):480–489
2. McCulley JP, Shine WE (2001) The lipid layer: the outer surface of the ocular surface tear film. Biosci Rep 21(4):407–418
3. Goldberg BB, Liu J-B, Forsberg F (1994) Ultrasound contrast agents: a review. Ultrasound Med Biol 20(4):319–333
4. de Jong N, Ten Cate FJ, Lancée CT, Roelandt JRTC, Bom N (1991) Principles and recent developments in ultrasound contrast agents. Ultrasonics 29(4):324–330
5. Stride E, Saffari N (2003) Microbubble ultrasound contrast agents: a review. Proc Inst Mech Eng H 217(6):429–447
6. Lindner JR (2004) Microbubbles in medical imaging: current applications and future directions. Nat Rev Drug Discov 3(6):527–533
7. Wilson SR, Burns PN (2010) Microbubble-enhanced US in body imaging: what role? Radiology 257(1):24–39
8. Dayton PA, Rychak JJ (2007) Molecular ultrasound imaging using microbubble contrast agents. Front Biosci J Virtual Libr 12:5124–5142
9. Ferrara K, Pollard R, Borden M (2007) Ultrasound microbubble contrast agents: fundamentals and application to gene and drug delivery. Annu Rev Biomed Eng 9:415–447
10. Kim DH. Mechanical properties, microstructure, and specific adhesion of phospholipid monolayer-coated microbubbles. Thesis PhD DUKE Univ Source DAI-B 6101 P 471 Jul 2000 177 Pages [Internet]. 1999 Oct [cited 2015 May 22]; Available from http://adsabs.harvard.edu/abs/1999PhDT........87K
11. Israelachvili JN (2010) Intermolecular and surface forces. Academic, San Diego, 706 p
12. Prausnitz JM, Lichtenthaler RN, de Azevedo EG (1998) Molecular thermodynamics of fluid-phase equilibria. Pearson Education, New Jersey, 1245 p
13. Epstein PS, Plesset MS (1950) On the stability of gas bubbles in liquid-gas solutions. J Chem Phys 18(11):1505–1509
14. Duncan PB, Needham D (2004) Test of the Epstein-Plesset model for gas microparticle dissolution in aqueous media: effect of surface tension and gas undersaturation in solution. Langmuir 20(7):2567–2578

15. Kim DH, Costello MJ, Duncan PB, Needham D (2003) Mechanical properties and microstructure of polycrystalline phospholipid monolayer shells: novel solid microparticles. Langmuir 19(20):8455–8466
16. Borden MA, Pu G, Runner GJ, Longo ML (2004) Surface phase behavior and microstructure of lipid/PEG-emulsifier monolayer-coated microbubbles. Colloids Surf B Biointerfaces 35(3-4):209–223
17. Witten TA, Wang J, Pocivavsek L, Lee KYC (2010) Wilhelmy plate artifacts in elastic monolayers. J Chem Phys 132(4):046102
18. Borden MA, Longo ML (2002) Dissolution behavior of lipid monolayer-coated, air-filled microbubbles: effect of lipid hydrophobic chain length. Langmuir 18(24):9225–9233
19. Borden MA, Longo ML (2004) Oxygen permeability of fully condensed lipid monolayers. J Phys Chem B 108(19):6009–6016
20. Lee S, Kim DH, Needham D (2001) Equilibrium and dynamic interfacial tension measurements at microscopic interfaces using a micropipet technique. 2. Dynamics of phospholipid monolayer formation and equilibrium tensions at the water-air interface. Langmuir 17(18):5544–5550
21. Kuhl TL, Leckband DE, Lasic DD, Israelachvili JN (1994) Modulation of interaction forces between bilayers exposing short-chained ethylene oxide headgroups. Biophys J 66(5):1479–1488
22. Orozco-Alcaraz R, Kuhl TL (2012) Impact of membrane fluidity on steric stabilization by lipopolymers. Langmuir 28(19):7470–7475
23. Chen CC, Borden MA (2011) The role of poly(ethylene glycol) brush architecture in complement activation on targeted microbubble surfaces. Biomaterials 32(27):6579–6587
24. Klibanov AL (2005) Ligand-carrying gas-filled microbubbles: ultrasound contrast agents for targeted molecular imaging. Bioconjug Chem 16(1):9–17
25. Dressaire E, Bee R, Bell DC, Lips A, Stone HA (2008) Interfacial polygonal nanopatterning of stable microbubbles. Science 320(5880):1198–1201
26. Malmsten M (1995) Protein adsorption at phospholipid surfaces. J Colloid Interface Sci 172(1):106–115
27. Christiansen JP, French BA, Klibanov AL, Kaul S, Lindner JR (2003) Targeted tissue transfection with ultrasound destruction of plasmid-bearing cationic microbubbles. Ultrasound Med Biol 29(12):1759–1767
28. Borden MA, Caskey CF, Little E, Gillies RJ, Ferrara KW (2007) DNA and polylysine adsorption and multilayer construction onto cationic lipid-coated microbubbles. Langmuir 23(18):9401–9408
29. Borden MA, Martinez GV, Ricker J, Tsvetkova N, Longo M, Gillies RJ et al (2006) Lateral phase separation in lipid-coated microbubbles. Langmuir 22(9):4291–4297
30. Lum AFH, Borden MA, Dayton PA, Kruse DE, Simon SI, Ferrara KW (2006) Ultrasound radiation force enables targeted deposition of model drug carriers loaded on microbubbles. J Control Release 111(1-2):128–134
31. Lentacker I, Smedt SCD, Sanders NN (2009) Drug loaded microbubble design for ultrasound triggered delivery. Soft Matter 5(11):2161–2170
32. Dove JD, Murray TW, Borden MA (2013) Enhanced photoacoustic response with plasmonic nanoparticle-templated microbubbles. Soft Matter 9(32):7743–7750
33. Feinstein SB, Ten Cate FJ, Zwehl W, Ong K, Maurer G, Tei C et al (1984) Two-dimensional contrast echocardiography. I. In vitro development and quantitative analysis of echo contrast agents. J Am Coll Cardiol 3(1):14–20
34. Li MK, Fogler HS (1978) Acoustic emulsification. Part 1. The instability of the oil-water interface to form the initial droplets. J Fluid Mech 88(03):499–511
35. Li MK, Fogler HS (1978) Acoustic emulsification. Part 2. Breakup of the large primary oil droplets in a water medium. J Fluid Mech 88(03):513–528
36. Feshtan JA, Chen CC, Kwan JJ, Borden MA (2009) Microbubble size isolation by differential centrifugation. J Colloid Interface Sci 329(2):316–324

37. Talu E (2007) Lipid-stabilized monodisperse microbubbles produced by flow focusing for use as ultrasound contrast agents and targeted drug delivery. ProQuest. 127 p

38. Gañán-Calvo AM, Gordillo JM (2001) Perfectly monodisperse microbubbling by capillary flow focusing. Phys Rev Lett 87(27):274501

39. Kim DH, Klibanov AL, Needham D (2000) The influence of tiered layers of surface-grafted poly(ethylene glycol) on receptor-ligand-mediated adhesion between phospholipid monolayer-stabilized microbubbles and coated glass beads. Langmuir 16(6):2808–2817

40. Borden MA, Sarantos MR, Stieger SM, Simon SI, Ferrara KW, Dayton PA (2006) Ultrasound radiation force modulates ligand availability on targeted contrast agents. Mol Imaging 5(3):139–147

41. Sirsi SR, Borden MA (2014) State-of-the-art materials for ultrasound-triggered drug delivery. Adv Drug Deliv Rev 72:3–14

42. Sheeran PS, Luois S, Dayton PA, Matsunaga TO (2011) Formulation and acoustic studies of a new phase-shift agent for diagnostic and therapeutic ultrasound. Langmuir 27(17): 10412–10420

43. Mountford PA, Sirsi SR, Borden MA (2014) Condensation phase diagrams for lipid-coated perfluorobutane microbubbles. Langmuir 30(21):6209–6218

44. Mountford PA, Thomas AN, Borden MA (2015) Thermal activation of superheated lipid-coated perfluorocarbon drops. Langmuir 31(16):4627–4634

45. Sheeran PS, Wong VP, Luois S, McFarland RJ, Ross WD, Feingold S et al (2011) Decafluorobutane as a phase-change contrast agent for low-energy extravascular ultrasonic imaging. Ultrasound Med Biol 37(9):1518–1530

46. Sheeran PS, Luois SH, Mullin LB, Matsunaga TO, Dayton PA (2012) Design of ultrasonically-activatable nanoparticles using low boiling point perfluorocarbons. Biomaterials 33(11): 3262–3269

47. Hoff L (2013) Acoustic characterization of contrast agents for medical ultrasound imaging. Springer, New Jersey, 218 p

48. Doinikov AA, Haac JF, Dayton PA (2009) Resonance frequencies of lipid-shelled microbubbles in the regime of nonlinear oscillations. Ultrasonics 49(2):263–268

49. Sirsi S, Feshitan J, Kwan J, Homma S, Borden M (2010) Effect of microbubble size on fundamental mode high frequency ultrasound imaging in mice. Ultrasound Med Biol 36(6):935–948

50. Marmottant P, van der Meer S, Emmer M, Versluis M, de Jong N, Hilgenfeldt S et al (2005) A model for large amplitude oscillations of coated bubbles accounting for buckling and rupture. J Acoust Soc Am 118(6):3499–3505

51. Choi JJ, Feshitan JA, Baseri B, Wang S, Tung Y-S, Borden MA et al (2010) Microbubble-size dependence of focused ultrasound-induced blood-brain barrier opening in mice in vivo. IEEE Trans Biomed Eng 57(1):145–154

52. Chomas JE, Dayton P, May D, Ferrara K (2001) Threshold of fragmentation for ultrasonic contrast agents. J Biomed Opt 6(2):141–150

53. van der Meer SM, Dollet B, Voormolen MM, Chin CT, Bouakaz A, de Jong N et al (2007) Microbubble spectroscopy of ultrasound contrast agents. J Acoust Soc Am 121(1):648–656

54. Dove JD, Borden MA, Murray TW (2014) Optically induced resonance of nanoparticle-loaded microbubbles. Opt Lett 39(13):3732

55. Katiyar A, Sarkar K, Jain P (2009) Effects of encapsulation elasticity on the stability of an encapsulated microbubble. J Colloid Interface Sci 336(2):519–525

56. Kwan JJ, Borden MA (2012) Lipid monolayer collapse and microbubble stability. Adv Colloid Interface Sci 183–184:82–99

57. Kwan JJ, Borden MA (2012) Lipid monolayer dilatational mechanics during microbubble gas exchange. Soft Matter 8(17):4756–4766

58. Garg S, Thomas AA, Borden MA (2013) The effect of lipid monolayer in-plane rigidity on in vivo microbubble circulation persistence. Biomaterials 34(28):6862–6870

59. Chatterjee D, Sarkar K (2003) A Newtonian rheological model for the interface of microbubble contrast agents. Ultrasound Med Biol 29(12):1749–1757
60. Sarkar K, Shi WT, Chatterjee D, Forsberg F (2005) Characterization of ultrasound contrast microbubbles using in vitro experiments and viscous and viscoelastic interface models for encapsulation. J Acoust Soc Am 118(1):539–550
61. Kwan JJ, Borden MA (2010) Microbubble dissolution in a multigas environment. Langmuir 26(9):6542–6548
62. Mer VKL (2014) Retardation of evaporation by monolayers: transport processes. Academic, New York, 298 p
63. Sarkar K, Katiyar A, Jain P (2009) Growth and dissolution of an encapsulated contrast microbubble: effects of encapsulation permeability. Ultrasound Med Biol 35(8):1385
64. Katiyar A, Sarkar K (2010) Stability analysis of an encapsulated microbubble against gas diffusion. J Colloid Interface Sci 343(1):42–47

Advancing Ultrasound Technologies for Tissue Engineering

Diane Dalecki and Denise C. Hocking

Contents

Abstract

The development of technologies that enable the fabrication of functional, artificial tissues is a major focus of the field of tissue engineering. Engineered tissues hold promise for repairing or replacing damaged tissues and organs or for use as in vitro tissue models for drug discovery and product testing. Ultrasound is emerging as a valuable, enabling technology for tissue engineering. This chapter focuses on innovative ultrasound-based technologies that have the capacity to

D. Dalecki (✉)
Department of Biomedical Engineering, University of Rochester, Rochester, NY, USA
e-mail: dalecki@bme.rochester.edu; ddalecki@ur.rochester.edu

D.C. Hocking
Department of Pharmacology and Physiology, University of Rochester, Rochester, NY, USA
e-mail: denise_hocking@urmc.rochester.edu

guide the fabrication of artificial tissues. Ultrasound fields are advantageous for tissue engineering because of their ability to noninvasively direct thermal and/or mechanosensitive processes within biological systems and scaffold materials with spatial and temporal fidelity. The chapter includes specific sections that discuss the development of ultrasound technologies with the capacity to affect scaffold fabrication processes, to control cell patterning volumetrically, to fabricate microvascular networks, and to control the spatial and temporal delivery of signaling molecules or bioactive chemicals. By offering new, noninvasive approaches to guide the fabrication of artificial tissues, ultrasound technologies hold exciting promise to advance the field of tissue engineering and regenerative medicine.

Introduction

The foundational goal for the field of tissue engineering is to fabricate living, artificial tissues from fundamental, raw materials of cells, scaffold materials, and bioactive signaling molecules. Development of tissue engineering strategies that enable the successful fabrication of functional artificial tissues holds revolutionary potential for replacing diseased or damaged tissues or organs. Engineered tissue constructs that mimic native tissue structure and function would also offer high-throughput, in vitro alternatives to animal models used currently for product testing and toxicology screening. However, many challenges still remain in achieving these transformative goals of tissue engineering. Critical obstacles in the field of tissue engineering include the need for new, enabling technologies for (i) scaffold fabrication processes, (ii) rapid and volumetric cell patterning to recreate native tissue architecture, (iii) fabricating physiologically relevant microvascular networks, and (iv) controlling the spatial and temporal presentation of growth factors and signaling molecules. Ultrasound-based technologies are emerging to offer novel solutions to these challenges in tissue engineering. In particular, this chapter focuses on innovative ultrasound techniques with exciting potential to guide the fabrication of functional artificial tissues. Ultrasound technologies for tissue engineering capitalize on the ability of ultrasound fields to interact with biomaterials through either thermal or mechanical mechanisms and thereby influence thermosensitive or mechanosensitive processes in biological systems or scaffold materials. Ultrasound offers numerous, unique advantages, as it is rapid, noninvasive, nontoxic, cost-effective, and adaptable to tissue engineering environments.

This chapter provides an overview of the exciting potential of ultrasound technologies for the field of tissue engineering. The chapter begins with an introduction to the goals, methodologies, and current challenges of tissue engineering and regenerative medicine (section "Tissue Engineering"). This is followed by a discussion of the advantages of ultrasound for tissue engineering and an introduction to

ultrasound technologies (section "Developing Ultrasound for Tissue Engineering"). A fundamental tutorial on the physical mechanisms by which ultrasound can interact with materials is also provided in section "Acoustic Mechanisms" to set the stage for discussions on how these acoustic mechanisms can be harnessed to develop new ultrasound-based technologies for the fabrication of engineered tissues. Subsequent sections provide discussion and representative examples of the development and translation of ultrasound-based technologies for scaffold fabrication (section "Ultrasound for Scaffold Fabrication"), cell patterning (section "Cell Patterning with Ultrasound"), microvascular tissue engineering (section "Ultrasound Technology for Microvascular Engineering"), and local delivery of signaling molecules, proteins, or bioactive chemicals ("Delivery of Biochemical and Signaling Molecules with Ultrasound"). The chapter concludes with a summary and look to the future for ultrasound technologies for tissue engineering and regenerative medicine.

Tissue Engineering

Introduction to Tissue Engineering and Regenerative Medicine

Severe organ damage or loss can result from a variety of conditions, including infectious diseases, trauma, cancer, and congenital anomalies. For over 50 years, tissue transplantation has been a successful therapy for treating end-stage organ failure [1]. Unfortunately, present demand for donor organs far exceeds the available supply, and future demand for replacement organs is expected to increase as the population ages. Currently, over 120,000 patients in the United States are awaiting organ transplantation; each day, an average of 20 patients die while waiting for donor organs (Organ Procurement and Transplantation Network, US Department of Health and Human Services). Additionally, for patients receiving organ transplants, treatment with immunosuppressant drugs to reduce immunologic rejection increases the risk of developing serious viral and fungal infections [2]. In response to these issues, tissue engineering and regenerative medicine (TE/RM) have emerged as potential therapeutic approaches to replace or regenerate diseased or destroyed organs and tissues. TE/RM merges biological and chemical sciences with engineering approaches to develop methods and materials that enable the reconstruction of various replacement tissues and organs of appropriate physiological and morphological function. In addition, there are a growing number of applications for engineered tissue outside of tissue replacement therapy. Engineered tissues would provide alternatives to traditional animal models used currently in pharmaceutical companies and government agencies for product and procedure testing, toxicology screening, drug discovery, and biological and chemical warfare detection.

In its basic practice, tissue engineering combines cells with either naturally derived or synthetic scaffold material to produce a three-dimensional (3D) construct. Typically, these nascent tissue constructs are subsequently exposed to a variety of different chemical and/or biophysical stimuli in an attempt to trigger normal developmental processes that mediate early tissue formation or repair in the

body. Using various combinations of cells and biomaterials, attempts have been made to fabricate many different types of tissue [3]. As examples, bilayered artificial skin substitutes have been produced by incorporating layers of neonatal fibroblasts and epithelial cells into either decellularized dermal matrices or synthetic, semipermeable membranes [4]. Tissue-engineered blood vessels have been produced by lining the inner wall of tubular scaffolds with endothelial cells, to provide a non-thrombogenic surface for blood flow, and adding an outer layer of fibroblasts and/or smooth muscle cells to provide vasoactive function [5]. The use of autologous cells, typically obtained from patient biopsies, in artificial tissues reduces the risk of complications arising from inflammation and immunologic rejection. However, this approach may not be feasible for patients with late-stage organ failure or with adult cell types that cannot be expanded in culture. In these cases, embryonic and adult stem cells are promising alternatives [6]. Stem cells can be expanded in culture in an undifferentiated state and then induced to differentiate into a wide variety of different cell types. Moreover, adult stem cells can be extracted from a variety of tissue sources, including bone marrow, fat, and placenta. Reprogramming of adult cells into pluripotent stem cells is also emerging as an alternative cell source [3].

In addition to sourcing the appropriate cells for replacement tissues, successful construction of engineered tissues requires the recreation of a biologically active extracellular environment that supports cell viability, promotes key cell functions, and enables 3D tissue development. During native tissue remodeling, the extracellular matrix provides cells with critical biomechanical and biochemical signals that control cell function and, in turn, guide tissue development. As such, Biomaterials used for tissue engineering must provide similar tissue-specific structural features and mechanical properties, as well as instructive cell adhesion sites to direct particular cell functions. In addition, tissue morphogenesis is carefully orchestrated by a variety of different growth factors and signaling molecules that are released and activated in complex spatial and temporal patterns [7]. As such, it has become increasingly clear that recreating an appropriate and dynamic scaffold microenvironment for implanted cells or engineered tissues is a key step to converting basic tissue engineering strategies into successful clinical treatments.

Scaffold materials under development for tissue engineering applications can be divided into two general categories: naturally derived (biologic) and synthetic. Natural biomaterials may be fabricated from individual proteins (e.g., fibrin, collagen, or silk) or polysaccharides (such as alginate, chitosan, or hyaluronan) that are readily extracted from tissues of vertebrates, invertebrates, or plants; these materials have been studied extensively for tissue engineering applications [8]. Acellular tissue matrices, derived from chemically and/or mechanically decellularized tissues or organs, are also being explored as natural composite biomaterials that largely retain the natural architecture and composition of the extracellular matrix of the target organ [9]. In the body, extracellular matrices provide tissues and organs with structural integrity and control cellular processes, including cell adhesion, migration, proliferation, and differentiation. Thus, natural biomaterials extracted or derived from extracellular matrices have a general capacity to support cell functions necessary for tissue regeneration. Type I collagen is the primary structural component of

native extracellular matrices and is the most abundant protein found in vertebrates [10]. Several factors make collagen I an attractive scaffold material, including its ease of isolation, low antigenicity and toxicity, and biodegradability [10]. Collagen can be processed into sponges, fibers, and films and has been FDA-approved for use in wound dressings and artificial skin [11]. However, much of the biological activity and mechanical strength of collagen I are lost during extraction, and thus, much effort has been directed at developing methods to produce a purified, biocompatible form of fibrillar collagen with improved bioactivity and strength. Exciting new technologies have also utilized a variety of natural biomaterials, including collagen, alginate, and decellularized extracellular matrices, as "bio-inks" for 3D organ printing [12].

Synthetic biomaterials are also widely utilized in tissue engineering applications due to their high biocompatibility, biodegradability, and versatility. Examples of synthetic materials include synthetic polymers, metals, and ceramics. A number of different biodegradable polyesters, including poly(glycolic acid) (PGA), poly(lactic acid) (PLA), polyethylene glycol (PEG), and poly(lactic-co-glycolic acid) (PLGA), are FDA approved for a variety of clinical applications, including sutures, devices, and joint replacements [13]. These polymers are composed of long chains of repeating subunits, and their physical properties, including porosity, mechanical properties, and degradation rate, can be customized through control of the chemical polymerization processes [13]. Similarly, degradation rates of many synthetic polymers can be predicted and controlled [13]. Three-dimensional synthetic scaffolds having a variety of shapes and sizes can be manufactured on a large scale via molding, extrusion, solvent casting, electrospinning, and gas foaming techniques [3]. Although synthetic polymers have many structural and production advantages over natural scaffolds, they lack the biological cues inherent in many naturally derived biomaterials. Therefore, extracellular matrix proteins, peptides, polysaccharides, and/or growth factors are often incorporated into synthetic biomaterials to provide cell adhesion sites and improve biological activity [3]. Overall, advances in both synthetic and natural scaffold design remain tempered by an inability to spatially and temporally recreate the complex 3D microenvironment that drives tissue regeneration in vivo.

Current Progress in Tissue Engineering and Key Challenges

Several promising TE/RM strategies have emerged during the past decade, including injecting autologous or allogenic cells directly into damaged tissue, implanting tissue analogs generated in vitro from cultured cells, and stimulating tissue regeneration in situ [14]. To date, only a few engineered tissues have reached clinical implementation [8]. One of the most significant advances has been in skin engineering, where several allogenic cell-based products are in clinical use, including Epicel®, Dermagraft®, and Apligraf®. An acellular alternative for skin regeneration is Integra®, an acellular matrix composed of bovine collagen, shark chondroitin-6-sulfate, and silicone [15]. In the United States, Carticel®, an autologous chondrocyte

implantation therapy, is the only FDA-approved therapy for regenerating articular cartilage. Several proprietary hydrogel matrices for chondrocyte culture and implantation are currently in clinical trials [16]. Additionally, bladder analogs, urethral segments, and vascular access grafts have been successfully implanted into patients, and clinical trials for artificial blood vessels, bronchial tubes, cornea tissue substitutes, and vaginal replacement constructs are underway [8]. However, to date, the fabrication of fully viable and functional organs that are of a larger size and possess a more complex and hierarchical cell and extracellular matrix organization has been unsuccessful [9].

It is widely recognized that the current lack of success in fabricating large, 3D tissues and organs, such as the liver, kidney, pancreas, and lung, is due primarily to two key challenges. Central to these challenges is the need to create 3D, bioactive scaffolds in which the complex micro-architecture of target tissues is spatially replicated, including the organization of various cell types, the organization and composition of the extracellular matrix, and the spatial and temporal availability of signaling molecules. A second critical factor involves the need to maintain cell viability throughout the tissue volume as the diffusion limitation of oxygen is exceeded. As such, advances in TE/RM strategies to produce complex tissues and organs will require developing technologies that have the capacity to (1) fabricate 3D scaffolds with appropriate biological activities and mechanical strength, (2) control the spatial organization and function of cells and signaling proteins in these scaffolds, and (3) rapidly establish a microcirculatory network within the engineered tissue for nutrient and gas exchange. Ultrasound technologies that aim to overcome these key challenges in tissue engineering are discussed in sections "Ultrasound for Scaffold Fabrication," "Cell Patterning with Ultrasound," "Ultrasound Technology for Microvascular Engineering," and "Delivery of Biochemicals and Signaling Molecules with Ultrasound."

Developing Ultrasound for Tissue Engineering

Advantages of Ultrasound for Tissue Engineering

Ultrasound is emerging as a versatile technology to advance the field of tissue engineering and regenerative medicine because it offers numerous unique advantages to direct artificial tissue fabrication [17, 18]. A prime advantage of ultrasound is that it provides a noninvasive energy source that can be localized to affect cells, scaffold materials, and/or signaling molecules. Ultrasound can be focused as a beam within tissues or biomaterials to exert site-specific and temporally controlled mechanical forces or heating that can be harnessed to influence thermosensitive or mechanosensitive processes in biological systems or scaffold materials. Details of the thermal and mechanical mechanisms for the interaction of ultrasound fields with biological tissues and non-biological materials are discussed further in section "Acoustic Mechanisms" below.

The versatility of ultrasound and the ease of adaptability of ultrasound instrumentation also enable the development of new ultrasound technologies for tissue engineering applications. Ultrasound instrumentation is relatively low-cost and portable, and a wide range of acoustic source geometries can be readily fabricated for specific tissue engineering design applications. Importantly, ultrasound devices are noninvasive and compact and thus can be easily incorporated into the sterile environments required for tissue engineering. Ultrasound exposure parameters (such as frequency and pulsing parameters) are highly controllable, allowing precise design of optimized spatial and temporal characteristics of ultrasound fields. Furthermore, ultrasound technologies can be incorporated into individual bioreactors, as well as scaled up to commercial fabrication processes. Overall, ultrasound-based technologies hold exciting potential to provide innovative solutions to challenges that currently limit advances in the fabrication of functional engineered tissues and organs.

Acoustic Mechanisms

Ultrasound fields can interact with tissues and materials through either thermal or nonthermal physical mechanisms [19–21]. Ultrasound is known to produce a wide range of biological effects in native tissues in vitro and in vivo [19–21]. Knowledge of acoustic mechanisms for effects of ultrasound on tissues provides the power to predict exposure conditions that produce specific biological effects. Thus, identification of the underlying mechanisms for effects of ultrasound on cells, tissues, and biomaterials is critical for the effective design and development of new ultrasound technologies for tissue engineering. The text below provides a short tutorial on the thermal and nonthermal physical mechanisms by which ultrasound can interact with tissues and biomaterials.

Absorption mechanisms convert ultrasound energy to heat. Heat can produce a wide range of responses in biological materials [20], and ultrasound-induced heating is the basis for the clinical use of ultrasound for physiotherapy and high-intensity focused ultrasound surgery. The magnitude of ultrasound-induced heating is dependent upon ultrasound field parameters and material properties of the medium supporting sound propagation. Material properties of relevance include the absorption coefficient, specific heat, density, and perfusion. For low amplitude (i.e., linear propagation) exposures, the absorption coefficient is simply a constant that is characteristic of the material. In native tissues, bone and teeth are among the tissues with the highest absorption coefficients. In comparison, soft tissues, such as liver and muscle, have absorption coefficients approximately an order of magnitude less than bone, while the absorption coefficient of water is comparatively minimal. Similarly, for comparable ultrasound exposures, the resultant ultrasound-induced heating would typically be greater in tissue engineering scaffold materials composed of plastics and polymers compared to water-based hydrogels. Thus, the absorption coefficient of the scaffold material and/or tissue is an important design parameter to consider when developing ultrasound technologies for tissue fabrication processes.

Acoustic field parameters also influence the extent of ultrasound-induced heating. Ultrasound exposure parameters of relevance to heating include the frequency, pressure amplitude, beam width, intensity, pulse duration, pulse repetition frequency, and total exposure duration. The magnitude of an ultrasound-induced temperature rise is directly proportional to the temporal average intensity [20]. Absorption coefficients of materials increase with increasing ultrasound frequency. At high amplitudes, nonlinear processes can result in waveform distortion, harmonic generation, and increased absorption [22]. Thus, an advantageous feature of ultrasound for tissue engineering is the ability to tune acoustic exposure parameters to noninvasively control heat generation and thermosensitive processes within tissues and biomaterials temporally and site-specifically.

Ultrasound fields can also interact with tissues and biomaterials through direct mechanical mechanisms [19]. Ultrasound is a mechanical wave, and propagation of ultrasound in materials produces cyclic variations in pressure, particle displacement, particle velocity, and particle acceleration. The forces associated with these particle oscillations cycle at the fundamental frequency of the ultrasound field. Second-order acoustic radiation forces can produce additional compressive, tensile, and shear forces. Acoustic radiation forces result from the transfer of momentum from the sound field to the medium of sound propagation [23]. These acoustic radiation forces are time-averaged forces and thus cycle at the pulse repetition frequency of the sound exposure. The magnitude and direction of the radiation force depend on characteristics of the sound field and the object in the field [23]. For example, for a plane wave incident on a perfect acoustic absorber, the radiation force acts in the direction of sound propagation, and the magnitude is directly proportional to the total power in the sound beam. In a fluid medium, the radiation force associated with a traveling wave field can produce bulk fluid flow in the direction of sound propagation termed acoustic streaming [20, 24]. In comparison, the radiation forces in a standing wave field vary sinusoidally in space and can result in the movement of cells or particles to the pressure nodes of the standing wave field [25–28]. Radiation torques exerted on particles can produce spinning or alignment of the particles in the sound field [20]. Harnessing the ability of ultrasound to exert site-specific forces noninvasively provides an innovative platform to exert biophysical stimuli during artificial tissue fabrication.

Acoustic cavitation is a general term that describes the interaction of a sound field with an existing gas bubble. In response to an ultrasound field of small amplitude, a gas bubble in liquid will oscillate radially around an equilibrium radius. The maximum response of a bubble to a sound field occurs when the acoustic frequency is equal to the resonance frequency of the bubble system. The resonance frequency is dependent on the initial radius of the bubble, as well as material parameters of the gas within the bubble and suspending medium. The radii of resonant bubbles are on the order of a few microns at frequencies relevant for biomedical ultrasound. The dynamic response of a gas bubble to sound exposure can be highly nonlinear, and many theoretical models have been developed to simulate microbubble cavitation [29]. Although a comprehensive discussion of acoustic cavitation is beyond the scope of this chapter, in general, the response of a gas bubble to ultrasound depends

upon the initial bubble size, acoustic pressure amplitude, frequency, and various damping mechanisms. Noninertial cavitation describes repetitive oscillations of a microbubble where the maximum expansion radius is less than twice the equilibrium bubble radius [20, 21]. The dynamics of noninertial cavitation are typically nonlinear, and the bubble oscillations can produce microstreaming, shear stresses, particle attraction, and heat generation, all of which are spatially localized near the oscillating microbubble [20, 21]. Inertial cavitation describes the rapid expansion of a microbubble to a radius greater than twice the equilibrium radius followed by a violent collapse of the microbubble to a fraction of the initial radius [30]. The inertial collapse of a microbubble can produce extraordinarily high temperatures and pressures, while the rebound of the microbubble can serve as a source of acoustic shock waves. High-speed liquid microjets can occur when microbubbles collapse asymmetrically. These microjets are capable of pitting metals and damaging cells and biomaterials. Inertial cavitation is also associated with a variety of sonochemically driven reactions including the formation of free radicals [31]. The generation of photons from inertial cavitation is termed sonoluminescence [20].

Acoustic cavitation is studied widely in biomedical and industrial fields, and various biological effects in vitro and in vivo can be attributed to acoustic cavitation [19–21, 32]. For in vitro experiments, gas nuclei capable of initiating cavitation are likely present unless directed efforts have been made to degas culture media and/or fluid samples. Tissues that naturally contain gas, such as those of the lung and intestine, are particularly susceptible to damage from ultrasound fields [19, 33, 34]. Ultrasound contrast agents are gas-filled microbubbles that are stabilized by protein, lipid, or polymer shells. The microbubbles are on the order of 1–10 μm in diameter and are used clinically to enhance backscatter to improve diagnostic imaging. Although initially developed for imaging applications, microbubble contrast agents are finding new therapeutic applications in areas including drug delivery, gene transfection, localized tissue destruction, and thrombolysis [35, 36]. Ultrasound contrast agents can be introduced directly in vitro or in vivo to enhance the extent of acoustic cavitation. Targeted contrast agents contain specific ligands on the bubble surface to provide site-specific localization of microbubbles to cells, proteins, or biomaterials. Acoustic radiation forces on microbubbles in a traveling wave field can result in translation of the microbubbles in the direction of sound propagation. Several manuscripts provide comprehensive reviews of the wide range of biological effects of contrast agents and ultrasound in vitro and in vivo [21, 32, 37].

Ultrasound Field Design

The previous section reviewed definitive physical mechanisms by which ultrasound fields can affect tissues and materials. Ultrasound fields offer a noninvasive, controllable source to spatially and temporally control localized heating, mechanical forces, and physical phenomena associated with acoustic cavitation. New ultrasound technologies for tissue engineering can harness these capabilities to affect

thermosensitive processes, control scaffold structure, and improve biological function. However, successful development of such ultrasound systems requires careful design of acoustic sources and exposure scenarios to specifically control desired heating, mechanical forces, and/or cavitation. Ultrasound exposure parameters that affect acoustic mechanisms include frequency, pressure amplitude, intensity, pulsing parameters (i.e., pulse duration, pulse repetition frequency), beam structure, and total exposure duration. Additionally, choice of scaffold material, presence of liquid media, and ultrasound exposure environment can all influence the extent of ultrasound-induced heating and/or the likelihood and extent of acoustic cavitation.

It is important to provide some words of caution on the potential for the design of sample holders and ultrasound exposure scenarios to influence acoustic mechanisms, and thereby introduce confounding effects on biological and biomaterial systems. Geometry and material properties of the sample holder employed for fabrication of engineered tissue can affect ultrasound fields within the holder. If sample holders made of materials with high absorption coefficients (such as plastics, polymers, and metals) are within the ultrasound beam, significant temperature increases and/or temperature gradients can occur by heat conduction in the biomaterial sample within the holder. Acoustic streaming of culture media or fluid within confined holder geometries can produce shear stresses that may affect mechanosensitive cells or biomaterials. Additionally, sample holders with acoustically reflecting interfaces, particularly from air interfaces, can produce complex sound fields within the holder volume including ultrasound standing wave fields. Standing wave fields contain pressure nodes (areas of minimum pressure) and antinodes (areas of maximum pressure) and spatially varying acoustic radiation forces. As an example, ultrasound exposure of samples within standard polystyrene well tissue culture plates can lead to significant confounding effects on the acoustic fields within the wells [38, 39]. Investigations in the literature often describe experimental scenarios where an ultrasound transducer is directly coupled to the bottom of a well in a tissue culture plate. The well is then filled with some combination of cells, liquid culture media, and/or scaffold material. In this exposure configuration, the interface between the culture media and air will act as a reflecting interface, and a standing wave field will be generated throughout the tissue well volume [38, 39]. Thus, depending on their distance from the interface, cells can be exposed to various pressures ranging from zero pressure amplitude at a nodal location to maximum acoustic pressure at an antinode. Additional complications of this exposure scenario include mode conversion and shear wave generation, reflections from the plate bottom, frequency-dependent resonances, and generation of displacements in the well at both the carrier frequency and pulse repetition frequency [38, 39]. Furthermore, acoustic coupling between wells on the plate can lead to generation of ultrasound fields within wells that are not the target of exposure [39]. Because of the many confounding effects that can be introduced by direct coupling of an ultrasound transducer to the bottom of a standard plastic tissue culture plate, cellular experiments in vitro employing such an exposure configuration are beyond the scope of review of this chapter. In the

development of new ultrasound technologies for tissue engineering, sample holders and exposure configurations should be designed to reduce the potential for confounding effects introduced by acoustic reflections and sample holder heating.

Ultrasound Imaging Technologies

Although this chapter focuses primarily on ultrasound technologies for artificial tissue fabrication, it is important to highlight that ultrasound imaging techniques are also providing new enabling technologies to advance the field of tissue engineering [18]. Technologies capable of imaging and quantitatively characterizing the properties of artificial tissues are critically needed to monitor the properties of engineered constructs during the fabrication process and postimplantation. Even though there are numerous imaging techniques available with unique imaging capabilities, such as confocal microscopy, multiphoton microscopy, second harmonic generation microscopy, and scanning electron microscopy, most of these technologies have distinct limitations that restrict their utility for monitoring tissue fabrication. Microscopy techniques typically have imaging depths less than ∼1 mm and very narrow focal widths, thereby limiting their capacity for larger volumetric imaging. Histology, biochemical techniques, and scanning electron microscopy are destructive techniques requiring extensive processing steps. Therefore, these techniques are not capable of longitudinal monitoring of tissue constructs during development. Furthermore, although microscopic imaging techniques can offer precise visualization of structure, they do not readily provide quantitative metrics of tissue properties.

In contrast, ultrasound imaging and quantitative tissue characterization techniques provide new capabilities for tissue engineering applications [18]. Ultrasound imaging offers real-time, noninvasive, and nondestructive visualization of engineered tissues and biomaterials. Conventional modalities, such as B-scan and Doppler, can provide rapid, volumetric imaging of tissue structure and fluid flow. High-frequency ultrasound imaging (nominally >20 MHz) offers improved spatial resolution, while still providing volumetric capabilities within hydrogel-based engineered tissue constructs [40, 41]. Importantly, quantitative ultrasound techniques employ various acoustic parameters (such as sound speed, absorption, backscatter) as metrics to quantitatively characterize the structural, biological, and material properties of engineered tissues. For example, the integrated backscatter coefficient has been employed as a quantitative metric to noninvasively characterize cell concentration [40] and collagen fiber microstructure [41] within engineered constructs. Furthermore, high-frequency parametric images of the integrated backscatter coefficient can be used to quantitatively visualize volumetric variations in cell concentration [40] or collagen microstructure [41]. Ultrasound elastography describes a variety of quantitative techniques that offer the capability to noninvasively and nondestructively measure and image the modulus of tissues and biomaterials [42]. In summary, ultrasound imaging and quantitative ultrasound

characterization techniques offer innovative, nondestructive approaches that can be employed to monitor the structural and mechanical properties of engineered tissues and biomaterials during the fabrication process and postimplantation.

Ultrasound for Scaffold Fabrication

From section "Developing Ultrasound for Tissue Engineering," it is evident that harnessing the capability of ultrasound fields to site-specifically and noninvasively influence thermal processes and exert mechanical forces presents exciting opportunities for developing new ultrasound-based technologies to direct the fabrication of engineered tissues. This section, and the subsequent three sections, present examples of how ultrasound technologies are advancing to meet key challenges in tissue engineering. This section focuses on how ultrasound techniques can be employed during scaffold fabrication processes to enhance the structure and/or functionality of biomaterial scaffolds. Developing new technologies that have the capacity to tune biomaterial scaffolds in order to recreate the physical and biochemical characteristics of native extracellular matrices is critical for advancing tissue engineering. Here, two avenues are presented as examples of approaches that incorporate ultrasound technologies into scaffold fabrication processes: one employs ultrasound to noninvasively affect collagen fiber microstructure and thereby influence cell functions and a second uses acoustic cavitation to affect the porosity of scaffold materials.

Type I collagen is the primary structural component of native extracellular matrices. Collagen I is widely investigated as a scaffold material for tissue engineering, and collagen-based products have been employed for wound dressings and skin substitutes. Importantly, the physical and biological properties of fibrillar collagens are strongly tied to variations in collagen fiber structure [43–45]. In turn, collagen fiber structure can be manipulated in vitro through mechanical forces, environmental factors, or thermal mechanisms [10, 46]. Thus, developing technologies that can direct collagen fiber structure noninvasively and site-specifically would provide a breakthrough approach to regulate the mechanical and biological properties of collagen-based biomaterials, and thereby control cellular responses during tissue repair. Moreover, advanced biomaterials with regionally defined variations in collagen fiber structure and function could provide spatial cues to instruct cell behavior and drive 3D tissue formation.

One newly developed ultrasound technology provides a noninvasive modality to control collagen fiber microstructure within 3D hydrogels during fabrication; this technique may provide a method to site-specifically increase the bioactivity of collagen hydrogels to drive cell responses, such as cell growth or migration [47]. Exposure of type I collagen to ultrasound during the polymerization process can alter collagen fiber size and density within the resultant hydrogel [47]. Scanning electron microscopy and second harmonic generation microscopy images showed that, under appropriate ultrasound exposure conditions, ultrasound exposure during collagen polymerization produces shorter, thinner collagen fibers compared to unexposed samples [47]. Ultrasound-induced temperature rises in the collagen gels

were modest (final temperatures <30 °C), and effects of ultrasound on collagen fiber microstructure were comparable to those produced by collagen polymerization at different temperatures [47]. Using focused ultrasound beams provides the added capability to site-specifically control collagen fiber structure to produce a single collagen hydrogel with distinct, regional variations in collagen fiber microstructures. For example, one study exposed the center of a cylindrical collagen sample during polymerization to produce a central core of short, thin collagen fibers within the beam volume, surrounded by longer, thicker collagen fibers outside the beam area (Fig. 1) [47]. More complex spatial variations in collagen microstructure could be produced by multiple-source configurations or ultrasound scanning capabilities.
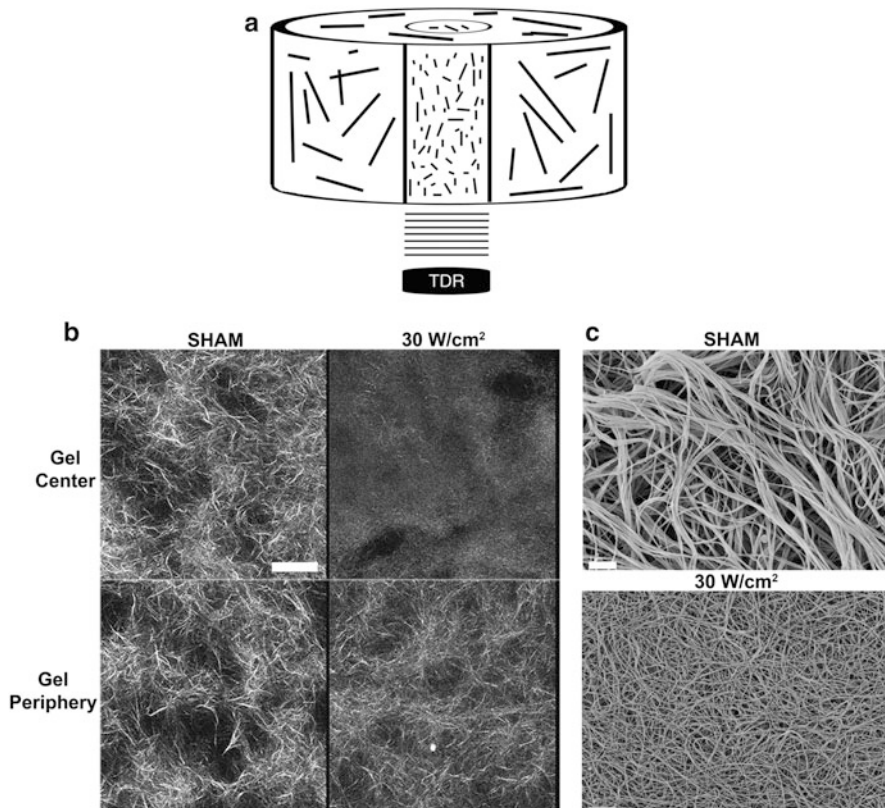
Fig. 1 Controlling collagen microstructure with ultrasound. (**a**) Schematic of the approach used to locally control collagen fiber microstructure within collagen hydrogels. A high-frequency, 8.3-MHz transducer (TDR), with a narrow beam (−6 dB = 0.6 cm), was directed at the center of a collagen sample. Exposures were performed during collagen polymerization. (**b**) Representative second harmonic generation images of collagen fibers within the center and periphery of sham- and ultrasound-exposed samples. Scale bar = 50 μm. (**c**) Representative scanning electron microscopy images taken from the center of sham or ultrasound-exposed collagen gels. Scale bar = 1 μm (Panels **b** and **c** reprinted with permission from Garvin et al. [47], Acoustical Society of America)

Interestingly, cells respond to ultrasound-induced alterations in collagen fiber micro-structure with increased rates of cell migration that were not observed in nonexposed, temperature-controlled samples, suggesting effects of ultrasound on collagen bioactivity occur through a nonthermal acoustic mechanism [47]. Thus, this ultrasound technology provides a noninvasive approach to control collagen fiber microstructure and thereby enhance biological activity of collagen hydrogels site-specifically.

Porosity is an important design characteristic for scaffold fabrication. Porous materials provide spaces and increased surface area for cell adhesion, proliferation, and migration. Additionally, the porosity of scaffold materials influences mass transport of nutrients and waste products within the scaffold volume. Although a variety of methods have been developed for introducing pore structures in bio-materials, many such approaches employ solvents that can compromise the biocom-patibility of the resulting scaffold. Ultrasound-based technologies can provide noninvasive methods for modifying the porosity of biomaterial scaffolds for tissue engineering applications. Acoustic cavitation is typically the underlying mechanism for effects of ultrasound on scaffold porosity. Physical phenomena associated with acoustic cavitation, such as microbubble oscillation, generation of high local tem-peratures, micro-jet formation, and microstreaming, can all alter scaffold porosity by introducing new pores, increasing pore connectivity, or enhancing mass transport through porous structures. Thus, to maximize cavitation activity, high-power, low-frequency ($\sim$20–50 kHz) ultrasound sources are typically utilized for ultra-sound technologies designed to modify scaffold porosity. These approaches are typically only suitable for fabricating scaffolds prior to seeding cells, as cell viability would be compromised by intense acoustic cavitation activity.

Several investigative teams have demonstrated the use of high-power, low-frequency ultrasound to affect pore structure in polymer scaffolds. In one approach, a solid-state foaming process was first used to prepare polylactic acid (PLA) scaffolds containing primarily closed-cell pores [48, 49]. Subsequent exposure of these prefabricated scaffolds to ultrasound (20 kHz, 750 W) increased inter-pore connectivity [49] and increased permeability of the scaffolds [48]. Using an alternate technique (supercritical CO_2 foaming) for prefabricating PLA foam scaffolds, Watson et al. [50] similarly found that low-frequency, high-power treatment of PLA scaffolds led to an increase in pore size, pore connectivity, and fluid transport into the scaffold. In another approach, ultrasound exposure of 3D electrospun polymer nanofibrous scaffolds increased pore size, porosity, and fiber thickness of the scaffolds, leading to enhanced cellular infiltration into the fibrous scaffolds [51]. Ultrasound techniques also hold potential to increase recellularization of decellularized native tissue scaffolds. Ultrasound exposure of decellularized patella tendon scaffolds increased spaces between collagen bundles leading to an increase in porosity and enhancement of recelluarization of the scaffold [52]. In summary, ultrasound technologies can provide noninvasive approaches to increase pore size, enhance pore interconnectivity, and improve fluid transport and cellular infiltration with biomaterial scaffolds.

Cell Patterning with Ultrasound

Recreating complex tissue architectures that are present in native tissues is a key challenge in the field of tissue engineering. Importantly, the spatial organization of cells provides critical cues that can direct cell behaviors essential for proper function of artificial tissues and organs. Various strategies are under development to control the spatial positions of cells within engineered constructs, each with its own set of limitations. Photolithography patterning of extracellular matrix proteins on substrates provides spatially organized sites for cell adhesion, but this approach is typically limited to two-dimensional patterning. Optical and magnetic forces have been used as methods for cells patterning. However, magnetic techniques require the attachment of magnetic particles to cells which can affect cell viability, while optical techniques are typically applied for single-cell manipulation. 3D bio-printing employs modified 3D inkjet printing technologies to pattern layers of spatially organized cells and biomaterials. Current 3D printing processes are time consuming, and temperatures and shear forces associated with 3D printing can affect cell behaviors and viability. Thus, there is a clear need for new technologies to rapidly and efficiently control the spatial organization of large volumes of cells within 3D-engineered constructs without producing adverse effects on cell function and survival.

Ultrasound can offer new solutions for cell patterning technologies for tissue engineering [17, 18]. Ultrasound standing wave fields (USWFs) can be employed to trap, levitate, or spatially organize particles or cells in suspending fluids [53]. An USWF is generated by the interference of two or more ultrasound fields. USWFs are characterized by regions of minimum acoustic pressure (nodes) and maximum acoustic pressure (antinodes). As an example, in an USWF generated between an ultrasound source and an acoustic reflector, the pressure nodes are spaced at intervals equal to one half the wavelength of the incident sound field. As discussed in section "Introduction to Tissue Engineering and Regenerative Medicine," acoustic radiation forces associated with an USWF vary sinusoidally in space. These primary acoustic radiation forces can actively direct particles or cells to pressure node locations [27, 28, 54]. Thus, by design of acoustic frequency, USWFs can predictably pattern cells or particles at defined spatial intervals. The magnitude of the acoustic radiation force depends upon the ultrasound exposure parameters and the material parameters of both the suspending media and the particles or cells [27, 28, 54]. In general, the magnitude of the acoustic radiation force on a particle in an USWF increases with increasing acoustic pressure amplitude, acoustic frequency, and volume of the particle [27, 28, 54]. Acoustic radiation forces exist only during sound exposure. In industrial and biotechnology applications, USWFs can be used to rapidly separate particles from suspending fluid media or direct particles to defined locations. When the USWF is removed, cells or particles in a fluid will sediment or return to a random distribution. In this way, filtration systems employ USWFs to rapidly sediment aggregated cells or particles from suspending fluids. Half-wavelength USWFs

have been used to create cell aggregates in suspension, and subsequently removal of the aggregates was proposed as a method to develop cell culture systems [55]. Alternatively, suspending media that undergo a phase change from liquid to solid during the ultrasound exposure can be employed to maintain the spatial patterning of cells or particles after removal of the sound field [26, 56–59].

Acoustic radiation forces associated with USWFs are the basis of an effective new technology for patterning cells in 3D tissue-engineered constructs [17, 26]. In this technology, cells are suspended in a type I collagen solution and exposed to an USWF to spatially pattern cells at pressure nodal locations [26]. A single transducer and reflector can be used to pattern cells in planar bands that are perpendicular to the direction of sound propagation and spaced at one half wavelength intervals (Fig. 2). More complex patterning geometries can be achieved with more than one acoustic source and/or reflector. Importantly, the acoustic patterning occurs rapidly and volumetrically throughout the engineered construct [17, 26]. Type I collagen is an abundant protein in native tissue, is widely utilized as a scaffold material for tissue
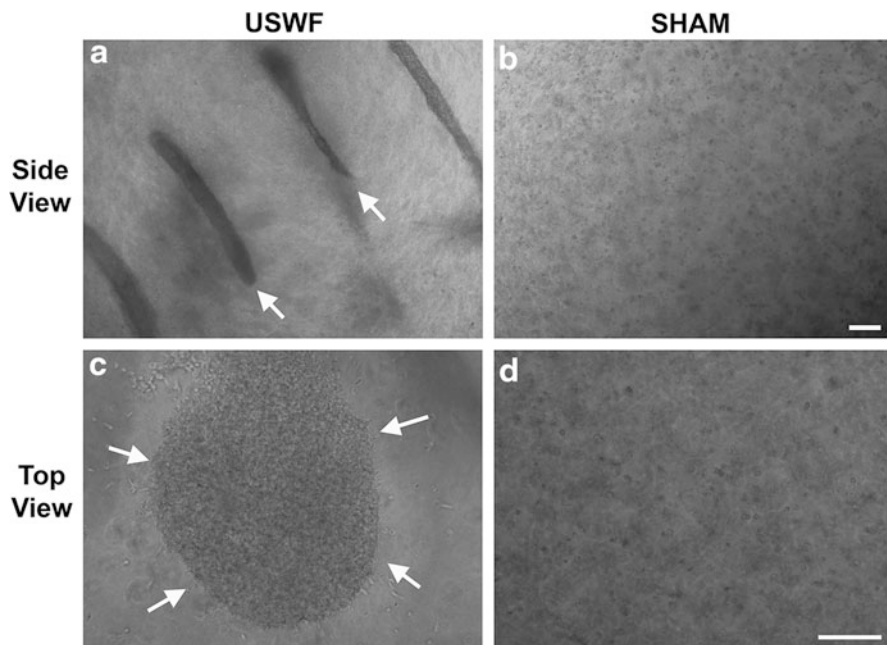
Fig. 2 Multicellular bands of endothelial cells form within 3D collagen hydrogels following exposure to USWF. Endothelial cells were suspended in an unpolymerized collagen type I solution and were exposed to a 1 MHz continuous wave USWF with 0.2 MPa peak pressure amplitude for 15 min. Sham samples were treated identically as USWF-exposed samples but were not subjected to the USWF. Representative phase-contrast images, taken 1 h after USWF exposure, show the spatial distribution of cells within USWF-exposed (**a**, **c**) and sham-exposed (**b**, **d**) collagen gels that were examined from both the side (**a**, **b**) and top views (**c**, **d**). *Arrows*, endothelial cell band. Scale bars, 200 μm (Reprinted from Ultrasound in Medicine and Biology, 37/11, Garvin et al. [56], with permission from Elsevier)

engineering, and undergoes a phase change from liquid to solid as temperature is increased. Thus, in this technology, USWF exposure is performed during the collagen polymerization process to "lock" the spatial pattern of cells in place after the sound field is removed. A key advantage of ultrasound is that the acoustic patterning is achieved noninvasively, thus maintaining sterile conditions necessary for tissue engineering. USWF exposures can be performed in modified tissue culture plates [26] or specially designed sample holders [17]. Acoustic patterning with USWF has been used to control the spatial organization of various cell types, including fibroblasts [26], human umbilical vein endothelial cells [56, 60], and human dermal lymphatic microvascular endothelial cells [17], within 3D collagen hydrogels. Importantly, USWF patterning of cells enhances cell function and promotes cell-mediated extracellular matrix reorganization, without adversely affecting cell viability [26].

Another ultrasound technology, also utilizing acoustic radiation forces, has been developed for patterning cells for tissue engineering applications. This technology employs acoustic droplet ejection and aqueous two-phase exclusion patterning to produce spatially patterned cocultures of cells on a substrate [61]. Specifically, acoustic radiation forces exerted on a liquid/air interface can lead to the ejection of liquid droplets from the liquid surface. In one study, the liquid used for droplet ejection was a solution of dextran and cells [61]. A plate placed above the liquid/air interface then captures the ejected droplet. Subsequent droplet ejection, combined with precise movement of the plate, can be used to fabricate defined patterns of cell-embedded droplets on the plate [61]. Employing more than one liquid/cell reservoir, each with a different cell type, provides the capability for multiplexed cell patterning [61]. Furthermore, after acoustic droplet patterning is complete, a final solution of polyethylene glycol (PEG) containing a final cell type can be added over the patterned droplets [61]. This ultrasound-based micropatterning technique provides a rapid, noncontact system for fabricating spatially patterned cell cocultures on a solid substrate.

Ultrasound Technology for Microvascular Engineering

A significant challenge to engineering complex tissues is the need to rapidly develop a vascular system to provide oxygen and nutrients to cells and remove metabolic waste products from the tissue construct. Some engineered tissues, such as skin substitutes, have relatively thin geometries that allow for mass transport by simple, passive diffusion. However, the fabrication of larger, 3D tissues requires new strategies for fabricating functional microvessel networks within engineered tissue constructs. Furthermore, vascularized 3D-engineered tissue constructs could provide realistic 3D in vitro models for drug discovery, toxicology testing, and product screening. Technologies capable of producing functional, small microvascular networks within 3D constructs are limited and remain in early stages of development. Vascularization strategies currently being pursued include scaffold functionalization, soft lithography and molding, 3D printing, and modular assembly. These approaches

face distinct limitations, as they can be time consuming, necessitate extended incubation times and secondary assembly processes, utilize sophisticated equipment and manufacturing processes, have confined geometry and/or limited dimensionality, and cannot be readily reduced to noninvasive applications.

To address this gap in technology, a new ultrasound technology has been developed to rapidly fabricate complex, microvessel networks within 3D-engineered collagen constructs [17, 56, 60]. In this approach, USWF-based acoustic patterning techniques (described in section "Cell Patterning with Ultrasound") are used to spatially organize endothelial cells within collagen hydrogels noninvasively [17, 56, 60]. Acoustic patterning occurs rapidly and hydrogels polymerize in approximately 15 min, thereby capturing the 3D endothelial cell patterns within the solidified gel. Importantly, USWF patterning of human endothelial cells into planar bands within collagen hydrogels leads to the rapid (1 day) emergence of capillary sprouts from the cell bands [56, 60]. Collagen fibers aligned in the direction of capillary sprout outgrowth, indicating USWF-patterned endothelial cells remodel their surrounding collagen matrix similar to natural capillary sprouting [56]. Over several days post-ultrasound exposure, USWF-fabricated microvessels continue to develop and mature into complex, anastomosing, lumen-containing microvessel networks throughout the full 3D volume of the collagen hydrogel (Fig. 3) [56, 60].

An important advancement of this ultrasound-based vascularization technology is that the morphology of the fabricated microvessel networks can be controlled by
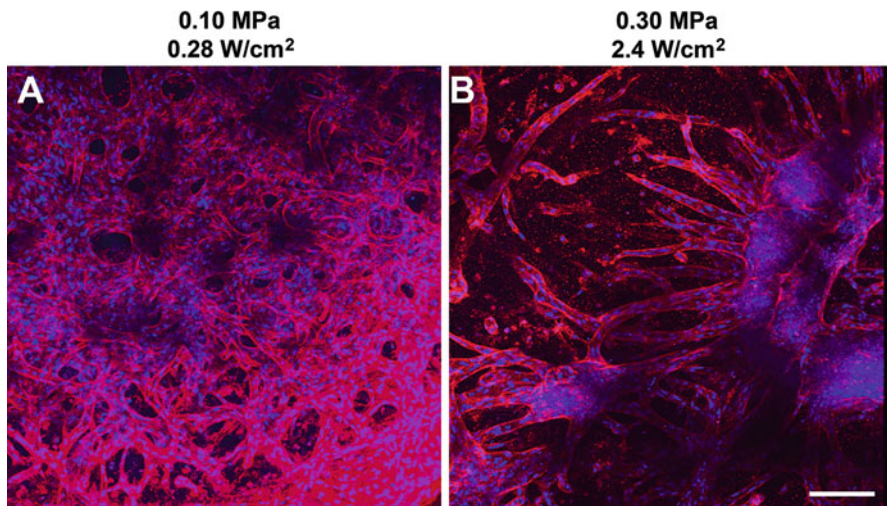
Fig. 3 Acoustic exposure parameters control microvessel network morphology. Unpolymerized solutions of type I collagen and endothelial cells were exposed to a 1-MHz ultrasound standing wave field with pressure amplitudes of either 0.1 MPa (**a**) or 0.3 MPa (**b**). Samples were incubated for 10 days and then stained for CD31 (*red*) to visualize endothelial cells. Cell nuclei were visualized by co-staining with DAPI (*blue*). Representative multiphoton z-stack images are shown. Scale bar, 50 μm (Reprinted with permission from Garvin et al. [60], Acoustical Society of America)

design of the USWF exposure parameters used for the initial cell patterning [56, 60]. Specifically, distinct microvessel morphologies have been fabricated by changing acoustic pressure amplitude [17, 56]. For example, USWF patterning (1 MHz) of endothelial cells at 0.1 MPa resulted in microvessel networks consisting of dense capillary-like morphologies throughout the collagen hydrogel [17, 56]. In comparison, USWF patterning at 0.3 MPa produced hierarchically branching, anastomosing networks between aligned vessel structures [17, 56]. Recall from section "Ultrasound Technology for Microvascular Engineering" that the frequency of an USWF controls the spacing between the patterned planar bands and the amplitude of the USWF controls the density of cells within each band. Thus, microvessel network morphology can be designed by appropriate choice of frequency and/or amplitude used for initial cell patterning. The ability of this USWF technology to noninvasively guide the fabrication of distinct microvessel network morphologies is a unique advantage of this vascularization technique.

Microvascular systems in native tissues are complex, consisting of arterioles branching to capillary beds that then give rise to venules. A further adaptation of this USWF-vascularization technology holds promise to fabricate such complex, physiologically relevant microvascular systems. In this method, sequential acoustic patterning is employed to fabricate a single, composite hydrogel-containing regions with distinct microvessel morphologies [17]. Specifically, a collagen/gel solution is placed in a holder and exposed to an USWF to pattern the cells to produce a desired microvessel network morphology [17]. Following polymerization, a second collagen/cell solution is overlaid over the first gel and exposed to a different USWF to pattern cells to produce a second desired microvessel network morphology [17]. In this fashion, composite hydrogels have been fabricated with distinct regions of hierarchically branching arteriole- or venule-like networks adjacent to regions containing capillary-like networks [17]. Note that exposing cell-embedded collagen gels to USWF after polymerization does not alter the initial cell patterning or affect cell viability [26].

An added complexity of native tissues is that they contain two independent vascular networks: the blood circulatory system and the lymphatic vascular system. Acoustic patterning of human dermal lymphatic microvascular endothelial cells has also been demonstrated to lead to rapid microvessel formation originating from cell-banded regions [17]. Thus, this USWF-vascularization technology has broad applicability for fabricating microvessel networks using different types and lineages of endothelial cells.

Delivery of Biochemicals and Signaling Molecules with Ultrasound

Tissue morphogenesis relies on the spatially and temporally orchestrated presentation of various signaling molecules to cells, including growth factors and extracellular matrix proteins. Thus, technologies that enable dynamic, controlled delivery of signaling molecules and/or bioactive chemicals are critical for advancing tissue

engineering. Ultrasound technologies are advantageous because they offer noninvasive approaches to control delivery. Furthermore, focused ultrasound beams provide excellent site-specific delivery capabilities, beam scanning allows for larger volumes of activation, and design of ultrasound exposure pulsing parameters and total exposure duration offers temporal control of delivery. Acoustic cavitation, ultrasound-induced heating, and/or acoustic radiation forces are the underlying physical mechanisms for different types of ultrasound-based delivery technologies. Thus, depending upon the underlying mechanism, ultrasound-based delivery methods may incorporate thermosensitive and/or mechanically sensitive materials or drug carriers. This section describes a variety of ultrasound-based delivery techniques, including those directed at controlling the expression of growth factors within engineered hydrogels, providing on-demand drug delivery with engineered constructs, and enabling intracellular delivery of drugs or genetic material.

A variety of ultrasound-based delivery technologies harness the mechanical activity associated with acoustic cavitation in their design. To maximize cavitation activity, these approaches can employ ultrasound contrast agents as a source of stabilized microbubbles. In these methods, ultrasound exposure of microbubbles, sometimes in combination with a drug delivery vehicle, provides spatial and temporal modulation of delivery. As an example of on-demand, ultrasound-induced drug release, one group developed a delivery system comprised of dye-carrier liposomes and microbubbles incorporated into an injectable cross-linking hydrogel [62]. Ultrasound exposure (20 kHz) of these microbubble/liposome constructs led to dye release in both in vitro and in vivo systems [62]. Furthermore, microbubbles themselves can be engineered to serve as drug delivery vehicles [63–65]. Additionally, coupling specific protein ligands on the microbubble surface provides cell-specific targeting [63, 64]. Material can also be delivered intracellularly using sonoporation, which is a process that transiently increases cell membrane permeability in response to ultrasound exposure. Choice of ultrasound exposure parameters affects the efficiency of membrane poration and the resultant cell viability [66–68]. Many studies have demonstrated that sonoporation with or without microbubbles can be an effective method for site-specific delivery of genetic material or drugs [35, 63–66, 69].

Acoustic droplet vaporization strategies also offer ultrasound-based capabilities for temporal and spatial modulation of growth factor release [70]. Acoustic droplet vaporization employs micron-sized emulsion droplets, typically comprised of perfluorocarbon liquids [71]. At 37 °C, the droplets remain as emulsions. However, upon exposure to ultrasound at appropriate amplitudes, the perfluorocarbon droplet is rapidly converted to a gas, forming a microbubble [71]. Microbubble formation is dependent upon ultrasound exposure parameters, droplet radius, and material properties of the perfluorocarbon droplet and suspending medium [71]. Double-emulsion formulations have been employed to incorporate growth factors within perfluorocarbon droplets [70]. In one study, fibrin hydrogels were fabricated containing double-emulsion droplets comprised of perfluorocarbon liquid and basic fibroblast growth factor (bFGF) [70]. Ultrasound exposure of the droplet-loaded hydrogels led to release of bFGF [70]. Focused ultrasound beams were employed, providing both

spatial and temporal control of growth factor release. As an additional consequence of acoustic droplet vaporization, the resulting microbubbles that were generated within the hydrogel added porosity and significantly increased the mechanical strength of the hydrogel [70].

The spatial localization of signaling molecules in relation to cells can affect cell behaviors and tissue morphogenesis. For examples, spatial gradients of growth factors can facilitate directed cell migration, and co-localization of cells and extra-cellular matrix proteins or protein mimetics can influence cell proliferation, adhesion, and migration. An USWF-based technology can be employed to noninvasively co-localize cells and signaling molecules or create spatial gradients. As described in section "Cell Patterning with Ultrasound," acoustic radiation forces associated with USWFs can spatially pattern cells within 3D hydrogels. However, the radiation force on a spherical particle is directly proportional to the particle volume. Thus, radiation forces exerted on soluble molecules are typically too small to produce spatial patterning. In a modification of the USWF-patterning technology described in section "Cell Patterning with Ultrasound," signaling molecules are first attached to either the cell surface or a biocompatible microparticle [17, 26]. USWFs are then used to spatially pattern cell- or microparticle-bound signaling molecules within hydrogels [17, 26]. As a demonstration of this approach, fibronectin was passively bound to cells prior to USWF exposure [26]. Fibronectin is a glycoprotein that can stimulate cell growth, contractility, and migration. USWF-mediated patterning of fibronectin-coated cells in collagen hydrogels produced high concentrations of fibronectin molecules co-localized to the USWF-patterned planar cell bands within the polymerized collagen gels [26]. This ultrasound technology offers a rapid, noninvasive methodology to produce patterns or spatial gradients of signaling molecules bound to cells or microparticles within hydrogel constructs.

Ultrasound-induced heating, in combination with thermosensitive materials, offers another approach for site-specific and temporally controlled drug/biochemical delivery. High-intensity, focused ultrasound has been employed to activate cells engineered with a heat-activated and ligand-inducible gene switch [72]. Ultrasound exposure of such cell-embedded fibrin constructs led to spatial and temporal control of expression of growth factors important for bone regeneration, specifically vascular endothelial growth factor (VEGF) and bone morphogenic protein 2 (BMP2) [72]. The ultrasound exposure produced limited effects on cell viability and scaffold structure [72]. An alternate thermally based approach employs temperature-sensitive liposomes. Several studies have demonstrated the effectiveness of local ultrasound-induced hyperthermia to control drug release from thermosensitive liposomes for in vitro or in vivo applications [73–76]. Furthermore, the combination of microbubbles and thermosensitive drug carriers provides opportunities for both thermal- and cavitation-based mechanisms for drug release [62, 77, 78].

Other drug delivery approaches rely on designed degradation or erosion of polymer materials to achieve temporal and spatial control of drug or chemical release. In these systems, ultrasound holds potential to influence the rate of release by enhancing erosion of carrier material through cavitation or by affecting local concentration gradients by streaming. For example, ultrasound exposure of a

protein-loaded, biodegradable copolymer significantly increased polymer degradation and increased release of protein from the construct [79]. Similarly, ultrasound-controlled release of an antibiotic from hydrogel carriers was demonstrated with low background release in the absence of ultrasound, suggesting the potential for site-specific on-off drug delivery with ultrasound technologies [80].

Conclusions and Future Directions

Ultrasound is advancing as a valuable tool for tissue engineering and regenerative medicine. Ultrasound fields are advantageous because of their capacity to noninvasively and site-specifically influence thermal processes and/or exert mechanical forces within biological systems and scaffold materials. Furthermore, from an engineering perspective, ultrasound fields are highly controllable, and acoustic sources can be readily incorporated within tissue engineering environments. Ultrasound technologies under development are directed at affecting scaffold fabrication processes, controlling cell patterning within 3D hydrogels, fabricating microvascular networks, and controlling the spatial and temporal presentation of biosignaling molecules within engineered tissues. Directions for further advances include engineering tissues comprised of multiple cell types, reconstituting native tissue microstructure within artificial scaffolds, and advancing nano- or microbubbles for targeted biochemical delivery within engineered tissues. Furthermore, the ability of ultrasound to act noninvasively offers breakthrough opportunities for achieving tissue engineering site-specifically in vivo. In summary, ultrasound technologies offer exciting new approaches to guide the fabrication of artificial tissues and advance the field of tissue engineering.

References

1. Nasseri BA, Ogawa K, Vacanti JP (2001) Tissue engineering: an evolving 21st-century science to provide biologic replacement for reconstruction and transplantation. Surgery 130:781–784
2. Patterson JE (1999) Epidemiology of fungal infections in solid organ transplant patients. Transpl Infect Dis 1:229–236
3. Atala A (2009) Engineering organs. Curr Opin Biotechnol 20:575–592
4. Shahrokhi S, Arno A, Jeschke MG (2014) The use of dermal substitutes in burn surgery: acute phase. Wound Repair Regen 22:14–22
5. Cleary MA, Geiger E, Grady C, Best C, Naito Y, Breuer C (2012) Vascular tissue engineering: the next generation. Trends Mol Med 18:394–404
6. Eberli D, Atala A (2006) Tissue engineering using adult stem cells. Methods Enzymol 420:287–302
7. Lutolf MP, Hubbell JA (2005) Synthetic biomaterials as instructive extracellular microenvironments for morphogenesis in tissue engineering. Nat Biotechnol 23:47–55
8. Atala A, Kasper FK, Mikos AG (2012) Engineering complex tissues. Sci Transl Med 4:160rv12
9. Badylak SF, Weiss DJ, Caplan A, Macchiarini P (2012) Engineered whole organs and complex tissues. Lancet 379:943–952

10. Shoulders MD, Raines RT (2009) Collagen structure and stability. Annu Rev Biochem 78:929–958
11. Cen L, Liu W, Cui L, Zhang W, Cao Y (2008) Collagen tissue engineering: development of novel biomaterials and applications. Pediatr Res 63:492–496
12. Pati F, Jang J, Ha DH, Won Kim S, Rhie JW, Shim JH et al (2014) Printing three-dimensional tissue analogues with decellularized extracellular matrix bioink. Nat Commun 5:3935
13. Vats K, Benoit DS (2013) Dynamic manipulation of hydrogels to control cell behavior: a review. Tissue Eng Part B Rev 19:455–469
14. Griffith LG, Naughton G (2002) Tissue engineering – current challenges and expanding opportunities. Science 295:1009–1014
15. Webber MJ, Khan OF, Sydlik SA, Tang BC, Langer R (2015) A perspective on the clinical translation of scaffolds for tissue engineering. Ann Biomed Eng 43:641–656
16. Madeira C, Santhagunam A, Salgueiro JB, Cabral JM (2015) Advanced cell therapies for articular cartilage regeneration. Trends Biotechnol 33:35–42
17. Dalecki D, Comeau EC, Raeman CH, Child SZ, Hobbs L, Hocking DC (2015) Guiding tissue regeneration with ultrasound in vitro and in vivo. Proc SPIE 9467:F1–F7
18. Dalecki D, Hocking DC (2015) Ultrasound technologies for biomaterials fabrication and imaging. Ann Biomed Eng 43:747–761
19. Dalecki D (2004) Mechanical bioeffects of ultrasound. Annu Rev Biomed Eng 6:229–248
20. NCRP (2002) Exposure criteria for medical diagnostic ultrasound: II. Criteria based on all known mechanisms. National Council on Radiaton Protection and Measurement, Bethesda
21. Nyborg W (2007) WFUMB safety symposium on echo-contrast agents: mechanisms for the interaction of ultrasound. Ultrasound Med Biol 33:224–232
22. Dalecki D, Carstensen EL, Parker KJ, Bacon DR (1991) Absorption of finite amplitude focused ultrasound. J Acoust Soc Am 89:2435–2447
23. Rooney JA, Nyborg WL (1972) Acoustic radiation pressure in a travelling plane-wave. Am J Phys 40:1825–1830
24. Nyborg W (1953) Acoustic streaming due to attenuating plane waves. J Acoust Soc Am 25:68–75
25. Dyson M, Pond JB, Woodward B, Broadbent J (1974) The production of blood cell stasis and endothelial damage in the blood vessels of chick embryos treated with ultrasound in a stationary wave field. Ultrasound Med Biol 1:133–148
26. Garvin KA, Hocking DC, Dalecki D (2010) Controlling the spatial organization of cells and extracellular matrix proteins in engineered tissues using ultrasound standing wave fields. Ultrasound Med Biol 36:1919–1932
27. Gor'kov L (1962) On the forces acting on a small particle in an acoustical filed in an ideal fluid. Sov Phy Dokl 6:773–775
28. Gould RK, Coakley WT (1974) The effects of acoustic forces on small particles in suspension. In: Bjorno L (ed) Finite amplitude wave effects in fluids: proceedings of the 1973 symposium. IPC Science and Technology Press, Guildford, pp 252–257
29. Faez T, Emmer M, Kooiman K, Versluis M, van der Steen AFW, de Jong N (2013) 20 years of ultrasound contrast agent modeling. IEEE Trans Ultrasound Ferr 60:7–20
30. Flynn HG (1982) Generation of transient cavities in liquids by microsecond pulses of ultrasound. J Acoust Soc Am 72:1926–1932
31. Suslick KS, Price GJ (1999) Applications of ultrasound to materials chemistry. Annu Rev Mater Sci 29:295–326
32. Dalecki D (2007) WFUMB safety symposium on echo-contrast agents: bioeffects of ultrasound contrast agents in vivo. Ultrasound Med Biol 33:205–213
33. Carstensen EL, Gracewski S, Dalecki D (2000) The search for cavitation in vivo. Ultrasound Med Biol 26:1377–1385
34. Dalecki D, Child SZ, Raeman CH, Cox C, Penney DP, Carstensen EL (1997) Age dependence of ultrasonically induced lung hemorrhage in mice. Ultrasound Med Biol 23:767–776

35. Ferrara K, Pollard R, Borden M (2007) Ultrasound microbubble contrast agents: fundamentals and application to gene and drug delivery. Annu Rev Biomed Eng 9:415–447

36. Qin S, Caskey CF, Ferrara KW (2009) Ultrasound contrast microbubbles in imaging and therapy: physical principles and engineering. Phys Med Biol 54:R27–R57

37. Miller DL (2007) WFUMB safety symposium on echo-contrast agents: in vitro bioeffects. Ultrasound Med Biol 33:197–204

38. Hensel K, Mienkina MP, Schmitz G (2011) Analysis of ultrasound fields in cell culture wells for in vitro ultrasound therapy experiments. Ultrasound Med Biol 37:2105–2115

39. Leskinen JJ, Hynynen K (2012) Study of factors affecting the magnitude and nature of ultrasound exposure with in vitro set-ups. Ultrasound Med Biol 38:777–794

40. Mercado KP, Helguera M, Hocking DC, Dalecki D (2014) Estimating cell concentration in three-dimensional engineered tissues using high frequency quantitative ultrasound. Ann Biomed Eng 42:1292–1304

41. Mercado KP, Helguera M, Hocking DC, Dalecki D (2015) Noninvasive quantitative imaging of collagen microstructure in three-dimensional hydrogels using high-frequency ultrasound. Tissue Eng Part C Methods 21:671–682

42. Parker KJ, Doyley MM, Rubens DJ (2011) Imaging the elastic properties of tissue: the 20 year perspective. Phys Med Biol 56:R1–R29

43. Korff T, Augustin HG (1999) Tensional forces in fibrillar extracellular matrices control directional capillary sprouting. J Cell Sci 112:3249–3258

44. Roeder BA, Kokini K, Sturgis JE, Robinson JP, Voytik-Harbin SL (2002) Tensile mechanical properties of three-dimensional type I collagen extracellular matrices with varied microstructure. J Biomech Eng 124:214–222

45. Yang YL, Motte S, Kaufman LJ (2010) Pore size variable type I collagen gels and their interaction with glioma cells. Biomaterials 31:5678–5688

46. Sander EA, Barocas VH, Fratzl P (2008) Biomimetic collagen tissues: collagenous tissue engineering and other applications. In: Collagen. Springer, US, pp 475–504

47. Garvin KA, VanderBurgh J, Hocking DC, Dalecki D (2013) Controlling collagen fiber microstructure in three-dimensional hydrogels using ultrasound. J Acoust Soc Am 134:1491–1502

48. Guo G, Ma Q, Zhao B, Zhang D (2013) Ultrasound-assisted permeability improvement and acoustic characterization for solid-state fabricated PLA foams. Ultrason Sonochem 20:137–143

49. Wang X, Li W, Kumar V (2006) A method for solvent-free fabrication of porous polymer using solid-state foaming and ultrasound for tissue engineering applications. Biomaterials 27:1924–1929

50. Watson NJ, Johal RK, Glover Z, Reinwald Y, White LJ, Ghaemmaghami AM et al (2013) Post-processing of polymer foam tissue scaffolds with high power ultrasound: a route to increased pore interconnectivity, pore size and fluid transport. Mater Sci Eng C 33:4825–4832

51. Lee JB, Jeong SI, Bae MS, Yang DH, Heo DN, Kim CH et al (2011) Highly porous electrospun nanofibers enhanced by ultrasonication for improved cellular infiltration. Tissue Eng Part A 17:2695–2702

52. Ingram JH, Korossis S, Howling G, Fisher J, Ingham E (2007) The use of ultrasonication to aid recellularization of acellular natural tissue scaffolds for use in anterior cruciate ligament reconstruction. Tissue Eng 13:1561–1572

53. Coakley WT, Hawkes JJ, Sobanski MA, Cousins CM, Spengler J (2000) Analytical scale ultrasonic standing wave manipulation of cells and microparticles. Ultrasonics 38:638–641

54. Gol'dberg Z (1971) Radiation forces acting on a particle in a sound field. In: Rozenberg L (ed) High intensity ultrasonic fields. Plenum Press, New York, pp 109–117

55. Bazou D, Coakley WT, Hayes AJ, Jackson SK (2008) Long-term viability and proliferation of alginate-encapsulated 3-D HepG2 aggregates formed in an ultrasound trap. Toxicol in Vitro 22:1321–1331

56. Garvin KA, Dalecki D, Hocking DC (2011) Vascularization of three-dimensional collagen hydrogels using ultrasound standing wave fields. Ultrasound Med Biol 37:1853–1864

57. Gherardini L, Cousins CM, Hawkes JJ, Spengler J, Radel S, Lawler H et al (2005) A new immobilisation method to arrange particles in a gel matrix by ultrasound standing waves. Ultrasound Med Biol 31:261–272

58. Gherardini L, Radel S, Sielemann S, Doblhoff-Dier O, Groschl M, Benes E et al (2002) A study of the spatial organisation of microbial cells in a gel matrix subjected to treatment with ultrasound standing waves. Bioseparation 10:153–162

59. Mazzoccoli JP, Feke DL, Baskaran H, Pintauro PN (2010) Development of multilayered cell-hydrogel composites using an acoustic focusing technique. Biotechnol Prog 26:600–605

60. Garvin KA, Dalecki D, Yousefhussien M, Helguera M, Hocking DC (2013) Spatial patterning of endothelial cells and vascular network formation using ultrasound standing wave fields. J Acoust Soc Am 134:1483–1490

61. Fang Y, Frampton JP, Raghavan S, Sabahi-Kaviani R, Luker G, Deng CX et al (2012) Rapid generation of multiplexed cell cocultures using acoustic droplet ejection followed by aqueous two-phase exclusion patterning. Tissue Eng Part C Methods 18:647–57

62. Epstein-Barash H, Orbey G, Polat BE, Ewoldt RH, Feshitan J, Langer R et al (2010) A microcomposite hydrogel for repeated on-demand ultrasound-triggered drug delivery. Biomaterials 31:5208–5217

63. Caskey CF, Hu X, Ferrara KW (2011) Leveraging the power of ultrasound for therapeutic design and optimization. J Control Release 156:297–306

64. Tsutsui JM, Xie F, Porter RT (2004) The use of microbubbles to target drug delivery. Cardiovasc Ultrasound 2:23

65. Unger EC, Porter T, Culp W, Labell R, Matsunaga T, Zutshi R (2004) Therapeutic applications of lipid-coated microbubbles. Adv Drug Deliv Rev 56:1291–1314

66. Fan Z, Chen D, Deng CX (2013) Improving ultrasound gene transfection efficiency by controlling ultrasound excitation of microbubbles. J Control Release 170:401–413

67. Karshafian R, Bevan PD, Williams R, Samac S, Burns PN (2009) Sonoporation by ultrasound-activated microbubble contrast agents: effect of acoustic exposure parameters on cell membrane permeability and cell viability. Ultrasound Med Biol 35:847–860

68. Pan H, Zhou Y, Izadnegahdar O, Cui J, Deng CX (2005) Study of sonoporation dynamics affected by ultrasound duty cycle. Ultrasound Med Biol 31:849–856

69. Cochran M, Wheatley MA (2013) In vitro gene delivery with ultrasound-triggered polymer microbubbles. Ultrasound Med Biol 39:1102–1119

70. Fabiilli ML, Wilson CG, Padilla F, Martin-Saavedra FM, Fowlkes JB, Franceschi RT (2013) Acoustic droplet-hydrogel composites for spatial and temporal control of growth factor delivery and scaffold stiffness. Acta Biomater 9:7399–7409

71. Kripfgans OD, Fowlkes JB, Miller DL, Eldevik OP, Carson PL (2000) Acoustic droplet vaporization for therapeutic and diagnostic applications. Ultrasound Med Biol 26:1177–1189

72. Wilson CG, Martin-Saavedra FM, Padilla F, Fabiilli ML, Zhang M, Baez AM et al (2014) Patterning expression of regenerative growth factors using high intensity focused ultrasound. Tissue Eng Part C Methods 20:769–779

73. Dromi S, Frenkel V, Luk A, Traughber B, Angstadt M, Bur M et al (2007) Pulsed-high intensity focused ultrasound and low temperature-sensitive liposomes for enhanced targeted drug delivery and antitumor effect. Clin Cancer Res 13:2722–2727

74. Grull H, Langereis S (2012) Hyperthermia-triggered drug delivery from temperature-sensitive liposomes using MRI-guided high intensity focused ultrasound. J Control Release 161:317–327

75. Kheirolomoom A, Lai CY, Tam SM, Mahakian LM, Ingham ES, Watson KD et al (2013) Complete regression of local cancer using temperature-sensitive liposomes combined with ultrasound-mediated hyperthermia. J Control Release 172:266–273

76. Mannaris C, Efthymiou E, Meyre ME, Averkiou MA (2013) In vitro localized release of thermosensitive liposomes with ultrasound-induced hyperthermia. Ultrasound Med Biol 39:2011–2020

77. Gourevich D, Dogadkin O, Volovick A, Wang L, Gnaim J, Cochran S et al (2013) Ultrasound-mediated targeted drug delivery with a novel cyclodextrin-based drug carrier by mechanical and thermal mechanisms. J Control Release 170:316–324
78. Yudina A, de Smet M, Lepetit-Coiffe M, Langereis S, Van Ruijssevelt L, Smirnov P et al (2011) Ultrasound-mediated intracellular drug delivery using microbubbles and temperature-sensitive liposomes. J Control Release 155:442–448
79. Agrawal CM, Kennedy ME, Micallef DM (1994) The effects of ultrasound irradiation on a biodegradable 50–50% copolymer of polylactic and polyglycolic acids. J Biomed Mater Res 28:851–859
80. Noble ML, Mourad PD, Ratner BD (2014) Digital drug delivery: on-off ultrasound controlled antibiotic release from coated matrices with negligible background leaching. Biomater Sci 2:839–902

Ultrasonic Drug Delivery Using Micelles and Liposomes

Ana M. Martins, Salma A. Elgaili, Rute F. Vitor, and
Ghaleb A. Husseini

Contents

Abstract

The encapsulation of drugs in nanocarriers revolutionized research in drug delivery, especially in cancer chemotherapeutics. Several nanosystems have been developed including liposomes, polymeric micelles, dendrimers, solid lipid nanoparticles, and others.

The surface of nanocarriers can be modified to alter their characteristics and improve their efficiency as drug delivery systems. The addition of polyethylene glycol chains, for example, increases the blood circulation time of nanocapsules and, in some cases, improves their stability.

A.M. Martins • S.A. Elgaili • R.F. Vitor • G.A. Husseini (✉)
Department of Chemical Engineering, American University of Sharjah, Sharjah, UAE
e-mail: amartins@aus.edu; salma.e.a@gmail.com; rvitor@aus.edu; ghusseini@aus.edu

Once the structure of nanocarriers is optimized, the next logical step is to explore the feasibility of using one or several trigger mechanisms to release their therapeutic contents at the required time and space. Abundant literature is available on both internal and external trigger mechanisms in cancer drug delivery. Internal mechanisms include changes in pH, enzyme concentration, and temperature, while external mechanisms include light, magnetic/electromagnetic waves, and acoustic power.

This review focuses on the utility of ultrasound and polymeric micelles in cancer drug delivery. The idea is to control the release of chemotherapeutics from micelles to cancerous cells by focusing the ultrasound waves on the diseased tissue while sparing other healthy cells in the body. Thus, the side effects of conventional chemotherapy can be minimized.

Abbreviations

AC	Alternating current
CMC	Critical micellar concentration
CW	Continuous wave US
DDS	Drug delivery system(s)
Dox	Doxorubicin
EPR	Enhanced permeability and retention
FA	Folic acid
FA-CLC/SPIO	Mixed micelles of folic acid-conjugated carboxymethyl lauryl chitosan and superparamagnetic iron oxide
HEMA	Hydroxyethyl methacrylate
ICAM-1	Intercellular adhesion molecule
IPN	Interpenetrating network
LFA-1	Leukocyte function-associated antigen
mAb	Monoclonal antibody
MDR	Multidrug resistance
MI	Mechanical index
PEG	Polyethylene glycol
PEG-b-PBLA	Polyethylene glycol-co-poly(beta-benzyl-L-aspartate)
PEG-PCL	Polyethylene glycol)-b-poly(caprolactone)
PEG-PE	Polyethylene glycol-phosphatidylethanolamine
PEG-PLLA	Polyethylene glycol-b-poly(L-lactide)
PEO	Poly(ethylene oxide)
PEO-b-PTHPMA	Copolymer of poly(ethylene oxide) and poly(2-tetrahydropyranyl methacrylate)
PFC_5	Perfluoropentane

PLA	Poly(lactic acid)
PLA-*b*-PEG	Copolymer of poly(lactic acid) and poly(ethylene) glycol
PPO	Poly(propylene oxide)
PTHPMA	Poly(2-tetrahydropyranyl methacrylate)
RES	Reticuloendothelial system
SLN	Solid lipid nanoparticles
US	Ultrasound

Introduction

Cancer is a leading cause of death in the western world [1]. Chemotherapy, a term first coined by the German physician and scientist Paul Ehrlich more than 100 years ago [2], is widely used as a cancer treatment, alongside surgery and radiotherapy. Several chemical compounds have been and are currently being researched as possible chemotherapeutic agents, but, in general, although efficient, they are not selective, killing both cancer cells and healthy cells. This leads to the development of serious side effects in patients undergoing treatment, such as hair loss, weight loss, nausea, fatigue, and decreased immunity [1]. Hence, there has been intense research in the area of drug delivery systems (DDS), engineered systems for the controlled spatial and/or temporal release of therapeutic drugs.

Nanoparticles are an essential part of a DDS. They are particles made of a defined stable material, which must be compatible with the human body, and their role is to carry the chemotherapeutic agent until this reaches the tumor site and then being able to release it. This way, there is a lower interaction of the drug with healthy cells, and also there is a decrease in the dose needed for the treatment than when using the free drug, which is economically desirable. There are several types of nanocarriers, namely, liposomes, micelles, dendrimers, nanotubes, solid lipid nanoparticles, nanoshells, quantum dots, and others [3].

Multifunctional nanoparticles can be engineered to target a certain site, usually based on specific characteristics of the cancer cells and, once there, an internal or external stimulus can be applied to trigger the release of the drug. Examples of internal stimuli are a change in pH, temperature, or enzyme activity, while external triggers include light, magnetic fields, heat, and ultrasound (US).

Ultrasound has been widely used in medicine for several decades due to its noninvasive nature. Its application in diagnostic imaging is well known [4]. Only recently, however, US has been tested as a trigger in DDS.

This chapter describes the recent advances on the use of polymeric micelles to encapsulate chemotherapeutic agents and the use of US as a trigger to promote the leakage of the drug from these nanocarriers.

Drug Delivery Systems

Diversity of Nanocarriers

There are several types of nanocarriers (Fig. 1 and Table 1). This paper focuses on polymeric micelles, but a brief description of other nanocarriers will be presented below.

One of the most widely researched nanoparticles, already in use in the clinical setting, are liposomes [5, 6]. Liposomes were discovered in the 1960s by Alec Bangham when conducting experiments with phospholipids. Liposomes are spherical structures with a size in the range of 20 nm to 1 μm comprised of a phospholipid bilayer membrane, similar to the cell membrane, surrounding an internal aqueous core. Due to the zwitterionic nature of the phospholipids, liposomes can be used to carry both hydrophilic and hydrophobic molecules, the first in their aqueous core, the latter in their hydrophobic membrane.

Micelles are smaller than liposomes with sizes ranging between 10 and 100 nm in diameter [7], with polymeric micelles having an average diameter of 20 nm [8]. Micelles are colloidal dispersions, consisting of amphiphilic surfactant molecules that aggregate spontaneously when in water, forming a spherical structure with a hydrophobic core that can encapsulate hydrophobic drugs [9]. Polymeric micelles will be further discussed in section "Triggered Release."

Dendrimers are small (1–20 nm diameter) synthetic, branched macromolecules, with a central core (ethylenediamine or ammonia) surrounded by multiple layers with active terminal surface groups [10]. The multiple hydrophobic or hydrophilic cavities that are formed in the interior of the dendrimer tridimensional structure are well suited for the encapsulation of molecules.

Solid lipid nanoparticles (SLN) are colloidal dispersions composed of solid lipids, such as waxes, fatty acids, and glycerides, stabilized by surfactants. In SLN, the drug can be entrapped inside the lipid matrix, encapsulated, or adsorbed to the surface of the particles [11].

Polymer-drug conjugates are drug delivery nanosystems composed of several drug molecules covalently attached to a polymer. Polymers used in this type of DDS include PEG, PGA, HPMA, and the drugs attached include Dox, camptothecin, docetaxel, and paclitaxel [12].

Other nanoparticles include quantum dots, niosomes, and carbon nanotubes [3, 13].

With such a diversity of nanocarriers, a pertinent question is: which one of these have been approved for clinical use? Recent review papers described which DDS are currently used in the clinical setting, as well as the ones undergoing clinical trials [14–17] (Table 2). In 2013, it was reported that 4,520 nanomedicines were undergoing clinical trials for cancer treatment [3].
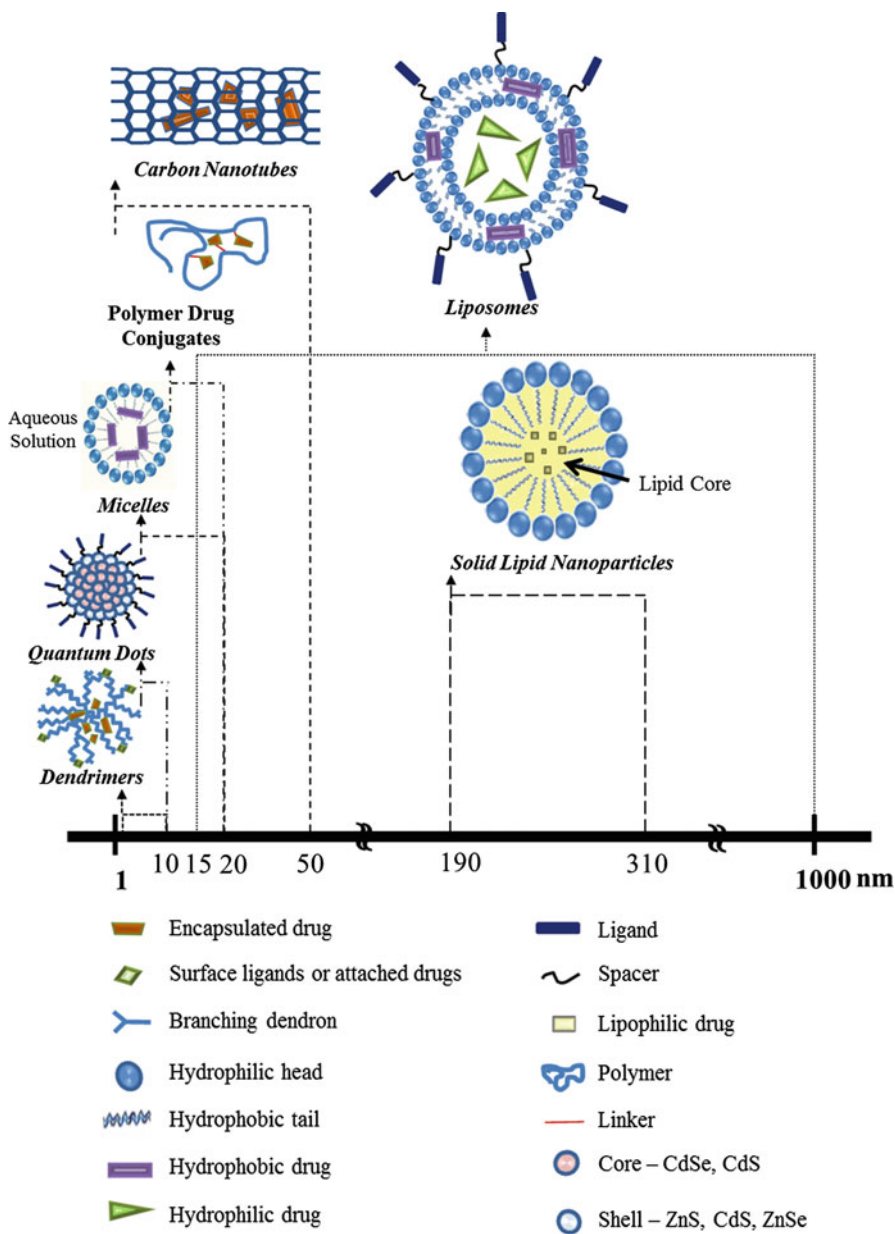
Fig. 1 Most used nanoparticles and their size ranges

Table 1 Types of nanocarriers used in drug delivery systems [14, 17]

Nanocarrier	Types	Composition	Examples
Drug conjugates	Polymer-drug conjugate	Linear polymers, drug	PGA, HPMA
	Antibody-drug conjugate	Targeted antibodies, drug	Gemtuzumab, brentuximab
	Polymer-protein conjugate	Polymer, anticancer protein	SMANCS
Lipid-based	Liposome	Phospholipids, cholesterol, others	DPPC, DOPE, DSPC, DPPE, DSPG
	Solid lipid nanoparticle	Lipids with low melting points	
Polymer-based	Dendrimers	Hyperbranched synthetic polymers	PAMAM
	Polymeric micelles	Amphiphilic block copolymers	Pluronic, PAA, PLA, PEG
	Polymeric nanoparticle	Glycan, cyclodextrin, Albumin	
	Protein nanoparticle		
Inorganic	Silica nanoparticle	Mesoporous silica	MCM-41, SBA-15
	Metal nanoparticle	Gold, iron oxide	
Viral-based		Self-assembled protein cages	CPMV

CPMV cowpea mosaic virus, *DPPC* 1,2-dipalmitoyl-sn-glycero-3-phosphocholine, *DOPE* 1,2-dioleoyl-sn-glycero-3-phosphoethanolamine, *DSPC* 1,2-distearoyl-sn-glycero-3-phosphatidyl-choline, *DSPE* 1,2-distearoyl-sn-glycero-3-phosphoethanolamine-*N*-poly(ethylene glycol)-2000, *DSPG* 1,2-distearoyl-sn-glycero-3-phosphatidylglycerol, *HPMA* *N*-(2-hydroxypropyl)-methacrylamide, *PAA* poly-(L-aspartate), *PAMAM* poly(amidoamine), *PEG* polyethylene glycol, *PGA* poly-(L-glutamate), *PLA* poly-(L-lactide), *SMANCS* styrene maleic anhydride neocarzinostatin

The EPR Effect

Chemotherapeutic drugs preferentially accumulate at the tumor location due to several physiological characteristics of tumors, which makes them distinguishable from normal tissues, such as pH, capillary structure, enzyme concentration, and others. The preferential extravasation and accumulation of macromolecules and nanoparticles at the tumor site is called the enhanced permeability and retention (EPR) effect, a phenomenon which was originally described by the group of Maeda in 1986 [18] and which has been extensively reviewed by this research group [19–21]. The EPR effect has been widely described in all types of cancer, excluding the hypovascular ones, such as prostate and pancreatic cancers [21]. However, a recent review of clinical trials showed that the efficiency of the encapsulated drug is only marginally higher than that of the free drug, a result which contrasts with that obtained in in vivo studies using animal models [22]. Apparently, the EPR effect depends on the tumor type, and in some tumors with irregular vascularity, it may be prevented due to low blood flow and high tumor interstitial fluid pressure. A very

Table 2 Different types of drug delivery systems that have been clinically approved [14, 17]

Drug delivery system	Nanoparticle/ polymer/protein/ antibody	Drug/protein	Cancer indication	Commercial name (approval date)
Antibody-drug conjugate	Brentuximab vedotin	MMAE	Non-Hodgkin lymphoma	Adcetris® (2011)
	Trastuzumab emtansine	DM1	Breast cancer	Kadcyla® (2013)
Liposomes	PEGylated liposomes	Doxorubicin	Kaposi's sarcoma, ovarian, breast	Doxil®/Caelyx® (1995)
		Doxorubicin	Kaposi's sarcoma, ovarian, breast	Lipo-Dox® (1998, Taiwan)
	Non-PEGylated liposomes	Cytosine arabinoside	Neoplastic meningitis	DepoCyt® (1999)
		Daunorubicin	Kaposi's sarcoma	DaunoXome® (1996)
		Doxorubicin	Breast	Myocet® (2000, Europe)
Polymer-protein conjugate	PEG	L-asparaginase	Leukemia	Oncaspar® (2006)
	Styrene maleic anhydride	Neocarzinostatin	Liver, renal	Zinostatin stimalamer (1994, Japan)
Polymeric micelles	PEG-PLA	Paclitaxel	Breast, lung, ovarian	Genexol-PM® (2007, South Korea)
Protein-drug conjugate	Albumin	Paclitaxel	Breast, pancreatic, non-small-cell lung	Abraxane® (2005)

DM1 maytansine derivative, *MMAE* Monomethyl auristatin E, *PEG* polyethylene glycol, *PLA* poly-(L-lactide)

important factor for the EPR effect is the tumor's hyper-permeable or *leaky* vasculature [20]. Due to a very fast angiogenesis, the capillary vessels of the tumors show a deficient structure; hence, it is easier for macromolecules and nanocarriers to extravasate into the tumor site than into a healthy tissue. Additionally, tumors have deficient lymphatic drainage systems, which allows for the extended retention of large molecules [20]. The EPR effect may also be enhanced due to the generation of factors that increase the permeability at the tumor site, such as prostaglandins, enzymes such as matrix metalloproteinases, vascular endothelial growth factor, nitric oxide, and others [18].

The so-called first-generation nanomedicine drugs are based on the EPR effect, also termed *passive targeting*. In contrast, *active targeting* involves the modification of the nanocarrier surface with a ligand, which selectively binds a receptor overexpressed in the membrane of the cancer cells. This will be further discussed in the following section.

Passive Versus Active Targeting

There are two broad types of targeting techniques, namely, passive and active [3, 5]. In *passive targeting*, the nanocarriers preferentially accumulate at the tumor site due to the EPR effect. In *active targeting*, besides the aid of the EPR effect, the nanocarrier has a feature that allows it to specifically target and interact with the cancer cells. Usually, the nanocarrier possesses a targeting moiety, such as a ligand, which is conjugated on its surface and is free to interact with a cell surface receptor overexpressed on the cancer cells [23]. The type of chemical modification of the nanocarrier surface depends on the type of receptor present on the surface of the tumor cells. Hence, active targeting can be generally defined as the use of targeting moieties or ligands to enhance the delivery of nanoparticles to the target tumor site, thus significantly increasing the therapeutic effects while decreasing the undesired side effects [23].

Several targeting moieties have been used in studies of targeting strategies, such as peptides, oligosaccharides, antibodies, aptamers, and low molecular weight molecules, the most widely used being folic acid [24]. The choice of the targeting moiety is also crucial since it affects the circulation time of the modified nanocarrier, its extravasation at the cancer site, its affinity for the cell receptor or antigen, and its cellular uptake [25]. Some examples will be discussed next.

Peptides are commonly used as targeting moieties in DDS. These small chains of amino acids are usually derived from sequences of proteins that bind to receptors in the cell membrane, such as intercellular adhesion molecule (ICAM-1), bombesin, leukocyte function-associated antigen (LFA-1), and others. Peptides have been investigated as targeting ligands in multifunctional nanoparticles used in triggered drug delivery for cancer therapy and imaging strategies [26].

Antibodies are widely used as targeting moieties due to their variety and specificity for receptors on the surface of cancer cells. Both human and nonhuman antibodies have been used in DDS research, but since the nonhuman may induce an immunogenic response, new methods are being investigated for the development of chimeric, fragmented, and humanized antibodies [27]. Monoclonal antibodies (mAb) are identical (clones) and monospecific and can be used in targeted cancer therapy, after the identification of which antigens are expressed on the surface of tumor cells [28]. There are several reports describing the use of monoclonal antibodies for targeted drug delivery [29–31].

Small molecular weight molecules have also been described as modifiers of nanocarriers used for targeted drug delivery. Carbohydrates such as galactose and mannose have been described [32], but folate is the most important one in this category since its receptor is overexpressed in many cancer cells due to the increased biosynthesis of nucleotide bases in these fast-dividing cells [33]. Folic acid, vitamin B_9, easily recognizes the folate receptor on the surface of several cancer cells in ovarian, brain, kidney, breast, lung, and other types of cancer [32, 34]. The inclusion of this molecule in DDS has been used in imaging [35] and therapeutic processes [32].

Aptamers, small molecules of single-stranded nucleic acids that can specifically bind proteins and peptides, have also been researched as targeting moieties in DDS [32, 36]. Their high specificity is due to the fact that they can fold into unique three-dimensional structures and target proteins including transcription factors and cell membrane receptors. They offer some advantages over other ligands, e.g., their high stability and low immunogenicity [36].

Other ligands have been described and were reviewed elsewhere [29–31].

In both passive and active targeting, it is essential that the nanocarrier remains in circulation long enough, which allows its accumulation at the desired location before release occurs.

Triggered Release

The aim of a good DDS is to deliver the encapsulated drug to the tumor site and release it there, thus avoiding healthy tissues and minimizing the side effects of the drug. The release of the drug from nanoparticles that reached the tumor site either by passive or active targeting can be controlled by triggers or stimuli, a process known as *triggered release* [37]. In this case, the nanocarriers have to be responsive to an external stimulus or to sense changes in the environment (internal stimulus) and release the drug load [38]. External triggers include hyperthermia, magnetic and electric fields, US and light, while changes in the pH of the environment, enzyme concentration, and/or redox potential are examples of internal triggers [6, 37–39].

The choice of the trigger depends on the type of nanocarrier used, the encapsulated drug, and the tumor environment. For example, it was observed that drug release from pH-sensitive micelles targeted with folic acid (named PHSM/f) was much higher at acidic pH (5.0) than at neutral pH [40]. Also, micelles can be synthesized with disulfide bonds that are sensitive to reduction by the antioxidant intracellular tripeptide glutathione, which concentrations are significantly different in healthy and tumor cells [38]. Although these are examples of internal triggers, micelles can also be designed to be sensitive to external ones, such as hyperthermia, US, magnetic and electrical fields, light, and others.

Ultrasound, the focus of this chapter, is considered one of the best trigger mechanisms in triggered drug delivery [6, 37], and it will be discussed in section "Ultrasound-Triggered Drug Release from Micelles."

Micelles

Polymeric Micelles

Micelles are colloidal nanocarriers made of amphiphilic molecules that spontaneously self-assemble and form a spherical monolayer structure of 10–100 nm in diameter when dissolved in water [7]. Amphiphiles are surface-active molecules that consist of a hydrophilic tail and a hydrophobic head [31]. Hence, the structure

of a micelle consists of an external hydrophilic corona and a hydrophobic core. Micelles can transport hydrophobic drugs and imaging agents in their hydrophobic cores [9], and recently, the preparation of core-inversible micelles that can sequester hydrophilic molecules in a hydrophilic core was also described [41] (Fig. 2). Additionally, polymeric micelles can transport drugs attached to the hydrophilic polymer of their corona [5]. When discussing micelles, a very important parameter to take into consideration is the critical micellar concentration (CMC), the concentration above which micelles assemble and form in water [29].

Micelles are not used widely in clinics yet (Table 2) but have several advantages over other nanocarriers: (i) they are biocompatible; (ii) they are easy to prepare and load with the drug; (iii) their small size allows their deep penetration into tissues and organs and increases the blood circulation time, since they escape renal excretion; (iv) the release of drugs from their core can be controlled; (v) they are stable in biological fluids; and (vi) they can be successfully used for drug solubilization [5, 8, 37, 42].

Polymeric micelles are formed from polymers with hydrophilic and hydrophobic monomers. Poly(ethylene oxide) (PEO) is widely used as the hydrophilic building block, while the hydrophobic monomers may be poly(propylene oxide) (PPO), poly (lactic acid) (PLA), or others [8, 9, 43]. The hydrophobic drug accumulates in the hydrophobic core of the micelle, while the hydrophilic PEO chains extend into the aqueous environments, stabilizing the micelles [37]. It has been observed that the pharmacokinetics and biodistribution of pharmaceuticals are enhanced when these are incorporated into polymeric micelles when compared to the free formulation [44].

Polymeric micelles of Pluronic® copolymer are widely used in DDS, especially in US-induced drug release. They are composed of triblock copolymers of PPO and PEO and have a hydrodynamic radius ranging between 5 and 20 nm at 37 °C, which allows their extravasation into the tumor [9, 37]. Besides the previously mentioned advantages of micelles in general, Pluronic® has several others [5, 9, 37]: (i) the
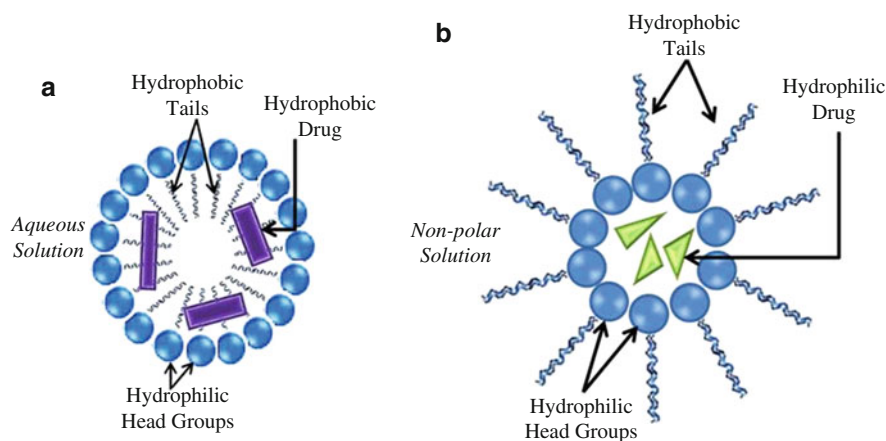
Fig. 2 Schematic of the structure of polymeric micelles. (**a**) Normal micelles in a polar solvent; (**b**) reverse micelles in a nonpolar solvent

ability to sensitize multidrug-resistant (MDR) cancer cells when used at low concentrations [45]; (ii) its high loading capacity; (iii) its increased shelf life when lyophilized; (iv) the low viscosity of its micellar solutions; (v) the fact that it can be sterilized by microfiltration; (vi) the ability to make it sensitive to a certain release trigger, as previously mentioned in section "Triggered Release"; (vii) its low in vivo toxicity [45]; and (viii) its enhanced structural stability and lower CMC when compared to micelles composed of low molecular weight surfactants. The physical and biological properties of Pluronic® compounds have been reviewed by Batrakova and coworkers [44, 45].

The most used type of Pluronic® micelles in research is Pluronic® P105 [8, 9, 29], composed of PEO and PPO blocks with the formula PEO_{37}-PPO_{56}-PEO_{57} [43]. P105 may exist as unimers, loose aggregates or dense micelles, depending on the solution concentration. These micelles have a CMC of ~1 wt.% at room temperature [46], but dense micelles that can encapsulate hydrophobic drugs form at concentrations 4 wt.% and above [47].

Polymeric micelles have several advantages as DDS, but their use in vivo is still challenging due to their recognition and elimination by the immune system and also due to stability problems when the micellar solution is diluted in the bloodstream [5, 37].

While circulating in the bloodstream, micelles adsorb proteins onto their surface and they are subsequently recognized by the reticuloendothelial system (RES) and cleared by phagocytosis, endocytosis, and/or other biological mechanisms. This can be prevented by covering the surface of the micelles with PEO that inhibits adsorption and opsonization [9]. Indeed, the hydrophilic PEO chains extend into the aqueous environment and associate with water molecules, leading to a steric repulsion of proteins, preventing their adsorption and further recognition of these *stealth* micelles by the RES [9]. This increases the circulation time of the micelles and enhances their accumulation at the tumor site by passive or active targeting [48]. Pluronic® micelles have the advantage of having PEO as an integral part of their structure, forming their coronas. The PEO corona, however, may pose problems for the micelles to interact with and enter the cells, where they would release their drug load. The use of sheddable polymers that allow the unmasking of the particles upon arrival at the target site has been studied. Further details on sheddable polymers and shedding techniques can be found on a review by Romberg et al. [49].

Another problem that arises when using polymeric micelles in vivo is their micellar stability. When injected into the bloodstream, the micellar solution may be diluted below the CMC, leading to their quick dissolution and the early release of the encapsulated drug [50]. One way to avoid this is to use higher concentrations of the polymer, but these may be toxic for the human body [43]. Research into this subject led to the design and synthesis of stabilized, cross-linked micellar formulations [51–55]. One of such formulations, named NanoDeliv™, was synthesized from P105 by creating an interpenetrating network (IPN) of the temperature-responsive N,N-diethylacrylamide polymer inside the hydrophobic core of the micelles [51]. NanoDeliv™ micelles are more stable upon dilution [51] and have a half-life of approximately 17 h [56]. The IPN expands at room temperature, allowing the accumulation of the drug in the core of the micelles but contracts when

the temperature is higher than 31 °C, thus trapping the drug. Hence, when the micellar solution is injected into the body at 37 °C, it is diluted, but the IPN prevents its dissolution and keeps the drug entrapped in the structure [51]. Although larger than the non-stabilized P105, the NanoDeliv™ are still small enough (~60 nm) to extravasate at cancer capillaries [8]. The group of Yang and coworkers [53] created a different type of stabilized micelles by the formation of cross-links in their outer shells. The size of these micelles was still small enough (100 nm), but they were significantly more stable than the non-stabilized ones.

Another approach to increase the micellar stability involves the optimization of the mass ratio of the hydrophilic and hydrophobic blocks that constitute the micelles [52]. Zeng and Pitt [54, 55] synthesized micelles with time-controlled degradation using PEO, N-isopropyl acrylamide (NIPAAm), and the polylactate ester of hydroxyethyl methacrylate (HEMA-lactate). The systemic circulation lifetime of this formulation could be controlled by changing the ratio of the copolymer concentration, and this DDS was shown to release the encapsulated drugs upon ultrasonication at 70 kHz.

Micellar Modifications for Active Targeting

The differences between passive and active targeting were mentioned in section "Passive Versus Active Targeting," and here, we shall discuss active targeting as a way to enhance the efficiency of polymeric micelles as DDS.

When using micelles as a DDS, several factors can be studied and modified to enhance their biodistribution and uptake, and these include the micellar composition, the drug encapsulated, and the tumor location [42]. The drug carrier, in this case, the micelle, is one of the most important components of the DDS, which can be modified to improve drug delivery. When used for passive targeting, which is based on the nanoparticle size, the formulation parameters are carefully selected in order to obtain micelles with an enhanced circulation half-life (previously mentioned) and that can easily extravasate at the tumor site. These stealth micelles are water soluble, have higher molecular weights than regular micelles, and higher structural stability [42]. The solubility of the drugs inside the micellar core, which also depends on the charge of the hydrophilic copolymers, can be enhanced by the addition of anioinic, nonionic, or zwitterionic surfactants [39].

In addition to passive targeting, polymeric micelles can be modified with ligand moieties, which can be attached to the hydrophobic blocks that form the micellar corona, to enhance active targeting [57].

One option to targeted delivery using micelles is to design *immunomicelles*, which consist of micelles with an antibody or antibody fragment (e.g., the Fab fragment) as a targeting moiety [28]. One of the first studies on the use of antibody-targeted micelles was done by Kabanov et al. [58], who reported the modification of Pluronic® P85 micelles with brain-specific polyclonal antibodies, as a way to

enhance the delivery of the drug haloperidol to mice brain. Monoclonal antibodies (mAb), derived from the IgG isotype antibody, have also been widely used for targeted cancer therapy [28]. Micelle-mAb conjugates are diblock copolymeric micelles with antibodies or antibody fragments (Fab, antigen-binding fragment) chemically attached to their surface. The first micelle-mAb to be synthesized used polyethylene glycol-phosphatidylethanolamine (PEG-PE) conjugated to the 2C5 mAb [28]. This antibody is reactive toward a wide variety of cancer cells, unlike the majority of anticancer mAb. The results showed that the antibodies conjugated to the micelles retained their activity and specificity, binding to several different cancer cells in vitro. In vivo experiments revealed an increased accumulation of these immunomicelles at the tumor site when compared to non-targeted micelles.

Polymeric micelles conjugated with folic acid have also been researched as targeted nanocarriers. Husseini et al. [59] synthesized Dox-encapsulating Pluronic® P105 micelles with a folate moiety and studied the Dox release triggered by 70-kHz LFUS at several power densities.

Presently, micelle-based DDS consisting of multifunctional nanocarriers are the most promising for anticancer therapies [29]. Drug delivery systems based on these multifunctional nanocarriers combine targeted (sections "Passive Versus Active Targeting" and "Micellar Modifications for Active Targeting") and targeted and triggered delivery (section "Triggered Release"). The combination of ligand targeting of cancer cells with the use of an internal or external stimulus to trigger the drug release from the nanocarrier ensures the highest specificity toward cancer cells with increased cytotoxicity and antitumor activity [60]. The use of stimuli-sensitive micelles in combination with a trigger for the drug release, in particular US, has been extensively studied by Husseini and coworkers [8, 9, 37, 43] and will be discussed in the following sections.

Ultrasound-Triggered Drug Release from Micelles

When using a DDS in anticancer therapy, it is necessary to optimize the rate of drug release from the nanocarrier in order to obtain the maximum efficiency and decrease the deleterious side effects that chemotherapy has on healthy cells. This is easily understandable: if the drug is released early, it may affect healthy tissues while preventing the drug to reach the intended tumor target, while if the release is too slow, the drug will not reach the necessary concentration to exert its therapeutic effect. The use of carefully designed nanocarriers sensitive to a certain stimulus or stimuli allows the time- and space-controlled release of the drug from the nanocarrier, the previously mentioned triggered release process. Several external triggers can be used for this purpose (see section "Triggered Release"), but here, we will focus on the use of US to trigger the release of the drug encapsulated in polymeric micelles.

Brief Introduction to the Physics of Ultrasound

Ultrasound has been widely studied as a trigger mechanism in DDS, due to the fact that it is safe, it is already being used for medical purposes, and it has a low cost. Ultrasound in medicine is mainly known as an imaging (diagnosis) technique without adverse side effects, although it may also be used for therapeutic purposes, e.g., physical therapy [61]. The physics of US has been recently reviewed [6]; here, a brief description will be presented.

What Is Ultrasound?

An ultrasound wave is a pressure wave (sound wave) that propagates through a medium and has frequencies of 20 kHz or higher, above the normal human hearing range (40 Hz to 20 kHz) [50, 62]. Just like any sound wave, US waves are sinusoidal and propagate by means of energy transfer between the molecules that constitute the medium, since they consist of cycles of alternating pressures: high pressure – *compression* – and low pressure – *rarefaction* [62].

Acoustic waves possess all the properties of a wave, i.e., attenuation (caused by dispersion due to energy losses while the wave propagates), reflection, refraction, amplification, absorption, and scattering [6]. Ultrasound waves, however, also have the capability of propagation on the surface of matter without traveling through it [63, 64].

Ultrasound waves propagate in a medium, namely, the *fluid medium*, by a series of compression and rarefaction states, and this propagation depends on the density of the material. Since it is a process where energy is transferred from molecules to molecules, the propagation is faster in solid medium than in liquid medium and is slower in gases [61]. In this process, the particles do not move, they just oscillate in place, while the energy is transferred, thus propagating the pressure wave. The physical nature of the ultrasonic waves explains how they can interact with cells and tissues, being able to shear open cells and nanoparticles. Usually, however, these physical forces are not able to cause these effects by themselves but only in the presence of gas bubbles [65, 66], as will be discussed in section "Mechanisms of US-Induced Micellar Drug Release and Cellular Uptake."

What Are the Parameters of Ultrasound?

Since acoustic waves are sinusoidal waves, they have the same important parameters that define any sinusoid. The high-pressure phases coincide with the upper peaks of the sinusoid, while the lower pressures coincide with the lower peaks. It is then possible to calculate wavelength (λ), frequency (1/T), amplitude of the wave, and speed (λ/T) of the wave [4].

The *frequency*, defined as the number of sinusoidal cycles per second (Hertz, Hz), is one of the most important parameters that defines the application of the US [67]. Low-frequency US (LFUS) refers to frequencies lower than 1 MHz, medium-frequency US usually ranges from 1 to 5 MHz, while high-frequency (HFUS) is greater than 5 MHz [43]. Higher frequencies ($\geq$1 MHz) have lower penetration depth and lower wavelengths, and they are used in medical diagnostic imaging [4].

The *power density*, commonly referred to as US intensity, is defined as the power carried per cross-sectional area of the US beam (W/cm^2) [50]. High intensities cause hyperthermia and are used for tissue ablation as an example. On the other hand, low intensities do not cause hyperthermia and are used for imaging purposes [4, 61].

The *mode of operation* is also a very important US parameter: in *continuous* mode (continuous wave, CW), the generated US wave is applied continuously for a determined period of time, while in *pulsed* mode, the wave is generated in a cycle of *on* and *off* periods that usually last a few seconds [68].

Although frequency, power density, and mode of operation are the main controllable parameters of US with a crucial importance in triggered drug delivery [69], it is also very important to consider *attenuation* that occurs while the wave passes through a medium. Attenuation is the intensity loss of the traveling wave, which occurs due to absorption and reflection phenomena. Attenuation depends on the frequency of US, decreasing as frequency decreases; hence, LFUS can penetrate tissues more deeply than HFUS [70]. Additionally, attenuation also depends on the medium through which the wave propagates: attenuation is very low in water and ultrasonic gel, but it is high in muscle and bone tissue [6]. This parameter is very important to consider when choosing the frequency of US to be used in different medical applications.

How Is Ultrasound Generated?

Ultrasound waves can be generated by an oscillating piezoelectric crystal, a transducer of the alternating current (AC) produced by an actuator [67] (Fig. 3). The transducer basically translates the applied voltage waveform into linear motion of

Fig. 3 Generation of ultrasound waves from an alternating current (*AC*) source
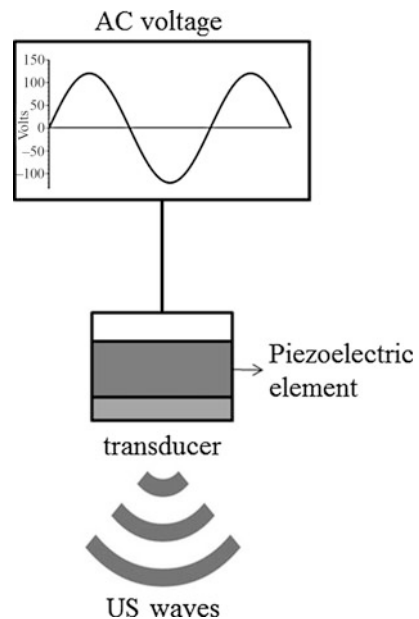
the transducer's face, producing the pressure waves that are transmitted into fluid or tissue through a medium or gel contacting the transducer.

Mechanisms of US-Induced Micellar Drug Release and Cellular Uptake

Interaction of US with Biological Systems

The interaction of US with biological systems is classified as thermal effects or nonthermal effects. Thermal effects are associated with the absorption of acoustic energy by body tissues and fluids, leading to hyperthermia [65]. Hyperthermia is very important in anticancer therapy, being used by itself, to heat the tumor, or as an adjuvant in DDS, to heat the tissues and/or as a trigger for drug release from temperature-sensitive nanocarriers [6, 50].

Nonthermal effects, which are usually exploited for triggered drug delivery, usually refer to cavitation, the formation, and oscillation of gas bubbles in the acoustic field in response to the oscillating pressure referred to previously [37]. Cavitation depends on the parameters of the US wave and only occurs after a certain threshold is achieved when the resonant frequency of the oscillating bubbles approaches the frequency of the ultrasonic field [37]. At low-pressure US amplitudes, *stable* (or non-inertial) cavitation occurs, during which the gas bubbles oscillate, slightly expanding and contracting [37, 71]. During stable cavitation, the size of the bubbles increases and microstreaming – circulating fluid flow around the bubbles – also occurs [72, 73]. This phenomenon has been described as enhancing drug delivery [74] and, if the pressure is high enough, it may shear open cells and nanoparticles (Fig. 4) [72, 75]. When the size of the bubbles approaches their resonant size and/or when the acoustic pressure increases, the oscillations become unstable and eventually lead to the collapse of the bubbles, generating extremely high pressures and temperatures and free radicals, a process known as *collapse* (or inertial) cavitation [37, 71, 74, 76, 77]. The mechanical index (MI) is another frequently used parameter related to ultrasound, and it is a measure of the probability of collapse cavitation occurring [78].

When the bubbles collapse near a solid surface, a directional sonic jet of liquid is produced [37, 76]. These events, if occurring near cells, will damage or even destroy them. Following the collapse, new, smaller bubbles form, and these may serve as cavitation nuclei, reinitiating the process [76]. In summary, both inertial and collapse cavitation may shear open both nanoparticles, such as micelles and liposomes, and cells, thus enhancing the drug delivery process by allowing the drug release and possibly allowing the direct entry of the drug into the cell cytosol [66, 75]. Several US-related parameters must be carefully controlled for cavitation and drug release to occur, such as the frequency, power density, duration of sonication, and position of the transducer [5].

Mechanisms of US-Triggered Drug Release

The knowledge of the properties of US, as well as the ways by which it interacts with matter, leads to the proposal of several mechanisms for US-triggered drug
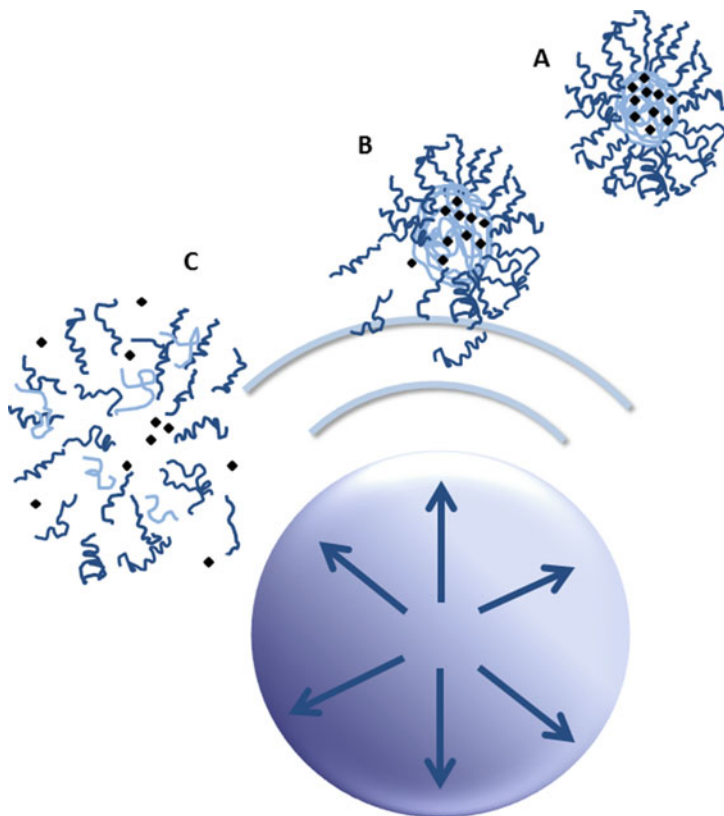
Fig. 4 Drug release from polymeric micelles triggered by ultrasound. (**a**) Intact micelle; (**b**) start of structural collapse of the micelle and initial release of the encapsulated agent; (**c**) complete collapse of the micelle and agent release due to the ultrasonic shockwave

delivery. The objective is to find a combination of acoustic parameters leading to a cavitational level and all associated effects that allow the delivery of the drug without killing the cells [50].

Several mechanisms have been proposed for US-triggered drug delivery, including drug release and cell drug uptake. These mechanisms are still being researched but seem to include [37, 50]: (i) disruption of the drug nanocarriers; (ii) enhanced drug transport and distribution in target tissues; (iii) enhancement of endocytosis and pinocytosis events, which increase drug uptake by the cells; and (iv) permeabilization of the cell membrane, which facilitates the transport of free and micelle-encapsulated drugs. Each of these mechanisms will be further discussed below.

Disruption of the Drug Nanocarriers

For the drug to be released from the nanocarriers, they have to be disrupted. The mechanical effects caused by US lead to the disruption of the drug carriers by shear

stresses and/or extreme stresses [79]. In the first case, when the shear stress caused by acoustic pressure and velocity gradients exceeds the cohesive forces of the nanocarrier, this will rupture and release the encapsulated drugs. On the other hand, the shock waves, microjets, extreme pressures, and temperatures and generation of free radicals caused by collapse cavitation all lead to the rupture of the drug carrier [37].

The disruption of the drug carrier triggered by US should occur at the tumor site, thus decreasing the deleterious side effects of chemotherapy. When the nanocarriers are polymeric micelles, this is particularly emphasized when pulsed US is used as a trigger. Polymeric micelles are capable of self-assembly: when the US is *on*, the drug is released from the micelles, but during the *off* US period, the drug that did not enter the cells can be re-encapsulated in the micelles that reform and circulate in the bloodstream again [80].

How does US increase the uptake of drugs – free or encapsulated – by the cell? Do these enter the cell by simple diffusion via endocytotic events, or does US induce transient pores in the cell membrane thus allowing the entrance? All mechanisms have been proposed, and while the first has been dismissed as having a major contribution, there are studies that support the other two.

Enhanced Drug Transport and Distribution in Target Tissues

This mechanism relies on the oscillatory movement of the fluid medium upon exposure to US, which increases the micro-convection phenomenon, thus enhancing the transport of molecules by simple diffusion [81]. This mechanism, which may occur even in the absence of cavitation, was suggested after the observation of drug distribution in poorly vascularized tumor tissues after exposure to US [79]. Diffusion, as the main mechanism of cellular drug uptake after US-triggered release from polymeric micelles, has been proposed but was dismissed by several experiments by the group of Pitt et al. [82–84].

When cavitation occurs, the drug transport is obviously enhanced by the convection currents generated from stable oscillating bubbles. The motion of the fluid near the drug (free or encapsulated) and the target tissues leads to the dispersion of the drug throughout the tissues. Additionally, when in the proximity of these bubbles, bodies that are denser than the fluid medium, such as drug carriers, are pushed toward the bubbles and eventually are sheared open and release their contents [72, 73].

Upregulation of Endocytosis/Pinocytosis

This mechanism suggests that the application of US upregulates the endocytosis and/or pinocytosis of the micelles encapsulating the drug by the tumor cells. Several in vitro cellular studies provided evidence for this mechanism, while others support the sonoporation mechanism discussed below (see section "Relevant In Vitro and In Vivo Studies" – in vitro cellular studies). In any case, this hypothesis concerns nonspecific endocytosis, since it is unlikely that cells possess receptors for polymeric micelles, rejecting the possibility of receptor-mediated endocytosis [37].

Cell Membrane Permeabilization

This mechanism suggests that the mechanical effects caused by the interaction of US with the cells cause the transient permeabilization of the cell membrane, facilitating the delivery of the drug to the target tissues [77]. Without bubble cavitation, hyperthermia is the major US effect, and this has little effect on cells [65]. When cavitation occurs, cells and drug-encapsulating nanocarriers are subjected to shock waves, microjets, and microstreaming, and this leads to the rupture of vesicles and the formation of pores in the cell membrane, enhancing the cell permeability [37, 77]. Blood vessel poration and rupture has also been noted [37]. Several studies support this mechanism, and these will be further discussed in section "Relevant In Vitro and In Vivo Studies."

Relevant In Vitro and In Vivo Studies

Most of the research done on ultrasound DDS using polymeric micelles as nanocarriers uses Pluronic®-based micelles, especially P105 [5, 37]. Other micellar formulations have also been used, and these are also briefly described in this section.

In Vitro Micellar Drug Release

The first evidence that US can release drugs from polymeric micelles came from in vitro studies. Most studies were performed using micelles encapsulating a fluorescent drug, such as the model drug calcein or the anticancer drug doxorubicin.

The group of Pitt and coworkers [85] designed an ultrasonic exposure chamber (Fig. 5) to measure the real-time fluorescence decrease due to drug release from polymeric micelles, especially Pluronic® P105, triggered by US. In this type of studies, the fluorescence inside the hydrophobic core of the micelle is higher, and it decreases when the fluorescent probe is released from the micelle and diluted in the medium.

In vitro studies investigated the effect of frequency on the efficiency of release. Ultrasound used for drug release usually ranges from 20 kHz to 16 MHz [74]. Using the ultrasonic chamber shown in Fig. 5, Husseini et al. [85] studied the effect of using 20–90 kHz pulsed US on the release of Dox and ruboxyl from polymeric micelles. The results showed that the release decreased with increasing frequencies, even when the power density increased, and this suggested an important role for cavitation in the process. Further studies by the same group showed a correlation between drug release and the appearance of subharmonic emissions and broadband noise, suggesting that collapse cavitation was involved [86].

Diaz de la Rosa and coworkers [87] also studied the effect of frequency on drug release from polymeric micelles and showed release at 70 kHz but no release at 476 kHz, even if inertial cavitation occurred at all frequencies. To explain this difference, the authors performed dynamic modeling studies of the bubble oscillation at 70 kHz and 500 kHz [80, 88] at different mechanical indices, a parameter that measures the probability of occurrence of collapse cavitation [89]. Their results
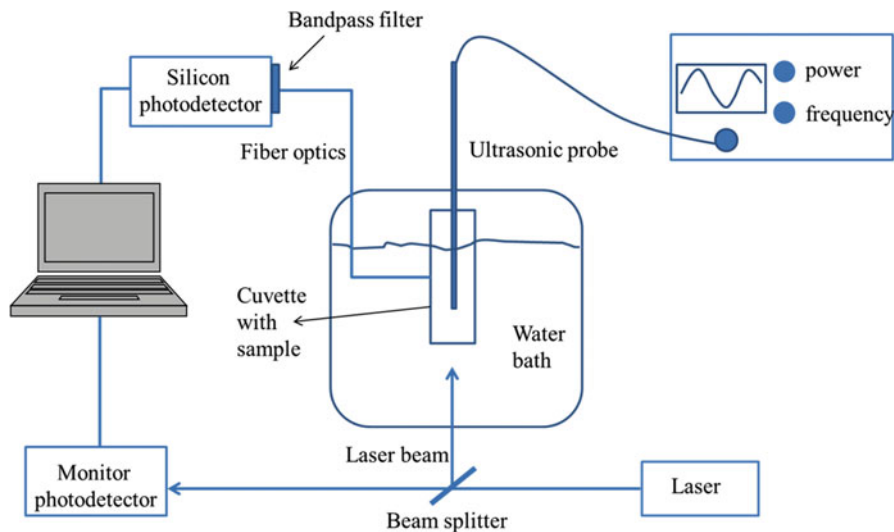
Fig. 5 Custom ultrasonic chamber designed by Husseini et al. [84]. The chamber detects real-time fluorescence, allowing the measurement of US-triggered drug release from polymeric micelles

showed different behaviors of the bubbles under the 70-kHz and 476-kHz ultrasonic fields, with two different routes to chaos, which explained the experimental results [80]. Further modeling studies by the same group showed that the drug release observed experimentally at 70-kHz US is due to an intermittent route to chaos, which does not occur at 476 kHz [80, 88].

Husseini et al. [85] studied the effect of changing power densities at a constant frequency on drug release from Pluronic® P105 micelles. They observed that as the power density increased, so did the release. At 70-kHz, the power density threshold required for drug release was on the range of 0.35–0.41 W/cm^2 [88]. When higher frequencies were applied, higher power densities had to be applied to obtain significant amounts of release [85].

Another factor that was studied was the use of pulsed US versus continuous wave (CW) US. In the same study mentioned previously, Husseini et al. [85] observed that when using pulsed US, the drugs were released while the US was *on*, but they were re-encapsulated in the micelles during the *off* period between short pulses. This provides a great advantage of this micellar system, since in vivo, when the micelles and the drug leave the diseased area, the drug will be re-encapsulated, thus decreasing the side effects due to the interaction of the drug with healthy cells. The kinetics of release and encapsulation was studied by the same group [90], and the results showed that a 20-kHz US pulse of 0.2 s was necessary to observe release, while the re-encapsulation required an *off* phase of 0.1 s. Maximum release occurred after 0.6 s insonation, and re-encapsulation occurred immediately after the pulse stopped and was also completed 0.6 s after

the beginning of the *off* period. The data obtained was described by simple physical models, and the best fit was obtained with a zero-order release and first-order re-encapsulation simple kinetics. New results were obtained and modeled in subsequent studies, using artificial neural network (ANN) [91] and chemical kinetic mechanistic models [92]. These studies investigated the drug release and re-encapsulation as functions of frequency, power density, micelle concentration, and temperature. Stevenson-Abouelnasr and coworkers [92] proposed four mechanisms for the release and re-encapsulation of Dox from P105 micelles using 20-kHz US with a power density of 0.058 W/cm^2: (i) micelle destruction and Dox release, (ii) cavitating nuclei destruction, (iii) micelles reassembly, and (iv) Dox re-encapsulation. While the first mechanism is due to cavitation, the second one is a slow partial recovery phase, when the re-encapsulation of a small amount of drug occurs. The last two mechanisms are independent of US. The modeling and sensitivity analysis of Dox release kinetics from P105 using an ANN model [91] showed that the drug release was inversely proportional to the US frequency and directly proportional to power density. The power density threshold to release at 20-kHz US was much lower (0.015 W/cm^2 at MI 0.15) than that at 70-kHz US (0.38 W/cm^2 at MI 0.40), emphasizing the role of inertial cavitation in the process. The same modeling strategy was further used to optimize the US parameters – US frequency, power density, pulse length, sonication duration – to achieve an optimal drug release at the tumor site via a model-predictive controller (MPC) [93, 94]. The parameters of the controller can then be adjusted to reach good reference signal tracking and sustain constant drug release.

Several studies were also performed to unravel the effect of micelle stabilization on the drug release rate. The release rate of Dox from stabilized and non-stabilized Pluronic$^®$ P105 micelles, triggered by 70-kHz US, was studied in vitro [95]. It was observed that Dox release from non-stabilized micelles (10 % release) was higher than from NanoDeliv™ stabilized ones (3 % release). Although 3 % is a low value, theoretically, the entire micellar drug load could be released if pulsed US was applied for a period long enough, in the presence of cells that compete for Dox. Another study by the same group [96] showed that the release rate of Dox from non-stabilized micelles is also significantly higher than from NanoDeliv™. Additionally, a study of the degradation kinetics of NanoDeliv™ micelles exposed to 70-kHz and 476-kHz US (both at MI 0.9), showed that, although US perturbs the IPN of the stabilized micelles, the degradation time is long when compared to the drug release rate, and no significant difference in the degradation rates could be observed after 2 h of insonation at both frequencies.

Temperature was studied as another factor that influences US-triggered drug release from polymeric micelles. The kinetic model developed by Stevenson-Abouelnasr et al. [92] was also used to study the kinetics of US-induced release and re-encapsulation of Pluronic$^®$ P105 micelles at different power densities and temperatures (namely, 25 °C, 37 °C and 56 °C) [97]. A negative correlation was reported between 70-kHz US power intensity and residual activation energy of the micelle destruction, and it was observed that an increase in temperature increased the rate of micelle destruction (a function accurately represented using the

Arrhenius equation) and decreased the rate of micelle reassembly. The ANN model developed by Husseini et al. [91] also predicted that Dox release is not dependent on temperature, suggesting that the major mechanism of release is not mainly due to the thermal effects of US. The same group [96] further studied the effect of temperature on Dox release and re-encapsulation from stabilized (NanoDeliv™) and unstabilized P105 micelles. Temperature did not have any effect on Dox release and re-encapsulation time constants for the unstabilized micelles. For the same temperature, the observed release was higher for the unstabilized micelles than for the NanoDeliv™, emphasizing the importance of the IPN in preserving the integrity of the micellar structure subjected to an external stimulus. On the contrary, no significant differences could be observed for the re-encapsulation rate constants of stabilized and unstabilized micelles.

The concentration of Pluronic® also influences the drug release from these polymeric micelles. The first evidence was published by Husseini et al. [85], who observed that the drug release was higher for lower concentrations of Pluronic® P105, possibly due to the higher local drug concentration in the hydrophobic core of the micelles, when the number of micelles was low. This study also provided evidence that the release was lower when the drug was deeply inserted into the micelle core. The ANN model developed by Husseini et al. [91] of the steady-state acoustic release of Dox from P105 micelles further indicated that higher release was obtained at lower copolymer concentrations.

The previously described studies used non-targeted Pluronic® P105 micelles, but targeted ones have also been studied. The first system combining polymeric micelles, targeting, and triggered release using US was described by Husseini and coworkers [59]. The polymeric micelles were synthesized with a folate moiety, and the release of encapsulated Dox was studied using 70-kHz US as a trigger. It was observed that Dox was released above a power density threshold of 0.55 W/cm^2, which again suggested the critical role of cavitation in the process. Above this threshold, the amount of drug release increased with increasing power densities but reached a maximum of 14 % release at 5.4 W/cm^2. A subsequent study by the same group [98] compared the kinetics of Dox release from folated and non-folated micelles exposed to 70-kHz US at different power densities. The results showed a higher percentage of release from folated micelles. Additionally, a mathematical model with a zero-order release and first-order re-encapsulation rate was used to fit the data and the existence of a power density threshold emphasized the importance of inertial cavitation for the drug release.

Although Pluronic® P105 has been the most researched type of polymeric micelles in acoustically-triggered drug delivery, several different formulations have been studied, including different types of Pluronic® and mixed micelle formulations. Ugarenko et al. [99], for example, synthesized DSPE-PEG$_{2000}$ (1,2-diasteroyl-*sn*-glycero-3-phosphoethanolamine-*N*-[amino(polyethylene glycol)-2000])-Pluronic® mixed micelles and studied the release of Dox and formaldehyde-releasing prodrugs, triggered by 20-kHz US at 100 W/cm^2. Upon micelle formation, it was observed that 60 % of Dox was encapsulated but no formaldehyde-releasing products. However, these were administered separately to

the Dox-loaded micelles. Upon exposure to US, 7–10 % of Dox was released from the micelles. This system was considered promising in cancer treatment, since it can potentially form cytotoxic DNA adducts in cancer cells.

Zhang and coworkers [100] designed and synthesized micelles of the block copolymer poly(lactic acid)-*b*-poly(ethylene) glycol (PLA-*b*-PEG), encapsulated Nile Red, and studied the release triggered by HIFU. They suggested an irreversible mechanism elicited by transient cavitation. The same group synthesized micelles of poly(ethylene oxide) and poly(2-tetrahydropyranyl methacrylate) (PEO-*b*-PTHPMA) [101] and also studied the effect of HIFU in this formulation. The observed disruption was due to the US-induced hydrolysis of 2-tetrahydropyranyl groups at room temperature.

In Vitro Cellular Studies

This section describes the main in vitro studies performed on polymeric micelles and US as a DDS. The uptake of Dox and other fluorescence molecules by cancer cells in vitro can be monitored by direct or indirect methods [8, 9, 37, 43, 102–104]. The direct methods measure the fluorescence of the cells by flow cytometry and/or fluorescence microscopy and also allow the study of the intracellular distribution of the drug. Indirect methods measure the depletion of the drug from the medium by using a spectrofluorometer.

In vitro cell studies provided evidence that US induces cavitation-related processes which mediate a synergistic effect between US exposure, pharmacological activity of the encapsulated drug, and polymeric micelles. The exposure to US releases the drug encapsulated in the nanocarriers and simultaneously enhances the intracellular uptake of micellar-encapsulated drugs, but different studies suggested different mechanisms of uptake, either the endocytosis of the carrier or the sonoporation of the cell membrane.

The first in vitro cellular study was performed by Munshi et al. [105] using Pluronic® P105-encapsulating Dox and 80-kHz US to study delivery of the agent to HL-60 human leukemia cells. The synergistic effect between US and encapsulated Dox was observed since the Dox IC_{50} was lowered from 2.35 to 0.19 mg/ml. Another study, using the same cell line and 70-kHz US [106] also showed a synergism between the Dox, polymeric micelles, and US. In the absence of US, the encapsulation protected the cells from the bioeffects of Dox, while the application of US triggered the drug release and/or uptake by the cells, causing DNA damage, as determined by the comet assay. Similar assays performed with NanoDeliv™ stabilized micelles [107] showed that these were able to protect cells from much higher Dox concentrations when compared to unstabilized micelles. Exposure to 70-kHz US led to a synergistic effect, similar to that observed on the previous study [106].

Several other in vitro studies on the drug release from Pluronic® micelles and cellular uptake induced by US were performed by the Pitt and Rapoport groups, using either LFUS or HFUS [82, 102–104]. Several US parameters were investigated, such as the power density, pulsed *vs.* CW US, insonation duration, and interpulse intervals. Marin et al. [102] studied the mechanism of US-induced drug

delivery to HL-60 cells in vitro. Using 20-kHz LFUS and Dox encapsulated in Pluronic® P105 micelles, they observed an increase in cellular drug uptake. They suggested that LFUS caused acoustic cavitation that induced both drug release from Pluronic® micelles and enhanced uptake of the micellar-encapsulated drugs. Additionally, the authors observed that, when using US, the same level of drug uptake could be attained when having a much lower extracellular concentration of drug.

The same group studied the effect of using CW or pulsed 20-kHz US on Dox uptake by the same cell line [103]. Drug uptake was observed in both cases, and the authors further studied the effect of the duration of the pulse (*on* period) and interpulse (*off* period) intervals. Dox uptake increased with increasing pulse duration from 0.1 to 2 s using the same total insonation time, and no significant effect of the interpulse interval could be observed, suggesting that the cells are very effective in competing with the drug re-encapsulation in micelles. The authors suggested two independents mechanisms that seem to control the acoustic-controlled drug uptake by the cells: (i) US-induced Dox release from micelles, with the consequent increase of the free drug in the medium; (ii) US-caused perturbation of the cell membrane with the consequent increase of the intracellular uptake of the micellar formulation.

In a study using different cell lines [104], the same group compared the drug release and cellular uptake when the cells were exposed to LFUS (20–100 kHz) or HFUS (1 MHz). They observed that the onset of acoustic cavitation at higher frequencies required much higher power densities than at low frequencies.

Rapoport and coworkers [84] studied the effect of copolymer concentration on the uptake of fluorescently labeled Pluronic® P105 micelles by ovarian carcinoma cell lines (A2780 drug sensitive and A2780/ADR MDR). Their data supported the internalization of drugs via fluid-phase endocytosis, followed by a nuclear accumulation enhanced by the use of the polymeric micelles and further increased by the application of 20-kHz US. The data also showed that the membranes of the endosomes and lysosomes of A2780/ADR MDR cells were more susceptible to the action of polymeric surfactants than those of drug-sensitive A2780 cells.

Pitt and coworkers [106–108] studied the differences between exposing HL-60 cells to free Dox, Dox encapsulated in Pluronic® P105, and Dox encapsulated in NanoDeliv™, with and without US. It was observed that, in the absence of US, cells exposed to free Dox were killed faster than those exposed to encapsulated Dox [106]. When exposed to 70- kHz US, however, the scenario was opposite: cells exposed to the encapsulated drug were killed at a faster rate than those exposed to the free drug. Hence, in the absence of US, the micelles protect the cells from the effects of the drug, and when US is used, the released Dox kills cells faster than the free drug. These studies also used the comet assay to monitor DNA damage caused by the treatment [106, 108]. They documented the correlation between cell death and DNA damage, thus indicating that apoptosis was the main mechanism of cell death caused by these insonation levels, not necrosis which irreversibly damages the cell membrane.

Howard and coworkers [109] used a different polymeric formulation – micelles of methyl-capped poly(ethylene oxide)-*co*-poly-(L-lactide) encapsulating the

anticancer drug paclitaxel – and also demonstrated the synergy between this system and US (1 MHz, power density 1.7 W/cm^2) used on a drug-resistant breast cancer cell line (MCF7/ADmt). In the absence of US, the micelles protected the cells from the toxic effects of the drug, but, upon exposure to the ultrasonic field, there was a dramatic increase in the accumulation of the micellar formulation inside the cells.

Similarly, Ugarenko et al. [99] demonstrated the previously described synergism, using Pluronic® P105 micelles stabilized with disteroyl-phosphoethanolamine-PEG200, encapsulating Dox, and 20-kHz US. They used this system in MDA-MB-231 breast cancer cells in vitro, and showed that, in the absence of US, the micellar system protected the cells from Dox, while upon application of US, 10 % of the drug was released and the cellular uptake was significantly increased. However, when US was applied for more than 5 s, the cells died, which emphasizes the importance of a careful control of all US parameters, when doing drug delivery research.

The groups of Pitt and Rapoport carried several studies [82–84] that demonstrated the uptake of micelles into cells, thus dismissing the proposed mechanism that US triggers the drug delivery from micelles outside the cells, followed by diffusion (see section "Mechanisms of US-Induced Micellar Drug Release and Cellular Uptake"). They designed Dox-encapsulating Pluronic® P105 micelles with the end hydroxyl groups labeled with a fluorescent probe possessing a different fluorescence than that of Dox. Studies of confocal microscopy and flow cytometry showed that, upon insonation, the labeled P105 micelles entered HL-60 cells and were distributed between the membrane, the cytosol, and other vesicles.

The same group further investigated whether the mechanism of cellular drug uptake triggered by US involved endocytosis/pinocytosis [82, 83]. A preliminary study [83], performed in the absence of US, used fluorescently labeled Pluronic® P105, and concluded that the aggregation state of the copolymer influenced the uptake by HL-60 cells, with unimers entering the cell by diffusion, while uptake of micelles occurred via fluid-phase endocytosis. A subsequent study [82] used Pluronic® P105 micelles labeled with a pH-sensitive fluorescent probe, which has higher fluorescence in acidic conditions, i.e., endosomes. Flow cytometry studies showed that, upon insonation with 70-kHz US, there was an increase in the fluorescent inside HL-60 and HeLa cells but no increase was observed inside endosomes and lysosomes. The researchers suggested that sonoporation was the main mechanism of US-enhanced drug uptake.

Sonoporation has been supported by several other studies, including the ones by Tachibana et al. [110–114], which provided direct evidence of this mechanism by using, for example, scanning electron microscopy. One of their early studies [111] used merocyanine 540 as a tracer and exposed HL-60 cells to 255-kHz US for 30 s. Results obtained by scanning electron microscopy showed the formation of pores in the cell membrane, which resulted in cell death. Another study [112], using the same cell line and the cytotoxic drug cytosine arabinoside, showed increased cell death upon exposure to 48-kHz US. Scanning electron microscopy showed some disruption of the cell membranes as well as a decreased number of microvilli, and it was hypothesized that this increased drug uptake. Saito and coworkers [115]

showed that sonoporation was implicated in the injury of corneal endothelium cells by US. They observed that some cells died due to necrosis, while others survived and recovered, with the membranes recovering integrity several minutes after the exposure. The experiments of Prentice et al. [116] also supported the sonoporation mechanism. They exposed MCF-7 breast cancer cells to high power densities of 1-MHz US and used atomic force microscopy to observe holes in the cell membranes. Stringham and coworkers [117] used a rat colon cancer cell line (DHD/K12 TRb) and the model drug calcein to unravel the relationship between cavitation and sonoporation. The cells were exposed to 476-kHz US at different power densities, and it was observed that, in these conditions, calcein entered and accumulated intracellularly, unlike in the absence of US. To test the hypothesis that inertial cavitation was directly related to the drug uptake, further experiments were performed at a pressure of 3 atm. At this higher pressure, it was observed that the accumulation of calcein inside the cells decreased. Since cavitation decreases as pressure increases at a constant US power density [118], these results proved the direct relation hypothesized by the authors. A similar result was obtained when using 1-MHz HFUS in an in vitro study with bovine endothelial cells [119]. Studies by Schlicher et al. [120], using flow cytometry coupled to electron and fluorescence microscopy, concluded similarly: the accumulation of calcein in prostate cancer cells was caused by the reversible increase in membrane permeability induced by acoustic cavitation caused by 24-kHz US. A paper by Zhou et al. [121] went further and reported the size of the pores produced in *Xenopus laevis* oocytes exposed to 1.075-MHz US.

Several studies, however, supported the endocytosis hypothesis of cellular drug uptake enhanced by US. Muniruzzaman et al. [83] investigated the effect of the copolymer aggregation state – micelles or unimers of Pluronic® P105 – on the intracellular uptake by HL-60 cells, in the absence of US. Their results suggested that below the CMC, the unimers enter the cell via simple diffusion, while micelles enter via fluid-phase endocytosis. A later study by the same group [84] used 20-kHz US and reported that sonication enhanced the rate of endocytosis of micelles by several types of human cell lines. In the same study, the intracellular distribution of Dox was studied by confocal microscopy, and its accumulation was observed in the nucleus. Sheikov et al. [122] provided evidence that US-enhanced pinocytosis in the endothelial cells that line brain arterioles and capillaries. The enhancement of endocytosis by US was also reported in human fibroblasts with no detectable cellular membrane injury [123].

As mentioned before, the mechanism of drug uptake is still being researched. A study by Meijering et al. [124], published in 2009, suggested that both mechanisms, endocytosis and sonoporation, contribute for drug cellular uptake induced by US. They studied microbubble-targeted delivery of therapeutic compounds to primary endothelial cells, using pulsed 1-MHz US, observing that both endocytosis and transient pore formation were involved in drug uptake, and that the contribution of endocytosis was dependent on the molecular size of the molecules to be delivered. Additionally, it has been suggested that different cells may respond differently to US and that maybe a general mechanism cannot be derived [5]. In

any case, the in vitro cellular studies provided evidence of the synergism between chemotherapy and US exposure, with US both enhancing the release of the drugs from the micelles and the uptake of the drug by the cells by creating transient pores in the cell membrane and/or increasing endocytosis.

In Vivo Research Using Animal Models

Several in vivo studies have been conducted since 2002 in order to test controlled delivery systems composed of polymeric micelles sequestering anticancer drugs and triggered using US in either rat or mouse models. It should be noted that, even in the absence of micellar systems, there is a decrease in tumor growth upon exposure to free drug and US, which confirms the synergistic effect between the pharmacological activity of the chemotherapeutic drug and US [37].

The first in vivo studies were performed by Nelson and coworkers [125, 126], who treated a group of 42 BDIX rats injected with a DHD/K12/TRb colorectal tumor cell line in both of their hind legs, with different concentrations of free Dox or Dox encapsulated in stabilized NanoDeliv™ micelles. The tumor in one leg was sonicated using 20- or 70-kHz US at different power intensities, duty cycles, and US application regimens (once or twice a week), while the other leg was left without sonication. An observable reduction of the tumor size was reported when the combined system was applied (micellar-encapsulated Dox and US), compared to the noninsonated, micellar-loaded Dox formulation and the free drug control. According to the authors, this could be due to the increased drug uptake by cancer cells when sonicated, or that the US assists the extravasation of the drug-loaded carriers into the tumor tissues.

Another in vivo experiment conducted by the same group [46] used immune-compromised athymic *nu/nu* mice model bearing ovarian carcinoma tumors and studied the effect of Pluronic® P105 and 1-MHz HFUS. The mice were treated with either micellar-encapsulated Dox or free Dox, and one group was insonated, while the control group was not exposed to US. It was observed that the intracellular encapsulated drug uptake by tumor cells was higher than the uptake by other sites or organs. The uptake by tumors was even more enhanced when localized sonication was applied, which resulted in an increase in mice survival rates when compared to noninsonated mice treated with a similar concentration of micellar Dox. More importantly, Dox did not accumulate in the heart, an organ which is severely affected by the cytotoxicity of this drug [127]. The advantage of using HFUS is due to the fact that it can be more precisely focused then LFUS and causes less sonolysis [85, 104].

Fluorouracil (5-FU) encapsulated in stabilized P105 micelles in conjunction with 20-kHz US was tested as a DDS in a BALB/c nude mice model inoculated with the WiDr human colon cancer cell line [128]. The group treated with US showed a significant reduction in tumor volumes, when compared to noninsonated groups, emphasizing the synergy resulting from the use of the combined delivery system, which became more evident for lower 5-FU concentrations.

Howard and coworkers [109] performed in vitro cellular studies using methyl-capped poly(ethylene oxide)-*co*-poly-(l-lactide)-tocopherol micelles encapsulating Paclitaxel further tested this formulation in vivo, in conjunction with 1-MHz

US. The results showed that this DDS was effective in the complete tumor regression in *nu/nu* mice inoculated with an MCF-7/ADM drug-resistant breast cancer cell line.

Gao and coworkers [129] studied the effect of 1- and 3-MHz US on the biodistribution of fluorescently labeled unstabilized and PEG-diacylphospholipid-stabilized Pluronic® P105 micelles in ovarian cancer-bearing *nu/nu* mice. The results showed that US enhanced the accumulation of the micelles in the tumors and that the degree of targeting depended on the local tumor sonication. A later study by the same group [130] used Dox encapsulated in Pluronic® P105 and mixed Pluronic® P105, PEG2000-diacylphospholipid and PEG-*co*-poly(beta-benzyl-L-aspartate) (PEG-*b*-PBLA) to treat the same mice cancer model and observed that 30 s of 1-MHz US increased the intracellular Dox uptake by eightfold. In a later study [131], *nu/nu* mice implanted with breast (MDA-MB-231) or ovarian cancer (A2780) cells were treated with Dox encapsulated in micelles of copolymers PEG-*b*-poly(L-lactide) (PEG-PLLA) or PEG-*b*-poly(caprolactone) (PEG-PCL) and loaded with perfluoropentane (PFC_5) nanoemulsions. The delivery system accumulated selectively in the tumor sites due to the EPR effect. This was followed by either 1- or 3- MHz US applied locally in order to release and increase the intracellular uptake of the encapsulated drug. The researchers suggested that this selective release of drug in tumor sites occurred mainly due to the collapse of the highly echogenic microbubbles developing from the nanodroplets that grew in size as a result sonication.

A group of researchers from Brigham Young University [132–134] conducted several in vivo experiments using BDIX rats bearing bilateral leg DHD/K12/TRb colorectal epithelial tumors. For their studies, they used US at 20- and 476-kHz at different pulse intensities as a trigger to release Dox from NanoDeliv™ micelles. The aims of the research were: (i) to study the pharmacokinetics of the drug, (ii) to quantitatively analyze the temporal Dox concentration profiles in cancerous and healthy rat tissues, and (iii) to study the effect of using different US frequencies (at the same MIs and temporal average intensities) on the development of cancer cells and drug delivery. Results showed that an initial, although not significant, accumulation of the drug in the blood-perfused organs, such as the liver and heart, took place. However, this accumulation decreased with time, when the drug started to preferentially accumulate in tumor tissues, with faster clearance rates from the healthy tissues achieved in the insonated groups when compared to the noninsonated groups. Consequently, this caused the tumors in the groups exposed to 20- and 476-kHz US to grow significantly slower than in the controls [134]. At 476-kHz, however, even if there was a tumor regression in treated groups, the differences in Dox concentration in cancerous cells were not significantly different between both groups, 6 h after the injection of the micellar system [132]. This result supported the main role of cell membrane permeabilization as the mechanism of drug uptake by cells, since it could not be explained by simple Dox release [132, 134, 135]. Additionally, these results were not obtained when the animals were exposed to US alone or to empty drug carriers, emphasizing the synergism between all these factors, just like in in vitro cellular studies.

A mouse model of breast cancer (spontaneous breast adenocarcinoma xenografted in female BALB/c mice) was used to study the dual application of 28-kHz and 3-MHz US when using a stabilized Pluronic® P105 micellar Dox system [136]. Dox was administered either free or encapsulated in the micelles, and some mice were exposed to US while a control group only received Dox in free form. As reported by the previous groups, it was observed that the US and polymeric micelle system were significantly more effective in facilitating drug accumulation in tumor cells when compared to either the free Dox or micellar noninsonated formulations. On the contrary, the concentration of Dox in non-tumor tissues was lower when micellar drug was used, compared to free drug. According to the authors, this was due to the role that US plays in cavitation and sonoporation.

Another set of experiments were conducted using docetaxel (DTX)-loaded P105/F127 mixed micelles in the treatment of male Sprague-Dawley rats and BALB/c nude mice models bearing Taxol-resistant human lung adenocarcinoma tumors (A549/Taxol) [137]. No US treatment was used in this work. The results obtained when the hybrid micellar formulation was used were compared to the results obtained from negative controls that were not treated at all and/or controls that received only the poorly soluble DTX and/or its commercially soluble form, Taxotere®. It was observed that the Taxol elimination half-life was extended when the micellar drug system was used. Moreover, the sizes of tumors injected with the DTX-hybrid micelles were significantly smaller than the sizes of the negative controls and the groups treated with Taxotere®. These promising results were probably due to the enhanced drug uptake by the tumor caused by the EPR effect, which indicates that such a system may be used in future clinical trials to overcome MDR in lung cancer.

Recently, the same group of researchers [138] developed a novel DDS composed of mixed micelles of folic acid-conjugated carboxymethyl lauryl chitosan (FA-CLC) and superparamagnetic iron oxide (SPIO) (FA-CLC/SPIO), sequestering camptothecin, and triggered using both magnetic and ultrasonic (1 MHz) fields. The system was tested against MDA-MB-231 (FA-positive) breast cancer cells implanted in 6−8-week-old female nude mice, and fluorescence and magnetic resonance imaging were used to confirm the active drug targeting of the system in vivo. It was observed that the therapeutic efficacy of this system was considerably enhanced when compared to other systems that used either the free drug or camptothecin-loaded FA-CLC/SPIO micelles triggered passively or actively (whether by US alone or the magnetic field alone). Nevertheless, it was recommended that extra caution should be taken in future experiments in order to prevent any possible unwanted accumulation of iron-containing vehicles in the liver when the cancer is located near this organ.

Clinical Trials and Uses

From the previous sections, it is clear that several micellar formulations have been and are being studied as possible chemotherapies, with or without the concomitant

use of US. However, so far, there are no FDA-approved micellar systems for the treatment of cancer [5, 139]. Some micellar formulations have been approved for use in other countries and several others are undergoing clinical trials around the world, as recently reviewed by Wicki et al. [17].

Genexol-PM$^®$ is a polymeric micelle composed of methoxy-PEG-poly(D,L-lactide) and encapsulating the chemotherapeutic drug Paclitaxel, which has been approved for the therapy of breast cancer in Europe and South Korea, and is undergoing clinical trials in the USA for the treatment of breast, small-cell lung, and pancreatic cancers [15, 16, 140]. This formulation is a regular micelle encapsulating the drug in its hydrophobic core, stabilized and soluble in water due to the PEG hydrophilic corona [15]. Paclital and NK105 are other Paclitaxel micellar formulations that are undergoing clinical trials for the treatment of ovarian and metastatic or recurrent breast cancer, respectively [16, 141]. Nanoxel, a micellar formulation of Paclitaxel, has also been approved for the treatment of breast cancer in India [17].

The combination of micelle-encapsulated drugs and US did not reach the clinical trial stage yet.

Conclusion and Future Directions

The high toxicity of potent chemotherapeutic drugs limits the therapeutic window in which they can be applied. This window can be expanded by controlling the drug delivery in both space and time such that non-targeted tissues are not adversely affected. This review chapter focuses on using US to control the release of antineoplastic agents from nanocarriers spacially and temporally. These nanovehicles include polymeric micelles and liposomes. The potential benefits of such controlled chemotherapy compels a thorough investigation of the role of US and the mechanisms by which US accomplishes drug release and/or enhances drug potency which is the focus of our drug delivery group.

As is widely known, the current practice in chemotherapy requires the use of high dosages of antineoplastic agents to increase its effectiveness on tumors which also results in detrimental side effects on healthy cells. These side effects significantly decrease the quality of life of the patient and result in several life-threatening conditions. Therefore, researchers have directed ample time to improve the practice of chemotherapy in an attempt to increase the effectiveness of the drug, which results in decreasing the need for high doses and in turn decreasing the side effects.

In addition to advancements in cancer drug delivery, other promising areas have evolved including, but not limited to, vaccines and gene delivery. The first area entails the discovery of the virus causing different cancers and vaccinating toddlers against each virus. On the other hand, gene delivery involves transfecting cancer cells with the intention of controlling or eliminating the DNA mutations. Gene delivery is divided into two main areas: viral and non-viral. Viral gene delivery involves the use of a virus to transfect the DNA of diseased cell. Its main drawback

is low specificity since the virus could transfect healthy cells in the process. Non-viral techniques include US, and they suffer from low transfection rates.

This chapter focused on drug delivery in cancer treatment with the utility of US. As mentioned above, this research area involves the sequestration of the drug inside nanocarriers designed to target the tumor cells specifically while sparing the healthy cells. Once at the tumor site, focused waves of US are used on the tumor to break open the carriers, releasing the drug into the cancer cells. The novelty of this line of research is the fact that it is the first combination of the two technologies, (i) nanocarriers or nanocapsules and (ii) US waves, to generate a new drug delivery methodology for cancer treatment.

When deciding on a drug delivery vehicle, several principles are examined to improve their performance including passive, ligand, and triggered targeting. Passive targeting is the main reason behind the success of liposomal Dox-Doxil (which achieved FDA approval in 1996). Passive diffusion takes place because of the leaky defective vasculature of cancerous tissues compared to health tissue. The extent to which passive diffusion improves drug accumulation at the tumor while reducing the systemic concentration is still being researched for a variety of chemotherapeutic agents and with different formulations of liposomes to achieve more efficient cancer treatments. Active targeting (or more correctly, ligand targeting) involves the decoration of targeting moieties unto the surface of drug delivery vehicles in the hope that receptor-mediated endocytosis will improve the antineoplastic accumulation at the tumor site via the key-and-lock mechanism. Naturally, the main obstacle faced by scientists in this area is to insure that the stability, drug efficiency, and other characteristics will not be affected by conjugating these molecules to these nanostructures. Some targeted nanocarriers have shown promising results in vitro, but the same improvement was not observed when tested in vivo. There is no doubt that ligand targeting will continue to be researched heavily to reach the optimal conditions of loading efficiency, moiety surface concentration, type of cancers that can be targeted, etc.

External and internal triggers constitute the third type of drug delivery targeting. External triggers including US, magnetic, electrical fields, and light have been reported widely in cancer treatment literature. Similarly, internal triggers (e.g., temperature variations, pH, and enzymes) have shown promise both in vivo and in vitro. This review has focused on the use of US as a trigger mechanism for several reasons. First, US waves can easily be focused on the tumor noninvasively. Additionally, the physics of US is very well understood and documented. US has also been used to induce hyperthermia (by increasing the temperature of the tissue to above 42 °C) which would be an added advantage to the use of this technique. More importantly, there is a well-documented synergism between the action of chemotherapeutic agents and US, thus rendering acoustic waves more attractive for this area of research.

In conclusion, we reiterate the importance of finding a multimodal drug delivery system that employs all three targeting techniques into one system that can be classified as a "magic bullet" in the fight against one of the most prevalent killers of the twenty-first century.

References

1. Jemal A, Bray F, Center MM, Ferlay J, Ward E, Forman D (2011) CA Cancer J Clin 61:69
2. DeVita VT Jr, Chu E (2008) Cancer Res 68:8643
3. Uchegbu IF, Siew A (2013) J Pharm Sci 102:305
4. Aldrich JE (2007) Crit Care Med 35:S131
5. Ahmed SE, Martins AM, Husseini GA (2015) J Drug Target 23:16
6. Moussa HG, Martins AM, Husseini GA (2015) Curr Cancer Drug Targets 15:282
7. Sutton D, Nasongkla N, Blanco E, Gao J (2007) Pharm Res 24:1029
8. Husseini GA, Pitt WG (2008) J Nanosci Nanotechnol 8:2205
9. Husseini GA, Pitt WG (2008) Adv Drug Deliv Rev 60:1137
10. Paleos CM, Tsiourvas D, Sideratou Z, Tziveleka L-A (2010) Expert Opin Drug Deliv 7:1387
11. Souto EB, Fangueiro J, Müller RH (2013) In: Uchegbu IF, Schätzlein AG, Cheng WP, Lalatsa A (eds) Fundamentals of pharmaceutical nanosciences. Springer, New York
12. Fante C, Greco F (2013) In: Uchegbu IF, Schätzlein AG, Cheng WP, Lalatsa A (eds) Fundamentals of pharmaceutical nanosciences. Springer, New York
13. Uchegbu IF (2013) In: Uchegbu IF, Schätzlein AG, Cheng WP, Lalatsa A (eds) Fundamentals of pharmaceutical nanoscience. Springer, New York, p 9
14. Cho K, Wang X, Nie S, Chen ZG, Shin DM (2008) Clin Cancer Res 14:1310
15. Peplow M (2014) Pharm J 292:467
16. Pillai G (2014) SOJ Pharm Pharm Sci 1:1
17. Wicki A, Witzigmann D, Balasubramanian V, Huwyler J (2015) J Control Release 200:138
18. Matsumura Y, Maeda H (1986) Cancer Res 46:6387
19. Maeda H (2001) Adv Enzyme Regul 41:189
20. Maeda H, Nakamura H, Fang J (2013) Adv Drug Deliv Rev 65:71
21. Maeda H, Wu J, Sawa T, Matsumura Y, Hori K (2000) J Control Release 65:271
22. Nichols JW, Bae YH (2014) J Control Release 190:451
23. Allen TM (2002) Nat Rev Cancer 2:750
24. Torchilin VP (2007) AAPS J 9:E128
25. Byrne JD, Betancourt T, Brannon-Peppas L (2008) Adv Drug Deliv Rev 60:1615
26. Yu B, Tai HC, Xue W, Lee LJ, Lee RJ (2010) Mol Membr Biol 27:286
27. Gu FX, Karnik R, Wang AZ, Alexis F, Levy-Nissenbaum E, Hong S, Langer RS, Farokhzad OC (2007) Nano Today 2:14
28. Torchilin VP, Lukyanov AN, Gao Z, Papahadjopoulos-Sternberg B (2003) Proc Natl Acad Sci U S A 100:6039
29. Oerlemans C, Bult W, Bos M, Storm G, Nijsen JF, Hennink WE (2010) Pharm Res 27:2569
30. Torchilin VP (2009) Eur J Pharm Biopharm 71:431
31. Torchilin VP (2007) Pharm Res 24:1
32. Yu MK, Park J, Jon S (2012) Theranostics 2:3
33. Zhao X, Li H, Lee RJ (2008) Expert Opin Drug Deliv 5:309
34. Shen Z, Li Y, Kohama K, Oneill B, Bi J (2011) Pharmacol Res 63:51
35. Ai J, Xu Y, Li D, Liu Z, Wang E (2012) Talanta 101:32
36. Shigdar S, Qiao L, Zhou SF, Xiang D, Wang T, Li Y, Lim LY, Kong L, Li L, Duan W (2013) Cancer Lett 330:84
37. Husseini GA, Pitt WG, Martins AM (2014) Colloids Surf B 123C:364
38. Mura S, Nicolas J, Couvreur P (2013) Nat Mater 12:991
39. Pitt WG, Husseini GA, Kherbeck LN (2013) In: Alvarez-Lorenzo C, Concheiro A (eds) Smart materials for drug delivery, vol 1. RSC Publishing, Cambridge, UK, p 148
40. Lee ES, Gao Z, Bae YH (2008) J Control Release 132:164
41. Huang W, Shi C, Shao Y, Lam KS, Luo J (2013) Chem Commun (Camb) 49:6674
42. Siepmann J, Siegel R (2012) Fundamentals and applications of controlled release drug delivery. Springer, New York
43. Husseini GA, Pitt WG (2009) J Pharm Sci 98:795

44. Batrakova EV, Kabanov AV (2008) J Control Release 130:98
45. Batrakova E, Li S, Li S, Venne A, Alakhov V, Kabanov A (1999) Pharm Res 16:1373
46. Rapoport NY, Christensen DA, Fain HD, Barrows L, Gao Z (2004) Ultrasonics 42:943
47. Rapoport N, Caldwell K (1994) Colloids Surf B 3:217
48. Kabanov AV, Batrakova EV, Melik-Nubarov NS, Fedoseev NA, Dorodnich TY, Alakhov VY, Nazarova IR, Kabanov VA (1992) J Control Release 22:141
49. Romberg B, Hennink WE, Storm G (2008) Pharm Res 25:55
50. Pitt WG, Husseini GA, Staples BJ (2004) Expert Opin Drug Deliv 1:37
51. Pruitt JD, Husseini G, Rapoport N, Pitt WG (2000) Macromolecules 33:9306
52. Sun Q, Radosz M, Shen Y (2012) J Control Release 164:156
53. Yang TF, Chen CN, Chen MC, Lai CH, Liang HF, Sung HW (2007) Biomaterials 28:725
54. Zeng Y, Pitt WG (2005) J Biomat Sci Polym 16:371
55. Zeng Y, Pitt WG (2006) J Biomater Sci Polym 17:591
56. Husseini GA, Christensen DA, Rapoport NY, Pitt WG (2002) J Control Release 83:303
57. Basile L, Pignatello R, Passirani C (2012) Curr Drug Deliv 9:255
58. Kabanov AV, Chekhonin VP, Alakhov V, Batrakova EV, Lebedev AS, Melik-Nubarov NS, Arzhakov SA, Levashov AV, Morozov GV, Severin ES et al (1989) FEBS Lett 258:343
59. Husseini GA, Velluto D, Kherbeck L, Pitt WG, Hubbell JA, Christensen DA (2013) Colloids Surf B 101:153
60. Rapoport N (2007) Prog Polym Sci 32:962
61. Hendee WR, Ritenour ER (2003) Medical imaging physics, 4th edn. Wiley, New York
62. Shriki J (2014) Crit Care Clin 30:1
63. Coltrera MD (2010) Otolaryngol Clin North Am 43:1149
64. Edwards H (2010) Ultrasound 18:100
65. Nyborg WL (2001) Ultrasound Med Biol 27:301
66. Rooney JA (1988) Ultrasound: its chemical, physical, and biological effects. VCH Publishers, New York, p 65
67. Hall DO, Selfridge AR (1995) US Patent 5,460,595A
68. Buldakov MA, Hassan MA, Zhao QL, Feril LB Jr, Kudo N, Kondo T, Litvyakov NV, Bolshakov MA, Rostov VV, Cherdyntseva NV, Riesz P (2009) Ultrason Sonochem 16:392
69. Rapoport N (2012) Int J Hyperthermia 28:374
70. Goss SA, Johnston RL, Dunn F (1978) J Acoust Soc Am 64:423
71. Wu J, Nyborg WL (2008) Adv Drug Deliv Rev 60:1103
72. Marmottant P, Hilgenfeldt S (2003) Nature 423:153
73. Nyborg WL (1982) Br J Cancer Suppl 5:156
74. Azagury A, Khoury L, Enden G, Kost J (2014) Adv Drug Deliv Rev 72:127
75. Rooney JA (1970) Science 169:869
76. Brennen CE (1995) Cavitation and bubble dynamics. Oxford University Press, New York, p 282
77. Ferrara KW (2008) Adv Drug Deliv Rev 60:1097
78. Church CC, Yang X (2005) J Acoust Soc Am 117:2530
79. Nomikou N, McHale AP (2010) Cancer Lett 296:133
80. Diaz de la Rosa MA, Husseini GA, Pitt WG (2013) Ultrasonics 53:377
81. Kaviany M (1986) Int J Heat Mass Transfer 29:2002
82. Husseini GA, Runyan CM, Pitt WG (2002) BMC Cancer 2:20
83. Muniruzzaman MD, Marin A, Luo Y, Prestwich GD, Pitt WG, Husseini GA, Rapoport N (2002) Colloids Surf B 25:233
84. Rapoport N, Marin A, Luo Y, Prestwich GD, Muniruzzaman MD (2002) J Pharm Sci 91:157
85. Husseini GA, Myrup GD, Pitt WG, Christensen DA, Rapoport NY (2000) J Control Release 69:43
86. Husseini GA, Diaz de la Rosa MA, Richardson ES, Christensen DA, Pitt WG (2005) J Control Release 107:253
87. Diaz de la Rosa MA (2007) High-frequency ultrasound drug delivery and cavitation, M.Sc. Thesis. Brigham Young University, Provo, UT

88. Diaz de la Rosa MA, Husseini GA, Pitt WG (2013) Ultrasonics 53:97
89. Parlitz U, Englisch V, Scheffczyk C, Lauterborn W (1990) J Acoust Soc Am 88:1061
90. Husseini GA, Rapoport NY, Christensen DA, Pruitt JD, Pitt WG (2002) Colloids Surf B 24:253
91. Husseini GA, Abdel-Jabbar NM, Mjalli FS, Pitt WG (2007) Technol Cancer Res Treat 6:49
92. Stevenson-Abouelnasr D, Husseini GA, Pitt WG (2007) Colloids Surf B 55:59
93. Husseini GA, Abdel-Jabbar NM, Mjalli FS, Pitt WG, Al-Mousa A (2011) J Franklin Inst 348:1276
94. Husseini GA, Mjalli FS, Pitt WG, Abdel-Jabbar N (2009) Technol Cancer Res Treat 8:479
95. Husseini GA, Diaz de la Rosa MA, Gabuji T, Zeng Y, Christensen DA, Pitt WG (2007) J Nanosci Nanotechnol 7:1028
96. Husseini GA, Diaz de la Rosa MA, AlAqqad EO, Al Mamary S, Kadimati Y, Al Baik A, Pitt WG (2011) J Franklin Inst 348:125
97. Husseini GA, Stevenson-Abouelnasr D, Pitt WG, Assaleh KT, Farahat LO, Fahadi J (2010) Colloids Surf A 359:18
98. Husseini GA, Kherbeck L, Pitt WG, Hubbell JA, Christensen DA, Velluto D (2015) J Nanosci Nanotechnol 15:2099
99. Ugarenko M, Chan CK, Nudelman A, Rephaeli A, Cutts SM, Phillips DR (2009) Oncol Res 17:283
100. Zhang H, Xia H, Wang J, Li Y (2009) J Control Release 139:31
101. Wang J, Pelletier M, Zhang H, Xia H, Zhao Y (2009) Langmuir 25:13201
102. Marin A, Muniruzzaman M, Rapoport N (2001) J Control Release 75:69
103. Marin A, Muniruzzaman M, Rapoport N (2001) J Control Release 71:239
104. Marin A, Sun H, Husseini GA, Pitt WG, Christensen DA, Rapoport NY (2002) J Control Release 84:39
105. Munshi N, Rapoport N, Pitt WG (1997) Cancer Lett 118:13
106. Husseini GA, El-Fayoumi RI, O'Neill KL, Rapoport NY, Pitt WG (2000) Cancer Lett 154:211
107. Pruitt JD, Pitt WG (2002) Drug Deliv 9:253
108. Husseini GA, O'Neill KL, Pitt WG (2005) Technol Cancer Res Treat 4:707
109. Howard B, Gao A, Lee S-W, Seo M-H, Rapoport N (2006) Am J Drug Deliv 4:97
110. Sivakumar M, Tachibana K, Pandit AB, Yasui K, Tuziuti T, Towata A, Iida Y (2005) Cell Mol Biol 51(Suppl):OL767
111. Tachibana K, Uchida T, Ogawa K, Yamashita N, Tamura K (1999) Lancet 353:1409
112. Tachibana K, Uchida T, Tamura K, Eguchi H, Yamashita N, Ogawa K (2000) Cancer Lett 149:189
113. Taniyama Y, Tachibana K, Hiraoka K, Aoki M, Yamamoto S, Matsumoto K, Nakamura T, Ogihara T, Kaneda Y, Morishita R (2002) Gene Ther 9:372
114. Taniyama Y, Tachibana K, Hiraoka K, Namba T, Yamasaki K, Hashiya N, Aoki M, Ogihara T, Yasufumi K, Morishita R (2002) Circulation 105:1233
115. Saito K, Miyake K, McNeil PL, Kato K, Yago K, Sugai N (1999) Exp Eye Res 68:431
116. Prentice P, Cuschierp A, Dholakia K, Prausnitz M, Campbell P (2005) Nat Phys 1:107
117. Stringham SB, Viskovska MA, Richardson ES, Ohmine S, Husseini GA, Murray BK, Pitt WG (2009) Ultrasound Med Biol 35:409
118. Bailey MR, Couret LN, Sapozhnikov OA, Khokhlova VA, ter Haar G, Vaezy S, Shi X, Martin R, Crum LA (2001) Ultrasound Med Biol 27:695
119. van Wamel A, Kooiman K, Harteveld M, Emmer M, ten Cate FJ, Versluis M, de Jong N (2006) J Control Release 112:149
120. Schlicher RK, Hutcheson JD, Radhakrishna H, Apkarian RP, Prausnitz MR (2010) Ultrasound Med Biol 36:677
121. Zhou Y, Kumon RE, Cui J, Deng CX (2009) Ultrasound Med Biol 35:1756
122. Sheikov N, McDannold N, Jolesz F, Zhang YZ, Tam K, Hynynen K (2006) Ultrasound Med Biol 32:1399

123. Hauser J, Ellisman M, Steinau HU, Stefan E, Dudda M, Hauser M (2009) Ultrasound Med Biol 35:2084
124. Meijering BD, Juffermans LJ, van Wamel A, Henning RH, Zuhorn IS, Emmer M, Versteilen AM, Paulus WJ, van Gilst WH, Kooiman K, de Jong N, Musters RJ, Deelman LE, Kamp O (2009) Circ Res 104:679
125. Nelson JL, Roeder BL, Carmen JC, Roloff F, Pitt WG (2002) Cancer Res 62:7280
126. Rapoport N, Pitt WG, Sun H, Nelson JL (2003) J Control Release 91:85
127. Chlebowski RT (1979) West J Med 131:364
128. Myhr G, Moan J (2006) Cancer Lett 232:206
129. Gao Z, Fain HD, Rapoport N (2004) Mol Pharm 1:317
130. Gao ZG, Fain HD, Rapoport N (2005) J Control Release 102:203
131. Gao Z, Kennedy AM, Christensen DA, Rapoport NY (2008) Ultrasonics 48:260
132. Staples BJ (2007) MSc Thesis, Brigham Young University, Provo, Utah, USA
133. Staples BJ, Pitt WG, Roeder BL, Husseini GA, Rajeev D, Schaalje GB (2010) J Pharm Sci 99:3122
134. Staples BJ, Roeder BL, Husseini GA, Badamjav O, Schaalje GB, Pitt WG (2009) Cancer Chemother Pharmacol 64:593
135. Staples BJ, Roeder BL, Pitt WG (2006) In: Annual meeting of the society for biomaterials. Pittsburgh
136. Hasanzadeh H, Mokhtari-Dizaji M, Bathaie SZ, Hassan ZM (2011) Ultrason Sonochem 18:1165
137. Chen L, Sha X, Jiang X, Chen Y, Ren Q, Fang X (2013) Int J Nanomedicine 8:73
138. Chen H, Chen M, Tung F, Liu T (2015) J Med Chem 58:3704
139. Elkhodiry MA, Momah CC, Suwaidi SR, Gadalla D, Martins AM, Vitor RF, Husseini GA (2015) J Nanosci Nanotechnol 15:1–19
140. Ledet G, Mandal T (2012) US Pharm 37:7
141. Hamaguchi T, Matsumura Y, Suzuki M, Shimizu K, Goda R, Nakamura I, Nakatomi I, Yokoyama M, Kataoka K, Kakizoe T (2005) Br J Cancer 92:1240

Near-Infrared Absorbing Nonmetallic Nanomaterials as Photoacoustic Contrast Agents for Biomedical Imaging

Lei Wang and Hao Wang

Contents

Abstract

Photoacoustic imaging (PIA) is an emerging whole-body imaging modality offering high spatial resolution, deep penetration, and high contrast in vivo. The photoacoustic (PA) signals are generated under the laser irradiation, where the optical energy is transferred to acoustic emissions and detected by an ultrasound transducer. A large amount of research in the last decade showed that near-infrared (NIR) absorbing nonmetallic nanomaterials such as organic dye-based nanoparticles, polymer-based nanoparticles, and carbon-based nanomaterials are promising PA contrast agents, which can increase the PAI performance, including

L. Wang • H. Wang (✉)
Laboratory for Biological Effects of Nanomaterials and Nanosafety, National Center for Nanoscience and Technology (NCNST), Beijing, China
e-mail: wanglei@nanoctr.cn; wanghao@nanoctr.cn

1163

the resolution, contrast, and depth of detection. Much effect has been devoted to developing new PA contrast agents. The current review focuses on the nonmetallic nanomaterials-based PA contrast agents for biomedical imaging.

Introduction

Photoacoustic imaging, also called optoacoustic or thermoacoustic imaging, is a PA effect-based imaging modality. The PA effect means that a matter absorbs a short-pulsed laser beam and converts its energy into heat partially. Pressure waves (ultrasound) are generated through thermo-elastic expansion of the matter, which are further detected by broadband ultrasonic transducers and converted into images. PAI combines high spatial resolution of ultrasonic imaging and high contrast of optical imaging [1–5]. Compared to other high-resolution volumetric optical imaging modalities widely used in the biomedical imaging field, including confocal microscopy and two-photon microscopy, which suffer from the limitation of depth less than 1 mm, PAI technology can overcome the limitation of depth and be detected up to a few centimeters deep in biological tissues [1]. Furthermore, the advantages of PAI involve real-time imaging in vivo and high spatial resolution without the use of ionizing radiation [4].

The PA effect was discovered by Alexander Graham Bell at 1880. Meanwhile, PA effect was unitized in the biomedical imaging field in recent years [6, 7]. At 2003, Wang et al. developed photoacoustic microscopy (PAM) and observe functional and structural PA imaging in vivo [8]. Razansky and Ntziachristos et al. used multispectral optoacoustic tomography (MSOT, a commercial PAI instrument) to image the mouse heart in 2012 [9]. Ntziachristos et al. and Wang et al. reviewed MSOT and photoacoustic tomography (PAT)-based PAI techniques and summarized their advantages at 2010 and 2012, respectively [10–12]. The depth of PAI based on PAM is scalable from 0.7 to 30 mm by varying the ultrasonic frequency from 75 to 3.5 MHz. Compared to PAM, MSOT can impart superior quantification and offer high-resolution in-depth imaging in three dimensions. The optimum of the PA instrumental setup can enhance PA imaging performance [13]. Meanwhile, PA contrast agents can also increase the imaging resolution, contrast, and depth of detection, [14, 15] which should satisfy (a) outstanding biocompatibility; (b) appropriate stability in vivo, specifically tolerance to sterilization and prolonged half-life stability; and (c) desirable targeting properties. Nanomaterials are promising PA contrast agents to satisfy the requirements. For example, the nanomaterials could be easily stabilized by PEG chains through covalent linkage or supramolecular approach to give prolonged half-life stability and biocompatibility. Furthermore, the modifications of targeting groups on the surface of nanomaterials are readily achievable through surface chemistry. The nonmetallic nanomaterial-based PA
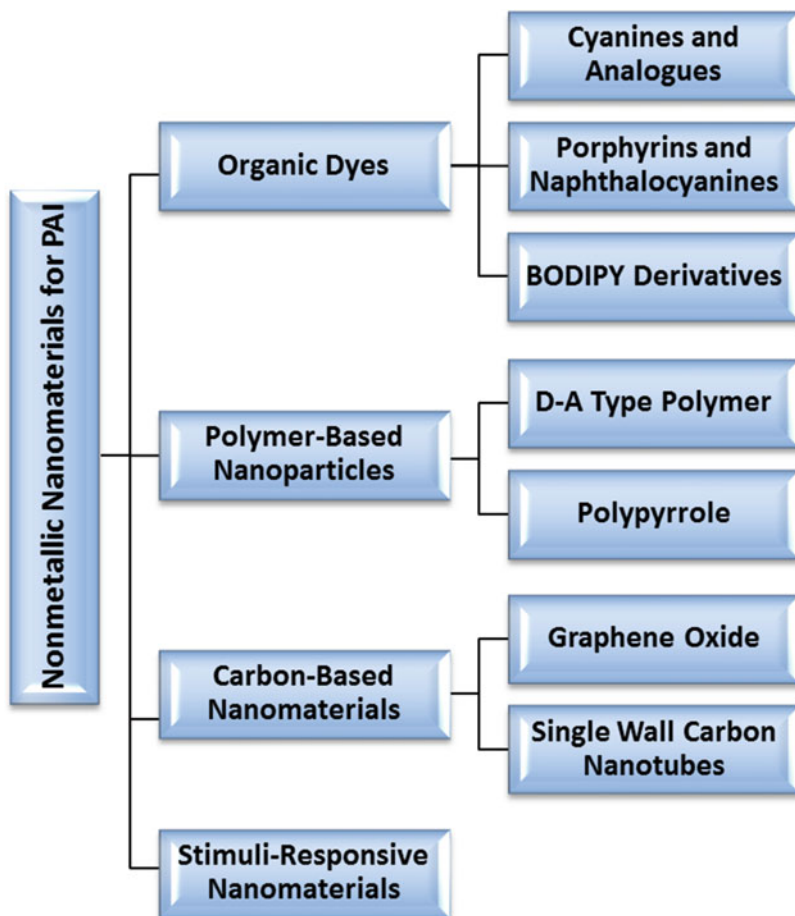
Fig. 1 Different classes of nonmetallic nanomaterials as PA contrast agents

contrast agents for biomedical imaging are reviewed as (i) organic dye-based nanoparticles, (ii) polymer nanoparticles, (iii) carbon-based nanomaterials, and (iv) stimuli-responsive nanomaterials (Fig. 1).

Organic Dye-Based Nanoparticles

Near-infrared window refers to NIR light ($\lambda = 650$–900 nm), which allows for deeper penetration, lower tissue absorption or scattering, and minimal autofluorescence. Organic dyes with a maximum absorption in the NIR range can be used for PAI. To gain efficient PA signals, organic dyes should have low-fluorescence quantum yield (lower ratio of photons emitted to photons absorbed, more of the absorbed energy can be converted into PA signal). The three types of organic dyes, e.g., cyanine, porphyrin,
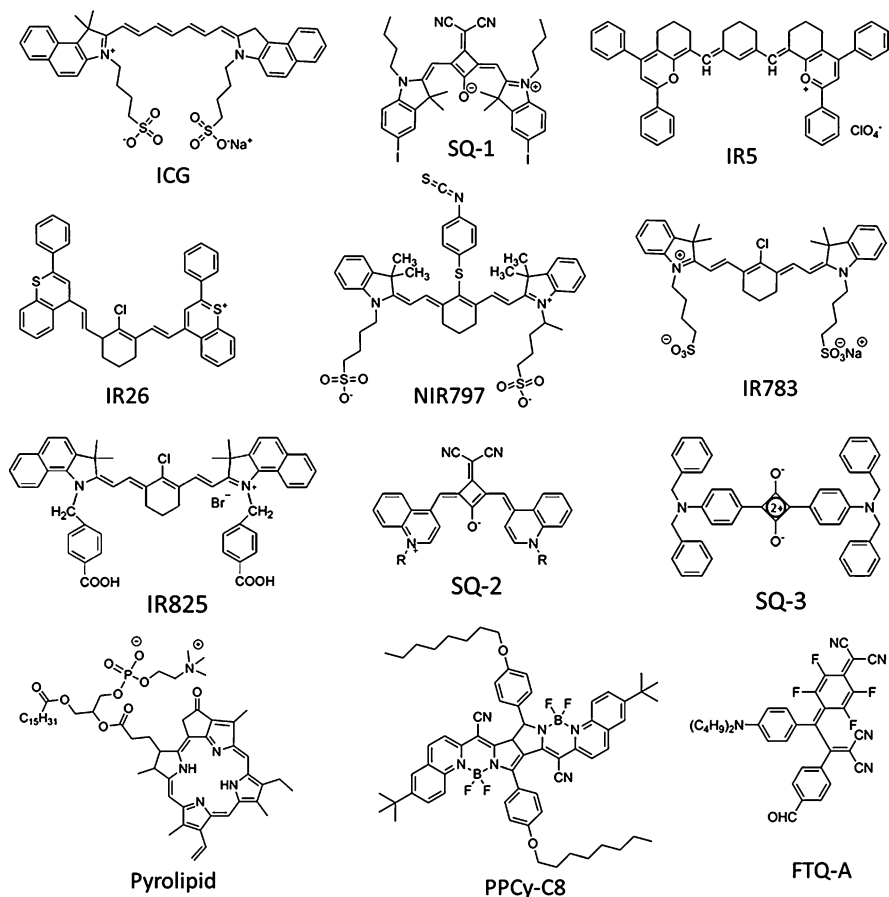
Fig. 2 The molecular structures of organic dyes with NIR absorbance

and boron-dipyrromethene (BODIPY) derivatives (Fig. 2), which can be used as PA contrast agents, have been explored by multiple research groups, especially these organic dye-based nanoparticles.

Cyanines and Analogues

Indocyanine green (ICG) is a Food and Drug Administration (FDA)-approved tricarbocyanine fluorescent dye. It has been used as a contrast agent for fluorescence imaging, which is one of the most commonly used medical imaging modalities. Recently, it was also developed as a PA contrast agent due to its simplicity, safety, and high sensitivity. However, certain drawbacks of free dye molecules, concerning its low stability, uncontrolled aggregation, and lack of targeting ability, have limited its application in biomedical imaging. Yoon et al. embedded ICG in a novel
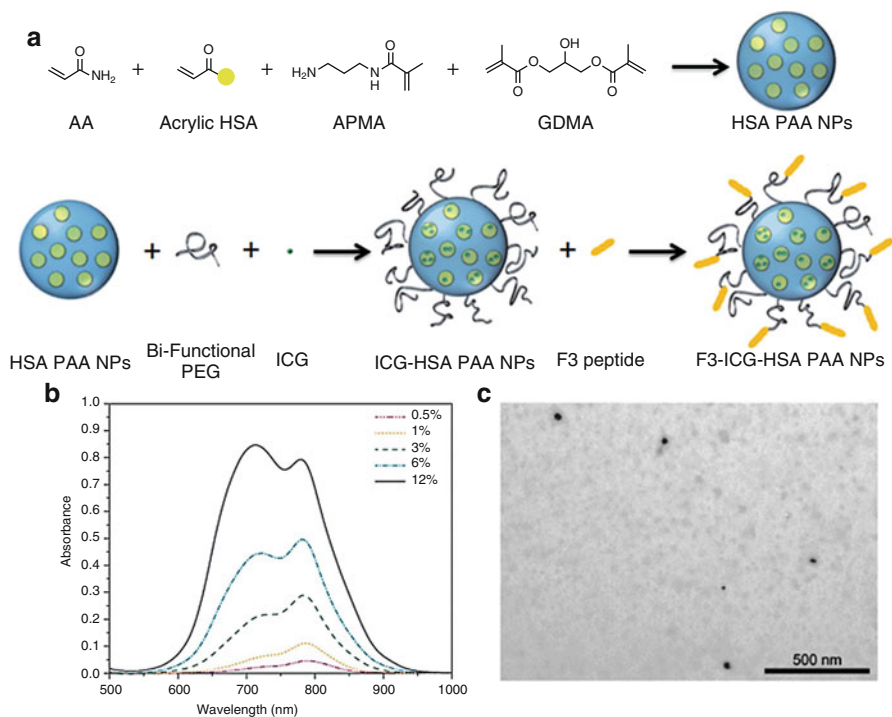
Fig. 3 (**a**) Synthesis of F3-(3 % ICG)-HSA-PAA NPs. (**b**) Absorption spectra of ICG-HSA-PAA NPs with different ICG contents. (**c**) TEM image of (3 % ICG)-HSA-PAA NPs (Reproduced with permission [16] Copyright 2013, Royal Society of Chemistry)

polymer–protein hybrid nanocarrier (Fig. 3a) to overcome the above limitations [16]. This nanocarrier was synthesized through pre-conjugation of human serum albumin (HSA) and amine-functionalized monomer, followed by polymerization using biodegradable cross-linkers, in a water-in-oil emulsion. The ICG dye was loaded into the HSA-conjugated polyacrylamide (PAA) nanoparticles (HSA-PAA NPs) through post-loading. The UV–Vis absorption spectrum of ICG-HSA-PAA NPs showed two strong peaks at 720 and 790 nm in the NIR range (Fig. 3b). The diameter of the dehydrated (3 % ICG)-HSA-PAA NPs was around 48 nm (Fig. 3c). The presence of hydrophobic pockets in the HSA-PAA NPs increased the chemical and physical stability of ICG by lowering the chemical degradation rates under physiological conditions. Furthermore, targeting peptide (F3 peptide) was attached to the surface of the NPs for selective delivery to specific cancer cell lines to obtain the targeting PA contrast agents. Wu et al. synthesized a class of dendrimers conjugated with an antitumor agent, gemcitabine (GEM) [17]. By using NIR-797 labeling (Fig. 4a), the accumulation and penetration in tumors of GEM-conjugated dendrimers were monitored by MSOT (Fig. 4b). The G4″-GEM signal intensity per unit tumor area and signal distribution area in tumors at different time points were quantified (Fig. 4c). The results indicated that GEM-conjugated dendrimers had
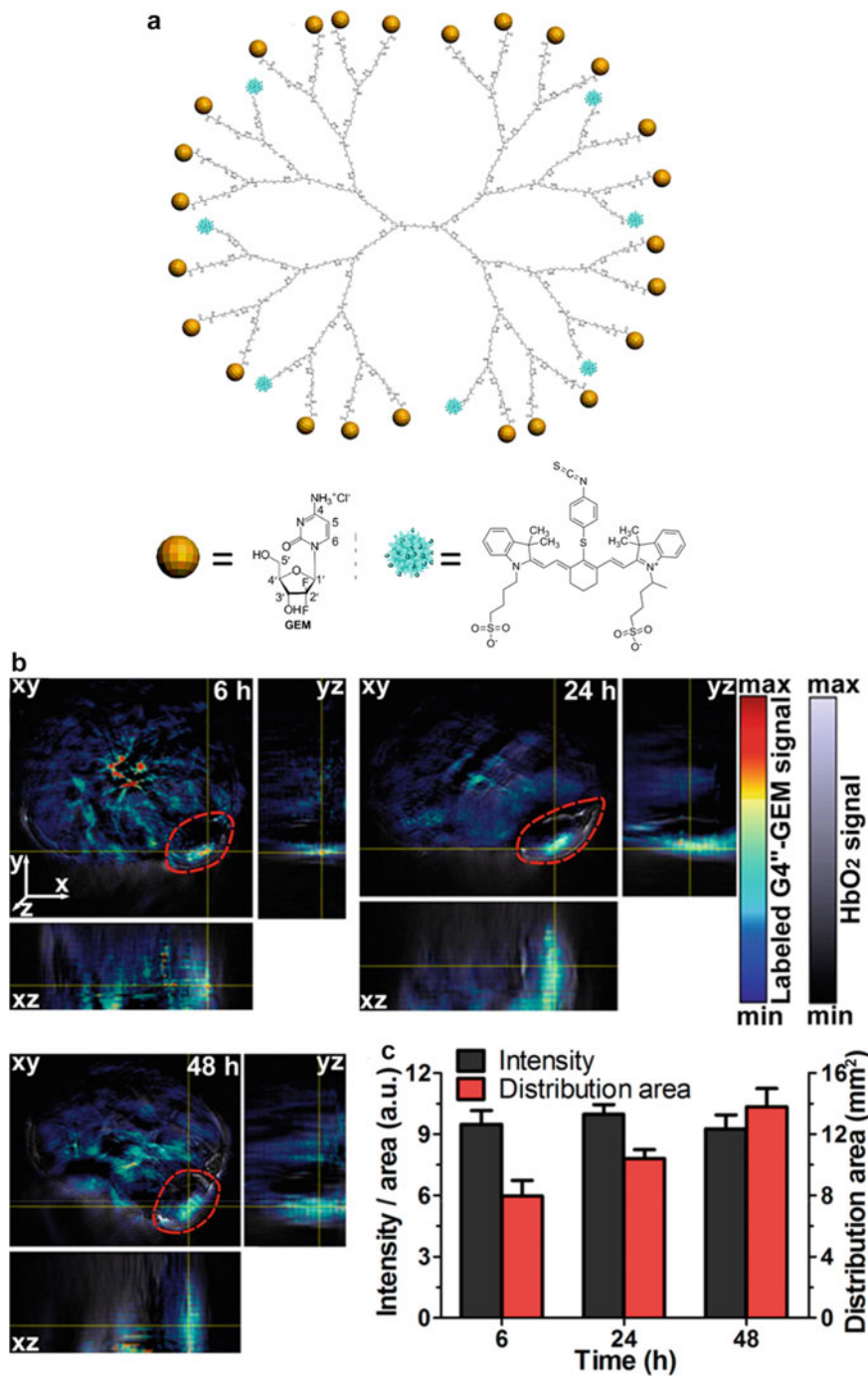
Fig. 4 (continued)

significant superiority over GEM-conjugated poly(amidoamine) (PAMAM) and lengthening the PEG segments on the periphery of the dendrimers could significantly improve the dendrimers' circulation time and tumor-targeting ability. Accordingly, their GEM-conjugated dendrimers with the longest peripheral PEG segments exhibited significantly higher antitumor activity compared to the GEM-conjugated PAMAM.

Wang and Würthner prepared NIR-absorbing and emission squaraine (SQ-1) dyes, which have good stability and high photoresistance. They modulated the aggregation of SQ-1 dyes in hydrophobic phospholipid bilayers of liposomes with variable mixing ratios of the SQ-1 dye and the liposome, to achieve dual NIR fluorescence and PA tomography dual-modular imaging (Fig. 5) [18]. The SQ-1 dye-loaded liposomes are typical vesicular structures with a size of 76 ± 15 nm (Fig. 6a), which is in accordance with the dynamic light-scattering (DLS) result (size: 103 ± 14 nm, PDI: 0.18). When doping minimal amounts of SQ-1 (1:500), molecularly dispersed SQ-1 in bilayers shows remarkable fluorescence (Fig. 6b). Interestingly, the PA signals are enhanced with the increase of SQ-1 in the nanoconfined bilayer region, which are due to the formation of SQ-1-based H-aggregates and enhanced thermal conversion efficiency (Fig. 6c, d). NIR fluorescence imaging in vivo indicated that the majority of SQ-1 $\subset$ L are enriched in the area where the blood vessels are generated, implying that the liposomal nanocarriers exhibit lower tumor tissue penetration capability after the vascular leakage. The research indicated that the importance of supramolecular modulation (monomer or aggregation) of NIR dyes loaded in the nanomatrix, which will determine the characteristics and application of the dye-doped nanomaterials [18]. Furthermore, they used the SQ-1-loaded pH-sensitive micelles as an activatable PA probe to investigate the NIR SQ-1 dye release profiles [19]. Zhao et al. reported the NIR squaraine dye (SQ-2) encapsulated micelles for in vivo fluorescence and PA bimodal imaging [20]. SQ-2 was encapsulated inside micelles constructed from a biocompatible nonionic surfactant (Pluronic F-127) to obtain SQ-2-encapsulated micelles (SQ-2 micelle) in aqueous conditions. The micelle encapsulation retained both the photophysical features and chemical stability of SQ-2. The SQ-2 micelle exhibited high photostability and low cytotoxicity in biological conditions. Unique properties of SQ-2 micelle in the NIR window of 800–900 nm enabled the development of a squaraine-based exogenous contrast agent for fluorescence and PA bimodal imaging above 820 nm. In vivo imaging using SQ-2 micelle, as demonstrated by fluorescence

---

Fig. 4 (**a**) The molecular structures of NIR-797 labeled dendrimer-GEM conjugates; (**b**) Orthogonal views of the MSOT images of an orthotopic 4 T1 tumor-bearing mouse at different time points after tail-vein injection of NIR-797-labeled G4″-GEM showing overlaid HbO$_2$ and NIR-797-labeled G4″-GEM signals. The 3D coordinate system defines the orientations and positions of the orthogonal views, and the dashed circles indicate the tumor regions. (**c**) Quantifications of the MSOT signal intensity of the NIR-797-labeled G4″-GEM per unit tumor area and its intratumoral distribution area that is acquired as a pixel area with a signal value > 0 within the tumor region of interest (ROI) at different time points after tail-vein injection of the NIR-797-labeled G4″-GEM (Reproduced with permission [17] Copyright 2014, American Chemical Society)
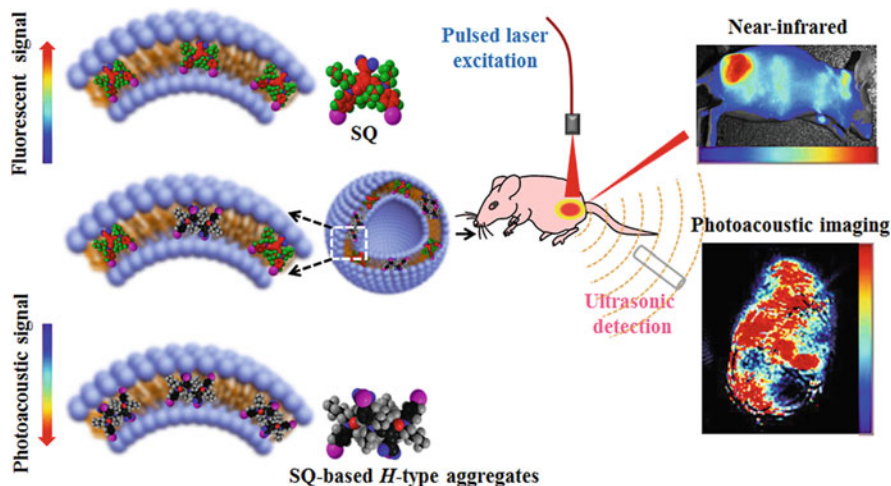
Fig. 5 Schematic diagram of the nanoconfined SQ assemblies in phospholipid bilayer and the utilization of these vesicles as probes for dual-modular tumor imaging in vivo (Reproduced with permission [18] Copyright 2014, American Chemical Society)

and PA tomography experiments in live mice, showed contrast-enhanced deep-tissue imaging capability. The usage of SQ-2 micelle proven by preclinical experiments in rodents reveals its excellent applicability for NIR fluorescence and PA bimodal imaging. Kohl and his coworkers introduced multifunctional nanoparticles loaded with NIR dyes (IR-5/IR-26) [21]. The nanoparticles showed excellent PA contrast properties as promising candidates for a resorbable PA contrast system. Li and Xing prepared IR-783 conjugated with dextran forming self-assembled nanoparticles, which could be utilized as pH-sensitive NIR nanoprobe for in vivo differential-absorption dual-wavelength PAI of tumors [22]. An et al. reported the albumin and NIR squaraine dye (SQ-3) nanoassemblies for PA imaging in vivo [23]. The SQ-3 dye was loaded and aggregated in albumin, which induced a NIR absorption at around 800 nm from the visible-light region. Thus, the PA signal could be generated in the tissue-transparent NIR optical window (700–900 nm). Blood analysis and histology measurements revealed that the nanocomplex could be used for PA tomography applications in vivo without obvious toxicity to living mice.

Recently, Wang and his coworkers introduced a bis-pyrene unit with strong hydrophobicity and large π-conjugation to the cyanine molecule to construct well-organized NIR-absorbing nanovesicles with super chemical and photostability (Fig. 7a) [24]. This is the first time that the cyanine dyes form vesicular nanoassemblies without templates (Fig. 7b, c). Interestingly, compared with the monomer and analogue ICG molecules, the stable nanovesicles showed significantly improved PA signal intensity and half-life in vitro and in vivo (Fig. 7d). The results demonstrated that supramolecular strategy could effectively improve the photophysical properties of building blocks. The hollow nanostructure could be potentially employed as a platform for delivery of various bioactive molecules for
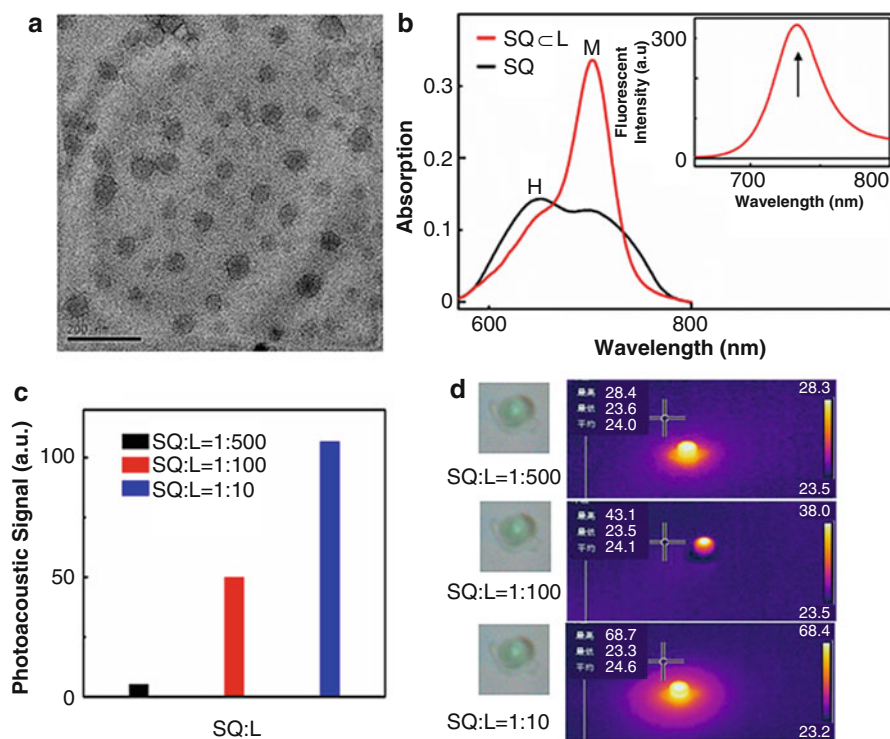
Fig. 6 (a) TEM images of SQ ⊂ L. (b) UV–Vis absorption spectra and the corresponding fluorescence intensity changes (*inset*, λex: 680 nm) of aggregated SQ (4 μM) in PBS and SQ monomers (4 μM) in SQ ⊂ L. (c) PA signal was enhanced with increasing ratio of SQ and phospholipid in liposomes from 1:500 to 1:10 (w/w). Error bar in (d) represented the SD of experimental duplicates. (d) Photothermal transformation photographs were taken from thermal camera (Reproduced with permission [18] Copyright 2014, American Chemical Society)

extensive biomedical applications. Liu and his coworkers engineered multifunctional nanomicelles for combined photothermal and photodynamic therapy under the guidance of multimodal imaging [25]. The multifunctional polymeric nanomicelle system containing a photosensitizer chlorin e6 (Ce6) was successfully fabricated, together with a NIR dye, IR825. The theranostic micelles could be utilized as a contrast agent for fluorescence and PA imaging of tumors in a mouse model. The combined photothermal and photodynamic therapy was carried out, achieving a synergistic antitumor effect both in vitro and in vivo.

Porphyrins and Naphthalocyanines

Porphyrin, a NIR dye, was utilized as PA contrast agents by Zheng and his coworkers [26–28]. The amphiphilic porphyrin derivative was prepared, which
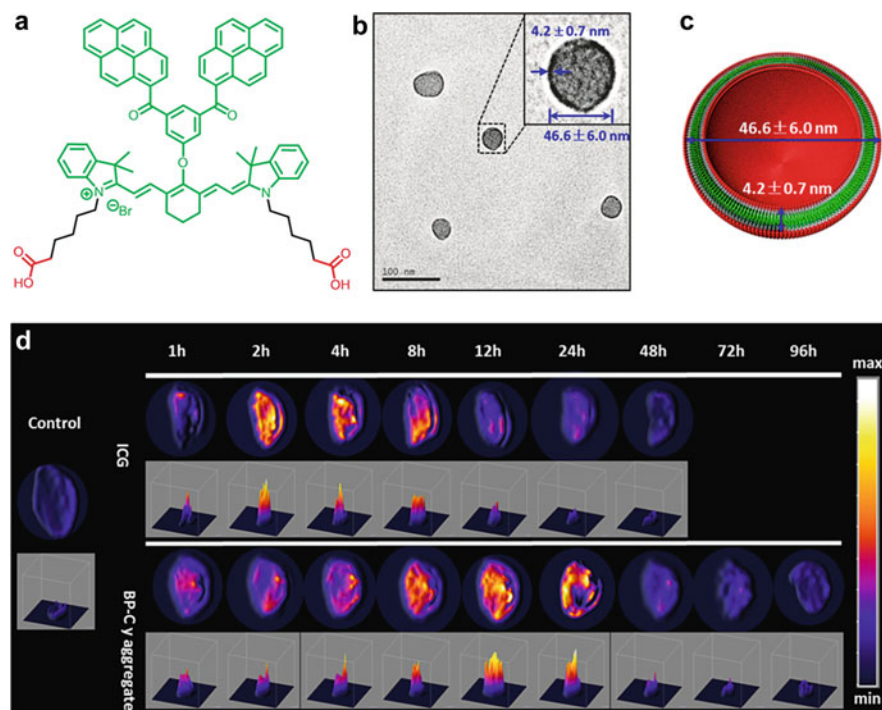
Fig. 7 (**a**) Molecular structures of BP-Cy. (**b**) TEM images of BP-Cy vesicles with negative staining. The expansions indicate the thickness of the bilayer membrane and the diameter of the vesicle in each case. (**c**) Schematic space-filling model for the vesicle. (**d**) In vivo model mice for PA imaging injected with ICG and BP-Cy aggregate (2.0×10^{-5} M, 200 μL) via tail vein and detected under laser irradiation (790 nm). The PA images were reconstructed by ImageJ (Reproduced with permission [24] Copyright 2015, Royal Society of Chemistry)

formed porphyrin bilayers (porphysomes) through self-assembly (Fig. 8a, b) [26]. The porphysomes showed large, tunable extinction coefficients at NIR region and unique PA properties. Hence, porphysomes enabled the sensitive visualization of lymphatic systems using PAT. As a nanomaterial, porphysomes could accumulate in tumors of xenograft-bearing mice, and laser irradiation could induce photothermal tumor ablation. Because of their organic nature, porphysomes were enzymatically biodegradable and induced minimal acute toxicity in mice (Fig. 8a). The optical properties and biocompatibility of porphysomes demonstrated the multimodal potential of organic nanoparticles for biomedical imaging and therapy. Similarly, Zheng also reported microbubbles (MBs) (Fig. 8c) as trimodal imaging agents (ultrasound, PA, and fluorescence) with the shell of amphiphilic porphyrin derivative molecules, which formed a single porphyrin-lipid layer [28]. The UV–Vis absorbance spectrum of the MBs in phosphate-buffered saline (PBS) displayed a Q-band peak at 704 nm, which is 37 nm red shifted from the porphyrin monomeric peak wavelength. This red-shifted peak is an indication of ordered aggregation of the
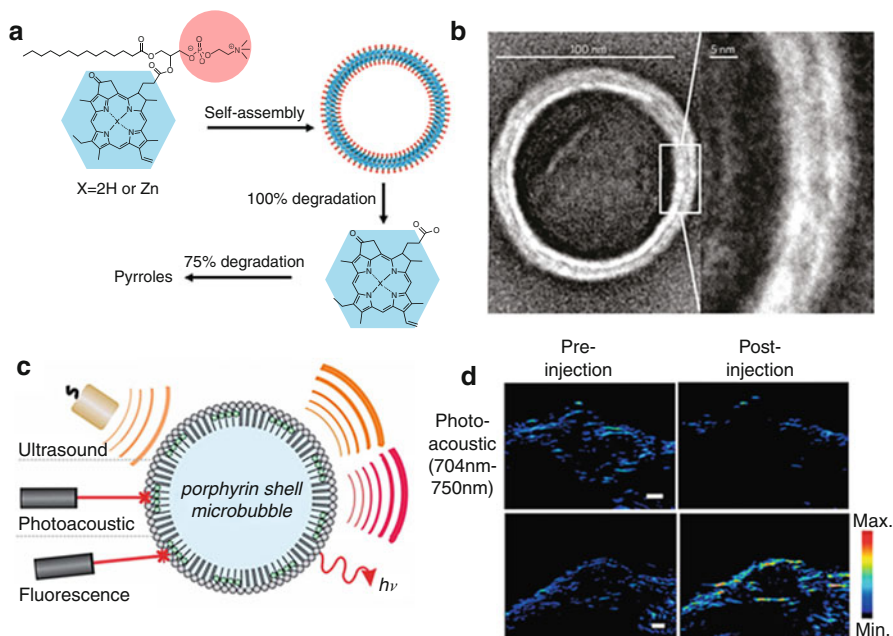
Fig. 8 (**a**) Schematic representation of a pyropheophorbide–lipid porphysomes and enzymatic degradation of the porphysomes. The phospholipid headgroup (*red*) and porphyrin (*blue*) are highlighted in the subunit (*left*) and the assembled nanovesicle (*right*). (**b**) Electron micrographs of negatively stained porphysomes (5 % PEG–lipid, 95 % pyropheophorbide–lipid). (**c**) Schematic of trimodal microbubbles. (**d**) In vivo imaging of MBs in a KB tumor xenograft at 10–30 s post intravenous injection of 280 μL of MB-PBS solution at a concentration of 2×10^9 MBs/mL (**a**, **b** reproduced with permission [26] Copyright 2011, Nature; **c**, **d** reproduced with permission [28] Copyright 2014, American Chemical Society)

porphyrins within the MB shell. PA images were pre- and post-injection of both MB formulations, and only the trimodal porphyrin shell MBs showed detectable increase in PA signal after injection (Fig. 8d).

Cai and his coworkers reported a family of naphthalocyanine-based nanomicelles that can avoid systemic absorption and provide good optical contrast for PA imaging (Fig. 9a) [29]. The naphthalocyanine dyes (Fig. 9b) were co-assembled with F127 into nanomicelles with the size of ~20 nm due to strong hydrophobicity (Fig. 9c). Interestingly, the free F127 could be removed without destroying the frozen micelle structures at 4 °C due to its temperature-sensitive CMC. The frozen nanomicelles (nanonaps) showed tunable and large near-infrared absorption intensity. Moreover, the nanonaps exhibited high stability and passed safely through the gastrointestinal tract. Hence, the nanonaps could be utilized to observe the two US/PA maximum intensity projections (MIPs) by tracing the movement of nanonaps through the intestine over a 30 min period (Fig. 9d). The indicated regions of interest showed, in real time, the out-of-plane passing of nanonaps through a transverse slice of the intestine. Compared to control regions B and C, which contained relatively constant
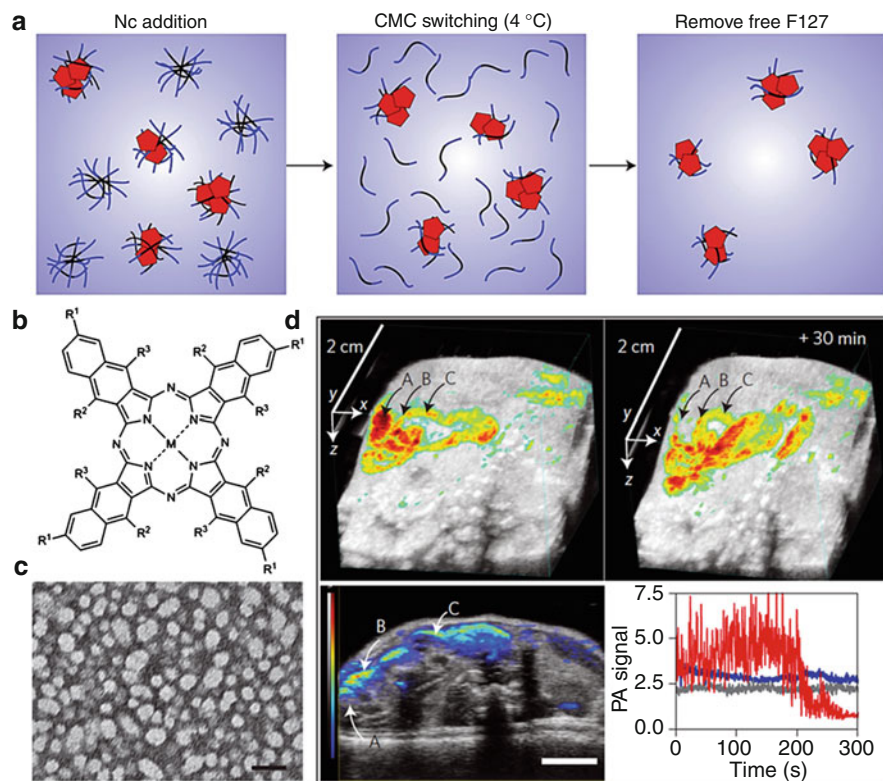
Fig. 9 (**a**) Generation of purified nanonaps. F127 PEO blocks are in *blue*, PPO blocks in *black*, and Nc dyes in *red*. (**b**) Chemical structure of naphthalocyanines used. ONc: M = 2H; R_1 = H; R_2, R_3 = O-$(CH_2)_3CH_3$. (**c**) Negative-stained TEM of dried nanonaps. Scale bar, 50 nm. (**d**) US (*gray*)/PA (color) MIPs of transverse slices, showing ONc nanonap intestinal transit over time. The MIP was used to orient the PA signal within a single slice of interest (*lower left*). Outflow quantification over time of nanonaps in area A (*red*) shown with reference to two others that maintained steady nanonap content in areas B (*blue*) and C (*gray*). The fluctuations in A are due to contractile inflow and outflow of nanonaps (Reproduced with permission [29] Copyright 2014, Nature)

nanoparticles volumes, nanonaps quantitatively exited from region A over 1 min and demonstrated peristaltic contractions in the process. Noninvasive, non-ionizing PA techniques were used to visualize nanonap intestinal distribution with low background and remarkable resolution and enabled real-time intestinal functional imaging with ultrasound co-registration.

BODIPY and Other Dyes

BODIPY with NIR absorbance as PA contrast agents was reported by Akers et al [30]. They found that the fluorescence quenching occurred in the formulation
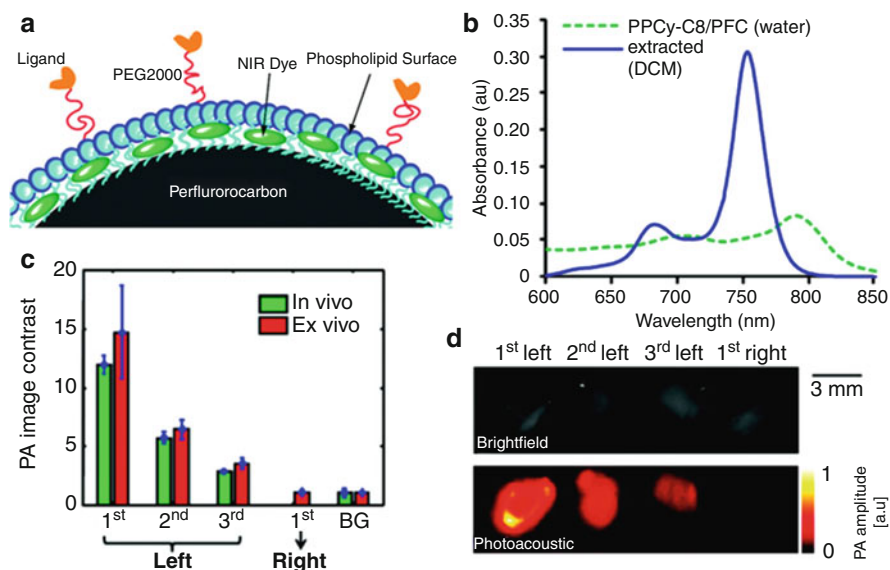
Fig. 10 (**a**) Schematic of dye-loaded PFC nanoparticles. The perfluorocarbon core is encapsulated in an amphiphilic phospholipid layer (*blue*) containing hydrophobic dyes (*green*). (**b**) Absorption of PPCy-C8/PFC nanoparticles in water and after extraction of the dye from liposome with dichloromethane (*DCM*). Absorption spectrum of PPCy-C8/PFC was corrected by the absorption of PFC with no dye. (**c**) Comparison of PA image contrasts quantified from in vivo and ex vivo results. *BG* background. (**d**) Bright-field and PA images of ex vivo lymph nodes 24 h after intradermal administration of PPCy-C8/PFC nanoparticles into the left forepaw of the rat (Reproduced with permission [30] Copyright 2011, American Chemical Society)

of NIR fluorescent dyes in nanoparticles resulted in enhanced contrast for PAI (Fig. 10a). They developed NIR dye-loaded perfluorocarbon-based nanoparticles for combined fluorescence and PA imaging with two kinds of NIR dyes and revealed distinct dye-dependent photophysical behavior. The pyrrolopyrrole cyanine (PPCy-C8) showed different absorbance behavior in dichloromethane (DCM) and aqueous solution (Fig. 10b). By controlling the quantity and ratio of PPCy-C8 in perfluoro-carbon nanoparticles, both optical and PA contrast can be tuned. Their results showed the benefit of nanomaterials for the enhancement of contrast by increasing the payload per particle. They also demonstrated that the PA and fluorescence detection system allowed detection of regional lymph nodes of rats in vivo with time-domain optical and PA imaging methods. The PAI contrasts were quantified from in vivo and ex vivo PAI results (Fig. 10c, d). Besides the above NIR-absorbing dyes, other organic NIR dyes have been developed and further utilized for PA bioimaging. Moreover, the perylene dye-based nanoparticles were successfully prepared and used to realize PAI of deep orthotopic brain tumor in mice models by Zhen Cheng [31]. Recently, the [2 + 2] click reactions by using amine-substituted aromatic precursors as donors and 7,7,8,8-tetracyano-2,3,5,6-tetrafluoroquino-dimethane (F$_4$-TCNQ) as acceptor molecules to afford donor–acceptor

chromophores, which have strong NIR absorption in the range of 700–900 nm. The series of dyes have potential in application as contrast agents for PAI.

Polymer-Based Nanoparticles

D-A-Type Polymer

Polymer-based nanoparticles have been exploited as nanocarrier for drug delivery over the past several years [32–34]. Recently, several polymers which possessed unique optical properties can be introduced as contrast agents for bioimaging [34]. D-A-type semiconducting polymer nanoparticles (SPNs) as a new class of NIR PA contrast agents with NIR light absorbing were developed by Pu et al. for PAI (Fig. 11a) [35]. The SPN1 shows stronger absorption than SPN2 at 700 nm (Fig. 11b). Similarly, the PA signals of SPN1 are much higher than that of SPN2 (Fig. 11c). Both the nanoparticles can generate stronger signals than the commonly used single-walled carbon nanotubes and gold nanorods (NRs) on a per mass basis (Fig. 11d), permitting the whole-body lymph node PA mapping in living mice at a low systemic injection mass. The SPNs possessed high structural flexibility and strong resistance to photodegradation and oxidation. Furthermore, by coupling SPNs to a cyanine dye derivative (IR775S) that was sensitive to ROS-mediated oxidation, they first demonstrated the NIR ratiometric PA probe (RSPN) for in vivo real-time imaging of reactive oxygen species (ROS) (Fig. 12a). The PA spectrum of RSPN showed three maxima at 700, 735, and 820 nm. In the presence of $ONOO^-$ and ClO^-, the PA peak from IR775S dyes almost disappeared, but the peak at 700 nm from SPN1 remained nearly the same. However, other ROS could not affect the PA spectrum (Fig. 12b). The ROS-responsive ratiometric PA measurement was realized in cells when they were in the resting state (Fig. 12c, d). Moreover, Liu and coworkers developed polymer PFTTQ (Fig. 13a) with NIR absorption and fabricated 1,2-distearoyl-sn-glycero-3-phosphoethanolamine-N-[methoxy(polyethylene glycol)-2000] encapsulated PFTTQ nanoparticles with good solubility and processability [36]. The PFTTQ nanoparticles with the intense NIR absorption, high nonradiative quantum yield, excellent photostability, and low cytotoxicity highlighted the great potential of processable PFTTQ nanoparticles for in vivo PA imaging (Fig. 13b, c).

Polypyrrole

Polypyrrole (PPy) as the PA contrast agent was reported in 2013 by Dai and his coworkers (Fig. 13d) [37]. They prepared PPy nanoparticles by aqueous phase polymerization using PVA as the stabilizing agent and $FeCl_3$ as an oxidation catalyst (Fig. 13e). The PPy nanoparticles were well dispersed in water with strong absorption in the 700–900 nm region and the PVA modified surface. Intravenous administration of PPy nanoparticles allowed imaging of the cerebral cortex of the mouse
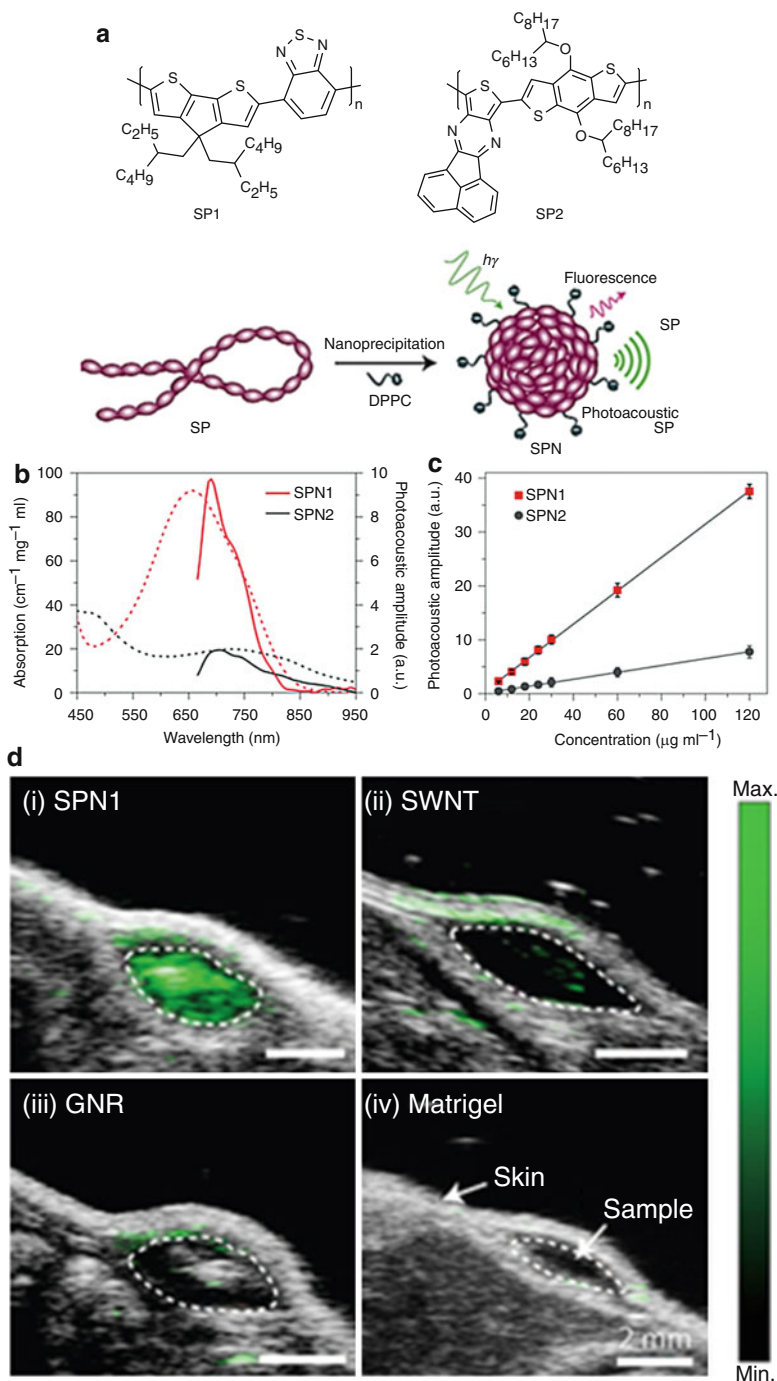
Fig. 11 (**a**) Molecular structures of SP1 and SP2 used for the preparation of SPN1 and SPN2, respectively. (**b**) UV–Vis absorption (*dashed lines*) and PA spectra (*solid lines*) of SPNs.

brain vasculature with greater clarity than the intrinsic signal from hemoglobin in blood. At 1 h post-injection, the PA signal remained essentially intense, indicating that a sufficient amount of PPy nanoparticles has long-circulating ability in blood. Moreover, no acute toxicity to the vital organs (e.g., heart, liver, lung, spleen, and kidney) was observed at 15 day post-injection, suggesting good biocompatibility of the PPy–PVA nanoparticles. PPy nanoparticles as PA contrast agents were also demonstrated by Liu [38].

Carbon-Based Nanomaterials

Graphene Oxide

Graphene, a shining star in the materials, exhibits many unique intrinsic photophysical properties, one of which is their strong optical absorbance in the NIR region. Graphene's derivatives are promising PA contrast agents with excellent PA contrast. For example, Jiang and He prepared graphene nanosheets from graphite particles with their π-conjugated aromatic structures, which exhibited nearly wavelength-independent absorption in the visible and NIR regions (Fig. 14a, b) [39]. For the first time, they demonstrated that the graphene nanosheets could generate strong PA signals with NIR excitation (Fig. 14c, d). Different from organic dye-based PA contrast agents, the photo-to-acoustic conversion was weakly dependent on the wavelength of NIR excitation. Recently, Dai's group first demonstrated that nano-sized reduced graphene oxide (nano-rGO) with noncovalent PEGylation exhibited sixfold higher NIR absorption than nano-GO, which was comparable to carbon nanotubes and gold-based nanomaterials [40]. This finding indicated nano-rGO can be used as a theranostic nano-agent in biomedicine. Similarly, Cai developed a nano-rGO, which was reduced by bovine serum albumin (BSA) protein from nano-GO with high stability and low cytotoxicity (Fig. 15a) [41]. The UV–Vis–NIR absorption spectrum of nano-GO showed a strong absorption peak at 232 nm. After BSA reduction, the absorbance of nano-rGO was significantly enhanced in the UV–Vis–NIR range (Fig. 15b). The PA signals produced by the nano-rGO were observed to be linearly dependent on the concentration ($R^2 = 0.99$) (Fig. 15c). Mice bearing MCF-7 tumor xenografts (80 mm^3 in size) were injected through the tail vein with 200 μL BSA-functionalized nano-rGO at a concentration of 1 mg/mL. The ultrasound and PA dual-modality images of a cross section crossed the center of the tumor were obtained and monitored up to 4 h after the injection (Fig. 15d–f). The

Fig. 11 (continued) (**c**) PA amplitudes of SPNs at 700 nm in an agar phantom as a function of mass concentration. $R^2 = 0.998$ and 0.997 for SPN1 and SPN2, respectively. (**d**) PA/ultrasound co-registered images of the nanoparticle–matrigel inclusions in mice at a concentration of 8 μg ml^{-1}. The images represent transverse slices through the subcutaneous inclusions (*dotted circles*) (Reproduced with permission [35] Copyright 2014, Nature)
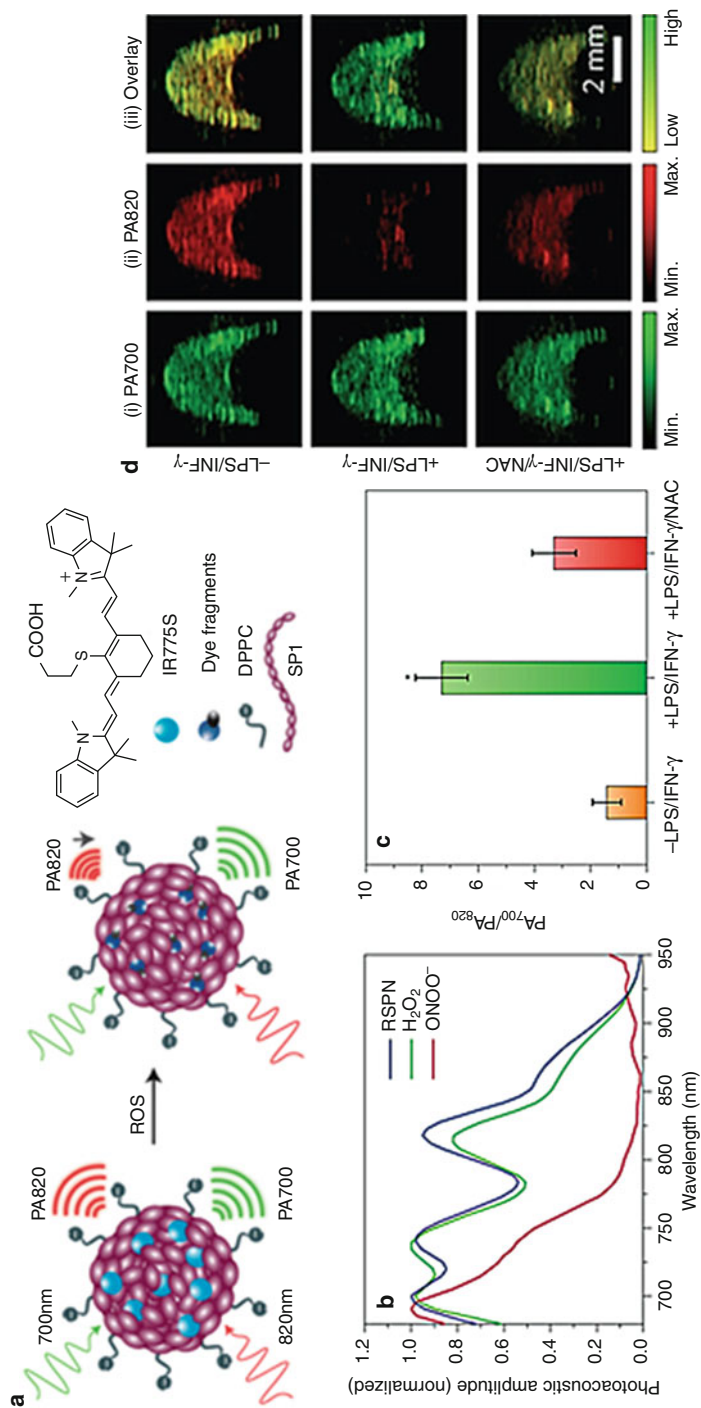
Fig. 12 (**a**) Proposed ROS-sensing mechanism. (**b**) Representative PA spectra of RSPN in the absence and presence of ROS. μM. (**c**) Quantification of the absorption ratio (PA700/PA820) for macrophage cell pellets with and without LPS/INF-γ or LPS/INF-γ/NAC treatment. Error bars represent standard deviations from four separate measurements. (**d**) PA images of macrophage RAW264.7 cell pellets (1.5×10^6 cells) without (*top*) or with (*middle*) stimulation with LPS/INF-g and with NAC protection (*bottom*). Cell pellets were inserted into an agar phantom and imaged with a pulsed laser tuned to (i) 700 nm or (ii) 820 nm. (iii) Overlays of images from (i) and (ii) (Reproduced with permission [35] Copyright 2014, Nature)
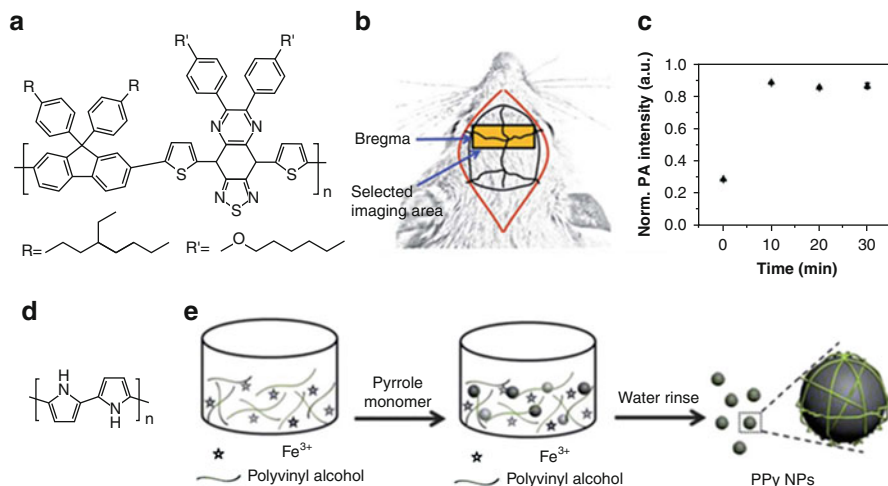
Fig. 13 (**a**) Chemical structures of the polymer PFTTQ. (**b**) The illustration of PA imaging of rat brain vasculature. (**c**) PA rat cortical vasculature C-scan images before and 10 min after injection of PFTTQ NPs. (**d**) Chemical structures of Ppy. (**e**) Schematic illustration of the formation of PPy NPs in an aqueous dispersion of water-soluble polymer–metal cation complexes (**a**–**c** : Reproduced with permission [36] Copyright 2014, Royal Society of Chemistry; **d**, **e**: Reproduced with permission [37] Copyright 2013, Royal Society of Chemistry)

prepared nano-rGO could be used as ready-to-use theranostic agents for both PAI and photothermal therapy in vitro and in vivo.

Other functional materials can be combined with GO for enhanced PA signals and multifunctional theranostic platform. Liu and coworkers designed a novel probe based on the rGO-iron oxide nanoparticle (IONP) nanocomposite, which was noncovalent functionalized with polyethylene glycol (PEG) for high stability in physiological environments [42]. Triple-modal fluorescence/MR/PAT for tumor imaging in vivo with rGO–IONP–PEG was realized to highlight the great potential of rGO nanoplatform-based functional materials for cancer theranostic applications. Chen and coworkers produced a novel photo-theranostic platform based on sinoporphyrin sodium (DVDMS) photosensitizer-loaded PEGylated graphene oxide (GO–PEG–DVDMS) for enhanced fluorescence/PA dual-modal imaging and combined PDT and PTT [43]. The GO–PEG carrier drastically improves the fluorescence of loaded DVDMS via intramolecular charge transfer. Concurrently, DVDMS significantly enhances the NIR absorption of GO for improved PA imaging and PTT. Similarly, Li and Yang afford the enhanced PA imaging by combining organic dye with GO [44]. The dye-enhanced GO was prepared utilizing the π–π stacking interactions between GO and ICG. The ICG–GO complex had a high absorbance in the NIR region and exhibited excellent photothermal and PA properties under NIR irradiation.

Qin, Yang, and Xing reported the design of a PA nanoprobe with the highest availability of optical-thermo conversion by using GO and dyes via π–π stacking
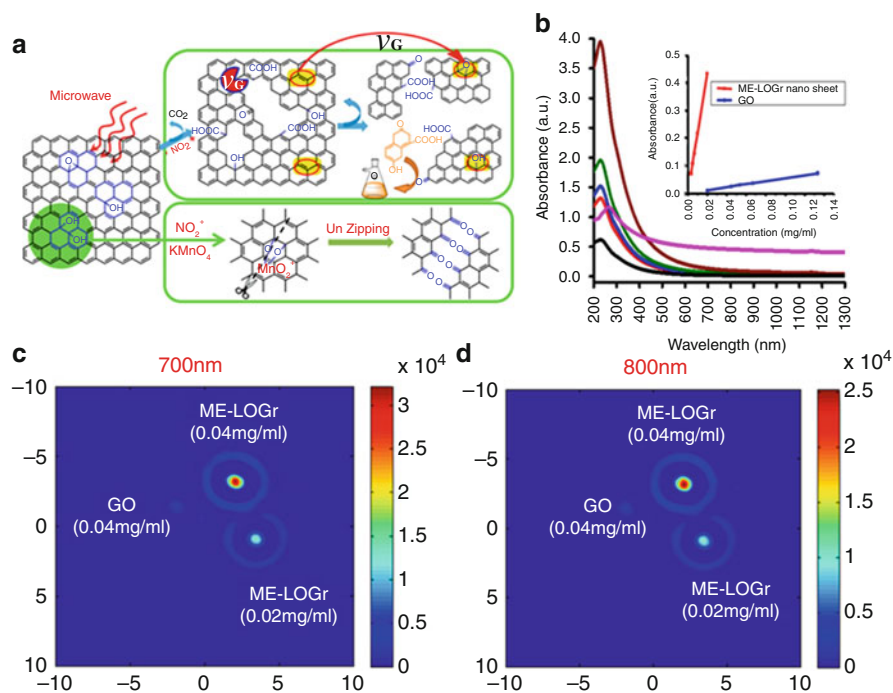
Fig. 14 (**a**) Schematic of the possible cutting mechanisms by microwave-assisted nitronium oxidation in the presence and absence of $KMnO_4$. v_C and v_G are referred to $v_{consumption}$ (reaction rate of defect consumption) and $v_{generation}$ (reaction rate of defect generation), respectively. (**b**) UV–Vis–NIR spectra of the GO sheets at different concentrations of 133.3 (*wine*), 66.7 (*olive*), 53.3 (*blue*), 44.4 (*red*), and 33.3 mg/L (*black*), respectively. For better comparison, the pink curve is 20 mg/L of microwave-enabled low-oxygen graphene (ME-LOGr) nanosheets. Inset shows the linear relationships between the absorption at 984 nm and the concentration of ME-LOGr nanosheets and GO (**c**) and (**d**) PA signal of GO and graphene nanosheets of different concentrations, illuminated with 700 and 800 nm laser. The color-coded vertical bar represents the strength of the PA signal generated. GO nanosheets were obtained via control-A experiment (Reproduced with permission [39] Copyright 2013, American Chemical Society)

interactions [45]. The GO served as a base material for loading dyes and quenching dye fluorescence via fluorescence resonance energy transfer (FRET) (Fig. 16a). Experiments verified that the designed fluorescence-quenching nanomaterials could produce stronger PA signals than the sum of the separate signals generated in the dye and the GO (Fig. 16b, c). The fluorescence-quenching nanomaterials as contrast agents were demonstrated to image the deep-seated tissues and tumors in living mice by enhancing PA contrast. PA therapy efficiency both in vitro and in vivo by using the fluorescence-quenching nanoprobes was found to be higher than with the commonly used PA therapy agents. The study demonstrated that quenching dye fluorescence via FRET would provide a valid means for developing high-efficiency PA nanoprobes.
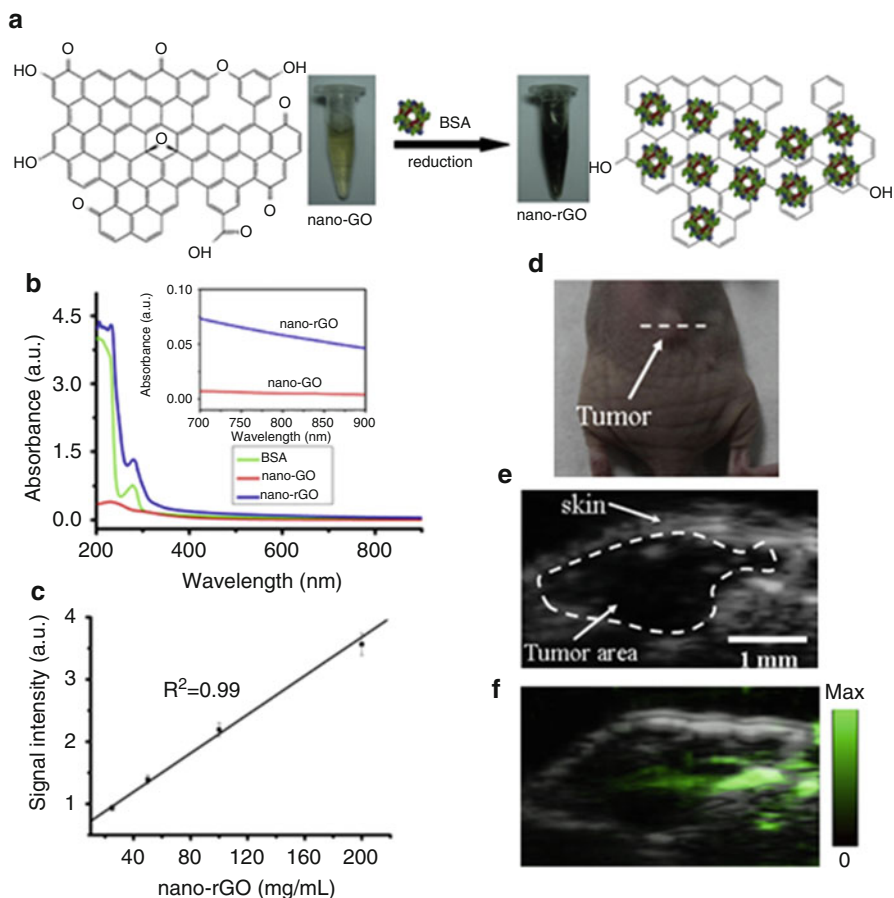
Fig. 15 (**a**) A scheme showing the preparation of nano-rGO from nano-GO using BSA as reductant and stabilizer. (**b**) UV–Vis–NIR absorption spectra of BSA, nano-GO, and nano-rGO. (**c**) The linear relationship between PA signal intensity and the concentration of nano-rGO and PA images of nano-rGO with different concentrations. (**d**) Digital photo of the mice-bearing MCF-7 tumor xenografts. (**e**) Ultrasound (*gray*) image of the tumor region. (**f**) Ultrasound and PA dual-modality images of the tumor region using nano-rGO as contrast agent (Reproduced with permission [41] Copyright 2013, Elsevier)

Single-Walled Carbon Nanotubes

Single-walled carbon nanotubes (SWNTs) had strong NIR absorption, which were widely exploited photothermal (PT) agents for cancer therapy with highly efficient light-to-heat conversion. Recently, PA properties of SWNTs under a pulsed light source were found and intensively investigated [46–48]. The PAI in vivo based on SWNTs contrast agents was firstly achieved by Zerda, Gambhir, and their coworkers [46]. They prepared a conjugation of cyclic Arg–Gly–Asp (RGD)-containing
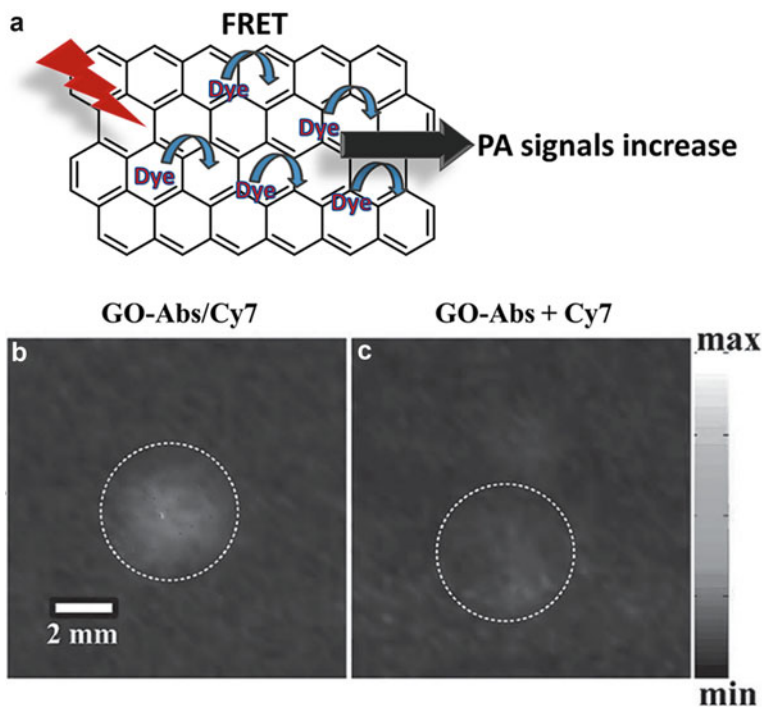
Fig. 16 (**a**) π–π stacking of dyes in close proximity to GO. GO quenches the dye fluorescence via FRET between dye molecules and GO. Using the pulse laser irradiation, the vast majority of absorbed light energy is converted to acoustic waves. The comparison of PA imaging contrast of tumors after being injected with GO–Abs/Cy7, GO–Abs, and Cy7. U87-bearing Balb/c nude mice ($n = 3$) was injected through the tail vein with GO–Abs/Cy7 (**b**), and separate GO–Abs and Cy7 solutions were injected simultaneously into the same mice (**c**). The *white dotted lines* on the images illustrate the approximate tumor edges (Reproduced with permission [45] Copyright 2015, Wiley Publishing Group)

peptides to SWNTs (SWNT-RGD) (Fig. 17a). The SWNT-RGD was stable in serum and showed NIR absorbance and PA properties (Fig. 17b, c). The SWNT-RGD was further attached to high affinity to $\alpha_v\beta_3$ integrin, which is overexpressed in tumor neovasculature. Intravenous injection of the targeted SWNT-RGD in mice led to 8 times higher PA signal in the tumor compared with mice injected with nontargeted SWNTs (Fig. 17d). Wang and Sitharaman took the advantage of high-optical-absorption contrast of SWNTs to realize the high-performance PAI [2, 47]. On the one hand, they validated and demonstrated the SWNTs could be utilized as PA contrast agents for biomedical imaging in vivo. On the other hand, PAI technique could detect, map, and quantify trace amounts of SWNTs in a variety of histological tissue specimens. The detection sensitivity of PAI technique to SWNTs could reach down to picogram (10^{-12} g) levels. PAI technique could provide complementary
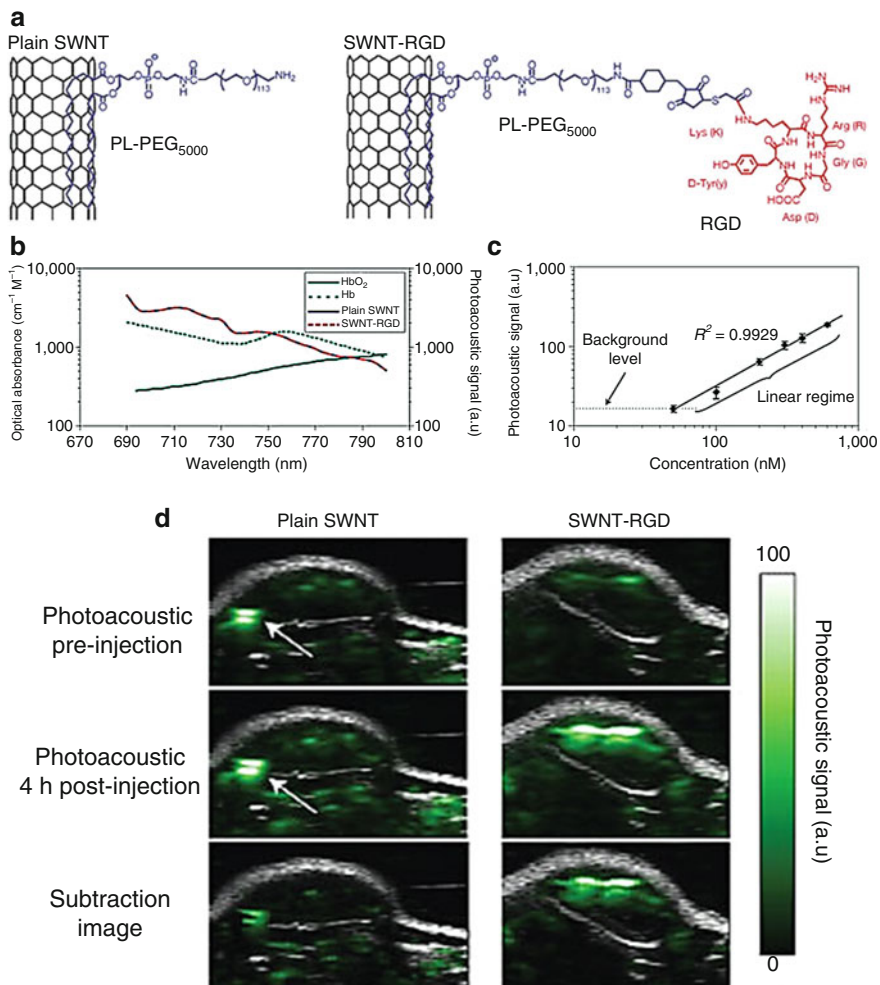
Fig. 17 (**a**) Illustration of plain SWNT and SWNT-RGD. The phospholipid binds to the sidewall of the SWNT connecting the PEG-5000 to the nanotubes. The RGD allows the SWNT to bind to tumor integrins such as $\alpha_v\beta_3$. (**b**) The PA spectra of plain SWNT and SWNT-RGD are overlaid on the known optical absorbance of HbO_2 and Hb. (**c**) The PA signal from each inclusion was calculated. The background level represents the endogenous signal measured from tissues. The error bars represent standard error ($n = 3$). (**d**) Ultrasound (*gray*) and PA (*green*) images of one vertical slice (*white dotted line*) through the tumor. The ultrasound images show the skin and tumor boundaries. Subtraction images were calculated as the 4 h post-injection image minus the preinjection image (Reproduced with permission [46] Copyright 2008, Nature)

information to existing electron and optical microscopy techniques in the histological analysis of tissue sections containing SWNTs.

In order to obtain excellent PA contrast agents, the synergistic effect of known NIR dyes was unitized by combination with SWNTs. Zerda et al. presented a family
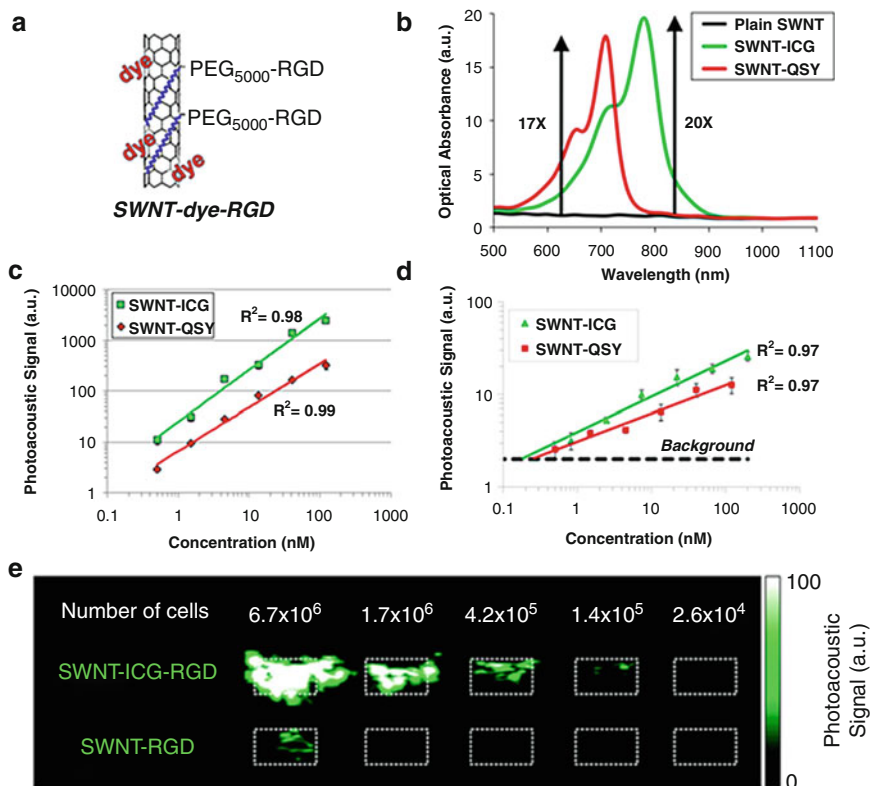
Fig. 18 (**a**) Illustration of a SWNT-dye-RGD particle. The dye (*red*) is attached to the SWNT surface through noncovalent π–π stacking bonds. Phospholipid–polyethylene glycol-5000 (*blue*) is conjugated to the targeting peptide (RGD) on one end and to the SWNT surface on the other end. (**b**) Optical spectra of SWNT-QSY (*red*) and SWNT-ICG (*green*). (**c**) The PA signal produced by SWNT-QSY and SWNT-ICG was observed to be linearly dependent on the particles' concentration ($R2 = 0.99$ and 0.98, respectively). (**d**) The PA signal from each inclusion was calculated using 3D regions of interest, and the "background" represents the endogenous signal measured from tissues. The error bars represent standard error ($n = 3$ mice). (**e**) PA vertical slice image through an agarose phantom containing increasing number of U87 cancer cells exposed to SWNT-ICG-RGD and plain SWNT-RGD particles. The signal inside the ROI (*dotted white boxes*) is not homogenous due to possible aggregates of cells (**a**–**d**: Reproduced with permission [49] Copyright 2012, American Chemical Society; **e**: Reproduced with permission [50] Copyright 2010, American Chemical Society)

of novel PA contrast agents that were based on the binding of small optical dyes to SWNTs (SWNT-dye) [49, 50]. They prepared five different SWNT-dye contrast agents using different optical dyes, creating five "flavors" of SWNT-dye nanoparticles. Furthermore, the SWNT-dyes were conjugated with cyclic Arg–Gly–Asp (RGD) peptides to molecularly target the $\alpha_v\beta_3$ integrins, which were associated with tumor angiogenesis (Fig. 18a). The new contrast agents, particularly, SWNT that was coated with either a fluorescence quencher, QSY
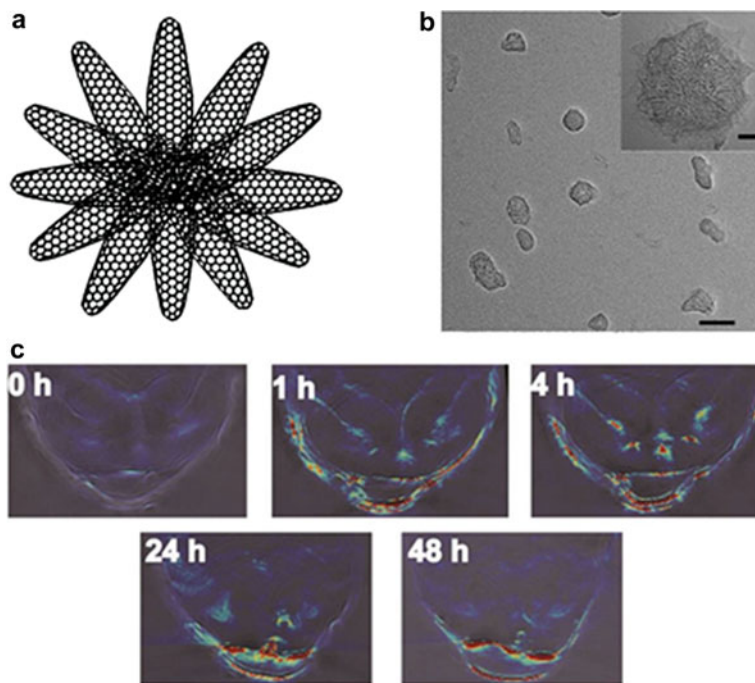
Fig. 19 (**a**) Illustration of a SWNHs/C 18 PMH-PEG. (**b**) TEM image of SWNHs/C 18 PMH-PEG; scale bar, 100 nm; *inset* scale bar, 20 nm. (**c**) Photoacoustic images of tumor in mice after intravenous injection with SWNHs/C 18 PMH-PEG for 1 h, 4 h, 24 h, 48 h (Reproduced with permission [52] Copyright 2014, Wiley Publishing Group)

(SWNT-QSY), or ICG (SWNT-ICG) exhibited 17 and 20 times higher molar extinction coefficient and over 100 times and 300 times higher PA contrast in living animals, respectively (Fig. 18b), compared to plain SWNTs, leading to sub-nanomolar sensitivities (Fig. 18c, d). Intravenous administration of these tumor-targeted imaging agents to tumor-bearing mice showed significantly higher PA signal in the tumor than that in mice injected with the untargeted contrast agent. Besides, the new contrast agent can detect $\sim$20 times fewer cancer cells than previously reported SWNTs (Fig. 17e). More importantly, the PA signals of SWNT-QSY and SWNT-ICG can be spectrally separated in living animals injected subcutaneously with both particles in the same location, opening the possibility for multiplexing in vivo studies.

A new type of carbon-based nanomaterials, single-walled carbon nanohorns (SWNHs) was recently developed with many advantages, such as suitable sizes (80–100 nm) for enhanced penetration and retention (EPR) and high purity with low toxicity (Fig. 19a, b) [51]. Shu and Wan reported the highly water-dispersible SWNHs as theranostic agents for PAI and PTT therapy for the first time [52]. They modified SWNHs with the poly(maleic anhydride-alt-1-octadecene-

poly(ethylene glycol)) (C 18 PMH-PEG) for high stability and biocompatibility. The as-prepared SWNHs/C 18 PMH-PEG not only can serve as an excellent photothermal agent but also can be used as a promising PAI contrast agent both in vitro and in vivo due to its strong absorption in the NIR region. The PAI result reveals that the SWNHs/C 18 PMH-PEG possesses ultra-long blood circulation time and can significantly be accumulated at the tumor site through the EPR effect. The tumor boundary can be clearly delineated after intravenous injection of SWNHs/C 18 PMH-PEG. The maximum accumulation of SWNHs/C 18 PMH-PEG at tumor site could be achieved at the time point of 24 h after intravenous injection (Fig. 19c). Therefore, a PAI-guided PTT platform based on SWNHs is proposed and highlights the potential theranostic application for biomedical uses. Wang and his coworkers developed C-dots with red emission from polythiophene phenylpropionic acid (PPA) as multimodal fluorescent, PAI, and thermal theranostics [53]. The as-prepared C-dots showed a broad absorption band in the visible to NIR region (400–800 nm) with red emission (from 500 to 800 nm with a peaked at 640 nm). Significantly, the prepared C-dots exhibited photothermal conversion efficiency as high as 38.5 % under 671 nm laser irradiation. At different excitation wavelengths, 350–600 nm (visible light) for red FL imaging and 671 nm (NIR light) for PA imaging and photothermal therapy (PTT) can be utilized for different functions. The study showed that as-prepared C-dots can be used as active agents in FL and PA imaging-guided PTT, thereby significantly broadening the biomedical applications of C-dots. These novel C-dots provide an excellent nanomaterial candidate for efficient theranostic applications.

Stimuli-Responsive Nanomaterials

The nanomaterials have been well developed as PA contrast agent for the biomedical fields. The structure and surface composition of the self-assembled nanomaterials can be controlled in well-defined chemical conditions for targeted imaging. However, the physiochemical parameters of prepared nanomaterials as well as designed biological functions will compromise due to the complicated bioenvironments. An alternative strategy, in situ construction of nanomaterials in biological conditions with signal transmutation to execute diagnostics and/or therapeutics, is developed recently. Xu and his coworkers founded supramolecular hydrogelation inside living cells in situ, which is triggered by enzyme with the fluorescence signals increasing due to the hydrophobic effect [54–56]. Rao and Liang reported a condensation reaction-induced hydrophobicity increase, resulting in aggregation to form nanostructures. The condensation reaction can be controlled by reduction or enzyme under physiological conditions with fluorescence, magnetic resonance, or radioactive readout [57–61]. Tang and Liu introduced aggregation-induced emission (AIE) effect-based supramolecular aggregation in living cells to monitor cell apoptosis, where the AIE molecules were released from their conjunction with peptide by caspase-3 [62–65]. The in situ constructive nanomaterials are generally realized from the small molecule with hydrophobic aggregatable units and hydrophilic
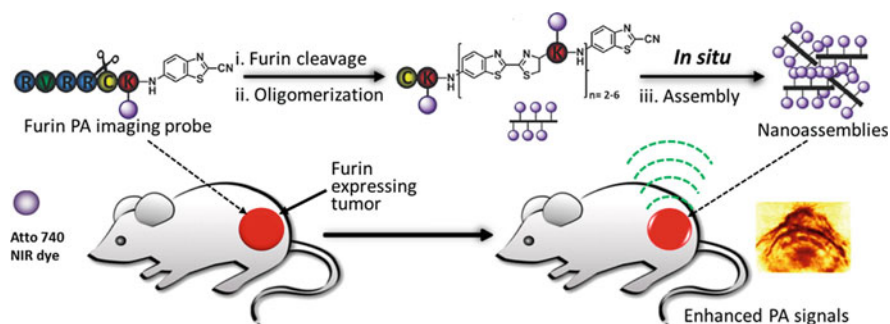
Fig. 20 Schematic illustration of activatable oligomerization-induced construction of nanoassemblies in situ for PA imaging of furin-like activity in vivo (Reproduced with permission [59] Copyright 2012, American Chemical Society)

responsive groups (prevent the aggregation due to hydrophilicity and steric hindrance). The hydrophobic aggregatable units self-assemble when the hydrophilic group leaving upon physiological condition stimuli. Meanwhile, Wang et al. reported supramolecular approach to realize the in situ formation of nanoassemblies in living cells, which involved the pH-responsive amphiphilic responsive carrier and aggregatable monomer bis-pyrene [66]. The nanocarrier delivered the bis-pyrene to the lysosomes of cells. In the acidic lysosomes, the bis-pyrene monomers were released and self-aggregated with turn-on signals. Similarly, the intelligent PA contrast agent with stimuli responsiveness will bring the PA signal enchantment due to the formation of nanomaterials upon stimuli to realize specific diagnosis/therapy functionality.

It is possible to construct nanomaterials as PA contrast agent in situ because the NIR dyes could quench the fluorescence and enhance intensity of PA signals when aggregation. For example, Rao and his coworkers introduced in situ condensation reaction and self-aggregation induced by enzyme, which provided PA contrast to report the enzyme activity in living subjects (Fig. 20) [59]. The molecular precursor includes furin-responsive peptide as a cage group, condensation reaction group, and NIR dyes. In furin overexpressing region, the molecular precursor was activated to accomplish the condensation reaction followed by the in situ aggregation to form nanoassemblies. Thus, the probe provided furin and furin-like activity in cells and tumor models by generating a significantly higher PA signal relative to furin-deficient and nontarget controls. This activatable PA probe could report enzyme activity in living subjects at depths significantly greater than fluorescence imaging probes.

Wang et al. rationally designed a responsive small-molecule precursor (P18-1) that simultaneously self-assembled into nanofibers in tumor sites that exhibited assembly induced retention (AIR) effect, which resulted in improved PA imaging signal and enhanced therapeutic efficacy (Fig. 21) [67]. The compound P18-1 was composed of purpurin 18 (P18) as the functional molecule, Pro–Leu–Gly–Val–Arg–Gly (PLGVRG) as the enzyme-responsive peptide linker, and Arg–Gly–Asp (RGD) as the targeting ligand. Initially, hydrophilic small-molecule P18-1 in physiological
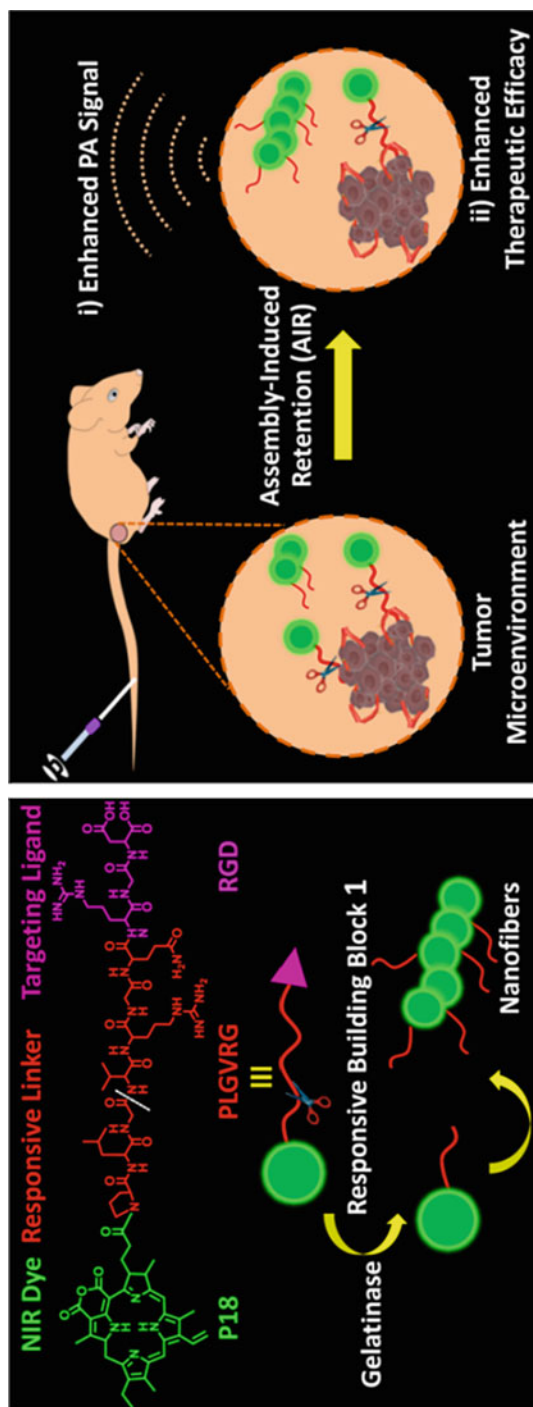
Fig. 21 Schematic illustration of the structure of P18-1 and it responsively self-assembled into nanofibers in tumor sites that exhibited AIR effect for improving PA imaging signal and tumor therapeutic efficacy (Reproduced with permission [67] Copyright 2015, Wiley Publishing Group)
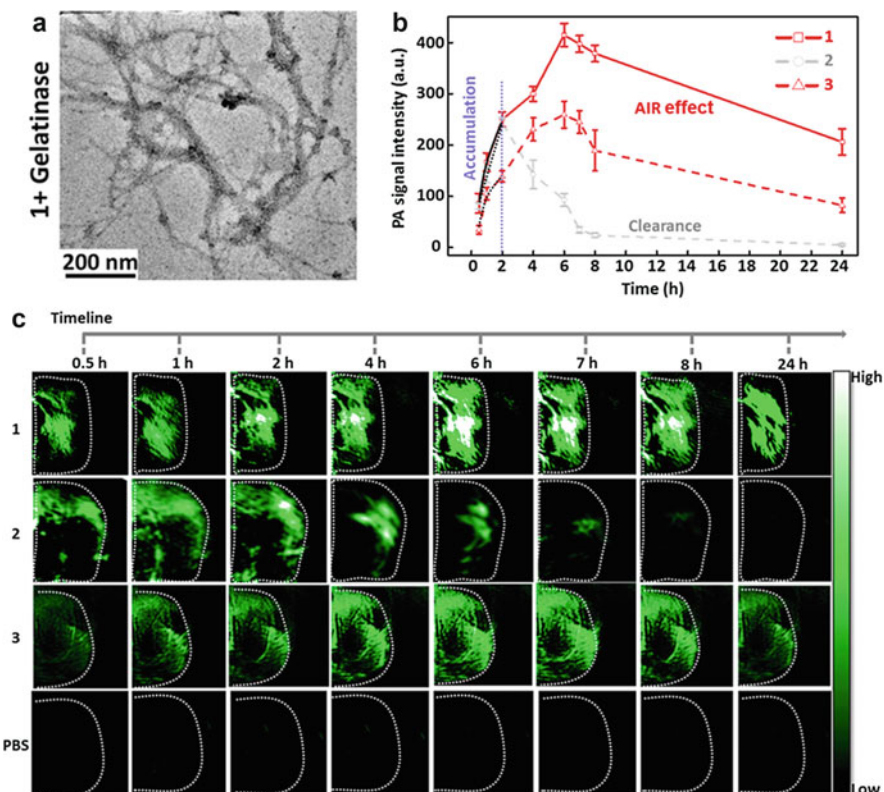
Fig. 22 (**a**) TEM image of self-assembled P18-1 after incubation with gelatinase in the buffer solution. (**b**) In situ quantification of PA signal intensity in tumor site with time increase from 0.5 to 24 h post-injection. (**c**) AIR effect of P18-1 in a tumor site was evaluated in U87 xenografted mouse model by monitoring long-term PA imaging signals. PA images in transverse sections of tumor up to 24 h after injection with P18-1, P18-2 (200 μM, 200 μL (PBS: DMSO = 95:5, v/v)), or PBS (200 μL (PBS: DMSO = 95:5, v/v)). All data are expressed as mean ± SD ($n = 3$). The statistical significances in P18-1 and P18-2 were determined using a two-sample Student's test (**$p \leq$ 0.01). (Reproduced with permission [67] Copyright 2015, Wiley Publishing Group)

environment readily diffused, extravasated, and targeted to $\alpha_v\beta_3$ integrins that overexpressed on cancer cell membranes. Then, gelatinase, which was overexpressed in tumor microenvironment, selectively cuts the PLGVRG linker. The residue of P18-1 with enhanced the hydrophobicity and reduced less steric hindrance self-assembled into nanofibers (Fig. 22a). Finally, the self-assembled fibrous nanostructures exhibited prolonged retention time in tumors that directly led to an enhanced PA signal and therapeutic efficacy (Fig. 22b). Intriguingly, P18-1 showed the maximum sevenfold higher retention concentration compared to that of the control molecule (P18-2) at 10 h post-injection owing to the AIR effect. Moreover, the half retention time ($\tau_{1/2}$) of P18-1 in tumor sites was up to 24 h, and $\tau_{1/2}$ of the P18-2 was only 4 h at the same condition (Fig. 22c). Eventually, the anhydride group of P18 in
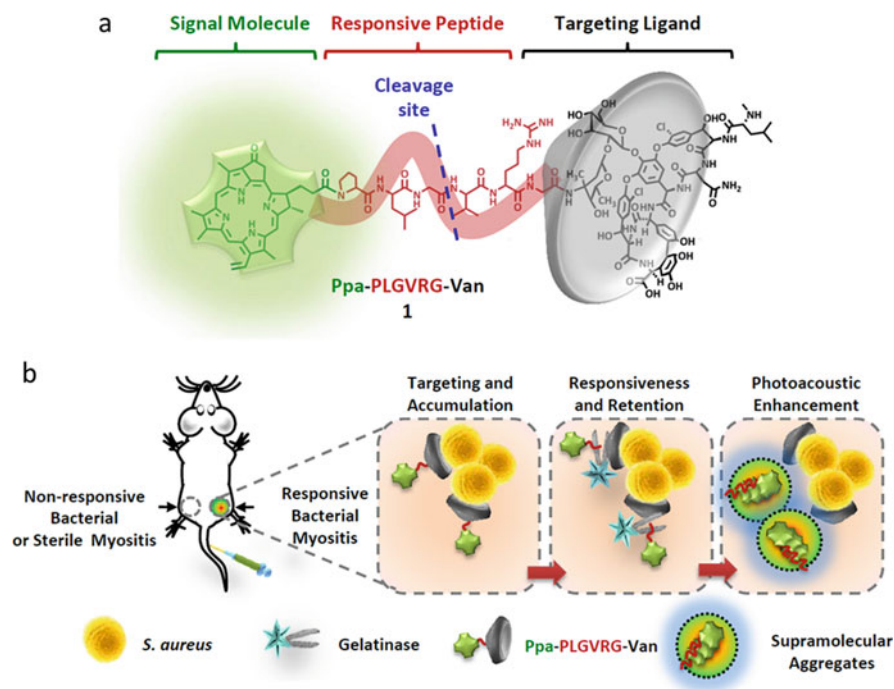
Fig. 23 (**a**) The molecular structure of Ppa–PLGVRG–Van as a building block for constructing supramolecular aggregates. (**b**) Illustration of bacterial infection imaging based on an in vivo aggregation strategy. Firstly, the targeting molecule (Van) causes Ppa–PLGVRG–Van to accumulate at the site of responsive bacterial myositis; then, the gelatinase produced by gelatinase-positive bacteria in the infectious microenvironment cleaves the peptide linker, triggering self-aggregation in situ; finally, the supramolecular aggregates significantly enhance the photoacoustic signal so that the bacterial infection can be detected by imaging (Reproduced with permission [68] Copyright 2015, Wiley Publishing Group)

nanofibers was slowly hydrolyzed and became a hydrophilic molecule that resulted in disassembly of assembly and excreted out of the solid tumor. The AIR effect based on the assembly of supramolecular structures in living systems will pave the way to develop novel functional nanomaterials for cancer diagnostics and therapeutics. By a similar strategy, they presented a new responsive photoacoustic contrast agent for specific and sensitive imaging of bacterial infection in vivo (Fig. 23a) [68]. The building block (Ppa–PLGVRG–Van 1) was designed and synthetically characterized, which is composed of pyropheophorbide-α (Ppa) as a signaling molecule, Pro–Leu–Gly–Val–Arg–Gly (PLGVRG) as an enzyme-responsive peptide linker, and vancomycin (Van) as a targeting ligand. The Ppa–PLGVRG–Van is selectively cleaved by gelatinase to form hydrophobic building blocks which readily self-aggregate in vitro and in vivo. Tissue-mimicking phantoms infected with various species of bacteria were created to confirm that aggregates formed in situ. The aggregation-induced enhancement of the photoacoustic signal can be explained by
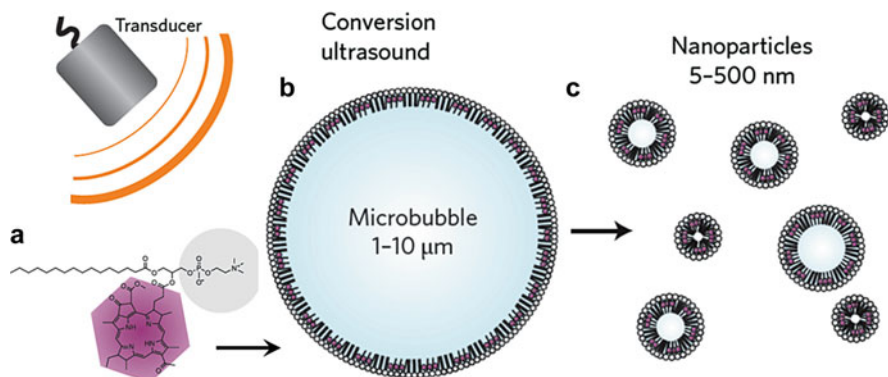
Fig. 24 Schematics of porphyrin microbubbles (*pMBs*) and their micro-to-nano conversion. (**a**) Molecular structure of BChl–lipid. (**b**) Self-assembled pMBs consist of a BChl–lipid shell encapsulating perfluorocarbon gas. (**c**) Porphyrin nanoparticles (*pNPs*) converted from pMBs via sonication with low-frequency, high-duty-cycle ultrasound (conversion ultrasound) (Reproduced with permission [71] Copyright 2015, Nature)

the increased heat conversion efficiency of aggregates compared to monomers, which was predicted by theory and confirmed experimentally. Thus, the specific accumulation and aggregation of Ppa–PLGVRG–Van in the microenvironment created by bacterial infection leads to a significant amplification of the PA signal in situ, which is consistent with theoretical predictions. The enhancement of the PA signal by in vivo self-aggregation can be used as the basis of a highly sensitive and specific system for imaging bacterial infections (Fig. 23b). The in situ responsive nanomaterials as PA contrast agent in living systems will provide new possibilities for biomedical applications such as tissue engineering, biosensing, bioimaging, and gene/drug delivery.

Converting monomeric compounds into supramolecular nanostructures by endogenous or external stimuli is increasingly popular because these materials are useful for imaging and treating diseases [69, 70]. At the same time, supramolecular nanostructures can also be converted from microstructures. Zheng et al. showed the in situ conversion of microbubbles to nanoparticles using low-frequency ultrasound (Fig. 24) [71]. The microbubble consists of a bacteriochlorophyll–lipid shell around a perfluoropropane gas (Fig. 25a). The encapsulated gas provided ultrasound imaging contrast, and the porphyrins in the shell conferred PA and fluorescent properties. On exposure to ultrasound, the microbubbles bursted and formed smaller nanoparticles that possessed the same optical properties as the original microbubble (Fig. 25b, c). The conversion was possibly realized in tumor-bearing mice upon ultrasound, where the PA signals kept for longer time (120 min) compared with that (2 min) of the tumor-bearing mice without ultrasound stimuli (Fig. 25d). The results indicated that the in situ construction of nanoassemblies could effectively deliver drugs to tumors or long-term PA imaging with enhanced permeability and retention (EPR) effect.
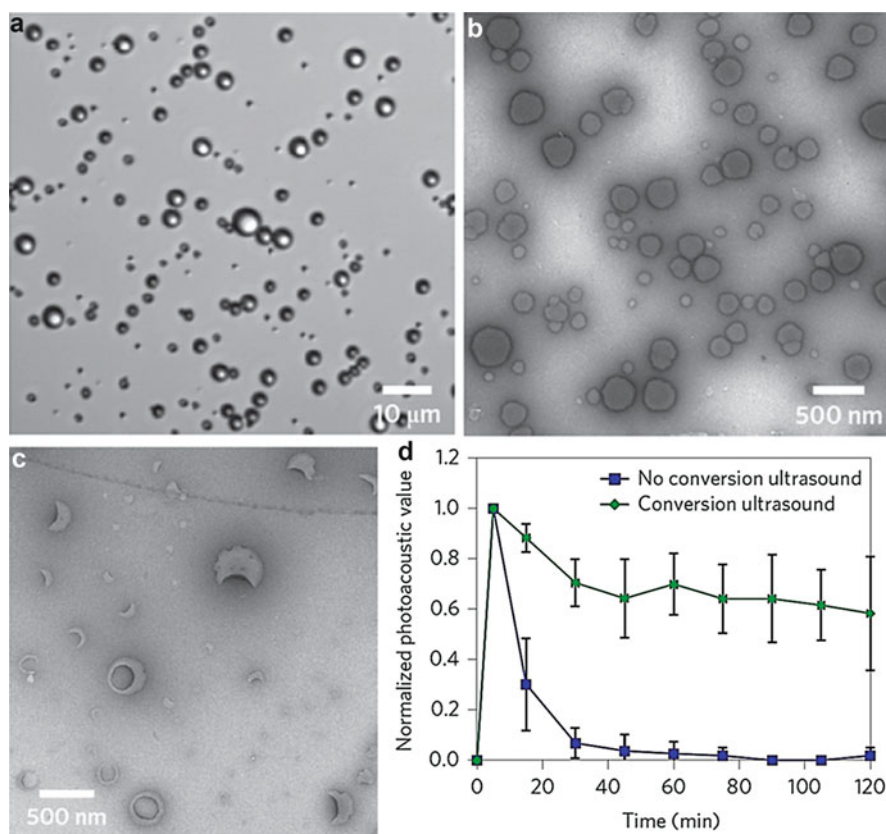
Fig. 25 (**a**) Light microscopy image of pMBs. (**b**) TEM image of pNPs formed from pMBs after ten ultrasound pulses. (**c**) TEM image of liposome-like structures formed from pNPs after placing pNPs in a vacuum. (**d**) Normalized PA signal over time in the tumor, with conversion ultrasound not applied (*blue*) or applied (*green*). PA values are normalized to the peak PA value. Mean $\pm$ 1 s.d. ($n = 3$). Only in tumors in which conversion ultrasound was applied does the pNP remain at the tumors site, indicating successful delivery to the tumor (Reproduced with permission [71] Copyright 2015, Nature)

Summary

PAI systems have been developed and commercialized as a real-time imaging technology for deep tissue with high resolution, which provides broad applications including imaging of tumor microenvironments, drug release, hemodynamics, oxygen metabolism, biomarkers, and gene expression. With the development of PAI instrument, new PA contrast agents should be designed and prepared for high-performance imaging. The nanomaterials show many advantages, such as high stability and long circulation time compared with small molecules. We have

reviewed the nanomaterials and their successful applications for PAI in the biomedical field. Especially, the in situ constructive and intelligent nanomaterials for PA imaging for disease diagnosis are emphasized. However, the use of the nanomaterials does not always run out of questions [72]. For examples, gold nanomaterials are discouraged by the unpredictable high cost. Copper-based nanomaterials face the problem of well-known pose neurotoxicity. Nonmetallic, especially, organic NIR dye-based nanomaterials are most promising contrast agents for PAI. On the one hand, many organic dyes pass through the FDA certification and are extensively used in clinics. On the other hand, one can control the PA properties (excitation wavelength and ultrasound intensity) of organic dye-based nanomaterials by adjusting the aggregation modes of organic dye molecules. Finally, the development of ligand-targeting and integrated diagnostics and therapeutics PA contrast agents is always the common goal of basic scientific research and clinical research. We believe that new preclinical PA contrast agents based on nanomaterials will offer a significant expansion of the diagnostic utility of PAI.

References

1. Xu M, Wang LV (2006) Photoacoustic imaging in biomedicine. Rev Sci Instrum 77(4):041101
2. Wang C, Ma X, Ye S, Cheng L, Yang K, Guo L, Li C, Li Y, Liu Z (2012) Protamine functionalized single-walled carbon nanotubes for stem cell labeling and in vivo raman/magnetic resonance/photoacoustic triple-modal imaging. Adv Funct Mater 22(11):2363–2375
3. Wang T, Yang Y, Alqasemi U, Kumavor PD, Wang X, Sanders M, Brewer M, Zhu Q (2013) Characterization of ovarian tissue based on quantitative analysis of photoacoustic microscopy images. Biomed Opt Express 4(12):2763–2768
4. Wang X, Xie X, Ku G, Wang LV, Stoica G (2006) Noninvasive imaging of hemoglobin concentration and oxygenation in the rat brain using high-resolution photoacoustic tomography. J Biomed Opt 11(2):024015
5. Li ML, Oh JT, Xie X, Ku G, Wang W, Li C, Lungu G, Stoica G, Wang LV (2008) Simultaneous molecular and hypoxia imaging of brain tumors in vivo using spectroscopic photoacoustic tomography. Proc IEEE 96(3):481–489
6. Dima A, Burton NC, Ntziachristos V (2014) Multispectral optoacoustic tomography at 64, 128, and 256 channels. J Biomed Opt 19(3):036021
7. Wang LV, Gao L (2014) Photoacoustic microscopy and computed tomography: from bench to bedside. Annu Rev Biomed Eng 16(1):155–185
8. Wang X, Pang Y, Ku G, Xie X, Stoica G, Wang LV (2003) Noninvasive laser-induced photoacoustic tomography for structural and functional in vivo imaging of the brain. Nat Biotechnol 21(7):803–806
9. Taruttis A, Claussen J, Razansky D, Ntziachristos V (2012) Motion clustering for deblurring multispectral optoacoustic tomography images of the mouse heart. J Biomed Opt 17(1):016009
10. Ntziachristos V, Razansky D (2010) Molecular imaging by means of multispectral optoacoustic tomography (MSOT). Chem Rev 110(5):2783–2794
11. Wang LV, Hu S (2012) Photoacoustic tomography: in vivo imaging from organelles to organs. Science 335(6075):1458–1462
12. Ntziachristos V (2010) Going deeper than microscopy: the optical imaging frontier in biology. Nat Method 7(8):603–614
13. Nie L, Chen X (2014) Structural and functional photoacoustic molecular tomography aided by emerging contrast agents. Chem Soc Rev 43(20):7132–7170

14. Li K, Liu B (2014) Polymer-encapsulated organic nanoparticles for fluorescence and photoacoustic imaging. Chem Soc Rev 43(18):6570–6597

15. Pan D, Kim B, Wang LV, Lanza GM (2013) A brief account of nanoparticle contrast agents for photoacoustic imaging. Wiley Interdiscip Rev Nanomed Nanobiotechnol 5(6):517–543

16. Yoon HK, Ray A, Lee Y-EK, Kim G, Wang X, Kopelman R (2013) Polymer-protein hydrogel nanomatrix for stabilization of indocyanine green towards targeted fluorescence and photoacoustic bio-imaging. J Mater Chem B 1(41):5611–5619

17. Wu W, Driessen W, Jiang X (2014) Oligo(ethylene glycol)-based thermosensitive dendrimers and their tumor accumulation and penetration. J Am Chem Soc 136(8):3145–3155

18. Zhang D, Qiao Z-Y, Mayerhoeffer U, Spenst P, Li XJ, Würthner F, Wang H (2014) Nano-confined squaraine dye assemblies: new photoacoustic and near-infrared fluorescence dual-modular imaging probes in vivo. Bioconjug Chem 25(11):2021–2029

19. Duan Z, Gao Y, Qiao Z-Y, Fan G, Liu Y, Zhang D, Wang H (2014) A photoacoustic approach for monitoring the drug release of pH-sensitive poly([beta]-amino ester)s. J Mater Chem B 2(37):6271–6282

20. Sreejith S, Joseph J, Lin M, Menon NV, Borah P, Ng HJ, Loong YX, Kang Y, Yu SW-K, Zhao Y (2015) Near-infrared squaraine dye encapsulated micelles for in vivo fluorescence and photoacoustic bimodal imaging. ACS Nano 9(6):5695–5704

21. Kohl Y, Kaiser C, Bost W, Stracke F, Fournelle M, Wischke C, Thielecke H, Lendlein A, Kratz K, Lemor R (2011) Preparation and biological evaluation of multifunctional PLGA-nanoparticles designed for photoacoustic imaging. Nanomed-Nanotechnol Biol Med 7(2):228–237

22. Huang G, Si Z, Yang S, Li C, Xing D (2012) Dextran based pH-sensitive near-infrared nanoprobe for in vivo differential-absorption dual-wavelength photoacoustic imaging of tumors. J Mater Chem 22(42):22575–22581

23. An F-F, Deng Z-J, Ye J, Zhang J-F, Yang Y-L, Li C-H, Zheng C-J, Zhang X-H (2014) Aggregation-induced near-infrared absorption of squaraine dye in an albumin nanocomplex for photoacoustic tomography in vivo. ACS Appl Mater Interfaces 6(20):17985–17992

24. An H-W, Qiao S-L, Hou C-Y, Lin Y-X, Li L-L, Xie H-Y, Wang Y, Wang L, Wang H (2015) Self-assembled NIR nanovesicles for long-term photoacoustic imaging in vivo. Chem Commun 51(70):13488–13491

25. Gong H, Dong Z, Liu Y, Yin S, Cheng L, Xi W, Xiang J, Liu K, Li Y, Liu Z (2014) Engineering of multifunctional nano-micelles for combined photothermal and photodynamic therapy under the guidance of multimodal imaging. Adv Funct Mater 24(41):6492–6502

26. Lovell JF, Jin CS, Huynh E, Jin H, Kim C, Rubinstein JL, Chan WCW, Cao W, Wang LV, Zheng G (2011) Porphysome nanovesicles generated by porphyrin bilayers for use as multimodal biophotonic contrast agents. Nat Mater 10(4):324–332

27. Huynh E, Lovell JF, Helfield BL, Jeon M, Kim C, Goertz DE, Wilson BC, Zheng G (2012) Porphyrin shell microbubbles with Intrinsic ultrasound and photoacoustic properties. J Am Chem Soc 134(40):16464–16467

28. Huynh E, Jin CS, Wilson BC, Zheng G (2014) Aggregate enhanced trimodal porphyrin shell microbubbles for ultrasound, photoacoustic, and fluorescence imaging. Bioconjug Chem 25(4):796–801

29. Zhang Y, Jeon M, Rich LJ, Hong H, Geng J, Zhang Y, Shi S, Barnhart TE, Alexandridis P, Huizinga JD, Seshadri M, Cai W, Kim C, Lovell JF (2014) Non-invasive multimodal functional imaging of the intestine with frozen micellar naphthalocyanines. Nat Nanotechnol 9(8): 631–638

30. Akers WJ, Kim C, Berezin M, Guo K, Fuhrhop R, Lanza GM, Fischer GM, Daltrozzo E, Zumbusch A, Cai X, Wang LV, Achilefu S (2011) Noninvasive photoacoustic and fluorescence sentinel lymph node identification using dye-loaded perfluorocarbon nanoparticles. ACS Nano 5(1):173–182

31. Fan Q, Cheng K, Yang Z, Zhang R, Yang M, Hu X, Ma X, Bu L, Lu X, Xiong X, Huang W, Zhao H, Cheng Z (2015) Perylene-diimide-based nanoparticles as highly efficient photoacoustic agents for deep brain tumor imaging in living mice. Adv Mater 27(5):843–847

32. Pan J, Liu Y, Feng S-S (2010) Multifunctional nanoparticles of biodegradable copolymer blend for cancer diagnosis and treatment. Nanomedicine 5(3):347–360

33. Pan J, Wan D, Bian Y, Sun H, Zhang C, Jin F, Huang Z, Gong J (2013) Fluorescent hydroxyapatite-loaded biodegradable polymer nanoparticles with folate decoration for targeted imaging. AIChE J 59(12):4494–4501

34. Li K, Pan J, Feng SS, Wu AW, Pu KY, Liu Y, Liu B (2009) Generic strategy of preparing fluorescent conjugated-polymer-loaded poly (DL-lactide-co-glycolide) nanoparticles for targeted cell imaging. Adv Funct Mater 19(22):3535–3542

35. Pu K, Shuhendler AJ, Jokerst JV, Mei J, Gambhir SS, Bao Z, Rao J (2014) Semiconducting polymer nanoparticles as photoacoustic molecular imaging probes in living mice. Nat Nanotechnol 9(3):233–239

36. Liu J, Geng J, Liao L-D, Thakor N, Gao X, Liu B (2014) Conjugated polymer nanoparticles for photoacoustic vascular imaging. Polym Chem 5(8):2854–2862

37. Zha Z, Deng Z, Li Y, Li C, Wang J, Wang S, Qu E, Dai Z (2013) Biocompatible polypyrrole nanoparticles as a novel organic photoacoustic contrast agent for deep tissue imaging. Nano-scale 5(10):4462–4467

38. Song X, Gong H, Yin S, Cheng L, Wang C, Li Z, Li Y, Wang X, Liu G, Liu Z (2014) Ultra-small iron oxide doped polypyrrole nanoparticles for in vivo multimodal imaging guided photothermal therapy. Adv Funct Mater 24(9):1194–1201

39. Patel MA, Yang H, Chiu PL, Mastrogiovanni DD, Flach CR, Savaram K, Gomez L, Hemnarine A, Mendelsohn R, Garfunkel E, Jiang H, He H (2013) Direct production of graphene nanosheets for near infrared photoacoustic imaging. ACS Nano 7(9):8147–8157

40. Hola K, Zhang Y, Wang Y, Giannelis EP, Zboril R, Rogach AL (2014) Carbon dots-emerging light emitters for bioimaging, cancer therapy and optoelectronics. Nano Today 9(5):590–603

41. Sheng Z, Song L, Zheng J, Hu D, He M, Zheng M, Gao G, Gong P, Zhang P, Ma Y (2013) Protein-assisted fabrication of nano-reduced graphene oxide for combined in vivo photoacoustic imaging and photothermal therapy. Biomaterials 34(21):5236–5243

42. Yang K, Hu L, Ma X, Ye S, Cheng L, Shi X, Li C, Li Y, Liu Z (2012) Multimodal imaging guided photothermal therapy using functionalized graphene nanosheets anchored with magnetic nanoparticles. Adv Mater 24(14):1868–1872

43. Yan X, Hu H, Lin J, Jin AJ, Niu G, Zhang S, Huang P, Shen B, Chen X (2015) Optical and photoacoustic dual-modality imaging guided synergistic photodynamic/photothermal therapies. Nanoscale 7(6):2520–2526

44. Wang Y, Fu YY, Peng Q, Guo S, Liu G, Li J, Yang H, Chen G (2013) Dye-enhanced graphene oxide for photothermal therapy and photoacoustic imaging. J Mater Chem B 1(42):5762–5767

45. Qin H, Zhou T, Yang S, Xing D (2015) Fluorescence quenching nanoprobes dedicated to in vivo photoacoustic imaging and high-efficient tumor therapy in deep-seated tissue. Small 11(22):2675–2686

46. De La Zerda A, Zavaleta C, Keren S, Vaithilingam S, Bodapati S, Liu Z, Levi J, Smith BR, Ma T-J, Oralkan O (2008) Carbon nanotubes as photoacoustic molecular imaging agents in living mice. Nat Nanotechnol 3(9):557–562

47. Avti PK, Hu S, Favazza C, Mikos AG, Jansen JA, Shroyer KR, Wang LV, Sitharaman B (2012) Detection, mapping, and quantification of single walled carbon nanotubes in histological specimens with photoacoustic microscopy. PLoS One 7(4):e35064

48. Zhou F, Wu S, Yuan Y, Chen WR, Xing D (2012) Mitochondria-targeting photoacoustic therapy using single-walled carbon nanotubes. Small 8(10):1543–1550

49. Zerda A, Bodapati S, Teed R, May SY, Tabakman SM, Liu Z, Khuri-Yakub BT, Chen X, Dai H, Gambhir SS (2012) Family of enhanced photoacoustic imaging agents for high-sensitivity and multiplexing studies in living mice. ACS Nano 6(6):4694–4701

50. Zerda A, Liu Z, Bodapati S, Teed R, Vaithilingam S, Khuri-Yakub BT, Chen X, Dai H, Gambhir SS (2010) Ultrahigh sensitivity carbon nanotube agents for photoacoustic molecular imaging in living mice. Nano Lett 10(6):2168–2172

51. Guldi DM (2007) Nanometer scale carbon structures for charge-transfer systems and photovoltaic applications. Phys Chem Chem Phys 9(12):1400–1420

52. Chen D, Wang C, Nie X, Li S, Li R, Guan M, Liu Z, Chen C, Wang C, Shu C, Wan L (2014) Photoacoustic imaging guided near-infrared photothermal therapy using highly water-dispersible single-walled carbon nanohorns as theranostic agents. Adv Funct Mater 24(42):6621–6628

53. Ge J, Jia Q, Liu W, Guo L, Liu Q, Lan M, Zhang H, Meng X, Wang P (2015) Red-emissive carbon dots for fluorescent, photoacoustic, and thermal theranostics in living mice. Adv Mater 27(28):4169–4177

54. Gao Y, Berciu C, Kuang Y, Shi JF, Nicastro D, Xu B (2013) Probing nanoscale self-assembly of nonfluorescent small molecules inside live mammalian cells. ACS Nano 7(10):9055–9063

55. Zhou J, Du X, Li J, Yamagata N, Xu B (2015) Taurine boosts cellular uptake of small d-peptides for enzyme-instructed intracellular molecular self-assembly. J Am Chem Soc 137:10040–10043

56. Gao Y, Shi JF, Yuan D, Xu B (2012) Imaging enzyme-triggered self-assembly of small molecules inside live cells. Nat Commun 3:1033–1040

57. Nejadnik H, Ye D, Lenkov OD, Donig JS, Martin JE, Castillo R, Derugin N, Sennino B, Rao J, Daldrup-Link H (2015) Magnetic resonance imaging of stem cell apoptosis in arthritic joints with a caspase activatable contrast agent. ACS Nano 9(2):1150–1160

58. Pu K, Mei J, Jokerst JV, Hong G, Antaris AL, Chattopadhyay N, Shuhendler AJ, Kurosawa T, Zhou Y, Gambhir SS, Bao Z, Rao J (2015) Diketopyrrolopyrrole-based semiconducting polymer nanoparticles for in vivo photoacoustic imaging. Adv Mater. doi:10.1002/adma.201502285

59. Dragulescu-Andrasi A, Kothapalli S-R, Tikhomirov GA, Rao J, Gambhir SS (2013) Activatable oligomerizable imaging agents for photoacoustic imaging of furin-like activity in living subjects. J Am Chem Soc 135(30):11015–11022

60. Gupta S, Chatni MR, Rao ALN, Vullev VI, Wang LV, Anvari B (2013) Virus-mimicking nano-constructs as a contrast agent for near infrared photoacoustic imaging. Nanoscale 5(5):1772–1776

61. Liang GL, Ren HJ, Rao JH (2010) A biocompatible condensation reaction for controlled assembly of nanostructures in living cells. Nat Chem 2(1):54–60

62. Hong Y, Lam JWY, Tang BZ (2011) Aggregation-induced emission. Chem Soc Rev 40(11):5361–5388

63. Kwok RTK, Leung CWT, Lam JWY, Tang BZ (2015) Biosensing by luminogens with aggregation-induced emission characteristics. Chem Soc Rev 44(13):4228–4238

64. Liang J, Tang BZ, Liu B (2015) Specific light-up bioprobes based on AIEgen conjugates. Chem Soc Rev 44(10):2798–2811

65. Shi HB, Kwok RTK, Liu JZ, Xing BG, Tang BZ, Liu B (2012) Real-time monitoring of cell apoptosis and drug screening using fluorescent light-up probe with aggregation-induced emission characteristics. J Am Chem Soc 134(43):17972–17981

66. Duan Z, Gao Y-J, Qiao Z-Y, Qiao S, Wang Y, Hou C, Wang L, Wang H (2015) pH-Sensitive polymer assisted self-aggregation of bis(pyrene) in living cells in situ with turn-on fluorescence. Nanotechnology 26(35):355703

67. Zhang D, Qi G-B, Zhao Y-X, Qiao S-L, Yang C, Wang H (2015) In situ formation of nanofibers from purpurin18-peptide conjugates and its assembly-induced retention effect in tumor sites. Advanced Materials Accepted 27(40):6125–6130

68. Li-Li Li, Huai-Lei Ma, Guo-Bin Qi, Di Zhang, Faquan Yu, Zhiyuan Hu, Wang H (2015) Pathological condition driven construction of supramolecular nano-assemblies for bacterial infection detection. Advanced Materials Accepted 28(2):254–262

69. Callmann CE, Barback CV, Thompson MP, Hall DJ, Mattrey RF, Gianneschi NC (2015) Therapeutic enzyme-responsive nanoparticles for targeted delivery and accumulation in tumors. Adv Mater 27(31):4611–4615

70. Chien M-P, Carlini AS, Hu D, Barback CV, Rush AM, Hall DJ, Orr G, Gianneschi NC (2013) Enzyme-directed assembly of nanoparticles in tumors monitored by in vivo whole animal

imaging and ex vivo super-resolution fluorescence imaging. J Am Chem Soc 135(50): 18710–18713

71. Huynh E, LeungBen YC, Helfield BL, Shakiba M, Gandier J-A, Jin CS, Master ER, Wilson BC, Goertz DE, Zheng G (2015) In situ conversion of porphyrin microbubbles to nanoparticles for multimodality imaging. Nat Nanotechnol 10(4):325–332

72. Wang X, Zhu M, Li J (2012) Biomedical effects and nanosafety of engineered nanomaterials: recent progress. Chin J Chem 30(9):1931–1947

Metallic and Upconversion Nanoparticles as Photoacoustic Contrast Agents for Biomedical Imaging

Kim Truc Nguyen, Sivaramapanicker Sreejith, and Yanli Zhao

Contents

K.T. Nguyen • S. Sreejith
Division of Chemistry and Biological Chemistry, School of Physical and Mathematical Sciences, Nanyang Technological University, Singapore, Singapore

Y. Zhao (✉)
Division of Chemistry and Biological Chemistry, School of Physical and Mathematical Sciences, Nanyang Technological University, Singapore, Singapore

School of Materials Science and Engineering, Nanyang Technological University, Singapore, Singapore
e-mail: zhaoyanli@ntu.edu.sg

Abstract

Photoacoustic imaging is an emerging biomedical technique. By using nonionized pulsed laser as the excitation source and ultrasound probe as the signal detector, this technique could afford noninvasive imaging for medical diagnostics. In this chapter, current biomedical imaging techniques are discussed and compared in terms of their pros and cons in clinical applications. The basic theory of photoacoustic imaging is elaborated. In order to gain better resolution as well as provide targeted imaging, photoacoustic contrast agents are often employed. Photoacoustic contrast agents such as metallic nanoparticles and upconversion nanoparticles are introduced, revealing promising potentials for clinical uses. Finally, the nanotoxicity of these nanomaterials for practical bioimaging is scrutinized. This chapter presents state-of-the-art research progress of using metallic and upconversion nanoparticles as photoacoustic contrast agents for biomedical imaging.

Keywords

Biomedical imaging • Confocal laser scanning microscopy (CLSM) • Dermoscopy (DS) • High frequency ultrasound imaging (HFUS) • Magnetic resonance imaging (MRI) • Novel imaging schemes • Metallic nanoparticles • Photoacoustic contrast agents • Photoacoustic imaging • Metallic and upconversion nanoparticles, contrast agents • Molecular photoacoustic imaging • Phenomenon of • Photoacoustic microscopy (PAM) • Photoacoustic tomography (PAT) • Photoacoustics based multi-modality imaging • Upconversion nanoparticles

Introduction

Diagnostics benefits the process of health and disease managements, which includes early detection of various diseases, injury assessment, and monitoring of treatment effects. To detect possible initiation or onset of a potential disease state in the tissue, any anomalies in terms of variations and shifts in the sizes or molecular compositions of the cellular components can serve as useful disease indicators. These potential indicators can be effectively monitored and studied by investigating the physical, mechanical, thermal, optical, and other tissue properties. Diagnostic procedures relying on human exteroceptive senses such as visual perception and auxiliary techniques such as histopathological tools, immunohistochemistry, and electron microscopy have been contributed significantly toward enhancing the diagnostic validity in current medicine. However, routine histology that remains the gold standard for the majority of diseases entails invasive procedures like excision biopsy of tissues inducing pain and inherent risks for scar formations and infections. The advent of novel biomedical imaging techniques embarks a methodological shift, where the conventional assay-based approaches are getting replaced by noninvasive imaging-based ones. Various noninvasive imaging modalities have been evolved over the years, and some of them have been translated for the

anatomical imaging. In this article, we review one of state-of-the-art noninvasive imaging techniques, i.e., photoacoustic imaging (PAI). Fundamental principles of PAI and its various forms of implementations are discussed along with highlighting metallic nanoparticles and upconversion nanoparticles as photoacoustic contrast agents.

Biomedical Imaging Techniques

In the past decades, several noninvasive imaging procedures have been evolved with increased diagnostic accuracy, and they are extensively used for performing a variety of clinical investigations [1]. In this context, we focus on the discussion of imaging techniques that are commonly used for soft tissue imaging to detect lesion sites. The widely used clinical imaging techniques include dermoscopy (DS) [2], high-frequency ultrasound (HFUS) [3], magnetic resonance imaging (MRI) [4], laser scanning confocal microscopy (LSCM) [5], and multiphoton microscopy (MPM) [6].

Dermoscopy (DS)

DS involves the usage of light-emitting diodes, digital cameras, and computer systems to perform noninvasive evaluation and differential diagnosis of various skin lesions in vivo [7]. The technique includes the diagnosis of pigmented skin lesions [2] such as the differentiation between malignant melanoma and benign melanocytic nevi, seborrheic keratoses, and basal cell carcinoma (BCC) for a broad range of nonpigmented and inflammatory skin diseases [8]. Figure 1 shows the images of various skin disorders obtained using DS. Although DS offers fast and cost-effective diagnosis, the procedure is restricted to only superficial skin layers and provides only low magnification of the diagnosed sites [9].

High-Frequency Ultrasound Imaging (HFUS)

HFUS often uses high-frequency (typically >5 MHz) ultrasonic waves to interrogate various contrasts of different tissues. Most diagnostic ultrasound imaging procedures involves the usage of piezoelectric ultrasound transducers associated with electronic instrumentation to send the ultrasound pulses into the tissues. Ultrasound images are reconstructed from the echo signals received from the tissues, where the received echoes reflect the acoustic properties of the tissues. Any variations in the acoustic impedances due to the differences in densities along the sound propagation path would be recorded and mapped. Ultrasound imaging has been widely used for various diagnostic applications [10] such as lymph node examination, tumor depth measurement, evaluation of inflammatory diseases like corticosteroids, plaque psoriasis, and systemic sclerosis, as well as examination of inflammatory morphological
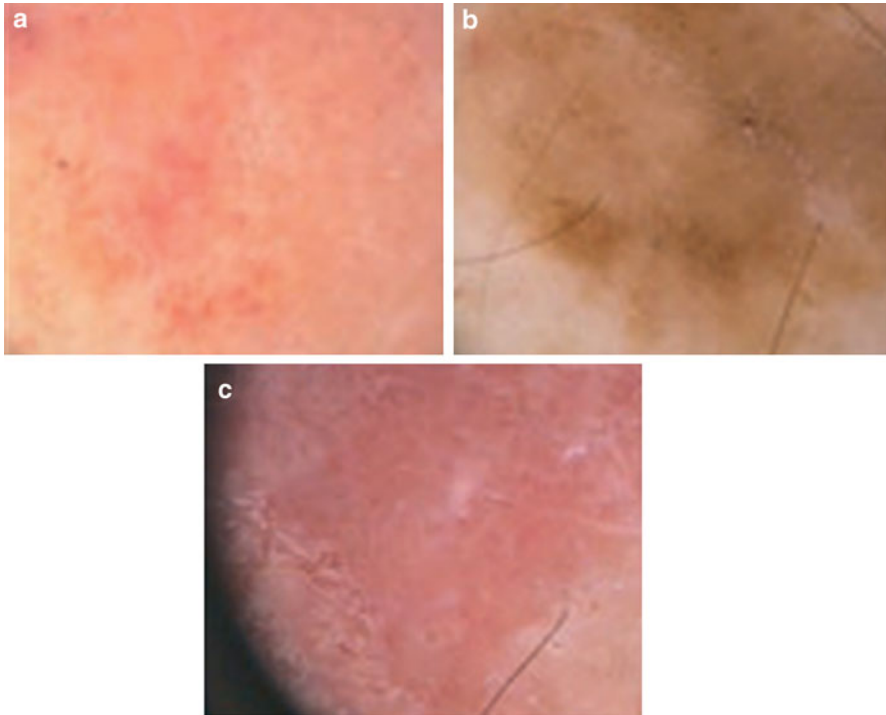
Fig. 1 Dermoscopic images of (**a**) actin keratosis, (**b**) stucco keratosis, and (**c**) pemphigus vulgaris (Adapted with permission from Ref. [9]. Copyright © 2011 John Wiley & Sons A/S)

structures and psoriatic arthritis. Furthermore, ultrasound imaging has also been used to define tumor margins preoperatively, so as to aid in the surgical treatment of skin tumors such as melanomas (Fig. 2a) and BCC [11]. Ultrasound imaging offers high penetration depth, wide field of view, and real-time imaging capability. However, it is challenged with poor image contrast and does not provide adequate resolution for performing cellular-level imaging.

Magnetic Resonance Imaging (MRI)

MRI that is based on the nuclear magnetic resonance (NMR) phenomenon maps the physiological and chemical structure of the tissues and provides their biochemical properties [4]. In clinical settings, MRI procedures are primarily conducted to study the lesion sites within soft tissues [12, 13]. Moreover, MRI-based diagnostic procedures have been also performed to evaluate various skin layers (Fig. 2b) and skin thickness and diagnosis of various diseases such as glomus tumor and unilateral lymphedema in skin tissues [14]. Although MRI procedures offer noninvasive
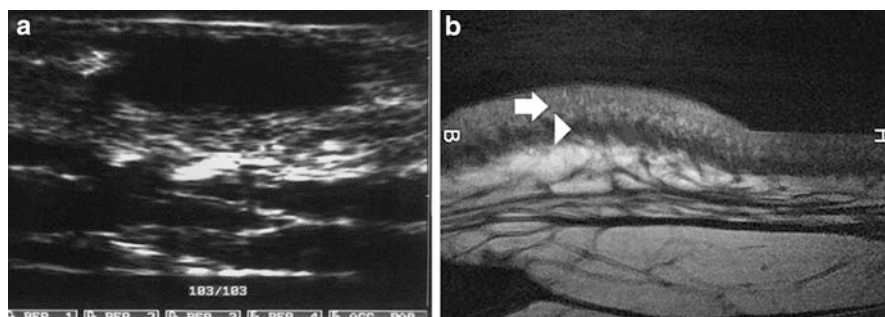
Fig. 2 (**a**) Cutaneous malignant melanoma of the right forearm. At 20 MHz HFUS, the lesion is shown as homogeneous hypoechoic nodule extending to the reticular dermis (Adapted with permission from Ref. [11]. Copyright © 1998, Elsevier Science Ireland Ltd). (**b**) T1 weighted spin echo image at the face obtained from 3–T MRI machine with well-distinguished superficial and deep dermis (*arrows*) (Adapted with permission from Ref. [14]. Copyright © 2009, European Society of Radiology)

imaging of soft tissues with very good penetration depth, they are often challenged with poor resolution, long interrogation time, high costs, and incapability of being used in patients with implants.

Confocal Laser Scanning Microscopy (CLSM)

CLSM is a noninvasive imaging technique that provides high-contrast images of the tissues with optical sectioning and high lateral and axial resolutions. The optical sectioning capabilities of CLSM technique are comparable with the conventional histological examinations, and therefore, the technique has been widely employed in various diagnostics and monitoring procedures, especially in dermatology. Its applications include imaging the topography of normal skin such as selective imaging of each layer of epidermis (Fig. 3), diagnosis of pigmentary disorders [15] such as melanoma [16] and nonmelanoma skin cancer [16], evaluation of inflammatory skin lesions such as allergic contact dermatitis, and psoriasis [17]. Current clinical diagnostic procedures have adopted CLSM technique to a great extent due to its noninvasiveness, high resolution, as well as real-time and optical sectioning capabilities. However, the penetration depth of CLSM is restricted, and CLSM can be operated only along the epidermal and superficial dermal structures and provides limited field of view [18].

Other Imaging Modalities

In addition to the described imaging modalities, other novel imaging schemes are evolving for imaging in biomedical diagnosis. These modalities include Raman spectroscopy [19], fluorescence remission spectroscopy and sensing [20], and
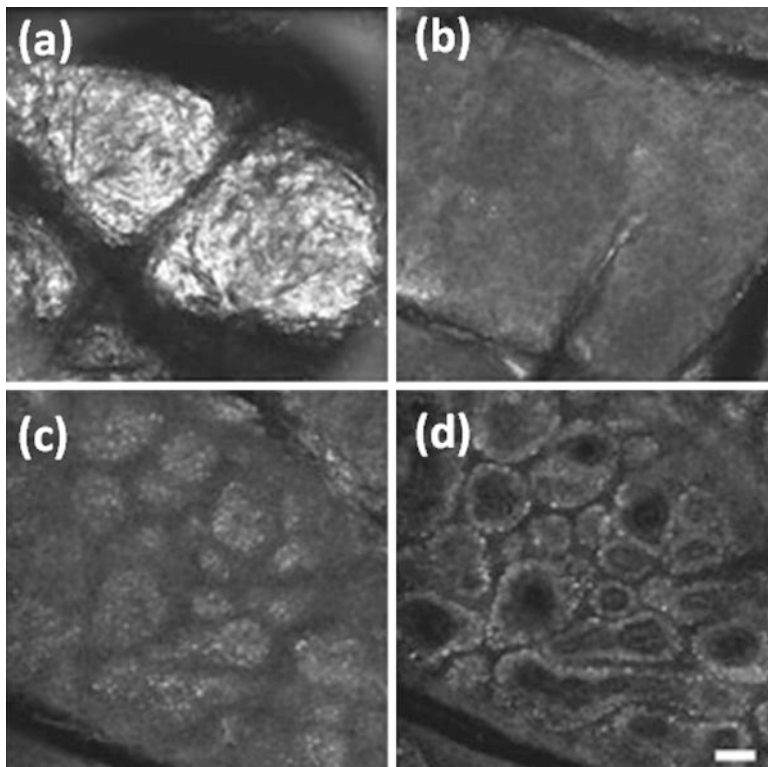
Fig. 3 Confocal images of normal skin taken from the forearm at the dorsal side of Fitzpatricks skin type III subject. (**a**) Stratum corneum, (**b**) keratinocytes in stratum spinosum, (**c**) basal cell layer observed as a cobblestone pattern of bright clusters of cells, and (**d**) dermo–epidermal junction. Scale bar 50 μm (Adapted with permission from Ref. [15]. Copyright © 2009 John Wiley & Sons A/S)

terahertz pulsed imaging [21]. Furthermore, combinations of two or more imaging techniques were also reported to provide synergetic complementary information from the diagnosed sites. Such techniques include the combination of multiphoton imaging with ultrasound and CLSM [9], fluorescence lifetime and spectral imaging with confocal microscopy [22], as well as other combination imaging modalities [23].

Table 1 summarizes the imaging performance of the imaging techniques currently used in biomedical imaging. Considering the diagnostic capabilities of each imaging technique, it is evident that the fundamental physical principles governing their operation impose certain limitations to their inherent resolution and penetration depth. Although imaging modalities such as HFUS and MRI offer sufficient penetration depth for imaging through various layers of tissues, they are challenged with limited spatial resolution for cellular-level imaging. DS has been widely used for recording and storing images of skin, but they often fail to map microscopic features

Table 1 Comparison of imaging modalities used in biomedical imaging

	DS	HFUS	MRI	CLSM
Resolution	>50 μm	32–500 μm	<100 μm	>0.5 μm
Penetration depth	Surface imaging	>8 cm	No limit	<300 μm
Advantages	Fast and cost-effective	High penetration depth, wide field of view, real-time imaging	High penetration depth, high accuracy	High resolution, real-time imaging, capable of optical sectioning
Disadvantages	Low penetration depth and magnification	Low resolution, low contrast	Low image contrast and imaging speed, expensive	Low penetration depth, small field of view

from the surface and subsurface of skin. Furthermore, high-resolution imaging modalities such as CLSM were found to operate within the photon ballistic regime, thereby limiting their penetration capabilities to less than 2 mm in human tissues. Nonconfocal optical imaging techniques are challenged with increased levels of photon backscattering from various layers of skin, leading to significant degradation in image quality due to the intense background noise [1, 24].

Current imaging limitations necessitate further investigations into the adoption of novel optical imaging schemes that can provide high-contrast images from greater depths with microscopic resolution. Over the past years, PAI has been evolved as a promising optical imaging modality that offers scalable spatial resolution beyond the optical diffusion limit (~1 mm). In addition, PAI also offers potential capabilities to derive multilevel information (structural, functional, and molecular) from the diagnosed sites [25]. Although a lot of studies in PAI have been primarily devoted toward cancer diagnostics and treatment guidance, suitable imaging contrast agents for PAI are still under investigation. In the following section, we discuss in detail about the principal theory of PAI and its potential contrast agents.

Photoacoustic Imaging in Biomedical Applications

Photoacoustic Phenomenon

The generation of acoustic waves by the absorption of electromagnetic energy is called photoacoustic effect [26]. The history of this phenomenon dates back to 1880 when Alexander Graham Bell reported the observation of sound generated by light [26]. Due to lack of appropriate light sources at that time, there was only a little progress for the research on the photoacoustic effect. Photoacoustics regained its attention due to the investigation performed by L. B. Kruezer in 1971, where photoacoustic effect was applied in detecting gas constituents by using laser-induced photoacoustic effect [27]. Photoacoustics has then been widely used in various areas
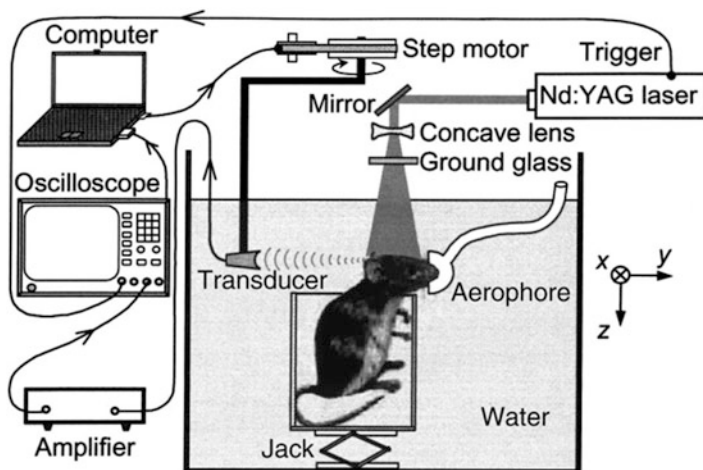
Fig. 4 Schematic illustration for PAI system (Adapted with permission from Ref. [36]. Copyright © 2003, Rights Managed by Nature Publishing Group)

pertaining to physics, chemistry, biology, engineering, and medicine. In particular, considerable research interests have been devoted to its applications for bioimaging applications [28–31].

The motivation that drove the development of PAI was to overcome the poor spatial resolution of optical imaging at greater depths and poor soft tissue contrast of ultrasound imaging. Further enhancement in penetration depth can be achieved by adopting radiofrequency (RF) or microwaves for photoacoustic excitation [32, 33], which falls under thermoacoustic imaging (TAI). PAI primarily involves the irradiation of biological tissues with pulsed lasers, where the absorption of the electromagnetic energy leads to local heating of the absorbers and the subsequent thermoelastic expansion results in the generation of broadband pressure waves (ultrasound). The initial distribution of absorbed photons should have exactly the same profile as the stress distribution when the generation of heat is fast enough so that both heat sources and acoustic sources do not move [34]. The pressure waves generated from the energy-absorbing centers propagate outside the tissues where they are detected by ultrasound transducers.

Considering the speed of sound in biological media and the temporal scales of time-resolved PA signals, an accurate localization of the optical absorber (photoacoustic signal source in this case) can be performed along the depth of the sample. Furthermore, by two-dimensional transverse scanning or by mathematical reconstruction of the time-resolved photoacoustic signals from multiple transducers, three-dimensional photoacoustic images can be formed. Figure 4 illustrates the block diagram of a typical PAI setup operated with multiple transducers. Owing to the fundamental physical principles of optical and acoustic wave propagation in biological tissues, PAI is restricted to operate within specific spatial resolution scales and penetration depths. As a consequence, there was often trade-off between imaging

depth and spatial resolution, so that specific PAI modalities were developed to provide either high resolution or deep penetration imaging capabilities.

Herein, the fundamental principles of PAI should be discussed. Laser energy is transformed to heat energy by the fast nonradiative relaxation of the excited states due to the absorption of the laser radiation by the medium. Subsequently, a pressure rise (ΔP) is formed due to the thermal expansion of the instantaneously heated tissue [35], and the pressure wave propagates omnidirectionally as ultrasonic waves throughout the tissue.

$$\Delta P = \frac{1}{\gamma}\frac{\Delta V}{V} = \frac{1}{\gamma}\beta\Delta T = \frac{1}{\gamma}\frac{\beta E_{abs}(z)}{\rho C_v} = \frac{\beta c_s^2}{C_p}H\mu_a = \Gamma H\mu_a \qquad (1)$$

where γ (Pa^{-1}) is the thermodynamic coefficient of isothermal compressibility:

$$\gamma = \frac{1}{\rho c_s^2}\frac{C_p}{C_v} \qquad (2)$$

where c_s (m/s) is the sound velocity in the medium, ΔV (cm^3) is the volume increase caused by the thermal expansion, V is the laser-irradiated volume initially at room temperature, ρ (g/cm^3) is the density of a medium, C_p (J/gK) is the heat capacity at constant pressure, and C_v is the heat capacity at constant volume. The pressure increase is proportional to the thermal coefficient of volume expansion β (K^{-1}) of the given medium and the absorbed energy density E_{abs} (J/cm^3), which in turn equals the product of the laser fluence H (J/cm^2) and the absorption coefficient of the medium μ_a (cm^{-1}). The expression $\frac{\beta c_s^2}{C_p}$ in Eq. 1 represents the Grüneisen parameter Γ that is a dimensionless, temperature-dependent factor proportional to the fraction of thermal energy converted into mechanical stress [35]. Hence, the variations in the optical absorption levels will be directly reflected on the amplitude of detected PA signals under same fluence conditions and this form to be the underlying physical principle of PAI. The spatial resolution and penetration depth of PAI are determined by the physical principles of both optical and acoustic wave nature. Spatial resolution of PAI is dependent on the quality of optical focusing as well as the operating parameters of the ultrasound transducer. For deep-penetrating PAI, the optical excitation determines the depth to which photons can propagate, and the frequency of the ultrasound determines the depth from which photoacoustic signals can be detected. Greater optical penetration can be achieved in the biological optical window ($\lambda_{excitation}$ = 600–1100 nm), where various tissue constituents exhibit less effective extinction coefficient. Since photoacoustic wave shows power-law dependence on its frequency, higher penetration depths in PAI can be achieved by using low-frequency ultrasound transducers.

Photoacoustic Imaging Techniques

Various forms of PAI have been evolved to image both microscopic and mesoscopic features from the surface as well as along depths of the tissues [29]. Based on the
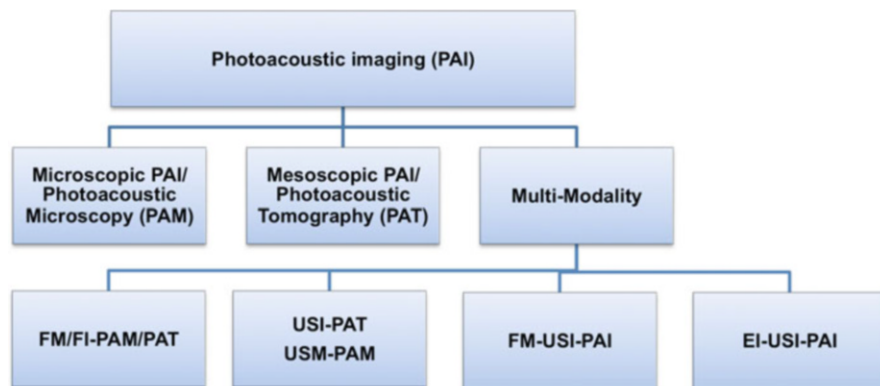
Fig. 5 Major forms of implementations in PAI. *FM* fluorescence microscopy, *FI* fluorescence imaging, *USI* ultrasound imaging, *USM* ultrasound microscopy, *EI* elasticity imaging

scales of achievable spatial resolution and levels of information, PAI modalities can be broadly classified into three major forms of implementation (Fig. 5), namely, microscopic PAI or photoacoustic microscopy (PAM), mesoscopic PAI or photoacoustic tomography (PAT), and integration of PAI with other imaging modalities (multimodality).

Photoacoustic Microscopy (PAM)

PAM technique primarily involves the usage of high-frequency transducers supported with focused or unfocused optical excitation and adequate two-dimensional transverse scanning to construct three-dimensional photoacoustic images. Axial resolution is primarily governed by the time-resolved detection of photoacoustic signals and pulse width of the optical excitation. Time-resolved detection of photoacoustic signals is directly dependent on the frequency of the ultrasound detector (higher the frequency, better the localization of the photoacoustic signal source) and the operating frequency of the receiver electronics (higher the frequency, finer the time-resolved detection of photoacoustic signals). Furthermore, the pulse width of the optical excitation should satisfy the conditions of thermal and stress confinements for the targeted size of the optical absorber. Lateral resolution in PAM is determined by the quality of the optical and acoustic focusing or by the overlap of the optical and acoustic foci.

Significant results have been reported in relation to multilevel PAM involved in lateral resolution scales varying from micrometers to few hundred nanometers [30, 37, 38]. However, considering the fundamental principles of high-frequency ultrasound propagation and optical focusing in biological media, the penetration depths in PAM are limited to few millimeters in biological tissues.

Photoacoustic Tomography (PAT)

In order to perform deep tissue imaging and to accelerate the imaging speeds, PAT technique using ultrasonic array detectors and near-infrared (NIR) optical excitations

has been widely used at the expense of the spatial resolution. PAT primarily involves the irradiation of the entire region of interest (ROI) by an expanded optical beam to generate the photoacoustic signals. The ultrasound detectors coupled at multiple locations around the ROI perform the time-resolved detection of the photoacoustic signals. By further subjecting to mathematical reconstruction routines, the signals form two-dimensional or three-dimensional photoacoustic images. Axial resolution in PAT again depends on the time-resolved detection of photoacoustic signals and pulse width of the optical excitation. However, lateral resolution is primarily governed by the physical dimensions and positioning of the ultrasound detectors. Depending on the excitation wavelengths, the penetration depth of PAT varies from few millimeters to several centimeters. By capitalizing on low optical attenuation at the biological optical window and low ultrasonic scattering, deep tissue PAI studies were performed with mesoscopic spatial resolution [39–41].

Photoacoustics-Based Multimodality Imaging

Considering the physical principles of individual imaging modalities as well as complex structural and biomolecular heterogeneities of tissues, it is impossible to extract all aspects of structural and molecular states of tissues from a single imaging modality with varying interrogation area, spatial resolution, and penetration depth. Therefore, the most widely used approach is to sequentially or simultaneously interrogate the subject through multiple imaging modalities. Such multimodal imaging systems have recently gained considerable interests. PAI in combination with other imaging modalities is therefore expected to further evolve. Since PAI provides optical absorption heterogeneities, it is always desirable to combine and assimilate complementary information such as optical scattering, fluorescence, and even nonoptical information. Complementary structural information based on acoustic heterogeneities was obtained using combined ultrasound and PAI systems [42–44].

Molecular Photoacoustic Imaging

Since PAI presents the potential strengths for mapping the optical absorption heterogeneities with multiscale resolution and varying depths in biological media, extensive investigations have been carried out toward the visualization of various biological processes at the molecular or cellular levels. Such an approach would facilitate detecting the onset of many diseases before any physical or visible anomalies are present, thus allowing early disease diagnosis, treatment, and better prognosis. Due to low optical absorption levels of molecular disease markers, molecular PAI (MPAI) technique requires the usage of exogenous bioconjugated contrast agents. By capitalizing on the imaging capabilities of PAI and the advent of novel molecular imaging probes, high-resolution deep tissue molecular imaging has now become reality. The widely used approach to perform MPAI is to employ bioconjugated nanoparticles, organic dyes, and reporter gene products as the contrast agents. These platforms enable to selectively enhance the imaging contrast for molecular targets and in some cases to provide functional information on dynamic processes inside the body.

Metallic and Upconversion Nanoparticles as Contrast Agents for Photoacoustic Imaging

In order to achieve better image resolution, photoacoustic contrast agents are used to enhance the signals from target site of inspection. Good candidates as photoacoustic contrast agents should possess the ability to transform the incident laser energy to heat energy by the fast nonirradiative relaxation process. In other words, optimal photoacoustic contrast agents should have high absorption coefficient at the laser wavelength while minimal quantum yield. In this aspect, organic dyes are usually not chosen due to their high quantum yield and fast photobleaching [45]. On the other hand, inorganic materials are in more favor of this application. PAI technique has been demonstrated with the help of different inorganic material-based contrast agents such as carbon nanotubes [46, 47], graphene-base hybrids [48–51], gold nanocrystals [52–56], silver nanocrystals [57, 58], iron oxide nanoparticles [59, 60], quantum dots [61], and recently upconversion nanoparticles [62]. Moreover, nanocrystals are easily controlled in size, shape, and surface functionality, which lead to tunable absorption wavelength in biological window (650–1100 nm). In this section, we highlight state-of-the-art studies using metallic and upconversion nanoparticles in PAI. Their unique morphology and composition leading to outstanding photoacoustic contrast enhancement will be discussed. In addition, the interactions of these nanomaterials with biological systems will also be explored.

Metallic nanocrystals possess numerous sizes, shapes, and components, which generate different plasmonic absorption wavelength and different stability in physiological conditions. Tuning plasmonic absorption wavelength of nanocrystals is no longer a difficult task. For example, one can control the length of gold nanorods (AuNRs) by changing the seeding and growth method to generate the precise longitudinal absorption wavelength (Fig. 6). Table 2 shows examples of various nanocrystals as PAI contrast agents.

We mainly discuss photoacoustic contrast agents with the absorption wavelength in the biology window on account of their deep tissue penetration and harmlessness to the pass-by tissues. The most common photoacoustic contrast agents are metal nanocrystals, which have the maximum absorption that can be easily tuned into NIR region. For instance, gold nanospheres were self-assembled by polymer encapsulation in order to generate the maximum absorption in NIR region (Fig. 7) [67]. These nanobeacons were then modified with biomolecules to facilitate their circulation and specific binding within the body. $\alpha_v\beta_3$-Integrin, a heterodimeric transmembrane glycoprotein, linked on nanobeacons (GNB_{160}) could greatly enhance neovascular homing specificity. While PAI alone could not differentiate photoacoustic signals derived from formed and stabilized neovessels, with $\alpha_v\beta_3$-GNB_{160} contrast enhancement, the PAI sensitively discriminated angiogenesis and microvasculature [68].

In addition, AuNRs are usually considered an alternative choice as PAI contrast agents. AuNRs offer distinct optical properties resulting from two surface plasmon bands corresponding to the transverse and longitudinal bands with the absorption maximum of longitudinal plasmon resonance in NIR region. A novel PAI contrast agent was developed based on PEGylated AuNRs as a passively targeted molecular
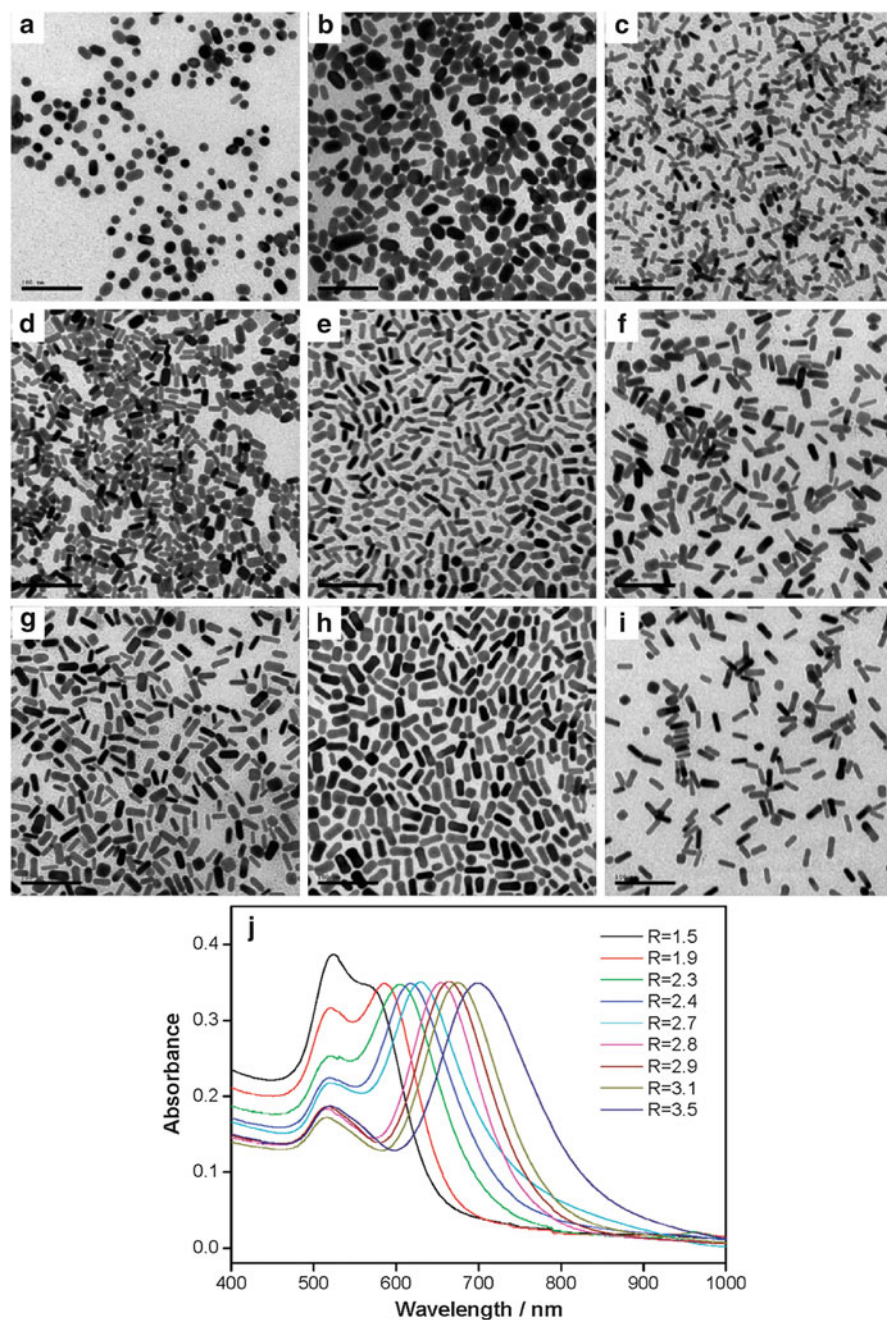
Fig. 6 TEM images of AuNRs with varying aspect ratios: (*A*) 1.5, (*B*) 1.9, (*C*) 2.3, (*D*) 2.4, (*E*) 2.7, (*F*) 2.8, (*G*) 2.9, (*H*) 3.1, and (*I*) 3.5. (*J*) UV–vis spectra of AuNRs with corresponding aspect ratios (Adapted with permission from Ref. [63]. Copyright © 2009, American Chemical Society)

Table 2 Various nanocrystals and their size, maximal absorption wavelength and extinction coefficient for PAI

Contrast agent	Diameter (nm)	Peak absorption wavelength (nm)	Extinction coefficient (M^{-1} cm^{-1})	Reference
Gold nanospheres	2–100	520–600	$(3.61 \pm 0.08) \times 10^6$ to $(6.06 \pm 0.03) \times 10^9$	[64]
Gold nanorods	Length = 51.0 ± 4.4 nm; Width = 14.1 ± 2.1 nm	850	$5.5 \pm 0.3 \times 10^9$	[65]
Gold nanorods	Length = 44.8 ± 4.1 nm; Width = 19.8 ± 2.9 nm	675	$3.3 \pm 0.3 \times 10^9$	[65]
Gold nanoshells	Diameter = 30.4 ± 4.4 nm; Thickness = 7.8 ± 2.2 nm	700–2200	8.3×10^9	[66]
Gold nanocages	50.3 ± 6.7	735	–	[55]
Silver nanoplates	25.3 ± 5.5	550	–	[58]
Silver nanoplates	60.9 ± 10.1	720	–	[58]
Silver nanoplates	128.0 ± 25.9	900	–	[58]
Silver nanoplates	218.6 ± 35.6	1080	–	[58]
Upconversion nanoparticles	24	NIR	–	[62]
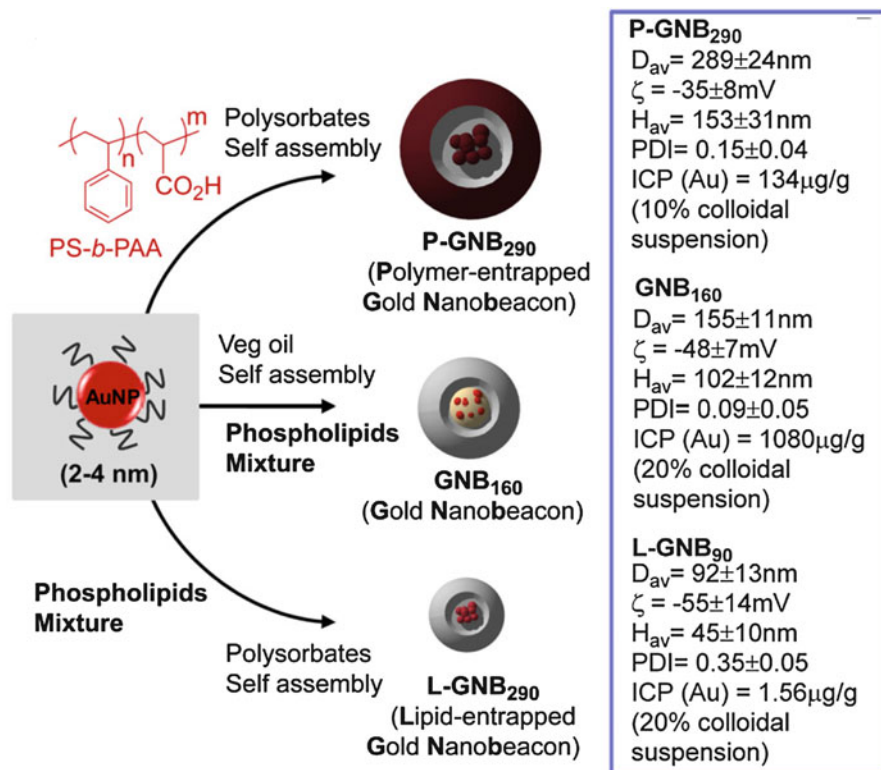
Fig. 7 Synthesis of different-sized gold nanospheres (Adapted with permission from Ref. [67]. Copyright © 2010 Elsevier Ltd)

imaging agent. Tumors were shown to have maximum gold content at 3 h post injection with 3.80 μg of gold per gram of tissue and also the peak value of photoacoustic signal [69]. Figure 8 shows the photoacoustic images of before and after 6 h post injection of AuNRs with different types of tumors including MDA-435S tumor as a positive control, 2008, HEY, and SKOV3 ovarian cancer cell lines. In a detailed study about concentration-dependent photoacoustic signal, there was a linear relationship ($R^2 = 0.95$) with a calculated detection limit of 0.40 nM AuNRs in the 2008 cell line.

Remarkably, photoacoustic signal generated from AuNRs can significantly be enhanced by a layer of silica coating. Silica-coated AuNRs can amplify the photoacoustic response without altering the optical absorption of AuNRs other than shifting it slightly to the red region (Fig. 9). This signal enhancement depends on the silica thickness in a biphasic way. The enhancement could be attributed to the changes in the interfacial heat conduction from gold to water through the silica layer. Moreover, silica coating also provides a facile platform for further functionalization of AuNRs.
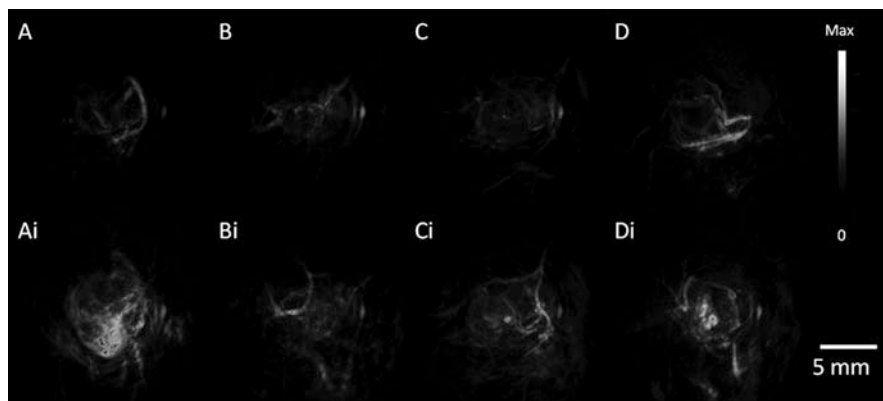
Fig. 8 Photoacoustic tumor imaging using PEGylated AuNRs as the contrast. Photoacoustic images (*top*) before and (*bottom*) after 6 h post tail-vein injection of 200 μL, 5.4 nM AuNRs (756 nm resonance). (*A, Ai*) MDA-435S tumor serving as a positive control. (*B, Bi*) 2008 tumor. (*C, Ci*) HEY tumor. (*D, Di*) SKOV3 tumor (Adapted with permission from Ref. [69]. Copyright © 2012, American Chemical Society)
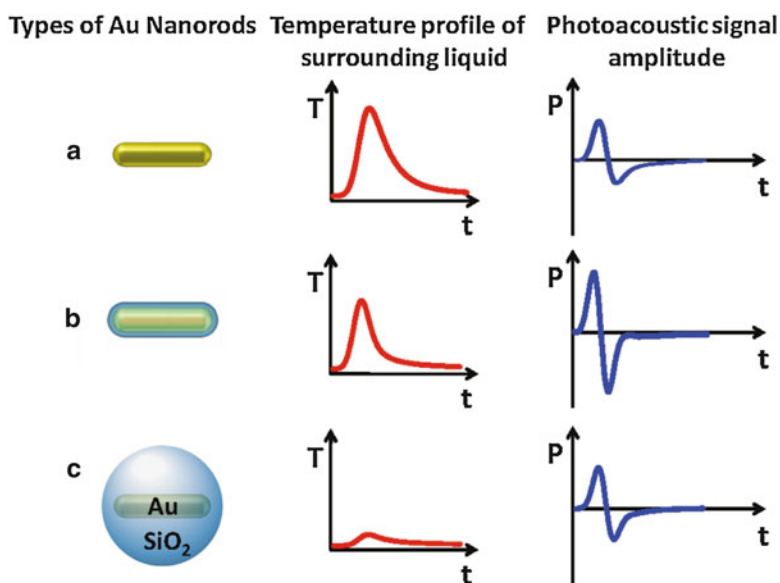
Fig. 9 (**a**) A bare gold nanorod with high interfacial resistance leads to broadened temperature profile and smaller amplitude of photoacoustic pressure signal. (**b**) Introducing a silica shell leads to minimal interfacial resistance between Au/SiO_2 and $SiO_2/water$, and results in sharper temperature profile. Because the temperature profile is at larger distance, the photoacoustic signal is increased. (**c**) A thick silica shell leads to broadened temperature peak and again a decrease in the photoacoustic signal, although the photoacoustic signal may still be higher than that of bare nanorod (Adapted with permission from Ref. [53]. Copyright © 2011, American Chemical Society)
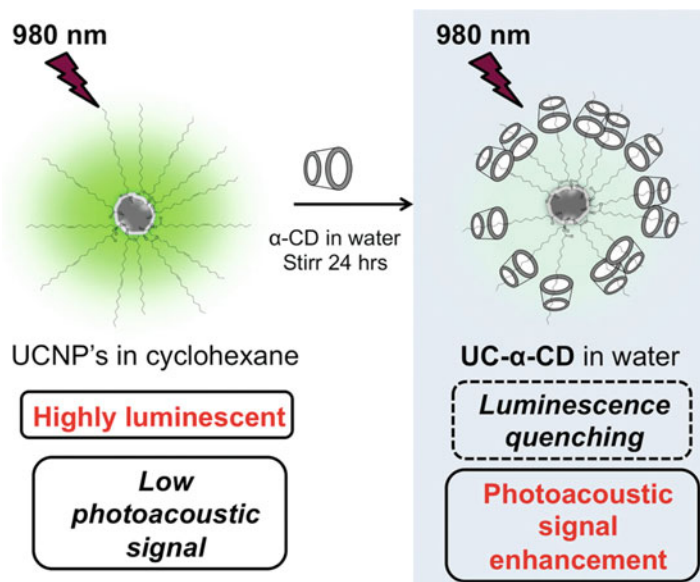
Fig. 10 Schematic illustration of luminescence quenching effect and subsequent photoacoustic signal enhancement from UC-α-CD in water (Adapted with permission from Ref. [62]. Copyright © 2014 WILEY-VCH Verlag GmbH & Co. KGaA, Weinheim)

Recently, a new type of photoacoustic contrast agent based on upconversion nanoparticles has been developed. Upconversion nanoparticles are known for their strong NIR absorption and high photoluminescence. When quenching the luminescence of upconversion nanoparticles, the laser incident energy is transferred to nonirradiative relaxation and thus photoacoustic signal is generated. Oleic acid-stabilized hexagonal-phased $NaYF_4:Yb^{3+},Er^{3+}$ (80:18:2) upconversion nanoparticles with a diameter of about 24 nm could undergo the phase transfer from organic phase to water medium by the surface modification with α-cyclodextrin (α-CD). This modification makes upconversion nanoparticles lose their luminescence property and at the same time enhance the photoacoustic signal of the final hybrid (UC-α-CD) (Fig. 10). From cytotoxicity studies, UC-α-CD was found to be noncytotoxic and suitable for in vivo PAI. Finally, in vivo localization of UC-α-CD in live mice for PAI at 980 nm excitation was carried out, proving that UC-α-CD could be used as an efficient contrast agent for diagnostic purposes (Fig. 11).

Challenges in the Use of Nanoparticles: Issues of Nanotoxicity

Tremendous potentials of nanomaterials to improve human lives are undisputed. However, the rapid advancement in nanotechnology will need to be carefully balanced with the toxicological risks [70, 71]. Nanotoxicology of some nanoparticles has been demonstrated in several biological systems [72]. The toxicity
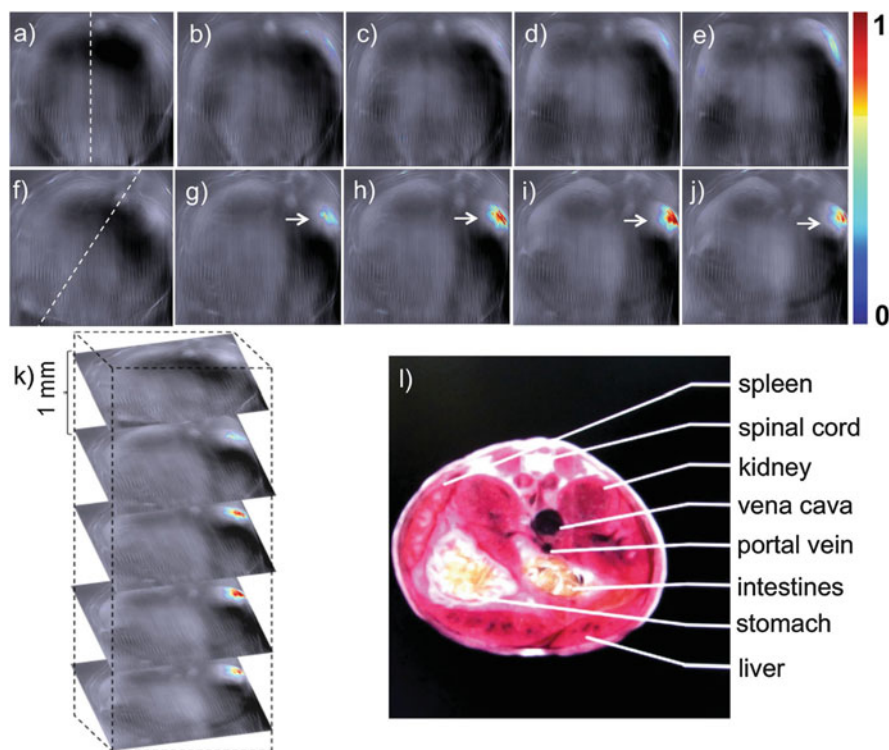
Fig. 11 Single-wavelength PAI of a live mouse anatomy at 980 nm. (**a**–**e**) Individual anatomy sections of the live mouse before intravenous injection of UC-α-CD. (**f**–**j**) Individual anatomy sections recorded after 35 min post-intravenous injection of UC-α-CD. Dashed lines in figures (**a**) and (**f**) indicate the positions of the mouse with respect to the viewer. Pointed areas in figures (**g**–**j**) indicate the localization of UC-α-CD. (**k**) Three-dimensional rendering of scanned area. (**l**) Schematic section corresponding to the analyzed area (Adapted with permission from Ref. [62]. Copyright © 2014 WILEY-VCH Verlag GmbH & Co. KGaA, Weinheim)

investigation is especially important for unbound nanoparticles such as those developed for uses in bioimaging as described in this chapter. Primarily, a small size of nanoparticles allows them to penetrate into every nook and cranny including intracellular space. The availability of high surface area–to-volume ratios also means that these small nanoparticles become more reactive as compared to large particles of the same material. These physical parameters coupled with the native bulk and surface reactivity of the nanoparticles give rise to their promising application potential in biological systems in ways that were never expected previously [73].

Effects of Nanoparticles on Cell Physiology

Once the barriers to enter into the body are breached, nanoparticles have the possibility to interact directly with cells and influence their behavior. There are

now a large amount of literature reports describing many physiological influences that nanoparticles can exert on various types of cells. Most of these studies focus on engineered nanoparticles including those for bioimaging. The effects that engineered nanoparticles can influence living cells range from acute cytotoxicity to less apparent outcomes such as inflammation and DNA damage. Acute cytotoxicity is the most direct and obvious outcome induced by nanoparticles. Nanocrystal semiconductors (quantum dots) have a great potential for various imaging purposes, but their toxic influence, especially in vivo, has been well described [74]. On the other hand, lanthanide nanoparticles are generally considered less toxic than quantum dots for bioimaging. Nonetheless, terbium-doped gadolinium oxide (Tb-Gd_2O_3) and dysprosium oxide (Dy_2O_3) nanoparticles resulted in decreased proliferation of human lung epithelial cells (BEAS-2B) and mouse fibroblasts (L929) after 48 h exposure at 200–2000 μg/mL [75]. Inflammation and oxidative stress induction are also possible outcomes of cellular interactions with nanoparticles. Zinc oxide (ZnO) nanoparticles, for example, have been shown to elicit reactive oxygen species (ROS) production and inflammation in BEAS-2B and mouse macrophages (RAW 264.7) [76]. Interestingly, in the same study, the authors found that cerium oxide (CeO_2) nanoparticles could suppress ROS production and induce cellular resistance to oxidative stress. In addition to the complexity of the mechanisms governing nanoparticle-cell interactions, the inflammatory potential of ZnO nanoparticles was found to be shape dependent [77]. A more sinister outcome of nanoparticle-cell interactions could be genotoxicity, which implies the possibility of nanoparticle-induced carcinogenesis in vivo. A number of different particle types have been demonstrated to induce genotoxicity in different biological systems. Tb-Gd_2O_3 nanoparticles were found to exert genotoxic pressure on human fibroblasts by profiling DNA damage via the detection of γ-H2AX expression after 24 h exposure at 1000 μg/mL [78]. In human fibroblasts with compromised p53 function, native cell-protective response was tipped toward carcinogenesis when subjected to the DNA damaging effects of ZnO nanoparticles [79]. In a more comprehensive in vivo study, titanium dioxide (TiO_2) nanoparticles introduced into mice through drinking water resulted in oxidative DNA damage, double-stranded DNA breaks, micronuclei formation, and DNA deletions [80].

Concentration, Biodistribution, and Clearance

Most of the nanotoxicology studies currently reported in literature examine the toxicity effects of relatively high concentrations of nanoparticles. On the other hand, there are emerging reports on more subtle cellular effects that low concentrations of nanoparticles can cause. Recently, it was demonstrated that TiO_2 nanoparticles at a concentration as low as 100 fg/mL could induce detectable autophagy in primary human keratinocytes over 24 h exposure [81]. Autophagy induction is generally a positive response to remove faulty entities within a cell in order to ensure survival, but it also plays a role in effecting the cell death [82]. The autophagy indicated in this study suggests that low concentrations of TiO_2

nanoparticles were enough to cause the damage. In addition to the concentration effect, there are also significant knowledge gaps in understanding the accumulation, distribution, and clearance of engineered nanoparticles in the body. Collectively, current lack of understanding the multifactorial landscape of nanotoxicology necessitates that toxicological evaluation of engineered nanoparticles for bioimaging should be tailored on a case-by-case basis within the specific context of the intended application.

Conclusion and Perspectives

A variety of noninvasive imaging modalities have been evolved for the imaging of tissues. However, state-of-the-art imaging modalities are mostly restricted to anatomical imaging of skin tissues and do not sufficiently provide high-resolution imaging capabilities through various layers of tissues. Since ultrasound scattering is about three orders of magnitude less than optical scattering in tissues, photoacoustic effect–based imaging modalities present a great potential for providing high-resolution images with improved penetration depth and rich optical contrast. Furthermore, the broadband nature of photoacoustic signal together with the usage of suitable focusing mechanisms offers scalable spatial resolution capabilities for PAI, leading to multiscale imaging of tissues [29]. Thus, PAI is expected to provide excellent diagnostic capabilities in dermatology, which can overcome the deficiencies of conventional technologies. Given the direct dependence of photoacoustic signals on optical absorption, selective optical excitation (irradiation with specific wavelengths) with wavelength sweeping and appropriate contrast agents such as AuNRs can be used to perform background free and targeted anatomical and molecular imaging. Nevertheless, the toxicological evaluation of these engineered nanoparticles should be tailored and evaluated prior to their usage in clinical settings. Considering the potential strengths of PAI for anatomical and molecular tissue imaging, it is anticipated that photoacoustic effect–based imaging modalities would be a prominent imaging tool with tremendous impacts across various domains of diagnostics.

References

1. Aspres N, Egerton IB, Lim AC, Shumack SP (2003) Imaging the skin. Australas J Dermatol 44:19–27
2. Argenziano G, Soyer HP, Chimenti S, Talamini R, Corona R, Sera F, Binder M, Cerroni L, De Rosa G, Ferrara G, Hofmann-Wellenhof R, Landthaler M, Menzies SW, Pehamberger H, Piccolo D, Rabinovitz HS, Schiffner R, Staibano S, Stolz W, Bartenjev I, Blum A, Braun R, Cabo H, Carli P, De Giorgi V, Fleming MG, Grichnik JM, Grin CM, Halpern AC, Johr R, Katz B, Kenet RO, Kittler H, Kreusch J, Malvehy J, Mazzocchetti G, Oliviero M, Özdemir F, Peris K, Perotti R, Perusquia A, Pizzichetta MA, Puig S, Rao B, Rubegni P, Saida T, Scalvenzi M, Seidenari S, Stanganelli I, Tanaka M, Westerhoff K, Wolf IH, Braun-Falco O,

Kerl H, Nishikawa T, Wolff K, Kopf AW (2003) Dermoscopy of pigmented skin lesions: results of a consensus meeting via the internet. J Am Acad Dermatol 48:679–693

3. Schmid-Wendtner MH, Burgdorf W (2005) Ultrasound scanning in dermatology. Arch Dermatol 141:217–224

4. Stefanowska J, Zakowiecki D, Cal K (2010) Magnetic resonance imaging of the skin. J Eur Acad Dermatol Venereol 24:875–880

5. Branzan AL, Landthaler M, Szeimies RM (2007) In vivo confocal scanning laser microscopy in dermatology. Lasers Med Sci 22:73–82

6. Tsai TH, Jee SH, Dong CY, Lin SJ (2009) Multiphoton microscopy in dermatological imaging. J Dermatol Sci 56:1–8

7. Zalaudek I, Argenziano G, Di Stefani A, Ferrara G, Marghoob AA, Hofmann-Wellenhof R, Soyer HP, Braun R, Kerl H (2006) Dermoscopy in general dermatology. Dermatology 212:7–18

8. Zalaudek I, Kreusch J, Giacomel J, Ferrara G, Catrical C, Argenziano G (2010) How to diagnose nonpigmented skin tumors: a review of vascular structures seen with dermoscopy: part I. Melanocytic skin tumors. J Am Acad Dermatol 63:361–376

9. Koehler MJ, Speicher M, Lange-Asschenfeldt S, Stockfleth E, Metz S, Elsner P, Kaatz M, König K (2011) Clinical application of multiphoton tomography in combination with confocal laser scanning microscopy for in vivo evaluation of skin diseases. Exp Dermatol 20:589–594

10. Dill-Müller D, Maschke J (2007) Ultrasonography in dermatology. J Dtsch Dermatol Ges 5:689–707

11. Cammarota T, Pinto F, Magliaro A, Sarno A (1998) Current uses of diagnostic high-frequency US in dermatology. Eur J Radiol 27:S215–S223

12. Padhani AR (2002) Dynamic contrast-enhanced MRI in clinical oncology: current status and future directions. J Magn Reson Imaging 16:407–422

13. Frisoni GB, Fox NC, Jack CR Jr, Scheltens P, Thompson PM (2010) The clinical use of structural MRI in Alzheimer disease. Nat Rev Neurol 6:67–77

14. Aubry S, Casile C, Humbert P, Jehl J, Vidal C, Kastler B (2009) Feasibility study of 3-T MR imaging of the skin. Eur Radiol 19:1595–1603

15. Kang HY, Bahadoran P, Ortonne JP (2010) Reflectance confocal microscopy for pigmentary disorders. Exp Dermatol 19:233–239

16. Nobre Moura F, Dalle S, Depaepe L, Durupt F, Balme B, Thomas L (2011) Melanoma: early diagnosis using in vivo reflectance confocal microscopy. Clin Exp Dermatol 36:209–211

17. Koller S, Gerger A, Ahlgrimm-Siess V, Weger W, Smolle J, Hofmann-Wellenhof R (2009) In vivo reflectance confocal microscopy of erythematosquamous skin diseases. Exp Dermatol 18:536–540

18. Koehler MJ, Lange-Asschenfeldt S, Kaatz M (2011) Non-invasive imaging techniques in the diagnosis of skin diseases. Expert Opin Med Diagn 5:425–440

19. Lieber CA, Majumder SK, Billheimer D, Ellis DL, Mahadevan-Jansen A (2008) Raman microspectroscopy for skin cancer detection in vitro. J Biomed Opt 13:024013

20. Wollina U, Schmidt WD, Koch A, Scheibe A, Erfurth F, Fassler D (2009) Fluorescence remission spectroscopy of psoriatic lesions and the effect of topical anthralin therapy. J Eur Acad Dermatol Venereol 23:1409–1413

21. Wallace VP, Fitzgerald AJ, Pickwell E, Pye RJ, Taday PF, Flanagan N, Thomas HA (2006) Terahertz pulsed spectroscopy of human basal cell carcinoma. Appl Spectrosc 60:1127–1133

22. Roberts MS, Dancik Y, Prow TW, Thorling CA, Lin LL, Grice JE, Robertson TA, König K, Becker W (2011) Non-invasive imaging of skin physiology and percutaneous penetration using fluorescence spectral and lifetime imaging with multiphoton and confocal microscopy. Eur J Pharm Biopharm 77:469–488

23. Vogler N, Meyer T, Akimov D, Latka I, Krafft C, Bendsoe N, Svanberg K, Dietzek B, Popp J (2010) Multimodal imaging to study the morphochemistry of basal cell carcinoma. J Biophotonics 3:728–736

24. Benati E, Bellini V, Borsari S, Dunsby C, Ferrari C, French P, Guanti M, Guardoli D, Koenig K, Pellacani G, Ponti G, Schianchi S, Talbot C, Seidenari S (2011) Quantitative evaluation of

healthy epidermis by means of multiphoton microscopy and fluorescence lifetime imaging microscopy. Skin Res Technol 17:295–303

25. Wang LV, Hu S (2012) Photoacoustic tomography: in vivo imaging from organelles to organs. Science 335:1458–1462

26. Bell AG (1880) On the production and reproduction of sound by light. Am J Sci 20:305–324

27. Kreuzer LB (1971) Ultralow gas concentration infrared absorption spectroscopy. J Appl Phys 42:2934–2943

28. Ntziachristos V, Ripoll J, Wang LV, Weissleder R (2005) Looking and listening to light: the evolution of whole-body photonic imaging. Nat Biotechnol 23:313–320

29. Wang LV (2009) Multiscale photoacoustic microscopy and computed tomography. Nat Photonics 3:503–509

30. Zhang HF, Maslov K, Stoica G, Wang LV (2006) Functional photoacoustic microscopy for high-resolution and noninvasive in vivo imaging. Nat Biotechnol 24:848–851

31. Razansky D, Distel M, Vinegoni C, Ma R, Perrimon N, Köster RW, Ntziachristos V (2009) Multispectral opto-acoustic tomography of deep-seated fluorescent proteins in vivo. Nat Photonics 3:412–417

32. Wang LV, Zhao X, Sun H, Ku G (1999) Microwave-induced acoustic imaging of biological tissues. Rev Sci Instrum 70:3744–3748

33. Kruger RA, Reinecke DR, Kruger GA (1999) Thermoacoustic computed tomography-technical considerations. Med Phys 26:1832–1837

34. Trevena DH (1966) Propagation of stress pulses across the interface between two immiscible liquids [5]. Nature 209:289

35. Oraevsky AA, Jacques SL, Tittel FK (1997) Measurement of tissue optical properties by time-resolved detection of laser-induced transient stress. Appl Opt 36:402–415

36. Wang X, Pang Y, Ku G, Xie X, Stoica G, Wang LV (2003) Noninvasive laser-induced photoacoustic tomography for structural and functional in vivo imaging of the brain. Nat Biotechnol 21:803–806

37. Maslov K, Zhang HF, Hu S, Wang LV (2008) Optical-resolution photoacoustic microscopy for in vivo imaging of single capillaries. Opt Lett 33:929–931

38. Rao B, Maslov K, Danielli A, Chen R, Shung KK, Zhou Q, Wang LV (2011) Real-time four-dimensional optical-resolution photoacoustic microscopy with Au nanoparticle-assisted subdiffraction-limit resolution. Opt Lett 36:1137–1139

39. Manohar S, Vaartjes SE, Van Hespen JCG, Klaase JM, Van Den Engh FM, Steenbergen W, Van Leeuwen TG (2007) Initial results of in vivo non-invasive cancer imaging in the human breast using near-infrared photoacoustics. Opt Express 15:12277–12285

40. Kim C, Erpelding TN, Jankovic L, Pashley MD, Wang LV (2010) Deeply penetrating in vivo photoacoustic imaging using a clinical ultrasound array system. Biomed. Opt Express 1:278–284

41. Ku G, Wang LV (2005) Deeply penetrating photoacoustic tomography in biological tissues enhanced with an optical contrast agent. Opt Lett 30:507–509

42. Kolkman RGM, Brands PJ, Steenbergen W, Van Leeuwen TG (2008) Real-time in vivo photoacoustic and ultrasound imaging. J Biomed Opt 13:050510

43. Niederhauser JJ, Jaeger M, Lemor R, Weber P, Frenz M (2005) Combined ultrasound and optoacoustic system for real-time high-contrast vascular imaging in vivo. IEEE Trans Med Imaging 24:436–440

44. Rousseau G, Blouin A, Monchalin J-P (2012) Non-contact photoacoustic tomography and ultrasonography for tissue imaging. Biomed Opt Express 3:16–25

45. Laufer J, Zhang E, Beard P (2010) Evaluation of absorbing chromophores used in tissue phantoms for quantitative photoacoustic spectroscopy and imaging. IEEE J Sel Top Quant 16:600–607

46. Zerda ADL, Liu Z, Bodapati S, Teed R, Vaithilingam S, Khuri-Yakub BT, Chen X, Dai H, Gambhir SS (2010) Ultrahigh sensitivity carbon nanotube agents for photoacoustic molecular imaging in living mice. Nano Lett 10:2168–2172

47. De La Zerda A, Zavaleta C, Keren S, Vaithilingam S, Bodapati S, Liu Z, Levi J, Smith BR, Ma T-J, Oralkan O, Cheng Z, Chen X, Dai H, Khuri-Yakub BT, Gambhir SS (2008) Carbon nanotubes as photoacoustic molecular imaging agents in living mice. Nat Nanotechnol 3:557–562

48. Nguyen KT, Sreejith S, Joseph J, He T, Borah P, Guan EY, Lye SW, Sun H, Zhao Y (2014) Poly (acrylic acid)-capped and dye-loaded graphene oxide-mesoporous silica: a nano-sandwich for two-photon and photoacoustic dual-mode imaging. Part Part Syst Char 31:1060–1066

49. Lalwani G, Cai X, Nie L, Wang LV, Sitharaman B (2013) Graphene-based contrast agents for photoacoustic and thermoacoustic tomography. Photoacoustics 1:62–67

50. Patel MA, Yang H, Chiu PL, Mastrogiovanni DDT, Flach CR, Savaram K, Gomez L, Hemnarine A, Mendelsohn R, Garfunkel E, Jiang H, He H (2013) Direct production of graphene nanosheets for near infrared photoacoustic imaging. ACS Nano 7:8147–8157

51. Sheng Z, Song L, Zheng J, Hu D, He M, Zheng M, Gao G, Gong P, Zhang P, Ma Y, Cai L (2013) Protein-assisted fabrication of nano-reduced graphene oxide for combined in vivo photoacoustic imaging and photothermal therapy. Biomaterials 34:5236–5243

52. Agarwal A, Huang SW, O'Donnell M, Day KC, Day M, Kotov N, Ashkenazi S (2007) Targeted gold nanorod contrast agent for prostate cancer detection by photoacoustic imaging. J Appl Phys 102:064701

53. Chen YS, Frey W, Kim S, Kruizinga P, Homan K, Emelianov S (2011) Silica-coated gold nanorods as photoacoustic signal nanoamplifiers. Nano Lett 11:348–354

54. Mallidi S, Larson T, Tam J, Joshi PP, Karpiouk A, Sokolov K, Emelianov S (2009) Multiwavelength photoacoustic imaging and plasmon resonance coupling of gold nanoparticles for selective detection of cancer. Nano Lett 9:2825–2831

55. Song KH, Kim C, Cobley CM, Xia Y, Wang LV (2009) Near-infrared gold nanocages as a new class of tracers for photoacoustic sentinel lymph node mapping on a rat model. Nano Lett 9:183–188

56. Sreejith S, Joseph J, Nguyen KT, Murukeshan VM, Lye SW, Zhao Y (2015) Graphene oxide wrapping of gold–silica core–shell nanohybrids for photoacoustic signal generation and bimodal imaging. ChemNanoMat 1:39–45

57. Homan K, Shah J, Gomez S, Gensler H, Karpiouk A, Brannon-Peppas L, Emelianov S (2010) Silver nanosystems for photoacoustic imaging and image-guided therapy. J Biomed Opt 15:021316

58. Homan KA, Souza M, Truby R, Luke GP, Green C, Vreeland E, Emelianov S (2012) Silver nanoplate contrast agents for in vivo molecular photoacoustic imaging. ACS Nano 6:641–650

59. Alwi R, Telenkov S, Mandelis A, Leshuk T, Gu F, Oladepo S, Michaelian K (2012) Silica-coated super paramagnetic iron oxide nanoparticles (SPION) as biocompatible contrast agent in biomedical photoacoustics. Biomed Opt Express 3:2500–2509

60. Grootendorst DJ, Jose J, Fratila RM, Visscher M, Velders AH, Ten Haken B, Van Leeuwen TG, Steenbergen W, Manohar S, Ruers TJM (2013) Evaluation of superparamagnetic iron oxide nanoparticles (Endorem®) as a photoacoustic contrast agent for intra-operative nodal staging. Contrast Media Mol I 8:83–91

61. Shashkov EV, Everts M, Galanzha EI, Zharov VP (2008) Quantum dots as multimodal photoacoustic and photothermal contrast agents. Nano Lett 8:3953–3958

62. Maji SK, Sreejith S, Joseph J, Lin M, He T, Tong Y, Sun H, Yu SW-K, Zhao Y (2014) Upconversion nanoparticles as a contrast agent for photoacoustic imaging in live mice. Adv Mater 26:5633–5638

63. Guo H, Ruan F, Lu L, Hu J, Pan J, Yang Z, Ren B (2009) Correlating the shape, surface plasmon resonance, and surface-enhanced Raman scattering of gold nanorods. J Phys Chem C 113:10459–10464

64. Liu X, Atwater M, Wang J, Huo Q (2007) Extinction coefficient of gold nanoparticles with different sizes and different capping ligands. Colloids Surf B: Biointerfaces 58:3–7

65. Lee K-S, El-Sayed MA (2005) Dependence of the enhanced optical scattering efficiency relative to that of absorption for gold metal nanorods on aspect ratio, size, end-cap shape, and medium refractive index. J Phys Chem B 109:20331–20338

66. Melancon MP, Lu W, Yang Z, Zhang R, Cheng Z, Elliot AM, Stafford J, Olson T, Zhang JZ, Li C (2008) In vitro and in vivo targeting of hollow gold nanoshells directed at epidermal growth factor receptor for photothermal ablation therapy. Mol Cancer Ther 7:1730–1739

67. Pan D, Pramanik M, Senpan A, Ghosh S, Wickline SA, Wang LV, Lanza GM (2010) Near infrared photoacoustic detection of sentinel lymph nodes with gold nanobeacons. Biomaterials 31:4088–4093

68. Pan D, Pramanik M, Senpan A, Allen JS, Zhang H, Wickline SA, Wang LV, Lanza GM (2011) Molecular photoacoustic imaging of angiogenesis with integrin-targeted gold nanobeacons. FASEB J 25:875–882

69. Jokerst JV, Cole AJ, Van de Sompel D, Gambhir SS (2012) Gold nanorods for ovarian cancer detection with photoacoustic imaging and resection guidance via Raman imaging in living mice. ACS Nano 6:10366–10377

70. Donaldson K, Stone V, Tran CL, Kreyling W, Borm PJ (2004) Nanotoxicology. Occup Environ Med 61:727–728

71. R. F. Service (2004) Nanotechnology grows up. Science 304:1732–1734

72. Oberdorster G, Oberdorster E, Oberdorster J (2005) Nanotoxicology: an emerging discipline evolving from studies of ultrafine particles. Environ Health Persp 113:823–839

73. Nel A, Xia T, Mädler L, Li N (2006) Toxic potential of materials at the nanolevel. Science 311:622–627

74. Yong KT, Swihart MT (2012) In vivo toxicity of quantum dots: no cause for concern? Nanomedicine (Lond) 7:1641–1643

75. Heng BC, Das GK, Zhao X, Ma LL, Tan TT, Ng KW, Loo JS (2010) Comparative cytotoxicity evaluation of lanthanide nanomaterials on mouse and human cell lines with metabolic and DNA-quantification assays. Biointerphases 5:FA88–FA97

76. Xia T, Kovochich M, Liong M, Mädler L, Gilbert B, Shi H, Yeh JI, Zink JI, Nel AE (2008) Comparison of the mechanism of toxicity of zinc oxide and cerium oxide nanoparticles based on dissolution and oxidative stress properties. ACS Nano 2:2121–2134

77. Heng BC, Zhao X, Tan EC, Khamis N, Assodani A, Xiong S, Ruedl C, Ng KW, Loo JS (2011) Evaluation of the cytotoxic and inflammatory potential of differentially shaped zinc oxide nanoparticles. Arch Toxicol 85:1517–1528

78. Setyawati MI, Khoo PK, Eng BH, Xiong S, Zhao X, Das GK, Tan TT, Loo JS, Leong DT, Ng KW (2012) Cytotoxic and genotoxic characterization of titanium dioxide, gadolinium oxide, and poly(lactic-co-glycolic acid) nanoparticles in human fibroblasts. J Biomed Mater Res A 101A:633–640

79. Ng KW, Khoo SP, Heng BC, Setyawati MI, Tan EC, Zhao X, Xiong S, Fang W, Leong DT, Loo JS (2011) The role of the tumor suppressor p53 pathway in the cellular DNA damage response to zinc oxide nanoparticles. Biomaterials 32:8218–8225

80. Trouiller B, Reliene R, Westbrook A, Solaimani P, Schiestl RH (2009) Titanium dioxide nanoparticles induce DNA damage and genetic instability in vivo in mice. Cancer Res 69:8784–8789

81. Zhao Y, Howe JL, Yu Z, Leong DT, Chu JJ, Loo JS, Ng KW (2012) Exposure to titanium dioxide nanoparticles induces autophagy in primary human keratinocytes. Small 9:387–392

82. Mizushima N, Levine B, Cuervo AM, Klionsky DJ (2008) Autophagy fights disease through cellular self-digestion. Nature 451:1069–1075

Part V

Food Processing

Ultrasonic Applications for Juice Making

Mehmet Başlar, Hatice Biranger Yildirim, Zeynep Hazal Tekin, and Mustafa Fatih Ertugay

Contents

Abstract

Nowadays, juice is one of the most popular beverages in food technology. Juice is easy to consume, delicious, and refreshing, and it is rich in vitamins, phytochemicals, and sometimes fiber, depending on the raw materials used. However, juice usually suffers from the loss of important nutrients and from compromised freshness and quality during thermal processing. Novel technologies for juice processing have therefore been developed to address the negative effects of thermal treatment. Among available technologies, ultrasound technology has a

M. Başlar (✉) • H. Biranger Yildirim • Z.H. Tekin
Faculty of Chemical and Metallurgical Engineering, Department of Food Engineering, Yıldız Technical University, Esenler, Istanbul, Turkey
e-mail: mbaslar@gmail.com

M.F. Ertugay
Department of Food Engineering, Erzincan University, Erzincan, Turkey

significant potential to produce good-quality, healthful, delicious, and affordable juice. At the same time, ultrasound technology is expressed to improve juice yield and extract some important compounds in the juice production. In recent years, many studies have been conducted on the effects of ultrasound technology on the shelf life, yield, bioactive components, natural color components, appearance, and rheological and physicochemical properties of juices. These studies have focused on efficient juice production using ultrasound technology alone or in combination with another technology. Along with pasteurization, ultrasound technology can be utilized as an important tool to develop and preserve the properties of juice. In this chapter, the possibilities and potential offered by ultrasound treatment to juice production technology are evaluated in light of recent studies.

Introduction

Vegetables and fruit have important positions in human diets due to their high vitamin and fiber contents. They also generally include phytochemicals such as beta carotene and other carotenoids, isothiocyanates, flavonoids, antioxidants, sulfides, and anthocyanins [47, 79]. These phytochemicals are beneficial for suppression of the formation of potential carcinogens and for prevention of cardiovascular and cerebrovascular diseases, hypertension, and stroke [41, 51, 100]. Fiber is also an important part of human diets; it remains mostly undigested and aids in elimination of harmful compounds through stool movement.

Juice is presently one of the most popular beverages in food technology. It is a product of vegetables and fruits that retains properties with very similar characteristics to the raw materials. Juice is easy to consume, delicious, and refreshing, and it is rich in vitamins, phytochemicals, and sometimes fiber, depending on the raw materials used. Juices can be more preferable for consumption than vegetables and fruits because a given amount of juice includes more nutrition than the same amount of fruits and vegetables, as long as nutritional losses are minimized during processing. The digestion of fruits and vegetables is also more complex and difficult than digestion of juices, so more of the nutritional value of fruit and vegetables is realized by drinking juice.

Juice production consists of many processes, including thermal treatments necessary for food safety and preservation of quality. High-temperature treatment denatures proteins, thereby inactivating microorganisms and enzymes that cause undesirable changes in juice and shorten its shelf life. Incomplete inactivation of enzymes will result in unwanted changes, such as enzymatic browning and cloudiness [15]. The enzymes polyphenol oxidase (PPO), pectin methyl esterase (PME), and peroxidase (POD) are generally found in fruit juices, with PME being the

predominant enzyme in various fruits [15, 70]. However, high temperature may change the biochemical, physicochemical, organoleptic (taste, aroma, flavor), and physical properties (color, viscosity) and nutritional values (vitamins, phenolic, etc.) of juices [22, 65]. For example, application of thermal treatments to fresh watermelon juice changed its color and dynamic viscosity and destroyed its lycopene content [64, 69]. More unwanted color changes occurred in apple juice following a thermal process than with a pulsed electrical field process (a nonthermal process) [20].

The current trend toward consumption of fresh, organic, or minimally processed foods with the highest product quality now demands that new processing methods be developed and applied by the food industry by determining juice acceptability to the consumer. When fruits and vegetables are first processed, their nutritional values are the highest, but once thermal treatments are applied to increase shelf life, the nutritional values start to decrease. However; if no treatments are applied, the food deteriorates because of harmful microorganisms and enzymes. Therefore, the search continues for nonthermal treatments that can prolong shelf life and minimize quality loss. The nonthermal treatments used in fruit juice processing have included ultrasound, UV light, high-intensity light pulses, pulsed electric fields, high hydrostatic pressure, supercritical carbon dioxide, dense-phase carbon dioxide, radiofrequency electric fields, γ-irradiation, ozonation, and flash-vacuum expansion [43]. Other alternatives include dielectric heating, ohmic heating, microwave heating, and radio frequency heating, used in combinations or as pretreatments [43].

The ultrasound process may minimize the effects on other quality parameters of fruit juices – for example, the content of heat-sensitive vitamins – because it is a nonthermal process [5]. The application of ultrasound to orange juice was reported to diminish its ascorbic acid content by only 5 % during processing, and the subsequent stability of ascorbic acid was enhanced during the storage period [45]. However, the viscosity of the juice affects the numbers of ultrasound-induced cavitation, so the juice composition may protect microbes and enzymes against the effects of cavitation [62]. Ultrasonication may also cause changes in the aroma profile and sensory attributes. Simunek et al. [78] examined the use of high-power ultrasound treatment for the pasteurization of apple juice and nectar and found that ultrasonic treatment caused the formation of new substances and/or the disappearance of existing ones when compared with untreated samples of juices and nectars [78].

Ultrasound processing, also called sonication, is used for extraction, homogenization, emulsification, drying, crystallization, cutting, and inactivation of microorganisms and enzymes. Microbial and enzymatic inactivation are essential for pasteurization of juices, and ultrasound, one of the nonthermal processes, has important potential in this respect. It does not have the common side effects of conventional thermal treatments on food nutritional and quality parameters, such as degradation of some vitamins, color, and proteins [72], and it has been approved by FDA since 2000, providing a potential 5 log reduction in juice microbial content [88] (Table 1).

High-power ultrasound applications have also been used for extraction of bioactive compounds (e.g., phenolics, flavonoids, ascorbic acid, and anthocyanins) found

Table 1 Effect of ultrasonic treatments on shelf life and microorganism inactivation

Juice	Treatment	Temperature (°C)	Microorganisms	Inactivation (cfu/mL)	Reference
Apple juice	Ultrasonic probe	40–60	Total mold and yeast	About 3 log	Ertugay and Başlar [32]
Tomato juice	Ultrasonic probe	30.6–39.9	Yeast	About 5 log	Adekunte et al. [4]
Apple cider	Ultrasonic probe	40 and 60	*Escherichia coli* K12	Up to 5.3 log; difference between sonication and thermal-alone treatments	[89]
Orange juice	Ultrasonic probe	40	*E. coli* ATCC 35218	2.2 log	Char et al. [19]
Purple cactus pear J.	Ultrasonic probe	38.4–78.2	Total plate count, Enterobacteria	Not detected	Zafra-Rojas et al. [99]
Chokanon mango juice	Ultrasonic bath	25	Coliform count, aerobic plate count, yeast and mold count	<0.72 log	Santhirasegaram et al. [73]
Apple juice	Ultrasonic bath	20	Total plate count and yeast and mold count	1.12 and 1.22 log, respectively	Abid et al. [2]
Kasturi lime juice	Ultrasonic bath	20	Total plate count and yeast and mold count	1.9 and 0.5 log, respectively	Bhat et al. [17]

in fruits and vegetables because ultrasound improved yield, productivity, and selectivity and decreased the required extraction time [21, 53, 92, 97]. Vilkhu et al. [92] reported that extraction yield was increased from 6 % to 35 % by ultrasound processing. A further benefit of decreased thermal effects and increased yield/productivity was that ultrasound technology improved the rheological and cloudy properties of the final juice product [23, 32].

Ultrasound treatment, which results from the conversion of electrical into mechanical energy by way of piezoelectric materials, generates successive compression and relaxation as sound waves pass through a fluid. The passing of the sound waves to the relaxation position causes the formation of bubbles and spaces with micrometer radii when the negative pressure overcomes the tensile force. These bubbles grow and collapse, generating a localized high temperature (approximately 2000–5000 °C) and pressure (approximately 10–100 MPa) [33]. The resulting high local temperature and pressure cause localized inactivation of enzymes and microbes without significantly increasing the total temperature, thereby providing effective pasteurization [85]. Ultrasound treatment was reported to provide a 5 log decrease in the content of food-borne pathogens in fruit juices [5, 72].

Despite the many benefits of ultrasound treatment on juice processing, some authors have reported negative effects on juice quality following ultrasound processing. For instance, some off-flavor was formed during orange juice production [95], and some adverse effects on the final product quality occurred due to ultrasound processing [58]. Overall, however, ultrasound has many advantages and relatively few disadvantages and is an effective nonthermal process that has been studied for several applications in food processing.

Ultrasound treatment is sometimes insufficient for inactivation of microorganisms and enzymes when used alone. It can, however, be used in combination with mild heat, pressure, or other methods for microbial inactivation, especially pathogens, to improve the effectiveness of the treatment [14, 26, 93]. A combination of ultrasound and thermal treatment is especially critical for enzyme inactivation.

Ultrasound technology presents important opportunities for juice technologies. This chapter summarizes the possibilities and potential offered by ultrasound treatment for juice production technologies, the advantages and disadvantages of ultrasound treatments, the types of ultrasonic applications, the effect of ultrasound treatment on juice quality, and the results from recent studies.

Novel Technologies for Juice Production

Novel food processing technologies are divided into two types: thermal and nonthermal. Novel processes based on nonthermal principles include ultrasound, pulsed electric fields (PEF), high-pressure processing (HPP), ultraviolet irradiation (UV), dense-phase carbon dioxide (DPCO2) or high-pressure carbon dioxide (HPCD), and ozone. All are based on unique principles, but none are thermal principles. Foodstuffs do not undergo high-temperature changes, so many of the negative effects caused by heat are avoided. Novel processes based on thermal principles include

ohmic heating, microwave, and radio frequency; these processes provide some advantages because of the rapid heat transfer, which increases product quality. Comparison of these novel technologies indicates the potential for high-quality juice production by nonthermal processes, although these too have some disadvantages. Nevertheless, these novel technologies for fruit and vegetable juice production, both alone and in combination, represent viable alternatives to the traditional thermal treatments such as pasteurization and sterilization.

The pulsed electric field (PEF) is one of the most attractive novel technologies because, when compared to the conventional technologies, the use of short pulses of electricity achieves a reduction in both processing time and thermal effects on the organoleptic and physical properties [66]. PEF, an effective nonthermal technology, consists of application of high-voltage (20–80 kV/cm) pulses to juice placed between two electrodes. PEF inactivates food-borne pathogens and spoilage microorganisms by electroporation and electrofusion mechanisms [12, 29, 65, 77]. Electroporation is a phenomenon whereby enlargement of pores and formation of new pores in the microbial cell membrane disrupts many important cellular activities. Electrofusion also causes mechanical fragility of the cell membrane due to changes in charge density between the intracellular and extracellular compartments [12]. The U.S. Food and Drug Administration (FDA) published a "letter of no objection" for the use of pulsed electric fields in 1995 and approved industrial application of PurePulse Technologies. Therefore, PEF is an approved method for juice production processes under conditions sustained by pure pulse technologies [11].

Much research has been published on microbial and enzymatic inactivation in food by PEF, but significantly less has appeared on the effect of quality parameters and food components. Research on the effects of PEF on food first appeared in 1990; the number of publications was approximately 150 in the 2000s and has increased since, to 5949, according to Food Science and Technology Abstracts (FSTA). Ortega-Rivas et al. [60] reported that high-voltage pulsed electric fields were effective as a nonthermal pasteurization process, providing a 6 log reduction in microorganism numbers and improving apple juice quality. The color of the apple juice was also lighter than in juice treated by ultrafiltration. Noci et al. [56] reported a microbial reduction of 5.4 log cycles and substantial inactivation of PPO and POD by PEF. Pasteurization of orange juice with a 35 kV/cm PEF treatment for 1500 μs completely inactivated POD [30]. Overall, the research results indicate that the sensory properties of juices are mostly preserved, pathogenic microorganisms and enzymes are inactivated, and the shelf life is extended (Table 2).

High-pressure processing (HPP) is another nonthermal food preservation method that acts by killing pathogenic and spoilage microorganisms by decreasing cell membrane permeability or causing lysis of the cell membrane and collapse of the noncovalent bonds under pressures of up to 400 MPa [39, 46]. The fundamental principle of high-pressure processing (HPP) is that liquid is compressed by a force applied to the liquid surrounding the product [10]. High-pressure treatments are related by two scientific principles: the Le Chatelier principle and the isostatic principle. The Le Chatelier principle shows that when a system in balance receives an impact from the outside, the system creates a new equilibrium in the impact-

Table 2 Effect of ultrasonic treatments on enzymes inactivation

Juice	Treatment	Temperature (°C)	Enzymes	Inactivation	Reference
Apple juice	Ultrasonic probe	40–60	PPO	D value changed between 12.9 and 146 min	Başlar and Ertugay [13]
Pineapple juice	Ultrasonic probe	54	PPO	Max 20 % decrease	Costa et al. [25]
Orange juice	Ultrasonic probe	<45	PME	Max 62 % decrease for 10 min	Tiwari et al. [83]
Tomato juice	Ultrasonic probe	50–75	PME	Inactivation rate was increased by 1.5–6 times	Terefe et al. [81]
Tomato juice	Ultrasonic probe	50–75	PG	Inactivation rate was increased by 2.3–4 times	Terefe et al. [81]
Tomato juice	Ultrasonic probe	61	PME	Inactivation rate was increased by 39–374 fold	Raviyan et al. [67]
Apple juice	Ultrasonic probe	20–60	PPO	3–94 % reduction for 10 min	Abid et al. [3]
Apple juice	Ultrasonic probe	20–60	POD	2–91 % reduction for 10 min	Abid et al. [3]
Apple juice	Ultrasonic probe	20–60	PME	3–93 % reduction for 10 min	Abid et al. [3]

reducing direction. The isostatic principle is based on Pascal's law/principle, which explains that pressure exerted on a fluid in a sealed and enclosed system equals the pressure applied to every point of the system surrounding the liquid at the same time [40, 90]. HPP is approved by the U.S. FDA as a method for juice preservation, and extensive research has investigated the application of HPP to juice.

Bayındırlı et al. [15] studied the effectiveness of HPP application on inactivation of pathogenic microorganisms, such as *Staphylococcus aureus* 485, *Escherichia coli* O157:H7 933, and *Salmonella enteritidis* FDA, and on enzymes, such as polyphenol oxidase and pectinesterase, in apple, orange, apricot, and sour cherry juices. They deduced that complete inactivation of these microorganisms was achieved by treatment at 350 MPa and 40 °C for 5 min and the polyphenol oxidase activity remaining in apple juice was 9 ± 2.2 % following application of a treatment at 450 MPa and 50 °C for 60 min. The pectinesterase activity remaining in orange juice after a treatment at 450 MPa and 50 °C for 30 min was 7 ± 1.6 %. Fernández et al. [75] investigated the antioxidant capacity, nutrient content, and sensory quality parameters of orange juice and an orange-lemon-carrot juice mix after high-pressure treatment and storage in different packaging. They deduced that HPP treatment and storage after treatment for 21 days at 4 °C did not cause significant differences in antioxidant capacity, vitamin C, sugar, or carotene content and that the total quality parameters after treatment were not substantially changed.

Ultraviolet (UV) technology is widely used to inactivate pathogenic microorganisms in food products. Ultraviolet light is an electromagnetic radiation with a wavelength between 200 and 400 nm. Decreases in ultraviolet light wavelength increase the efficiency of ultraviolet light. Therefore, the main antiseptic effects of UV against food-borne microbiological contaminants takes place in the UV-C band, which has the lowest wavelength (210–280 nm). UV-A tans human skin and UV-B burns skin and may cause cancer, but UV-C has a fatal effect on microorganisms [37].

The mechanism of inactivation is related to UV absorption by DNA/RNA. When UV-C is absorbed by thymine and cytosine in DNA, the structure of DNA is disrupted, and the proliferation of microorganisms is inhibited [18, 37]. UV radiation is also approved by the US FDA for juice preservation and provides a reduction of at least 5 log cycles in numbers of human pathogens and decreases the activity of undesirable enzymes [88]. Char et al. [19] investigated the inactivation of some microorganisms following a combined treatment using high-intensity ultrasound and UV-C light in fruit juice samples. UV-C radiation alone was sufficient to inactivate *E. coli* ATCC 35218, an *E. coli* cocktail, *S. cerevisiae* KE162, and a yeast cocktail in peptone water and clarified apple juice; however, UV-C alone did not provide sufficient microbial inactivation in squeezed orange juice. Zhang et al. [76] reported that a UV-C treatment was faster than HPP and was highly efficient at decreasing residual PME activity. However, HPP treatment resulted in fewer unwanted changes in lycopene content, dynamic viscosity, color, and browning of watermelon juice when compared to thermal and UV-C treatments. Treatment with high UV doses can therefore possibly cause nutritional and quality losses and formation of undesirable constituents. Adzahan [98] reported a 30 % loss in vitamin C content in apple cider at 14.3 mJ/cm^2 (UV doses), while [101] reported a 17 % vitamin C loss in orange juice at 100 mJ/cm^2.

Carbon dioxide is the main antimicrobial agent used against vegetative pathogens in high-pressure carbon dioxide (HPCD) or dense-phase CO_2 (DPCO$_2$) processing. CO_2 serves as a processing assisting agent and is an acceptable ingredient in foods and beverages. It also can be removed from juices by applying a mild vacuum at the final processing stage, prior to packaging [27, 50].

Ultrasonic Applications

Various applications of ultrasound processes have been researched to find new combinations for high-quality juice production, since ultrasound alone is often not sufficient to extend the shelf life of juice. Many studies have emphasized that the critical temperature range for ultrasonic inactivation of microbial and enzymatic activity is 50–60 °C [55, 59]. An ultrasound process combined with a mild thermal process is called thermosonication, which is one of the most suitable methods for juice processing. Martínez-Flores et al. [52] reported that thermosonication

(50–58 °C) extended the shelf life of carrot juice up to 14 days and retained substantial levels of some bioactive components. The shelf life of carrot juice increased with increasing treatment temperature. Wu et al. [96] reported that thermosonication (60–70 °C) inactivated PME by 90 %, noticeably decreased the particle size (<30 μm), and increased the viscosity to two- to fourfold. The authors suggest that thermosonication at 60–65 °C produced tomato juice that maintained its fresh-like properties. Similarly, thermosonication (60–75 °C) shortened the time for inactivation of PME up to 1.5–6 times and 2.3–4 times for polygalacturonase (PG) [81]. Başlar and Ertugay [32] reported that all molds and yeasts in apple juice were completely inactivated by thermosonication at 60 °C.

Thermosonication can be combined with high pressure in a process called manothermosonication (MTS); this is generally more successful than thermosonication alone. Guzel et al. [38] reported that *Listeria monocytogenes* and *Escherichia coli* suspended in apple and orange juices were inactivated by manosonication (MS) and MTS treatment. The study investigated the use of 100–200 kPa pressure and mild temperature (35 °C) for MS and 200 kPa pressure and 50–60 °C temperature for MTS. Both applications were more effective than ultrasound alone; however, only MTS showed a synergistic effect against microorganisms in juice. Jabbar et al. [42] reported that microorganisms in carrot juice were completely inactivated when treated with a combination of ultrasound and high hydrostatic pressure.

Better-quality juices are produced by combining a thermosonication process and another different nonthermal process, such as pulsed electrical fields and high-intensity light pulses. Walkling-Ribeiro et al. [94] reported that a thermosonication process (10 min at 55 °C) combined with a pulsed electrical field (PEF) treatment (40 kV/cm for 150 μs) was an effective alternative method to conventional pasteurization of orange juice. *Staphylococcus aureus* was inactivated by this combination at comparable levels to that achieved by conventional methods; however, the combination left a greater residual PME activity than conventional methods (12.9 % and 5.0 %, respectively). The shelf life of orange juice was extended up to 168 days by the combination, and the sensory attributes of this juice were rated as equivalent to a thermal treatment. A research study on the combination of thermosonication and PEF treatment, synergistic effect was conducted on *Cronobacter sakazakii* contamination in apple juice [7]. Munoz et al. [102] studied combinations of high-intensity light pulses and thermosonication for inactivation of *Escherichia coli* in orange juice but found no significant results.

Much research has investigated the combination of ultrasound and ultraviolet treatments, called photosonication [13, 19, 44, 74]. Başlar and Ertugay [13] reported the application of an ultrasonic probe and two or four ultraviolet lamps simultaneously as parallel treatments of apple juice sample placed in a beaker at 40 °C, 50 °C, and 60 °C. The photosonication treatment was better than ultrasonic treatment alone in terms of PPO inactivation, but the enzyme was still not completely inactivated. Char et al. [19] reported that ultraviolet light was more effective than

Table 3 Effect of ultrasonic treatments on cloudiness

Juice	Treatment	Temperature (°C)	Cloudiness	Change	Reference
Apple juice	Ultrasonic probe	40–60	Cloudiness level	Up to 16.9 times increase	Ertugay and Başlar [32]
Apple juice	Ultrasonic probe	40–60	Cloudiness stability	Up to 9.8 times increase	Ertugay and Başlar [32]
Apple juice	Ultrasonic bath	20	Cloudy	Up to 3.1 times increase	Abid et al. [2]
Orange juice	Ultrasonic probe	25	Cloud loss	Up to about 4 times decrease	Tiwari et al. [83]
Orange juice	Ultrasonic probe	10–30	Cloud value	Up to 2.7 times increase	Tiwari et al. [84]
Orange juice	Ultrasonic probe	32–38	Cloud value	Up to 2.16 times increase	Tiwari et al. [87]
Orange juice	Ultrasonic probe	25	Cloud value	Up to 2.22 times increase	Tiwari et al. [82]

ultrasonic treatment alone on decontamination of *E. coli* ATCC 35218 in apple juice. Inactivation of *E. coli* ATCC 35218 in orange juice by simultaneous treatment with ultraviolet light and ultrasound was more effective than ultraviolet light alone and ultrasound treatment alone. When combinations of ultrasound and UV-C treatment were applied to freshly squeezed Chokanan mango juice [74], the combination was reported to provide complete inactivation of coliforms and aerobic bacteria and significant reduction in yeast and mold counts. The author suggested the combination can be use as a hurdle technology to improve the quality of Chokanan mango juice. *Zygosaccharomyces bailii* in apple juice was inactivated with a combination of ultraviolet and ultrasound, rather than ultrasound alone [36]. Ultrasound treatment was also combined with pulsed light (PL) technology for inactivation of spoilage microorganisms in apple juice. The combination led to a reduction of 2.3–3.0 log cycles of spores (*Alicyclobacillus acidoterrestris* ATCC 49025) in apple juice and 6.4–5.8 log cycles for *Saccharomyces cerevisiae* [34].

Ultrasonic processes have been combined by treatments with some food additives, such as sodium benzoate, potassium sorbate, and alpha- and beta-pinene, for pasteurization of orange and apple juices against acid-adapted *Escherichia coli* O157:H7 [35]. The combination provided greater inactivation rates in both juices. Cheng et al. [23] studied the effects of carbonation (meaning that carbon dioxide is applied to a medium) and sonication on the quality of guava juice and found that carbonation provided more nuclei for cavitation. Ultrasonic treatment together with carbonation had no effect on microbial and polyphenol oxidase (PPO) inactivation; however, it stabilized cloudiness and the phenolic compound content. Similarly, Patil [61] reported that ozonation alone caused significant inactivation of *E. coli* in some fruit juice, while ozone application with combined ultrasound increased slightly the effectiveness of ozone (Table 3).

Effect of Ultrasound on Juice Quality

Shelf Life

One of the most important quality parameters regarding ultrasound applications for juices is the resulting shelf life of the product. The objective of pasteurization in conventional juice production is generally inactivation of thermostable enzymes (PME, PPO, and POD) rather than microorganisms because of the acidic properties of juice. In other words, microbial risks have already been eliminated under conditions where the enzymes of acidic juice are inactivated. However, the target for juice with a high pH is elimination of the microbial risk. The mechanisms of ultrasound treatment differ, so the target enzymes or microorganisms are not the same as those targeted with thermal process (Tables 1 and 2). The effects of the ultrasound process vary depending on the enzyme or microorganism. Therefore, the ultrasonic stability of microorganisms and enzymes in different food matrices should be determined carefully.

Ultrasound treatment of juice has been reported to be effective for the inactivation of enterobacteria [99], total yeasts and molds [32], aerobic plate count, coliform count, total yeast and mold count [73], and *Escherichia coli* [6]. Abid et al. [2] observed that total plate count was considerably decreased in samples sonicated for 60 and 90 min when compared to samples treated for 30 min and control samples. A significant decrease was also observed in yeasts and molds in all sonicated samples, but complete decontamination of the samples was not achieved. Bhat et al. [17] confirmed that the aerobic and total plate counts in kasturi lime (*Citrus microcarpa*) juice were significantly reduced by application of ultrasound for 60 min. In general, some microorganisms appeared resistant to ultrasonication and required longer treatment durations for destruction. Molds and yeasts, on the other hand, were more susceptible and showed significant reductions in the whole treated juices after ultrasonication for 30 and 60 min [17]. Another study showed that ultrasound combined with mild temperature elevations of 50 °C, 54 °C, and 58 °C increased the shelf life of carrot juice by 20 %, 40 %, and 60 %, respectively, when compared to a nontreated sample. The growth of enterobacteria for samples sonicated at 58 °C was only 2.02 log after 20 days of storage [52]. Adekunte et al. [4] reported that sonication alone was an effective application for obtaining the desired reduction (5 log) in yeast cells in tomato juice. On the other hand, ultrasound combined with heat treatment (thermosonication) enhanced the effectiveness of microbial inactivation and enabled a shorter processing time. Aadil et al. [1] reported that the microbial content of grapefruit juice was completely inactivated by thermosonication at 60 °C for 60 min, while the PME, POD, and PPO contents were reduced by 91 %, 90 %, and 89 %, respectively, by this same treatment. Terefe et al. [81] reported that PME affected the rheological characteristics of tomato-based products but was considerably inactivated by sonication-combined thermal treatment at temperatures higher than 50 °C. In another study, PME activity in tomato juice was reduced by 90 % by thermosonication at 60 °C, 65 °C, and 70 °C [96].

Several factors such as temperature, food matrix, pH, ultrasound intensity, and ultrasound processing time affect ultrasound application on enzyme inactivation. The enzymes (e.g., PPO) denature because of cell disruption, and higher ultrasonic intensities and longer processing times (376 W/cm^2 and 10 min) cause a significant reduction in enzyme activity (e.g., 20 % for PPO). However, ultrasound intensity has a negative effect on the overall protein concentration, so high intensity can cause nutritional protein loss as well [25].

Yield and Extraction

Ultrasonic treatments provide high yields and effective extractions by increasing the cutting power and generating microbubbles that increase the surface area and mass transfer based on the cavitation effect [8]. Lieu and Le [49] reported that ultrasonic treatment increased juice yield by up to 3.4 %, while shortening the treatment time threefold. Ultrasound-assisted enzymatic treatment also increased juice yield up to 2 % and shortened treatment time over fourfold when compared with traditional enzymatic treatment. The successive application of ultrasound and enzymatic treatment increased juice yield up to 7.3 %. Similarly, Nguyen and Le [57] reported that ultrasonic treatment alone increased the extraction yield by 10.8 % for juice production from pineapple mash. Ultrasonic treatment also enhanced the content of sugars, total acids, phenolics, and vitamin C.

Ultrasound application can enhance juice production by reducing the processing time and lowering energy consumption by improving mass transfer to and from interfaces. These effects considerably improve both application rate and final product yield [2, 63, 78]. The enhancement of mass transfer by ultrasonic application also has some other advantages; for example, ultrasound simplified the production of the date syrup but also increased the effectiveness of the antimicrobial components of the syrup and gave the product a better physical quality [31, 80].

Sensory Properties

Adverse effects on the sensory properties of juice during pasteurization processing include degradation of the desired ingredients and/or generation of undesirable flavors. One important reason for the use of alternatives to thermal processing is that nonthermal treatments prevent the loss of sensory properties that occurs during heat treatment of juice. Ertugay and Başlar [32] reported that apple juice treated at an ultrasound amplitude of 50 μm and a temperature of 50 °C for 10 min had the most acceptable aroma and flavor as determined by panelists. However, for a true benchmark in this type of work, pasteurization should be compared to ultrasonication based on the same feature of the juice. One such study confirmed that ultrasonic treatment (at 60 °C for 10 min) gave the greatest inactivation of PPO, indicating improvement of the sensorial properties compared to pasteurized juice. However, the properties of the ultrasonicated juice were inferior to those of untreated juice, probably because ultrasonic treatment can cause the formation of new compounds

due to the release of sequestered compounds and disintegration of compounds found in the raw material. Some ultrasonic treatments can improve the sensorial properties because of release and formation of new aromatic compounds, while other ultrasonic treatments (generally high intensity, temperature, and time) degrade these properties due to the generation of undesirable aromas or degradation of aromatic compounds. Vercet et al. [91] suggested that manothermosonication (MTS) could be the cause of metallic tastes via the effects of free radicals [78], although Simunek et al. [78] and Ertugay and Başlar [32] both reported that no metallic taste was detected by panelists in juice pasteurized with ultrasonic treatment. Simunek et al. [78] also identified new components in the apple juice and nectar and the loss of some original components following ultrasonic applications. For instance, ethyl 2-methylbutyrate was not detected in the untreated samples but accounted for 11.98 % of total aromatic compounds in pasteurized samples. The largest aromatic compound fraction was determined as 14.50 % after ultrasound treatment at an amplitude of 90 μm and a temperature of 60 °C for 6 min. On the other hand, ultrasound treatment had no adverse effects on the sensory properties of the juice [16].

    In general, the present research [32, 78] indicates that ultrasound causes less change or no change to the sensorial properties of juice when compared to pasteurized juice. At the same time, ultrasonic treatment at high intensity and/or temperature has the potential to cause adverse alterations in the sensorial properties of juice because of rapid isomerization of compounds and oxidative interaction with free radicals.

Bioactive Components

One of the important reasons for preferring juice consumption over consumption of the raw product is that juice contains high levels of bioactive compounds. High-heat treatment during pasteurization or sterilization processing of juices can lead to the disintegration of these bioactive components and other components vital to human health. Therefore, understanding the impact of ultrasound treatment on bioactive components is very important (Table 4).

    Some studies indicate that ultrasonic treatment increases the levels of bioactive compounds by improving the release of these components from the cells. For example, the bioactive components of apple juice were significantly increased after ultrasound application: The total phenolic values were higher in juice samples treated for 30, 60, and 90 min (768, 815 and 829 μg/g) than in nontreated apple juice (757 μg/g). Similar increases were also observed in flavonoid and flavonol content and in the total antioxidant capacity of the sonicated samples. The ascorbic acid value of the apple juice was improved by increasing the ultrasound treatment time, with the highest value observed in juice treated for 90 min [2]. On the other hand, the ascorbic acid content of orange juice was negatively influenced by ultrasonic temperature, amplitude, and treatment time. Ascorbic acid is thought to degrade due to sonolysis and oxidation reactions occurring during the ultrasound treatment [85]. The lycopene and anthocyanin contents of watermelon also decreased when ultrasound treatment was applied at high amplitude levels and long treatment times (>5 min). This temperature effect on lycopene levels has also been observed in juice

Table 4 Effect of ultrasonic treatments on bioactive components

Juice	Treatment	Temperature (°C)	Bioactive components	Change	Reference
Apple juice	Ultrasonic probe	40–60	Total phenolic component	<15 % decrease	Başlar and Ertugay [13]
Purple cactus pear J.	Ultrasonic probe	38.4–78.2	Total phenolic component	<30.5 % increase	Zafra-Rojas et al. [99]
Purple cactus pear J.	Ultrasonic probe	38.4–78.2	Ascorbic acid content	<17.9 % increase	Zafra-Rojas et al. [99]
Pineapple juice	Ultrasonic probe	54	Total phenolic component	Not sig.	Costa et al. [25]
Orange juice	Ultrasonic probe	10–30	Ascorbic acid	<2.05 % decrease	Tiwari et al. [85]
Chokanon mango juice	Ultrasonic bath	25	Total carotenoid content	<4.7 % decrease	Santhirasegaram et al. [73]
Chokanon mango juice	Ultrasonic bath	25	Ascorbic acid content	<38.5 % decrease	Santhirasegaram et al. [73]
Apple juice	Ultrasonic bath	20	Ascorbic acid	<34.04 % increase	Abid et al. [2]
Apple juice	Ultrasonic bath	20	Total phenolic component	<9.48 % increase	Abid et al. [2]
Apple juice	Ultrasonic bath	20	Total flavonoids	<30.18 % increase	Abid et al. [2]
Apple juice	Ultrasonic bath	20	Total flavonols	<44.1 % increase	Abid et al. [2]
Kasturi lime juice	Ultrasonic bath	20	Ascorbic acid	<6.68 % increase	Bhat et al. [17]
Kasturi lime juice	Ultrasonic bath	20	Total flavonoids	<42.3 % increase	Bhat et al. [17]
Kasturi lime juice	Ultrasonic bath	20	Total flavonols	<127.4 % increase	Bhat et al. [17]
Kasturi lime juice	Ultrasonic bath	20	Total phenolic	<27.36 % increase	Bhat et al. [17]

sonicated at 45 °C [68]. Başlar and Ertugay [13] reported a decrease in phenolic components following ultrasound treatment for long times at high temperature and amplitude; however, this decrease was not as substantial as that seen with pasteurization.

Thermal treatments can cause a significant decrease in total carotenoid content of juices, as oxidation damages the stability of the conjugated double-bond system of carotenoids [24, 48, 71]. On the other hand, chokanon mango juice samples sonicated for 15 and 30 min showed a significant increase in carotenoid content. However, the degradation of carotenoids occurred in samples sonicated for 60 min [73].

The total carotenoid content of carrot juice changes with ultrasonic treatment and storage when compared to control samples. A significant increase of 3.44 % was reported for total carotenoid content in carrot juice sonicated at 58 °C. This value was reduced during storage of the samples [52].

Rheological Properties

The rheological properties are identifying characteristics of fluid foods such as juice. The properties of juice can change during conventional heat treatments because of changes in the structural properties of the juice. Similarly, ultrasound treatment can usually induce some changes in juice rheological properties. Martínez-Flores et al. [52] reported that ultrasonic treatment caused significant increases in the viscosity of untreated carrot juice from 1.52 to 16.49 mPas. On the other hand, significant changes were observed in samples thermosonicated at temperatures of 50 °C, 54 °C, and 58 °C after 12, 14, and 20 days of storage, respectively.

The viscosity and pectin content increased with application of low-power ultrasound, which enhanced the clarity of the juice. On the other hand, application of high-power ultrasound can cause negative changes in juice rheology. Improvements in the clarity of the juice exposed to ultrasound significantly are due to cavitational collapse of bubbles that break down particles in the juice [21, 73]. The viscosity of grapefruit juice considerably increased in thermosonicated samples when compared to control samples. In general, increases in treatment time and temperature caused significant increases in viscosity of the samples, with the greatest results obtained by treatment at 60 °C for 60 min [1].

Cloudiness

Cloudiness is an important quality parameter that affects the appearance and flavor of the juice. It is determinative for consumer approval for some juices. It is related to the presence of particles composed of pectin, protein, cellulose, and lipids [1, 9]. The concepts of cloud value and cloud stability value are generally used for interpretation. The cloud value indicates the current turbidity levels, while cloud stability refers to the cloud value of the juice over time. Centrifugation at $4200 \times g$ for 15 min is equivalent to 1 year of storage [103].

Ultrasonic treatments affected cloudy parameters of juice at alot of reserach (Table 3). Aadil et al. [1] reported that the cloud value was considerably higher in thermosonicated grapefruit juice than in nonsonicated juice and the maximum value was obtained in juice thermosonicated at the maximum temperature and time tested (60 °C for 60 min). Cloud level and stability were both dependent on treatment time, temperature, and amplitude level. The best results were observed at the longest treatment time (10 min) and highest processing temperature (60 °C) and amplitude (100 μm). Cloud quality of the samples was slightly effected negative after 4 months of storage [32]. Cloud value of ultrasonicated apple juice was significantly altered

increasing according to nonsonicated apple juice [2]. According to results of a different study, cloud value in orange juice is considerably enhanced as a maximum increase of 270 % and the minimum increase observed as 125 % by ultrasound application [83]. Unlike the studies, Tiwari et al. emphasize low ultrasonic intensity, temperature, and treatment time increased more turbidity of orange juice.

Because of collapse of the cavitation bubbles formed on the surface, ultrasound caused to reduce the particle size in addition to the stability to the juices [23, 54]. This allows fine particles to remain in the supernatant after centrifugation and adds stability to the juice [99]. Investigation of the size of the particles in apple juice at an ultrasound amplitude of 100 μm and different temperatures showed that the particle size decreased with increasing processing temperature. At 60 °C, sonication converted particles to a soluble colloidal form [32]. The resulting reduction in particulates lowered the sedimentation value of the apple juice to 10–13 %. By contrast, ultrasonic application at 40 °C increased the sedimentation value to 30–32 %. The lower sedimentation at 60 °C treatment can be explained by cloud stability due to ultrasonic homogenization [32].

Color

Appearance is the main quality parameter in the choice of food products by consumers. Therefore, any ultrasonic process applied should improve or protect the appearance, especially color. Many studies have shown enhancement of customer preference for a product by improved color changes [13]. Processing temperature, treatment time, and ultrasound amplitude can all affect the color and degree of nonenzymatic browning of juices. Generally, minimal changes are observed on color levels. Apple juice ultrasonicated at an amplitude of 60 μm and a temperature of 40 °C for 6 min and apple nectar at 120 μm and 20 °C for 3 min yielded the most acceptable fruit juices. Some ultrasonic treatments improved the color properties when compared to untreated juice [78]. Other research has reported a significant difference between the color of ultrasonicated and nonsonicated apple juice, where the lowest L* and a* values and the highest b* values were observed in apple juice treated for 90 min [2]. Similarly, Adekunte et al. [5] reported that sonication reduced L*, a*, and b* values and increased the total color difference (TCD) and color index (CI) of tomato juice. On the other hand, ultrasound and thermal process increased nonenzymatic browning (NBE) and led to color changes and nutrient losses [28, 73]. The sonication and thermal treatment of juices caused a significant increase in the nonenzymatic browning of mango juices [73]. Nonenzymatic browning varied from 0.142 to 0.179 when compared to untreated orange juice (0.063) [84].

Physicochemical Properties

Some physicochemical properties, such as pH, soluble solids content, and titratable acidity, affect several juice qualities, including microbial, rheological, cloudiness,

appearance, and sensory properties. No considerable change was observed in pH, soluble solids content, and titratable acidity of sonicated apple juice [2], orange juice [83, 84], blueberry [86], kasturi lime juice [17], purple cactus pear juice [99], tomato juice [4], or Chokanon mango juice [73]. The pH value of the carrot juice thermosonicated at 58 °C was reduced after 20 days of storage (from 6.81 to 6.68), but no visible spoilage was apparent in the sample. A significant change was observed in titratable acidity of the same sample (treated for 58 °C) after 20 days of storage (from 0.30 % to 0.81 %) [52].

The electrical conductivity of liquid foods arises from the existence of nutrients such as vitamins, fatty acids, and proteins. The electrical conductivity of grapefruits can decrease because of the decreases in the mineral and vitamin contents of the sample during thermosonication [1].

Conclusions and Future Directions

Alone ultrasonic treatment is not sufficient for extending the shelf life of juices; therefore, it is commonly used in combination with a thermal process referred to as thermosonication. Various combinations of heat and sonication have been tested to extend the shelf life, but no method has yet been developed for application in the industrialization stage. Further research is needed for optimization of new processing combinations that incorporate ultrasonication. At the same time, it seems that some nonthermal process (UV and PEF) in commercialization stage is present. Despite shelf life of products produced by these methods being short, it is a preferable product due to high organoleptic characteristics. The success of the technologies has partially narrowed market and research interest for nonthermal processing of juice. However, ultrasonic treatment can provide significant advantages for the processing of juices: enhanced quality parameters, such as yield, extraction, cloudiness, rheological properties, and color as well as the shelf life. So it should focus on the area to improve the position of ultrasonic technique for juice technology in the future. In the future, it is estimated that use of ultrasound in fruit juice technology will spread due to its advantages over other technologies.

References

1. Aadil RM, Zeng X-A, Zhang Z-H, Wang M-S, Han Z, Jing H, Jabba S (2015) Thermosonication: a potential technique that influences the quality of grapefruit juice. Int J Food Sci Technol 50:1275–1282
2. Abid M, Jabbar S, Wu T, Hashim MM, Hu B, Lei S (2013) Effect of ultrasound on different quality parameters of apple juice. Ultrason Sonochem 20:1182–1187
3. Abid M, Jabbar S, Hu B, Hashim MM, Wu T, Lei S, Khan MA, Zeng X (2014) Thermosonication as a potential quality enhancement technique of apple juice. Ultrason Sonochem 21:984–990
4. Adekunte A, Tiwari BK, Cullen PJ, Scannel AGM, O'Donnel CP (2010) Effect of sonication on colour, ascorbic acid and yeast inactivation in tomato juice. Food Chem 122:500–507

5. Adekunte A, Tiwari B, Scannell A, Cullen P, O'donnell C (2010) Modelling of yeast inactivation in sonicated tomato juice. Int J Food Microbiol 137:116–120

6. Alighourci H, Barzegar M, Sahari MA, Abbasi S (2014) The effects of sonication and gamma irradiation on the inactivation of *Escherichia coli* and *Saccharomyces cerevisiae* in pomegranate juice. Iran J Microbiol 6:51–58

7. Arroyo C, Cebrián G, Pagán R, Condón S (2012) Synergistic combination of heat and ultrasonic waves under pressure for *Cronobacter sakazakii* inactivation in apple juice. Food Control 25:342–348

8. Awad TS, Moharram HA, Shaltout OE, Asker D, Youssef MM (2012) Applications of ultrasound in analysis, processing and quality control of food. Food Res Int 48:410–427

9. Baker RA, Cameron RG (1999) Clouds of citrus juices and juice drinks. Food Technol 53:64–69

10. Barba F, Esteve M, Frígola A (2012) High pressure treatment effect on physicochemical and nutritional properties of fluid foods during storage: a review. Compr Rev Food Sci Food Safety 11:307–322

11. Barbosa-Canovas GV, Altunakar B (2007) Pulsed electric fields processing of foods: an overview. In: Raso J, Heinz V (eds) Pulsed electric fields for the Food Industry- Fundamentals and applications. Springer, pp 3-22

12. Barbosa-Canovas GV, Gongora-Nieto MM, Pothakamury UR, Swanson BG (1999) Fundamentals of high-intensity pulsed electric fields (PEF). In: Preservation of foods with pulsed electric fields. Academic, San Diego

13. Başlar M, Ertugay M (2013) The effect of ultrasound and photosonication treatment on polyphenoloxidase (PPO) activity, total phenolic component and color of apple juice. Int J Food Sci Technol 48:886–892

14. Baumann AR, Martin SE, Feng H (2005) Power ultrasound treatment of *Listeria monocytogenes* in apple cider. J Food Prot 68:2333–2340

15. Bayındırlı A, Alpas H, Bozoğlu F, Hızal M (2006) Efficiency of high pressure treatment on inactivation of pathogenic microorganisms and enzymes in apple, orange, apricot and sour cherry juices. Food Control 17:52–58

16. Bevilacqua A, Speranza B, Campaniello D, Sinigaglia M, Corbo MR (2014) Inctivation of spoling yeasts of fruit juices by pulsed ultrasound. Food Bioprocess Technol 7:2189–2197

17. Bhat R, Kamaruddin NSBC, Min-Tze L, Karim AA (2011) Sonication improves kasturi lime (*Citrus microcarpa*) juice quality. Ultrason Sonochem 18:1295–1300

18. Bintsis T, Litopoulou-Tzanetaki E, Robinson RK (2000) Existing and potential applications of ultraviolet light in the food industry – a critical review. J Sci Food Agric 80(6):637–645

19. Char CD, Mitilinaki E, Guerrero SN, Alzamora SM (2010) Use of high-intensity ultrasound and UV-C light to inactivate some microorganisms in fruit juices. Food Bioprocess Technol 3 (6):797–803

20. Charles-Rodríguez A, Nevárez-Moorillón G, Zhang Q, Ortega-Rivas E (2007) Comparison of thermal processing and pulsed electric fields treatment in pasteurization of apple juice. Food Bioprod Process 85(C2):93–97

21. Chemat F, Huma Z, Khan MK (2011) Applications of ultrasound in food technology: processing, preservation and extraction. Ultrason Sonochem 18:813–835

22. Chen Y, Yu LJ, Rupasinghe HPV (2013) Effect of thermal and non-thermal pasteurisation on the microbial inactivation and phenolic degradation in fruit juice: a mini-review. J Sci Food Agric 93:981–986

23. Cheng LH, Soh CY, Liew SC, Teh FF (2007) Effects of sonication and carbonation on guava juice quality. Food Chem 104:1396–1401

24. Cortes C, Torregrosa F, Esteve MJ, Frigola A (2006) Carotenoid profile modification during refrigerated storage in untreated and pasteurized orange juice and orange juice treated with high-intensity pulsed electric fields. Agric Food Chem 54:6247–6254

25. Costa M, Fonteles T, Jesus A, Almeida F, Miranda M, Fernandes F, Rodrigues S (2013) High-intensity ultrasound processing of pineapple juice. Food Bioprocess Technol 6:997–1006

26. D'Amico DJ, Silk TM, Wu JR, Guo MR (2006) Inactivation of microorganisms in milk and apple cider treated with ultrasound. J Food Prot 69:556–563

27. Damar S, Balaban MO (2011) Effects of dense phase CO_2 on quality attributes of beverages. J Food Sci 347–358

28. Demirdöven A, Baysal T (2008) The use of ultrasound and combined technologies in food preservation. Food Rev Int 25:1–11

29. Altunakar B (2007) Food preservation by pulsed electric fields and selected antimicrobials. PhD thesis, Department of Biological Systems Engineering Washington State University Pulman, p 22

30. Elez-Martinez P, Soliva-Fortuny RC, Martin-Belloso O (2006) Comparative study on shelf life of orange juice processed by high intensity pulsed electric fields or heat treatment. Eur Food Res Technol 222:321–329

31. Entezari MH, Nazary SH, Khodaparast MHH (2004) The direct effect of ultrasound on the extraction of date syrup and its micro-organisms. Ultrason Sonochem 11:379–384

32. Ertugay MF, Başlar M (2014) The effect of ultrasonic treatments on cloudy quality-related quality parameters in apple juice. Innov Food Sci Emerg Technol 26:226–231

33. Feng H, Yang W (2011) Ultrasonic processing. In: Zhang HQ, Barbosa-Cánovas GV, Balasubramaniam VMB, Dunne CP, Farkas DF, Yuan JTC (eds) Nonthermal processing technologies for food. Blackwell Publishing, USA

34. Ferrario M, Alzamora SM, Guerrero S (2015) Study of the inactivation of spoilage microorganisms in apple juice by pulsed light and ultrasound. Food Microbiol 46:635–642

35. Gabriel AA (2015) Combinations of selected physical and chemical hurdles to inactivate *Escherichia coli* O157:H7 in apple and orange juices. Food Control 50:722–728

36. Gómez-Díaz JJ, Santiesteban-López A, Palou E, López-Malo A (2011) *Zygosaccharomyces bailii* inactivation by means of UV light and low-frequency ultrasound treatments. J Food Prot 74:1751–1755

37. Guerrero-Beltrán JA, Barbosa-Cánovas GV (2011) Ultraviolet-C light processing of liquid food products. In: Zhang HQ, Barbosa-Cánovas GV, Balasubramaniam VMB, Dunne CP, Farkas DF, Yuan JTC (eds) Nonthermal processing technologies for food. Blackwell, Ames

38. Guzel BH, Arroyo C, Condón S, Pagán R, Bayindirli A, Alpas H (2014) Inactivation of *Listeria monocytogenes* and *Escherichia coli* by ultrasonic waves under pressure at nonlethal (manosonication) and lethal temperatures (manothermosonication) in acidic fruit juices. Food Bioprocess Technol 7(6):1701–1712

39. Heinz V, Buckow R (2009) Food preservation by high pressure. J Consum Protect Food Safety 5:73–81

40. Heremans K (2002) High pressure bioscience and biotechnology: a century and a decade perspective. In: Hayashi R (ed) Trends in high pressure bioscience and biotechnology. Elsevier Science, Amsterdam, pp 1–6

41. Hertog MGL, Kromhout D, Aravanis C, Blackburn H, Buzina R, Fidanza F (1995) Flavonoid intake and longterm risk of coronary heart disease and cancer in the seven countries study. Arch Intern Med 155:381–386

42. Jabbar S, Abid M, Hu B, Hashim MM, Saeeduddin M, Lei S, Wu T, Zeng X (2014) Influence of sonication and high hydrostatic pressure on the quality of carrot juice. Int J Food Sci Technol 49:2449–2457

43. Jiménez-Sánchez C, Lozano-Sánchez J, Segura-Carretero A, Fernández-Gutiérrez A (2015) Review: alternatives to conventional thermal treatments in fruit-juice processing. Part 1: techniques and applications. Crit Rev Food Sci Nutr. doi:10.1080/10408398.2013.867828

44. Khandpur P, Gogate PR (2015) Effect of novel ultrasound based processing on the nutrition quality of different fruit and vegetable juices. Ultrason Sonochem 27:125–136

45. Knorr D, Zenker M, Heinz V, Lee D (2004) Applications and potential of ultrasonics in food processing. Trends Food Sci Technol 15(5):261–266

46. Knorr D, Heinz V, Buckow R (2006) High pressure application for food biopolymers. Biochim Biophys Acta 1764:619–631
47. Lako J, Trenerry V, Wahlqvist M, Wattanapenpaiboon N, Sotheeswaran S, Premier R (2007) Phytochemical flavonols, carotenoids and the antioxidant properties of a wide selection of Fijian fruit, vegetables and other readily available foods. Food Chem 101:1727–1741
48. Lee HS, Coates GA (2003) Effect of thermal pasteurization on valencia orange juice color and pigments. LWT-Food Sci Technol 36:153–156
49. Lieu LN, Le VVM (2010) Application of ultrasound in grape mash treatment in juice processing. Ultrason Sonochem 17(1):273–279
50. Liu Y, Hu X, Zhao X, Zhang C (2011) Inactivation of polyphenol oxidase from watermelon juice by high pressure carbon dioxide treatment. J Food Sci Technol 50:317–324
51. Marco DBF, Joseph V, John K (1997) Mechanisms of disease: antioxidants and atherosclerotic heart disease. N Engl J Med 337(6):408–416
52. Martínez-Flores HE, Garnica-Romo MaG, Bermúdez-Aguirre D, Pokhrel PR, Barbosa-Cánovas GV (2015) Physico-chemical parameters, bioactive compounds and microbial quality of thermo-sonicated carrot juice during storage. Food Chem 172:650–656
53. Mason TJ, Cordemans ED (1996) Ultrasonic intensification of chemical processing and related operations: a review. Trans Inst Chem Eng 74:511–516
54. Mason TJ, Paniwnyk L, Lorimer JP (1996) The use of ultrasound in food technology. Ultrason Sonochem 3(3):253–260
55. Mason TJ, Riera E, Vercet A, Lopez-Buesa P (2005) Application of ultrasound. In: Sun DW (ed) Emerging technology for food processing. Elsevier Academic Press, Londra
56. Noci F, Riener J, Walkling-Ribeiro M, Cronin DA, Morgan DJ, Lyng JG (2008) Ultraviolet irradiation and pulsed electric fields (PEF) in a hurdle strategy for the preservation of fresh apple juice. J Food Eng 85(1):141–146
57. Nguyen TP, Le VVM (2012) Application of ultrasound to pineapple mash treatment in juice processing. Int Food Res J 19(2):547–552
58. O'Donnell CP, Tiwari BK, Bourke P, Cullen PJ (2010) Effect of ultrasonic processing on food enzymes of industrial importance. Trends Food Sci Technol 21(7):358–367
59. Ohlsson T, Bengtsson N (2002) Minimal processing of foods with non-thermal methods. In: Ohlsson T, Bengtsson N (eds) Minimal processing technologies in the food industry. CRC Press LLC, Boca Raton, US
60. Ortega-Rivas E, Zárate-Rodríguez E, Barbosa-Cánovas G (1998) Apple juice pasteurization using ultrafiltration and pulsed electric fields. Food Bioprod Process 76:193–198
61. Patil S (2010) Efficacy of ozone and ultrasound for microbial reduction in fruit juice. Doctoral thesis, Dublin Institute of Technology
62. Patil S, Bourke P, Kelly B, Frías JM, Cullen PJ (2009) The effects of acid adaptation on Escherichia coli inactivation using power ultrasound. Innov Food Sci Emerg Technol 10:486–490
63. Patist A, Bates D (2008) Ultrasonic innovations in the food industry: from the laboratory to commercial production. Innov Food Sci Emerg Technol 9:147–154
64. Perkins-Veazie P, Collins JK (2004) Flesh quality and lycopene stability of fresh-cut watermelon. Postharvest Biol Technol 31:159–166
65. Qin BL, Pothakamury H, Vega H, Martin O, Barbosa-Canovas GV, Swanson BG (1995) Food pasteurization using high intensity pulsed electric fields. Food Technol 49(12):55–60
66. Quass DW (1997) Pulsed electric field processing in the food industry. A status report on pulsed electric field. Electric Power Research Institute, Palo Alto. CR- 109742, pp 23–35
67. Raviyan P, Zhang Z, Feng H (2005) Ultrasonication for tomato pectinmethylesterase inactivation: effect of cavitation intensity and temperature on inactivation. J Food Eng 70:189–196
68. Rawson A, Tiwari BK, Patras A, Brunton N, Brennan C, Cullen PJ, O'Donnell C (2011) Effect of thermosonication on bioactive compounds in watermelon juice. Food Res Int 44:1168–1173. doi:10.1016/j.foodres.2010.07.005

69. Rodrigo D, Cortes C, Clynen E, Schoofs L, Van Loey A, Hendrickx M (2006) Thermal and high-pressure stability of purified polygalacturonase and pectin methylesterase from four different tomato processing varieties. Food Res Int 39:440–448

70. Rodrigues S, Andre F (2012) Thermal treatment effects in fruit juice. In: Advances in fruit processing technologies, 2nd edn. CRC Press, Hoboken, pp 366–377

71. Rodriguez-Amaya DB (1997) Carotenoids and food preparation: the retention of provitamin a carotenoids in prepared, processed and store foods. OMNI, Washington, DC

72. Salleh-Mack SZ, Roberts JS (2007) Ultrasound pasteurization: the effects of temperature, soluble solids, organic acids and pH on the inactivation of *Escherichia coli* ATCC 25922. Ultrason Sonochem 14:323–329

73. Santhirasegaram V, Razali Z, Somasundram C (2013) Effects of thermal treatment and sonication on quality attributes of Chokanan mango (*Mangifera indica* L.) juice. Ultrason Sonochem 20:1276–1282

74. Santhirasegaram V, Razali Z, Somasundram C (2015) Effects of sonication and ultraviolet-C treatment as a hurdle concept on quality attributes of Chokanan mango (*Mangifera indica* L.) juice. Food Sci Technol Int 21(3):232–241

75. Fernández Garcia A, Butz P, Bognar A, Tauscher B (2011). Antioxidative capacity, nutrient content and sensory quality of orange juice and an orange-lemon-carrot juice product after high pressure treatment and storage in different packaging. Eur Food Res Technol 213(4–5):290–296

76. Zhang C, Trierweiler B, Li W, Butz P, Xu Y, Rüfer CE, Ma Y, Zhao X (2011). Comparison of thermal, ultraviolet-c, and high pressure treatments on quality parameters of watermelon juice. Food Chem 126:254–260

77. Simpson MV, Barbosa-Cánovas GV, Swanson BG (1995) Influence of PEF on the composition of apple juice. Internal report, Washington State University, Pullman, p 800

78. Simunek M, Jambrak AR, Petrovic M, Juretic H, Major N, Herceg Z, Hruskar M, Vukusic T (2013) Aroma profile and sensory properties of ultrasound-treated apple juice and nectar. Food Technol Biotechnol 51(1):101–111

79. Sun J, Chu Y, Wu X, Liu R (2002) Antioxidant and antiproliferative activities of common fruits. J Agric Food Chem 50(25):7449–7454

80. Tao Y, Sun D (2015) Enhancement of food processes by ultrasound: a review. Crit Rev Food Sci Nutr 55:570–594

81. Terefe NS, Gamage M, Vilkhu K, Simons L, Mawson R, Versteeg C (2009) The kinetics of inactivation of pectin methylesterase and polygalacturonase in tomato juice by thermoso-nication. Food Chem 117:20–27

82. Tiwari BK, Muthukumarappan K, O'Donnell CP, Cullen PJ (2008) Effects of sonication on the kinetics of orange juice quality parameters. J Agric Food Chem 56:2423–2428

83. Tiwari BK, Muthukumarappan K, O'Donnell CP, Cullen PJ (2009) Inactivation kinetics of pectin methylesterase and cloud retention in sonicated orange juice. Innov Food Sci Emerg Technol 10:166–171

84. Tiwari BK, Muthukumarappan K, O'Donnell CP, Cullen PJ (2009) Effect of low temperature sonication on orange juice quality parameters using response surface methodology. Food Bioprocess Technol 2:109–114

85. Tiwari BK, O'Donnell CP, Cullen PJ (2009) Effect of non- thermal processing technologies on the anthocyanin content of fruit juices. Trends Food Sci Technol 20:137–145

86. Tiwari BK, O'Donnell C, Cullen P (2009) Effect of sonication on retention of anthocyanins in blackberry juice. J Food Eng 93:166–171

87. Tiwari BK, O'Donnell CP, Muthukumarappan K (2009) Effect of sonication on orange juice quality parameters during storage. Int J Food Sci Technol 44:586–595

88. U.S. Food and Drug Administration (2000) Kinetics of Microbial Inactivation for Alternative Food Processing Technologies at http://www.fda.gov/Food/FoodScienceResearch/SafePracticesforFoodProcesses/ucm100158.htm

89. Ugarte-Romero E, Feng H, Martin SE, Cadwallader KR, Robinson SJ (2006) Inactivation of *Escherichia coli* with power ultrasound in apple cider. J Food Sci 71:102–108

90. Valdez-Fragoso A, Mujica-Paz H, Welti-Chanes J, Torres JA (2011) Reaction kinetics at high pressure and temperature: effects on milk flavor volatiles and on chemical compounds with nutritional and safety importance in several foods. Food Bioprocess Technol 4:986–995

91. Vercet A, Lopez P, Burgos J (1998) Free radical production by manothermosonitication. Ultrasonics 36:615–618

92. Vilkhu K, Mawson R, Simons L, Bates D (2008) Applications and opportunities for ultrasound assisted extraction in the food industry – a review. Innov Food Sci Emerg Technol 9:161–169

93. Villamiel M, de Jong P (2000) Inactivation of *Pseudomonas fluorescens* and *Streptococcus thermophilus in trypticase* soy broth and total bacteria in milk by continuous-flow ultrasonic treatment and conventional heating. J Food Eng 45:171–179

94. Walkling-Ribeiro M, Noci F, Riener J, Cronin DA, Lyng JG, Morgan DJ (2009) The impact of thermosonication and pulsed electric fields on *Staphylococcus aureus* inactivation and selected quality parameters in orange juice. Food Bioprocess Technol 2:422–430

95. Wong E, Vaillant F, Pérez A (2010) Osmosonication of blackberry juice: impact on selected pathogens, spoilage microorganisms, and main quality parameters. J Food Sci 75:468–474

96. Wu J, Gamage TV, Vilkhu KS, Simons LK, Mawson R (2008) Effect of thermosonication on quality improvement of tomato juice. Innov Food Sci Emerg Technol 9:186–195

97. Wu J, Lin L, Chau F-T (2001) Ultrasound-assisted extraction of ginseng saponins from ginseng roots and cultured ginseng cells. Ultrason Sonochem 8(4):347–352

98. Adzahan N (2006) Effects of ultraviolet treatment on water soluble vitamin retention in aqueous model solutions and apple juice. PhD thesis, Department of Food Technology, Cornell University, Ithaca

99. Zafra-Rojas QY, Cruz-Cansino N, Ramirez-Moreno E, Delgado-Olivares L, Villanueva-Sanchez J, Alanis-Garcia E (2013) Effects of ultrasound treatment in purple cactus pear (*Opuntia ficus-indica*) juice. Ultrason Sonochem 20:1283–1288

100. Zafra-Stone S, Yasmin T, Bagchi M, Chatterjee A, Vinson JA, Bagchi D (2007) Berry anthocyanins as novel antioxidants in human health and disease prevention. Mol Nutr Food Res 51:675–683

101. Tran MTT, Farid M (2004) Ultraviolet treatment of orange juice. Innov Food Sci Emerg Technol 5(4):495–502

102. Munoz A, Palgan I, Noci F, Morgan DJ, Cronin DA, Whyte P, Lyng JG (2011) Combinations of high intensity light pulses and thermosonication for the inactivation of escherichia coli in orange juice. 28(6):1200–1204

103. Stahle-Hamatschek S (1989) Cloud composition and its effect on cloud stability in natural cloudy apple juices (in German). Flussiges Obst 56(9):543–548

104. Altunakar B (2007) Pulsed electric fields processing of foods: an overview. In: Food preservation by pulsed electric fields and selected antimicrobials. p 22

Ultrasonic Applications for Food Dehydration

Mehmet Başlar, Ömer Said Toker, Salih Karasu, Zeynep Hazal Tekin, and Hatice Biranger Yildirim

Contents

Abstract

Food dehydration is a one of the oldest preservation methods based on simultaneous heat and mass transfer. The aim of the method is to remove the water from the food for prolonged shelf life by using an appropriate process. However, in the process of removing water from the food, there are practical difficulties due to the slow mass transfer that occurs in foods, depending on the food matrix and treatment conditions. Therefore, an ultrasonic treatment can be used in the dehydration process to increase the rate of mass transfer and to overcome these difficulties. At the same time, the rehydration properties of the dried foods can be improved by using ultrasonic wave creating microscopic channels, which may make moisture removal and gain easier. The treatment has been used to obtain high drying rates at the same temperatures or adequate drying rates at lower temperatures. In general, it has been used as different methods, such as ultrasound-assisted convective dehydration, ultrasound-assisted osmotic

M. Başlar (✉) • Ö.S. Toker • S. Karasu • Z.H. Tekin • H. Biranger Yildirim
Faculty of Chemical and Metallurgical Engineering, Department of Food Engineering, Yıldız Technical University, Esenler, Istanbul, Turkey
e-mail: mbaslar@yildiz.edu.tr; stoker@yildiz.edu.tr; skarasu@yildiz.edu.tr; zhazaltekin@gmail.com; hbiranger@hotmail.com

dehydration, ultrasound-assisted vacuum dehydration, and ultrasound-assisted freeze dehydration. The ultrasound has been used together with a dehydration process or as pretreatment in the methods as direct or indirect contact. In addition, other application- and apparatus-based ultrasound treatments have been improved during the dehydration process to enhance food quality.

Introduction

The human population is continuously increasing, whereas the world's food resources are declining. Efficient evaluation of food and energy resources and reduction of losses have therefore become important global issues. Reductions in food losses require the establishment of safe food production methods, processing with the most appropriate technologies, and use of appropriate preservation methods.

The term food preservation encompasses those processes designed to protect against microbial and biochemical factors responsible for food deterioration. Many methods may be used to prevent the deterioration of food, but most methods generally consider water activity as the dominant determinative condition leading to food deterioration because high water activity accelerates microbial growth and biochemical reactions. Therefore, controlling or reducing the water activity forms the basis of most of the food preservation methods, including dehydration.

Food dehydration has been used as a basic preservation method since ancient times. The basic aim of the dehydration process is to remove water from the food to prolong its shelf life and delay microbial and biochemical deterioration. Although the main objective of the dehydration processes is food preservation, it has many other purposes. Dehydration: (i) provides easier storage and transport; (ii) is an inexpensive preservation method; (iii) results in a denser nutrient content; (iv) produces intermediate or new products; and (v) simplifies and improves packaging. Numerous dehydration technologies and methods are in use today, including convective drying, spray drying, vacuum drying, freeze-drying, and infrared drying. Novel drying methods also continue to emerge to produce different, high quality, and economical dehydrated foods. These novel methods all have different properties when compared with other techniques, used alone or in combination.

The underlying principle of food dehydration is mainly simultaneous heat and mass transfer. Unlike dewatering and squeezing, dehydration processing uses evaporation to remove the water contained in the foods. The dehydration rate is an important criterion that determines product quality and cost-effectiveness and is generally controlled by the treatment temperature. However, practical difficulties often arise when removing water from a food; a particular problem is the mass transfer rate, which can be slow due to the food matrix and treatment conditions.

The removal of water can also be affected by a number of other conditions. An increase in the drying rate generally provides many advantages in terms of product quality and cost-effectiveness. Therefore, many drying technology methods have aimed to increase the drying speed. Ultrasound technology has a special place in drying technology because it accelerates the mass transfer process occurring during the drying.

Ultrasound is pressure wave oscillating that is above the threshold of perception by the human ear, in the frequency range of 20 kHz to 1 MHz. Ultrasound generates a series of effects on both internal and external resistance to moisture transfer in solids and liquids [1]. Cavitation is the main ultrasound mechanism in a liquid system. The moisture transfer rate from a solid food to the surrounding environment can be increased if cavitation is generated in the inner liquid phase of the food. Ultrasound generates a series of rapid compressions and expansions of the material in the solid. This is called the "sponge effect" and facilitates the flow of liquid out of the foods by creating microchannels that are suitable for fluid movement [2]. It is widely used in dehydration processes, as well as in preservation, crystallization, filtration, extraction, and cutting technologies. Ultrasound technology can show different effects in different systems because many factors, such as ultrasonic intensity, frequency, application form, pressure/vacuum, and temperature, affect its efficiency. However, the underlying mechanism of ultrasound involves acoustic cavitation, which can be divided into transient and stable forms.

Ultrasound waves create cavity bubbles by a series of compressions and rarefactions. If the ultrasonic intensity is above than 10 W/cm^2, the cavitating bubbles expand as they absorb ultrasonic energy and terminate in a violent collapse or implosion. This is defined as transient cavitation and it causes localized physical effects, such as very high temperature (about 5000 K), elevated pressure (about 2000 atm), shock waves, and high velocity water jets. This acoustic cavitation can be generally used in many processes, such as homogenization, emulsification, pasteurization, and depolymerization.

An ultrasonic intensity between 1 and 3 W/cm^2 generates generally stable cavitation (Feng and Yang 2011). This occurs at a low acoustic pressure and can lead to several acoustic effects, such as degassing and microstreaming. Stable cavitation oscillates the bubbles and causes a rapidly rotating mass of fluid in medium, which can create microcurrents and enhance heat and mass transfer [3].

Ultrasound-assisted (US-assisted) dehydration methods are based on a combination of the ultrasonic process with appropriate dehydration techniques. The ultrasound wave strongly accelerates mass transfer, so the ultrasound technique assists in dehydration by providing a high drying rate, thereby maintaining food quality. US-assisted dehydration has been combined with other forms of dehydration, including convective [4–6], osmotic [7–11], vacuum [12–15], and freeze-drying [16–18], in order to improve the overall effectiveness of the drying. In all these processes, ultrasound is employed to increase the drying rate and/or decrease the drying temperature. In addition, as in spray drying, some drying processes have been developed to generate products with better quality due to ultrasonic vibration.

The ultrasonic spray nozzle is one example: it has been developed for spray drying and ultrasonic spray freeze-drying [19, 20].

Investigation of US-assisted food dehydration has used ultrasonic waves created using either ultrasonic probes or ultrasonic baths. The ultrasonic device generally provides information about the ultrasonic intensity or acoustic cavitation. The ultrasonic bath creates stable cavitation, while the ultrasonic probe generally creates transient cavitation, depending on the treatment conditions. Therefore, the device and contact can significantly affect the dehydration and rehydration characteristics of food products. A further division arises due to the transfer of the ultrasonic wave to foods, via airborne ultrasound or contact ultrasound.

As its name implies, US-assisted food dehydration is usually supplementary to other drying applications. In many studies, ultrasonic treatment has generally been applied simultaneously to assist other dehydration methods. However, some researchers reported that ultrasonic pretreatment improved the dehydration/rehydration properties of products. Consequently, solution pretreatment is now used in the drying process or this process may be used as an alternative process on its own, as it can provide important advantages in drying [4, 21].

This chapter reviews different ultrasound-assisted dehydration processes, including convective, osmotic, vacuum, and freeze-drying applications, as well as the various types of ultrasonic equipment used. The mechanisms, applications, advantages/disadvantages, and recent investigations of ultrasound-assisted dehydration are also summarized.

Ultrasound-Assisted Convective Dehydration

Convective drying is one of the most widely used and oldest preservation methods in the food industry because of its ease of operation [22]. A considerable amount (12–25 %) of the overall industrial energy consumption is associated with the drying industry. This process gives food products a longer shelf life by reducing water activity. In this process, hot air with low humidity is used to remove moisture from the food material. The resulting reduction in the water activity provides some advantages to the food, such as preventing microbial growth and enzymatic activity and enabling easy packaging and transportation [23, 24].

Convective drying involves two types of water transfer resistances: the internal resistance to water movement inside the material and external resistance between the solid surface and the air [25, 26]. The convective drying process also has several disadvantages, such as high energy consumption, low dehydration rate, low product quality, high drying temperature, and long drying time [2, 22]. The slow moisture transfer rate is one of the main factors that lead to the long drying times, which reduces product quality and increases energy consumption. The length of the drying time is highly related to the falling rate period, which leads to high energy consumption and substantial loss of quality [27]. The nutritional and sensorial qualities of the final product are reduced during a long drying period at a high temperature due to thermal degradation of bioactive compounds and some color pigments [28].

Drying also affects the mechanical properties of the food material, such as texture and rehydration capacity [29].

Convective drying should therefore be improved by the use of other applications to overcome these difficulties. Several methods, including microwave, radio frequency, and ultrasound processes, have been combined with convective drying to increase the moisture transfer rate and to minimize quality losses in the final products [13, 30, 31]. Ultrasound technology, used in conjunction with convective drying, can provide additional advantages, such as reduced drying time and drying temperature, lower energy consumption, and preservation of color pigments (carotenoids, anthocyanin) and bioactive compounds (polyphenols and vitamin) in the dried products [32]. This process is referred to as US-assisted convective drying.

Ultrasound is a cyclic sound wave that is above the threshold of perception by the human ear, in the frequency range of 20 kHz to 1 MHz. Ultrasound generates a series of effects on both internal and external resistance to moisture transfer in solids and liquids [1]. Cavitation is the main ultrasound mechanism in a liquid system. The moisture transfer rate from a solid food to the surrounding environment can be increased if cavitation is generated in the inner liquid phase of the food. Ultrasound generates a series of rapid compressions and expansions of the material in the solid. This is called the "sponge effect" and facilitates the flow of liquid out of the foods by creating microchannels that are suitable for fluid movement [2]. US-assisted convective drying employs a frequency between 20 kHz and 40 kHz, generated by several different methods. These include the use of the complete drying chamber as an emitter [16], application of transducers within the drying chamber [33], and direct contact of the food with an emitter [34].

Beck et al. [6] investigated the effects of airborne ultrasound conditions on the drying behavior of a model food consisting of water, cellulose, starch, and fructose. They also determined the influence of airborne ultrasound at various power levels, drying temperatures, relative humidity of the drying air, and air speeds. They reported that drying time was significantly affected by the drying temperature and ultrasound power and was reduced by 21 % and 79 % at 50 °C and 70 °C, respectively, when applying 120 W ultrasound power. They concluded that ultrasound application reduced drying time significantly and improved the product quality.

Another study investigated the influence of the air temperature and the application of ultrasound on the convective drying kinetics of strawberry [5]. Drying time was reduced by 13–45 % by applying ultrasound, depending on the drying conditions. Drying times with no ultrasound application ranged from 3.3 to 5.5 h at 40–70 °C, while the times with ultrasound were 2.2–4.6 h.

Ultrasound application also positively affects the content of bioactive compounds and antioxidants in foods, in addition to its effects on drying kinetics. For example, Rodriguez et al. [35] examined the effects of ultrasound application, air velocity, and temperature on drying time and antioxidant capacity of thyme extracts. They found that extracts treated at air velocities of 1 and 2 m/s and air temperatures of under 60 °C showed an enhanced drying rate, a shortening of the processing time, and an increase in the antioxidant capacity when ultrasound was also applied. Another study

that examined the effects of ultrasound application on the drying behavior of clipfish reported that US-assisted convective drying at different temperatures (10 °C, 20 °C, and 30 °C) significantly reduced the drying time (by 10 %) at 10 °C and that ultrasound was more effective at a low drying temperature. The researchers also reported that the drying process at 20 °C with ultrasound application was faster than the same process without ultrasound at 30 °C.

Effect of ultrasound as a pretreatment application was investigated by Fernandes et al. [21]. It was reported that ultrasonic pretreatment of pineapple samples in distilled water between 10 and 30 min and overall drying time was reduced by 8 % [4]. They also concluded that the ultrasound-assisted osmotic dehydration incorporated more sugar than conventional osmotic dehydration and application of ultrasound increased the water effective diffusivity.

Effect of ultrasound pretreatment on drying kinetics, energy consumption, and selected quality properties of dried parsley leaves was investigated by Sledz et al. [36]. Ultrasound application with at 21 kHz, 12 W/g led to significant reduction of the drying time up to 29.8 % and the energy consumption by 33.6 % for parsley dried at 30 °C and 300 W.

The use of ultrasound as a pretreatment to air-drying of papaya was studied [37]. After application of ultrasound, effective water diffusivity and drying rate increased. Drying time reduced by about 16% and the papayas lost sugar (13.8 % in 30 min) during ultrasonic treatment.

The effect of ultrasound as a pretreatment application on drying kinetics and some quality parameters of apple was investigated by Nowacka et al. [38] They concluded that ultrasound increased drying time and showed positive effect on quality attributes of apple. The ultrasound treatment reduced drying time by 31 % in comparison to convective drying. The ultrasound treated apples showed between 9 % and 11 % higher shrinkage, 6–20 % lower density, and of 9–14 % higher porosity comparing the conventional process.

Several applications of ultrasound on convective drying are shown in Table 1. These studies showed that ultrasound can be successfully used in convective drying to reduce the drying time and enhance product quality. These studies also indicated that effect of ultrasound on drying time in the convective drying process is highly related to process parameters such as temperature and air velocity. The effect of ultrasound application can be readily observed at a low drying temperature and low air velocity. This can be explained by a dominant effect of higher temperature and high air velocity. Some authors also stated that ultrasound is more effective during the initial drying period. Further research is necessary to optimize the parameters of US-assisted convective drying to facilitate its use at the industrial scale.

Ultrasound-Assisted Osmotic Dehydration

Osmotic dehydration (OD) is mainly used as a predrying treatment prior to air-drying, freezing, freeze-drying, or vacuum-drying, in order to reduce energy consumption or the load of the following operations, to improve the quality of

Table 1 Ultrasound application on convective drying of some foods

Food materials	Parameters	Results	References
Apple slices	40–60 °C, 0–90 W, 1 m/s	The reduction in drying time was 46–57 % and the reduction in energy consumption was 42–54 %	Sabarez et al. [30]
Apple and red bell pepper	70°C, 42 W	Drying time savings of 23 % (red bell pepper) and 27 % (apple) were calculated for continuous ultrasound	Schössler et al. [18]
Egg plant	40 °C, 0–90 W	The drying time was shortened by 75 %	Puig et al. [39]
Clipfish	10–30 °C, 45 W	The drying time reduced by over 90 % at 10 °C, 32.2 % at 20 °C, and 8.3 % at 30 °C	Bantle and Hanssler [40]
Lulo (*Solanum quitoense* Lam.)	60C, 40 MHz	Sixteen odur-active volatiles of lulo (Solanum quitoense Lam.) were quantified	Forero et al. [41]
Parsley leaves	at 30 °C, 300 W	The reduction of the drying time up to 29.8 % and the energy consumption by 33.6 %	[36]
Thyme	40–80 °C, 1–3 m/s, 0–18.5 kW m^{-3}	Shortening the process time, minimizing energy consumption, and increasing the AC values of dried thyme extracts	Rodriguez et al. [35]
Strawberry	40–70 °C, 0–60 W	The reduction of drying time was 13–44 %	Gamboa-Santos et al. [5]

preserved food product, or to increase the shelf life of a product with high moisture content without changing its integrity. The process is based on the immersion of the food in a hypertonic (osmotic) solution that has low water activity and high osmotic pressure, or the direct implementation of the osmotic agent. Sucrose and sodium chloride (NaCl) are the most commonly used osmotic agents.

Osmotic dehydration reduces the water activity of the product, ranging between 0.95 and 0.90, so that microbial activity is inhibited. The treatment was first developed as a pretreatment technique for drying by Ponting et al. [42] and has been increasingly employed in various research studies [10, 43, 44].

The basis of osmotic dehydration is osmosis, which is based on removal of a fluid across a semipermeable membrane. When two solutions having different solute concentrations are separated by a semipermeable membrane, some ions or molecules are removed from the denser medium to less heavy medium until equilibrate. Energy is not expended during this transition. The cytoplasmic membrane of fresh fruits and vegetables, surrounding inner surface of the cell wall that consist of cellulosic and pectic substances, shows selective permeability. This membrane, acting as a semipermeable membrane during osmosis, only allows the passage of water and some low molecular weight soluble substances from the food product. Some of the soluble material in solution also diffuses into the product by countertransport because the

cell membrane is not completely semipermeable, but the withdrawal of water is greater than this solute transfer. The passage of water across the cell wall continues until the water concentrations on both sides reach equilibrium. Therefore, the osmotic dehydration process can be defined as the simultaneous diffusion of water and solutes [21, 43, 44].

The advantage of osmotic dehydration over other drying processes, such as convective drying and freeze-drying, is the minimization of losses of flavoring compounds, aromatic substances, and color. The process also occurs at low temperature, thereby preventing chemical reactions such as enzymatic browning [45, 46]. Osmotic dehydration not only removes water from the food but also provides a vehicle for addition of agents that lower water activity (such as sugar and salt), as well as vitamins, minerals, preservatives, and antioxidants to ensure the desired organoleptic, nutritional, and chemical contents of the food. This application is gaining in popularity in terms of obtaining products with better appearance and functional properties [47].

Mass transfer in osmotic dehydration is limited by some factors: resistance increasing with high viscosity of the osmotic solution and low density difference between the solid and solutions requiring additional mechanical (Rastogi et al. 2005). The mass transfer rate during osmotic dehydration depends on different factors, such as the concentration of the osmotic medium, temperature, agitation, food structure (porosity, etc.), the molecular weight of the osmotic agent, the sample-solution ratio, and the size and shape of the samples. The sample-liquid solution ratio is an important consideration and is usually retained between 3:1 and 1:4 in most studies [21, 37]. This sample–liquid solution ratio is desirable when considering the minimal amount of liquid that will ensure total immersion of the sample. The rate of osmotic dehydration increases as the concentration and temperature of the solution and its agitation increases. For example, higher temperature damages the cell membranes of the food, changes the structure of the material, and causes losses of nutrients. The shape and size of the material are also important parameters that should be taken into consideration during osmotic dehydration. Material with a large size will dehydrate more slowly because of the length of the diffusion path. Mass transfer rates in osmotic drying are very low and transfer completely stops after a certain period of time. Therefore, many pretreatment methods, such as vacuum processes, ultrasound, freeze/thaw, high hydrostatic pressure, microwave, pulsed electrical field, centrifugal force application, edible coatings, and supercritical CO_2, have combined with osmotic drying to increase the mass transfer rate [48–51].

Ultrasound-assisted osmotic dehydration (Fig. 1) is a dehydration process in which an osmotic solution is exposed to ultrasonic waves. The complex cellular surface of the material acts as an effective semipermeable membrane in the osmotic dehydration process. Water moves from the tissue into the hypertonic solution and the solutes from the osmotic solution moves into the treated material in the reverse direction [50]. Ultrasound in this case is used to enhance mass transport during osmotic dehydration. During the low-frequency power ultrasound application, ultrasonic waves (ranging from 20 to 100 kHz) induce a cavitation effect that influences the physicochemical and biochemical properties of the food. The cavitation causes a
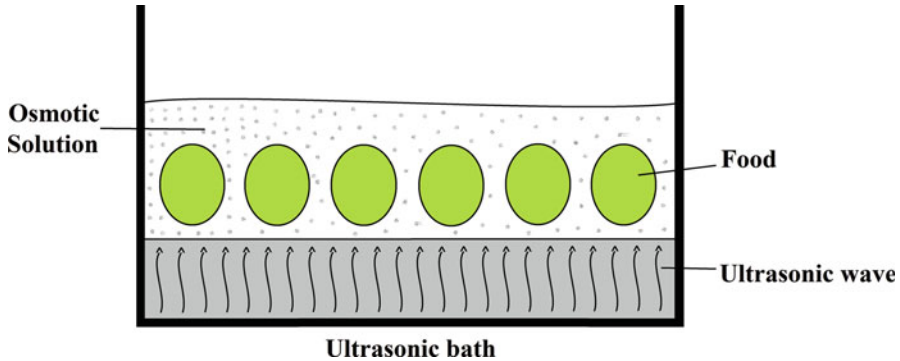
Fig. 1 Ultrasound-assisted osmotic dehydration

rapid series of contractions and expansions in the food tissue, which is usually referred as a sponge effect, as it is similar to when a sponge is squeezed and released repeatedly [10, 21]. Bubbles formed by cavitation collapse with differing intensities, or never collapse, depending on the temperature, pressure, food properties, and ultrasonic intensity and frequency. The bubbles are postulated to create microscopic channels or capillaries within the tissue during the application of ultrasound. This leads to the removal of water, contributes to the formation of the microscopic channels, and improves fluxes of osmotic solute to the intercellular of the dewatered food. This effect improves diffusion and osmotic processes and accelerates degassing. For that reason, ultrasound pretreatment can be used to reduce air-drying time [52–54]. In addition, according to some studies, ultrasound assisted osmotic dehydration increases the glass transition temperature of fruits and vegetables by altering the state of water in the structure [11]. The choice of appropriate parameters for ultrasonic application is a considerable issue. Thermal energy can cause local heating of the material during sonication and this is associated with the effect of cavitation, which may depend on the sequence, time, power, and frequency of the pulses [48].

The pretreatment is generally carried out at ambient temperature, since higher temperatures do not seem to enhance the effects of ultrasound application. In some studies, the research shows that low temperatures minimize food degradation and protect the natural aroma, color, and nutritive components of the food [10, 50, 55, 56].

Many recent studies have examined ultrasound-assisted osmotic dehydration as shown in Table 2. Studies on osmotic dehydration, ultrasound, and ultrasound-assisted osmotic dehydration have shown that many results can be obtained using different applications and different materials. Successful increases in water diffusivity and solid gains in reducing the drying time and cost have been achieved when ultrasound is combined with osmotic dehydration.

Nowacka et al. [10] investigated how ultrasound modulates the effects of osmotic drying on the microstructure and water state of kiwifruit. Kiwifruit slices were exposed to ultrasonic waves at a frequency of 35 kHz for 10, 20, and 30 min

Table 2 Ultrasound application on osmotic drying of some foods

Food Materials	Parameters	Results	References
Apple	40 °C, 50 °C, 60 °C, and 70 °C, 50 kHz.	Dry matter rate increases ranged from 23 % at 40 °C to 11 % in 70 °C after 3 h of dehydration. Dehydration was increased by 14–27 %	Simal et al. [54]
Broccoli	10, 20, 30, and 40 min at 35 °C, 40 kHz	US-assisted osmotic dehydration raised the glass transition temperature within 30 min	Xin et al. [11]
Cranberries	35 and 135 kHz	Color degradation, numerous cracks, and damage to the structure increased during application of high frequency ultrasound (130 kHz)	Shamaei et al. [51]
Kiwifruit	35 kHz for 10, 20, and 30 min	A positive effect on the mass transfer	Nowacka et al. [10]
Strawberry	0, 25, and 40 kHz	The reduction on total processing time, the increase on sugar gain, and the increase on water loss	Garcia-Noguera et al. [9]

when osmotic dehydration was carried out. The ultrasound pretreatment had a positive effect on the mass transfer. The authors noticed a creation of microstructure within the tissue and an increase in the average cross-sectional area of the cell [10].

Xin et al. [11] dehydrated broccoli using US-assisted osmotic dehydration to investigate the effect of trehalose and US-assisted osmotic dehydration on the state of water and glass transition temperature. The study compared US-assisted osmotic dehydration with conventional osmotic drying. In the first experiment, the broccoli samples were immersed in an osmotic solution containing trehalose (40 % w/w), NaCl (3 % w/w), and $CaCl_2$ (1 % w/w) at 35 °C for 2 h. In the other experiment, the samples were immersed in the same osmotic solutions and subjected to ultrasonic waves for 10, 20, 30, and 40 min at 35 °C in an ultrasonic bath at a frequency of 40 kHz. The amount of water loss and sugar gain in the samples increased in parallel with the processing time, whereas the sugar gain decreased in the samples treated for 40 min. Therefore, the processing time plays an important role in ultrasound-assisted osmotic dehydration of broccoli. The value of the glass transition temperature of samples osmotically dehydrated by the standard method was −27.52 °C to −23.31 °C, which represented about a 2.6 ° increase over 2 h. By contrast, US-assisted osmotic dehydration raised the glass transition temperature within 30 min [11].

US-assisted osmotic dehydration of apples was conducted by Simal et al. [54]. This study was carried out in 70°Brix sucrose solution at 40 °C, 50 °C, 60 °C, and 70 °C and a frequency of 50 kHz. The results confirmed the significant effect of ultrasound on the level of penetration of osmotic solutes into the apples. Dry matter rate increases ranged from 23 % at 40 °C to 11 % in 70 °C after 3 h of dehydration. Dehydration increased by 14–27 %, regardless of the temperature [54].

Shamaei et al., [51] investigated the effect of ultrasound with low (35 kHz) and high (130 kHz) frequency on the osmotic dehydration of cranberries. The samples were placed into osmotic solutions of 40 %, 50 %, and 60 % sucrose and 0.4 % and 8 % NaCl. Ultrasonic treatments were carried out at two frequencies (35 and 135 kHz). The use of low frequency ultrasound (35 kHz) was more favorable, based on the hardness and color of the dehydrated samples. On the other hand, color degradation, numerous cracks, and damage to the structure increased during application of high frequency ultrasound (130 kHz).

Garcia-Noguera et al. [9] researched the influences of the ultrasound pretreatment on the osmotic dehydration behavior of strawberries. In this study, the researchers implemented US-assisted osmotic dehydration to determine if drying time was reduced and water diffusivity increased. Strawberry halves were immersed in distilled water and in two different osmotic solutions (25–50 %) and then compared at four different times (10, 20, 30, and 45 min) and at three ultrasonic frequency levels (0, 25, and 40 kHz). These parameters were chosen to determine their effect on drying time, water loss, and soluble solids gains. Numerous results were obtained for osmotic dehydration combined with ultrasonic energy. The total processing time was reduced, the sugar gain was greater, and the water loss was larger when the sample halves were pretreated in 50 % sucrose solution for 45 min.

Consequently, ultrasound waves as US-assisted osmotic dehydration processes accelerate the movement of water from the food as well as allow better penetration of osmotic agents into food. Ultrasonic waves induce changes in cell structure and cause formation or widening of microchannels in the food tissue. Because ultrasonic waves severely broken down dense cell and therefore, parenchyma cell can be accelerate accumulation of osmotic agent to food materials, when it is immersed osmotic solution.

Ultrasound-Assisted Vacuum Dehydration

Vacuum dehydration is the dehydration of humid foods under pressure lower than zero. Lowering the pressure allows water removal at lower temperature so that the quality of the dehydrated food is improved over that prepared with traditional methods. The vacuum dehydration method has specific properties, such as prevention of oxidation, which separates it from conventional atmospheric dehydration methods because the sample does not come into contact with air during the vacuum dehydration process [57–59]. The vacuum dehydration can also decrease the dehydration time more than the traditional dehydration methods, making it a more energy-efficient dehydration process [27]. The short dehydration time and/or low drying temperature also help to retain the organoleptic and nutritional properties of food substances [58].

The dehydration of food products occurs at lower temperatures under vacuum because the boiling point of liquid removed during dehydration decreases in a vacuum. Therefore, heat- or oxygen-sensitive products, such as instant coffee, can benefit particularly by dehydration under vacuum. The trend toward natural and

organic food consumption has been increasing among consumers throughout the world. When people cannot obtain natural and organic foods easily or they want to consume foods in other seasons, they want their food to have minimal nutritional losses and a long shelf life. Therefore, temperatures should be kept at a minimum during the production process so that high quality dehydrated food can be produced.

Vacuum dehydration can also be performed easily by the use of indirect dryers, so food powders and ingredients of high quality are now being sold in the market with increasing volume and variety [60, 61]. The moisture content decreases with increase in porosity, so the porosity of fruits and vegetables increases during dehydration. For example, vacuum dehydrated food products such as papayas, bananas, and apples have higher porosities than the conventional and microwave dehydrated foods [62]. Vacuum dehydration also enables better flavor, less hydroscopic end products, and minimum product losses. The risk of occupational accidents, such as fires and explosions, is also limited by using vacuum drying because of the low or no oxygen content. On the other hand, a continuous drying process cannot be run as easily using a vacuum dryer as it can with an indirect dryer [60].

Vacuum dehydration can be recommended for use with heat-sensitive products but not generally for dehydration of all foods because it is an expensive operation with high maintenance costs [63, 64]. Experimental investigations are proceeding on vacuum dehydration using heat-sensitive materials such as carrot cubes [65], cranberries [66], and banana pieces [67]. Another disadvantage of vacuum dehydration is that heat transfer is not easy in a vacuum [64]. The dehydration defects can be reduced but vacuum dehydration cannot provide sufficient moisture removal from the center of samples to the surface, so the dehydration can result in a steep moisture slope in the surface layer of samples [68, 69].

Vacuum dehydration may require pretreatment or combination with other methods to improve the efficiency of the dehydration process. Vacuum dehydration is used as a pretreatment or in combination with microwave, freeze-drying, ohmic heating, superheated steam, hot air drying, or ultrasonic power.

Ultrasound-assisted vacuum (USV) dehydration is a method that combines vacuum dehydration and ultrasonic waves. This novel technique can be useful for faster food dehydration, production of the unique characteristics such as almost perfect rehydration rate, preferred sensory properties, nutritionally dense food, as well as for enhancing food quality and appearance. For instance, the ultrasound treatment has the potential to overcome the deficiencies of vacuum dehydration by accelerating mass transfer from the center of foods and expanding microchannels in the food matrix. As already discussed, ultrasound is an effective nonthermal technique that forms microchannels, like a sponge structure, by virtue of the continuous compression and release, and it produces cavitation so that both free and strongly bound water is removed easily. The drying rate increases without increasing the temperature of the material substantially [14, 52, 70]. The ultrasonic waves can also result in microdeformation of porous solid materials, which accounts for the formation of microchannels that improve diffusion and raise the convective mass transfer rate [14, 71, 72]. With these important properties, ultrasound improves vacuum

dehydration and the combination of ultrasound pretreatment and vacuum dehydration is preferable for greater moisture removal, increased mass transfer rates and effective diffusivity of water, and reduced overall processing time [33, 69, 73–76].

The USV dehydration has advantages of both of vacuum dehydration and ultrasonic treatment. The vacuum dehydration process generally occurs at lower atmospheric pressure (<101.330 kPa) and low temperature. If vacuum dehydration includes evaporation, the temperature should be higher than 0.01 °C and pressures should be between 0.612 and 101.330 kPa. Water found in the food can start to evaporate from the interface and emerge through the dry layer of the food. During evaporation, heat should be provided adequately to hold the temperature of the food above the boiling point of water because heat transfer can be a limiting factor under vacuum. The imposition of a vacuum dehydration lowers the temperature and pressure, and water starts to boil at a low temperature. Therefore, dehydration times are decreased by improved drying rates. Boiling creates bubbles within the liquid of the food and the bubbles are transported to the surface [63, 64].

In the USV dehydration technique, microchannels which provide chemical reactions in a solution are formed by acoustic cavitation so that mass transfer can increase. The acoustic cavitation is of two types: transient and stable cavitation. The stable cavitation can be formed by sound waves having fairly low ultrasound power of 1–3 W/cm^2 and generally contains gas and vapor while the transient cavitation can be formed with high ultrasound power of 10 W/cm^2. In stable cavitation, the shape of the bubbles is stable and bubbles have equilibrium sizes and their formation continues for a long time. The stable cavitation, unlike transient cavitation, does not damage the structural properties of food because no explosions occur during stable cavitation. Therefore, a low ultrasound power can be preferred under vacuum drying. Ultrasound generates cavitation so that moisture, which is strongly attached to solids, can be almost completely removed. The USV treatment is shown schematically in Fig. 2 [77–79].

Some research has investigated USV dehydration using ultrasonic waves applied in different ways: directly coupled to the food [12, 13], indirectly applied to the material [14, 15], and used as pretreatment [80]. Başlar et al. [13] showed that beef and chicken meat dehydrated by the USV technique at 55 °C, 65 °C, and 75 °C had shorter dehydration times. In the study, the USV technique was compared with vacuum and drying ovens. The meats were dehydrated in less time and with less energy consumption and more effective moisture diffusivity was obtained using USV.

The drying rate of beef and chicken increased with rising temperature but the moisture content reduction was fast and drying time was less at higher temperature, as reported for apple [81], pear [82, 83], and potato [84]. The drying kinetics of fillets was determined with ten thin-layer drying models at high fitting range ($R^2 =$ 0.9572–0.9982) and the least suitable model was the Thompson model. The most suitable model differed for each dehydration technique and meat [13].

Başlar et al. [12] dehydrated salmon and trout fillets using USV dehydration to decrease the dehydration duration at 55 °C, 65 °C, and 75 °C. The time required for dehydration of fillets by USV was less than that for dehydration carried out in
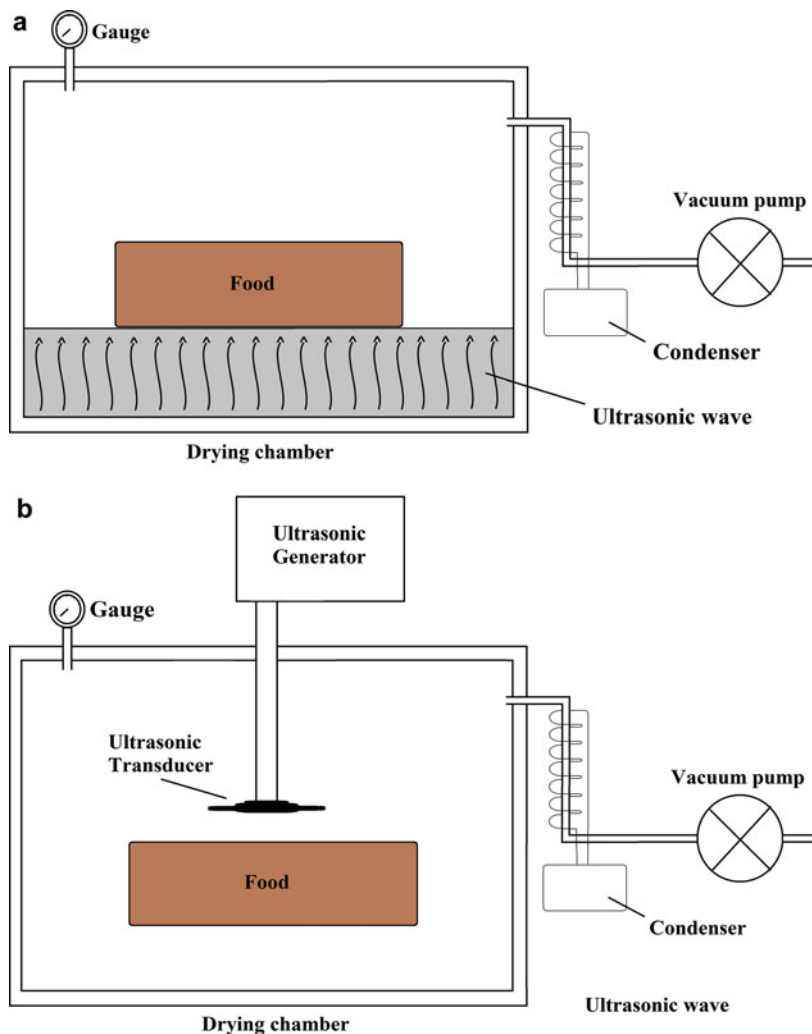
Fig. 2 Ultrasound-assisted vacuum dehydration: direct (**a**) and indirect (**b**)

vacuum and drying ovens. The time of dehydration of salmon and trout fillets using USV was decreased by 7.4 % and 27.4 %, respectively, compared to vacuum dehydration alone. The dehydration time was decreased by increasing the temperature for all dehydration techniques, but the greatest decrease occurred with the combined USV and vacuum dehydration techniques. The drying rate was increased with increasing temperatures with the USV technique, so that mass and heat transfers were higher at high temperature when ultrasound was applied. Garcia-Perez et al. [16] obtained similar results with carrot cubes dehydrated using the air velocity and ultrasonic power. The highest effective moisture diffusivity was also determined

by the USV technique and increased with increasing temperature. The drying kinetics of fillets was fitted to seven thin-layer drying models with R^2 values changed between 0.944 and 1.00. The most suitable model was the Page model [12].

The USV dehydration technique was first used as a combined drying method by [14], but the material was not food. In that study, wood was dehydrated using USV at a constant temperature (60 °C) and absolute pressure levels between 0.05 MPa and 0.08 MPa. The dehydration of wood is the most significant process for manufacturing of dried end products, so novel dehydration techniques were tested. The vacuum dehydration method was not sufficient to dry wood when the method was used singly, if the wood had a high initial moisture content. The control of surface and internal moisture content was also difficult and vacuum drying could not move out moisture from the center of the wood. When the temperature was increased to improve mass transfer, quality losses occurred in the wood.

Therefore, USV dehydration could be useful for improving the drying conditions. For instance, the effective diffusivity of the samples dehydrated with USV was found to be higher than that of the sample dried only with vacuum dehydration. The drying rate using USV dehydration was substantially faster than that using vacuum dehydration. When the absolute pressure was decreased, the drying rate was faster. The USV dehydration was a more useful technique in terms of removing free moisture, so it could be used to save energy and decrease the quality losses [14].

[15] examined the effects of USV dehydration at 25 °C and absolute pressure and found that ultrasonic waves could cause cavitation, as well as the formation of microchannels within the tissue of wood samples. A microscopy analysis revealed the formation of microchannels and other changes within the tissue of the wood samples. Ultrasound enhanced the temperature of wood during the course of dehydration. The final temperature of the wood samples was increased by decreasing the absolute pressure. As the propagation distance of the ultrasound was increased, the temperature was decreased. The increase in the drying rate and the decrease in the drying time were ensured by the small holes in the walls of the vessel and some ruptures, by interruption of some pits, removal of extracts from the wood ray cells, and the holes of the pits on parenchyma. Consequently, the temperature of the sample increased and microchannel formed within the tissue of the wood sample during USV dehydration, so that time of the dehydration process generally decreased, while the mass transfer rate, the wood specific permeability coefficient, and the effective water diffusivity increased [15].

Ultrasound pretreatment was applied during vacuum dehydration of Chinese catalpa wood. This dehydration method raised the effective water diffusivity, decreased the drying time of the wood, and enhanced the end product quality. In this study, after the wood samples were pretreated for three periods, at three absolute pressure levels, three ultrasonic power levels and room temperature, they were dehydrated at a constant temperature and pressure using a vacuum dryer to determine the effects of pretreatment parameters on vacuum dehydration characteristics. The formation of microchannels and other changes in the wood tissue structure were determined by microscopy. The effective water diffusivity was increased by increasing the ultrasound power level and the pretreatment time but was decreased with

Table 3 Ultrasound application on vacuum drying of some materials (food and other)

Materials	Parameters	Results	References
Beef	55 °C, 65 °C and 75 °C, 40 kHz, 590 W	Dehydration time decreased between 8.3 % and 37.5 %	Başlar et al. [13]
Chicken	55 °C, 65 °C and 75 °C, 40 kHz, 590 W	Dehydration time decreased between 10.8 % and 46.2 %	Başlar et al. [13]
Salmon fillets	55 °C, 65 °C and 75 °C, 40 kHz, 590 W	Drying time decreased between 7.4 % and 25.7 %	Başlar et al. [12]
Trout fillets	55 °C, 65 °C and 75 °C, 40 kHz, 590 W	Drying time decreased between 21.9 % and 27.4 %	Başlar et al. [12]
Wood	0,05 MPa and 0.08 MPa, 20 kHz, 100 W	Reduction on overall processing time, increase the mass transfer rate, increase wood specific permeability, and increase the effective water diffusivity	He et al. [14]
Catalpa wood	0.096–0.1 MPa, 20, 28 and 40 kHz, 1200 W	The dehydration time was reduced by decreasing absolute pressure	He et al. [15]

increasing absolute pressure. The dehydration time was reduced by decreasing absolute pressure. However, if ultrasound was applied at high power levels, the ultrasound pretreatment time was shortened [80]. Several applications of ultrasound on vacuum drying for some foods and other materials are shown in Table 3. Consequently, although USV dehydration is a novel drying technology, it is promising for industry by providing less drying time and energy consumption for both food drying. In addition, low temperature and short span drying features of USV dehydration accepts itself as a quality protective process.

Ultrasound-Assisted Freeze Dehydration

Freeze-drying, also known as lyophilization, is a widely used drying process that is especially performed for the prevention of loss of bioactive or nutritive compounds during drying. In this process, the temperature of the product is reduced below its freezing point and water vapor is formed from ice by sublimation at pressures lower than the triple point of water [18]. The shape, color, and flavor of the product can be maintained as the sample is freeze-dried at low temperature and pressure and the resulting sponge-like structure favors faster water penetration and recovery of the original characteristics during a rehydration process [85]. Freeze-drying enables preservation of the activity of nutraceuticals and pharmaceuticals, and flavor and aroma of food products [86].

These advantages of freeze-drying have led to its acceptance as the best drying method for keeping the fresh-like quality characteristics of the dried product [86].

However, despite its many advantages, its high cost due to operation and the long drying period, which ranges from several hours and to days, restricts its industrial application.

The freeze-drying process consists essentially of four parts:

 (i) Sublimation, which is responsible for 45 % of the energy consumption
 (ii) Vacuum, which accounts for 26 % of the energy consumed (the vacuum is used in the vacuum freeze-drying process; it is not used in the atmospheric process)
(iii) Condensation, which accounts for 25 % of the energy
(iv) Freezing, which accounts for 4 % [87]

Attempts to eliminate the disadvantages of freeze-drying have led to the use of different equipment as supplementary systems. Microwave-assisted freeze-drying is one of the potential drying methods that can reduce the duration of the freeze-drying period, while still maintaining the desired quality of the product [18]. Industrial application of this process is not promising because of difficulties that include corona discharges, melting, and overheating [87]. Adsorption freeze-drying and fluidized atmospheric freeze-drying are also technical improvements aimed at reducing the drying period and cost [18]. However, the desired quality was not attained in the products dried with these methods [87–89]. Therefore, the development of novel alternative techniques continues to overcome the drawbacks of the freeze-drying process.

US-assisted freeze-drying (US-AFD) is one promising technology that incorporates the positive effects of ultrasound into the drying process. Ultrasound at high power results in pressure variations at the gas/liquid interface, thereby accelerating removal of water from the food matrix [16]. Ultrasonic energy does not affect the main quality characteristics of the material dried and does not damage heat-sensitive compounds [16]. Therefore, ultrasound could be combined with freeze-drying to increase the efficiency of the freeze-drying technique. Bantle and Eikevik [33] dried peas at different temperatures using a high-intensity US-assisted atmospheric freeze-drying technique (US-AFD). They compared the drying rates of the AFD and US-AFD in order to observe ultrasound effect. The effective diffusion (D_{eff}) calculated using a modified Weibull model was 1.699×10^{-9}, 5.740×10^{-9}, and 12.303×10^{-9} m²/s for the samples dried with US-AFD at −6 °C, 0 °C, and 20 °C and 1.609×10^{-9}, 5.252×10^{-9}, and 12.228×10^{-9} m²/s for AFD, respectively. Comparison of the results indicated that ultrasound application and increasing temperature significantly accelerated the drying rate.

Bantle and Eikevik [33] reported an interaction between the ultrasonic pressure wave and the product that accelerated the water removal rate from the food matrix. The percentage increase of the D_{eff} value of US-AFD with respect to AFD was calculated as 5.3, 13.7, 9.3, 0.5, and 0.5 at −6 °C, −3 °C, 0 °C, 10 °C, and 20 °C, respectively. Examination of the first hours of the drying period showed that drying rate was higher in US-AFD than AFD; however, the rate was almost equal toward the end of the drying period. These findings show that US increased the drying rate when the dry layer was small, indicating that heat and mass transfer rate at the

interface between corresponding product and air is influenced by US. Comparison of the color values of the control and dried samples revealed that the L, a, and b values of the raw peas were 49.553, -16.167, and 41.57, respectively, while the color values of the samples dried with US-AFD at -6 °C, -3 °C, and 0 °C were very close to those of the raw samples, ranging from 50.033 to 50.933, -14.000 to -16.378, and 34.073–40.380, respectively. Higher temperatures caused significant changes in the color values.

Schössler et al. [18] studied the potential use of US-AFD for preservation of vegetables; specifically red bell pepper cubes. The aim of the study was to provide extra sublimation energy without heating the samples using ultrasound at an excitation amplitude of 6.7 μm. A significant increase in sample temperature was observed, which could be eliminated by adjusting the amplitude and interval of the ultrasound process. A reduction in the net ultrasound treatment time to 25 % and 14 % at the equal amplitude level resulted in a substantial decrease in sample temperature, which was very important for maintaining product quality. The pepper samples were ultimately dried under ultrasonic conditions (excitation amplitude of 4.9 μm, intermittent application of ultrasound with a net sonication time of 10 % at an interval of 10/90 s US/RP) that did not alter sample temperature with respect to freeze-drying. Ultrasound application influenced the moisture ratio of the samples for up to 16 h. The duration of freeze-drying and US-assisted freeze-drying were compared by fitting the Midilli model to the obtained drying curves. The required time was calculated considering the final moisture content of the sample as 10 % d.b. The times required for the conventional and US-AFD were calculated as 18.25 h and 16.16 h, indicating an 11.5 % time saving with ultrasound supply. This time saving is very important for the food industry in many aspects. The quality characteristics of the dried samples were compared by evaluating their bulk density values, color parameters, ascorbic acid content, and rehydration properties. No significant differences were found between quality parameters of the samples, meaning that the ultrasound treatment accelerated the drying process without damaging product quality.

Another material was carrot (*Daucus carota* var. Nantes) dried with power US-assisted freeze-drying (USAFD) at -10 °C and 2 m/s [17]. Fick's law was successfully used to model moisture content of the sample as a function of drying time. The D_{eff} value was calculated as 7.98×10^{-11} m²/s for USAFD and 4.62×10^{-11} m²/s for AFD, indicating that ultrasound accelerated the freeze-drying process with a reduction in drying time of 60 %. Rehydration characteristics and hardness values, chosen as textural parameters of the dried samples, were evaluated as quality criteria. The sample dried with USAFD rehydrated faster, but the hardness value of 3.76 N was not significantly different from the value of 3.34 for the AFD sample.

In another study, Santacatalina et al. [90] dried cubic apple samples (*Malus domestica* cv. Granny Smith) with power US-assisted atmospheric freeze-drying at different temperatures, in an attempt to overcome the low sublimation rate of atmospheric freeze-drying. The D_{eff} of AFD was calculated as 1.61×10^{-5}, 1.50×10^{-5}, and 1.08×10^{-5} m²/s at -5 °C, -10 °C, and -15 °C, respectively, and these values increased to 6.95×10^{-5}, 6.70×10^{-5}, and 3.60×10^{-5} m²/s as

Table 4 Ultrasound application on freeze drying of some foods

Food Materials	Parameters	Results	References
Apple	1–6 m/s, 50 W	D_{eff} values increased to 6.95×10^{-5}, 6.70×10^{-5}, and 3.60×10^{-5} m²/s as ultrasound applied at 50 W	Santacatalina et al. [90]
Carrot	−10 °C, 2 m/s	A reduction in drying time of 60 %	Santacatalina et al. [17]
Peas	−6 °C, 0 °C, and 20 °C	The significantly accelerated drying rate with ultrasound application and increasing temperature	Bantle and Eikevik [33]
Red bell pepper	6.7 μm	11.5 % time saving with ultrasound supply	Schössler et al. [18]

ultrasound was applied at 50 W. Different air velocities, ranging from 1 to 6 m/s, were tested and no regular trend was observed between air velocity and D_{eff} value. This finding might indicate that turbulence produced by high air velocity disrupts the ultrasonic field, resulting in a reduction in the acoustic energy influencing the sample [16]. The optimum air velocity was 2 m/s.

The results of these previous studies (Table 4), conducted on different fruits and vegetables, highlighted that the drying rate increased with ultrasonic treatment while having little adverse effect on the quality parameters of the samples. The extent of reduction in the drying time depended on the fruit and vegetable structure. Therefore, it is necessary to optimize this novel drying method by taking the fruit and vegetable type into consideration. US-assisted freeze-drying is a promising method for the food industry for drying food materials rapidly when compared with the other methods, without deteriorating the quality of the food samples.

Ultrasonic Apparatus

Spray drying is a process based on atomization at high temperature to produce dry powder from a liquid. Atomization divides the liquid into small particles of micron size by expulsion through an atomizer or spray nozzle. The process is generally carried out using mechanical atomization processes such as pressure atomization, two-fluid atomization, and spinning disk atomization. Mechanical atomization has no control on the final droplet size or the velocity and also requires more energy. By contrast, ultrasonic atomization can provide the desired droplet size distribution and the desired mean size by using only mechanical vibrations generated through transmission of electrical energy to a piezoelectric vibrating disk for generation of droplets. Ultrasonic atomizers use low vibrational energy; therefore, they overcome some disadvantages of conventional atomizing nozzles. The effect can be explained by two major hypotheses: capillary waves and cavitation [19].

Ultrasonic spray freeze-drying (USFD) is a technique that uses ultrasonic spray nozzles in a spray freeze-drying processing; it is a dehydration technique that

combines spray dehydration and freeze dehydration. D'Addioa et al. [20] used USFD to produce highly porous mannitol, lysozyme, and bovine serum albumin particles to demonstrate control over the particle size and aerodynamic properties. Therefore, the ultrasonic nozzle has potential for use in food and food additive production.

Conclusions and Future Directions

Ultrasonic treatments can potentially provide significant assistance in food dehydration because the dehydration process is defined as the simultaneous heat and mass transfers and accelerating both of these transfers is possible with ultrasonic treatments. In general, drying methods combined with ultrasound drying resulted in less drying temperature and duration. It's believed that these two advantages can prevent quality reducing effect for the corresponding material when compared with other drying techniques.

Many US-assisted methods have been developed and the US process has the potential to be combined with other drying processes. Recent developments in ultrasound applications and devices support the high potential for industrialization of US-assisted dehydration processes. Also low energy consumption of US methods can be considered as one of the major reasons for industrial choice of US. However, high technology and advanced applications are needed in order to apply modern preservation methods. In the meantime, there are controversies in effects of modern preservation methods on humans. There isn't a clear prediction on whether it is harmful or not upon next years. In terms of economics aspects, optimization, investment, and operating cost can be higher. Consequently, much research is needed for the optimization of the present methods and the development of new combinations that incorporate the recent developments in ultrasound applications and devices.

References

1. Mulet A, Carcel JA, Sanjuan N, Bon J (2003) Food Sci Technol Int 9(3):215
2. Mulet A, Cárcel JA, García-Pérez JV, Riera E (2011) In: Feng H, Barbosa-Canovas G, Weiss J (eds) Ultrasound technologies for food and bioprocessing. Springer, New York, p 511
3. Kiani H, Zhang L, Sun D (2014) Ultrasonic assistance for food freezing. In: Sun D-W (ed) Emerging technologies for food processing. Elsevier, Oxford, pp 498–500
4. Fernandes FAN, Gallao MI, Rodrigues S (2008) Effect of osmotic dehydration and ultrasound pre-treatment on cell structure: melon dehydration. LWT 41:604–610
5. Gamboa-Santos J, Montilla A, Cárcel JA, Villamiel M, Garcia-Perez JV (2014) Air-borne ultrasound application in the convective drying of strawberry. J Food Eng 128:132–139
6. Beck SM, Sabarez H, Gaukel V, Knoerzer K (2014) Enhancement of convective drying by application of airborne ultrasound – a response surface approach. Ultrason Sonochem 21(6):2144–2150
7. Fernandes FAN, Rodrigues S (2007) Ultrasound as pre-treatment for drying of fruits: dehydration of banana. J Food Eng 82:261–267

8. Fernandes FAN, Gallao MI, Rodrigues S (2009) Effect of osmosis and ultrasound on pineapple cell tissue structure during dehydration. J Food Eng 90:186–190

9. Garcia-Noguera J, Oliveira FIP, Gallao MI, Weller CL, Rodrigues S, Fernandes FAN (2010) Ultrasound-assisted osmotic dehydration of strawberries: effect of pretreatment time and ultrasonic frequency. Drying Technol 28:294–303

10. Nowacka M, Tylewicz U, Laghi L, Dalla Rosa M, Witrowa-Rajchert D (2014) Effect of ultrasound treatment on the water state in kiwifruit during osmotic dehydration. Food Chem 144:18–25

11. Xin Y, Zhang M, Adhikari B (2013) Effect of trehalose and ultrasound-assisted osmotic dehydration on the state of water and glass transition temperature of broccoli (*Brassica oleracea* L. var. botrytis L.). J Food Eng 119:640–647

12. Başlar M, Kılıçlı M, Yalınkılıç B (2015) Dehydration kinetics of salmon and trout fillets using ultrasonic vacuum drying as a novel technique. Ultrason Sonochem 27:495–502

13. Başlar M, Kılıçlı M, Toker O, Sağdıç O, Arici M (2014) Ultrasonic vacuum drying technique as a novel process for shortening the drying period for beef and chicken meats. Innovative Food Sci Emerg Technol 26:182

14. He Z, Yang F, Peng Y, Yi S (2013) Ultrasound assisted vacuum drying of wood effects on drying time and product quality. BioResources 8(1):855–863

15. He Z, Yang F, Peng Y, Yi S (2013) Effects of ultrasound on wood vacuum drying characteristics. Pro Ligno 9(4):693–699

16. García-Pérez JV, Cárcel JA, De La Fuente-Blanco S, Riera-Franco De Sarabia E (2006) Ultrasonic drying of foodstuff in a fluidized bed: parametric study. Ultrasonics 44:539–e543

17. Santacatalina JV, Cárcel JA, Simal S, Garcia-Perez JV, Mulet A (2012) Atmospheric freeze drying assisted by power ultrasound. In: International symposium on ultrasound in the control of industrial processes. Madrid

18. Schössler K, Jäger H, Knorr D (2012) Effect of continuous and intermittent ultrasound on drying time and effective diffusivity during convective drying of apple and red bell pepper. J Food Eng 108(1):103–110

19. Gogate PR (2015) The use of ultrasonic atomization for encapsulation and other processes in food and pharmaceutical manufacturing. In: Gallego-Juárez JA, Graff KF (eds) Power ultrasonics: applications of high-intensity ultrasound. Woodhead Publishing, Cambridge, pp 911–913

20. D'Addioa SM, Chana JGY, Kwoka PCL, Prud'homme RK, Chana HK (2012) Constant size, variable density aerosol particles by ultrasonic spray freeze drying. Int J Pharm 427:185–191

21. Fernandes FAN, Linhares FE Jr, Rodrigues S (2008) Ultrasound as pre-treatment for drying of pineapples. Ultrason Sonochem 15(6):1049–1054

22. Bantle M, Eikevik TM (2014) A study of the energy efficiency of convective drying systems assisted by ultrasound in the production of clipfish. J Clean Prod 65:217–223

23. Goyal RK, Kingsly ARP, Manikantan MR, Ilyas SM (2006) Thin-layer drying kinetics of raw mango slices. Biosyst Eng 95(1):43–49

24. Villa-Corrales L, Flores-Prieto JJ, Xamán-Villaseñor JP, García-Hernández E (2010) Numerical and experimental analysis of heat and moisture transfer during drying of Ataulfo mango. J Food Eng 98(2):198–206

25. Rossello C, Simal S, SanJuan N, Mulet A (1997) Nonisotropic mass transfer model for green bean drying. J Agric Food Chem 45(2):337–342

26. Simal S, Sánchez ES, Bon J, Femenia A, Rosselló C (2001) Water and salt diffusion during cheese ripening: effect of the external and internal resistances to mass transfer. J Food Eng 48:269–275

27. Chou SK, Chua KJ (2001) New hybrid drying technologies for heat sensitive foodstuffs. Trends Food Sci Technol 12:359–369

28. Mousa N, Farid M (2002) Microwave vacuum drying of banana slices. Drying Technol 20(10):2055–2066

29. Abbasi S, Azari S (2009) Novel microwave-freeze drying of onion slices. Int J Food Sci Technol 44:974–979

30. Sabarez HT, Gallego-Juarez JA, Riera E (2012) Ultrasonic-assisted convective drying of apple slices. Drying Technol 30(9):989–997
31. Dev SRS, Geetha P, Orsat V, Gariepy Y, Raghavan GSV (2011) Effects of microwave-assisted hot air drying and conventional hot air drying on the drying kinetics, color, rehydration, and volatiles of Moringa oleifera. Drying Technol 29(12):1452–1458
32. Kowalski SJ, Mierzwa D (2015), Ultrasound-assisted convective drying of biological materials. Drying Technol 33(13):1601–1613
33. Bantle M, Eikevik TM (2011) Parametric study of high-intensity ultrasound in the atmospheric freeze drying of peas. Drying Technol 29(10):1230–1239
34. Gallego-Juarez JA, Riera E, Blanco SD, Rodriguez-Corral G, Acosta-Aparicio VM, Blanco A (2007) Application of high-power ultrasound for dehydration of vegetables: processes and devices. Drying Technol 25(11):1893–1901
35. Rodriguez J, Melo EC, Mulet A, Bon J (2013) Optimization of the antioxidant capacity of thyme (Thymus vulgaris L.) extracts: management of the convective drying process assisted by power ultrasound. J Food Eng 119(4):793–799
36. Sledz M, Wiktor A, Rybak K, Nowacka M, Rajchert DW (2015) The impact of ultrasound and steam blanching pre-treatments on the drying kinetics, energy consumption and selected properties of parsley leaaves. Appl Acoust. doi:10.1016/j.apacoust.2015.05.006
37. Fernandes FAN, Oliveira FIP, Rodrigues S (2008) Use of ultrasound for dehydration of papayas. Food Bioprocess Technol 1:339–345
38. Nowacka M, Wiktor A, Śledź M, Jurek N, Witrowa-Rajchert D (2012) Drying of ultrasound pretreated apple and its selected physical properties. J Food Eng 113(3):427–433
39. Puig A, Perez-Munuera I, Carcel JA, Hernando I, Garcia-Perez JV (2012) Moisture loss kinetics and microstructural changes in eggplant (Solanum melongena L.) during conventional and ultrasonically assisted convective drying. Food Bioprod Process 90(4):624–632
40. Bantle M, Hanssler J (2013) Ultrasonic convective drying kinetics of clipfish during the initial drying period. Drying Technol 31(11):1307–1316
41. Forero DP, Orrego CE, Peterson DG, Osorio C (2015) Chemical and sensory comparison of fresh and dried lulo (Solanum quitoense Lam.) fruit aroma. Food Chem 169:85
42. Ponting JD, Watters GG, Forrey GG, Jackson RR, Stanley R (1966) Osmotic dehydration of fruits. Food Technol 20:125–131
43. Chiralt A, Talens P (2005) Physical and chemical changes induced by osmotic dehydration in plant tissues. J Food Eng 67:167–177
44. Shi J, Xue SJ (2009) Application and development of osmotic dehydration technology. In: Ratti C (ed) Food processing, in advances in food dehydration. CRC press, Boca Raton, pp 187–205
45. Rastogi NK, Raghavarao KSMS (2004) Mass transfer during osmotıc dehydratıon determina-tion of moisture and solute diffusion coefficients from concentration profiles. Food Bioprod Process 82(C1):44–48
46. Azoubel PM, Murr FEX (2004) Mass transfer kinetics of osmotic dehydration of cherry tomato. J Food Eng 61:291–295
47. Torreggiani D, Bertolo G (2001) Osmotic pre-treatments in fruit processing: chemical, physical and structural effects. J Food Eng 49:247–253
48. Chwastek A (2014) Methods to increase the rate of mass transfer during osmotic dehydration of foods. Acta Sci Pol Technol Aliment 13(4):341–350
49. Chemat F, Huma Z, Khan MK (2011) Applications of ultrasound in food technology: processing, preservation and extraction. Ultrason Sonochem 18:813–835
50. Rastogi NK, Raghavarao KSMS, Niranjan K, Knorr D (2002) Recent developments in osmotic dehydration: methods to enhance mass transfer. Trends Food Sci Technol 13:48–59
51. Shamaei S, Emam-Djomeh Z, Moini S (2011) Ultrasound-assisted osmotic dehydration of cranberries: effect of finish drying methods and ultrasonic frequency on textural properties. J Texture Stud. ISSN 0022–4901 43(2):133–141
52. Fernandes FAN, Rodrigues S (2008) Application of ultrasound and ultrasound-assisted osmotic dehydration in drying of fruits. Drying Technol 26(12):1509–1516

53. Mothibe KJ, Zhang M, Nsor-atindana J, Wang YC (2011) Use of ultrasound pretreatment in drying of fruits: drying rates, quality attributes, and shelf life extension. Drying Technol 29:1611–1621
54. Simal S, Benedito J, Sánchez ES, Rossello C (1998) Use of ultrasound to increase mass transport rates during osmotic dehydration. J Food Eng 36:323–336
55. Fernandes FAN, Rodrigues S, Law CL, Mujumdar AS (2011) Drying of exotic tropical fruits: a comprehensive review. Food Bioprocess Technol 4:163–185
56. Nowacka M, Tylewicz U, Balestra F, Rosa MD, Witrowa-Rajcherta D (2013) Microstructure changes of osmodehydrated kiwifruit sliced pretreated with ultrasound. In: Inside food symposium, Materiały Konferencyjne, 16. Leuven, 9–12 Apr 2013
57. Arevalo-Pinedo A, Murr FEX (2006) Kinetics of vacuum drying of pumpkin (Cucurbita maxima): modeling with shrinkage. J Food Eng 76:562–567
58. Wu L, Orikasa T, Ogawa Y, Tagawa A (2007) Vacuum drying characteristics of eggplants. J Food Eng 83:422–429
59. Ferenczi S, Czukor B, Cserhalmi Z (2014) Evaluation of microwave vacuum drying combined with hot-air drying and compared with freeze- and hot-air drying by the quality of the dried apple product. Period Polytech Chem Eng 58(2):111–116. doi:10.3311/PPch.7082
60. Mujumdar A (1987) Handbook of industrial drying. M. Dekker, New York, pp 156–157
61. Brown M (1999) Focusing on freeze-drying. Food Manuf 74(9):34–36
62. Kudra T, Mujumdar A (2002) Sonic drying. In: Advanced drying technologies. Marcel Dekker, New York
63. Ratti C (2009) Advances in food dehydration. CRC Press, Baco Raton, p 17
64. Chen X, Mujumdar A (2008) Drying technologies in food processing. Blackwell, Oxford, pp 225–232
65. Devahastin S, Suvarnakuta P, Soponronnarit S, Mujumdar AS (2004) A comparative study of low-pressure superheated steam and vacuum drying of a heat-sensitive material. Drying Technol 22:1845–1867
66. Gunasekaran S (1999) Pulsed microwave-vacuum drying of food materials. Drying Technol 17(3):395–412. doi:10.1080/07373939908917542
67. Thomkapanich O, Suvarnakuta P, Devahastin S (2007) Study of intermittent low-pressure superheated steam and vacuum drying of a heat-sensitive material. Drying Technol 25(1):205–223. doi:10.1080/07373930601161146
68. Avramidis S, Liu M, Neilson BJ (1994) Radio-frequency/vacuum drying of softwoods: drying of thick western red cedar with constant electrode voltage. For Prod J 44(1):41–47
69. Kanagawa Y, Yasujima M (1993) Effect of heat sources on drying time in vacuum drying of wood, International Conference on Wood Drying. Zvolen; Slovakia 292:164
70. Cohen JS, Yang TCS (1995) Progress in food dehydration. Trends Food Sci Technol 6(1):20–25
71. Tarleton ES (1992) The role of field-assisted techniques in solid/liquid separation. Filtr Sep 3:246–253
72. Fuente-Blanco S, Sarabia ERF, Acosta-Aparicio VM, Blanco- Blanco A, Gallego- Jua'rez JA (2006) Food drying process by power ultrasound. Ultrason Sonochem 44:523–527
73. Zhao F, Chen ZQ (2011) Numerical study on moisture transfer in ultrasound-assisted convective drying process of sludge. Drying Technol 29:1404–1415
74. Carcel JA, Garcia-Perez JV, Riera E, Mulet A (2011) Improvement of convective drying of carrot by applying power ultrasound-influence of mass load density. Drying Technol 29:174–182
75. Aversa M, Van der Voort AJ, De Heij W, Tournois B, Curcio S (2011) An experimental analysis of acoustic drying of carrots: evaluation of heat transfer coefficients in different drying conditions. Drying Technol 29:239–244
76. Jangam SV (2011) An overview of recent developments and some R&D challenges related to drying of foods. Drying Technol 29:1343–1357
77. Gong C, Hart DP (1998) Ultrasound induced cavitation and sonochemical yields. J Acoust Soc Am 104(5):2675–2682

78. Santos HM, Lodeiro C, Capelo- Martinez J-L (2009) The power of ultrasound. In: Ultrasound in chemistry: analytical applications. Weinheim, Wiley

79. Ashokkumar M (2011) Theoretical and experimental sonochemistry involving inorganic systems. Springer, Dordrecht, pp 2–5

80. He Z, Yang F, Yi S, Yi S, Gao J (2012) Effect of ultrasound pretreatment on vacuum drying of Chinese catalpa wood. Drying Technol 30(15):1750–1755. doi:10.1080/07373937.2012.713420

81. Akpinar EK, Bicer Y, Midilli A (2003) Modeling and experimental study on drying of apple slices in a convective cyclone dryer. J Food Process Eng 26:515–554

82. Doymaz I (2013) Experimental study on drying of pear slices in a convective dryer. Int J Food Sci Technol 48:1909–1915

83. Guiné RPF, Ferreira DMS, Barroca MJ, Gonçalves FM (2007) Study of the drying kinetics of solar-dried pears. Biosyst Eng 98:422–429

84. Falade KO, Solademi OJ (2010) Modelling of air drying of fresh and blanched sweet potato slices. Int J Food Sci Technol 45:278–288

85. Barbosa-Canovas GV, Vega-Mercado H (1996) Dehydration of foods. Chapman & Hall, New York

86. Nakagawa K, Ochiai T (2015) A mathematical model of multi-dimenisonal freeze-drying for food products. J Food Eng 161:55–67

87. Ratti C (2001) Hot air and freeze-drying of high-value foods: a review. J Food 49(4):311–319

88. Bell GA, Mellor JD (1990) Further developments in adsorption freeze-drying. CSIRO Food Res Q 50:48–53

89. Lombraña JI, Elvira CD, Villarán MC (1997) Analysis of operating strategies in the production of special foods in vials by freeze drying. Int J Food Sci Technol 32:107–115

90. Santacatalina JV, Fissore D, Cárcel JA, Mulet A, García-Pérez JV (2015) Model-based investigation into atmospheric freeze drying assisted by power ultrasound. J Food Eng 151:7–15

91. Feng H, Yang W (2011) Ultrasonic processing. Nonthermal processing technologies for food, In Eds: HQ Zhang, GV Barbosa-Cánovas, VMB Balasubramaniam, CP Dunne, DF Farkas, JTC Yuan. Blackwell Publishing, USA

92. Rastogi NK, Raghavarao KSMS, Niranjan K (2005) Developments in osmotic dehydration. Emerging technologies for food processing, Academic press 221–249

Ultrasonic Process Intensification for the Efficient Extraction of Nutritionally Active Ingredients of Polysaccharides from Bioresources

Ibrahim Alzorqi and Sivakumar Manickam

Contents

Abstract

To reduce the consumption of petroleum and common energy sources, it is important to look for alternative green techniques that are able to produce the same products and fulfill the same industrial applications. Power ultrasound is successful in inducing various physical and chemical transformations due to the intense pressure waves of the ultrasound in a liquid medium. Ultrasound energy could be considered as one of the new forms of energy which is promising for the applications of extraction involving the bioresources. This chapter presents the aspects of ultrasonic process intensification of the extraction of one of the most biologically active ingredients, namely, polysaccharides from diverse herbal materials. Number of studies has been surveyed and summarized to present their best outcomes in the applications of ultrasound in the extraction process.

I. Alzorqi • S. Manickam (✉)
Manufacturing and Industrial Processes Research Division, Faculty of Engineering, University of Nottingham Malaysia campus, Semenyih, Selangor, Malaysia
e-mail: Sivakumar.Manickam@nottingham.edu.my

Evidently, ultrasonic conditions provide better environment for isolating the bioactive compounds and more importantly with higher preservation of the bioactivity of extracted components.

Introduction

An increasing demand toward an effective, economic, and clean extraction process for the biologically active ingredients from herbs resulted into exploring a substantial number of newer extraction techniques. The newer extraction techniques focus on considerable cost/energy reduction, higher purity of the separated components, and preservation of bioactivity of the extracted components. Among many of the newer extraction technologies, ultrasound-assisted extraction (UAE) has been intensely exploited in these days. It is an efficient technique and thus being widely employed to extract a diverse range of active ingredients from herbs, with lower extraction time, and more importantly at lower temperatures. Besides, UAE is considered to be an economically feasible technique owing to its simple setup and easy handling and transportation and finally due to the requirement of smaller working area [1–4].

Ultrasound involves the application of frequencies ranging from 20 to 2000 kHz. It is based on a series of energy transformation chain as shown in Fig. 1 [5]. Acoustic power generated by transducers through converting the supplied electrical power into mechanical oscillation is responsible to produce millions of jets of microbubbles in the liquid medium of extraction. The created bubbles or cavities then grow and finally collapse at very small time intervals releasing large magnitudes of energy over a smaller area.

The whole phenomenon of formation, growth, and collapse of bubbles is referred as cavitation. The formed cavities create an eruption of the surrounding liquid and assist in increasing the mass transfer by breaking the cell wall of herbs and increasing the diffusion of active ingredients [6]. A range of factors that affect the ultrasonic extraction are the ultrasound frequency, the temperature of the medium, irradiation time, the amplitude of applied power, the ratio of solid herbal material to liquid solvent, the active cavitational zone, the diameter of ultrasound probe, and the type of sonication, i.e., indirect sonication (using an ultrasonic bath) or direct sonication (by probes). A careful consideration and selection of these factors with proper optimization will not only lead to an efficient extraction but also results into an economic extraction [7]. Thus, the successful application of UAE relatively depends upon the optimum operating conditions and the matrix of the plants subjected to ultrasound [1] which should be investigated carefully so that a higher yield of targeted active components and their bioactivity could be obtained. Significantly, these operational parameters could be optimized to obtain the best combination of
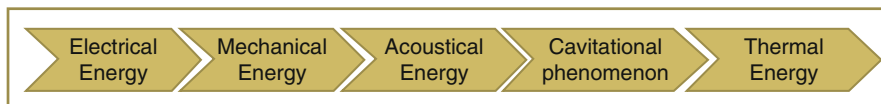
Fig. 1 The energy transformation chain in an ultrasound process [5]

their interacted ranges and meet the concentration and stiffness of the extracted herbal materials. Numerous studies examined the optimization of operational parameters for the best extraction of active ingredients from herbs. Among the different types of components that are extracted, the focus is on polysaccharides as they are one of the major dietary ingredients widely used in food, health, and nutritional applications. Specifically ultrasound has been employed and optimized to extract these polysaccharides from *Litchi* [8], *Boletus edulis* mycelia [9], *Asparagus officinalis* [10], *Longan* fruit pericarp [11], *Opuntia ala* [12], and *Ganoderma lucidum* at low frequencies (4, 6, and 8 kHz) [13]. Remarkably ultrasound has been found to enhance the water uptake and hydration of vegetable materials. It also provides greater penetration of solvent into the cellular materials, enlarges the pores of cells, and increases the contact surface area owing to the size reduction of herbal matrix [14]. More importantly ultrasound has been employed owing to its ability to effectively preserve the bioactivity of polysaccharides while increasing their extraction yield at shorter extraction time with less power consumption [11, 13, 15]. In this chapter the recent outcomes on the UAE technique, its physiochemical influence on the extraction process, types of ultrasonic reactors, and their utilization for the extraction of polysaccharides have been critically discussed.

Ultrasonic Cavitation Phenomena and Its Assistance in the Extraction

Since 1980, the extensive studies on the utilization of ultrasound have started. Ultrasound energy can be considered as one of the new forms of energy and promising in a wide range of technological applications. Ultrasound introduction leads to cavitation phenomenon which was observed only in the liquids, where each of the collapsing bubble could be illustrated as a micro-reactor. As a result of an increase in the reaction rates with ultrasonic cavitation, the interest in sonochemistry has dramatically increased in the recent years [16]. The chemical effects of ultrasound are known for many decades [17], and it is believed that the cavitation phenomena may lead to a significant degree of process intensification. Besides, employing ultrasonic energy resulted into considerable improvements in the physical processes such as extraction, emulsification, crystallization, etc.

Cavitation phenomenon is defined as the generation, subsequent growth, and collapse of smaller cavities, which consequently release large magnitudes of energy over a very small area, resulting in high densities of energy [18–20]. These cavities are created by microbubbles in the bulk of a liquid which act as nuclei. Due to the
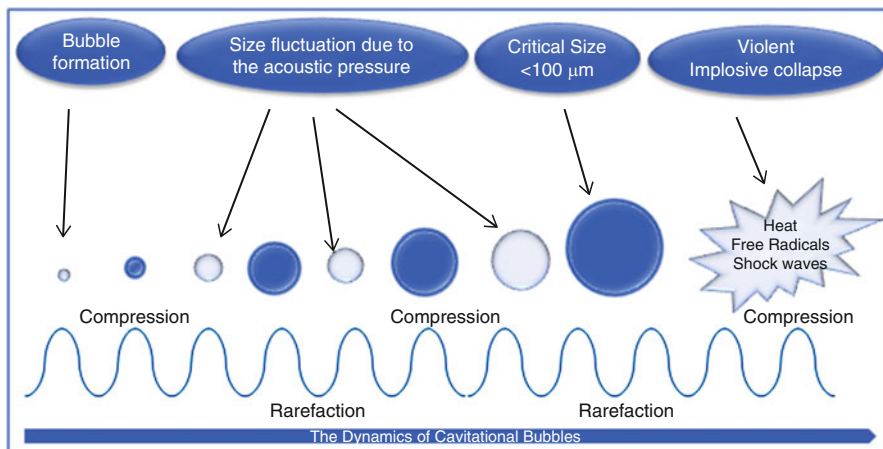
Fig. 2 The dynamics of a cavitational bubble during cavitation phenomenon [24]

acoustic field created by ultrasonic waves (20–100 MHz), these microbubbles undergo fluctuated motion in the form of repetitive compression and rarefaction cycles that lead to an increase in the overall bubble size (Fig. 2). It is deemed that these microbubbles enclose void of vapors or of dissolved volatile gases or reagents that are present in the bulk liquid. Accordingly, it is believed that during the sudden violent collapse of these cavities, intensive conditions in the form of localized hot spots of temperatures and pressures of 5000 K and 1000 bar, respectively, could be generated shortly where the bulk liquid is at ambient conditions. Such hot spots of high localized energy enhance the physical, chemical, and biological processes [2, 21–23].

Physical Effects of Ultrasound Cavitation

When the ultrasonic waves pass through a fluid medium, they create regions of higher and lower pressure variations which are known as acoustic pressure [25]. If the fluid medium represents a liquid phase, it may contain cavities of gas that form the nuclei for the formation of microbubbles (cavitation phenomena). These microbubbles start fluctuating in size in the form of compression and rarefaction cycles (acoustic cycles as shown in Fig. 2) when exposed to an acoustic field. Based on the extended number of acoustic cycles, the cavitation can be categorized into stable and non-stable forms. The non-stable form of cavitation is also classified into two types, namely, inertial and transient cavitation. The inertial cavitation can be illustrated by the extended number of acoustic cycles (many hundreds), which can occur for specific bubble sizes as well as acoustic pressures, that ends with a violent collapse for its bubbles to produce smaller ones (may be 30 times smaller than the

Fig. 3 The occurrence of transient cavitation near a solid surface and the resulted asymmetrical bubble collapse and the generation of liquid micro-jets [36]

original bubble size), while the transient cavitation is relatively considered to be short-life oscillation, due to the limited number of acoustic cycles (1–2) which could be observed at low frequencies (20–100 kHz) during the growth of bubbles until their violent eventual collapse [26–28].

The acoustic pressure created due to cavitation is strongly related to the amount of energy dissipated into the system. The dissipated energy has different flow patterns, based on the mechanism of dissipation. These patterns have been described by transient cavitation, steady streaming, micro-streaming, and micro-jetting. The "steady streaming" maybe resulted from a standing wave between two flat surfaces [25]. The reflection of sound on a solid surface or air-liquid interface simultaneously with the generation of a wave at the transducer results into the generation of standing waves.

Coalescence of small bubbles to form larger bubbles may occur during cavitation. Coalescence of small bubbles can be observed when they fly out of the sonication zone and were affected by the gravitational force. As a result of formation of larger bubbles, velocity and pressure variations can be noticed at microscale, which create fluid turbulence in the surrounding zone and cause micro-streaming that is considered to be the third type of energy flow pattern [29, 30]. Along with the formation of micro-streaming, due to the high pressure generated from the bubbles collapse, intense shock waves are propagated to produce turbulent micro-streaming in the surrounding fluid layers. The resulted micro-turbulent-streaming can be exploited to enhance the mass transfer in the extraction processes by breaking the cell wall of plants and animals [31, 32].

The fourth flow pattern of dissipating the acoustic energy is micro-jetting. When transient cavitation occurs near a solid surface, it creates asymmetrical bubble collapse and results in the generation of millions of micro-jets of liquid (Fig. 3). The generation of micro-jetting could be considered as one of the disadvantages of physical effects of ultrasonic cavitation, as it causes erosion and pitting adjacent to the solid surfaces of the process equipments. However, this can sometimes be considered as an advantage when the ultrasonic cavitation is involved in the extraction process or cleaning applications such as removing the hard aggregated layers from the solid surfaces [33–36].

Sonochemical Effects of Ultrasound Cavitation

With ultrasound cavitation, high energy is dissipated into the liquid system which leads to the generation of higher temperatures (few thousands of degrees) and pressures (few thousands of atmospheric pressures). Many chemical changes may occur due to the energy generated upon the collapse of cavitational microbubbles, represented by a number of chemical reactions that affect the overall system. The occurrence of these chemical reactions particularly takes place in the vapor phase inside the collapsed bubbles and within the surrounding fluid layer which results in the generation of primary and secondary radicals. These radicals subsequently enter into a number of reactions to produce chemically different molecules [2, 29, 34, 37, 38].

Based on the physiochemical properties of the sonicated medium, the amount of heat generated and hence the yield of radicals may change which influence a variety of chemical reactions. The relation between the maximum temperature reached upon the bubble collapse and the yield of radicals generated was reported by Ashokkumar et al., (2007). It was found that by achieving the maximum localized temperatures upon bubble collapse, the yield of generated radicals can be increased. Therefore, the effects of sonication power and external pressure of the cavitational bubbles have been intensely investigated besides changing the overall ambient temperature. Accordingly, it was found that increasing the sonication power and the external pressure and decreasing the bulk temperature of the sonicated medium lead to an increase in the temperature at the moment of bubble collapse and the yield of generated radicals [20, 29].

A second important factor that affects the yield of generated radicals is the size and the total number of cavitational bubbles generated. At a lower ultrasonic frequency (20 kHz), the largest size (100 μm) of cavitational bubbles can be achieved which continuously grow and lead to the generation of a larger amount of heat induced into the system, thereby resulting into releasing a higher number of radicals. In the investigation of ultrasound frequency and its potential effects on the industrial processes, it was found that the selected frequency has a direct effect on the size and total number of cavitational bubbles, thus the yield of generated primary radicals. For example, using an intermediate frequency range (200–500 kHz) may produce higher number of active cavitational bubbles and thus increases the yield of primary radicals per bubble [29]. Negatively, these radicals enter into a number of reactions and sub-reactions to produce chemically different molecules in the system [34, 38, 39]. For instance, primary free radicals of H and OH can be generated from the water vapor present inside the collapsed bubbles. These radicals in turn recombine to form hydrogen, hydrogen peroxide, or water molecules [40]. Different analytical methods are employed to quantify these generated radicals. Out of the methods, the iodide method is the most commonly employed method, which is based on the formation of hydrogen peroxide resulted from releasing the OH radicals in a sonicated water medium [41]. Thus, the iodine method has been used to estimate the amount of OH radicals generated in the system based on the amount of hydrogen peroxide resulted from the reaction of these radicals (Eqs. 1, 2, 3, and 4).

$$H_2O \rightarrow H + OH \tag{1}$$

$$H + H \rightarrow H_2 \tag{2}$$

$$OH + OH \rightarrow H_2O_2 \tag{3}$$

$$H + OH \rightarrow H_2O \tag{4}$$
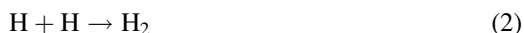
Significantly, the occurrence of chemical reactions leads to induce changes in the molecular structure and thus affects the bioactivity of the components. Therefore, to avoid such a problem, the physiochemical conditions (sonication power, temperature, and pressure) of the process should be carefully studied to diminish the interactive effects of generated radicals on the chemical reactions involved in the process. Interestingly, it was reported that the number of generated radicals can reach to its maximum value when the temperature inside the collapsed bubbles is maximized. Therefore, decreasing the ultrasonic power, and the bulk pressure, or increasing the bulk temperature help to decrease the total number of radicals generated due to the decrease in the internal temperature of the collapsing cavitational bubbles [41].

The degree of cavitation phenomena strongly depends on the relation between frequency and bubble size. The high pressure variations generated from a selected frequency lead to a rapid increase in the bubble size. For instance, the largest size (100 μm) of cavitational bubbles was found to be achieved at an ultrasonic frequency as low as at 20 kHz [27]. Accordingly such frequency was favorably followed in the electrical design of ultrasound systems. Although, a frequency of 20 kHz maintains a continuous growth of cavitational bubbles, it leads to higher amount of heat induced into the system and thus higher number of radicals released [29]. However, the same cavitational effects of 20 kHz could be obtained by changing the geometry of the ultrasonic system, for example, by changing the length of the emitter/transducer. It was reported that the ultrasonic bath designed with the operating frequency of 40 kHz gives the same cavitational effects as that of 20 kHz frequency if the length of the bonded transducers increased by two times to its original length [27]. Therefore, the interrelated factors, namely, power intensity, frequency, external temperature and pressure of the medium, and the vapor pressure of the solvent should be considered during the design of an ultrasonic cavitational reactor.

Selection of Solvent for Ultrasonically Assisted Extraction Process

Gogate (2008) reported the relation between the boiling point of a solvent and the cavitational activity. The optimum operating conditions in the cavitational process should be determined based on the bulk temperature and the right choice of extraction solvent. It was found that the vapor pressure of solvent has a direct interrelated effect on the maximum temperature and pressure achieved from the collapsed bubbles. Thus, an increase in the solvent vapor pressure may lead to a decrease in the maximum temperature and pressure of the collapsed bubbles. Therefore, if the intended process relies on the physical effects of cavitational

collapse, then using a low vapor pressure solvent and conducting at lower operation temperatures lead to achieving the maximum localized temperature and pressure upon bubble collapse. Accordingly, the size of bubbles will be increased due to an increase in the number of acoustic cycles of inertial cavitation. The maximum size reached by the cavitational bubbles is a crucial parameter to be considered with ultrasound dissipation, as it determines the cavitational intensity generated in the system by affecting the magnitude of pressure variations produced upon bubble collapse [2].

Sonochemical Reactors

The use of ultrasound cavitation in the biotechnology helps to overcome many challenges by achieving a significant reduction in the power required for the process line, space required for the installation of classical heating source and mixers, and the low amount of solvent required for extracting the active components from the herbal materials [3]. Generally, all the ultrasonic equipments share the same parts in the basic design of their system. First, the generator controls the level of power supplied to the electronic system. The electronic system controls the ultrasonic system which is the transducer. The majority of the electrical generator designed in a frequency range of 10–40 kHz is based on the industrial requirements and the type of applications. The second part is the transducer which is responsible for converting the electrical power into mechanical oscillations to produce the ultrasonic waves at a certain frequency. The most common type of transducers is the piezo-electric transducer (PZT) which is made-up of crystalline ceramic materials [4, 42]. The third part is the emitter which is considered to be the reactor of the ultrasonic system. It is responsible to dissipate the ultrasonic waves from the transducer into the medium. Mainly, the sonochemical reactors are classified into two types based on the way of introducing the ultrasonic waves, namely, ultrasonic bath and ultrasonic horn systems.

Ultrasonic Horn-Type Systems

This type of sonoreactors is represented by a horn system provided with a probe, and a sonotrode tip at the free end of the system (Fig. 4). The intensity of radiation can be varied and controlled by changing the shape of horn, which in turn determines the amount of amplification [27, 43]. It is suitable for small and relatively intermediate batch volumes, due to the limited active cavitational area around the ultrasonic tip (emitter). In general, the cavitational intensity found to be decreasing exponentially by moving away from the horn tip and vanishes at an approximate distance between 2 and 2.5 cm [44]. However, the active cavitational distance relates strongly to the frequency and the amount of electrical power supplied to the system. Therefore it is not recommended for large-scale commercial applications; especially those processes require longer residence time [2]. However, if the setup of ultrasonic-assisted
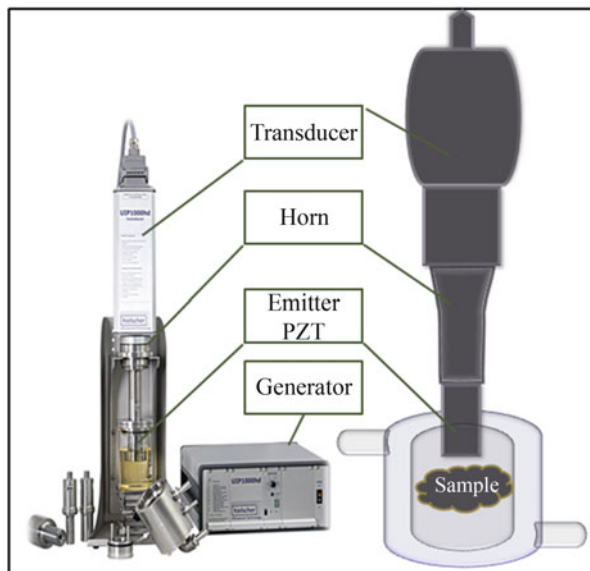
process considers exposing the liquid vertically to cover the high intensity region,
then this type of system could be used for a relatively larger scale. One of the
recommended solutions to overcome the limited batch volume is to use a circulation
or stirrer devise to be coupled with the ultrasound horn system. However, there are a
number of drawbacks affecting the use of this type of sonoreactors in the industry,
such as higher possibility of erosion and the particle shedding at the tip surface area
due to high power intensity and cavitational blocking [2]. Moreover, immersing the
probe directly into the liquid leads to an increase in the medium temperature quickly
as a result of direct contact between the solvent and the irradiation source.

Controlling the active zone of cavitation from horn-type ultrasonic systems is of
prime importance to ensure sufficient exposure of herbal materials to the acoustic
energy. This factor is considered to be essential for the determination of active
cavitational volume of the ultrasonic reactors. It influences directly the distance
traveled by the cavitational bubbles and the maximum size that could be reached by
the cavities (bubbles) in their life before their violent collapse [2, 45]. According to
Horst et al. (1996), the cavitational zone could be classified into three sections: high
cavitating region (Zone-1), cavitational transition region (Zone-2), and poor cavita-
tion region (Zone-3) (Fig. 5). A tip of an ultrasound horn acts as a point source and
the sound pressure is responsible for the cavitation. A decrease in the sound pressure
was observed by increasing the radiation distance. Therefore, when the sound
pressure approaches the threshold pressure (black threshold), the cavitational inten-
sity diminishes and finally vanishes beyond this pressure. Black threshold is the
lowest sound pressure at which cavitation could be observed [46].

Cavitation energy distribution within an ultrasonic extraction system was ana-
lyzed by measuring the cavitational intensity in the zone around the probe using an

Fig. 5 Classification of
cavitational zones
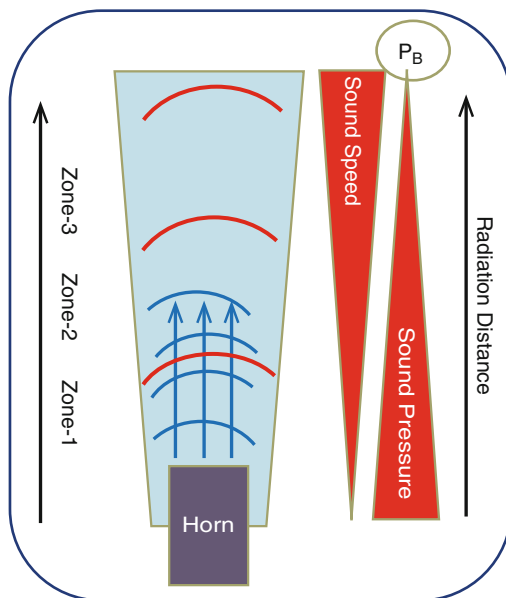
ultrasound energy meter (PB-500, Megasonics, USA). The ultrasonic energy was
first measured with pure water and found to be decreased remarkably from 16.49 to
4.22 W/cm^2 by increasing the distance from 1 to 6 cm away from the probe tip.
Significantly, the cavitational intensity decreased up to 2.82 W/cm^2 at 1 cm distance
after adding the powder of *Asparagus officinalis* to the extraction system. Accord-
ingly, the reduction in the cavitational intensity was attributed to the addition of
asparagus powder which absorbed the ultrasonic waves and suppressed the ultra-
sound energy which was totally diminished at 2.5 cm distance away from the probe
[10]. However, when they coupled the ultrasonic system with an agitator, the power
intensity was enhanced markedly to 9.42 W/cm^2 at a distance of 1 cm and the
cavitational intensity extended to reach a distance up to 4 cm due to an increase in the
contact between the particles of *Asparagus officinalis* and ultrasonic energy. Overall,
circulating the liquid may lead to an increase in the mass transfer rate and hence the
efficiency of overall extraction.

Ultrasonic Bath-Type System

The ultrasonic bath reactor is another type of sonoreactors, more flexible than the
horn type and can be used for any batch volume in laboratories as well as in
industries. The ultrasonic bath or cleaning bath can be described as a simple bath
reactor provided with an electrical generator and multiple number of transducers
(Fig. 6). The major advantage of using this type in the industry solves a number of
problems faced by the horn type, for example, erosion and cavitational blocking.
Increasing the number of transducers used in case of ultrasonic bath helps in

Fig. 6 Ultrasonic bath-type system
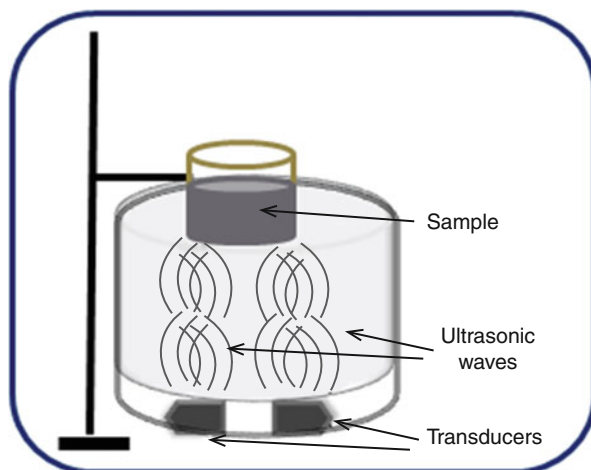
providing the same level of power dissipated into the system under low power intensities. Therefore the ultrasonic bath could be made with single, double, or multiple frequency, according to the number of transducers and equipment geometry [2].

There are different equipment geometries available for this type of ultrasound reactor. For example, if the transducers are attached at the bottom of an ultrasonic bath, the cavitational active zone will be vertically above the position of the transducers. Sometimes the transducers could be attached at both sides of an ultrasonic bath to provide horizontal zone of the cavitational activity. Many other types, i.e., triangular pitch reactor, hexagonal reactor with multiple frequency, and tubular-shape reactors with one or two irradiated ends, have been presented and effectively used for different applications [22, 46, 47, 48]. For processes that involve chemical reactions, the ultrasonic bath reactor is not recommended due to its low reproducibility and low intensity of power delivered to the sample. Nowadays, due to the increasing demand for these types of sonoreactors, they are manufactured widely by a large number of companies such as Hielscher, Branson, and Undatim, which are commonly used in the industries for different applications [43].

Ultrasonic-Assisted Extraction of Polysaccharides

Polysaccharides are longer branched chains of monosaccharide sugars (glucose), connected with each other by covalently bonded glycosidic linkages. They are considered as primary giant polymers due to their molecular weight which could reach up to 1×10^6 Da [49]. These active components of polysaccharides were effectively extracted by ultrasound which showed higher bioactivity [1, 8, 50–52]. Claver et al., (2010) optimized the ultrasonic extraction process to extract the polysaccharide components from Chinese malted sorghum. The optimum

operation conditions of 600 W of ultrasonic power, 4 min of irradiation time, and a ratio of solvent/herbal materials of 30 ml /1 g resulted into a maximum yield of polysaccharides of 17.6 %, which was very close to the predicted value of 17.08 % by a statistical response surface model [50].

During the extraction of polysaccharides from the root of *Valeriana officinalis L.*, the UAE was compared with the conventional hot water extraction method. The UAE had a remarkable influence in increasing the extractability of cellular polysaccharides (cellulose), as a result of cracking, peeling the outer surface cell-layers, and due to the size reduction of solid plant matrix. The ultrasonic horn system was provided with a 5 cm tip diameter which caused a high amount of acoustic energy dissipated into the system, due to the high contact surface area between the tip and the extraction medium. However, the sugar composition analysis of the resulted polysaccharides revealed that the easily accessible polysaccharides (starch) were likely degraded due to the damage that occurred from the implosion of cavitational bubbles which were exposed for a longer time (2 h) to ultrasound [52].

In a study for extracting the polysaccharides from the ethanol-insoluble plant residues from *Salvia officinalis*, a classical and an UAE were compared using polar (distilled water) and basic (diluted alkali of NaOH with 1 % and 5 % sequentially) media. The obtained results indicated that the majority (73 %) of the extractable cell wall polysaccharides were isolated using hot water at mild conditions with the addition of 1 % dil. NaOH. The application of UAE in the laboratory scale (50 g of ethanol-insoluble plant residues in 450 ml of distilled water) enhanced the yield of cell wall polysaccharides and the total extracts from 9.3 to 10 % and 34.3 to 39.9 %, respectively. Similar improvements were observed for pilot-scale experiments (2 kg of ethanol-insoluble plant residues in 30 lit of distilled water) upon the application of ultrasound. The yield of cell wall polysaccharides and the total extracts from *Salvia officinalis* increased from 2.4 % to 2.8 % and 10.3 % to 11.7 %, respectively [51].

Shirsath et al., (2012) indicated that the selection of extraction method toward obtaining a higher yield and purity for the extracted components depends on the nature of active ingredients, their thermal stability, and the matrix of materials subjected to the extraction [1]. Evidently, this was manifested in the study of Cheung et al., (2012), where three different types of medicinal mushrooms were exposed to the same operational conditions using two different extraction processes (UAE and hot water extraction, "HWE"). The yield of polysaccharide-protein complexes extracted from *G. frondosa* (UAE, 6.3; HWE 5.7, wt%) did not change significantly by changing the extraction technique. Conversely, the mushroom of *L. edodes* showed a remarkable increase in the yield with UAE (UAE, 12.4; HWE 6.57, wt %). However, an obvious decrease in the yield of polysaccharide-protein complexes was recorded (UAE, 1.61 wt%; HWE, 6.58 wt%) due to the application of UAE in the case of *C. Versicolor* mushroom [53].

Four ultrasonic parameters, i.e., power (7.2–40.3 W), time (10–30 min), temperature (40–80 °C), and the mixing ratio of solvent/herbal materials (10–30/g, vol/wt),

were optimized to extract the polysaccharides from *Ziziphus jujuba cv. jinsixiaozao*. The obtained optimal ultrasonic results were then compared with the control method, i.e., HWE. The yield and the purity of extracted polysaccharides were the indicator for the process performance in both the extraction techniques. The optimum results showed that the higher ultrasonic power (31.7 W) and the lower temperature (50 °C) were the optimal conditions to increase the yield of polysaccharides from 6.75 to 8.11 % within 20 min. Generally the ultrasonic power (31.7 W) and lower temperatures (45–53 °C) were the major factors that affected the yield of polysaccharides as compared with the nonsignificant effects of irradiation time and solid/solvent ratio [54].

Furthermore, the purity of polysaccharides achieved by UAE (28 %) was 1.2 times higher as compared to the classical HWE method under the operational conditions of 85 °C and 120 min [54]. These results could be attributed to the efficiency of UAE to enhance the mass transfer rate of polysaccharides and hence to increase their extractability due to the physical and mechanical actions of ultrasound cavitation on the cell wall of extracted materials.

A new ultrasonic extraction system was designed and optimized by Zhao et al. (2011) to extract the polysaccharides from *Asparagus officinalis* by employing a 2 L extraction scale. In comparison with the classical method of HWE, the optimal ultrasonic conditions (600 W of ultrasonic power, 46 min of ultrasonic irradiation time, and 35 ml/g solvent to solid ratio) resulted into a maximum yield of 3.134 %, which is higher than 2.253 % obtained by HWE within 120 min at 60 °C [10]. Thus, the proposed ultrasonic system of Zhao et al., (2011) achieved a remarkable improvement over the classical method in saving the time and energy. Moreover, the study covered investigations on the influence of ultrasonic system to the properties of produced polysaccharides such as molecular weight, sugar profile, and viscosity. The sugar composition analysis showed that the resulted polysaccharides contain glucose, fucose, arabinose, galactose, and rhamnose with an average molecular weight of 6.18×10^4 Da. The viscosity of polysaccharides extracted by the ultrasonic circulation system at 30 °C (26 mPa.s) was remarkably equal to the viscosity of the polysaccharides resulted from the HWE at 40 °C. Generally, the obtained results positively indicated that no significant change in the physical properties of the extracted polysaccharides occurs with the application of ultrasonic technique.

Studies also reported on the extraction of polysaccharides from *G. lucidum* under the influence of ultrasonic cavitation [13, 55–57]. The UAE was found to be suitable to preserve the bioactivity of polysaccharide components [55], where two fractions of isolated polysaccharides demonstrated their antioxidant and antitumor activities on the human breast cancer cells. With the low frequency ultrasound, a statistical design of response surface methodology was applied to optimize the extraction conditions by Chen et al. (2010). The optimum operational conditions were found to be: frequency, 8 kHz; temperature, 95 °C; time, 3 h; and water-to-solid ratio, 12:1 [13].

Conclusions and Future Directions

In this review, the aspects of ultrasonic energy in the process intensification of extracting and bioprocessing of active ingredients have been highlighted. Specific examples on the assistance of ultrasound in the isolation of polysaccharides from different herbal materials have been presented. The experimental investigations emphasize on the ability of power ultrasound to enhance the yield of isolated polysaccharides with higher preservation of their bioactivity. Remarkably, ultrasonic conditions provide better environment. However, the majority of these studies focus on the enhancement of extraction yield and the bioactivity of extracted components in a laboratory scale. A further scale-up should be experimented on a pilot or larger scale to increase the production and to provide fruitful dimensions for industrial applications. Proposing a continuous type of extraction setup with the aid of ultrasound has not been explored yet. Therefore, altering the geometry of ultrasonic-assisted extractor to overcome the limitations in the ultrasonic horn-type systems keeps the door open to achieve successful milestones in the food industries.

References

1. Shirsath S, Sonawane S, Gogate P (2012) Intensification of extraction of natural products using ultrasonic irradiations: a review of current status. Chem Eng Process Process Intesif 53:10–23
2. Gogate PR (2008) Cavitational reactors for process intensification of chemical processing applications: a critical review. Chem Eng Process Process Intesif 47:515–527
3. Vinatoru M (2001) An overview of the ultrasonically assisted extraction of bioactive principles from herbs. Ultrason Sonochem 8:303–313
4. Gallego-Juarez JA (2010) High-power ultrasonic processing: recent developments and prospective advances. Phys Procedia 3:35–47
5. Tang SY, Tan KW, Sivakumar M (2011) Ultrasound cavitation as a green processing technique in the design and manufacture of pharmaceutical nanoemulsions in drug delivery system In: Sanghi R, Singh V (eds) Green chemistry for environmental remediation, John Wiley & Sons, Inc., Hoboken, pp 153–208
6. Chemat F, Khan MK (2011) Applications of ultrasound in food technology: processing, preservation and extraction. Ultrason Sonochem 18:813–835
7. Gogate PR, Kabadi AM (2009) A review of applications of cavitation in biochemical engineering/biotechnology. Biochem Eng J 44:60–72
8. Chen Y, Luo H, Gao A, Zhu M (2011) Ultrasound-assisted extraction of polysaccharides from *Litchi* (*Litchi* chinensis Sonn.) seed by response surface methodology and their structural characteristics. Innovative Food Sci Emerg Technol 12:305–309
9. Chen W, Wang WP, Zhang HS, Huang Q (2012) Optimization of ultrasonic-assisted extraction of water-soluble polysaccharides from *Boletus edulis* mycelia using response surface methodology. Carbohydr Polym 87:614–619
10. Zhao Q, Kennedy JF, Wang X, Yuan X, Zhao B, Peng Y, Huang Y (2011) Optimization of ultrasonic circulating extraction of polysaccharides from *Asparagus officinalis* using response surface methodology. Int J Biol Macromol 49:181–187
11. Yang B, Zhao M, Shi J, Yang N, Jiang Y (2008) Effect of ultrasonic treatment on the recovery and DPPH radical scavenging activity of polysaccharides from *Longan* fruit pericarp. Food Chem 106:685–690

12. Cai W, Gu X, Tang J (2008) Extraction, purification, and characterization of the polysaccharides from *Opuntia milpa alta*. Carbohydr Polym 71:403–410
13. Chen X, Wang W, Li S, Xue J, Fan L, Sheng Z, Chen Y (2010) Optimization of ultrasound-assisted extraction of *Lingzhi* polysaccharides using response surface methodology and its inhibitory effect on cervical cancer cells. Carbohydr Polym 80:944–948
14. Toma M, Vinatoru M, Paniwnyk L, Mason T (2001) Investigation of the effects of ultrasound on vegetal tissues during solvent extraction. Ultrason Sonochem 8:137–142
15. Ebringerová A, Hromádková Z (2010) An overview on the application of ultrasound in extraction, separation and purification of plant polysaccharides. Cent Eur J Chem 8:243–257
16. Dahlem O, Demaiffe V, Halloin V, Reisse J (1998) Direct sonication system suitable for medium-scale sonochemical reactors. AIChE J 44:2724–2730
17. Richards WT, Loomis AL (1927) The chemical effects of high frequency sound waves I: a preliminary survey. J Am Chem Soc 49:3086–3100
18. Mason T (1991) Practical sonochemistry user's guide to application in chemistry and chemical engineering. Ellis Horwood, New York
19. Young FR (1989) Cavitation. McGraw-Hill, London
20. Leighton T (1994) The acoustic bubble. Acadamic Press, USA
21. Suslick KS (2001) Encyclopaedia of physical science and technology. Academic, San Diego
22. Gogate PR, Pandit AB (2001) Hydrodynamic cavitation reactors: a state of the art review. Rev Chem Eng 17:1–85
23. Sivakumar M, Pandit AB (2002) Wastewater treatment: a novel energy efficient hydrodynamic cavitational technique. Ultrason Sonochem 9:123–131
24. Newman C, Bettinger T (2007) Gene therapy progress and prospects: ultrasound for gene transfer. Gene Ther 14:465–475
25. Riley N (2001) Steady streaming. Annu Rev Fluid Mech 33:43–65
26. Yasui K (2002) Influence of ultrasonic frequency on multibubble sonoluminescence. J Acoust Soc Am 112:1405–1413
27. Povey MJ, Mason TJ (1998) Ultrasound in food processing. Blackie Academic and Professional, London
28. Hecht E (1996) Physics: calculus (445–450, 489–521). Brooks/Cole, Pacific Grove
29. Ashokkumar M, Lee J, Kentish S, Grieser F (2007) Bubbles in an acoustic field: an overview. Ultrason Sonochem 14:470–475
30. Elder SA (1959) Cavitation microstreaming. J Acoust Soc Am 31:54–64
31. Lin HY, Thomas JL (2004) Factors affecting responsivity of unilamellar liposomes to 20 kHz ultrasound. Langmuir 20:6100–6106
32. Simon RD (1974) The use of an ultrasonic bath to disrupt cells suspended in volumes of less than 100 μliters. Anal Biochem 60:51–58
33. Hagenson LC, Doraiswamy L (1998) Comparison of the effects of ultrasound and mechanical agitation on a reacting solid–liquid system. Chem Eng Sci 53:131–148
34. Luche JL, Bianchi C (1998) Synthetic organic sonochemistry. Plenum Press, New York
35. Lee J, Tuziuti T, Yasui K, Kentish S, Grieser F, Ashokkumar M, Iida Y (2007) Influence of surface-active solutes on the coalescence, clustering, and fragmentation of acoustic bubbles confined in a microspace. J Phys Chem C 111:19015–19023
36. Garbellini GS (2012) Ultrasound in electrochemical degradation of pollutants. InTech Rijeka, Croatia, 205–226
37. Mason T, Paniwnyk L, Lorimer J (1996) The uses of ultrasound in food technology. Ultrason Sonochem 3(3):S253–S260
38. Ashokkumar M, Mason TJ (2007) Sonochemistry. Kirk-othmer encyclopaedia of chemical technology. Wiley, New York
39. Mason TJ, Lorimer JP (2002) Applied sonochemistry. Wiley-VCH, Weinheim
40. Kentish S, Ashokkumar M (2011) The physical and chemical effects of ultrasound. In: Ultrasound technologies for food and bioprocessing. Springer, New York, pp 1–12

41. Ashokkumar M, Sunartio D, Kentish S, Mawson R, Simons L, Vilkhu K, Versteeg CK (2008) Modification of food ingredients by ultrasound to improve functionality: a preliminary study on a model system. Innovative Food Sci Emerg Technol 9:155–160
42. Aleixo PC, Júnior DS, Tomazelli AC, Rufini IA, Berndt H, Krug FJ (2004) Cadmium and lead determination in foods by beam injection flame furnace atomic absorption spectrometry after ultrasound-assisted sample preparation. Anal Chim Acta 512:329–337
43. Bermúdez-Aguirre D, Mobbs T, Barbosa-Cánovas GV (2011) Ultrasound applications in food processing. In: Ultrasound technologies for food and bioprocessing. Springer, New York, pp 65–105
44. Chivate M, Pandit A (1995) Quantification of cavitation intensity in fluid bulk. Ultrason Sonochem 2:S19–S25
45. Alzorqi I, Manickam S (2015) Effects of axial circulation and dispersion geometry on the scale-up of ultrasonic extraction of polysaccharides. AIChE J 61:1483–1491
46. Horst C, Chen YS, Kunz U, Hoffmann U (1996) Design, modelling and performance of a novel sonochemical reactor for heterogeneous reactions. Chem Eng Sci 51(10):1837–1846
47. Soudagar S, Samant S (1995) Semiquantitative characterization of ultrasonic cleaner using a novel piezoelectric pressure intensity measurement probe. Ultrason Sonochem 2:S49–S53
48. Gonze E, Gonthier Y, Boldo P, Bernis A (1998) Standing waves in a high frequency sonoreactor: visualization and effects. Chem Eng Sci 53:523–532
49. Wasser SP (2005) *Reishi* or *Ling Zhi* (*Ganoderma lucidum*). Encyclopaedia of dietary supplements, Marcel Dekker, New York, pp. 603–622
50. Claver IP, Zhang H, Li Qin Z, Huiming Z (2010) Optimization of ultrasonic extraction of polysaccharides from Chinese malted sorghum using response surface methodology. Pak J Nutr 9(4):336–342
51. Hromadkova Z, Ebringerova A, Valachovič P (1999) Comparison of classical and ultrasound-assisted extraction of polysaccharides from *Salvia officinalis L.* Ultrason Sonochem 5(4):163–168
52. Hromadkova Z, Ebringerova A, Valachovič P (2002) Ultrasound-assisted extraction of water-soluble polysaccharides from the roots of *valerian* (*Valeriana officinalis L.*). Ultrason Sonochem 9(1):37–44
53. Cheung YC, Siu KC, Liu YS, Wu JY (2012) Molecular properties and antioxidant activities of polysaccharide–protein complexes from selected mushrooms by ultrasound-assisted extraction. Process Biochem 47(5):892–895
54. Li JW, Ding SD, Xl D (2007) Optimization of the ultrasonically assisted extraction of polysaccharides from *Zizyphus jujuba cv. jinsixiaozao*. J Food Eng 80(1):176–183
55. Zhao L, Dong Y, Chen G, Hu Q (2010) Extraction, purification, characterization and antitumor activity of polysaccharides from Ganoderma lucidum. Carbohydr Polym 80(3):783–789
56. Huang SQ, Li JW, Wang Z, Pan HX, Chen JX, Ning ZX (2010) Optimization of alkaline extraction of polysaccharides from *Ganoderma lucidum* and their effect on immune function in mice. Molecules 15(5):3694–3708
57. Shi M, Zhang Z, Yang Y (2013) Antioxidant and immunoregulatory activity of *Ganoderma lucidum* polysaccharide (GLP). Carbohydr Polym 95(1):200–206

Ultrasound Processing of Milk and Dairy Products

Jayani Chandrapala

Contents

Abstract

The application of ultrasound to conventional dairy processes has the potential to provide significant benefits to dairy industry such as possible cost savings and improved product properties. Moreover, the appeal of ultrasound as a processing technique has been regarded safe compared to other emerging technologies. During the past decade, the technology has rapidly emerged as a mild nonthermal

J. Chandrapala (✉)

Advanced Food Systems Unit, College of Health and Biomedicine, Victoria University, Werribee, VIC, Australia

e-mail: Janage.Chandrapala@vu.edu.au

processing tool capable of replacing or assisting many conventional dairy processing applications such as inactivation of microbes and enzymes, homogenization and emulsification, creaming, crystallization, and functionality modifications within dairy systems. These aspects are highlighted in this chapter.

Introduction

Low-frequency, high-power ultrasound induces strong cavitation effects that influence the physical, mechanical, or chemical/biochemical properties of food systems [1]. In contrast, high-frequency low-power ultrasound generates physical effects that are comparatively gentle and can be utilized for noninvasive analysis, monitoring food materials, and nondestructive separations of multicomponent mixtures [2]. The application of high-power ultrasound in dairy processing may lead to the generation of physical forces that include cavitation, acoustic streaming, acoustic radiation, shear, micro-jetting, and shockwaves and chemical reactions that include the generation of very small amount of highly reactive radicals [3]. Both the physical forces and chemical effects are utilized in some applications while most dairy applications concentrated in solely utilizing the physical forces.

Microbial Inactivation

The dairy industry most commonly uses heat treatment to inactivate microorganisms as a means of preservation and ensuring food safety. However, thermal treatment causes significant changes to the composition and surface properties of the colloidal particles present and alters the physical properties of milk. Some changes such as those used to improve the texture of products like yogurt are desirable, while gel formation during the manufacture of ultrahigh temperature milk is highly undesirable [4]. Hence, novel preservation technologies that maintain the quality of milk have attracted some interest within the dairy industry. This trend toward the development of ultrasound as an alternative nonthermal technique is further driven by other advantages including reduced energy consumption, ability to target specific organisms, and no requirement for the introduction of preservatives [5].

Intense power and long contact times are required to inactivate microorganisms at ambient conditions in real food systems when ultrasound is applied alone [6, 7]. Hence, recent improvements recognize the combination of more than one established technique in combination with ultrasound such as heat

(thermosonication, TS), pressure (manosonication, MS), or heat and pressure (manothermosonication, MTS) and provide enhanced benefits for microbial inactivation. The effectiveness of microbial inactivation by these methods is dependent on the amplitude of the ultrasonic waves, exposure/contact time, volume of food being processed, the composition of the food including the types and initial number of the microbes present, and their aggregate state, viscosity of the medium, and the treatment conditions.

D'Amico et al. [8] showed that ultrasound treatment combined with mild heat (57 °C) for 18 min resulted in a 5-log reduction of *L. monocytogenes* in milk and a 5-log reduction in the total aerobic bacteria in raw milk. Juraga et al. [9] investigated the inactivation of *Enterobacteriaceae* in raw milk with the use of high-intensity ultrasound. Temperature (20 °C, 40 °C, and 60 °C), amplitude (120, 90, and 60 μm), and time (6, 9, and 12 min) were varied in the study. The results indicated significant inactivation of microorganisms under longer period of treatment with ultrasonic probe particularly in combination with higher temperature and amplitude. Use of ultrasound at 124 μm amplitude was effective without heat against spoilage microorganisms and potential pathogens including *E. coli*, *Pseudomonas fluorescens*, and *L. monocytogenes* even when inoculum loads of five times higher than permitted were present in raw and pasteurized milk [6]. In this study 100 % *E. coli* within 10 min, 100 % *Pseudomonas fluorescens* within 6 min, and 99 % *L. monocytogenes* within 10 min were reduced (Fig. 1). *Listeria monocytogenes* and *E. coli* were also thermosonicated in milk by others [10–12]. Gera and Doores [12] not only showed that pulsed sonication at 24 kHz caused mechanical damage to the bacterial cell wall and cell membrane when treated at temperatures between 30 °C and 35 °C but milk had a microbial protective effect with lactose exerting the most positive effect on bacterial survival. In a separate study, the synergistic effect of heat (63 °C) combined with sonication (24 kHz) was used to inactivate *Listeria innocua* and reduce the *mesophilic* bacteria count in raw whole milk by 0.69 log after 10 min and 5.3 log after 30 min [13] resulting in an extended shelf life [14]. Treating UHT milk with the same sonication parameters (63 °C and 24 kHz) prevented *mesophilic* growth higher than 2 log during ambient and refrigerated storage for 16 days [15]. Many documented outbreaks associated with infant formula are linked to *Cronobacter sakazakii*. Thermosonication at 20 kHz and temperatures up to 50 °C were used to inactivate *Cronobacter sakazakii* and reduce the microbial count in reconstituted infant formula by up to 7.04 $\log_{10}$ reduction after 2.5 min of treatment [16]. Thermosonication was also used against *Bacillus subtilis* [17], *Staphylococcus aureus* [18], *Salmonella typhimurium* [19], coliforms, and total plate counts [20] in milk.

Noci et al. [21] investigated the impact of thermosonication (TS) and pulsed electric field (PEF), individually and combined, on the survival of *Listeria innocua* 11288 (NCTC) in milk. TS (400 W, 160 s) without preheating declined *L. innocua* by 1.2 log10 cfu mL^{-1}, while shorter treatment times produced negligible inactivation. This highlighted the fact that TS was a hurdle rather than an effective standalone treatment [21]. Gabriel et al. [22] established the inactivation behavior

a

b
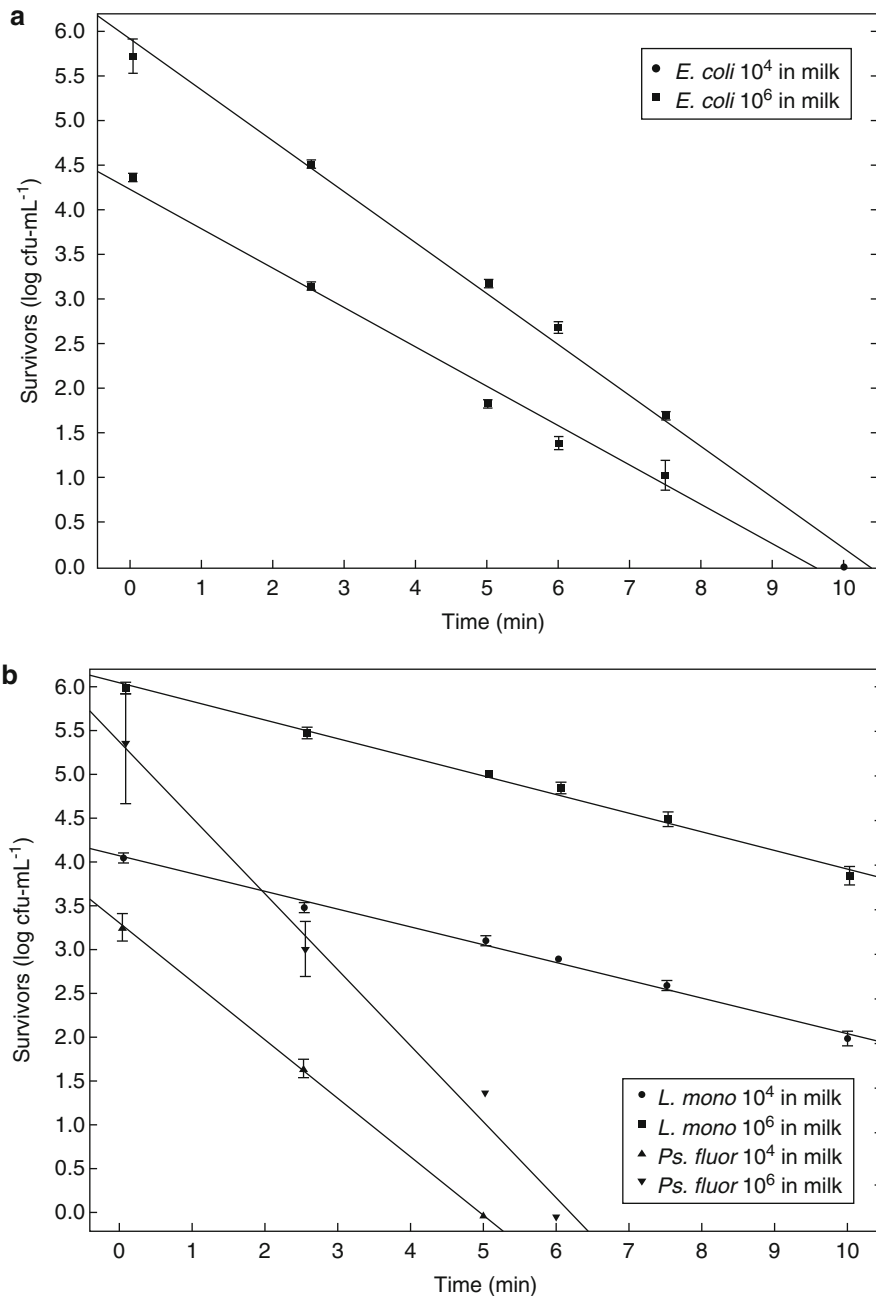
Fig. 1 The impact of ultrasonication at 20 kHz on (**a**) *Escherichia coli*, (**b**) *Listeria monocytogenes*, and *Pseudomonas fluorescens* at different starting concentrations in UHT milk [6]

of *Listeria monocytogenes* in nonfat, low-fat, and full-cream milk treated with multifrequency *Dynashock* ultrasound. Inactivation in all samples was biphasic, with an inactivation lag phase where injury accumulated, prior to log-linear inactivation phase. *L. monocytogenes* exhibited shortest lag phase of 20.57 min in full-cream milk. *L. monocytogenes* exhibited slowest log-linear inactivation rate of -0.24 log colony-forming unit cfu/min in full-cream milk and fastest inactivation rate of -0.37 log cfu/min in low-fat milk. Inactivation rate was slowest in full-cream milk at -0.24 log cfu/min and fastest in low-fat milk at -0.37 log cfu/min. Corrected decimal reduction time was shortest in full-cream milk at 24.81 min, followed by those in nonfat and low-fat milk at 29.17 and 30.64 min, respectively.

The main mechanism responsible for the ultrasonic microbial deactivation is the physical forces generated by acoustic cavitation. The asymmetric collapse of a cavitation bubble leads to a liquid jet rushing through the center of the collapsing bubble. Microorganisms that have hydrophobic surfaces will promote the collapse of cavitation bubbles on the surface and lead to severe damage of the cell wall (Fig. 2). Similarly, microstreaming effects can lead to the erosion of cell walls, again resulting in inactivation of the microorganisms. The effects of localized heating, free radical production causing DNA damage which in turn causes thinning of cell membranes are also crucial in the inactivation [23, 24]. Furthermore, the presence of a thick bacterial capsule (biopolymer layer) prevents cavitation bubbles from collapsing near the plasma membrane thus preventing the breakup of the bacterial cell [25]. On the other hand, the presence of a highly hydrated capsule may help absorbing the mechanical forces exerted on the bacterial cell. Gao et al. [25] proposed to consider the thickness and softness of the bacteria capsules as one of the most important parameters when using high-power ultrasound for the deactivation microbes.

Some microorganisms, in particular bacterial spores, are more resistant under certain conditions than others, and achieving inactivation can be relatively difficult. *Bacillus* and *Clostridium* spores were found to be more resistant to heat and similarly resistant to ultrasound [26]. Raso et al. [27] investigated the inactivation of *Bacillus subtilis* spores by ultrasonic treatments under pressure and combined pressure and heat treatment conditions. They showed that manosonication (MS) treatment at 500 kPa and 117 μm of amplitude for 12 min inactivated $\sim 99\%$ of the *B. subtilis* spore population. MS treatment (20 kHz, 300 kPa, 70 °C, 12 min) at 90 μm amplitude inactivated 75 % of the *B. subtilis* spore population; the same treatment at 150 μm amplitude inactivated 99.9 % of this population. The MS treatments at temperatures higher than 70 °C, which is manothermosonication (MTS), also led to more spore inactivation. In the range 70–90 °C, the combination of heat with a MS treatment (20 kHz, 300 kPa, 117 mm, 6 min) had a synergistic effect on spore inactivation. Table 1 highlights some other literature that has investigated the influence of different parameters on microbial inactivation of different dairy systems with the use of ultrasound.

The demand for food safety projected to rise annually in the world. The major trends associated with consumers in future are toward the use of dairy products that
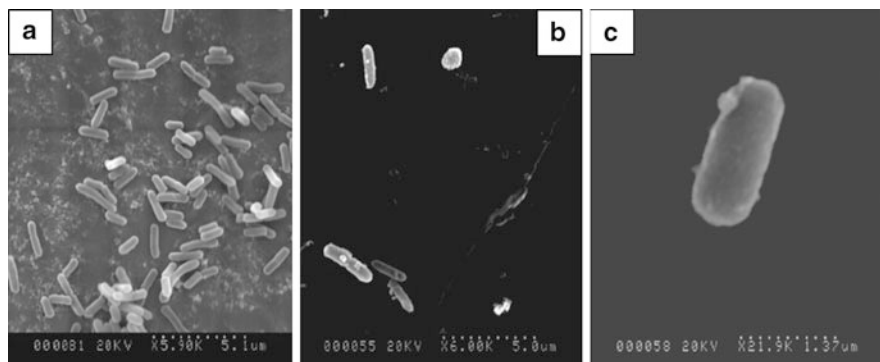
Fig. 2 SEM images of *L. Innocua* cells inoculated in raw whole milk (**a**) without treatment; (**b**) after 10 min of thermosonication treatment (63 °C and 120 μm) (20 kV, magnification 5.9 K); (**c**) closer view of a cell after treatment (20 kV, magnification 21.9 K) [28]

are less "heavily" preserved, high quality, more convenient, more "natural", free from additives, nutritionally healthier, and still with high assurance of microbiological safety. Ultrasound is a nondestructive-targeted technique without introducing preservatives. However, current research to enhance microbial inactivation in dairy systems by ultrasound is focused mostly in combination of another technique or combining ultrasound with other preservation factors [29] and moreover conducts in small-scale operations. Hence, the industry transition is yet to accelerate within the companies.

Enzyme Inactivation

Thermo-resistant enzymes in milk such as lipases and proteases that withstand UHT treatment can reduce the quality and shelf life of heat-treated milk and other dairy products. The potential of ultrasound to inactivate food enzymes has mostly been studied in model systems. General trends observed from all these studies suggested that thermo-labile enzymes were more sensitive to ultrasonication than heat-resistant enzymes. Such enzymes have been efficiently inactivated at tenfold the rate of thermal treatment alone, by MTS (20 kHz, 145 μm amplitude, and 650 kPa for protease, 117 μm amplitude and 450 kPa for lipase, 109–140 °C) treatment [32]. Molecular size and structure are thought to play a role in the sensitivity of enzymes to MTS, with large and less globular enzymes displaying more sensitivity [33].

The effectiveness of ultrasound for control of enzymatic activity is strongly influenced by many factors such as enzyme concentration, temperature, pH, and composition of the medium including treatment volume and gas concentration and processing variables such as sonotrode type and geometry, frequency, and acoustic energy density [34]. Enzyme inactivation generally increases with increasing US

Table 1 Some literature data on microbial inactivation in milk systems with regard to different parameters and combination of techniques

Target parameters	Food matrix	Target microbes	Conditions	Comments	Reference
Presence of butter fat	Fat-free milk Whole milk	L. innocua	400 W, 24 kHz, 63 °C/ 30 min 200 μm amplitude	Inactivation occurs in fat-free milk. Inactivation increased with increase in fat content. Mechanism: adhering of microbes to the newly formed fat globules and protected either by rough surface of the fat globules or by concealments within the globules providing a protective fat layer	[13]
Thermosonication (TS)	Raw whole milk	L. innocua Mesophilic bacteria	400 W 24 kHz	Pasteurization reduced 0.69 log and 5.5 log after 10 and 30 min. Combined with US 5 log reduction was achieved after 10 min	[14]
Thermosonication (TS)	Milk		400 W, 24 kHz, 63C 30 min Energy delivered: 129 mW/ml	Increased shelf life. Viable option for pasteurization	[30]
Different media Presence of lactose, casein, and β-LG	Whole milk Skim milk SMUF Phosphate buffer	E. coli L. monocytogenes	85 W/cm^2 24 kHz, 100 μm amplitude, pulsing 80 %	D values of 2.43, 2.4, 2.19 and 9.3, 8.61, 7.63 min for E. coli and L. monocytogenes was obtained, respectively, with whole, skim, and phosphate buffer. Presence of lactose showed significantly higher D values. Mechanism: stabilization of the bacterial membrane and proteins by lactose or accumulation of compatible solutes in the presence of lactose	[12]
Temperature Amplitude Time	Milk	S. aureus E. coli	20 kHz	Optimum conditions: T = 59.99 °C, time = 12 min, amplitude = 117.27 μm to S. aureus, and 110.41 μm to E. coli. Longer periods of time and with higher amplitude and temperature increased the inactivation of microbes	[31]

power, frequency, exposure time, amplitude, temperature, and pressure but decreases as volume of sample increases [35]. It has been reported that enzyme inactivation increases with an increase in solid content and decreases with increase in enzyme concentration [7]. No effect on milk enzymes was observed when ultrasound was applied without thermal treatment. However inactivation effects were reported when sonication was carried out above 61 °C. Similarly, TS (150 W, 20 kHz, 120 μm amplitude, 30–75.5 °C, 40.2–102.3 s) was reported to be more effective at inactivating milk enzymes (alkaline phosphatase, lactoperoxidase, and γ-glutamyl transpeptidase) than heat alone. However, the extent of inactivation was both enzyme and media specific [7]. Several studies have demonstrated that the effect of ultrasonic waves increases at higher total solid concentration [35]. In skim milk, the concentration of solids is lower than in whole milk resulting in a reduced ultrasonic effect. However, the concentration of enzymes in skim milk (alkaline phosphatase (AP) and gamma-glutamyl transpeptidase (GGTP)) is also lower than in whole milk leading to a more pronounced effect, as these enzymes are linked to fat globules and can be liberated by the ultrasound effect to the serum phase. As an example, the enhanced decrease of enzyme activity in whole milk than in skim milk by the effect of ultrasound and heat (75.5 °C; 102.3 s) could be due to the higher concentration of solids in the former [7]. Ertugay et al. [36] reported greater inactivation of LPO and AP enzymes which have a significant function in dairy processing at 40 °C compared to 20 °C.

According to the literature, inactivation of monomeric enzymes generally involves either defragmentation of the enzyme or formation into aggregates [37], whereas polymeric enzymes tend to fragment into monomeric subunits during ultrasonication primarily attributed to cavitation. In addition, the extreme agitation created by microstreaming could disrupt van der Waals interactions and hydrogen bonds in the polypeptide, causing protein denaturation [38]. Prolonged exposure to high-intensity ultrasound has been shown to inhibit the catalytic activity of a number of food enzymes due to the intense pressures, temperatures, and shear forces generated by the ultrasonic waves which denature protein. Özbek and Ülgen [39] reported that ultrasonic inactivation mechanisms depend on amino acid composition and the conformational structure of the enzyme. For example, splitting of the heme group from peroxidase by MTS was reported to inactivate the enzyme [40], while free radical-mediated deactivation of lipoxygenase by MTS was reported [41]. On the other hand, the inactivation of trypsin has been partly attributed to the large interfacial area created by ultrasound, which disrupts hydrophobic interactions and hydrogen bonds [38].

The combination of sonication with heat can assist thermal processing by reducing the thermal resistance of various enzymes. However, in some cases, solutions containing enzymes have been found to have increased activity following short exposures to ultrasound [1]. This may be due to the ability of ultrasound to break down molecular aggregates, making the enzymes more readily accessible for reaction. Therefore the key enzymes of concern to each dairy system should be investigated to ascertain the critical control parameters which can be specific to the enzyme, the dairy system, or both.

Homogenization

High-pressure homogenization is the most used technique within the dairy industry. In recent years, the use of ultrasound has attracted much interest [42–44] compared to microfluidization and high shear mixing due to its lower processing times and its controllable nature toward a desired favorable output [45]. However, there remains some uncertainty as to which technique is more efficient for homogenization and the primary mechanism for its effectiveness. Koh et al. [46] found that shear forces generated in the absence of cavitation were mainly responsible for homogenization effects with the use of high-pressure homogenization. Similar effects were found by the authors with the use of high-intensity ultrasound highlighting the minor contribution from cavitational effects toward homogenization. However, the efficiency of sonication toward homogenization is driven by several important factors such as power, frequency, amplitude, diameter of the ultrasonic probe, and the composition of the medium being sonicated.

High-power, low-frequency milk homogenization reporting a reduction in the size of milk fat globules has been widely studied [42–44]. Bermúdez-Aguirre et al. [30] showed that ultrasonic homogenization (400 W, 24 kHz, using a 22 mm probe) of milk at 63 °C for 30 min reduced the diameter of the milk fat globules to < 1 μm compared to the native fat globule size of 4.3 μm. Villamiel and de Jong [7] reported a milk fat globule size reduction of up to 82 % during continuous flow, high-intensity (150 W, 20 kHz, using a Branson sonifier with 18.76 mL cavity) ultrasonication of milk. Bosiljkov et al. [43] showed that an increase of the amplitude (20, 60, and 100 %) and time (2–15 min) of ultrasound (30 kHz, using 7 and 10 mm probes) significantly influenced the degree of homogenization of milk. Sonication disrupts the milk fat globule membrane (MFGM) and the resulting fat globules become heavily coated by proteins [30, 47]. Michalski et al. [47] stated that these complexes are stabilized neither by calcium bridges nor by hydrogen bonds, but through association of casein hydrophobic regions with lipid particles and possibly whey proteins. They further presumed that its αs_{2-} and κ-caseins are more likely to be involved in the complex. Fox et al. [48] suggested that van der Waals forces can also exist within casein–fat interactions.

High-fat dairy systems responded differently to sonication. This different behavior is totally dependent on processing conditions such as temperature, energy delivered, and processing times. Vijaykumar [49] studied the effect of thermosonication (60 °C, 20 kHz, 107–152 μm amplitude for 1–3 min) on cream samples containing 45.5 % fat content. They found increased viscosities where they attributed it toward the swelling of proteins. Cavitation caused by sonication can denature the proteins where it losses the tertiary structure or unfolding of globular proteins which in turn swells up resulting in increased hydrodynamic radius and greater molecular associations and thereby leads to viscosity increases. Furthermore, they stated that the specific area of fat globules of cream samples increased from 1.8–10.8 $\mu m^2 g^{-1}$ with thermosonication at 152 μm for 1 min.

Use of ultrasound as a homogenization technique in dairy processing is one of the limited number of processes that are mature enough to be implemented by the dairy

industry in large scale. With the development of large-scale equipment customized for specific dairy processing applications (Prosonix & Hilscher), it is anticipated that more work will be implemented by the dairy industry in coming years.

Creaming

Milk fat separation is a key process in producing some dairy products such as butter, cheese, yogurt, and skim milk. This is typically performed in large scale by centrifugal separators operated at high temperatures to maximize the separation efficiency. Juliano et al. [50, 51] used high frequencies (>400 kHz) than those associated with conventional food processing to destabilize fat and assist creaming in batch systems ranging in scale from mL to L as an alternative separation technology that can enhance the rate of milk creaming by gravitational sedimentation. This may provide advantages such as lower maintenance, less cleaning costs, and lower energy usage as it reduces the residence time of milk inside the ultrasonic separator. Moreover, no disturbance on the structure of fat globules is considered as an important aspect [2].

Leong et al. [52] established suitable ultrasonic parameters that enable successful separation of natural whole milk in large scale, demonstrating the importance of energy density and effectiveness of high-frequency ultrasound (1 and 2 MHz) to separate the small fat globules distributed in milk ($\sim$4 μm diameter) (Fig. 3). Furthermore, it was demonstrated that operation in the temperature range of around 25–40 °C is more optimal to the fat separation process due to the influence of temperature on the physical properties of the fat globules such as density, viscosity, and liquid/solid ratio [53]. When an ultrasonic standing wave is set up in a container, the fat globules distributed in the milk experience acoustic radiation forces that cause them to migrate specifically to the pressure antinodes. Since the acoustic forces are proportional to (radius)^3, the speed of response of the particles is a function of (radius)^2. Therefore larger particles will be driven to the node faster than smaller particles. As higher proportion of larger globules been represented by fat globules, then it's easy to separate the fat globules in milk (Fig. 3). The acoustic forces can be manipulated by adjusting the applied frequency and energy density.

One possible concern when using high-frequency ultrasound for the separation of milk fat is the potential for oxidation of fat to occur (i.e., lipolysis). Lipid oxidation and development of rancid off-flavors may greatly decrease the acceptability of lipid-containing dairy products. Consequently, ultrasound may have a detrimental effect on lipid functionality and integrity by promoting radical-driven oxidation processes which also consequently limit the application of power ultrasound to lipid-containing dairy systems. Juliano et al. [54] have shown that when sonicating milk within this high-frequency range used, oxidative volatiles derived from sonication were detectable above human sensory threshold limits only when very high specific energies were delivered to the milk. In contrast, Torkamani et al. [55] showed no significant oxidation of fat with sonication of cheddar cheese whey at similar frequencies and energy densities.

Fig. 3 Microscopy images obtained of (i) initial milk samples, (ii) bottom and (iii) top products after 20 min of sonication, with 1 MHz and sound source to reflector distance of 45 mm [52]
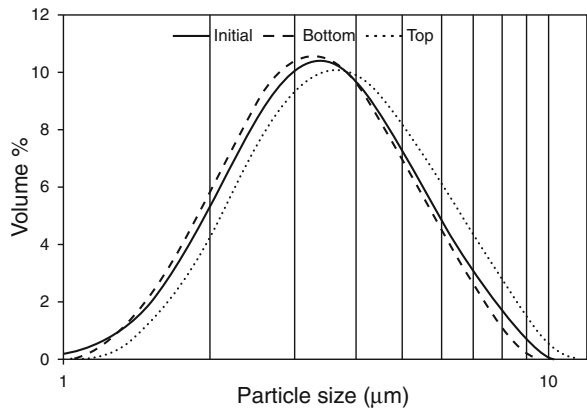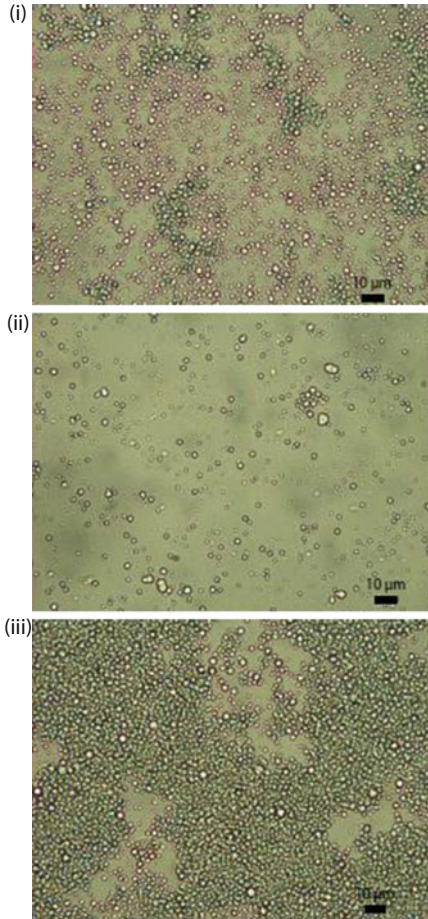
Another concern for using high-frequency ultrasound is the potential for alteration of fatty acids within the systems. The type of lipids that are present in foods is becoming of great importance to food manufacturers due to concern about "good" and "bad" lipids. Leong et al. [56] found that there was minimal production of monoglycerides and diglycerides upon sonication of triglyceride containing emulsions. Furthermore, Pandit and Joshi [57] found that high-energy inputs ($\sim$1000 J/mL) were required for hydrolysis of fatty oils by cavitation. However, lipids may also indirectly be modified by application of high-intensity ultrasound by influence the activity of lipases that may be used to alter lipids in milk systems.

Hence, these small-scale studies showed promising signs in using ultrasound as a fat separation technique within the dairy industry without any concerns. However, the cost involved within the initial stages of manufacturing ultrasonic equipments is of a hurdle for the dairy industry to embrace this technology in the near future.

Emulsification

Emulsification in dairy industry has been used through mechanical shaking, colloid mills, high- or ultrahigh-pressure homogenization, and microfluidization. However, ultrasonic emulsification offers several benefits over conventional emulsification methods such as improved energy efficiency, higher emulsion stability, lowered requirement of surfactants, and narrow-size distributions under controllable conditions [58, 59]. As an example, Jafari et al. [45] showed that increasing the microfluidization energy input beyond moderate pressures (40–60 kPa) led to overprocessing of emulsion droplets due to coalescence and found that decrease in emulsion droplet size <0.5 μm by microfluidization was not possible. In contrast, increased energy input helped to reduce emulsion droplet size with minimum re-coalescence of new droplets with US emulsification.

Ultrasound-assisted emulsification is influenced by many variables such as irradiation power, position of the ultrasonic source with liquid–liquid interface, tip diameter, vessel size, viscosity of the continuous phase, pre-emulsification, oil–water ratio, surfactant concentration, hydrostatic pressure, presence of dissolved gases, and exposure time [58–60]. Ultrasonic emulsification is primarily driven by cavitation, wherein collapse at or near the oil–water interface bubble causes disruption and mixing of the two phases, resulting in the formation of very fine emulsions [61]. Shear forces generated are very strong at low frequencies (e.g., 20 kHz) compared to 211 kHz, whereas an efficient emulsification is obtained at 20 kHz while a similar experiment at 211 kHz does not produce an emulsion. Only high-intensity, low-frequency ultrasound (16–100 kHz) is able to produce emulsions. Leong et al. [56] showed that pressures up to 400 kPa improved the efficiency of ultrasonic emulsification of food oils, whereas operating with ambient pressures over 450 kPa suppressed the cavitation activity and no emulsification could be achieved. Increasing the amount of gas in the system tends to increase the gas/vapor pressure ratio inside the bubbles which can cushion the bubble collapse and hence reduce the

shock wave intensity and thereby be less efficiently emulsified. In contrast, Behreud and Schubert [60] showed that increased concentration of gas neither influence the magnitude of the cavitational effects per unit volume nor the intensity of the cavitation collapse, although the energy dissipation per unit volume was found to control the particle size distribution of a system.

Recently, Shanmugam and Ashokkumar [62] demonstrated the possibility of incorporating novel food oils into milk systems by ultrasonic emulsification. A 20 kHz ultrasound horn was used to emulsify flaxseed oil in skim milk for delivering as a ready to drink formulae. A minimum process time of 3 min at an applied acoustic power of 176 W was sufficient to produce emulsion droplets with an average diameter of 0.64 μm. Furthermore, they found that those emulsions were stable for 9 days where no addition of surfactants was required to stabilize the emulsion. The authors attributed the stability of the emulsion due to the denatured whey proteins in the sonicated emulsion systems. Furthermore, they attributed the adsorption of proteins toward the emulsion surface stabilized the emulsion droplets due to the electrostatic repulsions and also highlighted the importance of residence time and power density toward achieving stable emulsions.

Although several studies have not been concentrated on formation of emulsions within the dairy industry, the increased trends toward ready to eat and drink dairy products may embrace the ultrasound as a technology toward manufacturing secondary dairy products with extended benefits of such as increased stability and less production times.

Ultrasound-Assisted Filtration

Membrane technology is currently used in the dairy industry for a variety of applications such as separation of milk components, concentration of protein levels prior to spray drying and water purification, and treatment of liquid effluents. One of the critical issues during filtration is the decline in permeate flux as a result of both concentration polarization and membrane fouling. Heat treatment of milk increases viscosity that will result in excessive membrane fouling due to pore blockage and cake formation [63], which in turn has a detrimental influence on the permeation rate and limits the economic efficiency of the processing operation. There are a number of different chemical (use of acid, alkali, enzymes, and hypochlorite) and physical (forward flushing and back flushing) methods currently used for cleaning a fouled membrane. These methods are time consuming, damage the membranes, cause secondary pollution, reduce the lifetime of the membrane, and are unsafe and/or expensive.

The application of ultrasound has proven to be an effective approach to enhance the flux to improve the cleaning of fouled membranes. It can be expected that the increased permeability observed due to sonication may have been affected by the physical processes caused by acoustic cavitation which may occur on the surface of the fouled membrane, on the solid material, and in the vicinity of the pores where the

dislodgement of particles that block the pores can be expected. Lamminen et al. [63] found increases in cleaned flux ratio as the power intensity of the system increased. This increase was attributed to an increase in the number of cavitation bubbles in the system and an increase in acoustic energy in the system by the cavitation bubbles. At the same time, although higher frequencies may have more cavitation bubbles, the bubbles are smaller in size and collapse less energetically; thus, they may not be capable of detaching particles from the cake layer as readily as lower frequencies [63–66]. Although, ultrasound has more positive attributes, cavitation may damage the membrane surfaces. At the highest powers (>12.2 W), some damage to the membrane was observed by Lamminen et al. [63], while at lower applied powers (<7.2 W), no damage to the membrane was found by Muthukumaran et al. [64, 65]. Hotrum et al. [67] hypothesized that non-inertial cavitation (cavitation bubble formation and bubble growth and oscillations) and acoustic streaming would be the main mechanisms of importance for the prevention of fouling of cheese milk whereas inertial cavitation which is the bubble collapse considered as an undesirable phenomenon due to the risk of erosion of equipment surfaces and or changes in the system. On the other hand, non-inertial cavitation induces microstreaming which can enhance the heat transfer, mass transfer, and membrane flux processes. However, they found that surface vibration may serve as a mechanism for prevention of a fouled layer.

Muthukumaran et al. [64] studied the ultrasonic cleaning of polysulfone ultrafiltration membranes fouled with dairy whey solutions. It was suggested that the ultrasonic effect is more significant in the absence of a surfactant but is less influenced by temperature and transmembrane pressure. Their experimental results in the whey ultrafiltration process revealed that ultrasound can significantly enhance the permeate flux, with an enhancement factor of between 1.2 and 1.7 across the full range. An increase of the mass transfer coefficient within the concentration polarization layer was also observed. In another study [65], they extended this aspect to consider the effect of ultrasonic frequency. Their results showed that the use of continuous low-frequency (50 kHz) ultrasound is most effective in both the fouling and cleaning cycles, whereas the application of intermittent high-frequency (1 MHz) ultrasound is less effective. Furthermore, their results showed that continuous low-frequency sonication generally reduces the components of the total flow resistance that are readily reversed during water flush [66]. This included the mass transfer resistance arising from both concentration polarization and labile protein deposits that are readily removed. Some other recent filtrations with the use of ultrasound in dairy processing are highlighted in Table 2.

Another recent study by Koh et al. [68] used a different approach in accompanying ultrasound to reduce the fouling of heat-treated dairy whey systems. They used ultrasound as a pretreatment process to break down big protein particles generated through thermal processing of whey protein solutions in order to improve the downstream ultrafiltration performance. The use of ultrasound followed after a heat treatment reduced membrane pore blockage and growth of the foulant cake layer greatly compared to heat-treated systems that has not been subjected to

Table 2 Some literature on use of ultrasound during filtration with regard to different parameters for dairy systems

Target	Food matrix	Conditions	Comments	Reference
Effects of different sonication modes with different frequencies on permeation flow and fouling during UF	Skim milk	Frequency = 37, 80 kHz, and tandem Modes = continuous, pulsed, sweeping, and degassing	Permeation flow increased with decreasing frequency Pulsed mode had the most effect on enhancement of flux and reduction of fouling percentage	[69]
Effects of ultrasound toward ultrafiltration of whey solution	2 % w/w whey protein solutions	Frequency = 30kHZ UF – cellulose membranes Power = 100 W	Ultrasound decreased the membrane fouling caused by concentration polarization Use of high-power US led to lowered retentions	[70]
Effects of ultrasound toward production and purification of peptides	Milk protein concentrates	Frequency = 20 kHz Power = 800 W Time = 4 min	A successful pilot scale membrane filtration was established as US-enhanced hydrolysis characteristics of proteins	[71]
Effects of ultrasonic waves on flux of MF	Fresh cow milk	Feed pressure = 0.5-0.8-1.4 bar Power = 20, 30, 50 W Distance between probe and surface = 2.6 and 4.4.cm	Higher flux was achieved with 0.5 bar, 40 W distance 2.6 CM Continuous irradiation increased flux by 33 % compared to pulsed irradiation	[72]

ultrasound. The extent of changes to pore blockage and cake growth was greater at higher solid concentration which leads to advantages of using ultrasound for processing of concentrated milk within the dairy industry.

These experiments have shown that the use of ultrasound in membrane processing within the dairy industry is generally positive (Table 2). However, there are conditions under which it can be less effective or even has a negative effect on filtration performance depending on circumstances. At present, the embracement of this technology by dairy industries has found to be slow mainly due to the need of processing line adjustments.

Sonocrystallization

Sonocrystallization is the use of power ultrasound to aid and control crystallization. The most effective sonocrystallization can be achieved when sound energy is delivered at the nucleation phase [73]. The use of ultrasound plays a key role in controlling the crystal structure and shape, decreasing the crystallization induction times, increasing yields, reducing size distribution, and increasing the rate of crystallization, which in combination increase the efficiency of some traditional processes, leading to cost effectiveness [74].

Lactose Crystallization

Lactose which is the most abundant component found in whey waste stream is removed in order to increase the further processing ability of these streams such as spray drying due to the fact that lactose makes the material sticky and thereby hard to process. A typical commercial process for lactose crystallization within the dairy industry can take up to 20 h to achieve a yield of ∼80 % crystallized lactose. Hence, a rapid recovery of lactose by ultrasound-assisted crystallization has been reported [73, 75]. The lactose recovery was found to be much higher.

In a typical reaction, crystallization takes place on the surface of existing crystals and these crystals act as nucleation sites. Cavitation bubbles act as nucleation sites [73, 75]. Shockwaves cause further agitation and bubble disruption increasing the number of nuclei available for nucleation [76], and the greater number of nuclei reduces crystal size, improves uniformity, and increases crystallization rate [77]. The cavitation hot spots where bubbles collapse are thought to be privileged nucleation centers, where the critical energy for crystal formation is decreased. Furthermore, the rapid collapse of bubbles reduces the crystallization temperature and thereby increases super saturation [78]. Even small changes in super saturation were found to significantly reduce the nucleation rate. The application of ultrasound can reduce the metastable zone width (MZW) which provides information for developing a controlled crystallization process, and this can have many significant benefits such as improved control over crystal size and habit. In comparison to mechanical agitation, ultrasound can provide more uniform mixing that can avoid unwanted zones of excessive super saturation in the vessel.

Patel and Murthy [79, 80] used sonocrystallization for lactose recovery from whey waste streams. The crystallization was reportedly completed with yields in the range of 80–92 % within 4 min of sonication. A recent study by Zisu et al. [81] used sonocrystallization at 20 kHz frequency to concentrated whey solutions containing ∼32 % lactose at ∼22 °C in a noncontact approach delivering a low applied energy density that varied between 3 and 16 J/mL. The control solution was passed through the ultrasonic rig at the appropriate flow rate without sonication. Crystallization of lactose in commercially concentrated whey was significantly increased by the application of ultrasound at a low-energy density of 3 J/mL and a flow rate of 2 L/min as can be seen from Fig. 4. Regardless of the sonication intensity and flow rate,
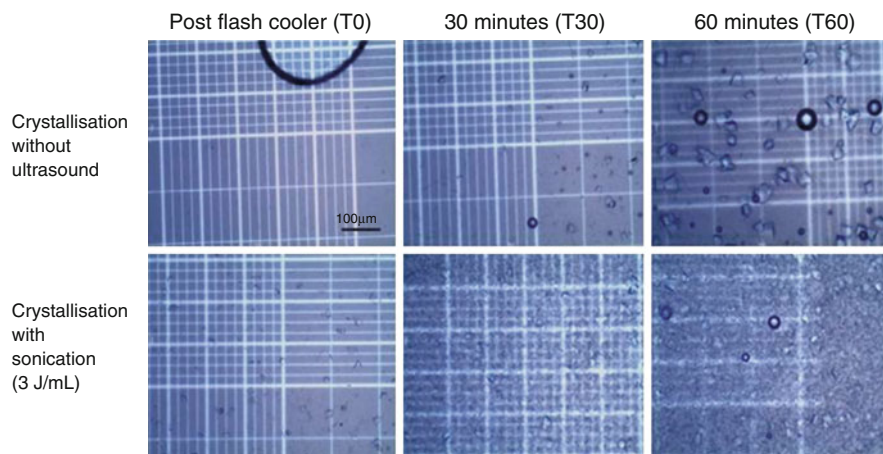
Fig. 4 Concentrated whey viewed under a light microscope at 10× magnification immediately after flash cooling at a flow rate of 2 L/min and after 60 min [81]

the least number of lactose crystals was observed in the control solutions. A greater number of lactose crystals were present in whey immediately after sonication at all energy densities (3–16 J/mL). Ultrasound generated a large number of nuclei resulting in the growth of many small crystals. The rate of sonocrystallization was greater than stirring for approximately 180 min but slowed down between 120 and 180 min as the metastable limit was reached. A second treatment with ultrasound at 120 min delivering an applied energy density of 4 J/mL stimulated further nuclei formation, and the rate of crystallization was maintained for >300 min. Yield on the other hand was limited by the solubility of lactose and could not be improved. The crystal size distribution was narrower than that with stirring and the overall crystal size was smaller. The study highlighted the importance of the conditions used for promoting crystallization.

Fat Crystallization

There has been considerable interest in the application of ultrasound with regard to crystallization of fats within the dairy industry [82, 83]. The crystal size and shape of fats within a product play a significant role to the texture and mouth feel. Martini et al. [82] studied the use of ultrasound as an additional processing condition to alter the crystallization behavior of anhydrous milk fat (AMF). It was shown that ultrasound decreases induction time of crystallization and generates smaller crystals and higher viscosities. However, the effectiveness of this technology depends entirely on the processing conditions. In contrast, Sizuki et al. [83] showed that ultrasound induced primary and secondary nucleations in the lipid, generating smaller crystals and as a consequence resulted in harder materials. Ultrasound affected hardness more efficiently when applied at higher crystallization temperatures (26 °C and 28 °C).

In addition to changes in hardness, AMF networks obtained after sonication were characterized by a steeper and sharper melting profile [83]. This research showed that ultrasound can be used as an additional processing tool to tailor the functional and physicochemical properties of lipids with the potential to be used in the processing of *trans*-free shortenings.

Ultrasound affects the rates of polymorph-dependant crystallization, crystal size, and morphology [82, 83]. A primary effect of sonocrystallization may be due to the high pressure generated when a sonication-induced cavity collapses. The different polymorphic forms have different stabilities that form specifically as a function of the supercooling temperature, mechanism, and lifetime of the collapsing bubbles. This points to the fact that ultrasound irradiation is an effective tool for controlling polymorphic crystallization of fats and reducing induction times. Furthermore, a range of crystal structures can be controlled. This means it is possible to tune the desired texture conditions for a particular dairy product. However, the ultrasound-induced cavitation that produces free radicals appears to have restricted the use of sonocrystallization for systems containing fats and oils, which are susceptible to oxidation by free radicals creating off-flavors [84]. On the contrary, Patrick et al. [85] reported that sonication at 66 kHz did not cause any off-flavor production due to oxidative changes to palm oil. Their results indicate that the optimum conditions for obtaining small crystals in the shortest time period are just below the cavitation intensity threshold.

Ice Crystallization

The ice crystal size directly influences the texture and taste of ice creams which are consumed in a frozen stage. The ice crystals are required to be as small as possible for a desired creamy mouth feel. When US is applied during the crystal growth phase, fragmentation of large crystals under acoustic stress will occur and lead to crystal size reduction. Ice cream contains up to 50 % by volume of entrapped air. Ultrasonic degassing can occur during the application of ultrasound and this process can result in undesirable modifications to the ice-cream texture. Acton and Morris [86] overcame this issue by increasing the initial gas content so that the proportion of air lost due to US can be compensated. But the question that remained unanswered was how much extra air needs to be added to obtain the desired texture.

Furthermore, high-intensity ultrasound may lead to fat oxidation which can lead to off-flavors and improper textures in ice creams. However, by keeping the cooling regime constant, it has been found that the structure of the crystallized product can be adjusted by varying the ultrasonic intensity [87]. Mortazavi and Tabatabai [88] found that application of 20 min-pulsed ultrasound resulted in the best sensory flavor, texture, and mouth feel evaluations of ice creams. Flavor and texture of samples prepared with 5 and 20 min pulse time also had better mouth feel than the control. Hence, the conditions need to be carefully monitored in using ultrasound on ice-cream applications.

The use of ultrasound for crystallization of lactose has been widely embraced by the dairy industry, although fat and ice crystallization aspects still remain in doubt due to its detrimental effects leading to consumer sensory concerns within dairy products. However, more work is needed to get the appropriate conditions optimized specific to a certain dairy product of interest.

Solubility of Dairy Powders

Rapid dissolution of dairy powders is desirable to avoid prolonged processing times, increased production costs, and reduced product quality. Micellar casein (MC) and milk protein concentrates (MPC) have generally poor solubility, which is known to decrease during storage, particularly at high ambient temperature and humidity [89]. The use of shear to accelerate the solubilization of these powders is therefore of interest. Some attempts have been made to produce high-protein dairy powders with increased solubility through the application of static high pressure [90], high shear [91], or ultrasound [91, 92] to concentrates, the addition of sodium caseinate or polydextrose [93], and the addition of mineral salts before drying [94]. A recent study by McCarthy et al. [95] showed that ultrasound (20 kHz/70.2 W) increased the solubilization of MPC powders with ultrasound (20 kHz/70.2 W). However, their study involved a stirring pretreatment step at 50 °C, which aids the dissolution of the powder particles to an extent. However, a thorough investigation of the effects of ultrasound on the dissolution of dairy powders was performed by Chandrapala et al. [96].

Chandrapala et al. [96] work investigates the effect of shear on powder solubilization by examining in detail the behavior of low-solubility MPC and MC powders during ultrasonication and was compared for low-shear overhead stirring, rotor-stator mixing, and high-pressure homogenization (Fig. 5). The initial solubility of the MPC and MC powders was between 60 % and 70 %. Ultrasonication achieved much more rapid solubilization of the powders, with 90–95 % solubility achieved in less than 10 min. The shear forces generated increase the mass transfer at the surface of these particles resulting in an increase in the rate of solubilization. To better contrast the solubilization behavior, the particle size distribution data can be compared for MPC and MC that had achieved approximately 80–100 % powder solubilization (Fig. 6). Ultrasonication appeared to be even more effective than rotor-stator mixing at breaking apart particle aggregates, presumably due to the high localized shear that can be created [97]. The average size of the largest particles was reduced for both MPC and MC powders to about 10–20 μm, with the emergence of a casein micelle peak at 200 nm now evident (Fig. 6). To observe if there were any structural changes to the proteins, native PAGE was performed on MPC solutions sonicated at different time intervals (30 s, 3 min, and 10 min) and compared to powder dissolved by low-shear overhead stirring. Bands representing casein, β-lactoglobulin, and α-lactalbumin and higher-molecular weight proteins such as immunoglobulins and BSA were all observed to remain unchanged after processing
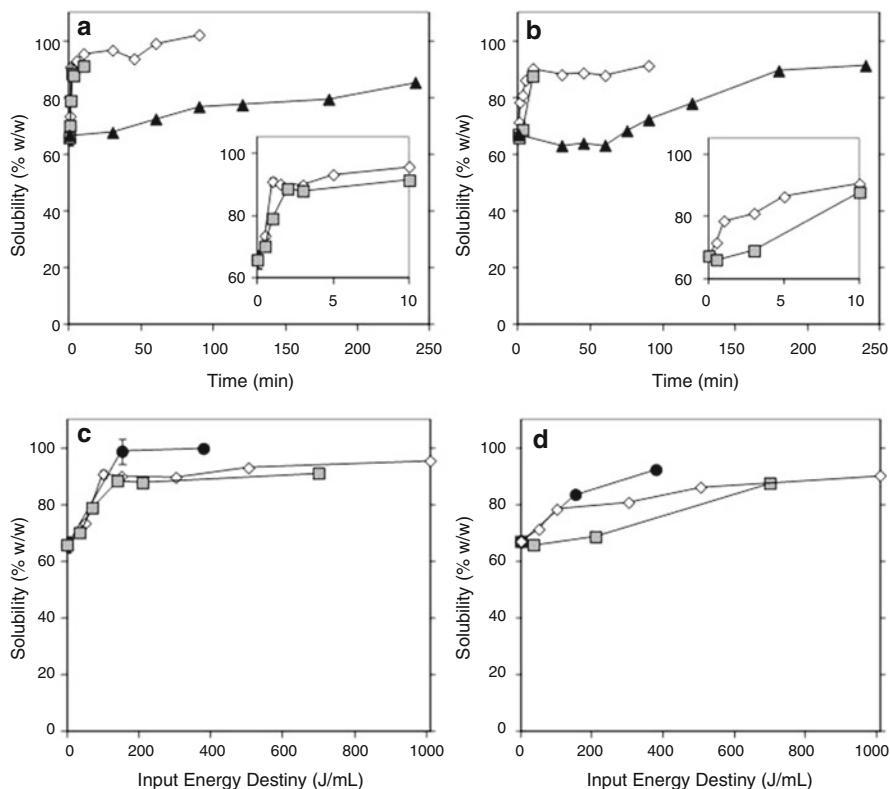
Fig. 5 Rate of solubilization of MPC (**a**) and MC (**b**) powders by sonication (◇), rotor-stator mixing (■), and low-shear overhead stirring (▲) and comparison of solubilization of MPC (**c**) and MC (**d**) powders by sonication (◇), rotor-stator mixing (■), and high-pressure homogenization (●) as a function of energy input [96]

by either sonication or homogenization [96]. This indicates that ultrasound did not have any noticeable effect on the individual protein components in the reconstituted milk or their interactions with each other. The current results suggest that these techniques only affect the large powder particles, increasing their rate of solubilization and disaggregating casein micelles without affecting the protein components liberated during dissolution.

Functionality Modification of Dairy Systems

Viscosity Modifications

Controlling the viscosity of food systems by ultrasound is one of the most promising processes that have been developed due to the facts that the process does not require any chemicals and additives, is simple and rapid, is cost effective, and will not
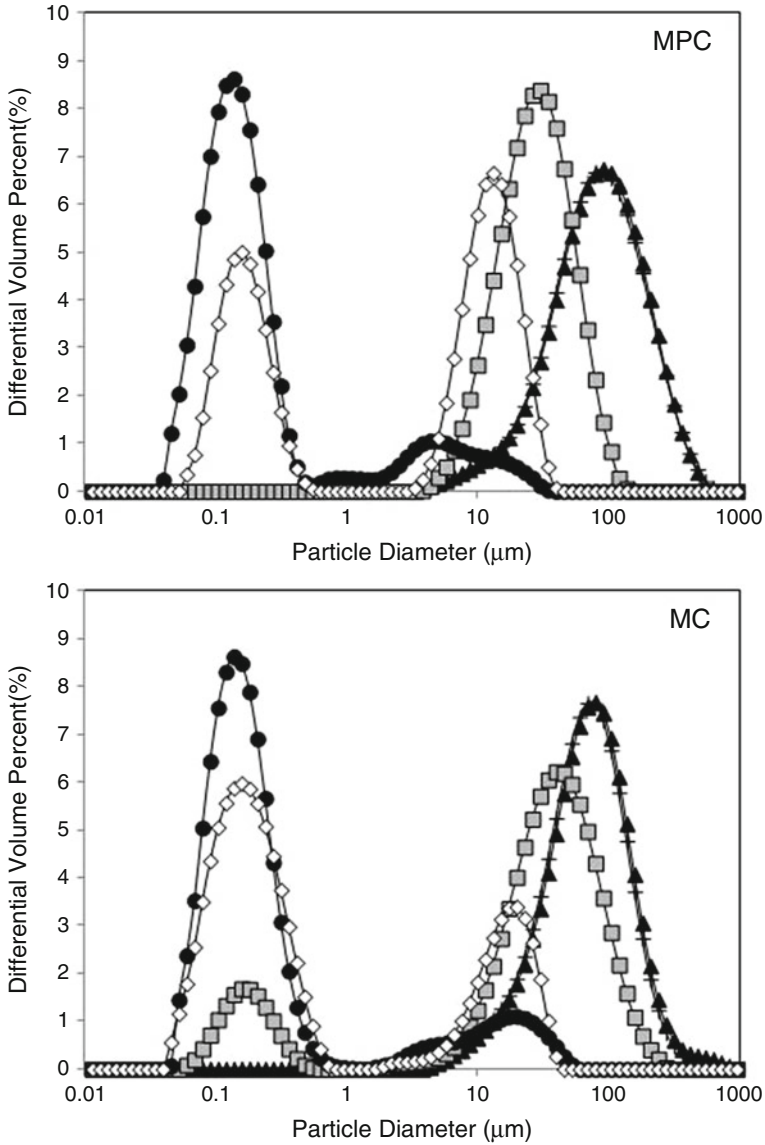
Fig. 6 Comparison of volume-weighted particle size distribution of MPC and MC powders solubilized to between 80 % and 100 % by different methods; ultrasonication (◇; sonicated for 3 min to 89 % and 81 % solubility of MPC and MC), rotor-stator mixing (■; mixed for 3 min and 10 min to 88 % solubility of MPC and MC), high-pressure homogenization (●; homogenized at 80 bar to 99 % and 84 % solubility of MPC and MC), and low-shear mixing time (▲; mixed for 240 min to 86 % and 92 % solubility of MPC and MC) [96]

induce large changes in the chemical structure of particles present in dairy systems which will be of a benefit.

Whey Proteins

During manufacture of whey protein powders, whey protein solutions consisting significantly high levels (4–15 % by weight) of protein are subjected to heat treatment. Issues with significantly increased viscosity of the protein solution ultimately limit the extent to which heat treatment is applied and the total solid concentration that can be used. The viscosity then increases further upon a second heat treatment during manufacture of secondary dairy products. Ashokkumar et al. [98, 99] and Zisu et al. [100] outlined a novel approach to overcome this problem. The application of ultrasound for a very short duration after such a heating step breaks down these aggregates and prevents their reformation on subsequent heating, thereby reducing the viscosity increase that is usually associated with this process (Fig. 7). This functionality (low viscosity) was preserved even after freeze or spray drying and then reconstitution into aqueous solution. Initially, it was argued that these observed viscosity changes might have been caused by the physical or chemical effects of acoustic cavitation. To investigate possible chemical effects due to radical generation, further experiments were carried out in which reconstituted whey protein concentrate (WPC) solutions were sonicated over a range of frequencies (20 kHz to 1 MHz) [98, 99]. It was found that whey solutions sonicated at 20 kHz showed the highest viscosity reductions [99, 100] even though 20 kHz ultrasound formed the least amounts of radicals [101]. The authors therefore attributed the observed viscosity reduction primarily to the physical forces generated during acoustic cavitation.

A thorough understanding of the mechanism of these ultrasound-assisted viscosity modifications was investigated by Chandrapala et al. [102]. The three types of main interactions within protein solutions were investigated: surface charge of the protein aggregates (indicative of electrostatic interactions), reactive thiol groups (indicative of thiol–disulfide interactions), and surface hydrophobicity (indicative of hydrophobic interactions). Interestingly, it was found that surface charge and reactive thiol groups remained unchanged with the sonication step applied in between the preheating and postheating steps (Fig. 8). However, the surface hydrophobicity of these aggregates was altered markedly (Fig. 8). Preheating denatures the whey proteins and thereby exposes the hydrophobic groups. This was indicated by an increase in the surface hydrophobicity of these preheated aggregates. This increase in surface hydrophobicity was greatly reduced with the introduction of a sonication step. It was speculated that sonication broke down the protein aggregate networks through physical shear caused by acoustic cavitation, leading to the formation of smaller aggregates with lower-surface hydrophobicity. These smaller aggregates are resistant toward further aggregation during postheating, thereby improving heat stability.

Similarly, Kresic et al. [103] also investigated the rheological and thermophysical properties of WPC and WPI solutions subjected to sonication. According to these results, the use of ultrasound changed the flow behavior and this was attributed to
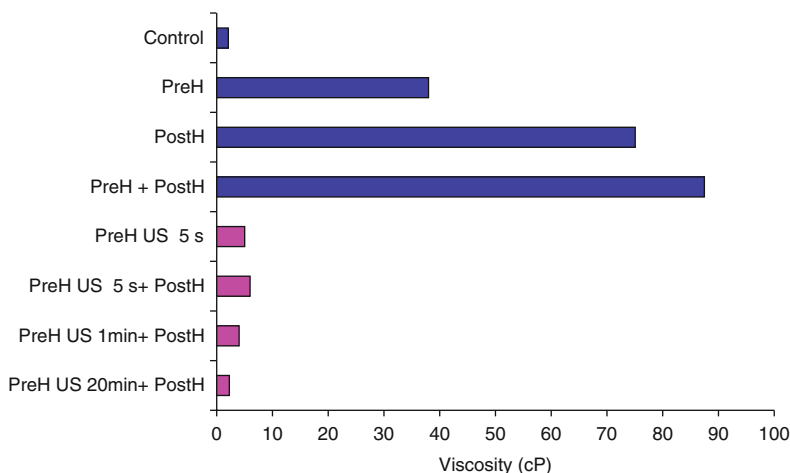
Fig. 7 The effects on solution viscosity for a 6.4 % protein (by weight) solution reconstituted from whey protein concentrate and sonicated with a 20-kHz horn at a calorimetric power of 31 W in a batch mode. Dark gray (*blue*) bars represent solutions without sonication; light gray (*pink*) bars indicate sonicated solutions. *PreH* preheating, *PostH* postheating, *US* sonication [99]

altered protein structure, namely, that the hydrophilic parts of amino acids are opened toward the surrounding aqueous phase, leading to an increased binding of water molecules. There has been some concern that the sonication of proteins in solution can lead to the formation of amyloid-type fragments [104]. This formation was observed when excessively high specific energy was delivered to a small volume. However, recent studies by Chandrapala et al. [105, 106] showed that no significant protein structural changes were observed up to 60 min of sonication, although these minor changes cannot be completely omitted from the observed functional property changes for both complex and model systems.

Casein + Whey Protein Mixtures

Although casein micelles are considered relatively stable particles, their composition and size respond to alterations in pH, temperature, and milk protein concentration [107]. It is possible that the localized high temperatures and shear forces created by sonication can physically alter the casein micelles or their interactions with other milk components. Madadlou et al. [108] found that the average size of reassembled casein micelles could be reduced by exposure to ultrasound (35 kHz frequency) for 6 h provided the pH was above 8. However it is unclear how this relates to native casein micelles since the reassembled casein particles were considerably larger (275 nm) and structurally and functionally different [109]. In another study involving true casein micelles in milk, a decrease in particle size resulting from sonication was observed. This particle size decrease was attributed to a reduction in casein micelle size by the authors, although this was not substantiated [110]. A recent study by Chandrapala et al. [111] showed that sonication did not appear to affect casein micelle size or composition or permanently affect the mineral balance in fresh skim
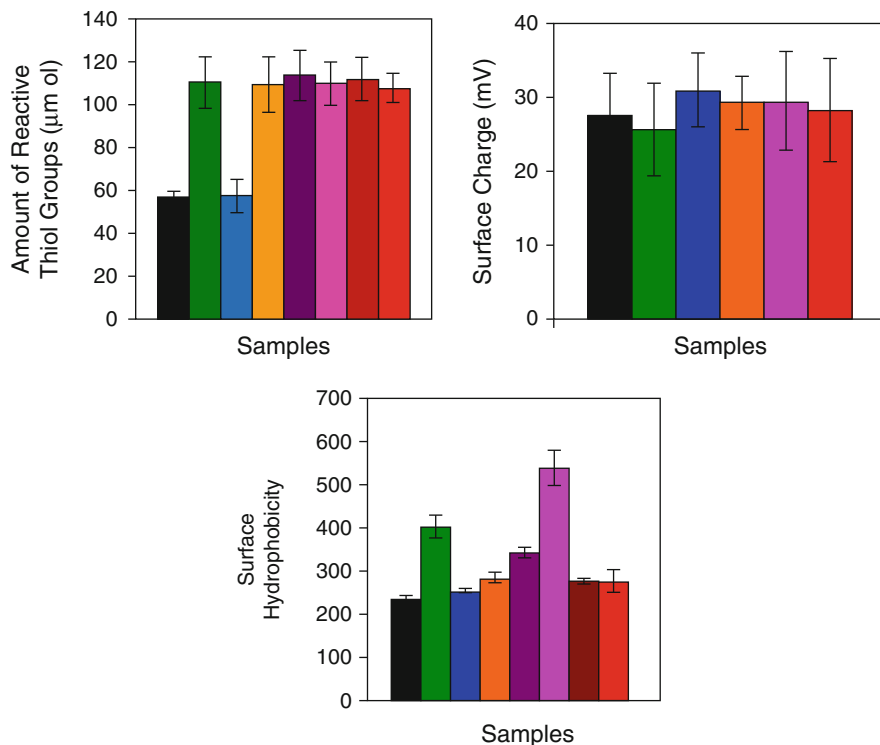
Fig. 8 Reactive thiols (*left*), surface charge (*middle*), and surface hydrophobicity (*right*) of proteins in heat-treated and sonicated 5 % (w/w) reconstituted WPC solutions. Colored bars from *left*: native (*black*), preheat (*green*), sonicated (*blue*), preheat + sonicated (*orange*), post-heat (excluding middle) (*purple*), preheat + post- heat (*pink*), sonicated + post-heat (dark *red*), preheat + sonicated + post-heat (light *red*) [102]

milk. Sonication did however reduce the size of the already small fat globules remaining in skim milk, appeared to break up whey protein aggregates and assisted in breaking apart casein micelle, non-micellar casein, and whey protein aggregates present in reconstituted casein powder systems. The results showed that controlled application of ultrasonic energy can help break up large casein and whey protein aggregates thereby influencing macroscopic properties such as viscosity, without inducing changes to the casein micelles or mineral balance. Similar results were obtained by Shanmugam et al. [112] when using up to 30 min of sonication, but prolonged sonication resulted in the partial disruption of some whey proteins from the whey–whey aggregates. In contrast, Liu et al. [113] found that casein micelles are disrupted at high pH values with sonication. In their study, reconstituted skim milk at 6.7–8 pH was sonicated at a specific energy input of 286 kJ/kg using 20 kHz. According to this study, ultrasound caused greater disruption of casein micelles causing release of proteins from the micellar to the serum phase at high pHs. Furthermore, they showed that the released proteins reassociated to form aggregates

of smaller size but with surface charge similar to that of casein micelles in the original milk. However, in other studies the dissociation of κ-casein was found to be dominant with increase in pH, which can result in an increase to the total protein content in the supernatants [114]. They hypothesized that it is due to a pH-dependent conversion of the native colloidal calcium phosphate (CCP) to an alternative form of calcium phosphate, which is less capable of maintaining the micellar integrity, particularly at higher pH values where the charges of the proteins are greater. Hence, it is arguable as to whether the effects observed by Liu et al. [113] under high pH conditions are just an ultrasound effect or a pH effect and/or a combination of both.

Milk Concentrates

Milk is often concentrated commercially to high solids in preparation for spray drying (typically 40–55 %). However, increasing the solid content, the viscosity of concentrated milk increases with time in a process known as "age thickening" by structural buildup through weak interactions between casein micelles that can be disrupted by mechanical shear [115]. High-power low-frequency ultrasound (20 kHz) has potential industrial application to reduce the viscosity and to control the rate of age thickening of concentrated skim milk. A recent study by Zisu et al. [116] investigated the high-intensity low-frequency ultrasound on concentrated skim milk to lower viscosity through the process of acoustic cavitation. Batch sonication for 1 min at 40–80 W and continuous treatment delivering an applied energy density of 4–7 J/mL reduced the viscosity of medium-heat skim milk concentrates containing 50–60 % solids. Viscosity was reduced by approximately 10 %, but this has improved to 17 % in highly viscous age thickened material. Sonication also showed changes in the shear-thinning behavior at shear rates below 150 s^{-1}. Although ultrasound lowered the viscosity of skim milk concentrated to 50 % solids, the treatment could only delay the rate of thickening once the aging process was established. It was only when ultrasound was activated during concentration that sonication prevented the viscosity of skim milk concentrates from increasing rapidly.

Gel Formation

A key aspect of yogurt is associated with the physical properties of the gel, which should possess a smooth textural character in mouth during consumption along with low serum separation during storage. Vercet et al. [117] studied the use of manothermosonication (MTS), to obtain tailored functional properties of the products. The application of ultrasound allowed elaboration of yogurts with rheological properties such as flow curves, apparent viscosity, yield stress, and viscoelastic properties superior to those of control yogurts elaborated with non-sonicated milk. The authors further showed that MTS yogurts had stronger structures, which resulted in higher

values of almost all of the many relevant rheological parameters. They suggested that ultrasound effects are mainly related to the cavitation phenomenon. As a result of the cavitation conditions, water molecules can be homolyzed, generating highly reactive free radicals that can react with and modify several molecules. Mechanical stress, generated either by shock waves derived from bubble implosion or from microstreaming derived from bubble's size oscillations, is also able to disrupt large macromolecules or particles. Reiner et al. [84] also found that compared to conventional yogurts, cultures from thermosonication (TS) milk had higher gelation pH values, greater viscosities, and higher water-holding capacities. The authors further stated that the structure was different; it showed a honeycomb-like network and exhibited a more porous nature. Similarly, Reiner et al. [118] found superior rheological properties of yogurts prepared from ultrasonicated milk than the yogurts prepared from conventionally heated milk. Further, Bermudez-Aguirre et al. [30] found only minor changes to the nutritional properties of milk after ultrasound, with the advantage of extending the shelf life of the product for more than 16 days at 4 °C without the use of intensive heat treatments. Wu et al. [119] reported that high-intensity ultrasound (90, 225, and 450 W, 20 kHz) significantly improved the viscosity and water-holding capacity and reduced syneresis of yogurt produced from sonicated milk. These effects are directly related to the yogurt structure, which is based on strings or clusters of casein micelles interacting physically with each other and with denatured serum proteins entrapping serum and fat globules. Furthermore, ultrasound could cause some qualitative changes in the fat globule membrane which would modify the ability of fat globules to interact with themselves and/or casein micelles, thereby improving the gelling properties.

In another study by Liu et al. [120], observed the renneting properties of reconstituted skim milk at 6.7–8 pH that were sonicated at a specific energy input of 286 kJ/kg using 20 kHz. It was shown that gelation attributes were significantly modified (i.e., faster gelation) in rennet gels made from milk sonicated at pH 8.0 and readjusted back to pH 6.7 compared to those made from milk sonicated at pH 6.7. The renneting properties were also modified (i.e., firmer gels) in milk sonicated at pH 6.7 compared to those of non-sonicated control milk. The modified renneting behavior was attributed to ultrasound-induced changes to the proteins in milk. Chandrapala et al. [121] looked at the phosphate-induced micellar casein gelation and the influence of sonication (20 kHz) to this process. Gels were formed by the addition of 7.6 mM tetrasodium pyrophosphate (TSPP) to 5 wt% micellar casein (MC) solutions. It was shown that sonication at 20 KHz and 31 W for up to 30 min changed the surface hydrophobicity of the proteins, whereas surface charge was unaltered. Sonication before the addition of TSPP formed a firm gel with a fine protein network and low syneresis. Conversely, sonication after TSPP addition led to an inconsistent weak gel-like structure with high syneresis (Fig. 9). Gel strength in both cases increased significantly after short sonication times, while the viscoelastic properties were less affected. Overall, the results showed that sonication can have a significant effect on gelation of micellar casein systems, but the state of the casein micelle prior sonication is a dominant factor and should be carefully controlled. Hence, the effects observed in the study by Liu et al. [113] can be confirmed as a
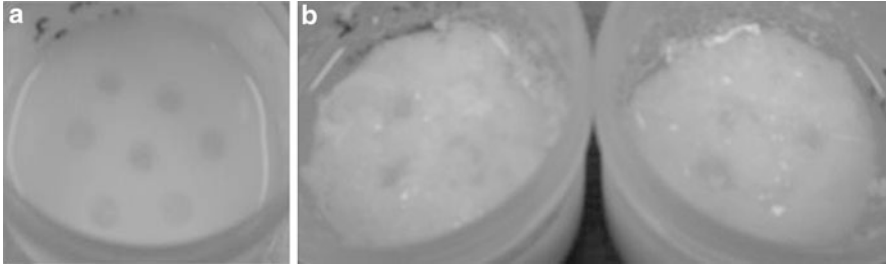
Fig. 9 Appearance of gels set by (**a**) sonication prior to TSPP addition and (**b**) TSPP addition after sonication [121]

combined effect of pH and ultrasound rather than just simply ultrasound being responsible.

The effect of sonication on milk gels has been reported. Acid gel firmness (G') was found to be altered when skim milk was ultrasonically treated prior to acidification, although the effect was attributed largely to denaturation of whey protein caused simply by temperature increases (up to about 95 °C) resulting from sonication performed without temperature control [114]. However, direct effects of ultrasound on casein micelles or individual caseins cannot be ruled out completely, although negligible effects were found on the individual caseins/casein micelles [111]. This may be because big multimeric protein complexes are more sensitive to the shearing forces created by microstreaming and bubble implosion than single-dissolved monomeric proteins.

Zisu et al. [122] also investigated the changes in heat-induced gelation properties of WPC systems. It was found that heat-set gels formed from WPC solutions that had been sonicated at 20 kHz showed higher gel strengths, reduced syneresis, and differences in gel microstructure, compared with gels made from non-sonicated WPC. Conversely, whey protein isolate (WPI) solutions were relatively unaffected by sonication, possibly reflecting the absence of larger aggregates in the initial solution or differences in composition. Adjustment of pH prior to ultrasound treatment did not result in significant differences compared with samples that were sonicated at neutral pH. This suggests that the mechanism for gel promotion is different from effects induced by pH changes. According to their results, the use of ultrasound changed the flow behavior and this was attributed to altered protein structure; the hydrophilic parts of amino acids are opened toward the surrounding aqueous phase, leading to increased binding of water molecules.

Foaming Capacity

Ultrasound has been used for many years in the study of estimating changes in protein conformation. Jambrak et al. [123] showed that ultrasound with a high-intensity (20 kHz) probe has a major effect on whey protein's functional properties such as solubility and foam ability. Their results showed that ultrasound of 40 kHz

frequency had less effect on whey protein than a 20 kHz probe. It was explained by the way of treatment. At probe treatment, the horn is inserted in solution which favors contact between tip and sample, whereas at baths flasks filled with solutions were immersed, so there was not direct contact with irradiating surface. A 15 min treatment using a 40 kHz bath showed the major impact: it decreased the conductivity of protein sample, increased solubility, and foaming ability of protein. The larger increases of foaming ability might be to the homogenization effect of ultrasound according to the authors. The homogenization effect of ultrasound usually disperses the protein and fat particles more evenly, which may improve the foaming property. During ultrasound treatment proteins probably became partially unfolded in structure which increases the foaming ability [123]. Ultrasound of 500 kHz did not impact the foaming ability of whey protein, but it affected solubility and conductivity.

Manipulating the functional properties of dairy ingredients is interesting from the point of protein functionality, although the actual mechanisms responsible for some observed effects are still under investigation. As mentioned earlier in this review, sonication of a liquid generates a number of different effects: mechanical vibration, agitation, shear forces, turbulence, acoustic cavitation, and free radicals. At this stage, it has been speculated that functional changes are due primarily to the physical effects of acoustic cavitation that slightly alter protein structure, since a higher-frequency ultrasound did not affect the functional properties of dairy ingredients. All these tailored desirable functional properties of end products with less nutritional loss and longer shelf lives are most welcoming for the wide use of ultrasound as an emerging technology in dairy streams.

Conclusion and Future Directions

Ultrasound is a promising technology suitable for a range of different applications in the dairy industry. In liquid media, the extreme physical forces generated by low-frequency, high-intensity ultrasound induces acoustic streaming, cavitation, shear, micro-jet, and shockwaves. These physical forces have been successfully used for the generation of dairy emulsions, functionality improvements of dairy systems, inactivation of microbes and enzymes, and crystallization of lactose, ice, and fat in dairy systems, among several other applications. High-frequency ultrasound on the other hand has been used to initiate rapid creaming of fat from milk. Ultrasound processing has advantages of achieving high product yields, minimizing flavor loss, increasing homogeneity, reducing energy requirements, reducing processing times, enhancing end-product quality, reducing chemical and physical hazards, and lowering the environmental impact, when compared with conventional dairy processes. Synergies with pressure and/or temperature have been reported but caution is advised to minimize nutritional losses and adverse flavor modifications if very high specific energies are to be delivered to the process.

Although the majority of these applications are only proven in the laboratory for a range of advantages, there is a high potential for large commercial scale-up

13. Rahman MS (1999) Handbook of food preservation. Marcel Dekker, New York

14. Patist A, Bates D (2008) Ultrasonic innovations in the food industry: from the laboratory to commercial production. Innov Food Sci Emerg Technol 9:147–154

15. Knorr D, Zenker M, Heinz V, Lee DU (2004) Applications and potential of ultrasonics in food processing. Trends Food Sci Technol 15:261–266

16. Villamiel M, van Hamersveld EH, de Jong P (1999) Review: effect of ultrasound processing on the quality of dairy products. Milchwissenschaft 54:69–73

17. Mason TJ, Paniwnyk L, Lorimer JP (1996) The uses of ultrasound in food technology. Ultrason Sonochem 3:S253–S260

18. Chandrapala J, Zisu B, Palmer M, Kentish S, Ashokkumar M (2011) Effects of ultrasound on the thermal and structural characteristics of proteins in reconstituted whey protein concentrate. Ultrason Sonochem 18:951–957

19. Ashokkumar M, Lee J, Zisu B, Bhaskarcharya R, Palmer M, Kentish S (2009) Sonication increases the heat stability of whey proteins. J Dairy Sci 92:5353–5356

20. Zisu B, Bhaskaracharya R, Kentish S, Ashokkumar M (2010) Ultrasonic processing of dairy systems in large scale reactors. Ultrason Sonochem 17:1075–1081

21. Suslick KS (1988) Ultrasound: its chemical, physical and biological effects. VCH Publishers, New York

22. Leighton TG (1994) The acoustic bubble. Academic, London

23. Ashokkumar M, Sunartio D, Kentish S, Mawson R, Simons L, Vilkhu K, Versteeg C (2008) Modification of food ingredients by ultrasound to improve functionality: a preliminary study on a model system. Innov Food Sci Emerg Technol 9:155–160

24. Mawson R, Knoerzer K (2007) A brief history of the application of ultrasonics in food processing. In: Proceedings of the 19th international congress on acoustics

25. Feng H, Yang W (2011) Ultrasonic processing. In: Zhang HQ, Barbosa-Canovas GV, Balasubramaniam VM, Dunne CP, Farkas DF, Yuan JTC (eds) Nonthermal processing technologies for food. Wiley-Blackwell, Oxford

26. McClements DJ (1995) Advances in the application of ultrasound in food analysis and processing. Trends Food Sci Technol 6:293–299

27. Villamiel M, de Jong P (2000) Inactivation of Pseudomonas fluorescens and Streptococcus thermophilus in trypticase soy broth and total bacteria in milk by continuous-flow ultrasonic treatment and conventional heating. J Food Eng 45:171–179

28. Ashokkumar M, Kentish S, Lee J, Zisu B, Palmer M, Augustin MA (2009) Processing of dairy ingredients by ultrasonication. PCT Int Patent Appl WO 2009/079691 A1

29. Ashokkumar M, Bhaskaracharya R, Kentish S, Lee J, Palmer M, Zisu B (2010) The ultrasonic processing of dairy products–an overview. Dairy Sci Technol 90:147–168

30. Zisu B, Lee J, Chandrapala J, Bhaskaracharya R, Palmer M, Kentish S, Ashokkumar M (2011) Effect of ultrasound on the physical and functional properties of reconstituted whey protein powders. J Dairy Res 78:226–232

31. Chandrapala J, Zisu B, Kentish S, Ashokkumar M (2012) The effects of high-intensity ultrasound on the structural and functional properties of α-lactalbumin, β-lactoglobulin and their mixtures. Food Res Int 48:940–943

32. Jambrak AR, Mason TJ, Lelas V, Herceg Z, Herceg IL (2008) Effect of ultrasound treatment on solubility and foaming properties of whey protein suspensions. J Food Eng 86:281–287

33. Zisu B, Schleyer M, Chandrapala J (2013) Application of ultrasound to reduce viscosity and control the rate of age thickening of concentrated skim milk. Int Dairy J 31:41–46

34. Gordon L, Pilosof AMR (2010) Application of high-intensity ultrasounds to control the size of whey proteins particles. Food Biophys 5:203–210

35. Madadlou A, Mousavi ME, Emam-Djomeh Z, Ehsani M, Sheehan D (2009) Sonodisruption of re-assembled casein micelles at different pH values. Ultrason Sonochem 16:644–648

36. Chandrapala J, Martin GJO, Zisu B, Kentish SE, Ashokkumar M (2012) The effect of ultrasound on casein micelle integrity. J Dairy Sci 95:6882–6890

13. Bermúdez-Aguirre D, Barbosa-Cánovas GV (2008) Study of butter fat content in milk on the inactivation of *Listeria innocua* ATCC 51742 by thermosonication. Innov Food Sci Emerg Technol 9:176–185

14. Bermudez-Aguirre D, Mobbs T, Barbosa-Canovas GV (2010) Processing of soft Hispanic cheese using thermosonicated milk: a study of physicochemical characteristics and storage life. J Food Sci 75:5548–5558

15. Bermudez-Aguirre D, Mobbs T, Barbosa-Canovas GV, Mawson R, Versteeg K (2009) Composition properties, physicochemical characteristics and shelf life of whole milk after thermal and thermosonication treatments. J Food Qual 32:283–302

16. Adekunte A, Tiwari BK, Scannell A, Cullen PJ, O'Donnell C (2010) Modelling of yeast inactivation in sonicated tomato juice. Int J Food Microbiol 137:116–120

17. Garcia ML, Burgos J, Sanz B, Ordonez JA (1989) Effect of heat and ultrasonic waves on the survival of two strains of *Bacillus Subtilis*. J Appl Bacteriol 67:619–628

18. Ordonoz JA, Aguilera MP, Garcia ML, Sanz B (1987) Effect of combined ultrasonic and heat treatment on the survival of a strain of *Staphylococcus Aureus*. J Dairy Res 54:61–67

19. Wringley D, Llorca N (1992) Decrease of *Salmonella typhimurium* in skim milk and egg by heat and ultrasonic wave treatments. J Food Prot 55(9):678–680

20. Villamiel M, Hamersveld V, De Jong J (1999) Review: effects of ultrasound processing on the quality of dairy products. Milchwissenschaft 54:69–73

21. Noci F, Walking-Ribeiro M, Cronin D, Morgan DJ, Lyng JG (2009) Effect of thermosonication, Pulsed electric field and their combination on inactivation of *L. innocua* in milk. Int Dairy J 19:30–35

22. Gabriel AA (2014) Inactivation of *L. monocytogenes* in milk by multifrequency power ultrasound. J Food Process Preserv. doi:10.1111/jfpp.12295

23. Bermudez-Aguirre D, Mobbs T, Barbosa-Canovas GV (2011) Ultrasound applications in food processing. In: Feng H, Barbosa-Canovas GV, Weis J (eds) Ultrasound technologies for food and bioprocessing. Springer, Science+Business Media, Germany. pp 65–105

24. Pagan R, Manas P, Alvarez I, Condon S (1999) Resistance of *Listeria monocytogenes* to ultrasonic waves under pressure at sublethal (manosonication) and lethal (manothermosonication) temperatures. Food Microbiol 16:139–148

25. Gao S, Lewis GD, Ashokkumar M, Hemar Y (2014) Inactivation of microorganisms by low frequency and high power ultrasound. A simple model for the inactivation mechanism. Ultrason Sonochem 21(1):446–453

26. Deghani MH (2005) Effectiveness of ultrasound on the destruction of *E. Coli*. Am J Environ Sci 1(3):187–189

27. Raso J, Palop A, Condon S (1998) Inactivation of *Bacillus subtilis* spores by combining ultrasonic waves under pressure and mild heat treatment. J Appl Microbiol 85:849–854

28. Bermudez-Aguirre D, Barbosa-Canovas GV (2008) Scanning electron microscopy of thermosonicated *Listeria Innocua* cells. In: Gutierrez Lopez GF, Weltichanes J, Parada Arias E (eds) Food engineering integrated approaches. Springer, NY. pp 287–294

29. Knorr D, Zenker M, Heinz V, Lee D (2004) Application and potential of ultrasonics in food processing. Trends Food Sci Technol 15:261–266

30. Bermudez-Aguirre D, Mawson R, Barbosa-Canovas GV (2008) Microstructure of fat globules in whole milk after thermosonication treatment. J Food Sci 73(7):E325–E332

31. Herceg Z, Jambrak AR, Celas V, Thagard SM (2012) The effect of high intensity ultrasound treatment on the amount of *S. aureus* and *E. coli* in milk. Food Technol Biotechnol 50:46–52

32. Vercet A, Lopez P, Burgos J (1997) Inactivation of heat-resistant lipase and protease from *Pseudomonas fluorescens* by manothermosonication. J Dairy Sci 80:29–36

33. Vercet A, Burgos J, Crelier S, Lopez-Buesa P (2001) Inactivation of proteases and lipases by ultrasound. Innov Food Sci Emerg Technol 2:139–150

34. Raso J, Pagán R, Condón S, Sala FJ (1998) Influence of temperature on the lethality of ultrasound. Appl Environ Microbiol 64:465–471

35. Sala FJ, Burgos J, Condon S, Lopez P, Raso J (1995) Effect of heat and ultrasound on micro-organisms and enzymes. In: Gould GW (ed) New methods of food preservation. Blackie Academic & Professional, London, pp 176–204

36. Ertugay MF, Yuksel Y, Sengul M (2003) The effect of ultrasound on lactoperoxidase and alkaline phosphatase enzymes from milk. Milchwissenschaft 58:593–595

37. Mawson R, Gamage M, Terefe MS, Knoerzer K (2011) Ultrasound in enzyme activation and inactivation. In: Feng H, Barbosa-Cánovas GV, Weiss J (eds) Ultrasound technologies for food and bioprocessing. Springer, Science+Business Media, Germany. pp 369–404

38. Tian ZM, Wan MX, Wang SP, Kang JQ (2004) Effects of ultrasound and additives on the function and structure of trypsin. Ultrason Sonochem 11(16):399–404

39. Ozbek B, Ulgen KO (2000) The stability of enzymes after sonication. Process Biochem 35:1037–1043

40. Lopez P, Sala FJ, Fuente JL, Condon S, Raso J, Burgos J (1994) Inactivation of peroxidase, lipoxygenase and polyphenol oxidase by manothermosonication. J Agric Food Chem 42:252–256

41. Lopez P, Burgos J (1995) Lipoxygenase inactivation by manothermosonication: effects of sonication parameters, pH, KCl, sugar, glycerol and enzyme concentration. J Agric Food Chem 43:620–625

42. Ertugay MF, Sengul M, Sengul M (2004) Effect of ultrasound treatment on milk homogenization and particle size distribution of fat. Turk J Vet Anim Sci 28:303–308

43. Bosiljkov T, Tripalo B, Brincic M, Jezek D, Karlovic S, Jagust I (2011) Influence of high intensity ultrasound with different probe diameter on the degree of homogenization (variance) and physical properties of cow milk. Afr J Biotechnol 10:34–41

44. Al-Hilphy ARS, Niamak AK, Al-Temimi AB (2012) Effect of ultrasonic treatment on buffalo milk homogenization and numbers of bacteria. Int J Food Sci Nutr Eng 2:113–118

45. Jafari SM (2007) Production of submicron emulsions by ultrasound and microfluidisation techniques. J Food Sci 82:478–488

46. Koh LLA, Chandrapala J, Zisu B, Martin GJ, Kentish S, Ashokkumar M (2014) A comparison of the effectiveness of sonication, high shear mixing and homogenization on improving the heat stability of whey proteins solutions. Food Bioprocess Technol 7:556–566

47. Michalski MC, Michel F, Geneste C (2002) Appearance of submicron particles in the milk fat globule size distribution upon mechanical treatments. Lait 82:193–208

48. Fox k, Holsinger VH, Caha J, Palansch MJ (1960) Formation of a fat-protein complex in milk by homogenization. J Dairy Sci 43:1396–1406

49. Vijaykumar S (2012) Effects of thermosonication on proteases and characteristics of milk and cream. MSc thesis, Iowa State University

50. Juliano P, Kutter A, Cheng LJ, Swiergon P, Mawson R, Augustin M (2011) Enhanced creaming of milk fat globules in milk emulsions by the application of ultrasound and detection by means of optical methods. Ultrason Sonochem 18:963–973

51. Juliano P, Temmel S, Rout M, Swiergon P, Mawson R, Knoerzer K (2012) Creaming enhancement in a liter scale ultrasonic reactor at selected transducer configurations and frequencies. Ultrason Sonochem 20:52–62

52. Leong T, Johansson L, Juliano P, Mawson R, McArthur S, Manasseh R (2014) Design parameters for the separation of fat from natural whole milk in an ultrasonic litre-scale vessel. Ultrason Sonochem 21:1289–1298

53. Leong T, Johansson L, Juliano P, Mawson R, McArthur S, Manasseh R (2014) Temperature effects on the ultrasonic separation of fat from natural whole milk. Ultrason Sonochem 21:2092–2098

54. Juliano P, Torkamani AE, Leong T, Kolb V, Watkins P, Ailouni S, Singh TK (2014) Lipid oxidation volatiles absent in milk after selected ultrasound processing. Ultrason Sonochem 21:2165–2175

55. Torkamani AE, Juliano P, Ailouni S, Singh TK (2014) Impact of ultrasound treatment on lipid oxidation of Cheddar cheese whey. Ultrason Sonochem 21:951–957

56. Leong T, Wooster T, Kentish S, Ashokkumar M (2009) Minimising oil droplet size using ultrasonic emulsification. Ultrason Sonochem 16(6):721–727
57. Pandit AB, Joshi JB (1993) Hydrolysis of fatty oils: effect of cavitation. Chem Eng sci 48:3440–3442
58. Abismail B, Conselier JP, Wilhelm AM, Delma H, Gourdon C (2000) Emulsification processes: online study by multiple light scattering measurements. Ultrason Sonochem 7:187–192
59. Juang R, Lin K (2004) Ultrasound assisted production of w/o emulsions on liquid surfactant membrane processes. Colloids Surf A Physiochem Eng Asp 238:43–49
60. Behreud O, Schubert H (2001) Influence of hydrostatic pressure and gas content on continues ultrasound emulsification. Ultrason Sonochem 8:271–276
61. Thompson LH, Doraiswamy LK (1999) Sonochemistry: science and engineering. Ind Eng Chem Res 38:1215–1249
62. Shanmugam A, Ashokkumar M (2014) Ultrasonic preparation of stable flax seed oil emulsions in dairy systems–physicochemical characterization. Food Hyd 39:151–162
63. Lamminen MO, Walker HW, Weavers LK (2004) Mechanisms and factors influencing the ultrasonic cleaning of particle-fouled ceramic membranes. J Memb Sci 237:213–223
64. Muthukumaran S, Kentish S, Stevens GW, Ashokkumar M, Mawson R (2007) The application of ultrasound to dairy ultrafiltration: the influence of operation conditions. J Food Eng 81:364–373
65. Muthukumaran S, Kentish S, Lalchandani S, Ashokkumar M, Mawson R, Stevens GW, Grieser F (2005) The optimisation of ultrasonic cleaning procedures for dairy fouled ultrafiltration membranes. Ultrason Sonochem 12:29–35
66. Muthukumaran S, Kentish S, Ashokkumar M, Stevens GW (2005) Mechanisms for the ultrasonic enhancement of dairy whey ultrafiltration. J Memb Sci 258:106–114
67. Hotrum NE, de Jong P, Akkerman JC (2015) Pilot scale ultrasound enabled plate heat exchanger-its design and potential to prevent biofouling. J Food Eng 153:81–88
68. Koh LL, Nguyen HH, Chandrapala J, Zisu B, Ashokkumar M, Kentish S (2014) The use of ultrasonic feed pre-treatment to reduce membrane fouling in whey ultrafiltration. J Memb Sci 453:230–239
69. Shahraki MH, Maskooki A, Faezian A (2014) Effect of various sonication modes on permeation flux in cross flow ultrafiltration membranes. J Environ Chem Eng 2:2289–2294
70. Abel M, Kiss ZL, Beszedes S, Hodor C, Keszthelyi-szabo G, Laszlo Z (2015) Ultrasonically assisted ultrafiltration of whey solution. J Food Proc Eng. doi:10.1111/jfpe.12177
71. Uluko H, Zhang S, Liu L, Li H, Cui W, Xue H, Zhao L, Sun Y, Lu J, Lu J (2014) Pilot scale membrane fractionation of ACE inhibitory and antioxidative peptides from ultrasound pretreated milk protein concentrate hydroxylates. J Func Foods 7:350–361
72. Mirzaie A, Mohammadi T (2012) Effect of ultrasonic waves on flux enhancement in microfiltration of milk. J Food Eng 108(1):77–86
73. Bund RK, Pandit AB (2007) Sonocrystallisation: effect on lactose recovery and crystal habit. Ultrason Sonochem 14:143–152
74. Deora NS, Misra NN, Deswal A, Mishra HN, Cillen PJ, Tiwari BK (2013) Ultrasound improved crystallization in food processing. Food Eng Rev 5:36–44
75. Bund RK, Pandit AB (2007) Rapid lactose recovery from paneer whey using sonocrystallization: a process optimization. Chem Eng Process 46:846–850
76. Guo Z, Zhang M, Li H, Wnag J, Kougoulos E (2005) Effect of ultrasound on anti-solvent crystallization process. J Crys Growth 273:555–563
77. Hem SL (1967) The effect of ultrasonic vibrations on crystallization processes. Ultrasonics 5(4):202–207
78. Kickling R (1965) Nucleation of freezing by cavity collapse and its relation to cavitation damage. Nature 206:915–917
79. Patel SR, Murthy VP (2009) Ultrasound assisted crystallization for the recovery of lactose in an anti solvent acetone. Crst Res Tech 44:889–896
80. Patel SR, Murthy VP (2011) Waste valorisation: recovery of lactose from partially deprotonated whey by using acetone as antisolvent. Dairy Sci Tech 91:53–63

81. Zisu B, Sciberras M, Jayasena V, Weeks M, Palmer M, Dincer T (2014) Sonocrystallisation of lactose in concentrated whey. Ultrason Sonochem 21(6):2117–2121

82. Martini S, Suzuki AH, Hartel RW (2008) Effect of high intensity ultrasound on crystallization behavior of anhydrous milk fat. J Am Oil Chem Soc 85:621–628

83. Sizuki AH, Lee J, Padilla SG, Martini S (2010) Altering functional properties of fats using power ultrasound. J Food Sci 75:208–214

84. Reiner J, Noci F, Cronin DA, Morgan DJ, Lyng G (2009) The effect of thermosonication of milk on selected physicochemical and microstructural properties of yoghurt gels during fermentation. Food Chem 114:905–911

85. Patrick M, Blindt R, Janssen J (2004) The effect of ultrasonic intensity on the crystal structure of palm oil. Ultrason Sonochem 11:251–255

86. Acton E, Morris GJ (1992) Methods and apparatus for the control of solidification in liquids. US Patent WO99/20420

87. Chow R, Blindt R, Chivers R, Povey M (2003) The sonocrystallisation of ice in sucrose solutions: primary and secondary nucleation. Ultrasonics 41(8):595–604

88. Mortazavi A, Tabatabai F (2008) Study of ice cream freezing process after treatment with ultrasound. World Appl Sci J 4(2):188–190

89. Havea P (2006) Protein interactions in milk protein concentrate powders. Int Dairy J 16:415–422

90. Udabage P, Puvanenthiran A, Yoo J, Versteeg C, Augustin MA (2012) Modified water solubility of milk protein concentrate powders through the application of static high pressure treatment. J Dairy Res 79:76–83

91. Augustin MA, Sanguansri L, Williams R, Andrews H (2012) High shear treatment of concentrates and drying conditions influence the solubility of milk protein concentrate powders. J Dairy Res 79:459–468

92. Yanjun S, Jianhang C, Shuwen Z, Hongjuan L, Jing L, Lu L, Uluko H et al (2014) Effect of power ultrasound pre-treatment on the physical and functional properties of reconstituted milk protein concentrate. J Food Eng 124:11–18

93. Carr A (2002) Monovalent salt enhances solubility of milk protein concentrate. In: New Zealand Dairy Board, Bhaskar NZ, Ganugapati Vijaya; Ram, Satyendra). Application: WO, 2002, pp 33

94. Schuck P, Davenel A, Mariette F, Briard V, Mejean S, Piot M (2002) Rehydration of casein powders: effects of added mineral salts and salt addition methods on water transfer. Int Dairy J 12:51–57

95. McCarthy NA, Kelly PM, Maher PG, Fenelon MA (2014) Dissolution of milk protein concentrates by ultrasonication. J Food Eng 126:142–148

96. Chandrapala J, Martin GJ, Kentish S, Ashokkuamr M (2014) Dissolution and reconstitution of casein micelle containing dairy powders by high shear using ultrasonic and physical methods. Ultrason Sonochem 21:1658–1665

97. Ashokkumar M, Lee J, Kentish SE, Grieser F (2004) Bubbles in an acoustic field: an overview. Ultrason Sonochem 14:470–475

98. Ashokkumar M, Kentish S, Lee J, Zisu B, Palmer M, Augustin M (2009a) Processing of dairy ingredients by ultrasonication. PCT Int Appl WO2009/079691A1

99. Ashokkumar M, Lee J, Zisu B, Bhaskarcharya R, Kentish S (2009) Sonication increases the heat stability of whey proteins. J Dairy Sci 92:5353–5356

100. Zisu B, Bhaskarcharya R, Ashokkumar M, Kentish S (2010) Ultrasonics processing of dairy systems in large scale reactors. Ultrason Sonochem 17:1075–1087

101. Devi S, Ashokkumar M, Grieser F (2005) The influence of acoustic power on multibubble sonoluminescence in aqueous solution containing organic solutes. J Phys Chem B 109:20044–20050

102. Chandrapala J, Zisu B, Palmer M, Kentish S, Ashokkumar M (2012) A possible mechanism to understand the ultrasound induced heat stability of whey protein concentrates. International nonthermal workshop, Melbourne

103. Kresic G, Lelas V, Jambrak AR, Herceg Z, Brncic SR (2008) Influence of novel food processing technologies on the rheological and thermophysical properties of whey proteins. J Food Eng 87:64–73

104. Stathopulos PB, Scholz GA, Hwang YM, Rumfeldt JA, Lepock JR, Meiering EM (2004) Sonication of proteins causes formation of aggregates that resemble amyloid. Protein Sci 13:3017–3027

105. Chandrapala J, Zisu B, Palmer M, Kentish SE, Ashokkumar M (2011) Effects of ultrasound on the thermal and structural characteristics of proteins in reconstituted whey protein concentrate. Ultrason Sonochem 18:951–957

106. Chandrapala J, Zisu B, Kentish S, Ashokkumar M (2012) The effects of high-intensity ultrasound on the structural and functional properties of α-Lactalbumin, β-Lactoglobulin and their mixtures. Food Res Int 48:940–943

107. Martin GJ, Williams R, Dunstan D (2007) Comparison of casein micelles in raw and reconstituted skim milk. J Dairy Sci 90:4543–4551

108. Madadlou A, Mousavi ME, Emam-Djomek Z, Ehsani M, Sheehan D (2009) Sonodisruption of reassembled casein micelles at different pH values. Ultrason Sonochem 16:644–648

109. Mounsey JJ, O'Kennedy BT, Kelly PM (2005) Influence of transglutaminase treatment on properties of milk and products made therefrom. Lait 85:405–418

110. Nguyen NH, Anema SG (2010) Effect of ultrasonication on the properties of skim milk used in the formation of acid gels. Innov Food Sci Emerg Technol 11:616–622

111. Chandrapala J, Martin GJ, Zisu B, Kentish S, Ashokkuamr M (2012) The effect of ultrasound on casein micelle integrity. J Dairy Sci 95:6882–6890

112. Shanmugam A, Chandrapala J, Ashokkumar M (2012) The effect of ultrasound on the physical and functional properties of skim milk. Innov Food Sci Emerg Technol 16:251–258

113. Liu Z, Juliano P, Williams R, Niere J, Augustin M (2014) Ultrasound effects on assembly of casein micelles in reconstituted skim milk. J Dairy Res 81(2):146–155

114. Anema SG, Klostermeyer H (1997) Heat induced, pH dependent dissociation of casein micelles on heating reconstituted skim milk at temperatures below 100°C. J Agric Food Chem 45:1108–1115

115. Snoeren THM, Brinkhuis JA, Damman AJ, Klok HJ (1982) The viscosity of skim-milk concentrates. Nether Milk Dairy J 36:305–316

116. Zisu B, Schleyer M, Chandrapala J (2012) Application of ultrasound to reduce viscosity and control the rate of age thickening of concentrated skim milk. Int Dairy J 1–3

117. Vercet A, Oria P, Quina P, Crelier S, Lopez P (2002) Rheological properties of yoghurt made with milk submitted and manothermosonication. J Agric Food Chem 50(21):6165–6171

118. Riener J, Noci F, Cronin DA, Morgan DJ, Lyng G (2010) A comparison of selected quality characteristics of yoghurts prepared from thermosonicated and conventionally heated milks. Food Chem 119:1108–1110

119. Wu H, Hulbert GJ, Mount JR (2001) Effects of ultrasound on milk homogenization and fermentation with yoghurt starter. Innov Food Sci Emerg Technol 1:211–218

120. Liu Z, Juliano P, Williams R, Niere J, Augustin M (2014) Ultrasound improves the renneting properties of milk. Ultrason Sonochem 21(6):2131–2137

121. Chandrapala J, Zisu B, Kentish S, Ashokkumar M (2013) Influence of ultrasound on the chemically induced gelation of micellar casein systems. J Dairy Res 80(2):138–143

122. Zisu B, Lee J, Chandrapala J, Bhaskarcharya R, Palmer M, Kentish S, Ashokkumar M (2011) Effect of ultrasound on the physical and functional properties of reconstituted whey protein powders. J Dairy Res 78:226–232

123. Jambrak AR, Mason T, Lelas V, Herceg Z, Hereg L (2008) Effect of ultrasound treatment on solubility and foaming properties of whey protein dispersion. J Food Eng 86:281–287

Application of Ultrasound Associated with Chemical Sanitizers for Food Products

Jackline Freitas Brilhante de São José

Contents

Abstract

Ultrasound is a form of energy generated by sound waves at frequencies that are too high to be detected by the human ear. Cavitation promotes the removal of dirt and food residues from surfaces and the inactivation of microorganisms. This phenomenon consists of formation, growth, and collapse of bubbles that generate a localized mechanical and chemical energy. There are indications that this technology can be used in the food industry, alone or associated with chemical sanitizers. The chemical and physical energy generated by acoustic cavitation promotes severe damage to the cell wall, resulting in the inactivation of microorganisms. The ultrasound can provide powerful disinfection, but its use for large-scale microbiological decontamination should be further evaluated, and in combination with other technologies, it could even provide excellent results. The

J.F.B. de São José (✉)
Departamento de Educação Integrada em Saúde, Federal University of Espírito Santo, Vitória, Brazil
e-mail: jackline.jose@ufes.br

use of ultrasound has also been implemented in the disaggregation of biofilms and the inactivation of microorganisms, which can help in the preservation of foods. Studies evaluating the use of ultrasound associated with others treatments, such as organic acids, hydrogen peroxide, and peracetic acid, have been conducted to provide a better understanding of the process and promote its application. Some authors suggest that the combination of ultrasound with other sanitizers can produce a synergistic effect. This chapter will discuss the application of ultrasound associated with chemicals products.

Introduction

The food industry has concerns about safety and quality of products. Recently, there has been great attention in new methods to guarantee the preservation of food without the use of additives. Thus, the food becomes safe and retains the food's nutritional value and sensory aspects. There is also a concern that the technologies applied should be related with low-energy consumption and should be cost competitive and environment-friendly. In this perspective, researches have been dedicated to new technologies used in food production and processing [1, 2].

Emerging strategies to preservation of food, such as pulsed electric field, high pressure, electrolyzed water, shortwave ultraviolet light (UV-C), irradiation, ozone, organic acids, nanoparticles, bacteriocins, and ultrasound treatments, have been usually studied for application in food industry. Ultrasound application has been an important topic of studies in food science and technology because of its promising effects in food processing and preservation [3–14].

Ultrasound is a technology that has been used with different objectives, such as communication with animals, the location of flaws in concrete buildings, chemical synthesis, the diagnosis or treatment of diseases, characterization of foods, and decontamination of surfaces and foods [13].

In food processing, the high-intensity ultrasound at low frequencies from 20 to 100 kHz is useful in inactivating microorganisms [15]. This inactivation is the result of a process called cavitation. Cavitation (Fig. 1) is the formation, growth, and collapse of bubbles that generate a localized mechanical and chemical energy [16, 17]. The inactivation effect of ultrasound has also been attributed to intracellular generation of cavitation, and mechanical shocks can impair the structural and functional cellular components until the cell lysis point [18]. The microbial death mechanism is mainly due to weakening of cell membranes, located heating, and production of free radicals. The destruction and disintegration of microorganisms by ultrasonic waves are related to the formation of bubbles during the cavitation process. Several studies [3, 8, 11, 14, 19, 20] demonstrated inactivation of
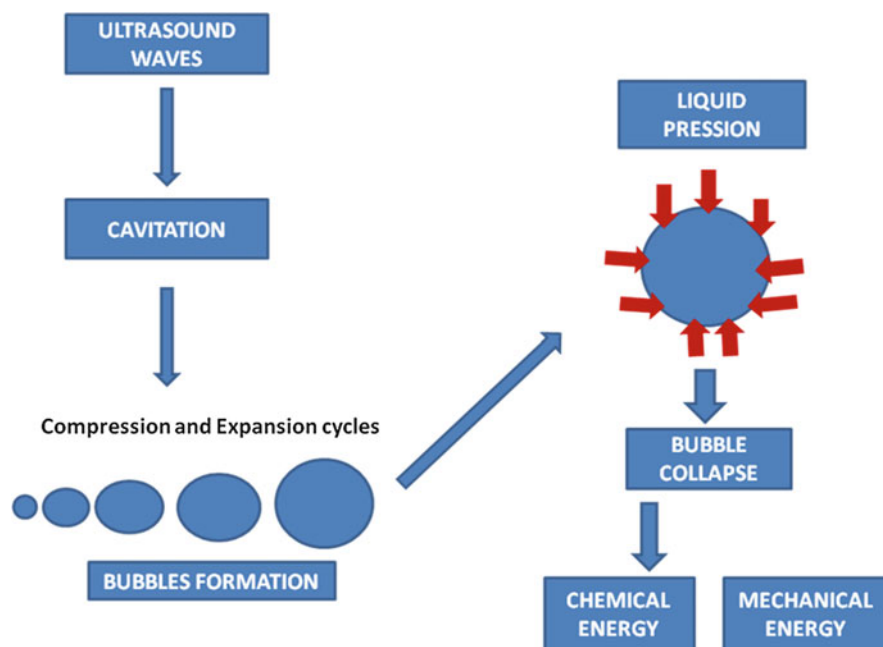
Fig. 1 Cavitation phenomenon and ultrasound mechanisms of action

microorganisms by ultrasound in combination or not with other treatments. The ultrasound alone can provide powerful disinfection, but its use for large-scale microbiological decontamination should be further evaluated, and in combination with other technologies, it could even provide excellent results [21].

The physical effect can be the main action that is involved on microbial cell death. However, it is known that the production of reactive compounds as peroxide hydrogen can promote the microbial disruption either [22]. When propagated through a biological structure, ultrasound promotes the compression and expansion of the medium particles, resulting in the production of a high amount of energy [15, 23].

Ultrasound offers advantages in terms of cost, productivity, and selectivity, with better processing time, improved quality, and reduced chemical damage and physical risks. Currently, the application of this technology has attracted attention for its role in environmental sustainability without causing damage, and it is therefore applicable to the concept of green technology [18]. Another important factor for the use of ultrasound in the food industry is the fact that it does not generate unpleasant odors and does not cause nutrient loss [15, 24], added to the fact of the possibility of being applied to room temperature and without heat generation [25].

Physical and chemical effects of ultrasound treatment are strongly associated with the amplitude of ultrasonic waves, exposure time, volume processed, food composition, and treatment temperature [13, 15]. These parameters modified the physical, chemical, and biochemical effects that can be observed with a variety of applications [4].

The determination of the frequency is very important and can affect the cavitation activity. The bubble size is inversely proportional to the frequency. Lower frequencies produce larger bubbles, and a higher energy is liberated [26].

Factors That Affect the Ultrasound Application

The characteristics of food can affect the application of high-power ultrasound. In highly viscous foods, ultrasound dispersion is difficult, thus reducing the frequency at which cavitation occurs. Lower frequencies are more effective in this case [27]. Other parameter is the pH of the medium or food. At a lower pH, inactivation rate of microorganisms is increased. Salleh-Mack and Roberts [28] observed a significant effect on the ultrasound inactivation (24 kHz/9 min), where a lower pH caused a major reduction in the count of microorganisms. Bacterial inactivation and the sonoprotective effect of milk components during the application of ultrasound (24 kHz at 30–35 °C) were observed by Gera and Doores [29]. The presence of lactose promote a increase on D values, suggesting that lactose exerted a protective effect on bacteria. São José et al. [13] suggested that when fresh-cut products are sanitized with ultrasound, some of the compounds of these foods can be released into the medium and exert a protective effect on bacteria.

The optimum temperature has to be determined to enhance the formation of cavitation. Salaleh-Mack and Roberts [28] evaluated ultrasound application and observed that ultrasound (24 kHz/9 min) improved the sensitivity of *E. coli* to thermal inactivation at increased temperatures. For some foods, as fruits and vegetables, the temperature increase is not appropriate. So, first it is necessary to evaluate the characteristics of the food and check the possibility of application of ultrasound associated with high temperature.

Application in Fruits and Vegetables

Fresh vegetables are frequently consumed in daily diets, and, in recent years, minimally processed fruit and vegetable consumption has increased [30]. Unfortunately, this demand promoted an increase in the frequency of outbreaks of foodborne illnesses related to these products [31].

Decontamination methods applied to fresh produce promote an increase in microbial safety and shelf life [32]. Sources of contamination are related to presence of pathogens in irrigation, wash waters, soil residue, insects, metals, and weeds [13]. It is important to mention about the care cleaning of fruits and vegetables before processing because fresh-cut produce is processed from a material grown in contact with soil and without any antimicrobial treatments. The washing and sanitization steps before cutting and during processing effectively reduce the risk of pathogen and residue contamination on fruits and vegetables from harvest and handling conditions [32, 33]. During sanitization, fruits and vegetables are subjected to an effective treatment to eliminate or reduce the number of pathogenic

microorganisms, without affecting the quality of product. The success of these procedures is related to several factors, such as time of washing, temperature, the method of washing, the type and concentration of the sanitizer, and the type of fresh-cut fruit or vegetable. Sanitizer should be selected so as to be effective in the elimination of pathogenic microorganisms and also be safe from toxicological aspects [13].

Commercial operations use wash treatments with chemical compounds as the essential step to reduce contamination on fresh fruits and vegetables. Sanitizing with chemical solutions influences the safety and preservation of these products. Sanitization step for the minimal processing of fruits and vegetables is very important, and it is vital to develop and evaluate new strategies that collaborate to the microbial safety of these products. These alternative methods could not result in the formation of toxic subproducts that put in danger human health and the environment [14].

Limitations in removal and inactivation of microorganisms from the surface of fruits and vegetables can be related to the presence of biofilms. Sanitizers are difficult to penetrate and destabilize in the biofilm structure. Therefore, it is necessary to evaluate methods that can remove these complex structures.

Among the new strategies that have been studied for application on sanitization step has been the use of ultrasound. Ultrasound has been adopted by the electronics industry to decontaminate surfaces, and its use has recently been recommended in sanitization step in the food industry. In recent years, many studies have evaluated the ultrasound application on food processing and preservation [3, 6, 11, 13, 15, 19]. Ultrasound application can be functional in the decontamination surface when associated to another strategies. This method improves antimicrobial action by weakening the cell wall which facilitates the penetration of sanitizers. The intense pressure generated during the use of ultrasound may contribute to the penetration of chemical oxidants through the cell membrane, and the cavitation process can assist the disintegration of microorganisms, which culminates in a higher efficiency of the sanitizing treatment. Therefore, ultrasound waves detach microorganisms from fruit and vegetable surfaces into sanitizer solutions and promote the exposure of microbial cells to sanitizer solutions. Thereby, ultrasound associated with sanitizers can show a synergistic effect [34].

Ultrasound and Chlorine Compounds

Easiest application, low cost, high antimicrobial activity, and complete dissolution in water of chlorinated agents make chlorine compounds attractive for frequent use in the fruit and vegetable industries [35]. The improper use of chlorine compounds can lead to water hyperchlorination, which can result in high concentrations of trihalomethanes and other byproducts that are known carcinogens [36]. Chlorinated compounds have been a focus of environmental concern [36, 37], and studies indicated that some emerging pathogens are more tolerant to chlorinated compounds, raising further concerns about the effectiveness and use of chlorine in the minimally processed food industry [35, 38]

Despite the restrictions of use, chlorinated compounds are still used. Considering the need to reduce their use, some studies have explored the evaluation of the use of chlorinated compounds in normal or reduced concentrations associated to ultrasound aiming to promote better inactivation of microorganisms.

Seymour et al. [3] reported that the combination of ultrasound (40 kHz/10 min) with sodium hypochlorite at 50 mg·L^{-1} resulted in the reduction of 1.2 log CFU·g^{-1} in *Salmonella* Typhimurium in lettuce compared with treatment with chlorine solution alone.

Apples treated with ultrasound at a 170 kHz frequency combined with 20 mg·L^{-1} chlorine dioxide showed a 4 log CFU.g^{-1} reduction in the population of contaminating *Salmonella* and *E. coli* O157: H7 [39].

Zhou et al. [40] observed that use of ultrasound contributed to a reduction of 0.7–1.1 log CFU·g^{-1} of *E. coli* O157: H7 in spinach in all treatments compared with treatments using only chemical sanitizers. Ayyildiz et al. [41] observed that a sequential combination of ultrasound and chlorine dioxide provided a 3.2–3.5 log reduction in the number of *E. coli* and total coliforms in raw wastewater, while the sum of the log reductions using individual treatments was 1.4–1.9 log CFU.mL.

Chen and Zhu [20] demonstrated that the use of chlorine dioxide in combination with ultrasound allows the maintenance of the postharvest quality in the Japanese plum (*Prunus salicina* L.).

Aday and Caner [42] evaluated effects of ultrasound and 6 mg/L chlorine dioxide combined or not on strawberry storage life and observed that these treatment were more beneficial for quality factors such as pH, total soluble solids, and texture compared with individual treatment.

Application of Ultrasound with Peracetic Acid

This sanitizer is produced by reaction between acetic acid and acetic anhydride with hydrogen peroxide in the presence of sulfuric acid which is the reaction catalyst function. It is a strong oxidizing agent and sanitizer with higher oxidative potential than of chlorine and chlorine dioxide [4].

The population of *Salmonella enterica* Typhimurium ATCC 14028 which adhered to the surface of cherry tomatoes was reduced by approximately 4 log CFU·g^{-1} in combination when ultrasound (40 kHz) and peracetic acid were used [11].

São José and Vanetti [14] evaluated the effect of ultrasound and chemical sanitizers to watercress, parsley, and strawberry and observed that combination of ultrasound and 40 mg/L peracetic acid resulted in reductions in aerobic mesophiles of approximately 6.5 log UFC/g and in mold and yeast ratios of 3.3 log UFC/g. However, this treatment caused watercress and parsley to darken. In the same study, all treatments with ultrasound promoted a reduction on firmness. The ultrasound treatments that were applied under conditions that would not impair sensory of nutritional properties did not effectively inactivate microorganisms.

Ultrasound application combined with peracetic acid did not promote virus reduction on recycled water reconditioning. Should be considered the frequency of ultrasounds because this can control the size of cavitation bubbles. This method can be a more environmentally friendly and toxicologically safer strategy for water reconditioning of the fresh-cut industry [43].

Application of Ultrasound with Organic Acids

Organic acids are GRAS (generally recognized as safe) and have the ability to inactivate foodborne pathogens [44]. These substances promote environmental pH reduction, disturbance of membrane transport and/or permeability, anion accumulation, or a decrease in internal cellular pH. Organic acids act rapidly and have a big spectrum of action [45].

Sagong et al. [19] evaluated the effect of ultrasound associated with lactic acid 1 % for 5 min on contaminated lettuce with S. Typhimurium and observed a reduction of 2.33 log CFU•g^{-1}. These same authors found that with combined treatment with ultrasound for 5 min, organic acids caused further reduction of 0.8–1.0 log CFU•g^{-1} of E. coli O157: H7, Salmonella Typhimurium, and L. monocytogenes compared to treatment with an organic acid alone.

Ansorena, Moreira, and Roura [46] evaluated the combined effect of ultrasound, citric acid, and thermal treatments on fresh-cut broccoli and observed retention of green color, microbial control, nutritional quality, and extending shelf life. These authors discuss that combination of treatments could reduce the required concentration of aqueous sanitizer and thermal treatment time.

The total aerobic bacteria and molds and yeasts on cherry tomatoes were reduced by 1.77 and 1.50 log UFC/g after the combined treatment of slightly acidic electrolyzed water and ultrasound [47]. In this same study, higher microbial reduction was observed with combined treatment in the strawberry samples but the reduction of cherry tomatoes was higher. This can be related to surface morphology differences between samples.

São José et al. [48] evaluated ultrasound and organic acids on green peppers and melon surfaces and observed that all treatments decreased the the number of adhered bacteria on green peppers and melon surfaces by more than 1.4 log CFU/cm^2. A higher removal of pathogens was observed after the use of a combination of ultrasound and 1 % lactic acid, which reduced the E. coli and Salmonella count by 2.9 and 2.8 log CFU/cm^2, respectively, on green peppers. For melons, the combination of ultrasound and lactic acid showed a reduction of 2.5 and 3.1 log CFU•cm^2 for E. coli and S. enteritidis, respectively. Acetic acid, a component of vinegar that is widely used for the sanitization of vegetables, reduced S. Enteritidis by 1.6 log CFU/cm^2 on green peppers. This same treatment reduced S. Enteritidis and E. coli by 1.4 and 1.8 log CFU/cm^2, respectively.

In Fig. 2 the effect of ultrasound and 1.0 % lactic acid in inactivation of Escherichia coli and Salmonella enterica serovar Enteritidis on green peppers and melon surfaces can be observed.
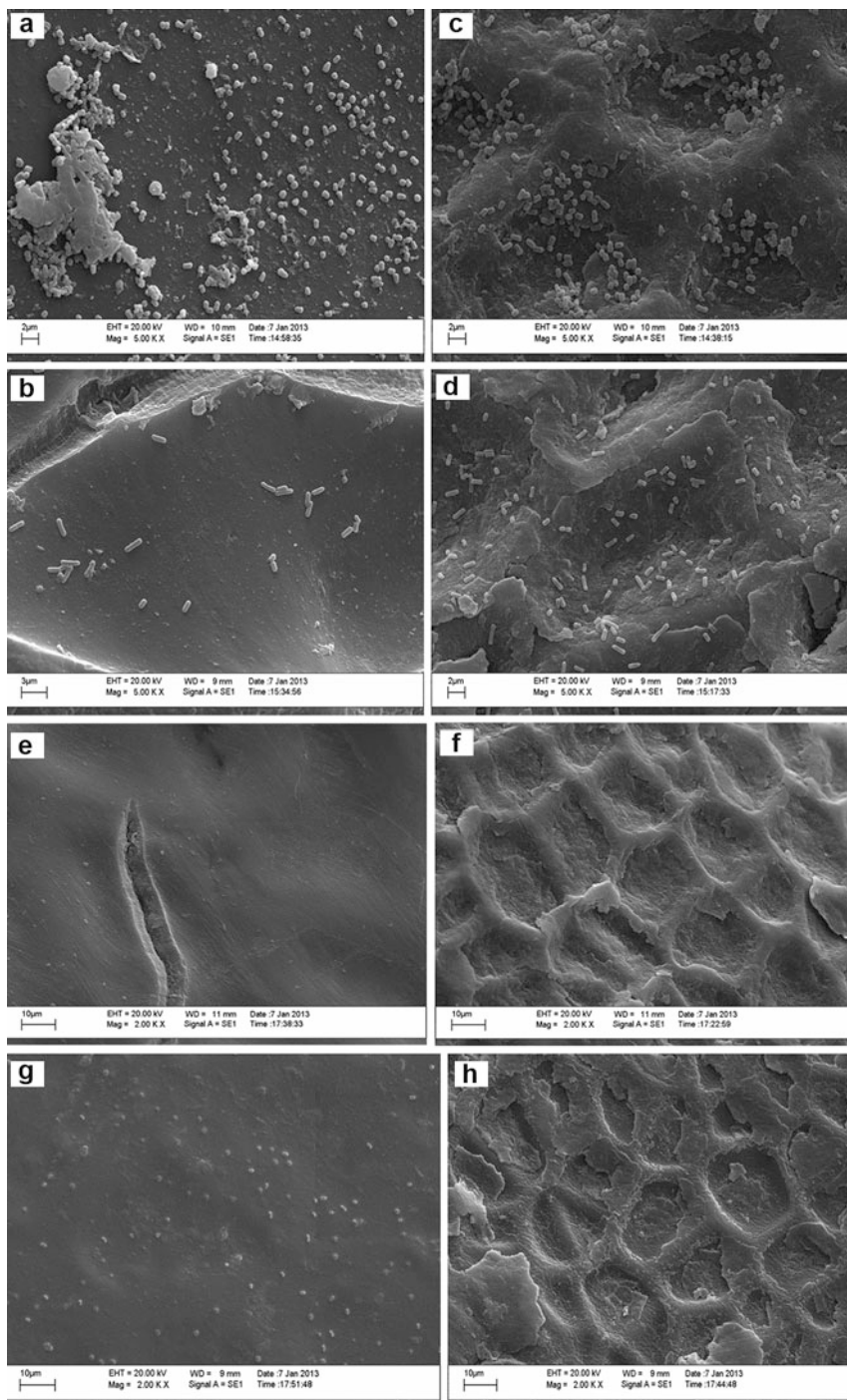
Fig. 2 (continued)

Velazquez et al. [49] used 1 % lactic acid on lettuce and observed a reduction of 1.7 log CFU/g of *E. coli* O157: H7. In the study of Huang and Chen [31], 1.0 % lactic acid was the most effective treatment, reducing *E. coli* O157: H7 on spinach by 1.9 log CFU/g.

São José et al. [50] evaluated the application of ultrasound and organic acids on surface pears and observed that the treatments removed more than 0.94 log CFU/cm^2. These results are comparable with chlorine sanitizing solution that reduces 1–2 logarithmic cycles in the initial count sanitized fruit.

Fruits and vegetables can be very difficult to clean because of their soft tissues that are easily damaged and irregular surfaces with microenvironments that protect microbes. Natural waxes on plant surfaces and oils and waxes commercially applied to plant surfaces can cause difficulty in the efficacy of sanitizers [51, 52].

Application of Ultrasound with Surfactants

Combination of sanitizer and surfactant can be better against microorganisms rather than using sanitizer alone. Surfactants consisting of amphipathic molecules can reduce interfacial tension. Thereby, surfactants can reduce hydrophobic interactions which are involved in bacterial adhesion and these can be removed from fruit and vegetable surfaces.

Iceberg lettuce and carrots were inoculated with *B. cereus* spores and treated with combinations of ultrasound and various concentrations (0.03–0.3 %) of surfactant (Tween 20, 40, 60, 80 and Span 20, 80, 85) solutions for 5 min. Combination of ultrasound (40 kHz) and 0.1 % Tween 20 promoted reduction on *B. cereus* spores of 2.49 and 2.22 log CFU/g on lettuce and carrots, respectively, without causing deterioration of quality [53].

The combination of ultrasound and detergent can promote greater reduction of cell surface than the isolated use of the detergent solution due to the cavitation phenomenon which releases mechanical energy in order to facilitate the contact of detergents/surfactants with the surface to be cleaned.

Application of Ultrasound with Nanoparticles

The low effectiveness in reducing contaminants in fresh-cut products, and the fact that the sanitizing chlorine results in the formation of harmful compounds to health, leads to development and evaluation of alternative sanitizers. The use of silver nanoparticles as antibacterial agent is relatively new.

Fig. 2 Photomicrographs of *E. coli* adhesion on green peppers (**a**) and melons (**c**); *S. enteritidis* adhesion on green peppers (**b**) and melons (**d**); removal of *E. coli* ATCC 11229 by application of ultrasound 40 kHz + 1.0 lactic acid for 2 min on green peppers (**e**) and melon surfaces (**f**); removal of *S. enteritidis* ATCC 13076 by application of ultrasound 40 kHz + 1.0 lactic acid on green peppers (**g**) and melon surfaces (**h**)

As one of multifunctional inorganic nanoparticles, zinc oxide is known to inactivate microorganisms. Nano-ZnO has been listed as GRAS by the US Food and Drug Administration. The combination of ultrasound and nano-ZnO coating promoted the slowdown of ethylene and carbon dioxide production and delayed the ripening process significantly in fresh-cut kiwifruit [54].

The silver nanoparticles have a broad action spectrum against gram-positive and gram-negative bacteria, molds, yeasts, and viruses. Regarding toxicity to animal cells, the metal is the silver that has the lowest toxicity. Silver nanoparticles have different applications such as catalysis in chemical reactions and microbial inactivation [55]. The efficient antimicrobial properties of silver nanoparticles caused it to be one of the most commonly used nanomaterials [56]. The inhibitory effect of Ag+ may be related to the adsorption of negatively charged bacterial cell wall and mobile deactivation of enzyme, disrupting the membrane permeability and ultimately leading to cell lysis and death [57]. Tiwari and Bihari [58] found that by treating $E.\ coli$ DH5 cells with 135 kHz for 15 min with nanoparticle solution with 25 g•mL^{-1}, a 50 % loss of viability was found, and this loss was equal to 40 % when cells were treated with ultrasound at 35 kHz associated with the nanoparticles. These same authors reported that the application of ultrasound ensures the entry of silver nanoparticles in the bacterial cell in which binding occurs initially with various sites on the membrane and cell wall.

The smaller particles with more surface area available to interact promote greater bactericidal effect than larger particles [59]. Ultrasound can facilitate the access of these nanoparticles to cell target.

Ultrasound and Other Chemical Compounds

In recent years, food industry focused on the use of natural compounds in food preservation. Plant extracts were used due to their antimicrobial and antioxidant properties. These substances interact in different forms with microbial cells [60].

Millan-Sango et al. [61] evaluated ultrasound combined to essential oil of oregano and observed that continuous ultrasound treatments led to a reduction of 2.65 ± 0.23 log CFU/cm^2 of $E.\ coli$ on the lettuce. Significant differences were found at 0.018 %, 0.022 %, and 0.025 % (v/v) both in continuous and pulsed US modes when compared with samples treated only with US. When continuous or pulse mode of US was combined with 0.025 % (v/v) of EO of oregano the result was synergetic. Essential oil combined with US could work synergistically on enhancing the inactivation of the tested bacteria [61].

Ferrante et al. [62] observed that thermosonication treatment at 45 °C, frequency of 20 kHz in combination with vanillin (1500 ppm) and citral (100 ppm), achieved a 6 log CFU/ml reduction of $L.\ monocytogenes$ in orange juice.

Yang et al. [63] investigated the effect of ultrasound (40 kHz, 10 min) and salicylic acid (0.05 mM) individually or in combination on blue mold, which is caused by $Penicillium\ expansum$ in peach fruit. The results showed that the

combination of ultrasound with salicylic acid were more effective than either individual treatment in controlling postharvest blue mold in peach fruit.

Muñoz et al. [64] has shown that the application of ultrasonic waves at 20 kHz of frequency, without nisin, produced a 0.30 log CFU/ml reduction in *L. innocua*. The addition of nisin at 2.50 mg/l resulted in a better antimicrobial effect of the ultrasound and promoted a reduction of 2.80 log CFU/ml of *L. monocytogenes*. Johnson et al. [65] reported that a combination of ultrasound treatment of 70 kHz for 2 h and the use of gentamicin sulfate on a biofilm reduced 97 % of the populations of *E. coli*. This fact is related to the ability of ultrasound to destabilize the cell membrane and allow the diffusion of the antibiotic through it.

Conclusion and Future Directions

Ultrasound has potential applications on food to control microbial contamination without changing their quality aspects. Some studies have shown that ultrasound treatment combined to chemical compounds could inactivate microorganisms. It is important for the application of ultrasound to understand the parameters (frequency, power, treatment time, etc.) to permit the efficiency of sanitization without promoting alterations on sensory quality and nutritional value of food. Ultrasound is an eco-friendly technology and has nonthermal properties, which also permits energy and cost savings.

Consumers demand food products with reduced values or absence of chemical compounds for microbial control. Ultrasound can permit this, and association of this with substances in reduced concentrations can increase the safety of fresh produce. Ultrasound can be a viable method for quality assurance and food safety. Further research should be encouraged to provide a better understanding of the process and promote its application. This would permit to identify the microbial inactivation mechanisms and understand the synergism when ultrasound is applied with another method.

References

1. Rollin F, Kennedy J, Wills J (2011) Consumers and new food technologies. Trends Food Sci Technol 22:99–111
2. Vidigal MCTR, Minim VPR, Simiqueli AA, Souza PHP, Balbino DF, Minim LA (2015) Food technology neophobia and consumer attitudes toward foods produced by new and conventional technologies: a case study in Brazil. LWT- Food Sci Technol 60:832–840
3. Seymour IJ, Burfoot D, Smith RL, Cox LA, Lockwood A (2002) Ultrasound decontamination of minimally processed fruits and vegetables. IJF Sci Technol 37(1):547–557
4. Knorr D, Zenker M, Heinz V, Lee DU (2004) Applications and potential of ultrasonics in food processing. Trends Food Sci Technol 15(5):261–266
5. Chemat F, Hoarau N (2004) Hazard analysis and critical control point (HACCP) for an ultrasound food processing operation. Ultrason Sonochem 11(3-4):257–260
6. Cameron M, McMaster LD, Britz TJ (2008) Electron microscopic analysis of dairy microbes inactivated by ultrasound. Ultrason Sonochem 15:960–964

7. Patil S, Bourke P, Kelly B, Frías JM, Cullen PJ (2009) The effects of acid adaptation on *Escherichia coli* inactivation using power ultrasound. Innov Food Sci Emerg Technol 10(4):486–490

8. Cao S, Hu Z, Pang B, Wang H, Xie H, Wu F (2010) Effect of ultrasound treatment on fruit decay and quality maintenance in strawberry after harvest. Food Control 21:529–532

9. Fava J, Hodara K, Nieto A, Guerrero S, Alzamora SM, Castro MA (2011) Structure (micro, ultra, nano), color and mechanical properties of *Vitis labrusca* L. (grape Berry) fruits treated by hydrogen peroxide, UV-C irradiation and ultrasound. Food Res Int 44(9):594–595

10. Arzeni C, Martinez K, Zema P, Arias A, Perez OE, Pilosof AMR (2012) Comparative study of high intensity ultrasound effects on food proteins functionality. J Food Eng 108(3):463–472

11. São José JFB, Vanetti MCD (2012) Effect of ultrasound and commercial sanitizers on natural microbiota and *Salmonella enterica* Typhimurium on cherry tomatoes. Food Control 24(1-2):95–99

12. Birmpa A, Sfika V, Vantakaris A (2013) Ultraviolet light and Ultrasound as non thermal treatments for the inactivation of micro-organisms in fresh read-to-eat foods. Int J Food Microbiol 167(1):96–102

13. São José JFB, Andrade NJ, Ramos AM, Vanetti MCD, Stringheta PC, Chaves JBP (2014) Decontamination by ultrasound application in fresh fruit and vegetables. Food Control 45:36–50

14. São José JFB, Vanetti MCD (2015) Application of ultrasound and chemical sanitizers to watercress, parsley and strawberry: microbiological and physicochemical quality. LWT- Food Sci Technol. doi:10.1016/j.lwt.2015.04.029

15. Piyasena P, Mohareb E, Mckellar RC (2003) Inactivation of microbes using ultrasound: a review. Int J Food Microbiol 87(3):207–216

16. Gogate PR, Kabadi AM (2009) A review of applications of cavitation in biochemical engineering/biotechnology. Biochem Eng J 44(1):60–72

17. Rastogi N (2011) Opportunities and challenges in application of ultrasound in food processing. Crit Rev Food Sci Nutr 51(8):705–722

18. Chemat F, Zill-e-huma, Khan MK (2011) Applications of ultrasound in food technology: processing, preservation and extraction. Ultrason Sonochem 18(4):813–835

19. Sagong HG, Lee SY, Chang PS, Heu S, Ryu S, Choi YJ, Kang DH (2011) Combined effect of ultrasound and organic acids to reduce *Escherichia coli* O157:H7, *Salmonella Typhimurium*, and *Listeria monocytogenes* on organic fresh lettuce. Int J Food Microbiol 145(1):287–292

20. Chen Z, Zhu C (2011) Combined effects of aqueous chlorine dioxide and ultrasonic treatments on postharvest storage quality of plum fruit (*Prunus salicina* L.). Postharvest Biol Technol 61(2-3):117–123

21. Joyce E, Phull SS, Lorimer JP, Mason TJ (2003) The development and evaluation of ultrasound for the treatment of bacterial suspensions. A study of frequency, power and sonication time on cultured *Bacillus* species. Ultrason Sonochem 10(6):315–318

22. Gao S, Lewis GD, Ashokkumar M, Hemar Y (2014) Inactivation of microorganisms by low-frequency high-power ultrasound: 1. Effect of growth phase and capsule properties of the bacteria. Ultrason Sonochem 21:446–453

23. Dolatowski ZJ, Stadnik J, Stasiak D (2007) Applications of ultrasound in food technology. Acta Sci Pol Technol 6(3):89–99

24. Lee SY, Baek SY (2008) Effect of chemical sanitizer combined with modified atmosphere packaging on inhibiting *Escherichia coli* O157:H7 in commercial spinach. Food Microbiol 25(4):582–587

25. Patist A, Bates D (2008) Ultrasonic innovations in the food industry: From the laboratory to commercial production. Innovative Food Science and Emerging Technology 9(2):147–154

26. Povey M, Mason T (1998) Ultrasound in food processing. Blackie Academic and Professional, London

27. Bermúdez-Aguirre D, Mobbs T, Barbosa-Cánovas GV (2011) Ultrasound applications in food processing. In: Feng H, Barbosa-Cánovas GV, Weiss J (eds) Ultrasound technologies for food bioprocess. Springer, New York, pp 64–105
28. Salleh-Mack SZ, Roberts JS (2007) The effects of temperature, soluble solids, organic acids and pH on the inactivation of *Escherichia coli* ATCC 25922. Ultrason Sonochem 14(3):323–329
29. Gera N, Doores S (2011) Kinetics and Mechanism of bacterial inactivation by ultrasound waves and sonoprotective effect of milk components. J Food Sci 76(2):m111–m119
30. Forghani F, Deog-Hwan O (2013) Hurdle enhancement of slightly acidic electrolyzed water antimicrobial efficacy on Chinese cabbage, lettuce, sesame leaf and spinach using ultrasonication and water wash. Food Microbiol 36(1):40–49
31. Huang Y, Chen H (2011) Effect of organic acids, hydrogen peroxide and mild heat on inactivation of *Escherichia coli* 0157:H7 on baby spinach. Food Control 22(8):1178–1183
32. Lopez-Galvez F, Ragaert P, Palermo LA, Eriksson M, Devlieghere F (2013) Effect of sanitizing formulations on quality of fresh-cut iceberg lettuce. Postharvest Biol Technol 85:102–108
33. Haute S, Tryland I, Veys A, Sampers I (2015) Wash water disinfection of a full-scale leafy vegetables washing process with hydrogen peroxide and the use of a commercial metal ion mixture to improve disinfection efficiency. Food Control 50:173–183
34. Yuting X, Lifen Z, Jianju Z, Jie S, Xingqian Y, Donghong L (2013) Power ultrasound for the preservation of postharvest fruits and vegetables. Int J Agric Biol Eng 6(2):116–125
35. Allende A, Selma MV, López-Gálvez F, Gil MI (2008) Impact of wash water quality on sensory and microbial quality, including *Escherichia coli* cross contamination, of fresh-cut escarole. J Food Prot 71:2514–2518
36. Rico D, Martín-Diana AB, Barat JM, Barry-Ryan C (2007) Extending and measuring the quality of fresh-cut fruit and vegetables: a review. Trends Food Sci Technol 18(7):373–386
37. Ruíz-Cruz S, Félix EA, Cinco MD, Osuna MAI, Aguilar GAG (2007) Efficacy of sanitizers in reducing *Escherichia coli* O157:H7, *Salmonella* spp. and *Listeria monocytogenes* populations on fresh-cut carrots. Food Control 18(11):1383–1390
38. Alvaro JE, Moreno S, Dianez F, Santos M, Carrasco G, Urrestarazu M (2009) Effects of peracetic acid disinfectant on the postharvest of some fresh vegetables. J Food Eng 95:11–15
39. Huang TS, Xu CL, Walker K, West P, Zhang SQ, Weese J (2006) Decontamination efficacy of combined chlorine dioxide with ultrasonication on apples and lettuce. J Food Sci 71(4): m134–m139
40. Zhou B, Feng H, Luo Y (2009) Ultrasound enhanced sanitizer efficacy in reduction of *Escherichia coli* O157: H7 population on spinach leaves. J Food Sci 74(6):m308–m313
41. Ayyildiz O, Sanik S, Ileri B (2011) Effect of ultrasonic pretreatment on chlorine dioxide disinfection efficiency. Ultrason Sonochem 18(2):683–688
42. Aday MS, Caner C (2014) Individual and combined effects of ultrasound, ozone and chlorine dioxide on strawberry storage life. LWT- Food Sci Technol 57(1):344–351
43. Sanchez G, Elizaquivel P, Aznar R, Selma MV (2015) Virucidal effect high power ultrasound combined with a chemical sanitizer containing peroxyacetic acid for water reconditioning in fresh-cut industry. Food Control 52:126–131
44. Akbas MY, Olmez H (2007) Effectiveness of organic acid, ozonated water and chlorine dippings on microbial reduction and storage quality of fresh-cut Iceberg lettuce. J Sci Food Agric 87(14):2609–2616
45. Alakomi HL, Skyttä E, Saarela M, Mattila-Sandholm T, Latva-Kala K, Helander IM (2000) Lactic acid permeabilizes gram-negative bacteria by disrupting the outer membrane. Appl Environ Microbiol 66(5):2001–2005
46. Ansorena MR, Moreira MR, Roura SI (2014) Combined effect of ultrasound, mild heat shock and citric acid to retain greenness, nutritional and microbiological quality of minimally processed broccoli (*Brassica oleracea* L.): an optimization study. Postharvest Biol Technol 94:1–13

47. Ding T, Ge Z, Shi J, Xu Y, Jones CL, Liu D (2015) Impact of slightly acidic electrolyzed water (SAEW) and ultrasound on microbial loads and quality of fresh fruits. LWT- Food Sci Technol 60:1195–1199

48. São José JFB, Medeiros HS, Bernardes PC, Andrade NJ (2014) Removal of *Salmonella enterica* Enteritidis and *Escherichia coli* from green peppers and melons by ultrasound and organic acids. Int J Food Microbiol 190:9–13

49. Velázquez LDC, Barbini NB, Escudero ME, Estrada CL (2009) Evaluation of chlorine, benzalkonium chloride and lactic acid as sanitizers for reducing *Escherichia coli* O157:H7 and *Yersinia enterocolitica* on fresh vegetables. Food Control 20(3):262–269

50. São José JFB, Medeiros HS, Bernardes PC, and Andrade NJ (2015) Ultrasound and organic acids in removal of *Salmonella enterica* Enteritidis and *Escherichia coli* from pears surfaces 33(1):118–128

51. Lima PM, São José JFB, Andrade NJ, Pires ACS, Ferreira SO (2013) Interaction between natural microbiota and physicochemical characteristics of lettuce surfaces can influence the attachment of *Salmonella* Enteritidis. Food Control 30(1):157–161

52. Fernandes PÉ, São José JFB, Arnez-Zerdas ERM, Andrade NJ, Fernandes CM, Silva LD (2014) Influence of hydrophobicity and surface roughness of mango and tomato in the adhesion of *Salmonella* Typhimurium and cleaning procedure using surfactin. Food Control 41:21–26

53. Sagong HG, Cheon H-L, Lee SY, Park KH, Chung MS, Ryu S, Choi YJ, Kang DH (2013) Combined effects of ultrasound and surfactants to reduce *Bacillus cereus* spores on lettuce and carrots. Int J Food Microbiol 160i(3):367–372

54. Meng X, Zhang M, Adhikari B (2014) The effects of ultrasound treatment and nano-zinc oxide coating on the physiological activities of fresh-cut kiwifruit. Food Bioprocess Technol 7:126–132

55. Choi O, Deng KK, Kim NJ, Ross L Jr, Surampalli RY, Hu Z (2008) The inhibitory effects of silver nanoparticles, silver ions, and silver chloride colloids on microbial growth. Water Res 42(1):3066–3074

56. Maynard AD, Aitken RJ, Butz T, Colvin V, Donaldson K, Oberdorster G, Philbert MA, Ryan J, Seaton A, Stone V, Tinkle SS, Tran L, Walker NJ, Warheit DB (2006) Safe handling of nanotechnology. Nature 444(16):267–269

57. Sambhy V, Macbride MM, Peterson BR, Sen A (2006) Silver bromide nanoparticle/polymer composites: dual action tunable antimicrobial materials. J Am Chem Soc 128:9798–9808

58. Tiwari DK, Behari J (2009) Biocidal nature of combined treatment of Ag-nanoparticle and ultrasonic irradiation in *Escherichia coli* DH5. Adv Biol Res 3(3-4):89–95

59. Panácek A, Kvitek L, Prucek R, Kolar M, Vecerova R, Pizurova N, Sharma VK, Nevecna T, Zboril R (2006) Silver colloid nanoparticles: synthesis, characterization, and their antibacterial activity. J Phys Chem B 110(33):16248–16253

60. Sango DM, Abela D, McElhatton A, Valdramidis VP (2014) Assisted ultrasound applications for the production of safe foods. J Appl Microbiol 116(5):1067–1083

61. David M-S, Anna ME, Valdramidis VP (2015) Determination of the efficacy of ultrasound in combination with essential oil of oregano for the decontamination of *Escherichia coli* on inoculated lettuce leaves. Food Res Int 67:145–154

62. Ferrante S, Guerrero S, Alzamora SM (2007) Combined use of ultrasound and natural antimicrobials to inactivate *Listeria monocytogenes* in orange juice. J Food Prot 70:1850–1856

63. Yang Z, Cao S, Cai Y, Zheng Y (2011) Combination of salicylic acid and ultrasound to control postharvest blue mould caused by *Penicillium expansum* in peach fruit. Innov Food Sci Emerg Technol 12(3):310–314

64. Muñoz A, Palgan I, Noci F, Cronin D, Morgan D, Whyte P, Lyng J (2012) Combinations of selected non-thermal technologies and antimicrobials for microbial inactivation in a buffer system. Food Res Int 47:100–105

65. Johnson LL, Peterson RV, Pitt WG (1998) Treatment of bacterial biofilms on polymeric biomaterials using antibiotics and ultrasound. J Biomater Sci Polym Ed 9:1177–1185

HACCP and HAZOP in Ultrasound Food Processing

Anne-Gaëlle Sicaire, Frédéric Fine, Maryline Vian, and Farid Chemat

Contents

Abstract

In the past few years, much interest has focused on the applications of ultrasound in food processing and technology. Many reports suggest effective benefits from combining ultrasound with classical techniques. Applications of ultrasound generally involve processes that can enhance rates, improve quality and/or safety, and reduce processing time. Ultrasound assistance has now become of significant importance when scaling up laboratory processes and can play a key role in implementing sustainable "green" technology.

A.-G. Sicaire (✉) • M. Vian • F. Chemat
Université d'Avignon et des Pays de Vaucluse, UMR 408, Equipe Green, Avignon, France
e-mail: anne-gaelle.sicaire@univ-avignon.fr; maryline.vian@univ-avignon.fr;
farid.chemat@univ-avignon.fr

F. Fine
Terres Inovia, Pessac, France
e-mail: f.fine@terresinovia.fr

Here we look at the concepts of hazard analysis and critical control points (HACCP) and hazard and operability (HAZOP) in the design of an ultrasonic food processing operation. These concepts are currently used as total quality management tools for the improvement of industrial operations. The HACCP program ensures the processing and production of safe foods by analyzing health hazards associated with processing, distribution, and consumption of foods, and in which the critical control points of the process are identified. The HAZOP analysis is used to identify hazardous working conditions in specific steps of a processing operation, taking into account the health effects of both contact and airborne ultrasound exposure.

Keywords

Ultrasound • HAZOP • HACCP • Critical control points

Introduction

In the past few years, much interest has focused on applying ultrasound in food processing. This technology has been increasingly used in processing, preservation, and extraction processes [1–6]. The applications of ultrasound in food processing are extensive and arise mainly from the physical effects of ultrasound. Sonication has been successfully applied to defoaming, degassing, cooking, cutting, freezing, drying, sterilizing, emulsifying, and homogenizing (Table 1) and can also be of interest for food preservation through its biochemical effects for the inactivation of microorganisms, spores, and enzymes. Sonication can break cell walls and denature enzymes, and when combined with other procedures, inactivation can be improved. Also, ultrasound can be used in assisted extraction procedures for the extraction of many target compounds contained in a wide range of matrices. These compounds of interest can then be further used for direct or indirect applications. Many reports suggest the effective benefits of combining ultrasound with classical techniques. Applications of ultrasound generally involve processes that can enhance rates, improve quality and/or safety, and reduce processing time. Ultrasound assistance plays a key role in implementing sustainable "green" technology.

The quality management tools in the food industry are becoming increasingly important to ensure safe food products processed in proper working conditions. Various methods are used to identify the risks that can occur. The concepts of hazard analysis and critical control points (HACCP) and hazard and operability (HAZOP) are used to ensure food safety and optimize efficiency and the management of risks affecting manufacturing processes, people, and the environment.

The HACCP system is a process that identifies and assesses the hazards and risks associated with the manufacture, storage, and distribution of foods. It implements the appropriate controls for the elimination or reduction of these hazards at specific points along the production line [7, 8].

Table 1 Application of ultrasound in food processing [6]

Application	Conventional methods	Ultrasound principle	Advantages	Products
Cooking	Stove Fryer Water bath	Uniform heat transfer	Less time Improving heat transfer and organoleptic quality	Meat Vegetables
Freezing/ crystallization	Freezer Freezing by immersion, by contact	Uniform heat transfer	Less time Small crystals Improving diffusion Rapid temperature decrease	Meat Vegetables Fruits Milk products
Drying	Atomization Hot gas stream Freezing Pulverization	Uniform heat transfer	Less time Improving organoleptic quality Improving heat transfer	Dehydrated products (fruits, vegetables)
Pickling/ marinating	Brine	Increasing mass transfer	Less time Improving organoleptic quality Product stability	Vegetables Meat Fish Cheese
Degassing	Mechanical treatment	Compression-rarefaction	Less time Improving hygiene	Chocolate Fermented products (beer)
Filtration	Filters (semipermeable membranes)	Vibrations	Less time Improving filtration	Liquids (juices)
Demolding	Greasing molds Teflon molds Silicone molds	Vibrations	Less time Reducing product losses	Cooked products (cake)
Defoaming	Thermal treatment Chemical treatment Electrical treatment Mechanical treatment	Cavitation	Less time Improving hygiene	Carbonated drinks Fermented products (beer)
Emulsification	Mechanical treatment	Cavitation	Less time Emulsion stability	Emulsions (ketchup, mayonnaise)
Oxidation	Contact with air	Cavitation	Less time	Alcoholic drinks (wine, whisky)
Cutting	Knives	Cavitation	Less time Reducing product losses Accurate and repeated cutting	Fragile products (cake, cheese)

The HAZOP system investigates potential deviations of operations from design conditions that could create process operation problems and hazards.

In the chemical industry, manufacturing processes are commonly adjusted to introduce new technologies such as ultrasound. However, in the food industry, the constraints of product image, the market, and dietary risks are such that any innovative technology must adapt to the manufacturing process and indeed to the whole production chain. The design of any ultrasound-assisted method for food processing must therefore be supported by HACCP and HAZOP analysis. These are important steps in approving products and food processes by standardization and certification. One of the major requirements for a food safety program is that it should be based on the principles of risk analysis and the study of critical points, as stated in the current edition of the *Codex Alimentarius* [9].

The design, construction, and start-up processes of processing or preservation assisted by ultrasound have to meet the specifications derived from the application of HACCP principles and HAZOP in sono-food processes.

HACCP

Definitions

HACCP stands for hazard analysis and critical control points [10]. The HACCP concept is a systematic approach to food safety management based on recognized principles designed to identify the hazards likely to occur at any stage in the food supply chain and put into place controls to forestall them [11]. It is a very logical system that covers all the stages in food production from production and harvest to consumption, via all the intermediate processing and distribution activities.

HACCP offers a number of advantages: most importantly, HACCP focuses on identifying and preventing hazards from food contamination. It permits more efficient and effective process administration, primarily because full record keeping, rather than spot daily statistics, enables investigators to see how well a firm is complying with food safety regulations over a period of time. The responsibility for ensuring food safety is placed appropriately on the food manufacturer or distributor, thereby helping food companies to compete more effectively in the world market and reducing barriers to international trade [12].

A critical control point (*CCP*) is a step in the flow diagram of the food process at which control measures can be applied. These CCPs are essential to prevent or eliminate a food safety hazard or reduce it to an acceptable level. Complete and accurate determination of CCPs is fundamental to controlling food safety hazards. If a hazard is identified at a step where control is necessary for safety, and where no control is performed, then the process has to be modified at that step, or at some earlier or later step, so as to include a control measure. In such a case, the added step is the CCP [13, 14].

Hazard analysis concerns any biological, chemical, or physical agent reasonably likely to cause illness or injury unless controlled. Thus the term "hazard" used here is limited to safety. Hazard analysis has to consider what control measures may be

applied to each hazard. Finally, the hazards associated with each step have to be listed along with the measures necessary to control them. More than one control measure may be required to control a specific hazard, and more than one hazard may sometimes be controlled by a specified control measure [14].

Food-contact surfaces are all those surfaces that may come into direct contact with human food during normal operating conditions. They include processing devices and support surfaces.

Quality control operation is a planned, systematic procedure that describes all the actions necessary to prevent food from being adulterated.

Principles

The HACCP system is based on a universally recognized set of seven principles. These are used to develop an HACCP plan for food. These principles reflect a framework developed on the basis of a combination of recognized, science-based, food safety considerations, and quality system characteristics [15]. This integration of basic food safety principles with the quality systems approach has been an important factor in the widespread recognition of the HACCP principles by food quality professionals [5].

The universally recognized seven principles of HACCP are:

- **Principle 1**: Conduct a hazard analysis of all raw materials and ingredients and each step (in the process flow diagram) used for preparation of the food product.
- **Principle 2**: Determine which raw materials and ingredients, and process steps, will be critical control points at which identified unacceptable hazards will be controlled.
- **Principle 3**: Establish critical limits or tolerances for each of the critical control points identified in Principle 2.
- **Principle 4**: Establish monitoring procedures for each of the critical control points identified in Principle 2.
- **Principle 5**: Establish corrective action procedures to be followed when monitoring of the critical control points reveals that the established critical limits have been exceeded or not been met.
- **Principle 6**: Establish verification procedures to confirm and provide confidence that the critical control points are being monitored effectively and are under control, and the HACCP plan for the product is operating effectively.
- **Principle 7**: Establish record keeping and documentation procedures for records and documents that are required by the HACCP plan.

Applications of Ultrasound

HACCP systems were initially designed and applied to the food manufacturing industry and are applicable throughout the food supply chain from raw material production through processing and distribution to final use by the consumer. The

system can also be applied to other products such as primary packaging or any of the different stages of food production where food safety is a fundamental issue [16]. If hazards are not controlled throughout the production chain, they may appear or develop later on. It is therefore essential to control the measures prescribed at each stage of the process, adopting a preventive approach for the entire supply chain [11].

HACCP in Ultrasound Food Processing

Quality Assurance

The entire food industry requires quality assurance provision for production monitoring, which involves testing products [17]. In some of these tests, long food treatment times are required, and destructive techniques are used. Ultrasound can be helpful in some of these tests. For example, low-intensity ultrasound has been used in the quality assessment of avocados, mangos, and melons according to ripeness state by evaluating ultrasonic parameters such as velocity and attenuation in relation to the physical characteristics of the medium. The quality of beef, chicken, cod, pork meat, milk, wine, sugar solutions, and oils has been evaluated with ultrasonic parameters, by applying the theory of how wave behavior (velocity and attenuation) relates to the physical composition of the medium [18]. Textures of products like cheese and cooked vegetables and the ripeness of fruits have all been determined using ultrasonic waves [19].

Despite its advantages, Chemat and Hoarau [20] suggest that ultrasound use in food engineering requires the setting up of an HACCP program in which the critical control points of food processing are identified, so that potential hazards in producing a safe quality product can be controlled.

Process Control

This HACCP program covers the activities carried out in transportation and reception of all materials to be used in the processing and packaging operations, storage, and warehousing of all materials and products at the food processing plant.

The HACCP processes should be systematic and successive, so flow charts must be prepared that include all the relevant steps, such as acquisition of raw materials, storage, formulation, preparation and melting, ultrasound treatment, heat exchange, aseptic packaging and finished product storage area, etc. (Fig. 1). Next, the accuracy of the flow chart should be verified by the HACCP team. If this team is unanimous, the flow chart should not be subsequently changed.

In this case, a theoretical typical food process can use ultrasound technologies to transform and preserve liquid products or semiliquid foods. In this theoretical process, the transformation (defoaming, degassing, emulsification, etc.) or preservative operation (pasteurization or sterilization) is continuous and requires a heat exchanger and an ultrasound probe or bath. The hazard to be studied (generally microbiological, physical, and chemical danger) is then selected by the quality team. In the ultrasound treatment, the critical processing factors are assumed to be the amplitude of the ultrasonic wave, the time of exposure/contact with the
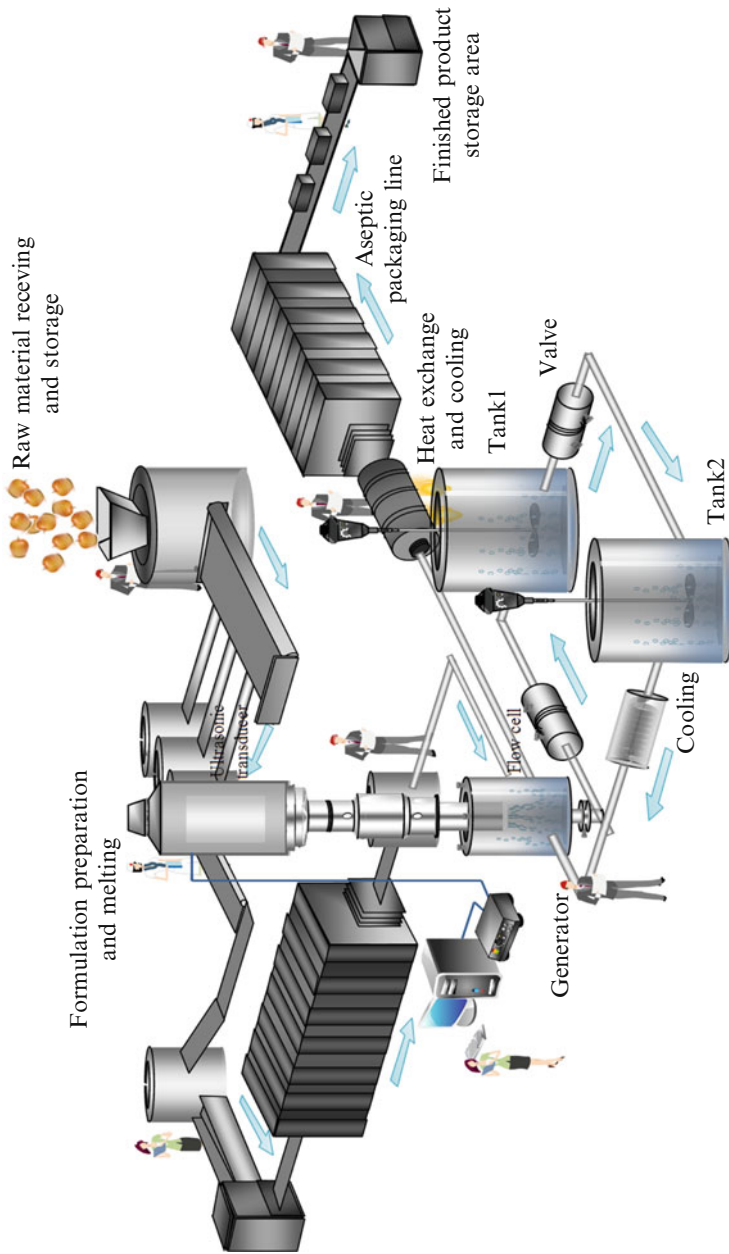
Fig. 1 A simplified flow diagram can be constructed for food processing using ultrasound technology (**a**) CCP = Critical Control Point. (**b**) Proceed to the next identified hazard in the described process. (**c**) Acceptable and unacceptable levels need to be determined within the overall objectives in identifying the CCPs of the HACCP plan
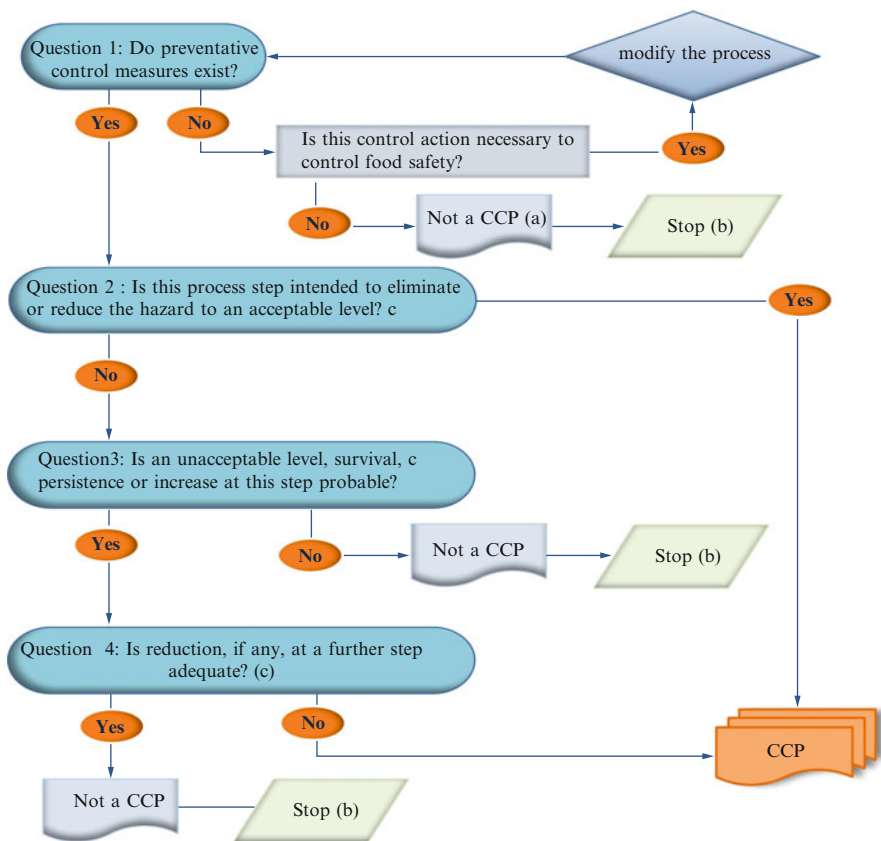
Fig. 2 Four questions should be included in the CCP decision tree of the HACCP system

microorganisms, the type of microorganism, the volume of food to be processed, the composition of the food, and the temperature of the treatment.

Understanding the potential hazards and manufacturing are essential for preparing a HACCP plan: some pollution may be eliminated sufficiently in the operation but not all. Therefore, knowledge of possible microbiological, chemical, physical, and biological hazards connected to the processes under evaluation is essential for the HACCP team. After the identification of existing hazards and control measures, a step or procedure is defined so that a food safety hazard can be prevented, eliminated, or reduced to acceptable levels. This step or control procedure is a critical control point (CCP). The selection of CCPs is made using a CCP decision tree (Fig. 2 and Table 2). This decision tree was designed to allow the HACCP team to ask specific, logical questions to help the determination of a true critical control point vs. a control point that could be handled under GMPs (Good Manufacturing Practices) or SOPs (Standard Operating Practices). However, the decision tree is not perfect and is mainly used to focus the team's attention on what should be used in an HACCP plan to control hazards.

Table 2 Deciding on critical control points (CCPs)

Processing steps	Questions of the CCP decision tree				Whether CCP or not	Main hazard
	Question 1	Question 2	Question 3	Question 4		
Raw materials and auxiliary material reception	Yes	Yes			CCP	Biological, chemical, and physical pollutions
Storage	Yes	No	Yes	Yes	Not	
Formulation, preparation, and melting						
Mixing	Yes	No	Yes	Yes	Not	Abuse of food additives
Curing	Yes	Yes			CCP	Contamination
Ultrasound treatment	Yes	No	Yes	No	CCP	Biological, chemical, and physical pollutions
Heat exchange						
Cooling	Yes	Yes			CCP	Pathogenic microbes
Boiling	Yes	Yes			CCP	Pathogenic microbes
Drying	Yes	No	Yes	Yes	Not	
Aseptic packaging	Yes	Yes			CCP	Pathogenic microbes
Finished product storage area	Yes	Yes			CCP	Pathogenic microbes

During the development of the HACCP plan, the HACCP team must draw up procedures to be followed if and when the monitoring of a CCP reveals that the critical limits are not respected, and therefore there is a loss of control of the hazard at the CCP. A product obtained during a processing step where the CCPs are not respected is a nonconforming product likely to be unsafe if consumed. Examples of verifications activities for CCPS that can help identify risks are given in Table 3.

HACCP Plan for Ultrasound Equipment/Hazard Analysis

The HACCP plan covers activities directed at design, construction, installation, performance, maintenance, and use of ultrasound equipment in a food processing plant. It also includes the calibration of the equipment used for monitoring and measuring parameters at any point in a process for the detection, elimination,

Table 4 Hazards associated with ultrasound processing

Origin	Hazard	Type	Severity	Applications concerned
Design and construction	Metals and plastics, oil, glass, pests, and other foreign bodies	Physical hazards	Low to high	Transformation/ preservation operation
Food-contact surfaces and non-respect of cleaning procedures	Toxic compounds, chemical migration, and microbiological proliferation and survival	Biological and chemical hazards	Intermediate to high	Transformation/ preservation operation
Environmental contaminants	Cross-contamination	Biological hazards	Low to high	Transformation/ preservation operation
Superheating: uneven heating time/inadequate power	Microbiological proliferation and survival	Biological hazards	Low to high	Transformation/ preservation operation

corrosion of the equipment, which can be damaged during normal operations, or by contact with raw materials, products, and cleaning equipment. Bath equipment, joints, and surfaces exposed to food contact must be smooth in order to prevent accumulation of substances [23, 24].

- *Installation of equipment*

  All ultrasound processing equipment should be installed so as to facilitate the use, cleaning, and maintenance of both the device itself and its immediate surroundings. After equipment is installed, it should be inspected and approved before being put into use under regular operating conditions. This inspection and approval should confirm that the equipment is able to perform the intended operation and avoid contamination.

- *Cleaned-in-place (CIP)*

  In some food processing operations, ultrasound equipment cannot be easily disassembled for cleaning between successive production runs, although it should be cleaned at the end of each use. These types of equipment are designated CIP equipment. Written procedures for cleaning and sanitizing CIP equipment are required [25].

Parameters of Ultrasonic Processing

Cavitation intensity is influenced by several physical parameters (wave frequency and amplitude, pressure, viscosity and temperature of the medium, etc.), but the geometries of the chamber and of the sonication horn are also key parameters. Since cavitation is limited to an area close to the transducer (the intensity of ultrasonic waves being inversely proportional to the square of the distance from the sonication tip), the effect of ultrasound depends on the shape and volume of the treatment chamber. Furthermore, cavitation should not take place too close to the horn's tip, as the bubbles generated could attenuate the effect by dispersing sonic waves. The

geometry and size of the horn also determine the energy transmitted to the medium. The characteristics of the treatment medium can also affect the intrinsic resistance of the microorganisms and the degradation of nutrients exposed to ultrasound.

HACCP in Ultrasound Food Preservation

The inactivation or inhibition of undesirable microorganisms is an essential part of food preservation. Food can become safe by treatments such as pasteurization and sterilization, or may possess intrinsic properties that contribute to safety, such as structure, low pH, and/or low water activity [26]. The goal of emerging technologies in food processing is to inactivate the initial population of microorganisms to a safe level with minimal damage to the product's quality attributes. In the HACCP program, the primary consideration is the prevention of contamination, cross-contamination, and deterioration of products by control of incoming raw materials, ingredients, packaging materials, and processing aids from the time they arrive at a food processing plant, their subsequent inspection, acceptance and storage until they are used, and control of the storage of semifinished and finished products starting from the time they are produced [27, 28]. Nevertheless, with some emerging technologies, microorganisms become more resistant over time to the action of specific factors such as pressure, electricity, or sound waves. In these cases, some reports show a positive effect on some microorganisms and enzymes when combined with other preservation techniques [29].

Ultrasound treatment can have lethal effects on microorganisms when applied with sufficiently high intensity (e.g., at frequencies above 18 kHz) [30]. Nevertheless, it has been shown that treatments only using ultrasound are often too gentle to reduce microbial populations. Sound waves should be applied together with other preservation factors in order to increase the effectiveness of the treatment. The use of ultrasound in combination with heat, pressure, or both seems a good option. The use of ultrasound, pressure, and heat along with low water activity (a_w) is a good combination for reducing resistant microbial populations in foods. The effect of pH, however, seems to be less significant when combined with ultrasound, and only a few reports focus on its effect [31].

In Table 5, the inactivation of some microorganisms is shown for different treatment media and operating conditions. With the combination of heat and ultrasound, substantial reductions in D values are obtained for *Listeria innocua* and *Salmonella*.

HAZOP

Definition

A hazard and operability (HAZOP) study is a formal, systematic, logical, and structured investigative study for examining potential deviations of operations from design conditions that could create process – operating problems and hazards [40]. It is one of the most structured techniques to identify hazards in a process plant

Table 5 Some examples of inactivation of microorganisms by ultrasound

Microorganisms	Treatment	Medium	Reductions	References
Listeria monocytogenes	20 kHz, ambient temperature, 200 kPa, or 400 kPa	Not specified	$D = 4.3$ min	[32, 33]
Salmonella spp.	160 kHz, 100 W by 10 min	Rice pudding	$D60\&S = 2.4$ min $D60 = 4.5$ min	[34]
Salmonella eastbourne	160 kHz, 100 W by 10 and 30 min	Peptone water	4 log reductions	[34, 35]
Salmonella typhimurium	30 min at 40 °C and 20 °C	Chocolate	26 % reduction with 10 min 74 % reduction with 30 min	[35]
Escherichia coli	700 kHz, 32 °C, 10 and 30 min	Skim milk	3 and 2.5 log reductions, respectively	[36]
Bacillus subtilis	20 kHz and 150 W, 100 °C	Distilled water, milk, and glycerol	63 % and 74 % reduction in glycerol, 79 % and 40 % reduction in milk, 70 % and 99.9 % in distilled water (depending on the species of *Bacillus*)	[37]
Yersinia enterocolitica	21–150 kHz, 30 °C and 200 kPa	Not specified	D from 4 to 0. 37 min depending on the amplitude	[38]
Staphylococcus aureus	24 kHz, 2–30 min, 3 W/cm^2	Orange juice	42–43 % reduction depending on the treatment time	[39]
Zygosaccharomyces bailii	Heat 55 °C with sonication at 20 Hz	Phosphate buffer (pH 7)	$D55 = 10.5$ min $D55\&S = 3.9$ min	[34]
Lactobacillus acidophilus	Heat at 60 °C, Ultrasound (110 kHz) assisted with temperature (60 °C)	Orange juice (pH 3.7)	$D60 = 70.5$ s $D60\&S = 43.2$ s	[3]

and aims to find all possible deviations from the normal functioning of process parameters.

There are basically four primary objectives in HAZOP study analysis:

1. Identify the causes of all deviations of changes from the intended design function.
2. Determine all major hazards and operability problems associated with any identified deviations.
3. Decide whether action is required to control the hazard or operability problems.
4. Ensure that the actions decided on are implemented and documented.

Principles

HAZOP study analysis is the key critical tool used throughout processing industries worldwide. The technique was designed to optimize the process and so improve performance. The purpose of the study is to provide a list of issues and recommendations for the prevention of each problem [41]. The HAZOP process is based on the following eight principles:

Principle 1: Identify conditions of risk and efficiency issues related to operations.
Principle 2: Establish corrective actions to prevent risks and condition efficiency problems.
Principle 3: Establish corrective actions to modify the procedure used in operation.
Principle 4: Establish a procedure control to verify the effectiveness of corrective action.
Principle 5: Establish a training program for staff.
Principle 6: Establish a system for recording actual data.
Principle 7: Establish monitoring procedures to verify the effectiveness of corrective action.
Principle 8: Update a diagram of the process with the corrective actions.

Applications of Ultrasound: The Nature of Potential Hazards of Ultrasound Equipment

Direct Effects on Operators

The main hazard the users may face is from accidental contact exposure to the ultrasonic waves. However, many industrial uses of ultrasound also incidentally generate and propagate high sound pressure levels in the air in the sonic and ultrasonic range. When this happens, a hazard may also arise from the ear's reception of the airborne ultrasound.

Direct Contact Exposures

Contact exposure happens when there is no intervening air gap between the transducer and tissue. This may be through direct intimate contact between the transducer and the tissue or it may be mediated by a solid or liquid. However, an air gap can diminish the ultrasonic energy transferred by orders of magnitude. Accidental immersion of a part of the body in a water bath excited by ultrasounds can cause tissue damage, and the energy transferred to the bone is approximately 65 % of that which is radiated; but if the part of the body is kept just out of the water, one million times less ultrasonic energy is transferred to it [42].

Devices such as ultrasonic equipment operating in a low-frequency range will readily cause tissue injury if and only if there is contact exposure. We know from anecdotal reports that at full ultrasonic power, contact exposure of a finger to the ultrasonic beam from an ultrasonic humidifier will cause sharp pain within seconds, likely due to overheating of the bone. However, when sonication is used for its destructive and violent effects, exposure to ultrasound in an ultrasonic bath operating

at high-power ultrasonic wave frequencies between 20 and 40 kHz is reported to have caused pain in the operator's hands [43].

Electricity

The ultrasound equipment is an electrical device that presents a potential danger to operators. Electricity is an invisible energy, which makes it even more dangerous during the electrical installation: it can cause electrical shock and burns and also be a potential fire hazard.

Indirect Effects on the Operator

Airborne Ultrasound

The major effects of airborne ultrasound in practice are the result of reception by the ear. The effects fall primarily into two categories: effects on the central nervous system and damage to the ear. These effects form the basis for exposure guidelines as they occur at lower sound pressure levels than those that can cause heating.

It has been reported that a 5-min exposure at selected frequencies in the range 17–37 kHz between 148 and 154 dB can reduce hearing sensitivity at subharmonic frequencies [44]. Slight losses also occurred occasionally at the third subharmonic. A number of subjective effects caused by airborne ultrasound have also been reported, including fatigue, headache, nausea, tinnitus, and disturbance of neuromuscular coordination. The effects of exposure to ultrasound on 18 young females working near a bank of "ultrasonic" cleaners were investigated [45]. These persons were exposed to both ultrasound and audible acoustic energy and complained of fatigue, headache, nausea, and tinnitus. The same symptoms were found in subsequent laboratory experiments in which human subjects were exposed to high-frequency acoustic radiation with audible components. When these same subjects were exposed to similar high-frequency energies, but without audible components, no complaints were made, leading Acton and Carson [45] to conclude that audible components had to be present for a subjective effect to be observed. They supported this theory by noting that women complained about these effects more than men. Since the exposed men were older and all had a history of noise exposure as well as high-frequency hearing losses, they assumed that the exposure radiations were largely inaudible to many of them [46].

Heating and Cavitation

Further information on the ultrasonic heating of humans has been reported [47], in the case of the use of an acoustical energy of 165 dB. Local heating in the crevices between the fingers caused burns almost instantly. Painful heating occurred after several seconds of exposure of larger surfaces such as the palm of the hand. In addition, it has been reported that mild heating in skin clefts is observed in the range 140–150 dB. Other non-auditory effects at these high levels included extremely disagreeable sensations in the nasal passages.

It can be concluded that acoustical energy greater than approximately 155 dB can cause harmful effects in humans exposed to airborne ultrasound, primarily as a result

of sound absorption and subsequently of heating. It is plausible that chronic lengthy exposures to levels between 145 and 155 dB might also be harmful, as they could raise body temperatures to mild fever levels during the exposure periods. However, high sound pressure levels have never yet been encountered in either commercial or industrial applications [45].

Ultrasound for Safe Use

Contact exposure to high-power ultrasound must be avoided at all times. High-power ultrasound is generally employed to cause a permanent physical change in a system. In order to ensure a safe use of high-power ultrasound, the following steps are recommended by the Safety Code 24, Guidelines for the Safe Use of Ultrasound from the Department of National Health and Welfare Ottawa, Ontario, Canada:

- Limited occupancy – Only operators qualified to use high-power ultrasound equipment or persons under strict supervision should be allowed within the boundaries of the controlled area while the equipment is operating.
- Responsibility of personnel – Personnel using high-power ultrasound, and safety inspectors in industry, should be knowledgeable about the possible harmful effects of ultrasound and about necessary protective measures.
- Other high-power ultrasound devices – Any high-power ultrasound device that might cause a person to receive contact exposure to the ultrasound should carry a label specifying that the device, or a certain part of it, should not be touched while it is operating. Where required, solid sources of ultrasound can be manipulated with suitable tools. The levels of low-power ultrasound used in nondestructive testing are such that, in general, there is little chance of harm occurring from brief accidental contact exposure. However, since biological effect data are still inconclusive, unnecessary contact exposure should be avoided.
- Warning signs – The warning sign for ultrasound radiation recommended for use is shown in Fig. 3. Warning signs should be placed on all high-power ultrasound devices. Accompanying each warning sign, there should also be a statement indicating the precautionary measures to be taken while the ultrasound power is on. Labels should also be placed on all ultrasonic cleaning tanks cautioning nearby personnel not to immerse hands or other parts of the body in the tank while it is operating.
- Protective measures for airborne ultrasound exposure – Safety procedures for the protection of personnel are similar to those used for audible noise. The objective is to ensure that ambient sound pressure levels do not exceed the recommended maximum permissible exposure level. This is achieved first by measuring the acoustical energy, and reducing exposure levels where required, preferably with engineering controls, reducing sound at its source or in its path by installing sound-absorbing material and containment baffles. If engineering controls are not possible, then ear protection should be used. Workers should be provided with ear protectors that reduce ultrasound levels at their ears.

Wearing a noise reduction
equipment

Risk of electrocution

Source of ultra ound
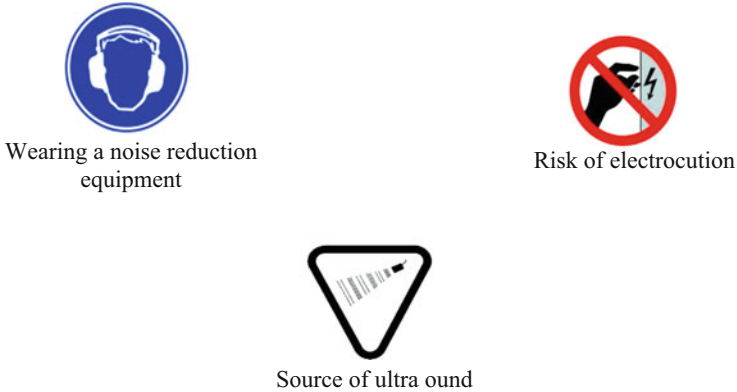
Fig. 3 Ultrasound warning signs

Conclusions and Future Directions

The design and construction of an ultrasound facility for food processing require both state-of-the-art equipment and common sense. The HACCP and HAZOP principles are key elements in the preparation of a strategy for manufacturing an ultrasound-treated product, with special attention given to product handling, treatment parameters, and equipment hygiene. Appropriate batch records must be kept and documented procedures implemented to ensure the industrial production of a safe product.

References

1. Krešić G, Lelas V, Jambrak AR, Herceg Z, Brnčić SR (2008) Influence of novel food processing technologies on the rheological and thermophysical properties of whey proteins. J Food Eng 87(1):64–73
2. Salleh-Mack SZ, Roberts JS (2007) Ultrasound pasteurization: the effects of temperature, soluble solids, organic acids and pH on the inactivation of Escherichia coli ATCC 25922. Ultrason Sonochem 14(3):323–329
3. Knorr D, Zenker M, Heinz V, Lee D-U (2004) Applications and potential of ultrasonics in food processing. Trends Food Sci Technol 15(5):261–266
4. Jafari SM, He Y, Bhandari B (2007) Production of sub-micron emulsions by ultrasound and microfluidization techniques. J Food Eng 82(4):478–488
5. Pingret D, Fabiano-Tixier A-S, Bourvellec CL, Renard CMGC, Chemat F (2012) Lab and pilot-scale ultrasound-assisted water extraction of polyphenols from apple pomace. J Food Eng 111(1):73–81
6. Khan MK, Chemat F, Zill-e-Huma (2011) Applications of ultrasound in food technology: Processing, preservation and extraction. Ultrason Sonochem 18(4):813–835

7. C. for F. S. NutritionApplied (2015) Hazard analysis & critical control points (HACCP) – HACCP principles & application guidelines [En ligne]. Disponible sur: http://www.fda.gov/Food/GuidanceRegulation/HACCP/ucm2006801.htm. [Consulté le: 11-mai-2015]

8. Council Directive 93/43/EEC on the hygiene of foodstuffs (1993) Official Journal of European Communities 14 Jun 1993

9. Chemat F, Nuns V, Pradeau C (2004) Contrôle et sécurité dans les procédés sono-agroalimentaires: HACCP et HAZOP. J Nat 16(1):47–52

10. Worsfold D, Griffith C (1995) A generic model for evaluating consumer food safety behaviour. Food Control 6(6):357–363

11. Codex Alimentarius Commission (1997) Recommended international code of practice. General principles of food hygiene. Annex to CAC/RCP 1-1969. Revision 3. Rome

12. Mortimore S (2000) An example of some procedures used to assess HACCP systems within the food manufacturing industry. Food Control 11(5):403–413

13. Notermans S, Gallhoff G, Zwietering MH, Mead GC (1995) Identification of critical control points in the HACCP system with a quantitative effect on the safety of food products. Food Microbiol 12:93–98

14. Hunter PR (1991) Application of Hazard Analysis Critical Control Point (HACCP) to the handling of expressed breast milk on a neonatal unit. J Hosp Infect 17(2):139–146

15. Damikouka I, Katsiri A, Tzia C (2007) Application of HACCP principles in drinking water treatment. Desalination 210(1–3):138–145

16. Pedro Javier Panisello PCQ (2001) Technical barriers to Hazard Analysis Critical Control Point (HACCP). Food Control 12(3):165–173

17. Bolton FJ (1998) Quality assurance in food microbiology — a novel approach. Int J Food Microbiol 45(1):7–11

18. Benedito J, Carcel JA, Gonzalez R, Mulet A (2002) Application of low intensity ultrasonics to cheese manufacturing processes. Ultrasonics 40(1–8):19–23

19. Chanamai R, Coupland JN, McClements DJ (1998) Effect of temperature on the ultrasonic properties of oil-in-water emulsions. Colloids Surf Physicochem Eng Asp 139(2):241–250

20. Chemat F, Hoarau N (2004) Hazard analysis and critical control point (HACCP) for an ultrasound food processing operation. Ultrason Sonochem 11(3–4):257–260

21. Scott VN (2004) How does industry validate elements of HACCP plans? Food Control 6:497–503

22. Baker DA (1995) Application of modelling in HACCP plan development. Int J Food Microbiol 25(3):251–261

23. Poliana Carolina Aleixo DSJ (2004) Cadmium and lead determination in foods by beam injection flame furnace atomic absorption spectrometry after ultrasound-assisted sample preparation. Anal Chim Acta 512(2):329–337

24. Wang J, Ma T, Zhang Z, Zhang X, Jiang Y, Dong D, Zhang P, Li Y (2006) Investigation on the sonocatalytic degradation of parathion in the presence of nanometer rutile titanium dioxide ($TiO2$) catalyst. J Hazard Mater 137(2):972–980

25. Gésan-Guiziou NAG (2007) Cleaning-in-place coupled with membrane regeneration for re-using caustic soda solutions. Sep Purif Technol 54(3):329–339

26. Soriano JM, Rico H, Moltó JC, Mañes J (2002) Effect of introduction of HACCP on the microbiological quality of some restaurant meals. Food Control 13(4–5):253–261

27. Vanne L, Karwoski M, Karppinen S, Sjöberg A-M (1996) HACCP-based food quality control and rapid detection methods for microorganisms. Food Control 7(6):263–276

28. Notermans S, Mead GC (1996) Incorporation of elements of quantitative risk analysis in the HACCP system. Int J Food Microbiol 30(1–2):157–173

29. Piyasena P, Mohareb E, McKellar RC (2003) Inactivation of microbes using ultrasound: a review. Int J Food Microbiol 87(3):207–216

30. Howard Zhang Q, Dorantes-Alvárez L, Gutiérrez-López GF, Yeom HW, Barbosa-Cánovas GV, Rodríguez JJ (2003) An update on some key alternative food processing technologies. In: Food science and food biotechnology. CRC Press, Boca Raton

31. Ana Cristina Soria MV (2010) Effect of ultrasound on the technological properties and bioactivity of food: a review. Trends Food Sci Amp Technol 7:323–331
32. Feng H, Barbosa-Canovas G, Weiss J (eds) (2011) Ultrasound technologies for food and bioprocessing. Springer, New York
33. Pagán R, Mañas P, Raso J, Condón S (1999) Bacterial resistance to ultrasonic waves under pressure at nonlethal (Manosonication) and lethal (Manothermosonication) temperatures. Appl Environ Microbiol 65(1):297–300
34. Earnshaw RG, Appleyard J, Hurst RM (1995) Understanding physical inactivation processes: combined preservation opportunities using heat, ultrasound and pressure. Int J Food Microbiol 28(2):197–219
35. Lee DU, Heinz V, Knorr D (2003) Effects of combination treatments of nisin and high-intensity ultrasound with high pressure on the microbial inactivation in liquid whole egg. Innov Food Sci Emerg Technol 4(4):387–393
36. Beyza Hatice Ulusoy CH (2007) The use of ultrasonic waves in food technology. Res J Biol Sci 2(4):491–497
37. Ordoñez JA, Burgos J (1976) Effect of ultrasonic waves on the heat resistance of Bacillus spores. Appl Environ Microbiol 32(1):183–184
38. Raso J, Pagán R, Condón S, Sala FJ (1998) Influence of temperature and pressure on the lethality of ultrasound. Appl Environ Microbiol 64(2):465–471
39. Chen C-Y, Anderson BO, Lo S-S, Lin C-H, Chen H-M (2010) Methicillin-resistant Staphylococcus aureus infections may not impede the success of ultrasound-guided drainage of puerperal breast abscesses. J Am Coll Surg 210(2):148–154
40. Rossing NL, Lind M, Jensen N, Jørgensen SB (2010) A functional HAZOP methodology. Comput Chem Eng 34(2):244–253
41. Noakes N, Chow CCL, Ko E, McKay G (2011) Safety education for chemical engineering students in Hong Kong: development of HAZOP Study teaching module. Educ Chem Eng 6(2): e31–e55
42. Berger BH (1984) Protection from infrasonic and ultrasonic noise exposure. J Occup Med 26(9):649–656
43. International Non-Ionizing Radiation Committee of the International Radiation Protection Association (1984) Interim guidelines on limits of Human exposure to airborne ultrasound. Health Phys 46:969–974
44. Parrack HO (1966) Effect of air-borne ultrasound on humans. Int J Audiol 5(3):294–308
45. Acton WI, Carson MB (1967) Auditory and subjective effects of airborne noise from industrial ultrasonic sources. Br J Ind Med 24(4):297–304
46. Chen H, Li X, Wan M (2006) The inception of cavitation bubble clouds induced by high-intensity focused ultrasound. Ultrasonics 44(Suppl 1):e427–429
47. Allen CH (1948) Some biological effects of intense high frequency airborne sound. J Acoust Soc Am 20(1):62

Ultrasonic Inactivation of Microorganisms

Shengpu Gao, Gillian Lewis, and Yacine Hemar

Contents

Abstract

High-power ultrasound has a great potential to become a nonthermal method for food preservation and shelf-life extension without affecting the quality and organoleptic properties of food products. While it is not yet used in the food

S. Gao
China Animal Disease Control Center, Slaughter Technology Center of Ministry of Agriculture of China, Beijing, China

G. Lewis
School of Biological Sciences, The University of Auckland, Auckland, New Zealand
e-mail: gd.lewis@auckland.ac.nz

Y. Hemar (✉)
School of Chemical Sciences, The University of Auckland, Auckland, New Zealand

The Riddet Institute, Plamerston North, New Zealand
e-mail: y.hemar@auckland.ac.nz

industry, it is an established, robust, flexible, and well-studied technology. In this chapter we review the current knowledge on the effect of high-power ultrasound, both low and high frequency, on the inactivation of microorganisms in aqueous solutions and model food systems. The main aim of the chapter is to relate the important parameters of ultrasonication and the properties of the microorganisms in order to obtain a fundamental understanding. For instance, the importance of the bacteria capsule is found to an important property for the resistance of bacteria to ultrasound. Similarly, the bacteria size and shape are important parameters, which might influence the inactivation of bacteria, depending on their state of growth (e.g., log phase vs stationary phase). Combination of hurdle technologies involving high-power ultrasound, such as manosonication, could offer further advantage in the use of nonthermal technologies for food preservation.

Keywords

Food preservation. *See* ultrasound bacterial inactivation • Hydrophilicity • Hydrophobicity • Microorganisms • Bacteria in food • Capsules and slime • pH • Size and shape • Cell appendages • Cell surface charge • Cell wall type • Growth • Bacteria with spores • Cavitation threshold • External pressure • Frequency • Viscosity and media

Introduction

The preservation of foods and their shelf-life extension has always been a priority for the food industry due to both food safety and economic considerations. Thermal processing, such as pasteurization, ultrahigh thermal (UHT), and canning, is extensively used. However in the case of some food products, these processes might affect their quality and the sensory (organoleptic) properties. Thus, the food industry has been continuously seeking new processing technologies as a replacement to the more conventional thermal technologies. These nonthermal process technologies include high hydrostatic pressure, cold plasma, and pulsed electric field; and food products treated with some of these novel technologies are already commercially available.

High-power ultrasound offers a great potential as a nonthermal process technology for food preservation. It is a robust, flexible, well-studied, and easy to implement technology. It can be operated in batch mode or in continuous mode in the case of liquid foods, offering the advantage of minimizing operator time if used in an industrial setup. However, when operated high-power ultrasonication does generate heat, which can be minimized using cooling systems.

Since one of the main aims of using novel process technologies is the inactivation of pathogenic microorganisms, this chapter focuses on the effects and mechanisms of both low- and high-frequency ultrasound treatment on microorganisms. A large volume of literature on the subject is already available, but not all of the available data will be reviewed in this chapter. The main objective of this chapter is to discuss high-power ultrasound inactivation of microorganisms in the light of the different

ultrasonication conditions, such as ultrasound power and ultrasound frequency, and the properties of the microorganisms, such as size, shape, and structure of their capsule. We have also tried to ensure that part of the chapter on microorganisms is easily accessible to the readers which are more familiar with ultrasound processing; and similarly parts of the chapter dedicated to ultrasound are written with the aim to be accessible to microbiologists.

Introduction to Microorganisms

Bacteria and Other Microorganisms in Food

Four main groups of microorganisms – bacteria, yeasts, molds, and viruses – are strongly related to food safety, as many of them can potentially cause foodborne diseases [95]. Bacteria, yeasts, and molds are the major causes for food spoilage.

Bacteria are single-celled, prokaryote microorganisms that show a broad range of specific morphologies including spherical (cocci), rod (bacilli), and curved (comma) shapes [90, 95]. The size of most bacteria is about 0.5–1.0 μm × 2.0–10 μm, and they can be arranged in clusters, chains, or tetrads [95]. A bacterium mainly includes a plasma membrane, cytoplasm, nucleoid with chromosomes, ribosomes, and inclusion bodies [110]. Some significant bacterial foodborne pathogens include *Campylobacter jejuni*, *Salmonella* species, *Escherichia coli*, *Listeria monocytogenes*, *Bacillus cereus*, *Clostridium botulinum*, *Clostridium perfringens*, *Shigella*, *Yersinia enterocolitica*, *Vibrio parahaemolyticus*, *Vibrio vulnificus*, *Staphylococcus aureus*, and *Enterobacter sakazakii* [25, 49, 108, 114].

Yeasts and molds are single-celled eukaryotes and multicellular eukaryotic microorganisms. *Saccharomyces cerevisiae*, as a typical yeast in foods, can cause food spoilage and generate alcohol and CO_2 [68, 95]. Viruses are regarded as noncellular microorganisms. Some viruses can cause foodborne diseases and some bacteriophages can lead to fermentation failure which indirectly affects the food qualities [95]. Yeast, molds, and viruses all have specific structure and sizes which imply that they can be affected differently by high-power ultrasound processing.

Microbial Growth

There are normally four stages in the growth of microorganisms: the lag phase, exponential phase (log phase), stationary phase, and death phase (Fig. 1) [74, 82]. During the lag phase, there is no instantaneous increase of the cell number when microorganisms are transferred into fresh media. Microbes reproduce markedly with a maximal division rate in the exponential phase, and the cell number remains stable and growth ceases in the stationary phase [63, 74, 82, 91, 96]. During rapid log growth phase, bacteria and other microorganisms are more sensitive to inactivation including radiation exposure and antimicrobial drugs [1, 112]. In the death phase, the cell number decreases logarithmically [90].
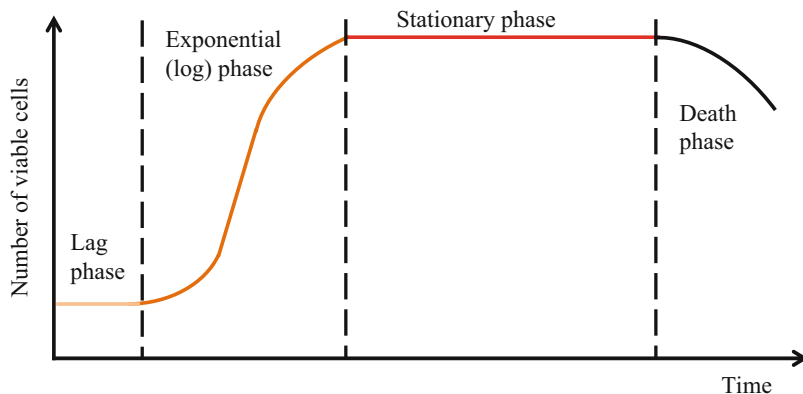
Fig. 1 Microbial growth curve in a closed system

Bacterial Cell Wall and Surface Properties

Cell Wall Type

Bacteria can be considered either gram positive or gram negative based on their response to gram staining, a system which was developed by Christian Gram in 1884 [90]. Gram-positive and gram-negative bacteria are stained in different colors due to their difference in cell wall structures. The structures of gram-positive and gram-negative cell walls are shown in Fig. 2. Gram-positive bacteria have a thicker and more robust cell wall than gram-negative bacteria [36]. Due to the different thickness of cell wall which results in various degrees of resistance to mechanical effects, the cell wall type is widely considered one of the main factors for influencing the ultrasound inactivation of bacteria.

A gram-positive cell wall is composed of many layers of homogeneous peptidoglycan or murein, which is about 20–80 nm thick and lies outside the plasma membrane, whereas gram-negative cells have a 2–7 nm peptidoglycan layer and a 7–8 nm thick additional structure called the outer membrane. Therefore, the cell wall of gram-positive cells is stronger than that of gram-negative bacteria because of the extra thickness of the peptidoglycan layer [36, 102, 120]. Also, gram-positive bacteria have a tighter adherent peptidoglycan layer than gram-negative bacteria [36].

The peptidoglycan structure is different between gram-positive cells and gram-negative cells. Peptidoglycan or murein is a complicated polymer that consists of numerous similar subunits; it contains sugar derivatives and several different amino acids. One type of amino acids called D-amino acids can protect cells from attacks by peptidases. Normally, the carboxyl group from the terminal D-alanine is linked to the amino group of diaminopimelic acid directly; however gram-positive cell walls generally contain a peptide interbridge as a link between the above two components. In contrast, there is no peptide interbridge for most gram-negative cell wall peptidoglycan. As a result, the peptidoglycan sac, linked and formed by the cross-links
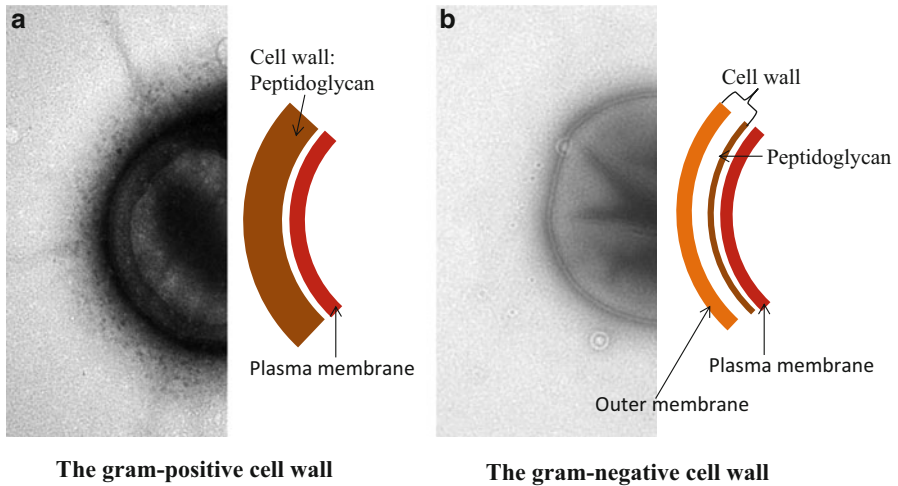
Fig. 2 Gram-positive and gram-negative cell walls. (**a**): a gram-positive envelope from *Staphylococcus epidermidis*; (**b**): a gram-negative envelope of *Enterobacter aerogenes*

between peptides and peptide interbridges, is stronger for gram-positive bacteria than that of gram negative [47, 56, 87, 102, 104, 117].

Hydrophobicity and Hydrophilicity

Hydrophobicity means that a particle or molecule is nonpolar and usually repels water, the molecule is unable to initiate hydrogen bonding, and the surface energy is normally low [78], whereas a hydrophilic molecule is polarized, thus is capable of hydrogen bonding, and can dissolve easily in water or other polar substances. Water is less structured when it surrounds a hydrophobic surface because of the function of intermolecular hydrogen bonding; in contrast, water is more structured when it is near a hydrophilic surface [11]. Surface hydrophobicity plays an important role in ultrasonication. It is expected that a hydrophobic surface will attract a cavitation bubble that processes a hydrophobic property.

Water contact angle (WCA) measurement is a significant method of examining bacterial cell surface hydrophobicity [78]. A high WCA indicates hydrophobicity and a low WCA is a reflection of hydrophilicity [11]. Microorganisms can be divided into three groups depending on the value of their WCA: hydrophobic (WCA $> 90°$), moderately hydrophobic (WCA $= 50° - 60°$), and hydrophilic (WCA $< 40°$) [78]. For example, it was found that *Enterobacter aerogenes* was moderately hydrophobic (WCA $= 62°$) and *S. cerevisiae* was hydrophilic (WCA $= 26°$) [78], whereas the water contact angle of *E. aerogenes* MBLA-0400 was 43° [77]. It was reported that *Staphylococcus epidermidis* was hydrophilic judging by the water contact angle measurement of 18.25° [35]. *S. epidermidis* ATCC 35983, *S. epidermidis* ATCC 35984, and *S. epidermidis* ATCC 12228 were hydrophilic, and their contact angles were 22°, 19°, and 10°, respectively, at pH 7 [42]. The hydrophobicities of seven strains

of *Bacillus subtilis* were measured, and the study found that the hydrophobicities varied among different strains [4]. The water contact angles of six strains, including ATCC 7058, ATCC 12432, ATCC 12695, ATCC 15129, ATCC 15476, and ATCC 15561, were less than 40°, and only ATCC 15811 was about 48°. Some researchers have characterized hydrophobic status for 27 species of bacteria based on adhesion and found that 44 % of the hydrophobic bacteria and 17 % of the hydrophilic bacteria were gram positive [72]. Moreover, the results varied with different methods, and the hydrophobicity status was also affected by the growth medium.

Cell Surface Charge

Bacteria in aqueous suspension are considered to be negatively charged [62], and bacteria such as *S. epidermidis, B. subtilis*, and *E. coli* were reported to have greater negative charges than positive charges [35]. However, bacteria surface charge effect on ultrasound inactivation is not known.

Capsules and Slime (Extracellular Polysaccharides)

There is a large structural layer that lies outside the cell wall of some bacteria, usually composed of polysaccharides called capsules or slime. They can potentially change the cell properties and thus influence the effects of ultrasound inactivation on bacteria. If it is well organized and difficult to wash off, the layer is considered to be a capsule; if the layer is unorganized and can be easily removed, it is called slime [10, 54, 60, 90]. There are several functions of capsules, including protecting bacteria against desiccation, resisting phagocytosis, expelling bacterial viruses and toxic materials, and protecting the host's defense mechanisms [40, 90, 118]. Capsules can be stained by India ink [118]. It was reported that capsules were found at both the stationary growth phase and exponential phase for *S. epidermidis* [50]. *S. epidermidis* RP62A (ATCC35984) was also a slime producer [116].

Cell Appendages

Cell appendages are the external features of bacterial cells including flagella, fimbriae, and pili, and they are not considered components of the cell wall. Flagella are threadlike locomotor appendages for motile bacteria that protrude from the plasma membrane and cell wall; they are about 20 nm in diameter and 15–20 μm long [90]. Fimbriae are short, hair-like appendages, composed of helically arranged protein subunits, which are on the surface of some bacteria and are thinner than flagella; pili usually are involved in bacterial mating [90]. The bacteria with fimbriae may affect the ultrasound inactivation, since they may dampen the mechanical effects induced by cavitation.

Ultrasound Inactivation of Bacteria and Other Microorganisms

There are mainly three groups of factors that affect the results of ultrasound treatment on the inactivation of bacteria and other microbes: first, the parameters affecting the cavitation threshold since bacterial inactivation is driven by cavitational effects;

second, the proprieties of the media; and last, the properties of the microbes. The factors affecting the cavitation threshold mainly include intensity and amplitude, frequency, temperature, and external pressure. The proprieties of media cover viscosity, volume, pH, and the initial number of bacteria. The characteristics of bacteria basically include gram-staining status, size and shape, bacterial capsules, bacteria species, spores, and growth phases.

Effects of Cavitation Threshold

Larger intensity causes more violent collapse of microbubbles than smaller intensity [70]. Thus, the inactivation rate of microorganisms generally increases with the increasing intensity of ultrasound. Microbes are more resistant to ultrasound at high frequencies than at low frequencies, which is mainly because in a short rarefaction and compression cycle, it is difficult for microbubbles to be produced. Further, because the vapor pressure increases quickly and cavitation bubbles are generated rapidly, bacteria and other microbes such as yeasts are more sensitive to ultrasonication at high temperature. Under high pressures, microbubbles can also collapse more rapidly and violently.

Effects of Intensity and Amplitude

Normally, the higher the intensity amplitude of ultrasound applied, the more inactivated the bacteria, since greater energy is released at higher intensity. It was found that the inactivation rate of *Mycobacterium* sp. 6PY1 increased with increased ultrasound power [6]. *E. coli* has been publicized widely for numerous outbreaks that have caused deaths [89]. Ultrasonic inactivation of *E. coli* XL1-Blue was investigated by using a horn-type sonicator utilizing the squeeze-film (i.e., sample was hold in a gap between two transducers) effect at 27.5 kHz with high power intensity [41]. The results showed that the inactivation rate of bacteria increased with increase in the amplitude of the vibrating face, which was more than 99 % in 180 s at an amplitude of 3 μm (p–p) and 2 mm squeeze film [41]. *E. coli* ATCC 25922 and NCTC 12900 suspensions also were examined by using ultrasound at different amplitude levels (0.4, 7.5, and 37.5 μm) [86]. It was found that there was a greater than 5-log reduction of *E. coli* by using ultrasound treatment for 15 min at 37.5 μm or less at 7.5 μm amplitude [86]. The disruption rate and protein release of *S. cerevisiae* were also found to increase with the increase in power from 120 to 600 W, when sonicated at 20 kHz [67].

A group of aerobic mesophilic microorganisms was ultrasonicated in date syrup at both 10 % and 25 % of total power (the exact power or intensity used was not reported), and the number of total microorganisms was significantly decreased at higher intensities than lower intensities [39]. However, it was reported that at low frequency, the inactivation rate of *Mycobacterium* sp. 6PY1 reached a constant level when the power increased to a certain value. And this was explained by stipulating that the number of cavitation bubbles becomes equal to the bacteria number [6, 59].

Effects of Frequency

It is difficult to determine whether low-frequency or high-frequency ultrasound is more efficient for the inactivation of bacteria because of the reasons stated above. Although shear forces produced in high-frequency ultrasound are less violent than those produced in low-frequency ultrasound, there are more hydroxyl radicals generated at low frequency. It was found that the kill rate at low-frequency high-power ultrasound (20 and 38 kHz) was significantly higher than at high-frequency low-power one (512 and 850 kHz) for the inactivation of *B. subtilis* [58]. The inactivation percentage of *Mycobacterium* sp. 6PY1 was lower at a high frequency (612 kHz) than at a low frequency (60 kHz) at the same power density (114 W/L), and the percentage was 43 % and 93 %, respectively [6]. It was also reported that *E. coli* and *Klebsiella pneumonia* had a continuous and significant decrease in numbers when treated by ultrasound with an intensity of 0.012 W/cm^3 for 15 min. At a frequency of 20 kHz, 6.06 % of live *E. coli* cells remained, while 18.9 % were still live when ultrasonicated at 40 kHz [57]. At a higher frequency (580 kHz), 57.2 % of *E. coli* cells were left and 75.5 % of *K. pneumonia* were left after 15 min, which was significantly more than at low frequency [57]. However, it was reported that the rate of inactivation of *E. coli* IAM 12058 was slightly higher at 500 kHz than at 20 kHz, under at the same sonication power (1.7–12.4 W) [61].

Effects of Temperature

Normally, bacteria are more sensitive to ultrasound treatment in an environment with high temperature. Increase in temperature results in an increase in vapor pressure [71], rapid generation of cavitation bubbles [37], and the viscosity of the media decreases; thus it lowers the ultrasound power threshold for the generation of cavitation.

Results from studies showed that ultrasonication at a mild temperature (50–60 °C) was more effective for microbial inactivation than ultrasonication under ambient temperature [30, 97]. The results on ultrasonication of *E. coli* ATCC 25922 showed that temperature had a significant effect on bacterial inactivation, where a 5-log reduction of *E. coli* was achieved in 3 min with no temperature control, while the optimum ultrasonication time was 10 min when the temperature was maintained at below 30 °C [99]. *S. epidermidis* suspensions (10^5 CFU/ml) were ultrasonicated by low-frequency ultrasound (20 kHz) in different suspension volumes (2, 5, and 10 ml), intensities (4 %, 10 %, 20 %, and 30 % of maximal energy output of 400 W), and ultrasonication times of 1 or 2 min [105]. Temperature was the main factor that affected the reduction of live bacteria, and *S. epidermidis* growth was minimal when temperatures exceeded 45 °C, while there was slight effect when temperatures were between 45 and 50 °C. In addition, it was found that ultrasound combined with temperature was significantly effective for reducing *Cronobacter sakazakii* (*Enterobacter sakazakii*) [2].

For yeast inactivation, it was found that ultrasonication could achieve a desired 5-log reduction in yeast cells *Pichia fermentans* at a moderate temperature (45 °C) [3]. *S. cerevisiae* cells were ultrasonicated in a Sabouraud broth at 35, 45, and 55 °C (20 kHz, wave amplitude in the range of 71–107 μm), and it was found that

inactivation at 55 °C and 45 °C increased significantly compared to 35 °C [48]. However, the increase in bacteria inactivation did not increase linearly with the increase in temperature [32, 66].

Effects of External Pressure

An increase of rapid and violent collapses of microbubbles occurs when external pressure increases [71]. For instance, D-values (the time it takes to inactivate 99 % of bacteria under well-defined processing conditions) for *Y. enterocolitica* decreased from 1.52 to 0.20 min when this bacterium was ultrasonicated at atmospheric pressure and 600 kPa [93]. However, other authors reported that increase of the pressure applied during sonication above a certain threshold (400 kPa) did not further improve bacterial inactivation [31, 93]. This was explained by the fact that ultrasonic field cannot overcome the cohesive forces due to high hydrostatic pressure applied, resulting in the decrease of the number of cavities generated [31, 93]. It was found that the upper limit was 300 kPa [66]. Inactivation of *E. coli* cells with ultrasonication, manosonication (MS), thermosonication (TS), and manothermosonication (MTS) was reported [66]. They found that the combination of ultrasonication with heat and/or pressurization significantly shortened the treatment time to obtain a 5-log reduction of bacteria. The inactivation of *B. subtilis* spores was tested using MS and combined MS/heat treatment [94]. It was found that approximately 99 % of the *B. subtilis* spores were inactivated at 500 kPa, with 117 μm of amplitude for 12 min by MS treatment, and there was a synergistic effect on spore inactivation by using heat treatment at 70–90 °C with MS at 20 kHz, 300 kPa, and 117 μm for 6 min [94]. The D-value decreased progressively during the ultrasonic inactivation of *C. sakazakii* with the increasing pressure—it had a 62 % decrease when pressure rose from 0 Pa to 100 kPa and a further 33 % decrease when the pressure changed from 200 to 300 kPa [14].

Media

Cavities cannot be generated easily in highly viscous media because the vibration of ultrasound waves is impeded [99]. There are still some disagreements about the effects of the sonicated volume, the pH of the medium, and the initial number of bacteria, on the inactivation of bacteria. However, many researchers indicated that bacteria and yeasts were more sensitive to ultrasound treatment when they are in low numbers.

Viscosity and Media

The effects of ultrasound inactivation on microorganisms are different when they are present in a food product compared to microbiological aqueous media. For instance, it was found that, after ultrasonication for 10 min, a 0.78-log reduction was achieved on *Salmonella* in milk, compared to a 4-log reduction when they were suspended in peptone water (160 kHz, 100 W) [64]. Cameron and co-workers isolated three

species of microbes from pasteurized milk, including *E. coli*, *S. cerevisiae*, and *Lactobacillus acidophilus*. After ultrasound treatment (20 kHz, 750 W), they reported that the reductions were more than 99 % for *E. coli* and *S. cerevisiae* and 72 % and 84 % for *L. acidophilus* when sonicated in saline solution and UHT milk, respectively [23]. The resistance to MS treatment for *C. sakazakii* was found to increase with decreasing in water activity [13]. In this case water activity was tuned by the addition of sucrose (44.4 % (w/v) of sucrose to achieve a water activity to 0.94). It is likely that the effect of water activity in this case is due to the increase in viscosity of the medium. In contrast, there was no significant difference in the inactivation rate of *E. coli* by ultrasound when using 0.1 M phosphate-buffered saline (PBS) or 0.9 % (w/v) sodium chloride (saline) [75]. This is again likely due to the fact that the viscosities of these two media are very similar.

Effect of the viscosity of the medium was suggested in the case of the inactivation of bacteria in milk system with different amounts of total solids. *Listeria innocua* ATCC 51742, in milks with different butterfat contents, was ultrasonicated (24 kHz, 120 μm amplitude, 63 °C) for up to 30 min [16]. The rate of inactivation increased with the decrease of fat content, and 2.5-, 3.2-, 4.5-, and 4.9-log reductions were obtained for milk with 3.47 %, 2 %, and 1 % butterfat and fat-free milk, respectively [16]. The effect of the media viscosity was also shown in the case of the inactivation of *E. aerogenes* dispersions in water or reconstituted milks of different concentrations, by low-frequency ultrasound (20 kHz, 8 W, sample volume 15 ml) [43]. The log reductions after 60 min sonication were 3.64, 2.73 (±0.23), 2.31, and 2.21 for the bacteria in water, 5 % milk (viscosity 1.072 mPa.s), 10 % milk (viscosity 1.293 mPa.s), and 15 % milk (viscosity 1.735 mPa.s), respectively.

Volume

Volume of bacteria used in different studies varies vastly from few milliliters to more than 1 l [65, 113]. The volumes used depend on the ultrasound equipment and the objective of the experiments. Normally the inactivation rate decreases with the increasing volume when the same ultrasound equipment and conditions are used. This is due to the fact that the actual ultrasonic energy delivered per milliliter of media (i.e., W/ml) is greater for a small volume of working suspensions than for a large one [51]. For instance, it was found that about 70 % and 30 % of *B. subtilis* were inactivated in volumes of 100 ml and 150 ml, respectively, while almost no bacteria were inactivated in a volume of 200 ml, when sonicated at 20 kHz for 15 min [58]. In another study, the effectiveness of ultrasound treatment of *Salmonella enteritidis* decreased when the volume of whole egg liquid was increased from 12.5 ml to 25 ml; a log reduction of 2.30 and 1.62, respectively, was reported [51]. The removal percentage of *E. coli* was 90, 86, and 85 % when treated in an ultrasonic bath at 42 kHz with a power of 70 W for 30 min, in volumes of 200, 400, and 600 ml, respectively [34]. These observations clearly suggested that the microbial inactivation is volume dependent, in order to achieve same effectiveness, higher power is required.

pH

The use of pH to assist ultrasound inactivation of bacteria has been also investigated. However, there are some discrepancies in the case of *E. coli* ATCC 25922 treated at pH 2.5 and 4.0 using both citric acid and malic acid for pH adjustment [99]. The study found the bacteria were slightly resistant to ultrasound at higher pH (5.1-log reduction) than in lower pH (5.4-log reduction), while the type of acid used did not affect the results significantly. However, it was reported that there were no significant differences in *D*-values when *S. cerevisiae* KE 162 was sonicated (20 kHz, 71.4 μm, 35 °C) at pH 5.6 and 3.0, and the *D*-values were 29.1 and 30.9 min, respectively [48]. It was also reported that the pH, ranging from 4.0 to 7.0, did not influence the effects of MS treatment (20 kHz, 117 μm, 200 kPa) on *C. sakazakii* [14]. Note that most studies focused on low-frequency ultrasound treatment, and that at the best of our knowledge, there are no reports on the effect of high-frequency ultrasound treatment of bacteria under different pH conditions. This fundamental knowledge is important, since pH may affect sonochemical reactions in high-frequency system.

Initial Microbial Number

The majority of publications reported that the ultrasound inactivation of bacteria is more efficient on low initial concentrations of microorganisms compared to high initial microorganism concentrations. It was reported that 99.9 % of *E. coli* K12 were inactivated within 3 min at a concentration of 4×10^6 CFU/ml, while 4 min was needed to achieve the same effect on a concentration of 2×10^9 CFU/ml (20 kHz, 12.57 W/cm^3) [53]. *S. cerevisiae* A50 was ultrasonicated by a horn-type sonicator at 27.5 kHz at a range of initial numbers (10^2 to 10^5 cell/ml), and low initial concentrations of cells were more sensitive to ultrasound (about 1.8-log reduction for 10^2 cell/ml) than high concentrations (about 0.3-log reduction for 10^5 cell/ml) [111]. However, it was also reported that there were no significant effects of the initial concentrations on the inactivation process. For instance, *Mycobacterium* sp. 6PY1 suspensions were inactivated by ultrasound at 20 and 612 kHz for 70 min, at concentrations of 2.15×10^{-3} to 1.4×10^{-2} mg protein/L. In this study the concentration was given as the amount of protein per liter. The results showed that independently of the concentration, a removal of approximately 93 % and 35.5 % at 20 and 612 kHz, respectively, was achieved [6].

Intuitively one would expect that the increase in number of microorganism will decrease the rate of inactivation, due to the increase in viscosity and the clumping of the microorganisms. However, other parameters, such as the bacteria characteristics and ultrasound energy, might also affect the relationship between the initial number and the extent of bacteria inactivation.

Properties of Microorganisms

The mechanisms of microorganism inactivation are normally due to the damage of cell structure including cell envelope disruption or physiological dysfunctions such

as function loss of key enzymes [69]. Different species of microbes have different sensitivities to ultrasonication. The idea that gram-positive bacteria are more resistant to ultrasonication than gram-negative bacteria has dominated in the literature for some time. However, recently some publications have shown that there is no significant difference in the inactivation of both types of bacteria. Disagreements were also reported when considering the shape and size of the microorganisms.

The Type of Cell Wall

Some reports showed that gram-negative bacteria were more sensitive to ultrasonic inactivation than gram-positive bacteria, due to the cell wall of gram-negative bacteria being thinner and weaker compared to that of gram-positive bacteria. This was reported as early as 1975 [5, 9]. More recently, gram-positive streptococci were reported to be more resistant to ultrasound than gram-negative bacteria group coliforms [19]. Ultrasound treatment (at 24 kHz and 1500 W/L for 60 min) resulted in average inactivation rates of 99.5 %, 99.2 %, and 99.7 % of the gram-negative bacteria *coliforms*, *fecal coliforms*, and *Pseudomonas* spp., respectively, while only 66 % and 84 % inactivation was reported for gram-positive bacteria *C. perfringens* and *fecal streptococci*, respectively, under the same ultrasound treatment conditions [36]. Gram-negative *E. coli* and gram-positive *L. acidophilus* isolated from pasteurized milk were ultrasonicated at 20 kHz and 750 W for 10 min. The results indicated that more than 99 % of *E. coli* was inactivated, but only 72 % and 84 % of *L. acidophilus* were inactivated in saline solution and UHT milk [23]. Ultrasonication of gram-negative bacteria including *E. coli*, *Pseudomonas aeruginosa*, and *Haemophilus influenzae*, as well as gram-positive bacteria *Enterococcus faecalis*, *S. aureus*, and *S. epidermidis*, was carried out by using an ultrasound generator at different temperatures (6–42 °C, 20 kHz) [75]. The results also showed that the gram-positive bacteria were more resistant to inactivation by ultrasound than the gram-negative bacteria. In another study, gram-positive bacterium *Streptococcus thermophilus* was found to be more resistant than the gram-negative *Pseudomonas fluorescens* (sonicated at 20 kHz) [115].

However, other researchers indicated that ultrasonication (26 kHz) of gram-positive *S. aureus* and *B. subtilis* and gram-negative *E. coli* and *P. aeruginosa* did not show any major differences [101]. Ultrasound experiments at 20 kHz performed on a mixture of gram-negative and gram-positive bacteria, including *E. coli*, *P. fluorescens*, *Chryseobacterium meningosepticum*, *L. acidophilus*, *Lactococcus lactis*, *B. cereus*, and *L. monocytogenes*, also did not show any relationship between gram status and the effects of ultrasonication [22]. These authors explained their observation by the fact that cytoplasmic membrane of these microorganisms consists of a lipoprotein bilayer, rather than cell wall, and thus very sensible to ultrasound inactivation.

Size and Shape

Larger cells were reported to be more susceptible to ultrasound than small cells [9, 81]. This is mainly because they have larger surface area, which results, under ultrasonication, in higher tensile forces than in the case of microorganisms with a

smaller surface area [57, 109]. Similarly, it was suggested that the larger cells of *K. pneumoniae* NCTC 418 were more sensitive to ultrasound treatment because of their large cross-sectional area [81]. Rod-shaped bacteria are also reported to be more sensitive than coccus-shaped cells [9] due to their cell surface to volume ratio [27]. However, as for gram status, it was also reported that there was no direct relationship between the size or shape of cells and the effects of ultrasonication [22].

Bacteria with Spores

Microbial spores are resistant to detrimental conditions including extreme temperatures and high or low pH [27, 73]. For example, it would require 4 h at 100 °C to destroy *Bacillus thermophilus* spores, and *B. subtilis* spores have been considered an indicator for the sterilization process because of their high resistance to thermal treatment [27]. Similarly, spore formers were also found to be more resistant to ultrasound than vegetative bacteria [36, 37]. However, ultrasonicated *Bacillus* spores were found to be more sensitive to heat treatment than non-ultrasonicated ones [83], since the cells had been pre-damaged by ultrasound treatment. In another study images of scanning electron microscope (SEM) confirmed the disruption and lysis of the *Bacillus globigii* spores and cracked spores and "pustules" near the surface of spores when subjected to ultrasound treatment [26].

Growth Phases

The effect of ultrasound on microorganisms in their different growth phase has not been extensively considered. It was however reported that dividing yeast cells were more vulnerable to ultrasonication than when in their stationary phase, because the dividing yeast cells or diploid cells were much larger than haploid cells [109]. Manosonication (20 kHz, pH 7.0 buffer, 117 μm, 200 kPa) of *C. sakazakii* showed that this bacterium was 1.6 times more resistant when in the stationary and death phases than when manosonicated in the log phase [14]. The microorganism growth phase can be very import if it affects the physical characteristics of the microorganism such as its size and shape. Recently Gao et al. [44] reported that *E. aerogenes* suspensions were more sensitive to ultrasonication (20 kHz frequency and sonication time of up to 20 minutes) in exponential growth phase than when they were in stationary phase. This was attributed to its change in morphology from a rodlike in the exponential phase to a coccus shape in the stationary phase.

Viruses

Viruses were also investigated as targets for ultrasound treatment. Three species of virus surrogates were examined including *Murine norovirus* (MNV-1), *Feline calicivirus* (FCV-F9), and MS2 bacteriophage, by using high-intensity ultrasound treatment at 20 kHz for 2 to 30 min [106]. However, the ultrasound treatment alone was not sufficient to inactivate these viruses in food such as orange juice. Thus, it was recommended that a combination of ultrasound with other processing techniques, such as heat and high pressure, is normally required to achieve virus inactivation. The bacteriophages ΦX174 and MS2 were treated different high-frequency ultrasound (582, 862, and 1142 kHz, 133 W) in combination with visible

light (conditions of visible light treatment were not given). It was found that these bacteriophages were sensitive to ultrasound treatment at the lower frequencies (582 and 862 kHz), and that ΦX174 was more resistant to ultrasound than MS2 [29].

Ultrasound as a Hurdle Technology

Although ultrasound treatment alone can inactivate some bacteria, however it still requires high power to reach a 100 % kill rate, which renders the technique expensive [12]. As a result, combinations with other inactivation technologies can be used to lower the processing cost and improve its efficiency. Typical methods which can be combined with ultrasound are thermal, high pressure, or both; resulting processes are termed manosonication (MS), thermosonication (TS), and manothermosonication (MTS) as mentioned above, respectively. Other technologies include pulsed magnetic fields (PMF), pulsed electric fields (PEF), high-intensity light pulses (HILP), ultraviolet (UV), supercritical carbon dioxide (SC-CO$_2$), and the addition of catalyst such as titanium dioxide (TiO$_2$) or disinfectants.

Some applications of MS and MTS have been covered previously in this chapter. In addition, MTS treatment at 300 kPa for 12 min inactivated 75 % to 99.9 % of *B. subtilis* spores at ultrasound amplitudes of 90 to 150 μm, and the inactivation of *B. subtilis* increased further when the processing temperature was increased to 70 °C [94]. Because of its relatively high viscosity, compared to water, combination of heat and ultrasound (MS) treatments has been used in the case of milk systems. It was found that *L. monocytogenes* and total aerobic bacteria can be inactivated with TS (20 kHz, 150 W, 118 W/cm^2, 18 min) [32]. A 4.82-log reduction of total aerobic bacteria was achieved with mild heat (57 °C) in raw milk compared to a 3.13-log reduction by ultrasound treatment alone. TS caused a 5.34-log reduction for *L. monocytogenes* in UHT milk, while only a 3.69-log reduction was achieved by sonication alone. It was also reported that the inactivation of *B. subtilis* in milk was more efficient by TS than either heat or ultrasonication alone (20 kHz, 150 W, 70 − 95 °C) [46]. The inactivation of *Listeria innocua* and mesophilic bacteria in raw whole milk by ultrasound treatment was studied using an ultrasonic processor (24 kHz, 120 μm, 400 W) [17]. When sonicated for 10 min, a 5-log reduction was achieved under mild temperature (63 °C); in contrast, a 5.3-log reduction was achieved using thermal pasteurization alone.

Ultrasound (20 kHz) and PEF and ultrasound and HILP, emerging nonthermal technologies, were also used for the inactivation of *E. coli* and *L. innocua* [80]. The combination of these two processes achieved a 4.0-log reduction for *E. coli*, compared to a 2.6-log reduction for each process alone. While the application of PEF and ultrasound achieved only a 1.6-log for *L. innocua*, this remained much higher than the reduction achieved by PEF (0.3-log reduction) or ultrasound (1.1-log reduction) alone [80]. In combination with HILP, the inactivation of *E. coli* (3.9-log reduction) was not much different from the levels of inactivation achieved by HILP alone (3.5-log reduction). In contrast, combination of ultrasound and HILP resulted in a 4.1-log reduction of *L. innocua* compared to a 2.7-log reduction by HILP alone and a 1.1-log

reduction by ultrasound alone. In addition, the combination of ultrasound and HILP resulted in a marked increase in the inactivation of *E. coli*, from a 2.7-log reduction for TS (24 kHz, 100 μm, 50 °C, 5 min) to nearly a 6-log reduction when TS and HILP treatments were used [79]. Ultrasound was also combined with PMF treatment to inactivate *E coli* ATCC 11775, but this did not achieve any significant difference compared to ultrasound treatment alone (20 kHz, 70 W) [100].

The combination of UV-C (ultraviolet radiation with a wavelength of 254 nm) and ultrasound (20 kHz) was also reported to be very effective on the inactivation of common fish pathogens such as heterotrophic bacteria and *Paramecium* spp. in recirculating aquaculture water, compared to ultrasound alone which was ineffective in inactivating these pathogens [15].

The SC-CO_2 technique is another nonthermal processing method used for bacteria inactivation. SC-CO_2 (350 bar, 36 °C) caused a 0.3-log reduction for *E. coli* DH1 in 5 min, and it achieved a 1-log reduction using high-power ultrasound treatment (30 kHz, 40 ± 5 W); the combination of these two methods resulted in a 8.5-log reduction [85]. Similarly, 2 min application of ultrasound and SC-CO_2 resulted in 7-log reduction for *S. cerevisiae* [84]. The main reasons for such a synergistic effect could be because the solubilization of CO_2 was enhanced and the transfer of cell-medium mass was accelerated by ultrasound [85].

TiO2 is sometimes used when ultrasonication is used for disinfection purposes [33, 36, 92]. The presence of TiO2 is believed to promote the formation of hydroxyl radicals by heterogeneous nucleation, and that it can also form TiO3 that can aggravate oxidative damage to bacteria. In addition, excitation of TiO2 by the thermal and sonoluminescence effects can lead to light-induced photocatalytic inactivation [33, 36, 92]. The addition of TiO2 during ultrasonication was reported to cause damage and accelerated peroxidation of the cell membrane of E. coli [92]. Another disinfectant trialed with ultrasound treatment is Korsolex AF, an aldehyde-free disinfectant that contained 5.1 % dodecylbispropylene diamine and 16.5 % laurylpropylene diamine [55]. The combination of ultrasound and Korsolex AF resulted in the inactivation of *S. aureus*, *P. aeruginosa*, and *Candida albicans*, while ultrasound alone (35 kHz, 0.66 W/cm^2 for 1 h) did not cause significant reduction in these bacteria. Biofilm was also treated by ultrasound, but ultrasound alone was not sufficient to inactivate the biofilm *E. coli* at either 70 kHz or 500 kHz, but it enhanced the killing by the antibiotic gentamicin [88].

Inactivation of Microorganisms in Solid Foods

Most of the researches dealing with the inactivation of microorganisms in food systems were carried out in model liquid food matrices such as water, juice, milk, fruit, and solid or semisolid foods such as vegetables, meat, and eggs (Table 1). Bacteria inactivation in liquid foods has been covered in previous sections. In this section, applications in semisolid or solid foods are reviewed. Applications of ultrasound for the treatment of solid foods include apples [52], strawberries [24, 103], plums [28], lettuce [18, 38, 52, 98], carrots [7, 103], cucumbers [103], cherry

Table 1 Some examples of ultrasound inactivation of microbes in foods

Product	Microbes	Initial number	Media volume	Treatments	Ultrasound conditions	Microbial log reduction	References
Model apple juice	*Escherichia coli* ATCC 25922	1×10^6 CFU/ml	50 ml	US	20 kHz, 0.4–37.5 μm, <30 °C; 0–15 min	0.4 μm: 3 7.5 μm: total inactivation in 6 min 37.5 μm: total inactivation in 3 min	[86]
Apple juice	*Alicyclobacillus acidiphilus* DSM14558^T, *Alicyclobacillus acidoterrestris* DSM 3922^T	1.91×10^5-5.82×10^5 CFU/ml	500 ml	US	25 kHz; 200–600 W; <50 °C; 1–30 min	Up to 4.56	[121]
Apple juice	*Saccharomyces cerevisiae* ATCC 4113	$>10^7$ CFU/ml	500 ml	TS	24 kHz; 120 μm; 60 °C; 30 min	Total inactivation	[122]
Apple juice	*Escherichia coli* K12 DSM 1607	N/A	40 ml	TS + LP	24 kHz; 100 μm (85 W/cm²); 40, 50 °C; 2.9, 5 min	TS: up to 2.7 PL: up to 4.9 TS + PL: up to 6	[79]
Apple juice	*Escherichia coli* O157: H7, *Listeria monocytogenes*, *Salmonella* spp., Yeast mixture	Stationary phase	1000 ml	US (Dynashock)/ US + UV-C	28, 45, 100 kHz; up to 600 W (50–100 %); 18.07–44.03 °C; 0–30 min	US: up to about 1.8 US + UV-C: 2.59 for *E. coli* O157: H7 in 15 min	[123]
Model orange juice	*Escherichia coli* (ATCC 25922, NCTC 12900)	1×10^6 CFU/ml	50 ml	US	20 kHz; 0.4–37.5 μm; <30 °C; 15 min	ATCC 25922. 7.5 and 37.5 μm: total inactivation NCTC 12900. 7.5 μm: 2.5; 37.5 μm: 2.7	[86]

Orange juice	Total mesophilic aerobes	N/A	1.4 L	US+/thermal	23, 500 kHz; 120–600 W (60 %); 17.9–88 °C; 15 min	0.1–1.7	[113]
Orange juice	Salmonella spp.	6- to 7-log CFU/ml	250 ml	US+ osmotic pressure	20 kHz; 50 ± 0.2 W, 48 μm (40 %), 0.83 W/ml; 25 ± 2 °C; 6.8–20.4 min	0.3–4.1	[125]
Tomato juice	Pichia fermentans DSM 70090	Stationary phase	80 ml	US	20 kHz; 0.33–0.81 W/ml, 24.4–61 μm; 25 ± 1.0 °C; 10 min	About 1 log to total inactivation	[2]
Milk	Pseudomonas fluorescens NIZO B337, Streptococcus thermophilus B8	10^7 CFU/ml	Up to 100 ml	US	20 kHz; up to 120 μm; 33–76 °C	P. fluorescens: 0.2–4.2 S. thermophilus: 0–2.7	[115]
Reconstituted skim milks	Enterobacter aerogenes	10^8 CFU/ml	20 ml	US	20 kHz, 8–9.2 W, <30 °C	5 wt% skim milk: 2.7, 10 wt% skim milk: 2.3 15 wt% skim milk: 2.2	[45]
Ultrahigh temperature (UHT) milk	Escherichia coli, Lactobacillus acidophilus, Saccharomyces cerevisiae	1×10^4 & 1×10^5 CFU/ml	40 ml	US	20 kHz; 750 W, 124 μm (100 %); 24–26 °C; 10 min	E. coli :4.4 L. acidophilus : 0.8 S. cerevisiae :2.1	[23]
Raw whole milk	Listeria innocua ATCC 51742	Around 10^7 CFU/ml	500 ml	TS/thermal	24 kHz; up to 400 W,40–120 μm (0.86–2.85 W/cm2); 63 ± 0.5 °C; 2–30 min	TS: 5 (10 min) Thermal: 5.3 (30 min)	[17]

(continued)

Table 1 (continued)

Product	Microbes	Initial number	Media volume	Treatments	Ultrasound conditions	Microbial log reduction	References
Reconstituted powdered infant formula	*Cronobacter sakazakii* (NCTC 08155 and ATCC 11467)	About 10^9 CFU/ml	50 ml	US	20 kHz; 24.4–61 μm; 25–50 °C; 10 min	>3	[3]
Raw milk	Total aerobic mesophilic bacteria (TAMB), coliform bacteria (CB)	TAMB: 8.6-log CFU/ml CB: 5.31-log CFU/ml	200 ml	US+ UV-C/thermal	24 kHz; 120 μm (240 W); <30/65 °C; 15/30 min	US+ UV-C (15 min) TAMB: 4.79; CB: 5.31 US (15 min). TAMB: 1.31; CB: 4.01 Thermal (30 min): TAMB: 3.28; CB: 5.31	[124]
Liquid whole egg	*Salmonella enteritidis*	Stationary phase	12.5–25 ml	US/US + thermal/US + PEF/US + HHP	20 kHz; 34.6–40 W; 5–55 °C; 30 s–5 min	US (5 min): 1 US+ Thermal (5 min): 1–2.3 US + PEF: 2.25–2.3 US + HHP (30–150 s): up to 3	[51]
Liquid whole egg	*Escherichia coli K12 DH 5a, Listeria seeligeri* NCTC 11289	*E. coli* ~ 10^8 CFU/ml *L. seeligeri* ~ 10^7 CFU/ml	10 ml	US/US + HHP	20 kHz; 24.6–42.0 W; iced water bath; up to 300 s	*E. coli*: 1–2 *L. seeligeri*: no inactivation	[65]

Tomato paste	*Lactobacillus sporogenes*	1×10^7 CFU/ml	N/A	US + ^{60}Co-γ irradiation	40 kHz; 60–120 W; 20 °C; 0–25 min	Up to total inactivation	(Ye et al. 2009)
Cherry tomatoes	*Salmonella enteritidis* serovar typhimurium ATCC 14028	6-7 log CFU/ml	N/A	US+ commercial sanitizers	40 kHz; 10 min	3.9	[20]
Lettuce	*Escherichia coli* O157:H7, *Salmonella typhimurium*, *L. monocytogenes*	10^9 CFU/ml	N/A	US + organic acids	40 kHz; 30 W/L; 5 min	2.75, 3.18, and 2.87	[98]
Strawberry	Bacteria, mold, and yeast	N/A	N/A	US	25, 28, 40, or 59 kHz; 20 °C; 10 min	According to frequency: *Bacteria:* 0.88, 0.79, 0.66, 0.26 *Mold and yeast:* 1.07, 0.97, 0.54, 0.22	[24]
Skin and meat surfaces of pork jowl	*Escherichia coli*, *Salmonella typhimurium*, *Yersinia enterocolitica*	10^7 or 10^4 CFU/ cm^2	N/A	US + high-pressure steam	30 to 40 kHz; 130 °C; 0.5–2 s	*E. coli* on skin 0.9–3.3, meat 1.0–2.5; *Salmonella* on skin 0.6–3.2; meat 0.4–2.1; *Y. enterocolitica* on skin 0.8–3.6; meat 0.6–2.1	[76]
Egg and eggshell	*Salmonella enteritidis*	7.78-log CFU	200 ml water	TS	24 kHz; 400 W, 60 µm; 54 °C; 5 min	4.8	[21]

Note: The list of abbreviations in the table are *CFU* colony-forming units of microorganisms, *US* ultrasound treatment, *TS* thermosonication, *LP* light pulses, *UV-C* ultraviolet C, *PEF* pulsed electric fields, *HHP* hydraulic high pressure, *N/A* not available

tomatoes [20], red bell peppers [8], spinach leaves [119], white cabbage [103], spring onions [103], and parsley [103]. Since cavitation, which is fundamental to bacteria inactivation, occurs in easily liquid media [107], solid foods need to be immersed in aqueous media during ultrasonication.

As an example, treatment of strawberries was performed by immersing the fruit into a water bath in an ultrasonic chamber at 20 °C and ultrasonicated at different frequencies (25, 28, 40, or 59 kHz) for 10 min [24]. As a result approximately a 0.3- to 0.9-log reduction for bacteria and a 0.2- to 1.1-log reduction for mold and yeast were achieved. The ultrasound treatment at 40 kHz resulted in a significant reduction of decay after 8 days of storage at 5 °C compared to non-treated strawberries. Note that the specific names of the microorganisms were not given in this work.

Because the rate of inactivation in solid or semisolid foods is very low, sanitizers are used in the aqueous medium to improve bacterial inactivation. For example, cherry tomatoes were ultrasonicated in the presence of commercial sanitizers (200 mg/L sodium dichloroisocyanurate or 40 mg/L peracetic acid) for 10 min, and an average of 3.9-log reduction of *Salmonella* typhimurium ATCC 14028 was achieved, compared to ultrasonication or immersion in the sanitizers alone (0.4- to 2.7-log reduction) [20]. When ultrasound treatment of lettuce was performed in the presence of organic acids, an additional 0.8- to 1.0-log reduction of *E. coli* O157:H7, *Salmonella* typhimurium, and *L. monocytogenes* was achieved [98].

In addition to the use of sanitizers, hurdle technologies are also employed. For instance, TS, the combination of thermal and ultrasound treatment (54 °C, 24 kHz, 400 W, 60 μm), was used to decontaminate eggshells, by sonicating a single egg immersed in 200 ml of water [21]. This process was found to be effective against *Salmonella enterica*, *S. enteritidis*, and *Salmonella* typhimurium (approximately a 5-log reduction was achieved on *S. enteritidis*), without affecting the physical characteristics of the eggshells.

In the case of meat samples, the effect of ultrasonication is dependent on the part of the cut that has been sonicated. The MS (in this case a combination of steam and ultrasound) of part of fresh pork jowl inoculated with bacteria showed that 0.6- to 3.6-log reductions were achieved for *E. coli*, *Salmonella* typhimurium, and *Y. enterocolitica* on the skin surface (0.5–2 s). In contrast, 0.4- to 2.5-log reductions were obtained for the meat surface of the pork jowl [76].

Conclusion and Future Directions

While the volume of published literature on bacteria is increasing, the variations in the ultrasound treatment conditions are different from one study to the other. These conditions such as ultrasound equipment, frequencies, ultrasound power and intensity, sample volume, temperature, and initial bacteria number are not always cited. Some of the parameters (e.g., power output) were not expressed in same manner, and some parameters in many publications were not even reported. In some publications the ultrasound conditions are not even given. Further, while ultrasound treatment is known to increase the temperature of the medium, most studies do not record the

maximum temperature reached during sonication. This is an important parameter, since temperature also contributes to the inactivation of bacteria. This makes quantitative comparison of the published results very difficult.

In this literature review, the topics related to ultrasound and bacteria are covered. Microorganisms are well studied and a concise literature exists. Similarly, fundamentals related to ultrasound, particularly ultrasound cavitation, are also well understood. However, there are clearly several gaps in the research works related to the inactivation of bacteria by ultrasound. Firstly, the exact mechanisms still not fully elucidated. While the effects of cavitation are generally offered as an explanation, the exact physics behind the breakup of a microorganism by cavitation is not well understood. Fundamental knowledge requires theoretical modeling of the inactivation of bacteria by ultrasound to confirm the proposed mechanisms. Most of the modeling performed on the experimental data is based on empirical models and is used to fit the data. These models are certainly useful and help compare using mathematical equations the effect of ultrasound on bacteria from a microorganism to another and for different ultrasonication conditions. Recently, Gao et al. [45] proposed a simple model based on the effect of ultrasound cavitation collapse near a microorganism. While this theoretical model agrees qualitatively with the experimental results, further work is needed to fine-tune the model as it still relies on fitting parameters (e.g., exact number of cavitation generated and the physical properties of the bacteria capsule).

The review of the literature performed in this chapter shows that there are clear limitation in the inactivation of some microorganisms, particularly those having thick capsules, such as gram-positive streptococci [44]. This calls to the use of hurdle technologies, including thermosonication and manosonication, since the heating temperature to be used can be lower than those needed in conventional heat or pressure treatments and thus can still result in a better sensory properties of the treated food. A promising method is the combination of supercritical carbon dioxide and sonication which, in addition to be highly effective in the case of some microorganisms (up to a 7-log reduction of *Saccharomyces cerevisiae* in juices), offers also the possibility of being implemented in as a continuous process [84].

Finally, while compared to high-frequency ultrasonication cavitation is important, generation of radicals and hydrogen peroxide when sonicating bacteria in aqueous systems is the dominant effect. More work is needed on the effect of high-frequency ultrasound; while this might not be relevant to the foods due to the amounts of hydrogen peroxide generated, it can be useful in non-food application such as water treatment and decontamination.

References

1. Abedi-moghaddam N, Bulić A, Henderson L, Lam E (2004) Survival of *Escherichia coli* to UV irradiation during exponential and stationary phases of growth. Journal of Experimental Microbiology and Immunology 5:37–43

2. Adekunte A, Valdramidis VP, Tiwari BK, Slone N, Cullen PJ, Donnell CP, Scannell A (2010) Resistance of *Cronobacter sakazakii* in reconstituted powdered infant formula during ultrasound at controlled temperatures: a quantitative approach on microbial responses. International Journal of Food Microbiology 142:53–59

3. Adekunte AO, Tiwari BK, Cullen PJ, Scannell AGM, O'Donnell CP (2010) Effect of sonication on colour, ascorbic acid and yeast inactivation in tomato juice. Food Chemistry 122:500–507

4. Ahimou F, Jacques P, Deleu M (2000) Surfactin and iturin A effects on *Bacillus subtilis* surface hydrophobicity. Enzyme and Microbial Technology 27:749–754

5. Ahmed FIK, Russell C (1975) Synergism between ultrasonic waves and hydrogen peroxide in the killing of micro-organisms. Journal of Applied Bacteriology 39:31–40

6. Al Bsoul A, Magnin JP, Commenges-Bernole N, Gondrexon N, Willison J, Petrier C (2010) Effectiveness of ultrasound for the destruction of *Mycobacterium* sp. strain (6PY1). Ultrasonics Sonochemistry 17:106–110

7. Alegria C, Pinheiro J, Gonçalves EM, Fernandes I, Moldão M, Abreu M (2009) Quality attributes of shredded carrot (Daucus carota L. cv. Nantes) as affected by alternative decontamination processes to chlorine. Innovative Food Science & Emerging Technologies 10:61–69

8. Alexandre EMC, Brandão TRS, Silva CLM (2013) Impact of non-thermal technologies and sanitizer solutions on microbial load reduction and quality factor retention of frozen red bell peppers. Innovative Food Science & Emerging Technologies 17:99–105

9. Alliger H (1975) Ultrasonic disruption. American Laboratory 10:75–85

10. An YH, Dickinson RB, Doyle RJ (2000) Mechanisms of bacterial adhesion and pathogenesis of implant and tissue infections. In: An YH, Friedman RJ (eds) Handbook of bacterial adhesion: principles, methods, and applications. Humana Press, Totowa, pp 1–27

11. An YH, Friedman RJ (2000) Appendix 1. In: An YH, Friedman RJ (eds) Handbook of bacterial adhesion: principles, methods, and applications. Humana Press, Totowa, pp 627–628

12. Antoniadis A, Poulios I, Nikolakaki E, Mantzavinos D (2007) Sonochemical disinfection of municipal wastewater. Journal of Hazardous Materials 146:492–495

13. Arroyo C, Cebrian G, Pagan R, Condon S (2011) Inactivation of *Cronobacter sakazakii* by manothermosonication in buffer and milk. International Journal of Food Microbiology 151:21–28

14. Arroyo C, Cebrian G, Pagan R, Condon S (2011) Inactivation of *Cronobacter sakazakii* by ultrasonic waves under pressure in buffer and foods. International Journal of Food Microbiology 144:446–454

15. Bazyar Lakeh AA, Kloas W, Jung R, Ariav R, Knopf K (2013) Low frequency ultrasound and UV-C for elimination of pathogens in recirculating aquaculture systems. Ultrasonics Sonochemistry 20:1211–1216

16. Bermúdez-Aguirre D, Barbosa-Cánovas GV (2008) Study of butter fat content in milk on the inactivation of *Listeria innocua* ATCC 51742 by thermo-sonication. Innovative Food Science & Emerging Technologies 9:176–185

17. Bermúdez-Aguirre D, Corradini MG, Mawson R, Barbosa-Cánovas GV (2009) Modeling the inactivation of *Listeria innocua* in raw whole milk treated under thermo-sonication. Innovative Food Science & Emerging Technologies 10:172–178

18. Birmpa A, Sfika V, Vantarakis A (2013) Ultraviolet light and ultrasound as non-thermal treatments for the inactivation of microorganisms in fresh ready-to-eat foods. International Journal of Food Microbiology 167:96–102

19. Blume T (2004) Improved wastewater disinfection by ultrasonic pre-treatment. Ultrasonics Sonochemistry 11:333–336

20. Brilhante São José JF, Dantas Vanetti MC (2012) Effect of ultrasound and commercial sanitizers in removing natural contaminants and *Salmonella enterica* Typhimurium on cherry tomatoes. Food Control 24:95–99

21. Cabeza MC, Cambero MI, de la Hoz L, García ML, Ordóñez JA (2011) Effect of the thermoultrasonic treatment on the eggshell integrity and their impact on the microbial quality. Innovative Food Science & Emerging Technologies 12:111–117

22. Cameron M (2007) Impact of low-frequency high-power ultrasound on spoilage and potentially pathogenic dairy microbes. University of Stellenbosch

23. Cameron M, McMaster LD, Britz TJ (2008) Electron microscopic analysis of dairy microbes inactivated by ultrasound. Ultrasonics Sonochemistry 15:960–964

24. Cao S, Hu Z, Pang B, Wang H, Xie H, Wu F (2010) Effect of ultrasound treatment on fruit decay and quality maintenance in strawberry after harvest. Food Control 21:529–532

25. Carlin F, Brillard J, Broussolle V, Clavel T, Duport C, Jobin M, Guinebretière M-H, Auger S, Sorokine A, Nguyen-Thé C (2010) Adaptation of *Bacillus cereus*, an ubiquitous worldwide-distributed foodborne pathogen, to a changing environment. Food Research International 43:1885–1894

26. Chandler DP, Brown J, Bruckner-Lea CJ, Olson L, Posakony GJ, Stults JR, Valentine NB, Bond LJ (2001) Continuous spore disruption using radially focused, high-frequency ultrasound. Analytical Chemistry 73:3784–3789

27. Chemat F, Zill e H, Khan MK (2011) Applications of ultrasound in food technology: processing, preservation and extraction. Ultrasonics Sonochemistry 18:813–835

28. Chen Z, Zhu C (2011) Combined effects of aqueous chlorine dioxide and ultrasonic treatments on postharvest storage quality of plum fruit (Prunus salicina L.). Postharvest Biology and Technology 61:117–123

29. Chrysikopoulos CV, Manariotis ID, Syngouna VI (2013) Virus inactivation by high frequency ultrasound in combination with visible light. Colloids and Surfaces B Biointerfaces 107:174–179

30. Ciccolini L, Taillandier P, Wilhem AM, Delmas H, Strehaiano P (1997) Low frequency thermo-ultrasonication of *Saccharomyces cerevisiae* suspensions: effect of temperature and of ultrasonic power. Chemical Engineering Journal 65:145–149

31. Condón S, Raso J, Pagán R (2004) Microbial inactivation by ultrasound. In: Cano MP, Tapia MS, Barbosa-Canovas GV (eds) Novel food processing technologies. CRC Press, Boca Raton, pp 423–442

32. D'Amico DJ, Silk TM, Wu JR, Guo MR (2006) Inactivation of microorganisms in milk and apple cider treated with ultrasound. J Food Prot 69:556–563

33. Dadjour MF, Ogino C, Matsumura S, Nakamura S, Shimizu N (2006) Disinfection of *Legionella pneumophila* by ultrasonic treatment with TiO_2. Water research 40:1137–1142

34. Dehghani MH (2005) Effectiveness of ultrasound on the destruction of *E. coli*. American Journal of Environmental Sciences 1:187–189

35. Dickson JS, Koohmaraie M (1989) Cell surface charge characteristics and their relationship to bacterial attachment to meat surfaces. Applied and Environmental Microbiology 55:832–836

36. Drakopoulou S, Terzakis S, Fountoulakis MS, Mantzavinos D, Manios T (2009) Ultrasound-induced inactivation of gram-negative and gram-positive bacteria in secondary treated municipal wastewater. Ultrasonics Sonochemistry 16:629–634

37. Earnshaw RG, Appleyard J, Hurst RM (1995) Understanding physical inactivation processes: combined preservation opportunities using heat, ultrasound and pressure. International Journal of Food Microbiology 28:197–219

38. Elizaquivel P, Sanchez G, Selma MV, Aznar R (2012) Application of propidium monoazide-qPCR to evaluate the ultrasonic inactivation of *Escherichia coli* O157:H7 in fresh-cut vegetable wash water. Food Microbiology 30:316–320

39. Entezari MH, Hagh Nazary S, Haddad Khodaparast MH (2004) The direct effect of ultrasound on the extraction of date syrup and its micro-organisms. Ultrasonics Sonochemistry 11:379–384

40. Franz CM, Stiles ME, Schleifer KH, Holzapfel WH (2003) Enterococci in foods - a conundrum for food safety. International Journal of Food Microbiology 88:105–122

41. Furuta M, Yamaguchi M, Tsukamoto T, Yim B, Stavarache CE, Hasiba K, Maeda Y (2004) Inactivation of *Escherichia coli* by ultrasonic irradiation. Ultrasonics Sonochemistry 11:57–60

42. Gallardo-Moreno AM, Navarro-Perez ML, Vadillo-Rodriguez V, Bruque JM, Gonzalez-Martin ML (2011) Insights into bacterial contact angles: difficulties in defining hydrophobicity and surface Gibbs energy. Colloids and Surfaces B Biointerfaces 88:373–380

43. Gao S, Hemar Y, Lewis GD, Ashokkumar M (2014) Inactivation of Enterobacter aerogenes in reconstituted skim milk by high-and low-frequency ultrasound. Ultrasonics Sonochemistry 21:2099–2106

44. Gao S, Lewis GD, Ashokkumar M, Hemar Y (2014) Inactivation of microorganisms by low-frequency high-power ultrasound: 1. Effect of growth phase and capsule properties of the bacteria. Ultrasonics Sonochemistry 21:446–453

45. Gao S, Lewis GD, Ashokkumar M, Hemar Y (2014) Inactivation of microorganisms by low-frequency high-power ultrasound: 2. A simple model for the inactivation mechanism. Ultrasonics Sonochemistry 21:454–460

46. Garcia ML, Burgos J, Sanz B, Ordoñez JA (1989) Effect of heat and ultrasonic waves on the survival of two strains of *Bacillus subtilis*. Journal of Applied Microbiology 67:619–628

47. Glauert AM, Thornley MJ (1969) The topography of the bacterial cell wall. Annual Review of Microbiology 23:159–198

48. Guerrero S, López-Malo A, Alzamora SM (2001) Effect of ultrasound on the survival of *Saccharomyces cerevisiae*: influence of temperature, pH and amplitude. Innovative Food Science & Emerging Technologies 2:31–39

49. Gurtler JB, Kornacki JL, Beuchat LR (2005) *Enterobacter sakazakii*: A coliform of increased concern to infant health. International Journal of Food Microbiology 104:1–34

50. Hogt AH, Dankert J, Feijen J (1985) Adhesion of *Staphylococcus epidermidis* and *Staphylococcus saprophyticus* to a hydrophobic biomaterial. Microbiology 131:2485–2491

51. Huang E, Mittal GS, Griffiths MW (2006) Inactivation of *Salmonella enteritidis* in liquid whole egg using combination treatments of pulsed electric field, high pressure and ultrasound. Biosystems Engineering 94:403–413

52. Huang T-S, Xu C, Walker K, West P, Zhang S, Weese J (2006) Decontamination efficacy of combined chlorine dioxide with ultrasonication on apples and lettuce. Journal of Food Science 71:M134–M139

53. Hunter G, Lucas M, Watson I, Parton R (2008) A radial mode ultrasonic horn for the inactivation of *Escherichia coli* K12. Ultrasonics Sonochemistry 15:101–109

54. Hussain M, Wilcox MH, White PJ (1993) The slime of coagulase-negative staphylococci: biochemistry and relation to adherence. FEMS Microbiology Reviews 10:191–207

55. Jatzwauk L, Schöne H, Pietsch H (2001) How to improve instrument disinfection by ultrasound. Journal of Hospital Infection 48:S80–S83

56. Jørgensen NOG, Stepanaukas R, Pedersen A-GU, Hansen M, Nybroe O (2003) Occurrence and degradation of peptidoglycan in aquatic environments. FEMS Microbiol Ecol 46:269–280

57. Joyce E, Al-Hashimi A, Mason TJ (2011) Assessing the effect of different ultrasonic frequencies on bacterial viability using flow cytometry. Journal of Applied Microbiology 110:862–870

58. Joyce E, Phull SS, Lorimer JP, Mason TJ (2003) The development and evaluation of ultrasound for the treatment of bacterial suspensions. A study of frequency, power and sonication time on cultured *Bacillus* species. Ultrasonics Sonochemistry 10:315–318

59. Jyoti KK, Pandit AB (2003) Hybrid cavitation methods for water disinfection: simultaneous use of chemicals with cavitation. Ultrasonics Sonochemistry 10:255–264

60. Kiers PJ, Bos R, van der Mei HC, Busscher HJ (2001) The electrophoretic softness of the surface of *Staphylococcus epidermidis* cells grown in a liquid medium and on a solid agar. Microbiology 147:757–762

61. Koda S, Miyamoto M, Toma M, Matsuoka T, Maebayashi M (2009) Inactivation of *Escherichia coli* and *Streptococcus mutans* by ultrasound at 500kHz. Ultrasonics Sonochemistry 16:655–659

62. Kohnen W, Jansen B (2000) Changing material surface chemistry for preventing bacterial adhesion. In: An YH, Friedman RJ (eds) Handbook of bacterial adhesion. Humana Press, Totowa, pp 581–589

63. Kolter R, Siegele DA, Tormo A (1993) The stationary phase of the bacterial life cycle. Annual Review of Microbiology 47:855–874

64. Lee BH, Kermasha S, Baker BE (1989) Thermal, ultrasonic and ultraviolet inactivation of *Salmonella* in thin films of aqueous media and chocolate. Food Microbiology 6:143–152

65. Lee DU, Heinz V, Knorr D (2003) Effects of combination treatments of nisin and high-intensity ultrasound with high pressure on the microbial inactivation in liquid whole egg. Innovative Food Science and Emerging Technologies 4:387–393

66. Lee H, Zhou B, Liang W, Feng H, Martin SE (2009) Inactivation of *Escherichia coli* cells with sonication, manosonication, thermosonication, and manothermosonication: Microbial responses and kinetics modeling. Journal of Food Engineering 93:354–364

67. Liu D, Zeng X-A, Sun D-W, Han Z (2013) Disruption and protein release by ultrasonication of yeast cells. Innovative Food Science & Emerging Technologies 18:132–137

68. Loureiro V (2000) Spoilage yeasts in foods and beverages. Food Research International 33:247–256

69. Manas P, Pagan R (2005) Microbial inactivation by new technologies of food preservation. Journal of Applied Microbiology 98:1387–1399

70. Mason TJ (1990) Sonochemistry: the uses of ultrasound in chemistry. The Royal Society of Chemistry Press, Cambridge

71. Mason TJ, Lorimer JP (1988) Sonochemistry: theory, applications and uses of ultrasound in chemistry. Ellis Harwood, Chichester, pp 1–50

72. McNamara CJ, Lemke MJ, Leff LG (1997) Characterization of hydrophobic stream bacteria based on adhesion to n-octane. Ohio J Sci 97:59–61

73. Moir A, Smith DA (1990) The genetics of bacterial spore germination. Annual Review of Microbiology 44:531–553

74. Monod J (1949) The growth of bacterial cultures. Annual Review of Microbiology 3:371–394

75. Monsen T, Lovgren E, Widerstrom M, Wallinder L (2009) In vitro effect of ultrasound on bacteria and suggested protocol for sonication and diagnosis of prosthetic infections. Journal of Clinical Microbiology 47:2496–2501

76. Morild RK, Christiansen P, Sorensen AH, Nonboe U, Aabo S (2011) Inactivation of pathogens on pork by steam-ultrasound treatment. J Food Prot 74:769–775

77. Mozes N, Léonard AJ, Rouxhet PG (1988) On the relations between the elemental surface composition of yeasts and bacteria and their charge and hydrophobicity. Biochemica et Biophysica Acta 945:324–334

78. Mozes N, Rouxhet PG (1987) Methods for measuring hydrophobicity of microorganisms. Journal of Microbiological Methods 6:99–112

79. Muñoz A, Caminiti IM, Palgan I, Pataro G, Noci F, Morgan DJ, Cronin DA, Whyte P, Ferrari G, Lyng JG (2012) Effects on *Escherichia coli* inactivation and quality attributes in apple juice treated by combinations of pulsed light and thermosonication. Food Research International 45:299–305

80. Muñoz A, Palgan I, Noci F, Cronin DA, Morgan DJ, Whyte P, Lyng JG (2012) Combinations of selected non-thermal technologies and antimicrobials for microbial inactivation in a buffer system. Food Research International 47:100–105

81. Nesaratnam ST, Wase DAJ, Blakebrough N (1982) The susceptibility to ultrasonic disintegration of *Klebsiella pneumoniae* NCTC 418. European Journal of Applied Microbiology and Biotechnology 15:56–58

82. Novick A (1955) Growth of bacteria. Annual Review of Microbiology 9:97–110

83. Ordoñez JA, Burgos J (1976) Effect of ultrasonic waves on the heat resistance of *Bacillus* spores. Applied and Environmental Microbiology 31:183–184

84. Ortuño C, Martínez-Pastor MT, Mulet A, Benedito J (2013) Application of high power ultrasound in the supercritical carbon dioxide inactivation of Saccharomyces cerevisiae. Food Research International 51:474–481

85. Ortuño C, Martínez-Pastor MT, Mulet A, Benedito J (2012) An ultrasound-enhanced system for microbial inactivation using supercritical carbon dioxide. Innovative Food Science & Emerging Technologies 15:31–37

86. Patil S, Bourke P, Kelly B, Frías JM, Cullen PJ (2009) The effects of acid adaptation on *Escherichia coli* inactivation using power ultrasound. Innovative Food Science & Emerging Technologies 10:486–490

87. Perkins HR (1963) Chemical structure and biosynthesis of bacterial cell walls. Bacteriological Reviews 27:18–55

88. Peterson RV, Pitt WG (2000) The effect of frequency and power density on the ultrasonically-enhanced killing of biofilm-sequestered *Escherichia coli*. Colloids and Surfaces B: Biointerfaces 17:219–227

89. Piyasena P, Mohareb E, McKellar RC (2003) Inactivation of microbes using ultrasound: a review. International Journal of Food Microbiology 87:207–216

90. Prescott LM, Harley JP, Klein DA (2002) Microbiology. McGraw-Hill Higher Education, Boston

91. Prosser JI, Tough AJ (1991) Growth mechanisms and growth kinetics of filamentous micro-organisms. Critical Reviews in Biotechnology 10:253–274

92. Rahman MM, Ninomiya K, Ogino C, Shimizu N (2010) Ultrasound-induced membrane lipid peroxidation and cell damage of *Escherichia coli* in the presence of non-woven TiO_2 fabrics. Ultrasonics Sonochemistry 17:738–743

93. Raso J, Pagan R, Condon S, Sala F (1998) Influence of temperature and pressure on the lethality of ultrasound. Applied and Environmental Microbiology 64:465–471

94. Raso J, Palop A, Pagan R, Condon S (1998) Inactivation of *Bacillus subtilis* spores by combining ultrasonic waves under pressure and mild heat treatment. Journal of Applied Microbiology 85:849–854

95. Ray B (2004) Fundamental food microbiology. CRC Press, Boca Raton

96. Russell JB, Cook GM (1995) Energetics of bacterial growth: balance of anabolic and catabolic reactions. Microbiological Reviews 59:48–62

97. Russell NJ (2002) Bacterial membranes: the effects of chill storage and food processing. An overview. International Journal of Food Microbiology 79:27–34

98. Sagong HG, Lee SY, Chang PS, Heu S, Ryu S, Choi YJ, Kang DH (2011) Combined effect of ultrasound and organic acids to reduce *Escherichia coli* O157:H7, *Salmonella* Typhimurium, and *Listeria monocytogenes* on organic fresh lettuce. International Journal of Food Microbiology 145:287–292

99. Salleh-Mack SZ, Roberts JS (2007) Ultrasound pasteurization: The effects of temperature, soluble solids, organic acids and pH on the inactivation of *Escherichia coli* ATCC 25922. Ultrasonics Sonochemistry 14:323–329

100. San Martin MF, Harte FM, Lelieveld H, Barbosa-Cánovas GV, Swanson BG (2001) Inactivation effect of an 18-T pulsed magnetic field combined with other technologies on *Escherichia coli*. Innovative Food Science & Emerging Technologies 2:273–277

101. Scherba G, Weigel RM, O'Brien WD Jr (1991) Quantitative assessment of the germicidal efficacy of ultrasonic energy. Applied and Environmental Microbiology 57:2079–2084

102. Schleifer KH, Kandler O (1972) Peptidoglycan types of bacterial cell walls and their taxonomic implications. Bacteriological Reviews 36:407–477

103. Seymour IJ, Burfoot D, Smith RL, Cox LA, Lockwood A (2002) Ultrasound decontamination of minimally processed fruits and vegetables. International Journal of Food Science and Technology 37:547–557

104. Shockman GD, Barrett JF (1983) Structure, function, and assembly of cell walls of gram-positive bacteria. Annual Review of Microbiology 37:501–527

105. Singer AJ, Coby CT, Singer AH, Thode HC Jr, Tortora GT (1999) The effects of low-frequency ultrasound on *Staphylococcus epidermidis*. Current Microbiology 38:194–196

106. Su X, Zivanovic S, D'Souza DH (2010) Inactivation of human enteric virus surrogates by high-intensity ultrasound. Foodborne Pathogens and Disease 7:1055–1061

107. Suslick KS (1988) Ultrasound: its chemical, physical and biological effects. VCH Publishers, New York, pp 1–64
108. Suzuki Y (1999) Restriction fragment length polymorphisms analysis by pulsed-field gel electrophoresis for discrimination of *Staphylococcus aureus* isolates from foodborne outbreaks. International Journal of Food Microbiology 46:271–274
109. Thacker J (1973) An approach to the mechanism of killing of cells in suspension by ultrasound. Biochemica et Biophysica Acta 240–248
110. Tortora GJ, Funke BR, Case CL (2013) Microbiology: an introduction. Pearson Education, Glenview
111. Tsukamoto I (2004) Inactivation of *Saccharomyces cerevisiae* by ultrasonic irradiation. Ultrasonics Sonochemistry 11:61–65
112. Twentyman PR, Bleehen NM (1973) The sensitivity of cells in exponential and stationary phases of growth to Bleomycin and to 1,3-bis(2-chloroethyl)-1-Nitrosourea. British Journal of Cancer 28:500–507
113. Valero M, Recrosio N, Saura D, Muñoz N, Martí N, Lizama V (2007) Effects of ultrasonic treatments in orange juice processing. Journal of Food Engineering 80:509–516
114. Velusamy V, Arshak K, Korostynska O, Oliwa K, Adley C (2010) An overview of foodborne pathogen detection: In the perspective of biosensors. Biotechnology Advances 28:232–254
115. Villamiel M, de Jong P (2000) Inactivation of *Pseudomonas fluorescens* and *Streptococcus thermophilus* in Trypticase® Soy Broth and total bacteria in milk by continuous-flow ultrasonic treatment and conventional heating. Journal of Food Engineering 45:171–179
116. Wang I-w, Anderson JM, Marchant RE (1993) Platelet-mediated adhesion of *Staphylococcus epidermidis* to hydrophobic NHLBI reference polyethylene. Journal of Biomedical Materials Research 27:1119–1128
117. Wilson M, McNab R, Henderson B (2002) Bacterial disease mechanisms: an introduction to cellular microbiology. Cambridge University Press, Cambridge
118. Yamada T, Ichiman Y, Yoshida K (1988) Possible common biological and immunological properties for detecting encapsulated strains of *Staphylococcus epidermidis*. Journal of Clinical Microbiology 26:2167–2172
119. Zhou B, Feng H, Luo Y (2009) Ultrasound enhanced sanitizer efficacy in reduction of *Escherichia coli* O157:H7 population on spinach leaves. Journal of Food Science 74: M308–M313
120. Zuber B, Haenni M, Ribeiro T, Minnig K, Lopes F, Moreillon P, Dubochet J (2006) Granular layer in the periplasmic space of gram-positive bacteria and fine structures of *Enterococcus gallinarum* and *Streptococcus gordonii* septa revealed by cryo-electron microscopy of vitreous sections. Journal of Bacteriology 188:6652–6660
121. Wang J, Hu X, Wang Z (2010) Kinetics models for the inactivation of Alicyclobacillus acidiphilus DSM14558(T) and Alicyclobacillus acidoterrestris DSM 3922(T) in apple juice by ultrasound. International. Journal of Food Microbiology 139:177–181
122. Marx G, Moody A, Bermudez-Aguirre D (2011) A comparative study on the structure of Saccharomyces cerevisiae under nonthermal technologies: high hydrostatic pressure, pulsed electric fields and thermo-sonication. International Journal of Food Microbiology 151:327–337
123. Gabriel AA (2012) Microbial inactivation in cloudy apple juice by multi-frequency Dynashock power ultrasound. Ultrasonics Sonochemistry 19:346–351
124. Şengül M, Erkaya T, Başlar M, Ertugay MF (2011) Effect of photosonication treatment on inactivation of total and coliform bacteria in milk. Food Control 22:1803–1806
125. Ye S, Qiu Y, Song X, Luo S (2009) Optimization of process parameters for the inactivation of Lactobacillus sporogenes in tomato paste with ultrasound and 60Co-γ irradiation using response surface methodology. Radiation Physics and Chemistry 78:227–233

Effect of Ultrasound Treatment on the Evolution of Solubility of Milk Protein Concentrate Powder

Bhesh Bhandari and Bogdan Zisu

Contents

Abstract

Low-frequency ultrasound has long been used to break and dissociate insoluble particles at a molecular level. In solution, power ultrasound of approximately 20 kHz generates sufficient shear to break agglomerates apart through acoustic cavitation, and this phenomenon has been reviewed in the context of powder solubility. Dairy powders are a dehydrated nonperishable globally important food

B. Bhandari (✉)
School of Land and Food Sciences, The University of Queensland, Brisbane, Australia
e-mail: bbhandari@uq.edu.au; b.bhandari@uq.edu.au

B. Zisu
School of Applied Sciences, College of Science, Engineering and Health, RMIT University, Melbourne, VIC, Australia
e-mail: bogdan.zisu@rmit.edi.au

commodity providing nutrition in both developed and developing regions around the world. The ability to rehydrate powders for use as food ingredients differs depending on the composition, processing history, and handling conditions with certain powders being more difficult to solubilize than others. In this chapter we focus mainly on the easily hydrated whey protein-based powders and the often more difficult powders to solubilize in the form of milk protein concentrates. Taking frequency into account, we discuss the use of high-power ultrasound as a method to aid powder solubilization through particle dissociation. Ultrasound as a technology is yet to be adopted commercially as a processing tool by the food-manufacturing industry, and limitations associated with the technique including equipment design are also discussed.

Introduction

Solubility: A Critical Functional Property of Dairy Powders

Dairy streams are highly perishable. Milk and other dairy streams are often dried and converted into powder for preservation to increase the shelf life of these otherwise rapidly perishable commodities, for storage stability, ease of handling, and transport without substantial loss of quality even at ambient temperatures. Spray drying is the globally preferred technology embraced by the dairy industry and together with the pre-drying processes of evaporative and/or membrane concentration will inevitably generate insoluble components.

In regions where milk supply exceeds consumption, milk is often spray dried for export to regions where dairying is unsustainable and local supply is unable to meet demand. Powders are regularly exported around the world to meet shortfalls in local milk supplies, and this process may also affect the solubility of powders. Spray-dried powders possess physical and functional properties including powder structure; particle size distribution; powder, bulk, and particle density; occluded air; and particle agglomeration which contribute to wettability, sinkability, dispersability, and solubility in solution. Solubility is a key functional attribute to industry and end users, and poorly soluble powders can cause processing difficulties and may result in quality and economic losses. Solubility is a measure of the final condition to which the constituents of the powder can be hydrated into solution. It is important to note that all powders have insoluble matter and not all constituents can be hydrated even in the most soluble powders. Solubility is dependent on the chemical composition and its physical state following the drying process. The processes of evaporative concentration and spray drying rely on thermal treatments which affect heat sensitive components and the severity of the heat treatment as well as the type of

drying generates denatured insoluble components [1]. Insolubility reflects the aggregate complex formation between denatured β-lactoglobulin and casein proteins and is referred to as the insolubility index. Adding to the complexity is the varied composition of pre-dried concentrates which also influence powder solubility. Factors directly affecting solubility are the presence of lactic acid, high mineral content in the form of salt ions, pH, and addition of heat-stabilizing agents added prior to spray drying [2].

Degradation of powder quality also occurs during storage affecting solubility by increasing the insoluble content. High protein powders and those with high lactose composition are prone to temperature degradation, and powders are often exported to regions around the world where the climate is hot or humid accelerating shelf-life degradation and increasing the insolubility index of powders.

Milk and milk-derived powders are often reconstituted for use in liquid products and solubility becomes a critical factor. Commercially, the reconstitution process is performed in the shortest time possible usually in a batch process relying on temperature and paddle mixing without strict consideration of the solubility profile of the powder. It is imperative for powders to rapidly solubilize during the reconstitution process and minimize storage sedimentation in resulting products. In the food industry, rapid dissolution properties are desirable to maximize processing times and prevent delays, increase production costs, and avoid the manufacture of products regarded as having poor qualities [3, 4].

Whey and Milk Protein Powders

This chapter focuses on two categories of commonly manufactured dairy powder: whey protein powders and milk protein powders.

Whey protein powders are manufactured with varying compositional characteristics and have many uses including infant formulations and diet food formulations and often used to standardize the protein content in preparation of yogurts. High-quality whey powders often exhibit good solubility properties.

Milk-based powders include skim milk and whole milk powders and are widely used as ingredients in many formulated foods including infant formula, soups, sauces, baked goods, and confectionery products to name a few. Similar to whey protein powders, these powders also typically exhibit good solubility properties.

Milk protein concentrates are a form of high-protein spray-dried powders (often exceeding 90 % protein) and due to the high nutritive and functional values are often used to standardize the protein content of milk in preparation for the use in the manufacture of secondary dairy products such as cheese, yogurts, and dairy-based beverages [5]. Milk protein concentrates are also used in the manufacture of confectionery, baked and ice cream products, soups, sauces, dessert products, ready-to-eat meals, and chocolate biscuits [6–9]. However, when it comes to solubility, this powder is often problematic and difficult to dissolve [3, 7]. Several studies have explored the protein conformation, functional properties, protein rehydration, and

solubility of reconstituted milk protein concentrate powders [10, 11]. Micellar casein and milk protein concentrate powders are less soluble at ambient temperatures in comparison with whey or milk powders requiring high temperatures to achieve adequate solubility during reconstitution [3, 7, 12]. Zwijgers [12] showed that the solubility of milk protein concentrate (MPC) could be improved significantly by raising the reconstitution temperature and by lengthening reconstitution times. In a commercial environment, however, this delays manufacturing processes reducing productivity, and if powders are poorly dissolved, there is a risk that product defects may occur resulting in further economic losses [5]. Due to this lack of solubility, a significant proportion of this chapter has been devoted to milk protein concentrate powders.

Power Ultrasound in Dairy Processing

Sound energy which is generated by a converter creates a continuous wave-type motion as it passes through a medium [13]. Ultrasound can be categorized in two general categories: high-frequency low-energy power ultrasound and low-frequency high-energy power ultrasound. Ultrasound when used as a processing tool is generally regarded as the sound waves emitted in the frequency range of 20 kHz to 1 MHz, also known as "power ultrasound." Depending on the sound wave frequency and the amplitude applied, a number of physical, chemical, and biochemical effects can be generated with the majority of food applications ranging in frequency between 20 and 40 kHz [14]. At these lower frequencies of the power ultrasound frequency range, acoustic cavitation effects occur and these are powerful enough to disrupt molecular bonding [15, 16]. Low frequencies (20–100 kHz), typical of most food applications, generally emit high pressures (70–100 MPa) [17] generating shock waves, turbulence, and physical effects through transient cavitation, and these dominate over chemical effects. At higher frequencies within the power ultrasound frequency range (>100 kHz), these powerful physical effects are gradually lost to generate predominantly H and OH radicals at the expense of physical shear. At even higher frequencies often above 1 MHz, the technology is mainly used for quality analysis, process control, and nondestructive inspection [18] to determine food properties, to measure flow rate, and to inspect the integrity of food packaging.

Although ultrasound technology has been implemented and applied commercially across various industries, the food industry has been slow to embrace the technology with few commercial applications. At the laboratory scale, ultrasound treatment has been used in a wide range of food applications including emulsification, extraction of bioactives, food preservation, mixing, meat tenderization, encapsulation of essential fatty acid, freezing of food, and quality evaluation [13, 19–25]. Its application also includes degassing of liquid foods, extraction of enzymes and proteins, inactivation of enzymes, induction of nucleation and crystallization, sterilization, filtration, and homogenization [26, 27]. Few of these applications are adopted commercially and this is particularly true for the dairy industry. Ultrasound is still considered novel in the dairy manufacturing; however, numerous

laboratory studies and some scale-up reports suggest that high-power low-frequency ultrasound has potential application in dairy manufacturing. These studies often focus on homogenization, viscosity reduction, controlling age-related thickening of milk concentrates, control and manipulation of whey and milk protein functional properties, sonocrystallization of lactose, and flocculation of milk fat to name a few [28–32]. Treatment times and energy intensities reported in some controlled laboratory studies indicate that energy requirements necessary to achieve a desired result can be small. Such possibilities may open new prospects for commercial implementation of ultrasound technology in the dairy industry.

Solubility is reported to be proportional to applied ultrasonic power and in addition to frequency; the applied energy density is paramount to controlling the solubility of reconstituted dairy powders. Adequate reporting of the applied energy density is also necessary for reproducibility, and this concept has been slow to be adopted in this emerging field of research. Zisu and Chandrapala [28], Koh et al. [33] and McCarthy et al. [34] have all emphasized the importance of appropriate representation of applied energy density according to Eq. 1:

$$\text{Energy density (J/mL)} = \text{Power drawn (W)} \times \text{Time (s)} / \text{Volume (mL)} \quad (1)$$

Defining and measuring energy density must take into account not only power (W) but also processing time and volume if working with a batch system or flow rate for continuous operation. The power delivered as ultrasonic energy, or calorimetric power (P), is determined by measuring the temperature change in water, in the absence of a cooling jacket, using Eq. 2 where Cpw is the heat capacity of water ($=4.18 \times 10^3$ J/kg K), M is the mass of water used (kg), ΔT is the change in temperature (K), and t is the duration of sonication (s) [35, 36]:

$$P = \text{Cpw } M(\Delta T/t) \quad (2)$$

The energy density in a batch system is calculated using Eq. 1. It is paramount that chilled water is circulated through a cooling jacket during sonication to maintain the solution temperature and avoid artifacts created by heat released as energy during sonication. In a continuous system, the applied energy density is determined by simply dividing the rated power (W) by the total flow rate in mL/s. This parameter provides information on the total sonication energy applied per mL of solution [28].

Also important is the need for ultrasonic equipment designed specifically for the food and dairy industries to maximize energy efficiency. Traditional horn-type sonicators typical of most power ultrasound applications were never designed to process food, and there is a complete absence of commercial manufacturing equipment available for the industry. Consequently this is a significant reason for the slow adoption of ultrasound technology by the food and dairy sectors. Ultrasonic equipment is traditionally designed to operate in direct contact with the material being treated (often fluid) and consists of a transducer to which a titanium sonotrode is attached. This is immersed into solution through which sound waves propagate and the energy density is greatest at the surface of the sonotrode, and this design may not

always be the most energy-efficient arrangement for dairy applications. An alternative to direct contact sonication employs a noncontact approach, and these sonication cells are designed with multiple low-power transducers attached to the outer surface of the metal cell eliminating the need for sonotrodes. Sound waves propagate through the metal surface and fluids are treated on the inner surface of the cell improving energy distribution. These sonication cells operate with lower power than sonotrodes but they distribute energy more efficiently, and this is paramount to designing equipment suited to the industry. A need for large-scale ultrasonic equipment compatible with the energy needs of the food and dairy industries and the recent surge of ultrasonic dairy research have the potential to prompt the development of dairy specific equipment for future adoption by the industry.

Power Ultrasound to Improve the Solubility of Reconstituted Dairy Powders

Several studies specifically show the disruption of larger insoluble aggregates following reconstitution of powders to aid solubility. The rapid dissolution of powders in solution is desired in food manufacturing to reduce processing times, to improve productivity, and to consistently produce good quality products. To do this at ambient temperature and across a wide temperature gradient has its challenges, and targeting insoluble aggregates and slow dissolution components is paramount. Low-frequency powder ultrasound has long been used to reduce agglomerate size. A technique such as sonication capable of improving the solubility of reconstituted powders can reduce hydration times and has potential industry application. Insoluble components of reconstituted dairy powders are similar in nature; that is, they are tightly bound agglomerated masses and by reducing their size to increase surface area will make them more soluble in solution.

It has been documented that high-power low-frequency sonication disrupts insoluble aggregates by reducing particle size in dairy solutions made from reconstituted powders [30, 37]. Sonicating reconstituted whey protein concentrate at 20 kHz also reduced the turbidity of solutions. Both these results were strongly correlated to particle size reduction resulting from treatment with high-intensity low-frequency sonication. Onwulata et al. [38] also reported similar reductions in aggregate size for whey proteins and caseins. The solubility of reconstituted whey protein concentrate [39] and whey protein isolate [26] solutions was improved following sonication at 20 kHz, and although not measured, this was possibly related to the reduction in the particle size of insoluble aggregates. These studies observed the effects of the ultrasound treatment on the functional properties of reconstituted whey protein powders at frequencies of 20, 40, and 500 kHz and concluded that low-frequency high-energy ultrasound treatment had significantly enhanced the solubility of the whey protein. This improvement in solubility was not observed at 500 kHz. However, due to the long duration of ultrasonic treatment without adequate temperature control, the solution temperature rose dramatically, which also is likely to have a

large contribution to the improvement of solubility. The effect of frequency was also supported by another study which showed that particle size was not reduced when sonicating reconstituted dairy powders at frequencies higher than 30 kHz where the physical forces of acoustic cavitation are weaker [37].

Frequency Is Critical to Solubility of Reconstituted Powders

Reconstituted Powders Sonicated at Low Frequency (20 kHz)

Ashokkumar et al. [29, 30] have shown that solution clarity of opaque 5 % and 15 % (w/w solids) whey protein solutions reconstituted from whey protein concentrate powder improved following low-frequency sonication at 20 kHz. After sonication (up to 60 min at 31 W), opaque solutions became translucent. This gradual improvement in solution clarity was attributed to the physical reduction in the size of the insoluble powder agglomerates to generate smaller particles as backed by particle size data. Prior to sonication, agglomerates were shown to reduce in size from an approximate average of 30 μm (with a range of 10–100 μm and occasionally exceeding 100 μm) to less than 1 μm as sonication time increased from 1 to 60 min (at 31 W) or as the power of sonication increased from 5 to 13, 31, and 51 W. The bulk effect was observed between 1 and 5 min, and the intensity due to larger aggregates was completely reduced within the first 10 min of sonication indicating the ultrasonic disruption of larger aggregates. A distribution corresponding to particles in the size range of approximately 0.1 μm continued to grow with increasing sonication time and power due to the disruption of larger insoluble aggregates. This was not believed to be related to the solubility of the proteins themselves since sonication did not increase the UV-visible absorption band corresponding to the whey proteins.

Reconstituted Powders Sonicated at Frequencies Greater than 20 kHz

Sonication of reconstituted whey protein solutions at frequencies higher than 20 kHz where the physical effects of acoustic cavitation are reduced did not have the same result. Ashokkumar et al. [29] also showed that sonication at frequencies of 213, 355, and 647 kHz did not affect insoluble agglomerates of whey protein solutions reconstituted to 8 % (w/w solids), and the particle size of solutions remained unchanged after sonication for 1 min at 5, 13, 31, and 51 W [29, 30]. Chemiluminescence was measured to confirm acoustic cavitation. At 213 kHz frequency, the chemiluminescence increased relative to power from 5 W to 13, 31, and 51 W after sonication for 1 min; however, without the physical effects observed at 20 kHz frequency, the particle size remained unchanged.

Solubility of Reconstituted and Sonicated Milk Protein Powders

Because of the high milk protein content, interactions between milk protein molecules will vary depending on its structural properties and the environmental circumstances (relative humidity, temperature, storage time, etc.) [8, 40]. Therefore, it may result in the modification of functional behavior of the hydrolysates compared to the intact protein such as altered solubility, viscosity, sensory properties, and foaming properties [41, 42].

Solubility expresses the ability to maintain a stable suspension in water [43]. It is one of the key functional properties of milk concentrate powders as an indicator of milk protein denaturation and aggregation. Milk protein concentrate powders not only show low solubility at ambient temperature in comparison with milk powders, but they require high temperatures to achieve adequate solubility during reconstitution [3, 8, 12]. Adding to this, MPC powders are prone to protein degradation during storage resulting in further solubility problems. Generally speaking, protein in the denatured and aggregated state exhibits poor emulsifying ability, foaming ability, and solubility [44]. Hevea [8] and McKenna [41] also confirmed that poor solubility of high milk protein powders was probably related to strong interactions between β-lactoglobulin and κ-casein. Furthermore, Havea [8] described two types of interactions in the molecule of proteins for the formation of insoluble material. One was based on covalent bonds. They consisted of inter- and intramolecular disulfide bonds which were formed via sulfhydryl oxidation reaction or sulfhydryl–disulfide interchange. The other one was non-covalent bonds, which included hydrophobic, hydrogen bonding, ionic, and other weak interactions. It also concluded most of the protein–protein interactions occurred through hydrophobic bonds. Thus, a solubility test can also be a useful tool to examine and investigate the molecular stability of milk protein concentrates.

High-power low-frequency ultrasound has been used to achieve rapid solubility of micellar casein and milk protein concentrate powders during reconstitution at ambient temperatures. Sonicating at 20 kHz frequency increased the initial solubilities of reconstituted milk protein powders from approximately 70 % to more than 90 % in the first three minutes of treatment with the bulk improvement occurring during the first minute of sonication [45]. After 10 min of sonication, close to 100 % solubility was achieved. There was a strong correlation between the particle size of reconstituted powders and solubility in response to the applied energy density of sonication showing gradual reduction with longer treatment times. A comparison of the rehydration of powders by stirring alone could only achieve approximately 85 % solubility after 4 h. Particle size distribution was used to support the solubility data.

Milk powders contain large vacuoles on the surface of powder particle formed during the spray-drying process with the bulk of the protein found on the outer shell [46]. It has been documented that during powder rehydration, agglomerates are disrupted into primary particles together with the simultaneous release of material from the powder particles into the surrounding aqueous phase [47]. The latter is considered a rate-limiting step. Ultrasonic degradation of the external particle layer

would explain the size reduction which helps the powder to dissolve by acoustic cavitation initiating the release of material to the aqueous phase at a faster rate.

In a separate study, the effects of power ultrasound were also studied on the dissolution properties of milk protein concentrate powders [34]. Low-frequency (20 kHz) high-intensity ultrasound (70.2 W) was used to reconstitute 5 % (w/w) powder, and the dissolution rate was compared to a conventional methods of dispersion by stirring. Rehydration of powder by stirring at 50 °C resulted in a typical two-step dissolution model, whereby the solubilization of larger particles coincided with the formation of a smaller particle population over time. Dispersal of reconstituted powders by sonication significantly accelerated the solubility process, achieving > 90 % levels of powder solubilization within 1 min of treatment at an energy density of 21.1 J/mL. However, in this study the temperature was uncontrolled during treatment and rose to over 70 °C during sonication contributing to solubility and potentially causing protein denaturation and aggregation. The rehydration process for milk protein concentrate powders involving conventional dissolution by stirring for 10 min at 50 °C achieves < 90 % powder dissolution.

A different approach to powder solubility was investigated by Yanjun et al. [48] studying the effect of power ultrasound pretreatment on the physical and functional properties of reconstituted milk protein concentrate. The impact of low-frequency 20 kHz power ultrasound pretreatment was investigated. Prior to spray drying of the powders, ultrafiltered and diafiltered milk protein retentates were sonicated at 12.50 W for 0.5, 1, 2, and 5 min. The particle size of these concentrates reduced from 28.45 μm to 0.13 μm after 0.5 min of sonication and then spray dried. The solubility of these pretreated powders reconstituted to 5 % (w/w solids) increased significantly from 35.78 % to 88.30 % after 5 min of ultrasonic pretreatment. The microstructure of these powder confirmed results, with small particles formed and trapped in dents of large particles. Sodium dodecyl sulfate–polyacrylamide gel electrophoresis showed no significant change in protein molecular weight indicating that the effects of low-frequency sonication are predominantly physical, thereby disrupting insoluble aggregates without changing protein conformation. Similar results were observed for reconstituted whey protein powders as discussed earlier in this chapter.

Effect of Ultrasound Treatment on the Solubility of Milk Protein Concentrate Powders Aged During Storage

In a previously unpublished study by Yu Song, Arnaud Mimouni, and Bhesh Bhandari, the effect of ultrasound treatment on the evolution of solubility of milk protein concentrate was studied in greater detail. Fresh and aged milk protein concentrates were treated with low-frequency high-energy ultrasound (20 kHz) after rehydration, and its effect on the solubility of reconstituted powders was observed.

Different scholars reported that with an increase in storage temperature, the solubility of the milk protein concentrate was lost at a faster rate [6, 8, 41]. Kher

et al. [9] found that dried milk protein powders lost solubility on storage and this further detracted from their functional performance in many food applications. McKenna [41] also mentioned that after 6 months storage at 20 °C, there were two layers formed at the particle surface. The first layer was composed of β–lactoglobulin and the other layer was made up of aggregated casein micelles. They formed a water-impermeable layer which therefore decreased the solubility. Anema et al. [5] have shown that the decrease in solubility of milk protein concentrate powders could be entirely accounted for by the reduced solubility of the casein micelles. A possible mechanism for the decrease in solubility with storage is the formation of a network of cross-linked proteins through hydrophobic and/or hydrogen bonding rather than covalent bonding at the surface of the powder acting as a barrier to water transport and subsequently inhibiting the hydration of the MPC85 particles. McKenna et al. [46] have microscopic evidence of movement of some protein out of the micelle and forming a monolayer of close packed micelles at the surface of the particles. They further postulated that cross-linking of micelles by nonmicellar proteins and by the close association of micelles at the surface.

In the study by Yu Song, Arnaud Mimouni, and Bhesh Bhandari, the objective of the research was to observe the effect of short-term low-frequency high-power energy ultrasound treatment on the solubility of the milk protein concentrate powders during aged storage.

The soluble solid and total nitrogen in the supernatant after rehydration were examined in order to achieve the goal. Milk protein concentrate powder containing 85 % protein was stored at 25 °C and relative humidity (RH) of 52.9 % for 30 days. The powder samples were then rehydrated into distilled water at 25 °C for 20 min followed by ultrasound treatment at 20 kHz for 1 min. The samples were then centrifuged at 25 °C and $4000 \times g$ for 10 min and filtered with a glass microfiber filter paper. The soluble solid test and total nitrogen test were conducted on both supernatant and suspension to examine the solubility of fresh and aged reconstituted powder samples.

Both soluble solid and crude protein content in supernatant increased significantly after ultrasound treatment ($p < 0.05$), which indicated that ultrasound treatment had improved the solubility of both the fresh and aged powders during rehydration. An increase of the temperature of the sample solution during ultrasound treatment had also contributed to the improvement of the solubility.

Storage and Analysis of MPC85

Commercially produced milk protein concentrate powder (85 % of protein) was used in these experiments. Milk protein concentrate powder 85 % (MPC85) contained milk proteins (82.4 % w/w) which has an equal proportion of casein and whey proteins, lactose (4 % w/w), ash (7.3 % w/w), and fat (1.6 % w/w). Distilled water was the rehydration medium which was used to dissolve MPC85 in these experiments.

10 g of fresh MPC85 powder was initially taken out of cold storage (4 °C) and spread thinly on a petri dish and then stored in vacuum-sealed P_2O_5 desiccators (RH close to 0 %) for 2 days to reach to ambient temperature and moisture content standardization. Randomized complete block design was adopted in this experiment to allocate different samples into the desiccators. The samples were transferred into storage desiccators which contained saturated salt solution of magnesium nitrate, Mg $(NO_3)_2 \cdot 6H_2O$. This saturated salt solution allowed the MPC85 powder to equilibrate at relative humidity (RH) of 52.9 %. The samples were stored at 25 °C for 30 days and then removed from storage for solid content and total nitrogen analyses.

Solubility was measured according to the methods of Havea [8] and Singh [7] which describe a mass fraction method to test the solubility of MPC85. After 30 days storage at 25 °C, 10 g of MPC85 powder was slowly poured in to 190 g of water under controlled conditions (25 °C and agitation rate at 220 rpm), and then after 20 min rehydration, 50 mL of suspension was centrifuged at 4000 × g for 5 min at 25 °C. The supernatant was then filtered under a vacuum (GF/A microfiber filter paper, 1.6 μm pore size). Duplicate 6 mL of the supernatant and the same amount of powder suspension were taken for soluble solid test. They were firstly poured into an aluminum cell and covered with 30–40 g of dried sand. After that, the cells were stored in the oven at 102 °C for 24 h and cooled down in P_2O_5 desiccators for 2–3 h for total solid determination.

The value of total solids in the filtrate of the supernatant from each sample was compared to that in the suspension to give the mass fraction of dissolved material, which is expressed as percentage (w/w) of dry powder.

The solubility percentage was calculated as Eq. 3:

$$\text{Solubility } (\%) = \frac{\text{Weight of total solids of supernatant}}{\text{Weight of total solids of powder suspension}} \times 100\% \quad (3)$$

The total nitrogen was analyzed from 2 mL of supernatant and powder suspension with a LECO CNS-2000 Combustion Analyzer. Fresh and aged MPC85 samples were treated with ultrasound to determine its effect on solubility immediately after the addition of powder to water and after hydration for 20 min. 200 g of MPC85 powder suspensions was placed in a 250 mL flat bottom conical flask and then sonicated with a 20 kHz ultrasonic probe. The probe with its 1.2 cm titanium tip was immersed in the suspension and the suspension was treated for 1 min (400 W maximum power). During the rehydration process, samples were observed with a compound light microscope. 10 g of fresh MPC85 powder was placed into 190 g water at 25 °C and observed under light microscope at ×800 magnification. Suspension samples were then treated with ultrasound for 15, 30, 45, and 60 s and observed. Samples were also allowed to hydrate for 20 min and observed at 5 min intervals.

The study was replicated and each value represents the means of two measurements. Analysis of variance (one-way ANOVA) was determined with a significant level of 5 %. The values statistically different are marked by the same letter (a) and the values statistically similar are marked with another letter (b).
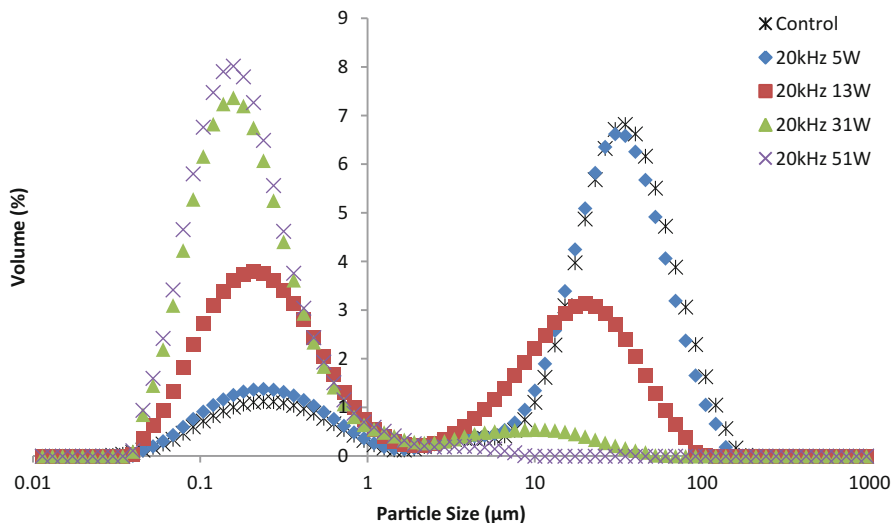
Fig. 1 Particle size reduction of 8 % (w/w) reconstituted whey protein concentrate powder sonicated at 20 kHz at 5, 13, 31, and 51 W (Adapted from Ashokkumar et al. [29])
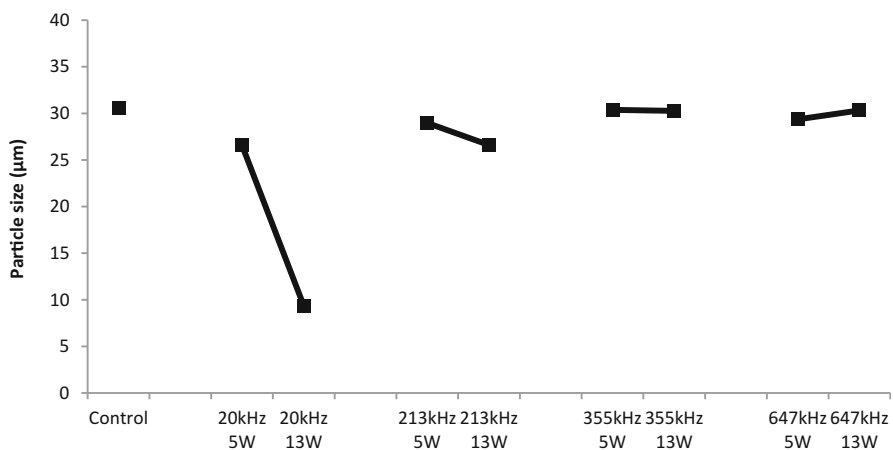
Fig. 2 Particle size of 8 % (w/w) reconstituted whey protein concentrate powder sonicated at 20, 213, 355, and 647 kHz (Adapted from Ashokkumar et al. [29])

Solubility of Sonicated MPC85 Powders During Storage

Ultrasound treatment significantly enhanced the soluble solid content in the super-natant after 20 min rehydration of both fresh and aged MPC85 powder. Figure 1 shows that the soluble solid content in the supernatant after 20 min of rehydration improved significantly with 1 min of ultrasound treatment ($p < 0.05$). Even though

Fig. 3 Solubility of stirred (◆) and sonicated (●) micellar casein powder during reconstitution as a function of time at ambient temperature (Adapted from Zisu and Chandrapala [45])
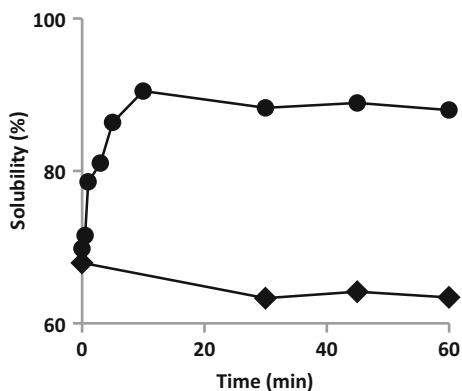
the solid content dropped from 69.97 % to 45.88 % after 30 days of aged storage, the solubility of reconstituted powder improved to 97.15 % and 98.4 % for fresh and aged MPC85 powder after treated with ultrasound for 1 min.

This result was confirmed by the total nitrogen test. Figure 2 reveals that after 1 min of ultrasound treatment at 20 kHz, the crude protein in the supernatant significantly increased by 30.86 % and 60.65 % for fresh and aged MPC85 powder, respectively ($p < 0.05$). The similar trend in experiment result between the soluble solid test and total nitrogen test indicates that low-frequency high-energy ultrasound considerably enhanced the solubility of the reconstituted MPC85 powder aged during storage.

Temperature control was not adopted in this study and the temperature of the MPC85 suspension increased after ultrasound treatment. After only 1 min of ultrasonic treatment, the heat energy generated by acoustic cavitation increased the suspension temperature from approximately 25 °C to approximately 32.5 °C (data not shown). Both Gaiani et al. [4] and Mistry and Hassan [49] report that high protein milk powders have low solubility at the room temperature but this improved as the temperature increases, and it is possible that temperature also contributed to the solubility in this experiment. However, considering the very short treatment time (1 min), the temperature contribution to solubility for reconstituted MPC85 powder is likely to be insignificant in comparison with ultrasonic treatment. It is reasonable to assume that acoustic cavitation and the shock waves generated by cavitation were the main contribution to the ultrasound effect [27].

Microscopic examination shows air bubbles forming when fresh MPC85 powder makes contact with water, indicating the absorbance of water into powder internal vacuoles (Fig. 3). With ultrasound treatment, the air bubbles collapsed and the surface tension between the powder and water was overcome which increased the rate of powder wetting, sinking, dispersing, and dissolving. It is noticeable that in both situations (with or without 20 min rehydration prior to ultrasound treatment), there were fewer MPC85 particles observed after ultrasound treatment (Figs. 3 and 4). The absence of the large particle indicates that the MPC85 powder gradually dissolved in water and milk protein solubilized to its micellar form (Fig. 4).
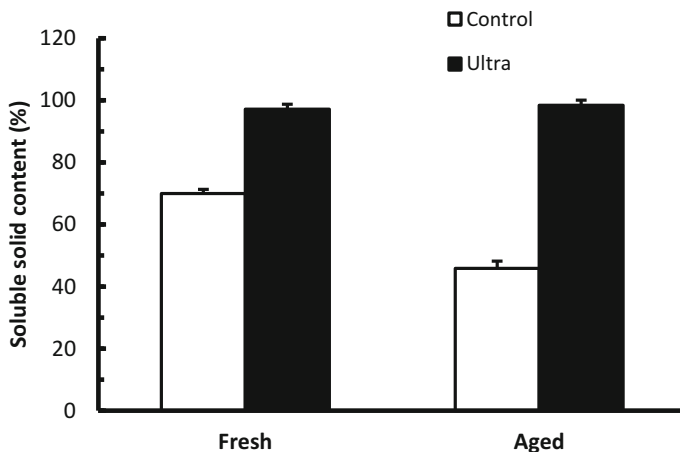
Fig. 4 Soluble solid content of reconstituted MPC85 powder before and after ultrasound treatment for 1 min at 20 kHz (Song, Mimouni and Bhandari, unpublished data)
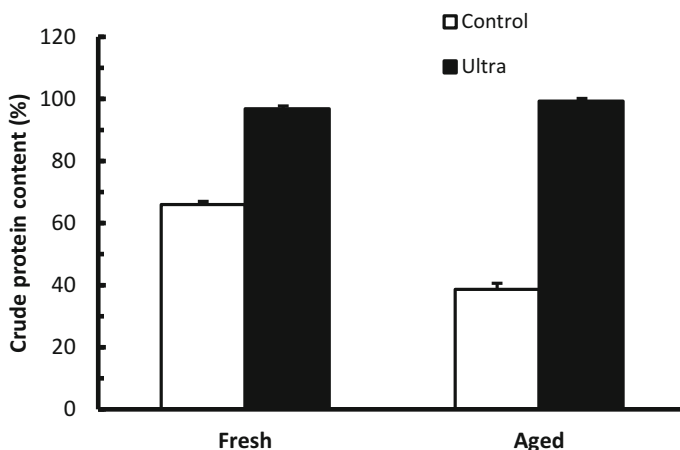
Fig. 5 Crude protein content of MPC85 powder before and after ultrasound treatment for 1 min at 20 kHz (Song, Mimouni, and Bhandari, unpublished data)

This experiment confirms the hypothesis for the rehydration process of MPC85 powder which was proposed by Minouni et al. [47]. Mimouni et al. [47] found that rehydration occurs in two steps. They are the disruption of the agglomerates into primary particles followed by simultaneous release of the material from the powder particles into surrounding aqueous phase. The latter is considered as the rate-limiting step. Hence, sonication may disrupt the agglomerates easily with shear forces generated by acoustic cavitation and thereby initiating the release of material to the aqueous phase at a faster rate. Furthermore, they stated that during powder rehydration, the vacuoles would be expected to fill with water. Thus, on hydration,
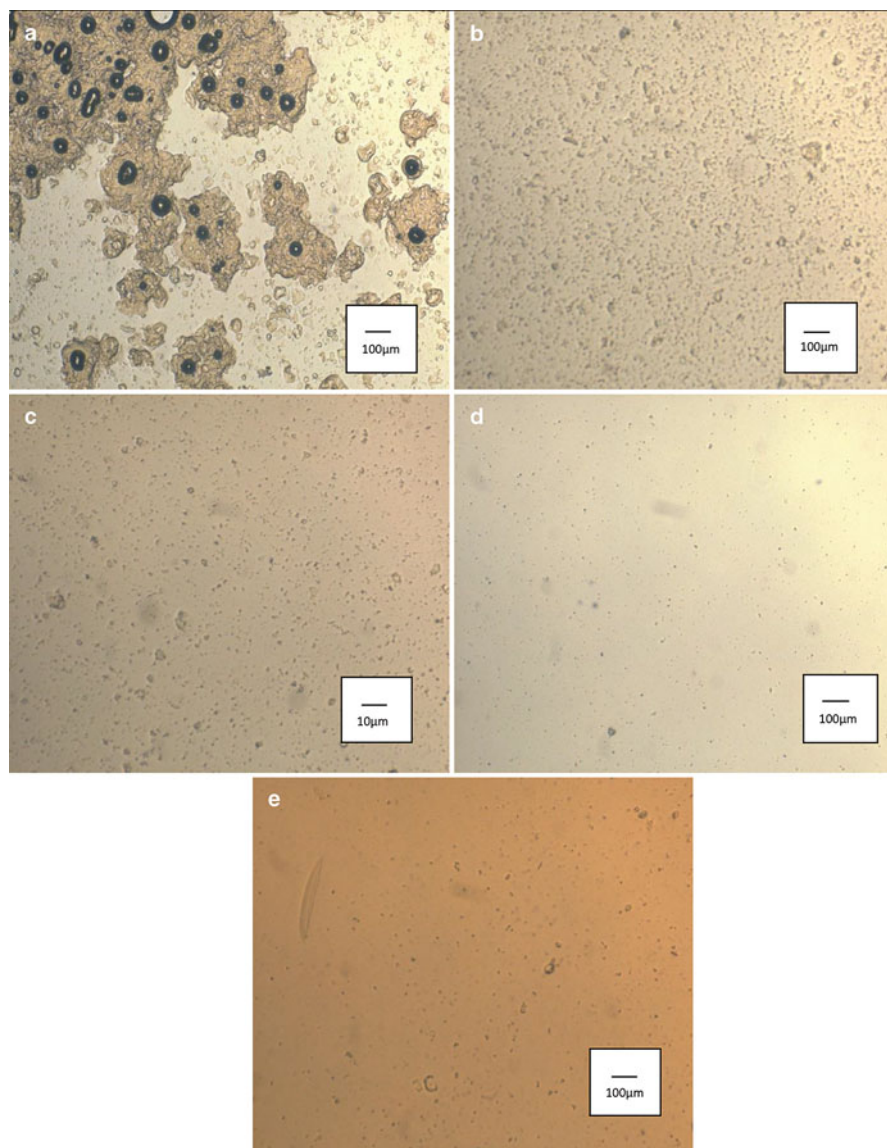
Fig. 6 Rehydration of MPC85 powder at 25 °C with 20 kHz ultrasound treatment viewed at ×800 magnification immediately after the addition of powder to water. Ultrasound treatment time: 0 s (**a**), 15 s (**b**), 30 s (**c**), 45 s (**d**), and 60 s (**e**) (Song, Mimouni, and Bhandari, unpublished data)

the bulk of the protein is expected to be in an outer shell. Mechanical degradation of the external layer of the particles would therefore lead to a limited decrease in their size, until sufficient material was dispersed at which point the particles would be expected to collapse or fully dissolve. Results presented in this study show that the
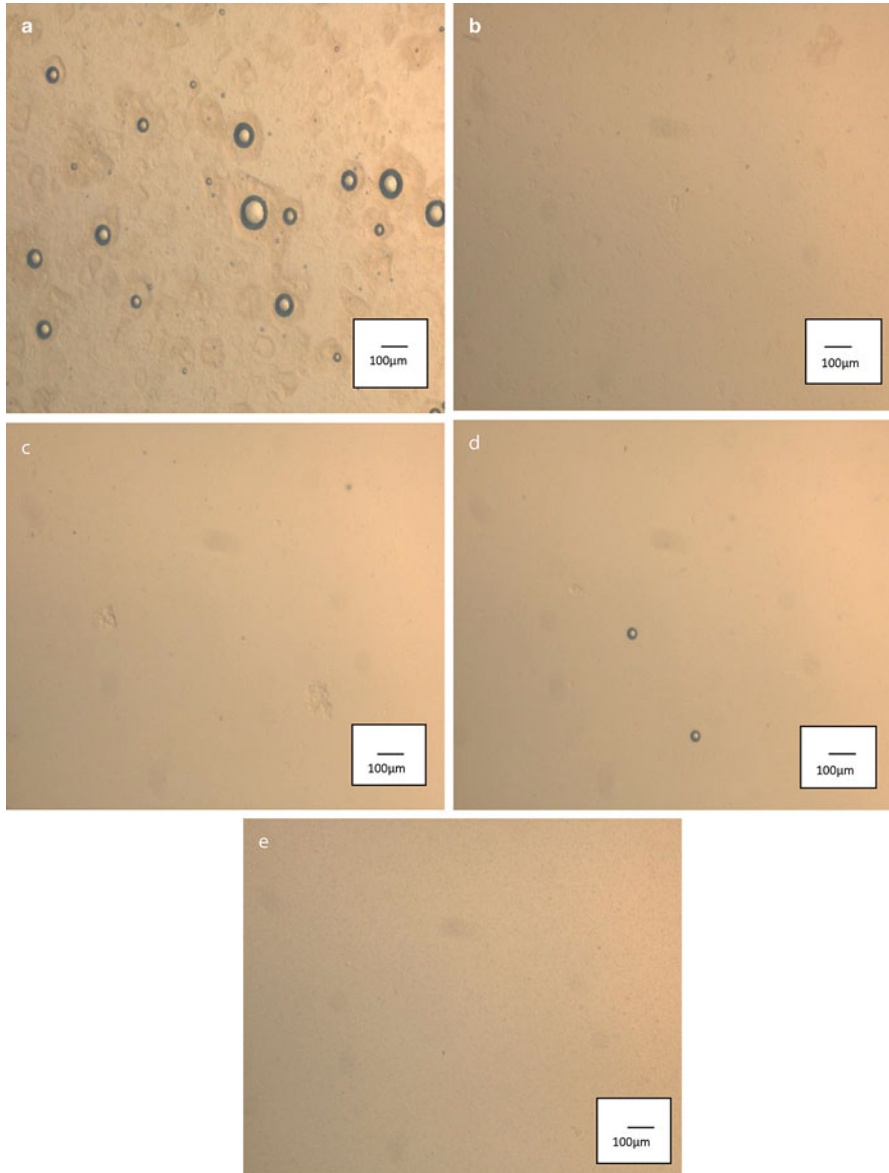
Fig. 7 Rehydration of MPC85 powder after 20 min hydration at 25 °C with 20 kHz ultrasound treatment viewed at ×800 magnification. Ultrasound treatment time: 0 s (**a**), 15 s (**b**), 30 s (**c**), 45 s (**d**), and 60 s (**e**) (Song, Mimouni, and Bhandari, unpublished data)

agglomerates present at the very beginning of the rehydration process were disrupted due to the mechanical energy from ultrasound treatment. The interaction between the casein micelles in the primary powder particles was then disrupted with the increase

in applied ultrasound energy. Thus the network of interacting micelles was disrupted and single micelles were released into solution, resulting in the solubilization of the larger milk particle aggregates (Figs. 5, 6, and 7).

Conclusions and Future Directions

Spray-dried dairy powders possess many physical and functional properties of which solubility is critical. Solubility is a measure of the final condition to which the constituents of the powder can be hydrated into solution and is a key functional attribute to industry and end users. Although ultrasound technology is yet to be adopted by the dairy industry, recent studies have demonstrated its potential. In solution, low-frequency power ultrasound of approximately 20 kHz was used to generate sufficient shear to break agglomerates apart through acoustic cavitation, and this phenomenon was applied to improve the solubility of reconstituted dairy powders. Ultrasound substantially improved the rate of solubilization in whey protein and milk protein-based powders. It is hypothesized that ultrasound accelerates a two-stage rehydration process by disruption of large agglomerates into primary particles followed by simultaneous release of the material from the powder particles into surrounding aqueous phase. Sonication disrupts large agglomerates, thereby initiating the release of material to the aqueous phase at a faster rate. Continuous reduction in the size of powder particles occurs until complete dispersed is reached at which point the particles collapse or fully dissolve.

References

1. Tamime AY (ed) (2009) Dried milk products. Dairy powders and concentrated milk products. Blackwell, Oxford, UK, pp 231–245
2. Singh H, Newstead DF (1992) Aspects of proteins in milk powder manufacture. In: Fox PF (ed) Advanced dairy chemistry, vol 1, 2nd edn, Proteins. Elsevier, New York, pp 735–765
3. Fang Y, Selomulya C, Ainsworth S, Palmer M, Chen XD (2011) On quantifying the dissolution behavior of milk protein concentrate. Food Hydrocoll 25:503–510
4. Gaiani C, Schuck P, Scher J, Desobry S, Banon S (2007) Dairy powder rehydration: influence of protein state, incorporation mode, and agglomeration. J Dairy Sci 90:570–581
5. Anema SG, Pinder DN, Hunter RJ, Hemar Y (2006) Effects of storage temperature on the solubility of milk protein concentrate (MPC85). Food Hydrocoll 20:386–393
6. Anema SG, Li YM (2003) Association of denatured whey proteins with casein micelles in heated reconstituted skim milk and its effect on casein micelle size. J Dairy Res 70:73–83
7. Singh H (2007) Interactions of milk proteins during the manufacture of milk powders. Lait 87:413–423
8. Havea P (2006) Protein interactions in milk protein concentrate powders. Int Dairy J 16:415–422
9. Kher A, Udabage P, McKinnon I, McNaughton D, Augustin MA (2007) FTIR investigation of spray-dried milk protein concentrate powders. Vib Spectrosc 44:375–381
10. Pavlovskaya G, McClements DJ, Povey MJW (1992) Ultrasonic investigation of aqueous-solutions of a globular protein. Food Hydrocoll 6:253–262

11. Suzuki N, Tamura Y, Mihashi K (1996) Compressibility and specific volume of actin decrease upon G to F transformation. Biochim Biophys Acta-Protein Struct Mol Enzymol 1292:265–272
12. Zwijgers A (1992) Outline of milk protein concentrate. Int Food Ingredients 3:18–23
13. Povey MJW (1998) Ultrasonics of food. Contemp Phys 39:467–478
14. Mason TJ (1998) Power ultrasound in food processing – the way forward. In: Povey MJW, Mason TJ (eds) Ultrasound in food processing. Blackie Academic %26 Professional, London, pp 105–126
15. Earnshaw RG (1998) Ultrasound: a new opportunity for food preservation. In: Povey MJW, Mason TJ (eds) Ultrasound in food processing. Blackie Academic %26 Professional, London, pp 183–192
16. Hem SL (1967) The effect of ultrasonic vibrations on crystallization processes. Ultrasonics 5:202–207
17. Laborde JL, Bouyer C, Caltagirone JP, Gerard A (1998) Acoustic bubble cavitation at low frequencies. Ultrasonics 36:589–594
18. Mizrach A (2008) Ultrasonic technology for quality evaluation of fresh fruit and vegetables in pre- and postharvest processes. Postharvest Biol Technol 48:315–330
19. Coupland JN (2004) Low intensity ultrasound. Food Res Int 37:537–543
20. Curt C (1994) Evaluation of emulsion stability – principle, applications, advantages and drawbacks. Sciences Des Aliments 14:699–724
21. Demirdoven A, Baysal T (2009) The use of ultrasound and combined technologies in food preservation. Food Rev Intl 25:1–11
22. Jafari SM, He YH, Bhandari B (2007) Role of powder particle size on the encapsulation efficiency of oils during spray drying. Drying Technol 25:1081–1090
23. Jiranek V, Grbin P, Yap A, Barnes M, Bates D (2008) High power ultrasonics as a novel tool offering new opportunities for managing wine microbiology. Biotechnol Lett 30:1–6
24. Vilkhu K, Mawson R, Simons L, Bates D (2008) Applications and opportunities for ultrasound assisted extraction in the food industry – a review. Innovative Food Sci Emerg Technol 9:161–169
25. Zheng L, Sun DW (2006) Innovative applications of power ultrasound during food freezing processes – a review. Trends Food Sci Technol 17:16–23
26. Jambrak AR, Mason TJ, Lelas V, Herceg Z, Herceg IL (2008) Effect of ultrasound treatment on solubility and foaming properties of whey protein suspensions. J Food Eng 86:281–287
27. Knorr D, Zenker M, Heinz V, Lee DU (2004) Applications and ultrasonics in food potential of processing. Trends Food Sci Technol 15:261–266
28. Zisu B, Bhaskaracharya R, Kentish S, Ashokkumar M (2010) Ultrasonic processing of dairy systems in large scale reactors. Ultrason Sonochem 17:1075–1081
29. Ashokkumar M, Kentish SE, Lee J, Zisu B, Palmer M, Augustin MA (2009) Processing of dairy ingredients by ultra-sonication, PCT International Application WO 2009079691 A1
30. Muthupandian A, Bhaskaracharya R, Kentish S, Lee J, Palmer M, Zisu B (2010) The ultrasonic processing of dairy products –an overview. Dairy Sci Technol 90:147–168
31. Leong T, Johansson L, Juliano P, Mawson R, McArthur S, Manasseh R (2014) Design parameters for the separation of fat from natural whole milk in an ultrasonic litre-scale vessel. Ultrason Sonochem 21:1289–1298
32. Dincer TD, Zisu B, Vallet CGMR, Jayasena V, Palmer M, Weeks M (2014) Sonocrystallisation of lactose in aqueous system. Int Dairy J 35:43–48
33. Koh LLA, Chandrapala J, Zisu B, Martin GJO, Kentish SE, Ashokkumar M (2014) A comparison of the effectiveness of sonication, high shear mixing and homogenisation on improving the heat stability of whey protein solutions. Food Bioprocess Technol 7:556–566
34. McCarthy NA, Kelly PM, Maher PG, Fenelon M (2014) Dissolution of milk protein concentrate (MPC) powders by ultrasonication. J Food Eng 126:142–148
35. Contamine RF, Wilhelm AM, Berlan J, Delmas H (1995) Power measurement in sonochemistry. Ultrason Sonochem 2:S43–S47

36. Kimura T, Sakamoto T, Leveque JM, Sohmiya H, Fujita M, Ikeda S, Ando T (1996) Standardization of ultrasonic power for sonochemical reaction. Ultrason Sonochem 3:S157–S161
37. Zisu B, Lee J, Chandrapala J, Bhaskaracharya R, Palmer M, Kentish SE, Ashokkumar M (2011) Effect of ultrasound on the physical and functional properties of reconstituted whey protein powders. J Dairy Res 78:226–232
38. Onwulata CI, Konstance RP, Tomasula PM (2002) Viscous properties of microparticulated dairy proteins and sucrose. J Dairy Sci 85:1677–1683
39. Kresic G, Lelas V, Jambrak AR, Herceg Z, Brncic SR (2008) Influence of novel food processing technologies on the rheological and thermophysical properties of whey proteins. J Food Eng 87:64–73
40. Mistry VV, Pulgar JB (1996) Physical and storage properties of high milk protein powder. Int Dairy J 6:195–203
41. McKenna AB (2000) Effect of processing and storage on the reconstitution properties of whole milk and ultrafiltered skim milk powders. Institute of Food Nutrition and Human Health, no. Palmerston North, Massey University
42. Thomas MEC, Scher J, Desobry-Banon S, Desobry S (2004) Milk powders ageing: effect on physical and functional properties. Crit Rev Food Sci Nutr 44:297–322
43. Birchal VS, Passos ML, Wildhagen GRS, Mujumdar AS (2005) Effect of spray-dryer operating variables on the whole milk powder quality. Drying Technol 23:611–636
44. Tamime AY (2007) Structure of dairy products. Blackwell, Oxford, xvi + 288 pp
45. Zisu B, Chandrapala J (2015) High power ultrasound processing in milk and dairy products. In: Datta N, Tomasula P (eds) Emerging dairy processing technologies: opportunities for the dairy industry. Wiley-Blackwell, Chichester/Hoboken
46. McKenna AB, Lloyd RJ, Munro PA, Singh H (1999) Microstructure of whole milk powder and of insolubles detected by powder functional testing. Scanning 21:305–315
47. Mimouni A, Deeth HC, Whittaker AK, Gidley MJ, Bhandari BR (2009) Rehydration process of milk protein concentrate powder monitored by static light scattering. Food Hydrocoll 23:1958–1965
48. Yanjun S, Jianhang C, Shuwen Z, Hongjuan L, Jing L, Lu L, Uluko H, Yanling S, Wenming C, Wupeng G, Jiaping L (2014) Effect of power ultrasound pre-treatment on the physical and functional properties of reconstituted milk protein concentrate. J Food Eng 124:11–18
49. Mistry VV, Hassan HN (1991) Delactosed, high milk protein powder. 2. Physical and functional properties. J Dairy Sci 74:3716–3723

Sonocrystallization of Lactose

Theory, Practice, and Future Directions

Tuna D. Dincer and Bogdan Zisu

Contents

Abstract

Sonocrystallization as an emerging science and technology has great potential to improve and change current methods of processing, resulting in significant cost and energy savings and opening up new applications in lactose crystallization.

Lactose crystallization is reported to be slow and unpredictable. Seeding is not used in industry and nucleation is achieved by rapid cooling. The problem with

T.D. Dincer (✉)
Food Science and Technology Program, School of Public Health, Faculty of health Sciences, Curtin University, Bentley, WA, Australia
e-mail: T.Dincer@curtin.edu.au

B. Zisu
School of Applied Sciences, College of Science, Engineering and Health, RMIT University, Melbourne, VIC, Australia
e-mail: bogdan.zisu@rmit.edi.au

conventional lactose crystallization is long induction times and large metastable zone width which makes the process unpredictable and difficult to control. Therefore, improved control of the lactose crystallization process has particular significance for the dairy industry.

In the last 10 years, there have been a significant number of reported applications of ultrasound in lactose crystallization. Most of the work reported utilized ethanol as anti-solvent to provide methods of whey proteins and lactose recovery without concentrating to high solid content. More recently, sonocrystallization from aqueous lactose solutions and concentrated whey has been reported for pharmaceutical and food industry applications. With the availability of equipment of industrial scale, it is anticipated that sonocrystallization of lactose in industrial scale may become a reality in the near future.

Introduction

Lactose is the major carbohydrate in milk and produced from whey which is the by-product of cheese making. Lactose is the major constituent of many concentrated and dried milk and whey products and widely used as a food ingredient and as carrier in tablets in pharmaceutical industry. Lactose represents 35 % of the total solids in milk and is the principal constituent in many dairy products, ranging from about 40 % in whole milk powder to 70 % in whey powder. Therefore, the properties of several dairy products, especially concentrated and dehydrated products, are dominated by certain properties of lactose, especially its solubility, crystallization behavior, and mutarotation.

Lactose is an interesting and complicated system for both crystallographers and manufacturers. An important difference from most other crystal growth systems is that an aqueous lactose solution is a pseudo-ternary system: molecules of both α and β forms of lactose are present which tend to reach mutarotation equilibrium. Thus, α-lactose monohydrate crystals never grow from a pure environment: their growth medium always contains β-lactose in a quantity of the same order of magnitude as the α-lactose itself [1]. The presence of β-lactose not only reduces the driving force for crystallization of α-lactose monohydrate but also significantly affects the crystal morphology, and as a result, a tomahawk shape forms (Fig. 1a). α-Lactose monohydrate can be observed in a variety of shapes, depending on the conditions of the crystallization: prisms (Fig. 1b), diamond, pyramid, and tomahawk, but this is purely a matter of variation in morphology; the crystal lattice is always the same [2]. The commonest shape is the tomahawk.
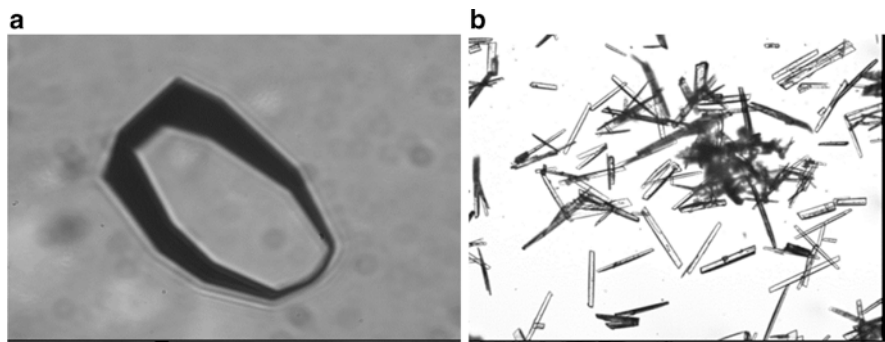
Fig. 1 Tomahawk- and prism-shaped α-lactose monohydrate crystals [5]

The crystal structure was determined by Fries et al. [3]. The unit cell contains two molecules of lactose and two of water. Lactose molecules are oriented with their long axis parallel to the **b** direction with the glucose moieties toward the –**b** direction. Michaels and van Kreveld [4] assumed a highly specific interaction between α-lactose molecules of the lattice and the β-lactose molecule in the solution, most explicitly at the $(0\overline{1}0)$ and $(0\overline{1}1)$ faces. Because the molecules of both anomers have the same β-galactosyl moiety, the α-lactose molecules of the crystal might form bonds as easily as with the galactose moiety of both α and β molecules. Once integrated, β-lactose molecules would further inhibit growth of α-lactose at that growth site. This could explain the shape of the α-lactose monohydrate crystal which displays a polar character: very small or missing $(0\overline{1}0)$ face and a large (010) face. The crystal morphology is dominated by the $(0\overline{1}\,\overline{1})$, $(0\overline{1}1)$, and (010) faces. α-Lactose monohydrate crystals grown in the absence of β-lactose are prism shaped and display similarly sized (010) and $(0\overline{1}0)$ faces (Fig. 1b).

The medium lactose crystallizes out and adds an extra layer of complexity due to the presence of proteins, mono- and divalent ions, etc., in whey [6]. Lactose phosphate which is produced during cheese making selectively attaches to the (010) face and reduces the growth rate [7, 8]. The variability of solubility of lactose in different industrial permeate [9] was reported which also impacted on controlling lactose crystallization in the industrial scale. Furthermore, these impurities are seasonal, and in industry different sources of whey are often mixed which makes controlling lactose crystallization difficult at industrial scale. Therefore, any improvements in controlling nucleation and also crystal size distribution would make significant improvement in the dairy industry.

Crystallization

Crystallization is a separation and purification technique that is widely used in food, chemical, and pharmaceutical industries. Crystallization is defined as a phase change where solute dissolved in liquid forms an orderly solid structure. Only a certain amount of solute can dissolve in liquid at a given temperature. This is called solubility concentration and the solution is at equilibrium. Solutions can be supersaturated either by removing solvent by evaporation, cooling, or addition of an anti-solvent. Supersaturated solutions are not at equilibrium and try to reach an equilibrium state by precipitating excess solute. Supersaturation is the driving force for crystallization. Undersaturated solutions are stable and will not crystallize. Supersaturated solutions on the other hand are either unstable or metastable [10]. As can be seen from supersolubility diagram of lactose (Fig. 2), in labile solutions, spontaneous nucleation is expected. The zone between solubility and supersolubility curves is called the metastable zone, and the probability of homogeneous nucleation is zero. The metastable zone width is influenced by factors such as fluid dynamics and presence of impurities, and spontaneous nucleation does not occur [10].

Crystallization proceeds with the formation of a new solid phase from solution (nucleation) and addition of molecules into this nuclei created (crystal growth) [11].

Nucleation is the process where solutes in liquid transform into crystal lattices and can take place through either primary or secondary nucleation. In homogeneous primary nucleation, molecules arrange themselves into a crystal lattice without external assistance. In heterogeneous primary nucleation, a solid foreign particle or surface provides apportion of the energy for nucleation which means it requires lower energy. Primary homogenous nucleation has the highest energy barrier and therefore only occurs in the labile zone. Primary heterogeneous nucleation occurs in

Fig. 2 Supersolubility diagram [11]
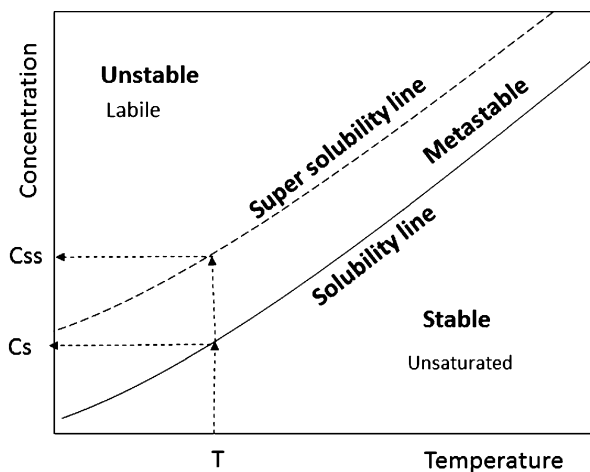
the metastable zone without any seed crystals in solution. As soon as crystals form, they lead formation of secondary nuclei due to attrition or contact and have a lower energy barrier than primary nucleation.

Primary nucleation prevails only at the initial stage of crystallization. Once a sufficient number of nuclei form and supersaturation drops into the metastable regime, secondary nucleation becomes the dominant mechanism for nuclei generation.

Crystal growth is a combination of two main steps: firstly, mass transport from solution to the crystal surface by volume diffusion or convection and then, secondly, incorporation of growth units into the crystal lattice through surface integration processes [12]. The overall growth rate is determined by the slower of these processes. If the rate of transportation of molecules onto the crystal surface is slower than the rate of incorporation of growth units into the crystal surface, the rate will be diffusion controlled. As the relative crystal-solution velocity is increased, the rate of growth increases up to a certain point and then remains constant. The growth above this point is controlled by surface integration.

Different faces may have different growth rates, depending on how readily they incorporate the crystal growth units. The morphology of a crystal is determined by the growth rates of each face: faster-growing faces usually grow out and disappear; slow-growing faces, being large, determine the morphology.

The interplay between secondary nucleation and crystal growth determines the final crystal size distribution and also the recovery of crystals. Controlling final crystal size and crystal size distribution is paramount in industrial crystallization. Therefore, any improvements in controlling nucleation and also crystal size distribution would make significant improvement to industrial crystallization.

Sonocrystallization

Sonocrystallization is the application of power ultrasound (frequencies from 10 to 100 kHz) to the crystallization process [13]. Studies on systems other than lactose have shown that sonocrystallization generally exhibits four features which do not occur in crystallization without sonication. These are faster primary nucleation, ease of nucleation, initiation of secondary nucleation, and production of smaller and purer crystals [14]. Faster primary nucleation means the metastable zone width is reduced with the application of ultrasound. Sonication was reported to alter the nucleation mechanism which was apparent as a strong reduction in the apparent order of nucleation. In order to establish a relationship between cavitation and ultrasound, several theories have been postulated, but the contribution of ultrasound to crystallization is still unclear [15].

These effects are attributed to localized high temperatures (5000 K) and pressures (2000 atm) created by imploding bubbles formed as a result of acoustic cavitation generated by high-intensity sound waves passing through solutions [16]. Localized high temperatures would be expected to decrease supersaturation therefore reduce the driving force. On the other hand, subsequent rapid cooling might play a

significant part in increasing supersaturation. Localized high pressures may reduce the crystallization temperatures. Furthermore, cavitation bubbles may act as nucleation sites by lowering the energy required for nucleation.

The ability of the ultrasound to cause cavitation depends on many factors, such as the frequency and intensity of ultrasound, properties of the liquid, and ambient conditions [17]. In liquid media, ultrasonic irradiation and cavitation in liquid- and solid-liquid systems can enhance reaction rate and product yield and facilitate mass transfer and reactant diffusion [18].

Ultrasound was reported to induce primary nucleation in a particle-free solution at lower supersaturations. For example, Li et al. [18] reported that by varying ultrasound power, duration, and solution volume, the mean size, crystal size distribution (CSD), and crystal shape can be perfectly controlled in spectinomycin hydrochloride crystallization. Sonocrystallization has been used to replace conventional seeding generating extremely small seed crystals for drug delivery [19]. Nuclei induced by ultrasound result in larger crystals during cooling crystallization [20].

Application of ultrasound was reported to reduce induction time [14, 21, 22]. The time elapses before formation of a measurable amount of crystals are called induction time, and it consists of formation of nuclei and growth of these nuclei. Assuming the time formation of a stable nucleus is much higher than the time necessary for the nucleus to reach a detectable size, the time it takes to reach a certain number of nuclei correlates to nucleation rate:

$$\mathbf{t_N} \propto \frac{\mathbf{N_N}}{\mathbf{J_{Hom}}} \tag{1}$$

$$\mathbf{J_{Hom}} = \mathbf{K_{hom}exp}\left[\frac{4}{27}\,\frac{\boldsymbol{\gamma}_s^3\mathbf{V}_m^2\boldsymbol{\beta}^3}{(\mathbf{T}\,\mathbf{k_B}\,\vartheta\boldsymbol{\alpha}\mathbf{lnS})^2}\right] \tag{2}$$

Combining two equations and taking the logarithm, induction time can be linearized, and K_{hom} and γ_{hom} can be calculated from the intercept and the slope of the line:

$$\ln\left(\mathbf{t_{ind}}\right) = \ln\left(\frac{\mathbf{N_c}}{\mathbf{K_{hom}}}\right) + \frac{4}{27}\,\frac{\boldsymbol{\gamma}_s^3\mathbf{V}_m^2\boldsymbol{\beta}^3}{\mathbf{k_B^3}\,\boldsymbol{\alpha}^2\vartheta^2\mathbf{T}^3}\,\frac{1}{\mathbf{ln^2s}} \tag{3}$$

In literature it has been shown that $\ln(t_{ind})$ versus $1/(\ln^2 S)$ consists of two linear segments: at high supersaturations, homogeneous nucleation, and, at lower supersaturations, heterogeneous nucleation. Lyezko et al. [21] reported that ultrasound reduced induction time significantly in potassium sulfate solution. Increasing the power input further reduced the induction time and reduced the slope and the intersection of the $\ln(t_{ind})$ versus $1/(\ln^2 S)$ plot. Ultrasound was reported to decrease the interfacial energy so the size of critical radius was reduced. On the other hand, for anti-solvent crystallization of roxithromycin, the slope was not affected by ultrasound, but the intercept was reduced [14].

Ultrasonic equipment consists of the electrical power generator, transducers, and emitters. For sonocrystallization two types of emitters are used: one using water baths and the other one using a horn [23]. Water baths have been used traditionally due to availability and low cost. They usually operate at 20–40 kHz, volumes vary between 0.5 and 25 L, power ranges from 40 W to 1000 W, and they are widely used for cleaning surfaces. More recently ultrasonic horns have become available, and reported use has increased for higher-intensity applications. It is important that the power applied or energy delivered to solutions is measured and reported correctly. Power represents the strength of the treatment which indicates the power of the ultrasonic wave. Power intensity (power irradiance) is defined as the power transmitted to the medium from the sonorod tip surface (W/m^2). As power is related to energy, it is possible to report ultrasonic energy delivered rather than power taking time of sonication into consideration (1 J = 1 W.s).

Application of ultrasound will convert the acoustic energy into heat regardless of the mechanism of the dissipation. Experimentally, this can be measured by measuring the temperature increase of the solution, and the heat dissipated can be calculated from an energy balance [24]:

$$Q = mC_p\Delta T \tag{4}$$

where Q is energy input in Watts, m sample mass, Cp heat capacity of the sample, and ΔT change in temperature.

This means all application of ultrasound will generate heat unless cooling is simultaneously applied. The temperature rise will be a function of ultrasound power applied, the volume of the solution, and the size of cavitation bubbles. At 20 kHz, a bubble grows to the largest size of 60–100 μm and generates a relatively large amount of heat [24].

Furthermore, only a fraction of the electrical energy applied to transducers to generate ultrasound is converted into acoustic energy. This will depend on the type of the equipment. For example, for ultrasonic water baths, DSA 100 and DSA 150 (China), power ranges from 60 to 150 W, and at 20 and 40 kHz, the relationship between power used and power dissipated is given in Fig. 3. Power used was measured with a wattmeter, and power dissipated was calculated by measuring the temperature change after a defined period of sonication at different power levels with 2.6 L of water (minimum water level). More power is delivered at 20 kHz than 40 kHz and efficiency is slightly higher (Fig. 3a). Approximately 50 % of the power is dissipated into solution. Power intensity was low and changed between 0.01 and 0.05 W/g. As water baths require two third minimum filled with water, the intensity applied cannot be increased by decreasing weight of sample. On the other hand, weight of sample can be varied by using ultrasonic horns. For example, for an ultrasonic horn (Sonics and Materials 650 with 13 mm rod), using 300 g water, power dissipated and intensity can be increased by increasing amplitude. Maximum efficiency is around 45 % and maximum intensity is 0.5 W/g at 100 % amplitude (Fig. 2b). It must also be noted that when the ultrasonic horn is on standby, it uses 55 W power. By changing the weight of solution, the ultrasound intensity applied

Fig. 3 Ultrasonic power, efficiency, and intensity for (**a**) ultrasonic bath, (**b**) and (**c**) ultrasonic horn
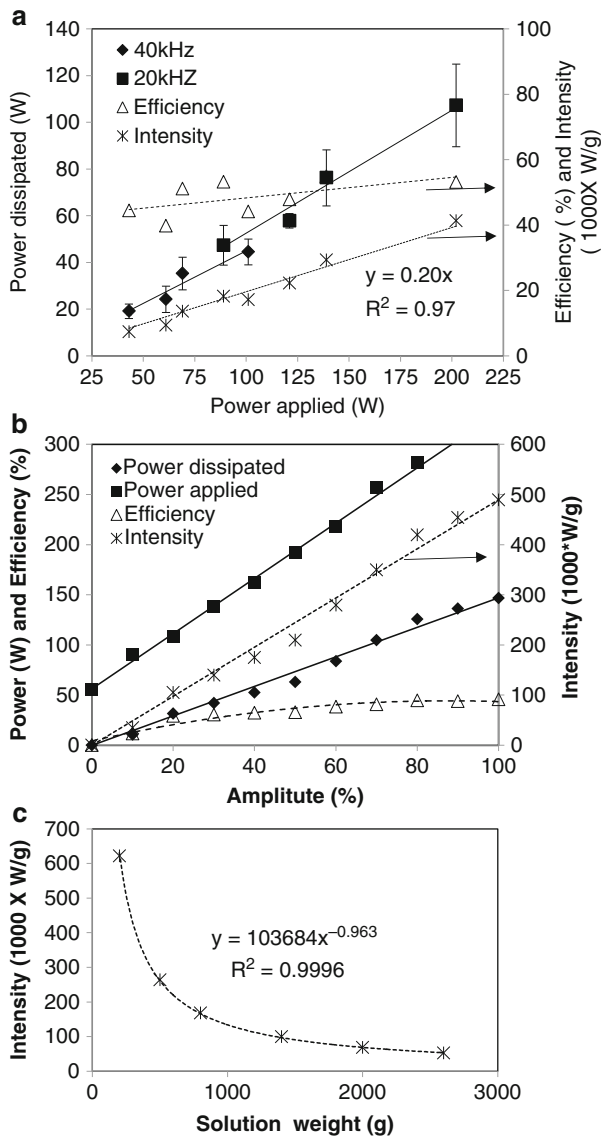
can be changed (Fig. 3c). Maximum intensity would be around 0.6 W/g (200 g water), but a significant amount of heat generated needs to be controlled. At low power densities, ultrasonic baths are slightly more efficient than horns. For 2.6 L water and 200 W power consumption, the ultrasonic horn delivers 0.035 W/g, while ultrasonic bath delivers 0.04 W/g (unpublished data). Lyczko et al. [21] reported the dissipated power represents 40 % of the electrical power consumed by the generator.

Nalajala and Moholkar [25] investigated the physical mechanism of sonocrystallization and reported that the shock waves created by ultrasound affect nucleation, while micro-turbulence governs the growth rate. The nucleation rate was reported to be an order of magnitude higher, but reduction in growth rate was reported as comparable to a mechanically agitated system for KCl.

Ruecroft, Hipkiss, and Maxted [26] reported that when bulk-phase mass transfer is rate limiting, ultrasonic treatment will enhance the growth rate by increasing the diffusion of growth units to the crystal surface. Dennehy [27] describes sonocrystallization as a central technique within the tool box of chemists and engineers for exerting control over particle size.

Lactose Crystallization

Lactose crystallization is complicated as lactose exists in two anomeric forms and mutarotation of each form into each other. When α-lactose monohydrate is added in excess to water with agitation, a specific amount dissolves rapidly, which is called the initial solubility of α-lactose monohydrate. As some of the α-lactose is converted into β-lactose, more α-lactose dissolves until the final equilibrium solubility is attained. The equilibrium solubility of lactose increases with temperature [2] and is lower in other solvents such as ethanol [28] and slightly higher in whey [29]. More lactose can be dissolved in solution by heating, and upon cooling, the solution will hold more lactose than its equilibrium solubility. This is called supersaturation and it is the main driving force for crystallization. It is expressed with respect to either lactose concentration or α-lactose concentration. Visser [30] derived a formula for S of α-lactose in which the influence of β-lactose on solubility of α-lactose is taken into account. Visser's equation is:

$$S = \frac{C}{C_S - FK_m(C - C_S)} \tag{5}$$

C = total lactose concentration, g anhydrous lactose per 100 g water
C_S = final solubility of lactose, g anhydrous lactose per 100 g water
F = a temperature-dependent factor for depression of solubility of α-lactose by β-lactose
K_m = β/α ratio of lactose in mutarotation equilibrium at the relevant temperature

Butler [32] has expressed supersaturation as absolute alpha lactose supersaturation C_α-$C_{\alpha s}$ by using Visser's equation:

$$C_\alpha - C_{\alpha S} = \frac{C_S - FK_m(C - C_S)}{K_m + 1} \tag{6}$$

Fig. 4 Updated lactose
supersolubility diagram in
terms of glact/100 g water
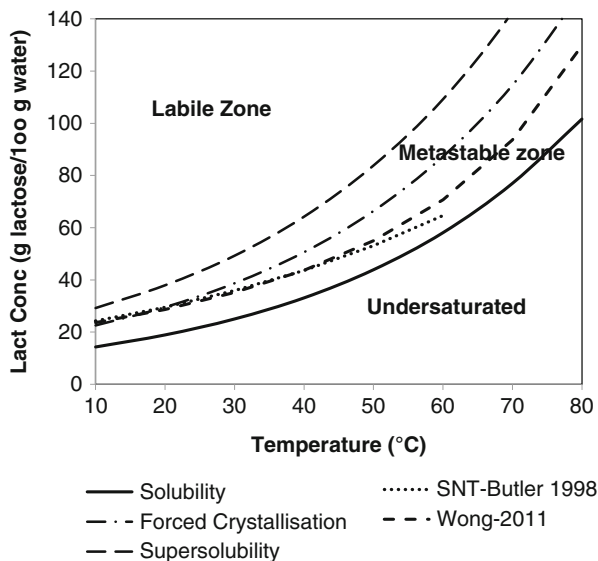
For nucleation (primary) to occur, Herrington [28] reported that lactose solution needs to be cooled to 30 °C, lower than the solubility value. This corresponds to around 2.1 times the initial solubility and is called supersolubility (Fig. 4).

Due to the presence of foreign particles (dust, impurities), surfaces (propellers), or mixing, nucleation (primary heterogeneous) of lactose occurs at relatively lower levels of supersaturation (1.6 times the solubility). This is called forced crystallization. This zone is sometimes called the intermediate zone [31]. More recently, the metastable zone has been investigated in great detail to assist industrial lactose crystallization. Butler reported a secondary nucleation threshold below which no nucleation is observed [32]. Wong et al. investigated the appearance of the first lactose seeds in stirred seeded lactose systems and derived an equation for lactose concentrations at which the first nuclei were detected as a function of temperature: $C = 0.1634\ e^{(0.0155T)}$ (C lactose (g/g water)) [33]. This was the same relationship developed by Vu et al. [34]. Temperatures at which transmission starts decreasing significantly (induction time) and corresponds with the supersolubility curve. The solubility, supersolubility, SNT, and metastable limits in terms of lactose/100 g water are:

Solubility [32] $C = 10.788\ e^{(0.021T)}$
SNT [32] $C_{SNT} = e^{(2.389+0.0287T)}$
First detection [35] $C = 16.34\ e^{(0.0155T)}$

Lactose supersolubility diagram describes the extent of crystallization as a function of temperature and concentration and is a great tool for controlling crystallization. For example:

Fig. 5 Literature nucleation rates of lactose
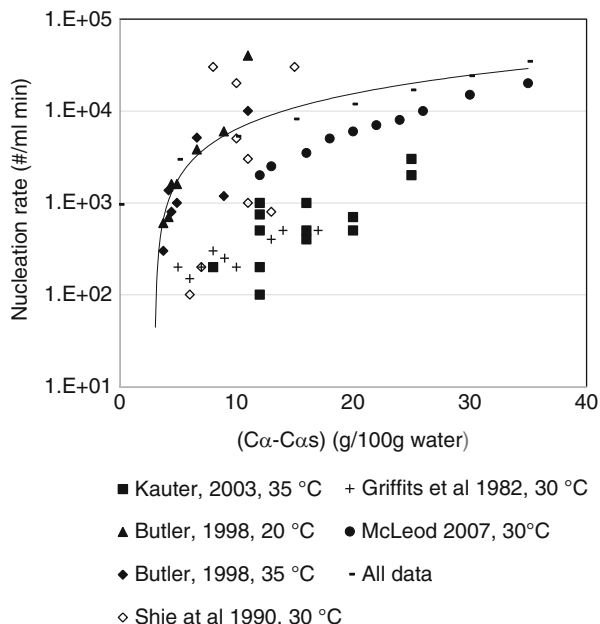
- Neither growth nor nucleation can take place in the unsaturated zone.
- Spontaneous nucleation can take place in the labile zone.
- Lactose crystals grow in metastable and labile zones.
- No nucleation will occur below secondary nucleation threshold even in the presence of seeds.
- Below the forced crystallization curve, crystal growth is promoted, while secondary nucleation is minimized.
- Above the forced crystallization curve, nucleation is promoted.

Once a sufficient number of nuclei have formed, crystal growth occurs. The rate of crystallization is then affected by temperature, supersaturation, surface area available growth, viscosity, agitation, and rate of mutarotation [31]. The rate of mutarotation is influenced directly by the temperature of the solution; it proceeds faster at high temperatures and very slowly at temperatures near the freezing point. Thus, temperature has the opposite effects on mutarotation and crystallization. This means that by cooling the concentrate too fast or to a very low temperature, crystallization proceeds quickly, but completion of crystallization takes longer; slow mutarotation results in a small amount of β-lactose being transformed into α-lactose for further crystallization. The interplay between nucleation and crystal growth determines final yield and crystal size distribution.

Nucleation of lactose has been studied and reported extensively [32, 36–39] (Fig. 5). Variation within the same studies highlights difficulties in measuring nucleation rates. Also different measurement techniques and equipment used cause variations in measurements. Nucleation rate increases with increasing

Fig. 6 Literature growth rates of lactose at 30 °C
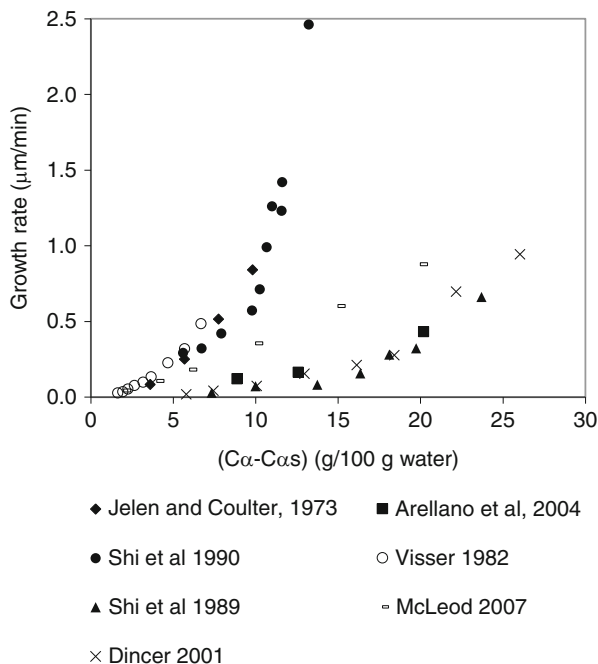
supersaturation, seed load, agitation, and impurity content and decreases with temperature [37, 40].

Crystallization kinetics of α-lactose monohydrate have been studied extensively (Fig. 6). Three main classes of study can be identified. The first is ex situ large single crystal growth with photographic measurement as developed by van Kreveld and Michaels [41] in a rotating flask. They have measured the growth rates of all major faces at 30 °C and two supersaturations. It was observed that there was no growth on the $(0\overline{1}0)$ face and slight growth on the $(0\overline{1}\,\overline{1})$ face at high supersaturations. The main growth was the movement of the (010) face in the +**b** direction and slight growth on the (110), (100), and (1–10) faces (Fig. 1). Later, Visser [42] used this method in his work on natural growth inhibitors in lactose and measured the growth rates of the (010) and the (100) faces in a stagnant system. The second method is in situ measurements of overall growth rates in a static environment. Shi et al. [43], Arellano et al. [44], and Dincer et al. [45] used this method to measure the overall growth rate for a contact and spontaneous nucleation and seeded systems, respectively. Shi's results have suggested that each crystal grows at its inherent constant rate, but different crystals have different growth rates. The third method is measurement of overall crystallization rate. Jelen and Coulter [46] and McLeod [37] measured growth rates in batch crystallizers as a weight increase per unit crystal surface area, and Shi et al. [39] in a continuous cooling crystallizer.

The photomicroscopic cell growth rates are an order of magnitude slower than the other measurement methods. Crystal sizes were less than 100 μm in
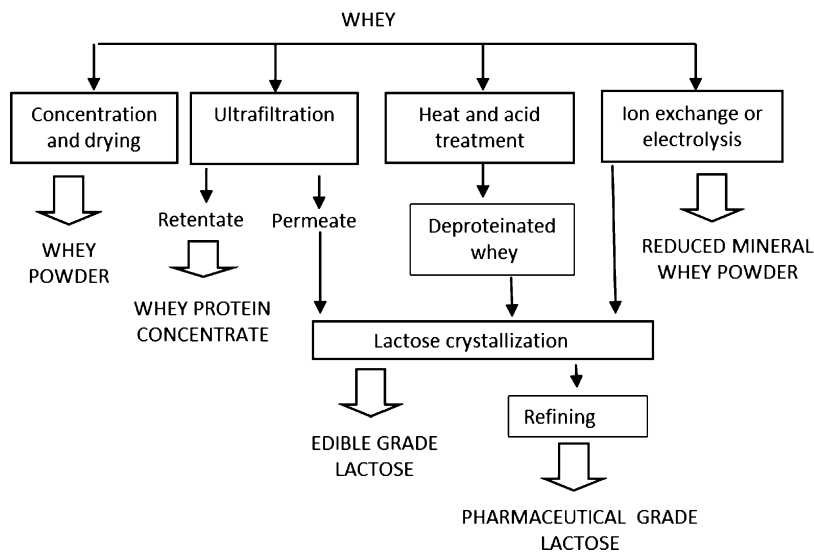
Fig. 7 Processing scheme for manufacturing major whey product [6]

photomicroscopic cell growth, while larger crystals 300–600 μm in cooling experiments and 1 cm large crystals were used in single crystal experiments. Within a lactose population, a wide variation of growth rates were reported [43, 45]. When large crystals were preselected, faster growth rates were measured. Crystals less than 100 μm were found to grow at the same rate in stagnant and flow environment. It was reported that up to 0.4–0.6 μm/min, growth rates are not diffusion controlled [45]. On the other hand, the growth rates of larger crystals (300–600 μm) increased with stirring up to 300 rpm, which was double the growth rates in stagnant solution [37]. Furthermore, the number average growth rates of a population of crystals are measured with the photomicroscopic method, while mass average growth rates are measured with other methods. The linear extrapolation technique to calculate the growth rate in the cooling crystallizer overestimates actual growth rates by neglecting the high number of slow-growing crystals [47], curvature at small sizes (less than 40 μm) in the semilogarithmic population density versus crystal size plot.

Growth rates of lactose crystals in industrial permeate were reported to be 50 % faster and [32] and the same as in aqueous solution [37] in two different studies.

All whey products contain significant amount of lactose; therefore, lactose crystallization is an important part of production of whey powder, whey protein concentrate, food, and edible-grade lactose. Figure 7 shows the main products produced from whey.

Whey from cheese and casein manufacture is the major source of lactose production. Whey contains almost 6–7 % dry matter: 70–80 % of this dry matter is lactose, 10–15 % is protein, 7–15 % is ash, and around 1 % is fat. Calcium, phosphorus, iron, potassium, and sodium are the main elements constituting the ash content. The composition of whey changes depending on the type of cheese

Fig. 8 Simplified version of lactose crystallization in whey powder and lactose manufacturing

```
Cheese Whey          Whey permeate
     ↓                    ↓
Concentration        Concentration
     ↓                    ↓
Flash Cooling        Flash Cooling
     ↓                    ↓
Crystallisation      Crystallisation
     ↓                    ↓
Spray drying         Decantation ────→  Refining
     ↓                    ↓                ↓
Packaging            Washing          Filtration
     ↓                    ↓                ↓
Whey powder          Drying           Crystallisation
                         ↓                ↓
                     Packaging         Drying
                         ↓                ↓
                     Edible grade      Packaging
                     lactose             ↓
                                       Pharmaceutical
                                       grade lactose
```
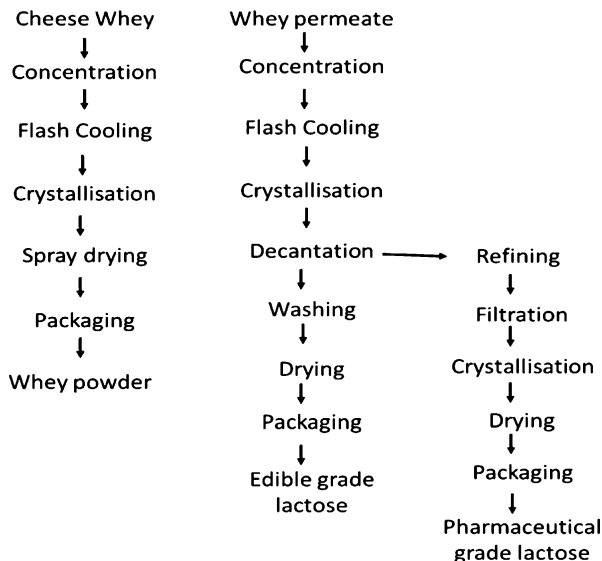
produced [48]. Raw whey from cheese factories contains low level of curd fines, which are removed by a combination of settling, screening, and centrifugation. The remaining fat content is removed by separation, and sweet whey needs to be pasteurized for microbiological quality.

Lactose is crystallized from whey, permeate, or decalcified permeate (Fig. 8). The major steps for producing lactose are protein removal, concentration, crystallization, separation, and drying.

Removal of proteins is usually done by ultrafiltration, and it reduces the viscosity in the concentrated solutions and permits concentrating to higher solid contents. Concentration of whey up to 50–70 % total solids is done by evaporation. Crystallization is initiated either spontaneously or by seeding with a small quantity of lactose crystals, usually in batch crystallizers by flash cooling, and crystallization proceeds with cooling usually to 20 °C. Cooling rates depend on the product specification. Depending on the specific product or processing objective, the desired lactose crystal size varies. For example, large crystals are desired in lactose production to enable recovery, while smaller crystals less than 20 μm are required for spray-dried whey powders. Cooling the concentrates too fast or to a very low temperature results in longer crystallization times as a result of slow mutarotation, i.e., only a small amount of β-lactose is transformed into α-lactose to promote further crystallization. Cooling rates between 1 and 4 °C/h allow mutarotation and crystallization to proceed at reasonable rates [31]. The process is slow and takes 12–24 h. Narrow crystal size distributions are desired, and, therefore, after initial nucleation, crystallizers are operated below the forced crystallization curve to maximize growth and minimize nucleation. Formed crystals can then be separated by centrifugation and washed and dried. Crude lactose is refined to produce pharmaceutical-grade lactose

by treatments to remove color, residual protein, and salts. In the refining process, decolorizing carbon removes impurities; HCl and lime are used to improve the action of carbon and removal of proteins. The carbon and the precipitated impurities are removed by filtration. The treated solution is then filtered and evaporated, and crystallization is initiated by seeding at low supersaturation to minimize graining. Crystallization of lactose is much more rapid in concentrated syrup than from whey. Then the crystals are centrifuged, washed, and dried. Commercial lactose manufacture is different from plant to plant.

The problem with conventional lactose crystallization is long induction times and large metastable zone width (MSZW) which makes the process unpredictable and difficult to control [49]. Therefore, improved control of the lactose crystallization process has particular significance for the dairy industry [50].

Sonocrystallization of Lactose

The first reported applications of ultrasound in lactose were to generate seed crystals with narrow crystal size distribution. Butler called these crystals as common history seeds as they were nucleated at the same time with ultrasound and grown under identical conditions [32]. Vu et al. [51] used ultrasound and ethanol as an anti-solvent to generate fine lactose seeds to make seed slurries with fine lactose particles for the dairy industry.

Since then, sonocrystallization of lactose has been reported in aqueous solution and whey at bench scale using ultrasonic baths and horns. There have also been two pilot-scale trials. Details of literature on sonocrystallization of lactose are given in Table 1. Early work concentrated on rapid lactose recovery from whey and utilized anti-solvent to achieve supersaturation and low-intensity ultrasound rather than energy-intensive concentration and cooling. The aim was to recover lactose from whey to reduce the biological oxygen value (BOD) and reduce the environmental impact of whey disposal. Later the attention moved to using high-intensity ultrasound for production of pharmaceutical-grade lactose and improving control of industrial lactose crystallization without the use of anti-solvent. The impact on morphology and β-lactose incorporation and the impact on nucleation rate were also investigated.

Lactose Recovery

Bund and Pundit [52] first reported sonocrystallization of lactose in aqueous solution using an ultrasonic bath (20 kH, 120 W) with 85 % ethanol as an anti-solvent and yielded recovery of 92 % lactose within 5 min compared to 15 % recovery with agitation alone. The speed and efficiency of this process are due to insolubility of lactose in ethanol and also increased cavitation due to lower vapor pressure of the solution [52]. Lactose solution is 200 times supersaturated using lactose solubility in

Table 1 Recovery of lactose with different methods

	Anti-solvent	System	Recovery (%)	Crystal size (μm)	T (°C)	Lactose (%)	C/Cs	Sonication time	Total time	Refs.
Ultrasonic bath with anti-solvent	Ethanol 84 %	Aqueous	92		30	17.5	230	5 m	5 m	[52]
		Paneer whey	92		7	55 % TS	350	NO	60 m	[56]
		Paneer whey	90		7	15	350	20 m	20 m	[54]
	Acetone 75 %	Aqueous	83	2.5	30	16		4 m	4 m	[57]
		Paneer whey	80	2.5–6.5	30	15		15 m	15 m	[58]
Ultrasonic horn	Ethanol 40–60 %	Aqueous	75–86	10–40	25	20–30		10 s on 10 s off	120	[53]
	No	Aqueous	44	101	Cooling 90–40 °C	30	2.1	Control no sonication	20 h	[59]
			48	93		40	3.2		12 h	
			53	86		50	4.7		8 h	
			83	27	20	30	2.1	5 m	5 m	
			84	22		40	3.2			
			84	15		50	4.7			
			76	80		30	2.1	45 s	5 h	
			78	79		40	3.2			
			79	78		50	4.7			
Pilot scale	Ethanol 75 %	Aqueous	NR	5–40	25	25		10–360 m	10–360 m	[53]
	No	Conc. whey	75–80	40	Cooling down	32	~2.5	1–3 m	24	[60]

ethanol water mixture as reported by Kougoulos et al. [53]. It was observed that nucleation was substantially reduced, and available supersaturation was utilized for growth in the presence of proteins. This technique was later applied to partially deproteinated paneer whey (resembles cottage cheese whey) from buffalo milk [54]. Addition of ethanol also resulted in precipitation of minerals as well resulting in high ash content in lactose [55]. Reduction of final pH to 2.8, continuous sonication at 7 °C with stirring, and seeding (1 %) resulted in 90 % lactose recovery within 20 min with 98 % lactose and 2 % protein.

Acetone as an anti-solvent produced similar results to ethanol. 90 % recovery was achieved after 4 min of sonication in aqueous lactose solution [57] and 80 % from paneer whey after 15 min of sonication [58].

The most comprehensive study on sonocrystallization of lactose was published by Kougoulos et al. in 2010 on the influence of ultrasound and anti-solvent on crystal habit and particle size especially investigating the effect of ethanol addition time using a P100 20 kHz sonic system with 8 mm ultrasonic probe in a 100 ml reactor [53]. Ultrasound was not observed to increase the lactose recovery after two hours of crystallization but reduced the crystal size.

There is the only study reported on recovery without anti-solvent. Dhumal et al. [59] looked at sonocrystallization of lactose to engineer lactose crystals with desired size and shape for dry powder inhalers (DPI). Sonocrystallization was used to replace conventional seeding generating extremely small seed crystals for drug delivery [19]. Nuclei induced by ultrasound result in larger crystals during cooling crystallization [20]. When grown in glycerine, lactose with smooth surfaces and narrow PSD suitable for DPI can be grown. A sonorod (Sonics and Materials, Vibra Cell, VCX 750) was used for sonication, but the amplitude was not reported. Control (only stirring), sonicated for 5 min, sonicated for 45 s and stirred for 3 h, and sonicated and glycerine added. Solutions without sonication produced yields of 44 %, 48 %, and 53 % after 20, 12, and 8 h for 30 %, 40 %, and 50 % solutions, respectively. Typical tomahawk-shaped lactose crystals were formed. On the other hand, all three concentrations yielded 83–84 % lactose crystals after 5 min of ultrasonication and crystal sizes of 27, 22, and 15 μm with increasing concentration. At higher concentration, the crystal size was smallest due to the increased rate of nucleation at high concentration. 45 s of ultrasonication followed by 3 h of stirring produced 78–80 % yield with 80 μm average crystal size. From the images of the crystals published, sonication produces prism-shaped crystal compared to conventional tomahawk-shaped crystal, and upon standing, crystal grows in **b** direction, producing crystals longer in **c** direction and not in **b** direction. This occurred after very high-intensity sonication.

Despite promising results for sonocrystallization of lactose using ethanol as an anti-solvent, no report of industrial or even small-scale applications have been reported in the literature. This is mainly due to the large amount of ethanol requirements: 5–6 times the volume of whey. Furthermore, ethanol needs to be separated from solution. Flammability of ethanol also limits its use as an anti-solvent.

Crystal Morphology

Different morphologies of lactose crystals have been reported in the literature
(Fig. 9). A needle or a prism-shaped morphology was reported in the presence of
anti-solvent and in combination of ultrasound and anti-solvent [52, 55]. These
crystals were reported to be 98 % lactose but the β-lactose content was not reported.
The addition time of ethanol was found to be the most significant effect on particle
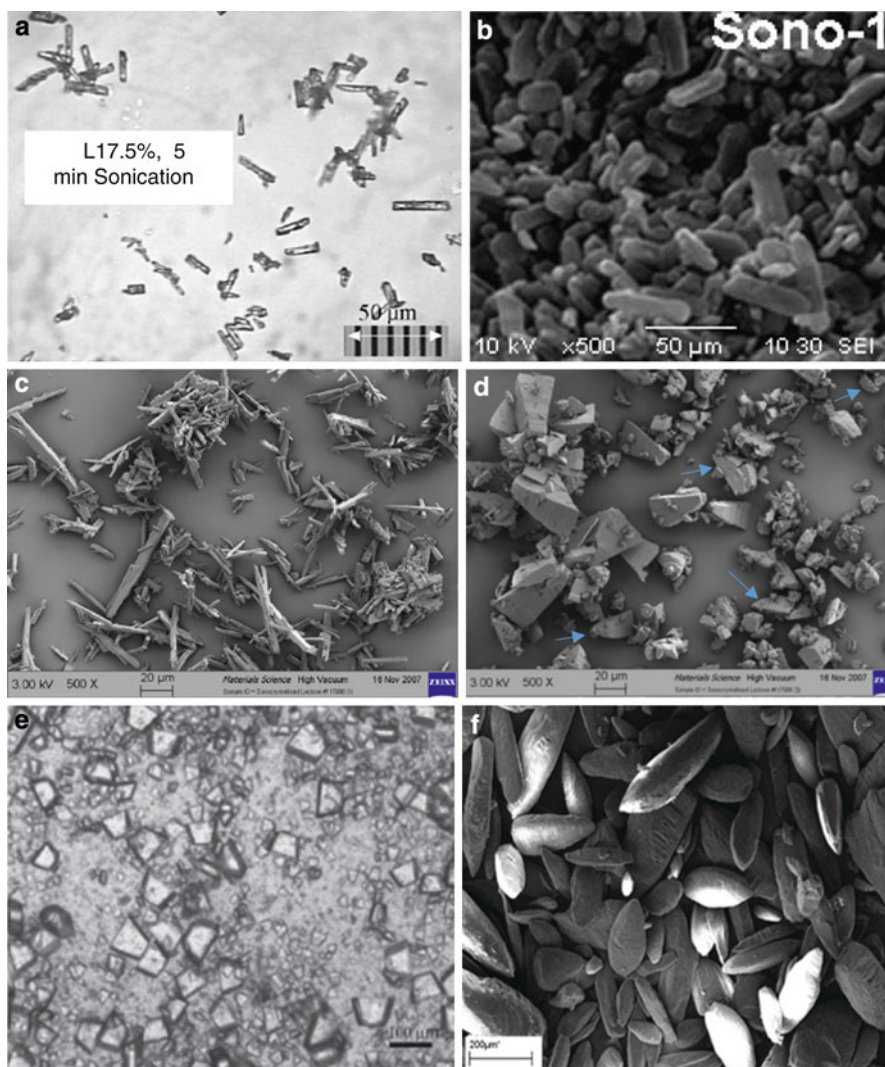
Fig. 9 Different morphologies of lactose crystals obtained via sonocrystallization. (**a**) Needle-
shaped crystals [52]. (**b**) Needle-shaped crystals [53]. (**c**) Needle-shaped crystals [53]. (**d**)
Tomahawk-shaped crystals [53]. (**e**) Lactose in concentrated whey [60]. (**f**) LactoSonic [61]

size and morphology of lactose crystals [53]. Rapid ethanol addition times resulted in needles, rods, and mixture of plates/rod crystals. With slower additions tomahawk crystal morphology was observed. Faster addition times increase the precipitation pressure due to increased supersaturation.

Rod-shaped lactose crystals were reported to have contained up to 45 % β-lactose. It must be noted that these crystals appear to have curved faces and unusual morphologies. Both alpha and beta lactose crystals can be visually identified. Tomahawk-shaped crystals were reported, and it was identified that up to 30 % β-lactose content did not alter the typical tomahawk morphology. This result can be disputed as individual β-lactose crystals are visible; therefore, the β-lactose content of tomahawk-shaped crystal should be less than 30 %. These rod-shaped crystals are quite different than the prism- or needle-shaped crystals reported by Bund [52].

Sonocrystallization in aqueous solutions resulted in prism-shaped crystals (rectangular pyramid) which were reported not to contain any β-lactose [59]. Prism-shaped α-lactose monohydrate crystals formed in aqueous solutions when the supersaturation was very high. At 30 % and 40 % lactose concentration, prisms are not observed in aqueous solutions. It appears that ultrasound had an impact on either surface diffusion or the mutarotation rate.

This is due to the relationship between precipitation pressure and morphology. The fastest-growing face of α-lactose monohydrate crystal is actually the (011) face in the absence of β-lactose. When β-lactose is present and precipitation pressure is low, β-lactose prevents the attachment of a new layer of molecules and slows the growth rate. But with increased precipitation pressure due to increased supersaturation, the inhibition of β-lactose decreases, and at the same time β-lactose is incorporated into the crystal lattice as well as α-lactose which increases the β-lactose content of the resultant crystal.

Induction Time and Nucleation Rate

The impact of ultrasound on induction time has been investigated and compared to stirring [62]. It was observed that ultrasound had a significant effect in reducing induction times (Fig. 10). Induction times are, on average, an order of magnitude shorter with sonication (0.15 W/g) compared to stirring (300 rpm) which in turn means faster nucleation rates. At low supersaturations the influence of ultrasound on nucleation is much more significant that at high supersaturation. Nucleation rates increased faster with sonication compared to stirring with increasing concentrations (Fig. 11). Application of ultrasound induced significantly faster nucleation at concentrations of approximately 15 g/100 g lower than stirring which implies that the metastable zone width is narrowed by ultrasound. Nucleation rates increased with increasing concentration for both sonication and stirring. However, the effect of ultrasound was more prominent at low supersaturation (in the intermediate zone, between relative lactose supersaturations of 1.6 and 2.1) [48]. Similar results were reported in other literature [14, 18].

Fig. 10 Induction times for
sonicated and stirred lactose
solutions at 22 °C [62]
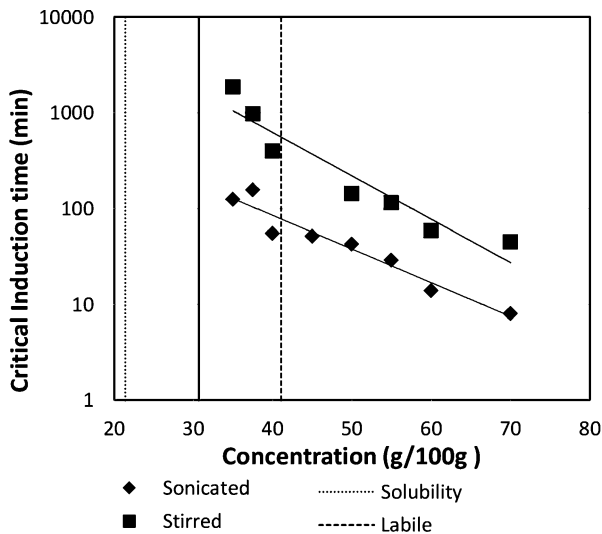
Fig. 11 Nucleation rates of
lactose with and without
ultrasound (Modified from
[62])
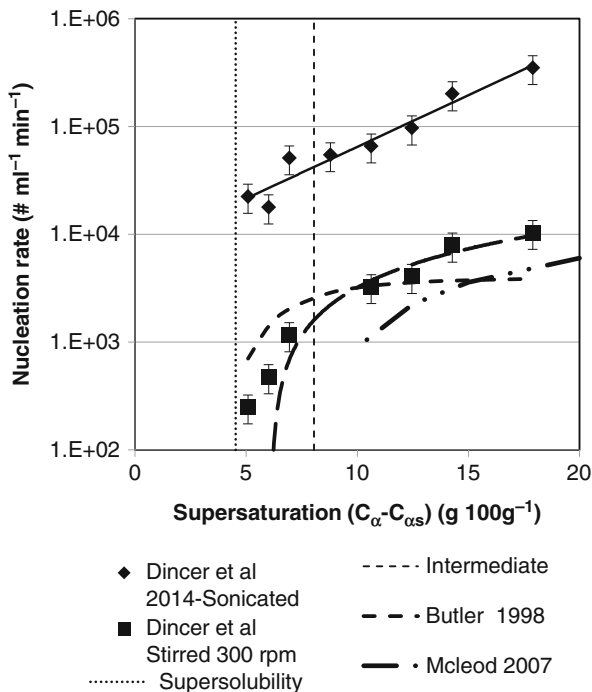
A plot of $\ln(t_{ind})$ versus $\ln^{-2}(S)$ differentiates between homogeneous and hetero-
geneous nucleation with different slopes [11] (Fig. 12). Homogeneous nucleation
involves spontaneous formation of nuclei in the absence of foreign particles and
occurs at high concentrations. Existence of foreign particles or surfaces reduces the

Fig. 12 The impact of sonication on induction time (Modified from [62])
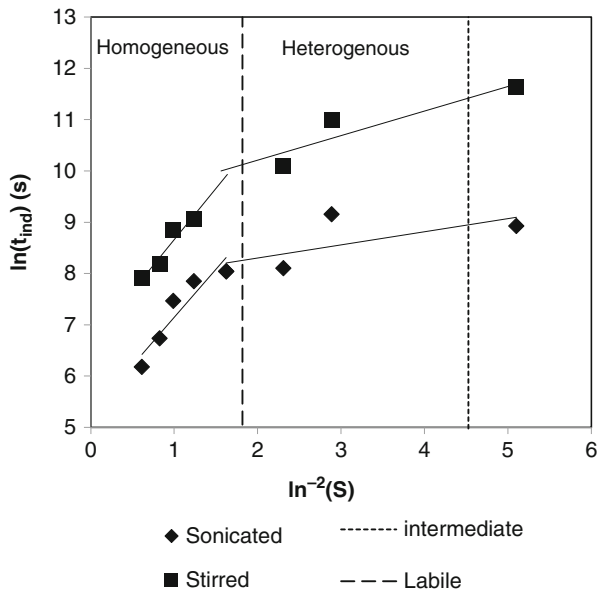
energy barrier for crystal formation, and nucleation occurs at lower supersaturations [12]. A change of mechanisms was observed. In the labile zone (above the supersolubility line), the similar slopes for sonication and stirring indicated that ultrasound did not have any impact on surface energy. In the heterogeneous nucleation zone, the slope of the sonicated is lower than the stirred experiments. A similar result was reported for tolazamide [63]. At high supersaturation, homogeneous nucleation is higher than heterogeneous nucleation; therefore, it dominates. At low supersaturation, the rate of homogeneous nucleation is so small so that nucleation is mainly heterogeneous nucleation. Application of ultrasound affects heterogeneous nucleation. The decrease in slope with sonication in the heterogeneous nucleation zone is an indication of decreased surface energy which results in a decrease in the size of the critical nucleus [21].

The Impact of Power

Sonocrystallization of lactose has been reported in ultrasonic baths, with horns and flow systems at a wide range of powers and energies (Table 2). In ultrasonic bath experiments, the impact of low ultrasound energies delivered was increased with the use of ethanol anti-solvent. The supersaturation of 200–300 times allowed rapid recovery of lactose. In aqueous solutions without anti-solvent, maximum supersaturation (C/Cs) was 2.23, and ultrasound energy delivered was an order of a magnitude higher than bath experiments. For example:

Table 2 Literature ultrasound power and energies applied

	Power (W)		Sample vol (L)	Ethanol %	Sonication time	Energy J/ml	Yield %	Refs.
	App.	Diss.						
Water bath	120	42	0.065	85	5 min	4	90	[52]
Water bath	120	42	0.190	95	20 min	16	80	[54]
P100	10–30	75	60–80	66–75	10–120 min	75–1100	70–86	[53]
Sonolab SL250	100	50	2.1	0.1	63–168 s	3–16		[60]
Vibra Cell VCX750	560[a]	280	0.13–0.15	–	45 s, 5 min	130–600	74–84	[59]
Vibra Cell VCX 600	46–380	50 % P_{app}	0.3	–	15 s to 16 min	7–400	NA	[62]
Prosonitron P500 flow cell	500	250	80	75	10–360 min	90–3240	NR	[53]
Prosonitron P500 noncontact	250–600		6.4	–	32–96 s	3–15	~80 %	[60]
Hielscher UIP1000hd	1000	500		–		4	NM	[60]

[a]Estimated 50 % efficiency

Fig. 13 The impact of
ultrasound power on
induction time
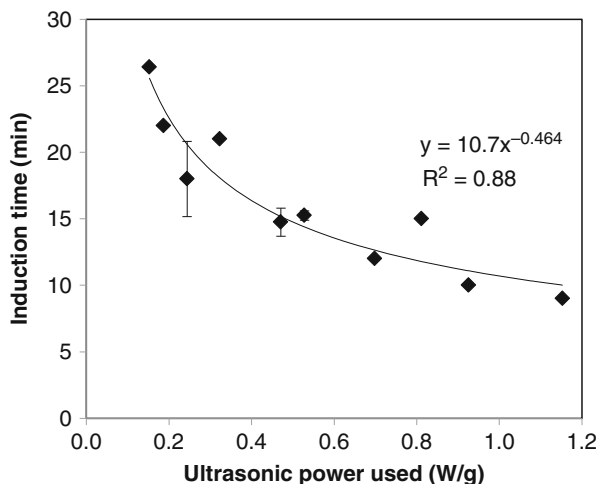
- Ultrasonic bath, 4 J/g: 90 % recovery after 5 min of sonication from 17 % lactose solution with 85 % ethanol addition
- Ultrasonic horn, 600 J/g: 80 % recovery after 5 min of sonication from 23 % lactose solution

The effect of ultrasound power on induction time and nucleation rate was investigated at 60 g/100 g lactose concentration and compared with stirring [62]. Induction times were found to decrease with increasing power. For sonication, a rapid decrease was observed until around 0.15 W/g power intensity (140 W, 30 % amplitude), and then the effect decreased (Fig. 13). Increasing stirring speed decreased induction time up to 600 rpm. Above this, formation and incorporation of large number of air bubbles into solutions resulted in increased induction times. In order to compare power used by sonication and stirring, nucleation rates were plotted as a function of power intensity applied. Stirring consumes less energy compared to sonication, but it was not possible to increase the nucleation rate with increasing stirring speed (Fig. 14). The benefit of reduced induction time with increasing power density needs to be weighed against the increase in energy consumption. However, energy requirement will decrease with increasing concentration, which was associated with decreased induction times.

Growth Rate
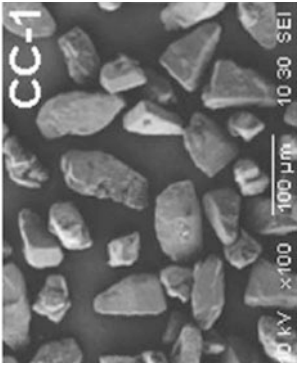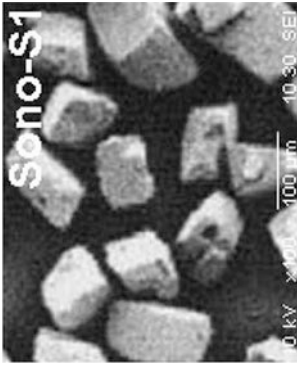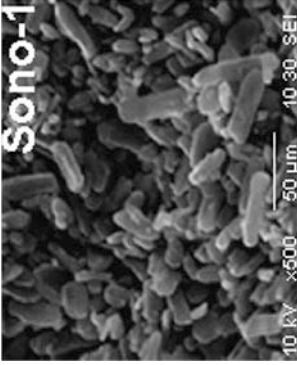
The effect of ultrasound on lactose crystal growth is not widely reported. Firstly, measuring growth rates of lactose crystals during sonication is not straightforward. Secondly, morphology of lactose crystal is complicated. Most of the studies concentrated on ultrasound induced primary nucleation. In the labile zone, nucleation is more prominent than crystal growth. Growth rates cannot simply be calculated by

Fig. 14 The effect of ultrasound power input on nucleation rate (♦ sonicated, ■ stirred)
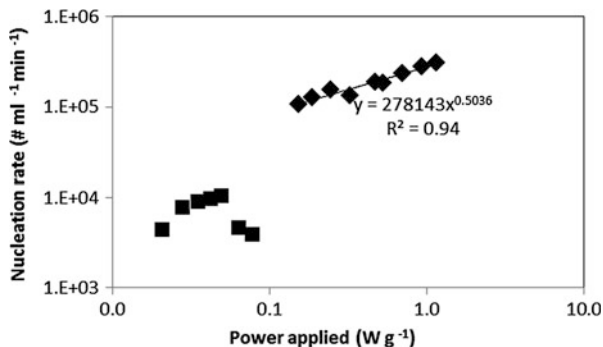
dividing final crystal time with duration of sonication. This is the change in average crystal size with time, not the crystal growth rate. It is highly influenced by nucleation. For example, average crystal sizes were reported to decrease with increasing supersaturation [52], sonication [59], and increasing power. Concluding that growth rates were reduced with supersaturation or ultrasound is not warranted. It is not physically possible to get accurate measurement of crystal growth rates under sonication in the labile zone as it will always be affected by nucleation unless experiments are conducted in a seeded system. Sonocrystallization of lactose was investigated, and data was provided by Dhumal et al. [59] to calculate growth rates with and without ultrasound. Final crystal size and duration of sonication for saturated lactose solutions were reported for (1) stirred at 300 rpm for 5–10 h, (2) sonicated for 45 s and stirred for 3 h, and (3) sonicated for 5 min. Calculated growth rates and applied power densities are given in Table 3 with crystal growth rates calculated using the equation derived by Butler [33]. Control crystals were grown for 10 h and yielded around 50 % lactose recovery, while samples sonicated for 45 s and stirred for 3 h yielded around 80 % recovery. Lactose concentration of 30 % (w/w) corresponds to 43 g lactose/100 g water, and at 25 °C, it lies below the supersolubility curve in the metastable zone. Growth rates reported in literature under these conditions are very similar to calculated stirring only growth rates. According to crystal size measurements, growth rates double following 45 s sonication and increases 30 times with 5 min sonication. In the literature, it was reported that when bulk-phase mass transfer is rate limiting, ultrasonic treatment will enhance the growth rate by increasing the diffusion of growth units to the crystal surface [26] and micro-turbulence governs the growth [25]. It was also reported that growth rates below 0.4 and 0.6 $\mu m \ min^{-1}$ are integration controlled at 30 °C [64, 65]. Therefore, increasing mass transfer rate is not expected to increase growth rate in sonicated samples. One of the difficulties associated with lactose crystals is that morphology can change significantly, and it may become difficult to assign faces to the crystals. Under standard conditions, crystal growth occurs in **b** direction with the (010) face fastest growing away from the tip of the crystal. The morphology of crystals after 5 min sonication is prism shaped. Measuring the length of the crystal does not provide comparison of growth rates with tomahawk-shaped crystals. It is very

Table 3 Lactose crystal growth rates with and without sonication [59]

Lactose (%)	Growth rates (µm/min)			
	Literature [32]	Stirring only	Sonicated and stirred (90 J/ml)	Sonicated (600 J/ml)
30	0.19	0.17	0.41	5.4
40	0.88	0.20	0.42	3.0
50	2.67	0.28	0.42	2.7

interesting that sonicated crystals grew faster in the **c** direction. At this supersaturation needle formation is not expected. The XRD patterns of prism-shaped crystals showed no β-lactose incorporation, and it may be possible that ultrasound has an impact on surface diffusion of α-lactose molecules on the $(0\overline{1}\,\overline{1})$ face. There has been no research on the impact of ultrasound either on the rate of mutarotation or surface diffusion reported in the literature.

Ultrasound was reported to have no effect on crystal growth rate (60 g/100 g, at 22 °C) when sonicating at 0.46 W g^{-1} and stirring at 300 rpm [62]. Sonication resulted in significantly faster nucleation rates than stirring. The change in the average crystal size (average growth rate) under constant sonication or stirring was found to be within experimental error at 0.14 μm min^{-1}. Formation of secondary nuclei during experiments was unavoidable as sonication or stirring was applied continuously. This resulted in widening of the crystal size distribution. The relative standard deviation for sonication was found to be higher than for stirring. This growth rate agrees with other lactose crystal growth rates given in the literature [45]. The same crystal morphology of a tomahawk was observed for sonicated and agitated crystals.

Bund also reported crystal growth rates of needle-shaped crystals after sonication with 85 % ethanol as an anti-solvent [52]. Growth rate was decreased from 2 μm/min to 1 μm/min in 10 min of sonication, consistent with reduced supersaturation after 90 % lactose recovery within 5 min.

The impact of ultrasound on lactose crystal growth rate has not been fully understood and warrants further investigation.

Pilot-Scale Sonocrystallization

There has been two pilot-scale sonocrystallization of lactose trials reported in literature both using a noncontact Prosonitron P500 flow sonicator [60].

Kaugulas et al. [54] used ethanol as an anti-solvent, and total crystallization time was 360 min. Ethanol was added at 10, 60, 120, and 360 min, and ultrasound was applied continuously during ethanol addition. Resulting crystals were found to have significant β-lactose incorporation, and different morphologies were observed, and this was a significant step forward in the implementation of sonocrystallization as a viable technology.

Recently sonocrystallization was applied to whey powder production [60]. A Prosonitron P500 noncontact sonicator was installed in-line with a commercial manufacturing process immediately following flash cooling. Concentrated whey (30 ± 1 °C containing 55 % solids of which 25 % was lactose) was diverted to the sonicator at the desired flow rate. Sonication was performed in a single pass at 250–600 W and flow rates of 4–12 L/min to achieve applied energy densities of 3–15 J/mL. Control samples were passed through the ultrasonic rig at the appropriate flow rate without sonication. Sonicated and control wheys were crystallized in bench scale following a similar cooling curve to commercial production.

Fig. 15 Crystallization profile of lactose in stirred and sonicated concentrated whey [60]
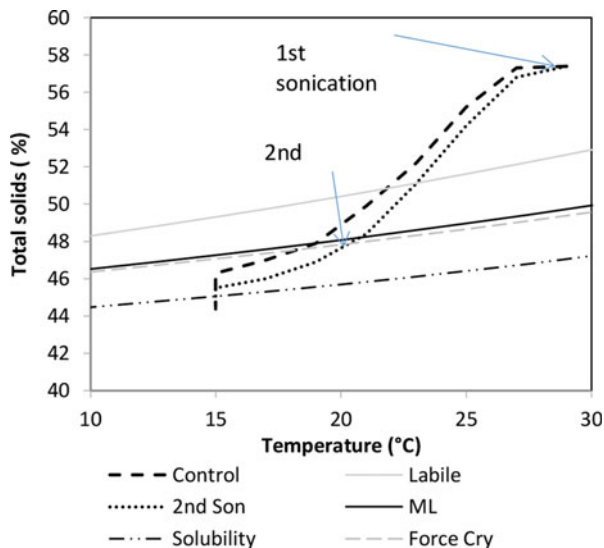
Sonocrystallization resulted in a faster rate of crystallization compared to control for up to 200 min. When a second sonication treatment was applied using a sonorod (UIP 100hd, Hielscher Ultrasonics GmbH, Germany, 1 kW) delivering an applied density of 4 J/ml, crystallization rate improved to 300 min, but ultimately both approached yielded around 80 % crystallized lactose. The main benefit was the size reduction and smaller variation in crystal size. The average crystal size for sonicated whey was 38.39 ± 10.02 μm and for stirred 57.9 ± 17.71 μm. No change in morphology was observed with sonication. A fast rate of reaction can be maintained for longer by applying a second ultrasonic treatment at the metastable limit to stimulate further nuclei formation. Although the yield of crystallized lactose is limited by the solubility of lactose, the resulting crystals are smaller than conventional stirring, and the process delivers greater control of the crystal size distribution. Results indicate that multiple ultrasonic treatments to create a pulsing effect may yield the maximum amount of crystallized lactose in a shorter time than conventional stirring (Fig. 15).

The hypothesis based on multiple ultrasonic treatments was confirmed in a separate experiment (Fig. 16). Concentrated whey (30 ± 1 °C) was fed to crystallization tanks post evaporation at a flow rate of 700 mL/min for 180 min. Sporadic primary lactose crystallization occurred during the filing process, but it was only after 180 min when the crystallization process was initiated that lactose crystallization was controlled. Constant sonication of the concentrated whey in the crystallization tank between 180 and 800 min at an energy density of 2 J/mL and a flow rate of 700 mL/min allowed maximum lactose crystallization to occur at approximately 500 min. This was only limited by lactose solubility. A similar level of crystallization was reached by stirring without ultrasonic treatment at approximately 900 min.
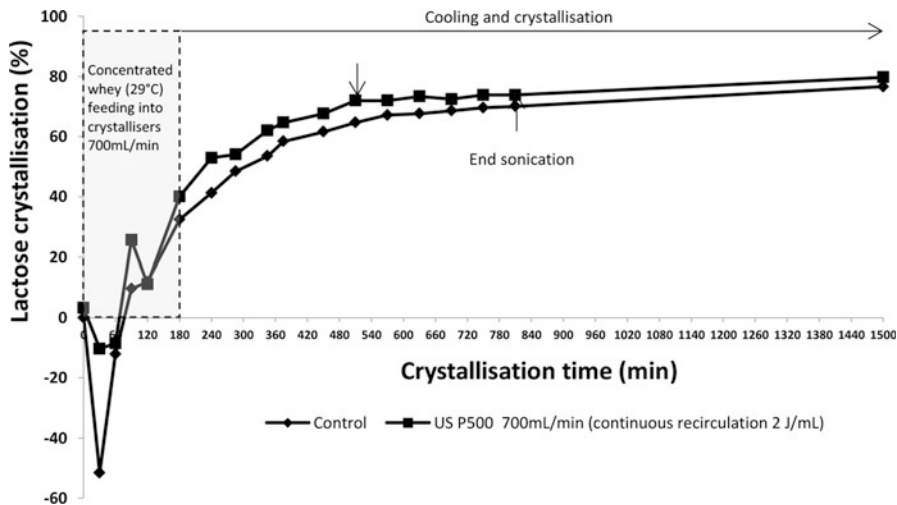
Fig. 16 Crystallization profile of lactose in concentrated whey during stirring (control) and sonication by continuous recirculation at 2 J/mL [66]
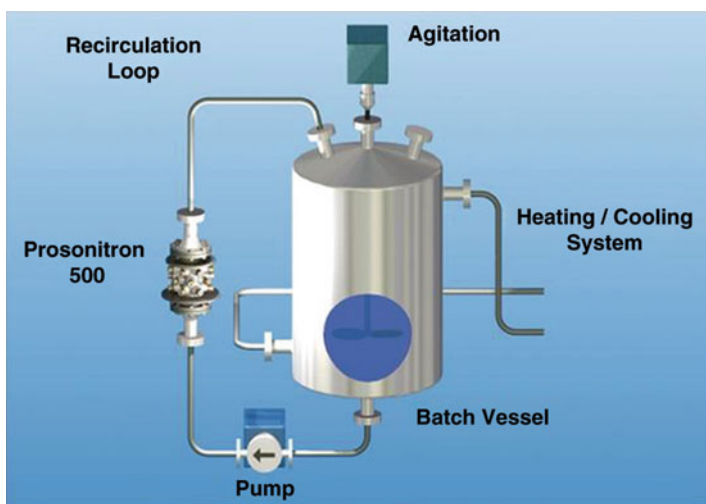
Fig. 17 Prosonix particle rounding technology [61]

Exposure to multiple ultrasonic treatments is believed to promote constant primary and secondary nucleation of lactose crystals.

The only sonocrystallized commercial product, LactoSonic, was reported to be commercially available for inhalation drug therapy (Fig. 17). It is produced by Prosonix particle rounding technology (PRT) which improved the morphology of lactose crystals with improved packing density, enhanced flow properties, and storage stability [61]. In LactoSonic production the Prosonitron 500 model

noncontact sonicator was configured in a recirculation loop, with an existing batch crystallizer. Crystal slurry was recirculated to create the desired morphology with in situ ultrasonic (cavitation) milling, Ostwald ripening, and interparticle collision. Prosonix also reported using a combination of ultrasound and anti-solvent for various pharmaceutical applications.

Future Trends

Although sonocrystallization is a mature technology in the pharmaceutical and fine chemical area, its implication to food is still in its infancy stage and needs further investigation [15]. Ultrasound is an emerging technology in dairy processing, and despite promising published data in the area of sonocrystallization, it has not been applied at industrial scale but may become a viable technology as its benefits are better understood. The impact of ultrasound on mutarotation rates and surface diffusion rates of lactose molecules has not been investigated. If ultrasound was shown to increase mutarotation rate, it may increase growth rates and shorten crystallization times. With the availability of pilot-scale sonicators, it is expected the processing conditions will be optimized and cost of processing will be reduced.

Conclusion

Sonocrystallization as an emerging science and technology has great potential to improve and change current methods of lactose crystallization. Sonocrystallization of lactose has been studied in both anti-solvent and aqueous systems. More recently, pilot-scale trials have been reported for both aqueous solutions and concentrated whey for pharmaceutical and food applications. Sonocrystallization was shown to reduce induction times and increase nucleation rate. Around 90 % lactose recovery was reported within a few minutes of sonication with the aid of ethanol as an anti-solvent at 4–16 J/ml ultrasonic energy. Around 80 % yield was achieved in aqueous solutions, but significantly higher energies were needed (130–600 J/ml). For industrial lactose crystallization of concentrated whey, application of continuous ultrasound at lower energy levels (>2 J/mL) resulted in a faster rates of crystallization with potential to reduce the processing times of existing batch crystallization processes. With the increasing availability of pilot- and commercial-scale sonicators and the expanding interest in ultrasound as a technology, there is great anticipation that sonocrystallization of lactose may lead to industrial applications.

References

1. Visser RA (1980) A natural crystal growth retarder in lactose. Neth Milk Dairy J 34:255–275
2. Nickerson TA (1988) Fundamentals of dairy chemistry, 3rd edn. Van Nostrand Reihold Co, New York

3. Fries DC, Rao ST, Sundaralingam M (1971) Structural chemistry of carbohydrates III. Crystal and molecular structure of alpha lactose monohydrate. Acta Crystallogr B27:994

4. Michaels AS, Van Kreveld A (1966) Influence of additives on growth rates in lactose crystals. J Dairy Sci 20:163–181

5. Dincer TD (2001) Mechanisms of lactose crystallisation. Ph.d., Curtin University of Technology, Perth

6. Zadow JG (1992) Whey and lactose processing. Elsevier Applied Science, New York

7. Lifran EV, Vu TTL, Durham RJ, Hourigan JA, Sleigh RW (2006) Lactose phosphate and its origin in cheesemaking: a case study. Australian J Dairy Technol 61(2)

8. Lifran EV, Vu TTL, Durham RJ, Hourigan JA, Sleigh RW (2007) Crystallisation kinetics of lactose in presence of lactose phosphate. Powder Technol 179:43–54

9. Wong SY (2011) A systematic approach to optimization of industrial lactose crystallization. University of Wisconsin-Madison, USA

10. Tavare NS (1995) Industrial crystallization: process simulation analysis and design. Plenum Press, New York

11. Mullin JW (2001) Crystallization, 3rd edn. Butterworth-Heinemann Ltd., Oxford

12. Hartel RW (2001) Crystallisation in foods. Barbosa-Canovas, G.V. An Aspen Publication, Gaithersburg, Maryland, USA

13. Paradkar A, Dhumal R (2012) Ultrasound assisted particle engineering. In: Chen D, Sharma SJ, Mudhoo A (eds) Handbook on applications of ultrasound sonochemistry for sustainability. CRC Press, Boca Raton, FL, USA

14. Luque de Castro M, Priego-Capote F (2007) Ultrasound-assisted crystallisation (sonocrystallisation). Ultrason Sonochem 14:717–724

15. Deora NS, Misra NN, Deswal A, Mishra HN, Cullen PJ, Tiwari BK (2013) Ultrasound for improved crystallisation in food processing. Food Eng Rev 5:36–44

16. Zisu B, Bhaskaracharya R, Kentish S, Ashokkumar M (2010) Ultrasonic processing of dairy systems in large reactors. Ultrason Sonochem 17:1075–1081

17. Mason T, Lorimer J (2002) Applied sonochemistry. Wiley-VCH, Weinhiem

18. Li H, Li H, Guo Z, Liu Y (2006) The application of power ultrasound to reaction crystallisation. Ultrason Sonochem 13:359–363

19. Li H, Wang J, Boa Y, Guo Z, Zhang M (2003) Rapid sonocrystallisation in salting out process. J Cryst Growth 247:192–198

20. Louhi-Kultanen M, Karjalainen M, Rantanen J, Huhtanen M, Kallas J (2006) Crystallisation of glycine with ultrasound. Int J Pharm 320:23–29

21. Lyczko N, Espitalier F, Louisnard O, Schwarzentruber J (2002) Effect of ultrasound on the induction time and the metastable zone widths of potassium sulphate. Chem Eng J (Lausanne) 86:233–241

22. Virone C, Kramer H, Rosmalen V (2006) Primary nucleation induced by ultrasonic cavitation. J Cryst Growth 294:9–15

23. Povey MJ, Mason TJ (eds) (1998) Ultrasound in food processing. Blackie Academic & Professional, London

24. Kentish S, Ashokkumar M (2011) The physical and chemical effects of ultrasound. In: Feng HO, Weiss J (eds) Ultrasound technologies for food and bioprocessing. Springer, Dordrecht

25. Nalajala V, Moholkar V (2011) Investigation in the physical mechanisms of sonocrystallisation. Ultrason Sonochem 18:345–355

26. Ruecroft G, Hipkiss D, Maxted T (2005) Sonocrystallization: the use of ultrasound for improved industrial crystallization. Org Proc Res Dev 9:923–932

27. Dennehy RD (2003) Particle engineering using power ultrasound. Org Proc Res Dev 7:1002–1006

28. Herrington BL (1934) Some physical chemical properties of lactose I. The spontaneous crystallisation of supersaturated lactose solution. J Dairy Sci 17:533

29. Bhargava A, Jelen P (1996) Lactose solubility and crystal growth as affected by mineral impurities. J Food Sci 61(1):180–184

30. Visser RA (1982) Supersaturation of alpha lactose in aqueous solutions in mutarotation equilibrium. Neth Milk Dairy J 36:89–101
31. Fox P, McSweeney P (1998) Dairy chemistry and biochemistry. Blackie Academic and Professional, London
32. Butler B (1998) Modelling industrial lactose crystallisation. Ph.D. University of Queensland, Brisbane, Australia
33. Wong SY, Bund RK, Connelly RK, Hartel RW (2012) Designing a lactose crystallisation process based on dynamic modeling. J Food Eng 111:642–654
34. Vu TTL, Hourigan JA, Sleigh RW, Ang MH, Tade MO (2003) Metastable control of cooling crystallisation. In: European symposium on computer aided process engineering, 2003. pp 527–532
35. Wong SY, Bund RK, Connelly RK, Hartel RW (2011) Determination of the dynamic metastable limit for α-lactose monohydrate crystallisation. Int Dairy J 21:839–847
36. Madsen HEL, Boistelle R (1979) Growth kinetics of the (001) face of hexatriacontane in solution. J Cryst Growth 46:681–690
37. Mcleod J (2007) Nucleation and growth of alpha lactose monohydrate. Ph.D., Massey University, Palmerston North, New Zealand
38. Griffiths R, Paramo G, Merson R (1982) Preliminary investigation of lactose crystallization using the population balance technique. Food Process Eng 78(218):118–128
39. Shi Y, Liang B, Hartel RW (1990) Crystallization kinetics of alpha lactose monohydrate in a continuous cooling crystallizer. J Food Sci 55(3):817–820
40. Kauter M (2003) The effect of impurities on lactose crystallisation. University of Queensland, Brisbane, Australia
41. van Kreveld A, Michaels A (1965) Measurement of crystal growth of alpha lactose. J Dairy Sci 48:259–265
42. Visser RA (1982) Growth of non-ionic lactose at various temperatures and supersaturations. Neth Milk Dairy J 36:167–193
43. Shi Y, Hartel W, Liang B (1989) Formation and growth phenomena of lactose nuclei under contact nucleation conditions. J Dairy Sci 72(11):2906–2915
44. Arellano MP, Miguel J, Bouchon P (2004) Development of a digital video-microscopy technique to study lactose crystallisation kinetics in situ. Carbohydr Res 339:2721–2730
45. Dincer TD, Ogden MI, Parkinson GM (2009) In situ investigation of growth rates and growth rate dispersion of α-lactose monohydrate. J Cryst Growth 311:1352–1358
46. Jelen P, Coulter S (1973) Effects of supersaturation and temperatures on the growth of lactose crystals. J Food Sci 38:1182–1185
47. Liang B, Shi Y, Hartel RW (1991) Growth rate dispersion effects on lactose crystal size distributions from continuous cooling crystalliser. J Food Sci 56(3):848–854
48. Hourigan JA, Lifran EV, Vu LTT, Listiohadi Y, Sleigh RW (2012) Lactose: chemistry, processing and utilisation. In: Augustin GWSMA (ed) Advances in dairy ingredients. Wiley-Blackwell & IFT Press, Oxford, pp 31–69
49. Patel SR, Murthy VP (2012) Lactose recovery processes from whey: a comparative study based on Sonocrystallisation. Sep Purif Rev 41:251–266
50. Westergaard V (2010) Milk powder technology evaporation and spray drying. Niro A/S, Soeborg
51. Vu TTL, Durham RJ, Hourigan JA, Sleigh RW (2003) Fine seed preparation for crystallisation process. In: Chemeca 2003: products and processes for the 21st century, Adelaide, 2003. Institute of Engineers, pp 964–971
52. Bund R, Pandit A (2007) Sonocrystallisation: effect on lactose recovery and crystal habit. Ultrason Sonochem 14:143–152
53. Kougoulos E, Marziano I, Miller PR (2010) Lactose particle engineering: influence of ultrasound and anti-solvent on crystal growth and habit. J Cryst Growth 312:3509–3520
54. Bund RK, Pandit AB (2007) Rapid lactose recovery from paneer whey using sonocrystallisation: a process optimisation. Chem Eng Process 46:846–850

55. Bund RK, Pandit AB (2007) Rapid lactose recovery from buffalo whey by use of ['Janti-solvent, ethanol'. J Food Eng 82(3):333–341
56. Bund R (2005) Waste management and recovery of valuable products from food industry waste streams. Mumbai University, Mumbai
57. Patel S, Murthy Z (2009) Ultrasound assisted crystallisation for the recovery of lactose in an anti-solvent acetone. Cryst Res Technol 44(8):889–896
58. Patel SR, Murthy VP (2010) Optimisation of process parameters by taguchi method in the recovery of lactose from whey using sonocrystallisation. Cryst Res Technol 45(7):747–752
59. Dhumal R, Biradar S, Paradkar A, York P (2008) Ultrasound assisted engineering of lactose crystals. Pharm Res 25(12):2835–2843
60. Zisu B, Sciberras M, Jayasena V, Weeks M, Palmer M, Dincer TD (2014) Sonocrystallisation of lactose in concentrated whey. Ultrason Sonochem 21:2117–2121
61. Manufacturing Chemists (2009) Particle engineering with ultrasound. Manufacturing Chemists, London
62. Dincer TD, Zisu B, Vallet CGMR, Jayasena V, Palmer M, Weeks M (2014) Sonocrystallisation of lactose in aqueous system. Int Dairy J 35:43–48
63. Kuldipkumar A, Kwon GS, Zhang GGZ (2007) Determination of growth mechanism of tolazamide by induction time measurement. Cryst Growth Des 7(2):234–242
64. van Kreveld A (1969) Growth rates of lactose crystals in solutions of stable anhydrous alpha lactose. Neth Milk Dairy J 23:158–275
65. Dincer TD, Ogden MI, Parkinson GM (2009) Crystal growth mechanisms of the (010) face of alpha lactose monohydrate crystals. J Cryst Growth 311:2427–2432
66. Zisu B (2014) An innovative approach to tailoring the functional characteristics of dairy ingredients. In: Paper presented at the IFT14 Annual Meeting and Food Expo, New Orleans, LA, USA, June 21–24, 2014

Ultrasound in Dairy Filtration

Li Ling Apple Koh

Contents

Abstract

Membrane filtration is commonly used in the dairy industry for the fractionation and concentration of dairy fluids. However, the economic efficiency of the use of membrane filtration systems is limited by membrane fouling, a phenomena which results from the buildup of particles on the surface and within the pores of the membrane. Several modifications have been proposed to reduce membrane fouling and enhance membrane performance. One such example is through the use of ultrasonics. This chapter addresses the application of ultrasound on membrane fouling by dairy solutions using two different modes – ultrasonic pretreatment of the feed prior to filtration and concurrent sonication alongside filtration.

L.L.A. Koh
Singapore University of Technology and Design, Singapore, Singapore
e-mail: apple_koh@sutd.edu.sg

Introduction

In the dairy industry, membrane filtration is used in various stages of product manufacture. In particular, microfiltration (MF) is used as an alternative approach for the separation of caseins from whey proteins in cheese making. The clarified whey is then processed by ultrafiltration (UF) to produce a concentrate stream of whey proteins. To produce lactose concentrate, the UF permeate can be further processed in a nanofiltration (NF) or reverse osmosis (RO) membrane unit.

A major problem in membrane operations is fouling as it directly affects productivity. The main effect of fouling is a sharp reduction in permeate flux that cannot be resolved while the process is running due to a buildup of particles on the surface and within the pores of the membrane [1]. In order to restore the original flux, costly and lengthy cleaning cycles are required [2]. Often, regular cleaning is insufficient and a new membrane unit is required. The economic feasibility of membrane technology is thus heavily dependent on the rate and extent of fouling [3].

In the past decades, many research groups have looked to better their understanding on the effects of fouling so as to fabricate a material with enhanced membrane performance. In addition, several modifications, as part of retrofitting existing membrane units, have also been proposed to reduce membrane fouling during processing. Lastly, various cleaning methods have also been developed to make cleaning cost effective for the restoration of membrane separation efficiency after fouling. This chapter focuses on the use of ultrasound in membrane filtration of dairy fluids in two very different ways – pretreating the feed using ultrasound prior to filtration and concurrent sonication alongside the filtration unit. In addition, the use of ultrasound as a cleaning technique is explored. Before that, the flux reduction phenomenon observed in membrane filtration is briefly discussed.

Flux Reduction in Membrane Filtration

The reduction in flux during membrane filtration is governed by two phenomena: concentration polarization (CP) and fouling. Both CP and fouling bring about additional resistance to filtration and occur predominantly on the feed side of the membrane surface [4]. Figure 1 shows the flux-time comparison for CP and fouling. CP begins almost immediately at the start of a filtration run and is stable throughout
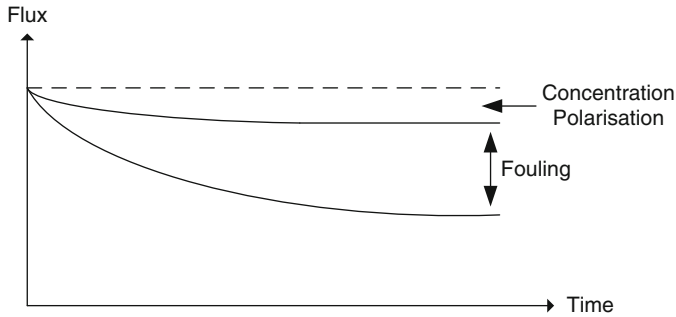
Fig. 1 Permeate flux behavior with respect to time for both concentration polarization and fouling (Adapted from Mulder [4]. Reproduced with permission from Springer.)

filtration [5, 6]. In the long run, a gradual flux decline is often observed, signifying a buildup of deposits on the surface of the membrane or in the pores of the membrane. Here at this stage, the buildup of deposits forms a cake layer. When the effects of fouling have been fully developed, the flux approaches a steady value such that any further flux decline is due to cake compression and consolidation [7, 8].

Membrane Resistance

In the absence of osmotic pressure effects, the flux through the membrane is given as follows:

$$J = \frac{\Delta P}{\mu_p R_T'} \tag{1}$$

where J is the permeate flux (m^3/m^2.s), ΔP is the pressure drop across the membrane (Pa), μ_p is the viscosity of the permeate (Pa.s), and R'_T is the total resistance of flow in the filtration unit (m^{-1}).

Ideally, the only resistance toward mass transfer is due to the membrane and this is known as the membrane resistance, R'_M. However, CP, which is prevalent in all filtration systems, results in the formation of a highly concentrated boundary layer at the membrane surface. This also exerts a resistance to mass transfer, R'_{CP}. A gel layer may also be formed when there is a high concentration of retained solutes at the membrane surface, exerting a resistance R'_G. In addition, there is also a resistance due to pore blockage by solutes on the porous membrane, R'_B. It is also possible for some solute to be adsorbed onto the surface of the membrane, providing a resistance R'_A. Thus, the total resistance accounts for the resistance due to the membrane, CP, gel layer, pore blockage, and adsorption:

$$R'_T = R'_M + R'_{CP} + R'_G + R'_B + R'_A \tag{2}$$
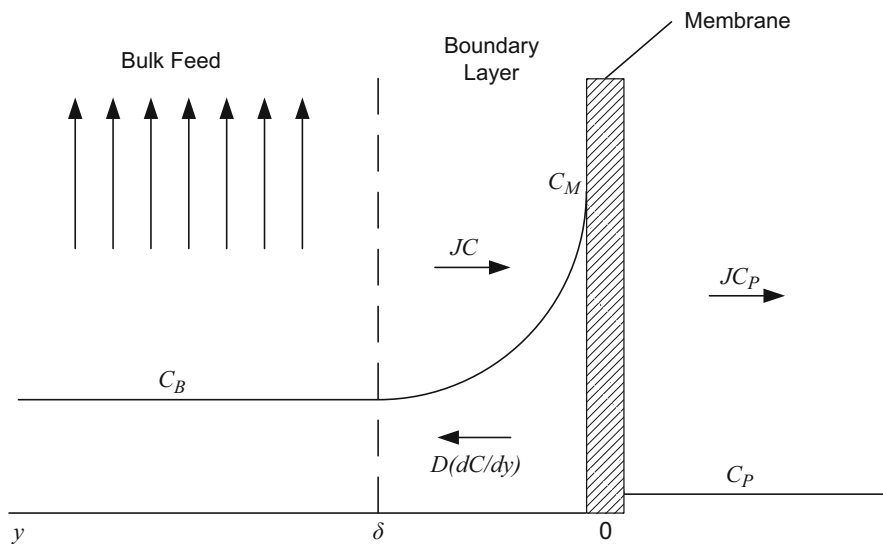
Fig. 2 Schematic representation of film model theory for concentration polarization (Adapted from Mulder [4]. Reproduced with permission from Springer.)

Concentration Polarization

In membrane filtration systems, the separation of the solute from the processing fluid results in an increase in solute concentration near the membrane surface, giving rise to a boundary layer generated at the membrane surface [9]. This is known as concentration polarization and is a reversible phenomenon whereby its effects can be minimized by varying the operating conditions during filtration. As there is a high solute concentration at the membrane surface, by Fick's law of diffusion, there is a tendency for the solute to diffuse back into the bulk feed solution. This is termed as back diffusion. At steady state, the mass transfer in the CP boundary layer is known as the film model theory, as shown in Eq. 3 and Fig. 2.

$$JC - JC_P = -\mathcal{D}\frac{dC}{dy} \tag{3}$$

where C is the concentration of solute (kg/m^3), C_P is the concentration of solute in the permeate (kg/m^3), $\mathcal{D}$ is the diffusion coefficient of the solute (m^2/s), and y is the distance from the membrane (m).

In this model, the rate of back diffusion ($-\mathcal{D}\frac{dC}{dy}$) is equal to the difference between the molar flux of convective transport of the solute toward the membrane (JC) and the rate of permeate flux (JC_P). The above equation assumes that the diffusion coefficient remains constant at all concentrations. In the absence of fouling, Eq. 3 becomes:

$$\frac{J\delta}{\mathcal{D}} = \ln\left(\frac{C_M - C_P}{C_B - C_P}\right) \tag{4}$$

where C_B is the bulk concentration of the solute (kg/m^3), δ is the thickness of the CP boundary layer (m), and C_M is the concentration of the solute at the membrane surface at $y = 0$ (kg/m^3). The ratio $\mathcal{D}/\delta$ is the mass transfer coefficient k_{CP} and is assumed to be independent of solute concentrations and flux [10]. The mass transfer coefficient is usually obtained from mass transfer correlations and is discussed briefly by Koh et al. [11].

Equation 4 is the classical equation used to quantify CP during UF and can only be used in mass transfer-controlled systems whereby the permeate flux is pressure independent. Assuming that there is total solute rejection at the membrane surface and $C_P = 0$, Eq. 4 becomes:

$$J = k_{CP}\ln\left(\frac{C_M}{C_B}\right) \tag{5}$$

In most membrane filtration operations, the feed concentration is kept constant. Hence, in order to overcome CP, the only solution is by improving the mass transfer coefficient [2]. Mass transfer coefficient is a function of cross-flow velocity, diffusion coefficient of the solute, density of the feed solution, and filtration configuration and dimensions.

In some cases, the concentration of the solute at the membrane surface increases such that the solute concentration reached the upper limit of the solubility of the solute in the solvent. At this point, the solute precipitates out and a gel layer develops. This critical solute concentration is known as the gel concentration or gel point (C_G) and is dependent on the type, size, shape, and chemical structure of the solute. Once the gel layer is formed, the solute concentration within this layer remains constant at C_G, as shown in Fig. 3. This gel layer exerts an additional resistance to the mass transfer of solute permeating through the surface. Under such conditions, $C_M = C_G$ and is known as the gel polarization model. Equation 5 becomes:

$$J = k_{CP}\ln\left(\frac{C_G}{C_B}\right) \tag{6}$$

This model is only applicable to macromolecular solutions and colloidal suspensions. Further, the model is not able to account for the change in feed properties, such as viscosity and density, as the concentration changes [12].

Fouling

The deposition of particles on the membrane surface or in the pores of the membrane is commonly known as fouling. The decline in permeate flux due to fouling is

Gel Layer   Membrane

Boundary
Layer

Bulk Feed

$C_M = C_G$

JC

JC_P

C_B

$D(dC/dy)$

C_P

δ 0
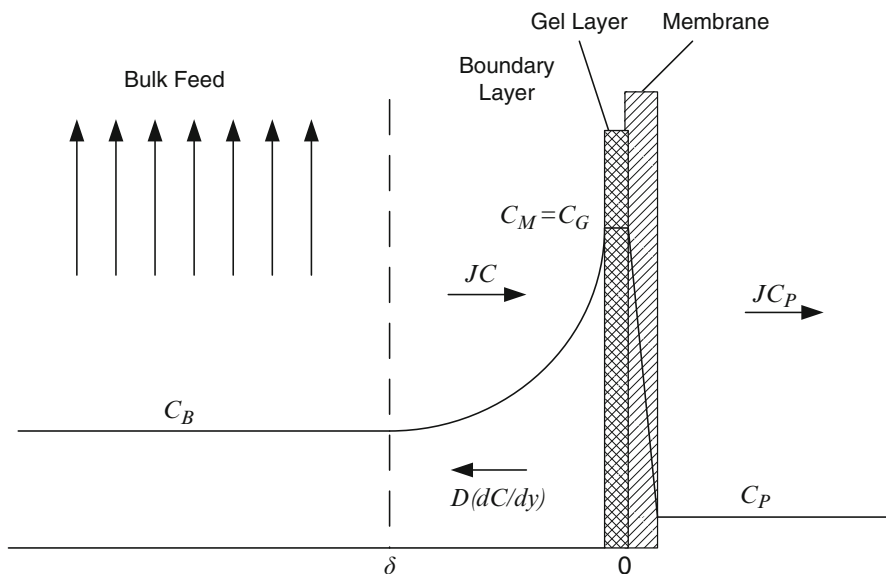
Fig. 3 Schematic representation of gel polarization model (Adapted from Mulder [4]. Reproduced with permission from Springer.)

due to the irreversible alteration in membrane properties caused by physical and chemical interactions between the membrane and the foulants [10]. Fouling occurs mainly in MF and UF as porous membranes are highly susceptible to fouling. There are three main fouling mechanisms, as shown in Fig. 4, in MF and UF membranes – (i) adsorption of foulant onto the membrane surface or within the membrane pores, leading to the blocking of pores, (ii) buildup of cake layer on the membrane surface, and (iii) cake compression [13, 14]. Cake compression is rarely observed in practice.

Unlike CP, fouling occurs slowly with time and may lead to an alteration in membrane selectivity. For example, the fouling layer controls membrane selectivity in the separation of casein from whey proteins by MF. This is known as a dynamic or secondary membrane of polarized solutes and causes MF membranes to behave like UF membranes. The result is a high rejection of both casein and whey proteins. To minimize the formation of a dynamic membrane, Cheryan [12, 16] and Lawrence et al. [17] recommend operating at high cross-flow velocities of 4–7 m/s and low transmembrane pressure (TMP) of less than 40 kPa. These operating conditions increase the wall shear stress for casein MF.

Many empirical models have been developed to predict fouling phenomena of ideal solutions. However, it is hard to apply these models to real systems due to the involvement of complex physical and chemical factors. Commonly used models include the pore blockage model and the cake filtration model. A description of these models can be found in Koh et al. [11].

Fig. 4 A plot of t/V against V shows the graphical representation of the transition in the various fouling mechanisms with time, where t is time (s) and V is the volume of permeate (m^3) (Adapted from Muthukumaran [15])
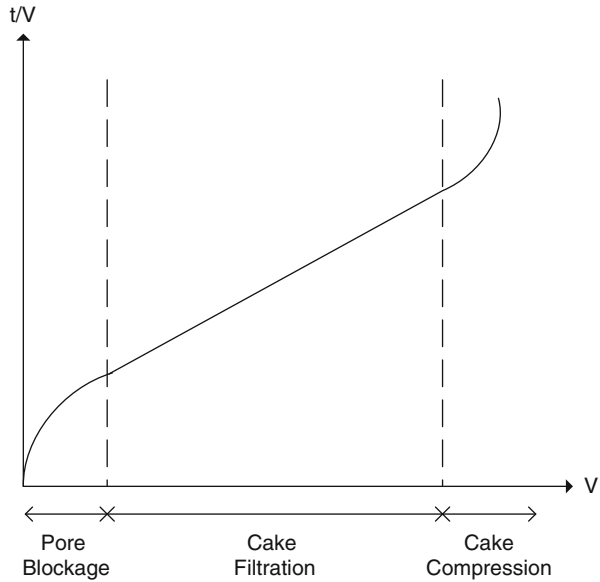
Ho and Zydney [18] developed a model that accounts for fouling as a result of pore blockage and cake layer formation in the same system. They assumed that the initial flux decline arises from pore blockage by large aggregates on the membrane surface. The flux through the blocked pores (J_B) is given by:

$$J_B = \frac{\Delta P}{\mu \left(R_M' + R_B' \right)} \quad (7)$$

where μ is the viscosity of the feed solution (Pa.s). As the filtration progresses, more particles settle on the membrane surface, adding resistance for the fluid to flow through the blocked pores and forming a cake layer on the membrane surface. This cake layer is formed due to the interaction between the retained solutes itself or with other components or membrane. It is commonly observed in the filtration of a feed that consists of proteins, organics, and colloids. Therefore, the filtrate flux through the fouled membrane is equal to the sum of the flow rate through the open and blocked pores, as shown in Eq. 8.

$$J = J_W \left[\exp\left(-\frac{a\Delta PC_b}{\mu R_M'} t \right) + \left(\frac{R_M'}{R_M' + R_P} \right) \left(1 - \exp\left(-\frac{a\Delta PC_b}{\mu R_M'} t \right) \right) \right] \quad (8)$$

$$R_P = \left(R_M' + R_{po} \right) \sqrt{1 + \frac{2f'R'\Delta PC_b}{\mu_f \left(R_M' + R_{po} \right)^2} t} - R_M' \quad (9)$$

where J_w is the flux through the clean membrane (m^3/m^2.s) and R_P is the resistance of the protein deposit (m^{-1}). The flow through the open pores corresponds to the

classical pore blockage model and is described by the first term within the brackets in Eq. 8. The second term in the equation represents flow through the blocked pores. Here, the permeate flux is characterized by the pore blockage parameter (α), the initial resistance of the deposit (R_{po}), and the cake growth factor ($f'R'$) and is dependent on these three factors. The pore blockage parameter, which represents the rate of pore blockage, is equal to the membrane area blocked per unit mass of protein convected to the membrane surface and is an indication of the protein aggregate size [15]. The initial resistance of the deposit is the resistance of a single protein aggregate, while the cake growth factor shows the rate of increase of the protein layer resistance with time due to the growth of the protein cake layer.

Although there are different models available to describe different fouling mechanisms, Ho and Zydney [18] showed that there is no need for that as their combined pore blockage and cake filtration is in agreement with experimental data for the constant pressure filtration of bovine serum albumin (BSA) solutions for a range of protein concentrations and TMP. Through this, they have showed that their model is able to determine and describe the smooth transition from pore blockage to cake filtration regime. Further work by these authors showed that the model is also in good agreement for the filtration of lysozyme, pepsin, immunoglobulin G, and myoglobin [19] and the MF of BSA-lysozyme and BSA-pepsin mixtures [20]. In addition, Muthukumaran et al. [21] obtained a good fit between the model and the experimental data in the UF of whey protein concentrate 80 (WPC80) with and without in situ ultrasound.

Cleaning Procedure

As fouling is an irreversible phenomenon, the physical and chemical changes that develop during the process occur throughout filtration [6]. Although changes in operating conditions during filtration may increase the flux temporarily, it is ineffective in reducing fouling effects in the long run. Hence, to alleviate the problem of low flux, cleaning or replacement of the membrane is necessary.

Membrane cleaning technologies include hydraulic, mechanical, and chemical methods [11]. Back flushing is a common hydraulic cleaning technique. Although back flushing improves permeate flux during filtration and delays the need for cleaning, a possible setback is the control of back pressure in large systems [11, 22]. Mechanical cleaning is a traditional cleaning method that is not extensively used. It involves the use of brushes or sponge balls that must be properly cleaned or disinfected to reduce any microbial growth. Further, mechanical cleaning is only applicable to surface cleaning and does not remove material within the pores of the membrane [10]. Thus, mechanical cleaning is typically performed in conjunction with other methods, such as chemical cleaning.

Chemical cleaning can either be done manually or cleaning in place (CIP). A CIP system is defined as the circulation of cleaning liquid through processing lines, pipes, and ancillary equipment without dismantling any part of the system. A typical cleaning cycle for membrane units in the dairy industry might involve product

removal; prerinse with water; alkali recirculation at 50 °C and pH 10.8–11.0; intermediate rinse with water; acid recirculation at 50 °C and pH 2.0–2.2; intermediate rinse with water; alkali recirculation at 50 °C, pH 10.8–11.0, and 180 ppm of free chlorine; and final rinse with water.

Two detergent recirculation steps are required as dairy processes consist of both protein and mineral deposits – alkali recirculation is performed to remove fat and protein, while acid clean is used to remove minerals. Chlorine, in the form of sodium hypochlorite, is also used in cases where the bulk of the deposit is proteinaceous to ensure effective disinfection. As acid tends to tighten the pores of the membrane and give low permeate flux upon starting up a new run, the cleaning cycle generally finished off with an alkali clean before a final rise with water is performed.

The cleaning efficiency is checked by measuring the pure water flux at a defined temperature, pressure, and flow rate at the end of a cleaning cycle and comparing it with the initial pure water flux obtained before a process run. This is expressed as the percentage flux recovery. A low percentage flux indicates insufficient cleaning, while a high percentage suggests efficient cleaning. 100 % flux recovery is rarely achieved. Although water flux measurement is a common way to quantify for cleaning efficiency, Trägårdh [23] observed that a high water flux does not necessarily guarantee good operational flux and suggested measuring the product permeate flux in the following run as a better indication for membrane cleaning efficiency.

Membrane Filtration in the Dairy Industry

In the dairy manufacturing industry, the main foulants are proteins (both native and denatured) and calcium phosphate. Dairy whey, an important dairy product due to its significant protein and lactose content, consists of β-lactoglobulin (β-LG), which accounts for the majority of the whey proteins, and α-lactalbumin (α-LA, approximately 20 %), along with small amounts of bovine serum albumin (BSA) and immunoglobulins. Glover [24] established that β-LG contributed more to membrane fouling than α-LA due to the ability of β-LG to form protein sheets on the membrane surface.

In addition, Marshall and Daufin [7] have shown that protein adsorption is influenced by the hydrophobicity of the membrane surface and the electrostatic forces between charged proteins and the membrane. At the initial stages of fouling, the interactions between the protein and membrane dictate the fouling behavior, while protein-protein interactions determine this behavior at later stages. Calcium was also found to play a role in protein cake formation by forming protein-protein and protein-membrane bridges.

Precipitation of salts and scaling of the membrane surface occurs when sparingly soluble salts in the feed stream are concentrated during filtration beyond their solubility. A dominant salt foulant in dairy feeds is calcium phosphate due to supersaturation in the aqueous phase. It displays reverse solubility whereby its solubility decreases with increasing temperature [8]. With increasing pH, the degree of calcium phosphate precipitation also increases as calcium becomes less

soluble [8]. Thus, low temperatures and pH are utilized in the industry to reduce calcium phosphate scaling on the membrane surface and within the pores. Calcium phosphate precipitation during membrane filtration can also be reduced upon addition of calcium-sequestering agents such as ethylenediaminetetraacetic acid (EDTA) or citrate to the feed. This reduces the ionic calcium concentration before filtration.

Nyström et al. [25] have reported that uncharged components, such as lactose, are unlikely to create fouling. This hypothesis was also substantiated by van der Horst [26] who did not observe fouling due to lactose during filtration of whey components. Lipids are also found to have no impact on UF membrane fouling unless the feed has a high lipid content [7, 27].

In this section, the use of ultrasound in membrane filtration of dairy fluids is discussed – to increase the permeate flux during membrane filtration and to improve cleaning efficiency after fouling.

Use of Ultrasound for In Situ Flux Enhancement

A significant research focus has been in the field of fouling minimization or control. A way to minimize fouling during filtration is through the addition of turbulence promoters to filtration units. These turbulence promoters increase the shear rate near the membrane surface by enhancing turbulence and back transport of solutes. This prevents particle deposition and reduces fouling. Some examples of turbulence promoters are vibratory shear-enhanced filtration and rotating disk modules. Akoum et al. [28, 29] have observed an increase in permeate flux by 300–400 % in these systems when compared to a standard spiral wound membrane. With this modified membrane filtration unit, it is observed that there is a higher pressure drop, which leads to greater energy consumption; Krstić et al. [30], however, believed that this is more than compensated by the flux improvement achieved. It is important to note that these vibrating equipments are expensive and difficult to scale-up.

More recently, the use of ultrasonic equipment to improve flux has been widely studied. Similar to the addition of a turbulence promoter, the ultrasonic unit is installed alongside a filtration unit to generate an ultrasonic field which can induce localized flow disturbances through vibration and cavitation and enhance turbulence near the membrane surface. The use of an ultrasonic field hence reduces the effects of CP. Muthukumaran et al. [15, 21, 31] studied the use of ultrasonics at low power levels and found that it can significantly enhance permeate flux during filtration of whey due to bubble collapse and acoustic streaming at the membrane surface. This leads to the generation of microjects which scour the membrane surface and promote back transport of deposits to the bulk solution, resulting in increased mass transfer coefficient within the concentration polarization layer. In addition, these deposits were broken down and the cake layer was found to be less compressible and looser. Mirzaie et al. [32] obtained similar results in the MF of milk where a high flux enhancement factor of 490 % was obtained at a pressure of 0.5 bar, ultrasonic power

of 40 W, and frequency of 20 kHz. Although an increase in mass transfer coefficient of water across the membrane was widely reported, Kokugan et al. [33] observed that ultrasound was not effective at removing foulants that were lodged inside the pores of the membranes.

Maskooki et al. [34] explored the use of intermittent high-frequency ultrasound to reduce membrane fouling and observed an increase in fouling at high transmembrane pressure. The authors suspected that the reduction in permeate flux may be due to the foulants redepositing into the pores of the membrane under the influence of the ultrasonic field and the formation of a more densely compacted cake layer. This shows that the operating conditions need to be optimized for ultrasound to create a positive effect on membrane filtration performance.

A study by Teng et al. [35], who investigated the effect of ultrasound positions on permeate flux during UF of a mixture of bovine serum albumin (BSA) and lysozyme, speculated that the enhancement in permeate flux may also be the result of a temporary change in the protein structure caused by the shear forces that are generated by ultrasound. The authors have also reported no change in protein aggregate size was observed before and after sonication. Other researchers have also found that ultrasound can change the quaternary and/or tertiary structure of proteins [36].

Although ultrasound has proven to be effective in increasing productivity, there is a discrepancy in the literature regarding the structural integrity of the membrane when exposed to ultrasonic waves. Masselin et al. [37] and Wang et al. [38] observed damage when polymeric membranes were used, while other studies showed no structural changes to the membrane surface [15, 31, 32, 39–41]. Muthukumaran et al. [15, 39] have concluded that the impacts to the structural integrity of the membrane during filtration with ultrasonic enhancement are a function of the power intensity of the ultrasonic field and the distance between the transducer and membrane. Kallioinen et al. [42], who investigated the influence of ultrasonic treatment on different membrane materials, also concluded that high ultrasonic intensity, together with close transducer-membrane distance, is the cause to membrane damage. As a consequence, it is recommended that low ultrasonics (US) intensity is used for membrane filtration processes. Gondrexon et al. [43] summarized the works done in the areas of US in filtration systems and found that most studies, which are carried out at low US intensity, below 5 W/cm^2, and low frequency, 20 to 100 kHz, reported that the membrane's intrinsic permeability remained unaltered and no structural damage was observed.

Lamminen et al. [44], on the other hand, studied the effect of ultrasonic frequency and length of treatment time on the structural integrity of the membrane and reported that no damage to the membrane was found for periods of over an hour of sonication. The authors stated that the membranes, which are more resistant to high temperatures and pressures, should be used to reduce the possibility of surface damage. In addition, Lamminen et al. [44] reported that cleaning was more effective when the transducer was facing the fouled surface as a result of acoustic streaming.

Use of Ultrasound as a Pretreatment Method

In feed pretreatment, the feed solution is treated and its properties are altered before filtration to stabilize or remove foulants. Heat treatment, pH adjustment, addition of complexing agents, precipitation, and pre-microfiltration are common examples of the methods used in feed pretreatment. Early works by Hickey et al. [45] showed that an increase in feed temperature and pH prior to UF, as a form of feed pretreatment, led to an increase in permeate flux as bulk calcium phosphate crystals, which would otherwise precipitate in the pores of the membrane, were formed and readily flushed from the system. However, this method was not commonly used as there was a decrease in protein retention [46]. Here, the use of ultrasonic treatment upstream of membrane filtration is explored in detail as a feed pretreatment technique.

To date, ultrasonic pretreatment has not been widely investigated. Hakata et al. [47] investigated the effect of ultrasonic pretreatment in the MF of an activated sludge lagoon effluent and observed a greater initial flux decline with increasing sonication time. They attributed the decrease to rapid pore blockage due to an increase in the proportion of smaller particles resulting from greater fragmentation of suspended solids. Conversely, when the effluent is pretreated by both coagulation and sonication, the permeate flux is higher than either treatment alone. It was thus speculated that this was due to a change in physicochemical properties of the effluent organic matter, which led to enhanced coagulation and resulted in the formation of a cake layer having a lower resistance to flow [47]. They also reported a 30 % increase in flux recovery and reduced irreversible membrane fouling when the feed was sonicated for 2 min using a 45 kHz ultrasonic bath with a power intensity of 107 W.

More recently, Koh et al. [48] explored the use of ultrasound for pretreatment of WPC80 solution before UF. It was observed that pretreatment of the 5 wt% feed through sonication alone, at an energy density of 31 J/ml, did not affect the flux decline pattern when compared to the native, untreated feed. At a solid concentration of 10 wt%, the pretreated feed showed a small but significant flux reduction with the native feed having a steeper initial flux decline (Fig. 5). Using Ho and Zydney's combined pore blockage and cake filtration model [18], the pore blockage parameter and cake growth factor during UF of the sonicated feed for both 5 and 10 wt% were slightly lower than that of the native feed. These results were consistent with those obtained when ultrasonics was applied directly to the UF module [21]. The authors [48] speculated that the reduced pore blockage parameter is the result of a reduction in protein aggregate size upon sonication, while the lowered cake growth factor may be due to the formation of a less compressible cake. In both feed types, the protein concentration in the permeate remained low at 0.05 wt%. Overall, ultrasonic pretreatment of the feed did not improve productivity substantially. This may be due to the small protein aggregate size and low viscosity of the native WPC80 solution; hence, the use of more concentrated protein solutions might lead to more positive results.

Application of ultrasonic pretreatment on the UF of fresh whey was also investigated [48]. The pore blockage parameter of the sonicated fresh whey feed was higher than that of the native feed. It was stated that this may be the result of the
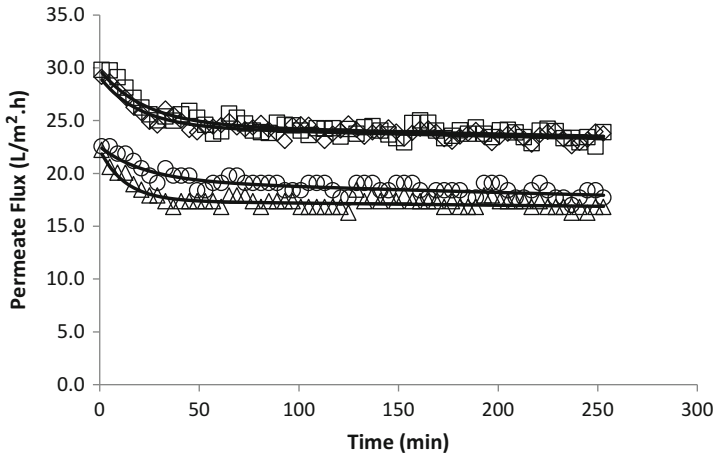
Fig. 5 Flux decline analysis for 5 and 10 wt% native and US WPC80 feeds. Experimental data are represented by symbols ($\Diamond$ 5 wt% Native, $\square$ 5 wt% US, Δ 10 wt% Native and $\circ$ 10 wt% US), while solid curves are model calculations using Eqs. 8 and 9, Ho and Zyndey's combined pore blockage, and cake filtration model [18] (Adapted from Koh et al. [48]. Reproduced with permission from Elsevier.)

reduction in size of both the whey protein aggregates and residual fat globules, which may have blocked the pores more readily. A slightly higher permeate flux and lower cake growth factor, when compared to the native feed, were also reported.

The same research group also investigated a combination of heat and ultrasonic pretreatment (PreH + US) to alleviate membrane fouling. The combination of heat and ultrasound was explored as it was found to improve the heat stability of whey protein solutions [49]. When a heated solution of denatured and aggregated proteins is sonicated, there is a dramatic decrease in protein aggregate size and viscosity. These reductions are attributed to the disruption of hydrophobic interactions by shear forces that are generated during acoustic cavitation [49, 50]. The protein aggregate size and viscosity of the preheated and sonicated whey solution remained low upon further heating, overcoming the problems of poor heat stability in reconstituted powders [49]. The authors [48] thus believed that with such a reduction in viscosity, it may alleviate membrane fouling and enhance downstream spray dryer productivity while producing heat-stable powders. The particle size and viscosity of the WPC80 solutions are presented in Tables 1 and 2, respectively.

Comparing a 5 wt% WPC80 feed that has undergone only heat treatment (PreH) and a feed which was preheated and sonicated (PreH + US), a clearer distinction in flux reduction data was observed by Koh et al. [48]. The authors also performed the experiments at higher solid concentration for the heat-treated feeds. It was observed that both pore blockage and cake growth increased with increasing solid concentration for all PreH feeds, while these two parameters remained low for the PreH + US feeds, as shown in Figs. 6 and 7. The increase in pore blockage for PreH feeds was due to the increase in the number of larger, denser protein aggregates, which were

Table 1 Summary of volume-weighted average particle size of 5 and 10 wt% native and sonicated WPC80 solutions and 5, 10, 12, and 15 wt% PreH and PreH + US WPC80 solutions (Adapted from Koh et al. [48]. Reproduced with permission from Elsevier.)

Feed concentration (wt%)	Native	Sonicated	PreH	PreH + US
5	24.7 ± 0.1	0.19 ± 0.001	35.0 ± 1.6	1.5 ± 0.2
10	37.5 ± 0.7	1.1 ± 0.6	48.1 ± 1.6	5.3 ± 0.1
12			56.6 ± 1.8	12.5 ± 0.1
15			77.9 ± 2.9	32.1 ± 0.8

Table 2 Summary of apparent viscosity (mPa.s) at a shear rate of 200 s^{-1} of 5 and 10 wt% native and sonicated WPC80 solutions and 5, 10, 12, and 15 wt% PreH and PreH + US WPC80 solutions (Adapted from Koh et al. [48]. Reproduced with permission from Elsevier.)

Feed concentration (wt%)	Native	Sonicated	PreH	PreH + US
5	3.2 ± 0.1	3.0 ± 0.1	10.0 ± 1.3	3.0 ± 0.1
10	4.5 ± 0.1	4.1 ± 0.1	61.6 ± 0.7	7.7 ± 0.1
12			134 ± 0.1	9.0 ± 0.0001
15			202 ± 0.1	10.9 ± 0.001
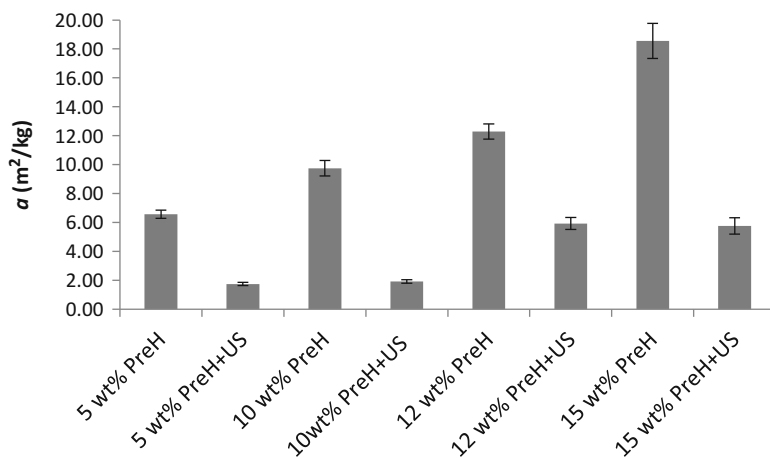
Fig. 6 Comparison of best-fit values of the pore blockage parameter (α) of 5, 10, 12, and 15 wt% WPC80 feeds using Ho and Zydney's combined pore blockage and cake filtration model [18] (Adapted from Koh et al. [51])

formed upon heating, with increasing solid concentration. This resulted in a greater flux reduction. On the other hand, the aggregates in the PreH + US feeds were partially broken down by sonication, leading to lower pore blockage values. Similarly, an increase in solid concentration saw an increase in the cake growth factor for PreH feeds due to the formation of denser cake layers with a higher resistance to flow, while sonication reduces this cake growth factor due to a lower fraction of protein contributing to the growth of the deposit.
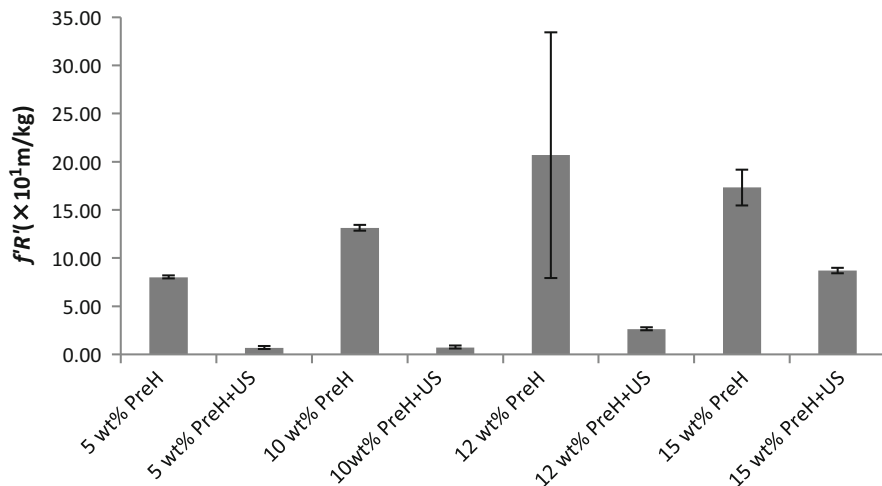
Fig. 7 Comparison of the best-fit values of the cake growth factor ($f'R'$) of 5, 10, 12, and 15 wt% WPC80 feeds using Ho and Zydney's combined pore blockage and cake filtration model [18] (Adapted from Koh *et al.* [51])

Based on the gel polarization model, Koh et al. [48] reported that sonication delayed the "gelling" of the protein. PreH feeds had a lower gel concentration due to the denaturation of the proteins as a result of heating, which allows the proteins to "gel" at lower concentrations. Conversely, a larger gel concentration is observed in the PreH + US system. This shows that sonication delays the "gelling" of the proteins and coincides with the results obtained using the combined pore blockage and cake filtration model, where the PreH + US systems have lower pore blockage and slower cake growth.

In addition, no change to the protein concentration in the permeate was observed in all systems. The authors thus concluded that feed pretreatment through both heat and ultrasound can provide a viable approach to the production of concentrates for use in heat-stable powders through UF. However, both water flux and zeta potential results showed that 100 % flux recoveries are not achieved in either of the heat-treated feeds. This may be due to the inability of the cleaning chemical agents to break down and dissolve the large, denatured protein aggregates. It was reported that the PreH + US feed had a higher flux after chemical cleaning than that of the PreH feed as the PreH + US feed has a smaller proportion of large aggregates in addition to a higher proportion of foulants that are removed by water flushing.

Use of Ultrasound in Membrane Cleaning

Previously, ultrasound was found to be an effective cleaning technique in many industries. Examples of ultrasonic cleaning are removal of particles from semiconductor wafers [52] and removal of scale and oxides from steep strip [53]. The use of

ultrasound was thus considered as an alternative cleaning method for fouled membranes. Similar to the use of ultrasound for fouling minimization, ultrasonic cleaning generates microjets, which scour the membrane surface and break down layers of deposits into smaller particles while preventing their redeposition by keeping them in suspension. In addition, ultrasound enhances turbulence within the cleaning solution. The improved cleaning efficiency through the use of ultrasound was proven by Muthukumaran et al. [54] who observed an improvement in the cleaning efficiency of polysulfone UF membranes that were previously fouled with whey solutions. In another study, Maskooki et al. [34] reported that the use of intermittent high-frequency ultrasound at 1 MHz for cleaning is less effective than continuous low-frequency ultrasound of 50 kHz.

Further, greater cleaning efficiencies were observed at low frequencies and high acoustic powers [44, 54–57]. Lamminen et al. [44] and Caia et al. [58] attributed the observed increase in cleaning efficiency to an increase in the number of cavitation bubbles and an increase in the size of the cavitating zone, as a result of high pressure amplitude of the sound wave with increased ultrasonic power intensity to the system [59]. With that, greater turbulence was also reported due to the increase in intensity of bubble implosion [60]. There are also reports of lower cleaning efficiencies at high ultrasonic frequencies as higher frequencies generate smaller cavitation bubbles, which may be incapable of dislodging the foulants from the membrane surface [21, 31, 34, 61, 62]. In addition, Watkinson [63] found that the ultrasonic effect was shown to be more significant in the absence of surfactants and was less dependent on temperature and pressure. As seen in ultrasonic enhancement to minimize fouling, there are inconsistent results regarding the structural integrity of the membrane upon ultrasonic cleaning.

Future of Ultrasonic Units in Dairy Processing

Although promising results are reported through the use of ultrasonic technology in membrane filtration processes, the scale-up of this unit to larger scale has not been investigated widely. Ashokkumar [64] believed that this is due to the lack in development of appropriate large-scale food processing equipment. Large-scale filtration with ultrasonic enhancement is also thought to be expensive due to its perceived high energy consumption [46]. Koh et al. [48] have previously shown that feed pretreatment, through the use of heat and ultrasound or ultrasound only, has the potential to reduce energy requirements in the UF of whey due to its low viscosity and resulting low cross-flow pressure drops. However, this energy saving must be offset against the energy demand of sonication itself.

In addition, most laboratory- and pilot-scale studies were performed using horn sonicators, which involved direct contact between the ultrasonic horn and the fluid to be processed. Riener et al. [65] reported a "rubbery" aroma upon sonication of milk with a 24 kHz, 22 mm diameter horn at a temperature of 45 °C. This is particularly undesirable and can impede the application of ultrasound in dairy processing. The "rubbery" aroma was found to be less intense at lower sonication powers but could

not be totally eliminated. In addition, upon sonication, an increase in volatile compounds was observed. They speculated that this was the result of the production of aldehydes from sonication-induced lipid oxidation. Ashokkumar [64] stated that long sonication contact time may also result in the contamination of the processing fluid due to the emission of metal particles from the tip of the horn.

Indirect sonication, such as through the use of tubular sonicators, may be more suitable for processing of food and dairy fluids. However, Ashokkumar [64] reported that there are only a few ultrasonic equipment manufacturers who are developing reactors with transducers attached on the exterior to avoid direct contact between processing fluids and the transducers. Therefore, combined efforts by the physical chemists, engineers, physicists, and food technologists is needed in the development of new equipment.

Conclusions

Ultrasonics in membrane fouling and cleaning studies presented here in this chapter would benefit from further investigation into the effect of ultrasound on the taste, odor, nutritional value, and allergenic properties of the final dairy products. This is of paramount importance to ensure that ultrasound does not add off-flavors and unsafe by-products to the products that are for human consumption. In addition, these acoustic methods are shown to be promising at the laboratory scale; however, most of these developments have scale-up and economic issues that require further investigation.

References

1. Eykamp W (1995) In: Noble RD, Stern SA (eds) Microfiltration and ultrafiltration. Elsevier, New York, pp 1–43
2. Cheryan M (1986) Ultrafiltration handbook. Technomic, Lancaster
3. James BJ, Jing Y, Chen MD (2003) Membrane fouling during filtration of milk – a microstructural study. J Food Eng 60:431–437
4. Mulder M (1996) Polarisation phenomena and fouling. Kluwer, Dordrecht, pp 416–464
5. Mulder MHV (1995) In: Noble RD, Stern SA (eds) Polarization phenomena and membrane fouling. Elsevier, New York, pp 45–84
6. Makardij A, Chen XD, Farid MM (1999) Microfiltration and ultrafiltration of milk: some aspects of fouling and cleaning. Food Bioprod Process 77:107–113
7. Marshall AD, Daufin G (1995) Physico-chemical aspects of membrane fouling by dairy fluids. International Dairy Federation, Brussels, pp 8–35
8. Rice G (2008) Membrane separation of calcium salts from dairy ultrafiltration permeates, in Department of Chemical and Biomolecular Engineering. The University of Melbourne, Australia
9. Richardson JF, Harker JH, Backhurst JR (2002) Membrane separation processes. Butterworth-Heinemann, Oxford, pp 437–474
10. Zeman LJ, Zydney AL (1996) Microfiltration and ultrafiltration: principles and applications. Marcel Dekker, New York

11. Koh LLA, Ashokkumar M, Kentish SE (2013) In: Tamime AY (ed) Membrane fouling cleaning and disinfection. Wiley-Blackwell, Chichester
12. Cheryan M (1998) Ultrafiltration and microfiltration handbook. Technomic Publishing Company, Lancaster
13. Xu-Jiang Y, Dodds J, Leclerc D, Lenoel M (1995) A technique for the study of the fouling of microfiltration membranes using two membranes in series. J Membr Sci 105:23–30
14. Lindau J, Jönsson AS (1999) Adsorptive fouling of modified and unmodified commercial polymeric ultrafiltration membranes. J Membr Sci 160:65–76
15. Muthukumaran S (2005) Ultrasonic enhancement of dairy ultrafiltration membrane processes, in Department of Chemical and Biomolecular Engineering and School of Chemistry. The University of Melbourne, Australia
16. Cheryan M, Alvarez JR (1995) In: Noble RD, Stern SA (eds) Food and beverage industry applications. Elsevier, New York, pp 415–465
17. Lawrence ND, Kentish SE, O'Connor AJ, Barber AR, Stevens GW (2008) Microfiltration of skim milk using polymeric membranes for casein concentrate manufacture. Sep Purif Technol 60:237–244
18. Ho C-C, Zydney AL (2000) A combined pore blockage and cake filtration model for protein fouling during microfiltration. J Colloid Interface Sci 232:389–399
19. Palacio L, Ho C-C, Zydney AL (2002) Application of a pore-blockage – cake-filtration model to protein fouling during microfiltration. Biotechnol Bioeng 79:260–270
20. Palacio L, Ho CC, Prádanos P, Hernández A, Zydney AL (2003) Fouling with protein mixtures in microfiltration: BSA–lysozyme and BSA–pepsin. J Membr Sci 222:41–51
21. Muthukumaran S, Kentish SE, Ashokkumar M, Stevens GW (2005) Mechanisms for the ultrasonic enhancement of dairy whey ultrafiltration. J Membr Sci 258:106–114
22. Caric M, Akkerman JC, Milanovic S, Kentish SE, Tamime AY (2009) In: Tamime AY (ed) Technology of evaporators, membrane processing and dyers. Wiley-Blackwell, West Sussex
23. Trägårdh G (1989) Membrane cleaning. Desalination 71:325–335
24. Glover FA (1985) Ultrafiltration and reverse osmosis for the dairy industry. National Institute for Research in Dairying, Reading
25. Nyström M, Kaipia L, Luque S (1995) Fouling and retention of nanofiltration membranes. J Membr Sci 98:249–262
26. van der Horst HC (1995) Fouling of organic membranes during processing of dairy liquids. International Dairy Federation, Brussels, pp 36–52
27. Kulozik U (1995) Water rinsing in reverse osmosis and ultrafiltration. International Dairy Federation, Brussels, pp 136–150
28. Al-Akoum O, Ding LH, Jaffrin MY (2002) Microfiltration and ultrafiltration of UHT skim milk with a vibrating membrane module. Sep Purif Technol 28:219–234
29. Akoum O, Jaffrin MY, Ding L-H (2005) Concentration of total milk proteins by high shear ultrafiltration in a vibrating membrane module. J Membr Sci 247:211–220
30. Krstić DM, Tekić MN, Carić MĐ, Milanović SD (2002) The effect of turbulence promoter on cross-flow microfiltration of skim milk. J Membr Sci 208:303–314
31. Muthukumaran S, Kentish SE, Stevens GW, Ashokkumar M, Mawson R (2007) The application of ultrasound to dairy ultrafiltration: the influence of operating conditions. J Food Eng 81:364–373
32. Mirzaie A, Mohammadi T (2012) Effect of ultrasonic waves on flux enhancement in microfiltration of milk. J Food Eng 108:77–86
33. Kokugan T, Kaseno FS, Shimizu M (1995) Ultrasonic effect on ultrafiltration properties of ceramic membrane. Membrane 20:213–223
34. Maskooki A, Kobayashi T, Mortazavi SA, Maskooki A (2008) Effect of low frequencies and mixed wave of ultrasound and EDTA on flux recovery and cleaning of microfiltration membranes. Sep Purif Technol 59:67–73

35. Teng M-Y, Lin S-H, Juang R-S (2006) Effect of ultrasound on the separation of binary protein mixtures by cross-flow ultrafiltration. Desalination 200:280–282
36. Villamiel M, de Jong P (2000) Influence of high-intensity ultrasound and heat treatment in continuous flow on fat, proteins, and native enzymes of milk. J Agric Food Chem 48:472–478
37. Masselin I, Chasseray X, Durand-Bourlier L, Lainé J-M, Syzaret P-Y, Lemordant D (2001) Effect of sonication on polymeric membranes. J Membr Sci 181:213–220
38. Wang X-l, X-f L, X-q F, Chen R, Gao B (2005) Effect of ultrasound irradiation on polymeric microfiltration membranes. Desalination 175:187–196
39. Muthukumaran S, Kentish SE, Stevens GW, Ashokkumar M (2006) Application of ultrasound in membrane separation processes: a review. Rev Chem Eng 22:155–194
40. Chen D, Weavers LK, Walker HW, Lenhart JJ (2006) Ultrasonic control of ceramic membrane fouling caused by natural organic matter and silica particles. J Membr Sci 276:135–144
41. Chai X, Kobayashi T, Fujii N (1998) Ultrasound effect on cross-flow filtration of polyacrylonitrile ultrafiltration membranes. J Membr Sci 148:129–135
42. Kallioinen M, Mänttäri M (2011) Influence of ultrasonic treatment on various membrane materials: a review. Sep Sci Technol 46:1388–1395
43. Gondrexon N, Cheze L, Jin Y, Legay M, Tissot Q, Hengl N, Baup S, Boldo P, Pignon F, Talansier E (2015) Intensification of heat and mass transfer by ultrasound: application to heat exchangers and membrane separation processes. Ultrason Sonochem 25:40–50
44. Lamminen MO, Walker HW, Weavers LK (2004) Mechanisms and factors influencing the ultrasonic cleaning of particle-fouled ceramic membranes. J Membr Sci 237:213–223
45. Hickey MW, Hill RD, Smith BR (1980) Investigations into the ultrafiltration and reverse osmosis of wheys 1. The effects of certain pretreatments. N Z J Dairy Sci Technol 15:109–121
46. Brans G, Schroën CGPH, van der Sman RGM, Boom RM (2004) Membrane fractionation of milk: state of the art and challenges. J Membr Sci 243:263–272
47. Hakata Y, Roddick F, Fan L (2011) Impact of ultrasonic pre-treatment on the microfiltration of a biologically treated municipal effluent. Desalination 283:75–79
48. Koh LLA, Nguyen HTH, Chandrapala J, Zisu B, Ashokkumar M, Kentish SE (2014) The use of ultrasonic feed pre-treatment to reduce membrane fouling in whey ultrafiltration. J Membr Sci 453:230–239
49. Ashokkumar M, Lee J, Zisu B, Bhaskarcharya R, Palmer M, Kentish S (2009) Sonication increases the heat stability of whey proteins. J Dairy Sci 92:5353–5356
50. Chandrapala J, Zisu B, Palmer M, Kentish S, Ashokkumar M (2011) Effects of ultrasound on the thermal and structural characteristics of proteins in reconstituted whey protein concentrate. Ultrason Sonochem 18:951–957
51. Koh LLA (2013) Ultrasonics as a new platform technology in dairy processing, in Department of Chemical and Biomolecular Engineering and School of Chemistry. The University of Melbourne, Australia
52. Kuehn T, Kittelson D, Wu Y, Gouk R (1996) Particle removal from semiconductor wafers by megasonic cleaning. J Aerosol Sci 27:S427–S428
53. Goode BJ, Jones RD, Howells JNH (1998) Ultrasonic pickling of steel strip. Ultrasonics 36:79–88
54. Muthukumaran S, Kentish S, Lalchandani S, Ashokkumar M, Mawson R, Stevens GW, Grieser F (2005) The optimisation of ultrasonic cleaning procedures for dairy fouled ultrafiltration membranes. Ultrason Sonochem 12:29–35
55. Wakeman RJ, Tarleton ES (1991) An experimental study of electroacoustic crossflow microfiltration. Chem Eng Res Des 69:386–397
56. Li J, Sanderson RD, Jacobs EP (2002) Ultrasonic cleaning of nylon microfiltration membranes fouled by Kraft paper mill effluent. J Membr Sci 205:247–257
57. Kobayashi T, Kobayashi T, Hosaka Y, Fujii N (2003) Ultrasound-enhanced membrane-cleaning processes applied water treatments: influence of sonic frequency on filtration treatments. Ultrasonics 41:185–190

58. Cai M, Wang S, Zheng Y, Liang H (2009) Effects of ultrasound on ultrafiltration of Radix astragalus extract and cleaning of fouled membrane. Sep Purif Technol 68:351–356
59. Sivakumar M, Pandit AB (2001) Ultrasound enhanced degradation of Rhodamine B: optimization with power density. Ultrason Sonochem 8:233–240
60. Leighton TG (1994) The acoustic bubble. Academic, San Diego
61. Juang R-S, Lin K-H (2004) Flux recovery in the ultrafiltration of suspended solutions with ultrasound. J Membr Sci 243:115–124
62. Popović S, Djurić M, Milanović S, Tekić MN, Lukić N (2010) Application of an ultrasound field in chemical cleaning of ceramic tubular membrane fouled with whey proteins. J Food Eng 101:296–302
63. Watkinson WJ (2008) In: Tamime AY (ed) Chemistry of detergents and disinfectants. Blackwell Publishing, Oxford
64. Ashokkumar M (2015) Applications of ultrasound in food and bioprocessing. Ultrason Sonochem 25:17–23
65. Riener J, Noci F, Cronin DA, Morgan DJ, Lyng JG (2009) Characterisation of volatile compounds generated in milk by high intensity ultrasound. Int Dairy J 19:269–272

Ultrasonic Separation of Food Materials

Thomas Leong

Contents

T. Leong (✉)
Faculty of Science, Engineering and Technology, Department of Mechanical and Product Design Engineering, Hawthorn, Swinburne University of Technology, Melbourne, Australia

School of Chemistry, The University of Melbourne, Melbourne, VIC, Australia

Department of Chemical and Biomolecular Engineering, The University of Melbourne, Melbourne, VIC, Australia
e-mail: tleong@mail.com

Abstract

High-frequency ultrasonic sound waves with a frequency >400 kHz have recently been used in various applications as a means to enhance the recovery of food materials in multicomponent mixtures. The premise of ultrasonic separation is to achieve significant enhancements to separation processes without altering the physical or chemical integrity of the food product. The application of ultrasonic standing waves leads to specific positioning of individual droplets or particles at the pressure nodes or antinodes within a reactor that increases the probability for them to agglomerate or coalesce into larger entities more rapidly. Increased particle sizes promote flotation or sedimentation and therefore enhance the predisposition of material mixtures for separation. This chapter will detail the main principles behind this technology and how it can be implemented into existing food processing lines. Application of this technology in food processing will be shown, showcasing commercial success in the palm oil milling industry and future potential in dairy and bioproducts.

Introduction

The ultrasonic processing of food has been investigated for many years, with applications largely focused in the frequency range spanning 20–100 kHz [1]. This region is commonly labeled the "power ultrasound" region. Here, a phenomenon known as *acoustic cavitation* may occur. This is when pressure waves from the applied ultrasound cause existing dissolved gas in liquid solutions to form bubbles that expand and contract. Such bubbles will grow over time due to coalescence and mass transfer and upon reaching a bubble diameter known as the resonant size, collapse. The collapse event is often of high intensity and leads to temperature increases up to 10,000 K and emission of pressure shockwaves of several hundred atmospheres within the local space of the collapsing bubble. These physical effects can be harnessed usefully in the initiation of intense shearing, mixing, and heating and is applicable for food processing applications such as emulsification, homogenization, extraction, or thermal treatment (details of these processes can be located in other chapters of this book).

Ultrasonic separation is a technology that typically uses high-frequency ultrasound (>0.4 MHz to several MHz) to separate food droplets and/or particles suspended in fluids [2]. At these higher frequencies, the violent cavitation bubble collapse that leads to enhanced shear and physical disruption in liquid systems is reduced and becomes almost negligible. Firstly, the cavitation threshold increases with increasing ultrasonic frequency such that collapse events become less likely to occur. Furthermore, the resonance size of collapsing bubbles is also inversely

proportional to the sound wave frequency. With a lowered resonance size, bubble collapse events occur with less momentum such that at frequencies greater than 1 MHz, these collapse events become relatively benign. As such, ultrasonic separation differs from typical sonoprocessing applications in that it aims to achieve "gentle" processing by avoiding violent bubble collapse.

Separation Techniques in Food Systems

There are a number of conventional food separation processes including centrifugation, sedimentation or clarification, chemical-induced flocculation, and membrane filtration units. These separation processes are well established and robust unit operations. Nevertheless, they bear a number of potential issues including but not limited to: (1) high energy consumption, (2) excessive shear that may damage the integrity of the product, (3) product fouling that limits throughput or requires extensive cleaning, (4) slow separation rates, and (5) excessive use of chemicals. Ultrasonic separation can be used alone or combined with these technologies to enhance process efficiencies.

Three main roles are identified in which ultrasonic separation is likely to be most useful in the food industry. The first is flocculation or aggregation enhancement, whereby the application of ultrasonic standing waves within an existing clarification or chemical flocculation system dramatically enhances the rate at which separation occurs, thereby reducing the residence time and/or chemical requirement. Reduced cost, increased throughput, and lowered environmental footprint can be achieved.

The second is based on the predisposition or pretreatment of food material upstream to an existing separation unit operation. This strategy is particularly effective in the treatment of food, that is, of a heterogeneous nature, such as those containing solids, liquids, and liquid product trapped in solids. An example is the mesocarp material of crushed palm fruit. The application of ultrasonics not only initiates aggregation of material such that the rate of separation occurs faster in the downstream clarification process, but the mild physical shear provided by the ultrasound can assist to liberate more product [3]. This can provide higher recovery of product from the solid phase and also reduces potential energy requirements through faster and more efficient downstream separation. Major energy savings can be achieved when combined with existing separations such as centrifugation.

Finally, the choice of megasonic separation parameters such as frequency, power level, and residence time can be tuned to selectively remove particles of a specific size. It can therefore be used as a tool for the fractionation of food ingredients dispersed within a continuous phase. Examples of components that may have increased value resultant from fractionation into streams with higher nutritional or structural benefit include fats, proteins, carbohydrates, and fibers. For this purpose, ultrasonic fractionation is a technique that is complementary to existing membrane separation processes.

Theory

Primary Acoustic Radiation Force

When a sound wave is reflected upon itself, the reflected wave can superimpose to form what is known as an acoustic standing wave. Such waves are characterized by regions of high local pressure where constructive superimposition occurs, known as pressure antinodes, and regions of minimum local pressure where destructive interference occurs, known as pressure nodes.

When a standing wave field is sustained in a medium containing a suspension of food particles or droplets, the wave will be partially scattered by the particles if there is an acoustic impedance mismatch between the fluid and the material of the particles. The scattering of the wave will produce what is known as the primary acoustic radiation force. This force acts on the particles and droplets, such that they are moved toward either the node or antinode of the standing wave depending on the acoustic contrast factor.

The acoustic contrast factor depends on the density and compressibility of the particles and their surrounding medium. The contrast factor can be calculated using:

$$\emptyset = \frac{5\rho_p - 2\rho_l}{2\rho_p + \rho_l} - \frac{\beta_p}{\beta_l} \tag{1}$$

where ρ is the density, β is the compressibility, and the subscripts l and p refer to the liquid medium and the particles, respectively [4]. Particles move toward the pressure nodes of the standing wave when the contrast factor has a positive sign and toward the pressure antinodes when the contrast factor has a negative sign. As a rule of thumb, food ingredients which have a density less than the surrounding fluid have a contrast factor that drives them toward the pressure maxima. Those with a density higher than the surrounding fluid will be driven toward the pressure minima. The positioning of individual droplets or particles on pressure nodes or antinodes within the standing wave will cause them to aggregate or coalesce rapidly into larger entities. Figure 1 shows a schematic representation of particles moving toward pressure nodal planes and pressure antinodal planes.

The study of acoustic radiation forces dates back to the work of King [5]. His work focused on understanding the behavior of spherical incompressible particles in acoustic fields. Yosioka and Kawasima [4] extended the work of King calculating the acoustic forces for compressible particles in planar acoustic waves as:

$$F_{ac} = -\frac{4\pi}{3} r^3 k E_{ac} \phi \sin(2kx) \tag{2}$$

where r is the particle radius, $k = \frac{2\pi}{\lambda}$ the wave number, λ is the wavelength of sound, E_{ac} the specific energy density, x the distance from a nodal point of the standing wave, and ϕ is the acoustic contrast factor. Gor'kov [6] generalized the work of
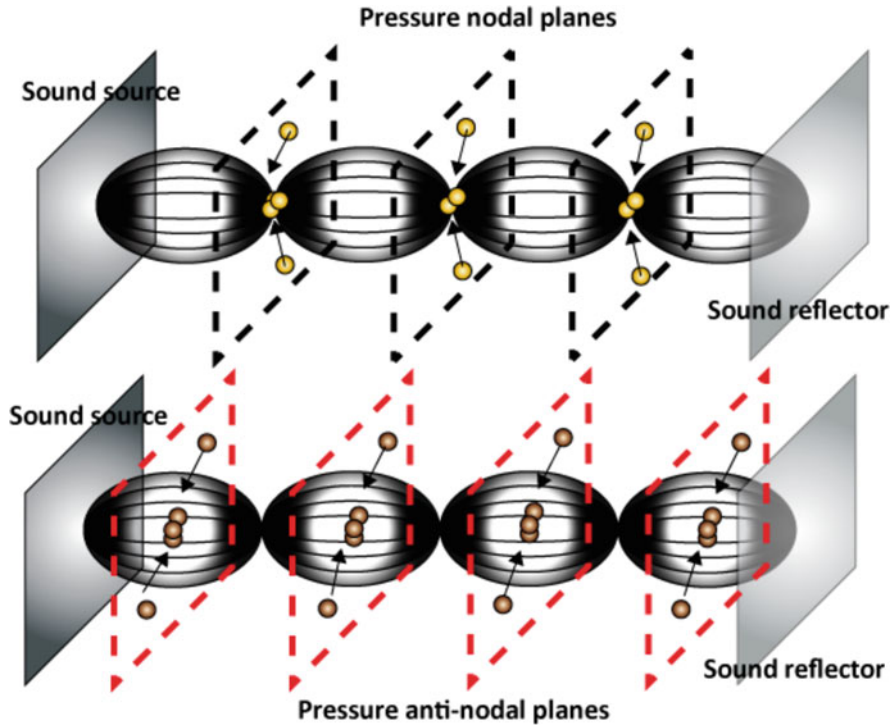
Fig. 1 Migration of food materials within an acoustic standing wave field (Reprinted with permission from Leong et al. [2] Copyright 2013 American Chemical Society)

Yosioka and Kawasima calculating the acoustic forces for compressible particles subjected to any acoustic field. Following Gor'kov's approach, the acoustic radiation force F_{ac} can be obtained from the acoustic force potential U_{ac} as [7]:

$$F_{ac} = \nabla U_{ac} \tag{3}$$

where the acoustic force potential has been derived by Gor'kov [6] as:

$$U_{ac} = \frac{4\pi}{3} r^3 \left[f_1 \frac{1}{2\rho_l c_l^2} \langle p_1^2 \rangle - f_2 \frac{3}{4} \rho_l \langle v_1^2 \rangle \right] \tag{4}$$

$$f_1 = 1 - \frac{\kappa_p}{\kappa_l} \tag{5}$$

$$f_2 = \frac{2(\rho_p - \rho_l)}{(2\rho_p + \rho_l)} \tag{6}$$

κ and ρ are compressibility and density, while the subscripts l and p stand for "liquid" and "particle" (droplet or a solid particle), respectively. The terms $\langle p_1^2 \rangle$ and
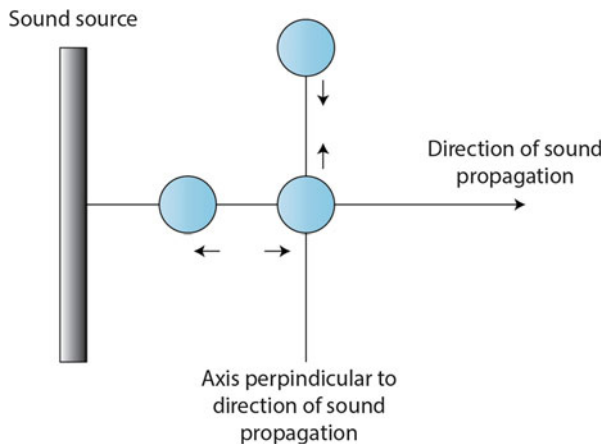
$\langle v_1^2 \rangle$ are the mean square pressure amplitude fluctuation of the sound field and of the particle velocity, respectively, and can be determined by solving the Helmholtz equation [8, 9]. The acoustic radiation force potential from a transducer element has been visualized by FEM [10].

The ability to separate food particles from the bulk fluid phase also depends on the applied frequency and amplitude level of the ultrasound used. The size of the food particles in question influences the selection of these parameters. Separation is not possible or very difficult if either the frequency or acoustic intensity is too low to manipulate particles which have a very small particle size. This can be overcome by applying very high-frequency ultrasound, as was demonstrated Yantchev et al. who used 40 MHz ultrasound to manipulate submicron particles inside a microfluidic chamber [11]. However, it is not possible to use such high frequencies in large-scale systems due to the strong attenuation such high-frequency ultrasound experiences with distance. An alternative method to manipulate small particles is by using seeding particles [12] or a flocculating agent that promotes smaller particles to stick together.

Additional Forces Acting on Particles

Once particles are displaced to either the nodal or antinodal planes, additional forces that act over short distances called "secondary acoustic forces" or "Bjerknes forces" come into play. These forces tend to attract particles together within the plane, enhancing the probability of collisions and hence aggregation and coalescence into larger collections of particles. Bjerknes forces are originated by the scattering of sound off neighboring particles [13]. The direction of these forces depends on the angle between the distance vector separating two particles and the direction of the sound field. Generally, these forces attract particles to one another once particles have moved into the nodal or antinodal planes (Fig. 2).

Once particles or droplets are grouped together on a plane, they may flocculate into bigger aggregates or coalesce into larger droplets. Clusters of particles or larger droplets can flocculate or cream at a faster rate if there is a density difference between the liquid medium and the material of the particle or droplet. This is due to buoyancy or gravitational force as follows:

$$F_B = \frac{4}{3}\pi r^3 g\left(\rho_l - \rho_p\right) \tag{7}$$

where g is gravity. Particles moving in a viscous liquid will also experience the Stokes drag force F_D. For small particles it is reasonable to neglect the particles' inertia and to assume that they are always moving in a local steady state [14]. For low Reynolds number the drag force F_D is given by Stokes Law as:

$$F_D = 6\eta\pi r\left(v_l - v_p\right) \tag{8}$$

where η is the viscosity of the fluid, v_l is the velocity of the fluid, and v_p is the velocity of the particle.

Acoustic Streaming

Acoustic streaming is the time-independent flow generated by the attenuation of an acoustic wave. This is an important factor for acoustic separation technologies because streaming exerts drag and shear on particles, influencing their behavior and movement within an acoustic field [15]. Typical effects of acoustic streaming on particle manipulation by acoustic radiation force were explained by Spengler [16]. Spengler's study of yeast cells manipulated in an ultrasound chamber detailed observations of cell motion with changing patterns and velocities over time that caused cells to be dragged around the chamber by streaming. In large-scale applications streaming can be severe and override the acoustic radiation forces, disturbing or even eliminating the formation of particle bands established at pressure nodal planes.

Acoustic streaming is caused by the attenuation of the sound field. Wave attenuation can be caused by viscous attenuation in the medium; scattering on particles, droplets or bubbles; or friction between a vibrating wall and the surrounding fluid. Zarembo [17] considered three main types of acoustic streaming: (1) Eckart streaming, (2) Rayleigh streaming, and (3) boundary layer Schlichting streaming. The latter two are considered microstreaming events because the length scale is of the order of magnitude of a wavelength for the case of Rayleigh streaming, and orders of magnitude smaller than a wavelength for the case of Schlichting streaming. Eckart streaming, on the other hand, is a large-macroscale streaming condition because the length scale of this flow pattern is significantly greater than the wavelength. An illustrative diagram of Eckart and Rayleigh streaming is shown in Fig. 3.

Schlichting streaming is a boundary layer-driven acoustic streaming, arising from the friction between the vibrating fluid medium in contact with a solid wall or vice versa, a vibrating wall in contact with a fluid. This effect is confined to a thin

Fig. 3 Eckart and Rayleigh acoustic streaming. Eckart streaming propagates through the medium from the sound source and occurs without the requirement for a standing wave to be generated. Rayleigh streaming requires a standing wave consisting of pressure nodal and antinodal regions to develop (Reprinted with permission from Leong et al. [2] Copyright 2013 American Chemical Society)
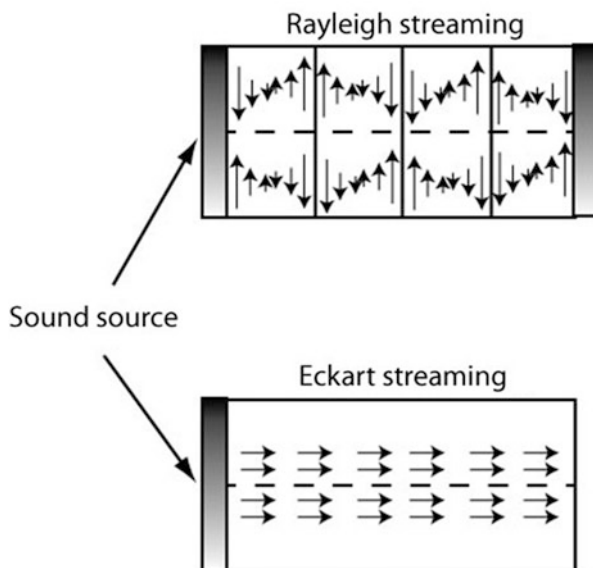
viscous boundary layer (called the shear-wave layer or the Stokes layer) [18]. Once the Schlichting streaming is established within the boundary layer, it provides a strong force that drives fluid toward the outside of the layer. In the case of standing waves, the streaming that occurs between pressure nodes and antinodes is called Rayleigh streaming.

Eckart streaming is due to the attenuation of the acoustic energy across the bulk of the fluid. When the medium attenuates the wave, a proportion of the acoustic energy is absorbed by the fluid, heating it up. The viscous acoustic attenuation coefficient for a plane sound wave was derived by Stokes as:

$$\alpha = \frac{2v(2\pi f)^2}{3c^3} \tag{9}$$

From Eq. 9 it can be seen that attenuation is proportional to viscosity and to the square of the frequency. This means that streaming effects tend to become more intense with increasing frequency. In high-power ultrasonic operations, there is also a formation of a fast-jet streaming called "Stuart" streaming. According to Lighthill [19], at higher powers Stuart streaming takes the form of an inertially dominated turbulent jet.

Design and Operating Guidelines

This section will cover the design and operating principles relevant to large-scale food processing using ultrasonic separation. For specific reactor design concepts, the reader should refer to the review by Leong et al. [20]. The design aspects of

microfluidic separation devices have also been extensively covered in the public domain and will not be presented in this chapter. Readers interested in design aspects and scaling laws in continuous microfluidic systems are encouraged to read the reviews by others [14, 21–23].

Design Parameters

The effectiveness of ultrasonic separation is underpinned by the ability to generate a stable, strong acoustic standing wave field inside the separation reactor. To achieve this, important design considerations are required. The distance of separation between the transducer and reflector should be designed to optimize the energy density and standing wave quality factor. The alignment and placement of transducers within the separation reactor should also be considered and positioned to optimize energy delivery.

Energy Density and Quality Factor

The quality factor (or Q factor), determined from the electrical impedance spectrum [24], is an important property in resonating systems such as standing waves. It represents the ratio of acoustic energy achieved in the resonator to the power applied to the generator. This factor is especially relevant in microfluidic devices for estimating the acoustic energy density (see Eq. 10) [25] but can also be relevant in the design of larger-scale separation reactors.

$$E_{ac} = \frac{PQ}{2\pi f} \tag{10}$$

where P is the active power consumption and the quality factor, Q, is at the frequency f [26]. The power consumption can be determined from the online active power meter integrated with the ultrasonic power supply. The Q factor is influenced by parameters such as the transducer-reflector distance. A higher acoustic energy density generates a stronger acoustic radiation force (see Eq. 2) and hence is expected to enable more rapid particle separation.

Transducer-Reflector Distance

The maximum effective distance to achieve a constant standing wave field upon reflection is limited by attenuation of the sound wave in the fluid medium. The higher the ultrasonic frequency, the more strongly attenuated it becomes. Thus, ultrasound in the MHz region generally has shorter effective working distances to achieve a strong standing wave field, compared with lower-frequency ultrasound. Strong attenuation may also give rise to undesirable acoustic streaming in the form of Eckhart streaming currents, which can disrupt effective separation from occurring.

Thus, the transducer-reflector distance is a critical design consideration, as separation with high frequencies will not operate effectively if the incident sound
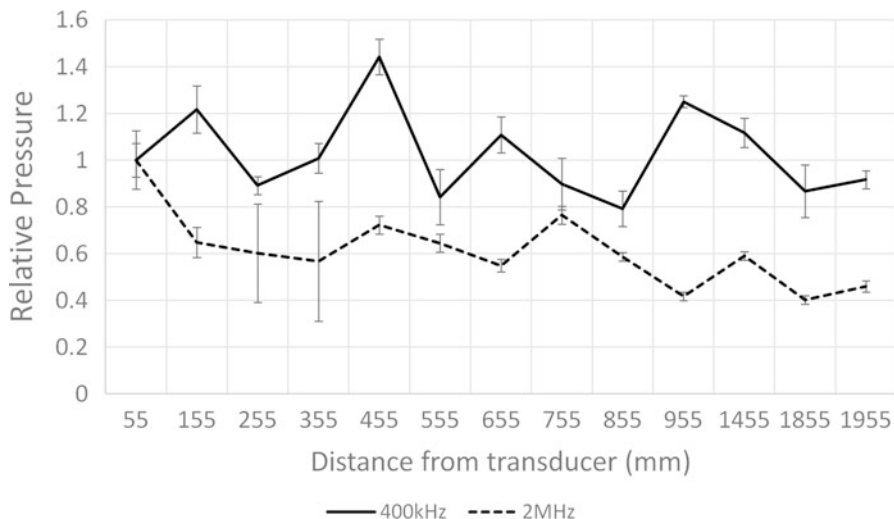
Fig. 4 Change in pressure relative to the pressure measured at 55 mm from the surface of the transducer for 400 kHz and 2 MHz transducers. No reflector plate except for the vessel wall at 2,100 mm was used for these measurements (Reprinted from Leong et al. [28], Copyright 2015, with permission from Elsevier)

wave becomes too attenuated before it can be reflected by the opposing wall. For example, in the work by Leong et al. [27], transducer-reflector distances greater than 85 mm became less effective in achieving skimming of cream from milk when using dual 1 and 2 MHz frequency ultrasound. Leong et al. [28] demonstrated with high-frequency 2 MHz ultrasound that sound pressures declined significantly with distance beyond 55 mm in a large experimental chamber (Fig. 4). By contrast, mid-frequency 400 kHz ultrasound was found to penetrate a significantly longer distance (up to 2 m) without significant decline in pressure level.

Number of Nodes/Antinodes

The number of pressure nodes and antinodes within the standing wave generated is dependent on the distance between the sound source and reflector, the reflector thickness, as well as the frequency. The higher the frequency and the greater the distance to the reflector, the larger the number of available sites (nodes/antinodes) for food material to accumulate. It is worth noting that the spacing between each node and antinode is a quarter wavelength of the ultrasound frequency.

Transducer Alignment

The alignment and positioning of transducers and the reflector within the reactor to generate standing waves should be considered with respect to (a) the direction of material flow inside the reactor, either horizontally or vertically, and (b) the alignment of multiple transducers in parallel or perpendicular reactor walls. Note that a perfectly parallel alignment between transducer and reflector/transducer, while
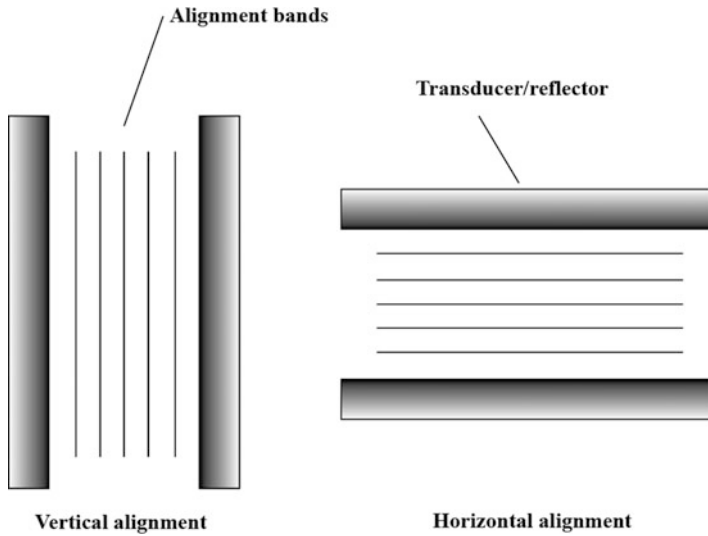
Fig. 5 Depiction of vertical alignment of the transducer and/or reflector for ultrasonic separation (Taken from Leong et al. [20] with permission of Springer. Copyright Springer Science+Business Media New York 2015)

offering optimal reflection, may cause potential transducer damage if high energy density is confined to a small geometrical volume.

Horizontal Versus Vertical Alignment of the Material Bands with Material Flow

A vertical or horizontal alignment refers to whether the transducer or reflector is positioned in a way that the nodal/antinodal bands that are formed are aligned in the vertical or horizontal plane (see Fig. 5). Where gravity is a necessary mechanism for enhanced separation (i.e., product collects at the top or bottom of the container), a vertical alignment is more amenable to separation since once product is aggregated to a sufficient size, the product can sediment or rise rapidly due to buoyancy. A horizontal alignment, however, hinders this natural rise/fall since product must pass through aligned bands that can "trap" the aggregated material prior to eventual rising/falling beyond the active processing region. Applying ultrasound in pulses can intermittently release product trapped in the horizontally aligned bands but would consequently decrease the energy input to the system per unit time.

Parallel Versus Perpendicular Multiple Transducer Arrangement for Enhanced Energy Density

This design criterion is considered only when using multiple transducers to increase the density of the energy input. An increased energy density can be beneficial to accelerating particle accumulation and hence separation. In this case, the transducer plates can be arranged facing each other (parallel) or orthogonal (perpendicular),

and either position has been shown to be effective [29]. Parallel alignment can be envisioned to be more likely to achieve effective superposition when using identical frequency (or wavelength multiple) transducers. Perpendicular alignment may create more regions where particle accumulation can occur.

An issue to consider when deciding which alignment is most suitable is the effective penetration distance of the frequency used for separation. For frequencies >1 MHz, the geometrical transducer-reflector distances >85 mm become less effective for separation due to attenuation and increased acoustic streaming. This was evidenced in reduced effectiveness for milk fat skimming [27].

Here, the minimum transducer-reflector distance is the width of the reactor, which must be designed to fit the transducers. Parallel alignment has the advantage of allowing close positioning of the transducers when facing each other. Very short transducer-reflector distances, or in this case transducer-transducer distances, can be realized even with large surface area plates when using a parallel alignment. The use of parallel transducers has been shown to work at batch scale, although additional adjustments may be needed to avoid direct sound radiation into the transducer, which may cause damage to the piezoceramics due to excessive heating. If necessary, transmission plates designed with optimal thickness for sound transmission can be used to position the transducers externally [30], which may allow for a more durable system for continuous processing.

A perpendicular alignment on the other hand is limited by the size of the transducer. Large transducers will increase the width of the separation chamber. In some cases, this width may be too large to allow for sufficient sound penetration due to sound wave attenuation (e.g., if high frequencies are used). This reduces the effectiveness and efficiency of the separation.

Operating Parameters

The achievement of successful separation is contingent on employing suitable operating conditions that (a) do not damage the transducers employed, (b) do not damage the food material being separated, and (c) enable effective and efficient separation.

Choice of Frequency
In principle, sound waves of any frequency can be used to establish a standing wave by which to manipulate suspended food materials. The selection largely depends on the type of material being separated. It should be noted however that the primary and secondary acoustic radiation forces scale with the applied frequency. That is, the higher the frequency, the stronger the force that is applied to the particles. Small particles require a stronger force to manipulate. There is also a requirement that the wavelength of the applied sound wave be smaller than the particle or droplet that is to be manipulated.

To separate small particles in the range between 1 and 10 μm, it is recommended to use a high-frequency ultrasound in the 1–4 MHz range to maximize the acoustic

radiation forces in the system. When applying higher-frequency ultrasound >2 MHz, considerations must be made to the limitations in vessel geometry that arise from attenuation of high-frequency ultrasound.

For particles or liquid droplets that are >10 μm, it can be advantageous to use a slightly lower-frequency ultrasound in the range between 400 kHz and 1MHz for the separation processes. These lower frequencies are less attenuated, and hence larger geometry reactors can be feasibly operated [28]. Larger geometries are more amenable to high-throughput processing and also increase the number of nodes/antinodes established within the acoustic standing wave, such that there is a larger number of locations where food material can collect and separate. An example where mid-frequency ultrasound was employed successfully for a large-scale food manufacturing operation is in the predisposing of palm oil product from the palm mesocarp material. Here, an ultrasound frequency of 600 kHz was successfully employed to process flow rates up to 45 tons/h [20].

Frequencies in the power ultrasound region can also be used to manipulate particles and droplets, but the lowered acoustic radiation forces and strong physical disruption and mixing effects associated with these frequencies make them less suitable.

Temperature of Operation

The limits of operation temperature are defined by (a) the physical limits of the ultrasonic transducer and (b) the temperature by which the food material begins to deteriorate from excessive heating.

Most transducers are capable of operating with temperatures up to 80 °C [20], depending on the specifications provided by the manufacturer. For hot processes, such as in edible oil production, it is advised not to have transducers placed in direct contact with the fluid. Instead, a transmission plate system [20, 30] is recommended whereby the transducer is positioned external to the fluid in the food reactor and the sound wave is transmitted through a stainless steel layer with an optimal thickness for transmission. In this case, a thickness that is a half-wavelength multiple of the applied frequency leads to optimal transmission. On the contrary, a plate thickness that is an odd multiple of a quarter wavelength leads to ideal reflection.

The temperature of the food medium will heat up as ultrasound is applied, due to attenuation of the sound wave. In this case, mechanical energy from the sound wave is transformed to heat, and heat flow also occurs between the compression and rarefactions of the oscillation cycle. Most food systems deteriorate in quality as they are heated. High temperatures may lead to denaturation of proteins, vitamins, and other components. Designs should include a cooling jacket or heat sink as necessary to maintain the integrity of the food material.

In some food systems, there exist optimal temperature ranges in which ultrasonic separation works more effectively. The temperature influences the physical properties of the food medium, influencing its density, viscosity, compressibility, and solid-liquid properties. These changes also influence acoustic properties such as the speed of sound and attenuation. In the ultrasonic separation of milk fat, Leong et al. [31] found that temperatures in the range between 20 and 60°C provided more

optimal separation, compared to milks that were chilled at cold room temperatures ~5–13°C. The reason proposed was due to a balance between the liquid-solid ductility as milk fat transitioned from semisolid to liquid and the presence of immunoglobulins present in whole milks.

Energy Density

The acoustic energy density is an important parameter along with the ultrasonic frequency that affects the magnitude of the acoustic radiation forces imparted on the particles distributed in the food medium. Increasing the energy density enables the initiation of more rapid separation of food materials and so can enable higher volumetric throughput either in batch or continuous separation processes. Higher energy density can be achieved by (a) reducing the volume being processed within the active region and (b) using dual transducers aligned in parallel positioned within close proximity.

However, one should be mindful that increasing energy density will also promote stronger acoustic streaming flows in the system. Such flows may be detrimental to separation in that it can perturb the collection of aggregated materials.

Residence Time and Specific Energy

Residence time is linked with energy density. To achieve desired output targets, food materials should experience sufficient duration of exposure to the ultrasonic standing wave in order to collect and aggregate to sufficiently large size such that it will separate spontaneously from the system. Typically, the food material needs to be subject to a defined specific energy that is conditional on the volume processed and the energy density delivered. Smaller particles and/or droplets will require a longer residence time to be aggregated to sufficiently large size for separation. Other factors which may influence this will include if the aggregation of food materials is reversible (i.e., weak interactions) or irreversible (i.e., coalescence, strong interactions). For materials that experience weak interparticle interactions, separation effectiveness can be improved by using a flocculent that will hold smaller particles more strongly together during sonication.

Operation Modes

Ultrasonic separation is amenable to operation modes ranging from batch to fully continuous. The choice largely depends on the outcome desired from the separation. For example, fully continuous operation enables high-throughput product treatment, whereas batch separation enables control of residence time to achieve targeted final output compositions, which may be advantageous for certain applications, e.g., in "fractionation" type processes. Some of the key design questions to consider in designing a reactor for either batch or fully continuous operation, such as product collection and process controls, are outlined. The principles would be similar in semi-batch and semicontinuous flow separation processes.

Batch (Single Unit)

Batch reactors can be relatively straightforward to design and operate and can be a useful first step toward developing a scale-up process for any potential ultrasonic food separation application. These reactors will inevitably consist of a fixed processing volume where standing waves are established. The food material to be separated will be loaded into the interrogation volume, processed, and then removed. High-density materials will sediment to the base of the reactor; low-density material will rise to the top of the reactor by buoyancy. Inlets and outlets located strategically to maximize product recovery after separation are necessary to ensure efficient product collection. The required duration of processing (i.e., residence time) will be determined by the energy input, volume processed, and the rate at which collected food material will separate by buoyancy or sedimentation. One of the possible advantages of batch separation is that the residence time, which influences the extent of separation, can be more effectively controlled for a given batch of food material and hence may be more suitable, e.g., for fractionation-type applications.

Continuous Flow

The design of continuous systems is more challenging to implement and operate since forces arising from product flow must be balanced with the acoustic forces during separation. The advantage however is that higher throughput can be achieved.

Whereas microscale systems can implement flow-split devices to harvest product [2], large-scale food systems have standing waves consisting of many nodal planes that make this impossible. Instead, overflow and underflow devices are the most amenable method to collect product. High-density material will collate at the bottom of the reactor and can be intermittently swept through the underflow area of the chamber. Low-density material will float to the top and can, by slow flow motion, be displaced to an overflow collection area. Carefully designed control systems must be put in place in order to maintain product quality (i.e., target concentrations for the separation process). For example, parameters such as energy input or rate of product flow can be adjusted to tailor the resultant separation achieved at the outlets.

The rate of product flow however must be below a certain Reynolds number to ensure laminar flow (which is dependent on the cross section of the flow area). For cylindrical pipes, this value is ~2,000. Flow regimes which are extremely turbulent are generally not suitable for megasonic separation, since mixing of the product will occur in such a situation, preventing effective separation. Nevertheless, the acoustic radiation force can in some cases be strong enough to overcome the mixing that occurs during processing. Separation can be successful in the presence of high mixing and flow if there is additional mechanism such as coalescence or flocculation that can hold collected food material together.

Continuous flow ultrasonic separation can be a useful addition to existing processing operations, where the predisposition or pretreatment of product prior

to a downstream separation unit will provide a benefit for the recovery of a high-value material post-decantation or centrifugation. In this situation, the ultrasonics serve to initiate agglomeration and/or coalescence of suspended food material, as well as enhance the extraction of product that may be trapped in solid raw materials. This intervention enhances the rate at which the downstream process achieves separation and also increases the recoverable yield of the food material. One example in which such an operation has been proven useful is in the palm oil milling industry, where the predisposition of material enhances the recoverable oil from the plant mesocarp [3].

Applications

This section will assess designs established to date at various scales for a range of applications. The most prominent example is the continuously operating separation reactor implemented in a high-tech palm oil mill, where the ex-screw press feed is treated for increased palm oil recovery. Other examples are the utilization of ultrasonics for milk fat separation and fractionation, algal cells in the production of algal oils, and bacteria, yeasts, and other cells in fermentation systems.

Applications of Ultrasound for Palm Oil Separation

A typical palm oil milling operation in Malaysia may experience a loss of recoverable product in the effluent with a potential revenue of >$200,000 USD per year. The application of ultrasonic separation technology to existing plant operations can be effective in minimizing product loss and to enhance clarification efficiency.

Juliano et al. [3, 32] successfully demonstrated the ability to enhance oil recovery from the extract obtained from pressed oil palm fruit mesocarp at lab and pilot scale. This success has recently been extended to full-scale commercial operation, capable of processing throughput of up to 45 tons per hour (Fig. 6). The system depicted can be applied directly to existing palm oil mills. Here, the feed coming directly from the ex-screw press is passed through a vertical chamber where droplets of palm oil product are predisposed into larger droplets. An additional recovery of between 1% and 10 % product is achieved in the process, which eliminates virtually any oil being lost to the effluent stream.

The success of the ultrasonic application is due to the ultrasound (applied at 600 kHz frequency) generating physical "rubbing" of the plant material. This activity assists the extraction of oil from the vegetal matter. The oil in the bulk liquid is then coalesced into larger droplets by the acoustic standing waves, resulting in faster oiling-off by gravity settling in downstream processing. Thus, ultrasonic application in this case improves the total recoverable oil and the rate of separation.

The use of this technology has revolutionized the design of future palm oil plants where the environmental footprint can be significantly reduced by decreasing the

Fig. 6 (**a**) Schematic representation of the megasonic palm oil separation reactor: the rectangles represent a transducer/transmission plate setup; (**b**) photograph of the commercially operating megasonic reactor (@45 t/h; 4 × 600 kHz, 1 kW each) (Taken from Leong et al. [20] with permission of Springer. Copyright Springer Science +Business Media New York 2015)
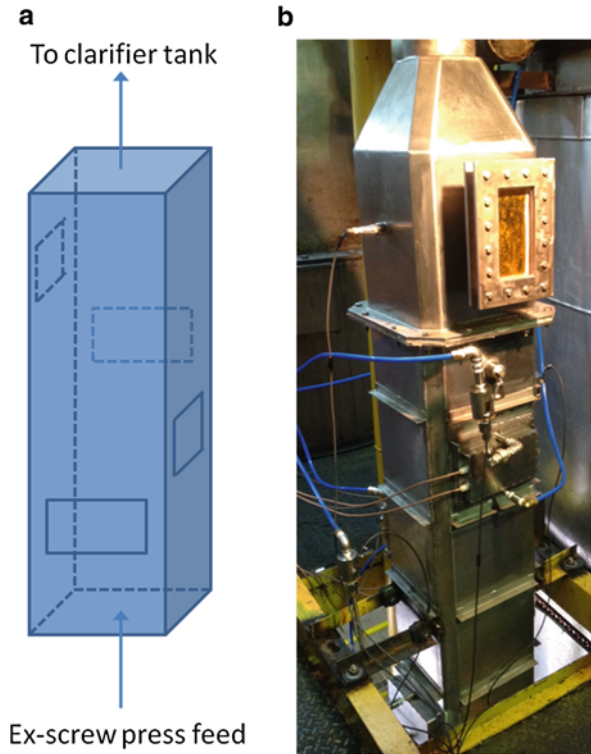
volumes utilized in the vertical clarification tanks, the amount of decanter centri-fuges, and the oil loss into effluents. For a typical palm oil milling operation, this equates to an increased profit averaging between $500,000 and $2,000,000 USD per year.

Enhanced Creaming of Milk Fat Globules

The dairy products we consume and enjoy such as milk, cheese, and butter have usually undergone a separation process that removes or concentrates the fat in the milk to a product specification defined by the manufacturer. In the dairy industry, this separation is typically achieved by using a centrifuge, which removes the fat from milk by application of intense g-forces by rapid spinning. Since milk fat is a valuable commodity, a common practice involves removing all of the fat from the milk and recombining the separated cream as required back into the skimmed milk to make products with standardized fat concentrations.

Traditionally, separations were performed simply by letting the cream in milk rise to the top where it could be skimmed off. Such practices are slow, requiring many hours to achieve sufficient separation. They are however still performed

today, primarily by cheese makers like those in Northern Italy famed for Parmesan and Romano cheeses [33]. These cheese makers continue to apply these traditional methods, since it creates milk with a fat size distribution that contributes to the unique flavors in these cheeses. The process creates a point of differentiation that cannot be achieved using centrifugation [34]. Ultrasonic separation has been recognized as a complementary technology that can significantly enhance the separation rate of fat from milk by "natural" methods [27].

When an acoustic standing wave is applied to volume of milk, the fat globules collect at the pressure antinodes, which can be observed as "bands" of fat globules. This phenomenon was observed by Miles et al. [35] in a small cuvette container. The milk fat globules collecting and concentrating at the pressure antinodes have an enhanced probability to aggregate into larger floccules. As fat globules collect into larger floccules, they begin to rise more rapidly to the surface due to the increased hydrodynamic radius as described by Stokes' Law [36].

A first-approach scale-up (up to 6 L volume) in a batch system was demonstrated by Juliano et al. [29] using a recombined milk emulsion. For a recombined milk emulsion, rapid separation could be achieved using ultrasound at an operating frequency of 400 kHz in a vessel with a transducer-to-reflector distance between ~18 and 20 cm. At these distances, a frequency of 1 MHz was less effective than 400 kHz and a frequency of 2 MHz again less effective than 1 MHz. The parameters found to achieve rapid separation of a recombined milk emulsion, however, were not successful in separating fat globules in natural whole milk within the same vessel [37]. Several reasons can be attributed to this. Natural whole milk has different properties, namely, particle size distribution and surface composition, compared to a recombined milk emulsion. The mean particle size is smaller in natural whole milk and so requires high-frequency ultrasound or strong acoustic energy density to manipulate effectively. In order to effectively apply high-frequency ultrasound >1 MHz, the geometry with respect to the distance between transducer and reflector should also be small to minimize attenuation.

Leong et al. [27, 31] applied these concepts to achieve separation using natural whole milk. Leong et al. showed that higher-frequency ultrasound, in this case >1 MHz, could effectively manipulate and separate the fat globules present in natural whole milk provided that a short transducer-reflector separation distance (between 30 and 85 mm) was used. Furthermore, the application of dual transducers in a parallel arrangement was found to influence more rapid skimming of fat due to the ability to achieve a higher energy density per unit volume.

Leong et al. [31] also showed that there is an "optimal" temperature range over which the rate of milk fat separation is greatest. In this case, a temperature range between 20 and 60 °C offered fast separation of milk fat in the experimental trials.

Leong et al. [38] have recently highlighted the ability of ultrasonic separation to initiate fractionation of milk fat globules into streams with enhanced proportions of small or large fat globules. These streams may have potential for creating dairy products with enhanced microstructure. This was achieved by manipulating the duration of processing and collecting product at defined intervals at specific locations within the reactor.

Notably, it was established that the milk fat became distributed in the separation vessel after sonication, such that the smallest fat globules were retained toward the bottom of the vessel and large-sized fat globules were enriched within the cream collected near the top of the vessel. These fractions positioned at the top and bottom of the vessel can be collected specifically by overflow/underflow. Similar techniques can be used to split streams of food ingredients containing specific particle size distributions.

Microbial and Algal Cell Separation

A diverse group of prokaryotic and eukaryotic photosynthetic microorganisms known as microalgae can be used to produce edible oils and other biofuels that can be used as an attractive alternative sustainable energy source. These algae are grown in aqueous medium such as water, but their separation, often by centrifugation, is identified as being energy intensive. The use of ultrasonic standing waves to concentrate microalgae is identified as a significant advancement toward improving their dewatering efficiency. Ultrasonic separation has been used to separate the algal cells from water [39, 40]. Bosma et al. [39] applied 2.1 MHz to algae flowing continuously through a small volume and achieved a separation efficiency of over 90 %, albeit at low flow rates of only 4–6 L per day. Although production flow rates are currently low, continued work to scale up ultrasonic separation systems by applying key concepts as detailed in this chapter will bring these products closer to market.

Fermentation Products

Ultrasonic separation can also be used as an alternative cell-retention system for fermentation and cell culturing applications [41]. Recombinant proteins, amino acids, and antibodies are some examples of the high-value products which can be delivered in these applications. Studies have shown that selective retention of viable versus nonviable cells is possible [42] reducing the need to "bleed out" product during operation, thereby improving production. Such systems are commercially available with the development of BioSep™, and could also be readily implemented into food applications such as fermentation tanks in the beer and wine industry.

BioSep™ units are available from throughputs as small as 10 L/day up to 200 L/day. Gorenflo et al. [41] found that these types of systems performed reliably and achieved separation efficiencies between dead and viable cells of greater than 95 %. Typical operation employs a stop time of 9 s (for run time of 120 s) to facilitate the removal of cells out of the acoustically active region. The advantage of ultrasound separation in such applications is that the technique is relatively simple and offers nearly maintenance-free operation by reducing the need to periodically bleed out product. The high-frequency ultrasound employed limits any potential physical or chemical change to the product, thereby preserving the quality.

It should be noted the 20-fold scale-up from 10 L per day perfusion rates to 200 L per day was based on using four parallel compartments in one separator with a single controller. This is because scale-up is limited by the geometry in which a strong standing wave can be established when using high-frequency ultrasound.

To be successful in the food industry and to accommodate the large throughputs required in beer and wine processing, scale-up to several tons per day is essential. For achieving these higher flow rates, a further scale-out of the process by using several 200 L/day reactors is recommended, since increasing the size of the separation chamber or flow rate through the chamber may reduce the overall efficiency of the system. Alternatively, different design configuration, including adjustments of the process conditions, may offer reasonable performance without the requirement of simple numbering up, which may be cost prohibitive due to the high capital costs of not only the ultrasonic transducers but also the reaction chambers themselves.

Future Applications

Potential designs can be established for a number of other applications such as effluent treatments, separation of starch suspensions, and water recycling. These reactors will have similar design considerations to the abovementioned applications. The scale of the process will determine the required throughputs, and the nature of the material to be separated will influence the selection of the appropriate operating parameters. For example, the ultrasonic frequency selection will be governed by the material to be separated and its properties such as particle size, density, and compressibility. This in turn determines the suitable geometries that can be designed for the separation reactor. To achieve the required throughputs, scale-up may be achievable if lower frequencies (<600 kHz) are used, whereas scale-out by using many parallel units may be necessary to maintain separation effectiveness in the process should a high frequency be required. Understanding these principles will ensure that a successful design is produced.

Conclusions and Future Directions

The application of ultrasonic separation technology to food manufacturing processes shows great promise. Recent advances have led to an improved understanding that will facilitate the development of high-throughput ultrasonic separation reactors. Even though there are few reactors currently operating at full-scale industrial processing, there is large potential for growth of this technology into the food industry as a separation enhancing tool to increase process efficiencies and production.

References

1. Chemat F, Khan MK (2011) Ultrason Sonochem 18:813
2. Leong T, Johansson L, Juliano P, McArthur SL, Manasseh R (2013) Ind Eng Chem Res 52:16555
3. Juliano P, Swiergon P, Mawson R, Knoerzer K, Augustin MA (2013) J Am Oil Chem Soc 90:579
4. Yosioka K, Kawasima Y (1955) Acustica 5:167
5. King LV, Roy P (1934) Soc Lond A Math 147:212
6. Gor'kov LP (1962) Sov Phys Dokl 6:773
7. Barnkob R, Augustsson P, Laurell T, Bruus H (2010) Lab Chip 10:563
8. Trujillo FJ, Juliano P, Barbosa-Cánovas G, Knoerzer K (2014) Ultrason Sonochem 21:2151
9. Trujillo FJ, Knoerzer K (2011) Ultrason Sonochem 18:1263
10. Johansson L, Evander M, Lilliehorn T, Almqvist M, Nilsson J, Laurell T, Johansson S (2013) Ultrasonics 53:1020
11. Yantchev V, Enlund J, Katardjiev I, Johansson L (2010) J Micromech Microeng 20
12. Augustsson P, Magnusson C, Grenvall C, Lilja H, Laurell T (2010) Micro total analysis systems 2010. Groningen
13. Mettin R, Akhatov I, Parlitz U, Ohl CD, Lauterborn W (1997) Phys Rev E 56:2924
14. Bruus H (2012) Lab Chip 12:1014
15. Spengler J, Jekel M (2000) Ultrasonics 38:624
16. Spengler JF, Coakley WT, Christensen KT (2003) Aiche J 49:2773
17. Zarembo LK (1971) In: Rozenberg LD (ed) High-intensity ultrasonic fields. Plenum Press, New York, p 137
18. Sadhal S (2012) Lab Chip 12:2292
19. Lighthill J (1978) J Sound Vib 61:391
20. Leong T, Knoerzer K, Trujillo FJ, Johansson L, Manasseh R, Barbosa-Cánovas GV, Juliano P Food Eng Rev 7:298
21. Groschl M (1998) Acta Acust United Acust 84:632
22. Hawkes JJ, Coakley WT (2001) Sensor Actuators B-Chem 75:213
23. Lenshof A, Laurell T (2011) Jala-J Lab Autom 16:443
24. Schmid M, Benes E, Sedlaczek R (1990) Meas Sci Technol 1:970
25. Woodside SM, Piret JM, Gröschl M, Benes E, Bowen BD (1998) AIChE J 44:1976
26. Burger W, Groschl M, Trampler F, Benes E (1993) Conference proceedings, Butterworth-Heinemann, Oxford, UK. pp. 507
27. Leong T, Johansson L, Juliano P, Mawson R, McArthur S, Manasseh R (2014) Ultrason Sonochem 21:1289
28. Leong T, Coventry M, Swiergon P, Knoerzer K, Juliano P (2015) Ultrason Sonochem 27:22
29. Juliano P, Temmel S, Rout M, Swiergon P, Mawson R, Knoerzer K (2013) Ultrason Sonochem 20:52
30. Michaud M, Leong T, Swiergon P, Juliano P, Knoerzer K (2015) Ultrason Sonochem 26:56
31. Leong T, Juliano P, Johansson L, Mawson R, McArthur SL, Manasseh R (2014) Ultrason Sonochem 21:2092
32. Juliano P, Swiergon P, Lee KH, Gee PT, Clarke PT, Augustin MA (2013) J Am Oil Chem Soc 90:1253
33. Caplan Z, Melilli C, Barbano D (2013) J Dairy Sci 96:2011
34. Ma Y, Barbano D (2000) J Dairy Sci 83:1719
35. Miles CA, Morley MJ, Hudson WR, Mackey BM (1995) J Appl Microbiol 78:47
36. Lamb H (1993) Hydrodynamics. Cambridge university press, Cambridge, UK
37. Temmel S (2012) Friedrich-Alexander-Universitat Erlangen-Nurnberg
38. Leong T, Johansson L, Mawson R, McArthur SL, Manasseh R, Juliano P (2016) Ultrason Sonochem 28:118

39. Bosma R, van Spronsen WA, Tramper J, Wijffels RH (2003) J Appl Phycol 15:143
40. Brennan L, Owende P (2010) Renew Sustain Energ Rev 14:557
41. Gorenflo VM, Smith L, Dedinsky B, Persson B, Piret JM (2002) Biotechnol Bioeng 80:438
42. Trampler F, Sonderhoff SA, Pui PWS, Kilburn DG, Piret JM (1994) Biotechnology 12:281

Index